CODEN: JASMAN ISSN: 0001-4966

The Journal of the Acoustical Society of America

Vol. 111, No. 1, Pt. 1 January 2002

(Continued)

THE JOURNAL OF THE ACOUSTICAL SOCIETY OF AMERICA VOL. 111, NO. 1, PT. 1, JANUARY 2002

CONTENTS—*Continued from preceding page*

(Continued)

THE JOURNAL OF THE ACOUSTICAL SOCIETY OF AMERICA VOL. 111, NO. 1, PT. 1, JANUARY 2002

CONTENTS—*Continued from preceding page*

(Continued)

THE JOURNAL OF THE ACOUSTICAL SOCIETY OF AMERICA VOL. 111, NO. 1, PT. 1, JANUARY 2002

CONTENTS—*Continued from preceding page*

ERRATA

CUMULATIVE AUTHOR INDEX

Document Delivery: Copies of journal articles can be ordered from *DocumentStore*, our online document delivery service (URL: http://documentstore.org/).

CODEN: JASMAN

The Journal of the Acoustical Society of America

ISSN: 0001-4966

Vol. 111, No. 1, Pt. 2 January 2002

FOREWORD

THEORETICAL STUDIES

EXPERIMENTS AND ANALYSIS

HUMAN AND ANIMAL ACCEPTABILITY STUDIES

(Continued)

CONTENTS—*Continued from preceding page*

REGULAR ISSUE PAPERS

CUMULATIVE AUTHOR INDEX

ACOUSTICAL NEWS—USA

Elaine Moran
Acoustical Society of America, Suite 1NO1, 2 Huntington Quadrangle, Melville, NY 11747-4502

Editor's Note: *Readers of this Journal are encouraged to submit news items on awards, appointments, and other activities about themselves or their colleagues. Deadline dates for news items and notices are 2 months prior to publication.*

Announcement of the 2002 Election

In accordance with the provisions of the bylaws, the following Nominating Committee was appointed to prepare a slate for the election to take place on 24 May 2002:

Patricia K. Kuhl, *Chair*	Bennett M. Brooks
Anthony A. Atchley	D. Vance Holliday
David T. Blackstock	Marjorie R. Leek

The bylaws of the Society require that the Executive Director publish in the *Journal* at least 90 days prior to the election date an announcement of the election and the Nominating Committee's nominations for the offices to be filled. Additional candidates for these offices may be provided by any Member or Fellow in good standing by letter received by the Executive Director not less than 60 days prior to the election date and the name of any eligible candidate so proposed by 20 Members or Fellows shall be entered on the ballot.

Biographical information about the candidates and statements of objectives of the candidates for President-Elect and Vice President-Elect will be mailed with the ballots.

CHARLES E. SCHMID
Executive Director

The Nominating Committee has submitted the following slate:

FOR PRESIDENT-ELECT

Ilene J. Busch-Vishniac

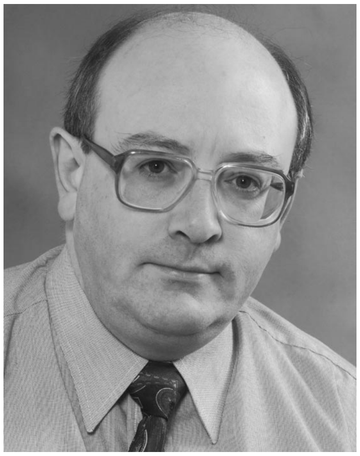

Gilles A. Daigle

FOR VICE PRESIDENT-ELECT

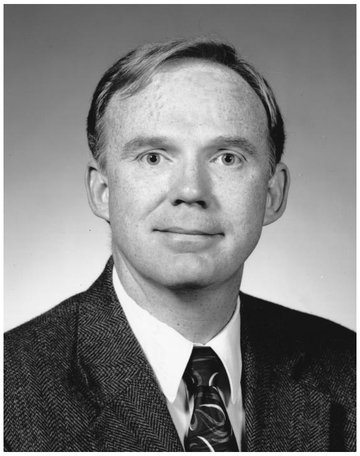

Anthony A. Atchley

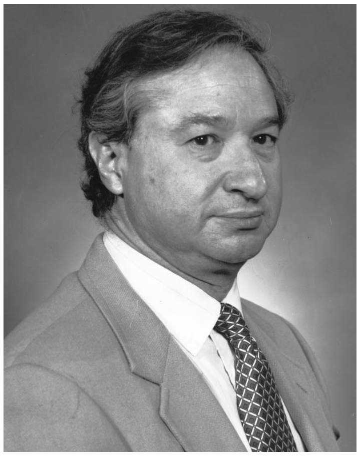

Sabih I. Hayek

FOR MEMBERS OF THE EXECUTIVE COUNCIL

Fredericka Bell-Berti

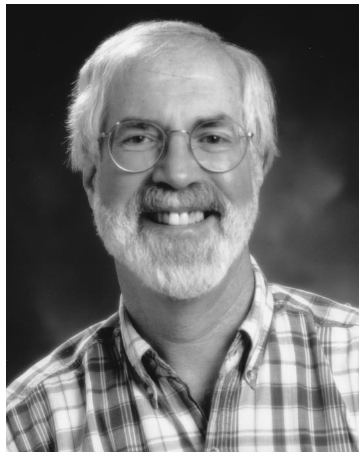

Steven M. Brown

Judy R. Dubno

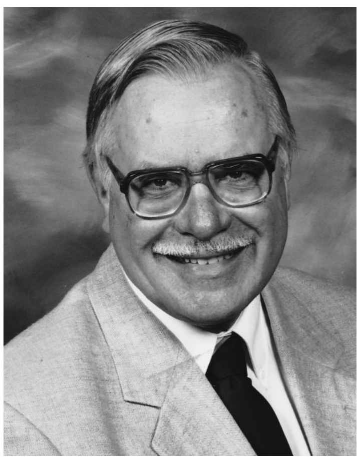

Lawrence L. Feth

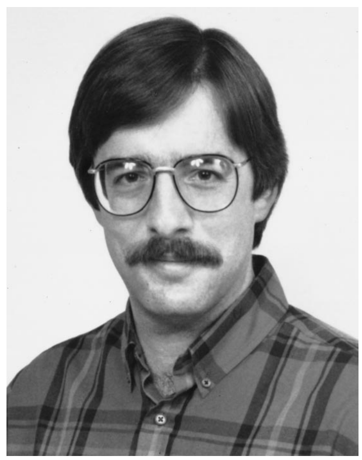

Ronald A. Roy

Sigfrid D. Soli

USA Meetings Calendar

Listed below is a summary of meetings related to acoustics to be held in the U.S. in the near future. The month/year notation refers to the issue in which a complete meeting announcement appeared.

2002

21–23 Feb. National Hearing Conservation Association Annual Conference, Dallas, TX [NHCA, 9101 E Kenyon Ave., Ste. 3000, Denver, CO 80237; Tel.: 303-224-9022; Fax: 303-770-1812; E-mail: nhca@gwami.com; WWW: www.hearingconservation.org/index.html].

10–13 March Annual Meeting of American Institute for Ultrasound in Medicine, Nashville, TN [American Institute for Ultrasound in Medicine, 14750 Sweitzer Lane, Suite 100, Laurel, MD 20707-5906; Tel.: 301-498-4100 or 800-638-5352; Fax: 301-498-4450; E-mail: conv_edu@aium.org; WWW: www.aium.org].

3–7 June 143rd Meeting of the Acoustical Society of America, Pittsburgh, PA [Acoustical Society of America, Suite 1NO1, 2 Huntington Quadrangle, Melville, NY 11747-4502; Tel.: 516-576-2360; Fax: 516-576-2377; E-mail: asa@aip.org; WWW: asa.aip.org]. Deadline for receipt of abstracts: 1 February 2002.

19–21 Aug. INTER-NOISE 2002, Dearborn, MI [INTER-NOISE 02 Secretariat, The Ohio State University, Department of Mechanical Engineering, 206 West 18th Ave., Columbus, OH 43210-1107; E-mail: hp@internoise2002.org].

2–6 Dec. Joint Meeting: 144th Meeting of the Acoustical Society of America, 3rd Iberoamerican Congress of Acoustics, and 9th Mexican Congress on Acoustics, Cancun, Mexico [Acoustical Society of America, Suite 1NO1, 2 Huntington Quadrangle, Melville, NY 11747-4502; Tel.: 516-576-2360; Fax: 516-576-2377; E-mail: asa@aip.org; WWW: asa.aip.org/cancun.html].

2003

28 April–2 May 144th Meeting of the Acoustical Society of America, Nashville, TN [Acoustical Society of America, Suite

1NO1, 2 Huntington Quadrangle, Melville, NY 11747-4502; Tel.: 516-576-2360; Fax: 516-576-2377; E-mail: asa@aip.org; WWW: asa.aip.org].

10–14 Nov. 145th Meeting of the Acoustical Society of America, Austin, TX [Acoustical Society of America, Suite 1NO1, 2 Huntington Quadrangle, Melville, NY 11747-4502; Tel.: 516-576-2360; Fax: 516-576-2377; E-mail: asa@aip.org; WWW: asa.aip.org].

2004

24–28 May 75th Anniversary Meeting (145th Meeting) of the Acoustical Society of America, New York, NY [Acoustical Society of America, Suite 1NO1, 2 Huntington Quadrangle, Melville, NY 11747-4502; Tel.: 516-576-2360; Fax: 516-576-2377; E-mail: asa@aip.org; WWW: asa.aip.org].

27 Nov.–3 Dec. 146th Meeting of the Acoustical Society of America, San Diego, CA [Acoustical Society of America, Suite 1NO1, 2 Huntington Quadrangle, Melville, NY 11747-4502; Tel.: 516-576-2360; Fax: 516-576-2377; E-mail: asa@aip.org; WWW: asa.aip.org].

Cumulative Indexes to the *Journal of the Acoustical Society of America*

Ordering information: Orders must be paid by check or money order in U.S. funds drawn on a U.S. bank or by Mastercard, Visa, or American Express credit cards. Send orders to Circulation and Fulfillment Division, American Institute of Physics, Suite 1NO1, 2 Huntington Quadrangle, Melville, NY 11747-4502; Tel.: 516-576-2270. Non-U.S. orders add $11 per index.

Some indexes are out of print as noted.

Volumes 1–10, 1929–1938: JASA and Contemporary Literature, 1937–1939. Classified by subject and indexed by author. Pp. 131. Price: ASA members $5; Nonmembers $10.

Volumes 11–20, 1939–1948: JASA Contemporary Literature and Patents. Classified by subject and indexed by author and inventor. Pp. 395. Out of Print.

Volumes 21–30, 1949–1958: JASA, Contemporary Literature and Patents. Classified by subject and indexed by author and inventor. Pp. 952. Price: ASA members $20; Nonmembers $75.

Volumes 31–35, 1959–1963: JASA, Contemporary Literature and Patents. Classified by subject and indexed by author and inventor. Pp. 1140. Price: ASA members $20; Nonmembers $90.

Volumes 36–44, 1964–1968: JASA and Patents. Classified by subject and indexed by author and inventor. Pp. 485. Out of Print.

Volumes 36–44, 1964–1968: Contemporary Literature. Classified by subject and indexed by author. Pp. 1060. Out of Print.

Volumes 45–54, 1969–1973: JASA and Patents. Classified by subject and indexed by author and inventor. Pp. 540. Price: $20 (paperbound); ASA members $25 (clothbound); Nonmembers $60 (clothbound).

Volumes 55–64, 1974–1978: JASA and Patents. Classified by subject and indexed by author and inventor. Pp. 816. Price: $20 (paperbound); ASA members $25 (clothbound); Nonmembers $60 (clothbound).

Volumes 65–74, 1979–1983: JASA and Patents. Classified by subject and indexed by author and inventor. Pp. 624. Price: ASA members $25 (paperbound); Nonmembers $75 (clothbound).

Volumes 75–84, 1984–1988: JASA and Patents. Classified by subject and indexed by author and inventor. Pp. 625. Price: ASA members $30 (paperbound); Nonmembers $80 (clothbound).

Volumes 85–94, 1989–1993: JASA and Patents. Classified by subject and indexed by author and inventor. Pp. 736. Price: ASA members $30 (paperbound); Nonmembers $80 (clothbound).

Volumes 95–104, 1994–1998: JASA and Patents. Classified by subject and indexed by author and inventor. Pp. 632. Price: ASA members $40 (paperbound); Nonmembers $90 (clothbound).

BOOK REVIEWS

P. L. Marston
Physics Department, Washington State University, Pullman, Washington 99164

These reviews of books and other forms of information express the opinions of the individual reviewers and are not necessarily endorsed by the Editorial Board of this Journal.

Editorial Policy: *If there is a negative review, the author of the book will be given a chance to respond to the review in this section of the Journal and the reviewer will be allowed to respond to the author's comments. [See "Book Reviews Editor's Note," J. Acoust. Soc. Am.* ***81****, 1651 (May 1987).]*

Structure-Borne and Flow Noise Reductions (Mathematical Modeling)

Sung-Hwan Ko, Sangwoo Pyo, and Woojae Seong

Seoul National University Press, Seoul, Korea, 2001.
ISBN: 89-521-0258-4.

A submerged body, moving fast enough through a fluid medium, creates a turbulent flow which generates pressure fluctuations on the body. These, in turn, cause the structure to vibrate, giving rise to what is known as flow noise. This monograph deals primarily with the response, the consequent radiation, and the sound transmission and reflection by the submerged structure due to the near-field pressure fluctuations of the turbulence. The principal author of the book, as a result of his almost 30 years tenure at the Naval Undersea Warfare Center, is a leading expert in the theoretical understanding of flow noise reduction, the primary objective of this monograph. His coauthors have been working with him during his stay at the Seoul National University and have themselves been conducting research in structural acoustics over the last decade. The monograph is the outgrowth of special lectures presented at the University by the principal author, and consists of seven chapters.

Chapter 1 is introductory in nature, and presents the basic concepts of reflection and transmission of normally and obliquely incident waves at the planar interface between two fluid media, and a fluid layer of constant thickness. The treatment here is fairly standard and essentially derived from many of the classic and more modern books on the theory of acoustics.

Chapter 2 goes on to discuss transmission and reflection, etc., when the intermediate layer between fluid media is that of a finite-thickness solid using the structural theory of thin elastic plates, usually referred to as flexural vibrations of plates. Also treated is that of a fluid–plate composite layer, and propagation through a two-dimensional flexible duct where the duct walls are again thin plates modeled using plate flexural vibration theory. The examples and numerical results come primarily from the principal author's publications in the *Journal of the Acoustical Society of America*. One slight shortcoming that I found in this chapter is that, when considering the surface waves at a fluid–plate interface, the authors discuss only the fluid-loaded flexural wave. A more complete discussion of the physical meaning of the other roots of the dispersion relation would have been useful, especially since, some years ago, much discussion on this phenomenon took place.

In Chap. 3 the authors treat the reduction of the pressure fluctuations by a fluid layer, modeled as an acoustic baffle, overlaying a thin elastic plate used to represent the submerged body's hull. Other more complicated configurations are also treated in this chapter. This is the first chapter in which finite elastic plates as opposed to plates of infinite extent are discussed. The principal author and colleagues were responsible for five of the eight references in this chapter, and again most of the numerical results were taken from them.

Chapter 4 introduces the theory of elasticity for use in later chapters where consideration is given to thicker plates whose thickness is more comparable in size to the shear wavelength than those considered in earlier chapters (plate thickness less than one-twentieth of the shear wavelength). In addition to deriving the classic elastodynamic equations, the authors present the relationships for reflection at an interface between a fluid and an elastomer, and transmission through an infinite-extent elastic layer. Wave propagation through a duct with the walls modeled as elastic layers is also treated in this chapter.

Chapter 5 uses the formulations derived in the previous chapter to study structure-borne noise reduction achieved by various configurations of baffles, again in the form of infinite-extent layers, but now modeled as elastic layers. Thus, Chap. 5 is related to Chap. 4 as Chap. 3 is to Chap. 2. The final section of this chapter is entitled, "Signal reception by a velocity sensor on an air-voided elastomer layer." The motivation for such a configuration is that the elastomer layer serves to reduce interfering signals emanating from the back plate, while the response of the velocity sensor to an incoming signal is enhanced relative to that of a pressure sensor at the same location.

The final two chapters are devoted to turbulent flow noise reduction. Chapter 6 begins with a treatment of the frequency-wave number spectrum of the turbulent boundary layer pressure fluctuations. The authors settle on the use of a Corcos spectrum for the various calculations and trade-offs presented in the final two chapters. The authors then go on to calculate the boundary layer noise levels that would be measured using a variety of flush-mounted hydrophone configurations. Among these are point hydrophones, an array of point hydrophones, rectangular hydrophones, an array of rectangular hydrophones, and a number of different geometric shapes, such as circular, triangular, etc. Also treated are the effects of different shading functions applied to the above shapes.

This book serves as a most comprehensive and excellent summary of the theoretical work done for modeling the reduction of structure-borne and flow noise generated by the turbulent flow generated on bodies as they move through their contiguous fluid environments. It will undoubtedly become a valuable addition to the libraries of graduate students and researchers interested in the growing field of transport system noise reduction.

DAVID FEIT
Signatures Directorate
Carderock Division Naval Surface Warfare Center
9500 MacArthur Boulevard
West Bethesda, Maryland 20817

Advanced Mathematical Methods in Science and Engineering

Sabih I. Hayek

Marcel Dekker, New York, 2000.
749 pp. Price: $195.00 hardcover ISBN: 0824704665.

The first question that one may ask is "Do we need another book on Advanced Mathematical Methods?" The answer to that question is a resounding yes if the book is to be used as a textbook or a reference tool for the person whose interest is in the acoustic/vibration area or in the mechanical/aerospace/civil engineering field. The unique features of this book are the insights and the details provided into the mathematical analysis of the many acoustics/vibrations examples and problems. The theory in each chapter is supplemented by numerous examples and problems (with solutions provided at end of book) taken from the vibration and heat transfer fields. While the book is aimed at the senior and graduate level class, it can

 0001-4966/2002/111(1)/15/2/$19.00

also serve as a very good reference book. The graduate student will receive an appreciation for the mathematical details that go into the analysis of typical problems. The researcher will find this book an excellent reference point for many classical vibration and acoustic problems. The book is easy to read and has many figures used to illustrate physical problems and to facilitate the understanding of complex mathematical procedures.

The book consists of nine chapters: Chap. 1—Ordinary Differential Equations; Chap. 2—Series Solutions of Ordinary Differential Equations; Chap. 3—Special Functions; Chap. 4—Boundary Value (BVP) and Eigenvalue Problems; Chap. 5—Complex Variables; Chap. 6—Partial Differential Equations; Chap. 7—Integral Transforms; Chap. 8—Green's Functions; Chap. 9—Asymptotic Methods.

Chapters 1–3 cover the basic mathematical methods suitable for the junior or senior level engineering student.

Chapter 4 deals with BVP and eigenvalue problems. Most of the examples and problems are drawn from vibration of strings, beams, and rods and are solved by using Fourier series techniques. Of particular interest to the reader may be the eight examples presented in the chapter and the 18 problems given at the end of the chapter illustrating classical vibrating systems with different types of realistic boundary conditions.

Chapter 5 covers classical complex variables theory with the residue theorem, inverse Laplace transform, and Riemann sheets being given full attention. The sections on inverse Laplace transform focuses on problems encountered in vibration of typical systems.

Chapter 6 deals with partial differential equations. The equations presented are the heat diffusion, membrane and plate vibration, and acoustic wave equations as applied to propagation/reflection. Laplace, Poisson, and Helmholtz equations are solved in infinite and finite domains. Cartesian, cylindrical, and spherical coordinates are considered. A wide array of realistic problems is solved with 40 unique problems devoted to vibration/acoustic and another 40 devoted to heat diffusion. The solution to each of these problems is given in the back of the book.

Chapter 7 presents Fourier, Hankel, and Laplace transform techniques as applied to heat flow and wave propagation in strings, membranes, and plates. The relationship between sine, cosine and complex Fourier transform is presented. Six vibration and six heat flow examples are worked out. Twenty-nine vibration problems are given at the end of the chapter.

Chapter 8 covers Green's function and applies the technique to vibration of strings and heat flow in Cartesian, cylindrical, and spherical coordinates. Dirichlet and Neumann conditions in one, two, and three dimensions are covered. Examples and problems address beams and membranes on elastic foundations.

Chapter 9 covers asymptotic methods such as steepest descent and saddle point that are widely used in acoustic radiation problems. The WKBJ method is also covered. Solutions to differential equations with irregular singular points and solutions to equations with large arguments are also presented.

Five appendices covering infinite series, special functions, and orthogonal coordinates are also given. A list of over 130 books is in the bibliography.

What makes this book different from others in the applied mathematics area is the presentation and discussion of the many acoustic/vibration problems of interest to the reader of this journal. I have found myself surprised at finding most of the mathematical techniques that I have used over the years in one book. I know that I will keep this book handy, and will refer to it in my research and in the graduate classes where classical vibration problems are encountered.

MAURO PIERUCCI
Department of Aerospace and Engineering Mechanics
San Diego State University
San Diego, California 92182-1308

BOOKS RECEIVED

Foundations of Engineering Acoustics. F. J. Fahy. Academic Press, San Diego, 2000. 784 pp. $84.95 *hc* ISBN 0122476654.

Linear Elastic Waves. J. G. Harris. Cambridge University Press, New York, 2001. 208 pp. $69.95 *hc* ($24.95 *pb*) ISBN 0521643686 *hc* (052164383X *pb*).

Seismic Ray Theory. V. Cerveny. Cambridge, New York, 2001. 720 pp. $130.00 *hc* ISBN 0521366712.

Canonical Problems in Scattering and Potential Theory Part 1: Canonical Structures in Potential Theory. S. S. Vinogradov, P. D. Smith, and E. D. Vinogradova. Chapman & Hall/CRC, Boca Raton, 2001. 392 pp. $74.95 *hc* ISBN 1584881623.

Foundations of Stuttering. Marcel E. Wingate. Academic Press, San Diego, 2001. 450 pp. $75.00 *hc* ISBN 0127594515.

Real-Time Adaptive Concepts in Acoustics: Blind Signal Separation and Multichannel Echo Cancellation. D. W. E. Schobben. Kluwer Academic Publishers, The Netherlands, 2001. 170 pp. $87.00 *hc* ISBN 0792371097.

Musical Imagery. R. I. Godoy and H. Jorgensen (Eds.). Swets & Zeitlinger, The Netherlands, 2001. 332 pp. $89.00 *hc* ISBN 9026518315.

How Can We Keep from Singing: Music and the Passionate Life. J. O. Goldsmith. Norton, W. W. & Company, Inc., New York, 2001. 236 pp. $22.95 *hc* ISBN 039302024X.

Vision Models and Applications to Image and Video Processing. C. J. van den Branden Lambrecht (Ed.). Kluwer Academic Publishers, Boston, 2001. 240 pp. $120.00 *hc* ISBN 0792374223.

Identification and Control of Mechanical Systems. Jer-Nan Juang and Minh Q. Phan. Cambridge University Press, New York, 2001. 384 pp. $80.00 *hc* ISBN 0521783550.

Mechanical Engineer's Handbook. D. B. Marghitu (Ed.). Academic Press, Incorporated, San Diego, 2001. 880 pp. $69.95 *hc* ISBN 012471370x.

Thin Film Magnetoresistive Sensors. S. Tumanski. Institute of Physics Publishing, Bristol, 2001. 446 pp. $120.00 *hc* ISBN 0750307021.

REVIEWS OF ACOUSTICAL PATENTS

Lloyd Rice
11222 Flatiron Drive, Lafayette, Colorado 80026

The purpose of these acoustical patent reviews is to provide enough information for a Journal reader to decide whether to seek more information from the patent itself. Any opinions expressed here are those of reviewers as individuals and are not legal opinions. Printed copies of United States Patents may be ordered at $3.00 each from the Commissioner of Patents and Trademarks, Washington, DC 20231. Patents are available via the Internet at http://www.uspto.gov.

Reviewers for this issue:

GEORGE L. AUGSPURGER, *Perception, Incorporated, Box 39536, Los Angeles, California 90039*
ALIREZA DIBAZAR, *Dept. of BioMed Engr., Univ. of Southern Calif., Los Angeles, California 90089*
HASSAN NAMARVAR, *Dept. of BioMed Engr., Univ. of Southern Calif., Los Angeles, California 90089*
DAVID PREVES, *4 Deerfield Drive, Princeton Junction, New Jersey 08550*
DANIEL RAICHEL, *2727 Moore Lane, Fort Collins, Colorado 80526*
CARL J. ROSENBERG, *Acentech, Incorporated, 33 Moulton Street, Cambridge, Massachusetts 02138*
WILLIAM THOMPSON, JR., *The Pennsylvania State Univ., University Park, Pennsylvania 16802*

5,926,995

43.30.Nb AUDIBLE FISHING LURE HAVING A SOUND EMITTING CHAMBER

Eugene Dubois, assignor to Bass Pro Trademarks, L.P.
27 July 1999 (Class 43/42.31); filed 22 May 1997

A floating fishing lure features an interior tubular chamber that contains two metallic balls. The lure naturally floats with a nose-up attitude so that the balls are at the rear and bottom of the upward tilted chamber. As the lure is retrieved with a jerk of the fishing line, the attitude of the lure changes so that it becomes parallel to the surface of the water, the balls roll forward and impact the front of the chamber, thereby producing a clicking noise. If the tension in the line is released, the lure returns to its nose-up attitude, the balls roll backwards striking the rear end of the chamber, producing another clicking noise.—WT

5,751,659

43.30.Yj CERAMIC MASS LOADED LONGITUDINAL VIBRATOR

Matthias M. Giwer, Arlington, Virginia
12 May 1998 (Class 367/158); filed 29 September 1969

A Tonpilz-type sonar transducer features a motor section with two concentric stacks of annular discs of piezoceramic rather than one stack with the same cross sectional area. The transducer is totally enclosed in a gas tight housing which is lined on its interior surface with pressure release material. The housing is back filled with an argon and methane mixture. The alleged advantages of this design are improved shock resistance, improved voltage breakdown characteristics, and low side and back radiation.—WT

5,949,742

43.30.Yj DIFAR SENSOR

John Lionel Delany and David Edwin James Buckingham, assignors to Ultra Electronics Limited
7 September 1999 (Class 367/188); filed in the United Kingdom 11 September 1995

A DIFAR sensor comprises two circular end masses **2** and **4** that constitute an inertial mass, four sensor elements located at the ends of two orthogonal diameters (only sensor element **30** is tagged in this cross-sectional view), and screw-threaded adjustment elements **38** and **40** that bear

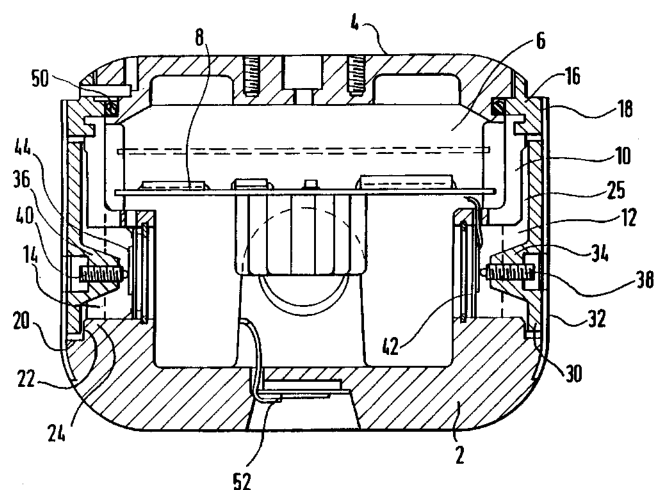

against piezoelectric transducer elements **42** and **44**, respectively. The signals from the diametrically opposite transducers are processed so as to form the difference between the outputs of the corresponding sensor elements. The screw adjustment feature allows for adjustment of the forces transmitted to the transducers after the entire unit has been assembled. A waterproof elastomeric skin **32** seals the unit. An omnidirectional hydrophone **52** located in a recess of base mass **2** provides a measurement of the acoustic pressure.—WT

5,959,939

43.30.Yj ELECTRODYNAMIC DRIVING MEANS FOR ACOUSTIC EMITTERS

Rune Tengham and Magnus Zetterlund, assignors to Unaco Systems AB
28 September 1999 (Class 367/174); filed in Norway 28 June 1995

The patent describes a method for driving flextensional underwater transducers. Flexible tie rods **5** are driven by electrodynamic actuators **6** and **7**, resulting in lever-assisted motion of ‘‘fastening devices’’ **2**. This appears

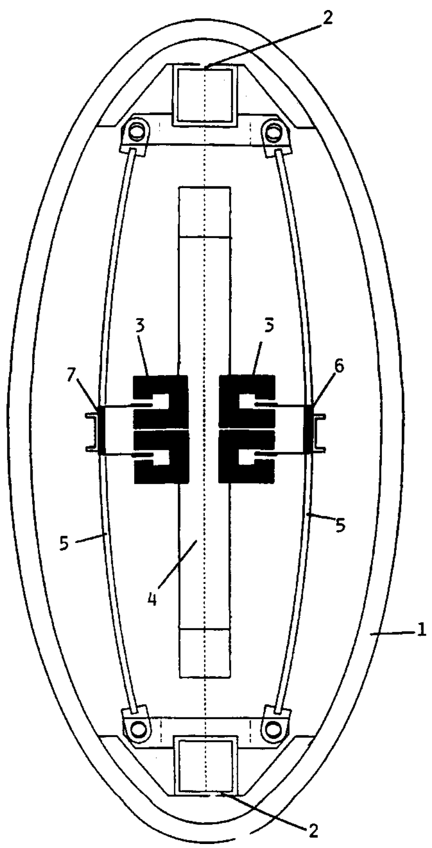

to be a little like connecting two electrical transformers back-to-back, but it is a practical way to couple almost any number of drive motors to a single spheroidal diaphragm.—GLA

5,939,818

43.38.Fx PIEZOELECTRIC TRANSFORMER, ITS MANUFACTURING METHOD AND ITS DRIVING METHOD

Hiroyo Hakamata, assignor to NEC Corporation
17 August 1999 (Class 310/359); filed in Japan 15 February 1995

A composite piezoelectric structure consists of two piezoelectric blocks **111** and **114** with electrode surfaces **112**, **113**, **115**, and **116** that are polarized in the thickness direction as indicated by the arrow **Ya** plus two other piezoelectric blocks **121** and **122** that are oppositely polarized from each other in the longitudinal direction as indicated by the arrows **Yc** and **Yd**. Items **123**, **124**, and **125** are also electrodes. An alternating voltage is applied between the electrode pairs **112–113** and **115–116**. Through 3–1

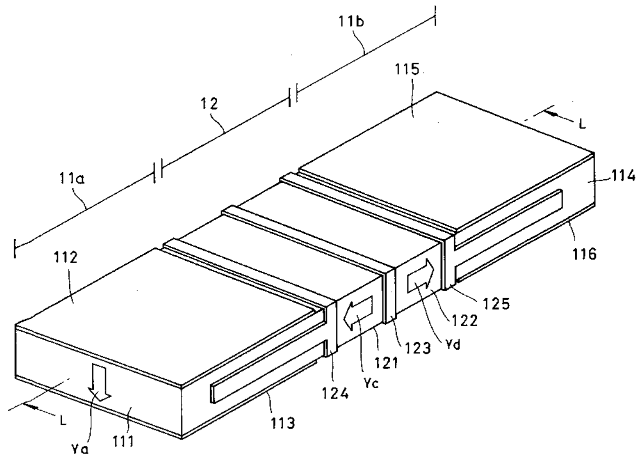

coupling, this excites the entire structure into longitudinal vibrations. When the excitation frequency is near the longitudinal resonance frequency of the entire structure (in this case, when the length of the structure equals 1.5 wavelengths) a significant voltage is generated between electrode **123** and either electrode **124** or **125**. Several other embodiments of the concept are discussed.—WT

5,945,769

43.38.Fx WAVE DRIVEN MOTOR

Reiji Mitarai and Hiroaki Takeishi, assignors to Canon Kabushiki Kaisha
31 August 1999 (Class 310/317); filed in Japan 26 August 1991

A flat annular ring is constructed from a large number of like-polarized piezoelectric wedge-shaped segments. By a judicious choice of the phases of cyclic signals applied to these segments, traveling waves are excited in the ring. These waves, in turn, are converted into a torque generation device.—WT

5,969,463

43.38.Fx ENERGY TRAPPING PIEZOELECTRIC DEVICE AND PRODUCING METHOD THEREOF

Yoshihiro Tomita *et al.*, assignors to Matsushita Electric Industrial Company, Limited
19 October 1999 (Class 310/320); filed in Japan 10 July 1996

This patent discusses various techniques for shaping a piezoelectric plate and for arranging the electrode patterns on the plate in order to excite a pure thickness mode of vibration.—WT

5,973,441

43.38.Fx PIEZOCERAMIC VIBROTACTILE TRANSDUCER BASED ON PRE-COMPRESSED ARCH

K. Peter Lo *et al.*, assignors to American Research Corporation of Virginia
26 October 1999 (Class 310/330); filed 15 May 1997

An electromechanical transducer is discussed that can provide tactile stimulation of the human body and thereby convey warning information about the environment in situations where other forms of information transmittal are not applicable or are compromised. The transducer or actuator is realized as a rectangular bimorph (two PZT plates sandwiching a steel plate) supported along two parallel edges and free at the other two and which is precompressed and predeflected into an arch shape. The electrical excitation is a large amplitude, short, e.g., 5 to 10 cycles, burst of energy at a resonance frequency of the bimorph that causes the curved plate to buckle. The buckling phenomenon results in greater sensations to the human skin, even through clothing, than sensations resulting from the vibrating plate alone.—WT

6,154,552

43.38.Hz HYBRID ADAPTIVE BEAMFORMER

Walter S. Koroljow and Gary L. Gibian, assignors to Planning Systems, Incorporated
28 November 2000 (Class 381/313); filed 14 May 1998

Integrated circuit technology allows hearing aid designers to include sophisticated signal processing in their products. For example, microphone arrays can be mounted on eyeglasses, allowing the sound pickup angle to be reduced in noisy environments. Further improvement can be realized by controlling the pattern lobes in such a way as to minimize pickup of interfering sounds. The invention is a sophisticated method for digitally implementing this kind of dynamic control.—GLA

5,966,438

43.38.Si METHOD AND APPARATUS FOR ADAPTIVE VOLUME CONTROL FOR A RADIOTELEPHONE

Eric D. Romesburg, assignor to Ericsson, Incorporated
12 October 1999 (Class 379/387); filed 5 March 1996

The invention applies to hands-free operation of cellular telephones and the like, particularly in moving vehicles. If the driver turns up the volume to overcome background noise, the cheap little loudspeaker overloads and speech intelligibility becomes worse, not better. The preceding two sentences summarize the first page and a half of the patent. It then goes on to describe a combination of noise suppression, echo canceling, dynamic volume control, and limiting that attempts to maintain best possible intelligibility by simultaneously compensating for background noise and loudspeaker limitations.—GLA

5,983,192

43.38.Si AUDIO PROCESSOR

Stephen C. Botzko and David M. Franklin, assignors to PictureTel Corporation
9 November 1999 (Class 704/500); filed 8 September 1997

Video teleconferencing techniques employ a variety of methods to pick up and distribute audio signals. The trick is to minimize transmission bandwidth and avoid signal degradation at the same time. The invention mixes and analyzes uncompressed audio and then selectively distributes time-compressed composite signals to various outputs. This is done in a manner that provides high signal quality while avoiding end site overload. The patent is interesting and informative.—GLA

6,026,169

43.38.Vk SOUND IMAGE LOCALIZATION DEVICE

Junichi Fujimori, assignor to Yamaha Corporation
15 February 2000 (Class 381/61); filed in Japan 27 July 1992

Delay-controlled panning of monophonic sources can produce virtual images over a wider area than conventional level-controlled panning, but it has its own set of problems, including front–rear ambiguity. The circuitry described here allows placement of a virtual sound source anywhere in the lateral plane, plus adjustment of apparent height. All of this is accomplished without resorting to head-related transfer functions.—GLA

6,038,323

43.38.Vk STEREOPHONIC IMAGE ENHANCEMENT SYSTEM FOR USE IN AUTOMOBILES

Michael L. Petroff, assignor to Harman Motive, Incorporated
14 March 2000 (Class 381/1); filed 17 November 1997

Most automobile stereo systems include a simple panning control so that the preferred listener (driver or passenger) can achieve a reasonably good balance between the levels of left and right channels. A number of patents have been issued for more exotic schemes that attempt to provide acceptable stereo reproduction for both listeners simultaneously. The inventor argues that sound reproduction characteristics in this environment cannot be modeled as relative delay between left and right channels. Instead, nonlinear phase shift over a 1-oct band (150–300 Hz) is used to supply stereo clues to each listener. The preferred embodiment uses simple filters to provide a symmetrical improvement in imaging for driver and passenger.—GLA

6,173,061

43.38.Vk STEERING OF MONAURAL SOURCES OF SOUND USING HEAD RELATED TRANSFER FUNCTIONS

John Norris and Timo Kissel, assignors to Harman International Industries, Incorporated
9 January 2001 (Class 381/309); filed 23 June 1997

The patent title deliberately uses the word ‘‘sources’’ because the invention is intended for use in multi-track stereophonic recording. Instead of conventional level-controlled panning, each track can be located or dynamically moved anywhere in space when reproduced through headphones or a

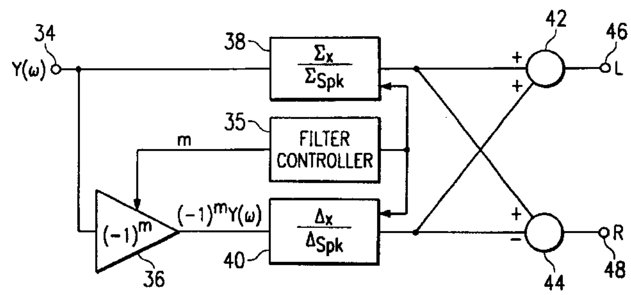

pair of loudspeakers. Although the basic techniques employed to (hopefully) achieve this result are not new, a number of improvements on prior art are disclosed in the patent.—GLA

6,231,710

43.50.Gf METHOD OF MAKING COMPOSITE CHAMBERCORE SANDWICH-TYPE STRUCTURE WITH INHERENT ACOUSTIC ATTENUATION

Eric Herup *et al.*, assignors to the United States of America as represented by the Secretary of the Air Force
15 May 2001 (Class 156/173); filed 4 June 1999

This patent describes an innovative structure called ChamberCore that is designed to provide broadband acoustic attenuation. It is damage tolerant, easy to manufacture, and can drastically reduce acoustic transmission through a structure, especially as a muffler for space launch vehicles. The ChamberCore is composed of tubes that create chambers in a honeycomb core between two faceplates. The structure has no weak interface between the facesheets and honeycomb core, as is often found in traditional sandwich-type structures. Additionally, each chamber has a hole to it through the inner facesheet, effectively converting it into a Helmholtz resonator.—CJR

6,248,423

43.50.Gf ACOUSTICAL AND STRUCTURAL MICROPOROUS SHEET

James A. Clarke and Charles A. Parente, assignors to Vought Aircraft Industries, Incorporated
19 June 2001 (Class 428/131); filed 14 August 1997

A sheet of steel is finely perforated with free electron laser technology. The resulting sheet becomes a structural element as for a jet engine with noise-suppressing qualities.—CJR

6,250,036

43.50.Gf SOUND CONTROL SYSTEM FOR STEEL ROOF DECKS

C. Lynn Nurley *et al.*, assignors to Loadmaster Systems, Incorporated
26 June 2001 (Class 52/537); filed 1 March 2000

The adjoining sheets of a steel roof deck diaphragm are separated from each other by nonmetallic strips of felt spacers, positioned between the overlapping side edges of the metal sheets. This prevents the generation of noise resulting from relative movement of the corrugated sheets.—CJR

6,244,378

43.55.Ev DUAL SONIC CHARACTER ACOUSTIC PANEL AND SYSTEMS FOR USE THEREOF

Ralph D. McGrath, assignor to Owens Corning Fiberglas Technology, Incorporated
12 June 2001 (Class 181/292); filed 11 December 1998

This composite sandwich panel has two faces and a honeycomb core. One face is perforated so that the cells act as Helmholtz resonators that can be tuned to the same or different frequencies. The other face is available as

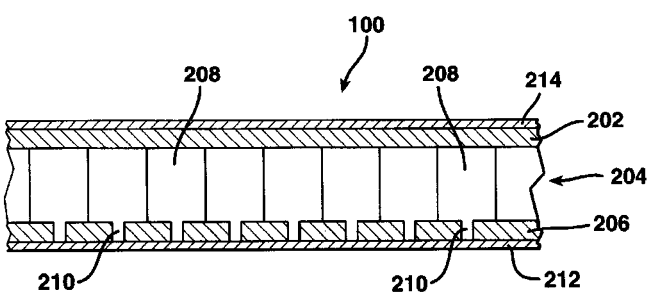

a broad sound-absorbing surface or a sound-diffusing surface. The panels can be applied to a ceiling or hung vertically in a room.—CJR

6,223,483

43.55.Ti VIBRATION DAMPING MECHANISM AND ANTI-EARTHQUAKE WALL MATERIAL

Isamu Tsukagoshi, Higashi-ku, Nagoya-shi, Aichi-ken, Japan
1 May 2001 (Class 52/167.1); filed 14 September 1999

The vibration damping mechanism described in this patent provides strength and rigidity to a building and, at the same time, provides a capability of damping vibrations. Two plates are separated by a space that is

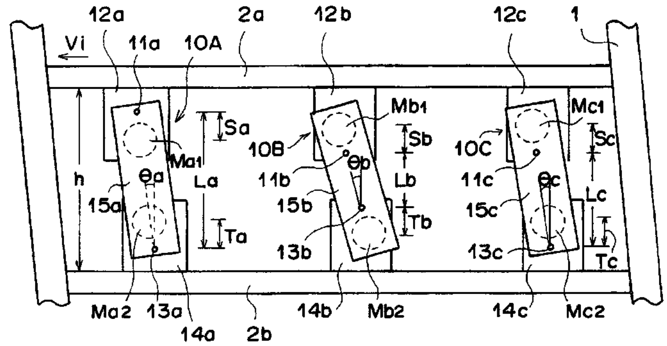

filled with a viscoelastic body. Deformation and movement of the viscoelastic body absorbs vibration energy, as from an earthquake.—CJR

6,237,302

43.55.Wk LOW SOUND SPEED DAMPING MATERIALS AND METHODS OF USE

J. Robert Fricke, assignor to Edge Innovations & Technology, LLC
29 May 2001 (Class 52/720.1); filed 25 March 1998

The composition described in this patent reduces vibrations in a built-up structure, including both damping of structure-borne vibrations and reduction of radiated airborne noise. The composition is either a mixture of at least two different granular materials, or it is a single granular material having a bulk sound speed of less than 90 m/s. The damping properties of a mixture can be calculated from the bulk densities and stiffnesses of its individual components. Built-up structures for which this composition could be helpful for damping are any composite of beams, plates, joints, and other structural components that are connected to form a nominal single unit, such as bridges, electronics cabinets, sports equipment, and automobiles. The method of the invention places the granular material in intimate contact with the structure and so defines a damped structural member.—CJR

6,236,313

43.58.Gn GLASS BREAKAGE DETECTOR

Kenneth G. Eskildsen *et al.*, assignors to Pittway Corporation
22 May 2001 (Class 340/550); filed 28 October 1997

Past glass breakage detectors of the simplest kind merely detect the presence of high-frequency sound. These are said to trigger easily on keys rattling and hand claps. More expensive units use more filters and watch for a pattern consisting of an initial pulse, followed by a low-frequency sound due to the flexing of the glass, and the final breaking sounds. This patent describes a low-cost device with five separate filters but without the temporal pattern detector. The filter responses are adjustable to maximize detection in the particular installation, for a particular type of glass, and so forth.—DLR

6,249,091

43.60.Bf SELECTABLE AUDIO CONTROLLED PARAMETERS FOR MULTIPARAMETER LIGHTS

Richard S. Belliveau, Austin, Texas
19 June 2001 (Class 315/312); filed 8 May 2000

The device applies to stage lighting control. Audio signals received by the proposed device's audio transducer are processed and converted into a control signal for varying stage lighting according to preset parameters. A digital communication scheme is applied by the operator who can establish the manner in which the multiparameter lighting device reacts to specific audio signals.—DRR

6,252,967

43.60.Cg REDUCING ACOUSTIC FEEDBACK WITH DIGITAL MODULATION

Kendall G. Moore *et al.*, assignors to Acoustic Technologies, Incorporated
26 June 2001 (Class 381/93); filed 21 January 1999

Sound reaching a microphone is converted into an electric signal, in the form of an inaudible, digitally modulated signal that is combined with the traditional electrical signal from the microphone, amplified, and converted into sound waves from the loudspeaker. Any sound traveling from the loudspeaker to the microphone has to include the inaudible component representing the original sound. The inaudible component is separated out from the audible component, and the original sound is reconstructed in a digital demodulator. The reconstructed original sound is subtracted from the signal from the microphone, thereby reducing any echoes and canceling feedback. Digital modulation includes any form of shift keying, including coherent and noncoherent techniques for modulating frequency, phase, or amplitude. The patent is similar in purpose to earlier United States Patents 5,412,734 and 5,649,018 by Thomasson; they differ principally in that the older Thomasson methods are essentially analog procedures using FM and PWM (pulse width modulation) carriers rather than the digital technique described in the present patent.—DRR

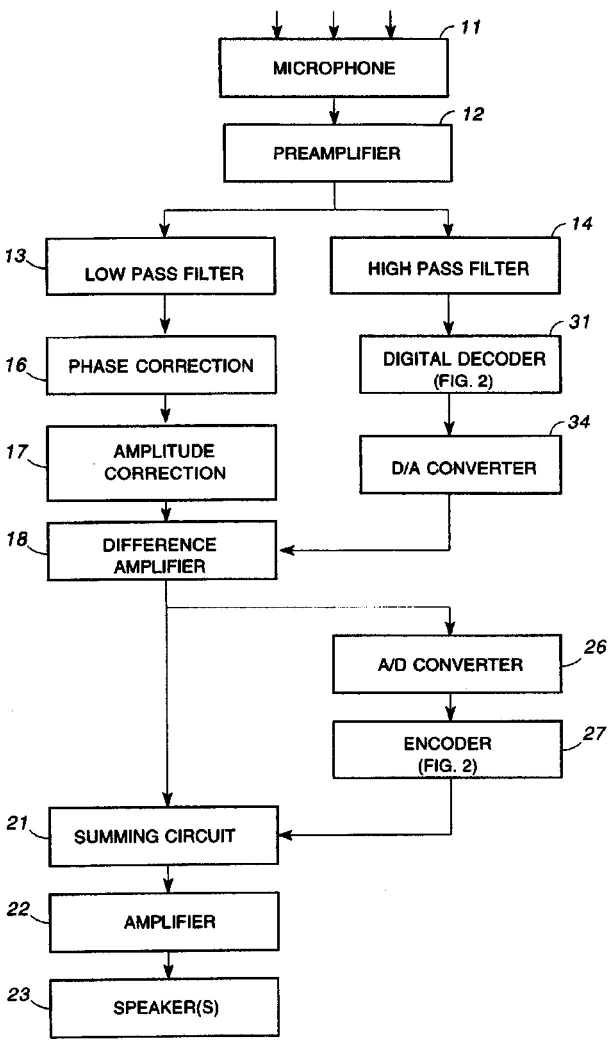

6,252,968

43.60.Cg ACOUSTIC QUALITY ENHANCEMENT VIA FEEDBACK AND EQUALIZATION FOR MOBILE MULTIMEDIA SYSTEMS

Anand Narasimhan and Ganesh Nachiappa Ramaswamy, assignors to International Business Machines Corporation
26 June 2001 (Class 381/103); filed 23 September 1997

Mobile equipment tends to yield distorted signals due to the quality of the reproduction equipment (think low-cost loudspeakers, e.g.) and the environment. According to the inventors, "the computational complexity must be kept to a minimum because mobile systems have limited resources and the solution should not result in excessive delays in audio reproduction." The device uses a "training signal" consisting of a set of pure frequency tones to estimate the characteristics of the reproduction medium. These single-frequency tones are passed through the reproduction medium to generate an output signal, which in turn is passed through a set of subband filters. Each of the subband filters passes at least one of the tones. The characteristics of the reproduction medium are then estimated by passing the output signal through the set of sideband filters. Based on the estimated characteristics of the reproduction medium, a set of subband inverse filters is constructed. Before passing the audio signal through the reproduction medium, the signal is sent through the set of inverse filters. This allegedly improves the quality of the audio signal after it passes through the reproduction medium.—DRR

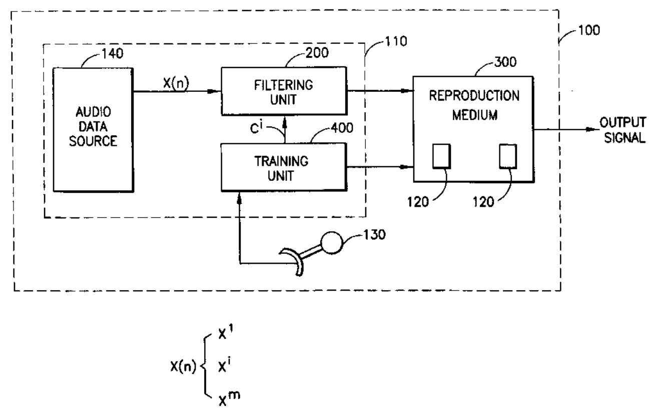

6,243,679

43.60.Lq SYSTEMS AND METHODS FOR DETERMINIZATION AND MINIMIZATION A FINITE STATE TRANSDUCER FOR SPEECH RECOGNITION

Mehryar Mohri *et al.*, assignors to AT&T Corporation
5 June 2001 (Class 704/256); filed 21 January 1997

The method described in this patent is said to achieve optimal reduction of size and redundancy of a weighted and labeled graph. The employed method assigns the contents to the arcs in the graph and then evaluates the weight of each path between states by examining the relationship between the labels. The algorithm then assigns the weight to each arc and determines the graph by removing redundant arcs with the same weights. The minimization of the graph is performed by collapsing a portion of the states in the graph in a reverse determination manner.—AAD

6,241,683

43.60.Qv PHONOSPIROMETRY FOR NON-INVASIVE MONITORING OF RESPIRATION

Peter T. Macklem *et al.*, assignors to Institut de recherches cliniques de Montréal (IRCM); McGill University
5 June 2001 (Class 600/529); filed in Canada 20 February 1998

In this device, a patient's tracheal sound signal is converted into a respiratory flow signal in order to compensate for the poor signal-to-noise ratio. The transformed signal is used when the sound signal occurs above a certain threshold. Interpolated signals are used when the sound signal falls below the threshold. The result is a breath volume indication. The start or stop of respiration can be detected by analyzing the sound signal. A wearable embodiment of the device can provide an immediate indication or alarm when breath volume indicates a need for medical attention.—DRR

6,244,376

43.60.Qv STETHOSCOPE HEAD

Artemio Granzotto, Zürich, Switzerland
12 June 2001 (Class 181/131); filed in Switzerland 13 May 1997

This is another design variation of the common stethoscope, one that does not appear to be terribly innovative. The design features a bell-shaped resonance body. A capsule within the bell-shape resonance volume contains the membrane, and it accommodates the lumen of a tube leading to the earpiece.—DRR

6,245,025

43.60.Qv METHOD AND APPARATUS FOR MEASURING FETAL HEART RATE AND AN ELECTROACOUSTIC SENSOR FOR RECEIVING FETAL HEART SOUNDS

Miklós Török *et al.*, H-1141 Budapest, Hungary
12 June 2001 (Class 600/500); filed 17 August 1998

This device has a twofold purpose: the first is to identify fetal heart sounds with improved reliability and the second is to implement low-power electronic circuitry enabling portable designs that provide for long-term home monitoring. The method utilizes the characteristic curves of first and second heart sounds. These first and second sounds are based on the differences in the frequency spectrum measured in a relatively short time window and on the estimation of the power measured in two frequency bands in the frequency range of fetal heart sounds. Digital filtering and selective power estimation are used to compute a power time function at the two test frequencies. The test frequencies can be varied to accommodate individual fetal parameters in order to enhance the distinction between the first and second sound. The microphone embodiment given here seems to be of rather conventional design.—DRR

6,251,077

43.60.Qv METHOD AND APPARATUS FOR DYNAMIC NOISE REDUCTION FOR DOPPLER AUDIO OUTPUT

Larry Y. L. Mo and Richard M. Kulakowski, assignors to General Electric Company
26 June 2001 (Class 600/455); filed 13 August 1999

The device relates to ultrasonic diagnostic systems which measure the velocity of blood flow using Doppler techniques. Background noise is suppressed using adaptive noise-reduction low-pass filters. A pair of adaptive low-pass filters is incorporated into two audio Doppler channels to suppress the background noise in the audio Doppler data. The low-pass filter can be implemented in the frequency domain, i.e., before the inverse fast Fourier transform (IFFT) operation, or in the time frequency domain, i.e., after the IFFT operation. Maximum frequency traces are channeled into a filter selection block which determines the filter cutoffs of the low-pass filters.—DRR

6,247,474

43.60.Rw AUDIBLE SOUND COMMUNICATION FROM AN IMPLANTABLE MEDICAL DEVICE

Daniel R. Greeninger *et al.*, assignors to Medtronic, Incorporated
19 June 2001 (Class 128/899); filed 29 April 1998

This patented device provides improved communication with an implantable medical device (IMD) in order to program the IMD or to retrieve IMD information and provide warnings to the patient of possible IMD malfunction. The IMD includes an audio transducer that emits audible sounds including voiced statements or musical tones stored in an analog memory. Sounds are played on command or in response to a warning trigger event.

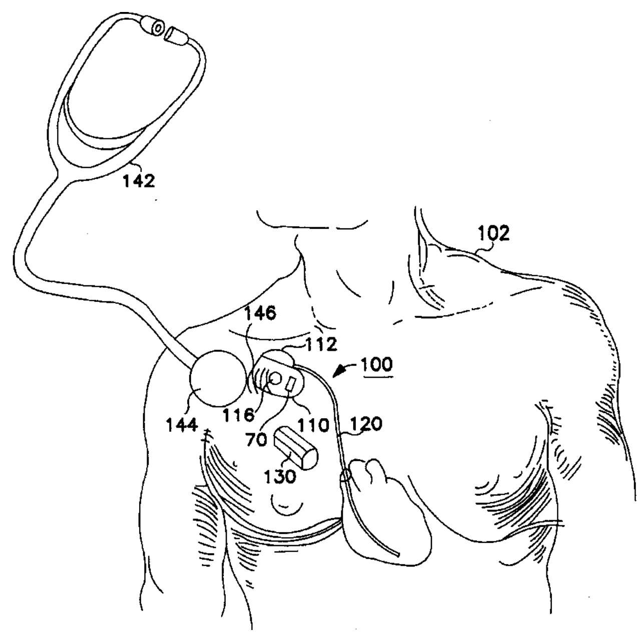

The transmission may consist of the audible signal alone or it may include rf transmission of stored data and parameters. In order to conserve energy, the audible sounds are generated at a low volume that cannot be heard without the aid of external amplifier or stethoscope. Voiced warnings of battery depletion or imminent delivery of a therapy are voiced at louder levels so that the patient can take notice and take appropriate action.—DRR

6,231,521

43.64.Jb AUDIOLOGICAL SCREENING METHOD AND APPARATUS

Peter Zoth *et al.*, Munich, Germany
15 May 2001 (Class 600/559); filed 17 December 1998

A variety of testing methods have been used in the past to detect hearing problems in infant children. Early detection of problems is an important factor in taking suitable corrective measures. However, the available testing equipment has typically been expensive and has required skilled

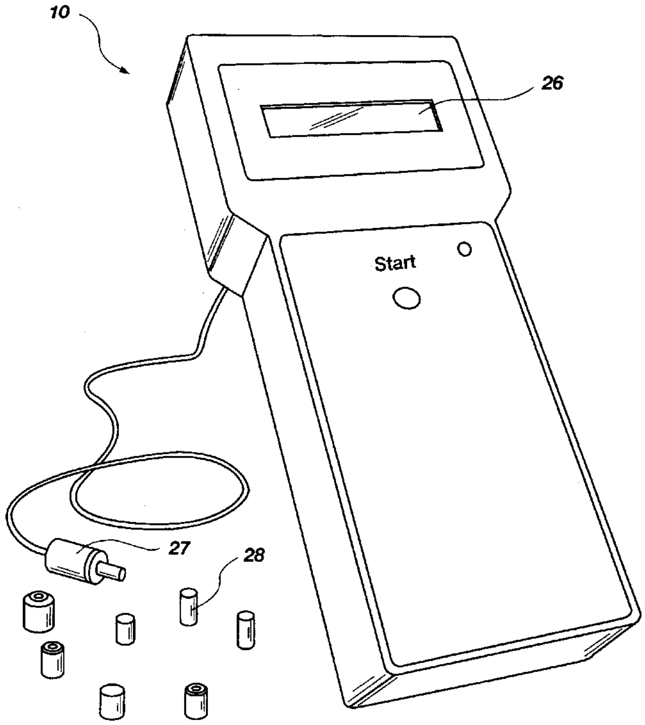

operators. These factors have limited the application of these tools. The patent describes a small, low-cost device which produces a test pulse at the ear and records the evoked otoacoustic emission. The result is automatically analyzed by an embedded processor which is said to have less than 1% false negative errors.—DLR

6,250,255

43.64.Ri METHODS AND APPARATUS FOR ALERTING AND/OR REPELLING BIRDS AND OTHER ANIMALS

Martin L. Lenhardt and Alfred L. Ochs, assignors to Virginia Commonwealth University
26 June 2001 (Class 119/713); filed 6 August 1998

Methods are continually being sought to chase away birds from airports, power lines, wind turbines, glass windows, and other objects that birds might inadvertently strike during flight. The patent covers an embodiment for generating an external signal to alert animals in danger and/or to repel them from specific areas. The system uses external stimuli such as,

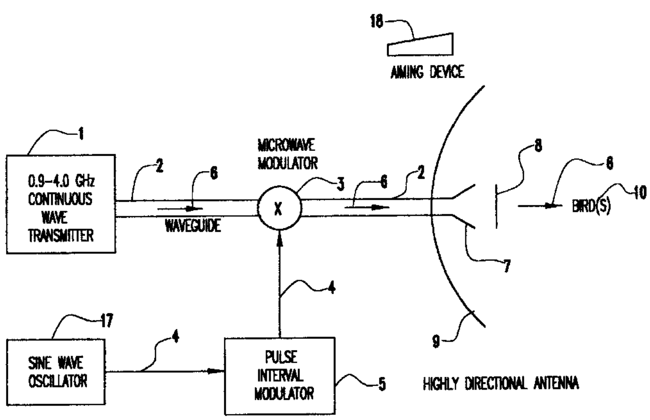

e.g., pulsing microwaves, vibration, or ultrasonic sound waves in order to alert animals of danger and/or to repel those animals from specific areas. The signals may provide a reversible unpleasant sensation in the animals so that they will be chased away from a specific area, such as an airport, and they are hopefully deterred from returning to that area.—DRR

6,228,020

43.66.Ts COMPLIANT HEARING AID

Roger P. Juneau *et al.*, assignors to Softear Technologies, L.L.C.
8 May 2001 (Class 600/25); filed 18 December 1997

The inside of an elastomeric, soft-bodied, hearing instrument is completely filled with a soft fill material that encapsulates the electronic components within. The exterior of the soft hearing aid, which is mounted on a hard faceplate, is made without modifying the ear impression and is said to seal well in the ear canal, enabling higher gain before acoustic feedback oscillation occurs. The soft outer surface of the hearing aid is virtually nonabsorbent, impervious to cerumen and discoloration, and is said to not need to be returned as frequently for modification as hearing aids made of hard acrylic.—DAP

6,229,900

43.66.Ts HEARING AID INCLUDING A PROGRAMMABLE PROCESSOR

Joseph R. G. M. Leenen, assignor to Beltone Netherlands B.V.
8 May 2001 (Class 381/314); filed in the World IPO 18 July 1997

The performance of a hearing aid for different listening conditions may be changed by the wearer by transferring new control signals from a remote location. At least one set of instructions is loaded into the remote control from an external device such as a personal computer and then transmitted to a receiver in the hearing aid. The new instruction signals are stored in a memory in the hearing aid which controls a programmable processor that determines the electroacoustic performance of the instrument. For binaural fittings, control signals are transmitted to both hearing aids in response to a single selection by the wearer of new instructions on the remote control.—DAP

6,231,604

43.66.Ts APPARATUS AND METHOD FOR COMBINED ACOUSTIC MECHANICAL AND ELECTRICAL AUDITORY STIMULATION

Christoph von Ilberg, assignor to Med-El Elektromedizinische Gerate Ges.m.b.H
15 May 2001 (Class 623/10); filed 26 February 1998

Persons with more severe hearing loss are likely to have more hair cells that are destroyed or not functioning properly. In such cases, traditional hearing aid stimulation is not always effective. Effective electrical stimulation of the auditory nerve does not always require that hair cells be intact. This patent describes a system in which acoustical/mechanical stimulation is utilized for that part of the audio frequency range hair cells are healthy and electrical stimulation for that frequency range which contains damaged hair cells.—DAP

6,240,192

43.66.Ts APPARATUS FOR AND METHOD OF FILTERING IN AN DIGITAL HEARING AID, INCLUDING AN APPLICATION SPECIFIC INTEGRATED CIRCUIT AND A PROGRAMMABLE DIGITAL SIGNAL PROCESSOR

Robert Brennan and Anthony Todd Schneider, assignors to dspfactory Limited
29 May 2001 (Class 381/314); filed 16 April 1997

A programmable DSP core or other type of microcontroller controls the parameters of a fixed-processing, hard-wired application specific integrated circuit (ASIC). Both circuits are placed on the same chip for easier packaging in small hearing aids. A filterbank in the ASIC splits the input signal into frequency bands. The number of channels in the filterbank is adjustable and their center frequencies may be shifted simultaneously. The DSP varies parameters such as channel gain of each band in response to input signal changes.—DAP

6,231,500

43.70.Dn ELECTRONIC ANTI-STUTTERING DEVICE PROVIDING AUDITORY FEEDBACK AND DISFLUENCY-DETECTING BIOFEEDBACK

Thomas David Kehoe, Monte Sereno, California
15 May 2001 (Class 600/23); filed 22 March 1994

This patent begins with an excellent and extended discussion of the causes, nature, and treatment of stuttering, as far as is known by the medical community. Several improvements to a previously patented biofeedback treatment system are then described. The device processes the user's speech, detecting stuttering, measuring voice pitch and muscle activity, and extracting a glottal excitation signal from the speech input. Several forms of biofeedback to the user are provided.—DLR

6,210,166

43.71.Ky METHOD FOR ADAPTIVELY TRAINING HUMANS TO DISCRIMINATE BETWEEN FREQUENCY SWEEPS COMMON IN SPOKEN LANGUAGE

William M. Jenkins *et al.*, assignors to Scientific Learning Corporation
3 April 2001 (Class 434/185); filed 17 December 1997

This interactive computer system is designed to test for and modify the frequency perception deficits said to be common in the condition known as language learning impairment. A pattern of frequency sweeps is presented to the subject. When the user correctly identifies the sweeps using mouse, keys, or other inputs, the presentation is altered by decreasing interstimulus intervals or increasing the rate or number of sweeps.—DLR

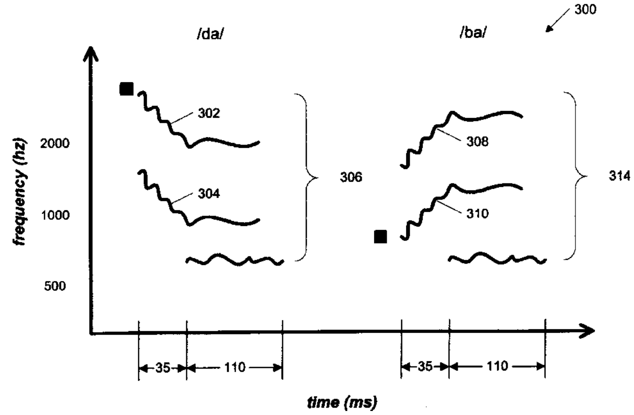

6,224,384

43.71.Ky METHOD AND APPARATUS FOR TRAINING OF AUDITORY/VISUAL DISCRIMINATION USING TARGET AND DISTRACTOR PHONEMES/GRAPHEMES

William M. Jenkins *et al.*, assignors to Scientific Learning Corporation
1 May 2001 (Class 434/185); filed 17 December 1997

This patent is another in a long series sponsored by the present assignee based on the premise that a person suffering from a particular form of perceptual deficit known as language learning impairment can, with training, overcome the condition. See, for example, United States Patent 6,210,166, reviewed above. Here, the task is to identify an enhanced target sound presented within a sequence of distractor sounds. As the subject's performance improves, the degree of enhancement is reduced, finally approximating normal speech. The enhancement consists of stretching the duration in regions of rapid frequency transitions.—DLR

6,236,965

43.72.Bs METHOD FOR AUTOMATICALLY GENERATING PRONUNCIATION DICTIONARY IN SPEECH RECOGNITION SYSTEM

Hoi-Rin Kim and Young-Jik Lee, assignors to Electronic Telecommunications Research Institute
22 May 2001 (Class 704/254); filed in the Republic of Korea 11 November 1998

This patent describes a method for automatically generating a pronunciation dictionary for accurately recognizing a new word not registered in the recognition system. The neural network used to build the dictionary is a back-propagation-trained multi-layer perceptron which generates phoneme and word models of new words. In this method, the pronunciation patterns of a large-scale pronunciation dictionary can be learned without resorting to phonetic knowledge. Finally, a pattern comparison section compares the word models with the extracted features so as to output the closest candidate word as the recognition result.—HHN

6,208,960

43.72.Ew REMOVING PERIODICITY FROM A LENGTHENED AUDIO SIGNAL

Ercan F. Gigi, assignor to U.S. Philips Corporation
27 March 2001 (Class 704/220); filed in the European Patent Office 19 December 1997

The basic issue here is stretching the duration of a speech signal. During voiced portions, this is easily done by duplicating fundamental periods. However, during voiceless intervals, an unwanted periodicity is introduced. This is overcome by staggering and randomizing the durations of the duplicated speech segments.—DLR

6,253,171

43.72.Ew METHOD OF DETERMINING THE VOICING PROBABILITY OF SPEECH SIGNALS

Suat Yeldener, assignor to Comsat Corporation
26 June 2001 (Class 704/208); filed 23 February 1999

This patent describes a method of computing a voicing value for each frequency band of a speech spectrum to improve output speech quality in a speech coding application. The method is based on determining a voicing probability indicating a percentage of unvoiced and voiced energy. The original and synthetic speech spectra **2** are divided into multiple bands **3** and

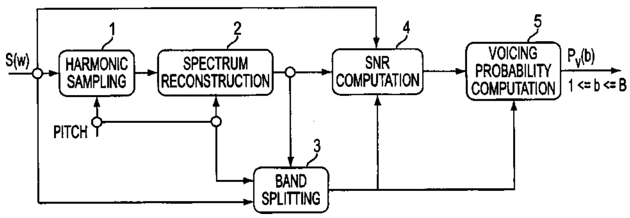

are compared harmonic by harmonic. A voicing determination is made by comparing the difference with an adaptive threshold. The voicing probability **5** for each band is then estimated based on the amount of energy in the voiced harmonics in that decision band.—HHN

6,219,640

43.72.Fx METHODS AND APPARATUS FOR AUDIO-VISUAL SPEAKER RECOGNITION AND UTTERANCE VERIFICATION

Sankar Basu *et al.*, assignors to International Business Machines Corporation
17 April 2001 (Class 704/246); filed 6 August 1999

This patent essentially proposes a wide variety of methods for combining features from acoustic and video analyses for use in identifying or verifying the speaker's identity. Suggested applications range from biometric measurement for security purposes to the indexing of recorded material, such as TV news broadcasts. Feature extraction uses well-known methods, such as cepstrum, discriminant analysis, and perceptual linear prediction for speech and Fischer linear discriminants or "face space distance" measures for facial features.—DLR

6,208,968

43.72.Ja COMPUTER METHOD AND APPARATUS FOR TEXT-TO-SPEECH SYNTHESIZER DICTIONARY REDUCTION

Anthony J. Vitale *et al.*, assignors to Compaq Computer Corporation
27 March 2001 (Class 704/260); filed 16 December 1998

This patent is concerned with the use of a rule system to reduce the size of an on-line phonetic dictionary. Each dictionary entry contains a graphemic (spelled) version and a phonetic version of each word. In a first pass, all of the entries are eliminated for which the phonetic component can be exactly generated from the graphemic component. Additional passes apply various methods of deriving words from root forms, or vice versa. Only the unique and nonderivable forms are kept in the final dictionary.—DLR

6,226,614

43.72.Ja METHOD AND APPARATUS FOR EDITING/CREATING SYNTHETIC SPEECH MESSAGE AND RECORDING MEDIUM WITH THE METHOD RECORDED THEREON

Osamu Mizuno and Shinya Nakajima, assignors to Nippon Telegraph and Telephone Corporation
1 May 2001 (Class 704/260); filed in Japan 21 May 1997

This method for generating more natural-sounding synthetic speech is based on a three-level system of controls. The top, or semantic, level includes emotional state and dialog status conditions. These are mapped to a

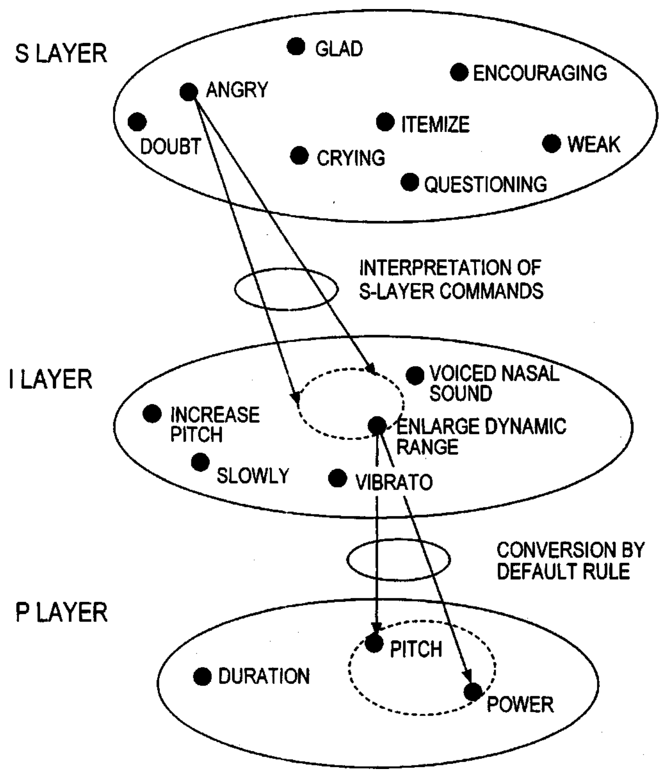

mid-range interpretation level which specifies broad phonetic characteristics. These are, in turn, mapped to the low-level player commands, which specify the low-level phonetic details.—DLR

6,212,501

43.72.Ja SPEECH SYNTHESIS APPARATUS AND METHOD

Osamu Kaseno, assignor to Kabushiki Kaisha Toshiba
3 April 2001 (Class 704/258); filed in Japan 14 July 1997

The patent describes a system for intermixing rule-based synthesis and analysis-based synthesis in order to achieve a more natural speech output. In many speech synthesis applications, portions of the text material can be prerecorded to capture the natural prosodic patterns. For other variable por-

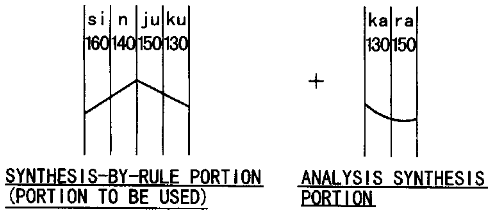

tions of text, the speech must be generated by rules. From the confusing patent text, it appears that the rule-generated prosodic patterns are adjusted for both pitch and phase so as to incorporate prerecorded portions wherever possible.—DLR

6,225,914

43.72.Ja AUTOMATIC VOICE DEVICE FOR FIRE EXTINGUISHER

Linsong Weng, assignor to Hugewin Electronics Company, Limited
1 May 2001 (Class 340/692); filed 9 February 2000

This speech synthesis application includes a motion detector and a speech synthesis chip packaged into the housing of a fire extinguisher. When the extinguisher is picked up, the voice output chip produces a sequence of fire-fighting assistance messages.—DLR

6,230,131

43.72.Ja METHOD FOR GENERATING SPELLING-TO-PRONUNCIATION DECISION TREE

Roland Kuhn *et al.*, assignors to Matsushita Electric Industrial Company, Limited
8 May 2001 (Class 704/266); filed 29 April 1998

Methods are described for building and using decision trees to convert spelled text to phonetic transcriptions suitable for speech synthesis. Two kinds of trees are considered. The first, called a ‘‘letter-only’’ tree, processes the spelled input letter by letter and contains information at each node for asking yes/no questions about the spelled text input. The second type, a ‘‘mixed’’ tree, processes both the original spelled input and the phonetic output of the first tree. Node information on this tree generates yes/no questions about both types of input streams. For example, the phonetic sequences can be checked for validity in the language, eliminating illegal output strings. The patent describes how the trees are built from the available training data.—DLR

6,208,359

43.72.Kb SYSTEMS AND METHODS FOR COMMUNICATING THROUGH COMPUTER ANIMATED IMAGES

Minoru Yamamoto, assignor to Image Link Company, Limited
27 March 2001 (Class 345/473); filed 23 April 1996

This audio/visual communication system generates an animated image at the receiving location which is intended to approximate the sender’s voice characteristics and movements. A rather novel analysis method, referred to

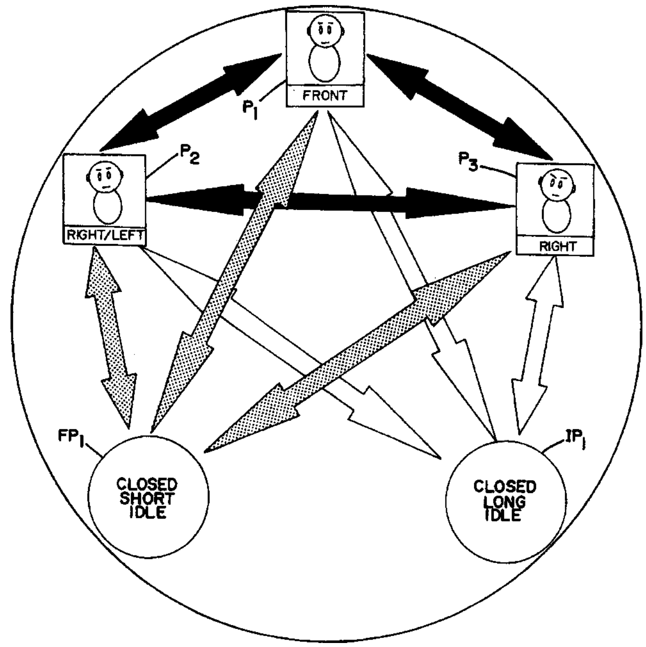

as ‘‘frequency-shifted waves,’’ is used to extract voice amplitude, pitch, and spectral structure as primary parameters. These are used, in turn, to derive further parameters, such as lip position and certain emotional states.—DLR

6,253,172

43.72.Lc SPECTRAL TRANSFORMATION OF ACOUSTIC SIGNALS

Yinong Ding *et al.*, assignors to Texas Instruments, Incorporated
26 June 2001 (Class 704/219); filed 16 October 1997

This patent introduces an improved method of pitch modification or spectral transformation by approximating the desired spectrum envelope with a whitened spectrum envelope of the frequency scaled signal. At the recognition stage, frequency compression may be needed to place the speech into a desired frequency band while preserving the shape of the envelope of

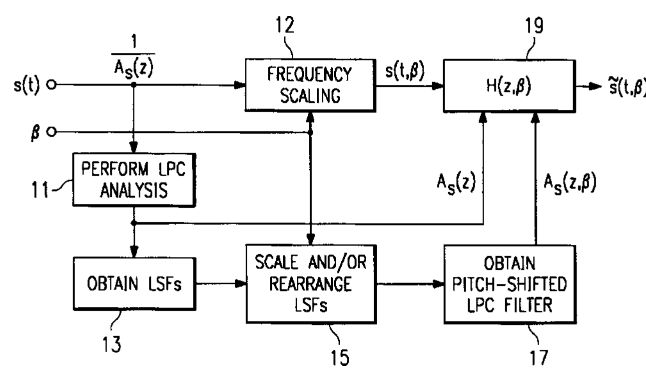

the short-time speech spectrum. After calculating the speech and desired envelope spectra, the approximation is produced by LPC analysis **11**, obtaining linear spectrum frequencies (LSF) **13**, scaling **15**, and transforming the scaled LSFs back to LPC **17**.—HHN

6,205,426

43.72.Ne UNSUPERVISED SPEECH MODEL ADAPTATION USING RELIABLE INFORMATION AMONG *N*-BEST STRINGS

Patrick Nguyen *et al.*, assignors to Matsushita Electric Industrial Company, Limited
20 March 2001 (Class 704/255); filed 25 January 1999

This speech recognition speaker model adaptor uses a relatively reliable method of recognition to update the model for use by the basic recognition system. Each of the *N*-best solutions from an initial pass of the basic recognizer is scored by a weighting technique based on likelihood scores and by a nonlinear thresholding function. The resulting ''reliable'' information is used to update the speaker model using known methods, such as maximum likelihood linear regression (MLLR) or maximum *a posteriori* (MAP).—DLR

6,208,966

43.72.Ne TELEPHONE NETWORK SERVICE FOR CONVERTING SPEECH TO TOUCH-TONES

Andrew Frederick Bulfer, assignor to AT&T Corporation
27 March 2001 (Class 704/251); filed 29 September 1995

This speech recognition application is intended to be added to an existing telephone interaction program which uses DTMF (Touch Tone) tones to make menu selections. The patented system recognizes the spoken digits, and the words ''star'' and ''pound,'' and generates the corresponding DTMF tones. Such a capability may be useful in a ''hands-free'' situation as well as with a rotary-dialed phone.—DLR

6,212,499

43.72.Ne AUDIBLE LANGUAGE RECOGNITION BY SUCCESSIVE VOCABULARY REDUCTION

Nobuyuki Shigeeda, assignor to Canon Kabushiki Kaisha
3 April 2001 (Class 704/254); filed in Japan 25 September 1998

This patent does not say that the described speech recognizer is limited to a small vocabulary, but it must be so. The reference database is organized as a tree by sequential syllables. When the user speaks a phrase, the signal is first processed by a spectral subtraction noise reducer. A formant analysis is then done on each input frame, proceeding in a syllable-by-syllable fashion, matching each syllable to the next level of the reference tree. If recognition ambiguities arise at any time, a list of alternatives is displayed for user intervention.—DLR

6,219,643

43.72.Ne METHOD OF ANALYZING DIALOGS IN A NATURAL LANGUAGE SPEECH RECOGNITION SYSTEM

Michael H. Cohen *et al.*, assignors to Nuance Communications, Incorporated
17 April 2001 (Class 704/257); filed 26 June 1998

This is a diagnostic tool for analyzing and evaluating interactive telephone dialogs. During simulated or actual use of the interactive telephone system, a detailed trace is recorded including the state of the dialog system, the prompt played, the spoken phrase, the recognition grammar, recognition results, and the system latency time. The diagnostic tool includes a method of computing an overall performance score for each dialog tested.—DLR

6,223,150

43.72.Ne METHOD AND APPARATUS FOR PARSING IN A SPOKEN LANGUAGE TRANSLATION SYSTEM

Lei Duan and Alexander M. Franz, assignors to Sony Corporation; Sony Electronics, Incorporated
24 April 2001 (Class 704/9); filed 29 January 1999

This patent describes a language parser which combines a speech recognizer using morphological analysis with a shift-and-reduce parsing system. The speech recognizer is based on known hidden Markov modeling techniques, but uses the parse status together with the morphological analysis to specify the recognition probabilities. The final parse tree is then passed to a target language synthesizer which reproduces the spoken input in a different language. Relatively little is said about the synthesis portion of the system.—DLR

6,223,160

43.72.Ne APPARATUS AND METHOD FOR ACOUSTIC COMMAND INPUT TO AN ELEVATOR INSTALLATION

Miroslav Kostka and Paul Friedli, assignors to Inventio AG
24 April 2001 (Class 704/275); filed in the European Patent Office 22 May 1997

This speech recognition application takes the form of a wrist watch or other portable device worn by a person, such as a hotel patron, who frequently uses a specific elevator system. The user can request a destination

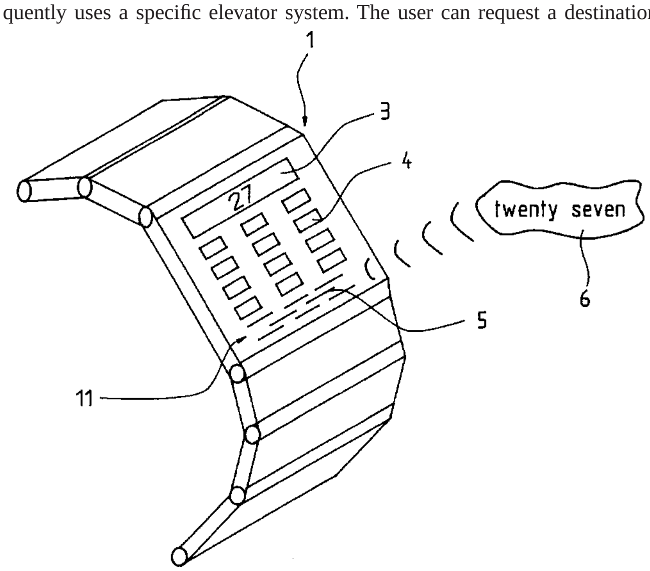

floor from some location near the elevators. A reply advises the user when a reserved elevator is nearing the user's departure floor.—DLR

6,224,636

43.72.Ne SPEECH RECOGNITION USING NONPARAMETRIC SPEECH MODELS

Steven A. Wegmann and Laurence S. Gillick, assignors to Dragon Systems, Incorporated
1 May 2001 (Class 764/246); filed 28 February 1997

In order to increase the recognition accuracy in ASR systems, this patent uses a two-pass identification process. In the first pass, the input speech sample is analyzed using parametric speech recognition techniques to identify speech units (e.g., phonemes). In the second pass, the input speech sample is further evaluated against the first-pass phonemes to identify the actual word. The second pass is a nonparametric speech recognition process in which the input sample is compared against the actual training observations. This tends to produce more accurate recognition results.—AAD

6,230,111

43.72.Ne CONTROL SYSTEM FOR CONTROLLING OBJECT USING PSEUDO-EMOTIONS AND PSEUDO-PERSONALITY GENERATED IN THE OBJECT

Takashi Mizokawa, assignor to Yamaha Hatsudoki Kabushiki Kaisha
8 May 2001 (Class 702/182); filed 6 August 1998

This patent describes the control system for an autonomous device capable of personal interactions using humanlike characteristics, such as emotions and personality. We might assume the intended devices would include artificial pets and the like. Outputs from the speech recognition system are sent to commanded and autonomous behavioral control units and to emotion and personality forming units, all of which govern the device's subsequent actions.—DLR

6,230,122

43.72.Ne SPEECH DETECTION WITH NOISE SUPPRESSION BASED ON PRINCIPAL COMPONENTS ANALYSIS

Duanpei Wu *et al.*, assignors to Sony Corporation; Sony Electronics, Incorporated
8 May 2001 (Class 704/226); filed 9 September 1998

This patent relates to an effective noise reduction method in ASR systems. The noise in the input signal is suppressed by splitting the input signal into different frequency subbands and weighting each band based on a Karhunen–Loeve transformation (KLT). According to the patent, the noisy signal in each band is projected onto the KLT subspace of the background noise correlation matrix from the same band. The projected vectors are then weighted with values estimated from background noise data.—AAD

6,233,561

43.72.Ne METHOD FOR GOAL-ORIENTED SPEECH TRANSLATION IN HAND-HELD DEVICES USING MEANING EXTRACTION AND DIALOGUE

Jean-Claude Junqua *et al.*, assignors to Matsushita Electric Industrial Company, Limited
15 May 2001 (Class 704/277); filed 12 April 1999

This patent introduces a speech translation system for hand-held devices. For example, an (English) buyer **20** wishes to communicate with a (Japanese) salesperson **22** in order to purchase a piece of merchandise. A speech recognizer **26** or **36** converts the spoken request into a digital format. A speech-understanding module **28** or **38** determines semantic components

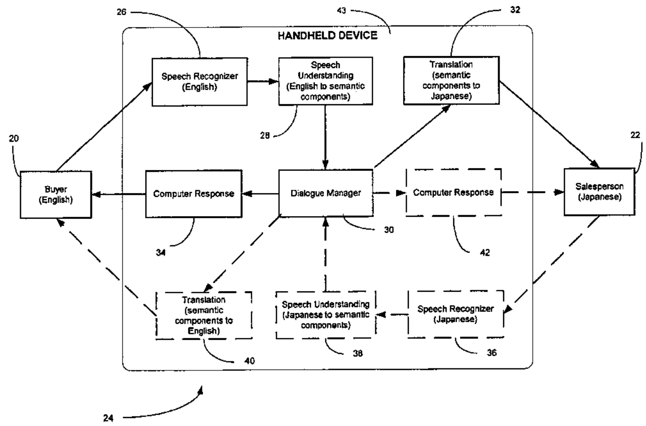

of the spoken request. Then a translation module **32** or **40** translates the spoken request from the original language to the target language. Computer response module **34** or **42** is multimodal in being able to provide a response to a user via speech synthesis, text, or graphic images.—HHN

6,253,175

43.72.Ne WAVELET-BASED ENERGY BINNING CEPSTAL FEATURES FOR AUTOMATIC SPEECH RECOGNITION

Sankar Basu and Stephane H. Maes, assignors to International Business Machines Corporation
26 June 2001 (Class 704/231); filed 30 November 1998

This patent relates to estimation of the location of the formant frequencies of the acoustic speech signal in a probabilistic or deterministic manner as a function of time. The system utilizes a wavelet-transform-based spectrum (wastrum) to extract the frequency, amplitude, and bandwidth components from the signal. The spectral components in the resulting plane are dynamically tracked via the K-Means clustering algorithm. According to the patent, the discussed method is robust with respect to noise.—AAD

Comment on "Eigenmode analysis of arbitrarily shaped two-dimensional cavities by the method of point matching" [J. Acoust. Soc. Am. 107, 1153 (2000)]

J. T. Chen,[a] M. H. Chang, I. L. Chung, and Y. C. Cheng
Department of Harbor and River Engineering, National Taiwan Ocean University, Keelung, Taiwan

(Received 6 July 2000; revised 20 August 2001; accepted 21 August 2001)

The method of point matching proposed by Kang and Lee [J. Acoust. Soc. Am. **107**, 1153–1160 (2000)] is revisited. This method can be seen as a single-layer potential approach from the viewpoint of imaginary-part dual BEM developed by Chen *et al.* [J. Chin. Inst. Eng. **12**, 729–739 (1999)]. Based on the concept of double-layer potential, an innovative method is proposed to deal with the problem of spurious eigensolution for the Neumann problem. Also, the acoustic mode is analytically derived for the circular cavity. Both the analytical study for a circular case and numerical result for a square cavity show the validity of the proposed formulation. [DOI: 10.1121/1.1410966]

PACS numbers: 43.20.Ks, 43.20.Rz [ANN]

I. INTRODUCTION

Kang and Lee[1,2] presented a so-called method of point matching for the eigenproblems. Also, they termed the nondimensional dynamic influence function (NDIF) method in another paper.[3] Mathematically speaking, they are equivalent in essence. Based on the concept of radial basis function (RBF) expansion,[4] the method can be seen as one kind of the radial basis expansion since RBF is a function of the radial distance between the observation point and the boundary point. Since only boundary nodes are required, this is a meshless method and can be called the boundary node method. This method also belongs to the Trefftz method[5] since the approximation bases satisfy the governing equation. The main advantage of this method is simple in data preparation and no integration is required in comparison with the boundary element method (BEM). However, two disadvantages of the NDIF method,[3] spurious eigenvalues and ill-conditioned behavior, were pointed out by Chen *et al.*[6] Although many examples of the Dirichlet types were successfully worked out,[3] spurious eigensolutions occurred[1,2,6] when this method was extended to solve for the Neumann problems. Kang and Lee[1,2] filtered out the spurious eigenvalues by using the net approach, which can cancel out the embedded spurious eigenvalues. However, two influence matrices must be calculated. Based on the dual formulation developed by Chen and Hong,[7] the influence function[1–3] of the NDIF method is nothing but the imaginary part of the fundamental solution $[U(s,x)=iH_0^{(1)}(kr)]$.[8,9] The NDIF method[3] can be seen as a single-layer potential approach from the viewpoint of the imaginary-part dual BEM.[6,9] Also, the main difference between the NDIF method and the imaginary-part BEM is the distribution of density function, as shown in Table I. The former one lumps the density on the boundary point; the latter one distributes density along the boundary.[6,9] The spurious eigensolutions originate from the improper approximation of null operator since insufficient number of constraints is obtained. Many methods including the real-part, imaginary-part, and multiple reciprocity methods (MRM), suffer the problems of spurious eigenvalues since information is lost. The real-part dual BEM was developed by Chen's group and many references can be found.[8,10] Particularly, the imaginary-part formulation also results in an ill-conditioned matrix since the condition number for the influence matrix is always very large.[6] Many approaches have been employed to filter out the spurious eigensolution and to extract the true eigensolution, for example, a dual method using the residue technique, SVD (singular value decomposition) updating terms and updating documents, and the generalized SVD technique. For the circular case, it was proved by using circulants and degenerate kernels that the Kang and Lee method causes the problems of spurious eigensolutions and ill-conditioned behavior since these problems are inherent in the imaginary-part formulation.[6,9]

In this Letter, the Kang and Lee method is found to be the single-layer potential approach from the viewpoint of the imaginary-part dual formulation.[8,9] We will propose a double-layer potential approach to avoid the occurrence of a spurious eigensolution that has been filtered out using the net approach for the Neumann problems by Kang and Lee.[1,2] The acoustic modes will be derived analytically in the discrete system of a circle case using circulants and degenerate kernels. Both an analytical study and a numerical experiment will be considered to examine the solution.

II. A UNIFIED THEORY USING DUAL FORMULATION

As mentioned earlier, spurious eigenvalues occur in the real-part BEM or MRM formulation. Also, the imaginary-part dual BEM results in spurious eigensolutions.[9] Here, we will analytically derive the true and spurious eigensolutions in the discrete system for a circular domain by using the imaginary-part dual BEM.[9] The degenerate kernels and circulants are employed to study the discrete system in an exact form. The unified theory is summarized in Table I and the comparison between the Kang and Lee method and the present method is made. The symbols in Table I follow the

[a]Author to whom correspondence should be addressed. P.O. Box 7-59, Keelung, Taiwan. Electronic mail: jtchen@mail.ntou.edu.tw

TABLE I. Comparisons of the nondimensional influence function method and the imaginary-part dual BEM.

Method	Imaginary-part dual BEM by Chen *et al.* (Ref. 6)	Nondimensional dynamic influence function by Kang *et al.* (Refs. 1–3)
Auxiliary system	$J_0(k\|\mathbf{x}-\mathbf{s}\|)$	$J_0(k\|\mathbf{x}-\mathbf{s}\|)$
Density	Distributed on boundary using constant element	Concentrated on discrete points
Solution representation for field or boundary data	$0=\Sigma_j\int_{B_j}\{(T(s_j,x_i)u(s_j)-U(s_j,x_i)t(s_j)\}dB(s_j)$	$u(x_i)=\Sigma J_0(k\|x_i-s_j\|)A_j$
	$0=\Sigma_j\int_{B_j}\{(M(s_j,x_i)u(s_j)-L(s_j,x_i)t(s_j)\}dB(s_j)$	$u(x_i)=\sum \frac{\partial J_0(k\|x_i-s_j\|)}{\partial n_{s_j}}B_j$
Eigenequation for	UT method: $U_{ij}t_j=0$	UL method: $(\mathrm{SM})_{ij}A_j=0$
the Dirichlet problem	LM method: $L_{ij}t_j=0$	TM method: $(\mathrm{SM}_s)_{ij}B_j=0$
Eigenequation for	UT method: $T_{ij}u_j=0$	UL method: $(\mathrm{SM}_x)_{ij}A_j=0$
the Neumann problem	LM method: $M_{ij}u_j=0$	TM method: $(\mathrm{SM}_{xs})_{ij}B_j=0$
Influence matrix	$U_{ij}=\int_{B_j}U(s_j,x_i)dB(s_j)$	$(\mathrm{SM})_{ij}=J_0(k\|x_i-s_j\|)$
	$T_{ij}=\int_{B_j}T(s_j,x_i)dB(s_j)$	$(\mathrm{SM}_s)_{ij}=\frac{\partial J_0(k\|x_i-s_j\|)}{\partial n_{s_j}}$
	$L_{ij}=\int_{B_j}L(s_j,x_i)dB(s_j)$	$(\mathrm{SM}_x)_{ij}=\frac{\partial J_0(k\|x_i-s_j\|)}{\partial n_{x_i}}$
	$M_{ij}=\int_{B_j}M(s_j,x_i)dB(s_j)$	$(\mathrm{SM}_{sx})_{ij}=\frac{\partial^2 J_0(k\|x_i-s_j\|)}{\partial n_{x_i}\partial n_{s_j}}$
Spurious eigenequation	UT method: $J_n(k\rho)=0$	UL method: $J_n(k\rho)=0$[a]
for the Dirichlet problem	LM method: $J_n'(k\rho)=0$	TM method: $J_n'(k\rho)=0$
True eigenequation	UT method: $J_n(k\rho)=0$	UL method: $J_n(k\rho)=0$[a]
for the Dirichlet problem	LM method: $J_n(k\rho)=0$	TM method: $J_n(k\rho)=0$
Spurious eigenequation	UT method: $J_n(k\rho)=0$	UL method: $J_n(k\rho)=0$[b]
for the Neumann problem	LM method: $J_n'(k\rho)=0$	TM method: $J_n'(k\rho)=0$
True eigenequation	UT method: $J_n'(k\rho)=0$	UL method: $J_n'(k\rho)=0$[b]
for the Neumann problem	LM method: $J_n'(k\rho)=0$	TM method: $J_n'(k\rho)=0$
Condition number	$\frac{\mathrm{Max}(h_n)}{\mathrm{Min}(h_n)}$,[c] $n=0,1,2,...$	$\frac{\mathrm{Max}(h_n)}{\mathrm{Min}(h_n)}$, $n=0,1,2,...$

[a]Example is available in Ref. 1.
[b]Example is not available in Ref. 1.
[c]h_n can be λ_l, μ_l, ν_l, or δ_l.

dual formulation of Chen and Hong.[7] Based on the imaginary-part dual BEM, the solution can be represented by

$$u(x_i)=\sum_{j=1}^{2N} U(s_j,x_i)A(s_j), \tag{1}$$

$$t(x_i)=\sum_{j=1}^{2N} L(s_j,x_i)A(s_j), \tag{2}$$

$$u(x_i)=\sum_{j=1}^{2N} T(s_j,x_i)B(s_j), \tag{3}$$

$$t(x_i)=\sum_{j=1}^{2N} M(s_j,x_i)B(s_j), \tag{4}$$

where x_i is the ith observation point, s_j is the jth boundary point, u and t are the potential and its normal derivative, $A(s_j)$ and $B(s_j)$ are the unknown concentrated densities at s_j, $2N$ is the number of boundary points, and the four imaginary-part kernels in the dual formulation can be expressed in terms of degenerate kernels[9] as shown below:

$$U(s,x)=\frac{-\pi}{2}J_0(kr) = -\sum_{m=-\infty}^{\infty}\frac{\pi}{2}J_m(kR)J_m(k\rho)\cos[m(\theta-\phi)], \tag{5}$$

$$T(s,x)=-\sum_{m=-\infty}^{\infty}\frac{\pi k}{2}J_m'(kR)J_m(k\rho)\cos[m(\theta-\phi)], \tag{6}$$

$$L(s,x)=-\sum_{m=-\infty}^{\infty}\frac{\pi k}{2}J_m(kR)J_m'(k\rho)\cos[m(\theta-\phi)], \tag{7}$$

$$M(s,x)=-\sum_{m=-\infty}^{\infty}\frac{\pi k^2}{2}J_m'(kR)J_m'(k\rho)\cos[m(\theta-\phi)], \tag{8}$$

in which $x=(\rho,\phi)$, $s=(R,\theta)$ in the polar coordinate, J and J' are the Bessel functions of the first kind and its derivative, respectively. For simplicity, we consider the same problem of a circular domain.[1–3] Since the rotation symmetry is preserved for a circular boundary, the four influence matrices in Eqs. (1)–(4) are denoted by $[U]$, $[T]$, $[L]$, and $[M]$ of the circulants with the elements

$$K_{ij}=K(R,\theta_j;\rho,\phi_i), \tag{9}$$

where K can be U, T, L, or M, ϕ_i and θ_j are the angles of observation and boundary points, respectively. Based on the theory of circulants and the relation between the Riemann sum and integral,[6,9] we have

$$\lambda_l=-N\pi J_l(k\rho)J_l(k\rho), \tag{10}$$

$$\mu_l=-N\pi k\rho J_l'(k\rho)J_l(k\rho), \tag{11}$$

TABLE II. The true and spurious eigenvalues for circular and square cavities using the single- and double-layer potential approaches.

		Circular cavity		Square cavity	
Boundary value problem	Eigensolution	Single-layer potential approach	Double-layer potential approach	Single-layer potential approach	Double-layer potential approach
Dirichlet problem	True eigensolution	$J_m(k\rho)=0$	$J_m(k\rho)=0$	$k_{mn}=\sqrt{\left(\frac{m}{L}\right)^2+\left(\frac{n}{L}\right)^2}\pi$ $(m,n=1,2,3,...)$	$k_{mn}=\sqrt{\left(\frac{m}{L}\right)^2+\left(\frac{n}{L}\right)^2}\pi$ $(m,n=1,2,3,...)$
	Spurious eigensolution	$J_m(k\rho)=0$	$J'_m(k\rho)=0$	$k_{mn}=\sqrt{\left(\frac{m}{L}\right)^2+\left(\frac{n}{L}\right)^2}\pi$ $(m,n=1,2,3,...)$	$k_{mn}=\sqrt{\left(\frac{m}{L}\right)^2+\left(\frac{n}{L}\right)^2}\pi$ $(m,n=0,1,2,3,...)$
	True eigenmode	$J_m(k\rho)e^{in\theta}$ $(m,n=0,1,2,3,...)$		$\sin\left(\frac{m\pi x}{L}\right)\sin\left(\frac{n\pi x}{L}\right)$ $(m,n=1,2,3,...)$	
Neumann problem	True eigensolution	$J'_m(k\rho)=0$	$J'_m(k\rho)=0$	$k_{mn}=\sqrt{\left(\frac{m}{L}\right)^2+\left(\frac{n}{L}\right)^2}\pi$ $(m,n=0,1,2,3,...)$	$k_{mn}=\sqrt{\left(\frac{m}{L}\right)^2+\left(\frac{n}{L}\right)^2}\pi$ $(m,n=0,1,2,3,...)$
	Spurious eigensolution	$J_m(k\rho)=0$	$J'_m(k\rho)=0$	$k_{mn}=\sqrt{\left(\frac{m}{L}\right)^2+\left(\frac{n}{L}\right)^2}\pi$ $(m,n=1,2,3,...)$	$k_{mn}=\sqrt{\left(\frac{m}{L}\right)^2+\left(\frac{n}{L}\right)^2}\pi$ $(m,n=0,1,2,3,...)$
	True eigenmode	$J_m(k\rho)e^{in\theta}$ $(m,n=0,1,2,3,...)$		$\cos\left(\frac{m\pi x}{L}\right)\cos\left(\frac{n\pi x}{L}\right)$ $(m,n=0,1,2,3,...)$	

$$\nu_l=-N\pi k\rho J_l(k\rho)J'_l(k\rho), \tag{12}$$

$$\delta_l=-N\pi k^2\rho J'_l(k\rho)J'_l(k\rho), \tag{13}$$

where R is set to be ρ, $l=0,\pm1,\pm2,...,\pm(N-1)$, N, and λ_l, μ_l, ν_l, and δ_l are the eigenvalues of $[U]$, $[T]$, $[L]$, and $[M]$ matrices, respectively. The determinants for the four matrices can be obtained by multiplying all the eigenvalues. We summarize the true and spurious eigenvalues in Table II for the circular cavity using the single- and double-layer potential approaches. Also, the square case is included. Figure 1 shows the minimum singular value versus k using the single-layer potential approach for the Neumann problem. It is found that both the analytical and numerical results match well and indicate that spurious eigenvalues occur. Figure 2 shows the minimum singular value versus k using the double-layer potential approach for the Neumann problem. No spurious eigenvalues occur, as predicted theoretically. For a square cavity, Fig. 3 shows the minimum singular value versus k using the single-layer potential approach for the Dirichlet problem. No spurious eigenvalues are found. By using the double-layer potential approach, spurious eigenvalues appear as shown in Fig. 4 for the Dirichlet problem. For the Neumann problem of a square cavity, the single-layer potential approach results in spurious eigenvalues while these values disappear in a similar way to the circular case when the double-layer potential approach is employed.

By substituting the nth true eigenvalue for k in Eq. (10) and the nth true boundary mode into Eq. (1), we have

$$u_n(a,\phi)=\frac{N}{\pi}\sum_{l=0}^{2N-1}U(\rho,l\Delta\theta;a,\phi)\cos\left(\frac{\pi n}{N}l\right)\Delta\theta,$$
$$0<a<\rho,\quad 0<\phi<2\pi, \tag{14}$$

after considering the real part of the eigenvector, where $\Delta\theta=\pi/N$ is the increment of angle. By substituting the degenerate kernel of U using Eq. (5), Eq. (14) reduces to

$$u_n(a,\phi)=\frac{N}{\pi}\sum_{l=0}^{2N-1}\sum_{m=-\infty}^{\infty}\frac{-\pi}{2}J_m(ka)J_m(k\rho)$$
$$\times\cos(m(l\Delta\theta-\phi))\cos\left(\frac{\pi n}{N}l\right)\Delta\theta. \tag{15}$$

When N approaches infinity, the Riemann sum in Eq. (15) reduces to

$$u_n(a,\phi)=-N\pi J_n(ka)J_n(k\rho)\cos(n\phi),$$
$$0<a<\rho,\quad 0<\phi<2\pi. \tag{16}$$

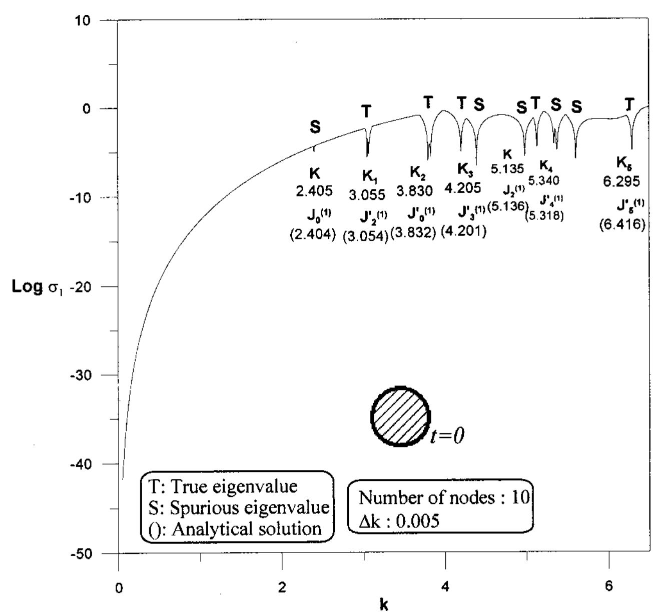

FIG. 1. The minimum singular value versus k using the single-layer potential approach for the Neumann problem of a circular cavity.

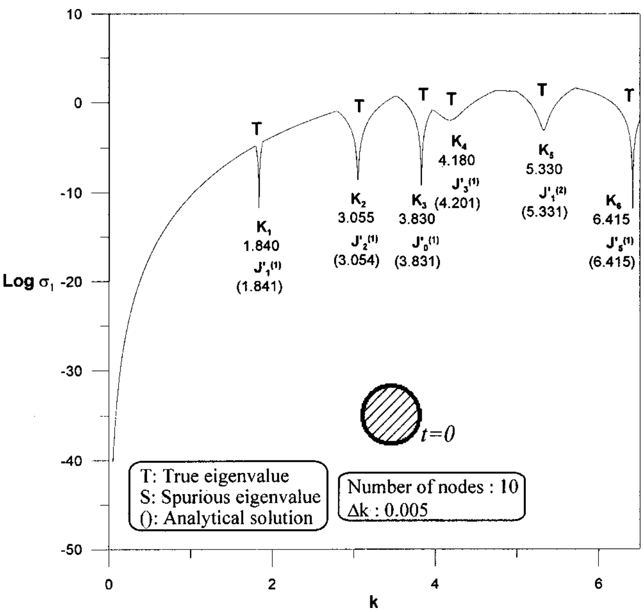

FIG. 2. The minimum singular value versus k using the double-layer potential approach for the Neumann problem of a circular cavity.

It can be analytically proved that the acoustic mode is found to be trivial since k satisfies the zero of $J_n(k\rho)$, as shown in Eq. (16). In the numerical implementation, the value of $J_n(k\rho)$ is not exactly zero. This is the reason why the contour plots for acoustic modes can be displayed in the papers of Kang and Lee, since a normalized value $J_n(k\rho)$ is divided.

III. CONCLUDING REMARKS

The NDIF method or the method of point matching was classified to be the single-layer potential approach from the viewpoint of imaginary-part dual formulation. The difference between the Kang and Lee method and imaginary-part BEM is the singularity distribution of the density function, where the former one lumps the density on the boundary point and the latter one distributes the density along the boundary. This method was extended to the double-layer potential approach for avoiding the occurrence of spurious eigensolutions encountered in the Kang and Lee method. By using the degenerate kernels and the analytical properties of circulants for a circular cavity, the spurious eigensolutions were studied analytically and the spurious eigenvalues disappeared. Also, the acoustic modes were analytically proved to be trivial. An additional example of a square cavity was also considered.

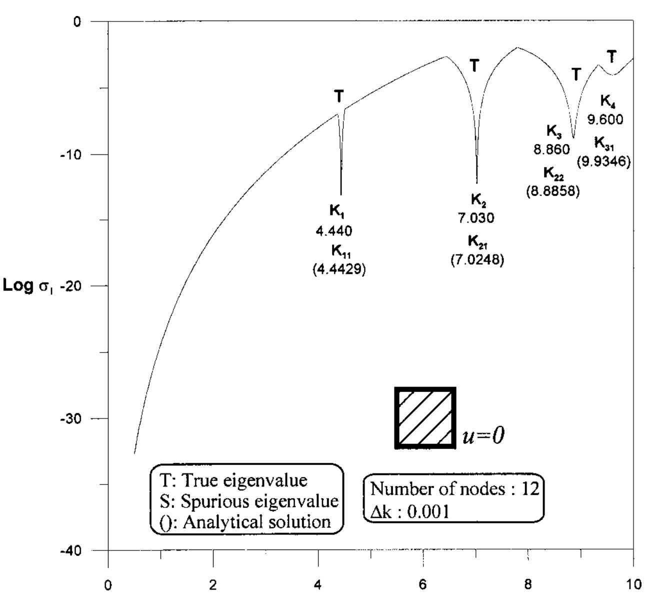

FIG. 3. The minimum singular value versus k using the single-layer potential approach for the Dirichlet problem of a square cavity.

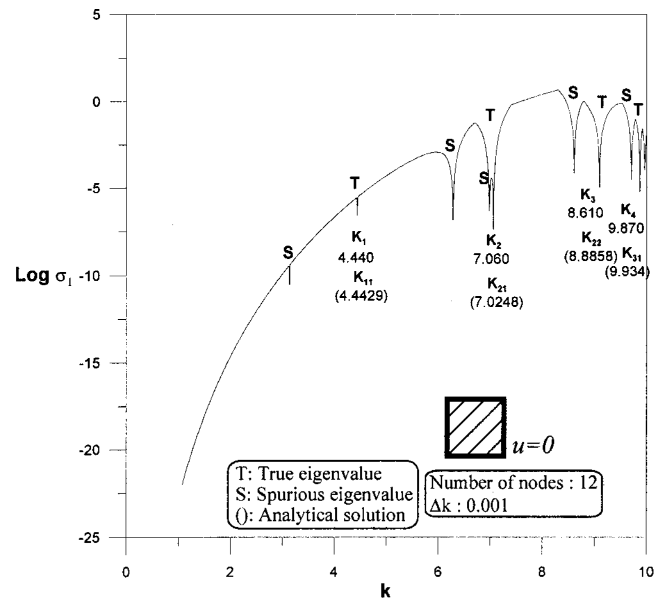

FIG. 4. The minimum singular value versus k using the double-layer potential approach for the Dirichlet problem of a square cavity.

[1] S. W. Kang and J. M. Lee, "Eigenmode analysis of arbitrarily shaped two-dimensional cavities by the method of point matching," J. Acoust. Soc. Am. **107**, 1153–1160 (2000).

[2] S. W. Kang and J. M. Lee, "Authors reply to the Comments on 'Vibration analysis of arbitrary shaped membranes using nondimensional dynamic influence function,' " J. Sound Vib. **235**, 171 (2000).

[3] S. W. Kang, J. M. Lee, and Y. J. Kang, "Vibration analysis of arbitrary shaped membranes using non-dimensional dynamic influence function," J. Sound Vib. **221**, 117–132 (1999).

[4] M. A. Golberg, C. S. Chen, and H. Bowman, "Some recent results and proposals for the use of radial basis functions in the BEM," Eng. Anal. Boundary Elem. **23**, 285–296 (1999).

[5] E. Trefftz, "Ein gegenstück zum ritzschen verahren," *Proceedings of the 2nd International Congress on Applied Mechanics, 1926*, pp. 131–137.

[6] J. T. Chen, S. R. Kuo, K. H. Chen, and Y. C. Cheng, "Comments on 'Vibration analysis of arbitrary shaped membranes using nondimensional dynamic influence function,' " J. Sound Vib. **235**, 156–171 (2000).

[7] J. T. Chen and H.-K. Hong, "Review of dual integral representations with emphasis on hypersingular integrals and divergent series," Trans. ASME, J. Appl. Mech. **52**, 17–33 (1999).

[8] J. T. Chen, "Recent development of dual BEM in acoustic problems," Comput. Methods Appl. Mech. Eng. **188**, 833–845 (2000).

[9] J. T. Chen, S. R. Kuo, and K. H. Chen, "A nonsingular integral formulation for the Helmholtz eigenprobles of a circular domain," J. Chin. Univ. Sci. Technol. **12**, 729–739 (1999).

[10] S. R. Kuo, J. T. Chen, and C. X. Huang, "Analytical study and numerical experiments for true and spurious eigensolutions of a circular cavity using the real-part dual BEM," Int. J. Numer. Methods Eng. **48**, 1401–1422 (2000).

Use of dual waves for the elimination of reverberations in drill strings (L)

Flavio Poletto[a)]
Istituto Nazionale di Oceanografia e di Geofisica Sperimentale—OGS, Borgo Grotta Gigante 42/c, 34010 Sgonico (Trieste), Italy

(Received 28 March 2001; revised 12 September 2001; accepted 15 October 2001)

Drill-string waves can be used to transmit acoustic and seismic information from the bottom hole to the surface. Because the drill string is a heterogeneous assembly, the investigated signal is disturbed by reverberations. Removal of the reverberations generated in the drill string is obtained by measuring acceleration and strain, which have opposite reflection coefficients and are used as dual waves. Addition of the dual waves makes it possible to remove part of the drill-string reflections and improve the signal-to-noise ratio. © *2002 Acoustical Society of America.*
[DOI: 10.1121/1.1427360]

PACS numbers: 43.40.Cw, 43.40.At, 43.20.Mv, 43.60.Dh [DEC]

LIST OF SYMBOLS

z	axial co-ordinate	m
A_i	drill-string cross-section	m^2
A_{bit}	drill-bit area	m^2
I_i	polar momentum of inertia per unit mass and length	m^4
E_i	Young modulus	GPa
μ_i	shear modulus	GPa
ρ_i	drill-string mass density	$m^{-3}\cdot kg$
ρ_{rock}	mass density of formation	$m^{-3}\cdot kg$
u_i	axial displacement	m
a_z	axial acceleration	$m\cdot s^{-2}$
θ_i	angular displacement	⋯
ε_z	axial strain	⋯
ε_θ	torsional strain	m^{-1}
V_{ax}	velocity of axial wave	$m\cdot s^{-1}$
V_{tor}	velocity of torsional wave	$m\cdot s^{-1}$
V_{rock}	P-wave velocity of formation	$m\cdot s^{-1}$
ω	angular frequency	s^{-1}
$k_i = k_{(\mathrm{ax})i}$	axial wavenumber	m^{-1}
$k_{(\mathrm{tor})i}$	torsional wavenumber	m^{-1}
$R_d = c_{d(\mathrm{ax})}$	reflection coefficient of axial displacement	⋯
$R_s = c_{s(\mathrm{ax})}$	reflection coefficient of axial strain	⋯
$T_d = t_{d(\mathrm{ax})}$	transmission coefficient of axial displacement	⋯
$T_s = t_{s(\mathrm{ax})}$	transmission coefficient axial strain	⋯
$R_{d(\mathrm{tor})}$	reflection coefficient of torsional displacement	⋯
$R_{s(\mathrm{tor})}$	reflection coefficient of torsional strain	⋯
$T_{d(\mathrm{tor})}$	transmission coefficient of torsional displacement	⋯
$T_{s(\mathrm{tor})}$	transmission coefficient of torsional strain	⋯
$R_{d(\mathrm{ax})0}$	drill-bit reflection coefficient of axial displacement	⋯
$R_{s(\mathrm{ax})0}$	drill-bit reflection coefficient of axial strain	⋯
Z	Z-transform	⋯
M_K	propagation matrix	⋯
$F_K(Z)$, $G_K(Z)$	propagation polinomials	⋯
$\mathcal{F}_{(s,a)}$	strain-to-acceleration shaping filter	⋯

I. INTRODUCTION

Drill-string waves can be measured for the transmission of information from the drill bit to the surface[1–3] and for seismic-while-drilling purposes.[4,5] These signals are disturbed by short- and long-period reverberations produced by the reflections occuring in the drill string. Inverse filtering of these reflections by using a data-dependent deconvolution operator is a basic processing step,[4] which may cause signal distortions when the data are affected by coherent noise. Acquisition of drill-string waves by using dual-sensor measurements is investigated in this work in order to reduce the presence of reflections and improve signal bandwidth and wave field interpretation. Dual measurements record waves reflected with opposite signs and make it possible to remove reflections of the drill-string waves from the acquisition phase. We consider acceleration and strain as dual waves—a similar approach is used by surface seismic with velocity and pressure waves.[6,7] Their coefficients are calculated for extensional and torsional components in drill strings of arbitrary materials. This analysis also shows that, unlike velocity and pressure, the transmitted acceleration and strain waves have the same amplitude variations in the drill-string sections.

The dual signals are shaped, scaled to fit the amplitude of the direct arrivals, and summed to separate the events produced by an odd number of reflections in the drill string and rig, reinforce the reflections of the formation ahead of the bit, and improve the signal-to-noise ratio. Effective separation requires the analysis of the complex wave fields reflected in the drill string with up- and down-going patterns.

The drill-string reflection patterns are discussed by Poletto and others.[8] They model the drill-string transmission

[a)]Electronic mail: fpoletto@ogs.trieste.it

line[8,9] to calculate the reflections of extensional and torsional waves, by assuming the seismic low-frequency approximation, and interpret the periodicities of signal and noise. In this analysis, the drill string is considered as an assembly of different tubes with different dimensions and impedances. It is divided into two main parts. The upper part is the section of the drill pipes, composed of a sequence of elements with more or less the same dimension and weight. The lower part is the bottom hole assembly (BHA). This part is more massive and its composition is rather complex. It is made of various components with different dimensions and mechanical characteristics. The most important are the heavy-weight drill pipes and drill collars. These BHA components cause important variations of impedance and strong reverberations in the drill-string waves.

At the low (i.e., seismic) frequencies, the wavelengths of the extensional-axial and torsional-transverse components are long compared to the drill-string diameter, and they are not dispersive. These vibrations propagate in the form of guided waves[10] and are recorded by the sensors placed on the rig and on the drill string. The surface-rig and downhole conditions and drill-string mechanical features influence the transmission modes and the quality of the signal, which can also be measured by using downhole tools inserted in the drill string.[11] Dual measurements are achieved by using axial and torsional accelerometers—in our analysis acceleration is equivalent to velocity and displacement—and strain gauges to measure axial and torsional strain—equivalent to force (i.e., weight-on-bit) and torque waves. These two different types (classes) of waves, related to displacement and strain, are denoted in the following text by subscripts d and s, respectively. Assuming the drill string as a sequence of cylinders with different lengths and weights we model it as a one-dimensional system of blocks and calculate the reflection coefficients $R_d = -R_s$ that characterize any interface between two tubes with different acoustic impedances.

II. REFLECTION COEFFICIENTS

The reflection coefficients for axial and torsional waves in strings formed of tubes of different materials and properties are computed. Assume two string blocks with density, Young and shear moduli, cross-section, and polar momentum of inertia per unit mass and unit length $(\rho_1, E_1, \mu_1, A_1, I_1)$ and $(\rho_2, E_2, \mu_2, A_2, I_2)$, respectively. For a tube with internal and external radii r_i and r_e, respectively, $I = (\pi/2)(r_e^4 - r_i^4)$. Let z be the axial coordinate and $e^{\imath(\omega t - kz)}$ be a (either displacement or strain) plane wave propagating with velocity $V = \omega k^{-1}$ in the positive z direction. In the low-frequency approximation, the string tube can be considered as a rod. The theoretical velocities of axial and torsional waves in a rod[12] are given by

$$V_{\mathrm{ax}} = \sqrt{E/\rho} \quad \text{and} \quad V_{\mathrm{tor}} = \sqrt{\mu/\rho}, \tag{1}$$

respectively. Requiring continuity of axial and angular displacement, force and couple moment, and phase at the interface (at $z=0$) between blocks 1 and 2 gives

$$u_1 = u_2 \quad \text{and} \quad \theta_1 = \theta_2, \tag{2}$$

$$E_1 A_1 \varepsilon_{(z)1} = E_2 A_2 \varepsilon_{(z)2} \quad \text{and} \quad \mu_1 I_1 \varepsilon_{(\theta)1} = \mu_2 I_2 \varepsilon_{(\theta)2}, \tag{3}$$

$$\frac{k_{(\mathrm{ax})1}}{k_{(\mathrm{ax})2}} = \sqrt{\frac{E_2 \rho_1}{E_1 \rho_2}} \quad \text{and} \quad \frac{k_{(\mathrm{tor})1}}{k_{(\mathrm{tor})2}} = \sqrt{\frac{\mu_2 \rho_1}{\mu_1 \rho_2}} \tag{4}$$

for the axial and the torsional components, respectively. The symbols u and θ are the relative axial and angular displacements, and $\varepsilon_z = \partial u / \partial z$ and $\varepsilon_\theta = \partial \theta / \partial z$ are the axial and angular strains.

The reflection coefficients at the interface are calculated for the axial component by using the relations (4) and substituting the plane wave solutions in Eqs. (2) and (3). The corresponding results for torsional waves are easily obtained by substituting E and A with μ and I, respectively.

A. Displacement waves

Let $u = e^{\imath(\omega t - k_1 z)}$ be a unit plane wave of axial displacement incident at the interface, where it is reflected with reflection coefficients R_d and transmitted with coefficients T_d. Using continuity Eq. (2), at $z=0$ we have $u + u_R = u_T$, where

$$u_R = R_d \, e^{\imath(\omega t + k_1 z)} \tag{5}$$

and

$$u_T = T_d \, e^{\imath(\omega t - k_2 z)} \tag{6}$$

are the reflected and transmitted displacements, respectively. We obtain $T_d = 1 + R_d$. Using the continuity of the forces [Eqs. (3)] gives

$$(1 - R_d) \, k_1 E_1 A_1 = T_d \, k_2 E_2 A_2 . \tag{7}$$

Hence, the amplitude of the axial strains corresponding to the unit displacement wave is $(1 - R_d) k_1$ and $T_d k_2$ in blocks 1 and 2, respectively.

The reflection coefficients are derived by using the previous relations and Eq. (4) and are

$$R_{d(\mathrm{ax})} = \frac{A_1 \sqrt{E_1 \rho_1} - A_2 \sqrt{E_2 \rho_2}}{A_1 \sqrt{E_1 \rho_1} + A_2 \sqrt{E_2 \rho_2}}$$

and (8)

$$R_{d(\mathrm{tor})} = \frac{I_1 \sqrt{\mu_1 \rho_1} - I_2 \sqrt{\mu_2 \rho_2}}{I_1 \sqrt{\mu_1 \rho_1} + I_2 \sqrt{\mu_2 \rho_2}},$$

for axial and torsional displacement waves, respectively.

B. Strain waves

Let us consider a unit strain plane wave $s = e^{\imath(\omega t - k_1 z)}$ incident at the interface, where it is reflected with coefficient R_s and transmitted with coefficient T_s. Using the continuity condition of the force at the interface, we obtain

$$E_1 A_1 (s + s_R) = E_2 A_2 s_T , \tag{9}$$

where

$$s_R = R_s e^{\imath(\omega t + k_1 z)} \tag{10}$$

and

$$s_T = T_s e^{\imath(\omega t - k_2 z)} \tag{11}$$

are the reflected and transmitted strain waves, respectively. Using Eq. (9) we calculate the discontinuity of the strain at $z=0$ and obtain the transmission coefficients as

$$T_s=\frac{E_1A_1}{E_2A_2}(1+R_s). \tag{12}$$

Now consider an incident strain wave of amplitude k_1, $s^{(1)}=k_1e^{\imath(\omega t-k_1z)}$, correspondent to the unit displacement incident wave (the simplification by $-i$ is here not relevant). Comparing the left-hand side term of Eq. (7) with the left-hand side term of Eq. (9) scaled by k_1, we have at $z=0$

$$(1+R_s)k_1=(1-R_d)k_1, \tag{13}$$

which gives

$$R_{s(\mathrm{ax})}=-R_{d(\mathrm{ax})} \quad \text{and} \quad R_{s(\mathrm{tor})}=-R_{d(\mathrm{tor})} \tag{14}$$

for axial and torsional waves, respectively. Comparing the right sides of Eq. (7) and (9) scaled by k_1 gives

$$T_sk_1E_2A_2=T_dk_2E_2A_2, \tag{15}$$

and

$$T_{s(\mathrm{ax})}=\frac{k_{(\mathrm{ax})2}}{k_{(\mathrm{ax})1}}T_{d(\mathrm{ax})} \quad \text{and} \quad T_{s(\mathrm{tor})}=\frac{k_{(\mathrm{tor})2}}{k_{(\mathrm{tor})1}}T_{d(\mathrm{tor})} \tag{16}$$

for axial and torsional waves, respectively. From Eq. (4) it follows that in drill strings assembled by tubes of the same elastic modulus and density $k_2=k_1$. In this case, as a consequence of Eq. (16), $T_s=T_d$, i.e., the transmitted strain wave propagates with the same transmission coefficient of the corresponding displacement wave, but with opposite reflection coefficients.

C. Reflection coefficient at the bit–rock contact

The reflection coefficient at the bit–rock contact is approximated by assuming extensional waves in the drill string and compressional plane waves in the formation.[13] This coefficient (denoted by the additional suffix 0) is obtained by substituting in Eq. (8) the impedance of the drilled rock for the string impedance $A_2(E_2\rho_2)^{1/2}$. This is given by $A_{\mathrm{bit}}V_{\mathrm{rock}}\rho_{\mathrm{rock}}$, where V_{rock} and ρ_{rock} are the P-wave velocity and the density of the formation drilled by a bit of cross-section A_{bit}. In this case, the drill string tube marked by the suffix 1 is a drill collar close to the bit. It can be shown—reasoning in a similar way to that already used to calculate the drill-string reflection coefficients—that we obtain again $R_{d(\mathrm{ax})0}=-R_{s(\mathrm{ax})0}$.

III. PROPAGATION OF DUAL WAVES

The drill-string, rig, and formation systems can be modeled as a transmission line to interpret the drill-string reflections,[8] and, for prediction purposes,[14] the reflection of the formation in the drill-string signal. Let the propagation in the transmission line be represented by the Z-transform of the time series, defined as $a_0+a_1Z^{-1}+\cdots+a_jZ^{-j}+\cdots$ for the time series a_j. Let the one-way delay in each discrete element of the transmission line be equal to $Z^{-1/2}$. The well-known[15] propagation matrix, which allows us to compute the down-going and up-going waves at each interface, is given by

$$M_J=\frac{Z^{J/2}}{\prod_{j=1}^{J}T_j}\begin{bmatrix} F_J(Z) & Z^{-J}G_J(Z^{-1}) \\ G_J(Z) & Z^{-J}F_J(Z^{-1}) \end{bmatrix}, \tag{17}$$

where

$$\begin{aligned} F_J(Z)&=F_{J-1}(Z)+R_JZ^{-1}G_{J-1}(Z), \\ G_J(Z)&=R_JF_{J-1}(Z)+Z^{-1}G_{J-1}(Z). \end{aligned} \tag{18}$$

Recursions (18), together with the initial conditions $F_1=1$ and $G_1=R_1$, give the functions $F_J(Z)$ and $G_J(Z)$ from reflection coefficients R_j, with $j=1,\ldots,J$. Equations (17) and recursions (18) allow us to calculate the displacement waves in the drill-string, rig, and layered formation systems. The drill-string reflection coefficients are given by Eq. (8). When calculating the strain waves, we use the opposite reflection coefficients [Eq. (14)] and, to take into account the discontinuous variation of the strain in tubes with different properties, we must use in the product of Eq. (17) the modified transmission coefficients given by Eq. (12).

A noticeable property of the propagation-matrix (17) is that the polynomials $F_J(Z)$ and $G_J(Z)$ contain an even and an odd number of reflection coefficients,[15] respectively. For this reason, $F_J(Z)$ is unchanged while $G_J(Z)$ simply changes its sign when passing from displacement to strain waves.

IV. SEPARATION OF REFLECTIONS

We consider the separation of the reflections occuring with an odd number of reflection coefficients—represented by polynomials $G_J(Z)$—with respect to the primary signals. Corresponding acceleration and strain waves have different waveforms. Assume equal instrumental response, and let the displacement be given as

$$u(\omega)=U(\omega)e^{\imath[\omega t-k(\omega)z]}. \tag{19}$$

The related strain is obtained by

$$\varepsilon_z=\frac{\partial u}{\partial z}=-\imath k(\omega)u(\omega), \tag{20}$$

and the acceleration by

$$a_z=\frac{\partial^2 u}{\partial t^2}=-\omega^2u(\omega). \tag{21}$$

Comparing Eqs. (20) and (21) gives the filter to shape the strain wave form into acceleration wave form—but we can also consider the filter shaping acceleration to strain—by

$$\mathcal{F}_{(s,a)}=\omega^2k^{-1}(\omega)e^{-\imath\pi/2}. \tag{22}$$

In the absence of dispersion (i.e., when $V=\omega k^{-1}$ is constant) we have

$$\mathcal{F}_{(s,a)}\propto\omega e^{-\imath\pi/2}. \tag{23}$$

The strain wave is shaped using the filter given by Eq. (23), scaled and summed to acceleration to remove the pattern of opposite reflections. The reflection layout is shown in Fig. 1. The method can be applied to the following.

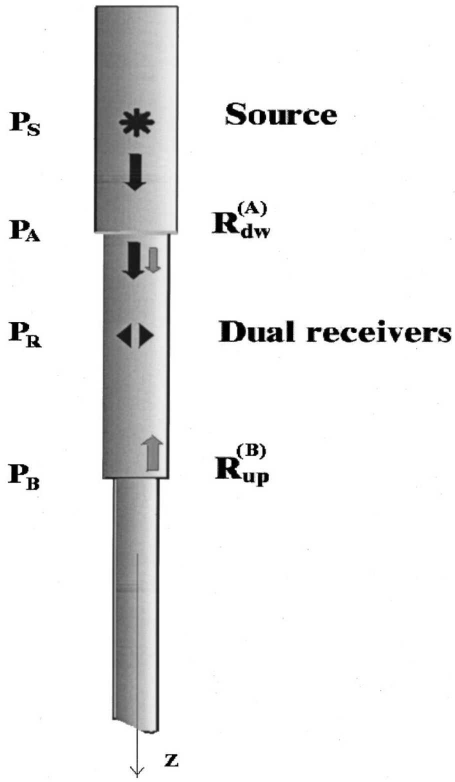

FIG. 1. The signal is produced by the source in P_S (denoted by a star) in the drill string and recorded by the dual sensors in P_R (denoted by two triangles). Two reflecting interfaces are located at P_A and P_B. Reflection coefficients at the downward (oriented with z direction) and upward (opposite to z direction) sides of the interfaces are represented. The transmitted signals and the down-going signals reflected two times—by the interface in P_B [with coefficient $R_{\mathrm{up}}^{(B)}$] and by the interface in P_A [with coefficient $R_{\mathrm{dw}}^{(A)}$]—have the same sign and cannot be separated. The up-going dual signals reflected once by the interface in P_B [with coefficient $R_{\mathrm{up}}^{(B)}$] have opposite signs and can be separated from the direct arrivals.

(1) Subtraction of rig reflections: The derrick-rig ghost reflection occurs in measurements at the top of the drill string. This reflection can be subtracted by using surface dual signals, while the transmitted bit signal is recorded with the equal sign. This allows us to separate the short-period rig and BHA reflections.
(2) The downhole drill string reflections in a signal recorded downhole near the bit can be subtracted. A similar analysis can be used to improve the reflections of the formation which are transmitted to the drill-string and used to predict the interfaces ahead of the bit.
(3) For signals measured at intermediate positions in the drill string, we distinguish between up-going and down-going reflections, which can be separated by using dual analysis (Fig. 1).
(4) Drill-string noise can be produced by contacts with the wall of the well. This noise can be analyzed with the support of numerical modeling to characterize the long-period reflections and determine the location of the noise source in the drill string.
(5) Dual fields provide information for deconvolving up-going waves by down-going waves, by assuming an unknown source signature.[7]

For example, field tests were measured using a downhole tool inserted in the heavy-weight drill pipes, in a position close to the drill collars and approximately 150 m above a bit, while drilling at 1160-m depth. In this case, about 48% of the energy of the short-period bottom-hole assembly reflections in the acceleration signal (i.e., the part of the reflections from the interface between drill pipes and heavy pipes) was removed by dual wave summation.

In summary, the use of dual measurements in drill strings is considered to characterize and separate the drill-bit signal reflections. This analysis suggests that the optimum position for a downhole tool inserted in the drill string is close to the bit. Dual measurements are also used to remove the rig reflections from surface pilot signals, and improve the analysis of the BHA reverberations.

ACKNOWLEDGMENTS

Acknowledgment is made to ENI-Agip for support of this research, José M. Carcione for useful comments and Massimo Malusa for his help in real data analysis.

[1] D. S. Drumheller, ''Acoustic properties of drill strings,'' J. Acoust. Soc. Am. **85**(3), 1048–1064 (1989).
[2] D. S. Drumheller and S. D. Knudsen, ''The propagation of sound waves in drill strings,'' J. Acoust. Soc. Am. **97**(4), 2116–2125 (1995).
[3] M. Hutchinson, V. Dubinsky, and H. Henneuse, ''An MWD Downhole Assistant Driller,'' Society of Petroleum Engineers, paper no. 30523 (1995).
[4] J. W. Rector III and B. P. Marion, ''The use of drill-bit energy as a downhole seismic source,'' Geophysics **56**, 628–634 (1991).
[5] F. Miranda, L. Aleotti, F. Abramo, F. Poletto, A. Craglietto, S. Persoglia, and F. Rocca, ''Impact of seismic while drilling technique on exploration wells,'' First Break **14**, 55–68 (1996).
[6] E. A. Robinson, M. Ewing, and J. L. Worzel, *Seismic Inversion and Deconvolution. Part B: Dual-sensor Technology* (Pergamon-Elsevier, Amsterdam, 1999).
[7] D. Loewenthal and E. A. Robinson, ''On unified dual fields and Einstein deconvolution,'' Geophysics **65**, 293–303 (2000).
[8] F. Poletto, M. Malusa, and F. Miranda, ''Numerical modeling and interpretation of drill-string waves,'' Geophysics **66**, 1569–1581 (2001).
[9] J. M. Carcione and F. Poletto, ''Simulation of stress waves in attenuating drill strings, including piezoelectric sources and sensors,'' J. Acoust. Soc. Am. **108**, 53–64 (2000).
[10] D. S. Drumheller, ''Extensional stress waves in one-dimensional elastic waveguides,'' J. Acoust. Soc. Am. **92**, 3389–3402 (1992).
[11] A. Leseultre, E. Lamine, and A. Jonsson, ''An instrumented bit: a necessary step to the intelligent BHA,'' Society of Petroleum Engineers, paper no. 39341 (1998).
[12] H. Kolsky, *Stress Waves in Solids* (Clarendon, Oxford, 1953).
[13] F. Poletto and M. Malusa, ''Reflection of drill-string extensional waves at the bit-rock contact,'' J. Acoust. Soc. Am. (submitted).
[14] M. Malusa, F. Poletto, and F. Miranda, ''Prediction ahead of the bit by using drill-bit pilot signals and reverse VSP,'' Geophysics, in press (2002).
[15] J. F. Claerbout, *Fundamentals of Geophysical Data Processing* (McGraw–Hill, New York, 1976).

Reduction of noise transmission through an aperture using active feedforward noise control (L)

J. Romeu, S. Jiménez, R. Capdevila, and N. Díaz
Acoustic Engineering Laboratory, LEAM, Technical University of Catalonia, UPC, Colom 11, Terrassa 08222, Spain

(Received 19 May 2000; accepted for publication 2 October 2001)

A local active noise control technique has been applied to reduce noise emission through an aperture in the wall of the enclosure. Pressure cancellation was effected at the center of an aperture of $0.3 \times 0.3\,\mathrm{m}^2$ for an enclosure of 2 m^3 volume, and the reduction in sound was measured at various locations at the aperture and at some distance from the enclosure. The results showed that sound pressure cancellation at the window implies emission attenuation through itself, and a relationship between attenuation at the window and outside the enclosure is confirmed. The behavior of attenuation results at the window is related to frequency, to the modal density of the sound field in the enclosure, and to the distance between the error microphone and secondary source. © *2002 Acoustical Society of America.* [DOI: 10.1121/1.1423928]

PACS numbers: 43.50.Ki [MRS]

I. INTRODUCTION

Enclosures are often used to attenuate noise from machinery, with a typical insertion loss (IL) of 15–20 dBA, which is usually enough for standard industrial environments. However, these enclosures must include a certain number of apertures for ventilation, manipulation, or material flow. These apertures transmit noise to the exterior, thereby acting as noise sources in themselves. Thus, attenuation of the enclosures is not as good as it could be.

One of the acoustic mechanisms of active noise cancellation in ducts is the reflection[1] of a primary wave by a secondary monopole source. Acoustic pressure at the secondary source position is maintained at zero by its action. Thus, the value of acoustic impedance is also zero and sound is perfectly reflected, although a compression is reflected as a rarefaction. Therefore, the secondary source provides a pressure release boundary condition and there is no transmission of sound downstream from the secondary source. Another acoustic mechanism is the absorption of noise by the secondary sources. In this case, there is no reflection of primary sound, but the pressure is equally maintained at zero downstream from the secondary source. In conclusion, both mechanisms provide a boundary condition that impedes sound transmission.

In waveguides, this boundary condition takes place at the location of the secondary source, due to plane wave propagation.[2–4] In free field, the zone of quiet is at the error microphone locations, and provides an acoustic shadow behind the error microphones.[5–9] Thus, a row of error microphones provides a boundary condition, which impedes sound transmission through the zone of quiet.

The aim of this project is to reduce noise transmission through an aperture in an enclosure, using active noise control techniques. Hence, global attenuation of the enclosure would be incremented by the elimination of these transmission paths. In order to decrease noise transmission, a boundary condition of low acoustic pressure will be forced in the transmission surface, using local active control strategies, because it is not necessary to reach a large area of attenuation. Our main objective is to achieve local attenuation at the window surface without any significant increase of sound pressure level in other areas of the enclosure.

II. LOCAL ACTIVE NOISE CONTROL

If sound pressure is cancelled at a point by means of a secondary source inside a room with diffuse sound field conditions, and the cancellation point is far from the secondary and primary sources, it is proven that the zone of quiet, within the pressure, is at least 10 dB below that due to the primary source, and is a sphere with a diameter of about one-tenth of a wavelength.[10] From the same theory, it can be found that an increase in pressure can occur at distances from the cancellation point which are longer than 0.16 λ, approximately.

A procedure that avoids increasing the sound pressure level inside the room consists in placing a secondary source next to the error microphone, so that the cancellation point is within the direct field of the secondary source. In this way, the sound power level of the secondary source is low compared to the primary source, and its contribution to the acoustic field amplitude in remote areas can be insignificant. This strategy is known as local active noise control. However, if the source is placed very near the error microphone, the diameter of the zone of quiet around the cancellation point tends to diminish. Considering point sources, it is confirmed that the space average modulus of pressure at those points, placed at a distance Δr from the cancellation point is determined by the expression[11]

$$\frac{\langle |p(r_{se}+\Delta r)|^2\rangle}{\langle |p_p(r_{se})|^2\rangle}=(1+k^2r_{se}^2)\left(\frac{\Delta r}{r_{se}}\right)^2, \tag{1}$$

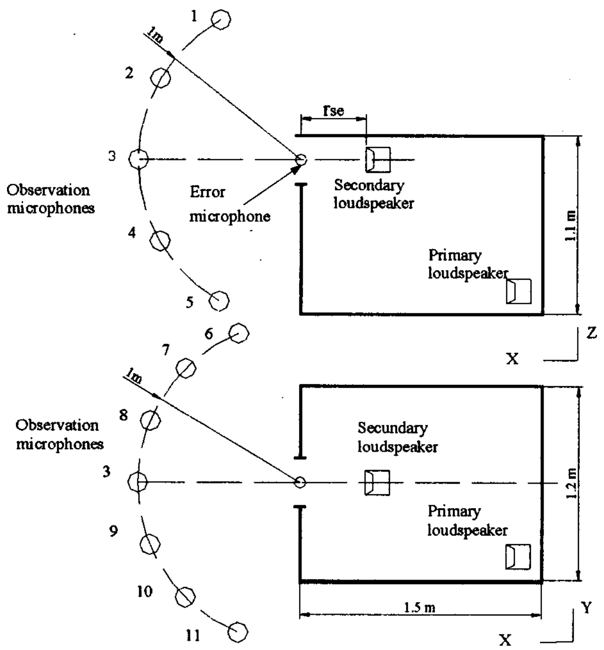

FIG. 1. Experimental setup. The error microphone is placed at the center of the aperture.

where r_{se} is the distance between secondary source and the error microphone, $\langle|p_p(r_{se})|^2\rangle$ is the space average squared modulus of the pressure at r_{se} from the secondary source before the cancellation, and $\langle|p(r_{se}+\Delta r)|^2\rangle$ is the space average modulus of the pressure at $r_{se}+\Delta r$ after the cancellation. When the secondary source is a flat piston and the error microphone is on its emission axis, it is shown that the zone of quiet also depends on the piston radius a and its relationship with the sound wavelength to be cancelled. When the piston radius is very small compared to the wavelength, the behavior of the source is similar to that of a monopole source.

III. EXPERIMENTAL SETUP

The experimental device (Fig. 1) is an enclosure with dimensions $1.2\times1.5\times1.1\,\mathrm{m}^3$. There is an aperture of $0.3\times0.3\,\mathrm{m}^2$ in a wall of the enclosure, where it is intended to carry out the acoustic noise control and prevent noise transmission from the interior of the enclosure to the exterior. This enclosure is placed in a laboratory of 204 m^3 and at a reverberation time of 1.2 s. The "cutoff" frequency for effective global control of the enclosed sound field[11] is about 53 Hz. This means that global active control in the room is not effective for frequencies above this value.

Primary noise is generated by a primary loudspeaker placed inside the enclosure at the furthest corner from the window, in order to excite the highest number of modes of the enclosure. The secondary source is a loudspeaker with a radius of 6 cm and the active noise control system is a typical DSP with a feedforward FXLMS algorithm. The reference signal is picked up directly from the function generator to avoid potential feedback contamination.

The cancellation point is in the middle of the window. Additional microphones (observation microphones) are placed to evaluate the area of acoustic pressure attenuation (see Fig. 2). Likewise, microphones are also placed outside

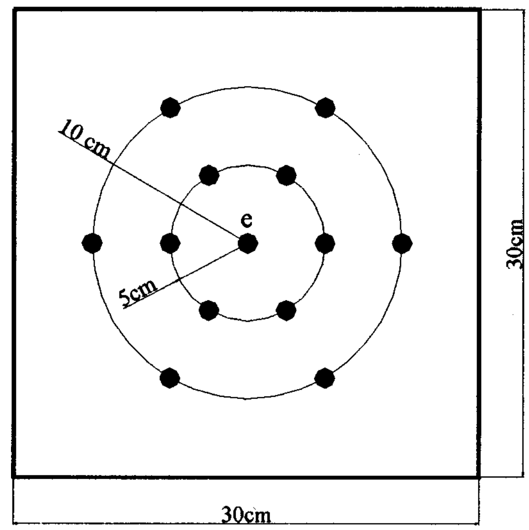

FIG. 2. Location of the observation microphones in the aperture. "e" means error microphone.

the enclosure, at a distance of 1 m from the window, so that the emission decrease can be evaluated. Several emission angles are covered both vertically and horizontally, showing sound level at 11 points (Fig. 1).

The enclosure response is shown in Fig. 3, where, for example, the resonance of the modes (1,0,0) and (0,1,0) (see Fig. 1 for x y z directions) at 120 and 146 Hz are clearly shown. For the studied range of frequency, all modes are still outstanding. The results obtained experimentally are similar to those obtained theoretically for the rectangular cavity, although there is some difference in the frequency value due to absorbing walls.[12]

IV. RESULTS

The experiments were developed for pure tone sounds between frequencies of 100 and 500 Hz, at intervals of 40 Hz and with distances between secondary source and error microphone of r_{se} equal to 15 and 45 cm.

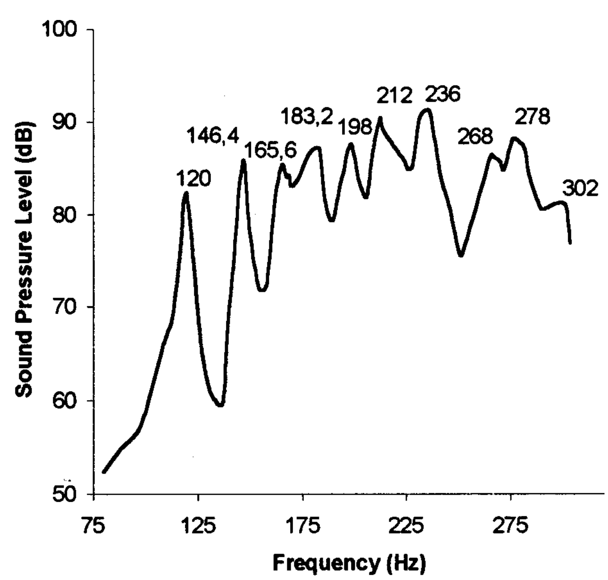

FIG. 3. Acoustic response of the enclosure.

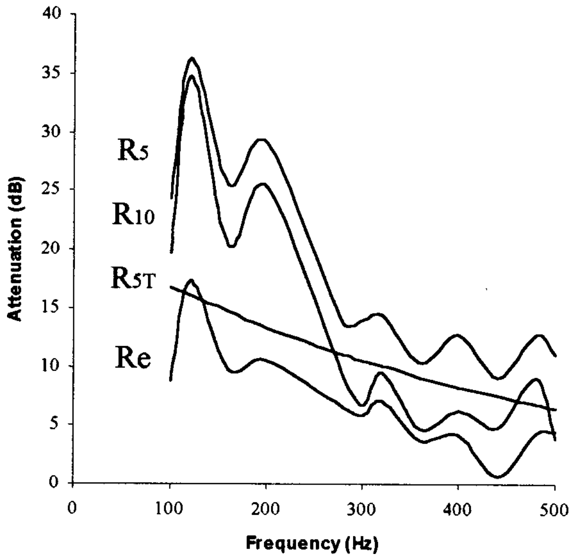

FIG. 4. R_5, R_{10}, and R_e values for $r_{se}=45$ cm. R_{5T} means theoretical attenuation according to Eq. (2), at 5 cm from the error microphone.

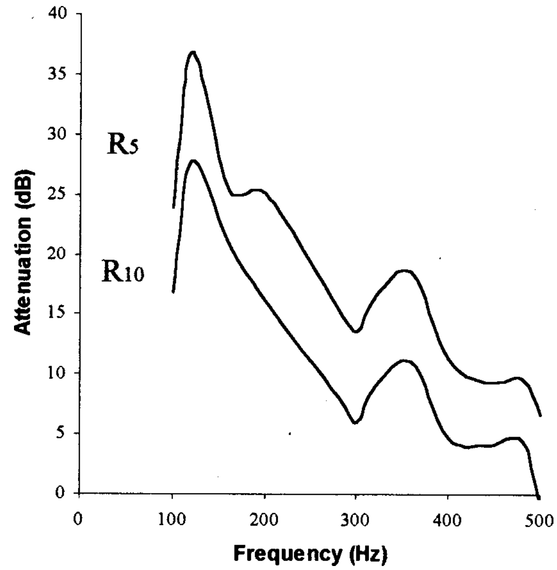

FIG. 5. R_5 and R_{10} values for $r_{se}=15$ cm.

The parameters R_5 and R_{10} are defined as the attenuation average of the microphones that were at 5 and 10 cm, respec tively, from the error microphone. R_e is the attenuation average of the microphones which were outside the enclosure. Figure 4 shows the attenuation results obtained as functions of frequency, for r_{se} equal to 45 cm. R_5 values are always higher than R_{10} ones, although there is a clear relationship between results for all frequencies.

The secondary source is a loudspeaker with a radius of 6 cm, so the ratio a/λ varies between 0.002 and 0.09 and hence the condition of point source can be assumed. Under these conditions, it is possible to determine the attenuation theoretically at distance Δr from the error microphone using Eq. (1), rewritten as

$$R_{\Delta r}=10\log\frac{\langle|p_p(r_{se})|^2\rangle}{\langle|p(r_{se}+\Delta r)|^2\rangle}$$
$$=10\log\frac{1}{(1+k^2r_{se}^2)(\Delta r/r_{se})^2}, \qquad (2)$$

where $R_{\Delta r}$ is attenuation in dB at distance Δr from the error microphone. It is then possible to determine the space average attenuation calculated by frequency for a given distance Δr and a specific position of the error microphone with regard to the secondary source, under diffuse sound field conditions. In particular, we can expect low modal density conditions in the low-frequency range, and consequently the results predicted by theory are not expected to converge with

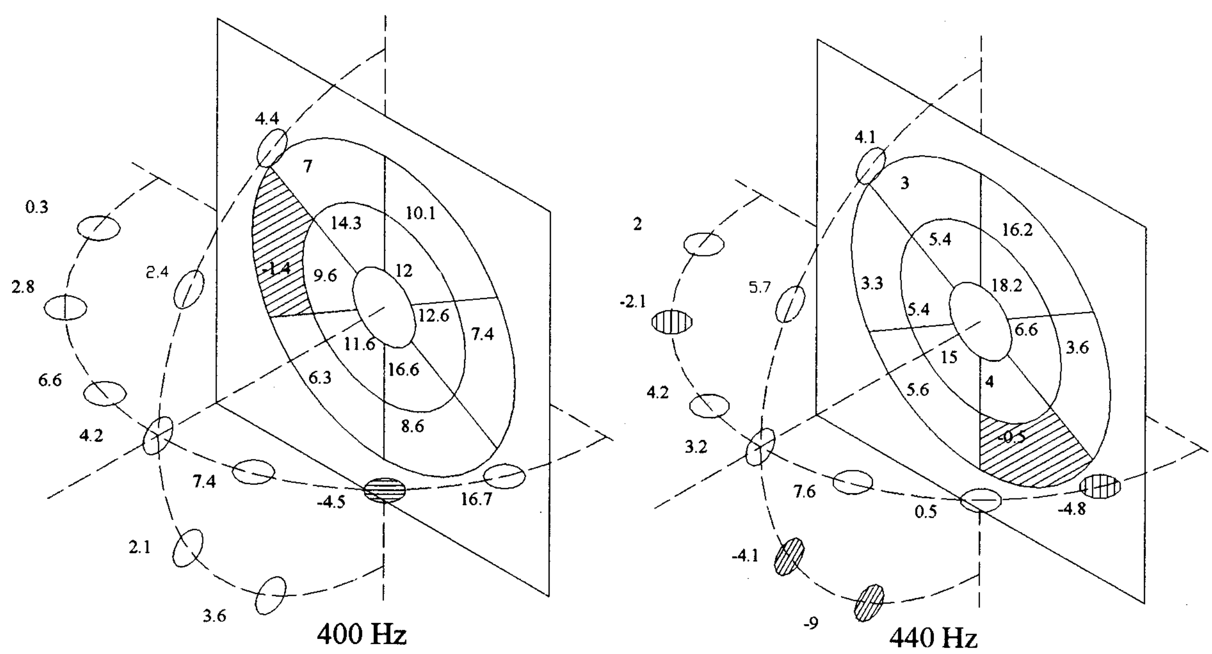

FIG. 6. Attenuation (in dB) at observation microphones placed in the aperture and outside the enclosure. It can be seen that increments in the aperture after control (dashed areas) cause increments outside the enclosure.

those obtained for these frequencies, because the physical cancellation mechanism is different.

It is interesting to compare the experimental results with these theoretical predictions. Diagram 4 shows the experimental space average attenuation for r_{se} equal to 45 cm. As expected, in most cases theoretical predictions are exceeded, especially at frequencies lower than 300 Hz. Higher attenuation is particularly obtained at 120 and 200 Hz. This effect can be caused by interaction of the enclosure acoustic field. The interior mode (1,0,0) coincides with 120 Hz, whereas the mode (1,0,1) corresponds to the frequency of 198 Hz. For both modes the secondary loudspeaker is not in a nodal plane. Therefore, global attenuation inside the enclosure is feasible, which would explain the high-level attenuation values obtained. For instance, attenuation at 120 Hz for r_{se} equal to 45 cm is almost the same as for Δr equal to 5 or 10 cm, which may indicate the cancellation of the mode (1, 0, 0) inside the enclosure.

The experimental results, from 300 to 500 Hz, follow the tendency of the theoretical Eq. (2), because the acoustic field inside the enclosure tends to adopt the characteristics of the diffused acoustic field as frequency increases.

It is also observed that for r_{se} 15 cm (Fig. 5), R_5 values are similar to those obtained with r_{se} equal to 45 cm, but the trend for R_{10} is different, with lower values for r_{se} equal to 15 cm, especially for frequencies above 300 Hz. This result is coherent with the theory exposed by Eq. (1) in diffuse field conditions. However, at 120 Hz, where global attenuation is suggested to take place, R_5 and R_{10} values are different from those obtained with r_{se} equal to 45 cm. In this case the error microphone may be in the direct field of the secondary loudspeaker and a process of local and nonglobal cancellation takes place because the acoustic power of the secondary source is lower than when r_{se} is 45 cm.

A. External attenuation

Attenuation measurements outside the enclosure were carried out only for r_{se} equal to 45 cm. The space average attenuation R_e for the 11 external microphones is also shown in Fig. 4, which is compared to attenuation on the transmission window for R_5 and R_{10}. It is easily observed that the tendency is the same for all averaged attenuations; therefore, we can assume a certain correlation between the attenuation at the window and the attenuation of transmission.

At low frequencies, it is verified that attenuation at all measurement points of the window leads to attenuation at all of the external points. However, at higher frequencies, increases in sound pressure levels at the window are detected, leading to increases at specific external points (see Fig. 6 for results at 400 and 440 Hz). Noise level increases at the window can be interpreted as areas of noise emission increase. However, this is unlikely to determine the directivity of the emission because the free field condition is not available.

V. CONCLUSIONS

The main conclusion is that sound pressure cancellation at the window implies emission attenuation. The use of techniques of local active noise control allows the attenuation area to be optimized without causing significant increases in other areas of the enclosure. In the studied case it is confirmed that as the secondary source is brought closer to the error microphone, the results tend to deteriorate due to the reduction of the zone of quiet.

The behavior of attenuation results at the window is related to the modal density of the sound field in the enclosure. At frequencies under 300 Hz, very high levels of attenuation are reached due to the interaction of the low modal acoustic field inside the enclosure. At frequencies over 300 Hz, the results tend to follow theoretical predictions for the diffuse field conditions, although differences of less than 5 dB are found. This could be caused by the complex phenomena that could take place in the aperture, such as the coupling of the enclosure and room sound fields, or the diffraction of sound around the edges of the aperture.

In conclusion, for the analyzed configuration, attenuation at the window (and therefore outside the window) is determined by the acoustic conditions inside the enclosure rather than by external conditions. The results are not related to the source characteristics. The results are only influenced by the enclosure, the aperture dimensions, the loudspeaker position, and the frequency.

ACKNOWLEDGMENTS

This work was supported by the CICYT program, Ref. TAP1999-0748, of the Spanish Ministry of Education and Culture.

[1] P. Nelson and S. Elliot, *Active Control of Sound* (Academic, Cambridge, 1993).
[2] K. Eghtesadi and H. Leventhall, ''A study of n-source active attenuator arrays for noise in ducts,'' J. Sound Vib. **91**(1), 11–19 (1981).
[3] M. J. M. Jessel and G. A. Magiante, ''Active sound absorbers in an air duct,'' J. Sound Vib. **23**(3), 383–390 (1972).
[4] J. Romeu, X. Salueña, S. Jimenez, R. Capdevila, and L. Coll, ''Active noise control in ducts in presence of standing waves. Its influence on feedback effect,'' Appl. Acoust. **62**, 3–14 (2001).
[5] S. Ise, ''Theory of acoustic impedance control for active noise control,'' Proc. InterNoise 94, pp. 1339–1342 (1994).
[6] S. Ise, H. Yano, and J. Tachibana, ''Application of active control to noise barrier,'' Proc. Int. Sym. Active Control of Sound and Vibration (1991), pp. 309–314.
[7] A. Omoto, K. Takashima, and K. Fujiwara, ''Active suppression of sound diffracted by a barrier: an outdoor experiment,'' J. Acoust. Soc. Am. **102**, 1671–1679 (1997).
[8] J. Guo and J. Pan, ''Analysis of active noise control in a free space,'' Proc. Active 95, pp. 649–660 (1995).
[9] J. Guo, J. Pan, and C. Bao, ''Actively created quiet zones by multiple control sources in free space,'' J. Acoust. Soc. Am. **101**, 1492–1501 (1997).
[10] S. Elliot, P. Joseph, A. Bullmore, and P. Nelson, ''Active cancellation at a point in a pure tone diffuse sound field,'' J. Sound Vib. **120**, 183–189 (1988).
[11] P. Joseph, S. Elliot, and P. Nelson, ''Near field zones of quiet,'' J. Sound Vib. **172**(5), 605–627 (1994).
[12] H. Kuttruff, *Room Acoustics* (Elsevier, London, 1991).

Second harmonic sound field after insertion of a biological tissue sample (L)

Dong Zhang,[a] Xiu-fen Gong, and Bo Zhang
State Key Lab of Modern Acoustics, Institute of Acoustics, Nanjing University, Nanjing 210093, China

(Received 8 March 2001; accepted for publication 1 October 2001)

Second harmonic sound field after inserting a biological tissue sample is investigated by theory and experiment. The sample is inserted perpendicular to the sound axis, whose acoustical properties are different from those of surrounding medium (distilled water). By using the superposition of Gaussian beams and the KZK equation in quasilinear and parabolic approximations, the second harmonic field after insertion of the sample can be derived analytically and expressed as a linear combination of self- and cross-interaction of the Gaussian beams. Egg white, egg yolk, porcine liver, and porcine fat are used as the samples and inserted in the sound field radiated from a 2 MHz uniformly excited focusing source. Axial normalized sound pressure curves of the second harmonic wave before and after inserting the sample are measured and compared with the theoretical results calculated with 10 items of Gaussian beam functions. © *2002 Acoustical Society of America.*
[DOI: 10.1121/1.1424868]

PACS numbers: 43.80.Cs, 43.80.Ev [FD]

I. INTRODUCTION

In the parabolic and quasilinear approximations, an analytical description for second-order sound fields of the sum-, difference-frequency, and second harmonic components in homogeneous media was well established by using the KZK equation and superposition of Gaussian beams.[1] However, in measuring or imaging the acoustic nonlinearity parameter of biological tissues, it is important to analyze the nonlinear field after inserting a sample, which is different from the propagation medium (distilled water). Saito studied this subject using a focusing source with a Gaussian distribution theoretically as well as experimentally.[2] Landsberger and Hamilton numerically investigated the second harmonic transmission and reflection at an interface for elastic solids by using the angular spectrum approach.[3] In the present letter, by using superposition of Gaussian beams and the KZK equation in quasilinear and parabolic approximations, an analytical description for the second harmonic generation after insertion of the sample is derived and expressed as a linear combination of self-and cross-interaction of Gaussian beams. Convergence of the summation of eigensolutions can generally be obtained with relatively few terms, resulting in a substantial computational saving over the direct numerical integration or the angular spectrum approach. In addition, a distinct advantage of the present method is that the solution of the second harmonic field can be interpreted physically. In the sound field radiated from a uniformly excited focusing source, four kinds of biological tissues are used as the samples and are inserted in the vicinity of the focus perpendicular to the beam axis for numerical calculation and experimental measurement. Comparison of the measured axial normalized sound pressure curves with the numerical calculations by using 10 items Gaussian function for the second harmonic wave before and after inserting the sample is presented.

[a]Present address: Department of electrical Engineering, Tohoku University, Sendai 980-8579, Japan; Electronic mail: dzhang@ecei.tohoku.ac.jp

II. FORMULATION OF THE PROBLEM AND ITS SOLUTION

As shown in Fig. 1, a focusing source with radius a and focusing length D located in a cylindrical coordinate system emits a sinusoidal sound wave with angular frequency ω and wave number k in the water. A sample with a thickness d is inserted perpendicular to the beam axis, the position of the front and back interfaces are z_1 and z_2, respectively. The density, sound velocity, and nonlinearity coefficient in the water are denoted as ρ, c, and β. The sound attenuation coefficients at the primary and secondary frequencies in the water are α_1 and α_2, respectively. For the sample, these parameters are denoted by a subscript x.

Complex velocity potentials $\phi_i(r,z)$ of the primary and second harmonic waves are used and can be decomposed as[4]

$$\phi_i(r,z)=q_i(r,z)\exp[-j(i\omega t-ikz)] \tag{1}$$

here and in the following, a subscript i ($i=1$ or 2) is corresponding to the primary and secondary waves, respectively. $q_i(r,z)$ is the complex pressure amplitude of $\phi_i(r,z)$. When $ka\gg 1$, by using the parabolic and quasilinear approximations, the KZK equation in the water can be expressed as

$$\begin{aligned}&\frac{1}{r}\frac{\partial}{\partial r}\left(r\frac{\partial q_1}{\partial r}\right)+j2k\frac{\partial q_1}{\partial z}+j2\alpha_1 kq_1=0,\\&\frac{1}{r}\frac{\partial}{\partial r}\left(r\frac{\partial q_2}{\partial r}\right)+j4k\frac{\partial q_2}{\partial z}+j4\alpha_2 kq_2=j\frac{\beta k^3}{c}q_1^2\end{aligned} \tag{2}$$

which satisfies the following source conditions:

$$q_1(r,0)=\left(\frac{u_0}{jk}\right)\exp(-jr^2/D),\quad r<a,$$

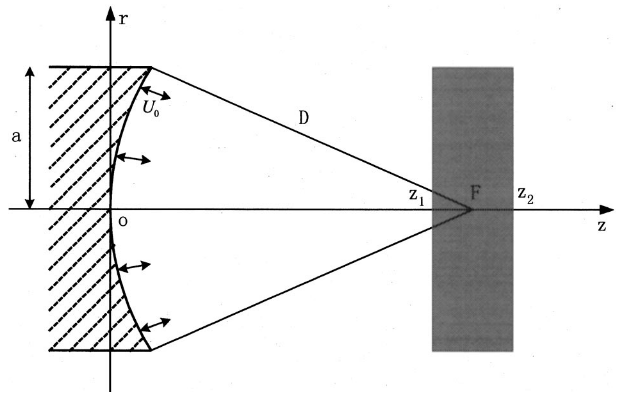

FIG. 1. Geometry for focusing source and insertion of a sample.

$$q_1(r,0)=0, \quad r>a \tag{3}$$
$$q_2(r,0)=0,$$

here u_0 is the amplitude of the source velocity. It has been reported that the distribution function of an axial symmetric source can be expressed as the superposition of Gaussian functions.[5]

$$q_1(r,0)=\sum_{n=1}^{N} A_n \exp[-B_n r^2], \tag{4}$$

where A_n and B_n coefficients are analogous to the optimized coefficients A_n^{opt} and B_n^{opt}, which can be obtained by computer optimization[5]

$$A_n=\frac{u_0 A_n^{\text{opt}}}{jk}, \quad B_n=\frac{B_n^{\text{opt}}}{a^2}+j\frac{k}{2D}. \tag{5}$$

From the principle of linear superposition, the primary field can be expressed as a linear summation of the fields radiated by these Gaussian sources; and the second harmonic field from the focusing source is thus a linear combination of self- and cross-interaction of the Gaussian beams. Therefore, $q_i(r,z)$ in the region $(z<z_1)$ can be obtained by substituting Eq. (4) into Eq. (2),

$$\begin{aligned} q_1(r,z)&=\sum_{n=1}^{N}\frac{A_n}{B_n}\frac{\exp[-\alpha_1 z]}{g_n(z)}\exp\left[-\frac{r^2}{g_n(z)}\right],\\ q_2(r,z)&=\sum_{n=1}^{N}\sum_{m=1}^{N}\frac{\beta k^2}{4c}\frac{A_n}{B_n}\frac{A_m}{B_m}\int_0^z G_1\exp[-G_1 r^2]\\ &\quad\times\frac{\exp[-2\alpha_1 z'-\alpha_2(z-z')]}{g_n(z')+g_m(z')}dz', \end{aligned} \tag{6}$$

where

$$g_n(z)=\frac{1}{B_n}+j\frac{2z}{k}$$

and

$$G_1=\left[\frac{g_n(z')g_m(z')}{g_n(z')+g_m(z')}+j\frac{z-z'}{k}\right]^{-1}.$$

Effective transmission coefficients for the fundamental and second harmonic components at an interface for a focused sound beam can be numerically calculated, respectively.[6] However, for the case of low concavity (half aperture angle for the focusing source <30°) and with the specimens whose material parameters do not differ greatly from the surrounding medium (distilled water), the focused beam could be regarded as a single normally incident plane wave at the interface.[2,7] Therefore,

$$q_i(r,z_{1+})=T_I q_i(r,z_{1-})$$

and (7)

$$q_i(r,z_{2+})=T_O q_i(r,z_{2-}),$$

here $T_I[=2\rho c_x/(\rho c+\rho_x c_x)]$ and $T_O[=2\rho_x c/(\rho c+\rho_x c_x)]$ are transmission coefficients for complex amplitude of velocity potential at the two interfaces. It should be noted that the reflections here are neglected, which is no disadvantage for biological tissues when short cw pulses are employed.

When in the region $z_1<z<z_2$, $q_i(r,z)$ satisfy the following KZK equation:

$$\begin{aligned} &\frac{1}{r}\frac{\partial}{\partial r}\left(r\frac{\partial q_1}{\partial r}\right)+j2k_x\frac{\partial q_1}{\partial z}+j2\alpha_{1x}k_x q_1=0,\\ &\frac{1}{r}\frac{\partial}{\partial r}\left(r\frac{\partial q_2}{\partial r}\right)+j4k_x\frac{\partial q_2}{\partial z}+j4\alpha_{2x}k_x q_2=j\frac{\beta_x k_x^3}{c_x}q_1^2. \end{aligned} \tag{8}$$

One can evaluate $q_i(z_{1-},r)$ at the first boundary by setting $z=z_1$ in Eq. (6). Then from Eq. (7), $q_i(z_{1+},r)$ can be derived and regarded as the boundary condition in Eq. (8). Therefore, $q_i(r,z)$ in the sample $(z_1<z<z_2)$ can be obtained as the following:

$$\begin{aligned} q_1(r,z)&=T_I\sum_{n=1}^{N}\frac{A_n}{B_n}\frac{\exp[(-\alpha_1 z_1)-\alpha_{1x}(z-z_1)]}{h_n(z)}\\ &\quad\times\exp\left[-\frac{r^2}{h_n(z)}\right],\\ q_2(r,z)&=T_I\sum_{n=1}^{N}\sum_{m=1}^{N}\frac{\beta k^2}{4c}\frac{A_n}{B_n}\frac{A_m}{B_m}\\ &\quad\times\int_0^{z_1}\frac{\exp[-(2\alpha_1 z')-\alpha_2(z_1-z')-\alpha_{2x}(z-z_1)]}{g_n(z')+g_m(z')}\\ &\quad\times G_2\exp[-G_2 r^2]dz'\\ &\quad+T_I^2\sum_{n=1}^{N}\sum_{m=1}^{N}\frac{\beta_x k_x^2}{4c_x}\frac{A_n}{B_n}\frac{A_m}{B_m}\int_{z_1}^{z}G_3\exp[-G_3 r^2]\\ &\quad\times\frac{\exp[-2(\alpha_1-\alpha_{1x})z_1-\alpha_{1x}z'-\alpha_{2x}(z-z')]}{h_n(z')+h_m(z')}dz', \end{aligned} \tag{9}$$

where

$$h_n(z)=\frac{1}{B_n}+j\frac{2z}{k_x}+j2z_1\left(\frac{1}{k}-\frac{1}{k_x}\right),$$

$$G_2=\left[\frac{g_n(z')g_m(z')}{g_n(z')+g_m(z')}+j\frac{z_1-z'}{k}+j\frac{z-z_1}{k_x}\right]^{-1},$$

$$G_3=\left[\frac{h_n(z')h_m(z')}{h_n(z')+h_m(z')}+j\frac{z-z'}{k_x}\right]^{-1}.$$

$q_i(z_{2-},r)$ at the second boundary can be obtained by setting $z=z_2$ in Eq. (9) and $q_i(z_{2+},r)$ can then be calculated with Eq. (7). Combined with Eq. (2), $q_i(r,z)$ beyond the sample $(z>z_2)$ can be expressed as follows:

$$q_1(r,z)=T_I T_O \sum_{n=1}^{N} \frac{A_n}{B_n} \frac{\exp[-\alpha_1 z_1-\alpha_x(z_2-z_1)-\alpha_1(z-z_2)]}{o_n(z)} \exp\left[-\frac{r^2}{o_n(z)}\right],$$

$$q_2(r,z)=\sum_{n=1}^{N}\sum_{m=1}^{N} T_I T_O \frac{\beta k^2}{4c}\frac{A_n}{B_n}\frac{A_m}{B_m}\int_0^{z_1} G_4 \exp[-G_4 r^2]\frac{\exp[-2\alpha_1 z'-\alpha_{2x}(z_2-z_1)-\alpha_2(z_1-z_2+z-z')]}{g_n(z')+g_m(z')}dz'$$
$$+T_O T_I^2 \sum_{n=1}^{N}\sum_{m=1}^{N}\frac{\beta_x k_x^2}{4c_x}\frac{A_n}{B_n}\frac{A_m}{B_m}\int_{z_1}^{z_2} G_5 \exp[-G_5 r^2]$$
$$\times\frac{\exp[-2(\alpha_1-\alpha_{1x})z_1-2\alpha_{1x}z'-\alpha_{2x}(z_2-z')-\alpha_2(z-z_2)]}{h_n(z')+h_n(z')}dz'+(T_O T_I)^2\sum_{n=1}^{N}\sum_{m=1}^{N}\frac{\beta k^2}{4c}\frac{A_n}{B_n}\frac{A_m}{B_m}$$
$$\times\int_{z_2}^{z} G_6\exp[-G_6 r^2]\frac{\exp[-2(\alpha_{1x}-\alpha_1)(z_2-z_1)-2\alpha_1 z'-\alpha_2(z-z')]}{o_n(z')+o_m(z')}dz', \tag{10}$$

where

$$o_n(z)=\frac{1}{B_n}+j\frac{2z}{k}+j2(z_1-z_2)\left(\frac{1}{k}-\frac{1}{k_x}\right),$$

$$G_4=\left[\frac{g_n(z')g_m(z')}{g_n(z')+g_m(z')}+j\frac{z_1-z'}{k}+j\frac{z_2-z_1}{k_x}+j\frac{z-z_2}{k}\right]^{-1},$$

$$G_5=\left[\frac{h_n(z')h_m(z')}{h_n(z')+h_m(z')}+j\frac{z_2-z'}{k_x}+j\frac{z-z_2}{k}\right]^{-1},$$

$$G_6=\left[\frac{o_n(z')o_m(z')}{o_n(z')+o_m(z')}+j\frac{z-z'}{k}\right]^{-1}.$$

Finally, the complex amplitude of the second harmonic sound pressure beyond the sample can be obtained from the relation $p_2(r,z)=2j\rho\omega q_2(r,z)$.

III. RESULTS

In order to verify the formulas obtained in this paper, we calculate the axial pressure amplitude for the second harmonic component from a uniformly excited focusing source when the sample is absent. For comparison, the same parameters in Ref. 4 are used in the calculation and our results agree well with that obtained in Ref. 4.

To study the second harmonic field after inserting the sample, a uniformly excited focusing source (2 MHz, $a=0.6$ cm, $D=5$ cm, Advanced Devices, USA) is employed for numerical calculation and experimental measurement. From Fig. 2(a), it can be found that the maximum value of the normalized axial pressure amplitude for the second harmonic component without the insertion of a sample is appeared at $z=4.2$ cm. Therefore, the center of the sample with thickness $d=2$ cm is chosen to be located at $z=4.2$ cm. The eggs used in measurement were bought from a supermarket and the porcine liver and fat were obtained freshly from a slaughterhouse, stored in 0.9% saline solution and studied within 6 hours. The degassed sample is carefully packed into a sample holder with polythene membrane windows at two sides. The ultrasonic parameters of samples are listed in Table I, in which the sound attenuation and velocity are measured by a pulse transmission method and nonlinearity coefficient is measured by insert substitution method.[8] Theoretical calculated results after the insertion of four kinds of biological specimens are also plotted as solid lines in Figs.

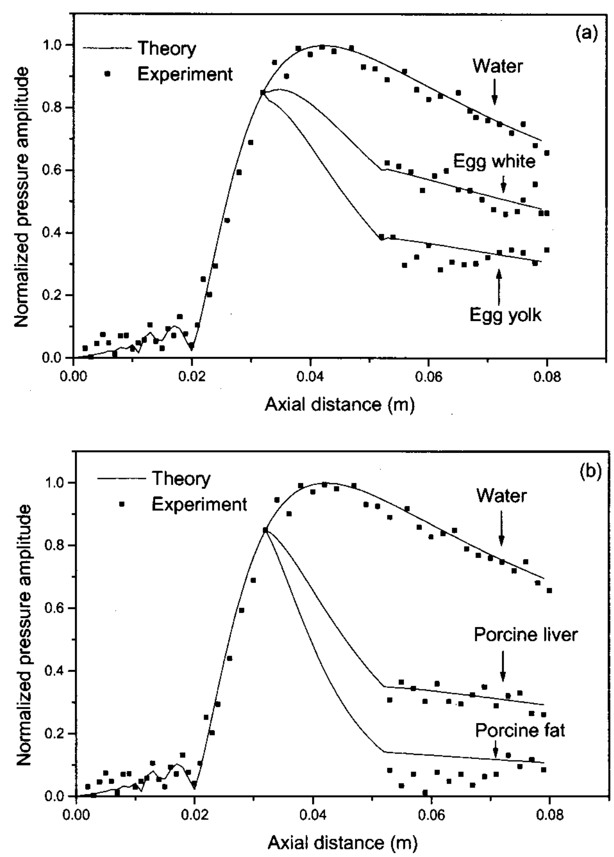

FIG. 2. Comparison of measured axial pressure amplitude with theory for second harmonic wave before and after inserting a sample (a) egg white and egg yolk and (b) porcine liver and porcine fat.

TABLE I. Ultrasound parameters for samples and distilled water in measurement (27 °C).

Sample	Density (g/cm^3)	Velocity (m/s)	Attenuation coefficient(m^{-1}) 2 MHz	4 MHz	β
Distilled water	0.997	1497			3.6[a]
Egg white	1.05	1542	6.5	18.3	3.6
Egg yolk	1.06	1520	18.5	54.6	5.0
Porcine liver	1.05	1588	21.4	44.2	4.45
Porcine fat	0.95	1445	43.3	94.4	5.5

[a]See Ref. 8.

2(a) and 2(b), where all curves are normalized so that the maximum pressure amplitude of the water becomes unity.

In measurement, a 2 MHz tone-burst signal is radiated from the focusing source and the source level should be adjusted to avoid shock formation to satisfy the quasilinear theory. The second harmonic signal 4 MHz is detected by a needle hydrophone (TNU001A, NTR Systems) with an active diameter of 1 mm. After amplification, the hydrophone output signal is sent to a spectrum analyzer (HP3585B). The experimental results for the second harmonic wave before and after inserting the sample are also shown in Figs. 2(a) and 2(b). It can be seen that (1) the experimental results are in agreement with the theoretical results, except that there are some oscillations due to inhomogeneity of the biological samples and low S/N ratio in measurement; (2) the theoretical model may be useful for nonlinear imaging in ultrasound microscopy.[6] In addition, it should also be noted that (1) due to the limitation of the superposition of Gaussian beams, the distance between the source and the first interface of the sample (z_1) should be greater than 0.12 times Fresnel distance; (2) the present theoretical model is also applicable to a piston source provided that Eq. (5) is modified.

IV. CONCLUSION

In this paper, in the quasilinear and parabolic approximations, an analytical description for the second harmonic sound field after inserting a sample is derived. In the theoretical analysis, sound diffraction, sound attenuation and nonlinear effect are considered. Four kinds of biological samples are used and inserted into the sound field radiated from a 2 MHz uniformly excited focusing source. The experimental results for the axial pressure amplitude of the second harmonic wave coincide with the theory. The present theoretical model may be extended to measure or image the acoustic nonlinearity parameter of biological tissues with consideration of the sound diffraction and attenuation.

ACKNOWLEDGMENTS

The authors wish to thank Professor F. Dunn for his valuable comments on the paper and his help in preparing the final version. The authors also wish to thank the National Natural Science Foundation of China (No. 19834040) and Natural Science Foundation of Jiangsu Province (No. BK99024)

[1]D. Ding, ''A simplified algorithm for the second-order sound fields,'' J. Acoust. Soc. Am. **108**, 2759–2764 (2000).
[2]S. Saito, ''Measurement of the acoustic nonlinearity parameter in liquid media using focusing ultrasound,'' J. Acoust. Soc. Am. **93**, 162–172 (1993).
[3]B. J. Landsberger and M. F. Hamilton, ''Second-harmonic generation in sound beams reflected from and transmitted through immersed elastic solids,'' J. Acoust. Soc. Am. **109**, 488–500 (2001).
[4]B. G. Lucas and T. G. Muir, ''Field of a finite-amplitude focusing source,'' J. Acoust. Soc. Am. **74**, 1522–1528 (1983).
[5]J. J. Wen and M. A. Breazeale, ''A diffraction beam field expressed as the superposition of Gaussian beams,'' J. Acoust. Soc. Am. **83**, 1752–1756 (1988).
[6]L. Germain, R. Jacques, and J. D. N. Cheek, ''Acoustic microscopy applied to nonlinear characterization of biological media,'' J. Acoust. Soc. Am. **86**, 1560–1565 (1989).
[7]S. D. Bennett, ''Approximate materials characterization by coherent acoustic microscopy,'' IEEE Trans. Sonics Ultrason. **SU-29**, 316–320 (1982).
[8]X. F. Gong, Z. M. Zhu, T. Shi, and J. H. Huang, ''Determination of the acoustic nonlinearity parameter in biological media using FAIS and ITD methods,'' J. Acoust. Soc. Am. **86**, 1–5 (1989).

Modal degeneracy in square wave guides

Brian J. McCartin[a)]
Applied Mathematics, Kettering University, 1700 West Third Avenue, Flint, Michigan 48504-4898

(Received 1 June 2001; revised 15 September 2001; accepted 11 October 2001)

Issues relating to modal degeneracy in a square wave guide are herein treated. Specifically, it is determined precisely which cutoff frequencies can be present, the multiplicity of each such frequency is ascertained, and a procedure is developed which provides a prescription for finding all the modes associated with each of these frequencies. As an added dividend, we characterize the family of harmonic series into which these frequencies naturally assemble. Just enough of the requisite number theory is included to make this account reasonably self-contained. © *2002 Acoustical Society of America.* [DOI: 10.1121/1.1424865]

PACS numbers: 43.20.Bi, 43.20.Mv, 43.40.Dx [JJM]

I. INTRODUCTION

A homogeneously filled cylindrical wave guide of square cross section with side a $(0 \leqslant x \leqslant a, 0 \leqslant y \leqslant a)$ possesses soft modes

$$\phi^S_{m,n} = \sin\frac{\pi m x}{a} \cdot \sin\frac{\pi n y}{a}; \quad m,n = 1,2,\ldots \tag{1}$$

and hard modes

$$\phi^H_{m,n} = \cos\frac{\pi m x}{a} \cdot \cos\frac{\pi n y}{a}; \quad m,n = 0,1,2,\ldots \tag{2}$$

which share the same cutoff frequency

$$f_{m,n} = \frac{\sqrt{m^2+n^2}}{2a}. \tag{3}$$

Because of the symmetry of the square, the modes where $m \neq n$ are degenerate in the sense that $\phi_{m,n} = \phi_{n,m}$. Whereas the nodal lines of $\phi_{m,n}$ are simply lines parallel to the sides of the square, such degenerate modes may be combined in-phase

$$\phi = [\cos\gamma \cdot \phi_{m,n} + \sin\gamma \cdot \phi_{n,m}] \cdot \cos(2\pi f_{m,n} t) \tag{4}$$

to produce truly exotic standing wave patterns (Ref. 1, p. 80). Furthermore, if combined out-of-phase

$$\phi = \phi_{m,n} \cos(2\pi f_{m,n} t) + \phi_{n,m} \sin(2\pi f_{m,n} t) \tag{5}$$

then travelling wave patterns arise in which the nodal lines move across the wave guide cross section in a cyclic fashion. Moreover, higher order degeneracy occurs, for example, whenever $m_1^2 + n_1^2 = m_2^2 + n_2^2$ since in this event we are confronted with many linearly independent modes all with the same cutoff frequency.

Discussion of such modal degeneracy is sporadic at best in the engineering literature (Ref. 2, p. 244) and the situation is only slightly improved in the acoustics literature (Ref. 3, pp. 206–207) amidst treatments of vibrating membranes and propagation in ducts. [This same degeneracy also occurs in the vibration of a square plate (Ref. 4, p. 184).] This is despite the fact that the problem has a rich history involving such notable scientists as Riemann (Ref. 5, Sec. 95), Lamé (Ref. 6, pp. 122–131), and Rayleigh (Ref. 7, pp. 312–317). It is the express purpose of this note to provide an essentially complete and self-contained treatment of this problem.

The acoustical significance of these results lies in their potential application to nearly square wave guides. Within such structures, the propagation of sound may be studied by classical perturbation procedures.[8] However, these approximation techniques require the *a priori* determination of the multiplicity of each eigenvalue together with a basis for the corresponding eigenspace.

II. FORMULATION

We are concerned with answering the following four interrelated questions concerning modal degeneracy:

(1) Which cutoff frequencies emerge from Eq. (3)?
(2) Precisely how many linearly independent modes correspond to each such frequency?
(3) Given a permissible cutoff frequency, is there an algorithm to list all (m,n) for which $f_{m,n}$ coincides with it?
(4) Can we group all of the allowed cutoff frequencies into disjoint "harmonic series" so that those within a group are all integer multiples of a "fundamental frequency"?

Rewriting Eq. (3) as

$$f_{m,n} = \frac{\sqrt{\ell}}{2a}, \quad \ell := m^2 + n^2, \tag{6}$$

reveals that our four questions above are equivalent to the following number theoretical considerations:

(1) Which integers, ℓ, are the sum of two squares?
(2) In how many ways may this be done?
(3) How may this be done?
(4) Can we partition the collection of all square roots of such integers into groups, each comprised of multiples of a "seed"?

[a)]Electronic mail: bmccarti@kettering.edu

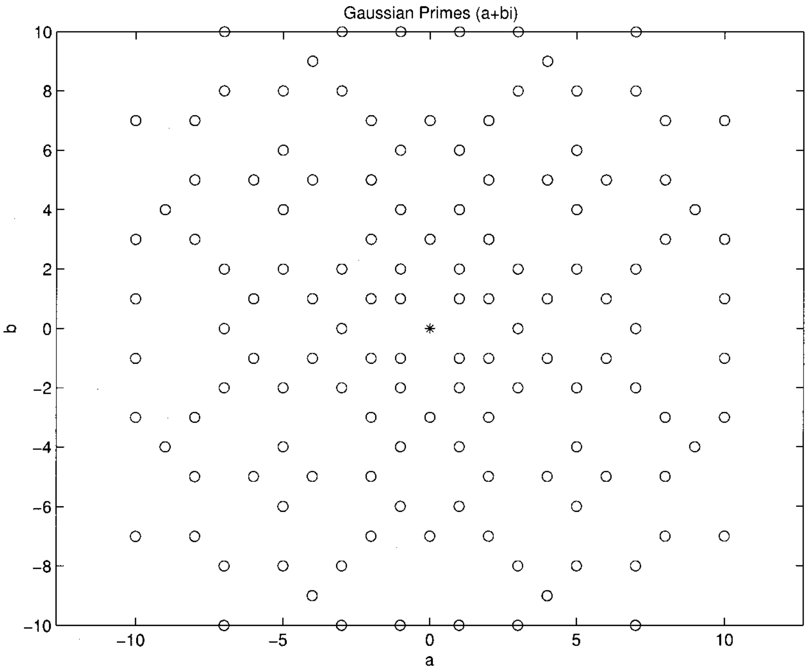

FIG. 1. The Gaussian primes in the complex plane.

III. NUMBER THEORY

The first three questions were answered by Fermat, Euler, and Gauss.[9] The answer to the last one appears here for the first time. Full proofs and further details are available in Ref. 10.

Whereas many results in elementary number theory hinge upon the prime factorization of an integer $\ell = p_1^{\pi_1} \cdot p_2^{\pi_2} \cdots p_k^{\pi_k}$, the questions raised above are best treated in the complex plane. Thus, we define the Gaussian integers to be the complex numbers $a+b\imath$ where a and b are integers. Consequently, they form a square lattice in the complex plane. Mathematically, they constitute a ring (Ref. 11, p. 370). The special values $u=\pm 1, \pm \imath$ are called the units and any two Gaussian integers differing only by a unit factor are called associates. The norm of a Gaussian integer is $N(a+b\imath) := a^2+b^2$.

A Gaussian integer, G, is said to be a Gaussian prime if its only factorizations are the trivial ones $G = u \cdot g$ involving unit factors, u. We now state, without proof, a characterization of the Gaussian primes. We begin with the straightforward observation that any odd real prime may be written as either $4k+1$ or $4k+3$. The Gaussian primes are then (Ref. 10, p. 18):

(1) The real primes of the form $4k+3$ and associates.
(2) The Gaussian integers for which $N(a+b\imath)=p$, p a real prime of the form $4k+1$.
(3) The Gaussian integers for which $N(a+b\imath)=2$, i.e., $1+\imath, 1-\imath, -1+\imath, -1-\imath$.

These are shown in Fig. 1 and are of sufficient visual allure to have inspired floor tilings and tablecloth weavings (Ref. 12, p. 34).

Through this characterization, we may now uncover the connection between Gaussian primes and our questions concerning sums-of-squares of integers. If we initially restrict our attention to real primes, $\ell = p$, then

$$\ell = p = m^2+n^2 = (m+n\imath)(m-n\imath) \tag{7}$$

requires that p either be equal to 2 or be of the form $4k+1$ since real primes of the form $4k+3$ cannot be factored as Gaussian integers. Conversely, if $p=2, 4k+1$ then it may be factored as in Eq. (7) and hence may be expressed as the sum of two squares in an essentially unique fashion (i.e., up to unit factors and the order of the factors).

Thus, the real primes naturally partition themselves into those that can or cannot be (uniquely) written as the sum of two squares. This is summarized in Table I. Observe that the first column is essentially a table of Gaussian primes since, for example, $41=4^2+5^2=(4+5\imath)(4-5\imath)=(-4-5\imath)(-4+5\imath)=(5+4\imath)(5-4\imath)=(-5-4\imath)(-5+4\imath)$ and thus yields the Gaussian primes $4\pm 5\imath$ and all of their associates. This table is easily constructed by putting all of the Gaussian

TABLE I. Partitioning of the primes.

Sums-of-squares	Not sums-of-squares
$2=1^2+1^2$	3
$5=1^2+2^2$	7
$13=2^2+3^2$	11
$17=1^2+4^2$	19
$29=2^2+5^2$	23
$37=1^2+6^2$	31
$41=4^2+5^2$	43
$53=2^2+7^2$	47
$61=5^2+6^2$	59
$73=3^2+8^2$	67
$89=5^2+8^2$	71
$97=4^2+9^2$	79
$101=1^2+10^2$	83

integers in order of increasing norm and identifying those with norm $p=2, 4k+1$.

This leads us to the final tool required from number theory, the prime factorization theorem. This fundamental result states that any real integer may be factored as (Ref. 10, p. 18)

$$\ell = 2^{\alpha_0}\cdot \prod_{p_i\equiv 1(\mathrm{mod}\ 4)} p_i^{\alpha_i}\cdot \prod_{q_j\equiv 3(\mathrm{mod}\ 4)} q_j^{\beta_j} \tag{8}$$

(where the p's and q's are real odd primes of the form $4k+1$ and $4k+3$, respectively), or in terms of Gaussian primes

$$\ell = [(1+\imath)(1-\imath)]^{\alpha_0}\cdot \prod_i [(a+b\imath)(a-b\imath)]^{\alpha_i}\cdot \prod_j q_j^{\beta_j}, \tag{9}$$

in a way that is unique up to units and order of factors.

IV. SOLUTION

We now supply complete answers to our four questions.

(1) An integer, ℓ, can be written as the sum of two squares if and only if each of the β_j is even, since in this and only this case Eq. (9) may be regrouped as $\ell=(m+n\imath)(m-n\imath)$ where $m+n\imath$ is given by

$$(1+\imath)^{\gamma_0}(1-\imath)^{(\alpha_0-\gamma_0)}\prod_i (a+b\imath)^{\gamma_i}(a-b\imath)^{(\alpha_i-\gamma_i)}\prod_j q_j^{\beta_j/2}, \tag{10}$$

and $m-n\imath$ is given by

$$(1+\imath)^{(\alpha_0-\gamma_0)}(1-\imath)^{\gamma_0}\prod_i (a+b\imath)^{(\alpha_i-\gamma_i)}(a-b\imath)^{\gamma_i}\prod_j q_j^{\beta_j/2}. \tag{11}$$

(2) Since $(1+\imath)^{\gamma_0}(1-\imath)^{(\alpha_0-\gamma_0)}$ and $(1+\imath)^{(\alpha_0-\gamma_0)}(1-\imath)^{\gamma_0}$ are associates, factors of 2 do not increase the number of possible groupings, Eqs. (10) and (11). Likewise, so long as all of the β_j are even, they also do not affect the number of such groupings. Thus, it is the middle term of Eq. (9) which alone determines the number of ways that ℓ may be expressed as the sum of two squares. Specifically, with

$$\alpha := \prod_{i=1}^{k} (\alpha_i+1), \tag{12}$$

the number of essentially distinct groupings is $\alpha/2$ if α is even and $(\alpha+1)/2$ if α is odd (i.e., ℓ is a perfect square or twice one). Thus, the number of linearly independent modes is equal to α unless ℓ is a perfect square in which case there are $\alpha+1$ (hard) or $\alpha-1$ (soft) independent modes.

(3) It is now straightforward to develop a general algorithm to reveal the modal structure corresponding to the cutoff frequency, Eq. (6). Begin by factoring ℓ as in Eq. (9) with the aid of Table I. Then, perform all of the groupings described by Eqs. (10) and (11). This process will yield all of the possible representations of ℓ as a sum of two squares and *ipso facto* all of the modes with the given cutoff frequency.

(4) From Eq. (3), we see that there is a harmonic series corresponding to every integer ℓ which is representable as the sum of two squares (so that all prime factors of the form $4k+3$ must appear to an even power) which is *not* divisible by a perfect square [and hence must have no factors of the form $4k+3$ and all of the α_i $(i=0,1,\ldots)$ in Eq. (8) must be equal to either 0 or 1]. Thus, for every seed, $s=2^{\alpha_0}\cdot\Pi_i p_i^{\alpha_i}$, with the α's so restricted, we may construct the corresponding harmonic series by multiplying s by the sequence of perfect squares. Note that, for soft modes, the seed $s=1$ is absent from its harmonic series which will also be missing any perfect square not divisible by any prime of the form $4k+1$. This is a consequence of $m\cdot n=0$ which produces $\phi^S_{m,n}=0$.

V. EXAMPLES

$\ell=\mathbf{9}=3^2=\underline{3^2+0^2}$. $\alpha=0+1=1$. Since ℓ is a perfect square, there are $\alpha-1=0$ soft modes and $\alpha+1=2$ hard modes [(3,0) and (0,3)].

$\ell=\mathbf{10}=2\times5=(1+\imath)(1-\imath)\cdot(2+\imath)(2-\imath)=(1+\imath)(2+\imath)\cdot(1-\imath)(2-\imath)=(1+3\imath)\cdot(1-3\imath)=\underline{1^2+3^2}$. Thus, there are $\alpha=1+1=2$ soft/hard modes [(1,3) and (3,1)].

$\ell=\mathbf{25}=5^2=(2+\imath)^2\cdot(2-\imath)^2=(3+4\imath)\cdot(3-4\imath)=\underline{3^2+4^2}=(2+\imath)^2\cdot(2-\imath)^2=\underline{5^2+0^2}$. $\alpha=2+1=3$. Since ℓ is a perfect square, there are $\alpha-1=2$ soft modes [(3,4) and (4,3)] and $\alpha+1=4$ hard modes [(5,0) and (0,5) and (3,4) and (4,3)].

$\ell=\mathbf{40}=2^3\times5=2^2[2\times5]=2^2[1^2+3^2]=\underline{2^2+6^2}$. Thus, there are $\alpha=1+1=2$ soft/hard modes [(2,6) and (6,2)].

$\ell=\mathbf{50}=2\times5^2=(1+\imath)(1-\imath)\cdot(2+\imath)^2(2-\imath)^2=(1+\imath)\times(2+\imath)^2\cdot(1-\imath)(2-\imath)^2=(-1+7\imath)\cdot(-1-7\imath)=\underline{1^2+7^2}=(1+\imath)(2+\imath)^2\cdot(1-\imath)(2-\imath)^2=(5+5\imath)\cdot(5-5\imath)=\underline{5^2+5^2}$. Thus, there are $\alpha=2+1=3$ soft/hard modes [(5,5) and (1,7) and (7,1)].

$\ell=\mathbf{65}=5\times13=(2+\imath)(2-\imath)\cdot(3+2\imath)(3-2\imath)=(2+\imath)(3+2\imath)\cdot(2-\imath)(3-2\imath)=(4+7\imath)\cdot(4-7\imath)=\underline{4^2+7^2}=(2+\imath)(3-2\imath)\cdot(2-\imath)(3+2\imath)=(8-\imath)\cdot(8+\imath)=\underline{8^2+1^2}$. Thus, there are $\alpha=(1+1)(1+1)=4$ soft/hard modes [(4,7) and (7,4) and (8,1) and (1,8)].

$\ell=\mathbf{234}=2\times13\times3^2$ belongs to the harmonic series sprouting from the seed $s=2\times13=26$ while $\ell=\mathbf{98\,000}=2^4\times5^3\times7^2$ springs forth from $s=5$. $\ell=100=10^2=2^2\times5^2$ produces both soft and hard modes while its seed $s=1$ and sibling sprout $\ell=\mathbf{196}=14^2=2^2\times7^2$ have no soft modes.

VI. CONCLUSION

In the preceding sections we have attempted to fill a lacuna in the acoustical literature pertaining to modal degeneracy in square wave guides. It should be noted that modal degeneracy can also occur in rectangular wave guides with commensurable sides. However, a treatment of this problem leads to a study of the diagonal quadratic form $\ell=m^2+k^2\cdot n^2$. This is of sufficiently greater complexity to warrant a separate treatment. Last, one should bear in mind that Table I may be extended indefinitely using built-in functions of both Mathematica (FactorInteger, Prime, and PrimeQ) and Maple (number theory [ ] and GaussInt [ ]).

[1] F. Pockels, *Über die partielle Differentialgleichung* $\Delta u+k^2u=0$ *(On the Partial Differential Equation* $\Delta u+k^2u=0$*)* (Teubner, Leipzig, 1891).

[2] R. B. Adler, L. J. Chu, and R. M. Fano, *Electromagnetic Energy Transmission and Radiation* (Wiley, New York, 1960).
[3] P. M. Morse and K. U. Ingard, *Theoretical Acoustics* (McGraw-Hill, New York, 1968).
[4] L. H. Donnell, *Beams, Plates, and Shells* (McGraw-Hill, New York, 1976).
[5] B. Riemann, *Partielle Differentialgleichungen und deren Anwendung auf physikalische Fragen (Partial Differential Equations and Their Application to Physical Problems)* (Zweite Auflage, F. Vieweg und Sohn, Braunschweig, 1876).
[6] G. Lamé, *Leçons sur la Théorie Mathématique de l'Élasticité des Corps Solides (Lessons on the Mathematical Theory of the Elasticity of Solid Bodies)*, Deuxième Édition (Gauthier-Villars, Paris, 1866).
[7] Lord Rayleigh, *The Theory of Sound*, 2nd ed. (Dover, New York, 1894).
[8] B. J. McCartin, "A perturbation procedure for nearly rectangular, homogeneously filled, cylindrical waveguides," IEEE Trans. Microwave Guided Wave Lett. **6**, 354–356 (1996), S 1051-8207(96)07485-5.
[9] L. E. Dickson, *History of the Theory of Numbers* (Chelsea, New York, 1952), Vol. II.
[10] E. Grosswald, *Representation of Integers as Sums of Squares* (Springer-Verlag, Berlin, 1985).
[11] G. Birkhoff and S. MacLane, *A Survey of Modern Algebra*, revised ed. (Macmillan, New York, 1953).
[12] R. K. Guy, *Unsolved Problems in Number Theory* 2nd ed. (Springer-Verlag, Berlin, 1994).

A *k*-space method for coupled first-order acoustic propagation equations

Makoto Tabei
Department of Electrical and Computer Engineering, University of Rochester, Rochester, New York 14627

T. Douglas Mast
Applied Research Laboratory, The Pennsylvania State University, University Park, Pennsylvania 16801

Robert C. Waag
Departments of Electrical and Computer Engineering and Radiology, University of Rochester, Rochester, New York 14627

(Received 11 June 2001; accepted for publication 8 October 2001)

A k-space method for large-scale simulation of ultrasonic pulse propagation is presented. The present method, which solves the coupled first-order differential equations for wave propagation in inhomogeneous media, is derived in a simple form analogous to previous finite-difference methods with staggered spatial and temporal grids. Like k-space methods based on second-order wave equations, the present method is exact for homogeneous media, unconditionally stable for ''slow'' $[c(\mathbf{r}) \leq c_0]$ media, and highly accurate for general weakly scattering media. In addition, unlike previous k-space methods, the form of the method allows straightforward inclusion of relaxation absorption and perfectly matched layer (PML) nonreflecting boundary conditions. Numerical examples illustrate the capabilities of the present k-space method. For weakly inhomogeneous media, accurate results are obtained using coarser temporal and spatial steps than possible with comparable finite-difference and pseudospectral methods. The low dispersion of the k-space method allows accurate representation of frequency-dependent attenuation and phase velocity associated with relaxation absorption. A technique for reduction of Gibbs phenomenon artifacts, in which compressibility and exponentially scaled density functions are smoothed by half-band filtering, is introduced. When employed together with this smoothing technique, the k-space method provides high accuracy for media including discontinuities, high-contrast inhomogeneities, and scattering structures smaller than the spatial grid resolution. © *2002 Acoustical Society of America.* [DOI: [10.1121/1.1421344]

PACS numbers: 43.20.Fn, 43.80.Qf, 43.35.Fj [ADP]

I. INTRODUCTION

This paper presents a method for computation of acoustic propagation in inhomogeneous media. The present method is an adaptation of the k-space method originally derived by Bojarski[1,2] and extended by several others.[3–5] As shown in Ref. 6, the k-space method has considerable advantages for large-scale simulations of ultrasonic propagation in soft tissues. The k-space method combines accurate spectral evaluation of spatial derivatives with a temporal iteration procedure that is exact for homogeneous media. For soft tissues, in which local medium properties show small variations around nominal background properties, this method provides excellent efficiency and accuracy compared to other approaches such as finite-difference and pseudospectral methods.[6,7]

Previous formulations of the k-space method for acoustic propagation have numerically solved second-order differential wave equations. Such formulations have some advantages, including conceptual simplicity and computational efficiency, since the acoustic fields are defined by only one independent variable, the acoustic pressure fluctuation, instead of acoustic pressure and vector particle velocity fluctuations. Propagation in inhomogeneous media including density variations can be computed using a simple transformation of the pressure variable (e.g., as in Refs. 5 and 6).

However, several desirable extensions to the k-space method are not possible using the usual second-order formulation. In particular, perfectly matched layer (PML) absorbing boundary conditions are not readily incorporated into current second-order k-space methods, while PMLs are easily formulated for coupled first-order acoustic propagation equations. Additionally, as derived in Ref. 8, the full wave equation incorporating relaxation absorption effects is of order $2+N$, where N is the number of relaxation processes employed. Relaxation effects can be incorporated more simply into numerical methods using coupled first-order acoustic propagation equations.[9]

Here, a k-space method is derived based on the coupled first-order differential equations for linear acoustic propagation. The method accounts for spatially varying sound speed, density, and relaxation absorption processes, and includes PML absorbing boundary conditions. The formulation of this method shows that the k-space method can be regarded as a finite-difference method containing linear correction operators. Use of staggered spatial and temporal grids increases the range of applicability for the method, and facilitates inclusion of relaxation absorption and PML boundary conditions. The close analogy between the method presented here and existing finite-difference methods allows extensions developed for finite-difference methods to be easily applied to the k-space method, and also allows current finite-difference algorithms to be improved by inclusion of the k-space operators introduced here.

The present k-space method is, like previous k-space methods based on second-order wave equations,[6] temporally exact for homogeneous media. For general media, the present method also has accuracy and efficiency advantages similar to previous k-space methods. Numerical results presented here show that the k-space method presented here has the high accuracy and stability characteristics of the original k-space method, including unconditional stability for media with $c(\mathbf{r}) \leqslant c_0$. The low numerical dispersion inherent to the k-space method allows the frequency-dependent absorption and physical dispersion associated with relaxation-process absorption to be accurately modeled.

A method for smoothing of discontinuous scattering media is also presented here. Together with the k-space method, this smoothing method is shown to provide accurate results for strongly scattering media and for media with structures smaller than the grid resolution. Numerical examples also demonstrate the efficiency of the present k-space method for large-scale computations of interest in ultrasonic imaging studies.

II. THEORY

A. Second-order and first-order *k*-space methods

The k-space method derived below is based on the coupled first-order linear acoustic propagation equations for a fluid medium of variable sound speed and density. For a lossless two-dimensional medium, these are[10]

$$\rho(\mathbf{r})\frac{\partial \mathbf{u}(\mathbf{r},t)}{\partial t} = -\nabla p(\mathbf{r},t)$$
$$\frac{1}{\rho(\mathbf{r})\,c(\mathbf{r})^2}\frac{\partial p(\mathbf{r},t)}{\partial t} = -\nabla \cdot \mathbf{u}(\mathbf{r},t), \tag{1}$$

where $\mathbf{u}$ is the (vector) acoustic particle velocity fluctuation with components u_x and u_y, p is the acoustic pressure fluctuation, $\rho(\mathbf{r})$ is the density of the medium, $c(\mathbf{r})$ is the sound speed of the medium, and $\mathbf{r}$ denotes the vector coordinate (x,y).

Many numerical methods for acoustic wave propagation have been based on Eq. (1). For example, in Ref. 11, ultrasonic propagation in an abdominal model was computed using a finite-difference method applied directly to the coupled equations.

The second-order wave equation corresponding to Eq. (1) is[10]

$$\nabla \cdot \left(\frac{1}{\rho(\mathbf{r})}\nabla p(\mathbf{r},t)\right) - \frac{1}{\rho(\mathbf{r})\,c(\mathbf{r})^2}\frac{\partial^2 p(\mathbf{r},t)}{\partial t^2} = 0. \tag{2}$$

This equation can be solved numerically by the k-space method. Below, a brief sketch of the k-space solution to Eq. (2) will be given and this solution will be analyzed to obtain a corresponding k-space method for coupled first-order propagation equations. For simplicity, the derivation will assume sound speed and density are constant, i.e., $\rho(\mathbf{r}) = \rho_0$ and $c(\mathbf{r}) = c_0$. A general derivation of the second-order k-space method is given in Ref. 6, while the first-order k-space method is straightforwardly extended to inhomogeneous media, as seen below.

For bandlimited signals such as typical ultrasonic pulses, very accurate spatial derivatives can be obtained by Fourier transformation of the pressure field.[12] This is the principle behind pseudospectral methods like that described in Ref. 13, in which the spatial derivatives from Eq. (1) are evaluated using discrete Fourier transformation and temporal iteration is performed using a fourth-order Adams–Bashforth/Adams–Moulton scheme. For the case of homogeneous sound speed and density, Eq. (2) can be written in the spatial-frequency domain as

$$\frac{\partial^2 \hat{p}(\mathbf{k},t)}{\partial t^2} = -c_0^2 k^2 \hat{p}(\mathbf{k},t), \tag{3}$$

where $\hat{p}(\mathbf{k},t)$ is the two-dimensional spatial Fourier transform of the acoustic pressure fluctuation $p(\mathbf{r},t)$.

A discrete form of the left-hand side of Eq. (3), obtained using a second-order-accurate finite-difference scheme, yields a crude pseudospectral method, expressed as

$$\frac{p(\mathbf{r},t+\Delta t) - 2p(\mathbf{r},t) + p(\mathbf{r},t-\Delta t)}{(\Delta t)^2} = -c_0^2\,\mathbf{F}^{-1}[k^2\,\mathbf{F}[p(\mathbf{r},t)]], \tag{4}$$

where $\mathbf{F}$ represents the two-dimensional spatial Fourier transform. In numerical implementations of Eq. (4), the spatial derivatives from the right-hand side of Eq. (3) are accurately represented using discrete Fourier transformation. Still, the discrete representation of the temporal derivative on the left-hand side is significantly dispersive. Current pseudospectral methods[12,13] typically use higher-order temporal integration schemes to decrease dispersion errors. However, for the homogeneous-medium case, temporal iteration can be performed exactly (e.g., without any dispersion) using the $k-t$ space scheme[6]

$$\frac{\hat{p}(\mathbf{k},t+\Delta t) - 2\,\hat{p}(\mathbf{k},t) + \hat{p}(\mathbf{k},t-\Delta t)}{(\Delta t)^2\,\mathrm{sinc}(c_0 \Delta t\,k/2)^2} = -(c_0 k)^2 \hat{p}(\mathbf{k},t), \tag{5}$$

where $\mathrm{sinc}(\mu) \equiv \sin(\mu)/(\mu)$. The temporal iteration scheme of Eq. (5) is mathematically equivalent to the scheme originally presented in Ref. 2. (A similar exact discretization for the linear part of the Korteweg–de Vries equation was presented in Ref. 14.)

As discussed in Ref. 6, the temporal exactness of this scheme follows from an exact discrete representation of the harmonic-oscillator differential equation, described in Ref. 15. Temporal iteration can be performed in the spatial-frequency domain, as done in Ref. 6 using a generalized form of Eq. (5). Alternatively, an equivalent iteration method employing the real-space pressure can be obtained by inverse spatial Fourier transformation of Eq. (5). The resulting iteration formula is

$$\frac{p(\mathbf{r},t+\Delta t)-2\,p(\mathbf{r},t)+p(\mathbf{r},t-\Delta t)}{(\Delta t)^2}$$
$$=-c_0^2\,\mathbf{F}^{-1}[k^2\,\mathrm{sinc}(c_0\Delta t\,k/2)^2\,\mathbf{F}[p(\mathbf{r},t)]]. \tag{6}$$

Below, the operation on the right-hand side of Eq. (6) is called the second-order k-space operator. This operator is defined as

$$[\nabla^{(c_0\Delta t)}]^2 p(\mathbf{r},t)\equiv-\mathbf{F}^{-1}[k^2\,\mathrm{sinc}(c_0\Delta t\,k/2)^2\mathbf{F}[p(\mathbf{r},t)]]; \tag{7}$$

the $(c_0\Delta t)$ superscript is meant to signify that the operators employed, while similar to the standard gradient operator, are also functions of the parameter $c_0\Delta t$.

The form of Eq. (6) suggests that the second-order k-space method can be considered a corrected finite-difference method in which the spatial Laplacian is replaced by the k-space operator. However, the k-space operator of Eq. (7) incorporates not only spectral evaluation of the Laplacian, but also a temporal correction term associated with the $k-t$ space iterator of Eq. (5).

To construct a k-space method for coupled first-order wave propagation equations, the second-order k-space operator can be factored into parts associated with each spatial direction. Below, this procedure is carried out for the two-dimensional case. An appropriate factorization is given by the first-order k-space operators

$$\begin{aligned}
\frac{\partial p(\mathbf{r},t)}{\partial^{(c_0\Delta t)^+}x}&\equiv\mathbf{F}^{-1}[ik_x\,e^{ik_x\Delta_x/2}\,\mathrm{sinc}(c_0\Delta t\,k/2)\mathbf{F}[p(\mathbf{r},t)]],\\
\frac{\partial p(\mathbf{r},t)}{\partial^{(c_0\Delta t)^+}y}&\equiv\mathbf{F}^{-1}[ik_y\,e^{ik_y\Delta_y/2}\,\mathrm{sinc}(c_0\Delta t\,k/2)\mathbf{F}[p(\mathbf{r},t)]],\\
\frac{\partial p(\mathbf{r},t)}{\partial^{(c_0\Delta t)^-}x}&\equiv\mathbf{F}^{-1}[ik_x\,e^{-ik_x\Delta_x/2}\,\mathrm{sinc}(c_0\Delta t\,k/2)\mathbf{F}[p(\mathbf{r},t)]],\\
\frac{\partial p(\mathbf{r},t)}{\partial^{(c_0\Delta t)^-}y}&\equiv\mathbf{F}^{-1}[ik_y\,e^{-ik_y\Delta_y/2}\,\mathrm{sinc}(c_0\Delta t\,k/2)\mathbf{F}[p(\mathbf{r},t)]],
\end{aligned} \tag{8}$$

so that

$$\left(\frac{\partial}{\partial^{(c_0\Delta t)^+}x}\,\frac{\partial}{\partial^{(c_0\Delta t)^-}x}+\frac{\partial}{\partial^{(c_0\Delta t)^+}y}\,\frac{\partial}{\partial^{(c_0\Delta t)^-}y}\right)p(\mathbf{r},t)$$
$$=[\nabla^{(c_0\Delta t)}]^2 p(\mathbf{r},t). \tag{9}$$

The spatial-frequency components k_x and k_y are defined such that $k^2=k_x^2+k_y^2$.

Using the operators of Eq. (8) within Eq. (1) enables construction of a first-order k-space method equivalent to Eq. (6). Application of the exponential coefficients from Eq. (8) requires the acoustic particle velocity variables u_x and u_y to be evaluated on grid points staggered by distances of $\Delta x/2$ and $\Delta y/2$, respectively. The resulting algorithm is

$$\begin{aligned}
\frac{u_x(\mathbf{r}_1,t^+)-u_x(\mathbf{r}_1,t^-)}{\Delta t}&=-\frac{1}{\rho(\mathbf{r}_1)}\,\frac{\partial p(\mathbf{r},t)}{\partial^{(c_0\Delta t)^+}x},\\
\frac{u_y(\mathbf{r}_2,t^+)-u_y(\mathbf{r}_2,t^-)}{\Delta t}&=-\frac{1}{\rho(\mathbf{r}_2)}\,\frac{\partial p(\mathbf{r},t)}{\partial^{(c_0\Delta t)^+}y},\\
\frac{p(\mathbf{r},t+\Delta t)-p(\mathbf{r},t)}{\Delta t}&=-\rho(\mathbf{r})\,c(\mathbf{r})^2\left(\frac{\partial u_x(\mathbf{r}_1,t^+)}{\partial^{(c_0\Delta t)^-}x}+\frac{\partial u_y(\mathbf{r}_2,t^+)}{\partial^{(c_0\Delta t)^-}y}\right),
\end{aligned} \tag{10}$$

where

$$\begin{aligned}
&\mathbf{r}_1\equiv(x+\Delta x/2,y),\quad \mathbf{r}_2\equiv(x,y+\Delta y/2),\\
&t^+\equiv t+\Delta t/2,\ \text{and}\ \ t^-\equiv t-\Delta t/2.
\end{aligned} \tag{11}$$

In Eq. (10), the coefficients c_0 and ρ_0 have been replaced by the spatially varying sound speed and density $c(\mathbf{r})$ and $\rho(\mathbf{r})$. Spatial staggering in Eq. (10) is implicitly incorporated into the spatial derivative operators employed. For example, the operators $\partial/\partial^{(c_0\Delta t)^+}x$ and $\partial/\partial^{(c_0\Delta t)^-}x$ defined by Eq. (8) correspond, by the shift property of Fourier transformation, to derivatives evaluated after spatial shifts of $\Delta x/2$ and $-\Delta x/2$, respectively.

Staggered temporal grids, discussed in the following section, have also been employed in Eq. (10). Notable is that the ordering of $(c_0\Delta t)^+$ and $(c_0\Delta t)^-$ operators is arbitrary depending on how the staggered grids are configured; however, for solution of coupled equations, the operators should be used in pairs such that the spatial shifting operations cancel out over any temporal interval of length Δt. Rationale for the use of spatial and temporal staggering is given in the following section.

The k-space method of Eq. (10) is straightforwardly shown to be equivalent to Eq. (5) for $c(\mathbf{r})=c_0$ and $\rho(\mathbf{r})=\rho_0$. Thus, this first-order k-space scheme is temporally exact for homogeneous media. As shown below, the method also provides high accuracy for media with properties are close to the background values, and in conjunction with an appropriate smoothing algorithm, yields high accuracy even for media including high-contrast discontinuities.

Theoretical stability limits for the present k-space method can be computed as described in Ref. 6; given neglect of density variations and assumption of a worst-case sound-speed variation $c(\mathbf{r})=c_{\max}$, the results are identical to those for the second-order k-space method. The resulting theoretical stability boundary is

$$\sin\frac{\pi\,\mathrm{CFL}}{2}\leqslant\frac{c_0}{c_{\max}}, \tag{12}$$

where CFL denotes the Courant–Friedrichs–Lewy number $c_0\Delta t/\Delta x$. Thus, like the original k-space method,[6] the k-space method derived above is also expected to be unconditionally stable for media with $c(\mathbf{r})\leqslant c_0$ everywhere.

As with the second-order k-space method, the first-order method of Eq. (10) can be regarded as a finite-difference method with correction factors that appear within the spatial derivative terms. The k-space algorithm of Eq. (10) is analogous to standard second-order-accurate finite-difference methods for computation of acoustic wave propagation[9,16] except that second-order-accurate spatial derivatives have been replaced by the k-space operators of Eq. (8) that incorporate spectral spatial accuracy as well as corrected temporal iteration.

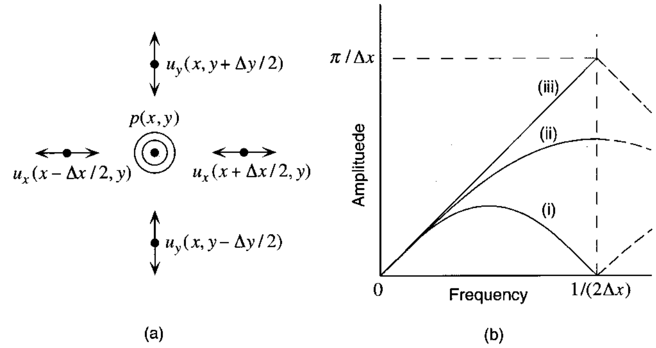

FIG. 1. Characteristics of discrete spatial derivative operators. (a) Sampling locations for spatially staggered grid. (b) Spatial-frequency response of first-derivative operators: (i) nonstaggered grid; (ii) staggered grid; (iii) ideal.

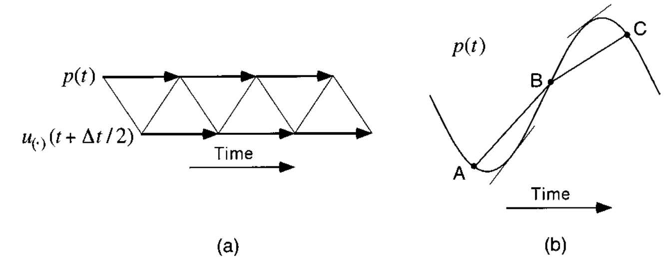

FIG. 2. Characteristics of discrete time derivative operators. (a) Time-staggered sampling for acoustic pressure and particle velocity. (b) Derivatives estimated using a staggered time scheme and true derivatives evaluated at the center of the time step.

B. Properties of staggered spatial and temporal grids

The temporal and spatial sampling configuration employed in the k-space method of Eq. (10) is directly analogous to staggered-space, staggered-time schemes employed in previous finite-difference methods.[9,16] Such staggered configurations are known to increase accuracy and stability for discrete representations of odd-order spatial and temporal derivatives.[12] For example, because the discrete Fourier transform is implicitly periodic, Gibbs phenomenon (ringing) artifacts result if the coefficients on the right-hand side of Eq. (8) have different values at the maximum spatial frequency $\pi/\Delta x$ and the minimum negative spatial frequency $-\pi/\Delta x$. The coefficient ik (which would correspond to a nonstaggered spatial grid) has a jump discontinuity of magnitude $2\pi/\Delta x$ at the transition between $k=\pi/\Delta x$ and $k=-\pi/\Delta x$. Coefficients of the form used in Eqs. (8) remove this discontinuity and, thus, can substantially reduce numerical artifacts in some cases, such as when the wave field is spatially undersampled. Accuracy and stability are particularly increased for media containing large discontinuities.[17]

Although staggering slightly increases the complexity of the k-space algorithm, the benefit from spatial staggering can be easily understood by examining the physical relationship between sound pressure and particle velocity. Figure 1(a) represents the spatial sampling locations for sound pressure and particle velocity in the present staggered grid. The arrow at each sampling location indicates the direction of particle motion represented by each parameter. In this configuration, a local change in sound pressure $p(x,y)$ immediately affects the adjacent particle velocities. On the contrary, in a nonstaggered grid configuration, in which p, u_x, and u_y are all sampled at the same grid points, symmetry prohibits a local change in sound pressure from immediately affecting the particle velocity components sampled at the same position. This effect limits the accuracy of computations for high-spatial-frequency components of the wave field.

Figure 1(b) shows the spatial-frequency response of the second-order-accurate discrete finite-difference operators for the first-order spatial derivative. Curve (i) shows the response for a nonstaggered center difference configuration, curve (ii) shows the corresponding response for the staggered grid center difference configuration, and curve (iii) shows the ideal frequency response for the continuous first-order derivative. Finite-difference schemes with higher-order accuracy show improved high-spatial-frequency response. Spectral computation of the first derivative on a staggered spatial grid, performed implicitly within the present k-space method, achieves this ideal frequency response up to the spatial Nyquist frequency $\pi/\Delta x$.

Figure 2 illustrates the characteristics of the temporal scheme employed. In panel (a), the temporal iteration process is shown for the staggered-time marching scheme. Because the time step is interleaved, time derivatives are evaluated based on values of spatial derivatives at the center of each time step. This staggering minimizes error when a crude time integration (Euler) scheme is employed. Panel (b) shows the difference between true derivatives (slopes of the tangential lines) and staggered finite differences (slopes of the straight lines between A, B, and C) at the center of each time step. Although time staggering reduces the error between the finite difference and the actual derivative, staggered finite-difference schemes still incur significant error with large time steps. This error is compensated in the k-space method by introducing a correction factor that leads to a temporally exact solution for a medium with constant sound speed. Although a temporally exact discrete solution can also be obtained using a nonstaggered grid,[15] staggered grids allow the necessary compensation to be performed using a single multiplicative factor. Use of a staggered time scheme also facilitates modeling of absorption, as shown in the next section. Thus, temporal staggering is important to the first-order k-space method.

C. Relaxation absorption and perfectly matched layers

The close analogy between the k-space method of Eq. (10) and standard finite-difference techniques[16] allows easy addition of features such as perfectly matched layer (PML) absorbing boundary conditions and relaxation-process absorption to the present k-space method.

In the following, the acoustic pressure fluctuation $p(\mathbf{r},t)$ is split into x and y components, $p(\mathbf{r},t)=p_x(\mathbf{r},t)+p_y(\mathbf{r},t)$. This splitting allows definition of direction-dependent absorption, which is necessary for incorporation of the PML.[9] Following the procedure applied to the finite-difference method in Ref. 9, the field equations are then written as a group of coupled first-order equations, with decay terms corresponding to relaxation absorbtion and to the PML. Discrete forms of these field equations are defined in a manner that provides high accuracy in the presence of large absorption.[9]

The (continuous) field equations for a PML medium with relaxation absorption can be written as

$$\rho(\mathbf{r})\left(\frac{\partial u_x(\mathbf{r},t)}{\partial t}+\alpha_x(\mathbf{r})\,u_x(\mathbf{r},t)\right)=-\frac{\partial(p_x(\mathbf{r},t)+p_y(\mathbf{r},t))}{\partial x}, \tag{13}$$

$$\rho(\mathbf{r})\left(\frac{\partial u_y(\mathbf{r},t)}{\partial t}+\alpha_y(\mathbf{r})\,u_y(\mathbf{r},t)\right)=-\frac{\partial(p_x(\mathbf{r},t)+p_y(\mathbf{r},t))}{\partial y}, \tag{14}$$

$$\kappa(\mathbf{r},t)\otimes\left(\frac{\partial p_x(\mathbf{r},t)}{\partial t}+\alpha_x(\mathbf{r})\,p_x(\mathbf{r},t)\right)=-\frac{\partial u_x(\mathbf{r},t)}{\partial x}, \tag{15}$$

$$\kappa(\mathbf{r},t)\otimes\left(\frac{\partial p_y(\mathbf{r},t)}{\partial t}+\alpha_y(\mathbf{r})\,p_y(\mathbf{r},t)\right)=-\frac{\partial u_y(\mathbf{r},t)}{\partial y}, \tag{16}$$

where $\alpha_x(\mathbf{r})$ and $\alpha_y(\mathbf{r})$ are dispersionless absorption parameters employed only within the PML and the $\otimes$ operator denotes temporal convolution. Equations (15) and (16) contain a generalized compressibility,[8] defined as

$$\kappa(\mathbf{r},t)\equiv\kappa_\infty(\mathbf{r})\,\delta(t)+\sum_{i=1}^{N}\frac{\kappa_i(\mathbf{r})}{\tau_i(\mathbf{r})}e^{-t/\tau_i(\mathbf{r})}H(t), \tag{17}$$

where $\kappa_\infty(\mathbf{r})$ is the usual compressibility $1/[\rho(\mathbf{r})c(\mathbf{r})^2]$, $\tau_i(\mathbf{r})$ is the relaxation time for the ith relaxation process, $\kappa_i(\mathbf{r})$ is the relaxation modulus for the ith-order relaxation process, with units of compressibility, and $H(t)$ is the Heaviside step function. The integration (convolution) terms in Eqs. (15) and (16) make these equations equivalent to second-order differential equations in time. The convolution terms can be simplified using properties of the Dirac δ function and Heaviside step function that appear in the generalized compressibility (17) as well as identities for convolutions involving time derivatives.[9] Thus, for example, the left-hand side of Eq. (15) can be written as

$$\begin{aligned}&\kappa_\infty(\mathbf{r})\left(\frac{\partial p_x(\mathbf{r},t)}{\partial t}+\alpha_x(\mathbf{r})\,p_x(\mathbf{r},t)\right)+\sum_{i=1}^{N}\frac{\kappa_i(\mathbf{r})}{\tau_i(\mathbf{r})}p_x(\mathbf{r},t)\\&\quad+\left[\sum_{i=1}^{N}\frac{\kappa_i(\mathbf{r})}{\tau_i(\mathbf{r})}e^{-t/\tau_i(\mathbf{r})}H(t)\left(-\frac{1}{\tau_i(\mathbf{r})}+\alpha_x(\mathbf{r})\right)\right]\\&\quad\otimes p_x(\mathbf{r},t).\end{aligned}$$

The last term in this latter expression is still a convolution of two time-dependent functions, and this form presents difficulties for numerical implementation. The difficulties can be resolved by introducing a state variable, which allows Eqs. (13)–(16) to be rewritten as a set of simultaneous first-order differential equations. The state variable employed here is a filtered version of the acoustic pressure fluctuation, defined as

$$S_i^{(\cdot)}(\mathbf{r},t)\equiv\left(\frac{e^{-t/\tau_i(\mathbf{r})}}{\tau_i(\mathbf{r})}H(t)\right)\otimes p_{(\cdot)}(\mathbf{r},t), \tag{18}$$

where $(\cdot)$ denotes x or y.

Using the state variables defined by Eq. (18), the continuous field equations are rewritten as the coupled first-order differential equations

$$\begin{aligned}&\frac{\partial u_x(\mathbf{r},t)}{\partial t}+\alpha_x(\mathbf{r})\,u_x(\mathbf{r},t)=-\frac{1}{\rho(\mathbf{r})}\frac{\partial(p_x(\mathbf{r},t)+p_y(\mathbf{r},t))}{\partial x},\\&\frac{\partial u_y(\mathbf{r},t)}{\partial t}+\alpha_y(\mathbf{r})\,u_y(\mathbf{r},t)=-\frac{1}{\rho(\mathbf{r})}\frac{\partial(p_x(\mathbf{r},t)+p_y(\mathbf{r},t))}{\partial y},\\&\frac{\partial p_x(\mathbf{r},t)}{\partial t}+\mu_x(\mathbf{r})\,p_x(\mathbf{r},t)\\&\quad=-\frac{1}{\kappa_\infty(\mathbf{r})}\left[\frac{\partial u_x(\mathbf{r},t)}{\partial x}-\sum_{i=1}^{N}\nu_i^x(\mathbf{r})\,S_i^x(\mathbf{r},t)\right],\\&\frac{\partial p_y(\mathbf{r},t)}{\partial t}+\mu_y(\mathbf{r})\,p_y(\mathbf{r},t)\\&=-\frac{1}{\kappa_\infty(\mathbf{r})}\left[\frac{\partial u_y(\mathbf{r},t)}{\partial y}-\sum_{i=1}^{N}\nu_i^y(\mathbf{r})S_i^y(\mathbf{r},t)\right],\\&\frac{\partial S_i^x(\mathbf{r},t)}{\partial t}+\frac{1}{\tau_i(\mathbf{r})}S_i^x(\mathbf{r},t)=\frac{p_x(\mathbf{r},t)}{\tau_i(\mathbf{r})},\\&\frac{\partial S_i^y(\mathbf{r},t)}{\partial t}+\frac{1}{\tau_i(\mathbf{r})}S_i^y(\mathbf{r},t)=\frac{p_y(\mathbf{r},t)}{\tau_i(\mathbf{r})},\end{aligned} \tag{19}$$

where

$$\mu_{(\cdot)}(\mathbf{r})\equiv\frac{1}{\kappa_\infty(\mathbf{r})}\sum_{i=1}^{N}\frac{\kappa_i(\mathbf{r})}{\tau_i(\mathbf{r})}+\alpha_{(\cdot)}(\mathbf{r}), \tag{20}$$

and

$$\nu_i^{(\cdot)}(\mathbf{r})\equiv\frac{\kappa_i(\mathbf{r})}{\tau_i(\mathbf{r})}-\kappa_i(\mathbf{r})\,\alpha_{(\cdot)}(\mathbf{r}). \tag{21}$$

Each of Eqs. (19) has the form

$$\frac{\partial R(\mathbf{r},t)}{\partial t}+\beta R(\mathbf{r},t)=Q(\mathbf{r},t), \tag{22}$$

where β is a constant that controls the decay of a field variable R. Following Ref. 9, the field equations can be transformed into a form that allows larger attenuations without numerical instability. This form is

$$\frac{\partial(e^{\beta t}R(\mathbf{r},t))}{\partial t}=e^{\beta t}Q(\mathbf{r},t). \tag{23}$$

Equations of this form can be discretized using the time-staggered scheme

$$\frac{e^{\beta(t+\Delta t)}R(\mathbf{r},t+\Delta t)-e^{\beta t}R(\mathbf{r},t)}{\Delta t}=e^{\beta(t+\Delta t/2)}Q(\mathbf{r},t+\Delta t/2), \tag{24}$$

and the equivalent form

$$R(\mathbf{r},t+\Delta t)=e^{-\beta\Delta t/2}(e^{-\beta\Delta t/2}R(\mathbf{r},t)+\Delta t\,Q(\mathbf{r},t+\Delta t/2)). \tag{25}$$

To obtain the final k-space scheme including PML and relaxation absorption, Eq. (25) is applied directly to Eqs.

(19). The spatial derivatives are replaced by the k-space operators (8), and the particle velocity variables u_x and u_y are evaluated on staggered spatial and temporal grids, as in the lossless algorithm of Eq. (10). The state variables $S_i^{(\cdot)}$ are evaluated using a staggered-time scheme. The final discrete field equations, written in a form suitable for direct numerical implementation, are

$$
\begin{aligned}
u_x(\mathbf{r}_1,t^+) &= e^{-\alpha_x(\mathbf{r}_1)\Delta t/2}\Bigg[e^{-\alpha_x(\mathbf{r}_1)\Delta t/2} u_x(\mathbf{r}_1,t^-) \\
&\quad - \frac{\Delta t}{\rho(\mathbf{r}_1)}\left(\frac{\partial(p_x(\mathbf{r},t)+p_y(\mathbf{r},t))}{\partial^{(c_0\Delta t)^+}x}\right)\Bigg], \\
u_y(\mathbf{r}_2,t^+) &= e^{-\alpha_y(\mathbf{r}_2)\Delta t/2}\Bigg[e^{-\alpha_y(\mathbf{r}_2)\Delta t/2} u_y(\mathbf{r}_2,t^-) \\
&\quad - \frac{\Delta t}{\rho(\mathbf{r}_2)}\left(\frac{\partial(p_x(\mathbf{r},t)+p_y(\mathbf{r},t))}{\partial^{(c_0\Delta t)^+}y}\right)\Bigg], \\
p_x(\mathbf{r},t+\Delta t) &= e^{-\mu_x(\mathbf{r})\Delta t/2}\Bigg[e^{-\mu_x(\mathbf{r})\Delta t/2} p_x(\mathbf{r},t) - \frac{\Delta t}{\kappa_\infty(\mathbf{r})} \\
&\quad \times\left(\frac{\partial u_x(\mathbf{r}_1,t^+)}{\partial^{(c_0\Delta t)^-}x} - \sum_{i=1}^{N} \nu_i^x(\mathbf{r})\, S_i^x(\mathbf{r},t^+)\right)\Bigg], \\
p_y(\mathbf{r},t+\Delta t) &= e^{-\mu_y(\mathbf{r})\Delta t/2}\Bigg[e^{-\mu_y(\mathbf{r})\Delta t/2} p_y(\mathbf{r},t) - \frac{\Delta t}{\kappa_\infty(\mathbf{r})} \\
&\quad \times\left(\frac{\partial u_y(\mathbf{r}_2,t^+)}{\partial^{(c_0\Delta t)^-}y} - \sum_{i=1}^{N} \nu_i^y(\mathbf{r})\, S_i^y(\mathbf{r},t^+)\right)\Bigg], \\
S_i^x(\mathbf{r},t^+) &= e^{-\Delta t/[2\tau_i(\mathbf{r})]}\left[e^{-\Delta t/[2\tau_i(\mathbf{r})]} S_i^x(\mathbf{r},t^-) + \Delta t\,\frac{p_x(\mathbf{r},t)}{\tau_i(\mathbf{r})}\right], \\
S_i^y(\mathbf{r},t^+) &= e^{-\Delta t/[2\tau_i(\mathbf{r})]}\left[e^{-\Delta t/[2\tau_i(\mathbf{r})]} S_i^y(\mathbf{r},t^-) + \Delta t\,\frac{p_y(\mathbf{r},t)}{\tau_i(\mathbf{r})}\right],
\end{aligned}
\tag{26}
$$

where the quantities μ and ν are defined by Eqs. (20) and (21), respectively.

This scheme provides spatial derivatives with spectral accuracy, temporal iteration that is exact for a homogeneous, lossless medium, and additional corrections that allow stable computations to be made in the presence of large absorption coefficients. The incorporation of relaxation processes allows simulation of realistic absorption in tissue, while use of the PML allows accurate computations to be carried out using small grid sizes. As shown below, the combination of these characteristics results in a powerful and flexible method for computation of ultrasonic propagation over long distances in inhomogeneous media such as soft tissues.

III. NUMERICAL METHODS

Numerical implementation of the present k-space method was accomplished using Eq. (26) directly. The k-space operators of Eqs. (8) were evaluated using two-dimensional discrete Fourier transforms, implemented using a fast Fourier transform (FFT) method.[18]

Initial conditions were chosen to specify a pulsatile incident plane wave with sinusoidal time variation and a Gaussian envelope. Boundary conditions were given by the perfectly matched layer (PML) on all sides of the grid. The absorption parameters α_x and α_y were tapered within the PMLs using formulas of the form[19]

$$\alpha_x = A\,\frac{c_0}{\Delta x}\left(\frac{x-x_0}{x_{\max}-x_0}\right)^4, \tag{27}$$

where x_0 is the coordinate at the inner edge of the PML, $x_{\max}$ is the coordinate at the outer edge of the grid, and A is the maximum absorption per cell, in nepers, within the PML. A PML thickness of 9 grid points, together with a maximum PML absorption A of 4 nepers per cell, were found to be sufficient to reduce boundary reflection and transmission coefficients below -90 dB for normally incident waves.

Relaxation-process absorption was implemented using two relaxation processes. The parameters κ_i and τ_i were chosen to approximate a linear dependence of absorption on frequency over the pulse bandwidth, using the formula for frequency-dependent absorption given in Ref. 8. The relaxation times chosen were

$$\tau_1 = \frac{1}{5\,f_{\max}}, \quad \tau_2 = \frac{2}{f_{\max}}, \tag{28}$$

where $f_{\max}$ is the nominal maximum frequency of interest. For a maximum frequency of 5 MHz, these are $\tau_1 = 40$ ns and $\tau_2 = 400$ ns. Given this choice of relaxation times, an absorption frequency dependence of 0.5 dB/cm/MHz is best approximated (in a least-squares sense) for the frequency range $0 < f < 5$ MHz by the compressibility coefficients $\kappa_1 = 0.004\,749\,\kappa_\infty$ and $\kappa_2 = 0.004\,562\,\kappa_\infty$.

Benchmark computations analogous to those described in Ref. 6 were carried out to test the accuracy and stability of the present k-space method. As in Ref. 6, time-domain scattered fields for cylindrical test objects were computed and quantitatively compared to an exact solution[20] using an L^2 error metric.[21] The primary test object was, as in Ref. 6, a cylinder with radius 2.0 mm and acoustic properties of human fat ($c = 1.478$ mm/μs, $\rho = 0.950$ g/cm^3)[11] in a background medium with acoustic properties of water at body temperature ($c = 1.524$ mm/μs, $\rho = 0.993$ g/cm^3). The incident pulse was a plane-wave with Gaussian temporal characteristics, a center frequency of 2.5 MHz, a temporal Gaussian parameter $\sigma = 0.25\,\mu$s, which corresponds to a -6-dB bandwidth of 1.5 MHz, and a central starting position of $x = -4.5$ mm at time zero. Time histories of the total pressure field were recorded, at 128 equally spaced ''measurement'' points spanning a circle of radius 2.5 mm concentric to the cylinder, using the interpolation method described in Ref. 6. Another benchmark employed the same configuration except that the cylinder had the density and sound speed of human bone ($c = 3.540$ mm/μs, $\rho = 1.990$ g/cm^3).[11]

In some cases, model media were smoothed before the computation to reduce errors associated with aliasing caused by discontinuities. Smoothing was applied by filtering analytic Fourier transforms of the inhomogeneities considered using the half-band spatial-frequency filter described in Ref. 6. This filter was found to give the most satisfactory results when applied to the quantities $\kappa_\infty(\mathbf{r})$ and $\rho(\mathbf{r})^{-\beta}$, where β is a small coefficient. The accuracy of computations was found not to depend strongly on the value of β employed; the value $\beta=1/6$ was used in the computations reported here.

A specific test of the smoothing method was implemented by computing scattering from a point (wire) scatterer with dimensions less than the grid resolution. The test object employed in this case was a point-like scatterer with acoustic properties of human bone ($c=3540$ m/s, $\rho=1.990$ g/cm^3) and a radius of 20 μm. Computations were performed with a spatial step of $\Delta x=0.0833$ mm (four points per nominal minimum wavelength of 0.333 mm) and a Courant–Friedrichs–Lewy number (CFL$\equiv c_0\Delta t/\Delta x$) of 0.1. For a k-space computation with smoothing, the model medium was obtained by the spatial-frequency filtering procedure described above applied to the analytic Fourier transform of the subresolution scatterer. For comparison, a computation using a discrete single-grid-point scatterer was also carried out. In this case, the scatterer sound speed and density were decreased so that the compressibility contrast γ_κ and the density contrast γ_ρ decreased in proportion to the relative increase in area, which corresponds (for a scatterer of dimensions much smaller than the wavelength) to constant scattering strength.[20] For a scatterer area of 0.0833 $\times 0.0833$ mm^2 (one grid point), this corresponds to a sound speed of 1.5897 mm/μs and a density of 1.0921 g/cm^3. Computational configurations were the same as for the 2.0-mm radius cylinder benchmarks, except that scattered fields (determined by subtracting the computed incident field in the absence of the scatterer) instead of total fields were compared to the corresponding exact solutions.

Implementation of relaxation absorption was tested in the k-space method by computing propagation of a plane-wave pulse in an absorbing medium. The pulse employed was a Gaussian-modulated sinusoid with a temporal Gaussian parameter of 0.25 μs. Propagation of this pulse was computed for a medium with absorption of 0.5 dB/cm/MHz (parameters τ_0, τ_1, κ_0, and κ_1 as given above), using a spatial step of $\Delta x=0.0833$ mm (4 points per nominal minimum wavelength). Waveforms were recorded at virtual measurement locations separated by 5 mm along the direction of propagation. The attenuation for the computed propagation was determined numerically as a function of frequency from the ratio of the two-pulse spectra, while the phase speed was determined numerically from the frequency-dependent phase change between the two pulses. These computed values were then compared with theoretical values, given by formulas available in Ref. 8.

An example computation, illustrating the performance of the present k-space method for large-scale problems relevant to ultrasonic imaging, was undertaken using a model tissue-mimicking phantom. This phantom is a 48-mm-diameter cylinder ($c=1.567$ mm/μs, $\rho=1.040$ g/cm^3) with two internal 10-mm diameter cylinders ($c=1.465$ mm/μs, $\rho=0.0940$ g/cm^3) and three internal 0.2-mm diameter wires ($c=2.600$ mm/μs, $\rho=1.120$ g/cm^3) in a background medium with properties of water ($c=1.509$ mm/μs, $\rho=0.997$ g/cm^3). The 48-mm cylinder also contained simulated random scatterers, implemented by applying a Gaussian random perturbation with rms amplitude 1% to the compressibility. The internal 10-mm cylinders and wires were not perturbed in this manner. The incident plane wave had a center frequency of 2.5 MHz, a -6-dB bandwidth of 1.7 MHz, and a propagation direction of 37° from the x axis, and was apodized using the window

$$A(\xi)=\{\mathrm{erf}[5(\xi+w_1/2+w_2/2)/w_2] - \mathrm{erf}[5(\xi-w_1/2-w_2/2)/w_2]\}/2, \tag{29}$$

where erf is the error function and ξ is an azimuthal distance along the initial wavefront. This window approximates a spatially limited plane wave of the width w_1 with tapered ends of width w_2. The window parameters employed for this example were $w_1=48$ mm (the diameter of the phantom) and $w_2=6$ mm. The grid size employed was 768×768 with a spatial step of 0.12 mm and a time step of 0.02 μs (CFL $=0.25$ based on the background sound speed).

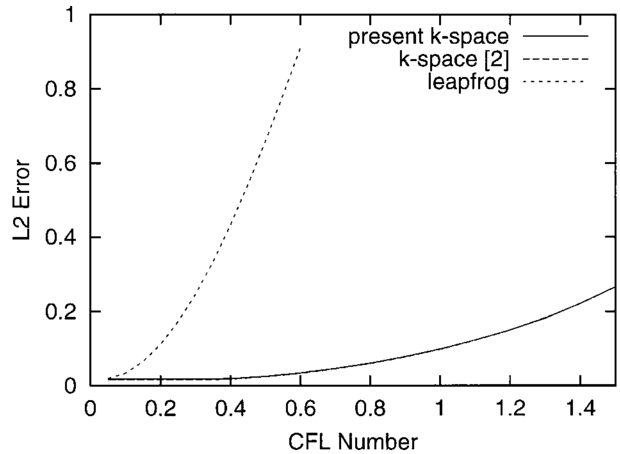

FIG. 3. Time-domain comparison of accuracy for the k-space and leapfrog pseudospectral methods as a function of CFL number. Each test used the ''fat'' cylinder of 2.0 mm radius and a spatial step size of 4 points per minimum wavelength.

IV. NUMERICAL RESULTS

The previous k-space method based on the second-order wave equation[2,5,6] has been shown in Refs. 6 and 7 to provide high accuracy for weakly scattering media. Spectral evaluation of spatial derivatives provides much higher accuracy than typical finite-difference methods for comparable spatial steps. The $k-t$ space iteration scheme of Ref. 2 provides unconditionally stable computations for media with $c(\mathbf{r})\leqslant c_0$ (Ref. 6) and allows large time steps to be employed while maintaining accuracy higher than comparable pseudospectral methods.[6,7]

Not surprisingly, the k-space method described here, which is based on coupled first-order wave propagation equations, has numerical properties very similar to those of the original k-space method. Figures 3 and 4, similar to Figs. 2 and 3 of Ref. 6, show the time-domain L^2 error as a function of the spatial and temporal sampling parameters. Figure 3, which shows computations made using the 2.0-mm-radius ''fat'' cylinder described above and a spatial step size of 4 points per minimum wavelength, show that the present k-space method exhibits temporal accuracy almost identical

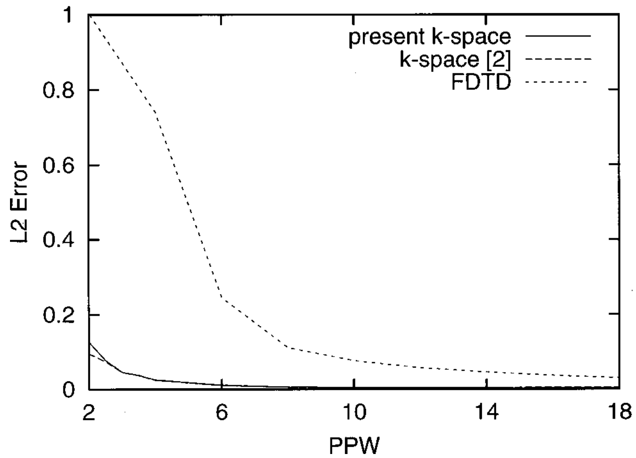

FIG. 4. Time-domain comparison of accuracy for the k-space and 2–4 finite-difference time-domain methods as a function of the spatial step size in points per minimum wavelength (PPW). Each test used the fat cylinder of 2.0-mm radius. CFL numbers were 0.5 for the k-space methods and 0.25 for the finite-difference time-domain method.

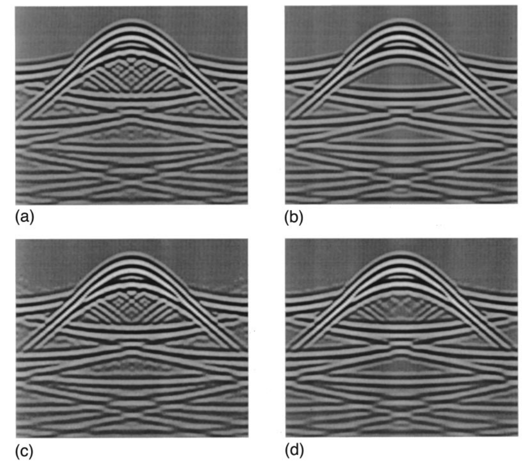

FIG. 5. Computed pressure waveforms at a receiver radius of 2.5 mm for a "bone" cylinder of radius 2.0 mm and a pulse center frequency of 2.5 MHz. The acoustic pressure is shown on a bipolar logarithmic scale with a 60-dB dynamic range. The horizontal range of each plot is 360°, covering the entire measurement circle starting with angle 0 (forward propagation). The vertical range of each panel corresponds to a temporal duration of 9 μs, with $t=0$ at the top of each plot. (a) Unsmoothed object; present k-space method, L^2 error 0.2292. (b) Smoothed object; present k-space method, L^2 error 0.0263. (c) Unsmoothed object; previous k-space method,[6] L^2 error 0.3060. (d) Smoothed object; previous k-space method,[6] L^2 error 0.2687.

to the k-space method of Ref. 6. Figure 3 also shows that both k-space methods provide much higher accuracy than a comparable pseudospectral method employing a leapfrog propagator (described in Ref. 6). Similar gains in accuracy have been obtained relative to a more sophisticated pseudospectral method incorporating fourth-order Adams–Bashforth iteration.[7] All three methods provide equivalent results for very small time steps (CFL numbers less than about 0.1), but the k-space methods maintain high accuracy up to a CFL number of about 0.4. In contrast, the leapfrog pseudospectral method rapidly increases in error for CFL numbers above 0.1.

The spatial accuracy of the present k-space method is compared to the previous k-space method[6] and to a 2–4 finite-difference method[11] in Fig. 4. Time-domain L^2 errors are shown, for the 2.0-mm-radius "fat" cylinder, as a function of the spatial step size (in points per wavelength, based on a nominal minimum wavelength of 0.333 mm). For these computations, the CFL number of the k-space computations was held constant at 0.5, consistent with the CFL-accuracy relationship shown in Fig. 3, while the CFL number of the finite-difference computations was held at an optimal value of 0.25.[21,22] Again, the present k-space method yields accuracy almost identical to that of the previous k-space method of Ref. 6. All three methods achieve high accuracy for finer grid spacings; however, the k-space methods achieve higher accuracy for much larger spatial step sizes. The L^2 error drops below 0.05 for k-space computations employing only 3 points per minimum wavelength, while achievement of the same accuracy criterion requires 14 points per minimum wavelength for the finite-difference computations.

Although the present k-space method and that of Ref. 6 yield nearly equivalent results for the benchmark case illustrated in Figs. 3 and 4, the use of coupled first-order equations in the present k-space method can provide greater accuracy for strongly scattering media. These advantages are illustrated using a benchmark computation for a 2-mm "bone" cylinder, introduced in Ref. 6. Since computations became unstable in this case for CFL numbers above about 0.2 [comparable to the theoretical upper stability limit of 0.2833 given by Eq. (12)], a CFL number of 0.1 was employed for the benchmark. Simulated waveforms obtained using the present k-space method and the previous k-space method of Ref. 6 are presented in Fig. 5 (computations carried out using the method of Ref. 6 were identical to those described in Ref. 6 except that the CFL number was reduced to 0.1). Both before and after smoothing of the model medium, the present k-space method achieves much higher accuracy than the previous method (L^2 error, relative to an exact series solution, was 0.2292 vs 0.3060 before smoothing, 0.0263 vs 0.2687 after smoothing). In addition, artifacts are greatly reduced in the computations employing the present k-space method. The waveforms obtained using the present k-space method with smoothing [panel (b)] are visually identical to those obtained from the exact series solution, shown in Ref. 6.

Further demonstration of the effectiveness of the present k-space algorithm, in conjunction with the smoothing methods used here, is given by Fig. 6. This figure illustrates numerical results for scattering from a bone-mimicking cylinder of sub-grid-resolution size (radius 0.02 mm [20 μm] compared to a spatial step of $\Delta x = 0.0833$ mm). The model medium, obtained by smoothing this subresolution cylinder using the methods described above, results in a scattered amplitude that is nearly identical to the exact solution. The corresponding discrete computation, which attempts to represent the subresolution scatterer using a single pixel with adjusted acoustic parameters, accurately obtains the waveform shape and delay, but incorrectly predicts the angle-dependent scattered amplitude. The accurate scattering computed for the half-band filtered medium indicates that the present k-space method, with smoothing of the kind used here, can account for structures with dimensions smaller than

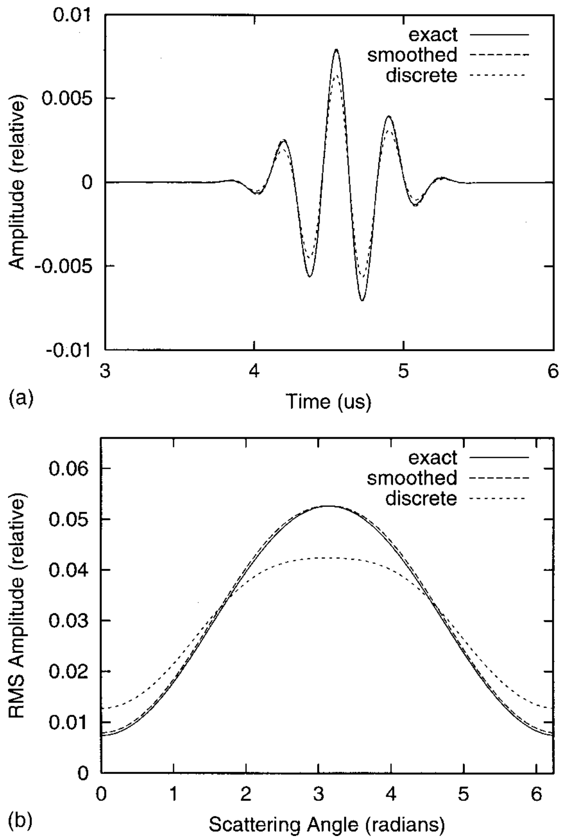

FIG. 6. Simulated scattering from a point (wire) scatter with radius 20 μm and acoustic properties of human bone. Each plot shows results for an exact series solution, a k-space solution using a half-band filtered representation of the subresolution scatterer ("smoothed"), and a single-pixel representation with equal scattering strength. (a) Backscattered signals. (b) The rms waveform amplitudes.

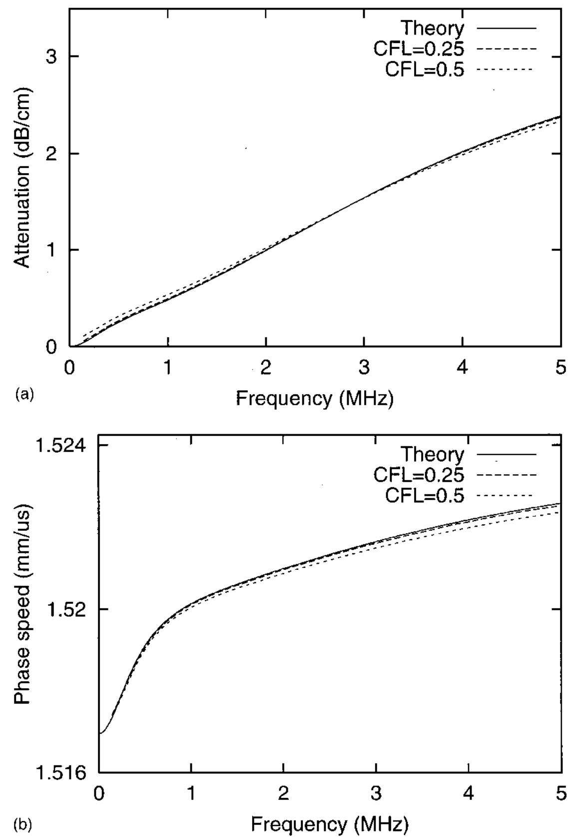

FIG. 7. Attenuation and phase speed for propagation of a pulse in a medium with two relaxation processes. Each panel shows theoretical values (Ref. 8) and values obtained using the present k-space method for two values of the CFL number. (a) Frequency-dependent attenuation. (b) Frequency-dependent phase speed.

the spatial step employed. Given sufficiently fine spatial sampling (4 points per minimum wavelength), scattering can be accurately computed from subgrid-sized structures located at arbitrary positions.

Results of the numerical test of relaxation absorption are illustrated in Fig. 7. Panel (a) shows theoretical and simulated attenuation values, while panel (b) shows theoretical and simulated values of the phase speed. The simulations are for two sizes of the time step corresponding to CFL$=$0.25 and CFL$=$0.5. The case with a smaller time step (CFL $=$0.25) agrees very well with the theory, while the case with a larger time step (CFL$=$0.5, as employed in the soft-tissue benchmark computations described above) shows good qualitative agreement. These results illustrate that the present k-space method with relaxation absorption can realistically simulate attenuation caused by soft tissues even for relatively coarse time steps.

Numerical results for the tissue-mimicking phantom example, described in the previous section, are illustrated in Fig. 8. This figure shows four snapshots of the spatially limited plane wave propagating through the phantom, causing coherent reflection from boundaries and wires as well as incoherent scattering from the random structure within the background cylinder. Notable is that smoothing of the medium has reduced any ringing artifacts to a level far below the low-level random scattering within the cylinder. Also notable is that the use of PML absorbing boundary conditions allows the computation shown to be performed efficiently (4063 CPU s on a 650-MHz Athlon processor for a simulation of duration 360 μs on a 768×768 grid). A hypothetical computation without absorbing boundaries, in which the grid size would be expanded to eliminate wraparound error within the region shown in Fig. 8, would require a grid size of approximately 4600×4600 points, resulting in a 35-fold increase in storage and computation time requirements.

V. DISCUSSION

The starting point for the k-space method introduced here is the previous k-space method based on the second-order wave equation.[2,6] Thus, a brief discussion of similarities and differences between these two methods is appropriate.

The two methods show identical accuracy for homogeneous media, since they are mathematically identical in this case. For weakly inhomogeneous media, both methods have similar performance in accuracy and stability. However, for stronger inhomogeneities such as the bone-mimicking cylinder benchmark described here, the two k-space methods differ significantly. The present method, based on the coupled first-order wave propagation equations, achieves much higher accuracy, although numerical evidence suggests that the present method has a lower stability threshold than the

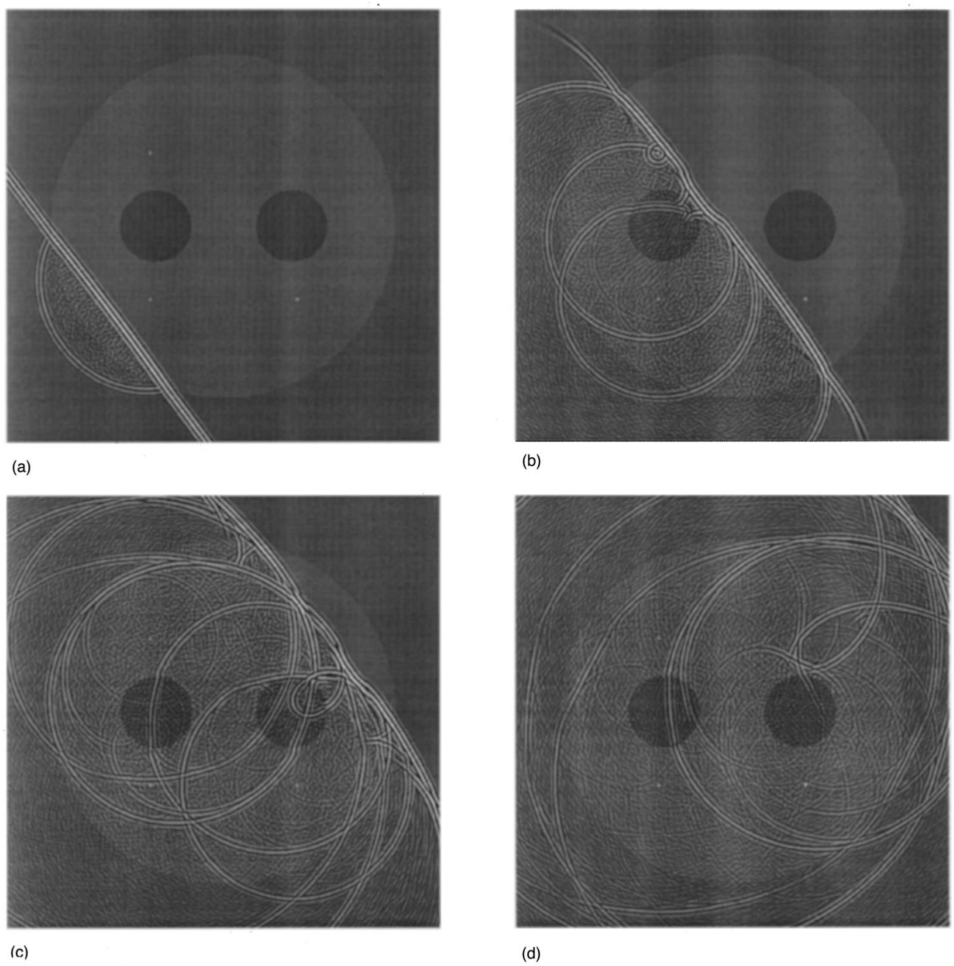

FIG. 8. Computed pressure fields for a 48-mm diameter tissue-mimicking phantom. Panels (a)–(d) show the total acoustic pressure at intervals of 12 μs, superimposed on an image of the phantom. The area shown in each panel is 61×61 mm. Wave fields are plotted using a bipolar logarithmic scale with a dynamic range of 60 dB.

method of Ref. 6. The increased accuracy of the present k-space method for high-contrast media, relative to previous k-space methods based on second-order wave equations,[6] occurs for several likely reasons. Since the k-space method for coupled first-order propagation equations can be written in a form involving no Fourier transforms of medium properties [Eq. (10)], some aliasing errors may be eliminated. In addition, the coupled first-order equations incorporate the density directly rather than within a derivative term, so that errors associated with inaccuracies in discrete derivatives of the density are also reduced.

The two methods also differ somewhat in computation and storage requirements. The method of Ref. 6 requires computation and storage of only one acoustic variable (the acoustic pressure fluctuation), while the present method requires computation of the pressure fluctuation as well as each vector component of the acoustic particle velocity fluctuation. Thus, for a constant grid size, the present k-space method requires somewhat greater storage and computation time than the method of Ref. 6. However, this difference is offset by the capability of the present k-space method to incorporate PML absorbing boundary conditions. For large computations, the high performance of the PML allows the grid size to be substantially reduced without introduction of wraparound or boundary-reflection errors, so that the present k-space method is often more efficient for practical problems. This advantage is potentially even more important for three-dimensional computations.

The present k-space method can also be compared with pseudospectral methods for coupled first-order propagation equations (e.g., Refs. 12, 13, and 17). Although both methods use Fourier transforms to accurately evaluate the spatial first-order derivative, the present k-space method also includes temporal correction terms, which were obtained by factoring the second-order k-space operator of Eq. (7) into the first-order operators of Eq. (8). As a result, the present k-space method utilizes two-dimensional Fourier transforms, while pseudospectral methods employ one-dimensional Fourier transforms for calculation of spatial derivatives. This difference leads to a slight increase in computational requirements associated with Fourier transforms. Typically, pseudospectral methods require eight sets of one-dimensional Fourier transforms per time step, while the present k-space method requires seven two-dimensional Fourier transforms per time step. However, the temporal correction provided by the k-space method eliminates the need for higher-order time schemes such as Adams–Bashforth and Adams–Moulton iteration, so that the k-space method may provide improved overall efficiency. This advantage occurs in part because the k-space method can provide accurate results for larger time steps (higher CFL numbers) than pseudospectral methods employing higher-order temporal iteration.[7]

Another advantage of the present k-space method is the close analogy between this method and the standard finite-difference time-domain method of Ref. 16. The present k-space method is algorithmically identical to the method of Ref. 16 except that second-order-accurate spatial derivatives have been replaced by the k-space operator of Eq. (8), which provides spectral accuracy in space, exact temporal iteration for homogeneous media, and high accuracy for general media. This close analogy has allowed relaxation absorption and PMLs, previously adapated to the corresponding finite-difference method,[9] to be straightforwardly incorporated into the present k-space method. The analogy allows great improvements in the performance and accuracy of existing finite-difference codes employing algorithms similar to those of Refs. 9 and 16 by the straightforward replacement of finite-difference spatial derivatives with the k-space operators of Eq. (8).

VI. CONCLUSIONS

The present k-space method, which numerically solves the coupled first-order differential equations for wave propagation in inhomogeneous fluid media, has been shown to hold a number of advantages for large-scale simulation of ultrasound–tissue interaction.

The method maintains the major advantages of previous k-space methods;[6] like those, the present method is spectrally accurate in space, temporally exact for homogeneous media, and highly accurate for modest medium variations. Furthermore, the form of the present method has allowed it to be extended with PML absorbing boundary conditions, relaxation absorption, and an effective approach to smoothing discontinuous scattering media. Since the present method can be interpreted as a finite-difference method with correction terms, existing finite-difference codes may be easily modified to take advantage of the accuracy available from the k-space method.

Numerical examples presented here have shown that the present k-space method has remarkable accuracy and stability characteristics, similar to previous k-space methods,[6] for computations involving weakly scattering media. The method, together with the smoothing approach presented here, provides higher accuracy for strongly scattering media. Since k-space methods allow highly accurate results to be obtained using coarse spatial and temporal sampling, the present k-space method, with the incorporation of PML absorbing boundary conditions and relaxation absorption, is particularly well-suited to realistic large-scale simulations for applications including ultrasonic imaging studies.

ACKNOWLEDGMENTS

This research was funded by NIH Grants Nos. HL 50855, CA 74050, and CA 81688, US Army Grant DAMD-17-98-1-8141, DARPA Grant N00014-96-0749, and the University of Rochester Diagnostic Ultrasound Research Laboratory Industrial Associates.

[1] N. N. Bojarski, ‘‘The *k*-space formulation of the scattering problem in the time domain,’’ J. Acoust. Soc. Am. **72**, 570–584 (1982).
[2] N. N. Bojarski, ‘‘The *k*-space formulation of the scattering problem in the time domain: An improved single propagator formulation,’’ J. Acoust. Soc. Am. **77**, 826–831 (1985).
[3] B. Compani-Tabrizi, ‘‘*K*-space formulation of the absorptive full fluid elastic scalar wave equation in the time domain,’’ J. Acoust. Soc. Am. **79**, 901–905 (1986).
[4] S. Finette, ‘‘Computational methods for simulating ultrasound scattering in soft tissue,’’ IEEE Trans. Ultrason. Ferroelectr. Freq. Control **34**, 283–292 (1987).
[5] S. Pourjavid and O. J. Tretiak, ‘‘Numerical solution of the direct scattering problem through the transformed acoustical wave equation,’’ J. Acoust. Soc. Am. **91**, 639–645 (1992).
[6] T. D. Mast, L. P. Souriau, D.-L. Liu, M. Tabei, A. I. Nachman, and R. C. Waag, ‘‘A *k*-space method for large-scale models of wave propagation in tissue,’’ IEEE Trans. Ultrason. Ferroelectr. Freq. Control **48**, 341–354 (2001).
[7] J. C. Mould, G. L. Wojcik, L. M. Carcione, M. Tabei, T. D. Mast, and R. C. Waag, ‘‘Validation of FFT-based algorithms for large-scale modeling of wave propagation in tissue,’’ Proc. IEEE Ultrason. Symp. 1999, **2**, 1551–1556 (1999).
[8] A. I. Nachman, J. F. Smith, and R. C. Waag, ‘‘An equation for acoustic propagation in inhomogeneous media with relaxation losses,’’ J. Acoust. Soc. Am. **88**, 1584–1595 (1990).
[9] X. Yuan, D. Borup, J. Wiskin, M. Berggren, and S. A. Johnson, ‘‘Simulation of acoustic wave propagation in dispersive media with relaxation losses by using FDTD method with PML absorbing boundary condition,’’ IEEE Trans. Ultrason. Ferroelectr. Freq. Control **46**, 14–23 (1999).
[10] A. D. Pierce, *Acoustics: An Introduction to its Physical Principles and Applications*, 2nd ed. (Acoustical Society of America, Woodbury, NY, 1989), Chap. 1.
[11] T. D. Mast, L. M. Hinkelman, M. J. Orr, V. W. Sparrow, and R. C. Waag, ‘‘Simulation of ultrasonic pulse propagation through the abdominal wall,’’ J. Acoust. Soc. Am. **102**, 1177–1190 (1998).
[12] B. Fornberg, *A Practical Guide to Pseudospectral Methods* (Cambridge University Press, Cambridge, 1996).
[13] G. Wojcik, B. Fornberg, R. Waag, L. Carcione, J. Mould, L. Nikodym, and T. Driscoll, ‘‘Pseudospectral methods for large-scale bioacoustic models,’’ Proc. IEEE Ultrason. Symp. 1997, **2**, 1501–1506 (1997).
[14] B. Fornberg and G. B. Whitham, ‘‘A numerical and theoretical study of certain nonlinear wave phenomena,’’ Philos. Trans. R. Soc. London **289**, 373–404 (1978).
[15] Ronald A. Mickens, *Nonstandard Finite Difference Models of Differential Equations* (World Scientific, Singapore, 1994).
[16] K. S. Yee, ‘‘Numerical solution of initial boundary value problems involving Maxwell’s equations in isotropic media,’’ IEEE Trans. Antennas Propag. **14**, 302–307 (1966).
[17] H.-W. Chen, ‘‘Staggered-grid pseudospectral viscoacoustic wave field simulation in two-dimensional media,’’ J. Acoust. Soc. Am. **100**, 120–131 (1996).
[18] M. Frigo and S. G. Johnson, ‘‘FFTW: An adaptive software architecture for the FFT,’’ Proc. ICASSP, **3**, 1381–1384 (1998).
[19] J. Mould, D. K. Vaughan, and L. Carcione, SPECTRALFLEX *User’s Manual* (Weidlinger Associates, Los Altos, CA, 1999).
[20] P. M. Morse and K. U. Ingard, *Theoretical Acoustics* (McGraw-Hill, New York, 1968), Chap. 8.
[21] R. L. Burden, J. D. Faires, and A. C. Reynolds, *Numerical Analysis* (Prindle, Weber, and Schmidt, Boston, 1978), Chap. 8.
[22] E. Turkel, ‘‘On the practical use of high-order methods for hyperbolic systems,’’ J. Comput. Phys. **35**, 319–340 (1980).

Low-frequency reflection characteristics of the s_0 Lamb wave from a rectangular notch in a plate

M. J. S. Lowe and O. Diligent
Department of Mechanical Engineering, Imperial College, London SW7 2BX, United Kingdom

(Received 8 February 2001; revised 4 October 2001; accepted 8 October 2001)

An analysis of the reflection of the fundamental Lamb mode s_0 from surface-breaking rectangular notches in isotropic plates is presented. The results are obtained from finite element time domain simulations together with experimental measurements. Very good agreement is found between the simulations and the measurements. Results are shown for a range of notch widths and depths, including the special case of a crack, defined as a zero-width notch. An interference phenomenon is identified which explains the periodic nature of the reflection coefficient when plotted as a function of notch width. Finally, an analysis using the S-parameter approach and both low and high frequency asymptotic analyses yields physical explanations of the nature of the reflection behavior from the cracks. It is found that the low frequency (quasistatic) approximation may be used accurately for cracks up to about a quarter of the plate thickness, provided that the quasistatic crack-opening function is chosen such that bending of the plate is omitted. At higher frequencies and depths the functions tend towards the high frequency (ray theory) predictions but these are never accurate models within the nondispersive frequency range of the s_0 mode. © *2002 Acoustical Society of America.* [DOI: 10.1121/1.1424866]

PACS numbers: 43.20.Mv [DEC]

I. INTRODUCTION

The motivation of the work presented here is the ultrasonic inspection (NDE) of plate structures to detect defects such as cracks or corrosion. There are many engineering structures which are composed of large areas of flat or curved plates, such as oil or chemical storage tanks, pressure vessels or pipelines. The routine inspection of these large areas to detect cracking or corrosion is very time consuming and thus expensive because conventional techniques require a test instrument to scan point by point in two dimensions over the whole area. An alternative for rapid inspection is to use ultrasonic Lamb waves which propagate along the plate and may be reflected by any defects. This can be done for example using a simple pulse-echo arrangement with a single transducer which is aligned to generate the waves in a chosen direction and then receive reflections from any defects.

However, the exploitation of Lamb waves for rapid inspection is hindered by the need to overcome their considerable complication compared to conventional methods. At any chosen frequency there may exist at least two modes, so that the interaction of a wave with a defect can result in a complicated multimode signal. The modes travel at different speeds and are dispersive, such that the shape of the multimode signal changes with distance along the plate. Also, the distributions of the stresses through the thickness of the plate differ from one mode to another, thus the nature of the modes needs to be understood in order to choose modes which are sensitive to the defects. Specific transducers which can excite and receive the chosen modes need also to be developed or selected with care.

Considerable progress in this topic has already been made. Work by Worlton[1,2] some 40 years ago identified the potential, in general, of using Lamb waves for inspection. Viktorov also contributed strongly to the understanding of Lamb waves, most notably in his well-known text.[3] In more recent years there has been a large and increasing number of publications relating to the exploitation of Lamb waves for the inspection of flat plate[4–11] or cylindrical shell[12–18] structures. Rayleigh waves have also been exploited for the detection and measurement of surface-breaking cracks, for example,[19,20] although such an approach is limited to localized detection of small cracks rather than long-range inspection. A large proportion of the literature has addressed the practical aspects of the application of guided waves to the inspection of pipes; this is in some ways a simpler problem than inspecting flat plates because the propagation is essentially unidirectional. However there remains a strong motivation to extend the findings on pipe inspection to the closely related two-dimensional problem of inspecting the area of a plate.[21]

The work presented in this paper addresses the fundamental case of the reflection of the low frequency symmetric mode (s_0) when it is incident at a simple surface-breaking crack or notch. The s_0 mode at low frequency has the attractive qualities for NDE of low dispersion and low leakage of energy if the plate is fluid loaded. Also, its stresses are almost uniform through the thickness of the plate so that its sensitivity to a defect is not dependent on the through-thickness location of the defect. The notch is assumed to be rectangular in section (with zero width in the case of a crack), is infinitely long and is aligned normal to the direction of wave propagation. Thus a plane strain assumption in the plane of the particle motion of the Lamb wave is sufficient for all considerations here. Studies of the interaction with notches such as this have already been performed by others. For example, Paffenholtz *et al.*[11] developed an inte-

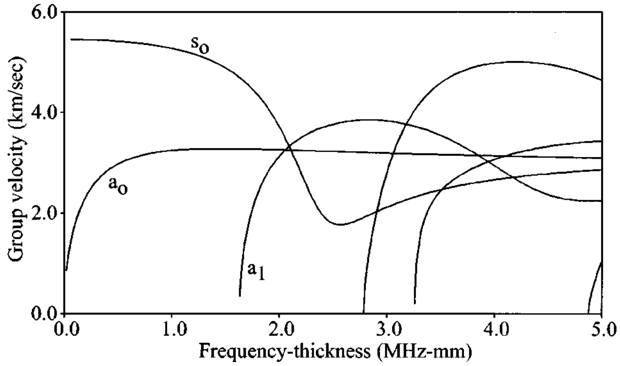

FIG. 1. Group velocity dispersion curves for Lamb waves in a steel plate.

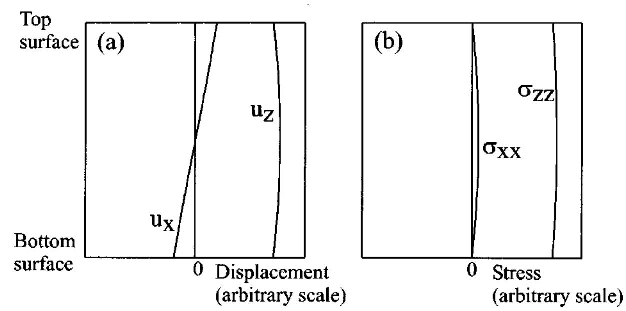

FIG. 2. Mode shapes of the s_0 mode at 1 MHz mm; (a) displacements, (b) stresses.

gral formulation to predict the interaction of a multimode signal, generated by a point impact source, with a crack; experimental measurements were also performed. Alleyne and Cawley[5] used finite element simulations and experiments to study the interaction of the a_0, s_0, and a_1 modes with a surface-breaking notch, the emphasis being on establishing the transmission coefficients. Cho and co-workers[7,8] have used a boundary integral method, together with experiments, to study the interaction of the a_0 and s_0 modes with an elliptical-shaped surface-breaking defect. In the present work we take the finite element and experimental approach of Alleyne and Cawley, but examine the reflection, rather than the transmission, of the s_0 mode. These results bring novelty by way of a systematic study of the reflection of the s_0 mode for ranges of frequency and notch dimensions. However, perhaps more significantly, we present an analytical interpretation of the results with the intention of bringing physical insight to the findings. Indeed the development of sound analytical interpretation of the fundamental cases such as these is considered to be particularly important: it is this understanding which will enable the much more complicated cases of realistic three-dimensional defects with waves incident in arbitrary directions to be tackled sensibly.

The paper starts with a brief review of the properties of the s_0 mode. The methodology which was used for the finite element time domain predictions and the setup for the experimental confirmations are then described. Results are then presented for both the finite element predictions and the measurements; they are compared and the nature of the behavior is examined. Finally an analytical study using the S-parameter technique[22] is used to further elucidate the observed behavior.

II. PROPERTIES OF THE s_0 MODE

Dispersion curves for the well-known Lamb waves in a steel plate are shown in Fig. 1. These group velocity curves indicate the speed of propagation of a wave packet and are therefore the curves of particular interest for long range propagation. Since the frequency axis may also be scaled with thickness, the scale is plotted as frequency-thickness for generality. Ideally for long-range NDE the s_0 mode is best exploited at very low frequency, where it is practically nondispersive. However resolution requirements normally force the frequency of choice upwards, so that a compromise is required, and indeed an optimum can be identified logically.[23] In practice the authors favor an approach to NDE in which the signals are kept as simple as possible; thus the upper bound of the frequency range of interest here is the cutoff frequency of the a_1 mode, about 1.6 MHz mm.

In its field structure the s_0 mode is very much the simplest of the Lamb modes, as illustrated by its mode shapes at 1 MHz mm, in Fig. 2. We use here the coordinate direction x to denote the normal to the surface of the plate, y to denote the normal to the plane strain, and z to denote the direction of propagation of the wave; displacements and stresses are u and σ, respectively. Only those components in the plane of the section and of any significant magnitude are shown. The mode shapes vary very little with the frequency; mainly at lower frequencies the magnitude of the displacement u_x diminishes with respect to u_z; similarly the stress σ_{xx} diminishes with respect to σ_{zz}. These simple shapes render the s_0 mode the most amenable to analytical examination, further motivating the focus on this mode for the work which is presented in Sec. VI. Also, of practical interest, the through-thickness uniformity of the σ_{zz} stress component indicates the equal sensitivity of the mode to defects at different depths, and the relatively low amplitude of the u_x displacement component results in minimal leakage of energy from the plate if it is immersed in an inviscid or low viscosity fluid.

III. METHODOLOGY FOR FINITE ELEMENT PREDICTIONS

The finite element modeling was performed in a two-dimensional domain, with the assumption of plane strain, using the program FINEL which was developed at Imperial College.[24] A schematic illustration of the spatial models is shown in Fig. 3. A plate of 3 mm thickness and 600 mm length was modeled for the predictions of the reflections from notches, the thickness being chosen for convenience to

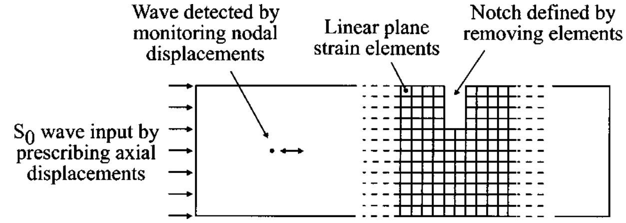

FIG. 3. Schematic illustration of finite element spatial discretization.

match the thickness of the plates which were used in the experimental work. The studies of the reflections from cracks assumed only 1 mm plate thickness, there being no experimental studies for comparison of these cases. In fact the choice of plate thickness for the models is arbitrary provided that the other spatial dimensions and the frequency are scaled to give the appropriate frequency-thickness product when comparing results; this scaling rule will be exploited in later discussion. The elements were defined to be perfectly square in shape, with 12 elements through the thickness of the plate when modeling notches and 16 elements through the thickness when modeling cracks. There were thus more than 50 elements per wavelength at the typical frequencies of study, substantially more than the threshold of eight elements per wavelength which the authors have found from experience to be a good limit for accurate modeling.[5,17] In fact the limiting criterion when designing the meshes for this study was the need for sensible spatial representation of the notches and cracks, rather than the accurate simulation of propagation.

Variants of the spatial model were set up to study rectangular notches and cracks of a range of dimensions. Each rectangular notch was created simply by removing elements, as illustrated in the figure. Two different depths of notch were considered, 17% and 50% depth, created by removing two and six elements, respectively, in the thickness direction. For each depth, a range of different widths was then studied. The models which were used to study cracks were created by disconnecting the elements at the nodes along the line defining the crack. Visually, therefore, there was no evidence of removal of material from the mesh, there was simply a discontinuity of the material. This approach has been found to be reliable in previous studies of guided wave interactions with cracks.[17] The cracks were surface breaking, aligned normal to the surface of the plate; they were thus equivalent to the rectangular notches but with zero width. Predictions were made for a range of different depths of crack.

The temporal model for the notch cases used a narrow band signal consisting of a five cycle tone burst of 400 kHz in a Hanning window, chosen to match the signal which was used in the experimental study. This was applied as a displacement boundary condition in the in-plane direction at all of the nodes at one end of the plate. The through-thickness profile of this boundary condition does not match perfectly the s_0 mode, however its symmetry ensured that only the s_0 mode was excited, the only other mode which could exist at this frequency being the antisymmetric a_0 mode. The crack studies used the same approach but with a wider band signal, consisting of a single cycle of 500 kHz in a Hanning window; this gives useful information from about 20 kHz to 1.4 MHz. Explicit time integration was used, assuming a diagonal mass matrix, thus avoiding the need for global matrix assembly or inversion in the finite element solutions. Constant duration time steps were taken, within the chosen limit of maximum allowable step length of 0.8 L/C, where L is the element length and C is the wave speed of the fastest wave present. This respects the stability limit of L/C for explicit time integration.[25]

The results of the simulations were obtained by monitoring nodal displacements at a location approximately mid-

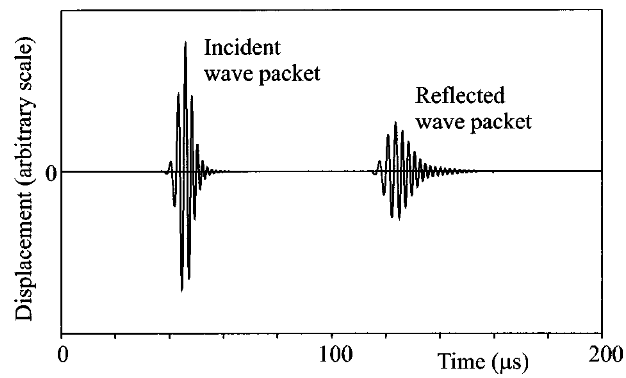

FIG. 4. Typical time record from finite element simulations; notch is 50% deep and 3 mm wide.

way between the excitation end of the plate and the notch or crack. The displacement in the in-plane direction (u_z) was monitored at the mid-thickness of the plate, thus ensuring that only the symmetric s_0 propagating mode was detected, since the antisymmetric a_0 mode has zero in-plane displacement at this depth. Since the monitoring location was some 60 plate thicknesses from the notch or crack, it was also considered that any nonpropagating modes which may be generated at the notch would not be recorded. A typical time record is plotted in Fig. 4, showing first the incident s_0 wave packet as it travels past the monitoring point, then the s_0 wave packet which is reflected from the notch. In this example the notch depth is 50% of the plate thickness and the width is 3 mm (equal to one plate thickness). Although there is some dispersion at this frequency, the incident wave packet shows reasonably accurately the shape of the signal which has been generated at the end of the plate. The reflected wave packet has traveled much further and shows evidence of significant dispersion; furthermore its shape is also affected by the nature of the reflection from the notch which has a finite width.

Processing of the signals to calculate the reflection coefficients of the s_0 mode was performed in the frequency domain. The frequency spectrum of the reflected wave packet was divided by that of the incident wave packet, giving the reflection coefficient for all frequencies in the bandwidth of the signal.

IV. EXPERIMENTAL PROCEDURE

Although the s_0 mode is the simplest and is nondispersive at low frequencies, it is in fact rather more difficult to work with experimentally than might be anticipated. A very popular means to excite and receive Lamb waves is by aligning a plane transducer at an angle to the surface of the plate, coupling the sound through a local fluid bath or through a solid angle block (so-called angle wedge transducer). However, the s_0 mode at low frequency has very little motion in the direction normal to the surface and so is not easily excited. At the same time the a_0 mode is very easily excited. Therefore, even when the angle of the transducer is set to match the s_0 mode, its spatial bandwidth (beam spread) is such that some of the unwanted a_0 mode is also excited.

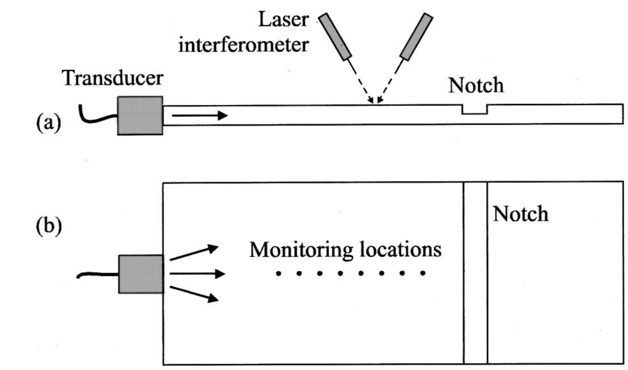

FIG. 5. Arrangement of notched plate, piezoelectric transmitter and laser receiver for experiments; (a) side view, (b) plan view.

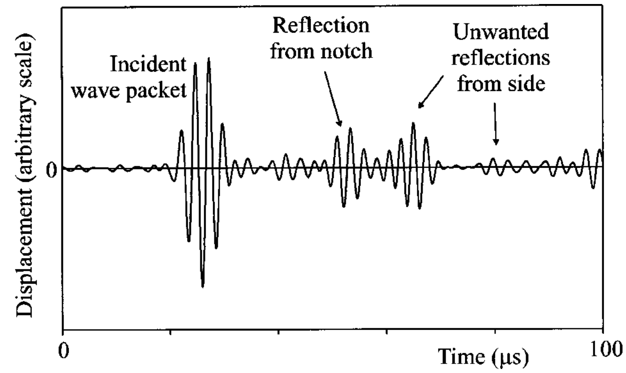

FIG. 6. Typical experimental time record; notch is 50% deep and 3 mm wide.

The main features of the experimental approach were thus designed with the aim of both exciting and receiving just the s_0 mode. The setup is illustrated in Fig. 5.

In excitation a plane wide-band piezoelectric transducer (Panametrics V301, 0.5 MHz center frequency) was positioned centrally at the end of the 3 mm thick plate. The transducer was coupled to the plate using a conventional coupling gel and held in position by a clamp. Care was taken in the preparation of the edge of the plate and in the positioning of the transducer in order to ensure that the excitation was as symmetric as possible with respect to the center line of the plate, so minimizing the excitation of the antisymmetric a_0 mode. Measurements of the signal at a single point on the surface of the plate at some distance from the edge were used to confirm that only the s_0 mode was present. This is easily observed because the s_0 mode is faster than the a_0 mode and so they arrive at separate times. The signal which was used for the reflection studies consisted of a five cycle tone burst of 400 kHz in a Hanning window; this was generated using a Wavemaker (Macro Design Ltd., UK) instrument.

The detection was achieved using a laser interferometer (Polytec OFV 2700, with dual differential fiber optic lines) to measure the displacement at the surface of the plate. Since the notch or crack reflects energy in both the s_0 and a_0 modes, it was again necessary to take steps to detect just the s_0 mode. Two measures were taken. First, the component of displacement in the direction parallel to the surface of the plate was measured, rather than the displacement normal to the plate; this in-plane displacement is very much larger than the normal displacement for the s_0 mode. The in-plane displacement was measured by using two laser beams aligned at an angle of 30 degrees to the normal: the difference between their two signals then gave the in-plane displacement. A thin retro-reflective tape was attached to the surface of the plate to enhance the optical backscatter. Second, the measurements were taken at a series of equally spaced positions along the plate, then a two-dimensional Fourier transform (2D–FFT)[26] was used to separate the s_0 and a_0 components. 64 points were used, with spacing of 1.04 mm, and the amplitudes were multiplied by a Hanning spatial window function. The 2D–FFT also helps to separate the wanted signal from other unwanted signals such as reflections from the sides of the plate.

Even though the in-plane displacement of the s_0 mode is relatively strong, the signals were in general quite weak. The quality of each displacement measurement was enhanced by taking 200 averages and by applying a band-pass filter. A typical signal which has been processed in this way is presented in Fig. 6, showing good signal-to-noise but at this stage still containing a significant quantity of unwanted components such as the edge reflections. The time trace shows the incident wave on its way to the notch, the reflection from the notch, which was in this case 50% deep and 3 mm wide, and some of these unwanted reflections which would later be removed by the 2D–FFT.

The s_0 reflection coefficient was calculated by dividing the frequency spectrum of the reflected s_0 signal by that of the incident signal. Although this gives results over the range of frequencies of the bandwidth, it was decided to use only the center frequency results because of the poor signal strength in the side bands.

One final treatment of the signals was to compensate crudely for the loss of amplitude caused by the spreading of the beam. Amplitudes were compared over a range of distances of propagation, without reflection. Apart from the very short distances near the source transducer, the amplitude variation was found to be described simply by an attenuation of 22 dB/m. The notch reflection measurements were thus increased according to this factor in order to represent the values to be expected from a plane wave front.

The reflection coefficient experiment was repeated for a total of 14 notched plates. There were two depths of notch, 17% and 50% of the plate thickness. The notch widths were 0.5, 1, 2, 3, 4, and 5 mm at 17% depth and 1, 1.5, 2, 3, 4, 5, 6, and 8 mm at 50% depth.

V. RESULTS

Figures 7 and 8 show the measured and predicted reflection functions for the 17% and 50% deep notches. The horizontal axis has been scaled to normalize the notch width to the plate thickness; thus these results may be applied equally to other thicknesses of plate provided that the frequency-thickness of 1.2 MHz mm is also retained. The experimental measurements and finite element predictions can be seen to agree well in both cases. Note that the ranges of the vertical axes of the two figures are not the same.

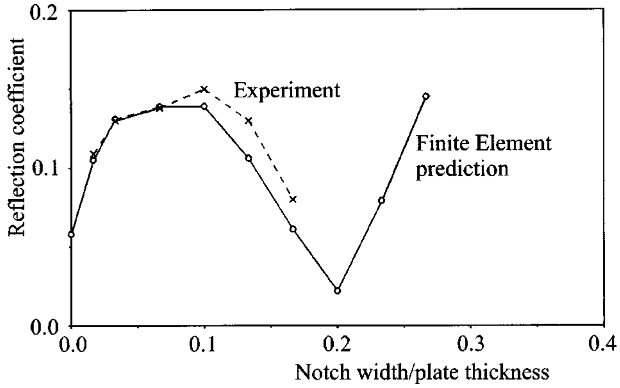

FIG. 7. Measured and predicted variation of s_0 reflection coefficient with notch width when notch depth is 17% of plate thickness; frequency-thickness product is 1.2 MHz mm.

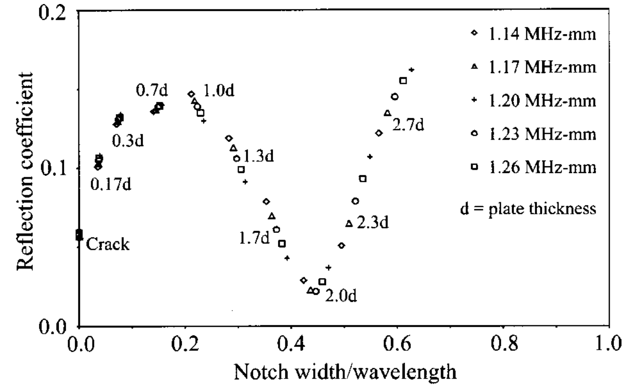

FIG. 9. Predicted variation of s_0 reflection coefficient with notch width normalized to wavelength, when notch depth is 17% of plate thickness; results for five similar frequency-thickness products.

The reflection starts at a low value when the notch width is zero (this is the crack case, considered only in the finite element work), then rises as the notch width is increased. The peak reflection then occurs when the notch width is about 10% of the plate thickness, then there is a low point at around 20% of the plate thickness, then an increase again. Additional finite element analyses (results not shown here) have shown that this pattern of peaks and troughs continues regularly as the notch width is further increased. Interestingly, the value of the peak of the reflection coefficient is approximately equal to the depth proportion of the notch: the maximum reflection coefficient for the 17% deep notch is about 0.15 and that for the 50% deep notch is about 0.6; this is in fact quite consistent with the high frequency (Kirchoff) approximation which will be discussed in Sec. VI.

In fact the significance of the peaks and troughs in the reflection functions is not the relationship of the notch width with the plate depth, but rather with the wavelength of the guided wave. Figures 9 and 10 show the finite element predictions plotted using this alternative normalization, notch width normalized to s_0 wavelength, on the horizontal axis. The finite element results in these figures for the frequency-thickness product of 1.2 MHz mm are the same as those in Figs. 7 and 8. The results for the other frequency-thickness products will be explained shortly. Now it can be seen, at least as a very rough approximation, that the maximum of the reflection function is when the notch width is about a quarter of a wavelength and the minimum is when it is about a half of a wavelength.

The reason for the peaks and troughs of the function is the interference between two signals which reflect from the notch, one from the start of the notch and the other from the end of the notch. The reflection from the end of the notch is, of course, retarded with respect to the signal from the start of the notch, so their superposition in the resulting reflected wave packet may be constructive or destructive, depending on the duration of the delay. Furthermore, the reflections from the start and end of the notch differ in phase too, the latter involving a phase reversal with respect to the former (one may anticipate this by observing that the geometric change at the start of the notch represents a reduction of impedance whereas that at the end of the notch represents an increase in impedance). Consequently the constructive interference occurs when the end reflection is half a cycle behind the start reflection, that is when the notch width is a quarter of a wavelength. Similarly, a notch width of half a wavelength delays the end reflection by one cycle, thereby causing cancellation of the signal. However, although helpful conceptually, this explanation is not strictly quantitative: the wave which travels between the start and end of the notch is not simply the s_0 mode but is a combination of s_0 and a_0 modes. Therefore the maxima and minima do not occur pre-

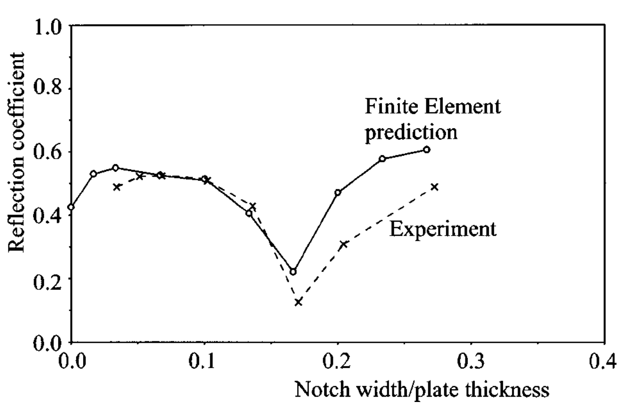

FIG. 8. Measured and predicted variation of s_0 reflection coefficient with notch width when notch depth is 50% of plate thickness; frequency-thickness product is 1.2 MHz mm.

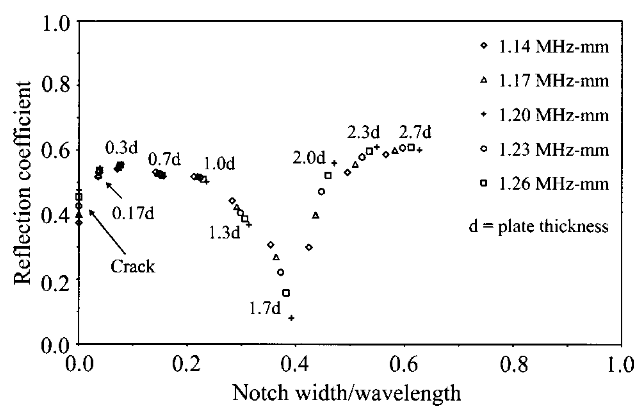

FIG. 10. Predicted variation of s_0 reflection coefficient with notch width normalized to wavelength, when notch depth is 50% of plate thickness; results for five similar frequency-thickness products.

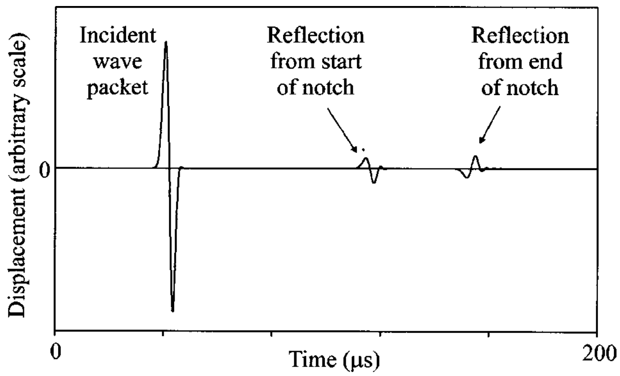

FIG. 11. Predicted time record showing incident and reflected signals for a very wide notch; notch depth is 17% of plate thickness and notch width is 33 plate thicknesses.

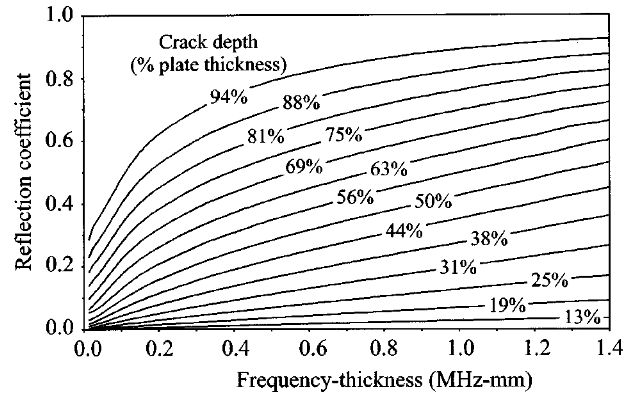

FIG. 12. Predicted spectra of s_0 reflection coefficient from a surface-breaking crack, for various depths of the crack.

cisely at the quarter and half wavelength positions, but at slightly smaller distances, because of the smaller wavelength of the a_0 contribution. This is particularly evident with the deeper of the two notches.

The two components of the reflection are readily seen by studying a very wide notch. Figure 11 shows the finite element predictions for the reflection of the s_0 mode from a notch whose depth is 17% of the plate thickness and whose width is 33 plate thicknesses. A single cycle signal has been used here in order that the phase of the reflections can be identified. The separate reflections from the start and end of the notch can be seen clearly. It is also evident that the reflection from the start of the notch is in the same phase as the incident signal whereas the signal from the end of the notch is in opposite phase.

Returning to Figs. 9 and 10, finite element results at four other frequency-thicknesses have been included in addition to the 1.2 MHz mm values. These additional data points were obtained by making use of the full width of the spectrum of the signal, an easy and reliable calculation with the noise-free finite element simulations. These extra values follow the same maxima and minima trends, but it is evident that they do not correspond precisely. For example, in Fig. 9 a line could be fitted reliably through the five points for 1.0 d but it would have a steeper downward slope than the overall trend line; the slopes of the 1.2 d and 1.7 d points would similarly be steeper. Thus the reflection functions are dependent not just on the ratio of the notch width to the wavelength but also on the frequency.

The dependence of the reflection coefficient on frequency was examined using the zero-width (crack) geometry and the wide band finite element simulations. The predicted reflection function spectra for 14 values of the crack depth are shown in Fig. 12. These show the reflection to be an increasing function of frequency and of crack depth. However, the rise of the coefficient with frequency is not linear, but tending towards a plateau; this is particularly evident for the deeper cracks. Figure 13 shows the same data plotted versus the crack depth for various values of the frequency-thickness product. An interesting outcome of the monotonic relationship with depth and with frequency is that the reflection coefficient could, in principle, be used to measure the depth of a crack. This would not be possible with most other guided wave modes because of their more complex through-thickness distributions of stresses. The nature of these functions will be examined in more detail in the following section.

VI. COMPARISON WITH ANALYTICAL SOLUTIONS FOR CRACKS

The findings of the reflection functions study provide a useful basis, in a look-up form, for anticipating the sensitivity of the s_0 mode to rectangular notches and cracks, for example, in NDE applications. However, as is usual with finite element studies, further analysis is needed in order to understand the nature of the phenomena. We consider here the simplest form of the notch, the crack, and present an analytical study which aims to bring some physical insight to the findings.

A well-established approach to the analytical study of reflection functions is the *S*-parameter technique.[22] The *S*-parameter is the coefficient of reflection or transmission of any mode of interest when a chosen mode is incident at any sort of discontinuity in a body. The method has been used in the analysis of scattering from defects in infinite bodies[27,28] as well as in wave guides.[15,29] The derivation is reached from the theories of mode orthogonality and reciprocity. A crack is a special case of a discontinuity: significant simplification of

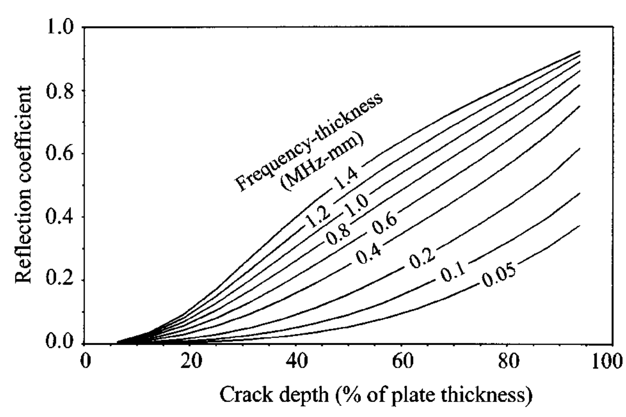

FIG. 13. Predicted s_0 reflection coefficient versus depth of the crack, for various frequency-thickness products.

the equations is possible because the tractions on the faces of the crack are defined to be zero. This results in the following equation:

$$\Delta S_{I,R}=\frac{i\omega}{4}\int_S \Delta u_I\cdot T_R\cdot\hat{n}\ dS. \tag{1}$$

$\Delta S_{I,R}$ is the reflection (or transmission) coefficient; this is the ratio of the particle displacement of the reflected wave R to that of the incident wave I. ω is the circular frequency; Δu_I is the vector of the displacements at the crack surface (normal and tangential) when the crack opens in response to the incident mode I; the amplitude of I is defined to be such that it transmits unit power flow per unit cross-sectional area of the wave guide. T_R is the stress field of a reflected mode R of unit power flow which would exist where the crack is located, but in an uncracked structure. $\hat{n}$ is the unit vector into the material in the direction normal to the crack face. Finally, the integral is calculated over the area S, which is the whole of the surface area (both faces) of the crack. The unit power flow of these two modes, P_I and P_R, respectively, is satisfied by

$$P_I=\frac{-i\omega}{4}\int_A (u_I\cdot T_{-I}-u_{-I}\cdot T_I)\cdot\hat{z}\ dA=1, \tag{2}$$

$$P_R=\frac{-i\omega}{4}\int_A (u_R\cdot T_{-R}-u_{-R}\cdot T_R)\cdot\hat{z}\ dA=1 \tag{3}$$

in which a negative subscript denotes that the displacement or stress is that which would exist in a wave which was traveling in the opposite direction to that of the power flow. The integral is over the cross-sectional area, A, of the wave guide and the unit vector $\hat{z}$ is in the direction of propagation of the power flow.

In the specific case of the analysis here, these equations may be simplified further to express the reflection coefficient of just the s_0 mode when the s_0 mode is incident. In this case Fig. 2 shows that the only significant component of stress is σ_{ZZ}, and furthermore, that it is approximately constant for all positions through the thickness of the plate. Thus only this stress and the z component of displacement (u_Z) need to be known in Eqs. (1)–(3). The approximate equation for the s_0 reflection coefficient is then

$$\Delta S_{s_0,s_0}=\frac{i\omega\sigma_{zz}}{4}\int_S \Delta u_z\hat{n}\ dS. \tag{4}$$

Equations (2) and (3) may similarly be simplified, in order to find the stress σ_{ZZ} of the power-normalized s_0 mode. Observing that the displacement u_Z is also approximately constant through the depth of the plate, the integration of these equations is straightforward. Also, the relationship between the stress and the displacement is the same as for a plane compression wave, that is $\sigma_{ZZ}=i\omega\rho C u_Z$, in which ρ and C are the density of the material and the phase velocity of the wave, respectively. Thus the expressions of the power-normalized displacement and stress which satisfy Eqs. (2) and (3) are

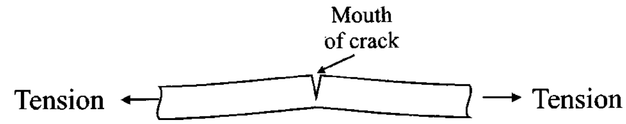

FIG. 14. Plate with edge crack and remotely applied tensile loading, showing also the possibility of bending of the plate at the crack.

$$u_z=\left(\frac{2}{\omega^2\rho CA}\right)^{1/2}, \tag{5}$$

$$\sigma_{zz}=i\left(\frac{2\rho C}{A}\right)^{1/2}. \tag{6}$$

The only remaining unknown for the solution of Eq. (4) is the displacement of the surface of the crack. A rigorous approach for obtaining this is to consider the tractions of all possible scattered modes, including the nonpropagating modes which exist just in the vicinity of the crack: relying on the orthogonality of the modes, it is possible to find a unique combination of all of them such that, together with the incident mode, the sum of all the tractions at the crack surface is null. A simpler approach, which we take here in the interests of gaining physical insight, is to approximate the crack displacement. We consider sequentially two limiting approximations, one for low frequency and one for high frequency, from which some interesting characteristics of the reflection behavior will be demonstrated.

A. Low frequency approach

The low frequency, or quasistatic, approach makes the assumption that the displacement at the crack surface can be calculated from an analysis of the response to a static stress field.[22] Such an assumption may be argued to be reasonable when the wavelength of the incident mode is very much larger than the geometric dimensions of the problem under consideration. In our application we thus consider very low frequencies such that the wavelength is much longer than the plate thickness and the crack length. There are two important features of this assumption: first, that the stress field can realistically be represented by an analysis which satisfies static equilibrium; second, that the stresses at locations remote from the crack are not relieved by the opening of the crack.

Static stresses and displacements at cracks are already well known for many structures, crack geometries and loadings, being the focus of much research in the field of fracture mechanics. In the present case of the s_0 reflection problem, the stress field in the incident wave is dominated by the in-plane stress component (σ_{zz}), and furthermore this is approximately uniform across the thickness of the plate for frequency-thickness products up to about 1 MHz mm. In the corresponding static analysis, this field is easily represented by the application of a tensile stress at the two ends of the plate at remote distances from the crack. An illustration of the static arrangement is shown in Fig. 14. A solution for the crack opening displacement (COD) at the mouth of the crack, in mode I (that is displacement discontinuities in the Z direction), has been established,[30]

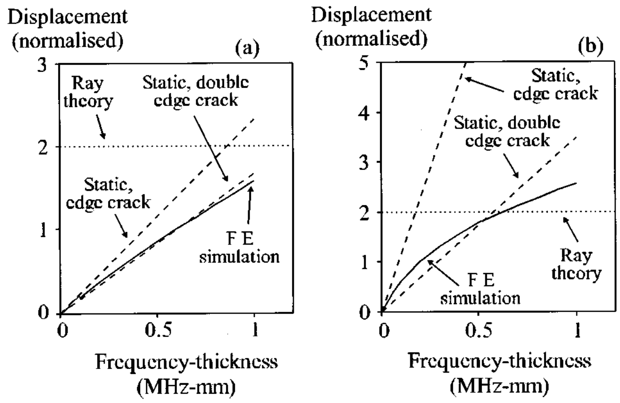

FIG. 15. Crack opening displacement (COD) at mouth of crack, showing static solutions, ray theory solutions and predictions of finite element simulations: (a) for 25% depth crack; (b) for 50% depth crack. Displacement is normalized to the in-plane displacement of the incident s_0 wave.

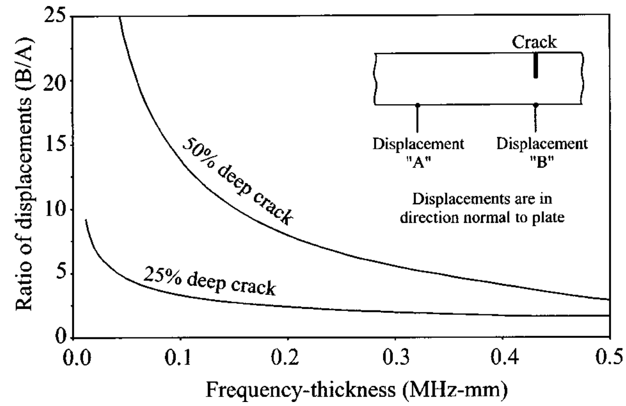

FIG. 16. Lateral displacement amplitude of surface of plate at location of crack, normalized to the same displacement component at a location remote from the crack; all data taken from the finite element simulations.

$$\mathrm{COD}_{\mathrm{mouth}} = \frac{4\sigma a}{E'} V, \tag{7}$$

where E' is the effective Young's modulus of the material, which in the present application is the plane strain modulus, a is the depth of the crack, and σ is the applied stress. The function V is, for a single-edge crack (SE),[30]

$$V_{\mathrm{SE}} = \frac{1.46 + 3.42(1 - \cos \pi a/2b)}{(\cos \pi a/2b)^2}, \tag{8}$$

in which b is the thickness of the plate. Substituting the power-normalized stress for the s_0 mode into Eq. (7), and the relationship between the stiffness and the velocity ($E' = \rho C^2$), and taking unit width of the plate (such that $A = b$), the crack opening displacement due to the power-normalized incident s_0 mode is

$$\mathrm{COD}_{\mathrm{mouth}} = \sqrt{\frac{32}{\rho C^3}} \frac{a}{\sqrt{b}} V. \tag{9}$$

The range of validity of the low frequency analysis can be assessed by examining the degree to which this prediction of the COD agrees with the (realistic) elastodynamic COD from the full finite element simulations, that is from the models which were used to predict the reflection coefficients in the earlier part of the paper. The COD was obtained simply by extracting the in-plane displacements at the two nodes at the crack mouth from the results of the simulations; the COD at the mouth is the difference between the displacement values at each side of the mouth. This comparison is made in Fig. 15, in which the results of Eq. (9) are labeled "Static, edge crack." Two cases are considered, in which the crack depth is, respectively, 25% and 50% of the plate thickness. The COD values have been normalized to the in-plane (Z) component of the displacement in the power-normalized incident wave. In both cases it can be seen that the initial slope of the static edge crack solution agrees with the finite element simulation. However, the solutions diverge very quickly, especially in the case of the deeper crack. Therefore the agreement is in general not good.

An interesting and important issue relating to the divergence of the curves is the extent to which the plate bends under the imposed tensile stress field. The static COD analysis includes bending of the plate, as illustrated in Fig. 14, the bending behavior enhancing the opening of the crack. However the true behavior is unlikely to include significant bending. This may be argued from two perspectives: first, that the stress field is not actually constant over long distances along the plate but varies sinusoidally, so that the region under tension may be very much shorter than is assumed in the static case; and second, that inertia may restrict the lateral dynamic motion. Both of these arguments lead to the expectation that the lateral motion of the plate may be significant at low frequencies but should reduce as the frequency is increased. This is indeed found to be the case when the finite element results are subjected to further scrutiny. Figure 16 shows the amplitude of the lateral displacement of the bottom surface of the plate at the location of the crack, for the whole range of frequencies, obtained from the finite element simulations. The displacement amplitude has been normalized to the same component of displacement at a location remote from the crack. The resulting curves show very clearly a dramatic enhancement of the lateral displacement at low frequency, then reduction as the frequency is increased. It can also be seen that, as should be expected, the lateral motion is greater for the deeper of the two cracks. These findings are consistent with results published by the authors on reflection functions in cracked pipes,[17,18] in which it was shown that there is negligible lateral motion of the pipes.

Therefore for further comparison we also include solutions here for a double-edge crack, in which there can be no plate bending. The double-edge crack is illustrated in Fig. 17. The dimensions have been kept such that the crack size is the same as in the single-edge case, thus the plate thickness has

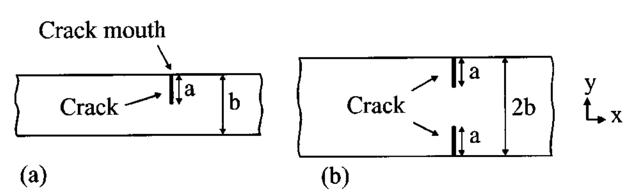

FIG. 17. Crack geometries: (a) edge crack; (b) double-edge crack.

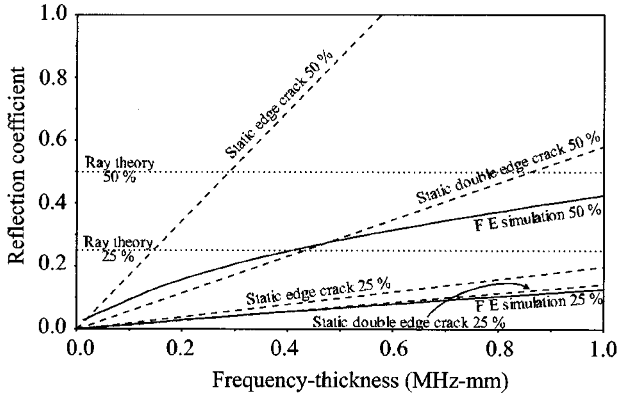

FIG. 18. Reflection coefficient predictions: comparisons of results from finite element simulations, static solutions, and ray theory solutions.

been doubled. The crack opening function for the double-edge crack (DE) is very similar to that for the single-edge crack (SE), except for the function V, which is now:[30]

$$V_{\mathrm{DE}}=\frac{1}{(\pi a/2b)}\left[0.454\sin\frac{\pi a}{2b}-0.065\left(\sin\frac{\pi a}{2b}\right)^3 -0.007\left(\sin\frac{\pi a}{2b}\right)^5+\cosh^{-1}\left(\sec\frac{\pi a}{2b}\right)\right]. \tag{10}$$

The results of the double-edge crack opening function, included in Fig. 15, show much better agreement with the finite element predictions. This is especially true for the smaller of the two cracks, in which case the agreement holds sensibly for the whole frequency range. Comparison of the two COD curves in each of parts (a) and (b) of the figure show also the significance of the plate bending component: the solutions for the single-edge COD and the double-edge COD differ by greater amounts as the crack depth is increased.

The next step in the analysis should, logically, be the prediction of the reflection function from the static COD results with Eq. (4). However this requires the COD profile for the whole of the crack, not just the COD at the crack mouth. The authors are not aware of published solutions for these profiles and so resorted instead to calculating them by static finite element analyses. The finite element model was spatially similar to that described earlier for the dynamic simulations, the key difference being that it was subjected just to a remote static tensile load. The model was run four times, thus yielding the full COD profiles for each of the two example crack depths, and for the single-edge and double-edge crack geometries. The results at the crack mouth were found to agree very closely with the published solutions.

The predictions of the reflection coefficient using these static COD profiles are shown in Fig. 18. It is no surprise to see that the degree of the agreement is very similar to that which was observed with the COD predictions in Fig. 15. Both the single-edge and the double-edge crack static solutions give quite reasonable predictions of the reflection from a 25% deep crack, the latter being particularly good. The reflection from the deeper crack is best predicted by the double-edge equations, once again demonstrating the benefit of omitting the bending behavior from the analytical model.

B. High frequency approach

The alternative approach for an approximate solution is to assume that the wavelength is very short compared to the dimensions of the crack. In this case a very simple ray analysis is possible in which the rays which arrive at the crack are assumed to be perfectly reflected and the rays which arrive at the remaining ligament of the plate are assumed to be perfectly transmitted. If one thinks of a wave with a very short wavelength arriving at some location on the crack surface, it seems quite reasonable to understand its reflection, locally, simply as the reflection of a plane wave from a free surface. Such an approach, known as ray theory or the Kirchoff approximation, has been widely employed in the study of the scattering of bulk waves in solid bodies.[31]

In the case under study here, the waves are not bulk waves, but it still seems reasonable to expect that this approach should work when the frequency is sufficiently high. The in-plane displacements and stresses of the s_0 mode are roughly uniform across the thickness of the plate and this particular mode is known to reflect perfectly from the free end of a plate without complications such as conversion to other modes.

The solution in this case is straightforward: since the rays reflect perfectly from the crack and transmit perfectly elsewhere, the reflection coefficient must simply be equal to the fractional depth of the crack. Therefore the reflection coefficient from the 25% deep and 50% deep cracks are 0.25 and 0.50, respectively. A key feature of these results is that, in contrast to the low frequency analysis, they are not functions of the frequency.

However, before using this result, we may go a little further in understanding the nature of this reflection by interpreting the ray theory in the context of the S-parameter approach. Consider the arrival and total reflection of a ray at the surface of the crack. In the same way as a plane wave reflects from a free surface, the reflection of the ray is characterized by a zero stress at the surface and a displacement which is exactly twice that of the displacement in the incident or reflected ray. The COD profile is thus very simple: it takes a constant value which is equal to twice the displacement of the incident mode. It differs furthermore from the static COD profiles in that it exists only at one face of the crack. Whereas the static analysis leads to a COD composed of the difference between the motions of the two faces (which are equal and opposite in the cases of this study), the ray analysis leads to a COD which is defined entirely by motion of the crack face on which the ray is incident; the other face does not move at all.

Since the COD profile is uniform, the integration of the S-parameter Eq. (4) is trivial. The integration is performed just over one face of the crack, using the displacement Δu_z which is equal to twice the value of the power-normalized displacement of the incident wave [Eq. (5)]:

$$\Delta u_z=2\left(\frac{2}{\omega^2\rho CA}\right)^{1/2}. \tag{11}$$

It is simple to demonstrate that this approach predicts unit amplitude reflection from the end of a plate as well as the coefficients of 0.25 and 0.50 for the two examples cited above.

The predictions of the ray analysis have been included for comparison in Figs. 15 and 18. The levels of these horizontal lines are consistently higher than the curves from the finite element simulations, but are at values which could sensibly be anticipated as high frequency asymptotes if the trends were to continue. Unfortunately, however, convergence to these lines at higher frequencies is physically impossible because the s_0 mode does not maintain the same simple displacement and stress profiles at higher frequencies. Indeed the limit of 1 MHz mm was chosen to be the highest frequency thickness for which the simplified analyses could be justified. At frequencies higher than this the stress and displacement mode shapes of the s_0 mode start to vary significantly through the thickness of the plate, thus invalidating the analytical solutions.

Thus it seems in general that a low frequency analysis can give good results when the frequency and the crack depth are small, provided that an appropriate COD model is employed. Considering a crack on one side of the plate which extends to about 25% of the depth of the plate, the quasistatic analysis based on a double-edge crack (so avoiding plate bending behavior) may be relied on to give usefully accurate predictions. It may reasonably be expected that the same is likely to be true for similarly small defects of other shapes, for example notches, subsurface cracks or angled cracks. For larger cracks, up to about 50% of the depth of the plate, the quasistatic solution is not accurate but is certainly much better than the ray theory solution. Overall, the trends of the reflection functions can be understood in terms of the transition from low frequency behavior to high frequency behavior. At low frequency the curves start with a linear slope which is a characteristic of the low frequency analysis, then level out towards a constant, frequency-independent, value which is a characteristic of the high frequency analysis.

VII. CONCLUSIONS

The finite element simulations, confirmed by experimental measurements, have provided a useful collection of reflection coefficient results for the s_0 mode reflecting from rectangular notches of various widths and depths. Furthermore, the examination of the results has identified the important phenomenon of the interference between the reflections from the two sides of the notch, which leads to a periodic shape of the reflection as a function of notch width, exhibiting evenly spaced maxima and minima. It has also been shown that the reflection function is characterized by both the geometric ratio of the wavelength to notch width and the frequency-thickness product. Whereas most applications of interest to the authors (guided wave NDE) do not have perfectly square notches, these observed characteristics are likely still to feature to some significant extent, and the understanding of their nature is important.

The findings of the analytical study of the reflection from cracks also has value in explaining the nature of the reflection behavior. Specifically, the trend of the functions from a linear slope at low frequency towards a frequency-independent constant at high frequency has been explained by the asymptotic quasistatic and ray theory analyses. As well as identifying here the useful range of parameters for which the asymptotic analyses may be used, the understanding of the phenomena will be useful for the interpretation of the observations of other cases of guided wave reflections when similar trends are observed.

[1] D. Worlton, ‘‘Ultrasonic testing with Lamb waves,’’ Nondestr. Test. (Chicago) **15**, 218–222 (1957).

[2] D. Worlton, ‘‘Experimental confirmation of Lamb waves at megacycle frequencies,’’ J. Appl. Phys. **32**, 967–971 (1961).

[3] I. A. Viktorov, *Rayleigh and Lamb Waves* (Plenum, New York, 1970).

[4] T. Mansfield, ‘‘Lamb wave inspection of aluminium sheet,’’ Mater. Eval. **33**, 96–100 (1975).

[5] D. Alleyne and P. Cawley, ‘‘The interaction of Lamb waves with defects,’’ IEEE Trans. Ultrason. Ferroelectr. Freq. Control **39**, 381–397 (1992).

[6] D. Alleyne and P. Cawley, ‘‘Optimization of Lamb wave inspection techniques,’’ NDT & E Int. **25**, 11–22 (1992).

[7] Y. Cho and J. Rose, ‘‘A boundary element solution for a mode conversion study on the edge reflection of Lamb waves,’’ J. Acoust. Soc. Am. **99**, 2097–2109 (1996).

[8] Y. Cho, D. Hongerholt, and J. Rose, ‘‘Lamb wave scattering analysis for reflector characterization,’’ IEEE Trans. Ultrason. Ferroelectr. Freq. Control **44**, 44–52 (1997).

[9] T. Ghosh, T. Kundu, and P. Karpur, ‘‘Efficient use of Lamb modes for detecting defects in large plates,’’ Ultrasonics **36**, 791–801 (1998).

[10] S. Rokhlin, ‘‘Resonance phenomena of Lamb waves scattering by a finite crack in a solid layer,’’ J. Am. Ceram. Soc. **69**, 922–928 (1981).

[11] J. Paffenholz, W. Fox, X. Gu, G. Jewett, S. Datta, and H. Spetzler, ‘‘Experimental and theoretical study of Rayleigh-Lamb waves in a plate containing a surface-breaking crack,’’ Res. Nondestruct. Eval. **1**, 197–217 (1990).

[12] W. Mohr and P. Holler, ‘‘On inspection of thin-walled tubes for transverse and longitudinal flaws by guided ultrasonic waves,’’ IEEE Trans. Sonics Ultrason. **SU-23**, 369–378 (1976).

[13] W. Bottger, H. Schneider, and W. Weingarten, ‘‘Prototype EMAT system for tube inspection with guided ultrasonic waves,’’ Nucl. Eng. Des. **102**, 356–376 (1987).

[14] J. Rose, J. Ditri, A. Pilarski, K. Rajana, and F. Carr, ‘‘A guided wave inspection technique for nuclear steam generator tubing,’’ NDT & E Int. **27**, 307–310 (1994).

[15] J. Ditri, ‘‘Utilization of guided elastic waves for the characterization of circumferential cracks in hollow cylinders,’’ J. Acoust. Soc. Am. **96**, 3769–3775 (1994).

[16] D. Alleyne and P. Cawley, ‘‘Long range propagation of Lamb waves in chemical plant pipework,’’ Mater. Eval. **55**, 504–508 (1997).

[17] D. Alleyne, M. Lowe, and P. Cawley, ‘‘The reflection of guided waves from circumferential notches in pipe,’’ J. Appl. Mech. **65**, 635–641 (1998).

[18] M. Lowe, D. Alleyne, and P. Cawley, ‘‘The mode conversion of a guided wave by a part-circumferential notch in a pipe,’’ J. Appl. Mech. **65**, 649–656 (1998).

[19] J. Rasmussen, ‘‘Prediction of fatigue using ultrasonic surface waves,’’ Nondestr. Test. (Chicago) **20**, 103–110 (1962).

[20] A. Testa and C. Burger, ‘‘A measurement of crack depth by changes in the frequency spectrum of Rayleigh wave,’’ *Novel Non-Destructive Testing Methods for Materials* (American Institute of Mining Metallurgical and Petroleum Engineers, New York, 1983), pp. 91–108.

[21] P. Wilcox, M. Lowe, and P. Cawley, ‘‘Lamb and SH wave transducer arrays for the inspection of large areas of thick plates,’’ in *Review of Progress in Quantitative NDE*, edited by D. Thompson and D. Chimenti (Plenum, New York, 2000), Vol. 19, pp. 1049–1056.

[22] B. Auld, *Acoustic Fields and Waves in Solids* (Krieger, Malabar, FL, 1990), Vol. 2.

[23] P. Wilcox, M. Lowe, and P. Cawley, ‘‘Long range Lamb wave inspection: the effect of dispersion and modal selectivity,’’ in *Review of Progress in Quantitative NDE*, edited by D. Thompson and D. Chimenti (Plenum, New York, 1999), Vol. 18, pp. 151–158.

[24] D. Hitchings, ‘‘FE77 User Manual,’’ Tech. Rep., Imperial College of Science, Technology and Medicine, London, UK, 1994.

[25] K.-J. Bathe, *Finite Element Procedures in Engineering Analysis* (Prentice-Hall, Englewood Cliffs, NJ, 1982).

[26] D. Alleyne and P. Cawley, ''A two-dimensional Fourier transform method for the measurement of propagating multimode signals,'' J. Acoust. Soc. Am. **89**, 1159–1168 (1991).
[27] B. Auld, ''General electromechanical reciprocity relations applied to the calculation of elastic wave scattering coefficients,'' Wave Motion **1**, 3–10 (1979).
[28] G. Kino, ''The application of reciprocity theory to scattering of acoustic waves by flaws,'' J. Appl. Phys. **49**, 3190–3199 (1978).
[29] W. Deutsch, ''Wave scattering from surface-breaking cracks sonified by a linear phased array,'' in *Review of Progress in Quantitative NDE*, edited by D. Thompson and D. Chimenti (Plenum, New York, 1999), pp, 71–78.
[30] H. Tada, P. Paris, and G. Irwin, *The Stress Analysis of Cracks Handbook* (Del Research Co., St. Louis, 1973).
[31] J. Achenbach, L. Adler, D. Kent Lewis, and H. McMaken, ''Diffraction of ultrasonic waves by penny-shaped cracks in metals: theory and experiment,'' J. Acoust. Soc. Am. **66**, 1848–1856 (1979).

The effect of fluid loading on radiation efficiency

M. L. Rumerman
Naval Surface Warfare Center, Carderock Division, Signatures Directorate (Code 7204), 9500 MacArthur Boulevard, West Bethesda, Maryland 20817-5700

(Received 16 April 2001; revised 27 September 2001; accepted 16 October 2001)

The metric ''radiation efficiency,'' used to estimate a panel's radiated acoustic power from a measure of its normal velocity, is typically derived under the condition of very light fluid loading. This paper shows that efficiencies calculated in this manner can significantly overestimate the radiated power when the condition of light fluid loading is not met, as can be the case for steel plates in water. It is also shown that, when fluid loading is not light, a baffled semi-infinite plate is not a good model for an interior support. Numerical results are presented for radiation efficiencies calculated for steel plates in water, and are compared to those calculated under the assumption of vanishing fluid loading. © *2002 Acoustical Society of America.* [DOI: 10.1121/1.1427359]

PACS numbers: 43.20.Tb, 43.40.Rj, 43.20.Rz [DEC]

I. INTRODUCTION

The metric ''radiation efficiency'' is used to convert a panel's vibration levels to radiated acoustic power by forming the four-factor product of panel mean-squared normal velocity, panel area, characteristic acoustic impedance of ambient medium, and radiation efficiency. The first substantial derivation, discussion, and application of a panel's radiation resistance appears to be due to Maidanik,[1] who presented results in terms of a normalized radiation resistance that later became known as radiation efficiency. In the ''classical'' application of radiation efficiency, the vibration field of a simply supported or clamped panel is assumed to be composed of in-vacuum modes. The power radiated by a given mode shape is then computed by using its Fourier transform and assuming the panel to lie in an infinite impedance coplanar baffle. By classifying modes in terms of ''corner,'' ''edge,'' and ''surface'' radiation, and applying the fraction of each type resonating in any broad frequency band, the overall radiation efficiency of the panel is estimated. This approach has been applied not only to panels that are homogeneous except for their perimeters, but to panels reinforced by interior ribs as well.

An assumption implicit in the derivation and use of these radiation efficiencies is that the fluid loading is ''light.'' This justifies the calculation of radiated power using the Fourier transforms of *in vacuo* modes of baffled plates and the treatment of interior ribs in the same manner as perimeter edges (when the rib impedances are large enough so that they effectively constrain the panel along their lines of attachment). Because the initial applications of radiation efficiency were to panels vibrating in air, this assumption was appropriate; however, the same approach has been applied to panels in water where the fluid loading may not be light. The purpose of this paper is to demonstrate that when the fluid loading is not light, the use of classical radiation efficiency can produce significant overestimates of radiated power.

Some aspects of this problem were examined by Davies,[2] who treated the problem of radiation due to a normal displacement wave freely propagating on a semi-infinite fluid-loaded membrane, and incident upon the membrane's supported edge. (In the present context, the differences between a ''membrane'' and a ''plate'' are unimportant.) Using a Wiener–Hopf analysis, he verified that the very light fluid-loading formulation yields a good approximation to the radiated power when a fluid-loading parameter μ, defined as the ratio of the membrane's (or plate's) mass impedance per unit area to the ambient acoustic medium's characteristic impedance, is greater than unity. Davies' results also indicate that, when μ is less than unity, the light fluid-loading approximation overestimates the radiated power. The present paper extends his contribution by comparing the radiation due to interior supports to the radiation due to baffled edges. It will be shown that not only does the light fluid-loading approximation overestimate the radiated power for baffled plates when $\mu<1$, but the baffled plate model overestimates the power radiated due to infinite impedance interior supports when $\mu<1$. For steel plates in water, the overestimate can be significant for frequencies and plate thicknesses of practical interest.

II. RADIATION DUE TO LINE FORCE

In order to illustrate why the problem arises, this section will consider a phase-invariant line force that drives an infinite plate bounding a semi-infinite acoustic medium. The problem may be formulated in terms of Fourier transforms of the spatial distribution of the excitation forces and the Green's function of the plate–fluid system. The latter is often referred to as the wave number or wave impedance. A discussion of this concept is given by Fahy.[3] The frequency–wave number impedances of the plate (in bending) and the acoustic medium are given by Eqs. (1) and (2), respectively, in which α is the transform variable (wave number) corresponding to the spatial variable and ω is the transform variable (radian frequency) corresponding to the temporal variable

$$Z_p(\alpha;\omega)=-i\omega M\left[1-\frac{\alpha^4}{k_b^4}\right];\quad k_b^4=\frac{M\omega^2}{D}, \tag{1}$$

$$Z_f(\alpha;\omega)=\frac{\rho\omega}{\sqrt{(k^2-\alpha^2)}};\quad k=\frac{\omega}{c}. \tag{2}$$

In Eq. (1), M is the mass per unit area of the plate, D is its bending rigidity, and k_b is the bending wave number of the plate at the particular frequency. In Eq. (2), ρ is the mass density of the ambient acoustic medium, c is its sound speed, and k is the acoustic wave number at that frequency. A time dependence $\exp(-i\omega t)$ is assumed, in which ω is equal to 2π times the frequency. When thin-plate theory is used for the bending model, the relationship in Eq. (3) applies, in which ρ_s is the mass density of the plate material, and c_c is the speed of compressional waves in the plate

$$\frac{\Gamma^2}{\mu}=\frac{\rho}{cM}\sqrt{\frac{D}{M}}=\frac{1}{\sqrt{12}}\frac{\rho c_c}{\rho_s c}, \tag{3}$$

where $\mu=\omega M/\rho c$ and $\Gamma=k/k_b$.

For steel plates in water, nominal parameter values are $\rho=1000$ kg/m^3, $c=1500$ m/s, $\rho_s=7800$ kg/m^3, and $c_c=5250$ m/s. With these values, the right-hand side of Eq. (3) is equal to 0.13. It is noted that Γ^2 is equal to the frequency divided by the plate's nominal bending coincidence frequency, and that Γ is the ratio of the *in vacuo* bending wave speed to the ambient acoustic wave speed (i.e., the bending wave Mach number).

Let a line force with temporal rms value per unit length F be located at $x=0$. The time-averaged power radiated per unit length of line force is given by Eq. (4a)

$$\Pi_F=\frac{F^2}{2\pi}\int_{-k}^{+k}\frac{\rho\omega}{\sqrt{(k^2-\alpha^2)}}\frac{d\alpha}{|Z_p(\alpha;\omega)+Z_f(\alpha;\omega)|^2}. \tag{4a}$$

When $\Gamma^4 \ll 1$, the evaluation of Eq. (4b) is obtained.

$$\Pi_F\approx F^2\frac{\rho}{2\omega M^2}\left(1-\frac{1}{\sqrt{1+\mu^2}}\right). \tag{4b}$$

This result was given by Maidanik,[4] who has an additional factor of 2 in the denominator of the right-hand side because he represented the line force in terms of its amplitude rather than this rms value. The asymptotic forms for very light fluid loading, $\mu \gg 1$, and heavy fluid loading, $\mu \ll 1$, are given by Eqs. (5a) and (5b), respectively,

$$\Pi_F\approx F^2\frac{\rho}{2\omega M^2}, \tag{5a}$$

$$\Pi_F\approx F^2\frac{\rho\mu^2}{4\omega M^2}. \tag{5b}$$

In defining radiation efficiency, the radiated power is divided by the fluid mass density, ρ; therefore, Eqs. (5) suggest that, at a given frequency, a plate in contact with an acoustic fluid of given mass density and sound speed may have a significantly smaller radiation efficiency than that plate in contact with an acoustic fluid having the same sound speed but much lower mass density. The line-force input admittance is also a factor in that it determines the magnitude of the force needed to satisfy the constraint. The idealizations discussed below consider the complete interaction between the plate and force.

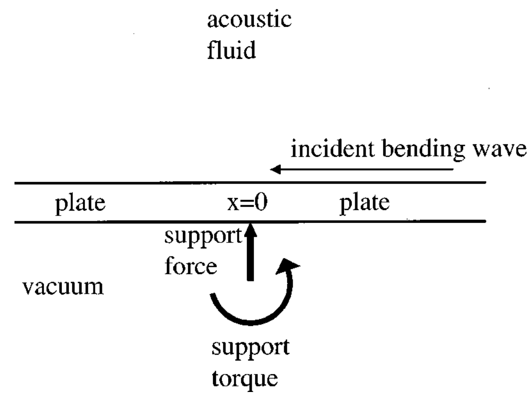

FIG. 1. Sketch of infinite plate configuration.

III. RADIATION DUE TO LINE SUPPORTS

Consider a free-bending wave given by $V_0\exp(-i\alpha_0 x)$, where V_0 is its rms normal velocity and α_0 is its wave number. The wave originates at $x=+\infty$ and propagates in the negative x direction on an infinite fluid-loaded plate that lies in the $x-y$ plane. In the absence of discontinuities on the plate, this wave does not radiate acoustic power if its wave speed is less than the speed of sound in the fluid, that is, if $\alpha_0>k$. The wave is normally incident upon an interior infinite impedance line support that lies along the line $x=0$. Two types of supports will be considered: (1) a knife edge that exerts only a force on the plate to null the normal velocity, and (2) a clamp that exerts both a normal force and a torque to null both normal velocity and bending rotation. These cases will be compared to that of a free-bending wave propagating on a semi-infinite plate and normally incident upon the clamped edge that it shares with a coplanar rigid baffle. Sketches of the infinite and semi-infinite plate configurations are given in Figs. 1 and 2. For both the infinite and semi-infinite plates, interaction of the incident wave and the supports results in radiated acoustic power.

A. General results

For the case of the interior support, whether knife edge or clamp, the rms force required to null the velocity is $F=V_0/|Y_F^i|$, where Y_F^i is the line-force input admittance given by Eq. (6)

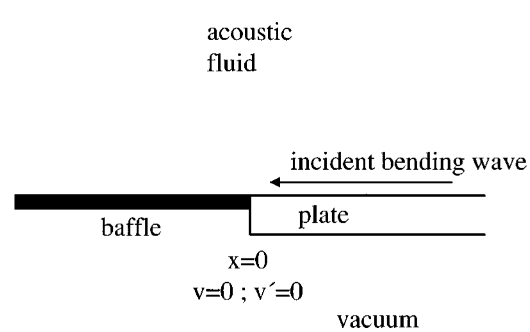

FIG. 2. Sketch of semi-infinite plate configuration.

$$Y_F^i = \frac{1}{2\pi}\int_{-\infty}^{+\infty} \frac{\exp(i\alpha x)}{Z_p(\alpha;\omega)+Z_f(\alpha;\omega)}\, d\alpha. \tag{6}$$

The time-averaged radiated power due to the force is obtained using Eq. (4a). At a clamped support, an rms torque $T=\alpha_0 V_0/|Y_T^i|$ is also required, where Y_T^i is the line-input admittance relating the torque to the rotation at the line of application, and is given by Eq. (7)

$$Y_T^i = \frac{1}{2\pi}\int_{-\infty}^{+\infty} \frac{\alpha^2 \exp(i\alpha x)}{Z_p(\alpha;\omega)+Z_f(\alpha;\omega)}\, d\alpha. \tag{7}$$

The time-averaged power radiated by the torque is given by Eq. (8)

$$\Pi_T = \frac{T^2}{2\pi}\int_{-k}^{+k} \frac{\rho\omega}{\sqrt{(k^2-\alpha^2)}} \frac{\alpha^2}{|Z_p(\alpha;\omega)+Z_f(\alpha;\omega)|^2}\, d\alpha. \tag{8}$$

Because at the drive line the plate rotation due to the force and the normal displacement due to the torque both vanish, the net powers due to the force and torque are uncoupled, and can be added to obtain the total power for the clamped support. The radiated powers for the corresponding cases of the semi-infinite baffled plates with simply supported and clamped edges are obtained using the Wiener–Hopf method.

B. Very light fluid loading

Very light fluid loading is obtained by letting the fluid mass density ρ become arbitrarily small, while keeping the sound speed, c, constant so that relevant wavelength ratios are maintained. In the limit of vanishing fluid mass density, the plates responses approach *in vacuo* values. The line force input admittance approaches $[k_b(1+i)/4\omega M]$, and the radiated power due to an interior support normal force is given by Eq. (9)

$$\Pi^{I,F} \approx \frac{8V_0^2}{\pi}\frac{\rho\omega}{k_b^2}\int_0^k \left(1-\frac{\alpha^4}{k_b^4}\right)^{-2} \frac{d\alpha}{\sqrt{(k^2-\alpha^2)}}$$

$$= \left[\frac{4-3\Gamma^2}{(1-\Gamma^2)^{3/2}} + \frac{4+3\Gamma^2}{(1+\Gamma^2)^{3/2}}\right]\frac{\rho\omega}{2k_b^2}V_0^2. \tag{9}$$

The line-torque admittance approaches $[k_b^3(1-i)/4\omega M]$, and the acoustic power radiated due to an interior support torque is given by Eq. (10)

$$\Pi^{I,T} \approx \frac{8V_0^2}{\pi}\frac{\rho\omega}{k_b^4}\int_0^k \alpha^2 \left|1-\frac{\alpha^4}{k_b^4}\right|^{-2} \frac{d\alpha}{\sqrt{(k^2-\alpha^2)}}$$

$$= \left[\frac{2-\Gamma^2}{(1-\Gamma^2)^{3/2}} - \frac{2+\Gamma^2}{(1+\Gamma^2)^{3/2}}\right]\frac{\rho\omega}{2k_b^2}V_0^2. \tag{10}$$

The power radiated due to an integer knife edge is given by Eq. (9) alone, and that radiated due to an interior clamp is found by adding the right-hand sides of Eqs. (9) and (10) to obtain Eq. (11)

$$\Pi_{cl}^I = \left[\frac{1}{\sqrt{(1+\Gamma^2)}} + \frac{3-2\Gamma^2}{(1-\Gamma^2)^{3/2}}\right]\frac{\rho\omega}{k_b^2}V_0^2. \tag{11}$$

The total velocity field on a semi-infinite clamped baffled plate under very light fluid loading is $V_0[\exp(-ik_bx)+i\exp(+ik_bx)-(1+i)\exp(-k_bx)]$, and the radiated power is given by Eq. (12)

$$\Pi_{cl}^B \approx \frac{8V_0^2}{\pi}\rho\omega\int_0^k (k_b^2+\alpha^2)^{-1}\left|1-\frac{\alpha^2}{k_b^2}\right|^{-2} \frac{d\alpha}{\sqrt{(k^2-\alpha^2)}}$$

$$= \left[\frac{1}{\sqrt{(1+\Gamma^2)}} + \frac{3-2\Gamma^2}{(1-\Gamma^2)^{3/2}}\right]\frac{\rho\omega}{k_b^2}V_0^2. \tag{12}$$

It is noted that, under very light fluid loading, the powers radiated by the interior clamped support and the baffled clamped edge are identical.

IV. CALCULATED RADIATION EFFICIENCIES

For two-dimensioinal (2D) configurations, radiation efficiency is obtained by dividing the time-averaged radiated power by the three-factor product of characteristic impedance of the ambient medium, the panel area (A), and the panel's mean-squared normal velocity

$$\sigma_{2\mathrm{D}} = \frac{\Pi}{\rho c A V_0^2}. \tag{13}$$

For a one-dimensional (1D) problem, the area is replaced by a length, L, and Π is the time-averaged power radiated per unit width of the plate in the direction parallel to the support

$$\sigma_{1\mathrm{D}} = \frac{\Pi}{\rho c L V_0^2}. \tag{14}$$

Because the plates modeled here are infinite or semi-infinite, there is no natural characteristic length, and L will be arbitrarily set equal to 100 cm. Additionally, rather than use the actual mean-squared velocity, which includes the contributions of incident, reflected, and transmitted velocity fields, the incident rms velocity, V_0, will be used as the reference velocity.

A. Illustrative example

Calculated results will be presented for a 1-cm-thick steel plate with water on one side, using the nominal material parameters given in Sec. II. Although the numbers have no significance in absolute terms, the definition provides a common basis for comparing the various configurations. Figure 3 presents radiation efficiencies for the infinite plate with an interior line support under normal water loading, and for a baffled plate with clamped edge under very light fluid loading (which is also the result for an interior clamped support under very light fluid loading). Figure 4 compares results for the semi-infinite baffled plate and infinite plate, each under normal water loading and having a clamped support.

B. Comments

For steel plates with water on one side, $\mu<1$ when $\Gamma^2<0.13$. Figure 3 dramatically illustrates the effects of fluid loading on the radiation efficiency of an interior support on an infinite plate. When $\Gamma^2<0.5$, the powers radiated by

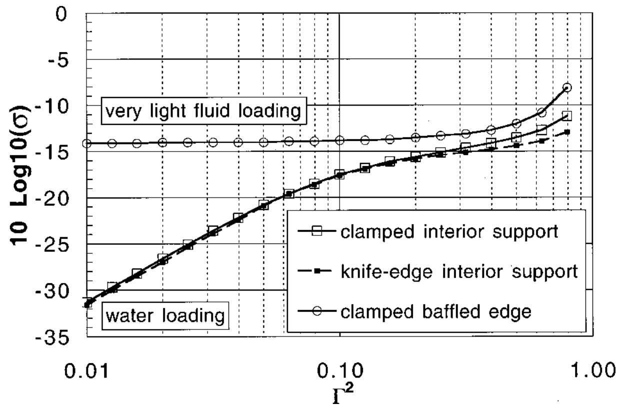

FIG. 3. Comparison of radiation efficiencies for normal water loading and light fluid loading.

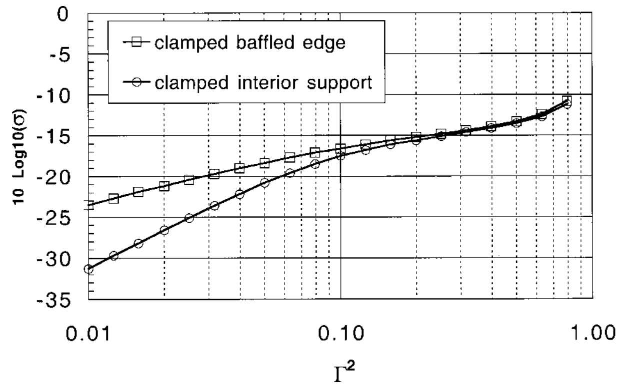

FIG. 4. Comparison of radiation efficiencies for semi-infinite baffled plate and infinite plate with clamped supports under normal water loading.

clamped and knife edge interior supports are almost identical. As Γ^2 decreases below 0.13, and μ decreases below unity, these values become increasingly less than the power radiated by the clamped edge (or clamped interior support) under very light fluid loading. (The condition of a simply supported edge, although a common model, is not a realistic boundary condition for a plate.) Figure 4 indicates that, when $\mu<1$, the baffled clamped edge model overestimates the power radiated by the interior clamped support.

V. DISCUSSION

The preceding analyses and calculations have indicated that the use of the classical light fluid-loading radiation efficiencies can significantly overestimate the radiation efficiencies of steel plates having one-sided water loading when $\mu<1$. (If the water loading is two-sided, the applicable inequality is $\mu/2<1$.) This was illustrated through the examples of an infinite plate having an interior infinite impedance knife edge or clamped support, and a baffled semi-infinite plate with a clamped edge.

The baffled-plated idealization is useful for plates in air when one panel is connected to another through a high impedance (translational and rotational) support. Under these conditions, the effectively clamped support inhibits panel coupling through a structural path and the light fluid loading makes coupling through the fluid path insignificant. The second panel effectively acts as a rigid baffle extension of the first; therefore, the infinite plate with clamped support and the semi-infinite baffled clamped plate have the same radiation efficiencies under very light fluid loading, as shown by Eqs. (11) and (12). The applicability of the baffle idealization to plates in water, however, is not always appropriate because the fluid path contributes to coupling between the plates, and the effect on radiated power can be significant.

An analysis of a situation in which the plate sections on opposite sides of the support are not identical requires some form of Wiener–Hopf procedure. One such implementation is given by Norris and Wickham,[5] who considered the problem of a fluid-loaded plate with a bending wave traveling towards its junction with a coplanar dissimilar plate. Their analysis was made specific to plates of the same material but different thickness, and one of their sample calculations is for steel plates in water reinforced by a clamped support along the junction line, with the second (receiving) plate twice the thickness of the first. They include a graph of radiated power vs frequency, and it can be shown that, below the coincidence frequency of the thicker plate, the results are comparable to those for a clamped uniform infinite plate of the smaller thickness. In this frequency range, a uniform, infinite-supported plate model appears to be adequate.

Line supports of infinite translational and rotational impedance were used in this paper to simplify the presentation of results and not obscure the points made regarding the importance of fluid loading in estimating radiation efficiency. If the supports are of finite impedance, as with ribs, these impedances must be combined with the corresponding input admittances of the plate to determine the resulting force and torque. The radiated power may then again be calculated using Eqs. (4a) and (8). Similarly, only situations that were phase-invariant in the direction of attachment were considered. Corresponding calculations can be performed for other than zero wave number for that direction, with similar results.

VI. CONCLUSIONS

The analysis in this paper has shown that the use of the classical, very light fluid-loading radiation efficiencies will overestimate the actual radiation efficiency when the fluid-loading parameter μ is less than unity. For steel plates with water on one side, this occurs at frequency-plate thickness products less than 3 kHz cm. When there is water on both sides of the plate, the applicable inequality is $\mu<2$, which occurs when the frequency-thickness product is less than 6 kHz cm. Statistical energy analysis codes that use radiation efficiency subroutines to compute radiated power will overestimate levels in these frequency ranges if fluid-loading effects have not been accounted for.

ACKNOWLEDGMENT

This work was supported by the Office of Naval Research Hydroacoustics Program: L. Patrick Purtell, Program Manager.

[1] G. Maidanik, ''Response of ribbed panels to reverberant acoustic fields,'' J. Acoust. Soc. Am. **34**, 809–826 (1962).
[2] H. G. Davies, ''Natural motion of a fluid-loaded semi-infinite membrane,'' J. Acoust. Soc. Am. **55**, 213–219 (1974).
[3] F. Fahy, *Sound and Structural Vibration* (Academic, Orlando, 1985), Chap. 3.
[4] G. Maidanik, ''The influence of fluid loading on the radiation from orthotropic plates,'' J. Sound Vib. **3**, 288–299 (1966).
[5] A. N. Norris and G. R. Wickham, ''Acoustic diffraction from the junction of two flat plates,'' Proc. R. Soc. London, Ser. A **451**, 631–655 (1995).

Theory of non-collinear interactions of acoustic waves in an isotropic material with hysteretic quadratic nonlinearity

Vitalyi Gusev
Laboratoire de Physique de l'Etat Condensé, UPRESA-CNRS 6087, Faculté des Sciences, Ecole Nationale Supérieure d'Ingénieurs du Mans, Université du Maine, 72085 Le Mans, France

(Received 1 December 2000; accepted for publication 17 April 2001)

A particular form of the energy potential (cubic in strains) is proposed, which leads to the bow-tie behavior of the nonlinear modulus in an isotropic material with hysteresis of quadratic nonlinearity. The nonlinear scattering of a weak probe wave in the field of a strong pump wave is analyzed. It is demonstrated that collinear interactions of the shear waves are allowed in materials with nonlinearity hysteresis. Both in collinear and non-collinear frequency-mixing processes the combination frequency is composed of the probe wave frequency and one of the even harmonics of the pump wave. In general, the developed theory predicts that in the presence of the hysteretic nonlinearity the number of possible resonant scattering processes increases. In particular, if frequency-mixing processes are forbidden in the material with the elastic quadratic nonlinearity (for a fixed ratio of primary frequencies), they may be allowed in the materials with hysteretic quadratic nonlinearity. Moreover, in materials with hysteresis of the nonlinearity the resonant frequency mixing for a fixed ratio of primary frequencies may be allowed for multiple mutual orientations of the primary wave vectors. [DOI: 10.1121/1.1382621]

PACS numbers: 43.25.Dc, 91.60.Lj, 91.30.Fn [MFH]

I. INTRODUCTION

There is currently a growing interest in nonlinear acoustic phenomena caused by hysteresis of nonlinearity in many types of mesoscopic materials.[1–7] For acoustics (which is, by definition, the mechanics of weak-amplitude disturbances) the lowest-order hysteretic nonlinearity is the most important. This is the so-called quadratic hysteretic nonlinearity.[4,6,7] Among the manifestations of the quadratic hysteretic nonlinearity are the observation of a quadratic dependence of the third harmonic amplitude on the excitation amplitude in some experiments,[8] the proportionality of the shift in the resonance frequency of a vibrating bar to the amplitude of oscillations,[7,9] self-modulation instability[10,11] and strong parametrically induced attenuation[12–15] of the acoustic waves in mesoscopic materials.

Unfortunately the existing theoretical models for the description of the nonlinearity hysteresis are one-dimensional.[4–6,16–18] They can be efficiently applied for the analysis of collinear[11–15,19,20] or quasi-collinear[21] interactions of the acoustic waves. But, for the analysis of non-collinear interactions of the acoustic waves a general tensor nonlinear stress/strain relationship should be modeled for the mesoscopic materials. In the present publication such model for hysteretic quadratic nonlinearity of an isotropic material is proposed and applied to the analysis of possible frequency-mixing processes in non-collinear longitudinal and shear waves.

A similar theoretical approach for quadratic elastic nonlinearity had been proposed more than 35 years ago.[22–24] Theoretical predictions for non-collinear three-wave acoustic interactions in elastic materials had been well confirmed by experiments (see references in the review article[25]) and have been subjected recently to the experimental verification in the mesoscopic (microinhomogeneous) materials (rocks) as well.[26,27] However, the question of the possible additional wave interactions allowed due to the presence of hysteretic quadratic nonlinearity has not been explored yet either theoretically or experimentally.

The theory developed in the following describes possible nonlinear non-collinear frequency-mixing interactions (due to nonlinearity hysteresis) between a strong (pump) wave creating a moving grating and a weak (probe) wave incident on this grating. Some of the predicted frequency-mixing processes are forbidden in the absence of the hysteretic quadratic nonlinearity or in the collinear geometry. It is expected that the proposed theory could be useful for the development of different methods for nonlinear acoustic tomography[28–30] based on non-collinear acoustic interactions, for the investigation of the acoustic wavefront reversal and for the analysis of the sound attenuation by noise in mesoscopic materials. In these and some other situations a three-dimensional (3D) model describing nonlinearity hysteresis in the case of an arbitrary low-amplitude (i.e., acoustic) loading of the material is necessary.

II. STRESS/STRAIN RELATIONSHIPS FOR MATERIALS WITH HYSTERESIS OF QUADRATIC NONLINEARITY

The final goal of the present publication is to identify all possible interactions of the acoustic waves (both longitudinal and shear) in materials with quadratic hysteretic nonlinearity. For this purpose the nonlinear constitutive relation (stress/strain relation) should be used. However, until now the description of nonlinearity hysteresis has been proposed only for one-dimensional (1D) processes. These nonlinear hysteretic relationships between normal stress and elongation[4–7,17] or between shear stress and shear strain[15,21] have been successfully applied for the description of collinear and quasi-collinear interactions of acoustic waves. But, they are not sufficient for the description of the non-collinear interactions and of interactions between the longitudinal and shear acoustic waves. For these purposes the general 3D relations between the stresses and strains in the materials with the hysteresis of the quadratic nonlinearity should be proposed.

The most straightforward way to derive the constitutive relations for an isotropic medium is to assume the existence of a "stress potential" (i.e., of an energy function), which depends on the strain invariants.[25,31–34] We are adopting this approach here. Thus, our first assumption is the existence of a stress potential in the hysteretic medium. Because we are interested in the lowest possible order (i.e., quadratic) nonlinearity in the stress/strain relation, in the expression for the energy we are retaining only cubic terms in strain. This is our second assumption. Both the first and the second assumptions are rather common.[22–25] The most important assumptions, however, are made relative to the form of the cubic terms in the stress potential because the form of these terms should reflect the basic properties of the medium with nonlinearity hysteresis.

It is confirmed by experiments[6,35–37] and it also follows from some theoretical models[6,16,17] that materials with hysteresis of the nonlinearity possess the property of end-point memory. The mechanical behavior of the material abruptly changes in the so-called end points where loading of the material is changed for unloading (or vice versa) and material remembers the latest end point (and under some conditions material remembers some of the previous end points as well). To take this phenomenon partially into account, we are evaluating the energy not relative to some undisturbed state of the material (as it is done in the nonlinear elasticity theory[25,31]), but relative to its state in the latest end point. This is our third assumption. It should be pointed out here that we are not modeling the total nonlinear stress/stress strain relationship but only its hysteretic part. The corresponding contribution to the energy function should be always negative to provide hysteretic lost work both when unloading follows loading, or loading follows unloading. To take this fact into account we assume that the energy function depends not on the invariants of the strain tensor (as in the nonlinear elasticity theory[25,31]) but on the absolute values of these invariants. Then, by choosing appropriate sign of the constant nonlinear parameters we are able to have only negative values of the hysteretic energy function for all possible deviations of the material from the end point. This is our fourth assumption.

Before implementing this assumptions it should be noted that finally the selection rules (energy and momentum conservation laws) for three-wave acoustic interactions in materials with quadratic hysteretic nonlinearity are controlled by the hysteresis in the stress/strain relationship (or, equivalently, by the bow-tie behavior of the elastic moduli). The form of the energy function we are choosing serves to derive a quantitative presentation of the hysteretic stress tensor and the hysteretic moduli, which correlates with their qualitative behavior known from the experiments. So, we believe that even if the form of the energy function (proposed in what follows) is incomplete, and, perhaps, it may be modified or improved in the future, the selection rules for the interaction of a weak probe wave with a strong pump wave (derived in what follows) will remain unchanged.

Our above formulated assumptions provide the rules for how the cubic terms in the classical presentation of the elastic energy[25,31] should be modified to get the description of the cubic terms in the presentation of the hysteretic energy W. The simplest term is

$$\begin{aligned} W_1 &= -\tfrac{1}{6}h_1|I_1(\varepsilon_{ij}-\varepsilon_{ij}^0)|^3 \\ &= -\tfrac{1}{6}h_1|\varepsilon_{mm}-\varepsilon_{mm}^0|^3 \\ &= -\tfrac{1}{6}h_1\,\mathrm{sign}[I_1(\hat{\varepsilon}-\hat{\varepsilon}^0)]I_1^3(\hat{\varepsilon}-\hat{\varepsilon}^0), \end{aligned} \tag{1}$$

where $h_1\geqslant 0$ is a non-negative constant (hysteretic nonlinear modulus), $I_1=\varepsilon_{mm}=tr(\hat{\varepsilon})$ is the first invariant of the strain tensor for which (as well as for the other second-range tensors) we are using in the following two types of notation, $\varepsilon_{ij}\equiv\hat{\varepsilon}$. Einstein's summation convection on repeated indices is assumed. In Eq. (1) ε_{ij}^0 is the strain tensor evaluated in the latest end point. Equation (1) satisfies all the above-formulated assumptions. With the help of Eq. (1) the corresponding contribution to stress tensor σ_{ij} is obtained by evaluating the variation of the energy with strain

$$\begin{aligned} \sigma_{ij}^{(1)} &= \frac{\delta W_1}{\delta\varepsilon_{ij}} = -\frac{1}{2}h_1|\varepsilon_{mm}-\varepsilon_{mm}^0|(\varepsilon_{mm}-\varepsilon_{mm}^0)\,\delta_{ij} \\ &\equiv -\tfrac{1}{2}h_1\,\mathrm{sign}[I_1(\hat{\varepsilon}-\hat{\varepsilon}^0)]I_1^2(\hat{\varepsilon}-\hat{\varepsilon}^0)\hat{I}, \end{aligned} \tag{2}$$

where $\hat{I}\equiv\delta_{ij}$ denotes the unit tensor. It should be noted here that the relation $\sigma_{ij}\equiv\partial W/\partial\varepsilon_{ij}$ defines the Lagrange's (or the second Piola–Kirchhoff's) stress tensor. However, in materials with nonlinearity hysteresis the nonlinearity of state equation significantly exceeds the so-called kinematic nonlinearity. In the analysis presented here the nonlinearity related to the difference between the Lagrange's and Euler's descriptions is completely neglected. In this case the stress tensor used here does not differ from the first Piola–Kirchhoff's stress tensor defined by $\sigma_{ij}\equiv\partial W/\partial u_{i,j}$ (where $u_{i,j}\equiv\partial u_i/\partial x_j$ is the displacement gradient tensor, u_i are the particle displacement components).

The corresponding contribution to elastic modulus c_{ijkl} is obtained by evaluating the variation of the stress with strain

$$\begin{aligned} c_{ijkl}^{(1)} &= \frac{\delta\sigma_{ij}^{(1)}}{\delta\varepsilon_{kl}} = -h_1|I_1(\hat{\varepsilon}-\hat{\varepsilon}^0)|\,\delta_{ij}\delta_{kl} \\ &= -h_1\,\mathrm{sign}[I_1(\hat{\varepsilon}-\hat{\varepsilon}^0)]I_1(\hat{\varepsilon}-\hat{\varepsilon}^0)\,\delta_{ij}\delta_{kl}. \end{aligned} \tag{3}$$

It should be pointed out that hysteretic moduli defined here are related to the moduli c'_{ijkl} traditionally introduced as $c'_{ijkl}\equiv\partial\sigma_{ij}/\partial u_{k,l}$ (Ref. 31) via the relation $c'_{ijkl}=(c_{ijkl}+c_{ijlk})/2$.

In accordance with Eq. (3) the hystereretic quadratic nonlinearity always leads to softening of the material. This conclusion correlates with the available experimental observations.[35,36] If after the latest end point $\partial I_1/\partial t>0$, then

$$c_{ijkl}^{(1)} = -h_1(I_1 - I_1^0)\,\delta_{ij}\delta_{kl}, \qquad (4)$$

where $I_1^0 \equiv I_1(\hat{\varepsilon}_0)$. If after the latest end point $\partial I_1/\partial t < 0$, then

$$c_{ijkl}^{(1)} = -h_1(I_1^0 - I_1)\,\delta_{ij}\delta_{kl}. \qquad (5)$$

For an arbitrary sequence of the end points the relations (3)–(5) describe experimentally observed[6,35,36] bow-tie behavior of the strain-dependent contribution to elastic modulus (Fig. 1).

The second possible cubic term in the hysteretic energy is

$$\begin{aligned} W_2 &= -\tfrac{1}{2}h_2 |I_1(\varepsilon_{ij} - \varepsilon_{ij}^0)| I_2(\varepsilon_{ij} - \varepsilon_{ij}^0) \\ &= -\tfrac{1}{2}h_2 \,\mathrm{sign}[I_1(\hat{\varepsilon} - \hat{\varepsilon}^0)] I_1(\hat{\varepsilon} - \hat{\varepsilon}^0) I_2(\hat{\varepsilon} - \hat{\varepsilon}^0), \end{aligned} \qquad (6)$$

where the hysteretic modulus $h_2 \geqslant 0$ and $I_2(\varepsilon_{ij}) = I_2(\hat{\varepsilon}) = \varepsilon_{mn}\varepsilon_{nm} = tr(\hat{\varepsilon}^2)$ is the second (second order in strain) invariant which is always non-negative (because of this it is unnecessary to introduce the modulus of I_2). With the help of Eq. (6) we derive

$$\begin{aligned} \sigma_{ij}^{(2)} = \frac{\delta W_2}{\delta \varepsilon_{ij}} &= -\frac{1}{2} h_2 \,\mathrm{sign}[I_1(\hat{\varepsilon} - \hat{\varepsilon}^0)]\{I_2(\hat{\varepsilon} - \hat{\varepsilon}^0)\hat{I} \\ &\quad + 2[I_1(\hat{\varepsilon} - \hat{\varepsilon}^0)](\hat{\varepsilon} - \hat{\varepsilon}^0)\}, \end{aligned} \qquad (7)$$

$$\begin{aligned} c_{ijkl}^{(2)} = \frac{\delta \sigma_{ij}^{(2)}}{\delta \varepsilon_{kl}} &= -h_2 \,\mathrm{sign}[I_1(\hat{\varepsilon} - \hat{\varepsilon}^0)][(\varepsilon_{kl} - \varepsilon_{kl}^0)\delta_{ij} \\ &\quad + (\varepsilon_{ij} - \varepsilon_{ij}^0)\delta_{kl} + I_1(\hat{\varepsilon} - \hat{\varepsilon}_0)\delta_{ik}\delta_{jl}]. \end{aligned} \qquad (8)$$

It is clear that in general the contribution Eq. (8) to the modulus depends both on the normal and shear strains, and that it predicts bow-tie behavior.

The third possible cubic term in the hysteretic energy is

$$\begin{aligned} W_3 &= -\tfrac{1}{3}h_3 |I_3(\varepsilon_{ij} - \varepsilon_{ij}^0)| \\ &= -\tfrac{1}{3}h_3 |I_3(\hat{\varepsilon} - \hat{\varepsilon}^0)| \\ &= -\tfrac{1}{3}h_3 \,\mathrm{sign}[I_3(\hat{\varepsilon} - \hat{\varepsilon}^0)] I_3(\hat{\varepsilon} - \hat{\varepsilon}^0), \end{aligned} \qquad (9)$$

where $h_3 \geqslant 0$ and $I_3(\varepsilon_{ij}) = I_3(\hat{\varepsilon}) = \varepsilon_{mn}\varepsilon_{np}\varepsilon_{pm} = tr(\hat{\varepsilon}^3)$ is the third (third order in strain) invariant. With the help of Eq. (9) we derive

$$\begin{aligned} \sigma_{ij}^{(3)} = \frac{\delta W_3}{\delta \varepsilon_{ij}} &= -h_3 \,\mathrm{sign}[I_3(\hat{\varepsilon} - \hat{\varepsilon}^0)](\varepsilon_{jp} - \varepsilon_{jp}^0)(\varepsilon_{pi} - \varepsilon_{pi}^0) \\ &= -h_3 \,\mathrm{sign}[I_3(\hat{\varepsilon} - \hat{\varepsilon}^0)](\hat{\varepsilon} - \hat{\varepsilon}^0)^2, \end{aligned} \qquad (10)$$

$$\begin{aligned} c_{ijkl}^{(3)} = \frac{\delta \sigma_{ij}^{(3)}}{\delta \varepsilon_{kl}} &= -h_3 \,\mathrm{sign}[I_3(\hat{\varepsilon} - \hat{\varepsilon}^0)][(\varepsilon_{lj} - \varepsilon_{lj}^0)\delta_{ik} \\ &\quad + (\varepsilon_{ik} - \varepsilon_{ik}^0)\delta_{jl}]. \end{aligned} \qquad (11)$$

In general the contribution Eq. (11) to the modulus depends both on the normal and shear strains, and it predicts a bow-tie behavior.

The contributions Eq. (1), Eq. (6), and Eq. (9) are all possible to obtain by the proposed modification of the cubic nonlinear terms in the classical presentation[25,31] of the elastic energy. However, it can be easily verified that (as also takes place in the case of the elastic quadratic nonlinearity) the modified nonlinear stresses [Eqs. (2), (7), and (10)] predict the absence of the interaction between pure shear waves. In other words, the proposed nonlinear relations do not describe the hysteresis in pure shear which is observed experimentally.[5,35] A possible reason for this discrepancy is in the fact that Eqs. (1), (6), and (9) are obtained (as is also done in the elasticity theory) by assuming that the energy should depend on the integer powers of the strain invariants. There exists no theoretical proof of this hypothesis. Lurie[32] cites in relation to this problem the following words of Truesdell: ‘‘Nature does not give preference to representation of functional relationships based upon power series,’’ and the following words of Rivlin: ‘‘Whatever ideas do not suffice, they are replaced by words such as simplicity or accessibility.’’ The power series in integer powers of the strain invariants are not sufficient to describe the nonlinearity hysteresis in shear. Because of this we have to include in the power series the noninteger powers of the strain invariants. However, following the idea of ‘‘simplicity’’ we will try to include as small a number of additional terms in the expression for cubic hysteretic energy as possible. It should be mentioned here that the noninteger powers of the third-order invariant (usually defined in nonlinear mechanics as the determinant of the strain tensor $\hat{\varepsilon}$) are commonly used to model even nonlinear elastic behavior of the materials [Ref. 32 (pp. 181–186), Ref. 33 (p. 105)]. The square root of the second invariant ($\sqrt{I_2}$) is one of the basic components of the hypoplasticity theory (see, for example, Refs. 38–41 and the references there in). The introduction into the elastic energy of a term proportional to $I_1\sqrt{I_2}$ (quadratic in strain) provides opportunity to describe some phenomena in a damaged medium (see Ref. 42 and references therein). In particular, the latter term may describe materials with different moduli in tension and compression.[43,44]

Following these ideas we propose to use, as elementary blocks for the construction of the cubic terms of the hysteretic energy, not the invariants I_2 and $|I_3|$ themselves but their powers $I_2^{1/2}$ and $|I_3^{1/3}|$, which are (similar to $|I_1|$) linear in strain magnitude. Note that the contributions W_1, W_2, and W_3 described above [Eqs. (1), (6), and (9)] are terms (cubic in strain) of power series in $|I_1|$, $I_2^{1/2}$, and $|I_3^{1/3}|$. However, with the latter elementary building blocks there are additional (cubic in strain) terms contributing to energy.

The additional cubic contribution to energy, which depends only on the second invariant, is

$$W_4 = -\tfrac{1}{3}h_4[I_2(\varepsilon_{ij} - \varepsilon_{ij}^0)]^{3/2} = -\tfrac{1}{3}h_4 I_2^{3/2}(\hat{\varepsilon} - \hat{\varepsilon}^0). \qquad (12)$$

We consider that the hysteretic modulus is non-negative ($h_4 \geqslant 0$) With the help of Eq. (12) we derive

$$\sigma_{ij}^{(4)} = \frac{\delta W_4}{\delta \varepsilon_{ij}} = -h_4[I_2^{1/2}(\hat{\varepsilon} - \hat{\varepsilon}^0)](\hat{\varepsilon} - \hat{\varepsilon}^0), \qquad (13)$$

$$\begin{aligned} c_{ijkl}^{(4)} = \frac{\delta \sigma_{ij}^{(4)}}{\partial \varepsilon_{kl}} &= -h_4\{I_2^{1/2}(\hat{\varepsilon} - \hat{\varepsilon}^0)\delta_{ik}\delta_{jl} + [I_2^{-1/2}(\hat{\varepsilon} - \hat{\varepsilon}^0)] \\ &\quad \times (\varepsilon_{kl} - \varepsilon_{kl}^0)(\varepsilon_{ij} - \varepsilon_{ij}^0)\}. \end{aligned} \qquad (14)$$

The contribution Eq. (14) to the modulus depends on both the normal and shear strains, and it predicts bow-tie behavior. Importantly, the proposed relationships Eqs. (12)–(14) allow the interaction of the pure shear waves in the medium with quadratic nonlinearity.

Here, we would like to mention once again very qualitatively the difference between the classical elastic theory[25,31] and the hysteresis model proposed here. In the classical theory the terms in energy, which are cubic in shear strain [for example, $\propto(\varepsilon_{21})^3$ in the plane shear wave propagating along the x_1 axis], are omitted on the basis of the reasoning that the energy should not depend on the sign of ε_{21} in an isotropic material. However, the terms $\propto|\varepsilon_{21}|^3$ are not forbidden by these reasons, and they are included in our model here by accounting for the terms $\propto I_2^{3/2}$ in the energy potential. The interaction of the pure shear waves in the medium with quadratic nonlinearity becomes possible.

The additional contribution to energy, which depends on the first and second invariants, is

$$\begin{aligned}W_5 &= -\tfrac{1}{2}h_5[I_1(\varepsilon_{ij}-\varepsilon_{ij}^0)]^2[I_2(\varepsilon_{ij}-\varepsilon_{ij}^0)]^{1/2}\\ &= -\tfrac{1}{2}h_5 I_1^2(\hat{\varepsilon}-\hat{\varepsilon}^0)I_2^{1/2}(\hat{\varepsilon}-\hat{\varepsilon}^0). \end{aligned}\tag{15}$$

It is assumed that $h_5 \geqslant 0$. With the help of Eq. (15) we derive

$$\begin{aligned}\sigma_{ij}^{(5)} &= \frac{\delta W_5}{\delta\varepsilon_{ij}} = -\frac{1}{2}h_5\{2I_1(\hat{\varepsilon}-\hat{\varepsilon}^0)I_2^{1/2}(\hat{\varepsilon}-\hat{\varepsilon}^0)\hat{I}\\ &\quad +[I_1^2(\hat{\varepsilon}-\hat{\varepsilon}^0)I_2^{-1/2}(\hat{\varepsilon}-\hat{\varepsilon}^0)](\hat{\varepsilon}-\hat{\varepsilon}^0)\}, \end{aligned}\tag{16}$$

$$\begin{aligned}c_{ijkl}^{(5)} &= \frac{\delta\sigma_{ij}^{(5)}}{\delta\varepsilon_{kl}}\\ &= -h_5\{I_2^{1/2}(\hat{\varepsilon}-\hat{\varepsilon}^0)\delta_{ij}\delta_{kl}+\tfrac{1}{2}I_1^2(\hat{\varepsilon}-\hat{\varepsilon}^0)\\ &\quad \times I_2^{-1/2}(\hat{\varepsilon}-\hat{\varepsilon}^0)\delta_{ik}\delta_{jl}+I_1(\hat{\varepsilon}-\hat{\varepsilon}^0)\\ &\quad \times I_2^{-1/2}(\hat{\varepsilon}-\hat{\varepsilon}^0)[(\varepsilon_{ij}-\varepsilon_{ij}^0)\delta_{kl}+(\varepsilon_{kl}-\varepsilon_{kl}^0)\delta_{ij}]\\ &\quad -\tfrac{1}{2}[I_1^2(\hat{\varepsilon}-\hat{\varepsilon}^0)I_2^{-3/2}(\hat{\varepsilon}-\hat{\varepsilon}^0)](\varepsilon_{kl}-\varepsilon_{kl}^0)(\varepsilon_{ij}-\varepsilon_{ij}^0)\}. \end{aligned}\tag{17}$$

The following additional contributions (cubic in strain) to the energy can be, in principle, constructed if we use $|I_3^{1/3}|$ as a building block in power series: $W\propto|I_3^{1/3}|I_1^2$, $W\propto|I_3^{1/3}||I_1|I_2^{1/2}$, $W\propto|I_3^{1/3}|I_2$, $W\propto I_3^{2/3}|I_1|$, and $W\propto I_3^{2/3}I_2^{1/2}$. However, in our opinion, it is possible to exclude most of them from the consideration on the basis of the following reasoning. Let us examine, for example, $W\propto|I_3^{1/3}|I_2$. The corresponding contribution to stress tensor will be $\sigma_{ij}\propto 2|I_3^{1/3}|\varepsilon_{ij}+\mathrm{sign}(I_3^{1/3})I_3^{-2/3}I_2\varepsilon_{im}\varepsilon_{mj}$. Let us imagine that there are only two nonzero strain components $\varepsilon_{12}\neq 0$ and $\varepsilon_{11}\neq 0$, but ε_{11} might be very small $(\varepsilon_{11}\to 0)$. Then, the evaluation of the normal stress component leads to $\sigma_{11}\propto\varepsilon_{12}^{8/3}\varepsilon_{11}^{-2/3}\to\infty$ when $\varepsilon_{11}\to 0$. It means that a shear wave might induce infinitely high stresses for the longitudinal wave propagation. The corresponding nonlinear contribution to elastic modulus diverges as well $(c_{1111}\propto\varepsilon_{11}^{-5/3}\to\infty)$ in the presence of a shear wave. That is why we exclude the term $W\propto|I_3^{1/3}|I_2$ from consideration. The similar arguments are valid for $W\propto I_3^{2/3}I_2^{1/2}$ $[\sigma_{11}(\varepsilon_{12}\neq 0,\varepsilon_{11}\to 0)\propto\varepsilon_{11}^{-1/3}\to\infty$, $c_{1111}(\varepsilon_{12}\neq 0,\varepsilon_{11}\to 0)\propto\varepsilon_{11}^{-4/3}\to\infty]$. In the case $W\propto I_3^{2/3}|I_1|$ the stress does not diverge $(\sigma_{11}(\varepsilon_{12}\neq 0,\varepsilon_{11}\to 0)\propto\varepsilon_{11}^{2/3}\to 0)$, but the nonlinear contribution to elastic modulus—does $[c_{1111}(\varepsilon_{12}\neq 0,\varepsilon_{11}\to 0)\propto\varepsilon_{11}^{-1/3}\to\infty]$. A similar situation takes place for $W\propto|I_3^{1/3}||I_1|I_2^{1/2}$ $[\sigma_{11}(\varepsilon_{12}\neq 0,\varepsilon_{11}\to 0)\propto\varepsilon_{11}^{1/3}\to 0$, $c_{1111}(\varepsilon_{12}\neq 0,\varepsilon_{11}\to 0)\propto\varepsilon_{11}^{-2/3}\to\infty]$. As a result (when using $|I_3^{1/3}|$) we get a single additional (cubic in strain) contribution to hysteretic energy with nondivergent stresses and moduli

$$\begin{aligned}W_6 &= -\frac{h_6}{2}|I_3^{1/3}|I_1^2 = -\frac{h_6}{2}\mathrm{sign}[I_3(\hat{\varepsilon}-\hat{\varepsilon}^0)]\\ &\quad \times I_3^{1/3}(\hat{\varepsilon}-\hat{\varepsilon}^0)I_1^2(\hat{\varepsilon}-\hat{\varepsilon}^0). \end{aligned}\tag{18}$$

It is assumed that $h_6\geqslant 0$. With the help of Eq. (18) we derive

$$\begin{aligned}\sigma_{ij}^{(6)} &= \frac{\delta W_6}{\delta\varepsilon_{ij}} = -\frac{1}{2}h_6\,\mathrm{sign}[I_3(\hat{\varepsilon}-\hat{\varepsilon}^0)]\{2I_1(\hat{\varepsilon}-\hat{\varepsilon}^0)\\ &\quad \times I_3^{1/3}(\hat{\varepsilon}-\hat{\varepsilon}^0)\hat{I}+[I_1^2(\hat{\varepsilon}-\hat{\varepsilon}^0)I_3^{-2/3}(\hat{\varepsilon}-\hat{\varepsilon}^0)]\\ &\quad \times(\hat{\varepsilon}-\hat{\varepsilon}^0)^2\}, \end{aligned}\tag{19}$$

$$\begin{aligned}c_{ijkl}^{(6)} &= \frac{\delta\sigma_{ij}^{(6)}}{\delta\varepsilon_{kl}}\\ &= -h_6\,\mathrm{sign}[I_3(\hat{\varepsilon}-\hat{\varepsilon}^0)]\{I_3^{1/3}(\hat{\varepsilon}-\hat{\varepsilon}^0)\delta_{ij}\delta_{kl}\\ &\quad +\tfrac{1}{2}[I_1^2(\hat{\varepsilon}-\hat{\varepsilon}^0)I_3^{-2/3}(\hat{\varepsilon}-\hat{\varepsilon}^0)][(\varepsilon_{lj}-\varepsilon_{lj}^0)\delta_{ik}\\ &\quad +(\varepsilon_{ik}-\varepsilon_{ik}^0)\delta_{jl}]+I_1(\hat{\varepsilon}-\hat{\varepsilon}^0)I_3^{-2/3}(\hat{\varepsilon}-\hat{\varepsilon}^0)\\ &\quad \times[(\varepsilon_{km}-\varepsilon_{km}^0)(\varepsilon_{ml}-\varepsilon_{ml}^0)\delta_{ij}+(\varepsilon_{im}-\varepsilon_{im}^0)\\ &\quad \times(\varepsilon_{mj}-\varepsilon_{mj}^0)\delta_{kl}]-[I_1^2(\hat{\varepsilon}-\hat{\varepsilon}^0)I_3^{-5/3}(\hat{\varepsilon}-\hat{\varepsilon}^0)]\\ &\quad \times(\varepsilon_{im}-\varepsilon_{im}^0)(\varepsilon_{mj}-\varepsilon_{mj}^0)(\varepsilon_{kn}-\varepsilon_{kn}^0)(\varepsilon_{nl}-\varepsilon_{nl}^0)\}. \end{aligned}\tag{20}$$

In the present version of the theory we restrict ourselves to the analysis of the acoustic wave interactions following from the above proposed six cubic terms W_1–W_6 in the hysteretic part of the energy function. From the mathematical point of view we are restricting ourselves to series in positive integer powers of $|I_1|$, $I_2^{1/2}$, and $|I_3^{1/3}|$. Here, it should be mentioned that it is difficult to find arguments to neglect *a priori* some terms containing negative powers of the elementary building blocks (for example, $W\propto I_1^4 I_2^{-1/2}$ or $W\propto|I_1^5|I_2^{-1}$). However, we are not including these terms in the analysis following the principle of simplicity. Only if the number of the parameters and terms introduced in the present theory is insufficient to describe experimental observations should additional terms then be incorporated in the energy function.

In relation to the use of negative powers of $|I_1|$, $I_2^{1/2}$, and $|I_3^{1/3}|$ the following should be mentioned as well. It is easily verified that the obtained description of hysteretic stresses [Eqs. (2), (7), (10), (13), (16), and (19) satisfy the representation theorem for hemitropic tensor-valued functions.[34] For the purposes of the present analysis it is important that this theorem describes which mathematical form should have the general nonlinear relationship between the stress tensor and the strain tensor in the isotropic materials.[32–34] The stress/strain relationships derived by us satisfy this theorem. Moreover, we may omit some of the terms in the derived relationships without losing isotropy.

For example, if we accept a hypothesis that the stress should depend on positive integer powers of $|I_1|$, $I_2^{1/2}$, and $|I_3^{1/3}|$ we can omit in the stress/strain relationships the terms containing the negative powers of these elementary blocks. If we do so the stresses $\sigma_{ij}^{(5)}$ and $\sigma_{ij}^{(6)}$ will be significantly simpler

$$\sigma_{ij}^{(5)} = -h_5 I_1(\hat{\varepsilon}-\hat{\varepsilon}^0) I_2^{1/3}(\hat{\varepsilon}-\hat{\varepsilon}^0)\hat{I}, \tag{21}$$

$$\sigma_{ij}^{(6)} = -h_6\,\mathrm{sign}[I_3(\hat{\varepsilon}-\hat{\varepsilon}^0)] I_1(\hat{\varepsilon}-\hat{\varepsilon}^0) I_3^{1/3}(\hat{\varepsilon}-\hat{\varepsilon}^0)\hat{I}. \tag{22}$$

However, even using Eq. (21) and Eq. (22) we still have no possibility to avoid the dependence of c_{ijkl} on the negative powers of $I_2^{1/2}$ and $|I_3^{1/3}|$. In particular, we have to consider the dependence of the modulus on the negative powers of $I_2^{1/2}$ if we want to describe experimentally confirmed hysteresis of shear nonlinearity. This reasoning demonstrates once again that our particular choice of the power series is finally motivated by the simplicity principle (although we have finally chosen not the simplest opportunity). It should be noted that elastic materials which have a "stress potential" (an energy function) are called hyperelastic.[32,34,39,45] From this point of view we have proposed above the description of hyperhysteretic materials. If we use Eqs. (21) and (22) instead of Eqs. (16) and (19) the material will still be isotropic; it will still possess the property of the nonlinearity hysteresis but it cannot be called hyperhysteretic.

The approach based on the utilization of the representation theorem is often used in nonlinear elasticity theory (see for example Ref. 32, Ref. 33, p. 95, Ref. 46, p. 193). We also have found a publication[47] where hysteresis was introduced in the behavior of the elastic coefficients responsible for compression motion (hysteresis related to shear motion was assumed to be negligible). Consequently, the model developed in Ref. 47 is rather far from being a general one. It should be also mentioned that in Ref. 47 the role of hysteresis in cubic (i.e., not in quadratic as here) nonlinearity was analyzed [see Eqs. (20) and (21) in Ref. 47].

We would like to note also the following. The assumptions adopted here that all the hysteretic modules $h_f (f = 1,2,3,4,5,6)$ are non-negative is sufficient to arrive at a non-negative energy density related to hysteresis and for softening of the material in the acoustic field. However, it is quite possible that not all of these assumptions are necessary. Perhaps, some of the h_f might be negative. From Eqs. (1), (6), (9), (12), (15), and (18) it follows, for example, that in a plane longitudinal wave (with $\varepsilon_{ij} = \varepsilon_{11}\delta_{i1}\delta_{j1}$) the sign of the total hysteretic energy is controlled by the sign of the parameter $(-1)[h_1 + 3(h_2+h_5+h_6) + 2(h_3+h_4)]$, which should be negative (but not necessarily should all h_f be separately positive). Currently the precise evaluation of the theoretical restrictions on the possible values of h_f is beyond our scope. In the variant of the theory presented here the modules h_f can be considered as phenomenological parameters, which are not necessarily positive.

The proposed description of the nonlinearity hysteresis does not cover all the memory properties of the materials with the hysteresis of the nonlinearity. In particular hysteretic materials may remember the previous absolute maximum and absolute minimum in the loading history.[6,37] It means that in general, when loading passes any of the previous end points there is a possibility that the obtained stress/strain relationships and the obtained expressions for the modulus should be modified. It is well known how with the use of the Preisach–Maergoyz space[6,16] these modifications can be done in the 1D case. For example, the description of the 1D periodic process with a single maximum and a single minimum over a period is given in Ref. 48. Surely, the Preisach–Mayergoyz space can be applied for the description of the memory effects in the general 3D case as well if the parameter (or the parameters) controlling the opening/closing of the hysteretic mechanical elements is identified. It is clear that for isotropic hysteretic materials this parameter should depend on the strain invariants. The most attractive possibility is to assume that the state of the hysteretic elements (i.e., are they opened or closed) is controlled only by the elastic energy density W^{el} (elastic stress potential). This assumption on the one hand is in accordance with our physical intuition that any transition between different states requires work and is accompanied by energy changes. On the other hand this assumption correlates with the fact that the sign of the elastic energy variation (the sign of the stress power)

$$\mathrm{sign}\left(\frac{\partial W^{\mathrm{el}}}{\partial t}\right) = \mathrm{sign}\left(\frac{\partial W^{\mathrm{el}}}{\partial \varepsilon_{ij}}\frac{\partial \varepsilon_{ij}}{\partial t}\right) = \mathrm{sign}\left(\sigma_{ij}^{\mathrm{el}}\frac{\partial \varepsilon_{ij}}{\partial t}\right),$$

is the most common loading criteria used by the investigators of hypoelasticity and plasticity[45,49] ($\sigma_{ij}^{\mathrm{el}}\partial\varepsilon_{ij}/\partial t > 0$ corresponds to loading). However, it is clear that the reality in general might be much more complicated. For example, in the general case there is no reason to assume that the role of shear and normal strains in closing/opening of the hysteretic elements is exactly proportional to their partial contributions to elastic strain energy W^{el}.

The extension of the Preisach–Mayergoyz theoretical approach to the case of an arbitrary 3D loading/unloading is beyond the scope of the present publication. For the purposes of the present analysis it is important that the above-derived model of the nonlinearity hysteresis is applicable without any modifications for the analysis of quasiharmonic (quasisinusoidal) processes which take place in the case of interaction of a strong harmonic (sinusoidal) pump wave with a weak probe wave. This statement is proved by the following arguments. To find the spectrum of the acoustic waves excited due to hysteretic nonlinearity we need to calculate the following integral:

$$\tilde{F}_i(\omega) = \int_{-\infty}^{\infty} \frac{\partial \sigma_{ij}^{(f)}}{\partial x_j} e^{i\omega t}\,dt = \int_{-\infty}^{\infty} c_{ijkl}^{(f)} \frac{\partial \varepsilon_{kl}}{\partial x_j} e^{i\omega t} dt, \tag{23}$$

where F_i denotes the ith component of the volume density of forces, ω denotes the cyclic frequency and $f = 1,2,3,4,5,6$. The highest in amplitude terms in Eq. (23) responsible for the processes of frequency mixing are proportional to the product of the pump (grating) wave amplitude and the probe wave amplitude. In the case of the quasiharmonic process these contributions do not depend on the possible long-term memory effects in hysteretic material. In fact, in the case of a weak modulation of the periodic grating by the probe wave the differences between any of the two end points corresponding to stop of loading (or between any of the end points corresponding to stop in unloading) are of the order of the probe amplitude. Because of this, possible changes in the derived stress/strain relationships and in the derived formulas for the nonlinear modulus (caused by the long-term memory effects) can be estimated as being proportional to the probe amplitude. These possible modifications may take place only in small time intervals near the end points. The duration of these intervals can be estimated as the time shift of the end point caused by the weak probe. So, these time intervals are also proportional to the probe amplitude. Consequently, the contribution of long-term memory effects to the integral in Eq. (23) is proportional to the square of the weak probe amplitude and is negligible (in comparison with the leading terms which are proportional to the product of the pump and probe amplitudes).

Thus, it follows that the description in Eqs. (3), (8), (11), (14), (17), and (20) of the hysteretic contribution to nonlinear modulus can be used for the description of nonlinear scattering of a weak probe by a strong sinusoidal pump wave. However, it should be mentioned that stress/strain relationships [Eqs. (2), (7), (10), (13), (16), (19)] should be additionally modified by including some residual stresses, which do not depend on the current strain ε_{ij} (and, consequently, they do not influence hysteretic contributions to modulus) but depend on the prehistory of the process. The description of how the necessary modification should be done in the case of a periodic process with a single maximum and a single minimum over a period (the so-called "simplex" process[50]) can be found in Ref. 48. In the following we are using the proposed model [Eqs. (3), (8), (11), (14), (17), (20)] for the strain-induced variation of the elastic modulus in isotropic hysteretic materials for the analysis of nonlinear scattering of a weak harmonic acoustic wave (probe) in the field of a strong harmonic acoustic wave (pump) in the general case of their non-collinear interaction.

III. FREQUENCY MIXING IN ISOTROPIC MATERIALS WITH NONLINEARITY HYSTERESIS

With the above-proposed description of the nonlinear hysteretic part of the constitutive (stress/strain) relationship, the derivation of the nonlinear wave equation is straightforward. In the equation of motion

$$\rho_0 \frac{\partial^2 u_i}{\partial t^2} = \frac{\partial}{\partial x_j}(\sigma_{ij}^L + \sigma_{ij}^{NL})$$

(where ρ_0 denotes the density of the material and u_i denotes the ith component of the particle displacement vector) we use the classical presentation for the linear elastic part σ_{ij}^{L} of the strain tensor and we assume that in the nonlinear part $\sigma_{ij}^{\mathrm{NL}}$ of the stress tensor the hysteretic quadratic terms dominate over the traditional elastic quadratic nonlinearity. So, we consider that $\sigma_{ij}^{\mathrm{NL}} = \sigma_{ij}$, where $\sigma_{ij} = \Sigma_{f=1}^{6} \sigma_{ij}^{(f)}$ is the sum of the contributions described in the previous section. The equation of motion can then be presented in the form

$$\left[\frac{\partial^2}{\partial t^2} - c_T^2 \Delta - (c_L^2 - c_T^2)\,\mathrm{grad\,div}\right]\mathbf{u} = \frac{1}{\rho_0}\mathbf{e}_i F_i,$$

$$F_i \equiv \frac{\partial \sigma_{ij}}{\partial x_j} \equiv c_{ijkl}\frac{\partial \varepsilon_{kl}}{\partial x_j}, \tag{24}$$

where $c_{L,T}$ denote the longitudinal and shear linear acoustic wave velocity, respectively, $\mathbf{e}_i$ are the unit vectors of the rectangular coordinate frame, and $c_{ijkl} = \Sigma_{f=1}^{6} c_{ijkl}^{(f)}$ is the sum of the hysteretic contributions to nonlinear modulus described in Sec. II. It should be mentioned that, because we are neglecting kinematic nonlinearity in comparison with hysteretic one, the right-hand side in the equation of motion has the same form both for the first and the second Piola–Kirchhoff's stress tensor. Also, because we are restricting ourselves here to the analysis of quadratic nonlinearity, only the linear part of the strain tensor contributes to Eq. (24) [that is, in Eq. (24) $\varepsilon_{kl} = (1/2)(\partial u_k/\partial x_l + \partial u_l/\partial x_k)$]. In the frame of Eq. (24) we are applying the traditional approach to analyze the interaction of the acoustic waves.[22,23] It is assumed that both the pump (grating) wave field $\mathbf{u}_g$ and the probe wave field $\mathbf{u}_p$ satisfy separately in the first approximation the linearized wave equation (24) [i.e., in the absence of the right-hand side (r.h.s.)]. It is assumed that the displacement fields $\mathbf{u}_g$ and $\mathbf{u}_p$ are known. In the second approximation the solution of Eq. (24) is assumed to have the form $\mathbf{u} = \mathbf{u}_g + \mathbf{u}_p + \mathbf{u}_s$, where $\mathbf{u}_s$ is the acoustic field (signal) generated due to the nonlinear term on the r.h.s. It is assumed that $\mathbf{u}_s$ is so small that it does not contribute to the r.h.s. in the second approximation. So, only $\mathbf{u}_s$ contributes to the left-hand side (l.h.s.) of Eq. (24) and only $\mathbf{u}_g + \mathbf{u}_p$ should be substituted in the r.h.s. in the second approximation. Consequently we arrive at the inhomogeneous wave equation for the signal (with the known r.h.s., which is, in fact, the nonlinear source of the scattered signal wave). Moreover, if we are interested in frequency-mixing wave interactions the terms in the r.h.s. which depend only on $\mathbf{u}_g$ or only on $\mathbf{u}_p$ should be omitted because they contribute only to collinear processes of the generation of higher harmonics in pump and probe waves.[4,21] Among the terms on the r.h.s., which depend both on $\mathbf{u}_g$ and $\mathbf{u}_p$, only the terms of the highest order in magnitude should be retained. These are the terms proportional to the product of the pump and probe wave amplitudes.

If we are considering the solution in the form of a superposition of plane waves

$$\mathbf{u} = \int\int\int d^3\mathbf{k}_s' \int_{-\infty}^{\infty} d\omega_s' \tilde{\tilde{\mathbf{u}}}_s(\mathbf{k}_s', \omega_s') e^{i\mathbf{k}_s'\mathbf{r} - i\omega_s' t},$$

and we apply a Fourier transform both in space and time

$$\frac{1}{(2\pi)^4}\int\int\int d^3\mathbf{r}\int_{-\infty}^{\infty} dt(\ldots)e^{-i\mathbf{k}_s'\mathbf{r} + i\omega_s t}$$

to both parts of Eq. (24) the result will be

$$([-\omega_s^2 + c_T^2 k_s^2 + (c_L^2 - c_T^2)\mathbf{k}_s(\mathbf{k}_s]\tilde{\tilde{\mathbf{u}}}_s(\mathbf{k}_s, \omega_s))$$

$$= \frac{1}{\rho_0}\mathbf{e}_i \tilde{\tilde{F}}_i(\mathbf{k}_s, \omega_s), \quad \mathbf{e}_i \tilde{\tilde{F}}_i(\mathbf{k}_s, \omega_s) \equiv \tilde{\tilde{\mathbf{F}}}(\mathbf{k}_s, \omega_s). \tag{25}$$

Here, we use double "$\sim$" for the notation of the Fourier transform of a function simultaneously in time and in space. The solution of Eq. (25) may contain in general both longitudinal (displacement vector $\mathbf{u}_{Ls}$ is parallel to the wave vector $\mathbf{k}_s$) and transverse (displacement vector $\mathbf{u}_{Ts}$ is perpendicular to the wave vector $\mathbf{k}_s$) wave components

$$\mathbf{u}_s=\mathbf{u}_{Ls}+\mathbf{u}_{Ts}. \tag{26}$$

With the help of Eq. (26) we transform Eq. (25) into

$$[c_L^2k_s^2-\omega_s^2]\tilde{\tilde{\mathbf{u}}}_{Ls}(\mathbf{k}_s,\omega_s)+[c_T^2k_s^2-\omega_s^2]\tilde{\tilde{\mathbf{u}}}_{Ts}(\mathbf{k}_s,\omega_s)$$
$$=\frac{1}{\rho_0}\mathbf{e}_i\tilde{\tilde{F}}_i(\mathbf{k}_s,\omega_s). \tag{27}$$

The parts $k_{si}\mathbf{k}_s/k_s^2$ of the basis vectors $\mathbf{e}_i$, which are parallel to $\mathbf{k}_s$, contribute to the longitudinal acoustic wave. Here, $k_{si}\equiv\mathbf{k}_s\mathbf{e}_i$. The parts $\mathbf{e}_i-k_{si}\mathbf{k}_s/k_s^2$, which are perpendicular to the wave vector $\mathbf{k}_s$, contribute to shear wave. Consequently, Eq. (27) can be separated into two parts

$$\begin{aligned}\tilde{\tilde{\mathbf{u}}}_{Ls}&=\frac{1}{c_L^2k_s^2-\omega_s^2}\frac{k_{si}\mathbf{k}_s}{k_s^2}\frac{1}{\rho_0}\tilde{\tilde{F}}_i(\mathbf{k}_s,\omega_s),\\ \tilde{\tilde{\mathbf{u}}}_{Ts}&=\frac{1}{c_T^2k_s^2-\omega_s^2}\left(\mathbf{e}_i-\frac{k_{si}\mathbf{k}_s}{k_s^2}\right)\frac{1}{\rho_0}\tilde{\tilde{F}}_i(\mathbf{k}_s,\omega_s).\end{aligned} \tag{28}$$

If we are interested in the dependence of the signal on time, the inverse Fourier transform of Eq. (28) in frequency should be performed and this can be done in the complex plane by calculating the residues in the poles of the multipliers $(c_{L,T}^2k_s^2-\omega_s^2)^{-1}$. In other words, these multipliers provide the description of the dispersion relation for the longitudinal and transverse signal waves

$$k_s^2=\omega_s^2/c_L^2,\quad k_s^2=\omega_s^2/c_T^2, \tag{29}$$

respectively. In the present analysis we are not interested in the pulsed processes and, consequently, we will not perform the inverse Fourier transform in time of Eq. (28). However, we will use the relations in Eq. (29) later for the identification of the wave processes allowed in the considered hysteretic medium by the conservation laws. Also, we are not interested in the present analysis in the description of the interaction between the acoustic beams but rather in the derivation of selection rules for the interaction of the plane waves. These selection rules for the allowed frequency-mixing processes might be different in the medium with hysteresis of quadratic nonlinearity from those in the medium with elastic quadratic nonlinearity. If the selection rules are found, the accounting for the beam character of the acoustic fields (and, as a result, the accounting for a finite pump–probe interaction volume) can be accomplished similar to the case of the elastic quadratic nonlinearity.[22,23] To find the selection rules for the resonance frequency-mixing processes it is sufficient to substitute plane acoustic waves both for the pump (grating) and probe in the r.h.s. of Eq. (28).

Let us demonstrate the procedure for the derivation of the selection rules using $c_{ijkl}^{(1)}$ of Eq. (3) as an example. In this case the components of the nonlinear volumetric force are

$$\begin{aligned}F_i^{(1)}=c_{ijkl}^{(1)}\frac{\partial\varepsilon_{kl}}{\partial x_j}&=-h_1|I_1(\hat{\varepsilon}-\hat{\varepsilon}^0)|\frac{\partial\varepsilon_{kk}}{\partial x_i}\\&=-h_1|I_1(\hat{\varepsilon}-\hat{\varepsilon}^0)|\frac{\partial}{\partial x_i}I_1(\hat{\varepsilon}).\end{aligned} \tag{30}$$

The next step is the evaluation of the Fourier image of the force in the frequency domain

$$\begin{aligned}\tilde{F}_i^{(1)}(\mathbf{r},\omega_s)&=\frac{1}{2\pi}\int_{-\infty}^{\infty}dt\,F_i^{(1)}e^{i\omega_s t}\\&=\frac{1}{2\pi}\sum_{m=-\infty}^{\infty}\int_{t_m}^{t_{m+1}}dt\,F_i^{(1)}e^{i\omega_s t}.\end{aligned} \tag{31}$$

In Eq. (31) the integration should be done separately between each pair of the consequent end-point time moments (t_m and t_{m+1}), because the behavior of the force in Eq. (30) changes each time when the system passes an end point. In the absence of the probe the end points are controlled by the pump field of a plane acoustic wave and coincide with the moments of strain maximum and minimum. And, these moments also correspond to maximum and minimum of the first invariant in the plane acoustic wave. Let us denote the end points in the pump (grating) wave by $t_m^{(0)}$. And let us consider without loss of generality that even m indexes correspond to maximum in strain. So, in the absence of the probe wave the evaluation of the force spectrum [when Eq. (30) is substituted in Eq. (31)] is straightforward

$$\begin{aligned}\tilde{F}_i^{(1)}(\mathbf{r},\omega_s)=\frac{h_1}{2\pi}\sum_{m=-\infty}^{\infty}(-1)^m\int_{t_m^{(0)}}^{t_{m+1}^{(0)}}dt[I_1(\hat{\varepsilon}_g)-I_1(\hat{\varepsilon}_g^0)]\\ \times\frac{\partial}{\partial x_i}I_1(\hat{\varepsilon}_g)e^{i\omega_s t}.\end{aligned} \tag{32}$$

Here, as elsewhere in this outline, the index "0" in the strains indicates the values of the strain evaluated in the latest end point. Without loss of generality we may consider that the pump wave (which creates the grating) propagates along the x_1 axis

$$\hat{\varepsilon}_g=\hat{\varepsilon}_g^A\cos(\mathbf{k}_g\mathbf{r}-\omega_g t)=\hat{\varepsilon}_g^A\cos(k_gx_1-\omega_g t). \tag{33}$$

Here, and in what follows, the index "A" will be attributed to the amplitudes of the strain. Then, it is clear that the term $\partial I_1(\hat{\varepsilon}_g)/\partial x_i$ in the integrand of Eq. (32) is equal to zero in the end points [because in the traveling wave of Eq. (33) $\partial/\partial x_i=\partial/\partial x_1=-(k_g/\omega_g)\partial/\partial t$]. This observation is very important because it provides opportunity even in the presence of a probe wave (a weak one, with $\hat{\varepsilon}_p^A\ll\hat{\varepsilon}_g^A$) to neglect a shift of the end points caused by the probe and also neglect a possible difference between the end points (in loading and unloading) and the extrema of the first invariant. In fact, the latter difference may occur only in a small time interval (proportional to $\hat{\varepsilon}_p^A$) near $t_m^{(0)}$ (and $t_{m+1}^{(0)}$) and the shift of the end points is also proportional to $\hat{\varepsilon}_p^A$. Then, because in the small interval in the vicinity of $t_m^{(0)}$ (and $t_{m+1}^{(0)}$) the deviation of $\partial I_1(\hat{\varepsilon}_g+\hat{\varepsilon}_p)/\partial x_i$ from zero will be also proportional to $\hat{\varepsilon}_p^A$, the contributions of these two considered effects to the integral in Eq. (31) will be proportional to $(\hat{\varepsilon}_p^A)^2$. These contributions are negligible in comparison with the contributions proportional to $\hat{\varepsilon}_g^A \hat{\varepsilon}_p^A$. Consequently, $\tilde{F}_i^{(1)}(\mathbf{r},\omega_s)$ in Eq. (31) can be evaluated as though both the end points and the extrema of I_1 coincide with the extrema of the strain tensor in the plane pump wave. We have checked that this result is general in the sense that (in the considered case of a probe wave which is significantly weaker than the pump wave) both the end points and the extrema of the strain invariants (I_1, I_2, I_3) can be approximated by the extrema of the strain in the pump wave (both in the longitudinal and in the shear). This result provides opportunity to always use $t_m^{(0)}$ and $t_{m+1}^{(0)}$ as the integration limits. Thus, in the general case (that is, even in the presence of the probe wave) the relation (31) can be approximated by

$$\tilde{F}_i^{(1)}(\mathbf{r},\omega_s)=\frac{1}{2\pi}\int_{-\infty}^{\infty} dt\, F_i^{(1)} e^{i\omega_s t}$$

$$=\frac{1}{2\pi}\sum_{m=-\infty}^{\infty}\int_{t_m^{(0)}}^{t_{m+1}^{(0)}} dt\, F_i^{(1)} e^{i\omega_s t}. \tag{34}$$

In the particular case described by Eq. (30), retaining in the r.h.s. of Eq. (34) only the terms proportional to $\hat{\varepsilon}_g^A \hat{\varepsilon}_p^A$, we derive

$$\tilde{F}_i^{(1)}(\mathbf{r},\omega_s)=\frac{h_1}{2\pi}\sum_{m=-\infty}^{\infty}(-1)^m\int_{t_m^{(0)}}^{t_{m+1}^{(0)}} dt\Big\{[I_1(\hat{\varepsilon}_g)-I_1(\hat{\varepsilon}_g^0)]$$

$$\times\frac{\partial}{\partial x_i}I_1(\hat{\varepsilon}_p)+[I_1(\hat{\varepsilon}_p)-I_1(\hat{\varepsilon}_p^0)]$$

$$\times\frac{\partial}{\partial x_i}I_1(\hat{\varepsilon}_g)\Big\}e^{i\omega_s t}$$

$$=\frac{h_1}{2\pi}\sum_{m=-\infty}^{\infty}(-1)^m\int_{t_m^{(0)}}^{t_{m+1}^{(0)}} dt\Big\{[\varepsilon_{nn}^g-\varepsilon_{nn}^{g0}]\frac{\partial}{\partial x_i}\varepsilon_{kk}^p$$

$$+[\varepsilon_{kk}^p-\varepsilon_{kk}^{p0}]\frac{\partial}{\partial x_i}\varepsilon_{nn}^g\Big\}e^{i\omega_s t}. \tag{35}$$

However, it is straightforward to verify that the term in Eq. (35), which contains $\varepsilon_{nn}^{g0}=(-1)^m\varepsilon_{nn}^A$ as a multiplier, does not contribute to frequency mixing. It depends on the frequency of the probe wave but does not depend on the frequency of the grating

$$\sum_{m=-\infty}^{\infty}(-1)^m\int_{t_m^{(0)}}^{t_{m+1}^{(0)}} dt\left(-\varepsilon_{nn}^{g0}\frac{\partial}{\partial x_i}\varepsilon_{kk}^p\right)e^{i\omega_s t}$$

$$=-\varepsilon_{nn}^{gA}\sum_{m=-\infty}^{\infty}\int_{t_m^{(0)}}^{t_{m+1}^{(0)}} dt\left(\frac{\partial}{\partial x_i}\varepsilon_{kk}^p\right)e^{i\omega_s t}$$

$$=-\varepsilon_{nn}^{gA}\int_{-\infty}^{\infty} dt\left(\frac{\partial}{\partial x_i}\varepsilon_{kk}^p\right)e^{i\omega_s t}.$$

This term contributes to the shift of the propagation velocity of the probe wave in the field of the pump wave.[4,21] This shift is proportional to the amplitude of the grating. Because of this observation, in the following analysis of the frequency-mixing processes we omit the terms proportional to the strain of the grating evaluated in the end points. Thus, from the above-presented analysis we conclude that the part of the nonlinear volumetric force (related to $c_{ijkl}^{(1)}$) which might be effective in the frequency mixing can be approximated by

$$F_i^{(1)}\approx -h_1\,\mathrm{sign}[I_1(\hat{\varepsilon}_g)-I_1(\hat{\varepsilon}_g^0)]$$

$$\times\left[\frac{\partial}{\partial x_i}(\varepsilon_{kk}^p\varepsilon_{ll}^g)-\varepsilon_{kk}^{p0}\frac{\partial}{\partial x_i}\varepsilon_{ll}^g\right]. \tag{36}$$

This is Eq. (36), which should be substituted in Eq. (34) to get the spectrum of the forces active in frequency mixing.

The evaluation, which is similar to one given above, provides the description of active volumetric forces related to the other hysteretic moduli. For example

$$F_i^{(2)}\approx -h_2\,\mathrm{sign}[I_1(\hat{\varepsilon}_g)-I_1(\hat{\varepsilon}_g^0)]\left[\frac{\partial}{\partial x_i}(\varepsilon_{kl}^p\varepsilon_{kl}^g)\right.$$

$$-\varepsilon_{kl}^{p0}\frac{\partial}{\partial x_i}\varepsilon_{kl}^g+\frac{\partial}{\partial x_j}(\varepsilon_{ij}^p\varepsilon_{ll}^g)-\varepsilon_{ij}^{p0}\frac{\partial}{\partial x_i}\varepsilon_{ll}^g$$

$$\left.+\frac{\partial}{\partial x_j}(\varepsilon_{kk}^p\varepsilon_{ij}^g)-\varepsilon_{kk}^{p0}\frac{\partial}{\partial x_j}\varepsilon_{ij}^g\right], \tag{37}$$

$$F_i^{(3)}\approx -h_3\,\mathrm{sign}[I_3(\hat{\varepsilon}_g)-I_3(\hat{\varepsilon}_g^0)]\left[\frac{\partial}{\partial x_j}(\varepsilon_{ik}^p\varepsilon_{kj}^g)\right.$$

$$\left.-\varepsilon_{ik}^{p0}\frac{\partial}{\partial x_j}\varepsilon_{kj}^g+\frac{\partial}{\partial x_j}(\varepsilon_{jk}^p\varepsilon_{ki}^g)-\varepsilon_{jk}^{p0}\frac{\partial}{\partial x_j}\varepsilon_{ki}^g\right]. \tag{38}$$

Note that all these forces are active only if the grating is introduced by a longitudinal wave because both I_1 and I_3 are zero in the shear plane wave. Consequently, it is useful to simplify Eqs. (36)–(38) by fixing the amplitude of the plane longitudinal (L) pump (grating) wave

$$\hat{\varepsilon}_g^A=\hat{\varepsilon}_{gL}^A=\varepsilon_{11}^g\delta_{il}\delta_{j1}, \tag{39}$$

and by assuming wave propagation along the x_1 axis $[\partial\varepsilon_{11}^g/\partial x_k=(\partial\varepsilon_{11}^g/\partial x_1)\delta_{k1}]$. Then, Eqs. (36)–(38) take the form

$$F_i^{(1)}(L)\approx -h_1\,\mathrm{sign}(\varepsilon_{11}^g-\varepsilon_{11}^{g0})$$

$$\times\left\{[(\varepsilon_{kk}^p-\varepsilon_{kk}^{p0})\delta_{i1}]\frac{\partial\varepsilon_{11}^g}{\partial x_1}+\frac{\partial\varepsilon_{kk}^p}{\partial x_i}\varepsilon_{11}^g\right\}, \tag{40}$$

$$F_i^{(2)}(L)\approx -h_2\,\mathrm{sign}(\varepsilon_{11}^g-\varepsilon_{11}^{g0})\Big\{[(\varepsilon_{i1}^p-\varepsilon_{i1}^{p0})+(\varepsilon_{kk}^p$$

$$-\varepsilon_{kk}^{p0})\delta_{i1}+(\varepsilon_{11}^p-\varepsilon_{11}^{p0})\delta_{i1}]\frac{\partial\varepsilon_{11}^g}{\partial x_1}$$

$$+\left[\frac{\partial\varepsilon_{ij}^p}{\partial x_i}+\frac{\partial\varepsilon_{11}^p}{\partial x_i}+\frac{\partial\varepsilon_{kk}^p}{\partial x_1}\delta_{i1}\right]\varepsilon_{11}^g\Big\}, \tag{41}$$

$$F_i^{(3)}(L)\approx -h_3\,\mathrm{sign}(\varepsilon_{11}^g-\varepsilon_{11}^{g0})\Big\{[(\varepsilon_{i1}^p-\varepsilon_{i1}^{p0})+(\varepsilon_{11}^p-\varepsilon_{11}^{p0})\delta_{i1}]\frac{\partial\varepsilon_{11}^g}{\partial x_1}+\Big[\frac{\partial\varepsilon_{i1}^p}{\partial x_1}+\frac{\partial\varepsilon_{1j}^p}{\partial x_j}\delta_{il}\Big]\varepsilon_{11}^g\Big\}. \tag{42}$$

Here, we introduced the argument "L" in the l.h.s. of Eqs. (40)–(42) to note that the pump is longitudinal. In evaluating $F_i^{(4)}$ we use the Taylor expansion

$$I_2^{1/2}(\hat\varepsilon_g-\hat\varepsilon_g^0+\hat\varepsilon_p-\hat\varepsilon_p^0)\equiv\sqrt{tr[(\hat\varepsilon_g-\hat\varepsilon_g^0+\hat\varepsilon_p-\hat\varepsilon_p^0)^2]}\approx\sqrt{tr[(\hat\varepsilon_g-\hat\varepsilon_g^0)^2]}\Bigg\{1+\frac{tr[(\hat\varepsilon_g-\hat\varepsilon_g^0)(\hat\varepsilon_p-\hat\varepsilon_p^0)]}{\sqrt{tr[(\hat\varepsilon_g-\hat\varepsilon_g^0)^2]}}\Bigg\},$$

and we derive

$$F_i^{(4)}\approx -h_4\Bigg\{\frac{tr[(\hat\varepsilon_g-\hat\varepsilon_g^0)(\hat\varepsilon_p-\hat\varepsilon_p^0)]}{\sqrt{tr[(\hat\varepsilon_g-\hat\varepsilon_g^0)^2]}}\frac{\partial\varepsilon_{ij}^p}{\partial x_j}+\sqrt{tr[(\hat\varepsilon_g-\hat\varepsilon_g^0)^2]}\frac{\partial\varepsilon_{ij}^p}{\partial x_j}+\frac{1}{\sqrt{tr[(\hat\varepsilon_g-\hat\varepsilon_g^0)^2]}}\Big[(\varepsilon_{kl}^g-\varepsilon_{kl}^{g0})(\varepsilon_{ij}^g-\varepsilon_{ij}^{g0})\frac{\partial\varepsilon_{kl}^p}{\partial x_j}+(\varepsilon_{kl}^g-\varepsilon_{kl}^{g0})(\varepsilon_{ij}^p-\varepsilon_{ij}^{p0})\frac{\partial\varepsilon_{kl}^g}{\partial x_j}+(\varepsilon_{kl}^p-\varepsilon_{kl}^{p0})(\varepsilon_{ij}^g-\varepsilon_{ij}^{g0})\frac{\partial\varepsilon_{kl}^g}{\partial x_j}\Big]-\frac{tr[(\hat\varepsilon_g-\hat\varepsilon_g^0)(\hat\varepsilon_p-\hat\varepsilon_p^0)]}{(tr[(\hat\varepsilon_g-\hat\varepsilon_g^0)^2])^{3/2}}(\varepsilon_{kl}^g-\varepsilon_{kl}^{g0})(\varepsilon_{ij}^g-\varepsilon_{ij}^{g0})\frac{\partial\varepsilon_{kl}^g}{\partial x_j}\Bigg\}.$$

The latter equation looks very different from Eqs. (36)–(38). However, it becomes very similar to Eqs. (40)–(42) when the pump wave is specified. In the case of the longitudinal grating of Eq. (39), we get

$$F_i^{(4)}(L)\approx -h_4\,\mathrm{sign}(\varepsilon_{11}^g-\varepsilon_{11}^{g0})\Big\{[(\varepsilon_{i1}^p-\varepsilon_{i1}^{p0})+(\varepsilon_{11}^p-\varepsilon_{11}^{p0})\delta_{i1}]\frac{\partial\varepsilon_{11}^g}{\partial x_1}+\Big[\frac{\partial\varepsilon_{ij}^p}{\partial x_j}+\frac{\partial\varepsilon_{11}^p}{\partial x_1}\delta_{i1}\Big]\varepsilon_{11}^g\Big\}. \tag{43}$$

Note that $\mathrm{sign}(\varepsilon_{11}^g-\varepsilon_{11}^{g0})$ appears in Eq. (43) because in the considered case

$$\sqrt{tr[(\hat\varepsilon_g-\hat\varepsilon_g^0)^2]}=|\varepsilon_{11}^g-\varepsilon_{11}^{g0}|=(\varepsilon_{11}^g-\varepsilon_{11}^{g0})\mathrm{sign}(\varepsilon_{11}^g-\varepsilon_{11}^{g0}).$$

Importantly, the modulus $c_{ijkl}^{(4)}$ can be controlled by the shear grating as well. If we fix the amplitude of the plane transversal (T) pump wave

$$\hat\varepsilon_g^A=\hat\varepsilon_{gT}^A=\varepsilon_{21}^g(\delta_{i1}\delta_{j2}+\delta_{i2}\delta_{j1}), \tag{44}$$

and assume its propagation along the x_1 axis $(\partial\varepsilon_{21}^g/\partial x_k)=(\partial\varepsilon_{21}^g/\partial x_1)\delta_{k1}$, then the active volumetric force $F_i^{(4)}$ becomes

$$F_i^{(4)}(T)\approx -\sqrt{2}h_4\,\mathrm{sign}(\varepsilon_{21}^g-\varepsilon_{21}^{g0})\times\Big\{[(\varepsilon_{i1}^p-\varepsilon_{i1}^{p0})+(\varepsilon_{21}^p-\varepsilon_{21}^{p0})\delta_{i2}]\frac{\partial\varepsilon_{21}^g}{\partial x_1}+\Big[\frac{\partial\varepsilon_{ij}^p}{\partial x_i}+\frac{\partial\varepsilon_{21}^p}{\partial x_2}\delta_{i1}+\frac{\partial\varepsilon_{21}^p}{\partial x_1}\delta_{i2}\Big]\varepsilon_{21}^g\Big\}. \tag{45}$$

Note that $\mathrm{sign}(\varepsilon_{21}^g-\varepsilon_{21}^{g0})$ appears in Eq. (45) because in the considered case

$$\sqrt{tr[(\hat\varepsilon_g-\hat\varepsilon_g^0)^2]}=\sqrt{2}|\varepsilon_{21}^g-\varepsilon_{21}^{g0}|=\sqrt{2}(\varepsilon_{21}^g-\varepsilon_{21}^{g0})\mathrm{sign}(\varepsilon_{21}^g-\varepsilon_{21}^{g0}).$$

The argument "T" is introduced in the l.h.s. of Eq. (45) to mention that the pump is the shear wave.

Similarly, the general presentations of $F_i^{(5)}$ and $F_i^{(6)}$ are rather complicated, but they become much simpler for the pump waves described by Eq. (39) and Eq. (44).

$$F_i^{(5)}(L)\approx -h_5\,\mathrm{sign}(\varepsilon_{11}^g-\varepsilon_{11}^{g0})\times\Bigg\{\Big[\frac{1}{2}(\varepsilon_{i1}^p-\varepsilon_{i1}^{p0})+(\varepsilon_{kk}^p-\varepsilon_{kk}^{p0})\delta_{i1}+\frac{3}{2}(\varepsilon_{11}^p-\varepsilon_{11}^{p0})\delta_{i1}\Big]\times\frac{\partial\varepsilon_{11}^g}{\partial x_1}+\Big[\frac{\partial}{\partial x_i}(\varepsilon_{ll}^p+\varepsilon_{11}^p)+\frac{1}{2}\frac{\partial\varepsilon_{ij}^p}{\partial x_j}+\frac{\partial}{\partial x_1}\times\Big(\varepsilon_{ll}^p-\frac{1}{2}\varepsilon_{11}^p\Big)\delta_{i1}\Big]\varepsilon_{11}^g\Bigg\}, \tag{46}$$

$$F_i^{(5)}(T)\approx -\sqrt{2}h_5\,\mathrm{sign}(\varepsilon_{21}^g-\varepsilon_{21}^{g0})\times\Big\{[(\varepsilon_{kk}^p-\varepsilon_{kk}^{p0})\delta_{i1}]\frac{\partial\varepsilon_{21}^g}{\partial x_1}+\frac{\partial\varepsilon_{kk}^p}{\partial x_i}\varepsilon_{21}^g\Big\}. \tag{47}$$

For the simplification of $F_i^{(6)}$ (which can be supported only by the longitudinal pump wave), we used the Taylor's expansions; for example,

$$I_3(\hat\varepsilon_g-\hat\varepsilon_g^0+\hat\varepsilon_p-\hat\varepsilon_p^0)\equiv tr[(\hat\varepsilon_g-\hat\varepsilon_g^0+\hat\varepsilon_p-\hat\varepsilon_p^0)^3]\approx tr[(\hat\varepsilon_g-\hat\varepsilon_g^0)^3]\Bigg\{1+3\frac{tr[(\hat\varepsilon_g-\hat\varepsilon_g^0)^2(\hat\varepsilon_p-\hat\varepsilon_p^0)]}{tr[(\hat\varepsilon_g-\hat\varepsilon_g^0)^3]}\Bigg\}.$$

$$F_i^{(6)}(L) \approx -h_6 \operatorname{sign}(\varepsilon_{11}^g - \varepsilon_{11}^{g0}) \times \left\{ \left[\frac{1}{2}(\varepsilon_{i1}^p - \varepsilon_{i1}^{p0}) + 2(\varepsilon_{kk}^p - \varepsilon_{kk}^{p0})\delta_{i1} + \frac{1}{2}(\varepsilon_{11}^p - \varepsilon_{11}^{p0})\delta_{i1} \right] \frac{\partial \varepsilon_{11}^g}{\partial x_1} + \left[\frac{\partial \varepsilon_{kk}^p}{\partial x_i} + \frac{\partial \varepsilon_{11}^p}{\partial x_i} + \frac{1}{2}\frac{\partial \varepsilon_{i1}^p}{\partial x_1} + \left(\frac{\partial \varepsilon_{kk}^p}{\partial x_1} - \frac{\partial \varepsilon_{11}^p}{\partial x_1} + \frac{1}{2}\frac{\partial \varepsilon_{ij}^p}{\partial x_j} \right)\delta_{i1} \right] \varepsilon_{11}^g \right\}. \tag{48}$$

Surely, the derived formulas (40)–(43) and (45)–(48) can be additionally simplified if we specify the mode of the probe wave (longitudinal or shear) and the polarization of the probe wave in the case of the shear probe (that is, the polarization in the plane or out of the plane fixed by $\mathbf{k}_g$ and $\mathbf{k}_p$). However, it is not necessary for the analysis presented here. Essential for our analysis is that there are only three types of different terms contributing to all eight calculated $F_i^{(f)}(L,T)$. These terms can be presented as proportional to

$$-h_f \operatorname{sign}(\varepsilon_{kl}^g - \varepsilon_{kl}^{g0})\varepsilon_{ij}^p \frac{\partial \varepsilon_{kl}^g}{\partial x_t},$$

$$h_f \operatorname{sign}(\varepsilon_{kl}^g - \varepsilon_{kl}^{g0})\varepsilon_{ij}^{p0} \frac{\partial \varepsilon_{kl}^g}{\partial x_t}, \tag{49}$$

$$-h_f \operatorname{sign}(\varepsilon_{kl}^g - \varepsilon_{kl}^{g0}) \frac{\partial \varepsilon_{ij}^p}{\partial x_t} \varepsilon_{kl}^g .$$

The form of the terms in Eq. (49) provides opportunity to predict a frequency of the nonlinearly scattered signal ω_s on the base of the following simple qualitative analysis. In fact, if the pump wave in Eq. (49) is a monochromatic wave of frequency ω_g, then the alternating sign function in Eq. (49) has a period $2\pi/\omega_g$ and its spectrum contains ω_g and all its odd harmonics. In other words the spectrum of $\operatorname{sign}(\varepsilon_{kl}^g - \varepsilon_{kl}^{g0})$ contains all the frequencies $(2n+1)\omega_g$ ($n=0,\pm 1, \pm 2,...$). Then, for monochromatic probe wave of frequency ω_p the equations (49) and (34) predict that ω_s is excited by simultaneous mixing of ω_p, ω_g, and $(2n+1)\omega_g$. As a result ω_s is combined of probe frequency ω_p and even harmonics $2n\omega_g$ of the pump wave [see Eq. (55) below]. The possibility of simultaneous excitation of the signal wave at different frequencies (corresponding to different *n*) is caused by the discontinuous variation of elastic module with strain (Fig. 1). The considered hysteretic nonlinearity may be characterized in its quantitative manifestation as being quadratic in amplitude and at the same time in its qualitative manifestations as being odd (not cubic but of an infinite order).

Of course the terms in Eq. (49) contribute to $F_i^{(f)}(L,T)$ with a combination of *i, j, k, l,* $t=1,2,3$ that is not arbitrary. For example, in $F_i^{(f)}(L,T)$ l is always equal to 1, while k might be only 1 or 2. However, if we want to find the frequency spectrum of the nonlinear forces, it appears to be simpler to find the spectrum of the contributions in Eq. (49) and then use the particular values of the indexes when substituting in the particular $\tilde{F}_i^{(f)}(L,T)$. It also appears simpler

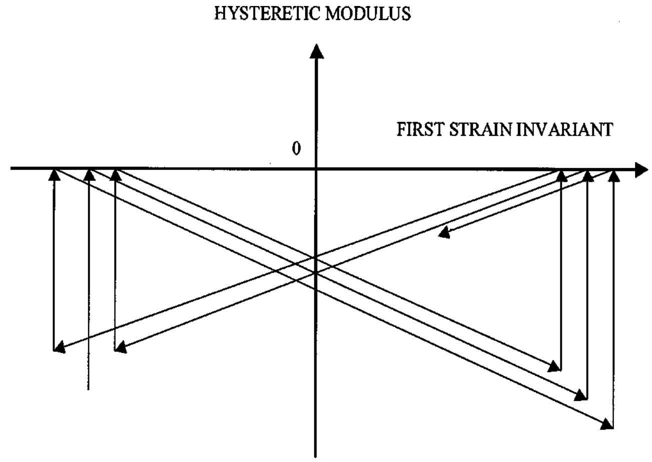

FIG. 1. Variation of strain-dependent contribution to nonlinear modulus accompanying strain variation in materials with hysteretic quadratic nonlinearity. A particular case, where the loading/unloading of the material is controlled only by the first strain invariant, is presented. The arrowheads indicate the path direction with increasing time.

not to fix the propagation direction of the pump wave (along the x_1 axis) before the evaluation of the $\mathbf{k}$ spectrum $\tilde{\tilde{F}}_i^{(f)}(L,T)$.

Accordingly, we evaluate the contributions of the terms in Eq. (49) to the spectrum of the volumetric forces by considering a very general case

$$\varepsilon_{kl}^g = \varepsilon_{kl}^{gA} \cos(\mathbf{k}_g \mathbf{r} - \omega_g t), \quad \varepsilon_{ij}^p = \varepsilon_{ij}^{pA} \exp[i(\mathbf{k}_p \mathbf{r} - \omega_p t)], \tag{50}$$

where ω_g and ω_p are considered to be positive. In accordance with (50) the position of the strain extremums are defined by

$$t_m^{(0)} = \frac{\mathbf{k}_g \mathbf{r} - \pi m}{\omega_g}. \tag{51}$$

In Eq. (51) $m=0,\pm 1,\pm 2,...$ is an integer number. Note that even m correspond to maxima [in accordance with the convention adopted in Eq. (32)]. Then, the contribution of the first term in Eq. (49) to the frequency spectrum of the nonlinear forces is

$$\begin{aligned} \tilde{F}_1^{(f)}(\omega_s) &\equiv \frac{1}{2\pi} \int_{-\infty}^{\infty} dt\, e^{i\omega_s t} \times \left[-h_f \operatorname{sign}(\varepsilon_{kl}^g - \varepsilon_{kl}^{g0}) \varepsilon_{ij}^p \frac{\partial}{\partial x_t} \varepsilon_{kl}^g \right] \\ &= -\frac{1}{2\pi} h_t \varepsilon_{kl}^{gA} \varepsilon_{ij}^{pA} (k_g)_t e^{i\mathbf{k}_p \mathbf{r}} \sum_{m=-\infty}^{\infty} (-1)^m \times \int_{t_m^{(0)}}^{t_{m+1}^{(0)}} dt\, e^{i(\omega_s - \omega_p)t} \sin(\mathbf{k}_g \mathbf{r} - \omega_g t), \end{aligned}$$

where $(k_g)_t$ is the projection of $\mathbf{k}_g$ on the x_t axis. After the integration over time and substitution of Eq. (51) we get

$$\tilde{F}_I^{(f)}(\omega_s) = -\frac{1}{2\pi} h_t \varepsilon_{kl}^{gA} \varepsilon_{ij}^{pA} \frac{(k_g)_t}{\omega_g} e^{i[\mathbf{k}_p + (\omega_s - \omega_p/\omega_g)\mathbf{k}_g]\mathbf{r}} \times \frac{\exp[i(\omega_s-\omega_p)/\omega_g]+1}{((\omega_s-\omega_p)/\omega_g)^2-1} \times \sum_{m=-\infty}^{\infty} e^{-i(\omega_s-\omega_p/\omega_g)\pi m}.$$

We apply the formula

$$\sum_{m=-\infty}^{\infty} e^{i\alpha\pi m} = 2\sum_{n=-\infty}^{\infty} \delta(\alpha - 2n)$$

for the summation. Here, δ denotes the delta function. The final presentation for $\tilde{F}_I^{(f)}(\omega_s)$ is

$$\tilde{F}_I^{(f)}(\omega_s) = -\frac{2}{\pi} h_t \varepsilon_{kl}^{gA} \varepsilon_{ij}^{pA} (k_g)_t \sum_{n=-\infty}^{\infty} \frac{1}{4n^2-1} e^{i(\mathbf{k}_p + 2n\mathbf{k}_g)\mathbf{r}} \times \delta(\omega_s - \omega_p - 2n\omega_g).$$

Applying to the latter result the 3D Fourier transform in space, we get

$$\tilde{\tilde{F}}_I^{(f)}(\mathbf{k}_s, \omega_s) = -\frac{2}{\pi} h_t \varepsilon_{kl}^{gA} \varepsilon_{ij}^{pA} (k_g)_t \times \sum_{n=-\infty}^{\infty} \frac{1}{4n^2-1} \delta^3(\mathbf{k}_s - \mathbf{k}_p - 2n\mathbf{k}_g) \times \delta(\omega_s - \omega_p - 2n\omega_g). \tag{52}$$

Here, δ^3 denoted the 3D delta function. The results for the two other types of the terms in Eq. (49) are obtained by similar manipulations

$$\tilde{\tilde{F}}_{II}^{(f)}(\mathbf{k}_s, \omega_s) = \frac{2}{\pi} h_t \varepsilon_{kl}^{gA} \varepsilon_{ij}^{pA} (k_g)_t \left(\frac{\exp(-i\pi\omega_p/\omega_g)+1}{2} \right) \times \sum_{n=-\infty}^{\infty} \frac{1}{[2n + (\omega_p/\omega_g)]^2 - 1} \times \delta^3(\mathbf{k}_s - \mathbf{k}_p - 2n\mathbf{k}_g)\, \delta(\omega_s - \omega_p - 2n\omega_g), \tag{53}$$

$$\tilde{\tilde{F}}_{III}^{(f)}(\mathbf{k}_s, \omega_s) = -\frac{2}{\pi} h_t \varepsilon_{kl}^{gA} \varepsilon_{ij}^{pA} (k_p)_t \sum_{n=-\infty}^{\infty} \frac{2n}{4n^2-1} \times \delta^3(\mathbf{k}_s - \mathbf{k}_p - 2n\mathbf{k}_g)\, \delta(\omega_s - \omega_p - 2n\omega_g). \tag{54}$$

With the help of the obtained Eqs. (52)–(54) the spectrum of all forces can be found if necessary.

For the current analysis it is important that in accordance with (52)–(54) the conditions for the resonance nonlinear scattering of a weak acoustic probe wave in the field of a strong pump wave can be described by the following conservation laws (synchronism conditions):

$$\omega_s = \omega_p + 2n\omega_g, \tag{55}$$

$$\mathbf{k}_s = \mathbf{k}_p + 2n\mathbf{k}_g, \tag{56}$$

with $n = 0, \pm 1, \pm 2, \ldots$. Note that in the particular case of $n = 0$ the probe wave is not scattered, though its propagation velocity and attenuation are modified by the presence of the grating. In the case of the copropagating and counterpropagating primary waves these effects were studied in Refs. 15 and 19. The terms in Eqs. (52)–(54) with $n \neq 0$ can also contribute to the considered effects in the degenerate case where the frequency of the probe wave ω_p coincides with the frequency of the grating ω_g or with one of its higher harmonics. It should not be forgotten that the terms of the form $h_f \operatorname{sign}(\varepsilon_{kl}^g - \varepsilon_{kl}^{g0}) \varepsilon_{kl}^{g0} (\partial \varepsilon_{ij}^p / \partial x_t)$, which are not active in frequency mixing [and, because of this, were omitted in Eqs. (40)–(43), (45)–(48)], should also be included in the analysis. We are planning to present the analysis of the induced anisotropy in the probe wave velocity dispersion and the probe wave attenuation in one of the forthcoming publications.

In the present publication we use the conservation laws (55), (56) together with the dispersion relations (29) for the acoustic signal [and the dispersion relations similar to (29) for the pump and probe acoustic waves] to analyze only frequency-mixing processes ($n \neq 0$) in materials with hysteresis of quadratic nonlinearity.

(1) It can be easily verified that the conditions (55), (56) allow the synchronous interaction of collinear waves of the same mode without mode conversion. In other words, in the case of collinear $\mathbf{k}_g$ and $\mathbf{k}_p$ the interaction of the longitudinal waves leads to the excitation of the longitudinal acoustic signals at all sum/difference frequencies given by $\omega_s = \omega_p + 2n\omega_g$ ($n = \pm 1, \pm 2, \ldots$). The collinear interaction of the shear probe with shear pump leads to the excitation of the shear acoustic signal at all $\omega_s = \omega_p + 2n\omega_g$ ($n = \pm 1, \pm 2, \ldots$). The collinear resonant interactions of the different modes (that is, the interaction between the longitudinal and shear waves) are forbidden. The collinear interactions with mode conversion (that is, the excitation of the shear/longitudinal acoustic signal in the interaction of the longitudinal/shear probe and pump waves) are forbidden as well.

(2) The description of the possible non-collinear interactions between the probe and pump waves is summarized in Table I. In this table $|n|$ is positive and, consequently, $\omega_s = \omega_p + 2|n|\omega_g$ corresponds to sum frequency excitation while $\omega_s = \omega_p - 2|n|\omega_g$ corresponds to difference frequency excitation. The type of the process (i.e., the sum or difference frequency excitation) is specified in the third column in Table I together with the mode of the scattered signal wave. The first two columns specify the acoustical modes of the probe and of the grating, respectively. In the fourth and the fifth columns the obtained solutions for the angle φ between $\mathbf{k}_g$ and $\mathbf{k}_p$ in the case of the resonant interaction and the frequency limits, where the resonant interaction is allowed, are given. Here, the parameter $c \equiv c_T/c_L$ denotes the ratio of the shear and longitudinal velocities, and the parameter $a \equiv 2|n|\omega_g/\omega_p$ denotes the ratio of the frequencies, which are combined in the nonlinear process. As was described in Ref. 15 (for the 1D case), in a medium with the hys-

TABLE I. Interaction cases which produce a scattered non-collinear wave in materials with quadratic hysteretic nonlinearity. Compact notations: $a\equiv 2|n|\omega_g/\omega_p$ ($|n|=1,2,3,...$), $c\equiv c_T/c_L$.

	1 Probe mode (ω_p)	2 Grating mode (ω_g)	3 Signal mode (ω_s)	4 $\cos\varphi$	5 Frequency limits
1	T	T	L $\omega_{sL}=\omega_{pT}+2\vert n\vert\omega_{gT}$	$c^2-(1-c^2)\frac{a^2+1}{a}$	$\frac{1-c}{1+c}<a<\frac{1+c}{1-c}$
2	L	L	T $\omega_{sT}=\omega_{pL}-2\vert n\vert\omega_{gL}$	$\frac{1}{c^2}-\frac{(1-c^2)}{c^2}\frac{a^2+1}{a}$	$\frac{1-c}{1+c}<a<\frac{1+c}{1-c}$
3	L	T	L $\omega_{sL}=\omega_{pL}+2\vert n\vert\omega_{gT}$	$c-\frac{(1-c^2)}{c}\frac{a}{2}$	$0<a<\frac{2c}{1-c}$
4	L	T	L $\omega_{sL}=\omega_{pL}-2\vert n\vert\omega_{gT}$	$c+\frac{(1-c^2)}{c}\frac{a}{2}$	$0<a<\frac{2c}{1+c}$
5	L	T	T $\omega_{sT}=\omega_{pL}-2\vert n\vert\omega_{gT}$	$\frac{1}{c}-\frac{(1-c^2)}{c}\frac{1}{2a}$	$\frac{1-c}{2}<a<\frac{1+c}{2}$
6	T	L	L $\omega_{sL}=\omega_{pT}+2\vert n\vert\omega_{gL}$	$c-\frac{(1-c^2)}{c}\frac{1}{2a}$	$\frac{1-c}{2c}<a<\infty$
7	T	L	L $\omega_{sL}=\omega_{pT}-2\vert n\vert\omega_{gL}$	$c+\frac{(1-c^2)}{c}\frac{1}{2a}$	$\frac{1+c}{2c}<a<\infty$
8	T	L	T $\omega_{sT}=\omega_{pT}-2\vert n\vert\omega_{gL}$	$\frac{1}{c}-\frac{(1-c^2)}{c}\frac{a}{2}$	$\frac{2}{1+c}<a<\frac{2}{1-c}$

teresis of quadratic nonlinearity each phonon of a weak probe wave can be combined with the $2|n|$ phonons of a strong pump wave ($|n|=1,2,3,...$). Note that the considered frequency-mixing process with $|n|=1$ has been identified recently in the experiments with sandstones.[51]

In our Table I the first five rows are of precisely the same form as the whole similar table presented by Jones and Kobett for the allowed interactions in materials with the elastic quadratic nonlinearity (Table I in Ref. 22). The one-to-one transformation between the first five rows of our Table I and Table I from Ref. 22 is achieved by the change in the notation for the frequencies $\omega_p\Leftrightarrow\omega_1$, $2|n|\omega_g\Leftrightarrow\omega_2$. Here, ω_1 and ω_2 are the frequencies of the primary waves in Ref. 22. In the case of the interaction between different acoustic modes ω_1 denotes the frequency of a longitudinal wave. The interaction cases described in the rows 6 to 8 in our Table I are formally additional in comparison with the cases identified for materials with elastic quadratic nonlinearity. These formally additional interaction cases appear because in our problem of the interaction between a weak probe wave and a strong pump wave in a hysteretic medium the primary waves are not equivalent (as they are in the problem considered in Ref. 22). In our case only the strong pump wave (the grating) can contribute simultaneously few phonons ($2|n|$) to the scattered signal. It means that in order to specify a particular process in our problem it is insufficient to say that the primary waves belong to different acoustic modes (as it is stated in the rows 3 to 5 in Table I of Ref. 22). We also have to specify a mode of the grating (i.e., is it a transversal as in the rows 3 to 5 of our Table I, or it is a longitudinal as in the rows 6 to 8 of our Table I). This is the reason for the appearance of the formally additional interaction cases in the materials with hysteretic quadratic nonlinearity. The formally additional cases in the rows 6 to 8 of our Table I appear as a result of an asymmetry in the primary waves, which was introduced by us in the problem in order to get analytical solutions. The rows 6 to 8 in Table I can be obtained from the rows 3 to 5 by changing there $a\Rightarrow 1/a$. All six rows (3 to 8) in our Table I can be obtained from the three rows (3 to 5) in Table I from Ref. 22 if we consider two different opportunities $a=\omega_2/\omega_1=2|n|\omega_g/\omega_p$ and $a=\omega_2/\omega_1=\omega_p/2|n|\omega_g$. That is why we are calling the interaction cases in the rows 6 to 8 of our Table I only formally additional.

The principal difference in the physics of frequency-mixing phenomena in materials with elastic and with hysteretic quadratic nonlinearity is related to the fact that in the latter case it is not the frequency of the pump wave itself but this is the even harmonics of the pump wave frequency that contributes to the combination (sum of difference) frequency. Because of this, even if the ratio ω_g/ω_p of the grating and the probe frequencies is fixed, there is an additional parameter $|n|=1,2,3,...$, which is very important in the inequalities imposing the frequency limits for the synchronous interaction (the fifth column in Table 1). Let us examine, for example, the process described in the first row in Table I (i.e., $T+T\Rightarrow L$). The value $|n|=1/2$ formally provides the description of the frequency mixing in a medium with elastic quadratic nonlinearity. The inequality in the fifth column (in the case $|n|=1/2$) divides the space of the primary frequencies in three parts

$$\text{(I)}: \ \frac{\omega_g}{\omega_p}<\frac{1-c}{1+c},$$
$$\text{(II)}: \ \frac{1-c}{1+c}<\frac{\omega_g}{\omega_p}<\frac{1+c}{1-c}, \quad \text{(III)}: \ \frac{1+c}{1-c}<\frac{\omega_g}{\omega_p}. \tag{57}$$

The excitation of the sum frequency in the elastic medium in the region (III) is forbidden. Because in the hysteretic medium the parameter $|n|=1,2,3,...$ is larger than $\frac{1}{2}$, then from the third inequality in Eq. (57) it follows that

$$\frac{1+c}{1-c}<2|n|\frac{\omega_g}{\omega_p}. \tag{58}$$

Consequently the excitation of the sum frequency in the region (III) is forbidden in the hysteretic materials as well.

In the region (II) a single process of sum-frequency excitation (possible for a single mutual orientation of $\mathbf{k}_g$ and $\mathbf{k}_p$) is allowed in the elastic medium. In this region $|n|$ sum-frequency resonant excitation processes may be allowed in the medium with the nonlinearity hysteresis ($\omega_s=\omega_p+2\omega_g, \omega_s=\omega_p+4\omega_g,\dots,\omega_s=\omega_p+2|n|\omega_g$) if the inequality

$$2|n|\frac{\omega_g}{\omega_p}<\frac{1+c}{1-c}$$

holds. The sum-frequency generation processes are forbidden in the region (II) in the hysteretic materials if the inequality (58) holds starting from $|n|=1$.

In the region (I) the excitation of the sum frequency is forbidden in the elastic medium. In this region $m+1$ processes are allowed in materials with quadratic hysteretic nonlinearity $[\omega_s=\omega_p+2(k-m)\omega_g,\ \omega_s=\omega_p+2(k-m+1)\omega_g,\ \dots,\ \omega_s=\omega_p+2k\omega_g$, k and m are positive integer numbers, $k>m]$, if

$$\frac{1-c}{1+c}<2(k-m)\frac{\omega_g}{\omega_p}, \quad 2k\frac{\omega_g}{\omega_p}<\frac{1+c}{1-c}$$

for some values of k and m. Sum-frequency excitation is forbidden in the region (I) in the hysteretic medium if the inequality (58) holds starting from $|n|=1$.

Another typical illustrative example is obtained from the analysis of rows 3 and 6 in Table I. In accordance with row 3 (in our Table I and also in Table I of Ref. 22) and row 6 in our Table I the excitation of the longitudinal sum-frequency signal in the interaction of the different modes ($L+T\Rightarrow L$) is forbidden in the elastic medium if

$$\frac{2c}{1-c}<\frac{\omega_g}{\omega_p}.$$

However, this process is always allowed in the medium with nonlinearity hysteresis for sufficiently large $|n|$ if the grating is created by a longitudinal wave. In fact, in accordance with row 6 in Table I there is always an infinite number of the allowed processes with $|n|$ satisfying the inequality

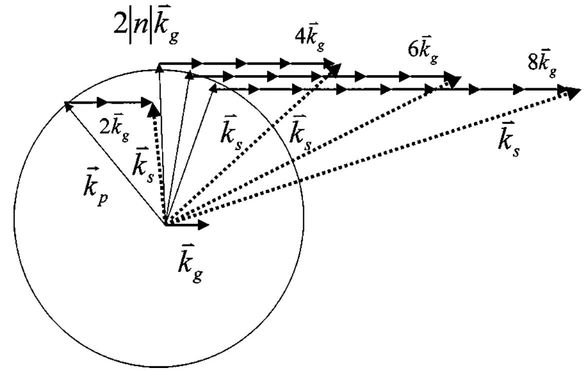

FIG. 2. Geometrical illustration of the synchronism condition $\mathbf{k}_s=\mathbf{k}_p+2|n|\mathbf{k}_g$ in the case of longitudinal sum-frequency excitation $\omega_s=\omega_p+2|n|\omega_g$ in the process of a weak shear probe wave scattering by a strong longitudinal grating. Thin vectors correspond to probe wave vectors $\mathbf{k}_p$. Their ends are on the circle of the radius $|\mathbf{k}_p|=6|\mathbf{k}_g|$ (because $\omega_p=3\omega_g$ is assumed in the figure). Thick vectors correspond to pump wave vector $\mathbf{k}_g$ and the wave vectors of its even harmonics ($|n|=1,2,3,4$). The dotted-line vectors correspond to nonlinearly scattered signal wave vector $\mathbf{k}_s$.

$$\frac{1-c}{2c}<2|n|\frac{\omega_g}{\omega_p}.$$

As a consequence there is an infinite number of the mutual orientations of $\mathbf{k}_g$ and $\mathbf{k}_p$, for which resonant scattering is possible. We illustrate this graphically in Fig. 2. For the presentation in Fig. 2 it was assumed that $c=c_T/c_L=1/2$ and $\omega_T/\omega_L=3$. Then, in accordance with row 3 in Table I the excitation of the sum frequency in the process $L+T\Rightarrow L$ is forbidden in the elastic medium and also in the hysteretic if the pump wave is shear. However, in accordance with the sixth row in Table I the same process but in the case of the longitudinal pump ($\omega_{sL}=\omega_{pT}+2|n|\omega_{gL}$) is allowed for all $|n|=1,2,3,...$. Figure 2 illustrates the momentum conservation $\mathbf{k}_{sL}=\mathbf{k}_{pT}+2|n|\mathbf{k}_{gL}$ in the considered scattering process for the different values of $|n|=1,2,3,4$. In accordance with Table I in the considered case $\cos\varphi=(1/2)-(9/8)(1/|n|)$. Consequently, for sufficiently large values $|n|\geqslant 10$ the resonance angles are close to $\pi/3$ and the scattered wave propagates nearly collinear with the pump wave.

We see that in general the presence of hysteretic nonlinearity may increase the number of possible angles for synchronous scattering of non-collinear acoustic waves in materials.

IV. CONCLUSIONS

In the developed theory the particular form of energy potential (cubic in strains) is proposed, which leads to the bow-tie behavior of the nonlinear modulus in an isotropic material with hysteresis of quadratic nonlinearity. The nonlinear scattering of a weak probe wave in the field of a strong pump wave is analyzed. It is demonstrated that collinear interactions of shear waves are allowed in materials with nonlinearity hysteresis. Both in collinear and non-collinear frequency-mixing processes the combination frequency is composed of the probe wave frequency and one of the even harmonics of the pump (the grating) wave ($\omega_s=\omega_p+2n\omega_g$). Note that recently the frequency-mixing process of the predicted type has been observed experimentally[51] for

$n=1$, though the directivity pattern of the interaction (that is, $\mathbf{k}_s=\mathbf{k}_p+2n\mathbf{k}_g$) has not been verified. In general the developed theory predicts that in the presence of hysteretic nonlinearity the number of possible resonant scattering processes increases. In particular, if frequency-mixing processes are forbidden in a material with elastic quadratic nonlinearity (for a fixed ratio of primary frequencies), they may be allowed in materials with hysteretic quadratic nonlinearity. Moreover, in materials with hysteresis of nonlinearity resonant frequency mixing for a fixed ratio of primary frequencies may be allowed for multiple mutual orientations of the primary wave vectors $\mathbf{k}_p$ and $\mathbf{k}_g$. To verify the predictions of the developed theory the experiments similar to those described in Refs. 26 and 27 are necessary. The developed theory is expected to become useful in the nonlinear tomography of mesoscopic materials.

ACKNOWLEDGMENTS

The work was supported in the frame of the Contract No. DGA/CNRS.

[1] J. N. TenCate, D. E. Smith, and R. Guyer, ''Universal slow dynamics in granular solids,'' Phys. Rev. Lett. **85**, 1020–1023 (2000).
[2] R. A. Guyer, J. TenCate, and P. Johnson, ''Hysteresis and the dynamic elasticity of consolidated granular materials,'' Phys. Rev. Lett. **82**, 3280–3283 (1999).
[3] R. A. Guyer and P. Johnson, ''Nonlinear mesoscopic elasticity: Evidence for a new class of materials,'' Phys. Today **52**, 30–35 (1999).
[4] V. Gusev, W. Lauriks, and J. Thoen, ''Dispersion of nonlinearity, nonlinear dispersion, and absorption of sound in micro-inhomogeneous materials,'' J. Acoust. Soc. Am. **103**, 3216–3226 (1998).
[5] I. A. Beresnev and K.-L. Wen, ''Nonlinear soil response—a reality?,'' Bull. Seismol. Soc. Am. **86**, 1964–1978 (1996).
[6] R. A. Guyer, K. P. McCall, and G. N. Boitnott, ''Hysteresis, discrete memory, and nonlinear wave propagation in rock: A new paradigm,'' Phys. Rev. Lett. **74**, 3491–3494 (1995).
[7] V. E. Nazarov, L. A. Ostrovsky, I. A. Soustova, and A. M. Sutin, ''Nonlinear acoustics of micro-inhomogeneous media,'' Phys. Earth Planet. Inter. **50**, 65–73 (1988).
[8] V. E. Nazarov, ''Nonlinear acoustic effects in annealed copper,'' Akust. Zh. **37**, 150–156 (1991) [Sov. Phys. Acoust. **37**, 75–78 (1991)].
[9] V. E. Nazarov, L. A. Ostrovskii, I. A. Soustova, and A. M. Sutin, ''Anomalous acoustic nonlinearity in metals,'' Akust. Zh. **34**, 491–499 (1988) [Sov. Phys. Acoust. **34**, 284–289 (1988)].
[10] P. P. Dimitriu, ''Self-modulation instability and recurrence phenomena in vibration-induced steady-state sinusoidal ground vibration,'' Phys. Earth Planet. Inter. **50**, 74–82 (1988).
[11] V. Gusev, ''Self-modulation instability in materials with hysteretic quadratic nonlinearity,'' Wave Motion **33**, 145–153 (2001).
[12] V. E. Nazarov, ''Sound damping by sound in metals,'' Acoust. Lett. **15**, 22–25 (1991).
[13] V. E. Nazarov, ''Nonlinear acoustic effects in annealed copper,'' Akust. Zh. **37**, 150–156 (1991) [Sov. Phys. Acoust. **37**, 75–78 (1991)].
[14] V. E. Nazarov, ''Attenuation of sound by sound in annealed copper,'' Akust. Zh. **37**, 825–826 (1991) [Sov. Phys. Acoust. **37**, 432 (1991)].
[15] V. Gusev, ''Parametric attenuation and amplification of acoustic signals in the media with hysteretic quadratic nonlinearity,'' Phys. Lett. A **271**, 100–109 (2000).
[16] D. J. Holcomb, ''Memory, relaxation, and microfracturing in dilatant rock,'' J. Geophys. Res. **86**, 6235–6248 (1981).
[17] Y. Ohsaki, ''Some notes on Masing's law and non-linear response of solid deposits,'' J. Fac. Eng., Univ. Tokyo (B) **35**, 513–536 (1980).
[18] I. D. Mayergoyz, *Mathematical Models of Hysteresis* (Springer, Berlin, 1991).
[19] V. Gusev, H. Bailliet, P. Lotton, and M. Bruneau, ''Interaction of the counterpropagating acoustic waves in the media with nonlinear dissipation and in the hysteretic media,'' Wave Motion **29**, 211–221 (1999).
[20] V. Gusev, ''Parametric acoustic source in a medium with hysteretic quadratic nonlinearity,'' Acoust. Lett. **22**(2), 30–34 (1998–2000).
[21] V. Gusev, C. Glorieux, W. Lauriks, and J. Thoen, ''Nonlinear bulk and surface shear acoustic waves in materials with hysteresis and end-point memory,'' Phys. Lett. A **232**, 77–86 (1997).
[22] G. L. Jones and D. R. Kobett, ''Interaction of elastic waves in an isotropic solid,'' J. Acoust. Soc. Am. **35**, 5–10 (1963).
[23] J. D. Childress and C. G. Hambrick, ''Interactions between elastic waves in an isotropic solid,'' Phys. Rev. **136**, A411–A418 (1964).
[24] L. H. Taylor and F. R. Rollins, Jr., ''Ultrasonic study of three-phonon interactions. I. Theory,'' Phys. Rev. **136**, A591–A596 (1964).
[25] L. K. Zarembo and V. A. Krasilnikov, ''Nonlinear phenomena in the propagation of elastic waves in solids,'' Usp. Fiz. Nauk **102**, 549–586 (1970) [Sov. Phys. Usp. **13**, 778–797 (1971)].
[26] P. A. Johnson, T. J. Shankland, R. J. O'Connel, and J. N. Albright, ''Nonlinear generation of elastic waves in crystalline rock,'' J. Geophys. Res. **92**(B5), 3597–3602 (1987).
[27] P. A. Johnson and T. J. Shankland, ''Nonlinear generation of elastic waves in granite and sandstone: Continuous wave and travel time observations,'' J. Geophys. Res. **94**(B12), 17729–17733 (1989).
[28] A. M. Sutin and V. E. Nazarov, ''Nonlinear acoustic methods of crack diagnostics,'' Radiophys. Quantum Electron. **38**(3–4), 109–120 (1995).
[29] S. N. Zaitsev, I. A. Soustova, and A. M. Sutin, ''Nonlinear interaction of acoustic emission pulses with harmonic test wave,'' Akust. Zh. **46**, 496–502 (2000) [Acoust. Phys. **46**, 427–432 (2000)].
[30] T. Sato, A. Fukusima, N. Ishida, ''Nonlinear parameter tomography system using counterpropagating probe and pump waves,'' Ultrason. Imaging **7**, 49–59 (1985).
[31] L. D. Landau and E. M. Lifshitz, *Theory of Elasticity* (Pergamon, New York, 1959).
[32] A. I. Lurie, *Nonlinear Elasticity Theory*, North-Holland Series in Applied Mathematics, Vol. 36 (North-Holland, Amsterdam, 1990).
[33] A. D. Drozdov, *Finite Elasticity and Viscoelasticity* (World Scientific, Singapore, 1996).
[34] S. S. Antmann, *Nonlinear Problems of Elasticity*, Applied Mathematical Sciences, Vol. 107 (Springer, New York, 1995).
[35] G. N. Boitnott, ''Experimental characterization of the nonlinear rheology of rock,'' Int. J. Rock Mech. Min. Sci. **34** (3–4), paper No. 033 (1997).
[36] A. N. Tutunku, A. L. Podio, A. R. Gregory, and M. M. Sharma, ''Nonlinear viscoelastic behavior of sedimentary rocks. II. Hysteresis effects and influence of type of fluid on elastic moduli,'' Geophysics **63**, 195–203 (1998).
[37] V. S. Yamshikov, V. L. Shkuratnik, and A. V. Lavrov, ''Memory effects in rocks (review),'' J. Mining Sci. **30**, 463–473 (1994).
[38] D. Kolymbas, ''Computer-aided design of constitutive laws,'' Int. J. Numer. Analyt. Meth. Geomech. **15**, 593–609 (1991).
[39] D. Kolymbas, ''An outline of hypoplasticity,'' Arch. Appl. Mech. **61**, 143–151 (1991).
[40] D. Kolymbas, ''Hypoplastic constitutive equations with internal variables,'' Int. J. Numer. Analyt. Meth. Geomech. **19**, 415–436 (1995).
[41] E. Bauer, ''Calibration of comprehensive hypoplastic model for granular materials,'' Soils Found. **36**(1), 13–26 (1996).
[42] V. I. Erofeev, ''Plane stationary waves in damaged medium with microstructure,'' Akust. Zh. **40**, 67–70 (1994) [Acoust. Phys. **40**, 57–60 (1994)].
[43] R. M. Jones, ''Stress–strain relations for materials with different moduli in tension and compression,'' AIAA J. **15**(1), 16–23 (1977).
[44] V. E. Nazarov and L. A. Ostrovsky, ''Elastic waves in media with strong acoustic nonlinearity,'' Akust. Zh. **36**, 106–110 (1990) [Sov. Phys. Acoust. **36**, 57–60 (1990)].
[45] A. E. Green, ''Hypo-elasticity and plasticity. II,'' J. Rational Mech. Anal. **5**, 725–734 (1956).
[46] W.-F. Chen and A. F. Saleeb, *Constitutive Equations for Engineering Materials, Vol. 1: Elasticity and Modeling* (Elsevier, Amsterdam, 1994).
[47] D. W. Kosik, ''Propagation of a nonlinear seismic pulse in an inelastic homogeneous medium,'' Geophysics **57**, 949–963 (1993).
[48] V. Gusev, ''Propagation of acoustic pulses in material with hysteretic quadratic nonlinearity,'' J. Acoust. Soc. Am. **107**, 3047–3058 (2000).
[49] S. A. Collins and R. C. Bachus, ''Use of hypoelasticity to model the

behavior of sands,'' in *Constitutive Equations for Granular Non-Cohesive Soils*, edited by A. Saada and G. Bianchini (Balkema, Rottedam, 1988), pp. 201–223.
[50] K. E.-A. Van den Abeele, P. A. Johnson, R. A. Guyer, and K. R. McCall, ''On the quasianalytic treatment of hysteretic nonlinear response in elastic wave propagation,'' J. Acoust. Soc. Am. **101**, 1885–1898 (1997).
[51] K. E.-A. Van den Abeele, P. A. Johnson, and A. Sutin, ''Nonlinear elastic wave spectroscopy (NEWS) techniques to discern material damage. I. Nonlinear modulation spectroscopy (NWMS),'' Res. Nondestruct. Eval. **12**, 17–30 (2000).

Nonlinearity of acoustic waves at solid–liquid interfaces

Christ Glorieux[a] and Kris Van de Rostyne
Laboratorium voor Akoestiek en Thermische Fysica, Departement Natuurkunde, Katholieke Universiteit Leuven, Celestijnenlaan 200D, B-3001 Leuven, Belgium

Vitalyi Gusev
Laboratoire de Physique de l'Etat Condensé, UPRESA-CNRS 6087, Faculté des Sciences, Université du Maine, Ecole Nationale Supérieure d'Ingénieurs du Mans, 72085 Le Mans, France

Weimin Gao, Walter Lauriks, and Jan Thoen
Laboratorium voor Akoestiek en Thermische Fysica, Departement Natuurkunde, Katholieke Universiteit Leuven, Celestijnenlaan 200D, B-3001 Leuven, Belgium

(Received 19 January 2001; revised 13 July 2001; accepted 21 September 2001)

The small-amplitude and finite-amplitude propagation characteristics of laser line source excited and laser detected Scholte waves are investigated. Acoustic waves with Mach numbers up to 0.054 are observed at the interface between water and glass. In our case of a hard solid–liquid interface, the Scholte wave propagates very much like a bulk wave, for which the simple-wave equation holds. The experimental results are well fitted with this model, extended with an attenuation term. An anomalously large (compared with low amplitude viscous effects) attenuation reveals possible leakage of energy from the Scholte wave to bulk waves, through a mechanism of nonlinear mixing between the different wave modes and viscosity induced turbulence. [DOI: 10.1121/1.1420388]

PACS numbers: 43.25.Fe, 43.25.Ed, 43.25.Zx [SGK]

I. INTRODUCTION

The application of a laser to excite acoustic waves has considerably widened the possibilities to study thermoelastic properties of materials. Laser excitation and detection leads to a large bandwidth, because energy can be deposited in a material in a very short time and in a confined volume. In this article we report on experimental results for both linear and nonlinear propagation properties of laser excited and detected Scholte waves and leaky Rayleigh waves at a solid–liquid interface.[1] Scholte waves are interface waves, which are usually rather weakly confined at the interface between liquid and solid and carry information both on liquid and solid properties, as illustrated in Sec. II. In Sec. III, we report on experimentally observed waves with Mach number up to 0.054, which is quite high compared to many classical experiments. The results are analyzed in the framework of the thermoelastic equations for the linear properties and of a theoretical model describing nonlinear Scholte wave propagation for the high amplitude waves. Suggestions are made for an extension of the simple-wave equation with an attenuation term, in order to account for experimental anomalies, which may result from mode coupling between the Scholte waves and bulk waves or viscosity-induced turbulence at high Mach numbers.

II. SOLID–LIQUID INTERFACE WAVES

In isotropic bulk conditions the solutions of the thermoelastic equations are longitudinal and shear waves. In the presence of an interface, the induced symmetry breaking gives rise to the existence of specific interface waves, which are characterized by their propagation along the interface, and by their localization in the interface region. Without loss of generality we restrict to the configuration of an optically absorbing liquid and transparent solid. We consider acoustic waves which are thermo-elastically generated by the optical absorption of light of a laser source causing a heat distribution in the liquid given by

$$Q(x,y,z)=\frac{Q_0}{z_0}\exp\left(-\left(\frac{x}{x_0}\right)^2-\left(\frac{y}{y_0}\right)^2-\left(\frac{|z|}{z_0}\right)\right), \qquad (1)$$

with Q_0 the amplitude of the laser intensity, x_0 and y_0 the width in the x and y directions, respectively, and z_0 the optical absorption depth in the liquid ($z<0$ in the liquid, see Fig. 1). We consider the case of cylindrically focused light (Fig. 1): $x_0 \ll y_0$ and y_0 is much larger than all wavelengths within the experimental bandwidth. In the linear regime the solution for the displacements is described in detail in Refs. 1–5. The displacement u_y in the y direction is zero, the y dependence of the solutions for the displacements in the x and z directions can be neglected, and the interface-confined solutions of the thermo-elastic equations are waves propagating in the x direction with exponentially decaying wave amplitude components in the z direction.

In general, the dispersion equation or so-called Scholte equation,

$$\Delta(q(\omega))=(q^2+p_{T1}^2)^2-4q^2p_{T1}p_{L1}+\frac{\rho_2}{\rho_1}\frac{p_{L1}}{p_{1,2}}q_{T1}^4=0, \qquad (2)$$

has two solutions, corresponding to a leaky Rayleigh and Scholte wave, respectively. ρ_n are the densities, q

[a]Postdoctoral Researcher of Fonds voor Wetenschappelijk Onderzoek-Vlaanderen (FWO-V), on leave at Department of Chemistry, Massachusetts Institute of Technology, 77 Massachusetts Avenue, Cambridge, MA 02139.

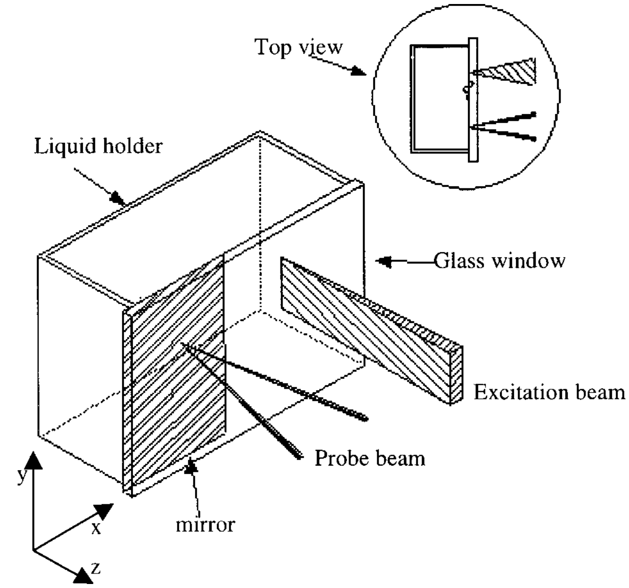

FIG. 1. Schematic diagram of the experimental setup: a laser line source along the (vertical) *y* direction excites left-going acoustic waves at the interface between the window and the liquid in the (horizontal) *x* direction. The *z* axis is perpendicular to the interface.

$=\omega/v_{R,S}$, $q_{L,T,n}=\omega/v_{L,T,n}$, and $p_{L,T,n}=\sqrt{q^2-q_{L,T,n}^2}$. ω is the radial frequency, v_L the longitudinal velocity, v_T the transverse velocity of the medium with index n ($n=1$ refers to the substrate and $n=2$ to the liquid. The sign of the square roots are such that the solution corresponds either to radiation away from the interface or, in the case of localization, to decay with increasing distance from the interface. Both waves have longitudinal and transverse components in the solid. The leaky Rayleigh (LR) wave penetrates over a distance $2\pi/q_L$ and $2\pi/q_T$ in the solid for *x* and *z* displacement, respectively. This mainly solid-borne wave attenuates with propagation due to the radiation of energy into the liquid under the Rayleigh angle $\theta_R=\cos^{-1}(v_{L2}/v_R)$ to the interface. The attenuation is larger as the wave is less supersonic with respect to the liquid and as the solid/liquid density ratio decreases. When the liquid is supersonic with respect to the solid, the leaky Rayleigh wave does not exist.[2] In contrast with the LR wave, the Scholte wave (neglecting thermo-viscous attenuation) travels unattenuated. The penetration depth in the solid is given by $1_{1S}^{-1}q_S^{-1}$ and by $1_{2S}^{-1}q_S^{-1}$ in the liquid, with $1_{nS}=\sqrt{1-(v_S/v_{Ln})^2}$. In the case of a large acoustic impedance mismatch between solid and liquid, the Scholte velocity v_S lies very close to v_{L2}, the longitudinal wave velocity of the liquid. As a result, 1_{2S} is smaller than 1, and the wave is only weakly localized. As a consequence, the characteristics of the Scholte wave are very close to the ones of an ordinary bulk wave in the liquid which propagates along the interface. This will be of importance for our experimental configuration glass-colored water, where $1_{2S}=\sqrt{1-(5130/1535.5)^2}=0.085$, and more than 90% of the energy is located in the liquid. For softer solids, or equivalently, less compressible liquids, the Scholte wave becomes more localized and slows down compared to the liquid bulk velocity.[2]

III. NONLINEAR SCHOLTE WAVE PROPAGATION: EXPERIMENTAL SETUP AND RESULTS

Using a transparent solid and a colored liquid absorbing pulsed laser light leads to interface waves with large Mach numbers (ratio between peak particle velocity and wave velocity).[6–9] Using a laser line source at a window-liquid interface thus yields a possibility to study nonlinear wave propagation. A *variant* of such a configuration, using ablation of a thin film of liquid or a soft coating, was exploited in Refs. 10 and 11 for studying nonlinear Rayleigh wave propagation. Especially Scholte waves are interesting, because their intrinsic nondispersive and nondiffracting character simplifies the analysis and renders information on the liquid.

Our experimental results for nonlinear Scholte waves were obtained using a cylindrically focused (75 μm$\times$15 mm) YAG laser beam for the excitation of waves along the interface between glass (longitudinal velocity $v_{L1}=5712$ m/s, transverse velocity $v_{T1}=3530$ m/s, density $\rho_1=2500$ kg/m^3) and an optically absorbing water–$CuCl_2$ solution (concentration 0.098 g/ml, density 1176 kg/m^3, bulk velocity 1535.5 m/s, optical absorption depth 324 μm). Interface waves were detected with an electronic bandwidth of 150 MHz by monitoring the deflection (differential detection of two fast photodiode signals) of a focused (focal width <10 μm) 10 mW HeNe beam reflecting at the interface (Fig. 1). By determining the dc signal change at different tilt angles of the sample, the system was calibrated to render absolute deflection angles (linearity range 0–0.5° deflection). The calibrated sensitivity was 110 V/rad. A more detailed description of the experimental setup has been published elsewhere (see, e.g., Refs. 3, 12, and 13). Pump energies of 1, 2, 5, 11, 15, and 18 mJ were used, corresponding to about 0.9 to 16 kJ/m^2 or 3 to 50 MJ/m^3 for the energy density in the heated region. These energy densities are sufficient to heat the liquid to a peak temperature of the order of several Kelvin up to tens of Kelvin. The (latent heat) energy density necessary to evaporate the liquid is 2260 MJ/m^3.

Given that a left-going displacement wave, $u_{z,x}(x,t)$ is given by

$$u_{z,x}(x,t)=\int_{-\infty}^{+\infty}u_{z,x}(\omega)\,\exp\,(i\omega t+ikx)\,d\omega, \tag{3}$$

then, in the absence of dispersion, the normal velocity is given by

$$\begin{aligned} v_z=\frac{\partial u_z}{\partial t}&=\int_{-\infty}^{+\infty}U_z(\omega)(i\omega)\,\exp(i\omega t+ikx)\,d\omega \\ &=\int_{-\infty}^{+\infty}U_z(\omega)(ikv_s)\,\exp\,(i\omega t+ikx)\,d\omega \\ &=v_s\frac{\partial u_z}{\partial x}. \end{aligned} \tag{4}$$

Thus, in a deflection setup, the signal, which is proportional to $\partial u_z/\partial x$, characterizes the normal velocity of the interface.

Figure 2 shows the intensity dependence of the signal at 2.5 mm [Fig. 2(a)] and at 11.5 mm [Fig. 2(b)] pump-probe

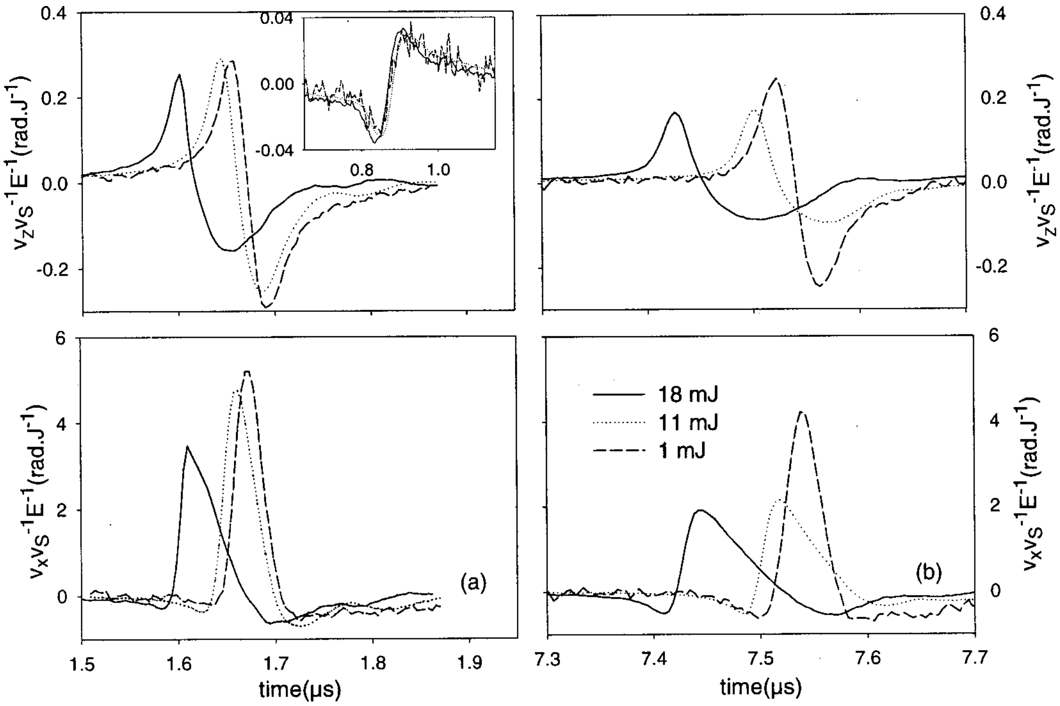

FIG. 2. Scholte wave intensity dependence at pump-probe distances 2.5 mm (a) and 11.5 mm (b), with pump energies of 1 mJ (dashed line), 11 mJ (dotted line), and 18 mJ (full line). The upper curves show the normal velocity and the lower curves the tangential velocity. The tangential velocity was deduced from the normal velocity using Eq. (4). Signals are normalized to their corresponding pump energies. The inset of (a) shows the leaky Rayleigh wave arrival.

distances. The normal velocity v_z was derived directly from the deflection angle signal [Eq. (4)]. The tangential velocity of the liquid v_x was calculated from the normal velocity v_z using their mutual Hilbert transform relation:[14]

$$v_x = -\frac{H(v_z)}{1_{2s}}. \tag{5}$$

The signals in Fig. 2 are normalized with the corresponding pump energy. Also the tangential velocity is represented in rad/J. The peak value of this quantity, multiplied by the corresponding pump energy, directly yields the Mach number M of the tangential displacement. The accuracy on M may be assessed from uncertainties in the calibration factor (110 ± 20) V/rad, used to convert the electronic signal amplitude to the deflection angle, and in the proportionality factor $1/1_{2S}=11.8\pm0.8$ in Eq. (5), used to calculate v_x from v_z.

The normalized leaky Rayleigh wave signal (shown in the inset of Fig. 2) had a velocity $v_R=3060\ \mathrm{m\cdot s^{-1}}$. Due to energy leakage into the liquid this wave decreased rather strongly (damping coefficient 40 $\mathrm{m^{-1}\ MHz^{-1}}$) with propagation distance and was not detectable at 11.5 mm. The Mach number with respect to the Rayleigh velocity for the LR velocity reached the significant level of 1.3×10^{-3} at the highest energy. However, due to the strong leakage of the LR wave, we do not expect strongly nonlinear propagation properties. An observed slight relative amplitude increase with pump energy was probably related to a nonlinear increase of excitation efficiency. Unfortunately, due to practical geometrical reasons, we could not investigate shorter pump-probe distances, where the LR reaches much higher amplitudes and thus probably shows nonlinear propagation behavior.

The normalized Scholte signal amplitude is significantly higher than the Rayleigh wave and decreases with increasing pump energy. Since this effect is contrary to the case of LR, and since the amplitude decrease is larger at larger pump-probe distance, it should be attributed to nonlinear effects in the propagation, rather than in the excitation. At 2.5-mm pump-probe distance [Fig. 2(a)], the slight excitation efficiency increase with pump energy is hidden by the dominating increase of attenuation with intensity. The nonlinear propagation effect of the Scholte wave is most clearly illustrated by the steepening of the leading wave front and the broadening of the trailing wave front. The nonlinear effect is not at all surprising. Though the experimental Mach number of the normal displacement remains moderate ($M=0.0046$), the large tangential displacement [Eq. (5): v_x is about 12 times larger than the normal displacement] has a Mach value up to 0.054. Note that the value of l_{2S}, used to calculate v_x from v_z, is subject to a significant uncertainty, since it depends critically on the small difference between the Scholte and bulk velocity. We assume here without proof that nonlinearity in itself does not influence this difference. The transition from quasi-linear to nonlinear propagation is clearly illustrated in Fig. 3. Figure 3(a) shows quasi-linear Scholte signals ($E=1$ mJ) for pump probe distances of 2.5, 6.5, and 11.5 mm. Signals at these positions for a pump energy of 18 mJ are plotted in Fig. 3(b). For the sake of comparison, the time axes for different propagation distances have been shifted with multiples of $\Delta x/v_S$ using the small amplitude Scholte velocity $v_S=1530\ \mathrm{m\cdot s^{-1}}$.

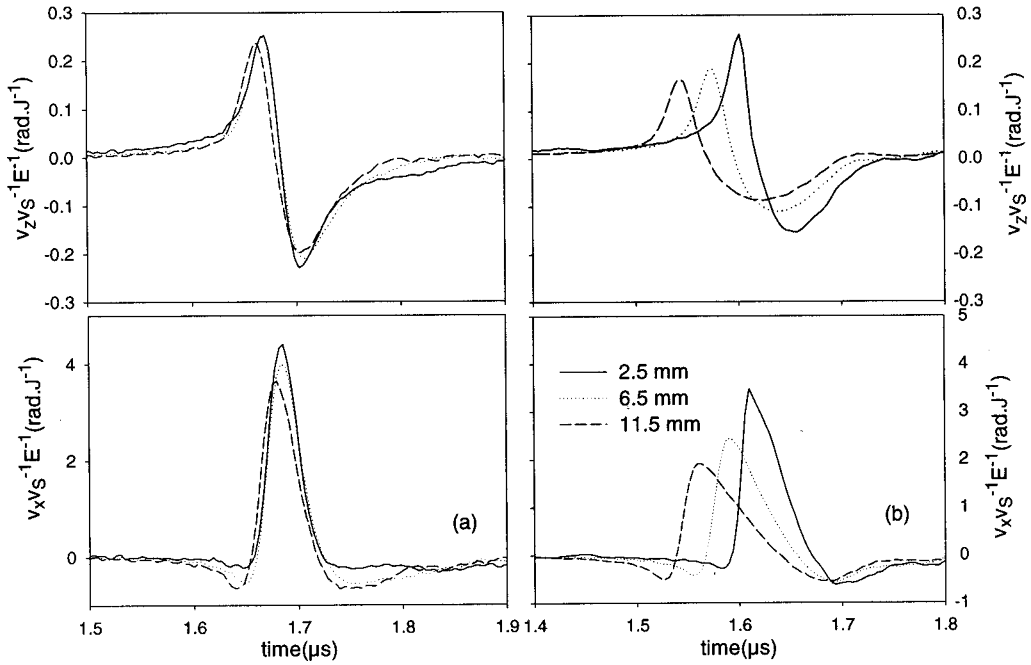

FIG. 3. Scholte wave signals at pump-probe distances 2.5 mm (full line), 6.5 mm (dotted line), and 11.5 mm (dashed line), for pump energies of 2 mJ (a) and 18 mJ (b). The upper curve shows the normal velocity and the lower curves the tangential velocity. The tangential velocity was deduced from the normal velocity using Eq. (4). Signals are normalized to their corresponding pump energies. The time axes for different propagation distances have been shifted with multiples of $\Delta x/v_S$, with $v_S=1530\ \mathrm{m\cdot s^{-1}}$, the small-amplitude value.

IV. NONLINEAR SCHOLTE WAVE PROPAGATION: THEORETICAL MODEL

Extensive work on the theory of nonlinear propagation of interface waves has been performed recently.[14,15] The nonlinear evolution of Scholte waves in time domain was elaborated by Gusev *et al.*[14] The evolution equation is given by

$$\frac{\partial v_x}{\partial \theta}=\frac{\varepsilon_1'}{v_{1,2}}v_x\frac{\partial v_x}{\partial \tau}-\frac{1}{2v_{L2}}\left\{\varepsilon_2'\frac{\partial}{\partial \tau}[v_x^2+(\mathrm{H}[v_x])^2]+\varepsilon_3'\frac{\partial^2}{\partial \tau^2}\left(\mathrm{H}\left[\mathrm{H}[v_x]\int^\tau v_x\,d\tau\right]+v_x\int^\tau v_x\,d\tau\right)\right\} \tag{6}$$

with H the Hilbert transform operator, $\tau=t-x/v_s$ the fast retarded time, θ the slow time variable. (The expressions for the scaled coefficients ε_1', ε_2', and ε_3' can be found in Ref. 14.) Note that Eq. (6) is essentially a modification of the simple-wave equation (see, e.g., Ref. 14), adapted for the specific localized character of Scholte waves. In our experimental configuration colored water-glass, the localization parameter $1_{2S}=0.085\ll 1$, such that ε_2' and ε_3' tend to zero and ε_1' tends to the Landau nonlinearity parameter $\varepsilon=1+B/(2A)$ ($\varepsilon=3.5$ for water,[16] A and B are the coefficients of the first and second terms, respectively, of the equation of state expressing pressure as a function of normalized density variations[17]). Therefore Eq. (6) is reduced to the simple-wave equation for longitudinal waves in liquids:[18]

$$\frac{\partial v_x}{\partial \theta}=\frac{\varepsilon}{v_{1,2}}v_x\frac{\partial v_x}{\partial \tau}. \tag{7}$$

In time domain, the simple-wave equation can be solved numerically using an amplitude-dependent propagation algorithm.[17] However, even if the propagation step is small, this algorithm encounters problems. At the point of shock front formation, the amplitude-dependent propagation evolution leads to a double-valued function, which is obviously not physical. In a real situation, this moment is anticipated by energy dissipation and thus never occurs. It is not straightforward how to implement this process numerically. In principle, thermo-viscous attenuation can be introduced by alternating every nonlinear propagation step Δx with the following low-pass filter convolution:

$$v_x(\tau)\rightarrow v_x(\tau)\otimes F(\tau), \quad \text{with } F(\omega)=\exp(-A_\omega\omega^2\Delta x). \tag{8}$$

A_ω is the thermo-viscous attenuation coefficient and ω is the angular frequency. $F(\tau)$ and $F(\omega)$ are each other's Fourier transform. Consequently, the simple-wave equation [i.e., Eq. (7) with the added linear term proportional to the second derivative of the particle velocity over fast time which describes sound absorption quadratic in frequency] is formally used instead of the simple-wave equation. Unfortunately, this alternation between nonlinear propagation and convolution steps is difficult to implement. The nonlinear propagation algorithm introduces a nonuniform time axis, which has to be made uniform in order to perform a standard numerical convolution. It is not obvious to assess the consequences of the interpolation going along with this and to define the minimum sampling rate required to avoid that the interpolation acts as a low pass filter by itself.

An all-frequency domain approach, as, e.g., implemented in Refs. 10, 11, 15, and 19, avoids most of this difficulty, and was already successfully applied in Refs. 10 and

11 to analyze the nonlinear propagation of large amplitude Rayleigh waves. As far as we know, there are two models in literature for nonlinear Scholte propagation in frequency domain. Fourier transforming Eq. (7) we arrive at the well-known frequency domain version of the simple-wave equation[20] [see, for example, Eq. (47) in Ref. 14]:

$$\frac{\partial \tilde{v}_x(\omega)}{\partial \theta} = \frac{-i\omega\varepsilon}{4\pi v_{L2}} \int_{-\infty}^{\infty} d\omega' \tilde{v}_x(\omega') \tilde{v}_x(\omega-\omega'), \tag{9}$$

with $\tilde{v}_x(\omega) = \int_{-\infty}^{+\infty} d\tau v_x(\tau) \exp(i\omega\tau)$. In dimensionless form after discretization, this reduces to

$$\frac{\Delta V_n}{\Delta X} = -\frac{in}{4}\left(\sum_{m=1}^{n-1} V_m V_{n-m} + 2\sum_{m=n+1}^{N} V_m V_{m-n}^*\right), \tag{10}$$

with $V_n = v_{x,n}/v_S$ $(n=1,\ldots,N)$, $v_{x,n} \equiv (2/N)\Sigma_{m=-N}^{N} v_x \times (t_m) \exp(i2\pi n t_m/T)$ the nth harmonic component of the v_x spectrum, $\Delta X = \Delta x/\bar{x}$. $\bar{x} = \lambda_0/(2\pi\varepsilon)$, $\lambda_0 = v_{1,2}T$, and T is the width of the time window of the waveform (about 400 ns for our experimental data). $\overline{x/M}$ can be seen as the shock formation distance for the longest wavelength component λ_0 in the wave.

A second model for the nonlinear Scholte wave propagation, developed by Meegan *et al.*,[15] describes the evolution of the harmonic components $v_{x,n}$ of a right propagating Scholte wave as

$$\frac{dv_{x,n}/v_s}{dx/\lambda_0} = \frac{\mu_1 n^2 \pi}{i\rho_1 v_s^2 \xi \eta_2}\left(2\sum_{m=n+1}^{N} R_{m,n-m} \frac{v_{x,m}}{v_s} \frac{v_{x,m-n}^*}{v_s} + \sum_{m=1}^{n-1} R_{m,n-m} \frac{v_{x,m}}{v_s} \frac{v_{x,n-m}}{v_s}\right) \tag{11}$$

with

$$R_{1,m} = R_{1,m}^{(1)} + \frac{1}{8} \frac{\rho_2 v_{L2}^8}{\rho_1 v_{T1}^8} \frac{\xi_0^{12}}{(1-\xi_0^2)} \frac{\beta + 4(\xi_0^{-4} - \xi_0^{-2})}{|1|+|m|+|1+m|},$$

$$\eta_2 = -\left(\frac{1-\xi_{T1}^2}{2\xi_{L2}}\right)$$

and

$$\xi_{L,T,i} = \sqrt{1 - v_s^2/v_{L,T,i}^2}.$$

$\xi_0 = v_s/v_{L2}$ and ξ and $R_{lm}^{(1)}$ are given in Refs. 15 and 19. Given the bulklike character of our experimental Scholte wave, $\xi_0 \cong 1$, the coefficients R_{lm} simplify to

$$\frac{R_{l,m}}{|R_{1,1}|} \cong \frac{4}{|l|+|m|+|l+m|}. \tag{12}$$

Equation (11) can be rewritten in discretized, dimensionless form as

$$\frac{\Delta V_n}{\Delta X} = -\frac{in}{4}\left(\sum_{m=1}^{n-1} V_m V_{n-m} + 2\sum_{m=n+1}^{N} \frac{n}{m} V_m V_{m-n}^*\right). \tag{13}$$

Equations (13) and (10) are similar in form and result, but not identical. Contrary to the equation of Gusev *et al.*, taking the bulk limit for Scholte waves, the equation of Meegan *et al.*[15] does not converge to the nonlinear evolution equation for bulk waves, but keeps a surface wave character. An elaboration on the reason for this is out of the scope of this article. For our analysis, given the strong bulklike wave character of the experimental Scholte waves, we have chosen to use the finite difference form of Eq. (10) to compare our data with theory. For our calculation the sampling frequency was $f_{\max} = 125$ MHz and $N = 50$ frequency components in the calculation was sufficient to accurately describe all the waveforms. This corresponds to a value of λ_0, the wavelength corresponding to the lowest frequency in the spectrum, of about 600 μm.

Due to the approximations made, the substrate properties have disappeared from the evolution calculation, and the liquid only affects the evolution via the scaling of the propagation variable x. Otherwise, the evolution calculation is uniquely determined by the spectral content and scaling of the starting waveform, and by attenuation effects. The effect of attenuation was implemented by alternating every nonlinear propagation step with a thermo-viscous convolution filtering step, which, in frequency domain, reduces to a multiplication:

$$V_n \rightarrow V_n \cdot F_n, \quad \text{with } F_n = \exp(-\bar{A} n^2 \Delta X), \tag{14}$$

and $\bar{A}$ is the dimensionless attenuation coefficient, which is related to the thermo-viscous attenuation coefficient A_ω by

$$A_\omega = \frac{\bar{A} \cdot X_{\max}}{4\pi^2 (f_{\max}/N)^2 x_{\max}}, \tag{15}$$

with $X_{\max} = x_{\max}/\bar{x}$.

This approach turned out to be more numerically stable than the addition of a second derivative attenuation term in Eq. (13), as was done, e.g., in Eq. (83) of Ref. 15.

V. NONLINEAR SCHOLTE WAVE PROPAGATION: DATA ANALYSIS

In order to compare the experimental curves with theory, we have taken, for the different pump energy levels, the experimental signal at $x_0 = 2.5$ mm pump-probe distance as the starting waveform of a nonlinear evolution calculation using the described frequency domain algorithm. The fit was optimized by minimizing the difference between the calculated and experimental amplitude spectra. A simple insertion of literature values $\varepsilon = 3.5$ and $A_{\omega,\mathrm{lit}} = 1.47 \times 10^{-15}$ s^2 m^{-1} (2.3 times the attenuation of pure water, estimate based on literature values[16] of the similar salt $ZnCl_2$ in water[21]) in the calculation did not yield a good fit. In order to clarify this discrepancy between experiment and theory, we have chosen to look for the best fitting couple ε, A_ω for each experimental dataset. Since nonlinear evolution calculations are rather time consuming, we have reduced the calculation complexity significantly by exploiting the favorable scaling properties of the dimensionless evolution Eq. (10) as follows. For a set of 25 dimensionless attenuation coefficients $\bar{A}$ between 7×10^{-6} and 2×10^{-4}, only one dimensionless evolution was calculated in a dimensionless coordinate X, with ΔX chosen small enough to ensure good convergence of the discretized

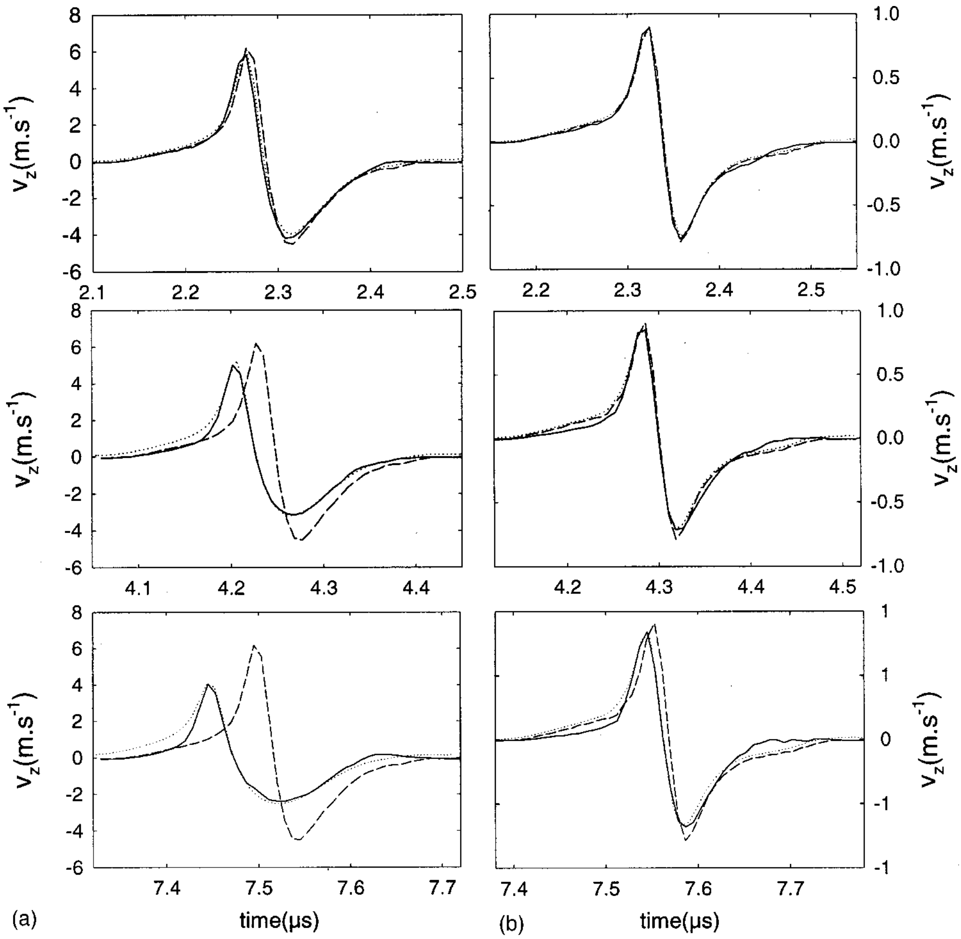

FIG. 4. Best fit (dotted curve) of the experimental signal (full line) at a pump-probe distance of 3.5 mm (upper figures), 6.5 mm (middle figures), and 11.5 mm (lower figures), for pump energies of 2 mJ (right figures) and 15 mJ (left figures). The dashed curve is the curve at pump-probe distance of 2.5 mm (the starting curve for the calculations), which has been shifted over the distance $\Delta x/v_S$.

calculation. This set of evolutions was compared to the normalized experimental dataset $V_{\exp,p}$ at $p=1,\ldots,P$ positions ($P=18$) between the second pump-probe distance $x_{\text{start}}=2.5$ mm and the final pump-probe distance $x_{\text{start}}+x_{\max}=2.5$ mm$+9$ mm$=11.5$ mm as follows. The value of $X_{\max}$ was searched (between 0 and 1200) such that the set of amplitude spectra $V_{\text{theor},p}\equiv V_{\text{theor}}(X=p\cdot X_{\max}/P)$ gave the best correspondence with the experimental set $V_{\exp,p}$. In this way the two-dimensional A, $X_{\max}$ search only required 25 evolution calculations. Note that our fit was based on the amplitude spectra of experimental data and theoretical calculations, rather than on the corresponding time domain signals (via Fourier transform). This was done in order to minimize time shift (or phase) errors due to inaccurate estimates of the (strongly temperature drift dependent) wave velocity, and to inaccuracies in the pump-probe position. The best fitting dimensionless parameters $A,X_{\max}$ were converted into the thermo-viscous attenuation coefficient A_ω and the parameter of nonlinearity ε_1' by Eq. (15) and

$$\varepsilon_1'=\frac{\lambda_0 X_{\max}}{2\pi x_{\max}}, \tag{16}$$

respectively. The latter relation follows from $\bar{x}=\lambda_0/(2\pi\varepsilon)$ and $\bar{x}=x_{\max}/X_{\max}$.

In Fig. 4, the fit result for the 15-mJ signal is shown in time domain for three positions. The experimental traces are fitted very well by the simple-wave equation, confirming our expectation that the nonlinear aspect of Scholte waves at a hard substrate interface is very similar to the case of ordinary bulk waves in the liquid. Fitting with the $\xi_0=v_S/v_{L2}\cong 1$ limit of the model of Meegan *et al.*[15] did not give substantially different fitting results. The fitting parameters for the 1, 2, 5, 11, and 18 mJ experimental data, together with the Mach numbers for v_x and v_z, are shown in Table I. The contour plot in Fig. 5 for the 15-mJ fit, and the intervals of confidence in Table I, give an idea on the uncertainty on the fitting parameters. For lower Mach numbers, the uncertainty on the fitting value is too large to draw conclusions. For the largest Mach numbers, the fitted nonlinear parameter $\varepsilon_{\exp}$ is systematically higher than 3.5, the literature value of pure water-glass Scholte waves,[15] though almost within the fitting uncertainty. Though useful for indicating the order of magnitude of the parameter, the fitting uncertainty on the experimental attenuation values is very large. However, the fitting values for the attenuation, between 2 and 15 times larger (increasing with signal amplitude) than the expected value for our water-copper chloride solution, which was estimated to be $A_{\omega,\text{lit}}=1.47\times 10^{-15}$ s^2 m^{-1}, deserve some attention. Though our finite probe size and detector bandwidth affect the experimental spectrum, and, via the starting spectrum, also the evolution calculations, the corresponding cutoff frequency is high compared to the overall spectral content, such that resulting smoothing effects are too weak to explain this discrepancy between theory and experiment. We have also verified that effects of heating are quasi-static on the time scale of the acoustic wave propagation, and, except for a

TABLE I. Experimental parameters and nonlinear fitting results.

E (mJ)[a]	M_{x0}[b]	M_{z0}[c]	$\overline{x}_{th}/M_{x0}$ (mm)	$\overline{A}$ ($\times 10^{-5}$)	$x_{\max}$	$\overline{x}_{\exp}/M_{x0}$ (mm)[d]	A_ω[e] ($\times 10^{-15}$ $s^2 \cdot m^{-1}$)	$\varepsilon_{\exp}$[e]
18	0.054	0.0046	0.54	6	500	0.33	14	5.6
				[3,13]	[100,1200]	[0.06,0.80]	[2,90]	[1.2,12]
15	0.048	0.0041	0.60	6	614	0.31	18	6.9
				[3,13]	[200,1100]	[0.10,0.55]	[3,45]	[2,12]
11	0.038	0.0033	0.76	5	844	0.28	20	9.5
				[4,12]	[300,1200]	[0.10,0.40]	[5,40]	[3,13]
5	0.020	0.0017	1.45	3	684	0.66	10	7.7
				[2,19]	[300,1100]	[0.29,1.05]	[2,35]	[3,13]
2	0.0069	0.000 58	4.21	2	195	6.7	2	2.2
				[0,20]	[100,700]	[3.4,24]	[0,60]	[1,7]
1	0.0035	0.000 30	8.29	24	22	114	3	0.25
				[0,50]	[5,50]	[25,250]	[0,60]	[0.05,0.60]

Note: [*,*] confidence intervals on parameters (one standard deviation on each side) in square brackets.
[a]E=pump energy.
[b]M_{x0}=initial Scholte wave Mach number for v_x component.
[c]M_{z0}=initial Scholte wave Mach number for v_z component.
[d]$\overline{x}_{th}/M_{x0}$ and $\overline{x}_{\exp}/M_{x0}$ are the theoretical, resp. fitted shock formation, distance for $\lambda=615$ μm, the largest wavelength in the calculated spectrum.
[e]Note that the literature value for $A_\omega=1.5\times10^{-15}$ $s^2\cdot m^{-1}$, $\epsilon=3.5$.

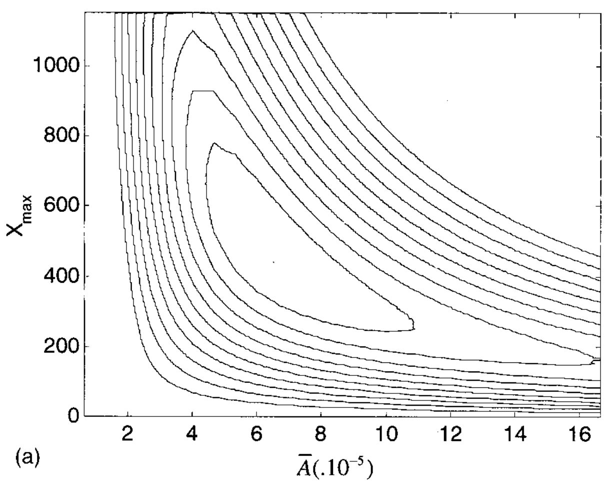

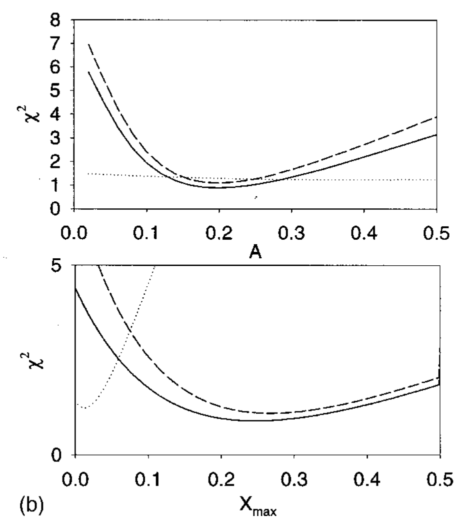

FIG. 5. Contour plot of $\chi^2 \equiv \Sigma_p (V_{\mathrm{theor},p} - V_{\exp,p})^2$ as a function of $\overline{A}$ and $X_{\max}$ for the 15-mJ signal. The best fit is found at $\overline{A}=0.12$ and $X_{\max}=0.30$ (a). (b) Shows the dependence of χ^2 on $\overline{A}$ (upper figure) and on $X_{\max}$ (lower figure) for energies of 15 mJ (full line), 11 mJ (dotted line), and 2 mJ (dashed line), as an illustration of the error of the fit parameters.

slow, global heating of the sample due to the supplied laser energy, thermal effects are limited to the excitation region. It is also doubtful that the high attenuation would be related to interface roughness, since this does not lead to an attenuation increasing with intensity, as in the experimental data.

Table I gives estimates for the shock formation distance, based on the fitting result for $X_{\max}$, experimental values for the Mach number M, and $\overline{x}=x_{\max}/X_{\max}$. The values (which are most reliable for the larger pump energies, where nonlinearity is clearly reflected in the signal) are smaller than, or of the order of, the coherence length of the quasi-synchronous interaction between the Scholte wave and the skimming bulk wave in liquid $[L=\lambda_0/2(1-v_s/v_{L2}))\approx 53$ mm] for the main harmonic components in the signal. The large coherence length is due to the deep penetration of the Scholte wave at the hard glass interface, which enhances the symmetry correspondence with bulk waves. In such a situation, coupling of Scholte and bulk wave most probably influences the wave propagation and may probably explain the anomalously large observed experimental attenuation. Mixing of Scholte wave with bulk waves frequency components introduces leakage, thus energy loss, or an apparent increase of attenuation, such as the one observed in our experiment. Mode coupling is expected to occur mostly for the larger components in the spectrum. Though difficult to quantify, nonlinear mode coupling may be related to the significant depletion around 15 MHz in the spectrum of Fig. 6(a) and around 25 MHz in Fig. 6(b). On the other hand, a decrease of amplitude in that spectral region is also seen in evolution simulations by the simple wave equation with attenuation term (though without mode coupling), using the same parameters as found for the experimental data. This indicates that this effect mainly reflects the combined effect of nonlinear mixing and subsequent attenuation of frequency components.

Several other effects may contribute to our anomalous large experimental attenuation. Increase of acoustic wave attenuation at high-amplitude monochromatic waves was already discussed by Beyer,[16] but that attenuation results from

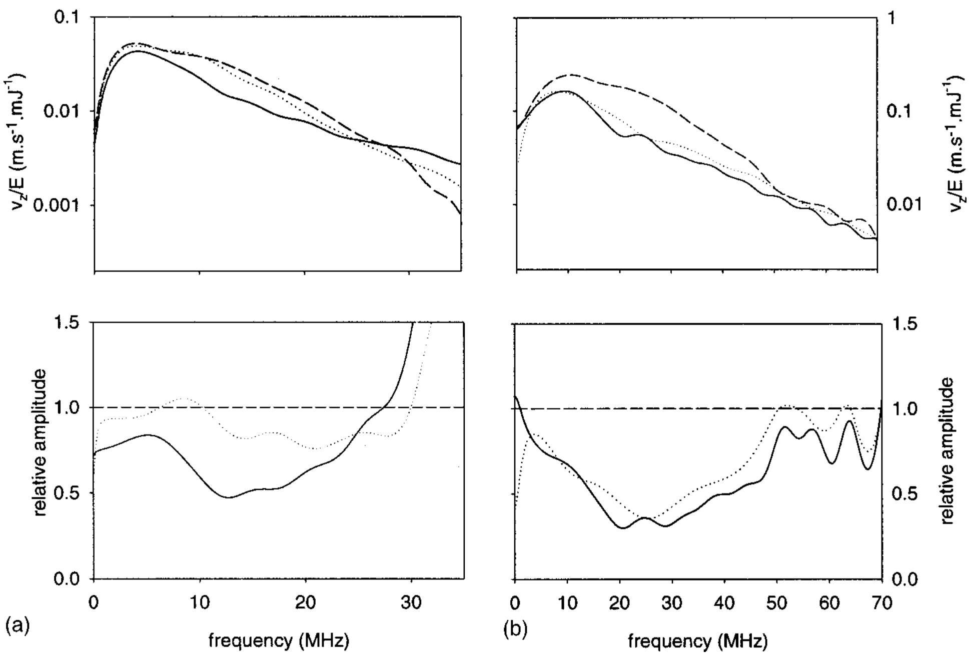

FIG. 6. Scholte wave amplitude spectrum at pump-probe distances 2.5 mm (a) and 11.5 mm (b), with pump energies of 1 mJ (dashed line), 11 mJ (dotted line), and 18 mJ (full line). The upper curves show the amplitudes normalized to their corresponding pump energies. In the lower curves, these amplitudes are normalized against the amplitudes of the 1-mJ signal.

the transfer of energy to higher harmonics, which we already take into account in our calculation. Also the onset of relaxation process (like salt-water dissociation or water-water dissociation) at high strains is theoretically possible. However, the indication of nonlinearly triggered relaxation phenomena is not conclusive: we have observed a very similar phenomenon for the system methanol-crystal violet, whose possible relaxation phenomena should be quite different from salt-water.

Also bubble formation is dissipative and thus a possible reason for attenuation. However, the time scale of a passing wave (60 ns) seems too fast compared to the time needed to form bubbles. Though difficult to model quantitatively, we believe that our high strain signals might evoke turbulence effects, which are irreversible, thus dissipative, and thus lead to attenuation effects.

We have estimated also the attenuation α_{BL} in the thermo-viscous boundary layer located near the solid–fluid interface using classical results for the propagation of quasi-plane pressure waves in wide ducts.[22,23] In classical theory α_{BL} is proportional to the square root of frequency and the ratio L_p/A of the pipe cross-section perimeter L_p to its area A. In the case of the plane Scholte wave the perimeter at the "pipe" occupied by the wave can be estimated as $L_p \propto 2(y_0 + l^s_{\mathrm{pen}})$. We remind here that y_0 is the length of the laser focus and l^s_{pen} denotes the Scholte wave penetration depth. However, only the solid–fluid interface participates in the wave absorption and, consequently, $L_p \propto y_0$. Thus, with $A \propto y_0 \cdot l^S_{\mathrm{pen}}$, we get $L_p/A \propto (l^S_{\mathrm{pen}})^{-1} \propto \lambda_S^{-1} \propto \omega$. As a result of this in the considered regime (we assume that l^S_{pen} significantly exceeds the viscous boundary layer thickness $\delta_v \equiv \sqrt{2v/\omega}$, where v is the kinematic viscosity of the fluid) $\alpha_{\mathrm{BL}} \propto \omega^{3/2}$. We estimated that at frequencies around 5 MHz the boundary layer attenuation is of the order of the theoretical bulk attenuation (which is proportional to ω^2) and, consequently, it cannot be responsible for the experimental observation of the attenuation of an order of magnitude higher. That is why currently we are not including the attenuation $\alpha_{\mathrm{BL}} \propto \omega^{3/2}$ in our computer simulation.

The strong tangential velocity gradients (dv_x/dx) over the shock front and normal velocity gradients (dv_x/dz), both due to the Scholte localization and, in particular, related to possible non-slip conditions at the liquid–solid interface (if the viscosity of the fluid is taken into account), are potential causes of turbulence in our system. To analyze the possibility of turbulence we have compared the conditions of our experiment with the known experimental results for closed pipes.[24,25] In the pipes the regime of turbulence is controlled by two parameters: the ratio R/δ_v of the tube radius R to the viscous boundary layer thickness δ_v and the Reynolds number defined as $\mathrm{Re} \equiv 2vR/v$, where v is the characteristic value of the particle velocity. For the Scholte wave we identify R with the Scholte wave penetration depth l^S_{pen}. Then we estimate that $R/\delta_v \sim 1^S_{\mathrm{pen}}/\delta_v \sim 2(\lambda_S/\delta_v) \sim \omega^{-1/2}$ exceeds 10^3 for frequencies below 40 MHz (i.e., practically in the whole frequency interval of interest, see Fig. 6). At the same time, with $v \approx Mv_S$ we estimate that $\mathrm{Re} \propto (2Mv_S l^S_{\mathrm{pen}})/v \propto 4/\pi M(\lambda_S/\delta_v)^2 - \omega^{-1}$ does not exceed 3×10^4 at frequencies above 1 MHz (i.e., practically in the whole frequency range of interest, see Fig. 6). In the range $\mathrm{Re} \leqslant 3\times10^4$, in accordance with Refs. 24 and 25 the weakly turbulent regime is possible. This regime is characterized by the generation of turbulence outside the boundary layer. It is well known[23,26] that in first approximation the turbulence effectively enhances viscosity and thermal diffusivity, leading to the increase of sound attenuation. However, bulk attenuation depends stronger on viscosity $(\sim v)$ than the boundary layer attenuation $(\sim \sqrt{v})$. This is the second reason why we are currently introducing bulk attenuation $(\sim \omega^2)$ and not the boundary layer attenuation in our computer simulations. Our estimates demonstrate that turbulence is a possible mechanism of the high attenuation of Scholte waves in

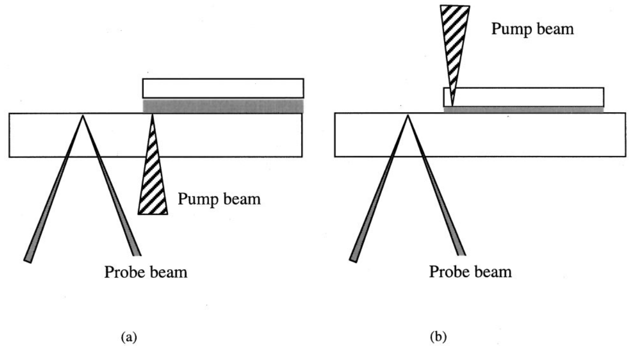

FIG. 7. (a) Schematic configuration for exciting waves at a liquid–solid interface, which are then mode converted into high-amplitude Rayleigh waves in the air-substrate region. (b) Configuration for exciting guided waves in a liquid layer between two substrates, which are then mode converted into high-amplitude Rayleigh waves in the air-substrate region.

our experiment. However, for a detailed analysis of this pos sibility, the dependence of the effective viscosity and thermal diffusivity (i.e., in the presence of turbulence) on the local parameters of the acoustic field should be incorporated in future theoretical models.

Remark that the used theoretical model does not take into account *possible* nonlinearities in the solid. Using the experimental values for v_z and relations between v_x and v_z in Refs. 1 and 15 we have calculated that our maximum Mach number for the velocities in the solid is 2×10^{-5}. It is also important that the acoustic energy is carried mainly inside the fluid due to weak localization of the Scholte wave in the liquid for our experimental situation. So four our case the nonlinear mechanisms of the liquid are dominating and the nonlinearity in the solid effectively does not play a significant role.[14] Nevertheless, we believe that the used mechanism for exciting highly nonlinear acoustic interface waves is suitable for the study of nonlinearity in solids. The strong intrinsic attenuation of leaky Rayleigh waves does not necessarily inhibit to look at nonlinear Rayleigh waves. By propagating large-amplitude Scholte and leaky Rayleigh waves excited in a short (to minimize leakage) solid–liquid region to a solid–air environment (detection region) both wave modes are efficiently converted into large amplitude Rayleigh waves [Fig. 7(a)]. Moreover, window–liquid–substrate configurations allow us to efficiently convert leaky Rayleigh waves excited at the window–liquid interface into bulk waves in the liquid, which are then mode converted into leaky Rayleigh waves at the liquid–substrate interface and eventually into Rayleigh (air–substrate) waves when the wave crosses from substrate–liquid to substrate–air [Fig. 7(b)]. The colored liquid–solid interface seems to be one of the most efficient existing mechanisms to excite very-large-amplitude interface acoustic waves.

VI. CONCLUSION

The results show that the propagation properties of Scholte waves opens an interesting new perspective for the investigation of solid–liquid interfaces. We have experimentally observed highly nonlinear Scholte waves and quantitatively analyzed the nonlinear propagation evolution. In our case of a high solid–liquid acoustic impedance mismatch, Scholte waves propagate very much like bulk waves, and the nonlinear propagation evolution are very well fitted by the simple-wave equation extended with an attenuation term. The good fits confirm the plausibility of the theoretical model. Interestingly, a too high fit value for the viscous attenuation coefficient was found. The most likely reason for this anomaly is mode coupling between the Scholte wave and skimming bulk wave in the liquid due to the short shock formation distance and large coherence length of their interaction in our experimental configuration. The role of the acoustically induced turbulence could also be important. Overall, we can conclude that the large magnitude and bandwidth of the waves which can be generated using this technique open an interesting perspective for the research of nonlinear behavior in solids and liquids, especially since many aspects of high nonlinearity are not yet fully understood.

ACKNOWLEDGMENTS

This work was supported by the Fund for Scientific Research Flanders (Belgium) (FWO Project No. G.0264.97), the EU INTAS program (Project No. 97-31680), and by U.S. National Science Foundation Grant No. DMR-9710140.

[1] V. E. Gusev, C. Desmet, W. Lauriks, C. Glorieux, and J. Thoen, J. Acoust. Soc. Am. **100**, 1514–1528 (1996).
[2] C. Glorieux, K. Van de Rostyne, K. A. Nelson, W. Gao, W. Lauriks, and J. Thoen, J. Acoust. Soc. Am. (in press).
[3] C. Desmet, V. E. Gusev, W. Lauriks, C. Glorieux, and J. Thoen, Prog. Nat. Sci. **6**, 390–393 (1996).
[4] F. Padilla, M. de Billy, and G. Quentin, J. Acoust. Soc. Am. **106**, 666–673 (1999).
[5] N. Favretto-Anres and G. Rabau, J. Acoust. Soc. Am. **203**, 193–208 (1997).
[6] M. W. Sigrist, J. Appl. Phys. **60**, R83–R122 (1986).
[7] G. Paltauf, H. Schmidt-Kloiber, and M. Frenz, J. Acoust. Soc. Am. **104**, 890–897 (1998).
[8] C. E. Bell and J. A. Landt, Appl. Phys. Lett. **10**, 46–48 (1966).
[9] T. E. McGrath, A. C. Beveridge, and G. J. Diebold, Appl. Phys. Lett. **73**, 1029–1031 (1998).
[10] A. Lomonosov, V. G. Mikhalevich, P. Hess, E. Y. Knight, M. F. Hamilton, and E. A. Zabolotskaya, J. Acoust. Soc. Am. **105**, 2093–2096 (1999).
[11] A. A. Kolomenskii, A. M. Lomonosov, R. Kuschnereit, P. Hess, and V. E. Gusev, Phys. Rev. Lett. **79**, 1325–1328 (1997).
[12] C. Desmet, V. E. Gusev, W. Lauriks, C. Glorieux, and J. Thoen, Appl. Phys. Lett. **68**, 2939–2941 (1996).
[13] C. Desmet, V. E. Gusev, W. Lauriks, C. Glorieux, and J. Thoen, Opt. Lett. **22**, 69–71 (1997).
[14] V. E. Gusev, W. Lauriks, and J. Thoen, IEEE Trans. Ultrason. Ferroelectr. Freq. Control **45**, 170–178 (1998).
[15] G. D. Meegan, M. F. Hamilton, Y. A. Il'inskii, and E. A. Zabolotskaya, J. Acoust. Soc. Am. **106**, 1712–1723 (1999).
[16] R. T. Beyer, in *Physical Acoustics, Principles and Methods; Vol. 2B*, edited by W. P. Mason (Academic, New York, 1965), pp. 231–264.
[17] K. Naugolnykh and L. Ostrovsky, *Nonlinear Wave Processes in Acoustics* (Cambridge U. P., Cambridge, 1998).
[18] O. Rudenko and S. Soluyan, *Theoretical Foundations of the Nonlinear Acoustics* (Consultants Bureau, New York, 1977).
[19] E. Y. Knight, M. F. Hamilton, Y. A. Il'inskii, and E. A. Zabolotskaya, J. Acoust. Soc. Am. **102**, 1402–1417 (1997).
[20] J. H. Ginsberg and M. J. Hamilton, *Nonlinear Acoustics* (Academic, San Diego, 1998).
[21] G. S. Darbari and M. R. Richelson, J. Chem. Phys. **53**, 859–866 (1969).
[22] A. D. Pierce, *Acoustics, An Introduction to its Physical Principles and Applications* (McGraw–Hill, New York, 1981).
[23] L. D. Landau and E. Lifshitz, in *Mécanique des Fluides* (Editions MIR, Moscow, 1971).
[24] J. R. Olson and G. W. Swift, Cryogenics **37**, 769–776 (1977).
[25] M. Ohmi and M. Iguchi, Bull. JSME **25**, 165–172 (1982).
[26] W. D. McComb, *The Physics of Fluid Turbulence* (Clarendon, Oxford, 1990).

Locating far-field impulsive sound sources in air by triangulation

Brian G. Ferguson, Lionel G. Criswick, and Kam W. Lo
Defence Science and Technology Organisation, P.O. Box 44, Pyrmont, NSW 2009, Australia

(Received 14 February 2000; revised 17 July 2001; accepted 19 July 2001)

The firing of a gun generates an acoustic impulse that propagates radially outwards from the source. Acoustic gun-ranging systems estimate the source position by measuring the relative time of arrival of the impulse at a number of spatially distributed acoustic sensors. The sound-ranging problem is revisited here using improved time-delay estimation methods to refine the source position estimates. The time difference for the acoustic wavefront to arrive at two spatially separated sensors is estimated by cross correlating the digitized outputs of the sensors. The time-delay estimate is used to calculate the source bearing, and the source position is cross fixed by triangulation using the bearings from two widely separated receiving nodes. The variability in the bearing and position estimates is quantified by processing acoustic sensor data recorded during field experiments for a variety of impulsive sound sources: artillery guns, mortars, and grenades. Imperfect knowledge of the *effective* speed of sound travel results in bias errors in the source bearing estimates, which are found to depend on the orientation of the sensor pair axis with respect to the source direction. Combining the time-delay estimates from two orthogonal pairs of sensors reduces these bias errors.
 [DOI: 10.1121/1.1402618]

PACS numbers: 43.28.Tc, 43.60.Gk [LCS]

I. INTRODUCTION

Historically, the military has viewed the accurate location and engagement of enemy indirect weapon systems as a vital factor on the battlefield. Sound ranging, which was first employed in World War 1, is the procedure used to locate guns and mortars by calculations based on the relative time of arrival of the sound impulse at several accurately located microphones. The time of arrival (travel time) depends on the local sound speed at each point along the acoustic propagation path from the source to the sensor. The relative time of arrival (commonly referred to as the differential time of arrival or simply, the time delay) is the difference in the times of arrival at two separate sensor positions. Passive ranging systems based on time-delay measurements at spatially distributed sensors assume isospeed sound propagation conditions when estimating the position of the source. Changing meteorological conditions lead to changing sound propagation conditions that can affect the accuracy of the source position estimates.

Although the location of artillery fire using acoustic means has traditionally been of military interest, it is the accuracy to which these sources of impulsive sound can be located that is of scientific interest.[1] The principles of sound ranging have not changed with time, and manually operated gun-ranging systems in the past have been limited by the magnitude of the error in the time-delay measurements, variously reported to be between 1 and 3 ms.[2,3] These historical systems employed an indirect method for time-delay estimation. First, each trace showing the variation of a sensor output with time is manually inspected for a ''break'' corresponding to the waveform of a gun-firing transient. Then, the beginning of the transient's waveform is taken as the time of arrival of the transient at the sensor. Finally, the time delay for a pair of sensors is calculated by taking the difference in the times of arrival of the transient at the two sensors. Errors arise because the time of the ''beginning'' of the transient tends to be subjective, especially in windy conditions when flow-induced noise at the sensor results in a low signal-to-noise ratio. The error in the time-delay estimate is equal to the sum of the errors in determining the two times of arrival.

In this paper, digital acoustic signal-processing techniques are used to reduce the time-delay measurement errors of traditional gun-ranging systems by an order of magnitude. The time delay for a pair of sensors is calculated automatically by cross correlating the outputs of the two sensors and then finding the time lag of the peak in the cross correlogram. The time-delay estimate obtained using this method can be interpreted as the time shift required for alignment of the transient waveforms received by the two sensors. An advantage of the cross-correlation method is that the time delay is measured directly, thus eliminating the errors associated with the indirect method. Also, the spatial correlation function of the flow-induced noise decreases with distance so that the effect of wind noise on the cross correlogram decreases as the sensor separation distance is increased; increasing the integration time also reduces the effect of wind noise. When the system errors are sufficiently small, the accuracy of the source position estimate depends on the wavefront angle-of-arrival variability for acoustic propagation in the atmosphere.

II. PASSIVE SOUND RANGING BY TRIANGULATION

The passive ranging of an acoustic source in the *near* field relies on measuring the curvature of the wavefront at the receiving array. For instance, knowing the sensor-separation distances and the isospeed of sound propagation in the medium, a three-element linear array can be used to estimate the range and bearing of the source by measuring the time delay between the center sensor and each of the other two sensors.[4–8] The radius of curvature of the wavefront is equal to the source range. For a source in the *far*

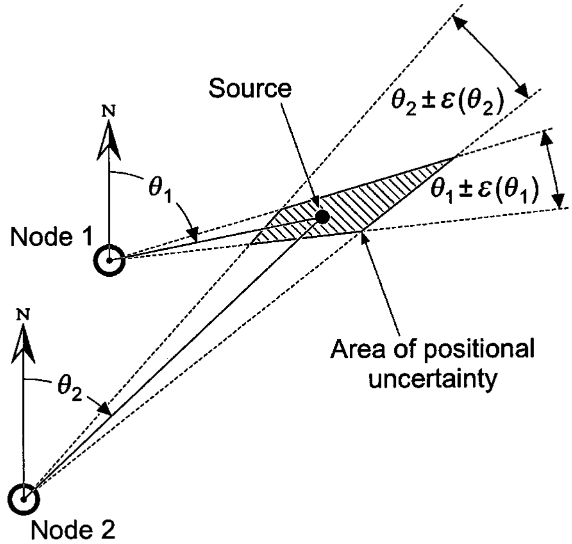

FIG. 1. Principle of triangulation using two widely separated nodes. Variability in the bearing estimates leads to an area of positional uncertainty within which the source lies.

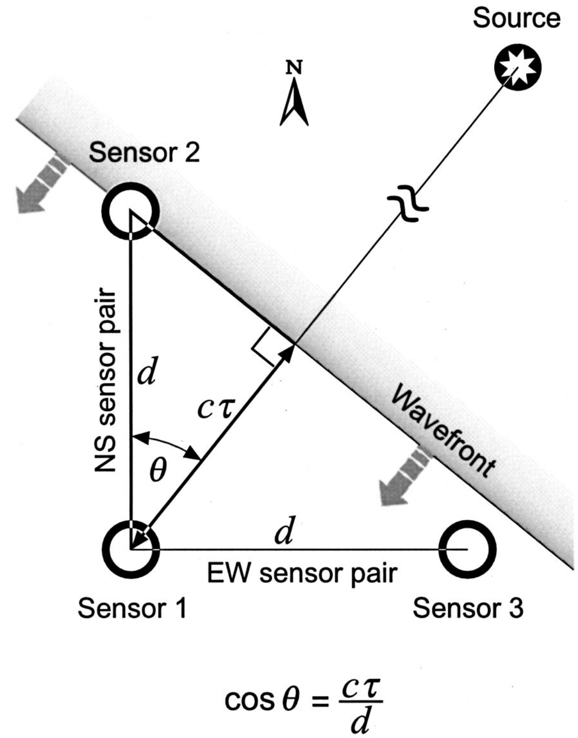

FIG. 2. Sensor configuration of each node. The source bearing is estimated here using the NS sensor pair—the product of the sound propagation speed c and the differential time of arrival τ divided by the sensor spacing d give the cosine of the relative bearing θ.

field, however, the wavefront arriving at a receiving node of closely spaced sensors is planar, so only the bearing can be estimated. In this case, a range estimate is derived by triangulation using the bearing estimates from multiple widely separated nodes whose positions are accurately known. The required processing to determine the optimal position estimate (in the presence of bearing measurement errors) using three or more nodes has been described elsewhere.[9] This paper considers triangulation using two nodes.

Figure 1 shows the principle of triangulation using two nodes. The source and the two nodes, labeled 1 and 2, are located on the $x-y$ plane at coordinates (x_s, y_s), (x_1, y_1), and (x_2, y_2), respectively, with the y axis pointing towards the north. The bearing lines from the two nodes intersect to determine a unique source location. Assuming line-of-sight propagation, the source position is given by

$$x_s = (y_s - y_1)\tan\theta_1 + x_1, \tag{1}$$

$$y_s = \frac{x_2 - x_1 + y_1\tan\theta_1 - y_2\tan\theta_2}{\tan\theta_1 - \tan\theta_2}, \tag{2}$$

where θ_n is the source bearing measured relative to the y axis at node n $(n=1,2)$, that is, with respect to north. The positional uncertainty of the source, represented by the shaded area in Fig. 1, is determined by the uncertainties, $\varepsilon(\theta_1)$ and $\varepsilon(\theta_2)$, in the source bearings, θ_1 and θ_2, respectively.

Figure 2 shows the sensor configuration of each node used in this paper. There are three sensors, labeled 1, 2, and 3. The coordinates of sensor 1 define the position of the node. Sensors 2 and 3 are located at a distance d (25 m) from sensor 1 in the north and east directions, respectively. Sensors 1 and 2 constitute the north–south (NS) sensor pair that is orthogonal to the east–west (EW) sensor pair consisting of sensors 1 and 3. The source bearing can be estimated using either pair of sensors or both.

An estimate of the source bearing with respect to the NS sensor pair axis (referred to as the NS source bearing) is given by

$$\theta_{\mathrm{NS}} = \cos^{-1}(c\tau_{12}/d), \tag{3}$$

where c is the speed of sound propagation in air (typically 340 m/s), and τ_{12} is the time delay between sensors 1 and 2. The source bearing with respect to the EW sensor pair axis (referred to as the EW source bearing), θ_{EW}, is estimated using the same expression but with τ_{12} replaced by τ_{13}, which is the time delay between sensors 1 and 3. The NS bearing can also be estimated by using the time delays from both pairs of sensors, which are orthogonal to each other

$$\theta_{\mathrm{NS}} = \tan^{-1}(\tau_{13}/\tau_{12}). \tag{4}$$

III. FIELD EXPERIMENT

A field experiment is designed to quantify the errors of the triangulation method for the passive ranging of distant impulsive sound sources in the atmosphere. Figure 3 shows (to scale) the surveyed positions of the source (a 105-mm artillery gun) and the receiving nodes. A grid square denotes an area of 1 km by 1 km. The ground-truth (survey) data are shown for the bearing and distance of the source with respect to each of the nodes, and for the internodal distance. The bearings are measured with respect to Grid North (GN).

When the gun fires, an acoustic transient signal propagates radially outwards from the source. The curvature of the spherical wavefront decreases with range and, when it arrives at each node in the far field, the wavefront is considered

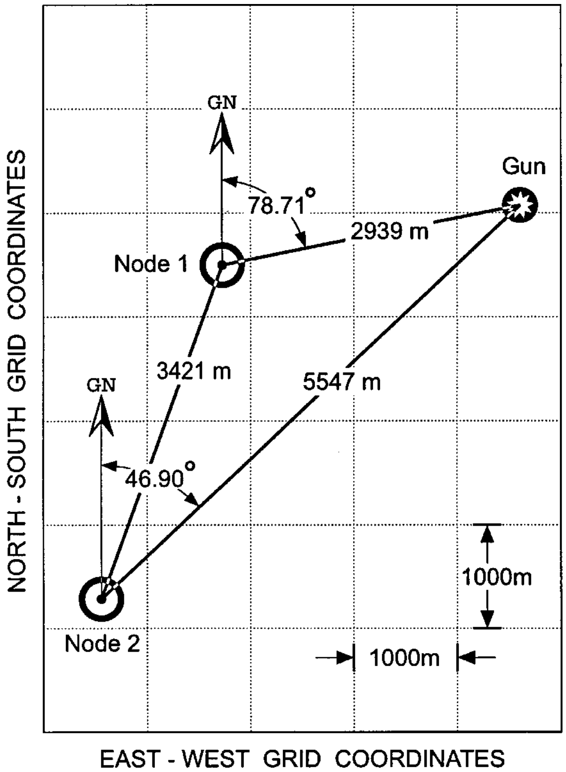

FIG. 3. Geometry of the field experiment. The distance from the source to each node and the distance between nodes are determined from the surveyed positions of the acoustic source (gun) and receiving nodes. The bearing of the source from each node is measured with respect to Grid North (GN).

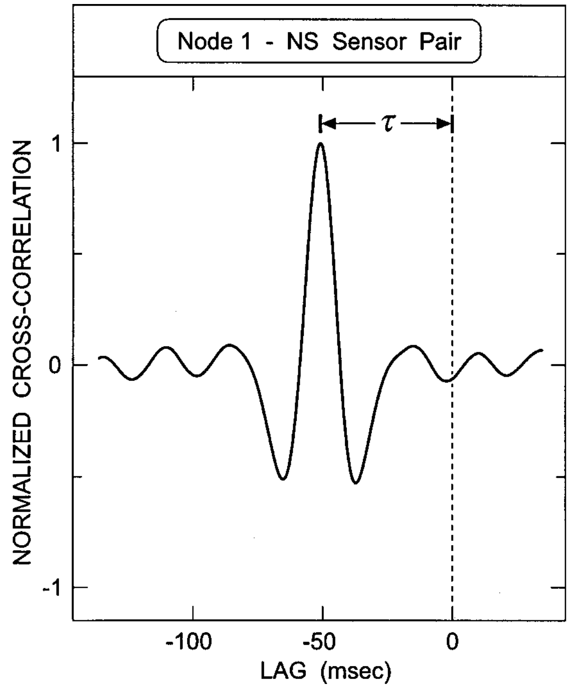

FIG. 4. Typical cross-correlation function of the gun-firing sound received by the NS sensor pair at node 1. The estimate of the differential time of arrival is given by the time lag τ at which the cross-correlation function attains its maximum value.

to be planar. Each of the sensor outputs is sampled at a rate of 20 000 times per second. The outputs of sensors 2 and 3 are each cross correlated with the output of sensor 1. The cross correlation is implemented in the frequency domain using a rectangular window function between 5 and 200 Hz, where most of the signal energy is contained. The integration or observation time is 0.2 s, which is short enough to ensure only one firing event occurs during the observation interval and yet much longer than the correlation time of noise. The signal-to-noise ratio at each sensor output exceeds 45 dB. Figure 4 shows a typical cross correlogram of the gun-firing sound received by the NS sensor pair at node 1 during the field experiment. The peak in the cross correlogram is well defined and its lag position gives an accurate estimate of the time delay between the two sensors. When the atmosphere is calm, the time-delay estimation accuracy is determined by the sampling period (0.05 ms), since the product of signal-to-noise ratio, integration time, and bandwidth is large. This represents an order of magnitude improvement in the time-delay measurement accuracy offered by early operational gun-ranging systems (quoted to be between 1 and 3 ms[2,3]). However, in practice, the time-delay estimation performance of any acoustic system depends strongly on atmospheric conditions. In the present experiment, the *minimum* standard deviation of the time delay estimates is 0.1 ms (observed for a gun-firing serial consisting of 22 events). For a time-delay error of 0.1 ms, the bearing estimate error using a single sensor pair is about 0.08° when the source direction is broadside to the sensor pair axis.

During the course of the field experiment, the gun is fired intermittently 206 times over a 20-h time period with the time intervals between firing serials being irregular. The source position of each firing event (gun primary) is computed by triangulation using the bearing estimates from nodes 1 and 2. (Note: Gun-ranging terminology refers to the firing of a shell as the "primary" and the bursting of the shell at the end of its trajectory as the "secondary.") Figure 5 shows the estimated source positions for all 206 firing events using the bearing estimates from the NS sensor pairs. Each grid square represents an area of 100 m by 100 m. Each white-filled circle represents a source position estimate. A black-filled square and a black-filled circle represent (respectively), the median and mean position estimates of all 206 events. The actual position (denoted by a black-filled triangle) corresponds to the surveyed position of the gun. The distance between the actual position and the *median* position estimate is 15 m, which is small considering that the gun is about 3 km from node 1 and 5.5 km from node 2. The distance between the actual position and the *mean* position is 25 m. The error covariance matrix is computed using all 206 position estimates. The result is then used to calculate the 1.5-sigma error ellipse, which is shown in Fig. 5 centered on the mean position estimate. About 74% of the source position estimates lie within this error ellipse. Due to the source-sensor node geometry, the spatial distribution of the position estimates (or error ellipse) is skewed towards the north of east, which is consistent with the direction of elongation of the positional uncertainty area shown in Fig. 1. Placing a third node to the south of the source would significantly reduce this elongation of the positional uncertainty area (that is, the error ellipse would appear more circular).

The accuracy of the source position estimates is deter-

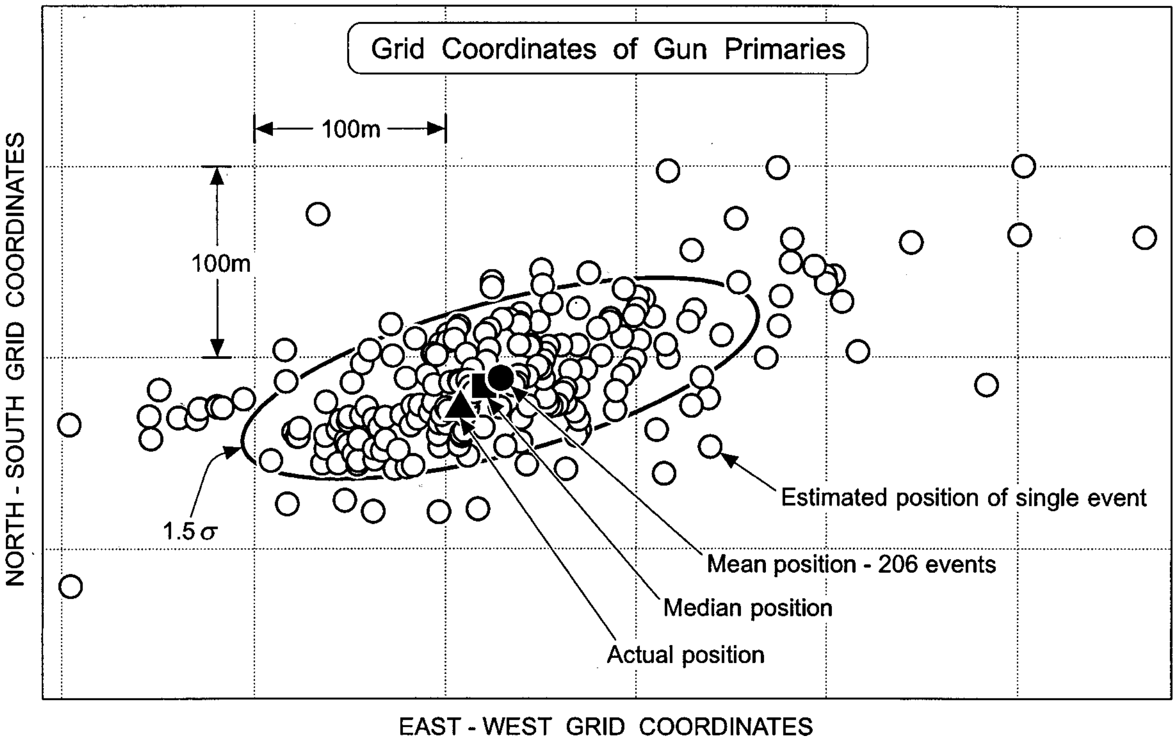

FIG. 5. Estimated grid coordinates for 206 gun-firing events and the 1.5-sigma error ellipse centered at the mean position estimate.

mined by the accuracy of the source bearing estimates. The source bearing error is equal to the difference between the bearing estimate (acoustic bearing) and the actual (surveyed) bearing of the source. Figures 6 and 7 show, for nodes 1 and 2, respectively, (a) the error in the (EW) source bearing estimated using the EW sensor pair and (b) the error in the (NS) source bearing estimated using both sensor pairs versus the error in the (NS) source bearing estimated using the NS sensor pair. The mean errors are shown in the figures as black-filled circles. It can be observed from Fig. 6(a) that for node 1, the variance of the source bearing errors using the EW sensor pair is larger than that using the NS sensor pair. Also, the source bearing estimates are biased in all cases, and the bias is larger when using the EW sensor pair.

The difference in bearing estimation performance using different sensor pairs is attributed to the direction of the source relative to the orientation of the sensor pair axis coupled with various factors such as time-delay estimation errors, imperfect knowledge of the speed of sound travel, and refraction of the acoustic wavefronts. The Appendix provides a brief statistical analysis of the bearing error due to each of these factors when using either a single pair of sensors or two orthogonal pairs of sensors. With a single pair of sensors, the bias and the variance of the bearing estimate always increase (regardless of the cause of the error) as the source direction tends to either of the end-fire directions of the sensor pair axis (that is, source bearing approaches $0°$ or $180°$). Assuming the errors are constant, Fig. 8 shows the predicted bearing error as a function of the actual source bearing for (1) an error of 5 m/s in the assumed sound speed (340 m/s); (2) an apparent source elevation angle of $6°$ (rather than the assumed value of $0°$) due to vertical refraction of the acoustic wavefronts; and (3) an error of 0.1 ms in the time-delay estimate. The bearing error is smallest when the source direction coincides with the broadside direction of the sensor pair axis (source bearing equals $90°$). The bearing error increases rapidly as the source direction approaches the end-fire direction (source bearing equals $0°$). With two orthogonal pairs of sensors, the bearing accuracy is not affected by the error in the assumed sound speed. Also, the bearing estimate actually represents the azimuth angle estimate, thus, vertical refraction of the acoustic wavefronts does not cause any bearing error. Furthermore, the bearing accuracy will be independent of the actual source bearing if the errors in τ_{12} and τ_{13} are statistically independent, zero-mean, and with the same variance.

The results shown in Figs. 6 and 7 suggest that for the present experiment, the bearing estimates from the NS sensor pairs at nodes 1 and 2 will provide the most accurate source position estimate. Figures 9(a) and 9(b) show the cumulative probability distributions of the source bearing errors for all 206 firing events using the NS sensor pairs at nodes 1 and 2, respectively, while Fig. 9(c) shows the cumulative probability distribution of the resulting source position errors. [Note that the source position error is defined here as the *distance* between the position estimate and the actual (surveyed) position of the source.] Figure 10 compares the cumulative probability distributions of the source position errors for all 206 firing events using the NS sensor pairs, the EW sensor pairs, and both NS and EW sensor pairs at nodes 1 and 2. This figure confirms that for the present experiment, the NS sensor pairs provide the best gun-ranging results but those obtained using both NS and EW sensor pairs are comparable. Table I(a) lists the source bearing errors and source position errors using the NS sensor pairs for cumulative probabilities of 0.5, 0.75, and 0.9; for example, there is a 75% probability

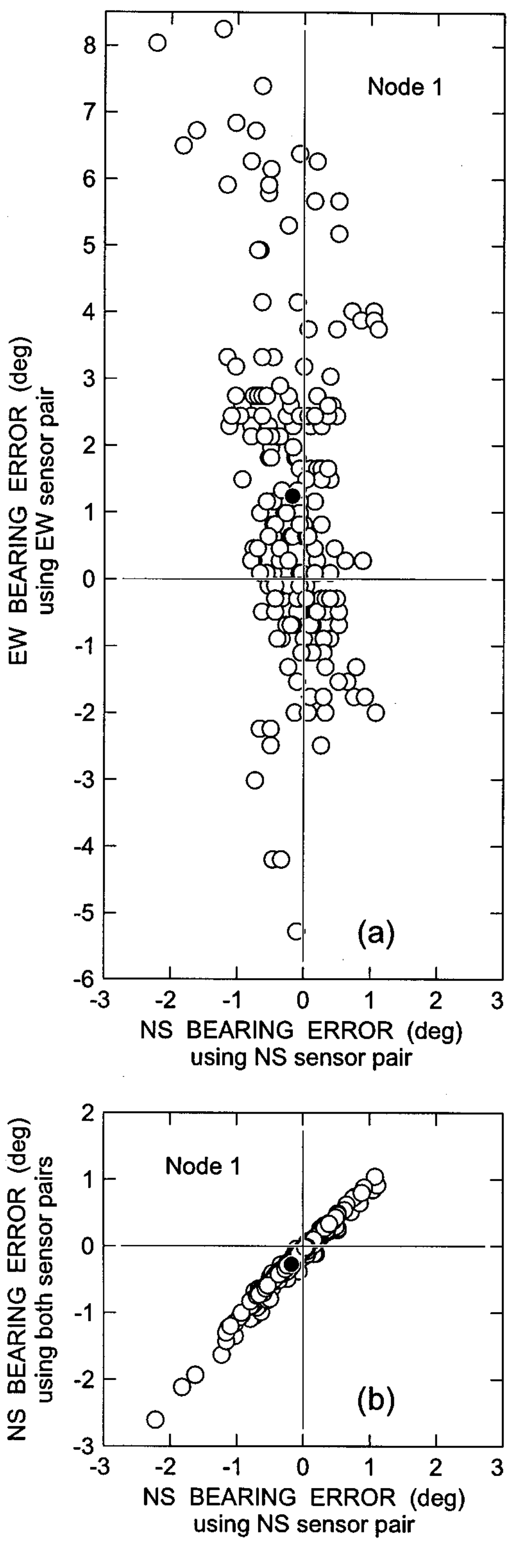

FIG. 6. For node 1: (a) Variation of the EW source bearing error using the EW sensor pair with the NS source bearing error using the NS sensor pair. (b) Variation of the NS source bearing error using both the NS and EW sensor pairs with the NS source bearing error using the NS sensor pair. The black-filled circle represents the mean bearing error.

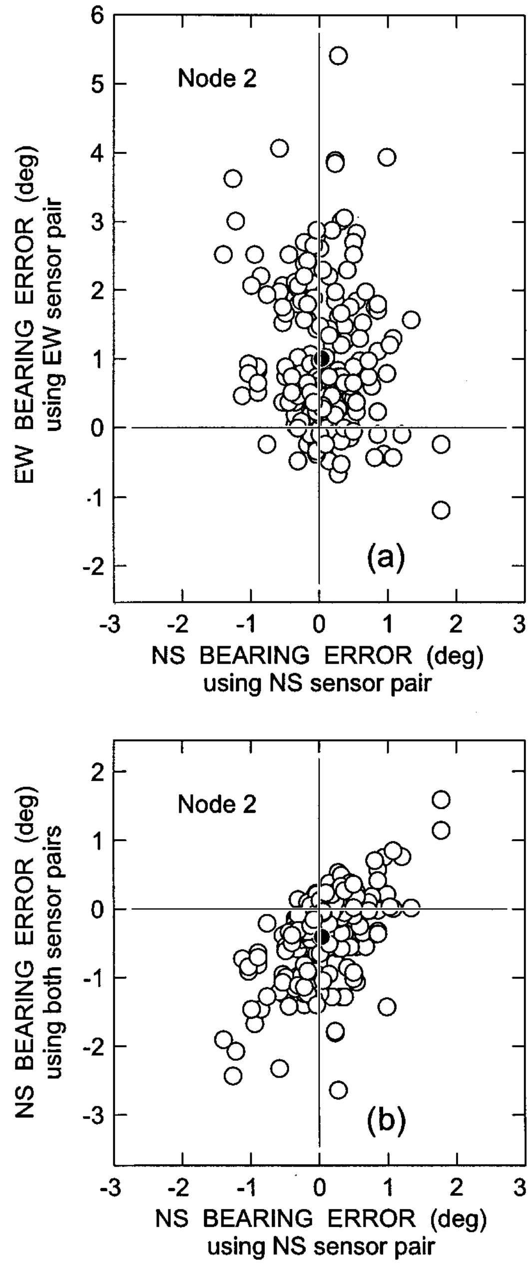

FIG. 7. For node 2: (a) Variation of the EW source bearing error using the EW sensor pair with the NS source bearing error using the NS sensor pair. (b) Variation of the NS source bearing error using both the NS and EW sensor pairs with the NS source bearing error using the NS sensor pair. The black-filled circle represents the mean bearing error.

that the source position error is less than 103 m. Tables I(b) and (c) list the corresponding results obtained using the EW sensor pairs and both NS and EW sensor pairs at the two nodes, respectively. The source position errors using the EW sensor pairs are roughly double those using the NS sensor pairs.

IV. METEOROLOGICAL EFFECTS

A. Ground wind and temperature variations

Meteorological effects on sound propagation have been reported for many years in the literature.[10,11] The effect of wind must be considered in sound ranging together with temperature.[2] The travel of sound is superimposed on that of the wind whose effect is usually more important than that of temperature. In the present experiment, the (ground) temperature varied from 13° to 16 °C, which corresponds to a

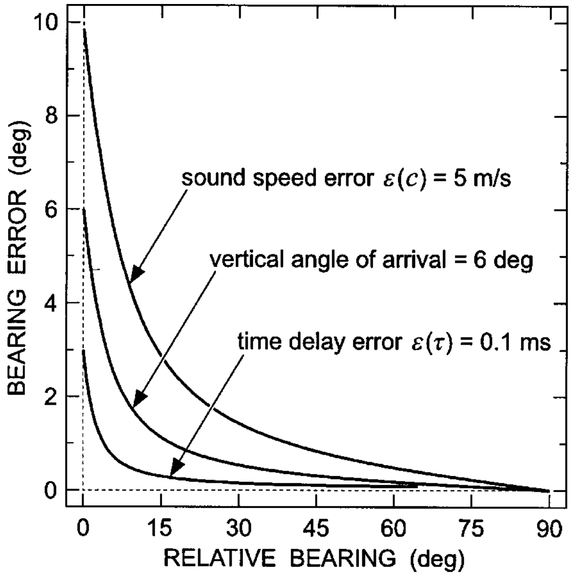

FIG. 8. Predicted bearing error as a function of the actual source bearing for (1) an error of 5 m/s in the assumed sound speed (340 m/s); (2) an apparent source elevation angle of 6° (rather than the assumed 0°); and (3) an error of 0.1 ms in the time-delay estimate. The bearing is measured with respect to the sensor pair axis.

sound-speed variation of 1.8 m/s, while the (ground) wind speed varied from 0 to 6 m/s over the 20-h period. The wind speed and direction, together with temperature, were logged every 2 min at node 1 *only*.

The effect of wind on sound-ranging system performance depends on the relative bearing of the source, that is, the direction of the source with respect to the orientation of the sensor pair axis. The speed of sound travel at node 1 (which was previously assumed constant at 340 m/s) is adjusted to include the effects of changes in wind velocity and temperature. Figure 11 shows a plot of the resulting EW source bearing error using the EW sensor pair against the NS source bearing error using the NS sensor pair at node 1 for each of the 206 firing events. Figure 12 shows the cumulative probability distributions of the source bearing errors using each of the sensor pairs (NS, EW) at node 1, with and without correction for the effects of wind- and temperature variations on the speed of sound travel. The difference in the source bearing errors using the NS sensor pair before and after the correction is found to be negligible. This is because the bearing estimate is insensitive to errors in the speed of sound travel when the source is near the broadside direction of the NS sensor pair. Comparing Fig. 11 with Fig. 6(a), the bias and variance of the source bearing errors using the EW sensor pair are reduced after correction for the effects of wind and temperature variations on the speed of sound travel; these reductions are represented by the shaded area in Fig. 12. However, the source bearing errors using the EW sensor pair are still larger (in a statistical sense) than those using the NS sensor pair after the correction. This is due to the fact that the source direction is near the end-fire direction of the EW sensor pair so that time-delay estimation errors and vertical refraction of the acoustic wavefronts have larger effects on the bearing accuracy of this sensor pair—see Fig. 8.

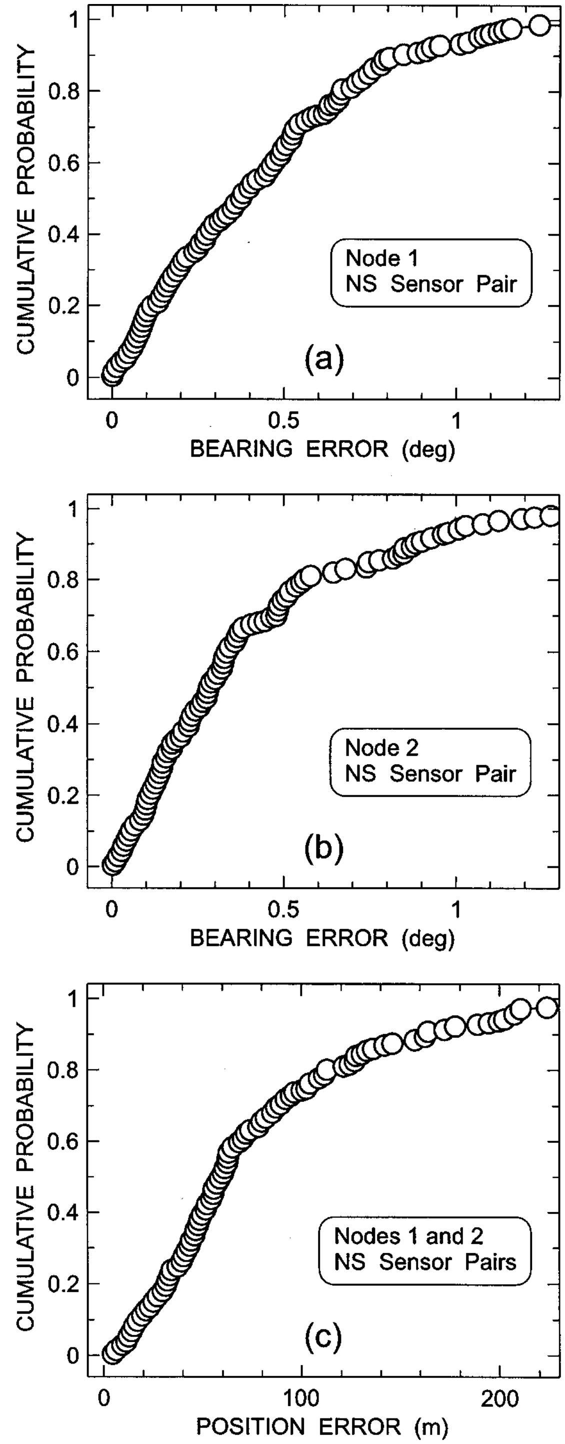

FIG. 9. (a) Cumulative probability distribution of the source bearing errors using the NS sensor pair at node 1. (b) Cumulative probability distribution of source bearing errors using the NS sensor pair at node 2. (c) Cumulative probability distribution of the source position errors using the NS sensor pairs at nodes 1 and 2.

B. Vertical refraction

The present source localization method assumes an isospeed sound propagation medium and hence straight-line propagation. However, the speed of sound propagation is dependent not only on ground wind and temperature, but also on conditions in the upper air. Knowledge of the vertical profiles of wind and temperature is required to determine the

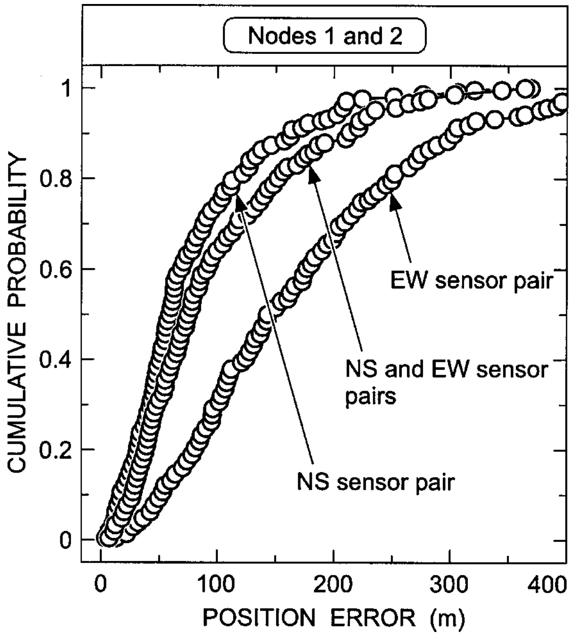

FIG. 10. Cumulative probability distributions of the source position errors using the NS sensor pairs, the EW sensor pairs, and both the NS and EW sensor pairs at nodes 1 and 2.

sound propagation path from the source to the sensor. Normally, with increasing height, there is a decrease in temperature and an increase in wind speed. These gradients of temperature and wind speed cause refraction of the wavefront in the vertical direction, and the acoustic wavefront arrives at the node with a finite elevation angle ϕ as depicted in Fig. 13. When the acoustic wavefront undergoes vertical refraction, it is the *apparent* bearing β (rather than the *actual* bearing θ) that is estimated by the NS (or EW) sensor pair. The cosine of the apparent bearing β (relative to the sensor pair axis) is equal to the product of the cosines of the azimuth angle θ (relative to the sensor pair axis) and elevation angle ϕ, that is, $\cos\beta=\cos\theta\cos\phi$. If the source is broadside to the sensor pair axis ($\theta=90°$), then the apparent bearing is equal to the azimuth angle ($\beta=\theta$) and is independent of ϕ, while at end-fire ($\theta=0°$) the apparent bearing is equal to the elevation angle ($\beta=\phi$). Thus, when using a single pair of sensors for bearing estimation, the effect of vertical refraction is minimal when the source direction is broadside to the sensor pair axis—see Fig. 8.

Ideally, knowledge of the apparent source elevation angle ϕ is required to compensate for the effect of vertical refraction of the acoustic wavefronts; otherwise, the source bearing estimates will be biased. An *effective* sound speed can be defined by $c_{\mathrm{eff}}=c/\cos\phi$, which includes the effects of ground wind and temperature variations in the numerator (c) and the effect of vertical refraction in the denominator ($\cos\phi$). For a given sensor spacing d, the effective sound speed c_{eff} maps the time delay τ to the azimuth angle of the source θ, that is, $\cos\theta=c_{\mathrm{eff}}\tau/d$.

The variability in the source bearing estimates caused by wavefront refraction effects can be observed in the present experiment by dividing the 206 firing events into nine groups; each group corresponds to a firing serial that lasted from 10 to 90 min. For each group of firing events (firing serial), the mean and standard deviation of the bearing estimates from each sensor pair at node 1 are calculated, and the results for the NS and EW sensor pairs are shown (respectively), in Fig. 14(a.1) for β_{NS} and Fig. 14(c.1) for β_{EW}. Here, a circle denotes the mean value and the error bars denote $\pm$ one standard deviation. Note that the bearing estimates (β_{NS}) from the NS sensor pair are measured with respect to Grid North and the bearing estimates (β_{EW}) from the EW sensor pair are measured with respect to Grid East. Similarly, the results for node 2 are shown in Fig. 14(a.2) for β_{NS} and Fig. 14(c.2) for β_{EW}. The bearing estimates from the NS (or EW) sensor pair are estimates of the apparent bearing β rather than the azimuth angle θ of the source. To estimate the azimuth angle θ of the source requires the use of both the EW and NS sensor pairs (see Appendix B 2). Figures 14(b.1) and 14(d.1) show for each firing serial the mean and standard deviation of the azimuth angle estimates (obtained using both sensor pairs at node 1) with respect to Grid

TABLE I. Values of the source bearing and position errors for specific values of cumulative probability (0.5, 0.75, and 0.9) using (a) the NS sensor pairs; (b) the EW sensor pairs; and (c) both the NS and EW sensor pairs, at nodes 1 and 2.

(a) North - South Sensor Pairs

Cumulative Probability	Bearing Error (°) Node 1	Bearing Error (°) Node 2	Position Error (m)
0.5	0.37	0.28	59
0.75	0.63	0.51	103
0.9	0.83	0.88	163

(b) East - West Sensor Pairs

Cumulative Probability	Bearing Error (°) Node 1	Bearing Error (°) Node 2	Position Error (m)
0.5	1.59	0.68	143
0.75	2.63	1.74	226
0.9	4.50	2.46	303

(c) Both NS and EW Sensor Pairs

Cumulative Probability	Azimuth Error (°) Node 1	Azimuth Error (°) Node 2	Position Error (m)
0.5	0.35	0.40	75
0.75	0.65	0.92	137
0.9	0.89	1.32	212

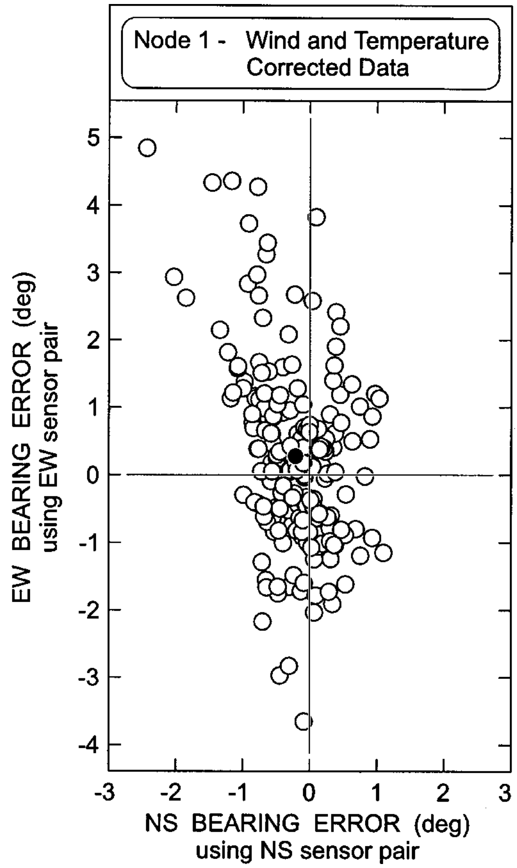

FIG. 11. For node 1: Variation with the NS source bearing error using the NS sensor pair of the EW source bearing error using the EW sensor pair, after correction for the effects of changes in wind velocity and temperature.

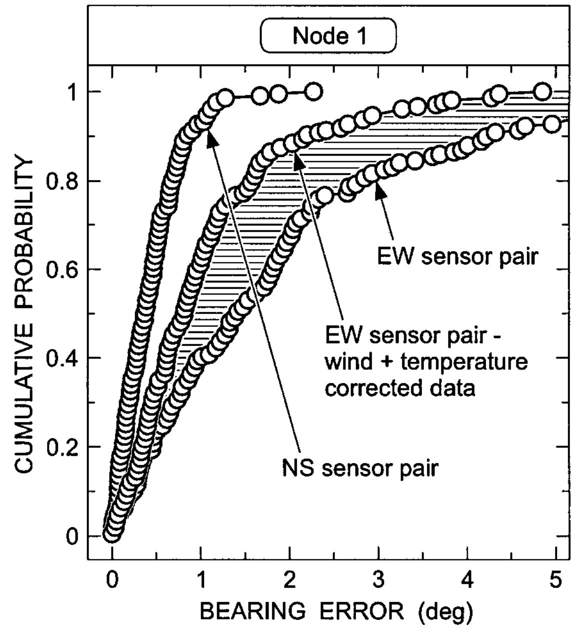

FIG. 12. Cumulative probability distributions of source bearing errors using the EW sensor pair at node 1, with and without correction for the effects of wind and temperature variations. The results for the NS sensor pair are also shown where the corrections for the effects of wind and temperature variations are negligible.

North and Grid East, respectively. The azimuth angle estimates with respect to Grid North θ_{NS} [see Fig. 14(b.1)] and Grid East θ_{EW} [see Fig. 14(d.1)] are complementary angles. Similarly, the results for node 2 are shown in Fig. 14(b.2) for θ_{NS} and Fig. 14(d.2) for θ_{EW}.

The biasing effect of *vertical* refraction on bearing estimation can be readily observed by comparing Fig. 14(c.1) for β_{EW} with Fig. 14(d.1) for θ_{EW}. The bias errors for β_{EW} are much larger than those for θ_{EW}. Vertical refraction of the acoustic wavefronts leads to β being a (positively) biased estimate of the actual bearing θ; the magnitude of the bias error is a maximum for the end-fire (0°) source direction and a minimum (zero) for the broadside (90°) source direction. The bias errors for β_{NS} [see Fig. 14(a.1)] are small because the source direction (78.7°) is near the broadside direction of the NS sensor pair axis. In comparison, the bias errors for β_{EW} [see Fig. 14(c.1)] are much larger because the source direction (11.3°) is near the end-fire direction of the EW sensor pair axis.

Figure 15 shows the corresponding results after correction for the effects of wind and temperature variations on the speed of sound travel. The remaining bias errors for the EW sensor pair after the correction [see Fig. 15(b) β_{EW}] are ascribed partly to the downward refraction of the wavefronts resulting from the prevailing vertical meteorological conditions (and partly to horizontal refraction as discussed in the next section).

C. Horizontal refraction

Horizontal refraction of the acoustic wavefronts shifts the azimuth angle θ of the source in a particular direction. For node 1, the bias errors in θ shown in Fig. 14(b.1) for θ_{NS} and Fig. 14(d.1) for θ_{EW} as deviations of the mean values from the actual value are attributed to *horizontal* refraction

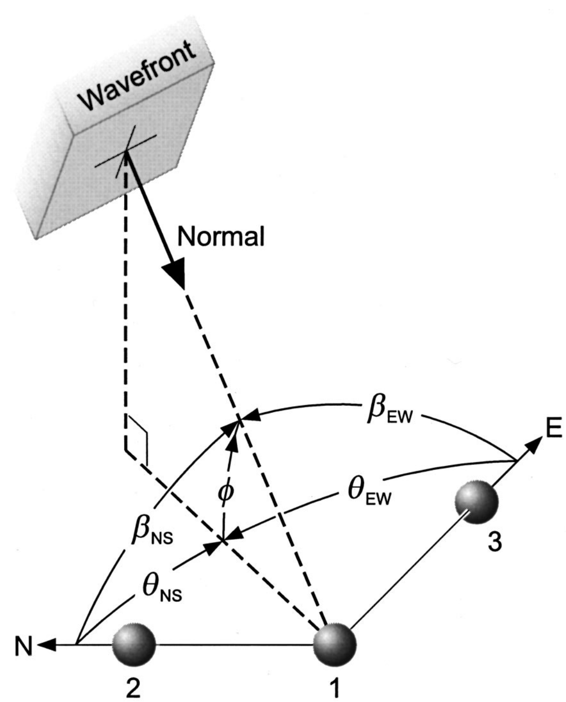

FIG. 13. An acoustic wavefront arrives at the sensor node with elevation angle ϕ due to vertical refraction; β and θ denote the respective apparent bearing and azimuth angles.

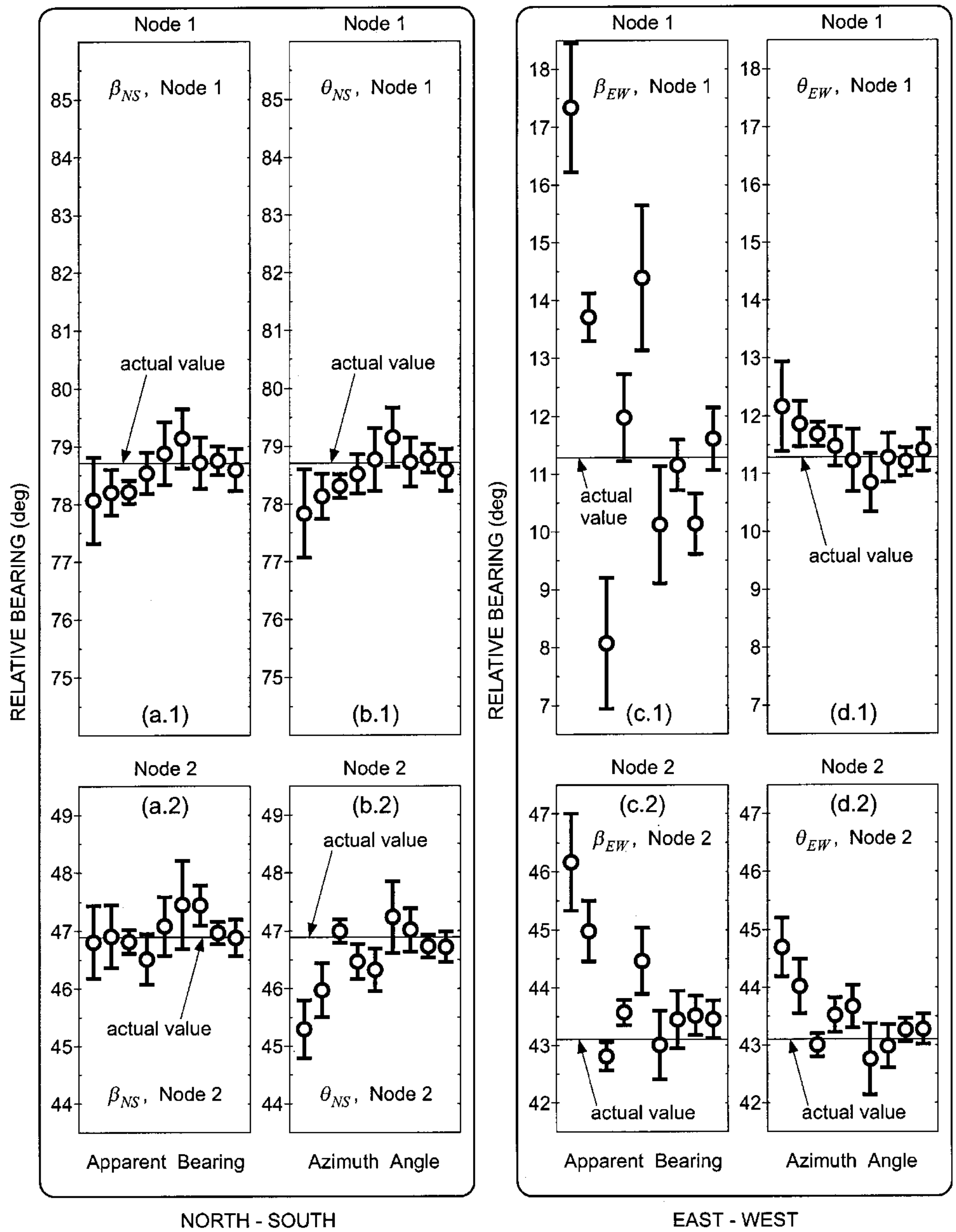

FIG. 14. Variability in the apparent bearing β and azimuth angle θ data at: Node 1—(a.1) β_{NS}; (b.1) θ_{NS}; (c.1) β_{EW}; (d.1) θ_{EW}; and Node 2—(a.2) β_{NS}; (b.2) θ_{NS}; (c.2) β_{EW}; (d.2) θ_{EW}.

of the acoustic wavefronts. Similar observations can be made for the node 2 results shown in Fig. 14(b.2) for θ_{NS} and Fig. 14(d.2) for θ_{EW}.

At node 2, the source is located at almost 45° with respect to the orthogonal axes of the sensor pairs, so the effects of wind/temperature variations and vertical refraction should be about the same for both sensor pairs. However, the bias errors of the bearing estimates from the NS sensor pair [see Fig. 14(a.2) β_{NS}] are smaller than those from the EW sensor pair [see Fig. 14(c.2) β_{EW}]. This unexpected result can be explained by the bias errors due to vertical and horizontal refraction compensating each other for the NS sensor pair. Such bias error compensation does not occur for the azimuth angle estimates from two orthogonal sensor pairs [see Fig. 14(b.2) θ_{NS}] because they are not affected by vertical refraction (only by horizontal refraction). It also explains why, for the present experiment, the source localization performance of the triangulation method is better when using the apparent bearings of the NS sensor pairs (β_{NS} from node 1 and β_{NS} for node 2) instead of the azimuth angles from both the NS and EW sensor pairs at the two nodes—compare Table I(a) with Table I(c).

V. OTHER OBSERVATIONS OF SOURCE BEARING VARIABILITY

Real data from two other field experiments are processed to extract information on the bearing variability of other impulsive sound sources: 155-mm guns, mortars, and grenades. Only a single node is deployed in these two ex-

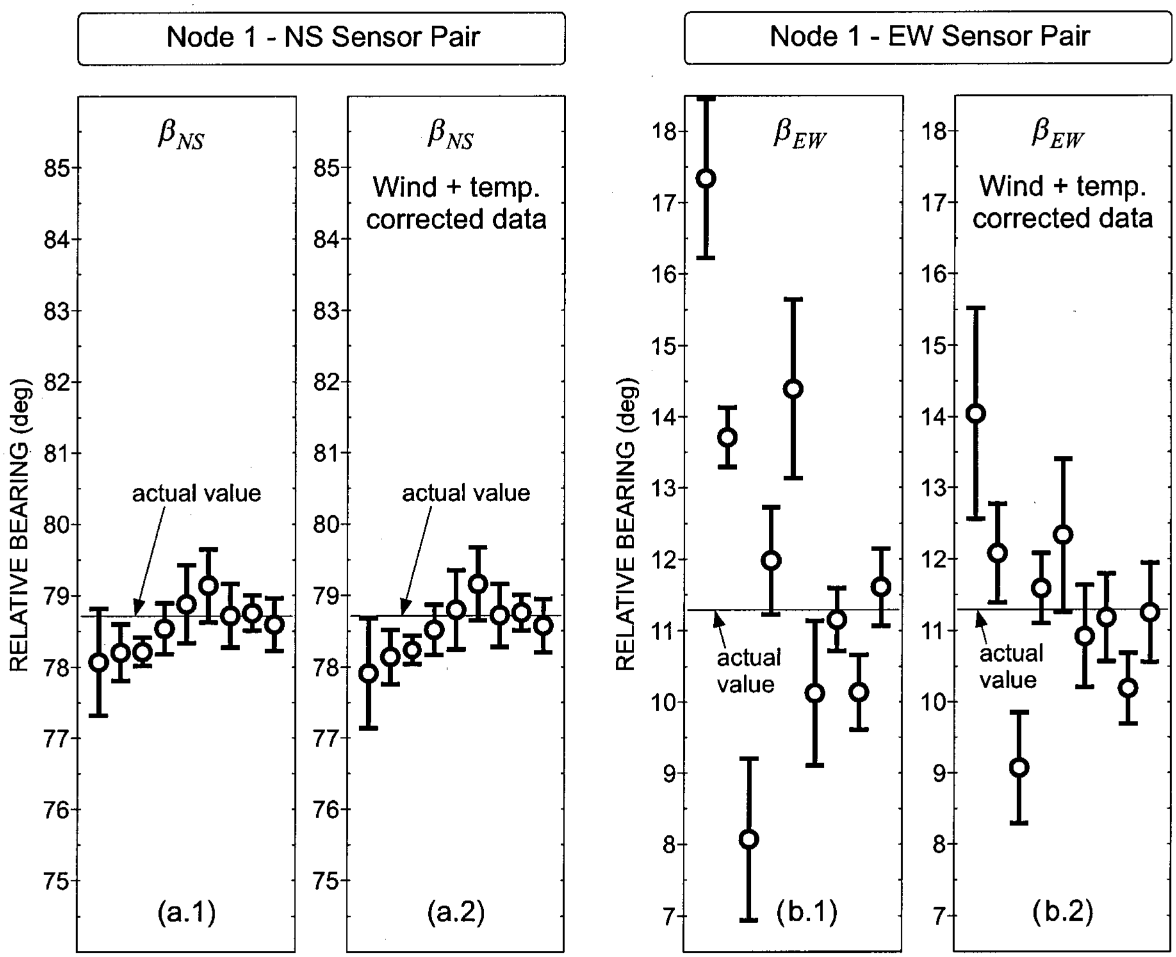

FIG. 15. For node 1: Variability in (a) the NS bearing (β_{NS}) data from the NS sensor pair and (b) the EW bearing (β_{EW}) data from the EW sensor pair *before* [(a.1), (b.1)] and *after* [(a.2), (b.2)] correction for the effects of wind and temperature variations.

periments, which were conducted on an opportunity basis. Accurate survey data for each source position and ground wind vector data are not available. The NS and EW sensor pairs are used, in turn, to estimate the (apparent) bearing of the source relative to the sensor pair axis.

The variability in the relative bearing estimates of the firing events is characterized using the mean and standard deviation, respectively, as measures of the central tendency and dispersion. For example, Fig. 16 shows the relative bearing observations of (155-mm) gunfire over two time periods of 62 min (period 1) and 17 min (period 2); there is a 58-min intermission between the gunfire serials. The estimated val-

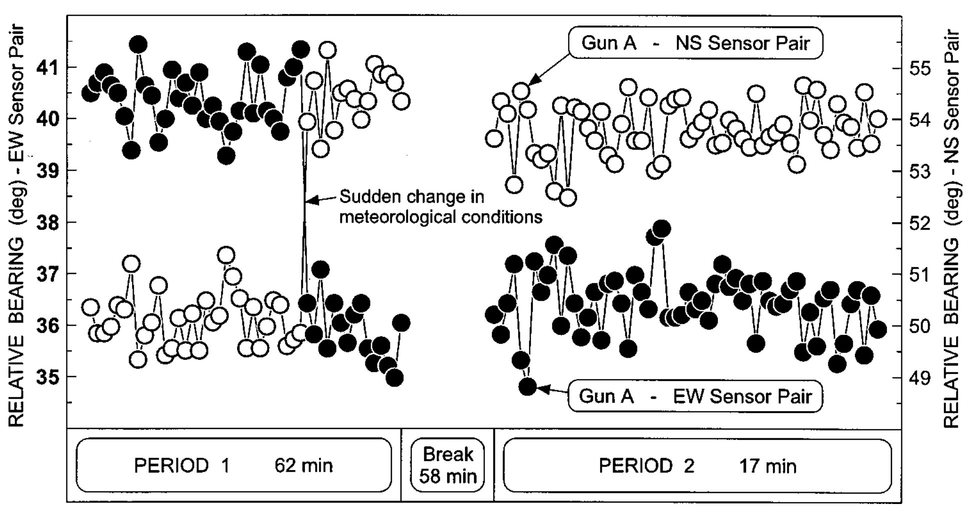

FIG. 16. Relative bearing data from the NS sensor pair and the EW sensor pair for a 155-mm gun (gun A) before, and after, a sudden change in the meteorological conditions.

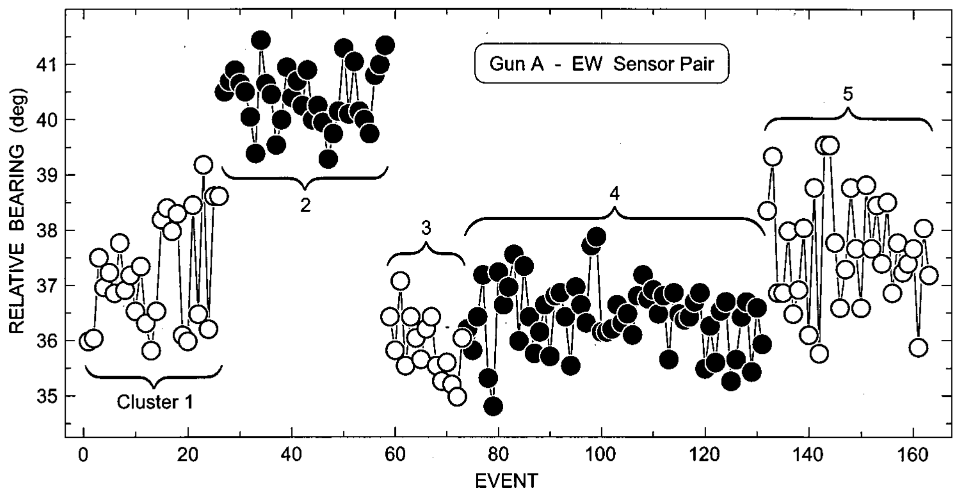

FIG. 17. Relative bearing data from the EW sensor pair for a 155-mm gun (gun A). The data are grouped as clusters, each cluster corresponding to a firing serial. Cluster 2 and 3 belong to the same firing serial, but are grouped separately due to the effect of a sudden change in meteorological conditions.

ues for the EW source bearing from the EW sensor pair are shown on the left-hand-side vertical axis (35–41°), and the estimated values for the NS source bearing from the NS sensor pair are shown on the right-hand-side vertical axis (49–55°). Initially, the variability in the bearing estimates resembles a random process and is attributed to the effects of time-delay estimation errors[8] and atmospheric turbulence.[12] Then, there is a discontinuity in the bearing estimates during period 1, which coincides with the arrival of a weather front and a sudden change in the meteorological conditions. The change in sound propagation conditions results in a systematic change of at least 4° in the source bearing estimates, which would have a significant impact on the source localization performance of the triangulation method. For the remainder of period 1, and for period 2, the variability in the bearing estimates again resembles a random process but with a different mean value. Random fluctuations in the atmosphere's wind and temperature fields produce random fluc-

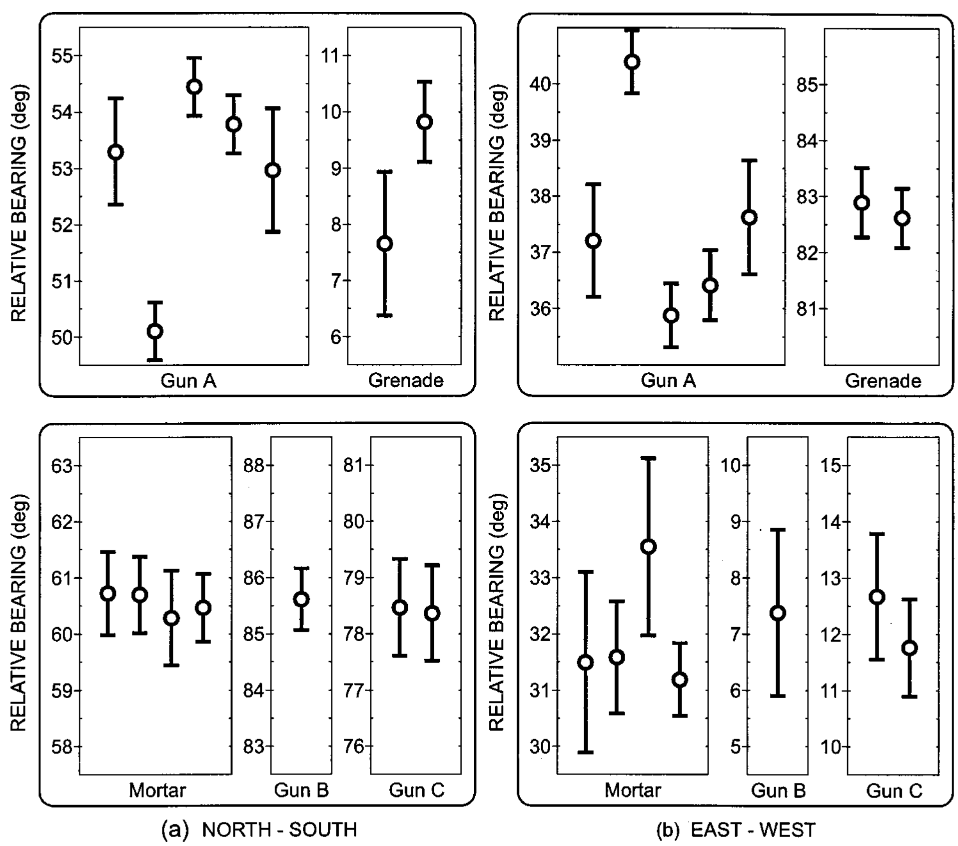

FIG. 18. Variability in the relative bearing data from (a) the NS sensor pair and (b) the EW sensor pair for all the sources studied during the other two field experiments. Each circle represents the mean value of the bearing data for a cluster (that is, a group of events corresponding to a firing serial) with the errors bars representing ± one standard deviation.

tuations in the intensity (acoustic scintillation) and orientation of the acoustic wavefronts (angle-of-arrival fluctuations) impinging on acoustic sensor arrays.[12]

In Fig. 16, the systematic change in the bearing estimates occurs over a short time period (minutes); however, changes are also observed to occur over longer time periods (hours to days). Figure 17 shows the EW source bearing estimates from the EW sensor pair for the same (155-mm) gun. The first cluster (denoted by white-filled circles) represents the observations on the first day (26 firings over 120 min). Clusters 2, 3, and 4 represent the observations on the second day (which are the same observations of the EW source bearing shown in Fig. 16). Cluster 5 represents the observations on the third day (32 firings over 90 min). The mean and standard deviation for each cluster are calculated and then plotted in Fig. 18(b)—gun A. The corresponding results for the NS source bearing estimates from the NS sensor pair are shown in Fig. 18(a)—gun A. For completeness, the rest of Fig. 18 shows the results for the primaries of other guns (B and C), a mortar firing serial, and an exploding grenade serial. The variability in the bearing estimates is larger when the source direction is near the end-fire direction of the sensor pair axis; for example, compare the results in Figs. 18(a) and 18(b) for grenade. These results are consistent with those for the artillery gun in the first field experiment [see Fig. 14(a.1) for β_{NS} and Fig. 14(c.1) for β_{EW}].

VI. CONCLUSIONS

Locating an impulsive sound source in air requires accurate time-delay measurements for the acoustic wavefront to travel between sensors, accurate survey information for the sensor positions, and knowledge of the effective speed of sound travel in the atmosphere. The variability in source bearing and position estimates is ascribed to the sound propagation medium being variable in both space and time. The variability in the source position estimates may be reduced by temporal averaging (observing many firing events from the same source over a long period of time) and by spatial averaging (observing the same firing event with many widely distributed nodes).

Source bearing errors resulting from atmospheric winds can be reduced by a prudent choice of sensor orientation, which is found to be preferable to adjusting the speed of sound travel to include the wind-speed variation observed in ground wind vector measurements taken in proximity to the sensors.

The apparent bearings from two orthogonal pairs of sensors can be decomposed into the constituent azimuth and elevation angles. Combining the time-delay estimates from two orthogonal pairs of sensors reduces the source direction bias errors caused by vertical refraction of the wavefronts and enables the source azimuth angle to be estimated directly without having to know the effective speed of sound travel.

ACKNOWLEDGMENTS

The authors gratefully acknowledge the technical discussions with their colleagues: Gary Speechley and Ron Wyber. The authors greatly appreciate the field trials support provided by the soldiers of 1 RISTA (Reconnaissance Intelligence Surveillance and Target Acquisition) Regiment, Australian Army and wish to recognize the leadership of their Commanding Officer (Lieutenant Colonel Rik Modderman).

APPENDIX A: SINGLE PAIR OF SENSORS

The source bearing θ is related to the time delay τ by Eq. (3). (All subscripts are dropped for simplicity.) Let $\Delta\theta$ be the error in the source bearing estimate. Denote $E[\cdot]$ as the ensemble average of the quantity in brackets. Then, $E[\Delta\theta]$ and $E[\Delta\theta^2]$ represent the bias error and mean-square error in the source bearing estimate, respectively.

1. Effect of time-delay error

By definition,

$$E[\Delta\theta^n]=\int_{-\infty}^{\infty}\left[\cos^{-1}\left(\frac{c(\tau+\Delta\tau)}{d}\right)-\theta\right]^n \times f_1(\Delta\tau)d\Delta\tau,\quad n=1,2,..., \tag{A1}$$

where $f_1(\Delta\tau)$ is the probability density function (PDF) of the time-delay estimate error $\Delta\tau$. By expanding the arc cosine function in Eq. (A1) as a Taylor series about the true value, and retaining the second-order and the first-order terms, respectively, it can be shown that

$$E[\Delta\theta]\cong-\frac{c}{d\sin\theta}E[\Delta\tau]-\frac{c^2\cos\theta}{2d^2\sin^3\theta}E[\Delta\tau^2], \tag{A2}$$

$$E[\Delta\theta^2]\cong\left(\frac{c}{d\sin\theta}\right)^2 E[\Delta\tau^2], \tag{A3}$$

where $E[\Delta\tau]$ and $E[\Delta\tau^2]$ are the bias error and mean-square error of the time-delay estimate, respectively.

2. Effect of sound-speed error

$$E[\Delta\theta^n]=\int_{-\infty}^{\infty}\left[\cos^{-1}\left(\frac{(c+\Delta c)\tau}{d}\right)-\theta\right]^n \times f_2(\Delta c)d\Delta c,\quad n=1,2,..., \tag{A4}$$

where $f_2(\Delta c)$ is the PDF of the sound-speed error Δc.

A second-order approximation of Eq. (A4) gives the bias error in the bearing estimate

$$E[\Delta\theta]\cong-\frac{\tau}{d\sin\theta}E[\Delta c]-\frac{\tau^2\cos\theta}{2d^2\sin^3\theta}E[\Delta c^2], \tag{A5}$$

where $E[\Delta c]$ and $E[\Delta c^2]$ are the bias error and mean-square error of the assumed sound speed, respectively. A first-order approximation of Eq. (A4) gives the mean-square error in the bearing estimate

$$E[\Delta\theta^2]\cong\left(\frac{\tau}{d\sin\theta}\right)^2 E[\Delta c^2]. \tag{A6}$$

3. Effect of vertical refraction

When there is vertical refraction, Eq. (3) provides an estimate of the *apparent* bearing β rather than the actual bearing (azimuth angle) of the source θ. This is because $c\tau/d=\cos\theta\cos\phi=\cos\beta$, where ϕ is the vertical refraction angle or the apparent source elevation angle. The bearing error due to vertical refraction is $\Delta\theta = \beta - \theta$, so

$$E[\Delta\theta^n] = \int_0^{\pi/2} [\cos^{-1}(\cos\theta\cos\phi) - \theta]^n f_3(\phi)\, d\phi,$$
$$n = 1,2,..., \tag{A7}$$

where $f_3(\phi)$ is the PDF of ϕ. The apparent bearing β is a (positively) biased estimator of the actual bearing θ because $\beta > \theta$.

APPENDIX B: TWO ORTHOGONAL PAIRS OF SENSORS

The source bearing θ is related to the time delays τ_{12} and τ_{13} by Eq. (4). (The subscript NS is dropped for simplicity.)

1. Effect of time-delay errors

$$E[\Delta\theta^n] = \int_{-\infty}^{\infty}\int_{-\infty}^{\infty} \left[\tan^{-1}\left(\frac{\tau_{13}+\Delta\tau_{13}}{\tau_{12}+\Delta\tau_{12}}\right) - \theta\right]^n$$
$$\times f(\Delta\tau_{12}, \Delta\tau_{13})\, d\Delta\tau_{12}\, d\Delta\tau_{13}, \quad n = 1,2,..., \tag{B1}$$

where $f(\Delta\tau_{12}, \Delta\tau_{13})$ is the joint PDF of the time-delay estimate errors $\Delta\tau_{12}$ and $\Delta\tau_{13}$.

Using a first-order approximation and assuming that $\Delta\tau_{12}$ and $\Delta\tau_{13}$ are (statistically) independent, zero-mean, and with the same variance $E[\Delta\tau^2]$, it can be shown that

$$E[\Delta\theta^2] \cong \left(\frac{c}{d}\right)^2 E[\Delta\tau^2]. \tag{B2}$$

2. Effect of vertical refraction

Equation (4) provides an estimate of the source azimuth angle θ, even when the acoustic wavefront undergoes vertical refraction. This is because the two sensor pairs are orthogonal and so $c\tau_{12}/d = \cos\theta\cos\phi$, $c\tau_{13}/d = \sin\theta\cos\phi$, where ϕ is the vertical refraction angle; dividing the second equation by the first gives $\tan\theta = \tau_{13}/\tau_{12}$. Thus, vertical refraction does not cause any error in bearing (azimuth angle) estimation using two orthogonal pairs of sensors. However, it may enhance the effects of other sources of errors on bearing estimation. For example, for a given vertical refraction angle ϕ, the mean-square bearing error due to time-delay estimation errors is given by

$$E[\Delta\theta^2] \cong \left(\frac{c}{d\cos\phi}\right)^2 E[\Delta\tau^2], \tag{B3}$$

which increases with ϕ.

[1] L. L. Beranek, ''Unsolved military noise problems,'' J. Acoust. Soc. Am. **24**, 769–772 (1952).

[2] ''Artillery Training—General Principles and Practice of Sound Ranging'' VI, Obs. Pam. No. 5, Chief of the Imperial General Staff, (UK) War Office (1957).

[3] T. R. Ford, ''Sound Ranging,'' Royal Australian Artillery Corps Training Manual 3, Pam. No. 7, 5–34 (1988).

[4] G. C. Carter, ''Time delay estimation for passive sonar signal processing,'' IEEE Trans. Acoust., Speech, Signal Process. **ASSP-29**, 463–470 (1981).

[5] G. C. Carter, *Coherence and Time Delay Estimation* (IEEE, New York, 1993).

[6] J. C. Hassab, B. W. Guimond, and S. C. Nardone, ''Estimation of location and motion parameters of a moving source observed from a linear array,'' J. Acoust. Soc. Am. **70**, 1054–1061 (1981).

[7] P. Heimdal and F. Bryn, ''Passive ranging techniques,'' in *Signal Processing*, edited by J. W. R. Griffiths, P. L. Stocklin, and C. Van Schooneveld (Academic, New York, 1973), pp. 261–269.

[8] B. G. Ferguson, ''Variability in the passive ranging of acoustic sources in air using a wavefront curvature technique,'' J. Acoust. Soc. Am. **108**, 1535–1544 (2000).

[9] D. J. Torrieri, ''Statistical theory of passive location systems,'' IEEE Trans. Aerosp. Electron. Syst. **AES-20**, 183–198 (1984).

[10] J. E. Piercy, T. F. W. Embleton, and L. C. Sutherland, ''Review of noise propagation in the atmosphere,'' J. Acoust. Soc. Am. **61**, 1403–1418 (1977).

[11] T. F. W. Embleton, ''Tutorial on sound propagation outdoors,'' J. Acoust. Soc. Am. **100**, 31–48 (1996).

[12] D. K. Wilson, ''Performance bounds for acoustic direction-of-arrival arrays operating in atmospheric turbulence,'' J. Acoust. Soc. Am. **103**, 1306–1319 (1998).

Passive ranging errors due to multipath distortion of deterministic transient signals with application to the localization of small arms fire

Brian G. Ferguson and Kam W. Lo
Defence Science and Technology Organization, PO Box 44, Pyrmont, NSW 2009, Australia

(Received 8 September 1999; revised 17 July 2001; accepted 19 July 2001)

A passive ranging technique based on wavefront curvature is used to estimate the ranges and bearings of impulsive sound sources represented by small arms fire. The discharge of a firearm results in the generation of a transient acoustic signal whose energy propagates radially outwards from the omnidirectional source. The radius of curvature of the spherical wavefront at any instant is equal to the instantaneous range from the source. The curvature of the acoustic wavefront is sensed with a three-microphone linear array by first estimating the differential time of arrival (or time delay) of the acoustic wavefront at each of the two adjacent sensor pairs and then processing the time-delay information to extract the range and bearing of the source. However, modeling the passive ranging performance of the wavefront curvature method for a deterministic transient signal source in a multipath environment shows that when the multipath and direct path arrivals are unresolvable, the time-delay estimates are biased which, in turn, biases the range estimates. The model explains the observed under-ranging of small arms firing positions during a field experiment. © *2002 Acoustical Society of America.* [DOI: 10.1121/1.1402619]

PACS numbers: 43.28.Tc, 43.60.Gk [LCS]

I. INTRODUCTION

With the wavefront curvature passive ranging technique,[1–3] a linear array consisting of three spatially separated microphones can be used to estimate the position (range and bearing) of a broadband acoustic source. The first step is to estimate the differential time of arrival (time delay) of the signal at each of the two adjacent sensor pairs using cross-correlation; the middle sensor is common to both sensor pairs. The second step is a nonlinear transformation that converts the time-delay estimates to the position estimate. The range estimate is much more sensitive than the bearing estimate to time-delay estimation errors.

There are many sources of error that affect the time-delay estimation process including the finite signal-to-noise ratio (SNR) at the output of each sensor, finite signal bandwidth and integration time, phase mismatch between the sensors (and their associated receiver circuitries), atmospheric turbulence effects on sound propagation, and multipath distortion of the received signals. Time-delay estimation errors due to noise and turbulence are inherently random in nature and are usually assumed to be zero mean. The lower bound on the error variance of the time-delay estimation errors due to noise alone has been considered elsewhere,[4] along with the dependence of the error variances for the bearing and range estimates on the time-delay estimate error variance and the source–sensor array geometry.[1] Recently, the theoretical performance bounds for acoustic direction-of-arrival arrays operating in atmospheric turbulence have been derived, and the degradation in system performance due to turbulence, rather than noise, has been studied using several atmospheric turbulence models.[5]

Obviously, any bias errors in the time-delay estimates (such as those due to phase mismatch between the sensors) will introduce bias into the range estimate. Even if the time delay estimate errors are zero mean, the range estimate is inherently biased due to its nonlinear relationship with the time-delay estimates. This bias has been shown to be positive[6] (range is overestimated) and it represents a fundamental limit on passive ranging using wavefront curvature. Range bias may also be caused by incorrect modeling of the propagation paths and sound-speed profile, and sensor positional errors. Using a three-element linear array, Carter[7] discussed the passive ranging errors due to bowing (noncollinearity) of the sensors, and Quazi and Lerro[8] investigated the combined effects of noise and intersensor spacing errors on bearing and range estimates.

This paper discusses the effect of multipath distortion of deterministic transient signals on time-delay estimation using cross correlation, and its impact on passive ranging using wavefront curvature. It is assumed that the multipath structure for each sensor is constant for a given source–sensor array geometry. A case study on the ranging of small arms fire is presented using real data. For wideband acoustic signals in a nondispersive sound propagation medium and in a multipath environment, the output of a cross correlator will be the superposition of a desired response and a number of its amplitude-scaled and time-shifted replicas [see Eq. (8)]. The desired response results from the cross correlation of the *direct path* signal components at the outputs of the two sensors. The peak of the desired response provides an estimate of the differential time of arrival of the acoustic signal (via the direct paths) at the two sensors. An extraneous response (replica) results from the cross correlation of either an indirect path component or the direct path component at the output of one sensor with an indirect path component at the output of the other sensor. Because of the interference among the desired and extraneous responses, the peak locations of the overall response will be different from those of the individual responses, and so the time-delay estimate will be biased. The bias is particularly significant when the main lobes of the extraneous responses merge with the main lobe of the desired response into a single broader distorted lobe in the correlogram. This will be the case if the multipath and direct path arrivals are unresolvable. Algorithms which suppress the effects of multipath propagation (sometimes referred to as *dereverberation* algorithms) have been developed for simple propagation channels with only a few resolvable multipaths.[9,10] Recently, a cepstral prefiltering technique has been proposed for time-delay estimation for zero-mean random signals (such as speech) under general reverberation conditions.[11] This technique is not applicable here as the impulsive sound associated with small arms fire is modeled as a deterministic transient signal which is received at each of the spatially distributed sensors along with its multipath replicas.

It is noted that time-delay estimation for deterministic transients in the presence of multipath distortion has been reported in the literature[12] for underwater applications, where the "time delay" is defined as the time-lag position of the maximum noise-free correlation magnitude. Such work compares the performances of different second-order and higher-order correlation methods against noise without considering the biasing effect of multipath distortion on the time-delay estimation. In other work,[13] a generic sonar model is used to determine how different sound-speed profiles and their subsequent effect on refraction and multipath structure affect the time-delay estimation in realistic ocean environments. Standard deviations of the time delay estimates are compared with those predicted using an isovelocity profile assumption. Synthetic microphone signals have been used to study the effects of room reverberation on the performance of the maximum likelihood cross correlator in time-delay estimation.[14] Unlike the present paper, the source signal is a continuous random signal rather than a deterministic transient.

The remainder of this paper is organized as follows. Section II discusses the (biasing) effect of multipath distortion of deterministic transient signals on time-delay estimation using cross correlation. Computer simulation results are presented for illustration. Section III discusses the subsequent impact of multipath distortion on passive ranging using wavefront curvature. Section IV presents a case study on passive ranging of small arms fire using real data. The theoretical development in the previous sections is used to explain the resulting range estimate errors. Section V gives the conclusions.

II. EFFECT ON TIME-DELAY ESTIMATION

A. Theory

The cross correlation of the outputs of a pair of sensors, $x_1(t)$ and $x_2(t)$, over an observation period of T is given by

$$r_{21}(\tau)=\int_{-T/2}^{T/2} x_1(t-\tau)x_2(t)\,dt. \tag{1}$$

If the acoustic source of interest emits a *deterministic transient* signal $s(t)$, and $n_1(t)$ and $n_2(t)$ represent uncorrelated additive zero-mean noise terms, then the outputs of the two sensors in a multipath-free environment can be modeled as

$$x_1(t)=s(t)+n_1(t), \tag{2a}$$

$$x_2(t)=\alpha s(t-D)+n_2(t), \tag{2b}$$

where α $(0<\alpha\leqslant 1)$ is an attenuation factor and D is the time delay between the two sensors. Substituting Eqs. (2a) and (2b) into Eq. (1) and assuming the observation period is infinitely long $(T\rightarrow\infty)$ so that the effect of noise is reduced to zero, the following expression is obtained for the cross-correlation function:

$$r_{21}(\tau)=\alpha\int_{-\infty}^{\infty} s(t-\tau)s(t-D)\,dt=\alpha R_{ss}(\tau-D), \tag{3}$$

where $R_{ss}(\tau)$ is the autocorrelation function of $s(t)$ defined by

$$R_{ss}(\tau)=\int_{-\infty}^{\infty} s(t-\tau)s(t)\,dt. \tag{4}$$

Since $R_{ss}(\tau)\leqslant R_{ss}(0)$, it follows from Eq. (3) that $r_{21}(\tau)$ attains its global maximum at $\tau=D$. Thus, the time-lag value τ that maximizes $r_{21}(\tau)$ is an estimate of the time delay D.

For a more complex scenario where the received signals contain multipath reflections of the source signal, a simple model for the outputs of the two sensors is given by

$$x_1(t)=s(t)+\sum_{k=1}^{K_1} a_{1k}s(t-\tau_{1k})+n_1(t), \tag{5a}$$

$$x_2(t)=\alpha\, s(t-D)+\sum_{k=1}^{K_2} a_{2k}s(t-\tau_{2k}-D)+n_2(t), \tag{5b}$$

where the two summation terms represent the multipath reflections of the source signal for the respective sensors, K_n is the number of indirect path (multipath) arrivals at sensor n, τ_{nk} is the time delay between the direct path arrival and the kth indirect path arrival at sensor n, and a_{nk} $(0<a_{nk}\leqslant 1)$ is the attenuation factor of the kth indirect path arrival at sensor n, $n=1,2$. A more rigorous model would convolve the source signal with the impulse response of each propagation path (prior to summation). However, the simple model suffices to explain the effect of multipath distortion on time-delay estimation and hence will be used in the subsequent discussion. The multipath structure for each sensor is assumed to be constant (that is, α, D, a_{nk}, τ_{nk}, K_n are constants) for a given source–sensor array geometry.

Equations (5a) and (5b) can be written as

$$x_1(t)=h_1(t)*s(t)+n_1(t), \tag{6a}$$

$$x_2(t)=h_2(t)*s(t-D)+n_2(t)=h_2(t-D)*s(t)+n_2(t), \tag{6b}$$

where $h_1(t)$ and $h_2(t-D)$ are the impulse responses of the propagation channels for the respective sensors, defined by

$$h_1(t)=\delta(t)+\sum_{k=1}^{K_1} a_{1k}\delta(t-\tau_{1k}), \tag{7a}$$

$$h_2(t) = \alpha\,\delta(t) + \sum_{k=1}^{K_2} a_{2k}\delta(t-\tau_{2k}). \tag{7b}$$

Substituting Eqs. (5a) and (5b) into Eq. (1), and assuming $T \to \infty$ gives

$$r_{21}(\tau) = \alpha\,R_{ss}(\tau - D) + \alpha\sum_{k=1}^{K_1} a_{1k}R_{ss}(\tau - D + \tau_{1k}) + \sum_{k=1}^{K_2} a_{2k}R_{ss}(\tau - D - \tau_{2k}) + \sum_{k=1}^{K_1}\sum_{l=1}^{K_2} a_{1k}a_{2l}R_{ss}(\tau - D - \tau_{2l} + \tau_{1k}). \tag{8}$$

Alternatively, Eq. (8) can be derived by first rewriting Eq. (1) as (assuming $T \to \infty$)

$$r_{21}(\tau) = \int_{-\infty}^{\infty} X_1^*(f)X_2(f)e^{j2\pi f\tau}\,df, \tag{9}$$

where $X_n(f)$ is the Fourier transform of $x_n(t)$, $n=1,2$, and $*$ denotes complex conjugation. Taking the Fourier transform of both sides of Eqs. (6a) and (6b) and substituting the results into Eq. (9) gives (noting that all the noise terms vanish)

$$r_{21}(\tau) = \int_{-\infty}^{\infty} H_1^*(f)H_2(f)|S(f)|^2 e^{j2\pi f(\tau - D)}\,df, \tag{10}$$

where $H_n(f)$ is the Fourier transform of $h_n(t)$, $n=1,2$. Expressions for $H_1(f)$ and $H_2(f)$ can be derived from Eqs. (7a) and (7b) as

$$H_1(f) = 1 + \sum_{k=1}^{K_1} a_{1k}e^{-j2\pi f\tau_{1k}}, \tag{11a}$$

$$H_2(f) = \alpha + \sum_{k=2}^{K_2} a_{2k}e^{-j2\pi f\tau_{2k}}. \tag{11b}$$

Substituting Eqs. (11a) and (11b) into Eq. (10) and evaluating the resulting integral (inverse Fourier transform) gives Eq. (8).

In Eq. (10), $H_1^*(f)H_2(f)$ forms the "frequency-weighting function" in the frequency-domain implementation of the generalized cross correlator[15] for a pair of sensor outputs consisting of *only* the direct path signals. In other words, $H_1(f)$ and $H_2(f)$ can be considered as the frequency responses of the prefilters for the two noise-free signals $s(t)$ and $s(t-D)$, respectively. Any phase mismatch between the two prefilters will mean $H_1^*(f)H_2(f)$ is complex and will result in the time-delay estimate being in error. Eliminating the phase mismatch requires $H_2(f)$ to be a real scalar multiple of $H_1(f)$. From Eqs. (11a) and (11b), this will be the case if

$$K_1 = K_2, \quad a_{2k} = \alpha\,a_{1k}, \quad \tau_{2k} = \tau_{1k}. \tag{12}$$

Equation (8) indicates that the cross-correlator output $r_{21}(\tau)$ is a superposition of the desired response $R_{ss}(\tau - D)$ and a number of its amplitude-scaled and time-shifted replicas. The actual shape of $r_{21}(\tau)$ depends on the relative amplitudes and time shifts of $R_{ss}(\tau - D)$ and its replicas, or equivalently, on the multipath structure for each sensor. Let B be the signal bandwidth, and define $\Delta_{kl} = D + \tau_{2l} - \tau_{1k}$ for $0 \leqslant k \leqslant K_1$ and $0 \leqslant l \leqslant K_2$, where $\tau_{10} = \tau_{20} = 0$. If $|\tau_{2l} - \tau_{1k}| > 1/B$, then $R_{ss}(\tau - \Delta_{kl})$ and $R_{ss}(\tau - D)$ will be resolved. When the dominant replicas overlap or merge with $R_{ss}(\tau - D)$ and the resulting $r_{21}(\tau)$ is asymmetric about D, the time-delay estimate can be *significantly* biased. This is usually the case when the multipath and direct path arrivals are unresolvable. The bias can be positive or negative depending on the multipath structure for each sensor.

B. Simulations

For the purpose of illustration, consider a deterministic transient signal consisting of a damped sinusoid

$$s(t) = u(t)e^{-\beta t}\sin 2\pi f_o t, \tag{13}$$

where $u(t)$ is the unit step function. The signal bandwidth B is approximately equal to β. The autocorrelation function of the signal is given by

$$R_{ss}(\tau) = \frac{1}{4}e^{-\beta|\tau|}\left(\frac{1}{\beta}\cos\omega_o\tau - \frac{\beta\cos\omega_o|\tau| - \omega_o\sin\omega_o|\tau|}{\beta^2 + \omega_o^2}\right), \tag{14}$$

where $\omega_o = 2\pi f_o$. By choosing suitable values for β and f_o, this deterministic transient signal can be made to resemble closely the observed acoustic waveform resulting from the discharge of a firearm.

Assume $f_o = 200$ Hz and $\beta = 4f_o/3$. Figures 1(a) and (b) show the signal waveform and its autocorrelation function, respectively. Now suppose there is only one indirect path arrival at each sensor, that is, $K_1 = K_2 = 1$. Let $D = 0$ and $\alpha = 0.9$. Figure 1(c) shows the cross correlogram $r_{21}(\tau)$ calculated using Eq. (8) for the multipath condition: $a_{11} = 0.8$, $a_{21} = 0.4$, $\tau_{11} = \tau_{21} = 0.4/\beta$. The bias in the time-delay estimate is -0.206 ms, which appears to be small, but it can have a large influence on passive ranging using wavefront curvature (as will be shown later).

The theoretical development assumes an infinitely long observation time that is not realizable in practice. With a finite observation time, the finite SNR at each sensor output leads to a random error component in the time-delay estimate. However, for the assumed noise model, this random error component is zero-mean. Thus, the bias in the time-delay estimate is due to multipath distortion alone. Computer simulation results are now presented to illustrate the effect of multipath distortion on time-delay estimation when the SNR, signal bandwidth, and observation time are finite.

The sensor outputs are sampled at 12 kHz. The source signal $s(t)$ is the damped sinusoid shown in Fig. 1(a). The additive noises $n_1(t)$ and $n_2(t)$ in Eq. (2) are modeled as uncorrelated zero-mean Gaussian white noise sequences bandlimited to f_o. These two noise sequences are generated independently using a Gaussian random number generator followed by a lowpass filter with a cutoff frequency of f_o. The SNR, defined here as the ratio of the *peak* signal power

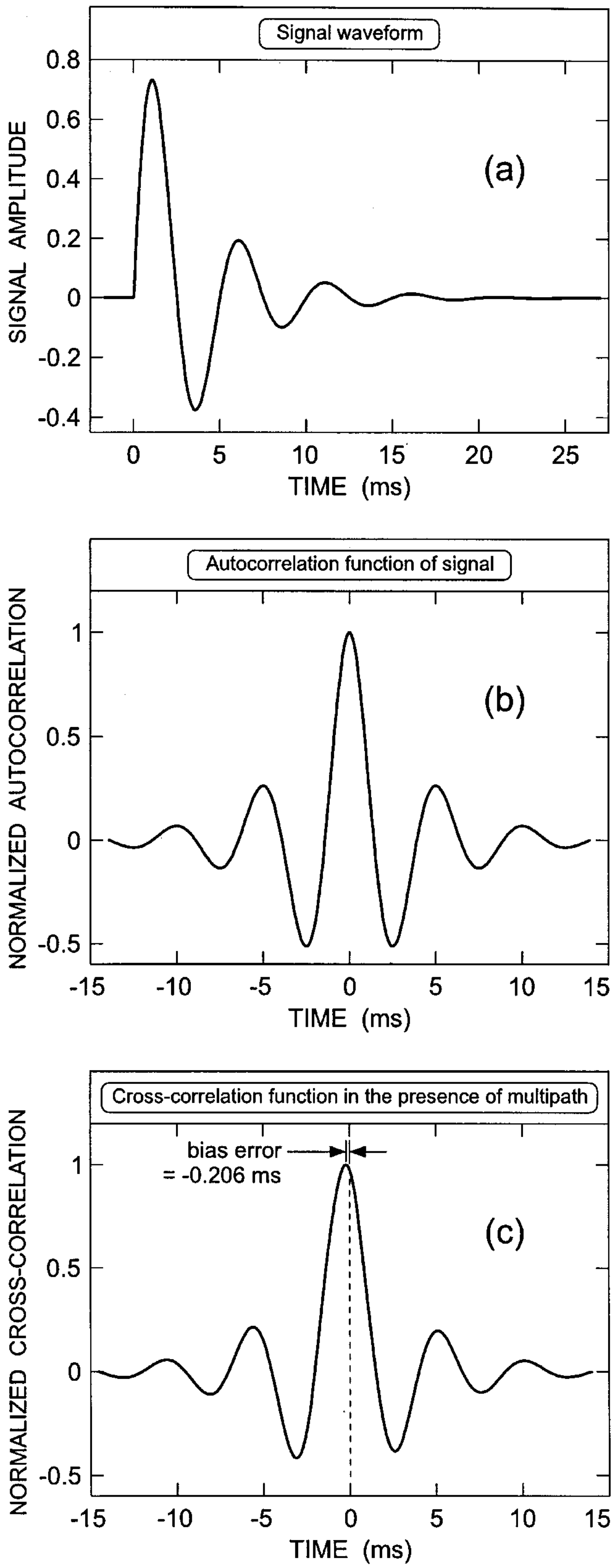

FIG. 1. (a) Waveform and (b) autocorrelation of a damped sinusoid signal with parameters: $f_o = 200$ Hz and $\beta = 4f_o/3$. (c) Cross-correlation $r_{21}(\tau)$ calculated using Eq. (8) for the signal in (a) with the multipath condition: $a_{11} = 0.8$, $a_{21} = 0.4$, $\tau_{11} = \tau_{21} = 0.4/\beta$; the time delay $D = 0$; and the relative attenuation factor $\alpha = 0.9$.

to the *average* noise power, is set to 40 dB. The multipath structure for each sensor is the same as that for Fig. 1(c). In a simulation run, two sensor output sequences each of length of 512 samples (which is much longer than the duration of the transient signal) are cross correlated. The time-delay estimate (which corresponds to the location of the cross-correlation peak) is refined using three-point quadratic interpolation[16] (also referred to as *inverse parabolic interpolation*[17]). The statistics of the time-delay estimates are compiled for a total of 100 000 runs. The left-hand side of Fig. 2 shows the histogram of the time-delay estimate data (*with* multipath distortion), which is found to be centered (biased) at a value of -0.206 ms, in agreement with the theoretical prediction for a single multipath arrival [see Fig. 1(c)]. Note that the random dispersion (or scatter) of the time-delay estimate data is due to noise alone. Also, the right-hand side of Fig. 2 shows the histogram of the time-delay estimate data *without* multipath distortion for which the bias is negligible.

In summary, for direct path sound propagation in the absence of multipath reflections, an unbiased estimate of the time delay is given by the time displacement at which the cross-correlation function attains its maximum value. The presence of multipath can distort the cross-correlogram resulting in the time delay estimate being biased.

III. IMPACT ON PASSIVE RANGING

A linear array consisting of three uniformly spaced sensors is used to estimate the range (and bearing) of an acoustic source using the wavefront curvature technique. The source–sensor array geometry is shown in Fig. 3, where the intersensor spacing is L and the range to the source from sensor n is R_n, $n = 1,2,3$. The time delay between sensor m and sensor n, D_{mn}, is defined as the differential time of arrival of the signal at the two sensors, that is, $D_{mn} = (R_m - R_n)/c$, where $m,n = 1,2,3$ and c is the isospeed of sound. Using the law of cosines and the fact that the sensors are collinear, it can be shown that the range to the source from the middle sensor (sensor 1) is given by[18]

$$R_1 = \frac{L^2 - c^2(D_{21}^2 + D_{31}^2)/2}{c(D_{21} + D_{31})}. \tag{15}$$

Also, it can be shown that the bearing of the source measured at the middle sensor with respect to the array axis is given by[18,19]

$$\theta_1 = \cos^{-1}\left\{ \frac{c}{2L}(D_{21} - D_{31}) + \frac{c^2}{4LR_1}(D_{21}^2 - D_{31}^2) \right\}. \tag{16}$$

If the sound speed and sensor spacings are known, then the source range and bearing can be estimated by replacing the time delays D_{21} and D_{31} by their estimates in Eqs. (15) and (16). In comparison with the range estimate, the bearing estimate is much less sensitive to time-delay estimation errors, especially when the source is far from the array. For example, the respective variances of the range and bearing estimate errors for a far-field source can be approximated by[1]

$$\sigma^2(\Delta R_1) \cong 2c^2(R_1/L_e)^4 \sigma^2(\Delta D_{32}), \tag{17a}$$

$$\sigma^2(\Delta \theta_1) \cong \tfrac{1}{6} c^2 (1/L_e)^2 \sigma^2(\Delta D_{32}), \tag{17b}$$

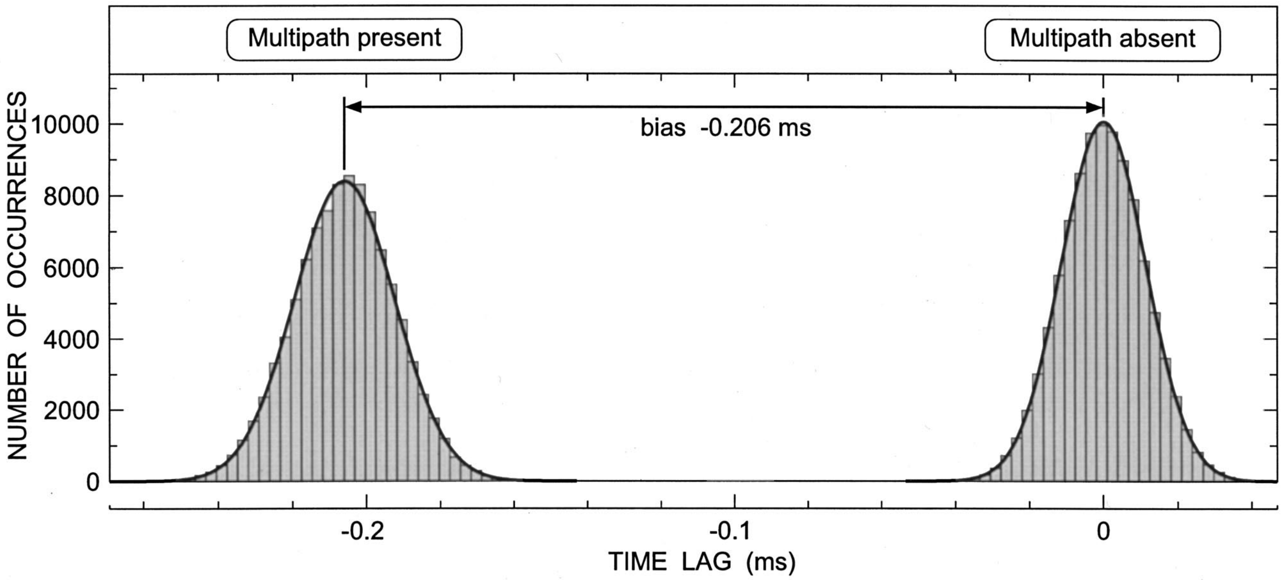

FIG. 2. Histograms of time-delay estimate data from computer simulations with and without multipath. SNR=40 dB. Left-hand side: multipath condition same as Fig. 1(c). Right-hand side: no multipath.

where $\sigma^2(\Delta D_{32})$ is the variance of the estimate error of D_{32}, and $L_e = L \sin\theta_1$ is the effective half-array length. These equations indicate that for a given $\sigma^2(\Delta D_{32})$, the variance of the range estimate error is larger than that of the bearing estimate error by a factor of $12R_1^4/L_e^2$. (Note that close agreement between theory and experiment for the variation of the range and bearing error variances with the effective half-array length has been reported recently for broadband sources of continuous sound in air.[3])

In general, the time-delay estimate error consists of a zero-mean random component and a bias term. When the estimates of the time delays D_{21} and D_{31} are unbiased (e.g., in the case where the errors are due to noise only), a second-order analysis has shown that the range estimate obtained using Eq. (15) is positively biased.[6] When the time-delay estimates are biased (e.g., in the case where the errors are due to both multipath distortion and noise), the ensemble average of the range estimate error (range bias) can be obtained using a first-order approximation, which is given by

$$E[\Delta R_1] \cong \frac{\partial R_1}{\partial D_{21}} \Delta D_{21}^b + \frac{\partial R_1}{\partial D_{31}} \Delta D_{31}^b, \tag{18}$$

where E is the ensemble average operator, ΔD_{n1}^b is the bias error in the estimate of D_{n1}, $n=2,3$, and the partial derivatives are evaluated at the true time delays. Using Eq. (15), it can be shown that

$$\frac{\partial R_1}{\partial D_{21}} = -\frac{c}{2} - \frac{L^2 - (cD_{21})^2}{c(D_{21}+D_{31})^2}, \tag{19a}$$

$$\frac{\partial R_1}{\partial D_{31}} = -\frac{c}{2} - \frac{L^2 - (cD_{31})^2}{c(D_{21}+D_{31})^2}. \tag{19b}$$

Since $D_{n1} \leq L/c$ for $n=2,3$, these partial derivatives are both negative. Thus, the effect of ΔD_{21}^b and ΔD_{31}^b on $E[\Delta R_1]$ will be either reinforced or canceled depending on whether they have the same sign or opposite signs. In the former case, $E[\Delta R_1]$ will have a sign opposite to those of ΔD_{21}^b and ΔD_{31}^b. Consequently, a sufficient (but not necessary) condition for the range estimate to be negatively (positively) biased is that the time-delay estimates are both positively (negatively) biased. To assess the effect of ΔD_{21}^b and ΔD_{31}^b on $E[\Delta R_1]$, consider the following numerical example. Let $R_1 = 190$ m, $\theta_1 = 90°$, $L = 5\sqrt{2}$ m, and $c = 346.5$ m/s. From the source–sensor array geometry, $D_{21} = D_{31} \cong 0.372$ ms. Suppose $\Delta D_{21}^b = \Delta D_{31}^b = 0.1$ ms due to multipath distortion. The first-order approximation gives $E[\Delta R_1] \cong -51$ m, or -27% of the actual range.

A similar first-order analysis can be performed for the bearing estimate. The ensemble average of the bearing estimate error (bearing bias) is approximately given by

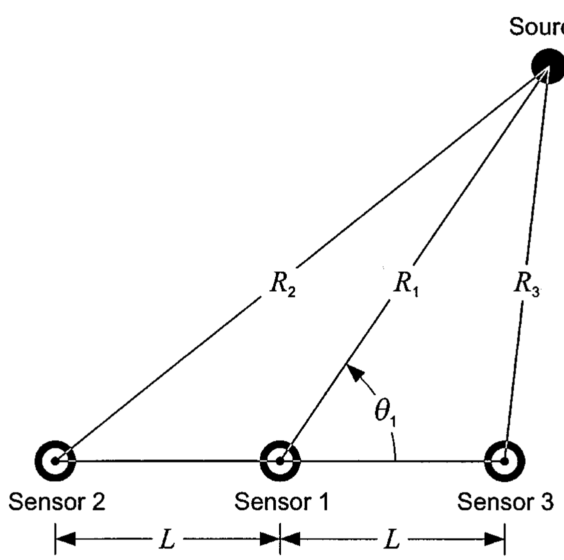

FIG. 3. Source–sensor array geometry for passive ranging using wavefront curvature.

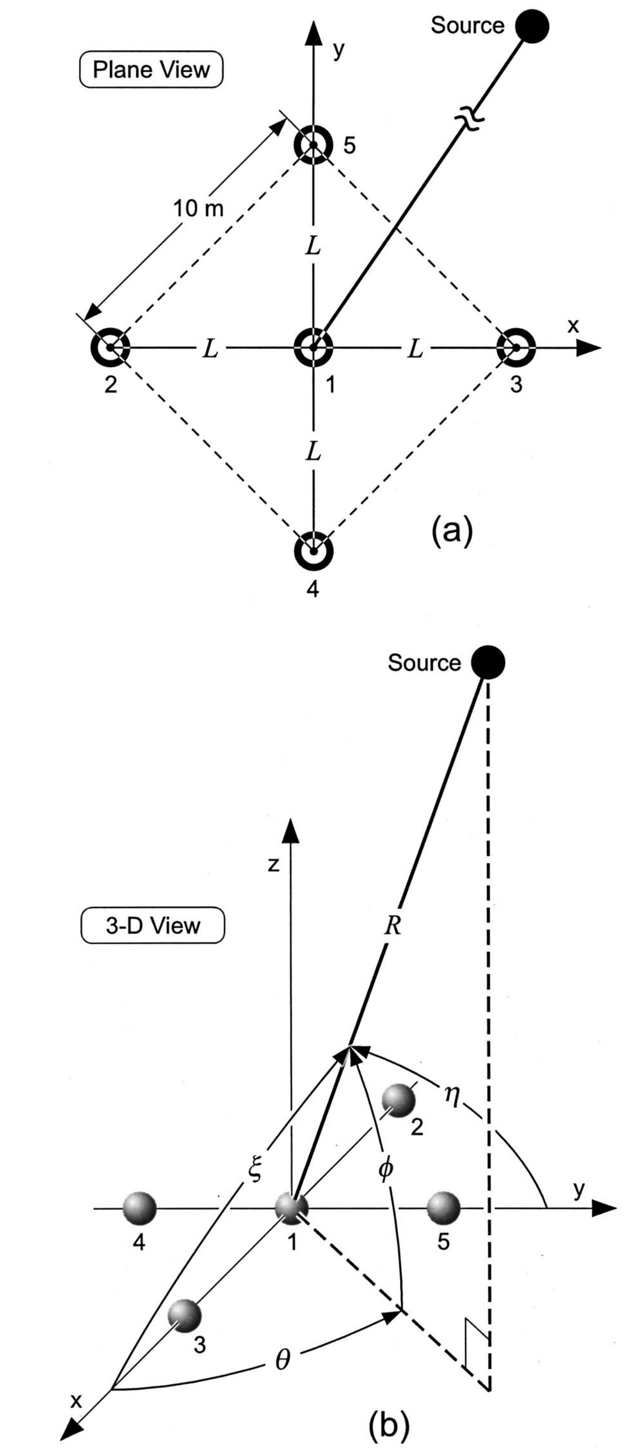

FIG. 4. (a) Plan view of sensor array geometry. (b) Spherical coordinates of source.

$$E[\Delta\theta_1] \cong \frac{\partial\theta_1}{\partial D_{21}}\Delta D_{21}^b + \frac{\partial\theta_1}{\partial D_{31}}\Delta D_{31}^b, \tag{20}$$

where the partial derivatives are evaluated at the true time delays. The expressions for these partial derivatives can be easily derived using Eq. (16). For a signal source far from the array, it can be shown that

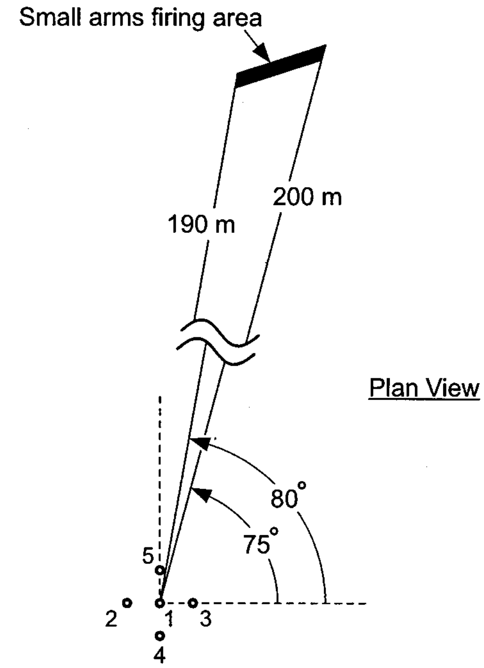

Sensor	Nominal position (x, y, z) (m)	Surveyed position (x, y, z) (m)
1	(0, 0, 0)	(0, 0, 0)
2	(-7.07, 0, 0)	(-6.90, 0, -1.55)
3	(7.07, 0, 0)	(6.87, 0.01, 1.67)
4	(0, -7.07, 0)	(-0.17, -7.03, 0.74)
5	(0, 7.07, 0)	(0.15, 7.04, -0.67)

FIG. 5. The source–sensor array configuration for small arms firing experiment.

$$E[\Delta\theta_1] \cong \frac{c}{2L_e}(\Delta D_{31}^b - \Delta D_{21}^b). \tag{21}$$

Therefore, ΔD_{21}^b and ΔD_{31}^b will have a smaller (larger) effect on $E[\Delta\theta_1]$ if they are of the same sign (opposite signs), which is the converse of the way that the signs of ΔD_{21}^b and ΔD_{31}^b affect $E[\Delta R_1]$. For the above numerical example where $\Delta D_{21}^b = \Delta D_{31}^b$, $E[\Delta\theta_1] \cong 0$; however, if ΔD_{21}^b becomes negative (while ΔD_{31}^b remains positive), then the first-order approximation for far-field sources [Eq. (21)] gives $E[\Delta\theta_1] \cong 0.28°$.

IV. CASE STUDY—PASSIVE RANGING OF SMALL ARMS FIRE

A. Array geometry

Equation (17) indicates that the range and bearing estimates from a three-sensor linear array become highly variable when the source direction approaches endfire (that is, as $\theta_1 \rightarrow 0$ or $\pi, L_e \rightarrow 0$). In practice, the coverage sector of the linear array is restricted to angles that are within $\pm 45°$ from broadside. Also, a linear array of omnidirectional sensors cannot resolve the left–right ambiguity of the source position. Installing a second linear array orthogonal to the first one provides full 360° coverage and resolves the left–right ambiguity problem. The resulting cross array is shown in Fig. 4(a), where there is a sensor at each corner of a 10 m $\times$ 10-m square and a sensor at the center. In other words, the two linear subarrays share a common sensor at the center, and both have an intersensor spacing of $L=5\sqrt{2}$ m. Subarray 1 (consisting of sensors 2, 1, 3) and subarray 2 (consisting of sensors 4, 1, 5) lie on the X axis and Y axis, respectively. Subarray 1 can be used to estimate the range R and bearing ξ (compound angle measured with respect to the positive X axis) which is related to the azimuth angle θ and elevation angle ϕ by $\cos\xi=\cos\phi\cos\theta$—see Fig. 4(b). Similarly, subarray 2 can be used to estimate the range R and bearing η (compound angle measured with respect to the positive Y axis) which is related to θ and ϕ by $\cos\eta=\cos\phi\sin\theta$—see Fig. 4(b).

B. Data acquisition and processing

The cross array is used to locate sources of small arms fire in a field experiment. Small arms fire generates both a shock wave and a blast wave. The shock wave originates from the bullet that travels at supersonic speed. For a supersonic projectile moving in a straight line at constant supersonic speed V, the surface of constant phase is a cone of apex angle given by[20] $\theta_V=2\theta_M=2\tan^{-1}[c/(V^2-c^2)^{-1/2}]$ where θ_M is the Mach angle. The blast wave originates from the muzzle whose position corresponds to the firing position; the acoustic energy is spread omnidirectionally and the surface of constant phase is a sphere. In the experiment, small arms are fired in an opposite direction to the sensor array and thus only muzzle blast waves are observed at the sensors. The source–sensor array geometry is shown schematically in Fig. 5, where there are five separate sources (firing positions) within the small arms firing area. The sources are distributed from 75° to 80° in azimuth at a 3° elevation angle, which corresponds to 75.02°–80.01° in ξ and 10.43°–15.29° in η. The distances to the sources from the central sensor (sensor 1) vary from 190 to 200 m. There are 69 separate firings from the five firing positions over a period of a few minutes, with the sequence of fire being random. The acoustic signal from each source is modeled as a deterministic transient, similar to the damped sinusoid shown in Fig. 1(a). The receivers are calibrated prior to measurement to ensure the effect of phase mismatch between the receiver channels is negligible. The sensor outputs are sampled at a frequency of $f_s=12$ kHz and the data are stored for subsequent processing.

Each of the firing events is automatically detected by testing the recorded data of the central sensor against a preselected threshold. For each detected event, a data sequence consisting of 2048 samples, centered at the time of detection, is extracted from the recorded data for each of the five sensors. Figure 6 shows segments of the typical data sequences extracted from the five sensors. Multipath propagation is evident as indicated by the small echoes in each received signal waveform following the strong (distorted) transient. A data length of 2048 samples is chosen for the following reasons: (i) Since the duration of the transient signal is about 100

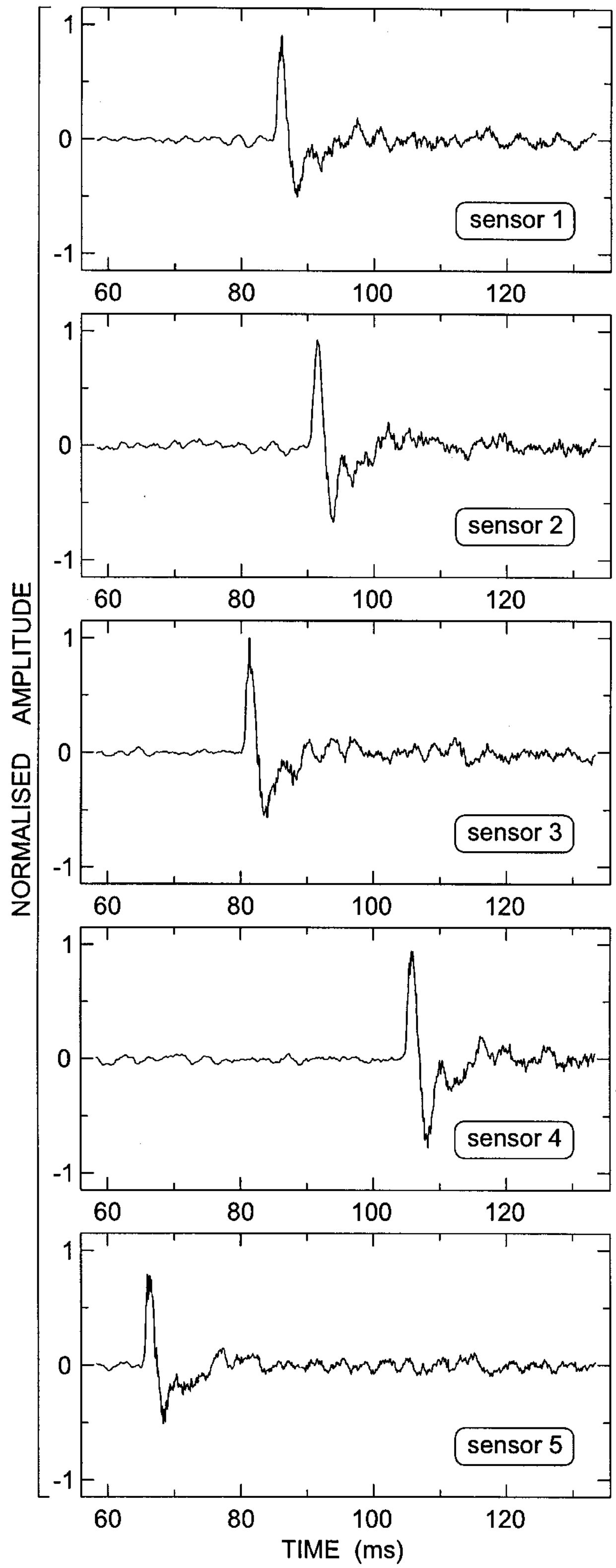

FIG. 6. Typical waveforms observed at the outputs of the five sensors during a firing event. The relative time delays are used to estimate the position of the source.

sampling periods and the maximum time delay is $(L/c)f_s \cong 245$ sampling periods, the data length ensures the complete transient signal is present in the data sequence for each sensor. (ii) The data length is short enough to avoid two transient signals, corresponding to two separate firing events,

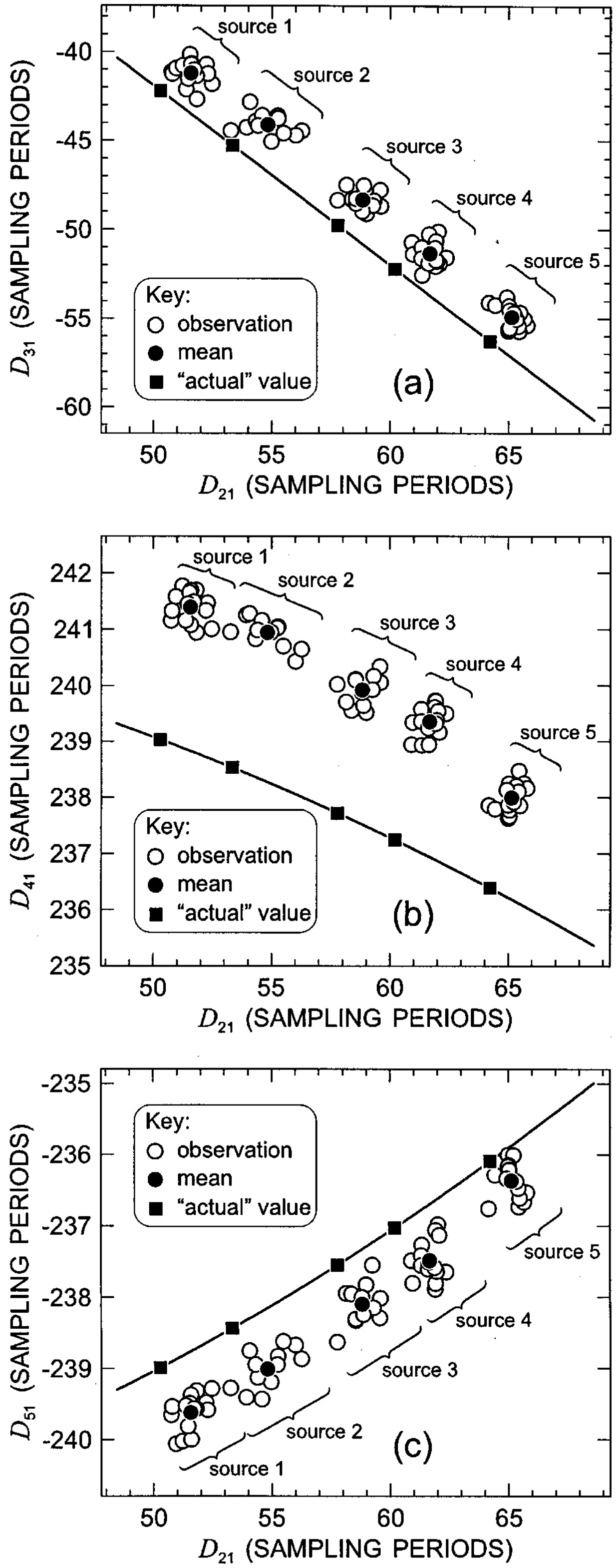

FIG. 7. Time delay for sensor pair $(n,1)$ versus time delay for sensor pair (2,1). (a) $n=3$. (b) $n=4$. (c) $n=5$. Unfilled circles: experimental data. Filled circles: centers of experimental data clusters. Squares: "actual" time delays. Solid line: theoretical relationship.

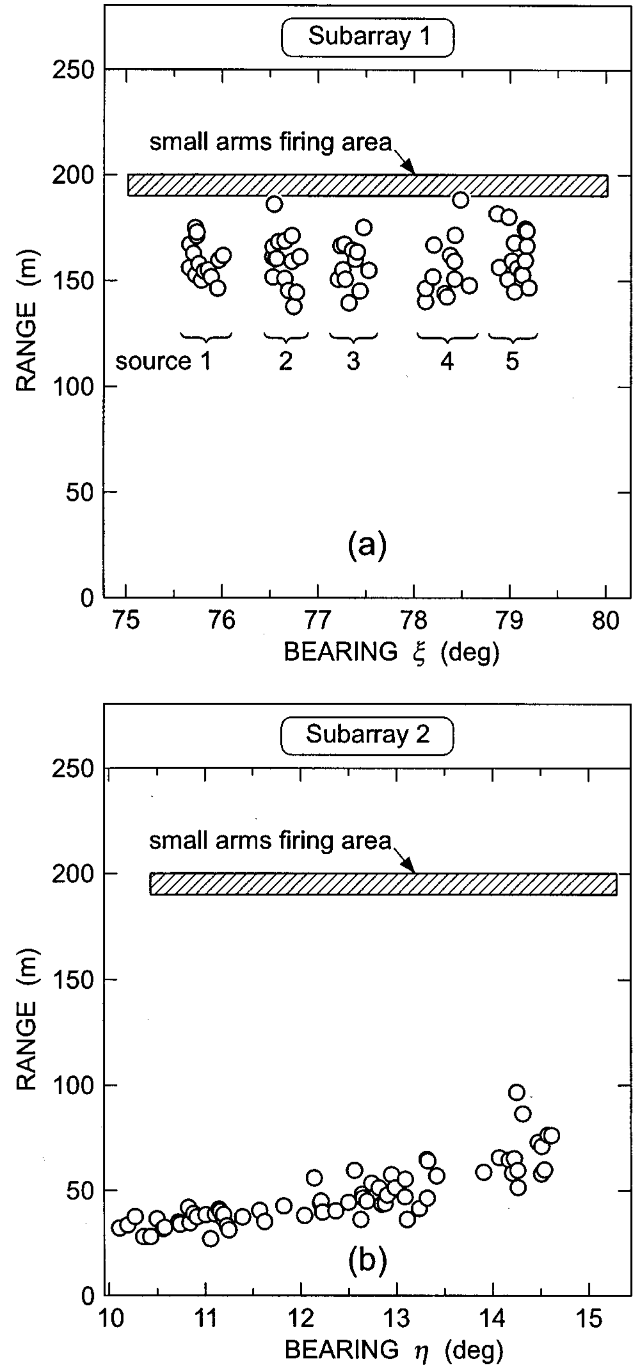

FIG. 8. Experimental results on range and bearing estimates obtained with (a) subarray 1 and (b) subarray 2.

being present in a data sequence. (iii) Most of the noise is below 200 Hz, so the data length is much longer than the noise correlation time of 60 sampling periods.

The data sequence of the central sensor is then cross correlated with the corresponding data sequence for each of the other four sensors. The cross correlation is implemented in the frequency domain using the fast Fourier transform (FFT). A rectangular spectral window from 50 to 500 Hz is used in the cross-correlation processing. The time delay estimates are refined using three-point quadratic interpolation.

C. Results and discussions

Figures 7(a)–(c) show the time-delay estimate data for the respective sensor pairs (3,1), (4,1), and (5,1) as the ordinates of the white-filled circles with the abscissas corresponding to the time-delay estimate data for sensor pair (2,1)—see Fig. 5 for the numbering of the sensors. These

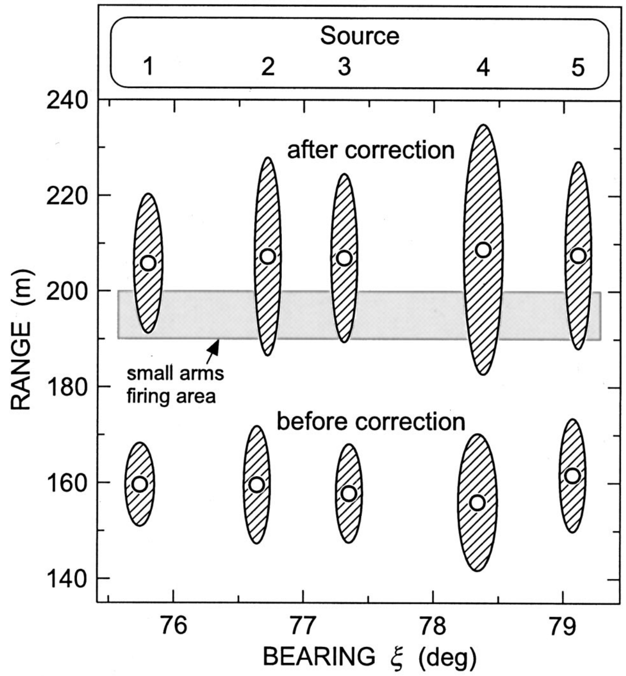

FIG. 9. Error ellipse representation for the uncertainty in the bearing and range estimates obtained with subarray 1 for each source. Lower row of ellipses—before correction of bias errors in time-delay estimates. Upper row of ellipses—after correction of bias errors in time-delay estimates.

graphical plots show the correlation between the time-delay estimate data for the 69 firing events. It can be seen that the data points are distributed into five clusters, which correspond to five separate sources. The center of each cluster, which is located at the mean coordinates of the data points of that cluster, is shown in the diagrams as a black-filled circle.

Using the wavefront curvature technique and assuming that the speed of sound in air $c=346.5$ m/s, the ranges and bearings of the five sources are estimated with subarray 1 (sensors 2,1,3) and then with subarray 2 (sensors 4, 1, 5). The results are shown in Figs. 8(a) and (b), respectively, with the shaded rectangle representing the small arms firing area. Note that the bearing refers to either ξ or η, depending on whether subarray 1 or 2 is used to locate the source. The five sources are resolved in Fig. 8(a) but not in Fig. 8(b). For subarray 1, all the bearing estimates lie within the limits of the actual source bearing distribution, which is not the case for subarray 2. All the source ranges are underestimated, especially those estimated using subarray 2. The source localization performance of subarray 2 is poor because the direction of each source is near the array's endfire direction. Conversely, subarray 1 provides better results because the direction of each source is near the array's broadside direction. With subarray 1, the mean value of the range estimate data for each source is less than 161 m, which is 29 m less than the lower limit of the actual source range distribution (190 m). With subarray 2, the mean values of the range estimate data for the five sources vary from 35 to 65 m, with the smaller value corresponding to the source with the smaller bearing η. In both cases, the range estimates for the five sources are all negatively biased.

The lower part of Fig. 9 shows a set of bearing-range

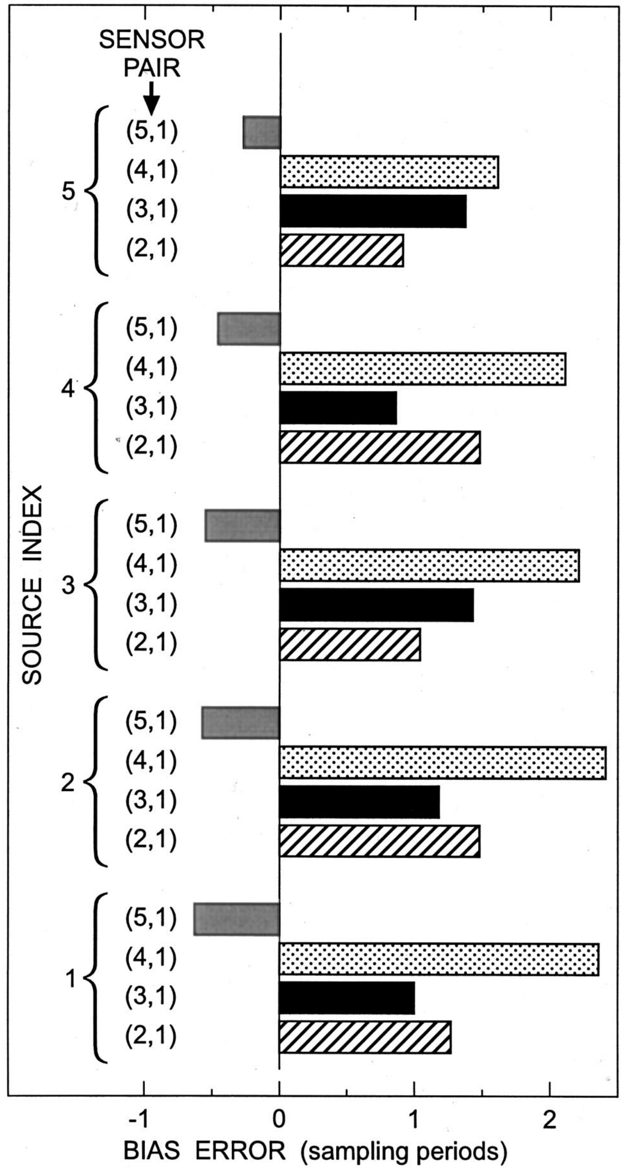

FIG. 10. The magnitude and sign of the bias in the time-delay estimate for each sensor pair and for each source.

error ellipses (labeled "before correction") which represents the uncertainty in the bearing and range estimates obtained with subarray 1 for the five sources. For each source, the mean values of the bearing and range estimate data define the center of the ellipse and the standard deviations of the bearing and range estimate data determine the half-lengths of the ellipse's minor and major axes, respectively.

Since the sensors are positioned on irregular ground on the side of a hill, one possible cause of the negative range bias is the noncollinearity of the sensor positions. To investigate this, the positions of the sensors are accurately surveyed (see the inset in Fig. 5) and then the surveyed (actual) sensor positions are used to calculate the time delays for all the sensor pairs for different source positions: $190\leqslant R\leqslant 200$ m, $75°\leqslant\theta\leqslant 80°$, $\phi=3°$. Finally, the calculated time delays for subarrays 1 and 2 are used, in turn, to estimate the source range and bearing using Eqs. (15) and (16), assuming the sensors of each subarray are collinearly located at their

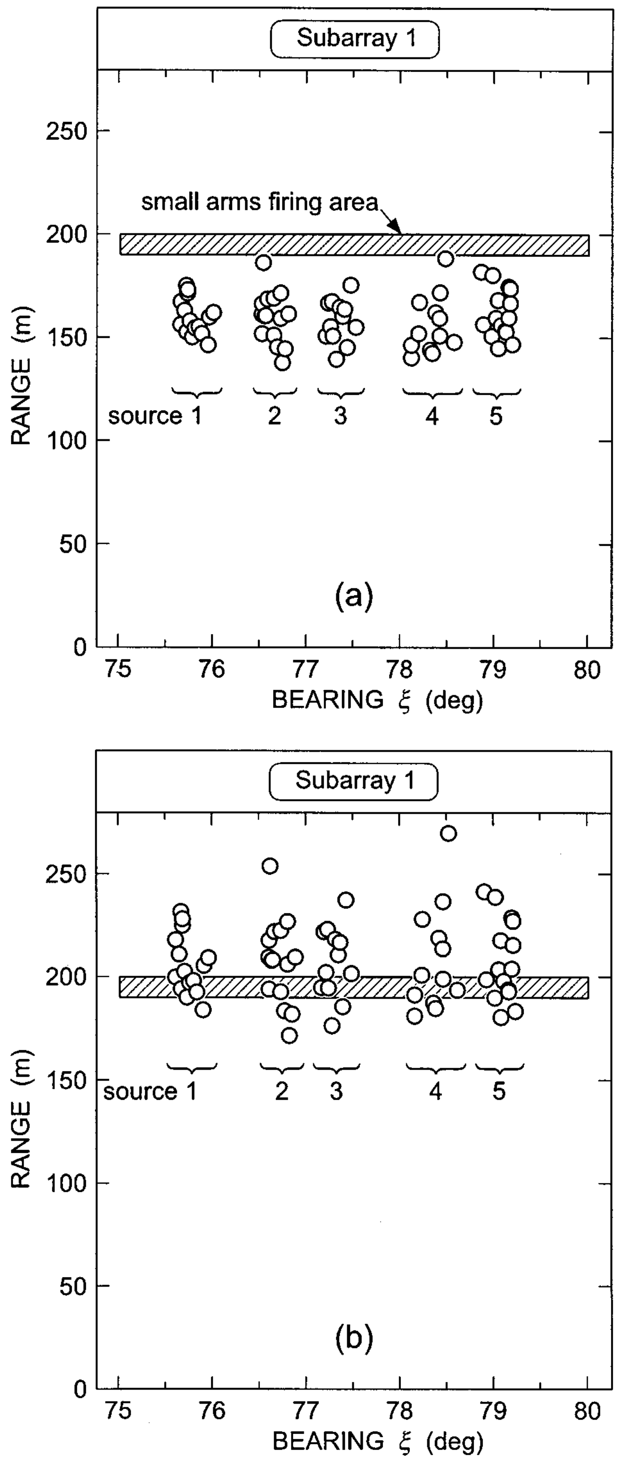

FIG. 11. Experimental results on range and bearing estimates obtained with subarray 1. (a) Before correction of bias errors in time-delay estimates. (b) After correction of bias errors in time-delay estimates.

nominal positions. For subarray 1, the source ranges are found to be overestimated by 9–12 m and the bearings ξ underestimated by 0.34°–0.47°. The source ranges are also overestimated using subarray 2. This over-ranging rules out the possibility of sensor noncollinearity being the cause of the negative range bias.

The negative range bias can also be caused by time-delay estimation errors. However, this cannot be due to the zero-mean random error components of the time-delay estimates, which include those due to noise and turbulence, as the resulting range bias would be positive.[6] As shown in Sec. III, the bias errors in the time-delay estimates can result in a negatively biased range estimate. Since the phase and amplitude responses of all the receiver channels are matched, the most probable cause of the bias errors in the time-delay estimates is multipath distortion of the received signals. The solid lines in Figs. 7(a)–(c) represent the time delays calculated previously using the *surveyed* sensor positions for sensor pairs (3,1), (4,1), and (5,1) versus those for sensor pair (2,1), respectively. Only the results for a source range of 195 m are shown because the results for the other source ranges (190–200 m) are almost the same. Each of the solid lines represents the relationship between the time delay for sensor pair (2,1) and the time delay for one of the other sensor pairs as the source bearing ξ varies between 75.02°–80.01° at a fixed range of 195 m. By comparing the results with the time-delay estimate data (indicated by the circles), it is clear that the time-delay estimates for the five sources are all biased.

To estimate the bias errors in the time-delay estimates for each source requires knowledge of the actual time delays, which in turn requires knowledge of the actual source range and bearing ξ. However, the source locations are only known to be within a certain area, therefore only the "best estimate" time delays can be obtained for each source, which are referred to here as the "actual" values. For a given source bearing, the variations in the time delays for the five sensor pairs are relatively small (in comparison with the bias errors) as the source range changes from 190 to 200 m. Therefore, the midvalue of the source range distribution (195 m) is used to obtain the actual time delays for each source. The source bearing is determined by assuming that bias errors in the time-delay estimates have negligible effect on the bearing estimate, and that the bearing estimate error is mainly due to noncollinearity of the sensors. The mean value of the bearing estimate data obtained previously for each source [see Fig. 8(a)] is corrected for the error due to sensor noncollinearity (0.34°–0.47°). Using the corrected mean value of the bearing estimate data and the midvalue of the source range distribution, the actual time delays for all the sensor pairs are then calculated for each source; these are shown as black-filled squares in Figs. 7(a)–(c). The bias in each time-delay estimate is calculated by subtracting the actual time delay from the mean of the corresponding time-delay estimate data. The above process is summarized in the Appendix. Figure 10 shows the magnitude and sign of the bias in the time-delay estimate for each pair of sensors and for each source.

By removing the bias from the time-delay estimate data for each sensor pair of subarray 1, and then using the resulting data in Eqs. (15) and (16), new estimates of the range and bearing are calculated for each source; the results are shown in Fig. 11(b). The original range-bearing data of Fig. 8(a) are reproduced as Fig. 11(a) for comparison purposes. The mean values of the new range estimate data for all five sources are larger than the midvalue (195 m) of the actual source range distribution by 11–14 m (5.6%–7.2%). The mean values of the new bearing estimate data are within

0.08° of the corresponding mean values of the original bearing estimate data shown in Fig. 11(a). (Thus, removing the bias errors from the time-delay estimates does not cause a significant change in the bearing estimate, and this justifies the previous assumption that the bias errors in the time-delay estimates have negligible effect on the bearing estimate.) Also, the upper part of Fig. 9 shows a set of bearing-range error ellipses (labeled "after correction") for the new range and bearing estimate data for each source. By comparing the upper and lower rows of error ellipses in Fig. 9, it can be seen that after correction of the bias errors in the time-delay estimates, the standard deviations of the range estimates are increased while those of the bearing estimates remain unchanged. This observation can be explained by the fact that after the bias correction, the variances of the time-delay estimates remain the same but the subarray "sees" the sources at longer ranges, and so the variances of the range estimates become larger. Equation (17a) suggests that the ratio of the standard deviations of the range estimates before, and after, the bias correction is approximately equal to the squared ratio of the average range estimates before, and after, the bias correction. This proposition has been verified numerically using the results shown in Fig. 9. On the other hand, the variances of the bearing estimates are independent of the source ranges according to Eq. (17b).

V. CONCLUSIONS

The passive ranging performance of the wavefront curvature method for a transient signal source in a multipath environment is degraded when the multipath and direct path arrivals are unresolvable because the time delays estimated using the cross-correlation technique are biased. Bias errors in the time-delay estimates result in the range estimates also being biased. In a field experiment conducted to locate sources of small arms fire, multipath distortion provides an explanation why the source ranges are significantly underestimated. Correction of the bias errors in the time-delay estimates results in a substantial improvement in the source range estimates. Once the bias errors in the time-delay estimates are removed, the source ranges are slightly overestimated by 11–14 m (5.6%–7.2%) due to the noncollinearity of the sensor positions.

ACKNOWLEDGMENTS

The authors gratefully acknowledge the contributions of their colleague Lionel Criswick to this paper and the field trial support provided by the Commanding Officer (Lieutenant Colonel Rik Modderman) and the soldiers of 1 RISTA Regiment, Australian Army.

APPENDIX: BIAS CORRECTION

The time-delay estimate data and the bearing estimate data obtained using subarray 1 are shown in Figs. 7 and 8(a), respectively. Denote the time-delay estimates for the sensor pair $(n,1)$ and the mth source as $\hat{D}_{n1,m}$, and their mean value as $\overline{\hat{D}}_{n1,m}$, where $1 \leqslant m \leqslant 5$ and $2 \leqslant n \leqslant 5$, the mean value of the bearing estimates for the mth source as $\overline{\hat{\xi}}_m$, and the time delay for the sensor pair $(n,1)$ and the source at range R and bearing ξ as $D_{n1}(R,\xi)$. The procedure used to correct the bias errors in the time delay estimates for source localization is summarized below.

(1) Using the surveyed sensor positions, calculate the time delays $D_{n1}(\overline{R},\xi_k)$ for all sensor pairs for different source positions: $75.02° \leqslant \xi_k \leqslant 80.01°$ and $\overline{R} = 195$ m.

(2) Substituting $D_{21}(\overline{R},\xi_k)$ and $D_{31}(\overline{R},\xi_k)$ into Eq. (16), obtain the source bearing estimates $\tilde{\xi}_k$ and the corresponding bias errors $\Delta\xi_k^b = \tilde{\xi}_k - \xi_k$. (Here, the bias errors are due to noncollinearity of the sensors in subarray 1.)

(3) For the mth source $(1 \leqslant m \leqslant 5)$, find $k(m) = \arg\min_k |\tilde{\xi}_k - \overline{\hat{\xi}}_m|$ and then compute $\overline{\hat{\xi}}_m^c = \overline{\hat{\xi}}_m - \Delta\xi_{k(m)}^b$. (This step removes errors in $\overline{\hat{\xi}}_m$ that are due to sensor noncollinearity, and $\overline{\hat{\xi}}_m^c$ is treated as the "actual" bearing of the mth source.)

(4) Using the surveyed sensor positions, calculate the "actual" time delays $D_{n1}(\overline{R},\overline{\hat{\xi}}_m^c)$ for all sensor pairs and all sources. (Here, $\overline{R}$ is treated as the actual source range.)

(5) Subtract $D_{n1}(\overline{R},\overline{\hat{\xi}}_m^c)$ from $\overline{\hat{D}}_{n1,m}$ to get the corresponding bias errors $\Delta D_{n1,m}^b$ in the time-delay estimates.

(6) Subtract $\Delta D_{n1,m}^b$ from $\hat{D}_{n1,m}$ to remove the bias errors in the time-delay estimates and then use the results for $n = 2,3$ in Eqs. (15) and (16) to estimate the source range and bearing.

[1] G. C. Carter, "Time delay estimation for passive sonar signal processing," IEEE Trans. Acoust., Speech, Signal Process. **29**, 463–470 (1981).
[2] C. Hassab, B. W. Guimond, and S. C. Nardone, "Estimation of location and motion parameters of a moving source observed from a linear array," J. Acoust. Soc. Am. **70**, 1054–1061 (1981).
[3] B. G. Ferguson, "Variability in the passive ranging of acoustic sources in air using a wavefront curvature technique," J. Acoust. Soc. Am. **108**, 1535–1544 (2000).
[4] G. C. Carter, *Coherence and Time Delay Estimation* (IEEE, Piscataway, NJ, 1993).
[5] D. K. Wilson, "Performance bounds for acoustic direction-of-arrival arrays operating in atmospheric turbulence," J. Acoust. Soc. Am. **103**, 1306–1319 (1998).
[6] K. B. Theriault and R. M. Zeskind, "Inherent bias in wavefront curvature ranging," IEEE Trans. Acoust., Speech, Signal Process. **29**, 524–527 (1981).
[7] G. C. Carter, "Passive ranging errors due to receiving hydrohpone uncertainty," J. Acoust. Soc. Am. **65**, 528–530 (1979).
[8] A. H. Quazi and D. T. Lerro, "Passive localization using time delay estimates with sensor positional errors," J. Acoust. Soc. Am. **78**, 1664–1670 (1985).
[9] H. C. So, P. C. Ching, K. C. Ho, and Y. T. Chan, "A novel constrained algorithm for delay estimation in the presence of multipath transmission," Proc. IEEE Int. Conf., Acoust., Speech, Signal Processing, 157–160 (1993).
[10] J. O. Smith and B. Friedlander, "Adaptive multipath delay estimation," IEEE Trans. Acoust., Speech, Signal Process. **33**, 812–822 (1985).
[11] A. Stephenne and B. Champagne, "A new cepstral prefiltering technique for esitmating time delay under reverberant conditions," Signal Process. **59**, 253–266 (1997).
[12] L. A. Pflug, E. I. George, W. I. Juliette, L. F. Robert, and J. H. Leclere, "Time-delay estimation for determininstic transients using second- and higher-order correlations," J. Acoust. Soc. Am. **94**, 1385–1399 (1993).
[13] E. Robinson and A. H. Quazi, "Effect of sound-speed profile on differen-

tial time-delay estimation,'' J. Acoust. Soc. Am. **77**, 1086–1090 (1985).
[14] B. Champagne, S. Bedard, and A. Stephenne, ''Performance of time delay estimation in the presence of room reverberation,'' IEEE Trans. Speech Audio Process. **4**, 148–152 (1996).
[15] C. H. Knapp and G. C. Carter, ''The generalized correlation method for estimation of time delay,'' IEEE Trans. Acoust., Speech, Signal Process. **24**, 320–327 (1976).
[16] G. Jacovitti and G. Scarano, ''Discrete time techniques for time delay estimation,'' IEEE Trans. Signal Process. **41**, 525–533 (1993).
[17] W. H. Press, S. A. Teukolsky, W. T. Vetterling, and B. O. Flannery, *Numerical Recipes in C,* 2nd ed. (Cambridge University Press, Cambridge, 1995).
[18] J. C. Hassab, ''Passive bearing estimation of a broad-band souce,'' IEEE Trans. Acoust., Speech, Signal Process. **32**, 426–431 (1984).
[19] G. C. Carter and P. B. Abraham, ''Estimation of source motion from time delay and time compression measurements,'' J. Acoust. Soc. Am. **67**, 830–832 (1980).
[20] A. D. Pierce, *Acoustics—An Introduction to its Physical Principles and Applications* (Acoustical Society of America, New York, 1994), pp. 606–615.

Quantifying uncertainty in geoacoustic inversion. I. A fast Gibbs sampler approach

Stan E. Dosso
School of Earth and Ocean Sciences, University of Victoria, Victoria, British Columbia V8W 3P6, Canada

(Received 9 March 2001; revised 7 August 2001; accepted 30 August 2001)

This paper develops a new approach to estimating seabed geoacoustic properties and their uncertainties based on a Bayesian formulation of matched-field inversion. In Bayesian inversion, the solution is characterized by its posterior probability density (PPD), which combines prior information about the model with information from an observed data set. To interpret the multi-dimensional PPD requires calculation of its moments, such as the mean, covariance, and marginal distributions, which provide parameter estimates and uncertainties. Computation of these moments involves estimating multi-dimensional integrals of the PPD, which is typically carried out using a sampling procedure. Important goals for an effective Bayesian algorithm are to obtain efficient, unbiased sampling of these moments, and to verify convergence of the sample. This is accomplished here using a Gibbs sampler (GS) approach based on the Metropolis algorithm, which also forms the basis for simulated annealing (SA). Although GS can be computationally slow in its basic form, just as modifications to SA have produced much faster optimization algorithms, the GS is modified here to produce an efficient algorithm referred to as the fast Gibbs sampler (FGS). An automated convergence criterion is employed based on monitoring the difference between two independent FGS samples collected in parallel. Comparison of FGS, GS, and Monte Carlo integration for noisy synthetic benchmark test cases indicates that FGS provides rigorous estimates of PPD moments while requiring orders of magnitude less computation time. [DOI: 10.1121/1.1419086]

PACS numbers: 43.30.Pc, 43.60.Pt [DLB]

I. INTRODUCTION

The problem of determining seabed geoacoustic properties from measured ocean acoustic fields has received considerable attention in recent years (e.g., Refs. 1–20). Geoacoustic inversion represents a strongly nonlinear inverse problem for which a direct solution is not available. A matched-field approach to this problem can be formulated by assuming a discrete model $\mathbf{m}=\{m_i, i=1,M\}$ representing the unknown geoacoustic and geometric parameters, with lower and upper bounds for each parameter, and by defining an error function $E(\mathbf{m})$ that quantifies the mismatch between the measured acoustic field and modeled replica fields. Substantial effort has been applied to the problem of estimating $\mathbf{m}$ by minimizing $E(\mathbf{m})$ via nonlinear optimization methods such as simulated annealing[1–6] (SA), genetic algorithms[6–13] (GA), and hybrid inversion algorithms.[14–18] However, relatively little work has been applied to the problem of estimating the uncertainties of these parameters in a rigorous manner.

For linear inverse problems with Gaussian-distributed random errors on the data, the probability distribution for the model parameters is also Gaussian, and straightforward analytic expressions can be derived to map the data uncertainties into parameter uncertainties based on the inverse operator for the problem.[21] For nonlinear problems (such as geoacoustic inversion), Gaussian data uncertainties do not imply Gaussian parameter uncertainties, and no general analytic solution is available. However, Bayesian inference theory provides a formalism for estimating parameter uncertainties for nonlinear inverse problems based on sampling theory. In a Bayesian formulation, the solution to an inverse problem is characterized by the posterior probability density (PPD) of the unknown model parameters. The PPD combines prior information about the model with the information provided by an observed data set. The data information is expressed in terms of the likelihood function defined by the statistical distribution of data errors. To interpret the multi-dimensional PPD in a useful manner, the state of information about model parameters is typically quantified in terms of moments of the PPD, such as the posterior mean, marginal probability distributions, and covariances, which provide parameter estimates and uncertainties. Estimating these moments involves computing multi-dimensional integrals of the PPD, which is usually carried out using sampling methods such as Monte Carlo integration or importance sampling. How to obtain unbiased sampling of these PPD moments and verify that the estimates have converged are key issues in Bayesian inversion.[22,23] Good overviews of the application of Bayesian inference to geophysical inverse problems are given by Tarantola[24] and Sen and Stoffa.[25,26]

Gerstoft[7] first applied a Bayesian formalism to compute marginal distributions and covariances for the geoacoustic inverse problem, using the final generations from several parallel GA inversions as the model sample and a semi-empirical probability weighting. This approach, which has been widely adopted (e.g., Refs. 8–11), provides a relative comparison between parameter estimates and an indication of the convergence of the optimization algorithm; however, as it is based on an empirically normalized data likelihood function, the resulting PPD is imprecise.[13] In an important work, Gerstoft and Mecklenbräuker[13] developed a rigorous likelihood-based approach to PPD estimation for geoacoustic inversion. In the applications they considered, fast estimation of PPD moments was deemed more important than precision,[13] and the PPD was again sampled using the final generation of GA inversions. This provided an efficient algorithm, sampling the PPD as a by-product of standard matched-field inversion. However, as the sampling distribution of GA is unknown, an unknown bias is introduced into the estimates.[13] In particular, the convergent properties of GA likely overestimate the PPD values around near-optimal models,[25,26] and a general convergence criterion was not applied.

In the present paper, the likelihood-based formulation for geoacoustic inversion of Gerstoft and Mecklenbräuker[13] is adopted, but a different approach is developed to sample the PPD, resulting in estimated distributions of a significantly different character. In particular, a Gibbs sampler (GS) approach is applied which provides an unbiased, asymptotically convergent sampling of the PPD.[24,25] Similar to SA optimization, GS is based on the Metropolis algorithm, first formulated to estimate integral properties of atomic systems in statistical mechanics.[27] In its basic form, GS can be computationally slow. However, just as modifications to the basic SA algorithm have produced much faster optimization algorithms (e.g., Refs. 4, 18, 28), the basic GS is modified here to greatly increase efficiency. These modifications, including rotating the parameter space to minimize correlations and adaptively determining effective perturbation sizes, lead to a practical algorithm referred to as the fast Gibbs sampler (FGS). Since the marginal PPDs are of primary interest for parameter uncertainties, a rigorous convergence criterion is developed based on intercomparison of the cumulative marginal distributions of two independent FGS samples collected in parallel.

The FGS algorithm is applied here to synthetic benchmark test cases[20] in which the statistical distribution of the data errors is known exactly. In such cases, Monte Carlo integration of the PPD and a standard GS approach converge asymptotically to the solution, and may be considered to provide numerical "ground truth," provided a consistent convergence criterion is applied. Comparisons of FGS, GS, and Monte Carlo results for these cases are used to validate the FGS approach. A companion paper[29] validates the FGS approach for a broadband, shallow-water geoacoustic experiment, including the attendant problem of estimating the data uncertainties (including both measurement and theory error).

The remainder of this paper is organized as follows. Sections II A and II B provide overviews of Bayesian inversion and principal approaches to PPD integration, while Sec. II C describes the GS approach and Sec. II D summarizes the Bayesian formulation for matched-field inversion. Section III develops the FGS algorithm, and Sec. IV compares FGS, GS, and Monte Carlo methods for synthetic benchmark test cases. Finally, Sec. V summarizes and discusses the results of this work.

II. THEORY

A. Bayesian formulation of inverse theory

This section summarizes the Bayesian formulation of inverse theory and the principal approaches applied to estimate integral properties of the PPD; more complete treatments can be found in Refs. 22–26. Let $\mathbf{m}$ and $\mathbf{d}$ represent model and data vectors, respectively, with elements m_i and d_i considered to be random variables. Bayes' rule, which follows from the definition of conditional probabilities, may be expressed

$$P(\mathbf{m}|\mathbf{d}) = P(\mathbf{d}|\mathbf{m})P(\mathbf{m})/P(\mathbf{d}), \tag{1}$$

where $P(\mathbf{m}|\mathbf{d})$ represents the conditional probability density function (PDF) of $\mathbf{m}$ given $\mathbf{d}$, $P(\mathbf{d}|\mathbf{m})$ is the conditional PDF of $\mathbf{d}$ given $\mathbf{m}$, $P(\mathbf{m})$ is the PDF of $\mathbf{m}$ independent of $\mathbf{d}$, and $P(\mathbf{d})$ is the PDF of $\mathbf{d}$. As the denominator of Eq. (1) is independent of $\mathbf{m}$, it can be considered a constant factor and the equation written as

$$P(\mathbf{m}|\mathbf{d}) \propto P(\mathbf{d}|\mathbf{m})P(\mathbf{m}). \tag{2}$$

When the observed data $\mathbf{d}^{\mathrm{obs}}$ are substituted into $P(\mathbf{d}|\mathbf{m})$, the result is interpreted as a function of $\mathbf{m}$, known as the likelihood function $L(\mathbf{d}^{\mathrm{obs}}|\mathbf{m})$, and Eq. (2) becomes

$$P(\mathbf{m}|\mathbf{d}^{\mathrm{obs}}) \propto L(\mathbf{d}^{\mathrm{obs}}|\mathbf{m})P(\mathbf{m}). \tag{3}$$

In Eq. (3), $P(\mathbf{m})$ is known as the prior PDF, representing the available *a priori* information of the model independent of the data. The likelihood function $L(\mathbf{d}^{\mathrm{obs}}|\mathbf{m})$ represents the information provided by the data. The PDF $P(\mathbf{m}|\mathbf{d}^{\mathrm{obs}})$ represents the state of information of $\mathbf{m}$ given both the prior information and the data and is known as the PPD.

The likelihood function is determined by the form of the data and the statistical distribution of the data errors, including both measurement and theory errors. In practice, it is often difficult to obtain an independent estimate of the error statistics, and simplifying assumptions are required to proceed. For the common assumption of unbiased Gaussian errors, the likelihood function is of the form

$$L(\mathbf{d}^{\mathrm{obs}}|\mathbf{m}) \propto \exp[-E(\mathbf{m})], \tag{4}$$

where $E(\mathbf{m})$ represent the error function appropriate to the state of available information (specific error functions are considered in Sec. II D). Hence, the PPD, Eq. (3), becomes

$$P(\mathbf{m}|\mathbf{d}^{\mathrm{obs}}) \propto \exp[-E(\mathbf{m})]P(\mathbf{m}), \tag{5}$$

or, when normalized,

$$P(\mathbf{m}|\mathbf{d}^{\mathrm{obs}}) = \frac{\exp[-E(\mathbf{m})]P(\mathbf{m})}{\int \exp[-E(\mathbf{m}')]P(\mathbf{m}')d\mathbf{m}'}, \tag{6}$$

where the domain of integration spans the multi-dimensional model space.

From the point of view of Bayesian theory, the PPD $P(\mathbf{m}|\mathbf{d}^{\mathrm{obs}})$ represents the general solution to the inverse problem. However, to interpret the PPD for multi-dimensional problems requires the computation of integral properties (moments) of the distribution, such as the posterior mean model, model covariance matrix, and marginal probability distribution for parameter m_i, which are defined, respectively, as

$$\langle \mathbf{m} \rangle = \int \mathbf{m}' P(\mathbf{m}'|\mathbf{d}^{\text{obs}}) d\mathbf{m}', \tag{7}$$

$$\mathbf{C_M} = \int (\mathbf{m}' - \langle \mathbf{m}' \rangle)(\mathbf{m}' - \langle \mathbf{m}' \rangle)^T P(\mathbf{m}'|\mathbf{d}^{\text{obs}}) d\mathbf{m}', \tag{8}$$

$$P(m_i|\mathbf{d}^{\text{obs}}) = \int \delta(m_i' - m_i) P(\mathbf{m}'|\mathbf{d}^{\text{obs}}) d\mathbf{m}', \tag{9}$$

where δ represents the Dirac delta function and higher-dimensional marginal distributions are defined in a manner similar to Eq. (9). These moments are of the general integral form

$$I = \int f(\mathbf{m}') P(\mathbf{m}'|\mathbf{d}^{\text{obs}}) d\mathbf{m}', \tag{10}$$

and provide estimates of the model parameters and their uncertainties. An alternative to using the posterior mean, Eq. (7), as parameter estimates is the maximum *a posteriori* (MAP) solution, defined as the model that maximizes $P(\mathbf{m}|\mathbf{d}^{\text{obs}})$. MAP estimates can be obtained efficiently using optimization methods (i.e., they do not require integration of the PPD), and are commonly used in geoacoustic inversion, although the mean has also proved useful.[30,31] In cases where the PPD is unimodal and symmetric the mean and MAP estimates coincide. For multi-modal or significantly asymmetric distributions, the MAP solution can provide more meaningful parameter estimates; however, the MAP estimate by itself provides no indication of the uncertainties or covariances associated with the model parameters.

B. Numerical integration of the PPD

In practice, much of the effort in Bayesian inversion is typically directed at evaluating multi-dimensional integrals of the PPD of the form of Eq. (10) in an efficient manner. This is typically carried out using sampling methods; this section provides a brief overview of principal sampling approaches.[22–26]

1. Monte Carlo methods

The Monte Carlo approach is based on drawing models at random from a uniform distribution over the domain of integration. By drawing models $\mathbf{m}_i, i=1,Q$ and calculating the posterior probability for each according to

$$P(\mathbf{m}_i|\mathbf{d}^{\text{obs}}) = \frac{\exp[-E(\mathbf{m}_i)]P(\mathbf{m}_i)}{\sum_{j=1}^{Q} \exp[-E(\mathbf{m}_j)]P(\mathbf{m}_j)}, \tag{11}$$

the desired integral quantities can be estimated as

$$I \approx \frac{\mathcal{M}}{Q} \sum_{i=1}^{Q} f(\mathbf{m}_i) P(\mathbf{m}_i|\mathbf{d}^{\text{obs}}), \tag{12}$$

where $\mathcal{M}$ represents the M-dimensional volume of integration. Monte Carlo methods provide an unbiased, asymptotically convergent estimate of the integral. In practice, convergence is established when a significant increase in sample size does not significantly change the estimate, or by intercomparing two Monte Carlo samples collected in parallel.

2. Importance sampling

Monte Carlo methods draw models from a uniform distribution over the model space; however, if large values of the integrand are concentrated in localized regions of the space, many of these models will not contribute significantly to the integral. The method of importance sampling is based on preferentially drawing samples from the regions that contribute most to the integral (i.e., important regions), thereby reducing the variance of the estimator for a given sample size. Let $g(\mathbf{m})$ denote the nonuniform sampling distribution from which Q models $\mathbf{m}_i$ are drawn, with the normalization condition

$$\int g(\mathbf{m}') d\mathbf{m}' = 1. \tag{13}$$

Equation (10) can then be written

$$\begin{aligned} I &= \int \left[\frac{f(\mathbf{m}') P(\mathbf{m}'|\mathbf{d}^{\text{obs}})}{g(\mathbf{m}')} \right] g(\mathbf{m}') d\mathbf{m}' \\ &\approx \frac{1}{Q} \sum_{i=1}^{Q} \frac{f(\mathbf{m}_i) P(\mathbf{m}_i|\mathbf{d}^{\text{obs}})}{g(\mathbf{m}_i)}. \end{aligned} \tag{14}$$

Note that the Monte Carlo method, Eq. (12), represents the special case of importance sampling, Eq. (14), with a uniform sampling function $g(\mathbf{m}) = 1/\mathcal{M}$.

Of obvious interest is the importance sampling function that produces the minimum-variance estimate for I; it can be shown that this is given by[22,32]

$$g(\mathbf{m}) = \frac{|f(\mathbf{m})| P(\mathbf{m}|\mathbf{d}^{\text{obs}})}{\int |f(\mathbf{m}')| P(\mathbf{m}'|\mathbf{d}^{\text{obs}}) d\mathbf{m}'}. \tag{15}$$

Unfortunately, this distribution cannot be applied in practice. Equation (15) contains an integral in the denominator that requires evaluation of $E(\mathbf{m})$ at all points in the model space; however, if this exhaustive enumeration is carried out there is clearly no need for importance sampling. The goal of importance sampling then is to choose a simple, practical function $g(\mathbf{m})$ that approximates Eq. (15), however crudely, while satisfying the normalization Eq. (13).[22,32] Section II C describes a sampling procedure (GS) which corresponds to a natural and elegant choice of importance sampling function, related to Eq. (15), that avoids enumeration of the model space. Finally, note that the importance-sampling estimate Eq. (14) is unbiased. However, if an unknown generating distribution $g(\mathbf{m})$ is employed that cannot be properly corrected for in the denominator of Eq. (14), an unknown bias will be introduced into the estimate.

3. Multiple MAP estimation

One approach to preferentially sampling important regions of the model space is to employ multiple runs of a global optimization method such as SA or GA to generate the Q model samples $\mathbf{m}_i$, an approach referred to as multiple MAP estimation.[25,26] The integral Eq. (10) can then be estimated according to

$$I \approx \sum_{i=1}^{Q} f(\mathbf{m}_i) P(\mathbf{m}_i|\mathbf{d}^{\text{obs}}), \tag{16}$$

where $P(\mathbf{m}_i|\mathbf{d}^{\text{obs}})$ is evaluated via Eq. (11). Since the generating distributions of GA and of SA with the usual fast cooling (i.e., cooling without achieving equilibrium at each temperature) are not known, the integral estimate cannot be corrected for the sampling function $g(\mathbf{m})$ in the denominator of Eq. (14), and the estimates will be biased [in terms of importance sampling, Eq. (16) assumes $g(\mathbf{m}_i)=1/Q$]. Further, since global optimizations concentrate their numerical effort in the regions of model space around optimal values, without correcting for the generating function, the integral will be overestimated in these regions.[25,26] Sen and Stoffa[25,26] recommend using all models sampled throughout a number of global optimization runs; applications that use only the final models could further overestimate the integral around optimal regions.

C. Statistical mechanics and the Gibbs sampler

The method of Gibbs sampling (GS) provides an efficient approach to unbiased sampling of PPD integrals in Bayesian inversion.[22–26] This approach, and the related method of SA, are based on an analogy with thermodynamic processes as described by statistical mechanics. According to this theory, the probability that a system of many atoms is in a state $\mathbf{m}$ with energy $E(\mathbf{m})$ is given by the Boltzmann or Gibbs distribution

$$P_G(\mathbf{m}) = \frac{\exp[-E(\mathbf{m})/T]}{\Sigma \exp[-E(\mathbf{m})/T]}, \tag{17}$$

where T represents the absolute temperature and the summation is over all possible states. Note that for nonzero T the probability distribution extends over all states, so that (unlike in classical physics) even at a low temperature there is a finite probability of the system being in a high-energy state. Further, transitions or perturbations to the system that increase E are permitted, although they are less probable than transitions that decrease E. Metropolis *et al.*[27] devised a simple scheme to simulate the behavior of a system in equilibrium by repeatedly perturbing the system and accepting perturbations for which a uniform random number ξ drawn from the interval [0, 1] satisfies the condition

$$\xi \leq \exp[-\Delta E/T]. \tag{18}$$

This procedure, known as the Metropolis algorithm (MA), accepts all perturbations that decrease E while accepting some perturbations that increase E with a probability that decreases with T. Gradually lowering the temperature while applying the MA simulates the evolution of the system to its ground state which represents the global minimum-energy configuration: this defines the optimization method of Metropolis SA.

Markov-chain analysis[23,26] of the MA verifies that after a large number of perturbations at a constant temperature, the equilibrium distribution is given by the Gibbs' PDF Eq. (17). Hence, the MA is referred to as a GS. Note that the MA samples from the normalized Gibbs' PDF without explicitly computing the denominator of Eq. (17) (known as the partition function in statistical mechanics) which involves an exhaustive enumeration of $E(\mathbf{m})$ over the model space. This achieves one of the requirements for importance sampling as discussed in Sec. II B. Further, comparison of the Gibbs PDF $P_G(\mathbf{m})$ from Eq. (17) with the PPD $P(\mathbf{m}|\mathbf{d}^{\text{obs}})$ from Eq. (6) indicates that the two are identical at temperature $T=1$ for the case of uniform prior distributions (the standard case in matched-field inversion). Hence, in the limit of a large number of perturbations, the MA at $T=1$ provides an unbiased sampling of the PPD $P(\mathbf{m}|\mathbf{d}^{\text{obs}})$. Employing the MA to generate $P(\mathbf{m}|\mathbf{d}^{\text{obs}})$ as the importance sampling function, i.e., $g(\mathbf{m})=P(\mathbf{m}|\mathbf{d}^{\text{obs}})$ in Eq. (14), the integral estimate simplifies to

$$I \approx \frac{1}{Q}\sum_{i=1}^{Q} f(\mathbf{m}_i). \tag{19}$$

Thus, unbiased estimates are computed directly from the set of Q models, with no requirement to weight the samples by estimated probabilities. For cases where the function $f(\mathbf{m})$ in I is approximately constant, the importance sampling function $g(\mathbf{m})=P(\mathbf{m}|\mathbf{d}^{\text{obs}})$ should provide a close approximation to the optimal (but unattainable) choice given by Eq. (15). However, even for cases where $f(\mathbf{m})$ is nonconstant, the GS provides an effective approach to estimating I. Section III describes the algorithm developed here for efficient GS as applied to geoacoustic inversion; however, first the adaptation of Bayesian inverse theory to the matched-field problem is briefly considered.

D. Application to matched-field inversion

A Bayesian approach was applied to matched-field inversion by Gerstoft and Mecklenbräuker;[13] for completeness, the approach is summarized here (in a somewhat different notation). Matched-field methods are generally based on matching the relative amplitude and phase of frequency-domain acoustic fields measured at an array of sensors. In practical cases, the data uncertainties (measurement and theory errors) are not well known, and simplifying approximations are required. Assuming complex, Gaussian-distributed random errors on N data at a single frequency, the likelihood function is given by[13,22]

$$L(\mathbf{m}) = \frac{1}{\pi^N|\mathbf{C_D}|}\exp[-(\mathbf{d}^{\text{obs}}-\mathbf{d}(\mathbf{m}))^{\dagger}\mathbf{C_D}^{-1}(\mathbf{d}^{\text{obs}}-\mathbf{d}(\mathbf{m}))], \tag{20}$$

where $\mathbf{C_D}$ is the data covariance matrix and † represents conjugate transpose. For multi-frequency data $\mathbf{d}_f^{\text{obs}}, f=1,F$ with errors assumed to be spatially uncorrelated and uncorrelated from frequency to frequency with an identical spectrum for each sensor, the data covariance at the fth frequency is $\mathbf{C_D}=\nu_f\mathbf{I}$, where the variance ν_f depends only on frequency and $\mathbf{I}$ is the identity matrix. The likelihood function for incoherent processing then becomes

$$L(\mathbf{m}) = \prod_{f=1}^{F} \frac{1}{(\pi\nu_f)^N}\exp[-|\mathbf{d}_f^{\text{obs}}-\mathbf{d}_f(\mathbf{m})|^2/\nu_f]. \tag{21}$$

However, Eq. (21) is not appropriate for matched-field applications, since the difference $|\mathbf{d}_f^{\text{obs}} - \mathbf{d}_f(\mathbf{m})|^2$ requires the modeled data $\mathbf{d}_f(\mathbf{m})$ include the complex source strength (magnitude and phase), which is generally not known. To remove this dependency, the replica data are taken to be

$$\mathbf{d}_f(\mathbf{m}) = S_f \mathbf{w}_f(\mathbf{m}), \tag{22}$$

where $\mathbf{w}_f(\mathbf{m})$ is the field computed via a numerical propagation model and S_f represents the complex source strength. Setting $\partial L / \partial S_f = 0$ to maximize L leads to

$$S_f = \mathbf{w}_f^\dagger(\mathbf{m}) \mathbf{d}_f^{\text{obs}} / |\mathbf{w}_f(\mathbf{m})|^2, \tag{23}$$

and hence to the likelihood function

$$L(\mathbf{m}) = \prod_{f=1}^{F} \frac{1}{(\pi \nu_f)^N} \exp[-B_f(\mathbf{m}) |\mathbf{d}_f^{\text{obs}}|^2 / \nu_f], \tag{24}$$

where $B_f(\mathbf{m})$ represents the (normalized) Bartlett mismatch function defined

$$B_f(\mathbf{m}) = 1 - \frac{|\mathbf{w}_f^\dagger(\mathbf{m}) \mathbf{d}_f^{\text{obs}}|^2}{|\mathbf{d}_f^{\text{obs}}|^2 |\mathbf{w}_f(\mathbf{m})|^2}. \tag{25}$$

From Eq. (24), the error function to be used in the PPD, Eq. (6), is given by

$$E(\mathbf{m}) = \sum_{f=1}^{F} B_f(\mathbf{m}) |\mathbf{d}_f^{\text{obs}}|^2 / \nu_f, \tag{26}$$

consisting of the sum of the Bartlett mismatches at each frequency, weighted by the ratio of the squared data magnitude to its variance. For experimentally measured acoustic data, an independent estimate of the data variance is often not available. In this case, under the assumption of independent, identically distributed errors at each sensor, a maximum-likelihood estimate of the variance $\hat{\nu}_f$ can be derived from the data themselves by setting $\partial L / \partial \nu_f = 0$ and evaluating the result at the maximum-likelihood model.[13] This approach is considered in detail for a shallow-water geoacoustic experiment in a companion paper.[29]

III. THE FAST GIBBS SAMPLER ALGORITHM

This section describes the FGS algorithm developed here for efficient sampling of the PPD for geoacoustic inversion. The algorithm applies the GS, described in Sec. II C, to the matched-field inverse problem, as formulated in Sec. II D. In particular, the error function $E(\mathbf{m})$ given by Eq. (26) is used in the MA at temperature $T=1$ to accumulate a large sample of models. From this sample, the GS importance sampling, Eq. (19), is applied to compute the desired PPD moments, as defined by Eqs. (7)–(9). For a sufficiently large sample of models, this procedure is guaranteed to converge to the desired PPD moments. Although GS provides an attractive approach to estimating integral moments of the PPD, in its basic form the method can be computationally slow. However, just as modifications to classical Metropolis SA have been developed which greatly increase the speed of convergence, the efficiency of the standard GS can be greatly improved. The FGS is based on several modifications, described below, which greatly increases the computational speed without affecting the estimates, as illustrated by synthetic examples in Sec. IV.

As described above, the FGS is based on applying the MA at $T=1$; however, the algorithm typically converges much faster by initiating at high T, cooling rapidly to $T=1$, and subsequently accumulating the sample (i.e., models accepted during the cooling stage are not retained in the sample). This procedure allows the actual sampling to begin at models that are reasonably probable. Initiating the sampling from an arbitrary model directly at $T=1$ generally results in the algorithm proceeding slowly through a sequence of improbable models until more probable regions of the model space are found. To negate the presence of these improbable models in the sample can require a much larger total sampling than would otherwise be needed. A similar approach was used by Basu and Fraser[33] to sample at the critical temperature in SA.

In addition to the initial cooling stage, several methods used to accelerate the convergence of SA are adapted to the same end for the FGS algorithm. These methods are based on determining parameter perturbation sizes and directions that provide an efficient search of the model space. For instance, a common approach in SA is to reduce the perturbation size as the inversion proceeds, thereby avoiding a prohibitively high perturbation rejection rate at low temperatures. For example, the method of fast simulated annealing[28] draws parameter perturbations from a Cauchy distribution about the current values, and decreases the distribution width linearly with temperature. Alternatively, the hybrid inversion method of adaptive simplex simulated annealing[18] decreases the size of Cauchy-distributed perturbations in an adaptive manner, based on the running mean of recently accepted perturbations. Since the asymptotic convergence of GS is based on random parameter perturbations uniformly distributed over the parameter bounds, uniform distributions are employed for all parameter perturbations in the FGS algorithm, with distribution widths (maximum perturbation sizes) determined adaptively as follows. Throughout the cooling stage of FGS (i.e., as $T \rightarrow 1$), the distribution width for each parameter is taken to be a factor k_1 times the maximum of the last K accepted perturbations (typically $k_1 = 2$ and $K=100$ during cooling). Let the distribution width for parameter m_i when $T=1$ is reached be given be u_i. Thereafter in sampling at $T=1$, the distribution width for parameter m_i is taken to be the greater of u_i or k_2 times the largest perturbation accepted to that point in sampling at $T=1$. The factor $k_2 = 2$ is typically adopted, although after a suitably large number of accepted perturbations (e.g., 1000), it can be reduced to a value closer to unity (e.g., $k_2 = 1.2$). In practice, it is found that stable maximum perturbation sizes are obtained relatively quickly, and remain essentially unchanged through the majority of the sampling. This procedure is designed to apply uniformly distributed perturbations of width approximately equivalent to the maximum perturbation size accepted with a noninfinitesimal probability at $T=1$. If this goal is achieved, the results of FGS should be virtually identical to standard GS (with a much lower rejection rate and resultant increase in efficiency), although the convergence proof for GS does not strictly apply. All results obtained to date (including those given in the following section) suggest that this approach works well; however, unusual cases could exist where it is not adequate (this is generally true for all heuristic methods, including SA and GA). The solution then is to use a larger value for k_2, at the cost of greater computational expense.

The direction of perturbations in model space is another important factor determining the efficiency of the sampling, particularly for inverse problems involving correlated or coupled parameters which produce narrow valleys in the error function E oriented obliquely relative to the parameter axes in model space. Since model perturbations in GS are typically applied parallel to the parameter axes, sampling along such valleys can be very inefficient (GA, which do not sample along parameter axes, may be less sensitive to correlations). To address this problem for SA inversion, Collins and Fishman[4] rotated the parameter space by applying an orthogonal transformation that diagonalized the covariance matrix of the error function gradient (estimated from a preliminary sampling of the model space). Parameter perturbations were then applied in the rotated (transformed) space, with the results rotated back to the original (physical) parameters. A similar procedure can be applied in FGS, although it is preferable to diagonalize the model covariance matrix, since it can be estimated directly from the sampling at $T=1$ (a similar procedure was applied by Jaschke and Chapman[19] in sampling at the critical temperature). It is found that a reasonably small preliminary sampling (e.g., 1000 accepted perturbations for each parameter) is sufficient, since the covariance matrix $\mathbf{C_M}$, Eq. (8), typically converges quite rapidly,[25,26] and since only a reasonable approximation to $\mathbf{C_M}$ is required to substantially improve sampling efficiency. The rotation matrix is determined from the eigenvector decomposition

$$\mathbf{C_M}=\mathbf{A}\,\mathbf{\Lambda}\,\mathbf{A}^T, \tag{27}$$

where $\mathbf{\Lambda}$ is a diagonal matrix with elements λ_i consisting of the eigenvalues of $\mathbf{C_M}$, $\mathbf{A}$ is an orthonormal matrix with columns $\mathbf{a}_i$ consisting of the corresponding eigenvectors, and T denotes transpose. The rotated parameters $\tilde{m}_i$ are determined by applying the orthogonal transformation

$$\tilde{\mathbf{m}}=\mathbf{A}^T\mathbf{m}. \tag{28}$$

Perturbations are applied in the rotated space where the parameter axes align with the dominant correlation directions of the original space. The result of each perturbation is rotated back to the original parameters according to

$$\mathbf{m}=\mathbf{A}\tilde{\mathbf{m}} \tag{29}$$

prior to evaluation of $E(\mathbf{m})$ and acceptance/rejection according to Eq. (18). The accepted models are accumulated (in addition to the preliminary sampling) until the sample converges (discussed below). To begin perturbing rotated parameters, the parameter bounds and maximum perturbation sizes for the physical parameters can be (approximately) transformed to the rotated space as follows. To determine bounds for the rotated parameters, a large number (e.g., 10^5) of models are randomly drawn within the physical parameter bounds and transformed to the rotated space. The minimum and maximum values obtained for each rotated parameter then serve as bounds in the rotated space [since this procedure does not require evaluation of $E(\mathbf{m})$, it is not computationally demanding]. A similar procedure can be applied to compute initial maximum perturbation sizes; thereafter, the width of the uniform distribution used to perturb each rotated parameter $\tilde{m}_i$ is taken to be a factor $k_2>1$ times the greater of the initial perturbation size and the largest accepted perturbation, as described above for physical parameters.

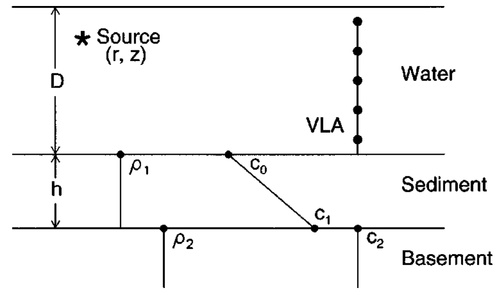

FIG. 1. Ocean environment for the synthetic test cases. In the first test case geometric parameters r, z, and D are known; in the second test case all parameters are unknown.

Finally, for meaningful integral estimates it is important to define a rigorous convergence criterion. The approach adopted here is to apply the FGS procedure in parallel to simultaneously collect two independent samples of models. During sampling, the PPD moments estimated from each sample are periodically compared; when the difference is suitably small, the procedure is considered to have converged and the final model sample is taken to be the union of the two independent samples.[22,23] This approach provides an automated, objective criterion that does not require rerunning the algorithm to verify convergence. Since the marginal probability distributions are of primary interest in the present work, the convergence criterion applied here is that the maximum difference between the cumulative marginal distributions for all parameters is less than a prescribed threshold ϵ, typically with $\epsilon=0.1$. Since the final sample is twice as large as the two independent samples, the difference between the final marginal distributions and the underlying ‘‘true’’ marginal distributions is generally expected to be less than the difference between the two samples.

IV. EXAMPLES AND ALGORITHM VALIDATION

This section illustrates and validates the FGS algorithm using two synthetic examples from the 1997 Geoacoustic Inversion Workshop[20] (Workshop97), which provided test cases designed to serve as benchmark standards for geoacoustic inversion. The importance of considering synthetic cases is that all sources of error are known, so no assumptions or approximations are required to apply the Bayesian analysis. In addition, the solutions can be directly compared to the true model. In a companion paper,[29] FGS is also validated for a measured acoustic data set from the Mediterranean Sea.

The general form for the test cases considered here is shown in Fig. 1. The environment is range independent and

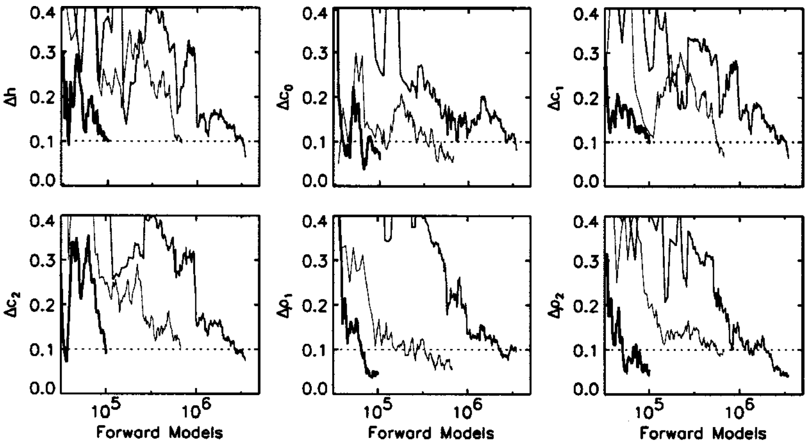

FIG. 2. Convergence of three approaches to estimating marginal PPDs for the first test case. Plots for each parameter show the maximum difference between the cumulative marginal distributions of two independent samples, as a function of the total number of forward model evaluations. Medium, thin, and thick lines indicate the Monte Carlo, GS, and FGS results, respectively. The dotted lines indicate the convergence threshold value of $\epsilon=0.1$.

consists of a sediment layer over a semi-infinite basement with nine geometric and geoacoustic parameters including water depth, D, source range and depth, r and z, sediment thickness, h, sound speeds at the top and bottom of the sediment layer, c_0 and c_1, sound speed of the basement, c_2, and the densities of the sediment and basement, ρ_1 and ρ_2, respectively. The synthetic data consist of acoustic fields at a frequency of 100 Hz measured at a vertical array of 20 sensors equally spaced over the water column. In the first test case (referred to as case SDc at Workshop97), the three geometric parameters are known, with values $r=1$ km, $z=20$ m, and $D=100$ m, leaving the six geoacoustic parameters as unknowns. In the second test case (referred to as WAa), all nine parameters are unknown. In both cases, the model parameterization is known, and the synthetic data and replica acoustic fields are computed using the normal-mode model ORCA,[34] with spatially white, complex Gaussian noise added to the data to yield a signal-to-noise ratio of SNR=20 dB (i.e., $\mathbf{C_D}=\nu\mathbf{I}$, with ν due to Gaussian errors of known variance).

A. Test case 1: Unknown geoacoustic parameters

The first test case was chosen as an example because, as one of the simplest cases from Workshop97, three different approaches to Bayesian inference could be applied, which proved prohibitively time consuming for the more challenging cases. The first approach consisted of the Monte Carlo method described in Sec. II B. The second approach consisted of a straightforward application of the GS described in Sec. II C, with an initial cooling stage to reach $T=1$ and perturbations drawn from uniform distributions over the entire search bounds for each parameter. The final approach consisted of applying the FGS algorithm as described in Sec. III, i.e., GS with an initial cooling stage, parameter rotations to minimize covariances, and uniform perturbation distributions with widths determined adaptively from the previously accepted perturbations. Convergence was established for each approach by collecting two independent samples in parallel, with termination requiring the maximum difference between the two cumulative marginal distributions for all parameters be less than $\epsilon=0.1$. The convergence of the three approaches for the first test case is illustrated in Fig. 2. In total, the Monte Carlo approach evaluated the error function $E(\mathbf{m})$ for approximately 7×10^6 models, requiring 30 h of CPU time on a 400-MHz PC. The GS algorithm evaluated approximately 7×10^5 models requiring 3 h of CPU time, and FGS evaluated about 10^5 models in 0.3 CPU hours.

The marginal probability distributions estimated using each of the three sampling approaches are compared in Fig. 3. This figure shows that the sediment thickness h and the sediment and basement sound speeds c_0, c_1, and c_2 are reasonably well determined, while the sediment density ρ_1 is poorly determined, and the basement density ρ_2 is completely undetermined. The marginal PPDs are essentially unimodal, with reasonably smooth and simple shapes. Importantly, it is apparent from Fig. 3 that there are no significant differences between the marginal distributions estimated by each of the three approaches to sampling. In fact, the maximum difference between the marginal cumulative distributions obtained by the three approaches is less than the convergence tolerance of $\epsilon=0.1$ (i.e., the distributions for each approach differ by less than the convergence threshold). It should be noted that although the PPD samples have been binned to produce histogram plots in Fig. 3, all three approaches treat the model parameters as continuous variables.

The consistency between the three approaches is further illustrated by the numerical estimates for the mean and stan-

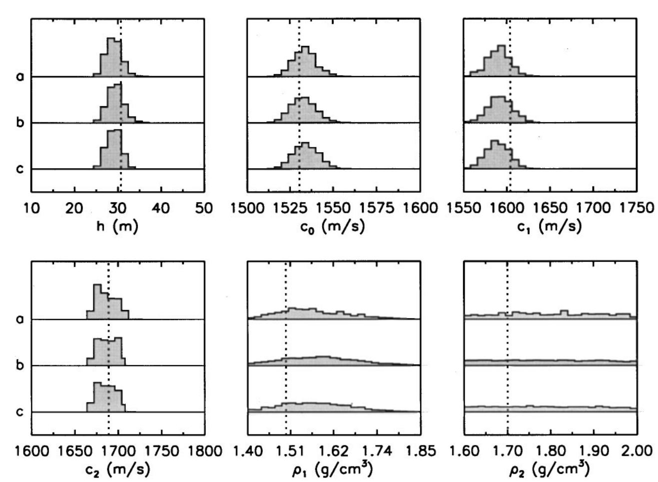

FIG. 3. Estimated marginal PPDs for the first test case. The distributions for each parameter were computed using (a) Monte Carlo integration, (b) GS, and (c) FGS. Dotted lines indicate the true parameter values, and the range of abscissa values indicates the parameter search bounds.

TABLE I. Summary of parameter means and standard deviations estimated for the first test case using three approaches to sampling.

Parameter	True value	Monte Carlo	GS	FGS
h (m)	30.7	29±2	29±2	29±2
c_0 (m/s)	1530.4	1534±7	1533±7	1534±7
c_1 (m/s)	1604.1	1591±13	1593±14	1590±13
c_2 (m/s)	1689.0	1687±11	1688±11	1687±11
ρ_1 (g/cm^3)	1.50	1.57±0.09	1.59±0.09	1.58±0.09
ρ_2 (g/cm^3)	1.70	1.80±0.1	1.79±0.1	1.79±0.1

dard deviation (square root of the diagonal elements of the covariance matrix) for each parameter, as given in Table I. Note that means and standard deviations were estimated from the M-dimensional PPD sample according to Eqs. (7) and (8), and do not simply represent one-dimensional (1D) moments derived from the marginal distributions. Since errors were included on the data, the estimated means are not expected to exactly reproduce the true parameter values. Table I indicates that the three approaches yield essentially identical mean and standard deviation estimates for each parameter.

To examine the parameter interdependencies, it is convenient to normalize the elements of the covariance matrix so as to remove the effects of differing parameter scales and units. This can be done be computing the model correlation matrix **R**, defined

$$R_{ij}=C_{M_{ij}}/\sqrt{C_{M_{ii}}C_{M_{jj}}}. \tag{30}$$

Elements R_{ij} are within $[-1, 1]$, with a value of 1 indicating perfect correlation between parameters m_i and m_j, -1 indicating perfect anti-correlation, and near-zero values indicating uncorrelated parameters (diagonal elements, or autocorrelations, are unity by definition). The correlation matrices estimated using each of the three approaches are given by solid lines in Fig. 4 and are indistinguishable. This figure indicates that reasonably strong positive correlations exist between h, c_1, and c_2, while weaker negative correlations exist between h and c_0 and between c_1 and c_0. Densities ρ_1 and ρ_2 are essentially uncorrelated with all other parameters. The dashed lines in this figure show the correlations corresponding to the covariance matrix used to define the parameter-space rotation in the FGS approach. This matrix, estimated from a preliminary sampling of 1000 values for each parameter from each of the parallel samples, clearly captures the dominant inter-parameter correlations.

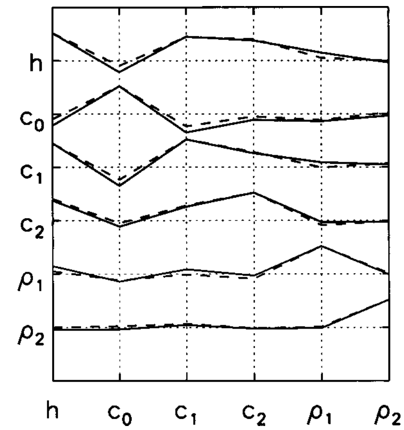

FIG. 4. Correlation matrix for the first test case. The solid lines indicate rows of the matrix estimated using Monte Carlo integration, GS and FGS (indistinguishable); the dashed lines indicates the preliminary estimate used to rotate the parameter space in FGS.

The above analysis indicates that PPD moments such as the mean, variance, covariance, and marginal distributions are accurately estimated via FGS, at small fraction of the computational effort of Monte Carlo integration or GS. To examine the FGS procedure more closely, Fig. 5 shows the sequence of error function values and model parameters that were accepted throughout the FGS sampling for one of the two parallel samples (the results for the other sample are similar). The values to the left of the first dotted line were obtained during the initial cooling stage, the values between dotted lines were obtained by perturbing the physical (unrotated) parameters, and the values to the right of the second dotted line were obtained by perturbing the rotated parameters. Figure 5 shows that the error function E decreases by several orders of magnitude during the cooling stage, obtaining values by the end of cooling that remain relatively constant for the remainder of the sampling. The model parameters initially vary widely within their bounds, but the variability decreases with cooling for all parameters except

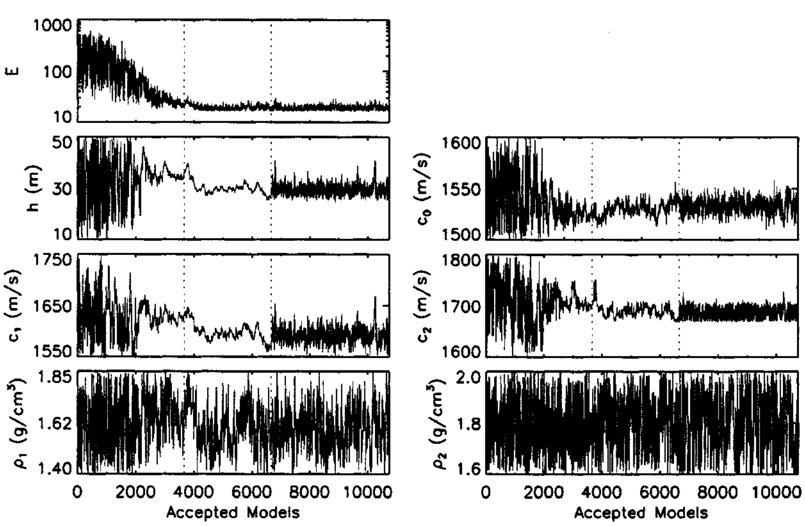

FIG. 5. Sequence of error function and parameter values for the models accepted in FGS sampling of the first test case. Dotted lines delineate intial cooling, unrotated sampling, and rotated sampling stages.

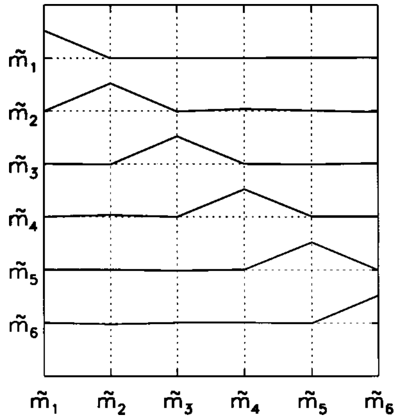

FIG. 6. Rows of the correlation matrix for the rotated parameters of the FGS sample of the first test case.

the basement density ρ_2. A total of 3000 accepted models were obtained by sampling the physical parameters (500 samples for each of the six parameters). During this stage, the parameters (except ρ_1 and ρ_2) wander relatively slowly. This behavior changes markedly at the transition to sampling in the rotated space, with the parameter values varying much more rapidly. The larger accepted perturbations, resulting from the mutual independence of the rotated parameters, provide a much more efficient sampling of the model space. It is interesting to note that the most dramatic change in the sampling character occurs for h and c_1, which correspond to the most strongly correlated parameters according to Fig. 4.

A final verification that the rotation matrix estimated from a relatively small sample effectively de-couples the parameters is given in Fig. 6, which shows the correlation matrix computed for the complete FGS sample in the rotated parameter space. This matrix obtained is an excellent approximation to the identity matrix, indicating that the level of correlation between parameters in the rotated space is indeed very small.

B. Test case 2: Unknown geoacoustic/geometric parameters

The second test case was chosen because it represents one of the most challenging cases from Workshop97, not only because it involves a larger number of unknowns (nine), but also because including the three geometric parameters introduces particularly strong interparameter correlations (illustrated below). Marginal PPDs were computed for this test case using both the GS and the FGS algorithms (Monte Carlo integration was also attempted, but was not close to convergence after 150 h of CPU time, and hence was abandoned). For convergence, the GS approach evaluated a total of 3.5×10^7 models requiring 140 CPU hours, while the FGS approach evaluated 3.8×10^5 models in 1.5 CPU hours. The convergence of the two approaches is shown in Fig. 7. Note that the characteristics of the GS convergence curves for D, r, and z are very similar, suggesting these parameters are strongly correlated. A similar observation applies to parameters c_1 and c_2. The convergence of GS is substantially slower for these parameters; however, FGS converges efficiently for all parameters.

The marginal PPDs estimated using the two approaches are shown in Fig. 8. The distributions are unimodal, smooth, and generally symmetric (with the exception of the distribution for c_2, which is notably asymmetric). Figure 8 shows that there are no significant differences between the marginal distributions estimated by the two methods, and the maximum difference between the cumulative distributions for each parameter is less than the convergence threshold of $\epsilon=0.1$. The consistency in results between the two sampling approaches is further illustrated by the excellent agreement between the numerical estimates for the parameter means and standard deviations given in Table II. In addition, the correlation matrices estimated by the two methods, shown in Fig. 9, are indistinguishable. This figure indicates near-unity correlations between r, z, and D, and between c_1 and c_2,

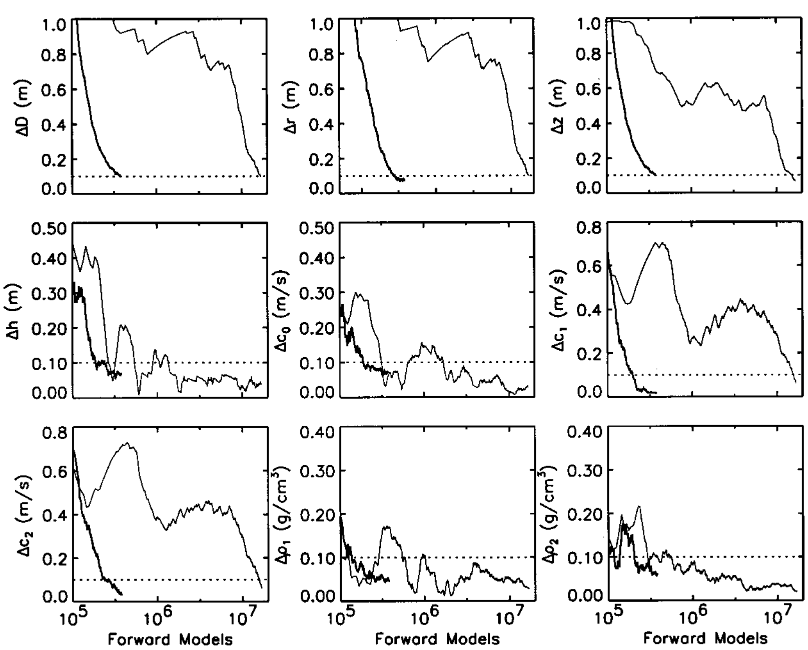

FIG. 7. Convergence of two approaches to estimating marginal PPDs for the second test case. Plots for each parameter show the maximum difference between the cumulative distributions of two independent samples, as a function of the total number of models evaluated. Medium and thick lines indicate the GS and FGS results, respectively. The dotted lines indicate the convergence threshold value of $\epsilon=0.1$.

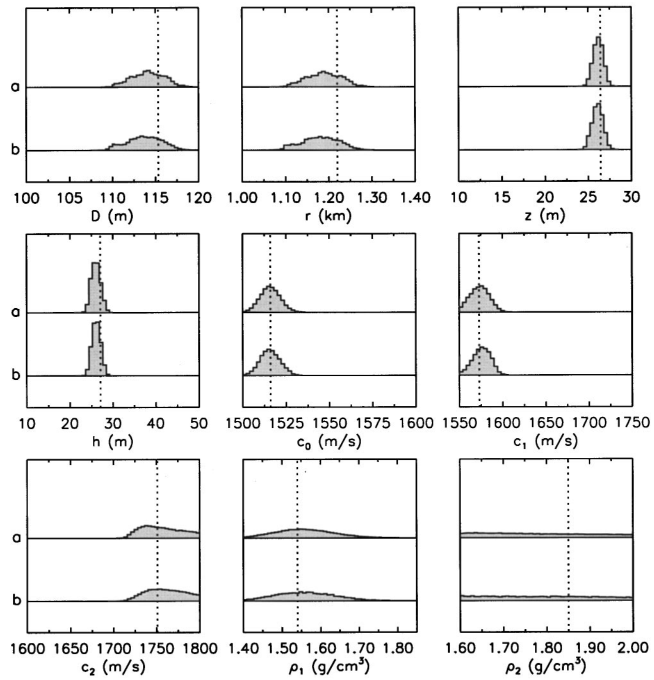

FIG. 8. Estimated marginal PPDs for the second test case. The distributions for each parameter were computed using: (a) GS, and (b) FGS. Dotted lines indicate the true parameter values, and the range of abscissa values indicate the parameter search bounds.

which lead to the slow convergence of GS for these parameters (Fig. 7).

Given the strong interparameter correlations indicated in Fig. 9, it is interesting to consider 2D marginal probability distributions for this test case, as given in Fig. 10. This figure shows that the 2D marginal PPDs for various combinations of r, z, and D and for c_1 and c_2 (i.e., pairs of correlated parameters) consist of narrow zones of high probability oriented obliquely with respect to the parameter axes. For comparison, Fig. 10 also includes 2D marginal PPDs for parameter pairs with little or no correlation. With perturbations parallel to the parameter axes, sampling along oblique zones for correlated parameters is a slow procedure, requiring a large number of small perturbations. However, in the rotated space, the axes align with the dominant correlation directions, allowing large perturbations and providing efficient sampling. The small-scale structure in the 2D marginal distributions of Fig. 10 results from under-sampling the distributions, since the convergence criteria for FGS is based on

TABLE II. Summary of parameter means and standard deviations estimated for the second test case using two approaches.

Parameter	True value	GS	FGS
D (m)	115.3	114±2	114±2
r (km)	1.22	1.18±0.4	1.19±0.4
z (m)	26.42	26.1±0.6	26.2±0.6
h (m)	27.1	26.1±1	26.0±1
c_0 (m/s)	1516.0	1515±6	1516±6
c_1 (m/s)	1573.0	1576±10	1574±11
c_2 (m/s)	1751.0	1759±21	1755±22
ρ_1 (g/cm^3)	1.54	1.56±0.8	1.56±0.8
ρ_2 (g/cm^3)	1.85	1.79±0.11	1.78±0.11

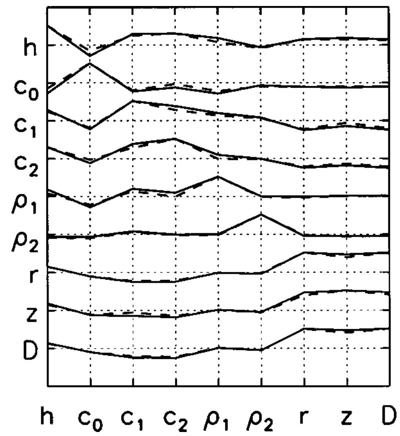

FIG. 9. Correlation matrix for the second test case. The solid lines indicate rows of the matrix estimated using GS and FGS (indistinguishable); the dashed lines indicates the preliminary estimate used to rotate the parameter space in FGS.

the 1D marginal distributions (convergence to smooth distributions in two dimensions is considerably more demanding and has not been required here).

To illustrate the FGS sampling for the second test case, Fig. 11 shows the sequence of accepted error function values and model parameters in a format similar to Fig. 5. Of particular note is the strongly correlated behavior between D and r, and the profound change in sampling upon parameter rotation for these and other parameters. The effectiveness of the rotation matrix computed from a relatively small initial sample is illustrated in Fig. 12, which shows the correlation matrix of the rotated parameters computed for the total FGS sample. The strong correlations present in the original parameter space (Fig. 9) have been almost completely removed, and the correlation matrix in Fig. 12 closely resembles the identity matrix.

C. Comparison to other approaches

The results of comparing FGS to GS and Monte Carlo integration in Secs. IV A and IV B indicate that FGS provides accurate estimates of PPD moments for geoacoustic inversion. Similar comparisons for different SNRs and for other benchmark test cases (not shown here) yielded identical conclusions. For all cases considered, the marginal probability distributions were found to be relatively simple and smooth functions, which has important consequences in terms of interpreting and understanding the PPD information content. It is interesting to note that marginal PPDs previously computed for the same (and similar) test cases using a GA-based multiple MAP estimator were of a decidedly different character, often sparse and spiky, with multiple isolated local maxima (e.g., Refs. 7–11, 13). This suggests that applying an unbiased sampler with a rigorous convergence criterion (as in FGS) can be a significant factor in determining the character of the PPD.

It is also interesting to compare the FGS analysis to qualitative observations often drawn from simple graphical methods. For instance, it is fairly common practice to appraise nonlinear inverse problems by plotting 1D and 2D cross-sections of the error E as a function of one and two

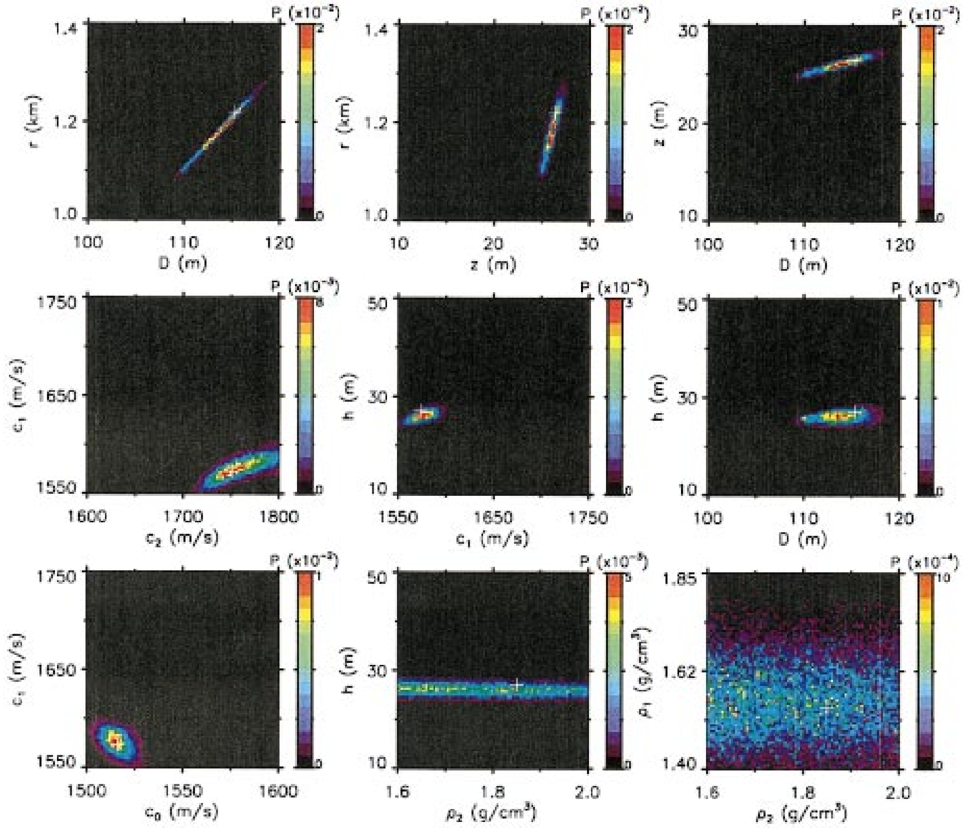

FIG. 10. Selected 2D marginal PPDs for the second test case. White crosses indicate the true parameter values. Distributions are scaled so a value of unity represents all samples concentrated into one pixel.

parameters, respectively, with the other parameters held fixed at their true values (for synthetic cases), or at their optimal values (for measured data). However, such cross-sections represent a highly constrained sampling which may not be representative of the parameter space. For example, Figs. 13 and 14 show 1D and 2D cross-sections of the parameter space for the second test case. The sharpness of the minima of E in cross-sections such as these is sometimes used to assess the relative sensitivity of the parameters. Based on this criteria, Fig. 13 indicates that D and r should be much better determined than z; however, according to Fig. 8, the opposite is true (this is due, of course, to parameter correlations). Further, parameter correlations are sometimes inferred from the angle between valleys in E and the parameter axes in 2D cross-sections. Based on this, Fig. 14 would suggest that there is little correlation between z and r or between z and D, while a negative correlation is suggested between c_1 and c_2 and between h and D. However, according to Figs. 9 and 10, all of these observations are incorrect. These examples show that simple cross-sections of a high-dimensional parameter space provide only limited information, and observations based on these should be treated with care. In contrast, the

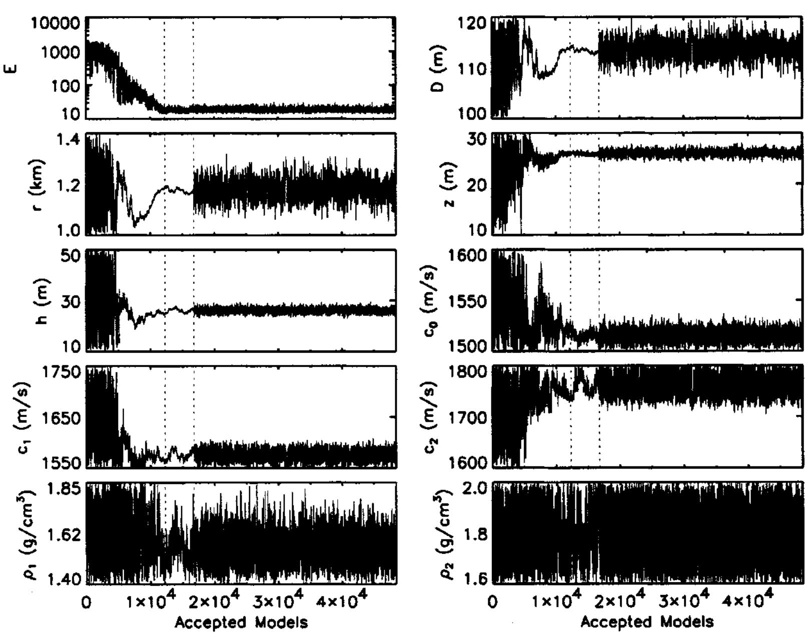

FIG. 11. Sequence of error function and parameter values for the models accepted in FGS sampling of the second test case. Dotted lines delineate intial cooling, unrotated sampling, and rotated sampling stages.

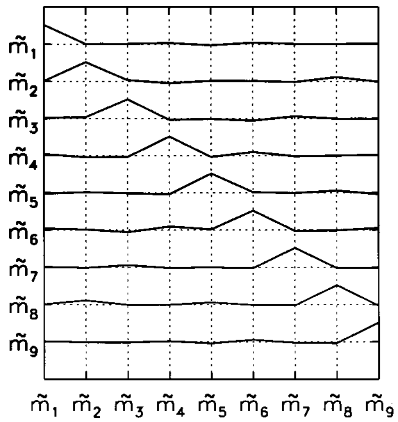

FIG. 12. Rows of the correlation matrix for the rotated parameters of the FGS sample of the second test case.

PPD, when properly sampled, provides results that are truly representative of the parameter space.

V. SUMMARY AND DISCUSSION

This paper developed a new approach to matched-field inversion for seabed geoacoustic parameters that emphasizes estimation of parameter uncertainties. The approach is based on Bayesian inference theory, which characterizes the solution to an inverse problem in terms of its posterior probability density. The PPD combines prior information about the model, such as parameter upper and lower bounds, with the information provided by an observed data set, quantified in terms of the likelihood function defined by the statistical distribution of the data errors. The multi-dimensional PPD is typically interpreted in terms of its moments, such as the posterior mean, covariance, and marginal probability distributions, which provide parameter estimates and uncertainties. Determining these properties requires estimating multi-dimensional integrals of the PPD using sampling methods such as Monte Carlo integration or importance sampling. Meaningful estimation of PPD moments requires an unbiased sampling algorithm with a rigorous convergence criterion.

The approach developed here consists of a Gibbs sampler based on the Metropolis algorithm, which provides an unbiased sampling of the PPD. The efficiency of standard GS was greatly increased by modifications similar to those used to accelerate the convergence of Metropolis SA. These modifications included: (i) an initial cooling stage to initiate sampling at equilibrium; (ii) sampling in a rotated parameter space to minimize inter-parameter correlations; and (iii) adaptively determining an effective maximum perturbation size for each parameter. Since the marginal PPDs are of primary interest here, the convergence criterion required the maximum difference between the cumulative marginal distributions of two independent samples collected in parallel decrease below a threshold value.

This fast Gibbs sampler algorithm was validated by comparison to Monte Carlo integration and to a standard implementation of GS for synthetic benchmark test cases in which the error statistics were exactly known. For each test case, the maximum difference between the resulting marginal distributions was smaller than the convergence threshold, and other PPD moments such as the mean, variance and covariance (scaled as parameter correlations) agreed to high precision; of the three approaches, FGS required orders of magnitude less computation time. In addition, the FGS algorithm is amenable to parallelization, and hence further substantial reductions in computation time are possible. The marginal PPDs obtained in each case were found to be relatively smooth and simple functions allowing straightforward interpretation of the information content for each unknown parameter. The calculation of PPD moments, such as mar-

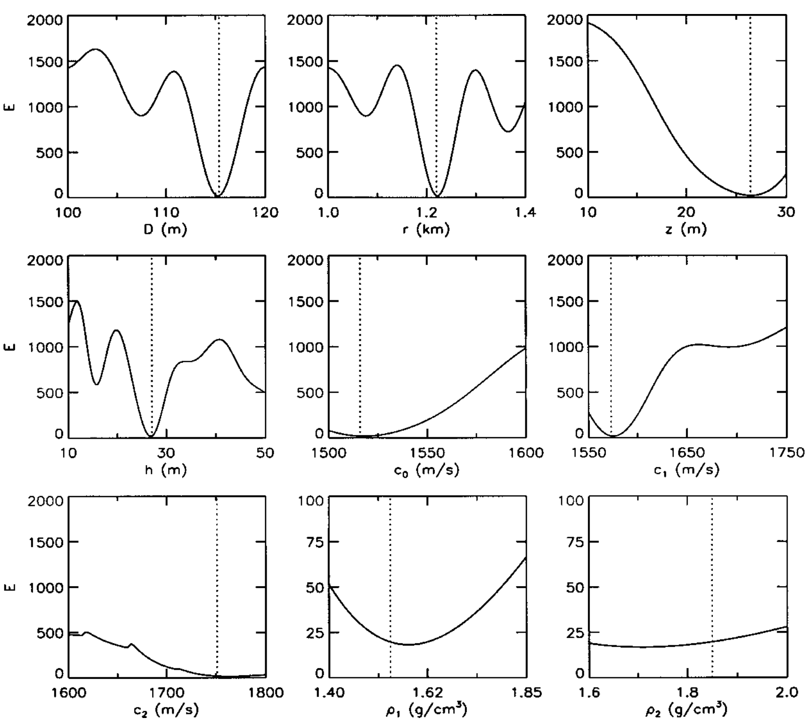

FIG. 13. 1D cross-sections of the error function $E(\mathbf{m})$ for the second test case. In each plot, parameters that are not varied are held at their true values. Dotted lines indicate the true value for the parameter being varied. Note the change in scale for E for ρ_1 and ρ_2.

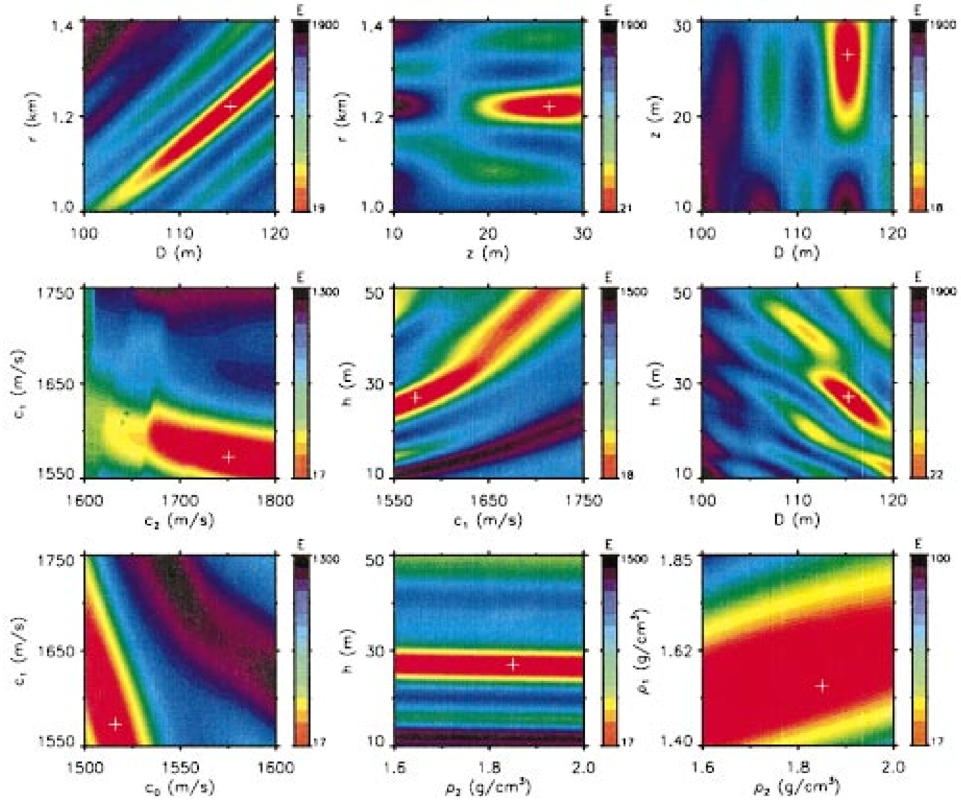

FIG. 14. Selected 2D cross-sections of the error function $E(\mathbf{m})$ for the second test case. In each plot, parameters that are not varied are held at their true values. White crosses indicate the true value for the parameter being plotted.

ginal distributions and covariances, can provide powerful tools for quantifying uncertainty and providing insight into the geoacoustic inverse problem.

ACKNOWLEDGMENTS

The author thanks Michael Wilmut for many helpful discussions on statistical methods. This work was supported by Office of Naval Research Grant No. N00014-96-1-0721.

[1] M. D. Collins, W. A. Kuperman, and H. Schmidt, ''Nonlinear inversion for ocean-bottom properties,'' J. Acoust. Soc. Am. **92**, 2770–2783 (1992).
[2] S. E. Dosso, M. L. Yeremey, J. M. Ozard, and N. R. Chapman, ''Estimation of ocean-bottom properties by matched-field inversion of acoustic field data,'' IEEE J. Ocean. Eng. **18**, 232–239 (1993).
[3] C. E. Lindsay and N. R. Chapman, ''Matched field inversion for geoacoustic model parameters using adaptive simulated annealing,'' IEEE J. Ocean. Eng. **18**, 224–231 (1993).
[4] M. D. Collins and L. Fishman, ''Efficient navigation of parameter landscapes,'' J. Acoust. Soc. Am. **98**, 1637–1644 (1995).
[5] M. R. Fallat and S. E. Dosso, ''Geoacoustic inversion for the Workshop97 benchmark test cases using simulated annealing,'' J. Comput. Acoust. **6**, 29–43 (1998).
[6] P. Gerstoft and Z-H. Michalopoulou, ''Global optimization in matched field inversion,'' *Proceedings of the Fourth European Conference on Underwater Acoustics*, edited by A. Alippi and G. B. Canneli (Italian National Research Council, Rome, 2000), pp. 27–32.
[7] P. Gerstoft, ''Inversion of seismoacoustic data using genetic algorithms and *a posteriori* probability distributions,'' J. Acoust. Soc. Am. **95**, 770–782 (1994).
[8] P. Ratilal, P. Gerstoft, and J. T. Goh, ''Subspace approach to inversion by genetic algorithms involving multiple frequencies,'' J. Comput. Acoust. **6**, 99–115 (1998).
[9] M. Siderius, P. Gerstoft, and P. Nielsen, ''Broadband geoacoustic inversion from sparse data using genetic algorithms,'' J. Comput. Acoust. **6**, 117–134 (1998).
[10] M. I. Taroudakis and M. G. Markaki, ''Bottom geoacoustic inversion by 'broadband' matched-field processing,'' J. Comput. Acoust. **6**, 167–184 (1998).
[11] M. I. Taroudakis and M. G. Markaki, ''Bottom geoacoustic inversion by matched field processing—A sensitivity study,'' Inverse Probl. **16**, 1679–1692 (2000).
[12] G. J. Heard, D. Hannay, and S. Carr, ''Genetic algorithm inversion of the 1997 geoacoustic inversion workshop test case data,'' J. Comput. Acoust. **6**, 61–71 (1998).
[13] P. Gerstoft and C. F. Mecklenbräuker, ''Ocean acoustic inversion with estimation of *a posteriori* probability distributions,'' J. Acoust. Soc. Am. **104**, 808–819 (1998).
[14] P. Gerstoft, ''Inversion of acoustic data using a combination of genetic algorithms and the Gauss–Newton approach,'' J. Acoust. Soc. Am. **97**, 2181–2190 (1995).
[15] M. R. Fallat and S. E. Dosso, ''Geoacoustic inversion via local, global and hybrid algorithms,'' J. Acoust. Soc. Am. **105**, 3219–3230 (1999).
[16] M. Musil, M. J. Wilmut, and N. R. Chapman, ''A hybrid simplex genetic algorithm for estimating geoacoustic parameters using matched-field inversion,'' IEEE J. Ocean. Eng. **24**, 358–369 (1999).
[17] M. R. Fallat, P. L. Nielsen, and S. E. Dosso, ''Hybrid geoacoustic inversion of broadband Mediterranean Sea data,'' J. Acoust. Soc. Am. **107**, 1967–1977 (2000).
[18] S. E. Dosso, M. J. Wilmut, and A. S. Lapinski, ''An adaptive hybrid algorithm for geoacoustic inversion,'' IEEE J. Ocean. Eng. **26**, 324–336 (2001).
[19] L. Jaschke and N. R. Chapman, ''Matched field inversion of broadband data using the freeze bath method,'' J. Acoust. Soc. Am. **106**, 1838–1851 (1999).
[20] A. Tolstoy, N. R. Chapman, and G. H. Brooke, ''Workshop97: Benchmarking for geoacoustic inversion in shallow water,'' J. Comput. Acoust. **6**, 1–28 (1998).
[21] W. Menke, *Geophysical Data Analysis: Discrete Inverse Theory* (Academic, Orlando, 1984).
[22] J. M. Hammersley and D. C. Handscomb, *Monte Carlo Methods* (Wiley, New York, 1964).
[23] W. R. Gilks, S. Richardson, and G. J. Spiegelhalter, *Markov Chain Monte Carlo in Practice* (Chapman and Hall, London, 1996).
[24] A. Tarantola, *Inverse Problem Theory: Methods for Data Fitting and Model Parameter Estimation* (Elsevier, Amsterdam, 1987).
[25] M. K. Sen and P. L. Stoffa, ''Bayesian inference, Gibbs' sampler and uncertainty estimation in geophysical inversion,'' Geophys. Prospect. **44**, 313–350 (1996).

[26] M. K. Sen and P. L. Stoffa, *Global Optimization Methods in Geophysical Inversion* (Elsevier, Amsterdam, 1995).
[27] N. Metropolis, A. Rosenbluth, M. Rosenbluth, A. Teller, and E. Teller, ‘‘Equation of state calculation by fast computing machines,’’ J. Chem. Phys. **21**, 1087–1092 (1953).
[28] H. Szu and R. Hartley, ‘‘Fast simulated annealing,’’ Phys. Lett. A **122**, 157–162 (1987).
[29] S. E. Dosso and P. L. Nielsen, ‘‘Quantifying uncertainty in geoacoustic inversion. II. Application to broadband, shallow-water data,’’ J. Acoust. Soc. Am. **111**, 143–159 (2002).
[30] D. F. Gingras and P. Gerstoft, ‘‘Inversion for geometric and geoacoustic parameters in shallow water: Experimental results,’’ J. Acoust. Soc. Am. **97**, 3589–3598 (1995).
[31] J.-P. Hermand and P. Gerstoft, ‘‘Inversion of broad-band multitone acoustic data from the YELLOW SHARK summer experiments,’’ IEEE J. Ocean. Eng. **21**, 324–346 (1996).
[32] W. H. Press, S. A. Teukolsky, W. T. Vetterling, and B. P. Flannery, *Numerical Recipes in FORTRAN* (Cambridge University Press, Cambridge, 1992).
[33] A. Basu and L. N. Fraser, ‘‘Rapid determination of the critical temperature in simulated annealing inversion,’’ Science **249**, 1409–1412 (1990).
[34] E. K. Westwood, C. T. Tindle, and N. R. Chapman, ‘‘A normal mode model for acousto-elastic ocean environments,’’ J. Acoust. Soc. Am. **100**, 3631–3645 (1996).

Quantifying uncertainty in geoacoustic inversion. II. Application to broadband, shallow-water data

Stan E. Dosso
School of Earth and Ocean Sciences, University of Victoria, Victoria, British Columbia V8W 3P6, Canada

Peter L. Nielsen
SACLANT Undersea Research Centre, Viale S. Bartolomeo, 400 19138 La Spezia, Italy

(Received 9 March 2001; revised 7 August 2001; accepted 31 August 2001)

This paper applies the new method of fast Gibbs sampling (FGS) to estimate the uncertainties of seabed geoacoustic parameters in a broadband, shallow-water acoustic survey, with the goal of interpreting the survey results and validating the method for experimental data. FGS applies a Bayesian approach to geoacoustic inversion based on sampling the posterior probability density to estimate marginal probability distributions and parameter covariances. This requires knowledge of the statistical distribution of the data errors, including both measurement and theory errors, which is generally not available. Invoking the simplifying assumption of independent, identically distributed Gaussian errors allows a maximum-likelihood estimate of the data variance and leads to a practical inversion algorithm. However, it is necessary to validate these assumptions, i.e., to verify that the parameter uncertainties obtained represent meaningful estimates. To this end, FGS is applied to a geoacoustic experiment carried out at a site off the west coast of Italy where previous acoustic and geophysical studies have been performed. The parameter uncertainties estimated via FGS are validated by comparison with: (i) the variability in the results of inverting multiple independent data sets collected during the experiment; (ii) the results of FGS inversion of synthetic test cases designed to simulate the experiment and data errors; and (iii) the available geophysical ground truth. Comparisons are carried out for a number of different source bandwidths, ranges, and levels of prior information, and indicate that FGS provides reliable and stable uncertainty estimates for the geoacoustic inverse problem. [DOI: 10.1121/1.1419087]

PACS numbers: 43.30.Pc, 43.60.Pt [DLB]

I. INTRODUCTION

The matched-field inverse problem of determining seabed geoacoustic parameters from measured ocean acoustic fields has received considerable attention in recent years (e.g., see references listed in Ref. 1); however, relatively little work has been applied to the problem of estimating the uncertainties of these parameters in a rigorous manner. This is an important problem, since without some indication of uncertainties, no confidence can be placed in the model parameters obtained by inversion. A companion paper[1] developed a fast Gibbs sampler (FGS) approach to this problem based a Bayesian formulation[2–6] that characterizes the solution in terms of its posterior probability density (PPD). The PPD combines prior information about the model with information from an observed data set expressed in terms of the likelihood function defined by the statistical distribution of the data errors. The FGS provides an unbiased sampling of the PPD yielding estimates of PPD moments such as marginal probability distributions and covariances, which provide quantitative measures of the parameter uncertainties. A rigorous convergence criterion is applied that requires the marginal distributions of two independent FGS samples collected in parallel agree to within a specified threshold. The FGS algorithm was validated in Ref. 1 for synthetic benchmark test cases[7] in which the statistical distribution of the data errors was precisely known. In such cases, uncertainty estimates from Monte Carlo integration of the PPD and from a standard Gibbs sampling approach provide unbiased estimates of the PPD moments to arbitrary accuracy (dependent on the convergence threshold). It was found that uncertainties estimated via FGS agreed with Monte Carlo and Gibbs sampling results to within the convergence threshold, while requiring orders of magnitude less computation time.

In applying Bayesian inversion methods to experimental data, the issue of quantifying the data errors becomes crucial. The statistical distribution of the data errors, including both measurement and theory errors, is usually not well known in practice, and for this reason the Bayesian approach has been criticized.[3,8] In the case of geoacoustic inversion, measurement errors typically include additive noise sources, instrument uncertainties and errors in sensor positions, while theory errors include factors such as an inexact formulation for the forward problem (e.g., neglect of elasticity, three-dimensional effects, roughness) and a simplified parameterization of the unknown geoacoustic and geometric properties. Given the lack of independent knowledge of the error statistics, to proceed with the Bayesian approach requires simplifying assumptions be made regarding the data likelihood function. Under the assumption of independent, identically distributed Gaussian errors, the variance can be estimated from the data themselves by minimizing the data misfit.[9] The approach adopted here to quantify the data uncertainty follows that of Gerstoft and Mecklenbräuker,[6] who showed that, under the above assumptions, a maximum-likelihood estimate can be formulated for the data variance in matched-field inversion. Since it is not known *a priori* how these assumptions influence the estimated PPD, it is important to validate the FGS results to establish that the parameter uncertainties obtained are meaningful. This is one of the major goals of the present paper. ''Ground-truthing'' uncertainty estimation is not a straightforward procedure, and there appears to be little previous work on this topic for the geoacoustic inverse problem.

With the model for the error statistics described above, FGS is applied here to estimate the uncertainties of the geoacoustic/geometric parameters of a broadband, shallow-water acoustic experiment.[10–12] The experiment, known as PROSIM'97, was carried out by the SACLANT Undersea Research Center in the Mediterranean Sea, off the west coast of Italy, at a site where previous geoacoustic and geophysical surveys had been performed.[13–15] The experiment consisted of towing a swept-frequency (300–850 Hz) source over gently sloping bathymetry, and recording the acoustic signals at a 48-sensor vertical array. Environmental properties such as the ocean sound-speed profile were measured at the experiment site; however, the bathymetry measurements along the source track were subject to relatively large errors due to experimental difficulties. The parameter uncertainties estimated for this experiment via FGS are validated in several ways. First, the widths of the marginal distributions are compared with the variability in the results of applying matched-field inversion to multiple independent data sets collected during the experiment. Second, the FGS results for experimental data are compared to corresponding results for synthetic test cases designed to closely simulate the experiment and data errors. Finally, the FGS results are compared to the available geophysical information for the region. The above comparisons are carried out for several different source bandwidths, source–receiver ranges, and levels of prior information (i.e., parameter search bounds). The results indicate that the FGS algorithm provides stable and reliable uncertainty estimates for the geoacoustic/geometric parameters. In addition, computation of the posterior covariance matrix provides information about inter-parameter correlations, which can provide insight into the causes of parameter uncertainties.

The remainder of this paper is organized as follows. Section II briefly describes the maximum-likelihood theory leading to the data variance estimates used in FGS analysis of measured acoustic fields. Section III describes the PROSIM'97 geoacoustic experiment and the results of previous acoustic and geophysical surveys in the study region. Section IV applies the FGS approach to the experimental data with the goal of validating the parameter uncertainty estimates and interpreting the experiment results. Finally, Sec. V summarizes and discusses the results of this paper.

II. THEORY: ERROR ESTIMATION FOR FGS ANALYSIS

The theory and implementation of the FGS inversion method are described in detail in the companion paper[1] and are not repeated here. However, to apply this method to experimental measurements requires an estimate of the data likelihood function which quantifies the statistical distribution of the data uncertainties, including both measurement and theory errors. Since independent information on this distribution is generally not available for measured ocean acoustic fields, simple and reasonable approximations must be made. Gerstoft and Mecklenbräuker[6] developed a useful approach to this problem for matched-field inversion, which is adapted in this section. The validity of this approach for FGS geoacoustic inversion is considered in Sec. IV.

Let vectors comprising N narrow-band data (complex acoustic pressure at an array of sensors) and M model parameters (unknown geoacoustic and geometric properties) be defined as random variables

$$\mathbf{d}=[d_1,d_2,\ldots,d_N]^T, \quad \mathbf{m}=[m_1,m_2,\ldots,m_M]^T, \tag{1}$$

respectively, where T denotes transpose. As described in Refs. 1 and 6, under the assumption that the data errors are complex, zero-mean Gaussian-distributed random variables that are spatially uncorrelated and uncorrelated from frequency to frequency with identical variance at each sensor, the likelihood function for incoherent processing of an observed multi-frequency data set $\mathbf{d}_f^{\mathrm{obs}}, f=1,F$ is given by

$$L(\mathbf{m})=\prod_{f=1}^{F}\frac{1}{(\pi\nu_f)^N}\exp[-|\mathbf{d}_f^{\mathrm{obs}}-\mathbf{d}_f(\mathbf{m})|^2/\nu_f], \tag{2}$$

where ν_f is the data variance at frequency f and $\mathbf{d}_f(\mathbf{m})$ represents the predicted (replica) data computed for model $\mathbf{m}$. For matched-field inversion, the dependence on the unknown complex source strength (magnitude and phase) S_f at each frequency can be made explicit by defining the replica data to be

$$\mathbf{d}_f(\mathbf{m})=S_f\mathbf{w}_f(\mathbf{m}), \tag{3}$$

where $\mathbf{w}_f(\mathbf{m})$ is the field computed via a numerical propagation model. Substituting this into Eq. (2) and explicitly identifying S_f and ν_f as unknown parameters leads to

$$L(\mathbf{m},\mathbf{S},\boldsymbol{\nu})=\prod_{f=1}^{F}\frac{1}{(\pi\nu_f)^N}\exp[-|\mathbf{d}_f^{\mathrm{obs}}-S_f\mathbf{w}_f(\mathbf{m})|^2/\nu_f], \tag{4}$$

where $\mathbf{S}=[S_1,\ldots,S_F]^T$ and $\nu=[\nu_1,\ldots,\nu_F]^T$. To remove the dependence on source strength, L is maximized over S_f by setting $\partial L/\partial S_f=0$, leading to the solution

$$S_f=\mathbf{w}_f^{\dagger}(\mathbf{m})\mathbf{d}_f^{\mathrm{obs}}/|\mathbf{w}_f(\mathbf{m})|^2, \tag{5}$$

where † represents conjugate transpose. Substituting Eq. (5) back into Eq. (4), the likelihood function can be written in the form

$$L(\mathbf{m},\boldsymbol{\nu})=\prod_{f=1}^{F}\frac{1}{(\pi\nu_f)^N}\exp[-B_f(\mathbf{m})|\mathbf{d}_f^{\mathrm{obs}}|^2/\nu_f], \tag{6}$$

where $B_f(\mathbf{m})$ represents the (normalized) Bartlett mismatch function at frequency f, defined

$$B_f(\mathbf{m})=1-\frac{|\mathbf{w}_f^{\dagger}(\mathbf{m})\mathbf{d}_f^{\mathrm{obs}}|^2}{|\mathbf{d}_f^{\mathrm{obs}}|^2|\mathbf{w}_f(\mathbf{m})|^2}. \tag{7}$$

To obtain a maximum-likelihood estimate of the data variance, Gerstoft and Mecklenbräuker[6] proceeded to set $\partial L/\partial\nu_f=0$ and evaluated the result at the maximum-likelihood model estimate $\hat{\mathbf{m}}$. The resulting variance estimate can be written

$$\hat{\nu}_f = B_f(\hat{\mathbf{m}})|\mathbf{d}_f^{\mathrm{obs}}|^2/N, \tag{8}$$

where the maximum-likelihood model $\hat{\mathbf{m}}$ for multi-frequency data with unknown variances is found by minimizing the objective function[6,16]

$$\Phi(\mathbf{m}) = \prod_{f=1}^{F} B_f(\mathbf{m}) \tag{9}$$

using a global or hybrid optimization scheme.

The derivation of the variance estimate Eq. (8) is based on the assumption of independent errors at each of N sensors. However, this assumption may not be valid for an array of sensors, as acoustic errors are known to be correlated over spatial scales defined by the propagating normal modes. In this case, Gerstoft and Mecklenbräuker[6] suggest replacing the number of sensors N in Eq. (8) with the number of uncorrelated sensors N_e, which is equivalent to the effective number of propagating modes (i.e., the number of modes carrying significant acoustic energy). Hence, the final expression for the variance estimate is

$$\hat{\nu}_f = B_f(\hat{\mathbf{m}})|\mathbf{d}_f^{\mathrm{obs}}|^2/N_e. \tag{10}$$

In practice, N_e can be estimated from a principal component analysis of the data covariance matrix[17] (illustrated in Sec. IV A).

To apply FGS to sample the PPD for experimental data, the (unknown) data variance ν_f is replaced with the variance estimate $\hat{\nu}_f$ given by Eq. (10). The error function applied in the PPD sampling, given by Eq. (29) of Ref. 1, then becomes

$$E(\mathbf{m}) = \sum_{f=1}^{F} B_f(\mathbf{m})|\mathbf{d}_f^{\mathrm{obs}}|^2/\hat{\nu}_f, \tag{11}$$

which consists of the sum of the Bartlett mismatches at each frequency, weighted by the ratio of the squared data magnitude to its estimated variance.

Given the assumed form of the data errors, it is useful for comparative purposes to define an ''effective'' signal-to-noise ratio (ESNR), which provides a measure of the signal level compared to all sources of error (measurement and theory), as quantified by the maximum-likelihood variance estimate. Ideally, the average per-sensor ESNR at frequency f would be defined

$$\mathrm{ESNR} = 10 \log \frac{|\mathbf{d}_f^{\mathrm{sig}}|^2}{|\mathbf{n}_f|^2}, \tag{12}$$

where $\mathbf{d}_f^{\mathrm{sig}}$ represents the signal and $\mathbf{n}_f$ represents the error (including measurement and theory error), with

$$\mathbf{d}_f^{\mathrm{obs}} = \mathbf{d}_f^{\mathrm{sig}} + \mathbf{n}_f. \tag{13}$$

However, since $\mathbf{d}_f^{\mathrm{sig}}$ and $\mathbf{n}_f$ are not known individually, a practical definition for an estimate to the ESNR, denoted $\mathrm{ES\hat{N}R}$, is given by

$$\mathrm{ES\hat{N}R} = 10 \log \frac{\langle|\mathbf{d}_f^{\mathrm{sig}}|^2\rangle}{\langle|\mathbf{n}_f|^2\rangle}. \tag{14}$$

Under the assumption that the error at each sensor is an independent, complex-Gaussian distributed random variable with variance ν_f, it follows that

$$\langle|\mathbf{n}_f|^2\rangle = \nu_f N, \tag{15}$$

$$\langle|\mathbf{d}_f^{\mathrm{sig}}|^2\rangle = |\mathbf{d}_f^{\mathrm{obs}}|^2 - \nu_f N, \tag{16}$$

and hence

$$\mathrm{ES\hat{N}R} = 10 \log \frac{|\mathbf{d}_f^{\mathrm{obs}}|^2 - \nu_f N}{\nu_f N}. \tag{17}$$

Replacing the variance ν in Eq. (17) with its estimate $\hat{\nu}$, given by Eq. (10), and replacing N with N_e leads to

$$\mathrm{ES\hat{N}R} = 10 \log \frac{1 - B(\hat{\mathbf{m}})}{B(\hat{\mathbf{m}})}, \tag{18}$$

which defines the $\mathrm{ES\hat{N}R}$ measure used in this paper.

Finally, it is interesting to note that the approach to estimating the variance from the data presented in this section has a straightforward physical interpretation in that it essentially applies the variance between the observed data and the data predicted for the optimal model as the estimated variance. To see this, note that if the maximization over variance, $\partial L/\partial \nu_f = 0$, is applied to Eq. (2) prior to considering source strength, the result is

$$\hat{\nu}_f = |\mathbf{d}_f^{\mathrm{obs}} - \mathbf{d}_f(\hat{\mathbf{m}})|^2/N, \tag{19}$$

representing the variance between measured and predicted data. Setting $\mathbf{d}_f = S_f \mathbf{w}_f$ in Eq. (19) and minimizing over S_f then leads to Eq. (5) for source strength, which when substituted back into Eq. (19) produces the variance estimate given by Eq. (8) (i.e., changing the order of the maximization steps does not change the final result).

III. PROSIM'97 GEOACOUSTIC SURVEY

A. Experiment and data

The PROSIM'97 shallow-water geoacoustic experiment was carried out by the SACLANT Undersea Research Center in the Mediterranean Sea off the west coast of Italy near Elba Island, as shown in Fig. 1. The experiment consisted of recording acoustic data at a vertical line array (VLA) of hydrophones due to several types of acoustic sources towed along a variety of tracks; only a subset of the (large) total data set is analyzed in this paper. The data considered here were generated by an acoustic transducer towed at approximately 12-m depth over a track with a gently sloping bottom (water depth of approximately 130–135 m). The source emitted a 0.5-s linear frequency-modulated signal that swept over the band 300–850 Hz approximately every 0.25 km in range along the track. The signals were measured at a bottom-moored, 48-sensor VLA, which spanned from 26 to 120 m depth with a 2-m hydrophone spacing. The acoustic pressure at each hydrophone was sampled at 3 kHz and transmitted from the VLA to the source ship via a radio-frequency data link, where it was recorded on optical disc. Environmental parameters such as the ocean sound-speed profile were recorded during the experiment; notably, however, the water-depth measurements along the source track

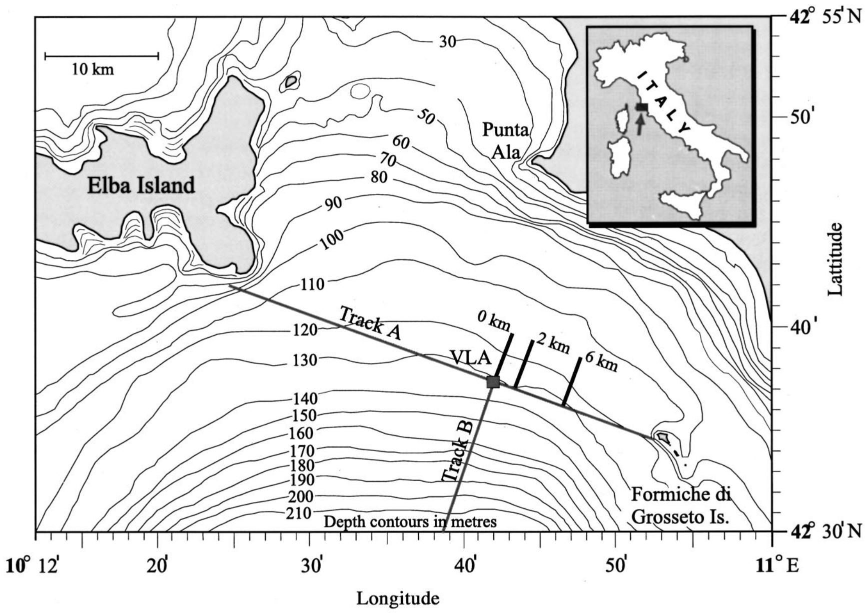

FIG. 1. Site of the PROSIM'97 geoacoustic experiment. Data analyzed in this paper were collected along source track A at ranges of 2–6 km southeast from the VLA.

were subject to large uncertainties due to poor calibration of the source ship's swath multi-beam echosounder.

The data analyzed here were recorded for a portion of the source track to the southeast of the VLA with source–receiver ranges of 2–6 km (Fig. 1). This track section was chosen so that the bottom slope was relatively uniform and the water depth varied by only a small amount, while ensuring long enough ranges that the far-field approximation could be applied in modeling the acoustic fields. An example of the recorded acoustic signals and ambient noise is shown in Fig. 2, in both the time and frequency domains, for the source at a nominal range of 4 km. The data to be inverted were taken to consist of the complex acoustic pressure at the array obtained by fast Fourier transforming the measured time series (the data at a sensor near 60-m depth in Fig. 2 were omitted due to low sensor gain). Because of the motion of the towed source and the swept-frequency character of the acoustic signal, ensemble averaging of data cross-spectral matrices was not possible; however, this should not present a problem, given the high SNR of the measured data (approximately 30–40 dB from Fig. 2). Further details of the PROSIM'97 experiment can be found in Refs. 10–12. FGS analysis is applied to the PROSIM'97 data in Sec. IV; first, however, the results of previous analysis of this experiment and of other

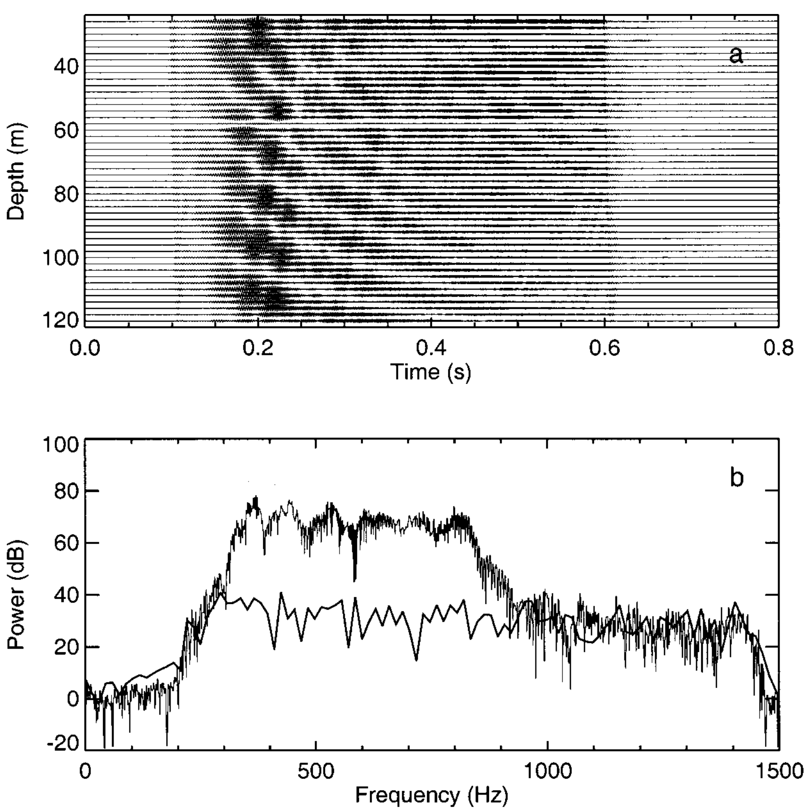

FIG. 2. Acoustic data recorded for a nominal source–receiver range of 4 km. (a) Shows time-domain data at the 48-sensor VLA (arbitrary origin time). (b) Shows frequency-domain data for a mid-water column receiver (arbitrary signal level) with the signal (plus noise) power indicated by the thin line and noise power (recorded prior to the signal) by the thick line.

geophysical and acoustic studies in the same region are briefly reviewed.

B. Previous experiment results

The PROSIM'97 experiment was conducted in the same region as the earlier Yellow Shark experiments,[13–15] which made use of both acoustic and geophysical measurements to determine seabed geoacoustic properties. Hence, the Yellow Shark results provide a relevant baseline for comparison with the results derived here. The geophysical studies included analysis of sediment core samples, high-resolution seismic surveys, and inversion of reflection coefficient versus angle data. These methods indicated that the seabed consisted of a thin, unconsolidated sediment layer of clays and silty clays overlying a basement of consolidated sediments (silt). The thickness of the upper sediment layer varied with range between approximately 3 and 10 m. The sound speed was approximately 1465 m/s at the top of the layer and 1495 m/s at the base, yielding a depth-averaged value of about 1480 m/s. Significantly, the sound speed of this layer was lower than that of water column, which varied between 1510 and 1520 m/s. The density and attenuation of the upper layer were approximately 1.5 g/cm^3 and 0.06 dB/λ, respectively, and the geoacoustic properties of the upper sediment layer varied only weakly with range. The basement layer had a sound speed of approximately 1530–1550 m/s, a density of 1.8 g/cm^3, and an attenuation of 0.1 dB/λ.

Several approaches were applied to the inversion of Yellow Shark acoustic data. Hermand and Gerstoft[13] inverted acoustic data (seven tones at frequencies of 200–800 Hz) using genetic algorithms with the normal-mode model SNAP.[18] The environment was considered mainly range-independent with unknown geometric and geoacoustic properties including a sound-speed gradient in the sediment layer. Gerstoft and Mecklenbräuker[6] also inverted multi-tone data using genetic algorithms and SNAP for a range-independent environmental model. Both of the above studies included marginal PPDs for geoacoustic parameters computed using a genetic-algorithms based sampling algorithm. Siderius and Hermand[14] inverted broadband (200–800 Hz) transmission-loss data from five ranges at a sparse array of four sensors. A range-dependent geoacoustic model was compiled by performing separate range-independent inversions for each of the five range segments, with the sediment and basement sound speeds and the sediment thickness as unknowns (geometry was assumed known). The inversions consisted of systematically varying the three geoacoustic parameters to obtain the best match to the measured data using the parabolic-equation model RAM.[19] Hermand[15] developed an inversion based on modeling the waveguide impulse response, and inverted broadband Yellow Shark data at a single hydrophone. Several processors were derived, and applied to a number of different parameterizations of a two-layer seabed (geometry was assumed known), including both range-independent and range-dependent environments (modeled with SNAP and the coupled-mode model C-SNAP,[20] respectively). The results of the above inversions yielded geoacoustic parameters in general agreement with the geophysical measurements. Overall, the systematic analysis that has been

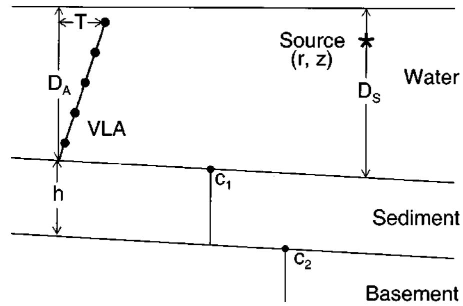

FIG. 3. Geoacoustic/geometric model parameters assumed for inversion of the PROSIM'97 field data.

carried out for the Yellow Shark geophysical and acoustic data, including uncertainty analysis and studying the effects of source range and frequency, makes this an excellent site to study new approaches to geoacoustic inversion.

Fallat *et al.*[11] carried out an initial analysis of the broadband data collected in the PROSIM'97 experiment using a hybrid matched-field inversion algorithm.[21] The model parameterization employed was based on a synthetic sensitivity study performed to identify the significant parameters, and consisted of the sediment layer thickness, h, the average sound speed of the sediment and basement, c_1 and c_2, and geometric parameters including the source range and depth, r and z, array tilt, T (defined as the horizontal offset of the top hydrophone), and the water depth at the source and the array, D_S and D_A. This model parameterization is illustrated in Fig. 3. The unknown geoacoustic parameters were considered range independent, but to accommodate the (weakly) range-dependent bathymetry, the adiabatic normal mode model PROSIM[22] was used to compute replica acoustic fields. Fallat *et al.*[11] independently analyzed recordings of multiple acoustic signals recorded during the experiment to examine the consistency of the inversion results. Their study concluded that the basement sound speed was reliably estimated, but that significant variation existed in the other parameter estimates. Table I summarizes the range of values obtained for geoacoustic properties h, c_1, and c_2 from the the Yellow Shark and PROSIM'97 experiments.

TABLE I. Summary of geoacoustic results in the PROSIM'97 survey region. GEO refers to geophysical measurements carried out during the Yellow Shark experiments; YS1, YS2, and YS3 refer to the Yellow Shark acoustic inversions of Refs. 13, 14, and 15, respectively; PRO refers to previous inversion of the PROSIM'97 acoustic data (Ref. 11); and FGS refers to the analysis of this paper. Note that the range of values for GEO includes the observed parameter variability with range or depth. For the acoustic surveys, the minimum and maximum inversion results are given (YS1 c_1 results represent an average over the gradient included in the sediment layer). FGS results represent the PPD mean plus/minus one standard deviation.

Analysis	h (m)	c_1 (m/s)	c_2 (m/s)
GEO	3–10	1465–1495	1530–1550
YS1	5–15	1465–1525	1520–1560
YS2	3–6	1463–1493	1551–1586
YS3	7–9	1465–1490	1525–1535
PRO	3–9	1465–1496	1522–1542
FGS	3–7	1465–1500	1527–1538

IV. FGS ANALYSIS

A. Model parameterization and data error estimation

To apply FGS analysis to the PROSIM'97 experiment first requires parameterizing the model of unknown geoacoustic/geometric properties and estimating the variance of the measured acoustic data. The model parameterization adopted here is the same as that used by Fallat *et al.*[11] in their analysis of the PROSIM'97 experiment, as described in Sec. III B and illustrated in Fig. 3. The density and attenuation in the sediment and basement were held fixed at the values determined by the Yellow Shark geophysical studies, described above. Replica acoustic fields were computed using the adiabatic normal-mode model PROSIM to accommodate the weak range dependence. Note that for efficiency, PROSIM computes only the propagating or trapped modes, and hence is accurate only in the far field. The bathymetry between source and receiver was taken to consist of a uniform slope from water depth D_S to D_A, with modal properties calculated at five intermediate points for the range-dependent modeling (previous studies indicated that this provided an adequate representation of the slope within the adiabatic approximation).[11,12] Since the model is parameterized in terms of range-independent geoacoustic parameters, acoustic inversion will recover integral averages of whatever range-dependent variation exists in the parameters between source and receivers. Similarly, since the upper sediment layer is parameterized with a homogeneous sound speed (following the sensitivity studies in Refs. 11 and 14), the sound speed recovered is expected to represent an average of the depth-dependent variation within this layer.

The second requirement for the FGS analysis is an estimate of the data error statistics. This paper will primarily consider acoustic data over the octave 300–600 Hz, although the effect of including the entire bandwidth is considered in Sec. IV C. Figure 2 indicates that the SNR of the measured acoustic data over the signal band is high (approximately 30–40 dB). However, for Bayesian inversion the data uncertainty must also include theory errors due to factors such as the simplified model parameterization and the approximate forward model described above, which typically dominate the variance at high SNR. Under the assumption of independent, identically distributed Gaussian errors, Eq. (10) provides a maximum-likelihood estimate of the data variance. To apply this estimate requires determining both the maximum-likelihood model $\hat{\mathbf{m}}$ and the effective mode number N_e. Maximum-likelihood models are determined here by minimizing objective function Eq. (9) using an adaptive hybrid matched-field inversion algorithm known as adaptive simplex simulated annealing.[23] The effective mode number can be estimated from a principal component analysis of the acoustic data as follows.[17] Acoustic fields recorded for the source at 16 ranges from 2 to 6 km were used to provide an ensemble average of the data covariance matrix. The eigenvectors of this matrix represent the principal components (empirical orthogonal functions) of the measured data, with the eigenvalues indicating the energy associated with each principal component (since 16 recordings were used in computing the data covariance matrix, there will be 16 nonzero eigenvalues). Since the set of principal components and the set of propagating modes both represent orthogonal bases for the acoustic data, the number of significant eigenvalues indicates the effective mode number. A suitable value can be estimated from the cumulative fractional energy η_n when n out of the total of $N_{pc}=16$ principal components (with nonzero eigenvalues) are included in the summation. With the eigenvalues μ_k, $k=1, N_{pc}$ ordered in decreasing magnitude, η_n is defined

$$\eta_n = \frac{\sum_{k=1}^{n} \mu_k}{\sum_{k=1}^{N_{pc}} \mu_k}. \tag{20}$$

Figure 4 shows curves for η_n as a function of n at frequencies of 300–600 Hz. By considering this figure, the effective

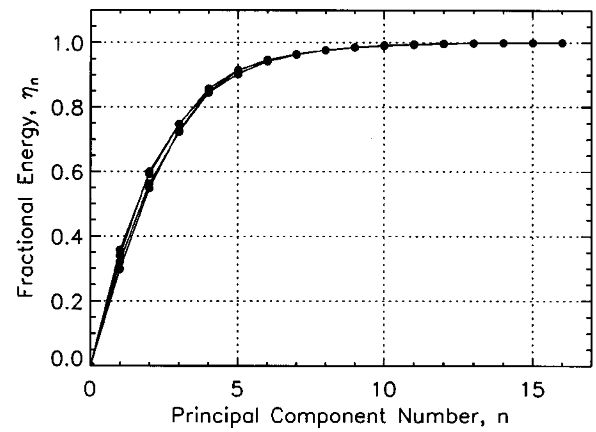

FIG. 4. Cumulative fractional energy η_n from principal component analysis of data for 16 source–receiver ranges from 2 to 6 km, as a function of the number of principal components n (curves shown for frequencies of 300, 400, 500, and 600 Hz).

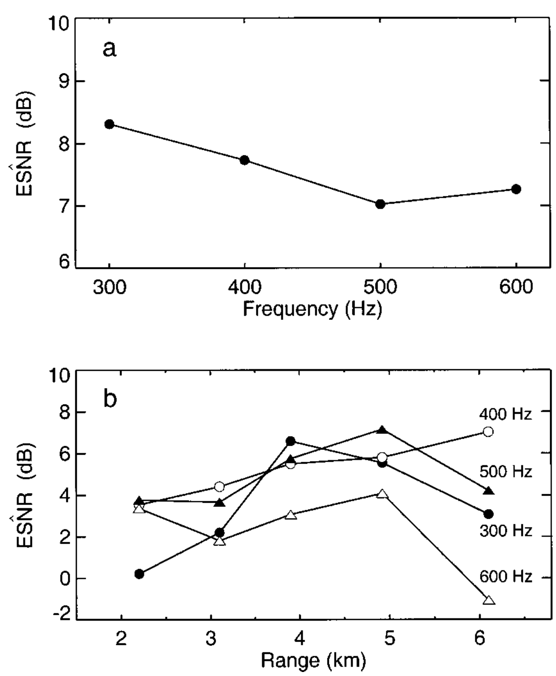

FIG. 5. Effective signal-to-noise ratio estimate $\widehat{\mathrm{ESNR}}$ of measured acoustic data used in FGS analysis. (a) Shows $\widehat{\mathrm{ESNR}}$ for single frequency inversions at 300, 400, 500, and 600 Hz for a nominal source range of 4 km. (b) Shows $\widehat{\mathrm{ESNR}}$ for multiple-frequency inversions for ranges of 2, 3, 4, 5, and 6 km.

mode number was taken to be $N_e = 5$ for all frequencies, since the first five principal components account for approximately 90% of the total acoustic energy, and the rate of change in η_n decreases significantly at about this value of n. It was found that the FGS analysis presented in Sec. IV B is not overly sensitive to the choice of N_e, in that a small variation (e.g., $N_e = 7$) did not significantly alter the results of the analysis.

Figure 5(a) shows the $\mathrm{ES}\hat{\mathrm{N}}\mathrm{R}$ calculated for single-frequency analysis at frequencies of 300, 400, 500, and 600 Hz using the acoustic fields measured for the 4-km source. Figure 5(b) shows the $\mathrm{ES}\hat{\mathrm{N}}\mathrm{R}$ when multi-frequency analysis is applied (i.e., data at multiple frequencies are inverted simultaneously) for source ranges of 2, 3, 4, 5, and 6 km. For multi-frequency analysis, the $\mathrm{ES}\hat{\mathrm{N}}\mathrm{R}$ is generally found to be somewhat lower at each frequency than for single-frequency analysis [e.g., compare the results in Fig. 5(a) with those at 4-km range in Fig. 5(b)]. The difference is likely due to the fact that the errors at each frequency are not fully independent (as assumed), and this deficit in information is represented by a lower $\mathrm{ES}\hat{\mathrm{N}}\mathrm{R}$. Figure 5(b) suggests a general increase in $\mathrm{ES}\hat{\mathrm{N}}\mathrm{R}$ with range out to 5 km. Since the signal level is higher at shorter ranges, the increase in $\mathrm{ES}\hat{\mathrm{N}}\mathrm{R}$ must be due to a decrease in the theory error with range. This could be due to improved validity of the far-field approximation in the normal-mode propagation model, and to the fact that high-angle propagation becomes less important at longer ranges, which de-emphasizes the inadequacies of the model parameterization at greater depths (e.g., use of a uniform basement). The somewhat unusual $\mathrm{ES}\hat{\mathrm{N}}\mathrm{R}$ values at 6-km range in Fig. 5(b) could be due to the fact that the water depth along the track stops increasing and begins decreasing at about this range (see Fig. 1), and hence the uniform slope assumed for the bathymetry is not completely valid.

B. FGS uncertainty analysis and validation

In this section, the FGS approach to Bayesian inversion, developed and validated for synthetic test cases in Ref. 1, is applied to the acoustic field data recorded during the PROSIM'97 experiment. Bayesian methods are sometimes criticized because of their explicit dependence on knowledge of the data error statistics.[3,8] In the present application to geoacoustic inversion, the actual error distribution is unknown, and the assumption is made of independent, identically distributed Gaussian errors, with the variance given by a maximum-likelihood estimate derived from the data. Since the applicability of these assumptions and their effect on the FGS analysis are not known *a priori*, it is important to validate the parameter uncertainty estimates obtained to have confidence in the analysis for experimental data. FGS is ap-

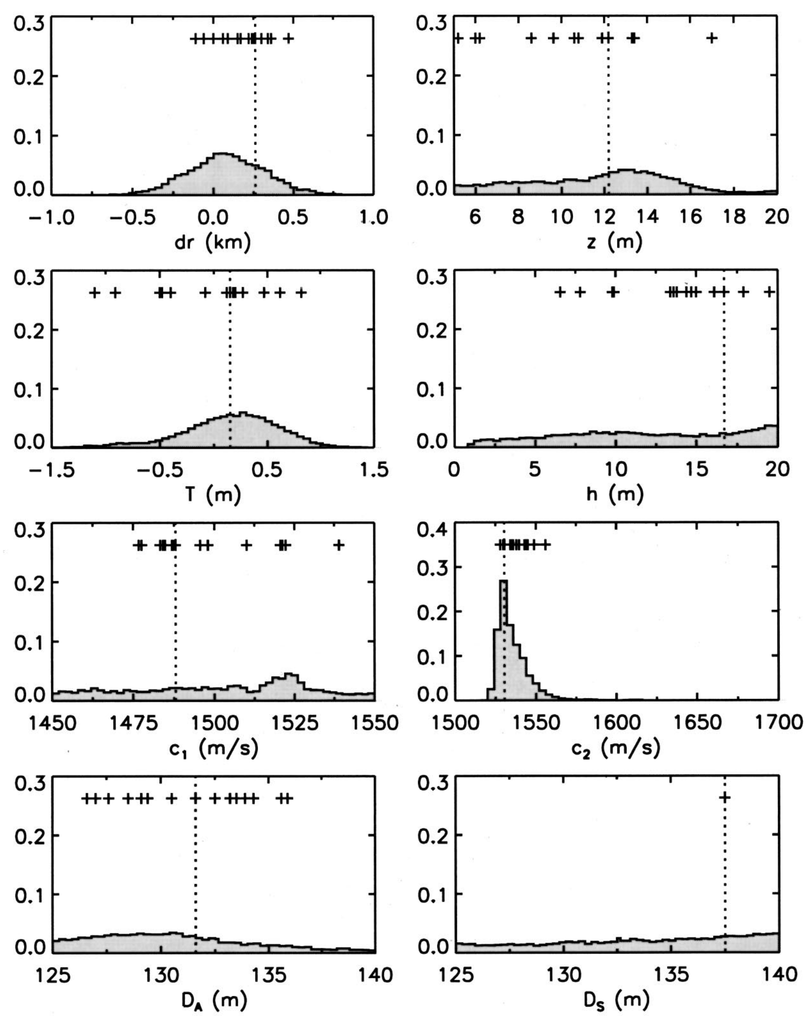

FIG. 6. Marginal probability distributions estimated from 400-Hz data for a nominal range of 4 km and wide search bounds (indicated by the range of abscissa values for each parameter). Crosses indicate the MAP model parameters obtained via matched-field inversion of 16 independent data sets recorded for 2–6 km range. Dotted lines identify the MAP parameters for the 4-km source.

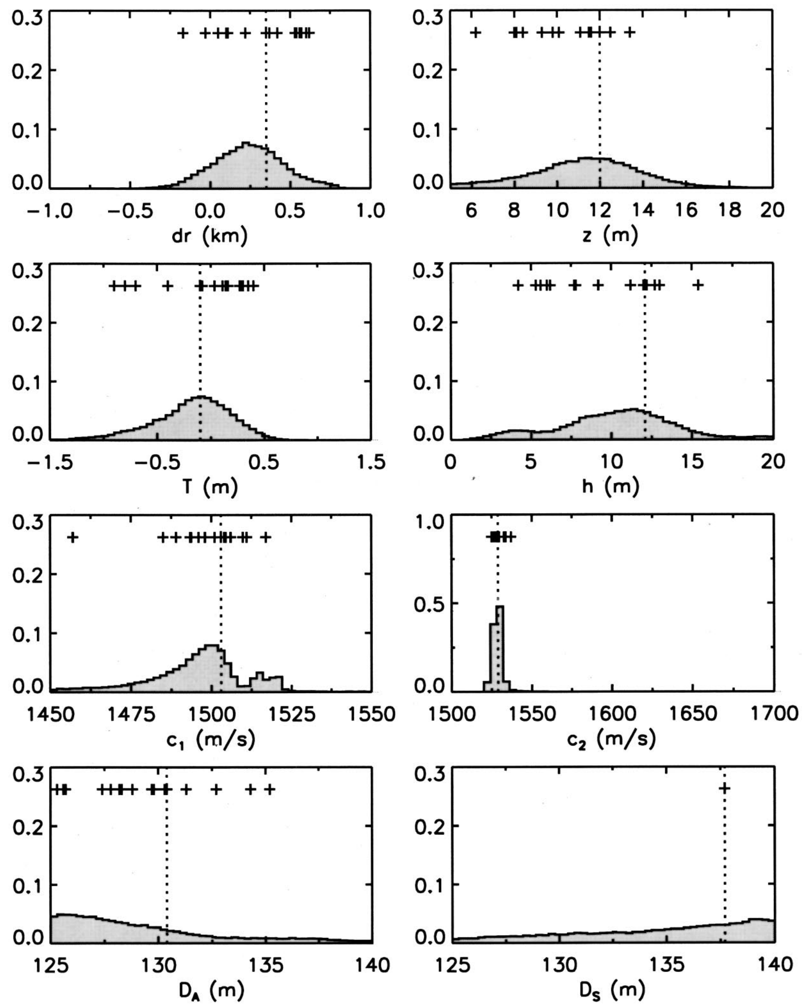

FIG. 7. Marginal PPDs estimated from multi-frequency (300, 400, 500, 600 Hz) acoustic data for a nominal source range of 4 km and wide parameter search bounds. Crosses indicate the MAP model parameters for 16 data sets collected for ranges of 2–6 km. Dotted lines identify the MAP parameters for the 4-km source.

plied here to a number of different source frequencies, source–receiver ranges, and levels of prior information, with the goal of interpreting the experiment results and validating the FGS approach for measured ocean acoustic data.

Figure 6 shows the marginal probability distributions for the eight geometric and geoacoustic parameters computed by applying FGS to the acoustic fields recorded at a single frequency of 400 Hz for the source at a nominal range of 4 km. The marginal distributions in Fig. 6 (and throughout this paper) are represented by histograms of the sampled models discretized into 50 bins. For display purposes, the plots are scaled so that a value of unity represents all probability concentrated in one bin. To convert this to a normalized probability value such that the integral over the parameter bounds (scaled to [0, 1]) is one, simply multiply the vertical scale by the number of bins. In Fig. 6, reasonably wide parameter search bounds (indicated by the range of abscissa values for each parameter plot) were adopted to assess the resolving power of the acoustic data with limited prior information. Note that the marginal distribution for the source range is expressed as the difference dr from the nominal range, rather than as range r itself. The marginal distributions obtained are smooth and relatively simple functions, although they are not symmetric or strictly unimodal for all parameters. Figure 6 shows that the source range, array tilt, and basement sound speed are resolved to varying degrees within their search bounds, but that other parameters (sediment thickness and sound speed and water depth at the source and array) are almost completely unresolved.

As a validity check of the FGS marginal probability distributions, Fig. 6 also includes the parameters of the maximum *a posteriori* (MAP) model solutions computed by minimizing the mismatch function Eq. (9) within the parameter search bounds for each of the 16 acoustic data sets recorded for source ranges of 2–6 km (the minimization was carried out using adaptive simplex simulated annealing[23]). The inversion results for the source at 4-km range (the range for which the marginal distributions were computed) are indicated by a dotted line. The idea here is that the variability in the MAP parameter estimates obtained by inverting multiple independent data sets should approximately reflect the relative parameter uncertainties of the marginal distributions. Given the fairly small number of available data sets and the fact that the actual environmental properties likely vary somewhat with range, this comparison is not intended to be rigorous. Nonetheless, Fig. 6 shows a reasonably good correspondence between the ''width'' of the marginal distributions and the variability in the MAP estimates for all parameters. In particular, the relatively small variation in the MAP estimates for the basement sound speed c_2 is in good agreement with the narrow marginal distribution for this parameter, while the much larger variation in MAP estimates for

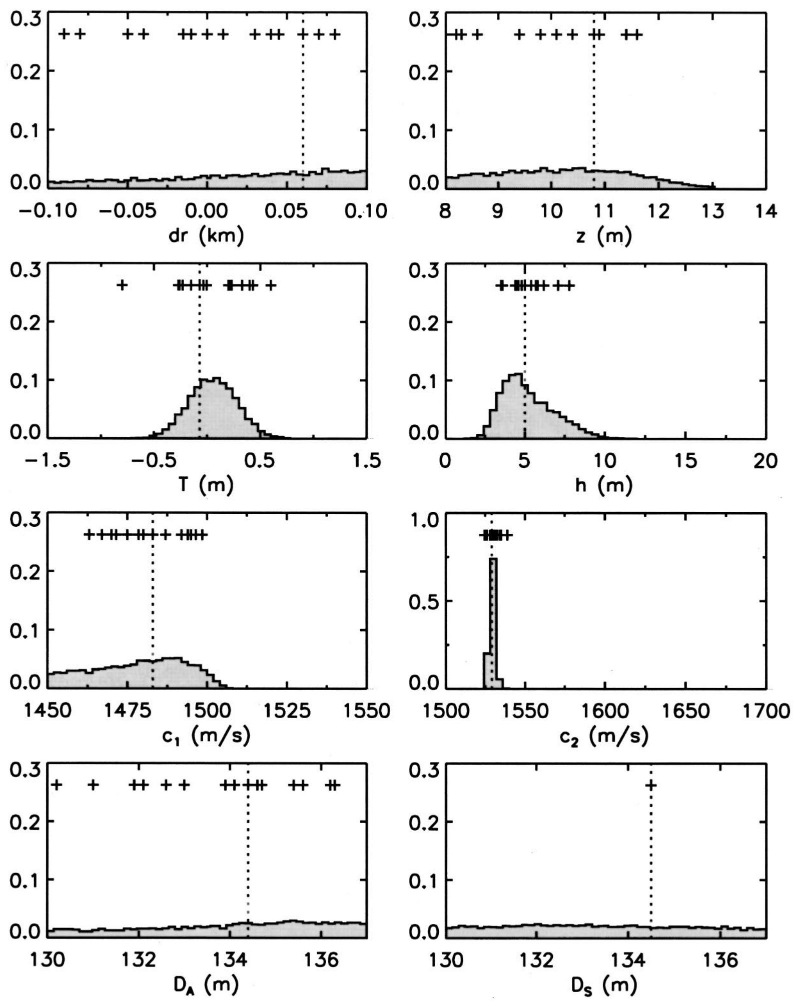

FIG. 8. Marginal PPDs estimated from multi-frequency (300, 400, 500, 600 Hz) acoustic data for a nominal source range of 4 km and narrow search bounds for geometric parameters except array tilt (parameter bounds indicated by range of abscissa values). Crosses indicate the MAP model parameters for 16 independent data sets collected for ranges of 2–6 km. Dotted lines identify the MAP parameters for the 4-km source.

the sediment sound speed and thickness, c_1 and h, reflect the wider probability distributions for these parameters. Note that since the water depth at the source D_S differed for each of the 16 data sets, only the result for the 4-km source is included in Fig. 6.

The marginal PPDs shown in Fig. 6 for acoustic data at 400 Hz indicate large uncertainties for the geoacoustic/geometric parameters, with the exception of the basement sound speed c_2. One approach to reduce these uncertainties is to include more data information in the analysis in the form of acoustic fields recorded at multiple frequencies. Figure 7 shows the marginal PPDs computed for data at frequencies of 300, 400, 500, and 600 Hz. In comparison with the single-frequency results (Fig. 6), the uncertainty is markedly reduced for a number of parameters in Fig. 7. For instance, the marginal distribution for c_1 and c_2 are considerably narrower, and parameters z and h are now clearly resolved within their search bounds. Figure 7 also shows the MAP parameter estimates obtained via hybrid inversion of independent multi-frequency data sets for 16 source ranges between 2 and 6 km. In comparison to the 400-Hz results shown in Fig. 6, the variation in the multi-frequency MAP estimates has decreased, particularly for h, c_1, and c_2. The spread in the independent MAP estimates is in good general agreement with the marginal distribution widths for all parameters. PPDs computed for other combinations of source frequencies are considered in Sec. IV C.

Figures 6 and 7 show that increasing the amount of data information can decrease the geoacoustic parameter uncertainties. Another approach is to improve the prior information by applying narrower parameter search bounds. In Figs. 6 and 7, wide search bounds were assumed for all parameters. Figure 8 shows the marginal PPDs computed for multi-frequency acoustic data when narrow search bounds are applied for the geometric parameters r, z, D_A, and D_S. In this case, the search bounds represent the actual experimental limitations of prior knowledge for these parameters (search bounds are indicated by the range of abscissa values for each parameter). Note that due to the difficulties with the echo-sounder on the source ship, the search bounds for the water depths are still relatively wide (130–137 m). In comparison to Fig. 7, the marginal distributions for parameters h and c_2 in Fig. 8 are substantially narrower, and the marginal distribution for c_1, although somewhat wider in Fig. 8, is in better agreement with the geophysical results which indicated an average sound speed in this layer of approximately 1480 m/s. The MAP model parameters computed for multiple independent data sets with narrow search bounds are also indicated in Fig. 8, and the spread in these parameters is again in good

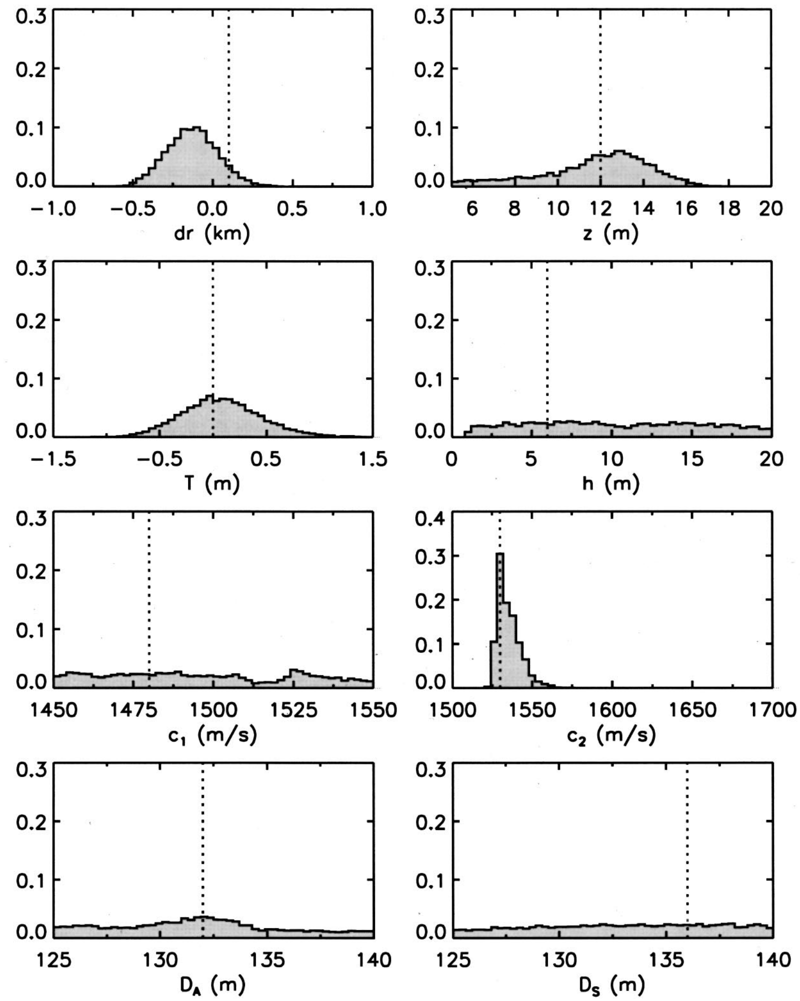

FIG. 9. Marginal PPDs estimated from noisy synthetic data at 400 Hz for a source range of 4 km using wide parameter search bounds. Dashed lines indicate the true parameter values.

general agreement with the estimated marginal distribution widths.

Another approach to validating the estimated PPD for measured data involves applying the FGS analysis to synthetic data computed to simulate the experimental data and errors as closely as possible. To this end, a model of the geoacoustic/geometric parameters was chosen to agree with the geophysical and acoustic survey results consisting of: $h=6$ m, $c_1=1480$ m/s, $c_2=1530$ m/s, $r=4$ km, $z=12$ m, $D_S=135$ m, $D_A=132$ m, and $T=0$ m. Synthetic acoustic data were computed for this model using the adiabatic normal-mode propagation model PROSIM. Since the errors for the experimental data were assumed to consist of independent, unbiased, Gaussian-distributed random variables with variance given by the maximum-likelihood estimate derived from the data, random errors with identical statistics were added to the synthetic acoustic data. FGS was applied to synthetic data computed in this manner for the source frequencies and parameter search bounds used in the analysis of the experimental data given in Figs. 6–8, with the results given in Figs. 9–11, respectively. In comparing the marginal PPDs computed for the simulated data to those for the measured data, it should be noted that since the actual data errors and the underlying geometric and geoacoustic parameters are not identical, the position of the maxima and the detailed structure of the marginal distributions may differ. However, if the error statistics assumed for the experimental data are valid, the width and general character of the marginal PPDs should be similar for measured and simulated data. Comparing Fig. 6 with Fig. 9, Fig. 7 with Fig. 10, and Fig. 8 with Fig. 11 indicates that this is indeed the case, with generally close correspondence in the character and width of the marginal PPDs for each parameter between the measured and simulated data. This correspondence is quantified in Fig. 12, which compares the standard deviation σ_i of the marginal distribution for parameter m_i (normalized by the width w_i of the parameter search bound) computed for both measured and simulated data. Figure 12 shows good agreement between the results for measured and simulated data, particularly for the case involving multi-frequency data with narrow search bounds for the geometric parameters shown in Fig. 12(c).

As further validation of the FGS approach, the marginal probability distributions computed for geoacoustic parameters h, c_1, and c_2 from the PROSIM'97 data are found to be in good general agreement with the results of previous geophysical and acoustic surveys in the region. In Table I, the uncertainties for these parameters are quantified by the PPD mean plus/minus one standard deviation, and compared with previous results. Although the geophysical results quoted (which include the observed parameter variability with depth and/or range) are not directly comparable to the FGS analy-

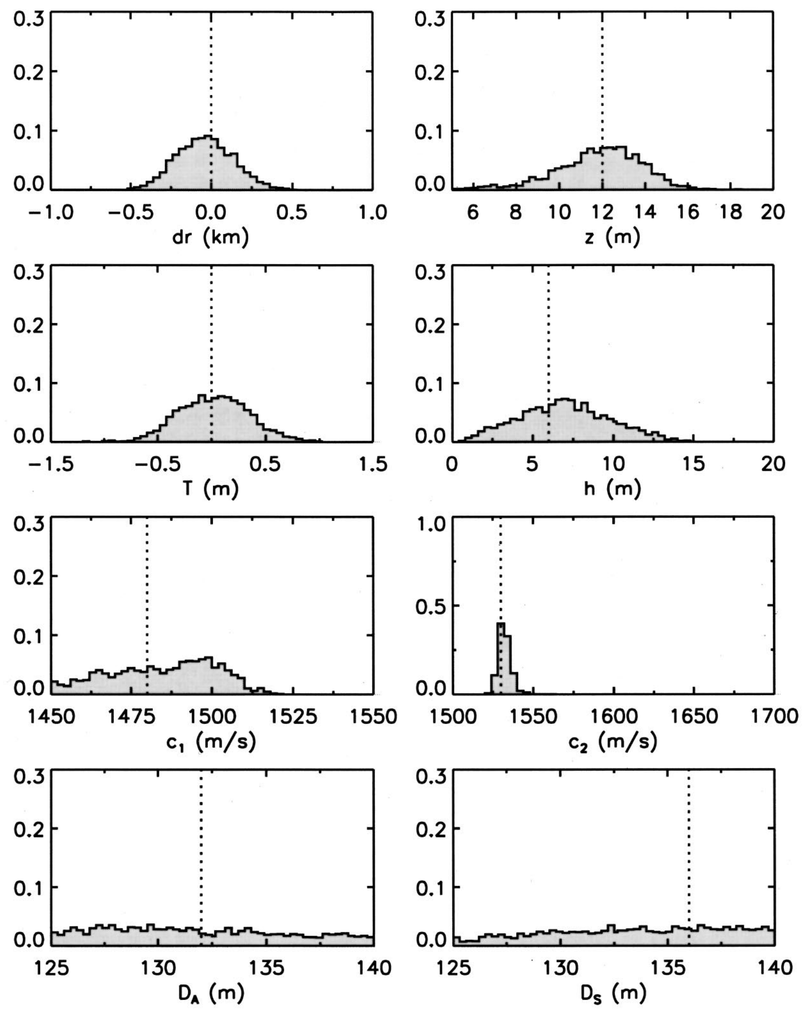

FIG. 10. Marginal PPDs estimated from noisy synthetic data at multiple frequencies (300, 400, 500, 600 Hz) for a source range of 4 km using wide parameter search bounds. Dashed lines indicate the true parameter values.

sis (which represents the uncertainty of range- and depth-integrated values), it is clear that both approaches yield similar parameter estimates. Furthermore, the FGS parameter uncertainties agree well with the variability (minimum and maximum values) obtained in previous acoustic inversions of the Yellow Shark and PROSIM'97 data sets.

C. PPD stability versus frequency and range

Section IV B illustrated marginal probability distributions computed from both single- and multiple-frequency data sets, and validated the distributions by comparison with multiple independent MAP inversions and analogous synthetic test cases. In this section, the stability of the marginal PPDs is considered as a function of both source frequency and range. To illustrate the dependence of the marginal PPDs on frequency, Fig. 13 shows the uncertainty distributions computed for the geoacoustic parameters using single-frequency data at 300, 400, 500, and 600 Hz, as well as the distributions obtained for multi-frequency data that included all of these frequencies (the multi-frequency result is the same as in Fig. 8). Narrow search bounds were applied for the geometric parameters (as per Fig. 8) in the FGS analysis. However, since the marginal distributions obtained for the geometric parameters in each case closely resemble those shown in Fig. 8, for simplicity, they are not included in the figure. Figure 13 shows that the marginal distributions obtained for the geoacoustic parameters using single-frequency data are simple, smooth functions that are very similar from frequency to frequency. This indicates that the PPD is stable with respect to frequency (i.e., it does not vary rapidly, change character, or fluctuate for small frequency changes), suggesting a consistency in the information content across the one-octave frequency band. However, more substantial differences in the marginal PPDs might be expected over wider frequency bands.

The single-frequency marginal distributions in Fig. 13 indicate poor resolution of the sediment parameters h and c_1 within their search bounds, while the basement sound-speed c_2 is reasonably well resolved. By comparison, the marginal PPDs computed for multi-frequency data are substantially narrower for all parameters, and the resulting distributions are in better agreement with the available independent geoacoustic information summarized in Table I. It is interesting to note from Fig. 13(a) that although all of the marginal distributions computed for single-frequency data indicate a substantial probability that the sediment layer has a thickness $h > 10$ m, the multi-frequency marginal PPD precludes this possibility. A similar observation can be made regarding sediment sound speeds $c_1 > 1505$ m/s. This indicates that simultaneous inversion of a multi-frequency data set can

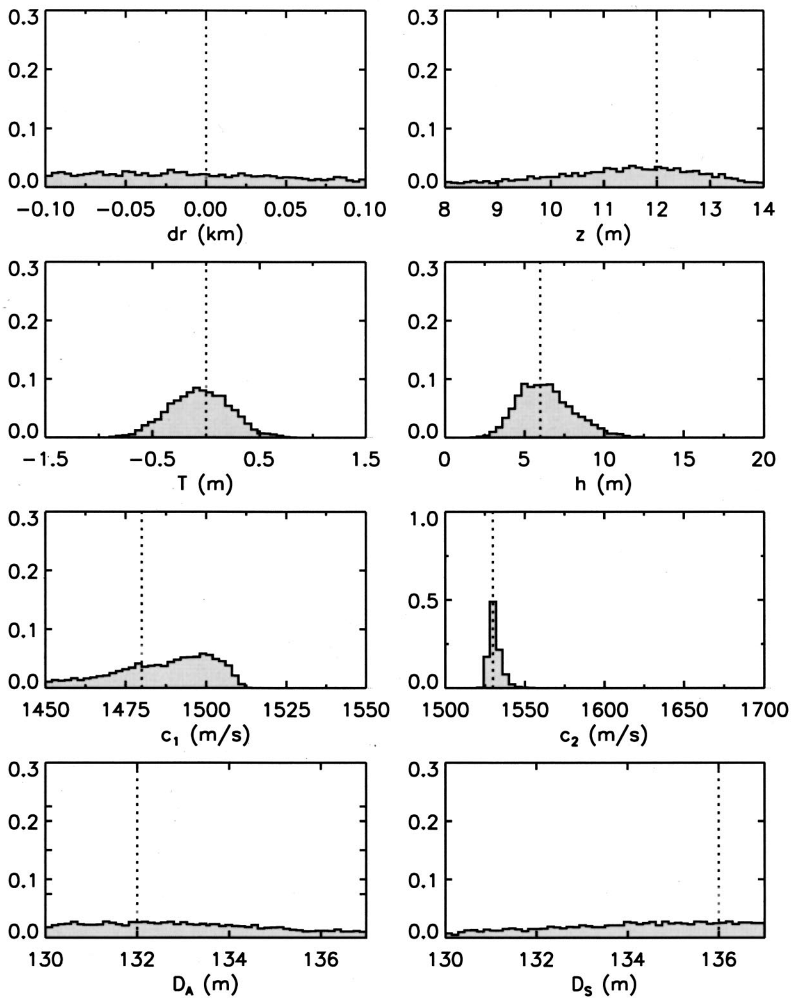

FIG. 11. Marginal PPDs estimated from noisy synthetic data at multiple frequencies (300, 400, 500, 600 Hz) for a source range of 4 km using narrow search bounds for geometric parameters. Dashed lines indicate the true parameter values.

eliminate ambiguities that are not precluded by data at any of the individual component frequencies.

To illustrate the improvement in the marginal distributions as a function of the frequency content, Fig. 14 shows marginal PPDs for the geoacoustic parameters computed using data at: 400 Hz; 300 and 400 Hz; 300, 400, and 500 Hz; and 300, 400, 500, and 600 Hz; and 300, 400, 500, 600, 700, and 800 Hz (cases 1–5, respectively). Comparing the marginal PPDs of cases 1 and 2 in Fig. 14 shows that including just two frequencies in the FGS analysis provides a substantial improvement over the single-frequency case for all geoacoustic parameters. Case 3 shows that including three frequencies provides a significant, but smaller, improvement, precluding sediment thicknesses $h > 10$ m and sound speeds $c_1 > 1505$ m/s. However, cases 3, 4, and 5 show that including four or more frequencies in the analysis does not result in a significant improvement over the three-frequency case. Hence, it appears that the most significant improvement in the marginal PPDs can be obtained using data at a fairly small number of frequencies over the octave band. This may indicate that data at relatively closely space frequencies do not contain significant linearly independent information. Greater improvements might be obtained by including data at frequencies over a wider band in the analysis. A similar analysis of marginal PPDs versus data frequency content was carried out by Gerstoft and Mecklenbräuker[6] and by Hermand and Gerstoft[13] for the Yellow Shark data; however, the results of those analyses are not easily interpreted as the genetic-algorithms based sampling method employed did not converge to simple, smooth distributions.

The dependence of the geoacoustic parameter uncertainties on the source range is illustrated in Fig. 15, which shows the marginal PPDs computed using multi-frequency data sets recorded for nominal ranges of 2, 3, 4, 5, and 6 km. This figure shows that the uncertainties for the sediment properties h and c_1 decrease somewhat with range from 2 to 4 km, while from 4 to 6 km the uncertainty distributions for all parameters are similar. This indicates general stability of the PPD as a function of range, with a weak range-dependence to the information content at shorter ranges. The wider uncertainty distributions for h and c_1 for source ranges of 2–3 km appear to be related to the lower $\widehat{\mathrm{ESNR}}$ values previously noted for these ranges in Fig. 5. To illustrate this point, Figs. 16 and 17 show marginal PPDs as a function of range computed for synthetic data with differing error statistics. In Fig. 16, the variance of the simulated data at each range was taken to be equal to the variance estimated from the measured data for the corresponding range, as indicated by the $\widehat{\mathrm{ESNR}}$ values given in Fig. 5(b). The widths of the resulting marginal PPDs are in good agreement with those for the measured data (Fig. 15), including the long distribution tails

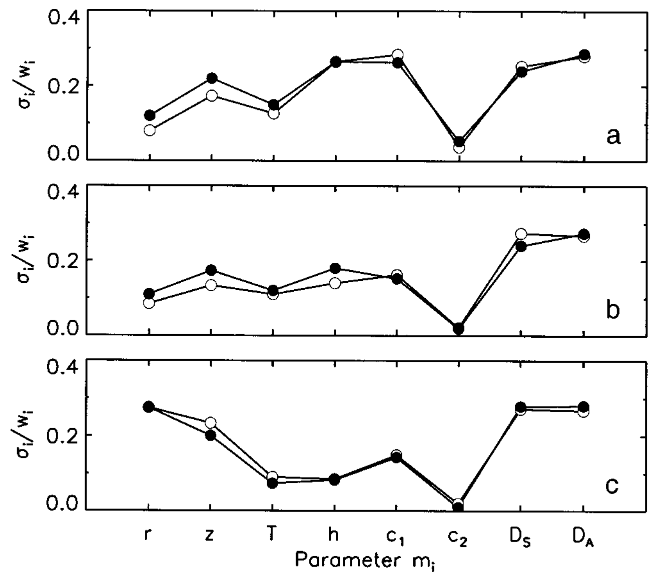

FIG. 12. Ratio of parameter standard deviation σ_i to search bound width w_i for FGS analysis of measured and synthetic data (solid and open circles, respectively). (a) shows results for 400-Hz data and wide search bounds (Figs. 6 and 9); (b) shows results for multi-frequency data and wide search bounds (Figs. 7 and 10); and (c) shows results for multi-frequency data and narrow search bounds (Figs. 8 and 11).

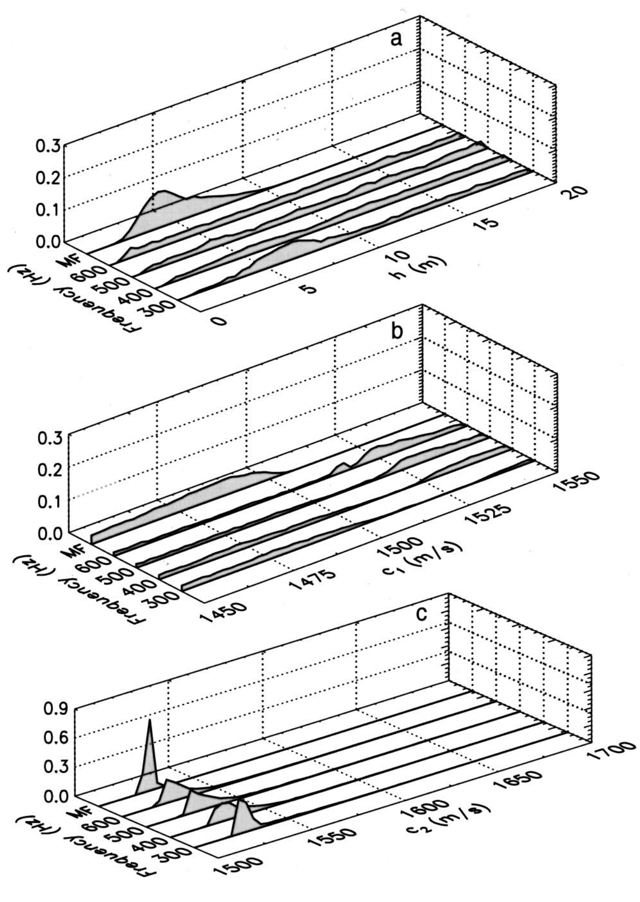

FIG. 13. Marginal PPDs for geoacoustic parameters h, c_1, and c_2 estimated from measured single frequency data at 300, 400, 500, and 600 Hz, and from multi-frequency (MF) data at all four frequencies. The nominal source range is 4 km, and narrow search bounds were applied for geometric parameters (not shown). For simplicity, histograms are represented by smooth functions.

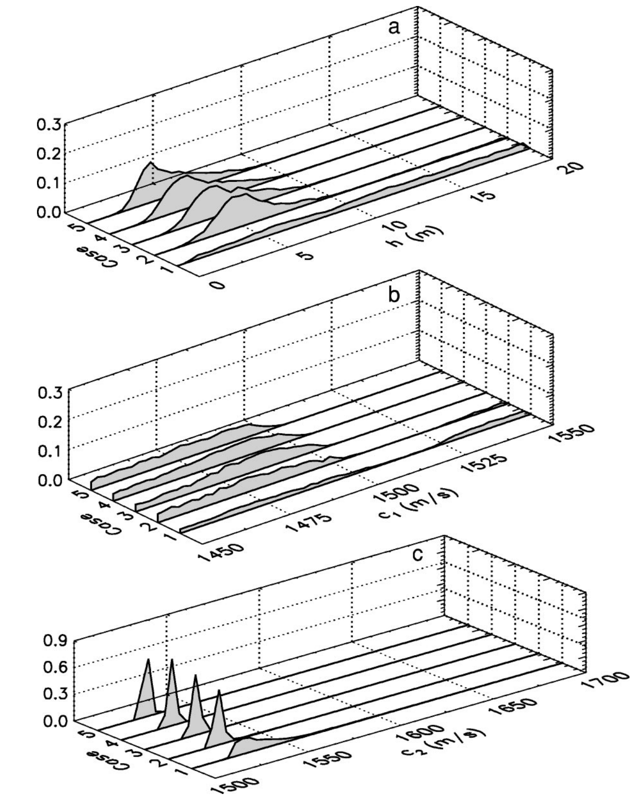

FIG. 14. Marginal PPDs for geoacoustic parameters h, c_1, and c_2 estimated from measured data with various frequency contents: case 1—400 Hz; case 2—300 and 400 Hz, case 3—300, 400 and 500 Hz; case 4—300, 400, 500, and 600 Hz; and case 5—300, 400, 500, 600, 700, and 800 Hz. Nominal source range is 4 km, and narrow bounds were applied for geometric parameters (not shown).

for large values of h and c_1 at the 2–3 km range. In Fig. 17, the variance of the simulated data at each range was taken to be equal to the variance estimated for the measured data at the 4-km range (i.e., the same variance was applied at all ranges). In this case, the marginal distributions for ranges of 2–3 km are narrower than those computed for the measured data; in particular, the long distribution tails for h and c_1, evident in Figs. 15 and 16, are absent in Fig. 17. Hence, the wider marginal distributions at short ranges appear to be accounted for by the larger data variances at these ranges.

D. Inter-parameter correlations

In the preceding sections, the PPD has been quantified in terms of marginal probability distributions for individual parameters, which effectively integrates out the dependence on all other parameters. Marginal distributions can be particularly useful for representing parameter uncertainties. However, insight into the causes of these uncertainties can often be obtained by examining the inter-dependencies between parameters. To quantify parameter inter-dependencies, the posteriori covariance matrix can be computed from the PPD sample accrued by the FGS algorithm, as described in Ref. 1. For display purposes, it is convenient to normalize the ele-

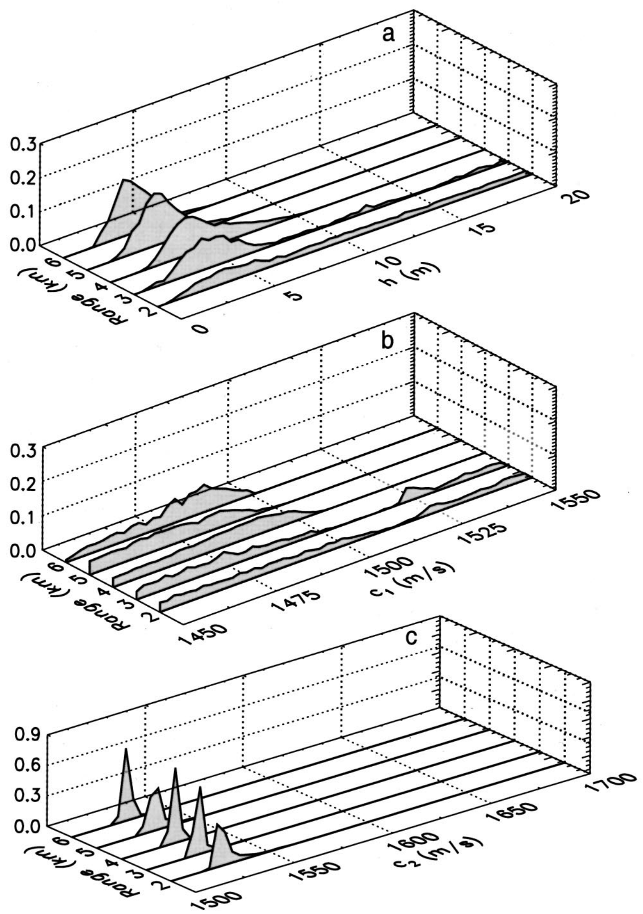

FIG. 15. Marginal PPDs for geoacoustic parameters h, c_1, and c_2 estimated from multi-frequency (300, 400, 500, 600 Hz) measured data for nominal source ranges of 2, 3, 4, 5, and 6 km and narrow search bounds for geometric parameters (not shown).

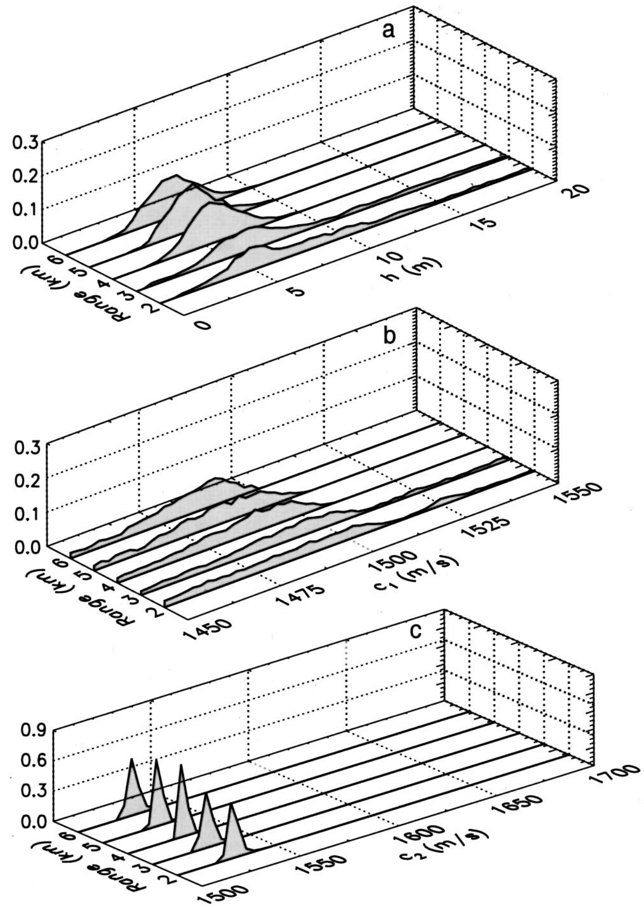

FIG. 16. Marginal PPDs for geoacoustic parameters h, c_1, and c_2 estimated from multi-frequency (300, 400, 500, 600 Hz) synthetic data for source ranges of 2, 3, 4, 5, and 6 km and narrow bounds for geometric parameters (not shown). The variances of the simulated data errors at each range were determined from measured data at that range [ESNRs given in Fig. 5(b)].

ments of the covariance matrix to remove the effects of differing parameter scales and units to produce the parameter correlation matrix $\mathbf{R}$ (defined in Ref. 1). Elements R_{ij} of the correlation matrix are within ± 1, with a value of $+1$ (-1) indicating perfect positive (negative) correlation between parameters m_i and m_j, and near-zero values indicating uncorrelated parameters (diagonal elements are unity by definition). Figure 18 shows the correlation matrices estimated for both measured and simulated data for a source at 4-km range and the three cases considered in Sec. IV B. In each case, good agreement is obtained between the two matrices. Figure 18(a) shows that for 400-Hz data and wide search bounds for the geometric parameters, the correlation matrix is dominated by the diagonal (autocorrelation) elements, and no significant inter-parameter correlations are evident. Figure 18(b) shows that for multi-frequency data and wide geometric bounds, a negative correlation between sediment thickness h and water depth D_A, and a positive correlation between h and sediment sound speed c_1 exist. Finally, Fig. 18(c) shows that for the most informative case of multi-frequency data and narrow geometric bounds, the following correlations exist: a strong negative correlation between h and both D_A and D_S, a positive correlation between D_A and D_S, and a positive correlation between h and c_1.

The inter-parameter correlations indicated in Fig. 18(c) can be illustrated further by plotting 2D marginal probability distributions for specific pairs of parameters, as shown in Fig. 19. In this figure, the marginal distributions are represented by 2D histograms, with each parameter discretized into 50 bins to obtain 2500 pixels. The distributions are scaled so that a value of unity represents all probability concentrated into one pixel (to convert to normalized probability, multiply by the number of pixels). In Fig. 19(a), the 2D marginal PPD for h and D_A clearly illustrates the strong negative correlation between these parameters, with the probability density confined to a fairly narrow elongated zone oriented with a negative slope relative to the parameter axes. The 2D marginal PPD for h and D_S, shown in Fig. 19(b), also indicates a negative correlation, although the probability distribution is somewhat more diffuse. The positive correlation between D_S and D_A can be discerned in Fig. 19(c) despite the highly diffuse distribution, and Fig. 19(d) clearly illustrates the positive correlation between h and c_1. Finally, Figs. 19(e)–19(i) show examples of 2D marginal PPDs for uncorrelated parameters. It should be noted that the small-scale structure in Fig. 19 results from undersampling of the 2D distributions since the convergence criterion for FGS is based on 1D marginal distributions.[1]

Simple physical explanations can account (at least in

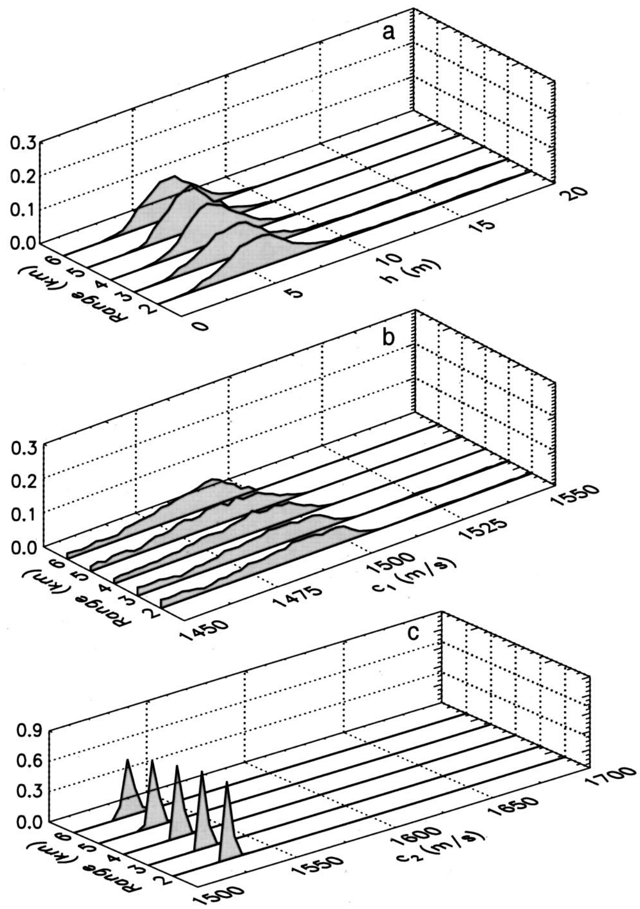

FIG. 17. Marginal PPDs for geoacoustic parameters h, c_1, and c_2 estimated from multi-frequency (300, 400, 500, 600 Hz) synthetic data for source ranges of 2, 3, 4, 5, and 6 km and narrow bounds for geometric parameters (not shown). The variances of the simulated data errors were determined from measured data at 4-km range in each case.

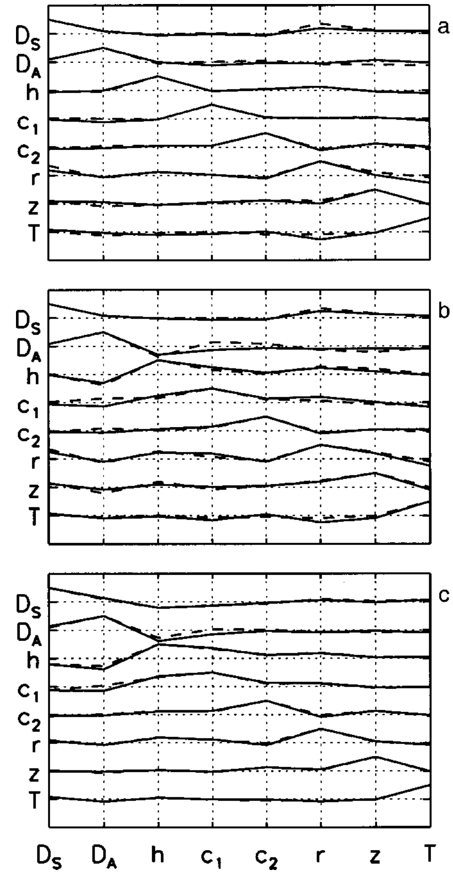

FIG. 18. Rows of the model correlation matrices estimated from measured data (solid lines) and synthetic data (dashed lines) for 4-km source range and the following cases: (a) 400-Hz data and wide search bounds; (b) 300, 400, 500, and 600 Hz data and wide bounds; and (c) 300, 400, 500, and 600 Hz and narrow search bounds for geometric parameters.

part) for the inter-parameter correlations indicated in Fig. 18(c) and Figs. 19(a)–19(d). The correlations between D_S, D_A, and h are likely related to the low sound speed of the upper sediment layer, which appears acoustically similar to the water. The water/sediment interface is therefore not well defined acoustically; however, the sediment/basement interface is well defined due to its larger sound-speed contrast. The fact that the same depth-to-basement can be obtained by increasing h while decreasing D_S and/or D_A (and vice versa) leads to the observed negative correlations between these parameters. The somewhat weaker positive correlation between D_S and D_A likely results from the fact that the bottom slope between source and array remains unchanged by either increasing or decreasing both of these quantities. Finally, the positive correlation between h and c_1 is likely related to the fact that the acoustic transit time through the sediment layer remains unchanged by either increasing or decreasing both sediment thickness and sound speed.

It appears that the strong inter-parameter correlations that exist between D_S, D_A, h, and c_1 together with the poor bathymetry control are responsible for the relatively large uncertainties in the PROSIM'97 acoustic inversion results for the sediment thickness and sound speed, as indicated in Figs. 8 and 16 and in Table I. The basement sound speed c_2, which is essentially uncorrelated with other parameters, is determined with significantly less uncertainty.

V. SUMMARY AND DISCUSSION

This paper applied Bayesian inference theory to estimate uncertainty distributions for geoacoustic and geometric model parameters from a broadband, shallow-water acoustic experiment carried out at a site where previous acoustic and geophysical studies had been performed. The experiment consisted of recording acoustic arrivals at a vertical array of sensors due to a swept-frequency (300–850 Hz) towed source. The posterior probability density of the model was sampled using a fast Gibbs sampler approach, and parameter uncertainties were quantified in terms of 1D and 2D marginal probability distributions, variances, and covariances (scaled as correlations). The PPD depends on the statistical distribution of the data errors, including both measurement and theory errors; however, independent information regarding this distribution is typically not available. To proceed, the errors were assumed to be due to independent, identically distributed Gaussian random processes at each (uncorrelated) sensor of the array, with the variance given by a maximum-likelihood estimate derived from the data themselves. Since the validity of this assumption is not clear *a priori*, an important goal of this work was to validate the parameter un-

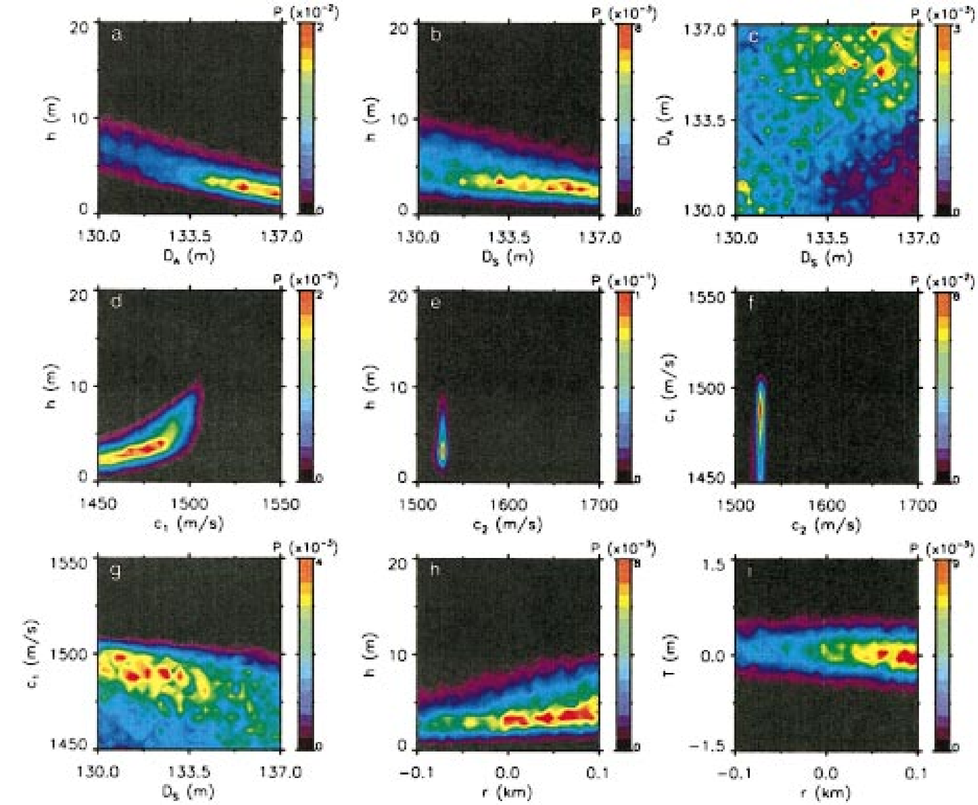

FIG. 19. 2D marginal probability distributions computed for measured data at 300, 400, 500, and 600 Hz with a source range of 4 km and narrow search bounds.

certainties derived from the FGS analysis. An effective signal-to-noise ratio was defined to measure the signal level relative to all sources of error (measurement and theory). While the SNR of the recorded signal relative to the ambient noise was approximately 30–40 dB across the source bandwidth, typical ESNR values were 2–8 dB.

FGS was applied to compute marginal probability distributions for the model parameters from single- and multi-frequency data, applying both wide and narrow search bounds for the geometric parameters as prior information. The marginal distribution widths decreased for multi-frequency data and for narrow search bounds. In each case, the width of the marginal distributions computed for a source at 4-km range agreed well with the variability in parameter estimates from independent MAP inversions for sources at 16 ranges from 2 to 6 km. In addition, marginal distributions computed for synthetic test cases designed to simulate the data and errors of the experiment were in close agreement with those computed for the experimental data. This indicates that the assumed error statistics are reasonable, and lead to meaningful uncertainty estimates for the model parameters. The agreement between the uncertainty results for experimental and synthetic data is particularly encouraging in that it illustrates that synthetic examples can provide realistic test cases for evaluating the analysis of measured data (i.e., benchmarking exercises). Finally, the range of geoacoustic parameter values from the FGS analysis were in good agreement with the results of previous geophysical and acoustic studies of the area.

Marginal distributions computed for single-frequency data sets at 100-Hz intervals indicated that the PPD was stable with respect to frequency. However, multi-frequency analysis yielded substantially better results, with the most significant improvement realized using data at three frequencies (i.e., there was little additional benefit to using more than three frequencies for the octave bandwidth considered). The PPDs were also found to be stable with respect to range over the interval 2–6 km, with slightly poorer results at the shorter ranges. This appeared to be the result of somewhat lower ESNR values at short ranges, possibly due to larger theory errors.

The marginal PPDs for the geoacoustic parameters indicated that the basement sound speed c_2 was determined to fairly high precision, but that the thickness h and sound speed c_1 of an upper sediment layer were less well determined. Correlation matrices and 2D marginal PPDs suggested the larger uncertainties were due to strong correlations between h and c_1 and between h and the unknown water depth at the source and array. The latter correlation is exacerbated by the low sound speed of the sediment layer (which appears acoustically similar to the water), and by the relatively poor prior knowledge of the water depth.

ACKNOWLEDGMENTS

The first author thanks Michael Wilmut for many helpful discussions on statistical methods, and Mark Fallat and Edward Chapin for preliminary data analysis. This work was supported by Office of Naval Research Grant No. N00014-96-1-0721.

[1] S. E. Dosso, ''Quantifying uncertainty in geoacoustic inversion. I. A fast Gibbs sampler approach,'' J. Acoust. Soc. Am. **111**, 129–142 (2002).
[2] A. Tarantola, *Inverse Problem Theory: Methods for Data Fitting and Model Parameter Estimation* (Elsevier, Amsterdam, 1987).
[3] M. K. Sen and P. L. Stoffa, *Global Optimization Methods in Geophysical Inversion* (Elsevier, Amsterdam, 1995).
[4] M. K. Sen and P. L. Stoffa, ''Bayesian inference, Gibbs' sampler and uncertainty estimation in geophysical inversion,'' Geophys. Prospect. **44**, 313–350 (1996).
[5] W. R. Gilks, S. Richardson, and G. J. Spiegelhalter, *Markov Chain Monte Carlo in Practice* (Chapman and Hall, London, 1996).
[6] P. Gerstoft and C. F. Mecklenbräuker, ''Ocean acoustic inversion with estimation of *a posteriori* probability distributions,'' J. Acoust. Soc. Am. **104**, 808–819 (1998).
[7] A. Tolstoy, N. R. Chapman, and G. H. Brooke, ''Workshop97: Benchmarking for geoacoustic inversion in shallow water,'' J. Comput. Acoust. **6**, 1–28 (1998).
[8] R. L. Parker, *Geophysical Inverse Theory* (Princeton University Press, Princeton, NJ, 1994).
[9] W. H. Press, S. A. Teukolsky, W. T. Vetterling, and B. P. Flannery, *Numerical Recipes in FORTRAN* (Cambridge University Press, Cambridge, 1992), p. 655.
[10] P. L. Nielsen, F. Bini-Verona, and F. B. Jensen, ''Environmental and acoustic data collected south of the island of Elba during the PROSIM'97 experiment,'' SACLANTCEN document SM-357, SACLANT Undersea Research Centre, La Spezia, Italy (1999).
[11] M. R. Fallat, P. L. Nielsen, and S. E. Dosso, ''Hybrid geoacoustic inversion of broadband Mediterranean Sea data,'' J. Acoust. Soc. Am. **107**, 1967–1977 (2000).
[12] M. R. Fallat, ''Simplex simulated annealing, a hybrid approach to geoacoustic inversion with application to Mediterranean Sea acoustic data,'' M.Sc. thesis, University of Victoria, Victoria, B.C., Canada (1999).
[13] J.-P. Hermand and P. Gerstoft, ''Inversion of broadband multitone acoustic data from the YELLOW SHARK summer experiments,'' IEEE J. Ocean. Eng. **21**, 324–346 (1996).
[14] M. Siderius and J.-P. Hermand, ''Yellow Shark Spring 95: Inversion results from sparse broadband acoustic measurements over a highly range dependent soft clay layer,'' J. Acoust. Soc. Am. **106**, 637–651 (1999).
[15] J.-P. Hermand, ''Broadband geoacoustic inversion in shallow water from waveguide impulse response measurements on a single hydrophone: Theory and experimental results,'' IEEE J. Ocean. Eng. **24**, 41–66 (1999).
[16] C. F. Mecklenbräuker and P. Gerstoft, ''Objective functions for ocean acoustic inversion derived by likelihood methods,'' J. Comput. Acoust. **6**, 1–28 (2000).
[17] T. B. Nelson and E. K. Westwood, ''Mode extraction from a VLA using singular value decomposition,'' J. Acoust. Soc. Am. **101**, 3025 (1997).
[18] F. B. Jensen and M. C. Ferla, ''SNAP—The SACLANTCEN normal mode acoustic propagation model,'' SACLANT Document SM-121, SACLANT Undersea Research Centre, La Spezia, Italy (1979).
[19] M. D. Collins and E. K. Westwood, ''A higher-order energy conserving parabolic equation for range-dependent ocean depth, sound speed, and density,'' J. Acoust. Soc. Am. **89**, 1068–1075 (1991).
[20] M. C. Ferla, M. B. Porter, and F. B. Jensen, ''C-SNAP: Coupled SACLANTCEN normal mode propagation loss model,'' SACLANT Document SM-274, SACLANT Undersea Research Centre, La Spezia, Italy (1993).
[21] M. R. Fallat and S. E. Dosso, ''Geoacoustic inversion via local, global and hybrid algorithms,'' J. Acoust. Soc. Am. **105**, 3219–3230 (1999).
[22] F. Bini-Verona, P. L. Nielsen, and F. B. Jensen, ''PROSIM broadband normal-mode model: A user's guide,'' SACLANT document SM-358, SACLANT Undersea Research Centre, La Spezia, Italy (1999).
[23] S. E. Dosso, M. J. Wilmut, and A. S. Lapinski, ''An adaptive hybrid algorithm for geoacoustic inversion,'' IEEE J. Ocean. Eng. **26**, 324–336 (2001).

An energy-conserving one-way coupled mode propagation model

Ahmad T. Abawi
SPAWAR Systems Center, San Diego, California 92152-5001

(Received 18 December 2000; revised 14 August 2001; accepted 24 August 2001)

The equations of motion for pressure and displacement fields in a waveguide have been used to derive an energy-conserving, one-way coupled mode propagation model. This model has three important properties: First, since it is based on the equations of motion, rather than the wave equation, instead of two coupling matrices, it only contains one coupling matrix. Second, the resulting coupling matrix is anti-symmetric, which implies that the energy among modes is conserved. Third, the coupling matrix can be computed using the local modes and their depth derivatives. The model has been applied to two range-dependent cases: Propagation in a wedge, where range dependence is due to variations in water depth and propagation through internal waves, where range dependence is due to variations in water sound speed. In both cases the solutions are compared with those obtained from the parabolic equation (PE) method. [DOI: 10.1121/1.1419088]

PACS numbers: 43.30.Bp [SAC-B]

I. INTRODUCTION

The coupled mode theory commonly used in acoustics was originally derived by Pierce[1] and Milder[2] from the wave equation for the velocity potential. In this formulation the field in a range-dependent waveguide is expanded in terms local modes with range-dependent coefficients (mode amplitudes). The application of the continuity of pressure and the vertical component of particle velocity allows a partial separation of the depth and range variables and yields a system of second order coupled differential equations for the mode amplitudes. However, as is pointed out by Rutherford and Hawker,[3] while the boundary condition of continuity of vertical component of particle velocity is correct for horizontal boundaries, when applied to problems with nonhorizontal boundaries, this boundary condition is only an approximation to the correct boundary condition of the continuity of the normal component of particle velocity. Rutherford and Hawker showed that one consequence of this approximation is nonconservation of energy. They used the WKBJ method to obtain a solution which satisfies both the proper boundary condition and conserved energy to first order in the slope of the nonhorizontal boundaries and interfaces. This problem was also addressed by Fawcett,[4] who derived a system of coupled mode equations which satisfies the correct boundary conditions. However, in addition to the two coupling matrices, which is typical of all coupled mode theories derived from the wave equation, the equations derived by Fawcett also contain two other so-called interface matrices. These matrices require a knowledge of the range derivatives of the local modes, which can only be computed approximately. The inaccuracy resulting from this along with the complexity involved in solving the system of differential equations make this an impractical computational method for solving range-dependent problems.

In an attempt to reduce the complexity involved in computing the coupling matrices, McDonald[5] used the original Pierce–Milder equations to argue that for a waveguide whose horizontal length scales are much larger than the acoustic wavelength only one of the two coupling matrices has significant contribution. By neglecting one of the coupling matrices and the horizontal derivative of the density, McDonald was able to derive an expression for the remaining coupling matrix in terms of local modes and their depth derivatives. The expression for the coupling matrix derived by McDonald was used by Abawi *et al.*[6] who derived a system of one-way coupled mode equations for the mode amplitudes. Although this method is a practical computational method for solving range-dependent problems, it still suffers from approximations made by neglecting one of the two coupling matrices. More importantly, since this method is based on the same boundary conditions as those used by Pierce and Milder, the energy among modes is not conserved.

The coupled mode model that is presented in this paper is derived, not from the wave equation, as is the case for the Pierce–Milder method, but from the equations of motion for the pressure and displacement fields. This method, which was first used by Shevchenko,[7] has common use in seismology and geophysics, Odom,[8] Maupin[9] and Tromp.[10] The derivation in this paper follows the derivation of Tromp. While the model derived by Tromp is for the general elastic waveguide, this model is derived for a waveguide consisting of fluid layers. Since the equations of motion constitute a system of two first order coupled differential equations, the coupled mode equations resulting from them only contain a single coupling matrix. Furthermore, this method provides a natural framework for applying the correct boundary and interface conditions without adding any more complexity to the numerical solution of the equations. In fact, it is shown in this paper that the proper application of the boundary and interface conditions not only simplifies the numerical computation of the coupling matrix by allowing it to be expressed in terms the local modes and their depth derivatives, it also makes it possible to show that the resulting coupling matrix is anti-symmetric, which guarantees the conservation of energy among modes.[3,6,10]

The method presented in this paper and the references cited in the above fall in the category of continuous coupled mode theory where the solution of the wave equation in a range-dependent waveguide is obtained by solving of a set of coupled differential equations. The solution for a range-dependent waveguide can also be obtained by the discrete coupled mode method.[11] In this method the range-dependent waveguide is approximated by range-independent stair steps and the coupled mode solution is obtained by matching the solutions of the wave equation for neighboring stair steps at their common boundary. This method is easy to implement numerically and has wide application in ocean acoustics. However, the method that is presented in this paper has two advantages over the discrete coupled mode method. The first advantage is it expresses the coupling matrix in terms of physical parameters and thus provides insight into the process of mode coupling by clearly showing what is responsible for it. The other, more important advantage is that this method in principle can be extended to handle propagation in three dimensions, where the discrete coupled mode method is designed for propagation in two dimensions and there is no obvious way to modify it to handle propagation in three dimensions.

This paper is organized in the following way. In Sec. II the coupled mode model is derived, where some of the details of the derivation are given in the appendices. In Sec. III the model is applied to two range-dependent propagation scenarios. The first one is propagation in a wedge, where range-dependence is entirely due to variations in water depth. The parameters used in this example are scaled to match those used by Coppens and Sanders[12] in a model tank experiment. The second example is propagation through internal waves, where range-dependence is entirely due to the variations in water sound speed. The parameters used in this example were those used in a test case in the Shallow Water Acoustics Modeling workshop.[13] In both of the above examples the results obtained from the coupled mode model are compared with those obtained from the parabolic equation (PE) method.[14]

II. DERIVATION OF THE COUPLED-MODE EQUATIONS

Consider the equations of motion with the x-axis in the direction of propagation

$$\partial_x p = \rho\omega^2 u_x,$$

$$\partial_x u_x = -\frac{p}{\rho c^2} - \hat{\mathbf{z}}\cdot\partial_z \mathbf{u},$$

$$\hat{\mathbf{z}}\cdot\mathbf{u} = \frac{1}{\rho\omega^2}\partial_z p.$$

In the above equations p is the pressure and $\mathbf{u}$ is the displacement vector. The pressure and the normal component of the displacement are continuous across any interface. This may be expressed as

$$[p]_-^+ = 0, \quad [\hat{\mathbf{n}}\cdot\mathbf{u}]_-^+ = 0,$$

where $[\zeta]_-^+ = \zeta_+ - \zeta_-$, the $+/-$ indicate the value of the parameter ζ just above/below the interface and $\hat{\mathbf{n}}$ is the unit vector normal to the interface.

The field quantities can be expressed as the sum of normal modes

$$p(x,z) = \sum_n p_n(z)e^{ik_n x}, \quad \mathbf{u}(x,z) = \sum_n \mathbf{u}_n(x,z)e^{ik_n x},$$

where p_n and $\mathbf{u}_n$ denote the normal modes. Substituting the above expressions into the equations of motion results in the following relationships for the modes

$$\begin{aligned}
&ik_n p_n = \rho\omega^2 u_n,\\
&ik_n u_n = -\frac{p_n}{\rho c^2} - \partial_z\left(\frac{1}{\rho\omega^2}\partial_z p_n\right),\\
&\hat{\mathbf{z}}\cdot\mathbf{u}_n = \frac{1}{\rho\omega^2}\partial_z p_n,\\
&[p_n]_-^+ = 0, \quad [\hat{\mathbf{z}}_n\cdot\mathbf{u}_n]_-^+ = 0.
\end{aligned} \tag{1}$$

In the above equations u_n denotes the x component of the displacement.

In a range-dependent environment the pressure and the displacement vector may be expressed as a sum of local normal modes with range-dependent coefficients, $c_n(x)$

$$\begin{aligned}
&p(x,z) = \sum_n c_n(x)p_n(z;x)e^{ik_n x},\\
&\mathbf{u}(x,z) = \sum_n c_n(x)\mathbf{u}_n(z;x)e^{ik_n x}.
\end{aligned} \tag{2}$$

In this notation the parametric range-dependence of the local modes at range x is indicated by the semicolon separating z and x.

Substitution of the above expansion into the equations of motion gives

$$\partial_x \sum_n c_n p_n e^{ik_n x} = \sum_n \rho\omega^2 c_n u_n e^{ik_n x},$$

$$\partial_x \sum_n c_n u_n e^{ik_n x} = \sum_n \left(-\frac{1}{\rho c^2}p_n - \hat{\mathbf{z}}\cdot\partial_z \mathbf{u}_n\right)c_n e^{ik_n x}.$$

Multiplying the first equation by $u_m e^{-ik_m x}$ and the second equation by $p_m e^{-ik_m x}$, adding the two equations and integrating along the depth of the waveguide gives

$$\begin{aligned}
&\sum_n \int_0^B \{(u_n p_m + p_n u_m)\partial_x c_n + c_n(p_m\,\partial_x u_n + u_m\,\partial_x p_n)\\
&\quad + ic_n k_n(u_n p_m + p_n u_m)\}e^{i(k_n - k_m)x}\,dz\\
&\quad = \sum_n \int_0^B \left\{-\frac{1}{\rho c^2}p_n p_m - \hat{\mathbf{z}}\cdot(\partial_z \mathbf{u}_n)p_m\right.\\
&\qquad \left. + \rho\omega^2 u_n u_m\right\} c_n e^{i(k_n - k_m)x}\,dz.
\end{aligned} \tag{3}$$

Since according to Eq. (1) $u_n = ik_n p_n/(\rho\omega^2)$, we find

$$2\,\partial_x(c_m)k_m+c_m\,\partial_x k_m=\sum_{n\neq m}A_{mn}c_n\,. \tag{4}$$

The details of the above derivation is given in Appendix B. In the above equation, A_{mn} is the coupling matrix given by

$$A_{mn}=-\Bigg[(k_n+k_m)\int_0^B\frac{1}{\rho}p_m\,\partial_x(p_n)dz+k_n\int_0^B p_n p_m \times\partial_x\left(\frac{1}{\rho}\right)dz+\left[\frac{k_n}{\rho}p_n p_m\partial_x h\right]_-^+\Bigg]e^{i(k_n-k_m)x}. \tag{5}$$

The above equation is not yet in the desired form, as it contains the range derivative of the modes, which is difficult to compute accurately. In the remainder of this section we will use the modal equations and the boundary and interface conditions to convert the above equation into one which only contains the local modes and their depth derivatives.

Consider the mode equations for mode n and mode m

$$\partial_z\left(\frac{1}{\rho}\partial_z p_n\right)+\frac{1}{\rho}(k^2-k_n^2)p_n=0, \tag{6}$$

$$\partial_z\left(\frac{1}{\rho}\partial_z p_m\right)+\frac{1}{\rho}(k^2-k_m^2)p_m=0. \tag{7}$$

The modal equation is obtained by substituting $u_n=ik_np_n/(\rho\omega^2)$ into the second equation in Eq. (1). Next evaluate

$$\int_0^B\{p_m\,\partial_x[\text{Eq. (6)}]-[\text{Eq. (7)}]\partial_x p_n\}dz.$$

This gives

$$\int_0^B\Bigg\{\partial_z\left(\partial_x\left(\frac{1}{\rho}\right)\partial_z p_n\right)p_m+\partial_z\left(\frac{1}{\rho}\partial_z(\partial_x p_n)\right)p_m +\frac{1}{\rho}p_n p_m\,\partial_x(k^2)+(k^2-k_n^2)\partial_x\left(\frac{1}{\rho}\right)p_n p_m +(k_m^2-k_n^2)\frac{1}{\rho}p_m\,\partial_x p_n-\partial_z\left(\frac{1}{\rho}\partial_z p_m\right)\partial_x p_n\Bigg\}dz=0.$$

The fifth term in the above equation can be written as

$$(k_m-k_n)(k_m+k_n)\int_0^B\frac{1}{\rho}p_m\,\partial_x p_n\,dz =-\int_0^B\Bigg\{\partial_z\left(\partial_x\left(\frac{1}{\rho}\right)\partial_z p_n\right)p_m+\partial_z\left(\frac{1}{\rho}\partial_z(\partial_x p_n)\right)p_m +\frac{1}{\rho}p_n p_m\,\partial_x(k^2)+(k^2-k_n^2)\partial_x\left(\frac{1}{\rho}\right)p_n p_m -\partial_z\left(\frac{1}{\rho}\partial_z p_m\right)\partial_x p_n\Bigg\}dz,$$

or

$$(k_m+k_n)\int_0^B\frac{1}{\rho}p_m\,\partial_x p_n\,dz =(k_n-k_m)^{-1}\int_0^B\Bigg\{\partial_z\left(\partial_x\left(\frac{1}{\rho}\right)\partial_z p_n\right)p_m +\partial_z\left(\frac{1}{\rho}\partial_z(\partial_x p_n)\right)p_m+\frac{1}{\rho}p_n p_m\partial_x(k^2) +(k^2-k_n^2)\partial_x\left(\frac{1}{\rho}\right)p_n p_m-\partial_z\left(\frac{1}{\rho}\partial_z p_m\right)\partial_x p_n\Bigg\}dz. \tag{8}$$

We would like to transfer all terms involving the range derivatives of the modes from inside the integral to the boundary term by using integration by parts. The first term can be written as

$$\int_0^B\partial_z\left(\partial_x\left(\frac{1}{\rho}\right)\partial_z p_n\right)p_m\,dz =\left[\partial_x\left(\frac{1}{\rho}\right)(\partial_z p_n)p_m\right]_-^+-\int_0^B\partial_x\left(\frac{1}{\rho}\right)(\partial_z p_m)(\partial_z p_n)dz.$$

Similarly, the second and the fifth terms can be written as

$$\int_0^B\partial_z\left(\frac{1}{\rho}\partial_z(\partial_x p_n)\right)p_m\,dz =\left[\frac{1}{\rho}\partial_z(\partial_x p_n)p_m\right]_-^+-\int_0^B\frac{1}{\rho}\partial_z(p_n)\partial_z(p_m)dz,$$

and

$$-\int_0^B\partial_z\left(\frac{1}{\rho}\partial_z p_m\right)\partial_x(p_n)dz =-\left[\frac{1}{\rho}\partial_x(p_n)(\partial_z p_m)\right]_-^++\int_0^B\frac{1}{\rho}\partial_z(p_n)\partial_z(p_m)dz.$$

Substituting these into Eq. (8) gives

$$(k_m+k_n)\int_0^B\frac{1}{\rho}p_m\,\partial_x p_n dz =(k_n-k_m)^{-1}\int_0^B\Bigg\{\left(-\partial_x\left(\frac{1}{\rho}\right)(\partial_z p_m)(\partial_z p_n)\right) +\frac{1}{\rho}p_n p_m\,\partial_x(k^2)+(k^2-k_n^2)\partial_x\left(\frac{1}{\rho}\right)p_n p_m\Bigg\}dz +\left[\partial_x\left(\frac{1}{\rho}\right)(\partial_z p_n)p_m+\frac{1}{\rho}\partial_x(\partial_z p_n)p_m -\frac{1}{\rho}\partial_x(p_n)(\partial_z p_m)\right]_-^+. \tag{9}$$

The boundary term in the above equation may be written as

$$\left[\partial_x\left(\frac{1}{\rho}\right)(\partial_z p_n)p_m+\frac{1}{\rho}\partial_x(\partial_z p_n)p_m-\frac{1}{\rho}\partial_x(p_n)(\partial_z p_m)\right]_-^+ =\left[\partial_x\left(\frac{1}{\rho}\partial_z p_n\right)p_m-\partial_x(p_n)\frac{1}{\rho}(\partial_z p_m)\right]_-^+.$$

Since the derivative along the interface of a continuous function f is continuous, we have

$$[\hat{\mathbf{T}}\cdot\nabla f]_{-}^{+}=0, \quad \text{where} \quad \hat{\mathbf{T}}=\hat{\mathbf{x}}+\frac{\partial h}{\partial x}\hat{\mathbf{z}}.$$

This gives

$$[\partial_x f]_{-}^{+}=-[\partial_x(h)\partial_z(f)]_{-}^{+}.$$

Since both p_n and $\partial_z p_n/\rho$ are continuous across the interface $z=h(x)$, the above boundary term can be written as

$$\left[\partial_x(h)\partial_z(p_n)\frac{1}{\rho}(\partial_z p_m)-\partial_x h\ \partial_z\left(\frac{1}{\rho}\partial_z p_n\right)p_m\right]_{-}^{+}.$$

With the help of the wave equation, Eq. (6), this may be written as

$$\left[\partial_x(h)\partial_z(p_n)\frac{1}{\rho}(\partial_z p_m)+\partial_x h\frac{1}{\rho}(k^2-k_n^2)p_n p_m\right]_{-}^{+}.$$

Substituting this into Eq. (9) and the result into Eq. (5) yields

$$\begin{aligned}(k_m-k_n)A_{mn}=\Bigg\{&\int_0^B\Bigg[[(k^2-k_nk_m)p_np_m\\&-\partial_z p_n\ \partial_z p_m]\partial_x\left(\frac{1}{\rho}\right)+\frac{p_np_m}{\rho}\partial_x(k^2)\Bigg]dz\\&+\partial_x h\Bigg[\frac{1}{\rho}\partial_z p_n\ \partial_z p_m+\frac{1}{\rho}(k^2\\&-k_nk_m)p_np_m\Bigg]_{-}^{+}\Bigg\}e^{i(k_n-k_m)x}.\end{aligned} \tag{10}$$

The expression for the coupling matrix given by the above equation is the main result of this paper. It shows the effect of mode coupling due to contribution from volumetric and bathymetric variations in the waveguide separately. The first part of the coupling matrix containing the integral is due to contribution from volumetric variations in the waveguide such as variations in sound speed and density as a function of range. The second part is due to contribution from bathymetric variations in range, i.e., variations in water depth, as is evident from the presence of $\partial_x h$.

The coupling matrix has two important properties. First, it is anti-symmetric, i.e., $A_{mn}=-A_{nm}^{\dagger}$. This implies that en-

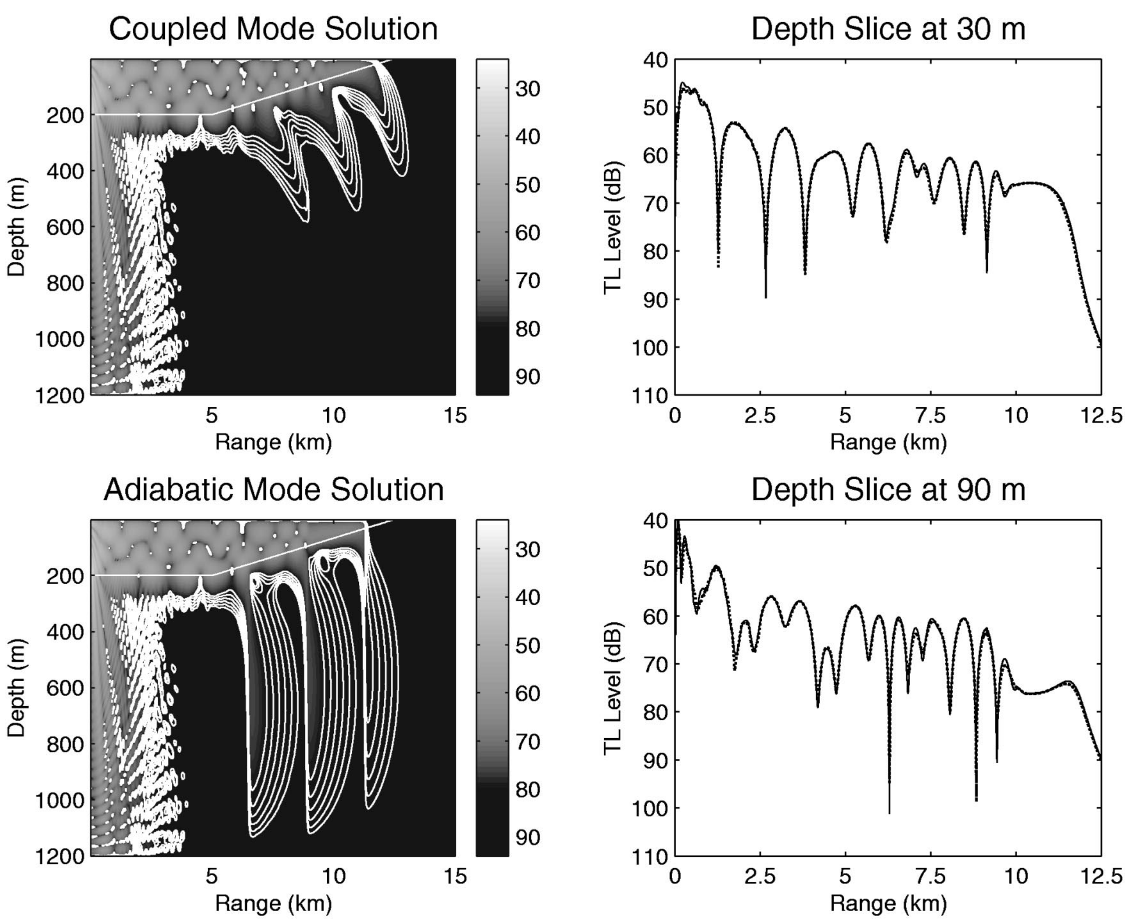

FIG. 1. Propagation in an oceanic wedge: The water depth is constant at 200 m for the first 5 km and it slowly decreases to zero in the next 7.5 km resulting in a wedge angle of 1.55 deg. The top left panel shows the acoustic field due a 25 Hz source placed at 180 m as a function range and depth computed using the coupled mode model. The bottom left panel shows the acoustic field computed using the adiabatic mode model. The top and bottom panels on the right show a comparison of the transmission loss as a function of range computed using the PE model (solid) the coupled mode model (dotted) for two receiver depths.

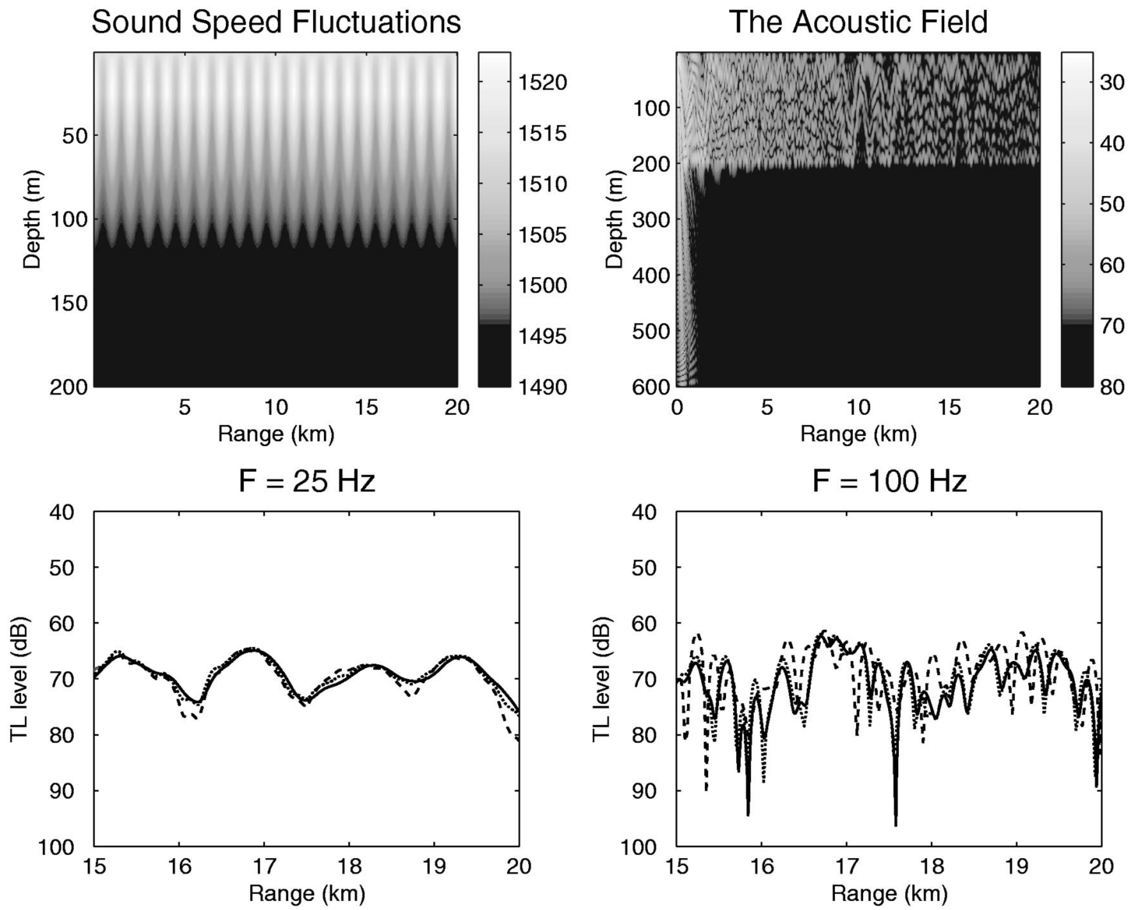

FIG. 2. Propagation through internal waves: The ocean environment consists of a 200 m layer over a bottom half space. The sound speed in the water is modeled to simulate fluctuations due to internal waves. The top left panel shows the sound speed fluctuations in the water. The top right panel shows the acoustic field in this environment due to a 100 Hz source placed at 100 m computed using the coupled mode model. The bottom two panels show a comparison of the transmission between the PE model (solid), the coupled mode model (dotted), and the adiabatic coupled mode model (dashed). The transmission loss is computed at a receiver depth of 100 m and for source frequencies of 25 and 100 Hz.

ergy is conserved among modes. Second, it only contains the modes and their depth derivatives. This means that the coupling matrix can easily be computed using the local modes and their depth derivatives, which can be obtained from any normal mode code such as KRAKEN.[15]

III. EXAMPLES

In this section the one-way coupled mode model developed in the previous section is applied to two range-dependent cases. In the first example we use the one-way coupled model to compute acoustic propagation an oceanic wedge wherein range-dependence is due to variations in the water depth. In the second example propagation through an ocean with internal waves is computed where the ocean environment is chosen such that range-dependence is entirely due to variations in sound speed. The results are compared with those obtained using the parabolic equation PE[14] method.

A. Propagation in a wedge

The ocean environment in this example is scaled to correspond to the model tank experiment reported by Coppens and Sanders.[12] The water depth is initially 200 m for the first 5 km and then it slowly decreases to zero in the next 7.5 km resulting in a wedge angle of approximately 1.55 deg. To approximate the branch cut integral in the modal representation of the field, a 1000 m deep false bottom is used. The waveguide consists of two isovelocity layers: a water layer over a bottom layer. The water sound speed is 1500 m/s and its density is 1.0 g/cm^3. The bottom sound speed is 1700 m/s with a density of 1.15 g/cm^3. The attenuation in the bottom is 0.5 dB/λ. A 25 Hz source is placed at 180 m. These environmental parameters are chosen to correspond to those used by Coppens and Sanders.

The acoustic field in the waveguide is computed using Eq. (2) with the modal coefficients, c_m, obtained from the solution of Eq. (4). The first order differential equation for the modal coefficients, Eq. (4), is solved by using fourth-order Runge–Kutta integration. To obtain the modes and the coupling matrix as a function of range, the wedge is divided into range-independent stair steps. The local modes and the local coupling matrix using Eq. (10) are computed in each stair step and updated in the differential equation. The step size in the two examples that are presented in this paper is 10 m. However, a step size of 50 m gives identical results.

The results of the above computation are shown in Fig. 1. The top left panel in Fig. 1 shows the acoustic field computed using the one-way coupled mode model described in this paper. It can be seen that as the water depth decreases, the water modes (there are three water modes in this example) cutoff in the form of discrete beams radiating into the bottom. The experimental data obtained by Coppens and Sanders show the exact same behavior. Jensen and Kuperman[16] used the parabolic equation method to model the acoustic propagation in this example and found results identical to those shown in the top left panel of Fig. 1. They interpreted the slow disappearance of the discrete water modes into the bottom as an indication that energy contained in a given mode does not couple into the next lower mode but couples almost entirely into the continuous mode spectrum. While this effect, which is a consequence of mode coupling, is implicitly accounted for in the parabolic equation (PE) formulation, the coupled mode model explicitly accounts for it through the coupling matrix. The two panels on the right in Fig. 1 show a comparison of the transmission loss computed using the one-way coupled model and the PE model for two receiver depths. The close agreement between the two models clearly demonstrates that the one-way coupled mode model correctly accounts for mode coupling. If the coupling matrix in the one-way coupled mode model are set equal to zero, the one-way coupled mode model reduces to the adiabatic mode model. The bottom left panel in Fig. 1 shows the acoustic field computed using the adiabatic mode solution. Observe that the adiabatic mode solution does not have the correct field behavior near cutoff. While in the coupled mode solution modes gradually radiate their energy to the bottom near cutoff, in the adiabatic mode solution this process occurs abruptly because there is no mechanism for the transfer of energy between modes.

B. Propagation in internal waves

The ocean environment in this example is one of the test cases used at the Shallow Water Acoustic workshop.[13] It consists of 200 m of water over a 400 m, isovelocity bottom. The bottom density 1.5 g/cm^3 and its sound speed was 1700 m/s. The sound speed profile and the velocity fluctuations due to internal waves in the water column are modeled according to[13]

$$c(z,r)=c(z)+\Delta c(z,r),$$

where

$$c(z)=\begin{cases}1515.0+0.016z & z<26\\ 1490(1.0+0.25(e^{-b}+b-1.0)) & z>26\end{cases}$$

and

$$\Delta c(z,r)=\frac{z}{25}e^{-z/25}\cos 2\pi r.$$

In the above $b=(z-200)/500$ and r is measured in km. The top left panel in Fig. 2 shows the sound speed profile for this example. The top right panel shows the acoustic field in the waveguide for a 100 Hz source place at 30 m. The bottom two panels in Fig. 2 show a comparison of the adiabatic normal mode and the coupled mode solutions with the PE solution for two source frequencies. In both cases the receiver depth is at 70 m. The coupled mode solution agrees well with PE solution at both frequencies while the adiabatic normal mode solution does not agree with the parabolic equation solution at all. This is more evident at the higher frequency where the effects of the internal waves, and thus the mode coupling due to them, is stronger.

ACKNOWLEDGMENTS

This work was supported in part by the Office of Naval Research Contract No. N0001496WX30305 and in part by the SPAWAR Systems Center Internal Research (IR) program Contract No. ZU548R8A01. The author would like to thank Dr. Bob Odom of the Applied Physics Laboratory at the University of Washington for useful discussions and for providing relevant references for this paper. The author also thanks the anonymous referees for their useful comments.

APPENDIX A: THE MODE ORTHOGONALITY RELATIONSHIP

The mode orthogonality equation is obtained by multiplying the mode equation (6) by p_m and Eq. (7) by p_n subtracting the resulting equations and integrating to give

$$\int_0^B\left[p_m\ \partial_z\left(\frac{1}{\rho}\partial_z p_n\right)-p_n\ \partial_z\left(\frac{1}{\rho}\partial_z p_m\right)\right]dz$$

$$+(k_m^2-k_n^2)\int_0^B\frac{1}{\rho}p_m p_n\ dz=0.$$

Integrating the first integral by parts results in boundary terms

$$p_m\frac{1}{\rho}\partial_z p_n\bigg|_0^B-p_n\frac{1}{\rho}\partial_z p_m\bigg|_0^B.$$

Since either the mode or its derivative is zero at the boundaries, there is no contribution from the above interface terms. What remains is

$$(k_m-k_n)(k_m+k_n)\ \int_0^B\frac{1}{\rho}p_m p_n\ dz=0.$$

For $m\neq n$,

$$(k_m+k_n)\int_0^B\frac{1}{\rho}p_m p_n\ dz=0,$$

and for $m=n$ we choose to normalize the modes such that

$$(k_m+k_n)\int_0^B\frac{1}{\rho}p_m p_n\ dz=2k_n\delta_{mn}.$$

APPENDIX B: DETAILS LEADING TO EQ. (4)

We start by multiplying the first equation in Eq. (1) by u_m and the second equation in Eq. (1) by p_m, adding the two equations and integrating to get

$$ik_n\int_0^B(p_n u_m+u_n p_m)dz$$

$$=\int_0^B\left(-\frac{p_n p_m}{\rho c^2}-\partial_z\left(\frac{1}{\rho\omega^2}\partial_z p_n\right)p_m+\rho\omega^2 u_n u_m\right)dz.$$

Integrating the middle term on the right-hand side by parts yields

$$\int_0^B \partial_z\left(\frac{1}{\rho c^2}\partial_z p_n\right)p_m\,dz=\left[\left(\frac{1}{\rho\omega^2}\partial_z p_n\right)p_m\right]_-^+ -\int_0^B\left(\frac{1}{\rho\omega^2}\partial_z p_n\right)\partial_z p_m\,dz.$$

Since the quantities inside the square brackets are continuous across the interface, the boundary term is zero. This results in

$$ik_n\int_0^B (p_n u_m+u_n p_m)dz=\int_0^B\left(-\frac{p_n p_m}{\rho c^2}+\frac{1}{\rho\omega^2}(\partial_z p_n)\times(\partial_z p_m)+\rho\omega^2 u_n u_m\right)dz. \quad \text{(B1)}$$

Next consider the following term in Eq. (1), which can be integrated to give,

$$\int_0^B \hat{\mathbf{z}}\cdot(\partial_z \mathbf{u}_n)p_m\,dz=[\hat{\mathbf{z}}\cdot\mathbf{u}_n p_m]_-^+-\int_0^B(\hat{\mathbf{z}}\cdot\mathbf{u}_n\;\partial_z p_m)dz. \quad \text{(B2)}$$

The continuity condition for the normal component of the displacement can be written as

$$[\hat{\mathbf{n}}\cdot\mathbf{u}_n]_-^+=[(-\hat{\mathbf{z}}+\partial_x h\hat{\mathbf{x}})\cdot\mathbf{u}_n]_-^+=0.$$

This gives,

$$[\hat{\mathbf{z}}\cdot\mathbf{u}_n]_-^+=(\partial_x h)u_n.$$

Since p_m is continuous across the interface, Eq. (B2) reduces to

$$\int_0^B \hat{\mathbf{z}}\cdot(\partial_z \mathbf{u}_n)p_m\,dz=[(\partial_x h)u_n p_m]_-^+-\int_0^B(\hat{\mathbf{z}}\cdot\mathbf{u}_n\;\partial_z p_m)dz.$$

Substituting this into Eq. (3) and using Eq. (B1) gives

$$\sum_n\left\{\partial_x c_n\int_0^B(u_n p_m+p_n u_m)dz+c_n\int_0^B(p_m\;\partial_x u_n+u_m\;\partial_x p_n)dz+c_n[(\partial_x h)u_n p_m]_-^+ e^{i(k_n-k_m)x}=0.\right.$$

Next substituting for $u_n=ik_n p_n/\omega^2\rho$ gives

$$\sum_n\left\{(\partial_x c_n)(k_n+k_m)\int_0^B\frac{1}{\rho}p_n p_m\,dz+c_n(k_n+k_m)\times\int_0^B(\partial_x p_n)\frac{p_m}{\rho}dz+c_n(\partial_x k_n)\int_0^B\frac{1}{\rho}p_n p_m\,dz+c_n k_n\int_0^B\partial_x\left(\frac{1}{\rho}\right)p_n p_m dz+c_n\left[(\partial_x h)\frac{k_n p_n p_m}{\rho}\right]_-^+ e^{i(k_n-k_m)x}\right\}=0. \quad \text{(B3)}$$

Using the orthogonality of the modes we find,

$$2\,\partial_x c_m k_m+c_m\;\partial_x k_m=\sum_{n\neq m}A_{mn}c_n,$$

where the coupling matrix, A_{mn} is defined by Eq. (10). For $m=n$ Eq. (B3) becomes,

$$2\,\partial_x c_n k_n+c_n\;\partial_x k_n+c_n k_n\int_0^B\left(2(\partial_x p_n)\frac{p_n}{\rho}+p_n^2\;\partial_x\left(\frac{1}{\rho}\right)\right)dz+c_n\left[(\partial_x h)\frac{k_n p_n^2}{\rho}\right]_-^+=0.$$

This can be written as

$$2\,\partial_x c_n k_n+c_n\;\partial_x k_n+c_n k_n\int_0^B\partial_x\left(\frac{p_n^2}{\rho}\right)dz+c_n\left[(\partial_x h)\frac{k_n p_n^2}{\rho}\right]_-^+=0.$$

It is shown in Appendix C that

$$\int_0^B\partial_x\left(\frac{p_n^2}{\rho}\right)dz=-\partial_x h\left[\frac{1}{\rho}p_n^2\right]_-^+, \quad \text{(B4)}$$

which gives

$$2\,\partial_x c_n k_n+c_n\;\partial_x k_n=0.$$

APPENDIX C: DERIVATION OF EQ. (B4)

The integral across the waveguide can be written as,

$$\int_0^B\partial_x\left(\frac{p_n^2}{\rho}\right)dz=\int_0^{h^+}\partial_x\left(\frac{p_n^2}{\rho}\right)dz+\int_{h^-}^B\partial_x\left(\frac{p_n^2}{\rho}\right)dz.$$

Each one of the above integrals can be written as,

$$\int_0^{h^+}\partial_x\left(\frac{p_n^2}{\rho}\right)dz=\partial_x\int_0^{h^+}\left(\frac{p_n^2}{\rho}\right)dz-\partial_x(h^+)\left[\frac{p_n^2}{\rho}\right]_{h^+},$$

and

$$\int_{h^-}^B\partial_x\left(\frac{p_n^2}{\rho}\right)dz=\partial_x\int_{h^-}^B\left(\frac{p_n^2}{\rho}\right)dz+\partial_x(h^-)\left[\frac{p_n^2}{\rho}\right]_{h^-}.$$

Substituting for these quantities we find

$$\int_0^B\partial_x\left(\frac{p_n^2}{\rho}\right)dz=\partial_x\int_0^B\left(\frac{p_n^2}{\rho}\right)dz-\partial_x h\left[\frac{p_n^2}{\rho}\right]_-^+.$$

The integral on the right-hand side is a constant which gives

$$\int_0^B\partial_x\left(\frac{p_n^2}{\rho}\right)dz=-\partial_x h\left[\frac{p_n^2}{\rho}\right]_-^+.$$

[1] A. D. Pierce, "Extension of the method of normal modes to sound propagation in an almost-stratifield medium," J. Acoust. Soc. Am. **37**, 19–27 (1965).
[2] D. M. Milder, "Ray and wave invariants for sofar channel propagation," J. Acoust. Soc. Am. **46**, 1259–1263 (1969).
[3] Steven R. Rutherford and Kenneth E. Hawker, "Consistent coupled mode theory of sound propagation for a class of nonseparable problems," J. Acoust. Soc. Am. **70**, 554–564 (1981).
[4] John A. Fawcett, "A derivation of the differential equations of coupled-mode propagation," J. Acoust. Soc. Am. **92**, 290–295 (1992).

[5] B. Edward McDonald, ''Bathymetric and volumetric contributions to ocean acoustic mode coupling,'' J. Acoust. Soc. Am. **100**, 219–224 (1996).

[6] Ahmad T. Abawi, Michael D. Collins, and W. A. Kuperman, ''The coupled mode parabolic equation,'' J. Acoust. Soc. Am. **102**, 233–238 (1997).

[7] V. V. Shevchenko, ''Irregular acoustic waveguides,'' Sov. Phys. Acoust. **7**, 389–397 (1962).

[8] Robert I. Odom ''A coupled mode examination of irregular waveguides including the continuum spectrum,'' Geophys. J. R. Astron. Soc. **86**, 425–453 (1986).

[9] V. Maupin, ''Surface waves across 2-d structures: A method based on coupled local modes,'' Geophys. J. **93**, 173–185 (1988).

[10] Jeroen Tromp, ''A coupled local-mode analysis of surface-wave propagation in a laterally heterogeneous waveguide,'' Geophys. J. Int. **117**, 153–161 (1994).

[11] R. B. Evans, ''A coupled mode solution for acoustic propagation in a waveguide with stepwise depth variations of a penetrable bottom,'' J. Acoust. Soc. Am. **74**, 188–195 (1983).

[12] A. B. Coppens and J. V. Sanders, ''Transmission of sound into a fast fluid bottom from an overlaying fluid wedge,'' Proceedings of Workshop on Seismic Propagation in Shallow Water (Office of Naval Research, Arlington, VA, 1978).

[13] ''Shallow water acoustic modeling workshop,'' September 1999, Naval Postgraduate School, Monterey, CA.

[14] Michael D. Collins, ''A slipt-step padé solution for the parabolic equation method,'' J. Acoust. Soc. Am. **93**, 1736–1742 (1993).

[15] Michael B. Porter, ''The kraken normal mode program,'' SACLANT Undersea Research Centre, La Spezia, Italy, Rep. SM-245, 1991.

[16] F. B. Jensen and W. A. Kuperman, ''Sound propagation in a wedge shaped ocean with penetrable bottom,'' J. Acoust. Soc. Am. **67**, 1564–1566 (1980).

Effective medium approach to linear acoustics in bubbly liquids

Steven G. Kargl[a)]
Applied Physics Laboratory, University of Washington, 1013 NE 40th Street, Seattle, Washington 98105

(Received 7 September 2000; revised 20 September 2001; accepted 19 October 2001)

Linear wave propagation through a bubbly liquid has seen a resurgence of interest because of proposed "corrections" to the lowest-order approximation of an effective wave number obtained from Foldy's exact multiple scattering theory [Foldy, Phys. Rev. **67**, 107 (1945)]. An alternative approach to wave propagation through a bubbly liquid reduces the governing equations for a two-phase medium to an effective medium. Based on this approach, Commander and Prosperetti [J. Acoust. Soc. Am. **85**, 732 (1989)] derive an expression for the lowest-order approximation to an effective wave number. At this level of approximation the bubbles interact with only the mean acoustic field without higher-order rescattering. That is, the field scattered from a bubble may interact with one or more new bubbles in the distribution, but a portion of that scattered field may not be scattered back to any previous bubble. The current article shows that modifications to the results of Commander and Prosperetti lead to a new expression for the effective wave number, which properly accounts for all higher orders of multiple scattering. [DOI: 10.1121/1.1427356]

PACS numbers: 43.30.Es, 43.20.Bi [SAC-B]

I. INTRODUCTION

Linear wave propagation through a host medium containing many small scatterers has been an active area of research since the pioneering work of Foldy[1] nearly a half century ago. In a multiple scattering theory,[1–5] one enumerates the interactions of each scatterer with an incident field and with the scattered fields from all other scatterers that comprise the assemblage, and, in principle, the total field at any location can be predicted. With sufficiently many scatterers the enumeration becomes intractable and the numerical evaluation is computationally intensive, hence an ensemble average is often applied to determine properties of the mean field. The primary result of the ensemble average is a reduction of the complex system of scatterers and host medium to an "effective medium."

Propagation of a mean field through a bubbly liquid is completely specified if the wave number spectrum for the "effective medium" can be determined. When a harmonic incident field encounters a distribution of identical scatterers, Foldy[1,6] found that the effective wave number satisfies

$$k_m^2 = k^2 + 4\pi N f, \tag{1}$$

where $\omega = ck$ is the angular frequency, and c and k are the speed of sound and wave number in the host medium without scatterers. The density of scatterers is N and f is a complex-valued scattering amplitude for a single scatterer in the host medium. The main assumption leading to (1) is that f accounts for the interaction of a scatterer with the mean field, which includes a contribution from the incident field as well as contributions from the scattered field. However, the scattered field from a given scatterer can interact with one or more new scatterers in the distribution, but a portion of this scattered field cannot return to any previously visited scatterers. Equation (1) provides a good estimate for k_m if the separation distance between nearest neighbors is sufficiently large. This means that the void fraction β is small such that β is defined as the ratio of the volume of gas to the total volume of a representative volume of the bubbly medium.

Recently, Ye and Ding[7] and Henyey[8] have reexamined the multiple scattering series as given by Foldy. These researchers use diagrammatic techniques to determine corrections to (1), which may be written as

$$k_m^2 = k^2 + 4\pi N F, \tag{2}$$

where F is an effective scattering amplitude that includes higher orders of multiple scattering. Ye and Ding found a second-order approximation, $F = f + i4\pi N f^3/2k$, by truncating the multiple scattering series. Henyey states that (2) is an *exact* expression for the effective wave number provided F can be determined, and, in fact, he postulates that F can be obtained from f by evaluating the acoustic scattering loss in terms of the effective medium. Additionally, Henyey reevaluated Ye and Ding's approximation and found $F = f + i4\pi N f F^2/(k + k_m)$ which agrees with Ye and Ding through $O(f^3)$.

A second approach to the problem of linear wave propagation through a bubbly liquid uses a continuum theory. The present article revisits the work of Commander and Prosperetti,[9] which is based on Caflisch *et al.*'s[10] rigorous foundations of van Wijngaarden's continuum model.[11,12] This approach applies a suitably chosen (volume or ensemble) average to the microscopic conservation laws and introduces averaged field variables. The resulting averaged governing equations replace the complex distribution of scatterers and host medium with a continuous effective medium.

Commander and Prosperetti's results are essentially that of an effective medium theory where the mean acoustic field is the relevant field that interacts with the scatterers [i.e., the discussion concerning contributions to the mean field following Foldy's approximation, (1), applies here]. A shortcoming

[a)]Electronic mail: kargl@apl.washington.edu

of their derivation is addressed, and the main result [see (6) in this work] includes all higher orders of multiple scattering at the level of approximations assumed by Caflisch *et al.* and Commander and Prosperetti (i.e., small void fractions).

The remainder of this article is organized as follows. In Sec. II we discuss the pertinent results of Commander and Prosperetti.[9] The notation used here is that of Commander and Prosperetti except in clearly noted situations where changes are required to avoid confusion. The primary results of this article are presented in Sec. III where an alternative expression for k_m^2 is given. Several numerical examples are given which demonstrate the conditions where higher-order multiple scattering effects become important and comparisons to available data are shown. The article concludes with Sec. IV.

II. BASIC EQUATIONS

This section lists the basic results from Commander and Prosperetti and the interested reader is referred to their article for the details.[9] When the bubbly liquid is replaced by an effective medium, the wave number spectrum is determined from the following set of equations:

$$k_m^2 = k^2 + 4\pi\omega^2 \int_0^\infty \frac{a n(a)\ da}{\omega_0^2 - \omega^2 + i(b_v + b_t + b_a)}, \tag{3a}$$

$$\omega_0^2 = \frac{1}{\rho a^2}\left[p_0 \Re(\Phi) - \frac{2\sigma}{a} \right], \tag{3b}$$

$$b_v = 4\mu\omega/\rho a^2, \tag{3c}$$

$$b_t = p_0 \Im(\Phi)/\rho a^2, \tag{3d}$$

$$b_a = \omega^2 k a. \tag{3e}$$

The number of bubbles per unit volume with equilibrium radius between a and $a+da$ is $n(a)da$. [Commander and Prosperetti use $f(a)$ for $n(a)$ while Foldy uses f to represent the scattering amplitude.] The angular frequency at resonance of a bubble with equilibrium radius a is defined in (3b) such that ρ is the ambient density of the host liquid and σ is the surface tension for an interface separating the host liquid from the gas within a bubble. The undisturbed pressure within the bubble is $p_0 = P_\infty + 2\sigma/a$ where P_∞ is the hydrostatic pressure at infinity and the second term is known as the Laplace pressure. Commander and Prosperetti group the viscous, thermal, and acoustic scattering loss mechanisms in a single expression $2\omega b$ whereas (3a) above explicitly displays the individual damping mechanisms defined in (3c)–(3e), respectively. The dynamic viscosity of the host liquid is μ, and the complex-valued function Φ is determined from consideration of the basic thermodynamics within the bubble. Detailed analysis by Prosperetti *et al.*[13] leads to

$$\Phi = \frac{3\gamma}{1 - i3(\gamma-1)\chi\{(i/\chi)^{1/2} \coth[(i/\chi)^{1/2}] - 1\}}. \tag{4}$$

The polytropic constant, $\gamma = C_p/C_v$, is the ratio of the specific heat of the gas at constant pressure to the specific heat of the gas at constant volume; the thermal diffusivity of the gas is $D = (\gamma-1)K_T T/\gamma p_0$; the thermal conductivity is K_T; the temperature is T; and $\chi \equiv D/\omega a^2$. Equations (3) and (4) are sufficient to determine the wave number spectrum for the linear propagation of an acoustic field through a bubbly liquid when higher-order multiple scattering effects can be ignored.

III. DISCUSSION

The proposed modification to the model constructed by Commander and Prosperetti involves a change to the bubble dynamics equation used [their Eq. (15)]. They chose Keller's equation for the radial pulsation of a bubble in the host liquid:

$$\left(1 - \frac{\dot R}{c}\right) R\ddot R + \frac{3}{2}\left(1 - \frac{\dot R}{3c}\right)\dot R^2$$
$$= \frac{1}{\rho}\left(1 + \frac{\dot R}{c} + \frac{R}{c}\frac{d}{dt}\right)\left(p - \frac{2\sigma}{R} - 4\mu\frac{\dot R}{R} - P\right). \tag{5}$$

The instantaneous radius of a bubble at location $\vec{x}$ is $R(a,\vec{x},t)$ and circumscribed dots indicate partial differentiation with respect to time. The pressure within the bubble is p and P is defined as the pressure at the position occupied by the bubble if the bubble were absent. Other bubble dynamics equations could have been selected (e.g., Gilmore, Herring-Trilling, etc.); however, Prosperetti and Lezzi[14] have shown that many of the nonlinear bubble dynamics equations are in the *same family* and should reduce to equivalent forms under linearization.

After the introduction of Keller's equation in their Eq. (15), Commander and Prosperetti state:

> It was first realized by Foldy[1] that, in a dilute mixture, to lowest order in β this quantity $[P]$ coincides with the average pressure defined in the previous section. In this limit, the bubbles do not interact with each other's field, but with the average field. An intuitive justification can be given as follows. *If the liquid quantities are interpreted in a volume-averaged sense*, it may be said that the pressure is, at time t, close to $P(\vec{x},t)$ nearly everywhere inside the averaging volume centered at $\vec{x}$. Large deviations from this value occur only in the immediate neighborhood of other bubbles. Let us now introduce into the averaging volume the bubble for which [their] (15) was written. Since the volume fraction is small, the probability of it ending up near another bubble is negligible. Furthermore, since the averaging volume must contain many bubbles, the effect on P of the addition of the new bubble can also be neglected.

where the emphasis is mine. The above passage correctly identifies the effect that a new bubble would have on the averaged pressure, but Commander and Prosperetti failed to argue the converse. Namely, *what is the effect of the other bubbles in the averaging volume on the new bubble*?

The proposed change is that Keller's equation should have been written in terms of the effective medium: $c \to c_m$

$=\omega/k_m$, $\rho\rightarrow\rho_m$, and $\mu\rightarrow\mu_m$. The linearization procedure remains unchanged. This leads to the fundamental result

$$k_m^2=k^2+4\pi\omega^2\int_0^\infty\frac{an(a)da}{\omega_{0m}^2-\omega^2+i(b_{vm}+b_{tm}+b_{am})},\quad(6a)$$

$$\omega_{0m}^2=\frac{1}{\rho_m a^2}\left[p_0\Re(\Phi)-\frac{2\sigma}{a}\right],\quad(6b)$$

$$b_{vm}=4\mu_m\omega/\rho_m a^2,\quad(6c)$$

$$b_{tm}=p_0\Im(\Phi)/\rho_m a^2,\quad(6d)$$

$$b_{am}=\omega^2 k_m a.\quad(6e)$$

In a dilute mixture, the approximate equalities $\omega_{0m}\approx\omega_0$, $b_{vm}\approx b_v$, and $b_{tm}\approx b_t$ hold because mixture laws for density and viscosity suggest that ρ_m and μ_m would have a negligible effect. For example, a void fraction of $\beta=0.01$ produces a 1% decrease in ρ and Arrhenius's mixture rule for viscosity[15] predicts an approximate 4% decrease in μ. Additionally, the surface tension remains unchanged because it is a local property at the interface separating the gas within a bubble from the surrounding host fluid. Finally, the important change is in the acoustic damping, (6e), which has the obvious interpretation that the bubble is radiating acoustic energy into an effective medium not the bubble-free host liquid. Equation (6) is the general and main result of this article.

Many of the previously cited papers investigate a canonical bubble distribution where all bubbles are identical. Insertion of a delta function bubble size distribution,

$$n(a)=N\delta(a-\overline{a}),\quad(7)$$

into (3a) yields

$$k_m^2=k^2+4\pi N\left[\frac{\omega^2\overline{a}}{\omega_0^2-\omega^2+i(b_v+b_t+b_a)}\right],\quad(8)$$

while the proposed expression (6a) gives

$$k_m^2=k^2+4\pi N\left[\frac{\omega^2\overline{a}}{\omega_{0m}^2-\omega^2+i(b_{vm}+b_{tm}+b_{am})}\right],\quad(9a)$$

$$\approx k^2+4\pi N\left[\frac{\omega^2\overline{a}}{\omega_0^2-\omega^2+i(b_v+b_t+b_{am})}\right],\quad(9b)$$

where $\overline{a}$ is the equilibrium radius of the bubbles. (Commander and Prosperetti use n for N.) The factor in square brackets in (8) is identified as f in (1). The factors in square brackets in (9a) and (9b) are equivalent to F in (2). Equation (8) was first derived by Carstensen and Foldy[6] [see their Eqs. (9-14) and (9-87)], and if Eq. (41) from Commander and Prosperetti is expressed in terms of wave numbers instead of sound speeds, then it would also agree with (8). The recent work of Sangani,[16] based on ensemble-averaged governing equations and pairwise bubble interactions, gives a result equivalent to (9b) [see the right-hand side of his Eq. (5.23)], but he provides neither a derivation nor a citation to the origins of this result.

To demonstrate the present model, a comparison to Silberman's data[17] is shown in Fig. 1. Figure 1(a) contains the

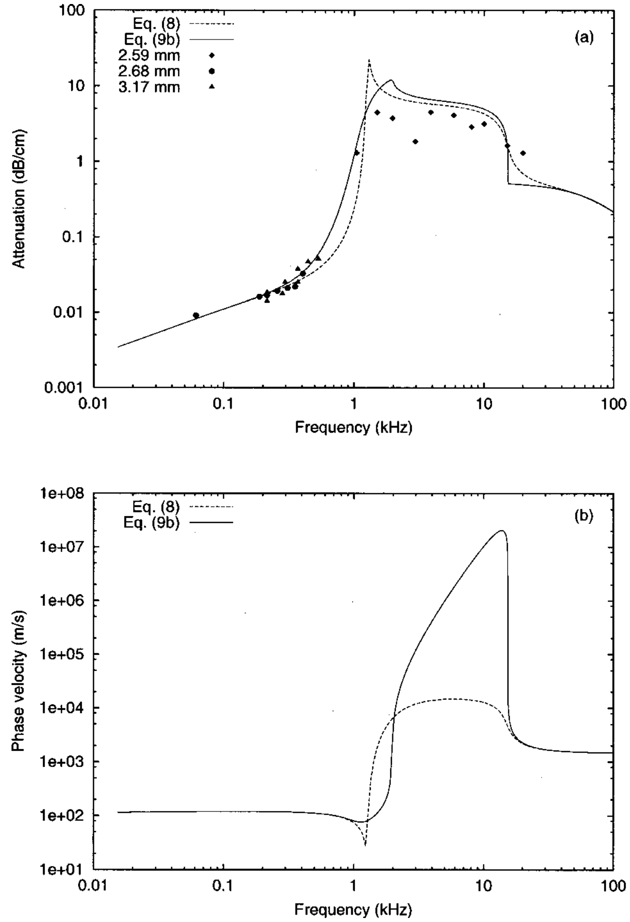

FIG. 1. (a) The attenuation for a delta-function bubble size distribution predicted by (3) (dashed line) and (6) (solid line). The data points are interpolated from Fig. 5 in Silberman's article. (b) The phase velocities predicted by (3) and (6).

attenuation measured by Silberman for three bubble sizes: 2.59, 2.68, and 3.17 mm, while the calculations use an equilibrium radius of $\overline{a}=2.68$ mm. The reported ambient temperature, pressure, and void fraction were $T=294.3$ K, $P_\infty=1.088\times10^5$ Pa, and $\beta=0.01$, respectively. All other material properties of the air and water are determined from standard empirical rules,[18] except $\gamma=1.4$ for all computations. The discrete data were interpolated from Fig. 5 in Silberman's article and correspond to those displayed in Fig. 5 of Commander and Prosperetti. The dashed and solid lines are (8) and (9b), respectively. Equation (9b) could have been expressed as a cubic polynomial in k_m and standard root finding techniques used, but a self-consistent iterative technique was implemented because the integral equation given in (6) must be solved iteratively. Figure 1(b) depicts the predicted phase velocity for these conditions. Interpolation of Silberman's phase velocity data was not attempted due to the overlap of several data points, and he only showed phase velocity measurements at frequencies below resonance where (8) and (9b) agree.

Several features are evident in Fig. 1. First, the sharp resonance peak predicted from (8) has been "smeared out" in the present model. This is easily understood by inspection of the denominator in (9b) and recognizing that the resonance condition is $\omega_0^2-\Im(b_{am})-\omega^2=0$ such that the chosen

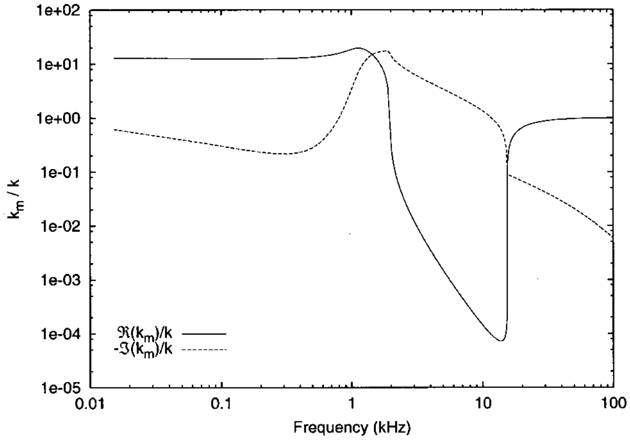

FIG. 2. A pictorial representation of the Kramers–Kronig dispersion relations shows the link between the real and imaginary parts of k_m. The salient feature is that the local rate of change in one component is reflected in the local behavior of the other component.

time convention of exp $(i\omega t)$ yields $\Im(b_{am})<0$. Not only does the peak shift to a higher "resonance frequency," the broadening occurs because $\Im(b_{am})$ is a function of ω. The second feature is that well above and well below the resonance frequency, (8) and (9b) agree, and these approach well-known asymptotic limits. The third feature evident in Fig. 1(a) is the cusp at the maximum attained attenuation calculated from (9b). The cause of the cusp is discussed later in connection with the fourth feature, which is the sharp transition in the attenuation near 15 kHz. The final, and perhaps most startling, feature appears in the phase velocity calculation depicted in Fig. 1(b). The phase velocity exceeds 1×10^7 m/s.

It should be recalled that in a dispersive medium the phase and group velocities are distinct, and if the medium exhibits "anomalous" dispersion, then the signal velocity is also distinct. In Stratton's discussion of these velocities,[19] he cautions: "It will probably be of more practical importance to the reader to know what certain common terms do not mean, than to attach to them a too precise physical significance." If a transmitter emits a finite-duration pulse in a dispersive medium, the earliest arrival of the pulse at a receiver is dictated by the signal velocity, and, in fact, the signal velocity is[20] c.

To understand the nature of the cusp and abrupt transition features in Fig. 1(a) and the predicted phase velocity, it is convenient to recall the Kramers–Kronig dispersion relations for the real and imaginary parts of k_m. Figure 2 depicts $\Re(k_m)/k$ and $-\Im(k_m)/k$ for the conditions corresponding to the Silberman data. It is clear from Fig. 2 that the cusp and abrupt transition features in the attenuation are due to the

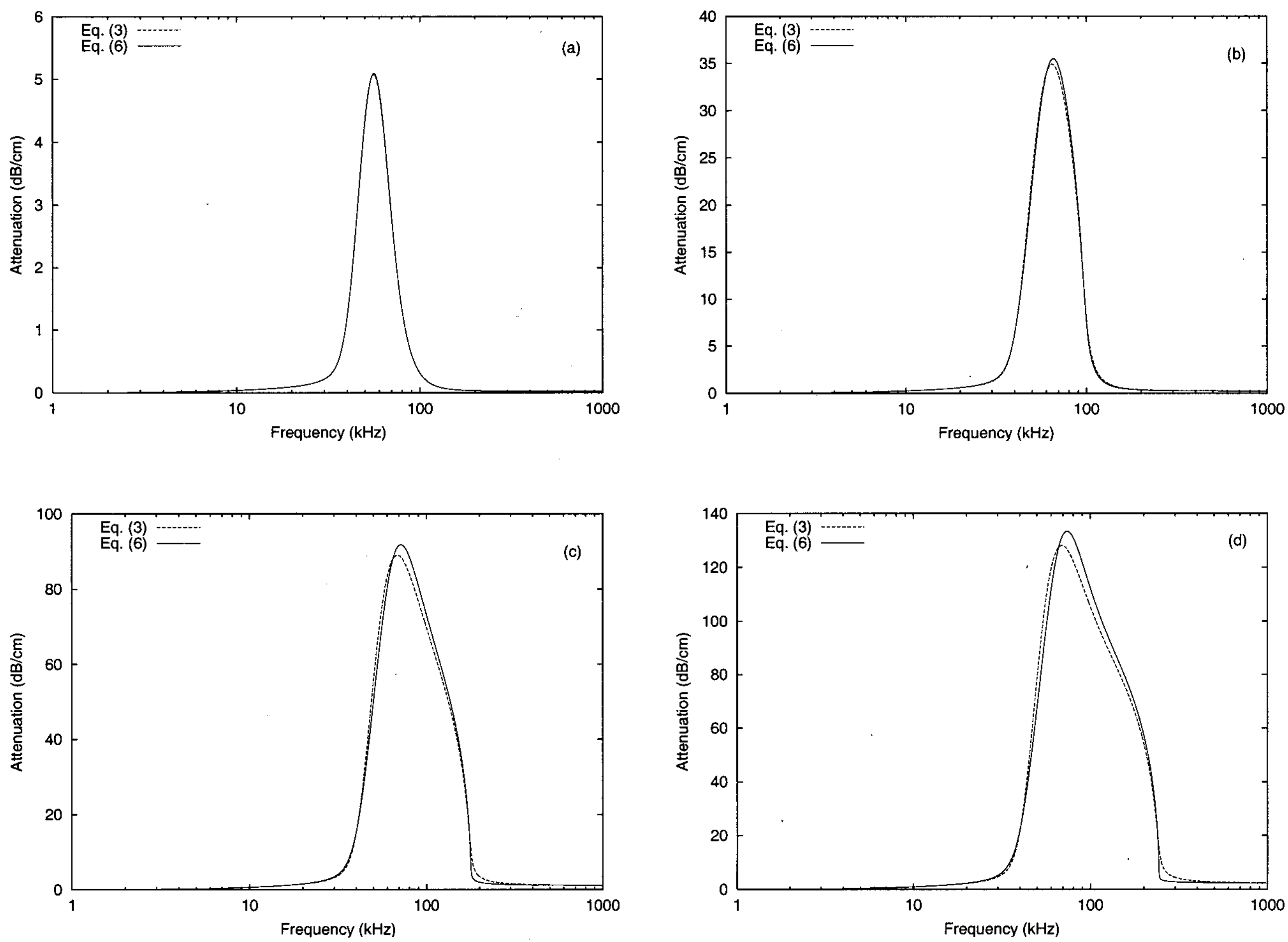

FIG. 3. The attenuation predicted by (3) (dashed line) and (6) (solid line) for several values of void fraction and the modified Gaussian bubble size distribution in (10). (a) $\beta=1\times10^{-5}$, (b) $\beta=1\times10^{-4}$, (c) $\beta=5\times10^{-4}$, and (d) $\beta=1\times10^{-3}$. The discrepancy between (3) and (6) is attributed to (6) properly including higher-order multiple scattering effects whereas (3) treats individual bubbles interacting with the mean acoustic field without higher order rescattering.

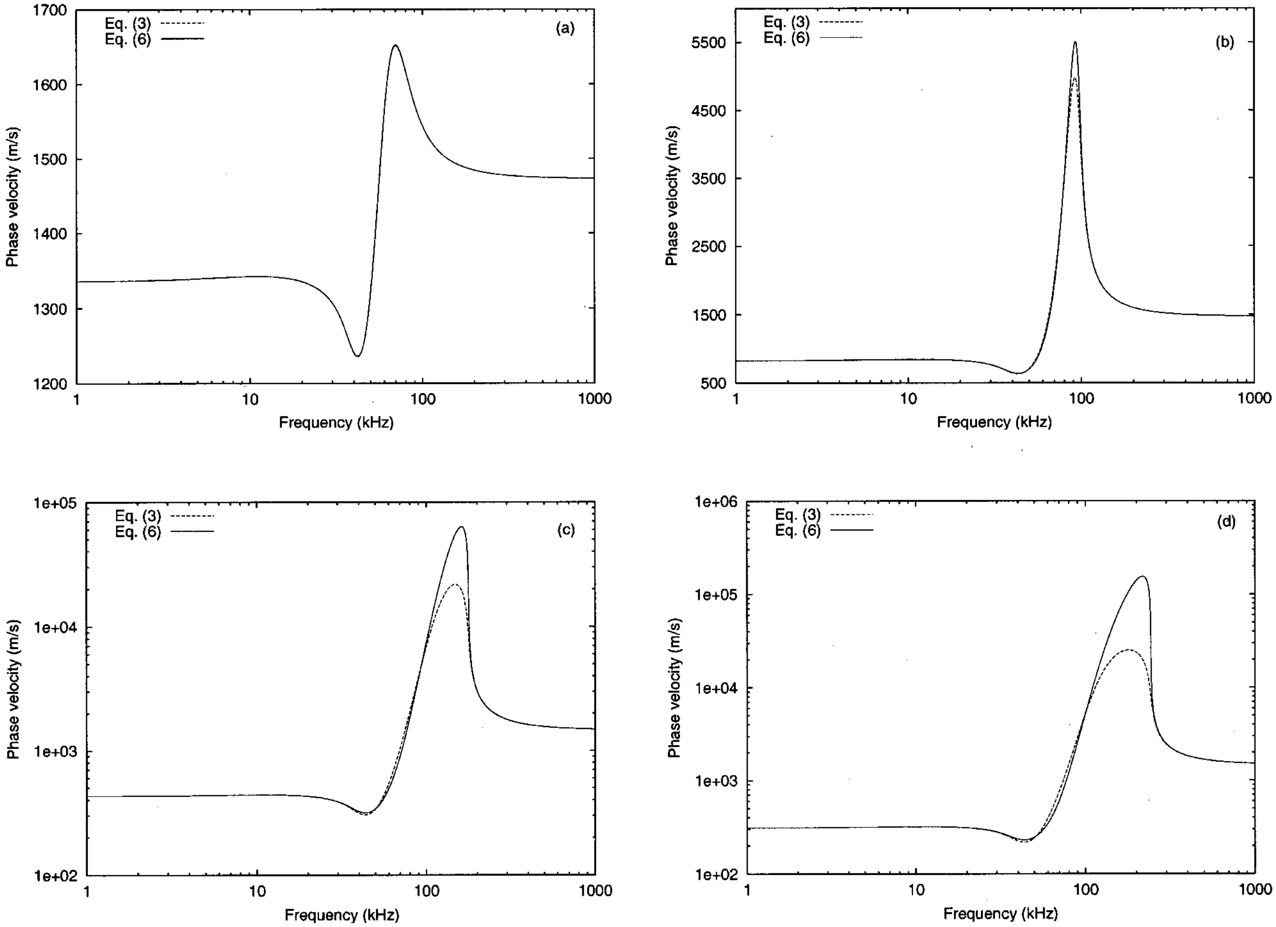

FIG. 4. The phase velocities corresponding to the attenuations shown in Fig. 3 for various void fractions: (a) $\beta = 1 \times 10^{-5}$, (b) $\beta = 1 \times 10^{-4}$, (c) $\beta = 5 \times 10^{-4}$, and (d) $\beta = 1 \times 10^{-3}$. The abscissas of (a) and (b) use a linear scale while (c) and (d) use a logarithmic scale.

local rate of change in $\Re(k_m)$. O'Donnell *et al.* have discussed local approximations to Kramers–Kronig dispersion relations,[21] and they show how local rates of change affect the nonlocal Kramers–Kronig relations. Henyey has pointed out that a step function in one component of k_m leads to a logarithmic singularity in the other component via the Kramers–Kronig relations.[22] Clearly, a local step function occurs near 15 kHz in $\Re(k_m)$, which accounts for both the abrupt transition in attenuation and the rapid transition from 1×10^7 m/s to approximately c.

Although the delta function distribution of (7) is convenient, it is seldomly, if ever, realized in experiments. Experiments designed to investigate departures of (6) from (3) due to higher-order multiple scattering will typically have some spread in the actual size distribution. One candidate distribution to consider is a modified Gaussian function:

$$n(a) = N[1 - \exp(-a_1 a)]\exp\{-a_2[(a - a_3)/a_3]^2\}. \tag{10}$$

The constants a_1, a_2, and a_3 control the knee in clamping the size distribution to zero, the width of the Gaussian distribution, and the radius at the peak of the Gaussian distribution, respectively. For the calculations depicted in Figs. 3 and 4, $a_1 = 0.95\ \mathrm{m}^{-1}$, $a_2 = 10$, and $a_3 = 4.9 \times 10^{-5}$ m, and a has the unit of meter in (10). The infinite integrals in (3a) and (6a) were truncated at 2×10^{-4} m, and the resulting definite integrals are computed using a 64-point Gauss–Legendre quadrature on 20 segments spanning the integration range. Figures 3(a)–(d) correspond to the following void fractions: $\beta = 1 \times 10^{-5}$, 1×10^{-4}, 5×10^{-4}, and 1×10^{-3}, respectively. The constant, N in (10), is determined from the void fraction. The computation of (3a) involves a single integration for each frequency whereas (6a) requires an iterative technique due to the dependence of (6e) on k_m.

The attenuation for the four void fractions is depicted in Fig. 3 while the corresponding phase velocities are shown in Fig. 4. At the lowest void fraction, $\beta = 1 \times 10^{-5}$, the attenuation and phase velocity predicted by (3a) and (6a) are indistinguishable. The interpretation is that higher-order multiple scattering effects can be ignored for (very) dilute bubble concentrations. Figures 3(b) and 4(b) for $\beta = 1 \times 10^{-4}$ show evidence of a departure between (3a) and (6a). Additionally, Figs. 3(c) and (d) and 4(c) and (d) show that as the void fraction becomes larger so does the discrepancy between the predicted attenuation and phase velocities. This is a clear indication that higher-order multiple scattering cannot be ignored when β exceeds approximately $\beta = 1 \times 10^{-4}$.

IV. CONCLUSIONS

Commander and Prosperetti developed an effective medium model for linear wave propagation in bubbly liquid by combining Keller's bubble dynamics equation for an isolated bubble in a pure liquid with the ensemble-averaged fluid dynamics equations of Caflisch *et al.* In this article it is argued that Keller's bubble dynamics equation should have been expressed for a bubble in the effective medium. This proposed modification yields (6), which in general must be solved by an iterative procedure. Numerous features of the new expression for k_m are worth noting.

A clear demarcation of the transition from void fractions composed from noninteracting bubbles to void fractions where higher-order multiple scattering becomes important occurs near $\beta = 1 \times 10^{-4}$. Wu and Jing[23] discuss ultrasound contrast agents, used in medicine for enhancing ultrasound images, in the context of nonlinear acoustics; however, one can infer from their article that the *in vivo* concentration of a contrast agent results in a void fraction on the order of 1×10^{-6} or smaller. Hence, the original results of Commander and Prosperetti are applicable for medical ultrasound in the linear acoustics regime.

When the void fraction is determined from a monodisperse bubble population and β is greater than 1×10^{-4}, several features become apparent. First, a softening of the resonance peak into a cusplike feature occurs. Second, an abrupt transition in the attenuation occurs when the real part of the scattering loss in (6e) approaches the scattering loss of (3e). The abrupt transition has been linked to the phase velocity, which can exceed 1×10^7 m/s, through Kramers–Kronig dispersion relations. The modified Gaussian distribution computations demonstrate that the sharp resonance peak and cusp feature of the monodisperse bubble population are completely removed. The modified Gaussian distribution does not contain a single, dominant bubble size, so one should anticipate a smooth, broad response throughout the frequency range corresponding to the resonance frequencies of the bubbles within the distribution. It is noted that the abrupt transition and large phase velocities are still evident in Figs. 3(c) and (d) and 4(c) and (d). Other distributions (not shown here) also exhibit the abrupt transition and large phase velocities.

ACKNOWLEDGMENTS

The author gratefully acknowledges Dr. Frank S. Henyey for the numerous discussions involving his work and the work of others. The Physical Acoustics Group at the Applied Physics Laboratory provided several opportunities to discuss the present research. This work was supported by the Office of Naval Research, Code 312OA.

[1] L. L. Foldy, ''The multiple scattering of waves,'' Phys. Rev. **67**, 107–119 (1945).
[2] M. Lax, ''Multiple scattering of waves,'' Rev. Mod. Phys. **23**, 287–310 (1951).
[3] M. Lax, ''Multiple scattering of waves. II. The effective field in dense systems,'' Phys. Rev. **85**, 621–629 (1952).
[4] P. C. Waterman and R. Truell, ''Multiple scattering of waves,'' J. Math. Phys. **2**, 512–537 (1961).
[5] J. G. Fikioris and P. C. Waterman, ''Multiple scattering of waves. II. Hole corrections in the scalar case,'' J. Math. Phys. **5**, 1413–1420 (1964).
[6] E. L. Carstensen and L. L. Foldy, ''Propagation of sound through a liquid containing bubbles,'' J. Acoust. Soc. Am. **19**, 481–501 (1947).
[7] Z. Ye and L. Ding, ''Acoustic dispersion and attenuation relations in bubbly mixture,'' J. Acoust. Soc. Am. **98**, 1629–1636 (1995).
[8] F. S. Henyey, ''Corrections to Foldy's effective medium theory for propagation in bubble clouds and other collections of very small scatterers,'' J. Acoust. Soc. Am. **105**, 2149–2154 (1999).
[9] K. W. Commander and A. Prosperetti, ''Linear pressure waves in bubbly liquids: Comparison between theory and experiments,'' J. Acoust. Soc. Am. **85**, 732–746 (1989).
[10] R. E. Caflisch, M. J. Miksis, G. C. Papanicolaou, and L. Ting, ''Effective equations for wave propagation in bubbly liquids,'' J. Fluid Mech. **153**, 259–273 (1985).
[11] L. van Wijngaarden, ''On equations of motion for mixtures of liquid and gas bubbles,'' J. Fluid Mech. **33**, 465–474 (1968).
[12] L. van Wijngaarden, ''One-dimensional flow of liquids containing small gas bubbles,'' Annu. Rev. Fluid Mech. **4**, 369–396 (1972).
[13] A. Prosperetti, L. A. Crum, and K. W. Commander, ''Nonlinear bubble dynamics,'' J. Acoust. Soc. Am. **83**, 502–514 (1988).
[14] A. Prosperetti and A. Lezzi, ''Bubble dynamics in a compressible liquid. Part 1. First-order theory,'' J. Fluid Mech. **168**, 457–478 (1986).
[15] A. Bondi, *Physical Properties of Molecular Crystals, Liquids, and Glasses* (Wiley, New York, 1968).
[16] A. S. Sangani, ''A pairwise interaction theory for determining the linear acoustic properties of dilute bubbly liquids,'' J. Fluid Mech. **232**, 221–284 (1991).
[17] E. Silberman, ''Sound velocity and attenuation in bubbly mixtures measured in standing wave tubes,'' J. Acoust. Soc. Am. **29**, 925–933 (1957).
[18] A. D. Pierce, *Acoustics—An Introduction to its Physical Principles and Applications* (Acoustical Society of America, Woodbury, NY, 1989).
[19] J. A. Stratton, *Electromagnetic Theory* (McGraw-Hill, New York, 1941), pp. 330–340.
[20] F. S. Henyey, ''Anomalous dispersion in ocean bubble clouds,'' J. Acoust. Soc. Am., submitted for publication (unpublished).
[21] M. O'Donnell, E. T. Jaynes, and J. G. Miller, ''Kramers–Kronig relationship between ultrasonic attenuation and phase velocity,'' J. Acoust. Soc. Am. **69**, 696–701 (1981).
[22] F. S. Henyey, private communication (unpublished).
[23] J. Wu and J. Tong, ''Measurements of the nonlinearity parameter B/A of contrast agents,'' Ultrasound Med. Biol. **24**, 153–159 (1998).

Development of an acoustic actuator for launch vehicle noise reduction

Benjamin K. Henderson, Steven A. Lane, and Joel Gussy
Air Force Research Laboratory, Space Vehicles Directorate, 3550 Aberdeen Avenue SE, Kirtland AFB, New Mexico 87117-5776

Steve Griffin
Boeing-SVS, 4411 The 25 Way, Suite 350, Albuquerque, New Mexico 87109

Kevin M. Farinholt
Department of Mechanical Engineering, Virginia Tech, 307 New Engineering Building, Blacksburg, Virginia 24061-0261

(Received 16 January 2001; accepted for publication 25 September 2001)

In many active noise control applications, it is necessary that acoustic actuators be mounted in small enclosures due to volume constraints and in order to remain unobtrusive. However, the air spring of the enclosure is detrimental to the low-frequency performance of the actuator. For launch vehicle noise control applications, mass and volume constraints are very limiting, but the low-frequency performance of the actuator is critical. This work presents a novel approach that uses a nonlinear buckling suspension system and partial evacuation of the air within the enclosure to yield a compact, sealed acoustic driver that exhibits a very low natural frequency. Linear models of the device are presented and numerical simulations are given to illustrate the advantages of this design concept. An experimental prototype was built and measurements indicate that this design can significantly improve the low-frequency response of compact acoustic actuators. [DOI: 10.1121/1.1420383]

PACS numbers: 43.38.Ar, 43.50.Ki [SLE]

I. INTRODUCTION

Acoustic mitigation in launch vehicles is particularly challenging due to the high excitation levels, the nondeterministic nature of the disturbances, and the strict mass, volume, safety, and cost constraints that must be met. During launch, noise levels in small launch vehicles can easily exceed 130 dB over the 0–200-Hz bandwidth, and can inflict damage to the payload. Without acoustic treatment to the fairing, acoustic levels above this bandwidth can approach 140 dB. The development of advanced composite fairings with reduced mass increases the acoustic transmission problem. Therefore, the interior acoustic response of next-generation launch vehicles is a critical concern for payload launch survivability.

Various types of active and passive noise treatments have been considered for launch vehicles to reduce interior acoustic levels during launch. Passive treatments are less effective at low frequency due to the limited amount that can be added. Recently, there has been research to investigate the feasibility of active structural acoustic control and active damping approaches to reduce low-frequency noise levels in launch vehicle fairings.[1,2] There has also been research to develop passive acoustic energy absorbers, which are designed to add damping to the lightly damped low-frequency acoustic modes of the fairing interior.[3] In both the passive and active approaches, diaphragm-type devices were mounted in sealed enclosures and used to couple with the interior acoustic volume. Therefore, the low-frequency response of the actuators was critical to the overall performance of the control approach. The actuators are able to more efficiently couple to the low-frequency acoustic modes of the launch vehicle by having a lower natural frequency. In the active damping approach, the low-frequency response of the actuators was enhanced using a servo-control loop.[4] In the case of passive acoustic attenuators, proper tuning of the device resonance was problematic due to the air-spring effect of the enclosure volume. The air spring of the enclosure can significantly increase the natural frequency of the acoustic actuator or passive damper. Since the actuators for either active or passive control approaches must be of small volume due to mission constraints, and since the actuator must be mounted in a sealed enclosure, the air spring of the enclosure volume becomes a significant problem impacting low-frequency performance.

The concept discussed in this work uses a novel approach to develop an acoustic actuator or passive damper mounted in a small sealed enclosure that exhibits a low natural frequency. This is accomplished in part by partially or completely evacuating the air from the enclosure to minimize the air-spring effect. Furthermore, the conventional diaphragm suspension is replaced with a buckling suspension system that exhibits a nonlinear spring rate. This suspension can be designed to support the large loads associated with the pressure difference across the diaphragm, while simultaneously exhibiting a low stiffness on the order of conventional speaker suspensions at the operating point.

In the following, a coupled model of the loudspeaker and the air spring of the mounting enclosure are developed. The theory and analysis of the buckling suspension and the effects of evacuating the enclosure are then presented. Numerical simulations are presented to demonstrate the advantages of this approach using the parameters of a typical loudspeaker. Finally, the development of a laboratory prototype is presented to experimentally demonstrate the concept. The prototype was designed as a passive system and did not include a voice coil in order to simplify fabrication. However, measurements of the experimental system were taken and used in simulations to predict the performance of a comparable active device.

II. THEORY

In this section, a coupled model of the electromechanical speaker dynamics and enclosure is presented. Then, the effects of implementing a nonlinear suspension and evacuating the enclosure are discussed. The system is modeled as a baffled piston, and the effects of the design parameters on the on-axis radiated sound pressure are computed to illustrate the design advantages.

At low frequency, the speaker responds as a simple mass-spring-damper system with an electromechanical force input. The mechanical dynamics can be modeled using a second-order differential equation,

$$m\ddot{x}(t)+d\dot{x}(t)+kx(t)=\psi i(t), \tag{1}$$

where $i(t)$ is the driving current, ψ is the actuator constant, $x(t)$ is the diaphragm displacement, m is the moving mass, d is the system damping, and k is the stiffness (inverse of compliance).[4] The electrical dynamics of the loudspeaker can be modeled as an inductor, a resistor, and a controlled voltage source in series. The inductance effect results from the voice coil, and the resistor models the direct current (dc) coil resistance. Typically, the mechanical and electrical systems are coupled by a magnetic field created by a permanent magnet. A voltage, $v_a(t)$, applied across the speaker input terminals pushes current through the voice coil, which moves the diaphragm. The movement of the voice coil within the magnetic field induces the flow of current in the opposite direction, which creates a back emf (electromotive force), modeled as a controlled voltage source. The back emf, $v_b(t)$, is proportional to the diaphragm velocity, $\dot{x}(t)$, by the actuator constant ψ. The electrical dynamics can be modeled by a first-order differential equation using Kirchoff's voltage law,

$$L\frac{di(t)}{dt}+R_{\mathrm{dc}}i(t)+\psi\dot{x}(t)=v_a(t), \tag{2}$$

where L is the coil inductance, and R_{dc} is the dc coil resistance.[4]

At low frequency, the enclosed air volume behaves as an air spring in parallel to the suspension and is simply added to the suspension stiffness, k. For an ideal gas under isothermal conditions, the air spring, k_a, is given by

$$k_a=\beta A^2=\frac{\rho_e c^2 A^2}{V}, \tag{3}$$

where

$$\beta\equiv\frac{\gamma P_0}{V}, \tag{4}$$

and A is the radiating area of the diaphragm, ρ_e is the density of the air in the enclosure, c is the sound speed, γ is the ratio of specific heat at constant pressure to specific heat at constant volume ($\gamma=1.4$ for air at standard temperature and pressure), P_0 is the static pressure of the enclosed air, and V is the volume.[5] If the enclosure is small, the air-spring stiffness may greatly exceed the speaker's suspension stiffness.

For simplicity, the enclosure-mounted loudspeaker can be modeled as a baffled piston radiating into free space. As such, the magnitude of the pressure response 1 m in front of the speaker is given by

$$\text{pressure amplitude at 1 m}=2\rho_o c|\dot{x}(t)|\left|\sin\left\{\frac{1}{2}\frac{\omega}{c}\left[\sqrt{1+\left(\frac{a}{r}\right)^2}-1\right]\right\}\right|, \tag{5}$$

where ρ_o is the ambient air density, $\dot{x}(t)$ is the diaphragm velocity, ω is the frequency of oscillation of the diaphragm, r is the distance from the piston (in this case $r=1$ m), and a is the diaphragm radius.[5] Together Eqs. (1), (2), and (5) form a coupled model relating the applied voltage to the radiated sound pressure.

Equations (3) and (4) indicate that the spring constant may be reduced by decreasing the radiating area, increasing the enclosure volume, changing the enclosure gas, or reducing the gas pressure. Increasing the enclosure volume is the conventional solution, although it has the disadvantage that speaker enclosures tend to be very large when low-frequency response is required. Values of γ for gasses that are both safe and readily available are fairly close to those of air, offering only a minimal improvement.

The other alternative, reducing the gas pressure, is more practical and advantageous. Assuming that the system is isothermal, the density of the air in the enclosure is directly proportional to the absolute pressure in the enclosure.[6] Therefore, a reduction in the internal pressure of the enclosure, accomplished by drawing a partial vacuum, translates directly into a reduction in the stiffness of the air spring.

The suspension of a conventional speaker diaphragm is relatively soft. As a consequence, even a small pressure difference between the front and back of a conventional speaker diaphragm would quickly "bottom-out" the speaker, preventing the diaphragm from operating properly. Conversely, if the suspension were redesigned to have large stiffness to oppose the load due to a significant pressure difference, it would have a very small excursion when driven at reasonable power levels, resulting in poor sound radiation. Additionally, the pressure difference resulting from a partial evacuation of the enclosure would likely cause significant deformation or even failure of the diaphragm itself. Therefore, the diaphragm must be designed to withstand the pressure loading.

A nonlinear, buckling suspension is proposed to provide a solution to the pressure loading effect resulting from evacuating the enclosure. It is desired to design a suspension to carry the large static pressure load while exhibiting a reduced stiffness at the operating point. In the ideal case, the suspension stiffness is reduced to a very small value at the

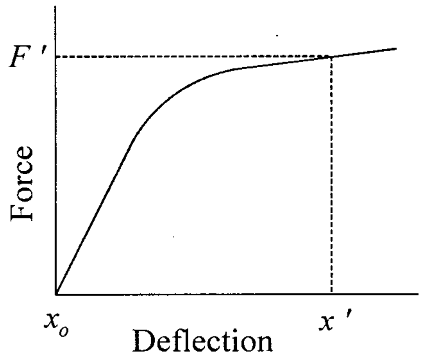

FIG. 1. Typical force versus deflection curve for a buckling slender beam.

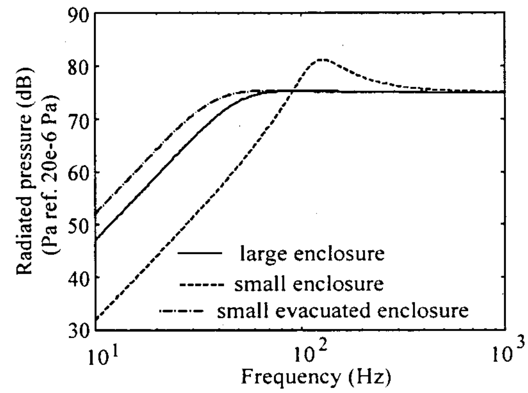

FIG. 2. On-axis radiated pressure simulation results.

desired interior pressure level. If the enclosure was completely evacuated, the air-spring stiffness would disappear completely, and the residual stiffness would result only from the nonlinear suspension element.

This desired nonlinear stiffness behavior has been observed in eccentrically loaded buckling beams.[7] Figure 1 presents a representative load curve (force versus deflection) for a slender beam with an initial eccentricity. As the loading force increases to the desired load value, indicated as F', the diaphragm deflects from its initial position, x_o, to the desired operating point, x'. The slope of the curve represents the stiffness, or spring rate, of the beam or support member. Notice that as the deflection increases, the slope of the curve, and hence the stiffness, decreases. This curve is valid as long as the material is not stressed beyond its elastic stress limit. It is desired to design a buckling support apparatus for the speaker system that behaves in this fashion. By careful design of the support apparatus, the stiffness can be made to approach zero at the operating point. This yields a system with very low stiffness contribution from the supporting apparatus. The damping of the buckling suspension can be optimized by the designer through material selection or passive damping treatments to achieve the desired performance.

III. SIMULATIONS

Using the coupled speaker-enclosure model presented in the previous section and the parameters of a typical loudspeaker listed in Appendix A, three simulations were computed for various configurations of an enclosure-mounted loudspeaker. In each case, the air-spring stiffness was computed using Eq. (3) and added to the value of k given in the Appendix. In the first case, the speaker was mounted in a 1-m^3 enclosure. This was contrasted to the response computed using a smaller, 0.0064-m^3 enclosure. The frequency response functions relating the voltage input to the on-axis radiated pressure output are given in Fig. 2. These plots show that the small volume enclosure significantly increased the resonance frequency of the speaker, which reduced the acoustic output at low frequencies by approximately 15 dB. The response using the 0.0064-m^3 enclosure system with a 90% vacuum is also shown in Fig. 2. In this simulation, it was assumed that the suspension stiffness was reduced to 10% of the suspension stiffness given in Appendix A, and that the damping of the nonlinear suspension was reduced by 50%. In this case, the resonance frequency of the enclosed speaker system was reduced below the frequency of the large enclosure system. Consequently, the low-frequency pressure response was increased by approximately 3 dB. Although this was an idealized simulation, it clearly illustrates the possible advantages of the proposed concept, specifically, improved low-frequency response with a relatively small enclosure volume.

IV. DEVICE REALIZATIONS

An active device can be built using a voice coil and magnet apparatus in order to be used as an acoustic actuator. However, without the voice coil and magnet, the device can be used as a passive acoustic attenuator. Acoustic attenuation is achieved by tuning the natural frequency of the device to couple to an acoustic mode of the fairing. This realization allows the device to couple with and add damping to a low-frequency acoustic mode.

Figure 3(a) is a schematic of a possible active realization of the device using a collapsible support mechanism. The support functions as the surround of a conventional speaker system by providing an airtight seal between the diaphragm and enclosure. Figure 3(b) is an illustration of a device with a rectangular geometry. By configuring the supports vertically, a trade-off is established between the maximum linear motion of the diaphragm and the overall device height. For actual launch vehicle implementations, both a low profile and low mass would be required. However, a large diaphragm stroke may be necessary due to the large acoustic levels experienced during launch.

V. EXPERIMENTAL SETUP AND PROCEDURE

A passive realization of the device shown in Fig. 3(b) was built and tested to experimentally investigate the effects of evacuating the enclosure and using a collapsible suspension. A diagram of the prototype device is given in Fig. 4. The base was constructed of aluminum, with interior dimensions of $0.212 \times 0.212 \times 0.0415\,\mathrm{m}^3$. Blue tempered spring-steel shims replaced both the suspension and surround components that might be expected in a conventional speaker. The spring-steel shims were affixed to the base and diaphragm with short aluminum shims, which were attached

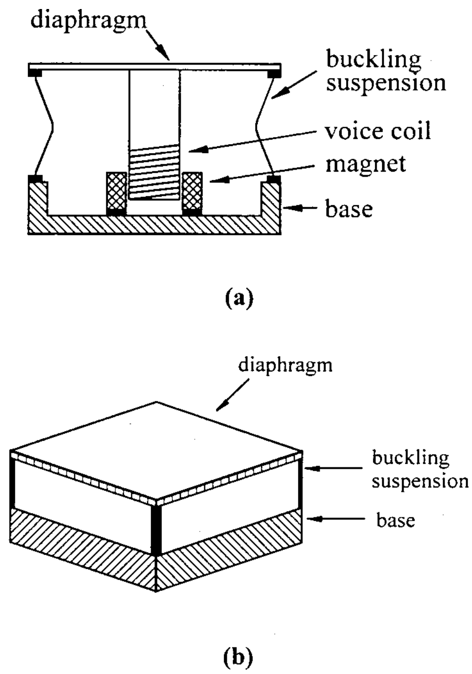

FIG. 3. Schematic (a) and illustration (b) of a device using buckling beams to support the diaphragm.

with screws to provide a rigid, clamped condition. The diaphragm consisted of an aluminum honeycomb structure sandwiched between two layers of carbon-epoxy composite. This material was chosen because of its low density and high strength. Three threaded holes were drilled into one side of the aluminum base to accommodate a vacuum pump connection, a relief valve, and a pressure gage.

Early experiments showed that extremely thin suspension shims were required to provide the necessary deformation while avoiding plastic deformation and fatigue. As a result, each of the four suspension members consisted of three 0.127-mm-thick layers. The three layers were not bonded, and thus carried no shear loads at their interfaces. The height of the suspension members was 55.7 mm, and each of the spring-steel members had a uniform initial prebend that resulted in a 4.7-mm initial out-of-plane displacement at mid-height. This curvature facilitates buckling behavior. The corners were covered with plastic patches, and gaps were sealed with silicone sealant to create a nearly airtight enclosure. The total initial volume of the enclosure was 0.0048 m^3.

Applying a series of downward displacements with a

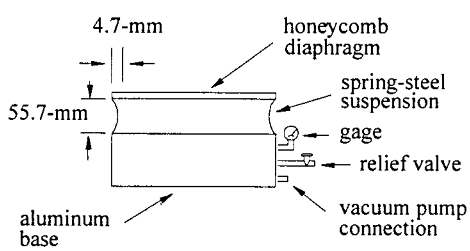

FIG. 4. Diagram of the experimental prototype.

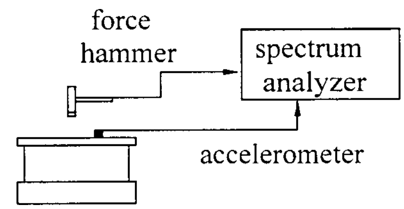

FIG. 5. Illustration of the experimental setup.

load cell and recording the resulting load cell voltage, which was proportional to force, yielded the load curve of the suspension. The measurements described in the next section were taken with the vacuum pump disconnected and the relief valve completely open to avoid any air-spring effects.

The natural frequency of the system was measured for the cases of no vacuum and with a partial vacuum. The partial vacuum was applied such that the suspension buckled without exceeding its elastic limit. The natural frequencies were measured using a force hammer, an accelerometer, and a spectrum analyzer as depicted in Fig. 5. The accelerometer was affixed to the center of the diaphragm with wax, and its output connected to the spectrum analyzer. The force hammer (with a force transducer) was connected to the secondary channel of the analyzer. The analyzer was set to record the transfer function between the force hammer and accelerometer in the frequency domain, with the force hammer serving as a trigger signal. Ten signals were averaged and recorded, and the natural frequency identified. The combined stiffness of the suspension and air spring was computed from the natural frequency measurements, since the moving mass was known, using the relation

$$k = m\omega_n^2, \tag{6}$$

where ω_n was the natural frequency in rad/s.[8]

The measured parameters of the system for the case of no vacuum and partial vacuum were used to compute the effective baffled piston model parameters. Electromechanical parameters for the model were assumed from the previous simulations. The model was then used to predict the effect that the partial vacuum and buckling suspension would have on the radiated pressure of an active realization of the experimental device.

VI. EXPERIMENTAL RESULTS

Figure 6 is a plot of the load curve for the experimental device. The slope of the curve at any point is a measure of the suspension stiffness at that displacement value. The results showed that the stiffness was high at low displacements and diminished with increasing displacement. Therefore, the

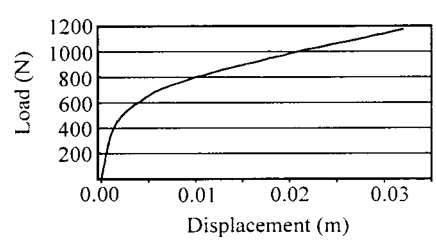

FIG. 6. Measured load curve of the buckling suspension.

device had a lower natural frequency at 0.02 m than at 0.005 m. Note that this load curve was measured with the relief valve fully open, so only the structural stiffness of the buckling suspension was measured. In the case of an internal partial vacuum, a distributed force occurs along the surface of the suspension that will alter the load curve shown in Fig. 6. This force must be taken into account when designing actual devices.

As the enclosure was evacuated, the natural frequency of the device was reduced from 175 to 59.5 Hz at maximum achievable vacuum. The measured natural frequency as a function of internal pressure is given in Fig. 7. Note that atmospheric pressure in Albuquerque, NM, where the experiments were conducted, was 84 kPa due to the altitude. The enclosure volume was also slightly reduced with increasing vacuum, since the diaphragm height was lowered as the suspension buckled.

To determine if the change in natural frequency was attributable to both the nonlinear suspension and the partial vacuum, consider a system using an equivalent volume (0.0032 m^3) with the same moving mass. If it is assumed that the suspension stiffness were to go to zero, and the only stiffness contribution resulted from the air spring as computed using Eq. (3), the resulting natural frequency would be 73.5 Hz. Since the measured natural frequency was less than 73.5 Hz, and because the suspension stiffness does not completely vanish, it is apparent that the air spring of the volume was significantly reduced by the partial vacuum.

Using the baffled piston model and the measured parameters of the experimental system listed in Appendix B, the effect of the buckling suspension and the partial vacuum on the radiated pressure was computed and is presented in Fig. 8. This simulation assumes that a voice coil and magnet can be added to the system without having a significant effect on the measurements obtained from the prototype device. This is reasonable since the mass of a voice coil is typically much less than the mass of the diaphragm used in this prototype. The damping ratio given in Appendix B was estimated from transfer function measurements of the prototype. The simulations predict that the evacuated system would provide a significant increase (approximately 20 dB) in the low-frequency acoustic output of the system.

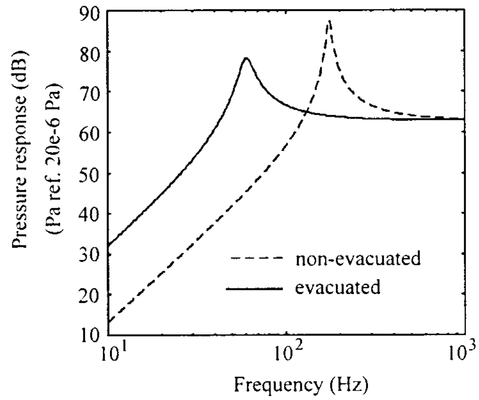

FIG. 8. Predicted on-axis radiated pressure response using experimental values of the prototype device.

VII. CONCLUSIONS

Simulations of a simple model of the proposed evacuated enclosure-mounted speaker indicated that a significant increase in the low-frequency acoustic output might be achieved relative to conventional speaker systems. A prototype device was built and tested, and demonstrated that a nonlinear suspension might be effectively used to support large pressure loads and yet provide low stiffness at the operating point. The results showed that partially evacuating the enclosure and using a nonlinear suspension significantly reduced the natural frequency of the prototype device. The performance of an active realization of the prototype device was predicted using a baffled piston approximation, and indicated an improvement in the low-frequency output of approximately 20 dB. Although the prototype device presented in this preliminary study is not practical for actual applications due to its size and mass, it does illustrate key design innovations proposed in this work.

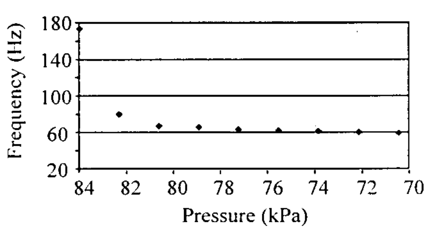

FIG. 7. Measured natural frequency of the prototype device as a function of internal pressure.

ACKNOWLEDGMENTS

This work was supported by the Air Force Research Laboratory, Space Vehicles Directorate, and by the Air Force Office of Scientific Research (AFOSR).

APPENDIX A: THEORETICAL MODEL

Loudspeaker parameters used in the simulations:

Moving mass, m:	0.05 kg
Stiffness, k:	3158 N/m
Damping constant, d:	7.5 N·s/m
Diaphragm radius, a:	10 cm
Force constant, ψ:	6.7 N/A
dc coil resistance, R_{dc}:	4.7 Ω
Inductance, L:	20 mH
Free air resonance, f_s:	40 Hz

Enclosure parameters:

Large enclosure:	1 m^3
Small enclosure:	0.0064 m^3

Other parameters:

Sound speed, c:	340 m/s
Air density, ρ_e:	1.21 kg/m^3

APPENDIX B: EXPERIMENTAL PROTOTYPE

Simulations parameters:

Moving mass, m:	0.453 kg
Damping ratio, ζ:	0.02
Diaphragm surface area:	0.047 m^2
Force constant, ψ:	6.7 N/A

dc coil resistance, R_{dc}:	4.7 Ω
Inductance, L:	20 mH
Enclosure volume without vacuum:	0.0048 m^3
Enclosure volume with partial vacuum:	0.0032 m^3
Natural frequency without vacuum:	175 Hz
Natural frequency with partial vacuum:	59.5 Hz

[1] S. Griffin, S. A. Lane, C. Hansen, and B. Cazzolato, ''Active structural acoustic control of a rocket fairing using proof-mass actuators,'' AIAA J. Spacecraft and Rockets **38**(2), 219–225 (2001).

[2] S. A. Lane, J. D. Kemp, S. Griffin, and R. L. Clark, ''Active acoustic control of a rocket fairing using spatially weighted transducer arrays,'' AIAA J. Spacecraft and Rockets **38**(1), 112–119 (2001).

[3] S. Griffin, S. A. Lane, R. L. Clark, and J. D. Kemp, ''Innovative passive mechanism for control of low frequency transmitted sound into a launch vehicle fairing,'' in *41st AIAA Structures, Structural Dynamics, and Materials Conference*, Atlanta, GA, April 2000.

[4] S. A. Lane and R. L. Clark, ''Improving loudspeaker performance for active noise control applications,'' J. Audio Eng. Soc. **46**(10), 508–519 (1998).

[5] L. E. Kinsler and A. R. Frey, *Fundamentals of Acoustics*, 3rd ed. (Wiley, New York, 1982), pp. 369–372 and 176–178.

[6] G. J. Van Wylen and R. E. Sonntag, *Fundamentals of Classical Thermodynamics*, 3rd ed. (Wiley, New York, 1986), pp. 43–47.

[7] F. B. Seely and J. O. Smith, *Advanced Mechanics of Materials*, 2nd ed. (Wiley, New York, 1959), pp. 585–595.

[8] D. J. Inman, *Engineering Vibration*, 2nd ed. (Prentice-Hall, Englewood Cliffs, 2001), p. 7.

Active control of road booming noise in automotive interiors

Shi-Hwan Oh,[a] Hyoun-suk Kim,[b] and Youngjin Park
Center for Noise and Vibration Control (NOVIC), Department of Mechanical Engineering, Korea Advanced Institute of Science and Technology (KAIST), Science Town, Taejon 305-701, Korea

(Received 13 August 2000; revised 19 September 2001; accepted 27 September 2001)

An active feedforward control system has been developed to reduce the road booming noise that has strong nonlinear characteristics. Four acceleration transducers were attached to the suspension system to detect reference vibration and two loudspeakers were used to attenuate the noise near the headrests of two front seats. A leaky constraint multiple filtered-X LMS algorithm with an IIR-based filter that has fast convergence speed and frequency selective controllability was proposed to increase the control efficiency in computing power and memory usage. During the test drive on the rough asphalt and turtle-back road at a constant speed of 60 km/h, we were able to achieve a reduction of around 6 dB of *A*-weighted sound pressure level in the road booming noise range with the proposed algorithm, which could not be obtained with the conventional multiple filtered-X LMS algorithm. [DOI: 10.1121/1.1420390]

PACS numbers: 43.50.Ki, 43.50.Lj [MRS]

I. INTRODUCTION

Active noise and vibration control with feedforward strategy[1–3] has been widely used in several practical applications such as the engine or exhaust noise control in passenger vehicles, passenger ships, turbo machinery, aircraft and vibration isolation systems.[4–11] One of the most difficult applications in which to implement active control is road booming noise attenuation[12–16] because of the nonlinear characteristics of road data and sensitivity of the transducer location on the control performance. Several studies[17–20] were carried out to estimate the control performance and select the location of reference transducer, error microphone, and loudspeakers for better performance in road-noise control. Because the road-noise characteristic is much different from one car to another and the transfer path from the tire to interior acoustics is complicated, the location of transducers for optimal reduction of noise and the expected reduction cannot be generalized for passenger vehicles. Road booming noise also has nonstationary characteristics caused by various road profiles and the change of driving speeds.

This paper sets out a strategy for attenuation of the road booming noise of a specific mid-size passenger vehicle with a 2000 cc engine; selection of the location and number of reference signals, appropriate positioning of control speakers, development of an efficient control algorithm for the experiment. Reference transducers and control speakers were optimally positioned by the experimental estimate of control performance using the multiple coherence function. An effective control algorithm is also developed to concentrate the control effort on the booming noise frequency band and increase the convergence speed. The hardware-in-the-loop simulation and experimental result are presented and the proposed control algorithm is compared with the conventional (constraint) filtered-X LMS algorithm through the simulation and experiment.

II. CHARACTERISTICS OF ROAD BOOMING NOISE

The nonstationary vibrations of front and rear wheels are generated by nonuniform road profiles and the change of vehicle speed. They propagate though the tire and complicated suspension system and finally generate structure-borne noise, impulsive noise, and other low frequency noise in the interior of the passenger vehicle. These noises lead to acoustical resonances in the interior of the passenger car and such resonant noise is called "road booming noise." There are several characteristics of road booming noise. First, the independent vibrations of four wheels generate it. So, it is hardly reduced by ANC with just one or two reference sensors. Second, the properties of road booming noise change continuously as the vehicle speed or road profile varies. The system from the wheel vibration to road booming noise is not linear because of the complexity of suspension system, transfer path, and the nonlinear interaction between vibration and sound, etc. It causes the road booming noise characteristics of each vehicle to be distinctive. Thus, the active control of road booming noise in the actual road test is rather difficult to achieve than the control in the laboratory setup.

The sound pressures of various road booming noises were detected from the microphone near the driver's headrest inside the vehicle while driven over some road profiles at several different speeds and its spectrum is shown in Fig. 1. No sports wheels were fitted. Four standard tires were attached to the test vehicle. It is hard to recognize the characteristics of booming noise from the original spectrum, but after *A*-weighting, the road booming noise component appears at around 250 Hz. On turtle-back, concrete, and rough asphalt roads at various vehicle speeds, the peak near 250 Hz did not change while those of other low frequencies were shifted. The undesired noise was influenced by the cavity mode behavior of the test vehicle. "Booming" indicates that

[a]Present address: Department of Satellite Control System, Satellite Division, Korea Aerospace Research Institute (KARI), P.O. Box 113, Yusung, Taejon 305-600, Korea; electronic mail: oshysh@kari.re.kr

[b]Present address: CTO, Digital Contents Laboratory, Emersys Corp., 404.KIPA, 48 Jang-Dong Yusung-Gu, Daejon 305-301, Korea.

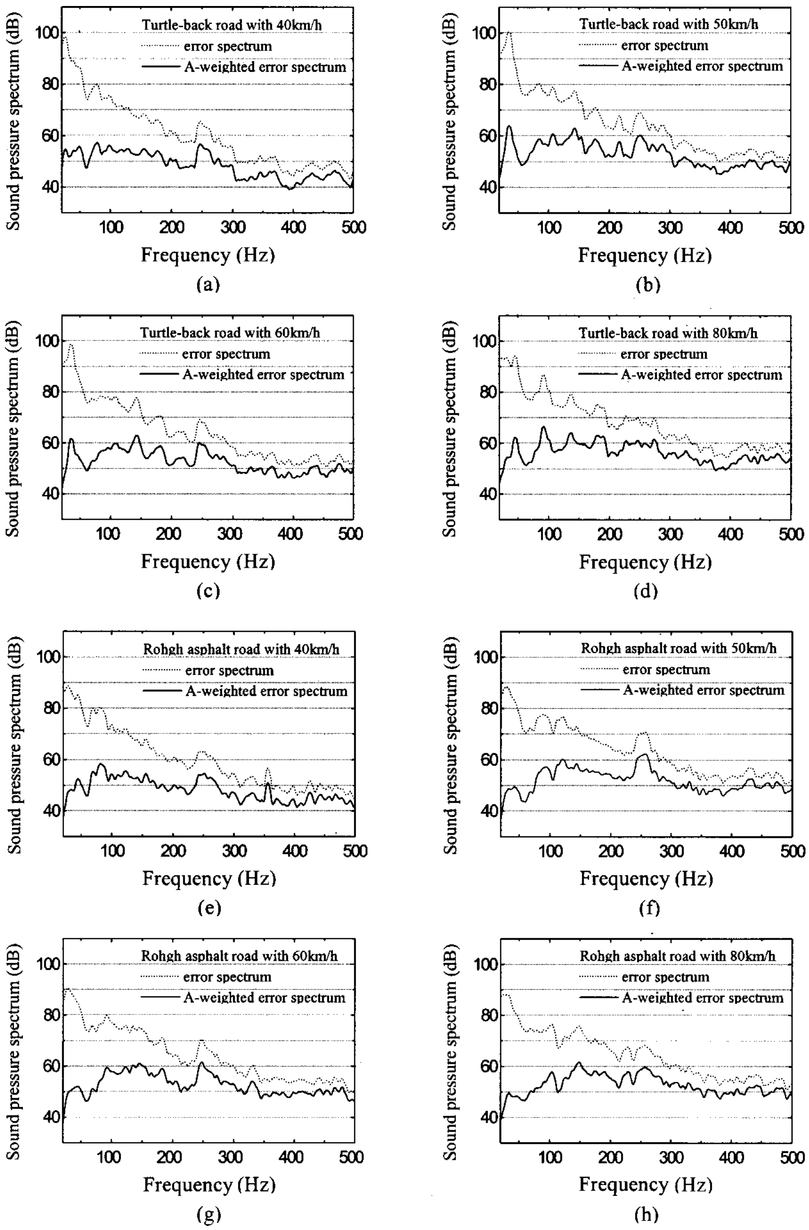

FIG. 1. The characteristics of road booming noise (*A*-weighted) sound pressure level inside the test vehicle driving a turtle-back road with (a) 40, (b) 50, (c) 60, and (d) 80 km/h, respectively, rough asphalt road with (e) 40, (f) 50, (g) 60, and (h) 80 km/h, respectively.

the noise is structure-borne. We did not test the correlation between the booming noise and the internal tire resonance.

III. SELECTION OF REFERENCE SIGNALS AND POSITIONING OF LOUDSPEAKERS

In order to select a set of reference transducers that offers the largest potential sound pressure level reduction, the multiple coherence method is generally used.[21] From the multiple coherence function, the incoherent output can be estimated as

$$S_{nn}(f)=(1-\gamma_{xy}^2(f))S_{yy}(f), \tag{1}$$

where S_{nn} is the incoherent output, γ_{xy}^2 is the multiple coherence function between the input and output, and S_{yy} is the uncontrolled output spectrum. The incoherent output is the sound pressure level at the error microphone that is not coherent with the input transducer. Therefore, the incoherent output can be used to determine the maximum reduction in sound pressure level a particular set of input transducers is capable of achieving. The maximum potential noise reduction in decibels is

$$\mathrm{NR}=-10\log(1-\gamma_{xy}^2(f)). \tag{2}$$

Road tests with various vehicles have shown that the ordinary coherence is often poor, less than 30%, between the signals from each individual accelerometer attached to the structure and the interior sound pressure signals. Several studies[14–20] had already used multiple reference signals to increase the coherence.

In order to determine the location and number of reference transducers to get a satisfactory reduction level of road booming noise for the passenger car, the following experiment was performed. Before the experiment, we selected sixteen possible candidates for a set of accelerometer locations in the suspension system, as shown in Fig. 2. The eight possible locations for the front and rear suspensions are symmetric. First, we got an error signal from a microphone placed on the driver's headrest and three acceleration signals from a

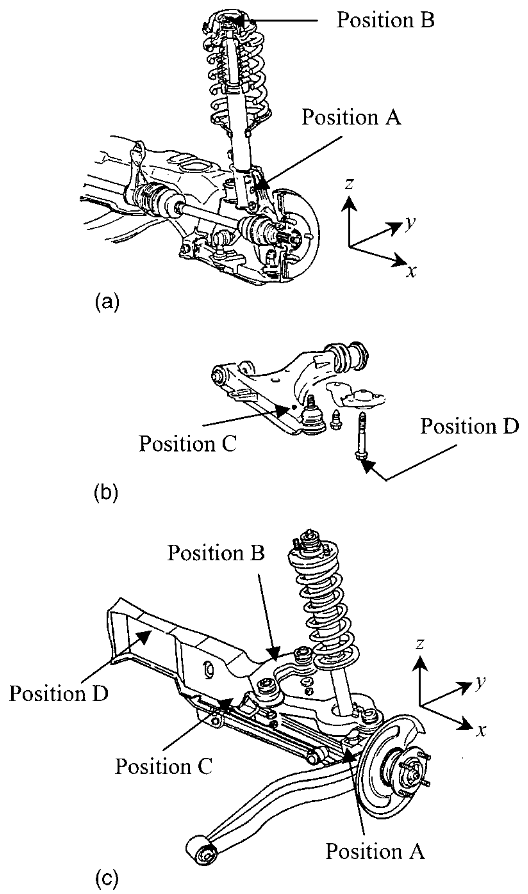

FIG. 2. Accelerometer locations: (a) front right suspension system (symmetric with front left); (b) lower arm of front right suspension system (symmetric with front left); (c) rear right suspension system (symmetric with rear left).

triaxial accelerometer attached to each candidate location while driving on the asphalt road at a constant speed of 60 km/h. The maximum possible reduction level for each reference candidate is listed in Table I. The result shows that it is hard to attenuate the road booming noise over 3 dB with only one triaxial accelerometer. Thus, by using four triaxial accelerometers, we got twelve reference signals and a microphone signal driving under the same condition. The accelerometers were located at position C for the front right and left suspension system and position A for the rear system on which it was easy to attach the sensors because the maximum reduction level for each position was similar. Multiple coherence functions were calculated for several combinations of acceleration signals and Fig. 3 shows the results. Because of the limited calculation power in real-time control process, the number of reference signals was limited to six. Comparing the results, it was found that the maximum attenuation of about 6 dB of the road booming noise band could be achieved with the front right and left acceleration signals (six channels). The front sound field was hardly correlated to the rear acceleration signals but to the front signals only in the booming frequency range, and the rear sound field was correlated to the rear signals only. From this experiment, for the case of a passenger car, an efficient positioning of six reference signals was decided on the two lower arms of the front wheels. The accelerometer signals for reference selection were not measured for turtle-back road drives because the booming noise for turtle-back road has particular frequency components, which are proportional to the vehicle speed under 200 Hz and do not appear for other roads. The reference locations determined by the coherence test for the turtle-back road may not be adequate for the general road condition.

Because the noise reduction level and convergence parameter of the LMS-based algorithm are affected by the secondary paths,[22] the appropriate positioning of loudspeakers was also determined using the measured reference and error microphone signals, which contain the primary and secondary path information.[23] Figure 4 shows the experimental setup to determine the loudspeaker position. The road booming noise control system can be written as

$$\mathbf{E}(f)=\mathbf{A}(f)+\mathbf{B}(f)\mathbf{W}(f), \tag{3}$$

where $\mathbf{E}(f)$ is an error vector in frequency domain, $\mathbf{A}(f)$ is the road booming noise, $\mathbf{B}(f)$ is a filtered reference, and $\mathbf{W}(f)$ is an adaptive filter. The information of transfer functions between the control speakers and error microphone is included in $\mathbf{B}(f)$, which depends on the speaker positions. The transfer functions were estimated for positions A, B, and C off-line. For each set of speaker locations, we calculated the optimum solutions of $\mathbf{W}(f)$ and the expected noise reduction levels from Eq. (3). The six accelerometers determined from the reference selection were used in the determination of speaker locations. Consequently, around 5–6 dB reduction could be expected when the speaker was located at the bottom behind the two front seats, i.e., position B.

IV. CONTROL ALGORITHMS

A. Leaky constraint multiple filtered-X LMS (CMFX LMS) algorithm

A *filtered-x* LMS (FX) LMS algorithm has been widely used in control applications. It is well known that the delay in the secondary path decreases the upper limit of convergence coefficient in this algorithm, so it is not as fast as an LMS algorithm in convergence of adaptive filter to the optimal solution. In order to reduce nonstationary signals effectively, a fast convergent algorithm is needed to track the

TABLE I. Maximum averaged reduction levels using one triaxial accelerometer.

Front left		Front right		Rear left		Rear right	
Position	NR (dB)	Position	NR (dB)	Position	NR (dB)	Position	NR (dB)
A	2.68	A	2.43	A	2.24	A	2.13
B	2.92	B	2.32	B	2.65	B	2.75
C	2.64	C	2.55	C	2.24	C	2.46
D	2.97	D	2.93	D	2.90	D	3.79

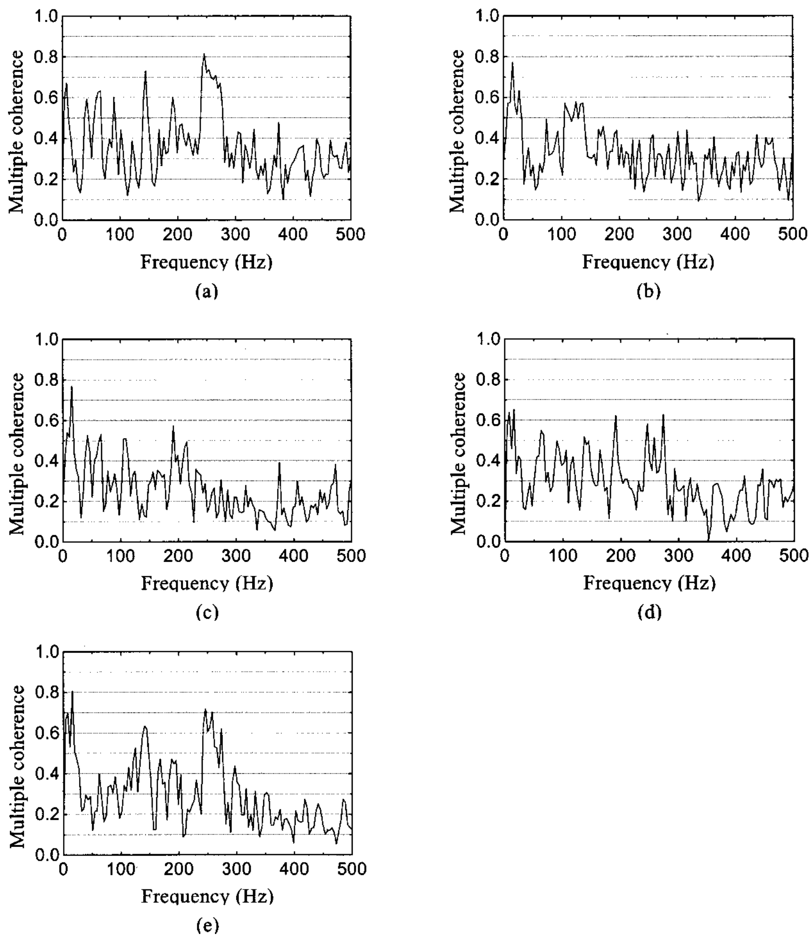

FIG. 3. Multiple coherence function between the error microphone and (a) front accelerometer signals (six channels; right and left *x, y, z* directions at front position C), (b) rear accelerometer signals (six channels; right and left *x, y, z* directions at rear position A), (c) four *x*-direction signals (four *x* directions at front position C and rear position A), (d) four *y*-direction signals (four *y* directions at front position C and rear position A), and (e) four *z*-direction signals (two *z* directions at front position C and rear position A).

undesired noise. In 1992 and 1994, a constraint *filtered-x* LMS (CFX LMS) algorithm, which has a convergence behavior similar to the LMS algorithm, was proposed by Bjarnason[24] and Kim[25] independently. It uses the constraint error instead of the error signal so that the time invariant assumption in the *filtered-x* LMS algorithm is not needed. Consequently, in the presence of a secondary path, the CFX LMS algorithm[26,27] recovers the upper limit of convergence coefficient that had been lowered by the delay in the secondary path.

In order to attenuate the road booming noise with a CFX LMS algorithm, it is necessary to extend the algorithm for a system with N references, K control speakers, and M error microphones. The mth error $e_m(k)$ and constraint error $e'_m(k)$ are expressed as

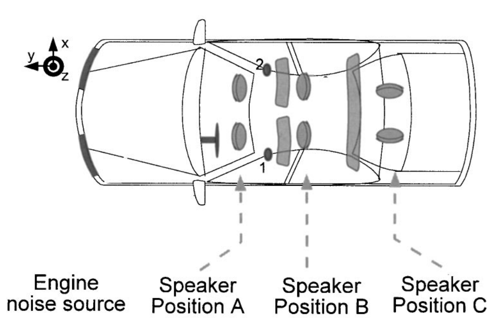

FIG. 4. Experimental setup to determine the position of the loudspeaker.

$$e_m(k)=d_m(k)+\sum_{n=1}^{N}\sum_{k=1}^{K}\sum_{j=0}^{L_h}\sum_{i=0}^{L} h_{mkj}w_{kni}(k-j)\times x_n(k-i-j), \tag{4}$$

$$e'_m(k)=d_m(k)+\sum_{n=1}^{N}\sum_{k=1}^{K}\sum_{j=0}^{L_h}\sum_{i=0}^{L} h_{mkj}w_{kni}(k)\times x_n(k-i-j), \tag{5}$$

where $d_m(k)$ is the undesired noise signal at the mth microphone, $x_n(k)$ is the nth reference, w_{kni} is the ith coefficient of the FIR-type adaptive filter $W_{kn}(z)$, i.e., $W_{kn}(z)=\Sigma_{i=0}^{i=L}w_{kni}(k)z^{-i}$ whose input is the nth reference and whose output goes to the kth control speaker, and h_{mkj} is the jth coefficient of the secondary path $H_{mk}(z)$, i.e., $H_{mk}(z)=\Sigma_{j=1}^{j=L_h}h_{mkj}z^{-j}$, which is located between the kth control speaker and the mth error microphone. The constraint error $e'_m(k)$ can be calculated by modifying $e_m(k)$ by eliminating $d_m(k)$ from Eqs. (4) and (5).

The weights in the CMFX LMS algorithm are updated by the steepest descent method. Derivation of the CMFX LMS algorithm that tries to minimize the cost function $e'^2_1(k)+e'^2_2(k)+\cdots+e'^2_M(k)$ is straightforward. To increase the stability bound and tracking performance, a leakage factor[28] was added in the update algorithm. The leaky CMFX LMS algorithm is summarized in Table II. The signal $fx_{mkn}(k)$ is a filtered signal of $x_n(k)$ through the error path

TABLE II. Summary of leaky CMFX LMS algorithm.

Given $x_n(k), e_m(k)$, $n=1,2,...,N$, $m=1,2,...,M$ at k step

$$fx_{mkn}(k)=\sum_{j=0}^{L_h} h_{mkj}x_n(k-j)$$

$$e'_m(k)=e_m(k)-\sum_{k=1}^{K}\sum_{j=0}^{L_h} h_{mkj}y_k(k-j)+\sum_{n=1}^{N}\sum_{k=1}^{K}\sum_{i=0}^{L} w_{kni}(k)fx_{mkn}(k-i)$$

$$w_{kni}(k+1)=(1-\alpha)w_{kni}(k)-2\mu\sum_{m=1}^{M} e'_m(k)fx_{mkn}(k-i)$$

$$y_k(k)=\sum_{n=1}^{N}\sum_{i=0}^{L} w_{kni}(k)x_n(k-i)$$

model $H_{mk}(z)$. The CMFX LMS algorithm is different from the MFX LMS algorithm only in that it uses $e'_m(k)$ instead of $e_m(k)$.

B. Leaky CMFX LMS algorithm with an IIR-based filter

When an FIR structure is used for an adaptive filter in active noise control, it needs a sufficiently large number of filter weights to achieve satisfactory control performance, especially for a lightly damped system. Using an IIR structure with a smaller number of weights can reduce the necessary computation power; however it may have instability or nonlinearity problems on updating the filter weights. In order to avoid these problems, an IIR-based filter,[29,30] which is a linear combination of fixed stable IIR filters, was proposed.

The selection of IIR bases is very important in a system-identification point of view. First, we need to consider the orthogonality between IIR bases, which means the impulse responses of IIR filter bases are orthogonal to each other. Otherwise, each weight of an IIR-based filter gives undesirable coupling effects in the updating process. If each IIR filter base has its own dominant frequency range, it is possible to control the undesired noise only in the selected frequency range. We can select the control frequency range by using these IIR filter bases appropriately. To get a decaying impulse response, exponential sine or cosine functions having their own dominant frequencies are considered as the impulse responses of an IIR filter base. These functions are not exactly orthogonal to each other, but approximately orthogonal if damping is small. We chose two elementary IIR filter bases as follows:

$$B_{i,c}(z)=\frac{1-e^{-\sigma_i T}Z^{-1}\cos\omega_i T}{1-2e^{-\sigma_i T}z^{-1}\cos\omega_i T+e^{-2\sigma_i T}z^{-2}},$$
$$B_{i,s}(z)=\frac{e^{-\sigma_i T}z^{-1}\sin\omega_i T}{1-2e^{-\sigma_i T}z^{-1}\cos\omega_i T+e^{-2\sigma_i T}z^{-2}}, \tag{6}$$

where the impulse responses of $B_{i,c}(z)$ and $B_{i,s}(z)$ are $e^{-\sigma_i t}\cos\omega_i t$ and $e^{-\sigma_i t}\sin\omega_i t$ in continuous-time domain, respectively. The time constant, σ_i, determines the decaying speed of the impulse response and it is an important design parameter affecting the control performance. Two IIR bases, $B_{i,c}(z)$ and $B_{i,s}(z)$ with real coefficients, represent an IIR base with a center frequency ω_i. The overall controller structure from the reference input to the control output using IIR bases is schematically drawn in Fig. 5.

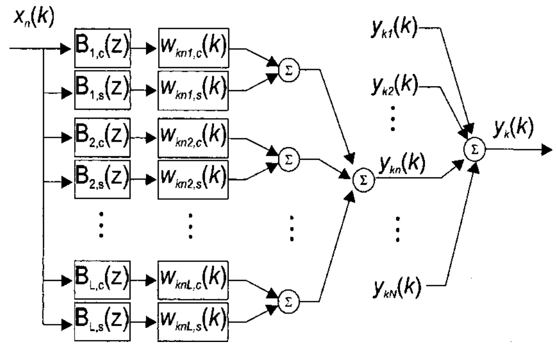

FIG. 5. Controller structure from the nth reference input to control output to the kth secondary source.

Let us define $B_i(z)$ with one pair of base filters as follows:

$$B_i(z)=[B_{i,c}(z)B_{i,s}(z)]^T. \tag{7}$$

To consider L frequency components in the IIR-based filter, there must be L IIR filter bases of Eq. (7).

Denoting $y_{nk}(k)$ as the control output to the kth secondary source due to the nth reference input, $y_k(k)$ can be obtained as the summation of $y_{nk}(k)$ for $n=1,2,...,N$ as follows:

$$y_k(k)=\sum_{n=1}^{N} y_{nk}(k), \tag{8}$$

where

$$y_{nk}(k)=\sum_{i=1}^{L} w_{kni}^T(k)u_{ni}(k), \tag{9}$$

$$w_{kni}(k)=[w_{kni,c}(k)\ \ w_{kni,s}(k)]^T, \tag{10}$$

$$u_{ni}(k)=B_i(z)x_n(k)=[u_{ni,c}(k)\ \ u_{ni,s}(k)]^T. \tag{11}$$

Scalar controller coefficients $w_{kni,c}(k)$ and $w_{kni,s}(k)$ are adaptive weights of $u_{ni,c}(k)$ and $u_{ni,s}(k)$, respectively. $u_{ni}(k)$ is the ith IIR filter output of $x_n(k)$ and its dimension is 2×1—like that of $B_i(z)$.

Because the proposed IIR-based filter does not have any nonlinearity or instability problems on updating the filter weights unlike the conventional adaptive IIR filters, it is easier to model a lightly damped system with an IIR-based filter.

Using this filter instead of an FIR filter, the mth error and constraint error can be written as follows:

$$e_m(k)=d_m(k)=\sum_{n=1}^{N}\sum_{i=0}^{L}\sum_{k=1}^{K}\sum_{j=0}^{L_h} h_{mkj}w_{kni}^T(k-j)u_{ni}(k-j), \tag{12}$$

$$e'_m(k)=d_m(k)+\sum_{n=1}^{N}\sum_{k=1}^{K}\sum_{j=0}^{L_h}\sum_{i=0}^{L} h_{mkj}w_{kni}^T(k)u_{ni}(k-j). \tag{13}$$

The leaky CMFX LMS algorithm with an IIR-based filter that tries to minimize the cost function $e_1'^2(k)+e_2'^2(k)$

TABLE III. Summary of leaky CMFX LMS algorithm with IIR-based filter.

Given $x_n(k), e_m(k)$, $n=1,2,...,N$, $m=1,2,...,M$ at k step

$$u_{ni}(k)=B_i(z)x_n(k)$$

$$fx_{mkn}(k)=\sum_{j=0}^{L_h} h_{mkj}x_n(k-j)$$

$$fu_{mkni}(k)=B_i(z)fx_{mkn}(k)$$

$$e'_m(k)=e_m(k)-\sum_{k=1}^{K}\sum_{j=0}^{L_h} h_{mkj}y_k(k-j)+\sum_{n=1}^{N}\sum_{k=1}^{K}\sum_{i=0}^{L} w_{kni}^T(k)fu_{mkni}(k)$$

$$w_{kni}(k+1)=(1-\alpha)w_{kni}(k)-2\mu\sum_{m=1}^{M} e'_m(k)fu_{mkni}(k)$$

$$y_k(k)=\sum_{n=1}^{N}\sum_{i=0}^{L} w_{kni}^T(k)u_{ni}(k)$$

$+\cdots+e'^2_M(k)$ is summarized in Table III, and its block diagram is presented in Fig. 6.

The filtered-$u_{ni}(k)$ signal through $H_{mk}(z)$, denoted as $fu_{mkni}(k)$, can be calculated as follows: $fu_{mkni}(k)=H_{mk}(z)u_{ni}(k)=H_{mk}(z)B_i(z)x_n(k)$, but this entails a high computational burden and requires a lot of memory. Since the filters $H_{mk}(z)$ and $B_i(z)$ are linear time-invariant filters, by reversing the filtering order of $H_{mk}(z)$ and $B_i(z)$, $fu_{mkni}(k)$ can be calculated more effectively as $fu_{mkni}(k)=B_i(z)fx_{mkn}(k)$.

V. HARDWARE-IN-THE-LOOP SIMULATION

The locations of the reference accelerometers, error microphones, and control speakers that had been determined in Sec. III were applied to the hardware-in-the-loop simulation and experiment. Two x direction (lateral) acceleration signals from the front wheels were not used on account of the limitation of calculation power, because the lateral motion has minimal correlation with interior noise. Accelerometers were attached symmetrically on the lower arms of front left and right wheels to measure the accelerations of the y and z directions (longitudinal and vertical). Two error microphones were located at the outer ears of two front seats and two commercial loudspeakers were positioned behind the front seats. The control performance is not sensitive to the nearby

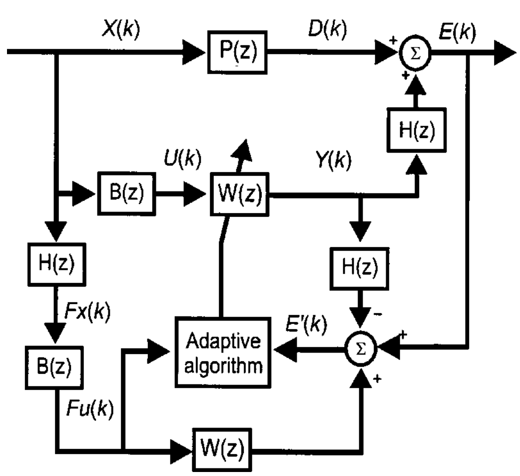

FIG. 6. Block diagram of CMFX LMS algorithm with IIR-based filter.

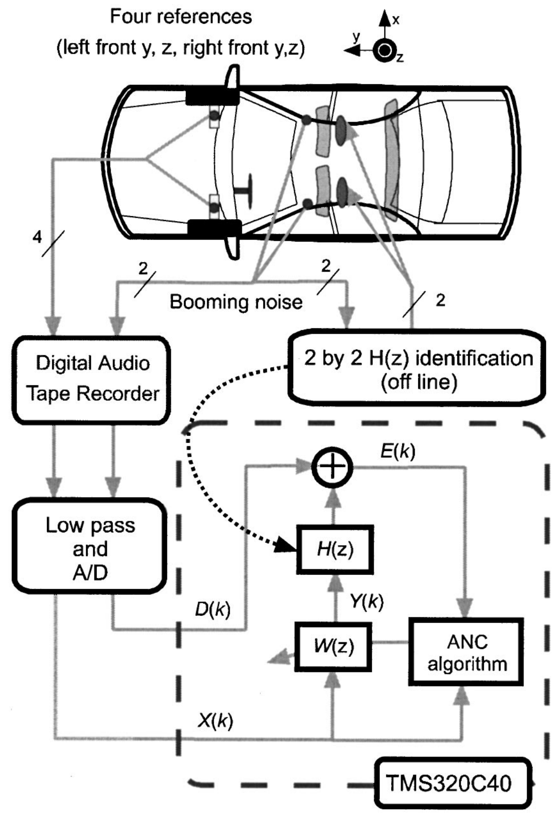

FIG. 7. Experimental setup for hardware-in-the-loop simulation.

change of loudspeaker locations. It can be shifted slightly for manufacturer's convenience. Thus, we developed an ANC system of four references, two secondary speakers and two error microphones, on the test car with the 2000 cc engine. Before carrying out a hardware-in-the-loop simulation, we recorded four accelerations and two error microphone signals while driving on a turtle-back road at a constant speed of 60 km/h. The simulations were carried out playing the record tape. Figure 7 illustrates the overall setup for hardware-in-the-loop simulation. Two microphone signals that are considered as the undesired noises and four reference signals were low-pass-filtered with cut-off frequency of 500 Hz and then A/D converted with a sampling frequency of 1000 Hz. A 2×2 secondary path was identified using two secondary speakers located behind the front seats. We carried out simulations using a DSP board equipped with a TMS320c40 chip.

The lengths of adaptive filters and the secondary path model with FIR type were 130 and 50, respectively. Nine IIR base pairs with center frequencies of 230, 235, 240, 245, 250, 255, 260, 265, and 270 Hz and damping coefficient of $\sigma_i=25$ are selected. IIR bases were concentrated on the road booming noise range.

Figure 8 shows the spectrum of the error microphone signal before and after control at the front right seat while driving on a turtle-back road at a speed of 60 km/h. Every sound pressure spectrum is A-weighted. It is easy to observe that the road booming component appears around 250 Hz from the noise spectrum of "before control."

Although the CFX LMS algorithm has better control performance than the conventional FX LMS for this application,[16] little reduction of noise was obtained with the

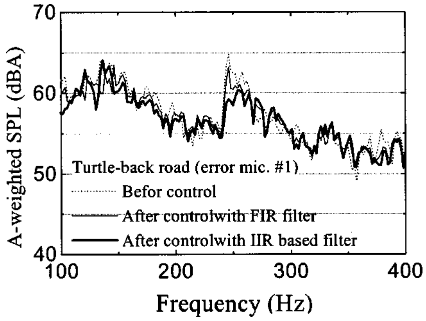

FIG. 8. Hardware-in-the-loop simulation results: Sound pressure level before and after control at the right front error microphone driving on a turtle-back road.

CMFX LMS algorithm while 5 dB of the peak value was reduced using the IIR-based filter in the road booming frequency range. There is no change out of the road booming frequency range when IIR-based filter is used. Driving at constant speed, the road booming noise was still nonlinear (in detail, time varying) because of the road condition, the complexity of suspension, transfer path, and interconnection between the vibration and sound. No reduction can be achieved for a small convergence coefficient with the MFX LMS algorithm and diverged rapidly for a small increment of convergence coefficient even in driving at a constant speed. If the booming noise had been time invariant for a constant driving speed, it could have been reduced with a conventional algorithm. The calculation powers of the two algorithms are almost equal. In this simulation, it is verified that the IIR-based filter is more efficient than an FIR filter for road booming noise which is concentrated in a narrow frequency band.

The length of the adaptive filter could not be increased more than 130 because of the calculation limit of the DSP hardware. For reference, the FIR filter length could be increased up to 300 taps and the reduction of 2 dB at the booming frequency was achieved for one secondary source and one error microphone configuration. The reason for the poor performance of the $4\times2\times2$ CMFX LMS is thought to be the insufficiency of the adaptive filter length. In most discrete-time control systems, the sampling frequency is usually chosen to be ten times the control target frequency for better performance. But in this application, we cannot raise it up over 1000 Hz on account of computation power although the control target frequency was about 250 Hz. Even if the sampling frequency is decreased in order to increase the filter length, the performance will be severely degraded. Reducing the number of filter coefficients while increasing the reference signal also degraded the performance in this simulation. Better performance can hardly be expected with an increasing number of references, as shown in Fig. 3. Another important reason is that the FIR filter tries to reduce error signals with more weighting for higher power components in the least-squares sense. The power of road booming noise under 200 Hz is dominant inside the car, so FIR adaptive filters will try to attenuate these low frequency components first. Since there is little coherence between the references and error signals in this frequency range, the weights of the adaptive filter fluctuate rapidly, thus consuming much of the

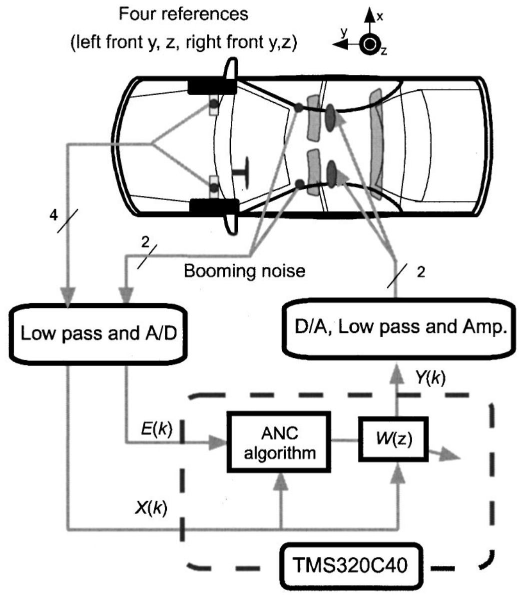

FIG. 9. Experimental setup.

control efforts. The effort to attenuate road booming near 250 Hz is comparatively small despite of higher coherence than in the low frequency range. These make the performance of the CMFX LMS algorithm worse in this application. To enhance the performance using the FIR filter, every reference signal was high-pass filtered, with a cut-off frequency of 150 Hz, and about 2–3 dB reduction of road booming noise was obtained, still below the reduction level of the IIR-based filter.

VI. EXPERIMENT

Real-time experimentation was executed while driving two types of road profiles (rough asphalt road and turtle-back road) at a constant speed of 60 km/h. Performance of the proposed CMFX LMS algorithm using an IIR base filter is compared with that using the conventional FIR filter. Filter length and all other parameters are chosen to be the same in the hardware-in-the-loop simulation for both algorithms. The overall experimental setup is presented in Fig. 9.

The attenuation of overall level of the *A*-weighted spectrums is plotted in Fig. 10. Spectrums of $e(k)$ before control, and after control using the FIR filter and IIR-based one are represented with a dotted line, solid line, and thick solid line, respectively. The conventional CMFX LMS algorithm achieves no remarkable reduction, and even the increment of the noise level is observed for the turtle-back road profile. It is because the signal power of the road booming component in the error microphone signal before *A*-weighting is significantly smaller than that of the noise component under 200 Hz as found in the hardware-in-the-loop simulation. A 5–6 dB reduction was achieved at the two error microphone positions in road booming frequency region near 250 Hz when the IIR-based filter was used. There is no apparent change of noise level out of the booming frequency range where IIR bases are not located. Because of the road booming noise characteristics, the CMFX LMS algorithm using a FIR filter tried to reduce low frequency range and little sound attenu-

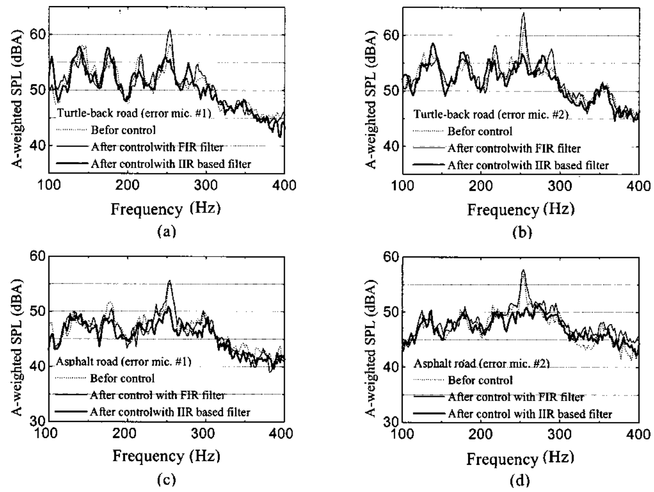

FIG. 10. Experimental results: Sound pressure level before and after control at the (a) right and (b) left error microphone driving on a turtle-back road, at the (c) right and (d) left error microphone driving on an asphalt road at a constant speed of 60 km/h

ation was achieved, whereas the IIR-based filter reduced noise effectively in the range of road booming. The *x* direction accelerometers of the front suspension position ''C'' may give some benefit to the turtle-back road results for 80 and 140 Hz peaks, but if such a reference location is selected, it is hard to expect enhanced control performance for the other road conditions, except for a turtle-back road. Thus, we did not select the *x* direction accelerometers of the front suspension position ''C.'' Road booming noises without/with control for a turtle-back road are greater and harsher than those for a course asphalt road. But the controlled sounds were slightly better than the uncontrolled sounds. Global reduction was not achieved in this study because only two error microphones were attached in front of the car. In order to achieve global reduction, more reference signals detected from the rear suspension system and error microphones would be needed, but the calculation power requirements would be increased substantially.

In this application, the sweet spot is located in a sphere with a diameter of 35–40 cm for 250 Hz noise, so if a driver moves his/her head, he/she can move outside the zone of cancellation with this single-input single-output configuration.

VII. CONCLUSION

Active control of road booming noise using four references, two control speakers, and two error microphones was investigated in the paper. The objective was to attenuate the road booming noise near the headrests of two front seats inside a passenger car. The characteristics of road booming noise of this car were examined and it was found that around 250 Hz was the dominant frequency range of booming noise for the test car. Four reference accelerometers were attached to both sides of the lower arms of the front wheels to maximize the reduction level through multiple coherence analysis. Two loudspeakers were also positioned appropriately to increase the control efficiency considering the primary and secondary paths. A leaky CMFX LMS algorithm with an IIR-based filter was adopted as a fast convergent and efficient algorithm having frequency-selective controllability to reduce time-varying signals effectively. Driving turtle-back and asphalt roads at a constant speed of 60 km/h, a 5–6 dB reduction of road booming noise was achieved at the error microphone positions through the hardware-in-the-loop simulation and experiment with the proposed control system. Comparable reductions could not be obtained with a MFX LMS algorithm or a CMFX LMS algorithm mainly because of the computational power limit. The proposed control system demonstrates the technical feasibility of active control of the road booming noise.

ACKNOWLEDGMENT

This work was financially supported by VRRC (Virtual Reality Research Center) in the ERC program of KOSEF and Brain Korea 21 project of Ministry of Science and Technology, Korea.

[1] B. Widrow and S. D. Stearms, *Adaptive Signal Processing* (Prentice–Hall, New York, 1985).
[2] P. A. Nelson and S. J. Elliott, *Active Control of Sound* (Academic, San Diego, 1992), Chap. 12, pp. 379–407.
[3] C. R. Fuller, S. J. Elliott, and P. A. Nelson, *Active Control of Vibration* (Academic, San Diego, 1996), Chap. 4, pp. 91–111.
[4] S. J. Elliott, I. M. Stothers, P. A. Nelson, A. M. McDonald, D. C. Quinn, and T. J. Saunders, ''The active control of engine noise inside cars,'' in Proceedings of Inter Noise 88, Poughkeepsie, New York, 1988, pp. 987–990.
[5] S. J. Elliott, P. A. Nelson, I. M. Stothers, and C. C. Boucher, ''In-flight experiment on the active control of propeller-induced cabin noise,'' J. Sound Vib. **140**, 219–238 (1990).
[6] C. R. Fuller and J. D. Jones, ''Experiment on reduction of propeller induced noise filed inside flexible cylinder,'' J. Sound Vib. **112**, 389–395 (1987).
[7] R. H. Cabell, H. C. Lester, G. P. Muthur, and B. N. Tran, ''Optimization of actuator arrays for aircraft interior noise control,'' in Proceedings of the Fifteenth AIAA Aeroacoustics Conference, Long Beach, CA, 1993, pp. 93–4447.
[8] A. J. Bullmore, P. A. Nelson, and S. J. Elliott, ''Theoretical studies of the active control of propeller-induces cabin noise,'' J. Sound Vib. **140**, 191–217 (1990).
[9] V. Martin, P. Vignassa, and B. Peseux, ''Numerical vibroacoustic modeling of aircraft for acoustic control of interior noise,'' J. Sound Vib. **176**, 307–332 (1990).
[10] W. Vonheesen, ''Practical experience with an active noise control installation in the exhaust gas line of a cogeneration plant engine,'' Acoustica **82** (Suppl 1), 195 (1996).
[11] S. Kim and Y. Park, ''Active control of multi-tonal noise with reference generator based on on-line frequency estimation,'' J. Sound Vib. **227**, 647–666 (1999).
[12] T. J. Sutton, S. J. Elliott, P. A. Nelson, and I. Moore, ''The active control of road noise inside vehicles,'' in Proceedings of Inter Noise 90, Gothenburg, Sweden, 1990, pp. 1247–1250.
[13] W. B. Ferren and R. J. Bernhard, ''Active control of simulated road noise,'' in Proceedings of the 1991 Noise and Vibration Conference, Traverse City, MI, 1991, pp. 69–82.
[14] T. J. Sutton, S. J. Elliott, A. M. McDonald, and T. J. Saunders, ''The active control of road noise inside vehicles,'' Noise Control Eng. J. **42**, 137–147 (1994).
[15] H. Sano, S. Adachi, and H. Kasuya, ''Active noise control based on RLS algorithm for an automobile,'' in Proceedings of Active 95, Newport Beach, CA, 1995, pp. 891–898.
[16] H.-S. Kim, Y. Park, and K.-H. Sur, ''Active noise control of road booming noise with constraint filtered-X LMS algorithm,'' in Proceedings of Inter Noise 96, Liverpool, UK, 1996, pp. 1155–1158.
[17] C. M. Heatwole, X. Dian, and R. J. Bernhard, ''Determination of the number of input transducers required for active control of road noise in-

side automobiles,'' in Proceedings of Noise-Con 93, Poughkeepsie, New York, 1993, pp. 207–212.

[18] C. M. Heatwole and R. J. Bernhard, ''The selection of active noise control reference transducers based on the convergence speed of the LMS algorithm,'' in Proceedings of Inter Noise 94, Yokohama, Japan, 1994, pp. 1377–1382.

[19] C. M. Heatwole and R. J. Bernhard, ''Reference transducer selection for active control of structure-borne road noise in automobile interiors,'' Noise Control Eng. J. **44**, 35–43 (1996).

[20] W. Dehandschutter and P. Sas, ''Active control of structure-borne road noise using vibration actuators,'' ASME J. Vibr. Acoust. **120**, 517–523 (1998).

[21] M. E. Wang and M. J. Crocker, ''On the application of coherence techniques for source identification in a multiple noise source environment,'' J. Acoust. Soc. Am. **74**, 861–872 (1983).

[22] G. Chen, T. Sone, and M. Abe, ''Effects of multiple secondary paths on convergence properties in active noise control systems with LMS algorithm,'' J. Sound Vib. **195**, 217–228 (1996).

[23] H.-S. Kim and Y. Park, ''A study on performance limit index of feedforward ANC,'' in Proceedings of Korean Society of Noise and Vibration Engineering, Kwang-Ju, Korea, 1995, pp. 161–164.

[24] E. Bjarnson, ''Noise cancellation using a modified form of filtered-X LMS algorithm,'' in Proceedings of Eusipco Signal Processing V, Brussels, Belgium, 1992.

[25] I.-S. Kim, H.-S. Na, K.-J. Kim, and Y. Park, ''Constraint filtered-X and filtered-U least-mean-square algorithm for the active control of noise in ducts,'' J. Acoust. Soc. Am. **95**, 3379–3389 (1994).

[26] H.-S. Na and Y. Park, ''The constraint least mean square error method,'' J. Korean Society of Noise and Vibration Engineering **4**, 59–69 (1994).

[27] H.-S. Na and Y. Park, ''Convergence analysis of the constraint Filtered-X LMS algorithm,'' in Proceedings of Inter Noise 95, Newport Beach, CA, 1995, pp. 485–488.

[28] K. Mayyas and T. Aboulnasr, ''Leaky LMS algorithm: MSE analysis for Gaussian data,'' IEEE SP **45**, 927–934 (1997).

[29] S.-H. Oh and Y. Park, ''Active noise control algorithm using IIR based filter,'' in Proceedings of Inter Noise 98, Christchurch, New Zealand, 1998, pp. 543–546.

[30] S.-H. Oh and Y. Park, ''Active noise control algorithm using IIR based filter,'' J. Sound Vib. **231**, 1396–1412 (2000).

A stability analysis of a decentralized adaptive feedback active control system of sinusoidal sound in free space

E. Leboucher, P. Micheau, A. Berry, and A. L'Espérance
G.A.U.S., Mechanical Engineering Department, Université de Sherbrooke, Sherbrooke, Québec J1K 2R1, Canada

(Received 28 February 2000; revised 12 June 2001; accepted 11 October 2001)

In some cases, the implementation of active control of sound in free space requires a large number of secondary sources and error sensors. In terms of control hardware, this may translate into considerable processing power requirement. A practical method to decrease processing power is to decentralize the control; that is, implement many single-input, single-output independent controllers operating simultaneously instead of a large multiple-input, multiple-output system. The main drawback of decentralized control is the risk of global instability. The purpose of this paper is to derive conditions under which globally stable control system behavior can be obtained in the case of adaptive feedback decentralized control for a sinusoidal disturbance. The main objective is to give practical conditions derived from the small gain theorem and the Nyquist criterion for the stability of the control system. These conditions only take into account the geometrical arrangement of the secondary sources and error sensors. This analysis involves a new parameter β called "*performance index*," which is associated with both the convergence of the individual controllers and the global stability of the system. Simulation and experimental results are shown to illustrate the effectiveness of the developed analytical tools.
[DOI: 10.1121/1.1427358]

PACS numbers: 43.50.Ki, 43.60.Gk [MRS]

I. INTRODUCTION

The active noise control of sinusoidal sound in free space has received considerable attention in the last few years. In a number of practical situations, the sound radiated in free space by extended sources needs to be globally reduced. This is the case of electrical power transformers, for example.[1] Nelson and Elliott have demonstrated that sound-power attenuation can be achieved by active control with secondary sources, loudspeakers for example, located in the near field of an extended radiator (also called the primary source).[2] An effective global attenuation of the sound power implies that the secondary sources must be in the vicinity of the radiator: the distance between each secondary source and the radiator must be less than $\lambda/4$, where λ is the acoustic wavelength.[3] The secondary sources are driven by a controller in order to cancel the sound field measured by error microphones, for example.

In this paper, the sound-power attenuation is based on the creation of one canceling point in front of each secondary source. Roughly speaking, each canceling point has the effect of creating a local zone of quiet; these individual zones of quiet must overlap in order to significantly reduce the noise downstream of the cancellation points. Fahnline[4] showed that global control of the sound field of an extended radiator can be achieved using a distribution of secondary point sources located sufficiently close to the radiator. When the secondary sources are driven such that the sound pressure is zero just outside the secondary source surface, then the sound pressure is zero everywhere past the surface. In practice, the resulting sound-power attenuation depends on the arrangement and density of secondary sources and the distance from canceling points to the radiator and secondary sources.[5] In addition, the main practical problem is to adequately drive the secondary sources in order to obtain the optimal sound-power attenuation. Because of the possibly changing properties of the controlled system (the loudspeakers, the microphones, and the propagation path) and the primary noise, the antinoise emitted by the secondary sources must be perfectly and continuously tuned by the controller in order to obtain the perfect destructive interference at the canceling points. This leads to an adaptive control system.

In practice, multichannel feedforward[6] or feedback[7] adaptive controllers are typically implemented. A feedback controller is very attractive because it requires only sound-pressure measurements at the canceling points; on the other hand, a feedforward controller needs an additional signal correlated with the primary noise. To adapt the controller, the most frequently employed algorithm in active control of sound is the *filtered x-LMS* algorithm. It requires a model of the transfer function between each secondary source and each canceling point. Thus, a considerable processing power is needed for multichannel systems: for M secondary sources and M error microphones the controller needs M^2 transfer functions. A technique called decentralized control has been developed in the last few years to avoid this problem and facilitate the hardware and design of the control system.[8] It consists of implementing an independent control system for each unit formed by a secondary source and its corresponding cancellation point. Because each independent controller does not take into account the other secondary sources, only the M direct transfer functions from each secondary source to the corresponding canceling point are needed.

The main drawback of such a decentralized control approach is the risk of instability when each independent controller works against the others. Previous work has proved that decentralized architecture can be used to efficiently implement adaptive multichannel feedforward control.[9] This prior study also defined a condition for the stability of the decentralized system which takes into account the positions of the secondary sources and canceling points. However, this condition appears to be rather conservative for large systems. Moreover, in the case of a periodic primary noise, an adaptive feedforward controller can be advantageously replaced by an adaptive feedback controller.[10] Experimental implementations on power transformers have demonstrated the efficiency of the decentralized adaptive feedback approach.[11] Nevertheless, stability problems due to the decentralized control strategy appeared during preliminary experiments. The purpose of this paper is to derive the conditions under which globally stable control system behavior can be obtained in the case of an adaptive feedback controller. The main objective is to give practical sufficient conditions for the stability which are only functions of the physical implementation of the control units and of the desired level of attenuation.

Section II presents a description of the independent adaptive feedback controllers which have been analyzed in this work. In the context of adaptive control system, stability means that the residual signal at the canceling points remains bounded, and convergence that the optimal feedback is reached asymptotically. The first condition for the stability is that the adaptation algorithm converges to its optimal values. The convergence of the adaptation process is considered in Sec. III. A parameter β called "*performance index*," which characterizes the state of the adaptation process, is introduced. The second condition for the stability is that the closed loop at each state of the adaptation process should be stable. In Sec. IV, two conditions for the stability of the closed loop based on the Nyquist criterion and the small gain theorem are proposed. These conditions depend on the geometrical arrangement of the control system (locations of the control loudspeakers and error microphones) and on the value of the performance index; they allow the stability to be predicted before practical implementation of the system. Moreover, a modification of the algorithm is suggested in Sec. IV in order to increase the global stability. Section V A presents an application of the theory to the active control of free-field noise using seven decentralized units. Finally, several acoustic experiments are described in Sec. VI. The practical effectiveness of the proposed criteria and algorithms is also discussed.

II. DESCRIPTION OF THE INDEPENDENT CONTROLLERS

A decentralized active noise control system of sinusoidal sound composed of M independent control units is considered. Each of these independent control units is composed of one loudspeaker, one microphone, and one controller, as illustrated in Fig. 1. This section describes the algorithm implemented in each independent controller, which is presented in Fig. 2. The independent controller drives the loudspeaker with the input signal u. The microphone located in front of the loudspeaker delivers the error signal e. The sound pressure measured by the error microphone results from the interference between the sinusoidal disturbance d and the sinusoidal antinoise which is modeled as the filtering of the input signal u by the loudspeaker–microphone transfer function h. The objective is to cancel the sinusoidal component of the error signal e. The control architecture implemented in each controller is an adaptive internal model control (IMC)[12] because it uses an internal model $\hat{h}$ of the loudspeaker–microphone transfer function in order to estimate the disturbance. The symbol (ˆ) denotes that the model $\hat{h}$ is an estimation of the real system h. The chosen structure for the model is a finite impulse response filter (FIR filter) with $N_{\hat{h}}$ coefficients noted $\hat{h}_k$. The estimation $\hat{d}$ of the disturbance d is computed with the internal model $\hat{h}$ from the error signal e and the input signal u

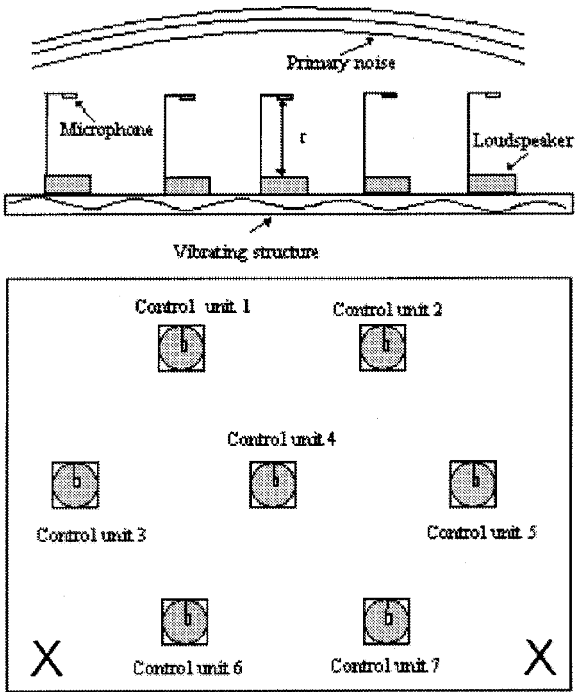

FIG. 1. Configuration of the control simulation. The vibrating structure is a square plate (2.4 m×2.4 m) 1 mm thick. Two loudspeakers (cross) located behind the plate are used to generate the primary acoustic field.

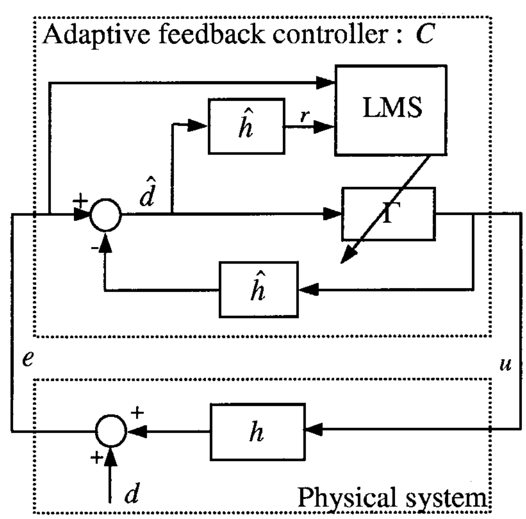

FIG. 2. Block diagram of an independent control unit.

$$\hat{d}(n)=e(n)-\sum_{k=0}^{N_{\hat{h}}-1}\hat{h}_k u(n-k). \tag{1}$$

The filtering by a FIR filter Γ with N_Γ coefficients of the estimated disturbance $\hat{d}$ generates the signal u that drives the loudspeaker

$$u(n)=\sum_{k=0}^{N_\Gamma-1}\Gamma_k\hat{d}(n-k). \tag{2}$$

In order to optimize the control filter coefficients Γ_j, a cost function equal to the instantaneous square of the net error $e^2(n)$ is defined. A steepest descent algorithm known as the filtered x-NLMS (normalized least-mean square) algorithm[13] is implemented to reach the optimal coefficients, i.e., the coefficients that minimize the cost function. The adaptation of the control filter is given by

$$\Gamma_k(n+1)=\Gamma_k(n)-2\mu(n)r(n-k)e(n), \tag{3}$$

where the reference signal $r(n)$ is obtained by filtering the estimated disturbance $\hat{d}(n)$ with the estimated transfer function $\hat{h}$

$$r(n)=\sum_{k=0}^{N_{\hat{h}}-1}\hat{h}_k\hat{d}(n-k). \tag{4}$$

Classically, in order to increase the convergence speed of the adaptation, the convergence coefficient $\mu(n)$ is a constant coefficient μ_0 normalized by an estimate of the instantaneous power of the reference signal $\hat{P}_r(n)$. For a stationary sinusoidal disturbance with frequency ω_0, the power of the reference signal $\hat{P}_r(n)$ is proportional to the power of the estimated disturbance, $\hat{P}_r=|\hat{h}(j\omega_0)|^2\hat{P}_{\hat{d}}$. However, in the case of decentralized control, the instantaneous power of the disturbance varies in time during the adaptation process because the antinoise generated by the other units is considered as disturbances. In order to limit these coupling effects, the convergence coefficient is defined as a constant coefficient μ_0 normalized by an estimate of the instantaneous power of the estimated disturbance $\mu(n)=\mu_0/[\hat{P}_{\hat{d}}(n)]$. This normalization is equivalent to the classical one, and it clearly describes the objective of the normalization: the adaptation process must be independent of the estimated disturbance.

III. ADAPTATION OF THE INDEPENDENT CONTROLLERS

In adaptive feedback theory, instability of the control system may have two causes: a nonconvergence of the adaptation process or an unstable feedback loop. In the following, these two causes of instability are investigated separately. In this section, the feedback loop is assumed stable and the slow adaptation process behavior of one controller is examined. In other words, the time scale of the adaptation process is assumed very slow in comparison to the dynamics of the feedback loop.

A. Problem formulation

Since the feedback loop is assumed to be stable, all signals (the estimated disturbance $\hat{d}$, the input u, the error e, the reference $\hat{r}$) are assumed to be sinusoidal with frequency ω_0, which is also the frequency of the primary disturbance d. The two main interests of the proposed adaptation process [Eq. (3)] are to allow a perfect self-tuning of the control filter and to adapt it when there is a very slow variation of the disturbance frequency ω_0. In the following, the tracking of the disturbance frequency is not considered.

The filtered reference signal being a sinusoidal signal, the control filter coefficients are assumed to be a sampled sinusoidal signal on a compact time support with a time-variant amplitude and phase:[14] $\Gamma_k(n)=A(n)\cos(\omega_0T_ek+\varphi(n))$ for $k=0,1,...,N_\Gamma-1$, and T_e is the sampling period. The frequency response of Γ is given by the following exact expression:

$$\Gamma(n,j\omega)=A(n)e^{j\varphi(n)}Q((\omega-\omega_0)T_e,N_\Gamma)+A(n)e^{-j\varphi(n)}Q((\omega_0+\omega)T_e,N_\Gamma), \tag{5}$$

where $Q(\nu,N)=\exp(j\nu(N-1)/2)[\sin(\nu N/2)]/[\sin(\nu/2)]$ is independent of both the amplitude and phase of the filter coefficients. Since $|Q(0,N_\Gamma)|=N_\Gamma$, and $|Q(2\omega_0T_e,N_\Gamma)|=0$ when T_e and N_Γ are chosen such that $\omega_0T_eN_\Gamma=m\pi$ with m an integer, it is possible to write $\Gamma(n,j\omega_0)=N_\Gamma A(n)e^{j\varphi(n)}$ when $\omega_0T_eN_\Gamma=m\pi$. Thus, the amplitude and phase of the control filter coefficients completely define the frequency response of the filter at ω_0. The convergence analysis of the adapted FIR filter can therefore be examined at the disturbance frequency; in other words, the convergence analysis of the N_Γ coefficients $\Gamma_k(n)$ can be stated in terms of the convergence analysis of the frequency response $\Gamma(n,j\omega_0)$.

B. Convergence to the optimum

The behavior of the filtered-x LMS algorithm in the time domain can be evaluated in the frequency domain if the adaptation process of the filter is slow.[15] Using Eqs. (1), (2), (3), and (4), the frequency response of the control filter at ω_0 is adapted according to the recursive scheme

$$\Gamma(n+1,j\omega_0)=\Gamma(n,j\omega_0)-2\frac{\mu}{|\hat{d}(n,\omega_0)|^2}\times\hat{h}^*(j\omega_0)\hat{d}^*(n,\omega_0)e(n,\omega_0), \tag{6}$$

where * denotes the complex conjugate and $\mu=\mu_0/4$. This expression of the update equation clearly shows that the steady state of the adaptation process $\Gamma(n+1,j\omega_0)=\Gamma(n,j\omega_0)$ is obtained when the sinusoidal component of the error signal equals zero $(e(n,\omega_0)=0)$. This condition defines the optimum value, or the convergence point, of the control filter $\Gamma^{\mathrm{opt}}(j\omega_0)$. From Eqs. (1) and (2), the error signal $e(n,\omega_0)$ is expressed as

$$e(n,j\omega_0)=[1+\hat{h}(j\omega_0)\Gamma(n,j\omega_0)]\hat{d}(n,\omega_0). \tag{7}$$

According to Eq. (7), the optimum value of the control filter associated with the steady state is only a function of the estimated model

$$\Gamma^{\mathrm{opt}}(j\omega_0)=-\frac{1}{\hat{h}(j\omega_0)}. \tag{8}$$

In order to establish the convergence of the adaptation process to the optimum value given by Eq. (8), Eq. (6) is expressed with $\Delta\Gamma(n,j\omega_0)=\Gamma(n,j\omega_0)-\Gamma^{\text{opt}}(j\omega_0)$ as

$$\Delta\Gamma(n+1,j\omega_0)=(1-2\mu|\hat{h}(j\omega_0)|^2)\Delta\Gamma(n,j\omega_0). \tag{9}$$

The update equation (9) can thus be written in the form of a geometric progression of common ratio $(1-2\mu|\hat{h}(j\omega_0)|^2)$ which converges without oscillation if the condition $0<\mu<1/[2|\hat{h}(j\omega_0)|^2]$ is verified.[15] It is therefore always possible to find a value of μ which ensures the convergence of the update equation of each control filter to its optimum value. Moreover, modeling errors of the estimated loudspeaker–microphone transfer function ($h\neq\hat{h}$) do not affect the convergence to the optimum (8). In other words, each adaptive feedback controller converges in spite of errors in the estimated model. It is important to note the difference with the adaptive feedforward controller which converges as long as the phase error of the estimated transfer function is less than $\pi/2$.[16] Thus, because the convergence of the adaptation is always ensured, the stability of the decentralized adaptive feedback active control system must be a property of the feedback loop.

C. The index of performance

To analyze the relation between the adaptation process and the feedback loop stability, a complex value called performance index is defined as follows:

$$\beta(n)=\frac{\Gamma(n,j\omega_0)}{\Gamma^{\text{opt}}(j\omega_0)}. \tag{10}$$

In other words, for each value of the control filter on its convergence path a value $\beta(n)$ is defined; this value is a measure of the adaptation process. The frequency response of the control filter during adaptation can be expressed using Eq. (5) and the relation $\Gamma(n,j\omega_0)=A_n e^{j\varphi(n)}$ as a function of $\beta(n)$

$$\begin{aligned}\Gamma(n,j\omega)=&\beta(n)\Gamma^{\text{opt}}(j\omega_0)Q((\omega-\omega_0)T_e,N_\Gamma)\\&+\beta(n)^*\Gamma^{\text{opt}}(j\omega_0)^*Q((\omega_0+\omega)T_e,N_\Gamma).\end{aligned} \tag{11}$$

For example, according to Eq. (9), and for an initial value $\Gamma(0,j\omega_0)=0$ the control filter value at any adaptation step is: $\Gamma(n,\omega_0)=\beta(n)\Gamma^{\text{opt}}(\omega_0)$ with the "performance index" $\beta(n)=1-(1-2\mu|h(\omega_0)|^2)^n$. Thus, for $n=0$ no control is accomplished, the performance index is $\beta=0$. For $n\to\infty$, the control filter converges towards the optimum value because $\beta\to1$, and a perfect rejection of the disturbance is realized $e(\infty,\omega_0)=0$.

D. Equivalent independent feedback controller

The adaptation process allows the convergence of the independent control filters to the optimum value defined by Eq. (8). When convergence is realized there is a perfect noise cancellation of the disturbance frequency at the microphone. In order to explain how the feedback loop rejects the disturbance frequency, it is necessary to derive the equivalent independent feedback controller, $C(s)=u(s)/e(s)$, which is presented in Fig. 2. From Eqs. (1) and (2), the equivalent independent feedback controller is

$$C(n,s)=[1+\Gamma(n,s)\hat{h}(s)]^{-1}\Gamma(n,s). \tag{12}$$

According to Eqs. (8), (10), and (12), the frequency response of the equivalent independent feedback controller at the disturbance frequency is $C(n,j\omega_0)=(1-\beta(n))^{-1}\Gamma(nj\omega_0)$. When $\beta(n)\to1$, the denominator of $C(n,j\omega_0)$ converges to zero, which implies a high gain at the disturbance frequency: $|C(n,j\omega_0)|\to\infty$. Thus, when there is a perfect attenuation, $\beta=1$, each equivalent independent feedback controller is characterized by a complex conjugate pair of poles centered at the disturbance frequency $s=\pm j\omega_0$. This is an essential similarity with the different techniques available for designing and implementing algorithms for the rejection of sinusoidal disturbances.[17] However, in spite of this necessary high gain at the disturbance frequency, each independent closed-loop system, alone (without interaction with the other units), can be assumed to be stable. The problem of the instability arises when all independent control units are physically coupled. The next section presents an analysis of this major problem.

IV. ANALYSIS OF THE FEEDBACK LOOP

The study of the adaptation process in the previous section shows that it is always possible to guarantee the convergence of the adaptation assuming a stable feedback loop. However, since the decentralized control doesn't take into account the different interactions between all the control units, some physical constraints must be satisfied in order to guarantee the stability of the overall system. This section presents the stability analysis of the feedback loop when the adaptation process is "frozen" at an iteration n. A value of the performance index β is associated with the "frozen state." To simplify the notation, the index n is omitted.

A. Decentralized feedback loop modeling

The M decentralized feedback controllers are equivalent to one classical feedback control structure representation shown in Fig. 2. Using matrix notations, the multichannel control system is modeled as

$$\mathbf{e}(s)=\mathbf{h}(s)\mathbf{u}(s)+\mathbf{d}(s), \tag{13}$$

with

$$\mathbf{e}(s)=[e_1(s),e_2(s),\ldots,e_M(s)]^T;$$

$$\mathbf{u}(s)=[u_1(s),u_2(s),\ldots,u_M(s)]^T;$$

$$\mathbf{d}(s)=[d_1(s),d_2(s),\ldots,d_M(s)]^T;$$

and the transfer matrix

$$\mathbf{h}(s)=\begin{bmatrix}h_{11}(s)&h_{12}(s)&\cdots&h_{1M}(s)\\h_{21}(s)&h_{22}(s)&\cdots&h_{2M}(s)\\\vdots&\vdots&\vdots&\vdots\\h_{M1}(s)&h_{M2}(s)&\cdots&h_{MM}(s)\end{bmatrix};$$

$h_{ij}(s)$ represents the transfer function between loudspeaker i and microphone j.

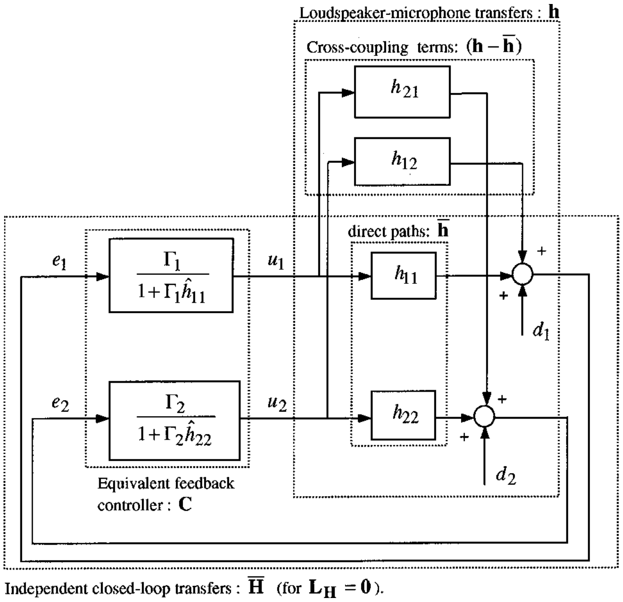

FIG. 3. Equivalent controller representation for a system of two control units.

The decentralized control system is modeled as

$$\mathbf{u}(s)=\mathbf{C}(s)\mathbf{e}(s), \tag{14}$$

where the equivalent feedback controller $\mathbf{C}(s)$ represents all equivalent independent controllers (12) in a square diagonal matrix (see Fig. 3)

$$\mathbf{C}(s)=[\mathbf{I}+\Gamma(s)\hat{\mathbf{h}}(s)]^{-1}\Gamma(s). \tag{15}$$

The independent control filters are represented in the square diagonal matrix: $\Gamma(s)=\mathrm{diag}(\Gamma_{11}(s),\ldots,\Gamma_{MM}(s))$; also, the estimated models of the physical system are represented in the square diagonal matrix $\hat{\mathbf{h}}(s)=\mathrm{diag}(\hat{h}_{11}(s),\ldots,\hat{h}_{MM}(s))$.

B. Performance of the control

Assuming the stability of the control system and $\beta\neq 1$, the noise attenuation at the various error microphones depends on the direction of the primary noise field.[18] An analysis of the noise attenuation during the adaptation is proposed in this section.

The global sound-pressure attenuation at the error microphones is defined by $\mathrm{Att}=20\log_{10}\|\mathbf{d}(\omega_0)\|_2/\|\mathbf{e}(\omega_0)\|_2$, where $\|\cdot\|_2$ denotes the Euclidean norm. The sensitivity operator of the feedback loop system $\mathbf{E}(s)$, defined as $\mathbf{e}(s)=\mathbf{E}(s)\mathbf{d}(s)$, is used to derive the maximum and minimum global sound-pressure attenuation achievable at the disturbance frequency ω_0. The bounds are given by the singular value decomposition of $\mathbf{E}(j\omega_0)$[18]

$$-20\log_{10}\overline{\sigma}(\mathbf{E}(j\omega_0))\leqslant \mathrm{Att}\leqslant -20\log_{10}\underline{\sigma}(\mathbf{E}(j\omega_0)), \tag{16}$$

where $\overline{\sigma}(\mathbf{E}(j\omega_0))$ and $\underline{\sigma}(\mathbf{E}(j\omega_0))$ are the maximum and minimum singular values of $\mathbf{E}(j\omega_0)$, respectively. The most favorable primary field causing the largest global attenuation is associated with $\underline{\sigma}(\mathbf{E}(j\omega_0))=\min\|\mathbf{E}(j\omega_0)\mathbf{d}(\omega_0)\|_2$ for $\|\mathbf{d}(\omega_0)\|_2=1$, while the least favorable primary field giving the smallest global attenuation is associated with $\overline{\sigma}(\mathbf{E}(j\omega_0))=\max\|\mathbf{E}(j\omega_0)\mathbf{d}(\omega_0)\|_2$ for $\|\mathbf{d}(\omega_0)\|_2=1$. According to the definition (10) of the index of performance, the matrix of control filters at the disturbance frequency is

$$\Gamma(j\omega_0)=-\mathbf{B}\hat{\mathbf{h}}^{-1}(j\omega_0), \tag{17}$$

where $\mathbf{B}=\mathrm{diag}(\beta_1,\ldots,\beta_M)$ is the diagonal matrix of the performance index of each unit. Using Eqs. (13), (14), (17), and $\mathbf{C}(j\omega_0)=[\mathbf{I}-\mathbf{B}]^{-1}\Gamma(j\omega_0))$ according to Eq. (15), the sensitivity operator at ω_0 is written as a function of local performance indices ($\mathbf{B}$)

$$\mathbf{E}(j\omega_0)=[\mathbf{I}+\mathbf{h}(j\omega_0)\hat{\mathbf{h}}^{-1}(j\omega_0)\mathbf{B}[\mathbf{I}-\mathbf{B}]^{-1}]^{-1}. \tag{18}$$

If $\mathbf{B}=\mathbf{0}$ then $\mathbf{E}(j\omega_0)=\mathbf{I}$; there is no attenuation. If $\mathbf{B}\to\mathbf{I}$ then $\mathbf{E}(j\omega_0)\to\mathbf{0}$; a perfect rejection is reached. The closer the matrix $\mathbf{B}$ is to the identity matrix, the better the global attenuation at the microphones. Equation (18) with (16) allows prediction of the maximal and minimal attenuation for any values of $\mathbf{B}$.

C. A necessary and sufficient condition for the stability

The Nyquist stability criterion[19] is classically used to analyze the stability of the feedback loop. However, the Nyquist stability criterion does not assume that each individual feedback loop is stable and that instability may arise from the interactions between the individual units. It thus seems important to quantify the interactions between the units because they may lead to instability of the decentralized control system. For this purpose, Morari proposed a stability criterion[12] deduced from the classical Nyquist criterion.

The multivariable Nyquist criterion is based on the analysis of the open-loop system $\mathbf{L}(s)=\mathbf{C}(s)\mathbf{h}(s)$. For an open-loop system without unstable pole, the closed-loop system is stable if and only if the encirclement count of the origin point of the map $\det(\mathbf{I}+\mathbf{L}(s))$ evaluated on the standard Nyquist D-contour equals zero, i.e., $N(0,\det(\mathbf{I}+\mathbf{L}(s)))=0$, where $N(0,g(s))$ denotes the net number of clockwise encirclements of the point (0,0) by the function $g(s)$. When poles are on the $j\omega$ axis (in the case $\mathbf{B}\to\mathbf{I}$), it is well established to realize very small detour around the poles to reform the Nyquist path.

However, the full system can be factored as $(\mathbf{I}+\mathbf{L}(s))=(\mathbf{I}+\mathbf{L_H}(s)\overline{\mathbf{H}}(s))(\mathbf{I}-\overline{\mathbf{h}}(s)\mathbf{C}(s))$, where the direct paths are represented by the square diagonal matrix

$$\overline{\mathbf{h}}(s)=\mathrm{diag}(h_{11}(s),\ldots,h_{MM}(s)). \tag{19}$$

The matrix of independent closed-loop transfers is defined as

$$\overline{\mathbf{H}}(s)=-\overline{\mathbf{h}}(s)\mathbf{C}(s)[\mathbf{I}-\overline{\mathbf{h}}(s)\mathbf{C}(s)]^{-1}, \tag{20}$$

and the matrix of relative errors is defined as

$$\mathbf{L_H}(s)=[\mathbf{h}(s)-\overline{\mathbf{h}}(s)]\overline{\mathbf{h}}^{-1}(s). \tag{21}$$

For example, Fig. 3 presents the matrices for a system of two control units. There are two independent closed-loop transfers; each of them is constituted of one direct path h_{ii} and one equivalent feedback controller $C_{ii}=\Gamma_i(1+\Gamma_i\hat{h}_{ii})^{-1}$. The interactions are represented by the cross-coupling terms; the output u_1 acts on the subsystem 2 via h_{21}, and vice versa, the output u_2 acts on the subsystem 1 via h_{12}.

According to Morari,[12] the following theorem can be stated: assume that $\mathbf{h}(s)$ and $\overline{\mathbf{h}}(s)$ have no unstable pole and that $\mathbf{H}(s)$ is stable, then, the closed-loop system is stable if and only if

$$N(0,\det(\mathbf{I}+\mathbf{L_H}(s)\overline{\mathbf{H}}(s))=0. \tag{22}$$

By using Eqs. (15) and (20), the matrix of independent feedback loop is $\mathbf{H}(s)=-\overline{\mathbf{h}}(s)\Gamma(s)[\mathbf{I}+\Gamma(s)(\overline{\mathbf{h}}(s)-\hat{\mathbf{h}}(s))]^{-1}$. Assuming a perfect estimation of the direct acoustic paths $\hat{h}_{ij}=h_{ij}$, the denominator of the latter matrix can be simplified, because $\overline{\mathbf{h}}(s)-\hat{\mathbf{h}}(s)=0$. The stability analysis using the criterion (22) therefore involves the following expression:

$$\mathbf{L_H}(s)\overline{\mathbf{H}}(s)=-[\mathbf{h}(s)-\overline{\mathbf{h}}(s)]\Gamma(s). \tag{23}$$

The stability criterion (22) together with Eq. (23) allows the stability of the feedback loop to be predicted, when the physical system $\mathbf{h}(s)$ and the adaptive filters are perfectly known. Moreover, the adaptive filters are completely defined by Eq. (11) as a function of the index of performance $\beta(n)$ and the physical system response at the disturbance frequency $\mathbf{h}(j\omega_0)$. Thus, for a given physical implementation of the control units, it is possible to predict the stability of the active noise system as a function of the index of performance.

D. A sufficient condition for the stability

According to the small gain theorem,[20] the closed-loop system is stable if the open-loop system $\mathbf{L_H}(s)\overline{\mathbf{H}}(s)$ is stable and satisfies the condition $\|\mathbf{L_H}(j\omega)\overline{\mathbf{H}}(j\omega)\|<1$ for all ω, where $\|\cdot\|$ denotes any compatible matrix norm.

According to Eq. (23), the upper bound of $\|\mathbf{L_H}(j\omega)\overline{\mathbf{H}}(j\omega)\|$ depends on the physical system $\mathbf{h}$ and the control filters Γ. Moreover, according to Eq. (11) the upper bound of the control filters is obtained at the disturbance frequency: $\|\Gamma(j\omega)\|\leqslant\|\overline{\mathbf{h}}^{-1}(j\omega_0)\mathbf{B}\|$ for all ω. Thus, the condition of stability is

$$\|[\mathbf{h}(j\omega)-\overline{\mathbf{h}}(j\omega)]\overline{\mathbf{h}}^{-1}(j\omega_0)\|<\|\mathbf{B}^{-1}\| \quad \forall\omega. \tag{24}$$

Under the assumption that all electroacoustic responses of the control loudspeakers and error microphones are frequency independent, each ''acoustic path'' of the physical matrix can be supposed to be frequency independent: $|h_{lm}(j\omega)|\cong|h_{lm}(j\omega_0)|$ for all l and m. Then, by assuming the norm 1, Eq. (24) becomes

$$|h_{mm}(j\omega_0)|>\beta_{\max}\sum_{\substack{l=1\\ l\neq m}}^{M}|h_{lm}(j\omega_0)|, \tag{25}$$

where $|\beta_m|\leqslant\beta_{\max}$ for all m with $\beta_{\max}$ a real positive number.

Equation (25) provides a sufficient condition for the stability of the closed-loop system during the process adaptation. When the process adaptation starts ($\beta_m=0$), the stability condition (25) is always verified. When the process adaptation converges toward the optimum ($\beta_m\rightarrow1$), the sufficient stability condition (25) becomes the condition for the matrix $\mathbf{h}(j\omega_0)$ to be diagonally dominant:[21] the sum of the interaction paths

$$\sum_{\substack{l=1\\ l\neq m}}^{M}|h_{lm}(j\omega_0)|$$

must be smaller than the direct path $|h_{mm}(j\omega_0)|$ for all paths m.

The expression (25) allows a sufficient condition on the stability of the closed-loop system to be expressed in terms of the maximum performance index and the physical system $\mathbf{h}$. However, it is possible that Eq. (25) is not satisfied, and yet the system is globally stable.

E. Introduction of a correction parameter: An improved algorithm

In the following we propose a modification of the algorithm aimed at increasing the stability of the control system. Roughly speaking, since each error microphone observes the antinoise generated not only by the corresponding loudspeaker but also by all other control loudspeakers, there is an error in the estimation of the disturbance. A way to increase the stability is to improve the estimation by each unit of the disturbance noise emitted by the primary source and/or to limit the effects of the other units. Under the assumption that units locally radiate the same antinoise, the internal model of each unit can be magnified in order to include the contributions of all nearest units $\hat{\mathbf{h}}=\alpha\overline{\mathbf{h}}$ with $\alpha\geqslant1$ a real scalar. Note that when $\alpha>1$, the sufficient condition (25) cannot be applied since it assumes a perfect estimation of the acoustic paths, $\overline{\mathbf{h}}=\hat{\mathbf{h}}$. The stability of the system must be tested according to the necessary and sufficient condition given by Eqs. (22) with (20) and (21).

V. PHYSICAL EXAMPLE

A. Preliminary considerations

In this section, we consider a simple physical example of a decentralized active noise control system and illustrate how the above stability conditions can be used to derive physical constraints for stability. The control system considered here is composed of M baffled coplanar control units operating in an anechoic environment (such as illustrated in Fig. 1). All the control loudspeakers are supposed to behave as baffled monopole sources and to have an electroacoustic response of L_s Pa m/V. The microphones are assumed to have an electroacoustic response of M_e V/Pa. The nondimensional physical coupling matrix $\mathbf{h}$ can be written as

$$\mathbf{h}(j\omega_0)=\frac{L_sM_e}{2\pi}\begin{bmatrix}\dfrac{e^{-jk_0r}}{r} & \cdots & \dfrac{e^{-jk_0r_{1M}}}{r_{1M}}\\ \vdots & \ddots & \vdots\\ \dfrac{e^{-jk_0r_{M1}}}{r_{M1}} & \cdots & \dfrac{e^{-jk_0r}}{r}\end{bmatrix}, \tag{26}$$

where k_0 is the acoustic wave number at the frequency ω_0, r the distance from each loudspeaker to its own microphone (assumed to be identical for all units), and r_{lm} is the distance between the loudspeaker l and the microphone m. The diagonal estimate of the coupling matrix used by the control system is thus $\hat{\mathbf{h}}(j\omega_0)=(L_sM_ee^{-jk_0r})/2\pi r\mathbf{I}$, with $\mathbf{I}$ the iden-

TABLE I. Maximum values of the performance index given by the small gain theorem and the Nyquist criterion for a control system composed of seven units at a frequency of 240 Hz for different values of the distance between each loudspeaker and microphone and different values of the gain α.

	Values of β_{max} given by the small gain theorem	Values of β_{max} given by the Nyquist criterion				
r (cm)	$\alpha=1$	$\alpha=1$	$\alpha=2$	$\alpha=3$	$\alpha=4$	$\alpha=5$
12	0.32	0.52	1	1	1	0.98
14	0.29	0.47	1	1	0.98	0.97
16	0.27	0.44	1	0.99	0.97	0.96
18	0.25	0.41	0.99	0.97	0.96	0.95
20	0.23	0.39	0.94	0.96	0.96	0.95
22	0.22	0.37	0.90	0.96	0.95	0.95
24	0.21	0.36	0.86	0.95	0.95	0.94
26	0.21	0.35	0.84	0.95	0.94	0.94
28	0.20	0.34	0.81	0.94	0.94	0.94
30	0.20	0.33	0.79	0.94	0.94	0.94
32	0.19	0.32	0.77	0.94	0.94	0.94
34	0.19	0.31	0.75	0.93	0.93	0.93
36	0.19	0.31	0.74	0.93	0.93	0.93
38	0.18	0.30	0.72	0.93	0.93	0.93
40	0.18	0.29	0.71	0.92	0.93	0.93
42	0.18	0.29	0.69	0.92	0.92	0.92
44	0.18	0.29	0.68	0.92	0.92	0.92

tity matrix. The sufficient stability condition (25) becomes:

$$\beta_{max} < \frac{1}{\sum_{\substack{l=1 \\ l\neq m}}^{M} \frac{r}{r_{lm}}} \quad \forall m. \tag{27}$$

According to Eq. (27), a perfect rejection of the sinusoidal disturbance ($\beta=1$ for all m) is obtained when

$$\sum_{\substack{l=1 \\ l\neq m}}^{M} \frac{r}{r_{lm}} \leqslant 1.$$

In the case of a control system composed of two control units, the condition becomes $r/r_{12} \leqslant 1$ (and $r/r_{21} \leqslant 1$). This condition always being physically satisfied, such a decentralized control system with two units will always be stable. Instability problems may thus appear for control systems composed of more than two control units.

B. Control system composed of seven control units

We now assume a control system composed of $M=7$ units as described in Fig. 1. Table I summarizes the maximum values of the performance index (β_{max}) for which this control system is stable according to the stability conditions deduced from the small gain theorem given by Eq. (27) and the Nyquist criterion condition (22) for different distances r between the control loudspeaker and the error microphone of each unit. A disturbance frequency of 240 Hz is considered in these simulations. The distance between any given unit and its neighbors was taken to be 20 cm. Several values of the gain parameter $\alpha=1$, 2, 3, 4, and 5 were considered for the calculation of β_{max} according to the Nyquist criterion condition, as discussed in Sec. IV E.

From these results, the stability condition derived from the small gain theorem appears to be much more conservative than the one deduced from the Nyquist criterion when $\alpha=1$.

Moreover, as expected, the stability of the control system is affected by the distance between each control loudspeaker and its associated error microphone. The value of β_{max} ensuring the stability of the control system decreases when r increases, which physically corresponds to a relative increase of the mutual interactions between the control units. Also, as expected the gain α has a beneficial effect on the global stability of the control system.

The control configuration of seven units with a distance $r=30$ cm was experimentally implemented. The experimental results are discussed in the next section. According to the results obtained from the simulation, in this configuration the system is nondiagonally dominant and is unstable for $\alpha=1$ and $\beta>0.33$. A gain $\alpha=4$ was therefore introduced in the experiment discussed hereafter. With such a gain, a stability limit $\beta_{max}=0.94$ is obtained from the Nyquist criterion (22). It thus allows a good control performance to be anticipated because the control filters are close to their optimum value.

VI. EXPERIMENTS

A set of experimental results is now presented to verify the accuracy of the theoretical results on the convergence of the adaptation, the stability of the feedback loop, and the control performances derived in the three previous sections. Three different configurations of the control system were experimentally investigated: The first case is a one-control unit; according to the results of Sec. III, a single controller converges toward the optimum given by Eq. (8). The second case is a control system composed of two control units separated by a distance of 20 cm. In Sec. V A, it was shown that such a control system always satisfies the diagonal dominant condition ($r_{ij}=r_{ji}>r\forall i,\ j=1,2$) and converges to the optimum. The third case involves seven units separated by a distance of 20 cm. It was shown in Sec. V A that the diagonal dominant condition is not satisfied in this case. Also, the Nyquist criterion predicts instability when $\beta=1$ in this configuration.

A. Description of the experimental controllers

Each control unit is composed of an electret error microphone, a fixed-point DSP (TMS320C50), an amplifier, and a baffled loudspeaker (diameter=7.5 cm). The feedback control algorithm is loaded on each fixed-point DSP board using a serial link with a personal computer. The signals are sampled at a sampling rate of 801 Hz. Each loudspeaker–microphone transfer function is modeled by an FIR filter of $N_{\hat{h}}=128$ coefficients. The identification of the coefficients is performed before control by an LMS algorithm for a white-noise excitation of the control loudspeaker. The adapted FIR filter Γ is composed of $N_\Gamma=32$ coefficients. The FIR filters $\hat{h}$ and Γ are used to compute $\hat{h}(j\omega)$ and $\Gamma(j\omega)$, respectively. A gain $\alpha=4$ is introduced in the algorithm, such that $4\hat{h}$ is used instead of $\hat{h}$ in Eq. (1). The primary acoustic field is generated by a vibrating plate on which the loudspeaker–microphone units are mounted. The vibrating plate is excited by two loudspeakers driven at the desired frequency. The primary loudspeakers are located behind the plate, at locations indicated in Fig. 1.

B. Control system composed of one control unit

The first test was realized with only one control unit and a disturbance frequency of 125 Hz. A distance of 30 cm was used between the control loudspeaker and the error microphone. The value of the performance index β at steady state calculated from the experimental values of $\hat{h}(j\omega_0)$, $\Gamma(j\omega_0)$, and Eq. (10) has a modulus of 1.002 and a phase of -2 deg. From these results, as predicted in Sec. III it can be concluded that a control unit working alone is stable and converges towards its optimum value defined by Eq. (8). Moreover, a 58-dB attenuation was measured at the error microphone. At the optimum, an almost-perfect cancellation of the disturbance is thus obtained at the error microphone.

C. Control system composed of two control units

The second experiment was realized with a control system composed of two control units separated by a distance of 20 cm. The distance between each loudspeaker and its own microphone and the frequency of the noise disturbance are the same as the previous case. This control system is experimentally observed to be stable at steady state as it was predicted by the small gain theorem in Sec. IV.

The experimental steady-state values of the two control filters were used to calculate the associated values of the local performance indices. The results are listed in Table II and show that each control unit has converged towards the optimum with a modulus close to 1 for the two local performance indices. The experimental steady-state values of the control filters were also used to plot the map of $\det(\mathbf{I}+\mathbf{L_H}(s)\overline{\mathbf{H}}(s))$ and check the Nyquist stability criterion as illustrated in Fig. 4. According to the Nyquist stability condition, the control system is stable. This is therefore in agreement with the experimental observation. The values of the residual sound pressure at each microphone presented in Table II show a significant noise, cancellation due to the control system at the error microphones.

TABLE II. Steady-state values of β_i and the corresponding attenuations at error the microphones for a system composed of two control units at 125 Hz for $r=30$ cm and $\alpha=4$.

Control unit	Sound-pressure level measured at the microphones before control (dB)	Attenuation after control (dB); Modulus and phase of β_i
1	90	Att=48, $\lvert\beta_1\rvert=0.95$, $\angle\beta_1=-3.2°$
2	90	Att=40, $\lvert\beta_2\rvert=1.01$, $\angle\beta_2=-1.9°$

D. Control system composed of seven control units

The third experiment was realized with seven independent control units in a configuration similar to Fig. 1. The separation between adjacent units was set to 20 cm, and the distance between each control loudspeaker and the corresponding error microphone was 30 cm. The frequency-domain simulations presented in Sec. V B show that for such a configuration with seven control units and for a correction gain $\alpha=1$, the small gain theorem predicts the instability for $\beta_{\max}>0.20$, and the Nyquist criterion predicts the instability for $\beta_{\max}>0.33$, which means that the decentralized control performs poorly in this case. The introduction of a correction gain $\alpha=4$ significantly increases the stability since in this case, the Nyquist criterion predicts the instability for $\beta_{\max}>0.94$. A value of $\alpha=4$ was therefore implemented in the experiments.

As an initial step, the physical matrix plant $\mathbf{h}$ was experimentally identified using 128-order FIR filters to model the transfer function between each control loudspeaker and each error microphone. A discrete time-domain computer

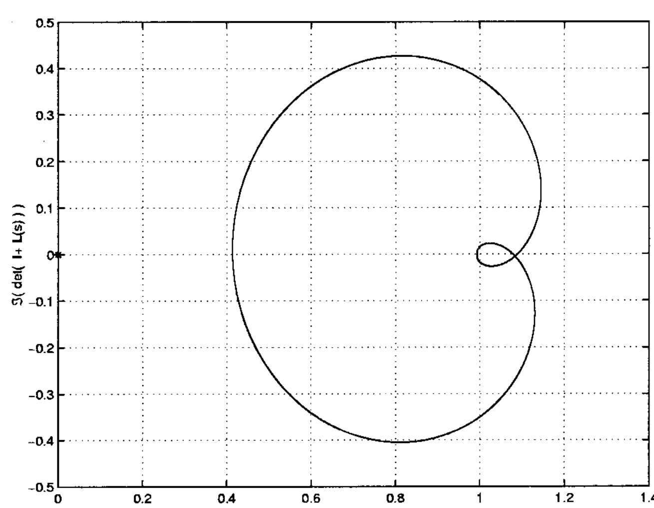

FIG. 4. Map of $\det(\mathbf{I}+\mathbf{L_H}(s)\overline{\mathbf{H}}(s))$ on the Nyquist D-contour obtained from the experimental values of the steady-state control filters for a system of two control units at 125 Hz and $\alpha=4$.

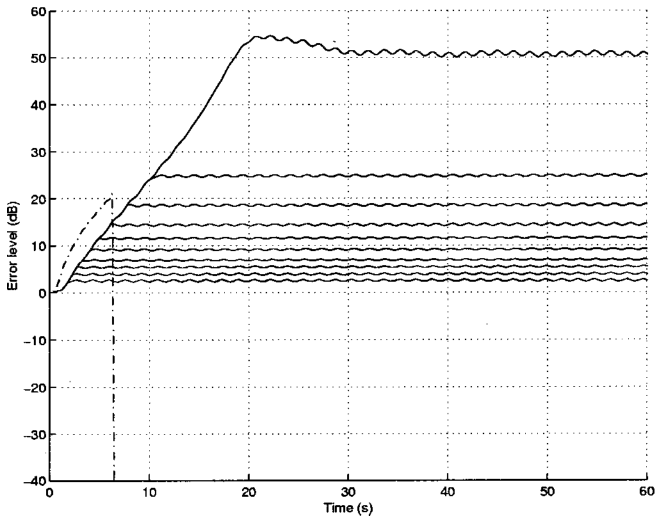

FIG. 5. Sum of the temporal squared error signals at the microphones obtained from the time-domain simulation of the control for a control system composed of seven units at a frequency of 240 Hz with $r=30$ cm for $\alpha=1$ (dashed line) and $\alpha=4$ (solid line).

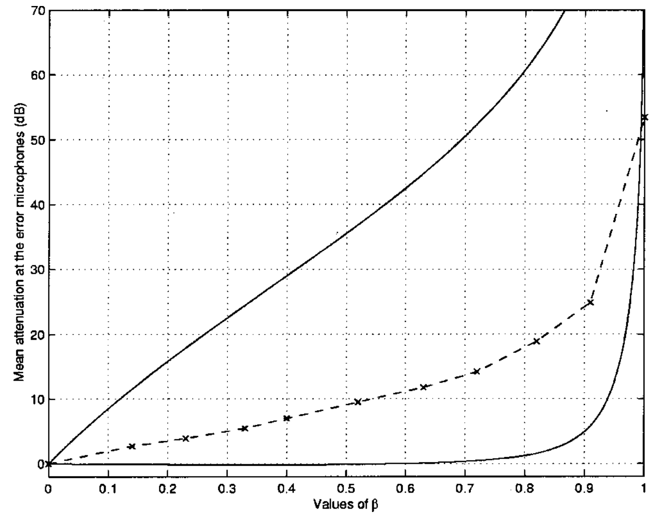

FIG. 6. Mean attenuation at the microphones versus β obtained by the singular value decomposition of the sensitivity operator $\mathbf{E}(j\omega_0)$ obtained at frequency of 240 Hz with the experimental values of the physical coupling matrix **h** (solid line) and obtained from the time-domain simulation of the control (cross-dash line) in the case of a control system composed of seven units separated by a distance of 20 cm. The distance between each loudspeaker to its microphone is equal to 30 cm and the gain $\alpha=4$.

simulation of the IMC feedback structure shown in Fig. 2 was implemented under SIMULINK for each control unit. The time-domain simulation used the experimental matrix plant **h**, as well as sampled values of the primary disturbance measured at the seven error microphone locations to represent the disturbance d at each error sensor. The time-domain simulation was then executed and stopped at various increasing times during the adaptation in order to assess the convergence and stability of the control system. The sum of the squared error signals obtained at the microphones is plotted as a function of time in Fig. 5 for $\alpha=1$ and $\alpha=4$; the oscillations of the error signal around a constant value indicate that the adaptation process has been stopped. The results of Fig. 5 show that the control system rapidly reaches the instability for $\alpha=1$, whereas it remains stable for $\alpha=4$. Based on these time-domain simulations, the values of the calculated performance index for a typical unit (the unit 1) and the averaged attenuation as a function of time during the adaptation process are listed in Table III for $\alpha=4$. These results indicate that the independent controllers are able to reach their optimum value ($\beta_i \to 1$ for all i) and almost perfectly reject the disturbance at each error sensor. Therefore, time-domain simulations based on the experimental matrix plant predict stability of the seven-unit system. The averaged sound-pressure attenuation obtained at the error microphones from the time-domain simulation is plotted as a function of the performance index in Fig. 6. As a comparison, the minimum and maximum averaged sound-pressure attenuation obtained from the singular value decomposition of the sensitivity operator $\mathbf{E}(j\omega_0)$ and the experimental physical matrix plant **h** were plotted on the same graph. As expected, the actual attenuation obtained from the time-domain simulation is bounded by the minimum and maximum attenuations given by the singular value decomposition of $\mathbf{E}(j\omega_0)$.

Finally, the control was experimentally tested with seven units and appeared to be stable. The steady-state values of the local performance index for each unit and the steady-state attenuation measured at each error microphone are summarized in Table IV. The experimental steady-state values of β_i show that one unit actually reached its optimum ($|\beta_6|=1$), whereas the others reached slightly suboptimal values ($|\beta_i|<1$ for $i\neq 6$). The experimental values however remain close to the maximum values deduced from the analysis in the frequency domain with the theoretical transfer

TABLE III. Values of the performance index of a typical unit at different frozen times of the adaptation process for a control system composed of seven units for $r=30$ cm and $\alpha=4$.

Time (s)	Values of β_1	Error level (dB)
2.2	0.14	2.7
2.4	0.23	3.9
2.9	0.33	5.5
3.4	0.40	7.0
4.2	0.52	9.5
5.0	0.63	11.8
6.3	0.72	14.2
6.9	0.82	18.9
7.3	0.91	24.9
19.6	1.00	53.4

TABLE IV. Steady-state values of β and the corresponding attenuations at the microphones for a system composed of seven control units at 240 Hz for $r=30$ cm and $\alpha=4$.

Control unit	Sound-pressure level measured at the microphones before control (dB)	Attenuation after control (dB); Modulus and phase of β_i
1	79	Att=15, $|\beta_1|=0.89$, $\angle\beta_1=-5°$
2	79	Att=20, $|\beta_2|=0.84$, $\angle\beta_2=-7.2°$
3	79	Att=16, $|\beta_3|=0.85$, $\angle\beta_3=-1.7°$
4	79	Att=12, $|\beta_4|=0.83$, $\angle\beta_4=-5.6°$
5	79	Att=29, $|\beta_5|=0.81$, $\angle\beta_5=-6.0°$
6	79	Att=25, $|\beta_6|=1.00$, $\angle\beta_6=-3.5°$
7	78	Att=28, $|\beta_7|=0.95$, $\angle\beta_7=-12.6°$

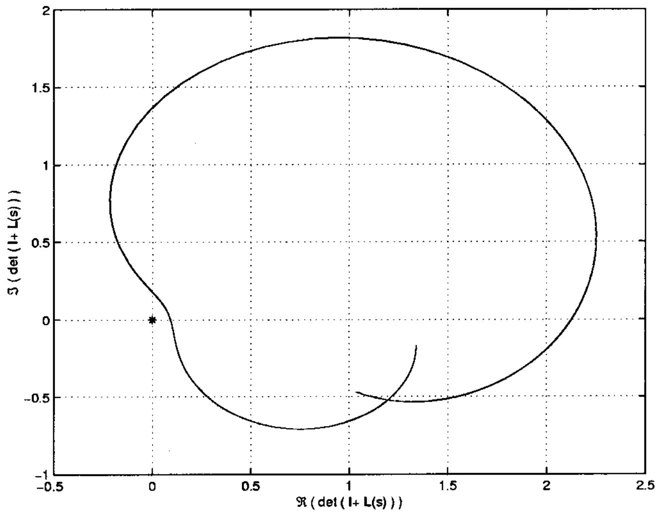

FIG. 7. Map of $\det(\mathbf{I}+\mathbf{L_H}(s)\overline{\mathbf{H}}(s))$ on the Nyquist D-contour obtained from the experimental steady-state values of the control filters for the control system of seven control units at 240 Hz when $\alpha=4$ and $r=30$ cm.

functions ($\beta_{\max}=0.94$) or the simulations in the time domain with the identified transfer functions ($\beta_{\max}=1$). The reason why some units reach only suboptimal values of β in the experiments has not yet been resolved. The experimental values of β_i were used to calculate the experimental control filters for each unit and plot the map of $\det(I+\mathbf{L_H}(s)\overline{\mathbf{H}}(s))$, Fig. 7. The check of the Nyquist criterion establishes that the control system is predicted to be stable, as was experimentally observed.

VII. CONCLUSIONS

This paper has presented the analysis and implementation of a decentralized adaptive feedback active noise control system of sinusoidal sound in free space. The active control system consists of an arrangement of multiple independent control units (a control loudspeaker, an error microphone, and a controller), each of which acts to create a point of zero sound pressure at the error microphone location. Each individual controller is a single-input single-output IMC (internal model control) feedback which is adapted by a steepest descent algorithm in order to minimize the total sound pressure at the corresponding error microphone. The main advantage of such a decentralized strategy is an important economy in terms of processing power for large systems, as compared to a centralized control strategy.

It was shown that, while it is possible to guarantee the convergence of the decentralized feedback to the optimum solution, global stability is not always satisfied. In order to quantify both the convergence and global stability of the feedback loop, a "performance index" β was introduced. The performance index is associated with the value of the individual control filters during convergence, relative to the optimal value of the control filters. The performance of the individual controllers increases with β, while the stability margin decreases with β. Two stability conditions which take into account the geometrical arrangement of the control sources and error sensors, as well as the value of the local performance index, were derived in order to assess the stability of the control system before its practical implementation. The first (sufficient) condition was deduced from the small gain theorem and essentially implies that the physical plant of the system should be diagonally dominant. The second (necessary and sufficient) condition was derived from the Nyquist criterion. A modification of the independent IMC controllers was suggested in order to increase the global stability of the system; the modification serves to improve the estimation by each unit of the primary disturbance and involves a gain parameter α in the IMC to amplify the control path model (transfer function between the control source and the corresponding error microphone). It was shown that a gain parameter $\alpha>1$ improves the global stability of the control system.

Simulations and experimental results were presented in the case of one, two, or seven independent units to control the sound field of a primary source in free space. The analytical tools developed proved to be useful in assessing the stability of the control system before it is experimentally implemented. The experiments also clearly demonstrate the effectiveness of decentralized control in situations where global stability is satisfied. Ongoing work involves the monitoring and control of the performance index of individual units in order to stop the convergence before instability is reached; also, the extension of decentralized control to structural systems is presently investigated.

[1] R. W. Stewart, J. M. McDonald, and S. Weis, "Active noise control of an electricity substation 275 kv transformer," Eng. Syst. Design Anal. **8**, 375–381 (1994).

[2] S. J. Elliot, P. Joseph, P. A. Nelson, and M. E. Johnson, "Power output minimization and power absorption in the active control of sound," J. Acoust. Soc. Am. **90**, 2501–2512 (1991).

[3] P. A. Nelson, A. R. D. Curtis, S. J. Elliot, and A. J. Bullmore, "The minimum power output of free field point sources and the active control of sound," J. Sound Vib. **116**(3), 397–414 (1987).

[4] J. B. Fahnline, "Active control of the sound radiated by vibrating body using only a layer of simple sources," J. Acoust. Soc. Am. **97**, 2249–2254 (1995).

[5] J. Guo and J. Pan, "Analysis of the active noise control in a free space," in *Proceedings of Active 95*, pp. 649–660, 1995.

[6] I. M. Stothers, S. J. Elliott, and P. A Nelson, "A multiple error LMS algorithm and its application to the active control of sound and vibration," IEEE Trans. Speech Audio Process. **ASSP-35**(10), 1423–1434 (1987).

[7] K. Fujita and M. Nishimura, "Active adaptive feedback control of sound field," JSME Int. J. **37**(3), 607–611 (1994).

[8] W. S. Levine, *The Control Handbook* (CRC Press, Boca Raton, 1996).

[9] S. J. Elliott and C. C. Boucher, "Interaction between multiple feedforward active control systems," IEEE Trans. Speech Audio Process. **2**(2), 521–530 (1994).

[10] B. Raphaely, S. J. Elliott, T. J Sutton, and M. Johnson, "Design of feedback controllers using a feedforward approach," in *Proceedings of Active 95*, pp. 863–874, 1995.

[11] A. L'Espérance, "New concept of active control of transformer noise. I. The active envelope," Can. Acoust. **28**(3), 8–9 (1998).

[12] M. Morari and E. Zafiriou, *Robust Process Control* (Prentice-Hall, Englewood Cliffs, NJ, 1989).

[13] B. Widrow and S. D. Stearns, *Adaptive Signal Process* (Prentice-Hall, Englewood Cliffs, NJ, 1985).

[14] B. Widrow, "Adaptive noise cancelling: Principles and applications," Proc. IEEE **63**(12), 1692–1716 (1975).

[15] G. Chen, "Evaluation of the convergence characteristics of the filtered-x LMS algorithm in the frequency domain," J. Acoust. Soc. Jpn. **16**, 331–339 (1995).

[16] S. J. Elliott and P. A. Nelson, *Active Control of Sound* (Academic, New York, 1992).

[17] A. L. Sievers and V. H. Flotow, ''Comparison and extension of control methods for narrow-band disturbance rejection,'' IEEE Trans. Signal Process. **40**, 2377–2391 (1992).
[18] S. Skogestad and M. Morari, ''Effect of disturbance direction on closed-loop performance,'' Ind. Eng. Chem. **26**, 2029–2035 (1987).
[19] A. G. J. MacFarlane and I. Postlethwaite, ''The generalized Nyquist stability criterion and multivariable root loci,'' Int. J. Control **25**(1), 81–127 (1977).
[20] C. A. Desoer and M. Vidyasagar, *Feedback Systems: Input–Output Proprieties* (Academic, New York, 1975).
[21] B. Noble and J. W. Daniel, *Applied Linear Algebra*, 2nd ed. (Prentice-Hall, Englewood Cliffs, NJ, 1977).

Social survey of community response to a step change in aircraft noise exposure

Sanford Fidell[a),b)] and Laura Silvati[a)]
BBN Technologies, 21128 Vanowen Street, Canoga Park, California 91303

Edward Haboly
Vancouver International Airport Authority, P.O. Box 23750, Airport Postal Outlet, Richmond, British Columbia V7B 1Y7, Canada

(Received 22 February 2000; revised 26 September 2001; accepted 28 September 2001)

Community response to a step change in aircraft noise exposure associated with the opening of a new runway at Vancouver International Airport was documented in two rounds of telephone interviews. One round of interviews was conducted 15 months prior to the start of operations on the new runway, while a second round of interviews was undertaken 21 months after the start of operations. The proportion of respondents who described themselves as "very" or "extremely" annoyed by aircraft noise in a residential area with increased aircraft noise exposure after the runway opening was markedly greater than that predictable from well-known dosage–response relationships. Analysis suggests that a good part of the "excess" annoyance is attributable to the net influence of nonacoustic factors.
[DOI: 10.1121/1.1423927]

PACS numbers: 43.50.Sr, 43.50.Lj [MRS]

I. INTRODUCTION

Most studies of the prevalence of community noise-induced annoyance concern steady-state circumstances of noise exposure. For example, neither FICON's (1992) analysis of the prevalence of annoyance associated with exposure to transportation noise nor that of Miedema and Vos (1998) addresses the time course of arousal and decay of noise-induced annoyance following changes in noise exposure. Two recent reviews of the effects of changes in noise exposure on annoyance (Fields *et al.*, 2000; Horonjeff and Robert, 1997) have noted the paucity and difficulty of developing information about effects of changes in noise exposure on the prevalence[1] of annoyance.

Horonjeff and Robert (1997) stress the importance of evaluating any changes in annoyance that may be associated with changes in aircraft noise exposure in the context of everyday fluctuations in aircraft noise exposure. Their concern is illustrated in Fig. 1, which contrasts annual time histories of daily aircraft noise exposure levels at opposite ends of the same runway at a major civil airport. The upper panel shows daily aircraft noise exposure levels at a noise monitoring station close to the arrival end of the runway. The lower panel shows daily aircraft noise exposure created by departures from the other end of the runway. The standard deviation of the former distribution of noise exposure levels is 2 dB, while that of the latter is 6.4 dB. Horonjeff and Robert suggest that the effect of an abrupt change in noise exposure (i.e., a step function) is more likely to be detected in the former case than in the latter.

Fields *et al.* (2000) further caution about the possibility that seasonal effects might distort comparisons of annoyance prevalence rates developed from interviews conducted at different times of year. They suggest that factors such as temperature, precipitation, wind velocity, and number of daylight hours may affect personal noise exposure because they can affect "the extent to which windows are open and the extent to which residents engage in out-of-doors activities around their homes."

Information about effects of changes in noise exposure on annoyance is scarce in large part because opportunities, resources, and appropriate site-specific circumstances for conducting longitudinal studies of reactions to changes in noise exposure are rare. Not surprisingly, systematic treatments and quantitative analyses of time constants of change in attitudes toward aircraft noise exposure, such as that described by Fidell *et al.* (1985), are also rare. Fidell *et al.* (1985) estimated that time constants for arousal and decay of community annoyance were on the order of months. It remains unclear, however, whether changes in prevalence rates of self-reported annoyance are transient, or whether they may persist for periods of many time constants following a change in noise exposure.

The degree of change in annoyance prevalence rate that is attributable to changes in noise exposure *per se* (as opposed to that attributable to nonacoustic factors) following a change in noise exposure also remains poorly understood. Fields *et al.* (2000) speculate in part that "heightened publicity...might make residents more aware of the effects of noise than would be expected in a steady-state [noise exposure] situation." They also note that changes in aircraft noise exposure sometimes occur after "bitter disputes during the planning process for the change," and that "Such resentment and residual bitterness might lead some residents to be more annoyed by the noise than otherwise."

Increases in air traffic at civil airports that may soon

[a)]Current affiliation: Fidell Associates, Inc., 23139 Erwin Street, Woodland Hills, CA 91367.
[b)]Electronic mail: fidell@pacbell.net

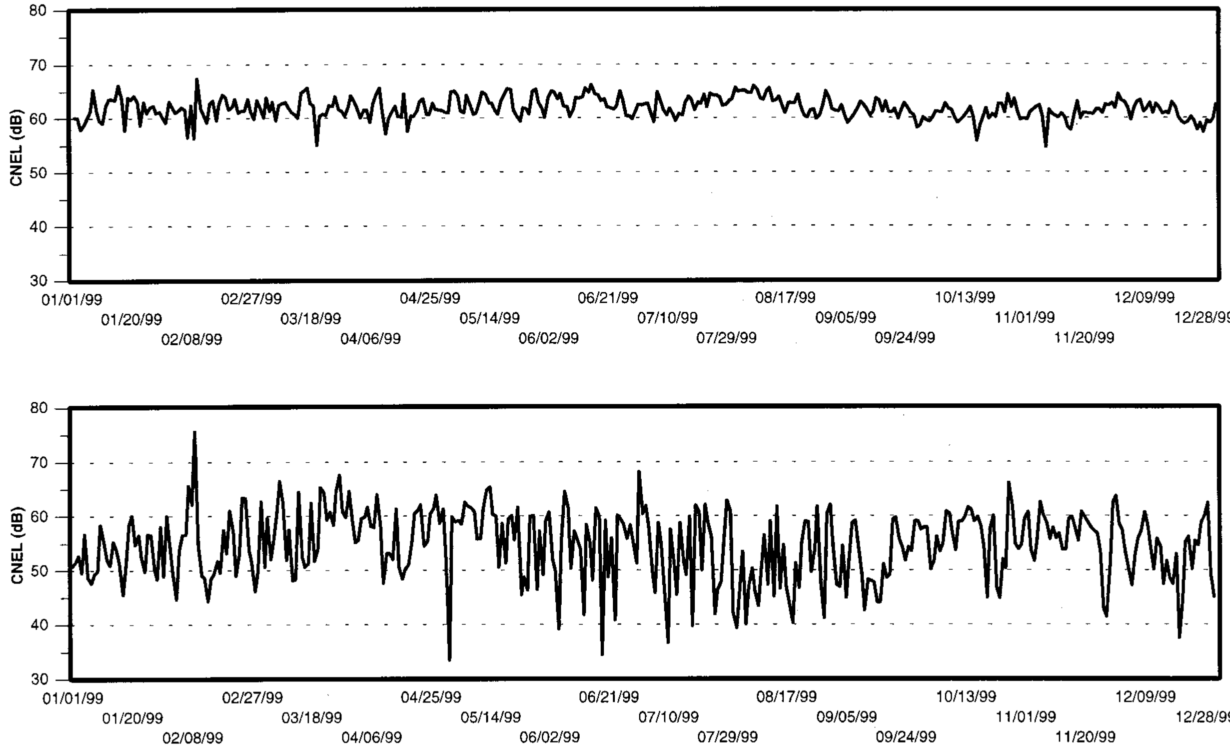

FIG. 1. Illustration of range of variability in daily aircraft noise exposure levels at opposite ends of the same runway at a large civil airport over the course of a year. Upper panel shows daily levels due to constant use of runway for arrivals; lower panel shows daily levels due to variable use of runway for departures.

accompany improvements in precision of navigation and modifications of air traffic control procedures may lead to greater temporal variability of aircraft noise exposure in airport-vicinity neighborhoods. It is therefore useful to seek improved understanding of temporal aspects of community response to changes in aircraft noise exposure.

The start of operations in November 1996 on a new runway (08L/26R) at Vancouver International Airport (YVR) in British Columbia, Canada presented an opportunity to document the effects of changes in aircraft noise exposure patterns in neighborhoods affected to varying degrees by changes in aircraft approach noise. Prior to November 1996, the south runway (08R/26L) and a crosswind runway (12/30) supported both arrival and departure operations at YVR. Since its opening, Runway 08L/26R has become YVR's primary landing runway between 7:00 AM and 10:00 PM, accommodating nighttime arrivals only under exceptional conditions. The south runway, which had been operational 24 hours a day, became the secondary landing runway and the primary departure runway, while the crosswind runway now supports few operations.

Aircraft landing on Runways 08L/R overfly residential areas immediately to the east of YVR, but initial segments of departure routes from Runways 26L/R overfly water rather than land. When Runway 08L/26R opened, a residential area about 3 miles to the east of the runway threshold became newly exposed to direct overflights of landing aircraft at altitudes as low as 600 feet AGL. Aircraft noise exposure due to landing operations on the 26 Runways decreased to varying degrees in areas to the south of the extended centerline of Runway 26L. Likewise, aircraft noise exposure due to (small numbers of) landing operations on Runway 12 decreased slightly in areas to the east of this crosswind runway. The net effect of these operational changes was to impose sudden but persistent shifts in long-term noise exposure levels in affected communities.

An initial round of telephone interviews was conducted in mid-August 1995 to determine the prevalence of aircraft noise annoyance in several neighborhoods prior to the opening of the runway. A second round of interviews was conducted in August 1998 to document changes in annoyance prevalence rates associated with the above changes in aircraft noise exposure.

II. METHOD

A. Selection of interviewing areas

Seven areas, composed in some cases of proximate but noncontiguous subregions of similar aircraft noise exposure and geographic relationships to the new runway, were selected for interviewing. All parts of the Burkeville/Brown Road neighborhood (composed of residences on opposite riverbanks) are beneath the extended centerline and very near the threshold of Runway 26L. Bridgeport is under the extended centerline of the new runway 26R, about 3 miles to the east. Several miles farther to the east, the neighborhoods of Hamilton/Annieville and Alex Fraser Bridge are beneath the extended centerlines of Runways 26L and 26R, respectively. Brighouse is located to the south of the extended centerline of Runway 26L. South Vancouver is located to the north of Runway 26L, while Marpole is located just beyond the threshold of Runway 26L, about 1 mile to the north.

B. Estimation of noise exposure

Version 4.11 of the U.S. Federal Aviation Administration's Integrated Noise Model (INM) was exercised to estimate Day-Night Average Sound Level (DNL) values for centroids of sampling areas during the calendar years preceding each round of interviews (1994 and 1997).[2] The range of estimated aircraft noise exposure levels within interviewing sites was in all cases less than ± 2 dB with respect to the noise level at the centroid of each site. The predominant aircraft noise heard by respondents in interviewing areas to the east of YVR was that of large jet transport aircraft on final approach to Runways 26L/R. These operations are aligned with the runway heading on a fixed glide slope for several miles to the east of YVR. Since cross-track dispersion of landing aircraft is small with respect to the slant range from the flight path above the extended runway centerline to respondents' homes, and because air traffic control procedures for aircraft approaching YVR were unchanged between rounds of interviews, flight track dispersion had little effect on the accuracy of estimation of aircraft noise exposure. The predominant aircraft noise in runway sideline interviewing areas to the north of Runway 26L was that produced by aircraft on or very near the ground, with negligible flight track dispersal.

Street traffic audible in the homes of respondents in the months prior to each round of interviews was that produced by local traffic on secondary streets. No major changes in surface street layout, circulation patterns, or average daily traffic between rounds of interviews affected street traffic noise levels between rounds of interviews.

C. Design of questionnaire

The same questionnaire administered to respondents in August 1995 (round 1) was administered a second time in August 1998 (round 2). The brief, structured questionnaire was composed of three open-response and seven closed-response category items.[3] The structure and wording of questionnaire items resembled those of other studies of community response to transportation noise from which dosage–response relationships have been inferred (e.g., Schultz, 1978; Fidell *et al.*, 1991; Green and Fidell, 1991; Miedema and Vos, 1998). The complete set of questionnaire items may be found in the Appendix.

The questionnaire was introduced as a study of neighborhood living conditions. The first explicit mention of noise occurred in Item 5 (''Would you say that your neighborhood is quiet or noisy?''), following preliminary questions about duration of residence, about the most and least favored aspects of neighborhood living conditions, and about the single most important neighborhood environmental issue. The next item (''Have you noticed any more or any less aircraft noise in your neighborhood over the past year, just since last summer?'') solicited information about sensitivity to change in aircraft noise exposure in the year preceding each round of interviews. Note that this wording does not require respondents to explicitly compare the annoyance of aircraft noise before and after the start of operations on the new runway.

Two subsequent items inquired about long-term annoyance with neighborhood street traffic noise and aircraft noise. The two final items solicited opinions about whether aircraft noise had disturbed sleep or interfered with conversation or listening to the radio or television.

D. Sampling and interviewing in the two rounds of study

Since Fidell and Jones (1975) have demonstrated a lack of substantive differences in the annoyance-related findings of panel and independent samples, and for reasons of cost effectiveness, independent random samples were drawn in the two rounds of interviews.[4] The sampling frame for the first round of interviews was assembled from residential telephone numbers listed within appropriate street address ranges for each interviewing area, taken from a print version of the then-current reverse telephone directory. The sampling frame for the second round of interviews was compiled from a digital database in which names and telephone numbers were associated with residential addresses within postal codes. The actual residential populations of the interviewing areas were stable between rounds of interviews. However, the sampling frame for the second round of interviews, assembled from newly available software and databases that permitted extraction of telephone numbers by geographically highly specific postal codes, was considerably larger than that of the first round.

On 20–24 August 1998, 3 years after the conduct of the first round of interviews on 17–20 August 1995, two dozen centrally supervised professional telephone interviewers made eight attempts (an initial attempt followed by seven callbacks at different times of day over the five-day period) to contact eligible respondents of randomly selected households. The opinions of one English-speaking, adult, verified household member were sought from each. Since Fields (1993) has shown that demographic variables such as age, sex, social status, income, education, home ownership, dwelling type, and length of residence have no reliable effect on reports of noise-induced annoyance, interviewers were instructed to conduct the interview with any adult, verified household member.

Interviewers from the same interviewing organization were formally trained prior to each round of interviews, and conducted several practice interviews. Central supervision of the interviewing process included real-time monitoring and confirmatory recalls for quality control purposes.

III. RESULTS

A. Summary of results of interviewing

Table I summarizes the mechanics of data collection for both rounds of study. Failure to complete an interview was due in most cases either to refusals or noncontacts after eight attempts. The total numbers of completed interviews in the first and second rounds of interviewing were 1000 and 1067, respectively. If the opinions of respondents in this survey are considered as simple random samples of populations of all

TABLE I. Disposition of telephone interview contact attempts by aggregated interviewing area.

		Burkeville and Brown Road	South Vancouver	Marpole	Bridgeport	Brighouse	Hamilton and Annieville	Alex Fraser Bridge	Total
Total telephone numbers in sampling frame	Round 1	283	1477	700	553	588	737	1129	5467
	Round 2	575	2535	3994	1466	4317	2003	1641	16 531
Nonsample[a]	Round 1	49	173	138	110	134	421	600	1625
	Round 2	151	1746	1396	272	2370	912	816	7663
Noncontacts (8 attempts)[b]	Round 1	135	744	384	196	216	151	255	2081
	Round 2	252	398	2342	976	1756	796	653	7173
Refusals	Round 1	21	269	93	87	102	69	120	761
	Round 2	84	153	98	63	44	124	62	628
Completed Interviews	Round 1	78	291	85	160	136	96	154	1000
	Round 2	88	238	158	155	147	171	110	1067
Completion rate[c]	Round 1	79%	52%	48%	65%	57%	58%	56%	57%
	Round 2	51%	61%	62%	71%	77%	58%	64%	63%

[a]Includes unsampled, disconnects, businesses, fax machines, modem lines, wrong addresses, changed numbers and non-English speaking households.
[b]Includes busy, no answer, call blocked, or answering machines after eight dialings.
[c]Completion rate calculated as follows: completed interviews ÷ [total−(nonsample+noncontact)].

residents of interviewing areas (including those not interviewed), estimates of confidence intervals may be derived by dichotomizing responses into respondents highly annoyed by noise exposure and respondents not highly annoyed. The 90% confidence intervals for high annoyance vary by questionnaire item and interviewing area from ±2.6% to ±7%.

B. Changes in aircraft noise exposure levels between rounds of interviews

Noise exposure contours were developed retrospectively from detailed information about actual aircraft operations in 1994 and 1997 (Vancouver International Airport Authority, 1994, 1997). The years 1994 and 1997 were selected as time periods appropriate to the time frame (“last year”) about which respondents were questioned. The composition and numbers of operations of the aircraft fleet serving YVR in the years prior to each round of interviews varied little from those experienced by the respondents at the times of interview. Total runway movements at YVR (an overall indication of airport activity) increased from 268 176 in 1995 to 298 174 in 1997 (the last full calendar years prior to two rounds of interviews), the equivalent of 1.1 dB in exposure units. The fleet serving YVR has consisted of 8% to 9% heavy aircraft (136 000 kg or greater), 26% to 32% single-aisle large jets (34 000 to 136 000 kg), and 59% to 66% regional jets or smaller propeller-driven aircraft (34 000 kg or less) from 1994 through 1998.

A software model of aircraft noise exposure was derived from knowledge of aircraft activity prior to each round of interviews, and reconciled against monitored noise exposure levels at monitoring sites near interviewing areas. These levels, shown in Table II, were estimated for respondent-weighted centroids of interviewing areas. The percentage of respondents highly annoyed by aircraft noise is also shown in the table.

The greatest increases in DNL between rounds of interviews occurred in Bridgeport (7 dB) and in Hamilton and Annieville (3 dB). Aircraft noise exposure levels varied little between rounds of interviews in other areas. Table II summarizes numbers of completed interviews in the seven interviewing areas (columns 4 and 5), and a noise exposure estimate weighted by the number of respondents who completed interviews within sampling subareas (columns 6 and 7).

C. Comparisons of responses in two rounds of interviewing

Comparisons of responses from the two rounds of interviews to selected questionnaire items are presented next. Although X^2 tests were conducted on actual counts, differences in responses to questionnaire items between rounds of interviews are expressed as percentages for the sake of convenience.

1. Notice of increases in aircraft noise (questionnaire items 6 and 6A)

Figure 2 compares the percentages of respondents who reported noticing more aircraft noise during the years prior to each round of study. Chi-square tests of the differences in numbers of respondents noticing more aircraft noise during the past year (versus those not noticing more aircraft noise) in rounds 1 and 2 were conducted in each interviewing area. A statistically significant difference in the percentage of respondents reporting that they had noticed an increase in aircraft noise during the past year was found in Bridgeport, where 69% of the respondents reported noticing more air-

TABLE II. Percent of respondents highly annoyed by aircraft noise exposure and estimated aircraft noise exposure levels by interviewing area and interviewing round.

Aggregated interviewing area	% HA		No. of completed interviews		Respondent-weighted DNL (dB)	
	Round 1	Round 2	Round 1	Round 2	Round 1	Round 2
Burkeville and Brown Road	16.7%	17.0%	78	88	71	70
South Vancouver	7.6%	8.4%	291	238	44[a]	44[a]
Marpole	10.6%	6.3%	85	158	53	53
Bridgeport	11.3%	51.6%	160	155	54	61
Brighouse	5.1%	4.8%	136	147	52	52
Hamilton and Annieville	0%	18.1%	96	171	46	49
Alex Fraser Bridge	4.5%	11.8%	154	110	50	51
Total no. of interviews			1000	1067		

[a]These DNL values are out of the range of available data on which the FICON relationship is based, and are consequently excluded from Fig. 6.

craft noise during the past year in round 2, in contrast to only 40% in the first round of interviews. This difference was unlikely to have arisen by chance alone ($X^2_{(1)}=26.7$, $p<0.007$). (Reports of increased notice of aircraft noise in the year prior to the first round of interviews are not attributable to changes in aircraft noise exposure levels.)

A statistically significant difference in the percentage of respondents reporting that they had noticed an increase in aircraft noise during the past year was found in Hamilton and Annieville, where 60% of the respondents reported noticing more aircraft noise during the past year in round 2, in contrast to only 22% in the first round of interviews ($X^2_{(1)}=35.3$, $p<0.007$). The percentage of respondents who noticed less aircraft noise during the past year is shown in Table III.

Figure 3 shows that large majorities of respondents at all sites who reported noticing increases in aircraft noise believed these increases were sizable (“moderate” or “considerable”). In Bridgeport, 86% of the respondents in round 2 (but only 72% in round 1) believed the increases in aircraft noise were sizable ($X^2_{(1)}=5.1$, $p<0.007$). The percentage of respondents in Hamilton and Annieville who believed that increases in aircraft noise were sizable increased from 71% to 81% from the first to second round of interviews, but the increase was not statistically significant.

2. Relative salience of high annoyance due to aircraft and street traffic noise (questionnaire items 7 and 8)

Figure 4 compares the percentages of respondents describing themselves as highly (“very” or “extremely”) annoyed by aircraft noise to those highly annoyed by street traffic noise in the two rounds of interviews. Points lying above the diagonal indicate a greater prevalence of high annoyance from aircraft noise than from street traffic noise.

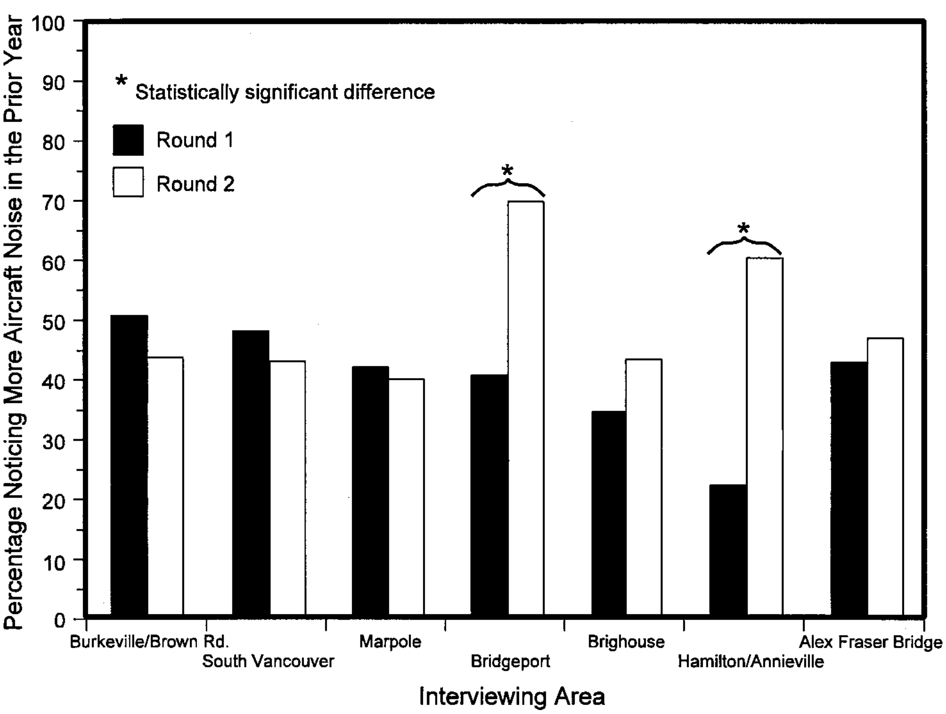

FIG. 2. Percentages of respondents noticing more aircraft noise during the prior year in the two rounds of interviews.

TABLE III. Percentage of respondents noticing less aircraft noise during the past year.

Interviewing area	Round 1	N	Round 2	N
Burkeville and Brown Road	5.1% (4)	78	23.9% (21)	88
South Vancouver	3.1% (9)	291	5.0% (12)	238
Marpole	4.7% (4)	85	3.8% (6)	158
Bridgeport	5.6% (9)	160	1.9% (3)	155
Brighouse	0.7% (3)	136	8.2% (12)	147
Hamilton and Annieville	3.1% (3)	96	3.5% (6)	171
Alex Fraser Bridge	2.6% (4)	154	8.2% (9)	110

Points lying below the diagonal indicate a greater prevalence of high annoyance from street traffic noise than from aircraft noise.

Changes in the relative annoyance of aircraft and street traffic noise are readily apparent among respondents in the Bridgeport and Hamilton and Annieville samples. Respondents in Hamilton and Annieville reported a greater prevalence of high annoyance due to aircraft noise in round 2, after having reported a greater prevalence of high annoyance due to street traffic noise round 1.

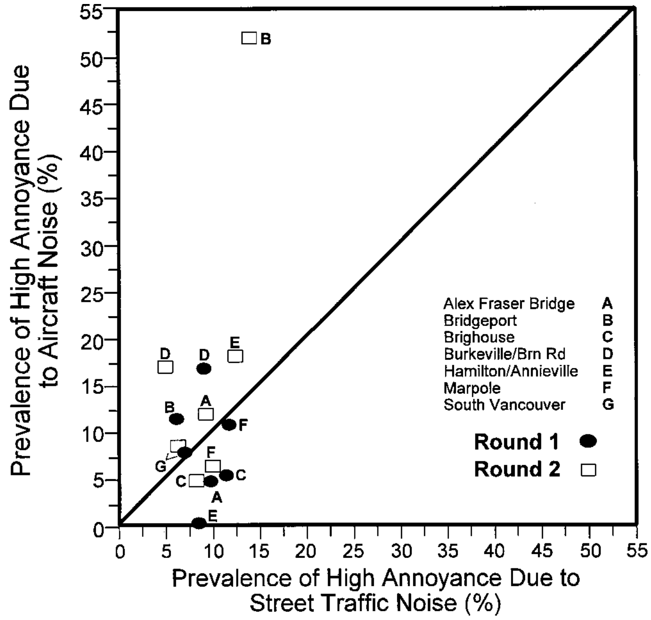

FIG. 4. Prevalence of high annoyance due to aircraft noise and street traffic noise in each interviewing area for the two rounds of interviews.

3. Differences in prevalence of aircraft noise-induced high annoyance (questionnaire items 8 and 8a)

As is evident from Fig. 5, the greatest increase in the prevalence of high annoyance due to aircraft noise was found in Bridgeport ($X^2_{(1)}=59.8$, $p<0.007$), where the percentage of respondents reporting high annoyance due to aircraft noise increased from 11% in round 1 to 52% in round 2. An increase in the prevalence of high annoyance due to aircraft noise between the rounds of interviews was also observed in Hamilton and Annieville ($X^2_{(1)}=19.7$, $p<0.007$). None of the respondents in Hamilton and Annieville had reported high annoyance due to aircraft noise in round 1, but 18% of respondents reported high annoyance in round 2. An increase from 5% to 12% of the respondents highly annoyed by aircraft noise in the Alex Fraser Bridge area was also observed from round 1 to round 2.

4. Differences in prevalence of aircraft noise-induced sleep disturbance (questionnaire item 9)

Figure 6 compares the percentages of respondents who reported aircraft noise-induced sleep disturbance during the past year in the two rounds of interviews. Greater percentages of respondents in round 2 than in round 1 reported sleep disturbance due to aircraft noise during the past year in all

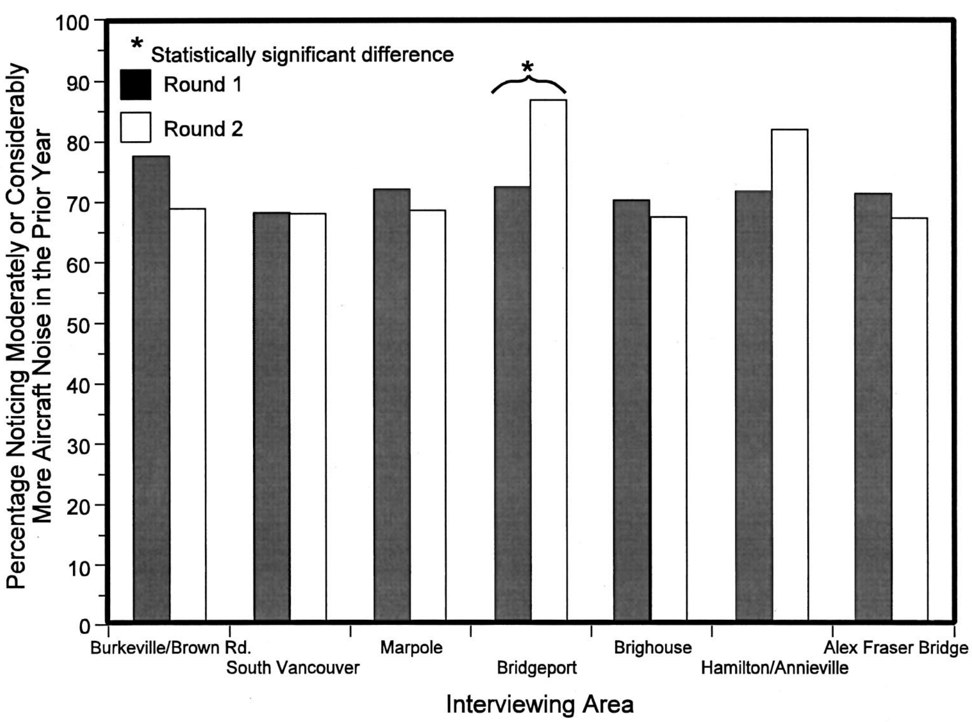

FIG. 3. Percentages of respondents noticing moderately or considerably more aircraft noise during the prior year in the two rounds of interviews.

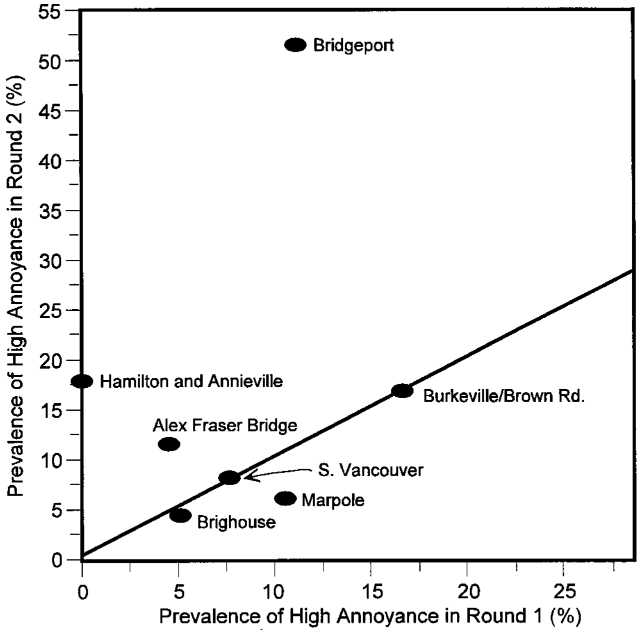

FIG. 5. Comparison of the prevalence of aircraft noise-induced high annoyance reported by respondents in Round 1 and Round 2.

interviewing areas. Statistically significant differences were found in Bridgeport ($X^2_{(1)}=27.5$, $p<0.007$), where 16% of respondents in round 1 and 43% of respondents in round 2 reported sleep disturbance due to aircraft noise, and in Hamilton and Annieville ($X^2_{(1)}=8.2$, $p<0.007$), where 5% of respondents in round 1 and 17% of respondents in round 2 reported sleep disturbance due to aircraft noise. Although an additional 15% of respondents in Burkeville/Brown Road reported aircraft noise-induced sleep disturbance in round 2, this finding was not statistically significant. Since Runway 08L/26R did not support nighttime overflights of the interviewing areas, any reported differences in sleep disturbance between the two rounds of interviews were without acoustic basis.

5. Differences in prevalence of aircraft noise-induced speech interference (questionnaire item 10)

Figure 7 compares the percentages of respondents in the two rounds of interviews who reported that aircraft noise had interfered with conversation or listening to the radio or television. Smaller percentages of respondents reported speech interference due to aircraft noise in round 2 than in round 1 in four interviewing areas. The only statistically significant differences were found in Bridgeport, where 47% of respondents in round 1 and 79% of respondents in round 2 reported that aircraft noise had interfered with conversation or listening to radio or television ($X^2_{(1)}=35.6$, $p<0.007$). An additional 13% of respondents in Hamilton and Annieville reported that aircraft noise had interfered with conversation or listening to radio or television.

IV. DISCUSSION

Table II (*v.s.*) summarizes percentages of respondents reporting high annoyance due to aircraft noise (columns 2, and 3), and estimated noise exposure (columns 6 and 7) in each of the seven interviewing areas. These are the values addressed in dosage–response analyses discussed in the following subsections.

A. Comparison of current findings with a well-known dosage–response relationship

Figure 8 shows the relationship between the prevalence of high annoyance in the present interviewing areas and a

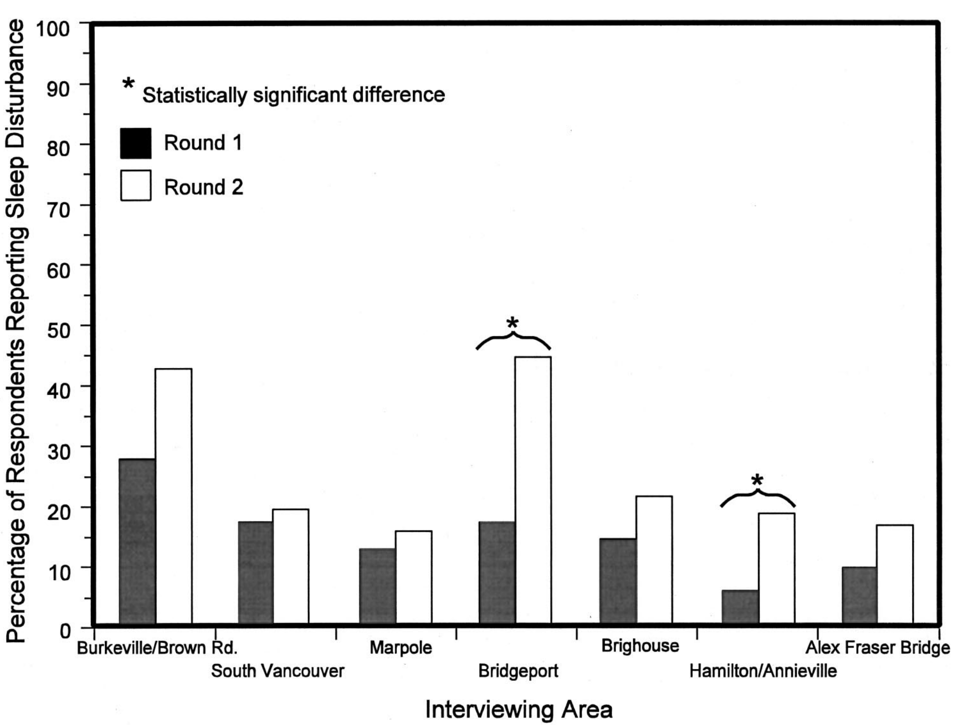

FIG. 6. Percentages of respondents reporting aircraft noise-induced sleep disturbance during the past year in the two rounds of interviews.

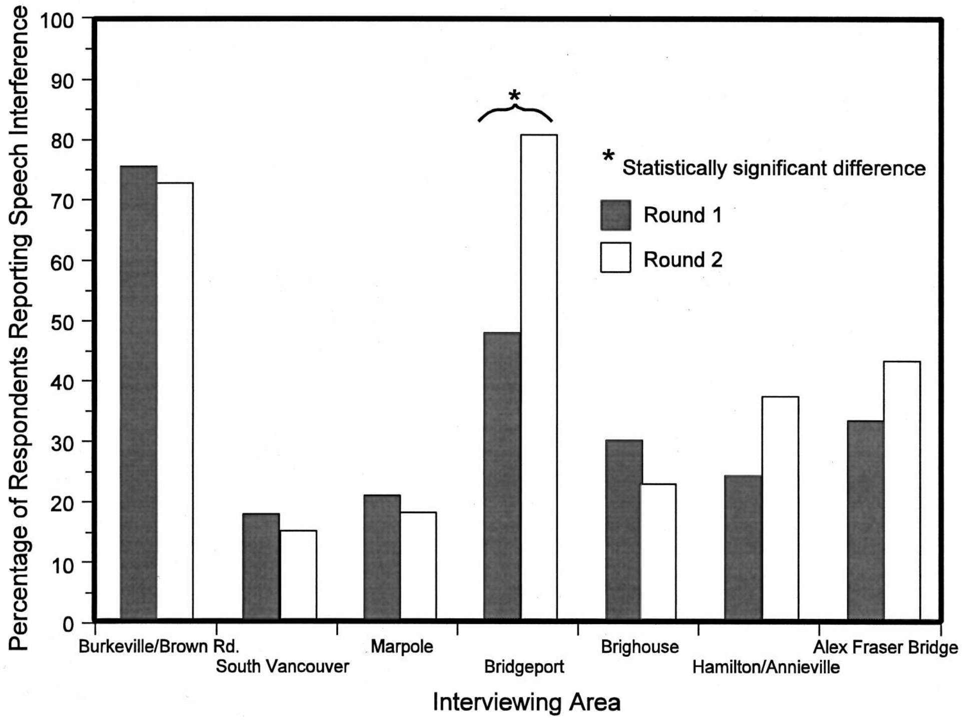

FIG. 7. Percentages of respondents reporting interference with conversation or listening to radio or television in the two rounds of interviews.

dosage–response relationship developed by FICON (1992). The data points show the prevalence of annoyance due to aircraft noise (item 8A) plotted against estimated DNL values in round 1 (triangles) and round 2 (rectangles). Ovals mark the mean of prevalence of high annoyance in 5-dB intervals. The error bars mark one standard deviation on either side of the mean prevalence of annoyance within 5-dB noise exposure intervals for 281 study sites and groupings of individuals within the same noise exposure ranges elsewhere (cf. Fidell, 1992).

The prevalence of high annoyance due to aircraft noise in the current interviewing areas is generally within one standard deviation of both the mean observed values for the 281 aircraft noise data points and of those predicted by FICON (1992). The notable exception is in Bridgeport, in which the prevalence of annoyance due to aircraft noise is considerably greater than that predicted by FICON.

B. Relative sensitivities to community noise exposure of current respondents and those elsewhere

Cumulative noise exposure alone, as quantified by DNL, does not account for all of the observed variability in the prevalence of noise-induced annoyance in different communities. In fact, all published dosage–response relationships based on a purely acoustic predictor variable leave a good deal of variance unexplained by noise measurements alone (cf. FICON, 1992; Job, 1988; Miedema and Vos, 1998). Nonacoustic factors that some speculate may account for the remainder of the variance include the economic dependence of a community (if not necessarily that of individuals) on the operation of a noise source, as well as a variety of attitudes about noise source operation, e.g., malfeasance, misfeasance, fear of crashes, necessity of noise exposure, controllability of noise exposure, etc.

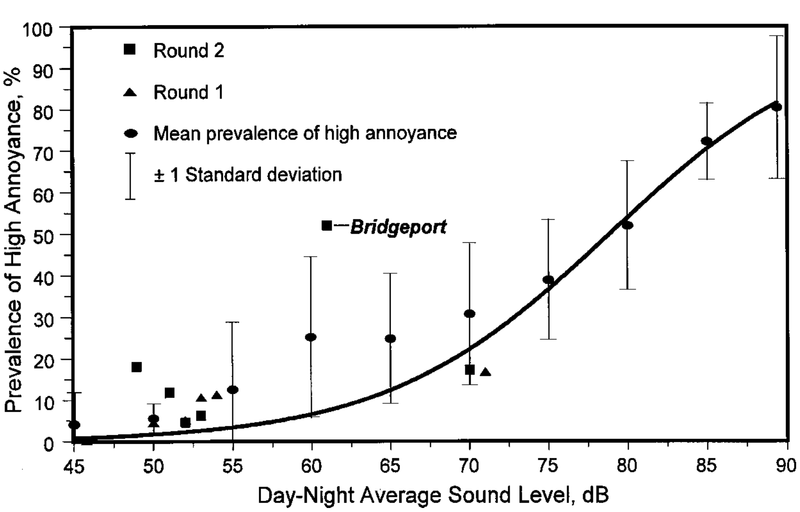

FIG. 8. Comparison of prevalence of high annoyance due to aircraft noise at YVR with FICON dosage–response relationship.

A quantitative model developed by Fidell *et al.* (1988) and Green and Fidell (1991) characterizes the aggregate effects of all nonacoustic determinants of annoyance judgments, and expresses them in a single parameter, D^*. A value of D^* may be interpreted as a value of DNL above which respondents describe themselves as highly annoyed by community noise exposure. The slope of the dosage–response relationship between noise exposure and prevalence of annoyance is fixed in this model by the effective (that is, duration-adjusted) loudness of the noise exposure, while the position of the dosage–response relationship along the abscissa is determined by the value of D^*. Systematic quantification of the aggregate effects of all nonacoustic influences on self-reports of noise-induced annoyance in terms of a single parameter is not intended to identify particular sources of response bias, but rather to reveal their net influence on self-reported annoyance prevalence rates.

The values of D^* as derived by the method of Green and Fidell (1991) from all points in the current data set were 68.5 dB in round 1, but 63.6 dB in round 2. The average D^* value observed by Green and Fidell (1991) for aircraft noise annoyance in the data set compiled by Fidell *et al.* (1991) was 70.2 dB. In other words, respondents in the second round of the current survey tolerated about 7 dB *less* noise exposure in their self-reports of high annoyance than airport neighborhood respondents elsewhere, whereas respondents in the first round of interviews had tolerated about 2 dB less noise exposure than respondents in airport neighborhoods elsewhere. This greater intolerance of aircraft noise in the second round of interviews suggests that a substantial portion of the apparent annoyance of aircraft noise exposure following the opening of the new runway is not attributable to changes in noise exposure alone.

C. Interpretation of reports of notice of change in aircraft noise

Many respondents at all sites reported noticing increases in aircraft noise in the years preceding each round of interviews. This finding is not inconsistent with the minor changes in the numbers and nature of aircraft operations at all sites in the year prior to the initial round of interviews, nor with the modest changes in noise exposure levels in certain of the interviewing areas prior to the second round of interviews. Questionnaire item 6 inquired about "notice"—that is, awareness—of change in aircraft noise, not about knowledge of cumulative sound exposure levels in neighborhoods attributable to aircraft operations.

Given the general awareness of the community and the controversy surrounding the highly publicized development of a new runway at YVR, it is hardly surprising that respondents would report notice of changes in aircraft noise. Unlike microphones, people's responses to aircraft noise exposure are determined by both acoustic and nonacoustic factors (Fields, 1993; Green and Fidell, 1991; Job, 1988). The question was not intended to confirm the calibration of noise modeling and monitoring systems, but rather to assess the degree to which respondents at various sites were sensitive to changes in noise exposure associated with the runway development. Reliable differences between rounds of interviews in rates of notice of change in aircraft noise were evident in only two of the seven interviewing areas.

V. SUMMARY

A disproportionately large and long-term increase was observed in the prevalence of self-reported high annoyance long after a step increase in aircraft noise exposure. Both the magnitude and the persistence of the elevation of the annoyance prevalence rate in a community three miles from the runway threshold nearly two years after the opening of a new runway are noteworthy. The greater-than-predicted increase in the prevalence of annoyance cannot be attributed to changes in noise exposure alone.

ACKNOWLEDGMENTS

The authors are grateful to the respondents for granting the interviews on which this study is based. The study was sponsored by the Vancouver International Airport Authority. Further methodological detail may be found in BBN Report 8247.

APPENDIX: SURVEY INSTRUMENT

ITEM 1. About how long have you lived at [street address]?
ITEM 2. What do you like <u>best</u> about living conditions in your neighborhood?
ITEM 3. What do you like <u>least</u> about living conditions in your neighborhood?
ITEM 4. What do you think is the single most important environmental issue in your neighborhood?
ITEM 5. Would you say that your neighborhood is quiet or noisy?

Follow up question if neighborhood was described as "noisy":

ITEM 5A. Would you say that your neighborhood is slightly noisy, moderately noisy, very noisy, or extremely noisy?
ITEM 6. While you've been at home during the past year, just since last summer, have you noticed any more or any less <u>aircraft noise</u> in your neighborhood?

Follow up question if more aircraft noise was noticed:

ITEM 6A. Have you noticed slightly, moderately, or considerably **more** <u>aircraft noise</u> during the past year?

Follow up question if less aircraft noise was noticed:

ITEM 6B. Have you noticed slightly, moderately, or considerably **less** <u>aircraft noise</u> during the past year?
ITEM 7. While you've been at home during the **past year**, have you been bothered or annoyed by <u>street traffic noise</u> in your neighborhood?

Follow up question if response to Item 7 was "yes":

ITEM 7A. Would you say that you were slightly annoyed, moderately annoyed, very annoyed, or extremely annoyed by <u>street traffic noise</u> in your neighborhood during the past year?
ITEM 8. While you've been at home during the **past year**, just since last summer, have you been bothered or annoyed by <u>aircraft noise</u> in your neighborhood?

Follow up question if response to ITEM 8 was "yes":
ITEM 8A. Have you been slightly annoyed, moderately annoyed, very annoyed, or extremely annoyed during the **past year** by aircraft noise in your neighborhood?

Second follow up question if response to ITEM 8 was "yes":
ITEM 8B. Generally speaking, are you more annoyed by noise from big jets, by noise from propeller planes, or by noise from other types of aircraft?
ITEM 9. While you have been at home during the past year, has your sleep been disturbed by aircraft noise at night? *Response categories were "yes" and "no."*
ITEM 10. While you have been at home during the past year, has aircraft noise interfered with conversation or listening to the radio or TV? *Response categories were "yes" and "no."*

[1]The term ''prevalence'' is used in its epidemiological sense, as implying a causal (noise exposure-related) as opposed to a noncausal (preexisting) ''incidence'' rate.

[2]Estimation of aircraft noise exposure over large areas by means of retrospective noise modeling is a standard and unavoidable practice in some circumstances. Areas for which noise exposure estimates have been produced in the present study are either close to flight paths or to the airport, in which areas the noise modeling software is most accurate. Software-produced aircraft noise exposure estimates were also checked for consistency with noise monitoring data. The noise exposure estimation procedures were consistent over rounds of interviews, so than any potential systematic errors of estimation apply equally to noise exposure estimates for both rounds of interviews.

[3]Discussions (not yet resolved) of alternate views about the preferred sequence, structure, and wording of questionnaire items for studies of noise-induced annoyance have occurred in the years following the conduct of the initial round of interviews in 1995. Consistency in questionnaire content in the second round of interviews precluded consideration of any such alternate questioning in the present study.

[4]Every experimental design is an exercise in economics. If the intervals between rounds of interviews are short enough and specifiable in advance, then for a given precision of measurement, the initial over-sampling and bookkeeping costs of a panel sample may be a cost-effective alternative to independent sampling in each round of interviews.

Federal Interagency Committee on Noise (FICON) (**1992**). ''Federal Agency Review of Selected Airport Noise Analysis Issues,'' in *Final Report: Airport Noise Assessment Methodologies and Metrics*, Washington, D.C.

Fidell, S. (**1992**). ''Interpreting findings about community response to environmental noise exposure: what do the data say?'' EuroNoise'92, London.

Fidell, S., and Jones, G. (**1975**). ''Effects of Cessation of Late-Night Flights on an Airport Community,'' J. Sound Vib. **42**(4), 411–427.

Fidell, S., Barber, D., and Schultz, T. J. (**1991**). ''Updating a dosage-effect relationship for the prevalence of noise-related annoyance,'' J. Acoust. Soc. Am. **89**, 221–233.

Fidell, S., Schultz, T. J., and Green, D. M. (**1988**). ''A theoretical interpretation of the prevalence rate of noise-induced annoyance in residential populations,'' J. Acoust. Soc. Am. **84**, 2109–2113.

Fidell, S., Silvati, L., and Fletcher, E. (**1995**). ''Social survey of community response to noise exposure near Vancouver International Airport,'' BBN Report No. 8105.

Fidell, S., Horonjeff, R., Mills, J., Baldwin, E., Teffeteller, S., and Pearsons, K. (**1985**). ''Aircraft noise annoyance at three joint air carrier and general aviation airports,'' J. Acoust. Soc. Am. **77**, 1054–1068.

Fields, J. M. (**1993**). ''Effect of personal and situational variables on noise annoyance in residential areas,'' J. Acoust. Soc. Am. **93**, 2753–2763.

Fields, J. M., Ehrlich, G. E., and Zador, P. (**2000**). ''Theory and Design Tools for Studies of Reactions to Abrupt Changes in Noise Exposure,'' NASA Contractor Report CR-2000-210280, NASA Langley Research Center, Hampton, VA.

Green, D., and Fidell, S. (**1991**). ''Variability in the criterion for reporting annoyance in community noise surveys,'' J. Acoust. Soc. Am. **89**, 234–243.

Horonjeff, R. D., and Robert, W. E. (**1997**). ''Attitudinal Responses to Changes in Noise Exposure in Residential Communities,'' NASA Contractor Report 97-205813, NASA Langley Research Center, Hampton, VA.

Job, R. F. S. (**1988**). ''Community response to noise: A review of factors influencing the relationship between noise exposure and reaction,'' J. Acoust. Soc. Am. **83**, 991–1001.

Miedema, H., and Vos, H. (**1998**). ''Exposure-response relationships for transportation noise,'' J. Acoust. Soc. Am. **104**, 3432–3445.

Schultz, T. J. (**1978**). ''Synthesis of social surveys on noise annoyance,'' J. Acoust. Soc. Am. **64**, 377–405.

Vancouver International Airport Authority (**1994**). Aeronautical Noise Management 1994 Annual Report.

Vancouver International Airport Authority (**1997**). Annual Report for 1997 Operations Data.

Inaccuracies in sound pressure level determination from room impulse response

Dejan G. Ćirić[a] and Miroslava A. Milošević
Faculty of Electronic Engineering, University of Niš, Beogradska 14, 18000 Niš, Yugoslavia

(Received 2 May 2001; revised 2 October 2001; accepted 13 October 2001)

The integration over discrete squared room impulse response (RIR) leads to the sound pressure level (SPL). However, certain inaccuracies in SPL determination appear as a consequence of influences of finite integration upper limit (UL) and noise. Due to that, these influences are investigated using two types of RIRs: those generated by simulation and those measured in the room. The investigations show that for RIRs with sufficiently small noise floors (below −20 or −15 dB) acceptably small inaccuracies are obtained if the integration UL is placed at $T/3$ (alternatively at $T/4$). A more general solution is to set UL at the knee representing the point where main decay intersects noise floor. For even smaller inaccuracies, it would be better to set UL at the point somewhat before the knee called optimal UL. The influences of finite integration UL and noise can also be reduced by implementation of finite UL compensation and noise subtraction. [DOI: 10.1121/1.1426375]

PACS numbers: 43.55.Br, 43.55.Ka, 43.55.Mc, 43.58.Fm [JDQ]

I. INTRODUCTION

The room impulse response (RIR) represents one of the most important room characteristics. The corresponding processing of the RIR can yield various room quantities and measurement parameters.[1–3] The focus of this paper is the steady-state mean-square pressure, that is the sound pressure level (SPL), obtained by the integration over squared RIR from zero to infinity.[4,5] In practice, this infinite upper limit (UL) of integration must be transformed into finite UL.

It has already been theoretically shown, excluding the influence of background noise (in the following called noise), that the integration up to $T/3$ or $T/4$ in SPL determination results in acceptably small error.[6,7] As an extension to this result, investigations of the influence of integration UL together with the influence of noise are performed here on a practical basis. Namely, the inaccuracy in SPL determination due to the integration over RIR of finite length is quantified. Not only has the finite length of RIR an important influence on inaccuracy, but also it matters whether the reverberant sound or noise is dominant in the part of RIR where the UL is placed. So, the investigations include the influence of noise and its power using the RIRs with various signal-to-noise ratios (SNRs). Besides, the number of averages required in order to obtain defined accuracy of SPL is analyzed.

Various approaches for reducing the influences of finite integration UL and noise are implemented including the setting of suitable UL and additional processing. The latter involves two correction techniques: noise subtraction for reducing the influence of noise, and finite UL compensation for reducing the influence of finite integration UL.

The mentioned influences are investigated on two types of RIRs with exponential decay. The first is obtained by simulation, using a proposed mathematical model, which enables generation of RIRs with known characteristics. The second type of response represents the RIRs measured in a particular room by the implementation of Maximum Length Sequence (MLS) technique[5–8] for a measurement system.[3,9]

II. SPL DETERMINATION FROM RIR

The integration over squared RIR $h^2(\tau)$ results in the steady-state mean-square pressure

$$p^2(t)=G\int_0^\infty h^2(\tau)\,d\tau, \tag{1}$$

where G is proportional to the source power.[4,5] When the MLS technique is implemented for measurement, the RIR represents a correlation function since it is obtained by cross-correlation of excitation signal and the response.[8] In the SPL determination from the RIR, the most important step is to calculate the overall energy as precisely as possible.[6,7] Of course, the integration UL cannot be infinite in practice, due to the finite length of measured RIR. As a consequence of this, all of the energy is not included in the calculation. However, since the RIR decays exponentially, most of the energy is concentrated in the response beginning. In this way, the integration over the early part of the RIR can yield an approximately correct result.[6] Nevertheless, there is a question of where the UL of integration should be set to obtain acceptable inaccuracy of SPL determination.

This problem becomes more complicated due to the influence of noise. The impulse decay representing the logarithmic plot of squared RIR consists of two parts: the first part where reverberation sound is dominant and the second part where the noise is dominant, as illustrated in Fig. 1. The point of intersection of these parts is the knee. In the vicinity of the knee, a significant influence of both reverberant sound and noise exists. In SPL determination, the integration UL should be set at the first part of RIR where reverberant sound is dominant. On the other hand, if the UL is placed at the

[a]Electronic mail: dciric@elfak.ni.ac.yu

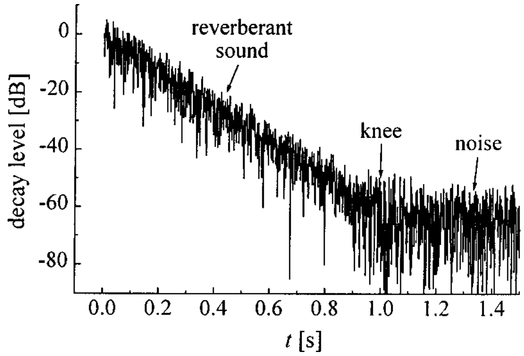

FIG. 1. The impulse decay of the simulated RIR with noise floor of −60 dB.

second part of RIR, the energy of the noise is added to the energy of reverberant sound, leading to bigger SPL than the right value. The energy of noise can also affect the accuracy of SPL determination if the UL is near the knee. In this case, by using only the first part of RIR for integration, UL is dislocated toward the response beginning and the length of the useful part of the response is further reduced, especially when noise has relatively big power.

III. INACCURACIES OF SPL DETERMINATION IN SIMULATED RIRS

A. Generating simulated RIRs

The most convenient way to investigate the influences of integration UL and noise is to use RIRs whose characteristics are all known and whose parameters can be controlled. Such RIRs can be generated by simulation, that is, by a corresponding mathematical model. For this purpose, the mathematical model given by the following expression

$$h(t)=\mathrm{sgn}(n_1(t))[e^{-kt/2T}r(t)+\sqrt{a}n_2(t)], \tag{2}$$

is used here, where $r^2(t)$ is a unit-mean multiplicative random process modeling fluctuations due to multiple reflected paths, a is the noise floor power, and $n_i(t)$ are the unit-variance noise processes. This model is based on a simple model for the squared RIR from Ref. 10. The time constant is changed here so that the impulse decay excluding the fluctuations and noise has the value of −60 dB for $t=T$, which is obtained for $k=13.815\,511$. Also, the model is extended by sgn function

$$\mathrm{sgn}(n_1(t))=\begin{cases}+1, & n_1(t)\geqslant 0\\ -1, & n_1(t)<0\end{cases}, \tag{3}$$

so that the simulated RIR comprises both positive and negative amplitudes in the part where the reverberant sound is dominant. This function does not influence the squared RIR remaining the same as in the mentioned simple model,[10] because it affects only the sign.

The process $r(t)$ is modeled as a Rayleigh fading process since it exhibits many of the characteristics of actual RIRs.[10] So, a random variable R is postulated in such a way that R^2 has an exponential probability density. The variable R can be generated as $R=\sqrt{(X^2+Y^2)/2}$, where X and Y are two independent zero-mean, unit-variance, normal random variables. The noise processes are modeled using Gaussian model. The mathematical model from Eq. (2) now enables generation of the simulated RIR, if there are four series of samples with Gaussian probability density. Two of them are used for noise processes $n_i(t)$ and the remaining two series are used for the random process $r(t)$. In order to obtain series with Gaussian probability density, a software module was developed.[3] The same set of four different series with Gaussian probability density can be used to generate RIRs with different SNRs by changing only the noise floor power, that is, parameter a in Eq. (2). But, the RIRs can be generated using different sets of four series, as well.

The noise floor power in the measured RIR can be different, depending on the measurement and the environment, that is, on ambient noise. So, it can range from a small value in comparison to the signal power up to a value close to the signal power. For example, a large value of noise floor power can be obtained in a receiving room with high ambient noise, in the measurement of sound insulation. The noise floor powers of simulated RIRs used in investigations here are in such a range that the noise floor levels (in the following noise floors representing $10\log a$) are between −5 dB and −60 dB. The absolute value of noise floor is approximately equal to the response SNR calculated in a standard way as the ratio of signal power to noise power. The signal power is calculated from the beginning of RIR, while the noise power is calculated from the second part of RIR where noise is dominant. All the simulated RIRs have the length of 2000 samples, that is, they have a duration of 2 s if the relative sampling interval is set on value of 1 ms. Due to the convenience, the value of T is set to 1 s. Figure 1 shows the impulse decay of a simulated RIR with noise floor of −60 dB, obtained by Eq. (2).

B. Influences of integration UL and noise

The integration UL can be set at various points of an RIR depending on a particular response. So, the points of RIRs ranging from 0.005 s to 1.5 s with steps of 0.001 s are used here as ULs. In this way, the UL is placed at the part of an RIR where reverberant sound is dominant, as well as at the part where noise is dominant. The lower limit of integration is placed at zero, as it is defined in Eq. (1).

In SPL determination, the steady-state mean-square pressures obtained from the simulated RIRs with various noise floors by Eq. (1) for various ULs are normalized by the corresponding pressure. This pressure is calculated from the RIR with noise floor of –60 dB by the same Eq. (1) in which the UL is set at the knee, and it represents approximately the right value of pressure. Setting UL at the knee introduces smaller inaccuracy than setting UL at the end of RIR, which will be analyzed later. The normalization pressure can be calculated with even smaller inaccuracy from an RIR with lower noise floor, but the inaccuracy introduced by using the RIR with noise floor of −60 dB is already negligible (smaller than 10^{-5} dB). By implementation of the described normalization, it is found that the reference value of SPL corresponding to normalized, the right level is approximately 0 dB. In this way, the calculated levels for various ULs (L_d)

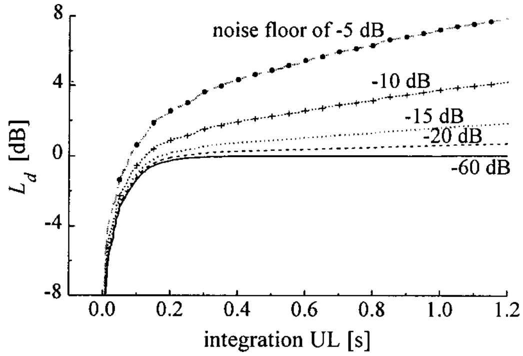

FIG. 2. The level deviations determined from simulated RIRs with various noise floors for various ULs.

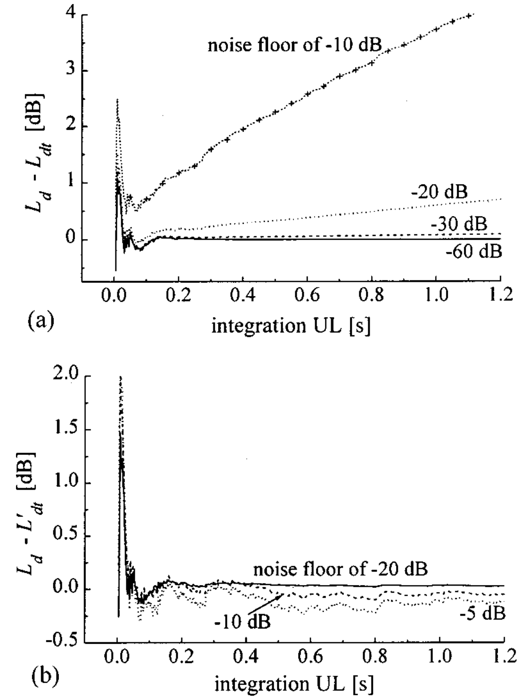

FIG. 3. The differences of the level deviations determined from the simulated RIRs with various noise floors and that one calculated by Eq. (4)(a), that is, by Eq. (6)(b).

directly represent the level deviations (the differences between the calculated levels and the right level).

The results of investigations show that considerable level deviation exists if the UL is set too close to the RIR beginning, so that a small range of response is integrated, as illustrated in Fig. 2. This deviation is negative because the calculated level is smaller than the right one, and it can be called "level decreasing." Level deviations above -1 dB appear in the RIR with noise floor of -60 dB, if the UL is placed at the points after 0.116 s (for that time, the RIR decays below -7 dB), while deviations above -0.1 dB appear for UL placed after 0.27 s. On the other hand, if UL is placed at the part of an RIR where noise is dominant or somewhat before, calculated level is bigger than the right one, that is, level deviation is positive and it can be called "level increasing." This level increasing becomes bigger as the UL is displaced toward the end of RIR and as the noise floor becomes bigger. It can reach a value of several decibels. This is why the integration UL should not be set in the part of an RIR where the noise is dominant.

The level deviation due to the finite integration UL can be theoretically obtained as

$$L_{dt} = 10\log(1 - e^{-kt_{ul}/T}), \tag{4}$$

where t_{ul} represents UL in time.[6,7] The level deviations determined from the simulated RIRs with relatively small noise floors are in good agreement with the deviation calculated by Eq. (4), as shown in Fig. 3(a). The noticeable differences in deviations in this example appear only if the integration UL is set close to the beginning of the RIR. Their absolute values drop below 0.3 dB for UL setting after 0.05 s, and they almost disappear for UL setting after 0.15 s. These differences are the consequence of response fluctuations. As the influence of fluctuations is bigger when the integration range is smaller, the noticeable differences exist only near the RIR beginning. On the other hand, the level deviations determined from the RIRs with higher noise floors (bigger than -20 dB) are considerably different from that calculated by Eq. (4). This is the consequence of the fact that the theoretically obtained level deviation in Eq. (4) does not take into consideration the influence of noise.

A procedure similar to that used in deriving Eq. (4) is implemented here to obtain theoretical level deviation, but including the influence of noise as well. For this purpose, the steady-state mean-square pressure is calculated by

$$p^2(t) = G\int_0^{t_{ul}} E\{h^2(\tau)\}d\tau = G\int_0^{t_{ul}} (e^{-k\tau/T} + a)d\tau, \tag{5}$$

where $E\{h^2(\tau)\}$ represents the expectation of squared RIR, which can be understood to be over the ensemble of random processes,[10] $r(t)$ and $n_i(t)$ from Eq. (2). In this way, the random processes and the cross-term $(2e^{-k\tau/2T}\sqrt{a})$, which is obtained by squaring the response $h(\tau)$, disappear in the integrated function. The solving of the previous integral and adequate normalization lead to the following level deviation

$$L'_{dt} = 10\log[1 - e^{-kt_{ul}/T} + (k/T)at_{ul}]. \tag{6}$$

The differences between the level deviations determined from simulated RIRs and the deviation calculated by Eq. (6) are now approximately equal to zero, as shown in Fig. 3(b), independent of the noise floor. Noticeable differences again exist only if the UL is placed close to the beginning of the RIR, as in Fig. 3(a), as explained above.

The described investigations were also performed on simulated RIRs generated using different sets of four series with Gaussian probability density. Level deviations obtained were similar to those presented in Fig. 2. However, there are relatively small differences between corresponding deviations especially in RIRs with higher noise floors, as shown in Fig. 4. Nevertheless, these differences do not greatly influence the conclusions.

Smaller level deviations, relative to those obtained by placing the UL at the part of the response where the noise is dominant, emerge if the UL is placed at the knee. Nevertheless, the calculated levels are again somewhat higher than the

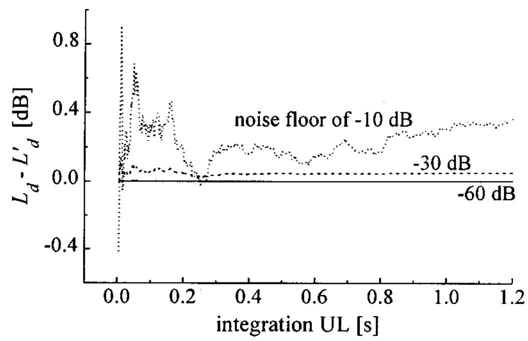

FIG. 4. The differences of level deviations determined from simulated RIRs generated by using two different sets of four series with Gaussian probability density $(L_d - L'_d)$.

right level. This increase becomes bigger with increasing noise floor, rising to about 1 dB, as shown in Fig. 5. Because of that, in RIRs with relatively high noise floors it is better to set the integration UL at a point placed somewhat before the knee. In this way, since UL is displaced toward the response beginning, the reduction of level due to finite UL is increased and, at the same time, the level increase due to the noise is reduced. Thus, the calculated level is closer to the right one. Setting UL at the point where level decrease due to finite UL is equal to level increase due to noise, results in level deviation of 0 dB. This point can be called optimal point or optimal UL.

Table I shows the points of RIRs with various noise floors where the integration UL should be set in order to obtain the right level. In all the RIRs except in the response with noise floor of -5 dB, the level deviation is very small (or equal to 0) if the integration UL is set at the point representing 0.7 value of the knee. Thus, for example, in RIR with a noise floor of -15 dB, the knee is at the point about 0.25 s distant from the response beginning, and UL should be placed at the point 0.175 s. For this UL, the calculated level is almost equal to the right one (the level deviation is 0.03 dB), while UL placed at the knee results in the level deviation of 0.34 dB. This analysis shows that SPL can be determined precisely enough even from an RIR with relatively high noise floor. However, more care should be given to the setting of integration UL.

Taking into consideration both the level decrease due to the finite integration UL and the level increase due to the

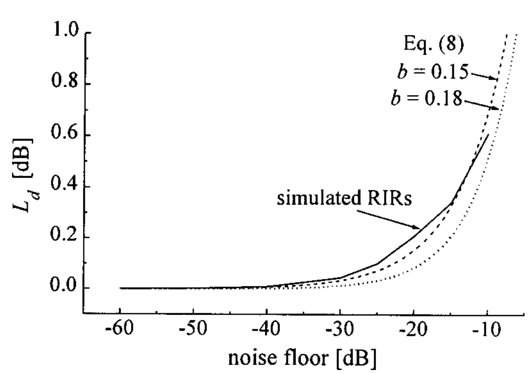

FIG. 5. The level deviations determined from simulated RIRs for the integration UL placed at the knee, and the deviations obtained by Eq. (8).

noise, relatively small inaccuracy in SPL determination is obtained for UL placed at $T/3$ or $T/4$ if the noise floor is not too high (not bigger than -20 or -15 dB). For example, UL at $T/3$ and $T/4$ results in level deviations of -0.04 and -0.13 dB, respectively, in RIR with noise floor of -60 dB. However, for an RIR with noise floor higher than the mentioned -20 or -15 dB, it is better to set UL at the knee. Even smaller inaccuracy (or no inaccuracy) is obtained for optimal UL placed somewhat before the knee.

IV. INACCURACIES OF SPL DETERMINATION IN MEASURED RIRS

In order to perform the mentioned investigations on measured RIRs, the measurements were carried out in one of the Laboratories at the Faculty of Electronic Engineering in Niš, which is similar to a classroom.[3,9] The simple PC based measurement system[3] developed at the Laboratory of Acoustics at this Faculty was used for the measurements of a number of RIRs in several points, by implementation of an MLS technique. Various noise floors in RIRs were obtained using various excitation signal levels. The RIRs with the same noise floor measured in various points lead to the similar results for the investigations performed. So, only the results obtained from RIRs measured in one point are presented in this section.

As in previous investigations, the calculated steady-state mean-square pressures are normalized by the corresponding pressure. It is calculated from the measured RIR with noise floor of about -50 dB, that is, with SNR of about 50 dB, in such a way that the integration UL is set at the knee. In order to compare in an easier way the results obtained from measured RIRs with those obtained from simulated responses, the values of UL are normalized here by the reverberation time of the laboratory, determined from broadband RIR (0.8 s). This time is approximately equal to the reverberation times at middle frequencies. The level deviations due to finite UL and noise in measured responses, shown in Fig. 6(a), are similar to those obtained in simulated responses with the same noise floor, The small differences between the corresponding deviations are presented in Fig. 6(b).

The knee of the RIR with noise floor of -10 dB is placed at the point about 0.145 s distant from the response beginning and the integration UL at the knee leads to the calculated level higher than the right one by about 0.7 dB. If the conclusions of the previous section are implemented, UL

TABLE I. The integration ULs leading to the right SPL $(L_d = 0$ dB) in simulated RIRs with various noise floors.

Noise floor [dB]	Knee [s]	UL [s] leading to $L_d = 0$ dB	UL/knee
-5	0.083	0.082	0.99
-10	0.167	0.126	0.75
-15	0.250	0.171	0.68
-20	0.333	0.233	0.70
-25	0.417	0.281	0.67
-30	0.500	0.331	0.66
-40	0.667	0.439	0.66
-50	0.833	0.552	0.66

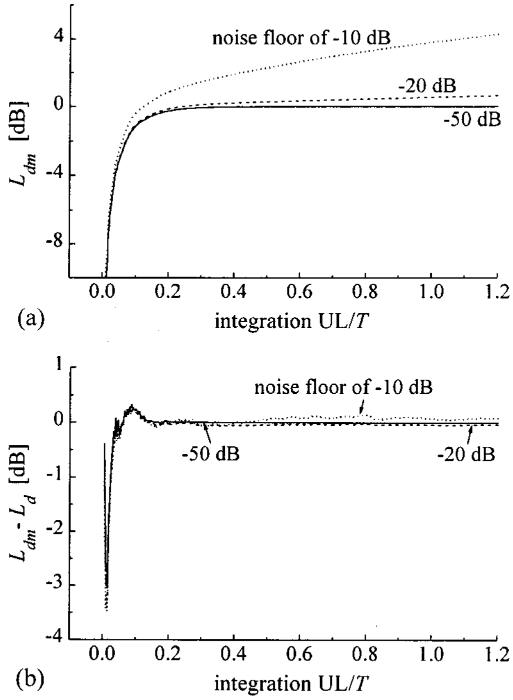

FIG. 6. The level deviations determined from measured RIRs with various noise floors (L_{dm}) (a) and the differences of these deviations and those determined from simulated RIRs (L_d) (b).

should be placed at the point obtained by multiplication of the time value of the knee by 0.7, that is, at the point 0.102 s. The integration over RIR up to this point results in the level deviation of about 0.07 dB. So, smaller deviation again appears if the UL is not placed at the knee, but somewhat before the knee.

V. NUMBER OF AVERAGES LEADING TO DEFINED LEVEL DEVIATION

Sometimes, even in MLS technique, the excitation signal level is too low in comparison to noise level (as can be found in the measurement of sound insulation). It can even happen that the RIR comprises only the noise. In such a case, averaging increases response SNR, that is, enabling the extraction of an appropriate RIR. Obtaining an adequate number of averages to reach a defined level deviation in SPL determination from the averaged RIR is presented in this section. An empirical formula for the estimation of the required number of averages (N) yielding the RIR from which SPL is determined with defined level deviation has already been derived in Ref. 4

$$N=[3.12e^{-bSNR_{BA}}/L_d]^{1.23}. \tag{7}$$

The constant b is equal to 0.18, while SNR_{BA} represents the broadband A-weighted SNR of response before averaging.

Now, the level deviations can be calculated from the preceding equation for each SNR and for $N=1$, that is, without the averaging because of which the index BA of SNR is omitted

$$L_d=3.12e^{-bSNR}. \tag{8}$$

These deviations are similar to the deviations determined from simulated RIRs with the integration UL placed at the

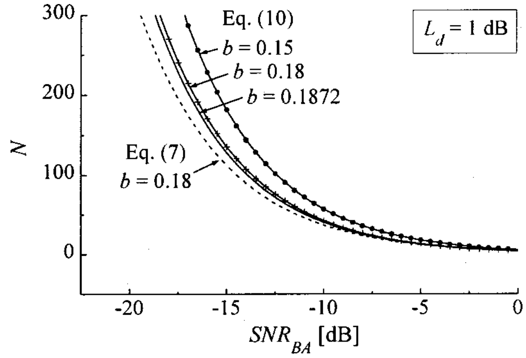

FIG. 7. The required number of averages leading to defined level deviation for UL placed at the knee calculated by Eq. (7) and by Eq. (10).

knee. The presentation of this is given in Fig. 5 using the previously described relationship that the absolute value of noise floor is approximately equal to SNR. Better agreement is obtained for $b=0.15$ in Eq. (8).

RIRs with the same SNR should lead to the same level deviation for the same integration UL, independent of the number of averages used to obtain them. So, Eq. (7) should result in such values of N for various SNR_{BA}'s and the same L_d, which lead to averaged responses with the same SNR. This can be obtained if the constant b gets the value of 0.1872 postulating that every doubling the number of averages results in improvement of SNR by 3 dB.

Another formula for calculation of the required number of averages yielding the defined level deviation for integration UL placed at the knee is derived here. Namely, the required SNR of response leading to the defined level deviation can be obtained based on Eq. (8). The difference between this SNR and SNR existing before averaging (SNR_{BA}) should be equal to the improvement of SNR obtained by averaging

$$\frac{1}{b}\ln\frac{3.12}{L_d}-SNR_{BA}=10\log N. \tag{9}$$

Solving the previous equation gives the required number of averages

$$N=10^{(1/10)((1/b)\ln(3.12/L_d)-SNR_{BA})}. \tag{10}$$

Unlike Eq. (7), this formula can be implemented for various constants b. Taking particular b, for various SNR_{BA}'s and the same L_d, it results in values of N, such that the averaged RIRs have the same SNR. Although Eq. (7) and Eq. (10) are different at the first sight, they result in the same N for $b=0.1872$. However, for other values of b, the numbers of averages obtained by these equations are different. As shown in Fig. 7, the influence of b on calculated number of averages is significant.

If SNR of response (SNR_{BA}) is too low (below 0 dB or 5 dB) for determination of right SPL using the optimal UL, the required number of averages enabling such determination is simply calculated from the required improvement of SNR obtained by averaging. Namely, the particular SNR of the response, which can be high enough for reliable determination of right SPL using optimal UL (for example, 8 dB or 10 dB), is defined as final SNR. The difference between this

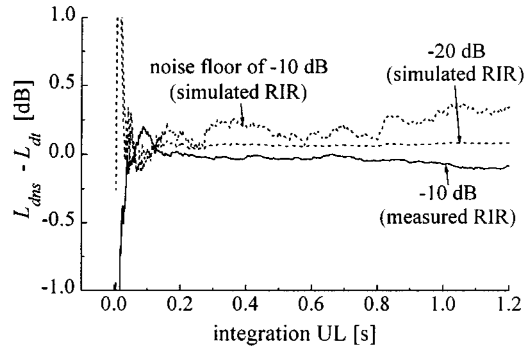

FIG. 8. The differences of the level deviations determined from the simulated and measured RIRs with various noise floors using noise subtraction (L_{dns}) and that one calculated by Eq. (4) (UL is normalized by T for measured response).

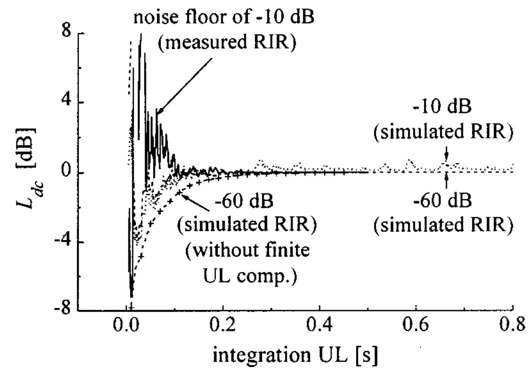

FIG. 9. The level deviations determined from simulated and measured RIRs with various noise floors implementing both noise subtraction and finite UL compensation (L_{dc}) (UL is normalized by T for measured response).

SNR and initial SNR_{BA} should be equal to the SNR improvement obtained by averaging. This leads to the required number of averages.

VI. NOISE SUBTRACTION AND FINITE UL COMPENSATION

As an alternative to the previously used approach of reducing the inaccuracies in SPL determination by setting appropriate UL, these inaccuracies can also be reduced by additional processing based on the implementation of two correction techniques. Namely, the inaccuracy caused by noise can be reduced by using the noise subtraction technique, while the inaccuracy caused by a finite UL can be reduced by using the technique called finite UL compensation.

The noise subtraction was previously used for increasing of the dynamic range of decay curve obtained by backward integration of RIR.[11] In this technique, the mean-square value of noise, calculated from the second part of response where the noise is dominant, is subtracted from squared RIR, before the integration. The response $h(t)$ comprising the noise can be presented by the sum of the RIR without noise $h_r(t)$ and the noise $n(t)$. If the mean-square value of noise $\overline{n^2}$ is now subtracted from the squared RIR, then the steady-state mean-square pressure is given by

$$p^2(t)=G\int_0^{\infty}\{h_r^2(\tau)+2h_r(\tau)n(\tau)+(n^2(\tau)-\overline{n^2})\}d\tau. \tag{11}$$

The second term in this equation $(2h_r(\tau)n(\tau))$ integrates to zero, as the noise can be either positive or negative.[11] The contribution of squared noise, that is, of noise energy, which is added to the energy of reverberant sound, is now reduced by subtraction of the mean-square value of the noise.

The investigations of implementation of this technique were performed on both simulated and measured RIRs. The obtained level deviations show that it represents an efficient technique for the reducing of inaccuracy of SPL determination due to noise. Namely, the earlier obtained level increase as a consequence of noise, now almost disappears. So, the deviations determined from the RIRs with various noise floors are similar. In this way, the differences between these deviations and the deviation calculated by Eq. (4) are considerably reduced, as shown in Fig. 8. Their values become close to zero, except for the described setting of UL close to the response beginning. It is worth mentioning that the noise subtraction technique is sensitive to accuracy of calculation of noise mean-square value. Thus, the reduction in influence of noise is dependent on this accuracy.

On the other hand, the consequence of finite integration UL in SPL determination leading to the inaccuracy is that the part of response energy from UL up to infinity is not included in the calculation. The loss of this part of energy can be offset by adding compensation energy to the energy calculated in the range from zero up to the UL. Multiplying the exponential decay term from Eq. (2) by the coefficient B representing the energy density at the zero point, the general expression for squared RIR without random processes and noise becomes $Be^{-kt/T}$. The compensation energy can be now calculated by

$$E_c=B\int_{t_{ul}}^{\infty}e^{-k\tau/T}\,d\tau=B\frac{T}{k}e^{-kt_{ul}/T}=-\frac{B}{A}e^{At_{ul}}, \tag{12}$$

where A is coefficient given by $A=\ln(D/B)/t_{ul}$, and D is the energy density at t_{ul} known as the mean noise energy density. The term energy density used for B and D means "temporal density, which is calculated by integrating over short time intervals."[2] In practice, the fluctuations of RIR can cause inaccuracy of the compensation energy calculation, so that this energy differs from the true loss.

In order to use RIR as long as possible for investigations of implementation of finite UL compensation, first the noise subtraction is implemented, and then finite UL compensation. In this way, correct implementations of these techniques should theoretically lead to level deviations equal to zero. However, when the integration UL is placed too close to the response beginning (up to 0.1 s from the beginning), the compensation energy is calculated with significant inaccuracy. This inaccuracy and the mentioned increased influence of fluctuations due to the smaller integration range cause level deviations that significantly vary from zero for UL placed close to the response beginning, as shown in Fig. 9. If the UL is placed far enough from the response beginning (after 0.1 s), the inaccuracy of compensation energy calculation is smaller and the level deviations tend to be approximately equal to zero. Beside being dependent on the UL, the accuracy of compensation energy calculation is dependent on the time range used for calculation of coefficients B and D as well. This range should not be too small due to the influence of response fluctuations, but it should also not be too big due to the decay of RIR energy.

VII. CONCLUSIONS

The integration over squared room impulse response (RIR) up to a finite upper limit (UL) in SPL determination leads to deviation of the calculated level from the right value. The investigations of the influences of both finite UL and noise performed here show that if the appropriate point of the response is set as UL, the level deviation is acceptably small. This appropriate point can be $T/3$ or $T/4$ for RIRs with sufficiently small noise floors—smaller than -20 or -15 dB. For RIRs with higher noise floors, it is better to displace UL toward the response beginning. The reason for this is that the calculated level can be considerably higher than the right level if the UL is placed at the part of response where the noise is dominant.

One general solution for UL setting, which can be implemented in RIRs with various noise floors, is to place the UL at the knee. This UL leads to relatively small level deviation, typically less than a decibel. However, for even smaller level deviation (tending toward zero), the integration UL should be placed at the point somewhat before the knee called the optimal UL. It is distant from the RIR beginning by a constant fraction of the interval to the knee. The investigations have shown that this constant should take the value of about 0.7 for RIRs with exponential decays. By implementation of the mentioned conclusions, SPL can be determined precisely enough from the RIRs with various noise floors, even with relatively high noise floors.

Another approach in reducing or even eliminating the influences of noise and finite UL relates to additional processing including noise subtraction and finite UL compensation. The noise subtraction is an efficient technique, enabling significant reduction of inaccuracy in SPL determination due to the noise. With the implementation of this technique, the UL can be set even at the end of response independently of noise floor, or the above mentioned approach for UL setting in responses with small noise floors can be applied. On the other hand, finite UL compensation is rather sensitive to the place where the UL is set in the response, and on the response fluctuations. Due to this, finite UL is correctly compensated only if UL is distant enough from the response beginning (e.g., 0.1 s). Thus, more care should be given to the implementation of finite UL compensation, especially if UL is placed too close to the response beginning. Beside the investigated influences, other factors such as non-exponential decay or non-stationary noise can influence the inaccuracy in SPL determination, and they can be the subjects of further study.

[1] J. S. Bradley and G. A. Soulodre, ''Objective measures of listener envelopment,'' J. Acoust. Soc. Am. **98**, 2590–2597 (1995).

[2] A. Lundeby, T. E. Vigran, H. Bietz, and M. Vorlander, ''Uncertainties of measurements in room acoustics,'' Acustica **81**, 344–355 (1995).

[3] D. G. Ćirić, ''Determination of Room Acoustical Quantities by Implementation of MLS Technique'' (in Serbian), Master's thesis, Faculty of Electronic Engineering, Niš, Yugoslavia (2000).

[4] W. Zuomin and W. T. Chu, ''Ensemble average requirement for acoustical measurements in noisy environment using the m-sequence correlation technique,'' J. Acoust. Soc. Am. **94**, 1409–1414 (1993).

[5] W. T. Chu, ''Impulse-response and reverberation-decay measurements made by using a periodic pseudorandom sequence,'' Appl. Acoust. **29**, 193–205 (1990).

[6] M. Vorlander and M. Kob, ''Practical aspects of MLS measurements in building acoustics,'' Appl. Acoust. **52**, 239–258 (1997).

[7] M. Vorlander and E. Mommertz, ''Guidelines for the application of the MLS technique in building acoustics and in outdoor measurements,'' Proc. Inter-noise 97, 1423–1428 (1997).

[8] J. Borish and J. B. Angell, ''An efficient algorithm for measuring the impulse response using pseudorandom noise,'' J. Audio Eng. Soc. **31**, 478–487 (1983).

[9] M. A. Milošević and D. G. Ćirić, ''Improvement of dynamic range of sound energy decay in room,'' Facta Universitatis, ser. Work. Liv. Env. Prot. **1**, 55–63 (1999) (available from University of Niš, Yugoslavia).

[10] D. R. Morgan, ''A parametric error analysis of the backward integration method for reverberation time estimation,'' J. Acoust. Soc. Am. **101**, 2686–2693 (1997).

[11] W. T. Chu, ''Comparison of reverberation measurements using Schroeder's impulse method and decay-curve averaging method,'' J. Acoust. Soc. Am. **63**, 1444–1451 (1978).

Judgments of noticeable differences in sound fields of concert halls caused by intensity variations in early reflections

Toshiyuki Okano
Takenaka Research and Development Institute, 1-5-1, Ohtsuka, Inzai, Chiba 270-1395, Japan

(Received 12 April 2000; revised 24 September 2001; accepted 12 October 2001)

In concert halls early reflections combine with the direct sound and with reverberation to determine the subjective rating of a room's acoustics. Of interest is how variations in the amplitudes of these early reflections are related to the subjectively just-noticeable differences (jnd) in several important acoustical parameters for their wide range encountered in existing halls. Investigated were four subjective parameters, apparent source width (ASW), loudness, intimacy and clarity, which are related to the physical measurements, [$1-\mathrm{IACC}_{E3}$], G, ITDG, and C_{80}, defined mathematically in Beranek [*Concert and Opera Halls: How They Sound* (Acoustical Society of America, New York, 1996)]. Forty-eight types of sound fields were chosen in which to make variations in the amplitudes of early reflections and were reproduced electro-acoustically by multiple loudspeakers in an anechoic chamber. The results indicate that ASW and loudness are more sensitive to changes in the levels of early reflections, and were the primary parameters investigated. Although the number of subjects available with enough experience in listening classical music is limited and the measured jnd is an initial estimation, the jnd of [$1-\mathrm{IACC}_{E3}$] is measured as 0.065 ± 0.015 in variations of sound field structures and the jnd of G was measured as 0.25 ± 0.15 dB, which is consistent with the results of previous studies. [DOI: 10.1121/1.1426374]

PACS numbers: 43.55.Fw, 43.55.Gx, 43.55.Hy [JDQ]

I. INTRODUCTION

At a listener's position in a concert hall, early reflections of the musical sound combine with the direct sound to create a major overall subjective impression that includes the quality of the musical performance and the quality of the acoustics of the hall, added to which is reverberation, another element that influences overall subjective impression. In the acoustical design of a concert hall, reflecting surfaces can be adjusted or augmented to vary the intensity of the reflections; thus, the need arises to know the significance of the difference in their intensity. Also, in simulations of musical sound fields knowledge of the accuracy of reflected sound levels is necessary. Serahim (1961, 1963) and Schubert (1969) investigated the minimum audible level of an early reflection for speech and musical signals. However, the size of the noticeable change in their intensities was not considered. Reichardt *et al.* (1967) measured the just-noticeable difference (jnd) for intensity variations in a single early reflection. The result suggested that the size of the jnd is related to the level of the reflection relative to its minimum audible level. This implies that a complex scheme is needed to determine the jnd, involving as parameters the minimum audible level with its delay, angle of incidence, and relationships to other reflections.

Between 1967 and 1995, a series of studies developed such physical measures as clarity index (C_{80}), loudness index (G), lateral energy fraction (LF), and interaural cross-correlation coefficient (IACC) that correlate with various perceived attributes of a sound field. C_{80} was developed by Reichardt *et al.* (1975) and Reichardt and Lehmann (1981); G by Lehmann (1976) and Barron and Lee (1988); LF by Barron (1971) and Barron and Marshall (1981); IACC by Keet (1968), Schroeder *et al.* (1974), Ando (1977), Hidaka *et al.* (1995), and Morimoto *et al.* (1995). Especially, Barron (1971) pointed out the necessity for significant levels of lateral reflections in concert halls and their contribution to enlarge "apparent source width" (ASW), an important subjective attribute of acoustical quality. Thus, the jnd in intensity variation in early reflections appears to be strongly connected to the ASW discrimination.

Cox *et al.* (1993) determined jnd values for changes of level in the first lateral reflection of a sound field which simulated that of a hall precisely. The results were converted to jnd values in LF and IACC. Those measures certainly correlate with ASW or "spatial impression" (SI), although the choice of whether to use LF or IACC differs among researchers. Cox *et al.* stated that the intensity variation in the first lateral reflection is more sensitively perceived by the difference in SI than any other attributes, but, their test sound field was limited to only one specific case. In this paper, a further goal is to confirm this finding in other types of sound fields. For example, in some halls the ceiling contributes the first reflection and may affect the perception of the lateral reflections that follow. Differences in the composition of a sound field might lead to different results.

Morimoto *et al.* (1995) determined the jnd of the interaural cross-correlation coefficient and found that its Weber's fraction is within a specific range from 0.2 to 0.3 for test sound fields with values of [1-IACC] from 0.1 to 0.5. However, their test sound field is limited to only two lateral reflections and to somewhat higher values of interaural cross-correlation coefficient than measured in actual concert halls. From the result of Cox *et al.*, Weber's fraction is calculated to be 0.11 for the reference sound field for [1-IACC] with a value of 0.67. It is necessary to confirm the findings for a wide range of conditions that corresponds to those in existing halls, in order to bridge the results of the two studies above.

Cox *et al.* also determined the jnd of the center time (Tc) and C_{80} as measures of clarity by varying the delay of early reflections and by varying the level and the starting delay of reverberation. Here, the effect of intensity variations of early reflections on clarity is a matter of interest. Although enlargements of an early reflection seem to increase the clarity from the definition of C_{80}, their experiment was not designed to include this case. In addition, their study did not cover the jnd of G that is also connected with the intensity variation in early reflections.

In a prior study, Okano (1993) made preliminary probes of the accuracy of early reflected sound levels in sound-field simulation, but at that time the relations between ASW and its measures were not always confirmed in a variety of sound fields. Subsequently, Hidaka *et al.* (1995) and Okano *et al.* (1998) found that the physical quantity $[1-\mathrm{IACC}_{E3}]$ as well as the low-frequency sound levels (G_{Elow} and its surrogate G_{low}, where G_{Elow} is a value in the early 80-ms part of an impulse response) was highly correlated with ASW and was an effective parameter in evaluating the acoustical quality of concert halls. IACC_{E3} is defined as the arithmetic average of interaural cross-correlation coefficients in the three octave bands with midfrequencies 500, 1000, and 2000 Hz obtained from the early 80-ms part of the binaural impulse responses of a sound field. This measurement was also found to be vitally important in the evaluation of opera houses (Hidaka and Beranek, 2000b). Recently, Okano (2000) reported on shifts in subjective image position in dependence on the amplitudes of very strong lateral reflections.

This study is intended to determine the jnd of relevant attributes of sound fields and their measures, in relation to intensity variations of early reflections, considering a variety of sound fields like those found in existing concert halls.

II. EXPERIMENTAL DESIGN

A. Listening test procedures

Test sound fields were electro-acoustically produced in an anechoic chamber with the multiple loudspeaker system shown in Fig. 1. The loudspeaker facing the subject produces the direct sound and the others produce the simulated reflections. Reverberant sound was supplied from four loudspeakers with elevation angles of 45° and horizontal angles of ±45° and ±135°. All loudspeakers are placed at 2 m from the subject.

A musical signal taken from the first four bars of the first movement of Mozart's 14th string quartet was recorded in an anechoic chamber. In the tests this signal was passed through various time-delay and amplitude controls to the various loudspeakers. Each signal combination was fed into the multiple loudspeaker system repeatedly. The Mozart musical motif was selected because in this experiment the direct sound is radiated from a central loudspeaker. A small performing group is closer in size to that type of sound source than an orchestra.

For each test, a subject compared two sound fields, one fixed and the other controlled by the subject: The fixed field was one of the reference fields to be described in Table I and

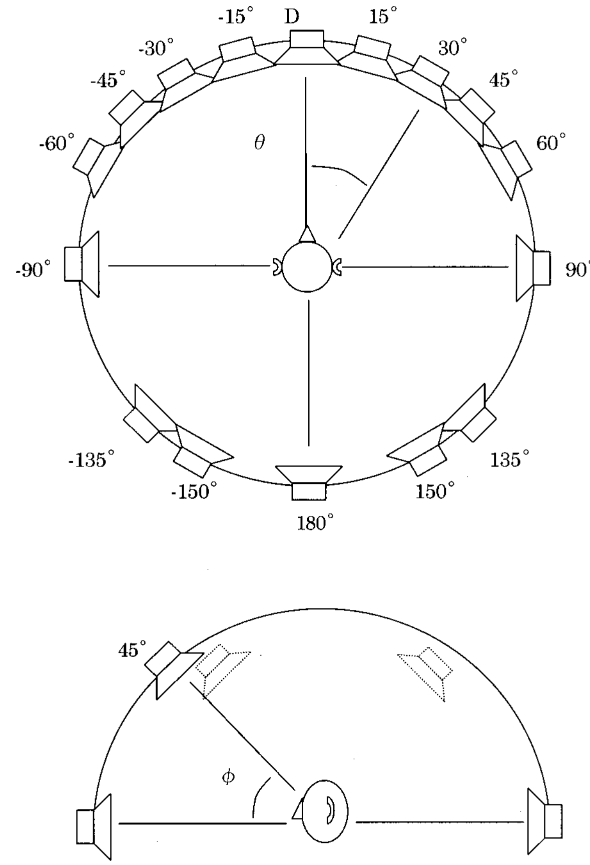

FIG. 1. Arrangement of multiple loudspeakers used for the listening test. Loudspeaker D radiates the direct sound and the subject always faces it. Other loudspeakers radiate early lateral reflections with different time delays and angles of incidence. The reverberant sound field is radiated from four loudspeakers placed at $\phi=45°$, $\theta=\pm45°$ and $\pm135°$.

the other was the same type of field, except that the amplitude(s) of one (or two, four) of the reflection(s) was/were under the control of the subject. The following is a typical procedure for type 1: Assume the reference field was N4R2 (Table I, 2nd column of series A). Each subject was instructed, before the first presentation, to compare the reference field with the trial field and to judge whether they were "different" or "same." This procedure of judgment is the same as that of Seraphim (1961, 1963), Schubert (1969), and Reichart *et al.* (1967), in which the absolute threshold level or the jnd in intensity variation of a reflection was measured. A further judgment was required here: if the two signals being compared sounded "different," (s)he was asked to name which attribute(s) seem to have changed when switching from one field to the other. There is a possibility that the subject might tend to name the difference incorrectly when several attributes changed simultaneously; for example, a change in ASW might be taken for a change in loudness. In order to minimize such confusion, the subject was asked to switch between the sound fields again and again until (s)he had confidence in naming the changed attribute. Actually, subjects repeated the switching many times in most of the judgments. Also, to minimize the confusion in naming, each presentation started with a distinct difference in the two signals.

At the beginning of each comparison (see Fig. 2), the

TABLE I. List of the direct sound and early reflections in relation to each reference sound fields. θ: azimuth angle, ϕ: elevation angle, ●: fixed components, ○: variable reflections.

Attributes of reflections					Name of reference sound fields															
			Angle of incidence		Series A				Series B								Series C			
Name	Delay (ms)	Amplitude	θ	ϕ	N4R2F	N4R2	N4R2N	N4C1	N1R1	N2R2	N8R2	N8A2	N8A4	N16R2	N16A2	N16A4	F4A2F	F4A2	F4A2N	F4C1
D1	0	0.71	0	0	●												●			
D2	0	1.00	0	0		●		●	●	●	●	●	●	●	●	●		●		●
D3	0	1.41	0	0			●												●	
W1	16	0.79	−30	0	○	○	○	●		○	○	●	●	○	●	●				
W2	20	0.75	30	0	○	○	○	●	○	○	○	●	●	○	●	●				
W3	23	0.72	−15	0										●	●	●				
W4	27	0.69	−60	0							●	○	○	●	○	○	○	○	○	●
W5	30	0.66	60	0							●	○	○	●	○	○	○	○	○	●
W6	33	0.64	15	0										●	●	●				
W7	46	0.56	45	0										●	●	●				
W8	64	0.48	−45	0										●	●	●				
W9	75	0.44	−90	0										●	●	●				
W10	78	0.43	90	0										●	●	●				
C1	20	0.75	0	45													●	●	●	○
C2	40	0.60	0	45	●	●	●	○			●	●	●	●	●	●				
C3	55	0.50	−45	45							●	●	○	●	●	○				
C4	60	0.52	45	45							●	●	○	●	●	○				
R1	50	0.54	180	0										●	●	●				
R2	70	0.46	150	0										●	●	●				
R3	80	0.42	−150	0	●	●	●	●			●	●	●	●	●	●	●	●	●	●

trial field was set to be very different from the reference field, i.e., 16 dB on the attenuator. This was expected to give a "different" response. After the subject's statement and naming, the attenuator was next changed from 16 to 8 dB and the subject made a new response. Assume that this response is also "different." Then, the attenuator was changed to "0" dB and the subject was expected to say "same." After that, the attenuator setting was increased to 4 dB and if the comparison was judged "different," the subject again named which, if any, of the attributes had changed. If the 4 dB setting was judged "same," the attenuator was increased to 8 dB. If the 4-dB setting was "different," the attenuator was set to 2 dB. Then succeeding tests were run with successively smaller changes in the attenuator until the difference between "different" and "same" responses was down to ±0.5 dB around some attenuator setting.

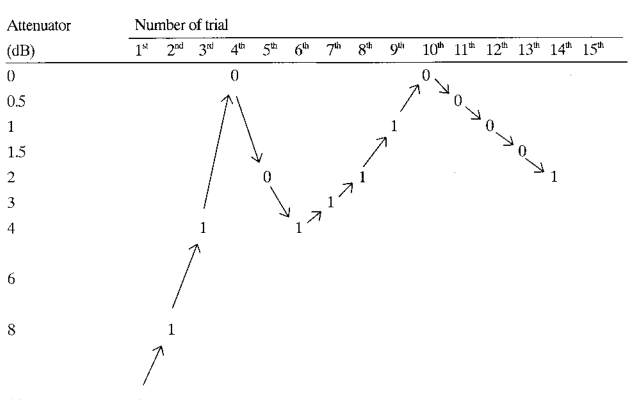

FIG. 2. A typical procedure of the listening test assuming the reference sound field N4R2 for type 1. The figure "0" indicates the judgment "same" and "1" indicates the judgment "different." Whenever the subjects judged "different," they were asked to name the subjective attributes of sound field they thought had been varied.

Whenever the subjects indicated a difference between a pair, they were asked to name the subjective attributes of the sound field they thought had been varied. Seven attributes were given to them as possibilities: "ASW," "envelopment," "loudness," "intimacy," "clarity," "timbre," and "echo disturbance." These attributes are often used to evaluate the acoustical quality of concert halls. The subjects were instructed to direct their attention to all seven of the attributes.

B. Test sound fields

The reference sound fields are listed in Table I. Included in each are the direct sound, discrete "reflected" components between 16 and 80 ms after the arrival of the direct sound, and the reverberation starting at 100 ms. The structure of the sound fields were selected as typical for two shapes of concert halls. Those test fields that have names starting with N in series A and B are for a shoebox-shaped hall and have a first reflection that is lateral. Those starting with F in series C are for a fan-shaped hall and have a first reflection that comes from in front (the ceiling). All of the sound fields in series A and C have four early reflections as their components. Series B shows variations in the number of early reflections of one, two, eight, and 16 including the fixed and the variable ones. The number of reflections is identified by the figures following the starting letters of N or F in the name of each test sound field, i.e., N8R2 means a shoebox-shaped hall with eight reflections—"R" and "2" are defined below.

D1, D2, and D3 are three possible direct sounds with amplitudes of 0.71, 1.0, and 1.41, respectively. This variation is related to the distance separating the source and the receiver during corresponding field measurements. The amplitudes of reflections do not vary as much. The name of reference sound fields having D1 as the direct sound is identified by a letter F and the name of those having D3 is identified by the letter N at the end. It means the ''listener's'' position in a concert hall would be ''far'' or ''near'' from the source compared to the normal amplitude of the direct sound:D2. The normal direct sound D2 assuming the distance between the source and the receiver would be 20 m. It approximates the distance from the center of a stage to the middle of an audience area in regular symphony halls. W1 to W10 indicate reflections from side walls; C1 to C4 reflections from *c*eilings; R1 to R3 reflections from *r*ear walls. Each reflection has associated with it a direction (depending on the loudspeaker), and a delay time and an amplitude determined by the length of the path traveled (see columns 2 and 3). No loss is assumed at the reflecting surface.

In Table I, the filled circles indicate components fixed in level, while the open circles indicate those whose amplitudes were simultaneously varied during the comparisons. Three types of variations are denoted by the second alphabetical letter in the names of reference sound fields. Those are, lateral reflections including the first reflection (R), lateral reflection excluding the first reflection (A), and a ceiling reflection (C). The number of variable reflections is identified by the figures following the letters. The reverberation time for each reference signal was 2.0 s except for N4R2F, N4R2, N4R2N, and F4A2, each of which had three possibilities in reverberation time, namely, 1.2, 1.6, and 2.0 s.

For each of the named signals (e.g., N8R2) there were two reference types: type 1 was for a *reference signal* for which the open circles were set to the levels in column 3 of Table I. For the comparison signal the subject could decrease the levels of the open circles by varying the numbers of decibels. *Type 1 was to determine the minimum audible variation in the amplitude(s) of the open-circle reflection(s)*. Thus, including the variation in reverberation times, 24 reference sound fields were used during type 1 tests.

Type 2 was for a *reference signal* with the open circles in Table I set to zero level. For the comparison signal the subject could increase the level of the open circles above zero by some number of decibels. *Type 2 was to determine minimum audible levels of the open-circle reflections*. Here, also, 24 reference sound fields were employed.

C. Physical measures of the test sound fields

Measured values for the principal parameters (e.g., RT, G,...) for each of the reference sound fields are listed in Table II. Each value for RT is an average value for two 1/1-octave bands with midfrequencies of 500 and 1000 Hz. Bass ratio (BR) was set at 1.0. Bradley and Soulodre (1997) found that a wide range of BRs has no effect on a subject's judgments of bass content. The reverberation times at the higher frequencies were decreased so as to simulate the air absorption effect. The values for G and C_{80} were measured by wideband pink noise. G and G_{Elow} are levels in dB relative to the level of the direct sound at 10 m from source in a free field. $[1-IACC_{E3}]$'s are derived from the measured binaural impulse responses using a dummy head at the listener's position. The values for initial-time-delay gap were read from the impulse responses.

The range among the test sound fields for those acoustical measures are: 2.0 to 1.2 s for RT; -1.0 to 3.7 dB for G; -6.1 to 1.0 dB for G_{Elow}; 0.02 to 0.91 for $[1-IACC_{E3}]$; and -5.7 to 2.0 dB for C_{80}; 16 to 40 ms for the initial-time-delay gap. Among existing halls, the values for those measures are approximately: 2.2 to 1.2 s for RT; 0 to 8 dB for G; -5 to -3 dB for G_{Elow}; 0.41 to 0.71 for $[1-IACC_{E3}]$; and -4 to 2.0 dB for C_{80}. The numbers are hall averages for the occupied RT condition and for the other parameters the halls were unoccupied (Beranek, 1996; Okano *et al.*, 1998). The values of the parameters for the occupied condition are expected to be approximately 2 dB lower for G, unchanged for $[1-IACC_{E3}]$, and 2 dB higher for C_{80} than those in the unoccupied condition, taken from existing concert hall data (Hidaka *et al.*, 2000a). The difference in G_{Elow} between the occupied and unoccupied condition is not expected to be as large as that for G because the early part of the impulse response should be less influenced by occupancy, similar to that found for $[1-IACC_{E3}]$. Beranek (1996) showed that the values for initial-time-delay gap for existing halls lie between 12 and 40 ms. Thus, these test sound fields have ranges in values close to those found among existing occupied halls.

D. Analysis of the subjective responses

When the subjects heard a difference between the paired signals, they named which of the seven subjective attributes of the sound fields they felt had changed. Envelopment and echo disturbance seldom were named. They confirm the knowledge that envelopment and echo disturbance relate primarily to late-arriving sounds. The attribute of timbre was named for more than half of the reference sound fields for type 1 by a subject, while other subjects rarely named it. For the test sound fields for type 2, another subject named timbre in many of the test sound fields, while others rarely named it. As a result, timbre was not reliably selected as a common perception among subjects. There was no suggestion that the test sound fields had acoustical defects such as echo disturbance and distinct coloration by the intensity variation in the early reflections. Thus, the four attributes ASW, loudness, intimacy, and clarity were found to be related to intensity variations in the early reflections.

The ''subjective responses'' in Table III are related to the ''attenuation of the variable reflections in dB,'' and indicate a part of the whole results showing the data for some reference sound fields for type 1, in the following ways: In the third column, ''0'' dB corresponds to the reference sound field, for which the variable reflections were at full amplitude. Note that for type 2, attenuation of ''∞'' dB corresponds to the reference sound field. Let us take N4R2 with an RT of 2.0 s as an example. When the attenuation was 1 dB, all judgments were ''same.'' For 2 dB, the parameter ASW was judged ''different.'' For each attenuation, at least four judgments were required when the judgment was very easy. When the

TABLE II. Measured values for acoustical parameters in each reference sound field.

Name of sound field	Att. in variable reflections (dB)	Acoustical parameters of sound field					
		RT (s)	G (dB)	G_{Elow} (dB)	$1—IACC_{E3}$	C_{80} (dB)	Δt_1 (ms)
			Series A				
N4R2F	0	2.0	1.5	−3.0	0.70	−2.5	16
	∞	2.0	0.6	−5.9	0.02	−5.7	40
	0	1.6	0.9	−3.0	0.70	−1.5	16
	∞	1.6	−0.1	−5.9	0.02	−4.7	40
	0	1.2	0.3	−3.0	0.70	−0.3	16
	∞	1.2	−1.0	−5.9	0.02	−3.5	40
N4R2	0	2.0	1.9	−1.9	0.58	−1.5	16
	∞	2.0	1.1	−4.4	0.02	−3.9	40
	0	1.6	1.4	−1.9	0.58	−0.5	16
	∞	1.6	0.4	−4.4	0.02	−2.9	40
	0	1.2	0.8	−1.9	0.58	0.7	16
	∞	1.2	−0.4	−4.4	0.02	−1.7	40
N4R2N	0	2.0	2.5	−0.6	0.42	−0.3	16
	∞	2.0	1.8	−1.8	0.02	−1.8	40
	0	1.6	2.0	−0.6	0.42	0.7	16
	∞	1.6	1.2	−1.8	0.02	−0.8	40
	0	1.2	1.5	−0.6	0.42	1.9	16
	∞	1.2	0.6	−1.8	0.02	0.4	40
N4C1	0	2.0	1.9	−1.9	0.58	0.7	16
	∞	2.0	1.7	−2.9	0.63	−2.0	16
			Series B				
N1R1	0	2.0	1.1	−3.9	0.38	−3.8	20
	∞	2.0	0.7	−6.0	0.02	−5.6	∞
N2R2	0	2.0	1.6	−3.2	0.65	−2.4	16
	∞	2.0	0.6	−6.0	0.02	−5.7	∞
N8R2	0	2.0	2.7	−0.4	0.83	0.2	16
	∞	2.0	2.0	−2.0	0.73	−1.3	27
N8A2	0	2.0	2.7	−0.4	0.83	0.2	16
	∞	2.0	2.2	−1.2	0.65	−0.8	16
N8A4	0	2.0	2.7	−0.4	0.83	0.2	16
	∞	2.0	2.0	−1.9	0.60	−1.4	16
N16R2	0	2.0	3.7	1.0	0.91	2.0	16
	∞	2.0	3.3	0.1	0.84	1.2	23
N16A2	0	2.0	3.7	1.0	0.91	2.0	16
	∞	2.0	3.4	0.7	0.84	1.5	16
N16A4	0	2.0	3.7	1.0	0.91	2.0	16
	∞	2.0	3.3	0.4	0.81	1.2	16
			Series C				
F4A2F	0	2.0	1.4	−3.7	0.62	−3.0	20
	∞	2.0	0.6	−5.6	0.02	−5.7	20
F4A2	0	2.0	1.8	−2.3	0.57	−1.9	20
	∞	2.0	1.1	−4.1	0.02	−3.8	20
	0	1.6	1.2	−3.3	0.57	−0.9	20
	∞	1.6	0.4	−4.1	0.02	−2.8	20
	0	1.2	0.6	−3.3	0.57	0.3	20
	∞	1.2	−0.3	−4.1	0.02	−1.6	20
F4A2N	0	2.0	2.4	−1.0	0.45	−0.5	20
	∞	2.0	1.9	−1.8	0.02	−1.6	20
F4C1	0	2.0	1.8	−2.3	0.57	−1.9	20
	∞	2.0	1.6	−2.8	0.69	−2.4	27

judgments were 50%–50%, about seven to ten responses were obtained in most of the cases. When the percentage of ‘‘different’’ judgments was 50% or higher, the two signals were judged ‘‘different.’’ When the percentage of different judgments was less than 50%, the two signals were judged ‘‘same.’’ For each of the ‘‘different’’ judgments, the subjects were asked which ones of the indicated subjective attributes were affected. In the N4R2 example, a 3-dB attenuation resulted in differences in loudness, ASW, and intimacy.

In type 1, an attenuation of 4 dB or greater usually caused differences in three of the four attributes. The subjective attribute ‘‘clarity’’ was hardly ever affected in this type.

In type 2, differences in three of the four attributes first occurred sometimes at an attenuation of 12 dB, sometimes at

TABLE III. Examples of subjective responses and measures of sound fields in reference sound fields and their variations, full amplitude of variable reflections as a reference (type 1). The reference sound fields are identified by the letters ''Ref.'' denoted in the right of attenuation values in the third column.

Name of reference sound field	Reverberation time (sec)	att. in variable reflections (dB)		Subjective responses				Strength G (dB)	Low-frequence sound level G_{Elow}	Interaural cross correlation coefficient				Clarity index C_{80} (dB)
										1-$IACC_E$				
				Loudness	ASW	Initmacy	Clarity			3B	500 Hz	1000 kHz	2000 kHz	
N4R2	2.0	0	Ref.	0	0	0	0	1.9	−1.9	0.58	0.43	0.71	0.59	−1.5
		1		0	0	0	0	1.8	−2.3	0.52	0.39	0.65	0.52	−1.9
		2		0	1	0	0	1.6	−2.7	0.46	0.35	0.57	0.45	−2.3
		3		1	1	1	0	1.5	−3.0	0.40	0.31	0.50	0.39	−2.6
		4		1	1	1	0	1.4	−3.2	0.35	0.27	0.44	0.34	−2.8
		8		1	1	1	0	1.3	−3.9	0.19	0.15	0.23	0.18	−3.5
N4R2	1.6	0	Ref.	0	0	0	0	1.4	−1.9	0.58	0.43	0.71	0.59	−0.5
		1		0	0	0	0	1.2	−2.3	0.52	0.39	0.65	0.52	−0.9
		2		0	1	0	0	1.0	−2.7	0.46	0.35	0.57	0.45	−1.3
		3		1	1	1	0	0.9	−3.0	0.40	0.31	0.50	0.39	−1.6
		4		1	1	1	0	0.8	−3.2	0.35	0.27	0.44	0.34	−1.8
		8		1	1	1	0	0.6	−3.9	0.19	0.15	0.23	0.18	−2.5

8 dB, and sometimes at 4 dB. The attribute clarity was affected only for large signal levels (smaller attenuator settings).

E. Subjects

Three subjects participated in the actual experiment. Two were musicians and the third was an acoustical engineer. All had normal hearing ability and had heard musical sounds at real concerts many times. In addition, all were trained, by participation in a pre-experiment period, to understand the meaning of each subjective attribute and to become accustomed to making the judgments. Each subject went through the above procedure twice for each reference sound field. Unfortunately, the number of subjects is small because of the difficulty in finding a greater number of subjects who were professionally related to hearing musical sounds. Two other persons with normal hearing ability tried the test. They were not musical instrument players, nor regular concert listeners. It seemed difficult for them to make confident and consistent responses during a pre-experiment period. They did not participate in the actual experiments. Consequently, as in Cox *et al.* (1993), all subjects were selected from a group of instrument players and regular concert listeners.

Because of the small numbers of subjects, differences among the response of each subjects, with respect to each of the four attributes of sound fields, were determined and are tabulated in Table IV. Those values indicate the deviation of each subject from the averaged response of the three in the amount of attenuation in decibels at which the rate of ''different'' judgment is 50%. A positive value means that the subject needs a larger difference between test sound fields to discriminate. Subject J was more sensitive and subject I was less sensitive in ASW, loudness, and intimacy compared to the average. For the clarity judgment, subject J was less sensitive and subject T was more sensitive. This result shows that the rank in sensitivity does not differ significantly among subjects at least for the attributes of ASW, loudness, and intimacy. The range of deviations among subjects in the attenuator values is ±0.9 dB in ASW, ±0.6 dB in loudness, ±1.1 dB in intimacy, and ±1.6 dB in clarity. These values correspond approximately to the ranges of the acoustical measures, ±10% in $IACC_{E3}$ for $IACC_{E3}$ of 0.5 or smaller, ±0.05 in $IACC_{E3}$ for $IACC_{E3}$ of 0.5 or larger, ±0.1 dB in G, and ±0.4 dB in C_{80}. The addition of further numbers of subjects would lead to more reliable averages of the jnd among listeners. However, the ranges of deviation in the acoustical measures derived here indicate that the data give an initial estimation that should apply to a larger group of regular concert listeners.

III. THE RANK ORDER IN SENSITIVITY AMONG ATTRIBUTES OF SOUND FIELDS IN JUDGMENT

The ranks in sensitivity among subjective attributes were derived from the analyzed subjective responses (See Table III for two examples). Among the four attributes, the most sensitive one is that judged ''different'' with the smallest variation in attenuator setting from the attenuator setting for the reference sound field. That is to say, it was determined to be the first attribute for the discrimination between the sound fields. Sometimes two or more attributes were determined to be the first attributes for the same reference sound field because the step in attenuation is not small enough to distinguish them. The second, third, and fourth attributes were

TABLE IV. Difference in responses among subjects. The attenuation values in decibel are indicated at which the rate of ''different'' judgment is 50% with respect to each attribute of the sound fields, relative to the averaged value for the three subjects. The positive values indicate that the subject needs larger difference to discriminate the sound fields than the average.

Subject	Attributes of sound fields			
	ASW	Loudness	Intimacy	Clarity
J	−0.8	−0.7	−1.3	+1.6
I	+1.0	+0.4	+0.9	−0.1
T	−0.1	+0.1	+0.4	−1.5

TABLE V. Rank order of the subjects' sensitivity to the four attributes of the sound fields. The number of reflections is fixed at four (series A and C) and the parameters are (1) the type of the first reflection (lateral) and the type of variable reflections (lateral, including a lateral reflection first); (2) the type of first reflection (ceiling) and the type of variable reflections (lateral, but excluding the first lateral); (3) the type of first reflection (lateral) and the type of variable reflections, (ceiling reflection, but a ceiling reflection was not first); (4) the type of first reflection (ceiling) and the type of variable reflections (ceiling, but with a ceiling reflection first). When the levels of the early reflections (indicated in Table I) are varied the values indicated here show the percentage of reference fields that the subjects judged the attribute to correspond to. Provided the values were 50% or greater, the bold figures indicate the highest percentage among the different rank orders for each of the four attributes. The maximum ranges in the acoustical measures between paired sound fields within this table are 0.6 for $[1-\mathrm{IACC}_{E3}]$; 1.0 dB for G; 2.6 dB for C_{80}; and 24 ms for initial-time-delay gap.

Type of the first reflection	Lateral				Ceiling			
Type of variable reflections	Lateral, including the first				Lateral, excluding the first			
	Attributes of sound field				Attributes of sound field			
Order in sensitivity	ASW	Loudness	Intimacy	Clarity	ASW	Loudness	Intimacy	Clarity
1st	**100%**	44%	**50%**		**100%**	40%		
2nd		**50%**	33%			**60%**	20%	
3rd		6%	17%	11%			**70%**	
4th				44%				10%
No difference				44%			10%	**90%**
Type of the first reflection	Lateral				Ceiling			
Type of variable reflections	Ceiling, not the first				Ceiling, the first			
	Attributes of sound field				Attributes of sound field			
Order in sensitivity	ASW	Loudness	Intimacy	Clarity	ASW	Loudness	Intimacy	Clarity
1st	50%	50%			50%		**100%**	
2nd						50%		
3rd								
4th								
No difference	50%	50%	**100%**	**100%**	50%	50%		**100%**

determined according to the order in sensitivity in discriminating the pairs of sound fields. When the judgment does not fall under ''different'' in any attenuation tested, that attribute is named ''no difference'' from that of the reference sound field.

Table V shows the results for the reference sound fields composed of the direct sound and four early reflections with the types of the first reflection and variable reflections as parameters. When the lateral reflections are the variable, ASW is always the most sensitive attribute among the four. Intimacy follows ASW for the sound fields for which the first reflection is included in the variables. When the first reflection is fixed, changes in intimacy are not found to be as sensitive regardless of whether the first reflection is from the lateral or ceiling. Loudness is not influenced by the type of variable reflections. Clarity is less sensitive than the others in any type of first reflection and variable reflection.

Table VI shows the same type of results for the reference sound fields having eight and 16 early reflections. Here, ASW is always the most sensitive attribute, followed by loudness. The order of intimacy is lower compared to the results with four reflections in Table V. However, intimacy

TABLE VI. Rank order of the subjects' sensitivity to the four attributes of the sound fields. The number of reflections is fixed at eight or 16 (series B) and the parameters are (1) the type of the first reflection (lateral) and the type of variable reflections (including the first reflection) and (2) same, but (excluding the first reflection). When the levels of the early reflections (indicated in Table I) are varied, the values indicated here show the percentage of reference fields that the subjects judged the attribute to correspond to. Provided the values were 50% or greater, the bold figures indicate the highest percentage among the different rank orders for each of the four attributes. The maximum ranges in the acoustical measures between paired sound fields within this table are 0.18 for $[1-\mathrm{IACC}_{E3}]$; 0.8 dB for G; 1.8 dB for C_{80}; and 11 ms for initial-time-delay gap.

Type of the first reflection	Lateral				Lateral			
Type of variable reflections	Including the first reflection				Excluding the first reflection			
	Attributes of sound field				Attributes of sound field			
Order in sensitivity	ASW	Loudness	Intimacy	Clarity	ASW	Loudness	Intimacy	Clarity
1st	**100%**	50%			**100%**	50%	13%	13%
2nd		**50%**	**75%**			**50%**	13%	13%
3rd							13%	
4th				50%				
No difference			25%	50%			**61%**	**74%**

TABLE VII. Rank order of the subjects' sensitivity to the four attributes of the sound fields. The number of reflections is fixed at four (series A and C) and the parameters are (1) the level of the direct sound (−3 dB); (2) same, but (0 dB); and (3) same, but (3 dB). When the levels of the early reflections (indicated in Table I) are varied, the values indicated here show the percentage of reference fields that the subjects judged the attribute to correspond to. Provided the values were 50% or greater, the bold figures indicate the highest percentage among the different rank orders for each of the four attributes. The maximum ranges in the acoustical measures between paired sound fields within this table are 0.6 for $[1-\mathrm{IACC}_{E3}]$; 1.0 dB for G; 2.6 dB for C_{80}; and 24 ms for initial-time-delay gap.

Level of the direct sound	−3 dB				0 dB				+3 dB			
	Attributes of sound field				Attributes of sound field				Attributes of sound field			
Order in sensitivity	ASW	Loudness	Intimacy	Clarity	ASW	Loudness	Intimacy	Clarity	ASW	Loudness	Intimacy	Clarity
1st	**100%**	**75%**	**62%**		**100%**	25%	16%		**100%**	38%	25%	
2nd		25%	13%			**67%**	42%	17%		**62%**	12%	
3rd			25%			8%	42%				**51%**	
4th				50%				17%				38%
No difference				50%				**66%**			12%	**62%**

follows ASW and loudness, especially when the first reflection is variable (left block). Clarity is also less sensitive than the others.

Table VII shows comparison of the results with the level of the direct sound as a parameter. Here, the number of early reflections is fixed at four and the variables are always from the lateral. Two types of the first reflection, lateral and ceiling are included. ASW is the most sensitive for all the reference sound fields, followed in order by loudness, and then by intimacy. A tendency is observed that loudness and intimacy are more sensitive when the direct sound is faint. Clarity, again, is less sensitive than the others in any level of the direct sound.

Table VIII shows the same kind of comparison with RT as a variable. The number of early reflections is fixed at four and the variables are always from the lateral. The results are the same as above—the ASW is always the most sensitive, clarity is less sensitive than the others, and loudness and intimacy lie in-between. Here, it is observed that very short reverberation time of 1.2 s. makes loudness and intimacy easier to discriminate.

Table IX shows a comparison of the number of early reflections as a parameter. The level of the direct sound is fixed at 0 dB, reverberation time is fixed at 2.0 s, and the first reflection is always lateral and variable. Regardless of the number of early reflections, it is the same observation that ASW is always the most sensitive attribute, clarity is less sensitive than the others, and loudness and intimacy lie in-between.

The maximum variation in C_{80} for each reference sound field was 1.4 ± 0.5 dB for type 1 and 1.5 ± 1.0 dB for type 2. On average, they cover about twice as large a range of variation in C_{80} as the jnd values of 0.67 ± 0.13 dB derived by Cox *et al.* (1993) and 0.9 dB by Bradley *et al.* (1999). This range of variations in C_{80} compared to its jnd is significantly smaller than that in $[1-\mathrm{IACC}_{E3}]$ (about five times as large as jnd on average) or that in G (about four times as large as jnd an average). This fact shows that the same size of intensity variation in early reflections makes a more distinct difference in ASW or loudness than clarity. Consequently, change in clarity appears to be masked by the changes in other attributes of ASW or loudness when those attributes are varied simultaneously. Although the size of variation in C_{80} is almost the same between the test sound fields of type 1 and type 2, differences in clarity were observed only in two among 24 reference sound fields for type 1, while about half of the reference sound fields were the case for type 2. It suggests that contribution to clarity by the addition of new early reflections is larger than that by the reinforcement of early reflections by their levels even if the increment in C_{80} is the same. Further study would be necessary to confirm this observation by an experiment more concentrated on clarity.

In some of the experimental sound fields, the second and following early reflections contributed to intimacy, but the study was not designed to clarify under what conditions this would generally be true.

The following are concluded from the above observations: (1) ASW is the most sensitive attributes among the

TABLE VIII. Rank order of the subjects' sensitivity to the four attributes of the sound fields. The number of reflections is fixed at four (series A and C) and the parameters are (1) reverberation time (2.0 s); (2) same, but (1.6 s); and (3) same, but (1.2 s). When the levels of the early reflections (indicated in Table I) are varied, the values indicated here show the percentage of reference fields that the subjects judged the attribute to correspond to. Provided the values were 50% or greater, the bold figures indicate the highest percentage among the different rank orders for each of the four attributes. The maximum ranges in the acoustical measures between paired sound fields within this table are 0.6 for $[1-\mathrm{IACC}_{E3}]$; 1.0 dB for G; 2.6 dB for C_{80}; and 24 ms for initial-time-delay gap.

Reverberation time (s)	2.0				1.6				1.2			
	Attributes of sound field				Attributes of sound field				Attributes of sound field			
Order in sensitivity	ASW	Loudness	Intimacy	Clarity	ASW	Loudness	Intimacy	Clarity	ASW	Loudness	Intimacy	Clarity
1st	**100%**	42%	25%		**100%**	25%	25%		**100%**	**62%**	**50%**	
2nd		**50%**	17%			**75%**	**62%**	13%		38%	13%	13%
3rd		8%	**50%**				13%				37%	
4th				25%				37%				37%
No difference			8%	**75%**				**50%**				**50%**

TABLE IX. Rank order of the subjects' sensitivity to the four attributes of the sound fields. The reflection is always from lateral and a variable. The level of direct sound, and reverberation time are fixed at 0 dB, and 2.0 s, respectively (series A and B) and the parameters are (1) number of reflections (four); (2) same, but (eight); (3) same; but (16); (4) same, but (one), and same, but (two). When the levels of the early reflections (indicated in Table I) are varied, the values indicated here show the percentage of reference fields that the subjects judged the attribute to correspond to. Provided the values were 50% or greater, the bold figures indicate the highest percentage among the different rank orders for each of the four attributes. The maximum ranges in the acoustical measures between paired sound fields within this table are 0.42 for $[1-\mathrm{IACC}_{E3}]$; 0.9 dB for G; 2.6 dB for C_{80}; and 11 ms for initial-time-delay gap.

Number of reflections	4				8				16			
	Attributes of sound field				Attributes of sound field				Attributes of sound field			
Order in sensitivity	ASW	Loudness	Intimacy	Clarity	ASW	Loudness	Intimacy	Clarity	ASW	Loudness	Intimacy	Clarity
1st	**100%**		50%		**100%**				**100%**	50%	50%	
2nd		50%	50%			**100%**	**100%**			50%		
3rd		50%										
4th				50%								
No difference				50%				**100%**			50%	**100%**

Number of reflections	1				2			
	Attributes of sound field				Attributes of sound field			
Order in sensitivity	ASW	Loudness	Intimacy	Clarity	ASW	Loudness	Intimacy	Clarity
1st	**100%**				**100%**	50%	50%	
2nd		**100%**	**100%**					
3rd						50%	50%	
4th								50%
No difference				**100%**				50%

four as long as the lateral reflections are variable. (2) Clarity is less sensitive than the other three attributes in regard to the intensity variation in early reflections. In this condition, changes in clarity are subject to masking by the attributes ASW, loudness, and intimacy. (3) Loudness follows ASW in sensitivity without being influenced significantly by differences in type of the first and variable reflections, the level of the direct sound, reverberation time, and the number of early reflections. (4) The first reflection contributes to intimacy regardless whether it is a lateral or a ceiling reflection. (5) Faint direct sound of -3 dB in the level and very short reverberation time of 1.2 s. makes loudness and intimacy easier to discriminate. The first item above confirmed the description by Cox *et al.* (1993) that the change in spatial impression was achieved without altering other subjective perceptions by decreasing the level of the first lateral reflection, and found the same observation is true for other types and variations in sound fields. In the following two sections, two primary attributes of ASW and loudness are discussed in relation to their measures.

IV. LOUDNESS IN RELATION TO Gs

Here, the measured Gs are taken to be surrogates for loudness. Extraction of the value of jnd in G was attempted from the subjective responses for loudness in response to a variety of variations in G among test sound fields. In Fig. 3, ΔG is the increment in G that was found to be "different" in the experiments (solid points) and the "same" (open points), where the circles indicate shoebox-shaped halls and the triangles indicate fan-shaped halls. The plots are made for three levels of the direct sound and three different reverberation times.

We see that most of the cases where ΔGs are 0.4 dB or larger they are subjectively "different" and most of the cases with ΔGs less than 0.1 dB are subjectively "same." Obviously, the spread from 0.1 to 0.4 is a transient region, and the jnd of ΔGs as a measure of loudness is in the range of 0.25 ± 0.15 dB. The range in this experiment is rather small compared to the jnd values, approximately 0.5 ± 0.2 dB in intensity discrimination for sinusoidal signals with intensity levels at 70 to 80 dB [Yost *et al.*, (1993), Fig. 2.2]. This result may be explained by the following facts. First, Morimoto *et al.* (1989) and Bradley and Soulodre (1995) suggest that apparent source width appears to be caused primarily by early reflections combined with the direct sound, and that it is distinguishable from the reverberant sound. Second, the energy of early reflections is subject to integration by hearing mechanism to combine with that of the direct sound while the energy of late arriving sound is not (Lochner *et al.*, 1958). These facts justify the interpretation that the subjects were inclined to find the difference within specifi-

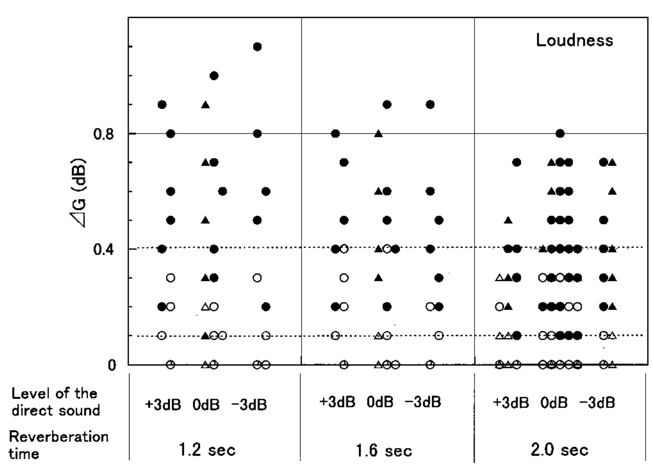

FIG. 3. Plots of subjective responses in loudness in relation to differences in G. Filled figures: subjectively different in loudness; open figures: subjectively the same in loudness. Circles: shoebox-type sound fields; triangles: fan-shape-type sound fields.

cally determined loudness of the apparent source that originates from direct sound and early reflections combined, rather than the change in total loudness.

Study of loudness perception shows that specific loudness determined for pure tone provides a better estimate of the loudness of target when it is presented in the context of other background sound (Moore, 1995, p. 133). Here, the apparent source and the reverberant sound are assumed to be target or background sound, respectively, because only the apparent sources are varied while the reverberant sound is kept constant. It should be emphasized that the subjects were never instructed to concentrate their attention to the apparent source or to any other portion of the test sound field. When ΔGs are derived from the early 80 ms of impulse responses, the values for the transient region are doubled to 0.5 ± 0.2 dB. It is identical to the jnd values for sinusoidal signals. This comparison can be applied when the masking of apparent source by reverberant sound is not large.

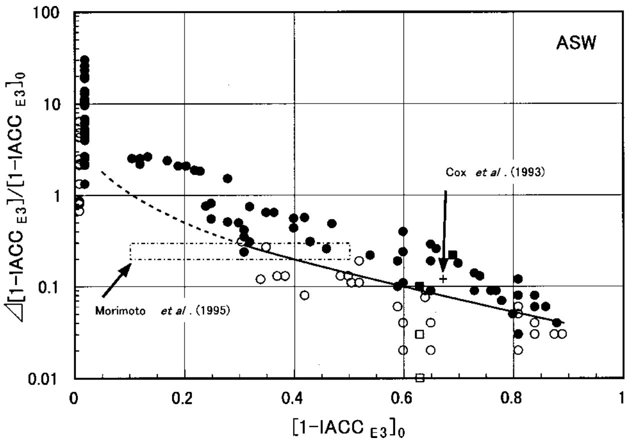

FIG. 4. Plots of subjective responses in ASW in relation to differences in $[1-\mathrm{IACC}_{E3}]$. The vertical axis indicates $\Delta[1-\mathrm{IACC}_{E3}]/[1-\mathrm{IACC}_{E3}]_0$: Weber fraction of $[1-\mathrm{IACC}_{E3}]$. It is a ratio of two $\Delta[1-\mathrm{IACC}_{E3}]$, the difference in $[1-\mathrm{IACC}_{E3}]$ between paired sound fields, and $[1-\mathrm{IACC}_{E3}]_0$ the smaller value of $[1-\mathrm{IACC}_{E3}]$ of the paired sound field. Filled figures: subjectively different in ASW; open figures: subjectively the same in ASW. Circles: lateral reflections as variables. Squares: a ceiling reflection as a variable.

V. ASW IN RELATION TO $[1-\mathrm{IACC}_E]$

In the previous study, $[1-\mathrm{IACC}_{E3}]$ and G_{Elow} were found to correlate to ASW (Okano *et al.*, 1998). G_{Elow} is defined as low-frequency sound level with frequency range below 355 Hz and within the early 80-ms part of the impulse response. Selection of these measures is based on the prior studies below. Combination of binaural dissimilarity and sound level as measures of ASW originate from Keet (1968). Morimoto *et al.* (1995) also support this combination. Barron and Marshall (1981) reported that spread of sound in width including the source broadening effect is observed for the frequency bands of 2 kHz or below. Blauert *et al.* (1986) showed that all frequency components of lateral reflection from 100 to 400 Hz contribute to enlarge ASW. Potter *et al.* (1995a) showed that IACC correlates to ASW better when it is measured for the frequency region from 250 to 2000 Hz than the cases from 70 to 2500 Hz or from 70 to 8000 Hz. Hidaka *et al.* (1995) showed that $[1-\mathrm{IACC}_{E3}]$ explains the difference of acoustical quality among existing halls more effectively than any other combination of bands, including the choice in the alternate measure of LF_E. They also showed that the influence of low-frequency sound levels below 355 Hz on ASW is twice as large as that of high-frequency sound levels above 355 Hz. Beranek, 1996, p. 510 found that there is a correlation between hall-averaged values of $[1-\mathrm{IACC}_{E3}]$ (measured for 500–2000-kHz bands) and LF_{E4} (measured for 125–1000-Hz bands). This fact is related to the report by Potter *et al.* (1995b) that frequency range centered at 600 Hz is the most important to ASW, because both measures include 500- and 1000-Hz bands in common. Okano *et al.* (1998) showed that the influence of the angle of incidence for a lateral reflection on ASW is limited to the frequency bands of 500 Hz or below. Both $[1-\mathrm{IACC}_E]$ and LF_{E4} cover this influence. When their angles of incidence are widely distributed, they also found that the influence of the number of reflections are observed in the bands of 1000-kHz or above. This is covered by $[1-\mathrm{IACC}_E]$ and not by LF_E. Consequently, $[1-\mathrm{IACC}_{E3}]$ and G_{Elow}, combined together, cover the principal frequency range of musical signals that is considered important for ASW.

Cox *et al.* (1993) derived the jnd of IACC as 0.075 in a sound field with intensity variation of the first lateral reflection. Davies *et al.* (1996) reported that the jnd of the change in energy in the low-frequency range, centered at 200 Hz of the early 80 ms of a impulse response, was measured to be 3.8 ± 0.2 dB. These values yield the ratio of 0.075/3.8 $=0.021$ dB. It means that the change in IACC of 0.02 corresponds to the change in low-frequency sound level of 1 dB. It is also shown in Hidaka *et al.* (1995), Fig. 12, that a difference of 5 dB in low-frequency sound level makes about the same change in ASW as an increase in $[1-\mathrm{IACC}_{E3}]$ of 0.1, resulting to a ratio of 0.02/dB. In the present test sound fields, the ratio between changes in $[1-\mathrm{IACC}_{E3}]$ and G_{Elow} is approximately 0.2/dB. Consequently, the effect of change in G_{Elow} on ASW is negligible because the effect of change in $[1-\mathrm{IACC}_{E3}]$ on ASW is ten times larger in the experiment designed. To be sure, it does not mean that G_{Elow} is not important. It just means that its effect is small enough in the scheme of present experiment compared to that of $[1-\mathrm{IACC}_{E3}]$.

Figure 4 shows the just-noticeable-differences (jnd) in ASW where it is assumed that $[1-\mathrm{IACC}_{E3}]$ is a surrogate measure of ASW. The vertical axis represents the Weber fraction for $[1-\mathrm{IACC}_{E3}]$, that is the difference in $[1-\mathrm{IACC}_{E3}]$ between the reference and trial sound field divided by $[1-\mathrm{IACC}_{E3}]_0$, where the suffix "0" means the smaller value of the two. Cases where "different" was judged are plotted as filled circles; cases where "same" was judged are plotted as open circles. For the cases with a ceiling reflection as a variable, they are plotted as filled squares or open squares next to each other. In some cases with a large number of reflections and a small attenuation, measures of image shift (Okano, 2000) indicated that the test sound fields happened to produce image shifts. Those plots are eliminated because they affect ASW quite differently. A curve is drawn between the "same" and "different" cases which clearly separates them. This curve indicates the jnd of ASW, where $[1-\mathrm{IACC}_{E3}]$ represents ASW. This jnd curve shows the same characteristic of the Weber fraction as that for sound level, in that it takes on large values near the threshold of sensation and becomes smaller as the sensation magnitude becomes larger (Yost *et al.*, 1993, pp. 22–24). Morimoto *et al.* (1995) published that the Weber fraction for measured IACCs was in the range of 0.2 to 0.3 for $[1-\mathrm{IACC}_{E}]_0$'s ranging from 0.1 to 0.5. Their result was close to that of Fig. 4, particularly in the range where $[1-\mathrm{IACC}_{E}]_0$'s are in the range of 0.3 to 0.5. In concert halls, the range of $[1-\mathrm{IACC}_{E3}]$'s is from 0.4 to 0.7 (Beranek, 1996, p. 517; Okano *et al.*, 1998, Fig. 6). For this range, the curve in Fig. 4 shows the jnd of $[1-\mathrm{IACC}_{E}]$ calculates to be in the range between 0.05 to 0.08. This value is close to the value of 0.075 measured by Cox *et al.* (1993) for a sound field with a reference value of 0.67 in calculated $[1-\mathrm{IACC}_{E}]$ by Ando's method (Ando, 1985, pp. 35–41).

Ando (1985, p. 132) showed that for a given angle of incidence, a variation in the level of the reflection affects $[1-\mathrm{IACC}_{E}]$ differently for each band. It suggests that, when the angles of variable reflections are limited to a specific angle, subjects possibly find the difference in a specific band at which the difference in $[1-\mathrm{IACC}_{E}]$ is mostly caused. When a difference causes in the specific band, specifically determined ASW in that band could be better able to explain the nature of judgements of differences, although $[1-\mathrm{IACC}_{E3}]$ is still assumed to be a measure of totally determined ASW of a sound field. In Fig. 5, the vertical axis represents the maximum value of Weber's fractions that is calculated for $[1-\mathrm{IACC}_{E}]$ in each of 500- 1000-, and 2000-Hz band. The abscissa, $[1-\mathrm{IACC}_{E}]_{0\text{-max}}$ indicates the smaller value of $[1-\mathrm{IACC}_{E}]$ within a pair of sound fields in the band at which the Weber's fraction is the maximum. It is drawn in the same manner as that of Fig. 4. Figure 5 shows the same kind of characteristics for the jnd of ASW, that the Weber's fraction becomes smaller as the magnitude of ASW increases; however, the slope of the curve that separates "different" and "same" plots is more moderate than that in Fig. 4. The curve in Fig. 5 shows that the jnd of $[1-\mathrm{IACC}_{E}]$ of the solo band is calculated to be approximately 0.08. The curve indicates that $[\Delta[1-\mathrm{IACC}_{E}]/[1-\mathrm{IACC}_{E}]_0]_{\max}$ takes a value of 0.2 when $[1-\mathrm{IACC}_{E}]_0$ is 0.4 for an example. Therefore, $\Delta[1-\mathrm{IACC}_{E}]_{\mathrm{jnd}}$ calculates to be 0.08, i.e., 0.2 multiplied by 0.4. Here, other kinds of frequency bands system such as critical band or any other models of auditory frequency filters would possibly be utilized. In such cases, the size of the jnd would have different values.

VI. DISCRIMINATION OF ACOUSTICAL QUALITY AMONG EXISTING CONCERT HALL

This study is not related to three of the six acoustical attributes listed in Beranek (1996, Chap. 15, p. 516). The three that are related are $[1-\mathrm{IACC}_{E3}]$ and G and the initial-time-delay gap. However, the initial-time-delay gap itself was not designated to vary directly during the test. The bass ratio and the surface-diffusivity index were constant in this test. The early decay time EDT itself was not an objective during each judgment in the hearing tests. Clarity, defined by the factor C_{80}, was not always found to be as sensitive an attribute as the intensity variation in early reflections. This is because the changes in the other attributes (such as ASW, loudness, and intimacy) masked the relatively small changes in clarity. Further, in the Beranek study, C_{80} was found to be highly correlated rather with the long-time reverberation time among existing halls, and that was also not an objective during each judgment in the tests.

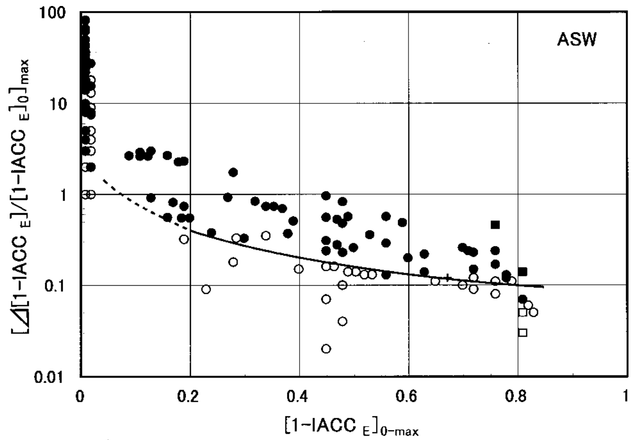

FIG. 5. Same as Fig. 4, but plots of subjective responses in ASW in relation to differences in $[1-\mathrm{IACC}_{E}]$ in solo band. The vertical axis indicates $[\Delta[1-\mathrm{IACC}_{E}]/[1-\mathrm{IACC}_{E}]_0]_{\max}$: the maximum value of Weber fraction of $[1-\mathrm{IACC}_{E}]$ among 500, 1000, and 2000-kHz bands. In each band, the ratio of two quantities $\Delta[1-\mathrm{IACC}_{E}]$ and $[1-\mathrm{IACC}_{E}]_0$, the smaller value of $[1-\mathrm{IACC}_{E}]$ of the paired sound field at the band, is calculated. The abscissa indicates $[1-\mathrm{IACC}_{E}]_{0\text{-max}}$: the value of $[1-\mathrm{IACC}_{E}]$ at the band that $\Delta[1-\mathrm{IACC}_{E}]/[1-\mathrm{IACC}_{E}]_0$ is the maximum. Filled figures: subjectively different in ASW; open figures: subjectively the same in ASW. Circles: lateral reflections as variables. Squares: a ceiling reflection as a variable.

The jnd of $[1-\mathrm{IACC}_{E3}]$ as contributors to ASW, and the jnd of G as contributors to loudness were found to be the range 0.065 ± 0.015 and 0.25 ± 0.15 dB, respectively, in a range of their values encountered in existing concert halls.

A plot of the subjective rank orderings of 19 concert halls (Beranek, 1996) is shown in Fig. 6 on a graph of $[1-\mathrm{IACC}_{E3}]$ vs G_{mid}. Here, G_{mid} indicates average of measured G values in the middle frequency bands of 500- and 1000 Hz 1/1 octave. Detailed data are shown in Table III of Okano *et al.* (1998). The solid circles indicate halls with rankings of A+ and A, the open circles with rankings of B+, and the solid triangles with rankings of B. Added are dotted lines adjusted in position to separate the categories. The halls in each subjective category, except for a couple of cases, are well separated by these lines. Here, the size of the jnd is intended to be compared to the subjective categories. The category B+ spans the range of more than 2 units of jnd in $[1-\mathrm{IACC}_{E3}]$ and many more units in G_{mid}, that is to say, a hall in the middle of this category range is subjectively different from any hall in the adjacent categories. This fact indicates that the category of rank ordering by Beranek (1996) has appropriate size to distinguish the difference in those acoustical attributes.

This paper is not an attempt to show that two parameters

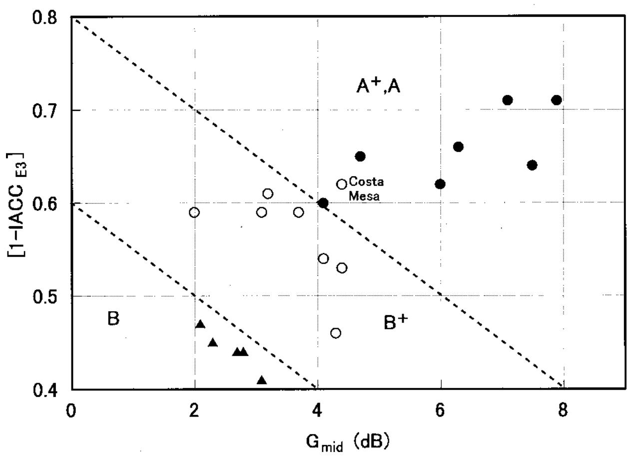

FIG. 6. Plots of $[1—\mathrm{IACC}_{E3}]$ and G_{mid} measured in existing halls in relation to the rank ordering by Beranek (1996). Data shows hall-averaged values in unoccupied condition. Filled circles: [A+, A] ranked halls; open circles: [B+] ranked halls; filled triangles: [B] ranked halls.

describe all of the acoustical quality of concert halls. The addition of other parameters, known to be important in concert halls, namely, reverberation time, initial-time-delay gap, bass ratio, and also envelopment will make the separation better. For example, the plot for Costa Mesa Hall is placed within the area of A^+ and A-ranked halls in spite of its ranking of B^+. This hall has a larger value of 31 ms in the initial-time-delay gap than the values ranging from 12 to 25 ms for the A^+ and A-ranked halls (Beranek, 1996, p. 517). Reichardt *et al.* (1967) showed that the jnd of initial-time-delay gap for the lateral reflection is 7 ms$\pm$0.6 ms. It is consistent with the following experimental results in this study. The first lateral reflection being variable, more than 10 dB of attenuation was necessary for intimacy to be found ''different'' when the delay difference between the variable and the first fixed reflection is 7 ms, and it needed only 3 dB of attenuation when the delay difference is 11 ms. The difference between the value of 31 ms for Costa Mesa Hall and the range of 12–25 ms for the A^+ and A-ranked halls is as large as the jnd of initial-time-delay gap and is significant.

VII. CONCLUSIONS

From the discussions above, the following points are emphasized:

(1) *Sensitiveness of ASW to changes in the level of early lateral reflections*: In the two types of concert halls simulated here, shoebox- and fan-shaped, variations in the amplitudes of early reflections were studied to learn their effects on the subjective attributes of ''ASW,'' ''loudness,'' ''intimacy,'' and ''clarity.'' In most cases, it is seen from Tables V to IX that ASW is the subjective attribute among the four that is the most sensitively picked up in regard to changes in the amplitude of early reflections. In no case was ASW less sensitive than any one of the others as long as the lateral reflection was variable. For the most part, changes in clarity possibly are masked by more distinct changes in the other attributes.

(2) *Determination of the jnd of [1—IACC] in a wide range of the value of [1—IACC]*: Although the value is an initial estimation because of the small number of available subjects, the previously reported jnd of [1—IACC] by Cox *et al.* (1993) was confirmed in the wide range of sound fields that is encountered in typical existing concert halls. The jnd in $[1—\mathrm{IACC}_{E3}]$ is measured as 0.065 ± 0.015 for the range of $[1—\mathrm{IACC}_{E3}]$ from 0.4 to 0.8. Here, for this range, it should be noted that the deviations in jnd among three subjects were within $\pm10\%$ in IACC_{E3}. The jnd in $[1—\mathrm{IACC}_{E}]$ in solo band among 500-, 1000-, and 2000- Hz 1/1 octave is measured as approximately 0.08 when it is assumed that the difference in ASW is picked up by the largest difference among the three bands.

(3) *Determination of the jnd of G by varying early reflections only*: Although the value is limited to be a rough estimation because of the small number of available subjects, the jnd of G is measured to be in the range of 0.25 ± 0.15. Here, it should be noted that the deviations in jnd among three subjects were within ±0.1 dB in G. When G's are derived from the early 80 ms of impulse response, the value is measured to be in the range of 0.5 ± 0.2.

(4) *Influence of the first reflection on intimacy*: The first reflection, whether it is from the ceiling or lateral, has considerable influence on intimacy.

These results, like those of a previous study, were derived with subjects who have sufficient experience in listening to classical music by playing musical instruments or by being an regular audience of concerts.

Comparison of these results with the subjective rankings of concert halls by Beranek (1996) shows that his middle rank, B+, is more than 2 jnd's in width in regard to the surrogate for ASW, and is much larger in width in regard to the surrogate for loudness. It is concluded that the categories in his ranking have significantly large size that is well distinguishable in those attributes.

ACKNOWLEDGMENTS

The author wishes to thank Dr. Takayuki Hidaka for his valuable discussions and his support for the study. He also wishes to thank Mr. Yasuo Makita for his valuable discussions in designing the test sound fields, Dr. Leo Beranek for comments and editorial assistance, and Dr. Yoichi Ando for his valuable discussions during the editorial period.

Ando, Y. (**1977**). ''Subjective preference in relation to objective parameters of music sound fields with a single echo,'' J. Acoust. Soc. Am. **62**, 1436–1441.

Ando, Y. (**1985**). *Concert Hall Acoustics* (Springer Berlin, Heidelberg).

Barron, M. (**1971**). ''The subjective effect of first reflections in concert halls—The need for lateral reflections,'' J. Sound Vib. **15**, 475–494.

Barron, M., and Lee, L.-J. (**1988**). ''Energy relations in concert auditonums. I,'' J. Acoust. Soc. Am. **84**, 618–628.

Barron, M., and Marshall, A. (**1981**). ''Spatial impression due to early lateral reflections in concert halls: The derivation of a physical measure,'' J. Sound Vib. **77**, 211–232.

Beranek, L. (**1996**). *Concert and Opera Halls: How They Sound* (Acoustical Society of America, New York).

Blauert, J., Möbius, U., and Lindemann, W. (**1986**). ''Supplementary psychoacoustical results on auditory spaciousness,'' Acustica **59**, 292–293.
Bradley, J., and Soulodre, G. (**1995**). ''The influence of late arriving energy on spatial impression,'' J. Acoust. Soc. Am. **97**, 2263–2271.
Bradley, J., and Soulodre, G. (**1997**). ''Factors influencing the perception of bass,'' J. Acoust. Soc. Am. **101**, 3135.
Bradley, J., Reich, R., and Norcross, S. (**1999**). ''A just noticeable difference in C_{50} for speech,'' Appl. Acoust. **58**, 99–108.
Cox, T., Davies, W., and Lam, Y. (**1993**). ''The sensitivity of listeners to early sound field changes in auditoria,'' Acustica **79**, 27–41.
Davies, W., Cox, T., and Lam, Y. (**1996**). ''Subjective perception of seat dip attenuation,'' Acustica **82**, 784–792.
Hidaka, T., Beranek, L., and Okano, T. (**1995**). ''Interaural cross-correlation, lateral fraction, and low- and high-frequency sound levels as measures of acoustical quality in concert halls,'' J. Acoust. Soc. Am. **98**, 988–1007.
Hidaka, T., Beranek, L., Masuda, S., Nishihara, N., and Okano, T. (**2000a**). ''Acoustical design of the Tokyo Opera City (TOC) concert hall, Japan,'' J. Acoust. Soc. Am. **107**, 340–354.
Hidaka, T., and Beranek, L. (**2000b**). ''Objective and subjective evaluations of twenty-three opera houses in Europe, Japan, and the Americas,'' J. Acoust. Soc. Am. **107**, 368–383.
Keet, W. (**1968**). ''The influence of early lateral reflections on the spatial impression,'' in Proceedings of the 6th ICA, Tokyo, Japan, E53–E56.
Lehmann, P. (**1976**). ''Über die ermittlung raumakusticher Kriterien und deren Zusammenheng mit subjektiven Beurteilungen der Horsamkeit,'' dissertation, TU Berlin, 1976.
Lochner, J., and Burger, J., (**1958**). ''The subjective masking of short time delayed echoes by their primary sounds and their contribution to the intelligibility of speech,'' Acustica **8**, 1–10.
Moore B. C. J. (**1995**). *Hearing* (Academic, San Diego).
Morimoto, M., and Maekawa, Z. (**1989**). ''Auditory spaciousness and envelopment,'' Proc. 13th Int. Congr. Acoust. Belgrade, 2, 215–218.
Morimoto, M., and Iida, K. (**1995**). ''A practical evaluation method of auditory source width in concert halls,'' J. Acoust. Soc. Jpn. **16**, 59–69.
Okano, T. (**1993**). ''Necessary accuracy for early reflections in sound field auralization,'' J. Acoust. Soc. Am. **94**, 1847.
Okano, T., Beranek, L., and Hidaka, T. (**1998**). ''Relations among interaural cross-correlation coefficient ($IACC_E$), lateral fraction (LF_E), and apparent source width (ASW) in concert halls,'' J. Acoust. Soc. Am. **104**, 255–265.
Okano, T. (**2000**). ''Image shifts caused by strong lateral reflections, and its relation to interaural cross correlation,'' J. Acoust. Soc. Am. **108**, 2219–2230.
Potter, J. M., Raatgever, J., and Bilsen, F. A. (**1995a**). ''Measures for spaciousness in room acoustics based on binaural strategy,'' Acta Acust. (Beijing) **3**, 429–443.
Potter, J. M., Bilsen, F. A., and Raatgever, J. (**1995b**). ''Frequency dependence of spaciousness,'' Acta Acust. (Beijing) **3**, 417–427.
Reichardt, W., and Schmidt, W. (**1967**). ''Die Wahmehmbarkeit der Veranderung von Schallfeldparametem bei der Darbietung von Musik,'' Acustica **18**, 274–282.
Reichardt, W., Alim, O., and Schmidt, W. (**1975**). ''Definition und Messgrundlage eines objektiven Masses zur Ermittlung der Grenze zwischen brauchbarer und Durchsichtigkeit bei Musikdarbietung,'' Acustica **32**, 126–137.
Reichardt, W., and Lehmann, U. (**1981**). ''Optimierung von Raumeindruck und Durchsichtigkeit von Musikdarbietungen durch Auswertung von Impulsschalltests,'' Acustica **48**, 174–185.
Schubert, P. (**1969**). ''Die Wahnehmbarkeit von Ruckwurfen bei Musik,'' Z. Hochfrequenztech. Electro-akust. **78**, 230–245.
Schroeder, M. R., Gottlob, D., and Siebrasse, K. F. (**1974**). ''Comparative study of European concert halls: Correlation of subjective preference with geometric and acoustic parameters,'' J. Acoust. Soc. Am. **56**, 1195–1201.
Seraphim, H. (**1961**). ''Über die Wahmehmbarkeit mehrerer Rückwürfe von Sprachscall,'' Acustica **11**, 80–91.
Seraphim, H. (**1963**). ''Raumakustische Nachbildungen mit eleltroakustischen Hilfsmitteln,'' Acustica **13**, 75–85.
Yost, W., Popper, A., and Fay, R. (**1993**). *Human Psychophysics* (Springer, New York).

Super-resolution in time-reversal acoustics

Peter Blomgren[a] and George Papanicolaou[b]
Department of Mathematics, Stanford University, Stanford, California 94305

Hongkai Zhao[c]
Department of Mathematics, University of California at Irvine, Irvine, California 92697-3875

(Received 3 May 2000; accepted for publication 27 September 2001)

The phenomenon of super-resolution in time-reversal acoustics is analyzed theoretically and with numerical simulations. A signal that is recorded and then retransmitted by an array of transducers, propagates back though the medium, and refocuses approximately on the source that emitted it. In a homogeneous medium, the refocusing resolution of the time-reversed signal is limited by diffraction. When the medium has random inhomogeneities the resolution of the refocused signal can in some circumstances beat the diffraction limit. This is super-resolution. A theoretical treatment of this phenomenon is given, and numerical simulations which confirm the theory are presented.
 [DOI: 10.1121/1.1421342]

PACS numbers: 43.60.Cg, 43.60.Gk, 43.20.Fn [JJM]

I. INTRODUCTION

In time-reversal acoustics a signal is recorded by an array of transducers, time-reversed, and then retransmitted into the medium. The retransmitted signal propagates back through the same medium and refocuses approximately on the source. The refocusing is approximate because of the finite size of the array of transducers (receivers and transmitters), which is called a *time-reversal mirror* (TRM; see Fig. 1). The possibility of refocusing by time reversal has many important applications in medicine, geophysics, nondestructive testing, underwater acoustics, wireless communications, etc., and has been studied in a variety of settings (Fink, 1997, 1999; Hodgkiss *et al.*, 1999; Dowling and Jackson, 1990). In the frequency domain, time reversal is equivalent to phase conjugation which has been studied extensively in optics (Porter, 1989).

Time-reversed signals propagate backwards through the time-independent medium and go through all the multiple scattering, reflections, and refraction that they underwent in the forward direction, which is why refocusing occurs. However, the size of the TRM is often small compared to the propagation distance, that is, the aperture of the time-reversal mirror is small, and only a small part of the advancing wave is captured and time reversed. In homogeneous media, the spatial resolution of the time-reversed signals is limited by diffraction and is inversely proportional to the aperture size and proportional to the wavelength times the propagation distance. In the notation of Fig. 1, the time-reversed and backpropagated signal due to a point source will focus in a region around the source with spatial width of order $\lambda L/a$. Here, λ is the wavelength of the carrier signal for the pulse, L is the distance from the source to the TRM, and a is the size of the TRM.

In underwater acoustics, typical parameters are: propagation speed $c_0 = 1.5$ km/s, wavelength $\lambda = 1$ m, propagation distance $L = 1-50$ km, TRM size $a = 50-100$ m. In nondestructive testing with ultrasound these lengths are scaled by a factor of 10^{-3}, so that typical wavelengths are $\lambda = 1$ mm.

If the medium is randomly inhomogeneous the focusing resolution of the backpropagated signal can be better than the resolution in the homogeneous case. This is referred to as *super-resolution*. Roughly speaking, the random inhomogeneities produce multipathing and the TRM appears to have an aperture that is larger than its physical size, an *effective aperture* $a_e > a$. This means that the recompressed pulse is narrower than in the homogeneous medium and we have super-resolution with a spatial scale of order $\lambda L/a_e$. This phenomenon was observed in underwater acoustics experiments (Dowling and Jackson, 1990; Hodgkiss *et al.*, 1999; Kuperman *et al.*, 1997) as well as in the ultrasound regime (Derode *et al.*, 1995; Fink, 1997, 1999).

An attempt at a theoretical explanation of super-resolution by multipathing is given in Dowling and Jackson (1992). This, however, requires *ensemble averages* in random media and does not account for the remarkable stability of the compressed pulse, without any averaging, as seen in the actual experiments. In Fig. 2, numerical computations with time-harmonic signals illustrate the lack of any resolution realization-by-realization, while on average the resolution is remarkable. For time-harmonic signals, time reversal is the same as phase conjugation on the TRM (usually called the *phase conjugation mirror*, in this setting).

The key to the statistical stability of time-reversed signals is their frequency spread. This stabilization of pulses has been seen in other contexts in stochastic equations and random media (Solna and Papanicolaou, 2000), but not in connection with time reversal, as it is presented and analyzed here.

In this paper, we explore analytically and numerically the phenomenon of super-resolution in time reversal in a regime of parameters where the effects of the random medium are fully developed. This regime can be described roughly as follows. The propagation distance, L, the carrier wavelength, λ, the aperture of the TRM, a, the correlation

[a]Electronic mail: blomgren@math.stanford.edu
[b]Electronic mail: papanico@math.stanford.edu
[c]Electronic mail: zhao@math.uci.edu

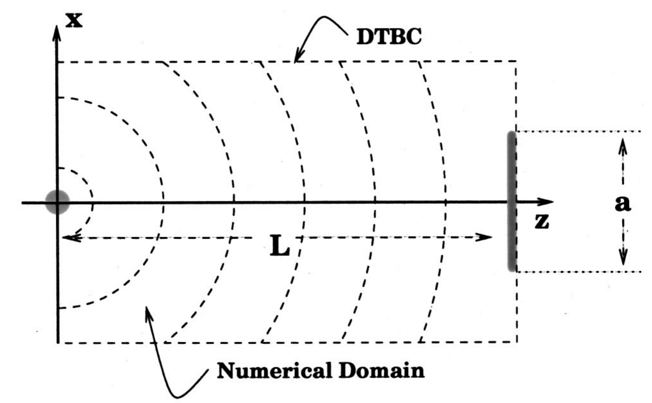

FIG. 1. Setting for time-reversal acoustics. A point source emits a wave, which is received on a screen of width a—the *time-reversal mirror* (TRM)— at a distance L from the source. The domain of numerical solution of the (parabolic) wave equation is shown with a dotted line, and DTBC stands for *discrete transparent boundary conditions*.

length of the medium fluctuations, l, and the variance of the sound-speed fluctuations, $\langle \mu^2 \rangle$, are scaled by a single parameter $\epsilon = \lambda/L$, which we assume to be small. We assume also that $l \sim \lambda$ and that $\langle \mu^2 \rangle \sim \epsilon$. In this regime

(i) The propagation distance is much larger than the correlation length of the inhomogeneities, which is large or comparable to the wavelength.

(ii) The aperture of the TRM is relatively small so that the effect of the random medium and multipathing can be felt.

(iii) The random fluctuations of the propagation speed are weak so that waves are scattered mostly in the forward direction.

Many situations in underwater acoustics and in ultrasound propagation fall into this regime. The objectives of this paper are to

(i) Systematically calculate statistics of the backpropagated phase-conjugated field using transport and Wigner equations in the frequency domain.

(ii) Derive an *effective aperture* formula for a TRM in random media. In particular, we show that the effective aperture for a finite aperture or Gaussian TRM is

$$a_e(L) = a\sqrt{1 + \frac{L^3\gamma}{a^2}},$$

where γ is a constant with dimensions of reciprocal length that depends on the statistics of the fluctuations of the propagation speed (see Sec. VII for details). It is assumed that the effective aperture is still small compared to the propagation distance, $a_e(L) \ll L$.

(iii) Show that for a pulse in the time domain, super-resolution is linked to the *effective aperture*, a_e, of the TRM, and that self-averaging due to the frequency spread of the signal makes super-resolution in time reversal statistically stable.

In Sec. II, we set up equations for backpropagated fields and quantities of interest in the frequency domain. In Sec. III, we introduce an invariant embedding approach in order to derive transport- and Winger equations for the time-reversed signal originating from a point source. Then, in Sec. IV, the diffraction limit for a homogeneous medium is calculated, in both the frequency and time domain for Gaussian and finite aperture TRMs. Scaling for the Wigner equation for the transport limit, from which the effective aperture will be derived, is introduced in Sec. V. Pulse stabilization in the time domain and the beam approximation are discussed in Secs. VI and VII, respectively. Details of the numerical implementation and numerical results are shown in Sec. VIII. The concept of dynamic TRM placement is introduced in Sec. IX and is explored with numerical simulations. Finally, in Sec. X we consider time reversal in a waveguide and show the results of several numerical simulations without discussing here the theory that explains them. In the Appendix we explain carefully the various scaling limits which lead to super-resolution and statistical stability in the time domain as described here.

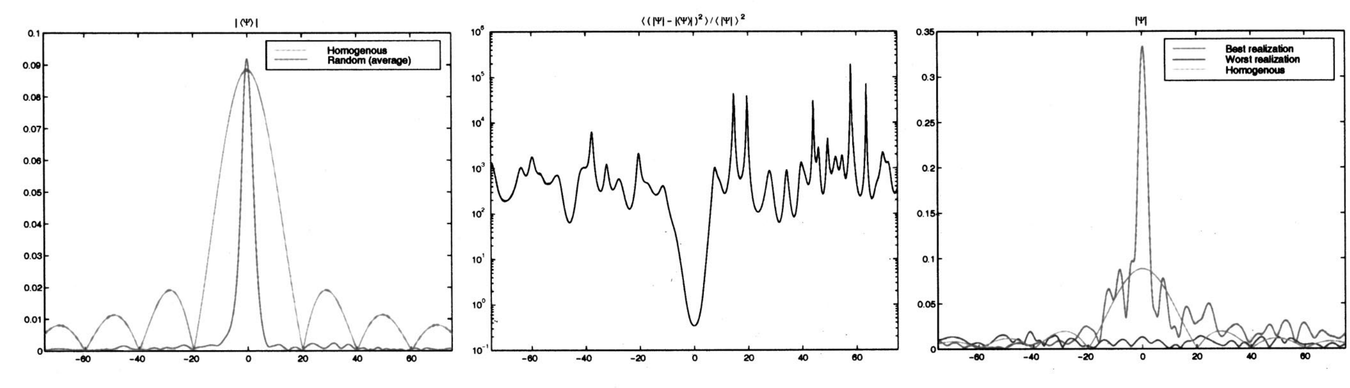

(a) Average (b) Relative Variance (c) Realizations

FIG. 2. Time-harmonic waves in random media. Propagation distance 1000 m, TRM width 50 m, width of numerical domain 150 m, width of random medium 112.5 m, contrast $\pm 5\%$, 428 realizations. (a) Amplitude of the mean: Homogeneous (light) and average over random realizations (dark) case. (b) Relative variance, $> \mathcal{O}(1)$ except for a very small interval. (c) Individual realizations that show super-resolution (high) as well as no resolution at all (low).

II. BACKPROPAGATED FIELDS

The time-reversed signal is synthesized from time-harmonic waves by the inverse Fourier transform. We start with the Helmholtz equation for time-harmonic waves $u(x,y,z)e^{-i\omega t}$

$$u_{xx}+u_{yy}+u_{zz}+k^2n^2(x,y,z)u=0. \tag{1}$$

Here, $k=\omega/c_0$ is the wave number, c_0 is a reference speed, $c(x,y,z)$ is the propagation speed and $n(x,y,z)=c_0/[c(x,y,z)]$ is the index of refraction. When the time-reversal mirror has small aperture (beam geometry) and the fluctuations in the propagation speed are weak, we can use the parabolic or paraxial approximation (see Tappert, 1977). We let $u=e^{ikz}\psi(x,y,z)$ and ignore backscattering in the Helmholtz equation (the term ψ_{zz}) to obtain a parabolic initial value problem for the wave amplitude ψ, in which the direction of propagation z plays the role of time (see Bamberger *et al.*, 1988)

$$2ik\psi_z+\Delta_\perp\psi+k^2(n^2-1)\psi=0,$$

$$\psi|_{z=0}=\psi_0(\mathbf{x};k),\quad \mathbf{x}=(x,y),$$

where $\Delta_\perp$ is the transverse Laplacian (2)

We note that the parabolic approximation is not valid in the immediate neighborhood of a point source. The full Helmholtz equation must be solved near the source and then matched with the parabolic equation further away from it. We will use a Gaussian beam in the frequency domain as an initial wave amplitude ψ_0, that is, a Gaussian in the transverse space coordinates. We take the pulse to be Gaussian in time as well, which means a Gaussian in the wave number k or frequency ω. By Fourier synthesis, the wave function in the time domain is given by

$$\Psi(t,x,y,z)=\int e^{i\omega(z/c_0-t)}\psi(x,y,z;\omega/c_0)d\omega. \tag{3}$$

We will also use a point source and consider it as the limit of a Gaussian in space whose width is very small or zero.

The Green's function $G(z,z_0;\mathbf{x},\xi;k)$ with a point source at (z_0,ξ) satisfies

$$2ikG_z+\Delta_\mathbf{x}G+k^2\mu(\mathbf{x},z)G=0,$$

$$G(z_0,z_0;\mathbf{x},\xi;k)=\delta(\mathbf{x}-\xi).$$

$$\text{Here,}\quad z>z_0,\quad \mu(\mathbf{x},z)=n^2(\mathbf{x},z)-1, \tag{4}$$

By reciprocity $G(z,z_0;\mathbf{x},\xi;k)=G(z_0,z;\xi,\mathbf{x};k)$. If the initial source distribution at $z_0=0$ is $\psi_0(\eta;k)$ then the wave field at $z=L$ is

$$\psi(\mathbf{y},L;k)=\int G(L,0;\mathbf{y},\eta;k)\psi_0(\eta;k)d\eta. \tag{5}$$

In time-reversal problems it is convenient to introduce the tensor product of two Green's functions

$$\Gamma(L,\mathbf{x},\mathbf{y};\xi,\eta;k)=G(L,0;\mathbf{x},\xi;k)\overline{G(L,0;\mathbf{y},\eta;k)},$$
$$\Gamma(0,\mathbf{x},\mathbf{y};\xi,\eta;k)=\delta(\mathbf{x}-\xi)\delta(\mathbf{y}-\eta), \tag{6}$$

because $\Gamma(L,\mathbf{y},\mathbf{y};\xi,\eta;k)$ describes the response, at the source plane, of a point source at η, whose signal is recorded on the TRM at $\mathbf{y}$, phase-conjugated, backpropagated and observed at ξ. In the following section we derive an equation for Γ, which is a form of invariant embedding.

Using $\Gamma(L,\mathbf{y},\mathbf{y};\xi,\eta;k)$, the time-harmonic, phase-conjugated, and backpropagated field at the source plane, $z=0$, can be written as

$$\begin{aligned}\psi^B(\xi,L;k)&=\int G(L,0;\mathbf{y},\xi;k)\overline{\psi(\mathbf{y},L;k)}\chi_A(\mathbf{y})d\mathbf{y}\\ &=\int\int\chi_A(\mathbf{y})\overline{\psi_0(\eta;k)}G(L,0;\mathbf{y},\xi;k)\\ &\quad\times\overline{G(L,0;\mathbf{y},\eta;k)}d\eta\, d\mathbf{y}\\ &=\int\int\chi_A(\mathbf{y})\overline{\psi_0(\eta;k)}\Gamma(L,\mathbf{y},\mathbf{y};\xi,\eta;k)d\eta\, d\mathbf{y}.\end{aligned} \tag{7}$$

Here, $\chi_A(\mathbf{y})$ is the aperture function for the TRM occupying the region A and is equal to 1 if $\mathbf{y}\in A$, and 0 otherwise. We use the same notation for other aperture functions as well. The backpropagated, time-reversed field is obtained by Fourier synthesis

$$\Psi^B(\xi,L,t)=\int\psi^B(\xi,L;\omega/c_0)e^{-it\omega}d\omega. \tag{8}$$

Here, t is *relative* time, on the scale of the pulse width. The travel time to and from the TRM has been eliminated.

III. INVARIANT EMBEDDING AND THE WIGNER EQUATION

From the equation for the Green's function $G(z,z_0;\mathbf{x},\xi;k)$, we can derive an equation for $\Gamma(L,\mathbf{x},\mathbf{y};\xi,\eta;k)$

$$2ik\frac{\partial\Gamma}{\partial L}+(\Delta_\mathbf{x}-\Delta_\mathbf{y})\Gamma+k^2(\mu(\mathbf{x},L)-\mu(\mathbf{y},L))\Gamma=0$$
$$\Gamma(0,\mathbf{x},\mathbf{y};\xi,\eta;k)=\delta(\mathbf{x}-\xi)\delta(\mathbf{y}-\eta). \tag{9}$$

Here, $\Delta_\mathbf{x}$ and $\Delta_\mathbf{y}$ are the Laplacians in the transverse variable $\mathbf{x}$ and $\mathbf{y}$, respectively. We introduce the following change of transverse variables:

$$\begin{aligned}&\mathbf{X}=\frac{\mathbf{x}+\mathbf{y}}{2},\quad \mathbf{x}=\mathbf{X}-\frac{\mathbf{Y}}{2}\\ &\mathbf{Y}=\mathbf{y}-\mathbf{x},\quad \mathbf{y}=\mathbf{X}+\frac{\mathbf{Y}}{2}\\ &\Delta_\mathbf{x}-\Delta_\mathbf{y}=(\nabla_\mathbf{x}-\nabla_\mathbf{y})(\nabla_\mathbf{x}+\nabla_\mathbf{y})=-2\nabla_\mathbf{X}\nabla_\mathbf{Y}.\end{aligned} \tag{10}$$

This transforms Eq. (9) into

$$\begin{aligned}&2ik\frac{\partial\Gamma}{\partial L}-2\nabla_\mathbf{X}\nabla_\mathbf{Y}\Gamma+k^2\left(\mu\left(\mathbf{X}-\frac{\mathbf{Y}}{2},L\right)-\mu\left(\mathbf{X}+\frac{\mathbf{Y}}{2},L\right)\right)\Gamma\\ &\quad=0,\\ &\Gamma(0,\mathbf{X},\mathbf{Y};\xi,\eta;k)\overset{\text{def}}{=}\delta\left(\mathbf{X}-\frac{\mathbf{Y}}{2}-\xi\right)\delta\left(\mathbf{X}+\frac{\mathbf{Y}}{2}-\eta\right).\end{aligned} \tag{11}$$

With the Fourier transform defined by

$$\hat{f}(p)=\frac{1}{(2\pi)^d}\int_{R^d} e^{ip\cdot x} f(x)dx,$$
$$f(x)=\int_{R_d} e^{-ip\cdot x}\hat{f}(p)dp, \tag{12}$$

and the scaling rule $\delta(x)=|\alpha|^d\delta(\alpha x)$ for δ functions in d dimensions, with $d=1,2$, here we introduce the Wigner distribution

$$W(L,\mathbf{X},\mathbf{P};\xi,\eta;k)=\frac{1}{(2\pi)^d}\int e^{i\mathbf{P}\cdot\mathbf{Y}}\Gamma(L,\mathbf{X},\mathbf{Y};\xi,\eta;k)d\mathbf{Y}. \tag{13}$$

It satisfies the Wigner equation (Fourier transform in $\mathbf{Y}$ of the Γ equation)

$$k\frac{\partial W}{\partial L}+\mathbf{P}\cdot\nabla_{\mathbf{X}}W=\frac{ik^2}{2}\int e^{-i\mathbf{Q}\cdot\mathbf{X}}\hat{\mu}(\mathbf{Q},L)\times\left[W\left(L,\mathbf{X},\mathbf{P}+\frac{\mathbf{Q}}{2}\right)-W\left(L,\mathbf{X},\mathbf{P}-\frac{\mathbf{Q}}{2}\right)\right]d\mathbf{Q}, \tag{14}$$

with the initial condition

$$W(0,\mathbf{X},\mathbf{P};\xi,\eta;k)=\frac{1}{(2\pi)^d}e^{-i\mathbf{P}\cdot(\xi-\eta)}\delta(\mathbf{X}-[\xi+\eta]/2). \tag{15}$$

Here, $\hat{\mu}(\mathbf{P},L)$ is the Fourier transform of $\mu(\mathbf{x},L)$ in the transverse variable $\mathbf{x}$. We can recover Γ from W by a Fourier transform, and in particular

$$\Gamma(L,\mathbf{y},\mathbf{y};\xi,\eta;k)=\int W(L,\mathbf{y},\mathbf{P};\xi,\eta)d\mathbf{P}. \tag{16}$$

Thus, the phase-conjugated, backpropagated time harmonic field is given by

$$\psi^B(\xi,L;k)=\int\int\overline{\psi_0(\eta;k)}\chi_A(\mathbf{y})\times\left(\int W(L,\mathbf{y},\mathbf{P};\xi,\eta,k)d\mathbf{P}\right)d\mathbf{y}\,d\eta, \tag{17}$$

in terms of the solution W of the Wigner equation (14).

IV. DETERMINISTIC DIFFRACTION LIMIT

In this section we will use the expression (17) for the backpropagated field and the invariant embedding and Wigner equations from Sec. III to calculate the deterministic diffraction limit for a time-dependent pulse, emanating from a point source in space.

For a homogeneous medium, with $\mu\equiv 0$, the solution to the Wigner equation (14) with the initial condition (15) is

$$W(L,\mathbf{X},\mathbf{P};\xi,\eta)=\frac{1}{(2\pi)^d}e^{-i\mathbf{P}\cdot(\xi-\eta)}\times\delta(\mathbf{X}-[\mathbf{LP}/k]-[\xi+\eta]/2). \tag{18}$$

Now, Eq. (16) gives

$$\Gamma(L,\mathbf{y},\mathbf{y};\xi,\eta;k)=\int W(L,\mathbf{y},\mathbf{P};\xi,\eta)d\mathbf{P}=\frac{1}{(2\pi)^d}\left(\frac{k}{L}\right)^d e^{-i(k/L)(\mathbf{y}-[\xi+\eta]/2)\cdot(\xi-\eta)}. \tag{19}$$

From this we get the following expression for the phase-conjugated and backpropagated time harmonic field:

$$\begin{aligned}\psi^B(\xi,L;k)&=\int\int\overline{\psi_0(\eta,k)}\chi_A(\mathbf{y})\frac{1}{(2\pi)^d}\times\left(\frac{k}{L}\right)^d e^{-i(k/L)(\mathbf{y}-[\xi+\eta]/2)\cdot(\xi-\eta)}d\mathbf{y}\,d\eta\\&=\left(\frac{k}{L}\right)^d\int\hat{\chi}_A\left(\frac{k}{L}(\eta-\xi)\right)\overline{\psi_0(\eta,k)}e^{i[k(\xi^2-\eta^2)/2L]}d\eta\\&=\left(\frac{k}{L}\right)^d e^{i(k\xi^2/2L)}\int\hat{\chi}_A\left(\frac{k}{L}(\eta-\xi)\right)e^{-i(k\eta^2/2L)}\overline{\psi_0(\eta,k)}d\eta.\end{aligned} \tag{20}$$

Here, $\hat{\chi}_A$ is the Fourier transform of the aperture function χ_A. If the source is a δ function in space (point source), $\psi_0(\eta)=\delta(\eta)$, then the expression for ψ^B simplifies to

$$\psi^B(\xi,L;k)=\left(\frac{k}{L}\right)^d e^{ik\xi^2/2L}\hat{\chi}_A\left(\frac{-k\xi}{L}\right). \tag{21}$$

We will now use this result for two different types of time-reversal mirrors. First, we consider a finite aperture TRM, from which we have edge diffraction effects. Then, we consider a TRM with a Gaussian aperture function. We comment briefly on the resolution limits in time reversal for these two kinds of TRMs.

A. Finite aperture TRM

For simplicity we consider only one transverse dimension, $d=1$. Let $\chi_A(y)$ be the indicator function of a TRM of size a centered at $y=0$. The Fourier transform of $\chi_A(y)$ is $\hat{\chi}_A(P)=\sin(Pa/2)/\pi P$. Plugging this into Eq. (21) gives

$$\psi^B(\xi,L;k)=\frac{1}{\pi\xi}\sin\left(\frac{k\xi a}{2L}\right)e^{ik\xi^2/2L}. \tag{22}$$

The diffraction-limited resolution can be measured by the distance ξ_F from the origin to the first *Fresnel Zone*, that is, the first zero of the phase-conjugated backpropagated field

$$\xi_F=\frac{2\pi L}{ka}=\frac{\lambda L}{a}. \tag{23}$$

If the pulse is a point source in space and a Gaussian in the time domain with carrier frequency ω_0, that is

$$\Psi_0(\eta,t)=\delta(\eta)\frac{1}{\sqrt{2\pi\sigma_t^2}}e^{-(t^2/2\sigma_t^2)}e^{-i\omega_0 t},$$
$$\psi_0(\eta,\omega)=\frac{1}{2\pi}\delta(\eta)e^{-[(\omega-\omega_0)^2\sigma_t^2/2]}, \tag{24}$$

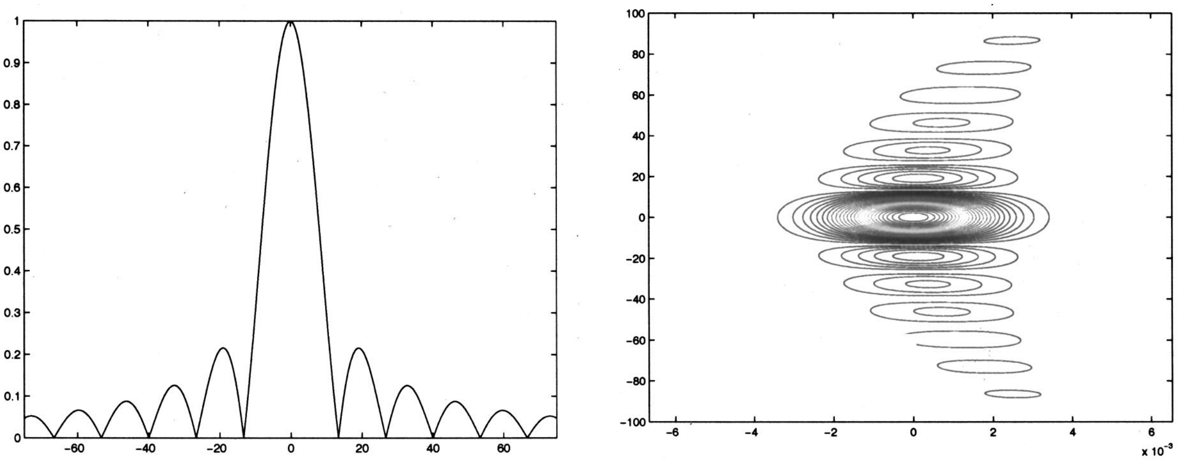

FIG. 3. The left figure shows the spatial diffraction pattern of the amplitude of (25) at time $t=0$. The right figure is a space-time contour plot of the amplitude of (25) and shows the parabolic shift in arrival time. Here, the pulse width is $\sigma_t=1.33$ ms, the TRM width $a=50$ m, the propagation speed is $c_0=1500$ m/s, the propagation distance is $L=1000$ m, and the period of the carrier is 0.22 ms at 4.5 KHz.

then the *time-reversed* and backpropagated signal in time at the source plane is

$$\begin{aligned}\Psi^B(\xi,L,t) &= \frac{1}{2\pi}\int \psi^B\left(\xi,L,\frac{\omega}{c_0}\right)e^{-[(\omega-\omega_0)^2\sigma_t^2]/2}e^{-i\omega t}d\omega \\ &= \int \frac{1}{(2\pi)^2 i\xi}\left(e^{(i\omega\xi a/2c_0L)}-e^{-(i\omega\xi a/2c_0L)}\right) \\ &\quad\times e^{(i\omega\xi^2/2c_0L)}e^{-[(\omega-\omega_0)^2\sigma_t^2/2]}e^{-i\omega t}\,d\omega \\ &= \frac{1}{(2\pi)^{3/2}i\xi\sigma_t}e^{-i\omega_0(t-(\xi^2/2c_0L))} \\ &\quad\times\{e^{(i\omega_0\xi a/2c_0L)}e^{-[(t-\xi^2/2c_0L)-\xi a/2c_0L]^2/2\sigma_t^2} \\ &\quad - e^{-i\omega_0\xi a/2c_0L}e^{-[(t-\xi^2/2c_0L)+\xi a/2c_0L]^2/2\sigma_t^2}\}. \end{aligned} \tag{25}$$

Diffraction from the two edges of the TRM is seen clearly. At the wavefront, where $t=\xi^2/2c_0L$, we have

$$\Psi^B\left(\xi,L,\frac{\xi^2}{2c_0L}\right) = \frac{\sqrt{2\pi}}{\sigma_t}\frac{1}{2\pi^2\xi}\sin\left[\frac{\omega_0\xi a}{2c_0L}\right]e^{-\xi^2/2[2\sigma_t c_0L/a]^2}. \tag{26}$$

If the width of the pulse in time σ_t is large compared to λ_0/c_0, the time period, then the variance of the Gaussian in Ψ^B is

$$\frac{2\sigma_t c_0L}{a}=\frac{2\sigma_t c_0}{\lambda_0}\frac{\lambda_0 L}{a}\gg\xi_F=\frac{\lambda_0 L}{a}. \tag{27}$$

Thus, the diffraction limit is determined by the carrier frequency. A plot of $\Psi^B(\xi,L,0)$ is shown in Fig. 3.

B. Gaussian TRM

We now consider the case where the aperture function, χ_A, is a normalized, isotropic Gaussian with variance a

$$\chi_A(\mathbf{y})\sim\frac{1}{(2\pi a^2)^{d/2}}e^{-|y|^2/2a^2}. \tag{28}$$

In this case, the phase-conjugated backpropagated time-harmonic field from a point source is

$$\psi^B(\xi,L;k)=\left(\frac{k}{2\pi L}\right)^d e^{-a^2k^2|\xi|^2/2L^2}e^{ik|\xi|^2/2L}. \tag{29}$$

The resolution of the refocused signal is proportional to the variance of this Gaussian, which is $\lambda L/a$.

If the pulse is a point source in space and a real Gaussian in time with carrier frequency ω_0, then

$$\begin{aligned}\Psi_0(\eta,t)&=\delta(\eta)\frac{1}{\sqrt{2\pi\sigma_t^2}}e^{-t^2/2\sigma_t^2}e^{-i\omega_0 t},\\ \psi_0(\eta,\omega)&=\frac{\delta(\eta)}{2\pi}e^{-[(\omega-\omega_0)^2\sigma_t^2/2]}.\end{aligned} \tag{30}$$

We use the inverse Fourier transform to synthesize the self-averaging, time-reversed, and backpropagated signal at the source plane

$$\begin{aligned}\Psi^B(\xi,L,t)&=\frac{1}{2\pi}\int\psi^B\left(\xi,L,\frac{\omega}{c_0}\right)e^{-[(\omega-\omega_0)^2\sigma_t^2]/2}e^{-i\omega t}\,d\omega\\ &=\frac{1}{2\pi}\int\left(\frac{\omega}{2\pi c_0L}\right)^d e^{-(a^2\omega^2\xi^2/2c_0^2L^2)}e^{i\omega\xi^2/2c_0L}\\ &\quad\times e^{-[(\omega-\omega_0)^2\sigma_t^2]/2}e^{-i\omega t}\,d\omega\\ &=\frac{1}{2\pi}\left(\frac{i}{2\pi c_0L}\right)^d\cdot\frac{d^d}{dt^d}[e^{-i\omega_0(t-[\xi^2/2c_0L])}\\ &\quad\times e^{-(a^2\omega_0^2\xi^2/2c_0^2L^2)}\sqrt{2\pi/[(a^2\xi^2/c_0^2L^2)+\sigma_t^2]}\\ &\quad\times e^{[i(t-[\xi^2/2c_0L])+[a^2\omega_0\xi^2/c_0^2L^2]]^2/[(2a^2\xi^2/c_0^2L^2)+2\sigma_t^2]}.\end{aligned} \tag{31}$$

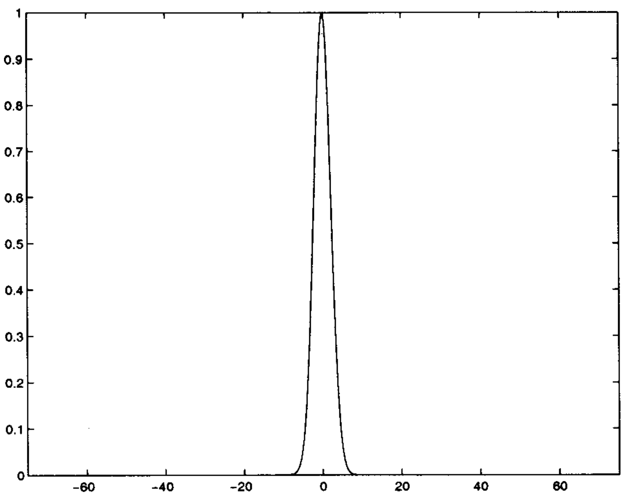

FIG. 4. The spatial shape of the compressed pulse with a Gaussian aperture function at time $t=0$, from (31). Here, the pulse width is $\sigma_t=1.33$ ms, the TRM width is $a=50$ m, the propagation speed is $c=1500$ m/s, propagation distance is $L=1000$ m, and the time period of the carrier is 0.22 ms. Note the absence of Fresnel zones for a Gaussian TRM.

Here, $\xi^2/2c_0L$ is the a parabolic shift in time of the front and $d=1,2$. A plot of the absolute value of this function at $t=0$ is shown in Fig. 4. When the aperture is small, $a/L \ll 1$, and the time duration of the pulse is large compared to the time period of the carrier, $\sigma_t \gg \lambda_0/c_0$, then the width of the compressed pulse in space is approximately $\lambda_0 L/a$. With the parameters as in Fig. 4, this ratio is 6.6 m, which is roughly the width at midlevel of the curve shown.

V. SCALED WIGNER EQUATION AND THE TRANSPORT LIMIT

In order to study the effect of random inhomogeneities we introduce a scaling of parameters as follows: (i) The wavelength λ is short compared to the propagation distance L and we let $\epsilon=\lambda/L \ll 1$ be a small, dimensionless parameter which scales all other variables. (ii) The wavelength is comparable to the correlation length, l, that is $l \sim \lambda$. This allows full interaction between the waves and the random medium, which is an interesting case to study. (iii) The fluctuations, $\mu=n^2-1$, of the index of refraction are weak and isotropic, $|\mu| \sim \sqrt{\epsilon}$. If the fluctuations are very strong or very anisotropic (as in a layered medium) the parabolic wave equation cannot be used. If they are very weak then stochastic effects will not be observable.

We want to analyze long-distance and long-time propagation, so we rescale the space variables by $\mathbf{x} \to \mathbf{x}/\epsilon$, $L \to L/\epsilon$. We do not rescale the time $t \to t/\epsilon$ in (8) because in this paper t is always *relative* time on the scale of the pulse width. So, it will remain of order one. The Green's function in the scaled variables is

$$
\begin{aligned}
G^{\epsilon}(L,0;\mathbf{x},\xi;k) &= G\left(\frac{L}{\epsilon},0;\frac{\mathbf{x}}{\epsilon},\frac{\xi}{\epsilon};k\right),\\
\Gamma^{\epsilon}(L,\mathbf{x},\mathbf{y};\xi,\eta;k) &= G^{\epsilon}(L,0;\mathbf{x},\xi;k)\overline{G^{\epsilon}}(L,0;\mathbf{y},\eta;k),
\end{aligned} \tag{32}
$$

and Γ^{ϵ} satisfies the scaled equation

$$
\begin{aligned}
&2ik\epsilon\frac{\partial\Gamma^{\epsilon}}{\partial L}+\epsilon^2(\Delta_{\mathbf{x}}-\Delta_{\mathbf{y}})\Gamma^{\epsilon}+k^2\sqrt{\epsilon}\\
&\qquad\times\left[\mu\left(\frac{\mathbf{x}}{\epsilon},\frac{L}{\epsilon}\right)-\mu\left(\frac{\mathbf{y}}{\epsilon},\frac{L}{\epsilon}\right)\right]\Gamma^{\epsilon}=0,\\
&\Gamma^{\epsilon}(0,\mathbf{x},\mathbf{y};\xi,\eta;k)=\frac{1}{\epsilon}\delta\left(\frac{\mathbf{x}-\xi}{\epsilon}\right)\delta\left(\frac{\mathbf{y}-\eta}{\epsilon}\right).
\end{aligned} \tag{33}
$$

The scaling of the initial conditions for Γ^{ϵ} is adjusted so that the wave energy is independent of the small parameter ϵ.

Since we are interested in the local coherence of wave fields, within a few wavelengths or correlation lengths, we introduce the scaled change of variables

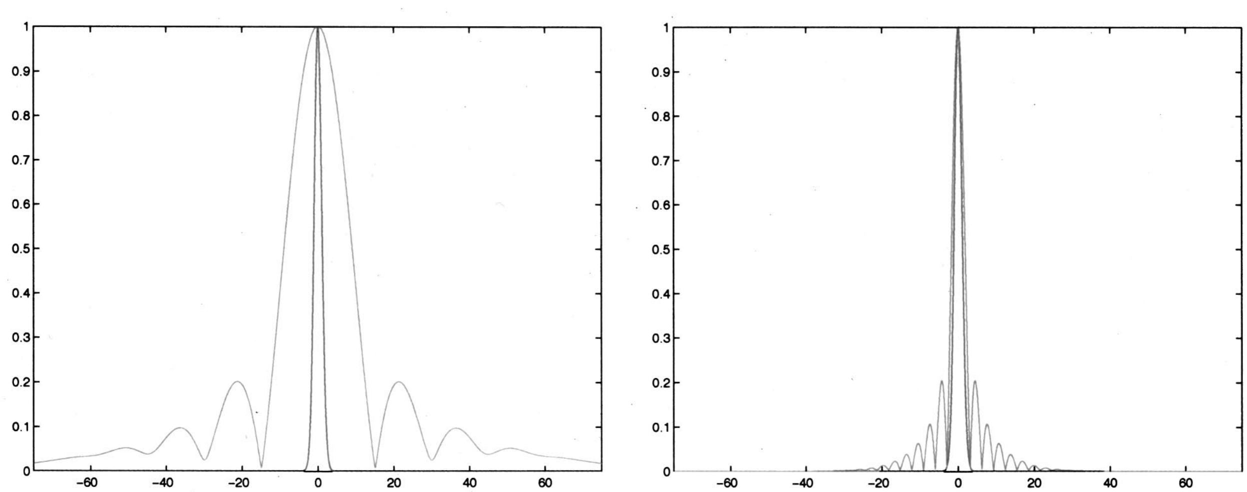

FIG. 5. Comparison of the theoretical formula (56) at time $t=0$, for a medium with $L=600$ m, $a_e=195$ m, $\gamma=2.12\times10^{-5}$ m^{-1}. The left figure shows a plot of (56) for a homogeneous medium, $\gamma=0$, with a TRM of width $a=40$ (light/wide Fresnel zone), and the random medium with $\gamma=2.12\times10^{-5}$ and $a=40$ (dark/narrow Fresnel zone). The right figure shows a plot of (56) for a homogeneous medium, $\gamma=0$, with $a=a_e=195$ (light), and the random medium with $\gamma=2.12\times10^{-5}$, and $a=40$ (dark). The match confirms the validity of (57). The values of a_e and γ originate from the numerical estimates of the effective aperture summarized in Table I in Sec. VIII.

$$\mathbf{X}=\frac{\mathbf{x}+\mathbf{y}}{2},\quad \mathbf{x}=\mathbf{X}-\frac{\epsilon\mathbf{Y}}{2},$$
$$\epsilon\mathbf{Y}=\mathbf{y}-\mathbf{x},\quad \mathbf{y}=\mathbf{X}+\frac{\epsilon\mathbf{Y}}{2}, \tag{34}$$

so that $\Delta_{\mathbf{x}}-\Delta_{\mathbf{y}}=(\nabla_{\mathbf{x}}-\nabla_{\mathbf{y}})(\nabla_{\mathbf{x}}+\nabla_{\mathbf{y}})=-2/\epsilon\nabla_{\mathbf{X}}\nabla_{\mathbf{Y}}$. In the new variables $\Gamma^{\epsilon}(L,\mathbf{X},\mathbf{Y};\xi;\eta;k)$ satisfies

$$2ik\frac{\partial\Gamma^{\epsilon}}{\partial L}-2\nabla_{\mathbf{X}}\nabla_{\mathbf{Y}}\Gamma^{\epsilon}+\frac{k^2}{\sqrt{\epsilon}}\left(\mu\left(\frac{\mathbf{X}}{\epsilon}-\frac{\mathbf{Y}}{2},\frac{L}{\epsilon}\right)-\mu\left(\frac{\mathbf{X}}{\epsilon}+\frac{\mathbf{Y}}{2},\frac{L}{\epsilon}\right)\right)\Gamma^{\epsilon}=0,$$
$$\Gamma^{\epsilon}(0,\mathbf{X},\mathbf{Y};\xi,\eta;k)=\frac{1}{\epsilon}\delta\left(\frac{\mathbf{X}}{\epsilon}-\frac{\mathbf{Y}}{2}-\frac{\xi}{\epsilon}\right)\delta\left(\frac{\mathbf{X}}{\epsilon}+\frac{\mathbf{Y}}{2}-\frac{\eta}{\epsilon}\right). \tag{35}$$

We again let $W^{\epsilon}(L,\mathbf{X},\mathbf{P};\xi,\eta;k)$ be the Fourier transform of $\Gamma^{\epsilon}(L,\mathbf{X},\mathbf{Y};\xi,\eta;k)$ in $\mathbf{Y}$, and then W^{ϵ} satisfies

$$k\frac{\partial W^{\epsilon}}{\partial L}+\mathbf{P}\cdot\nabla_{\mathbf{X}}W^{\epsilon}=\frac{ik^2}{2\sqrt{\epsilon}}\int e^{-(i\mathbf{Q}\cdot\mathbf{X}/\epsilon)}\hat{\mu}\left(\mathbf{Q},\frac{L}{\epsilon}\right)\times\left[W^{\epsilon}\left(L,\mathbf{X},\mathbf{P}+\frac{\mathbf{Q}}{2}\right)-W^{\epsilon}\left(L,\mathbf{X},\mathbf{P}-\frac{\mathbf{Q}}{2}\right)\right]d\mathbf{Q}, \tag{36}$$

with the initial condition

$$W^{\epsilon}(0,\mathbf{X},\mathbf{P};\xi,\eta;k)=\frac{1}{(2\pi)^d}e^{-i\mathbf{P}\cdot[(\xi-\eta)/\epsilon]}\delta\left(\mathbf{X}-\frac{\xi+\eta}{2}\right). \tag{37}$$

By the asymptotic theory which we review briefly in the Appendix, the average Wigner function $\langle W^{\epsilon}(L,\mathbf{X},\mathbf{P};\xi,\eta;k)\rangle\rightarrow W(L,\mathbf{X},\mathbf{P};\xi,\eta;k)$, as $\epsilon\rightarrow 0$, and W satisfies the transport equation

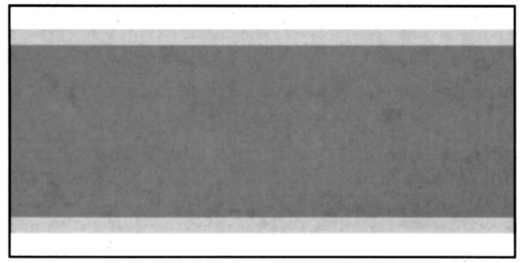

FIG. 6. Structure of the numerical domain: In the center strip the random medium is at full strength (75% of the thickness), then there is a smooth transition layer (5%–10%) where the strength decreases. In the outer layer the medium is homogeneous, allowing for effective implementation of discrete transparent boundary conditions.

$$k\frac{\partial W}{\partial L}+\mathbf{P}\cdot\nabla_{\mathbf{X}}W=\frac{\pi k^3}{4}\int\hat{R}\left(\frac{\mathbf{P}^2-\mathbf{Q}^2}{2k},\mathbf{P}-\mathbf{Q}\right)\times[W(L,\mathbf{X},\mathbf{Q};\xi,\eta;k)-W(L,\mathbf{X},\mathbf{P};\xi,\eta;k)]d\mathbf{Q},$$
$$W(0,\mathbf{X},\mathbf{P};\xi,\eta;k)=e^{[-i\mathbf{P}\cdot(\xi-\eta)/\epsilon]}/(2\pi)^d\delta\left(\mathbf{X}-\frac{\xi+\eta}{2}\right), \tag{38}$$

where R is the correlation function

$$R(z,\mathbf{x})=\langle\mu(\eta,\mathbf{y})\mu(\eta+z,\mathbf{y}+\mathbf{x})\rangle, \tag{39}$$

and $\hat{R}(p,\mathbf{P})$ is its Fourier transform in $(z,\mathbf{x})$, that is, the power spectral density of the fluctuations of the refractive index.

It is important to note that the initial condition for W in (38) depends on the small parameter ϵ, even though we have passed to the asymptotic limit in the equation. Small ϵ means high-frequency asymptotics, that is, long propagation distances compared to the wavelength, as well as long propagation distances compared to the correlation length, which produces the incoherent scattering terms on the right-side of the

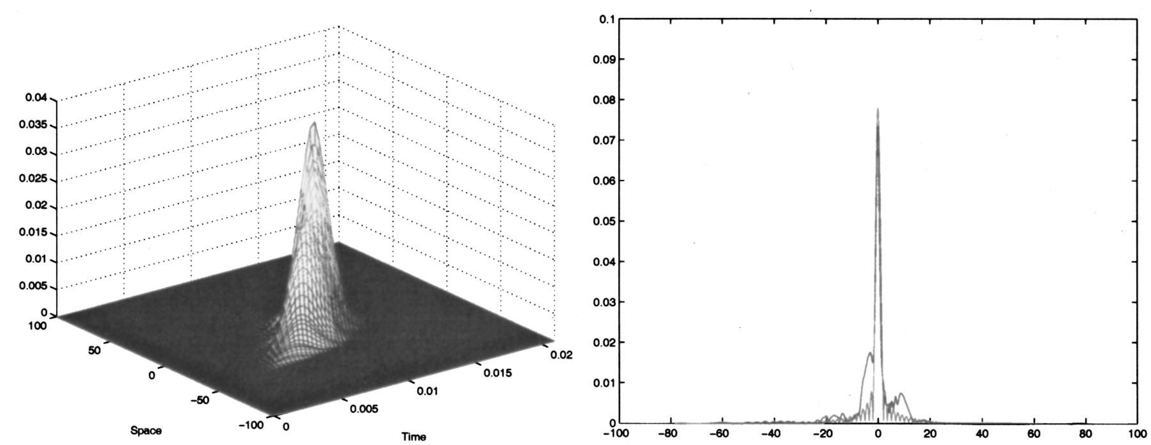

(a) TRM-received (b) Recompressed

FIG. 7. Numerical simulation of time reversal. The width of the time-reversal mirror and the numerical domain are 50, and 200 m, respectively. The maximum contrast is ±10%, that is $|\mu|\leqslant 0.1$. The left figure shows the signal as received on the TRM plane. This signal is restricted to the mirror, time-reversed, and re-emitted into the medium. The right figure shows a spatial section through the refocused signal. Here, the propagation distance is very short, only 200 m, or about 20 correlation lengths. We see that there is not enough randomness to observe super-resolution.

equation in (38). By keeping the ϵ dependence of the initial conditions we retain coherent diffraction effects in the transport approximation, which are clearly important in time reversal.

In the Appendix we discuss several scaling limits in which multipathing effects are relevant. We also discuss the validity of the paraxial approximation in these limits. In particular, the paraxial approximation may be violated in the transport limit, but its validity is restored in the narrow beam limit of Sec. VII.

VI. PULSE STABILIZATION

As we noted in the Introduction, time reversal of time harmonic or very narrow-band signals (phase conjugation) is statistically unstable. This means that

$$\langle \psi^B(\xi,L,k)\rangle = \int\int\left[\int W(L,\mathbf{y},\mathbf{P};\xi,\eta;k))d\mathbf{P}\right]\overline{\psi_0(\eta,k)}\chi_A(\mathbf{y})d\mathbf{y}\,d\eta \tag{40}$$

gives no information at all about the behavior of $\psi^B(\xi,L,k)$ for individual realizations of the medium, as demonstrated in Fig. 2, which is obtained by numerical simulations. How is it, then, that super-resolution in time reversal is clearly seen in a variety of physical experiments where there is no ensemble of random media or averaging? This issue is not addressed in the time-reversal literature and poor understanding of it tends to make super-resolution counterintuitive and somewhat mysterious, especially to those familiar with phase conjugation.

The explanation is that super-resolution is a time-domain phenomenon and it is the recompressed pulse in space *and* time that is statistically stable. Pulse stabilization in randomly layered media is well understood (Solna and Papanicolaou, 2000), and references therein, and the reason for this stabilization is similar to the one encountered in time reversal here. In the asymptotic limit of high-frequency, short correlations, and long propagation distances, described in the previous section, we also have statistical decorrelation of the wave functions for different frequencies. For $k\neq k'$ we have

$$\langle \psi^B(L,\xi,k)\psi^B(L,\xi,k')\rangle \approx \langle \psi^B(L,\xi,k)\rangle\langle \psi^B(L,\xi,k')\rangle, \tag{41}$$

in the limit $\epsilon\to 0$. This is the property that gives pulse stabilization in the time domain. To see this, we note that the time-reversed, backpropagated field is

$$\Psi^B(L,\xi,t)=\int e^{-i\omega t}\psi^B(L,\xi,\omega/c_0)d\omega, \tag{42}$$

and thus

$$\begin{aligned}\langle \Psi^B(L,\xi,t)^2\rangle &= \left\langle\left(\int e^{-i\omega t}\psi^B\left(L,\xi,\frac{\omega}{c_0}\right)d\omega\right)^2\right\rangle\\ &= \int\int e^{-i(\omega_1+\omega_2)t}\left\langle \psi^B\left(L,\xi,\frac{\omega_1}{c_0}\right)\right.\\ &\quad\times\left.\psi^B\left(L,\xi,\frac{\omega_2}{c_0}\right)\right\rangle d\omega_1\,d\omega_2\\ &\approx \int\int e^{-i(\omega_1+\omega_2)t}\left\langle \psi^B\left(L,\xi,\frac{\omega_1}{c_0}\right)\right\rangle\\ &\quad\times\left\langle \psi^B\left(L,\xi,\frac{\omega_2}{c_0}\right)\right\rangle d\omega_1\,d\omega_2\\ &= \langle \Psi^B(L,\xi,t)\rangle^2. \end{aligned}\tag{43}$$

This means that for any $\delta>0$, the probability

$$P\{|\Psi^B(L,\xi,t)-\langle\Psi^B(L,\xi,t)\rangle|>\delta\} \leqslant \frac{\langle(\Psi^B(L,\xi,t)-\langle\Psi^B(L,\xi,t)\rangle)^2\rangle}{\delta^2}\approx 0, \tag{44}$$

by the Chebyshev inequality and (43). That is

$$\Psi^B(L,\xi,t)\approx\langle\Psi^B(L,\xi,t)\rangle, \tag{45}$$

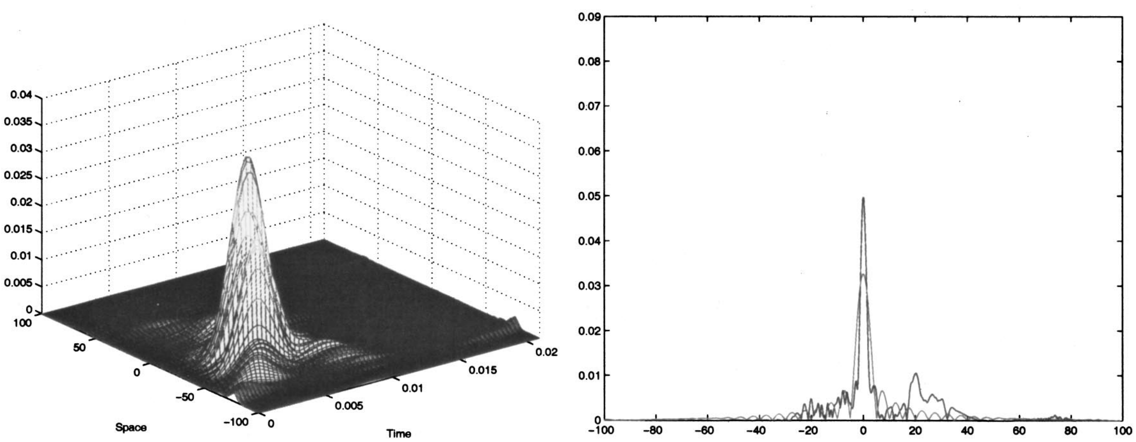

(a) TRM-received

(b) Recompressed

FIG. 8. In this simulation the propagation distance is 600 m. Now, we clearly see the super-resolution phenomenon: the peak of the recompressed pulse in the random medium (upper) is sharper than the one for the homogeneous medium (lower). (All other parameters are as in Fig. 7.)

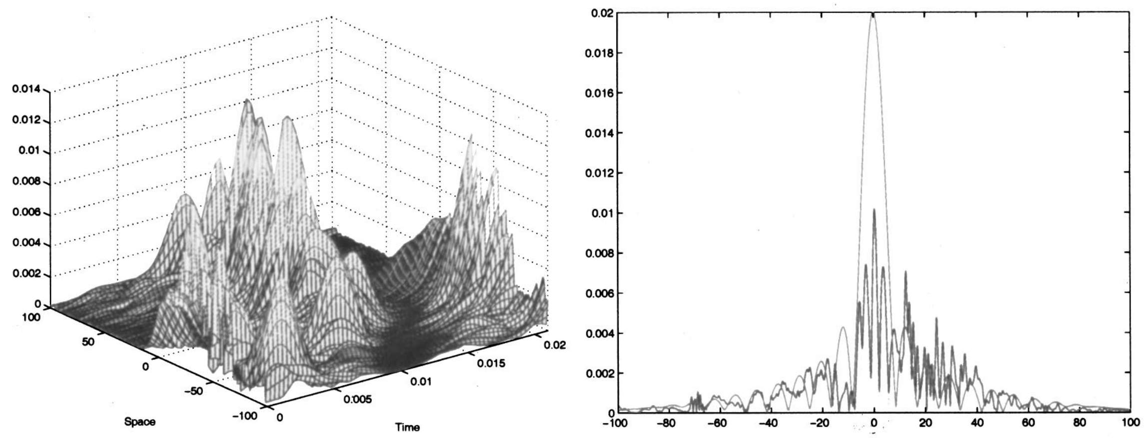

(a) TRM-received (b) Recompressed

FIG. 9. In this simulation the propagation distance is 1000 m. Although the first peak of the recompressed signal in the random medium is much narrower, there is really no super-resolution in this case because of the large sidelobes. The limits of the numerical simulations are discussed in Sec. II. (All other parameters as in Fig. 7.)

so that the time-reversed and backpropagated field is *self-averaging in this asymptotic regime*. Put in another way, averaging over frequencies is like averaging over realizations, *in the appropriate asymptotic regime*, as discussed in the Appendix. This is why super-resolution is observed in physical situations as well as in numerical simulations. In Sec. VIII we will discuss Figs. 7, 8, and 9, where the self-averaging property is quite clearly seen in the numerical simulations.

From (43) it is clear that, in general, fluctuation statistics of the time-reversed and backpropagated field depends on the two-frequency correlation function $\langle \psi^B(L,\xi,\omega_1/c_0)\psi^B(L,\xi,\omega_2/c_0)\rangle$. This differs substantially from its incoherent limit $\langle \psi^B(L,\xi,\omega_1/c_0)\rangle \times\langle \psi^B(L,\xi,\omega_2/c_0)\rangle$ only when $|\omega_1-\omega_2|\approx\epsilon(\omega_1+\omega_2)/2$. The two-frequency correlation function can be expressed in terms of the two-frequency Wigner function, for which a transport equation like (38) can be derived for its evolution in L. The additional information obtained this way affects only the tail of the time-reversed and backpropagated field, a phenomenon that is well understood in randomly layered media (Solna and Papanicolaou, 2000; Asch *et al.*, 1991). Tail behavior, that is, large-t behavior of (8), and hence two-frequency statistics, is important in a more refined theory of super-resolution where there are several sources of different strengths, in different but nearby locations in space as well as in time. We then want to find theoretical limits of when these sources can be discriminated in the time-reversed and backpropagated field, and for that we do need to know the tail behavior.

TABLE I. The table shows the propagation distance, L in meters; the numerically estimated effective aperture, a_e^E in meters; the corresponding estimate for γ, in inverse meters, using Eq. (57); a "theoretical" effective aperture, a_e^T, computed using (57) with $\gamma=2.12\times10^{-5}$ (the median of the estimated γ's); and the number of realizations used for each estimated pair of (a_e^E,γ). The other parameters are: TRM width, $a=40$ m; maximal contrast 10%, width of the numerical domain 150 m; width of the random media 112.5 m.

L	a_e^E	γ	a_e^T	N
300	77	2.00×10^{-5}	77	207
350	86	1.69×10^{-5}	92	418
400	104	1.83×10^{-5}	109	202
450	123	1.86×10^{-5}	127	202
500	150	2.11×10^{-5}	147	205
600	195	2.12×10^{-5}	190	213
650	217	2.08×10^{-5}	213	260
700	248	2.19×10^{-5}	238	202
750	266	2.05×10^{-5}	263	235
800	275	1.81×10^{-5}	289	201
850	293	1.71×10^{-5}	316	223

VII. BEAM GEOMETRY

We will assume from now on that the difference $\xi-\eta$ is of order ϵ and we will drop the ϵ in the phase of the initial

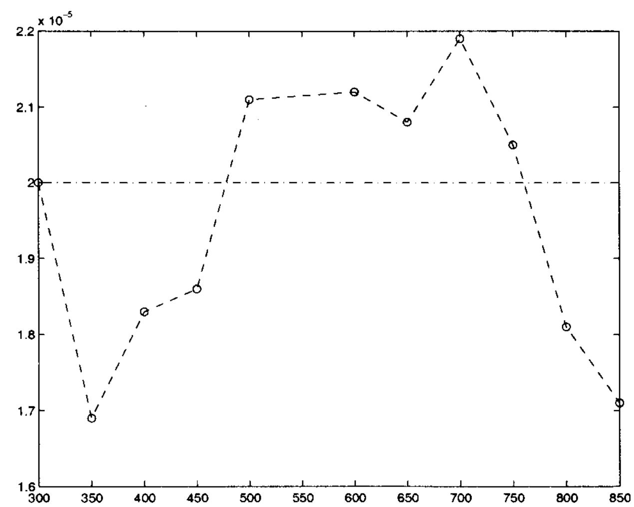

FIG. 10. The estimated values of γ for Table I. The estimate stabilizes as the propagation distance increases, *until* the numerical setup cannot capture adequately the multipathing and the rapidly growing effective aperture. In our setup we can simulate an effective aperture up to about twice the width of the random medium.

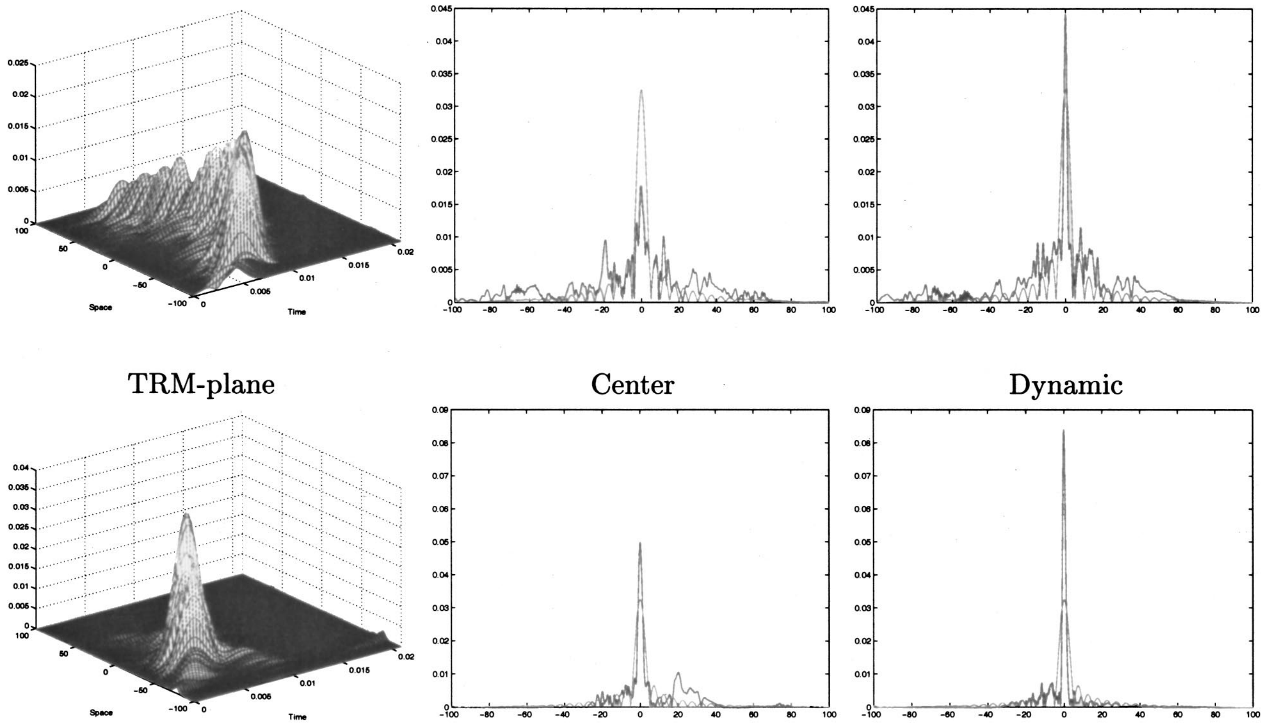

FIG. 11. Dynamic TRM placement: 600-m propagation. The left figure shows the pulse in space-time as received on the TRM plane. The center figure shows a spatial cut through the peak of the recompressed pulse using static TRM placement. The right figure shows a spatial cut through the peak of the recompressed pulse using optimal dynamic TRM placement. Note that each plot is for one random realization of the medium. The maximum contrast is 10%, that is $|\mu| \leqslant 0.1$. The TRM is 50 m wide and the numerical domain 200 m wide. The red curves correspond to time reversal in a homogeneous medium and the blue curves to time reversal in the random medium.

condition in the transport equation (38). This means that we will restrict our attention to the behavior of the time-reversed, backpropagated field in the vicinity of the source.

We will now introduce the *beam approximation* for the the solution W of the transport equation (38). This is simply a diffusion approximation in $\mathbf{P}$ space that is valid when the power spectral density $\hat{R}(p,\mathbf{P})$ is peaked near zero in the transverse wave number $\mathbf{P}$. We will describe this approxima-

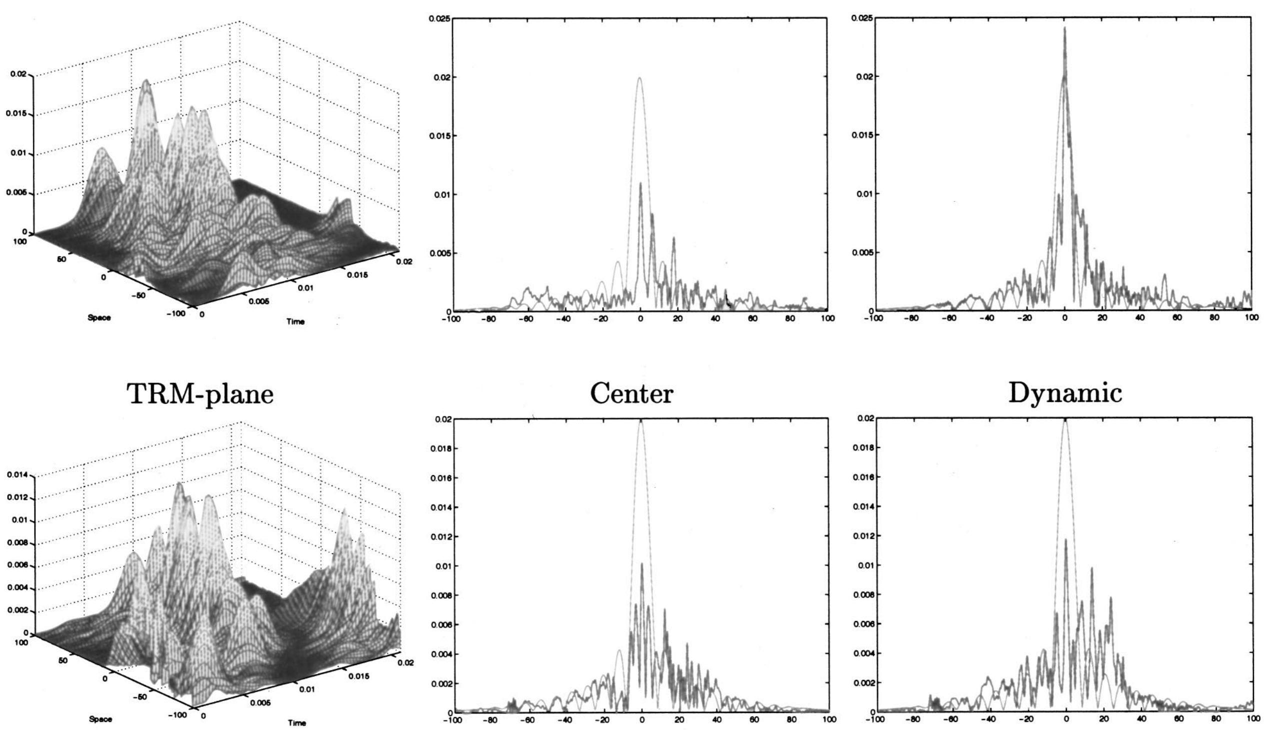

FIG. 12. Dynamic TRM placement: 1000-m propagation. (For parameter information see the caption for Fig. 11.)

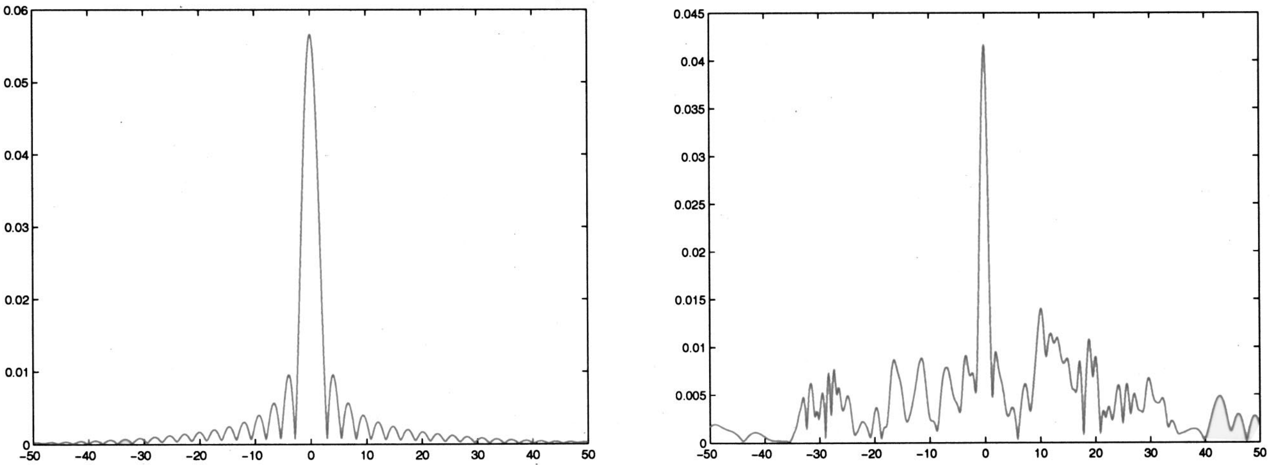

FIG. 13. The recompressed pulse for homogeneous (left) and random (right) media. The propagation distance is 800 m, the domain width is 100 m, and the maximal contrast is 10%. The boundary conditions are: *DTBC*. TRM width 100 m. Here, we can clearly see super-resolution as the recompressed peak is narrower in the random medium.

tion qualitatively without introducing a small parameter or doing a formal asymptotic analysis. We do this because it is a relatively simple and well-known approximation, and in any case does not involve high-frequency asymptotics or statistical considerations like the derivation of (38). The narrow-beam approximation is discussed further in the Appendix.

The physical basis for the narrow-beam approximation is this: When we are in the transport regime and the aperture of the TRM is small, that is, $a \ll L$ in Fig. 1, then only multiply scattered waves that stay near the z axis contribute significantly to the time-reversed and backpropagated field. So, the wave goes over many correlation lengths in the direction of propagation but only over a few in the transverse direction. This is what makes the power spectral density appear to be peaked in the transverse direction.

A quick derivation of the beam approximation is as follows. We expand W around the point $\mathbf{P}$ up to second order on the right side of (38) to obtain

$$k\frac{\partial W}{\partial L}+\mathbf{P}\cdot\nabla_{\mathbf{X}}W=\frac{\pi k^3}{4}\int \hat{R}\left(\frac{\mathbf{P}^2-\mathbf{Q}^2}{2k},\mathbf{P}-\mathbf{Q}\right)$$

$$\times[\nabla W(\mathbf{P})+\tfrac{1}{2}\nabla\nabla W(\mathbf{P})(\mathbf{Q}-\mathbf{P})]\cdot(\mathbf{Q}-\mathbf{P})\,d\mathbf{Q}, \quad (46)$$

$$W(0,\mathbf{X},\mathbf{P};\xi,\eta;k)=\frac{1}{(2\pi)^d}e^{-i\mathbf{P}\cdot(\xi-\eta)}\delta\left(\mathbf{X}-\frac{\xi+\eta}{2}\right),$$

where $\nabla\nabla W$ is the matrix of second derivatives of W. The gradient term on the right is zero because $\hat{R}$ is even, so (46) becomes

$$k\frac{\partial W}{\partial L}+\mathbf{P}\cdot\nabla_{\mathbf{X}}W=\frac{\pi k^3 D(\mathbf{P})}{8}\Delta_{\mathbf{P}}W(\mathbf{P}),$$
$$(47)$$
$$W(0,\mathbf{X},\mathbf{P};\xi,\eta;k)=\frac{1}{(2\pi)^d}e^{-i\mathbf{P}\cdot(\xi-\eta)}\delta\left(\mathbf{X}-\frac{\xi+\eta}{2}\right),$$

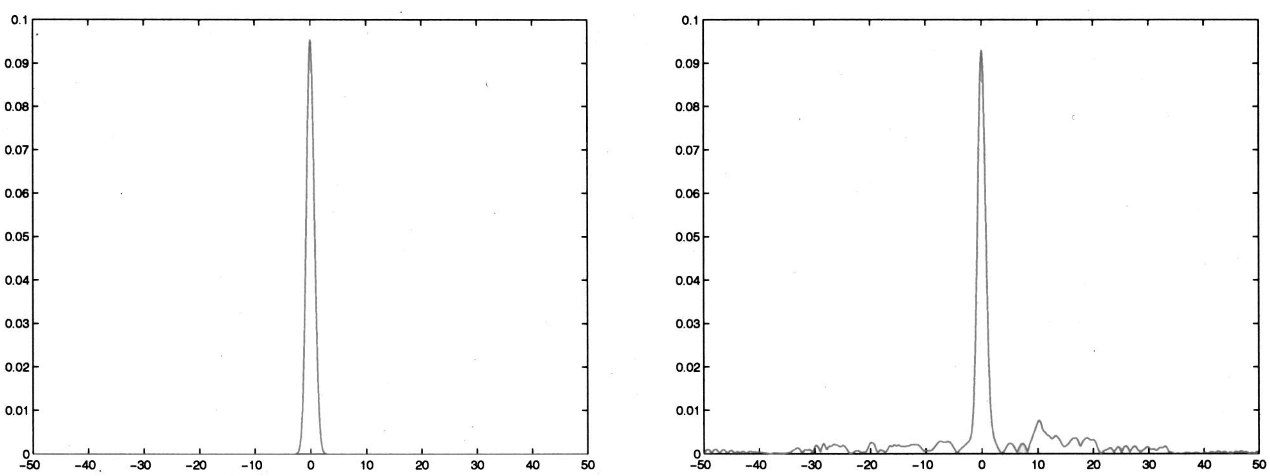

FIG. 14. Homogeneous medium on the left, random medium on the right. Here, we have *Waveguide* boundary conditions with TRM width 100 m. We capture all the energy inside the waveguide on the TRM, so the waveguide effect is much stronger than the random-medium effect. There can be no super-resolution in this setting.

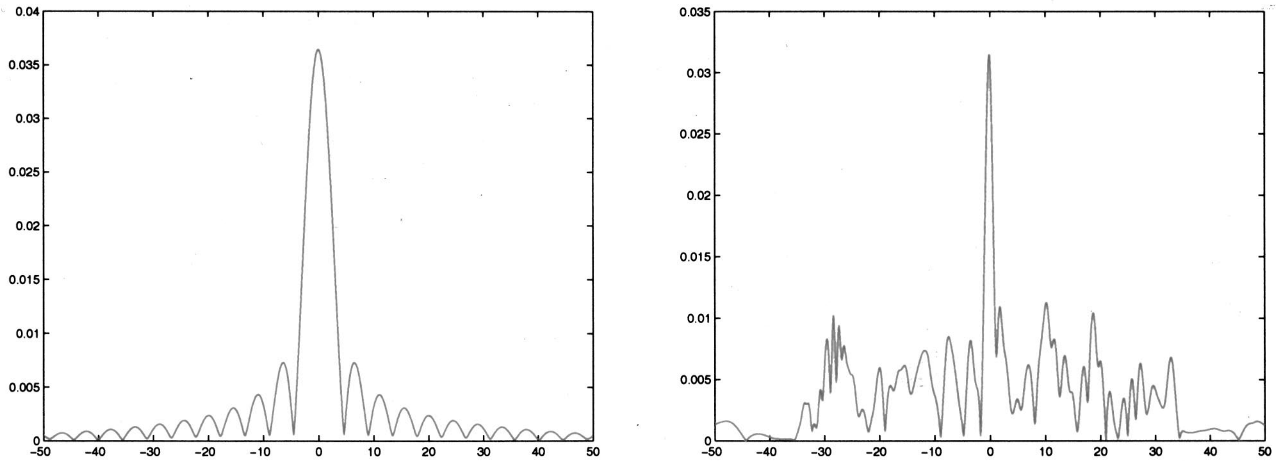

FIG. 15. Homogeneous medium on the left, random medium on the right. Type of boundary conditions: *DTBC* with TRM width 60 m. We can clearly see super-resolution as the recompressed peak is narrower in the random medium case. The fluctuations in the sidelobes are partly due to the fact that we are pushing the paraxial approximation beyond its limit; the 10% contrast is stretching the ''low-contrast'' assumption.

where $\Delta_{\mathbf{P}}$ is the Laplacian in wave number space and the wave number diffusion constant $D(\mathbf{P})$ is given by

$$D(\mathbf{P}) \stackrel{\text{def}}{=} \int \hat{R}\left(\frac{\mathbf{P}^2-\mathbf{Q}^2}{2k},\mathbf{P}-\mathbf{Q}\right)|\mathbf{P}-\mathbf{Q}|^2 d\mathbf{Q}. \tag{48}$$

When this wave number diffusion constant, which is a reciprocal length, is essentially independent of the wave number $\mathbf{P}$, then Eq. (47) is the narrow-beam approximation to the transport equation (38). In many interesting scaling limits the phase-space diffusion coefficient D does turn out to be constant, as we discuss in the Appendix.

For D constant, Eq. (47) can be solved by elementary methods. To get the time-reversed, backpropagated field we need $\Gamma(L,\mathbf{y},\mathbf{y};\xi,\eta;k)$, which is the inverse Fourier transform of W at $\mathbf{Y}=0$. Thus

$$\Gamma(L,\mathbf{y},\mathbf{y};\xi,\eta;k)= W(L,\mathbf{y},\mathbf{P};\xi,\eta;k)d\mathbf{P}$$

$$=\left[\frac{k}{2\pi L}\right]^d e^{-ik/L(\mathbf{y}-\xi+\eta/2)\cdot(\xi-\eta)} \times e^{-\pi k^2 DL(\xi-\eta)^2/2}. \tag{49}$$

Let

$$\gamma=\frac{\pi D}{8}. \tag{50}$$

Then, the mean phase-conjugated and backpropagated time-harmonic field is given by

$$\begin{aligned}\langle \psi^B(\xi,L,k)\rangle &= \int\int\left[\int W(L,\mathbf{y},\mathbf{P};\xi,\eta;k))d\mathbf{P}\right]\overline{\psi_0(\eta,k)}\chi_A(\mathbf{y})d\mathbf{y}\,d\eta \\ &=\left(\frac{k}{L}\right)^d e^{ik\xi^2/2L}\int \hat{\chi}_A\left(\frac{k}{L}(\eta-\xi)\right) \\ &\quad\times e^{-ik\eta^2/2L}\overline{\psi_0(\eta,k)}e^{-\gamma L k^2(\xi-\eta)^2}d\eta.\end{aligned} \tag{51}$$

Comparing this result with the exact solution of the deter-

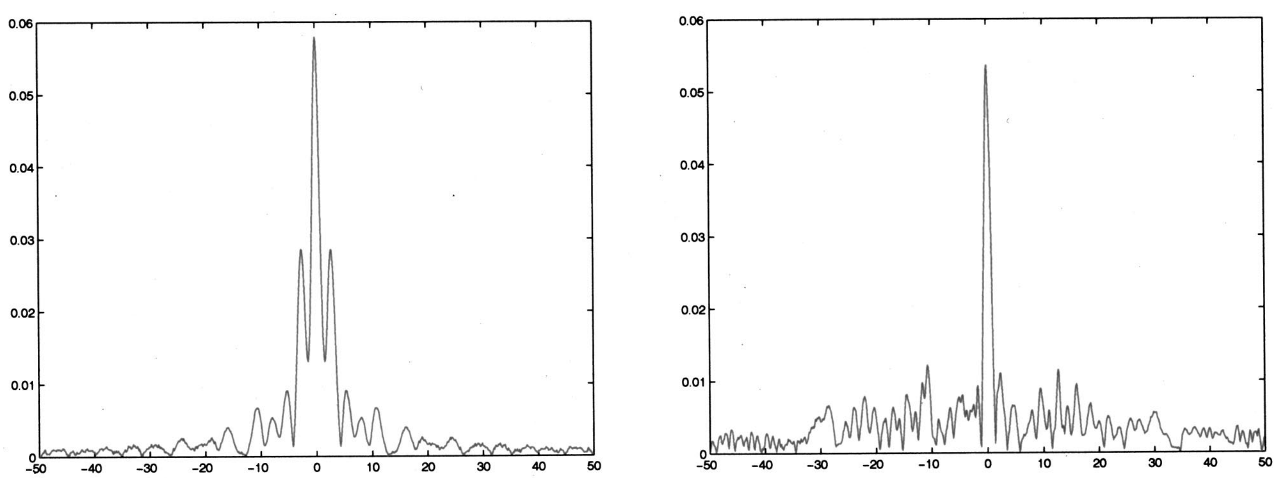

FIG. 16. Homogeneous medium on the left, random medium on the right. Type of boundary conditions: *Waveguide* with TRM width 60 m. The waveguide effects are quite strong, but an argument for super-resolution can be made, since the peak is better defined. Randomness does not, in any case, degrade the results.

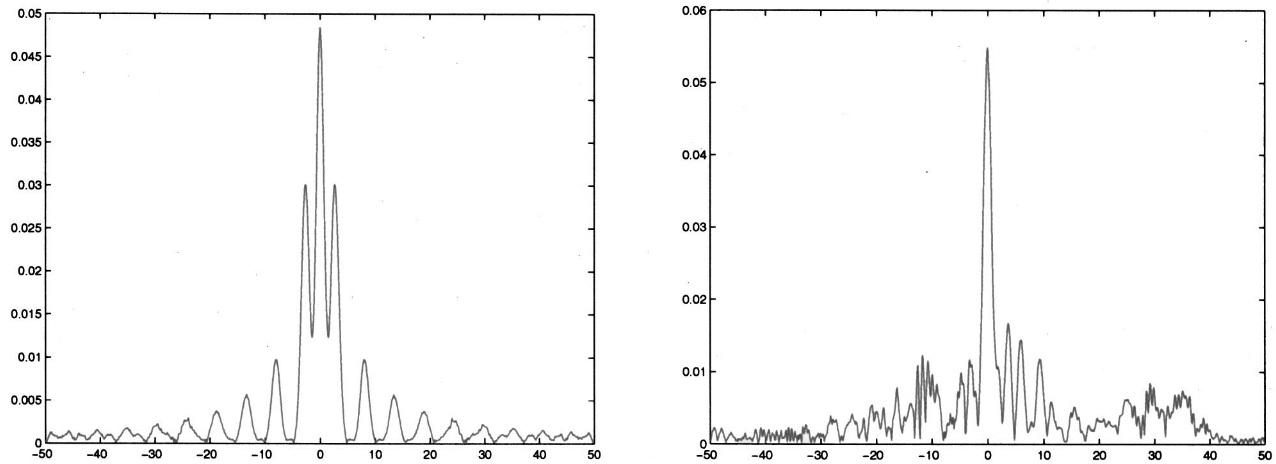

FIG. 17. Homogeneous medium on the left, random medium on the right. Type of boundary conditions: *Waveguide* with TRM width 50 m. The waveguide effects are quite strong, but there is super-resolution since the peak is better defined in the random medium.

ministic phase-conjugated and backpropagated field (20), we see that the effect of the random medium is just the Gaussian factor $e^{-\gamma L k^2(\xi-\eta)^2}$. Using (51) we can now compute an *effective aperture* for the phase-conjugated (or time-reversed) and backpropagated mean field due to a point source in the case of Gaussian TRM and finite aperture TRM, in both the frequency and the time domain.

A. Gaussian TRM

For a point source and a Gaussian aperture of the form (28), we obtain from (51)

$$\langle \psi^B(\xi,L;k)\rangle = \left(\frac{k}{2\pi L}\right)^d e^{-([a^2/2L^2]+\gamma L)k^2\xi^2} e^{ik\xi^2/2L}. \quad (52)$$

Comparing this with the deterministic field (29) we determine an *effective aperture* for the TRM for the mean time-harmonic wave

$$a_e = a\sqrt{1+\frac{2\gamma L^3}{a^2}}. \quad (53)$$

This result was also derived in a different way in Dowling and Jackson (1992). We will see that it is essentially universally valid in the beam approximation, both in the frequency- and in the time domain. It is clearly not valid unless

$$\frac{a_e(L)}{L} \ll 1, \quad (54)$$

which means that the *effective* TRM aperture size must be consistent with the beam approximation. From (53) and from the numerical experiments that we report in Sec. VIII, it is clear that $a_e(L) \gg a$ when the propagation distance L is large.

The self-averaging, time-reversed, and backpropagated field can be calculated exactly as in the deterministic case by replacing a with a_e in Eq. (31). If $a_e = a_e(L)$ is much smaller than the propagation distance L, as it must be by (54), then our analysis for the deterministic field carries over, which means that we get the same a_e in the time domain.

Super-resolution is now precisely the phenomenon of having the self-averaging, time-reversed, and backpropagated field be essentially equal to the deterministic field with a replaced by a_e, which is much larger than a for large L. The width in space of the recompressed field is proportional to $\lambda_0 L/a_e$, where λ_0 is the wavelength of the carrier wave.

B. Finite aperture TRM

With a finite aperture TRM the formula for the compressed pulse is more complicated. Stochastic, multipathing effects modify edge diffraction from the TRM, in the time domain, in a complicated way. The mean phase-conjugated and backpropagated time-harmonic field is

$$\langle \psi^B(\xi,L;k)\rangle = \frac{1}{\pi\xi}\sin\left(\frac{k\xi a}{2L}\right) e^{ik\xi^2/2L} e^{-\gamma L k^2 \xi^2}. \quad (55)$$

We do a Fourier synthesis to get the self-averaged, time-reversed, and backpropagated signal in the time domain for a point source, Gaussian pulse. The result is a combination of (25) and (31)

$$\begin{aligned}\Psi^B(\xi,L,t) &= \int \psi^B\left(\xi,L,\frac{\omega}{c_0}\right) e^{-[(\omega-\omega_0)^2\sigma_t^2]/2} e^{-i\omega t}\, d\omega \\ &= \int \frac{1}{2\pi i\xi}\left[e^{i\omega\xi a/2c_0L} - e^{-(i\omega\xi a/2c_0L)}\right] e^{i\omega\xi^2/2c_0L} e^{-(\gamma^2L\omega^2\xi^2/c_0^2)} e^{[(\omega-\omega_0)^2\sigma_t^2/2]} e^{-i\omega t}\, d\omega \\ &= \frac{1}{2\pi i\xi}\sqrt{\pi/[(\sigma_t^2/2)+(\gamma^2L\xi^2/c_0^2)]}\, e^{-i\omega_0(t-[\xi^2/2c_0L])} e^{-(\gamma^2L\omega_0^2\xi^2/c_0^2)} \\ &\quad \times\{e^{i\omega_0\xi a/2c_0L} e^{[i(t-[\xi^2/2c_0L])-i(\xi a/2c_0L)+(2\gamma^2L\omega_0\xi^2/c_0^2)]^2/[2\sigma_t^2+(4\gamma^2L\xi^2/c_0^2)]} \\ &\quad - e^{(-i\omega_0\xi a/2c_0L)} e^{([i(t-[\xi^2/2c_0L])+i(\xi a/2c_0L)+(2\gamma^2L\omega_0\xi^2/c_0^2)]^2)/[2\sigma_t^2+(4\gamma^2L\xi^2/c_0^2)]}\}. \end{aligned} \tag{56}$$

In Fig. 5 we show formula (56) at $t=0$, with various parameter values. We use the effective aperture formula

$$a_e = a\sqrt{1+\frac{2\gamma L^3}{(a/2)^2}}, \tag{57}$$

which is like the Gaussian TRM effective aperture formula (53) but with the constants adjusted using the numerical results presented in Sec. VIII.

In all calculations we use the estimate $\gamma=2.12\times10^{-5}\ \mathrm{m}^{-1}$ that we obtained from direct numerical simulations. This is discussed further in the next section.

The effective aperture formula (57), or (53), cannot be used when L so small that there is not enough multipathing, or so large that the beam approximation is not valid. We must have $a_e(L)\ll L$. Using (57), this means that $L\ll(8\gamma)^{-1}\approx 6$ km. The range 300–400 m to 1 km is roughly where the effective aperture formula is valid for random media like the one we simulated. At 600 m the effective TRM aperture is already 195 m, nearly five times larger than the physical size of the TRM, which is 40 m.

At the wavefront, $t=\xi^2/2c_0L$, expression (56) becomes

$$\begin{aligned}\Psi^B\left(\xi,L,t=\frac{\xi^2}{2c_0L}\right) &= \frac{1}{2\pi i\xi}\sqrt{\frac{\pi}{\frac{\sigma_t^2}{2}+\frac{\gamma^2L\xi^2}{c_0^2}}}\, e^{-[(a^2/4c_0^2L^2+(2\sigma_t^2\gamma^2L\omega_0^2/c_0^2))\xi^2/(2\sigma_t^2+(4\gamma^2L\xi^2/c_0^2))]} \\ &\quad \cdot\{e^{i\omega_0\xi a/2c_0L} e^{-(i2a\gamma^2\omega_0^2\xi^3/(2c_0^3\sigma_t^2+4c_0\gamma^2L\xi^2))} - e^{-i\omega_0\xi a/2c_0L} e^{i2a\gamma^2\omega_0^2\xi^3/(2c_0^3\sigma_t^2+4c_0\gamma^2L\xi^2)}\}. \end{aligned} \tag{58}$$

VIII. NUMERICAL SIMULATIONS

In this section we present the results of some numerical experiments highlighting the theoretical results of the previous sections. We transmit a time-dependent pulse through the random medium. It is synthesized from 64 frequencies, which allow for enough zero padding to avoid *aliasing* problems, and at the same time allow for a sufficient number of energy-carrying frequencies to resolve time-domain effects. The unit of length is the peak-energy wavelength, λ_0. We use a discretization with 10 points per wavelength, i.e., $\Delta x=\Delta z=0.1\lambda_0$. For the random medium fluctuations μ we take a Gaussian random field with exponential correlation, constructed spectrally. The correlation length is $\sim 10\lambda_0$, and the maximum contrast is 5%, or 10%.

We use a second-order accurate Crank–Nicholson (CN) discretization of the paraxial wave equation

$$2ik\psi_z+\psi_{xx}+k^2\mu\psi=0, \tag{59}$$

$$\begin{aligned}&2ik\delta_z^+\psi_{n,m}+\tfrac{1}{2}\delta_x^+\delta_x^-(\psi_{n,m}+\psi_{n+1,m}) \\ &\quad +\tfrac{1}{2}k^2(\mu_{n+1,m}\psi_{n+1,m}+\psi_{n,m}\psi_{n,m})=0,\end{aligned} \tag{60}$$

where

$$\begin{aligned}\delta_z^+\psi_{n,m} &= \frac{\psi_{n+1,m}-\psi_{n,m}}{\Delta z} \\ \delta_x^\pm\psi_{n,m} &= \pm\frac{\psi_{n\pm1,m}-\psi_{n,m}}{\Delta x}.\end{aligned} \tag{61}$$

This numerical approach may seem overly direct, for there are widely used phase-screen methods which do not require subwavelength resolution (Dashen *et al.*, 1985; Flatté *et al.*, 1987). However, for this series of numerical simulations we really wanted to resolve everything. Our code is limited to 2D. Extension of this direct approach to 3D is no longer viable in the long-range regime where we would want to use it. There are, however, good numerical methods for solving the paraxial wave equation in 3D (Bécache *et al.*, 1998).

We use discrete transparent boundary conditions (DTBCs) to limit the numerical domain while simulating an infinite medium. They are obtained by matching the interior CN-finite-difference-time-domain (CN-FDTD) scheme with an exact exterior CN-FDTD, yielding an exact *discrete* radiating boundary condition. This is worked out in detail in Arnold (1995).

We have validated our implementation of the DTBCs for long distances, up to 1000 m for random media and up to 5000 m for homogeneous media, by comparing the solutions in domains of width $x \in [-w,w]$ to the ones in domains of double the width, $x \in [-2w,2w]$. In a random medium, or a medium with scatterers, the DTBCs work very well as long as the random medium or the scatterers are sufficiently far away from the boundary. In practice this means about 4–5 λ, with a resolution of 10 points per λ. In this setting, the estimated error is of the order of machine precision.

In the numerical simulations we use a random medium at full strength in the center 75% of the numerical domain. The strength smoothly approaches zero in a region of 5%–10% of the domain width in order to avoid artificial reflections from the numerical random-homogeneous interface. In the outermost layer of the domain the medium is homogeneous. This allows for effective DTBCs (see Fig. 6).

The code is written entirely in MATLAB, compiled under MATLAB 5.2 with compiler 1.2 and MATLAB 5.3 with compiler 1.2.1. A typical simulation, with a 1000-m×200-m numerical domain, and 64 frequencies, completes in approximately 22 h, on a dual-Pentium III Xeon 550-MHz Linux workstation, where the embarrassingly parallel nature of the problem is exploited.

A. Numerical results

We show numerical results for propagation through random media with maximum fluctuations contrast of 10%, i.e., $|\mu| \leqslant 0.1$. This is actually quite a bit of randomness and is really pushing the validity of the paraxial approximation. The reason we use such high contrast is to observe super-resolution phenomena in a numerical domain that is manageable on a small network of workstations.

The width of the finite aperture TRM is 50 m, and the numerical domain in 200 m wide. Simulations for three different propagation distances are shown: (i) When the propagation distance is short, only 200 m. As can be seen in Fig. 7, this distance is too short for the randomness to have an impact on the resolution of the self-averaging, time-reversed, and backpropagated signal. (ii) With a propagation distance of 600 m the super-resolution effect is quite noticeable. The peak of the recompressed signal in the random medium is about 40% higher and quite a bit narrower than the one in the homogeneous medium. This is very stable from realization to realization; Fig. 8 shows a typical case. (iii) As we increase the propagation distance to 1000 m, more energy spills out of the domain by radiation through the boundaries, and multipathing contributing to super-resolution is lost. In Fig. 9 we are past the limit of what our numerical setup can do.

B. Numerical limits

For a given width of the numerical domain, and of the random medium, there is a limit to how long a propagation distance can be used in the numerical experiments. As the effective aperture a_e exceeds the size of the domain, the configuration can no longer accurately model an infinite medium. In Table I we show estimates for a_e and for the medium-characterizing parameter γ, in inverse meters, for different propagation distances with fixed domain and TRM widths.

It is reasonable to expect the growth of $a_e(L)$ with L for the finite aperture case to be similar to the one for a Gaussian aperture, that is, $\sim\sqrt{\gamma L^3}$ as in Eq. (53). We have found from the numerical simulations that a_e, a, and γ are related by Eq. (57), for a finite aperture TRM. If we use this formula to estimate γ, we might expect it to approach a constant as we sample an increasing part of the random medium. However, Table I and Fig. 10 show that this is not the case. Given the width of the numerical domain, there is a range of propagation distances for which the estimated γ is close to constant. For larger propagation distances there is a drop-off since the numerical setup cannot adequately capture the multipathing and the growing effective aperture. The numerical limitations of the effective aperture formula (57) are more severe in our setup than the theoretical ones coming from the beam approximation, which are discussed at the end of Sec. VII.

Our numerical calculations show that it is hard to simulate super-resolution with long propagation distances. We have used more than 200 time-harmonic realizations per propagation distance to estimate γ and a_e, whereas the self-averaging for Figs. 7–9 uses only 64 frequencies, and one realization of the random medium, and therefore cannot be expected to be as stable statistically. By using more frequencies, and widening the medium, these simulations should become more stable statistically.

IX. DYNAMIC TRM PLACEMENT

It is possible that the main part of the energy misses a statically placed time-reversal mirror. This can occur when the medium has a systematic drift (cross wind), or when the randomness is anisotropic. In such cases it may be advantageous to be able to move the TRM laterally so as to capture as much energy as possible. In this section we consider the effects of dynamic placement of the TRM. At this time, we do not have a theory that covers dynamic TRM placement, so the study is numerical.

We dynamically move the TRM with infinite speed, that is, we place the TRM in the optimal lateral location where it captures the most energy.

We show two realizations, each for the time-reversal experiment for a propagation distance of 600 m (Fig. 11) and 1000 m (Fig. 12), comparing the centered static placement with the dynamic placement. For the first realization in Fig. 11, the pulse energy is quite smeared out when it reaches the TRM plane, and the statically placed screen just barely manages to capture enough information to resolve the source. The dynamically placed TRM recompression is approximately three times better, and clearly super-resolves the source. In the second realization in Fig. 11, the pulse energy is still quite concentrated when it reaches the TRM plane, but it is a little bit off-center, so moving the mirror enhances the recompression.

As discussed earlier, in Sec. 2, the 1000-m propagation calculation cannot capture enough multipathing to give an accurate picture of super-resolution. However, as can be seen in the first realization shown in Fig. 12, dynamic placement can improve the recompression, even in this case. There are settings, as in the second realization, when the energy is too spread out, where dynamic placement does not help.

X. TIME REVERSAL IN A WAVEGUIDE

In this section we briefly explore numerically time reversal in random media where the boundaries are strongly *reflecting*, so that the energy gets trapped as in a *waveguide*. This is physically the case in underwater acoustics, where sound is reflected from the surface and from the bottom of the ocean, or in sound propagation in a channel.

Dirichlet- or Neumann-boundary conditions are, of course, a very simplified way to account for the physical boundaries where the surface is rippled, and the bottom rough. However, it is still of interest to see how the reflections off the boundaries and the randomness of the medium interact. We use homogeneous Dirichlet boundary conditions in our numerical simulations.

We compare time reversal through homogeneous and random media in a series of numerical calculations as follows. The numerical domain has width 100 m, the propagation distance is 800 m, and the maximum contrast, in the random case, is 10%. The first and third numerical experiments (Figs. 13 and 15), are standard time reversal in an infinite domain (radiating boundary conditions), with a statically placed TRM. The second and fourth experiments are in a waveguide with zero (Dirichlet) boundary conditions. In the second case (Fig. 14), the TRM is of the same width as the domain, so it captures all available energy and the recompressed signals are very good for both the homogeneous and random media. In the fourth, and most interesting case (Fig. 16), the TRM is 60 m (or 60% of the waveguide), and we clearly see how the randomness helps us achieve super-resolution. The sidelobes are eliminated by multipathing inside the waveguide.

We also consider smaller TRMs, in the same setting, to make sure that the results for 60 m (Fig. 16) are not special or a typical. In Fig. 17, where the TRM width is 50 m, we see clearly that the incoherence induced by the randomness dampens the sidelobes and the peak is much better resolved in the random case. This is super-resolution in a waveguide.

XI. SUMMARY AND CONCLUSIONS

We have presented a detailed analytical and numerical study of how multipathing in random media enhances resolution in time-reversed acoustics, that is, how super-resolution arises in random media. We have clarified, in particular, the statistical stabilization of the recompressed pulse in the time domain. We have also shown that when the propagation distance is large compared to the wavelength and the correlation length of the inhomogeneities, and the time-reversal mirror is small, there is an exact expression for the effective size of the TRM, its *effective aperture* (57), valid in both in the time- and frequency domain. Multipathing makes the effective size of the TRM much larger than its physical size. We have verified the theoretical results with careful and extensive numerical calculations, using exact nonreflecting boundary conditions in one transverse direction to simulate an infinite medium. Full two-dimensional transverse propagation is intractable on a workstation, at present, especially for long distances. This is because the discrete transparent boundary conditions are nonlocal.

ACKNOWLEDGMENTS

The work of P. B. and G. P. is supported by AFOSR Grant No. F49620-98-1-0211 and NSF-DMS-9971972.

APPENDIX: COMMENTS AND REFERENCES FOR THE TRANSPORT APPROXIMATION

The paraxial equation (2), or (4), is a Schrödinger equation in which z plays the role of time and the fluctuations $\mu = n^2 - 1$ are the random, ''time''-dependent potential. When these fluctuations are δ-correlated in z, then we have exact closed equations for moments of products of Green's functions

$$\left\langle \prod_{j=1}^{N} G(L,0,\mathbf{x}_j,\xi;k_j) \prod_{j=N+1}^{N+M} \overline{G(L,0,\mathbf{x}_j,\xi;k_j)} \right\rangle, \tag{A1}$$

where ξ is the source location, $\mathbf{x}_j$ are observation points, and the wave numbers k_j may be the same or different. This is done in Furutsu (1993) or in the articles in Tatarskii *et al.* (1993), and in a more mathematical way in Dawson and Papanicolaou (1984). In the case of two factors, $N = M = 1$, the product is denoted by Γ, and satisfies (9). The mean of its Fourier transform (13) is the mean Wigner function that now satisfies Eq. (38) *exactly*. The power spectral density $\hat{R}$ is a function of $\mathbf{P} - \mathbf{Q}$ only, so the transport equation (38) is a convolution equation and can be solved explicitly. One can then do the narrow-beam approximation as we did in Sec. VII, and this can be found in the literature in many places, in Furutsu (1993) as well as in this Appendix. The white noise or δ-correlation limit leading to (38) is also considered in Bouc and Pardoux (1984).

The mathematical idealization of having δ-correlated fluctuations is relevant in many situations in underwater acoustics and in many other propagation problems, as we will explain in this Appendix with a careful scaling of the problem. Using δ-correlated fluctuations is convenient analytically but may obscure other limits that are relevant, such as the high-frequency limit. This makes little difference for *single*-frequency statistics but it needs to be analyzed carefully in order to explain pulse stabilization in the time domain, as discussed in Sec. VI. That is why we presented the resolution analysis of time reversal in a random medium as we did here.

When backscattering is important, then the transport approximation is more involved and must be used carefully. A theory for the transport approximation using Wigner functions is given in Ryzhik *et al.* (1996), where many other references can be found. A recent survey of transport theory for random media is van Rossum and Nieuwenhuizen (1999). Time reversal in randomly *layered* media is analyzed in Clouet and Fouque (1997). Transport theory in a waveguide is considered in Kohler and Papanicolaou (1977).

1. Scaling I

We will now consider some specific scalings that result in the phase-diffusion equation (47), *and* have the frequency decorrelation property (41) that gives pulse stabilization.

We begin by rewriting the Schrödinger equation (2) or (4) in dimensionless form. Let L_z and $L_{\mathbf{x}}$ be characteristic length scales in the propagation direction, the distance L between the source and the TRM for example, and in the transverse direction, respectively, and k_0 a characteristic wave number. We introduce a dimensionless wave number $k' = k/k_0$ with $k_0 = \omega_0/c_0$ and ω_0 a central frequency. We rescale $\mathbf{x}$ and z by $\mathbf{x} = L_{\mathbf{x}}\mathbf{x}'$, $z = L_z z'$ and rewrite (2) in the new coordinates, dropping the primes

$$2ik\frac{\partial \psi}{\partial z} + \frac{L_z}{k_0 L_{\mathbf{x}}^2}\Delta\psi + k^2 k_0 L_z \sigma \mu\left(\frac{\mathbf{x}L_{\mathbf{x}}}{l}, \frac{zL_z}{l}\right)\psi = 0. \tag{A2}$$

The physical parameters that characterize the propagation problem are: (a) the central wave number k_0; (b) the strength of the fluctuations σ; and (c) the correlation length l. The length scales L_x, L_z, and the central wave length $\lambda_0 = 2\pi/k_0$ characterize the propagation regime that we wish to consider. The random fluctuations μ are normalized to have unit variance and unit correlation length. We introduce now three dimensionless variables

$$\delta = \frac{l}{L_{\mathbf{x}}}, \quad \epsilon = \frac{l}{L_{\mathbf{z}}}, \quad \beta = \frac{1}{k_0 l}, \tag{A3}$$

which are, respectively, the reciprocals of the *transverse scale* relative to correlation, the *propagation distance* relative to correlation, and the correlation length relative to the central *wavelength*. We will assume first that the dimensionless parameters β, σ, and δ are small

$$\beta \ll 1, \quad \sigma \ll 1, \quad \delta \ll 1. \tag{A4}$$

This is a regime of parameters where super-resolution phenomena as described here can be observed. It is a high-frequency regime ($\lambda \ll l, \beta \ll 1$), not the one on which this paper is based, but it is important physically and is easier to deal with analytically. The "transport" regime ($\beta \sim 1$) that we analyze in the paper is taken up later, as is the regime $\epsilon \ll 1$ that gives white noise.

The Fresnel number is defined by

$$\theta = \frac{L_z}{k_0 L_{\mathbf{x}}^2} = \beta\frac{\delta^2}{\epsilon}. \tag{A5}$$

After multiplying by θ we can rewrite the Schrödinger equation (A2) in the form

$$2ik\theta\psi_z + \theta^2 \Delta_{\mathbf{x}}\psi + \frac{k^2}{\epsilon^{1/2}}\mu\left(\frac{\mathbf{x}}{\delta}, \frac{z}{\epsilon}\right)\psi = 0, \tag{A6}$$

provided that we relate ϵ to σ and δ by

$$\epsilon = \sigma^{2/3}\delta^{4/3}. \tag{A7}$$

The asymptotic regime (A4) is realized with the ordering

$$\theta \ll \epsilon \ll \delta \ll 1, \tag{A8}$$

which implies that $\beta \ll 1$ also holds, corresponding to the *high-frequency limit*. We see from the scaled Schrödinger equation (A6) that this regime has the following interpretation. We have first take a *high-frequency* limit $\theta \to 0$, then a *white-noise* limit $\epsilon \to 0$, and then a *broad-beam* limit $\delta \to 0$. We will now discuss briefly and interpret these limits. A full analysis is given in Papanicolaou *et al.* (2001). Other orderings are considered in the next section.

For the high-frequency limit, especially in random media, we use the Wigner function as we explained before. Let $\psi_\theta(z,\mathbf{x})$ be a solution of the rescaled Schrödinger equation (A6). The Wigner function depends on the propagation distance z, the transverse position $\mathbf{x}$, and wave vector $\mathbf{p}$, and is given by

$$W_\theta(z,\mathbf{X},\mathbf{P}) = \int_{\mathbb{R}^d} \frac{d\mathbf{y}}{(2\pi)^d} e^{i\mathbf{P}\cdot\mathbf{Y}} \times \psi_\theta\left(z, \mathbf{X} - \frac{\theta\mathbf{Y}}{2}\right)\overline{\psi_\theta\left(z, \mathbf{X} + \frac{\theta\mathbf{Y}}{2}\right)}. \tag{A9}$$

It satisfies the evolution equation

$$\frac{\partial W_\theta}{\partial z} + \frac{\mathbf{P}}{k}\cdot\nabla_{\mathbf{X}}W_\theta = \frac{ik}{2\sqrt{\epsilon}}\int e^{i\mathbf{Q}\cdot\mathbf{X}/\delta}\hat{\mu}\left(\mathbf{Q}, \frac{z}{\epsilon}\right) \times \frac{W_\theta\left(\mathbf{P} - \frac{\theta\mathbf{Q}}{2}\right) - W_\theta\left(\mathbf{P} + \frac{\theta\mathbf{Q}}{2}\right)}{\theta}\frac{d\mathbf{Q}}{(2\pi)^d}.$$

In the limit $\theta \to 0$ the solution converges in a suitable weak sense, for each realization, to the solution of the random Liouville equation

$$\frac{\partial W}{\partial z} + \frac{\mathbf{P}}{k}\cdot\nabla_{\mathbf{X}}W + \frac{k}{2\sqrt{\epsilon}}\nabla_{\mathbf{X}}\mu\left(\frac{\mathbf{x}}{\delta}, \frac{z}{\epsilon}\right)\cdot\nabla_{\mathbf{P}}W = 0. \tag{A10}$$

The initial condition at $z = 0$ is that W equals the limit Wigner function $W_0(\mathbf{X},\mathbf{P})$ of the initial wave function. This is, of course, what we expect in the high-frequency limit since the characteristics of (A10) are the ray equations in the random medium.

We next consider the white-noise limit $\epsilon \to 0$ in the random Liouville equation (A10). Then, $W_\epsilon(z,\mathbf{X},\mathbf{P})$ converges weakly (in a probabilistic sense) to the stochastic process $W(z,\mathbf{X},\mathbf{P})$ that satisfies the Itô stochastic partial differential equation

$$dW = \left[-\frac{\mathbf{P}}{k}\cdot\nabla_{\mathbf{X}}W + \frac{k^2 D}{2}\Delta_{\mathbf{P}}W\right]dz - \frac{k}{2}\nabla_{\mathbf{P}}W\cdot d\mathbf{B}\left(\frac{\mathbf{X}}{\delta}, z\right). \tag{A11}$$

Here, $\mathbf{B}(\mathbf{X},z)$ is a Brownian random field, that is, a Gaussian process with mean zero and covariance

$$\langle B_i(\mathbf{X}_1, z_1)B_j(\mathbf{X}_2, z_2)\rangle = -\left(\frac{\partial^2 R_0((\mathbf{X}_1 - \mathbf{X}_2))}{\partial X_i \partial X_j}\right)\min\{z_1, z_2\},$$

where

$$R_0(\mathbf{X})=\int_{-\infty}^{\infty} R(s,\mathbf{X})ds,$$

$$R(z,\mathbf{X})=\langle \mu(s+z,\mathbf{Y}+\mathbf{X})\mu(s,\mathbf{Y})\rangle,$$

and

$$D=-\tfrac{1}{16}\Delta R_0(0),$$

which is the negative Laplacian of the reduced covariance R_0 at zero. We call Eq. (A11) the Itô–Liouville equation. Note that the Brownian field that enters the stochastic partial differential equation (A11) depends explicitly on the dimensionless correlation length δ in the transverse direction. Therefore, the limit process also depends on δ. Note also that the average of W, $\langle W(z,\mathbf{X},\mathbf{P})\rangle$, satisfies the phase-space diffusion equation (47) but with a diffusion constant D that differs from (48). The first argument of $\hat{R}$ in the integral in (48) is now set to zero, which then becomes the Fourier transform of the reduced covariance R_0. The D above agrees with (48) after this change. A detailed discussion of the white-noise limit is found in Papanicolaou *et al.* (2001), and the theoretical background of stochastic partial differential equations like (A11) is presented in Kunita (1997).

From the Itô–Liouville equation (A11) we can get closed equations for all the moments of the Wigner function W, not only for its mean but for moments with different wave numbers k as well. The wave number enters (A11) as a parameter. To have the decorrelation property (41), we need to show that

$$\begin{aligned}&\langle W(z,\mathbf{X},\mathbf{P};k_1)W(z,\mathbf{X},\mathbf{P};k_2)\rangle\\ &\quad\approx\langle W(z,\mathbf{X},\mathbf{P};k_1)\rangle\langle W(z,\mathbf{X},\mathbf{P};k_2)\rangle\end{aligned}\tag{A12}$$

for $k_1\neq k_2$. This is true in the limit $\delta\to 0$, as is explained in detail in Papanicolaou *et al.* (2001), because it is as if the Brownian fields $\mathbf{B}$ in (A11) have a spatial correlation of zero. After a scaling change this translates into decorrelation for different wave numbers.

We can summarize the results of performing the scaling limits $\theta\to 0$, followed by $\epsilon\to 0$, followed by $\delta\to 0$ by noting that they represent a precise analytical way to study the regime where the wavelength is much smaller than the correlation length (high-frequency limit), the propagation distance is much larger than the correlation length, and the fluctuations are weak (white-noise limit), and the transverse length scale is much larger than the correlation length $(\delta\to 0)$. The first two limits are fully compatible with the paraxial or parabolic wave approximation of Sec. II, while the last one requires that the beam, which is narrow because of the first two limits, must not be too narrow. Note that this scaling-limit analysis is different from the one we use in the paper, but appropriate for underwater acoustics. It leads to the same phase-space diffusion equation (47) for $\langle W(z,\mathbf{x},\mathbf{p})\rangle$, but the structure of the higher moments is different here, coming from (A11), than under the scaling followed in the paper. We now consider this scaling.

2. Scaling II

The second scaling we want to consider is the one described in Sec. V, where the wavelength is comparable to the correlation length, $\lambda\sim l$, the small parameter $\epsilon=\lambda/L_z\ll 1$, and the standard deviation of the fluctuations $\sigma\sim\sqrt{\epsilon}$. The scaled Schrödinger equation follows from (33) and has the form

$$2ik\epsilon\psi_z+\epsilon^2\Delta_{\mathbf{x}}\psi+k^2\epsilon^{1/2}\mu\left(\frac{\mathbf{x}}{\epsilon},\frac{z}{\epsilon}\right)\psi=0.$$

To connect with the precise scaling of (A6) we simply have to set $\theta=\epsilon$, $\delta=\epsilon$, and $\epsilon=\sigma^2$, which implies that $\beta=1$. This is the transport scaling. If, however, we want to follow this with the narrow-beam limit of Sec. VII, we must allow for different horizontal and vertical length scales by letting

$$\zeta=\frac{\epsilon}{\delta},\tag{A13}$$

which from (A5) gives

$$\zeta^2\theta=\epsilon\beta.$$

With $\sigma=\zeta\sqrt{\epsilon}$, the scaled Schrödinger equation is now

$$2ik\zeta^2\epsilon\beta\psi_z+(\epsilon\beta)^2\Delta_{\mathbf{x}}\psi+k^2\zeta^3\sqrt{\epsilon}\mu\left(\frac{\zeta\mathbf{x}}{\epsilon},\frac{z}{\epsilon}\right)\psi=0.$$

Letting $\epsilon\to 0$ with β and ζ fixed is the *transport limit*. Letting $\beta/\zeta\to 0$ is the high-frequency, phase-space diffusion limit, and letting $\zeta\to 0$ restores the validity of the parabolic approximation. We refer to these last two limits as the *narrow-beam approximation*.

The transport limit is analyzed in Ryzhik *et al.* (1996) and in Bal *et al.* (2001), where a rigorous proof of convergence of the mean Wigner function is given. It is the same as (38) in Sec. V except that we now have the parameters β and ζ, so that the average Wigner function satisfies

$$\begin{aligned}k\frac{\partial W}{\partial L}+\mathbf{P}\cdot\nabla_{\mathbf{X}}W=&\frac{\pi k^3\zeta^4}{4\beta^4}\\ &\times\int\hat{R}\left(\frac{\zeta^2(\mathbf{P}^2-\mathbf{Q}^2)}{2k\beta},\frac{\zeta(\mathbf{P}-\mathbf{Q})}{\beta}\right)\\ &\times[W(L,\mathbf{X},\mathbf{Q};\xi,\eta;k)\\ &-W(L,\mathbf{X},\mathbf{P};\xi,\eta;k)]d\mathbf{Q}.\end{aligned}\tag{A14}$$

The narrow-beam limit $\beta/\zeta\to 0$ followed by $\zeta\to 0$ comes from a two-term Taylor expansion of the integrand in (A14), leading to the phase-space diffusion equation (47), with the phase-space diffusion coefficient given by

$$D(\mathbf{P})=\int\hat{R}\left(\zeta\frac{\mathbf{P}\cdot\mathbf{Q}}{k},\mathbf{Q}\right)|\mathbf{Q}|^2d\mathbf{Q}.$$

We must now let $\zeta\to 0$ as well, otherwise the parabolic approximation itself may be violated. This will then give the same phase-diffusion coefficient obtained in the high-frequency limit (A8) of the previous section.

What we have not been able to show in Bal *et al.* (2001) is that in the transport limit the decorrelation property (A12) holds exactly. However, formal asymptotic analysis as well as numerical simulations indicate that this is true even though a mathematical proof is lacking at present.

Let us make some remarks that contrast the scaling limits of this and the previous section. The frequency decorrelation property is a consequence of the transport limit $\epsilon \to 0$ and does not depend on the narrow-beam limit $\beta/\zeta \to 0$ and $\zeta \to 0$. The narrow-beam limit not only gives an important analytical simplification leading to an easy-to-solve phase-space diffusion equation; it is in a way an essential part of the theory because without it the paraxial approximation is unlikely to hold in the transport limit. The validity of the paraxial approximation is, however, re-established after the narrow-beam approximation. Note also that $\zeta \to 0$ brings in the anisotropy between horizontal and transverse length scales that is needed in the paraxial approximation.

The *white-noise limit* corresponds to the ordering

$$\epsilon \ll \theta \ll \delta \ll 1, \tag{A15}$$

with $\sigma = \delta^{-2}\epsilon^{3/2}$. It is different from both the *transport limit* of this section

$$\epsilon \ll \beta \ll \zeta \ll 1, \tag{A16}$$

as well as the *high-frequency limit*

$$\theta \ll \epsilon \ll \delta \ll 1, \tag{A17}$$

(A8) of the previous section. However, our analysis (Papanicolaou *et al.*, 2001) shows that in all cases the average Wigner function satisfies the same phase-space diffusion equation (47). We expect that the structure of the higher-order moments, including the frequency decorrelation property, will also be the same but we can only show this in the high-frequency limit (A8) and the white-noise limit (A15), where the Itô–Liouville equation (A11) characterizes the Wigner function fully. The fact that several different asymptotic scale orderings lead to the same limit behavior explains why super-resolution and statistical stability in time reversal are seen very clearly both in physical experiments and in numerical simulations.

We also expect that the full-wave transport limit (Ryzhik *et al.*, 1996), without the paraxial approximation, will have the frequency decorrelation property and hence pulse stabilization. This has been seen clearly in full-wave numerical simulations in random media (Tsogka and Papanicolaou, 2001; Barryman *et al.*, 2001).

Arnold, A. (**1995**). ''Numerically Absorbing Boundary Conditions for Quantum Evolution Equations,'' in Proceedings of the International Workshop on Computational Electronics, Tempe, AZ.

Asch, M., Kohler, W., Papanicolaou, G., Postel, M., and White, B. (**1991**). ''Frequency content of randomly scattered signals,'' SIAM Rev. **33**, 519–626.

Bal, G., Papanicolaou, G., and Ryzhik, L. (**2001**). ''Radiative transport in a time-dependent random medium,'' J. Stat. Phys. (submitted).

Bamberger, A., Engquist, B., Halpern, L., and Joly, P. (**1988**). ''Parabolic wave equation approximations in heterogeneous media,'' SIAM (Soc. Ind. Appl. Math.) J. Appl. Math. **48**(1), 99–128.

Barryman, J., Borcea, L., Papanicolaou, G., and Tsogka, C. (**2001**). ''Imaging and time reversal in random media,'' Inverse Problems (submitted).

Bécache, E., Collino, F., and Joly, P. (**1998**). ''Higher-order Numerical Schemes and Operator Splitting for Solving 3D Paraxial Wave Equations in Heterogeneous Media,'' Technical Report 3497, INRIA: Institute National de Recherche en Informatique et en Automatique.

Bouc, R., and Pardoux, E. (**1984**). ''Asymptotic analysis of PDEs with wide-band noise disturbances and expansion of the moments,'' Stoch. Anal. Appl. **2**, 369–422.

Clouet, J. F., and Fouque, J. P. (**1997**). ''A time-reversal method for an acoustical pulse propagating in randomly layered media,'' Wave Motion **25**, 361–368.

Dashen, R., Flatté, S. M., and Reynolds, S. A. (**1985**). ''Path-integral treatment of acoustic mutual coherence functions for rays in a sound channel,'' J. Acoust. Soc. Am. **77**, 1716–1722.

Dawson, D. A., and Papanicolaou, G. (**1984**). ''A random wave process,'' Appl. Math. Opt. **12**, 97–114.

Derode, A., Roux, P., and Fink, M. (**1995**). ''Robust acoustic time reversal with high-order multiple scattering,'' Phys. Rev. Lett. **75**(23), 4206–4209.

Dowling, D. R., and Jackson, D. R. (**1990**). ''Phase conjugation in underwater acoustics,'' J. Acoust. Soc. Am. **89**, 171–181.

Dowling, D. R., and Jackson, D. R. (**1992**). ''Narrow-band performance of phase-conjugate arrays in dynamic random media,'' J. Acoust. Soc. Am. **91**, 3257–3277.

Fink, M. (**1997**). ''Time reversed acoustics,'' Phys. Today **50**, 34–40.

Fink, M. (**1999**). ''Time-reversed acoustics,'' Sci. Am. Nov., 91–97.

Flatté, S. M., Reynolds, S. A., and Dashen, R. (**1987**). ''Path-integral treatment of intensity behavior for rays in a sound channel,'' J. Acoust. Soc. Am. **82**, 967–972.

Furutsu, K. (**1993**). *Random Media and Boundaries: Unified Theory, Two-Scale Method, and Applications* (Springer, Berlin).

Hodgkiss, W. S., Song, H. C., Kuperman, W. A., Akal, T., Ferla, C., and Jackson, D. R. (**1999**). ''A long-range and variable focus phase-conjugation experiment in shallow water,'' J. Acoust. Soc. Am. **105**, 1597–1604.

Kohler, W., and Papanicolaou, G. (**1977**). *Wave Propagation in a Randomly Inhomogeneous Ocean*, Lecture Notes in Physics 70, Wave Propagation and Underwater Acoustics (Springer, Berlin).

Kunita, H. (**1997**). *Stochastic Flows and Stochastic Differential Equations* (Cambridge University Press, Cambridge).

Kuperman, W. A., Hodgkiss, W., Song, H. C., Akal, T., Ferla, C., and Jackson, D. R. (**1997**). ''Phase conjugation in the ocean,'' J. Acoust. Soc. Am. **102**, 1–16.

Papanicolaou, G., Ryzhik, L., and Solna, K. (**2001**). ''The parabolic approximation and time reversal in a random medium,'' SIAM (Soc. Ind. Appl. Math.) J. Appl. Math. (submitted).

Porter, R. P. (**1989**). *Generalized Holography with Application to Inverse Scattering and Inverse Source Problems*, Number XXVII in Progress in Optics (Elsevier Science, New York).

Ryzhik, L. V., Papanicolaou, G. C., and Keller, J. B. (**1996**). ''Transport equations for elastic and other waves in random media,'' Wave Motion **24**, 327–370.

Solna, K., and Papanicolaou, G. (**2000**). ''Ray theory for a locally layered random medium,'' Random Media **10**, 155–202.

Tappert, F. D. (**1977**). *The Parabolic Approximation Method*, Lecture Notes in Physics 70, Wave Propagation and Underwater Acoustics (Springer, Berlin).

Tatarskii, V. I., Ishimaru, A., and Zavorotny, V. U., editors (**1993**). *Wave Propagation in Random Media* (Scintillation) (SPIE and IOP, SPIE, Bellingham, WA; IOP, Philadelphia PA.)

Tsogka, C., and Papanicolaou, G. (**2001**). ''Time reversal through a solid–liquid interface and super-resolution,'' Inverse Problems (submitted).

van Rossum, M. C. W., and Nieuwenhuizen, T. M. (**1999**). ''Multiple scattering of classical waves: Microscopy, mesoscopy, and diffusion,'' Rev. Mod. Phys. **71**(1), 313–371.

Spectral shapes of forward and reverse transfer functions between ear canal and cochlea estimated using DPOAE input/output functions

Douglas H. Keefe[a)]
Boys Town National Research Hospital, 555 North 30th Street, Omaha, Nebraska 68131

(Received 20 June 2001; revised 8 October 2001; accepted 9 October 2001)

It is widely assumed that the distortion characteristics of the cochlea are uniform across its length, or at least across some portion of its length. For each distortion product otoacoustic emission (DPOAE) input/output (I/O) function across frequency, there is a corresponding cochlear I/O function defined over the cochlear source region. An assumption of distortion invariance is adopted such that these cochlear I/O functions are identical across tonotopic place, which is testable in the sense that a single nonlinear function should adequately describe the set of DPOAE I/O functions across frequency. If so, the differences in measured DPOAE I/O functions across frequency are produced by differences in the forward stimulus transmission to the generation site, and reverse DP transmission back to the ear canal. The absolute transfer-function magnitude is not determined by this technique, but the spectral shapes across frequency and between ears are determined. The role of middle-ear functioning is implicit in the I/O functions because of its controlling influence on these transfer functions. Results have been obtained using the average DPOAE I/O functions measured in a population of healthy ears [Gorga *et al.*, J. Acoust. Soc. Am. **107**, 2128–2135 (2000)], and support the hypothesis of cochlear-distortion invariance. The measured forward and reverse transfer functions have a general bandpass characteristic, and a more narrow-band structure with similarities to the behavioral threshold curve.
[DOI: 10.1121/1.1423931]

PACS numbers: 43.64.Bt, 43.64.Jb [BLM]

I. INTRODUCTION

There is evidence that the distortion characteristics of the cochlea are uniform along a major portion of its length. Sachs and Abbas (1974) proposed that such universal nonlinear functions are capable of describing basilar membrane (BM) nonlinearity. A single power law has been found adequate to account for the cubic distortion tone input/output (I/O) functions in the guinea pig cochlea (Withnell and Yates, 1998). More recently, it was found that the basilar membrane in the chinchilla cochlea vibrates with a compressive nonlinearity in the hook region (12–18 kHz) similar to that in the more apical region (5–9 kHz) (Rhode and Recio, 2000).

Cochlear modelers have posited invariant relationships across different sites in the cochlea. Based on measurements of BM motion by Rhode (1971), Zweig (1976, 1991) defined a cochlear scaling symmetry in that the BM envelope response to a pure tone at one frequency may be converted into an envelope response at a neighboring frequency by translating the envelope and adjusting its height. The scaling symmetry is assumed to be applicable to the mechanics of the mammalian cochlea across a major part of its length. Such scaling is imposed on the transfer function at a given ear-canal stimulus level, but the response varies nonlinearly with stimulus level. In cochlear models considered by de Boer (1997), the nonlinearities in cochlear mechanics reside in the functioning of outer hair cells (OHC)—a fixed nonlinear memoryless function between stereocilia deflection and output pressure by the OHC is assumed to be the same function at all locations on the BM.

The present research adopts as a working hypothesis the view that the distortion characteristics of the BM are uniform along a major portion of its length; this subset of its length is called the distortion-scaling region. It is widely agreed that nonlinearities in the generation of evoked otoacoustic emissions (EOAE) are intimately linked to BM nonlinearities. In particular, it is assumed that the I/O functions of distortion product otoacoustic emissions (DPOAE) are related to corresponding BM nonlinearities in the neighborhood of the generation region, and that these BM nonlinearities are similar across tonotopic locations.

It follows that the DPOAE I/O functions recorded in the ear canal at different frequencies are related to some "universal" nonlinear function of the BM I/O functions in the cochlea. Such DPOAE I/O functions are measured using a simultaneous presentation of a pair of pure-tone frequencies f_1 and $f_2 > f_1$. The relationship between ear-canal and cochlear responses is determined by the total forward transfer of energy at the f_1 and f_2 frequencies to the neighborhood of distortion product generation at the $2f_1 - f_2$ frequency (near the f_2 place for which the traveling-wave amplitudes of both f_1 and f_2 are large). This particular distortion-product (DP) order is the focus of attention because it tends to be of high amplitude in normal-hearing human ears (for f_2/f_1 close to 1.22). Once produced, the distortion product at the $2f_1 - f_2$ frequency propagates in the reverse direction back through

[a)]Electronic mail: keefe@boystown.org

the middle ear to the ear-canal microphone where it is recorded as a DPOAE.

II. THEORY

A schematic model of EOAE generation, which is drawn from Kemp (1980), is that the EOAE pressure P_{oae} measured in the ear canal is the output response to an input ear-canal stimulus pressure(s) P_{stim}, as modified by forward and reverse middle-ear transmission and forward and reverse cochlear transmission from the base to the generation site of the EOAE. The EOAE pressure is related to the stimulus pressure by

$$P_{\text{oae}} \sim T_m^R * T_c^R * C * T_c^F * T_m^F * P_{\text{stim}}, \tag{1}$$

in which the following functions are defined (from right to left): T_m^F is forward middle-ear transfer function from ear canal to cochlear base, T_c^F is forward cochlear transfer function from cochlear base to generation site, C is nonlinear cochlear EOAE generation function, T_c^R is reverse cochlear transfer function from cochlear generation site to base, and T_m^R is reverse middle-ear transfer function from cochlear base to ear canal.

Equation (1) includes the transformation of the stimulus energy due to forward propagation through the middle ear to the cochlear base (T_m^F), and forward propagation to the cochlear site of DPOAE generation (T_c^F). For the case of DPOAEs, the forward transmission functions are defined for each of the traveling waves at f_1 and f_2, although this fact is not explicitly represented in Eq. (1). The function C describes the generation of the distortion product as a function of the traveling wave amplitudes at the pair of stimulus frequencies. The generated DP reverse propagates to the cochlear base (T_c^R) and through the middle ear to the ear-canal microphone (T_m^R).

The reflection of the DP component at its tonotopic place is neglected, as are multiple internal reflections within the cochlea. The first approximation is reasonable because the response is dominated by distortion generated at the f_2 place at higher stimulus levels due to saturation at moderate levels of the emission component reflected at the DP place. There are contributions from the tonotopic place at low stimulus levels, but these occur at a reduced number of points on the I/O functions at these low stimulus levels and this reduces the overall contribution of tonotopic-place reflections in the numerical fits to be described. The second approximation is also reasonable because multiple internal reflections produce a fine structure in the DPOAE spectrum that tends both to saturate and to average out when averaging over DPOAEs measured in an ensemble of (healthy) ears. Such an ensemble-averaged data set is used in the present analysis. More detailed models of DPOAE generation and transmission have been described (Talmadge *et al.*, 1998).

Partitioning into linear and nonlinear components, the EOAE signal may be expressed as the product of a linear round-trip middle-ear transfer function $T_m^L = T_m^R * T_m^F$ and a nonlinear round-trip cochlear transfer/generation function $T_c^N = T_c^R * C * T_c^F$. The basilar membrane responds linearly to sine-tone stimulation at low stimulus levels (Zwicker and Schloth, 1984; Zweig, 1991), so that the product of cochlear transfer functions $T_c^R * T_c^F$ is independent of level. Any of the nonlinearities associated with the forward and reverse traveling waves (contributing to nonlinearities in the BM I/O function) may be partitioned into the unknown nonlinear cochlear function C. Hence, the EOAE can be schematically represented by the nonlinear function C, a total forward transfer function T_{mc}^F, and a total reverse transfer function T_{mc}^R defined by

$$T_{mc}^F = T_c^F * T_m^F, \quad T_{mc}^R = T_c^R * T_m^R, \tag{2}$$

in which the ratio of EOAE to stimulus pressure is

$$\frac{P_{\text{oae}}}{P_{\text{stim}}} = T_{mc}^R * C * T_{mc}^F. \tag{3}$$

This EOAE I/O function is proportional to the nonlinear cochlear function C at each frequency; all frequency dependence in the EOAE I/O function is determined by the spectrum of the total forward and reverse transfer functions. This conclusion does not strongly depend on the type of OAE or its manner of generation, except that there exists a localized region of generation that scales with the dynamical properties of the cochlear traveling wave, which means that C is independent of tonotopic frequency. It has been convenient to suppress explicit dependence on frequency. For DPOAEs that are the focus of subsequent numerical modeling, forward transfer functions can be defined at both f_2 and f_1 frequencies, but attention is paid to the forward transfer function at f_2 because the DPOAE generation site is close to the region of the maximum envelope at f_2. Adjusting the relative levels of the f_1 and f_2 primaries can adjust for relative differences in the corresponding pair of forward transfer functions across frequency, and these details are discussed in Appendix B. The reverse transfer function is evaluated at the $2f_1 - f_2$ frequency.

The first prediction from this model is that if one measures a collection of EOAE I/O functions across a set of different frequencies, then the underlying nonlinear function that describes the shape of the I/O function is identical across frequency. If no single nonlinear function is found to accurately describe the I/O functions across frequency, then the assumption of distortion invariance would be untenable.

Assuming that the first prediction is confirmed, then between any pair of I/O functions at two different frequencies, there is a unique forward translation and unique reverse translation of the first I/O function to the location of the second I/O function. The second prediction is that it is possible to measure the relative shift in the forward transfer function and the relative shift in the reverse transfer function, thus providing in a noninvasive manner and under *in vivo* conditions a unique decomposition of round-trip transmission in the middle ear and cochlea.

A. Example

Consider an idealized form of the nonlinear cochlear function C (Fig. 1). The BM input variable is the pressure difference acting across the BM in the forward-traveling wave from the cochlear base. Such a pressure difference is defined at each of the f_1 and f_2 frequencies in a DPOAE

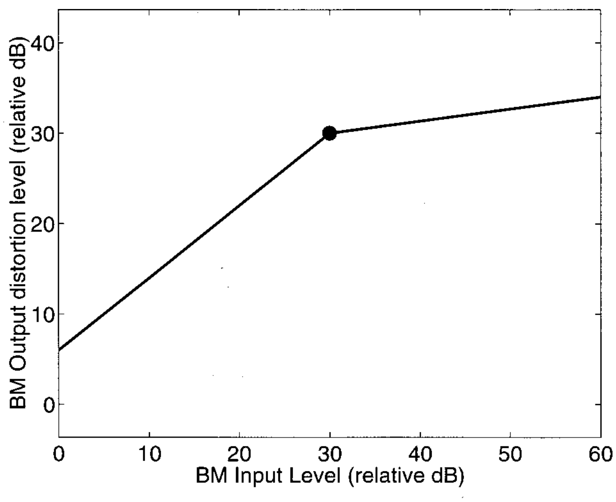

FIG. 1. Idealized nonlinear cochlear function C.

measurement, but for present purposes is defined for the pressure difference at the f_2 frequency. The BM output variable is the pressure difference acting across the BM in the reverse-traveling wave at the DP frequency $2f_1-f_2$. Both input and output BM variables are defined at the tonotopic location basal to which the BM responds approximately linearly, a location assumed (via cochlear invariance) to scale tonotopically across the range of stimulus frequencies. The breakpoint between the steeper and the more compressive lines, which is identified with a circle in Fig. 1, serves as a distinctive feature of this I/O pattern. It has been assumed that the same level of input excitation produces the same level of output distortion at any cochlear location. When this cochlear nonlinearity is indirectly assessed using an EOAE measurement, the ear-canal SPL is influenced by the forward and reverse transfer functions between ear canal and BM site of excitation.

Figure 2 shows a reference DPOAE I/O function measured at a particular reference frequency. It has the same general form as the nonlinear cochlear function in the preceding figure. A second curve shows the influence of attenuation in the forward transfer function, which shifts the entire I/O function along the horizontal stimulus axis, so that a higher stimulus level (by 20 dB) is needed to produce the same level of distortion.[1] Such a shift in forward transmission due to the presence of a conductive hearing loss is well known—Wever *et al.* (1941) showed such a horizontal shift in the I/O function of the cochlear potential versus stimulus level when a middle-ear pressure was applied to induce a conductive loss, thereby demonstrating the cochlear origin of distortion. Unlike cochlear potentials, EOAEs are also influenced by the reverse transfer function. The effect of a reverse transfer function, compared to the reference DPOAE I/O function, is illustrated by the third I/O function, which is translated vertically by a gain of 15 dB. This function and the reference I/O function have the same forward transfer function, so that the breakpoint occurs at the same ear-canal stimulus level ($L_2=40$ dB). The DPOAE source on the basilar membrane, once created, propagates back to the ear canal, but is filtered by its respective reverse transfer function.

If pairs of I/O functions were compared only in a low-level regime, in which the I/O function is characterized by a constant slope (which may, however, differ from a slope equal to one), it would be impossible to determine whether differences in intercepts on the L_2-axis are due to variations in forward or reverse transmission, or some combination thereof. There needs to be a change in the degree of nonlinearity to break the symmetry between horizontal and vertical translations on the the I/O function plane.

The next most general case is a pair of I/O functions that differ in both forward and reverse transfer functions—one example would be an I/O function with a relative attenuation of -20 dB in the forward direction, and a relative gain of $+15$ dB in the reverse direction. For this simple case of a two-slope I/O function, it is sufficient to measure the translation between the breakpoints of the I/O functions in order to obtain separate measurements of forward and reverse transfer function shifts. For the case of an arbitrary nonlinear I/O function that is assumed to be universal over some distortion scaling region of the cochlea, any pair of I/O functions with similar shape are related by horizontal and vertical translations.

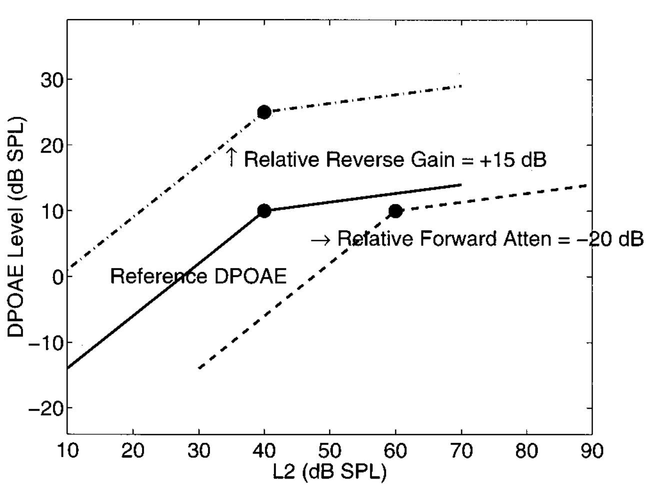

FIG. 2. DPOAE I/O functions at three frequencies with no attenuation (solid line), an attenuation in the forward transfer (dashed line), and an attenuation in the reverse transfer (dashed-dotted line).

III. MEASURED I/O FUNCTIONS AND ANALYSIS PROCEDURES

The goal of this study is to calculate the forward and reverse transfer functions in a population of healthy ears in which the average DPOAE I/O transfer function has been measured over a broad range of levels and frequencies. A set of DPOAE I/O transfer functions in healthy adult ears was reported by Gorga *et al.* (2000); this set of I/O functions constitutes the data analyzed in the present study. Each I/O function was the average over 70 subjects with normal hearing (pure tone thresholds not exceeding 10 dB HL at any test frequency, and normal 226-Hz tympanograms). The DPOAE level was measured at $2f_1-f_2$ for 12 primary levels (L_2 ranging from 10 to 65 dB SPL in 5 dB steps) and 9 pairs of test frequencies (f_2 ranging from 0.5 to 8 kHz in $\frac{1}{2}$-oct steps, and f_1 set such that $f_2/f_1=1.22$).

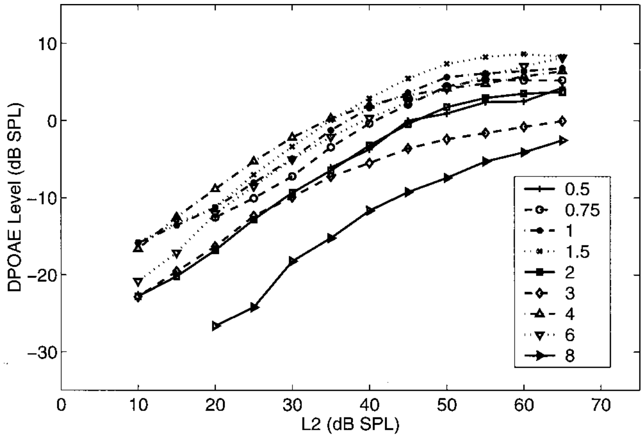

FIG. 3. DPOAE I/O function data at each f_2 frequency (in kHz).

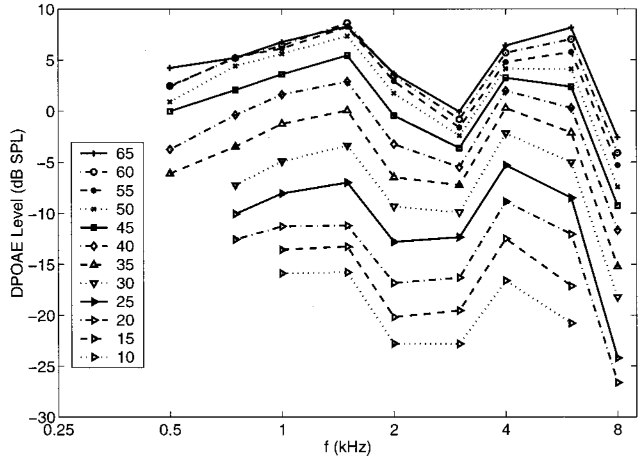

FIG. 4. DPOAE spectral (DP-gram) data at each L_2 level (in dB) listed in the legend.

The L_1 level was set to approximately maximize DPOAE level at this DP frequency in normal-hearing ears, with $L_1 = L_2$ at the highest test level and L_1 progressively larger than L_2 at lower test levels. In particular, $L_1 = L_2$ at 65 dB SPL level, and, otherwise, L_1 exceeds L_2 by a larger difference at smaller L_2's according to the following rule (Kummer *et al.*, 1998):

$$L_1 = 0.4 L_2 + 39. \tag{4}$$

This rule is similar to the asymmetry in L_1 and L_2 levels found by Gaskill and Brown (1990), and further refined by Whitehead *et al.* (1995). Gaskill and Brown provided a rationale for setting L_1 much larger than L_2 at low L_2 levels—the generation of the DPOAE near the f_2 place requires a much larger L_1 to produce a similar level of f_1 at this f_2 place than would be the case at higher L_2 levels. This is due to the fact that the traveling wave with frequency f_2 is both higher in level and more compressive at the f_2 place than is the traveling wave with frequency f_1 at the f_2 place. At higher L_2 levels, there is a broadening of each of the traveling wave envelopes, and hence a greater degree of overlap between f_1 and f_2, so that the optimum L_1 becomes comparable to L_2.

The measured average DPOAE I/O functions of Gorga *et al.* are plotted in Fig. 3, with each curve parametrized by the f_2 frequency. It is not immediately obvious whether all of these I/O functions can be described by the same underlying nonlinearity. An alternative representation of the data of Gorga *et al.* is as a set of DP-grams, i.e., in which DPOAE level is plotted versus f_2, with each curve parametrized by L_2 (Fig. 4). In this representation, it is obvious that the largest DPOAE levels are obtained at 1.5 kHz, and at 4–6 kHz. There is a region of lower level DPOAEs at 2 and 3 kHz, and the response falls off at the lowest and highest test levels. This general spectral pattern is similar to that previously observed (Lonsbury-Martin and Martin, 2001).

The standard deviations associated with these average I/O function levels have been plotted by Gorga *et al.* Their range of standard deviations extended from 5 to 11 dB across all data, with an average standard deviation of 7.8 dB. Based upon these measurements in 70 ears, the standard error of the mean corresponding to this average standard deviation is approximately 1 dB.

A. Specific choice of I/O functions

The example presented earlier used an idealized form of I/O function. Measured I/O DPOAE functions in healthy adult human ears are not adequately described by a double-linear fit. Yet, a reasonable approximation to such functions is a straight-line fit asymptotically at low stimulus levels, a transition region, and a saturating straight-line fit at moderate stimulus levels with a reduced slope. It is the broad transition region that is poorly fit by a pair of straight lines.

The approach described in this article is to fit all the (average) DPOAE I/O functions across all test frequencies with a universal nonlinear function that asymptotes at low and moderate stimulus levels to separate linear slopes, but which also allows a horizontal and vertical translation at each frequency to account for frequency-dependent shifts in the forward and reverse transfer functions. Because the standard error of the mean for the average DPOAE level (approximately 1 dB) is much less than the range of DPOAE levels (15 to 30 dB) across the L_2 levels at each f_2, the parameters of the fitting function should be insensitive to the variability in the averaged data. Parameter uncertainties were not formally calculated.

The fitting function is a rotated logistic function (Fig. 5), which has a broad transition region of the type found in measured DPOAE I/O functions. A standard logistic function is rotated such that its linear asymptote is fitted to the DPOAE I/O function at the lowest stimulus levels. The high-level regime of the rotated logistic function plays no significant role in modeling these data because the measured I/O functions in Fig. 4 remain in the compressive regime even at the highest stimulus levels used. The three global parameters needed to define this function are

(i) low-level slope of I/O function (in dB/dB),
(ii) saturation-region (compressive) slope of I/O function (in dB/dB), and
(iii) level difference (in dB) in rotated coordinates between the two straight-line asymptotes.

In addition, for each test frequency other than 1.0 kHz, there is a pair of parameters describing the translation of the I/O

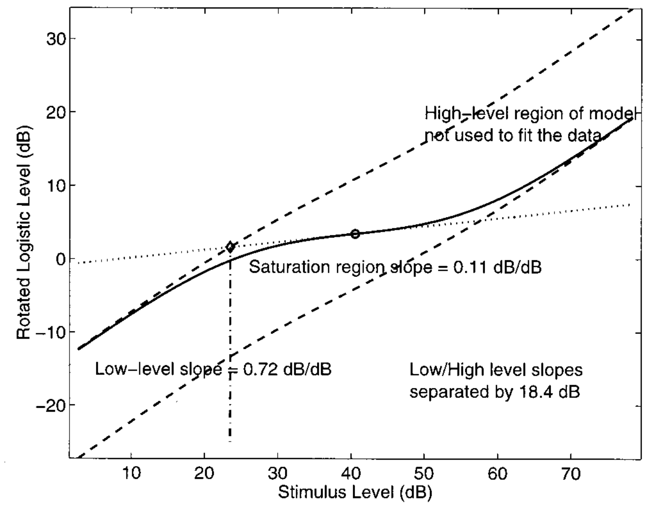

FIG. 5. Rotated logistic function used to model the I/O function data at $f_2 = 1$ kHz. At other frequencies, the model calculates horizontal and vertical translation levels (in dB).

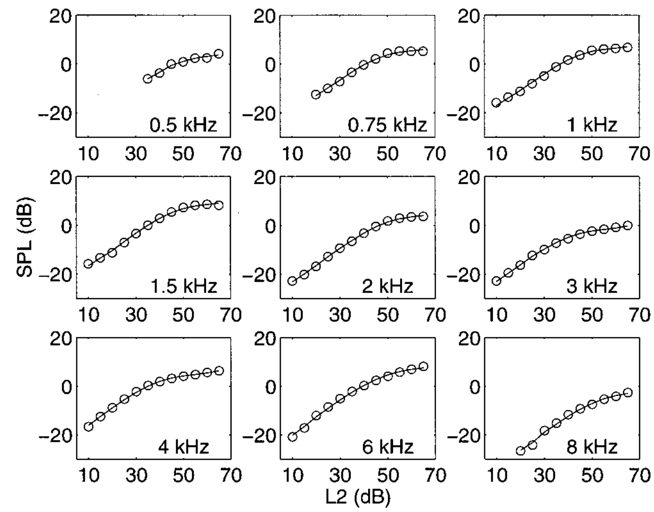

FIG. 6. DPOAE I/O function data and model fit at each f_2 frequency.

function horizontally and vertically. Thus, the I/O functions at the eight test frequencies other than 1 kHz were optimally fitted based on a single optimization using the Matlab Optimization Toolkit such that they were translated to overlap with the I/O function at 1.0 kHz.[2] There were 3 global parameters and $8\times2=16$ translational parameters for a total of 19 parameters to fit using $12\times9=108$ data points. The horizontal translation parameters provide the forward transfer function associated with f_2, and the vertical translation parameters provide the reverse transfer function associated with $2f_1-f_2$.

IV. RESULTS

Figure 5 shows the rotated logistic function that best fits the data: the low-level slope is 0.72 dB/dB, and the compressive slope is 0.11 dB/dB. The midpoint of the logistic function (labeled by the open circle) is calculated at each f_2 frequency in terms of the three global parameters. At $f_2 = 1$ kHz as in Fig. 5, the midpoint occurs at a level of 40 dB. The break point between the low-level and compressive regimes is defined as the level where the corresponding asymptotic straight lines intersect (denoted by the black diamond): this equals 23.5 dB in this example. This allows a quantitative definition of breakpoint for an I/O function that is slowly saturating. Although not of direct relevance to this study, a ''dynamic range'' of the nonlinearity is 18.4 dB for the fitted function.[3]

Figure 6 shows the measured I/O function and the model fit to the response at each f_2 frequency. Examples of more saturated responses are found from 0.75 to 2 kHz, while less saturated responses are found at lower and higher frequencies. This contrasts with the DPOAE responses that are larger in level at 1.5, 4, and 6 kHz. The agreement between each I/O function and the model is good at each test frequency, which suggests that the universal nonlinear function is able to represent the entire set of I/O functions, once the forward and reverse transfer functions are accounted for.

The overall accuracy of the fitting method is directly represented in Fig. 7, which plots the discrete values of the I/O functions at all nine test frequencies, after removing the horizontal and vertical translations associated with forward and reverse transmission. The single curve is the predicted I/O function at 1 kHz, plotted over the range of levels measured at that frequency. The translated I/O functions cluster closely to a universal nonlinear function, which supports the hypothesis of the existence of the distortion scaling region.

The DPOAE-derived forward transfer function level $[20\log T^F_{mc}(f_2)]$ is plotted in Fig. 8 versus f_2 relative to the level at 1 kHz, which is defined as 0 dB. This transfer function has local maxima at 1 and 4 kHz. Below 1 kHz, the forward transfer function increases with increasing frequency with a slope of 4–5 dB/oct. The level at 2 kHz is approximately −5 dB below the level at 1 kHz, and −9 dB below the level at 4 kHz. This suggests that less energy is transmitted to the f_2-place at 2 kHz than at neighboring frequencies.

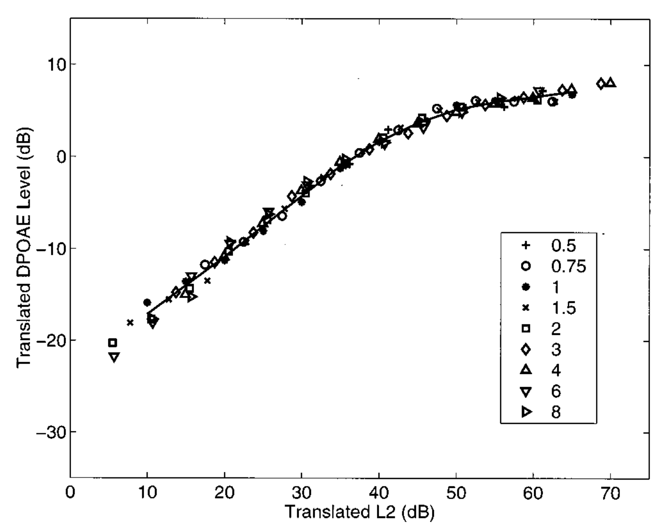

FIG. 7. Translated DPOAE I/O functions at all test frequencies (in kHz in legend) relative to I/O function at 1 kHz. The solid line is the predicted I/O function at 1 kHz across the range of 1-kHz test levels.

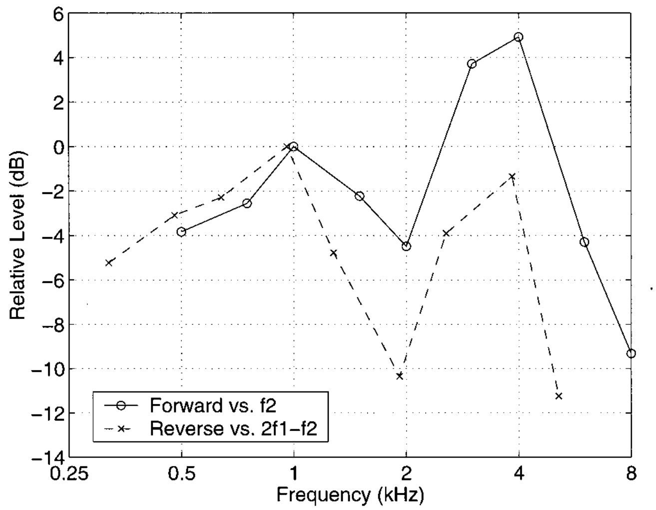

FIG. 8. Comparison of forward transfer function vs f_2 frequency and reverse transfer function vs $2f_1 - f_2$ relative to 0 dB at 1 kHz.

This reduction in forward transmission acts to reduce the DPOAE level at 2 kHz. Above 4 kHz, the forward transfer function decreases with increasing frequency with a steeper slope of -14 dB/oct.

Reverse transmission occurs at the DP frequency, so that the reverse transfer function $[20 \log T^{R}_{mc}(2f_1 - f_2)]$ is plotted as a function of $2f_1 - f_2$ (Fig. 8). The overall reverse transfer function has a band-limited shape qualitatively similar to the forward transfer function. This alignment shows that the spectral shapes of the forward and reverse transfer functions are similar: both transfer functions have maxima at 1 and 4 kHz, and a relatively sharp minimum at 2 kHz.

Differences are apparent in more detailed comparisons. The reverse transfer function notch at 2 kHz is 10 dB below that at 1 kHz, a deeper notch than in the forward transfer function. Above 4 kHz, the reverse transfer function decreases with a steeper slope of approximately -20 dB/oct, compared to -14 dB/oct for the forward transfer function.

It should be noted that similar optimization results were obtained with an alternative choice of nonlinear function—a function which asymptoted at high levels to a zero-slope condition according to a standard logistic function but which had a fixed linear slope at low stimulus levels. The calculated forward and reverse transfer functions were insensitive to the choice of nonlinear function, but the overall mean squared error was lower for the rotated logistic function. Hence, the rotated logistic function was chosen to calculate the forward and reverse transfer functions.

V. DISCUSSION

The extent to which one can accurately model a set of DPOAE I/O functions using a single nonlinear function was used as a test of the cochlear-invariance hypothesis. Were there a high degree of variance in the model fit represented in Fig. 7, the hypothesis would be rejected. The high degree to which the I/O functions across frequency can be translated onto a single nonlinear function is evident in Fig. 7. This supports the hypothesis that cochlear nonlinearity is independent of cochlear place over a range of tonotopic locations corresponding to the measurement bandwidth (f_2 varying from 0.5 to 8.0 kHz).

Explicit consideration of forward and reverse transfer functions provides a framework to account for the variations in DPOAE level across frequency based on the hypothesis of cochlear invariance. The forward and reverse transfer functions across frequency are influenced by variations in the forward and reverse middle-ear transfer functions, and the frequency dependence of cochlear transfer functions may also contribute a gradient in the response. Because the middle ear is a critical influence on both forward and reverse transmission, the derived forward and reverse transfer functions are compared to measurements of forward and reverse middle-ear transfer function measurements in the human temporal bones. The present results provide *in vivo* estimates of the relative levels of the forward and reverse transfer functions, but not their absolute gains. Because middle-ear experiments are usually performed under conditions in which the middle-ear cavities are surgically opened, it should be noted that the present derived transfer functions have been estimated under conditions in which the middle-ear cavities are in the normal closed configuration.

A. Forward transfer function

Measurements of forward middle-ear transfer functions in human temporal bones have been performed with the middle-ear cavities opened (Puria *et al.*, 1997; Hudde and Engel, 1998). Puria *et al.* measured the forward middle-ear pressure transfer function from the ear canal to the cochlear vestibule and found that the transfer function magnitude increased at low frequencies above 0.4 kHz with a slope of $+4$ dB/oct and decreased above 4 kHz with a slope of -8 dB/oct. The results in Fig. 8 show that the total forward transfer function increased with a slope of 4–5 dB/oct for frequencies between 0.5 and 1 kHz and decreased above 4 kHz with a slope of -14 dB/oct. Thus, the bandpass characteristic of the middle-ear pressure transfer function observed in human-cadaver ear measurements is evident in the present derived transfer functions based on *in vivo* DPOAE measurements. The low-frequency slopes are in agreement, but the high-frequency slope in the present results is steeper by a factor of -6 dB/oct. This discrepancy is discussed later. The human-cadaver ear measurements do not show the narrow-band structure between 1 and 6 kHz that is evident in the forward transfer function of Fig. 8; instead, the forward middle-ear pressure transfer function with the middle-ear cavities open is fairly flat between 0.5 and 4 kHz.

A narrow-band structure is known to exist in the average minimum audible pressure (MAP) at the eardrum (Killion, 1978), which is the SPL measured at the eardrum at the threshold of hearing. This MAP is plotted in Fig. 9. Note that all plots in this figure have been translated to coincide at 0 dB and 1 kHz. Based on the hypothesis that the spectral shape of the MAP is governed by the transfer function of the BM input relative to the eardrum SPL, it is expected that the forward transfer function should predict the spectral structure of the MAP. The original DPOAE response in the average healthy ear must first be transformed into a predictor of hear-

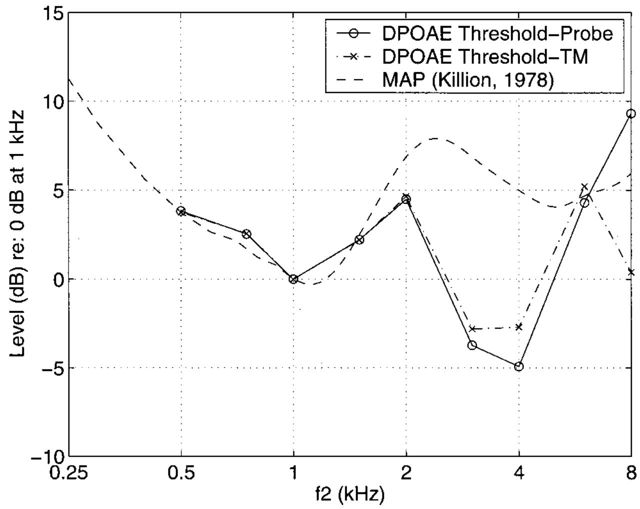

FIG. 9. Comparison of (1) predicted threshold level spectrum calculated from the inverse of the forward transfer function measurement using DPOAEs at the probe microphone (solid curve with symbol ○), (2) the threshold level spectrum adjusted from that in (1) by transforming the microphone position to the eardrum from the probe (dashed-dotted curve with symbol ×), and (3) the minimum audible pressure field response (long-dashed curve).

ing threshold, not by manipulation of the DP-gram but based on the derived forward transfer function. By inverting the forward transfer function data (from Fig. 8), a response termed the DPOAE threshold-probe curve is produced and plotted in Fig. 9.

Both the MAP and the DPOAE threshold-probe curve show a local minimum near 1 kHz, with good agreement at lower frequencies. The MAP has a local maximum (i.e., an elevated threshold) near 2.5 kHz, and a local minimum near 5 kHz. The DPOAE threshold-probe curve has a local maximum at a slightly lower frequency (2 kHz) and a local minimum also at a slightly lower frequency (4 kHz). The MAP increases slightly at frequencies above 5 kHz, whereas the DPOAE threshold-probe curve increases steeply from 4 to 8 kHz. The qualitative similitude in the placement of the maxima and minima supports the hypothesis that the behavioral (MAP) and DPOAE forward transfer function are influenced by a common factor.

Regarding the narrow-band structure of the MAP, Killion (1978) stated: "Perhaps the 2500 Hz sensitivity dip will ultimately be explained by the characteristics of the eardrum-to-basilar-membrane transformation," which is conceptually close to the present approach. From their transfer measurements in human-cadaver ears from eardrum to cochlear vestibule, Puria *et al.* (1997) investigated the extent to which the MAP can be explained as a detector of constant stapes acceleration, constant stapes volume-velocity, constant vestibule pressure, or constant power. They concluded that for frequencies above 150 Hz, the constant vestibule pressure detector was in approximate agreement with the MAP threshold curve, but they noted that none of the four physiological measurements exhibited the local maximum at 2.5 kHz found in the MAP. They point out the possibility that this local maximum "is due to the middle-ear cavities," which were open in their measurement conditions and thus functioned differently than under *in vivo* conditions. A middle-ear model of sound transmission shows that this local maximum is accurately predicted in frequency and relative level, and the local maximum is related to a broadly tuned middle-ear cavity resonance in the neighborhood of 3 kHz (Keefe *et al.*, 2001). It is expected that the DPOAE-derived forward (and reverse) transfer function should be influenced in a similar manner by this middle-ear cavity resonance, since it is an *in vivo* measurement.

A confounding factor is that the MAP is based on the SPL at the eardrum whereas the DPOAE-derived forward transfer function is based on the SPL measured back at the probe location. This produces deviations in the response at high frequencies, for which standing waves in the ear canal become important (Siegel, 1994). Appendix A describes an ear-canal model used to generate a DPOAE threshold-TM curve (see Fig. 9), which is similar to the DPOAE threshold-probe curve except referencing the stimulus pressure to the eardrum rather than the probe. The DPOAE threshold-TM curve does not account for the spectral characteristic of the MAP at and above 3 kHz. There is a common narrow-band structure in both responses that is probably influenced by the middle-ear cavity resonance. At 4 kHz, the DPOAE threshold-TM curve is closer to the MAP than is the DPOAE threshold-probe curve. At 8 kHz, the DPOAE threshold-probe response is larger than the MAP threshold, and the DPOAE threshold-TM response is smaller than the MAP threshold.

B. Reverse transfer function

The reverse transfer function (Fig. 8) plotted at the DP frequency $(2f_1-f_2)$ shows a similar narrow-band structure to that of the forward transfer function at the f_2 frequency. The spectral shapes of the forward and reverse transfer functions are similar in the human ear, in particular, the frequencies of the relative maxima and minima coincide to within experimental precision. This supports the theory that a common mechanism is responsible for the narrow-band structure. Having related the narrow-band structure in the forward transfer function to the existence of a resonance in the middle-ear cavity suggests that this resonance is also a necessary component in producing the narrow-band structure in the reverse transfer function.

This reverse transfer function differs from that predicted by Kemp (1980), which was based in part on predictions using the middle-ear model of Zwislocki (1962). With this middle-ear model and an ear canal having a volume of 0.7 cm^3, Kemp predicted a forward transfer function with a peak at 1 kHz and flat between 2 and 4 kHz, about 10 dB lower. The predicted reverse transfer function was a low-pass filter with cutoff near 1 kHz and falls by as much as 18 dB by 4 kHz. Neither of these spectral shapes is observed for the forward and reverse transfer functions derived in the present study. The Zwislocki middle-ear model used by Kemp was never intended for use over the broad frequency range of EOAEs, and lacks the desired accuracy in modeling forward and reverse transmission effects. Nevertheless, Avan *et al.* (2000) have used a variant of the Zwislocki model to accurately predict shifts in DPOAE responses based on measurements of acoustic reflex activation, pressurization, and mass-loading of the TM.

The reverse middle-ear transfer function has been measured under *in vivo* conditions in guinea pig (Magnan *et al.*, 1997). They remark on the need for close connections between research on EOAE and middle-ear mechanisms in order to quantitatively interpret EOAEs. Their technique requires an intracochlear sound source that makes it unsuitable for testing in human subjects.

The reverse middle-ear transfer function has been measured in human-cadaver ears with the middle-ear cavities open (Puria and Rosowski, 1996; Hudde and Engel, 1998). Puria and Rosowski (1996) measured the forward and reverse middle-ear pressure transfer functions between the ear canal at the TM and the cochlear vestibule in one human-cadaver temporal bone. Their measured forward and reverse transfer functions showed very different frequency dependences, and the reverse transfer function was shown to depend on the ear-canal loading. In one condition, an Etymotic ER10C probe was used to terminate the ear canal, apparently mounted close to the eardrum. The resulting reverse middle-ear transfer function has maxima at 0.8 and 2 kHz, a broad minimum at approximately 1.2 kHz, and a narrow, deep minimum at approximately 2.8 kHz. These maxima and minima are reminiscent of the pattern of maxima and minima in Fig. 8 for the reverse transfer function, but the frequencies do not coincide. Among the measurement differences are whether the middle-ear cavities are open or closed, and the distance of the ER10C probe from the eardrum.

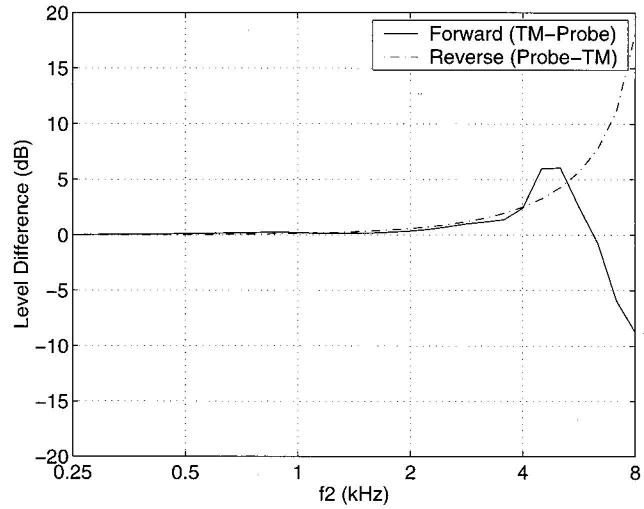

FIG. 10. The level difference is plotted for the transformation from probe SPL to eardrum SPL implicit in the forward transfer function (solid line), and from eardrum SPL to probe SPL implicit in the reverse transfer function (dashed-dotted line). The sign convention is such that at low frequencies, the eardrum SPL exceeds the probe SPL for forward transmission from a source (stimulus) at the probe, and the probe SPL exceeds the eardrum SPL for reverse transmission from a source (DPOAE) at the eardrum.

C. Implications

The high-frequency slope of the forward transmission function shows that the SPL at the TM is less than that at the probe above 6 kHz. This relation can be used to interpret the discrepancy in the high-frequency slope of the forward middle-ear pressure transfer function $p_{\mathrm{cv}}/p_{\mathrm{TM}}$ measured by Puria *et al.* (1997), in which p_{cv} represents the pressure in the cochlear vestibule. Suppose their measurement had been performed in an intact ear canal at the same location as the probe in the DPOAE experiments. Then the measured forward middle-ear pressure transfer function would be $p_{\mathrm{cv}}/p_{\mathrm{mic}}$, which can be expressed as

$$\frac{p_{\mathrm{cv}}}{p_{\mathrm{mic}}}=\frac{p_{\mathrm{cv}}}{p_{\mathrm{TM}}}\cdot\frac{p_{\mathrm{TM}}}{p_{\mathrm{mic}}}. \tag{5}$$

The left-hand side of the equation is the forward middle-ear pressure transfer function in the DPOAE measurement from the probe to the input of the cochlea. This relation states that this transfer function is the product of the forward middle-ear pressure transfer function measured at the TM and the forward transmission function from probe microphone to TM, defined by Eq. (A1). Because this latter ear-canal function falls off rapidly at high frequencies (see Fig. 10), it follows that the forward transfer function estimated from the DPOAE measurement at the probe microphone should fall off much more rapidly than the forward middle-ear pressure transfer function (at the TM). It was noted earlier that the DPOAE forward transfer function falls off at -14 dB/oct, while the forward middle-ear pressure transfer function falls of at -8 dB/oct, a difference of -6 dB/oct. Thus, the difference in the two slopes is in the predicted direction, although the slope of the forward ear-canal transmission function in Fig. 10 falls even more rapidly than -6 dB/oct. There is no simple analog to Eq. (5) for reverse transmission. The reverse transfer function is highly sensitive to probe placement in the ear canal, or, more generally, to the output terminating impedance of the ear canal as reacted to by an acoustical source on the eardrum (Puria and Rosowski, 1996).

A distinctive characteristic of the DP-gram is the notch at the f_2 frequency of 3 kHz at high stimulus levels. This is present in the DP-grams of Gorga *et al.* (2000) illustrated in Fig. 4, and a similar notch is evident in responses described by Lonsbury-Martin and Martin (2001). A major factor producing this notch is the deep minimum in the reverse transfer function at a $2f_1-f_2$ frequency near 2 kHz (Fig. 8)—note that $2f_1-f_2=1.92$ kHz when $f_2=3$ kHz.

This illustrates a potential clinical application of the results of this study. It may be possible to optimize the stimulus levels used in DPOAE testing by taking explicit account of the forward and reverse transfer functions between probe and cochlear source region. If the reverse transfer function is anomalously low for an f_2 frequency of 3 kHz, one might reasonably correct for that in testing at 3 kHz by using a higher stimulus level. At the very least, it should be recognized in the clinic that a low DPOAE level (e.g., at 3 kHz) does not necessarily mean that the cochlear distortion is reduced at such a frequency.

A conclusion of this study is that the assumption of cochlear invariance is supported. However, a confounding effect is that a single nonlinear function might fit the data in an acceptable manner even though the distortion may have, in fact, differed across frequency at different cochlear sites due to slightly different local distributions of energy on the BM in the f_1 and f_2 traveling waves. To address this confounding effect, a DP-gram test could be constructed based not on equal SPL at the probe microphone, but rather on equal cochlear distortion generated on the BM (based on measurements in a group of normal-hearing subjects). It may be possible to construct a set of ear-canal stimulus levels across frequency intended to produce equal cochlear distortion across frequency. An iterative approach to determine such a set of stimulus levels is proposed in Appendix B.

The DPOAE-derived forward and reverse transfer functions are each composed of the product of a middle-ear transfer function and a cochlear transfer function. Similarities have been discussed between the DPOAE-derived functions and the corresponding middle-ear pressure functions. The cochlear transfer function is defined between the basal end of the cochlea and the hypothetical location of the beginning of the nonlinear source region. The location of the nonlinear source region begins basal to the f_2 tonotopic location. In the linear regime, the cochlear transfer functions are defined in the forward direction at the f_1 and f_2 frequencies, and in the reverse direction at the $2f_1 - f_2$ frequency. The scaling symmetry hypothesis of Zweig (1991), if assumed to hold exactly, predicts that these cochlear transfer functions are constant across frequency.[4] If so, then the DPOAE-derived forward and reverse transfer functions represent the response of the middle ear.

This approach to measuring *in vivo* forward and reverse transfer functions may be useful in comparative studies of mammalian ears, based on measurements and analyses of DPOAE I/O functions. Measuring such data is noninvasive and might prove useful in assessing the bandpass characteristic of middle-ear transmission in a paradigm in which the middle-ear cavities are intact. This might complement experimental measurements of the middle-ear response (Rosowski, 1994).

This approach may also be useful in comparing middle-ear and cochlear transmission in neonatal versus adult human ears, and to test for possible differences in sources of distortion products. The middle-ear functioning in young children and neonates differs from that in adults (Keefe *et al.*, 1993, 2000). A noninvasive method to estimate forward and reverse transfer functions may be useful to better interpret the results of EOAE measurements in infants, and it has potential significance for clinical hearing screening programs. Similarly, in ears with mild conductive impairments for which DPOAEs can still be measured, the technique may have relevance to understanding the nature of forward and reverse conductive transmission losses. More research is needed to extend the approach to other EOAEs, and test the approach to individual ears with EOAE fine structure.

VI. CONCLUSIONS

The main conclusion of this study is that average measurements of DPOAE I/O functions across a wide range of levels and frequencies performed in a population of healthy human adult ears may be represented in terms of (1) a frequency-independent nonlinear function, and (2) separable forward and reverse transfer functions between the ear-canal probe and the cochlear source region. This supports the hypothesis that there exists a distortion scaling region on the basilar membrane across the tonotopic locations corresponding to f_2 frequencies between 0.5 and 8.0 kHz within which the functional form of the basilar membrane nonlinearity underlying DPOAE generation is essentially constant. The forward and reverse transfer functions have a general bandpass shape, and show an intermediate narrow-band structure with similarities to the behavioral MAP threshold curve.

ACKNOWLEDGMENTS

I appreciate the assistance of Michael Gorga, who provided the DPOAE I/O function data; he and Walt Jesteadt have given helpful critiques of the research. This research was supported by the NIH (R01 DC03784). A preliminary account of this research has been presented (Keefe, 2001).

APPENDIX A: EAR-CANAL TRANSFORMATIONS

The transfer functions estimated using the DPOAE I/O functions reference the stimulus pressure to the probe microphone, whereas most middle-ear transfer functions have been measured using a stimulus pressure at the eardrum. Thus, it is relevant to consider the influence of probe-to-eardrum transformations on both forward and reverse transfer functions.

1. Forward transmission

The forward probe-to-eardrum transformation is calculated using a cylindrical model of the ear canal, parameterized by an ear-canal diameter and length from the Etymotic ER-10C probe tip to the eardrum. Siegel (1994) has modelled the pressure transfer function between a DPOAE probe assembly and the eardrum with respect to the forward transfer of stimulus energy from the probe into the middle ear and cochlea, and has measured this pressure transfer function in the ear canal. To model acoustical transmission in the forward direction, the terminating impedance at the eardrum is required, for which Siegel ''loosely approximated'' the measured middle ear impedance data of Rabinowitz (1981). Since these data extended only up to approximately 4 kHz, an extrapolation would seem to have been required at higher frequencies. Siegel estimated the range of lengths between probe and eardrum to be 1.5–2.0 cm for an Etyotic ER10B probe assembly, which employs re-useable rubber tips. In contrast, the Etymotic ER10C probe used by Gorga *et al.* (2000) includes a softer disposable foam tip, which leads to a deeper insertion into the ear canal. Thus, the present model used a shorter length of 1.0 cm as well as an ear-canal diameter of 0.8 cm, which is a typical value to which the model is relatively insensitive. The average insertion depth in the subjects tested by Gorga *et al.* (2000) is unknown. The present model used the average middle-ear impedance (Z_{TM}) measurements of Margolis *et al.* (1999), for which the frequency range (0.13–11.3 kHz) encompasses the frequency range used in the set of DPOAE responses. A smooth-wall model of attenuation at the ear-canal walls was used, but results were essentially identical to those obtained when such losses were neglected.

The resulting predicted difference in SPL at the eardrum (with pressure p_{TM}) relative to the probe (with pressure p_{mic}) is shown in Fig. 10. This is based on the forward transformation incorporating the middle-ear impedance Z_{TM}, which for simplicity is expressed in the form without wall loss:

$$\left.\frac{p_{\mathrm{TM}}}{p_{\mathrm{mic}}}\right|_{\mathrm{Forward}}=\frac{1}{\cos(2\pi fL/c)+j(Z_c/Z_{\mathrm{TM}})\sin(2\pi fL/c)}. \tag{A1}$$

The length between the probe and TM is L, the characteristic impedance of the ear canal is Z_c, the frequency is f, the phase velocity of sound is c, and the complex time dependence is $e^{j2\pi ft}$. The general shape of the curve is similar to model results obtained by Siegel, except for a shift in frequency due to the shorter length used in the present model and overall reduced magnitudes of SPL differences. The maximum SPL differences that Siegel measured always exceeded 10 dB, larger than those predicted by the present model. The reasons for this discrepancy in the neighborhood of 5 kHz are unknown.

In this case, the SPL at the eardrum is slightly larger than the measured SPL at the probe at low frequencies, has a maximum response 6–7 dB larger near 5 kHz, and has a reduced response of −8 dB at 8 kHz. Thus, a measurement protocol with constant SPL at the probe, such as was used by Gorga *et al.* (2000), has the property that eardrum SPL's are larger at and above 4 kHz, and are attenuated at 8 kHz. Because of the variability in ear-canal dimensions and insertion depths, Siegel (1994) concludes that ''standing waves in the human ear canal lead to large errors in calibrating eardrum sound pressures at high frequencies'' in DPOAE measurements. The nature of the pattern of errors is that the DPOAE at the 4 kHz f_2 frequency would tend to be larger, because the stimulus SPL at the eardrum is larger than that calibrated at the probe (one must also track the forward transfer function at the f_1 frequency, but this is increased as well). The zero-crossing in the SPL difference level plot near 6 kHz (Fig. 10) indicates that the overall error might not be large, but high variability in responses may occur due to the markedly steep slope in the function (as influenced by individual differences). The DPOAE at the 8 kHz f_2 frequency would probably always be smaller than expected by the calibrated SPL at the probe, because the SPL at the eardrum would be smaller. Note that the effect of ear-canal length differs at the f_1 and f_2 frequencies.

The forward transformation at f_2 between probe and eardrum plotted in Fig. 10 is applied to the forward DPOAE transfer function data in Fig. 8 to generate the DPOAE Threshold-TM curve plotted in Fig. 9. The difference between the DPOAE Threshold-Probe and the DPOAE Threshold-TM curves is the probe-to-eardrum transformation.

2. Reverse transmission

The ear-canal length between the probe and the eardrum acts to filter not only the forward transmission of energy from the probe to the eardrum, but also the reverse transmission of the EOAE from the eardrum to the probe. At high frequencies, the EOAE pressure just in front of the eardrum does not equal the EOAE pressure measured by the probe microphone. Because this is reverse transmission, the roles of eardrum and microphone pressure are reversed from that of the forward transmission case [Eq. (10)], and the terminating impedance is the input impedance of the probe (Z_{probe}). The resulting equation (again without wall losses) that relates the microphone pressure to the source EOAE pressure at the TM is

$$\begin{aligned}\left.\frac{p_{\mathrm{mic}}}{p_{\mathrm{TM}}}\right|_{\mathrm{Reverse}}&=\frac{1}{\cos(2\pi fL/c)+j(Z_c/Z_{\mathrm{probe}})\sin(2\pi fL/c)}\\&\approx\frac{1}{\cos(2\pi fL/c)}.\end{aligned} \tag{A2}$$

This function is plotted as a level difference in Fig. 10 for the case that the probe is 10 mm from the eardrum. The figure facilitates comparison between forward and reverse transmission: the forward and reverse ear-canal level differences are not the same because the input impedance of the middle ear is quite different from the input impedance of the probe assembly. The reverse-transmission curve is drawn under the approximation that the magnitude of the probe impedance is much larger than the characteristic impedance of the ear canal; this approximation is given on the lower line of the above equation by neglecting the term proportional to Z_c/Z_{probe}. As with the probe considered by Siegel (1994), the Etymotic ER10C probe used by Gorga *et al.* (2000) has an input impedance that is primarily resistive and large compared to the characteristic impedance of an adult human ear canal.

Figure 10 illustrates that the perturbing effects of probe placement occur only at high frequencies for both forward and reverse transmission, and that the spectral shapes of these functions differ. Moreover, for the case of DPOAEs, the functions must be evaluated at different frequencies, because the forward transmission occurs at f_1 and f_2, while reverse transmission occurs at $2f_1-f_2$. The reverse transmission function is always positive over the range of $2f_1-f_2$ frequencies in the present analysis (<5.1 kHz), which means that the EOAE level measured by the microphone exceeds that which would be measured at the eardrum by as much as 4 dB or so. If one is interested in measuring DPOAEs at f_2 frequencies exceeding 8 kHz, the reverse ear-canal transmission effects can be large, exceeding 17 dB at a $2f_1-f_2$ frequency of 8 kHz. This high-frequency effect is extremely sensitive to the value of insertion length.

Beyond the effects predicted by Eq. (A2), it should be noted that the major complications arise in reverse transmission because the source is effectively in the cochlear vestibule at the base of the cochlea. The reverse transmission function from this source to ear-canal probe couples a middle-ear transfer function with the ear-canal transformation from eardrum to probe, and Eq. (A2) cannot be used to predict this coupling. This underlies the sensitive dependence of the reverse middle-ear transfer function on probe position that was pointed out by Puria and Rosowski (1996).

TABLE I. Forward transfer function level differences.

f_1 (kHz)	f_2 (kHz)	$\Delta L_{12}(f_2)$ (dB)
0.61	0.75	+1.7
0.82	1.00	+1.6
1.23	1.50	−1.9
1.64	2.00	−1.1
2.46	3.00	+4.6
3.28	4.00	−0.0
4.92	6.00	−5.3
6.56	8.00	−2.8

APPENDIX B: ON THE OPTIMUM $L_1 - L_2$ RATIO IN DPOAE MEASUREMENTS

This appendix describes how a knowledge of the forward transfer function may help in the selection of the optimal choice of $L_1 - L_2$ as L_2 is varied and as f_2 frequency is varied. An iterative procedure is proposed to obtain improved estimates of the forward and reverse transfer functions. Based on measurements in normal-hearing ears, the main idea is to select stimulus levels so as to normalize the input levels on the BM rather than normalizing SPL in the ear canal. Within such a stimulus set, it is important to give separate consideration to the L_1 and L_2 levels at the f_1 and f_2 frequencies. The ratio f_2/f_1 is assumed to be fixed at 1.22 in the following discussion.

The optimal forward transfer function levels L_1 and L_2 vary with f_2. Suppose L_2 is fixed at 40 dB SPL; then the rule of Eq. (4) is to set L_1 at 55 dB SPL, or 15 dB higher than L_2. Define the level difference $\Delta L_{12}(f_2)$ of the DPOAE-derived forward transfer function at f_2 relative to that at f_1, i.e.,

$$\Delta L_{12}(f_2) = 20 \log\left(\frac{T_{mc}^F(f_2)}{T_{mc}^F(f_1)}\right). \tag{B1}$$

The rule of Eq. (4) was implicitly based on a nominal condition in which the frequency dependence of the forward transfer function was not considered. This nominal condition is formalized by defining $\Delta L_{12}(f_2)$ to be zero at all f_2 frequencies. When the actual estimated $\Delta L_{12}(f_2) > 0$, there is greater transmission from the probe to the f_2-place region on the BM at the f_2 frequency than at the f_1 frequency, so that the nominal L_1 level predicted by Eq. (4) is too low to generate the nominal level of cochlear distortion. Conversely, when $\Delta L_{12}(f_2) < 0$, there is less transmission from the probe to the f_2-place region at the f_2 frequency than at the f_1 frequency, so that the nominal L_1 level predicted by Eq. (4) is too high.

Table I lists the level differences $\Delta L_{12}(f_2)$ calculated from the forward transfer function data using a spline interpolation of the data plotted in Fig. 8. The largest magnitudes in the level differences occur at f_2 frequencies in the range from 3–6 kHz. The intermediate $f_2 = 4$ kHz case is close to the nominal condition ($\Delta L_{12}(f_2) = 0$), because the forward transfer levels are similar at f_1 and f_2. The $f_2 = 3$ kHz case suggests that L_1 would be set too low in value by the rule of Eq. (4), and the $f_2 = 6$ kHz case suggests that L_1 would be set too high in value. The former is an additional factor that may account for the low DPOAE level at $f_2 = 3$ kHz. Thus, an analysis of the stimulus levels used in the original measurement and the resulting estimated forward transfer levels predict an apparent weak violation in cochlear invariance due to inaccuracies in satisfying the assumption that the relative level $L_1 - L_2$ is held constant across the BM. The only other f_2 frequency for which the magnitude of the level difference exceeds 2 dB is 8 kHz, for which the level difference is −2.8 dB. This has the same sign as the shift at 6 kHz.

In an experiment in which f_2/f_1 and L_2 are fixed, and f_2 and L_1 are each varied, the optimal L_1 at each f_2 frequency would be the level at which the DPOAE signal is maximized. This frequency-specific optimum may differ from the rule of Eq. (4). If $L_2 = 40$ dB SPL, the predicted nominal L_1 from Eq. (4) is 55 dB. If the forward transfer function varies across frequency, then one would expect the outcome of the experiment to give a distribution of optimum L_1 levels across the frequency range, but centered at 55 dB SPL. This experiment has been performed by Gaskill and Brown (1990). They tested eight different f_1 frequencies ranging from 2.16 to 3.2 kHz with $f_2/f_1 = 1.225$, and the L_1 levels at which the DPOAE level was maximized ranged from 54 to 67 dB SPL.[5] The fact that the optimum L_1 was not constant across frequency is consistent with the hypothesis that Eq. (4) is not optimized to include variations in forward transfer functions.

A thought-experiment is proposed to provide an iterative, self-consistent method for constructing stimulus levels in a manner to address this limitation, in which the present analysis coupled with the DPOAE data collected by Gorga *et al.* (2000) serves as the initial iteration. The forward transfer function obtained is used in the manner described above at each f_2 frequency to calculate an adjustment in L_1 at each choice of L_2 according to the value of $\Delta L_{12}(f_2)$. Data would be collected in the next iteration based on this new stimulus-level rule. The resulting forward transfer function would be used to update the new stimulus-level rule in the next round of iteration. The results are expected to converge with successive iterations to a self-consistent estimate of forward and reverse transfer functions, thereby providing a rule for choosing the $L_1 - L_2$ difference at each L_2 level and each f_2 frequency. A practical difficulty is the step of data collection in a large sample population of healthy ears, but even one further iteration would test the plausibility of the method. If the probe location from the eardrum were estimated, then the method could be refined to include the probe-to-eardrum forward and reverse transmission effects in the ear canal.

[1]The example cited of a 20-dB relative decrement in forward transmission is a hypothetical value, as is the subsequent example of a 15-dB relative increment in reverse transmission. The use of specific values is simply to illustrate the structure of forward and reverse transmissions as translations on the plane of the I/O function. There is no assertion that these specific values are physiologically realistic.

[2]The choice of 1 kHz as the reference frequency for fitting the I/O functions is arbitrary. Relative forward and reverse transfer functions may equally well be constructed using any other reference frequency.

[3]This dynamic range (18.4) is the perpendicular distance (dB) on the I/O function plane between the lower and upper asymptotically linear slopes. The dynamic range is often defined as the translation along the stimulus axis (the horizontal axis of the I/O function) between lower and upper slopes of slope 0.72 dB/dB. This latter dynamic range is 18.4/sin (arctan (0.72)) = 31.5 dB.

[4]In a more detailed cochlear model, an appropriate forward cochlear transfer function would be the pressure difference across the BM at any BM location relative to the pressure difference at the stapes. The scaling symmetry of Zweig (1991), which is used with the long-wavelength (WKB) approximation, predicts that this pressure difference scales. Thus, the forward cochlear transfer function has the same shape across frequency when translated to its tonotopic place. According to WKB theory, the reverse cochlear transfer function is equal in magnitude to that of the forward transfer function, and hence is also constant. The scaling approximation breaks down at low frequencies such that the traveling wave has a significant amplitude at the apical end of the cochlea.

[5]The manner in which the data of Gaskill and Brown (1990) are plotted is such that it is not possible to extract the maximum DPOAE level at each frequency.

Avan, P., Buki, B., Maat, B., Dordain, M., and Wit, H. P. (**2000**). ''Middle ear influence on otoacoustic emissions. I: Noninvasive investigation of the human transmission apparatus and comparison with model results,'' Hear. Res. **140**, 189–201.

de Boer, E. (**1997**). ''Connecting frequency selectivity and nonlinearity for models of the cochlea,'' Aud. Neurosci. **3**, 377–388.

Gaskill, S. A., and Brown, A. M. (**1990**). ''The behavior of the acoustic distortion product, $2f_1-f_2$, from the human ear and its relation to auditory sensitivity,'' J. Acoust. Soc. Am. **88**, 821–839.

Gorga, M. P., Nelson, K., Davis, T., Dorn, P. A., and Neely, S. T. (**2000**). ''Distortion product otoacoustic emission test performance when both $2f_1-f_2$ and $2f_2-f_1$ are used to predict auditory status,'' J. Acoust. Soc. Am. **107**, 2128–2135.

Hudde, H., and Engel, A. (**1998**). ''Measuring and modeling basic properties of the human middle ear and ear canal. Part III: Eardrum impedances, transfer functions and model calculations,'' Acta Acust. **73**, 242–247.

Keefe, D. H. (**2001**). ''Input/output functions of distortion product otoacoustic emissions predict the spectral shapes of the forward and reverse middle-ear transfer function,'' in *Abstracts of the 24th Midwinter Research Meeting of the ARO*, Des Moines (Association for Research in Otolaryngology), p. 25.

Keefe, D. H., Feeney, M. P., and Margolis, R. H. (**2001**). ''Energy transmission model of the fluid-filled middle ear and related pathologies,'' in *Abstracts of the 24th Midwinter Research Meeting of the ARO*, Des Moines (Association for Research in Otolaryngology), p. 220.

Keefe, D. H., Bulen, J. C., Arehart, K. H., and Burns, E. M. (**1993**). ''Ear-canal impedance and reflection coefficient in human infants and adults,'' J. Acoust. Soc. Am. **94**, 2617–2638.

Keefe, D. H., Folsom, R., Gorga, M. P., Vohr, B. R., Bulen, J. C., and Norton, S. (**2000**). ''Identification of neonatal hearing impairment: Ear-canal measurements of acoustic admittance and reflectance in neonates,'' Ear Hear. **21**, 443–461.

Kemp, D. T. (**1980**). ''Towards a model for the origin of cochlear echoes,'' Hear. Res. **2**, 533–548.

Killion, M. C. (**1978**). ''Revised estimate of minimum audible pressure: Where is the 'missing 6 dB'?'' J. Acoust. Soc. Am. **63**, 1501–1508.

Kummer, P., Janssen, T., and Arnold, W. (**1998**). ''The level and growth behavior of the $2f_1-f_2$ distortion product otoacoustic emission and its relationship to auditory sensitivity in normal hearing and cochlear hearing loss,'' J. Acoust. Soc. Am. **103**, 3431–3444.

Lonsbury-Martin, B. L., and Martin, G. K. (**2001**). ''Distortion product otoacoustic emissions,'' in *Otoacoustic Emissions Clinical Applications*, 2nd ed., edited by M. S. Robinette and T. J. Glattke (Thieme, New York), pp. 116–142.

Magnan, P., Avan, P., Dancer, A., Smurzynski, J., and Probst, R. (**1997**). ''Reverse middle-ear transfer function in the guinea pig measured with cubic difference tones,'' Hear. Res. **107**, 41–45.

Margolis, R. H., Saly, G. L., and Keefe, D. H. (**1999**). ''Wideband reflectance tympanometry in normal adults,'' J. Acoust. Soc. Am. **106**, 265–280.

Puria, S., and Rosowski, J. J. (**1996**). ''Measurement of reverse transmission in the human middle ear: Preliminary results,'' in *Diversity in Auditory Mechanics*, edited by E. Lewis, G. Long, R. Lyon, P. Narins, and C. Steele (World Scientific, Singapore).

Puria, S., Peake, W. T., and Rosowski, J. J. (**1997**). ''Sound-pressure measurements in the cochlear vestibule of human-cadaver ears,'' J. Acoust. Soc. Am. **101**, 2754–2770.

Rabinowitz, W. (**1981**). ''Measurement of the acoustic input immittance of the human ear,'' J. Acoust. Soc. Am. **70**, 1025–1035.

Rhode, W. S. (**1971**). ''Observations of the vibration of the basilar membrane in squirrel monkeys using the Mössbauer technique,'' J. Acoust. Soc. Am. **49**, 1218–1231.

Rhode, W. S., and Recio, A. (**2000**). ''Study of mechanical motions in the basal region of the chinchilla cochlea,'' J. Acoust. Soc. Am. **107**, 3317–3332.

Rosowski, J. J. (**1994**). ''Outer and middle ears,'' in *Comparative Hearing: Mammals*, edited by R. R. Fay and A. N. Popper (Springer-Verlag, New York), pp. 172–247.

Sachs, M. B., and Abbas, P. J. (**1974**). ''Rate versus level functions for auditory-nerve fibers in cats: tone-burst stimuli,'' J. Acoust. Soc. Am. **56**, 1835–1847.

Siegel, J. H. (**1994**). ''Ear-canal standing waves and high-frequency sound calibration using otoacoustic emission probes,'' J. Acoust. Soc. Am. **95**, 2589–2597.

Talmadge, C. L., Tubis, A., Long, G. R., and Piskorski, P. (**1998**). ''Modeling otoacoustic emission and hearing threshold fine structures in humans,'' J. Acoust. Soc. Am. **104**, 1517–1543.

Wever, E. G., Bray, C. W., and Lawrence, M. (**1941**). ''The effect of middle ear pressure upon distortion,'' J. Acoust. Soc. Am. **13**, 182–187.

Whitehead, M. L., Stagner, B. B., McCoy, M. J., Lonsbury-Martin, B. L., and Martin, G. K. (**1995**). ''Dependence of distortion-product otoacoustic emissions on primary levels in normal and impaired ears. II. Asymmetry in l_1/l_2 space,'' J. Acoust. Soc. Am. **97**, 2359–2377.

Withnell, R. H., and Yates, G. K. (**1998**). ''Onset of basilar membrane nonlinearity reflected in cubic distortion tone input-output functions,'' Hear. Res. **123**, 87–96.

Zweig, G. (**1976**). ''Basilar membrane motion,'' in *Cold Spring Harbor Symposia on Quantitative Biology* (Cold Spring Harbor Laboratory, New York), Vol. XL, pp. 619–633.

Zweig, G. (**1991**). ''Finding the impedance of the organ of Corti,'' J. Acoust. Soc. Am. **89**, 1229–1254.

Zwicker, E., and Schloth, E. (**1984**). ''Interrelation of different oto-acoustic emissions,'' J. Acoust. Soc. Am. **75**, 1148–1154.

Zwislocki, J. J. (**1962**). ''Analysis of middle ear function. Part I: Input impedance,'' J. Acoust. Soc. Am. **34**, 1514–1523.

Development of wide-band middle ear transmission in the Mongolian gerbil[a)]

Edward H. Overstreet III[b)] and Mario A. Ruggero[c)]

Institute for Neuroscience and Hugh Knowles Center, Department of Communication Sciences and Disorders, Northwestern University, 2299 North Campus Drive, Evanston, Illinois 60208-3550

(Received 20 April 2001; accepted for publication 24 September 2001)

Stapes vibrations were measured in deeply anesthetized adult and neonatal (ages: 14 to 20 days) Mongolian gerbils. In adult gerbils, the velocity magnitude of stapes responses to tones was approximately constant over the entire frequency range of measurements, 1 to 40 kHz. Response phases referred to pressure near the tympanic membrane varied approximately linearly as a function of increasing stimulus frequency, with a slope corresponding to a group delay of 30 μs. In neonatal gerbils, the sensitivity of stapes responses to tones was lower than in adults, especially at mid-frequencies (e.g., by about 15 dB at 10–20 kHz in gerbils aged 14 days). The input impedance of the adult gerbil cochlea, calculated from stapes vibrations and published measurements of pressure in scala vestibuli near the oval window [E. Olson, J. Acoust. Soc. Am. **103**, 3445–3463 (1998)], is principally dissipative at frequencies lower than 10 kHz. Conclusions: (a) middle-ear vibrations in adult gerbils do not limit the input to the cochlea up to at least 40 kHz, i.e., within 0.5 oct of the high-frequency cutoff of the behavioral audiogram; and (b) the results in both adult and neonatal gerbils are inconsistent with the hypothesis that mass reactance controls high-frequency ossicular vibrations and support the idea that the middle ear functions as a transmission line. [DOI: 10.1121/1.1420382]

PACS numbers: 43.64.Ha [BLM]

I. INTRODUCTION

The Mongolian gerbil is widely used as a model for studying the mammalian auditory system, including its development and aging. Therefore, it would be useful to understand the role of the middle ear in shaping the input to the cochlea in both adults and neonates of this species. However, the few studies that have measured ossicular vibrations in the middle ear of gerbils have often yielded inconsistent findings. For example: one study reported that the magnitude of stapes velocity in adult gerbils decayed at a rate of 6 dB/oct at frequencies higher than 1 kHz (Rosowski *et al.*, 1999), another found a relatively sharp peak of umbo sensitivity at about 4 kHz (Cohen *et al.*, 1993) and two others reported that the magnitude of ossicular velocity was relatively flat up to frequencies as high as 46 kHz (Olson and Cooper, 2000; Xue *et al.*, 1995). Similarly, one investigation in neonatal gerbils concluded that middle ear transmission improves by 25 dB between ages 14 and 16 days after birth (DAB) (Woolf and Ryan, 1988) while another reported that umbo vibrations for stimuli higher than 4 kHz did not change between 15 and 42 DAB (Cohen *et al.*, 1993).

In an effort to resolve the aforementioned discrepancies and to complement ongoing studies of basilar-membrane mechanics and its development at the hook region of the cochlea (Overstreet and Ruggero, 1998, 1999), the magnitude and phase characteristics of stapes vibrations were measured in adult and neonatal gerbils. Results in adults indicate that, contrary to an often-stated hypothesis, the inertial reactance of the middle ear does not restrict the input to the cochlea at least up to 40 kHz, i.e., a frequency within 0.5 oct of the cutoff of the gerbil behavioral audiogram. Results from neonates imply that middle-ear transmission improves considerably after 14 days of age, a period when the mass of the middle-ear ossicles increases substantially (Cohen *et al.*, 1992). The simultaneity of these developmental changes also clashes with the idea that ossicular vibrations are mass controlled at high frequencies. The ossicular vibration data in both neonatal and adult gerbils are consistent with the hypothesis that the mammalian middle ear functions as a transmission line (Olson and Cooper, 2000; Onchi, 1949, 1961; Puria and Allen, 1998; Wilson and Bruns, 1983; Zwislocki, 1962).

II. METHODS

A. Animal preparation

All experiments were conducted in accordance with guidelines of Northwestern University's Animal Care and Use Committee. Subjects were anesthetized adult and neonate Mongolian gerbils (*Meriones unguiculatus*). Breeding pairs were obtained from Tumblebrook Farms and a colony was developed. The ages of adult gerbils were between 90 and 160 DAB. Neonate gerbils were 14, 16, 18, and 20 day DAB (determined with a precision of ± 8 h), day zero being the day of birth. To help insure equal maturation rates, all litters were culled to six pups and only neonates weighing within one standard deviation of the norm for a given age

[a)]The substance of this article was part of a doctoral dissertation by the first author and was presented at a meeting of the Association for Research in Otolaryngology.

[b)]Current address: Advanced Bionics Corporation, 12740 San Fernando Road, Sylmar, CA 91342.

[c)]Electronic mail: mruggero@northwestern.edu

(Woolf and Ryan, 1985) were used. The norm is that the weights of the gerbils in grams roughly equal their age at least up to ~30 DAB (e.g., 14-DAB gerbils weigh about 14 g).

After sedation with a 0.01-ml subcutaneous injection of ketamine HC1 (100 mg/ml), gerbils were anesthetized with an initial intraperitoneal injection of sodium pentobarbital (48 mg/kg), later supplemented as needed to maintain deep anesthesia. During the course of the experiment the animals were kept hydrated by 0.10-cc intraperitoneal injections of Pedialyte (Abbott; each liter of this solution contains 45 mEq Na, 20 mEq K, 35 mEq Cl, 30 mEq citrate and 25 g dextrose), administered at ~90-min intervals. The gerbils were placed upon a vibration-isolation table (Technical Manufacturing Corporation, model No. 63-561) within a sound-insulated chamber (Industrial Acoustics Company). Rectal temperature was monitored and maintained at 39 °C by means of a servo-controlled battery-powered electrical heating pad wrapped around the animal. All gerbils were tracheotomized to maintain a patent airway but only animals older than 18 DAB were intubated. Intubation was not performed in younger animals because it was difficult to keep the requisite small-diameter trachea tubes free of fluid in the face of strong capillary forces. Instead, a clear air passage was maintained in neonates by lining the surgical opening to the trachea with cotton wicks.

The gerbil's head was firmly affixed to a custom-made holder which was heated to maintain normal cochlear temperature, counteracting the effects of deep anesthesia and the widely opened bulla (Brown *et al.*, 1983; Shore and Nuttall, 1985). The left pinna was removed to allow the insertion into the ear canal of a speculum containing the probe tube of a Knowles EK3103 miniature microphone. After opening the ventral aspect of the bulla, a ball silver-wire electrode was placed on the bone near the round window to record compound action potentials (CAPs) evoked by tone pips. The CAP thresholds as a function of stimulus frequency served as an ''audiogram'' to assess cochlear sensitivity, which often decreased with the passage of time. However, acute changes in cochlear sensitivity were not due to changes in stapes-vibration sensitivity, which was robust and remained nearly constant even post-mortem.

B. Sound system and its calibration

Acoustic stimuli were generated via a modified Radio Shack tweeter (Chan *et al.*, 1993) coupled to the ear speculum. The tweeter was driven with electrical sinusoids (1–40 kHz) digitally synthesized with a Tucker-Davis system under computer control. The sensitivity and phases of stapes vibrations in each gerbil ear were referenced to pressure in the ear canal using a ''hybrid calibration'' combining an ''*in situ* probe-tube calibration'' measured in that ear with an average ''artificial-cavity calibration.'' The *in situ* calibrations (thin solid lines in Fig. 1) were obtained with a miniature microphone fitted with a thin, small-diameter probe tube, whose tip was placed was placed within 2.5 mm of the tympanic membrane. The probe microphone had been previously calibrated against a 1/8-in. Brüel & Kjaer microphone in a

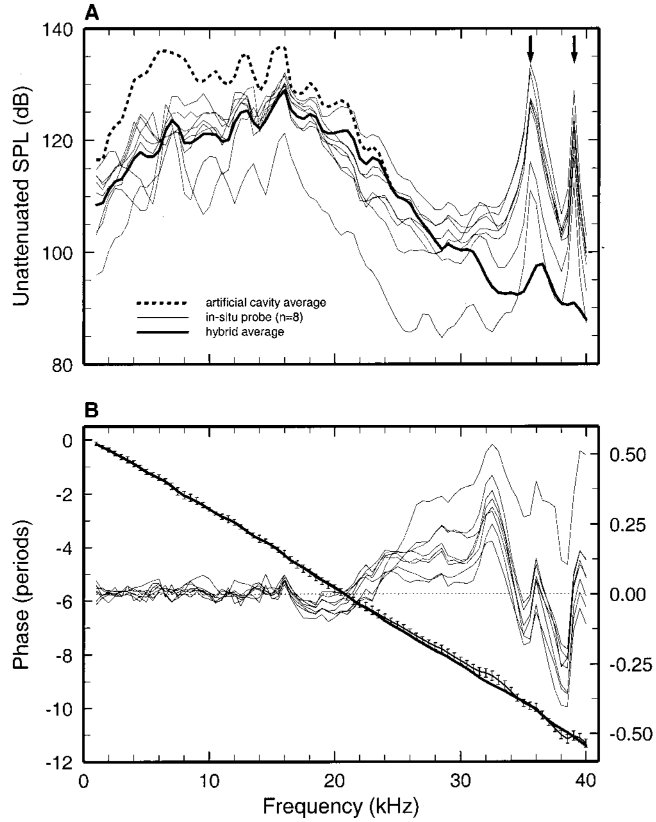

FIG. 1. Stimulus calibration. (a) The SPL produced by a constant and unattenuated voltage input to the earphone. The thin solid lines indicate *in situ* probe calibrations in the external ear canals of eight adult gerbils. The thick dashed line represents measurements in a small artificial cavity using a 1/8-in. condenser microphone. The thick solid line is the average of eight hybrid magnitude calibrations (see Sec. II), which were identical to the *in situ* calibrations at frequencies <16.5 kHz and identical to the artificial-cavity calibration (dashed line) at frequencies >25 kHz. (b) Vibration phases expressed relative to the voltage input to the tweeter. The standard deviations of the mean *in situ* calibration are indicated by brackets. The thick solid line is the average of the eight hybrid phase calibrations (see Sec. II). The thin solid lines indicate the phase differences between the *in situ* calibration and the hybrid calibrations in eight ears.

closed artificial cavity simulating the external ear canal of the gerbil. The ''artificial-cavity'' calibration was an average of three separate measurements.

At stimulus frequencies 16.5 kHz and lower, the magnitudes of the hybrid pressure calibrations were identical to those measured *in situ*; at frequencies higher than 25 kHz, they were identical to the magnitudes in the average artificial-cavity calibration; between 16.5 kHz and 25 kHz, the magnitudes were weighted averages of the *in situ* and artificial-cavity calibrations, with the weight of the latter increasing smoothly from nil at 16.5 kHz to 100% at 25 kHz. [The use of artificial-cavity calibrations in auditory investigations involving high-frequency stimuli was recently advocated by Pearce *et al.* (2001).] The phases of the hybrid calibration were obtained by adding pure delays of 162–165 μs to ''minimum'' phases computed (using the function RCEPS.M of MATLAB) from the magnitudes of the hybrid calibration, supplemented with a low-frequency terminal slope of 0 to +6 dB/oct, a slope of −6 dB/oct between 40 and 51 kHz, and a terminal high-frequency slope of −1000 dB/oct.

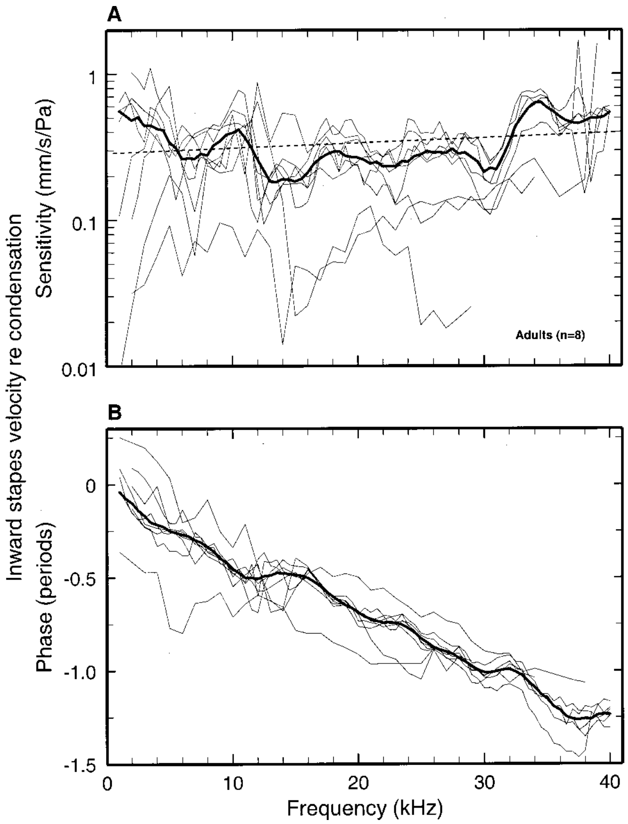

FIG. 2. Stapes velocity response to tones in adult gerbils. The magnitude [panel (a)] and phases [panel (b)] of stapes velocity sensitivity (mm/s/Pa) are plotted as a function of frequency for eight gerbils (thin lines). Central tendencies are indicated by medians (thick lines), which have been subjected to three-point smoothing to reduce jaggedness caused by unequal numbers of samples averaged at odd and even multiples of 500 Hz.

Figure 1 shows the magnitudes [panel (a)] and phases [panel (b)] of *in situ* probe-tube calibrations measured in eight gerbil ears (thin solid lines), the average artificial-cavity calibration (dashed lines), and the average of eight hybrid calibrations (thick solid lines). The latter served as references for the stapes vibration data in adults (Fig. 2). All *in situ* calibrations contained sharp magnitude peaks at the same frequencies [arrows in Fig. 1, panel (a)], probably because the probe tip was routinely placed in approximately the same location in each ear. As shown by panel (b), the phase differences between the *in situ* and hybrid calibrations were small at frequencies <16 kHz.

C. Stimulus protocol

CAP thresholds were measured using an automated procedure which, for each stimulus frequency, determined the sound pressure level (SPL, expressed in decibels referenced to 20 μPa) required to achieve a predetermined CAP magnitude (typically, 7 μV). Stimuli were 5-ms tone pips with onset phases randomized to cancel out cochlear microphonics and ramped with a 0.75 ms rise/fall time to efficiently synchronize the neural spikes without losing frequency resolution due to spectral spread.

Stimuli for the measurement of stapes vibrations were 5-ms tones presented every 50 ms with rise/fall times of 0.75 ms. Stapes velocity responses to 256–4096 stimulus repetitions were time averaged for each stimulus condition, depending upon the signal-to-noise ratio. Only averaged responses greater than 6 dB above the average noise floor were used.

D. Laser-velocimetry data collection and analysis

Stapes velocity was determined by means of a Dantec laser vibrometer consisting of a 20-mW He–Ne laser, a headstage, and a Doppler-frequency tracker (Ruggero and Rich, 1991). The laser light was targeted on a reflective glass microbead via an Olympus compound microscope equipped with a 20× ultra-long working-distance objective (Mitutoyo 20SL, N.A. 0.42). The bead (diameter: 20–30 μm) was placed on the head of the stapes near the incudo-stapedial joint. The angle between the laser beam and the axis of stapes vibration was less than 30 degrees. The electrical output signal of the vibrometer headstage was converted into a voltage proportional to target velocity by the Doppler-frequency tracker, whose output was digitized (16-bit resolution, sampling rate of 166 kHz) and stored on magnetic media in a computer. MATLAB programs were used to compute the discrete Fourier transforms of the time-averaged response waveforms. The velocity-response magnitudes and phases were imported into a spreadsheet (EXCEL) for further processing.

III. RESULTS

A. Specifying the pressure input to the middle ear

Specification of the acoustic stimulus at high frequencies is difficult because malleus vibrations result from a weighted spatial average of the local pressures and acoustic loads distributed across the surface of the tympanic membrane (Stinson and Khanna, 1989); "... above about 10 kHz ... it is not possible to define the acoustical input to the ear from sound pressure level measured at any single location" (Khanna and Stinson, 1985) (see also Stinson, 1985; Stinson and Shaw, 1982). Indeed, we found that referencing stapes vibrations to pressure calibrations measured *in situ* with a probe-tube introduced conspicuous valleys and peaks in velocity magnitude versus frequency curves at frequencies higher than 30 kHz, which closely mirrored the peaks and valleys, respectively, of the *in situ* calibrations [arrows in Fig. 1, panel (a)]. Since these irregularities (absent when vibrations were referenced to the constant voltage input to the earphone) appeared to be local and largely spurious features without counterpart in the effective pressure driving ossicular vibrations, stapes vibrations in the present study are referenced to hybrid pressure calibrations combining individual *in situ* calibrations (for frequencies <16 kHz) with a single average calibration measured in an artificial cavity (for frequencies >25 kHz) (see Sec. II).

B. Stapes vibrations in adult gerbils

Figure 2 shows the magnitudes and phases of stapes responses to tones measured in eight adult gerbils. Individual measurements (thin lines) and population medians (thick lines) are plotted as a function of stimulus frequency, with a

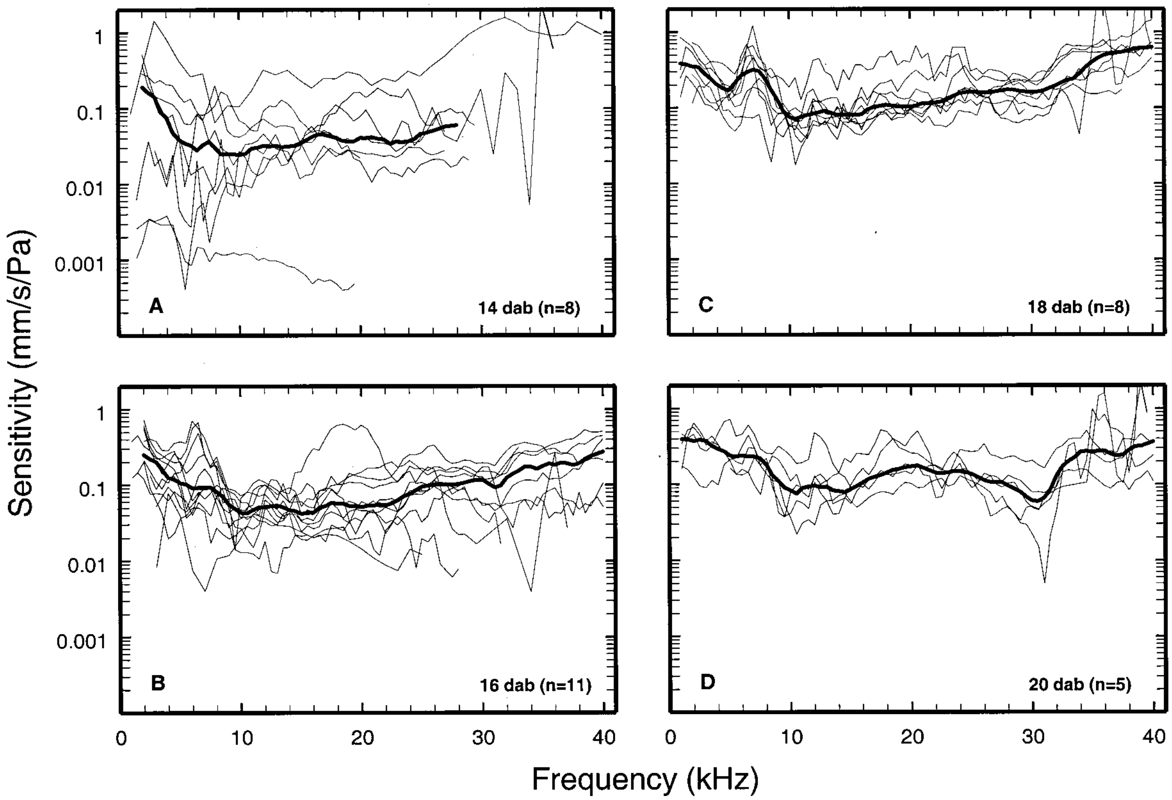

FIG. 3. The magnitude sensitivity of stapes responses to tones in neonatal gerbils. Each panel depicts responses from individual ears (thin lines) and population medians (thick lines). The median curves have been subjected to three-point smoothing to reduce jaggedness caused by unequal numbers of samples averaged at odd and even multiples of 500 Hz.

resolution of 500 or 1000 Hz. Panel (a) of Fig. 2 shows that, to a first approximation, sensitivity did not vary systematically as a function of frequency, with a mean magnitude of 0.34 mm/s/Pa in the 1–40 kHz range. [A straight-line fit to the median data points expressed in logarithmic coordinates (not shown) had a slope of +0.52 dB/oct.] The range of response magnitudes across ears was wide but, overall, variability was moderate, with interquartile ranges [brackets in Fig. 5, panel (a)] rarely exceeding 4 dB.

Panel (b) of Fig. 2 plots the phases of the velocity responses in the inward direction, referenced to condensation in the external ear canal near the tympanic membrane, as a function of stimulus frequency. At 1 kHz, stapes vibrations were nearly in phase with condensation, on average. At higher frequencies there was a steady, approximately linear, phase roll-off, so that stapes vibration lagged condensation by about 1.2 periods at 40 kHz. The median phase lags (thick line) were clustered around a straight line (not shown) with slope equivalent to a delay of 30 μs (95% confidence limits: 31.1 and 29.3 μs).

C. Stapes vibrations in neonate gerbils

Figures 3 and 4 show individual data and population medians for the magnitudes and phases, respectively, of stapes responses to tones measured in neonatal gerbils, grouped according to age (14, 16, 18, or 20 DAB). Stapes vibrations in 14-DAB gerbils were very variable and insensitive and could rarely be measured at frequencies higher than 26 kHz. Response variability became progressively smaller as a function of increasing age. This is especially evident in the phases of Fig. 4. Interquartile ranges in neonates 18–20 DAB (not shown) were comparable to those for adults (brackets in Fig. 5).

Figure 5 allows for comparison of the magnitude [panel (a)] and phases [panel (b)] of stapes vibrations as a function of age. Response magnitudes were larger in 16-DAB gerbils than in 14-DAB gerbils and still larger in 18- and 20-DAB gerbils. In gerbils aged 18 and 20 DAB, magnitudes approached adult values near 1 and 40 kHz but were less sensitive than in adults at 10–20 kHz. In that frequency range, adult sensitivity was some 12–20 dB larger than in neonates aged 14 or 16 days. Responses in neonates aged 14 days lagged adult responses at all frequencies. Response phases in neonates aged 16–20 days were similar to those of adults near 1 kHz but increasingly diverged at higher frequencies, with average slopes corresponding to group delays of 43, 35, and 32 μs for gerbils aged 16, 18, and 20 days, respectively (versus 30 μs for adults).

D. The input impedance of the adult gerbil cochlea

Using the data on stapes vibration in adult gerbils (Fig. 2) in conjunction with measurements of pressure in the perilymph of scala vestibuli (SV) near the oval window (Olson, 1998) and of the area of the stapes footplate [0.8 mm^2 (Cohen *et al.*, 1992)], we estimated the acoustic input impedance of the cochlea [SV pressure *re*: stapes volume velocity (Zwislocki, 1962)]. The magnitudes of the cochlear input

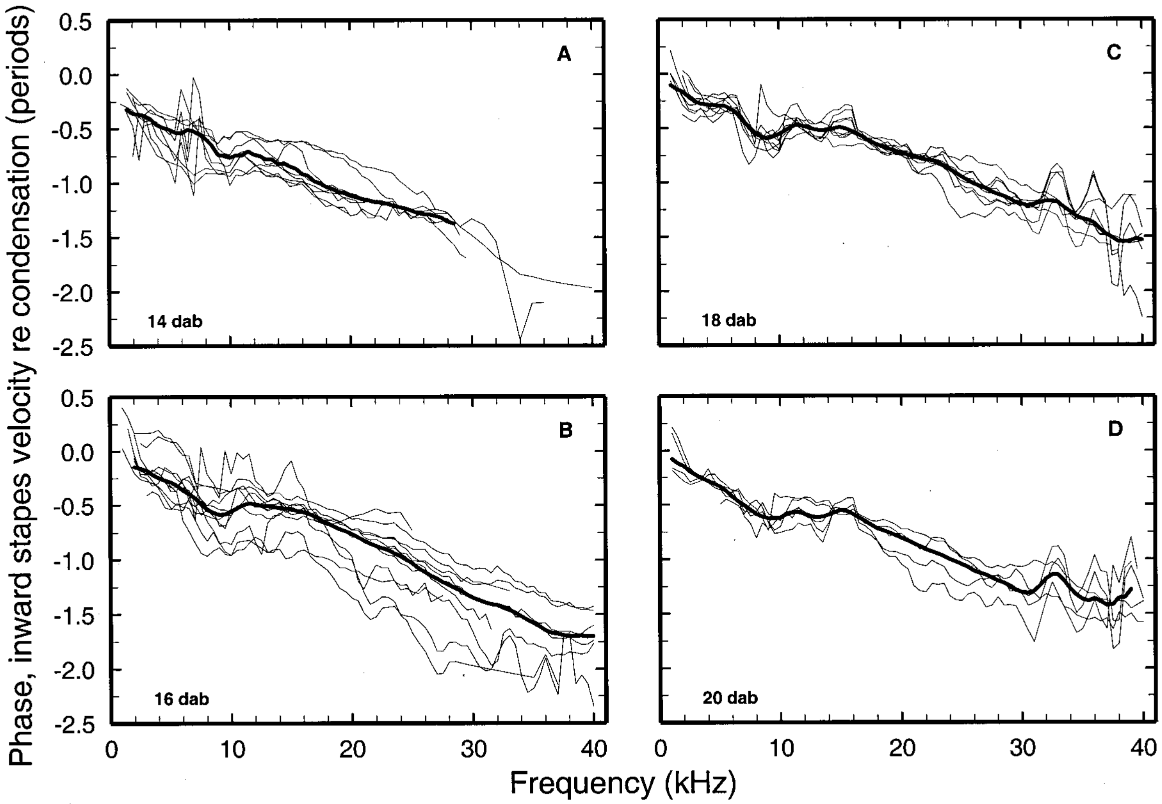

FIG. 4. The phases of stapes responses to tones in neonatal gerbils. The phases of peak inward velocity of the stapes footplate are expressed relative to peak condensation in the external ear canal, near the eardrum. Each panel depicts responses from individual ears (thin lines) and population medians (thick lines). The median curves have been subjected to three-point smoothing to reduce jaggedness caused by unequal numbers of samples averaged at odd and even multiples of 500 Hz.

impedance for the adult gerbil are shown in panel (a) of Fig. 6 as a function of stimulus frequency (open circles). In spite of irregularities, which probably reflect measurement errors in one or two laboratories (our own and Olson's), the input impedance is relatively invariant over a wide frequency range, amounting to 1.3×10^6 dyne.s.cm^{-5} (i.e., 1.3 cgs acoustic megohms or 130 MKS acoustic gigohms), on average.

Panel (a) of Fig. 6 also shows the magnitude of the cochlear input impedance for cat (Lynch *et al.*, 1982), guinea pig (Dancer and Franke, 1980), and chinchilla (Ruggero *et al.*, 1990). For guinea pig, input impedance magnitude was computed from averages of SV pressure (Dancer and Franke, 1980), stapes velocity (Dancer *et al.*, 1980), and stapes footplate area (Fernández, 1952) measured in different groups of subjects. For chinchilla, impedance magnitude was also computed using data from different subjects: stapes velocity (Ruggero *et al.*, 1990), SV pressure (Décory *et al.*, 1990), and stapes footplate area (Vrettakos *et al.*, 1988). For cat the estimate of impedance is presumably more reliable than for the other three species because it was derived from measurements of stapes vibration and SV pressure in the same individual ears (Lynch *et al.*, 1982). Nevertheless, the magnitude data for all four species are similar in showing relative independence from stimulus frequency, suggesting that cochlear input impedance is resistive. However, in a system with pure resistive impedance, impedance phases should be zero, whereas panel (b) of Fig. 6 shows that the impedance phases for the adult gerbil are about +45 degrees between 1 and 7 kHz and reach +135 degrees at the highest frequencies.

IV. DISCUSSION

A. Comparison of the present measurements of stapes vibrations with other ossicular-vibration data for adult gerbils

Figure 7 brings together all published measurements of the responses to tones of the stapes or malleus in adult gerbils. Panel (a) of Fig. 7 shows the response magnitudes, expressed as velocity amplitude divided by stimulus pressure, as a function of frequency. The present measurements of stapes vibration in gerbil (thick continuous lines) and those of Rosowski *et al.* [open circles (Rosowski *et al.*, 1999)] are similar in magnitude at 1 kHz but at higher frequencies they diverge rapidly. The magnitudes described by Rosowski *et al.* decayed at a rate of about 6 dB/oct between 1 and 10 kHz, whereas in the present study and another documented in an abstract (Olson and Cooper, 2000) the stapes velocity magnitudes were roughly flat in the frequency ranges 1–40 kHz and 8–40 kHz, respectively.

Figure 7 also depicts curves for recordings from the tympanic-membrane umbo, near the tip of the malleus (Cohen *et al.*, 1993; Xue *et al.*, 1995). In order to make the malleus magnitude data approximately comparable with stapes data, the former have been divided by a factor, 3.5,

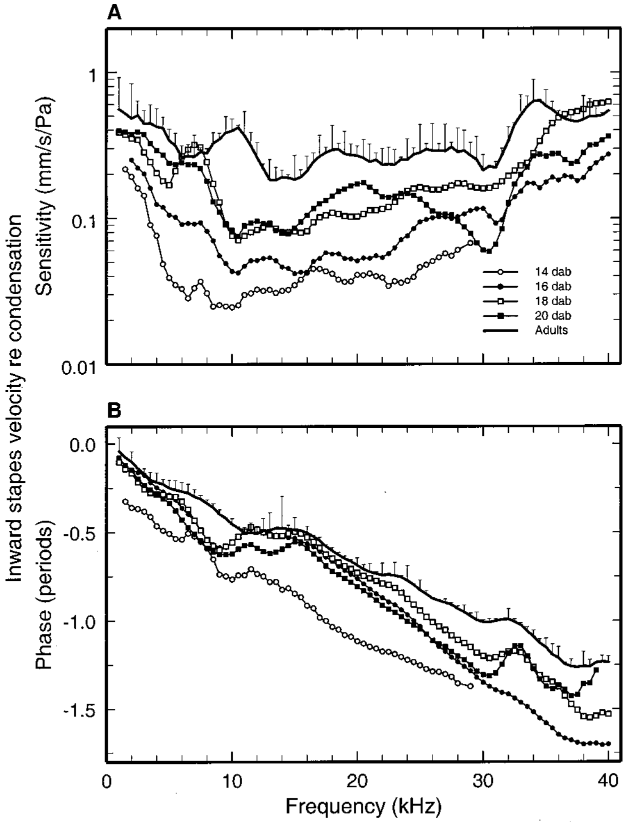

FIG. 5. Stapes velocity responses to tones in adult and neonatal gerbils. The median sensitivity magnitudes [panel (a)] and phases [panel (b)] of stapes velocity (from Figs. 2–4) are plotted as a function of frequency for adult gerbils as well as neonates aged 14, 16, 18, and 20 days. The curves for 14-DAB gerbils have been truncated at 26 kHz because stapes responses could be measured in only two animals. Interquartile ranges are indicated on the curves for adults (up brackets).

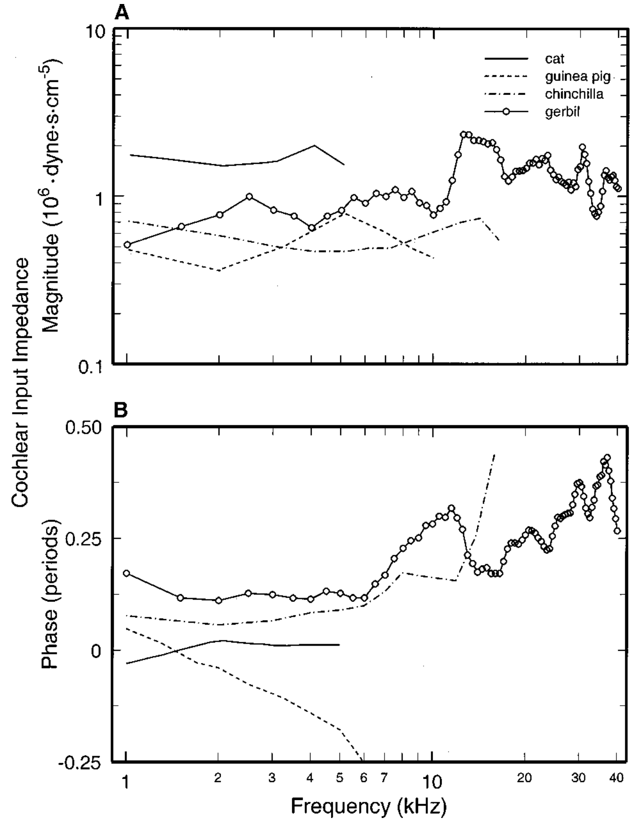

FIG. 6. The acoustic input impedance of the cochlea in gerbil and other species. The input impedance of the adult gerbil cochlea (open circles) was calculated using the present (point) measurements of stapes velocity, the area of the stapes footplate (Cohen *et al.*, 1992) and pressure in scala vestibuli (Fig. 6 of Olson, 1998). For comparison, the magnitude and phases of cochlear impedance are also shown for cat (Lynch *et al.*, 1982), chinchilla (Ruggero *et al.*, 1990), and guinea pig. For guinea pig, magnitudes are from (Dancer and Franke, 1980) and phases from (Rosowski, 1994), calculated from stapes velocity data of (Nuttall, 1974) and SV pressure of (Décory, 1989).

corresponding to the anatomical lever ratio of the gerbil middle ear (Rosowski *et al.*, 1999), on the assumption that this lever ratio translates into a constant reduction of velocity amplitude. Admittedly, this assumption probably does not hold at high frequencies (Rosowski *et al.*, 1999; Ruggero *et al.*, 1990). These derived stapes-vibration magnitudes differ from the present results in several respects but concur with them in indicating that transmission in the middle ear of adult gerbils does not decay substantially at high frequencies, at least up to 40–48 kHz, i.e., within 0.5 oct of the upper range of hearing in this species [57 kHz (Fay, 1988)].

Panel (b) of Fig. 7 gathers together all published response phases for stapes and malleus measured in the middle ears of adult gerbils. The present phases differ substantially in many respects from the stapes data of Rosowski *et al.* (1999) and the malleus data of Xue *et al.* (1995) but are consistent with stapes responses (not shown) reported in an abstract (Olson and Cooper, 2000).

The present results corroborate the results of some previous studies of the gerbil middle ear but not others: (a) with but one exception (Rosowski *et al.*, 1999), studies of ossicular response magnitudes in gerbil show that they do not decay substantially as a function of increasing frequency up to at least 40 kHz; (b) the present study and another (Olson and Cooper, 2000) [in contrast with those of Rosowski *et al.* (1999) and Xue *et al.* (1995)] found phase lags that increase more or less linearly with frequency. We do not know why there are large discrepancies among the results of several comparable investigations but we surmise that calibration errors played an important role in all studies, including the present one.[1]

B. Does mass reactance control middle-ear transmission of high-frequency signals?

Nearly three decades ago, Johnstone and Sellick (Johnstone and Sellick, 1972) marshalled convincing evidence against the then prevailing view (e.g., Dallos, 1973; Møller, 1963, 1965; Mundie, 1963; Zwislocki, 1962, 1963) that mass is the principal determinant of ossicular vibrations at high frequencies (see also Manley and Johnstone, 1974). Nevertheless, several subsequent discussions of middle-ear function have reiterated the mass-reactance hypothesis (e.g., Doan *et al.*, 1996; Hemilä *et al.*, 1995, 2001; Nummela, 1997; Relkin, 1988; Relkin and Saunders, 1980; Shaw, 1981). We argue here that this hypothesis is not supported by the newer middle-ear data (see also Rosowski, 1994).

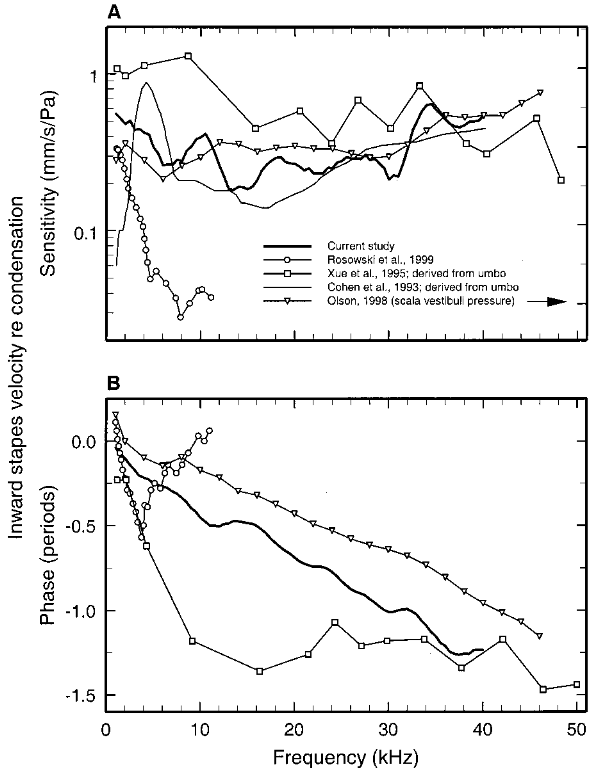

FIG. 7. Comparison of gerbil middle-ear responses to sound measured in several studies. A: sensitivity (*re*: stimulus pressure) of stapes velocity [present study and Rosowski *et al.* (1999)], umbo velocity (Cohen *et al.*, 1993; Xue *et al.*, 1995), and scala vestibuli pressure plotted as a function of frequency (Olson, 1998). The magnitude of the umbo data has been reduced according to the ossicular anatomical lever ratio, 3.5 (Rosowski *et al.*, 1999), to make it (approximately) commensurate with the stapes data. The scala vestibuli (SV) pressure gain (*re*: stimulus pressure) is indicated in the right ordinate (Olson, 1998). (b) Phases *re*: stimulus pressure of SV pressure (Olson, 1998), umbo velocity (Xue *et al.*, 1995), and stapes velocity [current study and Rosowski *et al.* (1999)].

If inertial reactance were the dominant factor limiting the high-frequency performance of the middle ear, ossicular vibrations should exhibit high-frequency velocity magnitudes with a slope of −6 dB/oct in the case of a first-order resonant system (Dallos, 1973). To investigate this question we constructed Table I, which shows that masslike behavior is not found in five of the six species in which ossicular responses have been measured at frequencies within 1 oct of the 60-dB high-frequency cutoffs of the behavioral audiograms. The one exception is a study of human temporal bones (Aibara *et al.*, 2001), which found a high-frequency slope of −7 dB.

If inertial reactance were the dominant factor limiting the high-frequency performance of the middle ear, ossicular velocity should exhibit a high-frequency phase plateau of −90 degrees, again for the case of a first-order system (Dallos, 1973). Such a plateau appeared consistent with the phase data of some early studies (e.g., Guinan and Peake, 1967) but the few more recent measurements of ossicular responses all indicate phase lags that accumulate well past −90 degrees and, most importantly, do not reach any obvious plateau (e.g., column 6 of Table I).

If mass controlled ossicular vibrations at high frequencies, the acoustic input impedance in the external ear canal near the tympanic membrane should be reactive at those frequencies. In fact, the input impedance of the middle ear is principally resistive except at low frequencies [e.g., in gerbil (Ravicz *et al.*, 1992) and in cat (Lynch *et al.*, 1994)]. Finally, it is noteworthy that loading the stapes (Johnstone and Taylor, 1971) or the tympanic membrane (Lynch, 1981) with additional masses causes only minimal changes in ossicular vibration.

To summarize, there is scant evidence favoring, and substantial evidence against, the hypothesis that the high-frequency responses of middle-ear ossicles are determined by mass reactance.

C. Does middle-ear transmission limit the upper frequency range of hearing?

It is often stated that high-frequency hearing is limited by the vibrations of the middle ear (Dallos, 1973; Hemilä *et al.*, 1995, 2001; Møller, 1963; Nummela, 1997; Zwislocki, 1975). One way to test this hypothesis is to ascertain whether middle-ear transmission exhibits a steep terminal slope at a frequency matching that of the cut-off of the behavioral audiogram in the same species [Table I, second column, from Fay (1988) and Heffner *et al.* (2001)]. As Table I indicates, measurements adequate to answer this question exist only for guinea pig. For this species, good matches between ossicular and behavioral high-frequency cutoffs has been observed in two studies (Manley and Johnstone, 1974; Wilson and Johnstone, 1975) but not in another (Cooper and Rhode, 1992). Thus, the resolution of this issue must await further measurements at frequencies bracketing those of the cutoffs of the behavioral audiograms.

D. The middle ear as a transmission line

The literature contains several proposals, both implicit and explicit, that the middle ear should be modeled as a transmission line, with distributed mass and stiffness (Olson and Cooper, 2000; Onchi, 1949, 1961; Puria and Allen, 1998; Wilson and Bruns, 1983; Zwislocki, 1962; see also Rabbitt, 1990), rather than as a lumped-parameter system. "In an ideal transmission line, terminated by the correct source and load impedance, a signal is transmitted without loss even at high frequencies, but with a delay" (Wilson and Bruns, 1983). The magnitudes and phases of the present stapes-vibration data and of the pressure data of Olson (1998) are consistent with the middle-ear model proposed by Puria and Allen (1998), which incorporates the transmission-line hypothesis. Especially striking are the nearly linear increases of phase lag of stapes vibration [Fig. 2, panel (b)] and scala vestibuli pressure [Fig. 7, panel (b)] as a function of increasing stimulus frequency, equivalent to group delays of 30 and 25 μs, respectively. Although linear increases of phase lag were not previously noticed in reports of ossicular vibrations, they can be gleaned in published data. For example, a delay of 36 μs can be computed from the phase lags of malleus vibration in cat (Decraemer *et al.*, 1990) which (probably not coincidentally) is identical to the delay derived by Puria and Allen (1998) from their own measurements of input impedance in the cat middle ear using a transmission-line model of

TABLE I. High-frequency slopes of magnitude-vs-frequency curves for ossicular responses to tones measured at frequencies approaching within one octave the 60-dB cut-off of audiometric thresholds. Roll-off slopes of the magnitude of ossicular vibration velocity at high frequencies compared to the limits of high-frequency hearing, i.e., frequency cutoff for 60-dB thresholds [from Hemilä *et al.* (1995), after Fay (1988), except for the hamster taken from Heffner *et al.* (2001)].

Species	60-dB cutoff of high-frequency hearing (kHz)	Ossicle	Frequency range for estimation of magnitude slope (kHz)	Slope of velocity-magnitude roll-off (dB/oct)	Phase lag *re*: condensation at highest frequency tested (degrees)	Reference for slopes
Mongolian gerbil	57	stapes	1–40	~0	~430	present work
		stapes	8–40	~0	not available	Olson and Cooper (2000)
		malleus	30–40	~0	not measured	Cohen *et al.* (1993)
		malleus	30–40	~0	~500	Xue *et al.* (1995)
Cat	78	malleus	1–50	−2.7	not measured	Cooper and Rhode (1992)
Guinea pig	49	malleus (free field)	25–50	−24 to −34	>470[a]	Manley and Johnstone (1974)
		incus	20–50	−14	not measured	Wison and Johnstone (1975)
		stapes	0.4–30	−1	not measured	Johnstone and Taylor (1971)
		stapes, incus	1–50	−2.2	not measured	Cooper and Rhode (1992)
Hamster	46.5	malleus (free field)	10–35	−1.8	not measured	Relkin and Saunders (1980)
Human	19	stapes	1–10	−7	~270	Aibara *et al.* (2001)
Rat	78	malleus (free field)	20–40	−9.7	not measured	Doan *et al.* (1996)

[a]Manley and Johnstone measured a 470-degree phase lag of the tip of the incus relative to the tip of the malleus at about 50 kHz (Manley and Johnstone, 1974); the phase lag of the incus with reference to pressure should be larger.

the tympanic membrane. Similarly, a delay of ~70 μs between 3 and 22 kHz may be computed from published phase lags of stapes vibration in chinchilla (Ruggero *et al.*, 1990).

E. Middle-ear transmission in neonatal gerbils

Middle-ear transmission in gerbils increases during the third postnatal week but is not fully mature by 20 days after birth. At 14 days after birth, stapes responses were less sensitive than in adults, e.g., by about 15 dB in the range 10 to 20 kHz (Fig. 5). Stapes responses grew larger with age but appeared to remain somewhat immature at 20 days after birth. No other stapes-vibration data for neonatal gerbils are available for comparison with the present measurements.

For stimuli 4–40 kHz, no significant sensitivity changes were found in umbo vibration in neonatal gerbils (Cohen *et al.*, 1993). At face value, these results indicate that the sound collection apparatus at the tympanic membrane of the gerbil is relatively mature at an early age, antedating the full development of signal transmission via the incus and stapes.

One study estimated the development of middle-ear function in gerbils by comparing the sensitivity of cochlear microphonics under normal acoustic stimulation and with the stapes artificially driven by a piezoelectric device (Woolf and Ryan, 1988). That study's conclusions—that middle-ear transmission improves by some 25 dB between 14 and 16 DAB and that its maturation is essentially complete by 18 DAB—contrasts both with the present stapes data and with the umbo data of Cohen *et al.* (1993).

F. Middle-ear transmission in neonatal hamsters, mice, and rats

Stapes vibrations have not been measured in neonates of any mammalian species other than the gerbil but results reminiscent of the present findings were obtained from the umbo of the tympanic membrane in golden hamsters (*Mesocricetus auratus*), mice, and rats. In golden hamsters, umbo vibrations of 20 and 25 kHz increase by 10 dB between 16 and 20 DAB and remain 10 dB less sensitive than in adults at 20 DAB (Relkin and Saunders, 1980). Between ages 10 and 60 DAB, the sensitivity of umbo responses to 32- or 34-kHz tones grow by 8 dB in mice (Doan *et al.*, 1994) and 15 dB in rats (Doan *et al.*, 1996).

G. Interpretation of the development of middle-ear transmission

Anatomical development data, which might help to explain our physiological findings of the maturing gerbil middle ear, are still meager. In the gerbil, the middle-ear ossicles are well ossified by 16 DAB (Finck *et al.*, 1972) and the area, depth, and appearance of the tympanic membrane reach mature values at 22–25 DAB, with most changes being completed by 20 DAB (Cohen *et al.*, 1992). Somewhat paradoxically, however, there is a large increase in ossicular mass between 16 and 42 DAB (Cohen *et al.*, 1992). [Bulla volume also increases significantly beyond 20 DAB and therefore may partly account for some of the data of Cohen *et al.* (1993), which were obtained with a closed bulla, but this change should not have influenced other measurements of stapes vibrations, such as our own, obtained with the bulla widely opened.] In neonatal rats the improvement of middle-ear sensitivity (Doan *et al.*, 1996) is also positively correlated with the growth in ossicular mass (the malleus and incus reach mature values of mass at 34 and 26 days) (Zimmer *et al.*, 1994).

On first consideration, it seems difficult to understand how an increase in ossicular mass could improve middle-ear transmission [since, by itself, inertial reactance should reduce transmission in proportion to the square of the stimulus frequency (Hemilä *et al.*, 1995)]. Two possibilities come to mind to resolve the apparent paradox. One is that the increase of ossicular mass with age has only minimal consequences on the ossicular moment of inertia, which is partly determined by the axis of rotation of the incudo-malleal complex. Another possibility is hinted at by the hypothesis that the tympanic membrane and the ossicular chain behave as a cascade of transmission lines (Puria and Allen, 1998; Wilson and Bruns, 1983). Taking this hypothesis as a point of departure, we speculate that in the adult gerbil middle ear the reactance of each shunt stiffness (at the malleus/incus and incus/stapes joints) is matched by the inertial reactance of each ossicle and that at the completion of ossification the ossicles of 16-DAB gerbils (Finck *et al.*, 1972) are as stiff as they ever will be. We propose that the subsequent large increase in mass reactance cancels out the preexisting stiffness reactance, thus extending the bandwidth of middle-ear transmission to adult values.

H. Summing up

Textbook treatments of the mammalian middle ear typically start out by comparing its performance to that of an ideal impedance-matching transformer but qualify this analogy by stating that a band-pass filter such as a simple resonant system is a more realistic model. Such a model is partly justified by some recent measurements in the middle ears of gerbils (Rosowski *et al.*, 1999) and humans (Aibara *et al.*, 2001). However, other studies [e.g., the present report and Olson and Cooper (2000)] contradict the resonant-system analogy and provide renewed justification for viewing the mammalian middle ear as a wideband transformer, perhaps implemented as a transmission line. It remains to be seen whether one of these contrasting views of middle-ear transmission eventually proves correct for the gerbil and perhaps other species.

ACKNOWLEDGMENTS

We thank Mary Ann Cheatham, Nigel Cooper, and one anonymous referee for their thorough reviews of previous versions of the manuscript, Andrei Temchin for much help with data processing and preparation of the final versions of the figures, and Jon Siegel for his assistance in the modification of the Radio Shack tweeter. We were supported by Grant No. R01-DC-00419 from the National Institute on Deafness and Other Communication Disorders (NIH).

[1]Some of the results in the present article differ from the corresponding ones in the Ph.D. dissertation on which it is based (Overstreet, 2000); a different method for the pressure calibration has been adopted here and some computational errors in the dissertation have been corrected.

Aibara, R., Welsh, J. T., Puria, S., and Goode, R. L. (**2001**). ‘‘Human middle-ear sound transfer function and cochlear input impedance,’’ Hear. Res. **152**, 100–109.

Brown, M. C., Smith, D. I., and Nuttall, A. L. (**1983**). ‘‘The temperature dependency of neural and hair cell responses evoked by high frequencies,’’ J. Acoust. Soc. Am. **73**, 1662–1670.

Chan, J. C., Musicant, A. D., and Hind, J. E. (**1993**). ‘‘An insert earphone system for delivery of spectrally shaped signals for physiological studies,’’ J. Acoust. Soc. Am. **93**, 1496–1501.

Cohen, Y. E., Bacon, C. K., and Saunders, J. C. (**1992**). ‘‘Middle ear development. III: Morphometric changes in the conducting apparatus of the Mongolian gerbil,’’ Hear. Res. **62**, 187–193.

Cohen, Y. E., Doan, D. E., Rubin, D. M., and Saunders, J. C. (**1993**). ‘‘Middle-ear development. V: Development of umbo sensitivity in the gerbil,’’ Am. J. Otolaryngol. **14**, 191–198.

Cooper, N. P., and Rhode, W. S. (**1992**). ‘‘Basilar membrane mechanics in the hook region of cat and guinea-pig cochleae: sharp tuning and nonlinearity in the absence of baseline position shifts,’’ Hear. Res. **63**, 163–190.

Dallos, P. (**1973**). *The Auditory Periphery—Biophysics and Physiology* (Academic, New York).

Dancer, A., and Franke, R. (**1980**). ‘‘Intracochlear sound pressure measurements in guinea pigs,’’ Hear. Res. **2**, 191–205.

Dancer, A., Franke, R., Buck, K., Smigielski, P., and Stimpfling, A. (**1980**). ‘‘Etude par interferometric laser des deplacements du tympan du cobaye sous l’action de sons purs et de bruits impulsifs,’’ Acustica **46**, 178–188.

Decraemer, W. F., Khanna, S. M., and Funnell, W. R. (**1990**). ‘‘Heterodyne interferometer measurements of the frequency response of the manubrium tip in cat,’’ Hear. Res. **47**, 205–217.

Décory, L. (**1989**). ‘‘Origine des differences interspecifiques de susceptibilité an bruit,’’ doctoral dissertation, Université de Bordeaux.

Décory, L., Franke, R. B., and Dancer, A. L. (**1990**). ‘‘Intracochlear pressure measurements in the cat, the chinchilla, and the guinea pig,’’ in *The Mechanics and Biophysics of Hearing*, edited by P. Dallos, C. D. Geisler, J. W. Matthews, M. A. Ruggero, and C. R. Steele (Springer-Verlag, Berlin), pp. 270–277.

Doan, D. E., Cohen, Y. E., and Saunders, J. C. (**1994**). ‘‘Middle-ear development. IV. Umbo motion in neonatal mice,’’ J. Comp. Physiol. [A] **174**, 103–110.

Doan, D. E., Igic, P. G., and Saunders, J. C. (**1996**). ‘‘Middle-ear development. VII: Umbo velocity in the neonatal rat,’’ J. Acoust. Soc. Am. **99**, 1566–1572.

Fay, R. R. (**1988**). *Hearing in Vertebrates: A Psychophysics Handbook* (Hill-Fay, Winnetka, IL).

Fernández, C. (**1952**). ‘‘Dimensions of the cochlea (guinea pig),’’ J. Acoust. Soc. Am. **24**, 519–523.

Finck, A., Schneck, C. D., and Hartman, A. F. (**1972**). ‘‘Development of cochlear function in the neonate Mongolian gerbil (Meriones unguiculatus),’’ J. Comp. Physiol. Psychol. **78**, 375–380.

Guinan, Jr., J. J., and Peake, W. T. (**1967**). ‘‘Middle-ear characteristics of anesthetized cats,’’ J. Acoust. Soc. Am. **41**, 1237–1261.

Heffner, R. S., Koay, G., and Heffner, H. E. (**2001**). ‘‘Audiograms of five species of rodents: implications for the evolution of hearing and the perception of pitch,’’ Hear. Res. **157**, 138–152.

Hemilä, S., Nummela, S., and Reuter, T. (**1995**). ‘‘What middle ear parameters tell about impedance matching and high frequency hearing,’’ Hear. Res. **85**, 31–44.

Hemilä, S., Nummela, S., and Reuter, T. (**2001**). ‘‘Modeling whale audiograms: effects of bone mass on high-frequency hearing,’’ Hear. Res. **151**, 221–226.

Johnstone, B. M., and Sellick, P. M. (**1972**). ‘‘The peripheral auditory apparatus,’’ Q. Rev. Biophys. **5**, 1–57.

Johnstone, B. M., and Taylor, K. J. (**1971**). ‘‘Physiology of the middle ear transmission system,’’ J. Otolaryngol. Soc. Austral. **3**, 226–228.

Khanna, S. M., and Stinson, M. R. (**1985**). ‘‘Specification of the acoustical input to the ear at high frequencies,’’ J. Acoust. Soc. Am. **77**, 577–589.

Lynch, T. J. III (**1981**). ‘‘Signal processing by the cat middle ear: Admittance and transmission, measurements and models,’’ doctoral dissertation, Massachusetts Institute of Technology.

Lynch, T. J. III, Nedzelnitsky, V., and Peake, W. T. (**1982**). ''Input impedance of the cochlea in cat,'' J. Acoust. Soc. Am. **72**, 108–130.

Lynch, T. J. III, Peake, W. T., and Rosowski, J. J. (**1994**). ''Measurements of the acoustic input impedance of cat ears: 10 Hz to 20 kHz,'' J. Acoust. Soc. Am. **96**, 2184–2209.

Manley, G. A., and Johnstone, B. M. (**1974**). ''Middle-ear function in the guinea pig,'' J. Acoust. Soc. Am. **56**, 571–576.

Møller, A. R. (**1963**). ''Transfer function of the middle ear,'' J. Acoust. Soc. Am. **35**, 1526–1534.

Møller, A. R. (**1965**). ''An experimental study of the acoustic impedance of the middle ear and its transmission properties,'' Acta Oto-Laryngol. **60**, 129–149.

Mundie, J. R. (**1963**). ''The impedance of the ear—a variable quantity,'' in *Middle Ear Function Seminar—Report #576*, edited by J. L. Fletcher (U.S. Army Medical Research Lab, Fort Knox, KY), pp. 63–85.

Nummela, S. (**1997**). ''Scaling and modeling of the mammalian ear,'' Comments Theor. Biol. **4**, 387–412.

Nuttall, A. L. (**1974**). ''Measurements of the guinea-pig middle-ear transfer characteristic,'' J. Acoust. Soc. Am. **56**, 1231–1238.

Olson, E. S. (**1998**). ''Observing middle and inner ear mechanics with novel intracochlear pressure sensors,'' J. Acoust. Soc. Am. **103**, 3445–3463.

Olson, E. S., and Cooper, N. P. (**2000**). ''Stapes motion and scala vestibuli pressure in gerbil,'' Assoc. Res. Otolaryngol. Mid-Winter Meet. Abst. 23, 114 (A).

Onchi, Y. (**1949**). ''A study of the mechanism of the middle ear,'' J. Acoust. Soc. Am. **21**, 404–410.

Onchi, Y. (**1961**). ''Mechanism of the middle ear,'' J. Acoust. Soc. Am. **33**, 794–805.

Overstreet, E. H. (**2000**). ''The development of basilar membrane mechanics in the mammalian cochlea,'' doctoral dissertation, University of Minnesota.

Overstreet, E. H., and Ruggero, M. A. (**1998**). ''Basilar membrane mechanics at the hook region of the Mongolian gerbil cochlea,'' Assoc. Res. Otolaryngol. Mid-Winter Meet. Abst. 21, 181 (A).

Overstreet, E. H., and Ruggero, M. A. (**1999**). ''The development of basilar membrane mechanics at the hook region of the Mongolian gerbil cochlea,'' Assoc. Res. Otolaryngol. Mid-Winter Meet. Abst. 22, 135 (A).

Pearce, M., Richter, C. P., and Cheatham, M. A. (**2001**). ''A reconsideration of sound calibration in the mouse,'' J. Neurosci. Methods **106**, 57–67.

Puria, S., and Allen, J. B. (**1998**). ''Measurements and model of the cat middle ear: evidence of tympanic membrane acoustic delay,'' J. Acoust. Soc. Am. **104**, 3463–3481.

Rabbitt, R. D. (**1990**). ''A hierarchy of examples illustrating the acoustic coupling of the eardrum,'' J. Acoust. Soc. Am. **87**, 2566–2582.

Ravicz, M. E., Rosowski, J. J., and Voigt, H. F. (**1992**). ''Sound-power collection by the auditory periphery of the Mongolian gerbil Meriones unguiculatus. I: Middle-ear input impedance,'' J. Acoust. Soc. Am. **92**, 157–177.

Relkin, E. M. (**1988**). ''Introduction to the analysis of middle-ear function,'' in *Physiology of the Ear*, edited by A. F. Jahn and J. Santos-Sacchi (Raven, New York), pp. 103–123.

Relkin, E. M., and Saunders, J. C. (**1980**). ''Displacement of the malleus in neonatal golden hamsters,'' Acta Oto-Laryngol. **90**, 6–15.

Rosowski, J. J. (**1994**). ''Outer and middle ears,'' in *Comparative Hearing: Mammals*, edited by R. R. Fay and A. N. Popper (Springer-Verlag, New York), pp. 172–247.

Rosowski, J. J., Ravicz, M. E., Teoh, S. W., and Flandermeyer, D. (**1999**). ''Measurements of middle-ear function in the Mongolian gerbil, a specialized mammalian ear,'' Audiol. Neuro-Otol. **4**, 129–136.

Ruggero, M. A., and Rich, N. C. (**1991**). ''Application of a commercially-manufactured Doppler-shift laser velocimeter to the measurement of basilar-membrane vibration,'' Hear. Res. **51**, 215–230.

Ruggero, M. A., Rich, N. C., Robles, L., and Shivapuja, B. G. (**1990**). ''Middle-ear response in the chinchilla and its relationship to mechanics at the base of the cochlea,'' J. Acoust. Soc. Am. **87**, 1612–1629.

Shaw, E. A. G. (**1981**). ''Eardrum representation in middle-ear acoustical network,'' J. Acoust. Soc. Am. Suppl. 1 **62**, S12 (A).

Shore, S. E., and Nuttall, A. L. (**1985**). ''The effects of cochlear hypothermia on compound action potential tuning,'' J. Acoust. Soc. Am. **77**, 590–598.

Stinson, M. R. (**1985**). ''The spatial distribution of sound pressure within scaled replicas of the human ear canal,'' J. Acoust. Soc. Am. **78**, 1596–1602.

Stinson, M. R., and Khanna, S. M. (**1989**). ''Sound propagation in the ear canal and coupling to the eardrum, with measurements on model systems,'' J. Acoust. Soc. Am. **85**, 2481–2491.

Stinson, M. R., and Shaw, E. A. G. (**1982**). ''Wave effects and pressure distribution in the ear canal near the tympanic membrane,'' J. Acoust. Soc. Am. Suppl. 1 **71**, S88 (A).

Vrettakos, P. A., Dear, S. P., and Saunders, J. C. (**1988**). ''Middle ear structure in the chinchilla: a quantitative study,'' Am. J. Otolaryngol. **9**, 58–67.

Wilson, J. P., and Bruns, V. (**1983**). ''Middle-ear mechanics in the CF-bat Rhinolophus ferrumequinum,'' Hear. Res. **10**, 1–13.

Wilson, J. P., and Johnstone, J. R. (**1975**). ''Basilar membrane and middle-ear vibration in guinea pig measured by capacitive probe,'' J. Acoust. Soc. Am. **57**, 705–723.

Woolf, N. K., and Ryan, A. F. (**1985**). ''Ontogeny of neural discharge patterns in the ventral cochlear nucleus of the mongolian gerbil,'' Brain Res. **349**, 131–147.

Woolf, N. K., and Ryan, A. F. (**1988**). ''Contributions of the middle ear to the development of function in the cochlea,'' Hear. Res. **35**, 131–142.

Xue, S., Mountain, D. C., and Hubbard, A. E. (**1995**). ''Electrically evoked basilar membrane motion,'' J. Acoust. Soc. Am. **97**, 3030–3041.

Zimmer, W. M., Rosin, D. F., and Saunders, J. C. (**1994**). ''Middle-ear development. VI: Structural maturation of the rat conducting apparatus,'' Anat. Rec. **239**, 475–484.

Zwislocki, J. J. (**1962**). ''Analysis of the middle-ear function. Part I. Input impedance,'' J. Acoust. Soc. Am. **34**, 1514–1523.

Zwislocki, J. J. (**1963**). ''Analysis of middle ear function. II. Guinea pig ear,'' J. Acoust. Soc. Am. **35**, 1034–1040.

Zwislocki, J. J. (**1975**). ''The role of the external and middle ear in sound transmission,'' in *The Nervous System, Vol. 3: Human Communication and its Disorders*, edited by D. B. Tower and E. L. Eagles (Raven, New York), pp. 45–55.

The use of distortion product otoacoustic emission suppression as an estimate of response growth

Michael P. Gorga,[a] Stephen T. Neely, Patricia A. Dorn, and Dawn Konrad-Martin
Boys Town National Research Hospital, Omaha, Nebraska 68131

(Received 18 June 2001; revised 17 October 2001; accepted 18 October 2001)

Distortion product otoacoustic emission (DPOAE) levels in response to primary pairs ($f_2=2$ or 4 kHz, L_2 ranging from 20 to 60 dB SPL, $L_1=0.4L_2+39\,\mathrm{dB}$) were measured with and without suppressor tones (f_3), which varied from 1 octave below to $\frac{1}{2}$ octave above f_2, in normal-hearing subjects. Suppressor level (L_3) varied from -5 to 85 dB SPL. DPOAE levels were converted into decrements by subtracting the level in the presence of the suppressor from the level in the absence of a suppressor. DPOAE decrement vs L_3 functions showed steeper slopes when $f_3<f_2$ and shallower slopes when $f_3>f_2$. This pattern is similar to other measurements of response growth, such as direct measures of basilar-membrane motion, single-unit rate-level functions, suppression of basilar-membrane motion, and discharge-rate suppression from lower animals. As L_2 increased, the L_3 necessary to maintain 3 dB of suppression increased at a rate of about 1 dB/dB when f_3 was approximately equal to f_2, but increased more slowly when $f_3<f_2$. Functions relating L_3 to L_2 in order to maintain a constant 3-dB reduction in DPOAE level were compared for $f_3<f_2$ and for $f_3\approx f_2$ in order to derive an estimate related to "cochlear-amplifier gain." These results were consistent with the view that "cochlear gain" is greater at lower input levels, decreasing as level increases. [DOI: 10.1121/1.1426372]

PACS numbers: 43.64.Ha, 43.64.Jb [BLM]

I. INTRODUCTION

Distortion product otoacoustic emissions (DPOAEs) are elicited when two pure tones, slightly different in frequency, are presented to the ear. They are low-level signals, produced within the cochlea, that propagate in the reverse direction through the middle ear and into the ear canal, where they can be measured with a microphone. These responses are generated by normal nonlinear mechanisms within the cochlea that are associated with outer hair cell (OHC) function. These nonlinear mechanisms are thought to provide amplification for low-level stimuli, in order to enhance the absolute sensitivity and sharp frequency selectivity that are characteristics of normal auditory function. These normal nonlinear mechanisms also provide compression as level increases, thus enabling the ear to encode stimulus level over a wide dynamic range. As a result of this association, it is common clinical practice to assume that the observation of DPOAEs would be consistent with normal nonlinear function and, therefore, normal hearing. Their absence would be consistent with the presence of cochlear (OHC-based) hearing loss, assuming that middle-ear function is normal. Of course, this view is simplistic in that it ignores the fact that DPOAEs do not completely disappear once any degree of hearing loss exists; rather, DPOAE level decreases as threshold increases, even though this relationship is variable (see below).

These observations have led to the use of DPOAEs as tools for identifying the presence of cochlear hearing loss, both as part of universal newborn hearing screening programs and as part of more general clinical applications. Much of the focus of previous work regarding the clinical utility of DPOAEs has been directed toward understanding the relation between these measures and auditory sensitivity (e.g., Martin *et al.*, 1990; Gorga *et al.*, 1993, 1996, 1997, 1999, 2000; Kim *et al.*, 1996; Dorn *et al.*, 1999). These efforts have been designed mainly to make dichotomous decisions in which, based on DPOAE findings, an ear is labeled as normal or impaired (as defined by pure-tone audiometric tests). As a result of these studies, it is now known that DPOAEs can identify the presence of hearing loss accurately at mid- and high frequencies, but are less accurate predictors of auditory status for lower frequencies. These frequency effects appear to be related to noise levels, which increase as frequency decreases. In addition, DPOAEs produce the fewest errors in diagnosis when moderate-level stimuli are used to elicit the response (Stover *et al.*, 1996; Whitehead *et al.*, 1992).

In other studies, DPOAE level or signal-to-noise ratio (SNR) have been correlated with audiometric threshold (Martin *et al.*, 1990; Probst and Hauser, 1990; Gorga *et al.*, 1997, 2002; Kimberley *et al.*, 1997; Kummer *et al.*, 1998; Janssen *et al.*, 1998), even within the range of hearing that is typically considered normal (Dorn *et al.*, 1998; Kummer *et al.*, 1998). Although there is some debate over the strength of the relationship (see Harris and Probst, 1997, for a review), these data showed that DPOAE level (or SNR) decreased as pure-tone thresholds increased up to thresholds of about 50–60 dB HL. For greater losses, no relation was observed because DPOAEs typically are absent. Still other studies have shown that DPOAE threshold (defined as some SNR) increases as audiometric threshold increases (Martin *et al.*, 1990; Gorga *et al.*, 1996; Dorn *et al.*, 2001).

In all of the above efforts, the primary focus was to determine the extent to which DPOAEs could be used to

[a]Electronic mail: gorga@boystown.org

dichotomously predict auditory status as normal or impaired, or to estimate the degree of threshold elevation. This approach is consistent with the view that DPOAEs are a byproduct of normal nonlinear cochlear behavior that resides in the OHC system. Since this nonlinear behavior probably is tied to normal threshold sensitivity (see Dallos *et al.*, 1980, for a review), damage to the OHCs results in the loss of nonlinear behavior and threshold elevation. A reduction or loss of DPOAEs is one manifestation of these changes to normal nonlinear function. In addition to threshold elevation, other changes occur as a consequence of damage to OHCs, including reduced frequency selectivity (e.g., Kiang *et al.*, 1976; Dallos and Harris, 1978; Liberman and Dodds, 1984) and reduction or elimination of suppression and intermodulation distortion (e.g., Dallos *et al.*, 1980; Kim, 1980). The slopes of functions relating cochlear responses to stimulus level (i.e., response growth) apparently depend on cochlear integrity as well. For example, the slopes of single-unit rate versus level functions, whole-nerve action potential (AP) masking functions, and basilar-membrane velocity versus level functions increase as a consequence of permanent or reversible cochlear insult (Evans, 1974; Sewell, 1984; Gorga and Abbas, 1981a, b; Ruggero and Rich, 1991). The majority of studies examining changes in frequency selectivity and increased response growth was conducted in animals. Still, all of these effects appear to be consequences of damage to the same underlying, nonlinear system.

The purpose of the present study is to determine whether DPOAE measurements can provide estimates of suprathreshold response properties in humans that are at least qualitatively similar to physiological measurements made in lower animals. Specifically, we were interested in knowing whether measures of response growth, derived from DPOAE suppression measurements, share similar characteristics with other measures of response growth, such as single-unit rate vs level functions. While DPOAE input/output functions also provide a measure of cochlear response growth, DPOAE suppression experiments have several advantages, in that they provide an opportunity to derive a measure of response growth for different frequencies at a fixed place along the cochlea. It is already known that DPOAE suppression tuning curves provide estimates of frequency selectivity and are useful in determining the generator site for DPOAEs (e.g., Brown and Kemp, 1984; Martin *et al.*, 1987; Abdala *et al.*, 1996). Data from some of these same studies, as well as others (Harris *et al.*, 1992; Kummer *et al.*, 1995; Abdala, 1998, 2001), reveal that DPOAE level varies with suppressor level, following trends that would be expected from more direct studies of suppression (Abbas and Sachs, 1976; Costalupes *et al.*, 1987; Delgutte, 1990; Ruggero *et al.*, 1992) and/or other measures of response growth, including rate vs level functions as a function of frequency for a fixed characteristic frequency (CF) or place (CP). We intend to extend that work by determining if DPOAE suppression can be used to describe response growth in much the same way decrements have been used in single-unit studies (Smith, 1977, 1979; Smith and Zwislocki, 1975; Harris, 1979; Harris and Dallos, 1979), in measurements of the whole-nerve AP (Abbas and Gorga, 1981; Gorga and Abbas, 1981a, b), and in auditory brainstem response (ABR) measurements (Gorga *et al.*, 1983) from lower animals. These data will be collected for a range of primary levels, with the additional goal of demonstrating changes in response growth and tuning as a consequence of stimulus level.

Furthermore, it has been proposed that the differences between the tip and the tail of a DPOAE suppression tuning curve provides an estimate that is related to the "gain of the cochlear amplifier" (e.g., Mills, 1998; Pienkowski and Kunov, 2001). As a final aspect of the present study, we will use a similar approach to provide this estimate as a function of primary level.

II. METHODS

A. Subjects

Thirteen young adults with normal hearing served as subjects for this study. All 13 subjects participated in studies in which $f_2=4$ kHz, while six of these subjects also participated in studies in which $f_2=2$ kHz. Each subject had thresholds of 20 dB HL (ANSI, 1996) or better for the octave- and half-octave frequencies from 0.25 to 8 kHz. In addition, each subject had normal middle-ear function on each day in which DPOAE data were collected. Normal middle-ear function was defined as a normal 226-Hz tympanogram. Approximately 15 h of data-collection time, divided among 7 to 9 sessions, was required at each f_2 for each subject, thus introducing the possibility of variation in probe placement across test sessions (see the description of calibration below).

B. Stimuli

All stimuli were produced by custom-designed software (EMAV, Neely and Liu, 1993) that controlled a soundcard (Fiji, Turtle Beach) housed in a PC. Separate channels of the soundcard were used to produce f_1 and f_2. The channel producing the lower-level primary frequency (f_2) was also used to produce a suppressor tone (f_3). These signals were delivered to the ear with an Etymotic ER-10C probe–microphone system that had been modified to remove 20 dB of internal attenuation on the sound-delivery side. This probe system includes two transducers for signal delivery and one microphone for recording signals in the ear canal.

Data were collected with f_2 frequencies of either 2 or 4 kHz. The ratio between primary frequencies (f_2/f_1) was approximately 1.25. For each set of suppression measurements at each f_2, the level of f_2 (L_2) was fixed at one of three levels (40, 50, 60 dB SPL for $f_2=2$ kHz) or one of five levels (20, 30, 40, 50, 60 dB SPL for $f_2=4$ kHz). Measurements for lower L_2 levels were not possible on a routine basis at 2 kHz, due to the increased variability observed at this frequency (see Figs. 3, 5, and 7 below). For each L_2, the level of f_1 (L_1) was set according to the equation, $L_1=0.4L_2+39$ dB (Janssen *et al.*, 1998). This approach results in the largest DPOAE level in subjects with normal hearing (Whitehead *et al.*, 1995; Kummer *et al.*, 1998, 2000; Janssen *et al.*, 1998). In the context of the present measurements, it may be helpful to think of each set of primary tones as a probe that elicits responses from the f_2 place, much the same way as probe tones are viewed during psychoacoustic or physiologic masking experiments. The suppressor tone (f_3) varied from about 1 octave below to approximately $\frac{1}{2}$ octave above f_2, with 16 f_3 frequencies for each L_2. The level of the suppressor tone (L_3) was varied from -5 to 80 or 85 dB SPL in 5-dB steps. For each f_2, L_2 combination, there were 336 conditions, including control conditions in which no suppressor was presented.

C. Procedures

Prior to each data-collection session, signal levels were calibrated in the ear canal, using the emission probe microphone. These levels subsequently were used to produce the specified levels for f_1, f_2, and f_3. There are other calibration techniques that might produce more reliable levels at the eardrum by avoiding problems such as standing waves (Siegel, 1994, 2002; Neely and Gorga, 1998). We have opted for the simpler approach in which the emission probe is used to measure SPL because of its ease of implementation.

For each stimulus condition, data were collected into two buffers. The contents of these buffers were summed, and the summed energy in the $2f_1-f_2$ frequency bin was used to estimate DPOAE level. The contents of the two buffers were subtracted in order to derive an estimate of noise level in the $2f_1-f_2$ frequency bin. This approach was followed in order to avoid problems associated with using the energy in several bins adjacent to $2f_1-f_2$, which would occur when f_3 frequencies are used that are close to f_2. By using the subtraction technique to estimate noise level, it was possible to place suppressor tones closer to f_2 than would ordinarily be possible if noise levels were estimated as the average energy in frequency bins surrounding f_2.

During data collection, measurement-based stopping rules were used, in which a run was terminated if the noise floor was below -25 dB SPL or after 32 s of artifact-free averaging, whichever occurred first. This stopping rule resulted in reliable estimates of DPOAE level for essentially all quiet conditions, where the mean signal-to-noise ratio (SNR) ranged from about 20 dB ($L_2=20$ dB SPL for $f_2=4$ kHz; $L_2=40$ dB SPL when $f_2=2$ kHz) to 35 dB or greater ($L_2=60$ dB SPL for both f_2 frequencies). These SNRs represent the effective range over which changes in DPOAE level could be measured as a result of the presence of the suppressor.

For each f_2, L_2 combination, a series of runs was conducted, in which f_3 was fixed at each of 16 frequencies. Figure 1 provides a summary of the stimulus paradigm. In this example, $f_2=4$ kHz, $f_1=3.2$ kHz, and L_2 and L_1 were fixed at 40 and 55 dB SPL, respectively. DPOAE levels (in response to each fixed f_2, L_2 combination) were measured while L_3 was varied over its entire range, thus producing a function in which DPOAE level was related to L_3 for each f_3. In each of these intensity series, the initial condition was a control condition, in which no suppressor was presented. The final condition in each series of f_3 frequencies also was a control condition. The DPOAE level from each experimental condition (i.e., each f_3, L_3 combination) was subtracted from the average DPOAE level from the two closest control conditions preceding and following the experimental condition. This process allowed us to convert DPOAE level changes due to the suppressor into a decrement (or amount of suppression) in dB. These DPOAE decrements were then plotted as a function of L_3, resulting in a series of 16 decrement vs L_3 functions for each f_2, L_2 combination. Decrements were chosen, based on previous neural work, in which it was shown that decrements in either single-unit discharge rate (e.g., Smith, 1979), whole-nerve APs (Abbas and Gorga, 1981), or ABR amplitudes (Gorga *et al.*, 1983) could be used as indirect measures of response to a masker. In addition, they represent the amount of suppression in dB. Finally, they partially control for differences in absolute response levels across subjects. In the present experiment, decrements are used to describe response growth to f_3 at the f_2 place.

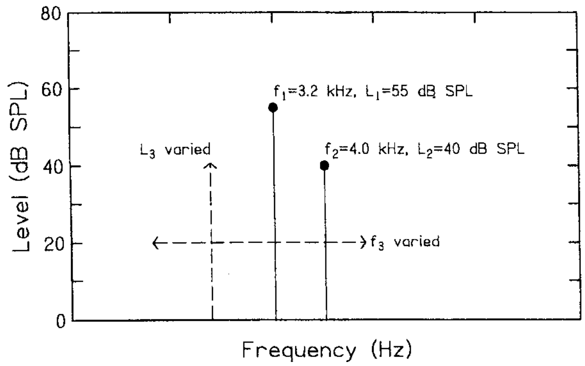

FIG. 1. Stimulus paradigm. In this example, $f_2=4$ kHz, $f_1=3.2$ kHz, $L_1=55$ dB SPL, and $L_2=40$ dB SPL. For each primary frequency and primary level combination, each of 16 f_3 frequencies was selected, its level was varied, and the DPOAE level elicited by the primaries was measured.

III. RESULTS

Implicit in experiments associated with DPOAE suppression measurements is the view that the two primary tones are used as probes or signals that are represented at a fixed cochlear place associated with f_2, and that holding the primary levels constant results in a constant response at this place. The repeatability of DPOAE levels for quiet conditions (no suppressor) would support this view for both f_2 frequencies. While the mean levels for control conditions varied across subjects, these levels were stable within each subject. When averaged across all subjects, the highest mean of the standard deviations (across subjects) for control conditions was 1.6 dB, which occurred when $f_2=2$ kHz and $L_2=40$ dB SPL. For all other f_2, L_2 combinations, the mean standard deviations for control conditions were about 1 dB. Thus, a relatively constant response was achieved for the control conditions in all subjects at both f_2 frequencies and at all L_2 levels.

A. DPOAE decrement vs suppressor level functions

Figure 2 shows individual and median decrement vs L_3 functions for the 16 f_3 frequencies surrounding an f_2 of 4 kHz. Medians were chosen here as the measure of central tendency in order to reduce the influence of outliers. In actuality, however, there was little difference between mean and median functions. In this example, L_2 was presented at 40 dB SPL. The panel in which $f_3=4.1$ kHz represents the

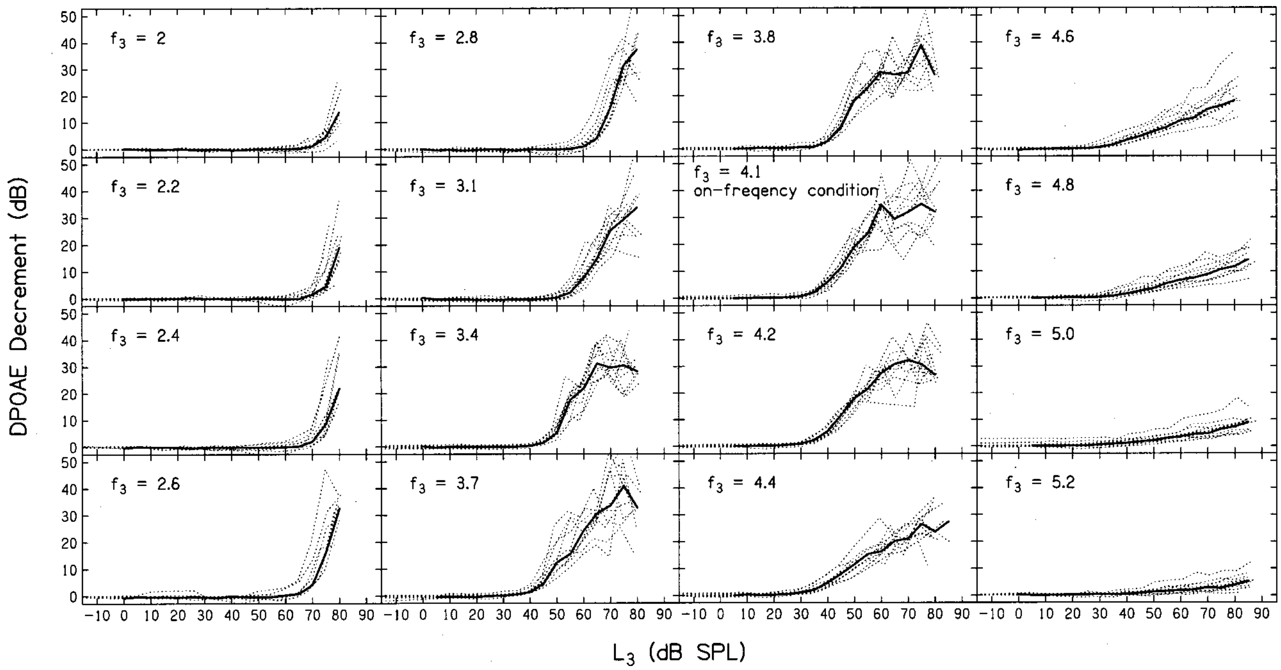

FIG. 2. Individual (dashed lines) and median (solid lines) DPOAE decrements as a function of L_3, with $f_2 = 4$ kHz and $L_2 = 40$ dB SPL. Within each panel, data are shown for a different suppressor frequency, f_3, which is noted within each panel.

condition in which f_3 frequency was closest to f_2. This condition ($f_3 = 4.1$ kHz) can be viewed as the on-frequency condition, when suppressor and probe frequencies are nearly equivalent. In the interest of space, individual data will be shown only for the case when $L_2 = 40$ dB SPL, although similar trends were observed for both lower and higher L_2 levels. Within each panel, the heavy line represents median data and the thin lines represent data from individual subjects. The apparent increase in variability when the decrement functions "saturate" (most evident when f_3 was between 3.4 and 4.2 kHz) is due to the fact that the response to the primary ($f_2 = 4$ kHz, $L_2 = 40$ dB SPL) has been decremented into the noise floor. Thus, the apparent variability on the saturated portion of these functions is actually due to the inherent variability in the noise.

Several trends may be observed in Fig. 2. First, the median decrement functions provide reasonable descriptions of the data from individual subjects, especially over the range of L_3 levels in which the decrement is increasing. Second, the lowest suppression threshold, defined as the lowest level

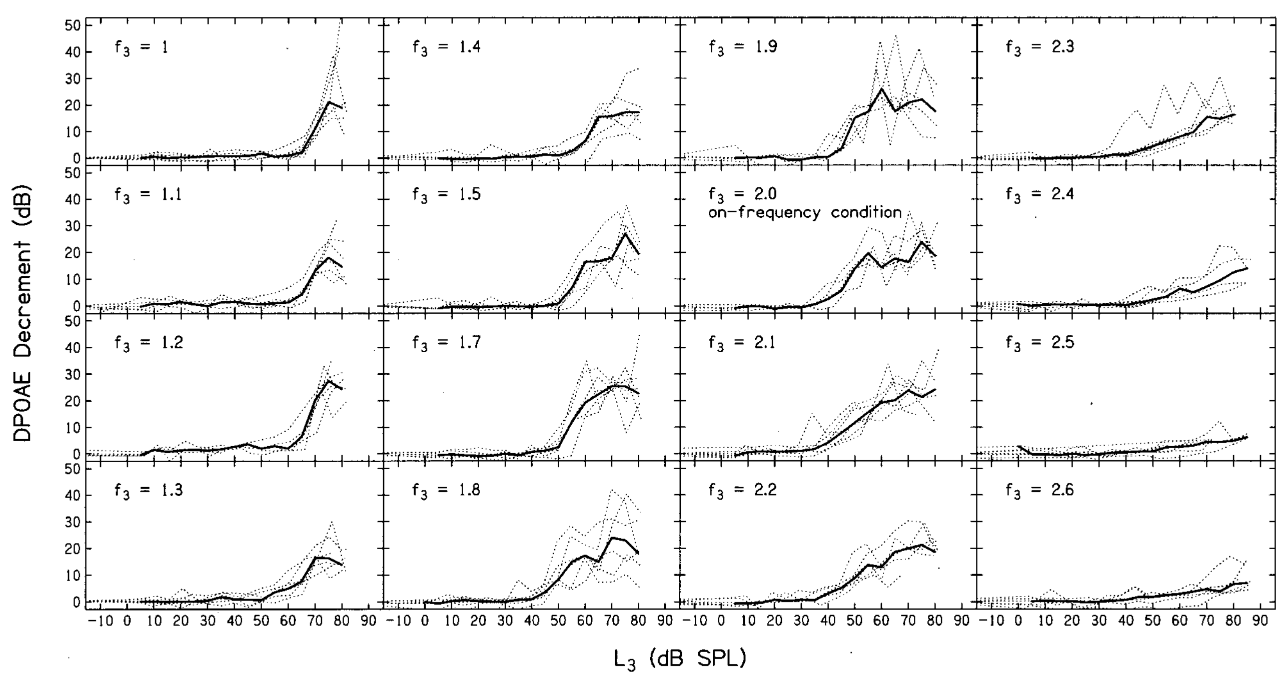

FIG. 3. Following the same convention used in Fig. 2, individual and median DPOAE decrements as a function of L_3, with $f_2 = 2$ kHz, $L_2 = 40$ dB SPL, and $L_3 = 55$ dB SPL.

at which the DPOAE level is first reduced by the suppressor, occurs for f_3 frequencies close to f_2. Thus, the onset of suppression occurs at the lowest level when $f_3 = 4.2$ kHz. Higher L_3 levels were required when f_3 moved away from this frequency. Third, the slopes of the decrement vs L_3 functions are frequency dependent. The steepest slopes occur for f_3 frequencies well below f_2. This trend is apparent in the left column of Fig. 2, in which f_3 was between about $\frac{1}{2}$ and 1 octave below f_2. As frequency increases, the slope decreases, with the most shallow slopes occurring for f_3 frequencies higher than f_2 (most evident in the right column of Fig. 2). Although previous DPOAE studies have not reported suppression data in this form, these frequency-dependent trends were evident in previous data as well (e.g., Kemp and Brown, 1983; Abdala, 1998, 2001; Kummer *et al.*, 1995).

Figure 3 shows decrement vs L_3 functions when $f_2 = 2$ kHz and $L_2 = 40$ dB SPL, following the format that was used in Fig. 2. The trends evident in Fig. 2 can also be seen here, although the data were less orderly compared to data when $f_2 = 4$ kHz. One difference between decrement functions at 2 kHz and those at 4 kHz was observed for low-frequency suppressors. The median functions in the left column of Fig. 3 (f_3 frequencies between $\frac{1}{2}$ and 1 octave below f_2) were characterized by a saturating portion at higher L_3 levels. This pattern was not observed for similar f_3, f_2 relationships when $f_2 = 4$ kHz (left column, Fig. 2). We cannot explain these differences in response patterns. We initially attributed the less-orderly results when $f_2 = 2$ kHz to the increased noise levels associated with measurements at this frequency. Evidence in support of this view was provided by the fact that longer averaging times were needed at 2 kHz. However, invoking increased noise levels to account for the differences in results is inadequate, since the stopping rules resulted in similar noise levels across f_2 frequencies. On the other hand, there are similarities in results across f_2 frequencies. For example, the median provided a reasonable description of individual data, there was increased variability at the saturating portion of the functions (representing the variability inherent in the noise), and the slopes of the decrement functions depended on the relation between f_3 and f_2. This latter observation was apparent on the high-frequency side of f_2 (right column of Fig. 3). The low-frequency effects were less clear at this f_2, compared to 4 kHz.

Figure 4 shows median DPOAE decrements as a function of L_3 when $f_2 = 4$ kHz and L_2 was at each of five different levels, ranging from 20 dB SPL (top panel) to 60 dB SPL (bottom panel). Data for f_3 frequencies less than f_2 are shown in the left column, while data for f_3 frequencies higher than f_2 are shown in the right column. Within each panel, the heavy line represents data for the condition in which f_3 was the closest to f_2 among the f_3 frequencies represented in the panel. The thin lines moving towards the right side of each panel represent data for other f_3 frequencies; the further the lines move towards the right side, the greater the difference in frequency between f_3 and f_2.

Several trends are obvious in this representation of the data. The lowest suppression thresholds are evident for f_3 frequencies close to f_2. For example, an L_3 of about 15 dB SPL when f_3 was either 4.1 or 4.2 kHz began to suppress the

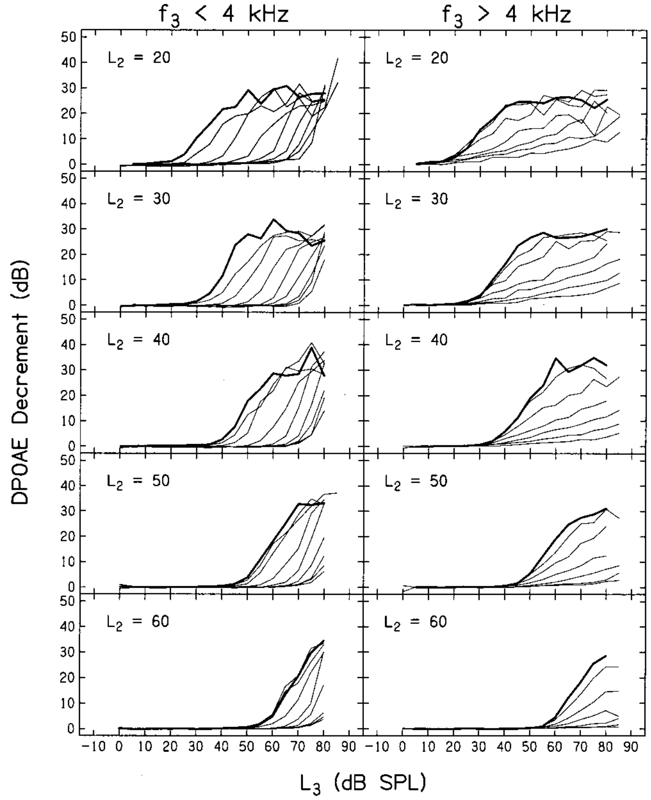

FIG. 4. Median DPOAE decrement vs L_3 functions for f_3 frequencies less than f_2 (left column) and for f_3 frequencies greater than f_2 (right column), when $f_2 = 4$ kHz. Within each panel, the parameter is f_3, with the heavy line representing data for the f_3 closest to f_2. The level of f_2 (L_2) varies within each column from 20 dB SPL (top panel) to 60 dB SPL (bottom panel).

response when $L_2 = 20$ dB SPL (left-most lines, top panel, right column). As f_3 increased, the level that just began to suppress the response increased. The same trends were evident for f_3 frequencies lower than f_2. Second, decrement (suppression) threshold increased with L_2. This can be seen in the systematic migration of the decrement functions towards the right as L_2 increased down each column. Third, the slope of the decrement vs L_3 function depended on the relationship between f_3 and f_2 as they had in the data summarized in Fig. 2. As in Fig. 2, the high-level portion of some of these functions should not be viewed as evidence of saturation; rather, these portions of the function represent the case when the response to the primary tones was suppressed into the noise floor.

In similar fashion, Fig. 5 represents median decrement vs L_3 data when $f_2 = 2$ kHz, following the format used in Fig. 4. Note here, however, that data are shown only for the cases when $L_2 = 40$, 50, or 60 dB SPL. Once again, the lowest suppression thresholds were observed when f_3 was close to f_2, and migrated to higher L_3 levels as L_2 increased (the progression down each column in the figure). In addition, the slopes of these functions were steepest for f_3 frequencies on the low side of f_2, decreasing as f_3 increases, much like the results that were observed when $f_2 = 4$ kHz. However, the orderly progression of these decrement functions relative to f_3, both in terms of threshold and in terms of slopes, were not as evident when $f_2 = 2$ kHz compared to the observation when $f_2 = 4$ kHz, especially for f_3 frequencies less than f_2.

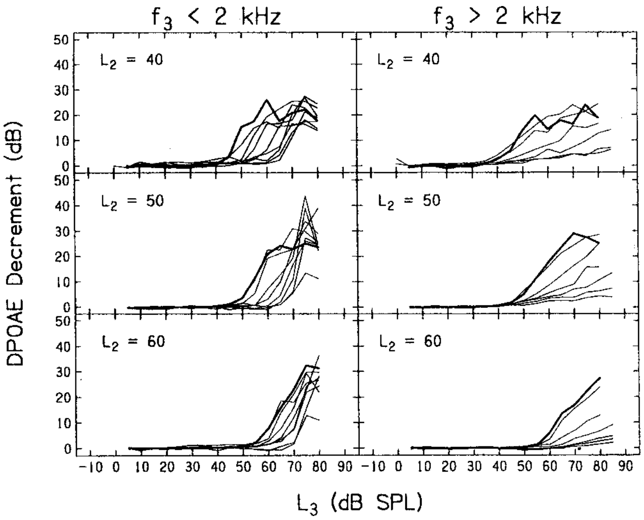

FIG. 5. Following the convention used in Fig. 4, median decrement vs L_3 functions when $f_2 = 2$ kHz.

B. Suppression tuning curves and slopes of decrement functions

Figure 6 shows median DPOAE suppression thresholds (top row) and slopes of the DPOAE decrement vs L_3 functions (bottom row) as a function of f_3 when $f_2 = 4$ kHz. Each column represents data for a different L_2. For the purposes of these tuning curves, suppression threshold was defined as the L_3 that resulted in a 3-dB reduction in DPOAE level from what was measured when the primaries were presented in the absence of a suppressor. This "threshold" was chosen because it could be estimated reliably, while it represents the level at which f_3 just begins to affect the response to the primary tones. This suppression threshold, however, was not estimated visually from decrement vs L_3 functions. Instead, the median decrement vs L_3 functions for each f_3 were transformed by the following equation:

$$D = 10 \log(10^{\mathrm{decr}/10} - 1), \tag{1}$$

and fit by a linear regression of D onto L_3. Lines were fit only to the range, $-5 < D < 20$. Each of these linear equations was then solved for the L_3 that resulted in a 3-dB decrement. According to the above equation, $D = 0$ when decr $= 3$ dB. The same linear regressions were used to provide slope estimates for the decrement functions.

The DPOAE suppression tuning curves shown in Fig. 6 have the lowest threshold when f_3 was close to f_2. This observation is not new, as it was evident in other studies that measured DPOAE suppression tuning curves for the $2f_1 - f_2$ DPOAE (Martin *et al.*, 1987, 1999; Harris *et al.*, 1992; Cianfrone *et al.*, 1994; Kummer *et al.*, 1995; Abdala *et al.*, 1996; Abdala, 1998, 2001). As f_3 moved away from f_2, the level necessary to reduce the response by 3 dB increased. The rate at which this increase occurred was more rapid on the high-frequency side of the tuning curve, compared to the low-frequency side. Although difficult to see in this representation, there was a slight shift in the frequency for which the lowest suppression threshold was observed, moving towards lower f_3 frequencies as L_2 was increased. Although variable, the slopes of the decrement functions generally decreased as f_3 increased. The steepest slopes were observed when f_3 was

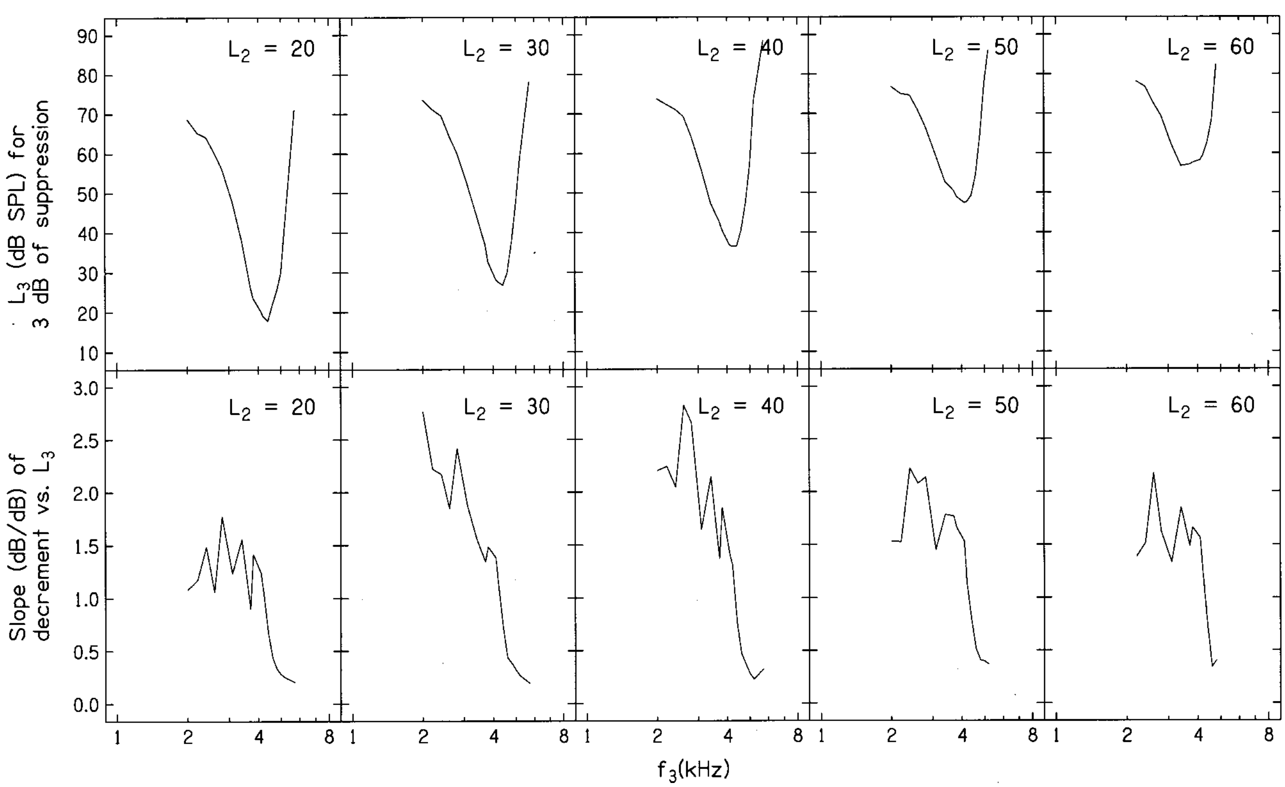

FIG. 6. Top: Suppressor level (L_3) as a function of suppressor frequency (f_3) that resulted in a 3-dB reduction in the DPOAE level elicited when the primaries were presented in quiet. Each of these DPOAE suppression tuning curves represents data for a different L_2. Bottom: Slopes of the decrement vs L_3 functions as a function of f_3. Each panel represents data for a different L_2.

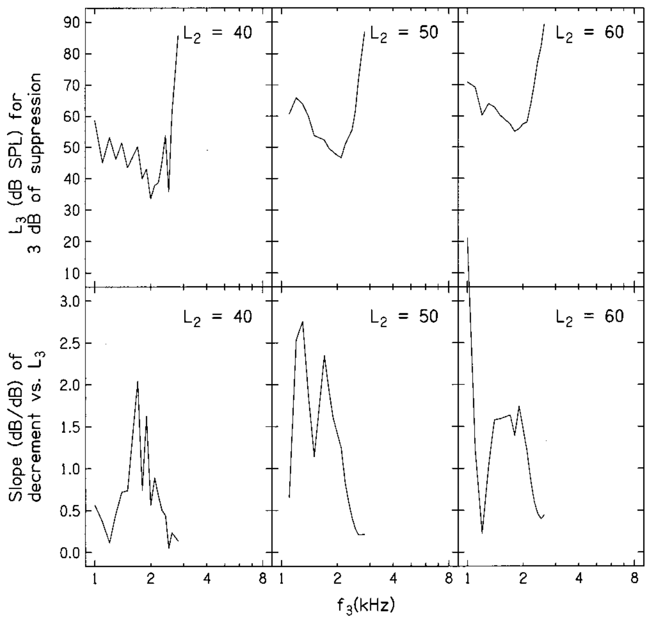

FIG. 7. Following the convention used in Fig. 6, DPOAE suppression tuning curves (top row) and slopes of DPOAE decrement vs L_3 functions (bottom row) for $f_2=2$ kHz.

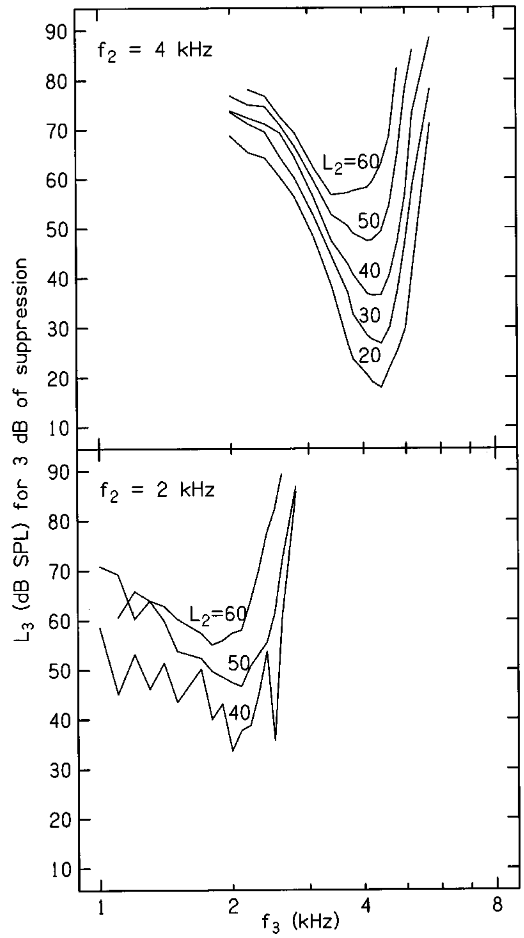

FIG. 8. The tuning curves from Figs. 6 and 7 are reproduced here. Top: $f_2=4$ kHz; bottom: $f_2=2$ kHz. Within each panel, the parameter is L_2.

about an octave below f_2, decreasing as f_3 increased. The shallowest slopes were observed for the highest f_3 frequencies relative to f_2. In most cases, there was a rapid transition between steep and shallow slopes as f_3 frequencies moved from below f_2 toward f_3 frequencies above f_2.

In comparison with previous DPOAE suppression data, Abdala (1998) reports a slope of between 1.2 and 1.4 dB/dB for low-frequency suppressors when $f_2=3$ kHz and $L_2=50$ dB SPL, and Kummer *et al.* (1995) show slopes between 1.5 and 2.0 dB/dB for low-frequency suppressors when $f_2=4$ kHz and $L_2=40$ dB SPL. In the present study, the slopes for low-frequency suppressors ranged from 1.5 to 2.5 dB/dB when $L_2=40$ dB SPL and from 1.5 to 2.0 dB/dB when $L_2=50$ dB SPL (see Fig. 6). For high-frequency suppressors relative to $f2$, all three studies reported rapid decreases in slope to values much less than 1 dB/dB.

Figure 7 displays equivalent DPOAE suppression tuning curves and slopes of decrement vs L_3 functions when $f_2=2$ kHz. Note that data are only shown for primary levels (L_2 levels) of 40, 50, and 60 dB SPL. This primary-level limitation is not thought to reflect fundamental differences in cochlear response properties at 2 kHz, compared to 4 kHz. As stated earlier, however, we cannot invoke differences in noise levels to account for differences in response patterns between 2 and 4 kHz because the measurement-based stopping rules resulted in near-equivalent noise levels across f_2 frequencies.

Some of the trends evident at 4 kHz were also present here. The lowest suppression threshold was observed for f_3 frequencies close to f_2. Higher thresholds were observed as f_3 moved away from f_2. Still, the pattern was more irregular at 2 kHz, compared to 4 kHz, especially when $L_2=40$ dB SPL. The low-frequency side of the suppression tuning curve for this condition was not monotonic. On the other hand, the two higher-level tuning curves at 2 kHz were similar in form to those observed at 4 kHz for similar L_2 levels. In addition, the most sensitive thresholds at 2 kHz occurred when f_3 was close to f_2, and the relation between L_2 and L_3 at these points was similar at 2 and 4 kHz.

The slopes of the decrement vs L_3 functions were less orderly when $f_2=2$ kHz compared to the case when $f_2=4$ kHz. While a rapid decrease in slope was observed as f_3 moved from just below f_2 towards higher frequencies, irregular slope patterns were observed on the low-frequency side of the functions relating slope to f_3. Thus, the data at 2 kHz showed the same frequency dependence that was evident at 4 kHz, but mainly for f_3 frequencies approximately equal to or higher than f_2. It is difficult to see any systematic relationship between slope and f_3 for f_3 frequencies $<f_2$.

Figure 8 reproduces the tuning curves from Figs. 6 and 7. The tuning curves at 4 and 2 kHz are shown in the top and bottom panels, respectively. The parameter within each panel is L_2. The slight migration of the tip towards lower f_3 frequencies as L_2 was increased can be seen in this representation of the data. In addition, 3 dB of suppression occurred when L_3 was roughly equal to L_2 for f_3 frequencies close to f_2. Similar trends were evident in other data, even though differences in the definition of "threshold" existed across studies (e.g., Harris *et al.*, 1992; Cianfrone *et al.*, 1994; Kummer *et al.*, 1995; Abdala *et al.*, 1996; Abdala, 1998, 2001; Pienkowski and Kunov, 2001). Note also that there

TABLE I. Q_{10}, slope of low-frequency segment (LF slope), and slope of high-frequency segment (HF slope) of suppression tuning curves. Data are provided from several previous studies, as well as from the present study. In addition to some differences in stimulus conditions, differences also existed across studies in how some of these estimates were obtained.

Study	f_2 (kHz)	L_2 (dB SPL)	Q_{10}	LF slope (dB/oct)	HF slope (dB/oct)
Harris *et al.* (1992)	4.0	40	2.97	38.9	128.3
Cianfrone *et al.* (1994)	3.3	62	2.24	25 to 35	100 to 115
Kummer *et al.* (1995)	3.975	40	3.5	43	234
Abdala *et al.* (1996)	3.0	50	3.2	39.5	82
Abdala (1998)	3.0	50	3.3	37	125
Abdala (2001)	3.0	45	3.5		
		65	2.5		
Present study	4.0	20	3.5	59	67
		30	3.4	52	89
		40	2.9	42	89
		50	2.7	37	82
		60	2.0	37	38

was a near-linear increase in suppression threshold with L_2 when f_3 was close to f_2. That is, the shift in L_3 necessary to result in a 3-dB reduction in DPOAE level was about 10 dB for every 10-dB increase in L_2. In contrast, the level necessary to reduce the response by 3 dB increased more slowly when f_3 was about an octave lower than f_2. This can be seen in the small range of L_3 levels on the low-frequency tail of the tuning curve, compared to the spacing when f_3 was approximately equal to f_2, at least when $f_2 = 4$ kHz.

In general, there were fewer data when $f_2 = 2$ kHz and there were aspects of the data at this f_2 frequency that were difficult to explain. Having said this, it is not our contention that cochlear function fundamentally differs between the 2-kHz and the 4-kHz places. Rather, we do not understand the reasons underlying the differences in the present measurements at these two frequencies. As a consequence of differences in variability, the limited range of L_2 levels, and the smaller number of subjects on whom data were available, we are less confident in our observations at 2 kHz compared to 4 kHz. Thus, the remainder of this paper will focus on the results at 4 kHz, where more data were available and less variability was evident.

A quadratic function was fit to three points on the tuning curves, including the point with the lowest threshold and one point on either side of this frequency. The minimum of the quadratic function was taken as the best frequency (the frequency for which suppression threshold was lowest). Based on these fits, the best frequency systematically decreased from 4.3 kHz when $L_2 = 20$ dB SPL to 3.5 kHz for $L_2 = 60$ dB SPL. That is, the best frequency decreased from 0.11 octaves above to 0.18 octaves below f_2 as L_2 increased from 20 to 60 dB SPL. At 3 kHz, Abdala (2001) observed a downward shift of about 0.07 octaves as L_2 increased from 45 to 65 dB SPL.

Table I provides a summary of tuning-curve characteristics from the present study and compares these estimates to similar estimates from previous DPOAE suppression tuning-curve studies. Stimulus conditions were chosen from these previous studies that were close to the stimulus conditions used presently. However, there was some variation in terms of f_2, L_2, the definition of suppression threshold, the range of f_3 frequencies, and the procedures used to estimate low- and high-frequency slopes of the tuning curves, which could affect agreement across studies. In the present study, low- and high-frequency slopes were determined by fitting the points on the tuning curve between the best frequency (defined by the quadratic function) and the point 20 dB above the threshold at the best frequency.

There is good agreement across studies in terms of Q_{10} (best frequency divided by the bandwidth at 10 dB above best threshold) and in the low-frequency slope of suppression tuning curves. There is less agreement in estimates of high-frequency slope, with the present values being on the low end of these estimates. This difference may relate to the way these slope estimates were derived. In general, however, there is good agreement among studies in terms of these three descriptions of tuning-curve shape. From the present data, it can be seen that, as expected, Q_{10}, and low- and high-frequency slopes decrease as L_2 increases. To the extent that these measures represent the frequency dispersion along the cochlea, that dispersion increases as stimulus level increases.

C. Growth of suppression as a function of L_2

Figure 9(A) plots the L_3 necessary for a 3-dB reduction in DPOAE level as a function of L_2 when $f_2 = 4$ kHz. The parameter in this figure is f_3, with solid lines representing data for f_3 frequencies $< f_2$, and dotted lines representing data for f_3 frequencies $> f_2$. These plots represent the amount by which the suppressor level (L_3) had to be increased as the signal level (L_2) was increased in order to maintain a constant amount of suppression (3 dB). Starting from the lower-left corner of this figure, the four dotted lines clustered together represent conditions in which f_3 was slightly higher than f_2. Data for progressively higher f_3 frequencies are represented by the dotted lines moving up this panel. In a similar fashion, the lowest solid lines represent data for f_3 frequencies that were close to but slightly lower than f_2. Data for progressively lower f_3 frequencies are represented by the solid lines moving up the panel. The lowest L_3 levels and the most linear (dB/dB) functions were ob-

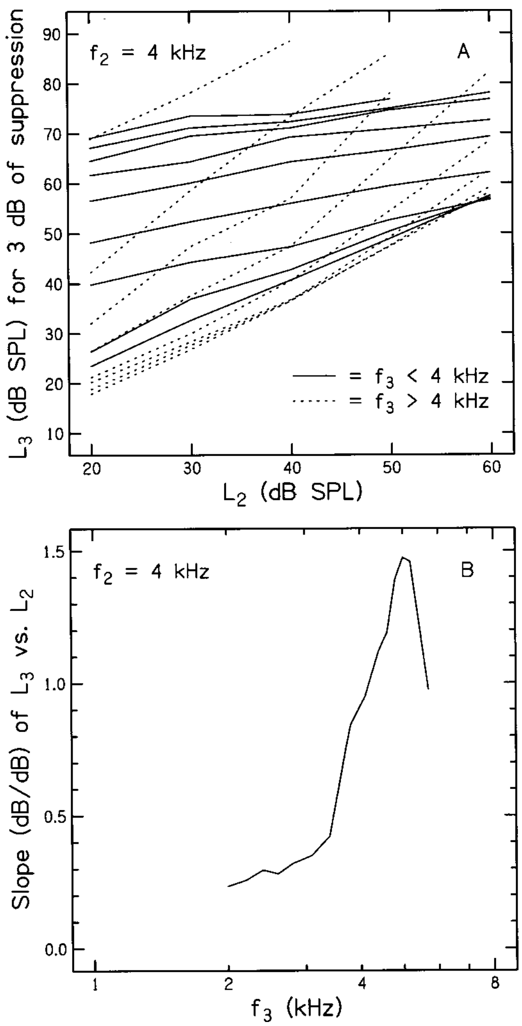

FIG. 9. Top: L_3 to produce a 3-dB reduction in DPOAE level as a function of L_2 for $f_2=4$ kHz. The parameter is f_3, with f_3 frequencies $<f_2$ shown as solid lines and f_3 frequencies $>f_2$ shown as dotted lines. Bottom: Slopes of the L_3 vs L_2 functions (top panel) as a function of f_3 frequency.

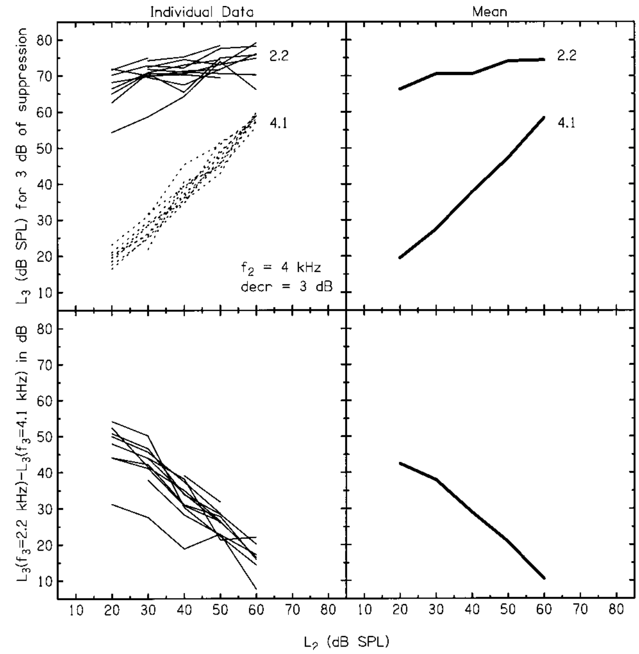

FIG. 10. Top row: L_3 necessary to produce a 3-dB reduction in DPOAE level as a function of L_2, when $f_2=4$ kHz. The parameter is f_3 frequency, as indicated within each panel. The left panel shows data for individual subjects, while the right panel shows mean data. Bottom: Gain as a function of L_2 for individual subjects (left panel) and averaged across subjects (right panel). Gain was defined as the difference in dB between the L_3 necessary to achieve a 3-dB reduction in DPOAE level when $f_3=2.2$ kHz and when $f_3=4.1$ kHz.

served for f_3 frequencies close to f_2, which can be likened to on-frequency conditions. In contrast, higher L_3 levels were needed to achieve a 3-dB reduction in DPOAE level when f_3 was higher than f_2; however, the L_3 level required to maintain a constant amount of suppression increased more rapidly, compared to the on-frequency case. When f_3 was less than f_2, higher L_3 levels also were needed. In these cases, however, the L_3 level necessary to maintain a constant 3-dB reduction in DPOAE level increased more slowly as L_2 increased. The data shown in Fig. 9(A) are the same as the tuning-curve data shown in the top panel of Fig. 8. Here, however, the effects of level for individual suppressor frequencies are more clearly shown.

Figure 9(B) plots the slope of the L_3 vs L_2 functions shown in Fig. 9(A). The slope is shallow at low f_3 frequencies relative to f_2. As f_3 approaches f_2, the slope increases rapidly, with a slope close to 1 dB/dB when f_3 and f_2 frequencies are approximately equal. As f_3 is increased further, the slope also increases. However, estimates of slope for f_3 frequencies above 5 kHz may not be reliable because they are based on fewer points. For some of these frequencies, the suppression criterion of 3 dB could be achieved only for low L_2 levels [see the top dotted line in Fig. 9(A)]. There is a transition in this slope function, such that the slopes are shallow and remain relatively constant at low f_3 frequencies, and then change abruptly and increase rapidly as f_3 increases further. The significance of this abrupt transition, which occurred at about 3.5 kHz, is unknown.

D. Tip-to-tail differences vs L_2

The top row of Fig. 10 plots the L_3 necessary to produce a 3-dB decrement as a function of L_2 for a frequency close to f_2 (4.1 kHz, dashed lines) and for a low frequency (2.2 kHz, solid lines) relative to f_2. Individual lines in the upper left-hand panel represent data from individual subjects. The lines in the right-hand panel represent means of the data shown on the left. The data shown here are equivalent to the data shown in Fig. 9(A). The representations in this figure differ from those shown in the previous figure, however, in that individual and mean data are presented for only two f_3 frequencies. Note that as L_2 increases, the level necessary to reduce the response by 3 dB also increases. However, the increase is more rapid when f_3 is close to f_2, compared to when f_3 is much lower than f_2. This is another representation of the changes in tip-to-tail differences that were evident in the tuning curves of Fig. 6, in which there were greater shifts in the tip versus the tail of the tuning curves as L_2 increased.

It can be argued that the "cochlear amplifier" for a specific place along the BM is active when that place is driven by its CF. Furthermore, it can be argued that the cochlear amplifier is less active when a specific place along the BM is driven by a frequency much lower than the CF for that place (e.g., Mills, 1998; Pienkowski and Kunov, 2001). Thus, a comparison of the "threshold" suppressor levels for a low-frequency suppressor vs a suppressor close to f_2 (i.e., the tip-to-tail difference) should provide an estimate that is related to the "gain" provided by the cochlear amplifier. These estimates are presented in the bottom row of panels in Fig. 10. The method used to obtain the present estimates of threshold differed slightly from the one described above in that $D=0$ was determined by linear interpolation instead of linear regression. The lines shown in the lower-left panel were derived by subtracting the L_3 for $f_3=4.1$ kHz from the L_3 for $f_3=2.2$ kHz, as a function of L_2. Each line represents the results for an individual subject. The line in the lower-right panel represents the mean of these data. As L_2 increases, the dB difference to maintain a constant response (3 dB of suppression) at the f_2 place decreases, going from about 45 dB when $L_2=20$ dB SPL down to 10 dB when $L_2=60$ dB SPL.

IV. DISCUSSION

We assume that the decrement in DPOAE level as a result of the suppressor (i.e., amount of suppression) is a measure of response to the suppressor at the f_2 place. That is, decrements provide indirect measures of response properties for a fixed cochlear place as a function of the frequency and level of the suppressor. In many ways, therefore, the assumptions associated with DPOAE suppression paradigms are similar to those made whenever physiological or psychophysical masking experiments are performed. Thus, one might view the present fixed-frequency, fixed-level primaries and the variable-frequency and variable-level suppressors the way one would view probes and maskers in masking or suppression studies. This framework might be useful as one considers the context within which the work reported here is interpreted.

As noted above, response patterns were not identical at 2 and 4 kHz. These differences in findings cannot be attributed to differences in noise level, because the measurement-based stopping rules resulted in near-equivalent noise levels for both f_2 frequencies. Control conditions were equally stable as well, thus suggesting that differences in response patterns were not the result of greater variability in DPOAE levels when $f_2=2$ kHz. Others have reported differences in DPOAEs from 2 kHz compared to 4 kHz. For example, He and Schmiedt (1993) noted that greater fine structure was evident in DPOAEs surrounding 2 kHz compared to 4 kHz. Konrad-Martin *et al.* (2001) reported data that revealed greater relative contributions to the ear-canal DPOAE from the reflection source (relative to the intermodulation source) at 2 kHz (compared to 4 kHz), an observation that is consistent with the greater fine structure noted by He and Schmiedt. The source(s) of these differences, and how they might influence the present results, are not known. For the purposes of simplicity, the discussion to follow will focus on results obtained when $f_2=4$ kHz. We remain perplexed, however, by the results when $f_2=2$ kHz, especially in view of the orderly behavior that was observed at 4 kHz.

A. DPOAE decrements as measures of response growth

Although previous studies reported DPOAE level (as opposed to DPOAE decrement) as a function of L_3 for a range of suppressor frequencies (e.g., Kemp and Brown, 1983; Kummer *et al.*, 1995; Abdala, 1998, 2001), the present results were similar to those reported previously. For example, Kummer *et al.* (1995) used an f_2 of 3.975 kHz an L_2 of 40 dB SPL, and an L_1 of 55 dB SPL, stimulus conditions that were nearly identical to one set of conditions in the present study. While we observed slightly steeper slopes for low-frequency suppressors, the overall pattern in their data [their Fig. 2(c)] was the same as we observed (present Fig. 6). Across all studies, changes in DPOAE level occurred more rapidly with suppressor level when the suppressor frequency was below f_2, with more gradual changes in DPOAE level when f_3 was greater than f_2.

Our preference for converting these data to decrements relates to the ease with which such conversions permit comparisons between DPOAE data and data derived from other measurements of cochlear response growth. In this form, these functions share many characteristics with other measures of response growth, including direct measurements from the BM, single-unit rate-level functions, whole-nerve AP decrement vs masker-level functions, and ABR decrement vs masker-level functions. For example, the suppressor levels at which threshold suppressive effects were observed depended on the relationship between f_3 and f_2. Assuming that DPOAE decrements describe the representation of f_3 at the f_2 place, then this relationship reflects how different frequencies are represented at a fixed place along the cochlea in much the same way as is evident in other measures of auditory function.

The slopes of these DPOAE decrement functions also share similarities with other measures of response growth. For example, the slopes of single-unit rate-level functions depend on the relationship between driver frequency and an individual fiber's CF (e.g., Sachs and Abbas, 1974). For driver frequencies much lower than CF, the slope of the rate-level function was steep, compared to the slopes when driver frequencies were higher than CF. Sachs and Abbas compared their single-unit data to the Mössbauer measurements of cochlear mechanics made by Rhode (1971). While Rhode's 1971 measurements were not as sensitive as more recent measures of cochlear mechanical responses, Sachs and Abbas were able to relate the two different measures. More recently, other direct measurements of BM motion have demonstrated a relationship between the slope of I/O functions and frequency for a fixed place along the cochlea (Ruggero and Rich, 1991; Ruggero *et al.*, 1997). These more recent data showed that when a particular place was driven at its CF, the slope of the I/O function was less steep compared to the case when the same place was driven at frequencies lower than CF. The present data, at least qualitatively, show the same systematic relationship between the slopes of the decrement vs L_3 functions and suppressor frequency, at least at 4 kHz. These observations are consistent with previous single-unit data (Sachs and Abbas, 1974; Schmiedt and Zwislocki, 1980), AP data in which the response to a probe was reduced by a masker (e.g., Abbas and Gorga, 1981), and direct BM measurements of response growth (Ruggero and Rich, 1991). Thus, it would appear that DPOAE decrement vs L_3 functions can be used as an indirect estimate of cochlear response growth as a function of frequency for a specific cochlear place. Quantitative comparisons, however, are not possible between the present data (in dB/dB) and either single-unit data (in spikes/s/dB) or basilar-membrane (in velocity/dB) measurements of response growth.

It may be possible, however, to compare the present results to previous single-unit (Abbas and Sachs, 1976; Costalupes *et al.*, 1987; Delgutte, 1990) and basilar-membrane (Ruggero *et al.*, 1992) recordings of suppression. As a general rule, the trends evident in the present results are consistent with the findings in these previous studies, including the dependence of slope on the relationship between suppressor frequency and best frequency (single-unit and basilar-membrane measurements) or f_2 (DPOAE suppression measurements). In some of these cases, however, direct comparisons are not possible because of differences in the ways suppression was measured. For example, Abbas and Sachs (1976) described the amount of suppression as a fractional response, relative to the discharge rate when the suppressor was not present. In those cases where more direct comparisons are possible, the present data are not in exact agreement with findings from lower animals. For example, Ruggero *et al.* (1992) observed slopes in the range from 0.65 to 1.42 dB/dB (mean$=$0.97 dB/dB) for suppressors below best frequency and slopes of 0.28 to 0.48 dB/dB (mean $=$0.36 dB/dB) for suppressors higher than the best frequency. The reduced slope of suppression observed for the basilar-membrane measurements may indicate reduced sensitivity of the animal preparation as a consequence of opening the cochlea. Alternatively, the differences in slope estimates may be due to fundamental differences between basilar-membrane suppression and DPOAE suppression. Delgutte (1990) observed slopes of about 2 dB/dB for suppressor frequencies 1 octave lower than CF and slopes of about 0.25 dB/dB for suppressors about $\frac{1}{4}$ octave above CF, but shallower slopes when differences in suppressive effects as a function of CF were taken into account. For one fiber with a CF close to the present f_2 (see Fig. 7, Delgutte, 1990), suppression grew with a slope less than 1.5 dB/dB for a suppressor 1 octave below CF.

B. Suppression tuning curves

The tuning curves described in this paper are similar in form to other measures of peripheral tuning, especially previously described DPOAE suppression tuning curves (e.g., Kemp and Brown, 1983; Abdala, 1998, 2001; Abdala *et al.*, 1996; Brown and Kemp, 1984; Harris *et al.*, 1992; Martin *et al.*, 1987, 1999; Kummer *et al.*, 1995; Cianfrone *et al.*, 1994). These DPOAE suppression tuning curves can be viewed as estimates of level as a function of frequency that results in a constant response (3 dB of suppression in the present study) at the f_2 place. While the data were more variable when $f_2=2$ kHz, the present results showed the expected pattern in which the lowest suppressor levels were needed when f_3 and f_2 frequencies were similar, with greater suppressor levels needed as f_3 moved away from f_2.

The most sensitive suppressor frequency shifted slightly towards lower frequencies as primary levels were increased (Fig. 8). Another way of stating this finding is that, for a given place, the frequency that is maximally represented at that place might change with level, an observation that has been made by others using more direct measurements of cochlear responses (e.g., Rhode and Recio, 2000). For example, Ruggero *et al.* (1997) observed about a 0.32-octave downward shift in best frequency as level changed from 10 or 20 dB SPL to 60 dB SPL. We observed a shift of about 0.30 octave (4.3 to about 3.5 kHz) over a similar range of levels. Thus, a basal spread of excitation is evident in cochlear mechanical responses, whether measured directly in animals or indirectly in humans.

C. Growth of suppression

In the data summarized in Fig. 9(A), an alternate approach was taken to describe response growth. Here, the suppressor (masker) level necessary to maintain a constant response was plotted as a function of L_2 (probe level). In this representation, it is evident that lower suppressor levels (L_3) were needed when f_3 was close to f_2, compared to when it was nearly an octave below f_2. For the on-frequency case, L_3 and L_2 were related linearly, such that it was necessary to increase L_3 by 10 dB for every 10-dB increase in L_2. In contrast, much smaller increases in L_3 were needed when f_3 was lower than f_2. Thus, the slopes of functions relating L_3 to L_2 [Fig. 9(B)] were 1 for conditions in which f_3 was approximately equal to f_2 and less than 1 for conditions in which f_3 was less than f_2. This means that the response to the suppressor (f_3) grew more rapidly than the response to the probe (f_2) at the f_2 place when $f_3<f_2$.

D. Compression ratio in normal ears

The summary in Fig. 10 might provide an estimate of the amount of compression for the on-frequency condition. When $f_3 \approx f_2$, both suppressor and probe are processed through the same input–output (I/O) function. Even though the I/O function is compressive, functions relating L_3 to L_2 grow linearly because they are treated similarly by the nonlinearity. In contrast, the response to a low-frequency suppressor at the f_2 place is less affected by the compressive nonlinearity, and probably grows more linearly. Thus, the slope of the function relating L_3 to L_2 for $f_3=2.2$ kHz (top row, Fig. 10) describes the interaction between responses to a stimulus that grows compressively at the f_2 place and one that grows linearly at the same place. In the present case, this slope estimate was 0.26 dB/dB, which compares favorably with values obtained from DPOAE I/O functions in normal-hearing humans (Dorn *et al.*, 2001), where the slope was 0.24 dB/dB, and is in the range of values (0.2 to 0.5 dB/dB) reported by Ruggero *et al.* (1997) for direct measurements from the chinchilla. The estimates from humans suggest that the normal ear compresses the input signal by a factor of about 4 from near-threshold levels to 60–70 dB SPL.

E. Indirect estimates of "gain"

While some have argued that the cochlear amplifier may have a "gain" of 1 (Allen and Fahey, 1992), others suggest that the mechanical responses of the cochlea are such that the displacements at any place are increased when that place is driven at its CF. Regardless of whether gain is provided by the cochlear amplifier, the fact remains that responses from normal cochleae are fundamentally different when a specific place is driven with an on-frequency stimulus, compared to responses when the same place is driven by a lower frequency. For example, Ruggero and Rich (1991) measured lower mechanical thresholds to a 9-kHz tone at a basal cochlear place, compared to the threshold for a 1-kHz tone at the same place. In addition, the I/O function for the 9-kHz tone was characterized by compression for moderate stimulus levels, whereas no compression was observed when the driver frequency was 1 kHz. Thus, the slope of the I/O function was steeper at 1 kHz. Furthermore, the I/O function at 9 kHz showed an elevated threshold and increased slope (approximating the slope at 1 kHz) when the animal was treated with furosemide. However, threshold and slope of the I/O function did not change at 1 kHz following furosemide administration.

Similar differences between on-frequency and low-frequency responses for a fixed cochlear place have been observed by others. For example, single-unit frequency threshold curves (FTCs) are characterized by low thresholds for CF tones, with increasing thresholds as driver frequency moves away from CF. Typically, these FTCs are characterized by a tail or low-frequency region, in which thresholds are elevated (relative to threshold at CF), but remain relatively constant. When OHC damage is sustained, thresholds for frequencies close to CF are elevated, with little or no change in the thresholds on the low-frequency tails of the FTC (e.g., Kiang *et al.*, 1976; Liberman and Dodds, 1984; Dallos and Harris, 1978). Stated differently, damage to the OHCs, which are thought to be closely related to cochlear-amplifier function, affected on-frequency responses more than low-frequency responses. Furthermore, Ruggero *et al.* (1997) compared premortem and postmortem velocity-vs-level functions, taking the difference between these conditions as a measure of gain (see their Fig. 16), on the assumption that the cochlear amplifier was functional prior to death, and disabled following death. This procedure resulted in gain estimates of 54 or 69 dB.

Taken together, these data suggest that a measure related to cochlear-amplifier gain may be obtained by comparing responses for on-frequency and low-frequency stimuli. In a sense, these two stimulus conditions may be viewed as including one in which the cochlear amplifier is active (on-frequency) and one in which it is not (low-frequency). Indeed, Mills (1998) took this approach in an effort to estimate cochlear-amplifier gain in gerbils. He compared tips and tails of DPOAE suppression tuning curves to derive gain estimates, choosing the intersection between the steeply sloped initial low-frequency portion and the more distant, low-frequency shallow-sloped tail of the tuning curve to define the low-frequency condition. More recently, Pienkowski and Kunov (2001) took a similar approach in humans. They showed that this estimate of gain decreased as threshold increased (even within the range of "normal hearing"), but studied only one primary level ($L_1 = 60$ dB SPL and $L_2 = 40$ dB SPL).

In the data from the present study, a sharp break on the low-frequency side of the DPOAE suppression tuning curves was not apparent. Furthermore, completely flat low-frequency tails were not observed. As a consequence, we used the lowest f_3 for which suppression was observed for a wide range of L_2 levels in the majority of subjects ($f_3 = 2.2$ kHz). The responses observed when $f_3 = 2.2$ kHz were viewed as responses that were not influenced by the cochlear amplifier at the place where $f_2 = 4$ kHz is represented (see Fig. 10). This approach results in a slightly larger estimate of gain compared to some of the other definitions that have been used, but the differences are small because the low-frequency tail has a shallow slope. We recognize the indirect nature of our overall approach, in addition to its limitations related to the somewhat arbitrary nature with which this frequency was selected. However, the decision to use the response to a low frequency relative to f_2 is not entirely arbitrary, given previous direct measurements of BM motion, single-unit FTCs, and DPOAE suppression data. Finally, we assumed that the cochlear amplifier was active for responses when f_3 approximated f_2 ($f_3 = 4.1$ kHz).

A comparison of suppression thresholds when $f_3 = 2.2$ kHz and $f_3 = 4.1$ kHz, therefore, was taken as an indirect estimate related to cochlear-amplifier gain. Examining these threshold differences for a range of L_2 levels provided an estimate that demonstrated that gain decreased as level increased (see Fig. 10). Depending on the appropriateness of the assumptions underlying this approach, these data provide an estimate related to cochlear-amplifier gain as a function of level in humans.

In an effort to compare the present results to more direct mechanical measurements, data reported by Ruggero *et al.* (1997) were used to estimate the dB difference between velocity-level functions at CF (10 kHz) and at a frequency (5 or 6 kHz) one octave below CF (see their Fig. 7). This approach to the mechanical data yielded gain estimates ranging from about 37 dB at 20 dB SPL to about 10 dB at 60 dB SPL, values that are close to the present, indirect estimates in humans.

In spite of the agreement between direct and indirect measures, there are other concerns with the conclusions from this study, beyond those associated with the underlying assumptions leading to estimates of gain. As noted earlier, response patterns were not as orderly at 2 kHz, compared to 4 kHz. We assume that cochlear function at the places where these two frequencies are represented is similar. Furthermore, the measurement-based stopping rules helped to equate noise levels for the two f_2 frequencies. Therefore, explanations that account for the differences in responses are not obvious. Furthermore, the present measurements require the use of a complex stimulus paradigm, with two tones serving as a probe signal, and a third tone serving as the suppressor. Opportunities exist for the generation of multiple distortion products and mutual suppression, both among stimulus tones and perhaps even among multiple distortion products.

F. Potential clinical significance

The inherent problems associated with paradigms like the one used here are unavoidable because direct measurements of BM motion and/or single-unit recordings are not possible in humans. While AP and/or ABR measurements are possible, both require a greater investment in recording time compared to DPOAEs, related to problems associated with the SNR for these neural measurements in humans. Averages including many samples, taking several minutes or longer, might be needed for one data point on an ABR decrement vs masker level function. While the SNR for AP measurements can be improved by placing an electrode either on the tympanic membrane or transtympanically on the promontory, such approaches are not routinely feasible in humans, including patients seen in the clinic. On the other hand, a single DPOAE decrement vs suppressor-level function can be obtained in 5–10 min or less, especially when $f_2 = 4$ kHz, a frequency for which the noise levels typically are low. This time could be shortened further if suppressor level were incremented in steps larger than 5 dB. To the extent that these DPOAE decrement functions provide an estimate of cochlear response growth at a specific place, the present data (as well as the data from others) suggest that objective estimates of response growth are possible in humans.

Furthermore, despite the complexity of the stimulus paradigm and the assumptions in the interpretation of these data, the similarity with previous data from lower animals suggest that estimates related to cochlear-amplifier gain are possible in humans. The work of Pienkowski and Kunov (2001) suggests that it might be feasible to design a paradigm that could be used to make similar estimates in patients whose hearing losses do not to completely eliminate the DPOAE. If successful under laboratory conditions, there may be clinical applications to these measurements. For example, these data may lead to a more quantitative approach to developing signal-processing schemes when fitting amplification (such as selecting a compression ratio), especially for infants and young children with hearing loss.

ACKNOWLEDGMENTS

This work was supported by a grant from the NIH (NIDCD RO1 DC02251). We thank Beth O'Connor for her help in figure preparation. We thank Dr. Brenda Lonsbury-Martin and two anonymous reviewers for their careful reading of this manuscript and for their many helpful suggestions.

Abbas, P. J., and Gorga, M. P. (**1981**). "AP responses in forward-masking paradigms and their relationship to responses of auditory-nerve fibers," J. Acoust. Soc. Am. **69**, 492–499.

Abbas, P. J., and Sachs, M. B. (**1976**). "Two-tone suppression in auditory-nerve fibers: Extension of a stimulus-response relationship," J. Acoust. Soc. Am. **59**, 112–122.

Abdala, C. (**1998**). "A developmental study of distortion product otoacoustic emission ($2\,f_1 - f_2$) suppression in humans," Hear. Res. **121**, 125–138.

Abdala, C. (**2001**). "Maturation of the human cochlear amplifier: Distortion product otoacoustic emission suppression tuning curves recorded at low and high primary levels," J. Acoust. Soc. Am. **110**, 1465–1476.

Abdala, C., Sininger, Y. S., Ekelid, M., and Zeng, F-G. (**1996**). "Distortion product otoacoustic emission suppression tuning curves in human adults and neonates," Hear. Res. **98**, 38–53.

Allen, J. B., and Fahey, P. F. (**1992**). "Using acoustic distortion products to measure cochlear amplifier gain on the basilar membrane," J. Acoust. Soc. Am. **92**, 178–188.

ANSI (**1996**). ANSI S3.6-1996, "Specifications for Audiometers" (American National Standards Institute, New York).

Brown, A. M., and Kemp, D. T. (**1984**). "Suppressibility of the $2\,f_1 - f_2$ stimulated acoustic emissions in gerbil and man," Hear. Res. **13**, 29–37.

Cianfrone, G., Altissimi, G., Cerevellini, M., Musacchio, A., and Turchetta, R. (**1994**). "Suppression tuning characteristics of $2\,f_1 - f_2$ distortion product otoacoustic emissions," Br. J. Audiol. **28**, 205–212.

Costalupes, J. A., Rich, N. C., and Ruggero, M. A. (**1987**). "Effects of excitatory and nonexcitatory tones on two-tone rate suppression in auditory-nerve fibers," Hear. Res. **26**, 155–164.

Dallos, P. J., and Harris, D. M. (**1978**). "Properties of auditory-nerve responses in the absence of outer hair cells," J. Neurophysiol. **41**, 365–383.

Dallos, P. J., Harris, D. M., Relkin, E., and Cheatham, M. A. (**1980**). "Two-tone suppression and intermodulation distortion in the cochlea: Effect of outer hair cell lesions," in *Psychophysical, Physiological and Behavioral Studies of Hearing*, edited by G. van den Brink and F. A. Bilsen (Delft University Press, Delft, The Netherlands), pp. 242–252.

Delgutte, B. (**1990**). "Two-tone rate suppression in auditory-nerve fibers: Dependence on suppressor frequency and level," Hear. Res. **49**, 225–246.

Dorn, P. A., Konrad-Martin, D., Neely, S. T., Keefe, D. H., Cyr, E., and Gorga, M. P. (**2001**). "Distortion product otoacoustic emission input/output functions in normal-hearing and hearing-impaired human ears," J. Acoust. Soc. Am. (in press).

Dorn, P. A., Piskorski, P., Gorga, M. P., Neely, S. T., and Keefe, D. H. (**1999**). "Predicting audiometric status from distortion product otoacoustic emissions using multivariate analyses," Ear Hear. **20**, 149–163.

Dorn, P. A., Piskorski, P., Keefe, D. H., Neely, S. T., and Gorga, M. P. (**1998**). "On the existence of an age/threshold/frequency interaction in distortion product otoacoustic emissions," J. Acoust. Soc. Am. **104**, 964–971.

Evans, E. F. (**1974**). "Auditory frequency selectivity and the cochlear nerve," in *Facts and Models in Hearing*, edited by E. Zwicker and E. Terhardt (Springer, New York), pp. 118–129.

Gorga, M. P., and Abbas, P. J. (**1981a**). "AP measurements of short-term adaptation in normal and in acoustically traumatized ears," J. Acoust. Soc. Am. **70**, 1310–1321.

Gorga, M. P., and Abbas, P. J. (**1981b**). "Forward-masking AP tuning curves in normal and in acoustically traumatized ears," J. Acoust. Soc. Am. **70**, 1322–1330.

Gorga, M. P., McGee, J., Walsh, E. J., Javel, E., and Farley, G. R. (**1983**). "ABR measurements in the cat using a forward-masking paradigm," J. Acoust. Soc. Am. **73**, 256–261.

Gorga, M. P., Neely, S. T., Bergman, B. M., Beauchaine, K. L., Kaminski, J. R., Peters, J., and Jesteadt, W. (**1993**). "Otoacoustic emissions from normal-hearing and hearing-impaired subjects: Distortion product responses," J. Acoust. Soc. Am. **93**, 2050–2060.

Gorga, M. P., Stover, L. J., and Neely, S. T. (**1996**). "The use of cumulative distributions to determine critical values and levels of confidence for clinical distortion product otoacoustic emission measurements," J. Acoust. Soc. Am. **100**, 968–977.

Gorga, M. P., Neely, S. T., and Dorn, P. A. (**1999**). "DPOAE test performance for *a priori* criteria and for multifrequency audiometric standards," Ear Hear. **20**, 345–362.

Gorga, M. P., Neely, S. T., and Dorn, P. A. (**2002**). "Distortion product otoacoustic emissions in relation to hearing loss," in *Otoacoustic Emissions: Clinical Applications*, 2nd ed., edited by M. S. Robinette and T. J. Glattke (Thieme Medical, New York), pp. 243–272.

Gorga, M. P., Neely, S. T., Ohlrich, B., Hoover, B., Redner, J., and Peters, J. (**1997**). "From laboratory to clinic: A large scale study of distortion product otoacoustic emissions in ears with normal hearing and ears with hearing loss," Ear Hear. **18**, 440–455.

Gorga, M. P., Nelson, K., Davis, T., Dorn, P. A., and Neely, S. T. (**2000**). "Distortion product otoacoustic emission test performance when both $2\,f_1 - f_2$ and $2\,f_2 - f_1$ are used to predict auditory status," J. Acoust. Soc. Am. **107**, 2128–2135.

Harris, D. M. (**1979**). "Action potential suppression, tuning curves and thresholds: Comparison with single fiber data," Hear. Res. **1**, 133–154.

Harris, D. M., and Dallos, P. J. (**1979**). "Forward masking of auditory nerve fiber responses," J. Neurophysiol. **42**, 1083–1107.

Harris, F. P., and Probst, R. (**1997**). "Otoacoustic emissions and audiometric outcomes," in *Otoacoustic Emissions: Clinical Applications*, edited by M.

S. Robinette and T. J. Glattke (Thieme, New York), pp. 151–180.

Harris, F. P., Probst, R., and Xu, L. (**1992**). "Suppression of the $2f_1-f_2$ otoacoustic emission in humans," Hear. Res. **64**, 133–141.

He, N-j., and Schmiedt, R. A. (**1993**). "Fine structure of the $2f1-f2$ acoustic distortion product: Changes with primary levels," J. Acoust. Soc. Am. **94**, 2659–2669.

Janssen, T., Kummer, P., and Arnold, W. (**1998**). "Growth behavior of the $2f_1-f_2$ distortion product otoacoustic emission in tinnitus," J. Acoust. Soc. Am. **103**, 3418–3430.

Kemp, D. T., and Brown, A. M. (**1983**). "A comparison of mechanical nonlinearities in the cochleae of man and gerbil from ear canal measurements," in *Hearing: Physiological Basis and Psychophysics*, edited by R. Klinke and R. Hartman (Springer, Berlin), pp. 82–88.

Kiang, N. Y-S., Liberman, M. C., and Levine, R. A. (**1976**). "Auditory-nerve activity in cats exposed to ototoxic drugs and high-intensity sounds," Ann. Otol. Rhinol. Laryngol. **85**, 752–768.

Kim, D. O. (**1980**). "Cochlear mechanics: Implications of electrophysiological and acoustical observations," Hear. Res. **2**, 297–317.

Kim, D. O., Paparello, J., Jung, M. D., Smursynski, J., and Sun, X. (**1996**). "Distortion product otoacoustic emission test of sensorineural hearing loss: Performance regarding sensitivity, specificity, and receiver operating characteristics," Acta Otolaryngol. (Stockh) **116**, 3–11.

Kimberley, B. P., Brown, D. K., and Allen, J. B. (**1997**). "Distortion product emissions and sensorineural hearing loss," in *Otoacoustic Emissions: Clinical Applications*, edited by M. S. Robinette and T. J. Glattke (Thieme, New York), pp. 181–204.

Konrad-Martin, D., Neely, S. T., Keefe, D. H., Dorn, P. A., and Gorga, M. P. (**2001**). "Multiple sources of distortion product otoacoustic emissions revealed by suppression experiments and inverse fast Fourier transforms," J. Acoust. Soc. Am. **109**, 2862–2879.

Kummer, P., Janssen, T., and Arnold, W. (**1995**). "Suppression tuning characteristics of the $2f_1-f_2$ distortion-product otoacoustic emission in humans," J. Acoust. Soc. Am. **98**, 197–210.

Kummer, P., Janssen, T., and Arnold, W. (**1998**). "The level and growth behavior of the $2f_1-f_2$ distortion product otoacoustic emission and its relationship to auditory sensitivity in normal hearing and cochlear hearing loss," J. Acoust. Soc. Am. **103**, 3431–3444.

Kummer, P., Janssen, T., Hulin, P., and Arnold, W. (**2000**). "Optimal $L1-L2$ primary tone level separation remains independent of test frequency in humans," Hear. Res. **146**, 47–56.

Liberman, M. C., and Dodds, L. W. (**1984**). "Single-neuron labeling and chronic cochlear pathology. III. Stereocilia damage and alterations of threshold tuning curves," Hear. Res. **16**, 55–74.

Martin, G. K., Lonsbury-Martin, B. L., Probst, R., Scheinin, S. A., and Coats, A. C. (**1987**). "Acoustic distortion products in rabbit ear canal. II. Sites of origin revealed by suppression contours and pure-tone exposures," Hear. Res. **28**, 191–208.

Martin, G. K., Ohlms, L. A., Franklin, D. J., Harris, F. P., and Lonsbury-Martin, B. L. (**1990**). "Distortion product emissions in humans. III. Influence of sensorineural hearing loss," Ann. Otol. Rhinol. Laryngol. Suppl. **147**, 30–42.

Martin, G. K., Stagner, B. B., Jassir, D., Telischi, F. F., and Lonsbury-Martin, B. L. (**1999**). "Suppression and enhancement of distortion-product otoacoustic emissions by interference tones above f_2. I. Basic findings in rabbits," Hear. Res. **136**, 105–123.

Mills, D. M. (**1998**). "Interpretation of distortion product otoacoustic emission measurements. II. Estimating tuning characteristics using three stimulus tones," J. Acoust. Soc. Am. **103**, 507–523.

Neely, S. T., and Gorga, M. P. (**1998**). "Comparison between intensity and pressure as measures of sound level in the ear canal," J. Acoust. Soc. Am. **104**, 2925–2934.

Neely, S. T., and Liu, Z. (**1993**). EMAV: Otoacoustic emission averager, Tech. Memo No. 17 (Boys Town National Research Hospital, Omaha, NE).

Pienkowski, M., and Kunov, H. (**2001**). "Suppression of distortion product otoacoustic emissions and hearing thresholds," J. Acoust. Soc. Am. **109**, 1496–1502.

Probst, R., and Hauser, R. (**1990**). "Distortion product otoacoustic emissions in normal and hearing-impaired ears," Am. J. Otol. **11**, 236–243.

Rhode, W. S. (**1971**). "Observations of the vibration of the basilar membrane in squirrel monkey using the Mossbauer technique," J. Acoust. Soc. Am. **49**, 1218–1231.

Rhode, W. S., and Recio, A. (**2000**). "Study of mechanical motions in the basal region of the chinchilla cochlea," J. Acoust. Soc. Am. **107**, 3317–3332.

Ruggero, M. A., and Rich, N. C. (**1991**). "Furosemide alters organ of cortin mechanics: Evidence for feedback of outer hair cells upon the basilar membrane," J. Neuro. **11**, 1057–1067.

Ruggero, M. A., Rich, N. C., Recio, A., Narayan, S. S., and Robles, L. (**1997**). "Basilar-membrane responses to tones at the base of the chinchilla cochlea," J. Acoust. Soc. Am. **101**, 2151–2163.

Ruggero, M. A., Robles, L., and Rich, N. C. (**1992**). "Two-tone suppression in the basilar membrane of the cochlea: Mechanical basis of auditory-nerve rate suppression," J. Neurophysiol. **68**, 1087–1099.

Sachs, M. B., and Abbas, P. J. (**1974**). "Rate versus level functions for auditory-nerve fibers in cats: Tone-burst responses," J. Acoust. Soc. Am. **56**, 1835–1847.

Schmiedt, R. A., and Zwislocki, J. J. (**1980**). "Effects of hair cell lesions on responses of cochlear nerve fibers. II. Single- and two-tone intensity functions in relation to tuning curves," J. Neurophysiol. **43**, 1390–1405.

Sewell, W. F. (**1984**). "Furosemide selectively reduces one component in rate-level functions from auditory-nerve fibers," Hear. Res. **15**, 69–72.

Siegel, J. H. (**1994**). "Ear-canal standing waves and high-frequency sound calibration using otoacoustic emission probes," J. Acoust. Soc. Am. **95**, 2589–2597.

Siegel, J. H. (**2002**). "Calibrating otoacoustic emission probes," in *Otoacoustic Emissions: Clinical Applications*, 2nd ed., edited by M. S. Robinette and T. J. Glattke (Thieme Medical, New York), pp. 416–441.

Smith, R. L. (**1977**). "Short-term adaptation in single auditory-nerve fibers: Some poststimulatory effects," J. Neurophysiol. **40**, 1098–1112.

Smith, R. L. (**1979**). "Adaptation, saturation and physiological masking in single auditory-nerve fibers," J. Acoust. Soc. Am. **65**, 166–178.

Smith, R. L., and Zwislocki, J. J. (**1975**). "Short-term adaptation and incremental responses of single auditory-nerve fibers," Biol. Cybern. **17**, 169–182.

Stover, L., Gorga, M. P., Neely, S. T., and Montoya, D. (**1996**). "Towards optimizing the clinical utility of distortion product otoacoustic emission measurements," J. Acoust. Soc. Am. **100**, 956–967.

Whitehead, M. L., Lonsbury-Martin, B. L., and Martin, G. K. (**1992**). "Evidence for two discrete sources of $2f_1-f_2$ distortion product otoacoustic emissions in rabbit. II. Differential physiological vulnerability," J. Acoust. Soc. Am. **92**, 2662–2682.

Whitehead, M. L., McCoy, M. J., Lonsbury-Martin, B. L., and Martin, G. K. (**1995**). "Dependence of distortion product otoacoustic emissions on primary levels in normal and impaired ears. I. Effects of decreasing L_2 below L_1," J. Acoust. Soc. Am. **97**, 2346–2358.

Effects of reversible noise exposure on the suppression tuning of rabbit distortion-product otoacoustic emissions

MacKenzie A. Howard[a)]
Neuroscience Program, University of Miami School of Medicine, Miami, Florida 33101-6960

Barden B. Stagner
Department of Otolaryngology, University of Miami School of Medicine, Miami, Florida 33101-6960

Brenda L. Lonsbury-Martin and Glen K. Martin
Neuroscience Program and Department of Otolaryngology, University of Miami School of Medicine, Miami, Florida 33101-6960

(Received 16 January 2001; revised 6 July 2001; accepted 21 September 2001)

Distortion-product otoacoustic emissions (DPOAEs) at $2f_1$-f_2 can be suppressed by the introduction of a third ''suppressor'' tone. Plotting the suppression of the DPOAE level against the changing frequency and level of the suppressor produces frequency-tuning functions referred to as suppression tuning curves (STCs). The dominant features of STCs, including their shape, are similar to the features of neural tuning curves (NTCs) recorded from single auditory nerve fibers. However, recent findings using reversible diuretics suggest that STCs do not provide the same measure of cochlear frequency selectivity as provided by NTCs. To determine if STCs are also insensitive to the adverse effects of excessive sounds, the present study exposed rabbits to a moderate-level noise that produced temporary threshold shift-like (TTS) effects on DPOAEs, and examined the influence of such exposures on STCs. DPOAEs were produced using primary tones with geometric-mean frequencies centered at 2.8 or 4 kHz, and with L_1 and L_2 values of 45/45, 50/35, 50/50, and 55/45 dB SPL. STCs were obtained before and during recovery for a period of approximately 2 h immediately following, and at 1, 2, 3, and 7 d post-exposure to a 2 kHz octave band noise, at levels and durations sufficient to cause significant but reversible reductions in DPOAE levels. STC data included tip center frequency, tip threshold, and Q_{10dB} measures of tuning for suppression criteria of 3, 6, 9, and 12 dB. Recovery was variable between animals, but all rabbits recovered fully by 7 d post-exposure. STC center frequencies measured during the TTS typically tuned to a slightly higher frequency, while tip thresholds tended to decrease and Q_{10dB} increase. Together, the results indicate that, despite similarities in the general properties of STCs and NTCs, these two types of tuning curves are affected differently following reversible cochlear insult. [DOI: 10.1121/1.1419094]

PACS numbers: 43.64.Jb, 43.64.Kc, 43.64.Bt, 43.64.Wn [LHC]

I. INTRODUCTION

A basic property of the auditory system involves frequency tuning, in which the receptive field of a sensory or neural component can be described in terms of the sound pressure that produces a criterion response as a function of varying stimulus frequency. Such a tuning-curve pattern typically has a sharp tip region for frequencies at which the auditory system component is most sensitive, and thus requires the lowest stimulus-input level to yield the criterion response. On average, these tuning curves tend to have fairly steep slopes on the high-frequency side and protracted tails on the low-frequency side, that extend more than a half octave below the more sensitive tip or characteristic frequency region. The classical example of tuning curves recorded in the auditory system is the neural tuning curve (NTC), measured electrophysiologically, for single cochlear nerve fibers (e.g., Kiang *et al.*, 1965).

Basilar membrane (BM) tuning can also be measured by recording the amplitude or velocity of membrane displacement at a particular place on the membrane to stimulus tones varied in frequency and level (e.g., Rhode, 1971; Ruggero and Rich, 1991). It has been shown that the frequency selectivity of cochlear nerve fibers can be directly related to the displacement of the BM in response to stimulation. Thus when recorded from a single animal, frequency tuning curves of both BM displacement and velocity mirror electrophysiologically recorded NTCs (Rhode, 1971; Narayan *et al.*, 1998). Based upon these findings, manipulations that affect NTCs can be assumed to have a counterpart in BM vibration. Thus poisoning the cochlea with ototoxic diuretics leads to similar changes in frequency selectivity for both NTCs (e.g., Evans and Klinke, 1982; Sewell, 1984) and BM tuning curves (Ruggero and Rich, 1991). Because BM tuning appears to be dependent upon a compressive nonlinearity, from which nonlinear phenomena such as DPOAEs arise, a rela-

[a)]Author to whom correspondence should be addressed. Department of Otolaryngology (B205), University of Colorado Health Sciences Center, 4200 East 9th Ave., Denver, CO 80262-0001, Voice: 303-315-7988, Fax: 303-315-8787. Electronic mail: mhoward@newssun.med.miami.edu

tionship among neural, BM, and DPOAE measures of tuning might be expected.

Aspects of DPOAE tuning are typically determined using response-suppression methods (Brown and Kemp, 1984; Kummer *et al.*, 1995; Abdala *et al.*, 1996; Martin *et al.*, 1998; Mills, 1998). Briefly, in the presence of the two eliciting primary tones at f_1 and f_2, a third suppressor tone, or f_3, is introduced. The f_3 tone is changed systematically in level and frequency to determine the combinations that suppress or reduce the DPOAE by some criterion amount (e.g., 3 dB). By holding the primary f_1 and f_2 tones constant and varying the level and frequency of the f_3 tone, a suppression-tuning curve (STC) can be described.

The dominant features of STC functions for the $2f_1$-f_2 DPOAE appear very similar to NTCs. For example, they consistently show low-frequency tails, sharp tips with a center frequency (CF) near the f_2 primary tone, and steep high-frequency slopes. The properties of STCs and NTCs have shown striking similarities in species as diverse as bats (Frank and Kossl, 1995) and lizards (Koppl and Manley, 1993). For example, in mustached bats some nerve fibers exhibit a steep low-frequency slope and a shallow high-frequency slope opposite to what is typically observed for NTCs. DPOAE STCs recorded at these frequencies also showed the same reversal of symmetry. Based upon such data, it could be assumed that DPOAE tuning accurately reflects neural tuning (Frank and Kossl, 1995).

Because NTCs can be used to determine the frequency selectivity of individual cochlear nerve fibers, the similarities between STCs and NTCs suggest that the former functions might somehow be used clinically to measure cochlear frequency selectivity at the level of the outer hair cells (OHCs). Comparisons between STCs from humans and neural responses, recorded as compound action potentials, have reported remarkable similarities between STCs and NTCs in both shape and detection threshold for both adults (Kummer *et al.*, 1995; Pienkowski and Kunov, 2001) and neonates (Abdala *et al.*, 1996; Abdala, 1998). In addition, measured human STCs have been compared to their psychophysical tuning curve (PTC) counterparts. Briefly, PTCs were found to be more sharply tuned in humans than STCs thus representing a result consistent with similar comparisons made between PTCs and NTCs in guinea pigs (Ryan and Dallos, 1975; Dallos *et al.*, 1977).

Comparison of STCs recorded from neonates and adults has uncovered significant differences in STC parameters between these groups. At certain frequencies, neonatal STCs are narrower (i.e., have a larger $Q_{10\mathrm{dB}}$), and have a steeper low-frequency slope (Abdala, 1998). More recent results comparing STCs in normal children with this earlier data have eliminated the possibility that these changes reflect aging processes (Abdala *et al.*, 2001). Such data strongly suggest that these types of changes correlate with a cochlear immaturity that is present just before birth, and can be detected in premature humans using DPOAE suppression methods. However, comparison of STCs from normal, age-matched adults, with STCs recorded from adults suffering from auditory neuropathy, showed that STCs are unaffected by this type of condition (Abdala *et al.*, 2000). Thus, analyzing STC parameters may yield information regarding some types of cochlear dysfunction, such as developmental immaturity, but will not be diagnostic for others.

In combination, it is tempting to interpret these data as evidence that STCs can be used noninvasively to directly measure cochlear frequency selectivity. However, despite the qualitative similarities between STCs and NTCs, a direct comparison between the two measures of frequency tuning in the peripheral ear may not be justified. One approach toward determining whether or not STCs represent a measure of cochlear frequency selectivity is to examine STCs in experimental subjects after making deliberate manipulations that have a known effect on both neural and basilar membrane tuning. For example, Martin *et al.* (1998) showed that STCs were not affected in the manner anticipated for NTCs, following cochlear insult with reversible ototoxic diuretics. In these experiments, STCs from rabbits injected with loop diuretics did not change appreciably in shape as might be expected for agents that drastically reduce DPOAE levels. Thus $Q_{10\mathrm{dB}}$ measurements of tip sharpness of the STC showed no significant differences between pre- and post-drug suppression, in the presence of DPOAE levels that had been reduced by about 20 dB. Such results are contrary to the effects of loop-diuretic administration on NTCs (Sewell, 1984) and basilar membrane tuning (Ruggero and Rich, 1991). These data elucidate a significant difference in the behavior of DPOAE STC functions and other measures of frequency tuning in the auditory system.

Another method of manipulating the frequency selectivity of the auditory system is to expose the ear to excessive sound. The after-effects of acoustic overstimulation on DPOAEs, NTCs, and BM tuning have been frequently documented in the literature. Thus when either a temporary or permanent threshold shift is induced by overexposure, the frequency selectivity exhibited by single cochlear nerve fibers deteriorates (e.g., Kiang *et al.*, 1976). These changes in tuning are exhibited in NTC functions as raised thresholds and decreased $Q_{10\mathrm{dB}}$ values, giving the curve a much flatter shape. As would be expected, acoustic trauma also disrupts BM tuning in the same way (Johnstone *et al.*, 1986). If STCs accurately reflect BM tuning, then following acoustic trauma STCs would also be expected to show increased thresholds and decreased $Q_{10\mathrm{dB}}$.

The purpose of the present study was to expand upon the previous work in rabbits to determine if the behavior of STCs following a noise-induced cochlear insult is similar to that observed following diuretic administration. Toward this end, STCs were measured before, directly after, and for an extended period of time after exposing rabbits to a noise producing a TTS. The TTS studies improved upon the diuretic experiments in that very sensitive, low level primary tones were employed for all measures to maximize the possibility of detecting significant changes in STC parameters. Additionally, the time course over which alterations in DPOAE levels were tracked was much longer than those used for the earlier diuretic experiments. A preliminary review of some aspects of this study was reported earlier (Howard *et al.*, 2000).

II. METHODS

A. Experimental animals

Subjects were five young adult rabbits (four pigmented, one albino), weighing from 2.2 to 3 kg. Prior to any DPOAE testing, animals were anesthetized with an intramuscular injection (ketamine 50 mg/kg, xylazine 10 mg/kg) and surgically fitted with a permanent head-restraint device using aseptic methods. Rabbits were given at least 3 wk to recover from the restraint-implant surgery before initiating the experimental protocol. During the course of the study, animals were provided with food and water *ad lib* in their home cages, within a standard vivarium facility, and were maintained on a routine 12:12 h light/dark cycle (lights on at 6:30 am). All experimental protocols were reviewed and approved by the Institutional Animal Care and Use Committee of the University of Miami School of Medicine.

B. DPOAE measurements

Awake rabbits were confined in a standard plastic restrainer and placed within a large, double-walled soundproofed chamber. The head of the rabbit was fixed firmly in place by attaching the surgically implanted headmount device to a bracket on the restrainer. Each set of DPOAE measurements typically included a DP-gram, i.e., DPOAE level as a function of frequency, with primary tone levels held constant, and several suppression response area (SRAs) measures described below. The DPOAE measurement techniques employed in the present study have been described in detail previously (Whitehead *et al.*, 1995). Briefly, f_1 and f_2 primary tones were produced by two D/A channels of a 16-bit digital signal processing (DSP) board (Digidesign, Audiomedia), mounted in a Macintosh IIci microcomputer. These primary-tone signals were transduced and presented to the closed ear canal by individual ER-2 (Etymotic Research) speakers. Sound pressure levels in the ear canal were measured using an ER-10 (Etymotic Research) microphone system. The ear-canal sound was sampled and averaged ($n=4$) by an A/D channel of the DSP board. A 4096-point fast Fourier transform (FFT) of the time sample was then performed by customized software. DPOAE and noise floor (NF) levels were extracted from the FFT. The DP-grams were collected at geometric mean (GM) frequencies $[\mathrm{GM}=(f_1 * f_2)^{0.5}]$, interspersed at 0.1-octave steps, from 1.414 to 18.37 kHz ($f_2=1.581$–20.549 kHz).

C. Suppression response areas

SRAs were obtained for each subject at the GM frequencies of 2.828 ($f_1=2.53$, $f_2=3.16$ kHz) and 4 kHz ($f_1=3.59$, $f_2=4.47$ kHz), which represent low-to-medium frequencies within the rabbit audibility range. SRAs were collected using four primary-tone levels at each GM frequency. Primary tones were either equilevel ($L_1=L_2=45$ and 50 dB SPL), or with $L_1>L_2$ ($L_1/L_2=50/35$ and 55/45 dB SPL). Previous studies indicated that these unequal level primary-tone combinations would show the most sensitivity to cochlear insults in rabbits (Whitehead *et al.*, 1995). When measuring SRAs, the suppressor or f_3 tone was digitally added to the f_1 channel. In each STC constructed from the relevant SRA, the suppressor level was increased systematically in 5-dB steps from 25 to 75 dB SPL, and its frequency stepped at 8 points/octave.

When stimulating with equilevel primary tone pairs at the 2.828 kHz GM frequency, f_3 was swept from 0.66 to 6 kHz. Preliminary data suggested that STCs for primary-tone pairs of unequal level tuned to slightly higher frequencies. Thus when unequal-level primary tone pairs at this GM frequency were used, f_3 was swept from 0.86 to 7.8 kHz. When using equilevel primary-tone pairs at the 4 kHz GM frequency, f_3 tones varied from 1 to 9.28 kHz, whereas f_3 tones for unequal primary tone pairs at the 4 kHz GM frequency were swept from 1.55 to 14.2 kHz. These data were obtained in a matrix of 270 frequency/level combinations, i.e., 27 frequencies by 10 levels.

One nonsuppressed "reference" DPOAE was recorded at the end of each of the frequency columns in the suppression matrix and thus represented the level of the control "unsuppressed" DPOAE. Total suppression level was calculated by subtracting the suppressed DPOAE level from the reference DPOAE level, based on the average of all 27 nonsuppressed control DPOAE levels. Comparison of SRAs produced with this average procedure with those produced by using control DPOAEs from each frequency column showed that STCs were not adversely affected using the mean-reference DPOAE method. This method was also useful in reducing noise in the SRAs as DPOAE levels approached the NF following cochlear insult. SRA contour plots were produced with each contour showing successive 3 dB increases in DPOAE suppression, i.e., 3–12 dB in 3-dB steps. Some pre-exposure data sets showed significantly lower unsuppressed DPOAE levels than others. This outcome was attributed to a poor fit of the microphone probe in the animal's ear canal. Data sets that were unreliable due to this type of error were excluded from further analyses.

D. Suppression tuning curves (STCs)

STCs were extracted from SRA contour plots as previously described in detail (Martin *et al.*, 1998). Briefly, a spreadsheet algorithm was developed to create the STCs and automatically extract the values of a number of tuning-curve parameters including center frequency, threshold, and $Q_{10\mathrm{dB}}$ of the tip of the curve, for the series of four suppression criteria of 3, 6, 9, and 12 dB. Preliminary analyses revealed that the overall outcomes were not dependent upon the suppression criteria employed. Thus the 6 dB criterion was adopted for all analyses to maintain sensitivity while keeping the data well above the NF.

E. Experimental protocol

DPOAE measurements, including DP-grams and SRAs for each set of primary-tone levels, at both GM frequencies, were recorded on at least three different days prior to exposing the rabbits to noise to ensure stable responses. DPOAEs were measured one final time immediately before the noise exposure episode. The rabbit was then placed in a large wire cage within a sound-proofed noise-exposure booth. Within this chamber, each rabbit was exposed to an octave band of noise (OBN), centered at 2 kHz, at rms levels varying from 95 to 100 dB SPL, for a period of at least 15 min. Noise level and exposure time were adjusted to ensure that each rabbit exhibited a DPOAE level decrement of $\geqslant$10 dB at 3 kHz. All loss measurements were taken from DP-grams in which primary tone levels were $L_1 = L_2 = 55$ dB SPL. For most subjects, a 15 min noise exposure was sufficient to produce DPOAE level decrements of this magnitude. One rabbit did not show a significant reduction in DPOAE level following the first noise exposure. This subject was allowed to recover for 2 wk before being exposed (30 min) to the identical 2 kHz OBN at a level of 100 dB SPL. This length of exposure was sufficient to induce a $>$10 dB DPOAE level decrement. Following noise exposure, rabbits were immediately returned to the plastic restrainer inside the DPOAE-measurement booth, and DP-grams and SRAs were measured continuously for approximately 2 h post-exposure. During this period, four complete sets of STCs, i.e., an STC for each level combination at both of the test GM frequencies, were obtained, from the lowest to the highest primary-tone levels at the lower test frequency, then progressing from low to high levels at the higher test frequency. A DP-gram was recorded between each complete set of STC measurements. Subjects were then returned to their home cages. DP-grams and SRAs were also measured 1, 2, 3, and 6 or 7 d following the noise-exposure session.

F. Statistical analysis

Simple linear regression models were fitted to post-minus pre-exposure data difference scores. Averaged post-exposure data collected during TTS (when unsuppressed DPOAE levels showed a decrement of $\geqslant$3 dB) were compared with averaged pre-exposure data using paired *t*-tests. The adopted level of statistical significance was $p < 0.05$ for all analyses. All statistical tests were performed using StatView (Abacus Concepts, v5.0). Outlying data points with values $>$3 SDs were excluded from the analysis due to the likelihood that these values represented anomalies arising from the inability of the STC algorithm to accurately track discontinuous or extremely irregular contours. No more than three outlying data points had to be removed from any set of data.

III. RESULTS

A. Pre-exposure STC measurements

Four sets of complete STC measurements were made on each rabbit on separate days before the noise-exposure episode was initiated. To ensure that the data being collected was reliable, simple regressions were performed comparing the last two of these data sets to each other. The test/retest regression models for each STC parameter were significant ($p < 0.001$). Average test/retest correlations (r) were 0.96 for STC CF, 0.72 for STC tip threshold, and 0.54 for $Q_{10\mathrm{dB}}$. The much lower test/retest reliability for $Q_{10\mathrm{dB}}$ again results from the difficulty in tracking irregular SRA contours. In all cases, it was clear, based on scatterplots of the data, that test/retest discrepancies were distributed equally on either side of the diagonal representing "no change" in the measured parameter. Values from the last two preliminary data sets, i.e., those taken the day before and immediately before exposure, for each of the three tuning-curve variables were averaged for each rabbit to create a baseline against which data obtained after noise exposure was compared.

B. Noise-induced DPOAE changes

Following noise exposure, DPOAE levels were diminished at test GM frequencies in all rabbits. However, DPOAEs gradually returned to normal over the course of several days. The largest reductions in DPOAE levels occurred at the test frequencies that were approximately one-half octave above the center frequency of the 2 kHz OBN, i.e., close to 3 kHz (i.e., 2.8–3.5 kHz). The average decrease in DPOAE level immediately following the OBN exposure, at the frequency of maximal loss, was 24 dB. DPOAE levels recorded at these frequencies were at the NF for some rabbits. Both the amount of the initial decrement in DPOAE level, and the period of time required for full recovery, varied among rabbits.

Figure 1A shows pre- and post-exposure DP-grams for two rabbits that experienced different amounts of DPOAE loss from the same noise exposure. It is clear from comparing the post-exposure open-square and open-circle curves for rabbits 48 and 58, respectively, that in addition to the amount of reduction in DPOAE level, they also varied somewhat with respect to the range of frequencies affected. Thus rabbit R58 (open circles) showed greater noise-induced reductions in DPOAE levels, over a broader frequency extent than did rabbit R48 (open squares). Data from both of the rabbits in this figure displayed increased DPOAE levels above 15 kHz, following OBN exposure. While this pattern was not exhibited by the other rabbits of the present study, high-frequency DPOAE level enhancements have been observed in previous studies following exposure to a 2 kHz OBN (Franklin *et al.*, 1991). None of the rabbits showed noticeable decrements in DPOAE levels below 1.8 or above 8 kHz that could be attributed to the OBN exposure. For all rabbits, DPOAE levels recovered fully by 1 wk post-exposure.

Figure 1B illustrates the recovery of DPOAE levels for a typical rabbit from immediately before (closed circles) to immediately following (open circles) and through 7 d post-exposure (gray diamonds) from 1 to 8 kHz, the region encompassing the OBN-induced shifts. At 7 d post-exposure, DPOAE levels were enhanced across all frequencies shown, including the region of noise-induced damage. Again, this post-exposure DP-gram pattern of enhancement during and after recovery was not repeated in every rabbit.

C. Noise-induced STC changes

Generally, it was not possible to measure STCs for the initial 2-h post-exposure period, i.e., immediately following noise exposure, because during this time DPOAE levels were typically at, or below, the NF. Sometimes, the rabbits were more restless following the exposure period, which increased the background noise levels, and also made suppression measurements less reliable at this time. With unsuppressed

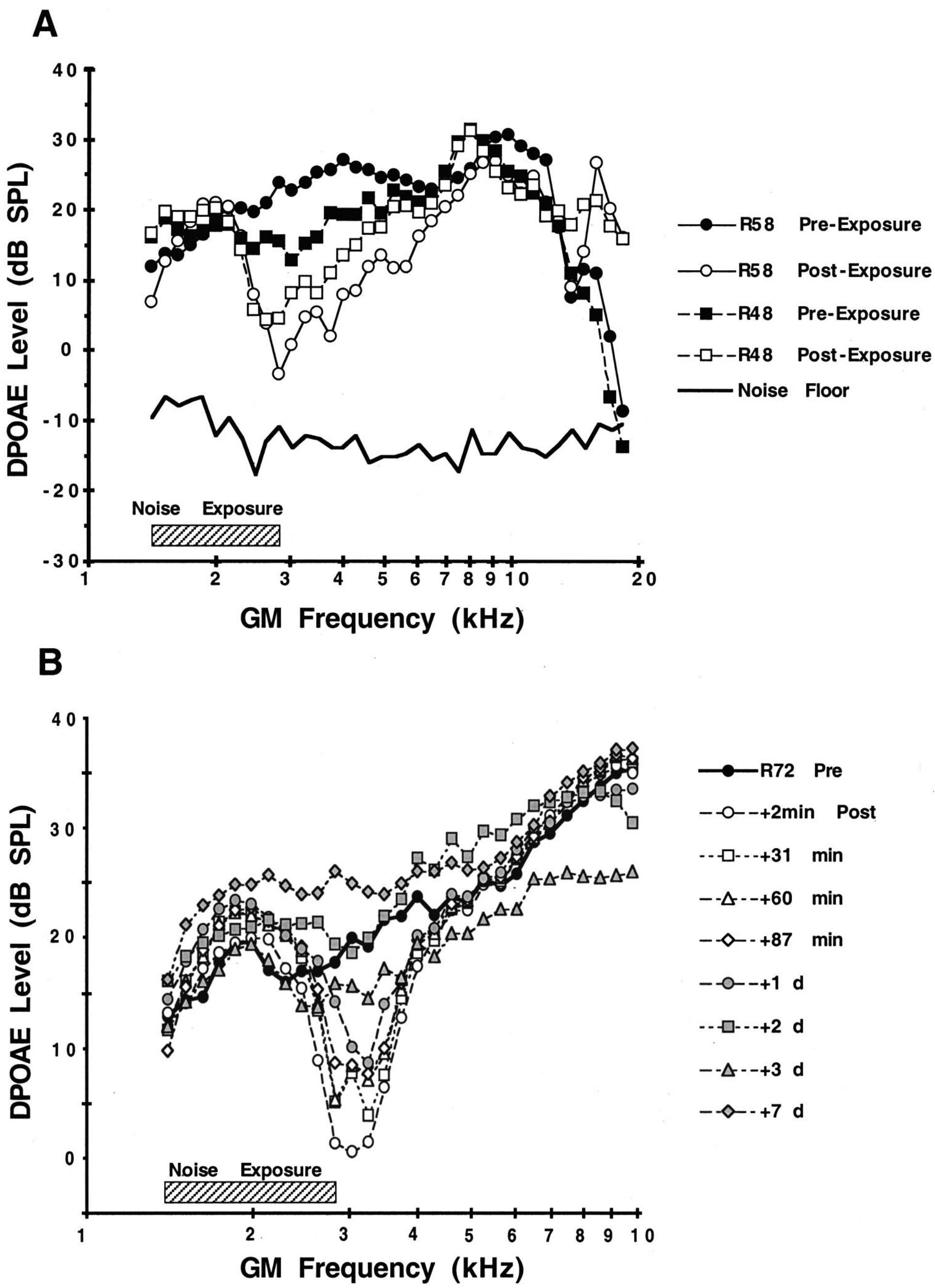

FIG. 1. DP-grams before and after OBN exposure. (A) DP-grams recorded from two rabbits, R48 (squares) and R58 (circles), both immediately before (closed symbols) and immediately after (open symbols) exposure. Each symbol represents the level of the measured DPOAE at the GM frequency of the two primaries tones with $L_1=L_2=45$ dB SPL. The solid line at the bottom of this plot indicates the noise floor. (B) Complete set of DP-grams for rabbit R72 from pre-exposure measurements (closed circles, solid line), through 7 d post-exposure (shaded diamonds, dotted line). The scales in this figure were optimized to show changes in the frequency range most affected by the OBN exposure more clearly. The figure legend indicates the post-exposure time for each DP-gram. The hatched bar at the bottom left of each plot represents the frequency range of the 95 dB SPL OBN exposure, for this as well as for the DP-grams illustrated below in Figs. 2 and 3.

DPOAE levels close to the NF, only the contours for the smaller amounts of suppression (e.g., 3 and 6 dB) could be obtained immediately following noise exposure.

Moreover, because DPOAE levels at frequencies near 3 kHz showed the greatest noise-reducing effects, STCs measured at the GM=2.828 kHz were slower to recover than those measured at the GM=4 kHz. Often, it was not until 3 d post-noise exposure that reliable STCs at 2.828 kHz could be measured. In contrast, it was possible to record some STCs at 4 kHz directly after noise exposure. These immediate post-exposure measures showed that those rabbits that were least susceptible to TTS did not show significant DPOAE level decreases at this higher 4 kHz test frequency. This was especially true when stimulating with primary tones at levels $\geqslant 50$ dB SPL.

Comparisons between pre- and post-exposure STCs from two different rabbits are shown in Figs. 2–3 for the two primary-tone GM frequencies of 2.828 and 4 kHz, respectively. The top row (A) of each of these figures contains a typical pre-exposure DP-gram recorded during collection of this particular data set (left column), SRAs (middle column), and STCs extracted at each of the four criteria levels (right column). The lower rows (B–F) show data sets obtained at various time points during recovery from noise exposure. Inset in the lower right of each STC is the $Q_{10\mathrm{dB}}$ measurement for the 6 dB suppression contour. The STC series illustrated in Fig. 2 is typical of all data collected, in that the largest post-exposure decrement in DPOAE level (B) was recorded during the first hour following exposure, with DPOAE level recovering over time to near baseline by 2 d (F) post-exposure. This same general pattern of recovery can be seen clearly in the DP-grams illustrated in Fig. 3 for

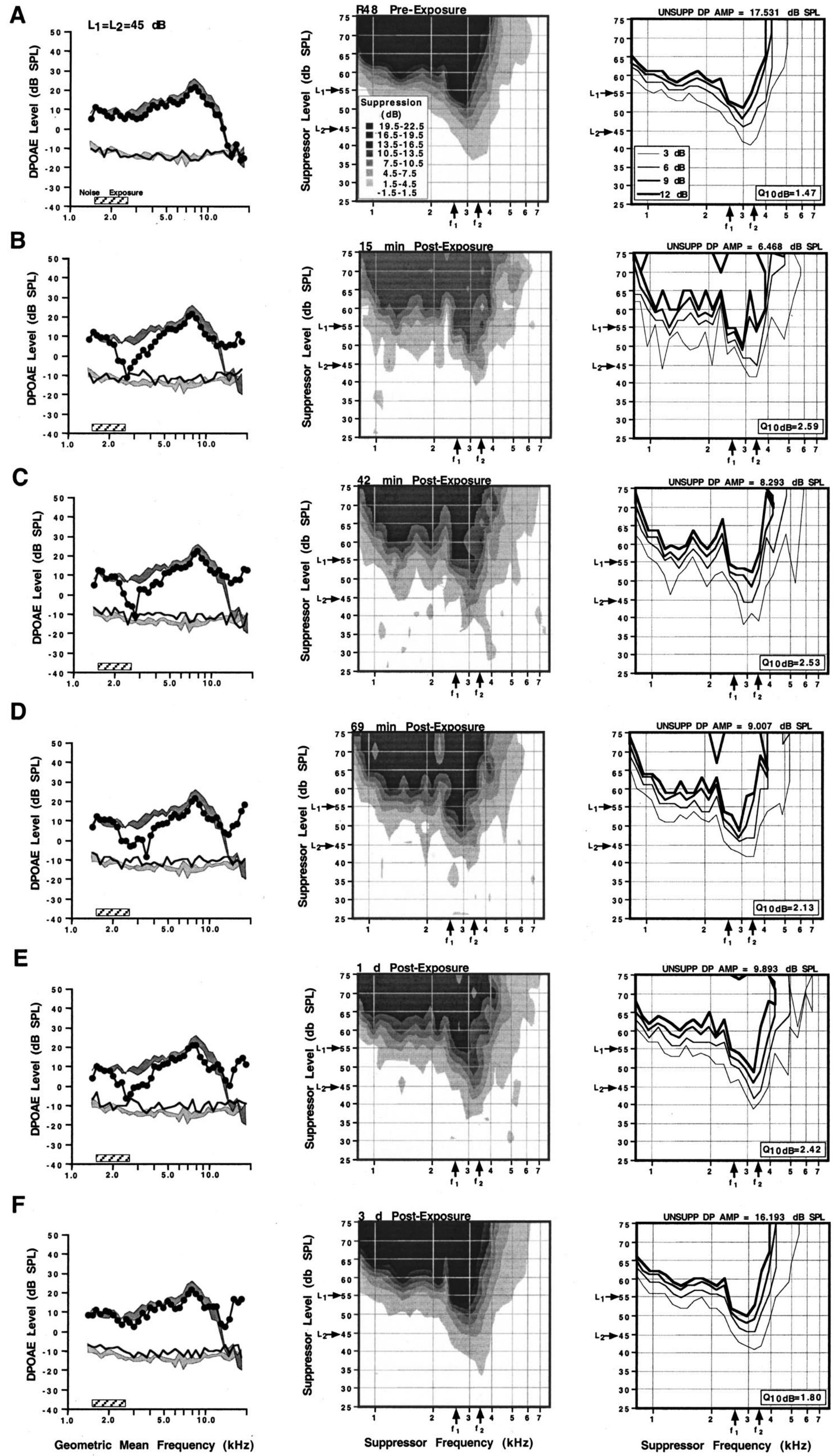

FIG. 2. Comparison of DP-grams (left column), SRAs (middle column), and the corresponding STCs (right column) recorded at 2.828 kHz before (A) and after (B–F) noise exposure for R48. Data collected produced prior to (A), 15 min (B), 42 min (C), 69 min (D), 1 d (E), and 3 d (F) following OBN exposure are illustrated. DP-grams show the frequency range and magnitude of the OBN-induced decrements in DPOAE level, as well as illustrate DPOAE recovery over time. The dark shaded regions in each DP-gram indicate mean pre-exposure ± 1 SD DPOAE levels. Light shaded regions in the lower portion of each plot indicate pre-exposure ± 2 SD NF levels. Unsuppressed DPOAE level for each measurement is noted at the top right of each STC plot. Inset at the bottom left in the STCs of A defines the level of DPOAE suppression, in 3 dB increments, produced by combinations of suppressor level and frequency. Arrows on the ordinates and abscissas of SRAs and STCs indicate the levels (L_1, L_2) and frequencies (f_1, f_2), respectively, of the primary tones. Suppression criteria levels from 3 to 12 dB are indicated by iso-suppression contours of increasing boldness in STCs. $Q_{10\text{dB}}$ values for the 6 dB STC are listed in the lower right corner of each figure.

another rabbit that exhibited a broader DPOAE-loss pattern than the one in Fig. 2.

Qualitative assessment of these figures reveals little difference in the general shape and size of STCs compared before and after noise exposure. The noticeable change is that the number of suppression contours recordable is dramatically reduced (e.g., Fig. 2B) when DPOAE levels were maximally decreased by the noise. Clearly there is no indication of elevation in STC tip thresholds. In fact, in Fig. 3C at 82 min post-exposure, when the DPOAE level was reduced by almost 20 dB, the 3 dB STC tip clearly occurs at a lower f_3 level.

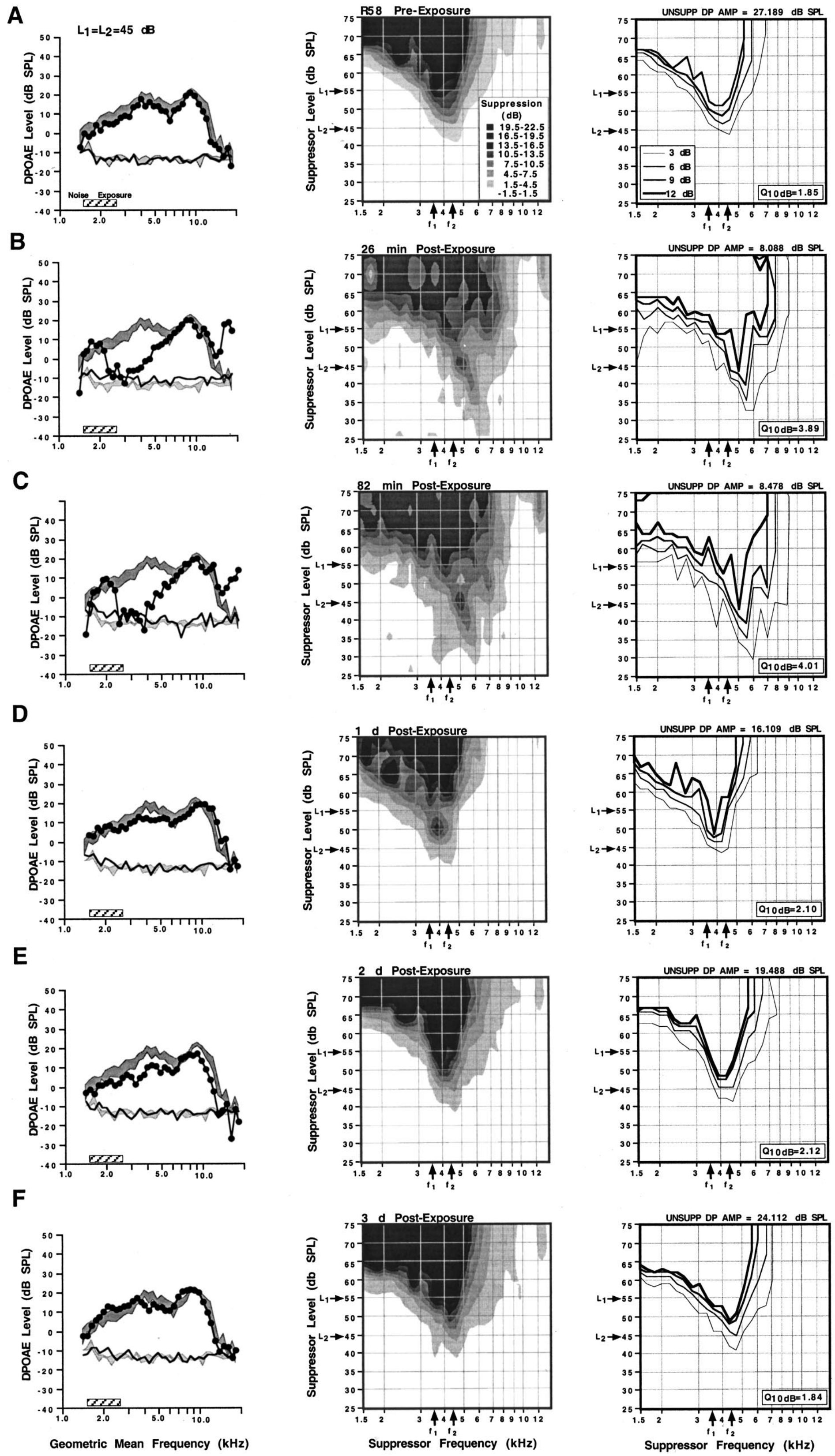

FIG. 3. Comparison of DP-grams (left column), SRAs (middle column), and the corresponding STCs (right column) recorded at 4 kHz before (A) and after (B–F) OBN exposure for R58. Illustrated are data sets collected prior to (A), 26 min (B), 82 min (C), 1 d (D), 2 d (E), and 3 d (F) following OBN exposure. See legend for Fig. 2 for details of these plots.

Because each rabbit was affected somewhat uniquely by the sound exposure in terms of the amount of DPOAE reduction, and the length of time to return to pre-exposure levels, changes in STC parameters are shown as a function of the unsuppressed DPOAE level, rather than as a function of time. This approach allows comparison of STCs at similar amounts of TTS in rabbits that experienced very different OBN-induced reductions in DPOAE levels.

The plots of Figs. 4A–C illustrate changes in STC tip CF, threshold, and Q_{10dB} relative to the relevant averaged pre-exposure data at the criterion suppression level of 6 dB. These plots include data from STCs recorded at both GM

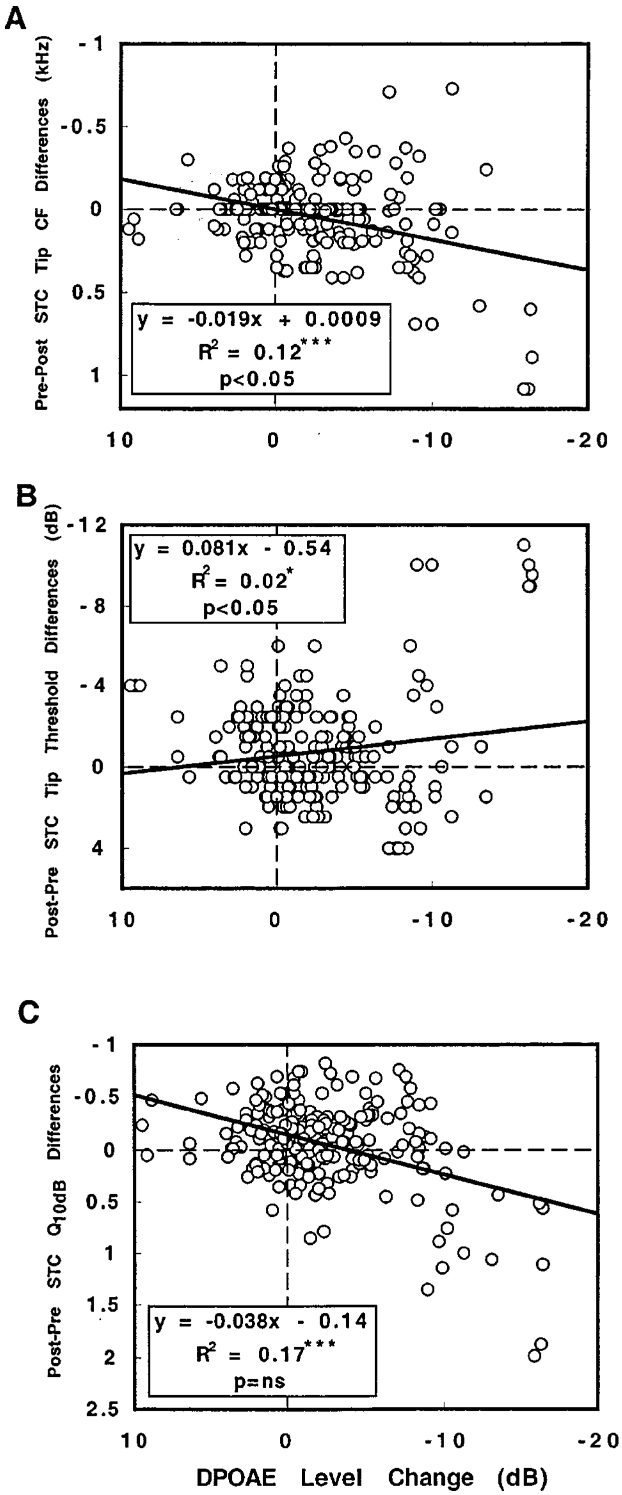

FIG. 4. Scatterplots of post- minus pre-exposure STC tip CF (A), tip threshold (B) and $Q_{10\mathrm{dB}}$ (C) differences paired with the corresponding noise-induced changes in DPOAE level for the 6 dB suppression criterion, for all primary-tone level combinations and all post-exposure measures. The solid line in each plot represents the simple regression model that best fits these data. The box in each plot contains the slope and intercept for each regression line, as well as the regression coefficient (R^2). Asterisks denote the particular level of significance achieved by each R^2 (* $p<0.05$, ** $p<0.01$, *** $p<0.001$). The p-value listed in each box indicates the level of significance of t-tests comparing pre-exposure data with data collected during >3 dB of DPOAE level decrements (ns=not significant). Dashed lines on the x- and y-axes in this figure, as well as in Figs. 5, 6, and 7, indicate no change from pre-exposure values.

frequencies and at all tone/level combinations. As shown in Fig. 4A, when the DPOAE level was reduced by 10 dB or more, following noise exposure (i.e., moving to the right along the abscissa), STC CFs tended to shift to a slightly higher frequency (i.e., moving downward along the ordinate) that was closer to f_2. Statistical comparison (paired t-test) of averaged preliminary STC CF values with CF values recorded during TTS revealed that this shift toward higher frequencies was significant ($t=-2.57$, $df=76$, $p<0.05$). Figure 4B illustrates the tendency for the STC tip threshold to decrease with greater amounts of DPOAE level reduction. A t-test revealed that these differences between pre-exposure STC thresholds and TTS thresholds were significant ($t=2.376$, $df=76$, $p<0.05$). Post-exposure $Q_{10\mathrm{dB}}$ measurements (Fig. 4C) showed a trend of increasing with greater amounts of OBN-induced DPOAE loss. However, t–tests comparing pre-exposure $Q_{10\mathrm{dB}}$ values with those recorded during TTS were not significant.

The solid line running through these plots indicates the simple regression models of each data set. While the regression coefficients (R^2) for these models are very low, due to the large amount of variability within each data set, the correlations indicated by the slopes of the regression models are significant for each STC parameter. Thus noise-induced decreases in the DPOAE level tended to be accompanied by small increases in STC CF and $Q_{10\mathrm{dB}}$, and small decreases in tip threshold.

Pre- and post-exposure data for the 6 dB suppression level were also analyzed separately for each of the combinations of primary-tone GM frequency and level. Illustrated in Fig. 5 are post- minus pre-exposure differences in STC tip CF stimulated with low ($L_1/L_2=45/45$ dB SPL; Figs. 5A, B) and high ($L_1/L_2=55/45$ dB SPL; Figs. 5C, D) primary-tone levels, at the primary-tone GM frequencies of 2.828 (Figs. 5A, C) and 4 kHz (Figs. 5B, D). Only STCs produced in the presence of higher level primary-tones, and at the higher GM frequency of 4 kHz (Fig. 5D), exhibited a significant correlation between DPOAE loss and increasing tip CF. T-tests between averaged pre-exposure measures and post-exposure measures recorded during TTS showed a significant increase in STC CF for only this combination of primary-tone level and frequency.

A similar analysis was performed on post- minus pre-exposure differences in STC tip threshold at each of the primary-tone level/frequency combinations (Fig. 6). The correlation between post-exposure DPOAE loss and decrease in tip threshold shown in Fig. 4B was present only in STCs produced in the presence of high level primary tones at the higher test frequency of 4 kHz (Fig. 6D). T-tests between averaged pre-exposure data and post-exposure tip thresholds recorded during TTS showed a significant decrease in STC tip threshold when DPOAE levels were diminished. STCs recorded at lower primary-tone levels at this test frequency showed an opposite correlation, with tip threshold increasing slightly with reduced DPOAE level (Fig. 6B). T-tests between pre- and post-exposure data recorded during the TTS condition indicated that tip threshold increases for these STCs were not significant. No correlation existed between post-exposure changes in tip threshold and the DPOAE level

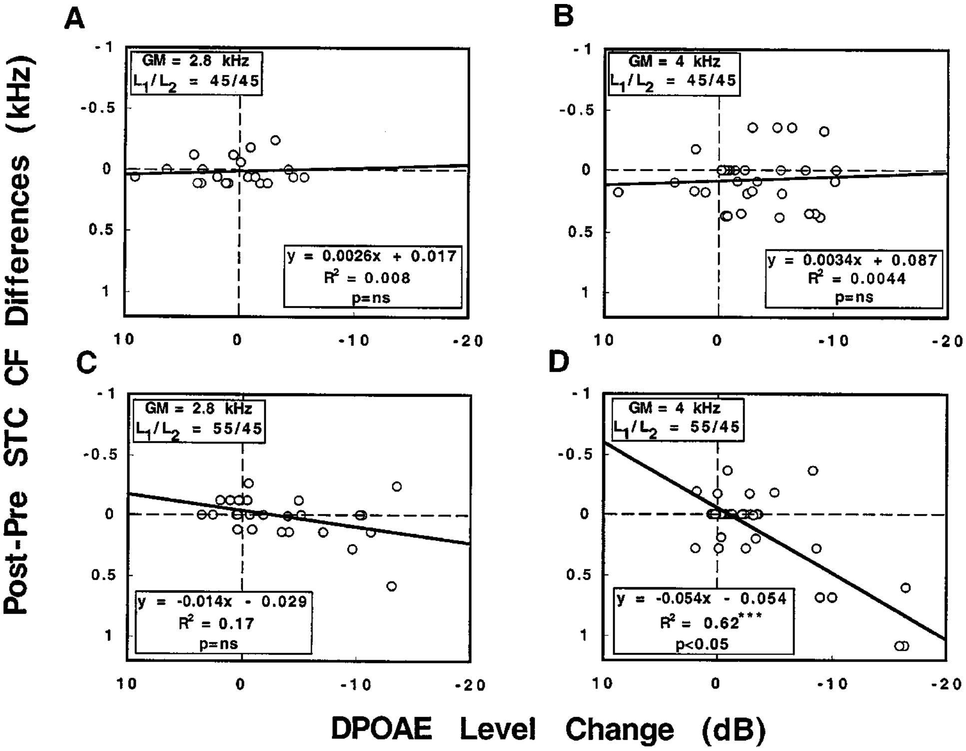

FIG. 5. Scatterplots of post- minus pre-exposure STC tip CF differences paired with the corresponding noise-induced changes in DPOAE level for four primary-tone frequency and level combinations at the 6 dB suppression level. Data collected using the primary-tone test frequencies of 2.828 kHz at low $[L_1/L_2=45/45$ dB SPL, (A)] and high $[L_1/L_2=55/45$ dB SPL, (C)] levels are illustrated in the left column. Data collected using these low (B) and high (D) primary-tone levels at the test frequency of 4 kHz are illustrated in the right column. Primary-tone stimulus parameters are listed in the box in the upper left of each figure. Simple regression models that best fit the data are indicated by solid lines running through each plot. The level of statistical significance of each R^2, as well as for pre/post *t*-tests, is denoted as in Fig. 4.

for STCs recorded at the lower primary-tone test frequency (Figs. 6A, C).

Post- minus pre-exposure differences in $Q_{10\mathrm{dB}}$ for different combinations of primary-tone test frequency and level are illustrated in Fig. 7. Data from STCs recorded in the presence of high level primary tones at both the 2.828 (Fig. 7C) and 4 kHz (Fig. 7D) GM test frequencies exhibited the same correlations between post-exposure DPOAE level reduction and $Q_{10\mathrm{dB}}$ increases as shown in Fig. 4C. During TTS, significant increases in $Q_{10\mathrm{dB}}$, as compared with pre-exposure data, were present only in the STCs recorded in the presence of high-level primary tones at the lower 2.828 kHz test frequency (Fig. 7C). Data collected when using lower-level primary tones displayed no correlations between changes in the DPOAE level and $Q_{10\mathrm{dB}}$ after OBN exposure at either test frequency.

IV. DISCUSSION

The purpose of this study was to gain a better understanding of how DPOAE suppression tuning is affected by a noise-induced cochlear insult, and to compare these findings

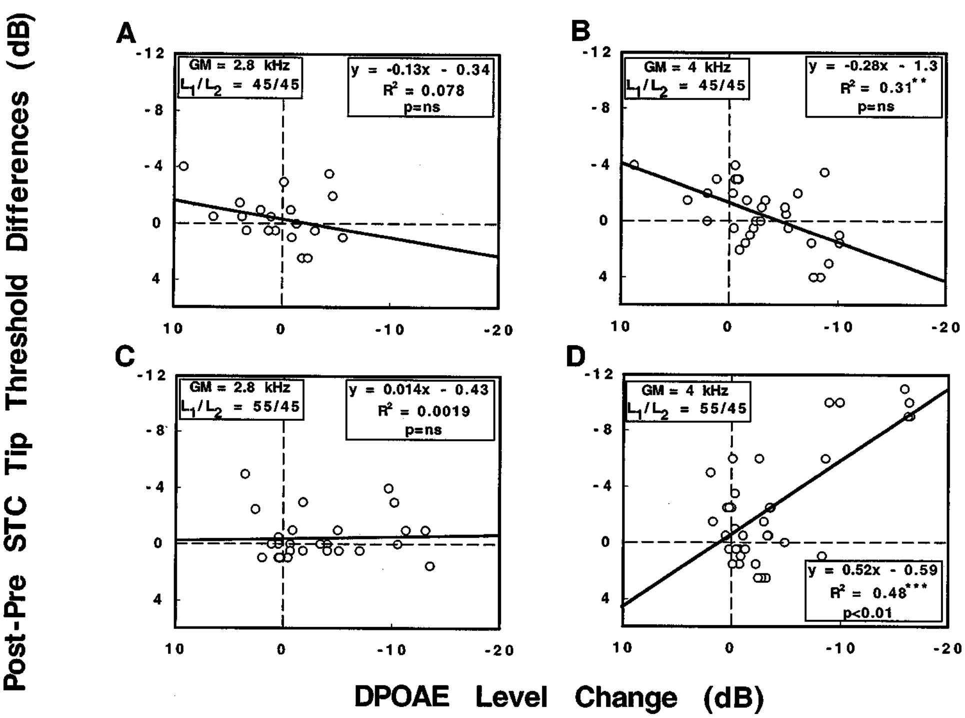

FIG. 6. Scatterplots of post- minus pre-exposure STC tip threshold differences paired with the corresponding noise-induced changes in DPOAE level for four primary-tone frequency and level combinations at the 6 dB suppression criterion. Primary-tone frequency and level combinations used to elicit DPOAEs for data shown in A, B, C, and D are identical to those in Fig. 5, and are listed in boxes in the upper left corner of each plot. Other plot details are identical to those described above for Fig. 5.

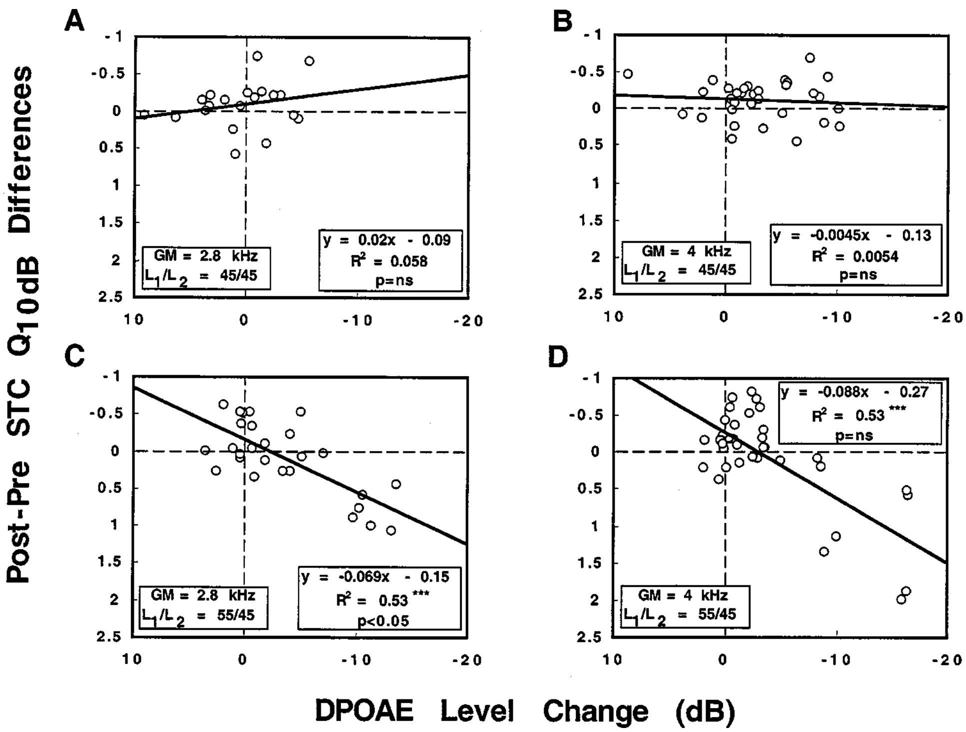

FIG. 7. Scatterplots of post- minus pre-exposure STC Q_{10dB} differences paired with the corresponding noise-induced changes in DPOAE level for four primary-tone frequency and level combinations at the 6 dB suppression criterion. Primary-tone frequency and level combinations used to elicit DPOAEs for data shown in A, B, C, and D are identical to those in Fig. 5, and are listed in boxes in the upper left corner of each plot. Other plot details are identical to those described above for Fig. 5.

with established effects of noise on neural frequency tuning. The major observation was that, while all five rabbits showed clear, significant, noise-induced reductions in DPOAE levels, DPOAE suppression tuning was not affected in the same way that similar insults disrupt psychoacoustic, neural, and BM tuning. Specifically, STCs measured during substantial noise-induced reductions in the DPOAE level of up to 15 dB, showed changes in both DPOAE tip thresholds and Q_{10dB} indices that tended to lead to a sharpening, rather than a broadening, of tuning. STC CFs also showed significant changes when DPOAE levels were reduced by noise exposure. This small shift in tuning towards higher frequencies (i.e., towards f_2) was in contrast to data collected in previous studies of the effects of cochlear insult on DPOAE STCs using reversibly ototoxic loop diuretics (Martin *et al.*, 1998). While the alterations in these three basic STC parameters of threshold, CF and Q_{10dB} all appeared to be relatively small, it was mainly the direction of these changes, in the presence of appreciable reductions in the corresponding DPOAE levels, that was different from the behavior of NTCs following cochlear insult.

The present results are clearly different from previous studies of both NTCs, and BM tuning, following sound overexposure. It has long been established that these types of functions, recorded before and after noise-induced cochlear insults, show large increases in tip threshold (e.g., Kiang *et al.*, 1976; Liberman and Beil, 1979; Smoorenberg and van Heusden, 1979; Salvi *et al.*, 1980). This tip-threshold elevation alone typically causes substantial broadening of the post-exposure NTC, which is reflected by decreases in the Q_{10dB}. A good comparison to the present DPOAE data on the effects of noise exposure on NTCs can be found in experiments conducted by Smoorenburg and van Heusden (1979). While their studies were performed on anesthetized cats, the level and duration of sound exposure were very similar to those used in the present work. Specifically, cat NTCs were recorded before, immediately following, and 6 h after induction of noise trauma. Thresholds for these functions were elevated immediately following noise exposure, but showed some recovery 6 h later. These NTCs from the Smoorenburg and van Heusden (1979) study clearly showed decreased frequency selectivity for the single nerve fibers, as measured by decreases in Q_{10dB}. In contrast, the rabbit STCs measured in the current study did not lose their sharp tuning, because there were no large increases in tip threshold as observed in the neural recordings of the Smoorenburg and van Heusden (1979) experiment.

While it would be ideal to perform both types of tuning measurements in the same animal following cochlear insult, the effects of sound exposure on NTCs has been well documented in the literature. Although STCs do show similar patterns and behaviors under some conditions, the present observations clearly demonstrate that these functions behave differently than NTCs. This is especially true following cochlear insults such as both reversible noise-induced threshold shifts (e.g., Smoorenburg and van Heusden, 1979) and reversible loop diuretic ototoxicity (e.g., Rubsamen *et al.*, 1995). Thus STCs cannot be used as a noninvasive measure of cochlear frequency selectivity in the straightforward way that invasive NTCs can.

The differences in STC and NTC behavior following acoustic trauma may be due, in part, to the way in which DPOAE suppression is produced. Two unique pure tones are required to generate a DPOAE, which, to produce an STC, is then suppressed by a third pure tone, that is varied in frequency and level. NTCs, on the other hand, are produced with a single pure tone, varied in frequency and level. The input of the second tone required to stimulate DPOAE generation adds several variables that must be accounted for. For example, STC sharpness can be influenced by the f_2/f_1 ratio.

This particular study used an f_2/f_1 ratio of 1.25 that consistently elicits robust DPOAEs in rabbits at the tested frequencies. However, earlier studies showed that decreasing f_2/f_1 ratios results in sharper STCs in both humans and gerbils (Brown and Kemp, 1984). For example, studies using very small f_2/f_1 ratios in bats produced STCs that were very similar in shape to single-tone elicited NTCs (Frank and Kossl, 1995).

Human STC parameters are also influenced by both test frequency (Abdala *et al.*, 1996) and primary-tone levels (Kummer *et al.*, 1995). Previous studies of rabbit STCs have shown similar results to human data (Martin *et al.*, 1998). The two test frequencies and the four sets of primary-tone levels for which STCs were collected in the present study were chosen because previous studies showed that they would be most sensitive to cochlear insult (Whitehead *et al.*, 1995). Preliminary pilot data showed that the major features of STCs were repeatable when these combinations of frequencies and levels were employed. The results from this study clearly show that the DPOAEs which are most sensitive to this type of cochlear insult, i.e., those recorded at the 2.828 kHz test frequency using lower primary-tone levels, did not display systematic changes in STC parameters during TTS (Figs. 5–7). On the other hand, the overall trends in the data, shown in Fig. 4, are largely due to changes in STCs elicited using higher primary-tone combinations, especially at the higher, 4 kHz test frequency.

Some differences between NTC and STC behavior may also be explained by the stimuli required to produce responses following cochlear insult. NTC functions are produced by plotting the stimulus level required to produce a detectable response in a single or group of cochlear nerve fibers, i.e., to reach threshold. Following cochlear insult such as sound trauma or ototoxic drug injection, the threshold of the NTC increases, and thus the sound pressure level of the stimulus must be increased to drive these nerve fibers to their threshold levels of activity. In other words, it is necessary to increase stimulus levels until a desired output level for the nerve fiber is reached. In contrast, STCs are produced by stimulating the auditory system at levels well above threshold. This involves suppressing the output of the system by criterion amounts, rather than plotting the minimum stimulus required to elicit a response. Following cochlear insult, stimulus levels from pre-exposure parameters do not need to be increased, because the system is often still producing a measurable response. While it may become impossible to measure all criterion suppression levels before the suppressed DPOAE reaches the NF level of the recording system, the STCs plotted in this study following noise exposure were produced without altering pre-noise stimulus parameters.

This difference in tuning measurement alone makes direct comparisons between STCs and NTCs somewhat difficult. For example, in the study by Smoorenburg and van Heusden (1979) mentioned above, production of post-noise NTCs required input levels 15–40 dB higher than pre-noise NTCs. Increases in the amplitude of the traveling wave on the BM of this magnitude could alone alter the frequency selectivity of cochlear nerve fibers. Analogously, increasing the f_2 input level, which could change the characteristics of traveling wave interaction on the basilar membrane, reduces the sharpness of STC tuning. Thus to make more realistic comparisons between NTCs and STCs, it may be necessary to equate the post-exposure measurement procedures by increasing the level of the primaries following OBN exposure, until the DPOAE is equal to pre-test levels.

The differences between pre- and post-exposure STC parameters recorded in these rabbits were similar to the differences between adult and neonatal STCs recorded in humans. While STCs do not appear to measure cochlear frequency selectivity in the same way that their neural counterparts do, the subtle changes in STC parameters noted in this study may reflect the presence of cochlear dysfunction, just as they may reflect cochlear immaturity in neonates. Since these changes are not systematic across all combinations of primary-tone frequency and level, and because STC behavior appears very similar in the presence of two very different types of cochlear dysfunction, i.e., immaturity and OBN overexposure, it may be difficult to use STCs as a diagnostic tool for specific types of cochlear dysfunction.

The results of the present study may be partly explained by the rules of saturating nonlinearities recently outlined by Fahey *et al.* (2000). Thus in a saturating nonlinearity, the suppressor must be within 10 dB of the supressee and the suppressor must be in the region of saturation for suppression to occur. This simple rule explains why in normal ears, STC tip thresholds are typically within 10 dB of the level of one of the primaries at threshold. In other words, when the level of f_3 is within 10 dB of one of the primaries, f_3 will begin to suppress the output of the nonlinearity. Following ototoxic or noise-induced cochlear insult, these rules still apply, leaving the tip threshold unchanged even though the shape of the nonlinearity may be altered. When the thresholds are perturbed by an insult to the cochlea, the saturation level of the nonlinearity may also be affected.

V. CONCLUSIONS

Tuning-curve functions can be produced to describe the frequency selectivity of different components of the auditory system. Comparison of different types of tuning curves, e.g., NTCs and STCs, has shown that they often demonstrate similarity in shape, but not necessarily in behavior. The purpose of the present study was to apply a traumatic noise exposure, which has a known effect on NTCs, and determine if STCs react in the same way following this insult. The DPOAE suppression data described here strongly suggests that STCs and NTCs are affected differently by this type of cochlear insult as measured by certain tuning parameters. The results of this study showed small increases in STC tip CF and $Q_{10\mathrm{dB}}$, along with decreases in tip threshold. This was in striking contrast to previous studies showing large increases in NTC tip threshold and corresponding decreases in $Q_{10\mathrm{dB}}$ values following noise exposure (e.g., Smoorenburg and van Heusden, 1979). However, these results reflect the differences seen between STCs recorded in adult and neonatal children, which are thought to reflect cochlear immaturity (Abdala, 1998). Such results indicate that STCs do not measure frequency tuning in the cochlea in the same way that

NTCs do, but probably reflect basic properties of suppression in nonlinear systems. Thus it is difficult to make assumptions about the frequency selectivity of the cochlea following cochlear insult based solely on the measurement of DPOAE STCs.

ACKNOWLEDGMENTS

This research was supported in part by funds from the Public Health Service (DC00613, DC03114, AG16893, DC04476), and funds from the University of Miami Chandler Chair. The technical assistance of D. Koivisto is gratefully acknowledged. M. A. Howard is a Lois Pope LIFE fellow.

Abdala, C. (**1998**). ''A developmental study of distortion product otoacoustic emission ($2f_1$-f_2) suppression in humans,'' Hear. Res. **121**, 125–138.

Abdala, C., Sininger, Y. S., and Starr, A. (**2000**). ''Distortion product otoacoustic emission suppression in subjects with auditory neuropathy,'' Ear Hear. **21**, 542–553.

Abdala, C., Visser-Dumont, L., and Ma, E. (**2001**). ''DPOAE suppression tuning: Cochlear immaturity or aging effects in adults?'' Abstr. Assoc. Res. Otolaryngol. **24**, 10.

Abdala, C., Sininger, Y. S., Ekelid, M., and Zeng, F.-G. (**1996**). ''Distortion product otoacoustic emission suppression tuning curves in human adults and neonates,'' Hear. Res. **98**, 38–53.

Brown, A. M., and Kemp, D. T. (**1984**). ''Suppressibility of the $2f_1$-f_2 stimulated acoustic emissions in gerbil and man,'' Hear. Res. **13**, 29–37.

Dallos, P., Ryan, A., Harris, D., McGee, T., and Ozdamar, O. (**1977**). ''Cochlear frequency selectivity in the presence of hair cell damage,'' in *Psychophysics and Physiology of Hearing*, edited by E. F. Evans and J. P. Wilson (Academic, London), pp. 249–258.

Evans, E. F., and Klinke, R. (**1982**). ''The effects of intracochlear and systemic furosemide on the properties of single cochlear nerve fibres in the cat,'' J. Physiol. (London) **331**, 409–428.

Fahey, P. F., Stagner, B. B., Lonsbury-Martin, B. L., and Martin, G. K. (**2000**). ''Nonlinear interactions that could explain distortion product interference response areas,'' J. Acoust. Soc. Am. **108**, 1786–1802.

Frank, G., and Kossl, M. (**1995**). ''The shape of $2f_1$-f_2 suppression tuning curves reflects basilar membrane specialization in the mustached bat, *Pteronotus parnellii*,'' Hear. Res. **83**, 151–160.

Franklin, D. J., Lonsbury-Martin, B. L., Stagner, B. B., and Martin, G. K. (**1991**). ''Altered susceptibility of $2f_1$-f_2 acoustic-distortion products to the effects of repeated noise exposure in rabbits,'' Hear. Res. **53**, 185–208.

Howard, M. A., Stagner, B. B., Martin, G. K., and Lonsbury-Martin, B. L. (**2000**). ''Effects of temporarily damaging noise on the suppression tuning of distortion-product otoacoustic emissions in rabbits,'' Soc. Neurosci. Abstr. **26**, 2198.

Johnstone, B. M., Patuzzi, R., and Yates, G. K. (**1986**). ''Basilar membrane measurements and the travelling wave,'' Hear. Res. **22**, 147–153.

Kiang, N. Y. S., Liberman, M. C., and Levine, R. A. (**1976**). ''Auditory-nerve activity in cats exposed to ototoxic drugs and high-intensity sounds,'' Ann. Otol. **85**, 752–768.

Kiang, N. Y. S., Watanabe, T., Thomas, E. C., and Clark, L. F. (**1965**). *Discharge Patterns of Single Fibers in the Cat's Auditory Nerve* (MIT, Cambridge, MA), Res. Monogr. 35.

Koppl, C., and Manley, G. A. (**1993**). ''Distortion-product otoacoustic emissions in the bobtail lizard. II. Suppression tuning characteristics,'' J. Acoust. Soc. Am. **93**, 2834–2844.

Kummer, P., Janssen, T., and Arnold, W. (**1995**). ''Suppression tuning characteristics of the $2f_1$-f_2 distortion-product emissions in humans,'' J. Acoust. Soc. Am. **98**, 197–210.

Liberman, M. C., and Beil, D. G. (**1979**). ''Hair cell condition and auditory nerve response in normal and noise-damaged cochleas,'' Acta Oto-Laryngol. **88**, 161–176.

Martin, G. K., Jassir, D., Stagner, B. B., and Lonsbury-Martin, B. L. (**1998**). ''Effects of loop diurectics on the suppression tuning of distortion-product otoacoustic emissions in rabbits,'' J. Acoust. Soc. Am. **104**, 972–983.

Mills, D. M. (**1998**). ''Interpretation of distortion product otoacoustic emission measurements. II. Estimating tuning characteristics using three stimulus tones,'' J. Acoust. Soc. Am. **103**, 507–523.

Narayan, S. S., Temchin, A. N., Recio, A., and Ruggero, M. A. (**1998**). ''Frequency tuning of basilar membrane and auditory nerve fibers in the same cochleae,'' Science **282**, 1882–1884.

Pienkowski, M., and Kunov, H. (**2001**). ''Suppression of distortion product otoacoustic emissions and hearing threshold,'' J. Acoust. Soc. Am. **109**, 1496–1502.

Rhode, W. S. (**1971**). ''Observations of the vibration of the basilar membrane in squirrel monkeys using the Mossbauer technique,'' J. Acoust. Soc. Am. **49**, 1218–1231.

Rubsamen, R., Mills, D. M., and Rubel, E. W. (**1995**). ''Effects of furosemide on distortion product otoacoustic emissions and on neuronal responses in the anteroventral cochlear nucleus,'' J. Neurophysiol. **74**, 1628–1638.

Ruggero, M. A., and Rich, N. C. (**1991**). ''Furosemide alters organ of Corti mechanics: Evidence for feedback of outer hair cells upon the basilar membrane,'' J. Neurosci. **11**, 1057–1067.

Ryan, A., and Dallos, P. (**1975**). ''Effect of absence of cochlear outer hair cells on behavioral auditory threshold,'' Nature (London) **253**, 44–46.

Salvi, R. J., Henderson, D., Hamernik, R., and Parkins, C. (**1980**). ''VIII nerve response to click stimuli in normal and pathological cochleas,'' Hear. Res. **2**, 335–342.

Sewell, W. F. (**1984**). ''The effects of furosemide on the endocochlear potential and auditory-nerve fiber tuning curves in cats,'' Hear. Res. **14**, 305–314.

Smoorenburg, G. F., and van Heusden, E. (**1979**). ''Effects of acute noise traumata on whole-nerve and single-unit activity,'' Arch. Oto-Rhino-Laryngol. **224**, 117–124.

Whitehead, M. L., McCoy, M. J., Lonsbury-Martin, B. L., and Martin, G. K. (**1995**). ''Dependence of distortion-product otoacoustic emissions on primary levels in normal and impaired ears. I. Effects of decreasing L_2 below L_1,'' J. Acoust. Soc. Am. **97**, 2346–2358.

On the frequency dependence of the otoacoustic emission latency in hypoacoustic and normal ears

R. Sisto[a)]
Dipartimento Igiene del Lavoro, ISPESL, Via Fontana Candida, 1, 00040 Monte Porzio Catone, Roma, Italy

A. Moleti[b)]
Dipartimento di Fisica, Universita di Roma "Tor Vergata," Via della Ricerca Scientifica 1, 00133 Roma, Italy

(Received 19 April 2001; revised 25 October 2001; accepted 29 October 2001)

Experimental measurements of the otoacoustic emission (OAE) latency of adult subjects have been obtained, as a function of frequency, by means of wavelet time-frequency analysis based on the iterative application of filter banks. The results are in agreement with previous OAE latency measurements by Tognola *et al.* [Hear. Res. **106**, 112–122 (1997)], as regards both the latency values and the frequency dependence, and seem to be incompatible with the steep $1/f$ law that is predicted by scale-invariant full cochlear models. The latency-frequency relationship has been best fitted to a linear function of the cochlear physical distance, using the Greenwood map, and to an exponential function of the cochlear distance, for comparison with derived band ABR latency measurements. Two sets of ears [94 audiometrically normal and 42 impaired with high-frequency ($f>3$ kHz) hearing loss] have been separately analyzed. Significantly larger average latencies were found in the impaired ears in the mid-frequency range. Theoretical implications of these findings on the transmission of the traveling wave are discussed.
[DOI: 10.1121/1.1428547]

PACS numbers: 43.64.Jb, 43.64.Kc, 43.64.Wn [BLM]

I. INTRODUCTION

According to literature (Probst *et al.*, 1991), the otoacoustic emission (OAE) latency is the delay between the click stimulus time and the time of the maximum of the evoked otoacoustic emission amplitude. Latency is physically due to the traveling time along the cochlear membrane from the base to the tonotopic site and back (cochlear round trip delay). A much smaller contribution comes from the transmission in the outer and middle ear. As tonotopic sites are distributed along the cochlea according to the Greenwood frequency mapping, latency is expected to be a function of frequency, with the lower frequency components traveling a longer cochlear path, thus being detected later as OAEs in the outer ear, hence the fundamental interest of measuring the latency as a function of frequency, by suitable time-frequency techniques, to get information about the physics of the acoustic signal transmission along the basilar membrane. The frequency resolved latency will be named spectral latency in the following.

Previous time-frequency measurements of the OAE spectral latency found indeed a clear frequency dependence, which was fitted to a power law:

$$\tau(f)=af^{b}, \tag{1}$$

with f in kHz, $a\approx 10$ ms and $b\approx -0.4$ (Tognola *et al.*, 1997). As the Greenwood map is a logarithmic function of the frequency, this power law is approximately equivalent to the exponential function of the cochlear distance that has been proposed for fitting the spectral latency versus cochlear distance relationship in studies of the derived band acoustic brainstem response (ABR) latency (Donaldson and Ruth, 1993).

Scale-invariant full cochlear models (Talmadge *et al.*, 1998) predict an inverse proportionality relationship between cochlear spectral latency and frequency $(b=-1)$, which is much steeper than that experimentally observed by Tognola *et al.* (1997). As this prediction is based on the same physical assumptions leading to some relevant predictions of the model (i.e., the generation mechanism of OAEs and their spectral quasiperiodicity), it is very important to clarify this issue, both experimentally and theoretically.

From a clinical point of view, a correlation between hearing loss and the degradation of many OAE parameters has been observed by many authors. As regards spontaneous OAEs (SOAEs), Moulin *et al.* (1991) and McFadden and Mishra (1993) found a correlation between the global presence of SOAEs and good hearing sensitivity. In the studies by Probst *et al.* (1987) and Sisto *et al.* (2001) it was shown that this correlation is local in the frequency domain. As regards transiently evoked OAEs (TEOAEs), Probst *et al.* (1987), Attias *et al.* (1995), and Lucertini *et al.* (1996), among many others, demonstrated the absence of TEOAEs in the audiometrically impaired frequency range, for hearing threshold levels higher than 20 dB. Prieve *et al.* (1993) and Hussain *et al.* (1998) showed also that the separation between normal-hearing and hearing-impaired ears was effectively performed above 1 kHz only, by analyzing TEOAE

a)Electronic mail: sisto@dil.ispesl.it
b)Electronic mail: moleti@roma2.infn.it

parameters such as response, signal-to-noise ratio (SNR), and reproducibility.

The sensitivity of OAE spectral latency to hearing loss has not been established yet, but the correlation between hearing loss and ABR latency has been analyzed by many authors, with interesting results. An increase of the ABR latency with hearing loss was generally observed (Rupa and Dayal, 1993; Watson, 1996). As regards the spectral latency, some derived band ABR results reported increased traveling wave velocity (TWV) associated to Meniere's disease (Thornton and Farrell, 1991; Kim *et al.*, 1994; Donaldson and Ruth, 1996), while others, using a tone burst technique, did not (Murray *et al.*, 1998). The correlation with noise-induced hearing loss was also observed by some authors (Don *et al.*, 1998), and the small ABR latency of the impaired frequency bands was explained as due to the reduced characteristic build-up time of the damaged cochlear filter. Previous studies had not found such a correlation (Kim *et al.*, 1994; Donaldson and Ruth, 1996). However, as the main contribution to both the ABR and the OAE latency is of cochlear origin, it is also interesting to study the correlation between hearing loss and OAE latency. As OAE latency is intrinsically frequency dependent, a frequency selective analysis is needed, also to avoid bias due to the different subject's OAE spectral composition. Time-frequency analysis techniques are now available (Wit *et al.*, 1994; Tognola *et al.*, 1997), which are capable, in principle, of providing a frequency-resolved OAE latency determination. It is important to understand if the sensitivity of the technique used for measuring the OAE spectral latency is sufficient to show a correlation with hearing impairment. If so, the OAE spectral latency could provide a useful parameter, in addition to other OAE parameters, such as amplitude and decay time (Sisto *et al.*, 2001), for developing tests of the cochlear functionality for screening or monitoring purposes.

The first aim of this work was to get accurate measurements of the latency-frequency relationship and to compare the results to other OAE and ABR spectral latency data, for testing the predictions of theoretical cochlear models. The second aim was to establish if a measurable correlation exists between OAE spectral latency and hearing impairment, by separately analyzing the latency data in two sets of normal and impaired ears.

This article is organized as follows: in Sec. II the data acquisition and analysis techniques are described, and the sources of systematic error are carefully evaluated; in Sec. III the theoretical models describing the cochlear transmission are discussed; in Sec. IV the results are presented and compared to previous results and theoretical predictions, and the correlation between hearing impairment and OAE spectral latency is evaluated; and in Sec. V the implications of these findings are discussed.

II. METHOD

In this work, TEOAE waveforms, recorded by the ILO-96 system (Otodynamics Ltd.) using the ‘‘nonlinear’’ paradigm, and pure tone audiograms have been analyzed. Two populations of young adults (20–30 years) males were studied: 94 normal-hearing ears of 47 subjects with no history of noise exposure and 42 hearing-impaired ears of subjects exposed to impulsive noise during their military training with firearms. All subjects underwent an otoscopy with removal of debris and wax from the ear canal, and an impedance test, before being analyzed for OAEs. Pure tone audiograms and TEOAEs were recorded in an acoustically shielded room. The audiometric test frequencies were 0.25, 0.5, 1, 2, 3, 4, 6, and 8 kHz. The ear was conventionally defined ‘‘normal’’ if no threshold shift higher than 20 dB was found over the whole frequency range. For 42 ears the audiograms showed threshold shifts of more than 20 dB at frequencies higher than 3 kHz. These ears with high-frequency hearing loss were defined ‘‘impaired’’ in this work. The average amount of hearing loss in the impaired ears is reported in Table I. A small set of four low-frequency impaired ears was not included in the cumulative analysis, because, as will be shown later, it is important to select an impaired set with homogeneous audiometric characteristics. The SSOAE recordings of the same subjects had been the object of a previous study (Sisto *et al.*, 2001), in which a statistical correlation between the presence of long-lasting OAEs and the audiometrically determined hearing impairment was found. Fast wavelet transform (Mallat, 1998) was performed by iterative application of perfect reconstruction FIR filter banks. The wavelet transform $W(f_i,t)$ of a signal s is obtained by computing the inner product of s with a set of basis functions ζ_i, named wavelets, as a function of the time shift t:

$$W(f_i,t)=\int s(t')\zeta_i(t'-t)\,dt'. \tag{2}$$

The wavelet functions $\zeta_i(t)$ are scaled (compressed) versions of a mother wavelet $\phi(t)$, whose Fourier transform is that of a bandpass filter, so the convolution integrals of Eq. (2) perform the bandpass filtering of s around the frequencies f_i. The functions $W(f_i,t)$, which will be called wavelet coefficients in the following, give a time-frequency representation of the evolution of the signal s. Alternative techniques, such as the short time Fourier transform (STFT), give a similar representation, but in the STFT case the frequency resolution is set, for all frequencies, by the inverse of the integration time, which, in turn, limits the time resolution. This typically gives an insufficient time resolution at high frequency and an insufficient frequency resolution at low frequency. The main advantage of the wavelet technique is indeed that the frequency and time resolution may be frequency-dependent, and chosen with some elasticity, according to the characteristics of the data to be analyzed. In this work, an iterative procedure computes the fast wavelet transform with a cascade of filterings followed by a factor 2 subsampling. This is mathematically equivalent to performing the convolution in-

TABLE I. Average hearing loss of the impaired ears.

	f (kHz)							
	0.25	0.5	1	2	3	4	6	8
Mean hearing loss	12	12	15	18	31	41	38	28
Standard deviation	2	3	7	15	16	18	21	20

tegrals of Eq. (2) with a set of wavelets scaled by a factor 2, whose shape depends on the parameters of the filters used. Filters corresponding to linear spline biorthogonal wavelets [for details on the properties and the parameters of this wavelet basis, see Mallat (1998)] have been used in this work. At the first step of the procedure the original waveform is both low-pass and high-pass filtered with a cutoff frequency $f_s/4$, where f_s is the data sampling frequency. The two filtered outputs are subsampled by a factor of 2. The high-passed subsampled output is directly the first wavelet coefficient, describing the time evolution of the signal in the frequency band extending from $f_s/4$ to $f_s/2$, while the low-passed subsampled output is fed to the input of the second step of the iterative procedure. The ith step of the iterative procedure selects a frequency band extending from $f_s 2^{-(i+1)}$ to $f_s 2^{-i}$, yielding a wavelet coefficient which is a function of time, representing the time evolution of the signal amplitude in the selected frequency band. Thus the frequency bandwidth is proportional to frequency, while the time step, i.e., the interval between subsequent time samples of the wavelet coefficient, doubles at each step of the procedure, due to subsampling. With this wavelet technique, the highest frequency bands benefit from the best time resolution, while at lower frequencies the time step increases, and the frequency resolution is better. As pointed out by Wit *et al.* (1994), the wavelet analysis method is particularly effective for studying the OAE spectral latency. This happens also because, due to the cochlear geometry, the highest frequencies have the shortest latencies, so they need a good time resolution, while the variable frequency bandwidth corresponds to a constant relative frequency resolution $\Delta f/f$. It should be added that, due to the logarithmic cochlear mapping, this means that each frequency band represents an interval of approximately equal length along the cochlear membrane.

The TEOAE ILO sampling frequency is 25 kHz. Thus a six-step wavelet analysis procedure yields six wavelet coefficients representing the time evolution of the six frequency bands: 0.195–0.39, 0.39–0.78, 0.78–1.56, 1.56–3.12, 3.12–6.25, and 6.25–12.5 kHz. In the following, for brevity, these octave bands will be labeled by the value of their geometrical average frequency, respectively, 0.28, 0.55, 1.10, 2.2, 4.4, and 8.8 kHz, which is approximately that corresponding to the central position of the cochlear region associated to each band. This frequency assignment is quite arbitrary, but it was considered to be the simplest model-independent choice. The time steps of the wavelet coefficients of the six bands are, respectively, 2.56, 1.28, 0.64, 0.32, 0.16, and 0.08 ms. Of course, other time-frequency techniques could provide a better frequency resolution (Tognola *et al.*, 1997). Octave bands were chosen because they give the advantage of collecting a large signal in each frequency band, giving a spectral latency measure that is less affected by the presence in the band of single long decay time OAEs (Sisto *et al.*, 2001). These spectral lines are characterized by a peculiarly slow decay, which could affect narrow-band high-frequency latency measurements, as will be shown in Sec. IV. In addition, octave band OAE spectral latency measurements can directly be compared to the results of derived band ABR latency studies, which typically use octave bands. A rough estimate of the signal-to-noise ratio (SNR) of each wavelet coefficient was obtained by evaluating the ratio between the rms value of that coefficient computed for the sum of the two ILO simultaneous acquisitions and that computed for the difference. This estimate of the SNR was used to select for the cumulative analysis only the data with a good reproducibility in the analyzed frequency band. A threshold was arbitrarily set at SNR$>$2 (6 dB). In the highest frequency band the response was very poor, mainly due to the limited bandwidth of the ILO click stimulus. In the lowest frequency band the latency measurements were influenced by the window. Thus, only the four intermediate frequency bands were actually used for OAE spectral latency measurements.

The method has been validated by applying it to synthesized signals of known time-frequency composition, to evaluate its timing accuracy and the systematic error introduced by the ILO window on the measurement of small latencies.

Due to the large interpersonal variability of the latency, a cumulative analysis was performed, separately for normal and impaired ears. The cumulative analysis was done as described next, using two slightly different algorithms, giving very similar results:

(1) The ear average (indicated by brackets in the following) of the wavelet coefficients $W(f_i,t)$ was performed for each audiometric category,

$$\langle W(f_i,t)\rangle = \frac{1}{N_{\text{ears}}}\sum_{k=1}^{N_{\text{ears}}} W(f_i,t), \tag{3}$$

and for each averaged coefficient the time of the maximum $t_{\max}(f_i)$ was found. The average spectral latency $\langle\tau(f_i)\rangle$ of the ith frequency band was defined as this $t_{\max}(f_i)$.

(2) The distribution of individual spectral latencies was obtained for each ear category, by finding $t_{\max,k}(f_i)$ for each ear. These distributions were compared by using the Student's *t*-test to evaluate quantitatively the statistical significance of the differences observed in each octave band between impaired and normal ears. The alternative definition of average spectral latency of the ith frequency band comes from the ear average of the $t_{\max,k}(f_i)$:

$$\langle\tau^*(f_i)\rangle = \frac{1}{N_{\text{ears}}}\sum_{k=1}^{N_{\text{ears}}} t_{\max,k}(f_i). \tag{4}$$

III. MODELS OF THE COCHLEAR TRANSMISSION

The OAE latency that has been experimentally measured in this work and in that by Tognola *et al.* (1997) is actually made up of two terms:

$$\tau(f) = \tau_c + \tau_{nc}, \tag{5}$$

where τ_c is the cochlear round trip delay and τ_{nc} is a noncochlear contribution, due to the transmission through the outer and middle ear. This last contribution is much smaller than τ_c and will be evaluated and considered in the next section. Its inclusion in Eq. (1) gives a correction to the best fit value of the parameter *b*, which has to be taken into account when a comparison is made to theoretical predictions on the cochlear latency τ_c.

The cochlear round trip delay for the frequency f resonating at $x(f)$, is given by

$$\tau_c(x(f))=2\int_0^{x(f)}\frac{dx}{\mathrm{TWV}(f,x)}, \tag{6}$$

where $\mathrm{TWV}(f,x)$ is the velocity of the traveling wave component of frequency f at the cochlear position x. Strictly speaking, as shown by Eq. (6), the OAE spectral latency measured at a frequency f provides information only about the path average of the inverse TWV, and only for the frequency f that is resonant at $x(f)$. Assuming, as a first step, a constant average inverse TWV, the cochlear latency is a linear function of $x(f)$:

$$\tau_c(x(f))=2x(f)\langle \mathrm{TWV}^{-1}\rangle, \tag{7}$$

where $\langle \mathrm{TWV}^{-1}\rangle$ is, as assumed, independent of frequency. It should be noted here that this functional dependence does not mean that $\mathrm{TWV}(f,x)$ is the same for all frequencies for any position x along the cochlea. Equation (7) is satisfied, for example, by any function $\mathrm{TWV}(f,x)$ that is a function of the ratio $x/x(f)$ between the cochlear position and that associated to the wave resonance for the frequency f. In fact, the cochlear latency would be given, in this case, by

$$\tau_c(x(f))=2\int_0^{x(f)}\frac{dx}{\mathrm{TWV}(x/x(f))}=2x(f)\int_0^1\frac{du}{\mathrm{TWV}(u)} =2x(f)\langle \mathrm{TWV}^{-1}\rangle. \tag{8}$$

The average over the cochlear path in Eq. (8) may be nonlinear, according to the functional form of $\mathrm{TWV}(f,x)$. The above simple assumption is not based on any theoretical cochlear model. Theoretical predictions about the analytical form of the TWV function come instead from full cochlear models. In such models the transmission along the cochlear membrane is ruled by a transmission line equation (Furst and Lapid, 1988; Talmadge *et al.*, 1998) with a parallel impedance term that is locally resonant at the frequency $f(x)$, given by the Greenwood map (Greenwood, 1990; Talmadge *et al.*, 1998):

$$x(f)=\frac{1}{k_\omega}\log_e\left(\frac{f_{\max}+f_0}{f+f_0}\right), \tag{9}$$

where $x(f)$ is the distance, in mm, along the cochlea, starting from the base, $k_\omega=0.1382\,\mathrm{mm}^{-1}$, $f_{\max}=20.655\,\mathrm{kHz}$, and $f_0=0.145\,\mathrm{kHz}$.

It should be reminded here that the inverse group velocity is given by

$$\mathrm{TWV}^{-1}(\omega,x)=\frac{\partial\,\mathrm{Re}(k(\omega,x))}{\partial\omega}, \tag{10}$$

where $\omega=2\pi f$ is the angular frequency and $k(\omega,x)$ is the wave number of the component of frequency ω at the cochlear position x.

The incompatibility of the experimental OAE latency data with the $1/f$ power law would have important theoretical implications. It is beyond the objective of this work to discuss the general problem of how to construct a model capable of correctly describing the physics of the signal transmission and amplification along the cochlear membrane. In the following it will be shown that the experimental evidence coming from OAE latency measurements may be effectively used as a constraint for theoretical models, and how models could be adapted to satisfy it. In the model by Talmadge *et al.* (1998), OAEs are interpreted as due to coherent reflection of the traveling wave near the tonotopic site. Most of the phenomenological characteristics of the OAE spectra (including quasiperiodicity and the relationship between different types of OAEs) are determined in these models by the phase behavior of the apical reflectance function. The $1/f$ law for latency is found in the scale-invariant limit, by integrating over the cochlear path the inverse of the group velocity associated to the Greenwood map, neglecting the scale-invariant breaking term f_0, and assuming a constant wave number at the reflection site, $k_c=7.5\,\mathrm{mm}^{-1}$. This scale-invariant prediction is

$$\tau_{S.i.}(x(f))=\frac{2k_c}{\omega k_\omega}\cong\frac{17}{f}\,\mathrm{ms}. \tag{11}$$

The same prediction comes from the phase variation of the apical reflectance function. These points are directly related to the interpretation of OAEs suggested by the model, and to the prediction of the OAE spectral quasiperiodicity, which is one of its most important results. It is therefore necessary to understand if and how such a model could be modified to become consistent with the experimental OAE latency measurements. In the following, this attempt will be made, analyzing the constraints on the form of the dispersion relation $k(\omega,x)$ implied by experimental findings, in a general theoretical framework using the transmission line formalism to describe the traveling wave transmission along the cochlear membrane (Furst and Lapid, 1988; Talmadge *et al.*, 1998).

In this class of models, the following relation is assumed to hold:

$$k(\omega,x)=\frac{\omega k_0}{\sqrt{\omega^2(x)-\omega^2+i\omega\Gamma(x)}}. \tag{12}$$

Exact scale invariance would be satisfied by any $k(\omega,x)$ that is a function of the ratio $\omega/\omega(x)$, if the scale-invariance breaking term f_0 of the Greenwood map [Eq. (9)] is neglected. This term becomes relevant at low frequency and may explain a deviation from the $1/f$ law below 1 kHz. As shown by C. Talmadge (private communication), the resonance term $i\omega\Gamma(x)$, which is also a scale-invariance breaking term unless a constant Q assumption be made ($Q=\omega/\Gamma$ is the resonance quality factor), may also explain a deviation from the $1/f$ law. The constant Q hypothesis seems to be contradicted by psychoacoustical measurements (Moore, 1978), indicating that tuning is an increasing function of frequency.

The inverse TWV may be computed from Eqs. (10) and (12), obtaining

$$\mathrm{TWV}^{-1}(\omega,x)=\frac{\partial\,\mathrm{Re}(k(\omega,x))}{\partial\omega} =\frac{\partial|k|}{\partial\omega}\cos\frac{\varphi}{2}+|k|\sin\frac{\varphi}{2}\,\frac{\partial}{\partial\omega}\left(\frac{\varphi}{2}\right), \tag{13}$$

where

$$\varphi=\tan^{-1}\left(\frac{-\omega\Gamma(x)}{\omega^2(x)-\omega^2}\right). \tag{14}$$

Far from the tonotopic site,

$$\omega(x)-\omega>2\Gamma(x), \tag{15}$$

the relation of Eq. (12) is approximately scale invariant, and the nonresonant contribution to cochlear latency is easily computed in the limit $Q\gg 1$:

$$\tau_{\text{far}}((f))=2\int_0^{x(f)-\Delta x}\frac{dx}{\text{TWV}(\omega,x)}$$

$$=\frac{k_0\sqrt{Q}}{2\omega k_\omega}\left(1+o\left(\frac{1}{Q}\right)\right), \tag{16}$$

where Δx is computed using the Greenwood map:

$$k_\omega\Delta x=2\Gamma/\omega=2/Q. \tag{17}$$

Near to the resonance

$$\omega(x)-\omega<2\Gamma(x), \tag{18}$$

the resonant contribution to cochlear latency is given by

$$\tau_{\text{res}}(x(f))=2\int_{x(f)-\Delta x}^{x(f)}\frac{dx}{\text{TWV}(\omega,x)}, \tag{19}$$

which may be computed numerically. The nonresonant contribution to cochlear latency, τ_{far}, turns out to be the dominant one, and its dependence on Q may account for the observed violation of the $1/f$ law. An accurate estimate of the empirical $\Gamma(x)$ relation would be useful to test this hypothesis. Equation (16), assuming

$$\Gamma(x)=\Gamma_0 e^{-k_\gamma x}, \tag{20}$$

with k_γ constant, implies, neglecting the correction due to τ_{res}, a latency-frequency relation which is still a power law of frequency, with

$$b=-1+\varepsilon, \tag{21}$$

where

$$\varepsilon=\frac{k_\omega-k_\gamma}{2k_\omega} \tag{22}$$

is a measure of the scale-invariance violation associated to the variation of Q.

In Figs. 1(a) and (b) the functions $\text{Re}(k(\omega,x))$ and $\text{TWV}^{-1}(\omega,x)$ are plotted, as computed from Eqs. (12) and (13), in the case $\varepsilon=0.35$.

In Fig. 2(a) the whole theoretical cochlear latency is plotted as a function of frequency, computed in the constant Q case ($\varepsilon=0$), in the case $\varepsilon=0.2$, and $\varepsilon=0.35$. The increase of the violation of the $1/f$ law with increasing ε is visible. In Fig. 2(b) the nonresonant and resonant contributions are separately plotted to show that the resonance gives a smaller and steeper contribution, which is independent on the Q profile and slightly modifies the simple prediction of Eq. (21). The tuning profiles $Q(x)$ associated to the three considered cases are shown in Fig. 2(c).

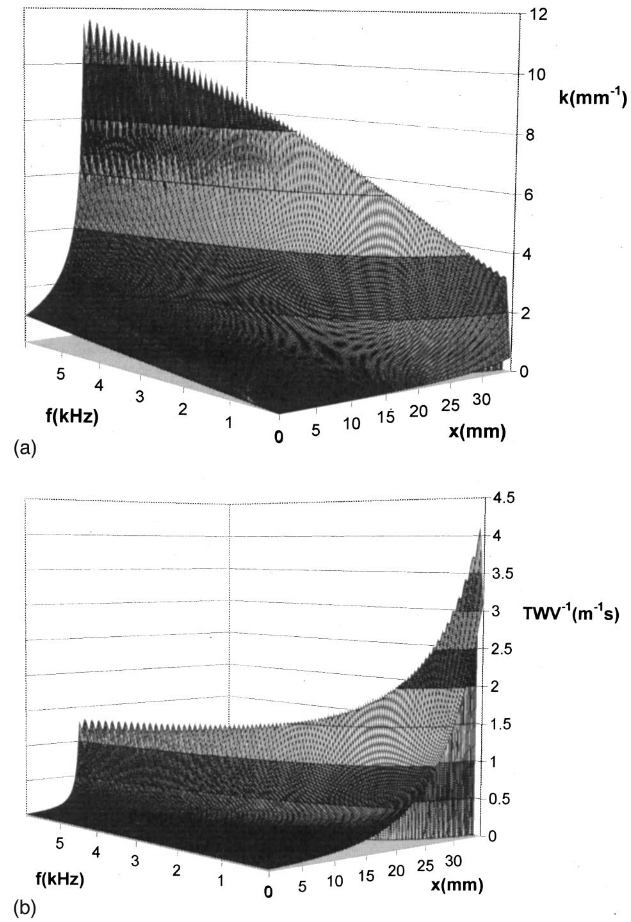

FIG. 1. Wave number $\text{Re}(k(f,x))$ (a) and associated $\text{TWV}^{-1}(f,x)$ (b), computed by using the cochlear transmission model of Eqs. (12)–(14) in the case $\varepsilon=0.35$. Spurious oscillations are a numerical spurious effect due to the finite resolution of the 2-D plot.

Another possible explanation of the OAE latency observations could be given by an explicit scale-invariance breaking in Eq. (12), which is obtained assuming a dependence on x of the parameter k_0.

In scale-invariant models, k_0^2, which may be interpreted as the product of the series inductance per unit length by the inverse parallel inductance per unit length of the equivalent transmission line (Furst and Lapid, 1988), is assumed to be independent of x. These quantities are related to the cochlear cross section and to the basilar membrane width and areal density (Talmadge *et al.*, 1998), which are not constant, and whose dependence on x could be approximately evaluated, in principle, from anatomical data. This is beyond the scope of the present work, in which no particular cochlear transmission model is actually proposed. In any case, as the parallel inductance $L(x)$ is also connected to the tonotopic frequency $\omega(x)$ by the resonance relation,

$$\omega(x)=\frac{1}{\sqrt{L(x)C(x)}}, \tag{23}$$

it is clearly reasonable to assume that $L(x)$ itself is some exponentially increasing function of the cochlear position x. Without hypothesizing a particular functional form of $L(x)$ based on anatomical data, an attempt is made here to find a

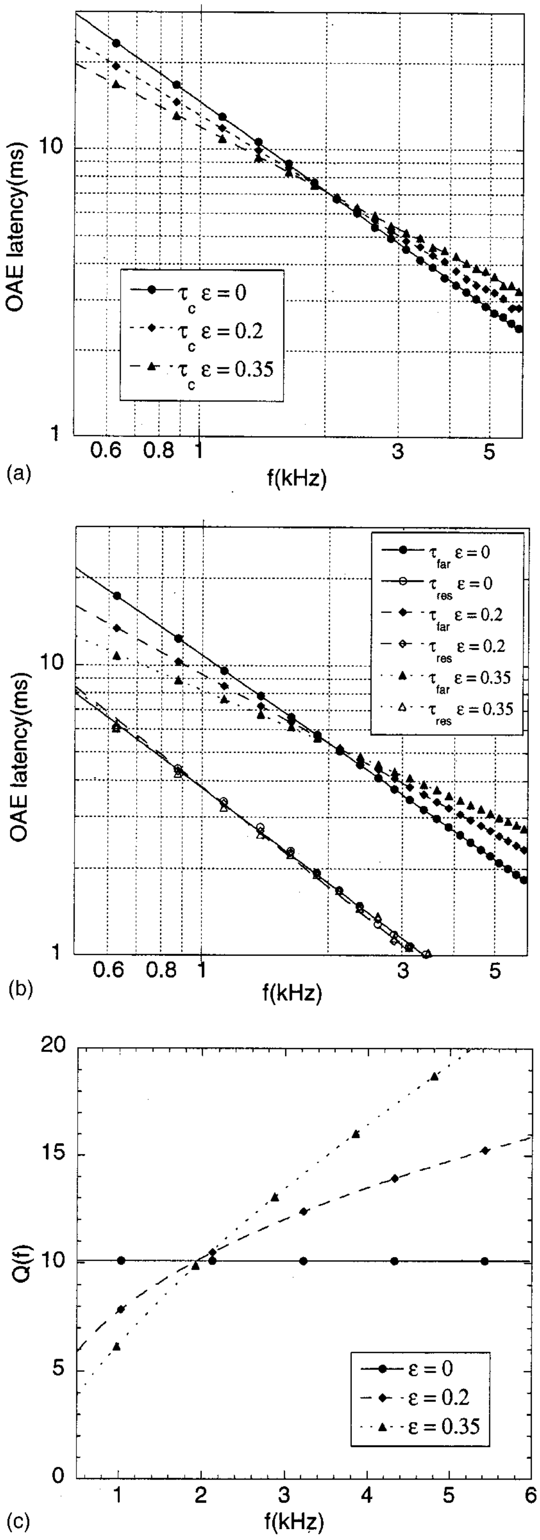

FIG. 2. Whole cochlear latency $\tau_c(x)$ (a) and nonresonant and resonant contributions to $\tau_c(x)$ (b), computed by numerical integration of Eq. (6), using the model of Eqs. (12)–(14), for three values of the scale-invariance breaking parameter ε [$\varepsilon=0$ (●), $\varepsilon=0.2$ (◆), $\varepsilon=0.35$ (▲)] associated to the variation of Q with frequency (c).

phenomenological dispersion relation giving the frequency dependence that is experimentally observed for the OAE latency.

The dispersion relation of Eq. (12) is easily extended to account for an exponential dependence on x of the inductance ratio:

$$k(\omega,x)=\frac{\omega k_{00}e^{-\alpha x}}{\sqrt{\omega^2(x)-\omega^2+i\omega\Gamma(x)}}, \tag{24}$$

where k_{00} and α are constants. The inverse TWV function may be computed as previously done. Assuming constant Q, and neglecting the scale-invariance breaking term in the Greenwood map, Eq. (24) implies again a latency-frequency relation which is approximately a power law of frequency, with

$$b=-1+\varepsilon. \tag{25}$$

In this case, the scale-invariance breaking parameter is defined as

$$\varepsilon=\frac{\alpha}{k_\omega}. \tag{26}$$

Of course, it is possible to assume both a variable Q and a dependence of k_0 on x, with a cumulative effect on the slope of the latency-frequency relationship.

Some further theoretical considerations need also to be made, regarding the comparison of OAE latency data to the results of ABR studies. Derived band ABR latency data seem to be accurately fitted by an exponential function of the cochlear path (Donaldson and Ruth, 1993):

$$\tau_{\mathrm{ABR}}(x)=A+Be^{Cx}, \tag{27}$$

where A, B, and C are fit parameters. The fact that derived band ABR latency data agree with this fit function suggested (Donaldson and Ruth, 1993) that the TWV is an exponentially decreasing function of the cochlear position, independent of frequency, given by the inverse of the derivative of the latency of Eq. (27) with respect to the cochlear position x:

$$\mathrm{TWV}(x)=\left(\frac{\partial\tau_{\mathrm{ABR}}(x)}{\partial x}\right)^{-1}=\frac{e^{-Cx}}{BC}. \tag{28}$$

It is interesting to note here that this empirical law is in agreement with Eqs. (21), (22), (25), and (26), with

$$C=k_\omega(1-\varepsilon). \tag{29}$$

It should also be pointed out here that the spectral latency data, whatever their frequency resolution, do not provide a function of the cochlear position x of the type

$$\tau_c(x)=\int_0^x\frac{dx'}{\mathrm{TWV}(x')}, \tag{30}$$

which would indeed permit us to correctly write Eq. (28). They provide instead the function of $x(f)$ defined in Eq. (6), where the factor of 2 accounts for the forward and backward propagation of the OAE signal. In other words, Eq. (27) is not defined, for any frequency, along the x axis, but rather along the curve $x(f)$ of Eq. (9), describing the Greenwood map in the x-f plane. Thus it is not correct to make the assumption that the TWV function must be given by Eq. (28) for all frequency components. This assumption was implicitly made in the mentioned derived band ABR latency stud-

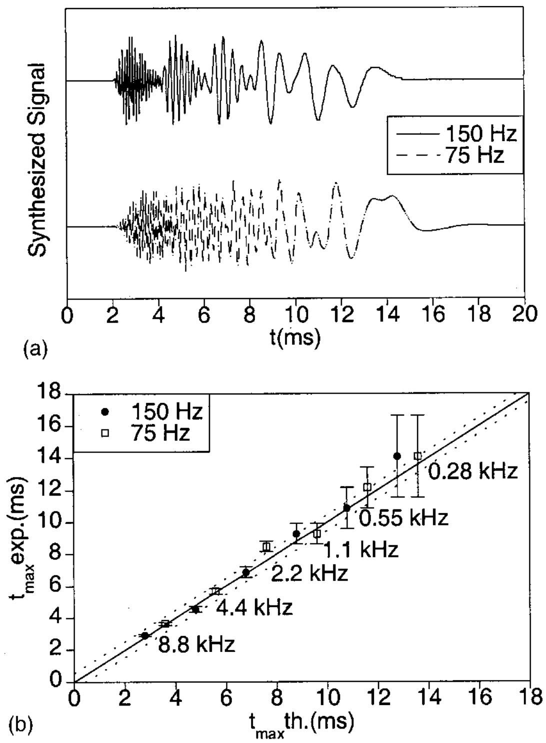

FIG. 3. Test of the timing accuracy of the wavelet method applied to synthesized waveforms. The two synthesized waveforms (a) are the sum of six gammatones of different decay constants ($\Gamma = 150$ Hz for the solid line and $\Gamma = 75$ Hz for the dashed line) spaced 2 ms in time. The measured spectral latency is plotted (b) versus the theoretical time of the maximum of each gammatone. The timing accuracy is better than 1 ms for all frequency components. Dotted lines indicate a ± 0.5 ms error. Labels refer to the gammatone main frequency.

ies, in which the TWV was estimated either by Eq. (28), or by assuming that the differences between the spectral latency of contiguous frequency bands were given by the corresponding cochlear path difference multiplied by the average inverse TWV. This warning has to be considered when comparing the OAE latency data with ABR latency data expressed in terms of TWV functions.

IV. RESULTS

Preliminary tests using synthesized waveforms have been performed to evaluate the precision and the systematic errors associated to the algorithm. In a first test a waveform made up of six gammatones, each belonging to one of the six frequency bands, and starting at different and known times, with 2-ms spacing, was used. No window was applied to this waveform. The gammatone (Wit *et al.*, 1994) is an oscillating function with a peaked envelope, which grows as t^3, and exponentially decays with a decay constant Γ:

$$\gamma(t) = \gamma_0 t^3 e^{-\Gamma t} \sin(\omega t). \tag{31}$$

Its amplitude peak is sharp, and its shape is similar to the TEOAE response at a single resonant frequency. In Fig. 3(b) the result of this test is presented, showing a very good agreement between the time of the maximum of the ith gammatone and that measured, in the corresponding frequency band, by the wavelet algorithm. This agreement was verified both for fast decaying gammatones ($\Gamma = 150$ Hz), producing

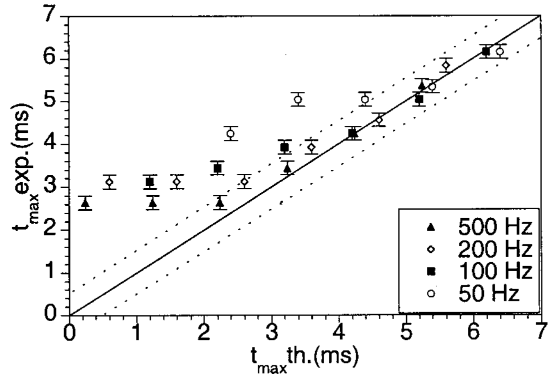

FIG. 4. Evaluation of the systematic latency measurement error due to the standard ILO window. The latencies of fast-decaying ($\Gamma = 500$ Hz) gammatones of frequency 4.4 kHz are correctly estimated (within ± 0.5 ms, marked by dotted lines) for latencies longer than 2.5 ms. For smaller decay constants the minimum measurable latency gradually increases, reaching the value of 4.5 ms for quasi-stationary gammatones of small decay constant, $\Gamma = 50$ Hz.

a waveform with clearly distinct peaks, each associated to one of the six gammatone frequencies, and for slowly decaying gammatones ($\Gamma = 75$ Hz), giving a more entangled waveform, similar to the real TEOAE waveforms [see Fig. 3(a)]. A second test was performed to evaluate the systematic error introduced by the ILO window. In fact, it should be noted that experimental high-frequency latencies are of the order of 5 ms, or smaller. The standard ILO window, starting at 2.5 ms, and reaching its maximum at 5 ms, could affect the measurement of such short latencies, and latencies shorter than 2.5 ms would not be measurable at all for this reason. This could be a serious source of systematic error, even if the rise of the window linear ramp is generally slower than the typical exponential decay (Sisto and Moleti, 1999) of the cochlear response in the first few ms. This problem has been carefully analyzed by doing a second simulation with gammatones. The aim of this test was to evaluate the shortest measurable spectral latency, as a function of the decay constant of the gammatone. In fact, the smaller the decay constant, the more the window ramp pushes forward in time the maximum of the unwindowed signal. Of course, this effect could also be analytically estimated, but it was also necessary to take into account the spectral distortion due to the window ramp. The results are shown in Fig. 4, where the spectral latency measured by the algorithm for a windowed 4.4-kHz gammatone starting at different times is plotted versus the time of the maximum of the unwindowed gammatone, for four different values of the gammatone decay constant. As expected, the systematic error is larger for small decay constants, and becomes negligible for values of the theoretical maximum time (of the unwindowed signal) ranging from 2.5 ms (for $\Gamma = 500$ Hz) to 5 ms (for $\Gamma = 50$ Hz). Thus this systematic error could be important in the highest frequency bands ($f > 4$ kHz), particularly when the TEOAE signal is dominated by high-frequency quasi-stationary OAEs. This is not the case for adult populations, in which most long-lasting OAEs (Sisto *et al.*, 2001) are found at lower frequencies (1–2 kHz), whose characteristic spectral latencies are larger. Thus the results of this work, in the four intermediate frequency bands, are not strongly affected by

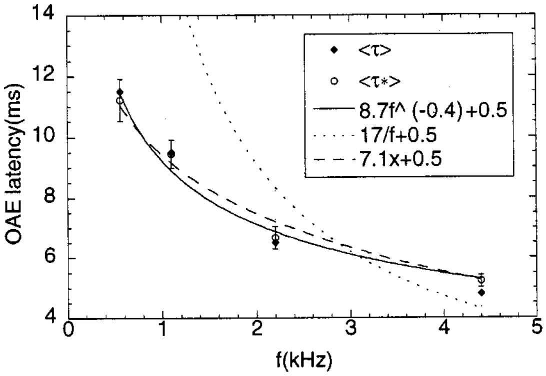

FIG. 5. Experimental average OAE spectral latencies for normal ears. The data are best fitted to Eq. (7), to the power law of Eq. (1), and to the $1/f$ law predicted by fully scale-invariant cochlear models, assuming in all cases a 0.5-ms noncochlear offset. Vertical error bars represent two sample standard deviations of the average latency $\langle \tau^*(f) \rangle$. The average latency $\langle \tau(f) \rangle$ computed as the time of the maximum of each average wavelet coefficient [Eq. (3)] is also plotted for comparison.

TABLE II. Comparison of the power law fit coefficients of the OAE latency-frequency relationship [Eq. (1)] found in this work with those found by Tognola *et al.* (1997), as a function of the stimulus intensity.

	a	*b*
Tognola (47 dB)	10.81	−0.43
Tognola (50 dB)	10.98	−0.47
Tognola (53 dB)	10.54	−0.43
Tognola (56 dB)	10.25	−0.46
Tognola (59 dB)	10.17	−0.48
Tognola (62 dB)	9.56	−0.44
Tognola (65 dB)	9.37	−0.45
Tognola (68 dB)	8.54	−0.40
This work (77 dB) (normal)	9.2	−0.37
This work (77 dB) (impaired)	10.5	−0.29

this error. A problem could arise, instead, in the application of such wavelet methods to the measurement of latencies in newborns and infants, in which intense long-lasting OAEs are often found at higher frequencies.

Another problem affecting the high-frequency data comes from the octave-band resolution. The TEOAE spectral response for adults is peaked between 1 and 3 kHz, and usually drops above 4 kHz, also due to the limited bandwidth of the ILO click stimulus. This means that the main contribution to the 6.25–3.12-kHz band is typically due to frequency components between 3 and 4 kHz, so it could be wrong to assign to the latency of the corresponding wavelet coefficient the central frequency of the band. A similar problem may affect the lowest frequency band, with the result of underestimating the slope of the latency-frequency relationship.

With these cautions, the algorithm was applied to the two populations of normal and high-frequency impaired ears. The average experimental spectral latency $\langle \tau^* \rangle$ of the normal ears is shown in Fig. 5 as a function of frequency. Error bars represent two sample standard deviations of the average latency. The data are in agreement to those by Tognola *et al.* (1997), as regards both the spectral latency absolute values and their frequency dependence. To allow comparison with their results, the data have been fitted to the phenomenological power law af^b, finding values of the two fit parameters ($a = 9.2$ ms and $b = -0.37$) similar to theirs, as shown in Table II. Taking into account the noncochlear contribution estimated later in this work, the best fit parameters of the power law fit slightly change: $a = 8.7$ ms, $b = -0.40$.

Following a suggestion by C. Talmadge (private communication) mentioning a method used by G. Long, a different analysis method has also been applied to a subset of our data. By visual comparison between our wavelet data and the TEOAE spectra, it is often possible to identify the wavelet contribution due to a given individual spectral line. In some cases it is also possible to identify successive peaks in the wavelet signal associated to consecutive cochlear echoes of the same spectral line, as shown in Fig. 6. The time delay between successive echoes is a measure of the cochlear round trip delay only, which does not suffer from the systematic errors introduced by the ILO window on high frequency latencies. The difference between the latency of the first echo and the delays between successive echoes has also provided a rough estimate of the noncochlear contribution, $\tau_{nc} = 0.5$ ms, that was used to fit the latency data. This method also permits, in principle, to assign a definite frequency to each latency value, eluding the octave-band resolution limit, which is intrinsic to this wavelet technique, but may be applied only to the subset of data for which an unambiguous line identification is possible. This selection could bias the results. It has been possible to apply the line identification method to 56 ears of the normally hearing population, with the result shown in Fig. 7, where the delay of the first echo is plotted. A steeper power law fits the data, with $b = -0.68$, which is closer to the ABR result, but still significantly different from the scale-invariance prediction. However, a larger statistical sample and a more accurate line identification procedure would be necessary to validate this result.

The data of Fig. 5 have also been fitted to a function of the cochlear path. As a first step, a linear function of $x(f)$ was used to fit the latency data: using Eqs. (6) and (9), the OAE spectral latency data were fitted to

$$\tau(f) = K \log_{10}\left(\frac{f_{\max} + f_0}{f + f_0}\right) + \tau_{nc}, \tag{32}$$

by varying the parameter K, which is related to the average

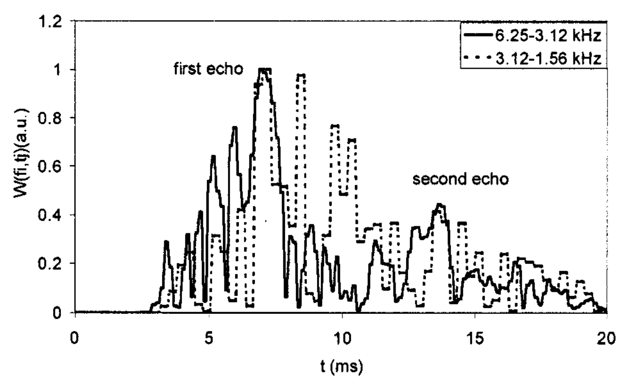

FIG. 6. Time evolution of the 6.25–3.12 and 3.12–1.56 kHz wavelet coefficients in one of the normal-hearing ears. Successive echoes of decreasing amplitude are visible.

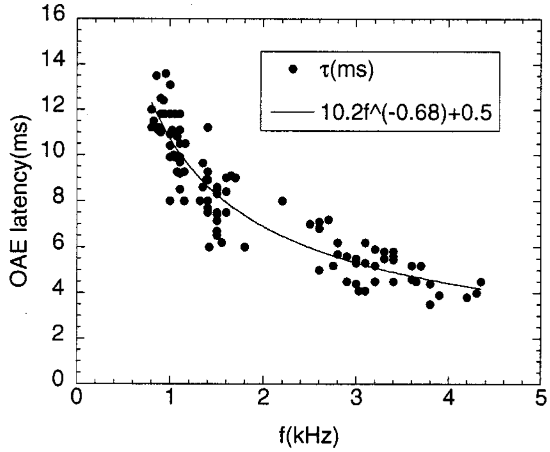

FIG. 7. Fit to the OAE latencies found by the line identification method of Fig. 6.

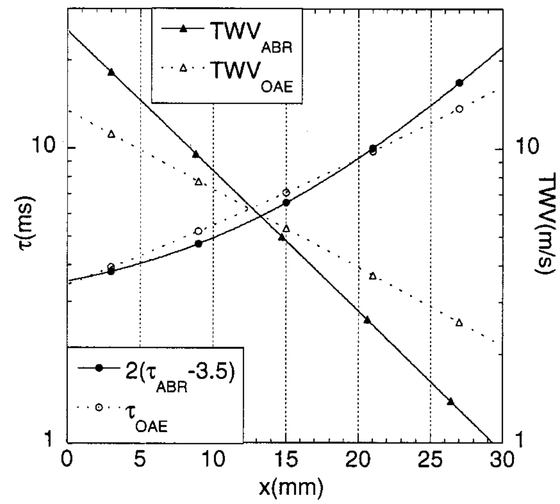

FIG. 8. Comparison of the functions $\tau(x)$ and $\mathrm{TWV}(x)$, computed according to Eqs. (34) and (28), with those reported by Donaldson and Ruth (1993) for the ABR latency and TWV. A 3.5-ms retrocochlear offset has been subtracted from the ABR latency prior to multiplying it by a factor of 2, to compare it with the OAE latency. Although the TWV functions are significantly different, the corresponding latency functions are quite similar in the range of the OAE latency measurements.

cochlear transmission speed (supposed independent of frequency) by

$$K=2(k_\omega \log_{10}(e))^{-1}\langle \mathrm{TWV}^{-1}\rangle. \tag{33}$$

The fit, as shown in Fig. 5, is quite good, considering that the single free parameter K was used, having fixed the three parameters k_ω, $f_{\max}$, and f_0 of Eq. (9) to the values reported in the literature. The fit was performed on the average spectral latency data shown in Fig. 5, and separately for each ear, providing a statistical distribution of the fit parameter K. The value of K obtained by the best fit of the average latencies was coincident, within the experimental uncertainties, with the average of the best fit values of K obtained for each ear, and was 7.1 ms for normal ears, corresponding to $(\langle \mathrm{TWV}^{-1}\rangle)^{-1}=4.9$ m/s.

The data were also fitted to the $1/f$ law, Eq. (11), predicted by scale-invariant full cochlear models. Such a steep frequency dependence is not compatible with the experimental results, as shown in Fig. 5, also taking into account a 0.5 ms noncochlear latency contribution.

The next step was comparing the data with ABR latency measurements. As mentioned in the previous section, ABR latency data are well fitted by Eq. (27), which is an exponential function of the cochlear path (Donaldson and Ruth, 1993). When comparing OAE to ABR latency data, one must consider that the outer, middle ear, and cochlear delays count twice in the OAE data, while, in the ABR latency, a significant retrocochlear delay of neural origin is present, which, for wave V, is on the order of 5 ms.

A fit of the OAE latency data was also attempted to an exponential function that could be compared to the ABR findings:

$$\tau(x)=2Be^{Cx}+\tau_{nc}. \tag{34}$$

This function is consistent with the TWV function of Eq. (28). Due to the logarithmic cochlear mapping this is essentially a power law of the frequency, approximately equivalent to

$$\tau(f)=2B\left(\frac{f_{\max}}{f}\right)^{C/k_\omega}+\tau_{nc}. \tag{35}$$

A good fit was obtained for $B=1.21$ ms and $C=0.061\ \mathrm{mm}^{-1}$, which correspond to the power law parameters:

$$a=2B(f_{\max})^{C/k_\omega}\approx 9.2\ \mathrm{ms} \tag{36}$$

and

$$b=-\frac{C}{k_\omega}\approx -0.44, \tag{37}$$

which are similar to those previously found by the direct fit to the phenomenological power law. The implicit cochlear latency offset, $B\approx 1.2$ ms, is not incompatible with typical ABR wave I latency values, which imply that any cochlear offset should be smaller than 1.5 ms.

The best fit values of the parameters B and C obtained by fitting the OAE latency data may be used to compute the functions $\tau(x)$ and $\mathrm{TWV}(x)$, according to Eqs. (34) and (28). These functions may be compared to those reported in derived band ABR latency studies, corresponding to Eqs. (27) and (28). In Fig. 8 this comparison is made with the results by Donaldson and Ruth (1993). They found a larger value of the parameter C, representing the inverse of the characteristic length scale of the latency-distance relationship, $C=0.11\ \mathrm{mm}^{-1}$, a smaller value of $B=0.36$ ms, and a parameter $A=4.9$ ms. To allow comparison between the OAE and ABR latency functions, a retrocochlear offset τ_{rc} must be subtracted from the ABR latency prior to multiplying it by a factor of 2. The functions $\mathrm{TWV}(x)$ are significantly different, but the corresponding functions $\tau(x)$, representing the actually observable quantity, are quite similar, within the cochlear range explored in this work, for $\tau_{rc}=3.5$ ms, which is on the order of the typical delay between waves I and V in ABR recordings. This observation may be considered as a warning that, as discussed theoretically in the previous section, one should be very careful when drawing

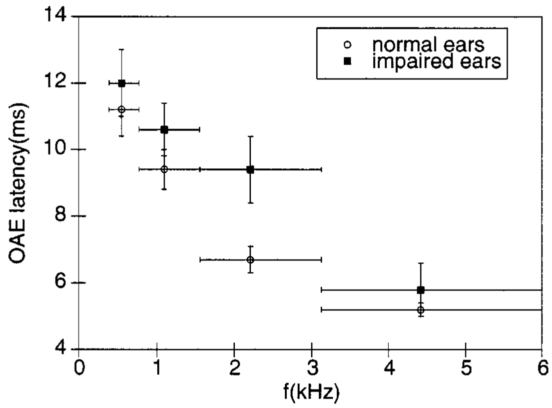

FIG. 9. Comparison between the experimental average OAE latencies of normal and high-frequency impaired ears.

conclusions on the detailed form of the TWV function starting from measurements of the spectral latency.

The average spectral latencies measured in the impaired ears are plotted in Fig. 9 as a function of frequency, compared to those of the normal ears, already shown in Fig. 5. A comparison between the parameters K, related to the average of the inverse TWV, measured in the two populations, was made. For the impaired ears the best fit parameter was $K_i = 8.3$ ms, while $K_n = 7.1$ ms was found for the normal ears. The fit to a power law also permits a comparison of the fit parameters a and b found for the two populations. As shown in Table II, the coefficients a and b are also different between the two populations. The statistical significance of the differences between normal and impaired ears has been evaluated by directly applying the Student's t-test to the two experimental spectral latency distributions. This test was performed on the distributions of the latencies, separately in the four frequency bands. A 95% confidence level has been conventionally used. The results of these tests are summarized in Table III. The probability associated to the parameter t resulted to be very small, particularly in the 2.2-kHz frequency band, immediately below the audiometric hearing loss range. This means, as will be discussed in the next section, that a statistically significant association exists indeed between OAE spectral latency and high-frequency audiometrically determined hearing loss.

V. DISCUSSION

The above experimental results on the OAE latency-frequency dependence and their new interpretation in the light of the Greenwood cochlear mapping are important from two different viewpoints. From a basic research point of view, the findings of this work, which are in quantitative agreement with earlier OAE latency measurements, show that the OAE spectral latency data may be fitted either by a simple linear function of the cochlear distance, or by an exponential function. This is in agreement with the results of derived band ABR latency studies, if one assumes a cochlear latency "offset" on the order of 1 ms. This offset could be explained as due to the slowing down phase of the traveling wave near the tonotopic site. As shown in the previous section, the fit to an exponential function of the distance is roughly equivalent to the fit to a power of the frequency. The $1/f$ law predicted by the cochlear model by Talmadge *et al.* (1998) is too steep to fit the data. The deviation from the scale-invariant prediction may be explained either by introducing an explicit scale invariance breaking associated to the dependence on x of the parallel inductance of the equivalent transmission line, or by taking into account the breaking due to the resonance. Both these possibilities have been examined analytically and with numerical simulations. It has been shown that both mechanisms could give a significant deviation from the $1/f$ law. It would be interesting to understand if the variation with x of these physical quantities (Q and/or k_0) that should be assumed to explain the OAE latency data is compatible with independent estimates coming from psychoacoustical and anatomical data.

From a clinical point of view, the comparison between normal and impaired ears has permitted us to show a statistically significant difference between the OAE latencies measured in the two populations. As the OAE latency is entirely of cochlear and precochlear origin, the comparison with ABR data could be very useful to separately analyze the effect of hearing impairment on cochlear and retrocochlear latency.

The clinical interest of the statistical dependence of the OAE spectral latency on the audiometrically determined hearing functionality is clear. The data of Fig. 9 show that the main difference between the normal and impaired ear latencies was found in the mid-frequency bands (1–2 kHz), while, for these subjects, the audiometric hearing impairment was found at higher frequencies (>3 kHz). This evidence could be qualitatively interpreted by assuming that the cochlear damage that is responsible for the audiometric hearing loss at a given frequency causes, in the corresponding cochlear region, a sharp variation of the parameters of the function $k(\omega,x)$. This corresponds to a decrease of the transmission speed for all frequencies in that cochlear region, mostly affecting the lower frequency latencies, while for the impaired frequency component a sharp variation of the wave vector is already given, in its tonotopic region, by the resonance itself.

This qualitative result is just an indication that this simple theoretical approach may be useful to investigate the cochlear transmission physics also for impaired subjects, and, conversely, that the latency observations of hearing-impaired subjects may provide important information for theoretical cochlear models. If the damage is also associated to a significantly decreased effectiveness of the active filter cochlear amplifier, the slowing down due to the resonance

TABLE III. Average OAE spectral latencies $\langle \tau^*(f) \rangle$ [Eq. (4)] measured in normal and impaired ears, and evaluation of the statistical significance of the difference by the Student's t-test. A 95% confidence level has been conventionally adopted.

	f (kHz)			
	4.4	2.2	1.10	0.55
$\langle \tau_n^*(f) \rangle$ (ms)	5.2 ± 0.1	6.7 ± 0.2	9.4 ± 0.3	11.2 ± 0.4
$\langle \tau_i^*(f) \rangle$ (ms)	5.8 ± 0.4	9.4 ± 0.5	10.6 ± 0.4	12.0 ± 0.5
$P_{n-i}(t)$	n.s.	10^{-6}	1.3×10^{-2}	n.s.

could also be reduced, giving impaired subjects latencies even shorter than those of the normal subjects, in the impaired range, as suggested by the results by Don *et al.* (1998). All these considerations suggest that the correlation between hearing loss and latency should be studied by taking into account the spectral features of both the latency and the hearing loss. High-resolution audiometric techniques and spectral latency measurements may be used to disentangle the effects of the various physical phenomena described in this work. The fact that the proposed experimental technique is sensitive enough to show the correlation between OAE latency and hearing loss is a new and important quantitative result. It means that latency versus frequency measurements, which are easily accomplished by analyzing standard TEOAE recordings by wavelet methods, could provide an additional indicator of cochlear functionality. This result supports the general idea of developing an indicator of the cochlear functionality based on a set of parameters coming from different analysis of the same transiently evoked OAE signal. Relatively long (40–80 ms) TEOAE recordings could be analyzed to measure the SSOAE amplitude, the long-lasting OAE decay time, and the OAE spectral latency. All these parameters have been shown to be correlated to cochlear damage (Sisto *et al.*, 2001), and could be effectively combined to build up a statistically significant indicator of the cochlear functionality.

VI. CONCLUSIONS

Experimental measurements of the TEOAE latency as a function of frequency, obtained by means of a time-frequency wavelet technique, have been presented, which are in agreement with previous OAE latency measurements (Tognola *et al.*, 1997), and show that the latency-frequency relationship is not compatible with the predictions of scale-invariant full cochlear models (Talmadge *et al.*, 1998). The data are in agreement with a linear dependence of latency on the cochlear path given by the Greenwood mapping, and good agreement has also been found with a weak exponential function of the cochlear path, which is also compatible with the ABR latency-cochlear distance relationship used in ABR studies.

A statistically significant difference has been found between the average mid-frequency OAE latencies measured in normal ears and in high-frequency hearing-impaired ears. It is the first time that direct evidence is presented of a correlation between hearing impairment and OAE spectral latency increase. This result implies that some latency-related parameter could be used, in addition to other OAE parameters, for developing complex cochlear functionality indicators for screening and monitoring purposes.

Some theoretical implications of the experimental findings on cochlear models based on the transmission line formalism have been discussed. The role of the possible scale-invariance breaking terms has been analyzed. The variation of Q with frequency could explain, to some extent, the violation of the $1/f$ relation between cochlear latency and frequency. It has been shown that the physically reasonable hypothesis of an exponential dependence on x of the inductive part of the parallel inductance of the equivalent transmission line could also recover a good agreement between the OAE latency data and an explicitly scale-invariant breaking cochlear model. From the theoretical viewpoint, this work shows that cochlear transmission models may be effectively used to predict the OAE latencies and their dependence on cochlear parameters, and that, conversely, OAE spectral latency data may be used to set important constraints on theoretical models.

ACKNOWLEDGMENT

We wish to thank Dr. M. Lucertini for having provided the data and for helpful discussions.

Attias, J., Furst, M., Furman, V., Reshef, I., Horowitz, G., and Bresloff, I. (**1995**). ''Noise-induced otoacoustic emission loss with or without hearing loss,'' Ear Hear. **16**, 612–618.

Don, M., Ponton, C. W., Eggermont, J. J., and Kwong, B. (**1998**). ''The effects of sensory hearing loss on cochlear filter times estimated from auditory brainstem response latencies,'' J. Acoust. Soc. Am. **104**, 2280–2289.

Donaldson, G. S., and Ruth, R. A. (**1993**). ''Derived band auditory brainstem response estimates of traveling wave velocity in humans. I: Normal-hearing subjects,'' J. Acoust. Soc. Am. **93**, 940–951.

Donaldson, G. S., and Ruth, R. A. (**1996**). ''Derived-band auditory brainstem response estimates of traveling wave velocity in humans: II. Subjects with noise-induced hearing loss and Meniere's disease,'' J. Speech Hear. Res. **39**, 534–545.

Furst, M., and Lapid, M. (**1988**). ''A cochlear model for acoustic emissions,'' J. Acoust. Soc. Am. **84**, 222–229.

Greenwood, D. D. (**1990**). ''A cochlear frequency position function for several species—29 years later,'' J. Acoust. Soc. Am. **87**, 2592–2605.

Hussain, D. M., Gorga, M. P., Neely, S. T., Keefe, D. H., and Peters, J. (**1998**). ''Transient evoked otoacoustic emissions in patients with normal hearing and in patients with hearing loss,'' Ear Hear. **19**, 434–449.

Kim, Y., Aoyagi, M., and Koike, Y. (**1994**). ''Measurement of cochlear basilar membrane traveling wave velocity by derived ABR,'' Acta Oto-Laryngol., Suppl. **511**, 71–76.

Lucertini, M., Bergamaschi, A., and Urbani, L. (**1996**). ''Transient evoked otoacoustic emissions in occupational medicine as an auditory screening test for employment,'' Br. J. Audiol. **30**, 79–88.

Mallat, S. (**1998**). *A Wavelet Tour of Signal Processing*, 2nd ed. (Academic, San Diego), pp. 255–272.

McFadden, D., and Mishra, R. (**1993**). ''On the relation between hearing sensitivity and otoacoustic emissions,'' Hear. Res. **71**, 208–213.

Moore, B. C. (**1978**). ''Psychophysical tuning curves measured in simultaneous and forward masking,'' J. Acoust. Soc. Am. **63**, 524–532.

Moulin, A., Collet, L., Delli, D., and Morgon, A. (**1991**). ''Spontaneous otoacoustic emissions and sensory-neural hearing loss,'' Acta Oto-Laryngol. **111**, 835–841.

Murray, J. G., Cohn, E. S., Harker, L. A., and Gorga, M. P. (**1998**). ''Tone burst auditory brain stem response latency estimates of cochlear travel time in Meniere's disease, cochlear hearing loss, and normal ears,'' Am. J. Otol. **19**, 854–859.

Prieve, B. A., Gorga, M. P., Schmidt, A., Neely, S., Peters, J., Schultes, L., and Jesteadt, W. (**1993**). ''Analysis of transient-evoked otoacoustic emissions in normal-hearing and hearing-impaired ears,'' J. Acoust. Soc. Am. **93**, 3308–3319.

Probst, R., Lonsbury-Martin, B. L., Martin, G. K., and Coats, A. C. (**1987**). ''Otoacoustic emissions in ears with hearing loss,'' Am. J. Otolaryngol. **8**, 73–81.

Probst, R., Lonsbury-Martin, B. L., and Martin, G. K. (**1991**). ''A review of otoacoustic emissions,'' J. Acoust. Soc. Am. **89**, 2027–2067.

Rupa, V., and Dayal, A. K. (**1993**). ''Wave V latency shifts with age and sex in normals and patients with cochlear hearing loss: development of a predictive model,'' Br. J. Audiol. **27**, 273–279.

Sisto, R., and Moleti, A. (**1999**). ''Modeling otoacoustic emissions by active nonlinear oscillators,'' J. Acoust. Soc. Am. **106**, 1893–1906.

Sisto, R., Moleti, A., and Lucertini, M. (**2001**). ''Spontaneous otoacoustic emissions and relaxation dynamics of long decay time OAEs in audiometrically normal and impaired subjects,'' J. Acoust. Soc. Am. **109**, 638–647.

Talmadge, C. L., Tubis, A., Long, G. R., and Piskorski, P. (**1998**). ''Modeling otoacoustic emission and hearing threshold fine structures,'' J. Acoust. Soc. Am. **104**, 1517–1543.

Thornton, A. R. D., and Farrell, G. (**1991**). ''Apparent travelling wave velocity changes in cases if endolymphatic hydrops,'' Scand. Audiol. **20**, 13–18.

Tognola, G., Grandori, F., and Ravazzani, P. (**1997**). ''Time-frequency distributions of click-evoked otoacoustic emissions,'' Hear. Res. **106**, 112–122.

Watson, D. R. (**1996**). ''The effects of cochlear hearing loss, age and sex on the auditory brainstem response,'' Audiology **35**, 246–258.

Wit, H. P., van Dijk, P., and Avan, P. (**1994**). ''Wavelet analysis of real ear and synthesized click evoked otoacoustic emissions,'' Hear. Res. **73**, 141–147.

Evidence that comodulation detection differences depend on within-channel mechanisms

Stephen J. Borrill and Brian C. J. Moore[a)]

Department of Experimental Psychology, University of Cambridge, Downing Street, Cambridge CB2 3EB, United Kingdom

(Received 27 April 2001; revised 24 July 2001; accepted 10 October 2001)

The threshold for detecting a narrow-band noise signal in the presence of one or more masking noise bands is higher when the signal and masker bands have the same envelope (i.e., are comodulated) than when they have independent envelopes. This is called a comodulation detection difference (CDD). CDD might be caused by perceptual grouping of the signal and masker bands when they are comodulated. This hypothesis leads to the prediction that some masking should occur for comodulated bands, even when they are widely separated in frequency. An alternative hypothesis is that CDD occurs because, when the signal and masker bands are independent, the signal band can be detected in the dips of the masker envelope. This leads to the prediction that CDD should only occur when the masker produces significant excitation at the signal place. Experiment 1 tested these predictions in a paradigm similar to two-tone masking. The signal was a 20-Hz-wide noise centered at 1500 Hz, and the masker consisted of two bands of noise on either side of the signal frequency, whose envelopes were either comodulated (condition C) or uncorrelated (condition U) with the envelope of the signal band. In a third condition (S), the signal band was replaced by a sinusoid. The frequency separation between the signal and masker bands, Δf, was varied from 100 to 1400 Hz. Thresholds were very similar for conditions U and S; thresholds declined progressively as Δf increased beyond 200 Hz, and reached the absolute threshold for $\Delta f = 1400$ Hz. For values of Δf from 200 to 1000 Hz, thresholds were higher for condition C than for conditions U or S (i.e., a CDD occurred), but for $\Delta f = 1400$ Hz thresholds for condition C also reached absolute threshold. In experiment 2, Δf was fixed at 600 Hz and conditions were included where only the upper or the lower masker band was correlated with the signal band. Also, the overall level of the masker was systematically varied. The results indicate that the magnitude of CDD is determined by the comodulation of the signal band with the masker band producing the most masking. Overall, the results support an explanation based on the spread of excitation and dip listening, rather than an explanation based on perceptual grouping.
[DOI: 10.1121/1.1426373]

PACS numbers: 43.66.Dc, 43.66.Mk [MRL]

I. INTRODUCTION

Several researchers have studied the ability to detect a noise-band signal, centered at frequency f_s, in the presence of one or more noise bands centered away from f_s. These bands have been referred to as masking bands, cue bands, or flanking bands (FBs), and their envelopes have either been correlated (comodulated) with that of the signal band, or uncorrelated with it. In many such experiments, the envelopes of the masking bands were correlated with each other, but not with that of the signal band envelope; the maskers in this case are referred to as ‘‘co-uncorrelated.’’ Typically, detection of the signal is better in the co-uncorrelated condition than when all bands, for both signal and masker, have the same envelope (correlated condition) (Cohen and Schubert, 1987; McFadden, 1987). The difference in threshold is often referred to as a ‘‘comodulation detection difference’’ (CDD). Also, thresholds are usually lower in the co-uncorrelated condition than when all bands are independent (all-uncorrelated condition); in fact, performance in the correlated and all-uncorrelated conditions tends to be very similar (McFadden and Wright, 1990; Wright, 1990).

In some ways, the stimuli used in experiments on CDD resemble those used in experiments on comodulation masking release (CMR) (Hall *et al.*, 1984a; Hall *et al.*, 1995; Moore, 1992). However, in the case of CMR, the task is usually to detect a sinusoidal signal centered in a band of noise (the on-frequency band), in the presence of one or more FBs. The envelopes of the FBs are either correlated with that of the on-frequency band (comodulated), or independent of it (uncorrelated). In CMR experiments, thresholds are lowest when the FBs are comodulated with the on-frequency band, whereas in CDD experiments thresholds are highest when the FBs are comodulated with the signal band.

Some researchers have suggested that both CMR and CDD depend partly on perceptual grouping processes. Common modulation of noise bands in different frequency regions may cause the noise bands to be perceptually fused, while independent modulation may cause them to be perceptually segregated (Bregman *et al.*, 1990; Darwin and Carlyon, 1995; Moore, 1997). In the case of CDD, it may be easier to detect a narrow-band noise when it is perceptually

[a)]Author to whom correspondence should be addressed.

segregated from the FBs (the co-uncorrelated condition) than when it is grouped together with the FBs (the correlated condition) (McFadden, 1987; Wright, 1990). In the case of CMR, when all of the masker bands are comodulated, the presence of the sinusoidal signal introduces a difference in modulation pattern in different frequency regions, and this might enhance the segregation of the signal from the background, thereby improving detectability.

If perceptual grouping on the basis of common modulation is responsible for both CDD and CMR, then one might expect the magnitude of CDD and CMR to vary in a similar way with modulation rate. This rate can be manipulated either directly or through variations in bandwidth of the noises; the average rate of envelope fluctuation increases with increasing bandwidth (Rice, 1954). CMR becomes smaller when the modulation rate of the maskers increases (Carlyon *et al.*, 1989) or when the masker bandwidth is increased (Schooneveldt and Moore, 1987; Hall *et al.*, 1988). However, Fantini and Moore (1994) showed that the difference in threshold between correlated and co-uncorrelated conditions (i.e., the amount of CDD) hardly changed with bandwidth. This suggests that different mechanisms underlie CMR and CDD.

Perceptual grouping may be regarded as a process that involves comparison of the outputs of auditory filters tuned to different center frequencies, i.e., an across-channel process. CDD has often been discussed in terms of an across-channel process (MacFadden, 1987; Wright, 1990). However, Fantini and Moore (1994) suggested that CDD might arise partly or exclusively from within-channel processes, i.e., from processes dependent on the output of a single auditory filter centered close to the signal frequency. They pointed out that in CMR experiments, the on-frequency band is usually similar in level to the FBs, while in CDD experiments, the signal band has a much lower level than the FBs. In CDD experiments, the amount of excitation evoked by the FBs at the signal band frequency would be similar to the excitation evoked by the signal band itself. Wright (1990) also considered the possibility that within-channel processes might account for CDD. However, she concluded that within-channel processes were not adequate to account for the results entirely. She argued that if CDD was caused by within-channel processes, then the magnitude of CDD should increase with decreasing frequency separation of the target and FBs. This was not found to be the case. It should be remembered, however, that the magnitude of CDD is specified as the difference between thresholds obtained in the different conditions (correlated, co-uncorrelated, and all-uncorrelated). On a within-channel explanation, there is no obvious reason why the *differences* between conditions should vary as a function of frequency separation between the signal band and FBs.

Some aspects of the results of Cohen and Schubert (1987) are more consistent with a within-channel explanation than with an across-channel explanation based on perceptual grouping. They measured CDD using a single FB centered at 1000 Hz with an overall level of 73 dB SPL and a signal band with variable center frequency. For an explanation based on perceptual grouping, there is no obvious reason why CDD should depend on whether the signal band is centered above or below the frequency of the masker band. In fact, CDDs up to about 10 dB were observed when the signal band was centered above the frequency of the masker band, but the CDDs were 2 dB or less when the signal frequency was below 800 Hz. Cohen and Schubert (1987) reasoned that when the envelopes of the signal and masker bands are independent, there will be times when the masker level is low and the signal level is high. Subjects may be able to listen for the signal in the ''dips'' of the uncorrelated masker, using the output of an auditory filter centered close to the signal frequency (Zwicker and Schutte, 1973; Buus, 1985; Moore and Glasberg, 1987a). Therefore, thresholds will be lower than when the masker and signal envelopes are correlated and no dip listening is possible.

The finding of a larger CDD when the signal was centered above the masker frequency could be related to the nonlinearity on the basilar membrane; input–output functions on the basilar membrane are highly compressive for frequencies close to the characteristic frequency, but become more linear for frequencies well below the characteristic frequency (Rhode and Robles, 1974; Sellick *et al.*, 1982; Ruggero *et al.*, 1997). In a CDD experiment, if the subject monitors a place on the basilar membrane tuned close to the signal center frequency, the response to the signal band will be compressive, while the response to a masker band centered well below the signal frequency will be linear. This tends to enhance the advantage gained from dip listening (Buus, 1985; Moore and Glasberg, 1987a; Nelson and Schroder, 1996; Wojtczak *et al.*, 2001).

In the present paper, we explore CDD using a stimulus paradigm similar to one that has been used in the past to measure the critical bandwidth or the auditory filter shape, namely two-tone masking (Zwicker, 1954; Patterson and Henning, 1977; Glasberg *et al.*, 1984a; Fastl and Schorer, 1986). In this paradigm, the threshold is measured for detecting a narrow-band noise signal with center frequency f_s in the presence of two sinusoids (at frequencies $f_s \pm \Delta f$). Two maskers are used to minimize off-frequency listening, i.e., the use of the output of auditory filters centered away from the signal frequency (Johnson-Davies and Patterson, 1979; O'Loughlin and Moore, 1981). A noise-band signal is used to reduce the influence of beats for small frequency separations between the signal and maskers. The inherent amplitude fluctuations in a narrow-band noise signal reduce the salience of beats as a cue (Egan and Hake, 1950; Zwicker and Fastl, 1990; Moore *et al.*, 1998). In some experiments, the masker has been composed of two bands of noise and a sinusoidal signal has been used (Fastl and Schorer, 1986). This also reduces the influence of beats as a cue.

In the experiments described here, two narrow bands of noise centered on either side of the signal frequency were used as maskers. The correlation of the masker bands with respect to the signal band was altered, allowing CDD to be measured. By comparing the results with those obtained using a sinusoidal signal, we hoped to gain some insight into the extent to which the results could be explained in terms of ''traditional'' (within-channel) masking processes. In the first experiment, the two masking bands were correlated with each other. We were particularly concerned with the question of whether there was significant masking in the correlated condition when the signal and masker bands were widely separated in frequency. A within-channel explanation leads to the prediction that masking in the correlated condition should only occur when the masker produces significant excitation at the signal ''place.'' Thus, the amount of masking in the correlated condition should approach zero at about the same signal–masker frequency separation as for the co-uncorrelated condition and the condition with the sinusoidal signal. On the other hand, it appears that perceptual grouping can occur for widely separated frequency bands; for example, CMR can occur when the on-signal and flanking bands are remote in frequency (Schooneveldt and Moore, 1987). If higher thresholds in the correlated condition are due to perceptual grouping of the signal and masker, some masking in that condition would be expected to occur even when the masker produces no excitation at the signal place. Thus, masking would be expected for the correlated condition at masker–signal frequency separations where there is no masking for the co-uncorrelated condition and the condition with the sinusoidal signal.

In the second experiment, we included conditions where either the upper or the lower masker band was correlated with the signal band, the other masker band being uncorrelated with the signal band. This was done to allow us to determine which of the two masker bands was most important in determining the amount of CDD. We used the results to test the prediction derived from a within-channel explanation of CDD, that the magnitude of CDD is determined by the correlation of the signal band with the masker band that produces the most masking; the correlation of the signal band with the other masker band should be of little importance.

II. EXPERIMENT 1

A. Method

1. Stimuli

The task was to detect a signal which was either a 20-Hz-wide band of noise or a sinusoid. The signal frequency (f_s) was 1500 Hz. The masker was composed of two 20-Hz-wide bands of noise which were correlated with each other. The bands were centered at frequencies of $f_s - \Delta f$ and $f_s + \Delta f$. The value of Δf was 100, 200, 300, 429, 600, 800, 1000, or 1400 Hz (the value of 429 Hz was included for comparison with the results of an earlier experiment, which is not reported here). One subject (GPM) was not tested with the 100- and 300-Hz values of Δf. There were three different signal conditions: correlated (where all three bands of noise had correlated amplitude modulation; co-uncorrelated (where the masking bands were correlated with each other, but the signal was uncorrelated); and sinusoidal (where the signal was a sinusoid).

The noise-band signal and maskers were generated digitally using either a Masscomp 5400 or a Silicon Graphics Indy computer. Two ''tracks'' were generated. The signal was put on one track and the maskers on the other. Each 20-Hz-wide band of noise was produced by adding together 201 sinusoids spaced 0.1-Hz apart, each with a random phase and amplitude (being drawn from a rectangular and Rayleigh distribution, respectively). Each band of noise was therefore a harmonic series with a 0.1-Hz fundamental. One full period (10 s) of each track was calculated, after which the track could be recycled, to create a continuous noise.

To make two bands correlated, the phase and amplitude of each component in one band were the same as for the analogous component in the other band. For example, the first components in the two bands had the same phase and amplitude, even though they had different frequencies. The signal and masker were played out simultaneously through twin 16-bit digital-to-analog converters (Masscomp DA04H) at a sampling rate of 16 000 Hz. They were low-pass filtered at 7 kHz using Kemo VBF8 filters (96 dB/oct slope) and then recorded onto separate channels of a digital audio tape (DAT–Sony 55ES). The tape was then played continuously for each condition. The sinusoidal signal was also generated digitally, with the same sampling rate, and was recorded onto DAT in the same way as for the noise-band signal.

The signal was gated with 50-ms raised-cosine ramps and with a steady-state duration of 300 ms. The signal was presented at random in one of three observation intervals which were marked by lights on the response box. The intervals were separated by 200 ms. The masker was gated simultaneously with the three intervals in which the signal might appear. The start of each trial was initiated by the subject's response on the previous trial. As the subjects did not respond after a fixed time, the noise samples on a specific trial were, in effect, randomly chosen from the continuously recycling signal and masker tracks.

Signal timing was controlled by a Texas Instruments 990/4 computer. Two analog multipliers (AD534L) connected in series were used as a gate. The gating voltage was derived from a 12-bit digital-to-analog converter. The signal level was controlled by a Charybdis model D programmable attenuator. The signal and masker were mixed using an active adder and then passed through a manual attenuator before being delivered to the left earpiece of a Sennheiser HD 414 headset. The masker bands each had a spectrum level of 65 dB (re: 20 μPa) and an overall level of 78 dB SPL.

A continuous low-pass noise was added to the stimuli to mask possible combination bands (Greenwood, 1971, 1972). The level of the low-pass noise was adjusted so that it had a spectrum level of 38 dB at the frequency $f_s - 2\Delta f$ (i.e., the frequency at which a cubic-difference band may have been present). No noise was used for values of Δf greater than $0.5 f_s$ (i.e., 750 Hz) as $f_s - 2\Delta f$ would be negative in these cases. In any case, the level of cubic distortion products is very low for large frequency separations of the primary components. The low-pass noise was produced by filtering a white noise (Hewlett Packard 3722A) using four 48 dB/octave low-pass filters (Kemo VBF/8) in series. The steep cutoff of 192 dB/oct was used to ensure that at small values of Δf there was as little masking as possible of the lower noise band. The −3-dB point of each filter was set to 1350, 1200, 1000, 800, and 400 Hz, for values of Δf of 100, 200, 300, 429, and 600 Hz, respectively.

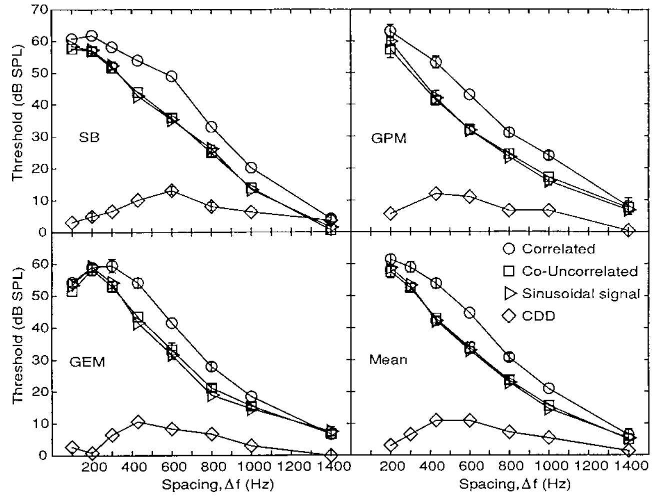

FIG. 1. Results of experiment 1, showing thresholds as a function of the frequency separation, Δf, of each masker noise band from the signal frequency. The bottom-right panel shows mean results, while the other panels show individual results. The signal was either a sinusoid (triangles), or a band of noise which was correlated (circles) or co-uncorrelated (squares) with the masker bands. The diamonds indicate the amount of CDD, defined as the difference between thresholds for the correlated and co-uncorrelated conditions. This is measured in dB, not dB SPL.

2. Procedure

Masked thresholds were estimated using a three-alternative, forced-choice method with an adaptive three-down, one-up procedure estimating the 79.4% point on the psychometric function (Levitt, 1971). The initial step size was 5 dB. After three reversals, the step size was decreased to 2 dB. A run was terminated after 12 reversals. The threshold was defined as the mean of the levels at the last eight reversals. Three thresholds estimates were obtained for each condition, and a fourth was obtained if the range of the first three exceeded 3 dB. The final threshold value was taken as the mean of these three (or four) estimates. Subjects were tested individually in a double-walled sound-attenuating booth. Feedback was provided on the response box.

3. Subjects

Three subjects participated, all with absolute thresholds less than 10 dB HL at all audiometric frequencies. Their mean absolute threshold at the signal frequency of 1500 Hz, determined using the same forced-choice procedure as described above, was 6 dB SPL. All subjects had experience with psychophysical experiments, having previously completed an earlier experiment measuring CDD with similar stimuli. All subjects were given as much practice as they needed to become stable on the conditions used (generally less than 4 h was needed).

B. Results and discussion

The results are shown separately for each subject in Fig. 1. The results are broadly similar across subjects. The bottom right-hand panel shows the mean results. Thresholds for all three conditions decline progressively with increasing frequency separation between the signal and masker bands, Δf, once the value of Δf exceeds 200 Hz. The lowest curve in each panel shows the amount of CDD, calculated as the difference between thresholds for the correlated and co-uncorrelated conditions. The CDD shows a maximum of 10–12 dB at separations of 429 and 600 Hz. The decline in CDD at small separations may have been caused by the interaction of the signal and masker bands in the peripheral auditory system, which would lead to beats and roughness. All subjects reported a roughness for $\Delta f = 100$ and 200 Hz. Note that, although the use of noise-band maskers reduces the salience of beats as a cue for signal detection, it does not completely prevent the use of such a cue. Indeed, the prominent envelope fluctuations in the 20-Hz-wide noise bands (Lawson and Uhlenbeck, 1950; Rice, 1954) were at much lower frequencies than the 100- and 200-Hz beats produced by interaction of the signal and masker bands, and so the former would have had little effect on the detectability of the latter (Dau *et al.*, 1997). The audible beats and roughness probably were responsible for the decrease in thresholds observed for subjects SB and GEM at the smallest frequency separations (recall that subject GPM was not tested at the 100-Hz separation). The decline in CDD for the smallest values of Δf probably occurred because the salience of beats and roughness was at least as great for the correlated as for the co-uncorrelated condition.

The decline in CDD for large values of Δf probably occurred because the masked thresholds in both the correlated and co-uncorrelated conditions approached the absolute threshold. Obviously, if the bands produce little or no masking in either condition, the CDD must be small. It is noteworthy that the amount of masking in the correlated condition did approach zero at large values of Δf. If the higher thresholds in the correlated condition were due to perceptual grouping of the signal and masker bands, one might expect some masking to occur in that condition even for very large frequency separations of the signal and masker bands. This was not the case.

A striking feature of the results is that thresholds are almost identical for the co-uncorrelated condition and for the condition in which the signal was a sinusoid. Recall that the latter condition is one which has been used in the past to estimate frequency selectivity; indeed, if the auditory filter is assumed to be roughly symmetrical on a linear frequency scale, the plot of signal threshold as a function of signal-to-masker frequency separation can be considered as directly representing the auditory filter shape at the signal frequency (Patterson and Henning, 1977; Glasberg *et al.*, 1984a; Fastl and Schorer, 1986). The masked thresholds in the correlated condition are higher than those for both the co-uncorrelated and sinusoidal signal conditions, for intermediate values of Δf. One possible explanation for the higher thresholds in the correlated condition has already been mentioned; in this condition the signal and masker bands may fuse perceptually, making it more difficult to detect the signal. But, as described above, this explanation is not consistent with the observation that the amount of masking in the correlated condition declined to zero for large values of Δf. A more plausible explanation is that the correlated condition does not allow the possibility of ‘‘dip listening,’’ while the other two conditions do; in the correlated condition the signal-to-noise

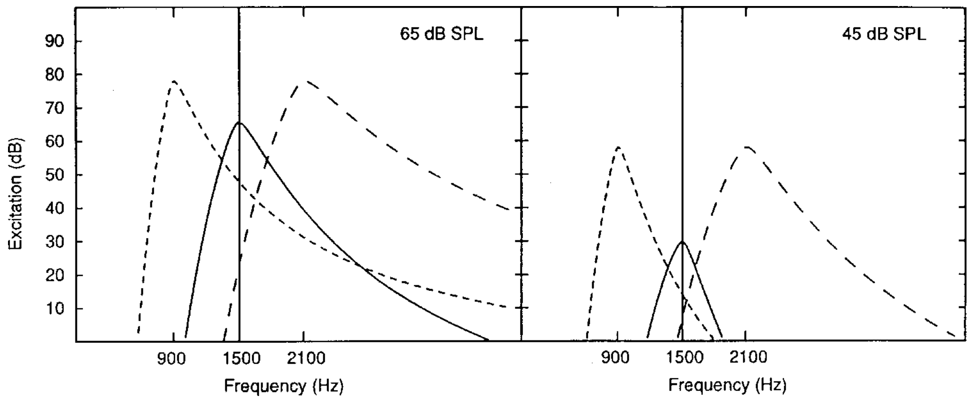

FIG. 2. Illustration of the rationale for experiment 2. Excitation patterns evoked by the masker (short- and long-dashed lines) and signal (solid lines) bands were calculated using the procedure described by Glasberg and Moore (1990) for masker spectrum levels of 65 (left) and 45 (right) dB. At the higher masker level, the excitation evoked by the lower band overlaps more with the signal excitation than the excitation evoked by the upper band. At the lower level, the overlap with the signal excitation is similar for the two masker bands.

ratio does not vary over time. This explanation is explored in more detail later in this paper.

III. EXPERIMENT 2. ASSESSING THE RELATIVE EFFECTS OF THE MASKING BANDS

A. Rationale

Experiment 1 used as a masker two narrow bands of noise which were linearly spaced on either side of the signal frequency. While the auditory filter is roughly symmetric on a linear frequency scale at moderate masker levels, it tends to become increasingly asymmetric, with a shallower low-frequency skirt, at high masker levels (Lutfi and Patterson, 1984; Moore and Glasberg, 1987b; Glasberg and Moore, 1990; Rosen *et al.*, 1998; Baker *et al.*, 1998; Glasberg and Moore, 2000). It seems likely that for the masker level used in experiment 1, the lower masker band produced more masking than the upper masker band. In experiment 2, the spectrum level of the masking bands was varied from 45 to 65 dB. One would expect that for the lowest level, the upper band would produce about as much masking as the lower band (Zwicker and Jaroszewski, 1982; Moore and Glasberg, 1987b; Rosen *et al.*, 1998). This is illustrated in Fig. 2, which shows excitation patterns of the masker and signal bands calculated using the procedure described by Glasberg and Moore (1990) for masker spectrum levels of 65 and 45 dB. At the higher masker level, the excitation evoked by the lower masker band overlaps with the signal excitation much more than the excitation evoked by the upper masker band. At the lower level, the overlap of signal and masker excitation is similar for the two masker bands.

In experiment 2, the correlation of each of the masker bands with the signal band was set independently; each could be either correlated or uncorrelated with the signal band and with the other masker band. The main question addressed was: is the magnitude of CDD determined by the correlation of the signal band with the masker band producing the most masking? If CDD is mainly based on within-channel processes, then one would expect this to be the case. For example, for a high masker level the lower masker band should produce more masking than the upper masker band. In this case, one can make the following predictions: (1) the threshold should be higher when the lower band is correlated with the signal band than when it is uncorrelated; (2) the threshold should be higher when only the lower masker band is correlated with the signal band than when only the upper band is correlated; (3) the threshold should be largely unaffected by whether or not the upper band is correlated with the signal band.

If CDD is determined by an across-channel process, then the magnitude of CDD will not necessarily be determined solely by the correlation of the signal band with the masker band producing the most masking. Indeed, for other phenomena that are assumed to depend on across-channel processes, such as CMR, increasing the number of correlated bands leads to a greater effect, while introducing one or a small number of uncorrelated bands lead to a marked disruption of the effect (Hall *et al.*, 1988; Hall and Grose, 1990; Hall *et al.*, 1990).

B. Method

1. Stimuli

The task was to detect a 20-Hz-wide noise signal centered at 1500 Hz. The signal was masked by two 20-Hz-wide bands of noise centered at 900 and 2100 Hz, corresponding to a Δf of 600 Hz; this value of Δf led to a large CDD in experiment 1. The masking noises had spectrum levels of 45, 55, and 65 dB SPL. They were generated in the same way as for experiment 1. A continuous low-pass noise with a -3-dB point of 400 Hz was presented with the maskers, to mask combination tones. The level of the noise was set so that its spectrum level at 300 Hz (the center frequency of the combination band at $2f_1-f_2$) was 27 dB lower than that of the masking bands. The low-pass noise was produced by filtering a white noise (Hewlett Packard 3722A) using four 48-dB/octave low-pass filters (Kemo VBF/8) in series.

To check that the low-pass noise would not produce a significant masking effect on the signal, a pilot experiment was conducted in which signal thresholds were measured without the narrow-band noise maskers. Only one subject was used for this. Three different noise spectrum levels were used; 18, 28, and 38 dB at 300 Hz. These correspond to the levels used in the experiment proper. The pilot experiment was also performed with no background noise at all. The background noise had a negligible effect on the signal threshold; even for the highest low-pass noise level, the amount of masking was less than 2 dB.

Five different combinations of signal–masker envelope correlation were used. The conditions were

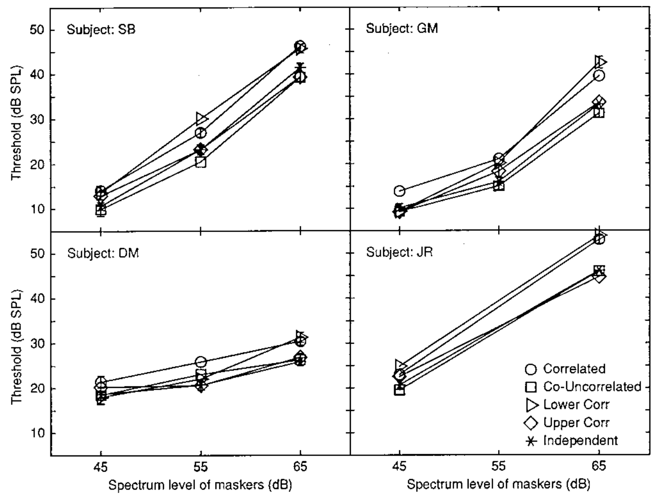

FIG. 3. Individual results of experiment 2, showing the signal threshold plotted as a function of the spectrum level of the maskers. Each symbol represents a specific condition, as indicated in the key.

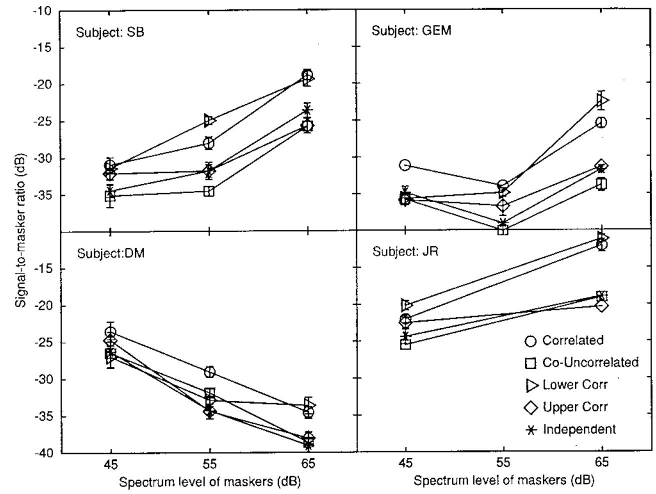

FIG. 4. The data from Fig. 3, replotted in terms of the ratio of signal level to masker spectrum level at threshold.

(1) Correlated: Both masker bands were correlated with the signal band.
(2) Co-uncorrelated: The two masker bands were correlated with each other but not with the signal band.
(3) Upper correlated: The upper masker band was correlated with the signal band while the lower band was uncorrelated.
(4) Lower correlated: The lower masker band was correlated with the signal band while the upper band was uncorrelated.
(5) Independent: All three bands had uncorrelated envelopes.

2. Procedure

The procedure was the same as for experiment 1.

3. Subjects

Four subjects participated, all with absolute thresholds less than 10 dB HL at all audiometric frequencies. Subjects SB, DM, and GEM had extensive experience in previous experiments on CDD. Subject JR was a new subject. All subjects were given as much practice as they needed to become stable on the conditions used (generally less than 4 h was needed). JR was given about 8 h of practice as she had no previous experience. JR was not tested at the middle noise level (55 dB SPL).

C. Results and discussion

The results for the individual subjects are shown in Fig. 3; signal thresholds are plotted as a function of masker spectrum level. Figure 4 shows the same data but with thresholds expressed as signal-to-masker ratio in dB. At the same relatively high masker level as used in experiment 1 (spectrum level of 65 dB, overall level of 78 dB SPL), the results fall clearly into two groups: the conditions in which the lower band was correlated with the signal band (correlated and lower correlated), which give higher thresholds, and the conditions in which the lower band was uncorrelated with the signal band (co-uncorrelated, upper correlated, and independent), which give lower thresholds. Thus, the correlation of the lower masker band with the signal band is the critical factor; the correlation of the upper band is unimportant. This is exactly as predicted by a within-channel account of CDD.

At the lowest masker level, one would expect the upper band of noise to produce a similar amount of masking to the lower band. Therefore, a within-channel explanation of CDD predicts that as the masker level is reduced, the correlation of the upper band with the signal band should become as important as the correlation of the lower band. The data are consistent with this prediction. At the lowest masker level, the condition giving the highest threshold, for three out of the four subjects, was the correlated condition, where both masker bands were correlated with the signal band. When only the lower or upper masker band was correlated with the signal band, thresholds tended to be slightly lower than for the correlated condition, but still slightly above those for the co-uncorrelated or independent conditions.

Perhaps the most clear-cut predictions relate to the asymmetric conditions, where either the upper or lower masker band was correlated with the signal band. For the highest masker level, thresholds are predicted to be higher for the lower correlated condition. For the lowest masker level, thresholds are predicted to be more similar for the two conditions. Figure 5 shows results for these two conditions. All four subjects show results that tend toward the predicted direction. A two-way within-subjects analysis of variance was performed with the factors correlation condition (lower correlated and upper correlated) and spectrum level (65 and 45 dB). Both main effects were significant: for correlation condition, $F(1,3)=14.16$, $p=0.033$; for level, $F(1,3)=26.57$, $p=0.014$. The interaction between correlation condition and spectrum level was also significant: $F(1,3)=114.79$, $p=0.002$. A Scheffé *post hoc* analysis showed that a significant difference between correlation conditions only occurred at the higher spectrum level ($p<0.01$).

The individual differences apparent in Fig. 5 are probably related to differences in the asymmetry of the auditory filter, and in the way that the asymmetry changes with level. Such individual differences have been demonstrated in pre-

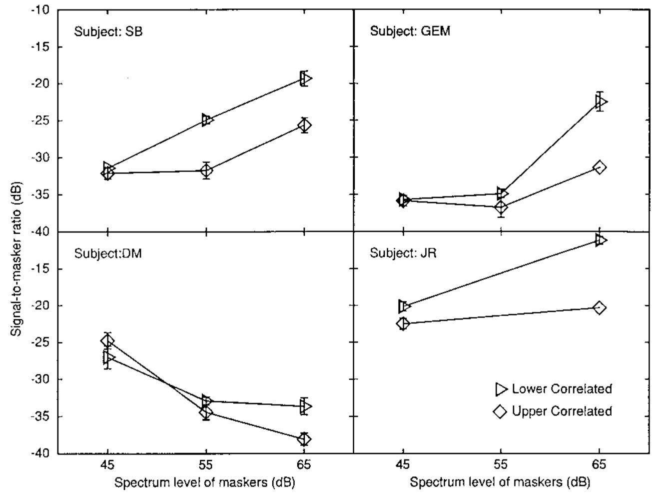

FIG. 5. Results for the lower correlated (triangles) and upper correlated (diamonds) conditions, showing the signal-to-masker ratio at threshold plotted as a function of masker spectrum level.

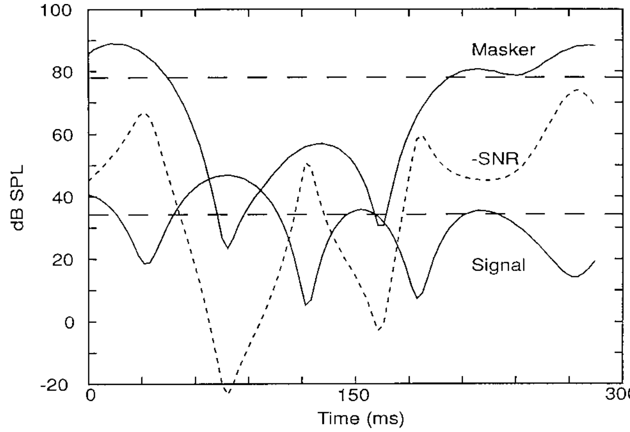

FIG. 6. An example of the envelopes produced by the method described in the text for uncorrelated signal and masker bands (solid lines). The masker level was 78 dB overall, and the signal level was set to the mean value determined in experiment 1 for the co-uncorrelated condition with $\Delta f = 600$ Hz. The noise-to-signal ratio is shown as the dashed line marked -SNR). The units for the SNR are, of course, dB, not dB SPL.

vious studies (Glasberg *et al.*, 1984b; Lutfi and Patterson, 1984; Rosen *et al.*, 1998). However, no direct measures were made of auditory filter asymmetry in the subjects of the present experiment.

In summary, the results of experiment 2 are entirely consistent with predictions based on a within-channel explanation of CDD. For an across-channel explanation, there is no obvious reason why the magnitude of CDD should depend on the correlation of the signal band with the masker band producing the greatest masking.

IV. A MODEL BASED ON DETECTION TIMES

A. Outline

In this section we present a model for CDD based on the output of a single auditory filter and the concept of ‘‘multiple looks’’ (Viemeister and Wakefield, 1991). The model operates on 300-ms segments of the masker and signal, as used in the experiments. A sliding window is used to select a number of sequential sections of the masker and signal. The output of the window is fed to a simulated auditory filter centered on the signal frequency. The level dependence of the filter is controlled by the instantaneous masker level in the chosen section. The signal-to-masker ratio at the output of filter is calculated and compared to a criterion ratio. If the signal-to-masker ratio is above the criterion, then that section is counted as providing a detection opportunity or ‘‘look’’ in which it is possible for the signal to be detected. The sliding window is advanced throughout the sample and the total number of detection opportunities is calculated, from which the cumulative detection time can be calculated. It is assumed that performance is monotonically related to the cumulative detection time.

A weakness of this model is that it operates on the signal-to-masker ratio at the output of the filter, rather than on the output of the filter *per se*. There is no explicit mechanism for determining the signal-to-masker ratio at any instant. We consider later on what sort of information might be used by the auditory system to select the ‘‘looks,’’ i.e., to know when the detection opportunities occur. We regard the model as a way of testing the idea that within-channel processes are sufficient to account for the data.

B. Detailed description

Bursts of signal and masker noise bands were calculated in a similar way to that used to make the stimuli. The duration of the each burst was 300 ms, the same as the steady-state portion of the stimuli. The masker and signal samples were separately analyzed. First, the root-mean-square (rms) value of the whole 300-ms sample was calculated; this corresponded to the overall level. Second, a sliding rectangular window 200 samples in size (12.5 ms) was applied to the sample. The window size was chosen to be comparable to the equivalent rectangular duration of the auditory temporal window measured by Moore *et al.* (1988) and Plack and Moore (1990). The window was placed at the start of the whole sample and the rms value of the 200-sample windowed segment was calculated. The difference between the rms value of the windowed segment and the overall rms value was used to calculate the level of the windowed segment. The window was then advanced by 50 samples (3.125 ms) and the rms level recalculated. The process was repeated until all 4800 samples had been covered.

Examples of the output of the sliding temporal integrator for co-uncorrelated signal and masker bands are shown by the solid lines in Fig. 6. For this example, the samples were not passed through a simulated auditory filter. The masker level was 78 dB overall, and the signal level was set to the mean value (about 34 dB) determined in experiment 1 for the co-uncorrelated condition with $\Delta f = 600$ Hz. The noise-to-signal ratio (shown as the dashed line marked -SNR) fluctuates markedly from moment to moment and reaches an extreme value of -20 dB, i.e., the signal-to-masker ratio reaches $+20$ dB. The horizontal lines represent the long-term rms levels of the masker and signal bands.

A block diagram of the operation of the model is shown in Fig. 7. The output of the sliding temporal integrator was

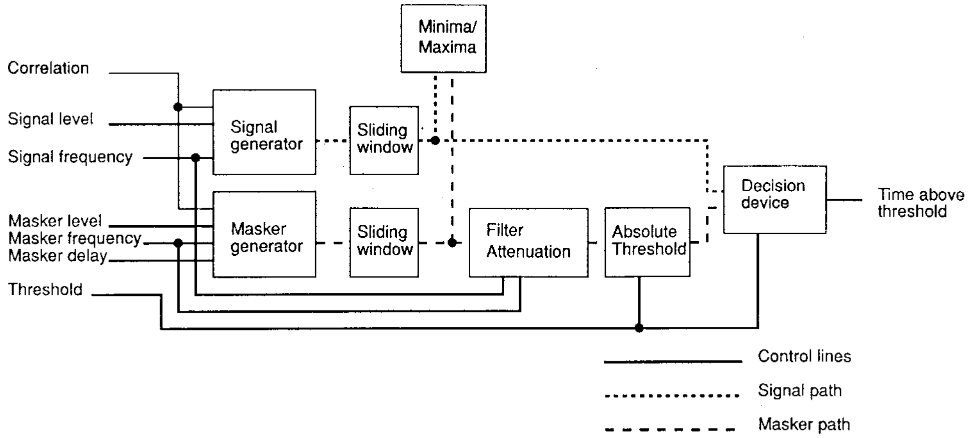

FIG. 7. A block diagram of the operations in the model.

passed to a simulated auditory filter centered at the signal frequency. (For ease of computation, the signal and masker were initially processed separately, and the signal was not passed through the filter. However, as the filter was centered at the signal frequency, and was assumed to have 0-dB gain at its tip, this had no effect on the outcome.) A rounded-exponential filter was used, based on the roex(p) filter described by Patterson *et al.* (1982). It is convenient to measure frequency in terms of the absolute value of the deviation from the center frequency of the filter, f_0, and to normalize this frequency variable by dividing by the center frequency of the filter. The new frequency variable, g, is

$$g=|f-f_0|/f_0. \tag{1}$$

The roex(p) filter shape is then given by

$$W(g)=(1+pg)\exp(-pg), \tag{2}$$

where W(g) is the intensity-weighting function describing the filter shape and p is a parameter which determines both the bandwidth and the slope of the skirts of the auditory filter. The higher the value of p, the more sharply tuned the filter.

To allow for the asymmetry of the filter, the parameter p was allowed to take different values on each side of the filter, i.e., p_l and p_u. Glasberg and Moore (1990) suggested that for an input level of 51 dB/ERB, p_l and p_u are roughly equal. They suggested further that p_u was almost invariant with level, whereas the value of p_l increases with increasing input level. We assumed, following Moore *et al.* (1997), that the value of p_l at an input level X (in dB/ERB) was given by the equation

$$p_{l(X)}=p_{l(51)}-0.35(X-51), \tag{3}$$

where $p_{l(51)}$ is value of p_l for an effective input level of 51 dB/ERB. This is a slightly modified form of the equation suggested by Glasberg and Moore (1990). The value of $p_{l(51)}$ was taken to be 34.1, as suggested by Glasberg and Moore for a center frequency of 1500 Hz. In combination, these equations allowed us to estimate the level of the masker at the output of the filter for any given long-term or short-term input masker level. The influence of the signal level on the filter shape was assumed to be negligible, as that level was very low compared to the masker level at the input to the filter.

The masker level and the signal level at the output of the filter were compared for each temporal position of the window and if the signal-to-noise ratio (SNR) was greater than a certain threshold value (the detection opportunity threshold, DOT), the segment was taken as providing a detection opportunity. The cumulative detection opportunity time was then incremented by 3.125 ms. To simulate the effect of absolute threshold, a constant was added to the output of the filter; the constant was chosen so that the predicted masked threshold would approach absolute threshold for large values of Δf. To choose an appropriate value for the DOT, the mean data from experiment 1 for $\Delta f=600$ Hz were used. The signal level at the input to the model was set to the mean threshold measured for the four subjects. Stimuli from both the correlated and co-uncorrelated conditions were applied to the model. The model was evaluated for several different values of the DOT, expressed as a signal-to-noise ratio. For both the correlated and co-uncorrelated conditions, 100 samples of the signal and masker were analyzed. The results are shown in Fig. 8.

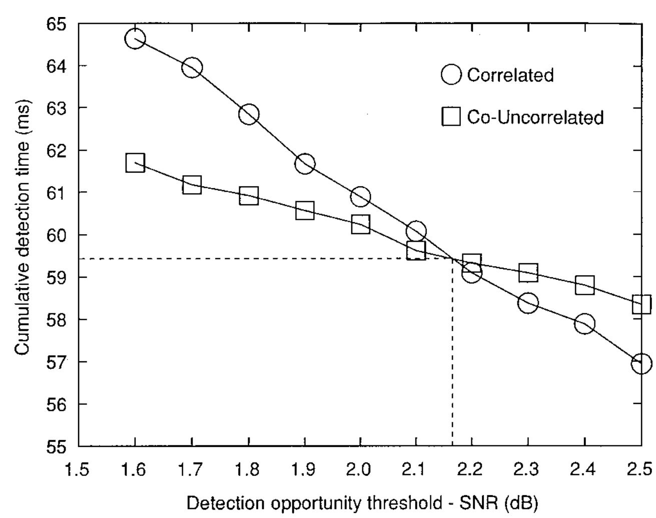

FIG. 8. Cumulative detection time plotted as a function of the signal-to-noise ratio required for a detection opportunity to occur (the detection opportunity threshold, DOT). Model outcomes are shown for the correlated condition (circles) and the co-uncorrelated condition (squares). The DOT and cumulative detection time are equal for the two conditions when the DOT equals 2.17 dB and the cumulative detection time equals 59.5 ms, as indicated by the dashed lines.

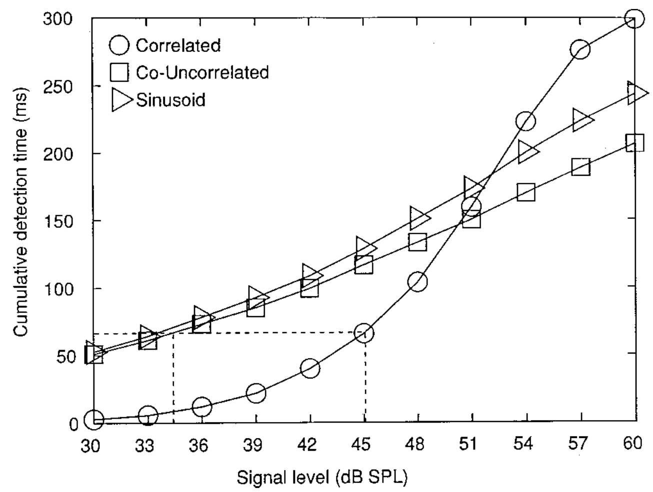

FIG. 9. Cumulative detection time plotted as a function of signal level for the correlated (circles), co-uncorrelated (squares), and sinusoid (triangles) conditions. The horizontal dashed line is plotted at the value of the cumulative detection time that is assumed to be required for threshold. Vertical dashed lines indicate the signal thresholds for the co-uncorrelated and correlated conditions.

For both the correlated and co-uncorrelated conditions, the cumulative detection time decreases as the DOT increases. This is not surprising for the co-uncorrelated condition, but it may not be immediately obvious why it occurs for the correlated condition; the reason is connected with the level dependence of the auditory filter. In the correlated condition, the input signal-to-masker ratio does not vary from moment to moment. However, when the masker level is at a momentary maximum, the filter becomes broader, thus giving a lower signal-to-masker ratio at the filter output than would be obtained with a level-independent filter. Similarly, when the masker level is at a momentary minimum, the filter becomes sharper and the signal-to-masker ratio increases. Hence, the signal-to-masker ratio at the output of the filter varies from moment to moment, even though the input ratio is fixed.

The decrease in cumulative detection time with increasing DOT is greater for the correlated than for the co-uncorrelated condition, and there is a DOT at which the cumulative detection time is the same for the two conditions. This DOT was the value chosen for use in the model. In other words, we assumed that a constant total detection time leads to constant performance. The DOT corresponded to a SNR of 2.17 dB. The corresponding cumulative detection time was 59.5 ms. The standard deviation of the cumulative detection time across the 100 samples of signal and masker, measured at the DOT of 2.17 dB, was 23 ms for the correlated condition and 16 ms for the co-uncorrelated condition.

C. Applying the model

The model as described here has the limitation that it allows for only one masking band. However, for the masker level used in experiment 1, the lower-frequency noise band would have dominated the masking. Therefore, it is reasonable to apply the model to the conditions of experiment 1, but taking only the lower-frequency masker band into account. Figure 9 shows the cumulative detection time as a function of signal level for the three conditions, correlated, co-uncorrelated, and sinusoidal, for $\Delta f = 600$ Hz, taking the DOT as corresponding to a SNR of 2.17 dB. At the criterion cumulative detection time of 59.5 ms, the signal levels in the correlated and co-uncorrelated conditions correspond to the mean obtained thresholds. This is, of course, as it should be, since the criterion cumulative detection time was selected to achieve this condition. More importantly, for the sinusoidal condition, the signal level at the criterion cumulative detection time corresponds very well with the mean obtained threshold; the predicted threshold is very slightly below that for the co-uncorrelated condition, which corresponds exactly to the obtained result.

If it is assumed that detectability is monotonically related to the cumulative detection time, then the functions in Fig. 9 should be monotonically related to psychometric functions. The model therefore predicts that the psychometric functions for the correlated and co-uncorrelated conditions should have different slopes. Indeed, the model predicts that at sufficiently high signal levels, a correlated signal should be more detectable than an uncorrelated signal. The reason for this is that at high signal levels the signal will always be above the masker level in the correlated condition. This is not true for the co-uncorrelated condition; even if the signal level is high enough for the signal to be highly detectable, there will be brief epochs when the SNR is below the DOT. However, the predicted crossover of the psychometric functions for the correlated and co-uncorrelated conditions might not be experimentally measurable, as performance might be close to ceiling for cumulative detection times above, say, 100 ms. The prediction of a difference in slopes of the psychometric functions in the region of masked threshold, is, however, experimentally testable. An experiment to be described in a future publication shows that the prediction is correct.

As a further test of the model, we used the model to predict the data for experiment 1, for the correlated and co-uncorrelated conditions (again taking into account only the masking effect of the lower masker band). We did not attempt to make predictions for values of Δf below 300 Hz, since, as argued earlier, the data for small values of Δf were probably influenced by beats and roughness, effects which are not incorporated in the model. The predictions are shown in Fig. 10. They reflect the general form of the data reasonably well; deviations can probably be accounted for by the simplified model of the auditory filter used in the model (which did not have a "tail" segment) and by the simple but probably inaccurate way of simulating the effect of absolute threshold. Overall, the model accounts well for the data.

V. DISCUSSION

We have presented evidence that CDD is not based on perceptual grouping processes, but probably depends on a within-channel process, similar to the process of "listening in the dips" (Zwicker and Schutte, 1973; Buus, 1985; Moore and Glasberg, 1987a; Hall *et al.*, 1995). We have also described a model of the way that this process might work. We do not claim that this is the only possibility, but it is a plausible one. The results do not rule out some role for across-

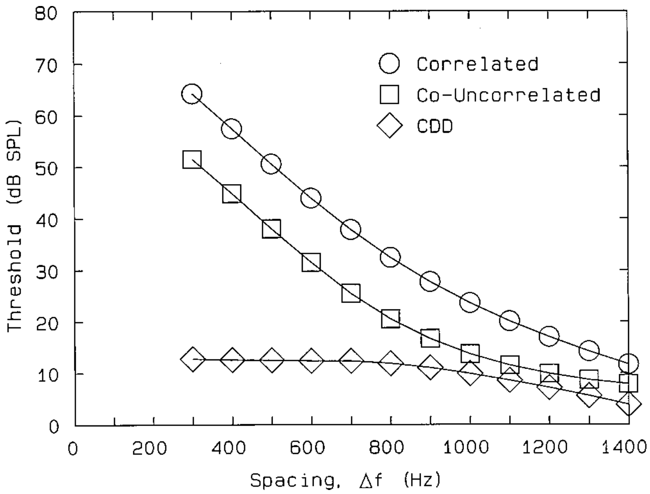

FIG. 10. Model predictions for the results of experiment 1 for the correlated (circles) and co-uncorrelated (squares) conditions. The predicted CDD (diamonds) is also shown.

channel processes, but the outcome of the modeling suggests that within-channel processes are sufficient to account for the results.

For within-channel explanations, such as that proposed above, it remains unclear exactly how subjects might be able to take advantage of moments when the SNR is relatively high. One possibility is that the presence of the signal is indicated by a reduced effective modulation depth, as the signal band will tend to "fill in" the dips in the masker band in the co-uncorrelated condition (Schooneveldt and Moore, 1989). In other words, a change in envelope distribution is the detection cue. Another possibility is that subjects are able selectively to extract information at times corresponding to dips in the masker envelope, as assumed in our model. They might do this by making use of changes in the temporal fine structure of the signal (Schooneveldt and Moore, 1987; Fantini and Moore, 1994); during times when the masker is dominant, the fine structure would correspond to the masker center frequency, while during the masker dips the fine structure would partly reflect the signal frequency.

It is also possible that across-channel information is used to indicate the appropriate times to listen; temporal dips at the outputs of channels tuned away from the signal frequency could be used to indicate the optimum times to use the output of the filter centered at the signal frequency (Moore, 1988; Buus *et al.*, 1996). For this type of explanation, information is extracted primarily from the output of a single auditory filter, but information from filters with other center frequencies indicates the optimum times at which to sample the output of the single filter. However, the results of experiment 2 suggest that across-channel information may not have been used to signal the appropriate times to listen. The upper noise band should have been as effective as the lower band in signaling these times, but for the highest masker level the correlation of the upper band with the signal band had no influence on signal thresholds.

We have argued that within-channel processes are probably sufficient to account for the main features of CDD. It is of interest that many aspects of CMR can also be accounted for by within-channel processes (Schooneveldt and Moore, 1987, 1989; Verhey *et al.*, 1999). However, in the case of CMR, some role for across-channel processes is generally accepted. For example, CMR can be produced by adding correlated bands of noise to the ear contralateral to that receiving the signal and on-frequency masker (Hall *et al.*, 1984b). It may be the case that perceptual grouping processes can sometimes help to reduce detection thresholds, as in the case of CMR (Hall and Grose, 1990), but that they rarely lead to increased detection thresholds. In a CDD paradigm, even if correlated masker and signal bands are perceptually grouped, the presence or absence of the signal may still be heard as a change in timbre.

ACKNOWLEDGMENTS

This work was supported by the MRC (UK). We thank Marjorie Leek and two anonymous reviewers for helpful comments on an earlier version of this paper.

Baker, R. J., Rosen, S., and Darling, A. M. (**1998**). "An efficient characterization of human auditory filtering across level and frequency that is also physiologically reasonable," in *Psychophysical and Physiological Advances in Hearing*, edited by A. R. Palmer, A. Rees, A. Q. Summerfield, and R. Meddis (Whurr, London).

Bregman, A. S., Liao, C., and Levitan, R. (**1990**). "Auditory grouping based on fundamental frequency and formant peak frequency," Can. J. Psychol. **44**, 400–413.

Buus, S. (**1985**). "Release from masking caused by envelope fluctuations," J. Acoust. Soc. Am. **78**, 1958–1965.

Buus, S., Zhang, L., and Florentine, M. (**1996**). "Stimulus-driven, time-varying weights for comodulation masking release," J. Acoust. Soc. Am. **99**, 2288–2297.

Carlyon, R. P., Buus, S., and Florentine, M. (**1989**). "Comodulation masking release for three types of modulator as a function of modulation rate," Hear. Res. **42**, 37–46.

Cohen, M. F., and Schubert, E. D. (**1987**). "The effect of cross-spectrum correlation on the detectability of a noise band," J. Acoust. Soc. Am. **81**, 721–723.

Darwin, C. J., and Carlyon, R. P. (**1995**). "Auditory grouping," in *Hearing*, edited by B. C. J. Moore (Academic, San Diego).

Dau, T., Kollmeier, B., and Kohlrausch, A. (**1997**). "Modeling auditory processing of amplitude modulation. I. Detection and masking with narrow-band carriers," J. Acoust. Soc. Am. **102**, 2892–2905.

Egan, J. P., and Hake, H. W. (**1950**). "On the masking pattern of a simple auditory stimulus," J. Acoust. Soc. Am. **22**, 622–630.

Fantini, D. A., and Moore, B. C. J. (**1994**). "Profile analysis and comodulation detection differences using narrow bands of noise and their relation to comodulation masking release," J. Acoust. Soc. Am. **95**, 2180–2191.

Fastl, H., and Schorer, E. (**1986**). "Critical bandwidth at low frequencies reconsidered," in *Auditory Frequency Selectivity*, edited by B. C. J. Moore and R. D. Patterson (Plenum, New York).

Glasberg, B. R., and Moore, B. C. J. (**1990**). "Derivation of auditory filter shapes from notched-noise data," Hear. Res. **47**, 103–138.

Glasberg, B. R., and Moore, B. C. J. (**2000**). "Frequency selectivity as a function of level and frequency measured with uniformly exciting notched noise," J. Acoust. Soc. Am. **108**, 2318–2328.

Glasberg, B. R., Moore, B. C. J., and Nimmo-Smith, I. (**1984a**). "Comparison of auditory filter shapes derived with three different maskers," J. Acoust. Soc. Am. **75**, 536–544.

Glasberg, B. R., Moore, B. C. J., Patterson, R. D., and Nimmo-Smith, I. (**1984b**). "Dynamic range and asymmetry of the auditory filter," J. Acoust. Soc. Am. **76**, 419–427.

Greenwood, D. D. (**1971**). "Aural combination tones and auditory masking," J. Acoust. Soc. Am. **50**, 502–543.

Greenwood, D. D. (**1972**). "Masking by combination bands: Estimation of the levels of the combination bands $(n+1)f_1 - nf_h$," J. Acoust. Soc. Am. **52**, 1144–1154.

Hall, J. W., and Grose, J. H. (**1990**). ''Comodulation masking release and auditory grouping,'' J. Acoust. Soc. Am. **88**, 119–125.
Hall, J. W., Grose, J. H., and Haggard, M. P. (**1988**). ''Comodulation masking release for multi-component signals,'' J. Acoust. Soc. Am. **83**, 677–686.
Hall, J. W., Grose, J. H., and Haggard, M. P. (**1990**). ''Effects of flanking band proximity, number, and modulation pattern on comodulation masking release,'' J. Acoust. Soc. Am. **87**, 269–283.
Hall, J. W., Grose, J. H., and Mendoza, L. (**1995**). ''Across-channel processes in masking,'' in *Hearing*, edited by B. C. J. Moore (Academic, San Diego).
Hall, J. W., Haggard, M. P., and Fernandes, M. A. (**1984a**). ''Detection in noise by spectro-temporal pattern analysis,'' J. Acoust. Soc. Am. **76**, 50–56.
Hall, J. W., Haggard, M. P., and Harvey, A. D. G. (**1984b**). ''Release from masking through ipsilateral and contralateral comodulation of a flanking band,'' J. Acoust. Soc. Am. Suppl. 1 **76**, S76.
Johnson-Davies, D., and Patterson, R. D. (**1979**). ''Psychophysical tuning curves: Restricting the listening band to the signal region,'' J. Acoust. Soc. Am. **65**, 765–770.
Lawson, J. L., and Uhlenbeck, G. E. (**1950**). *Threshold Signals*, Vol. 24, Radiation Laboratory Series (McGraw-Hill, New York).
Levitt, H. (**1971**). ''Transformed up–down methods in psychoacoustics,'' J. Acoust. Soc. Am. **49**, 467–477.
Lutfi, R. A., and Patterson, R. D. (**1984**). ''On the growth of masking asymmetry with stimulus intensity,'' J. Acoust. Soc. Am. **76**, 739–745.
McFadden, D., and Wright, B. A. (**1990**). ''Temporal decline of masking and comodulation detection differences,'' J. Acoust. Soc. Am. **88**, 711–724.
McFadden, D. M. (**1987**). ''Comodulation detection differences using noise-band signals,'' J. Acoust. Soc. Am. **81**, 1519–1527.
Moore, B. C. J. (**1988**). ''Dynamic aspects of auditory masking,'' in *Auditory Function: Neurobiological Bases of Hearing*, edited by G. Edelman, W. Gall, and W. Cowan (Wiley, New York).
Moore, B. C. J. (**1992**). ''Across-channel processes in auditory masking,'' J. Acoust. Soc. Jpn. (E) **13**, 25–37.
Moore, B. C. J. (**1997**). *An Introduction to the Psychology of Hearing*, 4th ed. (Academic, San Diego).
Moore, B. C. J., Alcántara, J. I., and Dau, T. (**1998**). ''Masking patterns for sinusoidal and narrow-band noise maskers,'' J. Acoust. Soc. Am. **104**, 1023–1038.
Moore, B. C. J., and Glasberg, B. R. (**1987a**). ''Factors affecting thresholds for sinusoidal signals in narrow-band maskers with fluctuating envelopes,'' J. Acoust. Soc. Am. **82**, 69–79.
Moore, B. C. J., and Glasberg, B. R. (**1987b**). ''Formulae describing frequency selectivity as a function of frequency and level and their use in calculating excitation patterns,'' Hear. Res. **28**, 209–225.
Moore, B. C. J., Glasberg, B. R., and Baer, T. (**1997**). ''A model for the prediction of thresholds, loudness and partial loudness,'' J. Audio Eng. Soc. **45**, 224–240.
Moore, B. C. J., Glasberg, B. R., Plack, C. J., and Biswas, A. K. (**1988**). ''The shape of the ear's temporal window,'' J. Acoust. Soc. Am. **83**, 1102–1116.
Nelson, D. A., and Schroder, A. C. (**1996**). ''Release from upward spread of masking in regions of high-frequency hearing loss,'' J. Acoust. Soc. Am. **100**, 2266–2277.
O'Loughlin, B. J., and Moore, B. C. J. (**1981**). ''Off-frequency listening: Effects on psychoacoustical tuning curves obtained in simultaneous and forward masking,'' J. Acoust. Soc. Am. **69**, 1119–1125.
Patterson, R. D., Nimmo-Smith, I., Weber, D. L., and Milroy, R. (**1982**). ″The deterioration of hearing with age: frequency selectivity, the critical ratio, the audiogram, and speech threshold,″ J. Acoust. Soc. Am. **72**, 1788–1803.
Patterson, R. D., and Henning, G. B. (**1977**). ''Stimulus variability and auditory filter shape,'' J. Acoust. Soc. Am. **62**, 649–664.
Plack, C. J., and Moore, B. C. J. (**1990**). ''Temporal window shape as a function of frequency and level,'' J. Acoust. Soc. Am. **87**, 2178–2187.
Rhode, W. S., and Robles, L. (**1974**). ''Evidence from Mössbauer experiments for non-linear vibration in the cochlea,'' J. Acoust. Soc. Am. **55**, 588–596.
Rice, S. O. (**1954**). ''Mathematical analysis of random noise,'' in *Selected Papers on Noise and Stochastic Processes*, edited by N. Wax (Dover, New York).
Rosen, S., Baker, R. J., and Darling, A. (**1998**). ''Auditory filter nonlinearity at 2 kHz in normal hearing listeners,'' J. Acoust. Soc. Am. **103**, 2539–2550.
Ruggero, M. A., Rich, N. C., Recio, A., Narayan, S. S., and Robles, L. (**1997**). ''Basilar-membrane responses to tones at the base of the chinchilla cochlea,'' J. Acoust. Soc. Am. **101**, 2151–2163.
Schooneveldt, G. P., and Moore, B. C. J. (**1987**). ''Comodulation masking release (CMR): Effects of signal frequency, flanking-band frequency, masker bandwidth, flanking-band level, and monotic versus dichotic presentation of the flanking band,'' J. Acoust. Soc. Am. **82**, 1944–1956.
Schooneveldt, G. P., and Moore, B. C. J. (**1989**). ''Comodulation masking release (CMR) as a function of masker bandwidth, modulator bandwidth and signal duration,'' J. Acoust. Soc. Am. **85**, 273–281.
Sellick, P. M., Patuzzi, R., and Johnstone, B. M. (**1982**). ''Measurement of basilar membrane motion in the guinea pig using the Mössbauer technique,'' J. Acoust. Soc. Am. **72**, 131–141.
Verhey, J. L., Dau, T., and Kollmeier, B. (**1999**). ''Within-channel cues in comodulation masking release (CMR): Experiments and model predictions using a modulation-filterbank model,'' J. Acoust. Soc. Am. **106**, 2733–2745.
Viemeister, N. F., and Wakefield, G. H. (**1991**). ''Temporal integration and multiple looks,'' J. Acoust. Soc. Am. **90**, 858–865.
Wojtczak, M., Schroder, A. C., Kong, Y.-Y., and Nelson, D. A. (**2001**). ''The effect of basilar-membrane nonlinearity on the shapes of masking period patterns in normal and impaired hearing,'' J. Acoust. Soc. Am. **109**, 1571–1586.
Wright, B. A. (**1990**). ''Comodulation detection differences with multiple signal bands,'' J. Acoust. Soc. Am. **87**, 292–303.
Zwicker, E. (**1954**). ''Die Verdeckung von Schmalbandgeräuschen durch Sinustöne,'' Acustica **4**, 415–420.
Zwicker, E., and Fastl, H. (**1990**). *Psychoacoustics—Facts and Models* (Springer, Berlin).
Zwicker, E., and Jaroszewski, A. (**1982**). ''Inverse frequency dependence of simultaneous tone-on-tone masking patterns at low levels,'' J. Acoust. Soc. Am. **71**, 1508–1512.
Zwicker, E., and Schutte, H. (**1973**). ''On the time pattern of the threshold of tone impulses masked by narrow-band noise,'' Acustica **29**, 343–347.

Relations among early postexposure noise-induced threshold shifts and permanent threshold shifts in the chinchilla

Roger P. Hamernik,[a] William A. Ahroon, James H. Patterson, Jr.,[b] and Wei Qiu
Auditory Research Laboratory, State University of New York, 107 Beaumont Hall, Plattsburgh, New York 12901

(Received 23 January 2001; revised 27 July 2001; accepted 24 October 2001)

Threshold shifts (TS) were measured at various times following a wide variety of noise exposures on over 900 chinchillas. An analysis of postexposure TS measures and noise-induced permanent threshold shift (PTS) showed that, across audiometric test frequency, there was a consistent relation between these variables of the form PTS (dB) $= \alpha(e^{\mathrm{TS}/\beta} - 1)$, where, for a given test frequency, α (dB) and β (dB) are constants. TSs were measured immediately following exposure (TS_0), 24 h after exposure (TS_{24}), and at several intermediate times in order to estimate the maximum TS (TS_{max}). Correlation between TS and PTS at the various test frequencies was highest for TS_{24}. An analysis of the 90th-percentile PTS showed a linear growth of PTS with TS_{24} of approximately 0.7 dB PTS/dB TS_{24}. These data provide some support, in the chinchilla model, for a variation of the three postulates originally presented by Kryter *et al.* [J. Acoust. Soc. Am. **39**, 451 (1966)]. Specifically: (i) TS_{24} is a consistent measure of the effects of a traumatic noise exposure. (ii) All exposures that produce a given TS_{24} will be equally hazardous. (iii) Noise-induced PTS in the most susceptible animals, following many years of exposure, is approximately equal to $(0.7)\mathrm{TS}_{24}$ measured after an 8-h exposure to the same noise. [DOI: 10.1121/1.1428545]

PACS numbers: 43.66.Ed, 43.50.Pn, 43.50.Qp [MRL]

I. INTRODUCTION

Temporary threshold shift (TTS) and compound threshold shift (CTS) measured on subjects following exposure to noise have been fundamental measures of the effects of a noise exposure on hearing in laboratory experiments using human and other mammalian species for more than 50 years. CTS differs from TTS in that the postexposure-shifted threshold recovers toward the preexposure levels but the recovery is not complete, leaving the subject with a permanent threshold shift (PTS). CTS is associated with a damaged sensory epithelium. Unlike the TTS experiments, which often used human subjects, experimentation that produced a CTS was invariably conducted on various nonhuman species.

Since it seemed reasonable to assume that temporary losses of hearing were somehow related to permanent losses (Reger and Lierle, 1954), the former simply being a milder manifestation of the latter, TTS experiments became very popular. While a considerable amount has been learned about the behavior of TTS and its relation to exposure parameters, the results have arguably had a modest impact on our knowledge of how noise-induced permanent threshold shift (NIPTS) accumulates over a working lifetime.

Data on TTS ultimately found their greatest practical application in noise-exposure criteria (e.g., Kryter *et al.*, 1966). Implicit in the development of the Kryter *et al.* document was the acceptance of three postulates: (a) TTS measured 2 min after an exposure (TTS_2) is a consistent measure of the effects of a single day's exposure to noise. (b) All exposures that produce a given TTS_2 will be equally hazardous; and (c) NIPTS following 10 years of exposure, 8 h/day is approximately equal to the TTS_2 measured after an 8-h exposure to the same noise. At the time these three postulates were published, their insecure foundations were clearly recognized. There is still not a sufficient database available from which the validity of these postulates can be assessed for industrial workers.

Auditory threshold shifts (TS) following noise exposure represent a complex response whose biophysical substrata are still not completely understood. The magnitude of the shift, whether a TTS or a CTS (Miller *et al.*, 1963), its frequency specificity, and its postexposure time course, which is dependent upon the magnitude of the TS, vary in a complex manner with the exposure stimulus parameters. The early stages of fatigue described by Hirsh and Ward (1952) and by Hirsh and Bilger (1955), in which TS was shown to have a diphasic profile during the first two minutes (TTS_2) postexposure, led to the adoption of TTS_2 as an index of the effects of an exposure, i.e., Kryter's postulate (a). As stimulus levels increased it became clear that complex TS dynamics was not just limited to the early postexposure period, but could also be found in the steady growth of TS over 8 to 12 h following a high-level exposure (Luz and Hodge, 1971; Hamernik *et al.*, 1988; Dancer *et al.*, 1991). This growth of TS has been associated with mechanical disruption of the structural integrity of the organ of Corti, and in animal models has been shown to be associated with sensory cell loss and NIPTS (Hamernik *et al.*, 1988).

An underlying rationale that pervades many of the TS studies is the desire to estimate PTS based upon some measure of TS. This goal has remained elusive despite some

[a] Electronic mail: roger.hamernik@plattsburgh.edu
[b] Also at U.S. Army Aeromedical Research Laboratory, P.O. Box 620577, Fort Rucker, AL 36362-5292.

novel attempts such as the use of time-integrated TS as an index of PTS (Sitler, 1972; Kraak, 1973). Thorough reviews of TS phenomena can be found in the literature (e.g., Ward, 1973; Kraak, 1981; Mills, 1986). This paper presents an analysis of the relation between TS measured at various postexposure times and the resulting PTS using a database obtained from over 900 chinchillas exposed to various noises.

II. METHODS

All data were obtained from chinchillas that were used in various noise-exposure experiments over a period of approximately 7 years in two different laboratories using different experimental protocols. All animals were made monaural by the surgical destruction of the left cochlea. Pure-tone thresholds were measured in each animal using either a behavioral avoidance-conditioning technique (Patterson *et al.*, 1993) or evoked-response audiometry (Ahroon *et al.*, 1996). The electrode for recording the auditory-evoked potentials (AEP) was implanted into the left inferior colliculus during the monauralizing surgery. Following surgery all animals were allowed to recover for 2 weeks before any preexposure testing began. All animals were awake during threshold testing. The average of at least three separate threshold determinations at each frequency obtained on different days was used to define the preexposure audiogram. Following a 30-day postexposure recovery period, thresholds were measured again on 3 different days and averaged for each animal to establish PTS. PTS was defined as the difference between the mean 30-day post- and preexposure audiograms.

The TS data obtained from the 936 chinchillas that were used in this analysis were separated into the following three data sets based on the type of noise exposure that was used.

Data set I ($N=192$): Acute exposures to broadband or narrow-band impacts having peak SPLs in the range 129 through 147 dB. All exposures lasted for 5 min. Thresholds were measured at 2 min, 1 h, 3 h, 6h, and 24 h postexposure at a number of frequencies using a behavioral avoidance-conditioning paradigm. Only thresholds at the octave intervals of 0.125, 0.250, 0.5, 1.0, 2.0, 4.0, and 8.0 kHz were used in the following analysis. Details of exposure and threshold testing procedures can be found in Patterson *et al.* (1993).

Data set II ($N=423$): Acute exposures to high-level, broadband impulses having peak SPLs in the range 150 through 160 dB. Exposures lasted from a fraction of a second (e.g., a single impulse) to 16.5 hours (e.g., 100 impulses; 1 impulse every 10 min). Thresholds were measured using evoked-response audiometry recorded from the inferior colliculus. TS measures were obtained 15 min, 2 h, 8 h, and 24 h postexposure at 0.5, 2.0, and 8.0 kHz. Details of the exposure and threshold testing protocols can be found in Ahroon *et al.* (1996).

Data set III ($N=321$): Five-day uninterrupted exposures to broadband impacts, octave bands of noise, or combinations of these two classes of noise. These exposures produced an asymptotic threshold shift (ATS) (Blakeslee *et al.*, 1978). Peak SPLs of the impacts ranged from 113 through 125 dB and rms levels of the octave band noises varied between 86 and 95 dB. Threshold shifts were obtained at 15 min, 2 h, 8 h, and 24 h postexposure at 0.5, 2.0, and 8.0 kHz. Details of the exposures and threshold testing protocols can be found in Ahroon *et al.* (1993).

Correlations between TSs and PTS, over a broad range of audiometric test frequencies, were possible only for data set I. Data from the three test frequencies measured in data sets II and III were used to verify and expand the observations made from data set I.

From the postexposure threshold recovery function for each animal, the following three TS measures were obtained for correlation with PTS at the corresponding frequency:

(1) TS_0: The first TS measured between 0 and approximately 20 min postexposure;
(2) TS_{max}: The maximum TS measured in the 0- to 24-h postexposure period (Hamernik *et al.*, 1988).
(3) TS_{24}: The TS measured 24 h following removal from the noise.

III. RESULTS AND DISCUSSION

The analysis presented below treats all TSs as equivalent, regardless of the type of noise exposure (continuous octave band, continuous non-Gaussian, impact or impulse) or frequency spectrum that produced the TS.

A. Scatter plots

Some perspective on the relation between TS and PTS can be obtained by plotting the PTS for each test frequency from each of the three data sets (together or separately) as a function of each of the three TS measures. An example of the resulting scatter plots for the 0.5-, 2.0-, and 8.0-kHz test frequencies for the entire data pool is shown in Fig. 1. The data at these frequencies represent the largest pool available for analysis ($n=936$). There is considerable variability in the data. For example, during the early postexposure period (TS_0) there are large numbers of animals that show $0<TS<80$ dB. After a 30-day recovery period, these same animals show $0<PTS<10$ dB. Similarly, animals with, for example, $60<TS<70$ dB can show $0<PTS<60$ dB. While some relatively small part of this variability is inherent in the experimental methods, the largest component most likely reflects variability in susceptibility (Ward, 1968) to noise, as has been often reported in the literature especially following impulse/impact noise exposures. For those animals with no PTS (i.e., $-5<PTS<5$ dB) the postexposure TSs can be considered TTSs. Also seen in Fig. 1 is a number of animals with $PTS<-5$ dB despite having a broad range of TSs, reflecting either inadequately defined pre- or postexposure thresholds or a ‘‘real’’ improvement in thresholds following noise exposure. The animals presented in this analysis had preexposure thresholds that were typically within ± 1 s.d. of the laboratory norms (Hamernik and Qiu, 2000) with typical test/retest reliability of ± 5 dB.

Because the data shown in Fig. 1 suggest both linear and nonlinear relations among the TS/PTS variables, a function that would allow nonlinear and (nearly) linear descriptions of the data of the form $PTS=\alpha(e^{TS/\beta}-1)$ was chosen to describe the results of the three data sets. This relation allows PTS to be zero with zero TS; it is nonlinear for small values

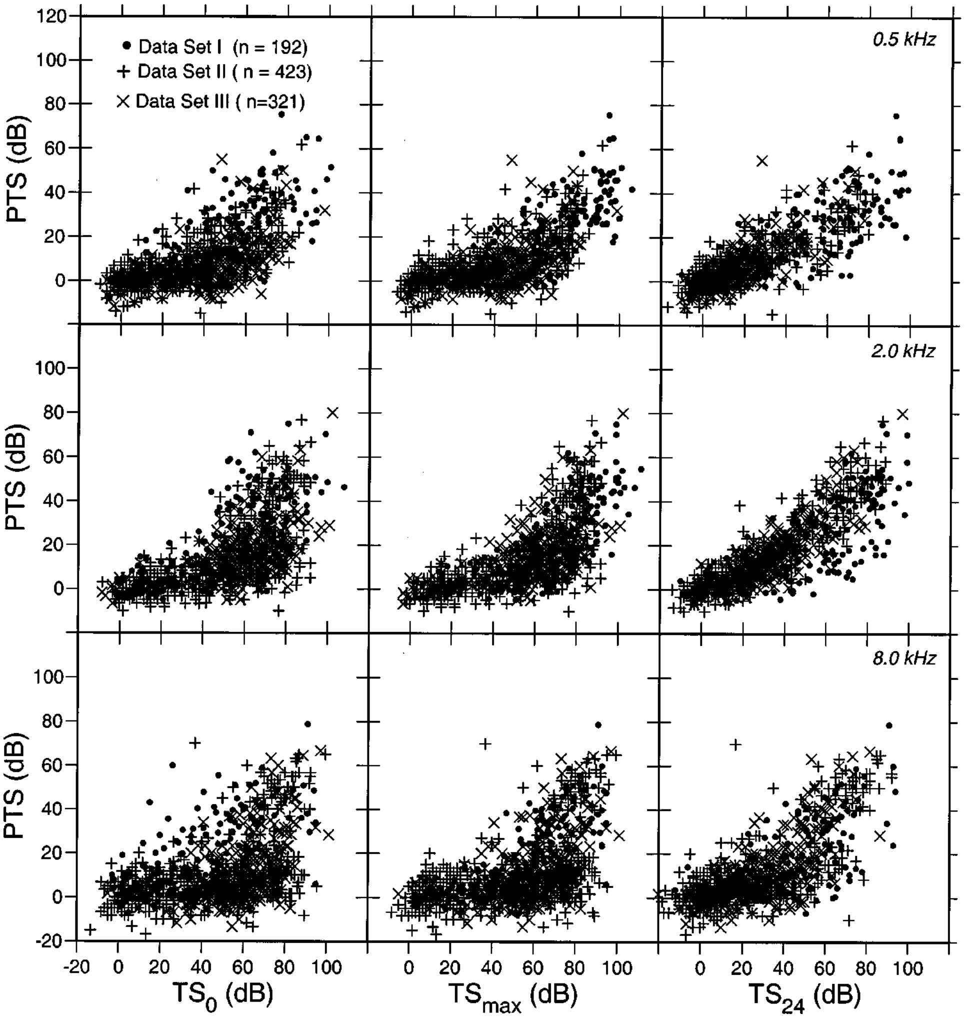

FIG. 1. Scatter graphs displaying threshold shift immediately following noise exposure (TS_0), maximum threshold shift (TS_{max}), and threshold shift 24 h following exposure (TS_{24}) with the corresponding permanent threshold shifts at the 0.5-, 2.0-, and 8.0-kHz test frequencies for data sets I, II, and III.

of the variable β and approaches linearity for larger values of β. A power series expansion of this function shows that the exponential becomes linear of the form $PTS=(\alpha/\beta)TS$, for large values of β, with a slope of α/β and a zero intercept. All bivariate regression and correlation analyses were computed using DELTAGRAPH PROFESSIONAL on a Macintosh computer. The constants α, β, and coefficients of determinance r^2, which were obtained following a nonlinear regression analysis, for each frequency and data set are shown in Table I. In general, the highest correlations were found for the TS_{24}/PTS relation. This was expected for at least two reasons. (i) Since many of the severe exposure conditions produced a growth of TS (Hamernik *et al.*, 1988) TS_0 will underestimate the PTS and (ii) a large part of the TTS component of CTS, which is arguably the most labile part, has recovered during the 24-h postexposure period (see also Pfander *et al.*, 1980). Also evident in this table are the typically smaller values of the constant β for the TS_{max} data compared to the TS_0 and TS_{24} data. This can be explained by noting that TS_{max} is equal to TS_0 for smaller (<30 dB) values of TS. At these levels of TS NIPTS is small but increases rapidly when there is a postexposure growth of TS (i.e., when $TS_0 < TS_{max}$).

The trends in this data are more clearly seen when the predictor TS measurements are collapsed into 5-dB bins and the mean TS within the bin is plotted against the mean PTS for that bin. Examples of such a data reduction at the 2-kHz test frequency for each of the data sets are shown in Fig. 2. [This statistical manipulation (or "pretreatment") has the added benefit of eliminating skewness in the predictor vari-

TABLE I. Coefficients of determinance (r^2) and the constants α (dB) and β (dB) for the exponential curve fit for the relation between PTS and TS_0, TS_{max}, and TS_{24} for all three data sets.

		TS_0			TS_{max}			TS_{24}	
kHz	r^2	α	β	r^2	α	β	r^2	α	β
				Data set I					
0.125	0.47	23.8	90.0	0.54	3.9	35.4	0.58	17.2	69.5
0.25	0.57	28.0	93.2	0.59	3.2	34.3	0.62	19.8	77.1
0.5	0.57	48.4	140.6	0.65	5.5	44.3	0.66	64.7	183.2
1.0	0.55	61.4	163.0	0.66	7.8	50.4	0.67	48.3	139.2
2.0	0.58	40.7	118.0	0.63	5.1	42.1	0.64	17.5	69.4
4.0	0.50	128.1	310.0	0.53	7.4	50.7	0.52	33.1	106.1
8.0	0.45	209.9	480.2	0.51	6.7	47.0	0.53	26.5	88.5
				Data set II					
0.5	0.49	6.1	46	0.54	8.4	58.5	0.66	64.7	183.2
2.0	0.54	7.2	46.6	0.59	1.7	29.1	0.85	39.2	96.0
8.0	0.33	6.4	49.6	0.32	3.5	36.9	0.64	9.9	45.1
				Data set III					
0.5	0.34	2.3	34	0.34	2.3	34.4	0.58	42.1	119.0
2.0	0.31	4.9	43.9	0.32	10.1	66.4	0.65	24.8	72.4
8.0	0.26	7.5	60.1	0.27	7.0	57.6	0.50	6.9	36.0

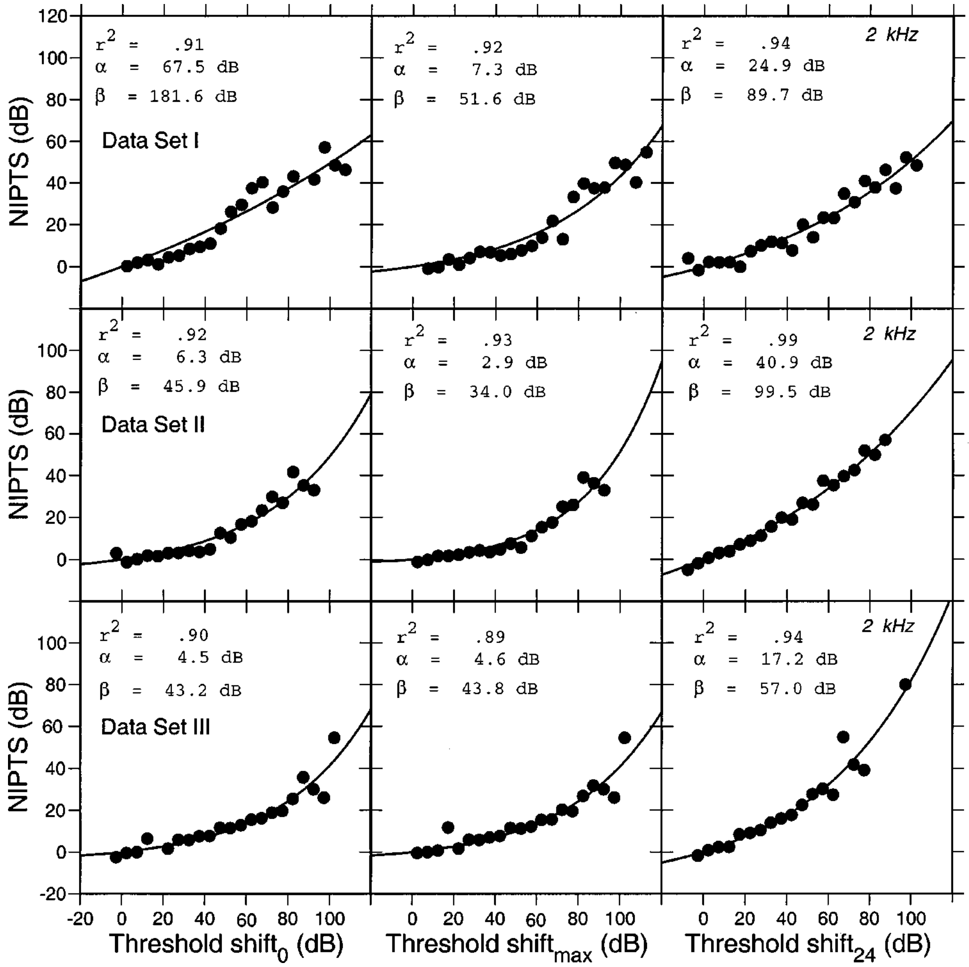

FIG. 2. The 5-dB bin reduction of the scatter plot data displaying threshold shifts immediately following noise exposure (TS_0), maximum threshold shift (TS_{max}), and threshold shift 24 h following exposure (TS_{24}) with the corresponding permanent threshold shifts at the 2.0-kHz test frequency for data sets I, II, and III. The solid curves represent a least-squares approximation to the exponential function $f(x) = \alpha(e^{TS/\beta} - 1)$.

ables.] In this figure, the abscissa represents the midpoint of a TS bin and the ordinate is the mean PTS for the subjects displaying the TS measure within the 5-dB bin. In general, the graphs for each data set and each frequency were similar and clearly show a positive relation between the TS variables and PTS. The 5-dB bin analysis, as expected, yields deceptively high correlation coefficients.

B. Percentile results

Noise-exposure criteria are typically designed to protect a certain percentile of the exposed population from an NIHL. Audiometric testing of employees in industrial settings is usually performed following a period of respite from the noise environment. With such considerations in mind the entire data set was analyzed using the same nonlinear function to relate TS_{24} to the median and 90th percentile PTS data. Figure 3 illustrates the exponential regression curves for the median (lower curve in each panel) and 90th percentile (upper curve) PTS within each 5-dB TS_{24} bin for the 0.5-, 2.0-, and 8.0-kHz test frequencies for each data set. Each median curve in Fig. 3 displays a nonlinear trend with increasing TS_{24} while the 90th percentile results generally show linear trends. Figure 4 presents the ratio of the α and β coefficients from the exponential least-squares analysis of percentile data from all three data sets. The slopes of these curves at $TS_{24}=0$ (i.e., ratio of α/β) for the median data are smaller than those of the 90th-percentile data, indicating a slow growth of NIPTS for relatively small values of TS_{24}. Surprisingly, the slopes of the 90th-percentile data are similar across frequency with a value of approximately 0.7, with no consistent change in the rate of growth of PTS with frequency. The linear growth of NIPTS with increasing TS_{24} in the 90th-percentile analysis suggests that, in the chinchilla model, a modification of the Kryter *et al.* (1966) postulate (c) with a factor of something less than 1.0 may be useful in estimating the NIPTS in the most susceptible chinchillas.

C. Multiple linear regression

The exponential least-squares regression described above relates a single predictor variable to the criterion PTS variable. Multiple regression and correlation methods allow the association of more than one predictor variable to a single-criterion variable. Because of the limited frequencies represented in the TS data of sets II and III a multiple regression analysis was best limited to data set I. Since PTS typically occurs over several audiometric test frequencies, such an analysis seemed appropriate. Thus, three sets of multiple regression and correlation analyses were performed using the PTS as the criterion variable and one of three TS measures as the predictor variables using the SPSS (Release 4) statistical package.

There are a number of multivariate regression techniques used to make predictions or measures of relation between a criterion variable and a set of predictor variables

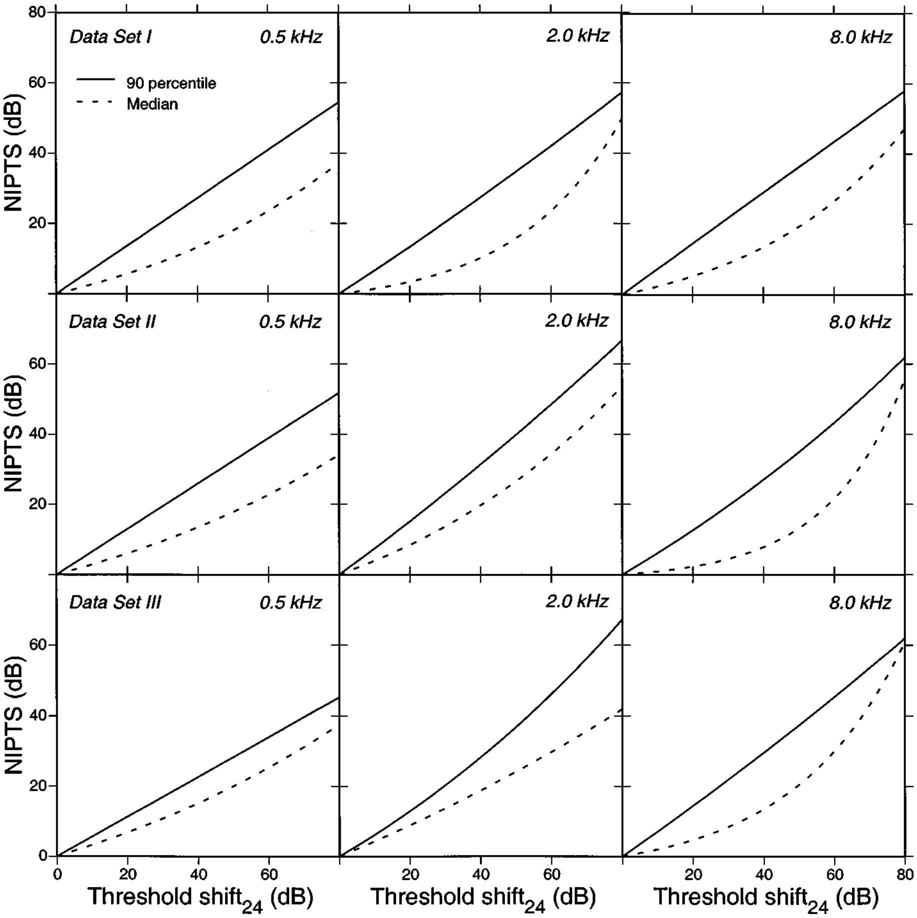

FIG. 3. Exponential least-squares regression lines showing the relation between TS_{24} and median PTS (lower curves) and 90th-percentile PTS (upper curves) at 0.5, 2.0, and 8.0 kHz for each of the three data sets.

(e.g., stepwise, forward entry, etc.). It seemed appropriate to reference any multiple correlations with the correlations between any of the TS measures and PTS at a single test frequency. Thus, the multiple regression/correlation model that was chosen for the analysis of the TS data performed separate bivariate regressions of the PTS (criterion variable) and the TS measure (predictor variable) at each test frequency. Following the calculation of the least-squares regression line and the associated r^2, multiple correlations were computed by adding the TS measures at other test frequencies in descending order of importance. The addition of additional variables was stopped when the change in the r^2 was not significantly increased ($\alpha = 0.05$). (That is, the analysis model specified a forced entry of the first predictor variable and then forward entry of any additional predictor variables.) For example, the r^2 between PTS at 2.0 kHz and TS_{24} at the 2.0-kHz test frequency was approximately 0.64. Following this calculation, the TS_{24} measure at the 1.0-kHz test frequency was added and the r^2 increased to approximately 0.66. At this point, adding any of the eight other TS_{24} measures did not cause a statistically significant increase in r^2 and therefore the multiple regression procedure stopped. This analysis was performed for all seven test frequencies and three predictor variables for data set I.

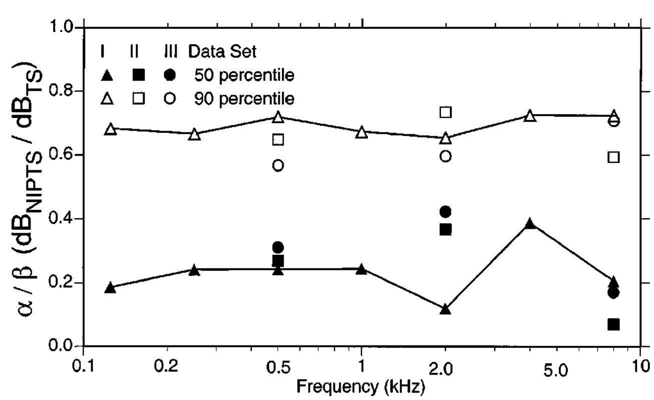

FIG. 4. The slope (α/β) of the regression line at TS$=0$ derived from the exponential least-squares regression equations between the median TS_{24} and the median and 90th-percentile PTS for all three data sets.

Table II lists the r^2 values from the multiple regression and correlation analyses. Each row in the table represents a summary of one complete multiple-correlation analysis. The first set of columns lists the results from the bivariate correlation. A second or third set of columns is presented if adding another TS measure at a specified frequency significantly improved the r^2 value reported in the previous column. Two things are apparent from this table. First, as noted above, the linear correlations between PTS and the TS measures are all relatively high. Second, while the incorporation of additional variables increases the correlation between the criterion and predictor variables for most test frequencies and predictor variables, this increase is relatively modest, ranging from no increase (TS_{max} at 0.125 kHz and TS_{24} at 0.125, 1.0, and 4.0 kHz) to 0.07 (TS_0 at 8.0 kHz). This largest difference represents a total of 7% (45% to 52%) change in r^2, reflecting a 7% increase in the amount of variability in PTS that could be explained based upon the variability of the TS_{24} variables.

TABLE II. Summary of multiple correlation analyses for data set I.

kHz	r^2	kHz	r^2	kHz	r^2
			TS_0		
0.125	0.4661	1.000	0.5041		
0.250	0.5675	1.000	0.6028		
0.500	0.5687	0.125	0.6037	2.000	0.6182
1.000	0.5536	2.000	0.5950	0.125	0.6117
2.000	0.5794	0.250	06029	8.000	0.6141
4.000	0.4987	1.000	0.5375		
8.000	0.4525	0.250	0.5163		
			TS_{max}		
0.125	0.5391				
0.250	0.5872	1.000	0.6450	0.125	0.6557
0.500	0.6492	0.125	0.6708		
1.000	0.6640	0.125	0.6763		
2.000	0.6335	1.000	0.6653		
4.000	0.5254	1.000	0.5651		
8.000	0.5104	1.000	0.5601		
			TS_{24}		
0.125	0.5770				
0.250	0.6170	0.125	0.6558	1.000	0.6726
0.500	0.6557	0.125	0.6888		
1.000	0.6687				
2.000	0.6432	1.000	0.6607		
4.000	0.5171				
8.000	0.5274	1.000	0.5606		

Thus, based on the large linear correlation coefficients and relatively mild improvements in prediction based on the incorporation of additional criterion variables, a multiple-correlation approach to this data is probably not warranted due to the rather large increase in complexity of models to predict PTS from TS measures.

IV. CONCLUSIONS

(1) The data presented in this report (Fig. 1) suggest that an exponential function of the form $PTS=\alpha(e^{TS/\beta}-1)$ is adequate to describe the relation between threshold shifts following a noise exposure and the concomitant permanent changes in hearing in the chinchilla.

(2) The correlations between TS and PTS were generally highest for the TS_{24} variable and lowest for the TS_0/PTS relation.

(3) The 90th-percentile NIHL is linearly related to TS_{24} with a slope of approximately 0.7, independent of test frequency.

Considering the above, the results presented in this paper provide support, in the chinchilla model of NIHL, for a modified version of the three Kryter *et al.* (1966) postulates mentioned in the Introduction. Specifically, (a) TS_{24} is a consistent measure of the effects of a single 8-h work-day exposure to noise. (b) All exposures that produce a given TS_{24} will be equally hazardous. Finally, considering that the 90th-percentile data shown in Fig. 3 are roughly similar for all three data sets; that data set III is derived from various 5-day asymptotic TS exposure paradigms and that the suggestion has been made that ATS represents an upper bound to the NIPTS to be expected from many years of exposure, then postulate (c) becomes NIPTS, in the most susceptible 10% of the chinchilla population, following 10 years of exposure, 8 h/day is approximately equal to (0.7) TS_{24} measured after an 8-h exposure to the same noise.

ACKNOWLEDGMENTS

This work was supported by Grant No. 1-R01-OH02317 from the National Institute for Occupational Safety and Health and Contracts Nos. DAMD17-91-C-1113 and DAMD17-91-C-1120 from the U.S. Army Aeromedical Research and Development Command. The views, opinions, and/or findings contained in this report are those of the authors and should not be construed as an official Department of the Army position, policy, or decision, unless so designated by other official documentation. Citation of trade names in this report does not constitute an official Department of the Army endorsement or approval of the use of such commercial items. In conducting the research described in this study, the investigators adhered to the *Guide for the Care and Use of Laboratory Animals*, prepared by the Committee on Care and Use of Laboratory Animals of the Institute of Laboratory Animal Resources, National Research Council [DHHS Publication No. (NIH) 86-23, revised 1985].

Ahroon, W. A., Hamernik, R. P., and Davis, R. I. (**1993**). ''Complex noise exposures: An energy analysis,'' J. Acoust. Soc. Am. **93**, 997–1006.

Ahroon, W. A., Hamernik, R. P., and Lei, S.-F. (**1996**). ''The effects of reverberant blast waves on the auditory system,'' J. Acoust. Soc. Am. **100**, 2247–2257.

Blakeslee, E. A., Hynson, K., Hamernik, R. P., and Henderson, D. (**1978**). ''Asymptotic threshold shift in chinchillas exposed to impulse noise,'' J. Acoust. Soc. Am. **63**, 876–882.

Dancer, A., Grateau, P., Cabanis, A., Vaillant, T., and Lafont, D. (**1991**). ''Delayed temporary threshold shift induced by impulse noises (weapon noises) in men,'' Audiology **30**, 345–356.

Hamernik, R. P., and Qiu, W. (**2000**). ''Correlations among evoked potential thresholds, distortion product otoacoustic emissions and hair cell loss following various noise exposures in the chinchilla,'' Hear. Res. **150**, 245–257.

Hamernik, R. P., Ahroon, W. A., and Patterson, J. H. (**1988**). ''Threshold recovery functions following impulse noise trauma,'' J. Acoust. Soc. Am. **84**, 941–950.

Hirsh, I. R., and Bilger, R. C. (**1955**). ''Auditory-threshold recovery after exposure to pure tones,'' J. Acoust. Soc. Am. **27**, 1186–1194.

Hirsh, I. R., and Ward, W. D. (**1952**). ''Recovery of the auditory threshold after strong acoustic stimulation,'' J. Acoust. Soc. Am. **24**, 131–141.

Kraak, W. (**1973**). ''Growth of TTS and course of recovery for different noises: Implications for growth of PTS,'' in *Proceedings Intl. Congress: Noise as a Public Health Problem*, edited by W. D. Ward (U.S. Govt. Printing Office, Washington, DC), pp. 293–299.

Kraak, W. (**1981**). ''Investigations on criteria for the risk of hearing loss due to noise,'' in *Hearing Research and Theory*, edited by J. V. Tobias and E. D. Schubert (Academic, New York), Vol. I, pp. 187–303.

Kryter, K. D., Ward, W. D., Miller, J. D., and Eldredge, D. H. (**1966**). ''Hazardous exposure to intermittent and steady-state noise,'' J. Acoust. Soc. Am. **39**, 451–464.

Luz, G. A., and Hodge, D. C. (**1971**). ''Recovery from impulse-noise induced TTS in monkeys and men: A descriptive model,'' J. Acoust. Soc. Am. **49**, 1770–1777.

Miller, J. D., Watson, C. S., and Covell, W. P. (**1963**). ''Deafening effects of noise on the cat,'' Acta Oto-Laryngol., Suppl. **176**, 1–91.

Mills, J. H. (**1986**). ''Effects of low and moderate-level sounds on hearing: Reger and Lierle (1954) revisited,'' in *Sensorineural Hearing Loss*, edited by M. J. Collins, T. J. Glattke, and L. A. Harker (University of Iowa Press, Iowa City), pp. 121–136.

Patterson, Jr., J. H., Hamernik, R. P., Hargett, C. E., and Ahroon, W. A. (**1993**). ''An isohazard function for impulse noise,'' J. Acoust. Soc. Am.

93, 2860–2869.
Pfander, F., Bongartz, H., Brinkmann, H., and Kietz, H. (**1980**). ''Danger of auditory impairment from impulse noise: A comparative study of the CHABA damage-risk criteria and those of the Federal Republic of Germany,'' J. Acoust. Soc. Am. **67**, 628–633.
Reger, S. N., and Lierle, D. (**1954**). ''Changes in auditory acuity produced by low and medium intensity-level exposures,'' J. Acoust. Soc. Am. **58**, 433–438.
Sitler, R. W. (**1972**). ''The effect of impulse noise on the auditory evoked response threshold of chinchilla,'' Ph.D. dissertation, Syracuse University, Syracuse, NY.
Ward, W. D. (**1973**). ''Adaptation and fatigue,'' in *Modern Developments in Audiology*, edited by J. Jerger (Academic, New York), pp. 301–344.
Ward, W. D. (**1968**). ''Susceptibility to auditory fatigue,'' in *Contributions to Sensory Physiology*, edited by W. D. Neff (Academic, New York), Vol. 3, pp. 191–226.

Detection of frequency modulation by hearing-impaired listeners: Effects of carrier frequency, modulation rate, and added amplitude modulation

Brian C. J. Moore[a)]
Department of Experimental Psychology, University of Cambridge, Downing Street, Cambridge CB2 3EB, England

Ewa Skrodzka[b)]
Institute of Acoustics, Adam Mickiewicz University, 85 Umultowska, 61-614 Poznan, Poland

(Received 6 July 2001; revised 5 September 2001; accepted 8 October 2001)

It has been proposed that the detection of frequency modulation (FM) of sinusoidal carriers can be mediated by two mechanisms: a place mechanism based on FM-induced amplitude modulation (AM) in the excitation pattern, and a temporal mechanism based on phase-locking in the auditory nerve. The temporal mechanism appears to be ''sluggish'' and does not play a role for FM rates above about 10 Hz. It also does not play a role for high carrier frequencies (above about 5 kHz). This experiment examined FM detection in three young subjects with normal hearing and four elderly subjects with cochlear hearing loss. Carrier frequencies were 0.25, 0.5, 1, 2, 4, and 6 kHz and modulation rates were 2, 5, 10, and 20 Hz. FM detection thresholds were measured both in the absence of AM, and with AM of a fixed depth ($m=0.33$) added in both intervals of a forced-choice trial. The added AM was intended to disrupt cues based on FM-induced AM in the excitation pattern. Generally, the hearing-impaired subjects performed markedly more poorly than the normal-hearing subjects. For the normal-hearing subjects, the disruptive effect of the AM tended to increase with increasing modulation rate, for carrier frequencies below 6 kHz, as found previously by Moore and Sek [J. Acoust. Soc. Am. **100**, 2320–2331 (1996)]. For the hearing-impaired subjects, the disruptive effective of the AM was generally larger than for the normal-hearing subjects, and the magnitude of the disruption did not consistently increase with increasing modulation rate. The results suggest that cochlear hearing impairment adversely affects both temporal and excitation pattern mechanisms of FM detection.
[DOI: 10.1121/1.1424871]

PACS numbers: 43.66.Fe, 43.66.Hg, 43.66.Ba [MRL]

I. INTRODUCTION

It has been proposed that the frequency discrimination of steady pulsed tones by normal-hearing listeners is largely based on temporal information (cues derived from phase locking) for frequencies up to 4–5 kHz (Moore, 1973a, b, 1974; Goldstein and Srulovicz, 1977; Sek and Moore, 1995; Moore, 1997; Micheyl *et al.*, 1998). Above 4–5 kHz, frequency discrimination is thought to depend on place mechanisms, based on changes in the excitation pattern (Moore, 1973b; Sek and Moore, 1995). The mechanisms underlying the detection of frequency modulation (FM) of sinusoidal carriers are thought to depend on the modulation rate. For sinusoidal modulation with rates above about 10 Hz, detection is probably largely based on excitation-pattern cues (Zwicker, 1956; Zwicker and Fastl, 1990; Moore and Sek, 1994, 1995; Saberi and Hafter, 1995; Sek and Moore, 1995). FM results in modulation of the excitation level at each place on the pattern, so the FM is effectively transformed into amplitude modulation (AM). Thus the FM can be detected as AM, either by using information from the single point on the excitation pattern where the AM is greatest (Zwicker, 1956; Zwicker and Fastl, 1990) or by combining information from different parts of the excitation pattern (Moore and Sek, 1994).

For very low FM rates (around 2 Hz), temporal information may also play a role (Moore and Sek, 1995, 1996; Plack and Carlyon, 1995; Sek and Moore, 1995); the short-term pattern of phase locking can be used to estimate the momentary frequency, and changes in phase locking over time indicate that FM is present. A similar temporal mechanism probably plays a role in the detection of FM of the fundamental frequency ($F0$) of harmonic complex tones, when those tones are bandpass filtered so as to contain only unresolved harmonics (Plack and Carlyon, 1994, 1995; Shackleton and Carlyon, 1994; Carlyon *et al.*, 2000). Indeed, for such tones, place information is not available at all, so subjects are forced to rely on temporal information.

The temporal mechanism may become less effective for modulation rates above about 5 Hz because it is ''sluggish,'' and cannot follow rapid changes in frequency. Consistent with this idea, thresholds for detecting FM of the $F0$ of harmonic complex tones containing only unresolved harmonics increase with increasing modulation rate over the range 1 to 20 Hz, reaching 20% (defined as the peak deviation in $F0$ divided by the mean $F0$) for a modulation rate of

[a)]Electronic mail: bcjm@cus.cam.ac.uk
[b)]Electronic mail: afa@main.amu.edu.pl

20 Hz (Carlyon *et al.*, 2000). In the case of sinusoidal carriers, performance does not change much with increasing modulation rate (Zwicker and Fastl, 1990; Moore and Sek, 1995, 1996; Sek and Moore, 1995), presumably because the place mechanism ''takes over'' from the temporal mechanism for modulation rates above 5–10 Hz.

Hearing-impaired people generally have higher FM detection thresholds (called hereafter FMDLs) than normal-hearing subjects. This might occur because their frequency selectivity is poorer than normal, disrupting the excitation-pattern mechanism (Pick *et al.*, 1977; Glasberg and Moore, 1986; Moore, 1998). Alternatively, or in addition, the use of cues based on phase locking may be impaired, either because phase locking itself is weaker than normal (Woolf *et al.*, 1981), or because temporal information is decoded via spatial cross correlation (Loeb *et al.*, 1983) or coincidence detection (Shamma and Klein, 2000), and these mechanisms are disrupted by changes in frequency-to-place mapping or traveling wave velocity associated with cochlear hearing loss (Ruggero, 1994).

Zurek and Formby (1981) measured FMDLs in ten subjects with sensorineural hearing loss (assumed to be mainly of cochlear origin) using a 3-Hz modulation rate and carrier frequencies between 125 and 4000 Hz. Subjects were tested at a sensation level (SL) of 25 dB, a level above which performance was found (in pilot studies) to be roughly independent of level. The FMDLs tended to increase with increasing hearing loss at a given frequency. For a given degree of hearing loss, the worsening of performance with increasing hearing loss was greater at low frequencies than at high frequencies.

Zurek and Formby suggested two possible explanations for the greater effect at low frequencies. The first is based on the assumption that two mechanisms are involved in coding frequency, a temporal mechanism at low frequencies and a place mechanism at high frequencies. The temporal mechanism may be more disrupted by hearing loss than the place mechanism. An alternative possibility is that, at low frequencies, absolute thresholds do not provide an accurate indicator of the extent of cochlear damage, since these thresholds may be determined by neurons with characteristic frequencies above the test frequency. For example, if the inner hair cells at a region of the basilar membrane tuned to low frequencies are damaged, then low frequencies may be detected via the ''tails'' of the tuning curves of neurons with higher characteristic frequencies. In extreme cases, there may be a dead region at low frequencies, with no functioning inner hair cells and/or neurons (Thornton and Abbas, 1980; Florentine and Houtsma, 1983; Turner *et al.*, 1983; Moore *et al.*, 2000; Moore, 2001).

Moore and Glasberg (1986) measured both FMDLs and thresholds for detecting AM (called hereafter AMDLs), using a 4-Hz modulation rate. They used subjects with moderate unilateral and bilateral cochlear impairments. Stimuli were presented at a fixed level of 80 dB SPL, which was at least 10 dB above the absolute threshold. The FMDLs were larger for the impaired than for the normal ears, by an average factor of 3.8 for a frequency of 500 Hz and 1.5 for a frequency of 2000 Hz, although the average hearing loss was similar for these two frequencies. The greater effect at low frequencies is consistent with the results of Zurek and Formby (1981). The AMDLs were not very different for the normal and impaired ears. The AMDLs provide an estimate of the smallest detectable change in excitation level. Moore and Glasberg (1986) also used the notched-noise method (Patterson, 1976; Glasberg and Moore, 1990) to estimate the slopes of the auditory filters, at each test frequency. The slopes, together with the AMDLs, were used to predict the FMDLs on the basis of Zwicker's excitation-pattern model. The obtained FMDLs were reasonably close to the predicted values. In other words, the results were consistent with the excitation-pattern model. This contrasts with results from normal-hearing subjects, for whom FMDLs for a 4-Hz modulation rate are not well predicted by an excitation-pattern model (Moore and Glasberg, 1989).

Grant (1987) measured FMDLs for three normal-hearing subjects and three subjects with profound hearing losses. The sinusoidal carrier was modulated in frequency by a 3-Hz triangle function. Stimuli were presented at 30 dB SL for the normal subjects and at a ''comfortable listening level'' (110–135 dB SPL) for the impaired subjects. For all carrier frequencies (100 to 1000 Hz), FMDLs were larger, by an average factor of 9.5, for the hearing-impaired than for the normal-hearing subjects. Grant also measured FMDLs when the stimuli were simultaneously amplitude modulated by a noise that was low-pass filtered at 3 Hz. The slow random amplitude fluctuations produced by this amplitude modulation would be expected to impair the use of cues for FM detection based on changes in excitation level. Consistent with the predictions of the excitation-pattern model, the random AM led to increased FMDLs. Interestingly, the increase was much greater for the hearing-impaired than for the normal-hearing subjects. When the random AM was present, thresholds for the hearing-impaired subjects were about 16 times those for the normal-hearing subjects.

As described earlier, it is likely that, for low modulation rates and for carriers below about 5 kHz, normal-hearing subjects can extract information about FM both from changes in excitation level and from phase locking (Moore and Sek, 1995; Sek and Moore, 1995). The random AM disrupts the use of changes in excitation level, but does not markedly affect the use of phase locking cues. The profoundly hearing-impaired subjects of Grant appear to have been relying mainly or exclusively on changes in excitation level. Hence, the random AM had severe adverse effects on the FMDLs.

Lacher-Fougère and Demany (1998) measured FMDLs for a 500-Hz carrier, using modulation rates of 2 and 10 Hz. They used five normal-hearing subjects and seven subjects with cochlear hearing loss ranging from 30 to 75 dB at 500 Hz. Stimuli were presented at a ''comfortable'' loudness level. The subjects with losses up to 45 dB had thresholds that were about a factor of 2 larger than for the normal-hearing subjects. The subjects with larger losses had thresholds that were as much as ten times larger than normal. The effect of the hearing loss was similar for the two modulation rates. Lacher-Fougère and Demany suggested that cochlear hearing loss disrupts excitation-pattern (place) cues and phase-locking cues to a roughly equal extent.

The present experiment was intended to provide further insight into the mechanisms underlying FM detection in subjects with moderate cochlear hearing loss. FMDLs were measured for a wide range of carrier frequencies (0.25–6 kHz) for modulation rates, f_m, of 2, 5, 10, and 20 Hz. Thresholds were determined when FM only was present and when the carriers in both intervals of a forced-choice trial were amplitude modulated at the same rate as the FM with a modulation index of 0.333. The added AM was intended to disrupt cues based on FM-induced AM in the excitation pattern. In a similar experiment conducted using normal-hearing subjects, Moore and Sek (1996) found that, for carrier frequencies up to 4 kHz, the deleterious effect of the added AM increased with increasing f_m. For the 6-kHz carrier, the deleterious effect was independent of f_m. This pattern of results was interpreted as being consistent with the hypothesis that both temporal and place mechanisms are involved in FM detection. The temporal mechanism is assumed to dominate for carriers below about 4 kHz, and for very low modulation rates; in these conditions the added AM had only a small disruptive effect. The place mechanism is assumed to dominate for high carrier frequencies, and for lower carrier frequencies when stimuli are frequency modulated at high rates; in these conditions the added AM had a larger disruptive effect.

We reasoned that if hearing-impaired subjects are able to use phase-locking information for low modulation rates (and for carriers below about 5 kHz), the added AM should have a relatively small effect for these rates, similar to the small effect found for normal-hearing listeners. However, if the extraction of phase-locking cues is disrupted, hearing-impaired subjects may rely on excitation-pattern changes for all modulation rates. In this case, the added AM should have a marked disruptive effect for all modulation rates.

II. METHOD

A. Procedure

FMDLs were measured using a two-interval two-alternative forced-choice task. On each trial, two successive stimuli were presented, one with sinusoidal FM and one without FM. The order of the two stimuli in each pair was random. Subjects were required to identify the interval with the FM by pressing the appropriate button on the response box. In some conditions, AM with a modulation depth, *m*, of 0.33 (corresponding to a peak-to-valley ratio of 6 dB) was added to both stimuli in a trial. This relatively small modulation depth was chosen to minimize AM-induced pitch fluctuations (Burns and Turner, 1986). A two-down one-up adaptive procedure was used (Levitt, 1971). The amount of FM was changed by a factor of 1.5 until four reversals had occurred, and by a factor of 1.25 for a further eight reversals. The threshold was estimated as the geometric mean of the amounts of FM at the last eight reversal points. Each threshold reported is the geometric mean of at least three (usually four) estimates. Subjects were tested in a double-walled sound-attenuating chamber. Correct-answer feedback was provided by lights on the response box.

B. Stimuli

The carrier frequency was 0.25, 0.5, 1, 2, 4, or 6 kHz. The overall level was 85 dB SPL for the hearing-impaired subjects and 70 dB SPL for the normal-hearing subjects; the level is specified as the estimated level at the eardrum. For the hearing-impaired subjects, the carrier was at least 10 dB above the absolute threshold for all frequencies tested, and in most cases was more than 20 dB above the absolute threshold (see Sec. II C). The modulation frequency, f_m, was 2, 5, 10, or 20 Hz. The starting phase of the FM for each stimulus was chosen randomly from one of four values: 0, $\pi/2$, π, and $3\pi/2$. Each stimulus had an overall duration of 1000 ms, including 20-ms raised-cosine rise/fall times. When AM was present, it was added with a phase of 180° relative to the FM. This differs somewhat from earlier experiments, where the relative phase varied randomly from one stimulus to the next (Moore and Glasberg, 1989; Moore and Sek, 1996). Pilot experiments using normal-hearing subjects indicated that the disruptive effect of the AM was almost unaffected by the phase of the AM relative to the FM.

Stimuli were generated using a Tucker-Davis array processor (TDT-AP2) in a host PC, and a 16-bit digital to analog converter (TDT-DD1) operating at a 50-kHz sampling rate. They were attenuated (TDT-PA4) and sent through an output amplifier (TDT-HB6) to a Sennheiser HD580 earphone. The headphone was chosen for its relatively smooth frequency response. This was important, since if the frequency response is irregular, FM can be transformed into a combination of FM and AM. Measurements using a probe microphone close to the eardrum (not using the subjects of the present experiment) and using a KEMAR manikin (Burkhard and Sachs, 1975) showed that the response was very flat (±0.6 dB) from 0.25 up to 1 kHz. The response showed a peak around 3 kHz, but with a smooth variation with frequency up to about 5 kHz. However, around 6 kHz, the response showed some irregularities, which varied from one ear to another. These irregularities might have led to detectable amounts of FM-induced AM when the FMDLs were relatively large.

Stimuli were presented to one ear only. For the hearing-impaired subjects, the ear with better hearing (averaged over the frequencies from 0.5 to 4 kHz) was tested. For the normal-hearing subjects, the test ear was the preferred ear of each subject.

C. Subjects

Three subjects with normal hearing and four subjects with mild to moderate hearing loss were tested. One normal-hearing subject was author ES. All other subjects were paid for their services. The normal-hearing subjects had absolute thresholds less than 20 dB HL at all audiometric frequencies and had no history of hearing disorders. Their ages ranged from 27 to 37 years. The audiograms for the test ears of the hearing-impaired subjects are shown in Fig. 1. The ages of the hearing-impaired subjects were 80, 61, 83, and 72 years, for TT, MP, GW, and AR, respectively. All losses were diagnosed as being of cochlear origin as indicated by lack of an air-bone gap; signs of loudness recruitment; normal tympanograms; and normal acoustic reflex thresholds. All hearing-

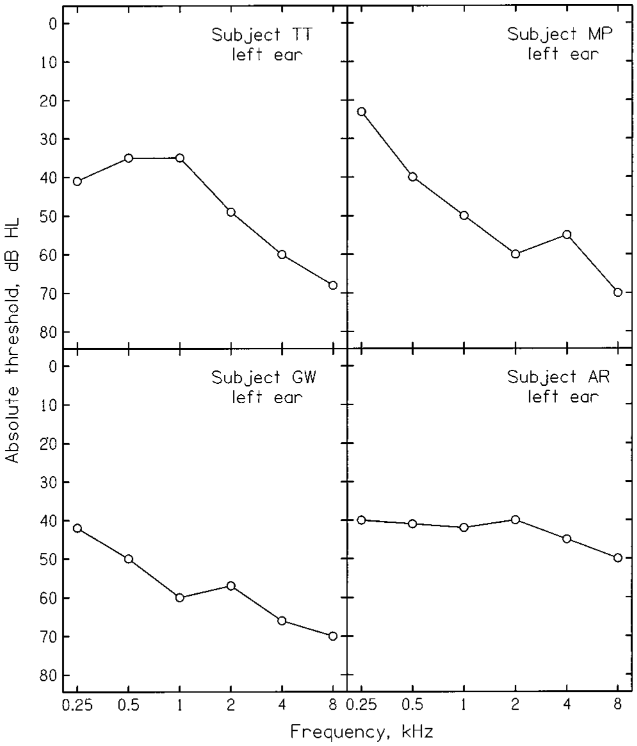

FIG. 1. Audiograms of the four hearing-impaired subjects.

impaired subjects were given the test for diagnosis of dead regions described by Moore *et al.* (2000). No evidence for dead regions was found. All subjects, including the hearing-impaired subjects, had extensive previous experience in psychoacoustic tasks, but not specifically in the detection of FM. All subjects received at least 2 h of practice on a selection of conditions from the present experiment, after which their performance appeared to be relatively stable; practice effects for FM detection appear to be relatively small (Moore, 1976).

III. RESULTS

The pattern of results was similar for the three normal-hearing subjects, and the mean results are shown in Figs. 2–5 by the short-dashed lines (detection of FM alone) and the long-dashed lines (detection of FM with added AM). The FMDLs are expressed as peak-to-peak deviation divided by the carrier frequency. The overall pattern of the results is similar to that found by Moore and Sek (1996). For the lower carrier frequencies, the disruptive effect of the added AM tends to increase with increasing modulation rate, but for the 6-kHz carrier there is little effect of modulation rate. The results differ somewhat from earlier results using similar stimuli (Moore and Glasberg, 1989; Moore and Sek, 1996) in that thresholds are not higher for the 6-kHz carrier than for the lower carrier frequencies. This may simply reflect individual differences, as frequency discrimination varies more across individuals at high frequencies than at medium frequencies (Nelson *et al.*, 1983). It is possible that the subjects in the present experiment used FM-induced AM (introduced by irregularities in earphone response) as a detection cue at 6 kHz. However, this seems unlikely, as the disruptive effect of the added AM was not greater at 6 kHz than at lower carrier frequencies.

To assess the statistical significance of the effects described above, a within-subjects analysis of variance (ANOVA) was conducted with factors carrier frequency, modulation frequency, and presence or absence of AM. The analysis was conducted on the logarithms of the FMDLs (expressed as a proportion of carrier frequency), as the vari-

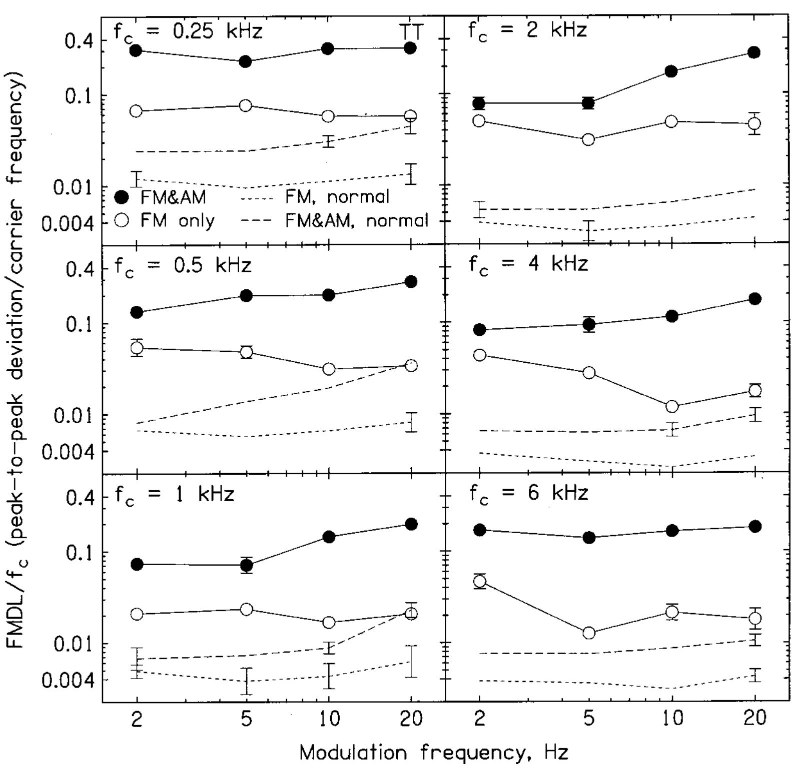

FIG. 2. FMDLs plotted as a function of modulation frequency. Each panel shows results for one carrier frequency. The circles indicate FMDLs for hearing-impaired subject TT, without (open circles) and with (filled circles) added AM. The short- and long-dashed lines show corresponding mean results for the normal-hearing subjects. Error bars indicate ± one standard deviation. They are omitted when they would span a range less than 0.1 log units (corresponding to a ratio of 1.26)

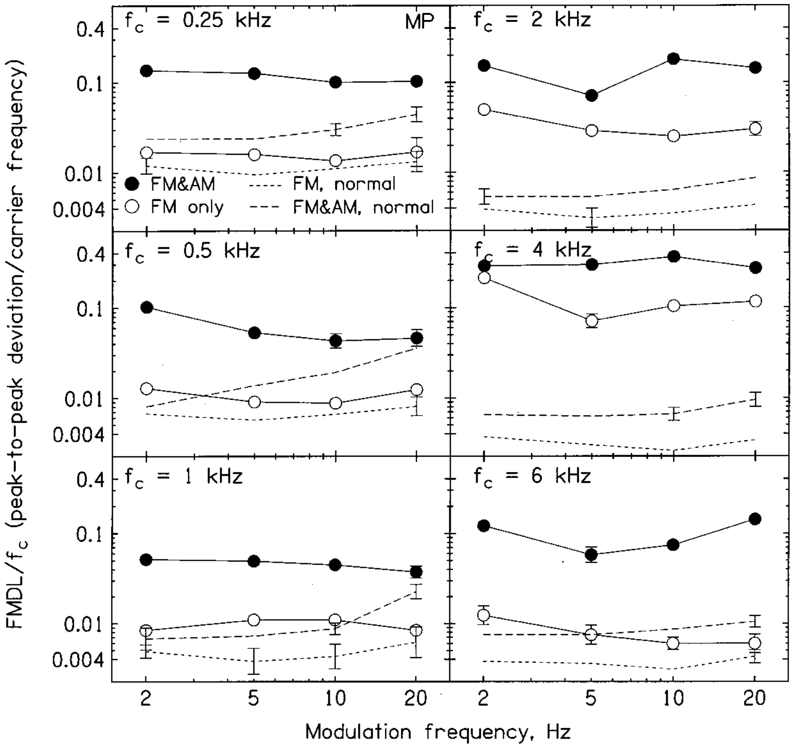

FIG. 3. As in Fig. 2, but for subject MP.

ability was more uniform across conditions with this transformation. The main effect of carrier frequency was significant; $F(5,10)=26.21$, $p<0.001$: the mean threshold was lowest at 2 kHz and highest at 0.25 kHz. The main effect of modulation rate was significant; $F(3,6)=46.87$, $p<0.001$: the mean threshold was highest for the 20-Hz rate. The main effect of presence or absence of AM was significant; $F(1,2)=41.9$, $p=0.023$: the added AM led to larger FMDLs. The interaction of the presence or absence of AM with modulation rate was significant; $F(3,6)=4.84$, $p=0.048$: the effect of the AM increased with increasing modulation rate. The interaction of carrier frequency and modulation rate was also significant; $F(15,30)=2.54$, $p=0.014$: this reflects the fact that for the 6-kHz carrier FMDLs did not vary markedly with modulation rate, while for the lower carrier frequencies FMDLs tended to increase with increasing modulation rate. However, the three-way interaction failed to reach significance at the 0.05 level.

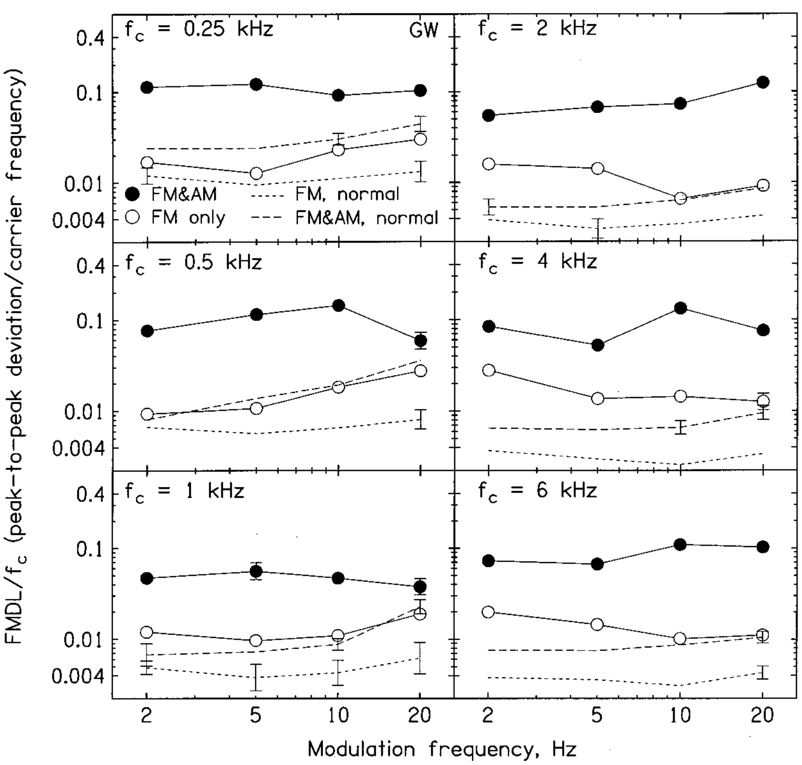

FIG. 4. As in Fig. 2, but for subject GW.

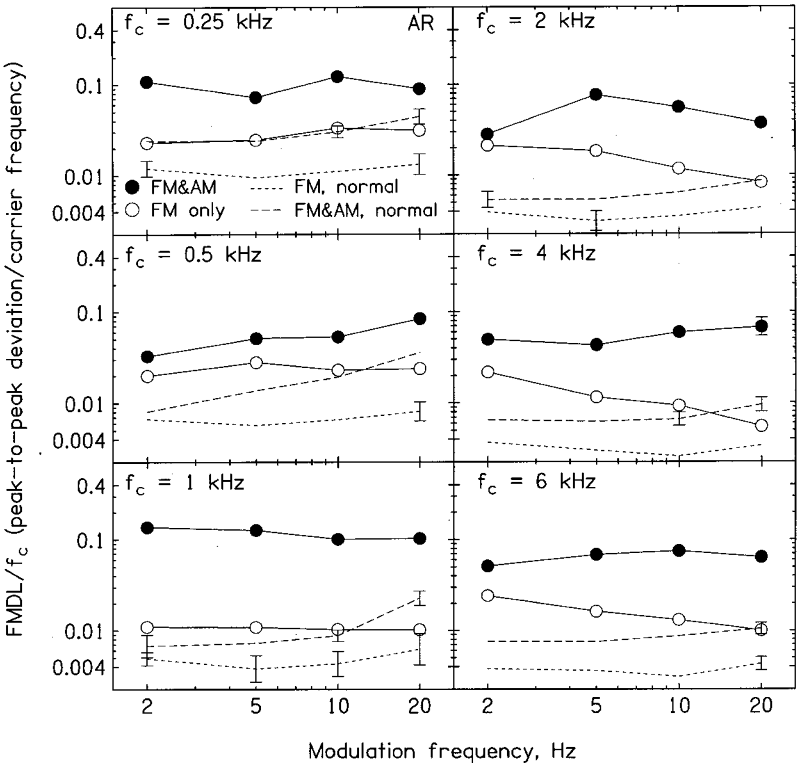

FIG. 5. As in Fig. 2, but for subject AR.

The individual results for the hearing-impaired subjects are shown in Figs. 2–5 by open symbols (FM alone) and filled symbols (with added AM). Generally, the FMDLs were markedly larger than for the normal-hearing subjects, and the disruptive effect of the AM was greater. Although the effect of the AM increased with increasing modulation rate in some cases (e.g., subject TT for carriers from 0.5 to 4 kHz, subject GW for carriers from 2 to 6 kHz, and subject AR for the 4-kHz carrier), this effect was not consistently observed and GW even showed a trend opposite to this for the 0.25-, 0.5-, and 1.0-kHz carriers. FMDLs did not vary markedly with carrier frequency, except for subject MP, who showed poorer performance for the 4-kHz carrier than for the other carriers.

Figure 6 shows the mean data for the normal-hearing (open symbols) and hearing-impaired (filled symbols) subjects. For the latter, the overall magnitude of the disruptive

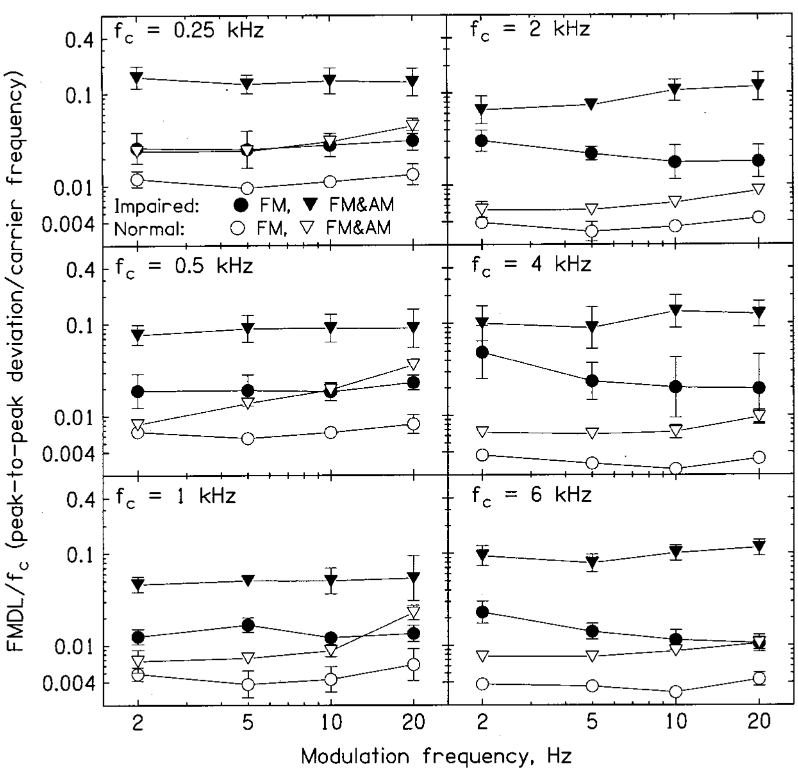

FIG. 6. Mean results for the normal-hearing subjects (open symbols) and the hearing-impaired subjects (filled symbols). Otherwise, as in Fig. 2.

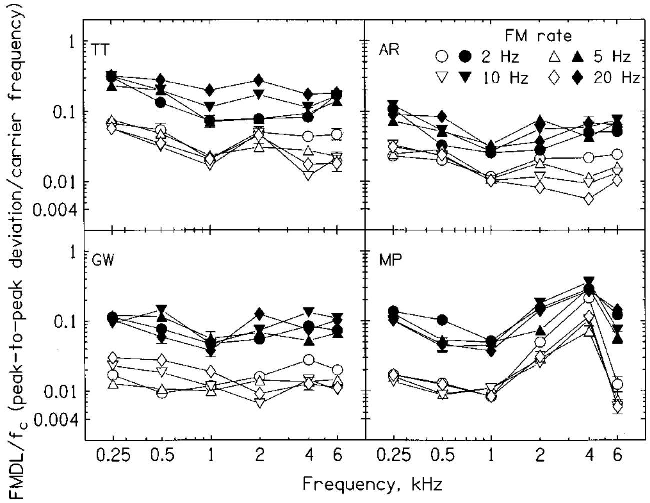

FIG. 7. FMDLs for the individual hearing-impaired subjects, plotted as a function of carrier frequency, with modulation rate as parameter. Open and filled symbols indicate FMDLs without and with added AM, respectively.

effect of the AM is similar across carrier frequencies. The effect is roughly independent of modulation rate for the three lowest carrier frequencies, but there is a trend for the effect to increase with increasing modulation rate for the three higher carrier frequencies.

Figure 7 shows the individual data for the hearing-impaired subjects plotted as a function of carrier frequency with modulation rate as a parameter. Open symbols indicate conditions with FM only, and filled circles indicate conditions with added AM. This figure shows more clearly the local increase in FMDLs at 4 kHz for subject MP. The reason why thresholds increased at 4 kHz and decreased at 6 kHz is not clear. Possibly, at 6 kHz he was able to use FM-induced AM produced by irregularity in the response of the earphone; without such a cue, his performance at 6 kHz might have been worse, as would be expected from his increasing hearing loss with increasing frequency. At 4 kHz, he was probably not able to use such a cue as the response of the earphone was smoother around 4 kHz. Consistent with this idea, for MP the added AM had a very large effect at 6 kHz, but a relatively small effect at 4 kHz.

For the three highest carrier frequencies, FMDLs in the condition without AM tend to decrease with increasing modulation frequency (in Fig. 7, the open circles are above the open diamonds for all subjects). In the condition with added AM, the FMDLs for high carrier frequencies do not show a consistent trend with changes in modulation frequency.

To assess the statistical significance of the effects described above, a within-subjects ANOVA was conducted with factors carrier frequency, modulation frequency, and presence or absence of AM. As before, the analysis was conducted on the logarithms of the FMDLs. The main effects of carrier frequency and modulation rate were not significant. The main effect of presence or absence of AM was highly significant; $F(1,3)=144.29$, $p<0.001$, performance being worse with the added AM. There was also a significant three-way interaction; $F(15,45)=3.22$, $p<0.001$. For the three lower carrier frequencies, the FMDLs hardly varied with modulation rate, regardless of whether or not AM was present. For the three higher carrier frequencies, FMDLs tended to decrease with increasing modulation rate when AM was absent. *Post hoc* tests based on the least-significant differences test showed that the FMDLs in the absence of AM were significantly lower for the 20-Hz rate than for the 2-Hz rate for the carriers of 4 and 6 kHz ($p<0.002$ and $p<0.01$, respectively). When AM was present, there was a slight trend for the FMDLs to increase with increasing modulation rate for the higher carrier frequencies, but this effect was significant only for the 2-kHz carrier ($p<0.05$).

IV. DISCUSSION

The relatively poor performance of the hearing-impaired subjects is consistent with the findings of earlier studies on FM detection, as described in the Introduction (Zurek and Formby, 1981; Moore and Glasberg, 1986; Grant, 1987; Lacher-Fougère and Demany, 1998). For example, Lacher-Fougère and Demany (1998) found that FMDLs were about a factor of 2 larger than normal for hearing-impaired subjects with mild losses, and as much as ten times larger than normal for subjects with larger losses. Our subjects had moderate losses, and had FMDLs that were three to eight times as large as normal.

The added AM produced a strong worsening in performance for the hearing-impaired subjects, even for low carrier frequencies and low modulation rates. For the 2-Hz modulation rate, the FMDL averaged across the four lowest carrier frequencies was a factor of 2.5 larger when AM was present than when it was absent. In contrast, the corresponding ratio for the normal-hearing subjects was only 1.45. Grant (1987) found an even larger disruptive effect of AM on FM detection for his profoundly hearing-impaired subjects; thresholds were increased by an average factor of 16. His greater effect is probably connected with the greater hearing loss of his subjects, who may have been relying exclusively on excitation-pattern cues, but for whom the excitation patterns would have been much broader than normal.

It has been argued in the past that the relatively small disruptive effect of AM at low modulation rates for normal-hearing subjects reflects the use of temporal information (Moore and Sek, 1996). The larger effect found for the hearing-impaired subjects suggests that they were not using temporal information effectively. Rather, the FMDLs were probably based largely on excitation-pattern cues (FM-induced AM in the excitation pattern), and these cues were strongly disrupted by the added AM.

An alternative explanation for the disruptive effect of the AM is that the AM led to level-dependent pitch shifts. For hearing-impaired subjects, sound level can have an abnormally large effect on the pitch of a pure tone, at both low and high frequencies (Burns and Turner, 1986). The AM-induced pitch fluctuations could make it more difficult to detect the FM of the stimuli. However, the AM depth used in our experiment produced only small fluctuations in level; the peak-to-valley ratio was 6 dB. The data of Burns and Turner (1986) suggest that a 6-dB change in level would typically lead to pitch shifts of less than 1%. This is small compared with the thresholds that we measured for our hearing-impaired subjects in the presence of the AM, which were typically around 10% of the carrier frequency. Thus, we believe that AM-induced pitch fluctuations probably made only a minor contribution to the disruptive effect of the AM on FM detection.

Another possible explanation for the disruptive effect of the AM is that, in the absence of AM, the detection of FM by the hearing-impaired listeners may have been based on the detection of loudness fluctuations; such fluctuations might be especially salient for subjects with sloping audiograms. The added AM would introduce prominent loudness fluctuations in both intervals of a 2-AFC trial, making the detection of FM-induced loudness fluctuations more difficult. This explanation is weakened by the finding that the added AM had a large disruptive effect even for frequencies where the audiogram was relatively flat, e.g., subject TT at 0.25 and 0.5 kHz, and subject AR at all frequencies. Also, even for frequencies where the audiogram was sloping, the FM-induced loudness fluctuations would have been small. The slopes of the audiograms of our subjects did not usually exceed 10 dB/oct. The FM detection thresholds in the absence of AM were typically around 2% (peak-to-peak), which means that the sensation level (SL) of the carrier would have fluctuated by less than 0.3 dB as a result of the FM. This would have produced only very small loudness fluctuations. We conclude that the hearing-impaired subjects probably did not detect the FM alone using FM-induced loudness fluctuations. Therefore, the effect of the AM on FM detection probably cannot be explained by disruption of these loudness cues.

Another factor that may have contributed to the large disruptive effect of the AM for the hearing-impaired subjects is that the effective ''internal'' modulation depth produced by the AM was larger for the hearing-impaired than for the normal-hearing subjects, because of the loss of cochlear compression in the former (Moore *et al.*, 1996). However, this does not provide an explanation for why the disruptive effect of the AM increased with increasing modulation rate for the normal-hearing subjects (for carriers below 6 kHz), but did not change consistently with modulation rate for the hearing-impaired subjects.

For the three higher carrier frequencies, FMDLs for the hearing-impaired subjects decreased with increasing modulation frequency up to 10 Hz when no AM was present; this effect was statistically significant at 4 and 6 kHz. A similar trend has been observed for normal-hearing subjects for high carrier frequencies in some earlier studies (Sek and Moore, 1995; Moore and Sek, 1996), although it was not clearly apparent for the normal-hearing subjects of the present study. The trend for improving performance with increasing modulation frequency up to 10 Hz is similar to that observed in studies of AM detection when the carrier is gated (Yost and Sheft, 1997); for a review, see Kohlrausch *et al.* (2000). It is consistent with the idea that the FM was detected via the AM that it introduced in the auditory system. However, for the three lower carrier frequencies, FMDLs in the absence of added AM did not change consistently with modulation frequency. Perhaps the lack of effect for these low frequencies reflects some residual ability to use temporal information for low modulation rates.

When AM was present, FMDLs did not change consistently with modulation rate for the hearing-impaired subjects; the effect of modulation rate was just significant at 2 kHz, but not for any other carrier frequency. The lack of effect of modulation rate when AM was present may have occurred because performance was limited by the imposed AM; essentially, subjects had to discriminate the change in AM depth produced by adding the FM to the AM. The task thus resembles an AM depth discrimination task, for which thresholds are roughly independent of modulation rate for rates up to 32 Hz and for moderate modulation depths (Ozimek and Sek, 1988).

Overall, the conclusions from this study are consistent with those of Lacher-Fougère and Demany (1998). The results suggest that both temporal and place mechanisms are adversely affected by cochlear hearing loss. The disruption of place mechanisms is not surprising, given the ample evidence that frequency selectivity is poorer than normal in subjects with cochlear hearing loss; for reviews, see Tyler (1986) and Moore (1998). The origin of the disruption of temporal mechanisms is somewhat uncertain. Phase locking to sinusoids was found to be abnormal in animal models of cochlear hearing loss in one study (Woolf *et al.*, 1981) but not in two others (Harrison and Evans, 1979; Miller *et al.*, 1997). Possibly, the decoding of temporal information depends on having a ''normal'' traveling were pattern on the basilar membrane (Loeb *et al.*, 1983; Shamma and Klein, 2000), and cochlear hearing loss changes the traveling wave sufficiently (Ruggero, 1994) to severely impair the extraction of temporal information.

It should be noted, however, that our hearing-impaired subjects were all elderly. It is possible that part of the reduced ability to make use of temporal information was related to the age of these subjects rather than to the hearing loss *per se*. Consistent with this idea, it has been shown that elderly subjects with near-normal audiometric thresholds have larger-than-normal thresholds for discriminating interaural time differences and smaller-than-normal binaural masking level differences (Strouse *et al.*, 1998).

V. SUMMARY AND CONCLUSIONS

In this study, we measured the ability of both normal-hearing and elderly hearing-impaired subjects to detect FM, using a wide range of carrier and modulation frequencies. FMDLs were measured both in the absence and presence of AM (in both intervals of a forced-choice trial). The AM was intended to disrupt cues for detection of FM based on FM-induced AM in the excitation pattern. The results showed that the hearing-impaired subjects performed markedly more poorly than the normal-hearing subjects. For the normal-hearing subjects, the disruptive effect of the AM tended to increase with increasing modulation rate, for carrier frequencies below 6 kHz. For the hearing-impaired subjects, the disruptive effective of the AM was generally larger than for the normally hearing subjects, and the magnitude of the disruption did not consistently increase with increasing modulation rate. The results suggest that cochlear hearing impairment adversely affects both temporal and excitation pattern mechanisms of FM detection.

ACKNOWLEDGMENTS

This work was supported by the Medical Research Council (UK). E.S. was partly supported by the State Committee for Scientific Research (Poland), Grant No. 8T11E01717. The authors thank Aleksander Sek and Brian Glasberg for their assistance and Kathy Arehart for helpful discussions and comments on an earlier version of this article. They also thank Marjorie Leek, Laurent Demany, and an anonymous reviewer for helpful comments.

Burkhard, M. D., and Sachs, R. M. (**1975**). "Anthropometric manikin for acoustic research," J. Acoust. Soc. Am. **58**, 214–222.

Burns, E. M., and Turner, C. (**1986**). "Pure-tone pitch anomalies. II. Pitch-intensity effects and diplacusis in impaired ears," J. Acoust. Soc. Am. **79**, 1530–1540.

Carlyon, R. P., Moore, B. C. J., and Micheyl, C. (**2000**). "The effect of modulation rate on the detection of frequency modulation and mistuning of complex tones," J. Acoust. Soc. Am. **108**, 304–315.

Florentine, M., and Houtsma, A. J. M. (**1983**). "Tuning curves and pitch matches in a listener with a unilateral, low-frequency hearing loss," J. Acoust. Soc. Am. **73**, 961–965.

Glasberg, B. R., and Moore, B. C. J. (**1986**). "Auditory filter shapes in subjects with unilateral and bilateral cochlear impairments," J. Acoust. Soc. Am. **79**, 1020–1033.

Glasberg, B. R., and Moore, B. C. J. (**1990**). "Derivation of auditory filter shapes from notched-noise data," Hear. Res. **47**, 103–138.

Goldstein, J. L., and Srulovicz, P. (**1977**). "Auditory-nerve spike intervals as an adequate basis for aural frequency measurement," in *Psychophysics and Physiology of Hearing*, edited by E. F. Evans and J. P. Wilson (Academic, London).

Grant, K. W. (**1987**). "Frequency modulation detection by normally hearing and profoundly hearing-impaired listeners," J. Speech Hear. Res. **30**, 558–563.

Harrison, R. V., and Evans, E. F. (**1979**). "Some aspects of temporal coding by single cochlear fibres from regions of cochlear hair cell degeneration in the guinea pig," Arch. Otolaryngol. **224**, 71–78.

Kohlrausch, A., Fassel, R., and Dau, T. (**2000**). "The influence of carrier level and frequency on modulation and beat-detection thresholds for sinusoidal carriers," J. Acoust. Soc. Am. **108**, 723–734.

Lacher-Fougère, S., and Demany, L. (**1998**). "Modulation detection by normal and hearing-impaired listeners," Audiology **37**, 109–121.

Levitt, H. (**1971**). "Transformed up–down methods in psychoacoustics," J. Acoust. Soc. Am. **49**, 467–477.

Loeb, G. E., White, M. W., and Merzenich, M. M. (**1983**). "Spatial cross correlation: A proposed mechanism for acoustic pitch perception," Biol. Cybern. **47**, 149–163.

Micheyl, C., Moore, B. C. J., and Carlyon, R. P. (**1998**). "The role of excitation-pattern cues and temporal cues in the frequency and modulation-rate discrimination of amplitude-modulated tones," J. Acoust. Soc. Am. **104**, 1039–1050.

Miller, R. L., Schilling, J. R., Franck, K. R., and Young, E. D. (**1997**). "Effects of acoustic trauma on the representation of the vowel /ε/ in cat auditory nerve fibers," J. Acoust. Soc. Am. **101**, 3602–3616.

Moore, B. C. J. (**1973a**). "Frequency difference limens for narrow bands of noise," J. Acoust. Soc. Am. **54**, 888–896.

Moore, B. C. J. (**1973b**). "Frequency difference limens for short-duration tones," J. Acoust. Soc. Am. **54**, 610–619.

Moore, B. C. J. (**1974**). "Relation between the critical bandwidth and the frequency-difference limen," J. Acoust. Soc. Am. **55**, 359.

Moore, B. C. J. (**1976**). "Comparison of frequency DL's for pulsed tones and modulated tones," Br. J. Audiol. **10**, 17–20.

Moore, B. C. J. (**1997**). *An Introduction to the Psychology of Hearing*, 4th ed. (Academic, San Diego).

Moore, B. C. J. (**1998**). *Cochlear Hearing Loss* (Whurr, London).

Moore, B. C. J. (**2001**). "Dead regions in the cochlea: Diagnosis, perceptual consequences, and implications for the fitting of hearing aids," Trends Amplif. **5**, 1–34.

Moore, B. C. J., and Glasberg, B. R. (**1986**). "The relationship between frequency selectivity and frequency discrimination for subjects with unilateral and bilateral cochlear impairments," in *Auditory Frequency Selectivity*, edited by B. C. J. Moore and R. D. Patterson (Plenum, New York).

Moore, B. C. J., and Glasberg, B. R. (**1989**). "Mechanisms underlying the frequency discrimination of pulsed tones and the detection of frequency modulation," J. Acoust. Soc. Am. **86**, 1722–1732.

Moore, B. C. J., and Sek, A. (**1994**). "Effects of carrier frequency and background noise on the detection of mixed modulation," J. Acoust. Soc. Am. **96**, 741–751.

Moore, B. C. J., and Sek, A. (**1995**). "Effects of carrier frequency, modulation rate and modulation waveform on the detection of modulation and the discrimination of modulation type (AM vs FM)," J. Acoust. Soc. Am. **97**, 2468–2478.

Moore, B. C. J., and Sek, A. (**1996**). "Detection of frequency modulation at low modulation rates: Evidence for a mechanism based on phase locking," J. Acoust. Soc. Am. **100**, 2320–2331.

Moore, B. C. J., Wojtczak, M., and Vickers, D. A. (**1996**). "Effect of loudness recruitment on the perception of amplitude modulation," J. Acoust. Soc. Am. **100**, 481–489.

Moore, B. C. J., Huss, M., Vickers, D. A., Glasberg, B. R., and Alcántara, J. I. (**2000**). "A test for the diagnosis of dead regions in the cochlea," Br. J. Audiol. **34**, 205–224.

Nelson, D. A., Stanton, M. E., and Freyman, R. L. (**1983**). "A general equation describing frequency discrimination as a function of frequency and sensation level," J. Acoust. Soc. Am. **73**, 2117–2123.

Ozimek, E., and Sek, A. (**1988**). "AM difference limens for noise bands," Acustica **66**, 153–160.

Patterson, R. D. (**1976**). "Auditory filter shapes derived with noise stimuli," J. Acoust. Soc. Am. **59**, 640–654.

Pick, G., Evans, E. F., and Wilson, J. P. (**1977**). "Frequency resolution in patients with hearing loss of cochlear origin," in *Psychophysics and Physiology of Hearing*, edited by E. F. Evans and J. P. Wilson (Academic, London).

Plack, C. J., and Carlyon, R. P. (**1994**). "The detection of differences in the depth of frequency modulation," J. Acoust. Soc. Am. **96**, 115–125.

Plack, C. J., and Carlyon, R. P. (**1995**). "Differences in frequency modulation detection and fundamental frequency discrimination between complex tones consisting of resolved and unresolved harmonics," J. Acoust. Soc. Am. **98**, 1355–1364.

Ruggero, M. A. (**1994**). "Cochlear delays and traveling waves: Comments on 'Experimental look at cochlear mechanics,' " Audiology **33**, 131–142.

Saberi, K., and Hafter, E. R. (**1995**). "A common neural code for frequency- and amplitude-modulated sounds," Nature (London) **374**, 537–539.

Sek, A., and Moore, B. C. J. (**1995**). "Frequency discrimination as a function of frequency, measured in several ways," J. Acoust. Soc. Am. **97**, 2479–2486.

Shackleton, T. M., and Carlyon, R. P. (**1994**). "The role of resolved and unresolved harmonics in pitch perception and frequency modulation discrimination," J. Acoust. Soc. Am. **95**, 3529–3540.

Shamma, S., and Klein, D. (**2000**). "The case of the missing pitch templates: how harmonic templates emerge in the early auditory system," J. Acoust. Soc. Am. **107**, 2631–2644.

Strouse, A., Ashmead, D. H., Ohde, R. N., and Grantham, D. W. (**1998**). "Temporal processing in the aging auditory system," J. Acoust. Soc. Am. **104**, 2385–2399.

Thornton, A. R., and Abbas, P. J. (**1980**). "Low-frequency hearing loss: Perception of filtered speech, psychophysical tuning curves, and masking," J. Acoust. Soc. Am. **67**, 638–643.

Turner, C. W., Burns, E. M., and Nelson, D. A. (**1983**). "Pure tone pitch perception and low-frequency hearing loss," J. Acoust. Soc. Am. **73**, 966–975.

Tyler, R. S. (**1986**). "Frequency resolution in hearing-impaired listeners," in *Frequency Selectivity in Hearing*, edited by B. C. J. Moore (Academic, London).

Woolf, N. K., Ryan, A. F., and Bone, R. C. (**1981**). "Neural phase-locking properties in the absence of outer hair cells," Hear. Res. **4**, 335–346.

Yost, W. A., and Sheft, S. (**1997**). "Temporal modulation transfer functions for tonal stimuli: Gated versus continuous conditions," Aud. Neurosci. **3**, 401–414.

Zurek, P. M., and Formby, C. (**1981**). "Frequency-discrimination ability of hearing-impaired listeners," J. Speech Hear. Res. **24**, 108–112.

Zwicker, E. (**1956**). "Die elementaren Grundlagen zur Bestimmung der Informationskapazität des Gehörs," Acustica **6**, 356–381.

Zwicker, E., and Fastl, H. (**1990**). *Psychoacoustics—Facts and Models* (Springer-Verlag, Berlin).

Binaural detection with narrowband and wideband reproducible noise maskers: I. Results for human

Mary E. Evilsizer
Hearing Research Center, Department of Biomedical Engineering, Boston University, 44 Cummington Street, Boston, Massachusetts 02215

Robert H. Gilkey
Hearing Research Center, Department of Biomedical Engineering, Boston University, 44 Cummington Street, Boston, Massachusetts 02215, Department of Psychology, Wright State University, Dayton, Ohio, and Human Effectiveness Directorate, Air Force Research Laboratory, Wright-Patterson Air Force Base, Ohio

Christine R. Mason, H. Steven Colburn, and Laurel H. Carney[a)]
Hearing Research Center, Department of Biomedical Engineering, Boston University, 44 Cummington Street, Boston, Massachusetts 02215

(Received 12 February 2001; revised 29 September 2001; accepted 1 October 2001)

This study investigated binaural detection of tonal targets (500 Hz) using sets of individual masker waveforms with two different bandwidths. Previous studies of binaural detection with wideband noise maskers show that responses to individual noise waveforms are correlated between diotic (N_0S_0) and dichotic (N_0S_π) conditions [Gilkey *et al.*, J. Acoust. Soc. Am. **78**, 1207–1219 (1985)]; however, results for narrowband maskers are not correlated across interaural configurations [Isabelle and Colburn, J. Acoust. Soc. Am. **89**, 352–359 (1991)]. This study was designed to allow direct comparison, in detail, of responses across bandwidths and interaural configurations. Subjects were tested on a binaural detection task using both narrowband (100-Hz bandwidth) and wideband (100 Hz to 3 kHz) noise maskers that had identical spectral components in the 100-Hz frequency band surrounding the tone frequency. The results of this study were consistent with the previous studies: N_0S_0 and N_0S_π responses were more strongly correlated for wideband maskers than for narrowband maskers. Differences in the results for these two bandwidths suggest that binaural detection is not determined solely by the masker spectrum within the critical band centered on the target frequency, but rather that remote frequencies must be included in the analysis and modeling of binaural detection with wideband maskers. Results across the set of individual noises obtained with the fixed-level testing were comparable to those obtained with a tracking procedure which was similar to the procedure used in a companion study of rabbit subjects [Zheng *et al.*, J. Acoust. Soc. Am. **111**, 346–356 (2002)]. [DOI: 10.1121/1.1423929]

PACS numbers: 43.66.Pn, 43.66.Dc [LRB]

I. INTRODUCTION

The task of detecting a pure-tone signal in a noise masker has been a critical tool used by psychophysicists to probe the mechanisms of hearing (e.g., Fletcher, 1940; Helmholtz, 1863). This simple task has been a building block of auditory theory, playing a role in the development of concepts, such as the critical band filter, and models for the integration of information across time as well as for the fundamental mechanisms of binaural hearing. Nevertheless, the mechanisms with which normal-hearing listeners perform this basic task are still not completely understood. Although it is often assumed that listeners base their decision on stimulus energy or a closely related statistic, this assumption has repeatedly been shown to conflict with observed data (see, for example, Gilkey, 1987; Kidd, 1987; Kidd *et al.*, 1989; Gilkey and Robinson, 1986; Isabelle and Colburn, 1991; Isabelle, 1995; Richards *et al.*, 1991; Richards, 1992; Richards and Nekrich, 1993). Moreover, evidence supporting the processing mechanisms incorporated in the classical psychophysical models are not obvious in recent physiological measurements (Young and Barta, 1986; Miller *et al.*, 1987; Rees and Palmer, 1988; Jiang *et al.*, 1997a, b; Palmer *et al.*, 1999, 2000). The limits of our understanding of the tone-in-nose detection task are perhaps most striking in the context of binaural masking experiments, where the relation between binaural and monaural processing is still not understood. Classical critical-band based models of binaural interaction fail to predict several significant features of the observed data, which suggests that integration of information across auditory channels must be included to explain the results (Zwicker and Henning, 1984; van de Par and Kohlrausch, 1999; Breebaart *et al.*, 2001; Trieurniet and Boucher, 2001). The failures of the classical models are even greater when predicting the results of binaural detection with reproducible noises, in which the details of responses to a set of individual

a)Author to whom correspondence should be addressed. Present address: Department of Bioengineering and Neuroscience, Institute for Sensory Research, Syracuse University, 621 Skytop Rd., Syracuse, NY 13244; electronic mail: laurel_carney@isr.syr.edu

repeated noise waveforms is investigated (Gilkey *et al.*, 1985; Isabelle and Colburn, 1991; Isabelle, 1995; Gilkey, 1990; Colburn *et al.*, 1997).

This article reports the first experiments in a series of studies that will utilize psychophysical measurements from humans, psychophysical measurements from rabbits, physiological recordings from the inferior colliculus of rabbits, and computational modeling to explore the processing governing tone-in-noise detection. This set of studies is linked by a common set of stimulus manipulations (masker bandwidth and interaural signal phase) and by a common set of reproducible noise maskers, which will allow direct comparison across studies of psychophysical, physiological, and model responses to individual noise-alone and signal-plus-noise waveforms.

This article examines human monaural and binaural detection for both narrowband and wideband maskers, which were generated from the same 25 noise waveforms such that the spectral components in the 100-Hz frequency region surrounding the 500-Hz tone were identical under wideband and narrowband conditions. Most efforts to describe tone-in-noise detection have considered only the parameters of the noise process and have ignored the statistics of the particular noise waveforms presented. In a typical experiment, each noise waveform is presented only once, and the average performance across a large number of masker samples is studied. Green (1964) used the term ''molar'' to refer to performance averaged across the ensemble of masker waveforms in this way. Another method is to consider each stimulus and predict the subjects' responses on a trial-by-trial basis. Green argued that a complete understanding of tone-in-noise detection would allow the experimenter to predict this ''molecular-level'' performance. In practice, incomplete knowledge of the internal noise of the listener and the sequential dependencies across trials makes trial-by-trial predictions impractical. Instead, a ''quasi-molecular'' approach can be employed, in which a set of reproducible noise waveforms is presented on multiple trials and the average response to each individual masker is analyzed. Several investigators have studied tone-in-noise detection using this approach (e.g., Pfafflin and Mathews, 1966; Ahumada and Lovell, 1971; Ahumada *et al.*, 1975; Siegel and Colburn, 1983, 1989; Gilkey *et al.*, 1985; Isabelle and Colburn, 1991; Isabelle, 1995). In most of these quasi-molecular-level studies, performance is described in terms of the probability of a ''target present'' response in one-interval experiments. Thus one measures the probability of correct detection, or a ''hit,'' (P_h) and probability of a false alarm (P_f) for each sample in the set of reproducible noises.

Modeling studies have been only moderately successful at explaining subject performance in reproducible-noise experiments, but they have raised several interesting theoretical questions, especially when results are compared across experimental studies (Gilkey *et al.*, 1985; Isabelle and Colburn, 1991; Isabelle, 1995). To a first approximation, the differences in hit and false-alarm rates across the ensemble of reproducible noises in a monaural or diotic detection task with wideband maskers (Watson, 1962; Ahumada *et al.*, 1975; Gilkey and Robinson, 1986) can be explained by sample-to-sample differences in the output of a simple critical-band-based energy-detector model. Nevertheless, energy-based models do not account for a substantial portion of the total variance in subject responses (e.g., Gilkey and Robinson, 1986), suggesting that energy at the output of a narrowband filter tuned to the target frequency may contribute to, but does not completely determine, the differences in responses observed across samples. Moreover, simple manipulations of stimulus parameters, such as masker bandwidth and the interaural phase of the signal tone, yield results that are not predictable by energy-related models.

The current study was designed in part to explore an apparent incongruity between studies with different masker bandwidths, notably the studies of Gilkey *et al.* (1985) and Isabelle and Colburn (1991). With a 500-Hz target and wideband (100–3000 Hz) maskers, Gilkey *et al.* (1985) found that the across noise-sample pattern of responses (hit rates and false-alarm rates) for the diotic (N_0S_0) condition was correlated with the pattern for the dichotic (N_0S_π) condition, even though the signal level was 10–15 dB lower for the dichotic condition. In contrast, with a 500-Hz target and narrowband ($\frac{1}{3}$-oct band) maskers, Isabelle and Colburn (1991) found that hit and false-alarm rates were uncorrelated between the N_0S_0 and N_0S_π conditions for two of their three subjects. In subsequent work, they showed that the across-sample differences in hit rate with narrowband maskers were not well predicted by energy-related models, including the equalization-cancellation (EC) model (Durlach, 1963) and cross-correlation models (Isabelle, 1995; Colburn *et al.*, 1997). The difference in masker bandwidths used in the two studies with reproducible noise was hypothesized to be the most likely reason for the discrepancy between these results (Isabelle and Colburn, 1991). Yet, if detection is based on energy in the response of narrow (i.e., critical-band) filters, then performance for tone-detection tasks with narrowband and with wideband maskers should be similar. Studies of binaural detection using random (nonreproducible) noise maskers have also concluded that there are differences in processing strategies between wideband and narrowband masker conditions, and between N_0S_0 and N_0S_π, especially for narrowband maskers (e.g., van de Par and Kohlrausch, 1999; Breebaart *et al.*, 2001).

The hypothesis that differences in bandwidth explain the differences in results between studies with reproducible noises can be tested by using pairs of narrowband and wideband maskers generated such that they are identical in the narrow band around the target frequency (i.e., approximately a critical band) and differ only outside the frequency range of the narrowband masker. Gilkey (1990) reported preliminary results comparing wideband and narrowband maskers in the same subjects; unlike Isabelle and Colburn (1991), Gilkey found that false-alarm rates were correlated across interaural configurations even with the narrowband maskers (although less so than with the wideband maskers). However, some of the subjects in Gilkey's study had unusual thresholds under the narrowband N_0S_π condition, which were substantially higher than those of Isabelle and Colburn's subjects. Said differently, Gilkey's subjects had similar thresholds under the N_0S_0 and N_0S_π conditions, suggesting that they may have been using similar strategies under both conditions and may not have taken full advantage of the additional binaural cues available in the N_0S_π condition.

The current study consisted of two experiments. The first experiment tested both diotic (N_0S_0) and dichotic (N_0S_π) detection of fixed-level tones in narrowband and wideband noise maskers. In the second experiment, a tracking procedure was used to control the signal level. In both experiments, performance was examined across the ensemble of noise samples (molar level) and on a sample-by-sample basis (quasi-molecular level). Because a companion study in rabbit (Zheng *et al.*, 2002) used a tracking procedure to study behavioral performance across noises, it was important to determine whether sample-level data obtained with two different procedures were comparable.

II. GENERAL METHODS

The subjects were four undergraduate students (three male and one female) aged 18–20 years with normal hearing. None of the subjects had prior experience with auditory experiments. The subjects were tested individually in an IAC (Industrial Acoustics Co., Bronx, NY) double-walled sound-attenuating booth. Both the masker and target stimuli were generated and combined using TDT (Tucker-Davis Technologies, Gainesville, FL) programmable equipment and presented to the subject via TDH-39 (Telephonics Corp., Farmington, NY) headphones.

A. Stimuli

To compare subject performance across masker bandwidths, narrowband and wideband noise maskers were created with related spectra. Twenty-five independent wideband, reproducible noise maskers were created that had a rectangular spectral envelope with a bandwidth of 100 Hz to 3 kHz, chosen to be consistent with the wideband masker bandwidth used in the study by Gilkey *et al.* (1985). The narrowband noise samples were obtained by digitally filtering the wideband noise samples so that the narrowband and wideband noise samples had identical phase and power spectra, component-by-component, in the 100-Hz frequency band, geometrically centered around 500 Hz (452 to 552 Hz). The narrowband masker was chosen to be similar to that of the narrowband masker employed by Isabelle and Colburn (1991). The long-term expected spectrum level of both the wideband and narrowband maskers was 40-dB SPL. Both the 500-Hz target and the masker were 300 ms in duration including a 10-ms rise/fall time with a cosine-squared ramp.

For each bandwidth, the N_0S_0 and N_0S_π stimulus conditions were each presented for approximately the same number of trials. Two different starting phases were studied for the N_0S_0 condition; half of the N_0S_0 trials were created by adding the tone with a 0° starting phase [$N_0S_0(0°)$], and the other half were created using a 180° starting phase [$N_0S_0(180°)$]. These two starting phases represent the stimulus combinations that make up the N_0S_π stimulus; the results for both starting phases of the N_0S_0 stimuli are useful for understanding and modeling the relation between diotic and dichotic conditions. Performance in the diotic case varies with the starting phase of the target tone (Gilkey *et al.*, 1985; Isabelle and Colburn, 1991). When analyzing the responses to the N_0S_0 stimuli, 50 target-masker combinations (the two starting phases for 25 different reproducible noises) were considered.

B. Experiment 1: Binaural detection with narrowband and wideband maskers

In experiment 1, responses were collected for detection of a 500-Hz tone under diotic and dichotic conditions with the wideband and narrowband sets of reproducible noise maskers.

1. Methods

a. Training. Training consisted of three tasks: a two-interval two-alternative forced-choice (2I,2AFC) tracking task with feedback, a one-interval fixed-level task with feedback, and a one-interval fixed-level task without feedback. Within each task, the interaural configuration and masker bandwidth varied across sessions according to a balanced Latin square, but were held constant within sessions. Each of these training tasks used random noise maskers (i.e., not reproducible noise).

First, the 2I,2AFC task with feedback was used to familiarize the subjects with the listening conditions and to provide an initial estimate of each subject's threshold, which was used to determine the initial tone level for subsequent fixed-level testing. The subject's task was to decide which of two stimulus intervals containing noise also contained a tone. The two-down–one-up tracking procedure estimated the 70.7% correct point on the psychometric function (Levitt, 1971). This procedure used 4-dB steps through the first two reversals and 2-dB steps for the remainder of the run. Ten to 15 runs of the 2I,21AFC task were completed; the exact number of runs depended on the variance of the threshold estimates. Each run consisted of 100 pairs of stimuli in which each interval of the pair had the same masker waveform.

Second, a one-interval, fixed-level task with feedback was employed to familiarize the subject with the task and to determine a signal level for each subject under each condition that would lead to a value of d' near unity, where $d' = z_h - z_f$, and z_h and z_f were the z-scores derived from the overall probability of a hit (P_h) across samples and the overall probability of false alarms (P_f) across samples, respectively (MacMillan and Creelman, 1991). Each run consisted of 100 trials using random noise at the bandwidth being tested. The tone levels in this task were +3, +1, and −1 dB with respect to the threshold determined by the 2I,21AFC tracking task. Two runs at each tone level were completed for each of the bandwidths and interaural configurations being tested. This sequence was repeated multiple times; levels were adjusted (with 1.0-dB resolution) until performance was stable and d' was approximately unity for the intermediate level tested. Random noise at the bandwidth being tested was used in all training trials that had feedback to prevent subjects from learning the unique characteristics of the reproducible noises.

Finally, the same one-interval task was repeated without feedback to determine if the levels estimated from the psy-

TABLE I. Tone level $(E_S/N_0)^1$ in dB, d', and β are shown for each subject, interaural configuration, and bandwidth (NB: narrowband, 100 Hz geometrically centered around 500 Hz; WB: wideband, 100–3000 Hz). The χ^2 and N^a values are given for performance across reproducible noise samples for both P_h and P_f. The r values are Pearson product-moment correlations for the first half of the trials versus the last half of the trials for each subject and condition. All of the χ^2 values and r values are significant $(p<0.01)$.[b]

Interaural configuration	BW	S	E_s/N_0	d'	β	P_h χ^2	P_h N	P_h r	P_f χ^2	P_f N	P_f r
N_0S_0	NB	S1	11.8	1.14	1.34	1115.0	96	0.88	907.1	96	0.82
		S2	11.8	0.98	1.14	1355.7	96	0.83	1397.2	96	0.81
		S3	12.8	0.77	1.00	309.0	96	0.60	216.2	96	0.59
		S4	12.8	1.32	0.75	498.6	62	0.71	605.4	62	0.56
	WB	S1	10.8	0.94	1.13	1778.8	96	0.93	932.0	96	0.84
		S2	9.8	1.01	1.09	1811.3	80	0.94	1406.4	80	0.88
		S3	13.8	1.05	1.01	499.3	64	0.66	200.8	64	0.52
		S4	10.8	0.72	0.89	882.8	64	0.84	590.4	64	0.77
N_0S_π	NB	S1	-6.2	0.82	0.86	186.6	64	0.72	212.3	64	0.69
		S2	3.8	1.07	1.12	224.4	64	0.73	357.4	64	0.91
		S3	1.8	0.71	0.97	107.7	88	0.76	93.2	88	0.74
		S4	-6.2	0.96	0.86	278.4	64	0.71	301.5	64	0.68
	WB	S1	-0.2	1.02	1.08	674.2	96	0.93	659.3	96	0.94
		S2	-2.2	1.11	1.02	370.1	56	0.87	552.9	56	0.96
		S3	4.8	0.80	0.94	133.4	96	0.64	164.3	96	0.68
		S4	0.8	0.89	0.90	316.3	64	0.79	342.1	64	0.87

[a] N is the number of trials per reproducible noise sample. The N for the N_0S_0 conditions is a combination of trials from the two tone phases.

[b] Because both of the tone phases are included in the N_0S_0 condition, there are 50 items; there are 25 items in the N_0S_π condition. Therefore, the degrees of freedom in the two conditions are 49 and 24 for N_0S_0 and N_0S_π, respectively, for the χ^2 test; 48 and 23 for N_0S_0 and N_0S_π, respectively, for Pearson's r.

chometric function would still yield a value of d' near unity with feedback turned off. If it did not, the tone level was again adjusted (with 1-dB resolution) to obtain a value of d' that was again near unity.

b. Testing. Four subjects completed a one-interval tone-in-noise detection task for which the subject had to respond either ''yes, the tone was present'' or ''no, the tone was not present.'' The 500-Hz tone was fixed at a level determined by the training tasks described above. Final analyses were conducted on results for a single tone level at which stable performance with a d' near unity was maintained over a complete set of runs (Table I).

The bias parameter β was calculated as a measure of the subject's tendency toward one response using the expression $\beta = e^{-0.5(z_h^2 - z_f^2)}$ (MacMillan and Creelman, 1991). A β value of 1 corresponds to no bias, so that the subject will respond ''tone'' and ''no tone'' equally often. β values greater than 1 indicate that the subject responds ''no tone'' more often; β values less than 1 indicate that the subject responds ''tone'' more often. The experimenter gave the subjects verbal feedback on the bias of their responses if the value of β for a session strayed more than 15% from unity.

Each testing session consisted of four identical sets of trials. Each set began with 20 practice trials with tone stimuli at a level 2 dB above the level that resulted in a d' of unity. Listeners were given feedback after each of the practice trials. Random noise at the bandwidth being tested was used in these practice trials to prevent subjects from learning the unique characteristics of the reproducible noises. Each set then continued with four runs consisting of 100 trials without feedback at the tone level chosen during the preliminary testing. Twenty-five reproducible noise masker waveforms were used in testing tone detection in each condition. Within each run, each noise sample was randomly presented exactly four times, two times with the tone and two times alone, so that each run consisted of 100 trials with no feedback. Each bandwidth and condition was tested for two to three sessions, which resulted in 56 to 96 trials for each signal-plus-noise and each noise-alone sample in each condition. The interaural configurations and noise masker bandwidths were randomized across sessions using a balanced Latin square.

2. Results and discussion

The molar-level results (i.e., averaged across noise samples) are shown in Table I, including E_S/N_0 in dB, d', and β, for the four combinations of interaural configuration (N_0S_0 and N_0S_π) and masker bandwidth (NB: narrowband, 100 Hz bandwidth; WB: wideband, 100–3000 Hz band). The other entries in Table I, χ^2, N, and r-values for hits and false alarms trials, will be discussed later in this work. Subject performance was near the targeted levels ($d'=1$, $\beta=1$) in all cases. Moreover, the performance levels (E_S/N_0 in dB) are comparable to those typically observed in molar-level experiments employing similar stimuli (reviewed in Durlach and Colburn, 1978). Because the d' values were not exactly one, and psychometric functions were not obtained in this study, exact values of the MLD cannot be determined. Nevertheless, approximate MLDs from these results range from about 9 dB to about 12 dB for the wideband maskers, and from about 8 dB to about 19 dB for the narrowband maskers. Most of these values are compatible with those that have typically been observed for similar conditions in the literature (reviewed by Durlach and Colburn, 1978). However, it should be noted that the results for subject 2 under the N_0S_π condition are unusual and indicate substantially worse molar-level performance under the narrowband condition than under the wideband condition (this subject has a relatively small MLD, about 8 dB, for the narrowband condition). Although there is no obvious explanation for this anomaly, considerable variability across subjects has been reported for performance in binaural detection tasks, particularly for narrow bandwidths (Bernstein *et al.*, 1998). In summary, these molar-level results are representative of those that would be expected in an equivalent experiment that did not employ reproducible noise maskers.

A summary of the molecular-level data can be seen in Fig. 1, in which the results for each subject under each binaural presentation mode and each masker bandwidth are shown separately in receiver operating characteristic (ROC) space. The top three rows of plots are for responses to narrowband stimuli, and the bottom three rows are for wideband stimuli; each row represents a particular interaural configuration. Each plotted character shows the proportion of hits (P_h) and the proportion of false alarms (P_f) for a particular noise sample; each character refers to the same noise sample in all panels. As can be seen, the characters are distributed broadly throughout the upper half of ROC space. The χ^2 values shown in Table I indicate that in each panel these across-sample differences in P_h and P_f are significantly greater than would be expected by chance alone and thereby indicate that the subjects' responses were driven by the properties of the individual noise-alone and signal-plus-noise samples. Said differently, some noise-alone and signal-plus-noise samples "sounded" more like they contained the target tone than others did. For example, Sample O can be seen in the upper right-hand corner of most of the panels, implying that this sample sounded like it contained the target tone on both noise-alone and signal-plus-noise trials under most conditions. In contrast, some samples appear below the positive slope diagonal in some conditions (e.g., sample A for all subjects in the N_0S_0 wideband condition with 180° tone phase), indicating that the effect of adding the target in these cases was to reduce the probability of a "yes" response. Said differently, adding the target made the sample sound less like it contained a target. Gilkey (1981) found that these cases with lower values of P_h than P_f tend to occur when the phase angle of the signal is such that adding the signal to the noise tends to reduce the energy in the noise near 500 Hz. These cases occurred in the present study predominantly in the two wideband N_0S_0 conditions.

The differences in performance on the tone-detection task across the set of reproducible noises were comparable to those reported in previous studies, based on a comparison of ROC plots (Gilkey *et al.*, 1985; Isabelle and Colburn, 1991) and χ^2 values (Isabelle and Colburn, 1991). Greater differences in responses across the set of reproducible noises for N_0S_0 than for N_0S_π can be observed in Fig. 1, and are also reflected in the χ^2 values in Table I (note that the numbers of trials for each condition must be taken into account when comparing χ^2 values). These greater differences in responses across noise samples for the N_0S_0 condition were also reported by Isabelle and Colburn (1991) and are consistent with the greater dependence of detection threshold on target phase for the N_0S_0 condition, which has been reported in previous studies of detection in reproducible noises (Gilkey *et al.*, 1985; Langhans and Kohlrausch, 1992). Examining these data at the quasi-molecular level indicates statistically significant sample-by-sample differences in subject responses that are not, by definition, considered in a molar level analysis. The goal of this series of articles is to utilize these sample-by-sample differences to determine the processing that the observer uses to judge the presence or absence of the target.

a. Comparison of responses across bandwidths. If the subjects base their judgments only on information within the auditory filter centered at the 500-Hz target frequency, then the effective stimuli under the wideband and narrowband conditions are identical. If so, the patterns of responses seen in the panels in the upper half of Fig. 1 should be identical to the corresponding patterns in the lower half of Fig. 1.

To examine this prediction more closely, the correlation between responses under the narrowband and wideband conditions is shown in Table II, separately for P_h and P_f, and for each binaural presentation mode and subject. For the N_0S_0 condition, the correlations for all of the subjects are significant for P_h; three of the four subjects are significantly correlated for P_f and the fourth subject shows positive, but insignificant, correlation. These results indicate that subjects are, to some degree, using the same information in the wideband and narrowband maskers (e.g., the information contained in the critical band centered at the target frequency) to make their judgments about the presence of the target in the N_0S_0 condition. However, a measure of the strength of these correlations in the context of the stability of subjects' performance can be obtained by comparison to the intra-subject correlations in Table I. The observed correlations of responses for the two bandwidths, while significant, are lower than might be expected based on the correlation between each subject's responses during the first half and second half of the runs (Table I), which was significantly greater than that across the two bandwidths. Tests of significant differences for non-independent correlations were used to compare the across-bandwidth correlation to the first-half–last-half correlations for N_0S_0 hits. Fourteen of the 16 resultant comparisons (2 bandwidths$\times$2 halves$\times$4 subjects) were significant at the 0.05 level. The significantly decreased correlation across bandwidths relative to the first-half–last-half correlation implies that information outside the 100-Hz band centered at the signal frequency affects the subject responses in the wideband condition. Consistent with this result is Gilkey and Robinson's (1986) ability to explain more of the sample dependence with a model that combined seven 50-Hz bands over a range of frequencies than they could with a single frequency band.

For the N_0S_π condition, none of the subjects show values of P_h that were significantly correlated across the bandwidths (Table II). For two subjects, P_f was significantly cor-

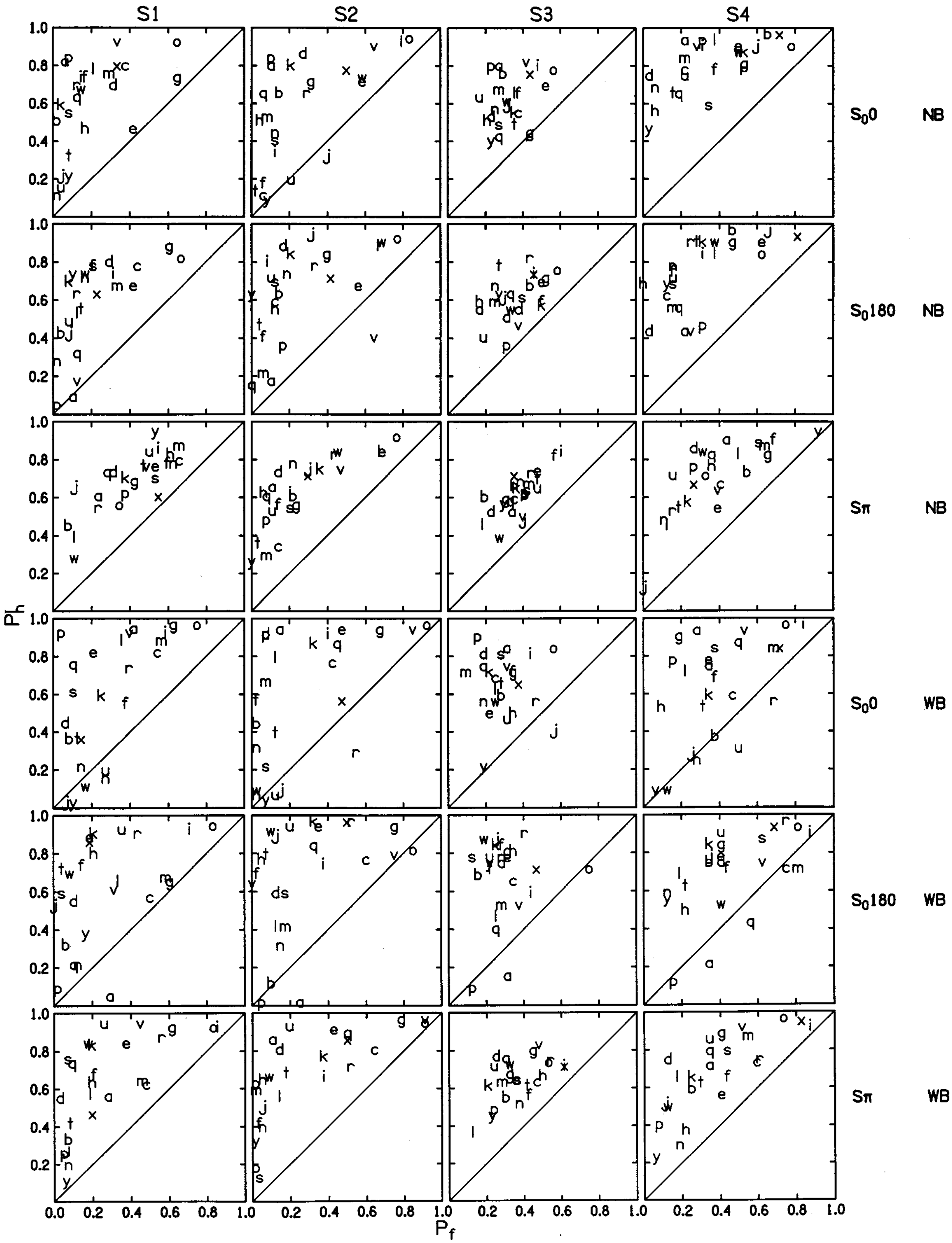

FIG. 1. P_h vs P_f for each reproducible noise sample ("a" through "y") for each subject (columns), bandwidth (top three rows versus bottom three rows), and interaural configuration (rows).

related across bandwidths, but these correlations were significantly lower than the comparable correlations between each subject's responses for the first and second halves of the runs (Table I). The weak or insignificant correlations across the two bandwidths implies that, for all subjects, N_0S_π responses in the wideband condition are influenced by information outside the critical band centered at the signal frequency, thereby lowering the correlation with responses in

TABLE II. Correlations between results for the wideband and the narrowband conditions. Pearson product-moment correlations are given for each subject and interaural configuration for both P_h and P_f. df=48 (N_0S_0), 23 (N_0S_π) (see note in caption for Table I).

Interaural configuration	Subject	r (P_h)	r (P_f)
N_0S_0	S1	0.72[a]	0.66[a]
	S2	0.51[a]	0.51[a]
	S3	0.43[a]	0.47[a]
	S4	0.38[a]	0.22
N_0S_π	S1	−0.06	0.20
	S2	0.26	0.48[b]
	S3	−0.03	0.47[b]
	S4	0.05	−0.08

[a]$p<0.01$.
[b]$p<0.05$.

TABLE III. Correlations between results for the two interaural configurations, N_0S_0 and N_0S_π. Pearson product-moment correlations are given for each subject and bandwidth. Note: Because the two tone phases were averaged for the N_0S_0 condition in the comparison to N_0S_π, all correlations have 23 degrees of freedom.

Bandwidth	Subject	r (P_h)	r (P_f)
NB	S1	−0.15	0.23
	S2	0.80[a]	0.92[a]
	S3	0.38	0.25
	S4	−0.50[b]	−0.17
WB	S1	0.77[a]	0.94[a]
	S2	0.75[a]	0.98[a]
	S3	0.43[b]	0.71[a]
	S4	0.86[a]	0.91[a]

[a]$p<0.01$.
[b]$p<0.05$.

the narrowband condition. Moreover, the effect of frequencies outside the critical band centered at the signal frequency appears to be substantially greater in the N_0S_π condition than in the N_0S_0 condition.

These results are compatible with the unpublished results presented by Gilkey (1990), who found significant correlations between values of P_f in wideband and narrowband N_0S_0 conditions, but substantially smaller (although still statistically significant for two out of three subjects) correlations between values of P_f in the wideband and narrowband N_0S_π conditions. The weak relation between wideband and narrowband responses in the N_0S_π condition is also consistent with subjective reports about the cues used in the N_0S_π condition for narrowband and wideband stimuli. Specifically, in the narrowband case, the ''width'' or ''shape'' of the binaural image is generally reported to provide a cue for detection; in the wideband case, the strength of the tonelike percept is reported to provide a cue for detection. These results are also consistent with the conclusions of van de Par and Kohlrausch (1999) and Breebaart *et al.* (2001) using random (nonreproducible) noise maskers across a range of bandwidths. However, they concluded that subjects were performing the task based on a single auditory filter centered at the target frequency in the wideband case, whereas integration across a number of different auditory filters was used in the narrowband case. The reproducible noise results presented here provide a means to test specific predictions of this and other models in future modeling studies.

c. Comparison of Responses across Interaural Configurations. The potential difference between results for wideband and narrowband conditions was first indicated when values of P_f and P_h were compared across interaural configurations for sets of reproducible narrowband maskers by Isabelle and Colburn (1991), who found weak and typically insignificant correlations, and for wideband maskers by Gilkey *et al.* (1985), who found significant correlations. However, these results were for different subjects and different reproducible noise samples. The current study allows this comparison within a single experiment. Based on the previous reports, it was expected that performance for N_0S_0 and N_0S_π conditions would be correlated under the wideband conditions and uncorrelated under the narrowband conditions. Table III shows that the responses of all four subjects were significantly correlated across interaural configurations with the wideband maskers, which is consistent with Gilkey *et al.* (1985). With the narrowband maskers, the responses of two subjects (S1, S3) were not significantly correlated for either signal-plus-noise trials (i.e., P_h) or noise-alone trials (i.e., P_f), the responses of one subject (S2) were positively correlated for both noise-alone and signal-plus-noise trials, and the responses of one subject (S4) were negatively correlated (but only for signal-plus-noise trials). These results are consistent with the diversity in response patterns across subjects reported by Isabelle and Colburn (1991) for narrowband maskers. (They reported one subject with significant positive correlations for both hits and false alarms, and two subjects with negative, but not significant, correlations.) These results suggest either that different processing strategies are used for different bandwidths or that masker components outside the critical band have a significant impact on the processing of stimulus components within the critical band.

d. Comparison of performance across subjects. The comparisons across bandwidths and interaural configurations presented above illustrate trends that were generally true for all subjects. For example, the P_h results for the N_0S_0 condition were strongly correlated across bandwidths for all subjects, and the P_h results for the N_0S_π condition were not correlated for any of the subjects

Intersubject correlations are shown in Table IV. The responses across reproducible noise maskers were significantly correlated for all pairs of subjects for the N_0S_0 condition for all cases, including both hits and false alarms and both narrowband and wideband maskers. N_0S_π results were also significantly correlated for all pairs of subjects for the wideband maskers, for both hits and false alarms. However, for the narrowband N_0S_π condition, only two subjects (S1 and S3) had significant positively correlated performance; one pair of subjects had a significantly negative correlation for performance on hits, and all other correlations were insignificant for the narrowband N_0S_π condition. The degree of variability in performance across subjects in this study was consistent with that reported for similar tasks by Bernstein *et al.* (1998).

TABLE IV. Correlations of responses between subjects. Pearson product-moment correlations are given for each subject pair under each interaural configuration and bandwidth. df=48(N_0S_0), 23 (N_0S_π) (see note in caption for Table I).

Interaural configuration	Bandwidth	Subject pair	r (P_h)	r (P_f)
N_0S_0	NB	S1-S2	0.54[a]	0.44[a]
		S1-S3	0.45[a]	0.56[a]
		S1-S4	0.45[a]	0.31[b]
		S2-S3	0.35[b]	0.50[a]
		S2-S4	0.55[a]	0.60[a]
		S3-S4	0.69[a]	0.61[a]
	WB	S1-S2	0.81[a]	0.63[a]
		S1-S3	0.66[a]	0.55[a]
		S1-S4	0.82[a]	0.56[a]
		S2-S3	0.69[a]	0.58[a]
		S2-S4	0.73[a]	0.58[a]
		S3-S4	0.71[a]	0.47[a]
N_0S_π	NB	S1-S2	−0.59[a]	−0.34
		S1-S3	0.50[b]	0.55[a]
		S1-S4	−0.05	0.19
		S2-S3	−0.19	−0.09
		S2-S4	−0.32	−0.16
		S3-S4	−0.18	−0.25
	WB	S1-S2	0.56[a]	0.69[a]
		S1-S3	0.63[a]	0.60[a]
		S1-S4	0.68[a]	0.77[a]
		S2-S3	0.62[a]	0.54[a]
		S2-S4	0.51[a]	0.61[a]
		S3-S4	0.62[a]	0.78[a]

[a]$p<0.01$.
[b]$p<0.05$.

C. Experiment 2: Comparison of tracking and fixed-level procedures

1. Methods

Experiment 1 was conducted at a fixed-tone level; however, a companion study (Zheng *et al.*, 2002) used rabbits that were studied with a tracking procedure. To explore potential differences in performance that might be related to these different testing procedures, a tracking procedure was used to retest two of the subjects from experiment 1 (S1 and S4), and the results of the two procedures were compared.

The same one-interval, yes–no task that was used in the fixed-level procedure of experiment 1 was used for the tracking procedure here, and the same fixed number of trials were included in each run. However, the tone-level in each tone-plus-noise trial was adjusted by following a two-down–one-up rule (Levitt, 1971). Tone levels were adjusted based on the subject's responses for tone-plus-noise trials only. For each track, 4-dB steps were used until there were two reversals and then 2-dB steps were used for the remainder of the run. The 70.7% correct detection threshold was calculated by averaging the reversals (after the step-size change) of each track. Signal trials that were presented at levels between one step above and two steps below the mean reversal level were used for the reproducible noise analysis, consistent with the analysis used in the companion study (Zheng *et al.*, 2002). Subject S1 was tested on narrowband conditions and subject S4 was tested on wideband conditions.

2. Results and discussion

Table V shows the summary of the data collected from these two subjects, which can be compared to their results in Table I for Experiment 1. With the tracking procedure, subject 1 shows a MLD of 16 dB for the narrowband condition and subject 4 has a MLD of 12 dB for the wideband condition. As can be seen, both molar-level (threshold values of E_S/N_0 in dB) and quasi-molecular-level (χ^2 and correlations between the first and last halves of the trials) results are comparable for the two experiments. Subject 1's threshold for the N_0S_π condition was higher by approximately 3 dB whereas subject 4's threshold was lower by 2 dB when performing the fixed-level experiment. Table VI shows that the sample-by-sample correlations between experiments 1 and 2 for both subjects were significant and positive for both hits and false alarms for all four combinations of bandwidth and interaural configuration. The results from the two testing procedures were strongly correlated for both subjects and for all conditions tested. Although these subjects were all tested extensively using fixed-level procedures before testing with the tracking procedures, it appears that tracking and fixed-level procedures yield similar results and that the results of our planned across-species comparisons would not be substantially obscured by this difference in procedure.

TABLE V. Experiment 2 results. Tone level (E_s/N_0) in dB is shown for each subject and condition. The values of χ^2 and N[a] are given for performance across reproducible noise samples for both P_h and P_f. The r values are Pearson product-moment correlations for the first half of the trials versus the last half of the trials for each subject and condition. All of the χ^2 values and r values are significant ($p<0.01$).[b]

Interaural configuration	BW	S	E_s/N_0	P_h			P_f		
				χ^2	N	r	χ^2	N	r
N_0S_0	NB	S1	12.8	302.1	88	0.62	370.6	160	0.71
N_0S_π			−3.2	291.6	94	0.91	204.3	160	0.74
N_0S_0	WB	S4	10.8	493.3	70	0.74	448.1	120	0.87
N_0S_π			−1.2	268.6	98	0.84	730.3	160	0.97

[a]N is the number of trials per reproducible noise sample. The N for the N_0S_0 conditions is a combination of trials from the two tone phases.
[b]Because both tone phases are included in the N_0S_0 condition, there are 50 items; there are 25 items in the N_0S_π condition. Therefore, the degrees of freedom in the two conditions are 49 and 24 for N_0S_0 and N_0S_π, respectively, for the χ^2 test; 48 and 23 for N_0S_0 and N_0S_π, respectively, for Pearson's r.

TABLE VI. Comparison of performance for the fixed-level versus tracking results. Pearson product-moment correlations between results for the two paradigms are shown.

Bandwidth	Interaural configuration	Subject	r (P_h)	r (P_f)
NB	N_0S_0	S1	0.79[a]	0.76[a]
	N_0S_π		0.85[a]	0.84[a]
WB	N_0S_0	S4	0.84[a]	0.77[a]
	N_0S_π		0.86[a]	0.91[a]

[a] $p<0.01$.

III. GENERAL DISCUSSION

This study tested subjects using a binaural detection task with wideband and narrowband noise maskers that had the same spectral components in the 100-Hz frequency region surrounding the 500-Hz tone. Comparisons of the results for the two bandwidth conditions reported here indicate that frequencies outside the 100-Hz band centered at the 500-Hz tone influence detection in both the N_0S_0 and N_0S_π conditions. The results are consistent with previous studies that focused on either wideband or narrowband reproducible noise maskers (e.g., Gilkey *et al.*, 1985; Isabelle and Colburn, 1991).

Comparison of the responses across the N_0S_0 and N_0S_π conditions for each of the masker bandwidths suggests that diotic and dichotic responses differ significantly due to the influence of frequencies outside a bandwidth that approximates the critical band. Dichotic processing is apparently much more influenced by the presence of frequencies away from the target frequency. These results provide motivation to extend models beyond the narrowband mechanisms that have been the focus of binaural detection models to date (Isabelle, 1995; Colburn *et al.*, 1997; cf. Breebaart *et al.*, 2001; Trieurniet and Boucher, 2001).

Future studies in this series will attempt to model these experimental results. Several challenges for such modeling studies are raised by these results. For example, responses across subjects generally were not correlated for the narrowband N_0S_π condition; therefore, it would not be possible to explain these data with a single model except by changing parameters from subject to subject. In general, performance across subjects was more highly correlated for the N_0S_0 condition than for the N_0S_π condition and was more correlated for the wideband condition than for the narrowband condition. The results of these comparisons suggest that subjects' listening strategies may change in a complex manner that is influenced by energy outside the critical band. In addition, different strategies for combining information across frequencies have been suggested by this and other studies. Whereas we conclude that energy outside the critical band influences detection in the wideband condition, others have concluded that cross-filter integration predominantly affects the narrowband condition (e.g., Breebaart *et al.*, 2001). These differences can be explored both by detailed modeling of the results across reproducible noise maskers, and with additional experimental studies in which the spectral contents are systematically varied both within and outside the critical band.

It has been established in detection studies with rabbits that differences in detection performance are observed across noise samples (Early *et al.*, 2001). A study of tone detection in rabbit using narrowband and wideband maskers and using the interaural configurations of the current study is the topic of the companion article (Zheng *et al.*, 2002). Similar trends across bandwidths and interaural configurations were found for the rabbits as were found for the human subjects in the current study. Future studies will pursue the problem of diotic and dichotic masking with signal-processing- and physiologically based models, and with physiological experiments.

ACKNOWLEDGMENTS

We acknowledge the helpful discussions and comments provided on earlier versions of this article by Susan J. Early, J. Michael Harrison, Armin Kohlrausch, and Fabio Idrobo. This work was supported by NIH NIDCD DC01641 (MEE, CRM, LHC) and NIH NIDCD DC00100 (HSC, RHG). Additional support was provided by AFOSR F49620-97-1-0231 (RHG).

[1] The level of the signal with respect to the masker was calculated as E_S/N_0=Tone level (dB SPL)−Noise spectrum level (dB SPL) $+10\ \log_{10}$ duration (s)/1 s.

Ahumada, A., and Lovell, J. (**1971**). "Stimulus features in signal detection," J. Acoust. Soc. Am. **49**, 1751–1756.

Ahumada, A., Marken, R., and Sandusky, A. (**1975**). "Time and frequency analysis of auditory signal detection," J. Acoust. Soc. Am. **57**, 385–390.

Bernstein, L. R., Trahiotis, C., and Hyde, E. L. (**1998**). "Inter-individual differences in binaural detection of low-frequency tonal signals masked by narrow-band or broadband noise," J. Acoust. Soc. Am. **103**, 2069–2078.

Breebaart, J., van de Par, S., and Kohlrausch, A. (**2001**). "An explanation for the apparently wider critical bandwidth in binaural experiments," in *Proceedings of the 12th International Symposium on Hearing: Physiological and Psychophysical Bases of Auditory Function*, edited by D. J. Breebaart, A. J. M. Houstma, A. Kohlrausch, V. F. Prijs, and R. Schoonhoven (Shaker, Maastricht, The Netherlands), pp. 153–160.

Colburn, H. S., Isabelle, S. K., and Tollin, D. J. (**1997**). "Modeling binaural detection performance for individual masker waveforms," in *Binaural and Spatial Hearing*, edited by R. H. Gilkey and T. Anderson (Earlbum, Englewood Cliffs, NJ), Chap. 25, pp. 533–555.

Durlach, N. I. (**1963**). "Equalization and cancellation theory of binaural masking-level differences," J. Acoust. Soc. Am. **35**, 1206–1218.

Durlach, N. I., and Colburn, H. S. (**1978**). "Binaural phenomena," In *Handbook of Perception: Hearing*, edited by E. Carterette and M. Friedman (Academic, New York), Vol. 4, pp. 365–466.

Early, S. J., Mason, C. R., Zheng, L., Evilsizer, M., Idrobo, F., Harrison, J. M., and Carney, L. H. (**2001**). "Studies of binaural detection in the rabbit using Pavlovian conditioning," Behav. Neurosci. **115**, 650–660.

Fletcher, H. (**1940**). "Auditory patterns," Rev. Mod. Phys. **12**, 47–65.

Gilkey, R. H. (**1981**). "Molecular psychophysics and models of auditory signal detectability," Ph.D. Thesis, Department of Psychology, Indiana University.

Gilkey, R. H. (**1987**). "Spectral and temporal comparisons in auditory masking," in *Auditory Processing of Complex Sounds*, edited by W. A. Yost and C. S. Watson (Erlbaum, Hillsdale, NJ), pp. 26–36.

Gilkey, R. H. (**1990**). "The relation between monaural and binaural tone-in-noise masking," Assoc. for Res. in Otolaryngol. (abstract) **13**, 165.

Gilkey, R. H. and Robinson, D. E. (**1986**). "Models of auditory masking: A molecular psychophysical approach," J. Acoust. Soc. Am. **79**, 1499–1510.

Gilkey, R. H., Robinson, D. E., and Hanna, T. E. (**1985**). "Effects of masker waveform and signal-to-masker phase relation on diotic and dichotic masking by reproducible noise," J. Acoust. Soc. Am. **78**, 1207–1219.

Green, D. M. (**1964**). "Consistency of auditory detection judgments," Psychol. Rev. **71**, 392–407.

Helmholtz, H. L. F. von (**1863**). *Die Lehre von den Tonempfindungen als physiologische Grundlage für die Theorie der Musik* (Vieweg und Sohn, Braunschweig, Germany). Translated as *On the Sensations of Tone as a Physiological Basis for the Theory of Music*, by A. J. Ellis from the 4th German edition, 1877 (Leymans, London, 1885) (reprinted by Dover, New York, 1954).

Isabelle, S. K. (**1995**). ''Binaural detection performance using reproducible stimuli,'' Ph.D. thesis, Boston University.

Isabelle, S. K. and Colburn, H. S. (**1991**). ''Detection of tones in reproducible narrow-band noise,'' J. Acoust. Soc. Am. **89**, 352–359.

Jiang, D., McAlpine, D., and Palmer, A. R. (**1997a**). ''Responses of neurons in the inferior colliculus to binaural masking level difference stimuli measured by rate-versus-level functions,'' J. Neurophysiol. **77**, 3085–3106.

Jiang, D., McAlpine, D., and Palmer, A. R. (**1997b**). ''Detectability index measures of binaural masking level difference across populations of inferior colliculus neurons,'' J. Neurosci. **17**, 9331–9339.

Kidd, G., Jr. (**1987**). ''Auditory discrimination of complex sounds: The effects of amplitude perturbation on spectral shape,'' in *Auditory Processing of Complex Sounds*, edited by W. A. Yost and C. S. Watson (Erlbaum, Hillsdale, NJ), pp. 16–25.

Kidd, Jr., G., Mason, C. R., Brantley, M. A., and Owen, G. A. (**1989**). ''Roving-level tone-in-noise detection,'' J. Acoust. Soc. Am. **86**, 1310–1317.

Langhans, A., and Kohlrausch, A. (**1992**). ''Differences in auditory performance between monaural and diotic conditions. I: Masked thresholds in frozen noise,'' J. Acoust. Soc. Am. **91**, 3456–3470.

Levitt, H. (**1971**). ''Transformed up-down methods in psychoacoustics,'' J. Acoust. Soc. Am. **49**, 467–477.

MacMillan, N. A., and Creelman, C. D. (**1991**). *Detection Theory: A User's Guide* (Cambridge U.P., New York).

Miller, M. I., Barta, P. E., and Sachs, M. B. (**1987**). ''Strategies for the representation of a tone in background noise in the temporal aspects of the discharge patterns of auditory-nerve fibers,'' J. Acoust. Soc. Am. **81**, 665–679.

Palmer, A. R., Jiang, D., and McAlpine, D. (**1999**). ''Desynchronizing responses to correlated noise: A mechanism for binaural masking level differences at the inferior colliculus,'' J. Neurophysiol. **81**, 722–734.

Palmer, A. R., Jiang, D., and McAlpine, D. (**2000**). ''Neural responses in the inferior colliculus to binaural masking level differences created by inverting the noise in one ear,'' J. Neurophysiol. **84**, 844–852.

Pfafflin, S. M., and Mathews, M. V. (**1966**). ''Detection of auditory signals in reproducible noise,'' J. Acoust. Soc. Am. **39**, 340–345.

Rees, A., and Palmer, A. R. (**1988**). ''Rate-intensity functions and their modifications by broadband noise for neurons in the guinea pig inferior colliculus,'' J. Acoust. Soc. Am. **83**, 1488–1498.

Richards, V. M. (**1992**). ''The detectability of a tone added to narrow bands of equal-energy noise,'' J. Acoust. Soc. Am. **91**, 3424–3435.

Richards, V. M., and Nekrich, R. D. (**1993**). ''The incorporation of level and level-invariant cues for the detection of a tone added to noise,'' J. Acoust. Soc. Am. **94**, 2560–2574.

Richards, V. M., Heller, L. M., and Green, D. M. (**1991**). ''Detection of a tone in a narrow band of noise: The energy model revisited,'' Q. J. Psychol. **43A**, 481–503.

Siegel, R. A., and Colburn, H. S. (**1983**). ''Internal and external noise in binaural detection,'' Hear. Res. **11**, 117–123.

Siegel, R. A., and Colburn, H. S. (**1989**). ''Binaural processing of noisy stimuli: Internal/external noise ratios for diotic and dichotic stimuli,'' J. Acoust. Soc. Am. **86**, 2122–2128.

Trieurniet, W. C., and Boucher, D. R. (**2001**). ''A masking level difference due to harmonicity,'' J. Acoust. Soc. Am. **109**, 306–320.

van de Par, S., and Kohlrausch, A. (**1999**). ''Dependence of binaural masking level differences on center frequency, masker bandwidth, and interaural parameters,'' J. Acoust. Soc. Am. **106**, 1940–1947.

Watson, C. S. (**1962**). ''Signal detection and certain physical characteristics of the stimulus during the observation interval,'' Ph.D. thesis, Indiana University, Bloomington, IN.

Young, E. D., and Barta, P. E. (**1986**). ''Rate responses of auditory-nerve fibers to tone in noise near masked threshold,'' J. Acoust. Soc. Am. **79**, 426–442.

Zheng, L., Early, S. J., Mason, C. R., Evilsizer, M. E., Idrobo, F., Harrison, J. M., and Carney, L. H. (**2002**). ''Binaural detection with narrowband and wideband reproducible noise maskers: II. Results for rabbit,'' J. Acoust. Soc. Am. **111**, 346–356.

Zwicker, E., and Henning, G. B. (**1984**). ''Binaural masking-level differences with tones masked by noises of various bandwidths and levels,'' Hear. Res. **14**, 179–183.

Binaural detection with narrowband and wideband reproducible noise maskers: II. Results for rabbit

Ling Zheng, Susan J. Early, and Christine R. Mason
Hearing Research Center, Department of Biomedical Engineering, Boston University, 44 Cummington Street, Boston, Massachusetts 02215

Fabio Idrobo and J. Michael Harrison
Department of Psychology, Boston University, Boston, Massachusetts 02215

Laurel H. Carney[a)]
Hearing Research Center, Department of Biomedical Engineering Boston University, 44 Cummington Street, Boston, Massachusetts 02215

(Received 12 February 2001; revised 29 September 2001; accepted 1 October 2001)

Binaural detection with narrowband and wideband noise maskers was examined by using a Pavlovian-conditioned eyeblink response in rabbits. The target was a tone at 500 Hz, and the maskers were ten individual noise samples having one of two bandwidths, 200 Hz (410 Hz to 610 Hz) or 2900 Hz (100 Hz to 3 kHz). The narrowband noise maskers were created by filtering the wideband noise maskers such that the two sets of maskers had identical spectra in the 200-Hz frequency region surrounding the tone. The responses across the set of noise maskers were compared across bandwidths and across interaural configurations (N_0S_0 and N_0S_π). Responses across the set of noise waveforms were not strongly correlated across bandwidths; this result is inconsistent with models for binaural detection that depend only upon the narrow band of energy centered at the frequency of the target tone. Responses were correlated across interaural configurations for the wideband masker condition, but not for the narrowband masker. All of these results were consistent with the companion study of human listeners [Evilsizer *et al.*, J. Acoust. Soc. Am. **111**, 336–345 (2002)] and with the results of human studies of binaural detection that used only wideband [Gilkey *et al.*, J. Acoust. Soc. Am. **78**, 1207–1219 (1985)] or narrowband [Isabelle and Colburn, J. Acoust. Soc. Am. **89**, 352–259 (1991)] individual noise maskers. © *2002 Acoustical Society of America.* [DOI: 10.1121/1.1423930]

PACS numbers: 43.66.Gf, 43.66.Pn, 43.66.Dc [LRB]

I. INTRODUCTION

Understanding the psychophysics and neurophysiology of the detection of a tone in a noise masker is one of the classic problems in auditory science. In the current study, a behavioral paradigm for the rabbit was used to investigate the detection of tones in wideband and narrowband maskers, and the correlation of detection results across bandwidths for a set of individual masker noise waveforms was investigated. These experiments were designed in parallel with a companion study on human subjects by Evilsizer *et al.* (2002). In both studies, narrowband maskers were derived from a set of individual wideband maskers such that the sets of stimuli had identical spectra in the narrow frequency band surrounding the target tone. Noise waveforms that were digitally stored, and were therefore reproducible, were used so that the details of responses across a set of masker waveforms could be investigated. Comparisons of results across bandwidths and across interaural configurations at each bandwidth provided information concerning the effect of masker frequencies outside the narrow frequency band that surrounds the tone frequency.

Two interaural configurations are frequently tested in studies of binaural detection with human listeners: a diotic N_0S_0 condition (in-phase masker and tone to the two ears) and a dichotic N_0S_π condition (in-phase masker and out-of-phase tone to the two ears). Several studies have measured binaural detection in animals (e.g., cat: Geesa and Langford, 1976; Wakeford and Robinson, 1974; budgerigar: Dent *et al.*, 1997; ferret: Hine *et al.*, 1994; rabbit: Early *et al.*, 2001). Most studies in other species have used free-field or near-field stimuli and have investigated binaural unmasking by changing the phase of the stimulus to one speaker placed near the animal. Studies in the rabbit allow the use of earmolds sealed into the ear canal, such that N_0S_0 and N_0S_π stimuli can be presented (Early *et al.*, 2001). Using this preparation, stimuli can be carefully controlled, allowing differences in performance across reproducible noise samples to be studied. Early *et al.* (2001) reported that responses were significantly different across reproducible noise samples and were correlated between N_0S_0 and N_0S_π; that study was limited to wideband noise maskers and tested only one tone phase for the N_0S_0 condition. In the current study, the set of stimulus conditions was expanded to provide responses that

[a)]Author to whom correspondence should be addressed. Present address: Department of Bioengineering and Neuroscience, Institute for Sensory Research, Syracuse University, 621 Skytop Rd., Syracuse, NY 13244; electronic mail: laurel_carney@isr.syr.edu

can be studied in parallel with results for human listeners (Evilsizer *et al.*, 2002); both studies were focused on comparing the responses across reproducible noise maskers at two bandwidths.

These studies were designed to address a discrepancy that exists in the human psychophysical literature concerning binaural detection studied with reproducible noise maskers. Gilkey *et al.* (1985) investigated detection of a 500-Hz tone using wideband (2900 Hz bandwidth, from 100 Hz to 3 kHz) reproducible noise maskers. They found significant differences in responses across noise samples and significant correlation of the responses between the N_0S_0 and the N_0S_π conditions. Isabelle and Colburn (1991) studied detection of 500-Hz tones using narrowband reproducible noise maskers (116 Hz bandwidth, from 445 to 561 Hz). They also found that there were significant differences in responses across narrowband noise samples; however, unlike the Gilkey *et al.* (1985) study, results were not significantly correlated between the N_0S_0 and N_0S_π conditions. The importance of this discrepancy lies in its implications for predictions of classical models for detection (reviewed by Colburn *et al.*, 1997), because the results for wideband and narrowband maskers should be identical if detection is influenced only by energy at frequencies within a critical band of the target frequency.

To address this discrepancy, the current study tested rabbits with a Pavlovian-conditioned eyeblink response in a detection task with 500-ms duration 500-Hz tones and narrowband and wideband noise maskers. Where possible, the parameters of this study were chosen to parallel those of the companion human study (Evilsizer *et al.*, 2002); due to the difference in species and test paradigms, there were differences between the studies. One such difference was the bandwidth of the narrowband maskers: the narrowband maskers in the companion study had a bandwidth of 100 Hz, whereas the narrowband maskers in the current study had a 200-Hz bandwidth (410 to 610 Hz). These stimuli were chosen based on preliminary results which suggested that performance in the rabbit was considerably more stable for the 200-Hz bandwidth than for 100 Hz, and performance levels differed between these bandwidths (Carney *et al.*, 2000). In addition, detection performance was found to be similar for 200-Hz and 3-kHz bandwidths in the current study, suggesting that the critical band of the rabbit is less than or equal to 200 Hz. The broader critical band of the rabbit is not surprising based on the fact that peripheral tuning is relatively broad in this species (Borg *et al.*, 1988).

As in the companion study, the wideband and the narrowband maskers in the current study were created with the same spectra in the 200-Hz band surrounding the tone frequency; the set of wideband maskers was filtered to obtain the set of narrowband maskers. The companion study used 25 reproducible noises; a subset of 10 of these noises was used in the current study, due to the limited number of tone-plus-noise trials that could be delivered in each behavioral test session. The total duration of stimuli differed between the two studies, but durations were chosen in an effort to study detection based on comparable effective stimulus durations (see later in this work). Finally, a tracking paradigm was used for most of the measurements in the current study, whereas most human studies of detection with reproducible noise maskers have used a fixed-level task (including the companion study Evilsizer *et al.*, 2002). In both the companion study and in the current study, a limited number of measurements were made to allow the comparison of results for the two stimulus-level-selection paradigms.

The aim of this study was to compare results for a tone-detection task with reproducible noise maskers for rabbit detection across bandwidths and interaural configurations and to test the hypothesis that rabbits exhibit the same trends in responses across conditions as human listeners. The use of reproducible noise maskers in psychophysical experiments such as these, as well as physiological experiments, provide data that are critical for testing models of binaural detection. Models of detection typically focus on the interactions of the target and masker in the response of a single auditory filter (or critical band). The responses presented here and in the companion article indicate that these models must be extended in future studies to include the influence of energy outside the critical band centered on the target in order to explain results for reproducible noises.

II. GENERAL METHODS

All experimental methods were approved by the Charles River Campus Institutional Animal Care and Use Committee at Boston University. The behavioral methods are similar to those reported by Early *et al.* (2001), and the ten wideband reproducible noise maskers were the same as in that study.

Three female Dutch-Belted rabbits (2.0–3.5 kg), with clean ear canals and normal distortion-product otoacoustic emissions (Lonsbury-Martin *et al.*, 1987), were the subjects in this study. The experiments were conducted in an IAC (Industrial Acoustics Co., Bronx, NY) double-walled sound-attenuating booth. Two-hour sessions were run daily. The animal sat in a custom-made open box and was wrapped in a towel. Stable positioning of the head was achieved with a bar surgically mounted on the skull using screws and dental acrylic. Each rabbit had earmolds that were custom-molded using a soft plastic material (Per-form H/H, Hal-Hen, Long Island City, NY).

A. Pavlovian eyeblink conditioning

Pavlovian eyeblink conditioning (reviewed in Gormezano *et al.*, 1983) was used to study binaural detection. The conditioned stimulus (CS) was a 500-Hz tone, and the unconditioned stimulus (US) was an electrical shock (0.9 mA, 60 Hz) delivered to electrodes positioned posterior to the orbit by a Med Associates (St. Albans, VT) constant-current shocker (ENV-410A). The shock occurred during the last 100 ms of the 500-ms duration tone. The choice of 500-ms duration for the tones and noise maskers and of a 400-ms delay to the onset of the US was based on previous studies of Pavlovian conditioning of the eyeblink response (e.g., Frey and Ross, 1968).

The onset of an eyeblink in the presence of the tone-plus-noise stimulus (CS) before the onset of the shock constituted a conditioned response (CR). Onset of the eyeblink after the shock constituted an unconditioned response (UR). The CS was always accompanied by the US.

An eyeblink on a tone-plus-noise trial with latency shorter than 400 ms was designated a CR. Allowing 100 ms for the execution of the eyeblink response, it was estimated that the first 300 ms of the tone-plus-masker stimulus determined the animal's response. The stimulus duration for the human study was set at 300 ms (Evilsizer *et al.*, 2002), thus providing roughly comparable effective stimulus durations across the studies.

Eyeblink responses to noise-alone trials were also recorded and analyzed. The eyeblink was monitored by a photodiode-phototransistor pair that was aimed at the edge of a small piece of white paper taped to the animal's eyelid to contrast with the animal's dark eye. The photodiode–phototransistor pair converted eyelid position into voltage. The onset of an eyeblink was determined automatically based on a criterion for the slope of the photodiode voltage.

Individual animals were initially trained with tones in quiet, and the level of the CS was fixed at a relatively high level (70 dB SPL) until the animal had CRs for 80% of the trials in a session. Two of the animals (R4 and R6) were subjects in a previous study (Early *et al.*, 2001) and had extensive experience in binaural detection with wideband maskers. All three animals were tested for about 30 sessions on a binaural detection task using noise maskers with several bandwidths (50 Hz, 200 Hz, 800 Hz, and 3 kHz) before being tested at the two bandwidths used in the current study. These 30 sessions were the only prior experience for R7 on the tone-plus-noise detection task.

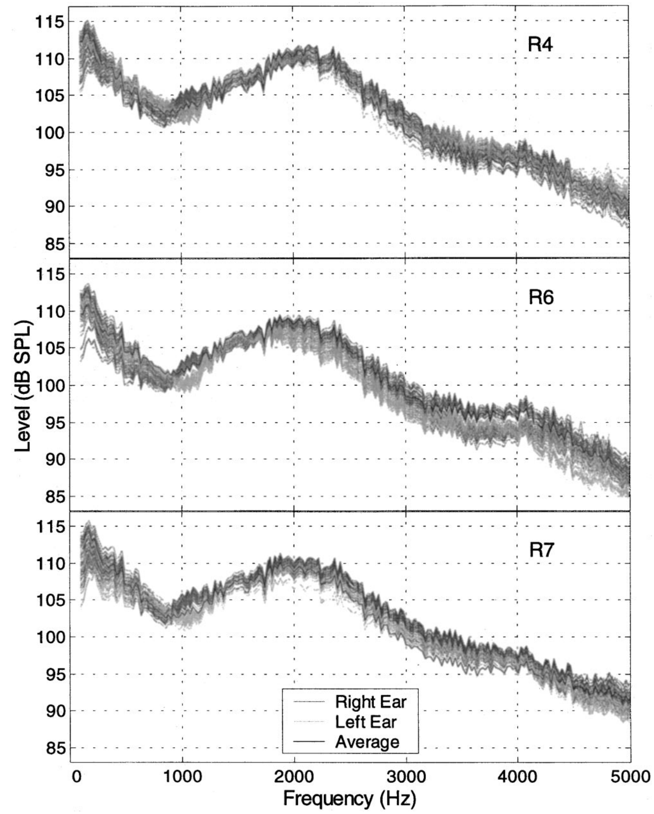

FIG. 1. Calibration curves for each ear of each animal (panels) for the 64 sessions in this study. Each curve is plotted as level in dB SPL as a function of frequency in Hz for the range 100–5000 Hz. The dark gray lines are the daily in-the-ear calibration curves for the right ear and the light gray lines are for the left ear. The black curve in each panel is the average calibration for that animal which was used to prefilter the stimuli delivered to both ears during the course of this study. See text for details of the acoustic calibration.

B. Acoustic stimuli

A Tucker-Davis Technologies (Gainesville, FL) System II was used to generate, low-pass filter (with corner frequency equal to 20 kHz), and present stimuli, record waveforms in the ear canal, and record eyeblink responses. Beyerdynamic DT-48 (Heilbronn, Germany) earphones were used to present the stimuli to the ear canals through the custom-made earmolds. The frequency response of the acoustic system (including the properties of the earphone, earmold, and ear canal) was characterized and used to create a prefilter that was applied to the stimuli. Each calibration was based on 64 500-ms duration white-noise samples that were presented and recorded using a probe-tube microphone (Etymotic ER-7, Elk Grove Village, IL) attached to the earmold. The amplitude spectra of the 64 noise recordings were averaged for each calibration curve.

The prefilter used to digitally compensate the reproducible noise waveforms for the shape of the frequency response was computed once for each rabbit on the basis of an average of several calibration curves that were obtained before data collection for this study began. This averaged calibration curve for each rabbit was calculated by averaging 16 to 20 calibration curves from both ears (8–10 from each ear) for that rabbit. The calibration curves included in the average calibrations varied by ± 5 dB between 200 Hz and 3 kHz, and varied slightly more (± 10 dB) at frequencies below 200 Hz. The repeatability of the calibrations across days is illustrated in Fig. 1.

The average calibration curve was used as the prefilter to ensure that identical waveforms were presented daily (Early *et al.*, 2001). However, the calibration curve of the acoustic system was still checked daily to ensure that there were no significant changes in the acoustics (e.g., related to position of the earmold) that could have introduced variability into the reproducible waveforms from day to day. Any significant difference between the daily calibration and the average calibration was investigated and resolved before daily testing began, typically by reseating the earmold within the ear canal. The set of ten reproducible noise maskers was created using digitized Gaussian noise samples that were pregenerated on the array processor of the TDT-II system at a sampling rate of 50 kHz. Band-limited noise maskers were obtained by applying a rectangular window in the frequency domain to the reproducible noise waveforms. The frequency window for the 200-Hz bandwidth noise maskers was geometrically centered at 500 Hz (410 to 610 Hz). The frequency window for the wideband maskers was 2900 Hz wide (100 Hz to 3 kHz). To create noises that had a flat spectrum in the ear canal, the amplitude spectrum of each band-limited white noise sample was divided by the averaged calibration curve for each rabbit. The mean spectrum level across all noises was fixed at 40 dB SPL.

A 500-Hz tone was the target stimulus. The tone level was set based on the averaged calibration curve. Both the tone and the masker had 500-ms durations, with 10-ms cosine-squared onset/offset ramps. Between tone-plus-noise trials there were many noise-alone trials (see later in this work); these stimuli were drawn from the same set of reproducible noises as the maskers in the tone-plus-noise trials. A 1-s interval followed each 500-ms trial.

The noise waveforms to the two ears were identical in all conditions (N_0). The tones presented to the two ears were either diotic (S_0) or were 180° out of phase (S_π). Previous studies that explored the phase-dependence of binaural detection (e.g., Gilkey *et al.*, 1985; Isabelle and Colburn, 1991) showed that N_0S_0 responses depend upon the starting phase of the tone. Therefore, half of the N_0S_0 stimuli in this study were created using tones with 0° starting phase [referred to as $N_0S_0(0°)$] and half were created with 180° starting phase [referred to as $N_0S_0(180°)$]. In addition to providing estimates of performance based on starting phases, these starting phases are the two components of the N_0S_π stimulus and are thus useful for analyses that compare responses across interaural configurations.

III. EXPERIMENT 1

The first experiment included tests of responses for narrowband and wideband maskers for both interaural configurations. In the companion study with human listeners (Evilsizer *et al.*, 2002), a fixed-level task was used to test performance across noise samples with the tone level fixed. A previous animal study (Early *et al.*, 2001) demonstrated that, with rabbits, a one-down–one-up track yielded results that were more stable over time as compared to testing at a fixed tone level (Carney *et al.*, 1998). Therefore, a tracking procedure was used for experiment 1 in the current study. The use of tracking versus fixed-level testing was further investigated in experiment 2.

A. Methods

Animals were tested with two masker bandwidths, 200 and 2900 Hz, and two binaural configurations, N_0S_π and N_0S_0; half of the N_0S_0 trials were $N_0S_0(0°)$ and half were $N_0S_0(180°)$. Only one condition was tested during a 2-h experimental session. Sixty-four sessions were run for each animal in eight sets. A set comprised eight sessions, with four sessions at each bandwidth. For each bandwidth there were two N_0S_0 sessions (one at each starting phase) and two N_0S_π sessions to match the number of sessions across the diotic and dichotic conditions. The eight sessions in each set were organized such that N_0S_0 conditions were tested in four consecutive sessions with bandwidth (narrowband and wideband) and tone starting phase (0° or 180° for N_0S_0) randomized, followed by four N_0S_π sessions. A new random sequence was determined for each odd-numbered test set, and the test order was reversed for the subsequent even-numbered set. Each rabbit had a different testing order. This strategy of changing interaural configurations only every few days was adopted after preliminary tests suggested that changing the interaural configuration (N_0S_0 vs. N_0S_π) on a daily basis resulted in performance that was less consistent over time. This method of ordering sessions allowed testing

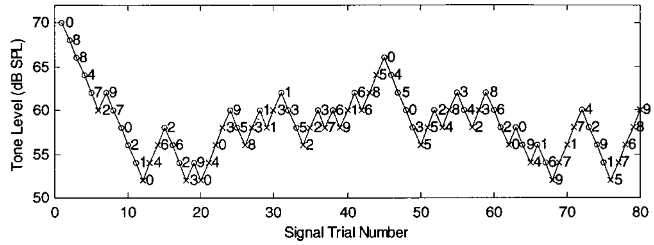

FIG. 2. A one-down–one-up track (R4, session 375, N_0S_π, narrowband noise maskers) for one behavioral session. Each point represents a tone-plus-noise trial. The number that labels each trial is the noise sample number (0–9). Each circle represents a CR; each x symbol represents a UR. The confidence interval for this track was 1.6 dB.

of all of the interaural configurations in a partially interleaved manner while still maintaining consistent performance over time.

A statistical power analysis of the data collected for a previous study (Early *et al.*, 2001) indicated that eight sessions for each condition would yield sufficient numbers of trials for each noise sample (approximately 40 trials/noise) to allow statistical testing of responses across reproducible noise samples. Therefore, at least eight test sessions were completed for each stimulus condition for the three rabbits in this study.

Each session consisted of a single track, an example of which is shown in Fig. 2. For each track, the tone level was initially set to 70 dB SPL and was adjusted from one tone-plus-noise trial to the next following a one-down-one-up rule, resulting in tracks that converged to a level at which CRs were present on 50% of the tone-plus-noise trials (Levitt, 1971). The step size was fixed at 2 dB. Each point in the representative track illustrated in Fig. 2 shows a tone-plus-noise trial; each CR (conditioned response, which precedes the shock) is indicated by a circle, and each UR (unconditioned response) is indicated by an x. The noise sample number used as the masker for each tone-plus-noise trial is indicated on the track.

Each trial was either a tone-plus-noise trial or a noise-alone trial. The noise masker in each trial was randomly chosen from the ten pregenerated reproducible noise samples. There were 33–47 noise-alone trials between each pair of tone-plus-noise trials, randomized such that tone-plus-noise trials occurred on average once per minute, with the interval between tone-plus-noise trials ranging from 49.5 to 70.5 s.[1] Animals were given a 1-min break after every 10 tone-plus-noise trials and a 3-min break after every 30 tone-plus-noise trials. Eighty to 90 tone-plus-noise trials were completed in a 2-h session.

Eyelid position was recorded during all tone-plus-noise trials and noise-alone trials. Occasionally, fidgeting or chewing by the animal resulted in fluctuations of the eye voltage signal that met the automated criterion for an eyeblink. This behavior was more common for one animal (R6) than for the other two. For this animal, the recorded eyeblinks on noise-alone trials were reviewed manually; trials that had obvious cyclic changes associated with chewing, or small, brief movements associated with fidgeting, were removed. The records removed were qualitatively different from typical eyeblinks, and represented approximately 1.5% of all noise-alone trials for this animal in the sessions that were included in the analysis. However, two sessions for this rabbit (R6) had an exceptionally large number (a factor of 5 higher than average) of noise-alone trials that were apparently affected by fidgeting and/or chewing behaviors; these sessions were excluded from further analysis, and those conditions were repeated on other days.

B. Data analysis

A confidence interval (Howell, 1992; Leek *et al.*, 2000) was computed to quantify the stability of a given track. The 95% confidence interval was calculated using the tone levels visited during the track, excluding the trials at the beginning of the track preceding the fourth reversal. If the confidence interval of a track was greater than 2.2 dB, it was excluded from analysis. Using this criterion, 1 out of 65 sessions was excluded from R4's data; 2 out of 66 sessions from R7's data; and 22 out of 88 sessions from R6's data. In the case of R6, most of the excluded sessions (20 of the 22) were for the narrowband N_0S_π condition (see later in this work).

The tone level at which CRs were present on 50% of the tone-plus-noise trials was determined by averaging the reversals (excluding the first four reversals of each track) across individual tracks. Tone-plus-noise trials at a tone level one step above and two steps at or below this level were included in the reproducible noise analysis (Early *et al.*, 2001). In order to test the statistical significance of performance differences across samples, a χ^2-test (Siegel and Colburn, 1989) was used in this study.

Because responses across the set of reproducible noises are affected by the starting phase of the tone (e.g., Gilkey *et al.*, 1985), responses were separated according to reproducible noise masker and starting phase of the tone into two sets of ten for the statistical analysis of the N_0S_0 results, thus creating a set of 20 stimuli for these analyses (ten for the $N_0S_0(0°)$ condition and ten for the $N_0S_0(180°)$ condition). One set of ten reproducible noises (with approximately the same number of overall trials as the combined N_0S_0 results) was used in the statistical analysis of the N_0S_π results. For comparison of responses across the N_0S_0 and N_0S_π conditions, the responses to each reproducible noise for the two starting phases of the tone for N_0S_0 were averaged together and then compared to the responses for the N_0S_π condition (Gilkey *et al.*, 1985).

C. Results and discussion

Three rabbits were tested over 3 to 4 months each. The session-by-session performance for each rabbit is shown in Fig. 3. Each point represents the mean signal level with respect to the noise level (E_s/N_0 in dB) for the reversals in the track (excluding the first four reversals). These E_s/N_0 values thus represent the mean across all ten reproducible noise waveforms of the signal-to-noise ratio that elicited responses on 50% of the tone-plus-noise trials. Only sessions with tracks that had a confidence interval size less than or equal to 2.2 dB are shown. This figure shows that the performance of all animals was relatively consistent across sessions, except

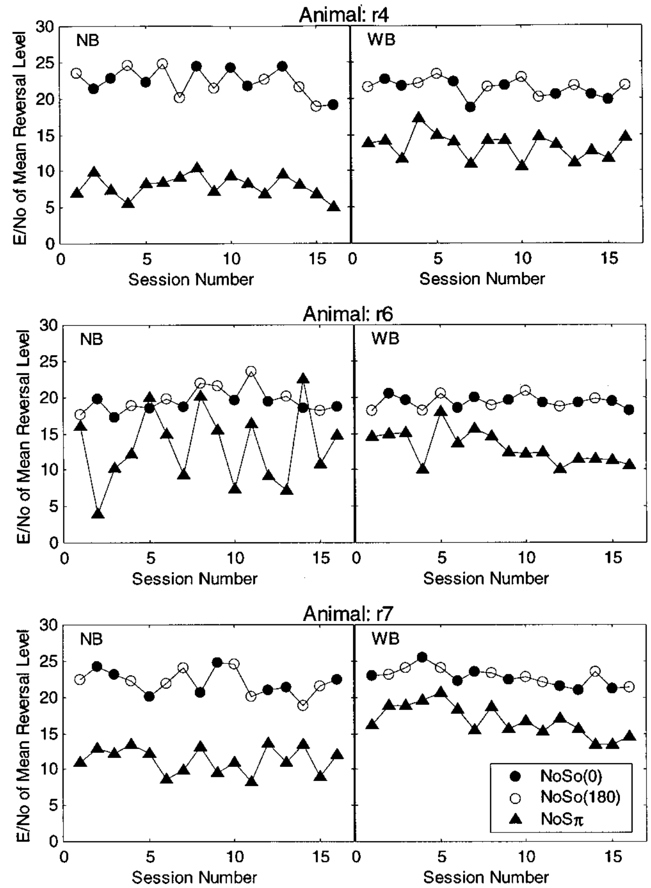

FIG. 3. The session-by-session mean reversal levels for three rabbits: R4, R6, and R7. In each plot, the left panels show results for narrowband maskers (NB); the right panels show results for wideband maskers (WB). Only sessions with a confidence interval less than or equal to 2.2 dB are shown.

for R6's performance for the narrowband N_0S_π condition.[2] Compared with R4 and R6, there is a slight downward trend over time in the mean reversals of R7. This improvement over time may be due to R7's more limited experience in binaural detection experiments before testing began.

Table I provides a summary of the experimental data for the three rabbits tested. E_s/N_0 in dB was calculated as:

$$\frac{E_s}{N_0} = \text{Tone level (dB SPL)} - \text{Noise spectrum level (dB SPL)} + 10\log_{10}\frac{\text{duration (s)}}{1\text{ s}}.$$

The duration used for this calculation was 400 ms, which is the entire duration of the CS before the onset of the US. The noise spectrum level was always 40 dB SPL.

The E/N_0 (in dB) for which the animals had CRs on 50% of the tone-plus-noise trials was within 1 dB across bandwidths for the N_0S_0 condition for all three rabbits (Table I). This result supports the assumption that the critical band for the rabbit is less than or equal to 200 Hz. Preliminary tests showed that the E_s/N_0 required for a 50% CR rate was reduced for a 100-Hz bandwidth masker (Carney *et al.*, 2000), thus the 200-Hz bandwidth was chosen for this ex-

TABLE I. Results from Experiment 1. χ^2 values are given for the results across reproducible noise maskers for tone-plus-noise and noise-alone trials.

Interaural configuration	Noise bandwidth[a]	Rabbit	Tone-plus-noise trials			Noise-alone trials	
			E_s/N_0[b]	χ^{2c}	N^d	χ^{2c}	N^d
N_0S_0	NB	R4	22.4	48.4[e]	78	63.5[e]	4978
		R6	19.5	32.2[f]	89	26.3	5181
		R7	22.1	37.1[e]	74	142.9[e]	4950
	WB	R4	21.4	74.3[e]	83	241.0[e]	4925
		R6	19.3	35.3[f]	93	48.1[e]	5228
		R7	22.8	87.0[e]	91	562.7[e]	4900
N_0S_π	NB	R4	7.9	28.4[e]	67	70.1[e]	5002
		R6	13.1	20.8[f]	43	16.7	4946
		R7	11.4	30.5[e]	69	73.2[e]	4955
	WB	R4	13.4	52.7[e]	68	379.7[e]	4911
		R6	13.0	27.3[e]	65	18.4[f]	5148
		R7	16.8	47.4[e]	69	478.0[e]	4927

[a]NB=200 Hz bandwidth; WB=100–3000 Hz.
[b]E_s/N_0 in dB of the stimulus at the mean reversal level of the tracks (50% CRs).
[c]χ^2 for the N_0S_0 conditions was calculated using 20 stimuli [ten for the $N_0S_0(0°)$ condition and ten for the $N_0S_0(180°)$ condition; 19 degrees of freedom]. There are nine degrees of freedom for the ten-stimulus N_0S_π condition.
[d]N is the average number of trials per reproducible noise sample. The N for the N_0S_0 conditions combines trials from the $N_0S_0(0°)$ condition and the $N_0S_0(180°)$ condition.
[e]$p<0.01$.
[f]$p<0.05$.

periment to ensure that the narrowband masker was at least as wide as the critical band. For the N_0S_π condition, E_s/N_0 in dB at the 50% CR level was lower for narrowband than for wideband maskers, as expected. As a result, the MLD (the difference in performance between N_0S_0 and N_0S_π) of all rabbits was larger for narrowband maskers than for wideband maskers. This trend was consistent with previous studies of human listeners (e.g., Bourbon and Jeffress, 1965; Metz *et al.*, 1968; Staffel *et al.*, 1990; Bernstein *et al.*, 1998; van de Par and Kohlrausch, 1999; Evilsizer *et al.*, 2002).

D. Responses across reproducible noises

According to a χ^2 test, the variability in responses across the set of reproducible noises was significantly ($p<0.05$) greater than would be expected due to chance for all rabbits and conditions for the tone-plus-noise trials (Table I). Figure 4 shows responses across the set of reproducible noises; percentages of trials with conditioned responses to tone-plus-noise trials (upper panels of each set) and percentages of noise-alone trials for which there were responses are shown. The variations in performance across noises, as well as across the bandwidths, interaural configurations, and rabbits, can be qualitatively seen by comparing the panels in Fig. 4; quantitative comparisons will be presented later in this work. $N_0S_0(0°)$ and $N_0S_0(180°)$ responses for each reproducible noise masker were averaged and plotted together for comparison to the N_0S_π responses (Fig. 4). For all rabbits, the overall percentage of conditioned responses on tone-plus-noise trials is approximately 50% (as expected for the one-up–one-down track), and the overall percentage of responses on noise-alone trials is very low, about 1%–5%. Spontaneous eye-blinks occur infrequently in the rabbit (1–3 per hour, Gormezano, 1966). The percentage of responses to noise-alone trials is higher for wideband maskers than it is for narrowband maskers, a result that is consistent across all rabbits.

E. Correlation across bandwidths

The correlations between the narrowband and wideband responses for individual rabbits are shown in Table II. As described earlier, the wideband maskers had the same spectra in the 200-Hz frequency band centered at 500 Hz as the narrowband maskers. If the responses in the presence of the different reproducible noise maskers were determined only by the masker spectrum near the tone frequency, i.e., if the spectrum outside this narrow band had no effect on detection, the narrowband results should have been highly correlated to the wideband results. Yet in most conditions, results for the two bandwidths were not significantly correlated. There was a significant correlation for one comparison (the N_0S_π tone-plus-noise trials) in a single rabbit (R7). The same rabbit was the only animal tested that showed correlated responses across the two bandwidths for the noise-alone trials, for both N_0S_0 and N_0S_π conditions.

For the N_0S_0 condition, the correlation of tone-plus-noise responses across the bandwidths was not significant but was always positive (Table II). This pattern was similar to that of the human study, which showed a significant effect of the frequency components outside of the narrow frequency band centered on the tone (Evilsizer *et al.*, 2002).

For the N_0S_π condition, the correlation of the tone-plus-noise trials across bandwidths was near zero for two of the three rabbits and was high for one rabbit (R7). This pattern was similar to that of the human subjects, for which the

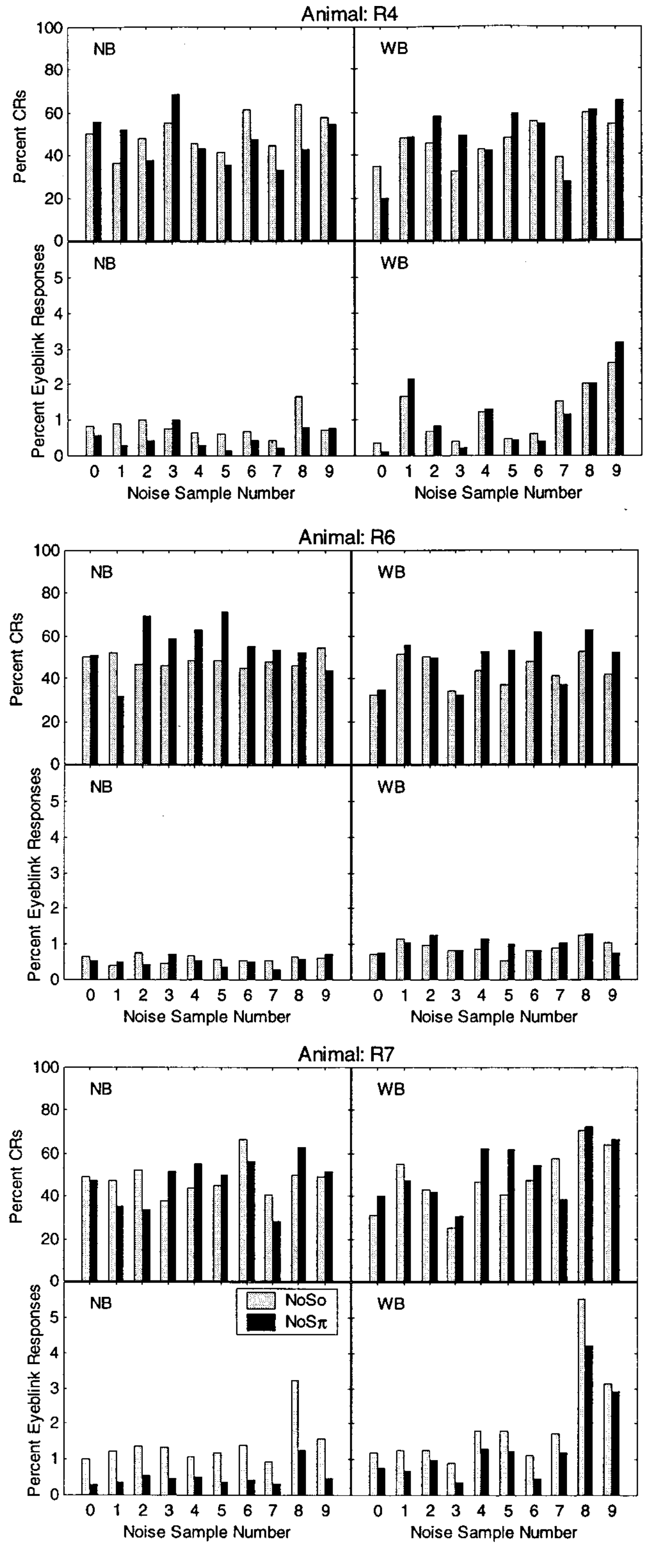

FIG. 4. Performance across reproducible noise maskers for the N_0S_0 and N_0S_π conditions for R4, R6, and R7. The left panels show results for narrowband maskers (NB), and the right panels show results for wideband maskers (WB). The responses to tone-plus-noise trials (upper panel) and to noise-alone trials (lower panel) are shown for each bandwidth. $N_0S_0(0°)$ and $N_0S_0(180°)$ were averaged for comparison to N_0S_π.

correlations of hits across bandwidths were near zero for three listeners, and positive but insignificant for one listener (Evilsizer *et al.*, 2002). The lack of strong correlation in tone-plus-noise and noise-alone results across bandwidths

TABLE II. Pearson's product-moment correlations between responses for wideband and narrowband maskers.

Interaural configuration[a]	Rabbit	Tone-plus-noise trials *r*	Noise-alone trials *r*
N_0S_0	R4	0.25	0.24
	R6	0.39	−0.29
	R7	0.33	0.80[b]
N_0S_π	R4	−0.03	0.12
	R6	−0.07	−0.37
	R7	0.64[c]	0.82[b]

[a]Responses for the N_0S_0 condition represent the combined data from the $N_0S_0(0°)$ condition and the $N_0S_0(180°)$ condition, resulting in 18 degrees of freedom. There were eight degrees of freedom for the ten-stimulus N_0S_π condition.
[b]$p<0.01$.
[c]$p<0.05$.

for these noise maskers, which have identical spectra in the frequency region near the tone frequency, suggests that the frequency components outside the 200-Hz frequency band affect the responses for the wideband condition.

F. Correlation across interaural configurations

The correlation between responses for the N_0S_0 and the N_0S_π conditions is shown in Table III. The responses for each of the reproducible noise maskers in the N_0S_0 condition were averaged across the two starting phases for comparison to the responses to the N_0S_π responses (Gilkey *et al.*, 1985). In general, the N_0S_0 and the N_0S_π responses were not significantly correlated for narrowband maskers, but were significantly correlated for wideband maskers for all three rabbits. This result suggests that similar physical properties of the noise may be affecting detection for both the N_0S_0 and the N_0S_π conditions in the wideband case, but that different stimulus characteristics may control the CR in the narrowband case.

Because the noise-alone trials were exactly the same for both the N_0S_0 and N_0S_π conditions, it might be expected that the performance on noise-alone trials would be correlated between the N_0S_0 and N_0S_π conditions. However, Table III shows that these responses were highly correlated for one

TABLE III. Pearson's product moment correlations between responses for the N_0S_0 and N_0S_π conditions. Note: To compare interaural configurations, the results for each reproducible noise for the $N_0S_0(0°)$ condition and the $N_0S_0(180°)$ condition were averaged together and then compared to the results for the N_0S_π condition, resulting in eight degrees of freedom for all correlations.

Noise bandwidth[a]	Rabbit	Tone-plus-noise trials *r*	Noise-alone trials *r*
NB	R4	0.31	0.48
	R6	−0.56	−0.04
	R7	0.27	0.97[b]
WB	R4	0.71[c]	0.97[b]
	R6	0.77[b]	0.44
	R7	0.67	0.98[b]

[a]NB=200 Hz bandwidth; WB=100–3000 Hz.
[b]$p<0.01$.
[c]$p<0.05$.

TABLE IV. Pearson's product moment correlations between rabbits.

Noise bandwidth[a]	Interaural configuration	Subject pair	Tone-plus-noise trails r	Noise-alone trials r
NB	N_0S_0	R4-R6	0.08	0.33
		R4-R7	0.14	0.83[b]
		R6-R7	0.25	0.10
	N_0S_π	R4-R6	−0.42	0.87[b]
		R4-R7	0.30	0.47
		R6-R7	0.11	0.30
WB	N_0S_0	R4-R6	0.75[b]	0.51[c]
		R4-R7	0.67[b]	0.62[b]
		R6-R7	0.59[b]	0.16
	N_0S_π	R4-R6	0.67[c]	0.19
		R4-R7	0.57	0.67[c]
		R6-R7	0.81[b]	0.36

[a]NB=200 Hz bandwidth; WB=100–3000 Hz. df=18 (N_0S_0) and 8 (N_0S_π); see note (a) in Table II.
[b]$p<0.01$.
[c]$p<0.05$.

rabbit (R7) for both narrowband and wideband maskers, and for one rabbit (R4) for wideband maskers only. This result implies that the strategy used on the tone-plus-noise trials may influence the responses to noise-alone trials.

These results showed the same trends as the companion human study, for which all comparisons across interaural configurations were significant for the wideband case, whereas no consistent trend was seen for the narrowband case (Evilsizer *et al.*, 2002). The responses to noise-alone trials tended to be more strongly correlated across interaural configurations for the wideband maskers than for narrowband maskers for both rabbit and human subjects.

The comparison of responses across interaural configurations in both the current and the companion study are also consistent with previously reported results. Gilkey *et al.* (1985) reported correlated results across interaural configurations when using wideband maskers, and Isabelle and Colburn (1991) reported uncorrelated results across interaural configurations when using narrowband maskers. The current and companion studies, which provide results for the same listeners and using stimuli that had identical spectra in the frequency region near the tone, support the hypothesis that the discrepancy between the two previous studies was due to the different bandwidths of the maskers (Isabelle and Colburn, 1991). The dependence on bandwidth of the relationship between the N_0S_0 and N_0S_π conditions also supports the conclusion that masker components well away from the tone frequency influence the detection results across reproducible noises.

G. Intersubject correlation

Table IV provides the correlation of responses across rabbits. For wideband tone-plus-noise trials, all three rabbit pairs were significantly correlated for the N_0S_0 condition, and two of three rabbit pairs were correlated for the N_0S_π condition. None of the pairs were correlated for the narrowband tone-plus-noise results for either interaural configuration. The noise-alone results showed weaker correlations across rabbits; two of six pairs were significantly correlated for the narrowband maskers, and three of six pairs were just significantly correlated for the wideband maskers.

These trends were similar to those in the companion study, which showed significant correlations across all subject pairs for the wideband maskers in both interaural configurations and relatively weak (though significant for the N_0S_0 condition) correlations for the narrowband maskers. Although the use of fewer reproducible noise maskers in the current study is probably responsible for the weaker statistical significance in many of the comparisons, all trends across conditions are comparable across the two studies.

H. Consistency of performance over time

Isabelle (1995) reported that the results for one set of reproducible noise maskers were stable for one human subject over several years. A similar result from one rabbit (R4) is shown here for two sets of data collected more than one year apart. One data set, from the study of Early *et al.* (2001) ("previous" data), was collected for at least ten sessions at one interaural configuration. The other data set ("current" data) was extracted from the larger data set of the current study that included two interaural configurations. A summary of the previous and current data sets is given in Table V. There was a strong correlation between the two data sets for tone-plus-noise trials for both the N_0S_0 and the N_0S_π conditions. Correlations between noise-alone responses for the

TABLE V. Comparison of previous and current data set. Note: These data were collected from R4 with wideband maskers. Because the previous data set included more sessions than the current set, it is characterized by higher χ^2 values.

Interaural configuration	Data set	E_s/N_0 for 50% CRs	Tone-plus-noise trials			Noise-alone trials		
			χ^2	N	r	χ^2	N	r
$N_0S_0(0°)$	Previous	22.5	85.9[a]	87	0.94[a]	187[a]	6167	0.83[a]
	Current	21.8	41.1[a]	39		95[a]	2454	
N_0S_π	Previous	13.0	62.3[a]	101	0.87[a]	212[a]	6851	0.58
	Current	13.3	52.7[a]	68		380[a]	4911	

[a]$p<0.01$, df=8.

TABLE VI. Comparison of tracking and fixed-level data from experiment 2.

Rabbit	Data set	E_s/N_0	Tone-plus-noise χ^2	N^a	r	Noise-alone χ^2	N^a	r
R4	Tracking	21.8	41.1^b	39	0.88^c	95^b	2454	0.85^c
	Fixed level	21.0	37.0^b	64		157^b	2470	
R7	Tracking	23.0	51.3^b	44	0.76^c	174^b	2456	0.81^c
	Fixed level	19.5	108^b	96		338^b	3702	

[a] N is the average number of trials per reproducible noise sample.
[b] $p<0.01$.
[c] $p<0.05$, df=8.

two data sets were significant for the N_0S_0 condition, and nearly significant for the N_0S_π condition.

IV. EXPERIMENT 2

A. Comparison of tracking and fixed-level procedures

As mentioned earlier, most reproducible noise tests in human listeners (Gilkey *et al.*, 1985; Isabelle and Colburn, 1991; Evilsizer *et al.*, 2002) have been conducted using a fixed-level procedure, but the rabbits were tested using a tracking procedure. In order to examine differences in performance caused by these different procedures, two rabbits were tested using a fixed-level procedure for a limited set of sessions.

B. Methods

One of the difficulties in performing these tests at a fixed level is due to the influence of changes in the overall performance on the results. The steep psychometric functions associated with this task (see Early *et al.*, 2001) can result in considerable differences in overall performance at a fixed level from day to day; a change in the percentage of CRs (especially if it drops below 50%) can influence the animal's performance over time (unpublished observations). The tracking paradigm, which automatically holds performance near 50% rate of CRs, generally results in consistent performance from session to session. In particular, if the animal misses a few trials in a row, the tracking paradigm automatically emphasizes the conditioning stimulus; increasing the level of the tone tends to reinforce the behavior, whereas leaving the tone at a fixed level can extinguish behavior if the percentage of CRs drops below 50%.

Because they had the most consistent performance across sessions, the fixed-level data were collected from R4 and R7 after experiment 1 was completed. The responses for the N_0S_0 condition with wideband maskers were more consistent than they were for other conditions (as quantified by the confidence interval statistic); therefore, this condition was tested using the fixed-level procedure and compared with the data from the tracking procedure.

C. Results and discussion

Table VI summarizes the experimental data from the tracking procedure and from the fixed-level procedure for the two rabbits. Because several months of tracking data were available for these animals, and their performance was relatively consistent over that time, it was possible to carefully choose the fixed levels to use for these tests. The responses for the two different experimental procedures were highly correlated for both animals for both tone-plus-noise and noise-alone results. Limited tests on human subjects in the companion study also showed strongly correlated results for the fixed-level task and tracking (Evilsizer *et al.*, 2002). Thus, the responses for N_0S_0 across sets of reproducible noise maskers for both bandwidths appear to be robust across these two test paradigms.

V. GENERAL DISCUSSION

In this study, three rabbits were tested with a tone-in-noise detection task using Pavlovian conditioning. Narrowband and wideband reproducible noise maskers with identical spectra in the 200-Hz frequency band centered on the tone frequency were used, and responses across reproducible noises were analyzed. The trends in the results reviewed here are generally consistent with those from the companion study in human listeners (Evilsizer *et al.*, 2002). The interpretation of the results from both of these studies and the data collected provide the basis for future modeling studies of diotic and dichotic detection with reproducible noise maskers.

The responses across reproducible noise samples show that, for each rabbit subject, there were significant differences across reproducible noise samples. The χ^2 values from rabbits (Table I) were lower than those for human listeners in the companion article, in part, perhaps, as a result of the use of fewer reproducible noise maskers in this experiment (Evilsizer *et al.*, 2002) (this is true even when comparable numbers of trials are used in the analysis). The smaller performance differences across reproducible noises for rabbit may be due to the Pavlovian conditioning paradigm used for these tests or to differences in sensitivity across the two species. The rabbits were also tested at higher E_s/N_0 levels than the humans; testing at higher signal-to-noise ratios is consistent with reduced differences in responses across reproducible noise maskers because the relative contribution of the noise waveform to the overall stimulus is reduced. Whether the difference in the performance levels was due to differences in auditory sensitivity, to differences in the sensitivity of the test procedure, or to other factors is a topic for further study.

Most of the comparisons between results for wideband and narrowband maskers (Table II) showed no significant correlation. Because the wideband and narrowband maskers had the same spectra around the tone frequency, the lack of correlation between wideband and narrowband performance suggests that frequency components outside the narrow band influence performance. Therefore, to explain these reproducible noise results with a model would require either a filter with a relatively wide passband or the combination of multiple filters covering a frequency range wider than the critical band. However, to explain these data, the model must also have similar thresholds for these two bandwidths for the N_0S_0 condition. This aspect of the results places a modeling constraint on either the nature of the information used at the output of a single filter, or on the ways in which information is combined across multiple filters.

Comparisons between the N_0S_0 performance and the N_0S_π performance (Table III) show that the responses on tone-plus-noise trials were not correlated for narrowband maskers, but were significantly correlated for wideband maskers. This result is consistent with the results from human listeners [i.e., the narrowband study of Isabelle and Colburn (1991), the wideband study of Gilkey *et al.* (1985), and the companion study of Evilsizer *et al.* (2002), which included both narrowband and wideband maskers]. Although the noise-alone trials were exactly the same for both the N_0S_0 and the N_0S_π conditions, the correlation across conditions was stronger for wideband than for narrowband maskers for both the rabbit and the human studies. This result suggests that the detection strategies used for tone-plus-noise trials may influence the performance for noise-alone trials.

The intersubject comparison (Table IV) shows that the results across animals were not correlated for narrowband maskers, but were significantly correlated for wideband maskers. This result indicates that one model may be sufficient to explain the wideband performance of all subjects, but that different models (or different model parameters) will be required for individual animals to explain the narrowband performance (Isabelle, 1995).

As with human subjects in the companion study, the responses of rabbit subjects varied significantly across noise samples for both narrowband maskers and wideband maskers, and performance was robust over time. An important aspect of this preparation is its potential for future electrophysiological experiments to investigate neural responses related to binaural detection. Physiological recordings from single neurons in the awake (and potentially behaving) rabbit preparation should contribute to an understanding of how different noise samples influence the firing of a single neuron. Future studies will concentrate on physiological recordings from these animals using the ten reproducible noises from these behavioral experiments. Combined with physiologically based modeling studies of both human and rabbit psychophysical results, these behavioral and physiological results should provide new insight to the classical problem of detection of a tone in noise.

ACKNOWLEDGMENTS

Research support was provided by NIH NIDCD DC01641. The Laboratory Animal Care Facility at Boston University has provided invaluable help with the longterm care of the animals in this study.

[1]In the current study, the proportions of conditioned responses for tone-plus-noise trials and of eyeblink responses for noise-alone trials are reported, rather than proportions of ''hits'' and ''false alarms.'' In the paradigm used, which was chosen to optimize conditioning, the *a priori* probability of a noise-alone trial was approximately 40 times greater than that of a tone-plus-noise trial. In addition, the animal was not forced to respond. The one-up-one-down tracking procedure described above kept the animal at a ''hit rate'' of approximately 0.5, and the ''false-alarm rate'' in this paradigm was approximately 0.02. In order to use the standard signal-detection terminology of hits, false alarms, and the metric d', the absence of responses on noise-alone trials must be regarded as correct rejections, and their absence on tone-plus-noise trials as misses. If the absence of responses on noise-alone trials were considered correct rejections, the animal would be operating in a proportion-correct range of about 0.97. Furthermore, the involuntary nature of the Pavlovian response runs counter to the notion of criterion placement in signal detection theory. Because of the differences between this paradigm and the traditional yes–no detection task used in humans, the use of the d' metric and associated terminology has been avoided here.

[2]Because some of R6's N_0S_π results were at a level comparable to her N_0S_0 results, her daily calibrations were checked before and after 15 sessions to ensure that no changes in earmold position had occurred during the session (perhaps as a result of movement by the animal) that would prevent proper delivery of the N_0S_π stimuli. No changes in calibration were observed that might have explained the large variation in the behavioral data for this condition for this animal.

Bernstein, L. R., Trahiotis, C., and Hyde, E. L. (**1998**). ''Inter-individual differences in binaural detection of low-frequency tonal signals masked by narrow-band or broadband noise,'' J. Acoust. Soc. Am. **103**, 2069–2078.

Borg, E., Engstrom, B., Linde, G., and Marklund, K. (**1988**). ''Eighth nerve fiber firing features in normal-hearing rabbits,'' Hear. Res. **36**, 191–201.

Bourbon, W. T., and Jeffress, L. A. (**1965**). ''Effect of bandwidth of masking noise on detection of homophasic and antiphasic tonal signals,'' J. Acoust. Soc. Am. **37**, 1180.

Carney, L. H., Mason, C. R., Harrison, J. M., and Idrobo, F. (**1998**). ''A classically conditioned rabbit preparation for the study of binaural masking level differences,'' in *Psychophysical and Physiological Advances in Hearing*, edited by A. R. Palmer, A. Rees, A. Q. Summerfield, and R. Meddis (Whurr, London), pp. 419–425.

Carney, L. H., Zheng, L., Evilsizer, M. H., Mason, C. R., Moscynski, S. J., Idrobo, F., and Harrison, J. M. (**2000**). ''Studies of binaural detection using reproducible noises with varied bandwidths in rabbit and human,'' 23rd meeting of the Association for Research in Otolaryngology.

Colburn, H. S., Isabelle, S. K., and Tollin, D. J. (**1997**). ''Modeling binaural detection performance for individual masker waveforms,'' in *Binaural and Spatial Hearing*, edited by R. H. Gilkey and T. Anderson (Erlbaum, Englewood Cliffs, NJ), pp. 533–555.

Dent, M. L., Larsen, O. N., and Dooling, R. J. (**1997**). ''Free-field binaural unmasking in Budgerigars,'' Behav. Neurosci. **111**(3), 590–598.

Early, S. J., Mason, C. R., Zheng, L., Evilsizer, M., Idrobo, F., Harrison, J. M., and Carney, L. H. (**2001**). ''Studies of binaural detection in rabbit using Pavlovian conditioning,'' Behav. Neurosci. **115**, 650–660.

Evilsizer, M., Gilkey, R. H., Mason, C. R., Colburn, H. S., and Carney, L. H. (**2002**). ''Binaural detection with narrowband and wideband reproducible noise maskers: I. Results for human,'' J. Acoust. Soc. Am. **111**, 336–345.

Frey, P. W., and Ross, L. E. (**1968**). ''Classical conditioning of the rabbit eyelid response as a function of interstimulus interval,'' J. Comp. Physiol. Psychol. **65**, 246–250.

Geesa, B. H., and Langford, T. L. (**1976**). ''Binaural interaction in cat and man. II. Interaural noise correlation and signal detection,'' J. Acoust. Soc. Am. **59**, 1195–1196.

Gilkey, R. H., Robinson, D. E., and Hanna, T. E. (**1985**). ''Effects of masker waveform and signal-to-masker phase relation on diotic and dichotic masking by reproducible noise,'' J. Acoust. Soc. Am. **78**, 1207–1219.

Gormezano, I. (**1966**). ''Conditioning and learning,'' in *Experimental Methods and Instrumentation in Psychology*, edited by J. B. Sidowski (McGraw–Hill, New York), pp. 383–420.

Gormezano, I., Kehoe, E. J., and Marshall, B. S. (**1983**). ''Twenty years of classical conditioning research with the rabbit,'' in *Progress in Psychobiology and Physiological Psychology*, edited by J. M. Sprague and A. N. Epstein (Academic, San Diego), pp. 197–275.

Hine, J. E., Martin, R. L., and Moore, D. R. (**1994**). ''Free-field binaural unmasking in ferrets,'' Behav. Neurosci. **108**, 196–205.

Howell, D. C. (**1992**). *Statistical Methods for Psychology* (Pws-Kent, Boston, MA), pp. 193–197.

Isabelle, S. K. (**1995**). ''Binaural detection performance using reproducible stimuli,'' Ph.D. dissertation, Boston University, Boston, MA.

Isabelle, S. K., and Colburn, H. S. (**1991**). ''Detections of tones in reproducible narrowband noise,'' J. Acoust. Soc. Am. **89**, 352–359.

Leek, M., Dubno, J., He, N., and Ahlstrom, J. (**2000**). ''Experience with a

yes-no single interval maximum-likelihood procedure,'' J. Acoust. Soc. Am. **107**, 2674–2684.
Levitt, H. (**1971**). ''Transformed up-down methods in psychoacoustics,'' J. Acoust. Soc. Am. **49**, 467–477.
Lonsbury-Martin, B. L., Martin, G. K., Probst, R., and Coats, A. C. (**1987**). ''Acoustic distortion products in rabbit ear canal. I. Basic features and physiological vulnerability,'' Hear. Res. **28**, 173–189.
Metz, P. J., von Bismarck, G., and Durlach, N. I. (**1968**). ''Further results on binaural unmasking and the EC model. II. Noise bandwidth and interaural phase,'' J. Acoust. Soc. Am. **43**, 1085–1091.
Siegel, R. A., and Colburn, H. S. (**1989**). ''Binaural processing of noisy stimuli: Internal/external noise ratios for diotic and dichotic stimuli,'' J. Acoust. Soc. Am. **86**, 2122–2128.
Staffel, J. G., Hall, J. W., Grose, J. H., and Pillsbury, H. C. (**1990**). ''N_0S_0 and N_0S_π detection as a function of masker bandwidth in normal-hearing and cochlear-impaired listeners,'' J. Acoust. Soc. Am. **87**, 1720–1727.
van de Par, S., and Kohlrausch, A. (**1999**). ''Dependence of binaural masking level differences on center frequency, masker bandwidth, and interaural parameters,'' J. Acoust. Soc. Am. **106**, 1940–1947.
Wakeford, O. S., and Robinson, D. E. (**1974**). ''Detection of binaurally masked tones by the cat,'' J. Acoust. Soc. Am. **61**, 1298–1300.

Effects of frequency-shifted auditory feedback on voice F_0 contours in syllables

Thomas M. Donath, Ulrich Natke, and Karl Th. Kalveram
Institute of Experimental Psychology, Heinrich-Heine-University, Düsseldorf, Germany

(Received 13 June 2001; accepted for publication 10 October 2001)

Previous studies have shown that, during continuous vocalization, voice fundamental frequency (voice F_0) is modified by frequency-shifted auditory feedback. In this study, the effects of frequency-shifted auditory feedback on voice F_0 contours were determined for the first two syllables of the nonsense word [tatatas]. Results show that voice F_0 is auditorily controlled with a long latency and responses are not interrupted by the onset and offset of phonation itself. Furthermore, after-effects were found in voice F_0 in trials after the termination of the frequency shift, which indicates that the response persists for several seconds. It is argued that the purpose of the auditory-vocal system is not to control voice F_0 precisely within single syllables, but rather on a supra-segmental level in the context of prosody.
[DOI: 10.1121/1.1424870]

PACS numbers: 43.70.Aj, 43.66.Hg [AL]

I. INTRODUCTION

Previous studies investigating the auditory-vocal system with the technique of frequency-shifted auditory feedback demonstrated that voice fundamental frequency (voice F_0) is monitored and controlled through a closed-loop negative feedback system with a relatively long latency of >100 ms and a nonlinear limiting property, which prevents corrective responses from exceeding a certain magnitude. When artificially increasing or decreasing the pitch of auditory feedback during vocalization, subjects change their voice F_0 in the opposite direction to compensate for the difference between perceived and intended pitch. However, no study has shown voice F_0 changes exceeding 60 cents for feedback frequency shifts between 100 and 600 cents (Elman, 1981; Burnett *et al.*, 1997; Larson, 1998; Natke and Kalveram, 2001). Also, no significant correlation between frequency shift and response magnitude has been found (Larson, 1998), which has led to the argument for a nonlinear limiting property (Larson *et al.*, 2000).

This current understanding of the nature of the auditory-vocal system is based almost exclusively on a paradigm in which the pitch of auditory feedback is modified unexpectedly while subjects vocalize continuously for several seconds (Elman, 1981; Burnett *et al.*, 1997; Larson, 1998; Jones and Munhall, 2000). Although this paradigm has provided much insight into the auditory-vocal system, it is not directly comparable to vocalization during speech. Speech is characterized by rapidly repeated onsets and offsets of phonation during the combination of vowels, voiced consonants, and voiceless consonants to form words and sentences. Therefore, the question arises whether the characteristics of voice F_0 control established so far also apply to speech, and which new aspects of F_0 control can be found by investigating phonation during speech. Utilizing a paradigm introduced by Natke and Kalveram (2001), in which subjects utter a nonsense word with frequency-shifted feedback, this study determined voice F_0 contours in syllables of the nonsense word ['ta:tatas]. In this way segmental and supra-segmental characteristics of voice F_0 control including latency, magnitude, speed, and duration of responses were measured.

The behavioral importance of precise voice F_0 production can be shown by examining the different informational aspects of prosody, of which F_0 is one dimension besides duration and amplitude. For a review of different aspects of prosody, see Cutler *et al.* (1997). First, there is evidence that prosodic information can have an effect on syntactic analysis. There is also evidence that listeners search actively for accented words to comprehend discourse structure because sentence accent varies depending on semantic context. For example, based on sentence context and the importance of words, a different noun would be stressed in the sentence "Joey gave a book to Mike." Tone languages such as Thai or Cantonese illustrate the potential of voice F_0 for lexical processing. In these languages, variations of F_0 in single syllables can distinguish between different meanings.

Prosody also conveys information about the emotional state of the speaker. Thus it becomes biologically important to realize the intended prosody. Yet another aspect of prosody is that individuals increase or decrease the similarity between their own and others' prosody depending on the situation. A socio-linguistic explanation for this phenomenon is that by matching prosody one can demonstrate social identification (Giles and Powesland, 1975). Since prosody plays a role in so many aspects of communication, it appears to be most important to control voice F_0 precisely.

A negative feedback system in auditory-vocal control would serve to stabilize voice F_0 by comparing the auditorily perceived pitch with an internal reference and adjusting voice F_0 in the opposite direction of deviations. Accordingly, the previously mentioned studies consistently found so-called *opposing responses* as a result of changes of the pitch of auditory feedback. Although the existence of a negative feedback system has been proven many times, the question remains why mean group responses fell within a range of approximately 30 to 60 cents while frequency shifts in most studies were 100 cents (one semitone) or even larger. Burnett *et al.* (1998) suggested that the control system might only be used as a fine-tuning mechanism for small magnitude F_0 fluctuations.

In a study by Larson (1998), subjects were instructed to change their voice F_0 either in the same or the opposite direction of the frequency shift or ignore the frequency shift. He reported that the first response was usually opposing with a latency of 100–150 ms, not strongly influenced by instructions and therefore automatic, while the second response appeared to be a reflection of voluntary mechanisms with latencies between 250 and 600 ms. Opposing responses with similar latencies have been found in other studies as well: 104–200 ms (Burnett *et al.*, 1997), 228 ms (Burnett *et al.*, 1998), and 243 ms (Larson *et al.*, 2000).

Besides opposing responses, also so-called *following responses* have been found (e.g., Burnett *et al.*, 1997; Larson, 1998). In the context of a negative feedback system, such responses would not be very useful because as voice F_0 is being correct in the same direction like the perceived deviation, the feedback F_0 would move away even further from the internal reference. However, following responses would be useful when adjusting voice F_0 to match an external reference. For example, when the F_0 of a piano note is higher than one's own voice F_0, voice F_0 has to be increased until it matches the external frequency. It is still unclear when or why following responses occur. Larson (1998) reports that following responses seem to occur more often when the frequency shift is larger.

Natke and Kalveram (2001) demonstrated that the closed-loop negative feedback mechanism found in experiments using continuous vocalization also applies to speech. In their study, the frequency shift was randomly activated before subjects uttered a three-syllable nonsense word. Thus the complete word was produced with frequency-shifted auditory feedback. Opposing responses were found in long-stressed, but not unstressed (short), first syllables. In the second syllables, opposing responses were found in both unstressed and long-stressed syllables. The authors concluded that long-stressed syllables are long enough for voice F_0 to be affected within them, whereas latencies of responses are too long for voice F_0 to be affected within unstressed and therefore short syllables. Furthermore, they suggested that in second short syllables, responses can be observed because latencies are equal to or less than the duration of preceding syllables.

In the study of Natke and Kalveram, average voice F_0 was calculated for entire syllables and latencies of response were not determined. However, the authors inspected F_0 contours of a limited number of trials and found onsets of responses approximately in the middle of long-stressed first syllables. Since the average response calculated in this way also reflects part of the syllable in which there is no change in F_0, the peak response in long-stressed first syllables was likely greater than the reported 25 cents. Overall the study revealed that the mechanism controlling voice F_0 works at the syllabic level in speech production and most likely applies to natural speech as well. There is also some evidence that the mechanism of voice F_0 control is not limited to relatively artificial settings, but is active during spontaneous speech as well. Natke *et al.* (2001) utilized frequency shifts of half an octave downwards and upwards during spontaneous speech in stuttering and nonstuttering persons. Nonstuttering persons responded with a decrease of global voice F_0 of 36 cents under the upward shift condition, but with no change under the downward shift condition.

Continuing the previous line of research, in this study the effects of frequency-shifted auditory feedback on voice F_0 contours in successive syllables were determined. In this way, temporal aspects of auditory-vocal F_0 control on segmental and supra-segmental level in syllable production were investigated.

II. METHOD

A. Subjects: Separation: Neckartenz-lingen

Twenty-two adults (11 women, 11 men) between 19 and 29 years of age participated ($M = 23$ years, s.d. $= 3.4$ years). Exclusionary criteria were a self-reported current speech disorder and a mother tongue other than German. A hearing screening assured that subjects had 20 dB HL or better pure-tone thresholds for the frequencies 0.25, 0.5, 1, 2, and 4 kHz bilaterally (audiometric test: Hortmann DA 323, Neckartenzlingen, Germany).

B. Apparatus

The subject's voice was frequency-shifted with a commercial device (DFS 404, Casa Futura Technologies, Boulder, CO), which works digitally (32 kHz, 14 bits) and had been modified with a relay to enable remote-switching between nonaltered auditory feedback and frequency-shifted auditory feedback. Auditory feedback was provided through sealed headphones (Blackhawk, DSP 5DX, Flightcom, Portland, OR), which have a built-in microphone to pick up subjects' voices and, according to the manual, attenuate air-conducted sound by approximately 24 dB SPL. Feedback volume was adjusted so that a sinusoidal tone of 440 Hz with 75 dB (A) at the microphone led to a headphones feedback volume of 70 dB (A). Subjects reported that this volume was comparable to auditory feedback during a normal conversation.

In order to mask bone conducted sound, low-pass-filtered white noise ($f_c = 900$ Hz) was presented at an intensity of 65 dB (A) during the experiment. Since there was no simple approach to the physical measurement of masking efficiency, our own and the subjects' observations served as an indicator. When the artificial feedback was turned off suddenly while the masking noise continued, subjects reported that to them it seemed as if they had stopped speaking because they could no longer hear their voice. This indicates that the masking level was sufficient to mask any speech sounds not presented through headphones. However, the masking level was still low enough for subjects to hear their voice clearly and distinctly over the noise.

The use of masking noise is debatable because it also masks the auditory feedback itself and thus the independent experimental variable. However, with masking subjects hear only the electronically processed feedback, as opposed to a mix of processed and bone-conducted sound. The latter had previously been described by subjects as a doubling of their voices, which presents a more serious interference with the independent experimental variable. Although in this study masking noise was used, Burnett *et al.* (1998) did not find that the presence or absence of masking noise had an effect on responses to frequency shift.

The vibrations of vocal folds were recorded with an electroglottograph (EGG; Laryngograph, Kay Elemtrics, Pine Brook, NJ). A commercial personal computer with stereo soundcard digitized the analog EGG signal and stored it with a sampling rate of 11 025 Hz and sampling resolution of 16 bits. In addition, the computer switched the frequency shift device between nonaltered and frequency-shifted auditory feedback. In addition to the microphone used for feedback, a second small microphone attached to the subjects' clothes picked up the acoustical speech signal. The acoustical signal was recorded along with the EGG signal. In this way the source of potential artifacts in the EGG signal could later be established more easily by inspecting the acoustical signal.

C. Procedure

Subjects had to speak the nonsense word [ˈta:tatas] at their habitual voice F_0 level. Furthermore, they had to speak at a speed and with a stress pattern indicated by a tone sequence presented through headphones. The tone sequence consisted of three 440-Hz sinusoidal tones. The first tone for the long-stressed syllable had a duration of 400 ms, the following two tones were each 200 ms long. The tones were separated by 40-ms pauses. The tone sequence was played twice, after which the subjects had 3.5 s to utter the word. Subjects were instructed to speak clearly, with normal volume, and with monotone voice (i.e., no voice F_0 variation). However, subjects were not informed that the feedback would be modified from time to time. Also, they were not specifically instructed to maintain their voice F_0 as a consequence of modified feedback. The playback of tones and recording of data was automated, so that subjects sat alone in a sound-insulated, but not reflection-free room.

To ensure that subjects uttered the nonsense word correctly, a training phase preceded the actual experiment. During the training phase, the tone sequence was played repeatedly in a loop while subjects simultaneously spoke along until they produced the word correctly at least five times in succession, as judged by the experimenter. Generally, subjects reached the criterion within ten trials.

The experimental phase consisted of 30 trials, each approximately 7 s long. The frequency of auditory feedback was shifted downward by 100 cents in 20% of all trials, resulting in six frequency-shifted trials. In these trials, the frequency shift was activated at the beginning of the tone sequence, so that auditory feedback, but not the tone itself, was frequency shifted from the very beginning of subjects' utterances. The frequency shift was deactivated without subjects' notice after they had uttered the nonsense word. Trials with frequency shift were arranged randomly with the limitation that at least two trials without frequency shift had to precede a frequency-shifted trial and the last trial could not be frequency shifted (see later in this work for explanations).

Additionally, a public speaking condition was introduced in a randomized fashion to investigate potential effects of a stressor (the presence of two listeners) on the auditory-vocal system. These results will be reported elsewhere (Donath *et al.*, 2001).

D. Data analysis

See Fig. 1 for a schematic illustration of data analysis.

Data were analyzed using MATLAB (The MathWorks Inc., Natick, MA). The raw EGG signal was first high-pass filtered (Butterworth-type, $f_c = 2$ kHz). Since the glottal closing is characterized by a steep increase of the EGG signal (Childers and Krishnamurthy, 1984), these increases were assessed by determining the maximums of the EGG signal's first derivative. The period between two closing instants equals the duration of one phonation cycle and its reciprocal equals the momentary F_0. The first detected closing instant defined the onset of phonation. F_0 contours were obtained for the vowels of the first two syllables.

Since the glottal closing instants and the F_0 values associated with them were spaced irregularly in time, F_0 contours with a fixed resolution of 0.1-ms steps were interpolated, so that averaging across trials and subjects became possible. In this way, for each vocalization an F_0 contour was obtained. The F_0 contours of single subjects were then truncated at the end, so that equal lengths were obtained. The shortest vowel duration determined the length of all F_0 contours for one subject. This approach was chosen to ensure that all portions of the F_0 contours for one subject were based on the total number of trials. To avoid F_0 contours being truncated excessively based on unusually short vowels, trials in which vowel duration was 25% shorter compared to all other trials were discarded. A total of 21 trials (7 PRE-trials, 6 FAF-trials, and 8 POST-trials) were discarded because of insufficient length or artifacts, resulting in a total of 383 trials for the first syllable and 388 trials for the second.

F_0 contours of vowels in words before (PRE), during (FAF), and after (POST) trials with frequency-shifted auditory feedback were analyzed. Accordingly, the truncated F_0 contours for each subject were averaged across the six trials preceding, the six trials during, and the six trials after frequency-shifted auditory feedback. The remaining 12 trials were not analyzed. Trials preceding frequency-shifted auditory feedback were used as reference trials, to which FAF- and POST-trials were compared for each subject. This approach was based on the assumption that subjects' voice F_0 should have returned to normal levels in PRE-trials because these were separated from FAF-trials by at least one trial without any frequency shift.

When examining subjects' F_0 contours, it became apparent that voice F_0 is not constant within single vowels. After averaging, voice F_0 still shows fluctuations, which might indicate that subjects have an individual voice F_0 contour during production of vowels. After a fast initial change, some subjects show a slow increase or decrease of voice F_0 over the course of vowel production. In case subjects have individual, nonrandom voice F_0 contours in vowels, the F_0

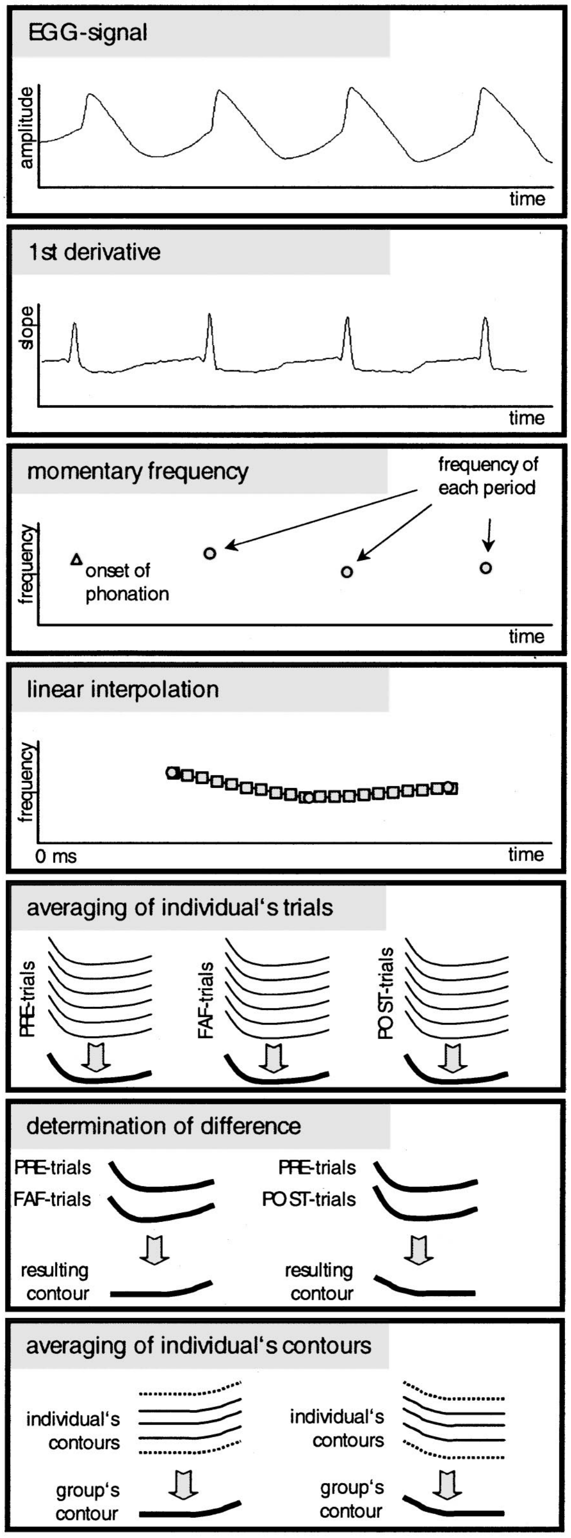

FIG. 1. Schematic illustration of the different steps during data processing. Step 1: The maxima of the first derivative of the digitized EGG signal are used to assess the glottal closings. Step 2: The frequency of each glottal period, i.e., the momentary voice F_0, is determined. The first glottal closing defines the onset of phonation. Step 3: A linear interpolation in a time pattern of 0.1-ms steps enables subsequent averaging of contours across trials and subjects. Step 4: PRE-, FAF-, and POST-trials are averaged for each subject. Step 5: The difference in cents between PRE- and FAF-trials as well as PRE-and POST-trials is determined. In this way, contours are created which reflect the variation based solely on frequency shift. Step 6: The contours are averaged across subjects.

variation solely due to frequency-shifted auditory feedback can be isolated by calculating the voice F_0 contour differences between FAF- and PRE-trials as well as POST- and PRE-trials. In other words, the voice F_0 variation shared by PRE-, FAF-, and POST-trials is removed, leaving only random variation and variation introduced by frequency-shifted feedback. Another advantage of using trials during the experiment as a reference is based on the large intra-individual variation of voice F_0. For example, Coleman and Markham (1991) found that habitual voice F_0 varies as much as plus/minus three semitones, and Jones and Munhall (2000) observed a significant steady increase in voice F_0 along 140 trials even without alteration of auditory feedback. Therefore, this approach should have minimized the error introduced by slow fluctuations of voice F_0 over the course of several trials.

In order to eliminate the interindividual variance due to the different pitches of the male and female subjects, whose habitual voice F_0 ranged from 99 to 251 Hz, and based on the reasoning previously described, the differences in cents between F_0 contours in PRE- and FAF-trials as well as PRE- and POST-trials were calculated for each data point. The resulting contours reflect the deviation of momentary F_0 during frequency shift and after its termination from normal productions under nonaltered auditory feedback, independently of the subjects' habitual voice F_0.

Based on previous research summarized in the Introduction and the closed-loop negative feedback system, one-tailed hypotheses about the differences between PRE- and FAF-trials and between PRE- and POST-trials were formulated. In order to test for differences in the initial and final portions of voice F_0 contours, they were arbitrarily divided into 25-ms intervals. Means for these intervals were calculated individually for subjects. However, since subjects' vocalizations were of unequal lengths, it had to be established which of the last 25-ms intervals was based on a reasonably high number of subjects. In our graphs, 0 ms corresponds to onset of phonation, which was defined by the first detected glottal closing. The voice F_0 contours begin at the point for which momentary voice F_0 values became available for all subjects, and therefore the graph reflects the entire group. The length of a glottal cycle is almost 10 ms in men and momentary voice F_0 values were "assigned" to the end of each cycle before interpolation and subsequent plotting. Therefore, momentary voice F_0 is not defined for the first few ms after onset of phonation. Consequently, the interval 0–25 ms after onset of phonation was not analyzed. By investigating the second 25-ms interval, it was ensured that the average voice F_0 used for testing is based on all subjects.

Wilcoxon rank sign tests were calculated for the intervals 25–50 ms ($N \geqslant 21$), 225–250 ms (long-stressed syllables, $N \geqslant 20$), and 75–100 ms (short unstressed syllables, $N \geqslant 17$) after onset of phonation.

It was hypothesized that several intervals would have a higher voice F_0 compared to PRE-trials. A compensatory response due to the downward frequency shift should occur once auditory feedback is processed and muscular changes take effect. Therefore, the last interval of the first long-stressed syllable in FAF-trials as well as the first and last

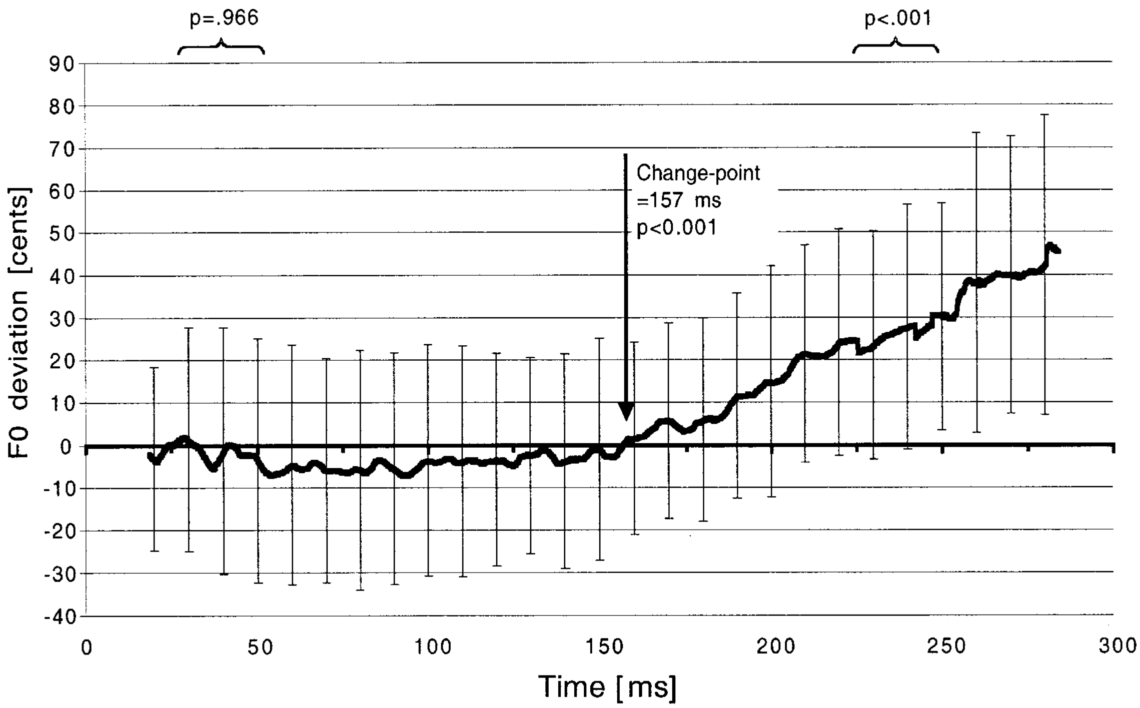

FIG. 2. Deviation of voice F_0 contour of the first (long) syllable of the nonsense word [ˈta:tatas] during frequency shift from trials before frequency shift, averaged across all subjects. Standard deviations across all subjects were plotted as bars with an arbitrarily chosen interval of 10 ms to visualize the variation of the contour. 0 ms is the onset of phonation, defined by the first glottal closing. The contour begins at the point for which voice F_0 data becomes available for all subjects (see Sec. II D for a more detailed description). The contour ends at the point for which n becomes less than 8. The two p-values are the results of Wilcoxon tests for interval deviations from 0. The latency of response was determined with the Castellan change-point test.

interval of the second unstressed syllable in FAF-trials should have a higher voice F_0. The compensatory response should last until corrected by the feedback not shifted in frequency. Therefore, the first interval of the first long-stressed syllable in POST-trials should also have a higher voice F_0. In this case the latency of the response will cause the first portion of the vowel to have a higher voice F_0 before returning to normal. Additional p-values were calculated as effect measures for intervals of syllables for which no changes in voice F_0 were assumed. (When interpreting p-values as effect measures, a high p-values indicates a lower probability for a difference and vice versa.) Since a normal distribution could not be assumed for responses, nonparametric Wilcoxon rank sign tests were calculated; one-tailed to test our hypotheses and two-tailed for other intervals.

The (average) latencies of responses in first syllables in FAF-trials and first syllables in POST-trials were determined based on a nonparametric approach to the change-point problem. The Castellan change-point test for continuous variables is related to the Mann–Whitney–Wilcoxon test and is described concisely in Siegel and Castellan (1988). This test estimates the (single) point of change in the distribution of a sequence and is more precise compared to approaches which estimate latency by determining the point at which a curve exceeds an arbitrarily chosen threshold (e.g., 2 s.d.). The latter approaches always overestimate latencies. The calculation of the test statistic posed a special problem: The time series of momentary fundamental frequencies to which the test was applied is the result of averaging across subjects and trials. Therefore, the actual number of data points can only be estimated, and data points are spaced irregularly in time. A very conservative approach was chosen. The minimum number of data points, based on which the time series could be created, is the average number of phonation cycles occurring over its length. This N is only a fraction of the actual number of data points, on which the contours are based, but yields a more realistic Z-score.

Since six tests were calculated, the significance level $\alpha = 5\%$ was corrected according to Bonferroni to $\alpha' = \alpha/6 \approx 0.008$. Additionally, the distribution of individual responses in second syllables during frequency shift and first syllables after termination of frequency shift were explored. Therefore, potentially existing groups of individuals exhibiting different response magnitudes because of low or high degree of audio-vocal control might be found. The correlation (Spearman-rho) between the two was calculated as well. In this way, a possible relationship between the degree to which vocal F_0 is auditorily controlled and the magnitude of adaptation, as indicated by effects in utterances following frequency-shifted trials, might be established.

III. RESULTS

A. First syllable during frequency shift

Figure 2 shows the voice F_0 deviation of FAF-trials from PRE-trials for first syllables. There is no significant difference between PRE- and FAF-trials in the interval 25–50 ms after vowel onset ($Z = -1.494$, $n = 21$, $p_{\text{2-tailed}} = 0.714$). Voice F_0 begins to increase during frequency-shifted auditory feedback after 157 ms, as determined with the Castellan change-point test ($Z = -5.541$, $n = 42$, $p_{\text{1-tailed}} < 0.001^*$). The response velocity is 339 cents/s in the inter-

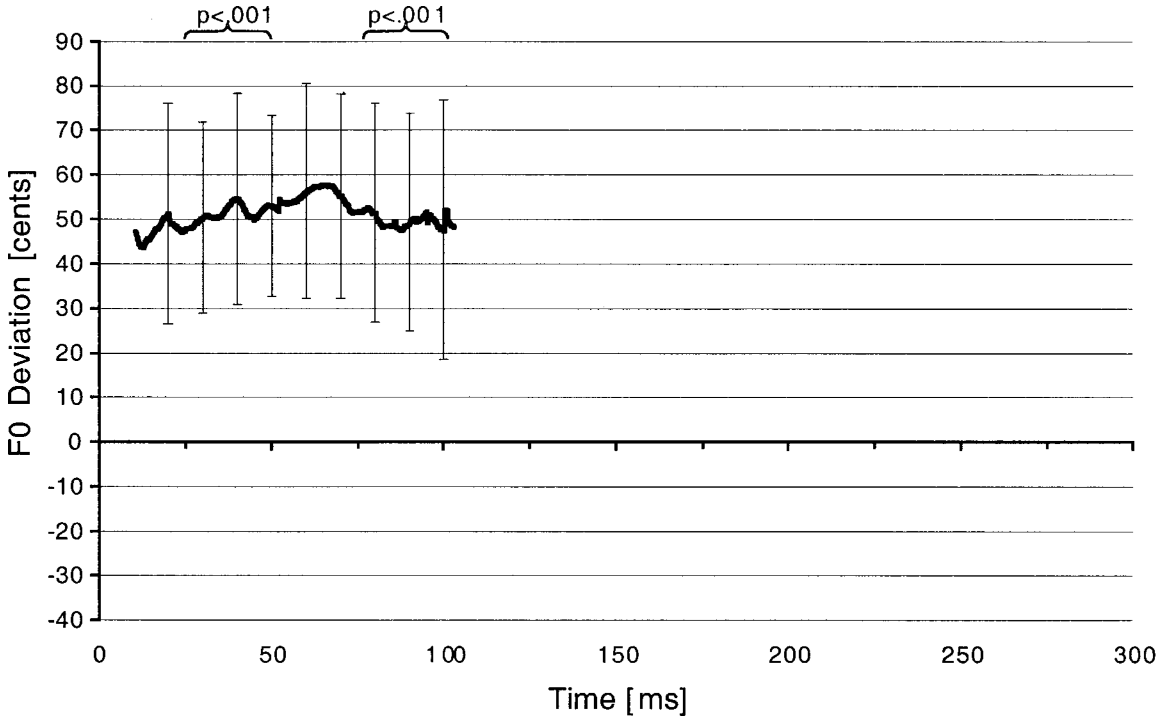

FIG. 3. Deviation of voice F_0 contour of the second (short) syllable of the nonsense word [ˈta:tatas] during frequency shift from trials before frequency shift. See caption for Fig. 1 for additional explanation.

val 150–250 ms after vowel onset, as measured by calculating the slope with a linear regression. In the interval 225–250 ms after vowel onset, mean voice F_0 is 28.3 cents higher than in PRE-trials ($Z = -3.380$, $n = 20$, $p_{\text{1-tailed}} < 0.001^*$).

B. Second syllable during frequency shift

Figure 3 shows the voice F_0 deviation of FAF-trials from PRE-trials for second syllables. In the interval 25–50 ms after vowel onset, mean voice F_0 is 51.5 cents higher than in PRE-trials ($Z = -3.924$, $n = 21$, $p_{\text{1-tailed}} < 0.001^*$). In the interval 75–100 ms after vowel onset, mean voice F_0 is 51.1 cents higher than in PRE-trials ($Z = -3.517$, $n = 17$, $p_{\text{1-tailed}} < 0.001^*$).

C. First syllable after termination of frequency shift

Figure 4 shows the voice F_0 deviation of POST-trials from PRE-trials for first syllables. In the interval 25–50 ms after vowel onset, mean voice F_0 is 20.6 cents higher than in PRE-trials ($Z = -3.099$, $n = 22$, $p_{\text{1-tailed}} < 0.001^*$). The Castellan change-point test indicates that voice F_0 begins to decrease after 171 ms ($Z = 4.854$, $n = 42$, $p_{\text{1-tailed}} < 0.001^*$). There is no significant difference between PRE- and POST-trials in the interval 225–250 ms after vowel onset ($Z = -1.791$, $n = 20$, $p_{\text{2-tailed}} = 0.074$).

D. Second syllable after termination of frequency shift

Figure 5 shows the voice F_0 deviation of POST-trials from PRE-trials for second syllables. There are no significant difference between PRE- and POST-trials in the interval 25–50 ms ($Z = -1.791$, $n = 20$, $p_{\text{2-tailed}} = 0.140$) and 75–100 ms after vowel onset ($Z = -2.123$, $n = 17$, $p_{\text{2-tailed}} = 0.033$).

E. Relationship between response magnitude during frequency shift and magnitude of effects after termination of frequency shift

To investigate the distribution of individual response magnitudes, the average response magnitude in the second short syllable during frequency-shifted auditory feedback was plotted for each subject (Fig. 6). The second syllable was chosen because the response is at its maximum and relatively stable, presumably reflecting the maximum of exercised control over phonation based on auditory feedback.

Exact Kolmogorov–Smirnov goodness of fit tests were calculated to test for a violation of normal distribution. For response magnitudes in second syllables under frequency shift, p is 0.912 ($Z = 0.529$ $n = 21$). For magnitudes of after-effects in first syllables after termination of frequency shift, p is 0.523 ($Z = 0.578$, $n = 21$).

To investigate a potential relationship between maximum response magnitude, which might reflect the amount of individual auditory-vocal control, and after-effects in the first syllable after termination of frequency shift, F_0 deviations of the beginning (25–100 ms) of the first syllable after termination of frequency shift were compared to the response magnitudes in second syllables during frequency shift. As seen in Fig. 6, there appears to be no obvious relationship between the two. Spearman-rho is 0.173 ($p_{\text{2-tailed}} = 0.454$, $n = 21$).

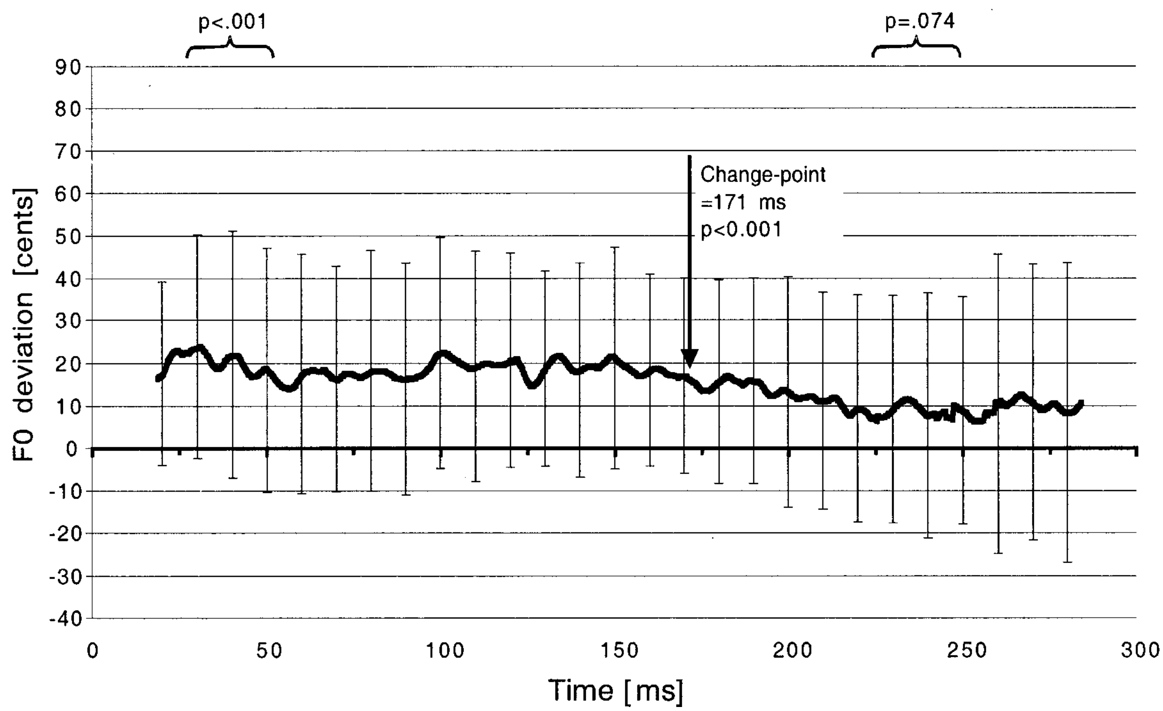

FIG. 4. Deviation of voice F_0 contour of the first (long) syllable of the nonsense word [ˈta:tatas] after termination of frequency shift from trials before frequency shift. See caption for Fig. 1 for additional explanation.

IV. DISCUSSION

The data in this study show several features of the auditory-vocal system with respect to F_0 control in speech. The data support the view of a negative-feedback system with a limiting property during production of vowels. The latency and duration of responses indicate that the auditory-vocal system is used to control voice F_0 on supra-segmental level, rather than within single syllables. Furthermore, voice F_0 adjustments based on auditory feedback remain for several seconds during pauses of speech.

A. Response latency

Adjustment of voice F_0 occurs after an interval, within which auditory feedback is processed, the efferents to the

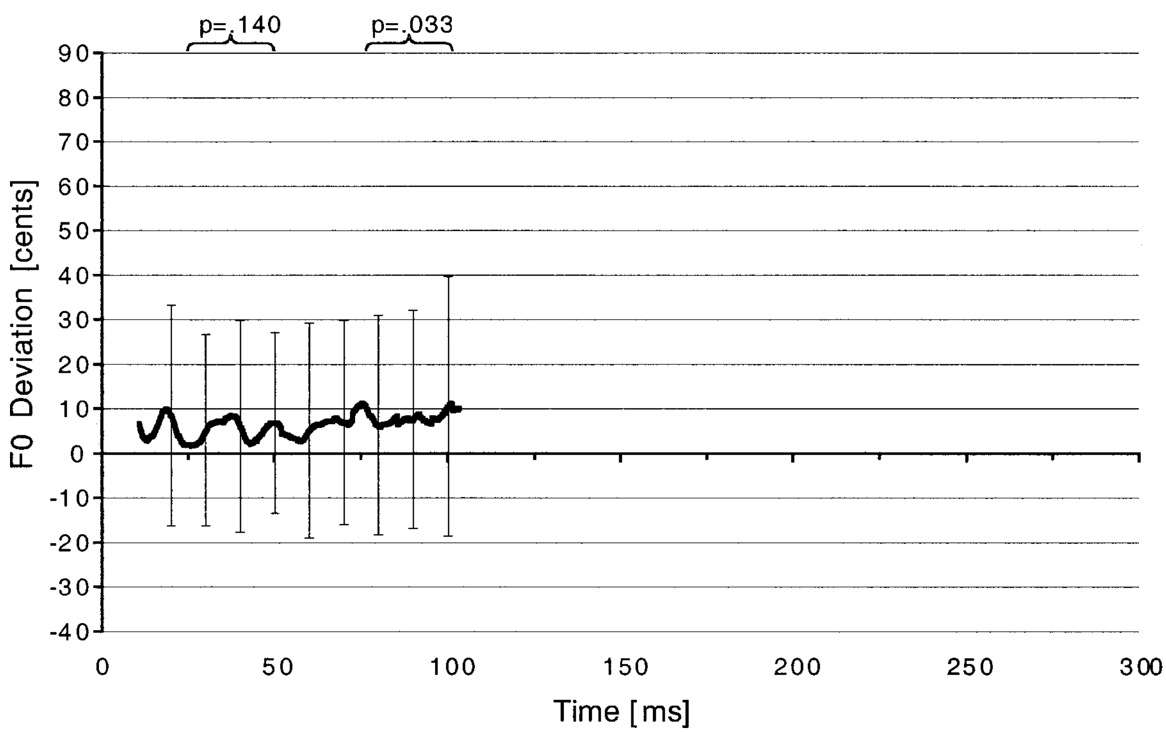

FIG. 5. Deviation of voice F_0 contour of the second (short) syllable of the nonsense word [ˈta:tatas] after termination of frequency shift from trials before frequency shift. See caption for Fig. 1 for additional explanation.

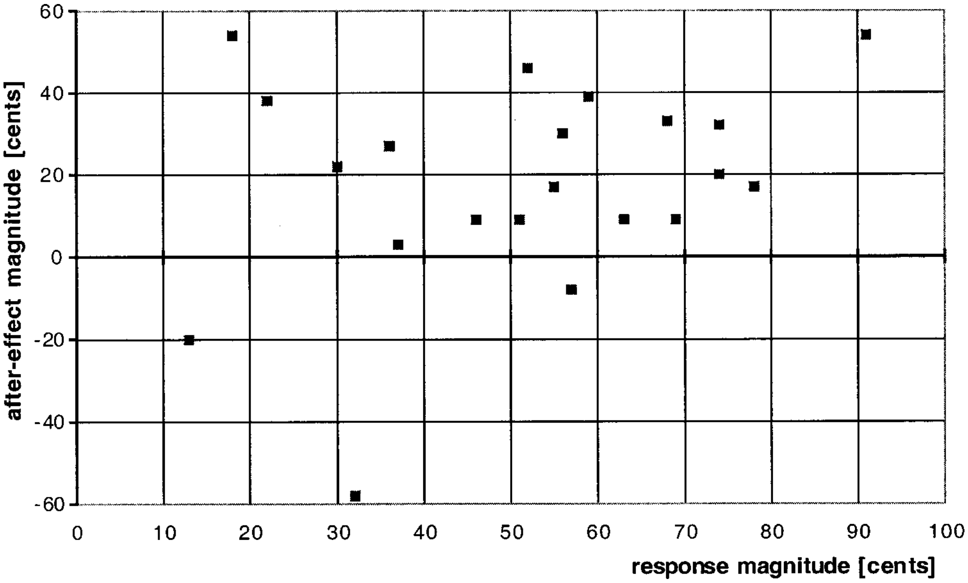

FIG. 6. Data from all subjects, illustrating individual response magnitudes in the second (short) syllable during frequency shift and magnitude of after-effects at the beginning of the first (long) syllable after termination of frequency shift. Magnitudes during and after frequency shift were calculated as mean differences to PRE-trials over the interval 25–100 ms after onset of phonation.

larynx are modified, and physical changes of the vocal folds take place. The long response latency of 157 ms prevents auditorily controlled realization of intended F_0 in short syllables and during the initial portion of long syllables. Therefore, auditory feedback would not be very useful for adjusting voice F_0 being realized during speech, but more useful in the regulation of voice F_0 in later segments or the learning of transformations between laryngeal configurations, subglottal air pressure, and the resulting voice F_0. The latter function of auditory feedback would be the basis for producing the correct voice F_0 at the onset of phonation during speech or singing. The first function could serve to adjust for temporarily changed conditions of the larynx and to control suprasegmental prosody.

It can be assumed that prosodic information is encoded in relative changes of voice F_0 rather than in absolute pitch; otherwise inter- and intraindividual variations in baseline voice F_0 would make prosodic decoding impossible. By monitoring the actually realized voice F_0 of syllables, adjustments can be made for later syllables, i.e., on a suprasegmental level. In this way, the relative differences in voice F_0 that encode information are produced more reliably.

B. Response magnitude

The maximum voice F_0 response in the opposing direction is approximately 50 cents in this study, even though a complete compensation would require a change of 100 cents. This maximum magnitude of response agrees well with earlier findings [Elman (1981): approximately 40–60 cents; Burnett *et al.* (1997): approximately 30 cents; Larson (1998): approximately 30 cents; Natke and Kalveram (2001): 15–65 cents], even though different paradigms such as continuous vocalization and speaking of nonsense words and frequency shifts varying from 100 to 600 cents were employed. These magnitudes of less than a semitone may seem small, but the compensation was easily audible in the audio records and falls well within natural prosodic variations. For example, at the end of questions voice F_0 increases around 100 cents (Bosshardt *et al.*, 1997).

Although previous findings and these results support the closed-loop model, no study has yet demonstrated a correlation between frequency shift magnitude and resulting response magnitude. This is not surprising because most studies have used frequency shifts of 100 cents and more, and only one used frequency shifts as low as 25 cents (Burnett *et al.*, 1998), while the responses seem to be limited to 30–60 cents. Therefore, the range in which a correlation between frequency shift magnitude and resulting response magnitude might be observed was not investigated systematically.

Several hypotheses, which do not necessarily exclude each other, are offered here to address the question why the response does not exceed approximately 30–60 cents regardless of frequency shift magnitude. First, besides auditory feedback, mechano-receptors in the vocal fold mucosa or proprio-receptors in the vocal fold muscles might play a role in voice F_0 regulation. Research on this topic is limited because of the invasive techniques necessary for experimental investigation. Reduced voice F_0 control was demonstrated after anesthetization of the superior laryngeal nerve (Tanabe *et al.*, 1975) and after anesthetization of the undersides of the mucosa of the vocal folds (Sundberg *et al.*, 1993). The different feedback channels would carry different information during frequency shift: proprioceptive and mechanoreceptive feedback would report actual voice F_0, whereas auditory feedback reports a deviation. The integration of feedback channels might limit the maximum response in a nonlinear fashion.

Another possibility might be that during speech (not singing), efferents controlling the larynx and modifying voice F_0 are only modified within close boundaries which reflect the small variations in F_0 occurring naturally in prosody. However, mean variations of 30–60 cents seem low compared to a s.d. of 15.87 Hz (corresponding to approximately 250 cents) of voice F_0 during reading of an unemotional, narrative text (Eady, 1982). Only the elimination of proprioceptive feedback combined with frequency shift of auditory feedback could isolate the role of auditory feedback and indicate its limitations for regulation. For example, Sundberg *et al.* (1993) demonstrated that anesthetization of the vocal folds reduces voice F_0 control. Although this approach decreases external validity considerably because of a complete loss of, rather than a variation of, proprioceptive feedback, it might be established to which degree (overlearned) motor programs limit voice F_0 variation based solely on auditory feedback.

When exploring individual subject's (average) responses in the second short syllable, it appears that response magnitudes are normally distributed around a mean magnitude of approximately 50 cents, ranging from 13 to 92 cents (Fig. 3). Therefore, it is not reasonable to assume a simple distinction between individuals who rely heavily or little on auditory feedback for voice F_0 control. Rather, there seems to be a continuum for the degree of auditory-vocal control. It could be that subjects whose voice F_0 is affected more strongly by auditory feedback also exhibit a stronger correlation between response magnitude and frequency shift magnitude. A future study might address this.

It might also be that voice F_0 in speech simply is not controlled very tightly. First, an external reference frequency for regulating voice F_0 is missing while speaking. When a reference tone of 440 Hz is provided, trained singers can match it with an accuracy of more than 1 Hz, which is a difference of approximately 4 cents (Sundberg, 1987). Furthermore, it has been shown that an unpredictable frequency shift can be completely compensated for in singing (Burnett *et al.*, 1997; Parlitz and Bangert, 1998). This indicates that the compensatory mechanism for voice F_0 can be very effective when a reference tone is represented internally, as in singing.

When speaking syllables, an intended voice F_0 may also be given for single syllables. However, in speaking, relative changes in voice F_0 would seem to be more important than realization of absolute voice F_0. Voice F_0 varies much more across gender and age than within one individual during normal speaking. Nevertheless, nonverbal information can be extracted from speech of children, women, and men with different voice registers. Therefore, relative changes must encode nonverbal information and not absolute voice F_0. Second, for precise comprehension of syllables and individual words, one would assume that voice F_0 is less important compared to formants and formant transitions, at least in languages such as English or German. Thus, it seems less important for the speaker to monitor and regulate fundamental frequency within syllables. This of course does not apply to tone languages, in which syllable voice F_0 contours have lexical function. Consequently, although a compensatory mechanism for voice F_0 at the syllabic level may exist, it seems that for languages such as English and German control of voice F_0 on supra-segmental level is more important (e.g., for word focus or conveyance of emotional states).

C. Response duration

Since in this study subjects had to utter a word, features of the supra-segmental nature of the auditory-vocal system could be examined. While a partial correction of a mismatch between intended and auditorily perceived voice F_0 occurs in the first syllables with a latency, the second syllables show a higher F_0 from the very beginning. Since syllables were separated by a voiceless consonant, phonation stopped between them. Therefore control of voice F_0 is continuous within single words and not interrupted by the onset and offset of phonation itself. It would seem plausible if such a continuous control scheme also applied to natural running speech.

Also in trials after the termination of frequency shift, the beginning of the first syllables still has a significantly higher F_0, even though auditory feedback is normal at that point and there had been a pause in speech for approximately 6 s. This indicates that the auditory-vocal system regulates voice F_0 of syllables in words produced several seconds later, based on information gathered in single syllables. Therefore there is evidence for a relatively fast, i.e., within a single word, and persisting adjustment of voice F_0 production based on auditory feedback. A detected deviation between intended and perceived voice F_0 is not only partially corrected, but also leads to adjustments in later vowels, which are separated by a pause. In trials after the termination of frequency shift, the intended voice F_0 is actually exceeded as a result of this adjustment. Thus there is clear evidence for the supra-segmental nature of auditory-vocal control. With normal auditory feedback in such trials, the mismatch is detected and voice F_0 decreases after a latency of approximately 170 ms, which is comparable to the 157 ms latency in frequency-shifted trials.

Voice F_0 is increased only by approximately 20 cents after termination of frequency shift, which is less than the approximately 50 cents during frequency shift. This may be the result of a ''decay.'' Over time, the magnitude of voice F_0 correction to be integrated with intended F_0 may decrease. This might be due to a memory effect; the voice F_0 correction ''fades'' as time passes. Future studies might investigate the characteristics of the temporal persistence of modifications based on auditory feedback.

It should be noted that these after-effects are different from the sensorimotor adaptation to auditory frequency shift demonstrated by Jones and Munhall (2000). They changed the pitch of auditory feedback in 1-cent steps from trial to trial until they reached a shift of 100 cents, maintained this shift for 20 trials, and finally returned feedback to normal pitch for 10 trials. Subjects gradually increased their voice F_0, although not to the extent necessary for a complete compensation. The last trials provided evidence for a sensorimotor adaptation. When subjects had heard their voice's pitch higher than their true voice F_0 and feedback became unexpectedly normal (i.e., seemingly lower than before), their voice F_0 increased, and vice versa. The authors state that ''subjects acted as if a remapping between perceived and produced pitch had taken place'' and compare their adaptation data to classic prism experiments (e.g., Held, 1965), in which subjects make errors in the opposite direction of visual prism displacement after a training period.

Interestingly, there is no relationship between the magnitude of responses in frequency-shifted trials, which might indicate the individual level of auditory-vocal control, and the magnitude of after-effects at the beginning of the following word. This indicates that individuals can have different levels of auditory-vocal control and ''adjustment decay rates,'' and that therefore these two aspects of the auditory-vocal system are mediated through independent mechanisms.

Although no subjects exhibited so-called following responses during frequency shift, two subjects showed after-effects in the opposite direction. Their voice F_0's are approximately 60 and 20 cents lower in trials after the termination of frequency shift compared to trials before frequency shift. At this point it is not clear whether this is a random effect or might reflect that some individuals exhibit a deviant voice F_0 control. More data would be needed to investigate this effect systematically and test it statistically. A future study might address this.

The very fast adjustment found in this study might reflect the need for quick and also persisting changes in control over laryngeal muscles, in order to consistently achieve the intended voice F_0 because of the complex neuro-physical processes involved in phonation. As has been previously suggested by Natke and Kalveram (2001), the relatively long latency prevents auditory feedback from efficient F_0 control within syllables. Voice F_0 in short syllables cannot be controlled auditorily at all, and voice F_0 in long syllables can only be adjusted after a rather long latency. Therefore, the picture that emerges is that auditory feedback is primarily used to adjust voice F_0 of following syllables, that is, on a supra-segmental level.

V. CONCLUSION

This study demonstrates that the paradigm of frequency-shifted auditory feedback during speaking of nonsense words can address several new aspects of auditory-vocal control during speaking. Rather than using auditory feedback for adjustment of voice F_0 in real time, the results point towards a role of the auditory-vocal system in supra-segmental monitoring and control of voice F_0. Based on auditory feedback, quick adaptations can be made to ensure that intended voice F_0 is produced and information is encoded properly in prosody.

ACKNOWLEDGMENTS

This research was supported by the Deutsche Forschungsgemeinschaft (DFG), Grant No. Ka 417/13-3.

Bosshardt, H. G., Sappok, C., Knipschild, M., and Hölscher, C. (**1997**). ''Spontaneous imitation of fundamental frequency and speech rate by non-stutterers and stutterers,'' J Psych. Ling. Res. **26**, 425–448.

Burnett, T. A., Senner, J. E., and Larson, C. R. (**1997**). ''Voice *F*0 responses to pitch-shifted auditory feedback: A preliminary study,'' J. Voice **11**, 202–211.

Burnett, T. A., Freedland, M. B., Larson, C. R., and Hain, T. C. (**1998**). ''Voice *F*0 responses to manipulations in pitch feedback,'' J. Acoust. Soc. Am. **103**, 3153–3161.

Childers, D. G., and Krishnamurthy, A. K. (**1984**). ''A critical review of electroglottography,'' CRC Crit. Rev. Biomed. Eng. **12**, 131–161.

Coleman, R. F., and Markham, I. W. (**1991**). ''Normal variations in habitual pitch,'' J. Voice **5**, 173–177.

Cutler, A., Dahan, D., and van Donselaar, W. (**1997**). ''Prosody in the comprehension of spoken language: A literature review,'' Lang Speech **40**, 141–201.

Donath, T., Natke, U., and Kalveram, K. T. (**2001**). ''Magnitude and latency of fundamental frequency response within syllables under frequency shifted auditory feedback and public speaking,'' in *Speech Motor Control in Normal and Disordered Speech*, Proceedings 4th International Speech Motor Conference (61–64), Nijmegen, The Netherlands, edited by B. Maassen, W. Hulstijn, R. D. Kent, and P. H. H. M. Van Lieshout (Uitgeverij Vantilt, The Netherlands).

Eady, S. J. (**1982**). ''Differences in the *F*0 patterns of speech: Tone language versus stress language,'' Lang. Speech **25**, 29–41.

Elman, J. L. (**1981**). ''Effects of frequency-shifted feedback on the pitch of vocal productions,'' J. Acoust. Soc. Am. **70**, 45–50.

Giles, H., and Powesland, P. E. (**1975**). *Speech Style and Social Evaluation* (Academic, London).

Held, R. (**1965**). ''Plasticity in sensory-motor systems,'' Sci. Am. **213**, 84–94.

Jones, J. A., and Munhall, K. G. (**2000**). ''Perceptual calibration of *F*0 production: Evidence from feedback perturbation,'' J. Acoust. Soc. Am. **108**, 1246–1251.

Larson, C. R. (**1998**). ''Cross-modality influences in speech motor control: The use of pitch-shifting for the study of *F*0 control,'' J. Commun. Dis. **31**, 489–503.

Larson, C. R., Burnett, T. A., and Kiran, S. (**2000**). ''Effects of pitch-shift velocity on voice *F*0 responses,'' J. Acoust. Soc. Am. **107**, 559–564.

Natke, U., and Kalveram, K. T. (**2001**). ''Fundamental frequency under frequency shifted auditory feedback of long stressed and unstressed syllables,'' J. Speech Lang. Hear. Res. **44**, 577–584.

Natke, U., Grosser, J., and Kalveram, K. T. (**2001**). ''Fluency, fundamental frequency, and speech rate under frequency-shifted auditory feedback in stuttering and nonstuttering persons,'' J. Fluency Disord. **26**, 227–241.

Parlitz, D., and Pangert, M. (**1998**) ''Short and medium motor responses to pitch shift: Latency measurements of the professional musicians's audio-motor loop for intonation,'' paper presented at the 16th International Congress on Acoustics and the 137th meeting of the Acoustical Society of America, Seattle, WA.

Siegel, S., and Castellan, N. J. (**1988**). *Nonparametric Statistics for the Behavioral Sciences*, 2nd ed. (McGraw-Hill, Boston).

Sundberg, J. (**1987**). *The Science of the Singing Voice* (Northern Illinois U.P., Dekalb, IL).

Sundberg J., Iwarsson J., and Billström, A. H. (**1993**). ''Significance of mechanoreceptors in the subglottal mucosa for subglottal pressure control in singers,'' presented at the 22nd Annual Symposium Care of the Professional Voice, Philadelphia.

Tanabe, M., Kitajima, K., and Gould, W. (**1975**). ''Laryngeal phonatory reflex: The effect of anesthetization of the internal branch of the superior laryngeal nerve-Acoustic aspects,'' Ann. Otol. Rhinol. Laryngol. **84**, 206–212.

Regulating glottal airflow in phonation: Application of the maximum power transfer theorem to a low dimensional phonation model

Ingo R. Titze[a)]
Department of Speech Pathology and Audiology and The National Center for Voice and Speech, 330 Wendell Johnson Speech and Hearing Center, The University of Iowa, Iowa City, Iowa 52242-1012

(Received 30 November 2000; revised 10 September 2001; accepted 18 September 2001)

Two competing views of regulating glottal airflow for maximum vocal output are investigated theoretically. The maximum power transfer theorem is used as a guide. A wide epilarynx tube (laryngeal vestibule) matches well with low glottal resistance (believed to correspond to the ‘‘yawn-sigh’’ approach in voice therapy), whereas a narrow epilarynx tube matches well with a higher glottal resistance (believed to correspond to the ‘‘twang-belt’’ approach). A simulation model is used to calculate mean flows, peak flows, and oral radiated pressure for an impedance ratio between the vocal tract (the load) and the glottis (the source). Results show that when the impedance ratio approaches 1.0, maximum power is transferred and radiated from the mouth. A full update of the equations used for simulating driving pressures, glottal flow, and vocal tract input pressures is provided as a programming guide for those interested in model development. [DOI: 10.1121/1.1417526]

PACS numbers: 43.70.Bk [AL]

I. INTRODUCTION

Speech language pathologists and singing teachers have generated two competing views (and accompanying behavioral strategies) about the management of airflow in phonation. On the one hand, there is the strategy of using a ‘‘sigh’’ to release air with the voice (Linklater, 1976; Colton and Casper, 1996; Brown, 1996), or using a *flow phonation mode* (Sundberg, 1987). This flow mode strategy helps to obtain maximum peak-to-peak glottal airflow. On the other hand, there is the opposite strategy of increasing the adduction of the vocal folds, as in *belt* (Sullivan, 1985; Bestebreurtje and Schutte, 2000) and some country-western singing (Sundberg *et al.*, 1999) to decrease both the average glottal flow and the peak flow for (perhaps) greater glottal efficiency. Even in some classical singing approaches, airflow reduction is sometimes encouraged by the mental image of ‘‘drinking in the air’’ rather than blowing out the air.

In this paper, a few data sets will be presented that simulate a ‘‘tight adduction’’ case and a ‘‘loose adduction’’ case with a computer model of phonation. One objective of the study is to show that both techniques can lead to an optimum acoustic output at the mouth, but the vocal tract configuration has to be matched to the glottal configuration. Tight adduction of the vocal folds requires a narrower supraglottal airway, whereas looser adduction requires a wider airway to maximize the output power. An underlying guiding principle is the maximum power transfer theorem in electric circuits and transmission systems, which states that the internal impedance of the source should match the impedance of the load for maximum power transfer.

A second objective of the study is to update the aerodynamic driving force equations for a low-dimensional model of vocal fold vibration in detail. Some changes have occurred since publication of the three-mass body-cover model (Story and Titze, 1995), particularly with regard to flow separation from the glottal wall and collision forces. In order to continue explorations with this low-dimensional body-cover model, it is important to provide the aerodynamic detail as a programming guide. This dual objective makes this paper somewhat of a nontraditional mixture between model development and a clinical application. But this mixture is justified by the fact that there is an unfortunate history of ‘‘modeling for modeling sake,’’ by this and other authors, with insufficient benefit to practitioners in voice and speech. This paper is an attempt to steer toward application while also maintaining a theoretical forward thrust.

II. THE MAXIMUM POWER TRANSFER THEOREM

For readers who are not familiar with the maximum power transfer theorem, a brief summary is provided. As illustrated in Fig. 1, assume a simple electric circuit with a voltage source v, an internal source resistance R_S, and a load resistance R_L. The current that flows is $i = v/(R_L + R_S)$ and the power delivered to the load is

$$p = i^2 R_L = v^2 R_L/(R_L + R_S)^2. \tag{1}$$

Now consider the variation of this power as the load resistance R_L is changed and the source resistance R_S and voltage v are held constant. For $R_L = 0$, the power is clearly zero. For R_L approaching infinity, the power is also zero, since the denominator in Eq. (1) is of higher power in R_L than the numerator. This suggests that there is an intermediate value of R_L for which the power is maximized. By differentiating p with respect to R_L in Eq. (1) and setting the derivative to zero, it is easily shown that the power is maximum for $R_L = R_S$, with a value $p = v^2/4R_S$. Figure 2 (top trace) shows

[a)]Electronic mail: ingo-titze@uiowa.edu

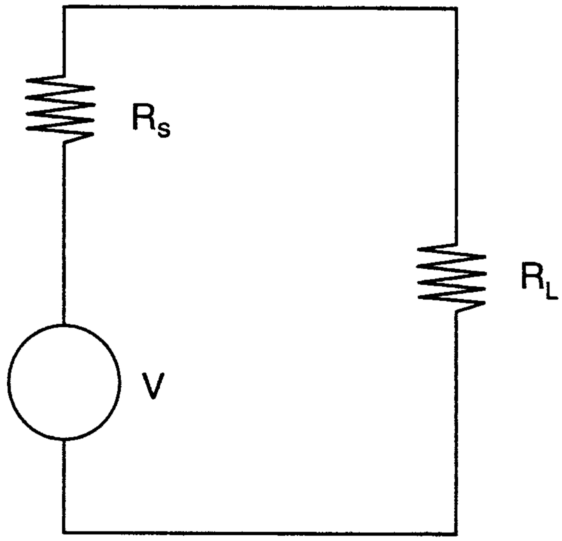

FIG. 1. Simple resistive circuit illustrating internal (source) resistance R_S and load resistance R_L.

the load power normalized to the maximum value, plotted as a function of R_L/R_S.

The circuit is not maximally *efficient*, however, when the power to the load is maximized. If we define efficiency as the ratio of load power to total power consumed in the circuit,

$$e=\frac{i^2R_L}{i^2(R_L+R_S)}=\frac{R_L}{R_L+R_S}, \tag{2}$$

then an equal amount of power is lost to the internal resistance as is delivered to the load, resulting in an efficiency of 50%. Maximum efficiency occurs when R_L becomes infinite (Fig. 2, bottom trace). Thus, there is a trade-off between maximum power transfer and maximum efficiency of power consumption in a simple circuit of this kind.

To apply the maximum power transfer principle to voice production, we must realize that pressure and flow are not as simply related to each other as voltage and current are in a resistive circuit. Since the acoustic load is a complex impedance, the quantitative nature of the maximum power theorem is not the same, but qualitatively the principle is expected to

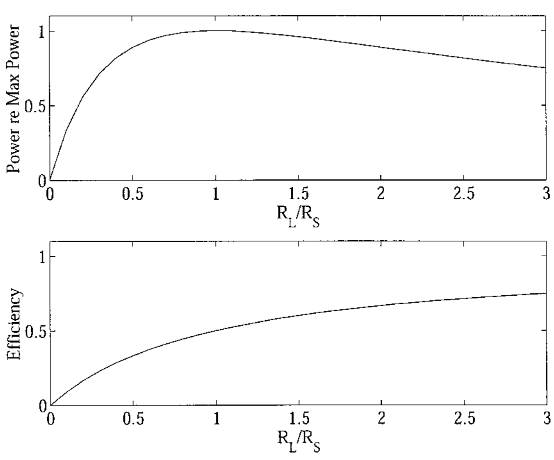

FIG. 2. (Top) power delivered to the load relative to maximum power $v^2/4R_S$, and (bottom) efficiency of power delivered to the load; both are plotted as a function of the load resistance to source resistance ratio R_L/R_S.

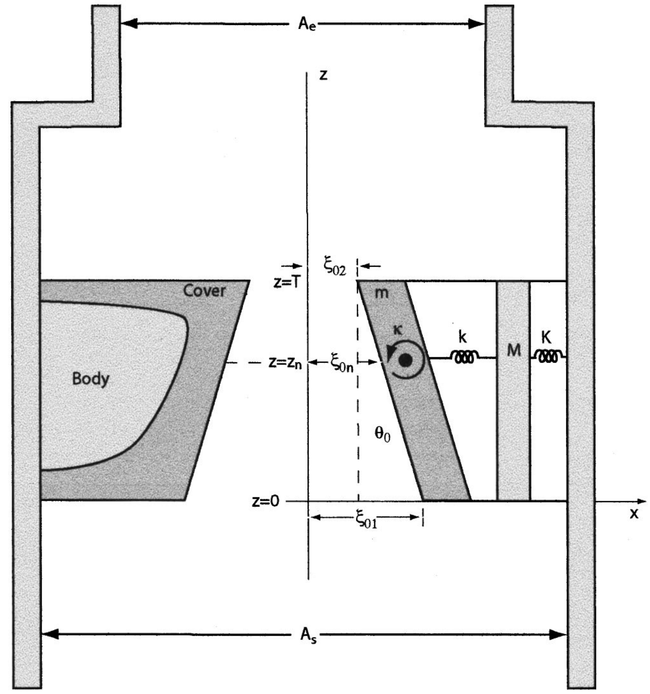

FIG. 3. Bar-plate representation of a body-cover model of the vocal folds.

be preserved: for maximum acoustic power to be delivered to the vocal tract, the internal glottal impedance should be of the same order of magnitude as the acoustic load impedance of the vocal tract. For maximum efficiency, the load impedance should be considerably higher than the glottal source impedance.

But vocal fold oscillation is a nonlinear process, for which glottal impedance calculations must be reinterpreted somewhat. The pressure source is steady (nonoscillatory), whereas the flow is nonsteady (oscillatory). For this reason, a time-domain simulation will be used to derive pressure–flow relations for various vocal tract geometries and then to determine maximum power transfer conditions numerically.

III. TIME-DOMAIN SIMULATION OF GLOTTAL AIRFLOW

A bar-plate version of the body-cover model of the vocal folds (Fig. 3) was used to vary glottal adduction of the vocal folds and the supraglottal area. The full mathematical details of the model are found in the Appendix. This low-dimensional model is patterned after Liljencrants (1991) in terms of the glottal configuration and is essentially equivalent to the three-mass model of Story and Titze (1995) in terms of its tissue characteristics. It is recognized that low-dimensional models with "bar" masses do not accurately represent partial glottal closure, which limits the normal variability of acoustic excitation of the vocal tract. In particular, cases for which the vocal folds do not collide and the mean glottal flow is excessive will not be representative of normal phonation. Although this may require some scrutiny of the data, the simplicity of models outweighs this acknowledged weakness. A high-dimensional finite element model (Alipour *et al.*, 2000) could have been used for this study, but not all of the mathematical details are yet available to everyone;

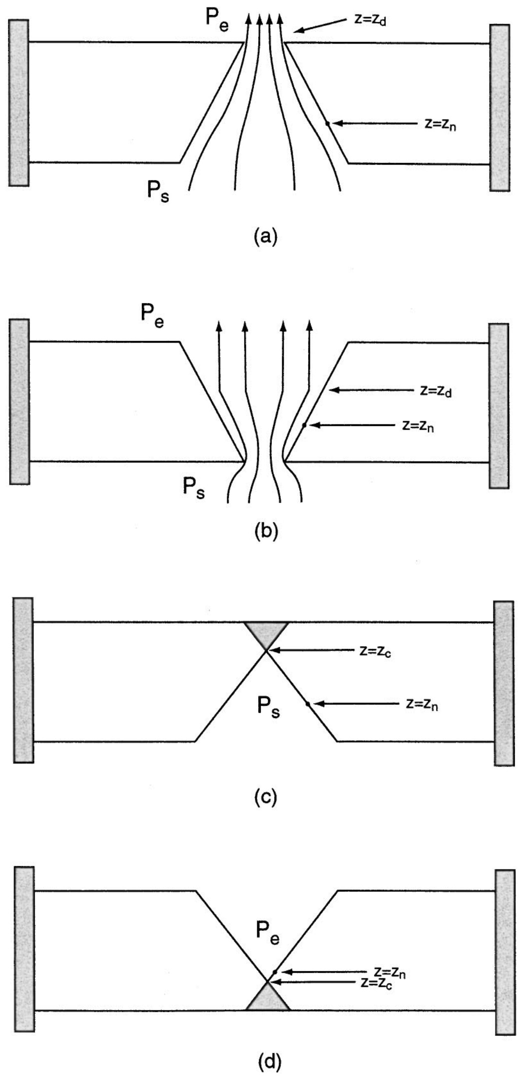

FIG. 4. Sketches used for intraglottal pressure calculations, (a) convergent glottis with no vocal fold contact, (b) divergent glottis with no vocal fold contact, (c) convergent glottis with contact on top, and (d) divergent glottis with contact at bottom.

hence, for sake of replication, the author selected this low-dimensional bar-plate model, which actually makes the study stronger if the hypotheses can be born out with this limited model. A strength of the current model is its full interactivity with the vocal tract. Acoustic pressures above and below the glottis not only define the transglottal pressure (and thereby the flow), but they also determine the driving forces on the vocal folds.

The exact equivalence between the tissue properties of the bar-plate and the three-mass versions of the body-cover model is investigated in a companion paper (Titze and Story, in press). The vocal fold configuration is controlled by ξ_{02}, the glottal half-width at the vocal processes, and θ_0, the pre-phonatory convergence angle of the glottis. The vocal tract configuration is controlled by the vowel shape and the epilaryngeal (supraglottal) tube area A_e. The subglottal area A_s is held constant for this study. Appropriate ratios of the control parameters are chosen to show under which conditions maximum power transfer occurs. Figure 4 shows various conditions of the glottis for contact and noncontact between the folds. The mathematics for the pressures and flows are given in the Appendix.

IV. PROCEDURE

A total of 120 simulations served as an initial data set for study. These were all simulations for which oscillation was either self-sustained (with limit cycles) or damped (with a point attractor). To simplify the parameter space, only two independent variables were chosen for investigation, the neutral glottal area at the top of the vocal folds ($2L\xi_{02}$ in Fig. 3), and the epilarynx tube area A_e. The convergence angle θ_0 was held constant (see below). The neutral glottal area could be negative to allow an initial vocal fold overlap. The epilarynx tube area was chosen to range between 0.2 and 2.0 cm^2 because such values were considered to be physiologically likely (Story, 1995).

The following parameters were held constant:

$P_L = 0.8\,\text{kPa}$ (lung pressure)
$A_s = 3.0\,\text{cm}^2$ (subglottal area)
$\theta_0 = 0.0333\,\text{rad} = 1.91°$ (convergence angle)
$K = 200\,\text{N/m}$ (body stiffness)
$k = 50\,\text{N/m}$ (cover stiffness)
$\kappa = 5\times10^{-5}\,\text{N m/rad}$ (torsional cover stiffness)
$M = 10^{-4}\,\text{kg}$ (body mass)
$m = 10^{-4}\,\text{kg}$ (cover mass)
$I = 10^{-10}\,\text{kg m}^2$ (cover moment of inertia)
$z_n = 0.5\,\text{T}$ (nodal point)
$B = 0.2(KM)^{1/2}$ (0.1 damping ratio of body)
$b = 0.2(km)^{1/2}$ (0.1 damping ratio of cover in translation)
$B_c = 0.2(\kappa I_c)^{1/2}$ (0.1 damping ratio of cover in rotation)
$L = 1.5\,\text{cm}$ (length of vocal fold)
$T = 0.3\,\text{cm}$ (thickness of vocal fold)
$\rho = 1.14\,\text{kg/m}^3$ (density of air)
$c = 350\,\text{m/s}$ (sound velocity of warm, moist air)
Vowel = /ɑ/ or /i/, 44 section vocal tract (see Fig. 6)
Nasal coupling = 0

With these parameters, the fundamental frequency of vocal fold oscillation was around 120 Hz, an average male speaking F_0. There was some variation of F_0 with neutral glottal area and epilarynx tube area, but that is not the focus of this investigation and was of little consequence.

V. RESULTS

Figure 5 shows the parameter space for oscillation when the vocal tract was configured as an /ɑ/ vowel. Circles indicate limit cycles (sustained oscillation) and dots indicate point attractors (damped oscillation). Note that oscillations were sustainable only for neutral glottal areas ranging from -0.15 to $+0.15$ cm^2 for the chosen viscoelastic constants of the bar-plate model. For the /i/ vowel, the oscillation space was more restricted, with most positive neutral areas yielding damped oscillation only.

Figure 6 shows a sample output for one simulation. On top is the vocal tract diameter function, showing, from left to right: trachea, epilarynx tube, pharynx, mouth, and nose. Below the diameter function are nine simulated wave forms, all 100 ms long, described in the figure caption. The neutral glottal area was -0.06 cm^2 (initially overlapped on top) and

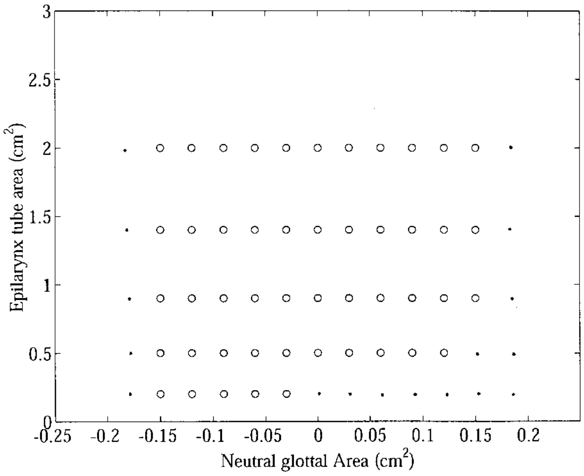

FIG. 5. Parameter space for oscillation. Circles indicate self-sustained oscillation (limit cycles) and dots indicate damped oscillation (point attractors).

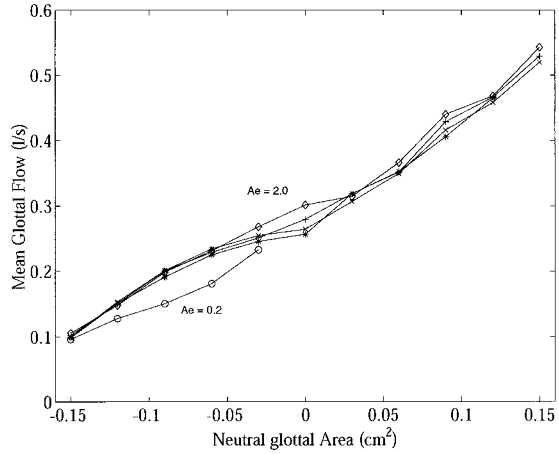

FIG. 7. Mean glottal flow vs neutral glottal area for five values of epilarynx tube area A_e. The lung pressure was kept at 0.8 kPa in all cases.

the epilarynx tube area was 0.5 cm^2. This particular case was chosen as an example because it shows a period-tripling bifurcation in the glottal area (labeled AG here). More severe bifurcations were seen in a number of cases, particularly for larger negative neutral areas (where the vocal folds further overlapped prior to oscillation). Such bifurcations created somewhat uneven power calculations, as will be seen later, because the vocal tract excitations differed slightly across cycles; but the overall results were not compromised severely by this unevenness. Power and flow calculations were performed on the wave forms labeled PO and UG in Fig. 6.

Figure 7 shows the mean glottal flow as a function of the neutral glottal area. Epilarynx tube area is the parameter on the curves. Note that this mean flow versus neutral area relation is essentially a proportionality, with little dependence on A_e, suggesting that *for mean flow, the glottis is a high impedance source*. The mean glottal area is considerably less than 0.2 cm^2, the smallest vocal tract area chosen. Since mean glottal flow is a more measurable quantity on human subjects than neutral glottal area, we will henceforth consider mean glottal flow to be one of the two independent control parameters. This is also the parameter that has the greatest clinical relevance in the management of airflow in phonation. Readers who wish to reconvert subsequent data sets back to neutral area can simply draw a straight line through the family of curves in Fig. 7 and use this line as a nomogram for reconversion.

For nonsteady (oscillatory) flow, a different picture is obtained. Figure 8 shows peak glottal flow as a function of mean glottal flow for this model. The data set shows the first important effect of A_e. Note that small values of A_e (0.2 and 0.5 cm^2) restrict the peak flow, but values of 1.0 cm^2 and

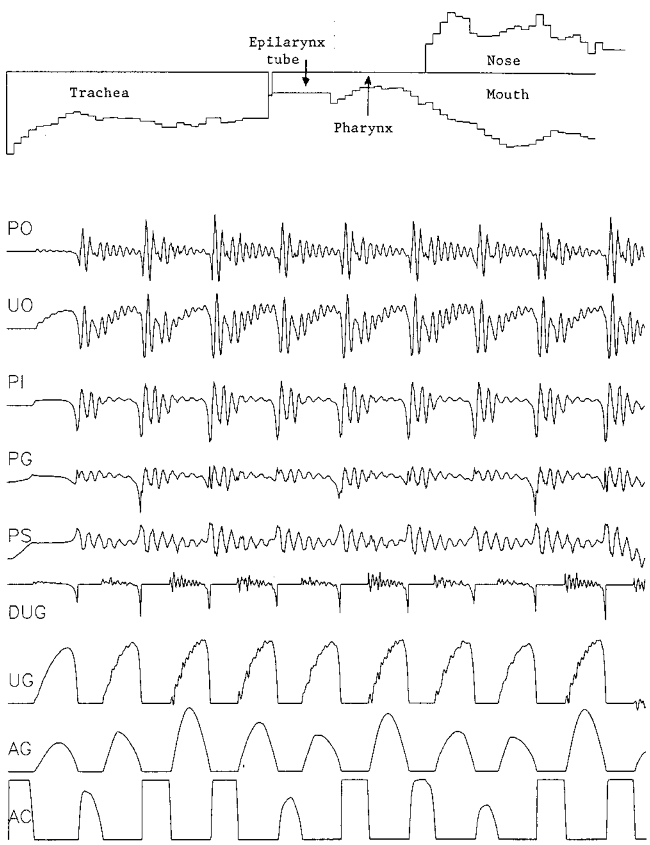

FIG. 6. Example of one of the simulations, showing from top to bottom: vocal tract diameter function, radiated mouth pressure (PO), mouth flow (UO), vocal tract input pressure (PI), intraglottal pressure (PG), subglottal pressure (PS), derivative of glottal flow (DUG), glottal flow (UG), glottal area (AG), and contact area (AC).

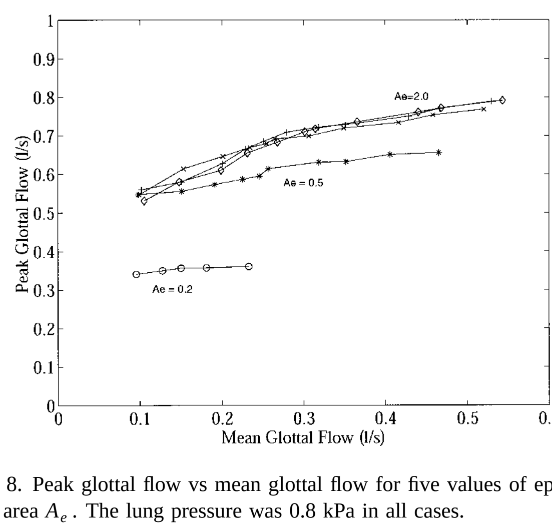

FIG. 8. Peak glottal flow vs mean glottal flow for five values of epilarynx tube area A_e. The lung pressure was 0.8 kPa in all cases.

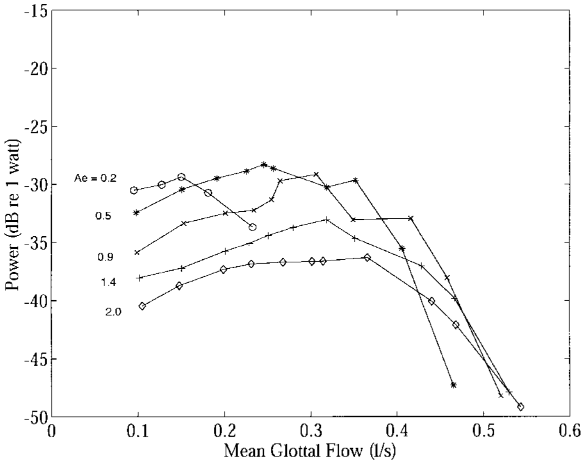

FIG. 9. Radiated oral power (in dB relative to 1.0 W) vs mean glottal flow for five values of epilarynx tube area A_e. The lung pressure was 0.8 kPa in all cases.

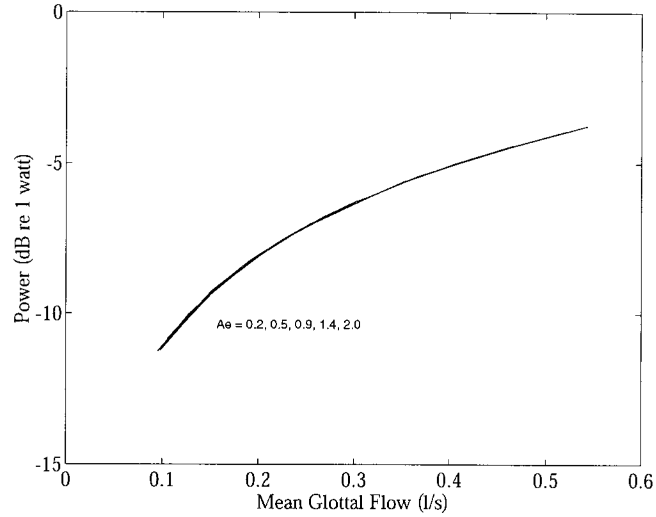

FIG. 10. Aerodynamic power (in dB relative to 1.0 W) vs mean glottal flow for five values of epilarynx tube area A_e. The lung pressure was 0.8 kPa in all cases.

higher have little effect on the peak flow. The peak flow is then governed only by the glottal resistance, not by the vocal tract impedance. We can therefore say that, acoustically, the glottis acts as a high impedance (constant flow) source only for values of $A_e > 1.0\ \mathrm{cm}^2$, with the internal glottal resistance limiting the flow. Sundberg (1987) has given glottal valving as an explanation of the "flow mode." The present results suggest that the "flow mode" appears to be governed more by epilarynx tube area than by glottal valving. As an example, for a mean glottal flow of 0.2 l/s, the peak flow can be essentially doubled by a 5:1 widening the epilarynx tube (from 0.2 to 1.0 cm^2). On the other hand, a 5:1 increase in mean glottal flow (from 0.1 to 0.5 l/s) increases the peak flow by only 50%.

The widening of the epilarynx tube to switch to a "flow mode" may not always be an advantage as far as vocal output power is concerned, as seen in Fig. 9. Here we show radiated oral power (in dB relative to 1 W) as a function of mean glottal flow for a simulated /ɑ/ vowel. This radiated power was computed as P_o^2/R_r, where P_o is the oral radiated pressure and R_r is the radiation resistance [$128\rho c/(9\pi^2)$; Flanagan, 1965]. Note that as the epilarynx tube area increases (top to bottom curve), the peak output power occurs for higher mean glottal flows. This is predicted by the maximum power transfer theorem; as the load impedance decreases, the source resistance must decrease also, thus maintaining an optimum R_L/R_S ratio. But the curves have too much of a downturn when the mean flow increases much beyond 0.3 l/s. The reason for this sharp downturn was given earlier; for bar masses, the glottal flow waveforms become nearly sinusoidal for positive neutral areas (no partial glottal closure). Since high frequencies radiate much better from the mouth than low frequencies, the radiated power suffers dramatically with decreased glottal adduction (as measured here by mean glottal flow). In a higher-dimensional model (Titze and Talkin, 1979; Alipour *et al.*, 2000), this can be remedied by allowing anterior–posterior variations in vocal fold contact. For the current bar-plate model, mean glottal flows above 0.3 l/s, for which there was no vocal fold collision, will henceforth be eliminated from the data sets for maximum power transfer considerations. This will make the proof of a downturn in the output power with increasing glottal width more difficult, but still possible with appropriate impedance ratios.

Consider now the aerodynamic power $P_L u_{\mathrm{mean}}$, where u_{mean} is the mean glottal flow. This is shown in Fig. 10. Since P_L was held constant, the relation must be a proportionality, which shows up as a logarithmic curve on a semilog plot. (Data points are not shown because the curves are so tightly overlapped.) The fact that the curve is identical for all values of A_e is an internal verification of the consistancy across A_e calculations, since the actual values plotted for u_{mean} were from different A_e curves.

Figure 11 shows glottal efficiency calculations, which (in dB) are simply the difference between the radiated output power in Fig. 9 and the aerodynamic power in Fig. 10. This glottal efficiency was expected to be a monotonically increasing function with mean glottal flow, as predicted in Fig. 2 (bottom trace), because the source resistance is decreasing.

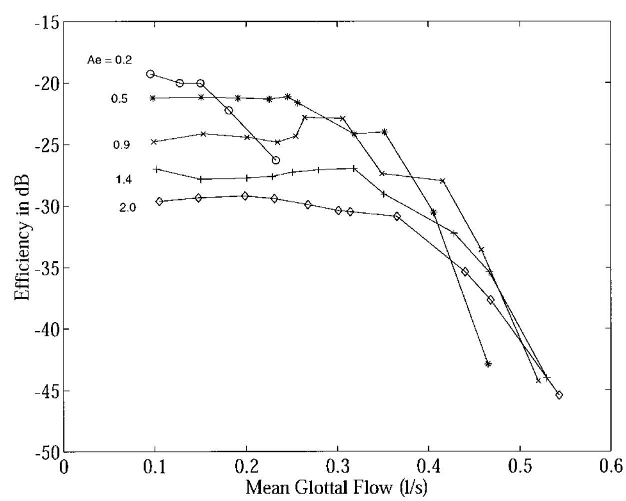

FIG. 11. Glottal efficiency (in dB relative to 1.0, or 100%) vs mean glottal flow for five values of epilarynx tube area A_e. The lung pressure was 0.8 kPa in all cases.

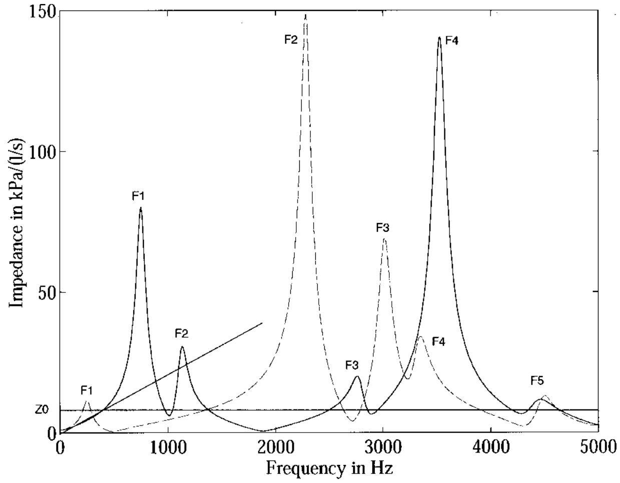

FIG. 12. Calculated input impedance of the vocal tract for the vowel /ɑ/ (solid curve) and the vowel /i/ (dashed curve). The sloping straight line is a low-frequency approximation. The horizontal straight line is the characteristic impedance of the epilarynx tube, $Z_0 = \rho c / A_e$.

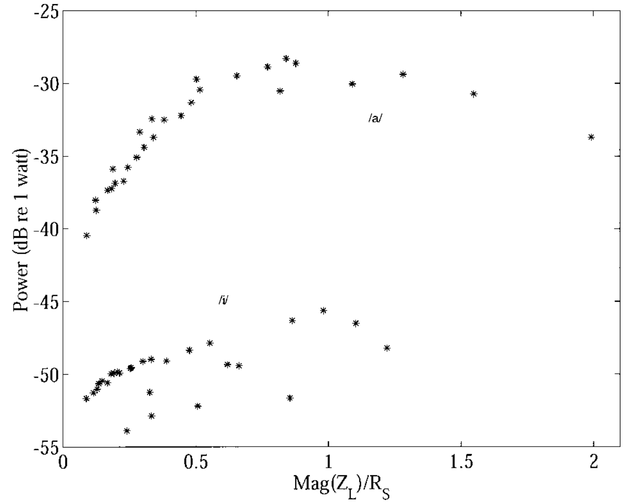

FIG. 13. Radiated oral power (in dB relative to 1.0 W) plotted against the ratio of magnitude of input impedance to glottal source resistance.

But, because of the aforementioned high frequency loss with no collision, and hence poorer radiation, the efficiency curves remained at best a constant (for low mean glottal flow) and at worst dropped off dramatically when mean flow was above 0.3 l/s.

To define a ratio similar to the R_L/R_S ratio for verification of the maximum power transfer theorem, the vocal tract input impedance was first calculated as outlined by Sondhi and Schroeter (1987) and Titze and Story (1997). For the /ɑ/ configuration shown on top of Fig. 6 (with no nasal coupling), the magnitude of the impedance is shown in Fig. 12 as a function of frequency. The solid curve is for the vowel /ɑ/ and the dashed curve is for the vowel /i/. Inspection of the real and imaginary parts of the impedance curves showed that, for low fundamental frequencies ($F_0 < F_1$), the impedance is essentially a positive (inertive) reactance, with the resistance playing a minor role. A straight-line approximation to this low-frequency impedance is also shown, computed as

$$Z_L = jZ_0(F_0/350), \tag{3}$$

where $j = (-1)^{1/2}$, and

$$Z_0 = \rho c / A_e, \tag{4}$$

the characteristic acoustic impedance of the epilarynx tube. Note that $Z_L = jZ_0$ occurs in Eq. (3) when $F_0 = 350\,\text{Hz}$. At this frequency, the straight-line impedance approximation crosses the constant horizontal line marked Z_0 on the vertical axis in Fig. 12.

Ideally, a source impedance match to the load impedance Z_L would be Z_L^*, its complex conjugate. This would be a compliant source impedance. But the glottal impedance is not compliant, which will make an impedance ratio a complex number. In terms of absolute magnitudes, however, the following ratio is defined:

$$\frac{\text{Mag}(Z_L)}{R_S} = \frac{(\rho c / A_e)(F_0/350)}{P_L / u_{\text{mean}}}, \tag{5}$$

where the glottal resistance R_S is taken to be the lung pressure divided by the mean glottal flow. This expression is limited by the straight-line approximation to the inertive rectance, which is good to F_0 slightly greater than $F_1/2$. In the simulation data sets described previously, this approximation was easily met, since F_0 was around 120 Hz and F_1 was 750 Hz for /ɑ/ and 250 Hz for /i/.

Figure 13 (top) is a replot of the entire family of data points for oral radiated power shown in Fig. 9 for the /ɑ/ vowel, with the abscissa now being the impedance ratio in Eq. (5). A second data set for the /i/ vowel (bottom) is added to the graph. Overall, the radiated power for /i/ is much less than for /ɑ/ because of the greater mouth constriction and smaller lip opening. Note that most of the points for each data set follow a curved path, and that maximization of radiated power occurs at the value of 1.0 for this impedance ratio. (As stated before, data points for $u_{\text{mean}} > 0.3\,\text{l/s}$ were eliminated for reasons described.) The similarity between these collections of data points and the idealized maximum power transfer curve (top of Fig. 2) gives support to the maximum power transfer theorem being applicable to vocal fold vibration. In particular, the steep rise before the peak and the more shallow decline after the peak lend credence to the hypothesis. The points falling lower than expected are mainly cases for which there was vocal roughness in the form of subharmonics.

VI. CONCLUSIONS

Mean glottal airflow (or, alternatively, glottal resistance) has been a target for optimizing vocal output power in voice therapy and singing training. The current investigation suggests that the optimization process should involve both the vocal tract and the vocal folds. It appears that an impedance matching between the two might take place. In general, a wide epilarynx tube (from the ventrical to the laryngeal vestibule) requires a low glottal resistance for maximum power transfer. Conversely, a narrow epilarynx tube requires a high glottal resistance (more adduction) for maximum power transfer. What Sundberg (1987) has called the “flow mode” appears to be a condition where the vocal tract impedance is considerably smaller than the glottal impedance, making the glottis a flow source acoustically, as for steady-flow (aerodynamic) conditions.

Vocologists (those who habilitate voices) have some choices in guiding a speaker or singer. If the desired (or acquired) voice quality is to be bright and "twangy," as in some forms of belting, gospel singing, or some regional dialects, the vocal tract can be more narrow in the epilaryngeal and pharyngeal region (Estill *et al.*, 1996; Story *et al.*, 2001). For such a vocal tract configuration, a well-adducted pair of vocal folds, with relatively high glottal resistance, would be a good match. Because of this higher glottal resistance, lung pressures would likely also be on the high side. Conversely, if the desired (or acquired) voice quality is to be "yawny," as in crooning, sobbing, or a mellow speech dialect (Estill *et al.*, 1996), the epilaryngeal and pharyngeal vocal tract can be wider. For this configuration, a lesser degree of adduction, with lower glottal resistance and probably lower lung pressure, is a good match.

It is already known that "yawn-sigh" is a good combination for voice therapy. Sigh involves a glottal posture with low glottal impedance that matches a "yawny" vocal tract. Less is known about the "twang-belt" combination in voice training and therapy. Here the voice is sometimes initiated with a creaky production, a tighter state of vocal fold adduction. This is a match for twang, a tighter vocal tract configuration. Some vocologists shy away from a twang-belt approach to voice therapy because they fear hyperfunction and excessive vocal fold collision. But since mean glottal flow is smaller, and hence presumably also the amplitude of vibration of the vocal folds, it is not clear that one or the other of these techniques is necessarily more healthy. For the time being, one must keep an open mind about high pressure, low flow production as a viable alternative to low pressure, high flow production. The choice depends to a large degree on the natural state of the vocal tract and the voice quality to be achieved with it.

As a future investigation, it would be worthwhile to examine if the subglottal (tracheal) impedance could assume a compliant characteristic to provide a true impedance match as a complex conjugate to the supraglottal impedance. It would also be instructive to test maximum power transfer for conditions where the fundamental frequency is at or above the first formant frequency. Research is presently ongoing in this area.

ACKNOWLEDGMENT

This work was supported by the National Institution of Health, Grant No. R01 DC02532-05.

APPENDIX

1. Equations of motion

The motion of the cover (plate) can be described with two degrees of freedom if we assume a rotation θ about a nodal point z_n (see Fig. 3) and a translation ξ of the nodal point,

$$I_c\ddot{\theta}+B_c\dot{\theta}+\kappa\theta=T_a, \tag{A1}$$

$$m\ddot{\xi}+b(\dot{\xi}-\dot{\xi}_b)+k(\xi-\xi_b)=F_a, \tag{A2}$$

where T_a is the applied aerodynamic torque, I_c is the moment of inertia for rotation of the cover, B_c is the rotational damping, κ is the rotational stiffness, m is the mass of the cover, b is translational damping, k is the translational stiffness, ξ_b is the displacement of the body, and F_a is the aerodynamic force at the nodal point. Similarly, the equation of motion for the body is written as

$$M\ddot{\xi}_b+b(\dot{\xi}_b-\dot{\xi})+k(\xi_b-\xi)+K\xi_b+B\dot{\xi}_b=0, \tag{A3}$$

where M is the mass, B is the damping, and K is the stiffness of the body.

2. Glottal area simulation

The glottal area for a left–right symmetrical bar-plate model is defined as

$$a(z)=2L[\xi_{0n}-(z-z_n)\tan(\theta_0+\theta)+\xi], \tag{A4}$$

where L is the length of the glottis and ξ_{0n} is the prephonatory displacement from the midline at the nodal point z_n, measured from the bottom of the vocal folds. With this area function, the glottal entry and exit areas are defined as

$$a_1=2L\ \mathrm{Max}\{\delta,[\xi_{0n}-(0-z_n)\tan(\theta_0+\theta)+\xi]\}, \tag{A5}$$

$$a_2=2L\ \mathrm{Max}\{\delta,[\xi_{0n}-(T-z_n)\tan(\theta_0+\theta)+\xi]\}, \tag{A6}$$

where δ is the minimum allowable area for glottal flow. Note that both the dynamic variables θ and ξ enter these equations for glottal area; since glottal area determines flow and also intraglottal pressure, aerodynamic coupling of the equations of motion (A1)–(A3) is guaranteed.

3. Aerodynamic driving pressure and driving torque

The assumed linear variation of the glottal area from entry to exit allows the pressure in the glottis to be integrated over the medial surface to obtain both the net driving torque on the cover and the net driving force on the body. Using ideal Bernoulli conditions for any point z upstream of the flow detachment point z_d [Figs. 4(a) and 4(b)]

$$P_s+\tfrac{1}{2}\rho v_s^2=P(z)+\tfrac{1}{2}u^2/a^2(z), \tag{A7}$$

where P_s is the subglottal pressure, v_s is the subglottal (trachea) particle velocity, $P(z)$ is the intraglottal pressure at any point z, u is the flow, and $a(z)$ is glottal area corresponding to the intraglottal pressure $P(z)$. Now let P_{kd} be defined as the kinetic pressure at the point of flow detachment and P_{ks} the kinetic pressure in the trachea,

$$P_{kd}=\tfrac{1}{2}\rho v_d^2, \tag{A8}$$

$$P_{ks}=\tfrac{1}{2}\rho v_s^2, \tag{A9}$$

where v_d is the particle velocity at flow detachment. Defining $a_d=a(z_d)$, the intraglottal pressure in the attached region is then

$$P(z)=P_s+P_{ks}-P_{kd}a_d^2/a^2(z). \tag{A10}$$

We now argue that the kinetic pressure P_{ks} in the trachea is negligible compared to P_s. Typically, P_s is on the order of 0.5–1.0 kPa in speech (Holmberg *et al.*, 1988), but can reach 5.0 kPa in singing (Bouhuys *et al.*, 1968). For a typical mean tracheal flow of 0.2 l/s (Holmberg *et al.*, 1988) and a tracheal cross section of 3 cm^2 (Story, 1995), the particle velocity is 67 cm/s, which leads to a kinetic pressure of 0.0002 kPa according to Eq. (11). Since this is several orders of magnitude lower than P_s, we will neglect P_{ks} from this point on.

The mean aerodynamic forces over the medial surface are now obtained by integration. For example, for the lower portion of a divergent glottis for which the detachment point z_d is *below* the nodal point z_n,

$$F_l = L z_d \frac{1}{z_d}\int_0^{z_d} P(z)\,dz + L(z_n - z_d)(P_s - P_{kd}), \tag{A11}$$

where we have assumed that the jet pressure above detachment is $P_s - P_{kd}$, the value obtained by letting $z = z_d$ in Eq. (A10). Performing the integration,

$$F_l = L P_s z_d - L P_{kd} a_d^2 \left[(-a^{-1}) \left(\frac{da}{dz} \right)^{-1} \right]_0^{z_d} + L(z_n - z_d)(P_s - P_{kd}). \tag{A12}$$

In evaluating the limits of this integration, it is necessary to assume that the glottal area gradient

$$\frac{da}{dz} = (a_d - a_1)/z_d \tag{A13}$$

is independent of z, but this assumption has already been made with linearization of the glottal area.

Defining $a_1 = a(o)$, we obtain the following for a *divergent* glottis:

$$F_l = L z_n P_s - L\left(z_n - z_d + \frac{a_d}{a_1} z_d \right) P_{kd} \quad \text{for } z_d \leqslant z_n. \tag{A14}$$

The upper force requires no integration because the jet pressure does not change from $z = z_n$ to $z = T$,

$$F_u = L(T - z_n)(P_s - P_{kd}) \quad \text{for } z_d \leqslant z_n. \tag{A15}$$

If the detachment point z_d is *above* the nodal point z_n, then for a *divergent* glottis,

$$F_l = L z_n \left(P_s - \frac{a_d^2}{a_n a_1} P_{kd} \right) \quad \text{for } z_d > z_n, \tag{A16}$$

$$F_u = L(T - z_n) P_s - L\left[(T - z_d) + \frac{a_d}{a_n}(z_d - z_n) \right] P_{kd} \quad \text{for } z_d > z_n, \tag{A17}$$

where $a_n = a(z_n)$ is the glottal area at the nodal point.

For a convergent glottis, the flow remains attached over the entire glottis [i.e., $z_d = T$ and $a_d = a_2 = a(T)$]. This allows Eqs. (A14)–(A17) to be replaced by two simpler equations,

$$F_l = L z_n \left(P_s - \frac{a_2^2}{a_n a_1} P_{kd} \right), \tag{A18}$$

$$F_u = L(T - z_n)\left(P_s - \frac{a_2}{a_n} P_{kd} \right), \tag{A19}$$

and the detachment point obviously does not need to be computed.

The total force F_a in Eq. (A2) is

$$F_a = F_l + F_u. \tag{A20}$$

To obtain the exact aerodynamic torque, we would need to integrate the differential torque $P(z) z\, dz$ over the entire plate surface. But we will employ an approximation that will lead not only to a simpler expression, but will also allow for a more direct comparison of the driving forces to those of the two-mass model (Ishizaha and Flanagan, 1972), and the three-mass model (Story and Titze, 1995). The torque approximation is obtained by using the two average forces F_l and F_u with their respective moment arms, $z_n/2$ and $(T - z_n)/2$,

$$T_a = F_l \left(\frac{z_n}{2} \right) - F_u \left(\frac{T - z_n}{2} \right). \tag{A21}$$

This is the torque used in Eq. (A1).

4. Calculation of the kinetic pressure at flow detachment

The only remaining unknown in the above-mentioned force and torque equations is the kinetic pressure P_{kd}. If we make the assumption that pressure recovery and flow reattachment are well downstream from the beginning of the jet, and that the jet pressure is constant, then the glottal exit condition can be written as

$$P_2 = P_d = P_e - k_e P_{kd}, \tag{A22}$$

where P_e is the (recovered) pressure in the epilarynx tube, P_2 is the exit pressure, and k_e is the pressure recovery coefficient (Ishizaka and Flanagan, 1972), written as

$$k_e = 2\,\frac{a_d}{A_e}\left(1 - \frac{a_d}{A_e} \right). \tag{A23}$$

Using once again Bernoulli's equation to the point of flow detachment,

$$P_s = P_d + P_{kd}, \tag{A24}$$

the kinetic pressure P_{kd} in all forgoing equations can be replaced by

$$P_{kd} = (P_s - P_e)/(1 - k_e). \tag{A25}$$

Now we use the Liljencrants (1991) and Pelorson *et al.* (1994) criterion for flow detachment,

$$a_d = a(z_d) = \mathrm{Min}(a_2, 1.2\, a_1). \tag{A26}$$

The nodal point area in the foregoing force and torque relations is defined as

$$a_n = \mathrm{Max}[\delta, 2L(\xi_{0n} + \xi)]. \tag{A27}$$

Substituting $z = z_d$ into Eq. (A4) and equating the result to $1.2\, a_1$ from Eq. (A5) yields the height of the separation point

$$z_d = \mathrm{Min}\left\{ T, \mathrm{Max}\left[0, -\frac{0.2}{\tan(\theta_0+\theta)} [\xi_{0n} + z_n \tan(\theta_0+\theta) + \xi] \right] \right\}, \tag{A28}$$

where the limits $0 < z_d < T$ have been imposed.

5. Driving pressures for glottal closure

When there is contact between portions of the vocal fold surfaces, we also need to invoke the hydrostatic pressure, defined here as the mean between the subglottal pressure and the supraglottal (epilaryngeal) pressure,

$$P_h = (P_s + P_e)/2. \tag{A29}$$

Consider three separate conditions for the driving force and torque as determined by the glottal configuration. The first condition is illustrated in Fig. 4(c) and applies to *upper contact only*:

$$a_1 > \delta, \quad a_2 \leqslant \delta, \tag{A30}$$

$$F_l = L z_n P_s \quad \text{for } z_c \geqslant z_n, \tag{A31}$$

$$F_u = L(z_c - z_n) P_s + L(T - z_c) P_h \quad \text{for } z_c \geqslant z_n, \tag{A32}$$

$$F_l = L z_c P_s + L(z_n - z_c) P_h \quad \text{for } z_c < z_n, \tag{A33}$$

$$F_u = L(T - z_n) P_h \quad \text{for } z_c < z_n. \tag{A34}$$

The second condition is for *lower contact only* [Fig. 4(d)]:

$$a_1 \leqslant \delta, \quad a_2 > \delta, \tag{A35}$$

$$F_l = L z_c P_h + L(z_n - z_c) P_e \quad \text{for } z_c < z_n, \tag{A36}$$

$$F_u = L(T - z_n) P_e \quad \text{for } z_c \leqslant z_n, \tag{A37}$$

$$F_l = L z_n P_h \quad \text{for } z_c \geqslant z_n, \tag{A38}$$

$$F_u = L(z_c - z_n) P_h + L(T - z_c) P_e \quad \text{for } z_c > z_n. \tag{A39}$$

The third condition is for *contact at both bottom and top*:

$$a_1 \leqslant \delta, \quad a_2 \leqslant \delta, \tag{A40}$$

$$F_l = L z_n P_h, \tag{A41}$$

$$F_u = L(T - z_n) P_h. \tag{A42}$$

In all expressions, the total driving force is again $(F_l + F_u)$ and the torque is evaluated by Eq. (A21) as before.

6. Calculation of contact point and contact area

The contact point z_c needs to be known for all the above-mentioned force and torque calculations. This point is determined by setting the medial surface displacement to zero. From Eq. (A4),

$$\xi_{0n} - (z_c - z_n)\tan(\theta_0 + \theta) + \xi = 0, \tag{A43}$$

which gives the result

$$z_c = \mathrm{Min}\left\{ T, \mathrm{Max}\left[0, z_n + \frac{\xi_{0n+\xi}}{\tan(\theta_0+\theta)} \right] \right\}, \tag{A44}$$

where the contact point is limited to the range $0 < z_c < T$. The vocal fold contact area is now easily computed as

$$a_c = L(T - z_c), \quad a_1 > 0, \quad a_2 \leqslant 0 \tag{A45}$$

$$= L z_c, \quad a_1 \leqslant 0, \quad a_2 > 0 \tag{A46}$$

$$= LT, \quad a_1 \leqslant 0, \quad a_2 \leqslant 0. \tag{A47}$$

7. Glottal area and glottal flow

If a wave-reflection analog is used for vocal tract acoustics (Liljencrants, 1985; Story, 1995), an analytic solution for the interactive flow is obtainable as described earlier (Titze, 1984). Subglottally, the relations for pressure and flow are

$$P_s = P_s^+ + P_s^-, \tag{A48}$$

$$u = \frac{A_s}{\rho c}(P_s^+ - P_s^-), \tag{A49}$$

where P_s^+ is a forward (rostrally) traveling wave in the trachea, P_s^- is a backward (caudally) traveling wave in the trachea, A_s is the subglottal tube area, c is the velocity of sound, and u is the glottal flow.

Similarly, the pressure and flow relations in the supraglottal region are

$$P_e = P_e^+ + P_e^-, \tag{A50}$$

$$u = \frac{A_e}{\rho c}(P_e^+ - P_e^-), \tag{A51}$$

where the subscript "e" stands for "epilarynx tube," which is immediately above the vocal folds. The known pressures in the above-given expressions are P_s^+ and P_e^-, the waves *incident* upon the glottis. The unknown pressures are P_s^- and P_e^+, the departing waves, and the total pressures P_s and P_e. In addition, the flow u is unknown. Thus, there are five unknowns in four equations, which suggests that another equation is needed for an analytical solution. This equation is Eq. (A25), rewritten here as

$$P_{kd} = \frac{1}{2}\rho \frac{u^2}{a_d^2} = \frac{(P_s - P_e)}{1 - k_e}. \tag{A52}$$

Substituting P_s and P_e from Eqs. (A48) and (A50) into Eq. (A52), and eliminating the unknown wave pressures P_s^- and P_e^+ from Eqs. (A49) and (A51) in favor of the known wave pressures P_s^+ and P_e^-, a quadratic equation for the flow u is obtained

$$u = \frac{a_d c}{(1-k_e)} \left\{ -\left(\frac{a_d}{A^*}\right) \pm \left[\left(\frac{a_d}{A^*}\right)^2 + \frac{4(1-k_e)}{\rho c^2}(P_s^+ - P_e^-) \right]^{1/2} \right\}, \tag{A53}$$

where

$$A^* = A_s A_e / (A_s + A_e) \tag{A54}$$

is an effective vocal tract area that includes both the tracheal tube and the epilarynx tube. In Eq. (A53), the plus sign is used when the second term in the square brackets is negative, and vice versa.

From an aerodynamic point of view, the glottal area is clearly a_d, the flow detachment area. But from a visual point of view, the area defined by light projected through the glottis is

$$a_g = \mathrm{Max}[0, \mathrm{Min}(a_1, a_2)]. \tag{A55}$$

This is the area that a photoglottograph would measure.

Alipour, F., Berry, D., and Titze, I. R. (**2000**). ''A finite-element model of vocal fold vibration,'' J. Acoust. Soc. Am. **108**, 3003–3012.

Bestebreurtje, M. E., and Schutte, H. K. (**2000**). ''Resonance strategies for the belting style,'' J. Voice **14**, 194–204.

Bouhuys, A., Mead, J., Proctor, D., and Stevens, K. (**1968**). ''Pressure-flow events during singing,'' Ann. N.Y. Acad. Sci. **155**, 165–176.

Brown, O. L. (**1996**). *Discover Your Voice* (Singular Publishing, San Diego).

Colton, R., and Casper, J. K. (**1996**). *Understanding Voice Problems*, 2nd ed. (Williams & Wilkins, Baltimore).

Estill, J., Fujimura, O., Sawada, M., and Beechler, K. (**1996**). ''Temporal perturbation and voice qualities,'' in *Vocal Fold Physiology: Controlling Complexity and Chaos*, edited by P. J. Davis and N. H. Fletcher (Singular Publishing, San Diego), pp. 237–252.

Flanagan, J. L. (**1965**). *Speech Analysis, Synthesis, and Perception* (Springer, New York).

Holmberg, E., Hillman, R., and Perkell, J. (**1988**). ''Glottal airflow and transglottal air pressure measurements for male and female speakers in soft, normal, and loud voice,'' J. Acoust. Soc. Am. **84**, 511–529.

Ishizaka, K., and Flanagan, J. L. (**1972**). ''Synthesis of voiced source sounds from a two-mass model of the vocal cords,'' Bell Syst. Tech. J. **51**, 1233–1268.

Liljencrants, J. (**1985**). ''Speech synthesis with a reflection-type line analog,'' Ph.D. dissertation, Royal Institute of Technology, Stockholm, Sweden.

Liljencrants, J. (**1991**). ''A translating and rotating mass model of the vocal folds,'' STL Quarterly Progress and Status Report 1, Speech Transmission Laboratory, Royal Institute of Technology (KTH), Stockholm, Sweden.

Linklater, K. (**1976**). *Freeing the Natural Voice* (Drama Book, New York).

Pelorson, X., Hirschberg, A., Van Hassel, R., Wijnands, A., and Auregan, V. (**1994**). ''Theoretical and experimental study of quasi-steady flow separation within the glottis during phonation: Application to a modified two-mass model,'' J. Acoust. Soc. Am. **96**, 3416–3431.

Sondhi, M. M., and Schroeter, J. (**1987**). ''A hybrid time-frequency domain articulatory speech synthesizer,'' IEEE Trans. Acoust., Speech, Signal Process. **35**, 955–967.

Story, B. H. (**1995**). ''Physiologically-based speech simulation using an enhanced wave-reflection model of the vocal tract,'' Ph.D. dissertation, University of Iowa.

Story, B., and Titze, I. (**1995**). ''Voice simulation with a body-cover model of the vocal folds,'' J. Acoust. Soc. Am. **97**, 1249–1260.

Story, B. H., Titze, I. R., and Hoffman, E. A. (**2001**). ''The relationship of vocal tract shape to three voice qualities,'' J. Acoust. Soc. Am. **109**, 1651–1667.

Sullivan, J. (**1985**). *The Phenomena of the Belt/pop Voice* (Sullivan, Denver).

Sundberg, J. (**1987**). *The Science of the Singing Voice* (Northern Illinois U.P., Dekalb).

Sundberg, J., Cleveland, T. F., Stone, R. E., and Iwarsson, J. (**1999**). ''Voice source characteristics of six premier country singers,'' J. Voice **13**, 168–183.

Titze, I. R. (**1984**). ''Parametrization of glottal area, glottal flow, and vocal fold contact area,'' J. Acoust. Soc. Am. **75**, 570–580.

Titze, I. R., and Story, B. H. (**in press**). ''Rulse for controlling low-dimensional vocal fold models with muscle activities,'' J. Acoust. Soc. Am.

Titze, I. R., and Story, B. H. (**1997**). ''Acoustic interaction of the voice source with the lower vocal tract,'' J. Acoust. Soc. Am. **101**, 2234–2243.

Titze, I. R., and Talkin, D. (**1979**). ''A theoretical study of the effects of various laryngeal configurations on the acoustics of phonation,'' J. Acoust. Soc. Am. **66**, 60–74.

Speech dynamic range and its effect on cochlear implant performance

Fan-Gang Zeng[a)]
Departments of Otolaryngology, Biomedical Engineering, and Cognitive Sciences, University of California, Irvine, California 92697

Ginger Grant[b)] and John Niparko
Department of Otolaryngology, Johns Hopkins University, Baltimore, Maryland 21287

John Galvin and Robert Shannon
House Ear Institute, Los Angeles, California 90057-1922

Jane Opie and Phil Segel
Advanced Bionics Corporation, Sylmar, California 91342

(Received 4 June 2001; accepted for publication 3 October 2001)

This study examines optimal conversions of speech sounds to audible electric currents in cochlear-implant listeners. The speech dynamic range was measured for 20 consonants and 12 vowels spoken by five female and five male talkers. Even when the maximal root-mean-square (rms) level was normalized for all phoneme tokens, both broadband and narrow-band acoustic analyses showed an approximately 50-dB distribution of speech envelope levels. Phoneme recognition was also obtained in ten CLARION implant users as a function of the input dynamic range from 10 to 80 dB in 10-dB steps. Acoustic amplitudes within a specified input dynamic range were logarithmically mapped into the 10–20-dB range of electric stimulation typically found in cochlear-implant users. Consistent with acoustic data, the perceptual data showed that a 50–60-dB input dynamic range produced optimal speech recognition in these implant users. The present results indicate that speech dynamic range is much greater than the commonly assumed 30-dB range. A new amplitude mapping strategy, based on envelope distribution differences between consonants and vowels, is proposed to optimize acoustic-to-electric mapping of speech sounds. This new strategy will use a logarithmic map for low-frequency channels and a more compressive map for high-frequency channels, and may improve overall speech recognition for cochlear-implant users.
 [DOI: 10.1121/1.1423926]

PACS numbers: 43.71.Es, 43.71.Ky, 43.66.Ts, 43.64.Me [CWT]

I. INTRODUCTION

A major goal in designing speech processors for cochlear implants is to optimally convert speech signals to electric currents that fit within an implant user's perceptual range. In order to make the softest speech sounds audible and the loudest still comfortable, it is important to know the dynamic range for speech sounds, the dynamic range for electric stimulation, and the appropriate conversion from speech sounds to electric currents. In clinical fitting procedures, selection of acoustic and electric dynamic ranges and conversion from acoustic amplitude to electric amplitude are part of the ''mapping'' process, which can play an important role in determining the outcome of cochlear-implant performance and satisfaction. Psychophysical studies have measured the dynamic range over a large electric parameter space and determined the appropriate conversion from acoustic amplitude to electric amplitude (e.g., Zeng and Shannon, 1992, 1994, 1995; Zeng, Galvin, and Zhang, 1998; Zeng and Galvin, 1999). However, less is known about how much speech information should be included in the input dynamic range for cochlear-implant speech processors (Fu and Shannon, 1999; Loizou, Dorman, and Fitzke, 2000). Here, we present new empirical data regarding the speech dynamic range and demonstrate its significance in cochlear-implant performance.

Ideally, a speech processor's input dynamic range (IDR) would be 120 dB, the typical dynamic range within which normal-hearing listeners process acoustic intensity information. This 120-dB acoustic dynamic range would then be converted into electric current values that evoke sensation between minimal to maximal loudness. However, the acoustic dynamic range must be greatly compressed to accommodate the substantially reduced range of electric stimulation for cochlear-implant listeners (about 10–20 dB; see Skinner *et al.*, 1997; Zeng and Galvin, 1999, and Table II of this study). Practically, because speech is likely the most important sound and usually has a smaller dynamic range than the 120-dB range, most implant devices have employed a much narrower 30–60-dB input dynamic range to better match the dynamic range of speech. In so doing, it is hoped that relative intensity changes from soft consonants to loud vowels are preserved perceptually for a cochlear-implant listener to understand speech.

[a)]Author to whom correspondence should be addressed. University of California, 364 Med Surge II, Irvine, CA 92697; electronic mail: fzeng@uci.edu
[b)]Present address: Cochlear Corporation, Englewood, CO.

Currently, there are more than 40 000 cochlear implant users worldwide. Nearly three-quarters of the implant users use the Nucleus device by Cochlear Corporation. In the Nucleus device, a fixed 30-dB range is used for the input dynamic range (User Manual, The Nucleus 22 Channel Cochlear Implant System, p. 4-SP). In the Med-El device, a fixed 60-dB input dynamic range is used (Stobich *et al.*, 1999). In the CLARION device, the input dynamic range can be varied between 20 and 80 dB for users of the simultaneous-analog-stimulation (SAS) strategy and between 10 and 60 dB for users of the continuous-interleaved-sampling (CIS) strategy (CLARION Device Fitting Manual, C9055003-002 Rev. C, p. 220). At present, the clinical fitting practice regarding the input acoustic dynamic range relies mostly on experience and lacks experimental validation.

It has long been assumed that speech has a roughly 30-dB dynamic range, based on classic acoustic analyses and statistical measurements on conversational speech (Dunn and White, 1940; Beranek, 1947; Fletcher, 1953). This 30-dB speech range has been used in many applications, including the Articulation Index (Kryter, 1962; ANSI, 1969, 1997). However, modern analyses using digital signal processing have shown a much wider speech dynamic range. Cox *et al.* (1988) measured distributions of short-term rms levels for conversational speech produced by 30 male and 30 female talkers. They found 40–50-dB distributions of the short-term rms speech levels in eight one-third octave bands covering a frequency range between 250 and 6300 Hz. Pavlovic (1993) noticed that speech dynamic range decreased from 50–60 to 30 dB when the constant of an exponential time window was increased from 13 to 200 ms. In addition, he found that an increase in vocal effort did not simply shift the speech dynamic range towards high values. Boothroyd *et al.* (1994) performed a similar analysis of seven phonemes produced by five female and five male talkers. They found that the overall dynamic range of these phonemes was 53 dB, and that the dynamic range was 37 dB even after adjustment in overall levels and high-frequency pre-emphasis. Stobich *et al.* (1999) calculated the distribution of envelope levels for 180 German sentences spoken by a male talker and found a dynamic range of 70 dB for these speech materials. Eddington (1999) found a 40–60-dB range in the distribution of envelope levels calculated over six frequency channels for TIMIT (Texas-Instruments-Massachusetts-Institute-of-Technology) sentences presented at a conversational level.

Perceptual studies also support the modern acoustic data that find the speech dynamic range to be greater than 30 dB. Studebaker *et al.* (1999) measured NU-6 word recognition at speech presentation levels from 64 to 99 dB SPL and speech-to-noise ratios from 28 to −4 dB. They found a slight increase in speech recognition scores (5 rau units) when the speech level was increased from 64 to 79 dB SPL. This suggests that, contrary to the commonly asserted 30-dB speech range, audibility continued to increase as the overall level increased. Moreover, if a 30-dB speech range were to be assumed, the lowest amplitudes for speech sounds would be 15 to 18 dB lower than the long-term rms level while the peak amplitudes would be 15 to 12 dB higher, according to ANSI (1969, 1997) specifications. If this were the case, word recognition should be similar between 16- and 28-dB speech-to-noise ratios. However, Studebaker *et al.* found significantly poorer speech recognition for the 16-dB than the 28-dB condition (by 5–25 rau units depending on the overall speech presentation levels). These results led Studebaker *et al.* to conclude that the effective dynamic range of speech must be at least 40–43 dB (28 dB + 15 or 12 dB).

In the present study, the distribution of envelope levels was measured for two widely used speech test materials: 12 vowels in /hVd/ format (Hillenbrand *et al.*, 1995) and 20 consonants in /aCa/ format (Turner, Souza, and Forget, 1995; Shannon *et al.*, 1999). Using either a broadband analysis or a narrow-band analysis from eight frequency channels, the data showed that these speech materials have an approximately 50-dB envelope level distribution. Speech recognition in cochlear-implant listeners was then measured as a function of the input dynamic range. Consistent with acoustic data, the perceptual data also showed that an input dynamic range of 50–60 dB produced optimal performance in cochlear implant users.

II. METHODS

A. Subjects

Ten CLARION (Advanced Bionics Corporation) cochlear-implant users participated in the experiment. The implant subjects' ages ranged from 21 to 56 years (average of 42 years). Each subject had at least 1 year of experience with the implant device prior to the experiment. Seven of the implant listeners used the CIS speech processing strategy, while the other three used the SAS strategy. All subjects were postlingually deafened, except for one subject (C4). All subjects were familiar with speech tests from previous clinical evaluations. Additional subject information is listed in Table I. Five normal-hearing (NH) listeners (age range of 21–36 years) also served as a control in the experiment. Local IRB-approved informed consent was obtained and all subjects were paid for their participation.

B. CLARION speech processors

In the experiment, cochlear-implant listeners used their preferred clinical programming parameters (or map) in the speech processors. User maps were uploaded from each subject's speech processor, stored in SOFTWARE-CLINICIAN (SCLIN) for Windows environment (CLARION Device Fitting Manual), and downloaded to a laboratory S-Series speech processor to minimize equipment-related variables. Speech recognition was conducted as a function of input dynamic range (IDR). There were six possible IDR settings with the CIS processing strategy (from 10 to 60 dB in 10-dB steps) and seven possible IDR settings with the SAS processing strategy (from 20 to 80 dB in 10-dB steps). No changes other than the IDR were made to an individual's map. Volume and sensitivity controls were kept constant at their normal settings within and between test sessions.

Figure 1 illustrates the mapping relationship between input dynamic range and electric dynamic range in CLARION cochlear implants. The x axis (input dynamic range in dB) determines the range of acoustic signals mapped into the

TABLE I. Biographical and audiological information for cochlear implant participants.

Subject	Age	Surgery date	Device	Strategy	Implant	Etiology
C1	66	11/16/89	S-Series	CIS	Left	Otosclerosis
C2	21	8/5/98	S-Series	CIS	Right	Unknown
C3	39	7/16/97	S-Series	CIS	Left	Unknown
C4	56	11/20/96	1.2	CIS	Left	Maternal rubella
C5	55	1/17/97	S-Series	CIS	Right	Congenital
C6	56	4/25/96	1.2	CIS	Left	Meningitis
C7	35	12/5/96	1.2	CIS	Right	Ototoxicity
S1	46	1/29/98	S-Series	SAS	Left	Unknown
S2	61	5/16/97	S-Series	SAS	Right	Meniere's
S3	76	7/9/98	S-Series	SAS	Right	Unknown

electric range in μA between threshold (T level) and the most comfortable loudness (M level). Because the x axis is logarithmic while the y axis is linear, a straight line on these axes indicates a logarithmic mapping between acoustic amplitude and electric amplitude. This logarithmic transformation has been verified psychophysically to restore normal loudness growth in electric stimulation (Eddington *et al.*, 1978; Zeng and Shannon, 1992; Dorman *et al.*, 1993).

For CLARION speech processors, conversions of acoustic to electric amplitudes depend on interactions among the sensitivity setting, the input dynamic range (IDR), and the electric dynamic range. The sensitivity setting determines the peak acoustic amplitude to be mapped to the maximal electric current that evokes the most comfortable loudness (M level). This peak acoustic amplitude is then used as the reference level (0 dB) for the input dynamic range, which can vary from 10 to 80 dB. An IDR setting of $-X$ dB means that only X dB of the acoustic range below the reference peak amplitude will be mapped to an implant user's electric dynamic range (between M and T levels). Acoustic amplitudes below the IDR setting stimulate at subthreshold levels ($<T$ level).

For example, an IDR setting of -50 dB (dashed sloping line) maps the 50-dB range below the 0-dB peak reference acoustic level into the audible electric dynamic range. Presumably, any acoustic level that is outside the input dynamic range will be mapped into either a subthreshold electric level ($<T$ level) or a constant saturating level ($=M$ level). Note, however, an interchangeable relationship between the IDR and the T-level settings. For instance, the same acoustic-to-electric amplitude map, as determined by the -50-dB IDR and the T-level settings (the dashed sloping line), can also be achieved by reducing the IDR setting to -40, -30, and -20 dB, while increasing the T level to $T1$, $T2$, and $T3$, respectively.

C. Stimuli

Vowel stimuli consisted of 12 tokens from five male and five female talkers in /hVd/ format (Hillenbrand *et al.*, 1995). Consonant stimuli consisted of 20 tokens from five male and five female talkers in /aCa/ format (Turner, Souza, and Forget, 1995; Shannon *et al.*, 1999). The Hillenbrand vowels were 16-bit.WAV files samples at 16 kHz, and the Turner/Shannon consonants were 16-bit.WAV files sampled at 44.1 kHz. All speech tokens were normalized based on the maximal rms level from a 50-ms running window. This maximal level most likely measured the level of the steady-state portion of the vowel.

These vowel and consonant stimuli were output via a PC soundcard (Turtle Beach MultiSound Fiji board), connected to one channel of a mixer (Tucker-Davis Technologies, TDT SM1). Continuous speech-spectrum-shaped noise was generated by passing white noise (TDT WG1) through a specially designed low-pass filter with a cutoff frequency at 608 Hz and a -12-dB/octave slope (Byrne *et al.*, 1994). The noise was delivered to another channel of the mixer where it was summed with the phonemic stimuli.

The summed speech and noise stimuli were amplified (Crown D-75) and presented to the listener via a Tannoy Reveal speaker mounted on a double-walled, sound-treated booth (IAC). Each subject was positioned in the center of the sound-treated room, facing the speaker (about 1 meter away, at 0° azimuth and at ear level). A calibration vowel /a/ was generated to have the same rms level as the average vowel level in both tests and to produce a conversational level of 65 dBA. The noise was attenuated via a programmable attenu-

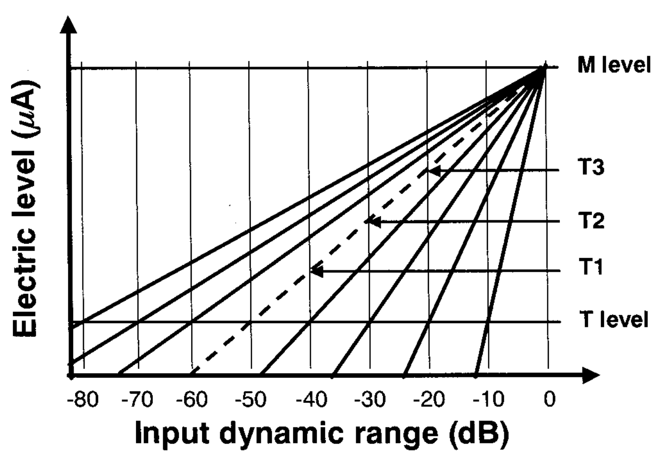

FIG. 1. Conversion from input dynamic range (x axis) to electric dynamic range (y axis) in CLARION devices. The reference acoustic level (0 dB) represents the peak amplitude, as determined by the sensitivity control, to be mapped to the most comfortable loudness level in electric stimulation (M level). Input dynamic range setting determine the range below the 0-dB reference acoustic level to be mapped into audible electric range between M and T levels. T level is electric threshold, representing 50% detection. Note the interchangeable relationship between IDR and T level settings in determining the acoustic-to-electric amplitude map (see the text in Sec. II B for detailed information).

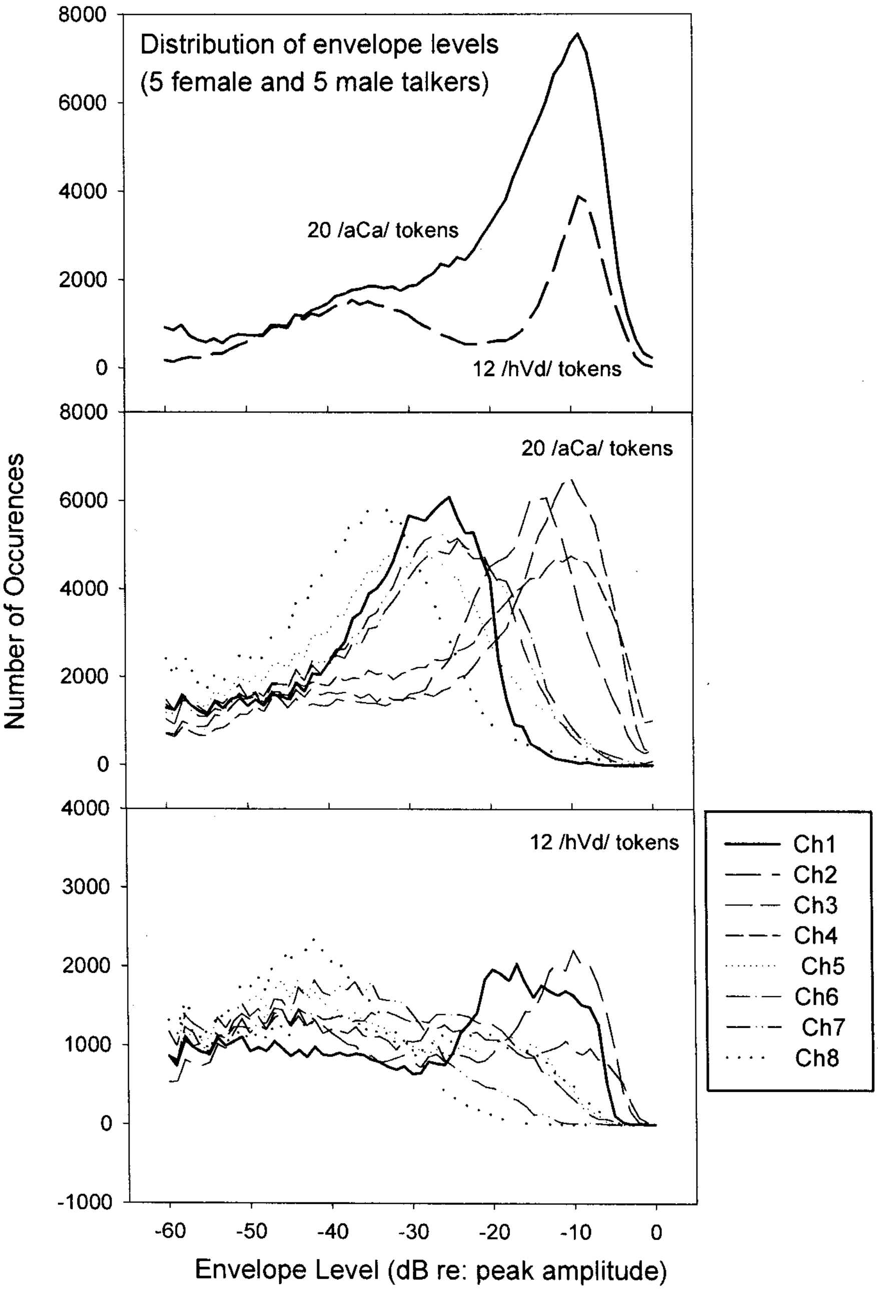

FIG. 2. Speech dynamic ranges in terms of envelope level distributions for the broadband condition (top panel) and the eight-narrow-band conditions (for consonants see the middle panel and for vowels see the bottom panel).

ator (TDT PA4) to achieve a +5-dB speech-to-noise ratio (i.e., the noise had a level of 60 dBA).

D. Procedures

Distribution of speech envelope levels was calculated for both broadband (250–6800 Hz) and narrow-band analysis. In the broadband analysis, the envelope of the acoustic signal was extracted by full-wave rectification and low-pass filtering (an Elliptical IIR filter with 160-Hz cutoff frequency and −6 dB per octave slope). The 160-Hz low-pass filter had an equivalent time window of roughly 6 ms, about half of the shortest integration value (13 ms) used in the Pavlovic study. A histogram recorded the number of occurrences for envelope amplitude (*re*: peak amplitude). Because coarticulation cues are always present in the adjacent sounds, the histogram also included contribution from the initial and final phonemes (/h/ and /d/ for vowels and /a/ for consonants). Because of the noise floor on the bottom of the distribution, the speech dynamic range was conservatively defined as the difference in the envelope levels producing between 5% and 99% accumulative occurrences. In the narrow-band analysis, the broadband signal was divided into eight narrow bands (fourth-order Elliptical IIR filters with cutoff frequencies at 250, 500, 875, 1150, 1450, 2000, 2600, 3800, and 6800 Hz, respectively). These filters approximately correspond to the frequency analysis filters used in the CLARION cochlear implant. The band-specific envelope was extracted and its amplitude histogram was constructed in the same way as for the broadband analysis.

Closed-set vowel and consonant recognition was measured separately using custom software (Robert, 1999). During each test, listeners heard five presentations of each phoneme spoken by each of the ten talkers; presentation of each

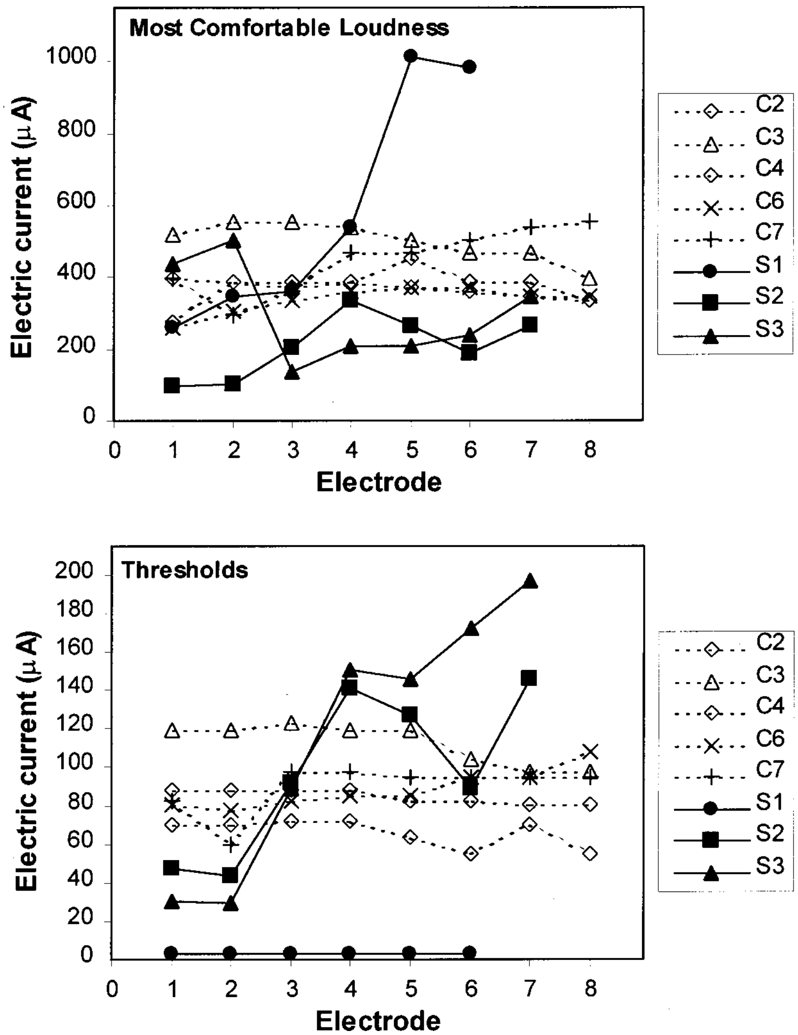

FIG. 3. Top panel displays the most comfortable loudness (M level) as a function of electrodes (x axis). Bottom panel displays threshold (T level) as a function of electrodes (x axis). Note both the greater intersubject- and intrasubject variability for the SAS users (filled symbols connected by solid lines) than for the CIS users (open symbols connected by dashed lines).

phoneme was randomized within the test. Listeners' responses to the stimuli were stored in a confusion matrix. No trial-by-trial feedback was given regarding the correctness of the response. Normal-hearing listeners listened to the original phoneme sounds in quiet and in noise (+5-dB S/N) with speech presented at 65 dBA. Implant listeners were tested first in quiet and then in noise. The test order of different input dynamic ranges was pseudorandomized. Each listener was given 15 min to acclimate to the experimental processor and was allowed to preview all stimuli before formal test sessions. Due to time limitation, some conditions were not tested.

III. RESULTS

A. Speech dynamic range

Figure 2 shows distribution of envelope levels for the /aCa/ and /hVd/ tokens in the broadband analysis (top panel) and for the /aCa/ tokens (middle panel) and the /hVd/ tokens (bottom panel) in the eight-channel analysis. First, note the dominant envelope level distribution at high levels for the broadband analysis. A small "bump" in the distribution at low levels (more obvious in the vowel envelope) most likely reflects the contribution from the lower-amplitude consonants. This is clearly illustrated in the narrow-band analysis, which shows a strong distribution at low levels for the high-frequency channels (dotted lines in the middle and bottom panels).

The broadband analysis (top panel) shows the acoustic dynamic range to be 47 dB (from −51 to −4 dB) for consonants and 46 dB (from −50 to −4 dB) for vowels. For the eight-channel condition, the consonant dynamic range is 41, 52, 51, 50, 47, 46, 47, and 45 dB for channel 1, 2, 3, 4, 5, 6, 7, and 8, respectively. On the other hand, the vowel dynamic range is 51, 51, 53, 49, 47, 47, 42, and 36 dB for channel 1,

TABLE II. Electric dynamic range in dB for five CIS users (C2, C3, C4, C6, and C7) and three SAS users (S1, S2, and S3). Note that S1 had six usable electrodes while S2 and S3 and seven usable electrodes.

Electrode	C2	C3	C4	C6	C7	S1	S2	S3
1	13.1	12.8	11.9	10.1	13.6		6.1	23.3
2	12.8	13.4	14.8	11.9	13.9	38.7	7.5	24.8
3	12.8	13.1	14.2	12.2	11.3	41.3	6.9	3.7
4	12.8	13.1	14.5	12.5	13.6	41.6	7.5	2.9
5	13.1	12.5	17.1	12.8	13.9	45.1	6.4	3.2
6	12.8	13.1	16.8	11.9	14.5	50.6	6.6	2.9
7	12.8	13.6	14.8	11.3	15.1	50.3	5.2	4.9
8	12.5	12.2	15.7	10.2	15.4			
Average	12.8	13.0	15.0	11.6	13.9	44.6	6.6	9.4
Std dev.	0.2	0.5	1.6	1.0	1.2	5.0	0.8	10.0

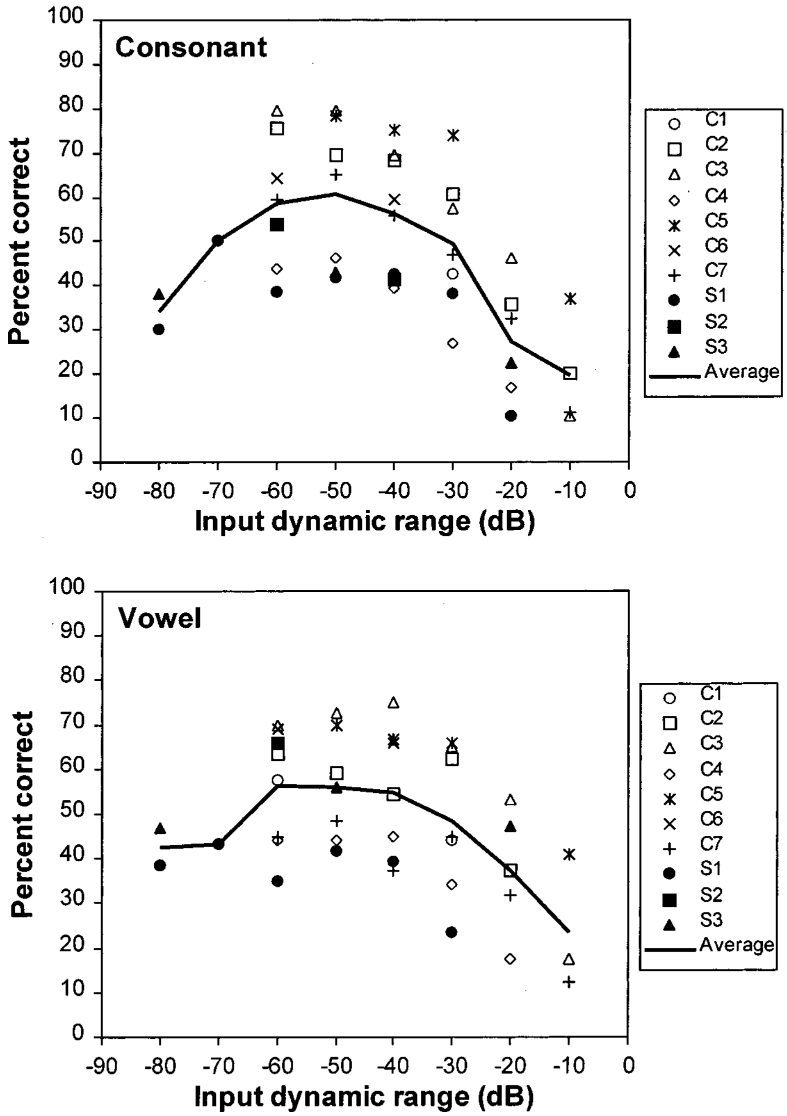

FIG. 4. Consonant (top) and vowel (bottom) recognition scores (*y* axis) in quiet as a function of the input dynamic range (*x* axis). Individual data are represented by symbols (unfilled symbols for CIS users and filled symbols for SAS users). The solid line represents the average data.

2, 3, 4, 5, 6, 7, and 8, respectively. Given these acoustic dynamic ranges, we shall see whether an input dynamic range setting of roughly 50 dB would produce optimal speech recognition in cochlear-implant users.

B. Electric dynamic range

Figure 3 shows the most comfortable loudness (*M* levels, top panel) and threshold (*T* levels, bottom panel) as a function of electrode position in 5 of the 7 CIS users and all 3 SAS users. These *M* and *T* levels are presented in microamps. Note the greater intersubject variability in both *M* and *T* levels for the SAS users compared to the CIS users. Also note the greater intrasubject variability across electrodes for the SAS users than the CIS users. The high *M* levels for subject S1 may actually be much lower as they approach the saturation portion of the current source in the CLARION S-series devices (CLARION Device Fitting Manual, p. 20).

Table II shows the calculated electric dynamic ranges, defined as the dB difference between *M* and *T* levels. Table II confirms the visual impression in Fig. 3 that the SAS users have both greater intersubject and intrasubject variability in dynamic range than the CIS users. The electric dynamic range averaged across electrodes was 12.8, 13.0, 15.0, 11.6, and 15.0 dB for the CIS users, C2, C3, C4, C6, and C7, respectively. On the other hand, the averaged electric dynamic range was 44.6, 6.6, and 9.4 dB for the SAS users, S1, S2, and S3, respectively. The unusually large dynamic range for S1 may actually be much lower and could be calculated by accessing the subject's internal device. Similarly, the variability in dynamic range across each subject's electrodes is much smaller (standard deviation ranges from 0.2 to 1.6 dB) for the CIS users than the SAS users (standard deviation ranges from 0.8 to 10.0 dB). The reasons for the differences between the CIS and SAS user results are not clear, but may be related to the difference in electrode configurations and stimulating waveforms between the two strategies.

C. Phoneme recognition in quiet

Figure 4 shows both the group average (line) and individual data (symbol). The top panel shows consonant recognition (*y* axis) as a function of input dynamic range (*x* axis), while the bottom panel shows vowel recognition (*y* axis) as a function of input dynamic range (*x* axis). For the five

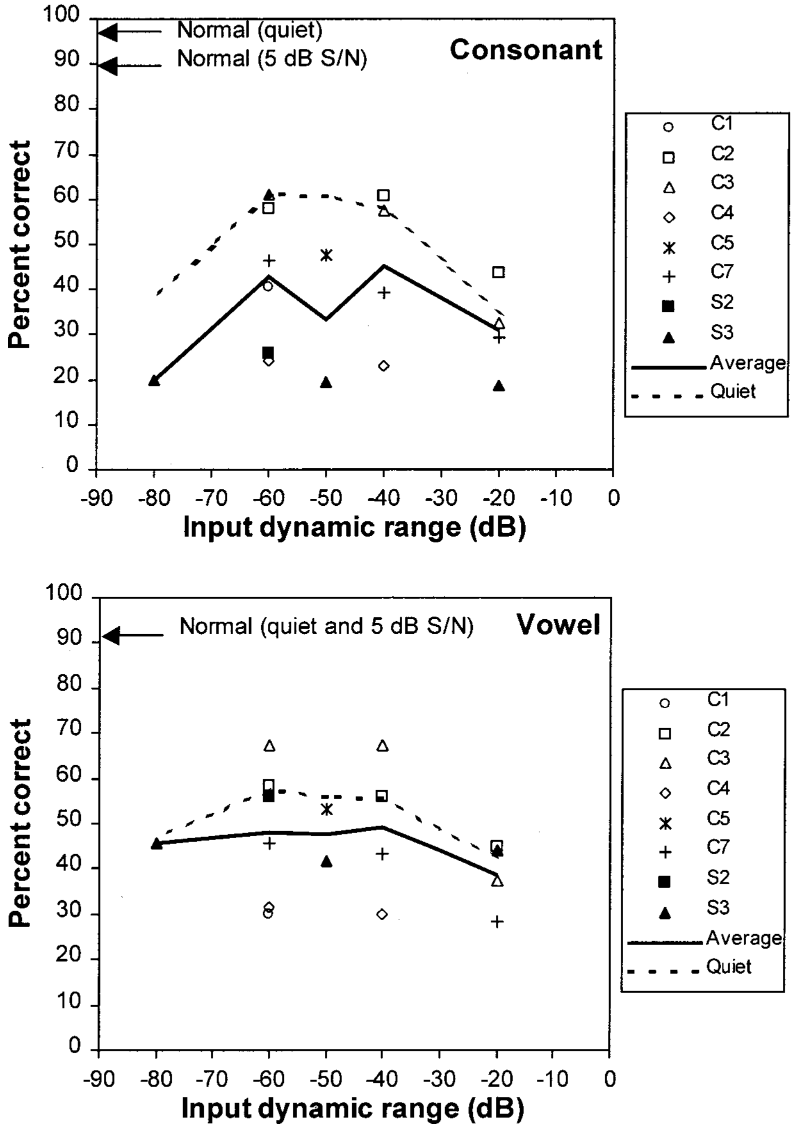

FIG. 5. Consonant (top) and vowel (bottom) recognition scores (y axis) in noise as a function of the input dynamic range (x axis). Individual data are represented by symbols (unfilled symbols for CIS users and filled symbols for SAS users). The solid line represents the average data. For comparison, the correspondent average data in quiet (see the text) are also included (dashed line). Arrow lines represent the average control data from five normal-hearing listeners.

normal-hearing listeners, the average score for consonant recognition was 97% and the score for vowel recognition was 93%. For the implant listeners, the best average score was about 40 percentage points lower than the normal-hearing controls; even the best individual score was still about 15 percentage points lower than the controls.

Average phoneme identification performance can be described by a nonmonotonic function, with best performance occurring at IDRs of −40 to −60 dB and decreased performance at lower and higher IDRs. Individual data showed a similar trend, but the range of performance varied greatly. Individual performance variability ranged between 30 and 45 percentage points for all except the −70- and −80-dB IDR conditions (data were collected in two of the three SAS users but could not be obtained in the CIS users at these IDRs).

A one-way analysis of variance (ANOVA) confirmed that the input dynamic range is a significant factor affecting speech recognition in CLARION cochlear-implant users [consonants: $F(7,36)=6.19$, $p<0.01$; vowels: $F(7,33)=2.79$, $p<0.05$]. A paired t-test indicated no significant difference in consonant recognition between the −50- and the −60-dB IDR conditions ($p>0.05$), but significantly poorer performance for the remaining narrower IDR conditions ($p<0.01$). For vowel recognition, there was no significant difference between −40-, −50-, and −60-dB IDR conditions ($p>0.05$); however, all produced better performance than the −10-, −20-, and −30-dB IDR conditions. No statistical test was conducted between the medium and the −70/−80-dB IDR conditions because of the small number of subjects. The present data suggest that the input dynamic range should be set to 50 dB or greater in order to achieve optimal speech performance in quiet.

D. Phoneme recognition in noise

Figure 5 shows consonant and vowel recognition as a function of input dynamic range for the 5-dB speech-to-noise ratio condition. For comparison, the dashed line shows the averaged data for the previous quiet condition. Because not all subjects were tested for every condition, the averaged data for the quiet condition is shown for only those conditions where corresponding, noise data were available. A paired t-test revealed that noise significantly lowered both consonant ($p<0.001$) and vowel recognition scores (p

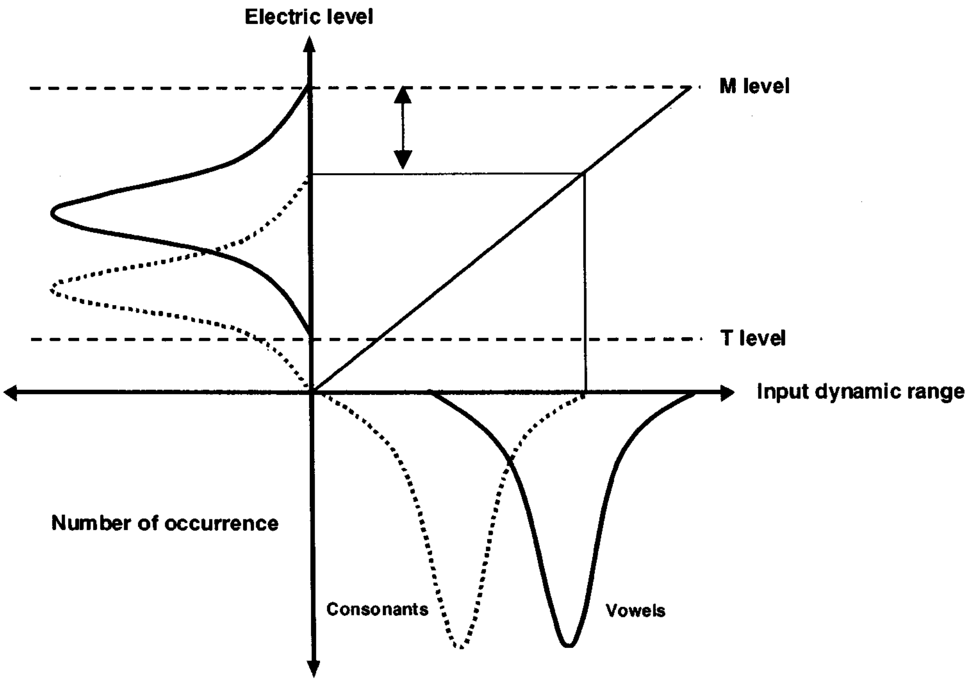

FIG. 6. Effects of envelope level distribution. I. Logarithmic mapping for both consonants and vowels. The right-bottom quadrant shows idealized acoustic envelope level distribution for consonants (dotted line) and vowels (solid line). The right-top quadrant shows the logarithmic acoustic-to-electric conversion. The left-top quadrant shows electric envelope level distribution. Note that a portion of low electric envelope levels is mapped below threshold (*T* level) and also that a portion of electric dynamic range is unused (indicated by the line with double arrowhead).

<0.01). The presence of noise seemed to "flatten" the consonant and vowel recognition functions observed in quiet. This trend is particularly apparent in vowel recognition performance. Average consonant recognition in noise was more degraded by wide IDR settings (a decrease of 20 percentage points for IDRs between -50 and -80 dB) than by narrow IDR settings (merely a decrease of 4 percentage points for the -20-dB IDR setting). CLARION fitting procedures recommend reducing the IDR to aid in noise suppression and to a limited extent, the present results support that recommendation. More detailed assessment of the effect of IDR settings on phoneme recognition in noise is difficult due to the large individual variability as well as the limited data collection in the present study.

IV. DISCUSSION

The present results have both theoretical and practical significance. Theoretically, the acoustic analysis results showed that multitalker phonemes have an approximately 50-dB distribution of envelope levels, which is much wider than the commonly assumed 30-dB speech dynamic range. In the broadband (250–6800 Hz) analysis, the distribution of consonant and vowel envelope levels, particularly the vowel envelope levels, showed a bimodal pattern (top panel in Fig. 2). This bimodal distribution disappeared in the narrow-band analysis (middle and bottom panels in Fig. 2), approximating a normal distribution with different means for different frequency bands. The high-frequency channels had a shifted

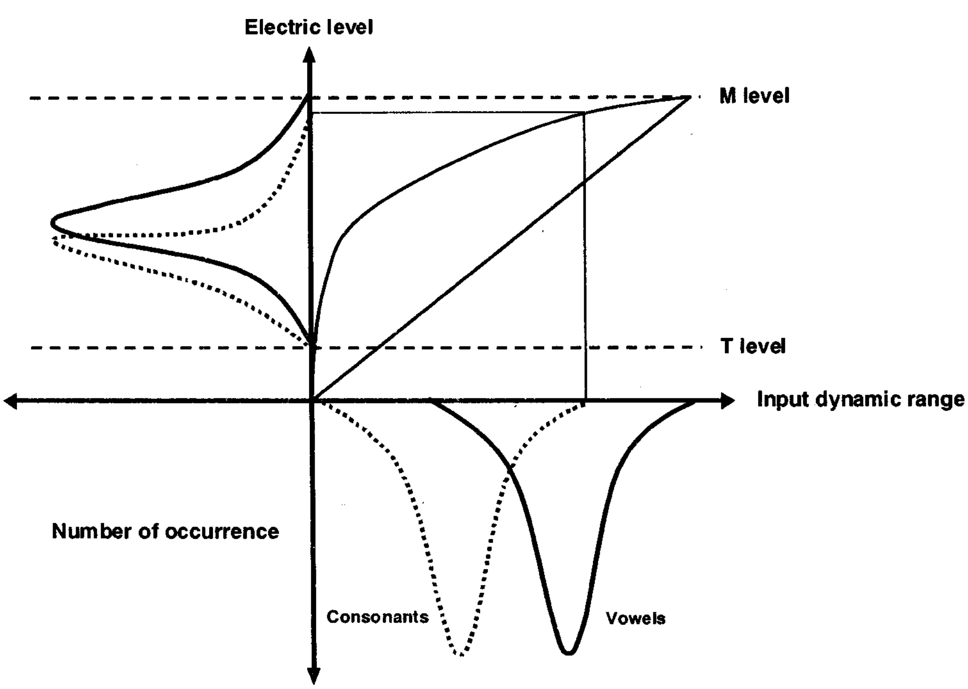

FIG. 7. Effects of envelope level distribution. II. Logarithmic mapping for vowels and more compressive mapping for consonants. The right-bottom quadrant shows idealized acoustic envelope level distribution for consonants (dotted line) and vowels (solid line). The right-top quadrant shows the logarithmic acoustic-to-electric conversion (straight line) for vowels and the more compressive conversion (curved line) for consonants. The left-top quadrant shows electric envelope level distribution. Note the improved use of electric dynamic range for consonants.

distribution towards lower envelope levels than the low-frequency channels. Presumably, the high-frequency channels carry mostly consonant information such as fricatives and stops, while the low-frequency channels carry mostly vowel information. In practical clinical fittings, this difference in envelope level distribution may significantly affect how consonants and vowels should be mapped into an implant user's audible electric range.

Acoustic-to-electric amplitude mapping has been studied extensively in users of auditory brainstem implants (Shannon, Zeng, and Wygonski, 1992), the Med-El/CIS-Link Ineraid devices (Boex *et al.*, 1995; Wilson *et al.*, 1999; Loizou, Poroy, and Dorman, 2000), and the Nucleus devices using either four-channel CIS-type processing (Fu and Shannon, 1998) or the SPEAK strategy (Zeng and Galvin, 1999). A general trend noted in these studies was that a more compressive map would produce better consonant recognition than a less compressive map, while the degree of compression appears to have a small opposite effect, if at all, on vowel recognition (Boex *et al.*, 1995; Zeng and Galvin, 1999). The present acoustic analysis can account for these observations.

Figure 6 shows a case where the acoustic envelope amplitude of both consonants (dotted line) and vowels (solid line) is mapped into the electric level using the same logarithmic function (assuming input dynamic range is in dB and electric level is in microamps). The two horizontal dashed lines represent the electric threshold (*T* level) and the most comfortable loudness (*M* level). Because the consonant envelope distribution was about 20 dB lower than the vowel envelope distribution (Fig. 2 middle and bottom panels), the consonants are likely to be mapped into a less-than-optimal electric range. First, some low envelope levels may be mapped into electric levels below threshold (the lower horizontal dotted line, top-left quadrant). Second, some of the upper portion of the electric dynamic range (indicated by the line with the double arrowhead) may not be utilized because few amplitude envelope levels ($<1\%$) are present. Third, most envelope levels are likely mapped into the lower portion of the electric dynamic range where intensity discrimination and modulation detection are both poor (Nelson *et al.*, 1996; Zeng *et al.*, 1998; Fu, 2000).

On the other hand, if a more compressive map is used for consonants, then all three undesirable effects can be alleviated. Figure 7 shows the same map as in Fig. 6 for vowels but a more compressive map for consonants (the curved line on the right-top quadrant). The compression will raise previously inaudible low envelope levels above threshold, reduce the unused portion of the electric dynamic range, and map more of the envelope into the upper electric dynamic range where intensity discrimination and modulation are optimal. One negative trade-off for the more compressive mapping is the possibility that some low-level noise may become audible. Another negative trade-off is the slightly distorted envelope level distribution (see the mapped consonant envelope distribution in electric domain, left-top quadrant). However, previous results on the effects of changing consonant-to-vowel ratios (Freyman, Nerbonne, and Cote, 1991) and amplitude compression (Souza and Turner, 1996; Van Tasell and Trine, 1996) indicated that this distortion should produce little, if any, decrease in consonant recognition.

Theoretically, under laboratory conditions in which the envelope level distribution for test materials is known, one can optimally set each channel's mapping function based on the mean and standard deviation of the envelope level distribution of that channel. Under realistic listening situations in which speech materials cannot be controlled and real-time processing is required, more compressive mapping for high-frequency channels relative to low-frequency channels will help map the consonant envelope levels into the full electric dynamic range. In other words, cochlear-implant users may achieve better overall speech recognition with a logarithmic map for low-frequency channels and a more compressive map for high-frequency channels. Such implementation is not feasible with the present clinical fitting systems. A future study using a research interface to the cochlear implant is required to implement the different mapping functions for different frequency channels and to evaluate its predicted improvement in speech recognition.

V. CONCLUSIONS

The present study measured the speech dynamic range using 20 consonants and 12 vowels spoken by five female and five male talkers. The present study also measured speech recognition in CLARION implant users as a function of input acoustic dynamic range. The acoustic and perceptual data support the following conclusions:

(1) The speech dynamic range is about 50 dB, much wider than the commonly assumed 30-dB dynamic range.
(2) An input dynamic range of 50–60 dB is required to support optimal speech recognition in cochlear implants.
(3) Current cochlear-implant users may benefit from a new amplitude mapping strategy that uses a logarithmic map for low-frequency channels and a more compressive map for high-frequency channels.

ACKNOWLEDGMENTS

The authors thank Lendra Friesen, Mark Robert, and John Wygonski for help in patient recruiting, speech test, and engineering support, respectively. We also thank Ginger Stickney, Rachel Cruz, Chris Turner, and two anonymous reviewers for comments on the manuscript. This study was supported by National Institutes of Health (Nos. RO1-DC-02267 and N01-DC-92100).

ANSI (**1969**). ANSI S3.5-1969, "American National Standards Methods for the Calculation of the Articulation Index" (American National Standards Institute, New York).

ANSI (**1997**). ANSI S3.5-1997, "American National Standards Methods for the Calculation of the Speech Intelligibility Index" (American National Standards Institute, New York).

Beranek, L. L. (**1947**). "The design of speech communication systems," Proc. Inst. Radio Eng. **35**, 880–890.

Boex, C. S., Pelizzone, M., Piloux, V., and Montandon, P. (**1995**). "Use of loudness scaling measurements to determine compressive mapping in speech processing for cochlear implants," Abstracts of 1995 Conference on Implantable Auditory Prostheses, p. 57.

Boothroyd, A., Erickson, F. N., and Medwetsky, L. (**1994**). "The hearing aid input: A phonemic approach to assessing the spectral distribution of speech," Ear Hear. **6**, 432–442.

Byrne, D., Dillon, H., Tran, K. (**1994**). "An international comparison of long-term average speech spectra," J. Acoust. Soc. Am. **96**, 2108–2120.

Cox, R. M., Matesich, J. S., and Moore, J. N. (**1988**). "Distributions of short-term rms levels in conversational speech," J. Acoust. Soc. Am. **84**, 1100–1104.

Dorman, M. F., Smith, L., Parkin, J. L. (**1993**). "Loudness balance between acoustic and electric stimulation by a patient with a multichannel cochlear implant," Ear Hear. **14**(4), 290–292.

Dunn, H. K., and White, S. D. (**1940**). "Statistical measurements on conversational speech," J. Acoust. Soc. Am. **11**, 278–288.

Eddington, D. K., Dobelle, W. H., Brackmann, D. E., Mladejovsky, D. E., and Parkin, J. L. (**1978**). "Auditory prostheses research with multiple channel intracochlear stimulation in man," Ann. Otol. Rhinol. Laryngol. **87** (Suppl 53), 5–39.

Eddington, D. (**1999**). "Speech Processors for Auditory Prostheses," NIDCD Contract N01-DC-6-2100, Final Progress Report.

Fletcher, H. (**1953**). *Speech and Hearing in Communication* (Van Nostrand, New York), pp. 69–88.

Freyman, R. L., Nerbonne, G. P., and Cote, H. A. (**1991**). "Effect of consonant–vowel ratio modification on amplitude envelope cues for consonant recognition," J. Speech Hear. Res. **34**, 415–426.

Fu, Q.-J. (**2000**). "Auditory temporal resolution and speech performance in cochlear implant users," J. Acoust. Soc. Am. **108**, 2600.

Fu, Q.-J., and Shannon, R. V. (**1998**). "Effects of amplitude nonlinearity on phoneme recognition by cochlear implant users and normal-hearing listeners," J. Acoust. Soc. Am. **104**, 2570–2577.

Fu, Q.-J., and Shannon, R. V. (**1999**). "Effect of acoustic dynamic range on phoneme recognition in quiet and noise by cochlear implant users," J. Acoust. Soc. Am. **106**, L65–70.

Hillenbrand, J., Getty, L. A., Clark, M. J., and Wheeler, K. (**1995**). "Acoustic characteristics of American English vowels," J. Acoust. Soc. Am. **97**, 3099–3111.

Kryter, K. D. (**1962**). "Methods for the calculation and use of the articulation index," J. Acoust. Soc. Am. **34**, 1689–1697.

Loizou, P. C., Dorman, M., and Fitzke, J. (**2000**). "The effect of reduced dynamic range on speech understanding: Implications for patients with cochlear implants," Ear Hear. **21**, 25–31.

Loizou, P. C., Poroy, O., and Dorman, M. (**2000**). "The effect of parametric variations of cochlear implant processors on speech understanding," J. Acoust. Soc. Am. **108**, 790–802.

Nelson, D. A., Schmitz, J. L., Donaldson, G. S., Viemeister, N. F., and Javel, E. (**1996**). "Intensity discrimination as a function of stimulus level with electric stimulation," J. Acoust. Soc. Am. **100**, 2393–2414.

Pavlovic, C. V. (**1993**). "Problems in the prediction of speech recognition performance of normal-hearing and hearing-impaired individuals," in *Acoustical Factors Affecting Hearing Aid Performance*, edited by G. A. Studebaker and I. Hochberg, 2nd ed. (Allyn and Bacon, Boston), pp. 221–234.

Robert, M. E. (**1999**). "CONDOR: Documentation for version 1.3©," House Ear Institute, Los Angeles, CA.

Shannon, R. V., Zeng, F.-G., and Wygonski, J. (**1992**). "Speech recognition using only temporal cues," in *The Auditory Processing of Speech: From Sounds to Words*, edited by M. E. H. Schouten (Mouton de Gruyter, Berlin), pp. 263–274.

Shannon, R. V., Jensvold, A., Padilla, M., Robert, M. E., and Wang, X. (**1999**). "Consonant recordings for speech testing," J. Acoust. Soc. Am. **106**, L71–74.

Skinner, M. W., Holden, L. K., Holden, T. A., Demorest, M. E., and Fourakis, M. S. (**1997**). "Speech recognition at simulated soft, conversational and raised-to-loud vocal efforts by adults with cochlear implants," J. Acoust. Soc. Am. **101**, 3766–3782.

Souza, P. E., and Turner, C. W. (**1996**). "Effect of single-channel compression on temporal speech information," J. Speech Hear. Res. **39**, 901–911.

Stobich, B., Zierhofer, C. M., Hochmair, E. S. (**1999**). "Influence of automatic gain control parameter settings on speech understanding of cochlear implant users employing the continuous interleaved sampling strategy," Ear Hear. **20**(2), 104–116.

Studebaker, G. A., Sherbecoe, R. L., McDaniel, D. M., Gwaltney, C. A. (**1999**). "Monosyllabic word recognition at higher-than-normal speech and noise levels," J. Acoust. Soc. Am. **105**, 2431–2444.

Turner, C. W., Souza, P. E., and Forget, L. N. (**1995**). "Use of temporal envelope cues in speech recognition by normal and hearing-impaired listeners," J. Acoust. Soc. Am. **97**, 2568–2576.

Van Tasell, D. J., and Trine, T. D. (**1996**). "Effects of single-band syllabic amplitude compression on temporal speech information in nonsense syllables and in sentences," J. Speech Hear. Res. **39**, 912–922.

Wilson, B. S., Lawson, D. T., Zerbi, M., and Wolford, R. D. (**1999**). "Speech processors for auditory prostheses," NIH Project NO1-DC-8-2105, Third Quarterly Progress Report.

Zeng, F.-G., and Galvin, J. J. (**1999**). "Amplitude compression and phoneme recognition in cochlear implant listeners," Ear Hear. **20**, 60–74.

Zeng, F.-G., Galvin, J. J., and Zhang, C. Y. (**1998**). "Encoding loudness by electric stimulation of the auditory nerve," NeuroReport **9**, 1845–1848.

Zeng, F.-G., and Shannon, R. V. (**1992**). "Loudness balance between acoustically and electrically stimulated ears," Hear. Res. **60**, 231–235.

Zeng, F.-G., and Shannon, R. V. (**1994**). "Loudness-coding mechanisms inferred from electric stimulation of the human auditory system," Science **264**, 564–566.

Zeng, F.-G., and Shannon, R. V. (**1995**). "Loudness of simple and complex stimuli in electric hearing," Ann. Otol. Rhinol. Laryngol. **104** (Suppl 166), 235–238.

Effects of phoneme class and duration on the acceptability of temporal modifications in speech[a]

Hiroaki Kato[b] and Minoru Tsuzaki[c]
ATR Human Information Processing Research Laboratories, Hikaridai, Seikacho, Kyoto 619-0288, Japan

Yoshinori Sagisaka[d]
ATR Interpreting Telecommunications Research Laboratories, Hikaridai, Seikacho, Kyoto 619-0288, Japan

(Received 3 July 1998; revised 9 July 2000; accepted 19 October 2001)

Human subjective acceptability of durational distortions in speech segments or portions is significantly affected by various segmental and sequential properties, e.g., the vowel color and temporal position in a word [Kato *et al.*, J. Acoust. Soc. Am. **101**, 2311–2322 (1997); **104**, 540–549 (1998)]. The current study focused on the effects of phoneme class and original duration of speech portions in isolated words. In experiment 1, the effect of four classes of phoneme, i.e., vowel, nasal, voiceless fricative, and silent closure, on the acceptable modification range was tested. Six listeners evaluated the temporal acceptability of each of 49 words where one of the steady-state portions was subjected to durational modification from −75 ms (for shortening) to +75 ms (for lengthening) in 7.5-ms steps. The results showed that the listeners' acceptable modification ranges were narrowest for vowels, and widest for voiceless fricatives and silent closures, with nasals in between. The mean acceptable ranges for the least vulnerable phoneme class, i.e., voiceless fricative and silent closure, reached 143% or more of that for the most vulnerable class, i.e., vowel. The observed variation in the acceptable modification range due to the different phoneme class was highly correlated with the inherent loudness in each phoneme class. A larger inherent loudness yielded a narrower acceptable range. Experiment 2 tested the effect of the original, as produced, duration of steady-state speech portions using 30 words where the factors of phoneme class and original duration were designed in a factorial way. The results showed that the original durations affected the listeners' absolute acceptable ranges; the ranges were narrower for shorter original durations. There was a significant interaction between the factors of phoneme class and original duration. The effect of the original duration was larger for vowels than for fricatives. This interaction could be accounted for by the difference in the temporal structure spanning beyond the modified portion itself. [DOI: 10.1121/1.1428543]

PACS numbers: 43.71.Es, 43.72.Ja, 43.70.Fq [JLH]

I. INTRODUCTION

Rules to assign segmental durations have been proposed for speech synthesis to replicate the segmental durations of naturally spoken utterances (Allen *et al.*, 1987; Bartkova and Sorin, 1987; Carlson and Granström, 1986; Campbell, 1992; Fant and Kruckenberg, 1989; Higuchi *et al.*, 1993; Kaiki and Sagisaka, 1992; Klatt, 1979; van Santen, 1994; Takeda *et al.*, 1989). The segmental durations provided by these rules generally have a certain amount of difference from the corresponding, naturally spoken durations. The effectiveness of a durational rule should be evaluated by how much such a difference is perceptually salient. With almost all previous rules, however, the average of the absolute difference, or error, of each segmental duration from its reference had been adopted as the measure of any objective evaluation.

In previous studies (Kato *et al.*, 1997, 1998), we pointed out a possible problem with this measure, i.e., it gives every segment the same weighting in evaluating errors. That is, it neglects the following factors which possibly affect the perceptual sensitivity to segmental durations: (1) interactions among errors in different segments, and (2) variations in segment attributes and phonemic contexts. Kato *et al.* (1997) examined the first factor and demonstrated that two durational errors occurring in consecutive vowel (V) and consonant (C) segments can be perceptually compensated by each other. Following that, Kato *et al.* (1998) focused on the second factor and revealed that perceptual sensitivity to durational errors is affected by a segment's temporal position in a word, its vowel quality, and the voicing of the following segments. This second study, however, tested only phonemically short vowels in words consisting of an open and light syllable succession, i.e., CVCVCVCV. The current study, therefore, continues the investigation of the second factor and expands the variety of segments or speech portions to be tested in the following two aspects: (1) phoneme class—consonantal classes are included in addition to the vowel

[a]Part of this work was done when the first author was also with the Graduate School of Science and Technology, Kobe University, and presented at the Fifth International Conference on Spoken Language Processing in Sydney, November, 1998.

[b]Current address: ATR Human Information Science Laboratories, Hikaridai, Seikacho, Kyoto 619-0288, Japan. Electronic mail: kato@atc.co.jp

[c]Current address: ATR Spoken Language Translation Research Laboratories, Hikaridai, Seikacho, Kyoto 619-0288, Japan.

[d]Current address: Graduate School of Global Information and Telecommunication Studies, Waseda University, Nishi-Waseda, Shinjuku, Tokyo 169-0051, Japan.

class, and (2) duration—phonemically long portions are included in addition to short vowels.

A. Influence of phoneme class on temporal sensitivity

Typical examples of the dependency of temporal sensitivity on the phoneme class can be found when comparing durational discriminability between vowel and consonant segments. Both Huggins (1972) and Carlson and Granström (1975) reported that the just noticeable differences (jnd's) for segmental durations are smaller for vowels than for consonants. Huggins manipulated the duration of a vowel /ɔ/ or a consonant /m, l, p, or ʃ/ embedded in a naturally spoken sentence, and asked his listeners to judge whether it was "normal," "too long," or "too short." The listeners were more sensitive to changes in the vowel duration than to changes in the consonant duration. Carlson and Granström employed a discrimination task for the differences in the duration of a vowel /a/ or a consonants /m, s, or t/ in isolated words, and found that their listeners' discriminability was remarkably higher for the vowel duration than for the consonant duration. Similarly, Bochner *et al.* (1988) reported that their listeners demonstrated greater acuity for changes in the durations of vowels (/i, ɪ, u, ʊ, a, ʌ/) than consonants (/p, t, k/).

The results of a study by Fujisaki *et al.* (1975), however, appear to contradict these three studies. Fujisaki *et al.* reported that durational jnd's are almost equal for all phoneme classes, regardless of whether they are vowels, nasals, voiceless fricatives, or silent closures. However, their task of the listeners in experiments was to judge the phonemic contrast depending on the segmental duration. This categorical judgment can obscure any potential effect of a difference in the phoneme class (Carlson and Cranström, 1975, commentary section). To summarize, therefore, previous studies suggested a general tendency of durational jnd's being shorter for vowels than for consonants, except in particular cases like when durational changes supply phonemic contrasts.

Although jnd's are precisely defined in the psychophysical sense, "acceptability" can be considered as another practical (and more direct) measure in the evaluation of durational rules. This "acceptability" measure, however, has rarely been investigated, except for several pioneering studies (Carlson and Granström, 1975; Sato, 1977; Sagisaka and Tohkura, 1984; Hoshino and Fujisaki, 1983). Carlson and Granström made compensatory temporal modifications on a vowel–consonant pair /as/ and on two consonants /st/ in a word *plasta* (to cover something with plastic). The listeners evaluated the acceptability of each modification on a scale from zero ("acceptable") to ten ("not acceptable"). The results showed that the acceptable ranges were narrower when the modifications included a vowel segment. The results therefore suggest that the durational change in the vowel influenced the acceptability more than that in the consonants. However, no direct comparisons were provided between the vowel and consonant segments. Neither did Sato's nor Sagisaka *et al.*'s study compare the effects between vowels and consonants. Hoshino *et al.*, in contrast, did measure the acceptability of the modifications in vowels and consonants separately, but they did not address the difference between vowels and consonants.

In summary, no direct experimental data exist showing the difference between vowels and consonants in evaluating the acceptability of durational changes. In particular, there seems to be no comparative study on the effect of different consonants, whereas the influence of different vowel qualities on the evaluation of acceptability has been investigated (Kato *et al.*, 1998). The first objective of the current study is, therefore, to provide a direct comparison among phoneme classes in terms of the acceptability of durational modifications. Four phoneme classes were chosen, i.e., vowel, nasal, voiceless fricative, and silence (silent closure).[1]

B. Influence of the original duration on temporal sensitivity

The current study also provides a comparison among different temporal properties of speech portions. The independent temporal variable to be tested is the duration of a speech portion that is acoustically continuous and, therefore, phonetically inseparable. In what follows, we refer to this portion as the "continuous portion" and to its duration as the "continuous duration."[2] This continuous portion starts with a segmental boundary and ends with either a segmental boundary or the end of the closure term in a stop articulation. It mostly coincides with a segment itself (e.g., a vowel or fricative) or a part of a segment (e.g., the closure of a stop), but it may span over linguistic (phonological and/or phonemic) boundaries. For instance, a geminate fricative as a whole is a continuous portion because it is phonetically inseparable; nevertheless, it can be phonologically separated into two parts by a syllabic boundary.

In a previous study, Kato *et al.* (1998) did not find any influence of the original duration or continuous duration on the perceptual sensitivity to durational modifications. However, all of their stimuli were taken from words having a homogeneous temporal structure (CVCVCVCV) and, therefore, the temporal variations of the tested portions were limited. The current study, in addition to using CV-syllable words, also uses words including much longer continuous portions, such as geminate obstruents and phonemically long vowels, and, naturally, there is a wide diversity in the stimulus duration. If a listener's acceptability judgment is based on the perceived distortion or temporal modification, and the temporal sensitivity roughly conforms to Weber's law, i.e., proportional to the base duration, then a wider variation of the base duration should show the perceptual effect as more salient. That is, the second objective of the current study is to reexamine the influence of the original duration on the acceptability of durational modifications using a sufficient variation of stimulus durations.

One should note that the duration of a continuous portion can also be described by discrete or linguistic measures, i.e., lengths of sounds quantized in terms of linguistic contrasts (e.g., the mora counting), instead of the continuous measure, i.e., the acoustic duration in milliseconds. Linguistic durations, however, are not always proportional to the corresponding acoustic durations, and even linguistic measures themselves are sometimes subject to controversy.

Therefore, it is difficult to control both continuous (acoustic) and discrete (linguistic) duration measures simultaneously in designing experimental conditions. In the current two experiments, we controlled the stimulus duration so as to have coherency in terms of the acoustic measure. This allowed us to estimate the extent of the accountability of psychoacoustical (i.e., non-language-specific) factors. Such an auditory-based approach has a potential advantage in providing perceptually valid notions that can be generalized across languages. Note, however, that we do not discard the notion of discrete or linguistic duration measures but supply an extensive discussion including them later in the general discussion section.

II. EXPERIMENT 1: EFFECT OF PHONEME CLASS

Experiment 1 aimed to test the dependency of acceptability evaluations for durational modifications on the difference in phoneme class.

A. Method

1. Material

The following four phoneme classes were chosen from among those tested in previous jnd studies: (1) vowel, (2) nasal, (3) voiceless fricative, and (4) silence (voiceless stop). To make our listeners focus on the temporal aspect of the material as much as possible, we chose test portions from among candidates whose durations were long enough, i.e., the phonemic quality of the test portions would not suffer from temporal manipulations over a reasonably wide range. If any phonemic quality changed, the listeners' judgments could no longer rely on a single criterion, i.e., the temporal cue. In these respects, the following groups of speech portions were employed for each of the phoneme classes tested.

(1) Vowels: Phonemically short /a/ vowels were used. The Japanese language has five vowels /a, i, u, e, o/ each of which has short and long phonemically contrastive variations. The short /a/ vowel has a relatively long inherent duration along with the short /e/ and /o/ in comparison with the short /i/ or /u/ (Sagisaka and Tohkura, 1984) and, therefore, can provide a sufficient durational margin for manipulation.

(2) Nasals and (3) voiceless fricatives: Since consonants in Japanese CV moras are usually shorter than those in the languages used in previous studies (e.g., English), it is difficult to manipulate their durations over a sufficient range to examine the temporal acceptability. For a shortening manipulation in particular, listeners possibly perceive a phonemic shift or an unusual articulation at the manipulated part, and then, they are no longer able to judge the acceptability of the stimulus word from the temporal aspect alone. Therefore, syllabic or moraic nasals and continuous portions including devoiced vowels[3] were chosen for the nasal and voiceless fricative classes, respectively. They are generally longer than regular (within-CV) nasal and fricative segments and provide sufficient consonantal durations comparable to those tested in previous studies. A moraic nasal (as in *Honda*) has the same phonological status as the CV-mora and has a comparable acoustic duration with a short vowel /a/. A devoiced vowel (as in *Hi̥tachi*) usually has a voiceless fricative quality like [ɸ], [s], [ʃ], [ç], [x], and [h]. When the preceding consonant is a voiceless fricative, a devoiced vowel continues from it, keeping the same phonetic quality. Note that the tested continuous portions were chosen from such concatenated pairs of a devoiced vowel and an adjacent voiceless fricative. In what follows, the term "devoiced vowel portion" refers to this concatenated, but continuous, voiceless fricative portion. A devoiced vowel portion, therefore, also has the same phonological status as the CV-mora and has a comparable acoustic duration with a short vowel /a/.

(4) Silence: The silent targets were chosen from the closures of geminate voiceless stops /pp, tt, kk/ (as in *Sapporo*) which have considerably longer silent closures than their single counterparts.

In addition to these four groups of speech portions, we included a fifth group of test portions, i.e., geminate fricatives. While the acoustic durations of vowels /a/, moraic nasals, and devoiced vowel portions are comparable with each other, those of silent closures in geminate stops are generally longer than the other three (150% or more). This means that there might be another explanatory variable, i.e., the base duration, in addition to the primary explanatory variable, i.e., the phoneme class. The geminate fricative /ss/ (as in *Nissan*) was, therefore, chosen as the fifth group to probe the influence of the base duration. The duration of the geminate fricative /ss/ is, in general, comparable with those of the longer test portions, i.e., silent closures in geminate stops, and its phoneme class matches one of those of the shorter three groups, i.e., voiceless fricatives.

2. Stimulus manipulation

The speech database from which the original material was taken and the method of stimulus manipulation were the same as those in our earlier papers (Kato *et al.*, 1997, 1998). Forty-nine words were selected from the ATR speech database (Kurematsu *et al.*, 1990). All of them are commonly used four-mora Japanese words.[4] To prevent any influence from the variety of lexical accent patterns[5] as much as possible, all of the tested words had the same accent pattern (low–high–high) at the first, second, and third moraic positions. The selected words were spoken naturally in isolation by one male speaker of Tokyo Japanese, a major dialect of Japanese, and were digitized at a 12-kHz sampling frequency with 16-bit precision.

The continuous portions whose durations were subjected to modifications ("target portions") were chosen from the second moraic position in the words. This positional condition was introduced to prevent the influence of the temporal position in the word on the acceptability evaluation, which was reported in a previous study (Kato *et al.*, 1998), as much as possible. Each duration of these target portions was manually measured from the spectrographic images of the original materials by professional phoneticians. The 49 selected tokens are listed in the Appendix (Table IV) with the phoneme class and measured continuous duration of each of the target portions. Table I summarizes the number of target portions and the average and standard deviations of the continuous durations for each of the stimulus groups.

The temporal modifications were made by a cepstral analysis and resynthesis technique with the log magnitude

TABLE I. The number of selected continuous portions for each of the stimulus groups in experiment 1, and the averages and standard deviations of their acoustic durations.

	Stimulus group					
	Short vowel	Moraic nasal	Devoiced vowel portion	Geminate stop	Geminate fricative	Total
No. of samples	10	14	11	7	7	49
Phoneme class	vowel	nasal	voiceless fricative	silence	voiceless fricative	
Average duration (ms)	115.5	121.6	113.0	192.9	224.3	
s.d. of durations (ms)	11.6	30.8	15.8	18.6	29.2	

approximation (LMA) filter (Imai and Kitamura, 1978), and were carried out at 2.5-ms frame intervals. The duration change was achieved by deleting or doubling every nth frame in the synthesis parameters throughout the target portion, where $(n-1)$ is the quotient of the total number of frames in the target divided by the number of frames to be deleted /doubled. The target portions were carefully trimmed out so as to exclude transient parts at both ends of the vowels and the on-and-after burst parts of plosives or affricates as much as possible, to prevent the modification of dynamic aspects around the phoneme boundaries which could conceivably have degraded the perceptual naturalness. Each of the target portions was shortened or lengthened over a range from -75 ms to $+75$ ms from the original duration in 7.5-ms steps, resulting in 20 different modification steps. Preliminary listening to all of the manipulated stimuli assured us that no phonemic shift had occurred in either the target portions or the surrounding phonemes. All of the stimuli were produced by a computer (SPARC Station 10, Sun Microsystems) at a 12-kHz sampling frequency with 16-bit precision. In total, 1029 word stimuli were prepared, i.e., (20 modification steps $+$ 1 unmodified) $\times$ 49 portions.

3. Procedure

The experimental procedure was the same as that in a previous study (Kato *et al.*, 1998). The stimuli were randomized and recorded onto a digital audiotape (DAT) through a D/A converter (MD-8000 mkII, PAVEC) and an anti-aliasing low-pass filter (FV-665, NF Electronic Instruments, $f_c = 5700$ Hz, -96 dB/oct) with a DAT recorder (DTC-55ES, SONY), and then presented diotically to the subjects through headphones (SR-Λ Professional, driven by SRM-1 MkII, STAX). A 4-s interval was inserted after each presentation for the subjects' response. The average presentation level was 73 dB SPL (A-weighted) measured with a sound level meter (Type 2231, Brüel & Kjær) through a condenser microphone (Type 4134, Brüel & Kjær) mounted on an artificial ear (Type 4153, Brüel & Kjær). The experiments were done in a sound-treated room whose average background noise level was 16 dB SPL (A-weighted), which was measured at the location of the subject with a sound level meter (Type 2231, Brüel & Kjær) and a condenser microphone (Type 4155, Brüel & Kjær).

The subjects were told that each stimulus word was possibly subjected to a temporal modification. Their task was to evaluate how acceptable each stimulus was as an exemplar of the token of that stimulus, using a seven-point rating scale ranging from -3 to 3, where -3 corresponded to "quite acceptable" and 3 corresponded to "unacceptable."[6] The subjects were asked to respond regarding only the temporal aspect of the stimuli as much as possible.

A total experimental run for each subject comprised of seven sessions. Seven of the 49 tokens were chosen for each session, and four repetitions of their 21 modified versions were randomly presented in the session. Therefore, each subject evaluated each stimulus four times in total. The seven tokens within a session were chosen from all of the five stimulus groups.

4. Subjects

Six adults with normal hearing participated in experiment 1. All of them were native speakers of Japanese.

B. Results

1. Measure of acceptability

The acceptability measure, referred to as the "vulnerability index," was the same as that used in a previous study (Kato *et al.*, 1998) to maintain consistency among the studies. To compute the vulnerability index, we first plotted the listeners' evaluation scores against the change in duration of the portion in question, and then a parabolic regression method as generally formulated below was applied to the plot,[7]

$$\text{Evaluation score} = \alpha(\Delta T - \beta)^2 + \gamma, \tag{1}$$

where ΔT denotes the change in duration; the unit of ΔT is not the relative duration but milliseconds. This regression was the best fitted polynomial function to the plot on the basis of the F-ratio criterion [$F(2,6171) = 1408.0$, $p < 0.0001$] (e.g., McCall, 1980). The coefficient of the second-order term or α of this parabolic curve was taken as the "vulnerability index," the objective variable of this study. This coefficient shows the rate of change in the evaluation score with a change in the durational modification; both the horizontal and vertical response biases can be separated out as β and γ. As shown in Eq. (1), α corresponds to the decrement[8] of the acceptability against a certain size of a temporal modification, and also to the width between the longer and shorter limits of the temporal modification, which yields a certain amount of acceptability decrement, i.e., an acceptable range. Therefore, α represents the vulnerability of a given continuous portion from the temporal modification. Figure 1 shows typical examples of individual fittings illus-

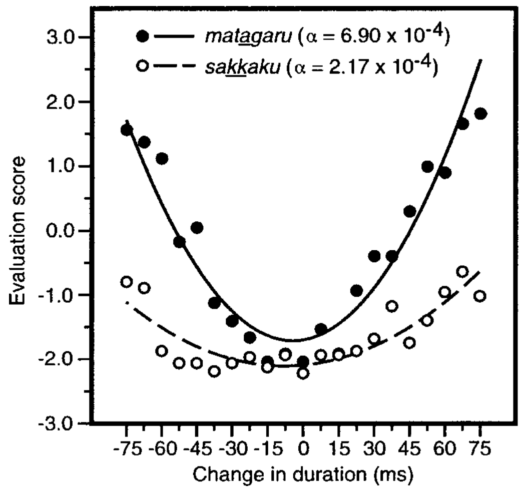

FIG. 1. An example illustrating a difference in acceptability-change between two different speech portions. The portions subjected to durational modification are marked with underlines in the legend. The scatter plots show that the evaluation score varies according to the durational change more drastically for the second vowel of the word "*matagaru* (to ride)" (filled circles) than for the silent closure of the geminate stop consonant in the word "*sakkaku* (illusion)" (open circles). The two regression curves trace this tendency. These are formulated as $y=0.000\,690(x+4.61)^2-1.71$ (solid line), and $y=0.000\,217(x+7.63)^2-2.10$ (dashed line).

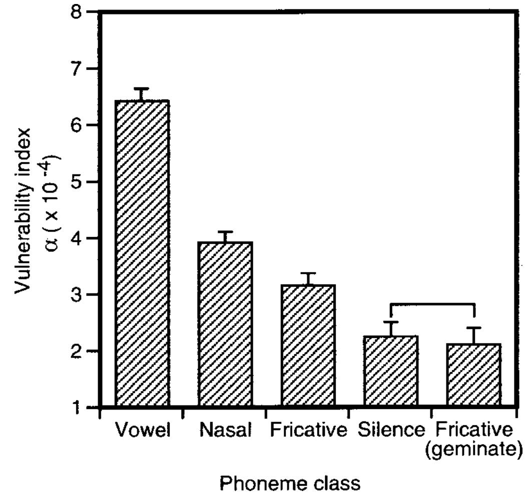

FIG. 2. The least squares means of the vulnerability index (α), i.e., the second-order polynomial coefficient of the fitting curve, for each phoneme class tested in experiment 1; they were calculated in the ANOVA procedure. A larger α implies a narrower acceptable range. The error bars show the standard errors. The difference between the two bridged bars is not statistically significant.

trating the difference in the acceptability change between two different target portions.

We applied a parabolic fitting to the evaluation scores for each of the 49 target portions per each of the six subjects, obtaining 294 fitting curves. Prior to the statistical analyses, we dropped unreliable data (fitting curves) on the basis of two criteria: (1) When α was not positive the fitting curve was dropped, because this suggests that the subject probably sensed no durational change for that particular token. (2) When the axis was extremely remote (more than six times sigma) from the distribution center of the entire data the fitting curve was dropped. In all, seven fitting curves were excluded, i.e., five eliminations by the first criterion, one elimination by the second, and one elimination by both criteria. Therefore, the dependent variable of experiment 1 consisted of 287 α scores.

2. Effect tests

The effect of *phoneme class* on the vulnerability index (α) was tested by a one-way ANOVA of repeated measures with *subject* as the blocking factor. The effect of *phoneme class* was found to be significant [$F(4,20)=53.1$, $p<0.001$]. As shown in Fig. 2, α was greatest for the vowels, next for the nasals, third for the fricatives, and smallest for the silent closures and fricatives in geminate consonants. Multiple comparisons among these average α's using Tukey–Kramer's HSD (the honestly significant difference) (SAS Institute, Inc., 1990) indicated the difference between any two average α's to be significant [$p<0.01$], except for the difference between the average α's of the geminate fricative and silence groups.

The averaged α score of the most vulnerable (i.e., susceptible to durational modifications) phoneme class, i.e., the vowel, became more than twice that of the least vulnerable class, i.e., the voiceless fricative or silence. This means that the least vulnerable phoneme class required more than 143% of the temporal modification of the most vulnerable class to yield the same acceptability decrement.

C. Discussion

The primary objective of the current study was to examine whether the acceptability for temporal modifications of continuous portions is affected by the phoneme class of modified portions. The results of experiment 1 showed significant effects due to the difference in the phoneme class. The listeners evaluated the temporal modifications of vowels as less acceptable than those of consonant portions regardless of whether they were nasals, voiceless fricatives, or silent closures. This tendency is in agreement with that predicted from literatures on jnd's for vowel and consonant durations in English or Swedish (Bochner *et al.*, 1988; Carlson and Granström, 1975; Huggins, 1972). In addition, the current experiment revealed nasals to be different from voiceless fricatives or silent closures.

To pursue a single variable that totally accounts for the observed relationship between the phoneme class and temporal sensitivity, we performed a loudness analysis[9] on the target speech of experiment 1. This was mainly because a previous study reported that the acceptability of modifications in a vowel duration correlates with the loudness inherent in each vowel quality (Kato *et al.*, 1998).

To estimate the inherent loudness for each phoneme class, we first calculated the loudness contour for each of the 49 target portions every 2.5 ms with a 30-ms rectangular window, in accordance with ISO 532 method B (ISO, 1975) assuming the diffuse field, using Zwicker *et al.*'s (1991) algorithm. Then, we picked out the median value from the entire loudness contour of each of the target portions as the representative loudness of that portion. Figure 3 shows these representative loudness values pooled for each phoneme

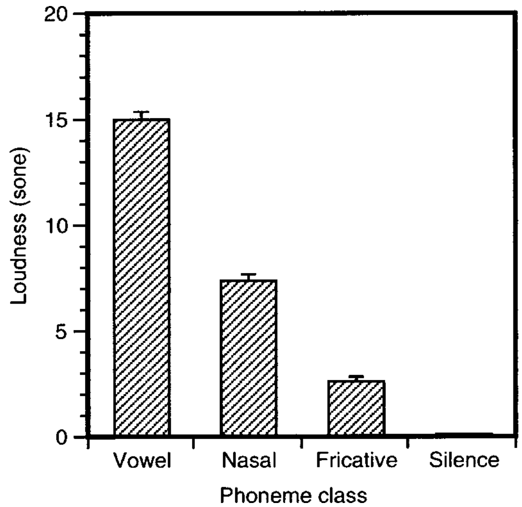

FIG. 3. The average loudness of the speech portions whose durations were subjected to temporal modification in experiment 1, as a function of the phoneme class. For the *silence* class, the background noise level was adopted. The error bars show the standard errors.

class. Multiple comparisons among the phoneme classes using Tukey–Kramer's HSD clearly indicated the difference between any pair of pooled loudness values as significant [$p<0.001$]. In fact, these loudness values, i.e., the estimated inherent loudness values, highly correlated with the phoneme class ($r=0.979$).

Furthermore, interestingly, the order of the phoneme classes by these loudness values was identical with that by the vulnerability indices (compare Figs. 2 and 3) except for the relation between the voiceless fricatives and silence. Therefore, these loudness values also have to correlate with the vulnerability index (α). The Pearson product-moment correlation coefficient (r) between the representative loudness and the α score based on the 49 target portions was 0.889. This high accountability of the loudness for the vulnerability index was comparable with that of the phoneme class where r was 0.888.

On the other hand, some results could not be accounted for by the factor of *phoneme class* or the inherent loudness. A significant difference was observed between the average α's of the devoiced vowel portions and geminate stops; these two stimulus groups differed from each other in both the phoneme class and the original duration. The difference between the average α's of the geminate stops and the geminate fricatives was, on the other hand, not significant; these two stimulus groups only differed in the phoneme class. Therefore, the difference of the average α's between the devoiced vowel portions and the geminate stops is more likely due to their difference in the original duration than to their difference in the phoneme class.

A problem now arises. If the difference between the α's of the devoiced vowel portions and the geminate stops is due to their durational differences, a similar durational effect should be observed in any phoneme class including the vowels. However, such an effect of the original duration was not observed in a previous study (Kato *et al.*, 1998) which measured α scores for vowel segments using the same procedures as those of the current study. Note, however, that the stimulus condition of the previous study differed from those of the current experiments. The previous study used only short vowels in a homogeneous syllable context, i.e., CVCVCVCV, and therefore the durational variation of the target segments was limited to a shorter range (less than 150 ms) than that used in the current study (87.5–220 ms). Experiment 2 was, therefore, designed to examine whether the effect of the original duration would be generally observed for similarly ranging portions as those of experiment 1, irrespective of differences in the phoneme class.

III. EXPERIMENT 2: EFFECT OF THE ORIGINAL DURATION

Experiment 2 systematically examined the effect of the original continuous duration on the acceptability of temporal modification in a given portion using two phoneme classes, i.e., vowel and voiceless fricative.

A. Method

1. Design

A two-way factorial design was applied. The first factor was the *phoneme class* of a continuous portion subjected to temporal modification. There were two levels in this factor, i.e., vowel and voiceless fricative. The second factor was the *original duration* of the portion in question. There were also two levels in this factor, i.e., short and long. The target portions for the short and long levels in the vowel class were chosen from phonemically short and long vowels, respectively. Those for the short and long levels in the voiceless fricative class were chosen from devoiced vowel portions and geminate obstruents, respectively. Other phoneme classes, e.g., nasal or silence, are unlikely to provide a comparable extent of durational variations in Japanese speech.

2. Material and procedure

Thirty four-mora Japanese words were selected as the original materials from the same database as in experiment 1. The target portions included ten short and ten long vowels, and five short and five long voiceless fricatives. The vowel quality of the vowel target portions was either /a/ or /o/. Five phonemically short /a/ materials were taken from among those used in experiment 1 in accordance with a criterion, i.e., that their α scores had been the five nearest to the median within that stimulus group. Five phonemically short /o/ materials were also chosen. For the long vowel materials, three phonemically long /a/ and seven phonemically long /o/ materials were chosen, i.e., ten /a:/ and /o:/ portions in total. The reason why the stimuli were taken from other vowels than /a/ vowels was that the source speech database did not include a sufficient number of long /a/ materials. A phonemically long /a/ is not lexically so frequent in Japanese. The vowel quality /o/ was chosen as a substitute because its inherent loudness, which has been suggested to affect the temporal acceptability (Kato *et al.*, 1998), is the closest to the inherent loudness of vowel quality /a/ among the four other vowel qualities in Japanese.

The original materials for the voiceless fricatives were a subset of those used in experiment 1. Five devoiced vowel

TABLE II. The number of selected continuous portions for each of the stimulus groups in experiment 2, and the averages and standard deviations of their acoustic durations.

	Stimulus group				
	Short vowel	Long vowel	Short fricative (Devoiced vowel portion)	Long fricative (Geminate fricative)	Total
No. of samples	10	10	5	5	30
Phoneme class	vowel	vowel	voiceless fricative	voiceless fricative	
Duration category	short	long	short	long	
Average duration (ms)	115.5	251.8	125.0	219.0	
s.d. of durations (ms)	11.0	25.7	17.7	17.1	

portions and five geminate fricatives were taken according to the same criterion as the short /a/ case previously mentioned. To reduce the size of the experiment and prevent subjects from unnecessary strain, a smaller number of tokens were taken for the fricative groups (five per group) than for the vowel groups. Relatively stable responses had been expected for the fricative groups because their tests were replications of those in experiment 1. The 30 selected tokens are listed in the Appendix (Table V). Table II summarizes the number of target portions and the average and standard deviation of the continuous durations for each of the stimulus groups.

The speaker of the original materials, the recording procedure, the manipulation method, and the procedure for the experimental run were the same as those in experiment 1.

3. Subjects

Nine adults with normal hearing participated in experiment 2. All of them were native speakers of Japanese. None of them participated in experiment 1.

B. Results

In accordance with the same procedures as in experiment 1, the vulnerability index (α score) was computed for each of the 30 target portions and each of the nine subjects, resulting in 270 α's. A two-way factorial ANOVA of repeated measures was performed with *phoneme class* and *original duration* as the main factors, and with *subject* as the blocking factor. The main effects of *phoneme class* and *original duration* were significant [$F(1,8)=51.9$, $p<0.0001$; $F(1,8)=67.0$, $p<0.0001$, respectively]. As shown in Fig. 4, α was greater for the vowels than for the voiceless fricatives, and similarly greater for the short targets than for the long targets. There was a significant interaction between both main factors (i.e., *phoneme class* and *original duration*) [$F(1,8)=14.7$, $p<0.005$]; the effect of *original duration* was larger for the vowels than for the voiceless fricatives. Multiple comparisons among the average α's of four stimulus groups using Tukey–Kramer's HSD (SAS Institute, Inc., 1990) indicated the difference between any two average α's to be significant [$p<0.05$], except for the difference between the α's of the long vowel and short voiceless fricative (devoiced vowel) portions.

C. Discussion

The objective of experiment 2 was to examine the effect of the original continuous duration on the acceptability of temporal modification under a systematic condition in which the factors of *original duration* and *phoneme class* were included in a factorial way. The effect of the phoneme class (similar to that observed in experiment 1) was replicated in experiment 2. The effect of the original duration for the voiceless fricatives was also replicated. The original duration was also found to affect the temporal vulnerability of vowels. A larger vulnerability index, i.e., a narrower acceptable modification range, was yielded for portions having a shorter original duration.

This tendency seems to be reasonable in the light of a general psychophysical law, i.e., Weber's law. Conforming to this law, a larger physical change is necessary for a longer base duration, i.e., the original continuous duration, to yield the same amount of perceived change. Note, however, that the acceptable range of a target portion, which is derived from α, is not exactly proportional to the corresponding original continuous duration, although they positively correlate with each other. The ratio of two acceptable ranges is considerably smaller than that of the corresponding original durations.

Experiment 2 also showed that there is a significant interaction between the factors of *phoneme class* and *original duration*. The effect of the original duration was larger for the vowels than for the voiceless fricatives. As seen in Table II, the difference in the average acoustic duration between

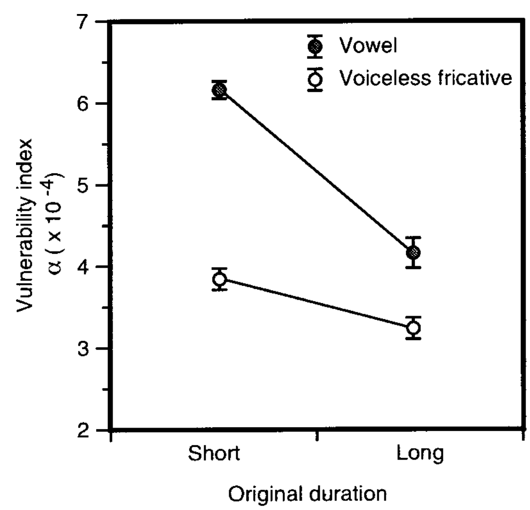

FIG. 4. The least squares means of the vulnerability index (α), i.e., the second-order polynomial coefficient of the fitting curve, for each stimulus group tested in experiment 2; they were calculated in the ANOVA procedure. A larger α implies a narrower acceptable range. The error bars show the standard errors.

the "short" and "long" groups is slightly larger for the vowel class. Nevertheless, the durational contrast in the vowel groups is not sufficiently larger than that in the voiceless fricative groups to account for the observed interaction on the basis of Weber's Law. An alternative source, therefore, should be taken into account for this interaction. Candidates of such a source are extensively discussed in the following section along with a further implication of the effect of the phoneme class.

IV. GENERAL DISCUSSION

This section tried to relate the acceptability measure, a perceptual measure of changes in phonetic durations, to measures of human sensitivity against changes in nonspeech durations. We thought it necessary to include this psychophysical discussion because it is important to estimate the extent to which conclusions and predictions based on the current study may be generalized. If they are psychophysically accountable, then we can infer what should happen in unknown languages or, e.g., other phoneme classes that have not been actually tested.

A. Effect of phoneme class

Differences in the phoneme class affected the acceptability of the durational modification in both experiments 1 and 2. One of the most promising psychoacoustic variables that can account for the effect of the phoneme class is the loudness of each target portion. As shown in Fig. 3, the phoneme class has a linear relation with the inherent loudness (the Pearson product-moment correlation coefficient $r=0.979$). Furthermore, the loudness of each target portion correlates with the vulnerability index (α) of that portion ($r=0.889$), as easily understood by comparing Fig. 3 with Fig. 2. This high accountability of the loudness for the vulnerability index is comparable with that of the phoneme class ($r=0.888$).

These facts suggest that the loudness measure can be a good index to predict differences in the temporal vulnerability of speech portions due to differences in the phoneme class. However, one should not generalize this accountability to any phoneme class other than those tested in the current study before confirming the psychophysical validity of the correlation between the stimulus loudness and the acceptability evaluation. We, therefore, tried to validate it according to the following two steps: the first step examined the correlation between acceptability and temporal sensitivity, and the second step examined the correlation between temporal sensitivity and loudness.

The first correlation seems to be plausible because the evaluation of the acceptability has to be based on the distortion that listeners had detected, that is, the durational jnd determines the baseline of the acceptable range. To support this notion, there are at least two examples showing the correlation in question. First, the influence of the phoneme class found in previous jnd studies (Bochner *et al.*, 1988; Carlson and Granström, 1975; Huggins, 1972) is generally in agreement with that of the current acceptability study; i.e., the listeners respond more sensitively to modifications in vowels than to those in consonants. Second, although the number of word tokens was not large, a correlation has been reported between the vulnerability index (α) and durational jnd as a result of a direct comparison using the same speech materials and the same listeners (Kato *et al.*, 1992).

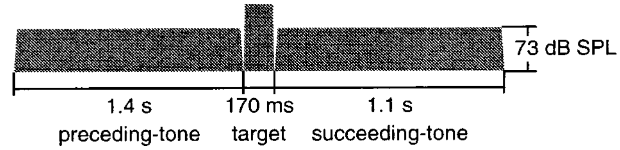

FIG. 5. Schematic examples showing the amplitudes of stimulus sequences used in the temporal discrimination test in Kato and Tsuzaki (1994). The horizontal and vertical axes refer to the time and level, respectively. All stimuli were 1-kHz tones. The level of the target portion was either 79, 76, 70, 67, 55 dB SPL, or silence. [Reproduced from Kato and Tsuzaki (1994).]

As for the second correlation, little evidence seems to be given by literature. Quantitative models dealing with the auditory acuity of filled durations, as long as the range of speech segments (about 50–300 ms) has been involved, have not taken into account stimulus loudness or intensity (Allan, 1979; Allan and Kristofferson, 1974). Additionally, experimental data has not appeared to support the relation between duration discrimination and stimulus intensity (Abel, 1972; Henry, 1948; Rammsayer, 1994). In these cases, although some intensity dependency has been observed during target stimulus presentation at an extremely low level (Henry, 1948) or under a low S/N condition (Creelman, 1962), no intensity effect has been found for a clearly audible stimulus.

However, it is important to point out that all of these studies presented the target signals only in isolation, while a segment in speech generally has preceding and/or succeeding other sounds, i.e., adjacent segments. The target portions in experiment 1 were also of the same case, because they were placed at the second moraic position within the four-mora words. Therefore, it appears necessary to examine the intensity effect under the condition that the target signals are temporally flanked by other signals, in addition to the traditional isolated presentation.

There is one example that deals with auditory temporal sensitivity under the stimulus conditions previously mentioned. Kato and Tsuzaki (1994) demonstrated the intensity effect on temporal discriminability for auditory durations surrounded by other sounds. Their stimuli were 1-kHz pure tones having an amplitude contour as shown in Fig. 5. The level of the target part whose duration was subjected to temporal modification was either 79, 76, 70, 67, or 55 dB SPL, corresponding to about 15 to 2.8 sone in loudness, or silence. The level and duration of the preceding and succeeding tones were fixed. The measured temporal jnd was correlated highly with the level of the target part as shown in Fig. 6. This figure was reproduced from Kato and Tsuzaki (1994) to clarify the difference among loudness categories, with each corresponding to the inherent loudness of each phoneme class tested in experiment 1. That is, 12–15, 6.5–8, and 2.8 sone referred to the loudness of the vowel, nasal, and voiceless fricative portions, respectively (see also Fig. 3). These results can be considered as evidence for the second correlation. Therefore, the accountability of loudness in the ob-

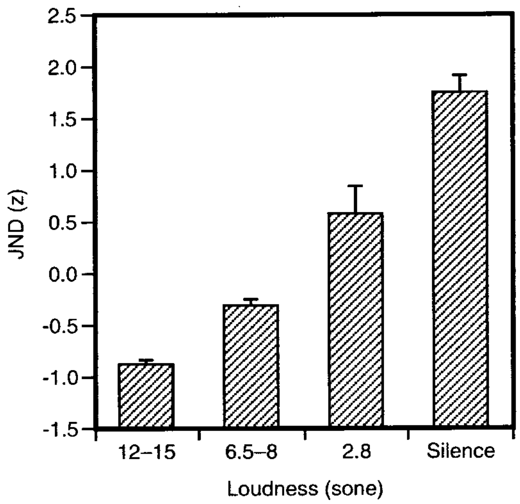

FIG. 6. The results of the temporal discrimination test in Kato and Tsuzaki (1994). The normalized just noticeable differences are shown. They are pooled over six subjects as a function of the level (translated to the loudness measure) of the target portion. Each category of the loudness measure roughly corresponds to the average loudness value of the vowel, nasal, voiceless fricative, or silence portions tested in the current study. The error bars show the standard errors. [Reproduced from Kato and Tsuzaki (1994).]

served effect of the phoneme class seems to be valid from the psychophysical point of view.

One may argue that the dynamic spectral nature of segments can be a cue to evaluate the size of a modification; nasals, voiceless fricatives, and obviously silences tend to have far less internal dynamics than vowels. Although we do not deny the possibility of such a spectral cue, it was unlikely the dominant effect in the current two experiments for the following reasons. First, the target portions of vowels were carefully chosen so as to exclude transient parts and the manipulations were given at steady-state parts as much as possible. Second, this factor is unlikely to be linear with the variations in the phoneme class, although it may have a certain effect in accounting for the differences between the vowels and the other three phoneme classes. Third, the listeners were asked to provide responses regarding only the temporal aspects of the stimuli. Although it was indeed difficult for them to be perfect, they tried their best to do so. The measure of loudness, on the other hand, is a more credible hypothesis because of its statistical accountability and psychoacoustical plausibility given earlier.[10]

B. Interaction between phoneme class and original duration

In experiment 2, a significant interaction was found between the factors of *phoneme class* and *original duration*. The effect of the original duration was larger for the vowels than for the voiceless fricatives. To account for this interaction, we consider, as a possible candidate, temporal cues that span beyond the target portion itself. In evaluating the temporal acceptability, the listeners could use the relative timings among the multiple portions or syllables surrounding the target portion. A major cue forming the perceptual timing of speech has been suggested to be the interval between vowel-onsets or vowel-onset asynchrony (VOA) by Sato

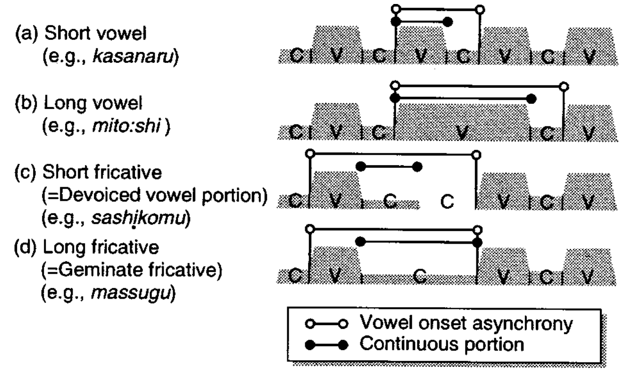

FIG. 7. Schematic examples showing the temporal structures of four-mora Japanese words for each stimulus group in experiment 2. The horizontal and vertical axes roughly refer to the time and loudness, respectively. ‘‘C’’ and ‘‘V’’ represent consonant and vowel portions, respectively. Note that the temporal alignment of each segment is highly idealized in these examples and that such rigid isochronous relations are rarely observed in actual Japanese speech.

(1977) through an observation of the production process; this was, then, empirically confirmed by Kato *et al.* (1996). The contribution of vowel onsets to the perceived timing has also been reported for English speech (Allen, 1972; Morton *et al.*, 1976).

To examine the role of VOA cues, we schematically illustrated the temporal structures of the speech materials used in experiment 2 and marked, thereon, the target portions and their VOAs (Fig. 7). As clearly seen in this figure, the VOA spanning over the short vowel (the vowel in the CV-mora) seems to be considerably shorter than that over the long vowel, whereas the VOA over the short fricative (devoiced vowel portion) is comparable with that over the long fricative (geminate fricative). Acoustic measurements of the actual stimulus words confirmed that the same tendency was found in the material of experiment 2 as summarized in Fig. 8. Whereas a clear contrast in the VOA between the ‘‘short’’ and ‘‘long’’ groups was observed for the vowels, no such tendency, or even the inverse tendency, was observed for the voiceless fricatives. Therefore, the observed interaction can be accounted for if we consider the difference in the VOA contrast as the source enlarging the effect of the original duration for the vowel class compared to the voiceless fricative class. These analyses suggest that the perceptual consequences of a given local modification or distortion may not solely be accountable by the change in the local duration itself but also by the changes in the intervals among the widely distributed multiple cues whereby the timing or rhythm is supplied.

C. Coherency of durational effects with discrete measures

To introduce an alternative implication about the effects of the original duration and the interaction observed in experiment 2, this subsection attempts to apply discrete or linguistic measures to the durations of target speech portions, rather than a continuous one, i.e., the acoustic duration.

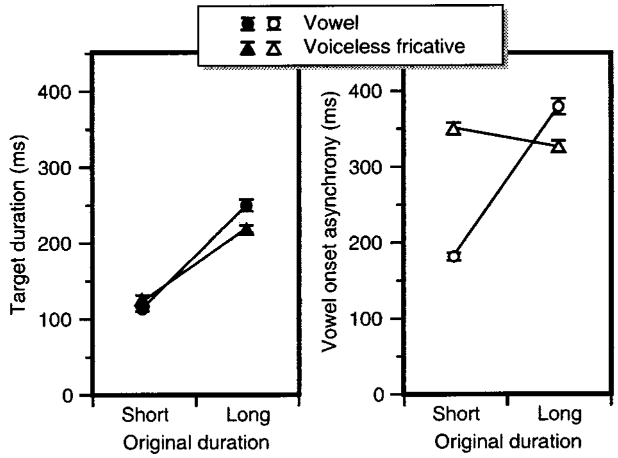

FIG. 8. The average and standard error of the measured duration of the target portions used in experiment 2 (copied from Table II and marked with closed symbols), and the measured intervals between the two vowel onsets (VOA) surrounding the target portions (marked with open symbols), as a function of the categorized target duration (short or long), i.e., the original duration. The short–long contrast of the original duration yields a much larger difference in VOA for the vowel class stimuli (open circles) than that for the voiceless fricative class stimuli (open triangles), while the difference in the target duration by the same contrast of the vowel class stimuli (closed circles) is similar to that of the voiceless fricative class stimuli (closed triangles).

1. Mora counting: A linguistic measure

First, the mora counting is examined. The notion of mora counting is used in phonology to handle the syllable weight, the relative durations of syllables when they are linguistically contrastive. The analysis of segments into moras is usually applied only to the syllabic nucleus (core vowel) and coda (final consonants), and not to the syllable onset (initial consonants), so that the presence or absence of an initial consonant does not change the mora counting or weight of a given syllable (Hyman, 1975; Kubozono, 1999). For instance, both of the two types of light syllables, V and CV, are counted as monomoraic and heavy syllables [(C)VV or (C)VC] are counted as bimoraic.

The mora, in several languages including Japanese, is frequently regarded as a basic unit of temporal regulation, as well as a unit by which the phonological distance is defined. If the quantity based on this unit were to be referenced as the base duration during the perceptual evaluation of temporal modifications, the observed durational effects would correlate with the mora counting of the target continuous durations. To test this possibility, we measured the target continuous durations by the mora counting and summarized them by stimulus groups in Table III.

The duration of a short vowel, a vowel in a CV-mora, is counted as monomoraic; although this duration shares one CV-mora with its consonantal partner, the initial consonant does not contribute to the mora counting according to the definition. The duration of a long vowel is counted as bimoraic in a similar way. The duration of a short fricative, i.e., a devoiced vowel portion, is counted as monomoraic because this portion has the same phonological status as a CV-mora. The duration of a long fricative, i.e., a geminate fricative, is counted as monomoraic; although it consists of a moraic obstruent (Kubozono, 1999; Vance, 1987), which is the final consonant of the first syllable of the word ($C_1V_1C_2$; subscript numerals show temporal moraic positions in a word), and the following short obstruent, which is the initial consonant of the CV-mora (C_3V_3), the initial consonant (C_3) again does not contribute to the mora counting.

These measurements reveal a sort of incoherence between the mora counting and the observed effects. That is, the short–long contrast in the voiceless fricative class does not show any difference in terms of the mora counting while it shows a significant difference in the acceptability evaluation. This fact, accordingly, does not support the notion that mora counting plays a role as a base duration in the current perceptual evaluation of temporal modifications.

2. Deviation from intact C–V alternation: An acoustic measure

The orthodox mora counting given above did not succeed in accounting for the observed effects probably because

TABLE III. Two discrete measures applied to the durational property of the target speech portions in experiment 2, i.e., the mora counting and the number of marker droppings. The first measure follows the definition in conventional phonology. The second measure is defined as the number of dropped temporal markers (phoneme boundaries) compared with the intact alternation of short consonants and vowels. The sequential structures of the words that embedded the target portions are shown along with example words. C and V stand for consonant and vowel segments. The subscript numerals show temporal moraic positions in words. Mora boundaries are marked by hyphens. A devoiced vowel is marked with an under-ring. The target continuous portions whose durations were subjected to temporal modification are underlined. The measure of the number of marker droppings is coherent with the observed durational effects, i.e., the main effect of the short–long contrast and the interaction (the stronger durational effect for the vowels than for the fricatives), while the measure of mora counting is not.

Stimulus group	CV sequence in the whole word	Example token	Mora counting	No. of marker dropping
Short vowel	$C_1V_1\text{–}C_2\underline{V_2}\text{–}C_3V_3\text{–}C_4V_4$	$ka\text{–}s\underline{a}\text{–}na\text{–}ru$	1	0
Long vowel	$C_1V_1\text{–}C_2\underline{V_2\text{–}V_3}\text{–}C_4V_4$	$mi\text{–}t\underline{o\text{–}o}\text{–}shi$	2	2
Short fricative (Devoiced vowel portion)	$C_1V_1\text{–}\underline{C_2\underset{\circ}{V}_2}\text{–}C_3V_3\text{–}C_4V_4$	$sa\text{–}\underline{sh\underset{\circ}{i}}\text{–}ko\text{–}mu$	1	1
Long fricative (Geminate fricative)	$C_1V_1\text{–}\underline{C_2\text{–}C_3}V_3\text{–}C_4V_4$	$ma\text{–}\underline{s\text{–}s}u\text{–}gu$	1	2

this counting does not consider any contribution of syllable-initial consonants. The reason why initial consonants, in general, have not been taken into account that much by phonological theory is that they are irrelevant in determining the phonological properties of a syllable (Hyman, 1975).[11] However, their relevance to acoustical properties is obvious, and, therefore, some psychoacoustical influence from their presence or absence seems to be inevitable. More specifically, the transitional part or boundary between consonant and vowel portions generally has a rapid and large acoustic change, e.g., a jump in intensity. Such an acoustic discontinuity can be used as one of the major markers that indicates the temporal structure or rhythm of a whole utterance (Kato *et al.*, 1997). In short, the presence or absence of syllable-initial consonants is always accompanied by the appearance or disappearance of such major temporal markers.

For a coherent implication of the observations in experiment 2, we compared the appearance or disappearance of these markers among different stimulus groups. The words that included short vowel targets consisted of only CV syllables as seen in Fig. 7(a). Since a stable and regular temporal alignment of the temporal markers was achieved in this alternation of short C and V, a clear and constant rhythm could be easily perceived from it. On the other hand, the temporal structures of words that included the targets in the other three stimulus groups, more or less, deviated from the regular C–V alternation [Figs. 7(b)–(d)]. The degree of such structural deviation can be defined, as given later in this work, using the number of temporal markers, i.e., C-to-V or V-to-C boundaries, that are dropped from the short C and V alternation.

In the case of words including short fricative targets (devoiced vowel portions), their temporal structures appeared to be the same as those including short vowel targets, $C_1V_1{-}C_2\underset{\circ}{V}_2{-}C_3V_3{-}C_4V_4$. However, as the devoiced vowel $\underset{\circ}{V}_2$ was actually a voiceless fricative and fused with the preceding consonant, there was, in fact, no acoustic discontinuity between the second consonant (C_2) and the following vowel ($\underset{\circ}{V}_2$). Accordingly, one temporal marker (C_2-to-$\underset{\circ}{V}_2$ boundary) could be regarded as having been dropped in comparison with the intact C–V alternation. The boundary between the devoiced vowel portion ($C_2\underset{\circ}{V}_2$) and the following consonant (C_3) had remained as a marker because C_2 and C_3 were different consonants in this stimulus group.

In the case of words including either long vowel or long fricative (geminate fricative) targets, two temporal markers could be regarded as having been dropped because their structures were either $C_1V_1{-}C_2V_2{-}V_3{-}C_4V_4$ or $C_1V_1{-}C_2{-}C_3V_3{-}C_4V_4$, where the boundary between the second and third mora ($V_2{-}V_3$ or $C_2{-}C_3$) did not have acoustic discontinuity. More specifically, both the V_2-to-C_3 and C_3-to-V_3 boundaries, and both the C_2-to-V_2 and V_2-to-C_3 boundaries, could be regarded as having been dropped from the intact C–V alternation in the long vowel and long fricative cases, respectively. These marker droppings from the intact C–V alternation are summarized in Table III.

Droppings of temporal markers from an intact C–V alternation imply degradation of the temporal regularity. A temporal modification given in an irregular temporal sequence is, in general, perceived less sensitively than that in a regular one (Tanaka *et al.*, 1994, for example). Assuming a similar degrading tendency of the temporal sensitivity with marker droppings also in experiment 2, the predicted effects on the α scores due to the short–long contrast in each phoneme class agree with the observed ones.

Finally, we should emphasize that this implication using the number of marker droppings, a discrete measure, and the implication using the VOA, a continuous measure introduced in Sec. IV B, are not mutually exclusive. Although they (apparently) focus on different aspects of the temporal measurement, both deal with a common source affecting the acceptability of a durational change, i.e., the temporal structure that spans beyond the local "target" portions. Therefore, the latter implication using the discrete or linguistic measure is not necessarily regarded as language specific but as one of the universal ways of figuring out the physical variations of temporal structures in speech.

V. CONCLUSIONS

The extent of acceptability decrement with temporal modifications in speech portions depended on the phoneme class of those portions whose durations were subjected to modification. The modification range for which a certain decrement of acceptability would be expected, i.e., the acceptable range, expanded with the phoneme class from vowel, nasal, then voiceless fricative or silence. The observed acceptability variations with the phoneme class correlated with the variation in loudness of the portion in question; the acceptable range narrowed as the portion became louder.

The extent of acceptability decrement with temporal modifications in speech portions also depended on the original, as produced, durations of the portions in question. The acceptable range expanded as the original duration increased. Interestingly, the degree of the effect by the original duration depended on the phoneme class. The effect was larger for the vowels than for the voiceless fricatives. This dependency could be accounted for by another source of the temporal structure, i.e., the vowel onset asynchrony (VOA). This dependency could be alternatively accounted for by a discrete measure representing the structural deviations of stimulus utterances from the regular C–V alternation.

An important implication of the current research is that an expanding acceptable range observed with changes in the phoneme class or original duration can be mostly accounted for by psychoacoustical terms, i.e., a reduced capability to discriminate temporal modifications as the loudness decreases or the original duration increases. It is probable that the acceptability of a speech portion coming in a different phoneme class and duration from those tested in the current study is, to a considerable extent, predictable from the psychoacoustical properties. There may, indeed, be other factors capable of affecting the acceptability evaluation. However, the results presented here demonstrate that we can expect a more valid (closer to human evaluation) measure than the traditional simple average of acoustic errors in evaluating durational rules by accounting for the loudness and original durations as weighting factors.

TABLE IV. Words used in experiment 1 in alphabetical order; portions whose durations were subjected to modification are marked in bold face. Attributes of each test portion, i.e., phonetic quality, phoneme class, and acoustic duration, and mean vulnerability indices (α's), are also given. The transcription of Japanese text is based on the Hepburn system (except that a moraic nasal is transcribed by an upper-case en). A devoiced vowel is marked with an under-ring. A top tie-bar marks a phoneme pair or triad that is inseparable in terms of phonetic segmentation. The phonetic symbols basically follow IPA usage.

Text	Phonetic quality	Phoneme class	Duration (ms)	$\alpha(\times 10^{-4})$
ba**N͡g**umi	[ŋ]	nasal	145.0	3.94
ba**k͡u̥**hatsu	[x]	fricative	125.0	1.86
bu**t͡su̥**karu	[s]	fricative	107.5	3.47
cho**kk**aku	silence	silence	182.5	2.29
da**N**ketsu	[ŋ]	nasal	95.0	3.17
ga**N**jitsu	[n]	nasal	125.0	4.35
ga**k͡k**ari	silence	silence	220.0	1.90
ha**N**doru	[n]	nasal	145.0	3.64
han**a**reru	[ɑ]	vowel	127.5	6.04
i**N**sotsu	[ɴ]	nasal	85.0	3.71
im**a**sara	[ɑ]	vowel	105.0	7.06
ji**s͡s**eki	[s]	fricative	210.0	2.11
ka**N͡g**eki	[ŋ]	nasal	157.5	2.43
ka**N**kaku	[ŋ]	nasal	102.5	3.45
ka**N**toku	[n]	nasal	90.0	4.34
kan**a**shimu	[ɑ]	vowel	120.0	5.18
kas**a**naru	[ɑ]	vowel	97.5	7.09
ka**s͡hi̥**kiri	[ʃ]	fricative	117.5	2.38
kat**a**meru	[ɑ]	vowel	102.5	7.30
ke**s͡s**aku	[s]	fricative	195.0	2.20
ki**N͡m**otsu	[m]	nasal	157.5	3.38
ko**k͡k**aku	silence	silence	175.0	2.22
ko**s͡hi̥**kake	[ʃ]	fricative	115.0	3.62
ma**Nn**aka	[n]	nasal	155.0	4.75
ma**ss**ugu	[s]	fricative	270.0	0.74
mat**a**garu	[ɑ]	vowel	105.0	6.90
mik**a**keru	[ɑ]	vowel	125.0	5.19
mi**s͡s**etsu	[s]	fricative	190.0	2.44
mi**t͡su̥**keru	[s]	fricative	87.5	2.92
mo**c͡hi̥**komu	[ʃ]	fricative	95.0	3.67
nar**a**beru	[ɑ]	vowel	122.5	6.54
na**t͡t**oku	silence	silence	190.0	2.93
o**s͡hi̥**komu	[ʃ]	fricative	135.0	3.01
ri**N**kaku	[ŋ]	nasal	85.0	5.06
sa**N**butsu	[m]	nasal	162.5	3.16
sa**k͡k**aku	silence	silence	172.5	2.17
sa**pp**ari	silence	silence	215.0	2.58
sa**s͡hi**komu	[ʃ]	fricative	117.5	3.34
sa**s͡s**oku	[s]	fricative	220.0	1.64
sa**s͡s**uru	[s]	fricative	235.0	2.22
se**k͡k**aku	silence	silence	195.0	1.59
shi**N**jiru	[n]	nasal	102.5	4.66
shin**a**biru	[ɑ]	vowel	127.5	6.28
ta**c͡hi̥**kiru	[ʃ]	fricative	102.5	3.69
ta**s͡s**uru	[s]	fricative	250.0	1.53
ta**s͡u̥**keru	[s]	fricative	137.5	2.62
u**c͡hi̥**komu	[ʃ]	fricative	102.5	4.14
ur**a**giru	[ɑ]	vowel	122.5	6.81
za**N**koku	[ŋ]	nasal	95.0	3.78

ACKNOWLEDGMENTS

We are grateful to Noriko Yoshikawa and Masako Tanaka for running the experimental procedures. We would like to thank Haruo Kubozono for his suggestions on terminology relating to phonetics and phonology, and Nick Campbell and Hideki Kawahara for their many helpful comments on early versions of this paper. We would also like to thank Yoh'ichi Tohkura for the initial impetus to the current study.

APPENDIX: PROPERTIES AND α SCORE OF EACH TESTED CONTINUOUS PORTION

Table IV shows the words used in experiment 1 in alphabetical order, and the phonetic quality, phoneme class, acoustic duration, and mean of vulnerability indices for each test portion.

Table V shows the words used in experiment 2 in alphabetical order, and the phonetic quality, phoneme class, categorized duration (short or long), acoustic duration, and mean of vulnerability indices for each test portion.

TABLE V. Words used in experiment 2 in alphabetical order; portions whose durations were subjected to modification are marked in bold face. Attributes of each test portion, i.e., phonetic quality, phoneme class, duration category, and acoustic duration, and mean vulnerability indices (α's), are also given. The transcription of Japanese text is based on the Hepburn system (except that a long vowel is marked with a subsequent length mark "**ː**"). A devoiced vowel is marked with an under-ring. A top tie-bar marks a phoneme pair that is inseparable in terms of phonetic segmentation. The phonetic symbols basically follow IPA usage.

Text	Phonetic quality	Phoneme class	Duration category	Duration (ms)	$\alpha(\times 10^{-4})$
ap**aː**to	[ɑ]	vowel	long	205.0	4.13
dep**aː**to	[ɑ]	vowel	long	200.0	4.35
fug**oː**ri	[o]	vowel	long	260.0	3.67
hir**o**garu	[o]	vowel	short	132.5	5.45
im**a**sara	[ɑ]	vowel	short	105.0	6.26
im**oː**to	[o]	vowel	long	227.5	3.75
ji**s͡s**eki	[s]	fricative	long	210.0	3.66
ka**s͡hi̥**kiri	[ʃ]	fricative	short	117.5	3.65
ke**s͡s**aku	[s]	fricative	long	195.0	3.86
kor**o**gasu	[o]	vowel	short	100.0	5.78
mat**a**garu	[ɑ]	vowel	short	105.0	6.53
min**o**gasu	[o]	vowel	short	120.0	6.60
mit**oː**shi	[o]	vowel	long	232.5	3.80
mit**o**reru	[o]	vowel	short	112.5	6.43
mi**t͡su̥**keru	[s]	fricative	short	87.5	4.98
mon**oː**ki	[o]	vowel	long	255.0	2.45
moy**oː**shi	[o]	vowel	long	220.0	3.47
nar**a**beru	[ɑ]	vowel	short	122.5	6.26
o**s͡hi̥**komu	[ʃ]	fricative	short	135.0	3.56
ot**oː**to	[o]	vowel	long	227.5	3.93
rek**oː**do	[o]	vowel	long	210.0	4.25
sa**s͡hi̥**komu	[ʃ]	fricative	short	117.5	4.42
sa**s͡s**oku	[s]	fricative	long	220.0	2.63
sa**s͡s**uru	[s]	fricative	long	235.0	3.22
shin**a**biru	[ɑ]	vowel	short	127.5	6.68
sum**aː**to	[ɑ]	vowel	long	202.5	4.77
ta**s͡s**uru	[s]	fricative	long	250.0	2.87
ta**s͡u̥**keru	[s]	fricative	short	137.5	4.30
tod**o**keru	[o]	vowel	short	107.5	6.14
ur**a**giru	[ɑ]	vowel	short	122.5	5.55

[1]When we changed the duration of voiceless stops, we just manipulated the duration of silent parts. We, therefore, use the term ''silent closure'' or ''silence'' to refer to the phoneme class corresponding to the voiceless stops.

[2]What ''continuous portion'' refers to is very similar to the ''continuant sound'' that was defined by Jacobson *et al.* (1954) in their distinctive feature theory, but differs from it in that the continuous portion may refer to the silent hold portion of a stop consonant; also, the continuant sound was implicitly defined as ranging within a single segment whereas the continuous portion may not.

[3]In Japanese, certain single vowels in certain positions of a word are often pronounced without vocal cord vibration. These vowels are called devoiced vowels. When a vowel is devoiced, we indicate it by a diacritic /V̥/. Vowel devoicing is most frequently observed with high vowels, i.e., /i/ and /u/, and it is most likely to occur when the vowels are placed between voiceless consonants, or are at the end of the word and are preceded by a voiceless consonant. There is also dialectal variation: in the Tokyo (i.e., eastern) dialect, vowels under the above conditions are devoiced with almost no exception, while such devoicing is less common in western dialects, such as the Osaka and Kyoto dialects. The lexical tone height (high or low)[5] of a vowel is not usually crucial to the devoicing of that vowel in Japanese (Tsujimura, 1996). In fact, all devoiced vowels tested in the current experiments were lexically categorized as high-tone segments.

[4]To maximize the freedom in word selection, we chose the materials from four-mora words which are lexically the most frequent in contemporary Japanese (Hashimoto, 1973; Yokoyama, 1981).

[5]A Japanese word has no lexical stress. Instead it has a pitch accent pattern, a combination of a high pitch and low pitch, each corresponding to a mora. The pattern provides lexical distinction like the stress pattern does in English.

[6]If the listeners were asked to rate the ''naturalness,'' they might have tended to use a strict criterion making it difficult for an informative evaluation to be maintained for the whole range of temporal modifications to be tested. To obtain information for a reasonably wide range of modifications, therefore, we chose the ''rating of acceptability'' over the ''rating of naturalness.''

[7]Although we could choose fitting functions other than polynomial fittings and/or could rescale the vertical axis to obtain an interval scale, we adopted the parabolic fitting on the raw evaluation scores owing to the advantage of its directly reflecting the subjects responses and its goodness of fitting.

[8]As we assigned a larger evaluation score to a more unacceptable or less acceptable impression, an increment of the evaluation score implies a decrement of the acceptability.

[9]Any usage of the word ''loudness'' in the current study means the loudness calculated by ISO-532 method B, unless otherwise stated. Although ISO-532B does not always provide excellent approximations for non-steady-state signals like speech, we adopted this method due to the advantage of its psychophysical basis instead of adopting power or intensity which incorporates no psychophysical considerations.

[10]In the same way, one may also argue that the $F0$ movement within segments serves as a cue to evaluate the size of a modification. We, however, regard that this factor had only minimum influence in the current experiments for the following reasons: (1) There were no remarkable differences between the $F0$ movements of vowel and nasal segments while there were obvious differences in the listeners' responses between the vowel and nasal cases. (2) The long vowel stimuli included two types of $F0$ patterns, i.e., high-to-high (flat) and high-to-low (falling). However, no systematic differences could be observed between the listeners' responses to these two stimulus subgroups.

[11]In a strict sense, the phonological function of syllable-initial consonants depends on languages. However, languages whose syllable-initial consonants have a phonological function are rare. Apparent exceptions include Pirahã and Eastern Popoluca, according to Blevins (1995).

Abel, S. M. (**1972**). ''Duration discrimination of noise and tone bursts,'' J. Acoust. Soc. Am. **51**, 1219–1223.

Allan, L. G. (**1979**). ''The perception of time,'' Percept. Psychophys. **26**, 340–354.

Allan, L. G., and Kristofferson, A. B. (**1974**). ''Psychophysical theories of duration discrimination,'' Percept. Psychophys. **16**, 26–34.

Allen, G. D. (**1972**). ''The location of rhythmic stress beats in English: An experimental study I and II,'' Lang. Speech **15**, 72–100, 179–195.

Allen, J., Hunnicutt, M. S., and Klatt, D. H. (**1987**). *From Text to Speech: The MITalk System* (Cambridge U. P., Cambridge, UK).

Bartkova, K., and Sorin, C. (**1987**). ''A model of segmental duration for speech synthesis in French,'' Speech Commun. **6**, 245–260.

Blevins, J. (**1995**). ''The syllable in phonological theory,'' in *The Handbook of Phonological Theory*, edited by J. A. Goldsmith (Blackwell, Oxford), pp. 206–244.

Bochner, J. H., Snell, K. B., and MacKenzie, D. J. (**1988**). ''Duration discrimination of speech and tonal complex stimuli by normally hearing and hearing-impaired listeners,'' J. Acoust. Soc. Am. **84**, 493–500.

Campbell, W. N. (**1992**). ''Multi-level timing in speech,'' doctoral dissertation, University of Sussex, Brighton, UK.

Carlson, R., and Granström, B. (**1975**). ''Perception of segmental duration,'' in *Structure and Process in Speech Perception*, edited by A. Cohen and S. Nooteboom (Springer-Verlag, Berlin), pp. 90–106.

Carlson, R., and Granström, B. (**1986**). ''A search for durational rules in a real-speech database,'' Phonetica **43**, 140–154.

Creelman, C. D. (**1962**). ''Human discrimination of auditory duration,'' J. Acoust. Soc. Am. **34**, 582–593.

Fant, G., and Kruckenberg, A. (**1989**). ''Preliminaries to the study of Swedish prose reading and reading style,'' Royal Institute of Technology, Speech Transmission Lab. Q. Prog. Status Report 2/1989, pp. 1–83.

Fujisaki, H., Nakamura, K., and Imoto, T. (**1975**). ''Auditory perception of duration of speech and non-speech stimuli,'' in *Auditory Analysis and Perception of Speech*, edited by G. Fant and M. A. A. Tatham (Academic, London), pp. 197–219.

Hashimoto, S. (**1973**). ''Several features of Japanese word accent,'' Trans. Inst. Electron. Commun. Eng. Jpn., Part D **56-D**, 654–661 (in Japanese with English figure captions).

Henry, F. M. (**1948**). ''Discrimination of the duration of a sound,'' J. Exp. Psychol. **38**, 734–743.

Higuchi, N., Shimizu, T., Kawai, H., and Yamamoto, S. (**1993**). ''Control of phoneme duration based on the movement of speech organs,'' J. Acoust. Soc. Jpn. (E) **14**, 281–283.

Hoshino, M., and Fujisaki, H. (**1983**). ''A study on perception of changes in segmental durations,'' Acoustical Society of Japan, Trans. Tech. Comm. Speech S82-75, 593–599 (in Japanese with English abstract and English figure captions).

Huggins, A. W. F. (**1972**). ''Just noticeable differences for segment duration in natural speech,'' J. Acoust. Soc. Am. **51**, 1270–1278.

Hyman, L. M. (**1975**). *Phonology: Theory and Analysis* (Holt, Rinehart and Winston, New York).

Imai, S., and Kitamura, T. (**1978**). ''Speech analysis synthesis system using the log magnitude approximation filter,'' Trans. Inst. Electron. Commun. Eng. Jpn., Part A **J61-A**, 527–534 (in Japanese with English figure captions).

ISO (**1975**). ''Acoustics—Method for calculating loudness level,'' International Organization for Standardization, ISO 532-1975 (E).

Jacobson, R., Fant, G., and Halle, M. (**1954**). *Preliminaries to Speech Analysis: the Distinctive Features and Their Correlates* (MIT, Cambridge, MA).

Kaiki, N., and Sagisaka, Y. (**1992**). ''The control of segmental duration in speech synthesis using statistical methods,'' in *Speech Perception, Production and Linguistic Structure*, edited by Y. Tohkura, E. Vatikiotis-Bateson, and Y. Sagisaka (IOS, Amsterdam), pp. 391–402.

Kato, H., and Tsuzaki, M. (**1994**). ''Intensity effect on discrimination of auditory duration flanked by preceding and succeeding tones,'' J. Acoust. Soc. Jpn. (E) **15**, 349–351.

Kato, H., Tsuzaki, M., and Sagisaka, Y. (**1992**). ''Acceptability and discrimination threshold for distortion of segmental duration in Japanese words,'' in *Proceedings of the 2nd International Conference on Spoken Language Processing* (University of Alberta, Edmonton, Alberta), pp. 507–510.

Kato, H., Tsuzaki, M., and Sagisaka, Y. (**1996**). ''Evidence for the predominance of vowel onsets to offsets in speaking-rate perception,'' in *Proceedings of the 3rd ASJ-ASA Joint Meeting* (Acoustical Society of Japan, Tokyo), pp. 1199–1204.

Kato, H., Tsuzaki, M., and Sagisaka, Y. (**1997**). ''Acceptability for temporal modification of consecutive segments in isolated words,'' J. Acoust. Soc. Am. **101**, 2311–2322.

Kato, H., Tsuzaki, M., and Sagisaka, Y. (**1998**). ''Acceptability for temporal modification of single vowel segments in isolated words,'' J. Acoust. Soc. Am. **104**, 540–549.

Klatt, D. H. (**1979**). ''Synthesis by rule of segmental durations in English sentences,'' in *Frontiers of Speech Communication Research*, edited by B. Lindblom and S. Öhman (Academic, London), pp. 287–299.

Kubozono, H. (**1999**). ''Mora and syllable,'' in *The Handbook of Japanese Linguistics*, edited by N. Tsujimura (Blackwell, Oxford), pp. 31–61.

Kurematsu, A., Takeda, K., Sagisaka, Y., Katagiri, S., Kuwabara, H., and Shikano, K. (**1990**). ''ATR Japanese speech database as a tool of speech recognition and synthesis,'' Speech Commun. **9**, 357–363.

McCall, R. B. (**1980**). *Fundamental Statistics for Psychology*, 3rd ed. (HBJ, New York).

Morton, J., Marcus, S., and Frankish, C. (**1976**). ''Perceptual centers,'' Psychol. Rev. **83**, 405–408.

Rammsayer, T. H. (**1994**). ''Effects of practice and signal energy on duration discrimination of brief auditory intervals,'' Percept. Psychophys. **55**, 454–464.

Sagisaka, Y., and Tohkura, Y. (**1984**). ''Phoneme duration control for speech synthesis by rule,'' Trans. Inst. Electron. Commun. Eng. Jpn., Part A **J67-A**, 629–636 (in Japanese with English figure captions).

SAS Institute, Inc. (**1990**). *SAS/STAT User's Guide, Version 6* (SAS Institute, Inc., Cary, NC), 4th ed., Vol. 2.

Sato, H. (**1977**). ''Segmental duration and timing location in speech,'' Acoustical Society of Japan, Trans. Tech. Comm. Speech S77-31, 1–8 (in Japanese with English abstract and English figure captions).

Takeda, K., Sagisaka, Y., and Kuwabara, H. (**1989**). ''On sentence-level factors governing segmental duration in Japanese,'' J. Acoust. Soc. Am. **86**, 2081–2087.

Tanaka, M., Tsuzaki, M., and Kato, H. (**1994**). ''Discrimination of empty duration in the click sequence simulating a mora structure,'' J. Acoust. Soc. Jpn. (E) **15**, 191–192.

Tsujimura, N. (**1996**). *An Introduction to Japanese Linguistics* (Blackwell, Oxford).

van Santen, J. P. H. (**1994**). ''Assignment of segmental duration in text-to-speech synthesis,'' Comput. Speech Lang. **8**, 95–128.

Vance, T. J. (**1987**). *An Introduction to Japanese Phonology* (SUNY, New York).

Yokoyama, S. (**1981**). ''Occurrence frequency data of a Japanese dictionary,'' Bull. Electrotechnical Laboratory Jpn. **45**, 395–418.

Zwicker, E., Fastl, H., Widmann, U., Kurakata, K., Kuwano, S., and Namba, S. (**1991**). ''Program for calculating loudness according to DIN 45631 (ISO 532B),'' J. Acoust. Soc. Jpn. (E) **12**, 39–42.

The relationship between the intelligibility of time-compressed speech and speech in noise in young and elderly listeners

Niek J. Versfeld[a] and Wouter A. Dreschler
Department of Clinical and Experimental Audiology, Academic Medical Center Room D2-330, Meibergdreef 9, 1105 AZ Amsterdam, The Netherlands

(Received 28 March 2001; revised 10 October 2001; accepted 10 October 2001)

A conventional measure to determine the ability to understand speech in noisy backgrounds is the so-called speech reception threshold (SRT) for sentences. It yields the signal-to-noise ratio (in dB) for which half of the sentences are correctly perceived. The SRT defines to what degree speech must be audible to a listener in order to become just intelligible. There are indications that elderly listeners have greater difficulty in understanding speech in adverse listening conditions than young listeners. This may be partly due to the differences in hearing sensitivity (presbycusis), hence audibility, but other factors, such as temporal acuity, may also play a significant role. A potential measure for the temporal acuity may be the threshold to which speech can be accelerated, or compressed in time. A new test is introduced where the speech rate is varied adaptively. In analogy to the SRT, the time-compression threshold (or TCT) then is defined as the speech rate (expressed in syllables per second) for which half of the sentences are correctly perceived. In experiment I, the TCT test is introduced and normative data are provided. In experiment II, four groups of subjects (young and elderly normal-hearing and hearing-impaired subjects) participated, and the SRT's in stationary and fluctuating speech-shaped noise were determined, as well as the TCT. The results show that the SRT in fluctuating noise and the TCT are highly correlated. All tests indicate that, even after correction for the hearing loss, elderly normal-hearing subjects perform worse than young normal-hearing subjects. The results indicate that the use of the TCT test or the SRT test in fluctuating noise is preferred over the SRT test in stationary noise. [DOI: 10.1121/1.1426376]

PACS numbers: 43.71.Gv, 43.71.Ky, 43.71.Lz [DOS]

I. INTRODUCTION

A conventional measure to determine the ability to understand speech in noisy backgrounds is the so-called speech reception threshold (SRT) for sentences (Plomp and Mimpen, 1979; Nilsson *et al.*, 1994; Versfeld *et al.*, 2000). Typically, simple, meaningful sentences are partially masked by noise, and the signal-to-noise ratio is varied in an adaptive manner such that the critical signal-to-noise ratio is obtained for which 50% of the sentences is completely intelligible. The critical signal-to-noise ratio, or SRT, defines to what degree speech information must be available to the listener in order to make it just intelligible. The SRT test usually utilizes stationary noise to mask the speech signal. It is known that models that operate in the spectral domain, such as the Articulation Index (AI, Fletcher, 1953), and its successor, the Speech Intelligibility Index (SII, ANSI, 1997) are able to make quite accurate predictions for the SRT with various types of noise masker. However, there are indications that especially elderly listeners have more difficulties with understanding speech in adverse listening conditions than young listeners (Konkle *et al.*, 1977; Gordon-Salant and Fitzgibbons, 1993, 1997), even after correction for the hearing loss. Presumably, other factors such as temporal resolution or cognitive demands may also play a significant role (Gordon-Salant and Fitzgibbons, 1993, 1997). Temporal acuity (such as backward masking, cf. Gehr and Sommers, 1999) appears to be most affected by age, in contrast to spectral masking (governed by the auditory filter bandwidth), which seems to remain unaffected as a function of age (Peters and Moore, 1992; Sommers and Gehr, 1998). It is conceivable that the SRT in stationary noise may not be the most appropriate measure to assess the effect of reduced temporal resolution.

An alternative manner to assess temporal acuity in relation to intelligibility is to measure the amount to which speech can be accelerated, or compressed in time. Experiments dealing with time-compressed speech go back to the fifties, where Fairbanks and Kodman (1957) measured word intelligibility as a function of time compression. From there on, time-compressed speech has been used for a variety of topics, including the detection of lesions of the brain stem and auditory cortex (e.g., Beasley *et al.*, 1972a, b; Kurdziel *et al.*, 1976; Beattie, 1986), central auditory processing, both in children (Riensche *et al.*, 1986; Bornstein, 1994; Stollman *et al.*, 1994; Stark *et al.*, 1995) and elderly listeners (Stollman and Kapteyn, 1994; Gordon-Salant and Fitzgibbons, 1997; Vaughan and Letowski, 1997), temporal processing and age effects (Konkle *et al.*, 1997; Gordon-Salant and Fitzgibbons, 1993, 1999), and hearing loss (Kurdziel *et al.*, 1975; Grimes *et al.*, 1984; Stuart and Phillips, 1998). Most recently, time-compressed speech has been used for the assessment of temporal processing in cochlear-implant listeners (Fu *et al.*, 2001). The technique itself has been used to reduce the time needed to listen to a message (Arons, 1992).

[a]Electronic mail: N.J.Versfeld@AMC.UvA.nl

With respect to time-compressed speech, a number of topics have not yet been addressed.

First, since both SRT and TCT measure aspects of speech intelligibility, it seems straightforward to study the relationship between these tests. From a theoretical point of view, there is no direct reason to expect SRT and TCT to be highly correlated. Thus, TCT might provide additional information to assess the speech perception capabilities of a given individual if it is not highly correlated to the SRT. It may give more insight into the differences in auditory and cognitive mechanisms involved with these different tests. Alternatively, if TCT and SRT indeed are highly correlated, it seems likely that the same auditory or cognitive mechanisms are underlying. Thus, the purpose of this paper is to assess the relationship between the SRT and TCT. To our knowledge, no paper has yet reported on this relationship (although several papers report on the combined effect of time compression and masking on intelligibility, e.g., Stollman and Kapteyn, 1994; Lacroix and Harris, 1979).

Second, the amount of time compression usually is expressed in a percentage. This does not cause any problems as long as single words are used, uttered by the same speaker. But, it is uncertain whether percentage compression is still a valid measure in the case of different speakers, using different speaking rates. To gain some insight into which measure is perceptually relevant, sentence materials are more appropriate than single-word materials. Unfortunately, only a few papers report on the perception of time-compressed sentences (Vaughan and Letowski, 1997; Gordon-Salant and Fitzgibbons, 1999; Fu *et al.*, 2001).

Third, most certainly due to the availability of the stimulus materials and the computational complexity, intelligibility of time-compressed speech is always measured at fixed time-compression rates (e.g., Beattie, 1986). It is known that fixed-stimuli methods may seriously suffer from ceiling and floor effects, unless the entire psychometric function is measured. Adaptive procedures do not have these problems, so measurements are much more efficient. In the literature, adaptive procedures in combination with time compression have never been reported. Only de Haan and co-workers (de Haan, 1977, 1982; de Haan and Schjelderup, 1978) devised a system with which the speech rate could be varied adaptively. They used this device to assess the relationship between intelligibility and comprehension of speech.

The present paper introduces a test where sentences are time compressed, and an adaptive method is used to define the threshold of intelligibility for time-compressed speech. In analogy to the SRT test, the time-compression threshold (or TCT) is defined as the speech rate (in syllables per second) for which half of the sentences are correctly perceived. In experiment I, normative data for the TCT test are presented for a group of young, normal-hearing subjects. In experiment II, both SRT in either stationary or fluctuating noise and TCT are measured for young and elderly normal-hearing or hearing-impaired listeners. The results of experiment II then are used to assess the relationship between SRT and TCT, and to assess the effect of age and hearing loss upon SRT and TCT.

II. EXPERIMENT I. DEVELOPMENT OF THE TCT TEST AND NORMATIVE DATA

A. Stimuli

Stimuli were 260 meaningful sentences (e.g., ''de bal vloog over de schutting'' [the ball flew over the fence], ''de voordeur bij de buren klemt'' [the neighbors' front door jams]), originally developed for a reliable measurement of the SRT in noise (Plomp and Mimpen, 1979). Each sentence consisted of 4 to 8 words, but always comprised 8 or 9 syllables. Half of this set was uttered by a female speaker (from Plomp and Mimpen, 1979), the other half by a male speaker (from Smoorenburg, 1986). This speech material (without any background noise) was time compressed by means of a modified pitch synchronous overlap add (PSOLA) technique (Moulines and Laroche, 1995). This technique performs duration reduction in the time domain, where it operates in a uniform manner over the entire sentence waveform. PSOLA preserves most physical characteristics of the speech signal, such as, for example, the spectral shape, the periodicity (pitch height), and the amplitude distribution. The PSOLA method has the property that it preserves the naturalness of speech, even at high time-compression rates. Each sentence was time compressed to 11 different degrees. For the male speaker, the speaking rates were $4.576/(0.85)^N$ syllables per second (syll/s), where N ranged between 0 (original speaking rate) and 10 (highest speaking rate). The original speaking rate was determined by manually counting the number of syllables of the entire set, and dividing this number by the total duration in seconds. For the female speaker, the speaking rates were $3.612/(0.85)^N$ syll/s, where again N ranged from 0 to 10. Each sentence was stored into a separate file, resulting in a total of 260 (sentences)$*$11 (speaking rates) $=$2860 files.

B. Subjects

Fourteen young, normal-hearing subjects (4 male, 10 female) participated. Their median age was 22 years and ranged from 20 to 29 years. Their pure-tone thresholds were 15 dB HL or better in their test ear at octave frequencies between 125 and 8000 Hz (inclusive). Subjects were mostly voluntary university students.

C. Procedure

Subjects were tested individually in a sound-insulated booth. Signals were played out via a SoundBlaster soundcard on a PC at a sample frequency of 15 620 Hz, low-pass filtered at 6.5 kHz, and subsequently fed to an InterAcoustics AC40 audiometer. Subjects received the signals via the audiometer's TDH 39P headphones over their best ear at a fixed level 75 dBA. Three subjects received the stimuli at a level of 60 dBA. (These subjects also participated in another listening experiment, not reported in this paper, that required this stimulus level.) The subject's task was to repeat the sentence he or she had just been presented. A sentence was scored if the listener repeated every word exactly. The speaking rate was varied adaptively via a one-up, one-down procedure. That is, if a sentence was repeated correctly, the speaking rate of the next sentence was increased. If the sentence was not repeated correctly, the speaking rate of the next sentence was decreased. This procedure makes the speaking rate converge to the point for which half of the (time-compressed) sentences is scored. In analogy to the procedure described by Plomp and Mimpen (1979), 13 sentences formed a list, and one list was required to estimate the threshold for the intelligibility of time-compressed speech, or the time-compression threshold (TCT). The TCT was estimated by taking the geometric mean of the speaking rate of the last ten sentences.

With the existing speech materials, 20 independent lists of 13 sentences each could be formed. Two of these were used as practice lists. The TCT test was interleaved with two SRT tests (reported on in experiment II). Every list occurred at the TCT test, but every subject received only 6 (out of 18) lists for the part dealing with the TCT; the remaining 12 lists were reserved for the SRT part. Lists and sentences within each list were always presented in a fixed order. Conditions (i.e., TCT and SRT), however, were arranged according to balanced design, wherein male and female speaker alternated between lists as well. Within a subject, each sentence was presented only once. The experiment (including the SRT test) lasted about 1 h.

D. Results and discussion

Per subject, 6 TCTs are available, 3 for a male speaker and 3 for a female speaker. In order to provide normative thresholds that are unbiased by learning effects, an analysis of variance (ANOVA) was performed. A three-way (''subject'' by ''speaker'' by ''repetition'') ANOVA showed no significant differences between the average threshold obtained in the first list presentation and the second or third list presentation ($F[2,26]=1.58$, $p>0.1$). Thus, no significant learning effect was observed. Also, a three-way (''repetition'' by ''speaker'' by ''level'') ANOVA was performed to assess the effect of level. No significant differences were found between the group of subjects that received the stimuli at presentation levels of 75 and 60 dBA ($F[1,72]=3.26$, $p>0.05$).

For the present group of 14 normal-hearing subjects, the raw data were pooled. Figure 1 displays the proportion of correct responses as a function of the speaking rate. Open and filled symbols represent results obtained with the male and female speaker, respectively. The solid line is a best fit (in a maximum-likelihood sense) of a logistic function to the data obtained with female speech. Similarly, the dashed line is a best fit for male speech. The speaking rate for which the proportion of correct responses is 0.5 is 12.5 syll/s for the female speaker and 12.8 syll/s for the male speaker. The logistic function is somewhat steeper for the male speaker than for the female speaker, but this difference is not significant ($z=1.1$, $p>0.1$).

Next, the data per list (i.e., the individual TCTs) were considered. The averages and 95%-confidence intervals of the 14 [subjects]$*$3 [repetitions]$=42$ TCTs are 12.3 syll/s and 1.86 syll/s for the female voice and 12.8 syll/s and 2.05 syll/s for the male voice, respectively. This means that if a TCT test is performed (e.g., in a clinical setting), a TCT lower than 10.5 syll/s is significantly worse than average. The former two ANOVAs show that the small difference between the average TCT of the male and female speaker (12.3 and 12.8 syll/s) is significant ($F[1,26]=5.49$ and $F[1,72]=4.69$, both $p<0.05$). Furthermore, the main effect of subject was significant ($F[13,26]=2.38$, $p<0.05$), but none of the interactions did reach the 5%-level of significance.

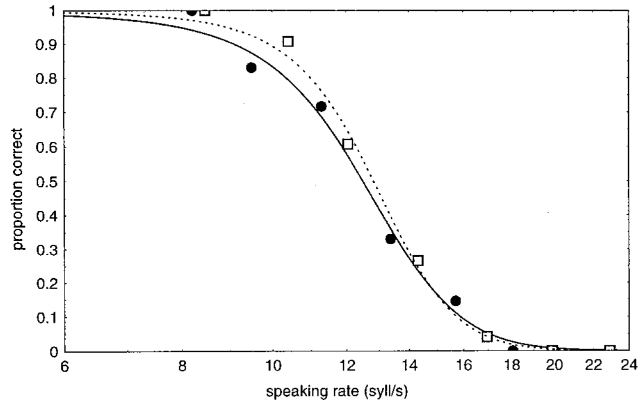

FIG. 1. Proportion of correct responses as a function of speaking rate (syll/s). Open and filled symbols indicate results obtained with the male and female speaker, respectively. The curves represent a best fit of a logistic function to the data.

The slight discrepancy between the two methods (maximum-likelihood method versus TCT averaging) is not only caused by the difference in the method of calculating the threshold, but mostly by the fact that with the TCT averaging only the last ten responses are taken into account (cf. Plomp and Mimpen, 1979), whereas with the maximum-likelihood method all except for the first responses are taken into account.

III. EXPERIMENT II. RELATIONSHIP BETWEEN TCT AND SRT

A. Stimuli

Stimuli were the same 260 sentences (20 lists) as described in experiment I. They were used in both the TCT and SRT test. With the SRT test, the speech was masked by running noise, and the spectrum of this noise was shaped according to the long-term average spectrum of the respective speaker. The noise was either stationary (Plomp and Mimpen, 1979) or fluctuating, resembling the amplitude modulations in a speech signal of a single speaker (cf. Festen and Plomp, 1990).

B. Subjects

In total, 49 subjects participated in this experiment. Fourteen of them also participated in experiment I. All subjects were fluent speakers of the Dutch language. The subjects' test ear was always their best ear. With this ear they were able to reach at least 80% speech discriminability for monosyllabic words in quiet. All subjects participated on a voluntary basis. According to age and hearing loss, they could be classified into four groups.

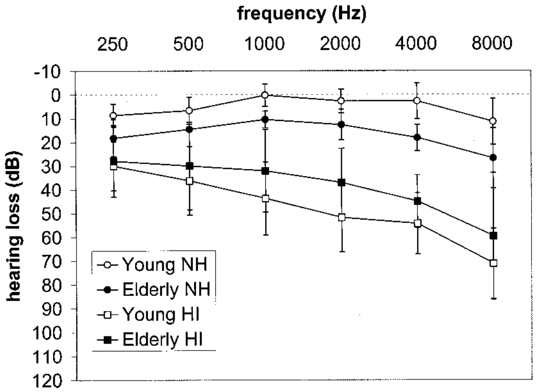

FIG. 2. Audiograms averaged across subjects for the four groups of subjects (see the legend). Error bars denote the standard deviations between subjects.

1. Young, normal-hearing subjects

Eighteen normal-hearing subjects (7 male, 11 female) participated. The median age was 23 years, ranging between 20 and 29 years. Their hearing was on average equal to or better than 10 dB HL at octave frequencies between 250 and 8000 Hz, with extremes up to 35 dB HL at 6000 or 8000 Hz. The average hearing loss is plotted in Fig. 2 as open circles. Error bars indicate the standard deviation between subjects. The TCT data of 14 subjects in this group have been used in experiment I.

2. Elderly, normal-hearing subjects

Eleven elderly, normal-hearing subjects (2 male, 9 female) participated. Their median age was 64 years and ranged from 58 to 70 years. Their pure-tone thresholds were 30 dB HL or better in their test ear at octave frequencies between 250 and 6000 Hz, with extreme values up to 60 dB HL at 8000 Hz. The average pure-tone threshold (in dB HL) is given in Fig. 2 as filled circles. Error bars indicate the standard deviation between subjects.

3. Young, hearing-impaired subjects

Eight young, hearing-impaired subjects (5 male and 3 female ranging in age from 15 to 35, median age 18 years) participated. Most of them were recruited from a local school for the hearing impaired. All suffered from sensorineural hearing loss (of which five were of hereditary origin, and three were of unknown origin), and their average pure-tone thresholds (in dB HL) are plotted in Fig. 2 as open squares. Error bars indicate the standard deviation between subjects. Apart from the hearing impairment, one subject suffered from additional speech and language problems, and for five subjects, parents were non-native speakers.

4. Elderly, hearing-impaired subjects

Twelve elderly, hearing-impaired subjects (6 male, 6 female) participated. Their median age was 63 years, ranging from 55 to 73 years. They suffered from mild-to-moderate (sensorineural) hearing loss, which all of them had acquired at later age. Their average pure-tone hearing loss is plotted in Fig. 2 as filled squares. Error bars indicate the standard deviation between subjects.

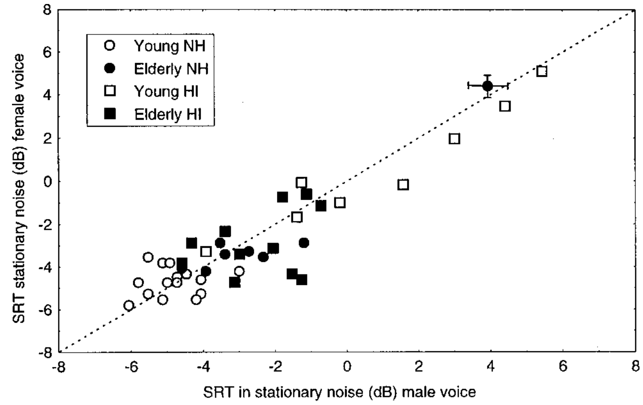

FIG. 3. SRT (dB) in stationary noise. Results obtained with the female speaker plotted as a function of results for the male speaker. The dashed line represents the points of equal SRT.

C. Procedure

With respect to the part dealing with the TCT test, the experimental procedure was that of experiment I. However, speech was presented at a minimum level of 60 dBA, and was at least 20 dB above threshold in quiet. For the individual subject, the masking noise of the SRT test was kept fixed, and was presented at a level equal to the speech in the TCT test. Speech-to-noise ratio was varied by variation of the speech level. The procedure with the SRT test was that described by Plomp and Mimpen (1979). Each list comprised 13 sentences. The subject's task was to reproduce the sentence he or she had just been presented. A sentence was scored if the listener repeated every word exactly. The speech-to-noise ratio was varied adaptively via a one-up, one-down procedure, converging to that speech-to-noise ratio (the speech reception threshold or SRT) for which half of the sentences are scored. The SRT was estimated by averaging the speech-to-noise ratio after the last ten sentences.

Lists and sentences within each list were presented in a fixed order. Male and female speaker alternated between lists. Conditions alternated in a balanced order, and were counterbalanced between subjects. Across subjects and within each subject, each condition and speaker occurred equally often. Within a subject, each sentence was presented only once. Therefore, apart from two practice lists, a subject received six lists with time-compressed speech, six lists with speech in stationary noise, and six lists with speech in fluctuating noise. The experiment lasted about 1 h.

D. Results and discussion

First, correlations between the results obtained for the different tests (i.e., SRT, TCT, male or female speaker) will be discussed. Second, results obtained for different subject groups will be compared. As in experiment I, no significant learning effects were observed, not even for the elderly group or hearing-impaired group.

1. Relationship between male and female speech

Figures 3–5 display the relationship between the results obtained with the male and female speaker, in the case of

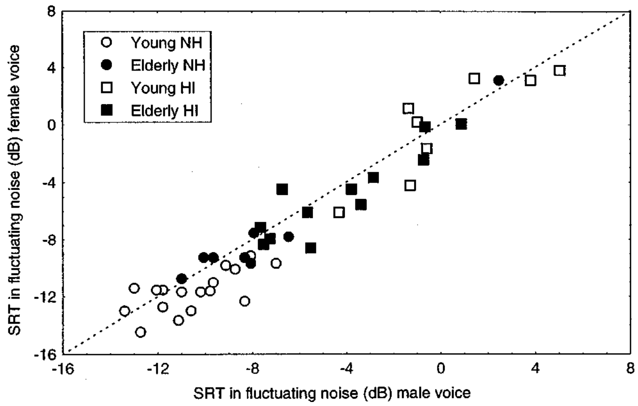

FIG. 4. As in Fig. 3, but for the SRT (dB) in fluctuating noise.

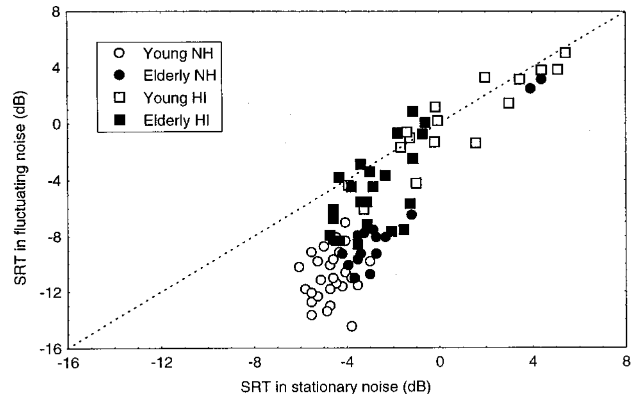

FIG. 6. SRT in fluctuating noise as a function of the SRT in stationary noise. Different symbols indicate the different groups of subjects (see the legend). The dashed line indicates the points of equal SRT.

SRT for stationary noise (hereafter denoted as $\mathrm{SRT_S}$), SRT for fluctuating noise (hereafter denoted as $\mathrm{SRT_F}$), and TCT, respectively. Figure 3 shows the results obtained for speech in stationary noise. The SRT obtained with the female speaker is plotted as a function of the SRT obtained with the male speaker. Different symbols indicate the four different subject groups. Each symbol represents the average of three SRT estimates. The standard error of this estimate is on average 0.5 dB for both speakers, and is indicated with error bars in one of the symbols to the top right of the figure. The dashed curve is a straight line indicating equal SRT. As can be seen from Fig. 3, the deviation from the symbols to the dashed line is small, but there seems to be a slight tendency for the female speaker to yield better results. Indeed, linear regression shows that the best-fitted straight line with unity slope significantly deviates from the dashed line, and the offset is 0.15 dB. Figure 4 shows similar results for fluctuating noise. Here, the offset is 0.65 dB. With time-compressed speech, thresholds obtained with male and female speech are also slightly different, as can be seen in Fig. 5. In contrast, performance for the female speech here is worse, and the difference between male and female speech is 0.55 syll/s. Correlation coefficients between the scores of the male and female speaker were 0.91 for the $\mathrm{SRT_S}$, 0.96 for the $\mathrm{SRT_F}$, and 0.92 for the TCT. In conclusion, differences between male and female speaker were significant, but small. In this paper, all results have been analyzed for the male and female speaker separately, as well as for the pooled data. In none of the cases were results significantly different, so in the remainder of this paper only the pooled data will be presented.

2. Relationship between $\mathrm{SRT_S}$, $\mathrm{SRT_F}$, and TCT

Figure 6 displays the relationship between $\mathrm{SRT_S}$ and $\mathrm{SRT_F}$. The dashed line indicates the points where $\mathrm{SRT_S}$ and $\mathrm{SRT_F}$ are equal. For young, normal-hearing listeners, the $\mathrm{SRT_S}$ is on average -4.7 dB, whereas the $\mathrm{SRT_F}$ is much better, namely -11.1 dB. Note that for subjects with a poor $\mathrm{SRT_F}$, $\mathrm{SRT_S}$ and $\mathrm{SRT_F}$ are about equal, whereas a relatively good performance for the $\mathrm{SRT_S}$ does not imply good performance for the $\mathrm{SRT_F}$.

Figure 7 displays the relationship between $\mathrm{SRT_S}$ and TCT. As SRT increases, TCT decreases, as to be expected. However, especially at higher SRTs, there is a considerable amount of scatter in the data. The correlation between the two data sets is 0.73. The correlation between $\mathrm{SRT_F}$ and TCT is considerably higher, namely 0.87. This relationship is depicted in Fig. 8.

3. Effect of age and hearing impairment on SRT and TCT

Table I displays for each subgroup the $\mathrm{SRT_S}$, $\mathrm{SRT_F}$, and TCT. (The values in parentheses are SII values and will be discussed below.) $\mathrm{SRT_S}$ and $\mathrm{SRT_F}$ for the group of young and

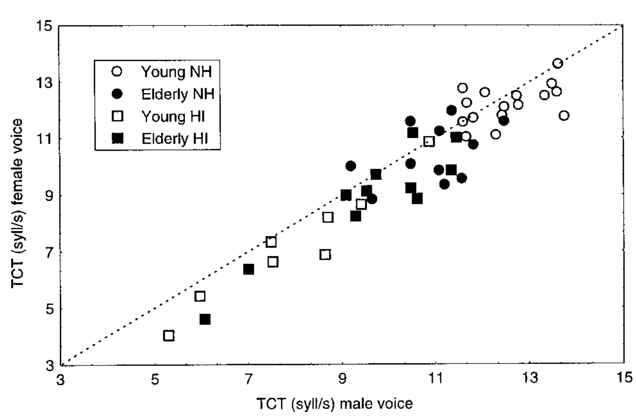

FIG. 5. As in Fig. 3, but for the TCT (syll/s).

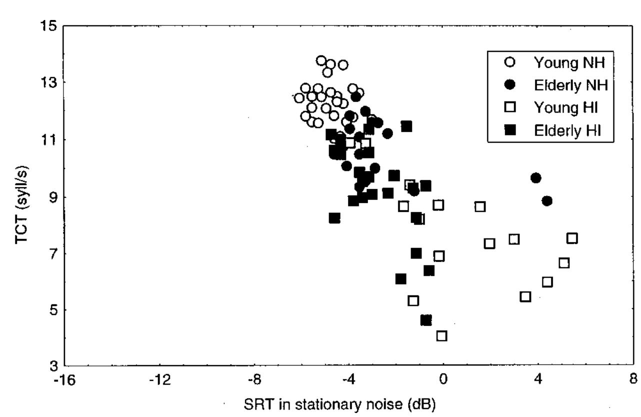

FIG. 7. TCT as a function of the SRT in stationary noise. Different symbols indicate the different groups of subjects (see the legend).

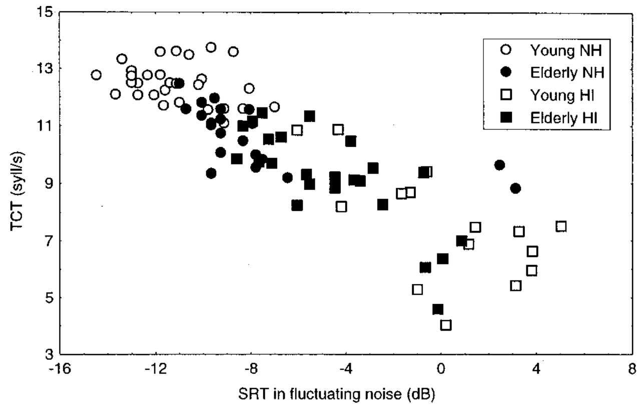

FIG. 8. TCT as a function of the SRT in fluctuating noise. Different symbols indicate the different groups of subjects (see the legend).

elderly normal-hearing subjects are in agreement with those reported in the literature (Festen and Plomp, 1990), and the difference between these two thresholds is about 6.4 dB. With elderly normal-hearing subjects, thresholds are somewhat poorer, but the difference between SRT_S and SRT_F still is 5.2 dB. The remarkable difference between the normal-hearing group and the hearing-impaired group is that the difference between SRT_F and SRT_S has practically vanished: 0.7 and 1.9 dB for the young and elderly group, respectively. Note that the SRT_S for both elderly groups is similar.

IV. GENERAL DISCUSSION

The results of experiment I showed that if the speaking rate was expressed in syllables per second, the psychometric functions for the male and female speaker practically overlap, and the difference is 0.3 syll/s. If one keeps in mind that the original speaking rate for the female speaker is on average 3.612 syll/s and for the male speaker 4.576 syll/s (ratio of 1.27), the finding that the two curves overlap to a high degree (ratio equal to 12.8/12.5=1.02) indicates that speaking rate expressed in syllables per second is a more perceptually relevant measure than percentage compression. Unfortunately, no distinction could be made between syllables per second and phonemes per second, since these two measures are highly correlated. However, the source of difficulty with speeded speech seems likely to occur at the phonemic level, with the possibility that consonant compression influences recognition performance more so than vowel compression or overall changes in sentence duration. Other factors, like rate of information processing, may be important as well.

In experiment II, it was observed that the difference between SRT for stationary and fluctuating noise was large for normal-hearing subjects and small for hearing-impaired subjects. This is in accordance with the results of Festen and Plomp (1990), and the difference in SRT is attributed to the notion that normal-hearing listeners are able to use the speech information at the time intervals when the level of the fluctuating masking noise is low. Due to loss of temporal acuity, hearing-impaired subjects often are not able to do so, causing the fluctuating noise to become smeared, behaving like stationary noise, such that the SRT_S and SRT_F are about equal. This is exactly what can be seen in Fig. 6. Subjects that perform well in fluctuating noise (low SRT_F) also perform well in stationary noise (low SRT_S), whereas the opposite is not true. This finding leads to the recommendation to conduct the SRT in fluctuating noise only, since it provides more information.

The finding that TCT correlates better with the SRT in fluctuating noise ($r=0.87$) than with the SRT in stationary noise ($r=0.73$) suggests that factors dealing with temporal processing play a dominant role. However, correlation is not as high as the correlation between male and female speech (r between 0.91 and 0.96). So, next to temporal factors, other factors may play a role. One factor may be cognition, for an increase in speech rate implies an increase in information rate which, in turn, requires a larger processing capacity. Thus, the TCT test also may provide information about the cognitive abilities. Especially in elderly subjects, processing capacities are said to decline (e.g., Gordon-Salant and Fitzgibbons, 1997; Salthouse, 1996). Unfortunately, the present data cannot be used to support this assertion, because differences in correlation are only small.

TCT and SRT in fluctuating noise correlate highly. Although time-compressed speech is less natural, it has the advantage that the test is far more time efficient. The duration of one TCT list was on average 83 s, whereas it was 113 and 120 s for the SRT test in stationary and fluctuating noise, respectively. Moreover, TCT may prove to be more successful with children, since the speech sounds funny and makes the task more challenging. However, TCT (and its relationship to SRT) for children has yet not been investigated.

To assess the effect of age on SRT and TCT, a two-way (age [2]$\times$hearing status [2]) ANOVA could be performed. However, the interpretation of the results of this ANOVA are contaminated by the fact that, especially for the young, hearing-impaired group, additional speech and language problems must have played a role, due to their hearing loss on the one hand, and, for five of the subjects, their non-native Dutch-speaking parents on the other hand. Indeed, the data show this poor performance. Therefore, scores between normal-hearing and hearing-impaired subjects cannot be compared. Also, normal-hearing young and elderly subjects cannot be directly compared, since the hearing loss for the elderly group was on average about 10 dB higher than for the young, normal-hearing group. To account for these differences in hearing loss, for every individual subject and condition, scores were converted to Speech Intelligibility Indices (SIIs, ANSI, 1997). For the sake of completeness, the data of all subjects were transformed.

TABLE I. Group-averaged results. For each group the mean SRT (in dB) and TCT (in syll/s) is given. In parentheses the corresponding SII value is given (see the text).

	SRT_S (dB)	SRT_F (dB)	TCT (syll/s)
Young, normal hearing	−4.8 (0.300)	−11.1 (0.089)	12.4 (0.321)
Elderly, normal hearing	−2.6 (0.365)	−7.8 (0.188)	10.7 (0.376)
Young, hearing impaired	0.8 (0.374)	0.1 (0.361)	7.6 (0.358)
Elderly, hearing impaired	−2.7 (0.308)	−4.6 (0.239)	9.2 (0.308)

Speech intelligibility index (SII)

The Speech Intelligibility Index (ANSI, 1997) is a calculation scheme that determines the part of the speech spectrum that is audible, i.e., is not below the absolute hearing level and not masked by interfering noise. For each frequency band (usually one-third-octave bands) the proportion of audible speech is calculated and these proportions are weighted summed, since not every band is equally important for speech intelligibility. This results in a number between zero and unity. Completely inaudible speech results in an SII of zero, completely audible speech in an SII of unity.

By definition, at the SRT, 50% of the sentences are perceived correctly. This critical speech-to-noise ratio can be converted to an SII value. Thresholds for subjects that need only little information for speech reception will yield low SII values. Thresholds for subjects that have problems with speech reception, on the other hand, will yield larger SII values. The advantage of using SII instead of SRT is that the SII takes into account the differences in threshold. Thus, it is quite conceivable that a hearing-impaired subject produces high SRTs but low SIIs, whereas a normal-hearing subject with poor speech processing capabilities produces high SIIs.

Table I displays, in parentheses, the SII group-averaged values for the four groups of subjects for the three conditions. SII values for SRT_S are between 0.3 and 0.4, indicating that roughly one-third of all speech information is necessary to reach the threshold of speech intelligibility with short, everyday sentences. Table I shows that, even after correction for the hearing loss, elderly, normal-hearing subjects perform worse than young, normal-hearing subjects ($F[1,27] = 104, p < 0.005$). Young, hearing-impaired subjects perform even worse, probably due to language problems. On the other hand, in contrast to the SRT_S values, elderly, hearing-impaired subjects perform rather well, reaching SII scores close to the young, normal-hearing group. It seems as if this group is very efficient in the use of speech information.

Unfortunately, SII is a purely spectral measure, i.e., it determines the part of the speech spectrum that exceeds the masking noise. It does not take into account the temporal characteristics of the noise. Therefore, thresholds obtained with time-compressed speech cannot be converted automatically to SII values, since the SII does not depend on the amount of time compression (because the noise spectrum and the speech spectrum do not depend on the amount of time compression). Yet, in order to be able to convert the TCT values to SII values, a simple addition was made to the SII calculation scheme. The SII for the unprocessed condition was calculated and simply multiplied with the amount of time compression, i.e., the sentence duration of the processed speech divided by the original duration. Thus, for example, if the duration of the time-compressed sentence was 0.6 times the original duration, the SII value also was multiplied with a factor 0.6. This calculation scheme can also be interpreted as removing the part of the information that has been removed by cutting out portions of the waveform. The group-averaged results of the SII calculations for the TCTs are given in Table I. The absolute values are very close to the ones corresponding to the SRT_S, and similar trends are even observed.

The SII model was not really developed for speech in fluctuating noise. Nonetheless, SRT_Fs were converted to SIIs, assuming it was stationary noise. The results are given in Table I. The absolute values do not have any meaning, but the relative values show that especially the young, hearing-impaired group has extreme difficulties in taking advantage of the fluctuating nature of the masking noise. Again, both groups of normal-hearing subjects benefit from the fluctuating characteristics, more than the elderly group of hearing-impaired subjects (who did perform well in stationary noise).

V. CONCLUSIONS

Two experiments with time-compressed speech have been reported. The first experiment provided normative data for time-compressed sentences. Speaking rate expressed in syllables per second appeared to be a more perceptually relevant measure than, e.g., compression rate. Young, normal-hearing subjects were able to understand 50% of the sentences at speaking rates of 12.5 syll/s.

The second experiment dealt with the relationship between the threshold for time-compressed speech (TCT) and speech-in-noise (SRT). Both stationary and fluctuating noise were used as a masker. Both young- and elderly normal-hearing and hearing-impaired subjects participated. The results show that (1) TCT correlates better with the SRT in fluctuating noise than with SRT in stationary noise, suggesting that factors dealing with temporal processing play a dominant role in the TCT; (2) SRT in fluctuating noise (and hence TCT) provides more information about the remaining hearing capacity than SRT in stationary noise; (3) even after correction for differences in hearing loss (by means of the SII), elderly subjects perform worse than young subjects in the normal-hearing population; (4) elderly, hearing-impaired subjects perform on average as well as young, normal-hearing subjects in stationary masking noise, but have considerably more difficulties in fluctuating noise.

With respect to audiological testing, the results show that SRT in fluctuating noise is recommended over SRT in stationary noise. One may even consider using TCT due to its time efficiency, despite the fact that time-compressed speech sounds less natural.

ACKNOWLEDGMENTS

The duration manipulation of the sentences was done with the software package GIPOS, developed by Ercan Gigi at the Institute for Perception Research (IPO), Eindhoven, the Netherlands. The first author acknowledges IPO for its hospitality and Ercan for his kind assistance. Marscha Krone, Bas Franck, and especially Maite Tromp are acknowledged for their part in the preparation and conduction of the experiment.

ANSI (**1997**). ANSI S3.5-1997, ''American national standard methods for the calculation of the speech intelligibility index'' (American National Standards Institute, New York).

Arons, B. (**1992**). ''Techniques, perception, and applications of time-compressed speech,'' Proceedings of 1992 Conference, American Voice I/O Society, 169–177.

Beasley, D. S., Forman, B. S., and Rintelmann, W. F. (**1972a**). ''Perception of time-compressed CNC monosyllables by normal listeners,'' J. Aud Res. **12**, 71–75.

Beasley, D. S., Schwimmer, S., and Rintelmann, W. F. (**1972b**). ''Intelligibility of time-compressed CNC monosyllables,'' J. Speech Hear. Res. **15**, 340–350.

Beattie, R. C. (**1986**). ''Normal intelligibility functions for the Auditec CID W-22 test at 30% and 60% time-compression,'' Am. J. Otol. **7**, 60–64.

Bornstein, S. P. (**1994**). ''Time compression and release from masking in adults and children,'' J. Am. Acad. Audiol. **5**, 89–98.

de Haan, H. (**1977**). ''A speech-rate intelligibility threshold for speeded speech and time-compressed connected speech,'' Percept. Psychophys. **22**, 366–372.

de Haan, H. (**1982**). ''The relationship of estimated comprehensibility to the rate of connected speech,'' Percept. Psychophys. **32**, 27–31.

de Haan, H. J., and Schjelderup, J. R. (**1978**). ''Threshold of intelligibility/comprehensibility of rapid connected speech: Method and instrumentation,'' Behav. Res. Methods Instrum. **10**, 841–844.

Fairbanks, G., and Kodman, F. (**1957**). ''Word intelligibility as a function of time compression,'' J. Acoust. Soc. Am. **29**, 636–644.

Festen, J. M., and Plomp, R. (**1990**). ''Effects of fluctuating noise and interfering speech on the speech-reception threshold for impaired and normal hearing,'' J. Acoust. Soc. Am. **88**, 1725–1736.

Fletcher, H. (**1953**). *Speech and Hearing in Communication* (Van Nostrand, New York).

Fu, Q.-J., Galvin III, J. J., and Wang, X. (**2001**). ''Recognition of time-distorted sentences by normal-hearing and cochlear-implant listeners,'' J. Acoust. Soc. Am. **109**, 379–384.

Gehr, S. E., and Sommers, M. S. (**1999**). ''Age differences in backward masking,'' J. Acoust. Soc. Am. **106**, 2793–2799.

Gordon-Salant, S., and Fitzgibbons, P. J. (**1993**). ''Temporal factors and speech recognition performance in young and elderly listeners,'' J. Speech Hear. Res. **36**, 1276–1285.

Gordon-Salant, S., and Fitzgibbons, P. J. (**1997**). ''Selected cognitive factors and speech recognition performance among young and elderly listeners,'' J. Speech Lang. Hear. Res. **40**, 423–431.

Gordon-Salant, S., and Fitzgibbons, P. J. (**1999**). ''Profile of auditory temporal processing in older listeners,'' J. Speech Lang. Hear. Res. **42**, 300–311.

Grimes, A. M., Mueller, H. G., and Williams, D. L. (**1984**). ''Clinical considerations in the use of time-compressed speech,'' Ear Hear. **5**, 114–117.

Konkle, D. F., Beasley, D. S., and Bess, F. H. (**1977**). ''Intelligibility of time-altered speech in relation to chronological aging,'' J. Speech Hear. Res. **20**, 108–115.

Kurdziel, S. A., Noffsinger, D., and Olsen, W. (**1976**). ''Performance by cortical lesion patients on 40% and 60% time-compressed materials,'' J. Am. Audiol Soc. **2**, 3–7.

Kurdziel, S. A., Rintelmann, W. F., and Beasley, D. S. (**1975**). ''Performance of noise-induced hearing-impaired listeners on time-compressed consonant–nucleus–consonant monosyllables,'' J. Am. Audiol Soc. **1**, 54–60.

Lacroix, P. G., and Harris, J. D. (**1979**). ''Multiplicative effects on sentence comprehension for combined acoustic distortions,'' J. Speech Hear. Res. **22**, 259–269.

Moulines, E., and Laroche, J. (**1995**). ''Non-parametric techniques for pitch-scale and time-scale modification of speech,'' Speech Commun. **16**, 175–205.

Nilsson, M., Soli, S. D., and Sullivan, J. A. (**1994**). ''Development of the Hearing In Noise Test for the measurement of speech reception thresholds in quiet and in noise,'' J. Acoust. Soc. Am. **95**, 1085–1099.

Peters, R. W., and Moore, B. C. J. (**1992**). ''Auditory filter shapes at low frequencies in young and elderly hearing-impaired subjects,'' J. Acoust. Soc. Am. **91**, 256–266.

Plomp, R., and Mimpen, A. M. (**1979**). ''Improving the reliability of testing the speech reception threshold for sentences,'' Audiology **18**, 43–52.

Riensche, L. L., Curran, C. E., and Porch, B. E. (**1986**). ''The assessment of reading readiness using multi-dimensionally scored time-compressed speech,'' J. Aud. Res. **26**, 1–4.

Salthouse, T. A. (**1996**). ''The processing-speed theory of adult age differences in cognition,'' Psychol. Rev. **103**, 403–428.

Smoorenburg, G. F. (**1986**). ''Speech reception in individuals with noise-induced hearing loss and its implication for hearing loss criteria,'' in *Basic and Applied Aspects of Noise-induced Hearing Loss*, edited R. J. Salvi, D. Henderson, R. P. Hamernik (Plenum, New York).

Sommers, M. S., and Gehr, S. E. (**1988**). ''Auditory suppression and frequency selectivity in older and younger adults,'' J. Acoust. Soc. Am. **103**, 1067–1074.

Stark, R. E., and Montgomery, J. W. (**1995**). ''Sentence processing in language-impaired children under conditions of filtering and time compression,'' Appl. Psycholing. **16**, 137–154.

Stollman, M. H. P., and Kapteyn, T. S. (**1994**). ''Effect of time-scale modification of speech on the speech recognition threshold in noise for elderly listeners,'' Audiology **33**, 280–290.

Stollman, M. H. P., Kapteyn, T. S., and Wegener Sleeswijk, B. (**1994**). ''Effect of time-scale modification of speech on the speech recognition threshold in noise for hearing-impaired and language-impaired children,'' Scand. Audiol. **23**, 39–46.

Stuart, A., and Phillips, D. P. (**1998**). ''Recognition of temporally distorted words by listeners with and without a simulated hearing loss,'' J. Am. Acad. Audiol **9**, 199–208.

Vaughan, N. E., and Letowski, T. (**1997**). ''Effects of age, speech rate, and type of test on temporal auditory processing,'' J. Speech Lang. Hear. Res. **40**, 1192–1200.

Versfeld, N. J., Daalder, L., Festen, J. M., and Houtgast, T. (**2000**). ''Method for the selection of sentence materials for efficient measurement of the speech reception threshold,'' J. Acoust. Soc. Am. **107**, 1671–1684.

Recognition of low-pass-filtered consonants in noise with normal and impaired high-frequency hearing

Amy R. Horwitz, Judy R. Dubno, and Jayne B. Ahlstrom
Department of Otolaryngology—Head and Neck Surgery, Medical University of South Carolina, 39 Sabin Street, Room 608, P.O. Box 250150, Charleston, South Carolina 29425

(Received 28 January 2000; accepted for publication 3 October 2001)

People with high-frequency hearing loss often complain of difficulty understanding speech, particularly in noisy environments. The reduction in audible high-frequency speech information provides one explanation. In addition, high-frequency hearing loss may reduce the contribution from the ''tails'' of high-frequency auditory nerve fibers, resulting in diminished availability of lower frequency speech cues. This study was designed to determine if high-frequency hearing loss results in speech-understanding deficits beyond those accounted for by reduced high-frequency speech information. Recognition of speech, both low-pass filtered and unfiltered, was measured for subjects with normal hearing and those with hearing loss limited to high frequencies. Nonsense syllables were presented in three levels of noise that was spectrally shaped to match the long-term spectrum of the speech. Scores for subjects with impaired high-frequency hearing were significantly poorer than scores for subjects with normal hearing. In the case of the low-pass-filtered speech, performance differences between groups could not be attributed to differences in speech audibility, as high-frequency speech cues were absent for all subjects. These results are consistent with the hypothesis that high-frequency fibers encode useful low-frequency speech information. [DOI: 10.1121/1.1427357]

PACS numbers: 43.71.Ky, 43.66.Sr [CWT]

I. INTRODUCTION

One of the most common complaints of people with high-frequency hearing loss is difficulty understanding speech in noisy environments. The reduction in audible *high-frequency* speech information provides at least part of the explanation. Indeed, the most widely applied model of speech recognition, the articulation index (AI) (French and Steinberg, 1947), is based upon the assumption that the contribution of a specific spectral region to speech recognition is determined solely by the audibility of that spectral region. However, speech-recognition deficits resulting from high-frequency hearing loss may not be limited to the loss of high-frequency speech information. For example, there is evidence that damage to the basal (i.e., high-frequency) region of the cochlea may be accompanied by physiological and behavioral changes such as (a) reduced contributions from the ''tails'' of high-frequency auditory nerve fibers (Kiang and Moxon, 1974); (b) reduced phase-locking and synchronization to low frequencies (Joris *et al.*, 1994); (c) disproportionate loss of activity from low-spontaneous-rate afferent fibers (Schmiedt *et al.*, 1996) and efferent fibers (Liberman *et al.*, 1990); (d) reduced intensity discrimination (Florentine, 1983); and (e) reduced temporal resolution, as measured by recovery from forward masking (Jesteadt *et al.*, 1982), modulation detection (Bacon and Viemeister, 1985), gap and decrement detection (Buus and Florentine, 1985; Moore *et al.*, 1993), and speech recognition in amplitude-modulated maskers (Bacon *et al.*, 1998; Eisenberg *et al.*, 1995).

These experimental results lead to the following question. Does high-frequency hearing loss result in speech understanding deficits beyond those accounted for by a reduction in high-frequency speech information? In previous behavioral experiments designed to answer this question (Van Tasell and Turner, 1984; Kim and Turner, 1988; Strickland *et al.*, 1994), subjects listened to speech that was filtered to remove high-frequency information. Accordingly, any contribution of basal fibers to recognition of this filtered speech was likely due to their role in encoding lower frequency speech components because high-frequency components of the speech were removed. Results of these experiments were equivocal and therefore the question remains unanswered. The first two studies (Van Tasell and Turner, 1984; Kim and Turner, 1988) found that speech recognition was poorer when high-frequency fibers were disrupted (by high-pass noise or hearing loss, respectively), whereas the third study (Strickland *et al.*, 1994) found no such effect. Interpretation of these contradictory conclusions is limited by variables not controlled across studies. For example, none of the studies included both of the following: (a) detailed measurements ensuring equal speech audibility for the relevant comparison conditions and (b) direct comparison of a group of subjects with high-frequency hearing loss and a group of subjects with normal hearing.

The design of the current study, in which both controls were included, provided an opportunity to assess the contribution of high-frequency fibers to the encoding of *lower frequency* speech information. It was hypothesized that listeners with high-frequency hearing loss would show deficits in recognition of low-pass filtered speech relative to listeners with normal high-frequency hearing. To appropriately test this hypothesis, speech audibility must be strictly controlled between the two groups. Therefore, the low-pass cutoff frequency of the speech and noise, as well as the minimum

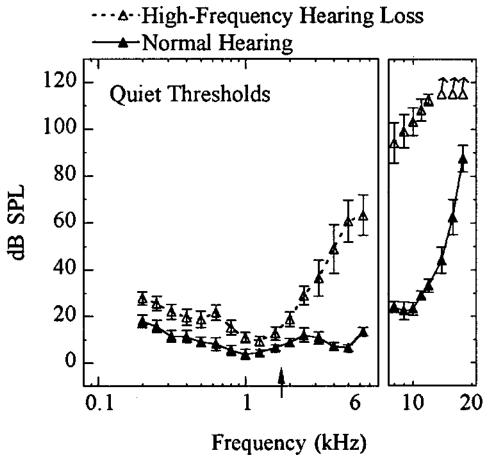

FIG. 1. Mean (±1 standard error) thresholds measured in quiet from 0.2 to 18 kHz for subjects with normal hearing (filled symbols) and for subjects with high-frequency hearing loss (open symbols). In the left panel, the arrow on the *x* axis indicates the cutoff frequency for the low-pass-filtered speech and noise. In the right panel, arrows indicate frequencies at which no subject responded at the maximum intensity presented.

background noise level, were selected so that the audibility of the filtered speech was equivalent for subjects with normal and impaired high-frequency hearing. The major focus of the study was a comparison of low-pass-filtered speech recognition scores for listeners with normal and impaired high-frequency hearing. In addition, an unfiltered speech condition was included to provide a baseline for comparison with scores for low-pass-filtered speech. A final condition included a high-pass-filtered noise masker intended to mask any speech information that might be carried by high-frequency fibers. As will be described, obtaining conclusive data when using a high-pass masker proved difficult.

II. METHOD

A. Subjects

Twelve subjects participated, all with immittance measures within normal limits. Six had normal hearing (five females, one male; age range: 21–35 years) and six had high-frequency hearing loss (two females, four males; age range: 66–79 years). Pure-tone thresholds were ≤20 dB HL (ANSI, 1996) at octave frequencies from 0.25 to 8.0 kHz for the normal-hearing subjects. For subjects with high-frequency hearing loss, thresholds were ≤20 dB HL (ANSI, 1996) at octave frequencies from 0.25 to 2.0 kHz and ≥30 dB HL (ANSI, 1996) at 3.0 kHz and above. One ear of each subject was selected for testing. For the subjects with impaired high-frequency hearing, the test ear was the ear with the lower thresholds at and below 2.0 kHz and/or the more elevated thresholds above 2.0 kHz. For normal-hearing subjects, test ear was selected randomly. Mean audiometric thresholds (in dB SPL) for both subject groups are shown in the left panel of Fig. 1. Although thresholds at frequencies ≤2.0 kHz were within "normal" limits for all subjects, thresholds at these frequencies for subjects with high-frequency hearing loss were higher than those of normal-hearing subjects (with a 9-dB mean difference for frequencies from 0.2 to 2.0 kHz). To provide an estimate of the functioning of the base of the cochlea, thresholds for pure-tone signals from 8.0 to 18.0 kHz were also obtained (using a Demlar audiometer and Koss earphones) and are shown in the right panel of Fig. 1.

B. Apparatus and stimuli

An insert earphone (Etymotic ER2) was used for stimulus presentation. This earphone was selected for its flat frequency response through 10 kHz to provide an extended bandwidth for the high-pass-filtered noise. Tonal signals were digitally generated (TDT DA3-4), 350-ms pure tones with 10-ms raised-cosine rise/fall ramps.

Speech signals were 66 consonant–vowel (CV) syllables and 63 vowel–consonant (VC) syllables formed by combining /b,tʃ,d,dʒ,ʒ,f,g,k,l,m,n,ŋ,p,r,s,ʃ,t,θ,ð,v,w,j,z/ and /ɑ,i,u/. Each of the 129 syllables was spoken by one male and one female talker without a carrier phrase, for a total of 258 syllables. [See Dubno and Schaefer (1992, 1995) for a more detailed description of the speech materials.] To provide a reasonable listening interval, the 258-item set was divided into four approximately equivalent lists such that each list contained 64 or 65 items and included all 23 consonants, three vowels, both talkers, and both consonant placements. Because the complete set of four lists was presented at least once for each condition, no effort was made to ensure strict equivalency among the four lists. Presentation order was randomized for items within each list and for the four lists within each 258-syllable set.

To control speech audibility over a range of signal-to-noise ratios, the masker was a spectrally shaped broadband noise with a $\frac{1}{3}$-oct band spectrum within 3 dB of the long-term average spectrum of the nonsense syllables. To generate this "speech-shaped" masker, Gaussian noise (TDT WG1) was routed through two cascaded, programmable $\frac{1}{3}$-oct band filters (Applied Research and Technology, IEQ) and recorded on digital audio tape (DAT). Output from the DAT was attenuated prior to mixing with the speech stimuli and presented at overall levels of 65, 71, and 77 dB SPL, for signal-to-noise ratios of 12, 6, and 0 dB, respectively. Digital speech waveforms were output from a 16-bit digital-to-analog converter (TDT DA3-4) at a sampling rate of 33 kHz, attenuated (TDT PA4), then mixed (TDT SM3) with one of three levels of speech-shaped masker. The speech and noise were then low-pass filtered (or not, depending on the condition), mixed (TDT SM3) with a high-pass-filtered noise masker (or not, depending on the condition), and delivered to the earphone. Speech level was expressed as that of a 1-kHz tone equal to the long-term rms level of the syllables. Overall speech level was set at 77 dB SPL prior to low-pass filtering. Due to the sloping characteristic of the unfiltered speech spectrum, the overall speech level changed by less than 1 dB following low-pass-filtering at 1.78 kHz.

For the condition in which the speech and speech-shaped masker were low-pass filtered, the mixed stimuli were routed through three cascaded programmable filters (two TDT PF1s and one Stanford Research Model 650) and low-pass filtered at 1.78 kHz. Slopes greater than 100 dB/oct were verified on a signal analyzer. The spectrum of the low-pass-filtered speech-shaped noise is shown by the dashed

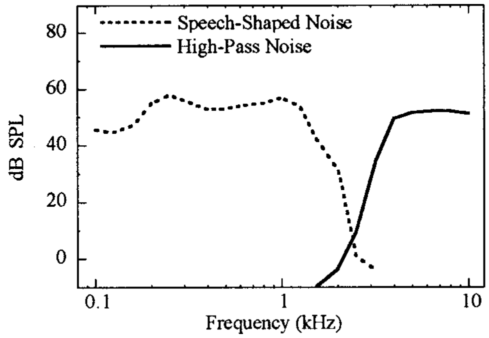

FIG. 2. Long-term rms $\frac{1}{3}$-octave band spectra for the low-pass-filtered speech-shaped noise (dotted line) and the 59-dB SPL high-pass noise (solid line). The overall level of the plotted speech-shaped noise is 65 dB SPL, the lowest level used.

line in Fig. 2. Long-term rms levels of the tones, speech, and speech-shaped noise were measured in a 2-cc coupler (B&K DB-0138 with Etymotic ER1-07 adapter).

A Gaussian noise was high-pass filtered (four cascaded TDT PF1s) at 3.75 kHz to create the high-pass noise which was then recorded on DAT. The slope was greater than 100 dB/oct as verified on a signal analyzer. The spectrum of the high-pass noise is shown by the solid line in Fig. 2. The presentation level of the high-pass masker was determined based on pilot data. To ensure that any disruption in speech recognition in the presence of high-pass noise was not due to unintentional downward spread of masking, each listener's thresholds at and below 2.0 kHz were measured with and without the high-pass noise. Indeed, the overall level of high-pass noise that was selected (91 dB SPL) because of its likelihood of masking the high-frequency fibers resulted in elevated thresholds for mid- and low-frequency signals. This finding is consistent with reports of "remote masking," whereby an intense high-pass noise causes mid- and low-frequency threshold elevation (e.g., Bilger and Hirsh, 1956; Keith and Anderson, 1969). To eliminate any remote masking confound, the level of the high-pass noise was reduced during pilot testing until thresholds between 0.2 and 2.0 kHz were unaffected by the presence of the high-pass noise. This process resulted in the use of a relatively low overall level for the high-pass masker (i.e., 59 dB SPL). The long-term rms level of the high-pass noise was measured in an ear simulator (B&K 4157). When measured in the 2-cc coupler used for the other noise and speech signals, the overall level of the high-pass noise was 44 dB SPL. This difference in overall level is due to differences in frequency response for the ER-2 earphone measured in the 2-cc coupler compared to that measured in an ear simulator, which more accurately approximates the response of the human ear, particularly in the high frequencies.

C. Procedures

1. Pure-tone thresholds

To obtain estimates of speech audibility across all test conditions, pure-tone thresholds were measured in quiet and in the presence of each masker using a single-interval (yes–no) maximum-likelihood psychophysical procedure similar to that described by Green (1993) and discussed in detail in Leek *et al.* (2000). Quiet thresholds were measured at $\frac{1}{3}$-oct center frequencies from 0.2 to 6.3 kHz. Masked thresholds were measured at selected $\frac{1}{3}$-oct center frequencies (i.e., 0.25, 0.5, 1, 1.6, 2, 2.5, 3.15, 4, and 5 kHz) for ten conditions. Specifically, thresholds were measured in the presence of (a) the high-pass masker alone, (b) three levels of the unfiltered speech-shaped masker, (c) three levels of the unfiltered speech-shaped masker plus the high-pass masker, and (d) three levels of the low-pass-filtered speech-shaped masker.

2. Speech-recognition scores

Following threshold testing, speech recognition was measured as follows. Subjects were familiarized with the testing procedure by listening to unfiltered syllables with no noise background. The set of possible consonants was presented on a computer monitor and subjects responded by pointing with a mouse. After an initial period during which the experimenter verbally reinforced subjects' responses, no feedback was provided. Prior to data collection, subjects also practiced responding to low-pass-filtered and unfiltered speech at all signal-to-noise ratios used for testing (i.e., 12, 6, and 0 dB). This training lasted between 1 and 2 h. At the start of each subsequent session, two practice runs were conducted but not scored. During data collection, presentation order was randomized for the three levels of speech-shaped noise (i.e., 65, 71, and 77 dB SPL) and, when applicable, for the two high-pass noise conditions (i.e., with and without high-pass noise).

First, to provide a baseline condition, speech-recognition scores were obtained for unfiltered speech presented in three levels of speech-shaped noise. Data for each condition consisted of the percentage of correct responses to one set of 258 syllables.

Next, to compare speech recognition between subject groups without audibility confounds, speech-recognition scores were obtained for low-pass-filtered speech presented in three levels of low-pass-filtered speech-shaped noise. To assess effects of high-pass-filtered noise, two sets of these scores were obtained, one with and one without high-pass noise. To reduce variance and increase statistical power, this block of low-pass-filtered conditions was repeated so that final scores for each condition were the percentage of correct responses to 516 syllables.

In all, speech-recognition scores were obtained in nine conditions: unfiltered speech in three levels of speech-shaped noise and low-pass-filtered speech in three levels of low-pass-filtered speech-shaped noise, with and without high-pass noise.

III. RESULTS AND DISCUSSION

A. Thresholds

1. Effects of speech-shaped noise

Mean masked thresholds (triangles) for the three levels of low-pass-filtered speech-shaped noise are plotted in Fig. 3. Mean quiet thresholds and the low-pass-filtered speech spectrum are included for reference. The bottom panel of Fig. 3 shows results for the lowest level of noise (i.e., 65 dB SPL). Mean masked thresholds (from 0.2 to 2.0 kHz) for the

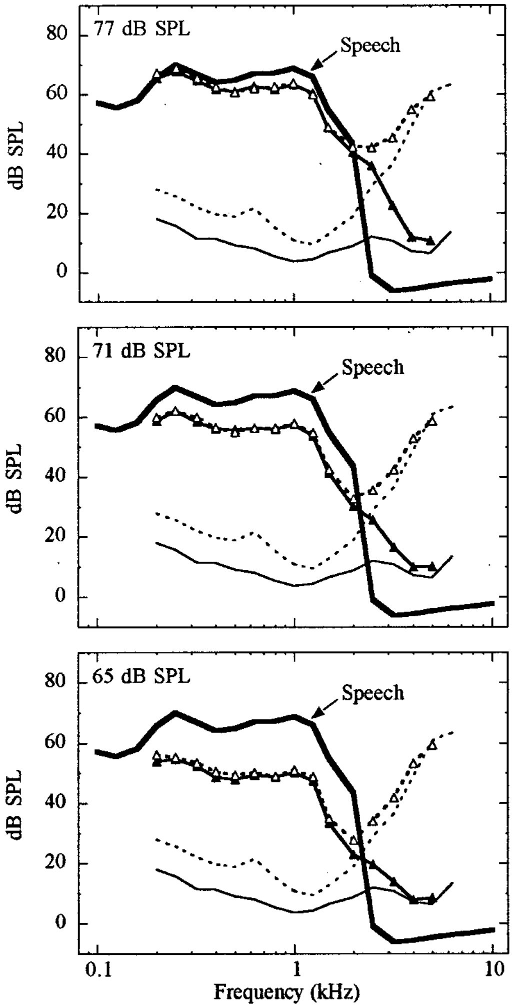

FIG. 3. Mean (±1 standard error) thresholds measured in low-pass-filtered speech-shaped noise for subjects with normal hearing (filled triangles) and for subjects with high-frequency hearing loss (open triangles). Replotted from Fig. 1 are quiet thresholds for subjects with normal hearing and for those with impaired high-frequency hearing (thin solid line and thin dashed line, respectively). The thick lines show the long-term rms $\frac{1}{3}$-octave band spectra for the low-pass filtered speech at 77 dB SPL. The top, middle, and bottom panels show results for speech-shaped noise at 77, 71, and 65 dB SPL, respectively.

subjects with normal hearing were within 2 dB of those for subjects with high-frequency hearing loss. Smaller differences in masked thresholds were obtained at the two higher levels of speech-shaped noise (i.e., 71 and 77 dB SPL) as shown in the middle and top panels of Fig. 3. Averaged across masker levels, mean masked thresholds (from 0.2 to 2.0 kHz) for subjects with normal hearing were within 1 dB of those for subjects with high-frequency hearing loss. Because speech audibility was determined by the speech-shaped masker and not by quiet thresholds, audibility of the low-pass filtered speech (as indicated by the difference between the thick line and the triangles in Fig. 3) was nearly identical for subjects with normal and impaired high-frequency hearing for all three masker levels. Thus, any observed differences in low-pass-filtered speech recognition cannot be attributed to differences in speech audibility between subjects with and without high-frequency hearing loss.

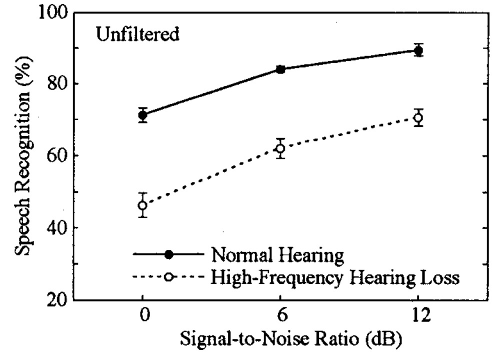

FIG. 4. Mean (±1 standard error) recognition scores for unfiltered speech in speech-shaped noise for subjects with normal hearing (filled circles) and subjects with high-frequency hearing loss (open circles) as a function of signal-to-noise ratio.

2. Effects of high-pass noise

Averaged across frequencies, group mean masked thresholds for pure tones from 0.25 to 2.0 kHz in the presence of the high-pass noise were within 1 dB of thresholds in quiet. These results confirm that the level of the high-pass noise was sufficiently low to avoid remote masking. Similar results were obtained for masked thresholds in the presence of speech-shaped noise (i.e., the addition of the high-pass noise affected group mean thresholds by less than 1 dB). Unless otherwise stated, threshold and speech-recognition scores reported throughout refer to those measured without high-pass noise. Speech scores obtained in the presence of the high-pass noise are presented in a later section.

B. Unfiltered speech recognition

Figure 4 shows results for the baseline condition that included both low- and high-frequency speech information. Unfiltered speech-recognition scores for subjects with normal high-frequency hearing were, on average, more than 20% higher than scores for subjects with impaired high-frequency hearing. Results of a repeated-measures analysis of variance (ANOVA) revealed that this difference between groups was significant ($F[1,10]=50.5$; $p<0.0001$). This finding is not surprising given the difference in the audibility of important high-frequency speech information for the two subject groups. Also as expected, recognition scores increased significantly with increasing signal-to-noise ratio ($F[2,20]=232.3$; $p<0.0001$). Finally, results of a repeated-measures ANOVA on rau-transformed scores indicated that there was no significant interaction between subject group and signal-to-noise ratio.[1]

C. Low-pass-filtered speech recognition

1. Effect of high-frequency hearing loss

To focus the investigation on the role of the base of the cochlea in encoding lower frequency information, the confounding influence of high-frequency speech audibility was removed. Recall that speech and noise were low-pass filtered at 1.78 kHz, and that all subjects had normal hearing through 2 kHz. Thus, for this condition, speech was presented only at those frequencies for which average masked thresholds were within 2 dB between groups and for which all subjects had

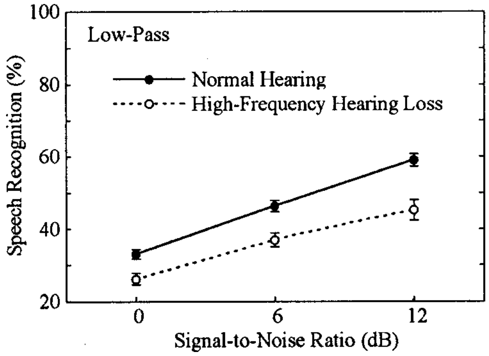

FIG. 5. Mean (±1 standard error) recognition scores for low-pass-filtered speech in low-pass-filtered noise for subjects with normal hearing (filled circles) and subjects with high-frequency hearing loss (open circles) as a function of signal-to-noise ratio.

normal hearing. Figure 5 shows mean low-pass-filtered speech-recognition scores for subjects with normal and impaired high-frequency hearing. In the absence of important speech cues above 2.0 kHz, scores for all subjects were reduced compared to those for unfiltered speech (compare Figs. 4 and 5). Importantly, if recognition scores were entirely dependent on the levels of the low-pass-filtered speech and noise, scores for subjects with normal and impaired high-frequency hearing should be equal. Instead, scores for subjects with high-frequency hearing loss averaged 10% lower than those for subjects with normal hearing. Results of a repeated-measures ANOVA revealed that this difference between subject groups was significant ($F[1,10]=15.8$; $p=0.003$). As signal-to-noise ratio was increased, average recognition scores increased significantly ($F[2,20]=426.7$; $p<0.0001$). In addition, the interaction between subject group and signal-to-noise ratio was significant ($F[2,20]=9.9$; $p=0.001$) and can be seen in the smaller difference between subject groups with decreasing signal-to-noise ratio. This finding is consistent with results from Kiang and Moxon (1974), which showed that representation of speech information carried by high-frequency auditory nerve fibers was degraded as signal-to-noise ratio decreased. That is, as observed here, the advantage for subjects with normal high-frequency hearing would be expected to be greatest for the most favorable signal-to-noise ratio, at which the high-frequency auditory nerve fibers are best able to encode lower frequency speech cues. Further, as signal-to-noise ratio decreases and less speech information is carried by high-frequency auditory nerve fibers, the difference in speech recognition between subjects with normal and impaired high-frequency hearing would be expected to decrease, as was the case here.

2. Estimating speech recognition using audibility calculations

Additional analyses using the AI were performed to determine if the significant group differences in speech recognition resulted from slight group differences in masked thresholds and corresponding differences in speech audibility. Previous studies (e.g., Dubno and Ahlstrom, 1995a,b) have shown that more accurate predictions of speech recognition may be obtained using speech audibility calculations based on subjects' masked thresholds rather than quiet thresholds and noise spectra. Therefore, AI calculations were based on subjects' masked thresholds measured at each of the three levels of the low-pass-filtered speech-shaped noise.[2] Speech scores were predicted from the normal transfer function relating the AI to consonant recognition established for the speech stimuli used in this experiment (Dirks *et al.*, 1990a,b). Averaging across level, when masked thresholds were taken into account, scores for subjects with normal hearing were predicted to be only 3% better than those for subjects with impaired high-frequency hearing. This predicted difference was due to slight differences in masked thresholds. However, observed scores for subjects with normal hearing were 11% better than those for subjects with impaired high-frequency hearing. To determine if significant group differences remained after accounting for masked thresholds, a repeated-measures ANOVA was performed using each listener's observed and predicted scores. The main effect of subject group remained significant ($F[1,8]=13.1$; $p=0.007$). Therefore, even when small differences in masked thresholds were taken into account, scores for subjects with impaired high-frequency hearing were poorer than those for subjects with normal high-frequency hearing.

3. Error analysis

It was of interest to determine if observed differences in overall scores between subject groups could be attributed to differences in confusions for particular types of speech information, such as place, manner, or voicing cues. The features of place, manner, and voicing are three categories thought to reflect different types of speech information. Because high-frequency auditory nerve fibers respond to lower frequency speech if presented with sufficient intensity (Kiang and Moxon, 1974), they may provide useful speech information such as formant cues used to distinguish place of articulation. Further, because high-frequency fibers can better preserve low-frequency timing information than low-frequency fibers (Kiang, 1975; Joris *et al.*, 1994), high-frequency fibers may be particularly well suited to provide speech periodicity and envelope information, which may help distinguish among manner classes and between voiced and voiceless consonants.

To examine error patterns, data obtained from individual listeners' stimulus-response confusion matrices were analyzed using the SINFA procedure (sequential information analysis; Wang and Bilger, 1973).[3] Results for place, manner, and voicing showed that more speech information was transmitted for subjects with normal high-frequency hearing compared to subjects with impaired high-frequency hearing. To broaden the analysis beyond place, manner, and voicing cues, error patterns were also assessed for the 23 individual consonants. Although a large range in information transmitted was observed across consonants, results for every consonant indicated that transmitted information was higher for subjects with normal high-frequency hearing than for subjects with impaired high-frequency hearing. Thus, differences between subject groups were not limited to isolated

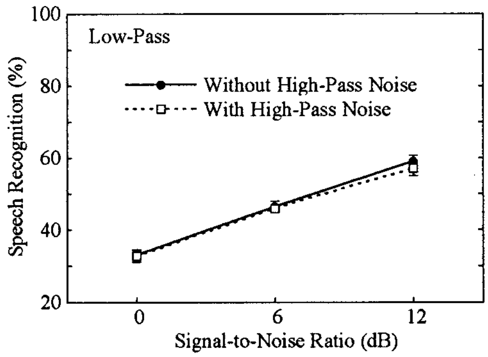

FIG. 6. Mean (± 1 standard error) recognition scores for low-pass-filtered speech in low-pass-filtered noise for subjects with normal hearing as a function of signal-to-noise ratio. Filled circles show scores without high-pass noise (replotted from Fig. 5) and open squares show scores in the presence of high-pass noise.

consonants or features. Instead, more global deficits were evident for subjects with impaired high-frequency hearing.

4. Effect and limitations of high-pass noise

Figure 6 shows mean speech-recognition scores for normal-hearing listeners with and without high-pass noise. The filled circles are replotted from Fig. 5 and show scores in the presence of speech-shaped noise alone. The open squares show scores in the presence of high-pass noise in addition to the speech-shaped noise. Speech recognition decreased slightly in the presence of the high-pass masker. Averaging across signal-to-noise ratio, scores decreased by 1% with the addition of the high-pass masker. Although a repeated-measures ANOVA indicated that this difference was significant ($F[1,5]=11.34$; $p=0.02$), its practical significance is questionable given its magnitude. This small effect of high-pass noise is difficult to interpret in light of the relatively low level of the noise and reveals an important problem with this approach. The high-pass noise level was selected to avoid downward spread of masking. However, at that noise level, it is not known if the high-pass noise was sufficiently intense to mask fibers in the base of the cochlea. This result serves as a reminder that studies of speech understanding with high-pass maskers may be difficult to interpret unless the effects of level, including downward spread of masking, are controlled.

5. Comparison with previous studies of lower frequency speech recognition

Looking at both overall speech-recognition scores and speech feature information, several similarities may be noted with previous studies of the role of high-frequency fibers in lower frequency speech recognition. Van Tasell and Turner (1984) measured speech recognition as a function of low-pass filtering and high-pass noise. Results for one listener with low-frequency hearing loss suggested that lower frequency speech recognition was largely due to the contribution of higher frequency fibers. In addition, high-frequency fibers appeared to play a role in transmitting both voicing and place information. Kim and Turner (1988) compared speech recognition between ears for listeners with unilateral high-frequency loss. Results were similar to the present study in that low-pass-filtered speech recognition was better for ears with normal compared to impaired high-frequency hearing. Further, similar to our results, differences in place information transmitted were measured between ears with and without high-frequency hearing loss. In contrast, there was little difference between ears in voicing information transmitted. Finally, in both the present study and that of Strickland *et al.* (1994), when using a high-pass noise to mask information carried by high-frequency fibers of normal-hearing listeners, little effect was seen for low-pass filtered speech recognition.

D. Possible effects of differences in age and lower frequency thresholds

A potential confound due to aging effects was difficult to avoid and should be acknowledged. This study required one group of subjects with normal hearing through the extended high-frequency range and a second group of subjects with substantial hearing loss above 2 kHz. These criteria resulted in selection of subjects that differed in age as well as hearing status. In this study, it was not possible to determine if age contributed to the differences in speech recognition observed between groups. Even if age effects were present, however, they would not detract from the importance of the finding of a deficit in low-frequency speech recognition for subjects with high-frequency hearing loss.

Perhaps related to age effects, another potential confound concerned differences in lower frequency pure-tone thresholds. Recall that whereas all subjects had ‘‘normal’’ low-frequency thresholds, subjects with high-frequency hearing loss had thresholds from 0.2 to 2 kHz that were, on average, 9-dB higher than those of normal-hearing subjects. However, given the spectrum and level of the speech-shaped masker used for all speech testing, differences in low-frequency thresholds did not result in differences in speech audibility between the two subject groups. Thus, from the perspective of the AI model, these differences in low-frequency thresholds in quiet should not result in differences in speech understanding. Alternatively, it is possible that slightly elevated lower frequency thresholds could reflect abnormal processing in this frequency range, which could in turn degrade lower frequency speech recognition. Whether or not such a potential deficit may be related to high-frequency hearing loss remains unclear.

IV. SUMMARY AND CONCLUSIONS

The role of high-frequency auditory nerve fibers in carrying mid- and low-frequency speech information has been difficult to determine, in part due to confounding effects of high-frequency speech cues and differences in speech audibility among subjects with normal and impaired hearing. This problem was addressed here by precisely controlling the spectra, bandwidth, and levels of speech and noise. Twelve subjects with normal hearing through 2.0 kHz participated; six had normal high-frequency hearing and the other six had impaired high-frequency hearing. Pure-tone thresholds and recognition of nonsense syllables were measured in several combinations of masker and filtering conditions. Results may be summarized as follows:

(1) Listeners with impaired high-frequency hearing showed deficits in recognition of unfiltered speech in noise compared to normal-hearing listeners. This deficit is likely related to the reduction in high-frequency speech audibility.
(2) Listeners with impaired high-frequency hearing showed deficits in recognition of low-frequency speech in noise compared to normal-hearing listeners. These results were not predicted on the basis of speech audibility because speech and noise were low-pass filtered and presented only at frequencies for which both groups had normal hearing and nearly equivalent masked thresholds. Instead, this result is consistent with the hypothesis that damage to the base of the cochlea results in a reduction in the encoding of lower frequency speech information.
(3) The use of a high-pass noise of sufficient intensity to assure that the fibers in the base of the cochlea are disrupted may result in elevated mid- to low-frequency thresholds. Therefore, studies using high-pass noise to model loss of contribution from high-frequency fibers should be undertaken with caution.

These findings may have clinical implications involving the nature of deficits accompanying high-frequency hearing loss and the provision of high-frequency amplification. The optimum degree of high-frequency amplification is currently unclear; results on this issue to date have been mixed (e.g., Murray and Byrne, 1986; Sullivan *et al.*, 1992). To the extent that deficits in speech recognition accompanying high-frequency hearing loss are caused by a reduction in restorable high-frequency speech information, amplification should be beneficial. However, due to unique properties of the basal region of the cochlea, speech-recognition deficits from basal damage may extend beyond the loss of high-frequency speech information. For example, damage to this region may also impair speech recognition as a result of reduced phase-locking and synchronization to low frequencies or a disproportionate loss of activity from low-spontaneous-rate afferent fibers and efferent fibers. To the extent that deficits in speech recognition accompanying high-frequency hearing loss are caused by these types of deficits, it is unknown if providing of high-frequency amplification would be beneficial. Indeed, recent results (e.g., Ching *et al.*, 1998; Hogan and Turner, 1998; Turner and Cummings, 1999) suggest that the provision of high-frequency amplification may result in a decrease in speech recognition for some listeners with severe high-frequency hearing loss.

Follow-up experiments are underway that include more realistic and complex listening situations. Recognition of nonsense syllables is a relatively straightforward task without involvement of cues from context, prosody, or memory. As such it was selected for this initial assessment. The next step is to include more complex conditions, such as listening to full words and sentences in temporally varying background noise. These conditions may reveal more information concerning deficits in speech recognition that accompany high-frequency hearing loss.

ACKNOWLEDGMENTS

This work was supported (in part) by Grant Nos. K23 DC00158 and R01 DC00184 from NIH/NIDCD and by the American Speech-Language-Hearing Foundation. The authors thank Fu-Shing Lee for advice on data analysis.

[1]When the ANOVA was performed on percent-correct scores, a significant interaction was observed between subject group and signal-to-noise ratio ($F[2,20]=4.4$; $p=0.025$). That is, the increase in recognition scores due to increasing signal-to-noise ratios differed for the normal-hearing and high-frequency hearing-impaired subjects. However, this result may have been influenced by recognition scores for normal-hearing subjects, which were in the 90% range. Accordingly, percent-correct scores were transformed into rationalized arcsine units (rau) to normalize the variance over the range of obtained scores (Studebaker, 1985) and then subjected to a second ANOVA that revealed a nonsignificant group by signal-to-noise ratio interaction. For all other conditions, percent-correct scores ranged from 20 to 64, with nearly identical corresponding rau-transformed scores. Thus, results from the other ANOVAs reported here were the same for percent-correct scores and rau-transformed scores. For simplicity, all remaining results are reported for percent-correct scores.

[2]These AI analyses were conducted on 10 of the 12 subjects. Two of the normal-hearing subjects were unavailable during the phase of data collection in which thresholds were measured in the three levels of the low-pass-filtered speech-shaped masker.

[3]These analyses were conducted using the Feature Information Transfer (FIX) program provided by Stuart Rosen at University College London.

ANSI (**1996**). ANSI S3.6-1996, "Specifications for Audiometers" (American National Standards Institute, New York).

Bacon, S. P., Opie, J. M., and Montoya, D. Y. (**1998**). "The effects of hearing loss and noise masking on the masking release for speech in temporally complex backgrounds," J. Speech Lang. Hear. Res. **41**, 549–563.

Bacon, S. P., and Viemeister, N. F. (**1985**). "Temporal modulation transfer functions in normal-hearing and hearing-impaired listeners," Audiology **24**, 117–134.

Bilger, R. C., and Hirsh, I. J. (**1956**). "Masking of tones by bands of noise," J. Acoust. Soc. Am. **28**, 623–630.

Buus, S., and Florentine, M. (**1985**). "Gap detection in normal and impaired listeners: The effect of level and frequency," in *Time Resolution in Auditory Systems*, edited by A. Michelsen (Springer, London), pp. 159–179.

Ching, T. Y. C., Dillon, H., and Byrne, D. (**1998**). "Speech recognition of hearing-impaired listeners: Predictions from audibility and the limited role of high-frequency amplification," J. Acoust. Soc. Am. **103**, 1128–1140.

Dirks, D. D., Dubno, J. R., and Bell, T. S. (**1990a**). "Problems in the prediction of speech recognition among normal-hearing and hearing-impaired listeners," J. Acoust. Soc. Am. Suppl. 1 **88**, S32.

Dirks, D. D., Dubno, J. R., Ahlstrom, J. B., and Schaefer, A. B. (**1990b**). "Articulation index importance and transfer functions for several speech materials," Asha **32**, 91.

Dubno, J. R., and Ahlstrom, J. B. (**1995a**). "Masked thresholds and consonant recognition in low-pass maskers for hearing-impaired and normal-hearing listeners," J. Acoust. Soc. Am. **97**, 2430–2441.

Dubno, J. R., and Ahlstrom, J. B. (**1995b**). "Growth of low-pass masking of pure tones and speech for hearing-impaired and normal-hearing listeners," J. Acoust. Soc. Am. **98**, 3113–3124.

Dubno, J. R., and Schaefer, A. B. (**1992**). "Comparison of frequency selectivity and consonant recognition among hearing-impaired and masked normal-hearing listeners," J. Acoust. Soc. Am. **91**, 2110–2121.

Dubno, J. R., and Schaefer, A. B. (**1995**). "Frequency selectivity and consonant recognition for hearing-impaired and normal-hearing listeners with equivalent masked thresholds," J. Acoust. Soc. Am. **97**, 1165–1174.

Eisenberg, L. S., Dirks, D. D., and Bell, T. S. (**1995**). "Speech recognition in amplitude-modulated noise of listeners with normal and listeners with impaired hearing," J. Speech Hear. Res. **38**, 222–233.

Florentine, M. (**1983**). "Intensity discrimination as a function of level and frequency and its relation to high-frequency hearing,'' J. Acoust. Soc. Am. **75**, 1375–1379.

French, N., and Steinberg, J. (**1947**). ''Factors governing the intelligibility of speech sounds,'' J. Acoust. Soc. Am. **19**, 90–119.

Green, D. M. (**1993**). ''A maximum-likelihood method for estimating thresholds in a yes–no task,'' J. Acoust. Soc. Am. **93**, 2096–2105.

Hogan, C. A., and Turner, C. W. (**1998**). ''High-frequency audibility: Benefits for hearing-impaired listeners,'' J. Acoust. Soc. Am. **61**, 1337–1351.

Jesteadt, W., Bacon, S. P., and Lehman, J. R. (**1982**). ''Forward masking as a function of frequency, masker level, and signal delay,'' J. Acoust. Soc. Am. **71**, 950–962.

Joris, P. X., Smith, P. H., and Yin, T. C. T. (**1994**). ''Enhancement of neural synchronization in the anteroventral cochlear nucleus. II. Responses in the tuning curve tail,'' J. Neurophysiol. **71**, 1037–1051.

Keith, R. W., and Anderson, C. V. (**1969**). ''Remote masking for listeners with cochlear impairment,'' J. Acoust. Soc. Am. **46**, 393–398.

Kiang, N. Y. S. (**1975**). ''Stimulus representation in the discharge patterns of auditory neurons,'' in *Human Communication and Its Disorders, Vol. 3*, edited by D. B. Tower (Raven, New York), pp. 81–96.

Kiang, N. Y. S., and Moxon, E. C. (**1974**). ''Tails of tuning curves of auditory-nerve fibers,'' J. Acoust. Soc. Am. **55**, 620–630.

Kim, M., and Turner, C. W. (**1988**). ''Low-pass speech recognition in high-frequency hearing-impaired subjects,'' Asha **30**, 193.

Leek, M. R., Dubno, J. R., He, N.-j., and Ahlstrom, J. B. (**2000**). ''Experience with a yes–no single-interval maximum-likelihood procedure,'' J. Acoust. Soc. Am. **107**, 2674–2684.

Liberman, M. C., Dodds, L. W., and Pierce, S. (**1990**). ''Afferent and efferent innervation of the cat cochlea: Quantitative analysis with light and electron microscopy,'' J. Comp. Neurol. **301**, 443–460.

Moore, B. C. J., Peters, R. W., and Glasberg, B. R. (**1993**). ''Effects of frequency on the detection of decrements and increments in sinusoids,'' J. Acoust. Soc. Am. **94**, 3190–3198.

Murray, N., and Byrne, D. (**1986**). ''Performance of hearing-impaired and normal hearing listeners with various high frequency cut-offs in hearing aids,'' Austral. J. Aud. **8**, 21–28.

Schmiedt, R. A., Mills, J. H., and Boettcher, F. A. (**1996**). ''Age-related loss of activity of auditory-nerve fibers,'' J. Neurophysiol. **76**, 2799–2803.

Strickland, E. A., Viemeister, N. F., Van Tasell, D. J., and Preminger, J. E. (**1994**). ''Is useful speech information carried by fibers with high characteristic frequencies?'' J. Acoust. Soc. Am. **95**, 497–501.

Studebaker, G. A. (**1985**). ''A rationalized arcsine transform,'' J. Speech Hear. Res. **28**, 455–462.

Sullivan, J. A., Allsman, C. S., Nielsen, L. B., and Mobley, J. P. (**1992**). ''Amplification for listeners with steeply sloping, high-frequency hearing loss,'' Ear Hear. **13**, 35–45.

Turner, C. W., and Cummings, K. J. (**1999**). ''Speech audibility for listeners with high-frequency hearing loss,'' Am. J. Audiol. **8**, 47–56.

Van Tasell, D. J., and Turner, C. W. (**1984**). ''Speech recognition in a special case of low-frequency hearing loss,'' J. Acoust. Soc. Am. **75**, 1207–1212.

Wang, M. D., and Bilger, R. C. (**1973**). ''Consonant confusion in noise: a study of perceptual features,'' J. Acoust. Soc. Am. **54**, 1248–1266.

Effects of prosodic factors on spectral dynamics. I. Analysis

Johan Wouters[a] and Michael W. Macon[b]
Center for Spoken Language Understanding, OGI School of Science and Engineering, Oregon Health & Science University, 20000 NW Walker Road, Beaverton, Oregon 98006

(Received 27 April 2001; revised 26 August 2001; accepted 23 October 2001)

The effects of prosodic factors on the spectral rate of change of vowel transitions are investigated. Thirty two-syllable English words are placed in carrier phrases and read by a single speaker. Liquid-vowel, diphthong, and vowel–liquid transitions are extracted from different prosodic contexts, corresponding to different levels of stress, pitch accent, word position, and speaking style, following a balanced experimental design. The spectral rate of change in these transitions is measured by fitting linear regression lines to the first three formants and computing the root-mean-square of the slopes. Analysis shows that the spectral rate of change increases with linguistic prominence, i.e., in stressed syllables, in accented words, in sentence-medial words, and in hyperarticulated speech. The results are consistent with a contextual view of vowel reduction, where the extent of reduction depends both on the spectral rate of change and on vowel duration. A numerical model of spectral rate of change is proposed, which can be integrated in a system for concatenative speech synthesis, as discussed in Paper II [J. Wouters and M. Macon, J. Acoust. Soc. Am. **111**, 428–438 (2002)].
[DOI: 10.1121/1.1428262]

PACS numbers: 43.72.Ar, 43.70.Fq, 43.70.Bk, 43.70.Aj [DOS]

I. INTRODUCTION

Prosody refers to suprasegmental aspects of speech such as phrasing, accent placement, stress, and speaking style. Although a number of studies have explored the effects of prosody on the degree of articulation of vowels or *vowel quality* (e.g., Lindblom, 1963; Fourakis, 1991; van Bergem, 1993; Sluijter and van Heuven, 1996), such acoustic-prosodic effects are rarely integrated in automatic speech-processing systems. As a result, important cues for robust speech recognition may be ignored, while synthetic speech often sounds overarticulated and requires a higher listening effort than natural speech (van Santen, 1997; Delogu *et al.*, 1998).

In the present paper, the effects of prosodic context on the spectral rate of change of vowel transitions are investigated. Based on results by Nelson (1983), Moon and Lindblom (1994) suggested that the spectral rate of change of vowel transitions depends on a speaker's *articulation effort*. In turn, we expect that the articulation effort depends on prosodic factors, such as the speaking style and the linguistic structure of a message. This motivates our hypothesis that the spectral rate of change of phonetic transitions increases with *linguistic prominence*, i.e., with the relative importance of a transition in an utterance given the linguistic-prosodic context.

In Sec. II E, the spectral rate of change is defined as the root-mean-square of the first three formant slopes. We design and analyze a balanced speech corpus to study the interaction between the spectral rate of change and prosodic factors such as stress, accent, word position, and speaking style. A numerical model is proposed to predict the spectral rate of change from prosodic factors. The results are consistent with a contextual view of vowel reduction, which can be integrated in a concatenative synthesis system. This is the topic of Wouters and Macon (2002), which is referred to as "Paper II" in the remainder of this paper.

Several researchers have investigated the effects of speaking rate and linguistic stress on the spectral structure of vowels. Lindblom (1963) measured formant frequencies at vowel nuclei in short and long vowels, and defined the difference between the measured values and the formant frequencies reached in long vowels as *target undershoot*. The degree of undershoot could be predicted based on the vowel duration and the difference between the target formant frequency and the formant value at the vowel onset. Gay (1978), on the other hand, found no effects of speaking rate or stress on vowel quality, even when the segmental durations changed substantially. Van Son and Pols (1990, 1992) compared formant targets and formant movements of Dutch vowels in normal and fast speech. The results contradicted the target undershoot model because the speaker achieved the same formant targets at both speaking rates, possibly by adapting his articulation style (van Son and Pols, 1992).

The target undershoot model regards vowel reduction as a consequence of contextual assimilation (Lindblom, 1963). A competing view on vowel reduction is that vowels shift towards a neutral target in faster speech and in unstressed syllables. This *centralization theory* was investigated by Fourakis (1991), who computed the distance between a neutral vowel target and vowels produced in different conditions of stress and speaking rate. The results did not support the centralization theory in the sense that individual vowels did not come closer to the neutral point in unstressed or fast speech. However, the vowel space shifted and decreased in size for the unstressed and fast conditions. In a recent study, Wrede *et al.* (2000) analyzed the spectral properties of vowels in a large corpus of spontaneous speech. They confirmed that the vowel space became smaller for shorter vowels,

[a]Electronic mail: wouters@ece.ogi.edu
[b]Deceased on 15 March 2001.

while the spectral rate of change in vowel onglides and offglides was not affected by the segmental durations.

Van Bergem (1993) reviewed the assimilation vs centralization argument and concluded that vowel reduction is the result of contextual assimilation, which frequently, but not necessarily, leads to a centralization of formant patterns. Van Bergem also demonstrated that several prosodic factors, apart from speaking rate, produce vowel reduction, such as syllabic stress, sentence accent, and word class. He argued that vowel reduction is not a result of duration changes, as assumed in Lindblom's (1963) target undershoot model, but that duration and vowel quality are both affected by prosodic factors and speaking style.

Strange (1989b,a) investigated the role of spectral dynamics in speech *perception*. She conducted intelligibility experiments with vowels in which the stationary regions or the transition regions were replaced by silence. Both vowel types yielded similar identification rates, and were slightly less intelligible than unmodified vowels. Based on similar silent-center experiments, Fox (1989) concluded that listeners rely on acoustic changes in transition regions rather than the transition endpoints to identify vowel targets, while van Son and Pols (1999) found that perceptual cues for consonant and vowel identification are distributed over transitions regions as well as targets. Furui (1986), in a series of experiments, showed that speech segments of 10 ms, excised at the point of maximum spectral change, contain the most important information for identification of consonant–vowel transitions. In spite of the perceptual importance of vowel dynamics, Watson and Harrington (1999) and Pitermann (2000) reported no improvements in automatic vowel classification when dynamic parameters were added to static features. Watson and Harrington (1999) argued that dynamic information, such as spectral rate of change, may be related to prosodic aspects of vowels rather than carrying phonetic information.

Moon and Lindblom (1994) reviewed the target undershoot model to account for differences between speaking styles. They modeled the speech motor mechanism as a second-order system, and represented the articulation effort by the system input force. The model expressed a linear relationship between the articulation effort and the speed of articulatory movements in the vocal tract. To reflect variations in the articulation effort, Moon and Lindblom added a formant rate-of-change parameter to the undershoot model. In a study of tongue movements in normal and fast speech, Flege (1988) also found that the peak velocity of the tongue was important to predict the undershoot of tongue movements. Similarly, Pitermann (2000) showed that in a database of [iVi] stimuli the formant rate of change increased with speaking rate, which reduced the degree of undershoot. In these and other studies (Nelson, 1983; van Bergem, 1993; Watson and Harrington, 1999), changes in tongue velocity or formant rate of change are viewed as the result of variations in the articulation effort.

Lindblom's (1990) Hyper & Hypo theory views phonetic variation as the result of a trade-off between economy of articulatory movement and communicative requirements. Depending on the speaker's articulation effort, different speaking styles can be produced ranging from sloppy, *hypo*-articulated speech to clear, *hyper*-articulated speech. This presents a new framework for studying vowel reduction. In long vowels or in hyperarticulated speech, the articulators may reach a stationary position corresponding to the vowel's phonetic target. In shorter vowels or in relaxed speech, the time available for the phonetic transition may be insufficient to reach the target, and undershoot occurs. If, for a given vowel duration, speaking effort is increased to speed up articulatory movements, then phonetic targets may be reached even in a short vowel.

In this work, we investigate the hypothesis that the spectral rate of change of vowel transitions varies with prosodic context. Based on the literature review, we expect a positive correlation between the linguistic prominence of vowel transitions and their spectral rate of change. Articulation effort is viewed as an underlying, ''hidden'' parameter in this process: during the production of linguistically prominent speech segments, the articulation effort increases, resulting in faster articulatory movements, and hence in a higher observed spectral rate of change. However, the relationship between articulation effort and articulatory movement, and between articulatory movement and spectral dynamics is not linear, and continues to be a topic of study (Nelson, 1983; Schoentgen and Ciocea, 1997). While the spectral rate of change may reflect relative changes in the articulation effort, for a given articulatory movement, the true value of the articulation effort is likely to remain hidden.

The present work extends Lindblom's (1990) Hyper & Hypo theory, in that variations in articulation effort are expected *throughout* a spoken utterance as well as across different speaking styles. A similar view was expressed by de Jong (1995), who measured tongue, jaw, and lip movements in monosyllabic words under varying conditions of stress, and concluded that the data were best explained by considering linguistic prominence as *localized hyperarticulation*.

This work also re-examines the notion of acoustic targets in the analysis of vowel reduction. Vowel reduction occurs when the ''ideal'' acoustic target of a vowel is not reached in fluent speech. In our view, such reduction is not well explained by postulating the existence of reduced or ''less ambitious'' acoustic targets. Rather, we agree with Moon and Lindblom (1994) that the acoustic realization of vowel is best described as the result of an interaction between phonetic context, vowel duration, and spectral rate of change. A closer investigation of this model of vowel reduction is presented in Sec. IV.

This study is limited to prosodic effects on the spectral *time dynamics* of sonorant speech. Other acoustic correlates of prosody reported in the literature include spectral balance (Sluijter and van Heuven, 1996) and intensity (Waibel, 1986). However, such effects may be more related to the vocal excitation or to a global shift in articulatory movements [e.g., lowered jaw (de Jong, 1995; van Son and Pols, 1992)], and are not investigated here.

II. METHODS

Three types of vowel transitions were studied: (1) liquid–vowel transitions; (2) diphthong transitions; and (3) vowel–liquid transitions. These transitions correspond to fairly large formant transitions, and were expected to vary appreciably due to changes in articulation effort. Similar transitions were studied by Moon and Lindblom (1994).

The transitions were placed in different prosodic contexts using carrier phrases, according to a balanced experimental design. This text corpus was read by a single speaker. Therefore, the present work aims to draw an accurate picture of the acoustic–prosodic characteristics of one speaker. The synthesis experiments in Paper II are based on the same speaker. Investigation of speaker-dependent effects is left for future work.

A. Prosodic factors

Previous studies have identified several prosodic factors that affect the degree of articulation of vowels. These include stress (van Bergem, 1993; Sluijter and van Heuven, 1996), pitch accent (Lindblom, 1963; Fourakis, 1991; van Bergem, 1993; de Jong, 1995; Sluijter and van Heuven, 1996), word length (Moon and Lindblom, 1994), word position (Lindblom, 1963), speaking rate (Kuehn and Moll, 1976; Flege, 1988; Fourakis, 1991; Gay, 1978; Pitermann, 2000; van Son and Pols, 1990, 1992), and word class (van Bergem, 1993). In this paper, we investigate the acoustic effects of four factors: (1) syllabic stress; (2) pitch accent; (3) word position; and (4) speaking style. These factors cover a broad range of the phenomena described in the literature, and are a first step in integrating knowledge about the spectral dynamics of vowels in a large domain text-to-speech synthesis system.

Stress is a lexical property of syllables in English words, indicating which syllable is, in some sense, stronger than the others (Sluijter and van Heuven, 1996). Two levels of stress are considered in this work, i.e., syllables receive either primary stress or are unstressed. In previous studies concerning prosodic–acoustic effects, syllabic stress was sometimes confounded with pitch accent. However, syllabic stress and pitch accent may have different acoustic correlates in fluent speech (van Bergem, 1993; Sluijter and van Heuven, 1996). Therefore, stress and accent are investigated independently here.

Several researchers have investigated the acoustic effects of pitch accent, whether in conjunction with syllabic stress or not (Lindblom, 1963; Fourakis, 1991; van Bergem, 1993; de Jong, 1995; Sluijter and van Heuven, 1996). For the present study, sentences were constructed to contain a single nuclear pitch accent. Words in a sentence are therefore considered either accented or not. Given the fixed structure of the sentences in the database, the nonaccented words of interest may precede the accent nucleus by two monosyllabic words, or follow the accent nucleus by one two-syllable word.

The final phrase boundary of a sentence affects the articulation effort of the word(s) preceding it. Lindblom (1963) varied the acoustic realization of vowels by placing words in a sentence-initial or sentence-final position, while Moon and Lindblom (1994) increased the number of syllables in a word to obtain shortening effects. In the present study, words are considered either sentence final or sentence medial. The sentence-medial words of interest are separated from the sentence boundary by three words.

TABLE I. Overview of the prosodic factors and levels considered in this study.

Factor	Stress	Accent	Position	Style
Level 1	Primary	Accented	Medial	Clear
Level 2	Unstressed	Nonaccented	Final	Fast
Level 3				Relaxed

The effect of speaking rate on vowel quality has been investigated by Kuehn and Moll (1976), Flege (1988), Fourakis (1991), Gay (1978), Pitermann (2000), van Son and Pols (1990, 1992), and others. Conflicting results were often found, due to the variety in *articulation styles* adopted by the speakers. In some studies, speakers were requested to increase their speaking rate while maintaining accurate pronunciations (van Son and Pols, 1990, 1992), or to speak at a tempo indicated by a metronome (Lindblom, 1963; Pitermann, 2000). In other cases, speakers spoke at a self-selected fast rate (Gay, 1978; Fourakis, 1991; Flege, 1988). In the present work, we follow Lindblom's (1990) proposal that speaking styles vary along a continuum from hypo- to hyperarticulated speech. Moreover, we expect that articulation effort and vowel duration behave in a rather independent way, allowing a speaker to articulate in a fast and clear manner, or in a slow and sloppy manner, or any combination in between. To investigate this, the speaker in our experiment read the same set of sentences in three different speaking styles. The recording protocol is explained in more detail in Sec. II C.

The prosodic factors and their levels are summarized in Table I. The levels are ranked according to their linguistic prominence. The sentence-medial level of the factor word position is considered here to be more prominent than the sentence-final level, corresponding to the fact that speakers generally de-emphasize words at the end of a declarative sentence. However, this does not imply that the last word of a sentence is always less prominent than preceding words, since the prominence structure of a sentence also depends on other prosodic factors, such as pitch accent.

To study the effects of the different prosodic factors on the spectral rate of change using a balanced experimental design, $2\times2\times2\times3=24$ prosodic conditions need to be considered for each phonetic transition in the database.

B. Speech corpus

The speech database was based on 30 two-syllable words with an ambiguous stress pattern in English. The words were selected from a lexicon to include at least one vowel transition involving a diphthong or a liquid. Most of the selected words have primary stress on the first syllable when used as a noun (e.g., *ab*stract), and primary stress on the second syllable when used as a verb (e.g., ab*stract*). The complete list is shown in Table II.

The selected words were placed in meta-linguistic carrier phrases of the form

(1) ''Please produce ... for him again.''
(2) ''The speaker will now produce... .''

TABLE II. Two-syllable words with ambiguous stress pattern.

abstract	impulse	research
chauffeur	increase	retake
debut	insert	rewrite
digest	incite/insight	romance
discharge	insult	surcharge
eighteen	Monroe	surveys
escort	narrates	transform
exploit	overt	transport
ferment	permit	trustee/trusty
import	pervert	upright

The resulting sentences are grammatically correct, independent of the syntactic properties of the inserted word. The first carrier phrase allows sentence-medial insertions of the target word and the second carrier phrase allows sentence-final insertions.

Pitch accent was varied by asking the speaker to emphasize either the target word, or the word ‘‘again’’ in the first carrier phrase, or ‘‘now’’ in the second carrier phrase. In total, the speaker was presented with eight typographically different sentences per two-syllable word, corresponding to different conditions of stress, accent, and sentence position. These sentences are shown in Table III for the target word ‘‘abstract.’’ Stressed syllables are underlined, while accented words appear in capitals. The sentences were repeated in three different speaking styles, producing 24 sentences per target word. Each sentence was recorded three times to improve the estimation of the spectral rate-of-change parameter, to be discussed in Sec. II E. The total number of utterances in the database is therefore $30\times24\times3=2160$.

C. Recording

The corpus was recorded in three sessions, each session corresponding to a particular speaking style. Sentences were grouped in blocks of eight per two-syllable word. These blocks were repeated three times per session and were randomly ordered per repetition. In the first repetition, the sentences within each block appeared as in Table III. In the second repetition, the order of stressed and unstressed syllables was reversed. In the third repetition, the sentence-medial and sentence-final conditions were reversed. This structured ordering per sentence block made it easier for the speaker to vary the desired prosodic factors for each new sentence. In each ordering, a sentence in which the target word was to be accented was followed by the same sentence with unaccented target, according to the tendency of a speaker to accent new information and deaccent given information (Halliday, 1967).

TABLE III. Presentation of the word ‘‘abstract’’ in different prosodic contexts, covering all combinations of stress, accent, and word position levels. Stressed syllables are underlined. Accented words appear in capitals.

(1) Please produce ABSTRACT for him again.
(2) Please produce abstract for him AGAIN.
(3) The speaker will now produce ABSTRACT.
(4) The speaker will NOW produce abstract.
(5) Please produce ABSTRACT for him again.
(6) Please produce abstract for him AGAIN.
(7) The speaker will now produce ABSTRACT.
(8) The speaker will NOW produce abstract.

The speaker was the second author, who speaks a northern dialect of American English without any strong regional influence. The speaker was required to correctly assign stress and pitch accents according to the typography of the sentences. This was achieved quite naturally after initial practice, and was helped by presenting the sentences in the order described above, as opposed to a completely random presentation. A sentence was repeated whenever the reading was not satisfactory to the speaker or to the experimenter.

The speaking styles were varied as follows. In the first session, the speaker read the sentences slowly and clearly, corresponding to a hyperarticulated speaking style. In the second session, the speaker read the sentences at a faster, but still comfortable rate. *Post hoc* analysis showed a 24% decrease in the vowel durations for the second session compared with the first session. In the third session, the speaker read the sentences in a more relaxed way than either the first or the second session. This resulted in a decrease in vowel durations of 30% compared with the first session.

The utterances were recorded in a sound-insulated booth, using a large-capsule condenser microphone. A laryngograph signal was simultaneously recorded to allow accurate marking of the glottal onset times for pitch-synchronous spectral analysis. The speech and the laryngograph signals were recorded directly onto a computer disk located outside of the sound-insulated booth, using a Delta 1010 external soundcard sampling at 48 kHz and 16 bits per sample. After the recording session, the speech and laryngograph signals were downsampled to 16 kHz for further processing.

D. Transition regions

The transitions of interest for this study were located in the sonorant regions of the two-syllable words. The following three *transition types* were considered:

liquid–vowel transitions; for example /ɹi/ in ‘‘**re**search;’’
diphthong transitions; for example /aɪ/ in ‘‘d**i**gest;’’
vowel–liquid transitions; for example /ʌl/ in ‘‘ins**ul**t’’

For the two-syllable words in Table II, most liquid–vowel or vowel–liquid transitions involve /ɹ/, while transitions with /l/ also occur. The diphthong transitions are mostly towards /i/, although the /oʊ/ and /ju/ diphthongs are also present. The transitions are summarized in Table IV. Some two-syllable words were included in Table II to cover /ɝ/ transitions, as in ‘‘ins**er**t.’’ However, since the realization of /ɝ/ corresponds more to a monophthong than to a diphthong, /ɝ/ transitions are not included in Table IV or in the analyses presented below. Hence, 39 phonetic transitions extracted from different two-syllable words remain.

The liquid–vowel transitions occur in syllable onsets, while the vowel–liquid transitions occur in syllable codas. In the remainder of this study, the three transition types will therefore be referred to as *onset*, *diphthong*, and *coda* transitions.

All transitions were excised from the recorded sentences using an automatic segmentation algorithm recently developed by Hosom (2000). This algorithm provides an objective

TABLE IV. Overview of the phonetic transitions extracted from different two-syllable words.

	Liquid–vowel	Diphthong	Vowel–liquid
	/l/–vowel	vowel–/i/	vowel–/l/
	/lɔɪ/ 1	/eɪ/ 5	/ʌl/ 2
	/ɹ/–vowel	/aɪ/ 4	vowel–/ɹ/
	/ɹi/ 4	/ɔɪ/ 1	/ɔɹ/ 4
	/ɹæ/ 3	vowel–/u/	/aɹ/ 2
	/ɹoʊ/ 2	/oʊ/ 4	/ɛɹ/ 1
	/ɹaɪ/ 2	/ju/ 1	/iɹ/ 1
	/ɹeɪ/ 1		
	/ɹʌ/ 1		
Total	14	15	10

criterion to partition the vowels into stationary and transition regions, thus avoiding possible inconsistencies in segmenting the transitions by hand. The segmentation system has reported a phoneme-level accuracy of 92.5% within 20 ms of manual labels for TIMIT sentences, which is close to agreements between human labelers reported in the literature [see Hosom (2000)]. Inspection of the phoneme labels for the present corpus revealed no obvious segmentation errors.

The automatic segmenter aligns hidden Markov model (HMM) states with the speech waveform, using a phonetic transcription of the utterance. Monophthongs are represented by three HMM states and liquids by two states. Diphthongs are modeled as a sequence of two monophthongs. Therefore, we defined the starting point b of each transition region $p_1 - p_2$ as the beginning of the last HMM state representing phoneme p_1, and the end point e as the end of the first HMM state representing phoneme p_2. To prevent estimation of the spectral rate of change in very short speech segments, b and e were corrected to be at least 20 ms away from the phoneme boundary between p_1 and p_2. In the next section, a spectral rate-of-change measure is developed which reflects the spectral dynamics at the center of a transition region, while being relatively insensitive to variations in the region boundaries.

E. Spectral rate of change

To investigate the effects of the prosodic factors, a measure of the spectral rate of change must be obtained for the transition regions described above. We denote this measure as RoC. One possible measure would be to extract spectral features such as mel-frequency-based cepstral coefficients (MFCC) at equidistant frames and compute the average Euclidean distance between successive frames across each transition region. However, preliminary experiments showed that such estimates were quite noisy even if smoothed delta MFCCs were computed (using a 5-point window), and did not correspond well with visual estimations of the rate of change in spectrograms. This is due partly to the fact that the MFCC distance reflects *all* spectral changes, including variations in spectral balance and frame-to-frame jitter.

For this study, a measure was needed that reflects the articulatory movements over the course of a phonetic transition. Therefore, we adopted a spectral rate-of-change measure based on formant trajectories, which follow the resonant frequencies associated with successive vocal-tract configurations. Formant tracking is known as a difficult problem in speech processing because the resonant frequencies of the vocal tract are not always observable in the output speech signal. However, for the present task the formants needed to be identified only in short regions of sonorant speech. A simple algorithm which finds the best path through a set of LPC poles was therefore able to correctly track the desired formants for most of the data. The LPC poles were computed from a mel-warped power spectrum, obtained via pitch-synchronous sinusoidal analysis of the speech signal (Wouters and Macon, 2000). About 40% of the transitions were manually checked, revealing tracking errors in less than 1.5% of the transitions.

After formant tracking, linear regression lines were fit to the formant trajectories in each transition region. A bell-shaped weighting function $w(t)$ was applied to improve the fit towards the center of the transition regions, making the regression lines less sensitive to the placement of the transition boundaries. The weighting function was defined as

$$w(t) = \sin(\pi t), \quad 0 < t < 1. \tag{1}$$

The weighted linear regression problem was solved using standard linear methods.

Since the transition regions were short (average 59 ms), the formant trajectories appeared as quasilinear and were closely approximated by the regression lines, except in the case of a formant tracking error. The slopes α_i of the regression lines describe the formant movements at the transition point between two phonemes. These slopes can be assumed as proportional to the peak velocity of the articulatory movement between the phoneme targets. Therefore, the regression line slopes can be considered as a measure of the relative articulation effort expended at the transition (Nelson, 1983; Moon and Lindblom, 1994).

Finally, the spectral rate of change of a transition region was defined as the normalized p norm of the absolute slopes $|\alpha_i|$ for a set of formants S_N

$$\mathrm{RoC} = \left(\frac{1}{N} \sum_{i \in S_N} |\alpha_i|^p \right)^{1/p}. \tag{2}$$

Different formant combinations were investigated using the analysis of variance (ANOVA) model to be discussed in Sec. III B. The percentage of variance (η^2) explained for different definitions of RoC increased when more formant slopes were included in the measure, as shown in Table V. One explanation why the model is more powerful for higher N is that the prosodic factors determine variations in the *articulatory movements*, which are reflected in different formants depending on the articulator(s) involved (e.g., effect of retroflex movement on $F3$).

For $N = 3$, the $p = 1$ norm explained less variance than the quadratic norm, as did a multiplicative combination of the three formant slopes (see Table V). Therefore, in the remainder of this paper, analysis will be based on the root-mean-square of the first three formant slopes, i.e., $p = 2$ and $N = 3$ in Eq. (2). Since the slopes were estimated from a mel-warped spectrum, the transitions of lower formants are weighted more heavily, in correspondence with the fre-

TABLE V. Percentage of variance (η^2) explained by the ANOVA model for different definitions of the spectral rate of change.

	RoC	$\eta^2 \times 100\%$
$N=1$	$F1$	51.08
	$F2$	70.86
	$F3$	56.73
$N=2,\ p=2$	$F1,F2$	70.54
	$F2,F3$	75.56
	$F1,F3$	66.30
$N=3,\ p=2$	$F1,F2,F3$	**75.68**
$N=3,\ p=1$	$F1,F2,F3$	74.68
	$\sqrt[3]{\lvert F1F2F3 \rvert}$	56.36

quency resolution of human hearing. No additional weighting of the formant slopes was performed.

III. STATISTICAL ANALYSIS

In this section the effects of the factors stress, accent, word position, and speaking style on the spectral rate of change of transitions in the database are investigated. First, the main effects of the prosodic factors are studied by comparing RoC means computed over specific subsets of the data. This provides a first insight into the data and suggests a refinement of the prosodic factor word position. Then, analysis of variance is performed to study the effects of interactions between the prosodic factors. Finally, a numerical model of the prosodic effects is proposed.

A. Main effects

In Fig. 1 the main effects of the prosodic factors are investigated by comparing the mean RoCs computed for each level of a prosodic factor. The estimated standard deviations of the means are also shown. The differences are significant in all cases ($p<0.01$, two-sided t-test), indicating that RoC is *higher* on average in stressed vs unstressed syllables, in pitch-accented vs unaccented words, and in sentence-medial vs sentence-final words. For the three speaking styles adopted in the corpus, RoC decreases in the relaxed style compared with the clear speaking style, and increases in the fast speaking style.

Figure 2 shows the effect of the sentence-medial vs sentence-final word position for onset, diphthong, and coda transitions, respectively, in the first and second syllable of the target words. The differences are significant for the onset

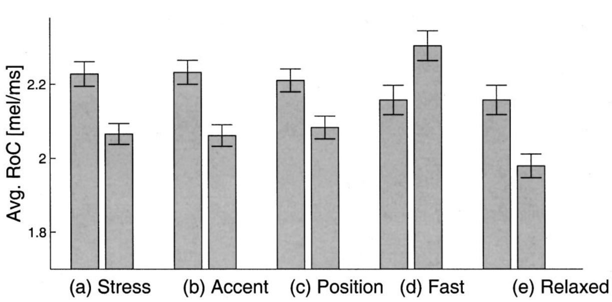

FIG. 1. Average spectral rate of change [mel/ms] for different subsets of the database: (a) stressed versus unstressed; (b) accented versus unaccented; (c) sentence medial versus sentence final; (d) clear versus fast style; (e) clear versus relaxed style.

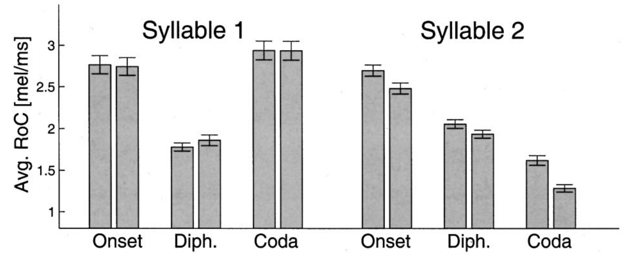

FIG. 2. Spectral rate of change [mel/ms] for sentence-medial versus sentence-final transitions, from left to right: Syllable 1: onset, diphthong, coda; Syllable 2: onset, diphthong, coda. The effect of the phrase boundary is significant only for the onset and coda transitions in the second, sentence-final, syllable.

and coda transitions in the second syllable ($p<0.05$, two-sided t-test). Hence, the spectral rate of change decreases in sentence-final transitions, but this effect is limited to the final syllable of a sentence, and is strongest for the syllable coda transition at the end of a sentence. For further analysis, we redefine the factor word position so that transitions in the second syllable of target words can be sentence final, but transitions in the first syllable are always considered sentence medial.

B. Analysis of variance

To study both the main effects and the interactions between the prosodic factors, analysis of variance (ANOVA) was performed. A six-way ANOVA was computed with stress, accent, position, style, transition type, and transition identity as independent variables and RoC as the dependent variable. Transition type (onset, diphthong, or coda) was added as an independent variable after exploratory analysis showed the importance of this factor. The transition identity refers to the phonemes involved in the transition, as summarized in Table IV. Hence, there are two levels for stress, accent, and position, three levels for style and transition type, and 39 levels for transition identity. The RoC measurements are balanced for the independent variables stress, accent, and style, but not for transition type, identity, and position. The latter is due to constraining the sentence-final word position level to transitions in the second syllable.

The ANOVA model describes the dependent variable as a sum of terms. However, in the case of spectral rate of change, a multiplicative model of the prosodic factors may be more appropriate. Such a model assumes that rapid articulatory movements are attenuated more as a result of prosodic factors, while slow movements vary less. To illustrate, if a spectral transition of 15 mel/ms decreases to 5 mel/ms for a certain prosodic factor, then with a multiplicative model a transition of 3 mel/ms decreases to 1 mel/ms. In the case of an additive model, a decrease in RoC by 10 mel/ms, regardless of the original RoC value, could lead to counterintuitive results: a transition of 3 mel/ms would be inverted to -7 mel/ms, unless additional constraints are imposed.

We computed the ANOVA both for RoC and for log(RoC). The results were comparable, but the interactions between the prosodic factors were somewhat less significant for log(RoC), indicating that the logarithmic transformation may better separate the main effects of the prosodic factors.

TABLE VI. Analysis of variance (ANOVA) of the logarithm of the rate-of-change measurements. The independent variables are transition identity, stress, accent, word position, speaking style, and transition type. For each factor, the degrees of freedom, sum of squares, F value, and significance are shown. Significant effects (<0.05) are marked with (*). No main effect was computed for transition type as the degree of freedom for this factor is zero after transition identity has been accounted for. To limit the size of the model, no interaction terms were computed for transition identity.

	Df	SS	F	Pr(F)
Main effects				
Identity	38	724.7	206.4	0.000*
Stress	1	2.4	26.4	0.000*
Accent	1	3.0	33.1	0.000*
Position	1	7.3	80.0	0.000*
Style	2	8.6	46.6	0.000*
2-way interactions				
Trans:stress	2	3.8	20.5	0.000*
Trans:accent	2	1.6	9.0	0.000*
Trans:position	2	2.9	15.9	0.000*
Trans:style	4	16.9	45.7	0.000*
Stress:accent	1	1.0	11.6	0.000*
Stress:position	1	0.0	0.4	0.500
Stress:style	2	0.2	1.5	0.209
Accent:position	1	0.0	0.2	0.648
Accent:style	2	0.0	0.4	0.656
Position:style	2	1.3	7.2	0.000*
3-way interactions				
Trans:stress:accent	2	0.0	0.0	0.947
Trans:stress:position	2	0.3	1.8	0.159
Trans:stress:style	4	0.1	0.4	0.799
Trans:accent:position	2	0.0	0.0	0.970
Trans:accent:style	4	0.4	1.1	0.320
Trans:position:style	4	0.5	1.4	0.207
Stress:accent:position	1	0.1	1.1	0.285
Stress:accent:style	2	0.1	0.7	0.453
Stress:position:style	2	0.2	1.3	0.252
Accent:position:style	2	0.1	0.8	0.445
4-way interactions				
Trans:stress:accent:position	2	0.2	1.5	0.203
Trans:stress:accent:style	4	0.2	0.6	0.627
Trans:stress:position:style	4	0.1	0.3	0.834
Trans:accent:position:style	4	0.1	0.2	0.887
Stress:accent:position:style	2	0.0	0.4	0.647
5-way interactions				
Trans:stress:accent:position:style	4	0.0	0.1	0.957
Residuals	2700	249.7		

Therefore, in Table VI the results for log(RoC) are reported. The same transformation was used for the results in Table V. In the remainder of this section, marginal means will be reported in percent change of RoC, corresponding to linear changes of log(RoC).

The analysis of variance confirms the main effects of stress, accent, position, and style shown in Fig. 1. The marginal means of the main effects indicate that RoC increases by 5.9% in stressed versus unstressed syllables, by 6.6% in accented versus nonaccented words, by 9.5% in sentence-medial versus sentence-final transitions, by 8.7% in fast versus clear speech, and by 4.7% in clear versus relaxed speech. A pairwise comparison between the means of the most prominent versus the least prominent prosodic condition, i.e., between stressed, accented, sentence-medial, and clear transitions versus unstressed, unaccented, sentence-final, and relaxed transitions, shows a cumulative effect of 21%.

The cumulative effect is not as high as the sum of the main effects, $5.9+6.6+9.5+4.7=26.7\%$, indicating that some of the interactions between the prosodic factors reduce the main effects. According to Table VI, the interactions between position and style and between stress and accent are significant. When the main effect of word position is combined with the effects of the interaction between word position and style, we find that the effect of word position is weaker in the relaxed speaking style (3.5%), while it is stronger in the clear speaking style (13.5%) and in the fast speaking style (11.5%). The interaction between accent and stress introduces modest (±2%) corrections to the main effects.

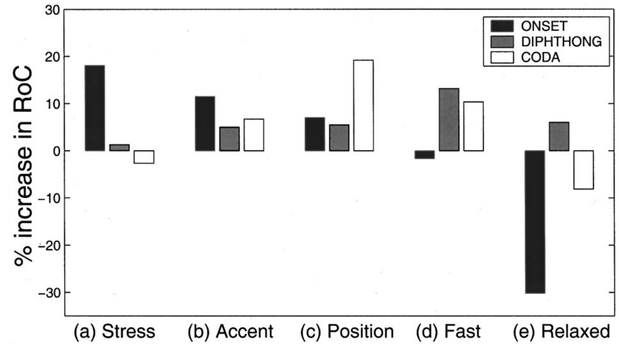

FIG. 3. Estimated parameters of the multiplicative model in Eq. (3). The parameters represent the relative increase in spectral rate of change (RoC) for syllable onset, diphthong, and coda transitions, when comparing (a) stressed versus unstressed syllables; (b) accented versus nonaccented words; (c) sentence-medial versus sentence-final transitions; (d) fast versus clear speech; and (e) relaxed versus clear speech.

Significant two-way interactions were found between the transition type and each of the prosodic factors. These interactions are now discussed in detail. A graphical representation of the prosodic effects for different transition types follows in Fig. 3. However, the data in Fig. 3 reflect the results of the multiplicative analysis discussed in Sec. III C and are somewhat different numerically from the ANOVA results discussed here.

The interaction between transition type and stress increases the main effect of stress for onset transitions, while neutralizing the effect for diphthong and coda transitions. When the marginal means of the interaction are combined with the main effect, RoC increases by 16% for stressed versus unstressed conditions in onset transitions. Diphthong transitions decrease by 2%, and coda transitions increase by 4%.

A similar interaction is observed between transition type and accent. For onset transitions, the main effect of pitch accent is reinforced (+13%), while it is smaller for diphthong (+3%) and coda (+5%) transitions.

The interaction between transition type and word position is in correspondence with Fig. 2 earlier. The effect of word position becomes smaller in onset (+7%) and diphthong (+4%) transitions, and larger in coda (+20%) transitions.

The interaction between transition type and speaking style results in slower onset transitions in the fast speaking style compared to the clear speaking style (−5%), and in dramatically slower onset transitions in the relaxed speaking style compared to the clear speaking style (−30%). Diphthong transitions are more rapid in the fast (20%) and relaxed (14%) styles, while coda transitions are more rapid in the fast style (13%) and practically the same in the relaxed style (3%), compared to the clear style. Flege (1988) observed the same asymmetry between vowel onset and coda transition rates. For several speakers, the velocities of onset tongue movements decreased in fast speech compared with normal-rate speech, while the velocities of coda movements increased. We believe this may be due to a hierarchical difference between syllable onsets and codas, which causes the dynamics of coda transitions to be dominated by preceding and following onset movements.

All other interactions between prosodic factors, including three-, four-, and five-way interactions, were not significant. When two-way interactions between transition *identity* and stress, accent, or position were computed, they were found to be highly significant ($p<0.0001$). However, since the interactions with transition identity have a large number of degrees of freedom, such interactions were excluded from the analysis shown in Table VI to avoid overfitting.

In Table VI, the percentage of variance (η^2) explained by transition identity alone is 70.6%. The percentage of variance explained by transition identity and the four prosodic factors with their interactions is 75.7%, or the prosodic factors account for 17% of the remaining variance. This is explored further in the next section.

C. A quantitative model of prosodic effects on spectral dynamics

Based on the analysis of variance, we propose a simple multiplicative model to predict the effects of prosodic context on the rate of change of vowel transitions in natural speech. This model can be integrated in a concatenative synthesis system, which is the topic of Paper II (Wouters and Macon, 2002). To reduce the complexity of the model, interactions between the prosodic factors, which were shown to be significant for stress and accent, and for word position and speaking style, are not taken into account. The effect of the transition type, however, is accounted for by estimating separate parameters for each transition type, i.e., syllable onset, diphthong, and coda transitions.

An advantage of the proposed model compared with the ANOVA model is that the parameters can be estimated without performing a logarithmic transformation. The distribution of the ANOVA prediction errors versus the fitted values is nonwhite for log(RoC), showing increasingly large errors for lower RoC values. Low RoC values are measured when the formant targets of two successive phonemes are close, as in /eɪ/ or /aɪ/. The effects of prosodic factors may be less reliable for such transitions, as the required articulation effort may be very low; hence, the transitions are produced with similar precision independent of prosodic context. To avoid boosting the importance of low RoC measurements through the logarithmic transformation, the parameters of the model in Eq. (3) were estimated through a nonlinear minimization of the prediction error.

The proposed model describes RoC as the product of five factors

$$\mathrm{RoC}=K_p\times\alpha(S)\times\beta(A)\times\gamma(P)\times\delta(Y). \tag{3}$$

TABLE VII. Estimated parameters for Eq. (3) when $\alpha(S=0)$, $\beta(A=0)$, $\gamma(P=\text{final})$, and $\delta(Y=\text{clear})$ are normalized to 1. The parameters in this table correspond with the values in Fig. 3 via $(\phi-1)\times100\%$, $\phi=\alpha...\delta$ (see the text).

	Onset	Diphthong	Coda
$\alpha(S=1)$	1.18	1.01	0.97
$\beta(A=1)$	1.11	1.05	1.07
$\gamma(P=\text{medial})$	1.07	1.05	1.19
$\delta(Y=\text{fast})$	0.98	1.13	1.10
$\delta(Y=\text{relaxed})$	0.70	1.06	0.92

K_p is determined by the transition identity, which reflects the phonetic context of a transition. The factors α to δ have a constant value depending on the level of stress (S), accent (A), word position (P), and speaking style (Y), respectively. These factors were estimated for each transition type independently.

The model in Eq. (3) requires estimation of one parameter for each level of a prosodic factor. We chose to normalize the prosodic factors by setting the parameters corresponding to the unstressed, unaccented, sentence-final condition in the clear speaking style to 1, i.e., $\alpha(S=0)=1$, $\beta(A=0)=1$, $\gamma(P=\text{final})=1$, $\delta(Y=\text{clear})=1$. The remaining parameters were then estimated by minimizing the squared error between the predicted RoCs and the experimentally found values, using a gradient-descent algorithm. This yielded the results shown in Fig. 3. In this figure, the parameters were normalized to $(\phi-1)\times100\%$, $\phi=\alpha...\delta$, to represent the relative increase in RoC in stressed versus unstressed syllables, accented versus nonaccented words, sentence-medial versus sentence-final transitions, fast versus clear speech, and relaxed versus clear speech. The effects are shown for syllable onset, diphthong, and coda transitions, respectively. The numerical values ϕ are given in Table VII.

The percentage of variance explained by the multiplicative model is defined as

$$\eta^2=1-\frac{E_{\mathrm{se}}}{\sigma^2}, \tag{4}$$

where E_{se} is the squared error between the measured RoC values and those predicted by the model in Eq. (3), and σ^2 is the variance of the RoC measurements. Using only the transition identities [parameters K_p in Eq. (3)], 60% of the variance is explained across onset, diphthong, and coda transitions. This increases to 67% when the prosodic factors are brought into the model. In Table VIII, η^2 is given for each transition type. The prosodic factors explain a larger part of the variance for the syllable onset transitions than for either diphthong or coda transitions. A possible explanation for this phenomenon is discussed in Sec. IV.

A considerable part of the variance left unexplained by the multiplicative model in Eq. (3) or by the ANOVA in Sec. III B is due to variations between the three repetitions in the corpus. These variations may be attributed in part to RoC measurement errors, for example during the segmentation of the transition regions or during formant tracking. Inconsistencies in the speaker's articulation may present another source of variation. An analysis of variance that included the repetition number of an utterance in addition to the factors in

TABLE VIII. Percentage of variance (η^2) explained by the multiplicative model in Eq. (3) for (1) the noisy RoC measurements, and (2) (between parentheses) the mean RoC across three repetitions. The table compares η^2 of a model including only K_p vs a model including K_p and the prosodic factors. The relative reduction in the unexplained variance ($1-\eta^2$) is shown at the bottom.

	Onset	Diphthong	Coda	All
K_p only	65 (74)	51 (66)	65 (79)	60 (72)
Full model	78 (88)	54 (70)	70 (85)	67 (80)
Rel. red.	37 (56)	6 (10)	13 (28)	18 (30)

Table VI showed a slightly significant interaction between speaking style and repetition ($p=0.03$). The corresponding marginal effects indicated that RoC dropped by 1.5% per repetition in the relaxed speaking style and by 1% per repetition in the fast speaking style, and increased by 2.6% per repetition in the clear speaking style. Variability in the speaker's articulation therefore contributes to the variance unexplained by the model in Eq. (3).

If the RoC measurement for a given phonetic transition in a given prosodic context is considered as a stochastic variable with mean μ and variance σ_ϵ^2, where σ_ϵ^2 reflects the measurement error and speaker variability, the average of the three RoC measurements per condition represents an unbiased estimator of μ, with variance $\sigma_\epsilon^2/3$. Re-estimation of the model in Eq. (3) using the average RoC yields parameters comparable to those in Table VII. The percentage of variance explained, however, increases to 72% when only the transition identities are considered, and to 80.5% when the prosodic factors are included. The results are again detailed in Table VIII for onset, diphthong, and coda transitions.

The large increase (about 12%) in explained variance due to averaging RoC indicates that the variance of one RoC measurement, σ_ϵ^2, is considerable. However, knowledge of the prosodic factors improves prediction of RoC both for noisy and for averaged RoC measurements, and explains about 8% of the variance across transition types. For onset transitions, the variance explained by the prosodic factors is around 14%, corresponding to a relative reduction in unexplained variance of 56% for the averaged RoC measurements, and 37% for the noisy RoC measurements.

IV. DISCUSSION

The results of this study suggest that the spectral rate of change of vowels increases in stressed syllables, as well as in accented and sentence-medial words, and in clearly articulated speech. These findings support the hypothesis that the spectral rate of change increases with linguistic prominence. As described in the Introduction, spectral rate of change is related to the articulation effort exercised by the speaker (Nelson, 1983; Moon and Lindblom, 1994). Therefore, our results resonate with de Jong's (1995) view of prominence as *localized hyperarticulation*.

Three types of spectral transitions were investigated: liquid–vowel, diphthong, and vowel–liquid transitions. Lindblom (1963), and others, showed that the degree of formant undershoot depends on the distance between the vowel target and the onset frequency at the consonant–vowel transition. Therefore, large formant transitions were preferred here to investigate the effects of prosodic context on the formant rate of change. We expect that variations in articulation effort, driven by changes in the prosodic context, may have similar effects on other vowel transitions. However, our data also showed significant interactions between the phonetic transition identity and the prosodic factors.

Two causes can be suggested for the interactions between transition identity and the prosodic factors. First, the relationship between articulatory movements and the spectral rate of change depends on the articulators involved. Hence, variations in articulation effort or in articulatory movements may affect certain spectral transitions more than others. Also, the prosodic context may have less impact on "easy" articulatory movements, which are close to a minimum expenditure of articulation effort (Nelson, 1983). Second, since the spectral transitions in this study were extracted from different English words, there may be effects of phonetic context outside the investigated diphone transitions. For example, competing demands on one articulator can constrain the spectral rate of change of a vowel transition. This could be the case for /oʊ–m/ in "romance," which features lip rounding in the diphthong transition /oʊ/ followed by a labial closure. Relatively large RoC values were measured for /oʊ/, indicating that the prosodic effects on the diphthong transition may be dominated by the labial closure.

The prosodic effects on the spectral rate of change are rather small in several cases (see Fig. 3). Hence, in a first approximation the spectral rate of change of vowels might be considered invariant across prosodic contexts and for different vowel durations. This is consistent with several observations in the literature (e.g., Gay, 1978; Hertz, 1991; Wrede *et al.*, 2000; Lindblom, 1963). On closer investigation, however, the spectral rate of change increases with the linguistic prominence of a phonetic transition. The effect becomes larger when several prosodic factors combine. For example, an onset transition in a stressed, accented syllable in clear speech is almost twice as fast as an unstressed, unaccented onset transition in relaxed speech, based on Eq. (3) and the parameters in Table VII.

The present results add support for a *contextual model of articulation*. According to this model, the extent of vowel reduction or the degree of coarticulation between sonorant phonemes depends on (1) the phonetic context; (2) the phoneme durations; and (3) the spectral rate of change of the phonetic transitions. This model is motivated physiologically by viewing phoneme durations and spectral rate of change as the result of two independent articulatory processes. While phoneme durations reflect the time intervals between successive articulatory gestures (Browman and Goldstein, 1992), spectral rate of change is related to the speaker's articulation effort. The time scheduled between articulatory gestures is to an extent independent from the articulation effort, so that speakers can control both their speaking rate and articulation style. However, the present study indicates that the articulation effort and gestural timing also covary with linguistic prominence.

It can be argued that spectral rate of change should not be viewed as an independent factor contributing to vowel reduction, but rather that variations in spectral dynamics result from changes in the acoustic targets in fluent speech. One way to predict such target shifts is to assume that vowels approximate a neutral target in reduced speech. However, as was discussed in the Introduction, such a centralization theory has not been validated by experimental data (Fourakis, 1991; van Bergem, 1993). Lindblom, on the other hand, successfully predicted acoustic target undershoot by considering phonetic context and by assuming a constant or speaking-style-dependent rate of change of phonetic transitions (Lindblom, 1963; Moon and Lindblom, 1994). We have refined this approach by investigating how the rate of change varies in different prosodic contexts. Assuming that our data result from shifts in the acoustic targets leaves open the question of how such reduced targets should then be predicted.

The contextual model of articulation may also explain the differences between the effects found for onset, diphthong, and coda transitions (see Fig. 3). The effects were largest and accounted for a higher percentage of the variance in the case of onset transitions, while they were weaker for diphthong and coda transitions. Similar asymmetries between onset and coda (or *offglide*) articulatory movements have been observed by Flege (1988) and Ostry *et al.* (1987). In the work by Kozhevnikov and Chistovich (1965), syllable onset movements were considered as elementary planning units of speech articulation, dominating offglide movements. Following this view, we speculate that the duration and articulation effort of a vowel *onset* may determine the extent of articulatory movement (i.e., the amount of target undershoot). The dynamics of the vowel coda then depend on the time available between the end of the preceding onset movement and the start of the next onset movement. The prosodic factors thus mainly impact onset transitions, and have fewer systematic effects on diphthong or coda transitions.

In this work, we have not investigated how well the total extent of articulatory movement, or the acoustic realization at the vowel center, can be predicted using measured values of the onset spectrum, duration, and spectral rate of change. One reason for this is that the formant trajectories in fluent speech do not always show an extremum or a stationary region within each vowel. In such case, the extent of one articulatory movement cannot be distinguished from the beginning of the next movement. We believe that an increased focus on spectral or articulatory dynamics may provide a more powerful tool to model vowel reduction in fluent speech, as opposed to the more traditional focus on target shifts.

Our analysis of the spectral dynamics in natural speech also stands in contrast with assumptions of vowel time invariance commonly made in speech synthesis and recognition systems. In most synthesis algorithms, vowel durations are controlled by uniformly time-stretching or time-compressing recorded speech units, for example using time-domain pitch-synchronous overlap-add (Moulines and Charpentier, 1990). As a consequence, the spectral rate of change increases in shortened vowels, and decreases in elongated vowels. Since vowel durations generally increase in stressed or accented positions (van Santen, 1992), as well as in clear speech, uniform time-stretching imposes a decrease in the

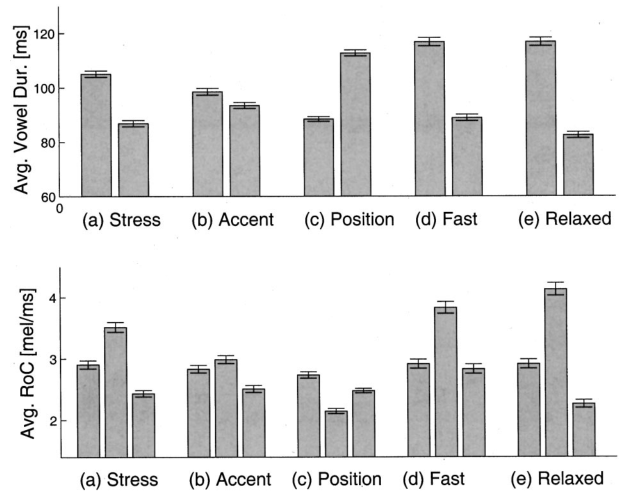

FIG. 4. Comparison of spectral dynamics in natural speech versus uniform time-warping. Top: Average vowel durations [ms] for (a) stressed versus unstressed; (b) accented versus nonaccented; (c) sentence medial versus sentence final; (d) clear versus fast; and (e) clear versus relaxed speech conditions. Bottom: Effect of time-warping linguistically prominent syllables using scaling factors derived from the top. Average rate of change [mel/ms] of syllable onset transitions is shown for (a) stressed, warped, and unstressed; (b) accented, warped, and nonaccented; (c) sentence medial, warped, and sentence final; (d) clear, warped, and fast; and (e) clear, warped, and relaxed speech conditions.

spectral rate of change in such cases, contrary to the behavior observed in the present data.

The difference between uniform time-warping and natural duration changes is illustrated in Fig. 4 for the present database. Average vowel durations are compared for minimal pairs differing in stress, accent, position, and speaking style (Fig. 4, top). The duration differences are consistent with results in the literature (van Santen, 1992). Using uniform time-scale modification to transform linguistically prominent syllables to their less prominent counterparts causes an increase in RoC for each prosodic factor except word position. This can be compared in Fig. 4 (bottom) with the actually measured RoC values for onset transitions. Except for word position, uniform time-warping increases the spectral rate of change where it should in fact decrease. The resulting speech is perceived as overarticulated.

In Paper II of this work, the perceptual importance of the spectral rate of change is investigated. We show that the contextual model of articulation can be integrated in algorithms for concatenative synthesis, by controlling the spectral rate of change of concatenated speech segments independently from duration modifications. As a result, different degrees of reduction can be achieved for units of a given acoustic database, according to the prosodic structure of a target utterance. The synthesized speech corresponds to a more natural articulation, which improves the perceptual quality.

The results in the present study were based on data from a single speaker. However, previous research has shown that speakers can differ with regard to the articulation strategy adopted in a given prosodic context. In some studies on the effects of speaking rate on vowel quality, subjects were free to choose between a hyperarticulated or hypoarticulated speaking style, which introduced significant interspeaker variations (Kuehn and Moll, 1976; Flege, 1988). Even when the speaking style is controlled more carefully, speakers still may use different strategies to signal stress or accent (Erickson, 1998; de Jong, 1995; Widera, 2000), or phrase finality (Byrd, 2000). More research is therefore needed to study the relation between linguistic prominence and spectral rate of change for other speakers, and to investigate the effects for different dialects. However, the present study fits in a synthesis paradigm that attempts to closely reproduce the voice of a specific speaker, as opposed to creating a statistical average of speakers. Synthesis experiments reported in Paper II are based on recordings from the same speaker investigated in this study.

V. CONCLUSION

An experimental database was designed to study the effects of prosodic factors on the spectral time dynamics of glide–vowel, diphthong, and vowel–glide transitions. The results indicated that the spectral rate of change increases with linguistic prominence, i.e., in stressed syllables, in accented words, in sentence-medial words, and in hyperarticulated speaking styles. The rate of change increased most in glide–vowel transitions, which occur at the syllable onset, while variations in diphthong and vowel–glide transitions were less predictable.

The present work suggests that, for a given phonetic context, vowel reduction depends on the interaction between the phoneme duration and the spectral rate of change. The rate of change reflects the articulation effort used by the speaker, while phoneme durations are determined by the timing of discrete articulatory gestures. Both factors depend on the prosodic context. A numerical model of the effects of prosodic factors on the spectral rate of change was proposed, which can be integrated in algorithms for automatic speech recognition or synthesis.

ACKNOWLEDGMENTS

This work was supported by the National Science Foundation under Grant No. LIS-0082718 to Michael Macon and Jan van Santen, and by Intel Corporation. The first author is also grateful to the three anonymous reviewers for their in-depth comments and references to related work.

Browman, C. P., and Goldstein, L. (**1992**). ‘‘Articulatory phonology: An overview,’’ Phonetica **49**, 155–180.

Byrd, D. (**2000**). ‘‘Articulatory vowel lengthening and coordination at phrasal junctures,’’ Phonetica **57**, 3–16.

de Jong, K. J. (**1995**). ‘‘The supraglottal articulation of prominence in english: Linguistic stress as localized hyperarticulation,’’ J. Acoust. Soc. Am. **97**, 491–504.

Delogu, C., Conte, S., and Sementina, C. (**1998**). ‘‘Cognitive factors in the evaluation of synthetic speech,’’ Speech Commun. **24**(2), 153–168.

Erickson, D. (**1998**). ‘‘Effects of contrastive emphasis on jaw opening,’’ Phonetica **55**, 147–169.

Flege, J. E. (**1988**). ‘‘Effects of speaking rate on tongue position and velocity of movement in vowel production,’’ J. Acoust. Soc. Am. **84**, 901–916.

Fourakis, M. (**1991**). ‘‘Tempo, stress and vowel reduction in American English,’’ J. Acoust. Soc. Am. **90**, 1816–1827.

Fox, R. A. (**1989**). ‘‘Dynamic information in the identification and discrimination of vowels,’’ Phonetica **46**, 97–116.

Furui, S. (**1986**). ‘‘On the role of spectral transition for speech perception,’’ J. Acoust. Soc. Am. **80**, 1016–1025.

Gay, T. (**1978**). ‘‘Effect of speaking rate on vowel formant movements,’’ J. Acoust. Soc. Am. **63**, 223–230.

Halliday, M. A. K. (**1967**). ‘‘Notes on transitivity and theme in English. II,’’ J. Linguistics, **3**, 199–244.

Hertz, S. (**1991**). ‘‘Streams, phones and transitions: Toward a new phonological and phonetic model of formant timing,’’ J. Phonetics **19**, 91–109.

Hosom, P. (**2000**). ‘‘Automatic time alignment of phonemes using acoustic-phonetic information,’’ Ph.D. thesis, Oregon Graduate Institute of Science and Technology, 20000 Walker Rd., Beaverton, Oregon 97006; also available at: http://cslu.ece.ogi.edu/publications

Kozhevnikov, V. A., and Chistovich, L. A. (**1965**). *Speech: Articulation and Perception*, JPRS 30,543 (Joint Publication Research Service, Washington, D.C.).

Kuehn, D. P., and Moll, K. L. (**1976**). ‘‘A cineradiographic study of VC and CV articulatory velocities,’’ J. Phonetics **4**, 303–320.

Lindblom, B. (**1963**). ‘‘Spectrographic study of vowel reduction,’’ J. Acoust. Soc. Am. **35**, 1773–1781.

Lindblom, B. (**1990**). ‘‘Explaining phonetic variation: A sketch of the H&H theory,’’ in *Speech Production and Speech Modelling*, edited by W. Hardcastle and A. Marchal (Kluwer Academic, Dordrecht), pp. 403–439.

Moon, S.-J., and Lindblom, B. (**1994**). ‘‘Interaction between duration, context, and speaking style in English stressed vowels,’’ J. Acoust. Soc. Am. **96**, 40–55.

Moulines, E., and Charpentier, F. (**1990**). ‘‘Pitch synchronous waveform processing techniques for text-to-speech synthesis using diphones,’’ Speech Commun. **9**(5/6), 453–467.

Nelson, W. L. (**1983**). ‘‘Physical principles for economies of skilled movements,’’ Biol. Cybern. **46**, 135–147.

Ostry, D. J., Cooke, J. D., and Munhall, K. G. (**1987**). ‘‘Velocity curves of human arm and speech movements,’’ Exp. Brain Res. **68**, 37–46.

Pitermann, M. (**2000**). ‘‘Effect of speaking rate and contrastive stress on formant dynamics and vowel perception,’’ J. Acoust. Soc. Am. **107**, 3425–3437.

Schoentgen, J., and Ciocea, S. (**1997**). ‘‘Kinematic formant-to-area mapping,’’ Speech Commun. **21**(4), 227–244.

Sluijter, A., and van Heuven, V. (**1996**). ‘‘Spectral balance as an acoustic correlate of linguistic stress,’’ J. Acoust. Soc. Am. **100**, 2471–2485.

Strange, W. (**1989a**). ‘‘Dynamic specification of coarticulated vowels spoken in sentence context,’’ J. Acoust. Soc. Am. **85**, 2135–2153.

Strange, W. (**1989b**). ‘‘Evolving theories of vowel perception,’’ J. Acoust. Soc. Am. **85**, 2081–2087.

van Bergem, D. R. (**1993**). ‘‘Acoustic vowel reduction as a function of sentence accent, word stress and word class,’’ Speech Commun. **12**, 1–23.

van Santen, J. P. H. (**1992**). ‘‘Contextual effects on vowel duration,’’ Speech Commun. **11**(6), 513–546.

van Santen, J. P. H. (**1997**). ‘‘Prosodic modeling in text-to-speech synthesis,’’ in Proceedings of EUROSPEECH, Keynote 19–28.

van Son, R. J. J. H., and Pols, L. (**1990**). ‘‘Formant frequencies of Dutch vowels in a text, read at normal and fast rate,’’ J. Acoust. Soc. Am. **88**, 1683–1693.

van Son, R. J. J. H., and Pols, L. (**1992**). ‘‘Formant movements of Dutch vowels in a text, read at normal and fast rate,’’ J. Acoust. Soc. Am. **92**, 121–127.

van Son, R. J. J. H., and Pols, L. C. W. (**1999**). ‘‘Perisegmental speech improves consonant and vowel identification,’’ Speech Commun. **29**(1), 1–22.

Waibel, A. (**1986**). ‘‘Recognition of lexical stress in a continuous speech understanding system—A pattern recognition approach,’’ in Proceedings of ICASSP, pp. 2287–2290.

Watson, C. I., and Harrington, J. (**1999**). ‘‘Acoustic evidence for dynamic formant trajectories in Australian English vowels,’’ J. Acoust. Soc. Am. **106**, 458–468.

Widera, C. (**2000**). ‘‘Strategies of vowel reduction—A speaker-dependent phenomenon,’’ in Proceedings of ICSLP, pp. I.552–555.

Wouters, J., and Macon, M. W. (**2000**). ‘‘Spectral modification for concatenative speech synthesis,’’ in Proceedings of ICASSP, pp. II.941–944.

Wouters, J., and Macon, M. W. (**2002**). ‘‘Effect of prosodic factors on spectral dynamics. II. Synthesis,’’ J. Acoust. Soc. Am. **111**, 428–438.

Wrede, B., Fink, G. A., and Sagerer, G. (**2000**). ‘‘Influence of duration on static and dynamic properties of German vowels in spontaneous speech,’’ in Proceedings of ICSLP, pp. I.82–85.

Effects of prosodic factors on spectral dynamics. II. Synthesis

Johan Wouters[a] and Michael W. Macon[b]
Center for Spoken Language Understanding, OGI School of Science and Engineering, Oregon Health & Science University, 20000 NW Walker Road, Beaverton, Oregon 97006

(Received 27 April 2001; revised 26 August 2001; accepted 28 August 2001)

In Paper I [J. Wouters and M. Macon, J. Acoust. Soc. Am. **111**, 417–427 (2002)], the effects of prosodic factors on the spectral rate of change of phoneme transitions were analyzed for a balanced speech corpus. The results showed that the spectral rate of change, defined as the root-mean-square of the first three formant slopes, increased with linguistic prominence, i.e., in stressed syllables, in accented words, in sentence-medial words, and in clearly articulated speech. In the present paper, an initial approach is described to integrate the results of Paper I in a concatenative synthesis framework. The target spectral rate of change of acoustic units is predicted based on the prosodic structure of utterances to be synthesized. Then, the spectral shape of the acoustic units is modified according to the predicted spectral rate of change. Experiments show that the proposed approach provides control over the degree of articulation of acoustic units, and improves the naturalness and intelligibility of concatenated speech in comparison to standard concatenation methods. © *2002 Acoustical Society of America.* [DOI: 10.1121/1.1428263]

PACS numbers: 43.72.Ar, 43.72.Ja, 43.71.An, 43.71.Es [DOS]

I. INTRODUCTION

In concatenative speech synthesis, segments of recorded speech or *acoustic units* are joined to generate target speech utterances. Many synthesis systems employ signal-processing methods to modify the duration and pitch ($F0$) of the acoustic units. Hence, a target prosody can be imposed that is independent of the duration and pitch of the units in the database. However, time- and pitch-scale modifications often reduce the naturalness of the acoustic units. This is partly due to artifacts introduced by the modification algorithms, but also to the fact that not enough acoustic–prosodic characteristics of the units are modified, such as aspects of vowel quality, spectral balance, intensity, and glottalization.

To avoid the use of speech modification in concatenative synthesis, a common approach is to expand the speech database with units in different prosodic contexts, and to search at run time for optimal units corresponding to the target utterance (i.e., Hunt and Black, 1996; Syrdal *et al.*, 2000; Takano *et al.*, 2001). It has been argued, however, that for synthesis of unrestricted text an unrealistically large number of such units would be needed, as the interactions between prosodic factors introduce a large number of contexts to be covered (van Santen, 1997; Edgington, 1997).

In this paper, an approach is presented to improve prosodic modification of acoustic units, by controlling the *degree of articulation* of sonorant phonemes. The approach is based on the results in Wouters and Macon (2002), which is referred to as "Paper I" for the remainder of this paper.

The degree of articulation can be defined acoustically as the *phonetic quality* of a phoneme segment, i.e., the extent to which the acoustic target associated with a phoneme is reached (Ladefoged, 1975). Control of the degree of articulation has significant potential to improve the naturalness and intelligibility of concatenated speech, since units selected from a small database often produce overarticulated or "choppy" speech, while units selected from a large database sometimes produce speech with an inconsistent or "patchwork quality" articulation style.

In formant synthesis, control of the degree of articulation is achieved relatively easily by redefining formant targets in certain phonetic and prosodic contexts (Klatt, 1987; Kohler, 1990). However, no consensus has been reached for predicting the desired formant targets depending on the prosodic or phonetic context, and description of the complete formant trajectories presents further challenges (Hertz, 1991; van Bergem, 1993). In concatenative synthesis, parametric control of formant targets is typically not available, due to problems with identifying and modifying formants in recorded speech.

In Paper I, we analyzed the spectral dynamics of vowel and liquid transitions in different prosodic contexts. The spectral rate of change, defined as the root-mean-square of the first three formant slopes, increased in linguistically prominent phoneme transitions, i.e., in stressed vs unstressed syllables, in accented vs unaccented words, in sentence-medial vs sentence-final words, and in clearly articulated speech vs reduced speech. These findings support the hypothesis that the speaker's *articulation effort* increases with linguistic prominence, resulting in faster articulatory movements and hence in a higher spectral rate of change (Nelson, 1983; Moon and Lindblom, 1994).

The results in Paper I are consistent with a *contextual model of articulation*. According to this model, the degree of articulation of a sonorant phoneme depends on (1) the phonetic context; (2) the phoneme duration; and (3) the spectral rate of change (Lindblom, 1963; Moon and Lindblom, 1994).

---
[a]Electronic mail: wouters@cse.ogi.edu
[b]Deceased on 15 March 2001.

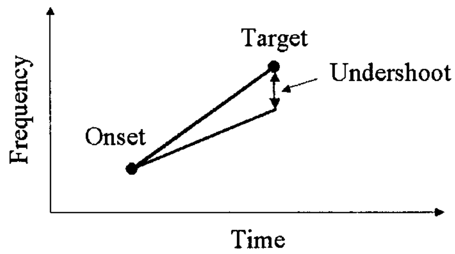

FIG. 1. Illustration of the contextual model of articulation for a hypothetical vowel formant. The target undershoot depends on the interaction between the phonetic context, the vowel duration, and the spectral rate of change.

Figure 1 illustrates this model for a hypothetical vowel formant. The difference between the formant target and the actual value reached at the vowel center is defined as the *target undershoot* (Lindblom, 1963). According to the contextual model of articulation, the amount of undershoot depends on the interaction between the phonetic context (i.e., the formant onset and target values), the phoneme duration, and the spectral rate of change (i.e., the formant slope). For a given duration and phonetic context, target undershoot occurs if the formant slope is below a critical value. However, if the vowel becomes longer, the target may be reached even with a moderate spectral rate of change. Similarly, if the onset and target formant frequencies are close, the target can be reached without requiring either a long vowel duration or a high spectral rate of change.

In most concatenative synthesis systems, methods are available to predict and modify phoneme durations, according to the prosodic structure of the target utterance. However, duration modification usually affects the spectral rate of change of the acoustic units, and does not enable control of the amount of target undershoot. Following the contextual model of articulation, we propose to control the spectral rate of change of acoustic units *independently* from their duration. Prediction of the desired spectral rate of change is based on the prosodic structure of the target utterance. The proposed method provides control of the degree of articulation of concatenated acoustic units, and improves the intelligibility and naturalness of synthesized utterances.

In Sec. II, a method is described to modify the spectral dynamics of acoustic units, using a line spectral frequency (LSF) representation. Prediction of the target LSF dynamics is based on the results of the statistical analysis in Paper I. High-quality speech is generated corresponding to the modified LSF spectra, using a sinusoidal+all-pole parametrization of the acoustic units.

In Sec. III, the proposed method is integrated in a text-to-speech (TTS) synthesis system. The naturalness of the proposed method is compared to standard concatenation techniques, using objective and subjective measures.

In Sec. IV, we investigate whether the perception of syllabic stress in concatenative synthesis can be improved using the proposed method. Silverman *et al.* (1990) and others have reported that the intelligibility of synthetic speech decreases for longer sentences and paragraphs, likely because several acoustic–prosodic cues are missing compared to natural speech. The stress experiment in Sec. IV is a first step towards determining whether control of the degree of articulation of acoustic units can improve the intelligibility of concatenated speech.

II. CONTROL OF DEGREE OF ARTICULATION IN CONCATENATIVE SPEECH SYNTHESIS

In this section, a method is proposed to integrate the contextual model of articulation in a concatenative synthesis framework. First, we describe a technique to modify the spectral shape of acoustic units, corresponding to a set of target spectral dynamics. The target dynamics are predicted based on the effects of prosodic factors analyzed in Paper I. Then, the parametrization of the speech signal is discussed, allowing spectral modification of acoustic units while maintaining the original speech quality.

A. Application of the contextual model of articulation

According to the contextual model of articulation, the degree of articulation of a sonorant phoneme in a given phonetic context depends both on the phoneme duration and on the spectral rate of change. This model can be integrated in a concatenative synthesis system, by predicting both the duration and the spectral rate of change of speech segments in a target prosodic context, and modifying the acoustic units accordingly. While duration modifications are commonly employed in concatenative synthesis systems, in this paper a method is proposed to control the spectral dynamics of acoustic units, independently from their duration.

One way to achieve independent control of the spectral rate of change and phoneme durations is to employ nonuniform time-warping. For example, if the spectral rate of change of a unit should decrease by 50%, this could be achieved by doubling the duration of phonetic transition regions inside the unit, and shortening stationary regions, for example, at the center of a phoneme. However, this technique requires segmentation of acoustic units into stationary and transition regions, which makes the approach sensitive to alignment errors. Also, no vowel reduction or target undershoot could be achieved without removing speech in phonetic transition regions, which may lead to increased spectral mismatch between concatenated speech units.

Rather than using time-warping, we represent the acoustic units by a set of spectral trajectories related to the resonant frequencies of the vocal tract. The rate of change of these trajectories can be modified, for example, using linear filtering. A filtering approach may not be optimal however, if the target rate of change, and hence the filter coefficients, vary continuously throughout an utterance, depending on the phonetic and prosodic context. Instead, the target trajectories can be computed as *maximum likelihood* trajectories, satisfying a set of static and dynamic constraints. This approach is explained in more detail below, for different spectral representations.

1. Formant trajectories

If a speech segment is represented by formant trajectories, where $f_{i,j}$ represents the jth formant at time points $i=1,...,N$, then new trajectories $x_{i,j}$ can be defined that are close to $f_{i,j}$, and satisfy a set of dynamic constraints, de-

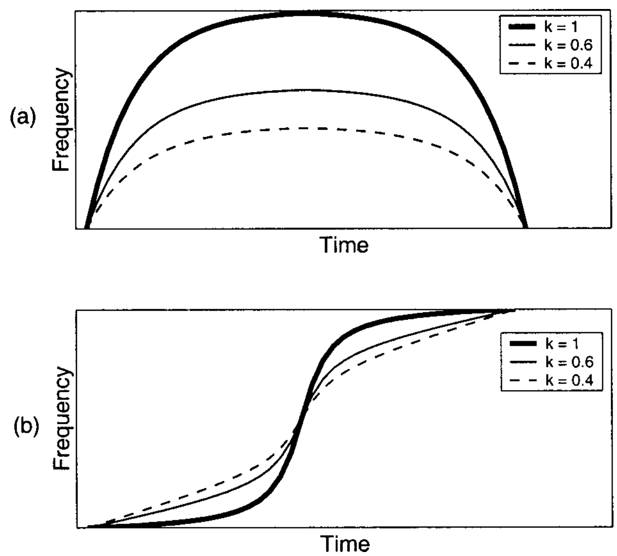

FIG. 2. Stylized formant trajectories and reduced versions obtained using Eq. (1).

noted as $\Delta f_{i,j}$. The new trajectories are found by minimizing the following cost function with respect to $x_{i,j}$

$$E=\sum_{i=1}^{N} (x_{i,j}-f_{i,j})^2+D\sum_{i=1}^{N-1} (\Delta x_{i,j}-\Delta f_{i,j})^2, \qquad (1)$$

where D is a weighting factor determining the relative importance of the static versus the dynamic constraints. This cost function was first proposed by Plumpe *et al.* (1998), to smooth spectral trajectories using statistically predicted $\Delta f_{i,j}$ parameters, in a hidden markov model (HMM) framework. The trajectories $x_{i,j}$ represent the maximum likelihood solution satisfying the static and dynamic constraints, if $f_{i,j}$ and $\Delta f_{i,j}$ are assumed to be normally distributed.

To modify the spectral rate of change, we specify the dynamic constraints $\Delta f_{i,j}$ as a scaled version of the local rate of change of the original formant trajectories

$$\Delta f_{i,j}=k_i\Delta f_{i,j}^{\mathrm{orig}}, \qquad (2)$$

where k_i is a time-varying scaling function. If k_i is set to a value smaller than 1, Eq. (2) expresses a reduction in the spectral rate of change, which was hypothesized in Paper I to correspond to a reduction in articulation effort in natural speech.

In Fig. 2, two stylized formant trajectories are shown along with their modified versions, when k is varied between 1, 0.6, and 0.4. Figure 2(a) represents a prototypical case of vowel reduction for one formant, where the difference between the trajectories at midpoint corresponds to the amount of target undershoot. Figure 2(b) does not demonstrate target undershoot, but represents different degrees of coarticulation between two sonorant phonemes for a single formant, resulting in less abrupt acoustic transitions.

For the stylized trajectories in Fig. 2, $\Delta f_{i,j}^{\mathrm{orig}}$ was set to $f_{i+1,j}-f_{i,j}$, and the weighting factor D was chosen such that the dynamic constraints $\Delta f_{i,j}$ were imposed most accurately.

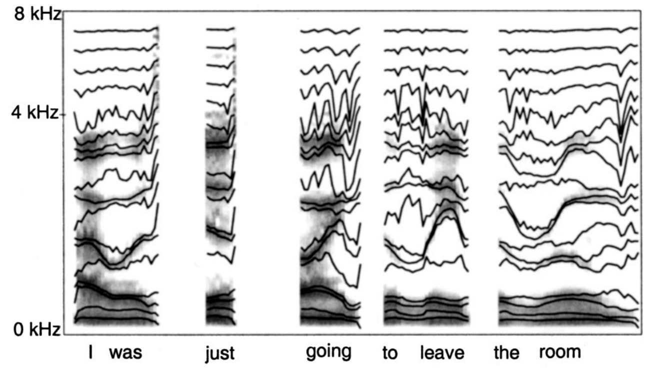

FIG. 3. Line spectral frequency trajectories overlaid on pitch-synchronous, mel-warped, spectrogram.

A value of $D=40$ was selected, as the trajectory shapes changed very little when D was increased further. Specification of the parameters k_i, $\Delta f_{i,j}^{\mathrm{orig}}$, and D in the context of an automated speech synthesis system is discussed below.

The endpoints of the trajectories in Fig. 2 were "frozen," by setting $x_{i,j}=f_{i,j}$ for $i=1, N$ in Eq. (2). This is also explained in the next section. Note that to create the reduced formant trajectories, no new vowel targets needed to be specified, nor was the vowel segmented into stationary and transition regions.

2. Line spectral frequency (LSF) trajectories

In concatenative synthesis, problems with formant detection prevent direct manipulation of the formant trajectories. Instead, the speech spectrum can be represented using line spectral frequencies (LSF), which are obtained automatically from LPC parameters. In this work, the LSFs are computed from a sinusoidal+all-pole representation of speech, as is discussed in Sec. II C.

In Fig. 3, LSF trajectories are overlaid on a pitch-synchronous, mel-warped, spectrogram. Because the distance between two closely placed LSFs corresponds to the bandwidth of an underlying LPC pole, the trajectories of close LSF pairs in Fig. 3 often coincide with formant trajectories. Hence, the LSFs are a suitable representation to enable modification of the formant dynamics. Another advantage of the LSF representation is that modified LSF parameters can be converted back to LPC filters that are stable as long as the ordering of the LSFs is preserved (Soong and Juang, 1984).

Equation (1) can be applied to control the spectral rate of change of the LSF trajectories, similar to the trajectories in Fig. 2. The modified LSF trajectories can then be converted back to speech using the sinusoidal+all-pole model discussed in Sec. II C below. However, application of Eq. (1) to each LSF trajectory independently does not preserve the distance between closely placed LSFs, resulting in formant widening or in the insertion of spurious high-energy peaks in the speech spectrum. Both artifacts degrade the perceptual quality of the resulting speech signal.

The distance between LSF pairs can be controlled by extending Eq. (1) with a third term

$$E=\sum_{i=1}^{N}\sum_{j=1}^{M}(x_{i,j}-f_{i,j})^2+\sum_{i=1}^{N-1}\sum_{j=1}^{M}D_1(i,j)(\Delta^i x_{i,j}-\Delta^i f_{i,j})^2$$
$$+\sum_{i=1}^{N}\sum_{j=1}^{M-1}D_2(i,j)(\Delta^j x_{i,j}-\Delta^j f_{i,j})^2, \tag{3}$$

where $f_{i,j}$ represents the initial LSF value at time i in trajectory j; $\Delta^i f_{i,j}$ is the desired time-derivative at i,j; $\Delta^j f_{i,j}$ is the desired LSF distance, normally set to $f_{i,j+1}-f_{i,j}$; $x_{i,j}$ is the new LSF value at time i in trajectory j; $\Delta^i x_{i,j}$ is the time derivative of $x_{i,j}$; $\Delta^j x_{i,j}$ is the LSF distance between $x_{i,j+1}$ and $x_{i,j}$; N is the number of time points in each LSF trajectory and M is the number of LSF trajectories, corresponding to the LPC model order.

If $\Delta^i x_{i,j}$ and $\Delta^j x_{i,j}$ are linear expressions of $x_{i,j}$, Eq. (3) is easily minimized by setting $dE/dx_{i,j}=0$, and solving the resulting set of linear equations using linear regression.

The weights $D_2(i,j)$ are specified so that the distance between closely placed LSFs is maintained, in order to preserve the bandwidths of the underlying formants. This can be achieved by setting $D_2(i,j)$ to a value inversely proportional to $|\Delta^j f_{i,j}|^2$. Similarly, the weights $D_1(i,j)$ are made proportional to $\Delta^i f_{i,j}$, so that the target spectral dynamics is imposed more accurately for rapidly changing LSFs, which often coincide with formant trajectories (see Fig. 3).

Therefore, the following formula was used for $D_1(i,j)$ and $D_2(i,j)$:

$$D_p(i,j)=a_p+b_p|\Delta^p f_{i,j}|^{c_p}, \quad p=1,2, \tag{4}$$

where $c_1=1$ and $c_2=-2$. The system parameters a_p and b_p were determined by generating a set of test sentences using different values for a_p and b_p, and retaining the values that produced the best perceptual results, through informal listening tests. No alternative values were investigated for c_1 or c_2. In future work, the parameters a_p, b_p, and c_p should be further optimized through tests with multiple listeners, or using a suitable objective quality measure.

In the present work, the contextual model of articulation is applied only in sonorant regions of speech. While the articulatory movements in nonsonorant speech may be governed by similar dynamics as in sonorant speech, the resonant frequencies of the vocal tract are usually not observable in the spectrum of nonsonorants, or must be separated from aperiodic signal components. Therefore, in our current system the trajectories $f_{i,j}$ are ''frozen'' at the sonorant boundaries, by replacing the relevant $x_{i,j}$ by $f_{i,j}$ in Eq. (3). An alternative boundary condition is to set $D_1(i,j)=0$ at the sonorant boundaries, allowing trajectory endpoints to change more freely. However, this approach may result in spectral discontinuities between sonorant and nonsonorant segments, and ignores the fact that the (hidden) articulatory dynamics in nonsonorant speech may still affect the trajectories in sonorant speech.

The cost function in Eq. (3) was first introduced by Wouters and Macon (2001) in the context of *unit fusion*. There, $\Delta^i f_{i,j}$ was defined to reduce spectral mismatch at concatenation points, by utilizing the spectral dynamics of external ''fusion'' units. The objective of the present paper is to improve the acoustic–prosodic characteristics of concatenated units, by specifying spectral dynamics $\Delta^i f_{i,j}$ that reduce mismatch between the degree of articulation of acoustic units in the database and in the target prosodic context. This is discussed in the next section.

TABLE I. Numerical values for prosodic factors, when $\alpha(S=0)$; $\beta(A=0)$; $\gamma(P=\text{final})$; $\delta(Y=\text{clear})$; and $\epsilon(W=\text{func})$ are normalized to 1.

	Onset	Diphthong	Coda
$\alpha(S=1)$	1.18	1.01	0.97
$\beta(A=1)$	1.11	1.05	1.07
$\gamma(P=\text{medial})$	1.07	1.05	1.19
$\delta(Y=\text{fast})$	0.98	1.13	1.10
$\delta(Y=\text{relaxed})$	0.70	1.06	0.92
$\epsilon(W=\text{cont})$	1.10	1.10	1.10

B. Effects of prosodic factors on $\Delta^i f_{i,j}$

In Paper I, a numerical model was developed that describes the spectral rate-of-change RoC of a phonetic transition as the product of five independent factors

$$\text{RoC}=K_p\alpha(S)\beta(A)\gamma(P)\delta(Y). \tag{5}$$

K_p is determined by the transition identity. The functions α to δ map the discrete level of four prosodic factors, i.e., stress (S); accent (A); word position (P), and speaking style (Y); to a numerical value. Hence, the functions α to δ modify the spectral rate of change RoC of a phonetic transition, depending on the prosodic context. The numerical values were estimated for liquid–vowel, diphthong, and vowel–liquid transitions, based on an experimental database, and are summarized in Table I. Since the liquid–vowel transitions occurred in syllable onsets and the vowel–liquid transitions occurred in syllable codas, the three transition types are referred to as *onset*, *diphthong*, and *coda* transitions.

The model in Eq. (5) can be exploited to control the degree of articulation of concatenated speech, by modifying the rate of change of acoustic units depending on the target prosodic context. The target spectral dynamics are defined as a scaled version of the original spectral dynamics of an acoustic unit

$$\Delta^i f_{i,j}=k_i\Delta^i f_{i,j}^{\text{orig}}, \tag{6}$$

where k_i is a scaling function corresponding to the ratio of the target prosodic factors of an acoustic unit and the original prosodic factors

$$k_i=\frac{\alpha(S^t)\beta(A^t)\gamma(P^t)\delta(Y^t)\epsilon(W^t)}{\alpha(S^o)\beta(A^o)\gamma(P^o)\delta(Y^o)\epsilon(W^o)}. \tag{7}$$

This expression for k_i was found by equating $\Delta^i f_{i,j}$ and $\Delta^i f_{i,j}^{\text{orig}}$ to RoC in Eq. (5) and substituting K_p. The superscripts t and o refer to the levels of the target and the original prosodic factors, respectively; ϵ is a prosodic factor related to word class, as is explained below.

The parameter k_i can be interpreted as a gain factor, increasing the spectral rate of change of an acoustic unit when the target utterance requires a higher degree of articulation than the original utterance, or, conversely, decreasing the spectral rate of change of a unit when the target utterance corresponds to a less prominent context than the original utterance. For example, if an acoustic unit occurs at the onset of a stressed syllable in the database, but is needed in an unstressed syllable during synthesis, the spectral rate of change is scaled by $k_i = 1/1.18 = 0.85$ (see Table I), reducing the rate of change by 15%.

Unfortunately, the numerical data available in Table I are sparse compared to the information needed to compute k_i for synthesis of unrestricted text. The prosodic factors studied in Paper I do not include all the factors known to have an effect on vowel quality, such as the syntactic category of a word (van Bergem, 1993), or word length (Moon and Lindblom, 1994). Furthermore, only two or three levels were studied per prosodic factor, ignoring effects of, for example, secondary syllabic stress, different pitch accents, and intermediate phrase boundaries. Therefore, the prediction of k_i described in this section is only a first approach to integrate the results from Paper I in a concatenative synthesis system.

In Paper I, significant differences were found between the prosodic factors for onset, diphthong, and coda transitions, indicating that the scaling function k_i is not constant throughout each syllable. Therefore, we use Eq. (7) to define k_i at the start- and end point of each vowel, taking the numerical values α to δ from the *onset* column in Table I at the start of a vowel, and from the *coda* column at the end of a vowel. Then, k_i is linearly interpolated for intermediate time points i in each vowel. In liquids and glides, k_i depends on the syllabic structure. In syllable codas, k_i is set to the endpoint value of the preceding vowel. In syllable onsets, the end points of k_i are set to the value of the neighboring sonorant, or to 1 at the transition with nonsonorants. Interpolation is used for the intermediate liquid/glide time points.

The linear interpolation scheme assumes that k_i changes gradually over the course of a syllable. The validity of this assumption could be tested by measuring the prosodic effects at different points in a syllable, while issues of time normalization and measurement accuracy for low RoC values would need to be resolved. One such set of measurements is provided by the diphthong data in Table I. The numerical values are comparable to those for coda transitions, which might be expected as the diphthong transitions often occur close to the syllable coda. However, the analysis in Paper I showed that the effects of the prosodic factors for diphthongs were estimated less reliably, possibly because the effects of the prosodic factors on the diphthong transitions were dominated by other articulatory constraints. Therefore, we decided to use only the onset and coda values in Table I to compute k_i.

In addition to the prosodic factors studied in Paper I, a factor based on word class, ϵ, was included in Eq. (7). This factor was normalized to 1 in function words, and was set to 1.1 otherwise, so that the spectral rate of change (i.e., articulation effort) is relatively lower in function words than in contents words (van Bergem, 1993).

In Eq. (6), $\Delta^i f_{i,j}^{\text{orig}}$ represents a smooth time derivative of $f_{i,j}$. Usually, the synthesis time points i of a target utterance are mapped to analysis time points $w(i)$ in the acoustic units, to perform time- and pitch-scale modifications. To avoid effects of $w(i)$ on $\Delta^i f_{i,j}^{\text{orig}}$, the time derivative is based on the LSF representation of the acoustic units prior to time- and pitch-scale modifications. In the present work, the derivative was computed using a 6-point finite impulse response (FIR) filter, corresponding to a low-pass smoothing operation convolved by the first-order difference. As the FIR filter produces LSF differences between the pitch-synchronous *analysis* time points, the filter output is further multiplied by the ratio of the original and the target fundamental frequency, to represent LSF differences between pitch-synchronous *synthesis* time points.

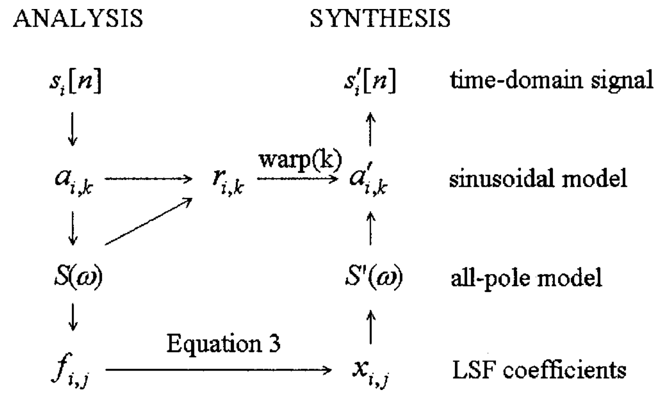

FIG. 4. Analysis/synthesis based on sinusoidal+all-pole model of speech.

C. Spectral modification

The LSF trajectories $x_{i,j}$, obtained by minimizing Eq. (3), must be transformed back to a speech signal with a perceptual quality comparable to that of unmodified acoustic units. A technique to achieve this was described in Wouters and Macon (2001), and is briefly reviewed here. Figure 4 summarizes the analysis/synthesis process.

During the analysis stage, each pitch-synchronous two-period speech frame $s_i[n]$ is represented by a harmonic estimate

$$\hat{s}_i[n] = \sum_{k=-L}^{L} a_{i,k} \exp(jk\omega_0 n), \tag{8}$$

where ω_0 is the fundamental frequency, L represents the number of harmonics, and $a_{i,k} = B_{i,k} \exp(j\phi_{i,k})$ are the complex sinusoidal amplitudes. The sinusoidal parameters are found by solving a complex regression, which minimizes the squared error between $s_i[n]$ and $\hat{s}_i[n]$ (Stylianou, 2001). From $a_{i,k}$, speech can be reconstructed that is practically indistinguishable from $s_i[n]$, by evaluating Eq. 8 pitch-synchronously and applying overlap-add (McAulay and Quatieri, 1986; Stylianou, 2001).

After sinusoidal analysis, an all-pole model is fit to the sinusoidal parameters. First, the power spectrum $|a_{i,k}|^2$ is mel-warped to improve the resolution of the all-pole model towards lower frequencies, corresponding to the frequency resolution of human hearing. To reduce bias of the all-pole spectrum towards the harmonic frequencies, the power spectrum is upsampled, using cubic interpolation in the log domain (Hermansky *et al.*, 1984). Then, correlation coefficients are obtained by an inverse discrete Fourier transform (IDFT) of the power spectrum. Application of the Levinson–Durbin algorithm to the correlation coefficients yields the all-pole (LPC) parameters. In the present work, an all-pole model of order $M=18$ was chosen for 16-kHz speech. The LPC parameters define a smooth, all-pole spectrum $S_i(\omega)=\sigma^2/A(e^{-j\omega})$, which is converted to LSFs $f_{i,j}$ by finding the roots of the polynomials $P(z)=A(z)+z^{-(M+1)}A(z^{-1})$ and $Q(z)=A(z)-z^{-(M+1)}A(z^{-1})$ (Itakura, 1975).

In the synthesis stage, waveforms $s_i'[n]$ must be determined corresponding to $x_{i,j}$. As illustrated on the right-hand side of Fig. 4, the LSF values $x_{i,j}$ corresponding to a synthesis frame are first converted to LPC coefficients, defining a smooth, all-pole spectrum $S_i'(\omega)$. The sinusoidal parameters $a_{i,k}'$ can then be obtained by evaluating $S'(\omega)$ at the harmonics of the target fundamental frequency ω_0', i.e., $a_{i,k}'=S_i'(k\omega_0')$. However, the all-pole envelope does not model some perceptually important characteristics of speech, for example by imposing a minimum-phase spectrum (Quatieri and McAulay, 1987). Choosing $a_{i,k}'=S_i'(k\omega_0')$ results in speech with a quality comparable to that of impulse-excited LPC.

A new method to predict $a_{i,k}'$ was proposed by Wouters and Macon (2001). The method is based on computing a spectral residual $r_{i,k}=a_{i,k}/S(k\omega_0)$ during speech analysis, and multiplying the target all-pole spectrum $S'(\omega)$ by a frequency-warped version of $r_{i,k}$. Resampling of the resulting spectrum produces the target sinusoidal parameters $a_{i,k}'$. The frequency warping is a monotonous, piecewise linear function, which maps dominant poles of $S(\omega)$ to dominant poles of $S'(\omega)$. Hence, residual characteristics $r_{i,k}$ around the spectral peaks or in the valleys of $S(\omega)$ are transferred to equivalent regions in $S'(\omega)$. As a result, perceptually important characteristics of $a_{i,k}$ are preserved in $a_{i,k}'$, while large residual values in the valleys of $S(\omega)$ do not degrade the shape of the target formant peaks, as occurs in modifications based on residual-excited LPC (RELP).

From $a_{i,k}'$, $s_i'[n]$ is computed by applying Eq. (8). A gain factor is applied to $s_i'[n]$ to ensure that the root-mean-square (rms) energy of the analysis frame $s_i[n]$ is preserved. Alternatively, the log rms energy contour of the acoustic units can be controlled similar to an LSF trajectory, in order to reduce the intensity of linguistically less prominent vowels, and to reduce energy mismatches at concatenation points.

III. TEXT-TO-SPEECH EXPERIMENT

A. Material

To evaluate the method in Sec. II, 80 English sentences were generated, using three different synthesis methods. The acoustic units were selected from a diphone table, and had been recorded in the context of small word groups or nonsense words. The speaker was the same person that recorded the database in Paper I. Hence, control of spectral dynamics based on the data in Table I should lead to a more accurate realization of this speaker's degree of articulation in fluent speech.

The sentences were synthesized using phoneme durations and fundamental frequency contours derived from natural sentences. Twenty sentences corresponded to short phrases recorded by the database speaker. Sixty other sentences were recorded by a different speaker, using a more lively speaking style. The "lively" sentences included several long words and function words, which introduce large variations in articulation effort in natural speech, and were expected to highlight quality improvements when controlling the degree of articulation in concatenated speech.

The sentences were synthesized using three different methods. These methods differed in their approach towards resolving spectral mismatch, either between two concatenated units (i.e., "concatenation errors"), or between the prosodic context of a given unit and the target utterance (i.e., "prosodic target errors"). The spectral structure of the acoustic units was modified in two of the three synthesis methods. Then, the units were combined using pitch-synchronous overlap-add to generate the final utterance.

The first synthesis method was a time-domain method. Time- and pitch-scale modifications were achieved using pitch-synchronous overlap-add (Moulines and Charpentier, 1990), and units were concatenated pitch-synchronously. No spectral modifications were performed. This method was denoted as "TD."

In the second method, spectral modification was enabled at the concatenation points. Concatenation mismatch between the LSF parameters of two units was spread linearly over an interpolation region, as described by Dutoit and Leich (1994). The interpolation region was limited to the phoneme in which a concatenation occurred, and it included at most 100 ms on each side of the concatenation point. This method was denoted as "LIN."

In the third method, the effects of prosodic factors were taken into account by specifying a scaling function k_i, as described in Sec. II B, and modifying the spectral shape of the acoustic units accordingly. Since the acoustic units consisted of diphones, spoken in a prosodically neutral context, their spectral transitions were assumed to be maximally articulated, i.e., $S^o=1$, $A^o=1$, $P^o=\text{medial}$, $Y^o=\text{clear}$, $W^o=\text{cont}$ in Eq. (7). The target prosodic factors were predicted automatically by the TTS engine, except for the speaking style, Y^t, which was set to *relaxed* for fast sentences (see below), and to *clear* otherwise. The third synthesis method was denoted as "PROS."

In the three synthesis methods, the log rms energy of the synthesis frames was treated similar to the LSF trajectories. Hence, in LIN, intensity mismatch between concatenated units was reduced using linear interpolation. In PROS, the time dynamics of the energy contour were controlled to reduce acoustic–prosodic mismatches.

B. Results

The performance of the three synthesis methods was compared objectively and subjectively. As an objective measure, mel-frequency cepstral (MFCC) distances were computed between the synthesized utterances and their natural examples, for the 20 sentences recorded by the database speaker. MFCC distances have been shown to correlate moderately well with perceptual distance measurements [e.g., $\rho=0.66$ in Wouters and Macon (1998), $\rho=0.67$ in Chen and Campbell (1999)], although not in the case of spectral discontinuities, as reported by Klabbers and Veldhuis (1998).

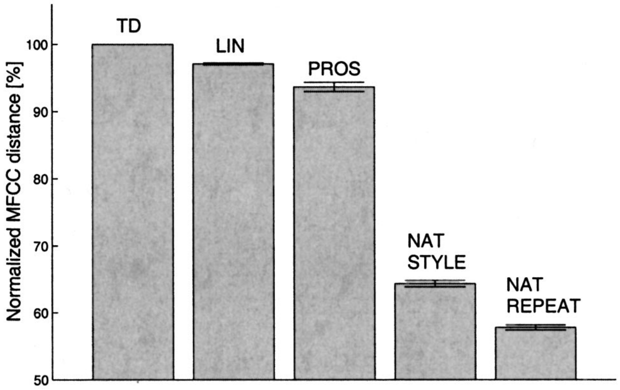

FIG. 5. Normalized MFCC distance between copy–prosody sentences and natural examples, for time-domain concatenation method (TD), linear interpolation of LSFs (LIN), control of prosodic effects (PROS). The normalized average distance between natural utterances is also shown, both across speaking styles and for repetitions within a given speaking style.

MFCC features are also commonly used in automatic speech recognition and to guide unit selection in speech synthesis (Hunt and Black, 1996).

The MFCC feature vectors were computed pitch-synchronously in sonorant phonemes, based on the sinusoidal+all-pole representation described in Sec. II C. The cepstral means were subtracted per sentence, to reduce the effect of differences in the recording conditions for the acoustic units and the example sentences. For each synthesis method m and sentence s, the objective distance $D(m,s)$ was defined as the root-mean-square Euclidean distance between the MFCC feature vectors of the synthesized utterance and of the natural example. $D(m,s)$ was divided by $D(\mathrm{TD},s)$, i.e., the distance obtained for the time-domain synthesis method, to normalize for sentence effects. The normalized distances were then averaged per synthesis method m.

The results are shown in Fig. 5. The three synthesis methods progressively decrease the distance between the concatenated and the natural utterances. These distances can be compared to the *intraspeaker variability*, or the average spectral distance between phonemically identical units recorded by the database speaker. The intraspeaker variability was computed using the phonetic transition regions described in Paper I. There, each sentence containing a particular phonetic transition was repeated nine times, i.e., three times for each of three speaking styles. As illustrated in Fig. 5, the average distance between repetitions of the phonetic transition across speaking styles was 63% of the average distance $D_{\mathrm{avg}}(\mathrm{TD},s)$. Within the same speaking style, the average distance between repetitions was 56% of $D_{\mathrm{avg}}(\mathrm{TD},s)$.

Figure 5 suggests that the proposed method has an effect equal in size to changes in speaking style in natural speech. However, the distance between concatenated speech and natural speech remains significantly larger than the intraspeaker variability. This can be attributed partly to the fact that the acoustic units in this experiment consisted of diphones, which are typically fully articulated and may have a different voice quality than is used in natural speech. The results show that the proposed method should be further improved to control the degree of articulation of concatenated units more accurately, and that other acoustic–prosodic characteristics, such as aspects of voice quality, should also be modified. While approaches based on selecting units from a large corpus of fluent speech may yield utterances closer to natural speech, we believe that the proposed method can further improve the naturalness of such utterances, by controlling the degree of articulation when prosodic target mismatch occurs.

TABLE II. Illustration of complementary version design when three pairs of synthesis methods, denoted as A, B, and C, need to be compared. The columns correspond to sentences and the rows correspond to listeners.

	S1	S2	S3	
L1	A	B	C	⋯
L2	B	C	A	
L3	C	A	B	
	⋮			

The three synthesis methods were also evaluated perceptually using the Comparative Mean Opinion Score (CMOS) test (ITU P.800, 1996). Fifteen subjects listened to pairs of synthesized utterances, and indicated their preference on a 7-point scale, ranging from ''A is much worse than B'' (−3) to ''A is much better than B'' (+3). All listeners were fluent speakers of American English. They listened over headphones in a sound-insulated booth, and could play the utterances several times before selecting a score.

For each sentence, three pairs of synthesis methods needed to be evaluated, i.e., TD-LIN, LIN-PROS, and TD-PROS. A complementary version design was adopted, to limit the duration of the test and to avoid training effects (van Santen, 1993). According to this design, subsequent listeners hear different synthesis pairs for each sentence, but each pair is evaluated equally often per sentence across listeners, and each listener hears each pair equally often across sentences. An example is shown in Table II, for the case where three pairs of synthesis methods need to be evaluated. The total number of sentences and listeners is also a multiple of 3. The ordering of the sentences and the synthesis methods within a pair is randomized per listener.

Thirty sentences were evaluated: nine ''fast'' sentences, nine ''neutral'' sentences, and 12 ''lively'' sentences. Additionally, one sentence for each group was presented as an example to the listeners at the beginning of each test session.

The sentences were generated as follows. Of the 20 sentences recorded by the database speaker, the phoneme durations were shortened by 20% for ten sentences, to generate fast speech. The remaining ten sentences were labeled as neutral speech. From the sixty lively sentences, 13 (i.e., 12 test sentences plus 1 example) were selected by finding the sentences for which the difference between the LIN and the PROS version was largest, using an objective distance measure as well as informal subjective comparisons. This preselection step was motivated by the fact that the proposed method does not always significantly alter the concatenated units, for example when there are no large formant movements or prosodic mismatches.

After presentation of the three example sentences, each listener evaluated the 30 remaining sentences using the complementary version design described above. Each lis-

TABLE III. Average perceptual scores of Comparative Mean Opinion Score (CMOS) test, on a scale from −3 to +3.

	LIN	PROS
TD	0.50±0.08	0.96±0.09
LIN		0.43±0.09

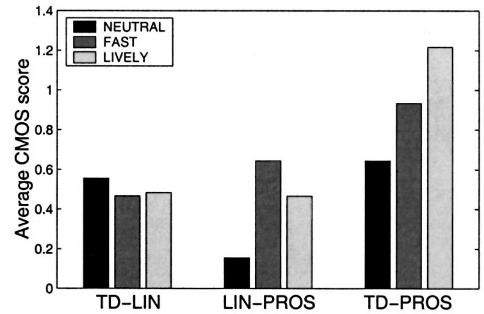

FIG. 6. Average CMOS scores for time-domain concatenation method (TD), linear interpolation method (LIN), and proposed method (PROS), for "neutral," "fast," and "lively" sentences.

tener evaluated one utterance pair per sentence, yielding a total of 30 judgments per listener. The average perceptual scores are shown in Table III, together with the standard error. The CMOS scores are highly significant ($p \ll 0.0001$ in each case). The linear interpolation method (LIN) improved the perceptual quality compared to the time-domain method (TD), while the proposed method (PROS) performed better than either TD or LIN. Analysis of the perceptual results per sentence group showed that the improvement of PROS compared to LIN was larger for the lively and fast sentences than for the neutral sentences. This is illustrated in Fig. 6.

As the CMOS scale ranged from −3 to +3, the results indicate that on average listeners rated PROS as "slightly better (+1)" than TD. This is a reasonable result, given that the proposed method operates only on the degree of articulation and on concatenation mismatches in sonorant speech segments, while other aspects of the synthetic utterances may still sound unnatural or disturbing.

In Fig. 7, spectrograms corresponding to one of the test sentences are shown for the three synthesis methods. Comparison between TD and LIN shows that linear smoothing can be effective when the specified interpolation region is appropriate and the line spectral frequencies on either side of a concatenation point underlie the same formants, such as in the words "was" and "the." In the PROS method, the dynamic constraints have reduced the spectral rate of change in the words "I was" and "leave," while smooth trajectories are obtained in the words "just" and "going." As can be seen from Fig. 7, the natural speech (NAT) is even more reduced in "I was" and "going" than was predicted by the PROS method. Hence, more work is needed to improve prediction and modification of the degree of articulation in concatenated speech.

The utterances discussed in this section are available at http://cslu.cse.ogi.edu/tts/demos/jasa02.

IV. STRESS PERCEPTION EXPERIMENT

Although current synthesizers attain high intelligibility scores for isolated words, long sentences or paragraphs are often harder to understand, or impose a higher cognitive load than natural speech (Silverman and Morgan, 1990; van Santen, 1997; Delogu *et al.*, 1998). In this section, an experiment is described to evaluate the potential of the proposed method to improve the perception of syllabic stress in con-

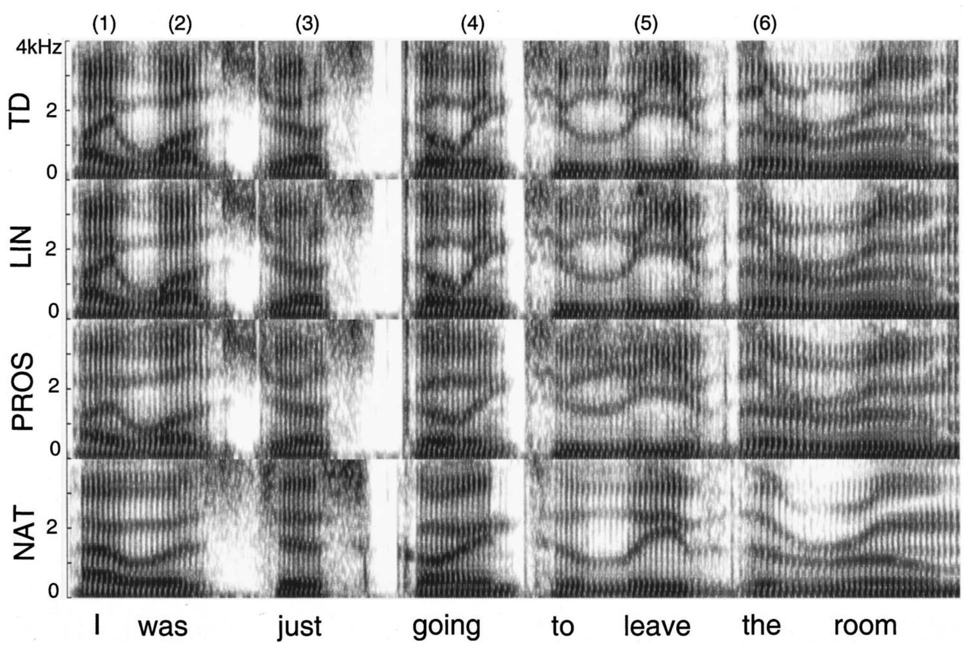

FIG. 7. Spectrograms corresponding to time-domain concatenation method (TD), linear interpolation of LSFs (LIN), control of prosodic effects (PROS). Detailed comparison, guided by the numbers at the top, shows that: the $F2$ rate of change is reduced by PROS in (1), the $F3$ discontinuity is removed by LIN and PROS in (2) and (6), the $F3$, respectively, $F2$, discontinuity is removed by PROS but not by LIN in (3) and (4), and the rate of change of $F2$ and $F3$ is reduced by PROS in (5).

TABLE IV. Utterances generated for each two-syllable word W. σ_1 and σ_2 refer to the first and second syllable of W, respectively. The rows indicate whether the pitch contour is normalized in W, whether the phoneme durations correspond to a stressed–unstressed pattern ($U1$) or unstressed–stressed pattern ($U8$), and whether σ_1 or σ_2 is spectrally reduced. The bottom row contains the results of the stress perception experiment, reported as the frequency $p(\sigma_1)$ with which the first syllable is perceived as stressed.

	$U1$	$U2$	$U3$	$U4$	$U5$	$U6$	$U7$	$U8$
Norm $F0$		x	x	x	x	x	x	
σ_1 short					x	x	x	x
σ_2 short	x	x	x	x				
σ_1 reduced				x		x	x	x
σ_2 reduced	x	x	x		x			
$p(\sigma_1)$ [%]	65	51	47	39	32	27	29	19

catenated speech. The experiment is a first step at determining whether control of acoustic–prosodic effects in addition to time- and pitch-scale modifications can increase the intelligibility of longer concatenated utterances.

In English, vowel quality is but one of the acoustic correlates of syllabic stress, next to pitch, duration, intensity, and spectral balance (e.g., Lindblom, 1963; Waibel, 1986; Sluijter and van Heuven, 1996). The present experiment tests (1) whether the proposed method alters the perceived vowel quality, and (2) what the effect is of variations in vowel quality on stress perception, for fixed values of pitch, phoneme durations, intensity, and spectral balance. If the experiment is successful, then the proposed method is a good candidate to improve the perception of stress in concatenative speech, by controlling the spectral shape of acoustic units in addition to time and pitch modifications.

A. Material

The test material consisted of 30 sentences, synthesized in eight different ways. The sentences were of the form "Please produce W for him," where W is a two-syllable word that can carry lexical stress on either syllable in English. For example, the word "digest" carries lexical stress on the first syllable σ_1 when it is a noun, and on the second syllable σ_2 when it is a verb. The two-syllable words were taken from the study in Paper I. The objective of the present experiment was to reduce σ_1 or σ_2 spectrally using the proposed method, and to study whether stress perception shifted away from the reduced syllable. Sluijter and van Heuven (1997) used a similar approach to evaluate the effect of spectral balance on stress perception, for the nonsense word "nana."

Eight utterances were generated per two-syllable word, as summarized in Table IV. The utterances were based on two natural recordings, which are denoted as $U1$ and $U8$ in Table IV. The speaker assigned syllabic stress to σ_1 in $U1$, and to σ_2 in $U8$. The speaker placed a nuclear pitch accent on the word "again," which followed the carrier phrase. This was done to avoid large pitch movements in σ_1 or σ_2, which would dominate stress perception and limit the effect of further stress manipulations. The accented word "again" was silenced out in the utterances generated for the perceptual test.

A straight line was fit to the original pitch contour of $U1$, to specify a target $F0$ without local pitch movements in W. A new utterance, denoted as $U2$, was generated with this target $F0$ in W, by modifying $U1$ using pitch-synchronous overlap-add (Moulines and Charpentier, 1990). Similarly, a pitch-normalized utterance, denoted as $U7$, was generated from $U8$.

A concatenated utterance, denoted as U', was generated by replacing the unstressed syllable σ_2 in $U1$ by the stressed version of σ_2 from $U8$. Hence, U' contained a sequence of two naturally stressed syllables, as can occur during unit selection when a desired unstressed unit is not found in the unit database.

U' was subjected to modifications of duration, pitch, and spectral shape, as follows. In $U3$ and $U4$, the phoneme durations of σ_2 in U' were changed to the unstressed (i.e., short) durations of σ_2 in $U1$. In $U5$ and $U6$, the phoneme durations of σ_1 in U' were changed to the unstressed durations of σ_1 in $U8$. The pitch contours were normalized in $U3$ and $U4$ as in $U2$, and in $U5$ and $U6$ as in $U7$. Then, σ_2 was spectrally reduced in $U3$ and $U5$, using the proposed method. Similarly, σ_1 was reduced in $U4$ and $U6$. The scaling values $\alpha(S=1)$ in Table I were raised by 10% to increase the amount of vowel reduction. The parameter $D_1(i,j)$ in Eq. (3) was also increased, so that the target spectral dynamics were imposed more accurately.

In the natural utterances $U1$ and $U2$, spectral reduction of σ_2 is the result of natural articulation processes. Similarly, σ_1 is naturally reduced in $U7$ and $U8$.

B. Results

The utterances were presented to 16 listeners, who were native speakers of American English, without known hearing problems. Each listener heard four utterances per word W, or 120 utterances, using the complementary version design described in Sec. III. The utterances were presented over headphones in a sound-insulated booth. The participants could listen several times to each utterance, by manipulating a graphical interface. Then, they were asked to classify W, by selecting one of two displayed words, corresponding to alternative stress patterns of W, e.g., "DIgest" and "diGEST". After making a selection, listeners proceeded to the next utterance.

The resulting classification scores, averaged over the 16 listeners, are shown in the bottom row of Table IV. The scores correspond to the frequency $p(\sigma_1)$ with which the first syllable was perceived as stressed for a particular utterance type. In Fig. 8, the classification scores are presented

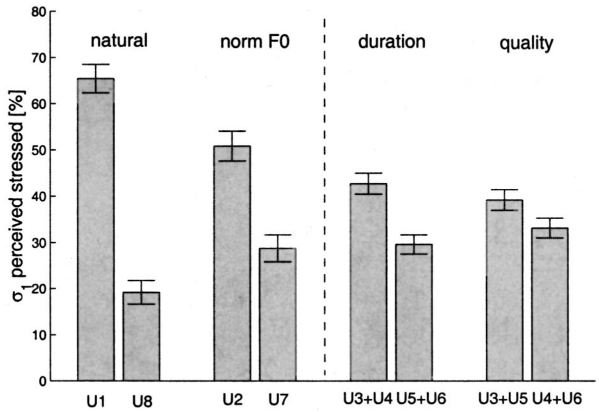

FIG. 8. Classification of first syllable as stressed for (a) natural utterances $U1$ and $U8$; (b) natural utterances with normalized pitch $U2$ and $U7$; (c) concatenated utterances grouped per durational stress pattern; and (d) concatenated utterances grouped per spectrally reduced syllable.

graphically, along with the estimated standard deviation of the mean. For the natural utterances $U1$ and $U8$, the first, respectively the second, syllable was intended to be stressed. The classification scores of 65.4% and 19.2% indicate that the intended stress pattern was not always perceived correctly, which may be attributed to the absence of a strong pitch accent and the lack of semantic information. Although no strong pitch accents occurred in W, the classification accuracy further decreased when pitch movements were normalized in $U2$ and $U7$.

For the utterances based on U', modifying the phoneme durations introduced an average difference of 13% in $p(\sigma_1)$ ($p<0.0001$, double-sided t-test), while modifying the vowel quality introduced an average difference of 6% in $p(\sigma_1)$ ($p=0.05$, double-sided t-test). The effects of duration and vowel quality modifications combined, so that when the second syllable is short *and* spectrally reduced, $p(\sigma_1)=46.7\%$ approaches the result for $U2$. When the first syllable is short *and* spectrally reduced, $p(\sigma_1)=27.5\%$ is slightly lower than the result for $U7$. Hence, the proposed method changes the degree of articulation of the concatenated units, so that the intended stress pattern is perceived more accurately.

The utterances discussed in this section are available at http://cslu.cse.ogi.edu/tts/demos/jasa02.

V. DISCUSSION

In the present paper, a method was presented to control the degree of articulation of sonorant units, by imposing dynamic constraints on the LSF trajectories. The method was motivated by the contextual model of articulation, according to which the degree of articulation of an acoustic unit depends on (1) the phonetic context; (2) the phoneme durations; and (3) the spectral rate of change. The proposed modifications were based on the numerical data obtained in Paper I, where the effects of prosodic factors on the spectral dynamics were analyzed for a balanced corpus. Experimental results showed that the modifications improved the naturalness and intelligibility of concatenated speech.

The proposed method does not require the (artificial) segmentation of speech units into stationary and transition regions, as would be required for an approach based on nonuniform time-warping. Rather, the dynamic characteristics of human speech articulation are integrated robustly, by specifying target spectral dynamics based on the local rate of change of the acoustic units. The method also allows specification of spectral dynamics that *increase* the degree of articulation of acoustic units, for example, to emphasize words or to adopt a clear, ‘‘didactic’’ articulation style. Using time-warping, no phonetic targets outside the range of the original acoustic units could be reached.

In the present work, the spectral constraints were applied only in sonorant speech segments, as the resonant frequencies of the vocal tract cannot be modeled in the spectrum of nonsonorant segments, or must be separated from aperiodic (i.e., noise-like) signal components. Hence, the end points of formant trajectories were ‘‘frozen’’ at the boundaries between sonorant and nonsonorant speech, often limiting the amount of spectral modification that could be achieved.

A solution to this problem would be to obtain a robust estimation of the resonant frequencies of the vocal tract, both in sonorant and nonsonorant speech, for example, by measuring the geometry of the vocal tract during speech recording. Such resonance trajectories could then be associated with the high-energy peaks of the spectrum in sonorant segments, while their dynamics could be controlled across sonorant and nonsonorant speech regions, according to the contextual model of articulation. Integration of such articulatory measurements in a concatenative synthesis system is a topic for further investigation. Another possibility is to extend the proposed method to all voiced phonemes, such as /v,z,ʒ,dʒ/ in English, and the voiced /h/. This could be achieved by splitting the speech signal into a deterministic and an aperiodic component (Stylianou, 2001; Yegnanarayana *et al.*, 1998), and applying the proposed method to the deterministic component only.

The present paper has addressed techniques to modify the degree of articulation of sonorant units; modification of other acoustic–prosodic characteristics, such as spectral balance, glottalization, or breathiness, was not discussed. The sinusoidal+all-pole model may present interesting possibilities for such modifications. For example, the spectral balance, which is related to the vocal force (Sluijter and van Heuven, 1996), may be modified by adding a slowly varying function to the sinusoidal amplitudes. Similarly, aspects of breathiness can be controlled by varying the ratio of the first harmonics in the sinusoidal representation (i.e., Doval and d'Alessandro, 1997).

In the experiments described in Secs. III and IV, the acoustic units were produced by the same speaker that recorded the database in Paper I. Hence, the spectral dynamics predicted using Table I should lead to more accurate synthesis of the articulatory behavior of this speaker. The data in Table I are also easily applied to acoustic units from different speakers. However, more research is needed to analyze the effects of speaker-dependent factors on the spectral dynamics.

VI. CONCLUSION

In this paper, an approach was described to integrate the effects of prosodic factors analyzed in Paper I in a concatenative synthesis framework. The generated speech utterances were more similar to natural utterances than speech produced by other methods, as measured by an objective distance measure. The perceptual quality of the proposed method was also preferred over standard concatenation methods.

A stress perception test showed that the proposed method can improve the intelligibility of concatenated speech, by controlling the degree of articulation of sonorant phonemes. Hence, the variations in the spectral dynamics measured in Paper I are not merely a ''production effect'' of natural speech; rather, the spectral dynamics were shown to have a communicative role by supporting the prosodic structure of a spoken message.

The modification techniques discussed in this paper show that it is possible to alter the formant structure of acoustic units, for example to generate target undershoot, while preserving the perceptual quality of the original recordings. The techniques increase the flexibility of concatenative synthesis systems, and open up new possibilities to explore the perceptual effects of quantative formant modifications in natural-sounding speech.

ACKNOWLEDGMENTS

This work was supported by the National Science Foundation under Grant No. LIS-0082718 to Michael Macon and Jan van Santen, and by Intel Corporation.

Chen, J.-D., and Campbell, N. (**1999**). ''Objective distance measures for assessing concatenative speech synthesis,'' in Proceedings of EUROSPEECH, pp. 611–614.

Delogu, C., Conte, S., and Sementina, C. (**1998**). ''Cognitive factors in the evaluation of synthetic speech,'' Speech Commun. **24**(2), 153–168.

Doval, B., and d'Alessandro, C. (**1997**). ''Spectral methods for voice source parameters estimation,'' in Proceedings of EUROSPEECH, pp. 533–536.

Dutoit, T., and Leich, H. (**1994**). ''On the ability of various speech models to smooth segment discontinuities in the context of text-to-speech synthesis by concatenation,'' in Proceedings of EUSIPCO, Vol. 1, pp. 8–12.

Edgington, M. (**1997**). ''Investigating the limitations of concatenative synthesis,'' in Proceedings of EUROSPEECH, pp. 593–596.

Hermansky, H., Fujisaki, H., and Sato, Y. (**1984**). ''Spectral envelope sampling and interpolation in linear predictive analysis of speech,'' in Proceedings of ICASSP, pp. 2.2.1–2.2.4.

Hertz, S. (**1991**). ''Streams, phones and transitions: Toward a new phonological and phonetic model of formant timing,'' J. Phonetics **19**, 91–109.

Hunt, A. J., and Black, A. W. (**1996**). ''Unit selection in a concatenative speech synthesis system using a large speech database,'' in Proceedings of ICASSP, pp. 373–376.

Itakura, F. (**1975**). ''Line spectrum representation of linear predictive coefficients of speech signals,'' J. Acoust. Soc. Am. Suppl. 1 **57**, S35.

ITU P.800 (**1996**). ''Methods for subjective determination of transmission quality,'' International Telecommunication Union (ITU), Recommendation P.800, http://www.itu.int

Klabbers, E., and Veldhuis, R. (**1998**). ''On the reduction of concatenation artefacts in diphone synthesis,'' *Proceedings of ICSLP*, Vol. 6, pp. 2759–2762.

Klatt, D. H. (**1987**). ''Review of text-to-speech conversion for English,'' J. Acoust. Soc. Am. **82**, 737–793.

Kohler, K. J. (**1990**). ''Segmental reduction in connected speech in German: Phonological facts and phonetic explanations,'' in *Speech Production and Speech Modelling*, edited by W. J. Hardcastle and A. Marchal (Kluwer Academic, Dordrecht), pp. 69–92.

Ladefoged, P. (**1975**). *A Course in Phonetics* (Harcourt Brace Jovanovich, San Diego).

Lindblom, B. (**1963**). ''Spectrographic study of vowel reduction,'' J. Acoust. Soc. Am. **35**, 1773–1781.

McAulay, R. J., and Quatieri, T. (**1986**). ''Speech analysis/synthesis based on a sinusoidal representation,'' IEEE Trans. Acoust., Speech, Signal Process. **34**(4), 744–754.

Moon, S.-J., and Lindblom, B. (**1994**). ''Interaction between duration, context, and speaking style in English stressed vowels,'' J. Acoust. Soc. Am. **96**, 40–55.

Moulines, E., and Charpentier, F. (**1990**). ''Pitch synchronous waveform processing techniques for text-to-speech synthesis using diphones,'' Speech Commun. **9**(5/6), 453–467.

Nelson, W. L. (**1983**). ''Physical principles for economies of skilled movements,'' Biol. Cybern. **46**, 135–147.

Plumpe, M., Acero, A., Hon, H., and Huang, X. (**1998**). ''HMM-based smoothing for concatenative speech synthesis, in Proceedings of ICSLP, 2751–2754.

Quatieri, T. F., and McAulay, R. J. (**1987**) ''Mixed-phase deconvolution of speech based on a sine-wave model,'' in Proceedings of ICASSP, pp. 649–652.

Silverman, H., and Morgan, D. (**1990**). ''The application of dynamic programming to connected speech recognition,'' IEEE ASSP Mag. **7**(3), 6–25.

Silverman, K., Basson, S., and Levas, S. (**1990**). ''Evaluating synthesiser performance: Is segmental intelligibility enough?,'' in Proceedings of ICASSP, pp. 981–984.

Sluijter, A., and van Heuven, V. (**1996**). ''Spectral balance as an acoustic correlate of linguistic stress,'' J. Acoust. Soc. Am. **100**, 2471–2485.

Sluijter, A., and van Heuven, V. (**1997**). ''Spectral balance as a cue in the perception of linguistic stress,'' J. Acoust. Soc. Am. **101**, 503–513.

Soong, F. K., and Juang, B.-H. (**1984**). ''Line spectrum pairs (LSP) and speech data compression,'' in Proceedings of ICASSP, pp. 1.10.1–1.10.4.

Stylianou, Y. (**2001**). ''Applying the harmonic plus noise model in concatenative speech synthesis,'' IEEE Trans. Speech Audio Process. **9**(1), 21–29.

Syrdal, A. K., Wightman, C. W., Conkie, A., Stylianou, Y., Beutnagel, M., Schroeter, J., Strom, V. Lee, K.-S., and Makashay, M. J. (**2000**). ''Corpus-based techniques in the AT&T nextget synthesis system,'' in Proceedings of ICSLP, Number 3601, III. 410.

Takano, S., Tanaka, K., Mizuno, H., Abe, M., and Nakajima, S. (**2001**). ''A Japanese TTS system based on multiform units and a speech modification algorithm with harmonics reconstruction,'' IEEE Trans. Speech Audio Process. **9**(1), 3–10.

van Bergem, D. R. (**1993**). ''Acoustic vowel reduction as a function of sentence accent, word stress and word class,'' Speech Commun. **12**, 1–23.

van Santen, J. P. H. (**1992**). ''Contextual effects on vowel duration,'' Speech Commun. **11**(6), 513–546.

van Santen, J. P. H. (**1993**). ''Perceptual experiments for diagnostic testing of text-to-speech systems,'' Comput. Speech Lang. **7**(1), 49–100.

van Santen, J. P. H. (**1997**). ''Prosodic modeling in text-to-speech synthesis,'' in Proceedings of EUROSPEECH, Keynote 19–28.

Waibel, A. (**1986**). ''Recognition of lexical stress in a continuous speech understanding system—A pattern recognition approach,'' in Proceedings of ICASSP, pp. 2287–2290.

Wouters, J., and Macon, M. W. (**1998**). ''A perceptual evaluation of distance measures for concatenative speech synthesis,'' in Proceedings of ICSLP, Vol. 6, pp. 2747–2750.

Wouters, J., and Macon, M. W. (**2001**). ''Control of spectral dynamics in concatenative speech synthesis,'' IEEE Trans. Speech Audio Process. **9**(1), 30–38.

Wouters, J., and Macon, M. W. (**2002**). ''Effect of prosodic factors on spectral dynamics. I. Analysis,'' J. Acoust. Soc. Am. **111**, 417–427.

Yegnanarayana, B., d'Alessandro, C., and Darsinos, V. (**1998**). ''An iterative algorithm for decomposition of speech signals into periodic and aperiodic components,'' IEEE Trans. Speech Audio Process. **6**(1), 1–11.

Shear wave focusing for three-dimensional sonoelastography

Zhe Wu and Lawrence S. Taylor
Department of Electrical and Computer Engineering, University of Rochester, Rochester, New York 14627

Deborah J. Rubens
Department of Radiology, University of Rochester Medical Center, Rochester, New York 14627

Kevin J. Parker
Department of Electrical and Computer Engineering, University of Rochester Medical Center, Rochester, New York 14627

(Received 4 April 2001; accepted for publication 20 September 2001)

A new vibration scheme is shown to provide localized vibration fields for three-dimensional sonoelastography imaging. The theoretical vibration distributions of double strip loads vibrating normally to the surface of a semi-infinite elastic space are calculated. A localization or focusing of shear waves inbetween the double-strip loads is predicted. Experimentally, two parallel rigid rectangular cross-section bars are mounted on an electromagnetic shaker. Driven by the signal source, the bars vibrate against the surface of a tissue-mimicking phantom. The double-bar source is also used to propagate shear wave into an *ex vivo* prostate phantom with a 6 mm ''tumor'' in it. A combination of high frequencies (400–600 Hz) is used to drive the double-bar applicator. In the phantom experiments, a shear wave focal zone with higher vibration amplitude and uniformity predicted by the theory was confirmed. The position of the focal zone is controllable when adjusting the separation of the bars as the theory shows. When this vibration scheme was used in a prostate phantom experiment, high-resolution tumor images with clear boundaries are obtained. The parallel bar is an ideal applicator to create more uniform vibration within a controllable localized volume. The field has uniformity especially in the direction along the bars. © *2002 Acoustical Society of America.* [DOI: 10.1121/1.1419093]

PACS numbers: 43.80.Cs, 43.80.Ev [FD]

I. INTRODUCTION

Low frequency shear waves can be used to reveal the mechanical properties of soft tissues and thus to detect and quantify hard lesions in the body (Parker *et al.*, 1990; Yamakoshi *et al.*, 1990). Since the three-dimensional (3D) tumor visualization and the measurement of the tumor volume are important in many cases (Egevad *et al.*, 1998), 3D sonoelastography is of great interest.

3D sonoelastography (Taylor *et al.*, 2000) is a technique that images hard lesions by acquiring a sequence of two-dimensional (2D) slices, which are subsequently assembled into a 3D volume. One of the challenges of this technique is to create a relatively uniform vibration field throughout the 3D region of interest. In sonoelastography, the lesion is detected by the local decrease in vibration amplitude caused by a hard (high shear modulus) lesion relative to the higher vibration in the softer (low shear modulus), surrounding tissue. In addition to direct imaging of vibration shear wave fields, it is also possible to estimate local values of Young's modulus within the regions of interest (Fu *et al.*, 2000).

The shear wave fields propagated in tissue are greatly influenced by the type of source that is employed. Yamakoshi *et al.* (1990) used a rectangular plate (20 mm by 60 mm) when using forced low frequency vibration to propagate shear waves in tissue phantoms. The vibration was normal to the surface of the phantom and the resulting vibration field was uniform along the longer side of the plate. Fu *et al.* (2000) later used a long rigid bar with a smaller rectangular cross section to create a plane-strain vibration field for reconstruction of the Young's modulus of a tissue phantom. The bar was mounted on a rigid column then driven normally to the phantom surface to create a plane strain state. Tanter *et al.* (2000) proposed a system for focusing shear waves for transient elastography imaging in which two bars with circular cross sections were placed beside the ultrasound transducer. Using this system on tissue phantoms they found that larger displacements were generated and shear waves penetrated deeper into the medium.

In this paper we show through theory developed by Miller and Pursey (1954) that the thin rectangular cross section bar (called a ''strip load'') of Fu *et al.* produces a beam pattern with a distinctive ''V'' shape. We then extend the analysis to the parallel-rod configuration employed by Tanter *et al.* and demonstrate how this presents a practical configuration for focusing shear waves for 3D image acquisition. The theoretical models are then confirmed by sonoelastography image experiments. To our knowledge, the beam patterns of single-strip load and double-strip load vibration sources have not previously been verified by both theoretical calculation and experimental verification.

In the first part of the paper, we will look at Miller and Pursey's theory. The single-strip load beam pattern is reviewed, and the theory is extended to double-strip loads. In the second part, experimental results on a tissue-mimicking phantom and *ex vivo* prostate phantom are presented. Experi-

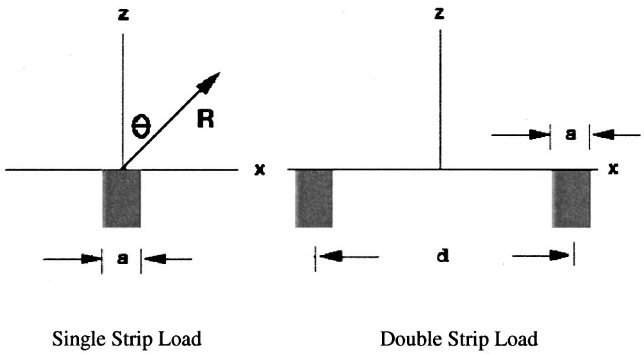

FIG. 1. Image explaining Miller and Pursey's coordinate system for both the single-strip load and the double-strip loads.

ment and theory are shown to agree and confirm that it is possible to create an extended region of shear vibration within elastic materials.

II. THEORY

Sonoelastography uses propagating shear waves to detect hard lesions surrounded by uniform softer tissues. Since a hard lesion is relatively less compliant to vibration than the soft tissue, localized regions of low vibration in the whole field correspond to the lesions. The vibration field is measured by Doppler ultrasound methods, which can map the peak vibration at any point in real time using the color Doppler mode.

To simulate the vibration field pattern of strip loads, we took advantage of Miller and Pursey's early work on mechanical radiators on an elastic half space in the following two cases.

A. A strip load with normal vibration

Consider a long thin strip placed in close contact with a semi-infinite large, uniform homogeneous elastic solid and vibrating normal to the surface of the medium (see Fig. 1). The solution for the vibration field in the far field is:

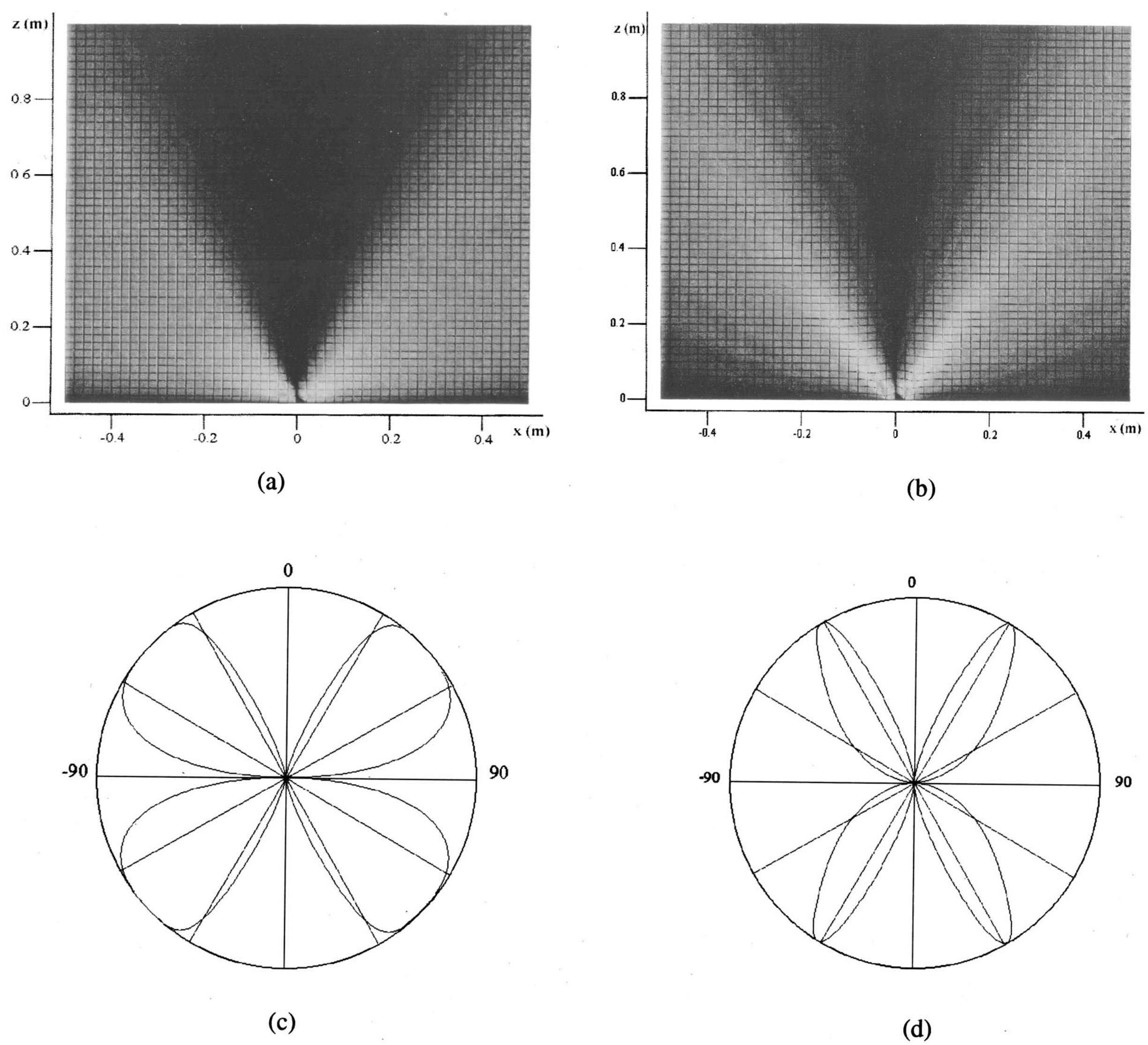

FIG. 2. Vibration fields of the single-strip shaking normal to the medium surface. (a) is Z direction field pattern and (b) is x direction field pattern. (c) is the angular distribution of u_z. (d) is the angular distribution of u_x.

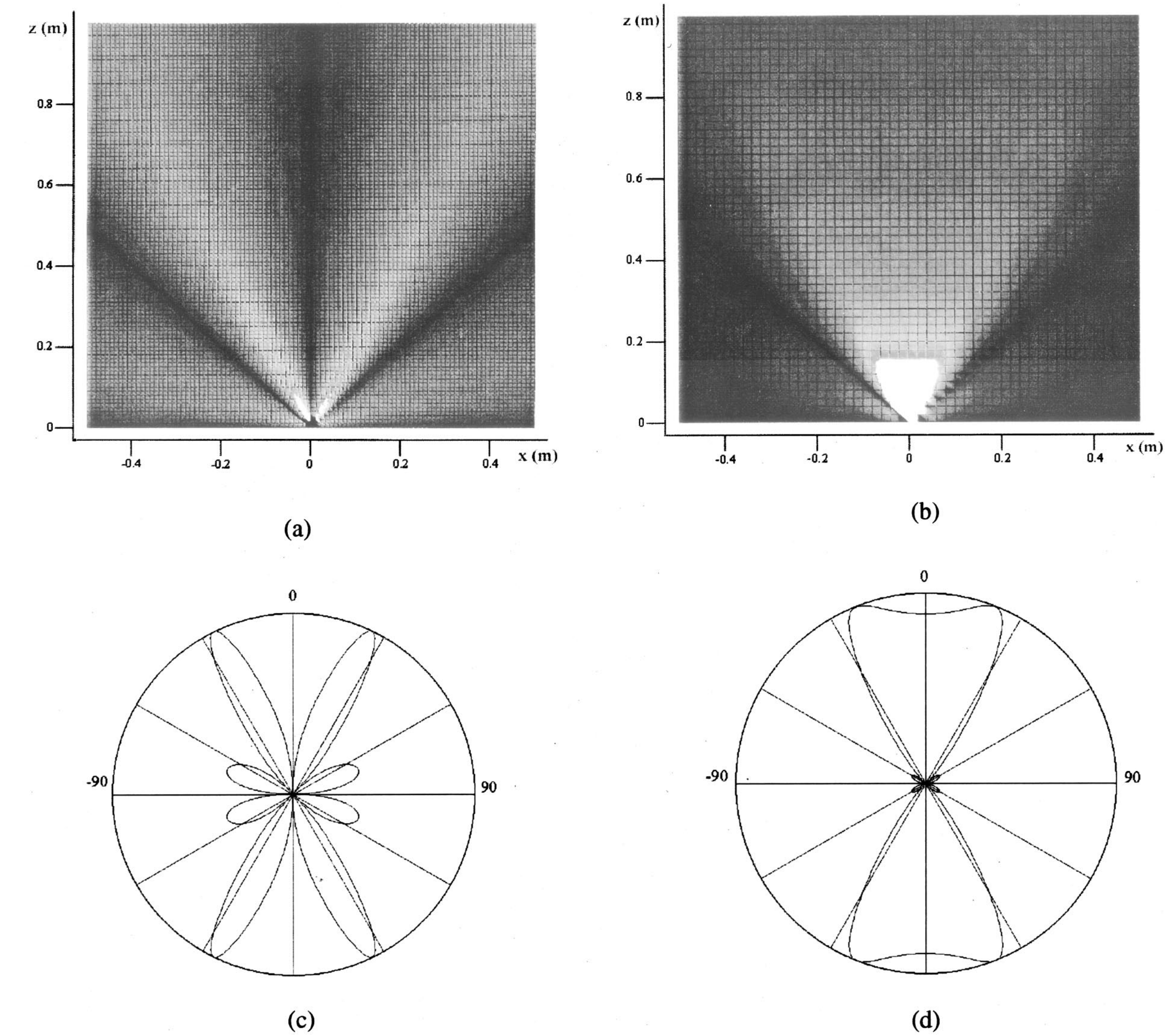

FIG. 3. Vibration fields of single-strip shaking tangential to the medium surface. (a) is the Z-direction field pattern, (b) is the x-direction field pattern, (c) is the angular distribution of u_z, and (d) is the angular distribution of u_x.

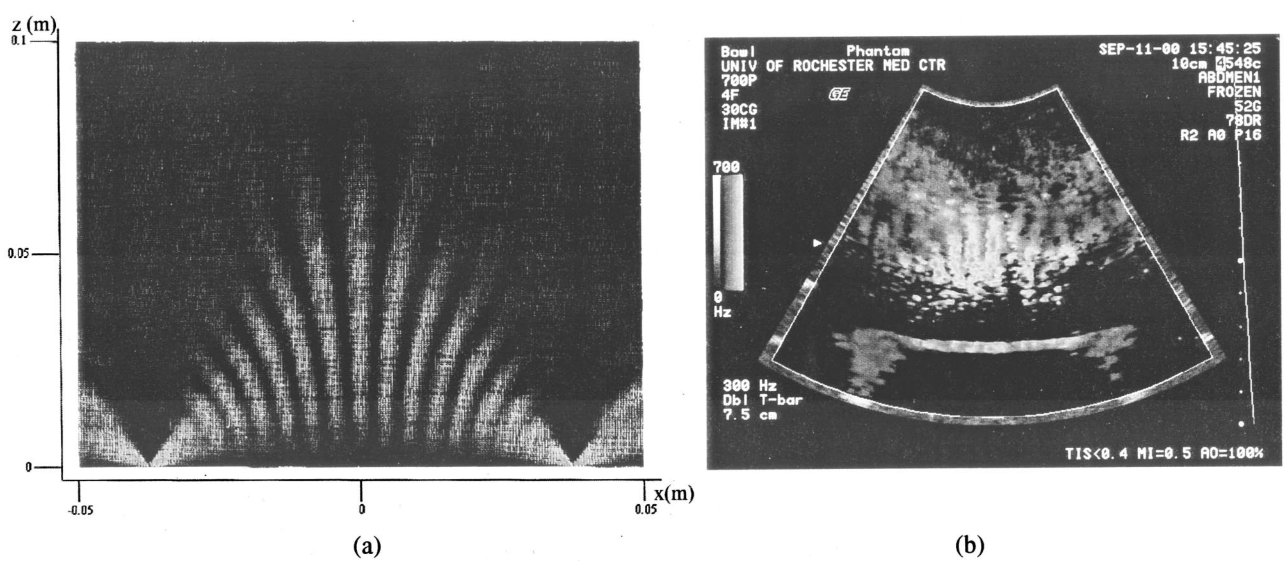

FIG. 4. Double-strip load beam patterns: (a) theoretical calculation of strip loads separated by 75 mm and (b) experiment result taken on Logiq 700. The green horizontal line near the bottom of (b) is the lower surface of the phantom.

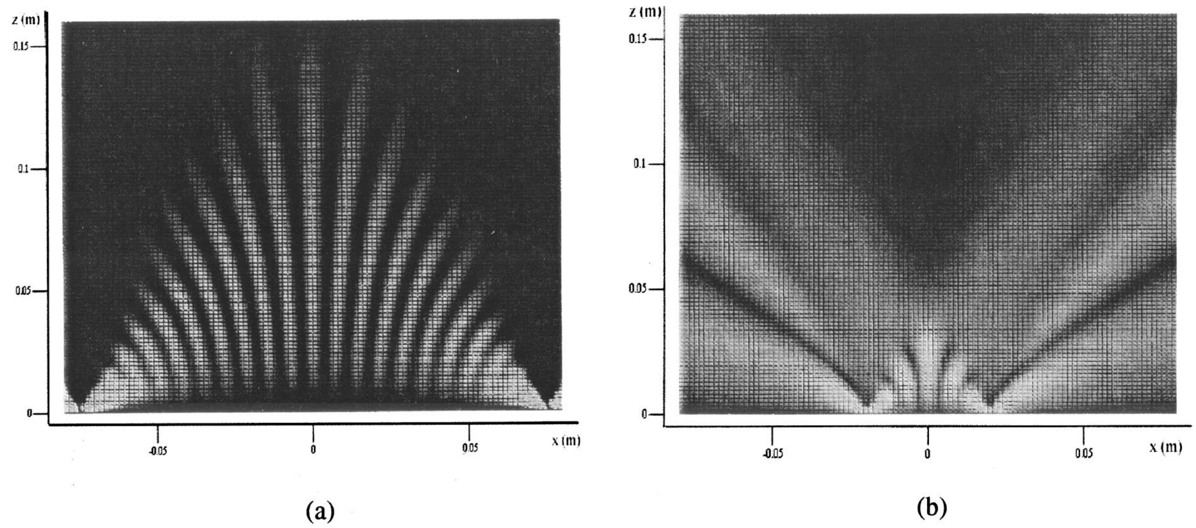

FIG. 5. Patterns change with separation: (a) separation between the two bars is 150 mm, and (b) separation between the two bars is 40 mm.

$$u_z = a \cdot e^{i\pi/4} \cdot \cos\theta \cdot \sqrt{\frac{2}{\pi \cdot R}} \cdot \frac{2\mu^{5/2} \cdot \sin^2\theta \cdot \sqrt{\mu^2 \cdot \sin^2\theta - 1}}{F_0(\mu \cdot \sin\theta)} \cdot e^{-i\mu R} + \frac{i \cdot \cos\theta \cdot (\mu^2 - 2 \cdot \sin^2\theta)}{F_0(\sin\theta)} \cdot e^{-iR}, \tag{1}$$

$$u_x = a \cdot e^{i\pi/4} \cdot \cos\theta \cdot \sqrt{\frac{2}{\pi \cdot R}} \cdot \frac{-\mu^{5/2} \cdot \sin 2\theta \cdot \sqrt{\mu^2 \cdot \sin^2\theta - 1}}{F_0(\mu \cdot \sin\theta)} \cdot e^{-i\mu R} + \frac{i \cdot \sin\theta \cdot (\mu^2 - 2 \cdot \sin^2\theta)}{F_0(\sin\theta)} \cdot e^{-iR}, \tag{2}$$

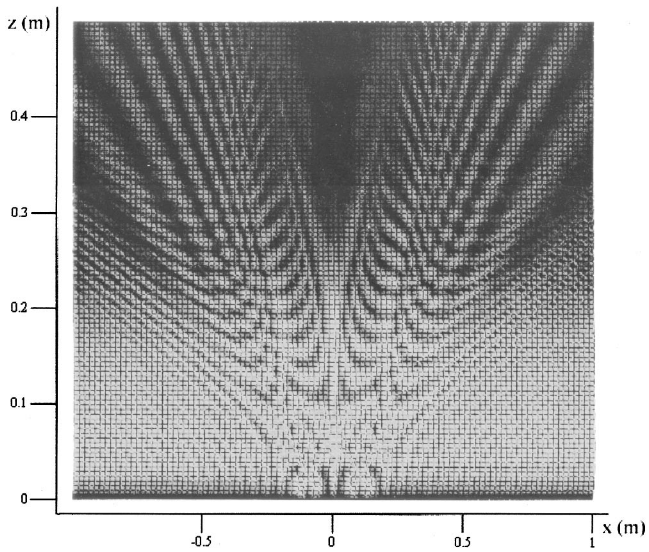

FIG. 6. Side view of the four-strip load beam pattern. From the image, we find a strong vibration region exists in the center of the four-strip load. It is highly focused (refer to the thin pencil-like pattern in the middle) within 20 cm from the load plane.

where u_z is the vibration amplitute in z direction, u_x is the vibration amplitute in the x direction. a is the width of the strip load, θ is the angle from the normal direction, and R is the distance from the origin. F_0 is defined as: $F_0 = (2x^2 - \mu^2)^2 - 4x^2 \cdot \sqrt{(x^2-1)\cdot(x^2-\mu^2)}$; $\mu = (c_{11}/c_{44})$; c_{11} is the bulk modulus and the c_{44} is the shear modulus.

B. Tangential excitation

Consider a long thin strip placed in close contact with a semi-infinite large, uniform homogeneous elastic solid and vibrating tangentially to the surface of the medium. In this case:

$$u_z = a \cdot e^{i(3\pi/4)} \cdot \cos\theta \cdot \sqrt{\frac{2}{\pi \cdot R}} \cdot \frac{-\mu^{7/2} \cdot \sin\theta \cdot \cos 2\theta}{F_0(\mu \cdot \sin\theta)} \cdot e^{-i\mu R} + \frac{\sin 2\theta \cdot \sqrt{\mu^2 - \sin^2\theta)}}{F_0(\sin\theta)} \cdot e^{-iR}, \tag{3}$$

$$u_x = a \cdot e^{i(3\pi/4)} \cdot \cos\theta \cdot \sqrt{\frac{2}{\pi \cdot R}} \cdot \frac{\mu^{7/2} \cdot \cos\theta \cdot \cos 2\theta}{F_0(\mu \cdot \sin\theta)} \cdot e^{-i\mu R} + \frac{2\sin^2\theta \cdot \sqrt{\mu^2 - 2 \cdot \sin^2\theta}}{F_0(\sin\theta)} \cdot e^{-iR}. \tag{4}$$

1. Waves separation

It is clear that Miller and Pursey's solution consists of two terms that travel at different velocities; one wave speed being μ times larger than the other. Our interpretation is that the faster one is a compressional wave and the slower one is a shear wave. To verify this, we examined the divergence of the slow traveling wave component and the curl of the faster component. In numerical assessments, they are both significantly close to zero, which agrees with the definitions of both types of waves.

We then neglect the compressional wave for the following two reasons. First, the wavelength of the compressional wave is typically as long as a few meters, which is not useful in resolving the lesions or other structures and cannot be supported in small centimeter sized organs. Second, since the

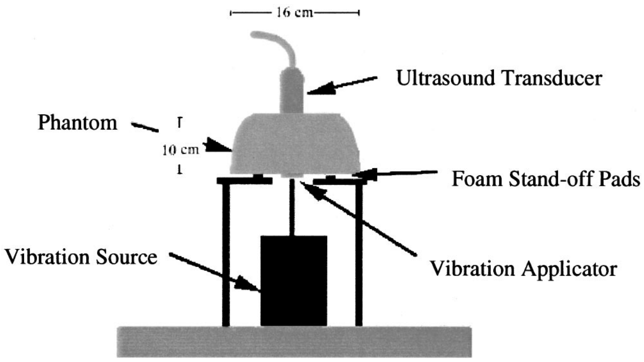

FIG. 7. Experimental setup for acquisition of the vibration images.

bulk modulus is nearly 1000 times larger than the shear modulus (Sarvazyan, 1995) in soft glandular tissue, the amplitude of the compressional wave is actually very small and thus has little contribution to the total pattern.

So, for a normal vibration strip source, the z component and the x component of the shear wave is:

$$u_z = a \cdot e^{i\pi/4} \cdot \cos\theta \cdot \sqrt{\frac{2}{\pi \cdot R}} \cdot \frac{2\mu^{5/2} \cdot \sin^2\theta \cdot \sqrt{\mu^2 \cdot \sin^2\theta - 1}}{F_0(\mu \cdot \sin\theta)} \cdot e^{-i\mu R}, \quad (5)$$

$$u_x = a \cdot e^{i\pi/4} \cdot \cos\theta \cdot \sqrt{\frac{2}{\pi \cdot R}} \cdot \frac{-\mu^{5/2} \cdot \sin 2\theta \cdot \sqrt{\mu^2 \cdot \sin^2\theta - 1}}{F_0(\mu \cdot \sin\theta)} \cdot e^{-i\mu R}. \quad (6)$$

For the tangential excitation strip source, the z component and the x component of the shear wave is:

$$u_z = a \cdot e^{i(3\pi/4)} \cdot \cos\theta \cdot \sqrt{\frac{2}{\pi \cdot R}} \cdot \frac{-\mu^{7/2} \cdot \sin\theta \cdot \cos 2\theta}{F_0(\mu \cdot \sin\theta)} \cdot e^{-i\mu R}, \quad (7)$$

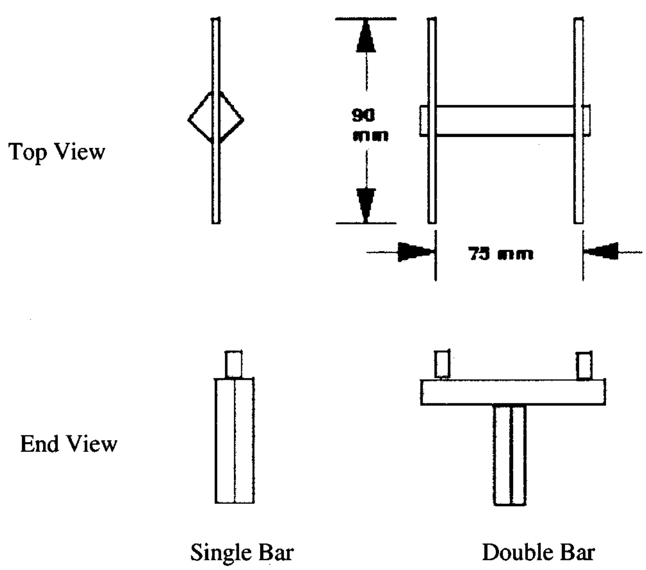

FIG. 8. Sketches and dimension of applicators used in the experiments.

$$u_x = a \cdot e^{i(3\pi/4)} \cdot \cos\theta \cdot \sqrt{\frac{2}{\pi \cdot R}} \cdot \frac{\mu^{7/2} \cdot \cos\theta \cdot \cos 2\theta}{F_0(\mu \cdot \sin\theta)} \cdot e^{-i\mu R}. \quad (8)$$

We plot the beam pattern and directivity functions of the propagating shear wave for both the normal source and the tangential source; see Figs. 2 and 3. One of the interesting features of the pattern is that the angular distribution of the vibration is frequency independent. This effect is observed in the experiments.

2. Superposition of strip loads

We next analyze a superposition of the vibration field created by two strip loads placed side by side with a separation of certain distance D. The left branch of the right strip load and the right branch of the left strip load interfere with each other and localize the energy into a small region (Fig. 4). Note that the beam pattern of the double-strip load is related to the wavelength of the propagating shear waves. In theory this provides us with an experimental method to measure the shear wave velocity in the material. The shear modulus can be further obtained from these values, although details of this are beyond the scope of this paper.

Theoretical simulations show the size of the focusing zone is dependent on the separation of the two strips. It can be roughly divided into two ranges. When the separation is large [150 mm as shown in Fig. 5(a)], the focal zone is a triangle located in between the two bars. As the separation reduces to 40 mm or less [as shown in Fig. 5(b)], the focal zone gradually becomes something more like the beam pattern of a single bar, which radiates energy mainly into a V-shape region. The focusing effect is no longer pronounced.

A further extension leads us to a four-strip load placed in a rectangular shape on a plane. All of the strips are infinitely long. As we expect, a region of higher vibration exists along the center axis of the four-strip load if they vibrate normal to their plane in-phase. Figure 6 shows the side view of the beam pattern of a four-strip load. The sharp, pencil-like pattern in the center of the image implies a highly focused vibration field along the center axis, along with an extended lateral region of high vibration.

III. MATERIALS AND METHODS

A Zerdine tissue phantom (CIRS: Norfolk, VA) was used for the experimental verification of the theory. The tissue-mimicking material has a sound speed near 1540 m/s, a Young's modulus of 20 KPa, and a shear modulus of 6.67 KPa. The phantom is bowl shaped with dimensions as shown in Fig. 7.

With the exception of a few small spherical inclusions in a different region, the phantom is isotropic and homogeneous with a uniform shear modulus. Samples of the phantom material were compression tested and the relaxation phenomenon observed indicated that the material has low shear viscosity. The resulting damping at high frequencies (above 300 Hz) insured that the displacement at the distal boundary of the phantom would be very small, so the bowl phantom is a good simulation of the semi-infinite space. Miller–Pursey

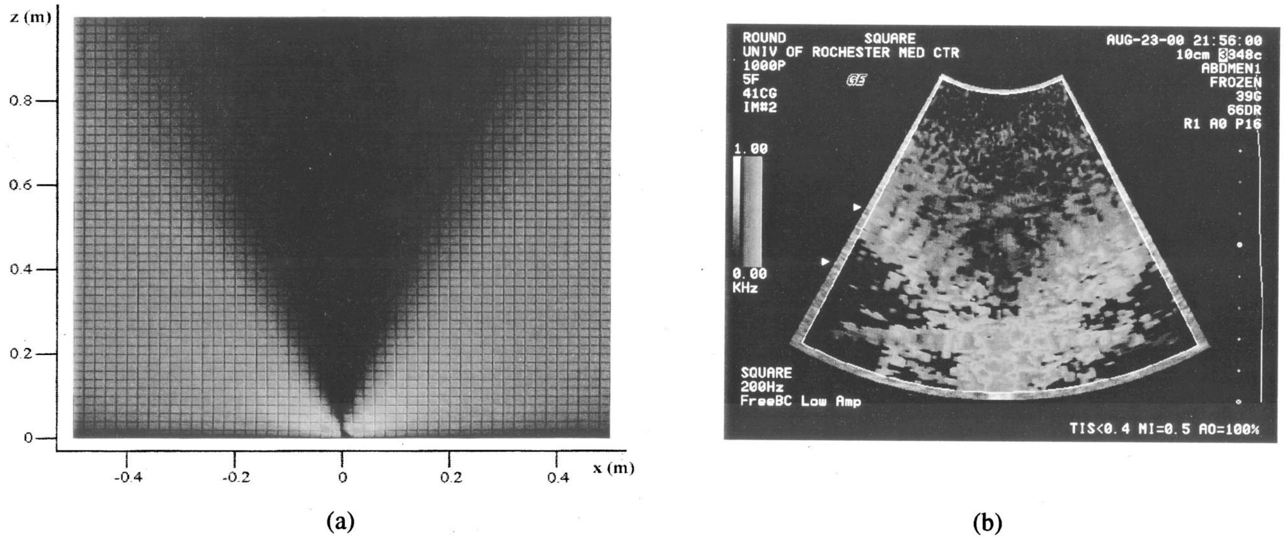

FIG. 9. Single-strip load beam patterns. (a) Theoretical calculation remapped into ultrasound curvilinear probe coordinates. The gray scale is also adjusted according to the digital filters used on the ultrasound machine. (b) Experimental result, taken on GE Logiq 700.

modeled the elastic half-space with stress-free boundary conditions on the surface. To approximate this condition, vibration was applied from below the phantom that was supported with three or four small pieces of closed cell foam cut into square sections approximately 10 mm thick and 15 mm on each side.

The infinitely long strip load was approximated by a rigid metal strip with a rectangular cross section 90 mm long, 6 mm wide, and 7 mm high supported on a column. The 6 mm edge was applied to the bottom surface of the phantom and driven normally to the phantom surface by a vibration shaker (Vibration Test Systems: Aurora, OH). Power to the shaker was provided by an audio amplifier driven either by a frequency generator when pure tones were used or by a harmonic waveform generator (Model #3511A Pragmatic Instruments: San Diego, CA) when multi-tone frequencies were used. Multi-tone signals were found effective in suppressing the modal patterns resulting from reflections off of the boundaries of the phantom (Taylor *et al.*, 2000). Multi-tone signals used in these experiments were, in our shorthand notation, w22 [200 267 333 400 Hz] with a mean frequency of 338 Hz and w37 [333 400 467 533 Hz] with a mean frequency of 440 Hz. All vibrations were applied as steady-state harmonic signals.

To image the beam pattern, the ultrasound transducer was applied from above, thus orienting the image plane normal to the long axis of the strip load and centering it about 45 mm from each edge. In this configuration, the applied force is a vector parallel to the image plane. A GE Logiq 700 ultrasound machine (GE Medical Systems: Milwaukee, WS) was modified to map Doppler variance to the screen in the color-flow mode. Doppler spectral variance is directly proportional to the square of the peak vibration amplitude (Huang *et al.*, 1990; Taylor *et al.*, 2000). See Figs. 8 and 7 for the experimental setup.

To perform a double-strip load focusing experiment, an

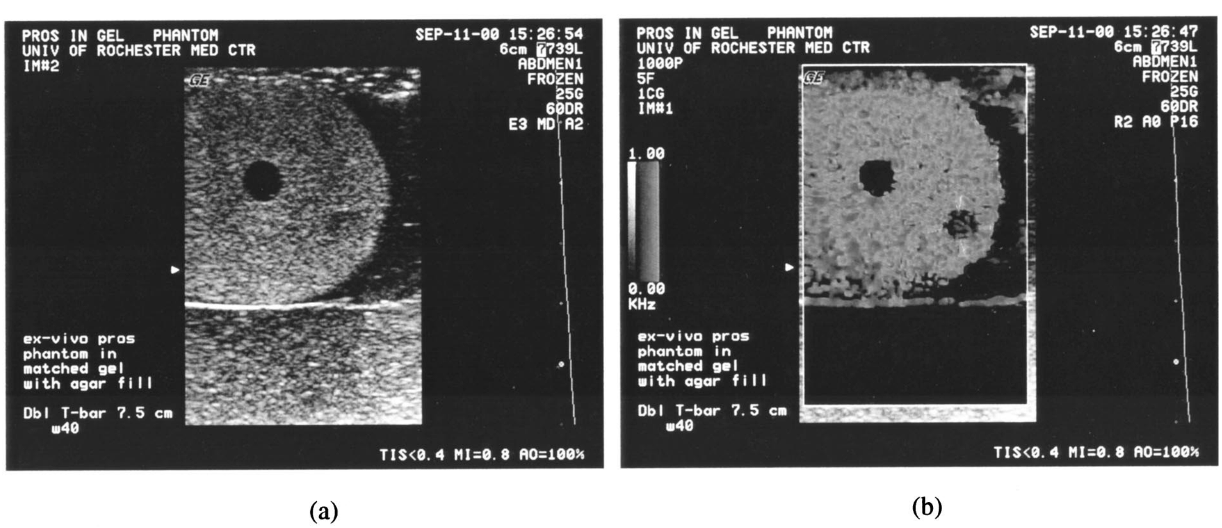

FIG. 10. Sonoelastography image of a prostate phantom with a hard lesion in the lower right quadrant. Double-strip loads are used as a vibration source. Separation between the two bars is 7.5 cm. The tumor size is approximately 6 mm in diameter. The central hole is the urethra-mimicking tube. (a) Conventional B-scan image of the phantom and (b) Sonoelastographic image of the phantom.

applicator was fabricated by mounting two rigid metal strips with a rectangular cross section 90 mm long, 8 mm wide, and 6 mm high in parallel on a rigid metallic bar. The centerline separation between the two parallel strips was adjusted to be 30, 50, or 75 mm.

IV. EXPERIMENTS AND RESULTS

We first compare the theory to the experiment for the single-strip load. Figure 9(b) shows the experimental beam patterns of single-strip load. We used a pure tone 200 Hz in this experiment. Since the imaging transducer detects vibration in the ''sector scan'' direction of the radiating ultrasound beam, the theoretical pattern is remapped from X-Y coordinates into the polar coordinates of the ultrasound probe and presented as a reference. The gray scale, representing the vibration amplitude, is also adjusted to simulate the imaging system response of GE Logiq 700 [Fig. 9(a)] (Taylor *et al.*, 2000).

The theory predicts that the shape of the strip load pattern is frequency independent. To verify this, we ran the frequency generator from 200 Hz to 400 Hz, stepping every 10 Hz. No change of the shape was observed within this range of frequency. A predictable and frequency-independent beam pattern is most useful for sonoelastography. Furthermore, the frequency independent feature of the strip load patterns enables us to apply the multi-frequency signal for reduction of modal artifacts (Taylor *et al.*, 2000).

In the double-strip load experiment, two parallel rigid rectangular cross-section bars with 75 mm separation were used. Driven by the signal source, the bars vibrate against the surface of a tissue-mimicking, bowl-shaped phantom, and a focal zone with higher vibration and uniformity predicted by the theory was confirmed. The position of the focal zone is controllable when adjusting the separation of the bars as the theory shows, as shown in Fig. 5.

The double bar was also used to propagate shear waves into a Zerdine *ex vivo* prostate phantom (CIRS: Norfolk, VA) in which there is a 6 mm ''tumor'' with a Young's modulus approximately seven times that of the surrounding medium. To better simulate the condition inside the body, the prostate phantom was surrounded by a gel phantom with similar elastic properties. A combination of high frequencies (400–600 Hz) is used to drive the double-bar applicator. High-resolution tumor images with clear boundaries are obtained, as shown in Fig. 10.

V. DISCUSSION

In our experimental studies, the vibrating applicator is typically placed beneath the sample shaking normally to the surface while the ultrasound probe is right above the sample. The ultrasound Doppler scanning principally measures the Z component (i.e., vertical component) of the vibration. For this reason, we are going to mainly discuss the u_z component of the normally shaking source.

Figure 2 shows that a normal vibrating single-strip load propagates shear wave into a V-shaped range. The angle between either branch (of u_z) and the normal direction is approximately 45 deg. This agrees very well with the experimental result (Fig. 9).

The shear waves from the double-strip loads meet and interfere inbetween the two loads. The interference effect localizes the energy into a small triangle region (Fig. 4). The height of the triangle is approximately half of the strip load separation. This information enables us to cover the region of interest by adjusting the separation of strip loads.

To verify that the shear wave field of strip loads is uniform along the axes of the strips, we moved the ultrasound probe from one end of the strips to the other, leaving a 1 cm margin on both ends. From the real-time image on the screen, the shape and magnitude of the vibration field appeared to be consistent.

When using a single frequency of vibration, the shear wave field of double-strip loads has some lobe-spacing effect due to spatially constructive and deconstructive interference. This can be eliminated by using multi-frequency signals in sonoelastography experiments where a uniform background is desired.

VI. CONCLUSION

We have shown through theory and experiments that a double-strip load can focus shear waves, which efficiently produces a stronger vibration field within a controllable region. From the nature of the applicator, the field is reasonably uniform along the strips. These features make double-strip loads a useful applicator for 3D sonoelastography. However, the idealized pattern given by theory and approximated in homogeneous, isotropic phantom experiments will not be realized in tissues. The additional complications of tissue boundaries, along with inhomogeneous and isotropic properties of some tissues, will modify the shear wave patterns. However, the general behavior of the double-strip line provides a useful standing point.

ACKNOWLEDGMENTS

This work was supported in part by the NSF/NYS Center for Electronic Imaging Systems, NIH grant No. 2 R01 AG16317-01A1, the University of Rochester Department of Radiology and Electrical and Computer Engineering and the General Electric Company (GE). The authors thank GE Medical Systems Division for the loan of the Logiq 700 ultrasound scanner used in the imaging experiments.

Egevad, L., Norberg, M., and Mattson, S. *et al.* (**1998**) ''Estimation of prostate cancer volume by multiple core biopsies before radical prostatectomy,'' Urology **52** (4), 653–658.

Fu, D., Levinson, S., Gracewski, S., and Parker, K. (**2000**). ''Noninvasive quantitative reconstruction of tissue elasticity using an iterative forward approach,'' Phys. Med. Biol. **45**, 1495–1510.

Huang, S. R., Lerner, R. M., and Parker, K. J. (**1990**). ''On estimating the amplitude of harmonic vibrations from the Doppler spectrum of reflected signals,'' J. Acoust. Soc. Am. **88**, 310–317.

Miller, G., and Pursey, H. (**1954**). ''The field and radiation impedance of mechanical radiators on the free surface of a semi-infinite isotropic solid,'' Proc. R. Soc. London, Ser. A **223**, 521–541.

Parker, K. J., Huang, S. R., Musulin, R. A., and Lerner, R. M. (**1990**). ''Tissue response to mechanical vibrations for 'sonoelasticity imaging','' Ultrasound Med. Biol. **16**, 241–246.

Sarvazyan, A. P., Skovoroda, A. R., Emelianov, S. Y., Fowlkes, L. B., Pipe, J. G., Adler, R. S., and Carson, P. L. (**1995**). ''Biophysical bases of elasticity imaging,'' in *Acoustical Imaging* (Plenum, New York), Vol. 21, pp. 223–240.

Tanter, M., Sandrin, L., Catheline, S., and Fink, M. (**1999**). ''Time-resolved 2D pulsed elastography,'' (abstract) Ultrason. Imaging **21**, 286.

Taylor, L. S., Porter, B. C., Rubens, D. J., and Parker, K. J. (**2000**). ''Three-dimensional sonoelastography: Principles and practices,'' Phys. Med. Biol. **45**, 1477–1494.

Yamakoshi, Y., Sato, J., and Sato, T. (**1990**). ''Ultrasonic imaging of internal vibrations of soft tissue under forced vibration,'' IEEE Trans. Ultrason. Ferroelectr. and Freq. Contr., **37**, 45–53.

Low-frequency acoustic pressure, velocity, and intensity thresholds in a bottlenose dolphin (*Tursiops truncatus*) and white whale (*Delphinapterus leucas*)[a]

James J. Finneran,[b] Donald A. Carder, and Sam H. Ridgway
Space and Naval Warfare Systems Center, San Diego, Code D35, 53560 Hull Street, San Diego, California 92152-5000

(Received 9 April 2001; revised 28 September 2001; accepted 2 October 2001)

The relative contributions of acoustic pressure and particle velocity to the low-frequency, underwater hearing abilities of the bottlenose dolphin (*Tursiops truncatus*) and white whale (*Delphinapterus leucas*) were investigated by measuring (masked) hearing thresholds while manipulating the relationship between the pressure and velocity. This was accomplished by varying the distance within the near field of a single underwater sound projector (experiment I) and using two underwater sound projectors and an active sound control system (experiment II). The results of experiment I showed no significant change in pressure thresholds as the distance between the subject and the sound source was changed. In contrast, velocity thresholds tended to increase and intensity thresholds tended to decrease as the source distance decreased. These data suggest that acoustic pressure is a better indicator of threshold, compared to particle velocity or mean active intensity, in the subjects tested. Interpretation of the results of experiment II (the active sound control system) was difficult because of complex acoustic conditions and the unknown effects of the subject on the generated acoustic field; however, these data also tend to support the results of experiment I and suggest that odontocete thresholds should be reported in units of acoustic pressure, rather than intensity. [DOI: 10.1121/1.1423925]

PACS numbers: 43.80.Lb [WA]

I. INTRODUCTION

It is often stated that the proper way to compare in-air and underwater hearing thresholds is on an acoustic intensity basis (e.g., Tavolga and Wodinsky, 1963; Johnson, 1966; Au, 1993) which is frequently taken to mean that the ear is an acoustic intensity detector (e.g., Ketten, 2000). The use of intensity, rather than pressure, is often desirable because intensity takes into account the characteristic impedances of the two media and represents net energy flow per time at threshold, regardless of the specific transduction principles involved. Acoustic intensity is related to the product of the acoustic pressure and particle velocity; thus, the measurement of acoustic intensity requires knowledge of the acoustic particle velocity as well as pressure.

Behavioral and physiological data indicate that some fish are sensitive to acoustic particle motion at low frequencies and close source distances and to acoustic pressure at higher frequencies and larger source distances (Cahn *et al.*, 1969; Fay and Popper, 1974; Buwalda, 1981). Because of their high sensitivity and wide audible frequency range, it seems likely that cetaceans are sensitive to acoustic pressure alone (Kastak and Schusterman, 1998), especially at high frequencies where acoustic particle motion amplitudes are small. However, there are few data on low frequency (i.e., below 1 kHz) underwater hearing thresholds in cetaceans (reviewed in Fay, 1988; Nachtigall *et al.*, 2000) and the existing data regarding possible cetacean sensitivity to acoustic particle motion at low frequencies are contradictory. Johnson (1966, 1967) reported no apparent sensitivity to particle motion in *Tursiops*; however, Turl (1993) reported a potential sensory modality shift in *Tursiops* (from pressure to particle motion) at frequencies between 50–150 Hz as the acoustic pressure was reduced to levels at or below ambient noise. Turl's study employed an up/down staircase method in a two-alternative, forced-choice paradigm. Hearing test tones were 1 s in duration; one-half of the trials were signal-absent (catch) trials. A unique feature of these data was the temporary plateau observed in the staircase data; that is, at lower frequencies (50–100 Hz), after a temporary plateau of 3–5 reversals, the subject began to respond consistently to signal-present trials without a corresponding increase in the false-alarm rate (false-alarm rates were less than 10% during these sessions). This continued until the tone levels were below ambient noise levels (approximately 20 dB below the temporary plateau). No temporary plateaus were observed at the higher frequencies tested (200–300 Hz), only a single plateau approximating the threshold. Turl obtained his data with the dolphin in open water at a distance of 1 m from the projector, where relatively large particle motions may have existed below 150 Hz.

This paper presents the results of a study designed to determine the relative contributions of acoustic pressure and particle motion to the low-frequency underwater hearing abilities of the bottlenose dolphin (*Tursiops truncatus*) and white whale (*Delphinapterus leucas*). This study was con-

[a] Portions of this work were presented at the 139th Meeting of the Acoustical Society of America, May 2000.
[b] Present address: Science Applications International Corporation, Maritime Services Division, 3990 Old Town Avenue, Suite 105A, San Diego, CA 92110.

ducted to verify Turl's results and to shed light on how to compare in-air and underwater hearing thresholds. The experimental approach was to measure underwater hearing thresholds while manipulating the relationship between acoustic pressure and particle velocity. This manipulation was achieved in two ways: (1) by placing the test subject at different distances from a single underwater sound source (experiment I), and (2) by using two sound projectors and an active sound control system to synthesize different pressure/particle velocity conditions at the location of the test subject (experiment II). Previous applications of active sound control in water have been confined to enclosed test chambers (e.g., Buwalda, 1981; Finneran and Hastings, 1999); therefore, in experiment II it was also necessary to determine the applicability of the active control technique to the open-water test environment used in this study.

II. BACKGROUND

The relationship between pressure and particle velocity at a point in space may be described by the specific acoustic impedance ratio ζ

$$\zeta=\frac{P}{\rho c V}, \tag{1}$$

where P is the complex pressure amplitude, V is the complex amplitude of a vector component of particle velocity, ρ is the medium density, and c is the sound speed. For a plane progressive wave, $\zeta=1$; within the near field of a monopole $\zeta \approx jkr$, where $j=(-1)^{1/2}$ and k is the wave number ($k=\omega/c$, where ω is the circular frequency). Acoustic impedance has important implications for energy transport because the phase relationship between pressure and particle velocity is analogous to the power factor in an electrical circuit and indicates the extent of cooperation between the "effort" (i.e., pressure) and the "flow" (particle velocity).

In acoustical systems power flow and energy transfer are often described using the acoustic intensity. The instantaneous acoustic intensity $\mathbf{I}(t)$, defined as $\mathbf{I}(t)=p(t)\mathbf{v}(t)$, represents energy transported per unit area and time. The instantaneous intensity may be split into two parts: the *active intensity* associated with the particle velocity component in phase with the pressure and the *reactive intensity*, which is associated with the particle velocity component in quadrature with the pressure (Fahy, 1995). The term *acoustic intensity* normally refers to the time-averaged (mean) active intensity (Kinsler *et al.*, 1982; Fahy, 1995); this quantity corresponds to local net transport of sound energy. In contrast, the reactive intensity represents local oscillatory transport of energy and has a mean of zero. For a single-frequency sound field the mean active intensity $\mathbf{I}$ may be written as

$$\mathbf{I}=\tfrac{1}{2}P[U\cos\theta_U\mathbf{i}+V\cos\theta_V\mathbf{j}+W\cos\theta_W\mathbf{k}], \tag{2}$$

where the particle velocity vector $\mathbf{V}=U\mathbf{i}+V\mathbf{j}+W\mathbf{k}$, θ_U, θ_V, and θ_W are the phase angles between P and U, V, and W, respectively, and $\mathbf{i}$, $\mathbf{j}$, and $\mathbf{k}$ are orthogonal unit vectors. For plane and spherical waves, $\underline{\mathbf{I}}$ reduces to $\overline{P}^2/\rho c$ in the direction of propagation, where $\overline{P}$ is the root-mean-squared (rms) pressure. For other conditions $\mathbf{I}$ must be calculated from the actual pressure and velocity. Unfortunately, the majority of acoustic stimuli used in hearing studies, both in-air and underwater, has been characterized with pressure measurements alone, making it impossible to determine the actual acoustic intensity in many circumstances. Often pressure thresholds are simply converted to units of acoustic intensity assuming plane progressive waves, which may not be valid, especially for enclosed sound fields at low frequencies.

In this study, the acoustic field was characterized using multiple pressure measurements (see Sec. III B); this allowed not only the acoustic pressure, but also the particle velocity and intensity to be determined at the subject's hearing threshold. Thresholds were measured at different acoustic conditions designed to present the subject with different combinations of pressure and velocity.

III. METHODS

A. Experimental subjects

Experimental subjects consisted of one male bottlenose dolphin (NAY, age 17 years, approximate weight 280 kg) and one female white whale (MUK, 32 years, 540 kg). Both animals were trained to produce audible "whistles" to hearing test tones (see Ridgway and Carder, 1997). The original training and recent test experience for each subject was limited to relatively high frequencies and/or far-field conditions, thus, prior to this study, neither animal had ever been systematically reinforced for responding to potential acoustic particle motion cues. The study followed a protocol approved by the Institutional Animal Care and Use Committee under guidelines of the Association for the Accreditation of Laboratory Animal Care.

B. Apparatus

Figures 1(a) and (b) show the experimental apparatus for experiments I and II, respectively. Both experiments were conducted in a 12×12-m floating, netted enclosure located in San Diego Bay. Water depth ranged from approximately 4–6 m. Ambient noise levels in San Diego Bay are highly variable, especially at the frequencies of interest here; thus, it was necessary to use masking noise to create a floor effect and reduce the interfering effects of varying ambient noise. The hearing thresholds presented in this study are thus masked thresholds, rather than "absolute" thresholds. Masking noise was generated using a personal computer and multifunction board (National Instruments PCI-MIO-16E-1), attenuated (HP 355C), filtered (Ithaco 4302), and amplified (experiment I, Hafler P7000; experiment II, Hafler Pro5000) before being input to an underwater sound projector (USRD J9). The masking noise frequency spectrum was compensated for the projector transmitting characteristics and acoustic standing waves using a digital filtering technique (Finneran *et al.*, 1999). The resulting noise (measured at the approximate location of the subjects' ears) was flat within ±3 dB over the range 50–1500 Hz. The masking noise spectral density level was 95 dB re:1 μPa^2/Hz. The noise projector was located 4 m behind each subject during experiment I [Fig. 1(a)] and 2 m in front of each subject during experiment II [Fig. 1(b)].

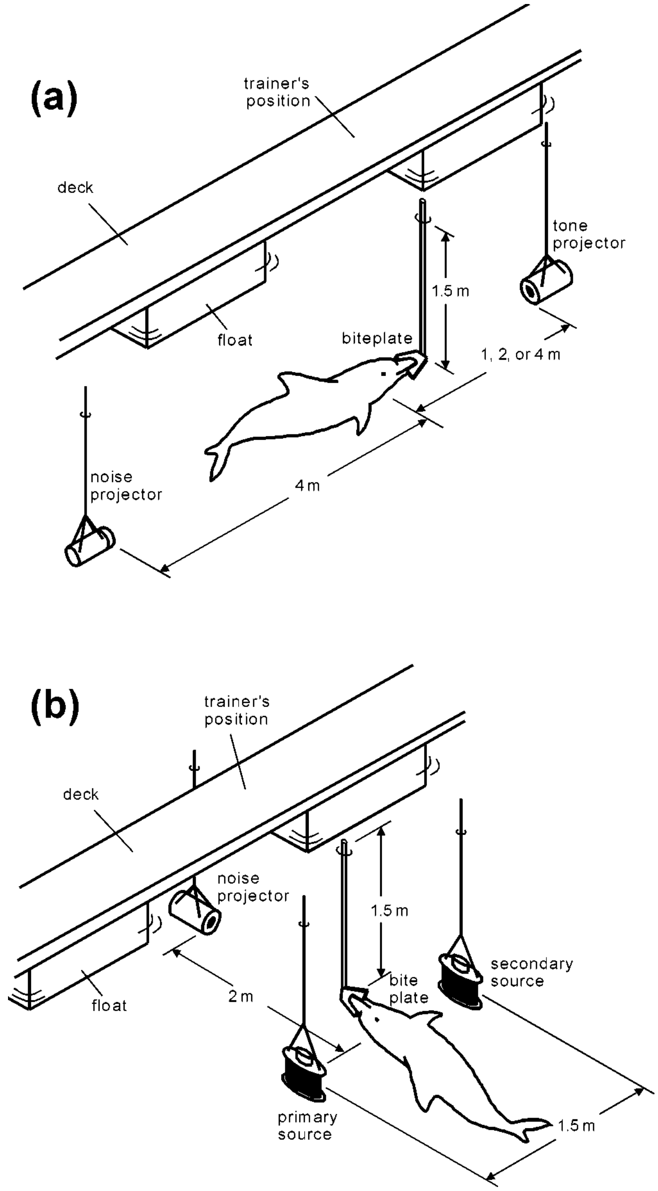

FIG. 1. Test setup for (a) experiment I and (b) experiment II.

Subjects were trained to station on a plastic biteplate attached to a polyvinyl chloride (PVC) frame submerged to a depth of 1.5 m. A receiving hydrophone (B&K 8105) was attached to the frame and used to measure the animal's whistle responses and other background noise. The hydrophone output was amplified (B&K 2692), bandpass filtered from 20 Hz to 20 kHz (Krohn-Hite 3CD8TL-20kg-N1U1 and 3BS8TH-20g-N1U1), and digitized using a second PCI-MIO-16E-1 multifunction board.

Experiment I featured a single-tone projector (USRD J13) located in front of the animal [Fig. 1(a)]. Hearing-test tones were generated using the PCI-MIO-16E-1, attenuated (Tucker-Davis PA4), filtered (Ithaco 4302), amplified (Hafler P7000), and input to the J13. The tone duration was 1 s, including 250-ms rise and fall times. Thresholds were measured at frequencies of 100 and 300 Hz and source distances of 1, 2, and 4 m. At both 100 and 300 Hz, the largest harmonic amplitudes were at least 30 dB below the fundamental.

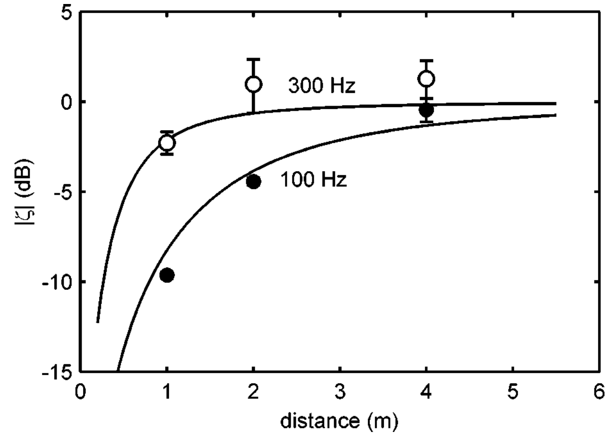

FIG. 2. Mean impedance ratio in the axial direction as a function of source distance for experiment I. Symbols: mean impedance ratio magnitudes from all tests conducted at 100 Hz (closed circles) and 300 Hz (open circles); Lines: theoretical impedance ratio for unbounded spherical wave propagation. The error bars indicate one standard deviation.

The acoustic field was characterized with the specific acoustic impedance ratio in the axial direction, ζ, at each distance. In this study, ζ was calculated from the transfer function measured between two hydrophones (B&K 8105) using

$$\zeta = \frac{jkd}{2}\,\frac{1+H_{12}}{1-H_{12}}, \tag{3}$$

where H_{12} is the (corrected) transfer function between the hydrophone signals and d is the distance between the hydrophones. This technique had the advantage that transfer function measurements may be corrected for any hydrophone amplitude and phase mismatch by repeating the measurement with the hydrophone positions interchanged (Chung, 1978).

Figure 2 shows the impedance ratio in the axial direction as a function of source distance. The symbols represent the mean impedance ratios from all tests conducted at 100 Hz (closed circles) and 300 Hz (open circles). The error bars indicate one standard deviation. The solid lines show the theoretical impedance ratio for unbounded spherical wave propagation. The agreement between the theory and the measured values was good close to the source but degraded at larger distances where contributions from reflected waves were more significant. The standard deviation also increased with source distance and frequency. Impedance ratios measured in the vertical and transverse directions were approximately an order of magnitude higher than those measured in the axial direction (i.e., particle motion amplitudes were relatively small in these directions). Table I summarizes the test matrix for experiment I. Subjects were tested at different distances in random order. Because of the larger variability in the acoustic field at 300 Hz (Fig. 2), approximately twice as many sessions were conducted at 300 Hz compared to 100 Hz.

Experiment II featured two underwater sound projectors (model 30 flextensional), positioned dorsal and ventral to the subject as illustrated in Fig. 1(b), and designated as the primary and secondary sources, respectively. In contrast to ex-

TABLE I. Experiment I test matrix. n indicates the number of threshold measurements for each subject at each test condition.

Freq. (Hz)	Distance (m)	$\lvert\zeta\rvert$ (dB)	$\angle\zeta$ (deg)	n (NAY)	n (MUK)
100	1	0.33	87	4	4
100	2	0.60	77	4	6
100	4	0.95	69	3	3
300	1	0.77	58	8	8
300	2	1.12	35	12	9
300	4	1.16	11	9	8

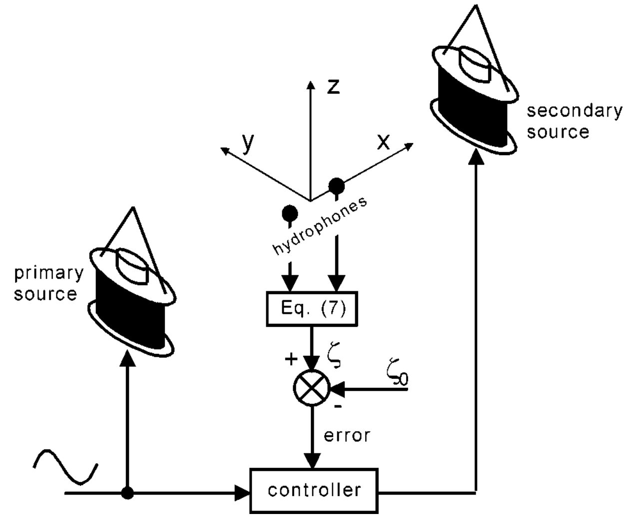

FIG. 3. Active control system configuration.

periment I, where subjects stationed with a "normal" orientation at the biteplate, during experiment II subjects were trained to station on their left side, i.e., with their median plane horizontal, and both ears located approximately in a vertical plane. The distance between the projectors was 1.5 m; the biteplate was located equidistant from each projector. The test frequency was 300 Hz. Tones for each projector were generated using a PCI-MIO-16E-1, attenuated (Tucker-Davis PA4), filtered (Ithaco 4302), amplified (Hafler P7000), and input to the model 30 transducer. The tone duration was 1 s, including 250-ms rise and fall times. The largest harmonic amplitudes were at least 30 dB below the fundamental.

During experiment II, an active sound control system (see Finneran and Hastings, 1999) was used to generate six different acoustic conditions, categorized by the specific acoustic impedance ratio ζ along the axis connecting the two projectors. These conditions were designated as: (1) low ζ; (2) primary only, (3) far field; (4) high ζ; (5) secondary only; (6) near field. *Primary only* and *secondary only* refer to cases where the secondary and primary sources, respectively, were turned off. *Far field* and *near field* refer to acoustic fields with $\zeta\approx 1$ and $\zeta\approx\exp(j\pi/2)$, respectively. The low-ζ condition featured a low-pressure/high-particle velocity. The high-ζ condition featured a high-pressure/low-particle velocity. Since the acoustic intensity is related to the product of the pressure and particle velocity component in phase with pressure, the intensity theoretically approached zero for the low-ζ, high-ζ, and near-field conditions. Table II lists the six conditions, the desired amplitude and phase of ζ at each condition, and the number of measurements obtained with each subject.

Figure 3 illustrates the operation of the active control system. Two hydrophones (B&K 8105), located at $x=20$ cm and $x=-20$ cm, were used to measure the pressure and estimate the impedance ratio in the x direction, ζ. The difference between ζ and the desired impedance ratio, ζ_0, was defined as the error ε. The error signal was input to a controller that adjusted the secondary source amplitude and phase to minimize $|\varepsilon|^2$ or $|\zeta-\zeta_0|^2$. The minimization was performed using a two-dimensional Pattern Search algorithm (Adby and Dempster, 1974). After this optimization of the secondary source amplitude and phase, ζ was measured using the switched-sensor technique (Chung, 1978). Mean values for the measured amplitude and phase of ζ for each of the six conditions are included in Table II. Differences between the desired and measured values of ζ were primarily a result of hydrophone amplitude and phase mismatches that could not be corrected during optimization (it was not practical to switch the hydrophone positions during optimization).

The acoustic fields for each condition of experiment II were characterized by measuring the complex pressure with a single hydrophone (B&K 8105) moved through grids of points in the $x-y$, $x-z$, and $y-z$ planes. The particle velocity and acoustic intensity vectors in each plane were calculated from the numerical gradient of the pressure measurements and Eqs. (1) and (2). Figures 4, 5, and 6 show, respectively, the measured pressure, velocity, and intensity in the $x-y$ plane for the six acoustic conditions listed in Table II; the panels (a)–(f) in Figs. 4–6 correspond to conditions 1–6 of Table II, respectively. The projector levels for each condition were adjusted so that the rms average of the pressures measured at $x=20$ cm and -20 cm was 136 dB *re*: 1

TABLE II. Experiment II test matrix.

Cond.	Description	Desired $\lvert\zeta\rvert$ (dB)	Desired $\angle\zeta$ (deg)	Measured $\lvert\zeta\rvert$ (dB)	Measured $\angle\zeta$ (deg)	n (NAY)	n (MUK)
1	low-ζ	−30	0	−30	17	9	11
2	primary only	⋯	⋯	−2	52	16	11
3	far-field	0	0	−1	7	6	5
4	high-ζ	20	0	18	35	6	5
5	secondary only	⋯	⋯	−2	−130	11	5
6	near-field	0	90	−1	87	5	5

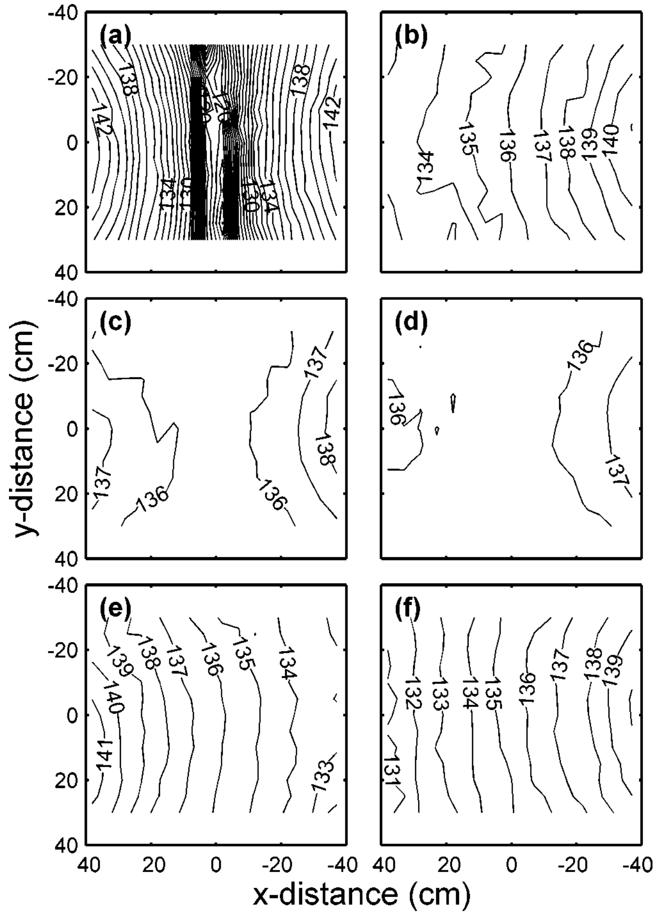

FIG. 4. Pressure amplitude contours measured in the $x-y$ plane for the (a) low-ζ; (b) primary-only; (c) far-field; (d) high-ζ; (e) secondary-only; and (f) near-field test conditions listed in Table II. Contour lines are separated by 1 dB.

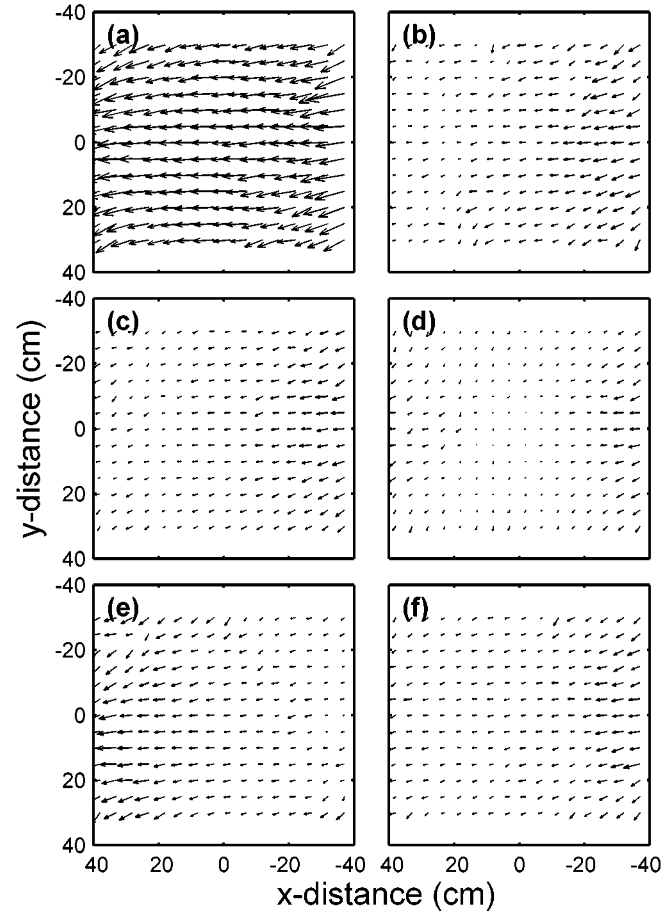

FIG. 5. Acoustic particle velocity in the $x-y$ plane for the (a) low-ζ; (b) primary-only; (c) far-field; (d) high-ζ; (e) secondary only; and (f) near-field test conditions.

μPa. The resulting acoustic fields were approximately axisymmetric and resembled those predicted from a model using a two spherical sources in unbounded water.

Figure 4 shows the pressure contours in the $x-y$ plane. Pressures were relatively uniform near the center of the $x-y$ plane, except in Fig. 4(a), the low-ζ condition, where large pressure gradients existed on either side of a central pressure minimum. Figure 5 shows the particle velocity vectors in the $x-y$ plane for each test condition. The velocity vectors were primarily directed along the x axis, except for the high-ζ condition [Fig. 5(d)], where the velocity was very small near the center of the field. The velocity was largest in the low-ζ condition [Fig. 5(a)]. Figure 6 shows the intensity vectors in the $x-y$ plane for each test condition. Figures 6(a), (d), and (f), the low-ζ, high-ζ, and near-field conditions, respectively, indicate small intensities at the center of the field. Acoustic intensity vectors were larger and more uniform in the primary-only, far-field, and secondary-only conditions [Figs. 6(b), (c), and (e), respectively]. Although some velocity and intensity vectors had significant amplitude in the y- and z directions, near the center of the field the intensity vectors were nearly parallel to the x axis and the other components were relatively small.

C. Procedure

Hearing threshold measurements began with the trainer directing the animal to station on the underwater biteplate. A series of trial presentations was then begun. Each trial consisted of a 3.5-s burst of masking noise (N) or a 3.5-s noise burst with a 1-s hearing test tone (S+N). The masking noise had 0.5-s rise and fall times. The noise burst for each trial was randomly generated; a single digital sequence was not repetitively used. Fifty percent of the trials were S+N. Subjects were trained to produce an audible whistle in response to S+N trials and to remain quiet during N trials. After each correct response (a whistle to S+N or no whistle to N), the subject was presented with a short "chirp" sound (0.25-ms duration, frequency sweep from 200–800 Hz with 0.05-ms rise/fall times, approx. 130 dB *re*: 1 μPa-rms) as feedback to indicate to the subject that they were correct on the previous trial. Subjects remained on the biteplate for a variable number of trials. After one to seven correct responses (determined randomly), an underwater buzzer was sounded as the signal for the subject to return to the surface for fish reward. The next series of trial presentations was then begun, if necessary. The magnitude of reinforcement was based on the performance of the subject.

Stimulus presentation began with ten warmup trials at a constant, suprathreshold level. Following these ten trials, the stimulus amplitude was adjusted using a modified up/down

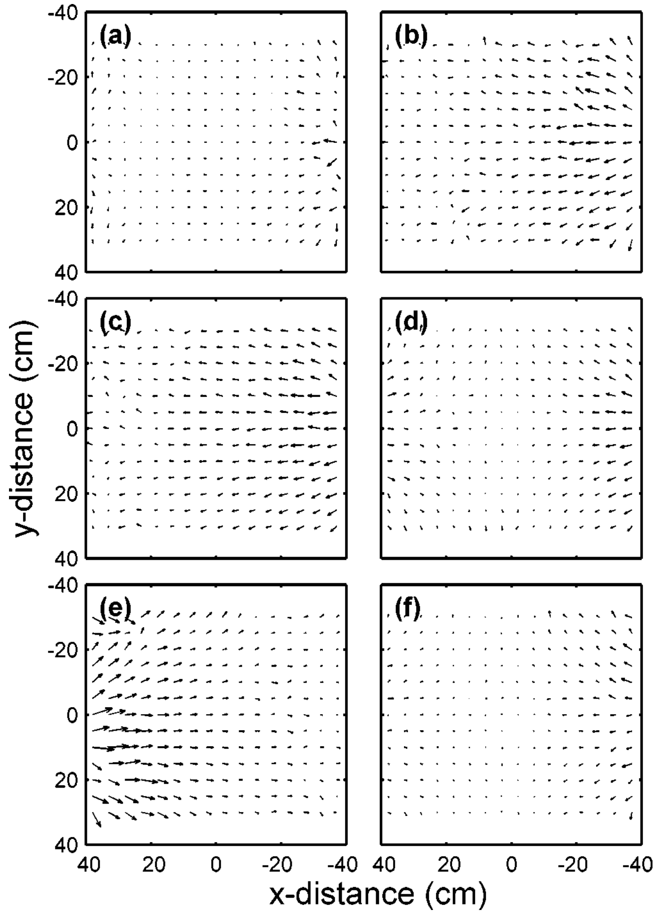

FIG. 6. Acoustic intensity in the $x-y$ plane for the (a) low-ζ; (b) primary-only; (c) far-field; (d) high-ζ; (e) secondary-only; and (f) near-field test conditions.

staircase procedure (Cornsweet, 1962): the amplitude was decreased by 4 dB following each hit (whistle response to S+N) until the first miss (no response to S+N), after which the amplitude was increased by 2 dB following each miss and decreased by 2 dB following each hit. The set of trials containing the first ten hit/miss and miss/hit reversal points was used to determine the threshold and the false-alarm percentage. The pressure threshold was defined as the mean pressure of the ten reversal points. Velocity and intensity thresholds were calculated from the pressure threshold and the measured acoustic impedance ratio ζ. Pressure and velocity thresholds are expressed in rms values.

The procedure for experiment II was identical to that above, with the exception that the secondary source amplitude was also adjusted using the staircase method to maintain the correct amplitude and phase relationship between the primary and secondary sources.

IV. RESULTS

The staircase data from experiments I and II followed the ''typical'' descending staircase pattern and no temporary plateaus and secondary descents were observed in either subject. More detailed results from experiments I and II are presented below.

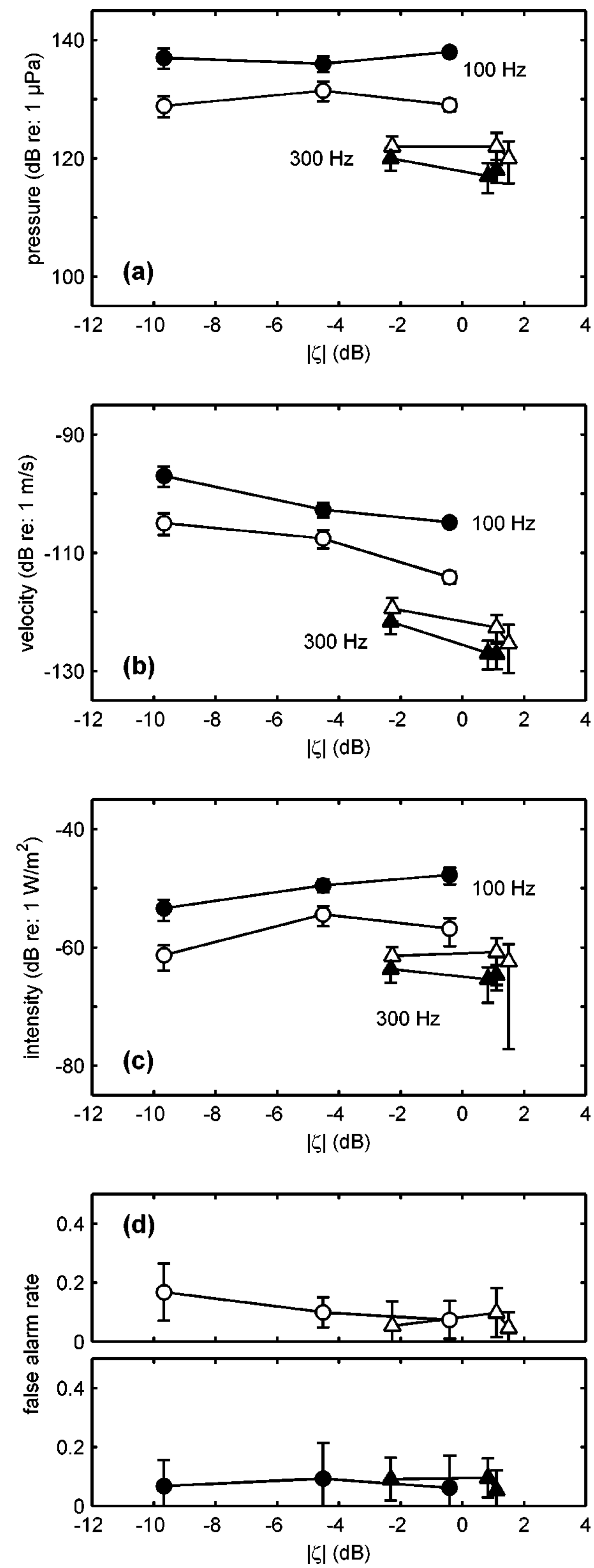

FIG. 7. (a) Pressure; (b) velocity; and (c) acoustic intensity thresholds measured at 100 Hz (circles) and 300 Hz (triangles) for subjects MUK (open symbols) and NAY (filled symbols) during experiment I. (d) False-alarm rates for MUK (upper) and NAY (lower) measured at 100 Hz (circles) and 300 Hz (triangles) during experiment I. In all plots, error bars indicate one standard deviation.

A. Experiment I

Figures 7(a), (b), and (c) show the measured pressure, velocity, and intensity thresholds, respectively, for subjects

NAY (filled symbols) and MUK (open symbols) at 100 Hz (circles) and 300 Hz (triangles) as functions of the mean acoustic impedance ratio from each test condition. Each data point represents the mean threshold for that particular distance and frequency. Error bars represent one standard deviation. Pressure thresholds were within 2 dB for each subject at a particular frequency. Velocity thresholds tended to decrease as the impedance ratio increased; intensity thresholds tended to increase with impedance ratio at 100 Hz but were relatively constant at 300 Hz. Differences between 300-Hz thresholds at 2 and 4 m were negligible, as expected, given the similarity between the acoustic conditions at these locations.

A multiple regression analysis with dummy coding was used to compare thresholds measured at 4 m to those measured at 1 and 2 m. Separate analyses were performed for each subject and frequency. The 4-m data set was chosen as the control because this position was intended to provide far-field acoustic conditions. The level of significance was 0.05. There were no significant differences in pressure thresholds for either subject at 100 or 300 Hz. There were significant differences between velocity thresholds in both subjects at 100 Hz [MUK, $F(2,10)=16.6$; NAY, $F(2,8)=22.5$] and 300 Hz [MUK, $F(2,22)=11.2$; NAY, $F(2,26)=15.2$]. Velocity thresholds at 1 m were significantly higher in both subjects at 100 Hz (MUK, $t=5.75$; NAY, $t=6.08$) and 300 Hz (MUK, $t=4.71$; NAY, $t=4.98$). For MUK, thresholds at 2 m were also significantly higher than those at 4 m ($t=3.73$). There were significant differences between intensity thresholds for NAY at 100 Hz [$F(2,8)=12.0$] but not at 300 Hz. At 100 Hz, the threshold at 1 m was significantly lower than at 4 m ($t=4.87$). For subject MUK, there were no significant differences between intensity thresholds at 100 or 300 Hz.

Figure 7(d) shows the mean false-alarm rates for MUK (upper) and NAY (lower) at 100 Hz (circles) and 300 Hz (triangles). The error bars indicate one standard deviation. False-alarm rates for MUK and NAY ranged from 0–0.30 and 0–0.25, respectively. A multiple regression analysis with dummy coding was also used to compare false-alarm rates at 4 m to those measured at 1 and 2 m; this analysis revealed no significant differences between false-alarm rates for either subject at 100 and 300 Hz.

B. Experiment II

Figures 8(a), (b), and (c) show the pressure, velocity, and intensity thresholds, respectively, for MUK (circles) and NAY (triangles) measured during experiment II plotted versus the mean impedance ratio at each test condition. Each data point represents the mean threshold at that test condition (see Table II). Error bars indicate one standard deviation. The solid lines are a visual aid and simply connect the mean threshold from each of the three distinct data groups. In general, pressure thresholds were relatively constant for each subject, except for the low-ζ condition, where thresholds were much lower. Velocity thresholds decreased with increasing impedance ratio. Intensity thresholds were relatively constant except for the near-field and high-ζ conditions, where the intensity thresholds were much lower.

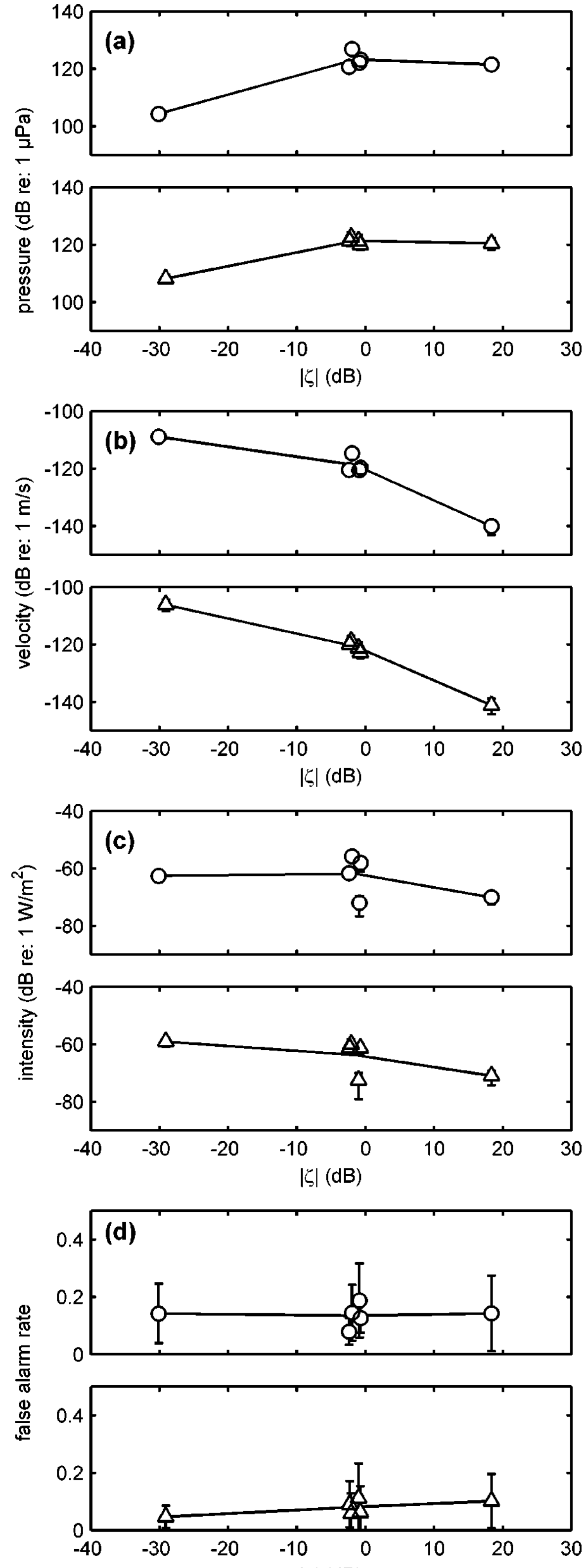

FIG. 8. (a) Pressure thresholds; (b) velocity thresholds; (c) acoustic intensity thresholds; and (d) false-alarm rates for MUK (circles) and NAY (triangles) measured during experiment II. Error bars indicate one standard deviation.

Differences between the mean thresholds at each condition were tested for significance using a multiple regression analysis with dummy coding. The far-field condition was used as the control data set. Separate analyses were performed for each subject; the level of significance was 0.05.

Far-field mean pressure thresholds were 123 and 120 dB *re*: 1 μPa for MUK and NAY, respectively. For each subject, thresholds were within 2 dB of these values except for the low-ζ condition, where pressure thresholds were 104 and 108 dB *re*: 1 μPa for MUK and NAY, respectively, and the primary-only condition, where thresholds were 127 and 123 dB *re*: 1 μPa for MUK and NAY, respectively. These differences were statistically significant [MUK, $F(5,36)=62.4$; NAY, $F(5,47)=26.7$]; thresholds at the low-ζ condition were significantly lower (MUK, $t=8.60$; NAY, $t=5.95$) and those at the primary only condition were significantly higher (MUK, $t=5.26$; NAY, $t=3.22$) in both subjects. For MUK, the mean threshold at the secondary-only condition (121 dB *re*: 1 μPa) was also significantly lower than the far-field condition ($t=8.60$), although the actual difference was only 2 dB.

There were significant differences from far-field velocity thresholds in both subjects [MUK, $F(5,36)=59.5$; NAY, $F(5,47)=105$]. Thresholds at the low-ζ condition were significantly higher (MUK, $t=10.5$; NAY, $t=16.1$) and those at the high-ζ condition were significantly lower (MUK, $t=3.32$; NAY, $t=2.23$) in both subjects. For MUK, the velocity threshold at the primary-only condition was also significantly higher than the far-field condition ($t=3.35$).

There were significant differences between intensity thresholds in both subjects [MUK, $F(5,36)=27.8$; NAY, $F(5,47)=13.7$]. Thresholds were significantly lower in both subjects at the near-field (MUK, $t=4.35$; NAY, $t=3.21$) and high-ζ (MUK, $t=4.25$; NAY, $t=3.26$) conditions. Intensity differences at the low-ζ condition were also significant, although MUK had a lower threshold ($t=3.42$) and NAY had a higher threshold ($t=2.75$) than the corresponding far-field value. The intensity thresholds for MUK at the primary-only and secondary-only conditions were also significantly higher and lower, respectively than the far-field condition (primary only, $t=3.63$; secondary only, $t=2.54$).

Figure 8(d) shows the mean false-alarm rates for MUK (circles) and NAY (triangles). The error bars indicate one standard deviation. False-alarm rates for MUK and NAY ranged from 0–0.33 and 0–0.29, respectively. A multiple regression analysis with dummy coding was used to compare false-alarm rates, with the far-field data again serving as the control set; this analysis revealed no significant differences between false-alarm rates for either subject.

V. DISCUSSION

A. Experiment I

The results of experiment I showed no significant change in pressure thresholds as the distance between the subject and the sound source was decreased. In contrast, velocity thresholds tended to increase and intensity thresholds tended to decrease as the source distance decreased. These data suggest that the subjects of this experiment were responding to the acoustic pressure alone and were not able to use acoustic particle motion cues as the source distance decreased. There were no temporary plateaus in the thresholds like those observed by Turl (1993). It is possible that Turl's subject responded to cues (other than acoustic) that indicated the presence of the signal or that the subject responded to tactile sensation associated with the stimulus. It is possible that the presence of masking noise in the current study affected the comparison with Turl's data; however, the masking noise projector was positioned at a sufficient distance to ensure far-field conditions at the subject and avoid large particle motions associated with the noise. The results of experiment I do agree with the observations made by Johnson (1966), who found no change in unmasked pressure thresholds measured at various positions in the near field of a source.

B. Experiment II

The active sound control system was successful at creating single-frequency acoustic fields with the desired pressure/particle velocity relationships. The control technique used in this study, which featured a pattern search algorithm, is particularly well-suited for synthesizing single-frequency sound fields with specific pressure/velocity conditions. The resulting fields were predicted reasonably well using a simple model consisting of two spherical sources in an unbounded medium.

The threshold data of experiment II are difficult to interpret, primarily because of complex acoustic conditions and the unknown effect of the subject's body on the acoustic field. The low-ζ condition featured a central pressure minimum surrounded by large pressure gradients (spatial velocity gradients also existed for the high-ζ condition but were not as severe as the pressure gradients associated with the low-ζ condition). The approximate dorso-ventral head size for the test subjects was 35–40 cm. Over this region in Fig. 4(a) the pressure varied by as much as 20 dB. These large pressure gradients had two potential effects. First, movement of a subject's head could have dramatically changed the received pressure; Fig. 4(a) indicates that movements as small as 5 cm would have resulted in a 6-dB difference in received pressure. Subject head movements within and between series of trial presentations were certainly greater than 5 cm. Second, because the peripheral transduction mechanisms in odontocetes are incompletely understood, the exact site where the acoustic pressure acts is unknown. Because the acoustic pressure in the center of the field varied dramatically over small distances, the net effect is that the actual received pressure is unknown. For example, if the rms average of the pressure at the outer surface of a subject's head is used, rather than the pressure at the center of the field, the resulting pressure thresholds approach those of the other test conditions. The low variability observed in the pressure thresholds at the low-ζ condition actually suggests that the subject was not experiencing the pressure within the central minimum; the pressure was apparently not varying substantially from trial to trial despite small differences in the subject's position. Because of these concerns, the threshold data from the low-ζ condition should be treated with skepticism.

The effect of subject's body on the acoustic field is difficult to determine. The acoustic field data in Figs. 4–6 were measured without the subject present. It was not practical to repeat these measurements with the subjects in place; thus, the exact acoustic field that each subject was exposed to is uncertain. This type of problem exists, to some extent, in all hearing studies based on minimum audible field measurements; however, in the present study, further errors may have been introduced because of the subjects' relatively large body size and short distance from the projectors, as well as loading effects the subjects may have had on the projectors. Pressure measurements obtained during test sessions confirmed the desired relationships between test conditions; e.g., substantially (i.e., 10–20-dB) smaller pressures during the low-ζ condition compared to the other test conditions; however, these data are to some extent anecdotal because the hydrophone was positioned to record the subject's whistle responses and was therefore not in the center of the field.

Although the data from experiment II are more difficult to interpret, some conclusions may be drawn. With the exception of the low-ζ data, which is suspect as described above, the experiment II data show that pressure thresholds were less dependent on the particular acoustic field conditions than velocity or intensity thresholds. Particle velocity thresholds at the high-ζ condition were much lower than those at the far-field, primary-only, secondary-only, and near-field conditions. Intensity thresholds at the near-field and high-ζ conditions were much lower than those measured from the far-field, primary-only, and secondary-only conditions. The comparison of intensity thresholds at the far-field and near-field conditions is particularly interesting because the pressure and particle velocity amplitude relationships were identical but the velocity phase was manipulated to be in phase (far-field condition) and in quadrature (near-field condition) with the pressure. The significant differences between these thresholds illustrates the potential danger of estimating intensity thresholds in complex sound fields from pressure measurements alone.

The primary-only and secondary-only conditions from experiment II imply some degree of receiving directivity at low frequencies. Pressure thresholds measured at the primary-only condition were 6- and 2 dB higher for MUK and NAY, respectively, than those at the secondary-only conditions. The projector was located dorsal to the subject during the primary-only test condition; thus, these data indicate higher pressure thresholds from sources located above compared to those below. A similar received directivity pattern was observed at 2 kHz by Schlundt *et al.* (2001) and may be the result of sound scattering and attenuation by the skull, air-filled sinuses, or within the nasal passages.

The false-alarm rates obtained in this study were relatively high compared to those obtained with MUK using a free-response paradigm in other studies (Finneran *et al.*, 2000; Schlundt *et al.*, 2000). Although the false-alarm rates were relatively high, there were no systematic differences between false-alarm rates at the different test conditions.

C. Pressure and intensity thresholds

To facilitate comparison with terrestrial mammal data, marine mammal hearing thresholds are sometimes reported in units of intensity, rather than pressure. In nearly all such studies, unbounded plane or spherical waves have been assumed and single-pressure measurements used to calculate the acoustic intensity. The majority of marine mammal hearing studies has been conducted in enclosed sound fields, however, where unbounded plane or spherical waves do not exist at low frequencies and the mean active intensity is not equal to $\overline{P^2}/\rho c$. The use of acoustic intensity has also led to confusion, in part, because the word *intensity* has been used to indicate instantaneous acoustic intensity, mean active intensity, or simply the amplitude or ''strength'' of a stimulus.

Kastak and Schusterman (1998) advocated reporting marine mammal thresholds in terms of acoustic pressure, rather than intensity, because the actual acoustic intensity is rarely measured and the likely sound transmission pathways in many species implicate acoustic pressure as the relevant cue. The results of the present study support this view.

Figures 7 and 8 illustrate the problem with using acoustic intensity to describe marine mammal underwater hearing thresholds: the intensity thresholds appear to depend on the acoustic field conditions, while the pressure thresholds do not. This suggests that underwater thresholds in odontocetes should be reported in units of acoustic pressure. If thresholds are reported in intensity units, sufficient acoustic field measurements must be made to either directly estimate the intensity (i.e., measure the pressure and particle velocity) or to verify plane or spherical wave propagation.

The use of acoustic pressure to describe odontocete hearing thresholds does not imply that specific terrestrial mammal damage risk criteria should be extrapolated to marine mammals on a simple pressure basis alone. Recent experimental measurements of temporary threshold shift (TTS) in odontocetes (Au *et al.*, 1999; Schlundt *et al.*, 2000; Finneran *et al.*, 2000) have indicated that much higher levels of acoustic pressure are required to induce TTS in these animals compared to what a simple extrapolation of terrestrial TTS pressure levels would predict.

VI. CONCLUSIONS

(1) The results of experiment I showed no significant change in pressure thresholds as the distance between the subject and the sound source was changed. In contrast, velocity thresholds tended to increase and intensity thresholds tended to decrease as the source distance decreased.
(2) The active sound control system was successful at creating single-frequency acoustic fields with the desired pressure/particle velocity relationships during experiment II.
(3) Interpretation of the results of experiment II was difficult because of the complex acoustic field and the unknown effects of the subject on the generated acoustic field; however, these data also tend to support the results of experiment I.
(4) Neither experiment produced a temporary plateau in the staircase data followed by a threshold decrease, as observed by Turl (1993). The results of both experiments tend to contradict Turl's suggestion of a sensory modality shift at low frequencies in *Tursiops*.
(5) The results of both experiments suggest that underwater marine mammal hearing thresholds be reported in units of pressure, rather than intensity.

ACKNOWLEDGMENTS

Animals were trained by Kim Miller, Jennifer Carr, Mark Todd, Randy Dear, Scott Peluso, Debbie Skaar, and Tricia Kamolnick. Luisa Luera and Jenny Briar assisted with data collection. We thank Carolyn Schlundt and Dr. David Helweg for technical assistance and helpful comments. Funding was provided by Dr. Robert Gisiner at the Office of Naval Research and the In-house Laboratory Independent Research (ILIR) Program at SPAWARSYSCEN San Diego. James Finneran was supported by a National Research Council Research Associateship.

Adby, P. R., and Dempster, M. A. H. (**1974**). *Introduction to Optimization Methods* (Chapman and Hall, London).

Au, W. W. L. (**1993**). *The Sonar of Dolphins* (Springer, New York).

Au, W. W. L., Nachtigall, P. E., and Pawloski, J. L. (**1999**). ''Temporary threshold shift in hearing induced by an octave band of continuous noise in the bottlenose dolphin,'' J. Acoust. Soc. Am. **106**, 2251(A).

Buwalda, R. J. A. (**1981**). ''Segregation of directional and nondirectional acoustic information in the cod,'' in *Hearing and Sound Communication in Fishes*, edited by W. N. Tavolga, A. N. Popper, and R. R. Fay (Springer, New York), pp. 139–171.

Cahn, P. H., Siler, W., and Wodinsky, J. (**1969**). ''Acoustico-lateralis system of fishes: Tests of pressure and particle-velocity sensitivity in grunts, *Haemulon sciurus and Haemulon parrai*,'' J. Acoust. Soc. Am. **46**, 1572–1578.

Chung, J. Y. (**1978**). ''Cross-spectral method of measuring acoustic intensity without error caused by instrument phase mismatch,'' J. Acoust. Soc. Am. **64**, 1613–1616.

Cornsweet, T. N. (**1962**). ''The staircase method in psychophysics,'' Am. J. Psychol. **75**, 485–491.

Fahy, F. J. (**1995**). *Sound Intensity*, 2nd ed. (E&FN Spon, London).

Fay, R. R. (**1988**). *Hearing in Vertebrates: A Psychophysics Databook* (Hill-Fay, Winnetka, IL).

Fay, R. R., and Popper, A. N. (**1974**). ''Acoustic stimulation of the ear of the goldfish (*Carassius auratus*),'' J. Exp. Biol. **61**, 243.

Finneran, J. J., and Hastings, M. C. (**1999**). ''Active impedance control in a cylindrical waveguide for generation of low frequency, underwater plane traveling waves,'' J. Acoust. Soc. Am. **105**, 3035–3043.

Finneran, J. J., Schlundt, C. E., Carder, D. A., Clark, J. A., Young, J. A., Gaspin, J. B., and Ridgway, S. H. (**2000**). ''Auditory and behavioral responses of bottlenose dolphins (*Tursiops truncatus*) and white whales (*Delphinapterus leucas*) to impulsive sounds resembling distant signatures of underwater explosions,'' J. Acoust. Soc. Am. **108**, 417–431.

Finneran, J. J., Carder, D. A., Ridgway, S. H., and Schlundt, C. E. (**1999**). ''Technique for the generation and frequency compensation of bandlimited white noise and its application in studies of masked hearing thresholds,'' J. Acoust. Soc. Am. **106**, 2130(A).

Johnson, C. S. (**1966**). ''Auditory thresholds of the bottlenosed porpoise (*Tursiops truncatus*, Montagu),'' U.S. Naval Ordnance Test Station Technical Publication 4178.

Johnson, C. S. (**1967**). ''Sound detection thresholds in marine mammals'' in *Marine Bioacoustics II*, edited by W. N. Tavolga (Pergamon, Oxford), pp. 247–260.

Kastak, D., and Schusterman, R. J. (**1998**). ''Low-frequency amphibious hearing in pinnipeds: Methods, measurements, noise, and ecology,'' J. Acoust. Soc. Am. **103**, 2216–2228.

Ketten, D. R. (**2000**). ''Cetacean Ears,'' in *Hearing by Dolphins and Whales*, edited by W. W. L. Au, A. N. Popper, and R. R. Fay (Springer, New York), pp. 43–108.

Kinsler, L. E., Frey, A. R., Coppens, A. B., and Sanders, J. V. (**1982**). *Fundamentals of Acoustics*, 3rd ed. (Wiley, New York).

Nachtigall, P. E. (**2000**). ''Psychoacoustic studies of dolphins and whales,'' in *Hearing by Dolphins and Whales*, edited by W. W. L. Au, A. N. Popper, and R. R. Fay (Springer, New York), pp. 330–363.

Ridgway, S. H., and Carder, D. A. (**1997**). ''Hearing deficits measured in some *Tursiops truncatus*, and discovery of a deaf/mute dolphin,'' J. Acoust. Soc. Am. **101**, 590–594.

Schlundt, C. E., Finneran, J. J., Carder, D. A., and Ridgway, S. H. (**2000**). ''Temporary shift in masked hearing thresholds (MTTS) of bottlenose dolphins, *Tursiops truncatus*, and white whales, *Delphinapterus leucas*, after exposure to intense tones,'' J. Acoust. Soc. Am. **107**, 3496–3508.

Schlundt, C. E., Carder, D. A. and Ridgway, S. H. (**2002**). ''The effect of projector position on the underwater hearing thresholds of bottlenose dolphins (*Tursiops truncatus*) at 2, 8, and 12 kHz,'' in *Echolocation in Bats and Dolphins*, edited by J. Thomas, C. Moss, and M. Vater (University of Chicago Press, Chicago) (in press).

Tavolga, W. N., and Wodinksy, J. (**1963**). ''Auditory capacities in fishes,'' Bull. Am. Museum Nat. Hist. **126**(2), 177–240.

Turl, C. W. (**1993**). ''Low-frequency sound detection by a bottlenose dolphin,'' J. Acoust. Soc. Am. **94**, 3006–3008.

A comparison of material classification techniques for ultrasound inverse imaging

Xiaodong Zhang[a] and Shira L. Broschat[b]
School of Electrical Engineering & Computer Science, Washington State University, P.O. Box 642752, Pullman, Washington 99164-2752

Patrick J. Flynn[c]
Department of Computer Science and Engineering, 384 Fitzpatrick Hall, University of Notre Dame, Notre Dame, Indiana 46556

(Received 2 September 2000; accepted for publication 2 October 2001)

The conjugate gradient method with edge preserving regularization (CGEP) is applied to the ultrasound inverse scattering problem for the early detection of breast tumors. To accelerate image reconstruction, several different pattern classification schemes are introduced into the CGEP algorithm. These classification techniques are compared for a full-sized, two-dimensional breast model. One of these techniques uses two parameters, the sound speed and attenuation, simultaneously to perform classification based on a Bayesian classifier and is called bivariate material classification (BMC). The other two techniques, presented in earlier work, are univariate material classification (UMC) and neural network (NN) classification. BMC is an extension of UMC, the latter using attenuation alone to perform classification, and NN classification uses a neural network. Both noiseless and noisy cases are considered. For the noiseless case, numerical simulations show that the CGEP–BMC method requires 40% fewer iterations than the CGEP method, and the CGEP–NN method requires 55% fewer. The CGEP–BMC and CGEP–NN methods yield more accurate reconstructions than the CGEP method. A quantitative comparison of the CGEP–BMC, CGEP–NN, and GN–UMC methods shows that the CGEP–BMC and CGEP–NN methods are more robust to noise than the GN–UMC method, while all three are similar in computational complexity. [DOI: 10.1121/1.1424869]

PACS numbers: 43.80.Qf, 43.60.Pt [FD]

I. INTRODUCTION

Breast cancer is a leading cause of women's death in the United States. Each year approximately 182 800 new cases of breast cancer are diagnosed and 40 800 women die.[1] The prognosis for breast cancer is directly correlated with the size of a tumor when detected. The smaller a tumor is when found, the better the chance of survival. Thus it is critical to detect breast cancer when it is at a treatable early stage. This requires a breast screening system with sufficiently high resolution.

X-ray mammography is widely used to detect breast cancer in post-menopausal women. However, for women under the age of 50 x-ray mammography has limited utility because breast tissue in younger women is dense, and dense tissue does not provide the contrast needed to readily image small tumors. This is not the case for ultrasound. Current ultrasound imaging technology is based on a pulse-echo approach in which only the reflected energy is used. However, this works poorly when strong scattering occurs as it does in the premenopausal female breast.[2–4] To account for this strong scattering, full wave inversion techniques can be used.

The full wave inverse problem involves a nonlinear Fredholm integral equation of the first kind which is known to be ill-posed. However, regularization schemes, such as Tikhonov or edge preserving (EP) regularization, can be employed to circumvent the ill-posedness.[5] The known quantities in the integral equation are the measured scattered field and the incident field, while the unknowns are the total field and the object function. The goal of the inverse scattering problem is to reconstruct the object function; the total field is itself a function of the object function. In recent years, much work has been conducted on the inverse problem.[6–18] Most of the algorithms that have been developed are optimization-based techniques, among which the most widely used are the Newton-type methods, the modified gradient (MG) method, and the conjugate gradient (CG) method. Two of the Newton-type methods used are the Gauss–Newton (GN) method[8,9] and the Newton–Kantorovich (NK) method.[11,13] In a comparative study Pichot *et al.* reported that the NK method outperforms the MG method.[17] Although the MG method eliminates the necessity for solving the forward scattering problem at each iteration, it was found to fail when used to reconstruct two large objects simulating the human body. One case was a cylinder with another off-center cylinder inside. The other was an elliptic object with two off-center cylinders inside. In contrast, the NK method was used to successfully reconstruct these two complex objects. Unfortunately, for a different problem with scattered data strongly corrupted by noise (signal-to-noise ratio SNR $=20$ dB or 10% of the maximum amplitude of the scattered data), the NK method diverged.[17] For the same problem, the

[a]Electronic mail: xzhang@eecs.wsu.edu
[b]Electronic mail: shira@eecs.wsu.edu
[c]Electronic mail: flynn@nd.edu

conjugate gradient method with edge preserving regularization (CGEP) converged and yielded satisfactory reconstruction. The CGEP method has also been successfully implemented to reconstruct experimental data.[16] Because of its robustness to noise, the CGEP was chosen for this work.

To reduce the computational cost of the CGEP algorithm, information about the anatomy of the breast and properties of its tissues are incorporated into the algorithm. In earlier work, Manry and Broschat exploited *a priori* information by introducing a material classification technique into the GN method.[9] The addition of material classification improved the rate of convergence of the GN method and also improved the accuracy of the reconstructions. However, the algorithm was found to be sensitive to noise. Motivated by the significant reduction in computational cost provided by the material classifier, a new material classification technique is introduced in this paper. The earlier classifier is termed univariate material classification (UMC) since it uses only values of the tissue attenuation coefficients during the classification process, although information about the sound speeds is also used during a post-classification process. Both classification techniques use a Bayesian classifier, but the new technique utilizes information about the attenuation coefficients and sound speeds of different tissues simultaneously and thus is called bivariate material classification (BMC). The BMC is introduced into the CGEP algorithm after completion of each iteration, and the resulting classified object is used in the next iteration.

In earlier work, a neural network (NN) classification technique was proposed.[18] The NN classifier was used with the CG method and was shown to significantly accelerate convergence of the CG method with better reconstruction accuracy. In this paper, we introduce the NN classifier in the CGEP method. Both the CGEP–NN and CGEP–BMC methods are used to reconstruct a full-sized, two-dimensional breast model. The breast model is the same one that was used in Ref. 9 and is described in the next section. It is composed of layers of skin, fat, and glandular tissue. Tumors and cysts of various sizes are embedded inside the glandular tissue. The model is $32\lambda \times 32\lambda$ in size, where λ is the wavelength in water at a frequency of 400 kHz ($\lambda = 3.72$ mm). It is discretized into 128×128 pixels and is illuminated successively by 128 plane waves at different angles.

Numerical simulations are conducted for both noiseless and noisy cases. By noise we mean that there exists signal noise in the scattered data and that the point-to-point ultrasound parameters of the same tissues vary.[9] Results are presented for a signal-to-noise ratio (SNR) of 70 dB for the scattered field measurements, although noisier cases were also studied. For the noiseless case, the CGEP–BMC correctly reconstructs the object and requires 40% fewer iterations than the CGEP method, while the CGEP–NN method correctly reconstructs the object and requires 55% fewer iterations than the CGEP method. For the noisy case, tumors and cysts are detectable for all three methods, and minimal tumors and a small cyst are correctly classified by the BMC and NN classifiers. However, some pixels are misclassified or are left unclassified. A quantitative comparison of the CGEP–BMC, CGEP–NN, and GN–UMC methods shows that the CGEP–BMC and CGEP–NN methods are more robust to noise than the GN–UMC method, while they all have comparable computational costs.

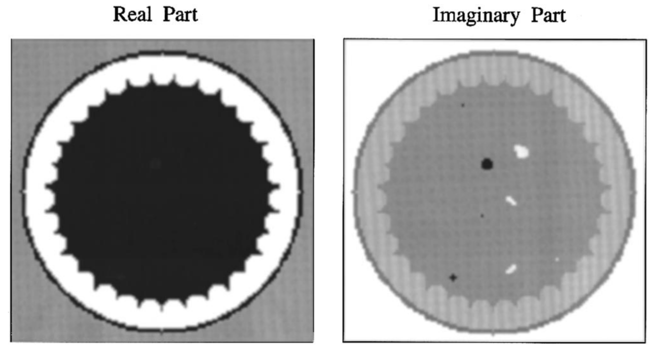

FIG. 1. True contrast for the breast model.

In Sec. II, the two-dimensional breast model is described. The CGEP method is discussed in Sec. III. In Sec. IV, the BMC classifier is presented, and in Sec. V, the neural network classifier is briefly discussed. Numerical results are presented in Sec. VI. Finally, concluding remarks are given in Sec. VII.

II. 2D BREAST MODEL AND SCATTERING GEOMETRY

The two-dimensional breast model used in the numerical simulations is shown in Fig. 1. In the real part of the object the tumors and cysts are difficult to discern, while they stand out in the imaginary part. The real part of the object depends mostly on the speed of sound while the imaginary part depends mostly on the attenuation. The lack of contrast in the real part reflects the similarity of the tissue sound speeds. On the other hand, the attenuations of glandular tissue, cysts, and tumors are distinct, and this is reflected in the imaginary part of the object.

The breast model is the same as that used in Ref. 9 and is discretized into 128×128 pixels, corresponding to an average breast with a 12-centimeter diameter. Simulations are performed at a frequency of 400 kHz with each pixel about 0.93 mm wide ($\lambda/4$ is water). Since inverse imaging is a full wave solution, it has a resolution of approximately $\lambda/4$. Thus, 400 kHz provides a resolution of less than a millimeter in water which should be adequate for breast imaging. The model is comprised of a skin layer 1.86 mm thick with an outer radius of 5.59 cm. Next a fat layer is constructed with an annular layer 5 mm wide and 1-cm fat lobes centered along the inner radius of the annulus. This geometry creates a highly refractive fat-glandular interface which provides a rigorous test of the imaging method. The breast interior is composed of glandular tissue and tumors and cysts of various sizes and shapes. Minimal tumors and a cyst one pixel in size (0.93 mm) are used to test the ability to image small objects. The model is assumed to be surrounded by water and is illuminated by 128 plane waves equally spaced around it. The scattered field is measured for each illumination along the four edges by 128 receivers on each edge. The measured scattered data for the true object are calculated using the

TABLE I. Typical tissue parameters at $f=400$ kHz.

Tissue	Speed [m/s]	Attenuation [m^{-1}]
Fat	1439.0	1.66
Glandular	1581.0	2.90
Skin	1586.0	3.36
Tumor	1573.0	6.58
Cyst	1584.0	0.46
Water	1490.0	0.0

BI–CGSTAB–FFT method.[19] Tissue parameters for the breast at a frequency of 400 kHz are listed in Table I as presented by Madsen *et al.*[20]

III. THE CONJUGATE GRADIENT METHOD WITH EDGE PRESERVING REGULARIZATION

Figure 2 shows the two-dimensional scattering geometry. The computational domain D is defined to be square. M receivers are located on a surface S enclosing D. The acoustic sound speed at r is denoted by $c(r)$, and the attenuation coefficient is $\alpha(r)$. The sound speed in the surrounding medium (here, water) is c_0, and the surrounding medium is lossless. The object is irradiated successively by plane acoustic waves at L different angles, $l=1,2,...,L$.

Assuming tissue density variations are negligible, i.e., that breast tissue is generally soft, the acoustic wave equation can be cast into integral equation form[21]

$$u_l(r)=u_l^{\mathrm{inc}}(r)+\int_D u_l(r')o(r')g(r,r')dr', \quad r\in D, \tag{1}$$

$$u_l^s(r)=\int_D u(r')o(r')g(r,r')dr', \quad r\in S \tag{2}$$

for the lth excitation where $u_l(r)$ is the total field, $u_l^{\mathrm{inc}}(r)$ is the incident field, $u_l^s(r)$ is the scattered field, and $g(r,r')$ is the Green's function. The object function $o(r)$ satisfies the relationship $o(r)=k_0^2\{[k^2(r)/k_0^2]-1\}$ where k_0 is the wave

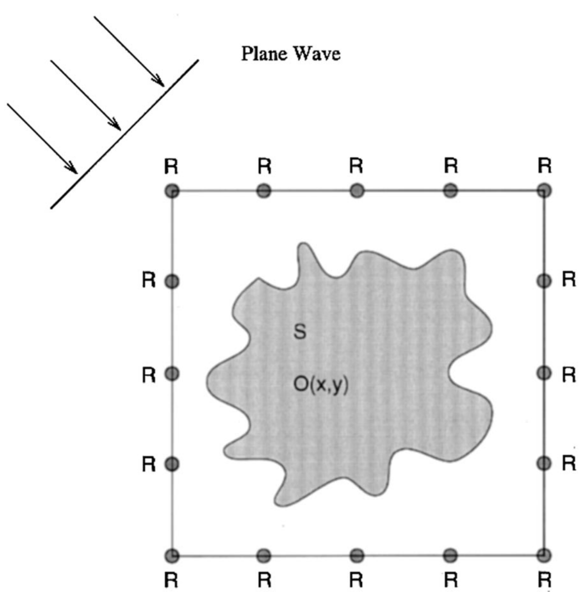

FIG. 2. Scattering geometry.

number in the background medium (water), and $k(r)$ is the wave number at r with $k(r)=[2\pi f/c(r)]-j\alpha(r)$. The term $\{[k^2(r)/k_0^2]-1\}$ is called the object contrast.

The goal of inverse imaging is to reconstruct the object function $o(r)$ using knowledge of the scattered data u^s. This problem is ill-posed by nature in the Hadamard sense[5]—i.e, the existence, uniqueness, and stability of the solution are not simultaneously ensured.[22] Using the moment method with pulse basis functions and point matching,[23] Eqs. (1) and (2) are converted to matrices with the domain D discretized into N square cells. This yields a nonlinear matrix system for each illumination l ($l=1,2,...,L$):

$$\vec{u}_l=(I-G_DO)^{-1}\vec{u}_l^{\mathrm{inc}}=\mathcal{L}(O)\vec{u}_l^{\mathrm{inc}}, \tag{3}$$

$$\vec{u}_l^s=G_SO\mathcal{L}(O)\vec{u}_l^{\mathrm{inc}}=G_SO\vec{u}_l, \tag{4}$$

where O is an $N\times N$ diagonal matrix with the diagonal elements forming the object vector $\vec{o}$, $\vec{u}_l^s$ is the $M\times 1$ scattered field vector, $\vec{u}_l$ is the $N\times 1$ total field vector, and $\vec{u}_l^{\mathrm{inc}}$ is the incident field vector. The subscript l indicates the lth illumination, and G_D and G_S are the $N\times N$ and $M\times N$ Green's function matrices, respectively. The elements for G_D and G_S are

$$G_{D_{ij}}=\int_{D_j} g(r_i-r')dr', \quad r\in D, \tag{5}$$

$$G_{S_{ij}}=\int_{D_j} g(r_i-r')dr', \quad r\in S, \tag{6}$$

where D_j is the area of the jth cell, and r_i is the center of the ith cell. G_D maps the domain D to domain D and G_S maps the domain D to domain S.

The inverse scattering problem requires solution of both a forward and an inverse problem. When the object is known, Eq. (3) is used to solve for the total field $\vec{u}_l$; the problem is well-posed and linear with respect to the incident field $\vec{u}_l^{\mathrm{inc}}$. This is the forward problem which is solved using the BI–CGSTAB–FFT method.[19,24] The total field of Eq. (3) is expressed in terms of basis functions, and the unknowns are the coefficients of these basis functions. This linear system is solved using the BI–CGSTAB method while the kernal of the integral operator is computed via FFTs. When the total field is known and Eq. (4) is used to solve for the object $\vec{o}$, the problem is nonlinear and ill-posed. This is the inverse problem. The ill-posedness inherent in Eq. (4) is more difficult to handle because of the nonlinearity.

A. The conjugate gradient technique

Since the CG method is an optimization approach, an error function must be defined

$$\vec{\rho}_l=\vec{u}_l^s-G_SO\mathcal{L}(O)\vec{u}_l^{\mathrm{inc}}, \tag{7}$$

where $\vec{u}_l^s$ is the true scattered data vector ($M\times 1$) for illumination by the lth source, O is an $N\times N$ diagonal matrix whose elements are the elements of the object vector $\vec{o}$ ($N\times 1$), $\vec{u}_l^{\mathrm{inc}}$ is the incident field vector ($N\times 1$), $\mathcal{L}(O)=(I-G_DO)^{-1}$, and the matrices G_D and G_S are defined by Eqs. (5) and (6), respectively. N is the number of cells into which the object is discretized, and M is the number of receivers per view. In addition, a cost functional is defined

$$\Phi = \frac{1}{2} w \sum_{l=1}^{L} \|\vec{\rho}_l\|^2, \tag{8}$$

where $\|\cdot\|$ is the Euclidean norm. Thus, the functional Φ is a measure of the discrepancy between the measured and calculated scattered data due to estimation of the object. As proposed in Ref. 10, the weight w is defined by

$$w = \left(\sum_{l=1}^{L} \|\vec{u}_l^s\|^2 \right)^{-1}, \tag{9}$$

where summation is over all sources. This choice ensures that the amplitude of the incident field has no impact on the function since $\vec{u}^s$ is linear in $\vec{u}^{\text{inc}}$.

The CG method involves several key updating equations:

$$\hat{\vec{o}}_{n+1} = \hat{\vec{o}}_n + t_n \vec{d}_n, \tag{10}$$

$$\vec{d}_{n+1} = -\vec{g}_{n+1} + \gamma_n \vec{d}_n, \tag{11}$$

where t_n is the step size along $\vec{d}_n$, $\vec{d}_n$ is the updating direction for the object at the nth iteration, $\vec{g}_n$ is the gradient of the cost functional at the nth iteration, and γ_n is the CG direction parameter. $\vec{o}_1$ is the initial guess, and $\vec{d}_1 = -\vec{g}_1$. Thus, we use the steepest descent direction to initiate the iterative process. Choices for t_n and γ_n are discussed below. The gradient of the cost functional is obtained from

$$\vec{g}_n = w \sum_{l=1}^{L} [\operatorname{diag}(\mathcal{L}(\hat{O}_n)\vec{u}_l^{\text{inc}})\mathcal{L}(\hat{O}_n)]^\dagger G_s^\dagger \vec{\rho}_{l,n}, \tag{12}$$

where $\mathcal{L}(O) = (I - G_D O)^{-1}$, † indicates the conjugate transpose, diag denotes the diagonal, and $\vec{\rho}_{l,n}$ is the difference between the measured and calculated scattered data at the nth iteration when the object is illuminated by the lth source. $\mathcal{L}(\hat{O}_n)\vec{u}_l^{\text{inc}}$ is essentially the total field at the nth iteration and is calculated for the forward problem.

To save computational time, a first-order approximation for t_n for large objects is used

$$t_n = \frac{\sum_{l=1}^{L} \langle \vec{\rho}_l, \vec{V}_l \rangle}{\sum_{l=1}^{L} \|\vec{V}_l\|^2}, \tag{13}$$

where $\vec{V}_l = G_s \{\mathcal{L}(\hat{O}_n)\}^T \operatorname{diag}(\vec{d}_n) \mathcal{L}(\hat{O}_n) \vec{u}_l^{\text{inc}}$, ''$T$'' means transpose, and the angle brackets denote the inner product.

There are many choices for the conjugate gradient direction parameter γ_n. In a previous study it was found that the recently proposed direction parameter given by

$$\gamma_n = \frac{\langle \vec{g}_{n+1}, \vec{g}_{n+1} \rangle}{\langle \vec{d}_n, \vec{g}_{n+1} - \vec{g}_n \rangle}$$

is the best choice for ultrasound inverse imaging.[25]

B. Edge preserving regularization

To further enhance the performance of the conjugate gradient method when the problem is strongly ill-posed and/or the scattered data is strongly corrupted, an edge preserving (EP) regularization technique is introduced into the conjugate gradient method. It allows smoothing of a homogeneous region while preserving edges in an image. It is a significant improvement over Tikhonov regularization[26,27] and, in addition, it is convenient to apply with the conjugate gradient method.

The original edge preserving regularization proposed by Lobel *et al.* was imposed on both the real and imaginary parts of the image.[10] For ultrasound imaging of the breast, edge preserving regularization is imposed on just the imaginary part of an image because only the imaginary part gives discernible results (see Fig. 1). Edge preserving regularization has the form

$$\Phi_R = \mu \sum_{p=1}^{N_{\text{lin}}} \sum_{q=1}^{N_{\text{col}}} \left(b_{p,q} \left\| \frac{\operatorname{Im}(\nabla o)_{p,q}}{\delta} \right\|^2 + \Psi(b_{p,q}) \right), \tag{14}$$

where Im indicates the imaginary part. μ is the regularization parameter which balances the data term and the regularization term. The parameter δ fixes the threshold level of the gradient norm above which a discontinuity is preserved and below which it is smoothed. For this project, δ was chosen empirically. The $b_{p,q}$ terms are real and continuous in $[0,1]$, p is the pixel number in the x direction, and q is the pixel number in the y direction. $(\nabla o)_{p,q}$ is the gradient of the object function at position (p,q). The $b_{p,q}$ terms record discontinuities, i.e., edges, in the imaginary part of the image. The function Ψ is given by[26]

$$\Psi(s) = s + \frac{1}{s} - 2. \tag{15}$$

The new cost functional is given by

$$\Phi_{\text{EP}} = w \sum_{l=1}^{L} \|\vec{\rho}_l\|^2 + \mu \sum_{p=1}^{N_{\text{lin}}} \sum_{q=1}^{N_{\text{col}}} \left(b_{p,q} \left\| \frac{\operatorname{Im}(\nabla o)_{p,q}}{\delta} \right\|^2 + \Psi(b_{p,q}) \right) \tag{16}$$

which depends on two variables, $\vec{o}$ and $b_{p,q}$. To minimize Eq. (16), we use successive over-relaxation, alternating minimization of Φ by fixing one of the two variables successively.

(1) When the $b_{p,q}$ terms are fixed, minimization of Eq. (16) is performed using the conjugate gradient method as discussed in the preceding section.
(2) When $\vec{o}$ is fixed, the values for the $b_{p,q}$ terms that minimize Φ_{EP} are unique and are given for each point (p,q) by the analytical expression

$$b_{p,q} = \frac{1}{2\sqrt{1 + \left(\frac{\|\operatorname{Im}(\nabla o)_{p,q}\|}{\delta} \right)^2}}. \tag{17}$$

Since $b_{p,q}$ gives the spatial gradient of the imaginary part of the object, it records information about discontinuities at each step of the algorithm. The values of $b_{p,q}$ from the previous step are used for the next estimate of the object. For simplicity, we assume the operators ∇ and Im are inter-

(a)

Z_1	Z_4	Z_7
Z_2	Z_5	Z_8
Z_3	Z_6	Z_9

(b)

-1	-2	-1
0	0	0
1	2	1

(c)

-1	0	1
-2	0	2
-1	0	1

FIG. 3. (a) 3×3 image region, (b) mask used to compute G_y at the center pixel, and (c) mask used to compute G_x at the center pixel. These masks are known as the Sobel operator.

changeable, $\mathrm{Im}(\nabla o)_{p,q} = \nabla(\mathrm{Im}(o_{p,q}))$. To simplify notation, we set $\mathrm{Im}(o_{p,q}) = Z_{p,q}$ so that $\mathrm{Im}(\nabla o)_{p,q} = \nabla Z_{p,q}$.

In image processing it is common to approximate $|\nabla Z_{p,q}|$ by[28]

$$|\nabla Z_{p,q}| = |G_{x_{p,q}}| + |G_{y_{p,q}}|, \tag{18}$$

where $G_{x_{p,q}}$ and $G_{y_{p,q}}$ are the gradient operators in the x and y directions, respectively. Sobel operators were chosen to compute the gradients because they provide both differencing and smoothing.[28] Since derivatives tend to enhance noise, smoothing is a particularly attractive feature. A Sobel operator operates on a 3×3 pixel section of an image as shown in Fig. 3 and is also known as a mask. The gradients at the center pixel, denoted Z_5, are given by

$$G_x = (Z_7 + 2Z_8 + Z_9) - (Z_1 + 2Z_2 + Z_3), \tag{19}$$

$$G_y = (Z_3 + 2Z_6 + Z_9) - (Z_1 + 2Z_4 + Z_7). \tag{20}$$

After the gradients for the center pixel have been determined, the masks are moved to the next pixel location and the procedure is repeated. The values along the four edges of the image are set to the values at the corners of the image. For our problem, the gradient of Φ_R with respect to the imaginary part of the contrast at location (p,q) is given by

$$\begin{aligned}\frac{\partial \Phi_R}{\partial Z_{p,q}} = \frac{1}{\delta^2}\{ & b_{p-1,q-1}(G_{y_{p-1,q-1}} + G_{x_{p-1,q-1}}) \\ & + b_{p,q-1}(2G_{y_{p,q-1}}) + b_{p+1,q-1}(G_{y_{p+1,q-1}} \\ & + G_{x_{p+1,q-1}}) + b_{p-1,q}(2G_{x_{p-1,q}}) \\ & + b_{p+1,q}(-2G_{x_{p+1,q}}) + b_{p-1,q+1}(-G_{y_{p-1,q+1}} \\ & + G_{x_{p-1,q+1}}) + b_{p,q+1}(-2G_{y_{p,q+1}}) \\ & + b_{p+1,q+1}(-G_{y_{p+1,q+1}} + G_{x_{p+1,q+1}})\},\end{aligned} \tag{21}$$

where

$$\begin{aligned}G_{x_{p,q}} = & (Z_{p+1,q-1} + 2Z_{p+1,q} + Z_{p+1,q+1}) \\ & - (Z_{p-1,q-1} + 2Z_{p-1,q} + Z_{p-1,q-1})\end{aligned}$$

and

$$\begin{aligned}G_{y_{p,q}} = & (Z_{p-1,q+1} + 2Z_{p,q+1} + Z_{p+1,q+1}) \\ & - (Z_{p-1,q-1} + 2Z_{p,q-1} + Z_{p+1,q-1}).\end{aligned}$$

The steps for the CGEP iteration procedure are

(1) Set initial guess.
(2) Repeat the following until convergence occurs.

(a) Minimize Eq. (16) with respect to $b_{p,q}$ when $\vec{o}$ is fixed. The updating equation for $b_{p,q}$ is given by Eq. (17).
(b) Minimize Eq. (16) with respect to $\vec{o}$ when the $b_{p,q}$ terms are fixed. Use the CG algorithm to estimate $\hat{\vec{o}}_{n+1}$ as discussed earlier.

The gradient of Φ_{EP} must now have two parts, the gradient $\vec{g}_1$ due to Φ and the gradient $\vec{g}_2$ due to Φ_R. Thus, $\vec{g} = \vec{g}_1 + \vec{g}_2$. Equation (13) is no longer valid and must be rederived to be completely rigorous. However, Eq. (13) is a reasonable approximation to the actual equation when μ is small. Since $\mu = 10^{-6}$ is chosen for this work, Eq. (13) is used. δ^2 is chosen empirically to be 250.

IV. BIVARIATE MATERIAL CLASSIFICATION (BMC)

To accelerate convergence of the CGEP algorithm, a new material classification technique is introduced into the CGEP iterations. It exploits knowledge of the material parameters, specifically the sound speed and attenuation, and thus the name bivariate material classification (BMC). Each pixel (p,q) of the object is represented by its sound speed x and attenuation y, and speed and attenuation are assumed to be both uncorrelated and Gaussian distributed. The BMC classifier is essentially a Bayesian classifier,

$$\wp = \max_c \frac{P(c)p(x,y|c)}{p(x,y)}, \tag{22}$$

where c is the tissue class type (e.g., cyst, fat, skin, tumor), $P(c)$ is the *a priori* probability of class c, $p(x,y|c)$ is the conditional probability density function given a class c, and $p(x,y) = \Sigma_c P(c)p(x,y|c)$ is the total probability density function. For convenience, attenuation values are weighted by a factor of 500. Since $P(c)p(x,y|c)/p(x,y)$ is the *a posteriori* probability $P(c|x,y)$ of a pixel (x,y) belonging to class c, $\wp \in [0,1]$. Thus $\wp$ is the maximum value of the *a posteriori* probability at pixel (x,y) for all classes considered. For example, after computation of the *a posteriori* probabilities for all classes considered, if fat tissue yields the maximum value, then the pixel at (x,y) is classified as fat and $\wp$ is set to be the *a posteriori* probability of fat. Information about the structure of the breast is also utilized. For example, it is known that skin tissue does not exist in the interior of the breast, and this fact is used to test for misclassification by the BMC classifier.

To implement bivariate material classification, we need values for the conditional probability density function (PDF) $p(x,y|c)$ and the probability $P(c)$ for each class. The strategy for finding these values is similar to the one proposed in Ref. 9 except that both the sound speed and attenuation are used. The conditional PDF $p(x,y|c)$ is assumed to be Gaussian, and the sound speed x and attenuation y are assumed to be independent. The mean values of both the sound speed and attenuation for all classes are already known, as shown in Table I. Thus, the task reduces to finding the variance of the conditional PDF and the probability $P(c)$. The reconstructed object is used to create histograms of the sound speed and attenuation, and these are used to estimate the variance and probability. For each histogram, a rectangular window is centered at the mean value for a particular class, and the width of the window is determined empirically. The probability $P(c)$ is estimated by the percentage of pixels within the window of each class. The variance of the conditional PDF is found in a similar manner.

Once the conditional PDF $p(x,y|c_j)$ and the probability $P(c_j)$ for $j=1,2,...,C$ are obtained, we are ready to perform classification for each pixel. However, there are situations when no decision should be made, for example, when it is equally likely that a pixel is two different tissue types. As proposed by Ref. 9, a ''rejection'' class is introduced to handle such situations. The rule for determining a rejection is

$$\text{If } \wp \geqslant 1-\mathfrak{R}, \text{ set tissue to } c, \text{ else reject.}$$

where $0 \leqslant \mathfrak{R} \leqslant 1$ is the rejection rate, a parameter for controlling classification. If $\mathfrak{R}=0$, then decisions from the Bayesian classifier are rejected; if $\mathfrak{R}=1$, then decisions are accepted. Thus $\mathfrak{R}$ is used as a measure of confidence in the ability to classify. The BMC classifier is used in the CGEP algorithm at every 10th iteration. $\mathfrak{R}$ is increased linearly from 0.5 to 0.9 from the 10th iteration to the 50th iteration. This has been found to give reasonable results.

Since decisions made by the Bayesian classifier can be incorrect, a ''clean up'' step is inserted after the Bayes classification step to prevent misclassification. The sound speed and attenuation of nonrejected pixels are checked to ensure that they fall within acceptable bounds. These bounds are chosen on the basis of the known ultrasound properties for the possible tissue types. For example, as indicated in Table I, the range of possible sound speeds is 1400 to 1800 m/s. If the bounds are exceeded, pixel identification is rejected. Location of the tissue type is also checked. For example, if a pixel is identified as skin tissue in the breast interior, it is rejected. The ''clean up'' procedure insures selection of tissue types that will most likely lead to a convergent solution.

V. NEURAL NETWORK CLASSIFICATION

The neural network classifier, proposed in Ref. 18, is also implemented with the CGEP method, and reconstructions are performed for the full-sized, 2D breast model. For details on neural network classification, see Ref. 18. Upon completion of the training state, the neural network configuration is 2–7–3, or 2 neurons in the first layer, 7 neurons in the second, and 3 neurons in the third. All activation functions are Log–Sigmoid. The initial learning rate is set to 0.09 and the momentum is set to 0.9. As with the BMC classifier, the NN classifier is used with the CGEP algorithm at every 10th iteration. A database is generated in the same manner as described in Ref. 18. The Matlab toolkit is used to train the neural network architecture.

VI. SIMULATION RESULTS

The CGEP, CGEP–BMC, and CGEP–NN methods were used to reconstruct the full-sized, 2D breast model discussed in Sec. II. Both noiseless and noisy cases were tested. By noiseless, we mean there is no signal noise in the scattered data and the mean values of the tissue parameters are used without variations. As in Ref. 9, for the noisy case, tissue losses are allowed to vary by 10% around the mean values, tissue sound speeds are allowed to vary by 2% (recall that sound speeds have considerably less impact on the imaginary part of the object than attenuation does), and the signal-to-noise ratio (SNR) of the scattered field measurements is set to 70 dB. The noise is meant to model both the system noise and point-to-point variations of the material parameters.

The three error measurements defined in Ref. 9 are the (1) relative residue error (RRE) which is defined as the normalized distance between the measured and computed scattered fields, (2) mean square error (MSE) which is defined as the normalized distance between the true and reconstructed objects, and (3) mean square error of the imaginary part (ImMSE) which is defined as the normalized distance between the imaginary part of the true and reconstructed objects. The latter is useful because only the imaginary part is used to distinguish a tumor from its surrounding tissue,

$$\mathrm{RRE}=\sqrt{\frac{\sum_{l=1}^{L}\|\hat{\vec{u}}_s-\vec{u}_s\|^2}{\sum_{l=1}^{L}\|\vec{u}_s\|^2}}, \tag{23}$$

$$\mathrm{MSE}=\frac{\|\hat{\vec{o}}-\vec{o}\|}{\|\vec{o}\|}, \tag{24}$$

$$\mathrm{ImMSE}=\frac{\|\mathrm{IMAG}(\hat{\vec{o}}-\vec{o})\|}{\|\mathrm{IMAG}(\vec{o})\|}, \tag{25}$$

where $\hat{o}$ indicates an estimated value.

The initial estimate used for the object function is the same one used in Ref. 9. The procedure for acquisition of the initial values is described in Ref. 9. Basically, they are obtained via two steps. The sound speed profile is acquired using either the Born approximation or the GN method for the real part of the object only—that is, the attenuation is set to zero. Once the sound speed profile has been calculated, the water, skin, fat, and glandular regions are located on the basis of pixel sound speeds. Termination of the algorithm occurs when $\mathrm{RRE}<1.0\times10^{-5}$ or when a maximum of 50 iterations has been performed. The material classifiers are introduced at the 10th iteration and are then used every 10 iterations thereafter. The timing for introduction of the classifiers is determined empirically.

All simulations were performed on a Cray T3E machine with 128 processors. Each simulation took from 3 to 6 wall-clock hours. A detailed flowchart for both algorithms is shown in Fig. 4.

A. Results without noise

Figure 5 shows the reconstructed images at iterations 10 and 50 for the CGEP method. At the 10th iteration, the tumors and cysts, even the minimal ones, are detectable. The reconstructed values at iteration 50 are quantitatively more accurate than those at iteration 10. Figure 6 shows the reconstructed results at iterations 10 and 40 for the CGEP–BMC

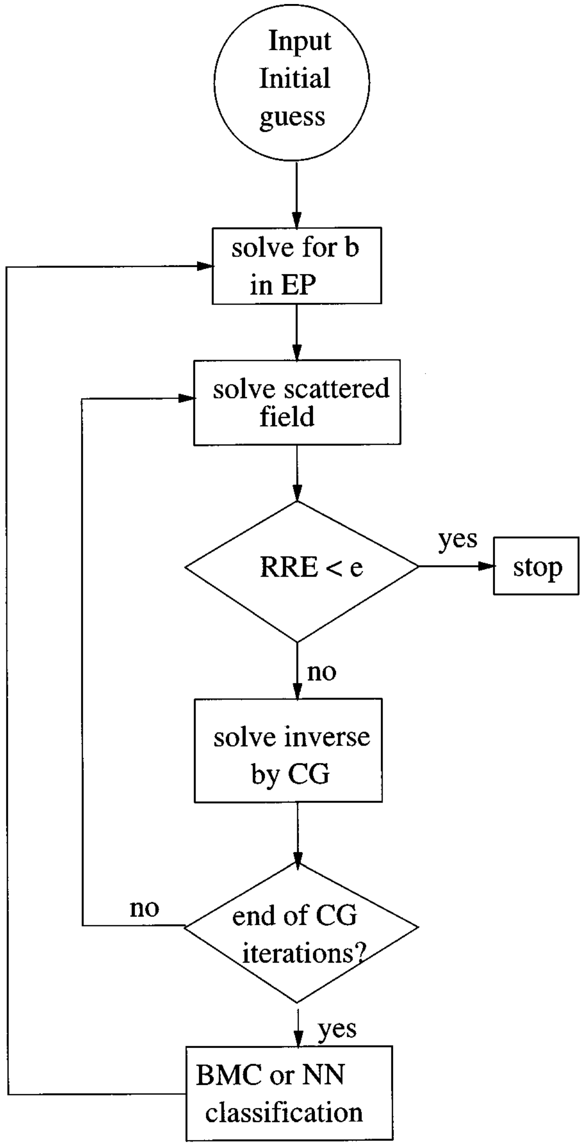

FIG. 4. Flowchart for the CGEP method with material classification.

method. At the 10th iteration, some pixels are left unclassified, but all the unclassified pixels are correctly classified at the 40th iteration. Figure 7 shows the reconstructed images at the 10th and 30th iterations for the CGEP–NN method. At the 30th iteration, the entire image is correctly classified.

The RRE curves for the CGEP, CGEP–BMC, and CGEP–NN methods are shown in Fig. 8. For the CGEP method, the RRE values decrease monotonically. Application of the classifiers at intervals of 10 iterations causes the RRE values to drop substantially except at the 20th iteration. At the 20th iteration, classification actually causes an increase in the RRE values. The decrease of the RRE values is desirable while the increase after classification is not unexpected. During classification some pixels are misclassified, and this misclassification causes the increase. The same phenomenon occurs in the MSE and ImMSE curves shown in Fig. 9. As can be seen on the flowchart Fig. 4, the classified object is used as an initial guess for the next series of CGEP iterations. This restarting strategy is beneficial to the CGEP algorithm since it results overall in smaller errors. The convergence of the

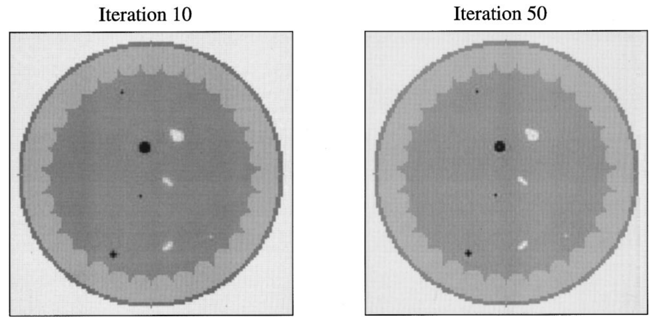

FIG. 5. Results fr the CGEP method without noise.

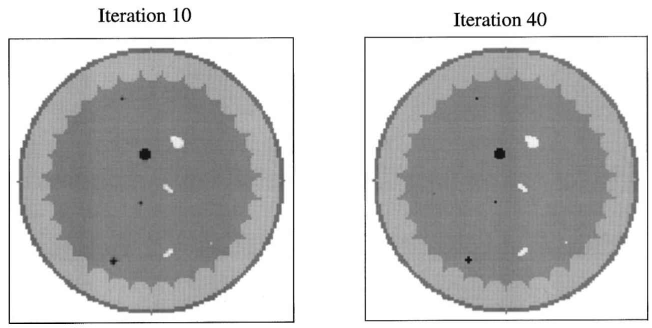

FIG. 6. Results for the CGEP–BMC method without noise.

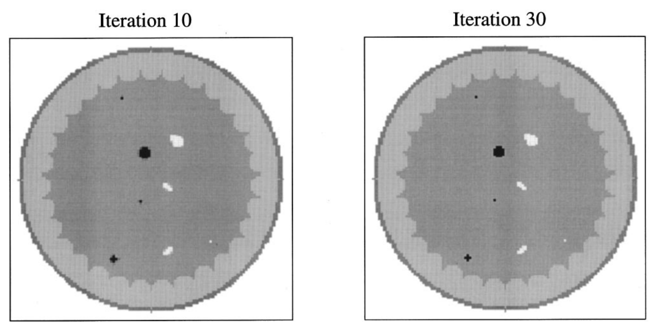

FIG. 7. Results for the CGEP–NN method without noise.

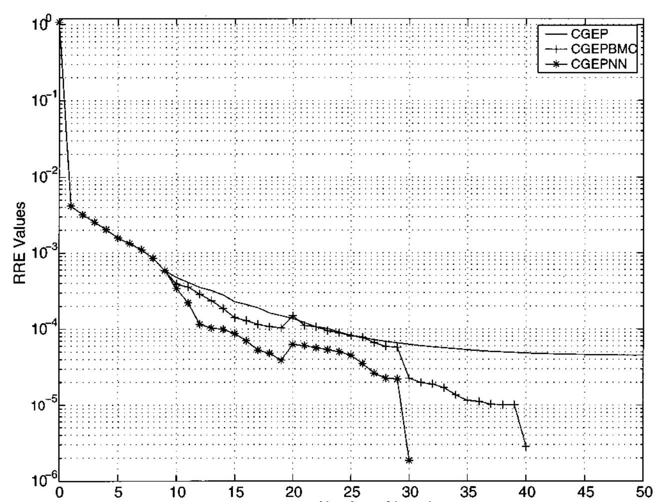

FIG. 8. RRE curves without noise.

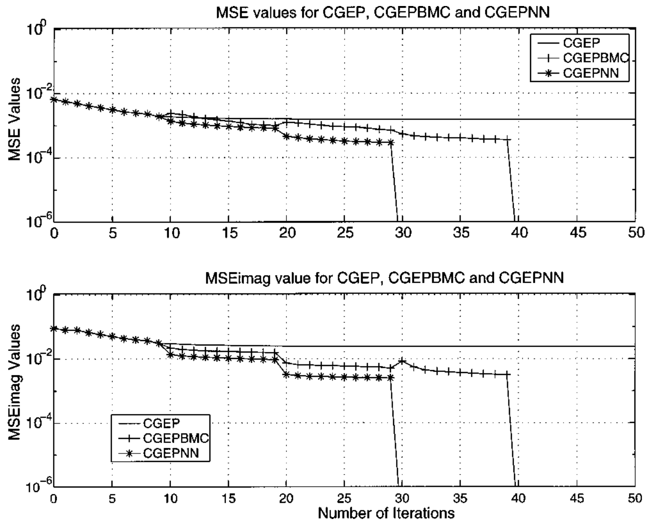

FIG. 9. MSE and ImMSE curves without noise.

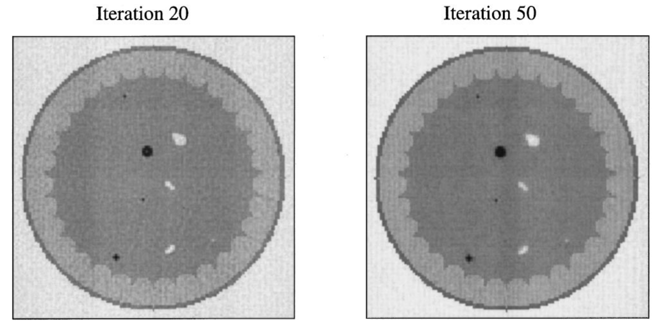

FIG. 10. Results for the CGEP method with noise.

CGEP method itself guarantees an eventual decrease in the error.

At the 40th iteration the RRE value for the CGEP–BMC method is 2.86×10^{-6}, and the RRE value for the CGEP–NN method at the 30th iteration is 1.85×10^{-6}. Both values are smaller than the predetermined criterion 10^{-5}. Thus the algorithms terminate.

Comparison of Figs. 5, 6, and 7 shows that the reconstructed images for the CGEP–BMC and CGEP–NN methods are more accurate than those of the CGEP method. Although both the CGEP–BMC and CGEP–NN methods correctly classify the object, the CGEP–NN method requires fewer iterations. For the noiseless case, the CGEP–BMC method requires 40% fewer iterations and the CGEP–NN method requires 55% fewer iterations than the CGEP method. Thus both the BMC and NN classifiers significantly reduce the number of iterations required and, hence, accelerate convergence.

Results for the CGEP–BMC and CGEP–NN methods are compared with those of the GN and GN–UMC methods reported in Ref. 9. Comparison of Figs. 6 and 7 with Fig. 4(b) in Ref. 9, which gives results for the GN–UMC method, shows that all three methods correctly classify the object, while the GN–UMC method takes the least number of iterations. In Table II we list the RRE, MSE, and ImMSE values after the final iteration of the CGEP, CGEP–BMC, CGEP–NN, GN, and GN–UMC methods. The RRE value for the CGEP method is an order of magnitude smaller than that of the GN method. Hence, reconstruction with the CGEP method is more accurate than with the GN method. In addition, the CGEP–BMC and CGEP–NN methods result in RRE values an order of magnitude smaller than that of the GN–UMC method.

B. Results with noise

Reconstruction results for the CGEP method with noise are shown in Fig. 10. Tumors and cysts are all detectable at both iterations 20 and 50. The reconstructed image at iteration 50 has smoother homogeneous regions than those at iteration 20. Figure 11 shows the reconstructed images at iterations 20 and 50 for the CGEP–BMC method. At iteration 20, notice that the minimal tumors and some pixels of the larger tumors are misclassified as glandular tissue, some cyst pixels are misclassified as glandular tissue, and some pixels are left unclassified. Some of the misclassified pixels are corrected at iteration 50. While all the tumors are correctly classified at iteration 50, the minimal cyst is still not. However, more pixels in the region of glandular tissue are left unclassified at iteration 20 than at iteration 50. Figure 12 shows the reconstruction images for the CGEP–NN method. Clearly all the tumors and cysts are correctly classified by both iterations 20 and 50. Also, there are more pixels left unclassified at iteration 20 than at iteration 50.

The RRE curves for the CGEP, CGEP–BMC, and CGEP–NN methods are shown in Fig. 13. Again we notice that the RRE values increase after classification has been applied. However, overall the RRE values decrease, although they decrease more slowly than those for the noiseless case. This is because the noisy case is more ill-posed. The CGEP–NN method results in a final value of RRE$=3.365\times10^{-4}$, and the CGEP–BMC results in RRE$=3.47\times10^{-4}$. Both are just slightly better than the final RRE value for the CGEP method RRE$=3.54\times10^{-4}$. The MSE and ImMSE curves for the CGEP, CGEP–BMC, and CGEP–NN methods are shown in Fig. 14. The values for the CGEP–NN method are smaller than for the CGEP and CGEP–BMC methods, indicating that reconstruction with the CGEP–NN is more accurate than with the CGEP–BMC method.

TABLE II. Error comparison for the CGEP, CGEP–BMC, CGEP–NN, GN, and GN–UMC methods without noise.

Error	CGEP	CGEP–BMC	CGEP–NN	GN	GN–UMC
RRE	4.527×10^{-5}	2.851×10^{-6}	1.858×10^{-6}	8.897×10^{-4}	1.914×10^{-5}
MSE	1.547×10^{-3}	0.0	0.0	1.726×10^{-3}	0.0
ImMSE	2.431×10^{-2}	0.0	0.0	1.726×10^{-2}	0.0

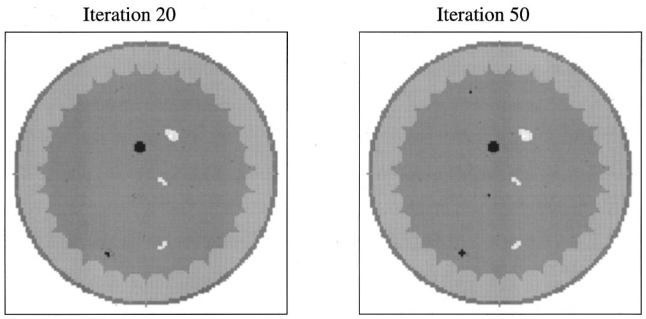

FIG. 11. Results for the CGEP–BMC method with noise.

Comparison of Figs. 11 and 12 with Fig. 7(b) in Ref. 9 shows that more pixels are misclassified with the GN–UMC method. The reconstructed images for the CGEP–BMC and CGEP–NN methods clearly have better visual contrast. The RRE, MSE, and ImMSE values for the last iteration of the CGEP, CGEP–BMC, and CGEP–NN methods and the best RRE, MSE, and ImMSE values for the GN and GN–UMC methods are listed in Table III. Although the RRE values for the CGEP–BMC and CGEP–NN methods are just slightly better than that of the GN–UMC method, the MSE values are an order of magnitude smaller than that of the GN–UMC method. This is also true for the ImMSE values. These results show that, as expected, the CGEP-based classification techniques are more robust to noise than the GN–UMC technique. With the CGEP method all error values decrease monotonically for both noiseless and noisy cases. However, when the GN method proposed in Ref. 9 is used for the noisy case, the ImMSE value at the ninth iteration is smaller than the value at the 20th iteration. The GN results diverge, while the CGEP results do not. The results shown are restricted to an SNR of 70 dB to facilitate comparison of the methods presented in this paper with the earlier GN–UMC method for which results are available only for 70 dB noise. In fact, it was found that the CGEP–NN method is able to detect tumors even at 40 dB.

C. Computational cost

The computational cost of the CGEP-based methods is dominated by the conjugate gradient iterations, which in turn are dominated by FFTs. The computational cost is $6N_{\mathrm{CGEP}}N_{\mathrm{fwd}}LN\log_2 N$, where N_{CGEP} is the product of the number of CG iterations and the number of edge preserving regularizations, N_{fwd} is the number of iterations for the forward solver, L is the number of sources, and N is the total number of cells into which the object is discretized. For a full-sized problem, N_{CGEP} is about 50 for an acceptable reconstruction and N_{fwd} is about 100. So the computational cost is $O(N^{5/2}\log_2 N)$. For the GN–UMC method, the computational cost is dominated by the GN method, whose computational cost as given in Ref. 8 is $4N_{\mathrm{GN}}(2N_{\mathrm{CG}}+N_{\mathrm{fwd}})LN\log_2 N)$ where N_{GN} is the number of Gauss–Newton iterations, N_{CG} is the number of conjugate gradient iterations used to approximate the inverse of the Jacobian matrix, and the other parameters are the same as for the CGEP method. L, N_{GN}, and N_{CG} grow as the edge dimension of the array, i.e., $N^{1/2}$.[8] Thus the cost for the GN method is $O(N^{5/2}\log_2 N)$ which is the same as that of the CGEP method.

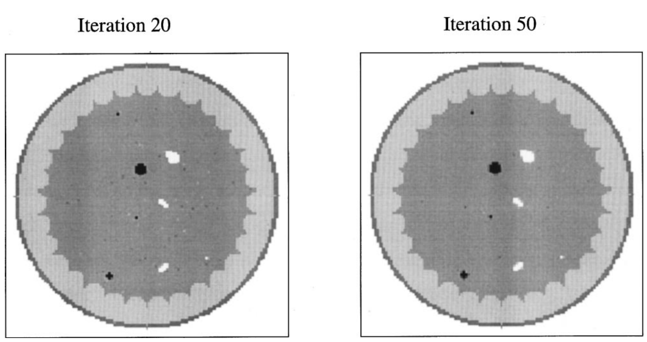

FIG. 12. Results for the CGEP–NN method with noise.

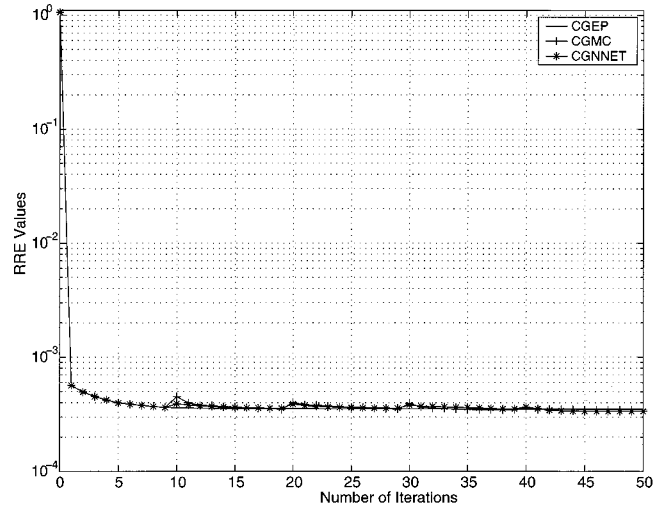

FIG. 13. RRE curves with noise.

VII. SUMMARY

In this paper, the CGEP method is used to solve the inverse problem for the detection of small breast tumors. The CGEP method is an iterative technique which is robust to noise but converges slowly. To accelerate convergence, a

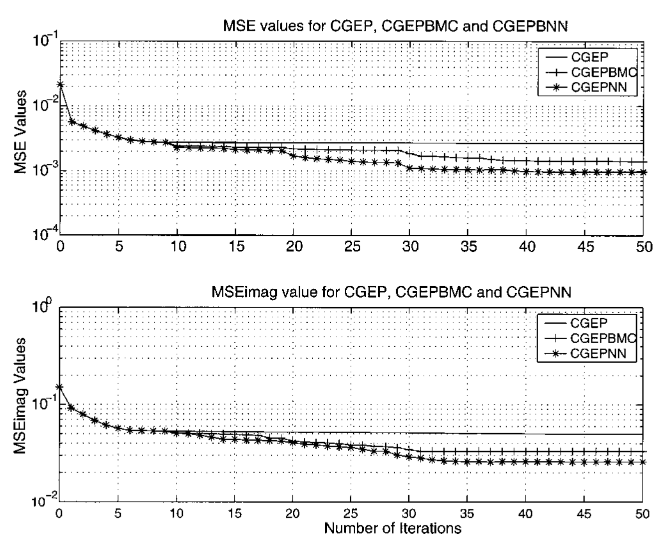

FIG. 14. MSE and ImMSE curves with noise.

TABLE III. Error comparison for the CGEP, CGEP–BMC, CGEP–NN, GN, and GN–UMC methods with noise.

Error	CGEP	CGEP–BMC	CGEP–NN	GN	GN–UMC
RRE	3.540×10^{-4}	3.470×10^{-4}	3.365×10^{-4}	3.593×10^{-4}	4.161×10^{-4}
MSE	2.702×10^{-3}	1.406×10^{-3}	9.707×10^{-4}	1.938×10^{-2}	1.920×10^{-2}
ImMSE	5.012×10^{-2}	3.302×10^{-2}	2.58×10^{-2}	0.1170	0.1008

new material classification technique is introduced as an extra step in the CGEP algorithm. The classifier, essentially a Bayesian classifier, is called bivariate material classification (BMC) since it simultaneously employs *a priori* knowledge of two breast tissue parameters, the sound speed and attenuation. The sound speed and attenuation for each type of tissue in the breast are assumed to be independently Gaussian distributed with known means but unknown variances. Histograms of the reconstructed images are used to estimate the variances and probability required by the classifier. A neural network (NN) classifier introduced in an earlier paper is used with the CGEP method as well. Both methods are used to reconstruct a full-sized, two-dimensional breast model for both noiseless and noisy cases. Numerical results show that the BMC and NN classifiers significantly reduce the number of iterations required for image reconstruction. In addition, the results are more accurate than that of the CGEP method without classification. For the noiseless case, the CGEP–NN method requires 55% fewer iterations and the CGEP–BMC method requires 40% fewer.

The CGEP-based methods are compared with each other as well as with the Gauss–Newton-based method (GN–UMC) proposed in Ref. 9. For the noiseless case, all three methods correctly classify the entire object. However, for the noisy case, the CGEP–BMC and CGEP–NN reconstructions are more accurate and yield smaller errors than those of the GN–UMC method. Thus the CGEP–BMC and the CGEP–NN methods are more robust to noise than the GN–UMC method. This is partly because information about both the sound speed and attenuation is used for classification in the CGEP–BMC and CGEP–NN methods, whereas only the attenuation is used for classification in the CN–UMC method. The CGEP-based methods do break down as the SNR is increased and start diverging at 60 dB, although the CGEP–NN method is still able to detect tumors even at 40 dB. The CGEP–BMC, CGEP–NN, and GN–UMC methods have comparable computational cost.

The CGEP–NN method gives slightly better results than the CGEP–BMC method. Differences between the two methods may be attributed to the fact that the neural network classifier is nonparametric, or distribution free, while the Bayesian classifier is parametric. For Bayesian classification to be correct, the accuracy of the distribution model is critical. However, the assumption that the sound speed and attenuation are independently Gaussian distributed is questionable. More time is required by the CGEP–BMC method than by the CGEP–NN method, although the CGEP–NN method requires a training state that can be time consuming. However, once the neural network architecture has been established, it can be re-used to perform classification.

ACKNOWLEDGMENTS

This work was supported by the National Science Foundation, Grant Nos. ECS-9711051 and EIA-9818212, and by the Carl M. Hansen Foundation.

[1] American Cancer Society, ‘‘Breast Cancer Facts and Figures—1997,’’ Atlanta, 1-800-ACS-2345, 1997.

[2] Q. Zhu and B. D. Steinberg, ‘‘Wavefront amplitude distribution in the female breast,’’ J. Acoust. Soc. Am. **96**, 1–9 (1994).

[3] R. J. Pauls and B. D. Steinberg, A refraction-based simulation to explore wavefront distortion in ultrasound mammography: Refraction-induced amplitude effects, Internal Report UP-14-92, Valley Forge Research Center, University of Pennsylvania, 1992.

[4] C. W. Manry and S. L. Broschat, ‘‘The FDTD method for ultrasound propagation through a two-dimensional model of the human breast,’’ J. Acoust. Soc. Am. **94**, 1774–1785 (1993).

[5] W. C. Chew, Y. M. Wang, G. Otto, D. Lesselier, and J. C. Bolomey, ‘‘On the inverse source method of solving scattering problems,’’ Inverse Probl. **10**, 547–553 (1994).

[6] W. C. Chew and Y. M. Wang, ‘‘Reconstruction of two-dimensional permittivity distribution using the distorted Born iterative method,’’ IEEE Trans. Med. Imaging **9**, 218–225 (1990).

[7] L. Liu, X. Zhang, and S. L. Broschat, ‘‘Ultrasound imaging using variations of the iterative Born technique,’’ IEEE Trans. Ultrason. Ferroelectr. Freq. Control **46**, 574–583 (1999).

[8] D. T. Borup, S. A. Johnson, W. W. Kim, and M.J. Berggren, ‘‘Nonperturbative diffraction tomography via Gaussian-Newton iteration applied to the scattering integral equation,’’ Ultrason. Imaging **14**, 69–85 (1992).

[9] C. W. Manry and S. L. Broschat, ‘‘Inverse imaging of the breast with a material classification technique,’’ J. Acoust. Soc. Am. **103**, 1538–1546 (1998).

[10] R. E. Kleinman and P. M. van den Berg, ‘‘A modified gradient method for two-dimensional problems in tomography,’’ J. Comput. Appl. Math. **42**, 17–35 (1992).

[11] A. Roger, ‘‘Newton-Kantorovitch algorithm applied to the electromagnetic inverse problem,’’ IEEE Trans. Antennas Propag. **29**, 232–238 (1981).

[12] A. Frenchois and C. Pichot, ‘‘Microwave imaging—complex permittivity reconstruction with a Levenberg-Marquardt method,’’ IEEE Trans. Antennas Propag. **45**, 203–215 (1997).

[13] N. Joachimowicz, C. Pichot, and J.-P. Hugonin, ‘‘Inverse scattering: An iterative numerical method for electromagnetic imaging,’’ IEEE Trans. Antennas Propag. **39**, 1742–1752 (1991).

[14] P. M. van den Berg, B. J. Kooij, and R. E. Kleinman, ‘‘Image reconstruction from Ipswich data—II,’’ IEEE Antennas Propag. Mag. **39**, 29–32 (1997).

[15] P. Lobel, R. Kleinman, C. Pichot, L. Blanc-Feraud, and M. Barlaud, ‘‘Conjugate gradient method for solving inverse scattering with experimental data,’’ IEEE Antennas Propag. Mag. **38**, 48–51 (1996).

[16] P. Lobel, L. Blanc-Feraud, C. Pichot, and M. Barlaud, ‘‘A new regularization scheme for inverse scattering,’’ Inverse Probl. **13**, 403–410 (1997).

[17] C. Pichot, P. Lobel, L. Blanc-Feraud, M. Barlaud, K. Belkebir, J. M. Elissalt, and J. M. Geffrin, ‘‘Gradient and Newton Kantorovich methods for microwave tomography,’’ in *Inverse Problems in Medical Imaging and Nondestructive Testing*, edited by H. W. Engl, A. Louis, and W. Rundell (Springer, New York, 1997), pp. 169–187.

[18] X. Zhang, S. L. Broschat, and P. J. Flynn, ‘‘A conjugate gradient-neutral network technique for ultrasound inverse imaging,’’ to appear in J. Comput. Acoust.

[19] H. A. van der Vost, ‘‘BI-CGSTAB: A fast and smoothly converging variant of BI-CG for the solution of nonsymmetric linear systems,’’ SIAM (Soc. Ind. Appl. Math.) J. Sci. Stat. Comput. **13**, 631–644 (1992).

[20] E. L. Madsen, J. A. Zagzebski, G. R. Frank, J. F. Greenleaf, and P.L. Carson, ''Anthropomorphic breast phantoms for assessing ultrasonic imaging performance and for training ultrasonographers: Part 2,'' J. Clin. Ultrasound **10**, 91–100 (1982).
[21] S. A. Johnson, F. Stegner, C. Wilcox, J. Ball, and M. J. Berggren, ''Wave equations and inverse solutions for soft tissue,'' Acoust. Imaging **11**, 409–424 (1982).
[22] A. Tikhonov, V. Arsenin, and F. John, *Solutions to Ill-Posed Problems* (Wiley, New York, 1997).
[23] R. F. Harrington, *Field Computation by Moment Methods* (MacMillan, New York, 1968).
[24] D. T. Borup and O. P. Gandhi, ''Calculation of high-resolution SAR distributions in biological bodies using the FFT algorithm and conjugate gradient method,'' IEEE Trans. Microwave Theory Tech. **33**, 417–419 (1985).
[25] X. Zhang, S. L. Broschat, and P. J. Flynn (unpublished).
[26] P. Charbonnier, L. Blanc-Feraud, G. Aubert, and M. Barlaud, ''Deterministic edge-preserving regularization in computed imaging,'' IEEE Trans. Image Process. **6**, 298–311 (1997).
[27] D. Geman and G. Reynolds, ''Constrained restoration and the recovery of discontinuity,'' IEEE Trans. Pattern Anal. Mach. Intell. **14**, 367–383 (1992).
[28] R. Gonzales and R. Woods, *Digital Image Processing* (Addison-Wesley, New York, 1992).

Variational method for estimating the effects of continuously varying lenses in HIFU, sonography, and sonography-based cross-correlation methods

Alex Alaniz[a)] and Faouzi Kallel
The University of Texas Medical School, Department of Radiology, Ultrasonics Laboratory, Houston, Texas 77030

Ed Hungerford
Department of Physics, University of Houston, Houston, Texas 77204

Jonathan Ophir
The University of Texas Medical School, Department of Radiology, Ultrasonics Laboratory, Houston, Texas 77030

(Received 28 April 2001; accepted for publication 7 October 2001)

The effects of high intensity focused ultrasound (HIFU)-induced continuously varying thermal gradients on sound ray propagation were modeled theoretically. This modeling was based on Fermat's variational principle of least time for rays propagating in a continuously varying thermal gradient described by a radially symmetric heat equation. Such thermal lenses dynamically affect HIFU beam focusing, and simultaneously create ultrasonic geometric and intensity distortions and artifacts in monitoring devices. Techniques which are based upon ultrasonic cross-correlation methods, such as elastography and two-dimensional temperature estimation, also suffer distortion effects and generate artifacts. [DOI: 10.1121/1.1424867]

PACS numbers: 43.80.Sh [FD]

I. INTRODUCTION

In the geometric limit, rays of sound are refracted when they traverse a boundary between two media with different speeds of sound. In sonography, refraction leads to a variety of geometric and intensity distortions, and to several artifacts (Ziomek, 1995).

In an attempt to predict the known distortions and artifacts created by spherical lenses, La Follette and Ziskin (1986) performed ray tracing simulations using simple trigonometric relations derived from Snell's law. In their work, simulated spherical lenses embedded in a uniform background medium were treated as regions with constant speed of sound V_1, while the uniform background medium was treated as a region with constant speed of sound V_2. Snell's law dictates that rays of sound which penetrate from a uniform region with a slower speed of sound V_2 into a lens with a faster speed of sound V_1, diverge. Conversely, Snell's law dictates that rays of sound which penetrate from a uniform region with a faster speed of sound V_2 into a lens with a slower speed of sound V_1, converge. Their computer simulations correctly predicted the known distortions and artifacts associated with fat or cystic, fluid-filled spherical lenses embedded in soft tissues. In this work we consider thermal lenses with continuously varying indices of refraction created by continuously varying temperature distributions.

The speed of sound in distilled water depends on the temperature of the water (Greenspan and Tschiegg, 1959). Between 0 °C and approximately 74 °C, the speed of sound of water rises from 1402.74 to 1555.47 m/s, and drops to 1543.41 m/s between approximately 74 °C and 100 °C. The approximate temperature 74 °C is an inflection point of the speed of sound in water as a function of temperature. Equation (1) in a following section describes the speed of sound of distilled water between 0 °C and 100 °C.

Given that the speed of sound in water depends on the temperature of the water, it follows that a continuously varying temperature distribution induced in a soft, water-based tissue by the attenuation of a high-intensity focused ultrasound (HIFU) beam due to absorption creates a continuously varying thermal lens within the soft, water-based tissue (Hynynen, 1997). In this discussion, the analysis of continuously varying thermal gradient lenses will be restricted to disks in the plane because (1) clinical two-dimensional ultrasound machines scan two-dimensional slices of three-dimensional volumes and (2) ellipsoidal, spherical, and cylindrical volumes may all be scanned across circular (disklike) cross sections (Fig. 1).

HIFU therapies conducted using Gaussian beam transducers produce approximately ellipsoidal, continuously varying thermal lenses (Wu and Nyborg, 1992; Hill *et al.*, 1994). Figure 1(a) depicts circular, disklike cross sections of an ellipsoid. Figure 1(a) applies to spheres as well since spheres are special cases of ellipsoids [Fig. 1(b)]. Continuously varying spherical lenses are included in this discussion as an extension of the work of La Follette and Ziskin (1986), which only considered spherical lenses with fixed indices of refraction. Figure 1(c) depicts circular, disklike cross sections of a cylinder. Cylindrical lenses may be generated in tissue phantoms using long, thin heating wires. Given the scanning nature of two-dimensional clinical ultrasound ma-

[a)]Electronic mail: akalaniz@hotmail.com; Post Doctoral Research Fellow, University of Houston, Department of Physics, 3211 Amerson Drive, Pearland, TX 77584.

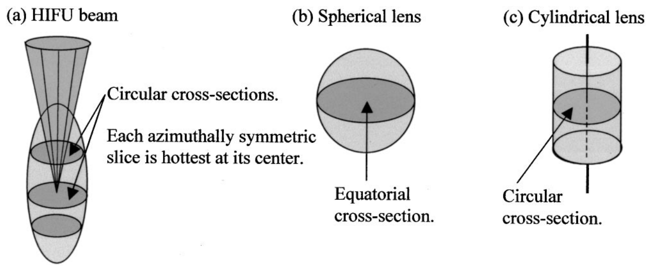

FIG. 1. Different sources of heat create different thermal gradients. (a) A Gaussian HIFU beam creates a Gaussian-shaped thermal lens. Cross sections orthogonal to the long axis of symmetry of the lens act as circular, radially decaying thermal lenses for two-dimensional scannings. (b) A spherical lens is created by a point source of heat located at the origin of the sphere. (c) A cylindrical lens is created in a gel phantom with a long, thin resistive heating wire.

chines, and the prevalence of ellipsoidal, spherical, and cylindrical lenses, it is natural to restrict this discussion to the optics of disks in the plane. This restriction also results in great mathematical simplifications as plane polar coordinates suffice to model the optics of the slices depicted in Figs. 1(a)–(c).

Given that spherical (or radial) lenses with constant indices of refraction create artifacts and distortions in sonography, it is expected that continuously varying radial lenses will also create artifacts and distortions (Le Floch and Fink, 1997). It follows, therefore, that continuously varying thermal lenses should create artifacts and distortions in all imaging modalities rooted in sonography, e.g., ultrasonic temperature mapping (Le Floch and Fink, 1997; Maas-Moreno and Damianou, 1996; Simon and Ebini, 1998) and elastography [a strain estimation modality (Ophir *et al.*, 1991)]. For example, as discussed in the next section, in the two-dimensional echo-shift temperature estimation method, the so-called ripple artifact reported by Simon *et al.* (1997) may be explained by the refraction of the ultrasound imaging rays by a HIFU-induced thermal lens. In elastography, which assumes a constant speed of sound, weak refraction leads to distortions of strain estimations, and strong refraction may cause decorrelation by causing rays from distinct A-lines to intersect, an effect which will be demonstrated in the following section.

II. A SIMPLE REFRACTION EXPERIMENT

Figure 2 summarizes results obtained from a heating experiment using a thin resistive Nichrome wire (32 AWG) as a heat source inside a gel/agar based phantom. The thin resistive Nichrome wire was inserted into a phantom made of a mixture of 225 Bloom gelatin (Kind & Knox, Inc., Sioux City, IA) and agar (Sigma®, St. Louis, MO). The agar was used to elicit acoustical scattering. Both ends of the wire were connected to a power supply. A dc current of 0.9 A was applied to the wire for a period of 4 min. This resulted in a delivered power to the wire of 3.4 W (the resistance of the 12 cm Nichrome wire was 4.15 ohms). The phantom was then allowed to cool down during 4 min. Radio frequency (rf) images from a plane perpendicular to the wire were acquired at intervals of 10 s. The rf images were acquired using a modified real-time linear array scanner (Diasonics Spectra II, Santa Clara, CA) that operates with dynamic receive focusing and a single transmit focal zone centered around 30 mm, a center frequency of 5 MHz, and a 40-mm field of view. The acquired images were then transferred to a desktop PC for off-line post-processing. Additional details about the experimental setup are presented in Kallel *et al.* (1999). Figure 2(a) shows the axial echo-shift resulting from the increased speed of sound due to the increased temperature around the wire. The axial component of the gradient of the echo-shift mapping shows the heated area as a bright circular area in Fig. 2(b). Figure 2(c) shows the lateral displacement component of the echo shift that resulted from the refraction of the ul-

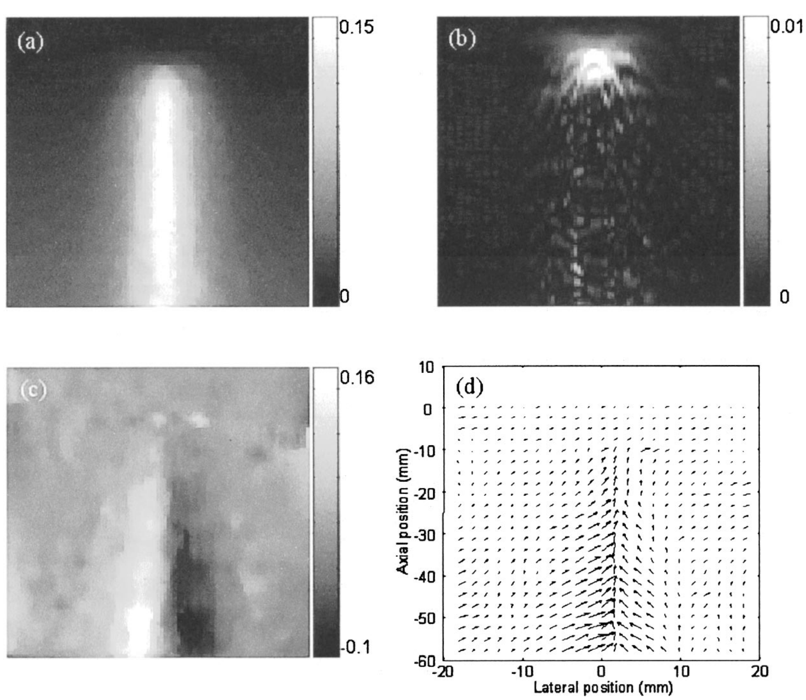

FIG. 2. Illustration of temperature-induced two-dimensional echo shift during a heating experiment. (a) Two-dimensional axial echo-shift. (b) Axial component of the gradient of the axial two-dimensional echo-shift map. (c) Two-dimensional lateral echo-shift. (d) Vector field of the two-dimensional echo-shift. The horizontal axis of the images (a)–(c) represents the lateral position in the phantom and the vertical axis represents the depth (axial position) in the phantom.

trasonic imaging beam by the thermal acoustic lens around the hot wire. The two-dimensional distribution of the lateral echo-shift was estimated using the technique proposed by Konofagou and Ophir (1998). Figure 2(d) illustrates the vector field of the two-dimensional echo shifts.

As shown in Fig. 2(b), there is a band of noise similar to the ripple noise reported by Simon *et al.* (1997) immediately behind the heated area around the wire. We believe that this noise is due to an apparent lateral echo-shift behind the heated area, which in turn was due to the refraction of the ultrasonic imaging beam. As can be seen, the lateral shift increases axially and laterally immediately behind the heated area. It increases with depth and reaches its highest value at the axis of symmetry of the heated area. As can be seen, the lateral displacement is even larger than the axial echo-shift particularly as the depth increases.

The ripple noise is explained by an increased decorrelation due to the use of the 1D axial displacement estimator method in the case of existing apparent lateral echo-shift across the imaging ultrasonic beam. Similar noise was reported in elastographic imaging (Kallel and Ophir, 1997; Kallel *et al.*, 1997). The lateral tissue displacement resulting from the applied axial compression resulted in a nonstationary decrease of the elastographic SNR. Konofagou and Ophir (1998) proposed an iterative correction for the effect of lateral tissue displacement on the elastogram. A similar technique can also be applied in order to reduce the ripple noise in the two-dimensional map of the heated area obtained using the echo-shift technique. Note that the heat-induced speed of sound mismatch may also cause refraction of the HIFU beam, which in turn may cause the focus of the HIFU beam to split into two small adjacent foci in the scanning plane. This was observed, but not reported, on many occasions during magnetic resonance imaging (MRI)-guided HIFU heating of canine livers (Righetti *et al.*, 1999). In the following two sections the refraction from acoustical thermal lenses is modeled theoretically and simulated numerically.

III. THEORY

A. Preliminary assumptions

As a first-order approximation, we shall consider the temperature-dependent speed of sound in simulated tissues or gel phantoms to be the same as the speed of sound in distilled water between 0 °C and 100 °C as determined by Greenspan and Tschiegg in 1959. That is, between 0 °C and 100 °C, we take the speed of sound to be given by

$$\begin{aligned} c(T(r)) = {} & 1402.736 + 5.033\,58\,T(r) - 0.057\,950\,6\,T^2(r) \\ & + 3.316\,36 \times 10^{-4} T^3(r) - 1.452\,62 \\ & \times 10^{-6} T^4(r) + 3.0449 \times 10^{-9} T^5(r). \end{aligned} \tag{1}$$

Equation (1) is not rounded for the sake of completeness. The precision expressed by it is likely far greater than can be expected for the speeds of sound in tissues or gel phantoms as a function of temperature.

B. The cylindrical lens

Figure 1(c) depicts a long, thin wire embedded in a gel phantom. The temperature distribution generated by the wire is azimuthally symmetric with respect to the wire. The temperature distribution for a given circular cross section of an azimuthally symmetric thermo-acoustic lens centered around the wire is given by the following two-dimensional Green's function in cylindrical coordinates:

$$T(r(t)) = T_l - \frac{Pt}{2\pi k_g l_w} \log\left(\frac{r}{r_w}\right). \tag{2}$$

The variable P is the ohmic heating power loss of the wire, t is a fixed time, l_w is the length of the long, thin wire, r_w is the radius of the wire, and T_I is the interface temperature between the wire and the phantom. The temperature decreases with increasing radius. At a sufficiently large radius r_b, the temperature returns to the unperturbed temperature of the simulated phantom, which we assume is large enough to act as a heat sink. Equation (2) substituted into Eq. (1) describes a cylindrical thermo-acoustic lens.

C. The spherical lens

The description of equatorial slices of spherical thermo-acoustic lenses, as shown in Fig. 1(b), are included in this section as a natural extension of the work of La Follette and Ziskin (1986) which involved only spherical lenses with constant indices of refraction. The temperature distribution generated by a point source of heat is spherically symmetric about the point source of heat, and is given by the following three-dimensional Green's function:

$$T(r(t)) = T_o + \frac{Q(t)}{4\pi k_g}\left[\frac{1}{r} - \frac{1}{r_b}\right], \tag{3}$$

where T_o is the physiological background temperature of the simulated phantom, $Q(t)$ is the heat energy deposited by the HIFU beam at time t, k_g is the thermal conductivity of the heated tissue, and r_b is the radius at which the temperature drops back to T_o. We assume the body is large enough to act as a heat sink. Equation (3) substituted into Eq. (1) describes an equatorial slice of a spherical thermo-acoustic lens.

D. Fermat's principle of least time

All rays of sound propagate along curvilinear paths which obey Fermat's principle of least time. Snell's law, in fact, is a special case of Fermat's principle of least time. Clearly, given the symmetries of the thermo-acoustic lenses described in this article, the best choice of coordinates for modeling sound ray trajectories are plane polar coordinates. Fermat's principle of least time expressed in polar coordinates states that rays of sound travel according to functions $\theta(r)$, which minimizes the integral

$$J = \int_{r_i}^{r_f} \frac{1}{c(T(r))} \sqrt{1 + r^2\left(\frac{d\theta(r)}{dr}\right)^2}\, dr = \int_{r_i}^{r_f} L(\theta, r)\, dr, \tag{4}$$

where $\theta(r)$ is the incident angle and $\theta(r+dr)$ is the refracted angle.

Note that the integral equation for J is expressed in terms of distance over speed, or time, and that $c(r)$ depends on a radial function such as given by Eq. (2) or (3) for $T(r)$. In order for J to be minimized, Eq. (4) must satisfy the Euler–Lagrange differential equation (Sagan, 1969). If $L(\theta;r)$ is the integrand of J, the Euler–Lagrange (ray tracing) equation is

$$\frac{d}{dr}\frac{\partial L}{\partial(d\theta/dr)}-\frac{dL}{\partial\theta}=0. \tag{5}$$

Application of Eq. (5) to the integrand of Eq. (4) yields

$$\frac{d\theta(r)}{dr}=\frac{Mc(T(r))}{r\sqrt{r^2-M^2c^2(T(r))}}, \tag{6}$$

where M is a constant of integration specified by the initial conditions of a ray according to

$$M=\frac{(d\theta/dr)_{t_o}r_o^2}{c(T(r_o))\sqrt{1+(d\theta/dr)_{t_o}r_o^2}}. \tag{7}$$

The variable r_o is the initial radius, usually taken to be r_b, $c(T(r))$ is the initial speed of sound, and $(d\theta/dr)t_o$ is the initial angle θ with respect to r. Unfortunately, beyond the simplest radial functions, e.g., $c(r)=Ar+B$, there are few closed-form solutions to Eq. (6) (Ziomek, 1995). In general, therefore, ray tracing usually requires numerical integration.

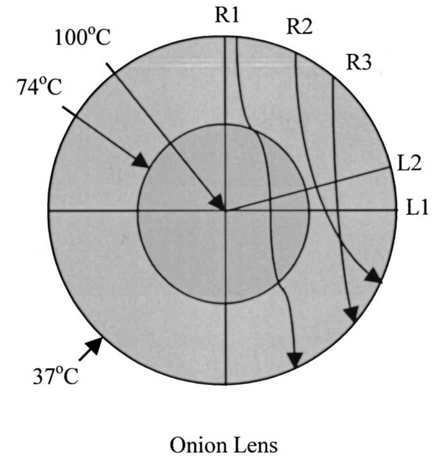

FIG. 3. An equatorial slice of a continuously warming spherical thermo-acoustic lens obeying Eq. (1) is depicted. Rays R1, R2, and R3 demonstrate the onion nature of the lens with the given temperature distribution which warms from 37 °C at its edge to 100 °C at its center. Ray R2 penetrates into increasingly warmer regions with increasingly faster speeds of sound. It diverges away from the origin of the lens until it reaches its point of closest approach to the origin, namely, at its intersection with line L2. The remainder of its trajectory is a reflection about line L2. Note that ray R3, having initiated its inbound path in a cooler region than ray R2, diverges less. Hence, rays R2 and R3 will intersect at some point. Ray R1 diverges from the center of the lens until it penetrates regions increasingly warmer than 74 °C, whereupon it begins converging towards the center of the lens. Its point of closest approach is line L1. The outbound trajectory of ray R1 becomes a reflection about line L1 with an exchange in handedness from right handed to left handed.

IV. SIMULATION OF A THERMO-ACOUSTIC SPHERICAL LENS

A. Rates of change

It is very important to note that while HIFU therapies last on the order of a few seconds to several tens of seconds, the time of flight of a ray of sound in a typical clinical ultrasound application is on the order of tenths of milliseconds. During 1 s, a ray of sound may travel as many as 1500 m, implying a speed of 1500 m/s. During 1 s, the linear dimensions of a surface of constant temperature (an isotherm) of a thermal lens may change on the order of 1 mm, implying a speed of 1 mm/s. Given this large disparity in speeds, the state of the temperature distribution of a *slowly* evolving thermal lens during the *brief* lifetime of a ray of sound may be considered to be nearly frozen in time. Thus, during the time of flight of a simulated ray of sound, we may approximate $T(r(t))$ by $T(r)$. Clearly, thermal lenses change shape as time runs from t to $t+dt$. The simulation must be done by snapshots.

B. Initial conditions

Consider the propagation of individual rays by numerical integration of Eq. (6). Initial conditions are required for each ray. The initial conditions for each ray may be chosen arbitrarily, but clinical ultrasound and HIFU beams are usually highly focused. To simulate focused clinical ultrasound or HIFU beams, thus, requires that the initial conditions for each ray be chosen such that they converge in some region as they propagate into the medium. In the simulation presented in this article, however, the initial conditions for individually simulated rays were chosen so that the rays commenced propagating in parallel. This choice allows the reader to see how initially parallel rays subsequently undergo differing extents of curvilinear warping as they propagate through regions of differing thermal gradients.

C. Onion lenses

As the temperature rises at the origin of a thermo-acoustic spherical lens from T_o up to 74 °C (the inflection point for the speed of distilled water as function of temperature), the speed of sound in water at the origin, as well as in the growing sphere of warming water, rises. This causes inbound rays heading towards the neighborhood of the origin of the thermal lens to diverge away from the center of the lens. If, after a while, the temperature of the water in the surrounding neighborhood of the origin of the lens exceeds 74 °C, the thermal lens becomes onionlike. It will have an inner shell with temperature $T_{\max}>74$ °C at $r=0$ dropping to just above 74 °C at some r_1, and an outer shell with temperature just below 74 °C at r_1+dr dropping to some cooler T_{biology} at some $r_2=r_b$. As before, rays initially inbound towards a neighborhood of the origin will diverge away from the origin between r_2 and r_1. However, any rays which are not sufficiently diverted away from regions warmer than 74 °C will begin to converge towards the origin between r_1 and $r\approx 0$ (Fig. 3). Outbound rays refract oppositely than inbound rays. The actual curved paths which individual rays follow within the continuously varying thermal lens depend on their initial conditions as given by (r_i,θ_i).

D. Summary

Note that for an inbound ray penetrating a continuously varying radial thermal lens, there will be a point of closest approach to the center of the lens (Fig. 3, rays R2 and R3). At the point of closest approach, the radical in Eq. (6) equals zero. These facts cut the amount of computation by half, as there is a mirror symmetry along the line from the origin of the spherical thermal lens to the point of closest approach. The numerical integration for an individual ray, thus, need only be performed up to its point of closest approach. The remainder of the trajectory follows directly by reflection about the axis of symmetry. Similar properties apply to rays which penetrate a core warmer than 74 °C. However, chirality is exchanged (Fig. 3, ray R1) at the point of closest approach.

E. A simulation of a spherical lens

Equation (3) substituted into Eq. (1) was used to model a continuously varying spherical thermo-acoustic lens for the simulation presented in this section. The value for $Q(t)$ was arbitrarily set to 1 J with t arbitrarily set to 2 s. The value of r_b at which the temperature cools back down to the initial temperature was arbitrarily chosen to be 1 cm. The arbitrary values were chosen to approximate values typical of HIFU surgeries involving focal intensities ranging from 750 to 1565 $\mathrm{W\,cm^{-2}}$ for periods of 8 to 20 s (Righetti *et al.*, 1999). For example, $(1500\ \mathrm{W\,cm^{-2}})\ (\pi\times(0.01\,\mathrm{m})^2)(2\,\mathrm{s})=0.94\,\mathrm{J}$. The thermal conductivity of water was taken to be $k_g=0.68\,\mathrm{W\,m^{-1}\,K^{-1}}$ at 370 K.

For the values given above, the outer shell of the onion lens runs between $r=1$ cm (at the biological temperature $T_o=37$ °C) and $r=0.240$ cm (at 74 °C). For the inner core of the lens, note that Eq. (3) diverges to infinity as r tends to 0. The temperature reaches 100 °C at $r=0.156$ cm. Since the temperature clearly does not reach infinity at $r=0$ cm, an artificial choice was made to let the temperature rise linearly from 100 °C at $r=0.156$ cm to 110 °C at $r=0$ cm. The speed of sound as a function of temperature was extrapolated to its value at 110 °C using Eq. (1).

The initial conditions for five inbound parallel rays starting at r_b were chosen to be $\theta_1=54.97°$, $\theta_2=62.66°$, $\theta_3=69.85°$, $\theta_4=76.73°$, and $\theta_5=83.41°$, respectively (Fig. 4). These angles correspond to $M_1=2.5\times10^{-6}$, $M_2=2.0\times10^{-6}$, $M_3=1.5\times10^{-6}$, $M_4=1.0\times10^{-6}$, and $M_5=0.5\times10^{-6}$, respectively. The initial angle values were derived by first solving for $(d\theta/dr)t_o$ in Eq. (7), and then for d in Eq. (8):

$$\left(\frac{d\theta}{dr}\right)_{t_o}=\frac{d}{r_b^2\sqrt{1-d^2/r_b^2}}, \tag{8}$$

where d is the adjacent side of a triangle and r_b its hypotenuse. The inverse cosine of each d value generated a θ_o value.

A step size of $\Delta r=1\times10^{-6}$ m was chosen. The precision implied by the values in this simulation were for the sake of the numerical quadrature. Any less precision would have resulted in no discernable physical effects. The value of

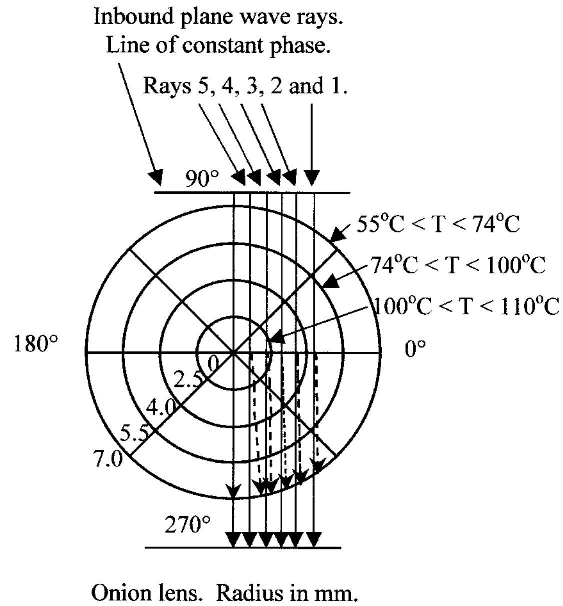

FIG. 4. In the absence of a thermal gradient, the rays of a plane wave (solid lines) propagate without distortion. In the presence of an onion lens, rays refract as depicted in Fig. 3. Quadrant 4 projects the refracted rays with the same initial conditions beside the unrefracted rays. The angular deviations (slightly exaggerated) are subtle. The effects, however, on cross-correlation techniques are much less subtle.

Δr necessary to propagate Eq. (6) is best computed using the measured echo time of the radial ray defined by the $\theta=90°$ radial in Fig. 4. As is evident from the echo shifts of Fig. 2(d) along the y-axis (or the $\theta=90°$ radial), the gradient of the lens $c(T(r))$ sampled by the $\theta=90°$ radial up to the center of the lens $c(T(0))$ is greater than for any other inbound ray in Fig. 4. As a consequence, the measured echo time, $e_{1,2}=2\Delta t_{r1=0,r2=rb}$, of the radial ray defined by the $\theta=90°$ radial undergoes the most reduction relative to its echo time prior to the heating process than any other nonradial inbound ray. In turn, this implies that the difference between the theoretical echo time for the radial ray defined by the $\theta=90°$ radial, namely, $e'_{1,2}=2J\ (r_1=0,r_2=r_b)$, and its measured echo time will be larger than for any other inbound ray for a given size of Δr. To calibrate Eq. (6) for a given maximum desired error, ε, the step size Δr must be less than or equal to the largest value of Δr such that $0\leqslant|e_{1,2}-e'_{1,2}|\leqslant\varepsilon$. For all inbound rays other than the radial ray defined by the $\theta=90°$ radial, the chosen step size $\Delta r_{\max}$ for the $\theta=90°$ radial makes the above inequality a strict equality. Note that for the radial ray defined by the $\theta=90°$ radial, $d\theta/dr=0$ in Eqs. (4), (6), and (7), which greatly simplifies the calculation of $e'_{1,2}$ when calibrating the value of $\Delta r_{\max}$.

The solid rays in Fig. 4 represent superimposed unperturbed inbound rays of sound. The dashed rays depicted in the figure represent numerically propagated inbound rays which began their inbound approach from $r_b=1$ cm at 37 °C. For the sake of amplifying the subtle refraction effects, only the portion of the lens extending to 0.7 cm is shown. The angular distortion effects are subtle on the scale shown. The effects on cross-correlation-based techniques which make differential comparisons are less subtle.

Inbound rays that do not penetrate the inner core of the

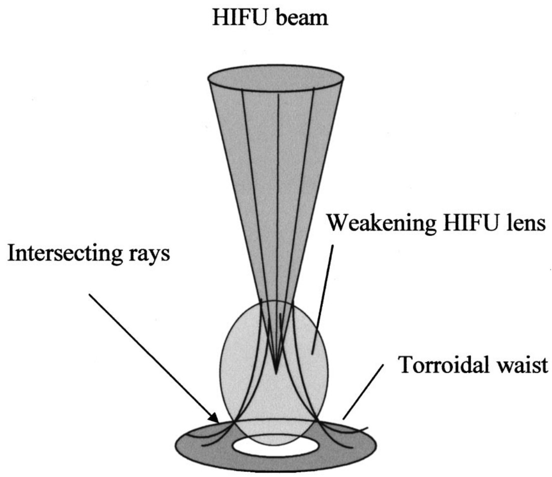

FIG. 5. Exaggerated HIFU beam splitting. Rays passing nearer the center of the lens diverge more than rays passing further from the center of the lens. This leads to intersection of rays in a torroidal waist region beyond the radially weakening spherical lens. The point of closest approach of an ''inner'' inbound ray occurs at a higher angle than for an ''outer'' inbound ray.

onion lens diverge until they reach their point of closest approach to the center of the lens. The further the point of closest approach is to the center of the lens for a given ray, the less is its divergence as it samples a smaller thermal gradient. This leads to the intersection of ''closer'' rays which diverge more with ''further'' rays which diverge less (Figs. 3 and 4). The dashed rays depicted in the fourth quadrant show such outbound convergence.

Inbound rays that penetrate the inner core will stop diverging and begin to converge as the speed of sound drops with decreasing radius. After such rays reach their points of closest approach to the center of the lens, their outbound paths become reflections of their inbound paths about the line passing through the center of the lens to the point of closest approach with an additional exchange between left-handedness and right-handedness. See ray R1 in Fig. 3.

V. EFFECTS AND DISTORTIONS

A. HIFU beam splitting

In Fig. 4, though it is subtle, there is a noticeable pinching effect acting on some of the propagated rays. Somewhere not far beyond the lens, it is clear that several of the rays will intersect. Since there is spherical symmetry, there will actually be a surface of revolution where rays intersect. This distributed region of intersecting rays is termed an optical waist, and is depicted in an exaggerated fashion in Fig. 5. The nearer the temperature of the target point gets to 74 °C, the greater will be the speed of sound, and thus the greater will be the ''diverging power'' of the thermal lens on inbound rays. ''Inner'' inbound rays beginning from nearer the longitudinal axis of a HIFU beam will be exposed to higher temperature gradients, and hence undergo more refraction than ''outer'' inbound rays further from the longitudinal axis of the HIFU beam. Thus the HIFU beam will eventually cause its own splitting/defocusing process resulting in the intersection of ''inner'' inbound rays with ''outer'' inbound rays in a toroidal waist region beyond the center of the spherical lens [observed but not reported in the work of Righetti *et al.* (1999)]. Clearly, the HIFU beam optics problem is a nonlinear, self-interacting problem.

B. Sonographic effects of continuous refraction

In sonography the speed of sound is assumed to be fixed, and all sound rays are assumed to propagate along rectilinear lines. Thermal lenses alter the speed of sound and lead to refraction. Refraction in turn distorts the paths of rectilinear rays into curved rays. The effects of a diverging thermal lens on sonography may be simulated by propagating rays from a simulated two-dimensional scan focused in the region of the thermal lens as in Fig. 1(a). When scanning across a thermal lens, the A-line rays will undergo the same splitting and collection into an optical waist as will the HIFU beam rays discussed in the section above. Clearly, the intersection of rays destroys the uniqueness properties of the ray tracing solutions. Intersections, moreover, will lead to interference/intensity effects. Phase and intensity information for each ray may be updated with each increment in Δr by keeping the wavelength λ fixed such that $c_{\text{local}} = f\lambda$.

C. Effects of continuous refraction on elastography

In elastography, local echo shifts (and therefore local tissue strains) are estimated from differential ultrasonic tissue displacements by echo shift cross-correlation methods (Ophir *et al.*, 1996). Since the speed of sound is assumed to be constant in elastography, any length distortions due to the refractive effects of thermal lenses will distort strain estimates. Length distortions, which would be considered negligible in sonography, are easily detected by the echo shift cross-correlation strain estimation methods used in elastography. Moreover, any intersection of rays from adjacent A-line elements will cause echo shift decorrelation even when ignoring other nonrefractive effects such as thermal expansion and swelling, and any protein denaturation which may irreversibly change the modulus of heat treated tissues (Alaniz, 2001; Chen and Humphrey, 1998).

D. Effects of continuous refraction on two-dimensional temperature estimation

In two-dimensional echo shift temperature estimation methods, heating and thermal expansion, rather than differential tissue displacements, result in echo shifts. The magnitudes of the estimated echo shifts, however, are generated with the same cross-correlation techniques used in elastography. In the temperature estimation method, however, estimated echo shifts, which are combinations of virtual axial strains due to variations in $c(T)$ and actual thermal axial strains, are used to make temperature estimations (Le Floch and Fink, 1997) rather than strain estimations. Thus the same artifacts and distortions which arise in elastography also arise in two-dimensional echo shift temperature estimation methods, and conversely, e.g., the so-called ripple artifact reported in the temperature estimation work of Simon *et al.* (1997), and in the elastography work of Kallel *et al.* (1999) (Fig. 2). According to Simon *et al.* (1997), sharp temperature gradients, corresponding to regions with sharp variations in the speed of sound, lead to the ripple (decorrelation) effect as the (length) distortions of the sound rays will be large.

VI. CONCLUDING REMARKS

Studies of the distortions and artifacts created by continuously varying thermal lenses in HIFU, clinical ultrasound, and clinical ultrasound-based cross-correlation techniques can be performed using Fermat's principle of least time. Continuously varying thermal lenses, such as those created by HIFU beams, distort rectilinear rays assumed in sonography into curved rays. Equation (6) is the ray tracing equation for circular cross sections of various types of thermal lenses. It may be used to propagate bundles of A-line and/or HIFU rays through thermal lenses with circular cross-sections. Hence, for a given level of acceptable error ε, Eq. (6) is useful for studying the effects of refraction on ultrasonic based cross-correlation monitoring of temperatures and strains caused by HIFU beams, as well as for modeling the nonlinear self-effects of the source HIFU beams upon themselves.

Before the defective lens of the Hubble Space Telescope was physically repaired, corrections to the optics of the known defective lens were performed mathematically on the light that was captured by the scientific instruments. In much the same way, it is possible to improve the imaging of clinical ultrasound machines used for HIFU monitoring given an equation for the speed of sound in a target tissue as a function of temperature. The same may be said for the dynamic problem of HIFU beam focusing. To do active optical corrections during a HIFU procedure, either the spatially and temporally varying temperature field, which defines the thermo-acoustic lens, must be assumed *a priori*, or it must be measured dynamically by some means, say, for example, by MRI. For ultrasound and ultrasound based cross-correlation techniques, an equation such as Eq. (1) could then be used to estimate the deviations in the echo times of individual rays. This would allow the transmit and receive delays of individual channels of an array to be adjusted accordingly. The same method applies, in principle, to HIFU transducers based on array technology.

Lastly, an extension of the work presented in this paper should include the effects of refraction on interference and intensity. Such an extension would complete the work of La Follette and Ziskin (1986).

ACKNOWLEDGMENTS

This work was supported in part by Program Project Grant No. P01-CA64597-07 from the National Cancer Institute to the University of Texas Houston Health Science Center.

Alaniz, A. (**2001**). ''Study of blended agar and gelatin gel phantoms for elastography by application of statistical mechanics and thermodynamics to dynamic stress-strain, X-Ray, and NMR data,'' Ph.D. dissertation, University of Houston, Houston, TX, pp. 2–6.

Chen, S. S., and Humphrey, J. D. (**1998**). ''Heat-induced changes in the mechanics of a collagenous tissue: pseudoelastic behavior at 37 °C,'' J. Biomech. **31**, 211–216.

Greenspan, M., and Tschiegg, C. E. (**1959**). ''Tables of the speed of sound in water,'' J. Acoust. Soc. Am. **31**, 75–81.

Hill, C. R., Rivens, I., Vaughan, M. G., and ter Haar, G. R. (**1994**). ''Lesion development in focused ultrasound surgery: a general model,'' Ultrasound Med. Biol. **20**(3), 259–269.

Hynynen, K. (**1997**). ''Review of ultrasound therapy,'' IEEE Ultrason. Symp., pp. 1305–1313.

Kallel, F., and Ophir, J. (**1997**). ''Three dimensional tissue motion and its effect on image noise in elastography,'' IEEE Trans. Ultrason. Ferroelectr. Freq. Control **44**, 1286–1296.

Kallel, F., Varghese, T., Ophir, J., and Bilgen, M. (**1997**). ''Non stationary strain filter: lateral and elevational decorrelation,'' Ultrasound Med. Biol. **23**, 1357–1369.

Kallel, F., Khirasaki, K., Alaniz, A., and Ophir, J. (**1999**). ''Monitoring low-power heat deposition with elastography,'' IEEE Ultrason. Symp.

Konofagou, E. E., and Ophir, J. (**1998**). ''A new elastographic method for estimation and imaging of lateral displacements, lateral strains, corrected axial strains and Poisson's ratios in tissues,'' Ultrasound Med. Biol. **24**(8), 1183–1199.

La Follette, P. S., and Ziskin, M. C. (**1986**). ''Geometric and intensity distortions in echography,'' Ultrasound Med. Biol. **12**(12), 953–963.

Le Floch, C., and Fink, M. (**1997**). ''Ultrasonic mapping of temperature in hyperthermia: the thermal lens effect,'' IEEE Ultrason. Symp., pp. 1301–1304.

Maas-Moreno, R., and Damianou, C. A. (**1996**). ''Echo-shifts. Part I. Analytical model,'' J. Acoust. Soc. Am. **100**, 2514–2521.

Ophir, J., Cespedes, E. I., Ponnekanti, H., Yazdi, Y., and Li, X. (**1991**). ''Elastography: a quantitative method for imaging the elasticity of biological tissues,'' Ultrason. Imaging **13**, 111–134.

Ophir, J., Cespedes, E. I., Garra, B. S., Ponnekanti, H., Huang, Y., and Maklad, N. (**1996**). ''Elastography: ultrasonic imaging of tissue strain and elastic modulus *in vivo*,'' Eur. J. Ultrasound **3**, 49–70.

Righetti, R., Kallel, F., Stafford, R. J., Price, R. E., Krouskop, T. A., Hazle, J. D., and Ophir, J. (**1999**). ''Elastographic characterization of HIFU-induced lesions in canine livers,'' Ultrasound Med. Biol. **25**(7), 1099–1113.

Sagan, H. (**1969**). *Introduction to the Calculus of Variations* (Dover, New York), pp. 52–53.

Simon, C., and Ebbini, E. S. (**1998**). ''Two-dimensional temperature estimation using diagnostic ultrasound,'' IEEE Trans. Ultrason. Ferroelectr. Freq. Control **45**(4), 1088–1099.

Simon, C., VanBaren P., and Ebbini, E. (**1997**). ''Quantitative analysis and applications of non-invasive temperature estimation using diagnostic ultrasound,'' IEEE Ultrason. Symp., pp. 1319–1322.

Wu, J., and Nyborg, W. L. (**1992**). ''Temperature rise generated by a focused Gaussian beam in a two-layer medium,'' Ultrasound Med. Biol. **18**(13), 293–302.

Ziomek, L. J. (**1995**). *Fundamentals of Acoustic Field Theory and Space-time Signal Processing* (CRC, Boca Raton), pp. 631–642.

Erratum: “Transforming echoes into pseudo-action potentials for classifying plants” [J. Acoust. Soc. Am. 110, 2198–2206 (2001)]

Roman Kuc
Department of Electrical Engineering, Yale University, New Haven, Connecticut 06520-8254

(Received 18 October 2001; accepted for publication 24 October 2001)

[DOI: 10.1121/1.1428553]

PACS numbers: 43.80.Ka, 43.64.Bt, 43.10.Vx [WA]

Figures 3(a), 4(a), 5(a), and 6(a) did not appear correctly. The images are presented correctly here.

FIG. 3. (a) Sycamore trunk.

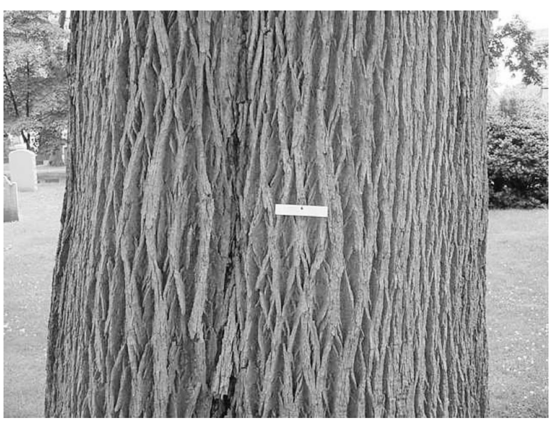

FIG. 4. (a) Norway maple.

FIG. 5. (a) Rhododendron.

FIG. 6. (a) Yew.

Sonic Boom Symposium

FOREWORD

The papers in this special collection primarily represent the work of individuals contributing to the Acoustical Society of America Sonic Boom Symposium held at the ASA's 136th meeting, Norfolk, VA, 15–16 October 1998. Similar to the 1965 and 1970 ASA Sonic Boom Symposia,[1,2] the purpose of the 1998 meeting was to provide a forum for government, industry, and university participants to present and discuss the current state of the art in sonic boom technology issues as well as new research results. The Symposium was cosponsored by the ASA's Physical Acoustics, Noise, and Animal Bioacoustics Technical Committees and consisted of three special sessions at the Norfolk meeting. Many invited authors had participated in earlier workshops on sonic boom sponsored by the National Aeronautics and Space Administration.[3–7] Symposium participants were strongly encouraged to submit manuscripts to JASA for possible publication based on their oral presentations with the goal to provide a set of peer-reviewed legacy papers for the next generation of sonic boom researchers, documenting the 1998 state of the art in the understanding of sonic booms including their generation, propagation, and effects on humans and animals. The authors are commended for producing the manuscripts here, and one hopes the collection will have a value even greater than simply the sum of each of the individual papers. JASA Associate Editors Louis C. Sutherland (Atmospheric Acoustics), Michael R. Stinson (Noise), and Whitlow W. L. Au (Animal Bioacoustics) handled the reviewing process for the manuscripts, and their work was invaluable along with that of the anonymous reviewers in improving the manuscripts and guiding them into this collection. Louis C. Sutherland also helped funnel two additional manuscripts on sonic booms, not directly associated with the 1998 Symposium, as additional contributions to this collection.

The symposium chairman appreciates the encouragement and support of JASA Editors-in-Chief Daniel W. Martin and Allan D. Pierce and Norfolk meeting General Chair Kevin Shepherd throughout this project. Many thanks belong to the ASA and the Symposium attendees, authors, anonymous reviewers, and JASA Associate Editors for making both the Symposium and this collection a successful reality.

[1] H. H. Hubbard, "Sonic-boom symposium: Foreword," J. Acoust. Soc. Am. **39**(5 Pt. 2), iv (1966).
[2] H. S. Ribner and H. H. Hubbard, "Sonic boom symposium: Foreword," J. Acoust. Soc. Am. **51**(2 Pt. 3), 671 (1972).
[3] *First Annual High-speed Research Workshop*, edited by A. H. Whitehead, Jr., NASA Conf. Pub. 10087, Pt. 1 (April 1992).
[4] *High-speed Research: Sonic Boom Volume 1*, edited by C. M. Darden, NASA Conf. Pub. 3172 (October 1992).
[5] *High-speed Research: Sonic Boom Volume 1*, edited by T. A. Edwards, NASA Conf. Pub. 10132 (February 1994).
[6] *High-speed Research: 1994 Sonic Boom Workshop—Atmospheric Propagation and Acceptability Studies*, edited by D. A. McCurdy, NASA Conf. Pub. 3279 (October 1994).
[7] *1995 NASA High-speed Research Program Sonic Boom Workshop Volume 1*, edited by D. G. Baize, NASA Conf. Pub. 3335 (July 1996).

VICTOR W. SPARROW
Symposium Chairman

Modification of sonic boom wave forms during propagation from the source to the ground

Henry E. Bass, Richard Raspet, James P. Chambers,[a] and Mark Kelly
The Jamie L. Whitten National Center for Physical Acoustics, University of Mississippi, University, Mississippi 38677

(Received 26 April 2000; revised 16 July 2001; accepted 27 July 2001)

A number of physical processes work to modify the shape of sonic boom wave forms as the wave form propagates from the aircraft to a receiver on the ground. These include frequency-dependent absorption, nonlinear steepening, and scattering by atmospheric turbulence. In the past two decades, each of these effects has been introduced into numerical prediction algorithms and results compared to experimental measurements. There is still some disagreement between measurements and prediction, but those differences are now in the range of tens of percent. The processes seem to be understood. The present understanding of sonic boom evolution will be presented along with experimental justification. [DOI: 10.1121/1.1404375]

PACS numbers: 43.28.Mw, 43.25.Cb [LCS]

I. INTRODUCTION

In the proceedings of the Sonic-Boom Symposium of 1965, Maglieri[1] noted that measured sonic boom rise times were quite variable. Pierce and Maglieri[2] analyzed measured data more carefully and noted that the rise times of sonic booms are typically 10 or more times that expected based only on viscous losses. Plotkin and George[3] plotted experimentally measured rise times as a function of shock overpressure and found that measured values were often three orders of magnitude or greater than expected. Both groups attributed the longer rise time to turbulence in the lower atmosphere. The early comparisons between measured and expected rise times were based upon viscous and thermal conduction as the only loss mechanisms.

Many early measurements of sonic boom rise times did not include simultaneous measurements of atmospheric conditions. These allowed the use of relative humidity as an adjustable parameter, which can give results which bracket experimental measurements. Pierce and Maglieri[2] and Plotkin and George[3] suggested that the anomalously long rise times were a result of scattering from atmospheric turbulence. By assuming turbulence strengths and scales, they were able to explain the observed relaxation times. The measurements they had to compare to did not include good measurements of the turbulence parameters so there was no way to determine what values should be used in the calculations. A statistical analysis by Raspet *et al.*[4] supported the assertion that turbulence plays a role in determining the shape of the leading edge of sonic booms, but at the time, there were no measurements of sonic boom wave forms with simultaneous measurements of turbulence so this hypothesis could not be tested.

Renewed interest in sonic booms in the 1980s provided support to conduct an experimental program designed to capture sonic boom wave forms along with comprehensive meteorological data. The measurements were conducted as a follow up to a Joint Acoustics Propagation Experiment (JAPE) conducted at White Sands New Mexico in the summer of 1991. The sonic boom measurements became known as JAPE-2. For the first time, simultaneous measurements of sonic boom wave forms, relative humidity (required for relaxation calculations), and turbulence characteristics (required for turbulence calculations) became available.

The effect of relaxation processes on the rise times of shock waves in the atmosphere has been acknowledged for many years.[5,6] In the early 1970s, the role of vibrational relaxation of nitrogen on absorption of sound in the atmosphere was identified and led to more accurate expressions for the vibrational relaxation times of all atmospheric constituents. In 1978, the absorption algorithm developed for the American National Standard ANSI S1-26-1978, "Method for calculation for the absorption of sound by the atmosphere,"[7] was incorporated into a finite wave propagation algorithm developed by Anderson[8] at the University of Texas to investigate the effect of vibrational relaxation on the propagation of explosion waves.[9] The resulting algorithm came to be known as SHOCKN. This algorithm was extended to predict the evolution of sonic boom wave forms propagating through a turbulent atmosphere.[10] Of particular interest has been the prediction of rise times of these sonic booms, since measured wave forms usually have rise times orders of magnitude greater than the rise times predicted from viscous and thermal losses. Atmospheric turbulence typically plays a major role in the increase in rise times measured at the surface of the earth. The rise time imposed by relaxation processes establish a base wave form to be perturbed by turbulence. Since turbulence most often increases the rise time, calculations based upon relaxation absorption and dispersion establish a lower limit.

The first predictions[9] from SHOCKN did not include dispersion which results from the same relaxation processes that give rise to atmospheric absorption. Dispersion was later included in calculations of the rise times of explosion waves and sonic booms propagated through a realistic stratified atmosphere.[10] Subsequent papers compared the predictions

[a]Electronic mail: chambers@olemiss.edu

of the SHOCKN algorithm to measurements of ballistic waves,[11] to steady state shock calculations,[12] as well as rise time predictions from time domain calculations, other frequency domain algorithms, and analytic solutions.[13] Other research investigated the propagation distance for a potential shock to ''heal,'' that is for an artificially lengthened or shortened rise portion of a wave to return within 10% of its steady state value.[14] The rapid advancement of computation and a few improvements to SHOCKN have resulted in improved calculations of interest in the study of sonic boom and blast wave rise times. This paper describes these improvements and presents modified results from the earlier papers.

The calculation algorithm is described in Sec. II. Section III investigates the effect of wave duration and shape on rise times of finite duration pulses. Section IV presents an improved calculation of ''healing'' distance for long duration shock waves. Section V presents results demonstrating the effects of vibration relaxation absorption and dispersion on explosion waves in the atmosphere. Turbulent scattering is discussed in Sec. VI and conclusions are presented in Sec. VII.

II. CALCULATION ALGORITHM

The Anderson algorithm[8] assumes that finite wave distortion and atmospheric attenuation and dispersion are independent over a sufficiently short distance step. The finite wave distortion is calculated in the time domain, the wave is then fast Fourier transformed, and the attenuation, dispersion, and geometrical spreading is applied to each Fourier component in the frequency domain. The inverse Fourier transform is then used to reconstruct the time domain wave form and the process repeated for the next distance step.

In practice, these are the calculation steps.

(1) The input wave is uniformly sampled in time.

(2) The maximum negative slope, $(dp/dt)_{\max}$ is determined and used to find the distance to shock formation,

$$d_{\text{shock}} = \rho_0 c^3 / \beta (dp/dt)_{\max}, \tag{1}$$

where β is the nonlinearity parameter, c is the frozen speed of sound, and ρ_0 the ambient density.

(3) The step size for calculation is chosen to be a fraction of the shock formation distance $(0.10 < \mathrm{f} < 0.25)$

$$d_{\text{step}} = \mathrm{f} d_{\text{shock}}. \tag{2}$$

(4) The time distortion applied to each point as a result of propagation a distance d_{step} is computed by

$$t_i' = t_i + \beta p(t_i) d_{\text{step}} / \rho_0 c^3, \tag{3}$$

where $p(t_i)$ is the pressure at time t_i.

(5) The wave is resampled so that the time samples are uniform.

(6) The fast Fourier transform is applied to the discretized time wave form to calculate the complex amplitude spectrum $A(f_i)$.

(7) Absorption and dispersion are computed at each frequency in the spectrum.

(8) The attenuation, relative dispersion, and geometrical spreading over the distance d_{step} are applied to the complex amplitude.

$$A'(f_i) = A(f_i) \sqrt{\frac{r(i-1)}{r(i)}}\, e^{-\alpha(f_i) d_{\text{step}}} e^{i \Delta\phi(f_i) d_{\text{step}}}, \tag{4}$$

where $\Delta\phi$ is the dispersion due to the changes in phase speed at each frequency. It should also be noted that cylindrical spreading applies due to the line source nature of the boom.

(9) The time wave form is reconstituted using the inverse fast Fourier transform. This process is repeated until the wave has propagated the required distance. It should be noted that for strong waves with peak pressures ($P_{\max} \geqslant 100$ Pa), the step sizes are routinely on the order of 1 cm and that propagation over distances of kilometers thus requires many steps.

Sampling requirements. Studies of the rise times of steady shocks[14] has led to the development of criteria for the sampling rate required for SHOCKN to match the results of weak shock theory for moderately strong impulses. SHOCKN was found to correctly predict the speed of propagation of the shock front of a steady state wave when there were at least eight to ten sample points on the rise portion of the wave form. The degradation when the number of sample points approach five or six was astonishing. This criteria was not satisfied for the shock waves with overpressures greater than 100 Pa in the earlier papers.[9–12] These calculations have been repeated and the results are presented below.

For sonic boom calculations, the sampling requirement leads to large numbers of sample points and very slow run times. For practical calculations of propagation of sonic booms at high pressure, we took advantage of the fact that if weak shock theory holds, the magnitude of the attenuation does not affect the nonlinear wave shape development.[11] The wave shape development can be calculated using artificially large attenuation in accordance with Eq. (11.3.10) of Ref. 15. The large attenuation increases the rise time and therefore reduces the sampling requirement. This technique allows the overall shape of the wave form to be preserved at the expense of detailed information of the rise time. When the overpressure drops to some lower level (300 Pa in this work), the artificial attenuation is removed and the proper thermoviscous and relaxational attenuation promptly reverts the rise time to its proper value. This reversion typically occurs within less than a few hundred meters of propagation[14] and less than 100 m in this work. This technique obviously cannot be used if detailed rise time information is desired for high pressure wave forms. In this case one must use a sufficiently high sample rate and allow the program to run for hours.

III. EFFECT OF WAVE DURATION ON THE RISE TIME

In a 1992 paper,[12] rise times predicted by SHOCKN for an N-wave propagating in the atmosphere were compared by Kang and Pierce[16] to those calculated for steady state wave forms in which the wave shape does not change with propagation distance. The 130-ms duration N-wave results agreed with the steady state case at high pressure when the rise portion of the wave was a small fraction of the half duration of the N wave (2%), but were much shorter (~40%) than steady state at lower pressures when the rise time was on the order of 14% of the half duration. An unrealistically long N

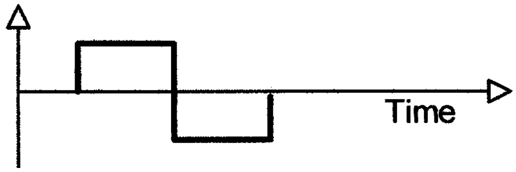

FIG. 1. Square pulse wave form utilized to mimic a steady state, step function shock in numerical propagation routines.

wave with a duration of 3 s was necessary to develop rise times closely approximating the steady state results at low pressure (10 Pa) (rise time 4% of the half duration).

In a later study of *healing time*,[14] a square pulsed wave form was used to simulate steady state rise time (see Fig. 1). The calculations of Ref. 12 have been repeated using this wave form. In this case the 130 ms total duration waves reproduce the steady state rise time results at 100 and 30 Pa, but the rise times are 50% shorter than steady state at 10 Pa. At this point, the rise time is about 8% of the half duration (see Fig. 2).

It appears that steady state calculations are only valid if the rise portion of the wave is on the order of a few percent of the half duration, even for the square waves used here. For sonic booms near the earth's surface, rise times are on the order of 10 ms, so steady state calculations are only valid for waves with durations greater than a few seconds. Given these constraints, it is therefore suggested that more accurate results can be achieved through the use of some form of marching solution that can handle arbitrarily changing propagation conditions.

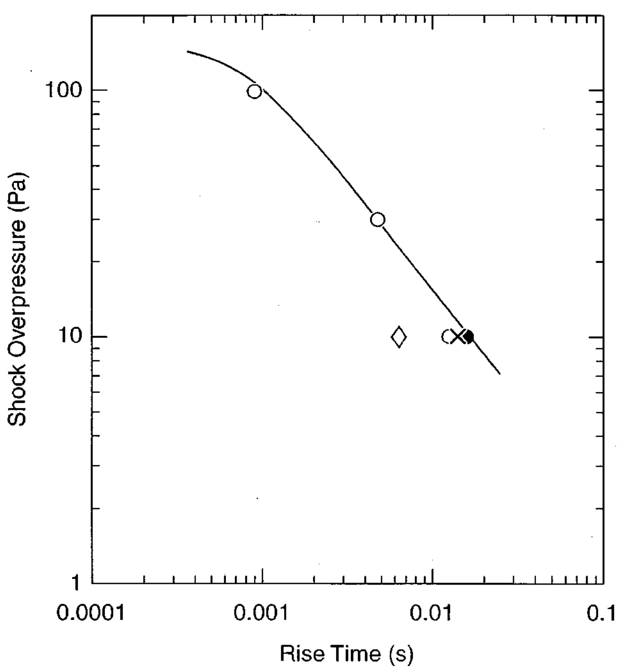

FIG. 2. Comparison of shock overpressure and rise time for steady state and transient wave forms. The solid line is the predicted rise time for a steady state shock from Kang and Pierce (Ref. 16). The symbols are the predicted rise time utilizing a square wave pulse of varying duration as a substitute for the steady state case. The duration of each pulse is ◇ 30 ms, ○ 130 ms, × 300 ms, and ● 3 s.

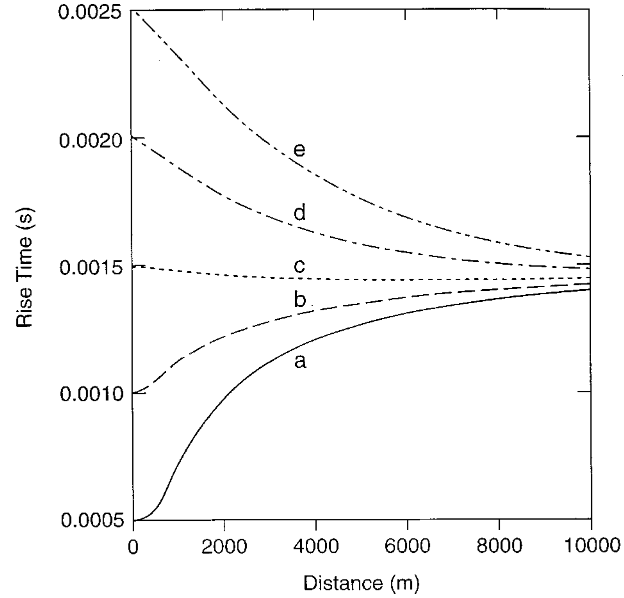

FIG. 3. Return of rise time to the steady state value for a 30-Pa square pulse propagating through a neutral atmosphere with 30% relative humidity. The initial rise times are (a) 0.5 ms, (b) 1.0 ms, (c) 1.5 ms, (d) 2.0 ms, and (e) 2.5 ms. The steady state rise time is 1.4 ms.

IV. HEALING DISTANCE

In calculations of the scattering of sonic booms by turbulence in the planetary boundary layer, it is often assumed that linear acoustics may be applied. To investigate this assumption, square pulses with varying rise times were propagated to determine how far the wave propagates before a disturbed rise time returns to within 10% of its steady state rise time. In the initial study,[14] a hyperbolic tangent rise portion of the wave was used which is typical of a wave form resulting from propagation through a gas whose attenuation is proportional to the frequency squared. In these cases, artificially lengthened rise times returned to the steady state value monotonically, but artificially shortened rise times would first become shorter, then return to the steady state. These calculations have been repeated using computed rise shapes as input. The rise portion of the wave is lengthened or shortened, then the wave is propagated until it returns to its steady state value. Figure 3 presents the results for a 30-Pa wave at relative humidities of 30%. The perturbed waves required over 4 km to return to within 10% of their steady state values.

These results agree with the earlier study, but do not display the nonphysical initial shortening of the rise times. Since the healing distances are much greater than the depth of the planetary boundary layer, even for relatively strong waves, linear theory can be used to calculate the effect of turbulence scattering on sonic booms with small error.

V. EFFECT OF ATTENUATION AND DISPERSION ON FINITE WAVE PROPAGATION

The steady state wave front thickness of a finite wave in a gas with attenuation proportion to frequency squared is given by

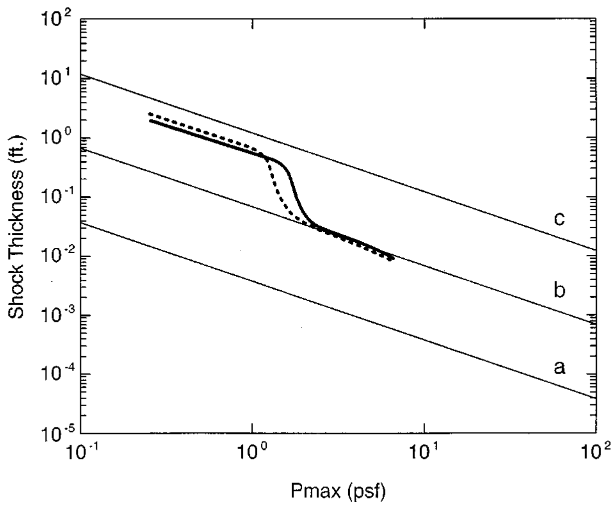

FIG. 4. Shock thickness vs overpressure for a 68-kg TNT explosive propagating through a neutral atmosphere with a relative humidity of 30% and temperature of 295 K. The thin solid lines are theoretical predictions for a steady state wave form propagating through an atmosphere with absorption described by Af^2. The coefficient "A" has been determined assuming (a) thermoviscous attenuation only, (b) thermoviscous attenuation combined with oxygen relaxation, and (c) thermoviscous attenuation combined with oxygen and nitrogen relaxation. The bold line is a model prediction for the transient blast wave with dispersion included and the dashed line with dispersion numerically removed. The rise time, in ms is equal to the shock thickness, in ft divided by the sound speed in ft/ms (1.13) and the abscissa scale can be converted to pascals by multiplying by 47.88 Pa/psf.

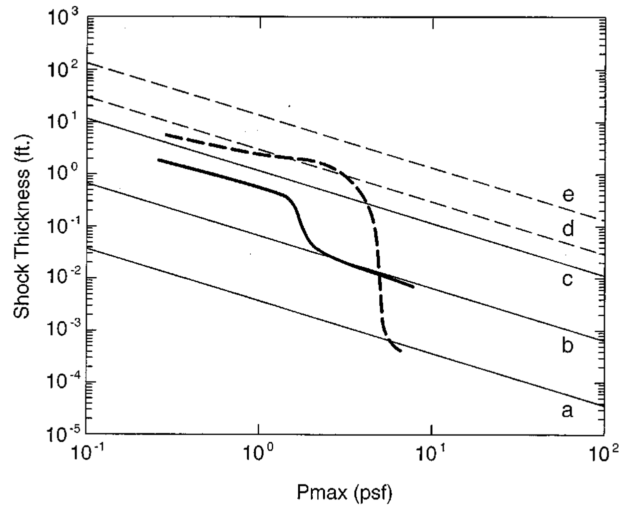

FIG. 5. Shock thickness vs overpressure for a 68-kg TNT explosive propagating through a neutral atmosphere with a relative humidity of 30% and 2% and temperature of 295 K. The thin solid lines are theoretical predictions for a steady state wave form propagating through an atmosphere with absorption described by Af^2 with 30% relative humidity. The dashed lines are the same with 2% relative humidity. The coefficient "A" has been determined assuming: (a) thermoviscous attenuation only for 30% and 2% relative humidity, (b) thermoviscous attenuation combined with oxygen relaxation for 30% relative humidity, (c) thermoviscous attenuation combined with oxygen and nitrogen relaxation for 30% relative humidity, (d) thermoviscous attenuation combined with oxygen relaxation for 2% relative humidity, and (e) thermoviscous attenuation combined with oxygen and nitrogen relaxation for 2% relative humidity. The bold lines are model predictions for the transient blast wave with 30% relative humidity (solid line) and 2% relative humidity (dashed line). Note that the thin solid lines are the same as in Fig. 4 and that the prediction utilizing thermoviscous attenuation only is the same for 30% and 2% relative humidity. The rise time, in ms is equal to the shock thickness, in ft. divided by the sound speed in ft/ms (1.13) and the abscissa scale can be converted to pascals by multiplying by 47.88 Pa/psf.

$$l_{\text{rise}}=\frac{8\rho_0}{\beta P_{\text{sh}}}\frac{c^4}{\omega^2}\alpha(f), \tag{5}$$

where $\alpha(f)$ is the attenuation at frequency f, and β is the parameter of nonlinearly. In the following calculations and figures, α has been assumed to have a form of $\alpha=Af^2$, where A has been determined by fitting straight lines to the standard atmospheric absorption calculations (Ref. 7) in those regions of frequency where relaxation transitions are not occurring. For instance, at a relative humidity of 20%, one can determine A for purely thermoviscous attenuation at a frequency of 200 kHz, for thermoviscous attenuation combined with O_2 relaxation at a frequency of 5000 Hz, and for thermoviscous attenuation combined with O_2 and N_2 relaxation at a frequency of 50 Hz.

In a 1983[10] paper concerned with the rise time of explosion waves from 68 kg of TNT in the atmosphere with and without dispersion, the figures published displayed results which were undersampled for pressures above 200 Pa. This undersampling could thus not yield rise times shorter than the sampling rate utilized. The dispersion in the calculation was also not calculated correctly due to interchange of equilibrium and frozen sound speeds. Figure 4 displays correct calculations of the explosion wave shock thickness in feet versus the overpressure in pounds per square foot (psf). As the explosion waves propagate and become weaker, the rise time transitions from a region where thermoviscous and O_2 vibrational relaxation attenuation determine the rise time of the wave to a region where the N_2 vibrational relaxation dominates. There is very little difference in rise times calculated with or without dispersion except in this transition region. In this region, dispersion increases the shock thickness by as much as 70%. The dispersion is greatest for frequencies in the rise portion of the wave near the N_2 relaxation frequency. The difference in phase changes due to varying propagation speeds of the Fourier components of the wave front leads to larger rise times. This conclusion is different from the conclusion in Ref. 10.

Figure 5 displays the rise time development of 68 kg of TNT in the atmosphere for different atmospheric conditions; $T=295\,\text{K}$, relative humidity=2% and 30%, and atmospheric pressure of 1 atm. For 30% relative humidity the relaxation frequencies are high enough so that the rise times at the highest pressures correspond closely to the steady state calculations for thermoviscous plus O_2 relaxation. As the pressures decrease, the rise times transition to those approaching the steady state value for attenuation due to thermoviscous, O_2 and N_2 relaxation. The explosion waves have a relatively short positive phase, so that the rise times at lower pressures are a significant fraction of the half duration, and the predicted rise times are approximately half that predicted by the steady state approximation.

The rise times calculated for 2% relative humidity correspond to only thermoviscous losses at the highest pressures. As the waves propagate and become weaker, the rise times increase to approximate the steady state rise times due to thermoviscous and O_2 relaxation. Inspection of the atmospheric attenuation curve at 2% relative humidity shows that

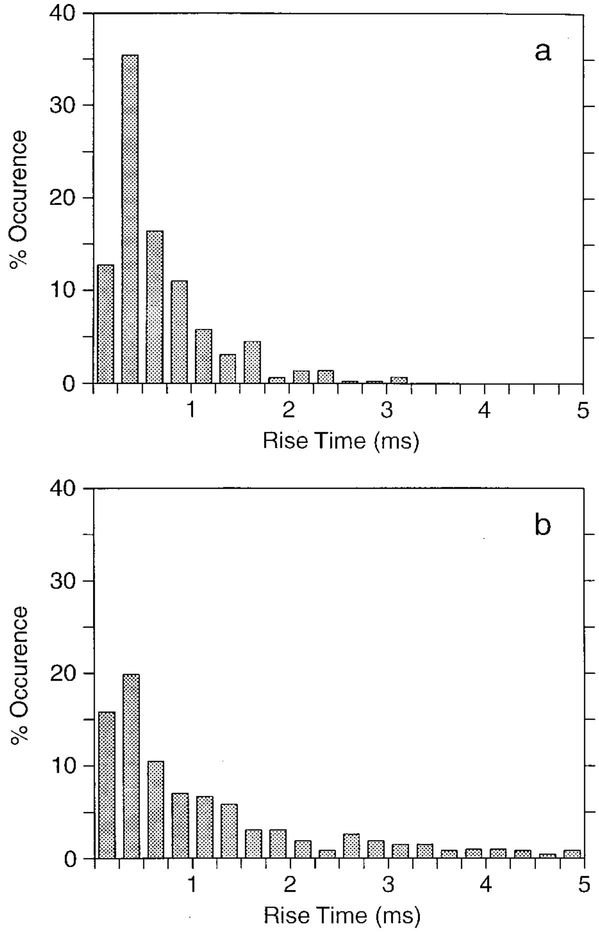

FIG. 6. Percent occurrence of rise times under mildly turbulent conditions: (a) measured data, (b) modeled data.

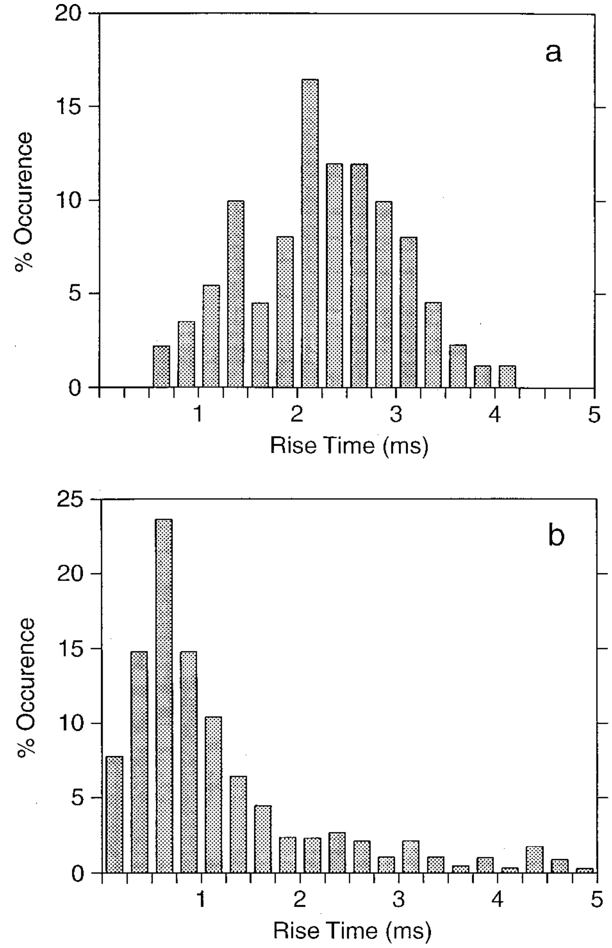

FIG. 7. Percent occurrence of rise times under moderately turbulent conditions: (a) measured data, (b) modeled data.

the O_2 and N_2 relaxation frequencies are quite close and that it is difficult to separate out the effects of the two. In this case, the duration effect must also be very large; the rise times are on the order of 20% of the positive phase duration of the wave. The high pressure behavior of the rise times is quite different from the behavior displayed in the 1983 paper. Specifically, the 1983 paper predicted improperly large rise times due to the use of an insufficient sampling rate.

VI. EFFECT OF TURBULENT SCATTERING ON FINITE WAVE PROPAGATION

Boulanger *et al.*[17] reported on the use of a scattering calculation to predict the effects of turbulence on sonic boom rise times and overpressures for different atmospheric conditions. The SHOCKN routine was utilized to propagate the wave form to the Planetary Boundary Layer and then linear scattering theory was utilized to include the influence of turbulent fluctuations from distributed turbules. Other authors have treated the problem in varying fashion.[18–20] The results of the calculation pursued here were compared to data collected at the JAPE-2 tests.[21,22] These tests provided simultaneous recordings of sonic boom pressure wave forms from T-38 aircraft along with detailed meteorological data. The recordings of each sonic boom were analyzed to determine the nature of the leading edge and the maximum overpressure. The individual records were collected together to form histograms as presented in Figs. 6 and 7 for mild and moderate turbulence conditions.

A scattering center-based calculation of continuous acoustic wave propagation through turbulence gave good results in earlier studies.[23] In addition, this method is flexible enough to allow for the prediction of sonic booms propagating through a realistic representation of the turbulence field including its spectrum and altitude dependence. Turbulence was represented in Ref. 17 by spherical turbules and is incorporated into the equation of propagation via a first Born approximation. This method offers a closed-form expression for the pressure which is convenient for use in computer simulation.

As mentioned earlier, a large number of individual measured sonic boom events were combined to create the histograms of rise times presented in Figs. 6 and 7. In a similar manner, a large number of simulations were conducted to model this data utilizing a synthesized T-38 wave form as an input. That is, turbules of varying sizes were randomly placed in the flight path of a sonic boom and the boom was propagated through this modeled atmosphere. This particular arrangement of turbules was randomly changed and the process was repeated until a statistically sufficient number of iterations were performed. In this manner it was possible to determine the most likely and possible rise times in the predicted data.

The model, as presented, overpredicts the change in rise times under mildly turbulent conditions and underpredicts the change under moderately turbulent conditions as seen in Figs. 6 and 7. The mildly turbulent conditions were described by $\langle \mu^2 \rangle = 1.5 \times 10^{-6}$ while the moderately turbulent conditions possessed a value of $\langle \mu^2 \rangle = 9.6 \times 10^{-6}$, where μ is the change in the index of refraction due to wind fluctuations which dominate those from temperature changes. It is suggested that previously neglected multiple scattering effects may account for the discrepancy.

VII. CONCLUSIONS

There has been good progress toward accurate predictions of sonic boom wave forms. A comprehensive propagation algorithm that includes only relaxation modifications to the wave form in the upper atmosphere (but including refraction) and the effect of turbulence in the lower atmosphere is still not available. Comparisons of calculations reported here, however, suggest that there is more work to be done to accurately include the effect of turbulence on sonic boom rise times. It may be necessary to include the actual speed of sound within turbules and multiple scattering. These problems will probably still be around when interest in sonic booms again surfaces.

ACKNOWLEDGMENTS

Much of the research supported here was supported by NASA Langley Research Center. The authors are especially indebted to Bill Willshire for effectively organizing JAPE-2 to acquire and share good data with us.

[1] D. J. Maglieri, ''Some effects of airplane operations and the atmosphere on sonic-boom signatures,'' J. Acoust. Soc. Am. **39**, S36–S42 (1966).

[2] A. D. Pierce and D. J. Maglieri, ''Effects of atmospheric irregularities on sonic-boom propagation,'' J. Acoust. Soc. Am. **51**, 702–721 (1972).

[3] K. J. Plotkin and A. R. George, ''Propagation of weak shock waves through turbulence,'' J. Fluid Mech. **54**, 449–467 (1972).

[4] R. Raspet, H. E. Bass, L. Yao, P. Boulanger, and W. E. McBride, ''Statistical and numerical study of the relationship between turbulence and sonic boom characteristics,'' J. Acoust. Soc. Am. **96**, 3621–3626 (1994).

[5] J. Piercy, ''Role of the vibrational relaxation of nitrogen in the absorption of sound in the air,'' J. Acoust. Soc. Am. **46**, 602–604 (1969).

[6] J. P. Hodgsen, ''Vibrational relaxation effects in weak shock wave in air and structure of sonic bangs,'' J. Fluid Mech. **58**, 187–196 (1973).

[7] ''Method for the calculation of the absorption of sound by the atmosphere,'' ANSI S1.26-1978, American National Standards Institute.

[8] M. O. Anderson, ''The propagation of a spherical *N* wave in an absorbing medium and its diffraction by a circular aperture,'' Masters thesis, Applied Research Laboratories, The University of Texas at Austin, 1974.

[9] H. E. Bass and R. Raspet, ''Vibrational relaxation effects on the atmospheric attenuation and rise time of explosion waves,'' J. Acoust. Soc. Am. **64**, 1208–1210 (1978).

[10] H. E. Bass, J. Ezell, and R. Raspet, ''Effect of vibrational relaxation on rise times of shock waves in the atmosphere,'' J. Acoust. Soc. Am. **74**, 1514–1517 (1983).

[11] H. E. Bass, B. A. Layton, L. N. Bolen, and R. Raspet, ''Propagation of medium strength shock waves through the atmosphere,'' J. Acoust. Soc. Am. **82**, 306–310 (1987).

[12] H. E. Bass and R. Raspet, ''Comparison of sonic boom rise time prediction techniques,'' J. Acoust. Soc. Am. **91**, 1767–1768 (1992).

[13] R. O. Cleveland, J. P. Chambers, H. E. Bass, R. Raspet, D. T. Blackstock, and M. F. Hamilton, ''Comparison of computer codes for the propagation of sonic boom wave forms though isothermal atmospheres,'' J. Acoust. Soc. Am. **100**, 3017–3027 (1996).

[14] R. Raspet, H. E. Bass, L. Yao, and W. Wu, ''Steady state rise times of shock waves in the atmosphere,'' Proceedings of the High Speed Research: Sonic Boom Conference, NASA Langley Research Center, 1992, pp. 109–115.

[15] A. D. Pierce, *Acoustics—An Introduction to its Physical Principles and Applications* (McGraw–Hill, New York, 1989), pp. 1–678.

[16] J. Kang and A. D. Pierce, ''Propagation of nonlinear transients, such as sonic booms, through an absorbing and relaxing atmosphere,'' J. Acoust. Soc. Am. Suppl. 1 **85**, S81 (1989).

[17] P. Boulanger, R. Raspet, and H. E. Bass, ''Sonic boom propagation through a realistic turbulent atmosphere,'' J. Acoust. Soc. Am. **98**, 3412–3417 (1995).

[18] B. Lipkins and Ph. Blanc-Benon, ''Numerical model for weakly non linear propagation of sound through turbulence, High Speed Research,'' 1994 Sonic Boom Workshop, Atmospheric Propagation and Acceptability Studies, NASA Conf. Publ. **3279**, 61–80 (1994).

[19] O. V. Rodenko and V. A. Khoklova, ''Statistics of sawtooth acoustic waves with random spatial modulation,'' Acoust. Phys. **40**, 111–115 (1994).

[20] A. D. Pierce, ''Propagation of acoustic pulses and sonic booms through small scale atmospheric turbulence,'' 16th AIAA Aeroacoustics Conference, Munich, 1995, pp. 95–105.

[21] B. W. Kennedy, R. O. Olsen, J. R. Fox, and G. M. Mitchler, ''Joint acoustic propagation experiment Project Summary,'' The Bionetics Corporation, Las Cruces, NM, September 1991.

[22] W. L. Willshire, Jr., D. P. Garber, and D. W. deVilbiss, ''The effect of turbulence on the propagation of sonic booms,'' Proceedings of the Fifth International Symposium on Long Range Sound Propagation, The Open University, Milton Keynes, England, May 1992.

[23] W. E. McBride, H. E. Bass, R. Raspet, and K. E. Gilbert, ''Scattering of sound by atmospheric turbulence: A numerical simulation above a complex impedance boundary,'' J. Acoust. Soc. Am. **90**, 3314–3325 (1991).

Propagation of finite amplitude sound through turbulence: Modeling with geometrical acoustics and the parabolic approximation

Philippe Blanc-Benon
Laboratoire de Mécanique des Fluides et d'Acoustique, UMR CNRS 5509, BP 163, 69131 Ecully Cedex, France

Bart Lipkens
Mechanical Engineering, Virginia Commonwealth University, Richmond, Virginia 23284-3015

Laurent Dallois
Laboratoire de Mécanique des Fluides et d'Acoustique, UMR CNRS 5509, BP 163, 69131 Ecully Cedex, France

Mark F. Hamilton and David T. Blackstock
Department of Mechanical Engineering, The University of Texas at Austin, Austin, Texas 78712-1063

(Received 26 April 2000; revised 26 June 2001; accepted 26 July 2001)

Sonic boom propagation can be affected by atmospheric turbulence. It has been shown that turbulence affects the perceived loudness of sonic booms, mainly by changing its peak pressure and rise time. The models reported here describe the nonlinear propagation of sound through turbulence. Turbulence is modeled as a set of individual realizations of a random temperature or velocity field. In the first model, linear geometrical acoustics is used to trace rays through each realization of the turbulent field. A nonlinear transport equation is then derived along each eigenray connecting the source and receiver. The transport equation is solved by a Pestorius algorithm. In the second model, the KZK equation is modified to account for the effect of a random temperature field and it is then solved numerically. Results from numerical experiments that simulate the propagation of spark-produced *N* waves through turbulence are presented. It is observed that turbulence decreases, on average, the peak pressure of the *N* waves and increases the rise time. Nonlinear distortion is less when turbulence is present than without it. The effects of random vector fields are stronger than those of random temperature fields. The location of the caustics and the deformation of the wave front are also presented. These observations confirm the results from the model experiment in which spark-produced *N* waves are used to simulate sonic boom propagation through a turbulent atmosphere. [DOI: 10.1121/1.1404378]

PACS numbers: 43.28.Mw, 43.25.Cb [LCS]

I. INTRODUCTION

When finite amplitude (or intense) sound, such as a sonic boom, propagates through a turbulent atmosphere, the propagation can be affected by turbulence. Atmospheric turbulence affects the perceived loudness of sound, mainly by changing its amplitude (peak pressure) and rise time (time portion between 10% and 90% of peak pressure). The results have been of importance for sonic booms because perceived loudness of the sonic boom when heard outdoors[1,2] is a large factor in determining the acceptability of supersonic flight.

Two propagation models are described here that calculate the nonlinear propagation of sound through turbulence. One is based on a geometrical acoustics approach and the other on a parabolic equation, namely, a modified KZK (Khokhlov–Zabolotskaya–Kuznetsov) equation.[3] Both approaches include a turbulence model that is used to generate individual realizations of a homogeneous, isotropic turbulent field.[4] Random temperature and velocity fields are generated. In the geometrical acoustics approach, linear geometrical acoustics is used to trace rays through each realization of the turbulent field. A nonlinear transport equation is then derived for the propagation along the rays. The transport equation is solved by a Pestorius type algorithm.[5] Absorption and dispersion are included in the model. In the second approach, a modified KZK equation that includes the effect of a random temperature field is solved numerically in the time domain. The main motivation for this work is to investigate to what extent finite amplitude effects alter the propagation of sound through turbulence, i.e., to determine the extent to which peak pressure and rise time distribution are altered. Results from numerical simulations of the propagation of spark-generated *N* waves through turbulence are reported.

In the first section, an overview of the turbulence model is presented. Next, the theory of linear geometrical acoustics is reviewed. A calculation of the probability density function of the occurrence of caustics is performed. Then, we derive the nonlinear transport equation along the eigenrays. In Sec. IV, the modification of the KZK equation to include the effect of a random temperature field is presented. Finally, numerical results are presented for the propagation of spark-produced *N* waves through turbulence.

II. TURBULENCE MODEL

Since we assume that the travel time of the acoustic wave through the turbulent medium is much smaller than the evolution time of the turbulent structures, we consider the turbulence frozen. The turbulent field is characterized as a sequence of independent realizations of a random scalar or vectorial field. Since the motivation of this work is a feasibility study, we limited this study to two-dimensional (2D) turbulent fields. We realize that a full 3D modeling of turbulent fields is necessary to accurately capture the effects of turbulence on sound propagation. The velocity **v** of a 2D isotropic random velocity field at a given point **x** is constructed[4,6] as a sum of N random incompressible Fourier modes, given by

$$\mathbf{v}'(\mathbf{x})=\sum_{i=1}^{N}\mathcal{U}(\mathbf{K}_i)\cos(\mathbf{K}_i\cdot\mathbf{x}+\phi_i),$$
$$\mathcal{U}\cdot\mathbf{K}_i=0. \tag{1}$$

The direction of the wave vector $\mathbf{K}_i$ and the phase ϕ_i are independent random variables with uniform distributions in order to ensure statistical isotropy and homogeneity. The amplitude of the velocity vector $|\mathcal{U}(\mathbf{K}_i)|$ is determined by the two-dimensional kinetic energy spectrum $E(K)$, where $K=|\mathbf{K}_i|$. For the results presented here we used an energy spectrum based on a Gaussian correlation function and a von Kármán energy spectrum, e.g., as described by Hinze[7] and Pao.[8]

For a field with a Gaussian longitudinal correlation function $f(r)=\exp(-r^2/L^2)$, the length scale L is related to the integral length scale L_f by

$$L_f=\frac{\sqrt{\pi}}{2}L.$$

For 2D Gaussian correlated fields the energy spectrum for velocity is given by

$$E(K)=\tfrac{1}{8}v'^2K^3L^4\exp(-K^2L^2/4), \tag{2}$$

where v'^2 is the mean square of the velocity fluctuations.

A 2D isotropic random temperature field T' can be constructed in the same way,[4] i.e.,

$$T'(\mathbf{x})=\sum_{i=1}^{N}\mathcal{T}(\mathbf{K}_i)\cos(\mathbf{K}_i\cdot\mathbf{x}+\phi_i). \tag{3}$$

The energy spectrum for temperature fields is slightly different from the one for the velocity:

$$G(K)=\tfrac{1}{2}\theta'^2KL^2\exp(-K^2L^2/4), \tag{4}$$

where θ'^2 is the mean square of the temperature fluctuations.

For each random field the same discretization of the energy spectrum is used. The length scales for the temperature and the velocity field are equal and the rms values θ' and v' are determined in such a way that the fluctuations of the index of refraction are the same for the scalar and the vectorial random field. At this point we must recall that the fluctuations of the index of refraction μ are related to the fluctuation of temperature T' and to the component v_1' of the velocity fluctuation in the direction of propagation of the incident wave:

$$\mu=-\frac{T'}{2T_0}-\frac{v_1'}{c_0}, \tag{5}$$

where T_0 is the ambient temperature, and c_0 is the ambient speed of sound.

Even though the Gaussian formalism is a very convenient one, it does not result in a realistic spectrum. This spectrum has a very sharp cutoff for high wave numbers, i.e., small turbulence scales, which is not observed in practice. Real spectra usually have a significant inertial range. The energy is not concentrated in structures of sizes roughly equal to L, but, on the contrary, is spread over both larger and smaller turbulent structures with length scales between an inner scale l_0 and an outer scale L_0. Changing the shape of the energy spectrum presents no special difficulty in our turbulence model. The number of Fourier modes is increased to correctly represent the bigger range of wave numbers. For some of the calculations presented here, we used a modified von Kármán spectrum. For 2D temperature fields, the energy spectrum $G(K)$ is written as:

$$G(K)=\frac{2\theta'^2L_0^{-5/3}}{\Psi\left(1,\frac{1}{6},\frac{1}{K_m^2L_0'}\right)}K\left(K^2+\frac{1}{L_0^2}\right)^{-11/6}\exp\left(-\frac{K^2}{K_m^2}\right), \tag{6}$$

where Ψ is the confluent hypergeometrical function and $K_m=5.92/l_0$.

III. LINEAR GEOMETRICAL ACOUSTICS

Linear geometrical acoustics is used to trace rays through each realization of the turbulence field. The classical formulation of linear geometrical acoustics[4,9,10] is well known. The step size ds in the integration of the geometrical acoustics equations is a function of the maximum wave number value K_{Max} that we consider in the turbulence energy spectrum and equals $ds=1/2K_{\mathrm{Max}}$. A fourth-order Runge–Kutta scheme is used to solve the system of differential equations. For source–receiver type problems it is necessary to find the eigenrays that connect source and receiver.

The standard formulations for ray trace equations, such as described by Pierce,[9] are used to trace acoustic rays through each realization of the turbulent field. The ray trace equations can be written in the form of

$$\frac{d\mathbf{x}}{ds}=\frac{1}{N}(\boldsymbol{\nu}+\mathbf{M}), \tag{7}$$

$$\frac{d\mathbf{p}}{ds}=\frac{1}{N}(\boldsymbol{\nabla}N-(\boldsymbol{\nabla}M)\cdot\mathbf{p}), \tag{8}$$

where $\mathbf{x}$ is the position vector of the ray trajectory parametrized by distance s. Here, $\mathbf{p}=p\boldsymbol{\nu}$ is a nondimensional wave vector given by $\mathbf{p}=\mathbf{k}/k_0$ and $k_0=\omega/c_0$, where $\mathbf{k}$ is the acoustic wave vector. The index of refraction is $N=c_0/c$, where c is the local speed of sound. The Mach number vector is $\mathbf{M}=\mathbf{v}/c$, where $\mathbf{v}$ is the fluid velocity vector.

The ray trajectory is completely determined by the initial conditions and the value of s. For a 2D plane wave the initial conditions are

$$\mathbf{x}(s=0)=\begin{pmatrix}0\\ y_0\end{pmatrix}, \tag{9}$$

$$\mathbf{p}(s=0)=\frac{N}{1+\mathbf{M}\cdot\boldsymbol{\nu}}\begin{pmatrix}1\\ 0\end{pmatrix}. \tag{10}$$

In order to obtain the local ray tube area, which is related to the local intensity of the wave, we need to trace the evolution of the two geodesic elements $\mathbf{R}=(\partial\mathbf{x}/\partial y_0)_s$ and $\mathbf{Q}=(\partial\mathbf{p}/\partial y_0)_s$. The geodesic elements describe the evolution of the wave front along each ray[10] and are given by

$$\frac{d\mathbf{R}}{ds}=\frac{1}{pN}(\mathbf{Q}-\boldsymbol{\nu}\boldsymbol{\nu}\cdot\mathbf{Q})-\frac{1}{N^2}(\boldsymbol{\nu}+\mathbf{M})\mathbf{R}\cdot\boldsymbol{\nabla}N+\frac{1}{N}\mathbf{R}\cdot\boldsymbol{\nabla}\mathbf{M}, \tag{11}$$

$$\frac{d\mathbf{Q}}{ds}=\frac{1}{N}[\mathbf{R}\cdot\boldsymbol{\nabla}\boldsymbol{\nabla}N-\mathbf{R}\cdot(\boldsymbol{\nabla}\boldsymbol{\nabla}\mathbf{M})\cdot\mathbf{p}-(\boldsymbol{\nabla}\mathbf{M})\cdot\mathbf{Q}]$$
$$-\frac{1}{N^2}(\mathbf{R}\cdot\boldsymbol{\nabla}N)[\boldsymbol{\nabla}N-(\boldsymbol{\nabla}\mathbf{M})\cdot\mathbf{p}], \tag{12}$$

with the appropriate initial conditions

$$\mathbf{R}(s=0)=\begin{pmatrix}0\\ 1\end{pmatrix}, \tag{13}$$

$$\mathbf{Q}(s=0)=\frac{\partial p(0)}{\partial y_0}\begin{pmatrix}1\\ 0\end{pmatrix}. \tag{14}$$

In this work we have considered two different random fields:

(1) The case of an inhomogeneous medium exhibiting only temperature fluctuations, called the scalar case; hence Eqs. (7), (8), (11), and (12) can be simplified by making use of $N^2=1+T'/T_0$ and $\mathbf{M}=\mathbf{0}$.
(2) The case of a medium exhibiting only velocity fluctuations, called the vectorial case, and Eqs. (7), (8), (11), and (12) can be simplified by making use of $N=1$.

A shortcoming of the linear solution is the appearance of caustics. When $\mathbf{R}$ vanishes, the pressure becomes infinite. In reality diffraction causes the pressure amplitude to be some finite value. In a turbulent medium, each individual ray reaches a caustic at some distance x from the source. To get information about this distance, we evaluate the probability density function of the occurrence of caustics by making use of the theory developed by Blanc-Benon *et al.*[11] For an initially plane wave propagating through two-dimensional isotropic turbulence, the probability density $P_2(\xi)$ of the distance ξ to the first caustic is

$$P_2(\xi)=\frac{\eta^2}{\sqrt{2\pi}\xi^{5/2}}e^{-\eta^4/6\xi^3}, \tag{15}$$

where η is equal to 1.85, ξ is the normalized distance $\xi=\mathcal{D}_2^{1/3}x$, and $\mathcal{D}_2$ is the diffusion coefficient. The quantity $\mathcal{D}_2$ is related to the effective spectral density $\Phi_{\mathrm{eff}}(K_x,K_y)$ by

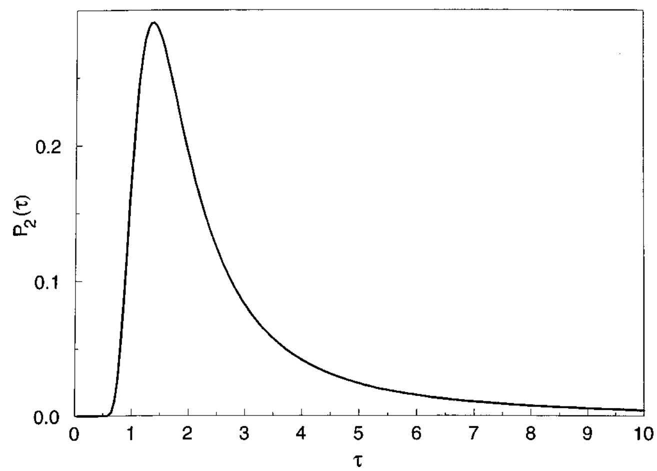

FIG. 1. Probability density function of occurrence of the first caustic for an initial plane wave.

$$\mathcal{D}_2=\pi\int_0^\infty K_y^4\Phi_{\mathrm{eff}}(0,K_y)\,dK_y\,, \tag{16}$$

with

$$\Phi_{\mathrm{eff}}(0,K_y)=\Phi_{cc}(0,K_y)+\frac{4}{c_0^2}\Phi_{11}(0,K_y). \tag{17}$$

The spectral density of the temperature fluctuations is Φ_{cc} and the spectral density of the velocity fluctuations v_1' is Φ_{11}. For two-dimensional Gaussian correlations functions of the random medium, it is straightforward to evaluate the diffusion coefficient $\mathcal{D}_2$:

$$\mathcal{D}_2=\mathcal{D}_{2,c}+\mathcal{D}_{2,v}=\frac{12\sqrt{\pi}}{L^3c_0^2}(\sigma_c^2+5\sigma_v^2), \tag{18}$$

where $\sigma_c^2=c_0^2\theta'^2/(4T_0^2)$ and $\sigma_v^2=v'^2$. The contribution to the diffusion coefficient $\mathcal{D}_2$ due to the temperature fluctuation is $\mathcal{D}_{2,c}$ and that due to the velocity fluctuation is $\mathcal{D}_{2,v}$. In Fig. 1 we plot the probability density of occurrence of the first caustic as a function of the normalized distance ξ. For short propagation distances there are no caustics. Then we observe a sharp peak at a fixed distance. The peak of the probability density function occurs at a normalized distance ξ equal to $\sqrt[3]{\eta^4/5}\simeq 1.33$. At larger distances, we observe a decay of the function $P_2(\xi)$ with propagation distance. In the paper by Blanc-Benon *et al.*[4] we showed that this decay is in agreement with the results of Kulkarny and White,[12] and of Klyatskin.[13]

IV. NONLINEAR TRANSPORT EQUATION

A lossless nonlinear transport equation is derived for the propagation of the waves along the eigenrays. Several assumptions are made in the development of the nonlinear equation and are listed here: (1) parameters of inhomogeneity vary slowly on the time scale of the characteristic signal duration, (2) the medium is frozen, i.e., during passage of the acoustic wave the turbulent field is constant in time, (3) self-refraction is not taken into account, i.e., first-order terms are sufficient in the ray equations while second-order terms are only important in describing the transport equation, (4) loss terms are neglected in the development of the ray path and transport equations, but absorption is added to the numerical algorithm and is dominated by thermoviscous absorption and dispersion of oxygen and nitrogen, (5) the fluid motion is isentropic, (6) ray acoustics approximation is used, (7) weak shock approximation is applied, i.e., only second-order terms are retained in the development of the transport equation.

Starting from the fundamental laws of fluid mechanics and making use of the above stated assumptions, we derive a transport equation. The derivation is lengthy and not presented here, but can be found, e.g., in Robinson.[14] The transport equation for the acoustic pressure p takes the form

$$\frac{\partial}{\partial s}\left[\frac{|A|}{\rho_0 c}|\boldsymbol{\nu}+\mathbf{M}|(1+\mathbf{M}\cdot\boldsymbol{\nu})p^2\right]-\frac{2\beta|A|}{\rho_0^2 c_0^4}p^2 p_{t'}=0, \tag{19}$$

where A is the ray tube area, β is the coefficient of nonlinearity, subscripts 0 denote ambient conditions, and t' is the retarded time coordinate given by $t'=t-\psi(\mathbf{x})$. The effects of passage through a caustic on small-signal waves may be approximated with $a\ -\pi/2$ phase shift in the frequency domain applied to each frequency component.[15] This is a valid approximation after the wave has passed through the caustic and has propagated back into the small signal domain. It does not present a valid prediction of the wave's behavior in the vicinity of the caustic. The next step is to transform the equation into the form of the homogeneous plane wave case.

First, let $\Pi=Kp'$, where

$$K=\sqrt{\frac{|A|\rho_{0s}c_{0s}}{|A_s|\rho_0 c}|\boldsymbol{\nu}+\mathbf{M}|(1+\mathbf{M}\cdot\boldsymbol{\nu})}, \tag{20}$$

where ρ_{0s}, A_s, and c_{0s} are, respectively, the density, initial ray tube area, and speed of sound at the source. The equation is now written

$$\frac{\partial\Pi}{\partial s}-\frac{\beta|A|\rho_{0s}c_{0s}}{|A_s|\rho_0^2 c_0^4 K^3}\Pi\Pi_{t'}=0. \tag{21}$$

Next, a transformation of the independent variable s, $Z(s)$,[14] is introduced:

$$\frac{dZ}{ds}=\frac{\beta|A|\rho_{0s}c_{0s}}{|A_s|\rho_0^2 c_0^4 K^3}\frac{\rho_{0s}c_{0s}^3}{\beta_{0s}}, \tag{22}$$

and the transport equation now takes the well-known form of Burgers equation[16] for lossless propagation of a finite-amplitude plane wave:

$$\frac{\partial\Pi}{\partial Z}-\frac{\beta_{0s}}{\rho_{0s}c_{0s}^3}\Pi\Pi_{t'}=0. \tag{23}$$

The distortion distance variable $Z(s)$ is given by Eq. (22), which can be rewritten as

$$\frac{dZ}{ds}=\sqrt{\frac{|A_0|}{|A|}\frac{\beta^2}{\beta_0^2}\frac{\rho_0 c_0^5}{\rho c^5}(1+\boldsymbol{\nu}\cdot\mathbf{M})^{-3}|\boldsymbol{\nu}+\mathbf{M}|^{-3}}. \tag{24}$$

The distortion distance variable Z describes the equivalent plane-wave distortion for a wave propagating in a random medium. Equation (23) is integrated numerically along the rays and yields the equivalent distortion value. The Burgers equation is solved numerically by a Pestorius-type algorithm.[5] The nonlinear distortion is applied in the time domain and absorption is applied in the frequency domain.

The computational strategy is then: (1) create realizations of the turbulent field, (2) find eigenrays that connect source and receiver, (3) apply Pestorius algorithm to solve nonlinear transport equation, (4) combine eigenrays to find the waveform at the receiver.

V. MODIFIED KZK EQUATION

Geometrical acoustics is primarily a linear and high frequency approach. Nonlinear effects are taken into account only when solving the nonlinear transport equation along the eigenrays. A second model, described below, was developed to include the effects of diffraction in addition to those of nonlinearity.

Boulanger *et al.*[17] used a turbules approach in which the scattering of sound by each turbule is calculated. The final waveform is calculated by summing over the scattering amplitude of each turbule. Using a Monte Carlo method, Sparrow *et al.*[18] have also studied the influence of atmospheric turbulence on sonic boom propagation, and they discussed the formation of caustics. Other researchers have developed numerical codes derived from discretizations of a wave equation. The latter approach was used in the study of sonic boom propagation in a quiet atmosphere, i.e., in the absence of turbulence.[19,20] The effect of turbulence on finite amplitude sound propagation was studied analytically by Pierce[21] and by Rudenko and Khokhlova.[22]

In order to include diffraction effects, we used the algorithm developed by Lee and Hamilton[3] that solves the KZK equation in the time domain. The KZK parabolic wave equation accounts for diffraction, absorption, and nonlinearity in directional sound fields. We modified the code as described below to include effects of inhomogeneities due to a random temperature field. The KZK equation is expressed here as

$$\frac{\partial p}{\partial z}=\frac{c_0}{2}\int_{-\infty}^{\tau}\nabla_\perp^2 p\,d\tau+\frac{\delta}{2c_0^3}\frac{\partial^2 p}{\partial\tau^2}+\frac{\beta p}{\rho_0 c_0^3}\frac{\partial p}{\partial\tau}, \tag{25}$$

where z indicates the nominal direction of propagation and $\tau=t-z/c_0$ the corresponding retarded time, where c_0 is the mean sound speed in a homogeneous medium. The index 0 denotes the mean values. The total pressure is $P(\mathbf{r},z,t)=P_0+p(\mathbf{r},z,t)$, where P_0 is undisturbed ambient pressure, and the operator $\nabla_\perp^2$ is the projection of the Laplacian in the plane that is normal to the z axis. The constants δ and β are medium-dependent thermoviscous absorption and nonlinearity parameters. Since we consider air at ambient condition, we have $\beta=1.2$. The right part of Eq. (25) is written as a sum over three terms that account for diffraction, relaxation, and nonlinearity. Relaxation due to the absorption in the atmosphere is implemented as done by Cleveland *et al.*[23] In the present investigation we focus on modifying the algorithm to account for inhomogeneity.

To include the effect of turbulence we need to add a term to the KZK equation. In order to reduce computation time, we perform the computations for two-dimensional

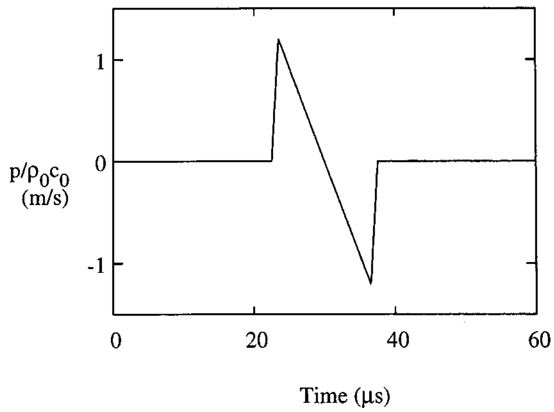

FIG. 2. Input waveform for the numerical experiment with the geometrical acoustics approach.

fields described by the Cartesian coordinates y and z. The effect of the random temperature inhomogeneities is included in the sound speed, and the local sound speed $c(y,z)$ is then written as $c(y,z)=c_0+c'(y,z)$. When the effect of weak sound speed fluctuations is incorporated into the KZK equation, the latter becomes

$$\frac{\partial p}{\partial z}=\frac{c_0}{2}\int_{-\infty}^{\tau}\nabla_{\perp}^2 p\, d\tau+\frac{\delta}{2c_0^3}\frac{\partial^2 p}{\partial \tau^2}+\frac{\beta p}{\rho_0 c_0^3}\frac{\partial p}{\partial \tau}+\frac{c'}{c_0^2}\frac{\partial p}{\partial \tau}. \tag{26}$$

It is this equation that we solved numerically.[3]

Only Gaussian temperature distributions $T(y,z)=T_0+T'(y,z)$ were used to simulate the turbulence. The initial waveform at $z=0$ is a plane N wave, slightly rounded to resemble the waveform produced by an electrical spark. The parameters of the N wave are similar to those used in the geometrical acoustics method.

VI. RESULTS

A. Geometrical acoustics approach

Results are presented for the case of 2D temperature or velocity turbulence fields with a Gaussian longitudinal correlation function, and for the case of a 2D temperature field with a von Kármán spectrum with a significant inertial range (Kolmogorov $-11/3$ law). The Gaussian fields are constructed as a sum of 100 Fourier modes with wave numbers equally spaced between a lower value of $0.1/L$ and a maximum value of $10/L$, where $L=2.5$ cm. In the case of the von Kármán spectrum (Juvé *et al.*[24]) the outer scale L_0 and the inner scale l_0 of turbulence are respectively set to 10 cm and 0.5 cm. The random field is generated with 100 Fourier modes spaced logarithmically between $0.3/L_0$ and $100/L_0$. The refraction index of the two random fields is given by $n=1+\mu$, where μ is the fluctuating part of the refraction index, $\mu=-T'/2T_0-v_1'/c_0$, where T_0 is the ambient temperature. The rms velocity fluctuation in the propagation direction v_1' is 2.5 m/s, and hence the rms temperature fluctuation θ' is 4.27 K. So the rms value of μ is the same for each random velocity or temperature field. Statistics are calculated over 100 realizations.

The initial waveform is that of an N wave similar to that produced by an electrical spark. Peak pressure is 500 Pa, duration is 15 μs, and rise time (time portion between 10% and 90% of peak pressure) is 1 μs (Fig. 2). Spark-produced N waves have been used successfully to simulate the sonic boom propagation through a turbulent atmosphere; see Lipkens.[25–27] The medium is air at ambient conditions with classical thermoviscous absorption, and O_2 and N_2 relaxation are included in the Pestorius algorithm.

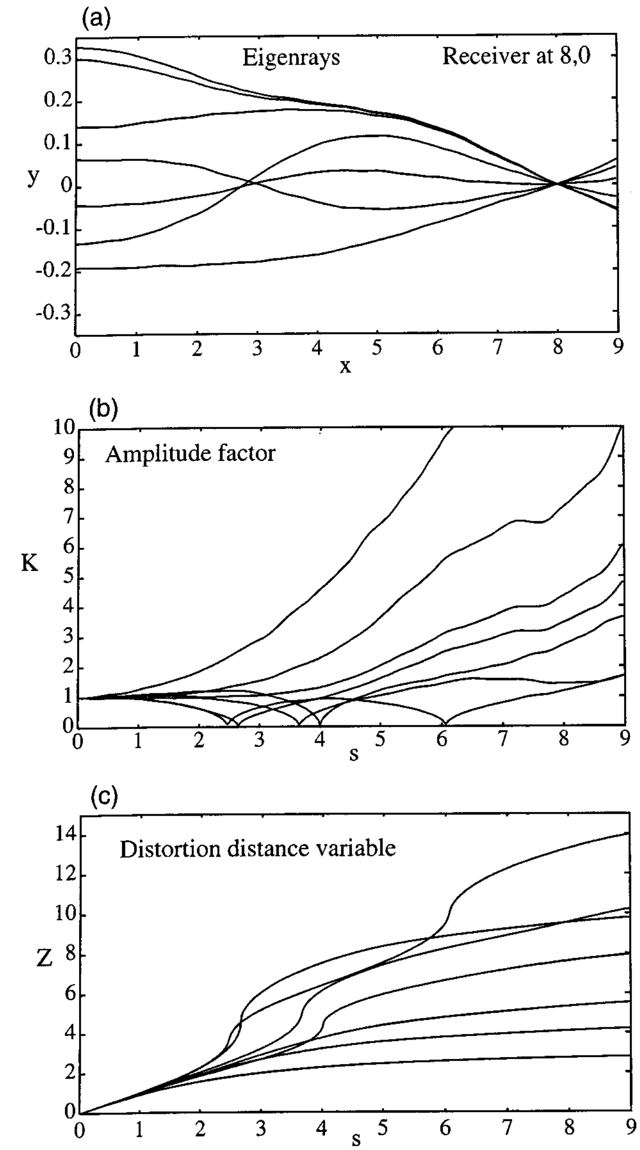

FIG. 3. Calculation example: (a) eigenrays, (b) parameter K, and (c) Z along each eigenray.

In Fig. 3 an example of a typical calculation is shown. In this particular case seven eigenrays [graph (a)] were found that connect the source with the receiver located at a distance of 8 m on the axis. Graph (b) shows the variation of the amplitude factor K along each eigenray. When the eigenray passes through a caustic, the amplitude factor K becomes zero, i.e., an infinite pressure amplitude which is a consequence of the linear geometrical acoustics assumption. The seven eigenrays in Fig. 3(b) can be classified in three categories. We observe that there is one eigenray that passes through two caustics before it reaches the receiver, three rays that pass through one caustic, and three rays did not yet pass

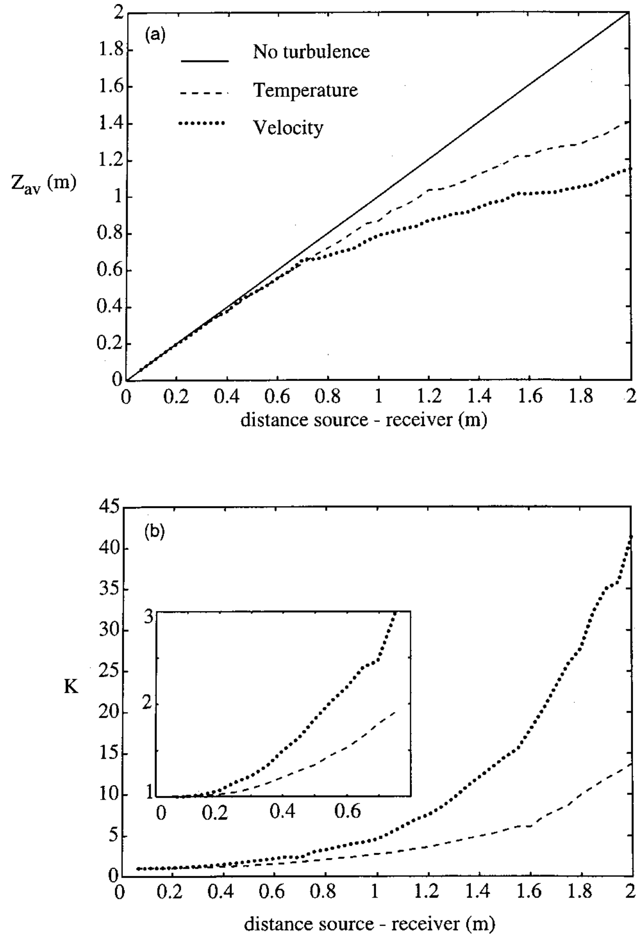

FIG. 4. Averaged results for parameters Z (a) and K (b) for Gaussian turbulent fields. Results are calculated by the geometrical acoustics approach.

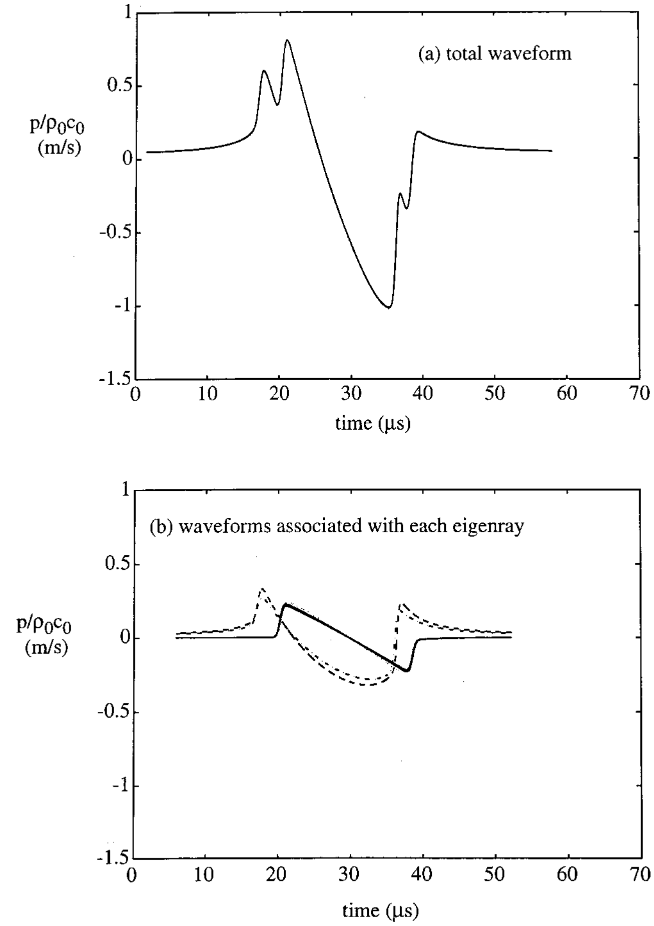

FIG. 5. Example of waveform calculation at the receiver. Graph (a) shows the total waveform and graph (b) shows the waveforms associated with each eigenray.

through a caustic. In graph (c) the distortion distance Z is plotted. For a plane wave in a homogeneous medium we would observe a straight line, i.e., $Z=s$. We see that when the wave passes through the caustic the distortion distance increases more rapidly. After a caustic, the distortion distance grows slower than an equivalent plane wave in a homogeneous medium. For the ray that passed through two caustics, the equivalent distortion distance is nearly 14 m. For one ray that did not propagate through a caustic, the equivalent distortion distance is slightly more than 2 m. The nonlinear

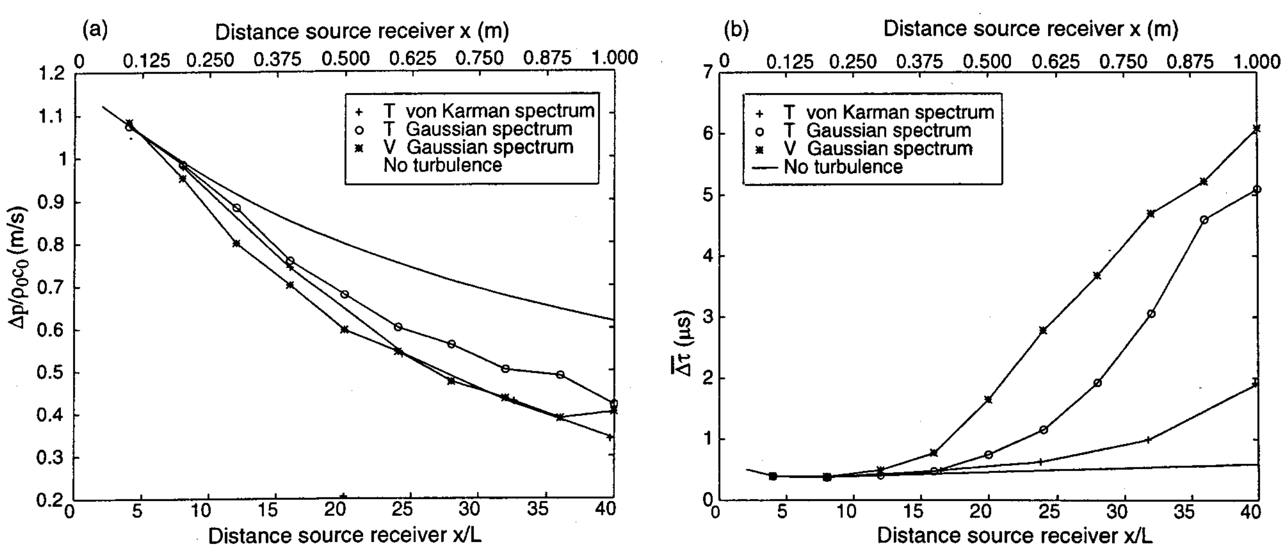

FIG. 6. Averaged normalized values of peak pressure (a) and rise time (b) of the total waveform for 100 realizations are plotted as a function of propagation distance x (m) and normalized propagation distance x/L, where $L=0.025$ m.

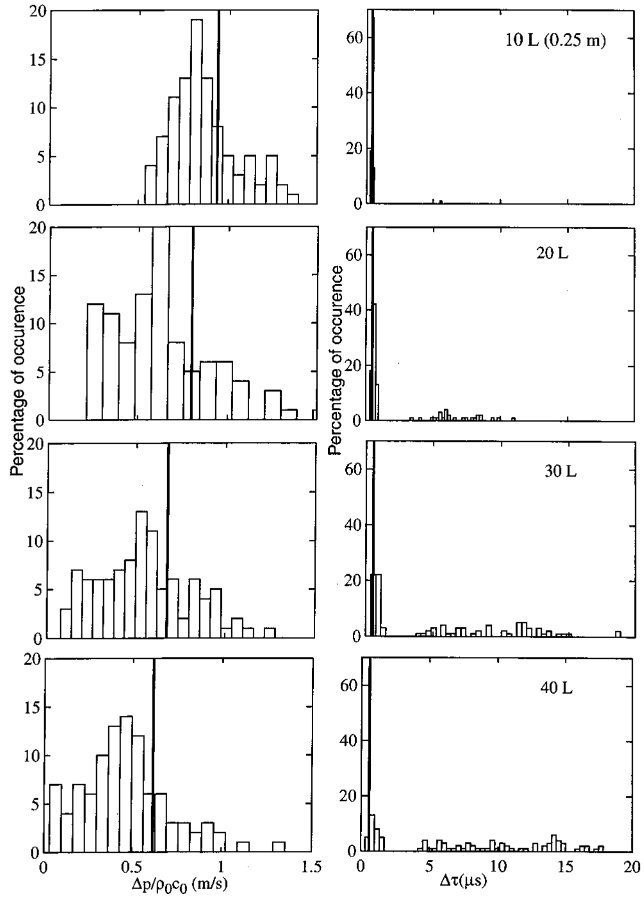

FIG. 7. Histograms of peak pressure and rise time at (a) $10L$, (b) $20L$, (c) $30L$, and (d) $40L$ for the geometrical acoustics model.

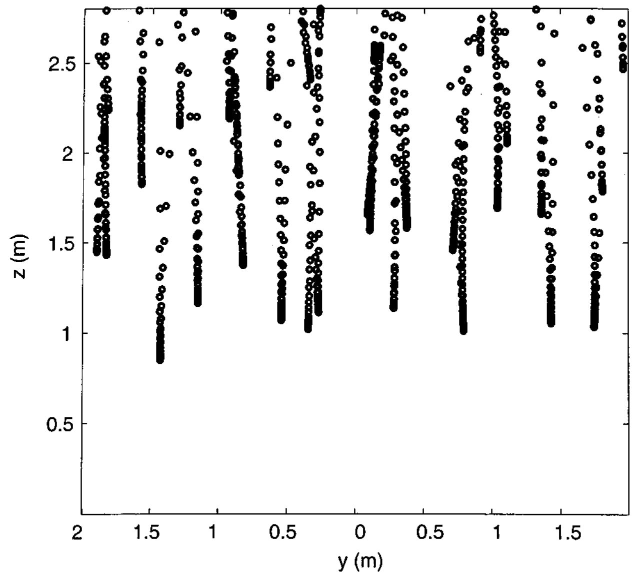

FIG. 8. Location of caustics calculated by the linear geometrical acoustics approach.

distortion will be very weak compared to the homogeneous case. In our previous work, it has been demonstrated that the presence of turbulence always results in a lower value of the age variable Z, i.e., the nonlinear distortion is weaker, and in an increase of the amplitude factor K (Lipkens *et al.*[28,29]).

In Fig. 4 the values of Z and K averaged over 100 realizations of a Gaussian field are presented. In graph (a) the value of Z is shown. Three curves are presented, i.e., for the no turbulence, temperature turbulence, and velocity turbulence cases. It is seen that the presence of turbulence always results in a lower value for the equivalent distortion distance. The effect is more pronounced when propagation distance increases, and stronger for the velocity turbulence. At a propagation distance of $x/L=80$, or $x=2$ m, the equivalent distortion distance for the velocity turbulence is slightly more than 50% than that for no turbulence. Graph (b) presents the values of the amplitude factor K. The factor increases rapidly with propagation distance, an indication that the amplitude of the waveform is less than that of a plane wave having propagated a similar distance in a quiet medium. Again, the effect is more pronounced for the velocity turbulence.

In Fig. 5 an example of a waveform calculation is presented. In this particular case five eigenrays were found that connect source and receiver. The waveform associated with each eigenray is shown in graph (a), while graph (b) shows the global waveform. Two waves have passed through a caustic and the other three have not. The latter three arrive at nearly the same time and are hard to distinguish.

The average values of peak pressure $\Delta p/\rho_0 c_0$ [graph (a)] and the rise time $\Delta\tau$ [graph (b)] calculated at different receiver distances are plotted in Fig. 6. The rise time is calculated as the time portion between 10% and 90% of the peak pressure of the total waveform. According to this definition, we note that the rise time is essentially determined by the differences in arrival times of the eigenrays when more than one eigenray is present. The peak pressure always decreases in the presence of turbulence. For the Gaussian correlation function, there is a small difference between the temperature and the velocity turbulence. At a distance of $x/L=40$ a decrease of 25% is observed. For the random scalar field (temperature) this effect is more pronounced when the field is modeled using a von Kármán spectrum.[30] For this case the generated random field is more realistic since the inertial range extends over two decades. On average the rise time is always increased by turbulence. The curves start to deviate from the no turbulence case when the rays pass through the first caustic. Using Eq. (18) we evaluate the diffusion coefficient for the scalar field $\mathcal{D}_{2,c}$ and the vectorial field $\mathcal{D}_{2,v}$ and then estimate the distance x of the peak of the probability density function, i.e., $x=1.33\mathcal{D}_2^{-1/3}$. For the Gaussian turbulence fields we have $x_T^G=0.324\,\mathrm{m}$ ($x_T^G/L\simeq 13$) for the temperature and $x_v^G=0.186\,\mathrm{m}$ ($x_v^G/L\simeq 7.4$) for the velocity. The occurrence of the first caustic at shorter distances for the velocity field explains the quicker departure from the no turbulence values. In the case of the temperature fluctuations modeled with a von Kármán spectrum [Eq. (6)], the maximum of the probability density function appears at $x_T^K=0.522\,\mathrm{m}$, i.e., $x_T^K=5.22\,L_0$. We note that the increase of the rise time is significant as soon as the propagation distance x/L reaches the estimated distance of the maximum of the probability density function.

The histograms of peak pressure and rise time for Gaussian temperature fields are shown in Fig. 7 for four

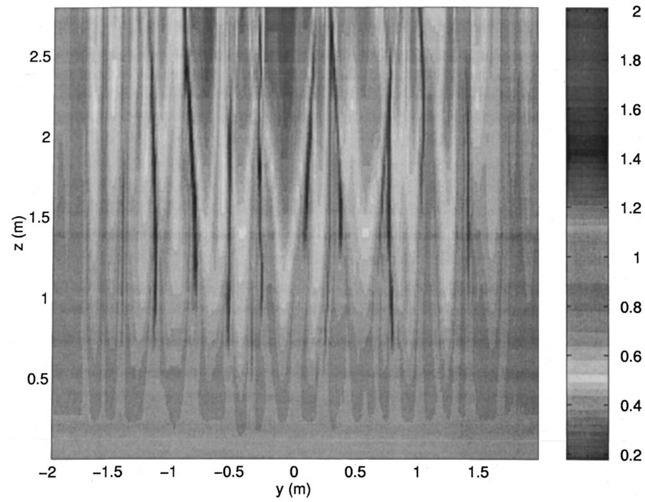

FIG. 9. Locations of peak pressure maxima of the wave obtained with the modified KZK approach.

propagation distances: $10L$, $20L$, $30L$, and $40L$. The solid line in each graph represents the no turbulence values of peak pressure and rise time. We observe that the distribution is asymmetric and that on average more peak pressures occur having values lower than for no turbulence. At the same time, a few large peak pressures are always present. Highest peak pressures are about twice that of the no turbulence value. The spread in peak pressure increases with propagation distance. The rise time distribution is also asymmetric and rise time is almost always increased by turbulence. With increasing propagation distance, large rise time values occur once the rays have passes through the first caustic. Maximum rise time values are an order of magnitude larger than the no turbulence value. Conclusions from the histograms are qualitatively the same as those from the model experiment with electrical sparks.[27]

B. Modified KZK approach

Our main interest in the use of a nonlinear parabolic wave equation was to study the evolution of the wave shape during its propagation in the turbulent media. A second motivation was to compare the effects of absorption and nonlinearity with the linear propagation effects. The initial plane wave parameters were equal to those used in the geometrical acoustics approach. The temperature fluctuations were modeled with 200 Fourier modes and a Gaussian turbulent spectrum ($L = 0.1$ m and $\theta' = 4.27$ K). The length scale corresponded to that of an experiment used to study the influence of thermal turbulence on phase fluctuations and in particular on the role played by random caustics on the occurrence of shocks in the wave front of the transmitted pressure field.[31–33]

First, we compare the results from the geometrical and KZK approach with regard to the location and appearance of caustics. The caustics are purely geometrical acoustic results, i.e., infinite amplitudes predicted at foci in the absence of diffraction. In the KZK approach, the effect of diffraction limits the value of the peak pressure at the focus of the wave.[34] However, at the focus, a high peak pressure is still

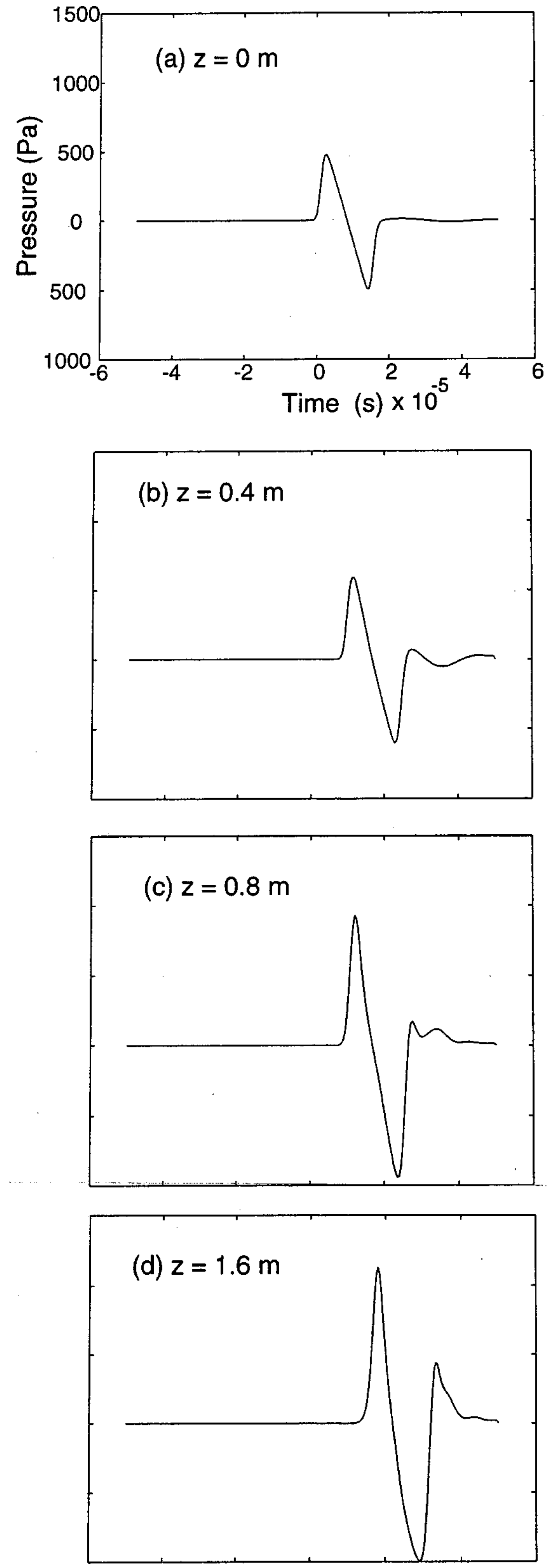

FIG. 10. Evolution of the N wave before and at a caustic. Calculation was done with the modified KZK approach for a Gaussian temperature field: (a) $z = 0.0$ m, (b) $z = 0.4$ m, (c) $z = 0.8$ m, and (d) $z = 1.6$ m.

obtained. In Figs. 8 and 9, we compare the value of the pressure maxima of the wave for the KZK approach case to the position of the caustics determined by the ray tracing approach. In Fig. 8, each dot represents the location of the first caustic along a ray path, and in Fig. 9 a map of the

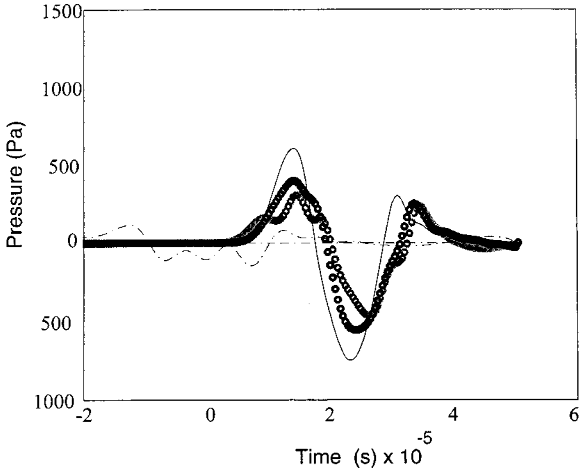

FIG. 11. Evolution of the *N* wave after propagation through a caustic. Calculation was done with the modified KZK approach for a Gaussian temperature field: (——) $z=2.0$ m, (●) $z=2.4$ m, (○) $z=2.8$ m, (–·–) $z=3.2$ m.

maximum pressure of the sound pulse is presented for each point in the spatial domain. Good agreement is seen between the position of the caustic and the maximum of the peak pressure. The agreement at the boundaries of the spatial domain is not as good because of the suppression of the turbulence field by the filter.

Next, we focus on the evolution of the *N* wave as it passes through one random caustic. The change of the waveform is shown in Fig. 10. The initial *N* wave is shown in graph (a). Graphs (b) and (c) show the waveform as it is propagating toward the caustic. We observe that the waveform becomes peaked. At the caustic [graph (d)] the biggest increase in peak pressure at the front and tail shock is observed. After the wave has passed through this caustic (Fig. 11), the wave is further distorted because it undergoes a phase shift. For large distances beyond the caustic ($z=3.2$ m) the wave front is no longer well defined because of the randomness of the propagating medium.

After propagating a certain distance through the turbulent medium, the wave shape can exhibit a wide variety of distortions. The effects that cause the distortion of the waveform are passage through a caustic, nonlinearity, and dissipation effects. In Fig. 12, examples of typical waveform distortion are shown. Figure 12 (a) shows the initial waveform. The rounded wave shape (graph b) occurs in an area where the sound speed is higher than c_0. In this case, the acoustical energy is transported from this area to a focusing area, and this process results in a decrease of the peak pressure. The nonlinear effects are weaker and the rise time increases compared with the no turbulence case. The peaked wave (graph c) occurs at a caustic as explained in the previous paragraph. A double peaked wave (graph d) is due to the superimposition of two consecutive wave fronts having slightly different

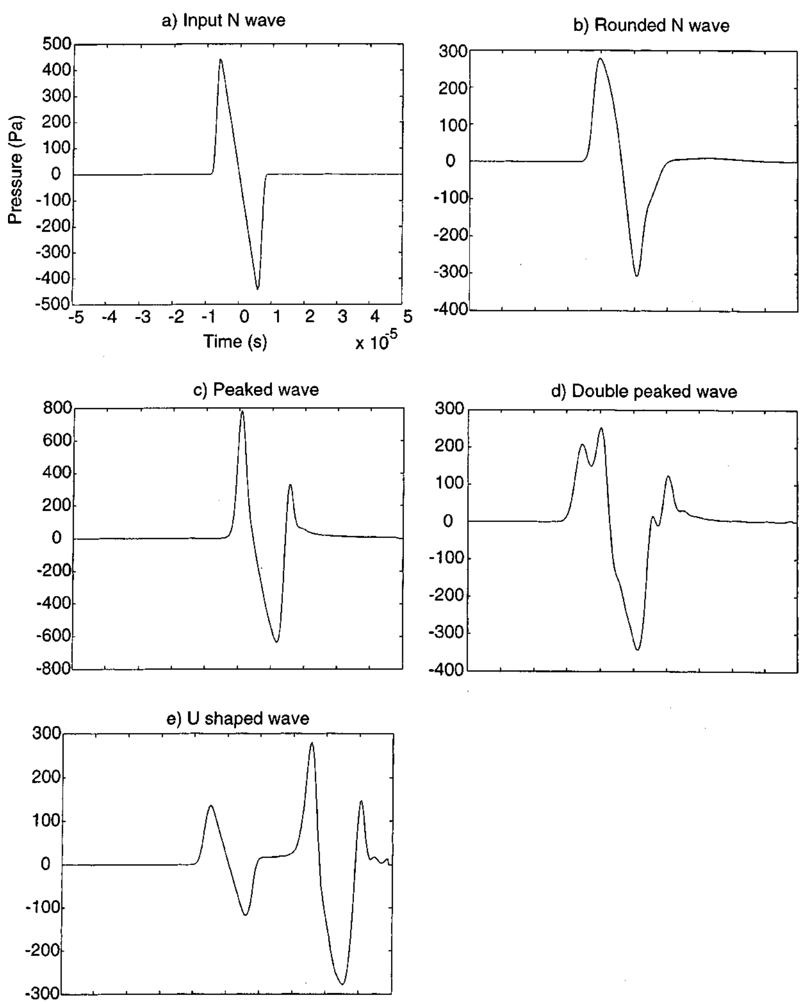

FIG. 12. Examples of distorted waveforms obtained with the modified KZK equation: (a) initial *N* wave, (b) rounded waveform, (c) peaked waveform, (d) double peaked waveform, and (e) U-shaped waveform.

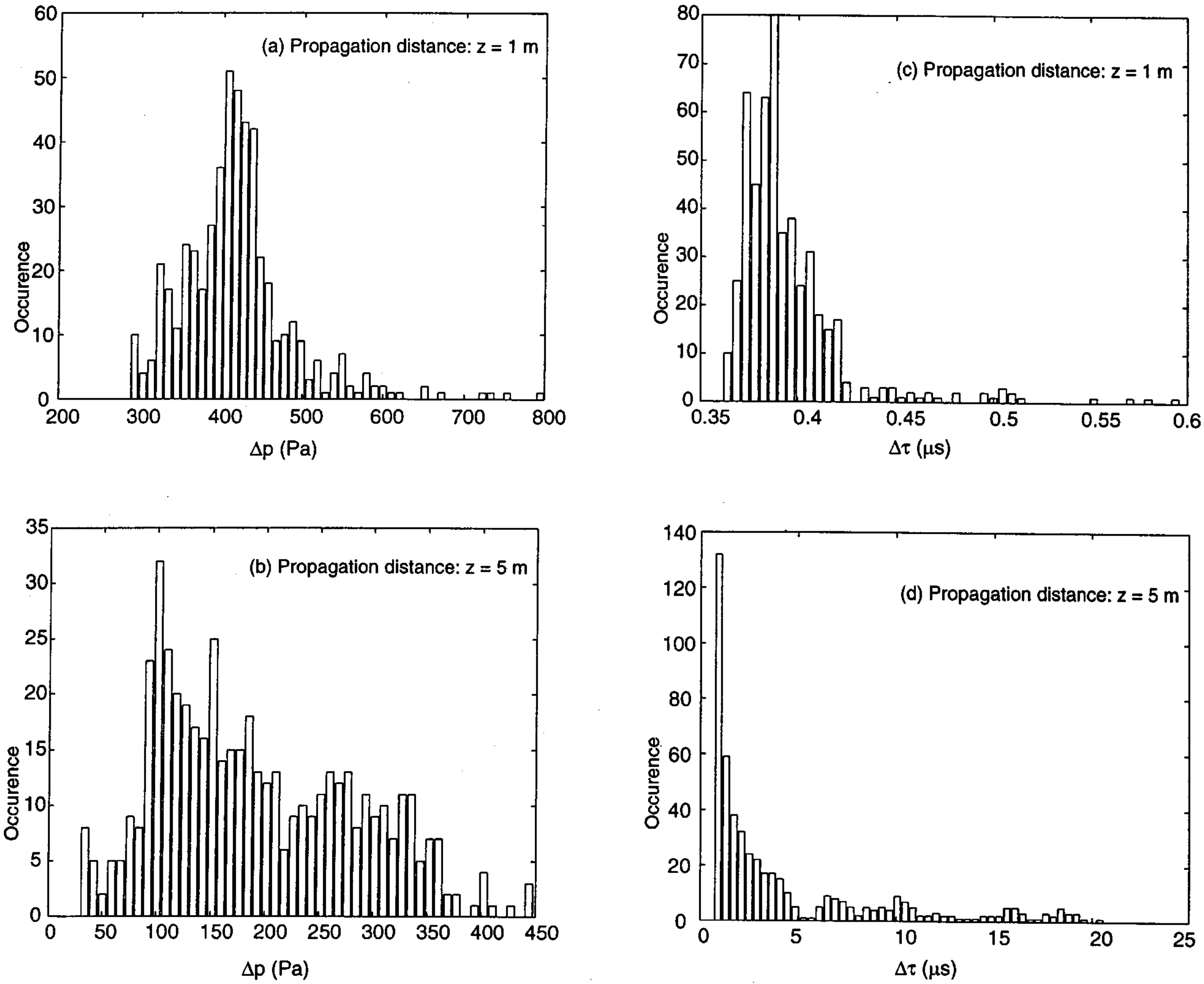

FIG. 13. Histograms of the peak pressure amplitude [(a) and (b)] and rise time [(c) and (d)] at a distance $z=1$ m and $z=5$ m from the source: results obtained with the modified KZK equation.

propagation times. A U-shaped waveform (graph e) is observed after a wave passes through a caustic.

Figure 13 shows the histograms of the peak pressure [graphs (a) and (b)] and rise time [graphs (c) and (d)] for two propagation distances $z=1$ m and $z=5$ m. For a propagation distance of $z=1$ m (i.e., $10\,L$) the expression for the probability of occurrence of the first caustic [Eq. (15)] indicates that only a few caustics exist. However, the distance of $z=5$ m (i.e., $50\,L$) is 3.85 times greater than the distance corresponding to the maximum of the probability density function ($x_T^G/L\simeq 13$). The distribution for the peak pressure is asymmetric and the mean peak pressure is smaller than the no turbulence case ($\overline{P}=430$ Pa at $z=1$ m; $\overline{P}=340$ Pa at $z=5$ m). The rise time histograms show that the turbulence almost always causes the rise time to increase when propagation distances increase. At the large distance $z=50\,L$, we note the appearance of a significant number of large values of the rise time. These conclusions are similar to those obtained with the geometrical acoustics method.

In order to obtain statistical information of peak pressure and rise time of the N waves, a spatial average over the y-direction of the computational domain was calculated for each realization. In Fig. 14, the average peak pressure amplitude [graph (a)] and rise time [graph (b)] are shown as a function of the propagation distance. Results are shown for three realizations of the turbulent field. It is observed that the average peak pressure decreases with increasing propagation distance. This decrease is also observed in the no-turbulence case and is caused by the effects of dissipation and relaxation. However, for the turbulence case, this decrease is more rapid and is in agreement with the results obtained in the geometrical approach (Fig. 6). This decrease is due to the focusing of the wave, since focusing also increases the dissipation rate. Moreover, the wave loses its coherence after propagation through a caustic, thereby increasing the duration and decreasing the peak pressure. The mean rise time increases with propagation distance. This result is in agreement with results of the geometrical acoustics approach. In absence of turbulence, rise time is decreased by effect of nonlinearity. An abrupt change of the slope of rise time increase is seen at a distance of the first caustics 1.3 m. The fact that turbulence always seems to increase the rise time is in agreement with the results of the spark produced N waves. The focusing of the waves at caustics seems to be of primary importance in explaining this behavior.

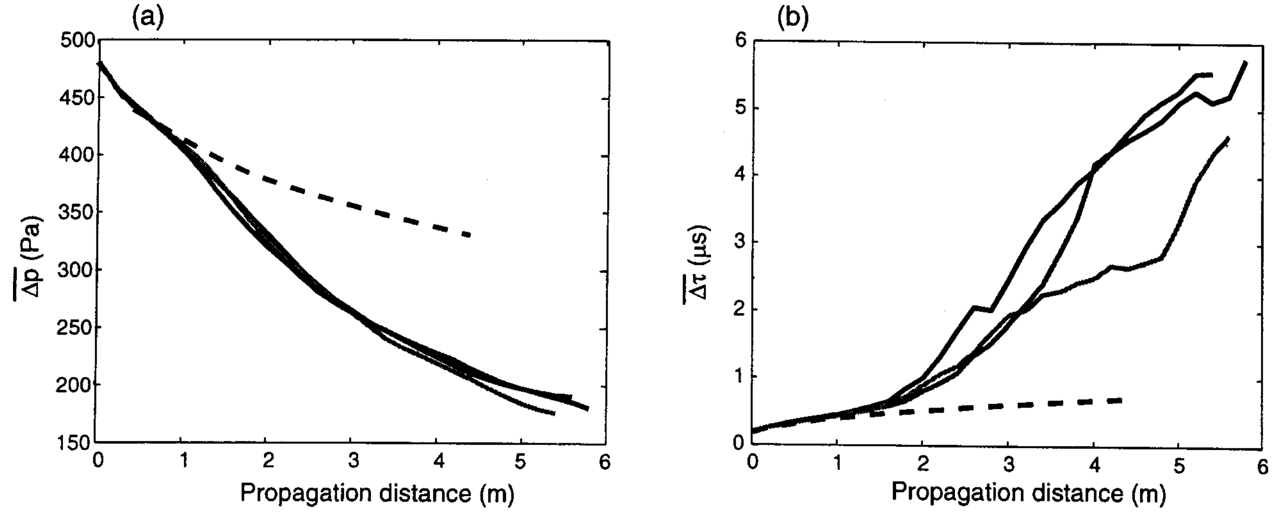

FIG. 14. Averaged peak pressure amplitude (a) and rise time (b) as a function of propagation distance: modified KZK equation. Results are shown for three realizations of a Gaussian turbulent field. The dashed line is the result for the no turbulence case.

VII. CONCLUSION

Two models are presented that describe nonlinear acoustic propagation through turbulence. The first model is based on a geometrical acoustics approach, in which a nonlinear transport equation is solved along the eigenrays. The second model is a modification of the nonlinear parabolic KZK equation. The modification is the inclusion of a random temperature field. Both models are then solved for individual realizations of a turbulent temperature or velocity field. The calculations are repeated and statistics are calculated.

The effect of turbulence on the waveform distortion, rise time, and peak pressure is calculated. It is shown that the nonlinear distortion in the presence of turbulence is weaker than without it. On average, peak pressure decreases in the presence of turbulence, and rise time increases. Peak pressure and rise time distributions are asymmetric. The effect of a velocity turbulence is more pronounced than that of a temperature field. The results confirm the observations of the model experiment.[27] We observed the same waveform distortion as was observed in the model experiment.[26]

In addition we calculated the probability density function for the occurrence of caustics. We showed that the location of caustics calculated by the geometrical acoustics method coincide with the peak pressure maxima calculated by the KZK method. The occurrence of caustics is shown to be responsible for the distortion of the waveform and the increase in variability of peak pressure and rise time.

ACKNOWLEDGMENTS

This research was supported in part by NATA Grant No. CRG941145. Funds for the first author were provided by a post-doctoral fellowship of the French Ministry of Education. C. Simand and P. Chary are gratefully acknowledged for their assistance with the numerical simulations. The authors gratefully acknowledge the many helpful suggestions provided by the reviewers.

[1] A. Niedzwiecki and H. S. Ribner, ''Subjective loudness of *N*-wave sonic booms,'' J. Acoust. Soc. Am. **64**, 1622–1626 (1978).
[2] J. D. Leatherwood and B. M. Sullivan, ''Subjective loudness response to simulated sonic booms,'' Proceedings, High-Speed Research Workshop on Sonic Boom, NASA Langley Research Center, Hampton, Virginia, edited by C. M. Darden, Vol. I, pp. 151–170 (1992).
[3] Y.-S. Lee and M. F. Hamilton, ''Time-domain modeling of pulsed finite-amplitude sound beams,'' J. Acoust. Soc. Am. **97**, 906–917 (1994).
[4] Ph. Blanc-Benon, D. Juvé, and G. Comte-Bellot, ''Occurrence of caustics for high-frequency acoustic waves propagating through turbulent fields,'' Theor. Comput. Fluid Dyn. **2**, 271–278 (1991).
[5] F. M. Pestorius, ''Propagation of plane acoustic noise of finite amplitude,'' ARL Technical Report No. 73-23, Applied Research Laboratories, The University of Texas at Austin (AD 778868) (1973).
[6] G. Comte-Bellot, C. Bailly, and Ph. Blanc-Benon, ''Modeling tools for flow noise and sound propagation through turbulence'' in *New Tools in Turbulence Modeling*, edited by O. Métais and J. Ferziger (Les Editions de Physique Springer, 1997), pp. 141–162.
[7] J. O. Hinze, *Turbulence* (McGraw-Hill, New York, 1959).
[8] Y. H. Pao, ''Transfer of turbulence energy and scalars quantities at large wave numbers,'' Phys. Fluids **11**, 1371–1372 (1968).
[9] A. D. Pierce, *Acoustics: An Introduction to Its Physical Principles and Applications* (McGraw-Hill, New York, 1981).
[10] S. M. Candel, ''Numerical solution of conservation equations arising in linear wave theory: Application to aeroacoustics,'' J. Fluid Mech. **83**, 465–493 (1977).
[11] Ph. Blanc-Benon, D. Juvé, V. E. Ostashev, and R. Wandelt, ''On the appearance of caustics for plane sound wave propagation in a moving random media,'' Waves Random Media **5**, 183–199 (1995).
[12] A. V. Kulkarny and B. S. White, ''Focusing of waves in turbulent inhomogeneous media,'' Phys. Fluids **25**, 1770–1784 (1982).
[13] V. I. Klyatskin, ''Caustics in random media,'' Waves Random Media **3**, 93–100 (1993).
[14] L. D. Robinson, ''Sonic boom propagation through an inhomogeneous, windy atmosphere,'' Ph.D. dissertation, Physics Department, University of Texas at Austin (1990).
[15] D. Ludwig, ''Uniform asymptotic expansions at a caustic,'' Commun. Pure Appl. Math. **19**, 215–250 (1966).
[16] D. T. Blackstock, ''Generalized Burgers equation for plane waves,'' J. Acoust. Soc. Am. **77**, 2050–2053 (1985).
[17] P. Boulanger, R. Raspet, and H. E. Bass, ''Sonic boom propagation through a realistic turbulent atmosphere,'' J. Acoust. Soc. Am. **98**, 3412–3417 (1995).
[18] V. W. Sparrow and A. D. Pierce, ''Simulations of sonic boom ray tube area fluctuations for propagation through atmospheric turbulence including caustics via a Monte Carlo method,'' in *High Speed Research, Sonic Boom Volume I*, NASA Conference Publication 3172, edited by C. M. Darden (1992), pp. 49–62.
[19] R. O. Cleveland, J. P. Chambers, H. E. Bass, R. Raspet, D. T. Blackstock, and M. F. Hamilton, ''Comparison of computer codes for the propagation

of sonic boom waveforms through isothermal atmospheres,'' J. Acoust. Soc. Am. **100**, 3017–3027 (1996).
[20] A. A. Piascek, ''A numerical study of weak step shocks that focus in two dimensions,'' Ph.D. dissertation, Department of Aerospace and Mechanical Engineering, Boston University, Massachusetts (1995).
[21] A. D. Pierce, ''Propagation of Acoustic Pulses and Sonic Booms through Small-Scale Atmospheric Turbulence,'' *16th AIAA Aeroacoustics Conference*, pp. 95–105, Munich (1995).
[22] O. V. Rudenko and V. A. Khokhlova, ''Statistics of sawtooth acoustic waves with random spatial modulation,'' Acoust. Phys. **40**, 111–115 (1994).
[23] R. O. Cleveland, M. F. Hamilton, and D. T. Blackstock, ''Time-domain modeling of finite-amplitude sound in relaxing fluids,'' J. Acoust. Soc. Am. **99**, 3312–3318 (1996).
[24] D. Juvé, Ph. Blanc-Benon, and P. Chevret, ''Sound propagation through a turbulent atmosphere: Influence of the turbulence model,'' in Proceedings of the Sixth International Symposium on Long Range Sound Propagation, Ottawa, Canada, pp. 270–282 (1994).
[25] B. Lipkens, ''Experimental and theoretical study of the propagation of *N* waves through a turbulent medium,'' Ph.D. dissertation, Department of Mechanical Engineering, University of Texas at Austin (1993).
[26] B. Lipkens and D. T. Blackstock, ''Model experiment to study sonic boom propagation through turbulence. Part I: Model experiment and general results,'' J. Acoust. Soc. Am. **103**, 148–158 (1998).
[27] B. Lipkens and D. T. Blackstock, ''Model experiment to study sonic boom propagation through turbulence. Part II: Effect of turbulence intensity and propagation distance through turbulence,'' J. Acoust. Soc. Am. **104**, 1301–1309 (1998).
[28] B. Lipkens and Ph. Blanc-Benon, ''Propagation of finite amplitude sound through turbulence: a geometrical approach,'' *Comptes Rendus Académie des Sciences Paris* T. 320, Série 2, pp. 477–484 (1995).
[29] B. Lipkens and Ph. Blanc-Benon, ''Numerical model for weakly nonlinear propagation of sound through turbulence,'' in High Speed Research, 1994 Sonic Boom Workshop, Atmospheric Propagation and Acceptability Studies, NASA Conference Publication 3279, edited by D. A. McCurdy (1994), pp. 61–80.
[30] C. Simand, ''Propagation d'un bang sonore dans l'atmosphere turbulente,'' Master Thesis, Ecole normale supérieure de Lyon (1996).
[31] Ph. Blanc-Benon and D. Juvé, ''Statistical properties of acoustic waves propagating through turbulent thermal fields,'' AIAA Paper No. 87-2727 (1987).
[32] Ph. Blanc-Benon and D. Juvé, ''Intensity fluctuations of spherical acoustic waves propagating through thermal turbulence,'' Waves Random Media **3**, 71–83 (1993).
[33] Ph. Blanc-Benon and D. Juvé, ''Dislocations in the wavefront of acoustic waves propagating through thermal turbulent fields,'' Forum Acusticum, Berlin, Acta Acustica CD-Rom 'Berlin99' ISBN3-9804568-5-4 (1999).
[34] A. T. Cates and D. G. Crighton, ''Nonlinear diffraction and caustic formation,'' Proc. R. Soc. London, Ser. A **430**, 69–88 (1990).

Sonic boom in the shadow zone: A geometrical theory of diffraction

François Coulouvrat
Laboratoire de Modélisation en Mécanique, Université Pierre et Marie Curie & CNRS (UMR n°7607), 8 rue du capitaine Scott, F75015 Paris, France

(Received 26 April 2000; accepted for publication 23 March 2001)

Geometrical acoustics predicts the amplitude of sonic booms only within the carpet. Inside the geometrical shadow zone, a nonlinear, geometrical theory of diffraction in the time domain is proposed. An estimation of magnitude orders shows that nonlinear effects are expected to be small for usual sonic booms. In the linear case, the matching to geometrical acoustics yields an analytical expression for the pressure near the cutoff. In the shadow zone, it can be written as a series of creeping waves. Numerical simulations show that the amplitude decay of the signal compares favorably with Concorde measurements, while the magnitude order of the rise time is correct. The ground impedance is shown to influence the rise time and peak amplitude of the signal mostly close to the cutoff. In the case of a weakly refractive atmosphere (low temperature gradient or downwind propagation), the transition zone about the cutoff is large, the transition is smooth, and the influence of ground absorption is increased.
[DOI: 10.1121/1.1371973]

PACS numbers: 43.28.Mw, 43.28.Fp, 43.25.Jb [LCS]

I. INTRODUCTION

Sonic boom is the noise associated with an aircraft flying at supersonic speeds. According to the classical theory (Whitham, 1952, 1956; Guiraud, 1965; Hayes *et al.*, 1969), sonic boom waveforms can be predicted within the frame of geometrical acoustics; sound propagates in the atmosphere along classical acoustic rays. These rays are launched perpendicular to the Mach cone formed by the airplane, but then deviate by refraction. In a quiescent, vertically stratified atmosphere, refraction leads to the formation of a shadow zone; only a limited area of the ground—the so-called "carpet"—is touched by direct rays (Fig. 1). Beyond the carpet edge, geometrical acoustics predicts no signal. Several computer codes [Hayes *et al.*, 1969; Thomas, 1972; Bass *et al.*, 1987 (SHOCKN); Robinson, 1991 (ZEPHYRUS); Cleveland, 1995 (THOR); Plotkin, 1998 (PCBoom3)] have been developed for predicting the sonic boom. They generally give good agreement with measured data, except close to the carpet edge where pressure amplitude is systematically overpredicted (Maglieri and Plotkin, 1995; Plotkin, 1998; Downing, 1998). Moreover, no computer code predicts sonic booms inside the shadow zone.

The exact solution in a particular case (Berry and Daigle, 1988; Pierce, 1989)—a point source in a stratified atmosphere with a specified sound speed profile—elucidates the physics of diffraction near the carpet edge: the limiting ray forming the shadow boundary sheds off creeping rays at the point of tangency with the ground (Fig. 2). Inside the shadow zone, these creeping waves propagate along the ground surface. Above the ground, the sound field emanates from rays diffracted by these creeping waves. The signal attenuation is explained by the energy lost as the creeping waves shed off more and more diffracted rays while propagating further into the shadow zone.

The solution of Pierce (1989) can be extended to an impulse signal (Raspet and Franke, 1988) by means of Fourier transform. However, Pierce's solution is strictly valid only for linear sound propagation from a point source, and cannot be extended without precaution to the sonic boom case. The first reason is that a supersonic aircraft radiates not spherical but conical wavefronts. More important, nonlinear effects severely affect sonic boom propagation. In order to describe the sonic boom in the shadow zone, it is necessary to separate two distinct steps: (1) nonlinear propagation in the atmosphere (from the source to the carpet cutoff) described by ray acoustics, and (2) diffraction near the cutoff. For this second step, we need a proper way for matching *locally* the ray description over the carpet to the creeping waves series in the shadow zone. For this article we proceed in a way similar to Bouche and Molinet (1994), who studied the shadow zone of a convex body in a homogeneous medium. We here extend their method to the case of an upward refracting atmosphere, and generalize it to a transient signal. It is also necessary to prove that nonlinear effects are negligible in the shadow zone, contrary to propagation above the carpet.

In Sec. II, a model equation—the unsteady Tricomi equation (Coulouvrat, 1997)—is derived for the sound field inside the shadow zone according to the geometrical diffraction process previously outlined. This equation includes nonlinearities. An estimation of the magnitude order of nonlinear versus diffraction effects shows that in usual cases, nonlinearities are expected to be small (Sec. III). In the linear case, it is then possible to properly match the solution of the unsteady Tricomi equation to the geometrical acoustics approximation inside the carpet (Sec. IV). This yields an analytical expression for the pressure field about the carpet edge, as a function of the incident field and ground impedance. This expression takes the form of a Fourier transform of the Fock integral in the frequency domain. Inside the shadow

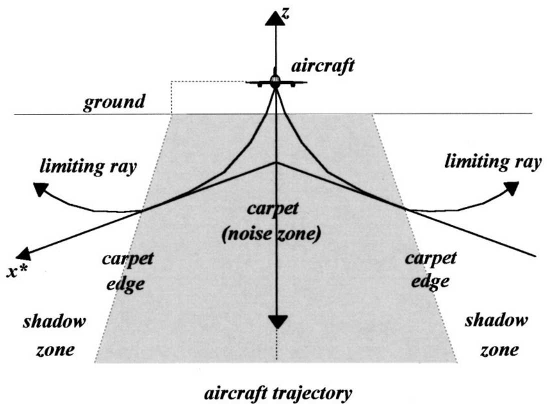

FIG. 1. The sonic boom carpet.

zone, the Fock integral can be written as an infinite series of creeping waves. Then, numerical simulations are performed for an incident ''*N*'' wave, over several different ground materials (Sec. V). The model of Attenborough (1983) is chosen for describing the ground impedance, as this model is considered a good description of rigid-frame porous materials for which data are available in the literature for typical outdoor ground surfaces. The numerical simulations are finally compared to Concorde measurements (Parmentier *et al.*, 1973) (Sec. VI). Results are established only for a quiescent, vertically stratified atmosphere. However, the influence of wind stratification will be discussed qualitatively.

Despite the extensive literature about sonic boom, little attention has been paid to diffraction effects near the carpet edge and inside the shadow zone. To our knowledge, the most recent theoretical work about sonic boom in the shadow zone was published by Onyeowu in 1975. Although relying also on the geometrical theory of diffraction briefly outlined above, Onyeowu's model suffers from several drawbacks which are overcome in the present work. First, Onyeowu did not evaluate the importance of nonlinear effects in the shadow zone. Second, he took into account only the first mode of the creeping wave series, an approximation which was not quantified. More important, the matching with geometrical acoustics was performed by Onyeowu through an empirical reflection coefficient varying between 1 (at the cutoff) and 2 (geometrical acoustics). To be consistent with the classical expression of the reflection coefficient of a grazing plane wave, the arbitrary value of 1 at the cutoff requires that the ground impedance is equal to zero. Therefore, his creeping waves dispersion relation is that over a perfectly pressure-release surface, an assumption which is inconsistant with the computation of a nonzero pressure field at the ground level. As a consequence, he cannot take into account finite ground impedances. Finally, no comparisons were made with in-flight data for the pressure amplitude decay. The influence of diffraction effects on the rise time of the signal was also not explored, though this is a crucial parameter for estimating the annoyance of outdoor sonic booms.

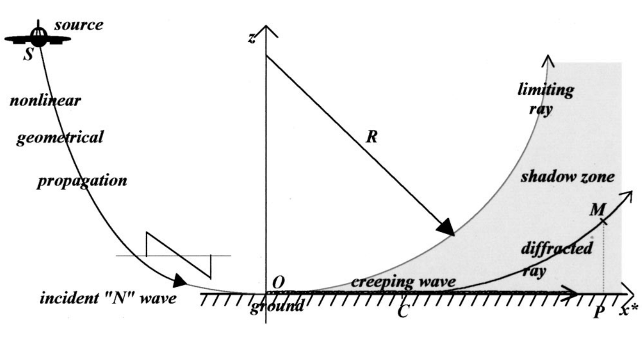

FIG. 2. Geometry of the problem in the shadow zone.

II. A NONLINEAR, GEOMETRICAL THEORY OF DIFFRACTION IN THE SHADOW ZONE

To estimate nonlinear effects inside the shadow zone, we propose a new, nonlinear, time-domain formulation of diffraction effects in the shadow zone. The detailed derivation of the generalized ''unsteady'' Tricomi equation has been published elsewhere (Coulouvrat, 1997) but will be briefly recalled here, as it is the basis for estimating nonlinear effects, and then deriving the analytical expression of the pressure field. According to the geometrical theory of diffraction, the acoustical path from the source S to the current observation point M in the shadow zone is the path SO from the source to the cutoff along the limiting ray, plus the ground path OC from the cutoff to the contact point of the diffracted ray with the ground, plus the path CM from the contact point to the current observation point along the diffracted ray (Fig. 2). Path SO is given by classical geometrical acoustics in a heterogeneous atmosphere. Provided altitude z is small compared to the radius of curvature of the limiting ray R, the propagation time ψ from the carpet edge O to the current point M is

$$\psi=(x^*+\sqrt{8z^3/9R})/c_0, \tag{1}$$

c_0 being the sound speed at the ground. The radius R is related to the sound speed vertical profile $c(z)$ by $R=-c_0/(dc(0)/dz)$. The present theory is limited to the case of an upward-refracting theory for which the sound speed gradient is negative at the ground level. The distance x^* between the cutoff and the projection P of the observation point on the ground is measured in the direction of the limiting ray. For steady horizontal flights, this direction makes a constant angle $\varphi=\sin^{-1}(c_0/\mathrm{M}c_{av})$ with the perpendicular to the carpet edge (Fig. 3), M being the Mach number and c_{av} the sound speed at the flight altitude.

Following a procedure similar to the one used for describing the vicinity of caustics (Pierce, 1989), Eq. (1) leads us to introduce the following dimensionless variables, which are better suited to the physics of the problem:

$$\begin{aligned}\tilde{t}&=(t-x^*/c_0)/T_{\mathrm{inc}}, \quad \tilde{x}=x^*/(2c_0T_{\mathrm{inc}}R^2)^{1/3},\\ \tilde{z}&=(2/c_0^2T_{\mathrm{inc}}^2R)^{1/3}z, \quad \tilde{p}_a=p_a/P_{\mathrm{inc}},\end{aligned} \tag{2}$$

where T_{inc} and P_{inc} are, respectively, the duration and the maximum amplitude of the incident pressure field at the cutoff (the field given by geometrical acoustics at the cutoff as if there was no ground).

Variable $\tilde{t}$ is introduced for the propagation time along the ground, $\tilde{z}$ for the diffraction boundary-layer thickness above the ground, and $\tilde{x}$ for the field attenuation as it penetrates into the shadow zone. Rewriting the fluid mechanics

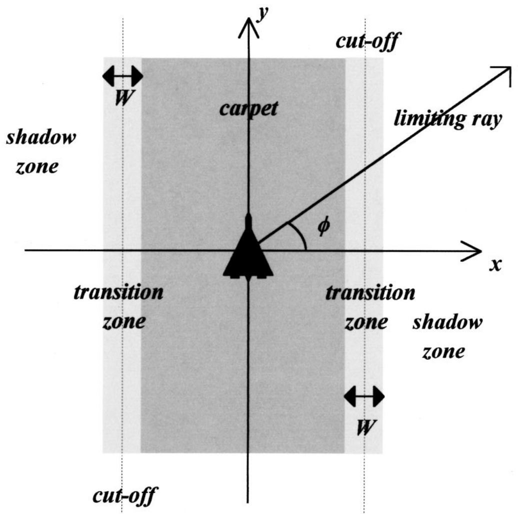

FIG. 3. The sonic boom carpet (view from top).

equations with this new system of coordinates, the dimensionless pressure field $\tilde{p}_a$ can be shown to satisfy Eq. (3) in the shadow zone:

$$\frac{\partial^2 \tilde{p}_a}{\partial \tilde{t} \partial \tilde{x}} = \frac{\partial^2 \tilde{p}_a}{\partial \tilde{z}^2} - \tilde{z} \frac{\partial^2 \tilde{p}_a}{\partial \tilde{t}^2} + \mu \frac{\partial^2 \tilde{p}_a^2}{\partial \tilde{t}^2}, \tag{3}$$

with ρ_0 the air density at ground level and $\beta = 1 + B/2A$ the nonlinearity parameter ($\beta = 1.2$ for air). The dimensionless parameter μ defined by

$$\mu = \beta \frac{P_{\mathrm{inc}}}{\rho_0 c_0^2} \left(\frac{R}{T_{\mathrm{inc}} c_0} \right)^{2/3} \tag{4}$$

is a measurement of quadratic nonlinear effects relative to diffraction effects. In Eq. (3), cubic nonlinear terms and second-order diffraction effects have been neglected. The right-hand side of Eq. (3) is identical to the nonlinear Tricomi equation obtained by Guiraud (1965) for describing the nonlinear sound field in the vicinity of caustics, while the left-hand side describes the field evolution as it penetrates into the shadow zone. The generalized nonlinear Tricomi equation (3) can easily be shown to be similar to the unsteady, small perturbation transonic potential equation in a stratified atmosphere. Therefore it may be called an "unsteady" Tricomi equation; here the "unsteady" term $\partial^2 \tilde{p}_a / \partial \tilde{t} \partial \tilde{x}$ describes the wave penetration inside the shadow zone.

Boundary conditions are of course different from that of aerodynamics, and are the following: (i) the pressure field vanishes at infinite times:

$$\tilde{p}_a(\tilde{t} = \pm \infty, \tilde{x}, \tilde{z}) = 0, \tag{5a}$$

(ii) it satisfies the impedance condition at the ground:

$$\hat{\tilde{p}}_a = \frac{i}{\omega T_{\mathrm{inc}}} \left(\frac{2 c_0 T_{\mathrm{inc}}}{R} \right)^{1/3} \frac{Z_s(\omega)}{Z_0} \frac{\partial \hat{\tilde{p}}_a}{\partial \tilde{z}} \quad \text{at } \tilde{z} = 0 \tag{5b}$$

[in Eq. (5b), $\hat{\tilde{p}}_a$ is the time Fourier transform of the pressure field, Z_0 and Z_s are respectively the air and ground surface impedance, and $\omega/2\pi$ the frequency], and (iii) it satisfies a radiation condition far from the ground in the shadow zone, similar to the one satisfied by the sound field reflected over a caustic (Guiraud, 1965; Seebass, 1971):

$$\tilde{p}_a \underset{\tilde{z} \to +\infty}{\sim} \tilde{z}^{-1/4} G(\tilde{x}, \tilde{t} - 2\tilde{z}^{3/2}/3), \tag{5c}$$

where the function $G(\tilde{x},.)$ is the (undetermined) outgoing waveform emanating from diffracted rays far over the ground at distance $\tilde{x}$. Equation (5c) can be equivalently written as a radiation condition specifying that there is no incident wave inside the shadow zone:

$$\left(\tilde{z}^{-1/4} \frac{\partial \tilde{p}_a}{\partial \tilde{z}} + \tilde{z}^{1/4} \frac{\partial \tilde{p}_a}{\partial \tilde{t}} \right) (\tilde{t}, \tilde{x}, \tilde{z} \to +\infty) = 0. \tag{5d}$$

The matching condition to geometrical acoustics will be detailed in Sec. IV.

TABLE I. Parameter estimation (aircraft flying at 11.000 m and Mach 2.0).

Atmosphere	Standard	Low gradient
Carpet width (km)	79	239
Incident pressure amplitude (Pa)	50	10
Parameter μ	0.03	0.1
Boundary-layer thickness H (m)	200	790
Matching zone width W (km)	4.8	44

III. MAGNITUDE ORDERS

The parameter μ [Eq. (4)] measures the relative magnitude order of nonlinear effects compared to diffraction around the cutoff and inside the shadow zone. Nonlinear effects are dominant during geometrical propagation from the aircraft down to the ground, and surely are negligible deep inside the shadow zone where amplitude is small and diffraction-induced attenuation dominant. The question remains on the importance of nonlinear effects around the cutoff. A moderate value of parameter μ would mean that nonlinearities are intimately coupled to diffraction there. The value of parameter μ is evaluated in Table I in two cases: first for a standard atmosphere, second for a low temperature-gradient atmosphere. As an example, we chose the case of an atmosphere having a 5 °C ground temperature, a constant gradient of −0.1 °C/km over 1 km above the ground, and then a constant gradient of −6.14 °C/km up to 11 km (Fig. 4). Above, it is identical to the standard atmosphere. Such an atmosphere can be viewed as a simple model for a quiet winter morning. According to Eq. (4), a small

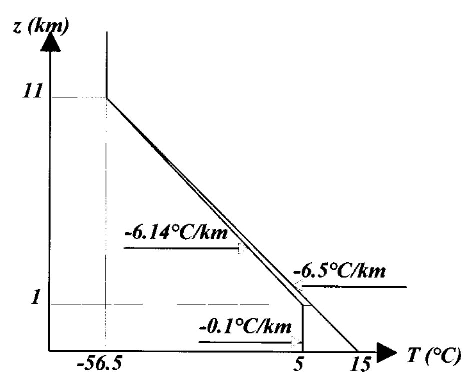

FIG. 4. Standard and low gradient atmosphere.

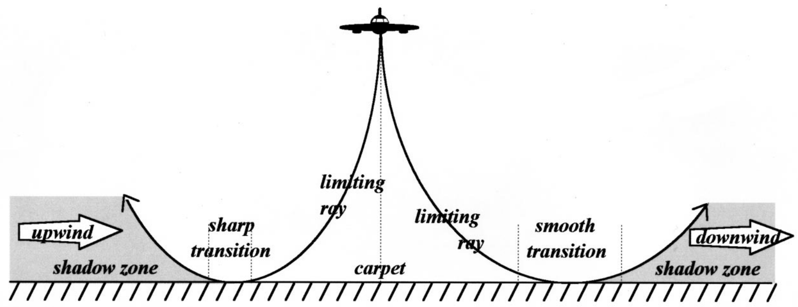

FIG. 5. Qualitative illustration of anisotropic wind effects.

temperature gradient, and consequently a large radius of curvature R, is expected to increase the relative importance of nonlinear effects in the shadow zone. However, a small temperature gradient also leads to an increase of the carpet width and a decrease of the incident pressure amplitude at the cutoff by geometrical attenuation, thus counterbalancing the decrease of the rays curvature. In order to take this into account, we computed the ray-tube area at the cutoff for the two different atmospheres; the ray-tube area for the low temperature gradient was found to be about 25 times larger. According to linear geometrical acoustics, we choose an incident pressure amplitude at the cutoff five times smaller. Additional decay due to nonlinear attenuation over a longer propagation path is expected to dampen even further the field at the cutoff. Compared values for the two different cases are collected in Table I. Results show that, in both cases, nonlinear effects are expected to be relatively small. However, this conclusion can be viewed only as provisional. The two cases studied in this article cannot be viewed as really representative of all atmospheric situations. Especially, the influence of wind gradients should be taken into account as indicated below. There could be some (probably rare) atmospheres almost uniform very near the ground but with very sharp gradients (of either temperature or wind) in altitude, which could lead to larger values. A statistical analysis relying on a long-term meteorological database is planned to be completed in a way similar to previous studies on sonic boom carpet widths (Heimann, 2001). Such a study would determine the probability (if any) of occurrence of meteorological situations implying significant nonlinear effects near the cutoff.

In Table I, two other characteristic lengths also are evaluated: the thickness H of the diffraction boundary layer above the ground, and the width W of the matching zone on each side of the cutoff. The thickness H is defined as the height at which the arrival time of the diffracted signal at point M inside the shadow zone differs from more than T_{inc} from the arrival time at point P on the ground (Fig. 2). The transition zone between the carpet, where geometrical acoustics is valid, and the true shadow zone in which the sound field decays exponentially, can be estimated by W (Fig. 3). This gives

$$H=\left(\frac{9Rc_0^2T_{\text{inc}}^2}{8}\right)^{1/3} \quad \text{and} \quad W=\cos\varphi(c_0T_{\text{inc}}R^2)^{1/3}. \tag{6}$$

It is to be noted that the characteristic width W is also Mach dependant, and increases with the Mach number. In Table I we note the large increase of the width of the matching zone in the low-gradient atmosphere. A large radius of curvature (weakly refractive atmosphere) leads to a smooth transition near the cutoff and a slow decay in the shadow zone, while a small radius of curvature (strongly refractive atmosphere) leads to a sharp transition and a rapid decay in the shadow zone. Such a qualitative conclusion can explain the asymmetry of the lateral peak amplitude distribution measured by Maglieri and Plotkin (1995) if we assume a windy atmosphere. An upwind propagation (small radius of curvature) leads to a shorter carpet, a sharper transition, and a stronger decay in the shadow zone, while a downwind propagation (large radius of curvature) leads to a wider carpet, a smoother transition, and a slower decay in the shadow zone. These qualitative effects are illustrated on Fig. 5. They are observed in the measurements reported by Maglieri and Plotkin (their Figure 16) for an XB-70 flying at Mach 2.0, if we assume an upwind propagation on the left side of the figure and a downwind propagation on the right side.

The detailed diffraction process in the shadow zone of a stratified, windy atmosphere remains rather intricate, though an approximate generalization of Pierce's solution was given recently by Li *et al.* (1998). One difficulty is that, if the ground wind is not constant, the creeping waves propagate over the ground along curved rays deviated by lateral winds. Moreover, in the windy case, rays are not normal anymore to the wavefront, so that Eq. (1) is not strictly valid anymore. However, if the atmosphere is vertically stratified, creeping waves propagate along straight rays, and the diffracted rays are normal to the wavefront at the ground level. In this case, we expect the diffraction process to be similar to the quiescent case, but with a modified radius of curvature taking into account the wind stratification:

$$R=-\frac{c_0+\vec{u}(0)\cdot\vec{n}}{[(dc/dz)(0)+(d\vec{u}/dz)(0)\cdot\vec{n}]}, \tag{7}$$

where $\vec{u}(z)$ is the horizontal wind speed and $\vec{n}$ is the unit horizontal vector along the Ox^* axis (oriented towards the shadow zone). As wind gradients are frequently comparable in magnitude order to temperature gradients, significant wind effects can thus be simply incorporated into the present model. Especially, very large radii of curvature are possible for downwind propagation, leading to effects similar to those observed for small temperature gradients [however, if the wind gradient is too large, the radius (7) will be negative in the case of downwind propagation, and the geometrical shadow zone will not exist any more].

IV. MATCHING TO GEOMETRICAL ACOUSTICS

In the linear case, it is possible to find an analytical expression of the sound field in the shadow zone by a proper matching to the geometrical acoustics approximation over the carpet. We proceed in a way similar to Bouche and Molinet (1994), who study the shadow zone of a convex body in a homogeneous medium. Their method is applied here to the case of an upward-refracting atmosphere. They suggest splitting the sound field into an incident geometrical part $\tilde{p}_a^{\mathrm{inc}}$ (the field given by geometrical acoustics at the cutoff as if there was no ground), and a diffracted part $\tilde{p}_a^{\mathrm{dif}}$ which takes into account ground effects and diffraction. First, an analytical approximation of the incident field near the cutoff is derived. The eikonal function can be evaluated along the limiting ray by a straightforward Taylor expansion:

$$\Psi(l)=\frac{1}{c_0}(l+l^3/6R^2+O(l^4/R^3)), \tag{8}$$

where l is the curvilinear coordinate along the limiting ray. At the same order of approximation, the equation of the wavefront cutting the limiting ray at the point of curvilinear coordinate l is

$$l=x+\frac{xz}{R}-\frac{x^3}{3R^2}+O(x^4/R^3), \tag{9}$$

so that the eikonal function in the vicinity of the carpet edge can be approximated by

$$\Psi(\overline{x})=\frac{1}{c_0}\left(x+\frac{xz}{R}-\frac{x^3}{6R^2}+O(x^4/R^3)\right). \tag{10}$$

Consequently, the incident pressure field is given near the cutoff by

$$\tilde{p}_a^{\mathrm{inc}}=F(\tilde{t}-\tilde{x}\tilde{z}+\tilde{x}^3/3), \tag{11}$$

$F(\tilde{t})$ being the (dimensionless) time waveform at the cutoff. It is easy to check that expression (11) is an *exact* solution of the linear Tricomi equation. It is then possible to determine by Fourier transforms the analytical expression of the acoustic field as a Fock integral (Pierce, 1989) in the vicinity of the carpet edge. We set

$$\tilde{p}_a=\int_{-\infty}^{+\infty}d\tilde{\omega}\int_{-\infty}^{+\infty}\hat{\tilde{P}}(\tilde{\omega},\tilde{K},\tilde{z})\exp(i(\tilde{K}\tilde{x}-\tilde{\omega}\tilde{t}))\,d\tilde{K}, \tag{12}$$

so that the incident Fourier component is equal to

$$\hat{\tilde{P}}^{\mathrm{inc}}=\frac{\mathrm{TF}^{-1}(F)(\tilde{\omega})}{|\tilde{\omega}|^{1/3}}\mathrm{Ai}\left(\frac{\tilde{K}\,\mathrm{sgn}(\tilde{\omega})}{|\tilde{\omega}|^{1/3}}-|\tilde{\omega}|^{2/3}\tilde{z}\right), \tag{13}$$

with $\mathrm{TF}^{-1}(F)$ the inverse Fourier transform of F, Ai the Airy function and Ai′ its derivative. The diffracted component is proportional to

$$\mathrm{Ai}\left(\left(\frac{\tilde{K}\,\mathrm{sgn}(\tilde{\omega})}{|\tilde{\omega}|^{1/3}}-|\tilde{\omega}|^{2/3}\tilde{z}\right)\exp\left(\frac{2i\,\mathrm{sgn}(\tilde{\omega})\pi}{3}\right)\right),$$

which is the solution of the (linear) unsteady Tricomi equation that satisfies the radiation condition Eq. (5d). The proportionality constant is determined by the impedance boundary condition Eq. (5b) satisfied by the *total* field. This completely determines the pressure field close to the cutoff. Returning to physical variables, one has (Coulouvrat, 1998)

$$p_a(x^*,z,t)=\mathrm{TF}\left(\left(\frac{2c_0R^2}{\omega}\right)^{1/3}\hat{P}(\omega,x^*,z)\mathrm{TF}^{-1}(F)(\omega)\right), \tag{14}$$

with

$$\begin{aligned}\hat{P}=\int_{-\infty}^{+\infty}dk\Bigg\{&\mathrm{Ai}\left(\tau-\frac{z}{l(\omega)}\right)\\&-\frac{\mathrm{Ai}'(\tau)-\varepsilon q\mathrm{Ai}(\tau)}{e^{2i\varepsilon\pi/3}\mathrm{Ai}'(\tau e^{2i\varepsilon\pi/3})-\varepsilon q\mathrm{Ai}(\tau e^{2i\varepsilon\pi/3})}\\&\times\mathrm{Ai}\left(\left(\tau-\frac{z}{l(\omega)}\right)e^{2i\varepsilon\pi/3}\right)\Bigg\}\exp(ikx^*),\end{aligned} \tag{15}$$

where $l(\omega)=(c_0^2R/2\omega^2)^{1/3}$ is a characteristic boundary-layer thickness at frequency ω, $\tau(\omega,k)=2(\omega/c_0)(k-\omega/c_0)l^2$, $\varepsilon=\mathrm{sgn}(\omega)$, and $q(\omega)=i[Z_0/Z_s(\omega)](|\omega|R/2c_0)^{1/3}$ is a measurement of finite ground-impedance effects at frequency ω.

In the shadow zone, we deduce from the residue theorem the expansion of integral (15) into a series of creeping waves:

$$\begin{aligned}p_a=\mathrm{TF}\Bigg\{&\mathrm{TF}^{-1}(F)(\omega)\\&\times\sum_n\exp(ik_nx^*)\frac{\mathrm{Ai}[b_n-(z/l)e^{2i\varepsilon\pi/3}]}{[\mathrm{Ai}'(b_n)]^2-b_n[\mathrm{Ai}(b_n)]^2}\Bigg\}.\end{aligned} \tag{16}$$

The residues $(b_n(\omega))_{n\in N}$ are the complex roots of the equation:

$$\mathrm{Ai}'(b_n)+e^{i\varepsilon\pi/3}q(\omega)\mathrm{Ai}(b_n)=0, \tag{17}$$

related to the complex wave number $(k_n(\omega))_{n\in N}$ of the creeping waves by

$$k_n=\frac{\omega}{c_0}\left(1+\frac{1}{2}\exp\left(\frac{-2i\varepsilon\pi}{3}\right)\frac{b_n}{(\omega l/c_0)^2}\right). \tag{18}$$

It is remarkable that, in the general case, the coefficients of the creeping waves series [Eq. (16)] are identical as those found by Berry and Daigle (1988) for a line source whose height tends to infinity. This means that, for a source located outside the diffraction boundary-layer, the way sound diffracts at the cutoff is ‘‘universal,’’ in the sense that it depends only on atmosphere properties near the ground and ground impedance, but *not* on the source. The dimensionless formulation even shows that the case of an incident ‘‘*N*’’ wave on a rigid ground can be made independent of any parameters. This property has been used by Truphème and Coulouvrat (1999) for comparisons with ‘‘BoomFile’’ experiments made by USAF (Lee and Downing, 1991).

V. SOUND FIELD AT THE CUTOFF

At the cutoff and on a perfectly rigid ground, the series (16) simplifies to

TABLE II. Parameters for outdoor ground surfaces.

Ground type	Ω	a	s_f	σ(kPa·s/m^2)	σ_{eff} (kPa·s/m^2)
Red-pine forest floor	0.529	1.65	0.9	50	77
Grass covered field	0.4	1.58	0.75	300	422
Bare sandy terrain	0.269	1.39	0.725	366	715
Barren sandy plain	0.379	1.27	0.725	1820	2524

$$p_a(t,x=0,z=0)=\left(-\sum_{n=0}^{+\infty}\frac{1}{b_n\mathrm{Ai}(b_n)}\right)F(t)=1.399F(t). \tag{19}$$

The incident pressure field on a rigid ground is thus amplified by a factor 1.399, instead of a factor 2 (mirror reflexion) deep inside the carpet. This classical result (Logan and Yee, 1962) proves that (i) the value of 1 postulated by Onyeowu for his empirical reflexion coefficient is not supported by theory, (ii) if only the first term is taken into account in the series expansion (19), one gets a value equal to 1.832 instead of 1.4, thus overestimating the cutoff amplitude by 31%.

However, the assumption of a rigid surface is not very realistic, especially at medium and high frequencies, for which parameter $q(\omega)$ cannot be neglected any more. Finite impedance effects lead to absorption by the porous ground material as sound grazes over the geometrical carpet. This results in lower amplitudes and finite rise times at the cutoff, and a larger attenuation in the shadow zone. For describing the ground material properties, the model of Attenborough (1983) gives the ground impedance as a complex, frequency-dependant function:

$$Z_s(\omega)=\frac{aZ_0}{\Omega\sqrt{[1+(\gamma-1)T(\sqrt{i}\mathrm{Pr}^{1/2}\lambda_P)][1-T(\sqrt{i}\lambda_P)]}}, \tag{20}$$

where a is the tortuosity ($a>1$), Ω is the porosity ($\Omega<1$), $\gamma=1.4$ is the ratio of the specific heats, and $\mathrm{Pr}=0.724$ is the Prandtl number. The parameter $\lambda_P=\sqrt{8\omega\rho_0 a^2/\Omega\sigma s_f^2}$ is the ratio of the mean pore size to the acoustic boundary layer thickness inside a pore, σ being the static flow resistivity and s_f a dynamical shape parameter. Function $T(x)$ is equal to $T(x)=2J_1(x)/xJ_0(x)$ with $J_n(x)$ the nth Bessel functions. Among the four parameters characterizing the material (a,Ω,σ,s_f), only the shape parameter is not directly measurable, but it varies little between 0.5 and 1. At low frequencies, acoustical absorption in the porous material can be described by a single parameter, the effective resistivity $\sigma_{\text{eff}}=s_f^2\sigma/\Omega$. For numerical simulations, we chose four outdoor ground surfaces, whose parameter values found in the literature (Attenborough, 1983, 1985) are recalled in Table II. Ground effects were evaluated for an incident ''N'' wave of duration 0.27 s and of normalized unit amplitude 1 over the four ground surfaces selected previously. Results are collected in Table III for the two different atmospheres described in Sec. III. Ground impedance effects are all the more pronounced as the (effective) flow resistivity of the ground material is smaller, as can be seen in Table III. However, even for a relatively rigid soil such as a barren sandy plain and a standard atmosphere, the signal rise time produced by ground porosity at the cutoff is of order 10 ms. It is comparable or longer than typical rise times resulting from propagation into a turbulent atmosphere over the carpet (generally between 1 and 10 ms, Bass *et al.*, 1998). Consequently, one can conclude that ground impedance effects *must* be taken into account to predict the rise time of sonic booms close to the cutoff on each side of the carpet edge. A low temperature gradient dramatically increases the influence of ground absorption, because of the increased width of the transition zone through which sound grazes over the ground. Very large rise times are forecast, which means much less annoying booms for outdoor hearing (annoyance for sonic boom indoors is primarily due to building rattle which depends on duration and peak pressure but very little on rise time). In a windy atmosphere, a similar effect can be expected on the downwind carpet side [long and smooth signals are reported by Maglieri and Plotkin (1995) on what we believe to be the downwind side of the carpet]. On the upwind side, influence of ground absorption will be smaller, leading to a cutoff field closer to the rigid ground case. One important conclusion is that ground diffraction and absorption effects are also important *inside* the carpet, over the distance W that can vary between a few kilometers to several tens of kilometers, depending on the atmospheric conditions. It is well known that the geometrical theory of diffraction used in the present model is not always valid deep inside the shadow zone, because of sound scattering by turbulence (Daigle *et al.*, 1986). However, the present model shows that diffraction effects can lead to large effects (low amplitudes and long rise times) also in regions where the theory is well established.

TABLE III. Calculated amplification factor and rise time at the cutoff; standard atmosphere/(**low gradient atmosphere**).

Ground nature	Amplification factor	Rise time (ms)
Rigid	1.40/(**1.40**)	0/(**0**)
Barren sandy plain	1.24/(**1.04**)	9.2/(**25.7**)
Bare sandy terrain	1.17/(**0.88**)	14.8/(**39.9**)
Grass-covered field	1.13/(**0.81**)	18.1/(**46.8**)
Red-pine forest floor	0.96/(**0.54**)	33.0/(**73.5**)

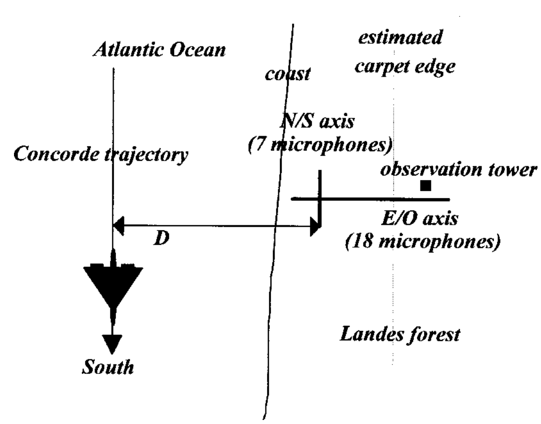

FIG. 6. Concorde test flights.

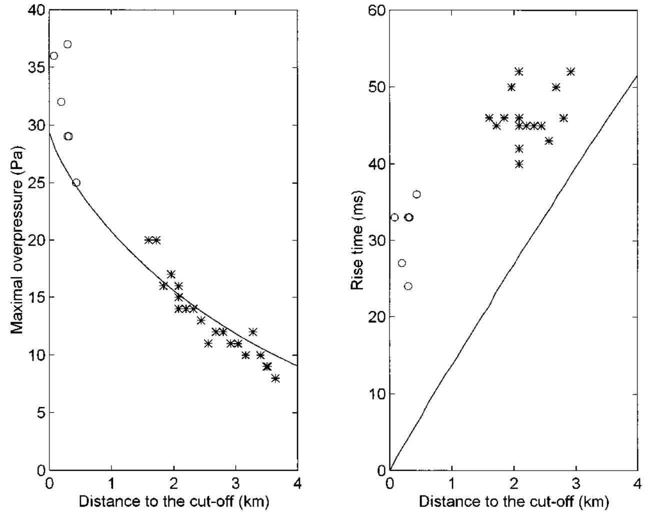

FIG. 7. Maximum overpressure and rise time in the shadow zone versus distance to the carpet cutoff over a rigid surface. Theory (solid line) and Concorde measurements (○ and ∗).

VI. COMPARISONS WITH CONCORDE TEST FLIGHTS

The sonic boom inside the shadow zone as predicted by theory will now be simulated numerically and compared to Concorde sonic boom measurements. Computation of sonic booms over a finite impedance ground surface requires several successive steps. (1) Calculate the Fourier transform of the incident pressure field by means of fast discrete Fourier transform algorithms (FFT). (2) For each frequency, solve the dispersion equation (17) for the selected number of creeping waves. (3) Calculate the series coefficient appearing in Eq. (16) and perform the series summation. (4) Compute the time signal by an inverse FFT.

As typical incident booms resembles ''*N*'' waves with two steep shock waves, it is necessary to retain a large number of frequencies ($\sim 2^{13}$). As the creeping waves series is slowly convergent, a high number of modes is necessary ($\sim$50). Consequently, step (2) in the numerical procedure is numerically time consuming if the ground surface is not perfectly rigid. For each frequency and each creeping mode, the dispersion equation is solved according to the procedure described by Raspet *et al.* (1991), by a Newton iterative algorithm. The frequency is increased step-by-step. The initial point of the Newton algorithm is the solution computed for the previous frequency and same mode number. For the lowest frequency, the initial point is the rigid case solution.

In 1973, Concorde test flights were conducted near the city of Biscarrosse (Gironde, France) along the Atlantic Coast. Concorde flew over the Atlantic Ocean in a north/south direction, and sonic boom signals were registered by microphones located in the Landes region, along two south/north and east/west axes (Fig. 6) (Parmentier *et al.*, 1973). Test flights were performed at different distances from the coast and at different Mach numbers. For some of the flights, Concorde trajectory was such that the microphones were partly or totally in the estimated shadow zone.

Numerical results are presented in Figs. 7–12 and compared to some Concorde sonic boom measurements. Figure 7 shows the computed maximum overpressures and rise times versus distance to the cutoff over a rigid ground. Results are compared to two Concorde test flights, one (indicated by circles) for which a few microphones were located inside the shadow zone close to the carpet edge, and one (indicated by stars) for which all microphones were located relatively deep inside the shadow zone. Numerical results were obtained for a standard atmosphere and an incident ''*N*'' wave of duration 0.27 s and 21 Pa amplitude. Simulations show that

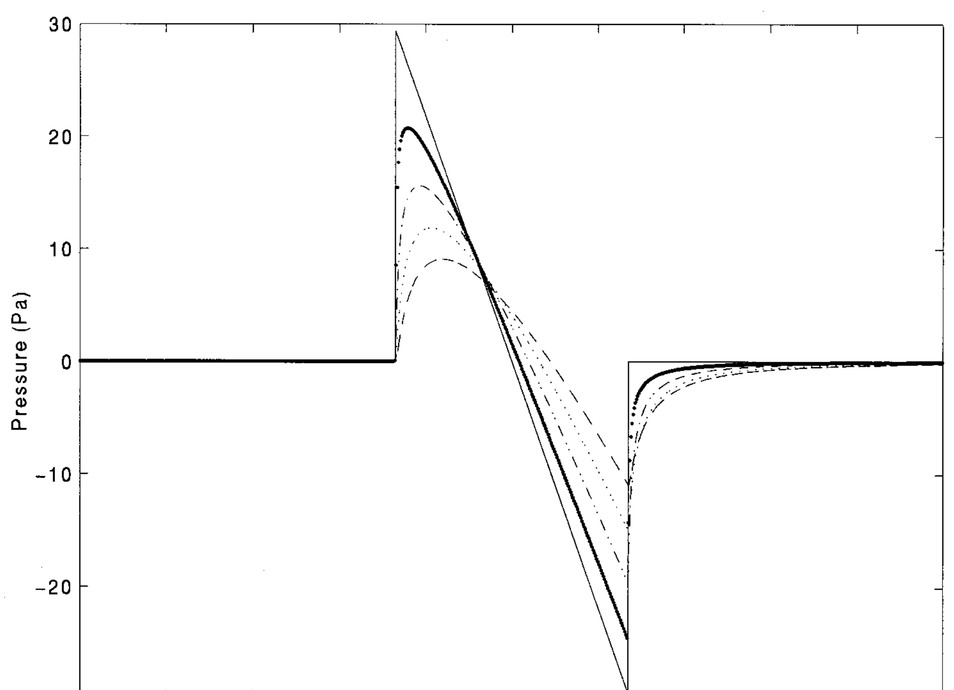

FIG. 8. Computed sonic boom pressure signals over a rigid surface at 0 (———), 1 (···), 2 (–.–.–), 3 (---), and 4 (–––) km from the cutoff.

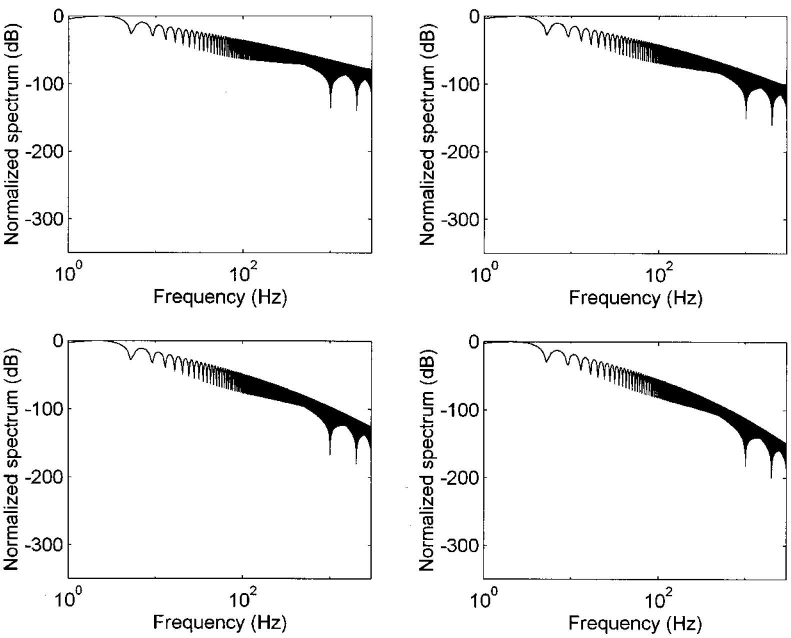

FIG. 9. Computed sonic boom pressure signals over a rigid surface. From left to right and top to bottom: normalized spectrum at 1, 2, 3, and 4 km from the carpet edge.

(i) the maximum overpressure decays almost exponentially with distance in the shadow zone; and

(ii) the rise time increases linearly with distance.

Comparisons indicate that the pressure field decay is in very good agreement with theory. The agreement is not so good for the rise time, but the rate of increase with distance is correct: the creeping wave's absorption results into long rise times in the deep shadow zone, of order 50 ms at 4 km. The computed rise time is probably underestimated because we have not taken into account (*i*) atmospheric turbulence and (*ii*) finite ground impedance. As shown previously, the influence of ground absorption on the finite rise time is expected to be significant near the cutoff. Taking into account that the rise time is extremely sensitive to the effects of even mild turbulence and the local conditions of the microphone emplacement, theoretical results can nevertheless be estimated satisfactory.

Figure 8 displays computed time signals at 0, 1, 2, 3, and 4 km from the carpet edge. We clearly observe the signal decay as it propagates deep into the shadow zone, and the rounding of the initial shock fronts because of diffraction-induced attenuation. The shock structure always spreads out *after* the initial shock front, as the creeping waves phase velocity is slightly smaller than the sound velocity. Figure 9 shows the normalized frequency spectrum (from 1 to 3000 Hz) of the signal at 1, 2, 3, and 4 km from the cutoff. It is obvious on the figure that the low-frequency spectrum remains unaltered during propagation, while the high-frequency content is strongly dampened by diffraction-induced attenuation. There is a 45-dB loss between 1 and 4 km at 1000 Hz, and a 70-dB loss at 3000 Hz. The maximum overpressure decay in the shadow zone is therefore due to the high-frequency attenuation, that spreads out the shock and erases the sharp pressure peak.

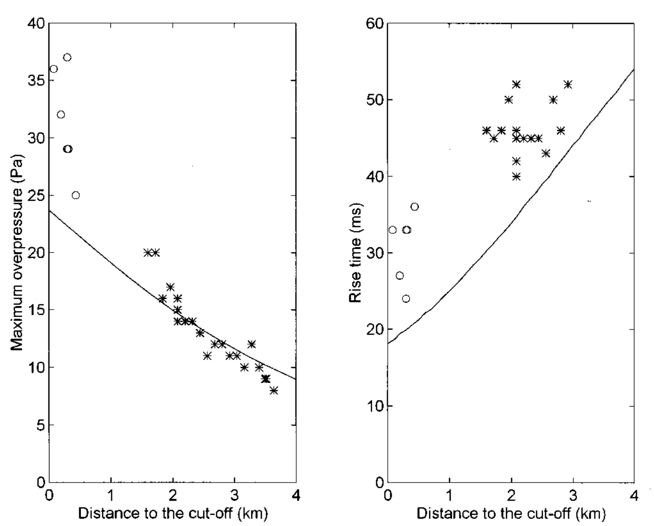

FIG. 10. Maximum overpressure and rise time in the shadow zone versus distance to the carpet edge over a grass-covered field. Theory (solid line) and Concorde measurements (○ and $*$).

Figures 10–12 present the same results, but with computations over a grass-covered field (see Table II for the corresponding values). It must be noted that deep inside the shadow zone, the maximum overpressure and rise time curves (Fig. 10) are very similar to those of the *rigid* case. This can be explained as follows: according to the definition of parameter q, the influence of finite ground impedance is mostly sensitive at high frequencies. As the high frequencies are the most attenuated, they completely disappear deep into the shadow zone. Consequently, sufficiently far from the cutoff, there remain only low frequencies which propagate almost as if the ground surface was rigid. On the contrary, close to the carpet edge, the ground impedance influence is major, with an increase of the rise time and a decrease of the maximum overpressure. Compared to Concorde sonic booms, the rise time is in better agreement there now, but the maximum overpressure is slightly underestimated near the

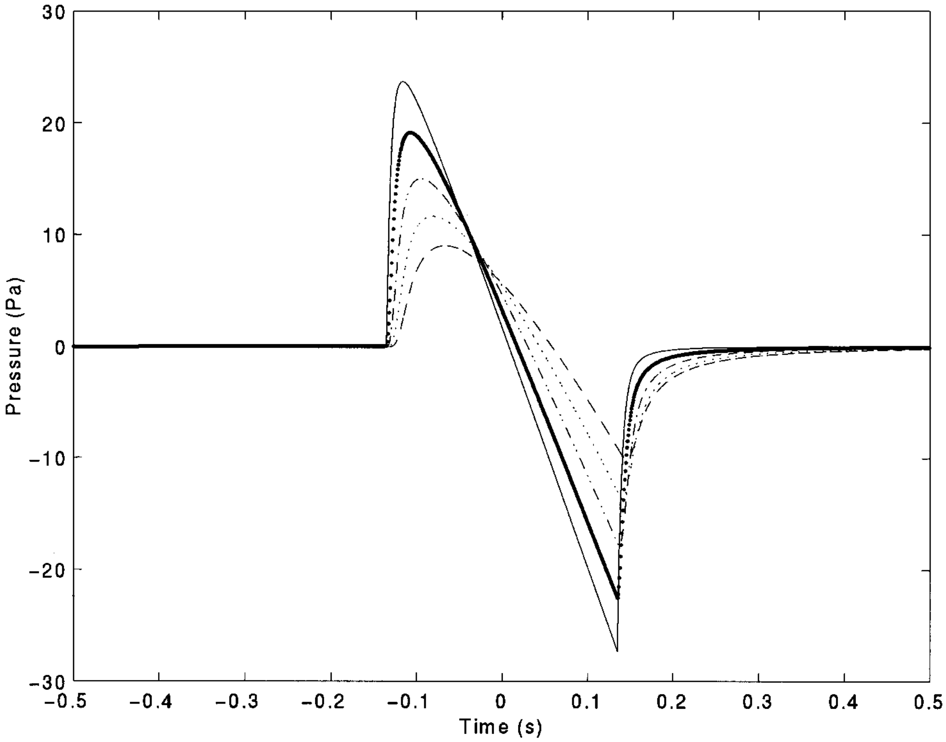

FIG. 11. Computed sonic boom pressure signals over a grass-covered field at 0 (———), 1 (···), 2 (–.–.–), 3 (---) and 4 (–––) km from the cutoff.

cutoff. Maybe part of the initial rise was due to atmospheric turbulence.

Figure 11 shows the pressure time signals at the same distances as Fig. 8, but over a grass-covered field. The major difference with the rigid case is that time signals look more rounded near the cutoff. Figure 12 outlines the dramatic effect of finite ground impedance on the high-frequency content of the signal spectrum: there is now a 160 dB loss at 3000 Hz between 1 and 4 km. All frequencies above 100 Hz are strongly attenuated, and the sonic boom will only be perceived as a low-frequency rumbling noise.

VII. CONCLUSION

We have presented a geometrical theory of diffraction in a temperature-stratified atmosphere for predicting sonic booms in the shadow zone. A genuine extension to include horizontal winds was also proposed. Compared to previous studies, the main new points are (*i*) the proper matching to the nonlinear geometrical acoustics approximation over the carpet, (*ii*) the evaluation of nonlinear effects, (*iii*) the influence of finite ground impedance, and (*iv*) the comparison to in-flight (Concorde) data. Comparisons with Concorde measurements show the theory provides a reasonable evaluation of diffraction effects, though only the magnitude order of the rise time can be estimated. Numerical simulations outline the dramatic effects of atmospheric and ground conditions. Low temperature gradients or downwind propagation can lead to a large increase of the transition zone around the cutoff. This results in extremely long rise times at the cutoff

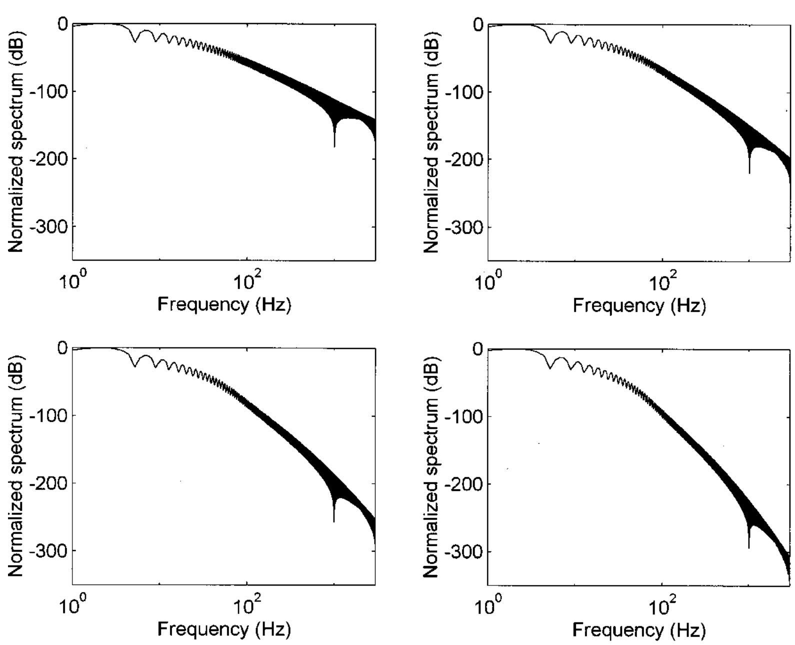

FIG. 12. Computed sonic boom pressure signals over a grass-covered field. From left to right and top to bottom: normalized spectrum at 1, 2, 3, and 4 km from the carpet edge.

as sound propagates over a finite impedance ground, even for a rather rigid ground. Further studies should take into account more realistic ground impedances (variable porosity or layered soils) and atmospheric turbulence.

ACKNOWLEDGMENTS

This work was supported by EADS Airbus SA, Toulouse, France. I am grateful to J.-P. Guiraud (LMM) and R. Etchevest (EADS Airbus SA) for helpful discussions. Concorde measurements were communicated by EADS Airbus SA. Comments of reviewers helped me to greatly improve this article.

Attenborough, K. (**1983**). ''Acoustical characteristics of rigid fibrous absorbents and granular materials,'' J. Acoust. Soc. Am. **73**, 785–799.

Attenborough, K. (**1985**). ''Acoustical impedance models for outdoor ground surfaces,'' J. Sound Vib. **99**, 521–544.

Bass, H. E., Layton, B. A., Bolen, L. N., and Raspet, R. (**1987**). ''Propagation of medium strength shock waves through the atmosphere,'' J. Acoust. Soc. Am. **82**, 306–310.

Bass, H. E., Raspet, R., Chambers, J. P., and Kelly, M. (**1998**). ''Modification of sonic boom waveforms during propagation from the source to the ground,'' Sonic Boom Symposium, 136th Meeting, Acoustical Society of America, J. Acoust. Soc. Am. **104**, 1830.

Berry, A., and Daigle, G. (**1988**). ''Controlled experiments of the diffraction of sound by a curved surface,'' J. Acoust. Soc. Am. **83**, 2047–2058.

Bouche, D., and Molinet, F. (**1994**). *Méthodes Asymptotiques en Electromagnétisme* (Springer, Berlin).

Cleveland, R. O. (**1995**). ''Propagation of sonic booms through a real, stratified atmosphere,'' Ph.D. dissertation, Department of Physics, The University of Texas at Austin.

Coulouvrat, F. (**1997**). ''Théorie géométrique non linéaire de la diffraction en zone d'ombre,'' C. R. Acad. Sci., Ser. IIb: Mec., Phys., Chim., Astron. **325**, 69–75 (in French, English abridged version).

Coulouvrat, F. (**1998**). ''Sonic boom beyond the carpet edge,'' *4th AIAA/CEAS Conference*, Toulouse, 2–4 June 1998, AIAA Technical Paper 98–2247, pp. 265–275.

Daigle, G., Embleton, T. F. W., and Piercy, J. E. (**1986**). ''Propagation of sound in the presence of gradients and turbulence near the ground,'' J. Acoust. Soc. Am. **79**, 613–627.

Downing, M. (**1998**). ''Summary of USAF sonic boom research,'' Sonic Boom Symposium, 136th Meeting, Acoustical Society of America, J. Acoust. Soc. Am. **104**, 1860.

Guiraud, J.-P. (**1965**). ''Acoustique géométrique, bruit balistique des avions supersoniques et focalisation,'' J. Mec. **4**, 215–267 (in French).

Hayes, W. D., Haefeli, R. C., and Kulsrud, H. E. (**1969**). ''Sonic boom propagation in a stratified atmosphere with computer program,'' NASA CR-1299, Washington.

Heimann, D. (**2001**). Effects of long-term atmospheric variability on the width of a sonic-boom carpet produced by a high-flying supersonic carpet, ARLO **2**, 73–78.

Lee, R. A., and Downing, J. M. (**1991**). ''Sonic booms produced by United States Air Force and United States Navy aircraft: measured data,'' Armstrong Laboratory, Air Force Systems Command, AL-TR-1991-0099.

Li, K. M., Ostashev, V. E., and Attenborough, K. (**1998**). ''The diffraction of sound in a stratified moving atmosphere above an impedance plane,'' Acust. Acta Acust. **84**, 607–615.

Logan, N. A., and Yee, K. S. (**1962**). ''A mathematical model for diffraction by convex surfaces,'' in *Electromagnetic waves*, edited by R. E. Langer (Univ. of Wisconsin, Michigan), pp. 139–180.

Maglieri, D. J., and Plotkin, K. J. (**1995**). ''Sonic Boom,'' in *Aeroacoustics of Flight Vehicles, Vol. 1, Noise Sources*, edited by H. H. Hubbard (Acoustical Society of America, New York), pp. 519–561.

Onyeowu, R. O. (**1975**). ''Diffraction of sonic boom past the nominal edge of the corridor,'' J. Acoust. Soc. Am. **58**, 326–330.

Parmentier, G., Mathieu, G., Schaffar, M., and Johe, Ch. (**1973**). ''Bang sonique de Concorde: enregistrement hors trace des variations de pression au sol. Centre d'Essais des Landes; 13 au 15 juin 1973,'' Institut Franco-Allemand de Recherches de Saint-Louis, RT-19/73 (in French).

Pierce, A. D. (**1989**). *Acoustics* (Acoustical Society of America, New York), Chap. 9, pp. 469–478.

Plotkin, K. J. (**1998**). ''State of the art of sonic boom modeling,'' J. Acoust. Soc. Am. **104**, 1830.

Raspet, R., and Franke, S. (**1988**). ''Residue series solution of impulse noise propagation into a shadow zone,'' J. Acoust. Soc. Am. **83**, 1964–1967.

Raspet, R., Baird, G. E., and Wu, W. (**1991**). ''The relationship between upward refraction above a complex impedance plane and the spherical wave evaluation for a homogeneous atmosphere,'' J. Acoust. Soc. Am. **89**, 107–114.

Robinson, L. D. (**1991**). ''Sonic boom propagation through an inhomogeneous windy atmosphere,'' Ph.D. dissertation, Department of Physics, The University of Texas at Austin.

Seebass, A. R. (**1971**). ''Nonlinear acoustic behavior at a caustic,'' Boeing Scientific Research Laboratory Document 01-82-1039.

Thomas, C. L. (**1972**). ''Extrapolation of sonic boom pressure signatures by the waveform parameter method,'' NASA TN D-6832.

Truphème, M.-A., and Coulouvrat, F. (**1999**). ''Détonation balistique (bang sonique) en bordure de carpette: comparaison entre les essais 'BoomFile' et la théorie géométrique de la diffraction,'' rapport final de stage de maîtrise de mécanique, Université de Versailles/Saint-Quentin-en-Yvelines (in French, English abstract).

Whitham, G. B. (**1952**). ''The flow pattern of a supersonic projectile,'' Commun. Pure Appl. Math. **5**, 301–348.

Whitham, G. B. (**1956**). ''On the propagation of weak shock waves,'' J. Fluid Mech. **1**, 290–318.

Model experiment to study sonic boom propagation through turbulence. Part III: Validation of sonic boom propagation models

Bart Lipkens[a)]

Applied Research Laboratories and Mechanical Engineering Department, The University of Texas at Austin, P.O. Box 8029, Austin, Texas 78713-8029

(Received 12 March 2000; revised 16 March 2001; accepted 23 March 2001)

In previous papers, we have shown that model experiments are successful in simulating the propagation of sonic booms through the atmospheric turbulent boundary layer. The results from the model experiment, pressure wave forms of spark-produced *N* waves and turbulence characteristics of the plane jet, are used to test various sonic boom models for propagation through turbulence. Both wave form distortion models and rise time prediction models are tested. Pierce's model [A. D. Pierce, "Statistical theory of atmospheric turbulence effects on sonic boom rise times," J. Acoust. Soc. Am. **49**, 906–924 (1971)] based on the wave front folding mechanism at a caustic yields an accurate prediction for the rise time of the mean wave form after propagation through the turbulence. [DOI: 10.1121/1.1371974]

PACS numbers: 43.28.Mw, 43.25.Cb [LCS]

I. INTRODUCTION

Recent efforts to develop a supersonic commercial airplane spurred interest in sonic boom research. The annoyance to sonic booms is an undesirable effect of supersonic flight, and presents a major obstacle to overland supersonic flight.

Peak pressure, rise time, and wave form shape are the main parameters that determine the subjective loudness of the sonic boom when heard outdoors.[1–5] The effect of atmospheric turbulence on sonic boom wave form distortion, peak pressure, and rise time has been studied, and several models have been developed that yield prediction for the waveform distortion and rise time.

Lipkens and Blackstock[6,7] showed that model experiments are successful in simulating the propagation of sonic booms through a turbulent atmosphere. Both the acoustic signal and the turbulence length scales were scaled down by the same factor. Electrical sparks produced *N* waves that propagated across a turbulent velocity field generated by a plane jet. The *N* wave form was measured by a wide band condensor microphone and the turbulence characteristics were obtained from hot-wire anemometry. After propagation through the turbulence, the wave form distortion of the *N* waves was similar to that of sonic booms, both in scale and in character.

The goal of this work is to use the model experiment data to test various sonic boom models for the propagation of booms through a turbulent atmosphere. These models have not been tested in a rigorous manner. When a correct scaling is obtained, the predictions from the sonic boom models should be applicable for the model experiment.

In Sec. II a brief overview is presented of the sonic boom models that we tested. In Sec. III the comparison of the model experiment results with the predictions from the sonic boom models is presented.

II. REVIEW OF SONIC BOOM MODELS

Sonic boom models for the propagation through the atmospheric turbulent boundary layer can roughly be divided into two categories. Some models yield estimates of the wave form distortion due to interaction with turbulence, while others emphasize the effect of turbulence on sonic boom rise time. Pierce and Maglieri[8] present an overview of the information that was available in the early 1970s of the effect of atmospheric irregularities on sonic boom propagation.

A. Distortion models

Pierce's model[9] is based on a combination of linear geometrical acoustics and diffraction effects. He considered a single layer of turbulence, whose assumed effect was to ripple the wavefront passing through the layer. Diffraction effects were then included in tracing the fronts to the ground. Low-frequency components diffract around small scale perturbations, while the high-frequency components propagate along rays with negligible diffraction. Therefore, diffraction washes out the focusing or defocusing of low-frequency components. The higher-frequency components of the sonic boom focus or defocus as determined by geometrical acoustics. Pierce argued that the propagation of the shocks is governed by geometrical acoustics, and that the expansion part of the sonic boom remains relatively undistorted because it is primarily composed of lower frequencies. Figure 1 shows the calculated signatures of a peaked and a rounded wave form obtained from a wave passing through a thin layer of turbulence, which causes a single parabolic ripple (concave or convex) of the wave front. Qualitatively, the model is able to yield a prediction for the spiking and rounding of the *N* wave, but the finer detail of the perturbations behind the

[a)]Present address: Mechanical Engineering, Virginia Commonwealth University, 601 West Main Street, Richmond, VA 23284-3015.

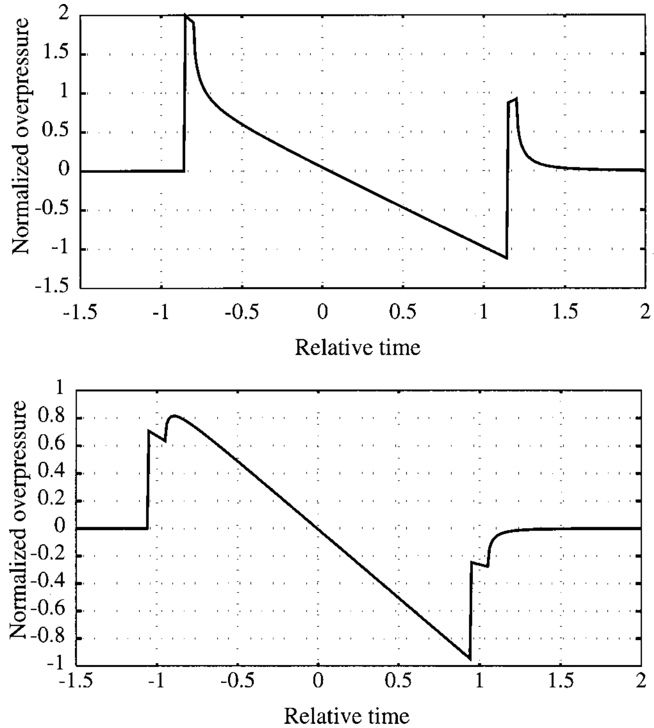

FIG. 1. Prediction of a spiked and rounded wave form.[9]

shock cannot be calculated. Another drawback of the model is that it does not provide any quantitative predictions for sonic boom data. Davy and Blackstock[10] demonstrated the effects of diffraction and refraction of electrical spark-produced N waves by a gas filled soap bubble. The sound speed of the gas inside the bubble determines whether the bubble acts as a converging or diverging lens. Their experiments showed that a soap bubble filled with helium rounds the wave form (diverging lens), while for an Argon-filled bubble, a spiked wave form (converging lens) is obtained. Ribner *et al.*[11] used a jet to study spiking and rounding of an N wave, generated by a shock tube. The signatures of N waves traveling upstream were of the spiked type, while signatures of downstream traveling waves were rounded. Refraction due to the mean flow pattern of the jet caused a focusing (upstream case) or defocusing (downstream case) of the wave. Ribner alluded to the existence of jets in the atmosphere and pointed out that they could be a viable mechanism for the spiking and rounding of sonic booms. Both experiments supported Pierce's model qualitatively.

Crow[12] applied first-order scattering theory of sound interacting with turbulence to transient wave forms. His model leads to a quantitative prediction of the perturbations behind the shock. The total wave is the sum of the incident wave unaffected by the turbulence and a scattered wave generated by the interaction of the incident wave with the turbulence. The main assumption is that the scattered wave is of first order in the fluctuations Δc associated with thermal fluctuations and $\Delta \mathbf{u}$ associated with mechanical turbulence. The partial differential equation that describes the pressure of the scattered wave[13] is

$$-\Box^2 p^S = D\{p^N\}, \tag{1}$$

where

$$\Box^2 = \nabla^2 - \frac{1}{c_0^2}\frac{\partial^2}{\partial t^2}$$

is the d'Alembertian, p^N is the incident wave, and p^S is the scattered wave. The incident N wave is modeled as a step function acoustic plane wave and has the form $p^N = \Delta p H(x_1 - c_0 t)$. Crow reasoned that a step shock is a good model since sonic boom measurements show that the most significant pressure perturbations are found behind the shock, an indication of the interaction between the shock and turbulence. The operator D has the form

$$D\{p^N\} = \frac{\partial}{\partial x_1}\left\{2m(\mathbf{x},t)\frac{\partial p^N}{\partial x_1}\right\}, \tag{2}$$

where

$$m(\mathbf{x},t) = (\Delta u_1 - \Delta c)/c_0,$$

is an effective Mach number, which combines the turbulent velocity fluctuations Δu_1 and temperature inhomogeneities Δc. Crow derived a formula which describes the mean-squared pressure perturbations. For turbulence of the form of the Kolmogorov inertial subrange, the mean-squared pressure perturbations take the form

$$\langle \psi^2(t)\rangle = (t_c/t)^{7/6}, \tag{3}$$

where

$$\psi(t) = p^S/\Delta p.$$

The parameter t is time relative to the arrival of the leading shock and

$$t_c = \frac{1}{c_0}(\sec\theta)^{11/7}\left[\int_0^{h_f} 1.33 c_0^{-2} h^{5/6} \epsilon_u^{2/3} dh\right]^{6/7}, \tag{4}$$

where ϵ_u is the turbulent energy dissipated per unit time by viscous stress, and

$$\sec\theta = M/(M^2-1)^{1/2},$$

where M is the flight Mach number. The integration limit h_f is the height of the atmospheric turbulent boundary layer. It is necessary to point out that Eq. (3) has a singularity at time $t=0$. The singularity is caused by the fact that this formula does not take a viscous subrange into account for the turbulence model. If a viscous subrange, i.e., a limit to the smallest possible eddy, is used, the value of $\langle \psi^2(0)\rangle \approx 10^8$, which Crow interpreted as having no physical meaning other than that the pressure perturbations near the shock front will be large. Figure 2 shows the variance in pressure, as predicted by Crow [Eq. (3)], for a value of $t_c = 2$ ms. Crow determined that typical values for t_c are in the range of 0.5–1.5 ms. The similar features for the bow and tail shock are explained by the fact that the turbulence is assumed to be frozen during the passage of the sonic boom.

Bauer and Bagley[14] used the results of a series of ballistic experiments to check the validity of Eq. (3). Bullets were fired into an open room, along one wall of which a turbulent jet was flowing. They gathered a large data set for several configurations of Mach number and turbulent jet velocities. They were able to confirm the correct order of magnitude of this equation. Pierce and Kamali[15] also tried to verify Eq. (3)

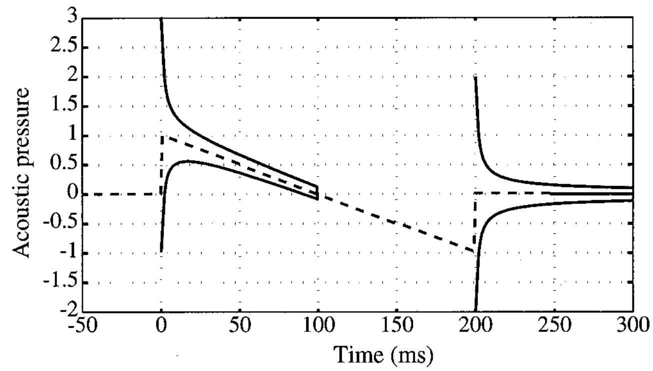

FIG. 2. Variance of acoustic pressure of a 200 ms duration N wave with a t_c value of 2 ms.[12]

by calculating the variance of a large set of sonic boom signatures and comparing it with the mean wave form. Their calculation showed agreement with the $-7/6$ power law prediction.

Pierce and Maglieri[8] mentioned several reservations to Crow's theory. First, according to Crow's scattering equation, the scattered wave and the incident wave are of the form $f(x+c_0t)$, which implies that no signal arrives earlier than the time $t+x/c_0$, regardless of the inhomogeneities. From geometrical acoustics, however, we know that there might be ray paths along which the signal travels faster than the ambient sound speed. Related to the problem of travel time is the question of shock arrival time. Is it the nominal arrival time from the theory or the actual arrival time? Crow used the latter, but a more detailed examination is warranted. Second, there is a question of how one compares the predicted variances $\langle \psi^2(t)\rangle$ with measured data. For each wave form time should start at the time of arrival of the shock, but for finite rise time wave forms this can lead to ambiguities. A uniform way to define arrival time is needed. Pierce and Maglieri also concluded from Crow's work that the probability of obtaining a spiked wave form is equal to that of a rounded wave form. They mentioned that this seems contrary to the results of Herbert, Hass, and Angell experiment,[16] in which rounded wave forms were more likely than spiked ones. Statistical analysis of the spark-produced N waves of Lipkens and Blackstock[7] also reveals that rounded waves are more prevalent than spiked waves.

Crow pointed out that his analysis could be extended to include plane waves of arbitrary shape. Plotkin[17] continued Crow's analysis for an incident wave of arbitrary form by representing it as a sum of infinitesimal steps. He was able to obtain an upper bound for the mean-squared pressure, which is given by

$$\langle (p_S)^2\rangle^{1/2} \leqslant \int_{-\infty}^{t}\left(\frac{t-\tau}{t_c}\right)^{-7/12}\frac{dp^N}{d\tau}\,d\tau. \tag{5}$$

This expression can be used to calculate an upper bound of the mean squared perturbation pressure of any incident wave form. As an example, we calculate an upper bound of the perturbation pressure for a ramp shock. The mean-squared pressure perturbation for a 1 ms ramp shock and a step shock is shown in Fig. 3. The value for Crow's characteristic time

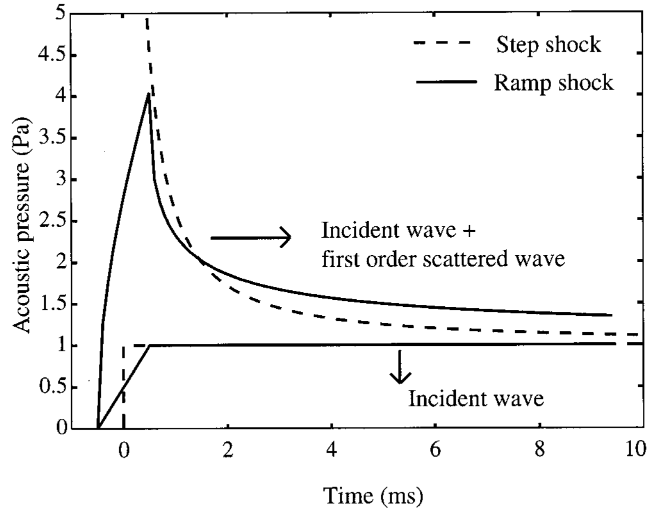

FIG. 3. Root mean-square perturbation pressure for a step shock and a ramp shock. The rise time of the ramp shock is 1 ms, and Crow's characteristic time is 1.5 ms.[17]

t_c is 1.5 ms. As one observes, the singularity that occurs for the step shock disappears for the ramp shock. The maximum pressure perturbation occurs at the end of the rise phase of the shock and is given by

$$\langle (p^S)^2\rangle_{\max}^{1/2} = \frac{12}{5}A\left(\frac{t_c}{t_0}\right)^{7/12}. \tag{6}$$

The decay of the perturbation pressure after the shock is nearly identical to Crow's solution for a step shock.

B. Rise time prediction models

Measured rise times of sonic booms generally range from 1 to 10 ms. If one uses a step shock model in a thermoviscous medium, then the Taylor shock thickness[18] can be calculated and is found to be of the order of 20–80 μs for typical sonic boom overpressures. The discrepancy between measured values of rise time and calculated values has been known for some time.[19] Turbulence was long supposed to be the responsible mechanism for the large rise times, especially since the measured rise times showed a considerable randomness. As pointed out later in this section, the mechanism responsible for large sonic boom rise time is molecular relaxation of oxygen and nitrogen. However, there is also experimental evidence[20,21] that sonic boom rise times further increase with increasing levels of atmospheric turbulence. An important question is whether turbulence changes the energy spectrum of the boom. Can scattering or some other process extract high-frequency energy from the wave? Garrick[22] compared the energy spectrum of a rounded sonic boom with that of a peaked sonic boom. The two spectra were very similar, and no change was apparent in the energy spectrum at high frequencies. Garrick's interpretation[22] is that turbulence causes a phase scrambling process for higher frequencies. Garrick, however, did not provide a mechanism responsible for the phase scrambling.

Pierce[23] explained anomalous rise time in terms of wave front folding at a caustic. The rippling of the wave front due to turbulence can lead to the formation of caustics (Fig. 4).

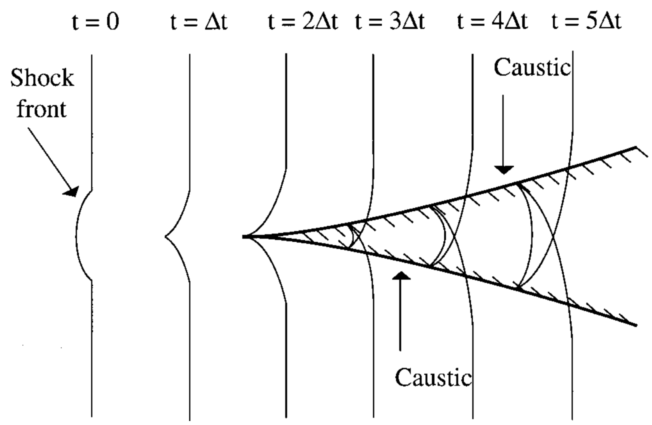

FIG. 4. Sketch showing the phenomenon of wave front folding at a caustic.[23]

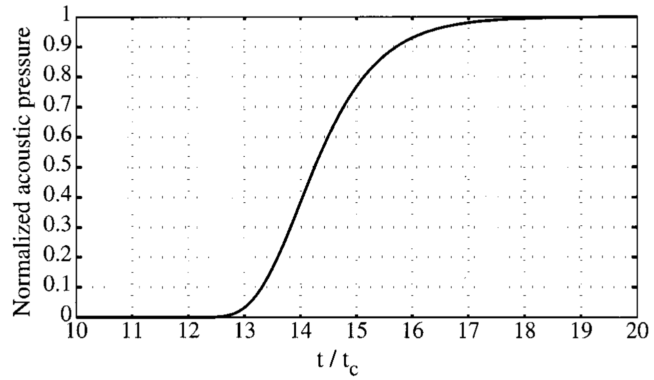

FIG. 6. Ensemble averaged signature of a sonic boom vs t/t_c, as derived by Pierce. The time origin corresponds to the first nonzero overpressure.[23]

After the wave front passes through the focus, wave front folding occurs. Pierce argued that folding occurs many times on a small scale as the wave propagates through the turbulence. The net effect would be that the pressure signature observed in the far field consists of many discrete shocks arriving at slightly different times (Fig. 5). The resulting pressure wave form would then exhibit an anomalously large rise time. Pierce pointed to the shadowgraphs, taken by Bauer and Bagley,[14] of shock waves propagating through a turbulent boundary layer as evidence of wave front folding.

Pierce's mathematical model is also based on the assumption of an incident step shock of the form $p = \Delta p_0 H(t - t_0 + x/c_0)$, where Δp_0 is the shock overpressure, t_0 is a reference time, i.e., time at which the shock nominally arrives at the receiver. The solution for the pressure at the receiver was represented as an adiabatic perturbation to the formal solution for a homogeneous medium when the normal component v_1 of the fluid velocity is specified on a particular plane as a function of time. This retarded-time solution is given by

$$p = \frac{\Delta p}{2\pi c_0 \overline{x_1}} \frac{d}{dt} \int \int H(t - t_0 - t_{TR} \overline{x_1}/c_0)\, dx_2\, dx_3, \qquad (7)$$

where $\overline{x_1}$ is the plane where v_1 is specified, $p = -\rho_0 c_0 v_1$ (plane wave assumption), and t_{TR} is the least travel time of an acoustic disturbance from a point $(\overline{x_1}, x_2, x_3)$ to the origin. Individual sample signatures are determined by the dependence of the travel time t_{TR} on x_2 and x_3 and thus consist of many shocks at random times. Pierce then determined the form of $t_{TR}(\overline{x_1}, x_2, x_3)$ by forcing Eq. (7) to agree with Crow's deterministic solution to first order in Δc and $\Delta \mathbf{u}$, which he considered to be random functions of space. Next, the mean rise time of sonic booms was calculated. The estimate of the mean rise time was based on the hypothesis that this should be the rise time of the average wave form. Artificial thickening of the shock front due to different arrival times was eliminated by computing the average as if all sample signatures began at the same time. Therefore, t_{TR} represents the least travel time. The ensemble averaged waveform then takes the form

$$\frac{\langle p(t) \rangle}{\Delta p_0} = \exp\{-E \hat{t}^{-1/6} e^{-b_1 \hat{t}^{7/6}}\}, \qquad (8)$$

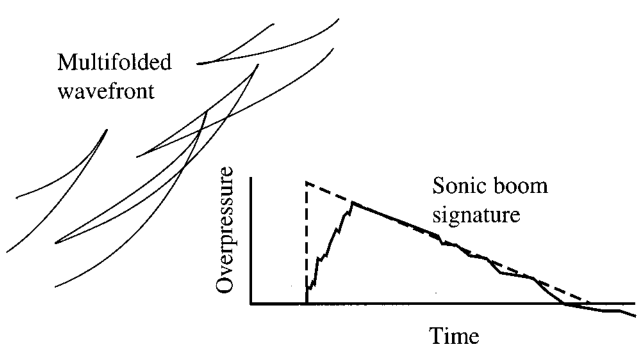

FIG. 5. Sketches of a multifolded wave front and a possible sonic boom signature corresponding to the passage of a multifolded shock.[23]

where $b_1 \approx 0.7$, $E = 6 \times 10^6$, where E is dependent on the structure of the turbulence, and $\hat{t} = t/t_c$, where t_c is Crow's characteristic time. The ensemble averaged wave form is plotted in Fig. 6. The rise time turned out to be of the order of 2 or $3t_c$. The rise time is extremely slowly varying with E. Diffraction is ignored in this approach.

George[24] raises several concerns with regard to Pierce's theory of multifolded shock fronts. One concern is that the theory is based on geometric acoustics and ignores diffraction. He also indicates that there does not seem to be any experimental evidence of microshocks. Pierce argues that his theory neglects the effects of viscosity but that in reality viscosity would tend to smear out the fine structure of the microshocks.

Plotkin[17] and Plotkin and George[25] proposed a perturbation theory to explain the large rise times. Their assumptions are that the high-frequency components of the shock front are scattered out of the front and that this process is offset by nonlinear steepening. The combination of both effects results in a larger than expected rise time. For propagation over large distances the rise time reaches an equilibrium value determined by the shock overpressure Δp and the turbulence parameters so that there is a balance between scattering and nonlinear steepening. Their analysis states that the parameter P, describing overpressure at a distance $-\xi$ behind the shock front, is governed by the Burgers equation

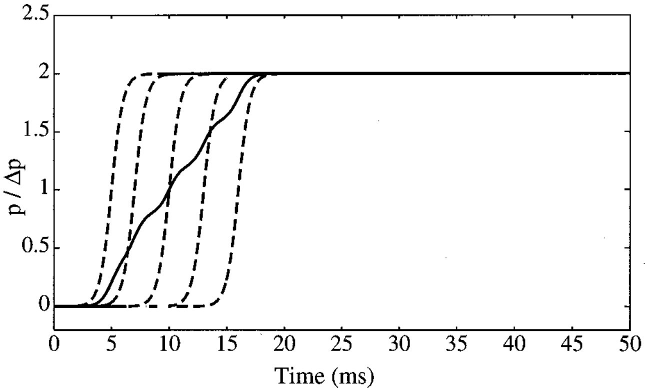

FIG. 7. Mean wave for a set of shocks with the same overpressure and rise time (2.2 ms), but different delay times. The rise time of the mean wave form is 11 ms.

$$\frac{\partial P}{\partial t}+\frac{c_0(\gamma+1)}{2\gamma}\frac{P}{p_0}\frac{\partial P}{\partial \xi}=\frac{L_0}{c_0}\langle(\Delta c+\Delta u_\parallel)^2\rangle\frac{\partial^2 P}{\partial \xi^2}, \qquad (9)$$

where $\Delta u_\parallel$ is the turbulent fluid velocity in the direction of propagation, γ is the specific heat ratio, and L_0 is the integral length scale of the turbulence. Except for a right side term that is a function of turbulence instead of viscosity, this equation is the same as Burgers equation for weak viscous shock propagation. From analogy with that equation, we can then infer that the right-hand side represents a dissipation term. Several assumptions are made in developing Eq. (9). The most important are that (1) the amplitude of the pressure and turbulence fluctuations are small so that the perturbation solution is valid, (2) the conditions for weak scattering are satisfied, (3) the shock thickness is much smaller than the turbulence macroscale, and (4) first-order perturbations need to be distinct from the shock front. In deriving the right-hand side of Eq. (9), Plotkin and George made the ergodic hypothesis so that the spatially averaged energy is equal to the averaged energy of an ensemble of realizations. Pierce[26] questioned it and presented a counter example to show the invalidity of the approximation.

The solution of Burgers' equation is well known[27,28] and Plotkin and George[25] used it to study the propagation of an initial step function shock of overpressure Δp_0. The wave form approaches an equilibrium shape with a rise time

$$\tau=\frac{16\gamma}{\gamma+1}\frac{p_0}{\Delta p_0}\frac{\langle(\Delta c+\Delta u_\parallel)^2\rangle L_0}{c_0^3}. \qquad (10)$$

In Ref. 17, Plotkin compares various sonic boom and explosion wave thicknesses to the theory. The theory shows reasonable agreement with the data.

Pierce and Maglieri[8] stated a number of reservations regarding the use of Eq. (10) for quantitative predictions. The most important is that the rise time of P is equal to the rise time of the ensemble averaged signature. However, the rise time of the ensemble averaged wave form is not necessarily the same as the average rise time of sample wave forms because of the spread in arrival times. This is illustrated in Fig. 7, where the mean wave (ensemble average) is shown for a set of shocks with the same rise time but slightly different delay times. Obviously, the rise time of the mean wave is an irrelevant upper bound to the average of the individual rise times and has no direct physical significance. George[24] and Plotkin and George[25] also discuss the problem of the rise time of the ensemble averaged wave form and mention that an ensemble average of shock waves may appear to have a thicker structure than any one wave. They indicate that the structure of an individual shock wave may be found by using their model provided that the propagation distance through turbulence is sufficiently long for the first scattered energy to have fallen behind the shock front.

The models of Pierce and Plotkin and George are examples of two different viewpoints of the large rise times of sonic booms. In Plotkin and George's model, the obtained rise time is the result of the balance between the scattering process and the nonlinear steepening. As such the rise time value is an equilibrium value. Pierce, on the other hand, models the rise time as a transient phenomenon that leads to increasingly larger values as the propagation distance through the turbulent atmosphere increases.

Ffowcs Williams and Howe[29] also examined the possible thickening of an initially sharp sonic boom by turbulence. They agreed that the irregular spiky structure of the sonic boom is caused by the interaction of the sonic boom with turbulence. Three distinct approaches to the turbulent origin of wave thickening were treated by them, namely (1) Lighthill's scheme[30] based on scattering theory with an assumed energy conservation between the specific incident wave and the mean rate of energy lost to the scattered field, (2) their reworking of the basic equations to describe properties of the mean wave established over many realizations, and (3) Plotkin and George's perturbation scheme. Their conclusion was that all three approaches actually lead to identical descriptions of the mean properties of the boom signature, i.e., Burgers' equation as derived by Plotkin and George. Ffowcs Williams and Howe stated that ''it is now apparent to us that the three approaches are essentially similar and describe only the stochastic mean wave, and that this mean gives only an irrelevant upper bound on shock thickness.'' The energy content of the mean wave decays according to Lighthill's formula, but because it relates only to the mean wave it should be regarded essentially as the decay of coherence of the wave front and not of the energy content of the actual wave. Their arguments are essentially similar to that of Pierce.

Ffowcs Williams and Howe also pointed out that the mean wave thickness, defined by Plotkin and George in Eq. (10), depends on the outer length scale of the turbulence, which in the atmosphere is on the order of 100 meters. They argue that smaller scale motions would be more efficient in affecting the wave rise phase because there would be a much smaller mismatch between interacting length scales. Ffowcs Williams and Howe used a theory that examines the propagation of short sound waves through turbulence in terms of a theory of multiple scattering. The theory was originally proposed by Howe[31] to study the rise time of sonic booms. Howe derived an integro-differential kinetic equation for the mean-square Fourier coefficients of waves propagating in inviscid turbulence. If only second-order effects are taken into account, the integro-differential equation reduces to the following diffusion equation for the distribution of acoustic energy in wave number space

$$\frac{\partial \mathcal{E}(\mathbf{k})}{\partial t} + c_0 \frac{\partial \mathcal{E}(\mathbf{k})}{\partial x_\parallel} = \frac{c_0 m^2 k^2}{2\Delta} \nabla_\perp^2 \mathcal{E}(\mathbf{k}), \tag{11}$$

where $\mathcal{E}(\mathbf{k})$ is the acoustic energy in wave number space and $x_\parallel$ is the space coordinate parallel to the wave number $\mathbf{k}$. $\nabla_\perp^2$ is the two-dimensional Laplacian operator in wave number space in the plane normal to $\mathbf{k}$. The length Δ is defined as

$$\frac{1}{\Delta} = \frac{\pi}{2u^2} \int_0^\infty \kappa E(\kappa) d\kappa, \tag{12}$$

and is of the same order of magnitude as the Taylor microscale, $E(\kappa)$ is the turbulence energy spectrum, and m is the turbulent Mach number. If the initial wave energy spectrum is given, then the solution of the spectrum due to propagation through the turbulence can be found. The solution can be used to calculate the shock thickness of the sonic boom. Ffowcs Williams and Howe introduced the following definition of shock thickness δ:

$$\frac{1}{\delta} = \frac{1}{(\Delta \overline{p_0})^2} \int_{-\infty}^{\infty} \overline{\left(\frac{\partial p}{\partial x}\right)^2} dx, \tag{13}$$

which excludes spurious contributions due to possible phase shift effects. Phase shifts were thus automatically excluded and large contributions due to the spiky structure of the wave profiles were averaged out. This definition seems indeed to provide an accurate time average of the rise time of individual realizations. The thickness of the mean wave form is

$$\delta = \delta_0 [1 + \mu(x)], \tag{14}$$

where

$$\mu(x) = 2 \int_0^x \frac{m(\xi)^2}{\Delta(\xi)} d\xi,$$

is the integrated scattering diffusivity. Interestingly, this definition predicts that $\delta = 0$ when $\delta_0 = 0$, which implies that a true shock remains a shock at least for propagation distances where the approximations made to find the solution are still valid. On the other hand, if the initial wave form has a finite rise time at the moment it enters the turbulent boundary layer, then Eq. (14) predicts thickening of the shock front. Ffowcs Williams and Howe calculated the thickening for typical atmospheric turbulence values and a Concorde type plane and found μ to have a maximum value of 0.3, which indicates at most an increase of 30% in the sonic boom rise time and that, therefore, turbulence cannot be the mechanism responsible for a large increase in rise time. Plotkin[32] argued that Ffowcs Williams and Howe's definition of shock thickness has no physical relation to shock thickness, but rather to the overall frequency content of the pulse. Since neither Plotkin and George's model nor Pierce's model account for the ultimate loss of acoustic energy, just its spatial relocation, one should not expect turbulence to have any effect at all on the shock thickness as defined by Ffowcs Williams and Howe. This argument is only partially valid since Ffowcs Williams and Howe's model is capable of explaining a redistribution of acoustic energy and the latter could be a viable mechanism for shock thickening. Another mechanism that could be responsible for shock thickening is a phase scrambling mechanism without changing the energy spectrum of the acoustic wave, as proposed by Garrick. This mechanism is not included in Ffowcs Williams and Howe's analysis and its omission must be considered a drawback for their model. The spatial relocation of acoustic energy, mentioned by Plotkin, can be caused by both effects, i.e., redistribution of acoustic energy and phase-scrambling process, but Ffowcs Williams and Howe are only able to account for one of those mechanisms. In the conclusion of their paper Ffowcs Williams and Howe refer to the work of Hodgson and Johannesen[33] and conclude that nonequilibrium gas effects (molecular relaxation) are responsible for the large rise time of sonic booms.

In absence of significant levels of turbulence, it is now well established that molecular relaxation of oxygen and nitrogen is responsible for the anomalous large rise time of sonic booms. Hodgson and Johannesen[33] were the first to demonstrate that weak shocks tend to attain a fully dispersed profile owing to nonequilibrium gas effects. They suggested a method to determine the thickness of a weak, fully dispersed shock in a single relaxing medium. Later, Hodgson[34] extended the model to include both oxygen and nitrogen relaxation and showed the effect on the sonic boom profile.

Bass *et al.*[35,36] proposed a molecular relaxation-based absorption theory, and suggested that when turbulence is absent, the molecular relaxation processes play the major role in determining the rise time. They calculated the shock rise time by using the numerical technique developed by Pestorius[37] and Anderson.[38] Classical absorption and molecular relaxation were accounted for in this model. Their results showed that the rise times computed with both absorption and dispersion included agree well with experimental data from their ballistic experiments, in which supersonic projectiles were fired in open air. Turbulence was also measured in their experiments. They concluded that atmospheric turbulence has little or no effect on measured shock rise times of the bullets fired in the experiment. However, it seems that an incorrect scaling was applied in their ballistic experiments. Therefore, one would not necessarily expect to see an effect of the turbulence.

Pierce[39] developed an augmented Burgers equation by including the effect of relaxation processes. Kang[40] derived the steady-state version of the augmented Burgers equation by using two assumptions. The first was to approximate the sonic boom as a step shock and the second was to assume a shock profile in steady state. His argument is that when the propagation distance is sufficiently long, one expects the shock profile to be fully developed. The shock profile then depends only on the shock overpressure and local properties of air. Results of Kang's calculation are shown in Fig. 8 where the theoretical rise time predictions are compared with measured rise times of sonic booms. In general the model yields a prediction of the right order of magnitude and the model results are almost an average of the measured data. Robinson[41] developed a numerical model that accounts for nonlinearity, classical absorption, relaxation, and stratification of the atmosphere. One interesting result of his work is

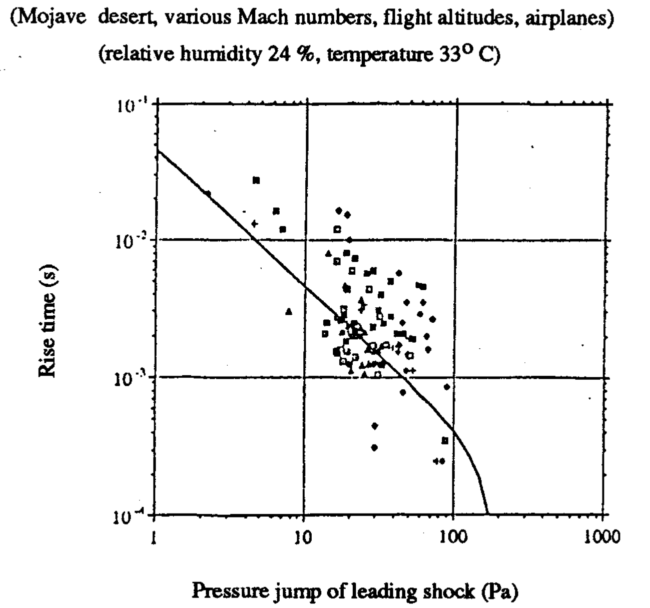

FIG. 8. Comparison of Kang's prediction for the rise time of a steady step shock with sonic boom measurements (Ref. 40).

that it does not show that the sonic boom reaches a steady-state profile by the time it hits the ground. His model also predicts the right order of magnitude of sonic boom rise times. The fact that the sonic boom does not reach a steady-state profile has also been shown by Cleveland.[42]

In summary, molecular relaxation is the main mechanism responsible for large rise times of sonic booms in absence of atmospheric turbulence. Rise times calculated from existent relaxation models are of the correct order of magnitude. The effect of atmospheric turbulence is to further increase sonic boom rise times. In the next section, model experiment data are used to test the different turbulence models. Do these models yield accurate quantitative predictions for the extra increase in rise time of sonic booms propagating in a turbulent atmosphere?

III. APPLICATION OF MODEL EXPERIMENT DATA TO TEST SONIC BOOM MODELS

Results from hot-wire anemometry and microphone measurements are used to test existing sonic boom models. A more detailed presentation of the model experiment design and apparatus is given in Ref. 43. The length scales of the spark-produced N waves and the turbulence of the model experiment are about a factor of 10 000 smaller compared with typical length scales of sonic booms and atmospheric turbulence.

A. Wave form distortion models

Crow's model[12] yields a formula for the pressure perturbations behind a steady shock. The dimensionless mean-squared pressure perturbation is given by Eq. (3). Plotkin[17] calculated an upper bound for the root-mean-square (rms) pressure perturbation for a ramp shock. It is straightforward to extend this analysis to an ideal N wave characterized by a peak pressure Δp, rise time t_0, and duration T_0 as is shown

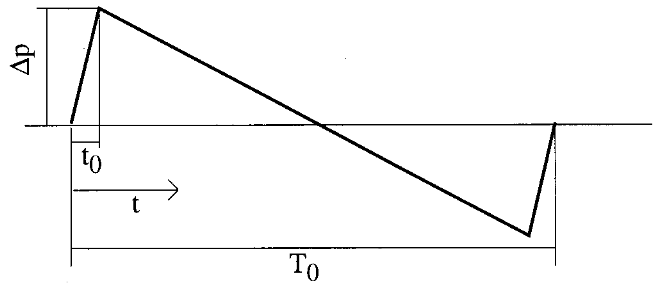

FIG. 9. Representation of an ideal N wave. Δp is peak pressure, t_0 is rise time, and T_0 is duration.

in Fig. 9. The upper bound of rms pressure perturbation was calculated for N wave parameters ($t_0 = 0.5\,\mu$s and $T_0 = 19\,\mu$s) that are typical for the model experiment. Hot-wire anemometry was used to measure the turbulent energy dissipation ϵ_u, which was found to be about 50 m^2/s^3 on the jet axis in the self-preserving region of the jet. The length of the turbulent layer is known. The turbulent energy dissipation was assumed to be constant over the turbulent layer, since the N waves propagated parallel to the nozzle height axis. The parameters of the experiment were used to calculate the integral [Eq. (4)] and the result is

$$t_c = 0.33\,\mu\text{s}. \tag{15}$$

The result of the rms pressure perturbation for the ideal N wave is presented in Fig. 10. It is observed that the maximum distortion occurs at the bow and tail shock location. The pressure perturbation at the bow shock is bigger than that of the tail shock as a result of the linear expansion between the two shocks.

The mean-squared pressure perturbation was calculated for six sets of 100 plane N waves measured after propagation through the turbulent layer. The jet nozzle velocity was, respectively, 0, 12.4, 18.3, 22.7, 26.6, and 31.3 m/s. A crucial point in this computation is the arrival time of each N wave. Crow's analysis does not take into account any variation of travel time variations, but a straight mean-squared calculation would be erroneous because of the phase shifts associated with each N wave. Therefore, in order to calculate the correct mean-squared pressure perturbation, we assumed that

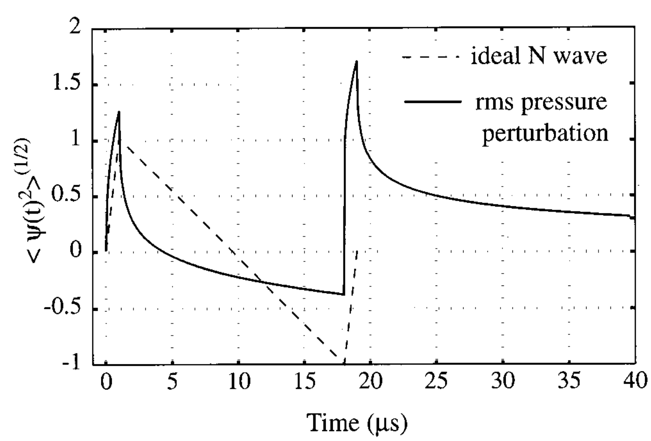

FIG. 10. The upper bound of the rms pressure perturbation for an ideal N wave.

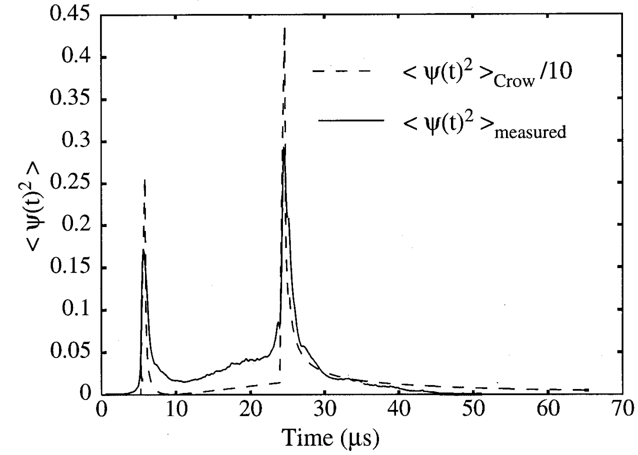

FIG. 11. Comparison of measured mean-squared pressure perturbation and the prediction of an upper bound of the rms pressure perturbation based on an extension of Crow's theory.

the time origin for each N wave is at the start of the wave form. Since the N waves have a finite rise time, it is necessary to determine the start of each N wave in a uniform way. It was decided to shift each signature so that the times corresponding to 50% of the peak overpressure coincide. This method results in a shift of the N waves that is more accurate than a time shift that would force the beginning of the wave forms to coincide. The latter is subject to more errors because of the existence of long precursors to some wave forms. To compute the mean-squared pressure perturbation, we subtracted the reference N wave recorded in the absence of turbulence from each N wave and squared the difference. An average is then calculated for the 100 N wave signatures. The result is compared with the theoretical curve, as is shown in Fig. 11 for a jet nozzle velocity of 31.3 m/s. The experimental curve has roughly the same shape as the theoretical curve. As expected, the extension of Crow's theory yields an upper bound for the maximum rms perturbation near the bow and tail shock. Table I contains the results of the calculation of Crow's characteristic time t_c, the upper bounds of the rms pressure perturbation near the bow and tail shock (from theory), and the measured maximum rms pressure perturbation near the bow and tail shock.

TABLE I. Comparison of rms pressure perturbation near the bow and tail shock as a function of jet nozzle velocity.

Jet nozzle velocity (m/s)	Charact. time (μs)	Measured rise time (μs)	$\langle\psi^2\rangle^{1/2}_{max}$ Bow shock theory	Bow shock exp.	Tail shock theory	Tail shock exp.
12.4	0.23	0.8965	1.333	0.216	1.129	0.322
18.3	0.32	1.1128	1.617	0.333	1.369	0.406
22.7	0.37	1.5100	1.760	0.343	1.490	0.343
26.6	0.41	1.8243	1.868	0.419	1.582	0.402
31.3	0.46	2.0674	1.998	0.410	1.692	0.538

B. Rise time prediction models

Pierce[15] developed an expression for the ensemble averaged wave form [Eq. (8)]. This equation takes into account different travel times for each N wave. The ensemble averaged wave form was calculated for six sets of measurements, each at a different jet nozzle velocity, and a time shift to each N wave was applied as described in the previous section. Figure 12 shows the measured ensemble wave form and the calculated one. Note that the calculation assumes a step shock and not an N wave. A good correlation is obtained between experiment and theory for the prediction of the bow shock. To further check this theory, we performed more experiments at different jet velocities and thus different values for Crow's characteristic time were obtained. Table II contains the numerical results of the rise time of Pierce's prediction and of the measured computed ensemble averaged wave form. Pierce's theory yields accurate predictions of the rise time of the ensemble averaged wave form. The relative error never exceeds 20%. Since Pierce's model is based on geometric acoustics, it is instructive to verify whether this assumption is met for the model experiment. For diffraction effects to be small, $\lambda L/L_0^2 \ll 1$, where λ is the wavelength, L

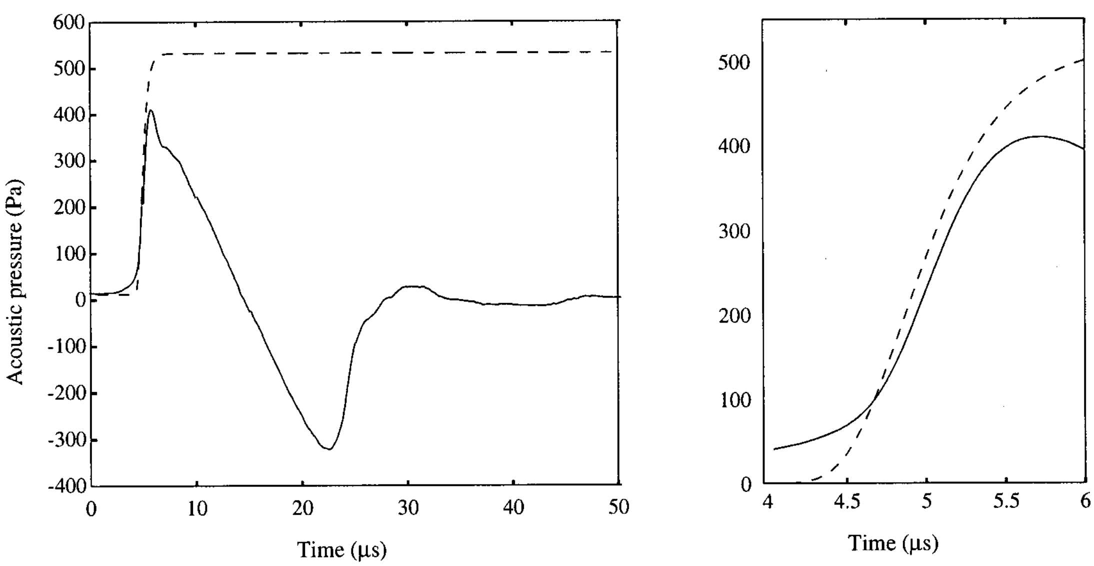

FIG. 12. Comparison of measured ensemble averaged mean wave form and Pierce's prediction.

TABLE II. Comparison of measured rise time of the ensemble averaged wave form and Pierce's prediction as a function of jet turbulence. The individual realizations are shifted in time in order that each wave form arrives at the same time.

Jet nozzle velocity (m/s)	Charact. time (μs)	τ_{Pierce} (μs)	$\tau_{\text{meas.}}$ (μs)
12.4	0.23	0.554	0.685
18.3	0.32	0.769	0.745
22.7	0.37	0.889	0.922
26.6	0.41	0.984	1.061
31.3	0.46	1.091	1.308

TABLE III. Comparison of measured rise time of the ensemble averaged wave form and Plotkin's prediction as a function of jet nozzle velocity. For the stochastic mean wave form individual realizations are not shifted in time, but the last column contains the rise time of the ensemble averaged wave form calculated with an arrival time correction.

Jet nozzle velocity (m/s)	Charact. time (μs)	τ_{Plotkin} (μs)	Stoch. mean $\tau_{\text{meas.}}$ (μs)	Time shifted $\tau_{\text{meas.}}$ (μs)
12.4	0.23	1.13	2.767	0.685
18.3	0.32	2.49	3.867	0.745
22.7	0.37	3.78	4.840	0.922
26.6	0.41	5.34	4.833	1.061
31.3	0.46	7.37	5.528	1.308

is the propagation distance, and L_0 is the integral length scale of the turbulence. For our experiment, $L_0=0.025$ m, and $L=0.5$ m. Wavelengths related to the shock structure of the N wave are $\lambda\approx 10^{-4}$ m, and for those related to the overall N wave length are $\lambda\approx 3\ 10^{-3}$ m. Therefore, for the shock structure $\lambda L/L_0^2=0.08$, and the propagation is mostly governed by geometric acoustics. For the larger length scales of the N wave, $\lambda L/L_0^2\approx 2.4$, and diffraction effects are important.

Plotkin and George[25] derived an expression for the rise time of an ensemble of step shocks propagating through turbulence [Eq. (10)]. First we check whether our model data satisfy the assumptions used in the derivation of this equation. The first assumption is that of small fluctuations in shock overpressure and turbulence velocity. For the data presented here, $\Delta p/p_0$ is 0.005, where Δp is the shock overpressure and p_0 is the ambient pressure. For the turbulence $\Delta u_\parallel/c_0$ is 0.008. The condition for weak scattering requires that $\Delta u_\parallel^2 L_0 L/c_0^2 T^2 \ll 1$, where T is the shock thickness. For our data this factor is about 6. Our model experiment does not satisfy the condition of weak scattering. The condition that the shock thickness T is much less than the integral length scale of the turbulence is easily satisfied. For the scattered energy to be distinct, $\lambda L/L_0^2 \geqslant \pi^2$. When we use a value of λ representative of the shock structure, we determine that this factor is about 0.3. Hence the condition of distinct scattered energy is not met. Therefore, we should expect that the value of rise time as given by Plotkin and George's model is an overestimate compared with the measured rise time data.

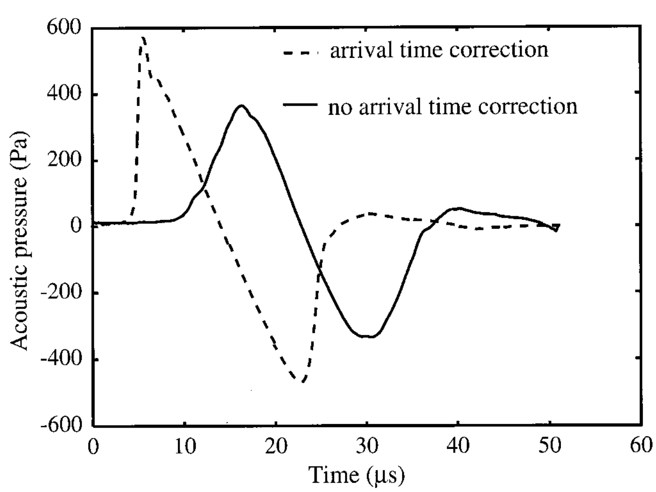

FIG. 13. Ensemble averaged waveform of 200 plane N wave signatures. The ensemble averaged wave form is computed with and without a correction for fluctuations in arrival time.

Although the conditions in our model experiment do not satisfy all of the assumptions of Plotkin and George's model, it is still instructive to compare the model experiment data with the prediction of Plotkin and George. We calculated the ensemble averaged wave form of the 200 recorded signatures with and without correction of arrival time. The rise time of this ensemble averaged wave form without correction does not have any physical significance and only serves as an upper bound for the actual rise time. The ensemble averaged wave forms with and without correction of arrival time are shown in Fig. 13. The rise time of the wave form calculated without a correction for arrival time is indeed much larger than that of the actual ensemble averaged wave form. We performed measurements at various jet nozzle velocities. The results of this experiment are summarized in Table III. It is seen that, compared with the rise time of the ensemble averaged wave form that is calculated with a correction for changes in arrival time, Plotkin and George's model yields an overprediction by a factor of 2–5 and the overprediction increases with increasing jet nozzle velocity. When the predicted rise times are compared with the values of the stochastic mean wave form without arrival time correction, a better correlation is obtained. As pointed out earlier, our experiments do not satisfy the conditions necessary to validate Plotkin and George's model. Given the conditions of our experiment, we expect an overestimate of the rise time.

The last model described in Sec. I is that by Ffowcs Williams and Howe.[29] Their model only yields an increase in rise time by a factor of about 30% at the most. The thicken-

TABLE IV. Comparison of measured rise time of the ensemble averaged wave form and Ffowcs William and Howe's prediction as a function of jet nozzle velocity. The parameter μ is the integrated scattering diffusivity.

Jet nozzle velocity (m/s)	μ	$\tau_{\text{F-H}}$ (μs)	$\tau_{\text{meas.}}$ (μs)
12.4	0.0027	0.687	0.685
18.3	0.0047	0.688	0.745
22.7	0.0067	0.690	0.922
26.6	0.0090	0.691	1.061
31.3	0.0116	0.693	1.038

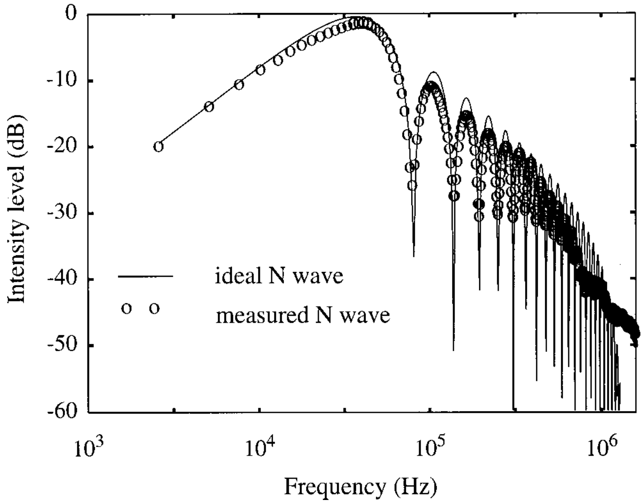

FIG. 14. Intensity spectrum of an ideal *N* wave and the *N* waves measured without turbulence.

ing of the shock is given by Eq. (14). The value of μ was calculated from the hot-wire anemometry data for the plane *N* wave experiments. Instead of Δ, we used the Taylor microscale to compute μ. Table IV contains the results of this calculation. Obviously, Ffowcs Williams and Howe's model yields an underestimate for the rise time. The model only yields a relative change of 1%, while the measurements show an increase in rise time by a factor of about 2 for a nozzle velocity of 31.3 m/s. An explanation for the failure of the model to provide an accurate estimate of the rise time is that this model only takes into account a redistribution of acoustic energy in wave number space, but it does not include a possible phase scrambling mechanism. In order to check whether the rise time increase might be caused by a shift in acoustic energy in wave number space, we calculated the averaged acoustic intensity spectrum of 100 *N* waves recorded in the absence of turbulence. In Fig. 14 the intensity spectrum is presented for an ideal *N* wave (as shown in Fig. 9) with the same rise time and duration as the measured *N* wave. Also shown is the averaged intensity spectrum of 100

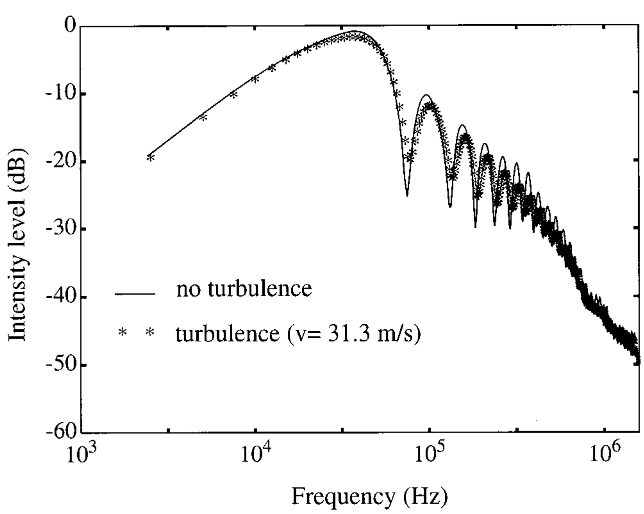

FIG. 15. Comparison of the averaged intensity spectrum of *N* waves measured with and without turbulence.

N waves recorded in the absence of turbulence. As is observed, the measured spectrum closely resembles that of an ideal *N* wave. The calculation was then repeated for a set of 100 *N* waves recorded after propagation through the turbulence. Figure 15 shows the results of this calculation. It is seen that after propagation through turbulence, the averaged spectrum still resembles the general shape of an *N* wave spectrum, but the peaks and nulls are more rounded. Therefore, the tenet that a redistribution of acoustic energy in wave number space is responsible for the thickening of the *N* waves is not conclusively supported by this graph, and it may explain why Ffowcs Williams and Howe's model only yields a very small increase in rise time of order 1%.

IV. CONCLUSION

The hot-wire anemometry data and the results from the microphone measurements are used to test sonic boom models. It is found that Crow's model yields an upper bound for the rms pressure perturbations. Typically, the predicted overpressures are larger by a factor of about 5. The rms pressure perturbation calculated according to the model shows the same dependence on time as the measured one.

Pierce's model for the prediction of the rise time of an ensemble averaged wave form that is corrected for changes in arrival time fits the measured data very well. Pierce's model is based on a wave front folding mechanism. It is essentially a transient model that leads to larger rise times for larger propagation distances through turbulence. Pierce's model is dependent on the smaller scale of the turbulence.

Plotkin and George's model is based on a balance between scattered energy out of the shock front and nonlinear steepening of the shock front. It is based on an equilibrium solution that is dependent on the outer length scale of the turbulence. Our model experiment conditions do not meet the assumptions made in their derivation, and validation of the model is not possible. Longer propagation distances are necessary to verify whether there is actually a balance between the scattered energy and the nonlinear steepening.

Our data seem to support Pierce's theory that the increase of rise times is indeed a transient phenomenon. Larger rise times occur for larger propagation distances. An extension of the current model experiment to longer propagation distances is necessary to confirm whether ever increasing rise times occur or whether an equilibrium is reached with a constant rise time. It is worthwhile to point out that within the parameters of this model experiment we are able to reproduce not only the distortion of sonic booms, but also the increase in rise time. Our statistics[6,7] parallel those of measured sonic booms[20] closely.

It is shown that Ffowcs Williams and Howe's model yields an underestimation of the rise time. Since their model only takes into account a redistribution of acoustic energy in frequency space and since no redistribution was measured, an increase in rise time cannot be expected. Since no significant redistribution of acoustic energy in the frequency space is measured, the tenet that a dispersion effect or a phase scrambling mechanism is responsible for the increase in rise time of plane *N* waves propagating through turbulence seems to be the correct interpretation.

ACKNOWLEDGMENTS

The author wishes to express his thanks to David T. Blackstock for many helpful discussions during the course of this work. This work is supported by a grant from NASA Langley Research Center (NAG-1-1204). Supervisor of the grant is Dr. G. L. McAninch.

[1] L. J. Shepherd and W. W. Sutherland, ''Relative annoyance and loudness judgments of various simulated sonic boom,'' NASA CR NAS-1-6193 Subcontract B-87017-US (1967).

[2] E. E. Zepler and F. R. P. Harel, ''The loudness of sonic booms and other impulsive sounds,'' J. Sound Vib. **2**(3), 249–256 (1965).

[3] D. R. Johnson and D. W. Robinson, ''Procedure for calculating the loudness of sonic bangs,'' Acustica **21**(6), 307–318 (1969).

[4] A. Niedzwiecki and H. S. Ribner, ''Subjective loudness of *N*-wave sonic booms,'' J. Acoust. Soc. Am. **64**, 1622–1626 (1978).

[5] A. Niedzwiecki and H. S. Ribner, ''Subjective loudness of minimized sonic boom waveforms,'' J. Acoust. Soc. Am. **64**, 1617–1621 (1978).

[6] B. Lipkens and D. T. Blackstock, ''Model experiment to study sonic boom propagation through turbulence. Part I: Model experiment and general results,'' J. Acoust. Soc. Am. **103**, 148–158 (1998).

[7] B. Lipkens and D. T. Blackstock, ''Model experiment to study sonic boom propagation through turbulence. Part II: Effect of turbulence intensity and propagation distance through turbulence,'' J. Acoust. Soc. Am. **104**, 1301–1309 (1998).

[8] A. D. Pierce and D. J. Maglieri, ''Effects of atmospheric irregularities on sonic-boom propagation,'' J. Acoust. Soc. Am. **51**, 702–721 (1972).

[9] A. D. Pierce, ''Spikes on sonic boom pressure waveforms,'' J. Acoust. Soc. Am. **44**, 1052–1061 (1968).

[10] B. A. Davy and D. T. Blackstock, ''Measurements of the refraction and diffraction of a short *N*-wave by a gas-filled soap bubble,'' J. Acoust. Soc. Am. **49**, 732–737 (1971).

[11] H. S. Ribner, P. J. Morris, and W. H. Chu, ''Laboratory simulation of development of superbooms by atmospheric turbulence,'' J. Acoust. Soc. Am. **53**, 926–928 (1973).

[12] S. C. Crow, ''Distortion of sonic bangs by atmospheric turbulence,'' J. Fluid Mech. **37**, 529–563 (1969).

[13] G. K. Batchelor, Symposium on Naval Hydrodynamics, Washington, Natl. Acad. Sci. (Publ. 515) (1957).

[14] A. B. Bauer and C. J. Bagley, Sonic boom modeling investigation of topographical and atmospheric effects, McDonnel-Douglas Corp., Long Beach, Calif., Rep. No. FAA-NO-70-10 (1970).

[15] A. D. Pierce and G. Kamali, ''Time dependence of variances of sonic boom waveforms,'' Nature (London) **234**, 30–31 (1971).

[16] G. A. Herbert, W. A. Hass, and J. K. Angell, ''A preliminary study of atmospheric effects on the sonic boom,'' *Aircraft engine noise and sonic boom*, AGARD Conf. Proc. 42, Advisory Group for Aerospace Res. and Devel., Neuilly Sur Seine, France (1969).

[17] K. J. Plotkin, ''The effect of atmospheric inhomogeneities on the sonic boom,'' Ph.D. Thesis, Department of Aerospace Engineering, Cornell University (1971).

[18] G. I. Taylor, ''The conditions necessary for discontinuous motion in gases,'' Proc. R. Soc. London, Ser. A **34**, 371–377 (1910).

[19] G. M. Lilley, ''The structure of shock waves at large distances from bodies traveling at high speeds,'' in *5th Congres Internationale d'Acoustique*, edited by Daniel E. Commins (Liege, Belgium, 1965), Vol. II, pp. 109–162.

[20] W. L. Willshire and D. W. DeVilbiss, ''Preliminary results from the White Sands Missile Range sonic boom propagation experiment,'' HSR Sonic Boom Workshop, NASA Langley Research Center, 1992. ARTICLE: in High Speed Research: 1992 Sonic Boom Workshop, C. M. Darden, ed., NASA CP 3172 (1992), pp. 137–149.

[21] R. A. Lee and J. M. Downing, Sonic boom produced by United States Air Force and United States Navy aircraft: measured data, AL-TR-1991-0099, Biodynamic Environment Branch, Biodynamics and Bioengineering Division, Armstrong Laboratory, Wright-Patterson Air Force Base, Ohio (1991).

[22] I. E. Garrick, Atmospheric effects on the sonic boom, Second Conference on sonic boom research, I. R. Schwartz, Ed., NASA SP-180 (1968).

[23] A. D. Pierce, ''Statistical theory of atmospheric turbulence effects on sonic boom rise times,'' J. Acoust. Soc. Am. **49**, 906–924 (1971).

[24] A. R. George, ''The effects of atmospheric inhomogeneities on sonic boom,'' *Third Conference on Sonic Boom Research*, NASA SP-255, I. R. Schwartz, Ed., pp. 33–57 (1971).

[25] K. J. Plotkin and A. R. George, ''Propagation of weak shock waves through turbulence,'' J. Fluid Mech. **54**, 449–467 (1972).

[26] A. D. Pierce, ''Comments on propagation of sonic booms and other weak nonlinear waves through turbulence,'' Phys. Fluids **15**, 952–954 (1972).

[27] J. D. Cole, ''On a quasi-linear parabolic equation occuring in aerodynamics,'' Q. Appl. Math. **9**, 225–236 (1951).

[28] E. Hopf, ''The partial differential equation $u_t+uu_x=\mu u_{xx}$,'' Commun. Pure Appl. Math. **3**, 201–203 (1950).

[29] J. E. Ffowcs Williams and M. S. Howe, ''On the possibility of turbulent thickening of weak shock waves,'' J. Fluid Mech. **88**, 563–583 (1973).

[30] M. J. Lighthill, ''On the energy scattered from the interaction of turbulence with sound or shock waves,'' Proc. Cambridge Philos. Soc. **49**, 531–551 (1953).

[31] M. S. Howe, ''Multiple scattering of sound by turbulence and other inhomogeneities,'' J. Sound Vib. **27**, 455–476 (1973).

[32] K. J. Plotkin, ''Review of sonic boom theory,'' AIAA 12th Aeroacoustics Conference, AIAA-89-1105, April 10–12, San Antonio, TX (1989).

[33] J. P. Hodgson and N. P. Johannesen, ''Real gas effects in very weak shock waves in the atmosphere and the structure of sonic bangs,'' J. Fluid Mech. **50**, 17–20 (1971).

[34] J. P. Hodgson, ''Vibrational relaxation effects in weak shock waves in air and the structure of sonic bangs,'' J. Fluid Mech. **58**, 187–196 (1973).

[35] H. E. Bass, J. Ezell, and R. Raspet, ''Effect of vibrational relaxation on rise times of shock waves in the atmosphere,'' J. Acoust. Soc. Am. **74**, 1514–1517 (1983).

[36] H. E. Bass, B. A. Layton, L. N. Bolen, and R. Raspet, ''Propagation of medium strength shock waves through the atmosphere,'' J. Acoust. Soc. Am. **82**, 306–310 (1987).

[37] F. M. Pestorius, Propagation of plane acoustic noise of finite amplitude, ARL Technical Rep. No. 73–23, Applied Research Laboratories, The University of Texas at Austin (AD 778868) (1973).

[38] M. O. Anderson, The propagation of a spherical *N*-wave in an absorbing medium and its diffraction by a circular aperture, ARL Technical Rep. No. 74-25, Applied Research Laboratories, The University of Texas at Austin (AD 787878) (1974).

[39] A. D. Pierce, *Acoustics: An Introduction to its Physical Principles and Applications* (McGraw-Hill, New York, 1981), pp. 547–562, 587–593.

[40] J. Kang, ''Nonlinear acoustic propagation of shock waves through the atmosphere with molecular relaxation,'' Ph.D. Thesis, Department of Mechanical Engineering, Pennsylvania State University (1991).

[41] L. D. Robinson, ''Sonic boom propagation through an inhomogeneous, windy atmosphere,'' Ph.D. Thesis, Physics Department, The University of Texas at Austin (1991).

[42] R. O. Cleveland, M. F. Hamilton, and D. T. Blackstock, ''Effect of stratification and geometrical spreading on sonic boom rise time,'' HSR Sonic Boom Workshop, NASA Langley Research Center, 1–3 June 1994. ARTICLE: in High Speed Research: 1994 Sonic Boom Workshop, D. A. McCurdy, ed., NASA CP 3279 (1994), pp. 19–38.

[43] B. Lipkens, ''Experimental and theoretical study of the propagation of *N* waves through a turbulent medium,'' Ph.D. Thesis, Mechanical Engineering Department, The University of Texas at Austin (1993).

Atmospheric turbulence conditions leading to focused and folded sonic boom wave fronts

Andrew A. Piacsek[a)]
Department of Physics, Central Washington University, Ellensburg, Washington 98926

(Received 12 July 2000; accepted for publication 9 April 2001)

The propagation and subsequent distortion of sonic booms with rippled wave fronts are investigated theoretically using a nonlinear time-domain finite-difference scheme. This work seeks to validate the rippled wave front approach as a method for explaining the significant effects of turbulence on sonic booms [A. S. Pierce and D. J. Maglieri, J. Acoust. Soc. Am. **51**, 702–721 (1971)]. A very simple description of turbulence is employed in which velocity perturbations within a shallow layer of the atmosphere form strings of vortices characterized by their size and speed. Passage of a steady-state plane shock front through such a vortex layer produces a periodically rippled wave front which, for the purposes of the present investigation, serves as the initial condition for a finite-difference propagation scheme. Results show that shock strength and ripple curvature determine whether ensuing propagation leads to wave front folding. High resolution images of the computed full wave field provide insights into the spiked and rounded features seen in sonic booms that have propagated through turbulence.
[DOI: 10.1121/1.1377631]

PACS numbers: 43.28.Mw, 43.25.Cb, 43.50.Vt [MRS]

I. INTRODUCTION

The stochastic nature of turbulence precludes a complete analytical solution to the problem of predicting how a sonic boom will distort after passing through the atmosphere's turbulent boundary layer (TBL). In order to predict the precise wave form observed at the ground, it would be necessary to specify the velocity, temperature, and density of the atmosphere within a considerable volume. The best we can hope for, then, is to predict the average effects of turbulence on certain broadly defined features of the wave form, and to compute the probability of certain extreme distortions, such as spikes, being present.

Studies of human response to sonic booms suggest that three main factors contribute to annoyance: peak amplitude, rise time, and overall spectral content.[1] Although they are related, there is some degree of independence among these factors. Clearly, a model for sonic boom propagation through turbulence should predict average values for these wave form characteristics as a function of general turbulence parameters. However, signatures of sonic booms created during test flights show considerable variability: Both peaked and rounded wave forms have been observed at different microphones during the same flight, and among different flights at the same microphone.[2] This suggests that a sonic boom distortion model should also predict probabilities of certain extreme wave forms.

Two distinct modeling approaches have received significant attention: Crow's scattering theory[3] and Pierce's model of wave front rippling leading to focusing and folding.[4,5] The main result of the first-order scattering theory is a power law dependence of rms pressure fluctuations on the distance of the observer behind the shock front (also expressed as time after shock arrival). This power law is in approximate agreement with experimental observations,[6] at least for times significantly later than the shock arrival. An extension by Plotkin and George to incorporate second-order scattering perturbations permitted a calculation of shock thickening[7] and a reformulation by Plotkin[8] yielded a calculation of the spectral content.

The scattering theory necessarily yields a statistical result, stemming from a statistical description of turbulence; it does not give a reliable prediction of a particular outcome for the fine-scale features of a sonic boom signature. It is not clear, then, whether this theory can give a satisfactory prediction of the probabilities of particular wave form shapes. Moreover, molecular relaxation and nonlinearity are incorporated into the first-order (linear) scattering theory in an ad hoc manner, leaving open the question of the significance of these effects on the mechanism of scattering.

This paper describes an effort to apply a numerical propagation scheme to Pierce's theory of rippled wave fronts. In this model, the first-order effect of turbulence is to refract the incoming steady-state sonic boom, producing a rippled wave front. Where the ripple is concave in the direction of propagation, the shock will focus and possibly form folded wave fronts and caustics. The pressure behind the shock (near the axis of focusing) is strongly influenced by diffracted waves originating along the wave front. Where the ripple is convex, geometric spreading leads to decreased amplitudes. Pierce showed that where focusing occurs, the shock front becomes spiked, and where defocusing occurs, the shock front becomes rounded.[4]

Wave front ripples will have many length scales, corresponding to the inertial subrange of turbulence scales. The cumulative effect of focusing and defocusing at many scales could conceivably produce a thickened shock front, as well as either a net peaked or rounded wave form with smaller

[a)]Electronic mail: piacsek@tahoma.cwu.edu

spikes superimposed. Pierce combined this approach with Crow's statistical model of turbulence and derived a probability density function for the arrival time of microshocks produced by focusing.[5] The staggered arrival of microshocks had the effect of thickening the overall shock. This analytical approach, while initially encouraging, rested on many assumptions and is somewhat difficult to interpret.

Since that time, computer speed and availability has reached the point where it is now the standard approach to numerically solve the equations suggested by these models of sonic boom propagation. For Pierce's model to yield a statistical prediction of sonic boom distortion, an initially plane wave front must be propagated through many realizations of turbulence, as in a Monte Carlo method, and statistics compiled from the many outcomes. One advantage of this "brute force" approach is that particular model outcomes may bear some resemblance to actual outcomes, unlike a solution that incorporates an ensemble average of turbulence effects. In this way, probabilities of particular outcomes (extremely peaked or rounded wave forms, for example) may be computed.

As a step in this direction, the present paper discusses numerical results obtained by propagating the positive phase of a sonic boom with singly and multiply rippled wave fronts. Turbulence is not incorporated directly into the propagation model, but serves only to produce the initial rippling. This simplification permits the study of wave form distortion as a function of propagation distance from a particular realization of wave front rippling. It also makes possible an interpretation of the role played by different rippling scales with regard to the location and magnitude of spikes or other identifiable features of the distorted wave form. Another advantage of assuming that the medium is inhomogeneous only within a single thin layer is the ability to assess the time scales of the evolution of certain features of wave form distortion, such as primary and secondary spikes. Results presented here suggest that some of these time scales are comparable to the propagation time through the entire atmospheric boundary layer; thus, it may be that distortions observed at the ground are, to first order, due to wave front rippling that occurs near the top of the boundary layer, since subsequent rippling may not have had sufficient time to develop features associated with focusing.

Section I describes the numerical experiment. A modified version of the NPE program by McDonald and Kuperman[9] is used to propagate the positive phase of a sonic boom-like N wave whose wave front is rippled. The precise form of the rippling is related to a simplified description of turbulence. As discussed previously, no turbulence is incorporated into the propagation model beyond the initial rippling.

A detailed discussion of the focusing behavior of a weak shock with a finite rise time is presented in Sec. II. This builds on previous work by the author[10] which examines the propagation of a step shock with a single concave ripple in the wave front. It is shown that two parameters, one associated with wave front curvature and the other with shock overpressure, govern whether geometric propagation predominates, such that wave front folding occurs beyond the focal point, or nonlinear effects predominate, causing the concave wave front to straighten. The range of parameter values corresponding to shock amplitudes and ripple scales typical of sonic booms entering the TBL is shown to encompass the transition between folding and shock dynamic behavior.

Numerical results for singly and multiply rippled wave fronts are presented in Sec. III. Different ripple dimensions and different observer locations are explored for singly rippled wave fronts. Finally, the case of a sonic boom wave front containing two ripple components is examined. Depending on the observer location, the multiply rippled wave front produces either extra spikes or a delayed onset of the shock peak.

II. NUMERICAL MODEL

A. Overview

A modified form of the NPE program developed by McDonald *et al.*[9,11] is applied to propagation of sonic booms with slightly curved wave fronts. The NPE is a time-domain approach that models first-order nonlinear wave propagation that may be diffracted at small angles from the primary axis. The linearized version of the NPE is essentially the time-domain equivalent of the parabolic equation often applied to sound beams. The frame of reference is an observer moving along the primary axis with the ambient sound speed, c_0; this eases constraints on the grid spacing and time step size needed for computational stability. Other features of the algorithm make it robust at handling steep gradients in the solution.

The NPE was developed primarily to model shock propagation underwater. To make the program suitable for sonic boom propagation, the effects of thermoviscous dissipation and molecular relaxation have been incorporated. With the primary direction of propagation coinciding with the x axis and assuming diffraction occurs only in the $x-y$ plane, our modified two-dimensional NPE can be written as follows:

$$\frac{\partial p}{\partial t}+\left(c_0+\beta\frac{p}{\rho c_0}\right)\frac{\partial p}{\partial x}+\frac{c_0}{2}\int_{\infty}^{x}\frac{\partial^2 p}{\partial y^2}\,dx'-\delta_{\mathrm{eff}}\frac{\partial^2 p}{\partial x^2}=0, \tag{1}$$

where p represents acoustic pressure, c_0 the ambient sound speed, β the parameter of nonlinearity, and δ_{eff} an effective dissipation coefficient that incorporates thermoviscous damping as well as the effect of molecular relaxation for a steady state shock.

It should be noted that this method of accounting for molecular relaxation is not strictly valid for a focusing shock, since focusing is not a steady-state process. Moreover, near focal points and caustics peak pressures may exceed 150 Pa, at which point vibrational energy states appear frozen to the passing shock front and no longer contribute to dispersive shock thickening. Modeling the effects of relaxation will be discussed in more detail in the following section.

A two-dimensional acoustic field, $p_0(x,y)$, is specified as the initial condition on the discretized coordinates (x_i,y_j). The algorithm then marches in time, solving a finite difference approximation of Eq. (1). At specified times, the solu-

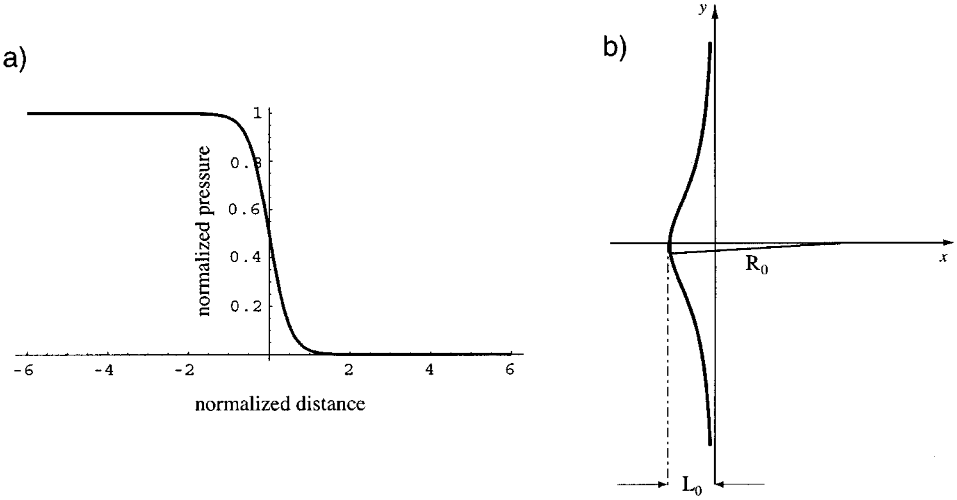

FIG. 1. (a) Wave front with parabolic ripple. R_0 is the radius of curvature at $y=0$; L_0 is the ripple amplitude. (b) Hyperbolic tangent profile of step shock. Distance along the x axis is normalized with respect to the shock width; pressure is normalized with respect to the shock amplitude.

tion array is written to disk, then rendered as a three-dimensional image. The high spatial resolution makes it possible to visualize the entire wave field as a smooth surface, in which the details of the shock front may be discerned.

The computational boundaries parallel to the x axis act as rigid, frictionless walls, reflecting incident waves without attenuation or phase shift. This type of boundary was chosen for its simplicity and reliability. However, with such simple boundaries, care must be taken to make the domain sufficiently large that, within propagation times of interest, reflected waves do not contaminate the solution near the shock front. It is also necessary to ensure that the initial wave front is perpendicular to these boundaries.

The acoustic pressure is set to zero everywhere ahead of the shock front. A grid tracking algorithm prevents the shock front from advancing too close to the front of the computational domain.

Computations were performed on a DEC Alpha workstation, with a typical grid size of 700 by 1000 points. With uniform grid spacing, the number of grid points needed to be large in order to achieve satisfactory resolution of the shock front while encompassing the entire positive phase of an N wave.

B. Initial conditions

The initial pressure field consists of the positive phase of an N wave that has a steady-state shock profile and a slightly curved wave front. In the vicinity of the shock, the wave form is described by a hyperbolic tangent function [shown in Fig. 1(a)]; behind the shock front, the wave form amplitude decreases linearly to zero. The hyperbolic tangent shock profile corresponds to the steady-state solution of Eq. (1) obtained when the initial condition is a planar step function. Traversing the x axis, the shock is specified by

$$p_0(x)=\frac{P_{\mathrm{sh}}}{2}\left(1-\tanh\frac{2x}{l_{\mathrm{sh}}}\right), \tag{2}$$

where P_{sh} denotes the peak shock pressure and l_{sh} is the Taylor length (which can be thought of as the shock width), given by

$$l_{\mathrm{sh}}=\frac{8\,\delta\rho_0 c_0}{\beta P_{\mathrm{sh}}}. \tag{3}$$

When only thermoviscous effects are considered, $\delta=\delta_{\mathrm{cl}}=1.86\times10^{-5}\ \mathrm{m^2/s}$ is the classical damping coefficient in air. In steady-state conditions, with the shock overpressure between 30 Pa and 120 Pa, the early portion of the shock rise is dominated by dispersion associated with O_2 relaxation.[12] The fully dispersed shock front has a rise profile that is similar to the hyperbolic tangent form produced by classical (thermoviscous) damping. The effects of O_2 relaxation can thus be modeled by replacing the classical dissipation coefficient with an effective dissipation coefficient, δ_{eff},[13]

$$\delta_{\mathrm{eff}}=\delta_{\mathrm{cl}}+c_{\mathrm{fr}}\tau_{\Delta C}=1.67\times10^{-3}\ \mathrm{m^2/s}, \tag{4}$$

where τ is the relaxation time of O_2, c_{fr} is the frozen shock speed, and Δc is the difference between the frozen and equilibrium shock speeds. The frozen shock speed corresponds to a shock rise time that is much shorter than the molecular relaxation time (such that molecular motion appears frozen to the shock), whereas the equilibrium sound speed corresponds to a shock with a sufficiently long rise time that molecular vibration states are always in equilibrium throughout the passage of the shock. Note that, in the limit of large shock amplitude, Δc approaches zero and δ_{eff} approaches δ_{cl}.

The wave front [depicted in Fig. 1(b)] lies nominally in the $y-z$ plane at $x=0$. The shallow ripple is specified as a variation along the y axis of the shock arrival time, $\tau_0(y)$, at $x=0$. An example of the form of $\tau_0(y)$, used in the case of a step shock with a single concave ripple, is

$$\tau_0(y)=\frac{L_0}{c_0}\left[1+\frac{L_0}{2R_0}\left(\frac{y}{L_0}\right)^2\right]^{-1}, \tag{5}$$

where L_0 is the maximum depth of the ripple and R_0 is the minimum radius of curvature of the wave front; both occur at $y=0$. Note that the ripple is symmetric about $y=0$; thus, the x axis shall be referred to as the "central axis." At large values of y, τ_0 approaches zero, so the wave front is nominally planar except in the vicinity of the central axis. Wave front curvature exists solely in the $x-y$ plane; the wave front is uniform along the z axis [normal to the page in Fig. 1(b)].

The geometry of focusing is then two dimensional.

It is convenient and instructive to define nondimensional parameters associated with this initial shock profile and wave front curvature. The shock thickness is described by the parameter $\mathcal{T}=l_{\mathrm{sh}}/L_0$, the wave front curvature is described by $\mathcal{C}=L_0/R_0$, and the shock amplitude is characterized by $\mathcal{P}=\beta P_{\mathrm{sh}}(\rho_0 c_0^2)^{-1}$. Each of these parameters corresponds to a physical process that plays some role during wave front focusing.

The shock thickness parameter, $\mathcal{T}$, can be associated with diffraction that occurs within the shock front, referred to here as ''inner diffraction.'' When $\mathcal{T}$ is zero, the shock front is perfectly abrupt and, in the absence of nonlinearity, propagates exactly according to geometric theory. This leads to a singularity in acoustic intensity at the point of first focus, $(x,y)=(R_0,0)$, where rays launched from the immediate vicinity of $y=0$ intersect. However, a nonzero value for $\mathcal{T}$ ensures that the shock amplitude will remain finite, even at the focal point, since frequencies comprising the shock front are not arbitrarily high and will diffract away from the wave front normal when the length scale of wave front curvature is comparable to that of the shock thickness (where $\mathcal{T}\approx 1$). Inner diffraction will always occur within a region arbitrarily near the focal point as long as $\mathcal{T}$ is nonzero.

The wave front curvature parameter, $\mathcal{C}$, indicates the amount of ''outer diffraction'' from points along the curved wave front. Diffracted waves originating from beyond the inflection points of the initial wave front are responsible for the familiar logarithmic amplitude profile behind the shock front at caustics.[14] $\mathcal{C}$ is inversely proportional to the time required for the shock to reach the focal point; it is directly proportional to the magnitude of diffraction effects behind the shock within a unit distance (or time) of propagation.

The shock strength parameter, $\mathcal{P}$, is directly proportional to the strength of nonlinear effects, such as steepening. This parameter can also be expressed in terms of the mach speed of the shock front, $M=v_{\mathrm{sh}}/c_0=1+0.5\mathcal{P}$.

These three parameters are completely independent of each other. Each represents the degree to which the corresponding physical effect governs the shock front evolution at $t=0$. By constructing several initial shock fronts that differ in the relative sizes of these parameters, it is possible to assess the relative importance of each physical process (inner diffraction, outer diffraction, and nonlinearity) upon the shock profile evolution near a focus.

It should be noted that these parameters are defined for the initial state, only. They are useful, nonetheless, because propagation in a homogeneous medium is determined by the initial state. The curvature parameter, $\mathcal{C}$, does not completely specify the initial wave front, but it does correspond to the rate at which diffraction effects contribute to the solution along the central axis.

The following briefly describes some numerical results showing that $\mathcal{P}$ and $\mathcal{C}$ govern whether a step shock with parabolic wave front curvature will propagate according to geometric acoustics or shock dynamics theory.

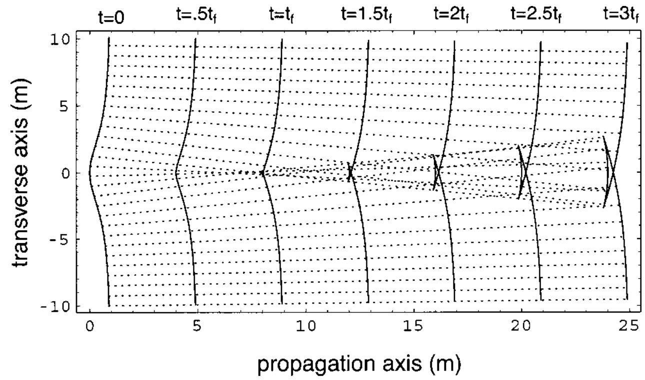

FIG. 2. Geometric evolution of initially concave shock front. Shown is a progressive sequence of wave fronts (solid lines) drawn at equal time intervals. The dashed lines are the ray trajectories.

C. Step shock with a single focus

Numerical experiments investigating the evolution of shock profiles in the region of a geometrical focus were carried out to examine the relative importance of diffraction and nonlinearity in the behavior of the shock front. The wave front is curved as described in Sec. II B, illustrated in Fig. 1(b), and the initial shock profile is the hyperbolic tangent function given by Eq. (2), shown in Fig. 1(a). Behind the shock front, the pressure amplitude is constant. Henceforth, this initial condition will be referred to as a ''step shock,'' with the understanding that the shock thickness is finite.

The step shock, rather than an N wave, was chosen for this preliminary investigation in order to have a computational array that was no larger than necessary to observe the evolution of the shock itself and the vicinity immediately behind it. Within this region, the slowly decreasing pressure field of a sonic boom-like N wave is nearly indistinguishable from a constant pressure field.

The numerical results for the initial condition just described are compared to the linear geometrical evolution of a discontinuous shock that has the same wave front curvature. Figure 2 depicts the geometrical propagation of the rippled shock; the solid curves are the wave front at successive time intervals, and the dashed lines trace rays that leave from the initial wave front on the left. After the point where rays first intersect $(t=t_f)$, the wave front becomes folded, forming the fish tail, or delta, pattern characteristic of this focusing geometry. Caustics are located at the extremes of the fish tail, $y_c(x)$, where the wave front folds back on itself. An observer located within these extremes $(-y_c(x)<y<y_c(x)$ at a distance x from the initial wavefront) experiences three shock fronts passing by, except at $y=0$, where two shocks are observed; outside this region only one shock is observed.

It is expected that nonlinear effects may prevent, or alter, the geometrical propagation shown in Fig. 2 because shock dynamic theory predicts self refraction of the wave front when the amplitude is locally increased.[15] The geometric result will serve as a reference to which numerical results can be compared.

Five different initial wave forms were created based on particular values for $\mathcal{C}$ and $\mathcal{P}$, most of which are within a range that is plausible for sonic booms. These are grouped into two sets of three wave forms; in each set, one parameter is constant while the other is varied.

In the first set, the ($\mathcal{C}$, $\mathcal{P}$) pairs are (0.025, 0.0001), (0.025, 0.0005), and (0.025, 0.0025). Here, shock amplitude (nonlinearity) is increasing while the shape of the wave front remains the same. For the second set, the values are (0.0125, 0.0005), (0.025, 0.0005), and (0.05, 0.0005). In this case, shock amplitude is constant as the initial wave front curvature increases (focal distance decreases). Note that the middle pair of values in each set is the same.

The initial pressure along the x axis at each y value was specified according to the hyperbolic tangent function, Eq. (2). The midpoint of the shock (where $p=0.5P_{\mathrm{sh}}$) lies at $x=-c_0\tau_0(y)$. The delay time, $\tau_0(y)$, is given by Eq. (5). The profile and the wave front, along with the variables that make up $\mathcal{P}$ and $\mathcal{C}$, are illustrated in Fig. 1.

The step size in the x direction, Δx, is chosen so that the steepest portion of the rise phase of the shock (from 10% to 90% of P_{sh}, a distance approximately equal to l_{sh}) is resolved by three grid points. The length of the computational domain in the x direction, L_x, is approximately four times the ripple depth, L_0. These dimensions require that the number of grid points in the x direction be at least $10/\mathcal{T}$.

The aspect ratio $\Delta y/\Delta x$ is restricted by the largest angle the wave front makes with respect to the y axis. To avoid an exaggerated staircase shape to the discretized wave front, the aspect ratio is made no larger than $\mathcal{C}^{-1/2}$.

The full wave field solution is rendered as a surface plot of acoustic pressure; the positive x axis points to the right (the direction of propagation). In most cases, the solution was carried out to five times the focal distance, R_0. The results for the first set, in which shock amplitude is varied, are shown in Fig. 3; the weakest shock is shown in plot (a), the strongest shock in plot (c).

The wave field in which nonlinearity is weakest clearly shows the folded wave front pattern predicted by geometrical acoustics; compare the plan view of Fig. 3(a) with the last wave front shown in Fig. 2. Specifically, there is a region along the transverse axis where an observer experiences three distinct shocks. At the edges of this region, the second and third shocks merge into one, where ray theory predicts a caustic. In Fig. 3(a), a secondary shock front can be seen extending beyond the caustics, its amplitude decaying with distance from the caustic. This secondary shock, not predicted by ray theory, is seen in the analytical solution of Obermeier[16] and in the experimental results of Sturtevant and Kulkarny,[14] where they are clearly associated with shock fronts diffracting from the sharp edges of the parabolic reflecting surface. In the present context, the secondary shock is believed to be composed of waves diffracted from regions of the initial shock front where the wave front curvature changes from convex to concave.

The evolution of the weakest shock along the central axis is shown in Fig. 4(a). Beyond the point of first focus (where the shock amplitude is largest), the double shock is apparent. The first shock is formed by the intersection of upper and lower parts of the original shock front; rays are crossing here, but not focusing. The second shock is the terminus of rays that have gone through a focus. Over time,

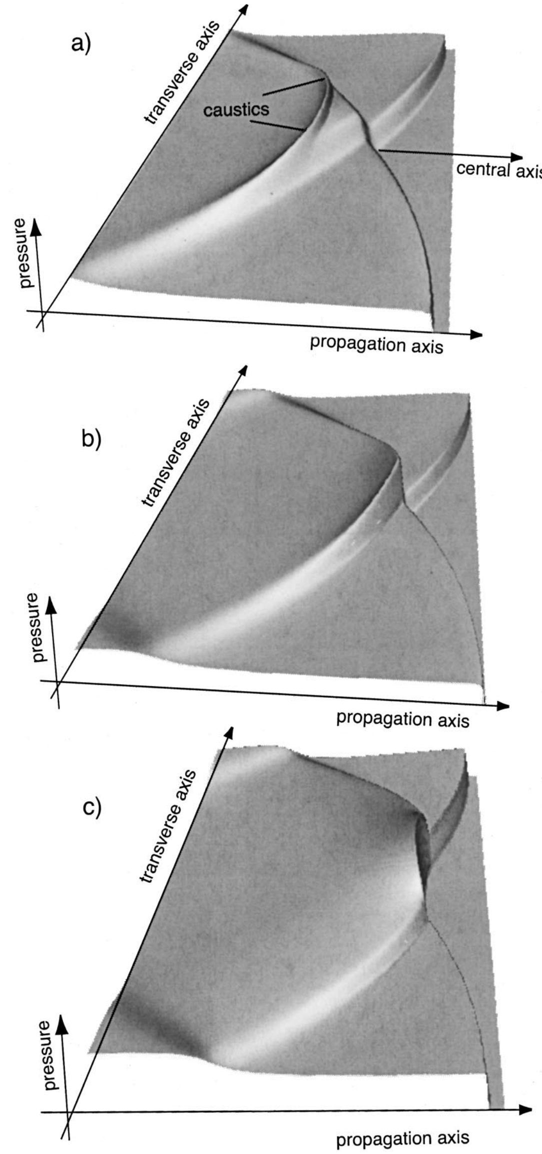

FIG. 3. Behavior of focusing step shock: dependence on shock strength. Shown are full wave field solutions at $t=5t_f$ for three initial conditions: (a) small initial shock amplitude (12 Pa); (b) moderate initial shock amplitude (60 Pa); (c) large initial shock amplitude (300 Pa). Wave front curvature is the same in each case.

the first shock advances relative to the second shock, which is a purely geometric phenomenon.

Note that the amplitude of the second shock decays more rapidly than that of the first shock; this is partly due to the more rapid geometric spreading of the central rays which make up the second shock, but is mostly the result of the nonlinear decay resulting from the rapid pressure decrease behind the second shock. Note also that a slight peak develops on the first shock, similar to what the main shock experiences at the outset. Diffraction from neighboring regions of the wave front (outer diffraction) destructively interferes with the field just behind both shocks on the axis of focus.

By contrast, the wave with the strongest shock amplitude, shown in Fig. 3(c), possesses a wave front that is still smooth and without caustics, consistent with the predictions of shock dynamics. In the vicinity of the central axis there is only one shock, referred to by Obermeier as the ‘‘shock

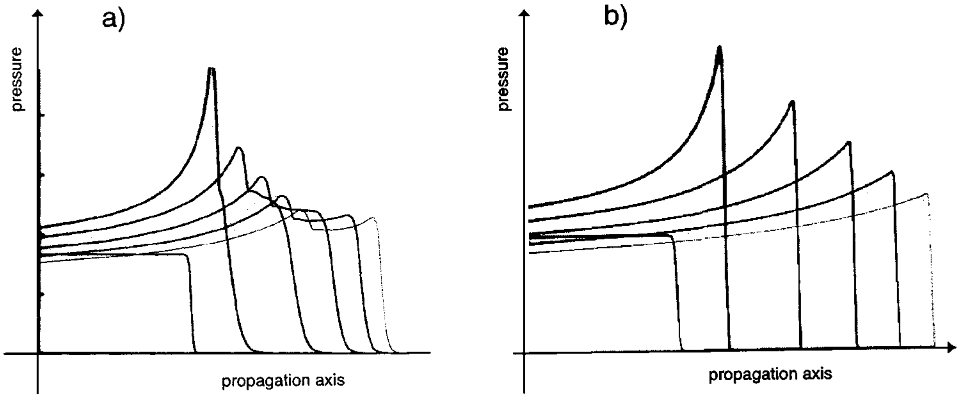

FIG. 4. Evolution of shock profiles along the axis of focus. (a) $\mathcal{C}=.025$, $\mathcal{P}=.0001$; shock front folds after the initial focus at $t=t_f$. (b) $\mathcal{C}=.025$, $\mathcal{P}=.025$; shock front does not fold. The initial amplitude in (b) is 25 times larger than in (a). Profiles are plotted at $t=0$, $t=t_f$, $t=2t_f$, $t=3t_f$, $t=4t_f$, and $t=5t_f$.

disk.'' Outside of this shock disk a second shock front is observed whose amplitude decays with distance from the central axis. This feature is also seen in the solution of Obermeier[16] and in the photographs of Sturtevant and Kulkarney.[14] At the top and bottom corners on the left-hand side of the plot can be seen wave fronts reflecting off the upper and lower boundaries.

The evolution of the wave form along the central axis is shown in Fig. 4(b). Note that the vertical scale is not the same as in plot (a) of the same figure; the initial shock amplitudes in the two cases differ by a factor of 25. With no folding, the pressure profile contains only a single shock, followed by a logarithmically decreasing overpressure. The shock amplitude decreases in accordance with the predictions of shock dynamics.

The shock front in Fig. 4(b) advances relative to the reference frame of the computational domain with speed $v_{\rm sh}-c_0=0.5c_0\mathcal{P}$, which is proportional to the shock amplitude. Thus, the shock speed is greatest along the central axis and decreases with distance from this axis, causing the wave front curvature to decrease with time.

The solution shown in Fig. 3(b) appears to represent a middle ground between geometric acoustics and shock dynamics; the wave front is neither folded, nor does it clearly show self-refraction. With this result as a reference ($\mathcal{P}=0.0005$ and $\mathcal{C}=0.025$), two further numerical trials were performed in which the initial wave front curvature was changed (shock amplitude is held constant). When $\mathcal{C}$ is increased from 0.025 to 0.05 (corresponding to a decrease in the focal distance, R_0), the wave exhibits geometric folding behavior, as shown in Fig. 5(a). When $\mathcal{C}=0.0125$, corresponding to a more shallow curvature, the wave is clearly in the shock dynamic regime, as shown in Fig. 5(b).

These numerical results confirm the presence of a transition between geometric and shock dynamic behavior for focusing shocks that have amplitudes and curvatures representative of sonic booms. References 16 and 14 show this transition for shocks with larger amplitudes and shorter focus lengths. Also demonstrated is the efficacy of describing a curved shock front with two nondimensional parameters, each quantifying the role played by nonlinearity or diffraction.[17]

III. SINUSOIDAL WAVE FRONT RIPPLING

A. Connection to atmospheric inhomogeneities

A simple model of atmospheric turbulence, adapted from Panofsky and Dutton,[18] describes turbulence as a collection of vortices. Each vortex is specified by a characteristic length (diameter), L_t, and a characteristic tangential

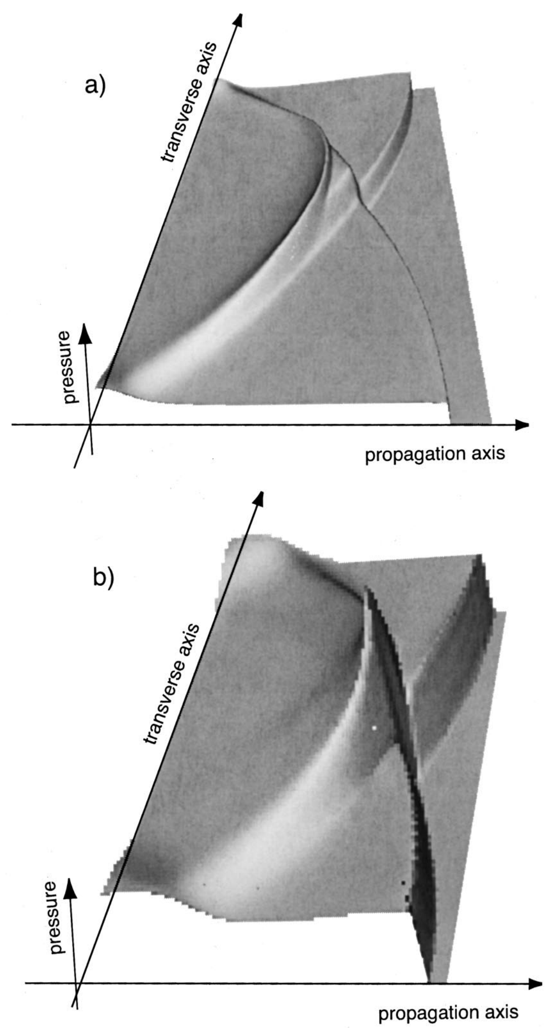

FIG. 5. Behavior of focusing step shock: dependence on wave front curvature. Shown are full wave field solutions at $t=5t_f$: (a) large initial curvature (short focal length); (b) small initial curvature (large focal length).

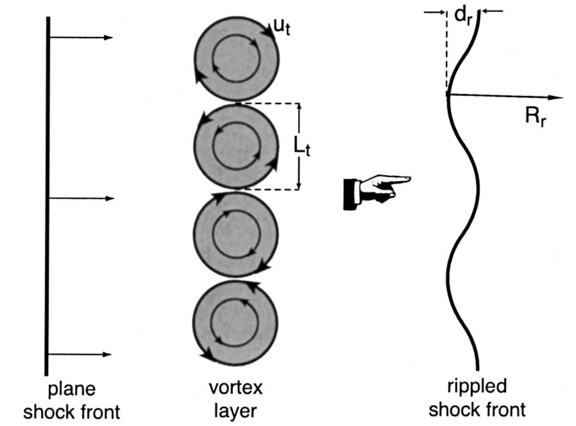

FIG. 6. Illustration depicting the rippling of an initially plane shock front due to a chain of vortices. Ripple parameters R_r and d_r can be expressed in terms of vortex parameters L_t and u_t.

speed, u_t, at the outer edge. Within this framework, one of the simplest realizations of turbulence is a thin layer consisting of a linear chain of identical vortices alternating in their direction of rotation, like a series of gears. An initially plane wave front passing through this vortex layer will become rippled in a way that is approximately sinusoidal with wave number $k_r = \pi/L_t$. This scenario is illustrated in Fig. 6.

The amplitude, d_r, and the minimum radius of curvature, R_r, of a sinusoidal ripple can be expressed (to first order) in terms of the vortex parameters as follows:

$$d_r = \frac{L_t u_t}{c}, \tag{6}$$

$$R_r = \frac{L_t c}{10 u_t}. \tag{7}$$

Note that d_r corresponds to L_0 of the parabolic ripple, described in Eq. (5). The nondimensional parameter associated with wave front curvature is then $\mathcal{C} = d_r/R_r = 10(u_t/c)^2$. Thus, even if u_t and L_t both independently characterize vortices, the focusing behavior of a rippled wave front, relative to the shock amplitude, depends only on u_t. This is physically plausible, since increasing the size of the vortex (while maintaining a constant outer velocity) will both increase the amplitude of the ripple and decrease the ripple wave number, with the net result that the ripple curvature is approximately constant.

The vortex layer just described can be interpreted as a realization of a single wave number component of turbulence. A more complete description of turbulence can be obtained via the superposition of many vortex streets within a thin layer, each representing a different component of turbulence. Wave front rippling from such a superposition of vortices will be a linear superposition of sinusoidal ripples that would result from each component alone. In this way, the effects of turbulence within a thin layer can be modeled directly with wave front rippling.

It should be emphasized that the rippling occurs along only one axis parallel to the wave front; the wave front is uniform along the other axis. The other important simplification is that the effects of atmospheric inhomogeneities are realized only for the initial condition. The numerical solution assumes a homogeneous medium.

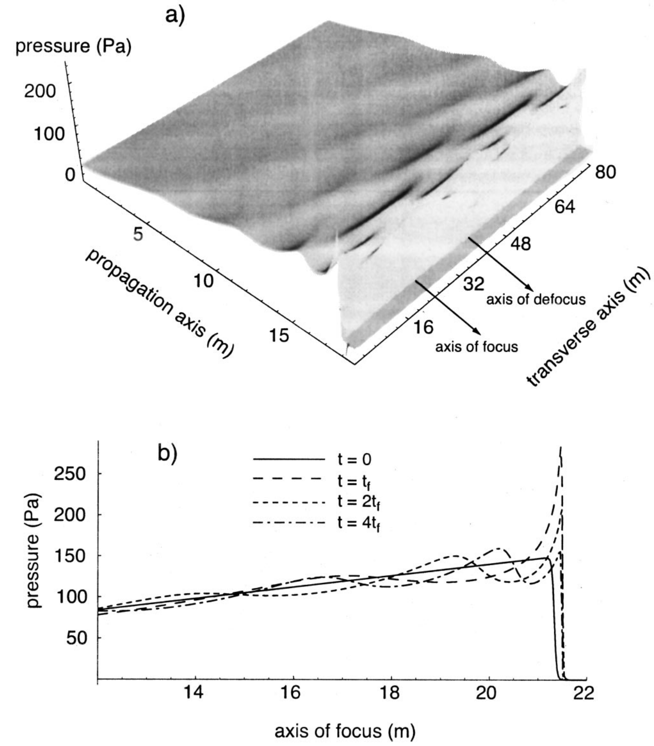

FIG. 7. Solution for positive phase of sonic boom with shallow sinusoidal ripple: case I. (a) Full pressure field at $t = 2.4$ s, (b) evolution of shock profile along axis of focus.

Section III B describes the numerical experiment that was conducted to assess the contributions to shock profile distortion from different scales of wave front rippling.

B. Description of the numerical experiment

The initial pressure field consists of the positive phase of an N wave with a sinusoidally rippled wave front. The wave form has approximately the shape of a right triangle: at the leading edge, the shock is described by the Taylor profile [Eq. (2)]; behind the shock, the overpressure decreases linearly to zero. The length of the pulse is 20 m, derived from a typical sonic boom duration of 120 ms.

Three cases, corresponding to different initial conditions, were studied. In cases I and II, the wave front is sinusoidally rippled from a single chain of vortices; in case III, the ripple has two wave number components. In each case the shock amplitude is 150 Pa ($\mathcal{P} = 0.0013$), resulting in a shock width of 0.1 m.

The first two cases have different initial wave front curvature. In case I, vortices with diameter $L_t = 20$ m and speed $u_t = 5$ m/s produce a ripple depth $d_r = 0.3$ m and focal distance $R_r = 128$ m; then $\mathcal{C} = 0.0024$ and $\mathcal{T} = 0.33$. In case II, vortices have diameter $L_t = 40$ m and speed $u_t = 12$ m/s, so that $d_r = 1.4$ m and $R_r = 112$ m; the resulting curvature is $\mathcal{C} = 0.0125$ and the thickness is $\mathcal{T} = 0.071$.

In case III, the wave front ripple has two components, described by parameters $\mathcal{C}_1 = 0.0125$ and $\mathcal{C}_2 = 0.0015$. This wave front was generated by adding a second component to

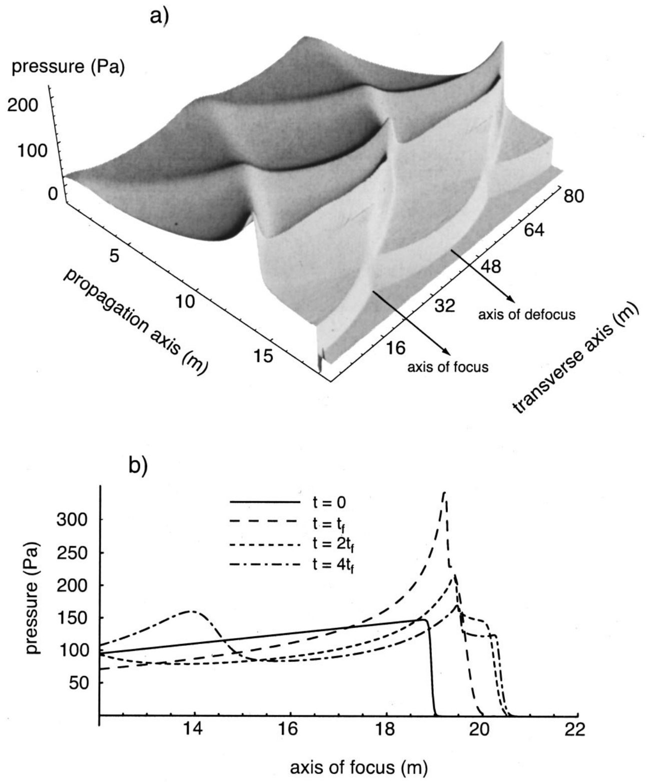

FIG. 8. Solution for positive phase of sonic boom with deep sinusoidal ripple: case II. (a) Full pressure field at $t = 1.6$ s, (b) evolution of shock profile along axis of focus.

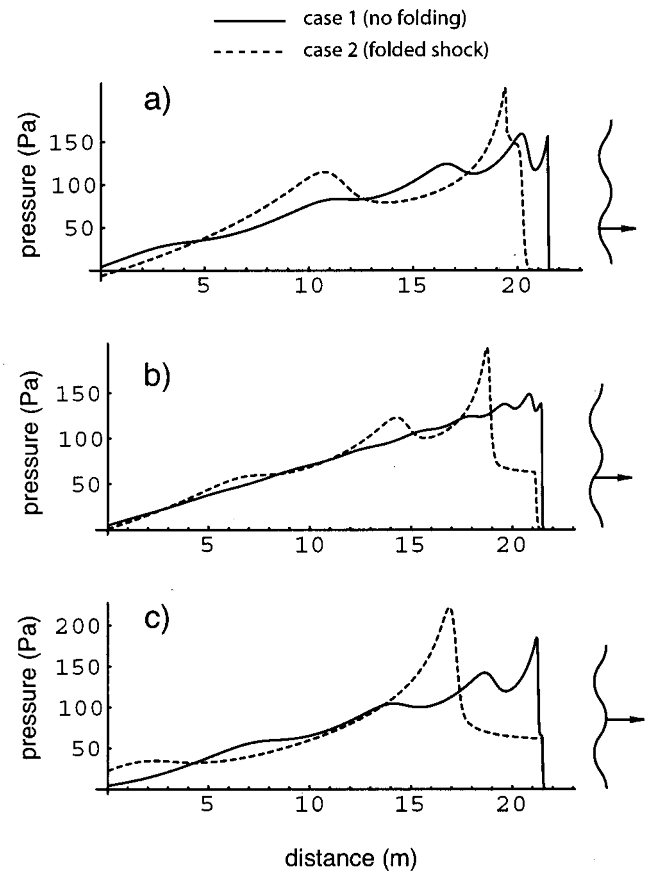

FIG. 9. Shock profiles of two sinusoidally rippled *N* waves that have propagated beyond the point of initial focus; one shock front has experienced folding (dashed curve), the other has not (solid curve). (a) Shock profiles recorded on axis of focus; (b) shock profiles recorded on the axis that intersects an inflection point on the initial wave front ripple; (c) shock profiles recorded on an axis of defocus.

the rippling of case II. The new component has a higher wave number, which is produced by smaller ($L_t = 8$ m) and slower ($u_t = 4$ m/s) vortices; most importantly (with regard to ripple curvature), the ripple depth of the second component is smaller: $d_r = 0.1$ m. An interesting feature of the higher wave number ripple component is that the ripple depth equals the shock thickness ($\mathcal{T} = 1$).

A final comment about the initial conditions should be made regarding the use of $\mathcal{C}$ to predict focusing behavior. In all three of the sinusoidal ripple cases $\mathcal{C}$ is equal to, or smaller than, the smallest value used in the step shocks with a parabolic ripple ($\mathcal{C} = 0.0125$). In the latter case, the shock did not fold. Since the amplitude of the sinusoidally rippled *N* waves is also larger, one might expect that they should all behave according to shock dynamics, if the parameter $\mathcal{C}$ may be meaningfully compared among different curvature shapes. The results suggest otherwise.

IV. RESULTS

A. Single ripple

Numerical results for case I (small wave front curvature) are summarized in Fig. 7 and the results for case II (large curvature) are shown in Fig. 8. Plot (a) in Figs. 7 and 8 shows the full wave field at a propagation distance well beyond the point of first focus; plot (b) shows the time evolution of the shock profile along the axis of focus indicated in plot (a).

These plots clearly show that the shock front in case I does not fold (it is nearly planar), while that of case II does fold. It is also evident that the peak amplitude on the axis of focus is larger in the folding case, where it occurs at the second shock (behind the leading shock). When the wave front does not fold, there is only one shock. These results confirm the shock dynamics prediction that strong nonlinear effects contribute to a decrease in the shock amplitude.[15]

The periodic form of the rippling produces a sort of interference (or ''waffle'') pattern behind the shock front in both cases. This corresponds to humps seen in the shock profiles. As propagation continues, the humps steepen and progress toward the shock front. In the case of no folding, the amplitude of the first hump eventually exceeds that of the shock [see Fig. 7(b)].

The observed pressure wave form depends on the location of the observer relative to the rippling in the wave front. The profiles in Figs. 7 and 8 show what would be measured by an observer situated along the axis of focus. An observer located at some other point on the transverse axis would measure a different wave form.

Figure 9 shows pressure profiles for both cases at three different observer locations along the transverse axis: the axis of focus, the axis of defocus, and a point midway between these. The folding shock exhibits significant variation along the transverse axis. Away from the axis of focus, the initial shock decreases in amplitude and advances relative to the larger second shock. By contrast, the shock front that does not fold thickens only slightly away from the axis of focus. At all three observation points, the folded shock exhibits the larger amplitude spike.

As with the parabolic wave front curvature, there must exist some shocks with sinusoidal rippling that exhibit neither definite geometric nor definite shock dynamic focusing behavior. Since the numerical results described previously correspond to initial conditions that are well within the realm of possible rippling produced by actual atmospheric turbulence, one may conclude that not all sonic booms will experience folding (at least if rippling shapes are approximately parabolic or sinusoidal).

B. Multiple ripples

The additional ripple component in case III is an independent source of spikes and other wave form distortions due to focusing, although the combined effects do not arise from a linear process of superposition. The initial wave front curvature of the additional ripple component is small enough ($\mathcal{C}=0.0015$) that it does not lead to wave front folding, unlike the larger scale ripple. Between the two ripple components there is zero phase difference at the axes of focus and defocus; both ripple components are focusing and defocusing together along these axes, albeit at different rates.

Results for case III can be compared with the single-component case II in Fig. 10. The pressure profiles of both cases are plotted together at three observer locations, with the dashed curved representing case III. The profiles all come from the full-field solution at $t=1.6\,\mathrm{s}$, at which point the shock has propagated approximately five times farther than the focal distance, R_r. The case III profiles, particularly along the axes of focus and defocus, exhibit small peaks in the vicinity of the shock front not seen in the corresponding case II profiles. Behind the main shock in each case, little difference is seen between the two cases. This is to be expected, because the smaller length scales (L_t and d_r) of the extra ripple component correspond to a smaller domain of influence in the field behind the shock front.

On the axis of focus, the case III profile exhibits a peak at the leading shock [Fig. 10(a)], compared to the smooth step bridging the first and second shocks seen in case II. This may be explained as the approximate superposition of the case II wave field with a nonfolding wave field similar to that seen in plot (a) of Fig. 7.

A somewhat more surprising result is the slight rounding (or delayed maximum) of the initial shock seen in the profile on the axis of defocus [Fig. 10(c)]. Simple superposition of folding and nonfolding wave fields does not satisfactorily explain the observed result.

One feature of these ripples that turned out to be less significant than anticipated is the shock thickness parameter, $\mathcal{T}=l_{\mathrm{sh}}/d_r$. When $\mathcal{T}\ll 1$, the shock is abrupt (as perceived by an observer sufficiently remote from the wave front to see that it contains many ripples); the more abrupt the shock, the better geometric theory (linear or nonlinear) will describe the evolution of the shock front.

If $\mathcal{T}$ is close to, or greater than, unity, as is true for the larger ripple wave number component in case III, the shock has a curvature comparable to its rise phase and would thus be far from the geometric approximation. In this case, it might be expected that, as focusing occurs, acoustic energy is readily diffracted away from ray paths, so that local increases in pressure are less pronounced.

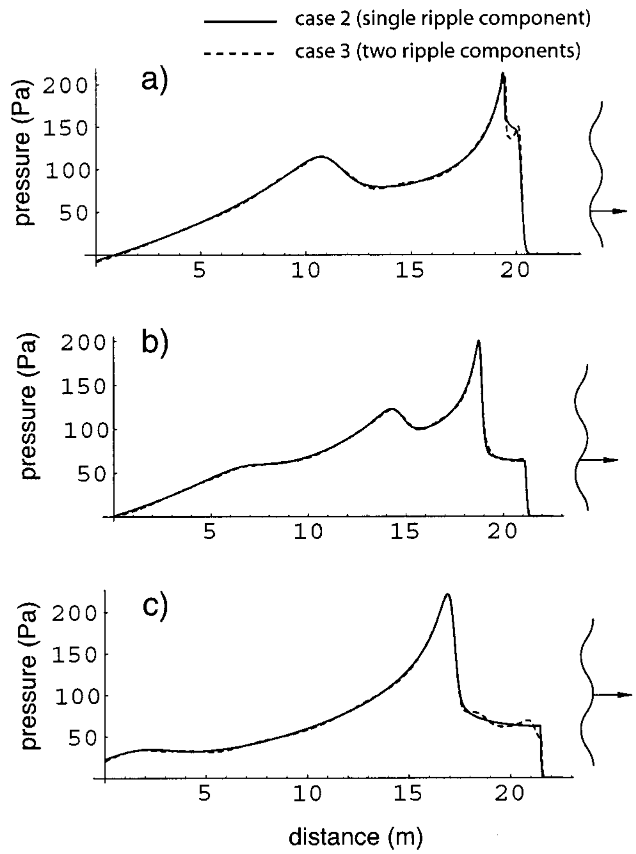

FIG. 10. Shock profiles of rippled N waves that have propagated beyond the point of initial focus; one shock front is rippled with a single sinusoid component (solid line), the other is rippled with two sinusoid components (dashed line). (a) Shock profiles recorded on axis of focus; (b) shock profiles recorded on the axis that intersects an inflection point on the initial wave front ripple; (c) shock profiles recorded on an axis of defocus.

The results demonstrate, however, that focusing of shallow ripples still produces distinct peaks at (and near) the shock front. An important implication is that even weak sonic booms (amplitudes less than 100 Pa), which are relatively thick due to molecular relaxation, will exhibit spiky features due to focusing.

V. CONCLUSIONS

A numerical study of the propagation of sonic booms with rippled wave fronts was performed in order to qualitatively and, to some extent, quantitatively evaluate the kind of wave form distortions that might be produced by various scales of wave front rippling. Via a simple model, rippling scales are associated with atmospheric turbulence parameters.

Whether folding of sonic boom wave fronts occurs depends on the amount of curvature present in the turbulence induced wave front rippling. Numerical results indicate that even for a relatively large amplitude (150 Pa), rippling produced by plausible turbulence conditions will result in a folded wave front. For a given wave front curvature, weaker shocks have a greater tendency to fold, implying that for weaker sonic booms, only the less energetic components of turbulence will produce ripples that do not lead to folding.

The wave form distortions associated with geometric wave front folding are distinctly different from those associated with shock dynamic wave front straightening. In both cases, continuous rippling along the wave front produces humps in the wave form behind the shock that advance and steepen. Folded shocks, however, exhibit a step between a leading shock and a stronger main shock; the time delay between these two shocks and the difference in their amplitudes increases significantly as an observer moves from the axis of focus to an axis of defocus.

Another discernible difference between folded and nonfolded shocks, regardless of observer location, is that folded shocks have large, distinct spikes (associated with the main shock), whereas nonfolded shocks have smaller spikes clustered near the shock front. This appears to be true for propagation distances between two and eight times the focal distance (the latter is typically between 50 and 100 m for sinusoidal ripples).

Finally, multiple ripple components independently appear to produce wave form distortions that are appropriate to their respective scales; at moderate propagation distances (between five and ten focal lengths), the combined effect on the pressure signature is approximately the superposition of these distinct processes. In particular, small peaks near the shock front are seen to be superimposed on the larger scale features when a second, smaller ripple component is added to the initial wave front.

Although the computational experiment simulated a very simple scenario, the particular outcomes contain many of the features seen in actual sonic boom recordings.[2] Among these are small spikes near the shock, large spikes far behind the shock front, and moderate rounding of the shock. One may also tentatively conclude that distortions due to small-scale focusing contribute high-frequency energy in the shock within moderate propagation distances beyond the initial rippling; as propagation continues, the smaller peaks near the shock front are steadily eroded by nonlinear steepening.

The present results are sufficiently encouraging to warrant pursuing more sophisticated numerical modeling of rippled wave fronts. Instead of constructing wave fronts from Fourier components, turbulence could be directly incorporated into the propagation scheme via velocity perturbations at each grid point. To make the problem computationally feasible, the sonic boom should be discretized on a nonuniform mesh, such that the very fine resolution is applied only near the shock front.

ACKNOWLEDGMENTS

The author wishes to acknowledge the scientific support and critical feedback, especially from John White and Doug Clarke, that he received while working on this project as a postdoctoral fellow at the Lawrence Livermore National Laboratory.

[1] A. Niedzwiecki and H. S. Ribner, J. Acoust. Soc. Am. **64**, 1622–1626 (1978).
[2] D. J. Maglieri, V. Huckel, H. R. Henderson, and N. J. McLeod, ''Variability in sonic-boom signatures measured along an 8000-foot linear array,'' NASA TN D-5040 (1969).
[3] S. C. Crow, ''Distortion of sonic bangs by atmospheric turbulence,'' J. Fluid Mech. **37**, 529–563 (1969).
[4] A. D. Pierce, ''Spikes on sonic-boom pressure wave forms,'' J. Acoust. Soc. Am. **44**, 1052–1061 (1968).
[5] A. D. Pierce and D. J. Maglieri, ''Effects of atmospheric irregularities on sonic-boom propagation,'' J. Acoust. Soc. Am. **51**, 7022–721 (1972).
[6] A. D. Pierce, ''Statistical theory of atmospheric turbulence effects on sonic-boom rise times,'' J. Acoust. Soc. Am. **49**, 906–924 (1971).
[7] K. J. Plotkin and A. R. George, ''Propagation of weak shock waves through turbulence,'' J. Fluid Mech. **54**, 449–467 (1972).
[8] K. J. Plotkin, ''The effect of turbulence on the loudness of minimized sonic boom signatures,'' NASA Conference on High-speed Research (1992).
[9] B. E. McDonald and W. A. Kuperman, ''Time domain formulation for pulse propagation including nonlinear behavior at a caustic,'' J. Acoust. Soc. Am. **81**, 1406–1417 (1987).
[10] A. A. Piacsek, ''A numerical study of weak step shocks that focus in two dimensions,'' Ph.D. thesis, Pennsylvania State University, 1995.
[11] B. E. McDonald and J. Ambrosiano, ''High-order upwind flux correction methods for hyperbolic conservation laws,'' J. Comput. Phys. **56**, 448–460 (1984).
[12] J. P. Hodgson, ''Vibrational relaxation effects in weak shock waves in air and the structure of sonic bangs,'' J. Fluid Mech. **58**, 187–196 (1973).
[13] J. Kang, ''Nonlinear acoustic propagation of shock waves through the atmosphere with molecular relaxation,'' Ph.D. thesis, Pennsylvania State University, 1991.
[14] B. Sturtevant and V. A. Kulkarny, ''The focusing of weak shock waves,'' J. Fluid Mech. **73**, 651–671 (1976).
[15] G. B. Whitham, ''On the propagation of weak shock waves,'' J. Fluid Mech. **1**, 290–318 (1956).
[16] F. Obermeier, ''On the propagation of weak and moderately strong curved shock waves,'' J. Fluid Mech. **129**, 123–136 (1983).
[17] W. L. Willshire, Jr. and D. W. Devilbiss, ''Preliminary results from the White Sands Missile Range sonic boom propagation experiment'' NASA Conference on High-speed Research, (1992), pp. 137–149.
[18] H. Panofsky and J. Dutton, *Atmospheric Turbulence: Models and Methods for Engineering Applications* (Wiley, New York, 1984), p. 35.

State of the art of sonic boom modeling[a)]

Kenneth J. Plotkin[b)]
Wyle Laboratories, 2001 Jefferson Davis Highway, Suite 701, Arlington, Virginia 22202

(Received 20 September 2000; accepted for publication 18 April 2001)

Based on fundamental theory developed through the 1950s and 1960s, sonic boom modeling has evolved into practical tools. Over the past decade, there have been requirements for design tools for an advanced supersonic transport, and for tools for environmental assessment of various military and aerospace activities. This has resulted in a number of advances in the understanding of the physics of sonic booms, including shock wave rise times, propagation through turbulence, and blending sonic boom theory with modern computational fluid dynamics (CFD) aerodynamic design methods. This article reviews the early fundamental theory, recent advances in theory, and the application of these advances to practical models.
[DOI: 10.1121/1.1379075]

PACS numbers: 43.28.Mw, 43.50.Lj [MRS]

I. INTRODUCTION

Sonic boom theory can be broadly divided into two parts. The first is fundamental theory: the understanding of what sonic boom is, its generation, and the principles of its propagation to the ground. The second part may be termed advanced topics, including details of shock rise times, propagation through turbulence, focusing, underwater penetration, and design tools.

The fundamentals of sonic boom theory were established and validated in the 1950s and early 1960s, and by the early 1970s were implemented into practical models. Over the past several decades, there have been requirements for design tools for an advanced supersonic transport, environmental assessment of launch vehicles, and environmental assessment of military aircraft operations. At the same time, there has been significant research in nonfundamental (but important) phenomena such as shock rise times and propagation through turbulence. Advances in both application models and research have taken place during a substantial growth in computing power and its widespread availability.

With the need for environmental assessments, the user base for models has expanded beyond specialists and researchers. There are now pure users who must calculate sonic booms as part of a larger system, with sonic boom modeling being only part of their work. An environmental analyst, for example, may model an entire airspace and flight operations in that airspace, then obtain the sonic boom associated with the supersonic parts of that scenario. Such a user may not understand anything about sonic boom other than interpretation of the final numbers on the ground. This is quite a contrast to users in the scientific community, who may use models developed by others but understand everything that those models are doing.

This article reviews fundamental sonic boom theory, advanced topics (and their status), and implementation of theory into models suitable for use by researchers and by pure users.

II. FUNDAMENTAL SONIC BOOM THEORY

A. Elements of fundamental theory

The basic elements of sonic boom theory are illustrated in Fig. 1, which shows a supersonic aircraft flying toward the left. Several wavefronts and the signatures at three distances are sketched. Sonic boom analysis is generally divided into three components: generation, propagation, and evolution.

A vehicle traveling at supersonic speeds **generates** a disturbance in the atmosphere. For slender vehicles or projectiles, this disturbance is governed by linearized supersonic flow theory,[1] and computed from supersonic area rule methods.[2–5] This is denoted in Fig. 1 as the ‘‘near field.’’ In traditional slender-body boom theory the disturbance is sufficiently weak that it behaves according to the acoustic approximation.

For blunt bodies (e.g., Space Shuttle Orbiter) the aerodynamic flow is inherently nonlinear, and the near field is more complex than slender body (acoustic limit) theory. Treatment of complex near fields is an advanced topic.

The disturbance **propagates** to the ground through the real atmosphere. There is a basic cylindrical spreading. This is modified by curvature of the wavefronts, as sketched in Fig. 1. The acoustic impedance also varies between the aircraft and the ground. Propagation is computed by the method of geometrical acoustics, as developed by Blokhintzev.[6] Keller[7] showed that geometrical acoustics applies to weak shock waves as well as the harmonic waves of Blokhintzev's formulation.

Because the basic acoustic propagation follows the rules of geometrical acoustics, it is possible for waves to converge and focus. Focusing does occur, and is an advanced topic.

The signature shape **evolves** as it propagates, as sketched, from ‘‘near field’’ to ‘‘mid-field’’ to ‘‘far field’’ in Fig. 1. This occurs because the signature, while weak, is still strong enough that over long distances nonlinear effects accumulate. Higher pressure parts of the signature travel slightly faster than ambient sound speed, and lower pressure

a)Presented at the Sonic Boom Symposium, 136th Meeting of the Acoustical Society of America.
b)Electronic mail: kplotkin@arl.wylelabs.com

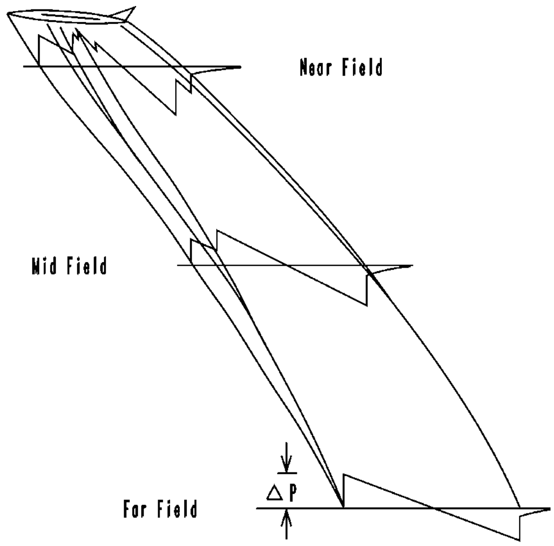

FIG. 1. Sonic boom generation, propagation, and evolution.

parts travel slightly slower. The distortion usually results in parts of the signature coalescing into shock waves, with a tendency for far-field signatures to become N-waves, as sketched in Fig. 1. The procedure for computing this distortion—and shock formation—was developed by Whitham,[8,9] and is known as Whitham's rule.

The boundaries between near-, mid-, and far-fields depend on particular circumstances. The near field is considered to be a region small enough that atmospheric gradients do not play a significant role. This is usually a few body lengths. Mid-field is where significant nonlinear distortion of the signature has occurred, but geometric features of the aircraft are still apparent. The far field is where the signature approaches an asymptotic shape, usually an N-wave. For small aircraft such as fighters, the far field is reached at distances as small as 5000 ft. For large aircraft, such as proposed 300-ft long supersonic transports, ground signatures from cruise above 50 000 ft can still be mid-field.

The near-field pressure field in the fundamental (slender body acoustic limit) theory is given by

$$\delta p(x-\beta r,r)=p_0\frac{\gamma \mathrm{M}^2 F(x-\beta r)}{(2\beta r)^{1/2}}, \tag{1}$$

where δp=overpressure associated with the wave, p_0=undisturbed ambient pressure, x=axial coordinate (body fixed), r=radius, γ=ratio of specific heats, M=Mach number, β=Prandtl–Glauert factor, $\sqrt{M^2-1}$, and

$$F(x)=\frac{1}{2\pi}\int_0^x \frac{A''(\xi)}{(x-\xi)^{1/2}}\,d\xi, \tag{2}$$

where A is the cross sectional area of the vehicle along cuts aligned with the Mach angle.

The quantity F, known as the F-function, represents the acoustic source strength, and when given by Eq. (2) is based on linearized supersonic flow area rule theory. Equation (1) represents cylindrical spreading of this acoustic disturbance in a uniform atmosphere. It is referred to as near field because the signature shape changes with distance due to nonlinear effects (per Whitham's rule). It is, however, a far-field radiating solution.

Equations (1) and (2) are written for axisymmetric bodies. Supersonic area rule theory introduced the concept of locally axisymmetric flow. If φ is the azimuth (i.e., angle in the roll direction), $F(x)$ is generalized to $F(x,\varphi)$, and is based on Mach cuts aligned with φ. As shown by Walkden,[5] lift can be included in this generalization, with the component of lift in each azimuthal direction becoming an equivalent area. This is a far-field result, valid at large radii where local cross-flow effects (usually present in the near field) are negligible. This is appropriate for sonic boom, where one is usually interested in the far field.

The source characteristics of the vehicle are embodied in $F(x)$. Whitham[8,9] applied nonlinear steepening to Eqs. (1) and (2) and obtained analytic solutions for the shock strength and duration of N-waves far from the vehicle. This solution contains the now-familiar result that shock strength decays as $r^{-3/4}$, rather than the acoustic decay of $r^{-1/2}$. An interesting result of Whitham's far-field solution is that the F-function appears only as the integral of its forward positive-pressure portion.

Figure 1 and Eqs. (1) and (2) are presented from an aerodynamics perspective, in body-fixed coordinates, with the boom viewed as waves. This is convenient for obtaining the pressure disturbance generated by the vehicle. For analysis of propagation in a real atmosphere, theory is shifted to an acoustics perspective, in atmosphere-fixed coordinates, with boom propagation viewed as rays. Figure 2 shows this shift in perspective. While either perspective is practical for steady flight, the use of body fixed coordinates for maneuvering flight confronts one with a non-Newtonian frame of reference. The ray perspective allows computation of propagation by geometrical acoustics, which is extremely well suited for analysis of acoustic waves through gradients and from moving sources.

In the ray perspective, Eq. (1) is rewritten as

$$\delta p(\tau)=p_0\frac{F(\tau)}{\sqrt{B}}, \tag{3}$$

where $\tau=t-a_0/s$, t=propagation time along ray, s=distance along ray, a_0=ambient sound speed, and B=amplitude factor accounting for ray tube area and acoustic impedance; these vary along each ray.

Note that δp and F in Eq. (3) are formally different functions than δp and F in Eqs. (1) and (2), but the differences are easy to reconcile. Details of the amplitude factor B, and of the application of Whitham's rule, can be found in Refs. 10 and 11, which are reviews of the fundamental theory. The above sets the stage for the discussion in this article.

B. Full implementations of fundamental theory

By the early 1960s, fundamental theory was well established. It included arbitrary aircraft maneuvers, ray tracing through a horizontally stratified atmosphere with winds, and evolution of the far-field boom for an arbitrary F-function.

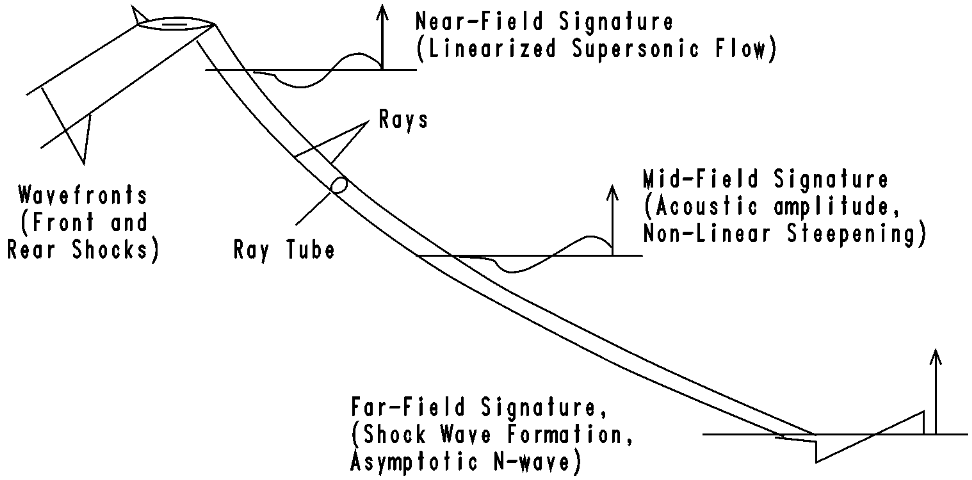

FIG. 2. Comparison between wave (vehicle fixed) and ray (atmosphere fixed) perspectives.

One of the widely known computer programs of that era was that of Friedman, Kane, and Sigalla,[12] published in 1963, and used extensively in analysis of the proposed Boeing 2707 SST of the 1960s. That program had most details correct, but had a discrepancy in the ray tube area formulation.

The first program generally regarded to have all of the details correctly implemented was that of Hayes, Haefeli, and Kulsrud,[13] in 1969. The report for this program (referred to as either the Hayes program or the ARAP program) contains complete expositions of the theory implemented, and is a valuable reference document. The program begins with an *F*-function source and implements a formulation of ray tracing analytically derived from Fermat's principle. Whitham's rule is applied via the concept of an *age parameter*, and shock coalescence is handled by numeric area balancing.

In 1972 Thomas[14] published a program that used quite different numeric algorithms from the Kane *et al.* and Hayes *et al.* models. Thomas' program computes ray paths by direct numeric integration of the eiconal (effectively applying Huygen's principle) and applies Whitham's rule via the analytic waveform parameter method. Rather than begin with an *F*-function, Thomas begins with a line of Δp at some radius, per the left-hand side of Eq. (1).

The differences between Hayes and Thomas for ray tracing and aging algorithms are of interest to specialists. From the user's perspective, both are equivalent and give the same results, with numeric precision typically in the range of three to five significant figures.

The difference between Hayes' use of the *F*-function and Thomas' use of Δp is, however, more profound than one might think. Equation (1) appears to show a direct relation and can be used to obtain Δp from an *F*-function. The Thomas program was developed so that one could directly input Δp from wind tunnel tests. Use of near-field wind tunnel data from simple bodies had been quite successful.[15,16] As noted earlier, however, the actual Δp in the near field does not necessarily correspond to the effective Δp from the *F*-function. This detail becomes significant when analyzing low boom supersonic aircraft, which are not particularly simple, and is one of the advanced topics discussed later.

A similarity between the Hayes and Thomas programs is that each computes a single point at a time: one run of either yields the boom at a single azimuth and flight time. Runs can be stacked to compute a number of points if a footprint or full mission analysis is required, but they are essentially single point programs.

These two programs are both nearly a third of a century old, which might leave the reader wondering why we are spending so much time on them. The reason is that both are full implementations of fundamental theory, accounting for arbitrarily maneuvering aircraft in arbitrary horizontally stratified atmospheres with wind. They are both still actively used today, and typify the core of what are termed full ray trace programs. Moreover, virtually every full ray trace sonic boom program in use today is evolved in one way or another from one of these two programs.

C. Simplified implementations of fundamental theory

While full implementation of fundamental theory (including arbitrary vehicle shape and atmosphere with winds) is complex enough to require computer implementation, the calculations themselves separate rather neatly into several distinct components. If analysis is limited to a windless atmosphere, numeric ray tracing can be performed one time for a surprisingly small set of parameters. George and Plotkin[17] presented charts that allowed manual computation of signature evolution under the flight track in a standard atmosphere.

Carlson[18] developed a very thorough, and much more useful, handbook procedure for calculation of N-wave booms from steady flight in a standard atmosphere. He presented this in the form of equations similar to Whitham's far field formulas, but with several factors associated with propagation through a standard windless atmosphere. These factors include the effect on amplitude and duration due to refracted ray paths, effects on amplitude and duration due to acoustic impedance gradients, and amplification due to reflection at the ground. Propagation off-track is included, so that boom can be computed across the width of the carpet. The integral of the *F*-function is represented by a normalized *shape factor* which is scaled according to aircraft size. Charts of shape factors are presented for a variety of aircraft, as are charts of the refraction and impedance factors for flight in a standard atmosphere. Carlson's method is valuable not only because it allows quick calculations of steady flight N-wave

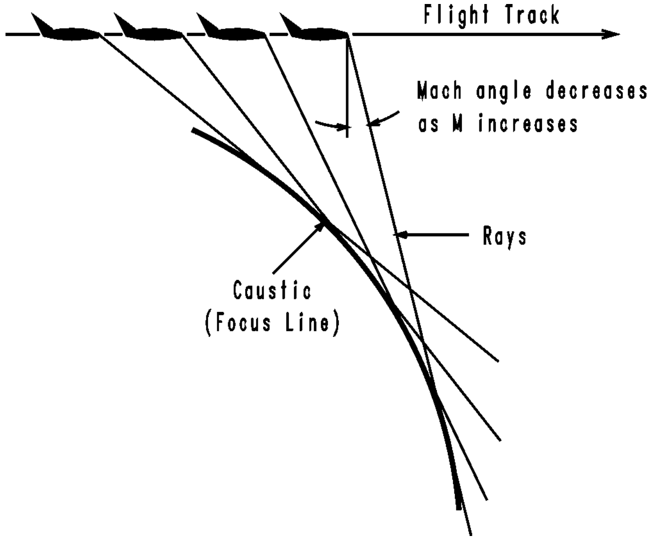

FIG. 3. Ray and caustic pattern for an acceleration focus.

booms, but also because it explicitly shows the scaling effect of parameters such as Mach number and aircraft length. The shape factors can be used to generate effective *F*-functions for use in full ray trace programs.

Another simplified approach was developed by Plotkin[19] for maneuvering aircraft in a windless atmosphere. It was noted that, for a given atmosphere, ray shapes depend only on the flight altitude and the initial vertical angle of the ray. Ray tube areas can be computed from ray shapes (trajectories of ray paths) and from derivatives of ray shapes with respect to vehicle flight parameters. Once these quantities are computed, calculation of boom for maneuvering aircraft becomes an algebraic exercise, with computational times about two orders of magnitude faster than that of a full ray trace program. This has made practical the computation of sonic booms from situations involving hundreds of operations.[20]

III. ADVANCED TOPICS AND PHENOMENA

A. Focused superbooms

With sonic booms traced to the ground via ray acoustics, it is easy to envision rays converging to a focus. Figure 3 illustrates focusing by an accelerating aircraft. An important facet of sonic boom focusing is that perfect lens-like focusing, involving a finite segment of wavefront to a point, does not occur. Focusing tends to be as illustrated, with only differential elements of the wave converging to a given point. There is a focal region along a *caustic* line, which forms an envelope of the rays. While diffraction at the caustic reduces the focus intensity, linear acoustic solutions for caustics are singular.[21] Guiraud[22] wrote the equations for focus of weak shock waves and developed a scaling law. Nonlinear effects cause the maximum focus amplitude to be finite, as observed in flight tests.[23] Figure 4 shows a typical signature along the caustic, compared with an N-wave. Amplitude is limited by both nonlinear effects and diffraction. The diffraction limit is frequency dependent, affecting low frequencies more than high frequencies, leading to a characteristic U-wave shape with the shocks peaked.

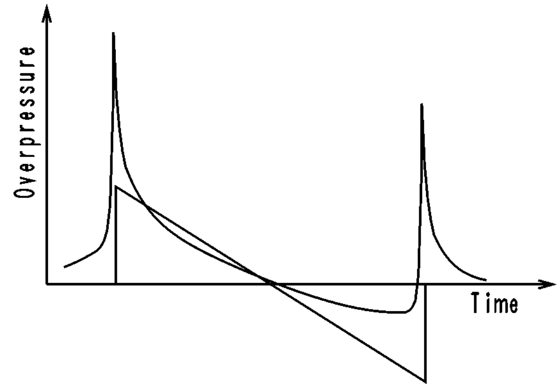

FIG. 4. Focused U-wave sonic boom compared with N-wave.

Gill and Seebass[24] obtained a numeric solution for focus of a step function at a caustic. Using Guiraud's scaling law, Plotkin and Cantril[25] extended a version of the Thomas code to apply Gill and Seebass' solution at focal zones. That code has evolved into PCBoom3,[26] which is still the only code to apply a full signature solution at foci.

Regions away from the caustic are of interest. In the region above the caustic, where rays cross, there are two types of boom: ordinary prefocus boom which has not yet passed through the caustic, and postfocus boom which has passed through the caustic. Postfocus booms are substantially attenuated, and have a U-wave shape more extreme than the focus shown in Fig. 4. Postfocus booms can be approximated by a Hilbert transform, a technique used in the TRAPS[27] and ZEPHYRUS[28] codes. PCBoom3 estimates the postfocus boom by taking the difference between the Gill–Seebass solution and the incoming prefocus boom.

There is an evanescent wave on the shadow side of the caustic. Fung[29] has developed numeric solutions for this wave, but those solutions have yet to be applied to a user program.

B. Shock rise times

Fundamental boom theory uses weak shock theory, where the structure of the shock waves is not addressed but the waves are understood to be thin. Flight tests showed sonic boom shocks to be substantially thicker than expected from classical absorption mechanisms. Long rise times—which are important because they affect perceived loudness of booms heard outdoors—occur partly from turbulence (discussed later) and partly from molecular relaxation. Pierce[30] has reviewed relaxation mechanisms in this symposium. The phenomenon is well understood, with shock structure being a balance between relaxation and nonlinear steepening. There are two approaches to computing shock structures. The first is the Pestorius[31] and Anderson[32] algorithm, where relaxation effects are applied in the frequency domain while steepening is computed in the time domain via Whitham's rule. The second is to use a Burgers equation formulation,[33] so that relaxation effects are computed in the time domain simultaneously with steepening.

Both computational methods have been successfully applied in specialized codes directed toward testing the corre-

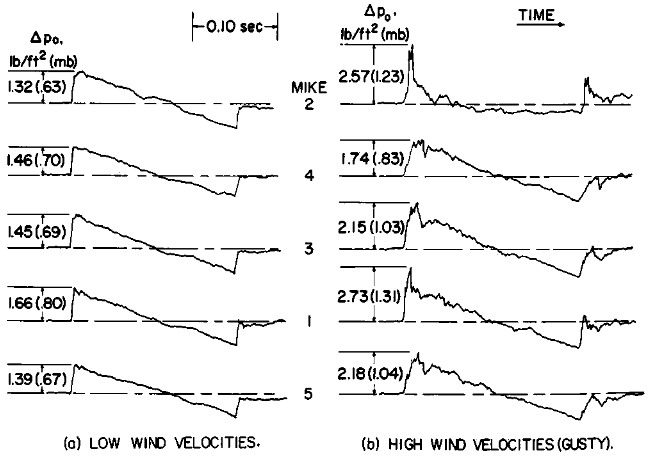

FIG. 5. Sonic booms measured under calm and turbulent atmospheric conditions (Ref. 35).

sponding theory. The Pestorius algorithm is implemented in ZEPHYRUS.[28]

PCBoom3[26] uses a simplified method. Based on flight test data,[34] a Taylor (hyperbolic tangent) shock structure is assumed, with a rise time of 1 ms-psf/Δp.

C. Turbulent distortion

Figure 5 shows sonic booms measured under calm and turbulent conditions.[35] Under turbulent conditions, booms are distorted in two ways. First, there is a ragged fine structure behind each shock. Second, shock rise times tend to be longer and variable. Crow[36] explained the fine structure by scattering theory. Crow's theory agrees well with flight test.[37] The effects of turbulence on rise times have been addressed by the competing theories of Plotkin and George[38] and Pierce.[39] It is generally accepted that turbulence plays a role in rise times, but definitive understanding of the mechanisms will probably require numeric solutions.

None of the current user models account for turbulent distortion.

D. Diffraction at carpet edge

Due to upward refraction, sonic boom carpets have a finite width. Booms observed near carpet edges are attenuated by ground impedance effects and by diffraction. Some analyses have been done on the effect of diffraction at the carpet edge, most recently by Coulouvrat[40] in this symposium. None of these theories have yet been applied to any of the user sonic boom prediction models.

E. Over-the-top booms

In the late 1970s, issues arose about secondary sonic booms—booms which had propagated upward, but were refracted downward in the thermosphere. Both the Hayes and Thomas programs had been written for application to primary booms—ones traveling downward—and could not follow this type of boom. The TRAPS program[27] was written to address this problem. It is a reformulation of the Hayes program, with the ability to trace rays in any direction. Over-the-top booms usually pass through a caustic. TRAPS uses a Hilbert transform to approximate the caustic passage, then resumes nonlinear propagation.

More recently, ZEPHYRUS[28] addresses over the top booms, in a manner similar to TRAPS.

F. Penetration into water

Because of concern about potential impacts on marine life, there is currently interest in the penetration of sonic booms into the ocean. Sparrow[41] and Cheng[42] have proposed theories for this penetration. Both theories use the airborne boom impinging on the water surface as an initial condition. To accommodate this requirement, PCBoom3 was adapted so that it would output, in addition to its usual quantities, ray angles and surface phase velocities required for both the Sparrow and Cheng models. Currently, neither underwater penetration theory is integrated into PCBoom3 or any other user model, but it is expected that this integration will happen fairly soon.

G. CFD matching

Equation (2), one of the foundation components of standard sonic boom theory, is essentially 1950s aerodynamic design technology. Aerodynamic design is now done using computational fluid dynamics (CFD), and there is a strong desire to use CFD solutions in place of Eq. (2).

As discussed earlier, δp in Eq. (1) is not just the signature taken on an arbitrary line parallel to the flight path. It must represent a far-field radiating source solution. An obvious approach to using CFD would be to carry CFD calculations out to distances where this condition is met. For complex configurations such as low-boom supersonic transports, however, this condition may not be met even at distances of five or ten body lengths.[43] Few CFD codes can be run to that distance. A method is required which can convert CFD results into equivalent far-field radiating source distributions.

George[44] investigated the reduction of under-track sonic boom by displacing it to the side. His analysis made use of multipoles. In the far field, all orders of multipole behave like Eq. (2), decaying as $1/r^{1/2}$. In the near field, each order multipole departs from this form. George developed analytical relations for these.

Page and Plotkin[45] exploited George's multipoles to match CFD solutions. They first obtained a CFD solution for δp on a cylinder about the vehicle being investigated. They fit multipoles to that solution, using George's full radius-dependent formulation. δp was then reconstituted, using the far-field formulation of each multipole. This method was implemented in MDBOOM,[46] a special limited-distribution version of PCBoom3.

H. Full footprints

All sonic boom models provide signatures at the ground. For many applications, the user needs a full footprint of some overall quantity, typically the maximum overpressure on the ground. Figure 6 shows a schematic footprint (contour chart of peak overpressure) for a focal zone, corresponding to the acceleration maneuver sketched in Fig. 3.

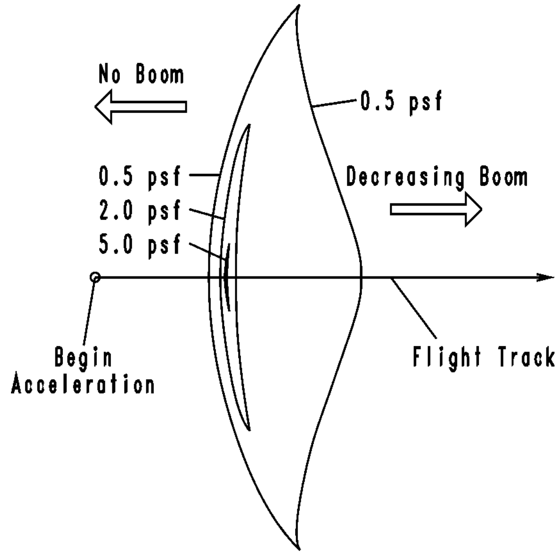

FIG. 6. Sonic boom footprint (overpressure contours) in a focal zone (not to scale).

At one time creating a footprint like Fig. 6 was a significant undertaking. Reference 47 contains footprints generated by an early version of PCBoom3 in the mid-1980s. Each footprint took several days to generate. Calculating boom at enough points on the ground would take one or two (sometimes three) overnight computer runs. Runs were pieced together manually, and contours were then drawn using a custom-written plotting program, directed toward a specific model pen plotter.

Today, the computations for a footprint such as those developed for Ref. 47 take only a few minutes, from start to finish. PCBoom3—which is aimed at production runs of single event footprints—has a menu interface that lets the user easily set up a run file. The boom calculations themselves can take only a few seconds, or at worst a minute or two. Drawing contours still requires some custom programming, but the bulk of the work is accomplished via readily available libraries. The contours appear on the user's computer screen virtually instantaneously. Thanks to the ubiquity of computer graphics and document production, the contours can be output to virtually any printer or plotter, or prepared in digital form for publication or to overlay on a map.

IV. CONCLUSIONS

A review has been presented of the state of the art of sonic boom modeling. Modeling means more than understanding phenomena: tools must be available which makes this available to the nonspecialist.

A number of particular models were discussed in this article. The following is a recap of the most significant of those models, and a summary of their features.

(i) Hayes (or ARAP)[13]—the first computer model regarded as having all details correct. It calculates boom for an arbitrarily maneuvering aircraft in an arbitrary horizontally stratified atmosphere.

(ii) Thomas[14]—a computer model developed by NASA shortly after Hayes, and with similar capabilities. It is notable for the use of the waveform parameter method of signature aging.

(iii) TRAPS[27]—developed for the purpose of tracing over-the-top booms. It follows Hayes' formulation, but uses ray distance (rather than altitude) as its independent variable, so that it can handle vertically turning rays. Accounts for the passage of a boom through caustics via a Hilbert transform. Accepts atmospheric data in standard meteorological format. Can smooth input trajectories via cubic spline fits.

(iv) ZEPHYRUS[28]—a reformulation of the basic Hayes method, aimed at incorporating as many physical effects as possible. Treats over-the-top booms similarly to TRAPS. Accounts for molecular relaxation shock structure by the Pestorius algorithm.

(v) PCBoom3[26]—evolved from the Thomas code, this program addresses focal zones by application of the Gill–Seebass focus solution and Guiraud's scaling law. Accepts initial signatures either as *F*-functions or Thomas-style δp, or can generate simplified Carlson *F*-functions from a built-in aircraft list. Computes boom footprints on the ground for a complete flight. Part of a system that includes a menu-driven user interface and graphical outputs of footprints and signatures. Variation MDBOOM[46] incorporates area-rule *F*-function calculation and the Page–Plotkin method for matching to CFD near-field solutions.

(vi) Carlson[18]—a manual procedure for computing N-wave booms in steady flight. Computes carpet width and boom signatures across the carpet. Includes shape factor charts for most aircraft, and also has a procedure for computing the shape factor. Well worth examining, even if you are going to use one of the computer programs.

A factor that must also be noted is that much of today's state of the art has been made feasible by the rapid growth of computer power. Boom calculations that were major undertakings a decade or two ago can now be performed in seconds or minutes.

ACKNOWLEDGMENT

This paper is dedicated to the memory of Professor A. Richard Seebass.

[1] W. D. Hayes, "Linearized Supersonic Flow," thesis, California Institute of Technology; reprinted as North American Aviation Report AL-222; available as Princeton University AMS Report 852 (1947).

[2] R. T. Whitcomb and T. L. Fischetti, "Development of a Supersonic Area Rule and an Application to the Design of a Wing-Body Combination Having High Lift-to-Drag Ratios," NASA RM L53H31a (1953).

[3] R. T. Jones, "Theory of Wing-Body Drag at Supersonic Speeds," NACA RM A53H18a (1953).

[4] H. Lomax, "The Wave Drag of Arbitrary Configurations in Linearized Flow as Determined by Areas and Forces in Oblique Planes," NACA RM A55A18 (1955).

[5] F. Walkden, "The Shock Pattern of a Wing-Body Combination, Far From the Flight Path," Aeronaut. Q. **IX**(2), 164–194 (1958).

[6] D. I. Blokhintzev, "The propagation of sound in an inhomogeneous and moving medium I," J. Acoust. Soc. Am. **18**, 322–328; also, *Acoustics of a*

Nonhomogeneous Moving Medium (Gostekhiazat, Moscow, USSR, 1946); translated as NACA TM-1399 (1946).
[7] J. B. Keller, ''Geometrical Acoustics. I. The Theory of Weak Shock Waves,'' J. Appl. Mech. **25**(8), 938–947 (1955).
[8] G. B. Whitham, ''The Flow Pattern of a Supersonic Projectile,'' Commun. Pure Appl. Math. **5**, 301–348 (1952).
[9] G. B. Whitham, ''On the Propagation of Weak Shock Waves,'' J. Fluid Mech. **1**, 290–318 (1956).
[10] A. R. Seebass, ''Sonic Boom Theory,'' J. Aircr. **6**(3), 177–184 (1969).
[11] K. J. Plotkin, ''Review of Sonic Boom Theory,'' AIAA-89-1105 (April 1989).
[12] M. P. Friedman, E. J. Kane, and A. Sigalla, ''Effects of Atmosphere and Aircraft Motion on the Location and Intensity of a Sonic Boom,'' AIAA J. **1**(6), 1327–1335 (1963).
[13] W. D. Hayes, R. C. Haefeli, and H. E. Kulsrud, ''Sonic Boom Propagation in a Stratified Atmosphere, with Computer Program,'' NASA CR-1299 (April 1969).
[14] C. L. Thomas, ''Extrapolation of Sonic Boom Pressure Signatures by the Waveform Parameter Method,'' NASA TN D-6832 (June 1972).
[15] H. W. Carlson, ''An Investigation of the Influence of Lift on Sonic-Boom Intensity by Means of Wind-Tunnel Measurements of the Pressure Fields of Several Wing-Body Combinations at a Mach Number of 2.01,'' NASA TN D-881 (1961).
[16] H. W. Carlson, ''Correlation of Sonic Boom Theory With Wind Tunnel and Flight Measurements,'' NASA TR R-13 (1964).
[17] A. R. George and K. J. Plotkin, ''Sonic Boom Amplitudes and Waveforms in a Real Atmosphere,'' AIAA J. **7**, 1978–1981 (1969).
[18] H. W. Carlson, ''Simplified Sonic Boom Prediction,'' NASA Technical Paper 1122 (1978).
[19] K. J. Plotkin, ''A Rapid Method for the Computation of Sonic Booms,'' AIAA-93-4433 (October 1993).
[20] K. J. Plotkin, ''CORBOOM Model for the Prediction of L_{Cdn} in Supersonic Flight Corridors,'' Wyle Research Report WR 91-11 (June 1991).
[21] D. Ludwig, ''Uniform Asymptotic Expansions at a Caustic,'' Commun. Pure Appl. Math. **XIX**, 215–250 (1966).
[22] J. P. Guiraud, ''Acoustique Geometrique, Bruit Ballistique des Avions Supersonique et Focalisation,'' J. Mec. **4**, 215–267 (1965).
[23] J.-C.-L. Wanner, J. Vallee, C. Vivier, and C. Thery, ''Theoretical and Experimental Studies of the Focus of Sonic Booms,'' J. Acoust. Soc. Am. **52**, 13 (1972).
[24] P. M. Gill and A. R. Seebass, ''Non-Linear Acoustic Behavior at a Caustic: An Approximate Solution,'' *AIAA Progress in Astronautics and Aeronautics*, edited by H. J. T. Nagamatsu (MIT, Cambridge, 1975).
[25] K. J. Plotkin and J. M. Cantril, ''Prediction of Sonic Boom at a Focus,'' Wyle Research Report WR 75-7 (October 1975); AIAA Paper 76-2 (January 1976).
[26] K. J. Plotkin, ''PCBoom3 Sonic Boom Prediction Model, Version 1.0e,'' Wyle Research Report WR 95-22E (October 1998).
[27] A. D. Taylor, ''The TRAPS Sonic Boom Program,'' NOAA Technical Memorandum ERL-87 (July 1980).
[28] L. D. Robinson, ''Sonic boom propagation through an inhomogeneous, windy atmosphere,'' Ph.D. thesis, University of Texas at Austin, 1991.
[29] K. Y. Fung, ''Shock Wave Formation at a Caustic,'' SIAM (Soc. Ind. Appl. Math.) J. Appl. Math. **39**(2), 355–371 (1980).
[30] A. D. Pierce, ''Rise profiles of initial shocks in sonic boom waveforms,'' J. Acoust. Soc. Am. **104**, 1829(A) (1998).
[31] F. M. Pestorius, ''Propagation of Plane Acoustic Noise of Finite Amplitude,'' Technical Report ARL-TR-73-23, Applied Research Laboratories, The University of Texas at Austin (August 1973).
[32] M. O. Anderson, ''The propagation of a spherical N-Wave in an absorbing medium and its diffraction by a circular aperture,'' Technical Report ARL-74-25, Applied Research Laboratories, The University of Texas at Austin (August 1974).
[33] J. Kang, ''Nonlinear Acoustic Propagation of Shock Waves Through the Atmosphere with Molecular Relaxation,'' Ph.D. thesis, The Pennsylvania State University, May 1991.
[34] A. D. Pierce and D. J. Maglieri, ''Effects of atmospheric irregularities on sonic-boom propagation,'' J. Acoust. Soc. Am. **51**, 702–721 (1972).
[35] D. A. Hilton, V. Huckel, and D. J. Maglieri, ''Sonic Boom Measurements During Bomber Training Operations in the Chicago Area,'' NASA TN D-3655 (1966).
[36] S. C. Crow, ''Distortion of Sonic Bangs by Atmospheric Turbulence,'' J. Fluid Mech. **37**, 529–563 (1969); NPL Aero Report 1260.
[37] G. Kamali and A. D. Pierce, ''Time Dependence of Variances of Sonic Boom Waveforms,'' Nature (London) **234**, 30–31 (1971).
[38] K. J. Plotkin and A. R. George, ''Propagation of Weak Shock Waves Through Turbulence,'' J. Fluid Mech. **54**(3), 449–467 (1972).
[39] A. D. Pierce, ''Statistical Theory of Atmospheric Turbulence on Sonic Boom Rise Times,'' J. Acoust. Soc. Am. **49**, 906–924 (1971).
[40] F. Coulouvrat, ''A nonlinear geometrical theory of diffraction for predicting sonic booms in the shadow zone,'' J. Acoust. Soc. Am. **104**, 1830(A) (1998).
[41] V. W. Sparrow, ''The effect of supersonic aircraft on the penetration of sonic boom noise into the ocean,'' J. Acoust. Soc. Am. **97**, 159–162 (1995).
[42] H. K. Cheng and C. J. Lee, ''A Theory of Sonic Boom Noise Penetration Under a Wavy Ocean,'' AIAA Paper 98-2958 (June 1998).
[43] M. Siclari and C. Darden, ''A Euler Code Prediction of Near to Mid-Field Sonic Boom Pressure Signatures,'' AIAA Paper 90-4000 (October 1990).
[44] A. R. George, ''Reduction of Sonic Boom by Azimuthal Redistribution of Overpressure,'' AIAA Paper 68-159 (1968).
[45] J. A. Page and K. J. Plotkin, ''An Efficient Method for Incorporating Computational Fluid Dynamics into Sonic Boom Prediction,'' AIAA-91-3275 (September 1991).
[46] K. J. Plotkin and M. J. Lucas, ''Calculation of Sonic Boom From Numeric Flowfield Solutions: MDBOOM Version 2,'' Wyle Research Report WR 89-19 (October 1989).
[47] K. J. Plotkin, ''Focus Boom Footprints for Various Air Force Supersonic Operations,'' Wyle Research Report WR 85-22 (1985).

Review and status of sonic boom penetration into the ocean

Victor W. Sparrow
Graduate Program in Acoustics, The Pennsylvania State University, 316B Leonhard Building, University Park, Pennsylvania 16802

(Received 20 April 2000; revised July 16, 2001; accepted July 19, 2001)

Since the 1970 Sonic Boom Symposium, held at the ASA's 80th meeting in Houston, TX, substantial progress has been made in understanding the penetration of sonic booms into the ocean. The state of the art at that time was documented by J. C. Cook, T. Goforth, and R. K. Cook [J. Acoust. Soc. Am. **51**, 729–741 (1972)]. Since then, additional experiments have been performed which corroborate Cook's and Sawyers' theory for sonic boom penetration into a flat ocean surface. In addition, computational simulations have validated that theory and extended the work to include arbitrarily shaped waveforms penetrating flat ocean surfaces. Further numerical studies have investigated realistic ocean surfaces including large-scale ocean swell. Research has also been performed on the effects of ocean inhomogeneities due to bubble plumes. This paper provides a brief overview of these developments. © *2002 Acoustical Society of America.*
[DOI: 10.1121/1.1402617]

PACS numbers: 43.28.Mw, 43.30.Zk [LCS]

I. INTRODUCTION

There has been substantial interest recently in the development of new concepts for supersonic passenger aircraft. In the early 1990's, it was decided that the sonic booms from such aircraft flying over land would not be acceptable to the public, and these aircraft now are envisioned to fly only on overwater routes. Some[1] have expressed concern that marine mammals may be disturbed by the sonic booms of such overwater flights, and NASA Langley Research Center, Hampton, VA has funded work to ascertain the noise impact of the High-Speed Civil Transport (HSCT) on underwater wildlife. The Air Force Research Laboratory (then known as the Armstrong Laboratory), Wright-Patterson Air Force Base, OH also has funded similar work regarding supersonic overwater military jet operations.

The purpose of this paper is to review the progress in understanding sonic boom penetration into the ocean since the 1970 Acoustical Society of America sponsored Sonic Boom Symposium, the second such meeting.[2] The first ASA Sonic Boom Symposium took place in 1965,[3] but ocean penetration was not discussed. The research at Penn State over the last few years will be emphasized. References are provided to the original published papers when possible. Although in early 1999 NASA decided it would cancel the High-Speed Research (HSR) program, the present work was motivated by the development of that programs' envisioned High-Speed Civil Transport (HSCT). Often the parameters of that hypothetical airplane will be utilized.

As seen in standard acoustics textbooks,[4,5] the acoustic wave field for a plane wave in one medium incident upon a half-space of another is well understood. Here, it is assumed that the interface between the two media (air and water) is perfectly flat and that the incident pressure wave is small in amplitude compared to the ambient pressure (the acoustic assumption). For sonic booms for the envisioned HSCT, the peak pressures just above or below the water surface are on the order of 100 Pa, and such amplitudes are small enough for linear acoustics to apply.

The present work examines the primary underwater influence of a supersonic aircraft overflight, that of an evanescent wave formed immediately below the ocean surface. This evanescent wave is created to match the pressure continuity boundary condition at the air–water interface. As will be more fully described later, the evanescent wave extends below the ocean surface approximately 100–200 m for an HSCT. Since marine mammals breathe air, and most species generally remain near the ocean surface except when diving for food,[6] the research reported here has focused exclusively on the sonic boom-induced evanescent waves in the top few hundred meters of the ocean. In contrast, in a series of papers Cheng and Lee[7–10] have sought the underwater sound levels at even greater depths. They suggest that certain sonic boom wave-number components match with ocean surface roughness features leading to propagating waves at certain frequencies. However, the Penn State work has examined only the first few hundred meters of the ocean, so no comparisons are presently available to Cheng and Lee's predictions. Currently there are no experimental measurements available for such greater depths either.

The next section of this paper will review the state of the art in sonic boom penetration into the ocean back in 1970. We will then review the experiments performed since, and the work at Penn State in two primary areas. First, for a flat, homogeneous ocean a technique for determining the underwater penetration for an arbitrarily shaped waveform via Fourier analysis will be described. The following section then will explain the specific computational aeroacoustic (CAA) numerical method used for understanding the penetration when the ocean is either nonhomogeneous or does not have a flat surface. Understanding this nontraditional numerical method is important because most off-the-shelf computational fluid dynamics (CFD) codes cannot model the transfer of acoustic energy across the high impedance mismatch between air and water. The accurate simulations described here model either the effects of wind waves on the ocean surface or the plumes of air bubbles immediately under the surface. Finally, this paper concludes with suggestions for future work.

II. STATE OF THE ART IN 1970

At the time of the 1970 Sonic Boom Symposium much was known about sonic booms propagating into the ocean. A paper by Cook, Goforth, and Cook[11] described a sound wave penetrating into the ocean given an incident N wave from a supersonic airplane above

(a) The wave would still be an N wave just below the surface.
(b) The wave would be attenuated and smoothed with increasing depth. The acoustic pressure would drop to a value of $\approx$10% of its value at the surface at a depth of $\approx$60% the length of the N wave.
(c) The 2–100-Hz overpressures are greater than 100 times the background noise levels. The sound-pressure levels can exceed ambient noise levels by up to 50 dB from the surface down to depths of 100–200 m.
(d) The sound-pressure levels are low enough not to cause physiological harm to marine life from a single overflight.

These descriptions of the penetrating wave were based on an analytical Fourier analysis available at the time, validated by model experiments.

One can easily decompose an incident sonic boom waveform via the Fourier transform into a superposition of plane waves of appropriate frequencies. Hence, one can determine the underwater sound field due to a sonic boom in air by superimposing the underwater contributions of each plane wave. This was the approach taken in the analytical predictions by Sawyers[12] and then in the more detailed analysis by Cook[13] that provide the theory for the above descriptions. Sawyers and Cook each assumed that the incident sonic boom waveform was an N wave. Sawyers' simple analytical expression for the underwater acoustic pressure due to an incident sonic boom is

$$\pi p_s = (2\tau-1)\tan^{-1}\left(\frac{\tau-1}{\zeta}\right) - (2\tau-1)\tan^{-1}\left(\frac{\tau}{\zeta}\right) + \zeta \log\left[\frac{\zeta^2+\tau^2}{\zeta^2+(\tau-1)^2}\right], \tag{1}$$

where $p_s = p/p_{\text{surface}}$ is nondimensionalized acoustic pressure, $\tau = t/T$ is nondimensionalized time, T is the sonic boom duration, ζ is a cleverly nondimensionalized depth defined below, log indicates a base e logarithm, and the inverse tangent functions are assumed to range from $-\pi/2$ to $\pi/2$. Cook's similar expressions used inverse tangent functions which instead ranged from 0 to π. In Eq. (1)

$$\zeta = \frac{z\sqrt{1-V^2/c_{\text{water}}^2}}{TV}, \tag{2}$$

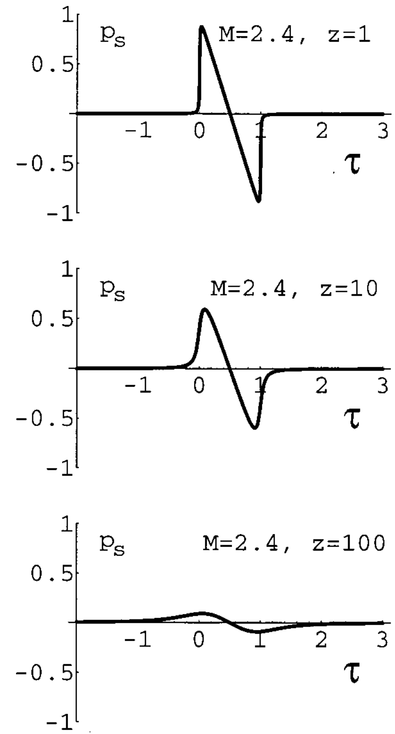

FIG. 1. Prediction of the decay of an N wave with depth using the Sawyers/Cook analytical theory. The nondimensionalized acoustic pressure is shown at depths of 1, 10, and 100 m. A Mach number of 2.4 is assumed.

where z is the depth in meters, V is the speed of the aircraft, and c_{water} is the speed of sound in the water. For an example of the decay of an N wave with depth from the envisioned HSCT using Eq. (1), see Fig. 1. To correctly interpret Eq. (1) for different aircraft speeds, one must recall that the duration T is a function of the speed V.[14] Applying this theory, one finds for an HSCT producing an N-shaped sonic boom of duration 0.3 s, flying at a Mach number in air of 2.4, that the sound field extends approximately 100–200 m below the water surface.

Here, the key assumptions of this analytical theory are that the water has a flat surface and is infinitely deep. As is explained in the next section, this theory further assumes that the aircraft is flying level at a speed no higher than Mach 4.4.

The sound wave underneath the water is not a propagating wave, but is formally called an inhomogeneous plane wave[4]—informally referred to as an evanescent wave. Each Fourier component of frequency decays with depth exponentially, proportional to $e^{-\omega T\zeta}$. Notice high frequencies are attenuated more than low frequencies. This is why the waveforms in Fig. 1 are smoother at the greater depths.

In 1995 Rochat and Sparrow analyzed these waveforms as a function of depth using a number of different sound descriptors including peak level and unweighted and weighted sound-exposure levels.[15] They found that peak level or unweighted sound-exposure level deceased somewhat slowly with depth but weighted sound metrics decreased more quickly. For example, at a depth of 128 m the unweighted sound-exposure level will decrease only 13.4 dB from the surface value, whereas the A-weighted sound-exposure level will drop 91.5 dB from the surface value.

The Sawyers/Cook analytical theory was validated by experiments of Waters and Glass.[16,17] To simulate sonic booms they exploded small dynamite caps over a flooded rock quarry with extensive underwater instrumentation, and their results agreed very well with the Sawyers/Cook analytical predictions.

III. EXPERIMENTS

Fairly soon after the 1970 Sonic Boom Symposium, Intrieri and Malcolm made underwater measurements of the sonic booms resulting from projectiles.[18] They also found good agreement with the Sawyers/Cook theory for projectile speeds below Mach 4.4. For projectile speeds above Mach 4.4, Intrieri and Malcolm measured an acoustic shock wave propagating into the water, unlike the evanescent waves seen for lower Mach numbers.

A sonic boom wave propagates directly into the water only when the angle of incidence of the boom is less than about 13.2° with respect to the normal to the water surface. There is no strong decay with depth as is predicted by the Sawyers/Cook theory, which is valid only for larger angles of incidence.[14] Therefore, during military aircraft maneuvers, such as in a steep supersonic dive, it should be possible to produce a propagating wave in the water. For example, ignoring atmospheric effects, an aicraft flying over the ocean at Mach 1.2 and diving at an angle steeper than 43.2° from level flight would produce a propagating wave in a flat ocean since $\sin^{-1}(1/1.2)\,\text{radians} - 13.2° = 43.2°$. However, such propagating waves are not expected during routine passenger aircraft operations since the sonic boom waves are expected to impact the water surface at angles greater than 13.2°.

Underwater measurements of sonic booms from real aircraft have been few until recently. Early underwater measurements of F-8 aircraft sonic booms were made by Young in 1968.[19] The results were inconclusive, probably because of the instrumentation available at the time and because the aircraft were barely supersonic, only flying at Mach 1.10 to 1.15 at 914.4 m (3000 ft.). Another early measurement was reported by Urick and Tulko in 1972, this time from a Navy F-4 airplane also flying at 304.8 m (1000 ft.) at Mach 1.1, again barely supersonic.[20]

The first well-instrumented, useful underwater measurement of aircraft sonic boom in the open literature was made accidentally by Desharnais and Chapman in 1996.[21,22] Desharnais and Chapman measured the Concorde sonic boom underwater using a vertical array of hydrophones off the Scotian shelf. Here, the Mach number was estimated to be Mach 2.02. They found good agreement for the vertical decay of acoustic energy below the ocean surface as predicted by the flat ocean analytical predictions of Sawyers[12] and Cook.[13] An even more recent, important experimental measurement of sonic booms is mentioned below.

IV. ARBITRARILY SHAPED WAVEFORMS AND A FLAT INTERFACE

Recently, Sparrow and Ferguson[23] developed an automated approach to predict the underwater sound field due to incident sonic booms which are not *N*-shaped, as assumed by Sawyers and Cook. This procedure allows one to take arbitrarily shaped sonic boom waveforms and determine the corresponding underwater sound field assuming a flat ocean. Complete details are given in Ferguson's M.S. thesis.[24]

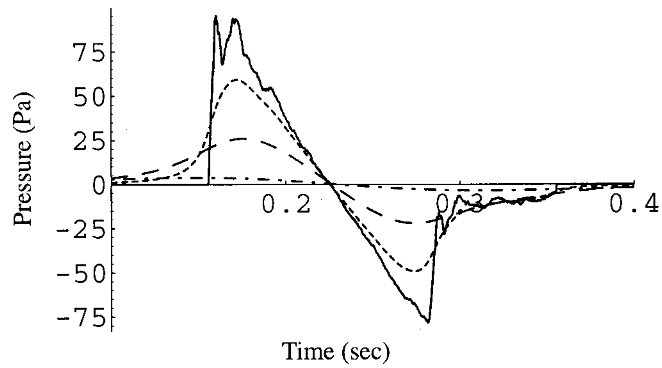

FIG. 2. Underwater predicted waveforms from a surface measured F-15 double-peaked wave at depths of 0 (solid), 4 (short dashes), 16 (long dashes), and 64 (dash/dot) meters. The horizontal axis is time in seconds and the vertical axis is pressure in pascals.

In short, the incident wave at the surface is Fourier analyzed in terms of its component wave numbers as

$$[\text{spectrum}] = \sum_{X=1}^{N_{\text{samp}}} p(x,z=0)\, e^{-j(2\pi/N_{\text{samp}})(K-1)(X-1)}. \tag{3}$$

In this expression, X is the spatial sampling variable, K is the wave number sampling variable, and N_{samp} is the number of samples in the spectrum. Written as a discrete Fourier transform, the above expression is implemented using the FFT algorithm. The [spectrum] is used to find the underwater sound pressure as

$$p(x,z) = \frac{2}{N_{\text{samp}}} \sum_{K=1}^{N_{\text{samp}}} [\text{spectrum}]\, e^{-z\mu k_o} e^{j(2\pi/N_{\text{samp}})(K-1)(X-1)}. \tag{4}$$

This is simply a superposition of the different wave-number components in the initial wave, now accounting for each wave-number component's decay with depth. Here, $\mu = \sqrt{1 - V^2/c_{\text{water}}^2}$, and the $e^{-z\mu k_0}$ term in Eq. (4) gives the appropriate wave-number-dependent exponential decay. The factor of 2 in front of the equation comes from the pressure doubling at the surface due to the boundary conditions.

The essential finding from this Fourier synthesis approach is that high frequencies in sonic booms do not penetrate very far beneath the ocean surface. One manifestation of this result is that a waveform measured in the air near the ground, and jagged because of the effects of atmospheric turbulence, will become smooth a few meters under the water surface. One can think of the ocean surface as an effective low-pass filter on the incident acoustic energy. As an example, Fig. 2 shows an F-15 doubled-peaked sonic boom measured in 1987.[25] Clearly the wave is smoothed after penetrating just 4 m under the surface. A previous study on standard noise descriptors of the penetrating sonic boom noise by Rochat and Sparrow[15] further confirms the low-pass filtering effect. Hence, this superposition method gives us considerable insight into the underwater sound field due to realistic incident sonic boom waveforms. As seen in the references,[24,26] the superposition procedure has been used to predict the underwater sound fields due to sonic booms created by supersonically maneuvering military aircraft.

Very recently, underwater measurements of the sonic booms of F-4 aircraft were made by Sohn *et al.*[27] They show excellent agreement between their measurements and the above-mentioned Fourier theory. This will be discussed further in Sec. VII.

V. A FINITE DIFFERENCE APPROACH

A. Motivation

The Fourier synthesis approach, however, does not allow for nonflat ocean surfaces. It also does not account for inhomogeneities in the media, such as ocean bubbles. Therefore, a more flexible approach, the finite difference method, has been employed to investigate the effects of more realistic ocean environments. The development of an appropriate finite difference method, however, was not straightforward.

The inherent difficulty with modeling sound waves propagating between air and water is the significant difference in characteristic impedance. The speed of sound and ambient density of air are approximately $c_{\mathrm{air}}=343\,\mathrm{m/s}$ and $\rho_{0,\mathrm{air}}=1.21\,\mathrm{kg/m^3}$, respectively. Similarly, for water $c_{\mathrm{water}}=1500\,\mathrm{m/s}$ and $\rho_{0,\mathrm{water}}=1000\,\mathrm{kg/m^3}$. The ambient temperature everywhere is assumed to be 20 °C. Hence, the ratio of the characteristic impedances is

$$\frac{(\rho_{0,\mathrm{water}}c_{\mathrm{water}})}{(\rho_{0,\mathrm{air}}c_{\mathrm{air}})}=3600, \tag{5}$$

a fairly large number. It is hard for acoustic energy to be efficiently transmitted, on a time-average basis, across such a boundary. In fact, sound in air is so effectively reflected by water that the water is usually modeled by a hard surface. Similarly, it is common practice in underwater acoustic studies to model an air interface as a pressure release surface, approximated by $p\approx 0$.

However, sound does penetrate across this surface as shown earlier. To find a finite difference method that can handle the two different media simultaneously, one must take into account the fact that the acoustic perturbation (denoted by a prime) of the density in the water is on the order of the ambient (denoted by a subscript zero) acoustic density of the air

$$\rho'_{\mathrm{water}}\sim\rho_{0,\mathrm{air}}. \tag{6}$$

Hence, most off-the-shelf computational fluid dynamic and computational aeroacoustic codes will fail at an air–water interface. This has been noted by Fricke,[28] who modeled underwater sound impinging on ice. Fricke's successful approach to the problem was to add appropriate nonlinear terms to his elastodynamic equations. A similar solution was attempted for the present situation, but it did not succeed because of recurrent numerical instabilities.

B. Derivation

The finite difference scheme that was found to work for the sonic boom penetration problem is a method borrowed from geophysics. Individuals interested in oil exploration regularly employ finite difference models which can handle vastly different media, e.g., oil, rock, water, gases, etc. The specific method employed for the present application was inspired by Sochacki *et al.*[29] Essentially an integral form of the wave equation is applied at the air–water interface rather than a discretization of the appropriate partial differential equation,[4] the inhomogeneous wave equation in terms of the acoustic pressure p

$$\frac{1}{\rho_0(\overline{x})c^2(\overline{x})}\frac{\partial^2 p}{\partial t^2}-\nabla\cdot\left(\frac{1}{\rho_0(\overline{x})}\nabla p\right)=0. \tag{7}$$

Here, the speed of sound $c(\overline{x})$ and ambient density $\rho_0(\overline{x})$ are written as functions of position $\overline{x}.$ It will be easier for us later to simplify this equation so we rewrite it as

$$a(\overline{x})\frac{\partial^2 p}{\partial t^2}-\nabla\cdot(b(\overline{x})\nabla p)=0, \tag{8}$$

where

$$a(\overline{x})=\frac{1}{\rho_0(\overline{x})c^2(\overline{x})}\quad\text{and}\quad b(\overline{x})=\frac{1}{\rho_0(\overline{x})} \tag{9}$$

are convenient mathematical constructions.

For simplicity we will only analyze the one-dimensional version of the method in detail. In 1D the above inhomogeneous wave equation becomes

$$a(x)p_{tt}=(b(x)p_x)_x, \tag{10}$$

where the subscripts denote appropriate partial derivatives. If we integrate both sides of this equation over the interval $-\epsilon$ to ϵ straddling the air–water interface at $x=0$, we have

$$\begin{aligned}\int_{-\epsilon}^{\epsilon}ap_{tt}\,dx&=\int_{-\epsilon}^{\epsilon}(bp_x)_x dx\\&=bp_x|_{-\epsilon}^{\epsilon}\\&=b(\epsilon)p_x(\epsilon,t)-b(-\epsilon)p_x(-\epsilon,t),\end{aligned} \tag{11}$$

and, thus

$$a^-\int_{-\epsilon}^{0}p_{tt}\,dx+a^+\int_{0}^{\epsilon}p_{tt}\,dx=b^+p_x(\epsilon,t)-b^-p_x(-\epsilon,t). \tag{12}$$

Here, the superscripts + and − indicate values for the appropriate sides of the boundary. Also note that in this form the derivative of the reciprocal of the ambient density, $1/\rho_0(x)=b(x)$, has been removed by the spatial integration. Since we expect $b(x)$ to jump at the air–water interface, eliminating the derivative of $b(x)$ is essential in obtaining a stable numerical method.

Now let $\epsilon\rightarrow\Delta x/2$ and approximate the two remaining integrals by assuming p_{tt} is constant over the appropriate spatial intervals. One has

$$\frac{\Delta x}{2}(a^++a^-)p_{tt}=b^+p_x(\epsilon,t)-b^-p_x(-\epsilon,t). \tag{13}$$

Using the standard finite difference notation of superscripts for time increments and subscripts for spatial positions, a simple finite difference version is obtained by using a second-order centered difference approximation for p_{tt}, while using first-order forward- or backward approximations for p_x

$$\left(\frac{(a^+ + a^-)\Delta x}{2\Delta t^2}\right)(p_0^{n+1} - 2p_0^n + p_0^{n-1}) = \frac{b^+}{\Delta x}(p_1^n - p_0^n) - \frac{b^-}{\Delta x}(p_0^n - p_{-1}^n). \tag{14}$$

This equation provides a simple explicit time-marching formula along the interface. Spatial position 0 is assumed to be exactly on the air–water interface, with position -1 in the air, and position $+1$ in the water.

The derivation for a two-dimensional version of the above interface equation is slightly more complicated, accounting for the possibility of the surface being curved. The result is

$$\begin{aligned}\frac{a_{j,k}}{\Delta t^2}(p_{j,k}^{n+1} - 2p_{j,k}^n + p_{j,k}^{n-1}) &= \frac{1}{\Delta x^2}[b_{j+1/2,k}p_{j+1,k}^n - (b_{j+1/2,k} + b_{j-1/2,k})p_{j,k}^n \\ &\quad + b_{j-1/2,k}p_{j-1,k}^n] + \frac{1}{\Delta z^2}[b_{j,k+1/2}p_{j,k+1}^n \\ &\quad - (b_{j,k+1/2} + b_{j,k-1/2})p_{j,k}^n + b_{j,k-1/2}p_{j,k-1}^n],\end{aligned} \tag{15}$$

where $a_{j,k} = \alpha a^+ + \beta a^-$. The variables α and β here denote the percentage of water or air, respectively, filling a grid block. An even more accurate method including grid refinement in the z direction has been derived and utilized by Rochat.[30,31]

C. Application

The method just given is only used at the interface between the air and water. Away from the interface the simplified wave equation

$$\frac{\partial^2 p}{\partial t^2} - c^2(\overline{x})\nabla^2 p = 0, \tag{16}$$

is valid. Because ocean bubbles significantly change the speed of sound, but not the ambient density, this form is also a good approximation if the water is inhomogeneous. One can use simple second-order centered differences on Eq. (16) and the resulting explicit difference system is stable under the standard Courant restriction for a two-dimensional system where $\Delta x = \Delta z$

$$c_{\max}\frac{\Delta t}{\Delta x} \leqslant \frac{\sqrt{2}}{2}, \tag{17}$$

where $c_{\max}$ indicates the maximum speed of sound is used. For us, $c_{\max} = c_{\text{water}}$.

For the research reported here, Rochat's grid refinement method was used near the interface. To make the resulting finite difference system as stable as possible the equations were solved on a large rectangular grid with the right and left boundaries taken to be rigid, so as to keep the interface scheme stable. The upper boundary was also taken to be rigid for convenience. For the lower boundary a standard absorbing boundary condition was applied.[32]

The simulations were started after an initial propagating sonic boom waveform was inserted into the air portion of the computational domain. Relative to the orientation of the air–water interface, the waveform's angle of incidence was matched to the Mach number of aircraft, chosen here to be $M = 2.4$. Because of the coarse grid used in the simulations, $\Delta x \approx 1$ m, a slightly rounded sonic boom waveform was usually utilized since an N-shaped wave would be severely affected by finite difference dispersion. See the references for details.[33,30,31]

VI. SUMMARY OF RESULTS

Because of space limitations, only a summary of the results of the studies can be given here. The interested reader can find the full details and numerous figures in the work of Rochat, and Rochat and Sparrow.[30,31]

A. Flat surface/homogeneous

For a typical result see Figs. 2 and 3 of Rochat and Sparrow's 1997 work[33] (there shown for $M = 1.4$). One sees the wave initially hitting the ocean surface and then reflecting, leaving the evanescent wave clearly below the ocean surface. Horizontal slices at appropriate depths in the water were found to agree with the work of Sawyers and Cook. Using their theory in 1995, Sparrow predicted that faster aircraft speeds would result in deeper penetrations of the sonic booms.[14] This prediction was confirmed by the finite difference simulations.

B. Ocean swell/homogeneous

To include the effects of ocean swell, also called wind waves, a straightforward trochoidal sea surface was employed having a wavelength equal to 20 times the ocean wave height, crest to trough. This ratio of 20 is a common ocean engineering approximation.[34] The simulations were run assuming that the incident sonic boom wave impinges on the ocean surface in the same direction that the wind waves are traveling. One can argue[7,8,30] that this would lead to the worst-case scenario for the possible focusing or defocusing of the acoustic energy. Corresponding to wind speeds of 0, 10, 20, and 30 knots, runs were made with average ocean wave heights in the open sea corresponding to 1.0, 1.4, 2.3, and 3.75 m, respectively.

It was noted that focusing did occur both above and below the ocean surface. It was found that as the wave height increased, the amount of focusing or defocusing increased over the case of a flat ocean. Higher Mach numbers also implied more focusing or defocusing. This focusing, however, never increased the peak sound levels from the sonic booms more than 1.5 dB. Thus, the amount of focusing and defocusing due to the wind waves seems negligible for noise impact studies, at least in the top layers of the ocean where marine mammals spend most of their time.

Slightly more complicated ocean surfaces composed of the superposition of several wave numbers were also investigated. Again, the amount of focusing or defocusing never increased the peak levels beyond 1.5 dB. The simulations also verified Cheng *et al.*'s assertion[7] that the effects of ocean swell on the focusing will be most appreciable for swell wavelengths comparable to or larger than the sonic boom's effective length.[35,30]

For each of the ocean surfaces studied, the surfaces were smooth enough that a Mach 2.4 sonic boom angle of incidence never produced a propagating wave in the water. However, Sohn *et al.*[27] have suggested that higher-speed aircraft (Mach 3 or higher) might produce sonic booms that will scatter a propagating wave into the water if the surface is rough enough. No finite difference simulations were attempted for sonic booms corresponding to such high Mach numbers.

C. Flat surface/inhomogeneous

The ocean in reality is not homogeneous, but has significant speed of sound variations near the surface because of air bubbles. Bubbles greatly increase the compressibility compared to degassed water, and hence the speed of sound significantly decreases for the low frequencies of interest in the present study.[36,37]

Two models for the ocean bubbles were examined. One model consisted of horizontal layers of constant speeds of sound which increased in value with increasing depth until about 8 m, where the ambient value of 1500 m/s was achieved. A second model included only a single bubble plume shaped like half a period of a sine-squared function, approximately 10 m wide and 10 m deep.

The results from a number of computational simulations show that the bubbles had little, if any, effect on the penetration of the sonic boom. In the bubble plume one might see a change in the sound level of 1 dB at most due to the presence of the bubbles. The speed of sound variations only extend a few meters below the ocean, and such features seem quite small compared to the size of the incident sonic boom. Nonresonant bubble scattering from spatially large distributions of bubbles just under the ocean surface can be a substantial effect for underwater propagation studies.[38] However, for a sonic boom incident from the air, the underwater bubbles can be thought of as a slight lowering of the ocean surface. Little to no additional sonic boom energy penetrates. The present findings suggest that future simulations might be able to ignore ocean bubbles entirely.

Recently, however, the question has been raised as to whether bubble plume resonances have been adequately accounted for in the model described here.[39] Underwater acousticians are just beginning to fully understand these resonances, and additional information on them would be needed to incorporate their influence into the present and future models of sonic boom penetration into the ocean. Extremely delicate and careful underwater experiments would be needed to verify any resonant interactions between impinging sonic booms and bubble plumes in the open ocean.

VII. RECENT FINDINGS OF SOHN *ET AL.*

As mentioned at the end of Sec. IV, Sohn *et al.*[27] have performed careful field measurements of sonic boom penetration into the ocean for low Mach number F-4 aircraft overflights. The waveforms received on a vertical hydrophone array agreed well with predictions made using the Fourier method described in Sec. IV. More important in relation to Sec. VI, however, the experimental findings indicated no underwater scattering of the sonic booms due to either a real ocean surface or real bubbles. Sohn *et al.* concluded that a homogeneous ocean with a flat surface seemed adequate for confidently predicting the environmental effects of overwater sonic booms. These conclusions corroborate the numerical results of Sec. VI, which all indicated that both ocean swell and ocean bubbles are negligible effects on sonic boom penetration.

VIII. CONCLUSIONS AND SUGGESTIONS FOR FUTURE WORK

This paper has reviewed the progress in understanding the penetration of sonic booms into the ocean since the 1970 Acoustical Society of America Sonic Boom Symposium, focusing on many of the results that have recently been generated at The Pennsylvania State University. Both a Fourier synthesis technique and a finite difference numerical method have been described, and numerous citations have been provided to detailed references for the specific findings. It was found that the underwater sound field due to an incident sonic boom is well described by the flat, homogeneous ocean analytical theory developed by Sawyers and Cook and the similar Fourier synthesis method of Sparrow and Ferguson. The effects of bubble plumes and of focusing due to wind waves on the ocean never increased or decreased the sound levels by more than 1.5 dB over the levels seen in a homogeneous, flat ocean. These predictions were made in the top few hundred meters of the ocean, the region where marine mammals spend the majority of their time.

The present research has assumed a deep ocean. In the future the effects of a finite depth ocean channel also should be examined. It is expected that bottom reflections and coupling effects will produce increased underwater sound levels when the water is less than approximately 300 m deep. One could also modify the finite difference programs developed in this research to account for nonlinear wave propagation effects near the ocean surface. Those effects are negligible for an HSCT, but would be important for modeling aircraft or projectiles flying close to the water surface.

ACKNOWLEDGMENTS

The author would like to recognize the very important contributions to this research of his former graduate students, Judy Rochat and Tracie Ferguson, who performed much of the work described here. This research was supported by the NASA Langley Research Center, Hampton, VA, and the Air Force Research Laboratory, Wright Patterson Air Force Base, OH.

[1] W. C. Cummings, ''Sonic booms and marine mammals: Informational status and recommendations,'' NASA CP-10132, pp. 219–231, 1993.
[2] H. Ribner and H. Hubbard, ''Sonic boom symposium: Forward,'' J. Acoust. Soc. Am. **51**(2), Pt. 3, 671 (1972).
[3] H. Hubbard, ''Sonic boom symposium: Forward,'' J. Acoust. Soc. Am. **39**(5), Pt. 2, IV (1966).
[4] A. D. Pierce, *Acoustics: An Introduction to Its Physical Principles and Applications* (Acoustical Society of America, Woodbury, NY, 1989).
[5] L. E. Kinsler, A. Frey, A. B. Coppens, and J. V. Sanders, *Fundamentals of Acoustics*, 3rd ed. (Wiley, New York, 1982).
[6] A. E. Bowles, Personal communication, Hubbs-Sea World Research Institute, San Diego, CA, 1995.
[7] H. K. Cheng, C. J. Lee, M. M. Hafez, and C. Y. Tang, ''Sonic boom propagation and its submarine impact: A study of theoretical and computational issues,'' AIAA paper 96-0755, 34th Aerospace Sciences Meeting, Reno, NV, 1996.
[8] H. K. Cheng and C. J. Lee, ''Submarine impact of sonic boom: A study comparing and reconciling results from two prediction approaches,'' in *Proceedings of Noise-Con 97* (Institute of Noise Control Engineering, Poughkeepsie, NY, 1997), pp. 399–404.
[9] H. K. Cheng and C. J. Lee, ''A theory of sonic boom noise penetration under a wavy ocean,'' AIAA paper 98-2958, 2nd AIAA Theoretical Fluid Dynamics Meeting, Albuquerque, NM, 1998.
[10] H. K. Cheng and C. J. Lee, ''Sonic boom noise penetration under a wavy ocean,'' J. Acoust. Soc. Am. **104**(3), Pt. 2, 1831 (1998).
[11] J. C. Cook, T. Goforth, and R. K. Cook, ''Seismic and underwater responses to sonic boom,'' J. Acoust. Soc. Am. **51**(2), Pt. 3, 729–741 (1972).
[12] K. N. Sawyers, ''Underwater sound pressure from sonic booms,'' J. Acoust. Soc. Am. **44**, 523–524 (1968).
[13] R. K. Cook, ''Penetration of a sonic boom into water,'' J. Acoust. Soc. Am. **47**(5), Pt. 2, 1430–1436 (1970).
[14] V. W. Sparrow, ''The effect of supersonic aircraft speed on the penetration of sonic boom noise into the ocean,'' J. Acoust. Soc. Am. **97**, 159–162 (1995).
[15] J. L. Rochat and V. W. Sparrow. ''Sound levels under the ocean due to sonic boom penetration,'' in *Proceedings of Inter-noise 95* (Institute of Noise Control Engineering, Poughkeepsie, NY, 1995), pp. 967–970.
[16] J. Waters and R. E. Glass, ''Penetration of sonic boom energy into the ocean: An experimental simulation,'' Hydrospace Research Corp., Final Report on Contract FA70-WAI-185, HRC TR 288, June (1970), available from NTIS/DTIC as AD 711 963.
[17] J. Waters, ''Penetration of sonic boom energy into the ocean: an experimental simulation,'' in *Noise and Vibration Control Engineering, Proceedings of the Purdue Noise Control Conference (1971)*, pp. 554–557.
[18] P. Intrieri and G. Malcolm, ''Ballistic range investigation of sonic-boom overpressures in water,'' AIAA J. **11**, 510–516 (1973).
[19] R. W. Young, ''Penetration of sonic booms into the ocean,'' J. Acoust. Soc. Am. **44**, 392 (1968).
[20] R. J. Urick and T. J. Tulko, ''Sonic booms in the sea: A recent observation,'' J. Acoust. Soc. Am. **52**(5), Pt. 2, 1566–1568 (1972).
[21] F. Desharnais and D. M. F Chapman, ''Underwater measurements of a sonic boom,'' in *Proceedings of OCEANS 97 MTS/IEEE* (IEEE, Piscataway, NJ, 1997), pp. 592–596.
[22] F. Desharnais and D. M. F. Chapman, ''Underwater measurements and modeling of a sonic boom,'' J. Acoust. Soc. Am. **104**(3), Pt. 2, 1848 (1998).
[23] V. W. Sparrow and T. Ferguson, ''Penetration of shaped sonic boom noise into a flat ocean,'' AIAA paper 97-0486, 35th Aerospace Sciences Meeting, Reno, NV, 1997.
[24] T. J. Ferguson. M. S. thesis, ''The effect of aircraft maneuvers on sonic boom noise penetration into a flat ocean,'' Graduate Program in Acoustics, University Park, PA, 1997.
[25] R. A. Lee and J. M. Downing, ''Comparison of measured and predicted lateral distribution of sonic boom overpressures from the United States Air force sonic boom database,'' J. Acoust. Soc. Am. **99**, 768–776 (1996).
[26] T. J. Ferguson and V. W. Sparrow, ''Effect of aircraft maneuvers on sonic boom penetration into the ocean,'' J. Acoust. Soc. Am. **101**(5), Pt. 2, 3103 (1997).
[27] R. A. Sohn, F. Vernon, J. A. Hildebrand, and S. C. Webb, ''Field measurements of sonic boom penetration into the ocean,'' J. Acoust. Soc. Am. **107**, 3073–3083 (2000).
[28] R. Fricke, ''Quasi-linear elastodynamic equations for finite difference solutions in discontinuous media,'' J. Comput. Acoust. **1**, 303–320 (1993).
[29] J. S. Sochacki, J. H. George, R. E. Ewing, and S. B. Smithson, ''Interface conditions for acoustic and elastic wave propagation,'' Geophysics **56**(2), 168–181 (1991).
[30] J. L. Rochat, Ph.D. dissertation, ''Effects of Realistic Ocean Features on Sonic Boom Noise Penetration into the Ocean: A Computational Analysis,'' Graduate Program in Acoustics, University Park, PA, 1998.
[31] J. L. Rochat and V. W. Sparrow, ''A computational analysis of sonic booms penetrating a realistic ocean interface,'' J. Acoust. Soc. Am. **109**, 899–908 (2001).
[32] V. W. Sparrow and R. Raspet, ''Absorbing boundary conditions for a spherical monopole in a set of two-dimensional acoustics equations,'' J. Acoust. Soc. Am. **87**, 2422–2427 (1990).
[33] J. L. Rochat and V. W. Sparrow, ''Two-dimensional focusing of sonic boom noise penetrating an air–water interface,'' AIAA J. **35**(2), 35–39 (1997). Also was AIAA paper 96-1751, AIAA/CEAS 2nd Aeroacoustics Conference, State College, PA, 1996.
[34] J. Gaythwaite, *The Marine Environment and Structural Design* (Van Nostrand Reinhold, New York, 1981).
[35] J. L. Rochat and V. W. Sparrow, ''Focusing of sonic boom noise penetration into a homogeneous wavy ocean: Complex surfaces and wavelength comparisons,'' J. Acoust. Soc. Am. **102**(5), Pt. 2, 3159 (1997).
[36] D. G. Crighton, A. P. Dowling, J. E. Ffowcs Williams, M. Heckl, and F. G. Leppington, *Modern Methods in Analytical Acoustics* (Springer, Berlin, 1992).
[37] T. G. Leighton. *The Acoustic Bubble* (Academic, San Diego, 1994).
[38] K. E. Gilbert, ''A stochastic model for scattering from the near-surface oceanic bubble layer,'' J. Acoust. Soc. Am. **94**, 3325–3334 (1993).
[39] T. G. Leighton, Personal communication, University of Southampton, Southampton, England, 1998.

Underwater measurements and modeling of a sonic boom[a)]

Francine Desharnais[b)] and David M. F. Chapman
Defence Research Establishment Atlantic, P.O. Box 1012, Dartmouth, Nova Scotia B2Y 3Z7, Canada

(Received 26 April 2000; revised 26 June 2001; accepted 26 July 2001)

During a sea trial on the Scotian Shelf, acoustic signals from a sonic boom were recorded on 11 hydrophones of a vertical array. The array spanned the lower 50 m of the water column above a sand bank at 76 m water depth. The source of the sonic boom was deduced to be a Concorde supersonic airliner traveling at about Mach 2. The waterborne waveform was observed to decay as an evanescent wave below the sea surface, as expected. The calm weather (sea state 1) resulted in low ambient noise and low self-noise at the hydrophones, and good signal-to-noise ratio on the upper hydrophones; however, the decreased signal amplitude is more difficult to detect towards the lower part of the water column. The period of the observed waveform is of the order 0.23 s, corresponding to a peak frequency of about 3 Hz. The shape of the measured waveform differs noticeably from the theoretical N-shape waveform predicted with Sawyers' theory [J. Acoust. Soc. Am. **44**, 523–524 (1968)]. A simple shallow-ocean geoacoustic model suggests that this effect may be caused in part by seismo–acoustic interaction of the infrasonic waves with the elastic sediments that form the seabed. [DOI: 10.1121/1.1404376]

PACS numbers: 43.28.Mw, 43.30.Ma, 43.30.Zk [LCS]

I. INTRODUCTION

To eliminate the sonic boom impact on people, supersonic commercial aircraft center their high-speed activities over water. As a consequence, a renewed interest in underwater sonic boom propagation is seen in the literature.[1–4] Although it is recognized[5] that the audible noise (or signal-to-noise ratio) of a sonic boom is not appreciable at depths more than 30–40 m, this shallow layer is inhabited by a large number of marine species, including whales. Therefore, it is important to understand the impact of supersonic flight over coastal areas.

During a sea trial in shallow water south of Nova Scotia, Canada, acoustic signals from an unexpected sonic boom were recorded on 11 hydrophones of a vertical array. Based on the event time and location, the source of the sonic boom was deduced to be a Concorde supersonic airliner in transit between Paris and New York, and traveling at about Mach 2. The fortuitous measurement proved to be of good quality due to the high signal-to-noise ratio at most hydrophones.

Very few underwater measurements of sonic booms are available in the literature. The scaled measurements of Waters[5] with dynamite caps as a source are a standard reference. Malcolm and Intrieri[6,7] have also made scaled measurements using gun-launched small cone-cylinder models with similar results. Although the above references measured underwater waveforms very close to those theoretically calculated, Young[8] measured sonic booms from a diving F-8 aircraft during a full-scale experiment, and observed waveforms that were strangely complicated. Subsequent to the measurements presented here, Sohn *et al.*[9] measured sonic booms generated by F-4 aircraft that generally agreed with analytical theories on sonic boom penetration underwater. The sonic boom measurement presented here shows interesting differences from the theoretically expected waveform. The uncontrollable parameters of this experiment, including the shallow-water environment and the use of a Concorde aircraft, make this data set unique, and generate questions as to the mechanisms influencing sonic boom signatures underwater. We hypothesize that the observed waveform was influenced by an interaction of the very low-frequency sonic boom energy with the particular seabed found at the experimental shallow-water site.

The following section reviews sonic boom basics, and discusses the underwater propagation of a sonic boom. The measurements are presented next, along with a full description of the experiment. Modeling of the measured underwater waveforms is also presented. The last section expands on the hypothesis of an interaction between the sonic boom acoustic energy and the seabed.

II. SONIC BOOM PROPAGATION

The propagation in air of a sonic boom is a well-known and well-documented phenomenon. As the aircraft reaches and overtakes the speed of sound in air, the overpressure disturbance called the sonic boom propagates along a cone-shaped trajectory originating at the aircraft and traveling at the same speed as the aircraft (Fig. 1). The intersection of the Mach cone with land, or in our case with the sea surface, is a one-sided hyperbola (dashed line in Fig. 1) also traveling at the supersonic speed of the aircraft.

The pressure signal as a function of time along the hyperbola approximates an N-shaped waveform at the earth's surface (Fig. 1). Pierce[10] and Maglieri and Plotkin[11] have shown that the following relationship can be used to describe accurately the duration T of a sonic boom:

[a)]Portions of this work were presented in "Underwater measurements of a sonic boom," Proceedings of Oceans '97 Conference, Halifax, NS, Canada, Vol. 1, October 1997, and "Underwater measurements and modeling of a sonic boom," Sonic Boom Symposium, 136th meeting of the Acoustical Society of America, Norfolk, VA, October 1998.

[b)]Author to whom correspondence should be addressed; electronic mail: francine.desharnais@drea.dnd.ca

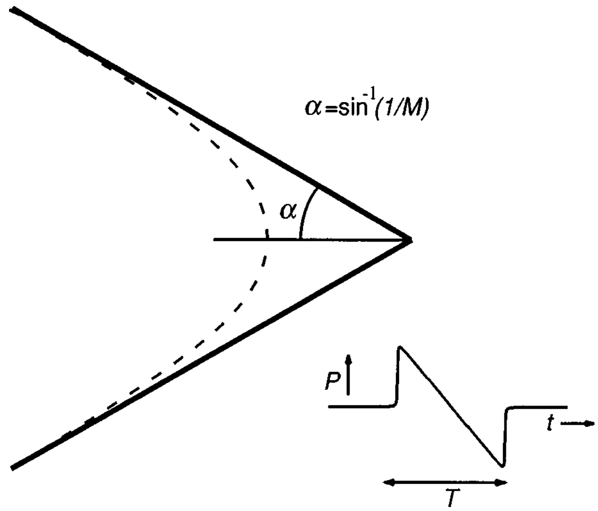

FIG. 1. Plan view of a Mach cone. The dashed line represents the intersection with the sea surface. The lower design represents an N-shaped sonic boom waveform.

$$T = k\frac{M}{(M^2-1)^{3/8}}, \tag{1}$$

where M is the Mach speed of the aircraft (or speed of the aircraft/speed of sound in air) and k is a constant related to the aircraft shape, altitude, and other physical parameters. The duration is typically of the order of 100 ms for a commercial supersonic aircraft.

At the sea surface, the airborne wave faces a large acoustic impedance contrast, as the speed of sound in water is closer to 1500 m/s (as opposed to ~343 m/s in air), and the density of water is ~1000 kg/m^3 (as opposed to ~1 kg/m^3 in air). If the speed of the aircraft is less than the speed of sound in water (approximately Mach 4.4 if the sound speed in air is taken as 343 m/s), the sonic boom, as shown in Fig. 2, is totally reflected by the sea surface for incident angles (normal to the sea surface) over 13.1° [arcsin(1/4.4)]. The Air France Concorde travels between Paris and New York at a cruise speed of Mach 2 (at an altitude of approximately 18 000 m). The associated sonic boom has an incident angle of 30°, implying that a total reflection of the sonic boom occurs at the sea surface.

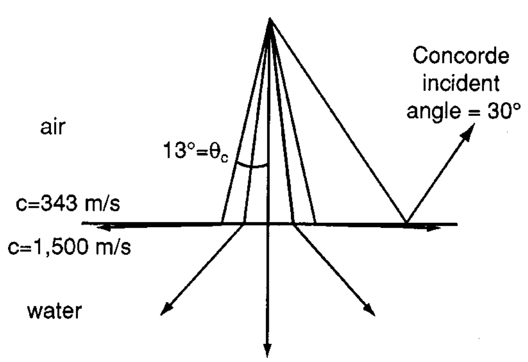

FIG. 2. For the sound speeds indicated on the diagram, a compressional sound wave will be transmitted through water for angles steeper than 13.1° only. The Concorde sonic boom wave has an angle of incidence on the order of 30°.

In the water, the acoustic field is an evanescent or inhomogeneous plane wave that propagates horizontally but decays with depth. (This field is necessary to satisfy the condition that the acoustic pressure is continuous across the interface.) The decay is frequency dependent: the lower frequencies penetrate deeper than the higher frequencies.

The first theory to explain the sonic boom penetration in the water was published by Sawyers.[12] The theory was later refined by Cook,[13] but the modifications were estimated to probably be too small to be measured experimentally. Sawyers' theory will therefore be used in this paper to model the experimental data. It expresses the pressure p of the sonic boom waveform as a function of depth with the following equation:

$$\pi\frac{p}{p_{\text{surface}}} = (2\tau+2\xi-1)\left[\tan^{-1}\left(\frac{\tau-\xi-1}{\zeta}\right) - \tan^{-1}\left(\frac{\tau-\xi}{\zeta}\right)\right] + \zeta\ln\left[\frac{\zeta^2+(\tau-\xi)^2}{\zeta^2+(\tau-\xi-1)^2}\right], \tag{2}$$

where p_{surface} is the reference pressure at the sea surface. The nondimensionalized parameters of (2) are defined as

$$\tau = \frac{t}{T}, \tag{3}$$

$$\zeta = \frac{z}{m\cdot T}, \tag{4}$$

$$\xi = \frac{x}{T\cdot V}, \tag{5}$$

$$m = \frac{V}{(1-V^2/c^2)^{1/2}}, \tag{6}$$

where t is the time (s), z the depth (m), x the horizontal distance (m) in the direction the sonic boom is traveling [i.e., the boom arrives at $(x,z)=(0,0)$ at $t=0$], V is the aircraft speed, and c is the sound speed in water (m/s). Sawyers' theory assumes the ocean surface to be flat, and does not account for bottom reflections (deep water).

Although (2) was derived with the simplifying assumption that the source of the sonic boom passes directly overhead at Mach number M, it is easily generalized to the case of an observation point away from the source track. If the source is at height h and the observation point is a horizontal distance y from the projection of the source track on the sea surface, then the track elevation angle θ is given by

$$\tan\theta = \frac{h}{y}. \tag{7}$$

The Mach cone may still be viewed as locally plane at the observation point, but the local angle of incidence α' is given by

$$\sin\alpha' = \frac{1}{M}\sqrt{1+(M^2-1)\cos^2\theta}. \tag{8}$$

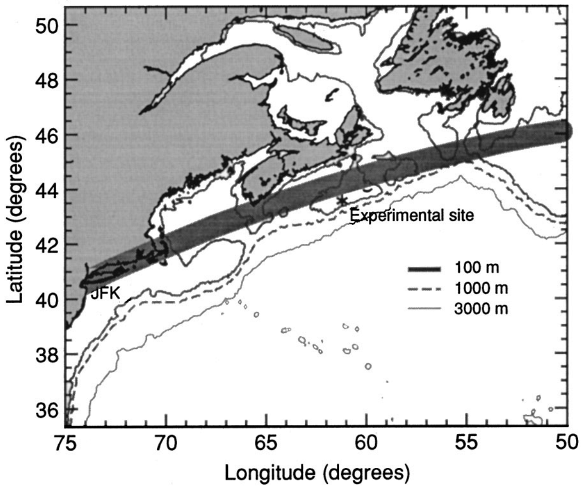

FIG. 3. Experimental area south of Nova Scotia. The dark gray zone represents the estimated trajectory of the Concorde.

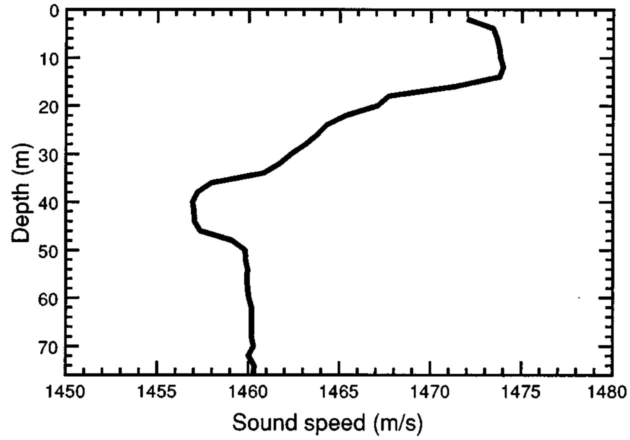

FIG. 4. Sound-speed profile as a function of depth, at the experimental site.

Off-track, the sonic boom is not traveling parallel to the source track, but in a direction forming the angle ϕ with the source track, where

$$\tan\phi = \sqrt{M^2-1}\cdot\cos\theta. \tag{9}$$

Also, the local horizontal speed of the sonic boom is not M, but M', where

$$M' = M\cos\phi = \frac{M}{\sqrt{1+(M^2-1)\cos^2\theta}}. \tag{10}$$

In summary, Sawyers' 2D theory still applies, but we must interpret α and M as local effective quantities.

It is understood that several factors can significantly alter the waveform of a sonic boom in a real environment, compared to this idealistic N-wave, such as secondary shock waves from various parts of the airframe, atmospheric stratification, and scattering at the ocean surface. These factors can affect the shape of the waveform in air, and affect the hypothesis that Sawyers' 2D theory applies for the 3D case, as supported by Eqs. (7)–(10). The details of the impact of scattering at the air/water interface are still being researched (Rochat and Sparrow,[14] and Cheng and Lee[15]), but a rough sea surface could potentially modify the underwater waveform if the sea state is appropriately high. In the absence of a measurement in air, as shown in the following section, an idealistic N-wave will be assumed.

III. MEASUREMENTS

The underwater acoustic measurements were taken in a shallow-water area on the Scotian Shelf (Fig. 3). The sonic boom was heard from the deck of C.F.A.V. QUEST at 9:17 AST (Atlantic Standard Time) on 28 May 1996. This time corresponded to the approximate time of passage of the Air France Concorde flying from Paris to New York (JFK Airport). The dark gray line in Fig. 3 represents an estimate of the Concorde path; the actual path is unknown, although Moncton Flight Center indicates that the path is normally 50 to 60 nm south of Nova Scotia, with a heading of 265°. The typical cruise speed of the Concorde is Mach 2.02 at an altitude of 18 288 m. We do not know if the Concorde had already started its descent to New York when the boom was heard at the experimental site.

The exact location of the experimental site is 43°27.6′ N 61°17.2′ W, over an area known as Western Bank. The water depth at this location is 76 m, over a sand bottom. The bottom properties are well-known for this general area and can be found in Osler.[16] The sound-speed profile at the site is shown in Fig. 4; the measurement was made with an expendable bathy-thermograph probe deployed at 8:08 AST on the same date. The weather was calm with a sea state of 1, 0.25-m swell (from 280°) and winds at 10 kn.

The data were collected with a vertical line array of 11 functioning hydrophones from 16.5- to 65-m depth. The spacing between the elements of the array varied between 0.9 and 9.5 m. The array was deployed independently from the ship, which was approximately 2.6 km away when the sonic boom was heard.

Examples of the recorded data are shown in Fig. 5 for the three hydrophone depths of 16.5, 33, and 57 m (dotted lines). The relative time is in seconds [time 0 corresponds to 9:17:36 AST (28 May 1996)] and the same relative shift was applied for the three hydrophones. The amplitude is also relative: 0.6 relative units corresponds to 1.714 Pa in calibrated units.[17] The original sampling frequency of the data is 2048 Hz. The data in Fig. 5 were smoothed with a 0.0122-s (25 points) moving average window to accentuate some of the features in the data, especially for the deeper hydrophones with a much lower signal-to-noise ratio. The solid lines in Fig. 5 represent modeling results which are discussed in the following section—they represent the modeled N-shaped waveform of the sonic boom for an underwater sensor.

The most striking feature in the data is the oscillation that follows the first N-shaped waveform. This oscillation is present at all depths (a longer moving average window would bring this out more clearly for the deeper hydrophones). The frequency of this oscillation is difficult to estimate since the moving average has the effect of smearing the waveform. At shallower depth, where the signal-to-noise ratio of the data is higher, the period can be estimated at 0.27 s. Using the approximation of Howes,[18] which states that the

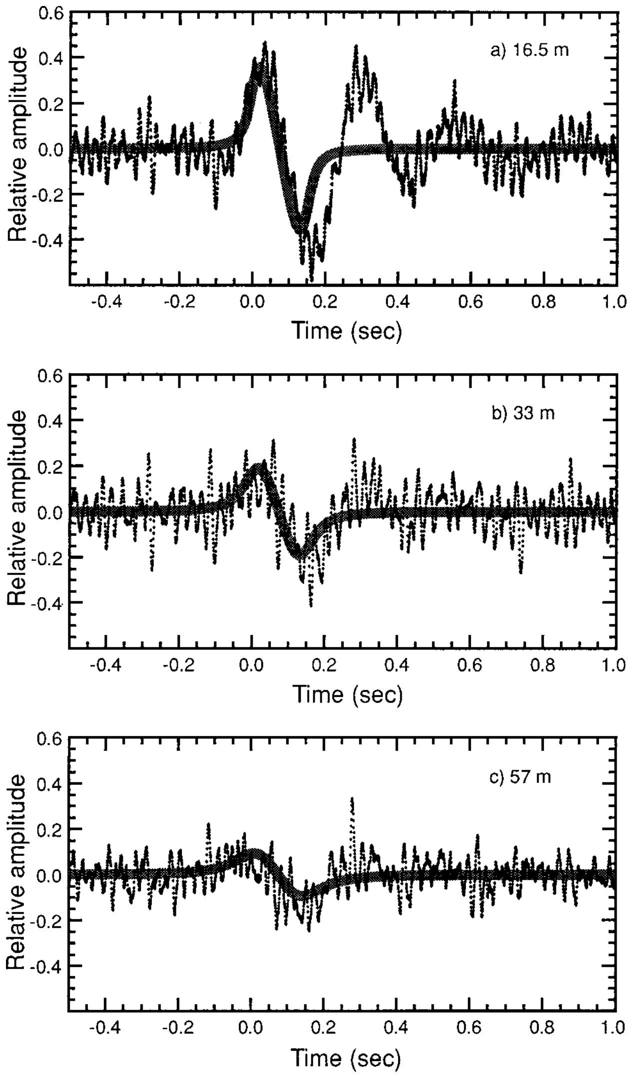

FIG. 5. Sonic boom data (dotted lines) and model (solid lines) for receivers at (a) 16.5-m; (b) 33-m, and (c) 57-m depth. The vertical scale is relative: 0.6 relative units correspond to 1.714 Pa for the data; the model amplitude is relative to the pressure at the sea surface.

effective acoustic period of the sonic boom N-wave is about 1.5 times its duration, the period of 0.27 s corresponds to a duration T of 0.18 s. This rough estimate is almost half the duration of 0.35 s which is expected for a Concorde flying at 18 000 m.[19]

The amplitude decreases with depth, as experimentally observed with the scaled experiments of Waters[5] and Intrieri and Malcolm.[6,7] The actual rate of decline as a function of depth is difficult to quantify since the experimental peak fluctuates largely with the background noise. Instead of using the peak, we decided to estimate the total broadband energy content (strictly speaking—the sound exposure) of the sonic boom by integrating the squared amplitude of the signal for a period of 7 s centered approximately on the sonic boom. This broadband rate of decay as a function of depth is shown in Fig. 6 (circles). A noise level was estimated over a 1-s period preceding the sonic boom, and subtracted from the signal level. In Fig. 6, the abscissa units have been scaled to be comparable with the modeling results (solid line) which are discussed in the following section.

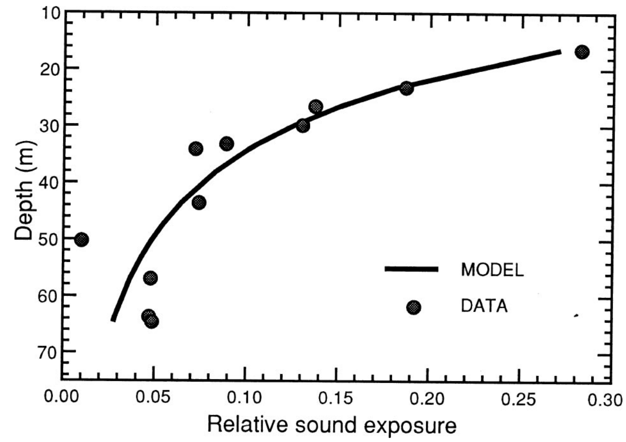

FIG. 6. Relative sound exposure (normalized to the sea surface) as a function of depth; solid line: model; circles: data.

A sonic boom duration T of 0.18 s would correspond to a peak frequency of approximately 3.7 Hz. Figure 7 shows the sound exposure spectrum density levels of the measured sonic boom for three different hydrophone depths. These spectra were obtained using 2.44 seconds of data centered on the sonic boom event. The data were padded with zeros for a fast Fourier transform (FFT) length of 8192 points, and a frequency resolution of 0.25 Hz in Fig. 7. The upper hydrophone shows a strong peak around 3.5 Hz, which is consistent with the peak frequency of the sonic boom calculated from its period in the time domain. The lower hydrophones also show a peak at 3.5 Hz, although of smaller amplitude. Secondary peaks near 1.5 and 2.75 Hz are also seen for the lower hydrophones. Background noise levels were estimated from a 1-s-long data sample preceding the sonic boom by 2 s. As for the sonic boom signal, the noise sample was padded with zeros to achieve an FFT length of 8192 points, and a frequency resolution of 0.25 Hz. Only below 6–7 Hz are the energy levels of the sonic boom higher than those of the background noise levels. The signal-to-noise ratio in the 3–4-Hz band was 25 dB for the shallowest hydrophone, and 10–15 dB for the deepest hydrophones.

The sound exposure spectrum density levels at frequencies of 2.75 and 3.5 Hz are plotted as a function of hydro-

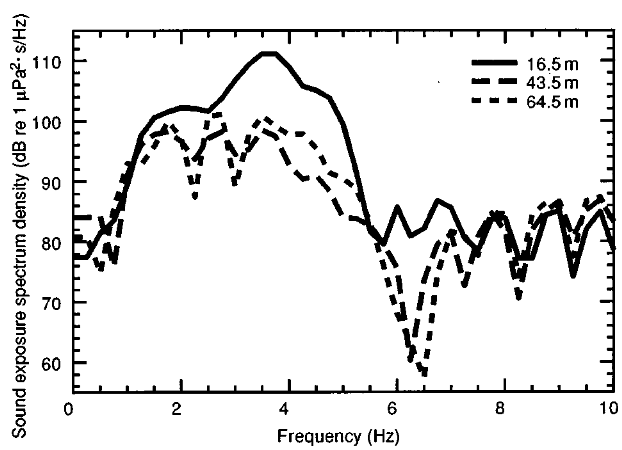

FIG. 7. Measured sonic boom sound exposure spectrum density (over 2.44 s) at 16.5, 43.5, and 64.5 m.

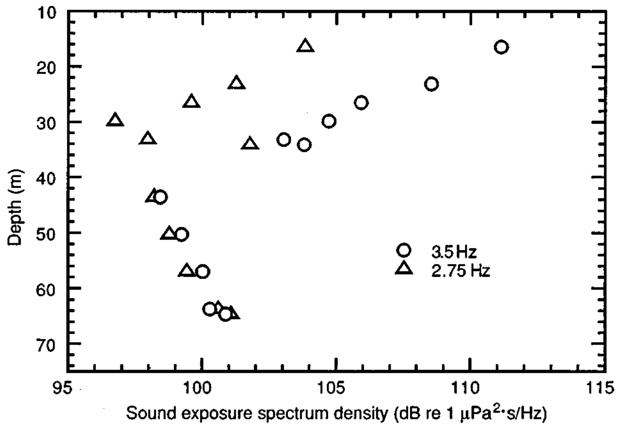

FIG. 8. Measured sound exposure spectrum density level as a function of depth at 3.5 Hz (circles) and 2.75 Hz (triangles).

phone depth in Fig. 8. Contrary to the sound exposure plotted in Fig. 6, the spectrum density at these two frequencies decreases with depth in the upper half of the ocean, but increases with depth in the lower half. This behavior will be discussed in more detail in Sec. V.

IV. MODELING OF THE SONIC BOOM TIME SERIES

The time series for each hydrophone was modeled using Sawyers' theory introduced in Sec. II. The main variables of Eqs. (2)–(6) are

(i) z, the depth in the water;
(ii) c, the sound speed in the water (taken here as 1470 m/s);
(iii) V, the speed of the aircraft; and
(iv) T, the duration of the sonic boom.

The first two variables of this list are known. The next two variables were estimated with a curve-fitting algorithm, assuming a horizontal distance [y in Eq. (7)] of 0 m. This last assumption has the effect of decreasing the estimated speed of the aircraft, since the ground speed of the sonic boom is slightly lower off-center of the contact hyperbola at the sea surface (see the discussion at the end of Sec. II).

Using the upper hydrophone data (with the highest signal-to-noise ratio), we estimated an aircraft speed of 600 m/s (Mach 1.75) and a boom duration of nearly 0.18 s. Using the full set of hydrophones, the estimated aircraft speed is 670 m/s (Mach 2) and the duration 0.16. Both speed estimates are believable from what we know of the typical Concorde cruising speed.

For a comparison with the data, the model results obtained with a speed of Mach 2 and a sonic boom duration of 0.16 s are shown in Fig. 5 for three different hydrophone depths. All amplitudes were scaled by a single correction factor to optimize the fit with the model. This procedure had to be used since we do not know the signal pressure at the sea surface (p_{surface}), there being no sensor at shallow depth.

The model fits the data better for the lower hydrophones than for the upper hydrophones. The misfit for the upper hydrophones is due to the boom duration, which seems too short in the model. However, it is difficult to judge how the original N-shaped waveform is modified by the oscillation following it. The amplitude of the signal fits equally well at all depths, suggesting that the amplitude correction factor used on the data was reasonable.

The rate of decay with depth was estimated for the model the same way as for the data. Since the amplitude is normalized to the surface [as we don't know p_{surface} in Eq. (2)], the sound exposure is normalized the same way (sound exposure=1 at the surface). The results are shown in Fig. 6. The model fits this feature of the data very well.

A major feature of the data from all hydrophones is a marked oscillation following the expected N waveform. Such a feature was not observed in the scaled experiments of Waters[5] and Intrieri and Malcolm,[6] nor in the full-scale data of Young[8] or Sohn *et al.*[9]

These oscillations cannot be explained by reflections from the ship at the sea surface, which might have been a problem if the ship had been closer to the array. Similarly, reflections from the seabed could not be great enough in amplitude to have the large effect seen on the upper hydrophones, considering the rapid decay of the sonic boom amplitude with depth.

It is possible that scattering at the sea surface affected the waveform underwater. A theoretical study by Cheng and Lee[15] indicates that this is a possibility at large depths when the sonic boom signature length is comparable to the surface wave length. A parallel study by Rochat and Sparrow[14] indicates that the effect should be negligible for surface wave amplitudes less than 1 m (0.25-m waves were observed during the experiment). Until further research confirms the extent of the sea-state impact on the actual sonic boom waveform, scattering cannot be ruled out.

Since we had no acoustic sensors in air (outside of human ears), we do not know what the waveform was in air. It is possible that the oscillation is due to refracted paths of the sonic boom in the high atmosphere. The only factor against this theory is a comment from the observer on deck (coauthor Chapman) who heard the distinct two-beat signal of the sonic boom. If the oscillation had been part of the air wave, one would expect the sound to be accompanied by "rumbles." Short of a better proof, high atmosphere refraction is kept as a potential explanation for the observed oscillations.

Another possibility, discussed in the following section, is that the ringing observed in the sonic boom time series is due to the excitation of a low-frequency seismic mode at the ocean/seabed boundary. Similar ringing effects were seen in land-based seismometers responding to sonic booms (see Cook and Goforth[20]). To explore this hypothesis, further modeling is required, including time-domain synthesis of wave trains.

V. MODELING THE INFLUENCE OF THE SEABED

Since the sonic boom measurement was unexpected, there was no in-air sensor to record the signal before it penetrated the sea surface, and it is difficult to know how much of the "anomalous" ringing of the waveform needs to be explained by ocean acoustic propagation effects, including possible interaction with the seabed. As the signal strength

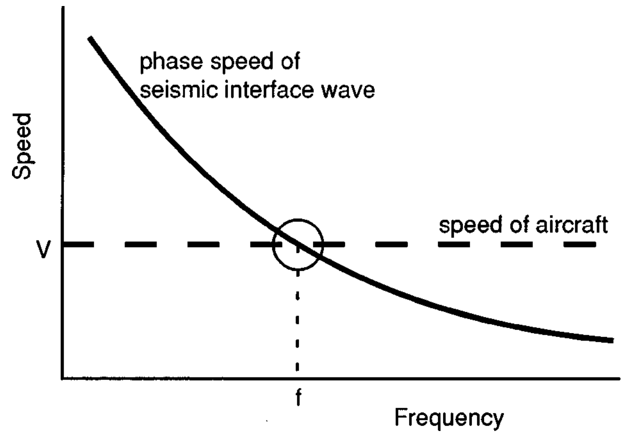

FIG. 9. Schematic diagram illustrating the excitation of a seismic interface wave of frequency *f* and speed *V* by the broadband energy of a sonic boom traveling at the same speed.

decays rapidly with depth in the water column, seabed effects would be more pronounced in shallow water, and virtually nonexistent in deep water. In this case the water depth of 76 m is sufficiently shallow to raise the possibility that the infrasonic component of the sonic boom signature could excite a seismo–acoustic interface wave in the seabed, and that this excitation could in part be an explanation for the observed "ringing" of the waveform. This does not preclude other physical mechanisms from contributing a similar effect.

The seabed interaction hypothesis is based on the following assumptions:

(i) the ocean is shallow enough to allow sufficient energy at the lowest frequencies of a sonic boom to penetrate through the water layer to the seabed below;
(ii) the seabed supports shear waves, and hence seismo–acoustic interface waves; and
(iii) the sonic boom has a frequency span and speed of advance that matches—and therefore excites—a seismo–acoustic wave at the ocean/seabed boundary.

An interface wave[21–24] can exist at the interface between two dissimilar elastic media (one may be a fluid). Although the wave propagates along the interface, it is evanescent in both perpendicular directions away from the interface, with most of the energy confined to a region about a wavelength deep on either side of the boundary. The shear speed in the sediments beneath the ocean typically increases monotonically with depth. The resulting seismo–acoustic interface wave is dispersive, with the phase speed decreasing as frequency increases. This is shown schematically in Fig. 9.

The sonic boom is a transient waveform moving with the aircraft at speed V; in the frequency domain, this translates into a broad spectrum of energy, each component of which moves with horizontal phase speed V. If the dispersion curve of the interface wave spans the same frequencies and has a range of phase speeds that brackets the aircraft speed, then it is possible for the sonic boom to excite an interface wave of speed V and peak frequency f, where (f,V) is the point at which the frequency and speed of the sonic boom match the frequency and speed of the interface wave. Since the interface wave has a compressional wave component in the overlying water layer, a hydrophone signal would display a resonant effect at this frequency in addition to the conventional sonic boom signature. However, for this effect to be noticeable, the water must be shallow enough that the amplitude of the sonic boom is not too small at the ocean bottom.

We have translated this hypothesis into a simple model: for a bottomless homogeneous ocean, each frequency component of a plane sonic boom N-wave gives rise to an evanescent wave in the water, decaying with depth. Introducing a reflecting bottom at a finite depth gives rise to a second wave evanescent in the opposite sense, having higher amplitude at the bottom and evanescing upwards. At the bottom, the amplitude and phase of the two waves are linked by a complex reflection coefficient that depends upon the properties of the water layer and the underlying seabed, which is assumed to be horizontally stratified. The acoustic field in the water layer is the sum of these two evanescent components. The bottom reflection coefficient becomes singular at pairs of (frequency, speed) values that correspond to a natural mode of oscillation of the water/seabed system, that is, a seismo–acoustic interface wave. This contributes a large additional oscillation to the time series of the waterborne portion of the sonic boom. The broadband sonic boom is a clapper that strikes the seabed, which obligingly rings like a bell.

Consider a simple model consisting of a homogeneous atmosphere, a homogeneous ocean of depth H, and a stratified seabed. Flat, parallel boundaries separate the layers. A plane wave of single frequency ω, horizontal wave number $k=\omega/V$, and unit amplitude, incident on the ocean from the air, is specularly reflected with very nearly unit amplitude, owing to the very large density difference between air and water, as shown by Chapman and Ward.[25] The pressure field in air is thus

$$P_a = e^{i(kx+q_a z-\omega t)} + e^{i(kx-q_a z-\omega t)}, \tag{11}$$

in which $q_a = k\sqrt{M^2-1}$ is the vertical wave number, and z is positive downwards. Note that the pressure at the sea surface is twice the amplitude of the incident wave.

In the water, the field is the sum of two components, an upward- and a downward-propagating plane wave. The pressure must be continuous across the boundary at the sea surface, and the complex amplitude ratio of the two components at the seabed must equal the plane-wave acoustic reflection coefficient of the seabed, R. This quantity will be determined by the underlying sediment layers. The pressure field in the water is thus

$$P_w = 2\,\frac{e^{i(kx+q_w z-\omega t)} + R\ e^{i2q_w H} e^{i(kx-q_w z-\omega t)}}{1+R\ e^{i2q_w H}}, \tag{12}$$

in which $q_w = k\sqrt{(V/c_w)^2-1}$ is the vertical wave number in the water. For $V<c_w$, this vertical wave number is imaginary, and the field components are evanescent in the vertical direction. If $|q_w|H$ is large, then we have the standard case of sonic boom penetration into "deep" water. If $|q_w|H$ is small, then acoustic reflection at the seafloor could become important, and we have a "shallow" water case.

The calculation proceeds as follows: the time series of the incident sonic boom N-wave is Fourier-analyzed into a

TABLE I. Simple geoacoustic model of ocean and seabed layers.

Layer no.	Thickness [m]	Density[a]	Compressional speed[b] [m/s]	Shear speed[b] [m/s]
1	76	1	1470	0
2	3.76	1.63	$1605.0-1.2i$	$166.7-0.2i$
3	6.36	1.68	$1618.5-1.2i$	$282.0-0.3i$
4	7.95	1.75	$1637.6-1.2i$	$352.0-0.3i$
5	9.19	1.84	$1660.4-1.2i$	$407.0-0.4i$
6	10.24	1.93	$1686.3-1.2i$	$453.4-0.4i$
7	infinite	2.1	$1950.0-0.4i$	$600-0.2i$

[a]Relative to water.

[b]Negative imaginary parts account for attenuation, although the effect in this case is negligible. (To convert to attenuation units of dB/wavelength, multiply by 54.6.)

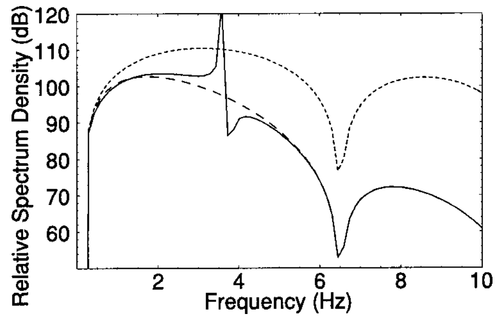

FIG. 10. Modeled sonic boom spectra at the sea surface (short dash), at 43.5-m depth in a shallow ocean with a nonelastic seabed (long dash), and at 43.5-m depth in a shallow ocean with an elastic seabed (solid).

spectrum with frequency-dependent amplitude and phase. A seabed geoacoustic environment is postulated, and the acoustic reflection coefficient R of the seabed is calculated as a function of frequency using standard techniques, as described in the Appendix. Using Eq. (12), the transfer function of each frequency component is calculated at a chosen hydrophone depth. The complex incident spectrum is multiplied by the complex transfer function to produce the complex spectrum of the signal transmitted to that depth. Finally, this complex spectrum is inverse-Fourier transformed to produce the modeled time series at the hydrophone.

We now describe the oceanographic and geoacoustic parameters used in our calculations, based on the best independent information that could be found on the geophysical structure of the seabed in the experimental area.[16] Table I shows the precise numerical parameters used. We assume a constant sound speed in water of 1470 m/s based on an average value of the actual sound-speed profile. The upper 37.5 m of the underlying sediment (sand) is modeled as 5 homogeneous sublayers closely approximating a medium with the following properties: the density (relative to water) has an average value of 1.8, with a linear gradient of 0.01/m; the compressional speed increases linearly from 1600 to 1700 m/s; and the shear speed has a power-law profile of the form $160\ z^{0.3}$ m/s (with the depth z in meters). The sub-bottom layer (till) is modeled as a homogeneous half-space. Attenuation is introduced by allowing all the speeds to have small imaginary parts. (See Ref. 21, p. 37; to convert to attenuation units of dB/wavelength, multiply by 54.6.)

Modeled frequency spectra at different hydrophone depths were calculated with this model for the input parameters mentioned above. For the calculations in this section, we assume that the duration of the N-wave is 0.225 s, the speed of the aircraft is 580 m/s (about Mach 1.75), and that the incident wave is an ''ideal'' N-wave with no distortions. The assumed duration T of 0.225 s is significantly longer than the duration of 0.16–0.18 s used in Sec. IV to fit the data in the time domain; however, the longer duration provides a main spectral lobe with the same general shape as the measured spectra shown in Fig. 7; moreover, the longer duration also provides a match of the modeled and measured spectral null at 6.25 Hz, which is quite sensitive to T. A duration of 0.225 s is also nearer the expected duration for a Concorde flying at high altitude, although lower than the presumed 18 000 m.

Figure 10 shows the modeled effect of the shallow ocean environment on the spectrum of an ideal sonic boom waveform at a submerged hydrophone, in particular the influence of shear waves in the seabed. (The levels in this figure have been arbitrarily adjusted to roughly match those in the measured data, as we have no information on absolute input levels). Three cases are shown: (a) the short dash denotes the spectrum just under the sea surface; (b) the long dash denotes the spectrum at 43.5-m depth with a nonelastic seabed (that is, the shear waves are ''turned off''); and (c) the solid line denotes the spectrum at 43.5-m depth with the elastic seabed described above.

Case (b) is essentially identical to the spectrum of an evanescent N-wave described mathematically by Sawyers[12] for the same hydrophone depth. Comparing with case (a), case (b) shows the filtering effect of the evanescent nature of the waterborne acoustic field: the evanescent penetration attenuates high frequencies more strongly. This shifts the spectral peak lower in frequency. The same calculation performed with a very deep seabed (not shown) results in a spectrum with levels only slightly lower than case (b), suggesting that the effect of a ''fluid'' seabed would be difficult to discern, at least for the environment under consideration.

Case (c), for which the shear waves are ''turned on,'' shows a prominent sharp resonance superimposed on the broad main lobe of the sonic boom spectrum, corresponding to the excitation of a seismo–acoustic interface wave at the seabed. For this combination of model parameters, the frequency of this resonance is 3.5 Hz. Additional model runs (not shown) indicate that, although the overall level of the broad main lobe decreases with increasing depth, the resonance strength of the superimposed resonance actually increases as the seabed is approached.

Note that the location of the resonance in the simple model with an assumed ideal incident sonic boom waveform coincides roughly with the ''extra'' energy shown in the experimental spectra in Fig. 7. This is significant, since the seabed model was not adjusted to achieve a ''best fit'' in any sense.

Figure 11 shows the resulting wave in the time domain. Cases (a)–(c) correspond to the corresponding cases of Fig. 10. Case (a), the short dash, is a replica of the incident ideal waveform, just under the sea surface. Case (b), the long dash, is indistinguishable from the waveform obtained from applying the theory of Sawyers[12] at the same hydrophone depth.

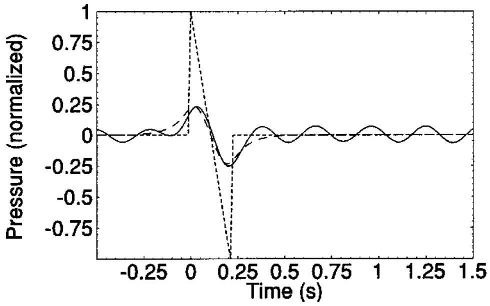

FIG. 11. Modeled time series at the sea surface (short dash), at 43.5-m depth in a shallow ocean with a nonelastic seabed (long dash), and at 43.5-m depth in a shallow ocean with an elastic seabed (solid).

The filtering effect of the evanescent penetration into the ocean ''rounds'' the shoulders of the ideal N-wave by progressively removing high frequencies. Case (c), the solid line, shows the results for the elastic seabed, with the shear waves turned on: the model produces oscillations in the time domain qualitatively similar to those observed in the experimental data. The ''Q'' of the model oscillations seems high compared with the data, leading to extended ringing before and after the main pulse. (This is not a computational artifact.) The oscillations are present at all depths. A discouraging aspect of the model is that it does not reproduce the large oscillations evident in the time series at the shallowest receiver, shown in Fig. 5(a).

Further support for the hypothesis of seabed interaction is shown in Fig. 12, which displays the modeled spectrum density level (in relative dB units) as a function of depth for the frequencies of 2, 3.1, and 3.5 Hz. The frequency of 3.5 Hz is centered on the peak of the seismic interface wave, and the amplitude of the peak increases for hydrophone depths closer to the seabed, indicating a strong bottom effect. For frequencies away from the seismic peak (e.g., 2.5 Hz which is nearer the peak frequency of the sonic boom), the levels decrease as a function of depth, as one would expect for a sonic boom signal in deep water. The frequency of 3.1 Hz in Fig. 12 is on the shoulder of the seismic peak of 3.5 Hz, and shows a behavior more similar to that seen in the data (see Fig. 8); that is, the level decreases with depth in the upper half of the water layer, and increases with depth in the lower half. The rate of increase/decrease of the levels as a function of depth, however, is higher in the data (Fig. 8) then for the modeled values (Fig. 12).

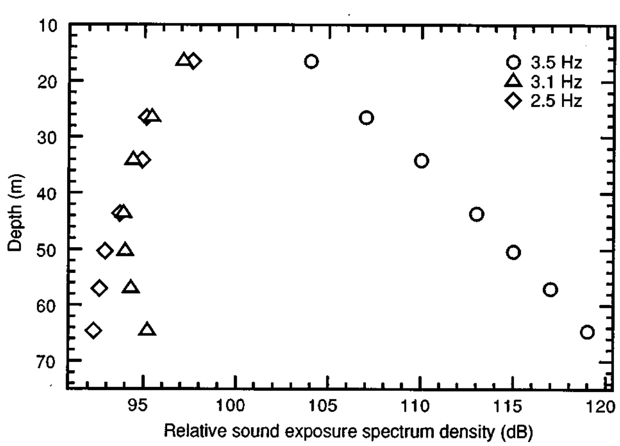

FIG. 12. Modeled sound exposure spectrum density levels as a function of depth at 3.5 Hz (circles), 3.1 Hz (triangles), and 2.5 Hz (diamonds).

The proposed simple propagation model coupled with a plausible geoacoustic environment shows the desired extra oscillations in the waveform, at least qualitatively. Clearly this simple model is incomplete, and it is likely that there are other physical mechanisms at work. One possibility is that we have oversimplified the water layer, as we have assumed a homogeneous layer, where the true profile is depth dependent. Also, model sensitivity studies indicate that the shear and density properties of the seabed are important, and a more realistic seabed (i.e., range-dependent layer properties) would presumably broaden and weaken the seismic resonance. The ocean wave scattering theory of Cheng *et al.*[15] may possibly explain the anomaly, but the ocean was calm during the experiment. Having no information about the incident waveform severely limits our investigations with this serendipitous data set. With this simple model, we cannot reproduce all the features of the observations; however, the modeling results indicate that seismo–acoustic wave excitation should not be overlooked as a mechanism leading to anomalous waveforms in shallow oceans.

VI. CONCLUSIONS

A sonic boom that originated from a supersonic Concorde aircraft was observed on 11 hydrophones of a vertical linear array located in shallow water. The waterborne waveform decayed as an evanescent wave below the sea surface. The first part of the observed waveform was modeled using Sawyers' theory.

The waveform was followed by some oscillations of a type not previously reported in the literature. The simpler explanation for these oscillations is that the sonic boom waveform in air was not a pure N-waveform, but one combined with high-atmosphere refraction which would look somewhat like the signals observed underwater. As we had no acoustic sensors in air, we cannot rule out this hypothesis.

The second hypothesis for the origin of these oscillations is an excitation of a low-frequency seismic mode at the ocean/seabed boundary. Tests were made with a simple model and it was found that some of the features of the underwater measurements, like the ringing in the time series, could be reproduced qualitatively. This phenomenon would restrict observations of these ringing events to shallow-water areas over shear-supporting seabeds, and the resulting oscillations potentially shorten the apparent period of the sonic boom signal. A more controlled experiment may be needed in order to corroborate either hypothesis.

ACKNOWLEDGMENTS

The authors would like to thank the experts met during the Sonic Boom Symposium of the 136th meeting of the Acoustical Society of America for their advice and multiple useful suggestions.

APPENDIX: ACOUSTIC REFLECTION FROM A LAYERED ELASTIC SEABED

For the purpose of this paper, the influence of the seabed on the waterborne acoustic waveform is encapsulated in the acoustic plane-wave reflection coefficient R, evaluated at fixed horizontal phase speed as a function of frequency. Simple models of the seabed assume all-fluid layers, but a more realistic model (especially at infrasonic frequencies) takes into consideration the elastic nature of the sediments.

In homogeneous elastic media, the wave equations of motion reduce to uncoupled wave equations for compressional (P) waves, vertically polarized shear (SV) waves, and horizontally polarized shear (SH) waves. When the medium becomes vertically stratified, the SH waves remain independent, but the P and SV waves become coupled through the gradient of the shear modulus. However, we need not consider SH waves any further, as they are not coupled to acoustic waves in the ocean (fluid) layer. In general, the remaining equations of motion are difficult to solve, and the usual strategy is to approximate continuous vertical stratification of material properties by a stack of many homogeneous layers. Within each layer, the fields are pure P and pure SV waves, and the continuous coupling is replaced by discrete coupling at the boundaries between the layers. With sufficiently fine layering, the stacked-layer method provides acceptably good results.

We follow Brekhovskikh[26] in his calculation of the reflection coefficient of a multilayered elastic medium, with some adaptations. We imagine a plane wave of frequency ω and horizontal wave number k incident upon a stack of elastic layers. (All the fields in all the layers will share the same horizontal wave number, due to Snell's law.) The particle velocity $\mathbf{u}$ in a given layer with compressional speed c_p and shear speed c_s is given by the vector expression

$$\begin{aligned}\mathbf{u}=&(c_p/\omega)[a_p(k\hat{\mathbf{x}}+q_p\hat{\mathbf{z}})e^{i(kx+q_pz)}+b_p(k\hat{\mathbf{x}}-q_p\hat{\mathbf{z}})e^{i(kx-q_pz)}]\\&+(c_s/\omega)[a_s(q_s\hat{\mathbf{x}}-k\hat{\mathbf{z}})e^{i(kx+q_sz)}\\&-b_s(q_s\hat{\mathbf{x}}+k\hat{\mathbf{z}})e^{i(kx-q_sz)}],\end{aligned}\tag{A1}$$

in which a_p, b_p, a_s, and b_s are the amplitudes of downward-traveling (a) and upward-travelling (b) compressional (p) and shear (s) waves at the top of the layer; $\hat{\mathbf{x}}$ and $\hat{\mathbf{z}}$ are the unit vectors in the horizontal and downward vertical directions, respectively, and q_p and q_s are the compressional and shear vertical wave numbers given by

$$q_p=\sqrt{(\omega/c_p)^2-k^2}\quad\text{and}\quad q_s=\sqrt{(\omega/c_s)^2-k^2}.\tag{A2}$$

The compressional and shear components of $\mathbf{u}$ satisfy the compressional and shear wave equations and represent longitudinal motion and vertically polarized transverse motion, respectively. From this field, the relevant velocity and stress components at the top of a layer are

$$u_x=(c_p/V)(a_p+b_p)+\sqrt{1-(c_s/V)^2}(a_s-b_s),\tag{A3a}$$

$$u_z=\sqrt{1-(c_p/V)^2}(a_p-b_p)-(c_s/V)(a_s+b_s),\tag{A3b}$$

$$\begin{aligned}\tau_{zz}=&i\omega V\rho[(c_p/V)(1-2c_s^2/V^2)(a_p+b_p)\\&-2(c_s^2/V^2)\sqrt{1-(c_s/V)^2}(a_s-b_s)],\end{aligned}\tag{A3c}$$

$$\begin{aligned}\tau_{xz}=&i\omega V\rho[2(c_s^2/V^2)\sqrt{1-(c_p/V)^2}(a_p-b_p)\\&+(c_s/V)(1-2c_s^2/V^2)(a_s+b_s)],\end{aligned}\tag{A3d}$$

in which $V=\omega/k$ is the horizontal phase speed and ρ is the bulk density of the layer. The associated velocity and stress components at the bottom of the layer of thickness h are obtained from Eqs. (A3a)–(A3d) by the substitutions

$$a_p\rightarrow a_pe^{i\varphi_p},\quad a_s\rightarrow a_se^{i\varphi_s},\quad b_p\rightarrow b_pe^{-i\varphi_p},$$

and (A4)

$$b_s\rightarrow b_se^{-i\varphi_s},$$

in which

$$\varphi_p=(\omega h/c_p)\sqrt{1-(c_p/V)^2}$$

and (A5)

$$\varphi_s=(\omega h/c_s)\sqrt{1-(c_s/V)^2}.$$

Across the boundary between two adjacent elastic layers (assumed to be "welded," the four velocity and stress components must be continuous. For a system of n layers consisting of $n-2$ finite layers sandwiched between two semi-infinite layers, there are $4n$ field variables, for which the $n-1$ boundaries provide $4n-4$ equations; however, there are four additional constraints, as the incident amplitudes in the semi-infinite layers must be specified. This leaves a system of $4n-4$ equations with $4n-4$ unknowns. For the seabed acoustic reflection coefficient calculation, the constraints would be $a_p^{(l)}=1$, $a_s^{(l)}=0$, $b_p^{(n)}=0$, and $b_s^{(n)}=0$, in which the superscript denotes the layer number. If a layer is fluid, the number of amplitudes and boundary conditions is reduced, as shear waves are not supported ($a_s=b_s=0$) and a "slip" condition exists at the layer boundaries, so that u_x need not be continuous across them. The object is to calculate the complex amplitude $b_p^{(l)}$, that is, the reflection coefficient R.

In vector form, the solution of this problem amounts to the inversion of a large block-diagonal matrix with many zero off-diagonal elements. (The boundary conditions only connect adjacent layers.) There are several methods of solution available, but we decided to code the problem in MATHEMATICA® and allow the LINEARSOLVE procedure to choose the optimal method.[27] The user chooses the layer thicknesses, densities, and wave speeds (both compressional and shear). Bulk attenuation of the waves within the layers is handled by adding appropriate small imaginary parts to the wave speeds. The computer model constructs the matrix of boundary condition equation at this stage, but the elements are still functions of frequency and horizontal phase speed (or grazing angle). For a given horizontal phase speed, the amplitude and phase R is then computed as a function of frequency. We partly validated our MATHEMATICA® computer code by comparing calculated reflection and transmission coefficients at a fluid/solid boundary with published results.[28]

In such a medium, there is the possibility of exciting a seismo–acoustic interface wave (or mode), which manifests itself naturally as a pole in the reflection coefficient. If the sediment layer were a homogeneous half-space, there would be only a single, slow, seismo–acoustic mode: the Scholte wave. This wave is nondispersive, as components at all frequencies travel at the same phase speed, which is identical to the group speed. In a depth-dependent shear-speed profile, there is a fundamental mode akin to the Scholte mode, but this mode is now dispersive: for a monotonically increasing shear speed, the phase speed decreases with increasing frequency. In addition to the fundamental mode, there may be other modes that superficially appear to be pure shear waves trapped by the upward-refracting profile. However, these modes are very weakly coupled to the water layer, and have little influence on the reflection coefficient. For the effect of the interface wave to be noticeable, the frequency and horizontal phase speed of the acoustic wave in the ocean must match the frequency and phase speed of the interface wave. If the acoustic wave is broadband, as in the case of the sonic boom, the interface wave will be excited at the frequency where the phase speeds match.

[1] V. W. Sparrow, ''The effect of supersonic aircraft speed on the penetration of sonic boom noise into the ocean,'' J. Acoust. Soc. Am. **97**, 159–162 (1995).
[2] V. W. Sparrow, ''The effect of aircraft speed on the penetration of sonic boom noise into a flat ocean,'' in Proceedings of High-Speed Research: 1994 Sonic Boom Workshop, NASA Conference Publication 3279 (1994), pp. 137–156.
[3] H. K. Cheng, C. J. Lee, M. M. Hafez, and W. H. Guo, ''Sonic boom propagation and its submarine impact: A study of theoretical and computational issues,'' in AIAA Paper 96-0755, 34th Aerospace Sciences Meeting and Exhibit, Reno, NV (1996).
[4] H. K. Cheng, C. J. Lee, M. M. Hafez, and W. H. Guo, ''Theoretical and computational studies on sonic boom propagation and its submarine impact,'' in Proceedings of High Speed Research Program: Sonic Boom Workshop, NASA Langley Research Center (1995).
[5] J. Waters, ''Penetration of sonic boom energy into the ocean: An experimental simulation,'' in Noise and Vibration Control Engineering, edited by M. Crooker, Proceedings of the Purdue Noise Control Conference, Purdue University, Lafayette, IN, 14–16 July 1971 (1971), pp. 554–557.
[6] P. Intrieri and G. Malcolm, ''Ballistic range investigation of sonic-boom overpressures in water,'' AIAA J. **11**, 510–516 (1973).
[7] G. Malcolm and P. Intrieri, ''Ballistic range investigation of sonic-boom overpressures in water,'' AIAA Paper 72-654, presented at the AIAA 5th Fluid and Plasma Dynamics Conference, Boston, MA (1972).
[8] R. W. Young, ''Penetration of sonic boom into the ocean,'' J. Acoust. Soc. Am. **44**, 392 (1968).
[9] R. A. Sohn, F. Vernon, J. A. Hildebrand, and S. C. Webb, ''Field measurements of sonic boom penetration into the ocean,'' J. Acoust. Soc. Am. **107**, 3073–3083 (2000).
[10] A. D. Pierce, *Acoustics: An Introduction to Its Physical Principles and Applications* (Acoustical Society of America, Woodbury, NY, 1989).
[11] D. Maglieri and K. Plotkin, ''Sonic boom,'' in Aeroacoustics of Flight Vehicles: Theory and Practice, Vol. 1: Noise Sources, edited by H. Hubbard, NASA Ref. Pub. 1258, Vol. 1, WRDC Tech Report 90-3052, August 1991, 532 (1991).
[12] K. Sawyers, ''Underwater sound pressure from sonic booms,'' J. Acoust. Soc. Am. **44**, 523–524 (1968).
[13] R. Cook, ''Penetration of a sonic boom into water,'' J. Acoust. Soc. Am. **47**, 1430–1436 (1970).
[14] J. L. Rochat and V. W. Sparrow, ''Two-dimensional focusing of sonic boom penetrating an air–water interface,'' AIAA J. **35**, 35–39 (1997).
[15] H. K. Cheng and C. J. Lee, ''A theory of sonic boom noise penetration under a wavy ocean,'' AIAA Paper 98-2958, 2nd AIAA Theoretical Fluid Mechanics Meeting, Albuquerque, NM (1998).
[16] J. C. Osler, ''A geo-acoustic and oceanographic description of several shallow water experimental sites on the Scotian Shelf,'' DREA Technical Memorandum 94/216, Defence Research Establishment Atlantic, NS, Canada (1994).
[17] Figure 5 has been published previously in Desharnais and Chapman [Proceedings of Oceans '97, Vol. 1, pp. 592–596 (1997)] with a different vertical scale. The version published here corrects for a small calibration error found later with the experimental system.
[18] W. L. Howes, ''Farfield spectrum of the sonic boom,'' J. Acoust. Soc. Am. **41**, 716–717 (1967).
[19] K. Plotkin, personal communication (1998).
[20] J. C. Cook and T. Goforth, ''Seismic and underwater responses to sonic boom,'' J. Acoust. Soc. Am. **51**, 729–741 (1972).
[21] F. B. Jensen, W. A. Kuperman, M. B. Porter, and H. Schmidt, *Computational Ocean Acoustics* (AIP, Woodbury, NY, 1993).
[22] J. C. Osler and D. M. F. Chapman, ''Seismo-acoustic determination of the shear wave speed of surficial clay and silt sediments on the Scotian Shelf,'' Can. Acoust. **24**, 11–22 (1996).
[23] J. A. Collins, G. H. Sutton, and J. I. Ewing, ''Shear-wave velocity structure of shallow-water sediments in the East China Sea,'' J. Acoust. Soc. Am. **100**, 3646–3654 (1996).
[24] S. E. Dosso and G. H. Brooke, ''Measurement of seismo-acoustic ocean-bottom properties in the high Arctic,'' J. Acoust. Soc. Am. **98**, 1657–1666 (1995).
[25] D. M. F. Chapman and P. D. Ward, ''The normal mode theory of air-to-water sound transmission in the ocean,'' J. Acoust. Soc. Am. **87**, 601–618 (1990).
[26] L. M. Brekhovskikh, *Waves in Layered Media*, 2nd ed., translated by R. T. Beyer (Academic, London, 1980).
[27] S. Wolfram, *The* MATHEMATICA® *Book*, 3rd ed. (Wolfram Media, Champaign, IL, 1996).
[28] K. Ergin, ''Energy ratio of the seismic waves reflected and refracted at rock–water boundary,'' Bull. Seismol. Soc. Am. **42**, 349–371 (1952).

Validation of sonic boom propagation codes using SR-71 flight test data

Lyudmila G. Ivanteyeva, Victor V. Kovalenko, Evgeny V. Pavlyukov, and Leonid L. Teperin
Central Aerohydrodynamic Institute (TsAGI), Moscow, Russia

Robert G. Rackl
The Boeing Company, M/S 67-ML, Box 3707, Seattle, Washington 98124-2207

(Received 26 April 2000; revised 26 June 2001; accepted 27 July 2001)

The results of two sonic boom propagation codes, ZEPHYRUS (NASA) and BOOM (TsAGI), are compared with SR-71 flight test data from 1995. Options available in the computational codes are described briefly. Special processing methods are described which were applied to the experimental data. A method to transform experimental data at close ranges to the supersonic aircraft into initial data required by the codes was developed; it is applicable at any flight regime. Data are compared in near-, mid-, and far fields. The far-field observation aircraft recorded both direct and reflected waves. Comparison of computed and measured results shows good agreement with peak pressure, duration, and wave shape for direct waves, thus validating the computational codes. © *2002 Acoustical Society of America.* [DOI: 10.1121/1.1404377]

PACS numbers: 43.28.Mw, 43.25.Cb [LCS]

I. INTRODUCTION

Since it is difficult to simulate sonic booms under laboratory conditions, the major investigative means are numerical analysis and flight testing. The expense of the latter leaves computation as the major method. Opportunities are rare for verifying sonic boom propagation codes based on flight test data.

The ZEPHYRUS sonic boom propagation code was developed by Robinson under NASA sponsorship in 1991 for level flight in a stratified atmosphere with horizontal winds.[1] It takes into account air absorption phenomena (Pestorius algorithm), and temperature and wind gradients, and has no restrictions when propagating near, and through, caustics and points on the propagation path with a horizontal tangent.

In 1995, NASA Dryden Flight Research Center acquired near-field, far-field, and ground sonic boom signature measurements during SR-71 flights at Mach 1.25 to 1.6 at various gross weights, concentrating on the non-N-wave region.[2] An F-16XL aircraft probed the SR-71 near-field signatures from close to the aircraft to more than 8000 ft. below. A slow-speed YO-3A aircraft measured the SR-71 sonic booms from 21 000 to 38 000 ft. below. Atmospheric data were recorded for each test day. The experimental data have been examined in a preliminary way by NASA in order to reject or correct problem data. In spite of some discrepancies in the data, they are a valuable source for code validation. This paper analyzes 59 near-field and 22 far-field signatures, including waves reflected off the ground, and U-shaped waves.

The objective of the present paper is to validate the ZEPHYRUS code by comparing its outputs with flight test results. This comparison is not direct and requires processing of experimental data and preparing initial data acceptable to the ZEPHYRUS code. A modified F-function is introduced in this paper to supply the initial data. The sonic boom generation and propagation code BOOM, developed by TsAGI, propagates the signal to a near-field point where it is handed off to the ZEPHYRUS code as initial data. The BOOM code is based on the Whitham F-function method, without accounting for atmospheric absorption. It cannot pass through caustics, but includes effects of vehicle acceleration and stratified three-component winds.[3–6] This code was used as an independent source of information when comparing the experimental data with ZEPHYRUS predictions.

II. PROCESSING OF EXPERIMENTAL DATA

Analysis of the experimental data showed that over the course of a short data-taking session of 40 s duration, the SR-71 flight parameters exhibit considerable variations: the aircraft decelerates, changes its heading, and so on. How these variations presented challenges to the present work is considered below. Note, however, that we require only a short portion of such a 40-s session—namely, the portion when the signal was emitted that is measured further away.

When measuring far-field disturbances, the YO-3A was flying at a Mach number of about 0.1; typical signal durations are similar to those measured on the ground, around 0.2 s. In this case the SR-71 motion instability is of no importance—the measurement devices were acquiring the disturbance generated by a current (''instantaneous'') state of the source.

The situation with the F-16XL aircraft is different. It flew at almost the same speed as the SR-71. The time intervals of boom probings are as long as several seconds. In this case an algorithm should determine the emission time in the SR-71 flight path and evaluate source flight parameters. Detailed analysis of submitted experimental data showed that experimenters managed to sustain the requirement of SR-71 steady flight with high accuracy in many but not all measurement sessions. Figure 1 serves as an example of irregular flight, which shows time histories of ''normal'' acceleration

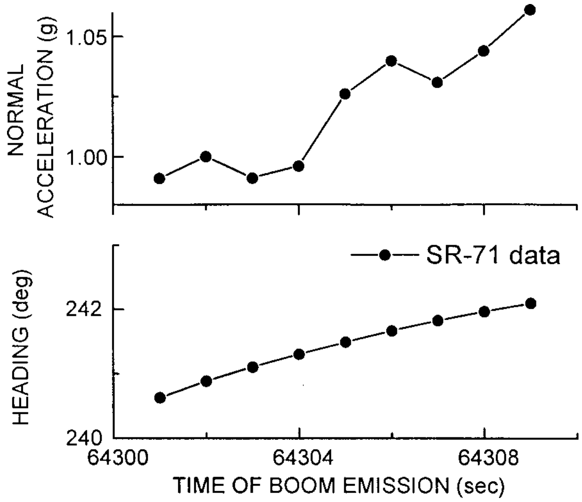

FIG. 1. Evolution of flight parameters during emission period.

(perpendicular to the flight track) and heading of the SR-71 aircraft during an emission period of interest.

The following explains the transformation of F-16XL probe data from the reference frame moving with the aircraft to one for a stationary observer.

The sonic boom problem is formulated for a body moving at a supersonic speed V; disturbances propagate along characteristic rays at the speed of sound; the overpressure time history $P(t)$ is determined in atmosphere-fixed coordinates. An equivalent problem is the calculation of the spatially dependent overpressure $P(x)$ along the x axis in vehicle-fixed coordinates. If an aircraft flies in steady, level flight in a homogeneous atmosphere, then the relationship between t and x coordinates is simple: $t = x/V$. In this case, transformation of the spatial pattern into the time domain is straightforward by considering the simultaneous arrangement of the source and receiver aircraft. Preliminarily, in the available experimental dataset, the receiver aircraft location was determined by the distance along the x axis back from a homogeneous atmosphere Mach cone under the assumption of uniform flow around the SR-71 at a Mach number averaged over the entire session. The assumption of steady, level, straight flight is very important here. For example, estimates suggest that at a receiver aircraft distance of 1000 m, a deviation in Mach number by 0.01 (more specifically, from 1.25 to 1.26) during a session results in deforming $P(x)$ by 17 m, which is equivalent to 0.05 s in $P(t)$ (with the total wave duration being about 0.15 s); a flight path inclination of 1 deg with respect to the horizon at M=1.25 leads to a time divergence of also about 0.05 s. Notable differences are expected to be associated with long sessions (longer than 10 s) with changes in heading when the source aircraft can displace transversely by large distances.

All variations of these kind are insignificant in a usual sense, but can unrecognizably change the overpressure profile. This irregularity is exemplified in Fig. 2 for sonic boom overpressure versus the distance to the bow shock, referred to the specific body length L (L=30 m). The example shown belongs to one of the "worst" in the sense that the variations of the flight parameters during measurement were considerable.

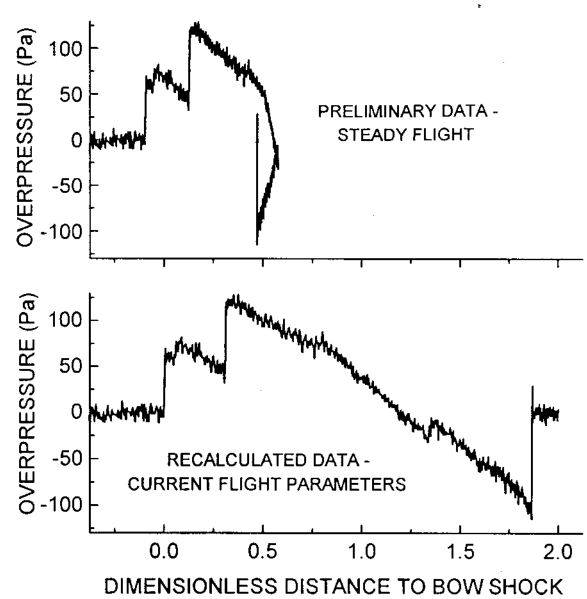

FIG. 2. Example of sonic boom wave transformation upon processing.

A simple recalculating procedure to improve the situation has been used. It takes into account current SR-71 values of Mach number, heading, and path inclination during the emission period. The processing program is based on the following procedure:

(i) the spatial position of the probing airplane F-16XL is taken as a starting point;
(ii) the point of sonic boom emission on the SR-71 path is computed;
(iii) experimental data at that point are used assuming uniform straight flight for the SR-71; and
(iv) spatial position of the F-16XL is calculated with respect to the SR-71 bow shock.

This procedure is carried out for all recorded F-16XL positions. Wind speed is considered only for displacement (shift) of the Mach cone.

It is seen from Fig. 2 that after processing, overpressure has developed into a reasonable shape. Overpressure for every F-16XL probing was corrected in such a way and then transformed into the atmosphere-fixed coordinates, as discussed before with velocity V averaged over the emission period.

III. INITIAL DATA

In order to compare theoretical and experimental data we require an initial disturbance near the body generating the sonic boom. The subject experiment is unique in providing special near-field measurements to obtain these initial disturbances. However, as is explained below, these data are not suitable for direct use even after transformation. The indicated disturbances depend on a number of parameters: distance between the aircraft-generator and point of measurement (R); atmospheric conditions along the signal path; flow conditions around the aircraft-generator, that is local Mach numbers, angles of attack, bank, yaw; body shape; settings of controls; engine flow conditions, etc.

Measurements were conducted at particular discrete values of these parameters which, as a rule, do not coincide with values necessary for use in sonic boom propagation calculations. Hence, interpolation of experimental data using all indicated factors should be performed. It is difficult to carry out. Sonic boom wave propagation is a nonlinear process. Locations of the shock waves and their number vary during propagation. Therefore, direct interpolation is wrought with significant errors.

Some extracts from the theory are useful in understanding how to overcome these difficulties. According to classical sonic boom theory,[3–5] overpressure signature $P(t)$ is calculated using the following equations:

$$P(t)=k_1F(\eta);\quad t=k_2[\eta-kF(\eta)];$$
$$\frac{F_2-F_1}{\eta_2-\eta_1}=\frac{1}{k};\quad (F_2+F_1)(\eta_2-\eta_1)=2\int_{\eta_1}^{\eta_2}F\,d\eta. \tag{1}$$

The first equation in (1) handles amplitude attenuation, the second transforms spatial coordinates into temporal ones, the third and fourth handle the process of shock formation, k, k_1, and k_2 are the waveform coefficients;[5] values F_1, F_2, η_1, η_2 bound the part of the signature which is merged into a shock. Initial data for wave propagation at the axis of a three-dimensional body may be formulated in terms of the Witham function $\Phi(x)$

$$F(\eta,\varphi)=\frac{\partial}{\partial\eta}\Phi(\eta,\varphi),\quad \Phi(\eta,\varphi)=\int_x^\eta\frac{S'(x,\varphi)}{\sqrt{\eta-x}}\,dx, \tag{2}$$

where $S'(x,\varphi)=(\partial/\partial x)S(x,\varphi)$ and the area $S(x,\varphi)$ of the equivalent body of revolution are computed taking into account lift and lateral force distributions

$$S(x,\varphi)=S_b(x,\varphi)+\frac{\beta}{2q}[Y(x,\varphi)\cos\varphi+Z(x,\varphi)\sin\varphi], \tag{3}$$

where $S_b(x,\varphi)$ is the area of projection onto the plane $\{x=0\}$ of body sections by the plane $x=x_1-\beta(z_1\sin\varphi+y_1\cos\varphi)$; x and η are coordinates along the free-flow velocity vector; φ is the angle between the vertical plane and the direction of boom propagation; and q is the dynamic pressure. In terms of nondimensionalized lift and lateral force coefficients, we have

$$S(x,\varphi)=S_b(x,\varphi)+S_{\text{ref}}\frac{\beta}{2}[C_L(x,\varphi)\cos\varphi+C_z(x,\varphi)\sin\varphi], \tag{4}$$

where S_{ref} is a characteristic area.

These relations demonstrate that the initial values for the sonic boom problem according to the linear theory are defined by

(i) body cross-sectional area distribution,
(ii) lift/lateral force distribution,
(iii) Mach number,
(iv) angle φ of boom emission.

The influence of Mach number is introduced by

(i) the multiplier $\beta=(M^2-1)^{0.5}$,
(ii) $C_L(x,\varphi)$ and $C_z(x,\varphi)$ distributions,
(iii) inclination of the sectioning plane (this does not significantly affect final results in the examined Mach number range).

If the angle φ is small, then $\cos\varphi\sim1-\varphi^2$, $\sin\varphi\sim\varphi$, $C_L\sim A+B\varphi^2$ (an even function of φ), $C_z\sim C\varphi$ (an odd function of φ), $S_b(x,\varphi)\sim D+E\varphi^2$ (an even function of φ). Here, coefficients A, B, C, D, and E do not depend on φ.

Therefore, using $\overline{C_L}(x,\varphi)=C_L(x,\varphi)/C_{Lt}$, where C_{Lt} is the lift coefficient for the entire body, at small angles φ we have

$$S(x,\varphi)=S_b(x)+S_{\text{ref}}\frac{C_L^*}{2}[\overline{C_L}(x)]+\overline{o}(\varphi), \tag{5}$$

where $C_L^*=C_L(M^2-1)^{0.5}$ is a combined parameter which establishes the dependence of $S(x,\varphi)$ on the lift coefficient of the body and on Mach number.

In addition, we have $C_L\sim A+B\gamma^2$ (an even function of bank angle γ), $C_L\sim A+B\delta^2$ (an even function of yaw angle δ); with this, $S(x,\gamma,\delta)=S(x)+\overline{o}(\gamma,\delta)$. Thus, at small values of φ, γ, and δ the function $S(x,\varphi)$ is almost independent of angles of bank, yaw, and emission; the function is mainly governed by distributions of lift and thickness along the axis.

Finite-difference flow-field computations in the examined Mach number range (Euler code[6]) have shown that normalized load $\overline{C_L}(x)$ varies little with C_L and M.

Finally, we have the functional dependence of $F(\eta,\varphi,\gamma,\delta)$ at small angles

$$F(\eta,C_L,M)=A(\eta)+C_L^*B(\eta), \tag{6}$$

where A and B are some coefficients, which depend on the body geometry (actual values of A and B are not of interest here). According to the first and the second equations from (1) it is possible to define a modified F function $[F_m(\eta)]$ such that it gives rise to a specified signature (that is, from body to the receiver location R) in an isentropic process without shock wave formations.

$$F_m(\eta)=P(\eta_R)/k_1;\ \eta=\eta_R+kP(\eta_R)/k_1;\ \eta_R=t/k_2. \tag{7}$$

Thus, we can ''return'' experimental profiles to the body axis and determine the modified F functions that generate the present sonic boom wave. It is important to note that the correct calculation with such a modified F function is possible only for distances $r>R$; at shorter values of r the real pattern will be replaced with a ''shockless'' profile. The operation with modified F functions allows isolating and removing from the analysis the influence of the strongest parameter—distance between aircraft-generator and aircraft-receiver.

At particular values of C_L and M the modified F function is computed as

$$F_m(\eta,C_L,M)=F_{m1}(\eta)+\frac{F_{m2}(\eta)-F_{m1}(\eta)}{C_{L2}^*-C_{L1}^*}(C_L(M^2-1)^{0.5}-C_{L1}^*), \tag{8}$$

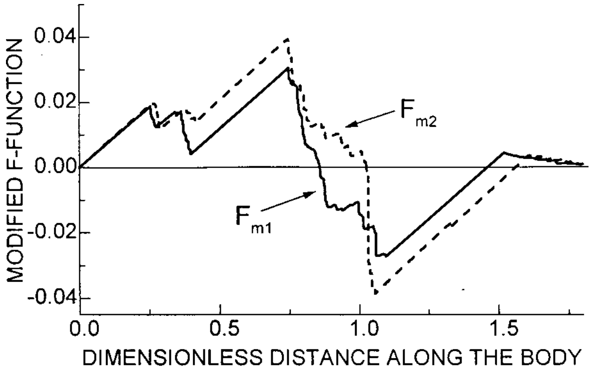

FIG. 3. Modified F function for two basic versions.

where $F_{m1}(\eta)$ and $F_{m2}(\eta)$ are two "basic" signatures. These signatures were selected taking into account the following factors: maximum possible difference in C_L^* and minimum distance R between the SR-71 and the F-16XL. As mentioned above, operation with modified F functions, derived from experimental profiles $P(t)$, can ensure correct results if the distance is larger than R at which the profiles were obtained. Therefore, the shorter R, the more widely the results are applicable. Note that versions with identical values of C_L^* are equivalent: the profiles differ through r only. This means that referring the profiles to a particular r will make them coincident.

Two equivalent profiles for two basic versions were considered. These profiles were referred to a single value of r and averaged in order to diminish the influence of random or extraneous factors (for example, deflection of aircraft controls) resulting in the following mean parameter values for M, lift coefficient C_L, and combined parameters C_L^*, mentioned above:

$$M=1.269, \quad C_L=0.0695,$$

$$C_{L1}^*=0.0532, \quad \text{basic version } 1(F_{m1}),$$

$$M=1.469, \quad C_L=0.122,$$

$$C_{L2}^*=0.1312, \quad \text{basic version } 2(F_{m2}).$$

The initial data thus obtained are valid for correct description of sonic boom wave evolution at distances below the SR-71 greater than 22.5 body lengths $(r/L>22.5)$. The shapes of these basic modified F functions are shown in Fig. 3.

For the ZEPHYRUS code, the initial data must be provided in the form of $P(t)$, instead of $F(\eta)$. Therefore, the BOOM code, which may operate with either a $P(t)$ or an $F(\eta)$ distribution, was used to transform a modified F function into $P(t)$ at $R/L=22.5$. This $P(t)$ distribution is used by the ZEPHYRUS code as an initial condition.

For convenience the measurements were subdivided into three groups: $r/L<22.5$, the near-field measurement on board F-16XL; $22.5<r/L<100$, the midfield measurement on board F-16XL; and $r/L>100$, the far-field measurement on board YO-3A.

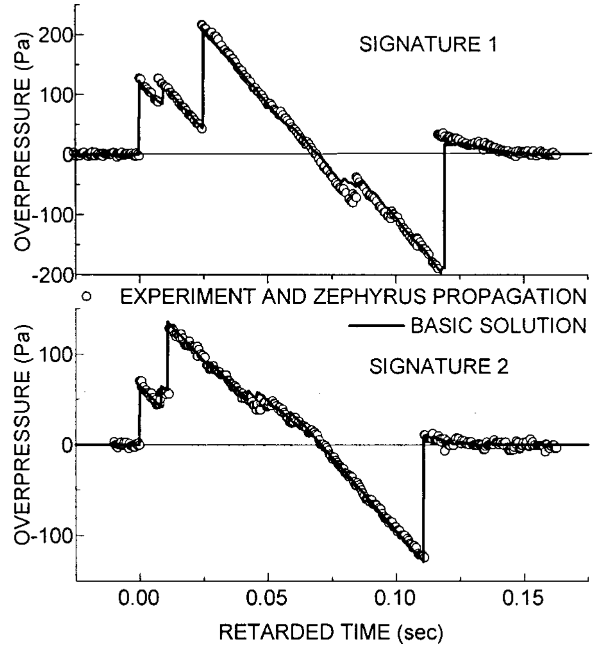

FIG. 4. Near-field comparison at $r/L=22.5$. Signature 1: $M=1.237$, $Z=9492$ m, $C_L=0.0997$, $\varphi=3.12°$. Signature 2: $M=1.509$, $Z=14\,749$ m, $C_L=0.1384$, $\varphi=0.08°$.

IV. NEAR-FIELD COMPARISONS

The technique of finding initial data was checked for each of 19 available near-field signatures. On the one hand, the above described method provides a $P(t)$ distribution at $R/L=22.5$ (the basic solution) using a modified F function. On the other hand, each of the experimentally obtained $P(t)$ distributions measured at $r/L<22.5$ may be propagated to $R/L=22.5$ by ZEPHYRUS or BOOM and, thereafter, compared to the previous basic solution. The reason for such comparison is that a good agreement of two distributions will confirm the correctness of the interpolation algorithm theory which is based upon discrete experimental measurements. In Fig. 4 two signatures with essential differences in SR-71 Mach numbers and lift coefficients are shown. SR-71 altitude (Z) and angle of boom emission (φ) are taken into account. ZEPHYRUS and BOOM outputs are very close (not distinguishable); therefore, BOOM's data are not presented here. Agreement of calculation and experiment in the near field is good. This fact validates the method of defining initial data for computation codes and suggests that involving other experimental profiles (in addition to the four profiles utilized) does not contribute anything new to the results.

V. MIDFIELD COMPARISONS

Midfield data associated with Ref. 2 are provided by 40 sonic boom signatures. As stated above, the theoretical results were obtained with the ZEPHYRUS and BOOM computer codes by utilizing an initial signature at $R/L=22.5$ and propagating it to the probing location.

Major irregularities occur in the measured waveforms mainly due to the generating aircraft's movement during the time period of sonic boom wave recording—more particularly, by changes in Mach number, heading, and altitude.

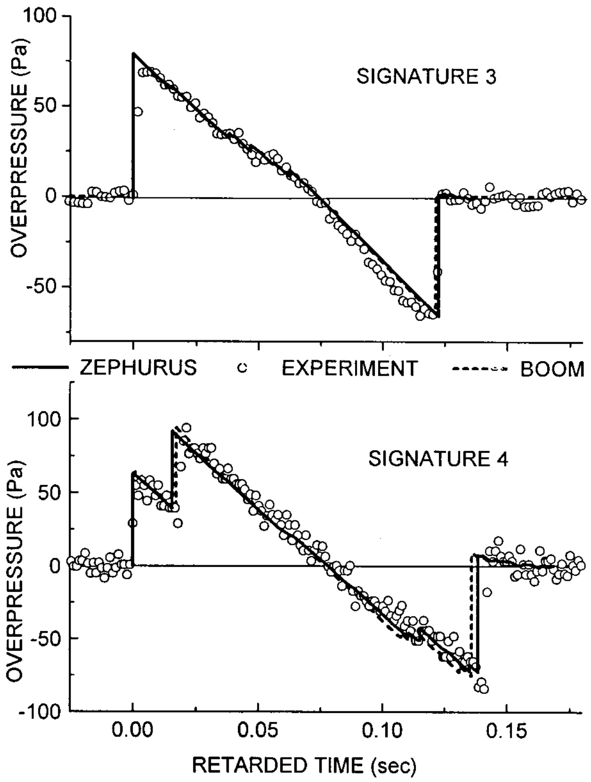

FIG. 5. Midfield comparison. Signature 3: $M=1.6$, $Z=14\,680$ m, $C_L=0.1096$, $r/L=56.5$, $\varphi=3.9°$. Signature 4: $M=1.252$, $Z=9313$ m, $C_L=0.0682$, $r/L=84.2$, $\varphi=-6.4°$.

Measured profiles are additionally tainted by measurement errors. These errors can be neither filtered out nor compensated for as the accuracy of measurement devices is not stated.

Examination and comparison of all midfield signatures made it possible to conclude that theoretical and experimental data converge rather well. Figure 5 shows two samples. The conducted comparison of computational and experimental outcomes in the midfield validated the ZEPHYRUS code over the r/L range from 22.5 to 85.0.

VI. FAR-FIELD COMPARISONS

The far-field measurements were conducted by the YO-3A aircraft. Sensors installed on each wing tip and on the top of the vertical tail of that aircraft recorded disturbances from the SR-71 and the F-16XL of various kinds: those received from above, reflected off the ground, and U-waves. Preliminary identification of the signals was carried out by NASA personnel. Used as criteria in relating a particular signal to a certain aircraft were the maximum amplitude in the wave and sonic boom wave duration.

The data comparison takes into account the Doppler effect associated with motion of the aircraft-receiver. The YO-3A flight speed was assumed to be 65 kn[2] and directed along the SR-71 speed vector. This adds a correction of about 0.005 to 0.01 s (depending on wind velocity at the YO-3A flight altitude) to the total duration of the sonic boom wave, which was around 0.15 to 0.20 s.

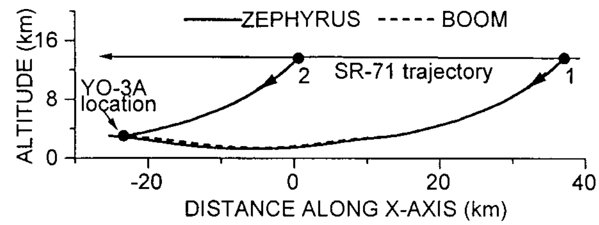

FIG. 6. Ray propagation in the far field. Point 1 is the SR-71 location at the emission time of the wave refracted through a point with a horizontal tangent. Point 2 is the SR-71 location at the emission time of the wave arrived from above.

Initial near-field data corresponding to the SR-71 aircraft flight conditions at the time of boom emission were computed for all far-field measurement sessions.

A. Ray propagation features

Actual flight conditions are not perfectly steady. An iterative numerical procedure for searching for boom emission parameters was created. The ray paths were calculated for certain time steps and boom emission angle; the emission parameters of the ray nearest the YO-3A aircraft was obtained. The searching procedure refined the parameters in a neighborhood with diminished step sizes up to obtaining a desirable accuracy of the ray hitting a signal registration spot.

Unfortunately, the time intervals of the submitted experimental data, as a rule, were insufficient for determining actual emission parameters for reflected waves. In those cases, flight trajectories were extrapolated under the assumption that the aircraft flew in steady level flight with flight parameters taken from the first second of the submitted data. Wind profile and aircraft heading, as a rule, encouraged additional curvature of the ray paths and enabled the occasional recording of U-waves. Differences of theoretical and experimental registration times of the signals arriving from above varied from flight to flight in the range from 2 to 6 s. This discrepancy cannot be completely compensated for by introducing reasonable variations in the flight parameters and weather conditions, even when introducing vertical wind. The difference between ZEPHYRUS and BOOM code outputs, however, is never more than 0.03 s.

Figure 6 exemplifies the ray propagation in the vertical plane computed by both ZEPHYRUS and BOOM codes. The calculations are conducted for identical flight and atmospheric conditions and angles of boom emission. Differences of ray paths are observed only in the area near the turning point (horizontal tangent). This is most likely explained by various methods of weather profile interpolation.

B. Waves from above

Twelve experimental far-field signatures were compared to ZEPHYRUS and BOOM outputs for the waves arriving from above. Specific features of such a comparison are shown in Fig. 7 for two variants with a significant difference in the combined lift parameter C_L^*. While analyzing this figure it should be noted that discrepancies may occur due to several factors: poor experimentation, data transformation errors, incorrect analyses, etc.

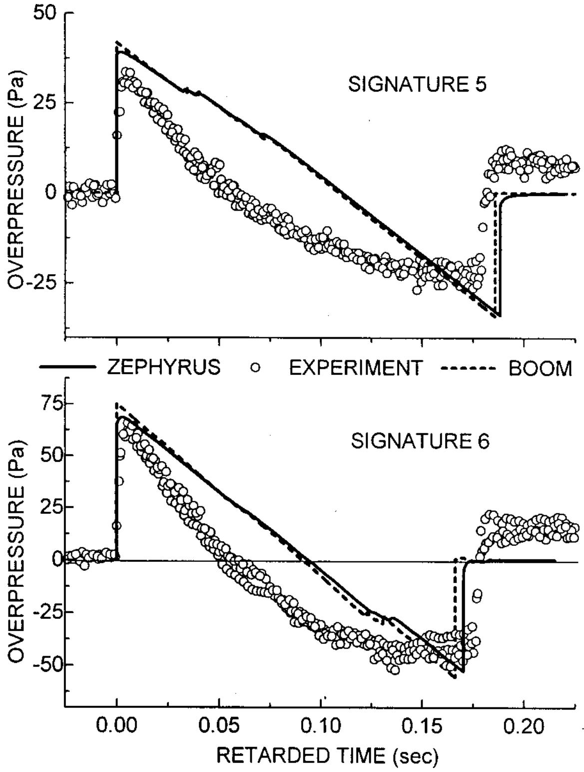

FIG. 7. Far-field comparison. Signature 5: $M = 1.505$, $Z_{\text{SR-71}} = 14\,478$ m, $Z_{\text{YO-3A}} = 3225$ m, $C_L = 0.1368$, $\varphi = 3.45°$. Signature 6: $M = 1.252$, $Z_{\text{SR-71}} = 9278$ m, $Z_{\text{YO-3A}} = 3084$ m, $C_L = 0.0908$, $\varphi = 15°$.

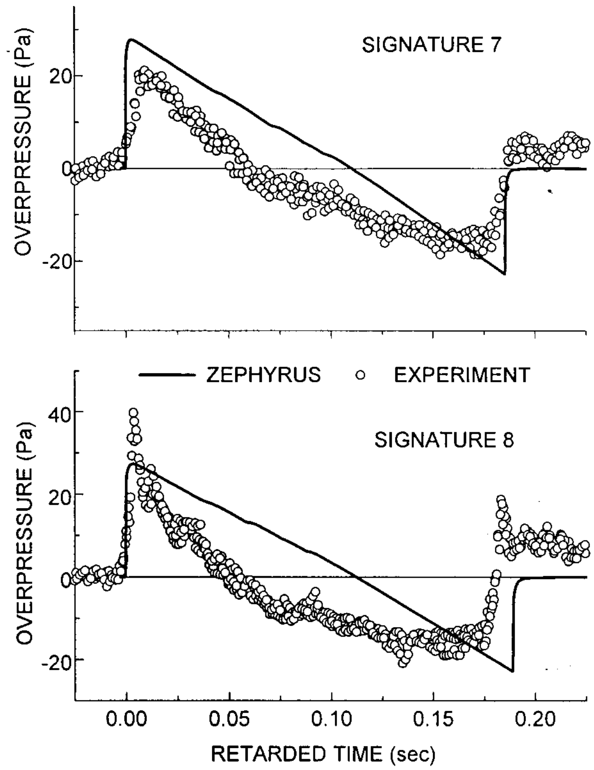

FIG. 9. Comparisons of sonic boom pressure time histories for waves reflected off the ground. Signature 7: $M = 1.50$, $Z_{\text{SR-71}} = 14\,613$ m, $Z_{\text{YO-3A}} = 3225$ m, $C_L = 0.1069$, $\varphi = 2.8°$. Signature 8: $M = 1.487$, $Z_{\text{SR-71}} = 14\,833$ m, $Z_{\text{YO-3A}} = 3110$ m, $C_L = 0.1189$, $\varphi = 3.6°$.

Reference 2 emphasizes that the bowed shape of the overpressure signatures is a consequence of filtering the microphone signals in the frequency range below 2 Hz. Thus, the considerable difference between calculated and experimental values in the central part of the signature should be attributed to instrument error.

The computer codes are correct in predicting fine details in the signature, for example when the disturbances from different areas of the vehicle do not produce a single resulting shock (N-wave). Three examples for different lift coefficients and similar flight and weather conditions are given in Fig. 8. The greater the lift coefficient, the stronger the disturbances off the wing and the greater the merging effect. Unlike the near- and midfield data, here one can distinguish the codes' results due to accounting for absorption and dispersion in ZEPHYRUS (as opposed to BOOM). The ZEPHYRUS code smooths sharp spikes.

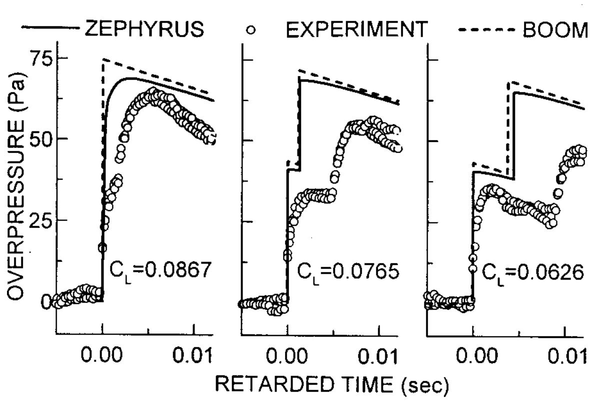

FIG. 8. Merging of two separate shocks.

C. Waves reflected off the ground, and U-waves

Overpressure in the waves reflected off the ground and U-waves was measured by microphones installed on the YO-3A slow-speed observation aircraft; these measurements have the same disadvantages as described before for the waves arriving from above.

The cases under study in this section feature the fact that rays propagate over very long paths. Note again that, as a rule, the emission point turns out to be located far beyond the SR-71 flight path portion which is covered by recorded data, i.e., it is not possible with the provided limited dataset to establish exactly at which point/altitude/flight conditions the signal was emitted.

The calculation of signals reflected off the ground assumes that the ground level is 701 m above MSL.

Also, the signals under study feature the fact that a long portion of the ray was in the low-altitude atmosphere and subjected to inhomogeneities usually called "low-altitude turbulence."

Two sample signatures are presented: one with a satisfactory comparison, and one where our waveform classification differs from NASA's preliminary analysis.

Two reflected wave signatures, among nine submitted, are shown in Fig. 9. Taking into account signal duration, its amplitude, and form, and the fact that ZEPHYRUS predicts an N-wave, signature 7 is classified as a wave reflected off the

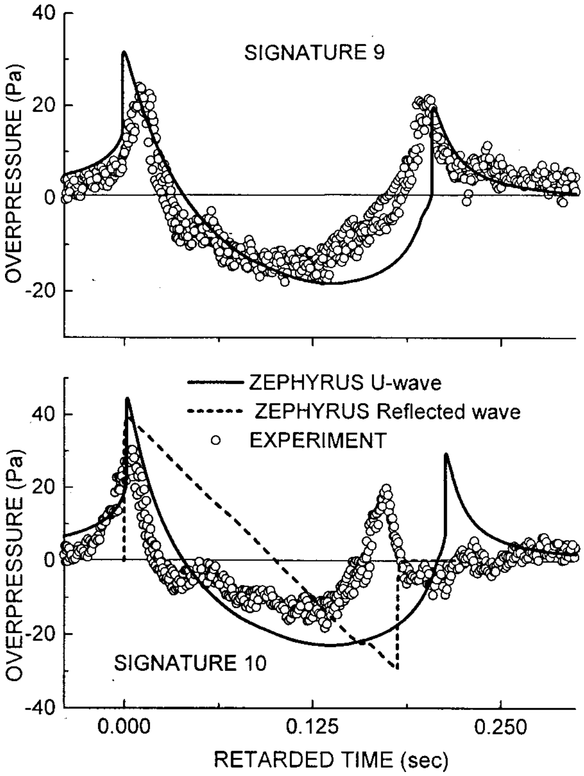

FIG. 10. Comparisons of sonic boom pressure time histories for U-waves. Signature 9: $M=1.254$, $Z_{\text{SR-71}}=9288$ m, $Z_{\text{YO-3A}}=3084$ m, $C_L=0.0908$, $\varphi=17.4°$. Signature 10: $M=1.259$, $Z_{\text{SR-71}}=9454$ m, $Z_{\text{YO-3A}}=3268$ m, $C_L=0.0765$, $\varphi_{\text{N-wave}}=4.1°$, $\varphi_{\text{U-wave}}=35°$.

ground. As for signature 8, it was preliminarily classified as a U-wave. In our opinion, according to the considerations mentioned above, this wave should also be classified as a reflected one.

The agreement of ZEPHYRUS outputs and experimental data in sessions with reflected waves is reasonable.

Concerning U-waves, it is possible to demonstrate qualitative agreement. The experimental data on this phenomenon are too sparse to be able to be more precise. There are only four such signatures in the examined dataset and, in addition, the experimental data for these versions are insufficiently detailed for preparing the initial data required for propagation analyses. Nevertheless, referring to Fig. 10, signature 9 is a U-wave. The prediction shows a rather satisfactory agreement with the experimental data. Signature 10 was classified as a U-wave, it really looks like a U-wave; however, ZEPHYRUS with actual emission parameters predicts an N-wave. Taking into account the bowed shape due to signal filtration and additional distortions when passing through a turbulent layer, it is possible to assume that this is most likely an N-wave. Figure 10 compares the experimental signature with the ZEPHYRUS N-wave prediction using a corresponding calculated value of boom emission $\varphi_{\text{N-wave}}$, and with a possible ZEPHYRUS U-wave prediction with an angle of boom emission $\varphi_{\text{U-wave}}$ which is substantially greater than $\varphi_{\text{N-wave}}$. The retarded time for the N-wave correlates with the experimental data.

It would be important and very useful to compare theoretical results with data provided by ground-based measuring devices. Notice that the present report stresses the features of comparison for near- and far fields (taking into account measurements by only the F-16XL and the YO-3A, respectively). The main difficulty in near-field processing is the accuracy of time-variable transformation into atmosphere-fixed coordinates. By contrast, far-field measurements suffer from errors in amplitudes. Measurements by arrays of ground-based sensors would provide supplementary data which could make the ZEPHYRUS validation procedure more complete and convincing. No such data were provided for this analysis.

VII. CONCLUSIONS

The ZEPHYRUS code was validated by employing two independent information sources: data from special-purpose sonic boom flight measurements carried out by NASA in 1995 by using the SR-71 aircraft as a generator of sonic boom waves, and the BOOM code developed at TsAGI.

Measured overpressure signatures in the near-field and midfield of the SR-71 aircraft as acquired by an F-16XL aircraft needed to be transformed to the variables inherent in sonic boom theory. Results of this transformation notably depend on both the variations in aircraft-generator movement parameters during a measurement session and errors in measuring the parameters characterizing flight conditions.

A method and computer software were developed for establishing near-field disturbance profiles for any SR-71 flight condition. These are based on a similarity parameter for the modified *F*-function that describes disturbance profiles for a domain around the body.

Establishing the initial data for computation required utilizing four profiles from the total profiles measured by F-16XL devices; the remaining profiles were used to validate the ZEPHYRUS code.

Analytical results from ZEPHYRUS and BOOM codes and experimental data for near- and midfield ($5<r/L<85$) compare well. Some differences are mainly caused by source aircraft motion instability and/or errors in flight parameter measurement.

When determining sonic boom wave emission points during the far-field analyses, a successive iteration procedure was used.

Analytical and experimental data on sonic boom wave arrival times at the YO-3A location were compared. The difference of this value for the waves arriving from above the YO-3A ranges from 2 to 6 s. Results from ZEPHYRUS and BOOM are almost identical, with differences not exceeding 0.03 s.

The comparison of experimental sonic boom wave signatures in the far field showed satisfactory agreement with ZEPHYRUS and BOOM codes' prediction. Differences are chiefly caused by filtering the low-frequency spectral part by the microphones used as sensors on the YO-3A. This factor is seen in the overpressure profile shape: the profile gets "bow-shaped" instead of the usual N-wave. Results from ZEPHYRUS and BOOM are almost identical; the effects of energy absorption and dispersion (taken into account by ZEPHYRUS) are revealed in smoothing the extrema of the signatures.

Sonic boom waves reflected off the ground are described correctly by ZEPHYRUS. Agreement of theoretical and experimental values in this case is reasonable. The experimental information provided is insufficient to judge the level of quality of computing the waves that have run through caustic points (U-waves).

ACKNOWLEDGMENTS

This work was supported by The Boeing Company. Many thanks to Mr. Robert D. Cuthbertson and Mr. Hugh W. Poling for assistance in providing the research.

[1] L. D. Robinson, ''Sonic Boom Propagation Through an Inhomogeneous, Windy Atmosphere,'' Ph.D. dissertation, University of Texas (1991).
[2] E. A. Haering, L. J. Ehernberger, and S. A. Whitmore, ''Preliminary Airborne Measurements for the SR-71 Sonic Boom Propagation Experiment,'' in NASA High-Speed Research Program Sonic Boom Workshop, NASA Conference Publication 3335, 12–13 September 1995; published July 1996.
[3] Yu. L. Zhilin, ''Attenuation Theory of Stationary and Nonstationary Shock Waves in Inhomogeneous Media,'' Trudy TsAGI, Vol. 1094 (1967).
[4] Yu. L. Zhilin, ''Sonic Boom From Aircraft Flying Along Arbitrary Trajectory in Stratified Atmosphere with Three-component Wind,'' *Aeromechanics* (Nauka, Moscow, 1976).
[5] Yu. L. Zhilin and S. L. Chernyshev, ''Algorithm for Searching Sonic-boom Profiles,'' Trudy TsAGI, Vol. 2110 (1981).
[6] Yu. L. Zhilin and V. V. Kovalenko, ''On Matching Near-field and Far-field Solutions in Sonic Boom Problem,'' Uch. Zap. TsAGI **XXIX** (3–4) (1998).

An analysis of the response of Sooty Tern eggs to sonic boom overpressures

Carina Ting[a] and Joel Garrelick
Anteon/Cambridge Acoustical Associates, Inc., Cambridge, Massachusetts 02140

Ann Bowles
Hubbs-Sea World Research Institute, San Diego, California 92109

(Received 27 April 2000; accepted for publication 19 March 2001)

It has been proposed that sonic booms caused a mass hatching failure of Sooty Terns in the Dry Tortugas in Florida by cracking the eggshells. This paper investigates this possibility analytically, complementing previous empirical studies. The sonic boom is represented as a plane-wave excitation with an N-wave time signature. Two models for the egg are employed. The first model, intended to provide insight, consists of a spherical shell, with the embryo represented as a rigid, concentric sphere and the albumen as an acoustic fluid filling the intervening volume. The substrate is modeled as a doubling of the incident pressure. The second, numerical model includes the egg-shape geometry and air sac. More importantly, the substrate is modeled as a rigid boundary of infinite extent with acoustic diffraction included. The peak shell stress, embryo acceleration, and reactive force are predicted as a function of the peak sonic boom overpressure and compared with damage criteria from the literature. The predicted peak sonic boom overpressure necessary for egg damage is much higher than documented sonic boom overpressures, even for extraordinary operational conditions. Therefore, as with previous empirical studies, it is concluded that it is unlikely that sonic boom overpressures damage avian eggs.
[DOI: 10.1121/1.1371766]

PACS numbers: 43.80.Gx, 43.50.Pn, 43.40.Ey [MRS]

I. INTRODUCTION

It has been suggested that sonic booms caused a mass hatching failure of Sooty Terns on the Dry Tortugas, Florida.[1] Notwithstanding the circumstantial evidence, this hypothesis is often quoted as proof that sonic booms harm wildlife.[2] Empirical studies in which chicken eggs were exposed to sonic boom-like impulsive noise sources[2,3] showed no resulting eggshell damage, and in fact the hatched chicks were observed to be normal. To date no complementary analytical study has been performed to support the empirical studies. This study fills that gap by providing a mathematical analysis of the response of avian eggs to sonic boom overpressures and interpreting these response predictions to determine the potential for sonic boom overpressures to damage avian eggs.

The analysis is performed at two levels of idealization. The first model is that of a spherical elastic shell with the embryo represented as an inertial concentric sphere and the albumen as an acoustic fluid that completely fills the intervening volume. This analytical model is intended to provide verification and insight for the second, higher fidelity numerical model. The numerical model accounts for the egg shape and includes an air sac. In both models the sonic boom is taken to be an incident acoustic plane wave with the classic N-wave time signature. In order to predict the potential for sonic boom overpressures to damage avian eggs, the peak shell stress, embryo acceleration, and reactive force at the substrate upon which the egg rests are computed as a function of the sonic boom overpressure and compared with damage criteria taken from the literature.

II. ANALYSIS

A supersonic overflight produces a sonic boom that impinges on an egg resting on an effectively rigid substrate, or baffle. The basic geometry of the sonic boom impingement is sketched in Fig. 1. The overpressure is modeled as a plane acoustic wave with the classic N-wave time signature. It is incident on the egg and substrate with a propagation vector having an elevation angle, α, measured from the vertical of $\alpha=\sin^{-1}(1/M)$, where $M=U/c$ is the local mach number with U the effective flight speed of the supersonic aircraft and c the local air sound speed. In equation form this is

$$\begin{aligned} P_{\mathrm{SB}}(x,y,t) &= \frac{P_i}{2}\left[\left(1-2\frac{t'}{\tau}\right)U_s(t') + \left(1+2\frac{(t'-\tau)}{\tau}\right)U_s(t'-\tau)\right], \\ t' &= t-\frac{1}{c}[x\sin\alpha - y\cos(\alpha)], \end{aligned} \tag{1}$$

with the Fourier spectrum of the sonic boom given by

$$\tilde{P}_{\mathrm{SB}}(x,y,\omega)=\tilde{N}(\omega)P_{\mathrm{plane}}(x,y,\alpha,\omega),$$

with

$$\tilde{N}(\omega)=\frac{P_i}{2}\left[\frac{i}{\omega}[1+\exp(i\omega\tau)]+\frac{2}{\tau\omega^2}[1-\exp(i\omega\tau)]\right],$$

[a] Current address: 236 Middlebrook Dr., Fairfield, CT 06430.

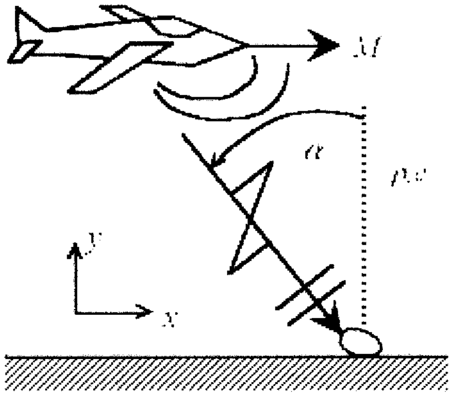

FIG. 1. Overall geometry and coordinate system for sonic boom incident on an egg resting on a rigid substrate.

and

$$P_{\text{plane}}(x,y,\alpha,\omega)=\exp(ik(x\sin\alpha-y\cos\alpha)). \tag{2}$$

In the above equation, we have assumed the harmonic time variation $\exp(+i\omega t)$, with time t and radial frequency ω. The variable $k=\omega/c$ is the acoustic wave number and τ is the duration of the sonic boom. The variable P_i represents the peak overpressure as typically measured; that is, at ground level assuming pressure doubling.

Two models of the egg are analyzed. In both cases the egg is treated as a linear system of continuous and lumped elements. The first model, used to obtain insight as well as verify the numerical results, takes the geometry to be spherically symmetric and thus separable, allowing for analytic response predictions of shell stresses and embryo accelerations, is described in Sec. A. The second, and more accurate, is numerical and includes asymmetric influences of the egg shape and air sac and the presence of a rigid substrate. It is presented in Sec. B.

A. Analytical model

The spherical analytic model of the egg is sketched in Fig. 2. The shell is treated as a thin, elastic spherical shell of radius, a and constant thickness h_s and the embryo is a rigid inertial sphere of radius a_e and mass M_e, concentric with the shell. The albumen is represented by an acoustic fluid of mass density ρ_a and sound speed c_a, that completely fills the volume between the embryo mass and the inside surface of the shell. Here, for the sake of simplicity, we maintain axisymmetry by considering only $\alpha=0$ or $M\gg 1$, i.e., high Mach number flights.

The rigid substrate upon which the analytical egg rests is assumed to have two effects. It doubles the incident pressure over the egg surface and it generates a reactive force that constrains the radial motion of the shell to be zero at $\theta=0$. This force, $\tilde{F}_R(\omega)$, is taken to be the resultant of a uniformly distributed pressure over the assumed circular contact area, $A_R=\pi a^2\Delta^2$, where Δ is one half the subtended polar angle. The solution to this problem is described below. Response function expressions are obtained in the frequency domain and, in turn, response time histories are computed numerically by taking their inverse Fourier transforms.

The harmonic equations of motion of a thin, isotropic, axisymmetric spherical shell driven by a radial pressure applied to the shell, may be expressed as[4]

$$\begin{aligned}\tilde{v}(\theta,\omega)&=\sum_{n=0}^{\infty} V_n\frac{d}{d\theta}P_n(\cos(\theta)),\\ \tilde{w}(\theta,\omega)&=\sum_{n=0}^{\infty} W_nP_n(\cos(\theta)),\end{aligned} \tag{3}$$

where the modal amplitudes V_n and W_n are given by the coupled equations

$$\begin{aligned}\begin{bmatrix}V_n\\W_n\end{bmatrix}&=\frac{-(1-v_s^2)a^2}{E_sh_s}\begin{bmatrix}a_{11}&a_{12}\\a_{21}&a_{22}\end{bmatrix}^{-1}\begin{bmatrix}0\\p_n\end{bmatrix}\\ a_{11}&=\Omega^2-(1+\beta^2)(v_s+\lambda-1)\\ a_{12}&=\beta^2(1-v_s-\lambda)-(1+v_s)\\ a_{21}&=-\lambda[\beta^2(v_s+\lambda-1)+(1+v_s)]\\ a_{22}&=\Omega^2-2(1+v_s)-\beta^2\lambda(v_s+\lambda-1)\\ \Omega&=\omega a\sqrt{\frac{\rho_s(1-v_s^2)}{E_s}},\quad \beta=\frac{h_s}{a\sqrt{12}},\quad \lambda=n(n+1),\end{aligned} \tag{4}$$

and the modal radial load is obtained from

$$p_n=\frac{(2n+1)}{2}\int_{-1}^{1}\tilde{p}(\theta,\omega)P_n(\cos\theta)d(\cos\theta), \tag{5}$$

where E_s is the shell material Young's modulus, and v_s is the Poisson's ratio, ρ_s the shell's mass density, and $P_n(\,)$ is the Legendre polynomial of order n. Vibration damping is provided by using the complex elastic modulus, $E_s\rightarrow E_s(1+i\eta_s)$, with η_s being the structural loss factor.

The total radial pressure applied to the shell consists of the external surface pressure $\tilde{p}_s(\theta,\omega)$, the internal pressure exerted by the albumen, $\tilde{p}_a(\theta,\omega)$, and the reactive pressure from the substrate interface, $\tilde{p}_R(\theta,\omega)$

$$\tilde{p}(\theta,\omega)=\tilde{p}_s(\theta,\omega)+\tilde{p}_a(\theta,\omega)+\tilde{p}_R(\theta,\omega), \tag{6}$$

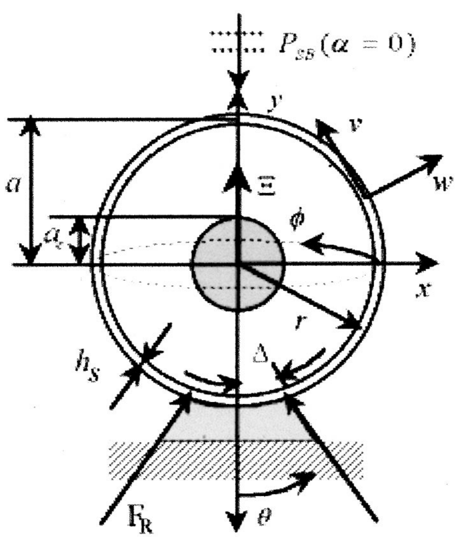

FIG. 2. Geometry, coordinate system, and degrees of freedom for spherical egg model.

with

$$\tilde{p}_R(\theta,\omega)=\tilde{F}_R(\omega)/A_R, \quad \theta<\Delta$$
$$=0 \quad \text{otherwise.} \tag{7}$$

Ignoring sound radiation from the surrounding air, the modal amplitudes of the external pressure on the sphere which is twice the incident pressure as given in Eq. (2), is[5]

$$(p_s)_n=\frac{2i}{(ka)^2}\frac{(2n+1)i^n}{h_n'(ka)}\tilde{N}(\omega), \tag{8}$$

where $h_n'(\,)$ is the derivative with respect to argument of the spherical Hankel function of the first kind of order n.

The albumen is modeled as an acoustic fluid and the internal pressure is governed by the acoustic wave equation. The modal components of the pressure in the internal fluid is

$$(p_a(r))_n=-i\omega Z_n(r,\omega)W_n, \quad a<r<a_e \tag{9}$$

where the modal impedance Z_n has a solution of the form

$$Z_n(r,\omega)=a_n j_n(k_a r)+b_n y_n(k_a r), \tag{10}$$

where $j_n(\,)$ and $y_n(\,)$ are spherical Bessel functions of order n, of the first and second kind, respectively, and $k_a=\omega/c_a$. The modal coefficients a_n and b_n are defined by enforcing continuity of radial displacement with the shell at $r=a$ and with the rigid spherical mass at $r=a_e$. The solution is

$$\begin{bmatrix} a_n \\ b_n \end{bmatrix}=\begin{bmatrix} j_n'(k_a a) & y'(k_s a) \\ (j_n'(k_a a_e)-i\rho_a c_a j_n(k_a a_e)Y_n) & (y_n'(k_a a_e)-i\rho_a c_a y_n(k_a a_e)Y_n) \end{bmatrix}^{-1}\begin{bmatrix} i\rho_a c_a \\ 0 \end{bmatrix}, \tag{11}$$

where Y_n is the translational admittance of the mass, given as

$$Y_{n=1}=-i\frac{4\pi a_e^2}{3\omega M_e}, \quad Y_{n\neq 1}=0. \tag{12}$$

To obtain the modal coefficients of the internal surface pressure of the shell, Eq. (9) is evaluated at $r=a$.

The modal coefficients of the support pressure at the substrate are obtained from Eq. (5) as

$$(p_R)_n=\frac{(2n+1)\tilde{F}_R(\omega)/A_R}{2(n+1)} \times[P_{n-1}(\cos\Delta)-\cos\Delta P_n(\cos\Delta)]. \tag{13}$$

It remains to solve for the value of $\tilde{F}_R(\omega)/A_R$ that enforces the boundary condition

$$\tilde{w}(\theta=0,\omega)=0. \tag{14}$$

Using Eqs. (4), (9), (13), and (14), this reaction force becomes

$$(\tilde{F}_R(\omega)/A_R)=-\frac{\displaystyle\sum_{n=0}^{\infty}\frac{a_{12}(p_s)_n}{\bar{D}}}{\displaystyle\sum_{n=0}^{\infty}\frac{a_{12}(p_R)_n}{\bar{D}}},$$

with

$$\bar{D}=a_{11}a_{22}-a_{12}\left(a_{21}-\frac{i\omega(1-v_s^2)a^2}{E_s h_s}Z_n(r=a,\omega)\right). \tag{15}$$

The solution for the shell displacements may now be obtained via substitution of Eqs. (8), (9), and (15) into Eqs. (4) and (6). The associated shell stresses are completely defined by these displacements and are provided by Timoshenko[6] with some modification of the coordinate system.

Finally, the vertical embryo acceleration is given by

$$\tilde{\ddot{\Xi}}=-\omega^2 Z_a^{n=1}(r=a_e,\omega)Y_{n=1}W_{n=1}. \tag{16}$$

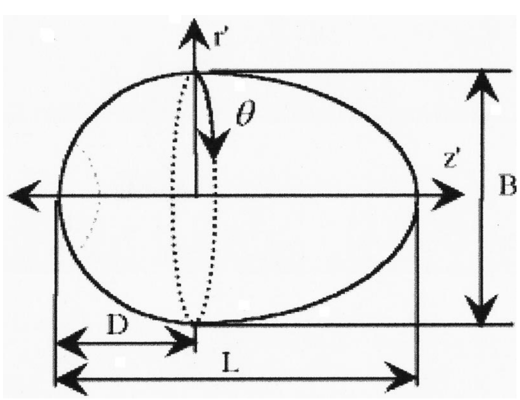

FIG. 3. Geometry and coordinate systems, for numerical egg model.

B. Numerical model

With this model, the geometry of the eggshell is treated with geometric fidelity and the air sac is represented along with the albumen and embryo. As before, the shell is modeled as thin and linearly elastic and is capable of both membrane and flexural stresses. However, now the embryo and air sac as well as the albumen are modeled as acoustic media. The model was solved numerically, using the cosmic Nastran finite-element analysis direct frequency solution. The eggshell is developed from QUAD4 bending and membrane plate elements. Acoustic fluid elements represent the albumen, egg yolk, and air sac. The acoustic elements were created using HEX6 solid elements with material properties set to simulate an acoustic behavior.[8] Consistent with the literature,[7] the shell geometry is characterized as a composite ellipsoid described in Fig. 3. The finite-element mesh is shown in Fig. 4. A mesh convergence was not performed, given the difficulty of specifying a simply supported boundary condition with the same equivalent contact area with a

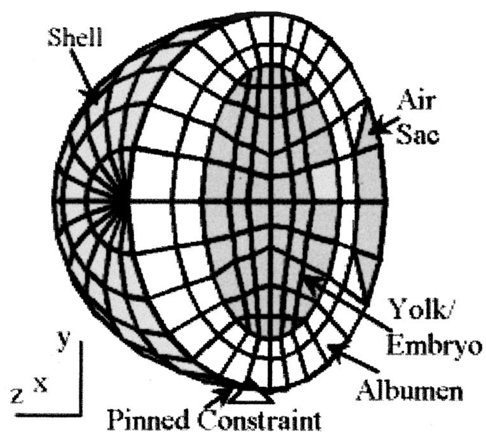

FIG. 4. Sketch showing finite-element mesh for the numerical egg model.

finer mesh. It was assumed that the mesh was adequate because meshing guidelines for the frequency range studied were used and there was good agreement between the numerical and analytical results.

The egg is positioned on the substrate so that the height of its center of mass is minimized. The substrate itself is taken to be rigid, and radiation loading on the egg is ignored. The surface pressure acting on the eggshell was computed for a plane wave incident on the egg in the presence of the rigid planar boundary using the computer code NASHUA.[9] The elastic egg is constrained such that there are zero shell displacements at the single shell–substrate interface node. The resulting reaction force vector is interpreted to be a uniformly distributed pressure, acting over the average of the areas of the elements adjacent to the constrained node.

III. NUMERICAL RESULTS

A. Model input parameters

In this section we describe the input parameters for our models. For a given air sound speed, which we take as 330 m/s, the sonic boom, represented as an N wave, is fully defined by the peak pressure and duration. Further, since all our models are linear, all response functions may be computed for a unit peak pressure and scaled accordingly. For the sonic boom duration, τ, we take 0.15 s, a representative value for U.S. Air Force fighter aircraft. Two incident elevation angles are considered, $\alpha = 0°$ and 56°, the latter simulating an overflight of roughly Mach 1.2.

Published data[10] indicate the basic structure and dimensions for eggs of a variety of bird species, including the Sooty Tern, are similar to those of common chicken eggs, for which there are a number of published sources of measured physical properties. Accordingly, the material and geometric parameters that we have chosen for our study are based on chicken egg data.[7] These parameters are summarized in Tables I and II.

TABLE I. Material properties for egg models.

Description	Symbol	Value
Shell elastic modulus	E_s	1.1×10^{11} Pa
Shell Poisson's ratio	v_s	0.3
Shell mass density	ρ_s	2000 kg/m^3
Shell loss factor	η_s	0.01
Albumen mass density	ρ_a	1000 kg/m^3
Albumen speed of sound	c_a	1500 m/s
Yolk mass density	ρ_y	1100 kg/m^3
Yolk speed of sound	c_y	1500 m/s

TABLE II. Egg dimensions.

Description	Symbol	Value
Thickness of shell	h_s	3.6 mm
Length of shell	L	5.7 cm
Largest breadth of shell	B	4.2 cm
Distance from largest breadth to blunt End	D	2.5 cm
Radius of spherical shell	a	2.3 cm
Radius of yolk/embryo	a_e	1.5 cm
Area of contact	A_R	0.15 cm^2

The elastic modulus of the shell is subject to considerable uncertainty, with values in the literature ranging from 1×10^{10} to 29×10^{10} Pa[11,12] The value chosen, which falls within this range, is consistent with values computed from ultrasonic measurements of the compressional wave speed commissioned for this study ($c_s = 6900$ m/s) and the measured shell density, using $E = \rho c^2$. For our spherical model the radius, a, was chosen by equating the sphere volume to that of the egg. The area of contact was chosen to be less than what we measured for a chicken egg resting on compacted sand (7.7 cm^2). The mass density of the albumen was measured directly, and its speed of sound was taken from the literature.[13] The properties of the embryo were assumed to be equivalent to that of a yolk, the mass density of which was measured directly and the speed of sound obtained from the literature.[13]

B. Egg failure criteria

Peak eggshell stress and peak embryo acceleration are chosen as our primary damage metrics. The corresponding failure criteria, that is, maximum allowable levels, are shown in Table III. As with the elastic modulus there is a good deal of spread in the published data for the ultimate eggshell stress. To err on the conservative side, the value of 1.2×10^7 Pa is the lowest reported in Voisy and Hunt,[11] where values between 1.2×10^7 and 5.6×10^7 are presented. The maximum embryo acceleration listed is taken from Blesch.[14] In this reference, experiments are described that indicate egg yolks subjected to the listed acceleration over a 1.5-ms period yield no damage on the cellular level. The duration is appropriate since, as will be seen, the computed embryo acceleration is a damped oscillatory motion with a period on the order of 1 ms.

TABLE III. Egg failure criteria.

Description	Value
Ultimate stress of shell	1.2×10^7 Pa
Maximum embryo acceleration	988.0 g (1.5-ms duration)
Force to break chicken egg	3.2 N

Finally, as a result of our study, a third failure criterion is proposed in Table III. It is the maximum allowable concentrated radial force that may be applied to the egg. During eggshell failure tests conducted for this study by the Department of Plastics Engineering at the University of Massachusetts at Lowell, it was found that egg failure correlated well with the force applied by the testing machine. It is therefore proposed as a more robust failure metric than ultimate stress. The value shown in Table III should be conservative because the eggs were placed between rigid platens for the tests, thus minimizing the area of contact, and in turn maximizing the stress.

C. Response predictions

In this section we present computed response predictions for our numerical model, with those from our analytical model to provide insight. The maximum flexural stress at the substrate interface is found to be the predominate stress. The embryo acceleration, Ξ, and the substrate reactive force on the egg, F_R, are also presented. All results are normalized to P_i, twice the value of the free-field peak overpressure to simulate the practice of referring to the strength of the sonic boom as that measured at ground level, as noted previously.

1. Analytical sphere model

Time histories computed for the shell stress, embryo acceleration, and substrate reactive force for the spherical egg described in Sec. II A are shown in Fig. 5. All three signatures suggest the response of a damped oscillator impulsively excited at $t=0$ and $t=1.5$ ms, the initiation and termination times of the N wave. (Although not readily apparent in the figure, the oscillations correspond to a frequency of 1040 Hz.) To pursue this notion further, consider a single degree of freedom, lumped parameter, damped oscillator. For the oscillator mass, M, we take the total mass of the egg. The spring stiffness is estimated as the local stiffness of the spherical shell statically loaded by a uniform radial pressure over a circular cap of area $A_R \ll 2ah_s$ (Ref. 15)

$$K \approx \frac{E_s h_s^2}{a}\left[0.42-0.116\frac{A_R}{ah_s}+0.023\left(\frac{A_R}{ah_s}\right)^2\right]^{-1}. \tag{17}$$

The dashpot constant B is estimated as $B=\eta K/\omega_0$, where ω_0 is the natural frequency of the oscillator. For the parameters provided in Tables I and II we predict a natural frequency of 980 Hz, comparing favorably with the 1040-Hz oscillations observed in Fig. 5.

Continuing with this simplified model, and assuming that the egg is small in terms of acoustic wavelength in air ($ka \ll 1$), the net translational force applied to the shell by twice the incident wave pressure becomes

$$\tilde{F}_{\text{egg}}(\omega) \approx i\omega\frac{2\pi a^3}{c_0}2\tilde{P}_{\text{SB}}(x=0,y=0,\omega), \tag{18}$$

which has the time signature of

$$F_{\text{egg}}(t)=\frac{2\pi a^3}{c}\frac{d}{dt}(2P_{\text{SB}}(x=0,y=0,t)),$$

where the location (x,y) is arbitrarily chosen to be (0,0). The solution to this forced problem is readily obtained. The reaction force, the force stored in the spring, K, is

$$\begin{aligned}F_R(t)=P_i\frac{2\pi a^3\omega_0}{c}\Big[&U_s(t)\exp\left(-\frac{\eta_s}{2}\omega_0 t\right)\sin\omega_0 t\\&+U_s(t-\tau)\exp\left(-\frac{\eta_s}{2}\omega_0(t-\tau)\right)\sin\omega_0(t-\tau)\Big],\\&\omega_0 a/c\ll 1,\quad \omega_0\tau\gg 1.\end{aligned} \tag{19}$$

The associated maximum stress in a thin spherical shell subject to a reaction force is[15]

$$\sigma_\theta(z=h_s/2,\theta=0)\approx\frac{F_R(t)}{h_s^2}\left[0.42-0.282\ln\left(\frac{A_R}{ah_s}\right)\right],\quad A_R<2ah_s. \tag{20}$$

The corresponding acceleration of the embryo and the entire egg is

$$\begin{aligned}\Xi(t)\approx P_i\frac{2\pi a^3\omega_0}{M_{\text{egg}}c}\cdot\Big[&U_s(t)\exp\left(-\frac{\eta_s}{2}\omega_0 t\right)\sin(\omega_0 t)\\&+U_s(t-\tau)\exp\left(-\frac{\eta_s}{2}\omega_0(t-\tau)\right)\\&\times\sin(\omega_0(t-\tau))\Big],\quad \omega_0 a/c\ll 1,\quad \omega_0\tau\gg 1.\end{aligned} \tag{21}$$

The agreement is good between predictions using the expressions in Eqs. (19), (20), and (21), and that from the full analytical model is good. The solution has the same charac-

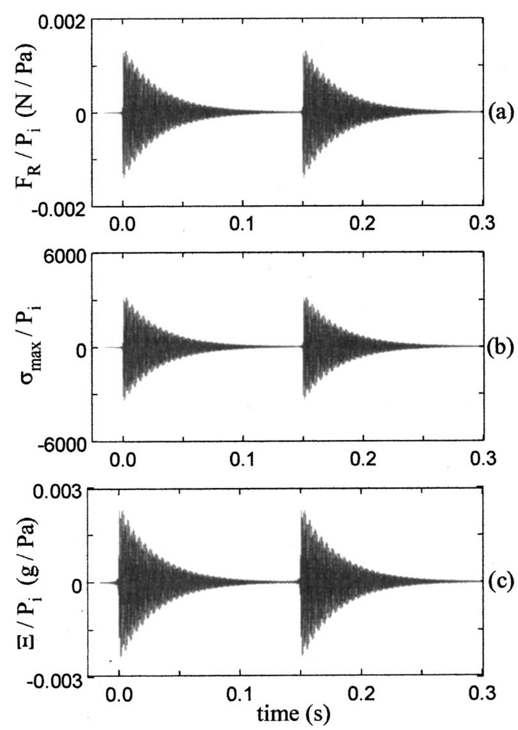

FIG. 5. Calculated response time histories to unit N-wave excitation from $\alpha=0$ sonic boom for analytic spherical egg model with assumed pressure doubling modeling the substrate. (a) reaction force at substrate; (b) peak stress; (c) embryo acceleration.

ter, and the difference between the lumped parameter peak stresses is within 17% of the full analytical model.

2. Numerical finite-element model

Before computing response time histories with the numerical model, a modal analysis of the model was performed. Consistent with our previous discussion, the fundamental frequency of the modeled egg with the point pinned boundary constraint was computed to be 960 Hz, with a mode shape indicative of the egg mass translating as a rigid body with elastic deformation limited to the immediate vicinity of the substrate constraint. The air sac and embryo do not seem to play any role, other than to affect the total mass of the egg.

To compare the numerical results with those from the analytical model, we initially consider the case with $\alpha=0$. First, for diagnostic purposes, we model the substrate as a doubling of the incident pressure field and a constraint, as was done for the analytical, spherical shell model. Although not presented here, the predictions are quite similar to the earlier predictions obtained for the analytical sphere and lumped parameter model described previously. The maximum shell stress is predicted to be slightly higher than that for the analytical sphere model, which may be attributed to the larger radius of curvature at the substrate–shell interface.

However, the nature of the time signatures for the egg response changes quite considerably when the full, most accurate model of the rigid substrate is employed. In this treatment, rather than the *a priori* doubling of the incident pressure, we account fully for the diffractive and reflective effects of the substrate. These results are shown in Fig. 6,

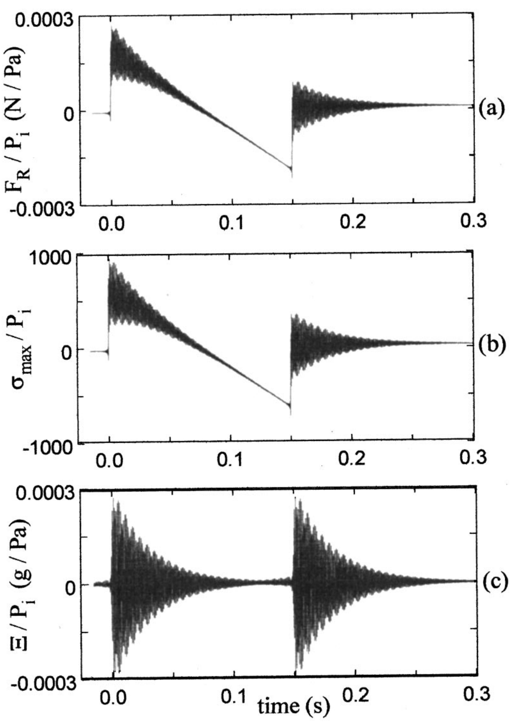

FIG. 6. Calculated response time histories to unit N-wave excitation from $\alpha=0$ sonic boom for numerical egg model with rigid baffle modeling the substrate. (a) reaction force at substrate; (b) peak stress; (c) embryo acceleration.

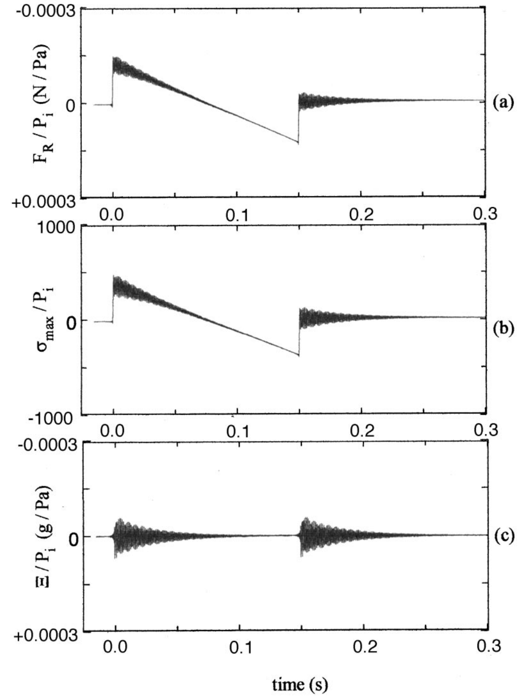

FIG. 7. Calculated response time histories to unit N-wave excitation from $\alpha=0$ sonic boom for numerical egg model with rigid baffle modeling the substrate. (a) reaction force at substrate; (b) peak stress; (c) embryo acceleration.

again with $\alpha=0$. The peak levels are observed to be significantly lower than those for the previous substrate model and the time signatures more closely resemble that of the incident N wave. For insight into this outcome, we can return to the simple lumped parameter model described earlier. The oscillator mass was driven by a net translational force produced by the $n=1$ modal component of the incident plane pressure wave evaluated at the shell surface in the analytical model. However, with the presence of the rigid substrate, the wave reflected from it propagates in the opposite direction. For the long acoustic wavelengths of interest, that is where the breadth of the egg, B, is much smaller than the acoustic wavelength, λ, this reduces the net translational force acting on the egg from the order of B/λ to $(B/\lambda)^2$.

Finally, in Fig. 7, we present results for the egg response with the full substrate model to an incident sonic boom with a more realistic $\alpha=56°$ and note that the predicted levels are roughly 50% of those predicted for $\alpha=0$.

IV. CONCLUSIONS

From Table IV we see that no damage is predicted with any of our response metrics, until the sonic boom overpressure reaches 12 000 Pa (250 psf). At this value, the reaction

TABLE IV. Peak overpressures required to cause failure.

Failure metric	P_i, Pa (psf) $\alpha=0°$, $M=\infty$	P_i, Pa (psf) $\alpha=56°$, $M=1.2$
Shell stress	1.3×10^4 (270)	2.6×10^4 (530)
Embryo acceleration	3.7×10^6 ($7.6\ 10^4$)	1.7×10^7 (3.6×10^5)
Reaction force	1.2×10^4 (250)	2.18×10^4 (460)

force may exceed its maximum tested value. Embryo accelerations are of acceptable level until the overpressure reaches much higher values. It is suggested that these values are conservative, as a result of the chosen damage criteria and presumed small shell–substrate contact area as well as the assumption of worst case $\alpha=0$ (corresponding to infinite Mach number).

Supersonic operations within military operating areas typically generate overpressures that are of considerably lower levels. For example, in 1992 an extensive sonic boom monitoring program was carried out in connection with a training program, primarily within the Elgin Military Operating Area near Caliente, Nevada.[16] Approximately one thousand missions were flown during the training period, the majority of the sorties with F-15 and F-16 aircraft. Monitoring sites were scattered throughout the area. The maximum peak overpressure recorded at any site was 910 Pa (19 psf). Another example was the controlled focused measured boom measurement study at Edwards AFB in 1994.[17] Here, the maximum recorded overpressure of 1000 Pa (21 psf) was generated by an aircraft in level acceleration about 2100 meters (7000 ft) above the ground.

Higher sonic boom levels are possible under highly unusual conditions. For example, sonic booms were recorded from F-4C aircraft flying low-level terrain-following profiles during Joint Task Force II operations at the Sandia Corporation Test Range near Topah, Nevada in 1968. The maximum peak overpressure was 6900 Pa (144 psf) for a flight at Mach 1.26 with a ground clearance of 29 meters (95 ft).[18] This is the highest recorded overpressure known to the authors. Yet even here, comparing this overpressure to that required for failure with $\alpha=56°$, we predict no failure with a safety factor of 3.2. Thus, we conclude that, even under the most extraordinary circumstances, sonic boom overpressures from practical aircraft maneuvers do not pose a potential threat of damage to avian eggs.

ACKNOWLEDGMENTS

The authors gratefully acknowledge the Armstrong Laboratory of Wright Patterson Air Force Base for their financial support, and Dr. Micah Downing for providing invaluable technical assistance and insight.

[1] O. L. Austin, Jr., W. B. Robertson, Jr., and G. E. Woolfender, ''Mass Hatching Failure in Dry Tortugas Sooty Terns,'' Proc. Int. Ornithological Cong. 15:627, 1970.

[2] A. E. Bowles, F. T. Aubrey, and J. R. Jehl, ''The effect of high amplitude impulsive noise on hatching success. A reanalysis of the Sooty Tern Incident,'' Noise and Sonic Boom Impact Technology Program, OL-AC HSD/YAH (NSBIT) Report #HSD-TP-91-0006, 1991.

[3] A. E. Bowles, M. Knobler, and M. E. Seddon, ''Effects of Simulated Sonic Booms on the Hatchability of White Leghorn Chicken Eggs,'' Occupational and Environmental Health Directorate, AL/OE-TR-1994-0179, 1994.

[4] M. C. Junger and D. Feit, *Sound, Structures, and Their Interaction* (The MIT Press, Cambridge, MA, 1972).

[5] Reference 4, p. 319.

[6] S. Timoshenko and S. Woinowsky-Krieger, *Theory of Plates and Shells* (McGraw-Hill, New York, 1959).

[7] A. L. Romanoff and A. J. Romanoff, *The Avian Egg* (Wiley, New York, 1969).

[8] G. C. Everstine, F. M. Henderson, and R. R. Lipman, ''Finite Element Prediction of Acoustic Scattering and Radiation from Submerged Elastic Structures,'' Nastran Users Colloquium, 1987.

[9] G. C. Everstine, and F. M. Henderson, ''Coupled Finite Element/Boundary Element Approach for Fluid–Structure Interaction,'' J. Acoust. Soc. Am. **87**, 1938–1947 (1990).

[10] D. F. Hoyt, ''Practical Methods of Estimating Volume and Fresh Weight of Bird Eggs,'' The Auk 96: 73–77 (1979).

[11] P. W. Voisy and J. R. Hunt, ''Review Paper: Measurement of Eggshell Strength,'' J. Texture Stud. **5**, 135–182 (1974).

[12] J. Lin, V. M. Puri, and R. C. Anantheswaran, ''Measurement of Eggshell Thermal-Mechanical Properties,'' Trans. ASAE **00001-2351/95/3806-1769**, (1995).

[13] C. Javanaud, R. R. Rahalkar, and P. Richmond, ''Measurement of Speed and Attenuation of Ultrasound in Egg White and Egg Yolk,'' J. Acoust. Soc. Am. **76**, 670–675 (1984).

[14] E. L. Besch, ''Morphological Changes in Avian Eggs Subjected to Accelerative Force,'' J. Appl. Physiol. **20**(6), 1241–1248 (1965).

[15] R. J. Roark, *Formulas for Stress and Strain* (McGraw-Hill, New York, 1954).

[16] K. D. Frampton, M. J. Lucas, and K. J. Plotkin, ''Measurements of Sonic Booms Due to ACM Training in the Elgin MOA Subsection of the Nellis Range Complex,'' Wyle Research Report WR 93-5, prepared for the Douglas Aircraft Company, 1993.

[17] M. Downing, N. Zamot, D. Morin, E. Wokki, S. Chung, K. Plotkin, and D. Maglieri, ''Controlled Focused Sonic Booms from Maneuvering Aircraft,'' J. Acoust. Soc. Am. **104**, 112–121 (1998).

[18] C. W. Nixon, H. K. Hille, H. C. Sommer, and E. Guild, ''Sonic Booms resulting from Extremely Low-altitude Supersonic Flight: Measurements and Observations on Houses, Livestock, and People,'' AMRL-TR-69-52, October, 1968.

Sonic booms of space shuttles approaching Edwards Air Force Base, 1988–1993

Robert W. Young
710 West 13th Avenue, Escondido, California 92025-5511

(Received 1 July 2001; revised 21 September 2001; accepted 1 October 2001)

From 1988 to 1993 13 sonic booms of space shuttles approaching Edwards Air Force Base were measured at a site 10 miles west of EAFB, with one to seven different sound level meters for each measurement. Results from five of these measurements are here presented. Maximum differences in measured levels between instruments for the same flight varied from 0 to 6 dB depending on the measurement descriptor and model of sound level meter. The average difference between predicted and measured values was 0.7±1.5 dB. For sound level meters with adequate bandwidth the waveforms measured varied from a near perfect N-wave to a more distorted form reflecting the influence of the varying condition of the atmosphere during propagation to the ground. [DOI: 10.1121/1.1420182]

PACS numbers: 43.28.Mw, 43.50.Lj [LCS]

I. INTRODUCTION

From 1988 to 1993 the author measured 13 of the sonic booms generated during landings of the Space Shuttle at Edwards Airforce Base (Young, 1998). Results of five of these measurements are presented. In Sec. II we describe the close-in flight paths of the Shuttle during landing phase, in Sec. III we describe the waveform and sound exposure spectrum, and in Sec. IV we describe the C- and A-weighted measurements and the predicted values for the C-weighted descriptors. Section V provides a short summary.

II. TRACKS AND PATHS OF SPACE SHUTTLES

Space shuttle Columbia, approaching landing at Edwards Air Force Base in California on 10 December 1990, passed almost directly over six microphones on the ground at latitude 34.8784° north, longitude 118.0354° west of Greenwich. The microphone position, marked by a + sign in Fig. 1, is about 10 miles west of Edwards. The ground there is about 800 m (2600 ft) above sea level. The ‘‘square-on-a-corner’’ symbol marks the origin from which the sonic boom expanded.

Dots along the track mark Columbia’s position every 15 s. As it slowed, dots are spaced closer together, up to landing on concrete Runway 22. The dot marked 0549Z identifies a reference ZULU (Greenwich) time. By the original radar and theodolite tables for every second supplied by Edwards Air Force Base, Time-Space Information Division (Marion Doran), one can find the latitude, longitude, altitude, and Mach number of Columbia.

A pseudo three-dimensional plot of one of the landings is given in Fig. 2. At 054900Z Columbia was 19.8 km (67.6 kft) above sea level, gliding at Mach 1.65. At 054922Z, Columbia was gliding at Mach 1.41, 17.7 km (58 kft) above ground, almost directly over the microphones.

Figure 3 shows the track of Atlantis approaching Edwards Air Force Base on 6 December 1988, landing on the 40 000-ft Runway 17. Dots connected by lines mark the position of Atlantis every 15 s. When Atlantis was starting its helical descent, the slant range was about 91 kft from shuttle to the cluster of microphones on the ground at the location marked by a plus sign at the lower left of the figure.

Figure 4 shows the path of Atlantis in pseudo-three dimensions. At the point at the top of the box, Atlantis was moving at Mach 1.44, altitude 65.5 kft above ground. Six minutes later Atlantis came to a stop on Runway 17.

III. WAVEFORM DESCRIPTION AND SOUND EXPOSURE SPECTRUM

As shown in Fig. 5 the sonic boom waveform of Columbia on 10 December 1990 was an almost ideal N-wave of duration near 400 ms. This reflects the fact that the measurement systems have the required bandwidth to register the true wave form of the transient signal (Crocker and Sutherland, 1968). The absolute positive and negative peak overpressure was 104 Pa (2.2 psf); the corresponding peak flaT sound pressure level is 134.3 dB.

Figure 6 shows the sonic boom overpressure waveform of the Atlantis flight on 6 December 1988. The positive peak overpressure was 57 Pa; the corresponding peak flaT sound pressure level PKT=129 dB. The negative peak overpressure was −40 Pa, corresponding to PKT=126 dB. Although the general wave shape was also a near-classical N-wave, there is an asymmetrical spike at the beginning of the ‘‘N-wave’’ which is followed by a smaller wave of perhaps one-tenth the initial amplitude. The duration of the N wave was 394 ms.

An efficient way to describe both magnitude and duration of a sonic boom (or any other transient sound) is to report its sound exposure level in an identified frequency band or bands. Sound exposure level is a level of a time integral of squared instantaneous sound pressure. Integration time need not be reported. For a theoretical N-wave of peak overpressure 104 Pa and duration 400 ms, the flaT sound exposure level is 125.6 dB.

Figure 7 shows by light wiggly lines near 0.25 Hz the sonic boom spectrum of Columbia landing of 10 December

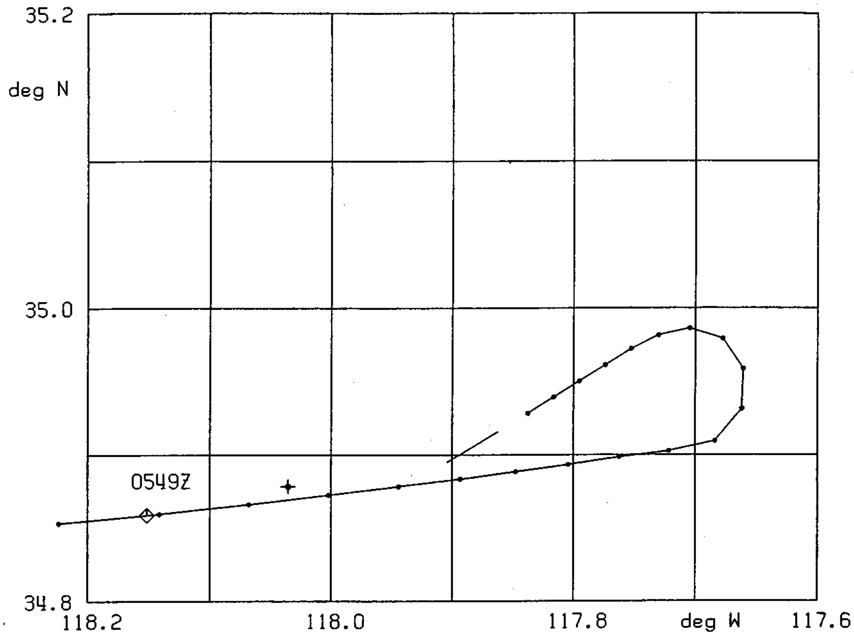

FIG. 1. Columbia track, 10 December 1990. (diamond), boom origin. (+), microphone.

1990. The ordinate is sound exposure spectrum level, abbreviated 1-Hz TSEL, for 1-Hz band flaT sound exposure level. The frequency scale is logarithmic to 100 Hz; the analysis bandwidth is 0.25 Hz. The characteristic spacing of the peaks in the frequency spectrum is 1/(Duration) or 2.54 Hz for the duration of 394 ms.

Superimposed on the basic plot of Fig. 7 is a theoretical overlay for sound exposure spectrum level of an ideal N-wave (Young, 1986; Sutherland *et al.*, 1990). The overlay grid consists of dots; at the upper right the 70-dB dotted line is marked 70; one frequency is labeled 10 Q, the Q being added to identify "theoretical."

An equation for the sound exposure spectrum level at a frequency f (in Hz) is given by

$$L_{\mathrm{E}}(f)=L_{pk}+10\,\lg\{[2/(\pi f)^2] \times|\sin(\pi fT)/(\pi fT)-\cos(\pi fT)|^2\}. \quad (1)$$

The calculated overlay in light dotted lines is for an N-wave of duration $T=100\,\mathrm{ms}$ and peak overpressure, L_{pk}, of 1 Pa (peak sound pressure level 94.0 dB).

To the extent of nine peaks in the spectrum in Fig. 7, the overlay matches experimental data very well, after the log scales are shifted for duration and peak pressure. The spectral peaks are spaced $2.5\,\mathrm{Hz}=1/T$. At $f=1$ Hz on the experimental plot, the sound exposure spectrum level (1-Hz SEL) read from the graph was 120 dB. When $L_E(f)=120\,\mathrm{dB}$, $f=1\,\mathrm{Hz}$, and $T=400\,\mathrm{ms}$ are substituted in Eq. (1), $L_{\mathrm{pk}}=133.9\,\mathrm{dB}$. This is in reasonable agreement with a peak sound pressure level 134.3 dB that is deduced from Fig. 7.

Figure 8 is a plot of the sound exposure spectrum level of the N-wave of Fig. 7, but now extended to 1000 Hz. The bin width and spacing are nominally 1000 Hz/800=1.25 Hz. The smoothly rounded curve of Fig. 7 in the vicinity of 2 Hz is now represented by a jagged curve in Fig. 8, with only two points per 2.5-Hz spacing in spectral peaks. A slight difference between the fundamental frequency of the N-wave, 1/400 ms=2.5 Hz, and the sampling frequency of the discrete Fourier transform may lead to the near cancellation of the spectral peaks in the vicinity of 300 Hz (see Fig. 7). At lower frequencies, the negative slope of the spectrum is 6 dB/oct as required by Eq. (1).

IV. C- AND A-WEIGHTED DESCRIPTORS

A. C-weighted overpressure

Figure 9 shows the overpressure waveform from Fig. 6 of the Atlantis (6 December 1988) sonic boom with the C-weighting weighting of the standard sound level meter.

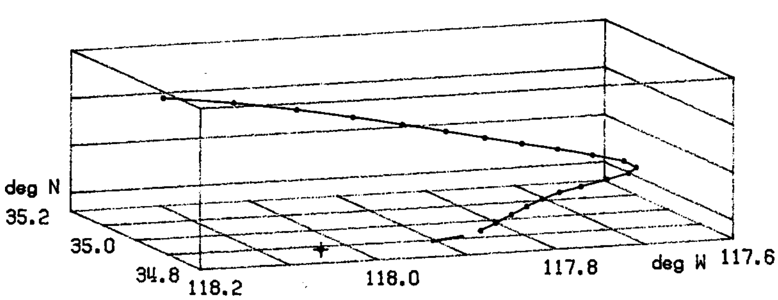

FIG. 2. Columbia path, 10 December 1990.

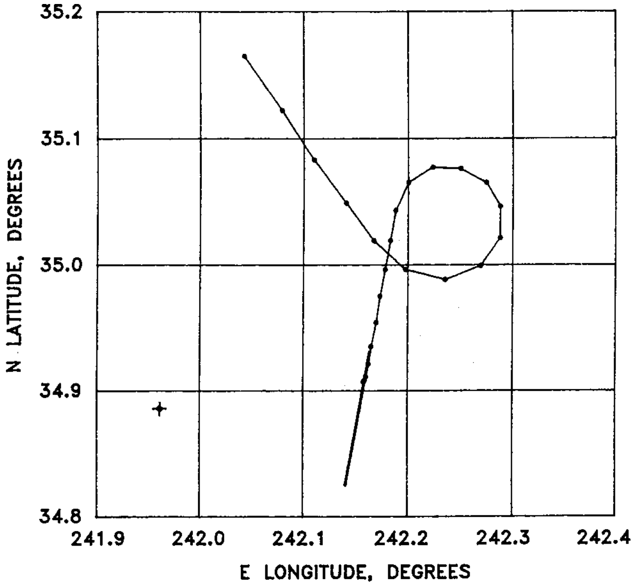

FIG. 3. Atlantis track, 6 December 1988.

The C-weighting no longer provides the necessary bandwidth to retain the true waveform of the sonic boom. The resulting waveform shows two very similar, mostly positive spikes, in place of a near-ideal-positive-negative N-wave. The duration between spikes is 394 ms.

The original overpressure wave was sensed by a Brüel & Kjaer Type 4147 microphone feeding a B&K Type 2631 microphone carrier system probably down 3 dB at 0.01 Hz and 10 kHz. The nominal C-weighting is flaT throughout much of the audio range, with roll-offs of −3 dB at 31.5 Hz and at 8 kHz. Since the usual Fourier analyzer does not include a C-weighting, for this investigation, the signal was routed through the C-weighting of a B&K Type 2230 sound level meter.

As can be seen in Fig. 9, the initial peak C-weighted overpressure for Atlantis was 37 Pa. The corresponding peak C-weighted sound pressure level is 125.4 dB. This is only 4 dB less than the peak flaT sound pressure level of the original N-wave.

B. C-weighted sound exposure spectrum level

Figure 10 shows the Atlantis C-weighted sound exposure spectrum level (1-Hz CSEL) up to 400 Hz. The analysis was performed by a Spectral Dynamics 380-13-13-5 FFT Signal Analyzer, set for 400 lines (bins) in the 400-Hz analysis band, resulting in a nominal bin width and spacing of 1 Hz. In view of the sonic boom duration of 394 ms, the fundamental frequency and spacing of peaks in the spectrum is 1.0 Hz. As a consequence, the spectrum in Fig. 10 lacks the detailed shape shown earlier in Fig. 7.

When Atlantis was descending at Mach 1.4 at an altitude of 17.7 km almost directly over the microphones, the C-weighted sound exposure level of the sonic boom

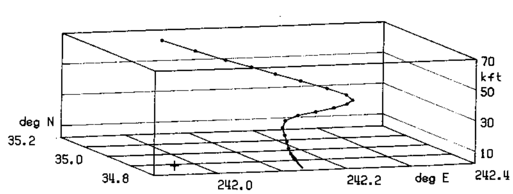

FIG. 4. Atlantis path, 6 December 1988.

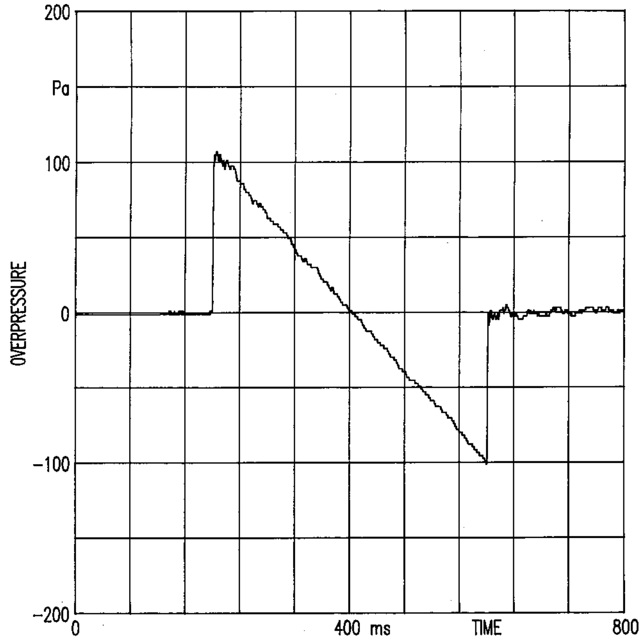

FIG. 5. Sonic-boom waveform of Columbia, 10 December 1990, 215007U, N-duration 400 ms; 800-ms time window. Positive peak flaT overpressure 104 Pa (2.2 psf); corresponding peak flaT sound pressure level, PKT=134.3 dB.

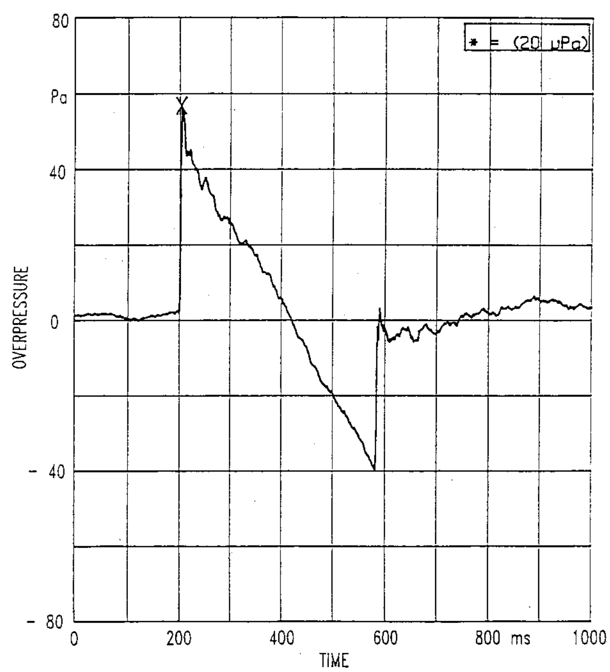

FIG. 6. Sonic-boom waveform of Atlantis, 6 December 1988, 153312U; N-duration, 394 ms; 1000 m time window. Positive peak flaT overpressure 57 Pa (1.2 psf); corresponding peak flaT sound pressure level=129 dB.

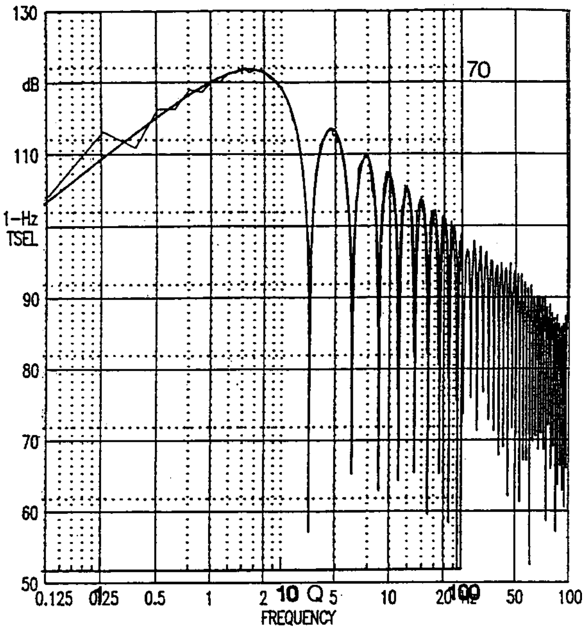

FIG. 7. Flat sound exposure spectrum level to 100 Hz of Columbia, 10 December 1990.

was 89 dB. Figure 10 shows that the maximum C-weighted sound exposure spectrum level falls roughly in the vicinity of 20 Hz.

C. A-weighted overpressure

The A-weighting of the standard sound level meter causes a response somewhat like that of the ear. The greatest sensitivity is in the vicinity of 3 kHz. Relative to response at 1 kHz, the response is −39.4 dB at 31.5 Hz and −2.5 dB at 10 kHz.

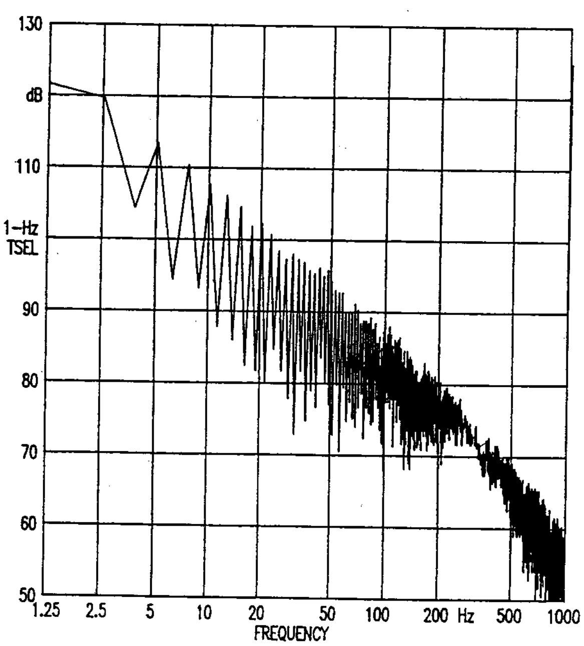

FIG. 8. Flat sound exposure spectrum level to 1000 Hz of Columbia, 10 December 1990.

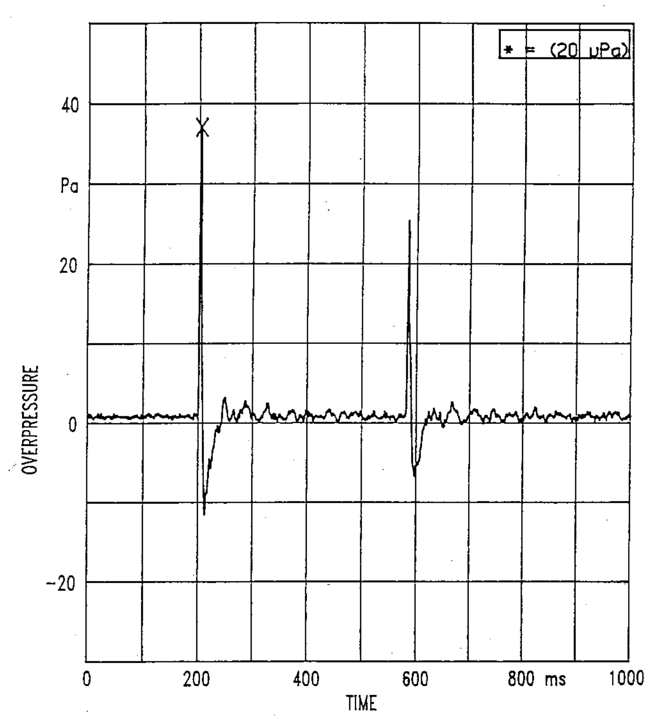

FIG. 9. C-weighted waveform of Atlantis sonic boom, 6 December 1988; 1000-ms time window. Peak overpressure +37 Pa (+0.8 psf); corresponding peak C-weighted sound pressure level=125.4 dB.

Figure 11 illustrates how the A-weighting transforms an original N-wave to brief initial and terminal spikes. The peak overpressure was 28 Pa; the corresponding peak A-weighted sound pressure level is 123 dB.

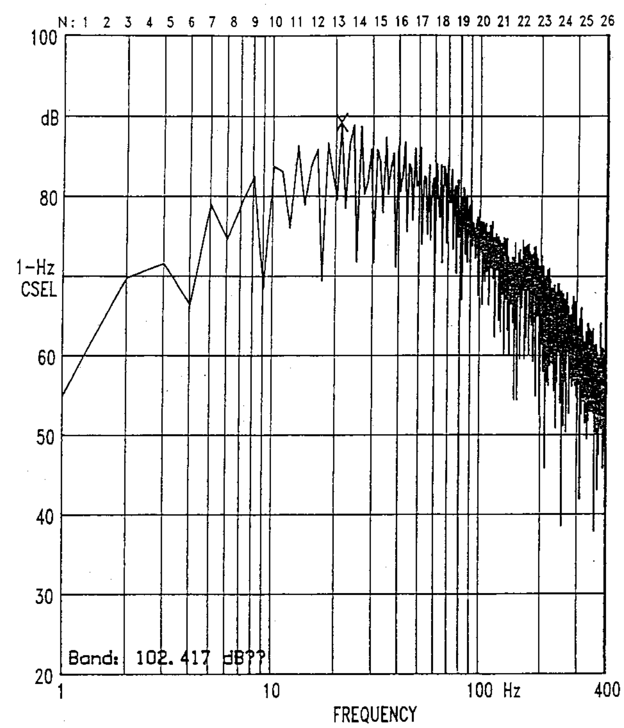

FIG. 10. C-weighted sound exposure spectrum level of Atlantis initial transient, 6 December 1988, analysis bandwidth, 1 Hz, CSEL=102.4 dB.

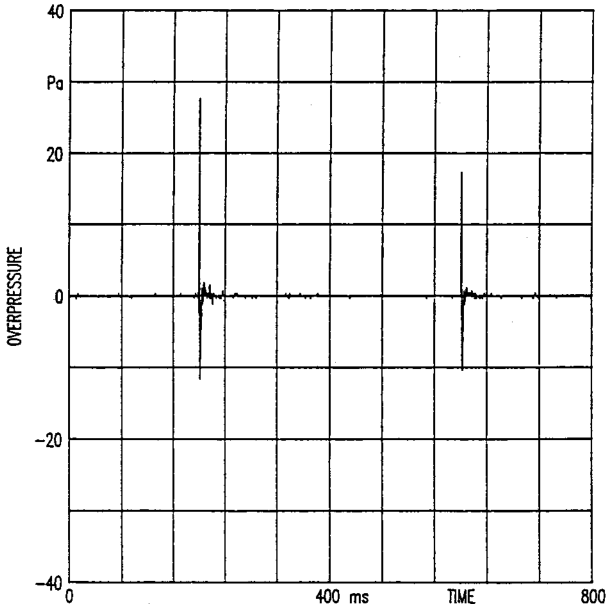

FIG. 11. A-weighted overpressure of Columbia sonic boom 10 December 1990.

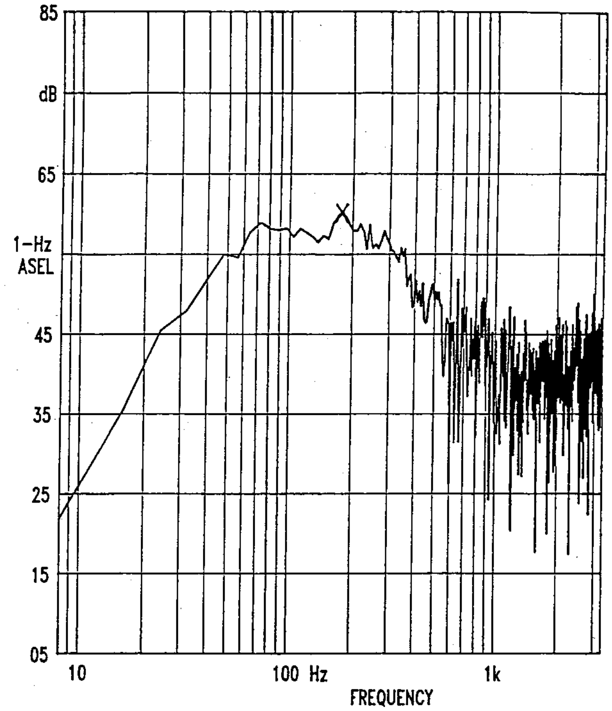

FIG. 12. A-weighted sound exposure spectrum level of Atlantis initial transient, 6 December 1988, analysis bandwidth, 1 Hz, ASEL=84 dB.

Figure 12 shows the A-weighted sound exposure spectrum level (1-Hz ASEL) when Atlantis at Mach 1.4 passed almost directly 17.7 km over Edwards Air Force Base. The figure shows that a dominant part of the A-weighted sound exposure level spectrum of a sonic boom lies between 50 and 800 Hz, with a broad maximum around 200 Hz. This is a range covered by most community noise monitors. If a monitor is provided with adequate response to sudden transients, the single monitor can serve for all kinds of sounds, steady and impulsive. However, the A-weighted measure may not adequately register the environmentally significant low-frequency content of many high-intensity impulsive sounds.

D. Comparison of measured and predicted sound levels for four sonic boom events

Table I is a summary of levels measured with seven different instruments for sonic booms of four space shuttles on four different dates approaching Edwards Air Force Base. Abbreviations for the measured values and the approximate average level relative to the flaT descriptors for this set of measurements are as follows:

Abbreviation	Descriptor	Approximate average level *re*: flaT (dB)
PKT	peak flaT sound pressure level	0
PKC	peak C-weighted sound pressure level	−1.2
PKA	peak A-weighted sound pressure level	−11.9
MXFC	maximum fast C-weighted sound pressure level	na
MXFA	maximum fast A-weighted sound pressure level	na
TSEL	flaT sound exposure level	0
CSEL	C-weighted sound exposure level	−17.0
ASEL	A-weighted sound exposure level	−33.8

Sixteen simultaneous measurements were possible for several of the descriptors using from two to four different instruments on each of the four flights. For comparison between these limited data for different instruments, the table lists the difference between the maximum and minimum values for any one set of measurements. These differences varied from 0 to 6 dB depending on the instruments and descriptors. The mean and standard deviation of these differences was 2.0±2.0 dB. For each of the eight descriptors, the standard deviations over the multiple measurements for the four nominally similar flights varied from ±0.4 dB (two or three measurements of peak levels) to ±2.6 dB (11 measurements of A-weighted sound exposure level).

Not included in Table I are data for a 394-ms sonic boom from the Atlantis landing 6 December 1988. At a lateral slant range of 91 kft from the track, the PeakFlat (PKT)

TABLE I. Summary of different measured levels of sonic booms caused by space shuttles about to land at Edwards Air Force Base; offset at nearest approach, slant range from origin of sonic boom to measuring site. Mach number and aircraft location at time when the sonic boom generated; air temperature shortly after boom.

Date				Position			Mach. No.	Temperature	
Instrument	Shuttle Flight	PKT	PKC	PKA	MXFC	MXFA	TSEL	CSEL	ASEL
10 December 1990	Columbia; Offset 3450 ft; Slant range 74 621 ft; Mach 1.67; 0 °C								
GR1982		130.7							
CEL 162SEL						93.9			89.6
CEL 493-238						99.7			92.4
B&K 2230					114.5			108.0	
RACAL 4D		135.1	133.2	122.8			126.3	110.4	92.3
TEAC DAT		134.3	132.5	122.9			125.8	108.5	92.8
	Average	133.4	132.9	122.9		96.8	126.1	109.0	91.8
	Max-Min	0.9	0.7	0.1		5.8	0.5	2.4	3.2
Galloway calculation		134.3						108.5	
Difference (Calculated−Measured)		0.9						−0.5	
11 April 1991;	Atlantis; Offset 27 400 ft; Slant range 85 479 ft; Mach 1.59; 6.0 °C								
GR1982		130.3							
CEL 162SEL									
CEL 493-238						91.7			86.0
B&K 2230					111.2				85.0
RACAL 4D								105.3	
TEAC DAT (1 kHz)		131.3					123.2		
TEAC DAT (100 Hz)							123.2		
	Average	130.8			111.2	91.7	123.2	105.3	85.5
	Max-Min	1.0					0.0		1.0
Galloway calculation		133.2						107.2	
Difference (Calculated−Measured)		2.4						1.9	
14 June 1991;	Columbia; Offset 13 000 ft; Slant range 83 378 ft; Mach 1.70								
GR1982		130.0							
CEL 162SEL						94.5			
CEL 493-238									89.6
RION NL-11									88.2
RACAL 4D								108.9	
	Average	130.0				94.5		108.9	88.9
	Max-Min								1.4
Galloway calculation		133.2						107.3	
Difference (Calculated−Measured)		2.4						−1.6	
30 January 1992;	Discovery; Offset 36 500 ft; Slant range 88 789 ft; Mach 1.61; 0.0 °C								
GR1982		131.2							
CEL 162SEL						92.4			87.4
CEL 493-238						98.4			92.2
RION NL-11					112.7			108.9	
B&K 2230								108.3	
RACAL 4D (1 kHz)		134.0		121.9			125.6	107.6	91.1
RACAL 4D (100 Hz)							125.2	108.4	
	Average	132.6		121.9	112.7	95.4	125.4	108.3	90.2
	Max-Min	2.8				6.0	0.4	1.3	4.8
Galloway calculation		133.6						107.6	
Difference (Calculated−Measured)		1.0						−0.7	
Overall average measured		132.1	132.9	122.5	112.8	95.1	124.9	108.3	89.7
standard deviation (N)		1.9(8)	0.4(2)	0.4(3)	1.3(3)	3.0(6)	1.2(6)	1.3(9)	2.6(11)
Average (Calculated−Measured)		1.9						−0.2	

level was 128 dB, PKC was 125 dB, PKA was 119 dB, MXFT was 118 dB, MXFC was 102 dB, and MXFA was 84 dB. These values are 3 to 11 dB below the comparable averages for the data in Table I. This may reflect in part, the greater slant range for this measurement.

By use of rectangular position coordinates and aircraft name at 1 s time intervals obtained from radar and theodolite tracking data supplied by Edwards Air Force Base, and by use of a simple theoretical model (Carlson, 1978), flight parameters for the sonic booms, such as the position of the supersonic aircraft when it generated a sonic boom could be calculated (Galloway, 1993). The slant ranges involved varied from about 75 to 89 kft. The calculated values for PKT and CSEL provided by Galloway using the Carlson model are included in Table I and show that, on the average, these calculated values differed by 1.9 and −0.2 dB, respectively, from the corresponding measured values.

V. SUMMARY

Results from 5 out of a series of 13 sonic boom measurements made from 1988 to 1993 from landing of the Space Shuttle are presented using data from two to seven different sound level meters simultaneously. The differences between the simultaneous measurements for the eight different sonic boom descriptors evaluated varied from 0 to 6 dB with a mean and standard deviation of 2.0±2.0 dB. Calculated values for the peak flat sound pressure level (PKT) and the C-weighted sound exposure level (CSEL) agreed with the average measured values within 1.9 and −0.2 dB, respectively. Wave forms for two of the events showed, in Fig. 5, a near perfect N-wave and, in Fig. 6, a slightly distorted form reflecting the influence of propagation through a turbulent atmosphere. The measured levels for the four nominally similar flights agreed within a standard deviation of ±1.5 to 1.7 dB for the flaT or C-weighted descriptors and ±2.1 to 2.7 dB for the A-weighted descriptors, reflecting the slightly greater variability in A-weighted levels for sonic boom signatures.

ACKNOWLEDGMENTS

William Galloway furnished shuttle positions for some of the measured sonic booms and provided predicted peak sonic boom overpressures and C-weighted sound exposure levels. Jon Francine from Hubbs-Seaworld Research Institute helped with the many measurements at Edwards Air Force Base. The Associate Editor provided helpful suggestions for the article. Evelyn Young gave complete support throughout the preparation of the article.

Carlson, H. W. (**1978**). ''Simplified sonic boom theory,'' NASA TP-1122.
Crocker, M. J., and Sutherland, L. C. (**1968**). ''Instrumentation requirements for measurement of sonic boom and blast waves—a theoretical study,'' J. Sound Vib. **7**, 351–370.
Galloway, W. J. (**1993**). Personal communication.
Sutherland, L. C., Brown, R., and Goerner, D. (**1990**). ''Evaluation of potential damage to unconventional structures by sonic booms,'' report by Wyle Laboratories for Human Systems Division, AF Systems Command, Brooks AF Base, HSD-TR-90-021.
Young, R. W. (**1986**). ''Efficient monitoring of aircraft noise near a military operating area,'' paper before NATO Conference, Aircraft Noise in a Modern Society, Mittenwald, Germany.
Young, R. W. (**1998**). ''Thirteen sonic booms of space shuttles approaching Edwards Air Force Base, 1988–1993,'' J. Acoust. Soc. Am. **104**, 1847–1848(A).

Relative rates of growth of annoyance of impulsive and non-impulsive noises

Sanford Fidell, Laura Silvati, and Karl Pearsons
BBN Technologies, A Unit of GTE Internetworking, 21128 Vanowen Street, Canoga Park, California 91303

(Received 27 April 2000; revised 19 January 2001; accepted 10 March 2001)

Twenty-nine people judged the relative annoyance of five variable level signals and 29 impulsive and non-impulsive fixed-level signals in an adaptive paired comparison study. Signals were presented for judgment as heard indoors in a facility capable of accurately reproducing the very low-frequency content of sonic booms. When the annoyance of sonic booms *un*accompanied by rattle was compared with that of sounds containing more higher-frequency energy (an aircraft flyover and an octave band of noise centered at 1 kHz), the relative rate of growth of annoyance, as expressed in C-weighted SEL units, was nearly 2:1. In other words, to maintain subjective equality of annoyance, each increase in level of sonic booms had to be matched by nearly twice the increase in level of an aircraft flyover or an octave band of noise centered at 1 kHz. Relative rates of growth of annoyance of sonic booms accompanied by rattle and of non-impulsive sounds, including both low- (63-Hz octave band of noise) and high-frequency energy (1-kHz octave band of noise and an aircraft flyover), were closer to 1:1. Relative rates of growth of annoyance for sonic booms unaccompanied by rattle and low-frequency sounds (63 Hz) were also about 1:1. These differences in relative rates of growth of annoyance of impulsive and non-impulsive sounds are as plausibly attributed to their relative low-frequency content as to impulsiveness *per se*. It may therefore be more useful for some purposes to express the annoyance of impulsive signals and other environmental noises containing substantial low-frequency energy in terms of effective (duration-corrected) loudness level rather than commonplace ASEL or CSEL. [DOI: 10.1121/1.1377630]

PACS numbers: 43.50.Qp, 43.50.Pn, 43.50.Lj [MRS]

I. INTRODUCTION

Prediction of the annoyance of sonic booms is more uncertain than prediction of the annoyance of subsonic aircraft noise. The latest report of the Committee on Hearing, Bioacoustics, and Biomechanics (CHABA) of the National Research Council of the annoyance of sonic booms (CHABA, 1996) indicates that either of two dosage–response relationships may predict the annoyance of sonic booms, depending on the circumstances of noise exposure.

Both methods of predicting the annoyance of impulsive noise require assumptions about the rate of growth of annoyance with sound level. One of the dosage–response relationships assumes that the annoyance of impulsive signals such as sonic booms increases at twice the rate of the annoyance of non-impulsive signals. The other dosage–response relationship assumes that the annoyance of sonic booms does not increase as rapidly with sound level.

Prior studies (e.g., Kryter, 1968; Leatherwood and Sullivan, 1994; and Schomer, 1994) have documented a variety of relative rates of growth of annoyance of impulsive and non-impulsive sounds. Figure 1 compares the results of regression analyses described by CHABA (1996) that link annoyance judgments with signal presentation levels. [The information summarized in Fig. 1 combines measurements made both indoors and outdoors. Schomer and Sias (1998) have noted that nonlinear increases in secondary emissions may affect the levels of rattling sounds as heard indoors.]

Figure 1 shows that only at lower noise levels do A-weighted sound levels of non-impulsive sounds increase at a rate of 2 dB for every 1-dB increase of the impulsive noise of the same judged loudness or annoyance. At levels greater than 85 dB ASEL[1] for non-impulsive sounds and 95 dB CSEL for impulsive sounds, the slope of the relationship steepens to approximate an equal increase in both impulsive levels (measured in CSEL) and non-impulsive levels (measured in ASEL) to maintain equal judged annoyance for the two types of sounds. The current study was undertaken to develop information about the relative rates of growth of annoyance of sonic booms and non-impulsive sounds with absolute sound level, and the influence of rattle[2] on these annoyance growth rates.

II. METHOD

A. Test signals and presentation levels

Subjects made 97 comparisons of the annoyance of pairs of signals in a two-alternative, forced-choice paired comparison protocol. Table I summarizes the signals heard at subject-controlled levels. The aircraft flyover, 63-Hz octave band of noise, and 1-kHz octave band of noise served as variable signals in 87 of the 97 comparisons. Simulated indoor sonic booms that varied in level from trial to trial were presented without accompanying rattle in 10 of the 97 comparisons.

Table II describes the test signals that were presented at fixed levels. The simulated indoor sonic booms were presented at seven fixed levels, with and without rattle, while the aircraft flyover and the bandlimited Gaussian noises were presented at a single level. The rattle that was added to the simulated sonic booms was a digital recording lasting approximately one second of the noise produced by vibrating

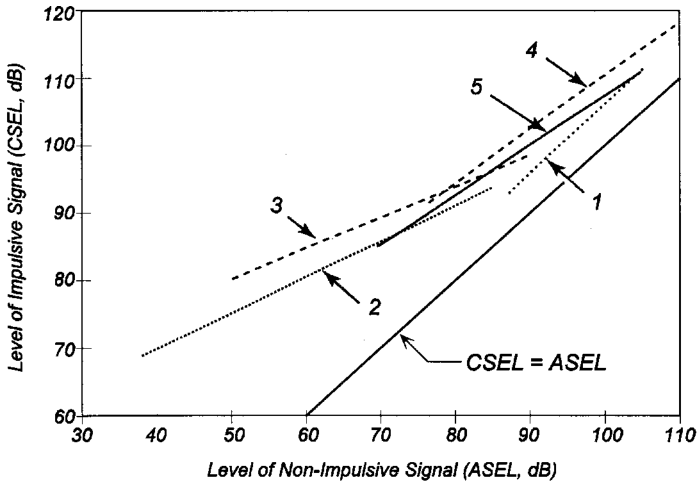

FIG. 1. Comparison of rates of growth of annoyance with at-ear level for impulsive and non-impulsive sounds reported in controlled-exposure studies.

Curve	Citation	Impulse	Comparison (Non-Impulse)	Environment	Measurements
1	Kryter (1968)	Boom	Aircraft	Indoor	Outdoor
2	Schomer (1994)	Blast	White noise	Indoor	Indoor
3	Schomer (1994)	Blast	Vehicles	Indoor	Outdoor
4	Leatherwood and Sullivan (1994)	Boom (speaker)	Aircraft (speaker)	Laboratory booth	Indoor
5	Leatherwood and Sullivan (1994)	Boom (speaker)	Aircraft (speaker)	Lecture hall	Indoor

crockery. Rattle was added only to the simulated booms presented at fixed levels, not to the booms that varied in level with test subjects' annoyance judgments. Rattle was added to the simulated sonic booms at such a low level that it did not meaningfully affect their A- or C-weighted SEL values. Although the simulated sonic booms varied in level by 25 dB over the range of fixed presentation levels, the rattle varied by only 20 dB over this range, due to minor nonlinearities in low-frequency sound reproduction.

Table III shows the presentation levels of all fixed signals. The Appendix contains spectra of the fixed sonic booms, as well as spectra of the maximum levels of the aircraft flyover, the 63-Hz and 1-kHz octave bands of noise, and the rattle signal. No adjustments were made to time patterns or spectra of signals presented for judgment at varying levels.

B. Test environment and procedures

All annoyance judgments were made at a fixed seating position in a low-frequency test facility that permitted controlled generation of impulsive waveforms with peak sound-pressure levels as great as 136 dB. The sealed enclosure test facility was 4.6 by 6.7 by 3.2 meters high. Subjects were seated individually inside this concrete chamber, facing a cloth curtain that was hung in front of a full-scale plaster wall. The wall was positioned in front of 12 low-frequency drive modules mounted on a rigid, airtight septum dividing the chamber into two volumes. Each drive module contained six servomotor-driven, specially stiffened, 15-in. loudspeaker cones. These drive modules reproduced the simulated sonic booms and the 63-Hz octave band of noise. Since the impulses passed through the plaster wall before they were heard by test subjects, they simulated sonic booms as heard indoors.

Two studio monitor loudspeakers, positioned behind the curtain but in front of the plaster wall, reproduced the aircraft overflight, the 1-kHz octave band of noise, and the rattling sounds accompanying some sonic booms. The order of presentation of the fixed and variable signals was randomized within trials. The order of presentation of signal pairs was independently randomized and fully interleaved, so that the order of presentation of signal pairs was also unpredictable.

C. Test subjects

Subjects were audiometrically screened prior to testing to within 20 dB of normal hearing (audiometric zero) over

TABLE I. Signals presented at variable (subject-controlled) levels.

Test signal	Description
Stage II Aircraft Overflight	
B-727 takeoff	Recorded commercial aircraft overflight (nominal duration=15 s)
Bandlimited Noise	
Octave band of Gaussian noise centered at 63 Hz	Nominal duration=2 s Nominal onset/offset time=0.1 s
Octave band of Gaussian noise centered at 1 kHz	Nominal duration=2 s Nominal onset/offset time=0.1 s
Simulated Sonic Booms	
Short sonic boom	Fighter aircraft sonic boom (nominal duration=100 ms) without accompanying secondary emissions
Long sonic boom	Fighter aircraft sonic boom (nominal duration=250 ms) without accompanying secondary emissions

TABLE II. Signals presented at fixed levels.

Test signal	Description
	Stage II Aircraft Overflight
B-727 takeoff	Recorded commercial aircraft overflight (nominal duration=15 s)
	Simulated Indoor Sonic Booms
Short sonic boom	Typical fighter aircraft sonic boom (nominal duration=100 ms) without secondary emissions
Short sonic boom	Typical fighter aircraft sonic boom (nominal duration=100 ms) with secondary emissions
Long sonic boom	Typical fighter aircraft sonic boom (nominal duration=250 ms) without secondary emissions
Long sonic boom	Typical fighter aircraft sonic boom (nominal duration=250 ms) with secondary emissions

the frequency range of 100 to 6000 Hz. Ten of the 29 test participants who judged the relative annoyance of the test signals were women ranging in age from 18 to 46, while 19 were men ranging in age from 18 to 40.

D. Solicitation of annoyance judgments

Subjects were instructed to indicate by a button push whether the first or second signal presentation of each trial was the more annoying. The durations of the signal presentation intervals were determined by the durations of the signals themselves. The duration of the response interval was determined by the subject's response latency.

Signal generation and presentation, as well as all other aspects of data collection, were under real-time computer control. Figure 2 diagrams the signal generation and presentation hardware. A maximum likelihood estimation algorithm described by Green (1990, 1995) and by Zhou and Green (1995) adaptively controlled signal presentation levels in real time, on the basis of test participants' ongoing decisions. The underlying psychometric function was assumed to be a cumulative Gaussian with a standard deviation of 10 dB. The value of the estimated point on the psychometric function was 50%: i.e., the point at which individual subjects judged the comparison (variable level) signal more annoying half of the time and the standard (fixed level) signal more annoying half of the time.

TABLE III. Presentation levels of fixed signals.

Test signal	Fixed presentation level
B-727 takeoff	95.6 dB ASEL
Short sonic boom with and without rattle	108.4 dB CSEL
	104.4
	100.4
	98.4
	96.4
	92.4
	88.4
Long sonic boom with and without rattle	107.9 dB CSEL
	103.9
	99.9
	97.9
	95.9
	91.9
	87.9

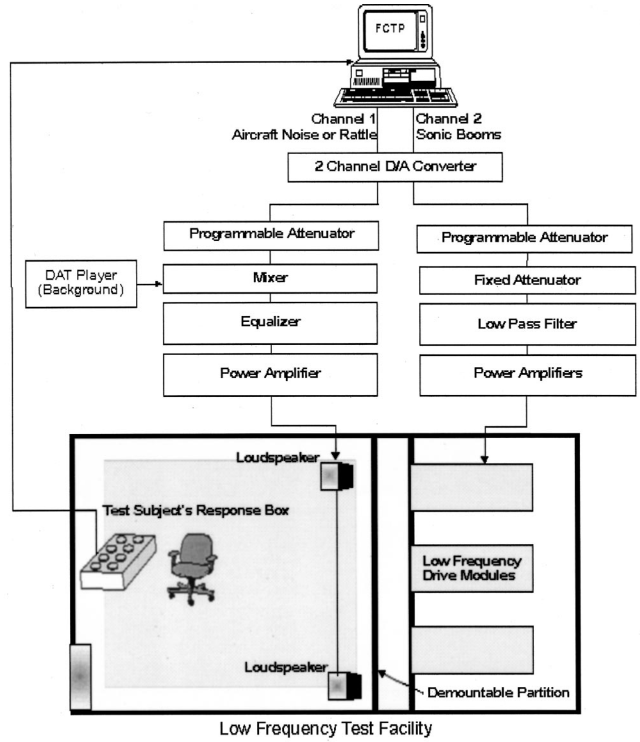

FIG. 2. Illustration of instrumentation controlling administration of test conditions in the low-frequency test facility.

The point of subjective equality of annoyance was approached by a binary search algorithm. Step sizes between trials ranged from a maximum of 30 dB (for the first 14 subjects) and 40 dB (for subjects 15 through 29), to a minimum of 2.5 dB. The maximum signal presentation level permitted was 110 dB. Twelve trials were administered for each determination of the relative annoyance of signal pairs, sufficient to yield a standard deviation of the threshold estimate of approximately 4 dB.

A long-duration digital recording of general urban noise with a highly compressed dynamic range, mixed with shaped Gaussian noise, was reproduced at all times that subjects were present in the test facility. The A level of the background noise at the subject's head position was approximately 36 dB.

III. RESULTS

A. Data collection and processing

The 97 signal pairs presented 12 times to each of 29 subjects yielded 33 756 paired comparison judgments. The 97 determinations of points of subjective equality of annoyance from the 29 subjects produced a total of 2813 data points.

B. Reliability of annoyance judgments

Points of subjective equality of annoyance arising from comparisons in which the same signals served as both fixed

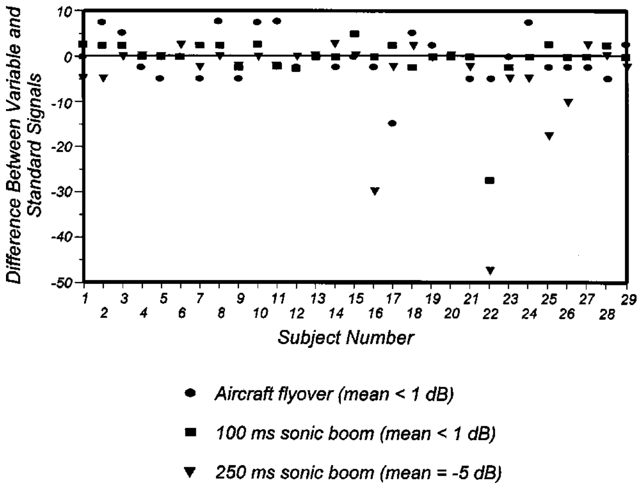

FIG. 3. Differences between the levels of the variable and fixed signals at the point of subjective equality when signals are compared against themselves.

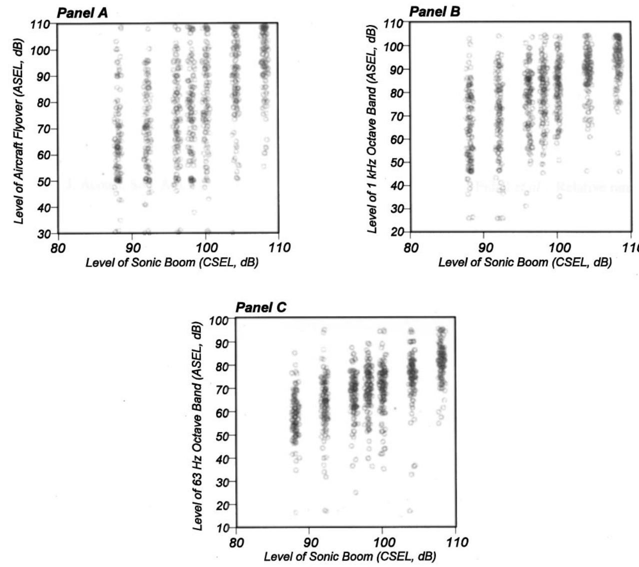

FIG. 4. Levels of aircraft flyover, 1-kHz octave band noise, and 63-Hz octave band noise when judged equally annoying to sonic booms for all test subjects.

and variable level signals provided one measure of the reliability of annoyance judgments. These pairs included three comparisons in which the aircraft flyover, the 100-ms sonic boom without rattle, and the 250-ms sonic boom without rattle served as both the fixed and variable signals.

Figure 3 shows the differences between the variable and fixed level signals at the points of subjective equality of annoyance for these three signal pairs for each test subject. The mean difference between the signals and themselves at the point of subjective equality was less than 1 dB for the aircraft flyover, less than 1 dB for the 100-ms sonic boom, but −5 dB for the 250-ms sonic boom. Large mean differences at the point of subjective equality of annoyance between the 250-ms sonic boom and itself for two subjects (see Fig. 3) are outliers attributable to lapses of attention. The mean difference between the 250-ms sonic boom and itself for the remaining subjects is less than 2 dB.

C. Summary of annoyance judgments

Figure 4 shows scatter plots of the levels of the aircraft flyover, the 1-kHz, and the 63-Hz octave bands of noise when judged equal in annoyance to sonic booms heard at seven fixed levels. These scatter plots display the variability observed at each level of the sonic booms. The levels of the 63-Hz octave band of noise (in the lower panel) cluster more closely than the other two variable signals when judged equally annoying to the sonic boom. Table IV shows mean levels of the aircraft flyover and the 63-Hz and 1-kHz octave bands of noise when judged equal in annoyance to the various sonic booms.

D. Analysis of variance of annoyance judgments

Annoyance judgments in which sonic booms at fixed levels were compared to the aircraft flyover or the two octave bands of noise at variable levels were analyzed together in an omnibus analysis of variance. This primary analysis provided simultaneous tests of the effects of type of variable signal, duration of sonic booms, presence of rattling sounds with sonic booms, and the presentation level of the fixed sonic booms on subjects' judgments of annoyance. Subsequent comparisons were performed of the rates of growth of annoyance due to impulsive and non-impulsive noise.

A 3 (signaltype)×2 (sonic boom duration)×2 (rattle condition)×7 (signal presentation level) repeated measures analysis of variance was conducted. The dependent variable was the level of the variable level signal when judged equal in annoyance to the sonic booms. Subjects made annoyance judgments at all levels of the four factors, yielding the 84 paired comparisons included in this analysis.

1. Main effects

A statistically significant effect of type of variable signal ($F_{(2,56)} = 23.04$, $p < 0.001$) indicated that subjects' annoyance judgments depended on which variable signals were compared to the sonic booms. The mean ASEL levels of the variable signals when judged equally annoying to the sonic booms were 78 dB (for the aircraft flyover), 79 dB (for the 1-kHz octave band of noise), and 69 dB (for the 63-Hz octave band of noise). In other words, the low-frequency octave band of noise was judged on average to be as annoying as a sonic boom at a level 10 dB lower than variable level signals with greater high-frequency content. Type of variable signal accounted for 21% of the variance in annoyance judgments.

Since no statistically significant effect of duration of sonic boom was observed, it was apparent that subjects did not discriminate between the annoyance of 250-ms and 100-ms sonic booms. A statistically significant effect of rattle was observed ($F_{(1,28)} = 97.71$, $p < 0.001$), however. The overall mean levels of the variable signals at the point of subjective equality were 78 dB when sonic booms were accompanied by rattle, but only 73 dB when sonic booms were not accompanied by rattle. This effect accounted for 6% of the variance in annoyance judgments.

TABLE IV. Mean ASEL values (in dB) of the aircraft flyover, 63-Hz and 1-kHz octave bands of noise when judged equal in annoyance to sonic booms presented at seven fixed CSEL values (in dB).

	Aircraft flyover				63-Hz Octave band				1-kHz Octave band			
	100-ms sonic boom		250-ms sonic boom		100-ms sonic boom		250-ms sonic boom		100-ms sonic boom		250-ms sonic boom	
Level of boom	Rattle	No rattle	Rattle	No rattle	Rattle	No rattle	Rattle	No rattle	Rattle	No rattle	Rattle	No rattle
88.2	73.6	62.6	68.6	59.2	62.1	53.6	60.2	54.8	71.9	60.4	67.4	58.8
92.2	72.1	64.7	73.5	64.7	67.0	58.5	65.7	60.5	73.3	62.9	76.2	66.6
96.2	77.2	70.3	79.7	70.3	68.3	65.7	69.3	62.6	81.2	73.5	80.0	72.7
98.2	78.3	73.4	78.5	72.8	71.3	67.5	70.8	67.5	82.6	77.5	82.5	75.6
100.2	82.7	79.2	77.5	81.8	72.0	69.2	69.6	68.8	83.9	80.6	82.0	82.6
104.2	92.2	82.3	90.3	85.3	75.9	73.7	76.1	73.1	87.6	85.9	90.3	87.6
108.2	90.5	97.4	97.5	97.1	81.1	80.8	82.3	80.3	92.9	94.3	94.6	92.1

A statistically significant linear trend of level of the sonic boom signals ($F_{(1,29)}=338.46$, $p<0.001$) was observed, indicating that subjects' annoyance increased linearly as the level of sonic booms increased. The level of sonic booms accounted for 69% of the variance in points of subjective equality among subjects. The overall mean levels of the variable signals when judged equal in annoyance to sonic booms, as well as the fixed levels of the sonic booms, are presented in Table V. The mean difference in level between the sonic boom and the variable signal when judged equally annoying was 22 dB.

2. Interactions

A small but statistically significant interaction (accounting for 1% of the variance in annoyance judgments) of type of variable signal with sonic boom presentation level was observed ($F_{(1,28)}=36.01$, $p<0.001$), since annoyance increased differentially with level of sonic boom for the various signal pairs (as shown in Fig. 5).

Another small but statistically significant interaction (accounting for 2% of the variance in annoyance judgments) of rattle with level of the sonic booms was also observed ($F_{(1,28)}=84.75$, $p<0.001$). Figure 6 shows that the level of the variable signal at the point of subjective equality of annoyance was higher when sonic booms were presented with rattle than when they were presented without rattle, especially at lower presentation levels.

TABLE V. Presentation levels of sonic booms, mean levels of variable signals, and their differences at points of subjective equality of annoyance.

Fixed presentation levels of sonic booms (CSEL) (dB)	Mean levels of variable signals when judged equal in annoyance to sonic booms (ASEL) (dB)	Difference (dB)
88	63	25
92	67	25
96	73	23
98	75	23
100	78	22
104	83	21
108	90	18
Mean difference between fixed and variable signals		22.4dB

E. Comparison of relative rates of growth of annoyance

Relationships of the rates of growth of annoyance for impulsive and non-impulsive noises were investigated through linear regression. Figure 7 shows mean levels of the variable signals when judged equally annoying to sonic booms with and without rattle. The three panels of this figure show that slopes of the relationships for sonic booms presented with rattle were steeper than those of sonic booms presented without rattle.

The relative rate of growth of annoyance was roughly 2:1 when booms without rattle were compared to the aircraft flyover (panel A). In other words, a 2-dB increase in the level of the aircraft flyover was judged to be as annoying as a 1-dB increase in the level of the sonic boom presented without rattle. However, the relative rate of growth of annoyance was only 1.3:1 when sonic booms with rattle were compared to the aircraft flyover: each 4-dB increase in the level of the aircraft flyover was judged to be as annoying as a 3-dB increase in the level of sonic booms presented with rattle.

The relative rate of growth of annoyance when sonic booms without rattle were compared with the 1-kHz octave band of noise was slightly greater than 2:1 (panel B of Fig. 7). The relative rate of growth of annoyance was 1.3:1 when

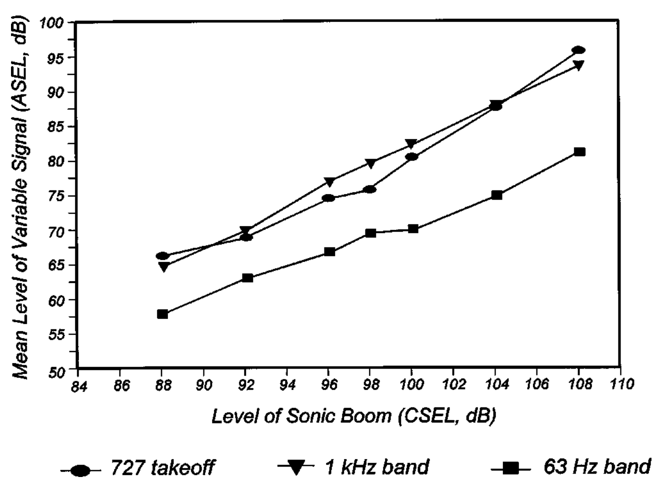

FIG. 5. Mean levels of the variable signals at points of subjective equality when compared to the aircraft flyover, 1-kHz and 63-Hz octave bands of noise.

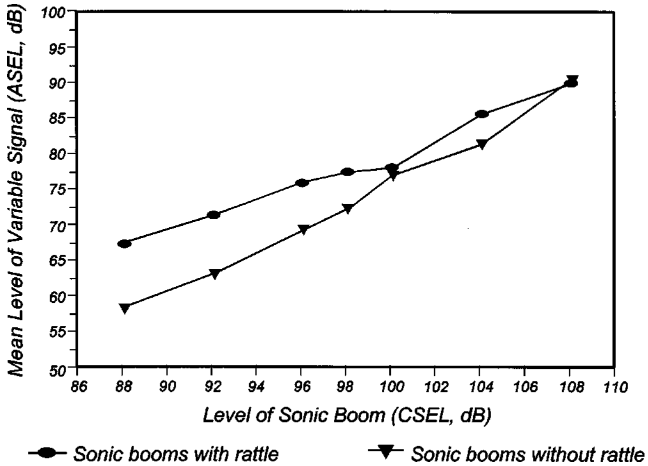

FIG. 6. Mean levels of the variable signals at the point of subjective equality of annoyance with sonic booms presented with and without rattle.

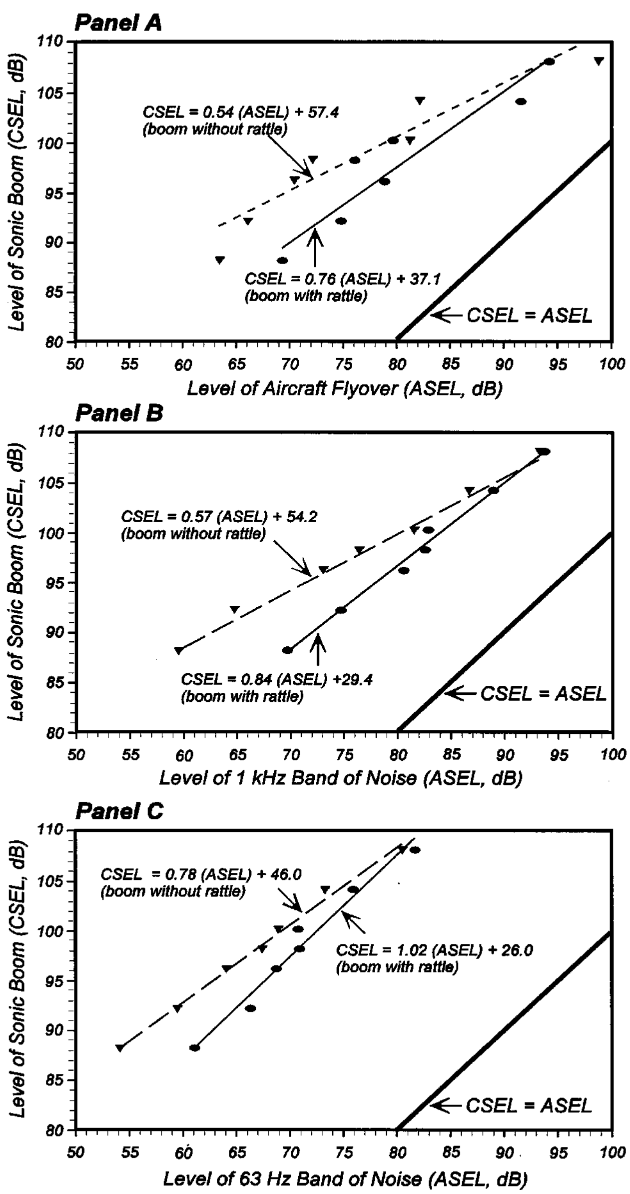

FIG. 7. Comparison of the rates of growth of annoyance of impulsive and non-impulsive noises.

sonic booms with rattle were compared to the 1-kHz octave band of noise: each 5-dB increase in the level of the 1-kHz octave band of noise was judged to be as annoying as a 4-dB increase in the level of the sonic boom accompanied by rattle.

Panel C of Fig. 7 shows that the relative rate of growth of annoyance was 1.3:1 when sonic booms without rattle were compared to the 63-Hz octave band of noise. The relative rate of growth of annoyance was 1:1 when sonic booms accompanied by rattle were compared to the 63-Hz octave band of noise was judged to be as annoying as a 1-dB increase in the level of the sonic boom accompanied by rattle.

The slopes of the regression lines (the reciprocals of the growth rates discussed above) range from 0.54 to 1.0.[3] These linear regressions account for essentially all of the variance in the annoyance judgments.

IV. DISCUSSION

A. Annoyance of simulated sonic booms

Averaged findings for all test subjects' judgments were readily interpretable, despite variability among individuals' annoyance judgments.

(i) Subjects were more annoyed by sonic booms accompanied by rattle than by sonic booms unaccompanied by rattle. The influence of rattle on the ratings of annoyance of sonic booms was more pronounced at lower than at higher noise levels.

(ii) Mean levels of the non-impulsive variable signals were 5 dB greater when judged equal in annoyance to sonic booms with rattle than without rattle.

(iii) Subjects did not differentiate between the annoyance of longer and shorter duration sonic booms.

Rattle may exacerbate noise-induced annoyance in field settings by calling attention to the occurrence of lower-level impulsive noises that might otherwise go unnoticed. Contextual and other nonacoustic factors also undoubtedly contribute to annoyance judgments of impulsive signals, in a manner such as that suggested by Green and Fidell (1991) and others for the case of general transportation noise. The effect of rattle *per se* on the annoyance of impulsive signals observed under controlled signal presentation conditions can nonetheless be evaluated independently of such other influences.

B. Relative rates of growth of annoyance among signals

The findings of some studies (e.g., Schomer, 1994) of the annoyance of a limited class of high-energy impulses reveal a 2:1 differential in the growth rates of annoyance of impulsive and non-impulsive sounds. This differential was observed only under a subset of conditions in the present study. In other conditions, the relative growth rates for impulsive and non-impulsive sounds were intermediate between 2:1 and 1:1.

One factor that can account for the observed differences in growth rates of annoyance in different comparisons is the

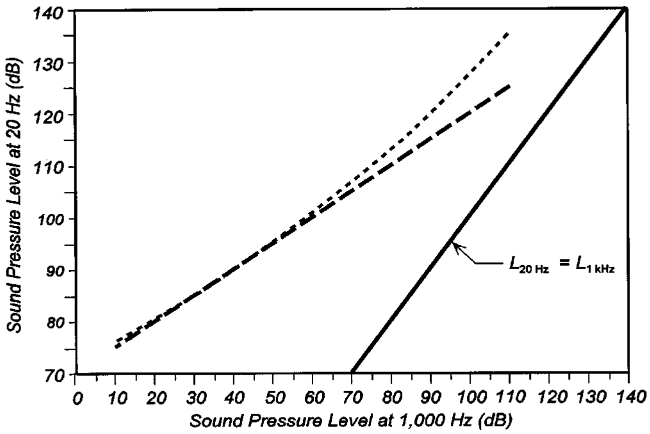

FIG. 8. Dashed line shows relative rate of growth of loudness of a 20-Hz tone with a 1-kHz tone, per ISO R 226 (1987). Solid line shows 2:1 growth rate.

loudness of low-frequency content of sounds heard at high absolute sound-pressure levels. The spacing of contours of equal loudness at low frequencies is much closer than at mid- or high frequencies. Thus, sounds containing energy at frequencies in the range of 20–200 Hz increase in loudness as their absolute levels increase at a faster rate than sounds containing energy at frequencies in the range of 500–5000 Hz.

Figure 8 illustrates the magnitude of this difference between low- and midfrequency growth rates per ISO R 226 (1987). The dashed line compares the predicted loudness of a low-frequency (20-Hz) tone with that of a midfrequency (1-kHz) tone. The relative rate of growth of loudness with level differs little from 2:1 (the upper solid line) at sound levels as great as 90 dB.

Figure 9 compares the relationships between the rates of growth of annoyance of impulsive and non-impulsive noises observed in the current study with those observed in other controlled exposure studies. The relative rates of growth of annoyance shown for the current study are in good agreement with those reported by Leatherwood and Sullivan (1994).

The present findings also indicate that when sonic booms without rattle are compared with low-frequency sounds (63-Hz octave band of noise), the rates of growth of annoyance are roughly comparable $(\text{slope}=0.78)$. However, when the same sonic booms are compared to sounds with greater high-frequency content (aircraft flyovers or an octave band of noise centered at 1 kHz) the growth rates of annoyance are closer to 2:1 (slope$=$0.54 and 0.57, respectively), in agreement with Schomer's findings. (Note that the minor differences in ranges of levels of simulated sonic booms and rattle over the 20-dB range of presentation levels may also have had some influence on the similarity of levels of booms with and without rattle at the points of subjective equality of annoyance.)

When the annoyance of sonic booms accompanied by rattle was compared with the annoyance of a low-frequency signal (63-Hz octave band of noise), the growth rates of annoyance were also found to be comparable $(\text{slope}=1.0)$. The

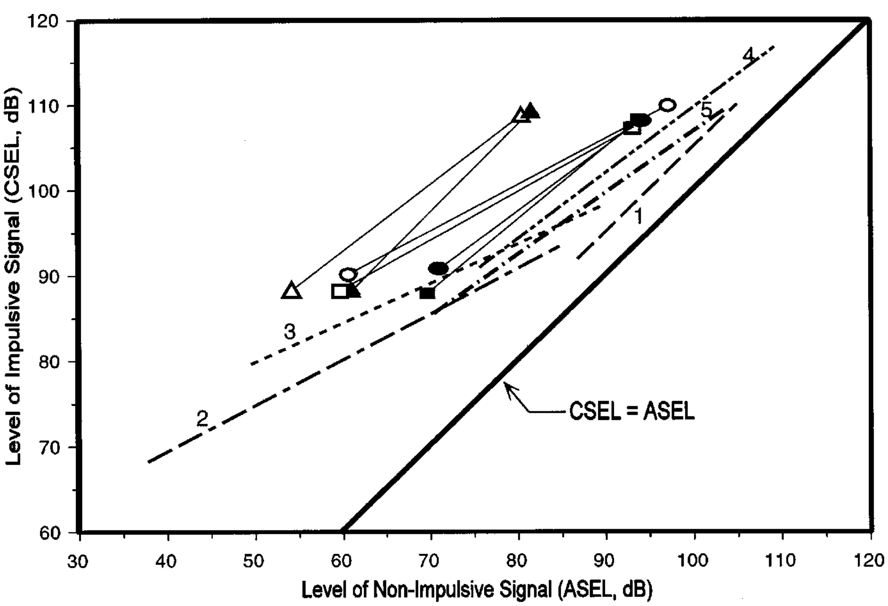

Curve/ Symbol	Citation	Impulse	Comparison (Non-Impulse)	Environment	Measurements
1	Kryter (1968)	Boom	Aircraft	Indoor	Outdoor
2	Schomer (1994)	Blast	White noise	Indoor	Indoor
3	Schomer (1994)	Blast	Vehicles	Indoor	Outdoor
4	Leatherwood & Sullivan (1994)	Boom	Aircraft (speaker)	Laboratory Booth	Indoor
5	Leatherwood & Sullivan (1994)	Boom	Aircraft (speaker)	Lecture Hall	Indoor
Ovals	Fidell *et al.* (1997)	Boom	Aircraft (speaker)	Sonic Boom Simulator	Indoor
Triangles	Fidell *et al.* (1997)	Boom	63 Hz octave band of noise	Sonic Boom Simulator	Indoor
Squares	Fidell *et al.* (1997)	Boom	1 kHz octave band of noise	Sonic Boom Simulator	Indoor

FIG. 9. Comparison of rates of growth of annoyance for impulsive and non-impulsive sounds reported in previous studies (dashed lines) to those reported in the current study (solid lines). Open symbols denote booms without rattle, whereas filled symbols denote sonic booms with rattle.

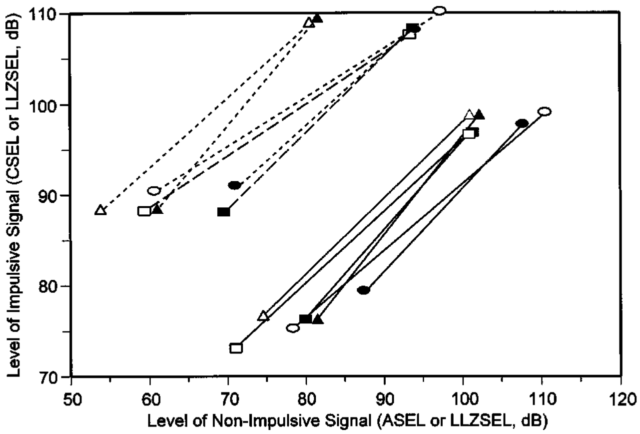

FIG. 10. Rates of growth of annoyance for impulsive and non-impulsive noise, in units of CSEL and ASEL (dashed lines) and LLZSEL (solid lines). Triangles represent 63-Hz band comparisons, squares represent 1-kHz band comparisons, and ovals represent aircraft flyover comparisons. Open symbols represent booms without rattle, and closed symbols represent booms with rattle.

predominant low-frequency content common to the two signals can account for this similarity in growth rates. When the same sonic booms with rattle are compared to sounds with lesser low-frequency energy (e.g., aircraft flyovers or a band of noise centered at 1 kHz) the growth rates of annoyance approach 1:1 (slopes = 0.76 and 0.87). The addition of rattle to a sonic boom dominated by low-frequency energy adds considerable high-frequency energy. This higher-frequency energy can account for the similarity in growth rates of annoyance between an aircraft flyover and band of noise centered at 1 kHz and sonic booms accompanied by rattle.

Figure 7 (v.s.) shows that at higher presentation levels of sonic booms, the presence of rattle is less prominent and the annoyance of the combination of rattle and sonic boom is similar to the annoyance of the sonic booms without rattle.

C. Loudness level interpretation of findings

Another perspective on the current findings may be gained by expressing signal levels at points of subjective equality of annoyance in terms of Zwicker's loudness level (Zwicker, 1977), a more complex spectral weighting procedure than the A- or C-weighting networks. Two recent studies of the annoyance of subsonic aircraft noise (Pearsons *et al.*, 1996, 1997) have shown that loudness levels calculated by Zwicker's procedures reduce the variability in judgments of the annoyance of aircraft overflight and other transportation noise with appreciable low-frequency content.

Figure 10 includes the findings shown in Fig. 9 (in which ASEL and CSEL values are plotted against one another for non-impulsive and impulsive sounds, respectively) as well as units of LLZSEL (SEL values for signals weighted by Zwicker's loudness level procedure). The dashed lines in the figure are plotted against ASEL and CSEL axes, while the solid lines are plotted against LLZSEL axes.

The displacements of the dashed and solid lines from one another merely reflect numerical differences between loudness level, A-weighted, and C-weighted sound levels of the same sounds. The tighter clustering of solid lines plotted in loudness level units indicates that the contributions of low-frequency energy to annoyance are better predicted by the loudness level noise metric than by the A- or C-weighting networks. In addition, the slopes of the lines in Fig. 10 are more similar to each other and are closer to 1:1 for growth of annoyance than the dashed lines, whose growth rates vary from 1:1 to 2:1.

D. Implications of findings

The observation that the annoyance of high-energy impulsive sounds grows twice as fast as that of non-impulsive sounds has been attributed by some to their impulsiveness *per se*. The present findings suggest that differences in the rates of growth of annoyance of impulsive and non-impulsive sounds heard at high sound levels can be equally plausibly attributed to their low-frequency content.

V. CONCLUSIONS

Judgments of the annoyance of impulsive and non-impulsive sounds support the following conclusions:

(1) Sonic booms accompanied by rattle were judged more annoying than those unaccompanied by rattle.
(2) The rate of growth of annoyance of a simulated sonic boom unaccompanied by rattle compared to an aircraft flyover was similar to that of a sonic boom compared to a 1-kHz octave band of noise. The two rates of growth were 1.9:1 and 1.8:1, respectively, or nearly 2:1.
(3) The rate of growth of annoyance of sonic booms unaccompanied by rattle compared to the 63-Hz octave band was 1.3:1, closer to 1:1.
(4) The rate of growth of annoyance of sonic booms accompanied by rattle compared to an aircraft flyover is similar to that of a sonic boom compared to a 1-kHz octave band of noise. The two rates of growth were 1.3:1 and 1.1:1, respectively, or about 1:1.
(5) The rate of growth of annoyance of sonic booms accompanied by rattle when compared with the 63-Hz octave band of noise was 1:1.
(6) The low-frequency content of impulsive sounds may control their annoyance rather than their impulsiveness *per se*.
(7) No distinction was observed between annoyance judgments of shorter- and longer-duration simulated sonic booms presented for judgment as heard indoors.
(8) Comparison of the growth of annoyance for impulsive and non-impulsive signals in terms of Zwicker's loudness level reduced the variability and suggested a uniform growth of 1:1 for all signals.

ACKNOWLEDGMENTS

The authors are grateful to the test participants for their diligence throughout their participation, and to Ms. Mary Westheimer for organizing the data collection effort. The study was sponsored by the U.S. Air Force Air Combat Command. Additional details of this study may be found in BBN Report 8213, ''Relative Rates of Growth of Annoyance of Impulsive and Non-Impulsive Noises'' (Fidell *et al.*, 1997).

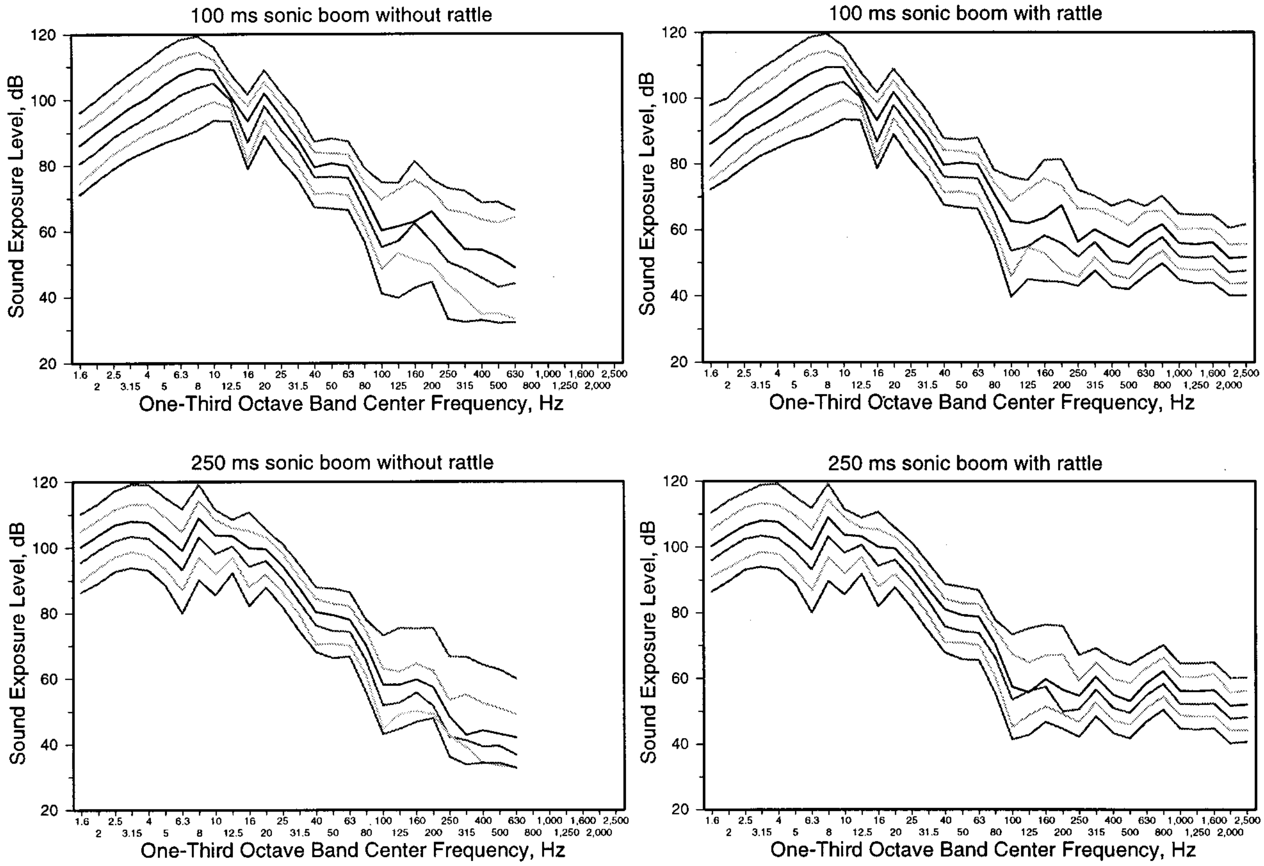

FIG. A1. One-third octave band spectral levels of sonic boom signals of short and long duration presented with and without rattle at seven levels.

APPENDIX: SPECTRA OF TEST SIGNALS

The four panels of Fig. A1 display one-third octave band spectra of the four simulated sonic booms presented at seven fixed levels. Figure A2 displays one-third octave band spectra of the maximum level at which the aircraft flyover, 63-Hz, and 1-kHz octave bands of noise were presented. The spectrum labeled "rattle only" is plotted at the highest level at which rattle was presented when accompanying simulated sonic booms.

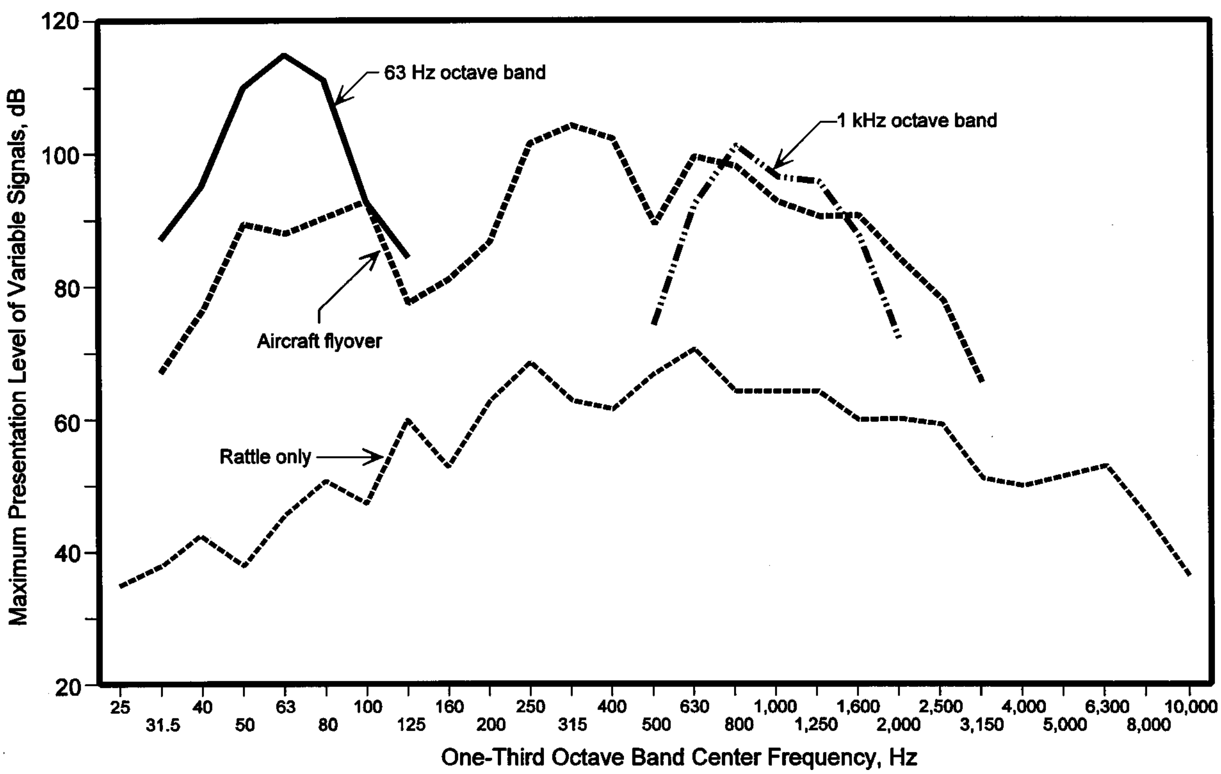

FIG. A2. One-third octave band spectral levels of three variable signals and rattle only at maximum presentation level.

[1]ASEL is the abbreviation for the decibel quantity ten times the logarithm to the base ten of the ratio of a given time integral of squared instantaneous A-weighted sound pressure, over a stated time interval or event, to the product of the squared reference sound pressure of 20 micropascals and reference duration of one second. Note: In symbols, the (A-weighted) sound exposure level is:

$$L_{\mathrm{AE}}=10\ \log\left\{\left[\int_0^T p_{\mathrm{A}}^2(t)\,dt\right]\Big/\ p_0^2 t_0\right\}=10\ \log(E/E_0)=L_{\mathrm{A}T}+10\ \log(T/t_0),$$

where p_{A}^2 is the squared instantaneous A-weighted sound pressure, a function of time t; for gases $p_0=20\ \mu\mathrm{Pa}$; $t_0=1$ s; E is sound exposure; $E_0=p_0^2 t_0=(20\ \mu\mathrm{Pa})^2\mathrm{s}$ is reference sound exposure. CSEL is the abbreviation for the same quantity calculated with C-weighting rather than A-weighting.

[2]The term ''rattle'' is used in its colloquial sense, since the secondary acoustic emissions of household paraphernalia are highly idiosyncratic and nonlinear with the acoustic energy applied to residential structures. The rattle added to certain test signals in this study was a digital recording, approximately one second in duration, of noise made by vibrating cups and saucers.

[3]Rates of growth of annoyance with level may be equivalently expressed as slopes (e.g., 0.5) as ratios (e.g., 2:1), or as reciprocals of slopes (e.g., 2.0).

Committee on Hearing, Bioacoustics, and Biomechanics (CHABA) (**1981**). ''Assessment of Community Response to High Energy Impulsive Sounds,'' *Report of Working Group 84, Committee on Hearing, Bioacoustics, and Biomechanics, National Research Council* (National Academy, Washington, D.C.).

Committee on Hearing, Bioacoustics, and Biomechanics (CHABA) (**1996**). ''Community Response to High-Energy Impulsive Sounds: An Assessment of the Field Since 1981,'' *Report of Working Group 102 of the National Research Council Committee on Hearing, Bioacoustics, and Biomechanics* (National Academy, Washington, D.C.).

Federal Interagency Committee on Noise (FICON) (**1992**). Final Report, Airport Noise Assessment. Methodologies and Metrics, Washington, D.C.

Fidell, S., Silvati, L., Pearsons, K., Howe, R., and Lind, S. (**1997**). ''Relative Rates of Growth of Annoyance of Impulsive and Non-Impulsive Noises,'' BBN Report No. 8213, The Environmental Company (under contract to the U.S. Air Combat Command), Charlottesville, VA.

Green, D. M. (**1990**). ''Stimulus selection in adaptive psychophysical procedures,'' J. Acoust. Soc. Am. **87**, 2662–2674.

Green, D. M. (**1995**). ''Maximum likelihood procedures and the inattentive observer,'' J. Acoust. Soc. Am. **97**, 3749–3760.

Green, D. M., and Fidell, S. (**1991**).

International Organization for Standardization (**1987**). ''Normal Equal Loudness Contours and Normal Thresholds of Hearing Under Free Field Listening Conditions,'' ISO Recommendation R 226, CH-1211 Geneva 20, Switzerland.

Kryter, K. D., Johnson, P. J., and Young, J. P. (**1968**). ''Psychological Experiments on Sonic Booms Conducted at Edwards Air Force Base,'' USAF Contractor Report AF 49(638), USAF National Sonic Boom Evaluation Office, Arlington, VA.

Leatherwood, J. D., and Sullivan, B. M. (**1994**). ''A Laboratory Study of Subjective Annoyance Response to Sonic Booms and Aircraft Flyovers,'' NASA Technical Memorandum 109113.

Pearsons, K., Howe, R., Sneddon, M., Silvati, L., and Fidell, S. (**1997**). ''Comparison of the predictors of the annoyance of commuter, Stage II and Stage III overflights as heard outdoors,'' NASA Contractor Report CR-97-205812, Langley Research Center, Hampton, VA.

Pearsons, K., Howe, R., Sneddon, M., and Fidell, S. (**1996**). ''Comparison of the Performance of Noise Metrics as Predictors of the Annoyance of Stage II and Stage III Aircraft Overflights,'' NASA Contractor Report 198348, Langley Research Center, Hampton, VA.

Schomer, P. D. (**1994**). ''New descriptor for high-energy impulsive sounds,'' Noise Control Eng. J. **42**(5), 179–191.

Schomer, P. D., and Averbuch, A. (**1989**). ''Indoor human response to blast sounds that generate rattles,'' J. Acoust. Soc. Am. **86**, 665–673.

Schomer, P. D., and Neathammer, R. D. (**1998**). ''The role of helicopter noise-induced vibration and rattle in human response,'' J. Acoust. Soc. Am. **81**, 966–976.

Schomer, P. D., and Sias, J. W. (**1998**). ''On spectral weightings to assess human response, indoors, to blast noise and sonic booms,'' Noise Control Eng. J. **46**(2), 57–71.

Schomer, P. D., Sias, J. W., and Maglieri, D. (**1997**). ''A comparative study of human response, indoors, to blast noise and sonic booms,'' Noise Control Eng. J. **45**(4), 169–182.

Zhou, B., and Green, D. M. (**1995**). ''Reliability of pure-tone thresholds at high frequencies,'' J. Acoust. Soc. Am. **98**, 828–836.

Zwicker, E. (**1977**). ''Procedure for calculating loudness of temporally variable sounds,'' J. Acoust. Soc. Am. **62**, 675–682.

Summary of recent NASA studies of human response to sonic booms

Jack D. Leatherwood,[a)] Brenda M. Sullivan,[b)] Kevin P. Shepherd, David A. McCurdy, and Sherilyn A. Brown
Structural Acoustics Branch, NASA Langley Research Center, Hampton, Virginia 23681

(Received 27 April 2000; accepted for publication 11 February 2001)

NASA Langley Research Center has conducted three groups of studies on human response to sonic booms: laboratory, ''inhome,'' and field. The laboratory studies were designed to: (1) quantify loudness and annoyance response to a wide range of shaped sonic boom signatures and (2) assess several noise descriptors as estimators of sonic boom subjective effects. The studies were conducted using a sonic boom simulator capable of generating and playing, with high fidelity, both user-prescribed and recorded boom waveforms to test subjects. Results showed that sonic boom waveform shaping provided substantial reductions in loudness and annoyance and that perceived level was the best estimator of subjective effects. Booms having asymmetrical waveforms were found to be less loud than symmetrical waveforms of equivalent perceived level. Subjective responses to simulated ground-reflected waveforms were fully accounted for by perceived level. The inhome study presented participants with simulated sonic booms played within their normal home environment. The results showed that the equal energy theory of annoyance applied to a variety of multiple sonic boom exposures. The field studies concluded that sonic boom annoyance is greater than that in a conventional aircraft noise environment with the same continuous equivalent noise exposure. [DOI: 10.1121/1.1371767]

PACS numbers: 43.50.Jh, 43.50.Pn, 43.50.Qp, 43.66.Lj [MRS]

I. INTRODUCTION

NASA Langley Research Center is supporting NASA High-Speed Research Program (HSRP) efforts to develop an updated technology base for future high-speed civil transport aircraft. A particular component of the HSRP effort supported extensively by Langley was assessment of the environmental impact of sonic booms in terms of loudness and annoyance effects. This area is important because of its influence on the operational and economic aspects of commercial supersonic flight. For example, if aircraft configurations based upon ''minimum-boom'' design considerations were permitted to fly overland routes, then the economic viability of such aircraft would be greatly enhanced. Achievement of minimum-boom designs involves tailoring the lift and volume distributions of an aircraft, and hence the shape of the boom signature, to minimize boom loudness, reduce subjective startle effects, and lessen indoor effects such as wall and window vibration and rattle. Reductions in loudness and other effects (such as startle) may be achieved by modifying boom waveforms in such a manner as to reduce the high-frequency components of the waveforms and decrease front- and/or rear-shock strengths.

Potential benefits of sonic boom shaping were described in studies[1,2] using subjective tests to assess the relative loudness of symmetrical *N*-wave booms defined by various combinations of rise time, duration, and peak overpressure. Results from these studies showed that, for constant peak overpressure, substantial reductions in subjective loudness could be achieved by increasing the rise time of the front and rear shocks. Additional studies[3,4] suggested that boom loudness could be reduced by replacing *N*-wave signatures with symmetrical signatures that achieved peak overpressure in two pressure steps instead of one. This method, referred to as front-shock minimization, entailed decreasing the strength associated with the initial pressure rise (front shock) and then allowing a slower pressure rise to maximum overpressure. Booms shaped in this manner would contain significantly less high-frequency energy and be less loud than an *N* wave of identical front-shock rise time and maximum overpressure.

NASA Langley Research Center has conducted three groups of studies on sonic booms: laboratory, ''inhome,'' and field. These three complementary parts consist of (a) laboratory studies, which have very good control over the sound stimuli that the subjects hear but require a very abnormal listening environment; (b) an inhome study where sounds are played through loudspeakers in people's homes, thus improving the realism of the environment but reducing the control over the sound field; and (c) field studies with completely normal environment but very poor knowledge of the precise details of the sound exposure. The ''acceptability'' of or ''annoyance'' caused by a sound is affected by many factors. In a laboratory situation, while some of these factors are under control, others may be missing. Thus, ratings of sounds can be considered as accurate relative to one another, but not in an absolute sense. The inhome study moves closer to absolute measurements and the field studies measure absolute, real reactions. Another question affecting assessment of a sound exposure is the combination of single events into a long-term multiple-event situation. Within the laboratory,

[a)]Retired.
[b)]Electronic mail: b.m.sullivan@larc.nasa.gov

TABLE I. Summary of sonic boom psychoacoustic laboratory experiments.

Experiment	Number of subjects	Description	Scaling method	In paper
1	32	Simulator validation	PC[a]	No
2	60	Boom shaping effects	NCS[b]	Yes
3	40	Scaling study, NCS[c]	NCS	No
4	40	Scaling study, ME[c]	ME[d]	No
5	40	Asymmetrical booms No. 1	ME	Yes
6	72	Indoor/outdoor booms	ME	Yes
7	48	Recorded booms	ME	Yes
8	48	Reflected booms	ME	Yes
9, 10, and 11	32, 32, and 32	Booms vs flyovers Nos. 1, 2, and 3[e]	NCS, PC, and NCS	No
12	48	Intermediate shock effects	ME	No
13 and 14	32 and 56	Asymmetrical booms Nos. 2 and 3	ME	Yes

[a]PC: method of paired comparisons.
[b]NCS: numerical (11-point) category scale.
[c]Reference 5.
[d]ME: method of magnitude estimation.
[e]Reference 6.

such combining of reactions is again unrepresentative of a realistic situation. The inhome study, however, is designed to enable the investigation of multiple-event environments.

The series of laboratory experiments (14 studies) were designed to (a) develop an improved understanding of sonic boom subjective effects; (b) quantify in a systematic and comprehensive manner the loudness and annoyance benefits due to intentional sonic boom shaping as well as distortions due to passage through walls, ground reflections, and atmospheric propagation; and (c) assess various noise descriptors as predictors of sonic boom subjective effects. This paper summarizes the more important findings of these studies. The 14 sonic boom experiments are listed in Table I, which gives a brief description of each experiment, number of subjects, scaling method used, and a notation as to whether or not results from the experiment are included in the present paper.

Langley Research Center also completed an inhome study in which simulated sonic booms were played through loudspeaker systems in people's homes. Various scenarios involving different numbers of booms at different levels were played, and the participants were required to give annoyance judgments at the end of each day's exposure.

The third part of Langley Research Center's program to study subjective response to sonic boom was a series of field studies in which the responses of community residents experiencing supersonic overflights and their boom exposures were measured. This study was unique in that no other study has investigated the reactions of people routinely exposed to sonic booms over a long time period. It will not be discussed here and is fully reported in the NASA report.[7] In summary, the study found that sonic boom annoyance increased as the number and/or level of the booms increased. Sonic boom annoyance is greater than that in a conventional aircraft environment with the same continuous equivalent noise exposure. Large differences noted in responses from two localities were not attributable to sonic boom exposure, but were explained in part by differences in attitudes towards the ''noise makers'' and differences in exposure to low-altitude, subsonic aircraft flyovers.

II. SONIC BOOM SIMULATOR

The experimental apparatus used in the laboratory studies was the Langley Research Center's sonic boom simulator. Construction details, performance capabilities, and operating procedures of the simulator have been described by Leatherwood, Shepherd, and Sullivan.[8] The simulator, shown in Fig. 1, is a person-rated, airtight, loudspeaker-driven booth, carpeted and lined with foam to reduce acoustic resonances, and free of loose objects capable of creating rattles. It is capable of accurately reproducing user-specified sonic boom waveforms at peak sound pressure levels up to approximately 138 dB, corresponding to overpressures up to about 190 Pa. Input

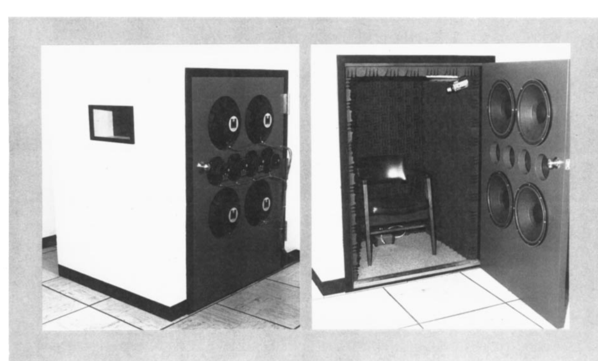

FIG. 1. NASA Langley sonic boom simulator.

waveforms were computer generated and preprocessed to compensate for nonuniformities in the magnitude and phase characteristics of the frequency response of the booth and sound reproduction system. Preprocessing was accomplished by the use of a digital broadband equalization filter described by Brown and Sullivan.[9] Plots of time histories of recordings made in the booth, such as are shown in Figs. 4 and 12, show good accuracy in reproducing boom shapes, with no evidence of room resonances. Maglieri and Plotkin[10] have stated that vibratory, auditory, and even visual factors may all affect human response to indoor sonic booms. Paulsen and Kasta[11] and Öhrström[12] have demonstrated that the presence of vibration can affect response to stimuli recorded or experienced inside buildings. Schomer and co-workers[13,14] reported that the presence of rattles strongly influences human response to noise inside buildings. Sounds such as helicopter noise and sonic boom, which contain considerable low-frequency energy, are likely to cause such rattles. However, a study[15,16] performed in a laboratory situation did not show the same influence from rattles, possibly because the rattling objects did not belong to the subjects so they were not concerned about the possibility of damage. The tests conducted in the Langley simulator were aimed at studying only the acoustical characteristics of *N* waves and shaped booms, and their effects on perceived loudness/annoyance; other effects, including building vibration, were not considered since it is believed that such effects cannot be meaningfully studied in a laboratory, but require a realistic field setting.

III. LOUDNESS OF FRONT-SHOCK-MINIMIZED (FSM) BOOMS

A. Description and purpose of study

This study (full details of which are published in Ref. 17) determined subjective loudness effects due to detailed and precise shaping of simulated sonic boom waveforms. Objectives were to: quantify the effects of sonic boom shaping on subjective loudness; assess several noise descriptors as subjective loudness predictors; and obtain preliminary data on waveform asymmetry effects. The study was conducted in the Langley sonic boom simulator using test subjects obtained from a subject pool of local residents. Subjective responses were obtained using a continuous 11-point numerical scale, with the end points labeled "not loud at all" and "extremely loud."

B. Stimuli for FSM study

The waveforms of the 180 test stimuli consisted of factorial combinations of four boom shaping parameters associated with the symmetrical front-shock-minimized (FSM) waveform shown in Fig. 2. The parameters were peak overpressure $\Delta p_{\max}$ of the waveform, front-shock rise time τ_1, secondary rise time τ_2, and ratio of front-shock overpressure to peak overpressure $\Delta p_f/\Delta p_{\max}$, denoted as the overpressure ratio. The factorial combinations consisted of five peak overpressures (ranging from 47.9 to 114.9 Pa); three secondary rise times (20, 30, and 50 ms); three front-shock rise

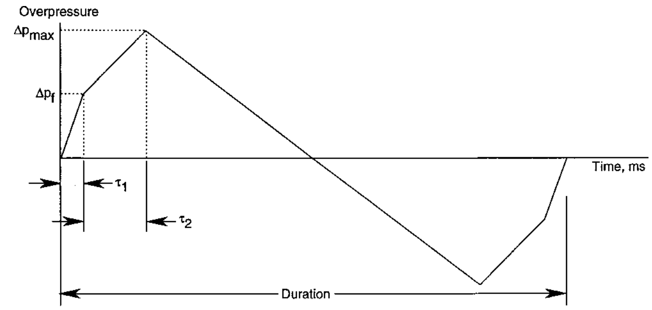

FIG. 2. Shape parameters for front-shock-minimized (FSM) sonic boom signatures: τ_1=front-shock rise time, τ_2=secondary rise time, $\Delta p_{\max}$=peak overpressure, and Δp_f=front-shock overpressure.

times (1, 2, and 4 ms); and four overpressure ratios (0.25, 0.50, 0.75, and 1.00). Duration of all FSM waveforms was 300 ms.

C. Front-shock-minimization results

Mean subjective loudness ratings for each factorial combination of peak overpressure, overpressure ratio, and front-shock rise time are displayed in Figs. 3(a)–(c). The loudness ratings were averaged over secondary rise time τ_2, since statistical analysis indicated they did not depend upon τ_2. Each plot in Fig. 3 contains results for a single front-shock rise time. Also shown in each plot (by the inverted triangles) are mean subjective loudness ratings for *N* waves which have the same rise time as the corresponding FSM waveforms. The *N*-wave data were obtained in an earlier unpublished laboratory experiment by two of the present authors.

Figure 3 shows that all FSM waveforms were rated as quiet as or quieter than *N* waves of comparable peak overpressures. Also, for a given loudness rating, the FSM waveforms had substantially higher peak overpressures than the *N* waves, except for those FSM waveforms for which $\Delta p_f/\Delta p_{\max}=1$ (called a flattop waveform). Thus, significant loudness reductions (relative to *N*-wave loudness) were realized, depending upon the particular combinations of FSM shaping parameters selected.

D. Comparison of noise descriptors

The noise descriptors selected for evaluation as loudness predictors were: flat-weighted sound exposure level (FSEL); *C*-weighted sound exposure level (CSEL); A-weighted sound exposure level (ASEL); Stevens Mark VII perceived level (PL) (modified as described in Ref. 4); and Zwicker loudness level (ZLL). Linear correlation coefficients between descriptor levels and mean loudness ratings were calculated for each descriptor. Detailed descriptions of the statistical analyses are given in the report.[17] The highest correlations occurred for ASEL, PL, and ZLL. Any one of these descriptors could be used to predict loudness with similar prediction accuracy.

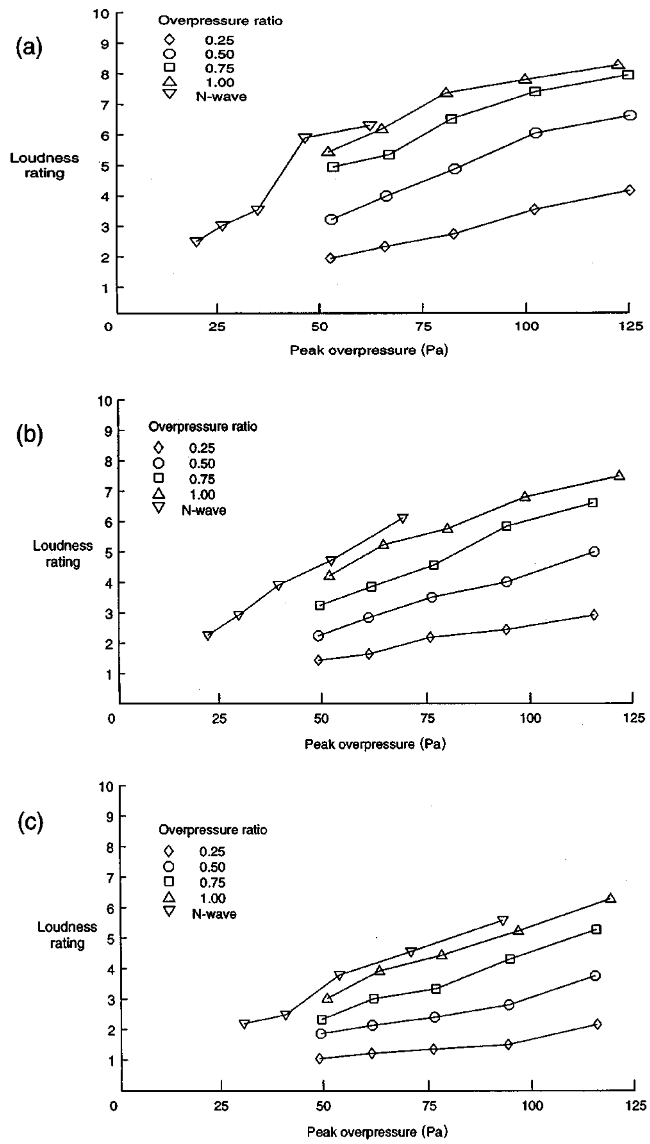

FIG. 3. Effect of peak overpressure level, overpressure ratio, and front-shock rise time on subjective loudness for front-shock-minimized signatures: (a) $\tau_1 = 1$ ms, (b) $\tau_1 = 2$ ms, and (c) $\tau_1 = 4$ ms.

IV. LOUDNESS AND ANNOYANCE OF SIMULATED INDOOR AND OUTDOOR SONIC BOOMS

A. Description and purpose of study

The previous study investigated the effects on loudness of boom shaping for booms as they would be heard outdoors. However, there remained a question as to whether the benefits would carry over to waveforms representative of booms heard indoors. Because of room acoustics and wall attenuation effects, indoor waveforms generally lack distinctive rise time characteristics and lose significant high-frequency spectral energy. The result is an increase in relative emphasis of low-frequency spectral components of the indoor waveforms which could introduce annoyance components not present in outdoor waveforms. If so, annoyance could perhaps be a more appropriate subjective criterion measure than loudness. These issues were addressed in a study[18] that: (1) investigated loudness and annoyance response to simulated indoor and outdoor *N*-wave and FSM waveforms; (2) determined the more appropriate criterion measure (i.e., loudness or annoyance) for assessing subjective effects; and (3) evaluated the five noise descriptors described in Sec. III as estimators of loudness and annoyance for both outdoor and indoor waveforms. Two groups of test subjects were used; one group made loudness judgments and the other made annoyance judgments. The scaling method used was magnitude estimation. The stimulus used as a standard was a symmetrical *N* wave with a front-shock rise time of 3 ms and peak overpressure of 42.6 Pa, which was assigned a loudness (or annoyance) value of 100. All stimuli were presented in a random order; thus, indoor and outdoor booms were intermingled. The test subjects were not told that the test sounds included ''indoor'' and ''outdoor'' booms; they simply heard a sound having a range of auditory characteristics. Thus, this experiment has no relevance to the determination of acceptable levels, either indoors or outdoors; it is solely concerned with changes in subjects' responses due to changes in the acoustical characteristics of the booms. The concept of ''perceptual constancy'' describes the tendency of people to judge sounds differently depending on their preconceptions of what is expected (or acceptable) indoors or outdoors.[19] Such findings apply to tests in which the subjects had some knowledge of the experienced (or simulated) situation, or some familiarity with what the test stimuli would sound like when heard indoors or out. In this experiment, relative responses to stimuli in a laboratory situation only were studied, and perceptual constancy is not a factor.

B. Stimuli for indoor/outdoor boom study

The test stimuli consisted of 135 simulated sonic boom waveforms. Forty-five of these represented outdoor waveforms and 90 represented indoor waveforms. The simulated outdoor waveforms consisted of the three boom types displayed in the top row of Fig. 4. These were: *N* waves, FSM waveforms with the ratio of front-shock overpressure to peak overpressure equal to 0.50, and FSM waveforms with a front-shock overpressure to peak overpressure ratio of 0.75. Front-shock rise times of 2, 4, and 8 ms were used for each boom type. All waveforms had durations of 300 ms. Both FSM waveforms had secondary rise times of 60 ms. The indoor waveforms were obtained by applying the two ''house filters'' shown in Fig. 5 to the outdoor waveforms. The filters are defined in the report[18] and were derived from measured data using steady-state, nonimpulsive sounds, as no data were available for impulsive sounds. One filter approximates the magnitude of the frequency-dependent noise reduction characteristics associated with transmission of sound into a typical residential structure with the windows open. The other filter represents the noise reduction characteristics with the windows closed. The waveforms obtained by applying these filters to the three outdoor boom types are shown in the middle and lower rows of Fig. 4, respectively. Phase effects were not simulated so waveforms measured in realistic indoor environments could look considerably different from these plots, but the spectral content would be similar.

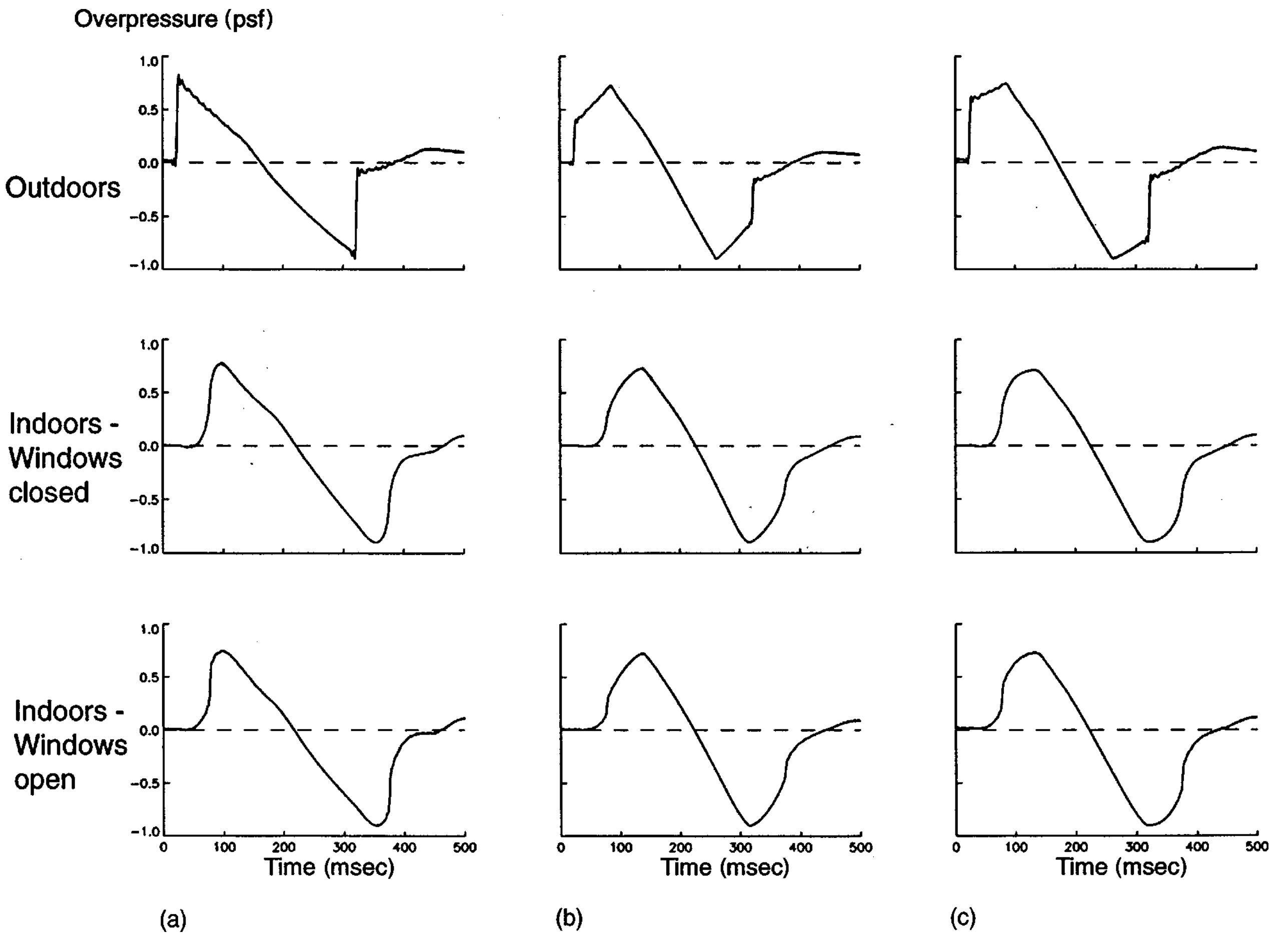

FIG. 4. Boom signatures measured in simulator for three boom types and three simulated listening conditions. Boom types are (a) *N* waves, (b) FSM with overpressure ratio of 0.5, and (c) FSM with overpressure ratio of 0.75. Front-shock rise time for all boom types shown is 2 ms. Simulated listening conditions are (i) outdoors; (ii) indoors, windows closed; and (iii) indoors windows open.

C. Comparison of noise descriptors

The predictive ability of each noise descriptor was determined as described in Sec. III. Correlation coefficients and standard errors of estimate for (a) the total stimuli set (135 waveforms); (b) the outdoor waveforms (45 waveforms); (c) the indoor, windows-open condition (45 waveforms); and (d) the indoor, windows-closed condition (45 waveforms) are presented in the report.[18] To summarize the results, first, the noise descriptor that performed most consistently (high correlations and low standard errors of estimate) under all conditions was PL. Second, with the exception of ASEL, correlation coefficients obtained for the annoyance criterion were insignificantly less than (within 1.5%) or exceeded those obtained for the loudness criterion. Thus, in an overall sense, annoyance was the more accurate subjective response criterion measure than loudness. The poorer performance of ASEL for the annoyance criterion was due to the low-frequency rolloff of the A-weighting filter which prevented ASEL from accounting for the effects of low frequencies which were the likely source of annoyance effects.

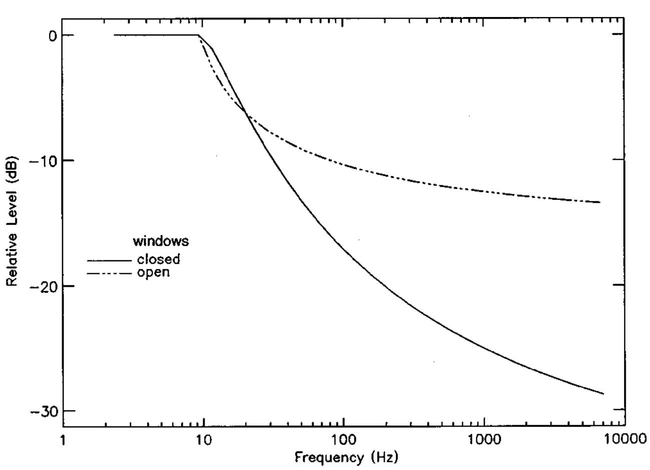

FIG. 5. Frequency response functions for windows-open and windows-closed house filters.

D. Loudness versus annoyance comparisons

The central tendency parameter used to characterize the loudness or annoyance estimates for each stimulus was the geometric mean of the subjective ratings. The logarithms of the geometric means are displayed in Figs. 6(a)–(c) as a function of the perceived level for the outdoor, indoor windows-closed, and indoor windows-open waveforms. Linear regression lines are also shown. Perceived level was used based upon its demonstrated ability to predict the loudness of shaped booms (see Sec. III) and its consistent performance as both a loudness and annoyance estimator in these studies.

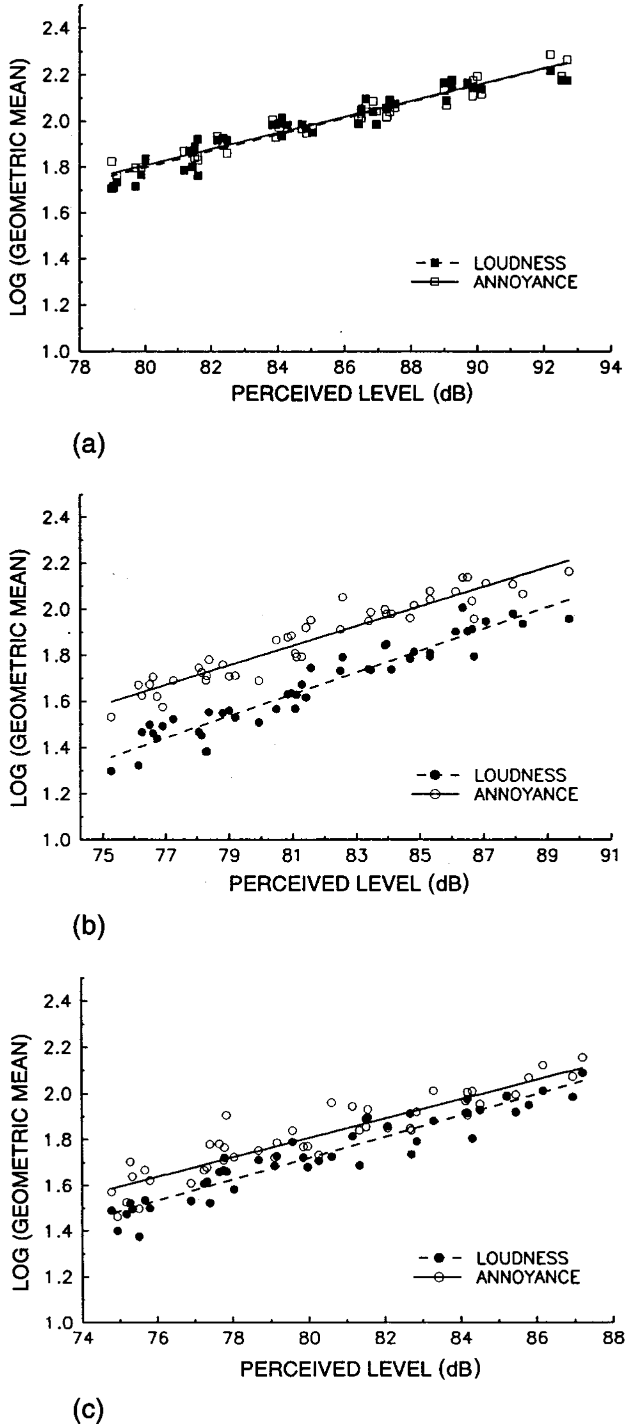

FIG. 6. Loudness and annoyance response comparisons for three simulated listening conditions: (a) outdoor condition; (b) indoor, windows-closed condition; and (c) indoor, windows-open condition.

Figure 6(a) shows that the numerical values assigned to loudness and annoyance for the simulated outdoor waveforms were identical. This implies that the outdoor waveforms did not contain annoyance components beyond those attributable to loudness. Numerical values of annoyance for the simulated indoor waveforms [Figs. 6(b) and (c)], however, were generally larger than those for loudness at equal PL, especially for the windows-closed waveforms. This implies that the indoor waveforms contained annoyance components beyond that due solely to loudness. Dummy variable analysis showed these differences to be statistically significant (probability <0.001) and that the slopes of the two lines in each figure were equal. In terms of PL, the difference between each pair of lines in Figs. 6(b) and (c) is 4.2 dB for the windows-closed condition and 1.6 dB for the windows-open condition. It is noteworthy that the difference between loudness and annoyance response increases with increasing low-frequency content in the waveform (outdoor condition to indoor windows open to indoor windows closed).

Based upon the above results, a preferred subjective criterion measure and subjective response estimator for booms heard indoors can be identified. The preferred criterion measure is annoyance and the preferred subjective response estimator is PL. Selection of annoyance as the criterion measure is based on (a) the presence of an additional annoyance component for the indoor waveforms (as evidenced by the higher annoyance scores) and (b) improved prediction accuracy when annoyance was the criterion. Selection of PL as the best metric was based on the demonstrated ability of PL to account for loudness effects of outdoor waveforms and annoyance effects of both indoor and outdoor waveforms. For booms heard outdoors either annoyance or loudness can be used as the criterion measure.

The subjective benefit to be derived from minimizing the boom shape was carried through from the outdoor situation to the indoors and was accounted for by the PL noise descriptor.

V. LOUDNESS OF GROUND-REFLECTED SONIC BOOM WAVEFORMS

A. Description and purpose of study

In an outdoor situation, a human observer is generally near a reflecting surface and, therefore, would hear at least two booms, one directly propagated from the aircraft (direct boom) and one reflected from the ground (reflected boom). The direct and reflected booms combine to form a composite waveform which is the waveform perceived and judged by the observer. A significant factor influencing the shape (and, consequently, subjective perceptions) of a composite waveform is the delay time of the ground-reflected boom. This is the time by which a reflected boom lags the direct boom and is a function of observer height and angle of incidence of the shock wavefront. The purpose of this study was to quantify the subjective loudness effects due to ground reflections of simulated *N*-wave and FSM waveforms. The study[20] also used magnitude estimation scaling.

B. Stimuli for reflected boom study

Each simulated composite waveform was defined by the combination of a direct boom waveform with a delayed version of the direct waveform with no change in phase or amplitude between the two. For each direct waveform six delay times were used. Thus, each direct waveform produced six unique composite waveforms. Twenty-four distinct direct waveforms were used and consisted of factorial combinations of two boom types, three front-shock rise times, and four peak overpressure levels.

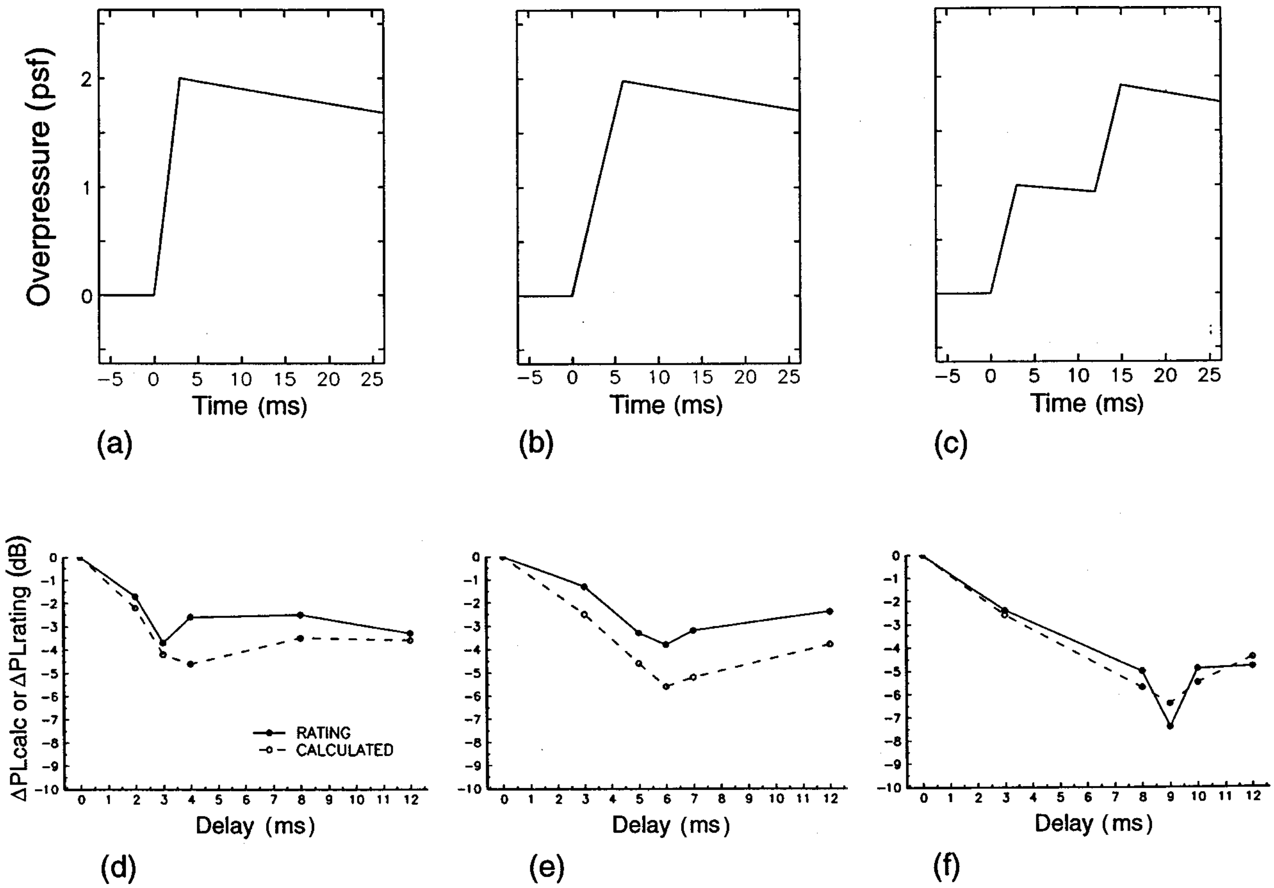

FIG. 7. Front portions of nominal composite boom signatures for *N* waves with added reflection at three delay times: direct boom has a rise time of 3 ms. (a) Delay time=0 ms, (b) delay time=3 ms, and (c) delay time=12 ms. Effect of varying delay time on calculated PL (dashed lines) and subjective response (solid lines) for *N* waves with rise times of 3, 6, and 9 ms, normalized to the values for zero delay time. (d) Rise time=3 ms, (e) rise time=6 ms, and (f) rise time=9 ms.

The two direct waveform types were *N*-wave and front-shock minimized. The FSM waveform had a front-shock overpressure to peak overpressure ratio of 0.5 and a secondary rise time of 60 ms. Front-shock rise times for each direct waveform type were 3, 6, and 9 ms. Duration for all direct waveforms was 300 ms. Six values of delay time were used to generate the six composite waveforms for each waveform type/front-shock rise time combination. Delays of 0, 3, and 12 ms were common to all combinations. The remaining three values of delay time for each combination were: delay time=front-shock rise time; and delay time=front-shock rise time ±1 ms. The direct waveforms having a 3 ms rise time included a delay of 8 ms. The front portions of nominal composite waveforms for an *N* wave, with a 3 ms rise time, combined with reflected waveforms having 0, 3, and 12 ms time delays are displayed in Figs. 7(a), (b), and (c). Figures 7(d), (e), and (f) show the effect upon calculated PL (dashed lines) of varying delay time for *N* waves with rise times of 3, 6, and 9 ms, normalized to the values for zero-delay time. Also shown is the effect on subjective rating (solid lines) normalized in the same way. Both calculated level and subjective rating reach a minimum at or close to the point where the delay time of the reflected *N* wave equals the *N*-wave rise time, that is, the reflected boom begins just when the direct boom reaches its maximum overpressure.

C. Delay versus no delay

Correlation and regression analyses (results presented in Ref. 20) were conducted to assess the five noise descriptors. They indicated that PL correlated highest with subjective loudness ratings and exhibited the lowest standard errors of estimate for all composite waveforms. These findings support the earlier recommendation that PL be selected as the descriptor of choice for general use in assessing sonic boom subjective effects. Since PL best accounted for loudness effects of composite waveforms containing reflections of varying time delay, subjective ratings of composite booms with nondelayed reflections should not differ significantly from those with delayed reflections when expressed in terms of PL. This is confirmed in Fig. 8, which compares subjective response to composite waveforms containing delayed reflections to those containing nondelayed reflections. The comparison is made in terms of the linear regression lines for each case and shows that, when expressed in terms of PL, subjective responses for the composite waveforms with delayed and nondelayed reflections were virtually identical. This does not imply, however, that the loudness of composite waveforms was independent of delay time. It simply means that any such effects were accounted for by PL. Overall, PL performed very well as an estimator of subjective loudness

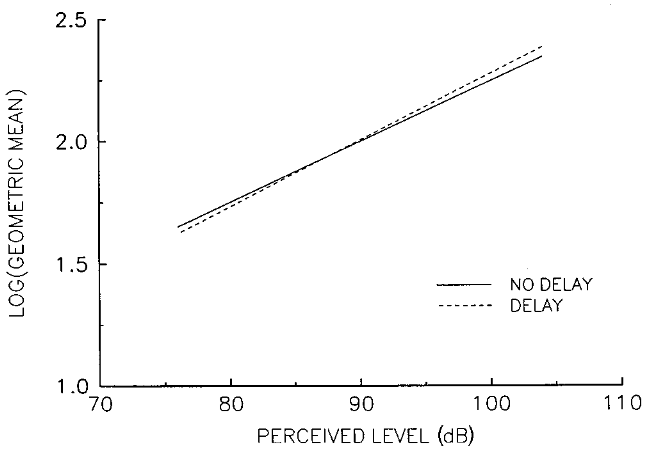

FIG. 8. Comparison of the linear regression lines relating subjective response to perceived level for the delay and no delay booms.

for sonic boom waveforms containing single reflections of varying time delay.

VI. LOUDNESS OF ASYMMETRICAL SONIC BOOMS

A. Description and purpose of study

Preliminary results in Sec. III implied that asymmetrical sonic boom waveforms may be less loud than symmetrical waveforms of equivalent PL. To explore this issue, three follow-up experiments, which utilized a wide variety of asymmetric waveforms, were conducted. Sonic boom waveform asymmetry was intentionally introduced by systematically varying the rise times and peak overpressures of the front and rear shocks of simulated *N*-wave waveforms. This process resulted in a set of waveforms in which the loudnesses of the front and rear portions of each waveform generally differed. The parameter used to define loudness asymmetry was the difference between calculated PL of the front shock and calculated PL of the rear shock of a waveform. Objectives of these studies were to (1) quantify subjective loudness as a function of both the magnitude and direction (that is, front louder than rear versus rear louder than front) of asymmetry; (2) compare loudnesses of symmetrical and asymmetrical waveforms having equivalent total PL; and (3) determine asymmetry effects for waveforms of varying duration.

B. Stimuli for waveform asymmetry studies

The stimuli for the first experiment[21] consisted of *N* waves in which the rise times and peak overpressures of the front and rear shocks were systematically and independently varied. Three rise times (2, 3, and 6 ms) and five front and five rear peak overpressure amplitudes were selected. Factorial combinations of these resulted in a stimuli set containing 225 unique waveforms, each of which had a duration of 300 ms. Front- and rear-shock loudness differences were attributable to peak overpressure differences (when front- and rear-shock rise times were equal), spectral differences (when front and rear rise times were unequal), or both.

The stimuli for the second experiment (unpublished) consisted of asymmetrical *N* waves having equal front- and rear-shock rise times. Loudness asymmetry for these waveforms resulted from differences in peak overpressure between the front and rear shocks. No loudness differences due to spectral effects were present. As in the first asymmetry experiment, each waveform duration was 300 ms. Rise times selected were 2, 3, and 6 ms. For each rise time two values of PL for the complete waveform were used; these were not the same across rise times. This experiment differed from the first asymmetry experiment in that 11 loudness asymmetry magnitudes were preselected for each unique combination of rise time and PL. Nominal loudness asymmetry magnitudes ranged from -20 to $+20$ dB, including a nominal asymmetry value of 0 dB. This resulted in a total of 66 waveforms defined by the factorial combinations of rise time, peak overpressure, and asymmetry magnitude.

The stimuli set for the third experiment (unpublished) used the same factors (three rise times, two levels of PL, 11 loudness asymmetry values) as the second asymmetry experiment except that each of the 66 waveforms was used in two versions, one with a duration of 100 ms and the other with a duration of 200 ms instead of 300 ms. This resulted in 132 waveforms. An additional group of 22 stimuli each having a duration of 300 ms and a rise time of 2 ms were included for comparison with findings of the first and second experiments. Thus, the total stimuli set for the third asymmetry experiment contained 154 waveforms.

C. Waveform asymmetry effects

Asymmetry magnitude and direction were defined by the expression "$\mathrm{PL}_f - \mathrm{PL}_r$," where PL_f is the calculated loudness of the front shock and PL_r is the calculated loudness of the rear shock. The value of this expression is the magnitude of asymmetry and the sign of the expression defines asymmetry direction. If $\mathrm{PL}_f = \mathrm{PL}_r$ the waveform is symmetrical. Typical results obtained in the first asymmetry experiment showing the effects of asymmetry magnitude and direction are displayed in Figs. 9(a)–(d) for waveform asymmetry magnitudes of approximately ± 4, ± 8, ± 12, and ± 16 dB. Each plot displays linear regression lines describing the relationship between the logarithms of the geometric means of the magnitude estimates and total perceived level for (a) waveforms which have zero or very small (within ± 1 dB) loudness asymmetry (solid lines); (b) waveforms with positive asymmetry (dotted lines); and (c) waveforms with negative asymmetry (dash-dotted lines). The solid lines, labeled as symmetrical, are identical in each plot.

The results of Fig. 9 indicate that loudness of asymmetrical signatures, for each asymmetry magnitude, was generally less than the loudness of symmetrical signatures of equivalent total PL. The magnitude of the loudness reductions increased as asymmetry magnitude increased and depended upon the direction of asymmetry. This is shown by consecutive inspection of Figs. 9(a)–(d). Generally, waveforms having negative asymmetry magnitudes were judged to be less loud than those having positive asymmetry magnitudes when compared on the basis of equivalent total PL. This effect increased with increasing absolute values of asymmetry magnitude.

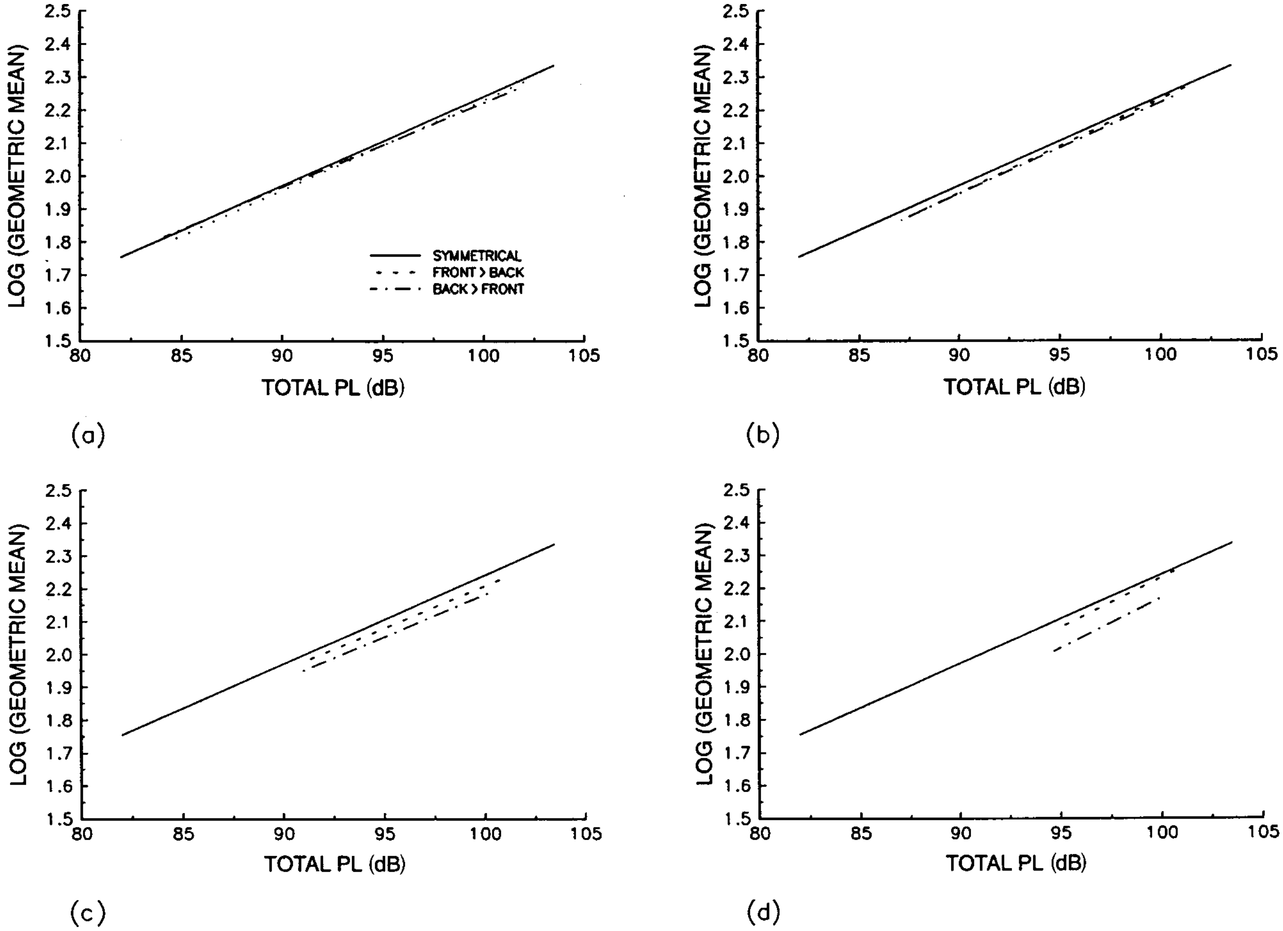

FIG. 9. Linear regressions of subjective response on total PL for four categories of *N*-wave signature asymmetry: (a) asymmetry≈±4 dB, (b) asymmetry≈±8 dB, (c) asymmetry≈±12 dB, and (d) asymmetry≈±16 dB.

The overall effect of waveform asymmetry on subjective loudness was separately determined for each experiment using the following procedure. Linear regression analysis was performed between the logarithms of the geometric means (dependent variable) and PL for the total waveforms (independent variable). The residuals, calculated from each analysis, contained the effects of waveform asymmetry and experimental error for a given experiment. By curve fitting the residual data using asymmetry magnitude (up to third order) as the independent variable, subjective loudness changes as a function of asymmetry magnitude were determined. These changes were then converted from subjective scale units to equivalent PL units using the regression coefficient obtained for PL. The equivalent PL values represent corrections to total calculated PL due to waveform asymmetry. Hereinafter they will be referred to as PL asymmetry corrections. For example, a PL asymmetry correction of −3 dB indicates that the total PL calculated for an asymmetrical waveform of interest overestimated the actual loudness by 3 dB.

PL asymmetry corrections obtained by applying the above procedure to the data for each experiment are shown in Fig. 10 as a function of asymmetry magnitude. Since the waveforms of the first and second asymmetry experiments were all of 300 ms duration, only the 22 waveforms of experiment 3 that had durations of 300 ms were used to determine the curve for experiment 3 in Fig. 10. Figure 10 shows that PL asymmetry corrections were generally negative when a rear shock was louder than a front shock and became increasingly negative with increasingly negative asymmetry magnitudes. At an asymmetry magnitude of approximately −20 dB, the PL asymmetry corrections were about −3 dB. For positive asymmetry magnitudes the PL asymmetry cor-

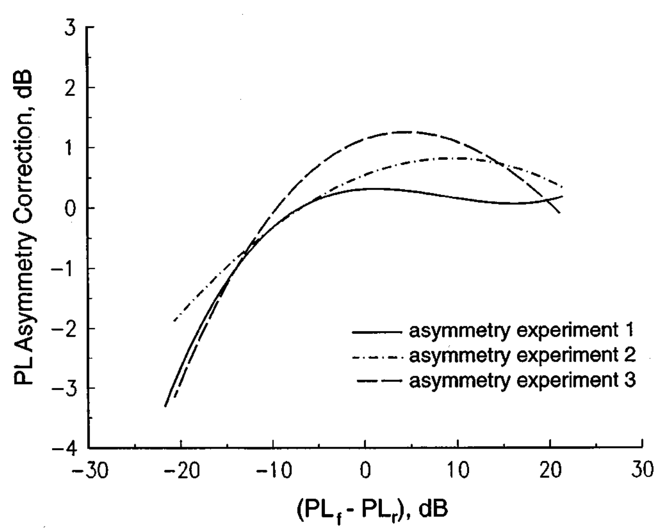

FIG. 10. *N*-wave asymmetry effect: correction to measured PL for waveforms of 300 ms duration.

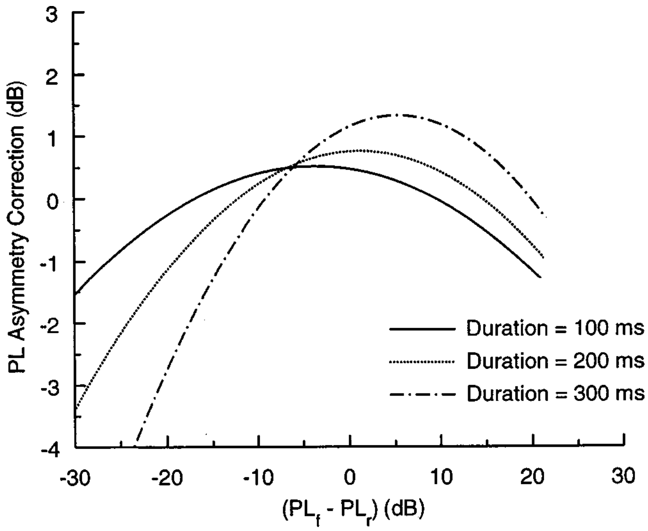

FIG. 11. *N*-wave asymmetry effect: correction to measured PL for waveforms of durations 100, 200, and 300 ms—third asymmetry experiment.

rections were relatively small (less than about ± 1 dB). Statistical analysis indicated that the differences between the three curves were not significant (probability <0.05).

The asymmetry effects obtained in the third asymmetry experiment for sonic boom waveforms of 100, 200, and 300 ms durations are presented in Fig. 11. These results show that asymmetry effects diminished and that the difference between positive and negative asymmetry decreased as the duration of the waveforms decreased.

The underlying auditory or perceptual mechanisms responsible for the asymmetry effects are unclear. Temporal masking does not appear to be an operative factor since the delay between the front and rear shocks was 300 ms and significant temporal masking effects are generally limited to delay times of less than 200 ms.[22] The temporal spacing between the front and rear shocks tends to rule out the single time constant model of loudness integration as a contributing factor to these results. One possible explanation might lie in the two time constant loudness integration model proposed by Ogura *et al.*,[23,24] which uses one time constant for signals of increasing intensity and another, much longer one for signals of falling intensity. Another possibility is that some type of ''psychological'' masking was present that caused the loudness, or presence, of a weaker front shock to divert, or mask, the attention of the subjects such that the effects of the rear shocks were not fully perceived. These ideas are speculative, however, and further research into asymmetry effects would be required in order to gain additional understanding of these results.

VII. LOUDNESS OF REALISTIC SONIC BOOM WAVEFORMS

A. Description and purpose of study

The studies discussed earlier used simple boom waveforms representing idealized booms predicted by theory and, consequently, were not representative of the many complex shapes that real booms can take after propagation through the atmosphere. For example, the shape of the front shock is affected by molecular relaxation and viscosity in ways that are fairly well understood. Turbulence, however, affects the waveforms in ways that can only be predicted statistically. Obviously, it was impractical to synthesize the many waveforms required to replicate an adequate sample of such a process in the sonic boom simulator. A more reasonable approach was to use ground-recorded waveforms obtained from actual aircraft flyovers. Fortunately, a collection of sonic boom waveform recordings obtained during tests at White Sands Missile Range was available[25] and was used to select the realistic waveforms used in this study.

The purpose of this study was to quantify subjective loudness response to a set of waveforms selected from those recorded at White Sands Missile Range. The selected waveforms represented several shapes that sonic booms may take when modified by turbulence. These shapes have been categorized by previous investigators[26] as: *N* waves, peaked waves (booms with one or more peaks on both front and rear shocks), rounded waves (booms with rounded front and rear shocks), and ''U-shaped'' waves (booms having two strong positive-going peaks).

B. Stimuli for realistic boom study

The test stimuli (see Ref. 27) consisted of simulator reproductions of recorded sonic booms from flyovers of F15 and T38 aircraft together with several computer-generated idealized waveforms. Thirteen recorded waveforms, having a range of rise times, were selected from the White Sands database. These consisted of: three *N* waves, four peaked waves, three rounded waves, and three U-shaped waves. Sample waveforms for three of these categories are shown in Fig. 12. In addition, three idealized *N* waves were included to provide a basis for comparing subjective response to realistic versus idealized waveforms. To simulate future supersonic transports more accurately, the F15 and T38 waveforms were ''stretched'' by increasing the time between the pressure shock at the front of the waveform and the similar shock at the tail. The shapes and rise times of the front and rear shocks were unchanged by this procedure. Each of the stimuli defined above was presented at five levels.

C. Loudness response to recorded waveforms

Since each boom category represented a ''shape'' that a boom may assume after propagation through atmospheric turbulence, any differences in loudness ratings between the various categories when viewed as a function of PL are indicative of an effect not accounted for by PL.

If these differences are small and statistically insignificant, it can be concluded that atmospheric alterations of the waveforms are accounted for by PL. Linear regression lines showing the relationship between the logarithm of the geometric means of the loudness magnitude estimates and PL for each boom category are presented in Fig. 12. As indicated in Fig. 12 the regression lines are tightly grouped and exhibit similar slopes. Statistical analysis confirmed that the regression lines were identical in both slope and intercept (probability<0.001). This does not mean that waveforms of different shapes but comparable peak overpressures were

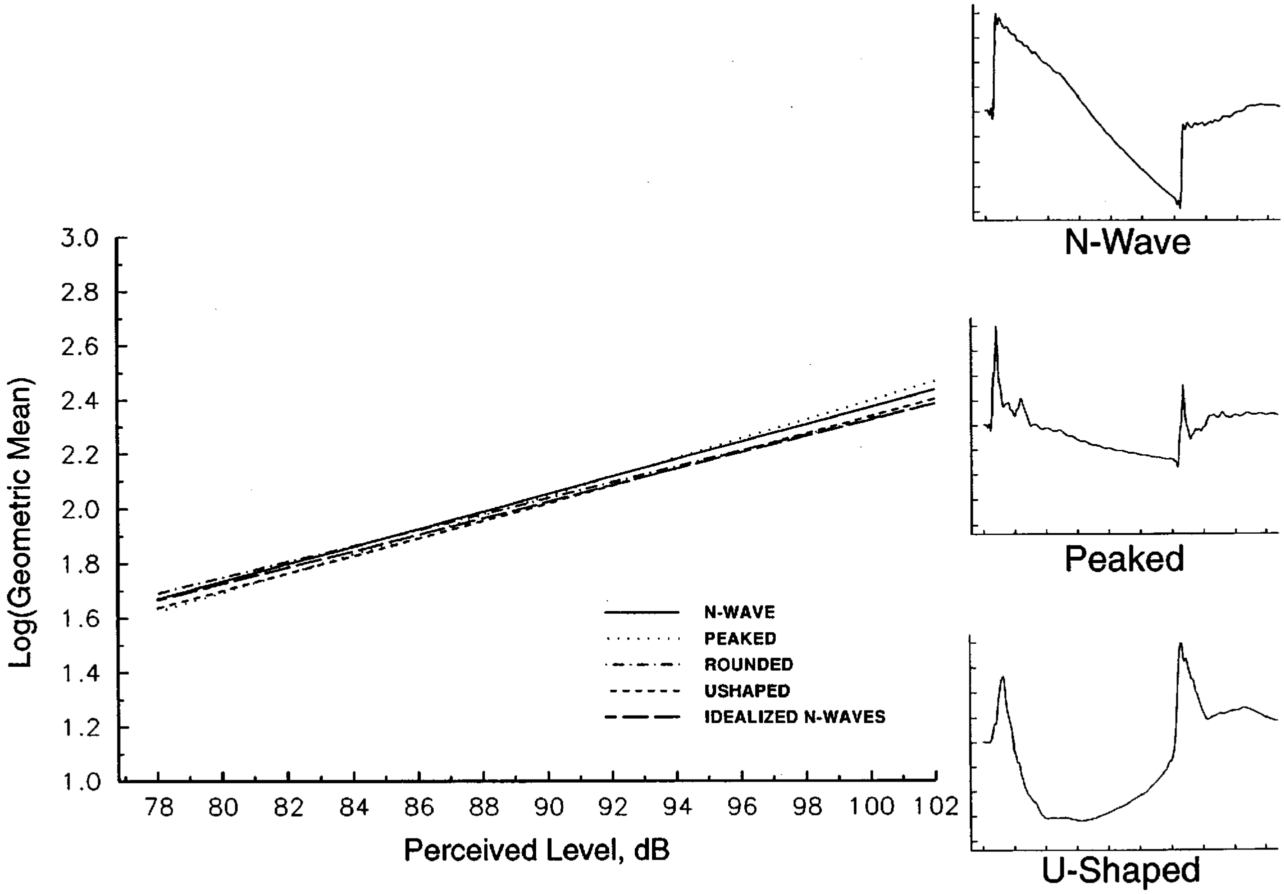

FIG. 12. Linear regression of subjective response on perceived level, for each of five boom categories, in terms of the PL descriptor, with example waveforms from three of the categories.

rated equally loud. In fact, this was not the case. The results do show that PL effectively accounted for the turbulence-induced shape differences between the recorded waveforms as well as the difference between the idealized *N* waves and the White Sands booms.

VIII. RESPONSE OF PEOPLE IN THEIR HOMES TO SIMULATED SONIC BOOMS

A. Description and purpose of study

In the inhome study,[28] a computer-controlled audio system played simulated sonic booms from a custom-recorded CD through loudspeakers installed in the test subject's home. The primary objective of the study was to determine the effect on annoyance of the number of sonic boom occurrences in a realistic environment. There is a trade off between noise level and number implicit in community noise ratings such as equivalent-continuous sound level (L_{eq}) and day–night average sound level (L_{DN}). The validity of this trade off has been questioned for cases where the daily number of sounds is low. Typically, these ratings have been tested around airports, which have large numbers of events. For expected exposure to sonic booms from commercial aircraft, the number of exposures would be small. Therefore, this test was designed to address the issue of small numbers of events.

Analysis of the data also addressed the questions: (1) How does the waveform shape and the level of the boom affect annoyance? (2) What is the effect of startle on annoyance? (3) Which noise descriptor best predicts annoyance to sonic booms?

The system was installed for eight weeks in each of 33 homes. One person per household was designated the subject and once a day was asked to respond to a number of questions presented on the computer's monitor. The loudspeakers were situated in the rooms most used by the subject and varied in number from two to four depending on the size of the home.

A 14 h daytime exposure period was chosen, during which a predetermined number of booms was played at randomized times. At the end of each test day, the subject answered a series of questions about his or her activities during the day. He or she was asked to give an overall annoyance rating to the total sonic boom exposure for the day (i.e., to all the sonic booms heard during the day) on a scale of 0 to 10. The subject was also asked if he or she was startled by any of the sonic booms during the day.

B. Stimuli for inhome boom study

The stimuli used in this test represented combinations of three boom waveforms, three A-weighted sound exposure levels, and seven boom occurrence rates. The three boom waveforms represented an *N* wave as heard outdoors, an *N* wave as heard indoors, and a front-shock-minimized boom as heard outdoors. All booms were symmetrical with 300 ms

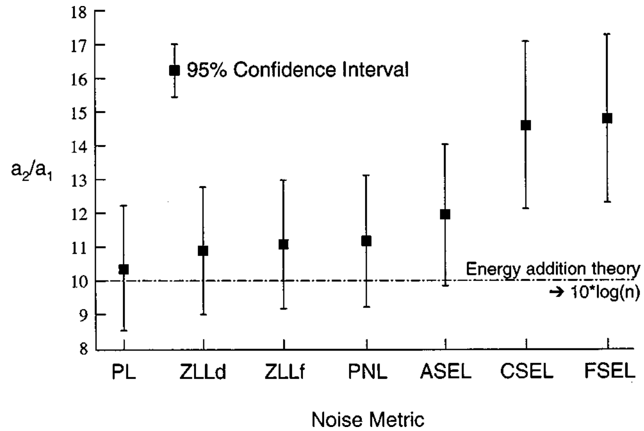

FIG. 13. Determination of log(N) coefficient in modeling the effect of number of sonic boom occurrences on annoyance. Annoyance$=a_0+a_1$ level $+a_2$ log(number of events).

duration and rise times of 4 ms. The FSM boom had a secondary rise time of 30 ms and an overpressure ratio of 0.3. The nominal ASEL levels used were 66, 70, and 74 dB. The occurrence rates were 4, 10, 13, 25, 33, 44, and 64 booms per day. Only one sonic boom waveform was presented each day. On most days the sonic boom was presented at only one level. On a few test days the boom was presented at two or three of the test ASEL levels.

C. Results of inhome boom study

The results of this study lead to the conclusion that annoyance increases as the number of sonic booms heard increases. This effect of number of occurrences can be modeled by the addition to the measured sonic boom level of the term $k\times\log$(number of booms). The value of k can be determined from the coefficients of a multiple regression equation as follows:

$$A=a_0+a_1\times[L+k\times\log(N)], \tag{1}$$

where A=annoyance rating, L=individual sonic boom level, and N=number of sonic boom occurrences. Expanding the equation gives

$$A=a_0+a_1\times L+a_1\times k\times\log(N). \tag{2}$$

Replacing $a_1\times k$ with a_2 gives the regression equation

$$A=a_0+a_1\times L+a_2\times\log(N), \tag{3}$$

where $a_2=a_1\times k$ and $k=a_2/a_1$. Figure 13 shows the value of k in terms of a_2/a_1 and the corresponding 95% confidence intervals on k as determined from multiple regression analyses for each of the noise descriptors. The descriptors used were flat-weighted sound exposure level; C-weighted sound exposure level; A-weighted sound exposure level; Stevens Mark VII perceived level (modified as described in Ref. 4); perceived noise level (PNL); Zwicker loudness level [diffuse field (ZLLd)]; and Zwicker loudness level [frontal field (ZLLf)]. As shown in Fig. 13, the calculated values of k ranged from 10 to 15, depending on the descriptor considered. Based on energy addition theory, the predicted value of k is 10, as indicated by the dashed line. For all but two of the descriptors, FSEL and CSEL, the 95% confidence interval about the calculated value includes this value. The most likely reason that the 95% confidence intervals for FSEL and CSEL do not include 10 is the slope of the loudness function. For a given overpressure, changes in rise time will affect the loudness and A-weighted values, but have little effect on CSEL or FSEL. Thus, the slope of the latter plotted against loudness will yield a relatively low value, which will translate into an apparent deviation from "equal energy" ($k>10$). Thus, the deviation from equal energy is most likely an artifact of CSEL and FSEL being poor predictors of loudness for the sounds included in this study.

Of the descriptors studied, PL was the best predictor of annoyance. The results of this study also showed the effects of waveform shapes were accounted for by the noise descriptors; startle increases annoyance; and the louder the boom is, the greater is the increase in annoyance caused by startle.

IX. SUMMARY

NASA Langley Research Center has conducted three groups of studies on sonic booms: laboratory, inhome, and field. These three complementary parts consisted of (a) laboratory studies, which have very good control over the sounds that the subjects hear but require a very abnormal listening environment; (b) an inhome study where sounds are played through loudspeakers in people's homes, thus improving the realism of the environment but reducing the control over the sound field; and (c) field studies with a completely realistic environment but poor knowledge of the precise details of the sound exposure.

NASA Langley Research Center conducted the laboratory studies to: (1) quantify loudness and annoyance response to a wide range of shaped sonic boom signatures and (2) assess several noise descriptors as estimators of sonic boom subjective effects. The studies were conducted using a sonic boom simulator capable of generating and playing, with high fidelity, both user-prescribed and recorded boom waveforms to test subjects. Results from the totality of the tests indicated that perceived level was the best estimator of subjective effects.

These studies included classical N-wave shapes and also front-shock-minimized waveforms, that is, waveforms that reach peak overpressure in two steps, consisting of an initial short-duration rise to an intermediate pressure Δp_f, followed by a considerably longer duration rise to the final peak overpressure $\Delta p_{\max}$. Test results showed that FSM waveforms were rated less loud than N waves of comparable peak overpressures. The amount of loudness reduction depended on the duration of the initial rise and the magnitude of the ratio $\Delta p_f/\Delta p_{\max}$.

Booms having asymmetrical waveforms, that is, the front and rear portions having different calculated PL, were found to be less loud than symmetrical waveforms of equal total perceived level. This effect was not accounted for by any of the noise descriptors. The magnitude of the loudness reduction increased as asymmetry increased and depended upon the direction of asymmetry, being larger when the rear portion of a waveform had a higher PL value than the front portion. Asymmetry effects diminished and became more "balanced" relative to the symmetrical condition as duration of the waveforms decreased.

Subjective responses to composite waveforms, each consisting of a direct plus a single simulated ground-reflected waveform, were fully accounted for by perceived level.

Perceived level also accounted for the effects on loudness of turbulence-induced shape distortion for a variety of recorded waveforms as well as the difference between the idealized N waves and recorded sonic booms.

Loudness and annoyance were determined to be equivalent criterion measures for simulated outdoor booms. For simulated indoor booms, annoyance was the better criterion measure based on (a) the presence of an additional annoyance component for the indoor waveforms (as evidenced by the higher annoyance scores) and (b) improved prediction accuracy when annoyance was the criterion. Selection of PL as the best metric was based on the demonstrated ability of PL to account for loudness effects of outdoor waveforms and annoyance effects of both indoor and outdoor waveforms.

An inhome study was conducted in which simulated sonic booms were played through loudspeaker systems in people's homes. Various scenarios involving different numbers of booms at different levels were played and the subjects were required to make annoyance judgements at the end of each day's exposure. The results of this study indicate that as the number of boom occurrences increased, the resulting annoyance increased in a manner consistent with equal energy theory.

[1] D. R. Johnson and D. W. Robinson, Acustica **18**, 241–258 (1967).

[2] A. Niedzwiecki and H. S. Ribner, J. Acoust. Soc. Am. **64**, 1617–1621 (1978).

[3] A. Niedzwiecki and H. S. Ribner, J. Acoust. Soc. Am. **64**, 1622–1626 (1978).

[4] K. P. Shepherd and B. M. Sullivan, "A loudness calculation procedure applied to shaped sonic booms," NASA Technical Paper **3134**, 1–10 (1991).

[5] S. McDaniel, J. D. Leatherwood, and B. M. Sullivan, "Application of magnitude estimation scaling to the assessment of human subjective loudness response of simulated sonic booms," NASA Tech. Memo. **107657**, 1–33 (1992).

[6] J. D. Leatherwood and B. M. Sullivan, "A laboratory study of subjective annoyance response to sonic booms and aircraft flyovers," NASA Tech. Memo. **109113**, 1–35 (1994).

[7] J. M. Fields, "Reactions of residents to long-term sonic boom noise environments," NASA Contractor Report **201794**, 1–157 (1997).

[8] J. D. Leatherwood, K. P. Shepherd, and B. M. Sullivan, "A new simulator for assessing subjective effects of sonic booms," NASA Tech. Memo. **104150**, 1–35 (1991).

[9] D. E. Brown and B. M. Sullivan, "Adaptive equalization of the acoustic response in the NASA Langley sonic boom chamber," in *Recent Advances in Active Control of Sound and Vibration*, edited by C. R. Fuller (Technomic, Lancaster, PA, 1991), pp. 360–371.

[10] D. J. Maglieri and K. J. Plotkin, "Sonic boom," in *Aeroacoustics of Flight Vehicles: Theory and Practice, Vol. 1, Noise Sources*, edited by H. H. Hubbard, NASA Reference Publication 1258 (1991), Vol. 1, pp. 550–556.

[11] R. Paulsen and J. Kasta, J. Sound Vib. **181**, 295–314 (1995).

[12] E. Öhrström, J. Sound Vib. **205**, 555–560 (1997).

[13] P. D. Schomer and R. D. Neathammer, J. Acoust. Soc. Am. **81**, 966–975 (1987).

[14] P. D. Schomer and A. Averbuch, J. Acoust. Soc. Am. **86**, 665–673 (1989).

[15] J. M. Cawthorne, T. K. Dempsey, and R. DeLoach, "Human response to aircraft noise-induced building vibration," in *Proceedings of the AHS/NASA/Army Specialists Meeting on Helicopter Acoustics*, May 22–24, Hampton, VA, NASA Conf. Publ. **2052**, 479–491 (1978).

[16] C. A. Powell and K. P. Shepherd, "Aircraft noise induced building vibration and effects on human response," in Proceedings of the 1989 International Conference on Noise Control Engineering (INTER-NOISE 89), 4–6 December (1989), Newport Beach, CA, pp. 567–572.

[17] J. D. Leatherwood and B. M. Sullivan, "Laboratory study of effects of sonic boom shaping on subjective loudness and acceptability," NASA Technical Paper **3269**, 1–25 (1992).

[18] J. D. Leatherwood and B. M. Sullivan, "Loudness and annoyance response to simulated outdoor and indoor sonic booms," NASA Tech. Memo. **107756**, 1–36 (1993).

[19] I. Flindell, "A laboratory study of the perceived benefit of additional noise attenuation by houses," NASA Tech. Memo. **85647**, 1–56 (1983).

[20] B. M. Sullivan and J. D. Leatherwood, "Subjective response to simulated sonic booms with ground reflections," NASA Tech. Memo. **107764**, 1–33 (1993).

[21] J. D. Leatherwood and B. M. Sullivan, "Effect of sonic boom asymmetry on subjective loudness," NASA Tech. Memo. **107708**, 1–30 (1992).

[22] E. Zwicker and H. Fastl, *Psychoacoustics: Facts and Models* (Springer, Berlin, 1990), p. 74.

[23] Y. Ogura, Y. Suzuki, and T. Sone, J. Acoust. Soc. Jpn. (E) **12**, 1–11 (1991).

[24] Y. Ogura, Y. Suzuki, and T. Sone, Noise Control Eng. J. **40**, 231–240 (1993).

[25] W. L. Willshire and D. W. DeVilbiss, "Preliminary results from the White Sands Missile Range sonic boom propagation experiment," NASA Conf. Publ. **1**, 137–149 (1992).

[26] D. J. Maglieri and K. J. Plotkin, "Sonic boom," in *Aeroacoustics of Flight Vehicles: Theory and Practice, Vol. 1, Noise Sources*, edited by H. H. Hubbard, NASA Reference Publication 1258 (1991), Vol. 1, pp. 524–539.

[27] B. M. Sullivan and J. D. Leatherwood, "A laboratory study of subjective response to sonic booms measured at White Sands Missile Range," NASA Tech. Memo. **107746**, 1–29 (1993).

[28] D. A. McCurdy, S. A. Brown, and R. D. Hilliard, "The effects of simulated sonic booms on people in their homes," AIAA Paper 95-0834, pp. 1–8, presented at the American Institute of Aeronautics and Astronautics 33rd Aerospace Sciences Meeting, Reno, NV (January, 1995).

Effects of sonic booms on breeding gray seals and harbor seals on Sable Island, Canada

Elizabeth A. Perry, Daryl J. Boness,[a)] and Stephen J. Insley
Department of Zoological Research, National Zoological Park, Smithsonian Institution, Washington, D.C. 20008

(Received 9 May 2000; revised 18 December 2000; accepted 22 December 2000)

The Concorde produces audible sonic booms as it passes 15 km north of Sable Island, Nova Scotia, where gray and harbor seals occur year round. The purpose of this research was to assess how sonic booms affect these seals. The intensity of the booms was measured and three types of data (beach counts, frequency of behavior, and heart rate) were collected before and after booms during the breeding seasons of the two species. In addition to the data taken during breeding, beach counts were made before and after booms during the gray seal moult. The greatest range in overpressure within a single boom was 2.70 psf during gray seal breeding and 2.07 psf during harbor seal breeding. No significant differences were found in the behavior or beach counts of gray seals following sonic booms, regardless of the season. Beach counts and most behaviors of harbor seals also did not differ significantly following booms, however, harbor seals became more vigilant. The heart rates of four gray seal mothers and three pups showed no clear change as a result of booms, but six male harbor seals showed a nonsignificant tendency toward elevated heart rates during the 15-s interval of the boom. These results suggest sonic booms produced by the Concorde, in level flight at altitude and producing on average a sonic boom of 0.9 psf, do not substantially affect the breeding behavior of gray or harbor seals.
[DOI: 10.1121/1.1349538]

PACS numbers: 43.80.Nd [WA]

I. INTRODUCTION

Marine mammal reaction to anthropogenic disturbance, such as boats, aircraft, seismic exploration, and human presence alone, is usually difficult to measure and much of the available information is anecdotal. Most of the data on disturbance responses come from short-term behavioral reactions such as termination of feeding or social interactions, and increase in vigilance (alertness) and/or avoidance responses (Richardson, 1995). There are a few studies of seals' reactions to aircraft overflights, but they rarely include measurements of sound levels (reviewed in Richardson, 1995).

The degree to which seals react to aircraft varies with characteristics of the flyover (Johnson, 1977; Kelly *et al.*, 1986). Variables such as the type, speed, flight path, and altitude of the craft affect disturbance responses in seals. For example, studies in which fixed wing aircraft were used for aerial surveys have reported altitude levels at which seals become disturbed and leave their haulout locations (e.g., Brueggeman *et al.*, 1990 as cited in Richardson, 1995; Osborn, 1985). Some species, such as bearded seals (*Erignathus barbatus*), appear to react more strongly to helicopters than fixed wing aircraft (Burns and Frost, 1979), although there are reports of walrus (*Odobenus rosmarus*) calf mortality caused by larger animals stampeding to the water when small aircraft approached (see Johnson *et al.*, 1989).

Characteristics of the seals and the season also play roles in the severity of a disturbance response. The number of animals and sex and age compositions of haulout groups appear to be important factors of how strongly the animals react to aircraft. Small groups of seals, groups composed primarily of young animals, and groups with mothers and pups tend to react most strongly (e.g., Salter, 1979). Male elephant seals showed a longer-lasting response to simulated sonic booms than females, while the response of California sea lions to the same stimulus varied with season (Stewart, 1982). During the breeding season females were more alert and males did not respond, but outside the breeding season more than half of the animals moved to the water. Some authors have speculated that dramatic disturbances can lead to increased pup mortality (e.g., Bowles and Stewart, 1980), as has been documented in walruses but not in Northern elephant seals or California sea lions (Stewart, 1982).

Generally, it is difficult to determine if seal reactions are to the sound stimulus and/or visual stimulus associated with the aircraft. Sonic booms generated by supersonic aircraft and rocket launches have caused California sea lions (*Zalophus californianus*) to stampede to the water, but not Northern elephant seals (*Mirounga angustirostris*) (Stewart *et al.*, 1993). In these cases the aircraft were not visible so the seals must have been responding to auditory stimuli alone.

With the potential for an increase in the use of supersonic commercial transport, it is important to assess how widespread and extensive the effects of sonic booms might be on marine mammals. The greatest impacts are likely to occur on breeding grounds that are within a few km of the flight paths of supersonic jets. There are presently few opportunities where such studies can be conducted, but one location is at Sable Island, Nova Scotia, Canada. Breeding

[a)]Author to whom correspondence should be addressed.

gray seals and harbor seals haul out on Sable Island and are exposed to sonic boom generated by the Concorde on its daily trans-Atlantic flights. Their reaction to these booms has never been documented although the Concorde has been passing the island since the 1970s.

Gray seals and harbor seals use Sable Island throughout the year. Gray seals give birth to their young from late December through January and females remain on the pupping grounds throughout lactation. Adult males maintain positions near females and compete for the opportunity to mate with them, on land, at the end of lactation (Boness and James, 1979). Female harbor seals give birth to and nurse a single pup on land during their breeding season in May and June. Unlike gray seals, harbor seal females forage at sea during lactation, most often leaving their pups behind on shore (Boness *et al.*, 1994) and mating occurs in the water (Allen, 1985; Coltman *et al.*, 1998) at the end of lactation.

Sonic booms could substantially affect gray and harbor seals in several ways. The booms could cause movement and activity that would interrupt normal maternal care, leading to a decrease in pup growth rate and weaning weight, which could affect future survival of young (e.g., Boness *et al.*, 1995). Booms could cause an increase in the direct mortality of pups through trampling or causing them to flee the beach and be exposed to shark predation or by becoming separated from their mothers prematurely and starving to death.

The purpose of this study was to assess the impact of sonic booms on gray and harbor seals on Sable Island during breeding. It also examined whether gray seals tended to leave the beaches in response to booms during their moult. Both of these species have been repeatedly exposed to the Concorde's sonic booms on Sable Island, and thus may show decreased responses due to habituation. If habituation has occurred, adult seals are likely to respond less than pups, which would not have previously experienced sonic booms.

II. METHODS

A. Study site

Data for this study were collected on Sable Island, Canada (44 °N, 60 °W), from 2–27 January 1997 during the gray seal breeding season and 26 May–17 June 1998 during the harbor seal breeding and gray seal moulting seasons. Sable Island is a 40-km long crescent-shaped sandbar in the Northwest Atlantic, 163 km from land.

The westbound flight track of the Concorde {50° 41′ N, 15° 00′ W; 50° 50′ N, 20° 00′ W; 50° 30′ N, 30° 00′W–49° 16′ N, 40° 00′ W; 47° 03′ N, 50° 00′ W–46° 1′ N, 53° 00′ W; 44° 14′ N, 60° 00′ W–42° 46′N, 65° 00′ W) passes 8.4 nautical miles, or 15.5 km, north of Sable Island. Sonic booms are regularly heard in association with these flights.

B. Sonic booms

Two Boom Event Analyzer Recorders (BEARs) with PCB, Inc., model 106B50 high intensity ICP pressure sensors (frequency response: ±5% between 0.5 and 8000 Hz) with built-in preamplifier and windscreens were provided by the Noise Effects Branch, Armstrong Laboratory, at Wright-Patterson AFB, OH. The BEARs (frequency response set from 0.5 to 2500 Hz; maximum peak overpressure 165 dB *re*: 20 μPa) were designed to capture the full waveform of impulsive acoustic events and store them in digital form (Lee and Downing, 1993). The BEARs were set up at inland locations to digitally record sonic booms during the gray seal breeding season. Maximum sound pressure levels (rms, dB *re*: 20 μPA) were taken from a Brüel & Kjær, model 2236 handheld sound level meter (SLM) positioned at one of four inland locations. Recordings were calibrated daily using a Brüel & Kjær 124-dB Pistonphone Calibrator.

During the harbor seal breeding season in the summer, sonic booms were recorded using a TEAC model RD-135T DAT recorder and PCB 106B50 microphone with power supply, stationed at an inland location. Recordings were calibrated twice daily using a Brüel & Kjær 124-dB Pistonphone Calibrator.

C. Behavior

To assess if animals would respond to sonic booms with a dramatic startle response by fleeing into the water, we counted the number of gray seals and harbor seals on shorelines before and after booms. To detect more subtle behavioral impacts, we used videotaped records. These data involved paired comparisons of behavior during set time intervals before and after booms. Finally, we measured physiological impacts by deploying heart rate transmitters on free-ranging animals and comparing heart rates before, during, and after booms.

The number of gray seals along the shoreline adjacent to the videotaping sites were counted before and after the booms, to record the number of animals that left the beach. The haul-out groups included adults and pups during the breeding season and all age classes during the moulting season. Beach counts of harbor seals were conducted at two locations. One location was along the circumference of Wallace Lake, a small inland lake where there was the highest density of mothers and pups, as well as males. The other was along the North Beach wherever there was a haul-out group. The number of harbor seals using Sable Island during the breeding season has declined and haul-out groups, consisting primarily of adult males, were small and dispersed.

During the gray seal breeding season, remote video stations were established in two inland locations overlooking groups of mothers, their pups, and adult males. The locations were chosen based on having a concentration of mothers and pups; 11 mother–pup pairs at one site and 14 at the other. We also needed a good vantage point for the video camera so that we could see all of the animals in the field of view and access the camera without disturbance to the animals. The animals were videotaped daily, from 0745 to 1130 h and from 1230 to 1600 h, using time-lapse video equipment (Furhman Diversified, Inc., Seabrook, TX). Mothers and their pups were paint-marked for identification and daily maps of individuals' locations were drawn at the beginning of each tape session to assist with identification on videotapes. All animals in the field of view that were identified were included in the analysis. Because the video setup was focused on the same group for the season, we were able to observe the same mother–pup pairs throughout their lactation.

We used two sampling designs to detect possible changes in gray seal behavior in response to the sonic booms. In one analysis we compared the behavior of gray seals during the minute in which the boom was recorded with a randomly selected minute during the afternoon taping session, prior to the afternoon boom. In the second analysis, we compared each animal's behavior during a 10-min period before and after the boom.

In the minute of the boom, when we expected to detect immediate, or startle, responses to the boom, all animals were scored as to whether they were inactive or exhibiting low-level activity (subtle body movements such as raising the head to scan the area, scratching, or stretching) or moving (any activity involving position or location changes). For animals nursing at the time of booms, nursing terminations were also recorded. For a control condition, the behaviors of the same individuals were recorded during a randomly chosen 1-min interval in the afternoon when there were no sonic booms. Comparisons of the proportion of observations in which animals were active, moving, or nursing between boom and control minutes were made using paired *t*-tests Because proportional data violate assumptions of normality, we used 500 randomizations of the data to calculate the probabilities of our test statistics (Manly, 1997).

During the 10-min interval immediately preceding and following boom events we expected to detect more subtle, long-lasting, or cumulative effects. We recorded the frequency of aggressive encounters, number of movements, distance moved in seal lengths, occurrences of nursing (on-teat time), and number of 1-min intervals in which low-level activities occurred.

Harbor seal behavior was recorded on real-time videos, using Sony model TR700 video recorders. As with the gray seals, we observed frequency of aggression, frequency and duration of vigilance (scanning) behavior, movements on the beach, and total distance moved (measured in seal lengths) by the harbor seals. We were uncertain how long the effects of disturbance might last in harbor seals so we used several different time intervals for paired comparisons of behaviors before and after booms. We compared behavior in the 30 s following booms to that by the same individuals in the 30 s prior to the boom, and repeated the process for 1 min, 3 min, and 5 min following and preceding the boom.

Bonferroni adjustments were applied to significance levels of individual behavior variables, to test the overall null hypothesis that sonic booms did not affect the behavior of gray or harbor seals at $\alpha = 0.05$ (Manly, 1997). Thus each of the four gray seal behavior variables were tested at a significance level of $\alpha = 0.0125$ and the five harbor seal variables were tested at $\alpha = 0.01$.

D. Heart rates

Heart rate monitoring units (Wildlife Computers, Inc., Isanti, MN) were deployed on five gray seal mother–offspring pairs and nine adult male harbor seals. Myocardial pacemaker electrodes (Medtronic, Inc.) were used on gray seals and salmon fishing hooks served as electrodes on harbor seals. Upon capture, gray seal females were sedated using Telazol® and harbor seals were given diazepam. Because handling and both drugs were likely to affect the seals' heart rates, we did not include heart rate data from the first 24 h following deployment of the units. The units were programed to store heart rate at 5-s intervals and were left on the animals for 4–13 days.

The heart rate receivers recorded heart rates ranging from 0 to 256 beats per min (bpm). Extreme readings were common and likely instrument artifacts (R. Hill, Wildlife Computers, pers. com.). To remove such artifacts we deleted any rates that were less than 4 bpm—the lowest reported heart rate in a seal (Thompson and Fedak, 1993). We also deleted any rates greater than 207 bpm because a frequency distribution showed a major peak at 207 bpm and individual records periodically showed long strings of 207 bpm, just as strings of zeros occurred.

Using the corrected data sets, gray seal heart rates were averaged over three time periods before booms (3 min, 2 min, and 1 min) and were compared using a repeated measures ANOVA to heart rates during the minute of booms, and to the 3-min, 2-min, and 1-min time period following each boom. Harbor seal heart rates were averaged over 3

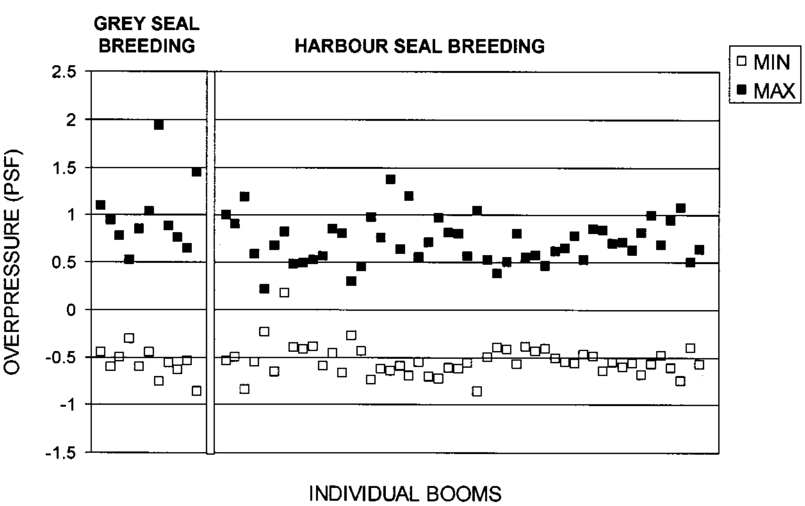

FIG. 1. Minimum and maximum overpressures of *N*-wave sonic booms recorded during the gray and harbor seal breeding seasons and gray seal moulting season on Sable Island, Nova Scotia.

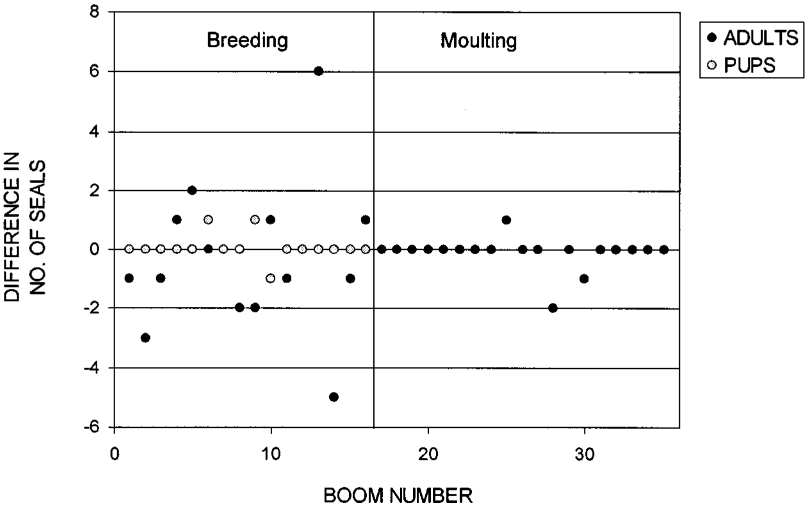

FIG. 2. Difference in number of gray seal adults and pups on beaches before and after sonic boom events during breeding and moulting seasons.

min, 2 min, and 1 min before the booms and compared, using a repeated measures ANOVA, to heart rates in the 15 s that booms occurred and 3-min, 2-min, and 1-min intervals following the booms.

III. RESULTS

A. Sonic booms

There was a range from 0 to 5 sonic booms heard daily during the gray seal and harbor seal breeding seasons. Generally there were three sonic booms each day, two between 0800 and 1000 h and one between 1730 and 1830 h. The times of events varied little between the two field seasons, making them easy to predict to within 15 mins.

During the gray seal breeding season, a total of 66 audible booms were documented, of which 12 were recorded by BEARs (Fig. 1) and 36 were measured by the sound level meter (SLM). There were high correlations between minimum (Pearson correlation, $r=0.997$) and maximum ($r=0.999$) overpressures and the maximum sound level ($r=0.999$) for the four booms that were recorded simultaneously by the two BEARs. There were also high correlations between the maximum sound levels registered by the BEAR units and the SLM (BEAR 17 and SLM: $r=0.938$; BEAR 18 and SLM: $r=0.907$). The mean minimum and maximum overpressure, based on data recorded by the BEARs, were -0.568 psf (s.d.$=0.142$) and 0.935 psf (s.d.$=0.355$), respectively. Sound pressure levels detected by the SLM ranged from 121.68 to 133.33 dB, with a mean of 114.21 dB (s.d.$=6.49$). The greatest range in overpressure within a single sonic boom during gray seal breeding was 2.70 psf.

During the harbor seal breeding season and gray seal moulting season we were able to record 50 (Fig. 1) of 70 noted sonic booms using the DAT recorder. The mean minimum and maximum overpressures were -0.541 (s.d. $=0.166$) and 0.716 psf (s.d.$=0.238$), respectively. The greatest range in overpressure within a single sonic boom in May/June was 2.07 psf.

B. Behavior

1. Beach counts

On 16 days of the gray seal breeding season we recorded the number of adults and pups on two portions of the shoreline before and after sonic boom events. Because we could not predict the exact time that a boom event would occur, two of our pre-boom counts were more than 15 min before the boom and, therefore, excluded from the analysis. There was no significant difference between the number of adults

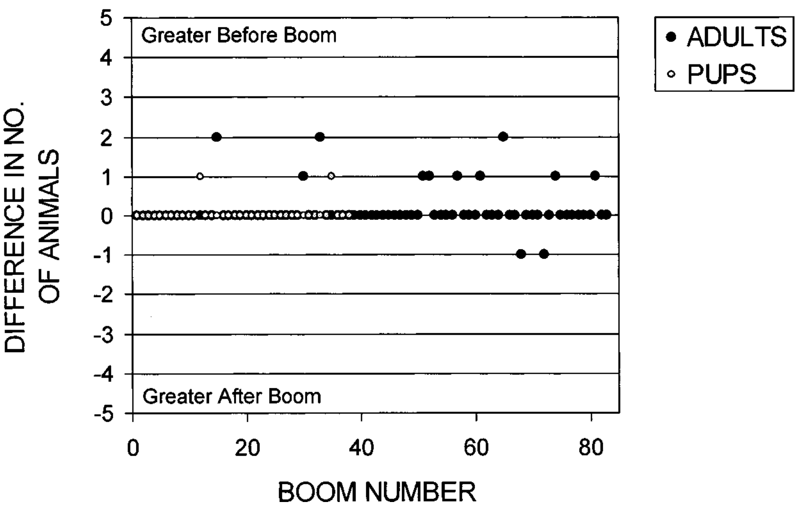

FIG. 3. Difference in number of harbor seal adults and pups on beaches before and after sonic boom events during their breeding season.

TABLE I. Results of the paired t-test comparing the occurrences of low-level activity, movement, and nursing between the minute of booms and control minutes for gray seal pups and adults. Probabilities for paired t-test following 500 randomizations are reported as $p_{\text{randomizations}}$. [Data are proportional and, therefore, violate assumptions of parametric tests. Randomizations of data allow use of parametric tests (Manly, 1997).]

	Behavior	Mean Boom	Mean Control	T	p	$p_{\text{randomization}}$
Pups $N=25$	Low-level activity	0.53	0.59	−0.74	0.464	0.470
	Movement	0.10	0.11	−0.15	0.879	0.858
	Nursing	0.05	0.03	0.75	0.458	0.542
Adults $N=28$	Low-level activity	0.82	0.78	0.95	0.348	0.374
	Movement	0.15	0.18	−0.86	0.396	0.428

on the beach before and after the boom (paired t-test; $t=1.07$, $df=13$, $p=0.304$), with pre-boom group sizes ranging from 14 to 37 adults. Neither was there a difference between the number of pups on beaches before and after booms (paired t-test; $t=0.366$, $df=13$, $p=0.72$; Fig. 2), with pre-boom pup counts ranging from 3 to 29.

We were also able to conduct gray seal beach counts before and after 21 sonic booms during their moulting period. All pre-boom counts were conducted no more than 1 min before the booms and groups were counted less than 1 min after booms. Group sizes before and after booms, which varied from 1 to 15 animals, were compared using nonparametric rank tests because the data were not normally distributed. There was no significant difference between pre- and post-boom counts (Wilcoxin Signed Rank Test; $W=3.00$, $p=0.50$; Fig. 2).

A total of 83 harbor seal counts, 33 at Wallace Lake and 50 on North Beach, were made before and after 55 different boom events (Fig. 3). Counts were made within 1 min prior to booms and within 1 min following booms. Group sizes on North Beach ranged from 1 to 20 adults and on the shoreline of Wallace Lake from 4 to 13 adults and 1 to 10 pups. We found that the number of pups on Wallace Lake shoreline did not change in response to booms (Wilcoxin Signed Rank Test; $W=-3.00$, $p=0.50$). We also found no difference in the number of adults before and after booms at either site (North Beach: $W=-6.00$, $p=0.25$; Wallace Lake: $W=-27.00$, $p=0.13$).

2. Observed behavior

Gray seal video recording sessions commenced on 4 Jan and continued until 27 Jan. At one site recordings provided data on 11 mother–pup pairs and 2 adult males during 30 sonic booms. At the second site, the behavior of 14 mother–pup pairs and 1 adult male was recorded for 24 booms.

Comparing behaviors in the minute of the boom to a randomly selected minute we found no significant differences overall in the occurrence of low-level activity ($t=-0.19$, $df=52$, $p=0.85$) or movement ($t=-0.80$, $df=52$, $p=0.45$) between boom and randomly selected control minutes. When separated by age class, neither pups nor adults differed significantly in the occurrence of low-level activity or movement between the boom minutes and control minutes (Table I).

A total of 27 gray seal nursing bouts were observed during the boom minutes and 15 were observed during the control minute. Of these 11 (41%) were interrupted during the boom and 8 (53%) during the control minute.

Likewise, when behavior data were analyzed using a 10-min period after the boom compared to 10 min before, there were no significant differences in behaviors for either pups or adults (Fig. 4). The mean activity level, measured as the number of 1-min intervals in which animals were active during each 10-min period, did not differ. Nor was there a mean difference in the number of times that animals changed location or the distance moved before and after booms, for either pups or adults (Table II).

As there were only 28 harbor seal pups born on Sable Island during 1998, and they were widely dispersed, only adult and sub-adult males were included in assessments of behavior. Harbor seal males spend about 40% of their time on land during the breeding season and much of this time is spent resting (Coltman *et al.*, 1997). They are rarely aggres-

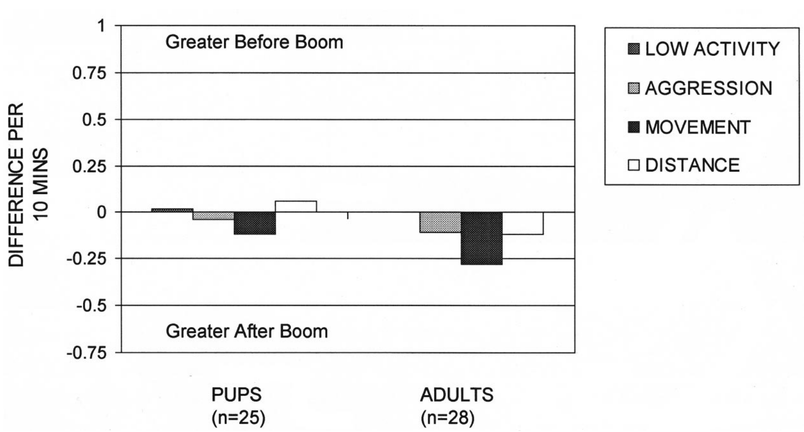

FIG. 4. Differences between gray seal adult and pup behaviors in the 10 min before booms and 10 min following booms.

TABLE II. Results of repeated measures ANOVA comparing the occurrences of low-level activity, aggression, movement, and distance moved between 10-min intervals immediately before and after booms for gray seal pups and adults. Probabilities for F-values following 500 randomizations are reported as $p_{\text{randomizations}}$. (These data were not normally distributed and, therefore, randomizations were used to calculate true probabilities for each F-value.)

	Behavior	Mean Before	Mean After	F	df	p	$p_{\text{randomization}}$
Pups	Low-level activity	0.54	0.55	0.22	1,24	0.6361	0.596
$N=25$	Aggression	0.01	0.03	2.43	1,24	0.1194	0.442
	Movement	1.07	1.22	0.63	1,24	0.4265	0.312
	Distance moved	0.87	0.87	0.00	1,24	0.9548	0.948
Adults	Low-level activity	0.77	0.78	0.29	1,27	0.5887	0.552
$N=28$	Aggression	0.44	0.52	1.28	1,27	0.2577	0.368
	Movement	1.19	1.40	1.70	1,27	0.1926	0.150
	Distance moved	1.03	1.23	1.15	1,27	0.2831	0.312

sive because mating and competition for mates occur at sea. Consequently, we found low frequencies of aggression in our 10-min samples before the boom and found no increase in incidence of aggression following booms in any of the four time intervals (Fig. 5). We also found little movement by males when they are settled on the beach and there was no increase in movement following booms, regardless of the length of the observation interval (Fig. 5).

Harbor seal males did become significantly more vigilant, both in frequency and duration, following sonic booms (Table III). The effect was most apparent in the 30 s following a boom and least apparent in the 5-min observation period. The difference in frequency of vigilance was still significant when comparing 5-min periods but the difference in duration was not, using the Bonferroni correction (Table III).

C. Heart rates

Of the ten units deployed on gray seals, seven provided useful data, two units were lost, and one unit failed. Heart rate data were obtained from four gray seal females and three pups. The number of booms encompassed in these data varied among individuals, ranging from 3 to 17.

Female gray seals had an average heart rate of 103.0 bpm (s.d. $=36.1$), which was lower than that of pups,

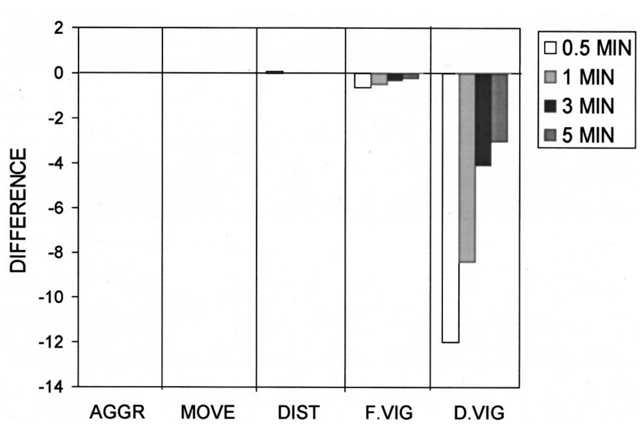

FIG. 5. Differences in five harbor seal behaviors between pre-boom time intervals and post-boom time intervals. Behaviors include aggression (AGGR), movement (MOVE), distance moved (DIST), frequency of vigilance (F.VIG), and duration of vigilance (D.VIG).

132.6 bpm (s.d. $=30.3$). In none of our three time-interval comparisons did heart rates differ between pre-boom, boom, and post-boom periods for either females or pups (Table IV).

The heart rates of harbor seal males ($n=6$) had a bimodal distribution with one peak below 55 bpm and the second peak above 80 bpm, as illustrated for three males in Fig. 6. In all three time-interval comparisons (1 min, 2 min, and 3 min before and after booms) we found a similar pattern in which heart rates before and after booms were consistently lower than those in the 15-s boom interval (Fig. 7). None of our comparisons were significant, but because of our small sample sizes we had low power to detect significant differences.

IV. DISCUSSION

We studied gray and harbor seals during breeding and gray seals during moulting on Sable Island, Nova Scotia, to assess how sonic booms affect their behavior. We collected three types of data: beach counts, behavior (social, spatial, and vigilance or low activity), and heart rates. Our general design was to collect these data on the same individuals before and after booms and to include all age and sex classes. Pups were expected to be more sensitive than juveniles and adults because the Concorde has been flying past Sable Island since the early 1970s and juvenile and adults may have become habituated to sonic booms. Pups, however, will not

TABLE III. Mean differences[a] in male harbor seal behaviors ($n=41$ sonic booms) within four different observation intervals.

	30 s	1 min	3 min	5 min
Frequency of aggression	0.02	0.01	−0.03	0.01
Frequency of movement	0.02	0.01	−0.03	−0.05
Distance moved	0.06	−0.02	−0.08	−0.11
Frequency of vigilance	−0.29[a] ($p=0.007$)	−0.48[a] ($p=0.006$)	−0.88[a] ($p=0.002$)	−1.09[a] ($p=0.009$)
Duration of vigilance	−6.02[a] ($p=0.0001$)	−8.39[a] ($p=0.001$)	−12.24[a] ($p=0.012$)	−14.95 ($p=0.056$)

[a]Difference = Pre-boom behavior − post-boom behavior.

TABLE IV. Mean heart rates (SEM) for gray seal females and their pups before, during and after sonic boom events. Pre-boom, boom, and post-boom time intervals over which heart rates were averaged are shown in the "Interval Durations" column.

	Interval durations	Pre-boom	Boom	Post-boom	Repeated measures ANOVA
Females	1 min–1 min–1 min	106.0 (9.7)	105.7 (11.7)	105.6 (12.2)	$F_{2,3}=0.009$, $p=0.99$
	2 min–1 min–2 min	104.4 (10.0)	105.7 (11.7)	105.6 (12.7)	$F_{2,3}=0.095$, $p=0.91$
	3 min–1 min–3 min	104.9 (10.4)	105.7 (11.7)	106.4 (12.3)	$F_{2,3}=0.192$, $p=0.83$
Pups	1 min–1 min–1 min	139.6 (4.2)	142.0 (3.5)	137.7 (2.1)	$F_{2,2}=1.876$, $p=0.27$
	2 min–1 min–2 min	139.8 (3.6)	142.0 (3.5)	138.4 (2.7)	$F_{2,2}=3.738$, $p=0.12$
	3 min–1 min–3 min	140.2 (3.6)	142.0 (3.5)	139.5 (2.4)	$F_{2,2}=1.877$, $p=0.27$

have been directly exposed to the booms prior to being born. Unfortunately, the dramatic decline in harbor seal births over the past few years, combined with their dispersed distribution, made it difficult to collect data on both pups and females of this species.

Disturbance responses such as abandonment of the beach, large-scale movements, or increased aggression may cause separations of mothers and pups and eventual starvation of pups. Likewise, abandonment of the beach, especially by young animals, might increase shark predation. Less direct effects that may be significant are disruptions to maternal care such as reduced suckling, which may lead to lower pup growth rates and weaning weights. Moulting seals have reduced metabolic rates compared to pre-moult periods (Ashwell-Erickson *et al.*, 1986), reducing the need for food. Moulting seals tend to spend more time hauled-out, which allows increased blood flow to the skin and warmer skin correlates with increased hair growth (Feltz and Fay, 1966; Ling, 1974). A frequent disturbance that forces seals into the water could prolong moulting, during which seals fast, by slowing hair growth. In addition, during the moulting fast, seals mobilize lipids stored in the blubber to meet metabolic needs (John *et al.*, 1987) and, therefore, extending the moult and accompanying fast could lead to reduced energy stores and slower recovery of body condition.

During a severe disturbance, animals would be expected to show avoidance behavior by racing to the water, which has been documented in harbor seals and other seal species (Stewart, 1981, 1993; Stewart *et al.*, 1993, 1996). In this study, the number of gray seal and harbor seal adults and pups on beaches during the breeding season did not change following booms, nor did the number of gray seals during the moulting season. Therefore, the seals were not sufficiently startled or disturbed to rush to the water when booms occurred.

Adult gray seals are aggressive on breeding grounds, with aggression occurring between all possible age-sex class comparisons. Some types of aggression occur more frequently toward the end of the breeding season and others earlier in the season (Boness *et al.*, 1982; Boness, 1984; Boness *et al.*, 1995). In addition, the incidence of aggression tends to increase as density on breeding beaches increases (Fogden, 1971), either through crowding or movement. As expected, we found that adult gray seals were more aggressive than pups, however, the incidence of aggression did not increase following booms. Gray seals also did not increase movements on the beaches following booms, which might have been expected if the animals were startled. In contrast to gray seals, harbor seals tend to be less aggressive on land, although male–male aggressive encounters do occur during the breeding season (Thompson, 1988). There was no change in the incidence of harbor seal aggression following sonic booms, nor did the frequency of movement change.

Other studies have shown an increase in vigilance or alertness as a disturbance reaction in seals (Bowles and Stewart, 1980; Stewart, 1981, 1993; Stewart *et al.*, 1996). We measured low-level activity in the gray seals, which would include changes in scanning behavior or vigilance, and found no differences following booms. Harbor seal males did become significantly more vigilant, both in frequency and duration, for up to 5 min following sonic booms. Studies of harbor seal vigilance have found that the frequency of vigilance varies with group size and composition as well as time of year (Renouf and Lawson, 1986; Terhune, 1985). Adult males become more vigilant as the breeding season progresses and when group sizes are small the frequency of individual vigilance increases. In this study, animals were observed during their mating season and group sizes ranged from 1 to 20 animals; therefore, the increased vigilance following sonic booms probably reflects a common tendency for these animals to be alert. The lack of movement to the water by seals suggests that the wariness produced is relatively mild.

A number of studies of birds and mammals have shown that heart rate is a sensitive indicator of arousal and that heart rate can dramatically increase when animals are disturbed or harassed (MacArthur *et al.*, 1979; Moen *et al.*, 1978; Thompson *et al.*, 1968). Few studies have reported seal heart rates, particularly of startled animals. Generally, pinniped heart rates drop when the animals enter periods of apnoea during diving, fright, or sleep and increase above resting heart rate when the animals are breathing following dives (Kooyman, 1989).

Variation in reported heart rates is extreme in seals, ranging from 4 bpm in a free-ranging gray seal during dives (Thompson and Fedak, 1993) to more than 171 bpm in a threatened harp seal pup (Lydersen and Kovacs, 1995). Fedak *et al.* (1988) report that the heart rate of gray seals in a swimming flume was between 110 and 120 bpm and that heart rates did not increase with exercise alone but did increase after multiple dives.

Gray seal pups had higher heart rates than adult females, as has been found in harp seals (Lydersen and Kovacs, 1995). However, neither the heart rates of gray seal mothers

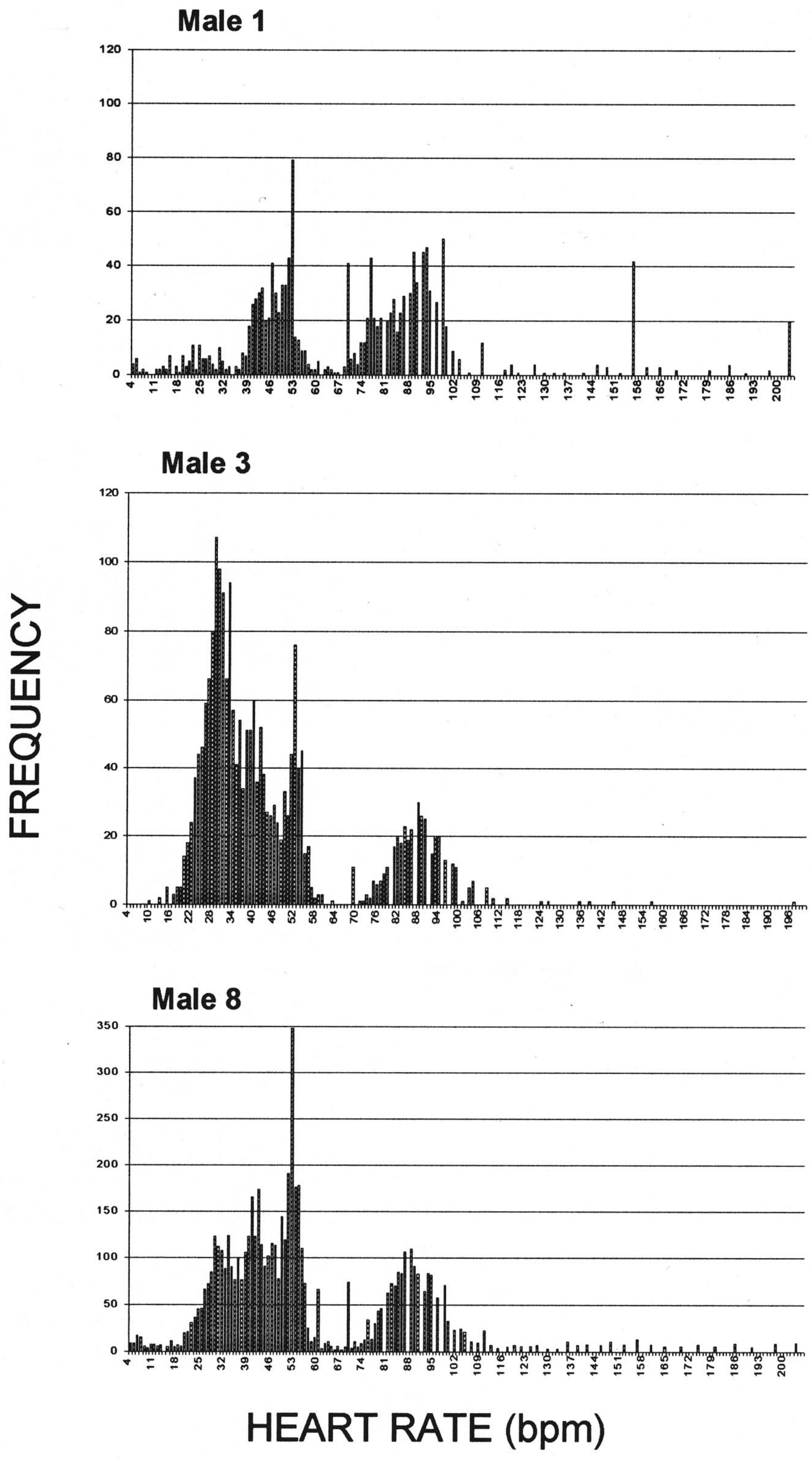

FIG. 6. Frequency distribution of heart rates for three adult males on 5 June 1998, after heart rates below 4 and above 204 bpm have been removed.

or pups differed among pre-boom, boom, and post-boom periods. When harp seal adults and pups are threatened by the approach or touch of a human, they alternate between states of apnoea, when heart rates drop to less than 35 bpm, and hyperventilation, when heart rates increase to over 150 bpm (Lydersen and Kovacs, 1995). Clearly, the gray seals in this study were not similarly stressed by sonic booms.

The heart rates of harbor seal males showed a trend in which their heart rates rose to an average of 66 bpm during the boom and returned to lower pre-boom rates immediately after. The difference in heart rates was not significant probably because the sample sizes were small. The harbor seal heart rates had a bimodal distribution with peaks between 30 and 55 bpm and another between 75 and 100 bpm. It is possible that the lower heart rate occurred while animals were sleeping and the higher heart rate occurred while animals were awake. Thus the increase in heart rates at the time of the boom would reflect that animals awoke from sleep.

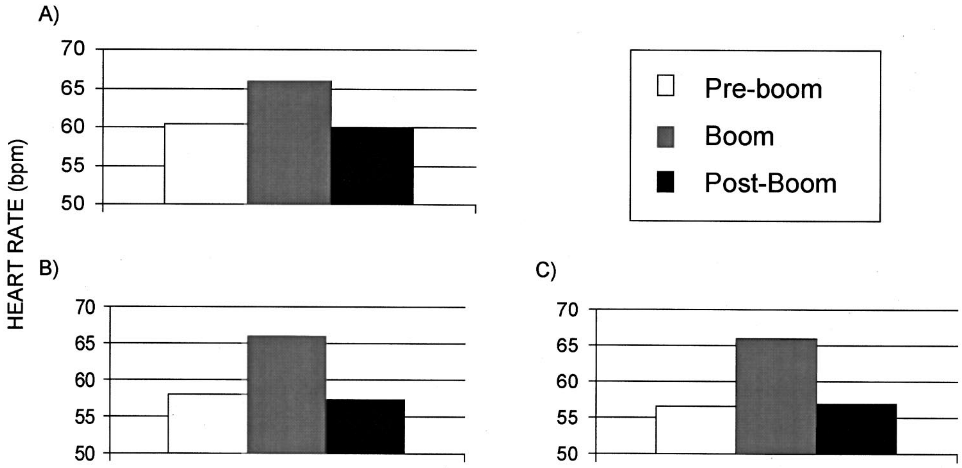

FIG. 7. Mean heart rates of adult male harbor seals ($n=6$) averaged over 15 s in which the boom occurred and (a) 1-min intervals ($F_{2,5}=2.211$, $p=0.160$), (b) 2-min intervals ($F_{2,5}=2.603$, $p=0.123$) and (c) 3-min intervals ($F_{2,5}=3.901$, $p=0.056$) before and after sonic booms.

Unfortunately, we do not have behavior data to confirm this suggestion. Nonetheless, the change in heart rates in response to booms demonstrated that the animals perceived the booms but, because the responses were minor and short-lived, the animals were not severely disturbed.

Based on our results, we suggest that sonic booms from the Concorde do not have substantial effects on the breeding behavior of gray and harbor seals on Sable Island. The lack of large-scale movements from the beaches to the water in response to the boom precludes the possibility that shark predation or separations of mothers and pups result from these particular sonic booms. Similarly, lack of increased movement on the beaches or increased aggression precludes the possibility of increased mother–pup separation or injury to animals. These behaviors, along with lack of evidence of suckling terminations in response to these booms, suggest that there is no reduction in quality of maternal care. The minor effects of increased vigilance and slight increase in heart rates of harbor seals are unlikely to substantively affect individual animals or the population.

Given the long history of sonic booms from the Concorde's flights near Sable Island and a steady increase of about 13% per year in the gray seal breeding population at Sable (Mohn and Bowen, 1996), it seems unlikely that there are any long-term cumulative effects of these booms on the breeding biology of Sable gray seals. It is more difficult to make such a clear statement about harbor seals since the breeding population at Sable Island is experiencing a major decline at the present time. However, during the twenty-some years of the Concorde flights near Sable Island, the harbor seal population increased substantially from 1987 through 1993 before beginning the substantial decline. It is therefore unlikely that these sonic booms are playing a role in this decline through cumulative effects.

In conclusion, our results show relatively minor or no affects of sonic booms produced by the Concorde on breeding harbor and gray seals. There are several points to consider in interpreting our results. First, the seals breeding on Sable Island have had at least 20 years to habituate to the booms and, therefore, we are not measuring responses at first exposure, with the exception of responses by pups. Second, the carpet booms of the Concorde in level flight over Sable Island produce a relatively minor form of disturbance (approximately 0.9 psf) in comparison to focused booms of greater intensity, such as those produced during low-altitude combat maneuvers. Therefore, it is important to note that the results presented here may not be generalizable to unexposed adult seals or to seals exposed to other types of sonic booms. Finally, we were unable to measure effects of the sonic booms on animals in the water. Sonic booms penetrate water and the impact will vary with oceanic wave conditions and aircraft speed (Sparrow, 1995; Rochat and Sparrow, 1997). Consequently, booms have the potential to affect animals that are in the water foraging or moving between foraging areas and breeding grounds.

V. SUMMARY

We studied gray and harbor seals during breeding and gray seals during moulting on Sable Island, Nova Scotia, to assess how sonic booms affect their behavior. We collected three types of data: beach counts, behavior (social, spatial, and vigilance or low activity), and heart rates. Our general design was to collect these data on the same individuals before and after booms. We deliberately tried to include all age and sex classes in our study since we might have expected different sensitivities for different classes. This would be especially true for pups compared to juvenile and adults because the Concorde has been flying past Sable Island since the early 1970s and juvenile and adults may have become habituated to sonic booms. Pups, however, will not have been directly exposed to the booms prior to being born. Unfortunately, the dramatic decline in harbor seal births over the past few years, combined with their dispersed distribution, made it difficult to collect data on pups especially, but on females as well.

Although the individual data sets may not be specifically biologically significant, taken together, if there were significant effects of booms on these measures or a group of them, it would point to a biologically significant impact on these species. For example, abandonment of the beach, large-scale movements, or increased aggression may cause separations of mothers and pups and eventual starvation of pups. Likewise, abandonment of the beach, especially by young animals, might increase shark predation. Less direct effects that may be significant are disruptions to maternal care such as reduced suckling, which may lead to lower pup growth rates and weaning weights. Moulting is a particularly energetically demanding period following shortly after another demanding period, breeding. Frequent disturbance that forces seals into the water could prolong moulting (during which seals fast) and lead to failures to recover body energy stores or to compromise the immune system, making seals more vulnerable to diseases.

However, our results from gray seals provided no evidence to suggest sonic booms from the Concorde had any effect on this species. No animals of any age or sex class left the beaches in substantial numbers in response to sonic booms, either during the breeding season or the moulting season. There was no indication of increased aggression or increased frequency of movement or distance moved on the breeding grounds by individual animals after booms. Suckling bouts did not appear to be interrupted by booms since the number of times suckling terminated during sampling periods did not differ between the boom periods and control periods. There was not even any apparent effect on low-level activity or vigilance behavior or heart rates for either adults or pups.

Results from the harbor seal study were similar with respect to beach counts and most behavior variables, but small effects were apparent in some behaviors and heart rates. Neither males, females, nor pups left the beaches in response to sonic booms, as evidenced by a lack of change in beach counts before and after booms. Aggression among seals on the beach was very low normally and showed no increase in response to sonic booms. The frequency of movement on land and distances moved before booms did not differ following booms. However, unlike gray seals, the frequency and duration of vigilance, or scanning behavior, did significantly increase following booms and this difference persisted for up to 5 min, although the effect began to diminish. Similar to the effect on vigilance behavior, heart rates increased during booms but diminished rapidly and returned to pre-boom levels.

Based on our results, we suggest that sonic booms from the Concorde do not have substantial effects on the breeding behavior of gray and harbour seals. The lack of large-scale movements from the beaches to the water in response to the boom precludes the possibility that shark predation or separations of mothers and pups result from sonic booms. Similarly, lack of increased movement on the beaches or increased aggression precludes the possibility of increased mother–pup separation or injury to animals. All of these behaviors along with lack of evidence of suckling terminations produced by booms point to no reduction in quality of maternal care. The minor effects of increased vigilance and slight increase in heart rates of harbor seals are unlikely to substantively affect individual animals or the population. Given the long history of sonic booms from the Concorde's flights near Sable Island and a steady increase of about 13% per year in the gray seal breeding population at Sable, it seems unlikely that there are any long-term cumulative effects on the breeding biology of Sable gray seals. It is more difficult to make such a clear statement about harbor seals since the breeding population at Sable Island is experiencing a major decline presently. However, within the twenty-some years of the Concorde flights near Sable Island, the harbor seal population increased substantially from 1987 through 1993 before beginning the substantial decline. It is therefore unlikely that the sonic booms are playing a role in this decline through cumulative effects.

ACKNOWLEDGMENTS

We wish to thank Suzanne Ambs, Don Bowen, Sara Iverson, and Jim McMillan for assistance in the field. Steve Beecroft, Mike Carter, Micah Downing, Bob Lee, and Mike Patterson provided technical assistance with sonic boom recording. Mary McNamara of Medtronics, Inc. suggested cardiac electrodes for the heart rate transmitters and Medtronics, Inc. donated electrodes to this study. Gerry Forbes, Officer in Charge of the Sable Island Meteorological Station (Canadian Department of the Environment), provided invaluable logistical support in the field and assisted with electronic equipment failure that threatened to prevent boom recordings, and other logistical support was provided by the Department of Fisheries and Oceans, Canada. Thanks to Dave Schneider for providing statistical advice. Funding for this study was provided by the National Air and Space Administration (NASA), the Smithsonian Institution, and the Friends of the National Zoo.

Allen, S. G. (**1985**). ''Mating behavior in the harbor seal,'' Marine Mammal Sci. **1**, 84–87.

Ashwell-Erickson, S., Fay, F. H., Elsner, R., and Wartzok, D. (**1986**). ''Metabolic and hormonal correlates of molting and regeneration of pelage in Alaskan harbor and spotted seals (*Phoca vitulina* and *Phoca largha*),'' Can. J. Zool. **64**, 1086–1094.

Boness, D. J. (**1984**). ''Activity budget of male gray seals, *Halichoerus grypus*,'' J. Mammal. **65**, 291–297.

Boness, D. J., and James, H. (**1979**). ''Reproductive behaviour of the gray seal (*Halichoerus grypus*) on Sable Island, Nova Scotia,'' J. Zool. **188**, 477–500.

Boness, D. J., Anderson, S. S., and Cox, C. R. (**1982**). ''Functions of female aggression during the pupping and mating season of gray seals, *Halichoerus grypus* (*Fabricius*),'' Can. J. Zool. **60**, 2270–2278.

Boness, D. J., Bowen, W. D., and Iverson, S. J. (**1995**). ''Does male harassment of females contribute to reproductive synchrony in the gray seal by affecting maternal performance?'' Behav. Ecol. Sociobiol. **36**, 1–10.

Boness, D. J., Bowen, W. D., and Oftedal, O. T. (**1994**). ''Evidence of a maternal foraging cycle resembling that of otariid seals in a small phocid, the harbor seal,'' Behav. Ecol. Sociobiol. **34**, 95–401.

Bowles, A., and Stewart, B. (**1980**). ''Disturbances to the pinnipeds and birds of San Miguel Island, 1979–1980,'' in *Potential Effects of Space Shuttle Sonic Booms on the Biota and Geology of the California Channel Oslands: Research Reports*, edited by J. R. Jehl, Jr. and C. F. Cooper (Cent. Mar. Stud., San Diego State University and HSWRI, San Diego, California), pp. 99–137.

Brueggeman, J. J., Malme, C. I., Grotefendt, R. A., Volsen, D. P., Burns, J. J., Chapman, D. G., Ljungblad, D. K., and Green, G. A. (**1990**). ''Shell Western E & P, Inc., 1989 Walrus Monitoring Program: The Klondike, Burger, and Popcorn Prospects in the Chukchi Sea'' (EBASCO Environmental, Bellevue, WA), Var pp.

Burns, J. J., and Frost, K. J. (**1979**). ''Natural history and ecology of the bearded seal, *Erignathus barbatus*,'' Environ. Assess. Alaskan Cont. Shelf, Final Rep. Princ. Invest., NOAA, Juneau, AK, **19**, 311–392.

Coltman, D. W., Bowen, W. D., and Wright, J. M. (**1998**). ''Male mating success in an aquatically mating pinniped, the harbour seal (*Phoca vitulina*) determined by microsatellite DNA markers,'' Mol. Ecol. **7**, 627–638.

Coltman, D. W., Bowen, W. D., Boness, D. J., and Iverson, S. J. (**1997**). ''Balancing foraging in the male harbor seal, an aquatically mating pinniped,'' Anim. Behav. **54**, 663–678.

Fedak, M. A., Pullen, M. R., and Kanwisher, J. (**1988**). ''Circulatory responses of seals to periodic breathing: Heart rate and breathing during exercise and diving in the laboratory and open sea,'' Can. J. Zool. **66**, 53–60.

Feltz, E. T., and Fay, F. H. (**1966**). ''Thermal requirements *in vitro* of epidermal cells from seals,'' Cryobiology **3**, 261–264.

Fogden, S. C. L. (**1971**). ''Mother–young behavior at gray seal breeding beaches,'' J. Zool. **164**, 61–92.

John, T. M., Ronald, K., and George, J. C. (**1987**). ''Blood levels of thyroid hormones and certain metabolites in relation to moult in the harp seal (*Phoca groenlandica*),'' Comp. Biochem. Physiol. **88A**, 655–657.

Johnson, B. (**1977**). ''Appendix 1. The effects of human disturbance on a population of harbor seals,'' in *Environmental Assessment of the Alaskan Continental Shelf. Annual Reports of Principal Investigators for the Year Ending March 1977*, Vol. 1, Receptors (Alaska Department of Fish and Game, U.S. Department of the Interior), pp. 422–431.

Johnson, S. R., Burns, J. J., Malme, C. I., and Davis, R. A. (**1989**). ''Synthesis of information on the effects of noise and disturbance on major haulout concentrations of Bering Sea pinnipeds,'' LGL Alaska Res. Assoc., Inc. (Anchorage, AK), p. 267.

Kelly, B. P., Quakenbush, L. T., and Rose, J. R. (**1986**). ''Ringed seal winter ecology and effects of noise disturbance. Final Report,'' in *Selected Protected Species Abstracts*, Minerals Management Service, Alaska OCS Office, Anchorage, AK, p. 89.

Kooyman, G. L. (**1989**). *Diverse Divers* (Springer-Verlag, Berlin).

Lee, R. A., and Downing, J. M. (**1993**). ''Boom Event Analyzer Recorder (BEAR): The USAF unmanned sonic boom monitor,'' 15th AIAA Aeroacoustics Conference, October 25–27, 1993, Long Beach, CA, AIAA Rep. 93-4431.

Ling, J. K. (**1974**). ''The integument of marine mammals,'' in *Functional Anatomy of Marine Mammals*, edited by R. J. Harrison (Academic, New York), pp. 1–44.

Lydersen, C., and Kovacs, K. M. (**1995**). ''Paralysis as a defence response to threatening stimuli in harp seals (*Phoca groenlandica*),'' Can. J. Zool. **73**, 486–492.

MacArthur, R. A., Johnston, R. H., and Geist, V. (**1979**). ''Factors influencing heart rate in free-ranging bighorn sheep: A physiological approach to the study of wildlife harassment,'' Can. J. Zool. **57**, 2010–2021.

Manly, B. F. J. (**1997**). *Randomization, Bootstrap and Monte Carlo Methods in Biology*, 2nd ed. (Chapman & Hall, New York), p. 399.

Mohn, R., and Bowen, W. D. (**1996**). ''Gray seal predation on the eastern Scotian Shelf: modeling the impact on Atlantic cod,'' Can. J. Fish. Aquat. Sci. **53**, 2722–2738.

Moen, A. N., Dellafera, M. A., Holler, A. L., and Buxton, B. A. (**1978**). ''Heart rates of white-tailed deer fawns in response to wolf howls,'' Can. J. Zool. **56**, 1207–1210.

Osborn, L. S. (**1985**). ''Population dynamics, behavior, and the effect of disturbance on haulout patterns of the harbor seal *Phoca vitulina richardsi*/Elkhorn Slough, Monterey Bay, California,'' B.A. Thesis, University of California, Santa Cruz, p. 75.

Renouf, D., and Lawson, J. W. (**1986**). ''Harbor seal vigilance: Watching for predators or mates?'' Biol. Behav. **11**, 44–49.

Richardson, W. J. (**1995**). ''Documented disturbance reactions,'' in *Marine Mammals and Noise*, edited by W. J. Richardson, C. R. Greene, Jr., C. I. Malme, and D. H. Thomson (Academic, San Diego, CA), pp. 240–324.

Rochat, J. L., and Sparrow, V. W. (**1997**). ''Two-dimensional focusing of sonic boom noise penetrating an air–water interface,'' AIAA J. **35**, 35–39.

Salter, R. E. (**1979**). ''Site utilization, activity budgets, and disturbance responses of Atlantic walruses during terrestrial haul-out,'' Can. J. Zool. **57**, 1169–1180.

Sparrow, V. W. (**1995**). ''The effect of supersonic aircraft speed on the penetration of sonic boom noise into the ocean,'' J. Acoust. Soc. Am. **97**, 159–162.

Stewart, B. S. (**1981**). ''Behavioral response of northern elephant seals and California sea lions on San Nicolas Island, California, to loud impulse noise,'' J. Acoust. Soc. Am. **70**, 84.

Stewart, B. S. (**1982**). ''Studies on the pinnipeds of the Southern California Channels Islands, 1980–1981,'' HSWRI Tech Rep. 82-137, p. 117.

Stewart, B. S., Francine, J. K., and Thorson, P. H. (**1993**). ''Biological effects of launch-specific related noise and sonic boom from the Titan IV rocket at San Miguel Island and South Vandenberg Air Force Base on 2 August 1993,'' HSWRI Tech Rep. 93-246, p. 22.

Stewart, B. S., Thorson, P. H., and Francine, J. K. (**1996**). ''Behavioral responses of pinnipeds and selected avifauna at Vandenberg Air Force Base and the northern Channels Islands to rocket noise and sonic boom during launch of a Titan IV K-22 rocket from SLC-4E, Vandenberg Air Force Base, on May 12, 1996,'' HSWRI Tech Rep. 96-254, p. 67.

Terhune, J. (**1985**). ''Scanning behavior of harbor seals on haul-out sites,'' J. Mammal. **66**, 392–395.

Thompson, D., and Fedak, M. A. (**1993**). ''Cardiac responses of gray seals during diving at sea,'' J. Exp. Biol. **174**, 139–164.

Thompson, P. (**1988**). ''Timing of mating in the common seal (*Phoca vitulina*),'' Mammal Rev. **18**, 105–112.

Thompson, R. D., Grant, C. V., Pearson, E. W., and Corner, G. W. (**1968**). ''Cardiac response of starlings to sound: Effects of lighting and grouping,'' Am. J. Physiol. **214**, 41–44.

Walker, B. G., and Bowen, W. D. (**1993**). ''Behavioural differences among adult male harbor seals during the breeding season may provide evidence of reproductive strategies,'' Can. J. Zool. **71**, 1585–1591.

The effect of a coastline on the underwater penetration of sonic booms

Joel Garrelick[a)]
Cambridge Acoustical Associates, Engineering and Information Technologies Group, Anteon Corporation, 84 Sherman Street, Cambridge, Massachusetts 02140

(Received 15 May 2001; accepted for publication 7 September 2001)

A simplified analysis is presented for the underwater noise levels from a steady supersonic flight traversing a coastline. The effect of the coast is to introduce a propagating noise component that does not exhibit the classic evanescent attenuation with depth for flights subsonic in water. Expressions are given to estimate the boundary of, and levels within, the coastal region where this component dominates. An illustrative example is presented. © *2002 Acoustical Society of America.* [DOI: 10.1121/1.1414702]

PACS numbers: 43.28.Mw, 43.30.Nb, 43.50.Lj [LCS]

I. INTRODUCTION

According to the classic analysis,[1–3] the spectral pressure that is transmitted underwater by the sonic boom from a steady level flight attenuates exponentially with depth, provided that $M = U/c_a < (c_w/c_a) \cong 4.4$, where U is flight speed, M the associated in-air Mach number, and (c_w/c_a) the ratio of sound speeds in water to air. The analysis takes the atmosphere and ocean to be homogeneous and the interface plane. Nevertheless, predictions from this analysis have recently been validated in the field.[4,5]

The classic analyses require that the incident pressure be stationary under the transformation $\zeta = x - Ut$, where x is distance along the flight path and t is time. The implication is that the flight continues for all time over an infinite ocean surface. An aircraft traversing a coastline is not amenable to the above transformation. The effect is to introduce a component of the underwater field that is not evanescent, but rather attenuates geometrically. As such, in deep or shallow water, there is a region where it dominates the overall pressure. This is analyzed below using a highly idealized, *ad hoc*, mathematical model.

II. ANALYSIS

We consider the geometry sketched in Fig. 1. An aircraft in level, steady, supersonic flight flies normal to the coastline, out to sea with a bottom of constant depth D. The coast itself is taken to be palisade-like, represented by a planar vertical, rigid, boundary. This simplifying assumption allows for a relatively simple explicit expression for the pressure field. The more general sloping coast is also tractable,[6] but it adds complexity deemed beyond the scope of this paper.

At zero lateral standoff, the spectral pressure of the sonic boom at the ocean surface is that of a plane acoustic wave with wave number ω/U along the flight path, that is,

$$\tilde{p}(x,z=0;\omega) = P_0(\omega)\exp(i\omega x/U) = P_0(\omega)\exp(ik_a x/M), \tag{1}$$

where $k_a = \omega/c_a$ is the in-air acoustic wave number, we assume that the time dependence is $\exp(-i\omega t)$, and that the amplitude $P_0(\omega)$ accounts for pressure doubling at the surface.

A. Coastal "footprint:" Infinite ocean depth

In the absence of the coastline, that is with Eq. (1) valid for all $-\infty < x < \infty$, and in the limit of deep water ($D \to \infty$), the underwater pressure is given by the classic expression[1]

$$\tilde{p}(x,z;\omega) = P_0(\omega)\exp(ik_a x)\exp[ik_w z\sqrt{(M_w^2-1)}/M_w], \tag{2a}$$

where $k_w = \omega/c_w$, and the underwater Mach number $M_w = U/c_w \cong M/4.4$. With M_w subsonic, i.e., $M_w < 1$, Eq. (2a) may be rewritten to highlight the exponential attenuation with depth,

$$\tilde{p}(x,z;\omega) = P_0(\omega)\exp(ik_a x)\exp[-|k_w|z\sqrt{1-M_w^2}/M_w]. \tag{2b}$$

To account for the presence of the coastline we retain Eq. (1) but limit it to the semi-infinite domain $x \geqslant 0$, that is we set

$$\begin{aligned}\tilde{p}(x,z=0;\omega) &= P_0(\omega)\exp(i\omega x/U)\\ &= P_0(\omega)\exp(ik_a x/M), \quad x \geqslant 0,\\ &= 0, \quad x < 0.\end{aligned} \tag{3}$$

Now, in addition to an evanescently attenuating field, we have a propagating pressure component associated with the (acoustically compact) near field around the origin, so-called "edge mode" radiation.[7] Its source strength is the net vertical force per unit coast length,

$$F(\omega) = P_0(\omega)\int_{-\infty}^{0}\exp(ik_a x/M)\,dx \to -iP_0(\omega)/(k_a/M). \tag{4}$$

Radiation from such a force is given by[8]

[a)]Electronic mail: jgarrelick@anteon.com

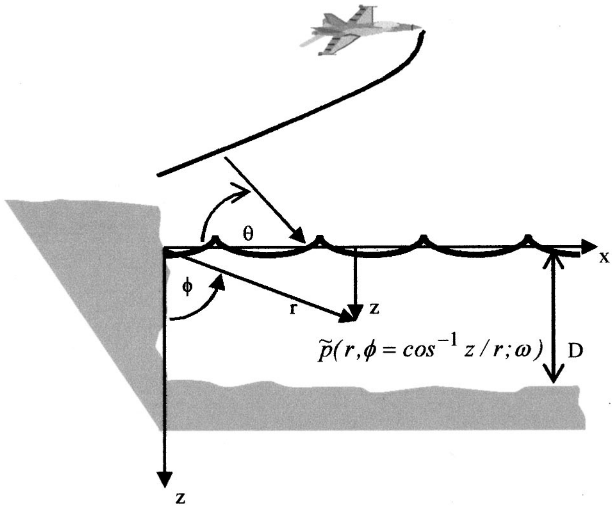

FIG. 1. Sonic boom from steady flight traversing coastline.

$$p(r,\phi;\omega)=i/2k_wH_1(k_wr)\cos\phi F(\omega)$$
$$\cong i(2\pi)^{-1/2}\exp(-i3\pi/4)\exp(ik_wr)$$
$$\times(k_w/r)^{1/2}\cos\phi F(\omega),\quad k_wr>1, \tag{5}$$

where H_1 is the Hankel function of the first kind, $r=\sqrt{x^2+z^2}$ is range, and $\phi=\cos^{-1}(z/r)$ is the elevation angle measured from a normal to the ocean surface. Substituting Eq. (4), we obtain

$$p(r,\phi;\omega)=(1/2)P_0(\omega)M_wH_1(k_wr)\cos\phi$$
$$\cong(2\pi)^{-1/2}P_0(\omega)M_w\exp[i(k_wr-3\pi/4)]$$
$$\times(k_wr)^{-1/2}\cos\phi,\quad k_wr>1. \tag{6}$$

The radiated field given by Eq. (6) satisfies the free ocean surface boundary condition through the $\cos\phi$ term. We may readily account for a rigid boundary condition along our vertical coast with an in-phase image source. Taking further advantage of our assumption of a spatially compact edge mode, this simply doubles the pressure in Eq. (6), yielding

$$p(r,\phi;\omega)=P_0(\omega)M_wH_1(k_wr)\cos\phi, \tag{7a}$$

or

$$p(r,\phi;\omega)\cong(2/\pi)^{1/2}P_0(\omega)M_w\exp[i(k_wr-3\pi/4)]$$
$$\times(k_wr)^{-1/2}\cos\phi,\quad k_wr>1. \tag{7b}$$

Thus, from Eqs. (2) and (7), the coastal region "footprint" where the evanescent field is short-circuited by propagating waves from the shoreline is defined by the inequality,

$$\exp(-k_wz\sqrt{1-M_w^2}/M_w)/(k_wz)\leqslant M_w(k_wr)/H_1(k_wr), \tag{8a}$$

or, at long range,

$$\exp(k_wz\sqrt{1-M_w^2}/M_w)/(k_wz)$$
$$\leqslant(2/\pi)^{1/2}(k_wr)^{-3/2}M_w,\quad k_wr>1. \tag{8b}$$

The above expression assumes a flight line normal to the coastline. However, it is worth noting that the phenomenon will also occur for a flight oblique to the coast, say one making an angle γ with its normal, provided that the projected wave number along the coastline remains supersonic in water, i.e., provided $\sin\gamma<(c_a/c_w)$. At larger angles, the coastline effect will (also) be evanescent. To represent absorption associated with acoustic propagation, one allows k_w to be complex, that is, $k_w\rightarrow k_w/\sqrt{(1-i\eta)}$.

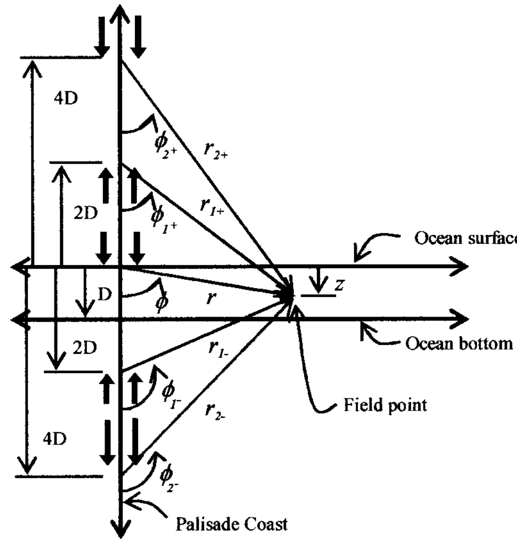

FIG. 2. Edge mode images representing the free ocean surface, the immovable ocean bottom, and the vertical coast.

B. Finite ocean depth

With our vertical coast, we may also readily account for a finite, immovable, ocean bottom, at constant depth D using the method of images,[9] the geometry of which is sketched in Fig. 2. Consequently, applying superposition, the solution is given by

$$p(r,\phi;\omega)=-P_0(\omega)M_w\Bigg\{H_1(k_wr)\cos\phi + \sum_{n=1}^{\infty}(-1)^n\sigma^n[H_1(k_wr_{n^+})\cos\phi_{n^+} - H_1(k_wr_{n^-})\cos\phi_{n^-}]\Bigg\}, \tag{9a}$$

or, at large range,

$$p(r,\phi;\omega)\cong-(2/\pi)^{1/2}P_0(\omega)M\exp(-i3\pi/4)\times(k_w/k_a)^{1/2}\Bigg\{\exp(ik_wr)(k_ar)^{-1/2}\cos\phi + \sum_{n=1}^{\infty}\sigma^n[\exp(ik_wr_{n^+})(k_ar_{n^+})^{-1/2}\cos\phi_{n^+} + \exp(ik_wr_{n^+})(k_ar_{n^-})^{-1/2}\cos\phi_{n^-}]\Bigg\},$$
$$k_wr>1, \tag{9b}$$

with $r_{n\pm}=r\sqrt{(2nD/r\pm z/r)^2+(\sin\phi)^2}$, $\phi_{n\pm}=\tan^{-1}[\sin\phi/(2nD/r\pm z/r)]$, and the "bottom bounce" reflection coeffi-

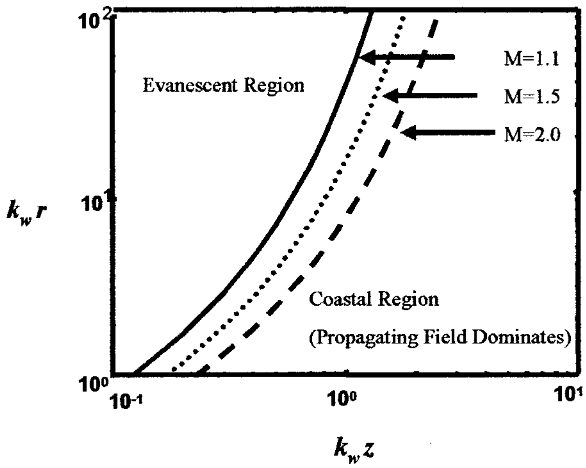

FIG. 3. Coastal region boundary for various values of M.

cient, $\sigma \leqslant 1$, is introduced, *ad hoc*, to represent bottom losses.

The total spectral pressure is the sum of Eqs. (2) and (9) and the associated time signatures of the components and/or the sum are given by the inverse transform(s),

$$p(r,\phi;t)=(1/2\pi)\int_{-\infty}^{\infty} p(r,\phi;\omega)\exp(-i\omega t)d\omega$$
$$=(1/\pi)\mathrm{Re}\left(\int_{-\infty}^{\infty} p(r,\phi;\omega)\exp(-i\omega t)d\omega\right). \quad (10)$$

III. ILLUSTRATIVE EXAMPLE

First, letting $D\rightarrow\infty$, the boundary of the coastal region given by Eq. (8b) is plotted in Fig. 3 for various Mach numbers M. The graph pertains to any and all spectral components of a sonic boom signature. It is universal in that the axes are nondimensional, receiver depth $(k_w z)$ and range $(k_w r)$. For example, with a sonic boom of duration 0.1, the spectrum will peak in the vicinity of about 10 Hz. At this frequency, with a receiver at depth say $z=30\,\mathrm{m}$ $(k_w z \cong 1.26)$, and letting $M=1.5$, the evanescent field is short-circuited at ranges $k_w r \leqslant 28.0$, or about $r \leqslant 670\,\mathrm{m}$. This range may extend out farther in the presence of strong reflections from an ocean bottom, with "hot spots" created where multiple received rays add constructively, or in the limit where a reverberant field is developed. However, the influence of the ocean bottom is perhaps more insightfully illustrated in the time domain, as shown in Fig. 4.

In this example we hypothesize a unit N-wave sonic boom signature of duration 0.1 s on the sea surface and $M=2$. The sea depth is taken to be 200 m and we assume a receiver at a depth of 30 m and range 50 m. Also, we take $\eta=0$, but allow for a frequency-invariant bottom bounce reflection loss of 3 dB $(\sigma=2^{-1/2})$.

The computed evanescent pressure using Eq. (2) is plotted versus time in Fig. 4(a) and the propagating field using Eq. (9b) in Fig. 4(b). For reference, in both figures, the surface signature is shown as a dotted line. Signatures were computed with a frequency resolution of 0.1 Hz up to 200 Hz. At this depth the peak value of the evanescently attenuating pressure has been reduced to about 12% of that at the surface. It also exhibits the characteristic pre- and post-spreading of the surface signature. At this range and depth, the peak level of the propagating component is higher, about 20% of the surface pressure. And at this moderate depth it arrives first, since it propagates at the speed of sound in water. Also, for the assumed depth one can clearly distinguish between the arrival of the direct and indirect paths. However, there are two contributions for each value of n in Eq. (9), or in other words for each number of bounces off the bottom, and they are not entirely separated.

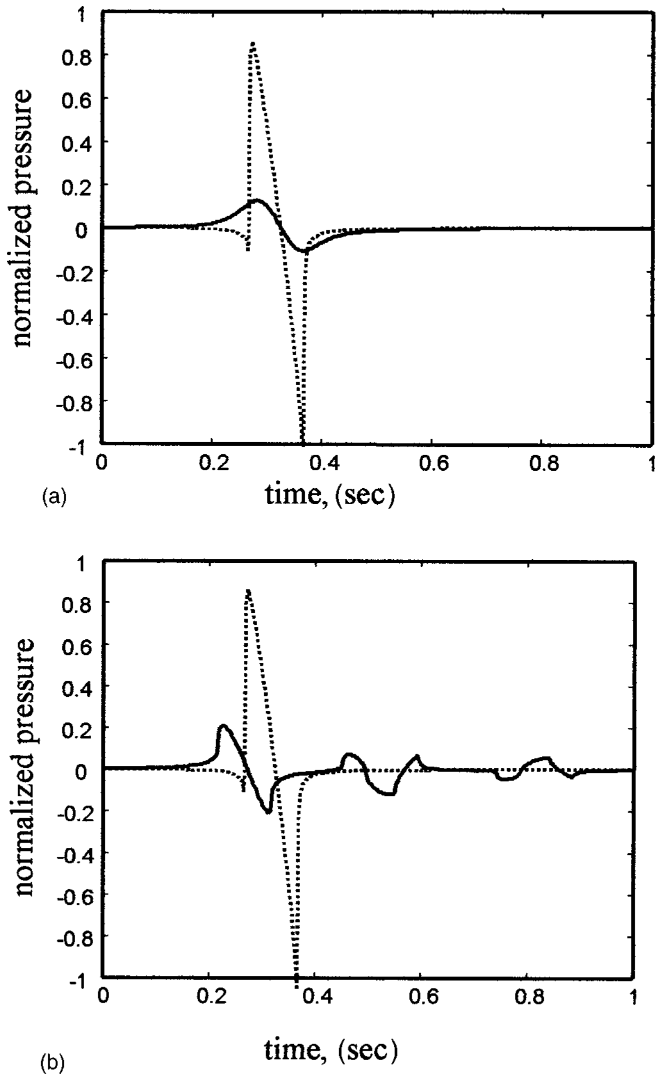

FIG. 4. Computed pressure components at a depth of 30 m and the range from the coast of 50 m for a 0.1 s unit N-wave at $M=2$: Ocean depth 200 m. (a) Evanescent component [Eq. (2)]. (b) Propagating component including bottom reflections [Eq. (9b)].

IV. CONCLUSIONS

The presence of a coastline introduces a propagating component to the classic evanescent underwater noise field from a steady supersonic flight. As a consequence, underwater noise levels may be enhanced over conventional values, the effect becoming more pronounced with increasing receiver depth and frequency.

ACKNOWLEDGMENT

The author gratefully acknowledges the support of the Air Force Research Laboratory and Marine Acoustics, Inc.

[1] K. N. Sawyers, ''Underwater sound pressures from sonic booms,'' J. Acoust. Soc. Am. **44**, 523–524 (1968).

[2] R. K. Cook, ''Penetration of a sonic boom into water,'' J. Acoust. Soc. Am. **47**, 1430–1436 (1970).

[3] V. W. Sparrow and T. Ferguson, ''Penetration of shaped sonic boom noise into a flat ocean,'' *35th Aerospace Sciences Meeting and Exhibit*, Reno, NV, 1997, AIAA Paper No. 97-0486.

[4] F. Desharnais and D. M. F. Chapman, ''Underwater measurements of a sonic boom,'' *Proc. Oceans 97/MTS/IEEE*, 1997, pp. 592–596.

[5] R. A. Sohn, F. Vernon, J. A. Hildcbrand, and S. C. Webb, ''Field measurements of sonic boom penetration into the ocean,'' J. Acoust. Soc. Am. **107**, 3073–3083 (2000).

[6] For example, E. Topuz and L. B. Felsen, ''Intrinsic modes: Numerical implementation in a wedge-shaped ocean,'' J. Acoust. Soc. Am. **78**, 1735–1745 (1985); also, Michael J. Buckingham, ''Theory of acoustic radiation in corners with homogeneous and mixed perfectly reflecting boundaries,'' *ibid.* **86**, 2273–2291 (1989).

[7] M. C. Junger and D. Feit, *Sound, Structures and Their Interaction*, 2nd ed. (MIT Press, Cambridge, MA, 1986), Sec. 5.8.

[8] E. Skudrzyk, *The Foundations of Acoustics* (Springer-Verlag, New York, 1971), Sec. 21.13 [with $k_z = 0$ and, from the surface impedance of a cylindrical filament, $\tilde{F}(\omega) \cong -i2\rho\omega R^2 V_0$].

[9] See Ref. 8, Sec. 18.16.

Seismic detection of sonic booms[a)]

Joseph E. Cates[b)] and Bradford Sturtevant
Graduate Aeronautical Laboratories, California Institute of Technology, Pasadena, California 91125

(Received 18 July 2001; revised 29 August 2001; accepted 30 August 2001)

The pressure signals from a sonic boom will produce a small, but detectable, ground motion. The extensive seismic network in southern California, consisting of over 200 sites covering over 50 000 square kilometers, is used to map primary and secondary sonic boom carpets. Data from the network is used to analyze three supersonic overflights in the western United States. The results are compared to ray-tracing computations using a realistic model of the stratified atmospheric at the time of the measurements. The results show sonic boom ground exposure under the real atmosphere is much larger than previously expected or predicted by ray tracing alone. Finally, seismic observations are used to draw some inferences on the origin of a set of "mystery booms" recorded in 1992–1993 in southern California.
[DOI: 10.1121/1.1413754]

PACS numbers: 43.28.Mw, 43.20.Dk [LCS]

I. INTRODUCTION

The seismic network in southern California routinely detects sonic booms from aircraft. The high density of sites and the extensive ground coverage of the network, over 50 000 square kilometers, provide a unique opportunity to study the long-range propagation of direct and indirect sonic booms.

In Sec. II, the fundamental features of sonic boom carpets under a realistic atmosphere are presented. The pressure signals from the N-wave signal in the atmosphere produce a small, but detectable, ground motion as outlined in Sec. III. Seismic data from three overflights are presented in Sec. IV: a west to east SR-71 pass at $M=3.15$, the landing of space shuttle Discovery, STS-42, at Edwards AFB, and the passage of shuttle Discovery over Washington and Oregon. Section V presents the results of an analysis of a set of "mystery booms" which occurred in California in 1992 and 1993.

II. ATMOSPHERIC PROPAGATION

For the propagation of sonic booms through the atmosphere, the linear theory of geometrical acoustics is applied. In geometrical acoustics, the shock front moves along rays with speed c relative to the surrounding medium, where c is the local sound speed. Following Pierce (1981), the ray-tracing equations can be written

$$\frac{d\mathbf{x}}{dt}=\frac{c^2\mathbf{s}}{\Omega}+\mathbf{v}, \tag{1}$$

$$\frac{d\mathbf{s}}{dt}=-\frac{\Omega}{c}\nabla c-\mathbf{s}\times(\nabla\times\mathbf{v})-(\mathbf{s}\cdot\nabla)\mathbf{v}, \tag{2}$$

where $\mathbf{n}$ is the unit normal to the wave, the medium moves with velocity $\mathbf{v}$, the wave-slowness vector $\mathbf{s}=\mathbf{n}/(c+\mathbf{v}\cdot\mathbf{n})$, and $\Omega=1-\mathbf{v}\cdot\mathbf{s}=c/(c+\mathbf{v}\cdot\mathbf{n})$. A stratified model is typically assumed for the atmosphere where properties vary only with altitude $[\mathbf{v}=\mathbf{v}(z),\ c=c(z)]$, and the vertical wind velocity is zero $(v_z=0)$. For this case, the equation for the change of $\mathbf{s}$ simplifies to a generalization of Snell's law. The horizontal components s_x and s_y must remain constant, while the vertical component is given by

$$s_z=\pm\left[\left(\frac{\Omega}{c}\right)^2-s_x^2-s_y^2\right]^{1/2}. \tag{3}$$

The ray equations become

$$\frac{dx}{dt}=\frac{c^2s_x}{\Omega}+v_x,\quad \frac{dy}{dt}=\frac{c^2s_y}{\Omega}+v_y,\quad \frac{dz}{dt}=\frac{c^2s_z}{\Omega}. \tag{4}$$

From the assumption of a stratified atmosphere, the right-hand side of Eqs. (4) are functions of altitude alone and can be integrated numerically from atmosphere profiles.

Rays are confined to regions of sound speed and wind speed where $s_z^2>0$. A turning point exists where s_z passes through zero and the ray changes direction of vertical propagation. For an atmosphere without winds, a ray will only turn horizontal at the altitude with sound speed

$$c(z^*)=\frac{c_0}{\cos\theta_0}, \tag{5}$$

where c_0 and θ_0 are the sound speed and ray angle to the horizontal at the point where the ray is emitted. For the case of a sonic boom, the ray is emitted at the complement of the Mach angle. Therefore, the ray turning points for an aircraft in straight and level flight are located at the altitude where the sound speed is equal to the velocity of the aircraft. For an aircraft flying at below the ambient sound speed at the ground, all rays will be turned and none will reach the ground. This critical Mach number is referred to as the cutoff Mach number. Rays which are turned at high altitude will reach the ground only if the sound speed is greater than that at the ground; otherwise, the ray will be channeled between an upper and lower turning point.

For long-range propagation in the atmosphere, the effect of winds cannot be neglected. For a stratified atmosphere with winds, the turning points for each ray depend on the ray

[a)]Portions of this work were presented as "Studies of sonic booms with seismic networks," 129th Acoustical Society of America meeting, 30 May–3 June 1995, Washington, DC.
[b)]Presently at Universal Music Group, Universal City, CA.

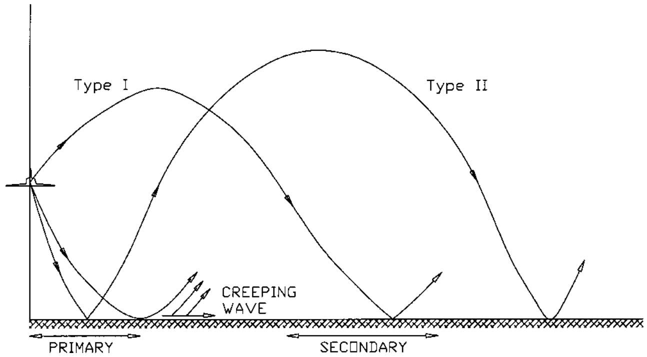

FIG. 1. Illustration of sonic boom carpets.

direction. It is convenient to define the effective sound speed seen by a ray moving in a particular direction $c_{\mathrm{eff}}=c_0+\mathbf{v}\cdot\mathbf{n}$. The turning point for a ray occurs at the altitude where

$$c_{\mathrm{eff}}(z^*)=\frac{c_0}{\cos\theta_0}, \tag{6}$$

which depends on the ray direction through the effective sound speed.

For a uniform atmosphere with no winds, the sonic boom forms a Mach cone which intersects the ground to produce the hyperbolae typically associated with the sonic boom footprint. For realistic atmosphere profiles, the sonic boom footprint becomes much more complex, as shown in Fig. 1. The primary carpet lies directly beneath the aircraft and consists of direct rays from the aircraft to the ground. The increasing temperature as rays approach the ground leads to the refraction of the rays upward which limits the width of the primary carpet. Outside of the primary carpet, a secondary carpet is formed of indirect rays which have propagated upward and been refracted back to the ground. Additional carpets are formed further from the aircraft flight path by rays which have reflected from the ground, returned to high altitude, and then back toward the ground. Even higher-order carpets exist further out from the flight path.

Between the primary carpet and secondary carpet, geometrical acoustics predicts a shadow region where no rays

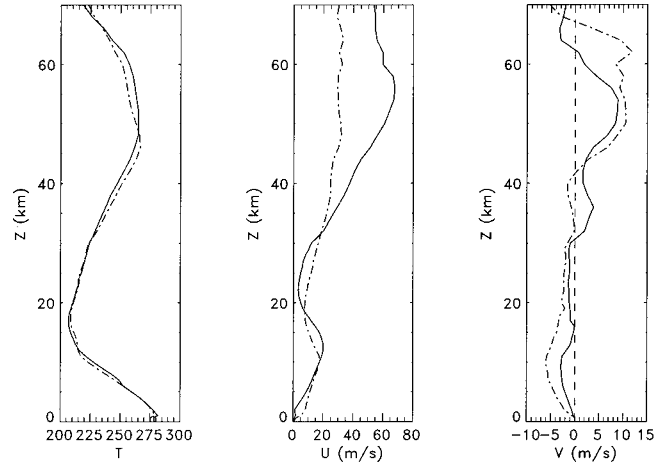

FIG. 2. Temperature and zonal (east/west, U) and meridional (north/south, V) wind component profiles for January (———) and November (–·–), Edwards AFB Range Reference Atmosphere.

reach the ground. However, the full theory of acoustics allows for a creeping wave launched at the edge of the primary carpet which propagates along the ground in the ray direction. The creeping wave is typically illustrated as a wave moving along the ground continually launching rays upward. Since the creeping wave sheds energy, the amplitude dies off exponentially with distance (Rickley and Pierce, 1980).

For the present analysis, the Range Reference Atmosphere for Edwards Air Force Base is used for wind and thermodynamic properties to 70 km altitude (Meteorology Group, Range Commanders Council, 1983). These profiles are comparable to the U.S. Standard Atmosphere, Supplemental Atmosphere (1966), and climatic data for the Pacific Missile Range, CA (de Violini 1967, 1969). In Fig. 2, profiles of temperature and zonal and meridional wind components are shown as a function of altitude from the monthly profiles for January and November. Zonal winds are positive when from west to east and meridional wind components are positive when from south to north. During the winter months, the zonal wind component shows strong stratospheric winds blowing from west to east. Meridional wind

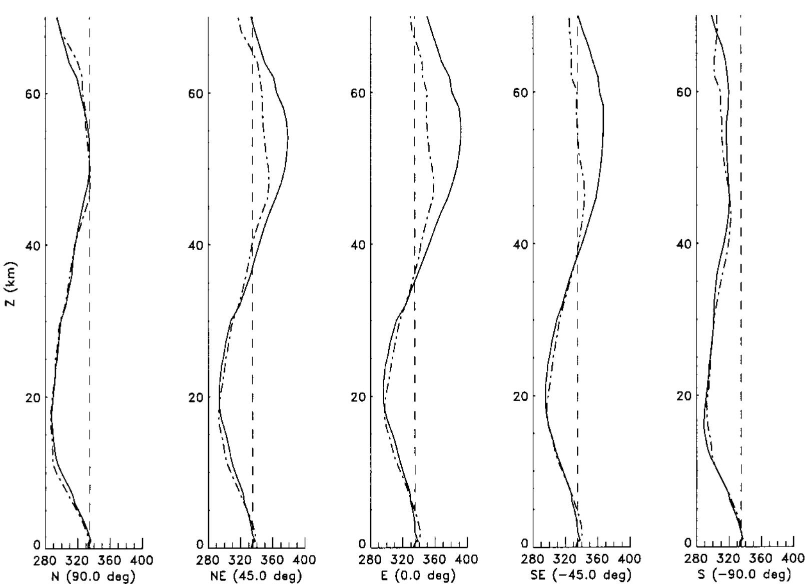

FIG. 3. Effective sound speed profiles for January (———) and November (–·–), Edwards AFB Range Reference Atmosphere.

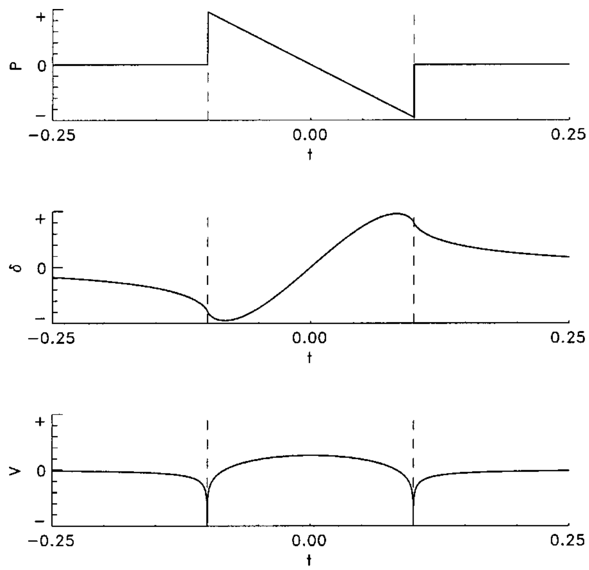

FIG. 4. Surface effects of pressure wave.

components are much weaker and tend to fluctuate in direction, although stronger meridional wind components are also found at stratospheric altitudes.

Effective sound speeds for five ray directions are shown in Fig. 3. Shallow rays traveling east will be turned downward toward the ground between 40 and 60 km altitude. The effective sound speed for rays traveling directly north or south is not sufficiently high at altitude to diffract the rays to the surface, but a significant area of high effective sound speeds exists even for the northeast and southeast directions. Rays traveling west will not be turned back to the ground at any altitude. The temperature rise in the stratosphere alone is not sufficient to return rays to the ground.

Examples of these atmospheric effects have been observed experimentally for sonic booms. Rickley and Pierce (1980) measured secondary sonic booms from Concorde flights along the East coast of the United States. Microphones captured similar indirect sonic booms from the Concorde refracted from the level of the stratosphere (40–50 km) which had propagated a horizontal range of over 165 km. These were followed several minutes later by low-frequency signals which had refracted from the level of the thermosphere (100–130 km) and propagated over ranges up to 1000 km (Balachandran *et al.*, 1977). Sonic boom signatures are often recorded past the nominal edge of the primary carpet; however, the occurrence of creeping waves is difficult to detect due to the similar effects of turbulent scattering (Onyeowu, 1975).

Although pointwise pressure measurements have been made for indirect sonic booms, fundamental questions about the size and shape of the indirect carpets and the shadow regions remain unanswered. Measurement of indirect sonic booms has traditionally been very difficult due to the locational dependence on the atmospheric conditions at high altitude and the wide geographic coverage required to resolve the carpets. As shown in the next section, existing seismic networks, such as the network in southern California which covers over 50 000 square kilometers, provide a very useful tool for analyzing the indirect sonic booms.

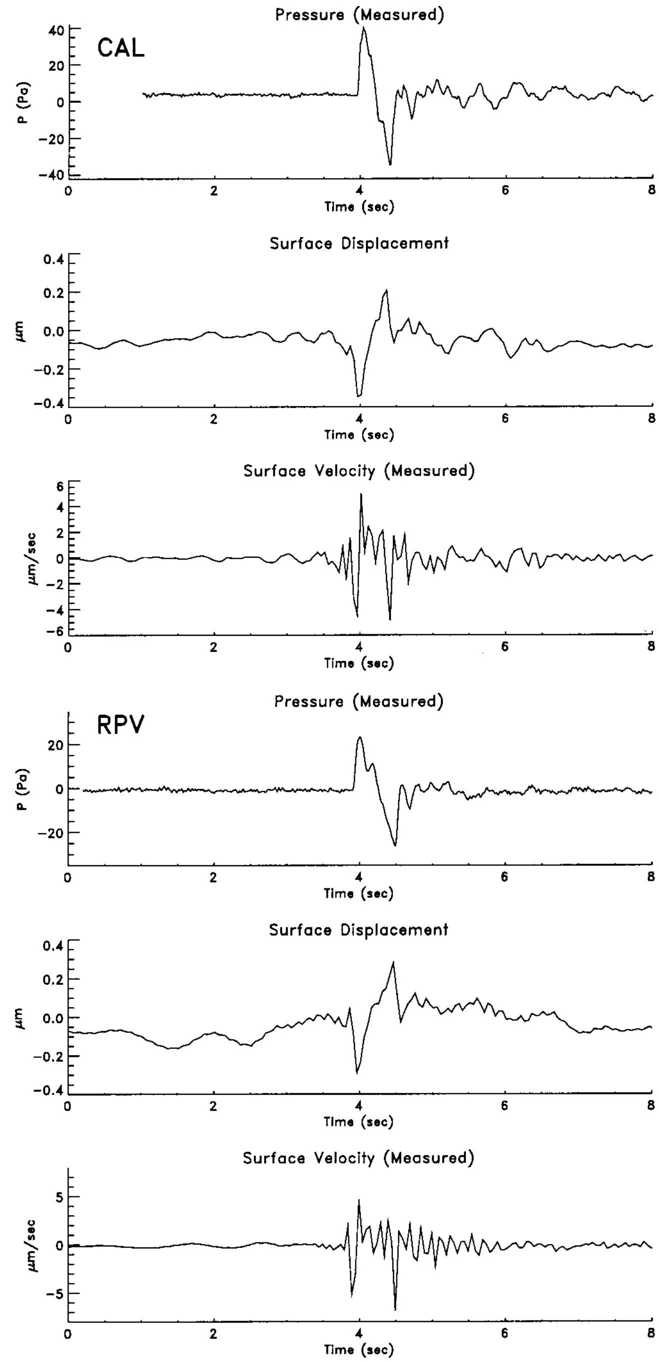

FIG. 5. Pressure, surface displacement, and surface velocity for TERRAscope sites CAL (Cal State LA) and RPV (Rancho Palos Verdes) for the reentry of space shuttle Endeavour, March 1995. (Data provided by Dr. H. Kanamori, Caltech Seismological Laboratory.)

III. SEISMIC DETECTION

Early use of seismographs in sonic boom research was primarily restricted to examining the effects of sonic booms on ground motion and the possibility of damage to structures or triggering of earthquakes (Cook and Goforth, 1970). These studies involved only a few seismograph instruments, often specifically emplaced for the overflights. Only recently have larger existing seismograph networks been used to detect sonic booms from aircraft and meteors (Kanamori *et al.*, 1992; Qamar, 1993).

Due to the much higher sound speed in the surface, the

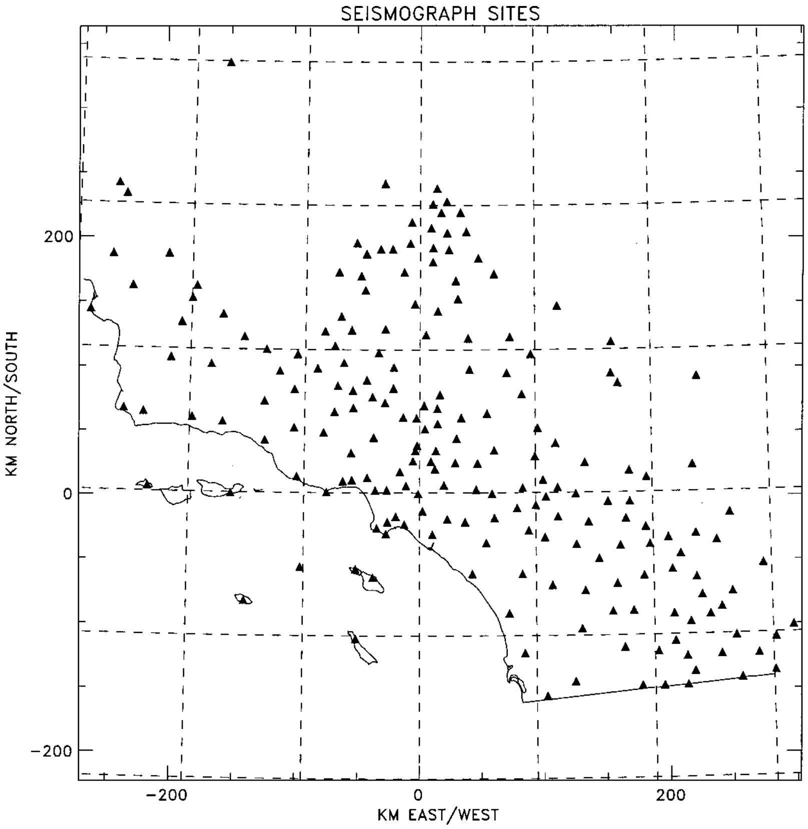

FIG. 6. Seismic stations in California used for the current study.

majority of the energy of the N-wave is reflected; however, several effects of the wave are observed in the ground. The primary effect of the pressure wave is the moving strain field in the surface immediately beneath the N-wave. A secondary, weaker effect is the production of coupled Rayleigh waves which follow the passage of the N-wave. In addition, irregularities in the ground properties and acoustic coupling with geographical features become local sources which radiate additional seismic waves. Since the wave speed is higher in the ground, precursor waves are often observed to arrive several seconds before the sonic boom (Cook and Goforth, 1970).

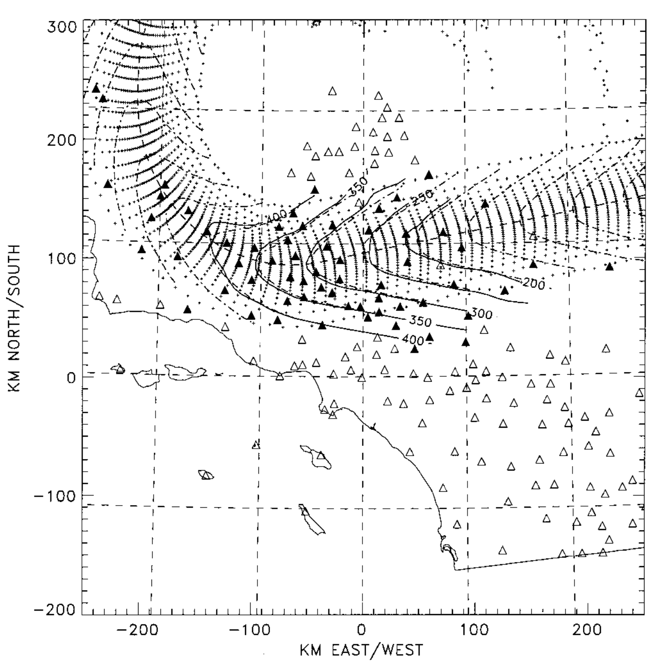

FIG. 7. Contours from seismic arrival times (———) compared with ray-tracing results (–·–) for SR-71 flight, 8 December 1993, at $M=3.15$, altitude 21 km. The small plus symbols represent where rays from ray-tracing intersected the ground.

If the shock wave is approximated as a moving normal load over an elastic half-space, the displacement and velocity of the surface can be computed from a superposition of solutions producing zero normal and shear stress at the boundary. Consider an incident wave moving along the surface at velocity U with pressure distribution

$$p(x,t)=p_0 e^{i\omega(t-x/U)}. \tag{7}$$

The vertical displacement u_z at the surface is given by

$$u_z(x,t)=-\frac{Up_0}{2\mu\omega}\left(\frac{\lambda+2\mu}{\lambda+\mu}\right)e^{i\omega(t-x/U)}, \tag{8}$$

where λ and μ are the elastic constants of the half-space (Ben Menachem and Singh, 1981). The surface velocity follows immediately by derivation of the displacement. The theoretical surface displacement and velocity predicted by Eqs. (7) and (8) for a pressure N-wave with duration $\tau=0.2$ are shown in Fig. 4. The surface velocity diagram shows the inverted U-type of signature characteristic of an N-wave for velocity seismograms. The two strong downward peaks correspond to the leading and trailing shock on the original N-wave.

Pressure transducers have been added to a number of the TERRAscope stations in southern California operated by the Caltech Seismological Laboratory. This allows direct comparisons between sonic boom pressures and surface velocity.

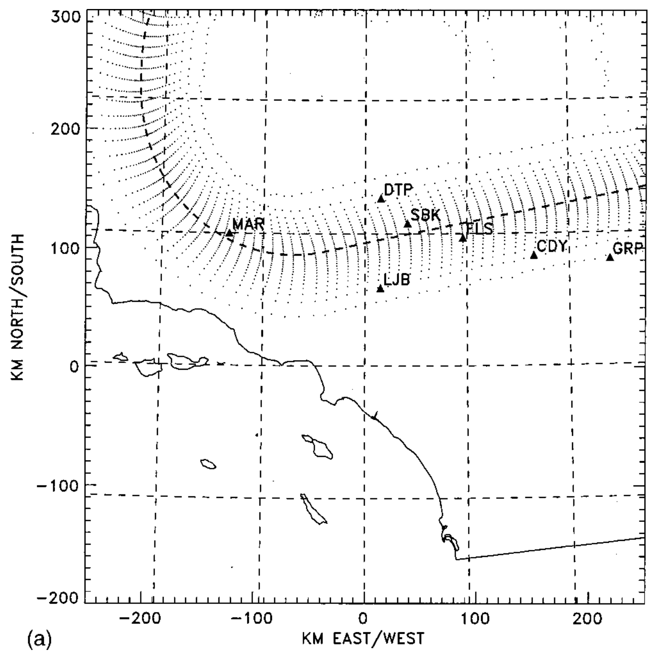

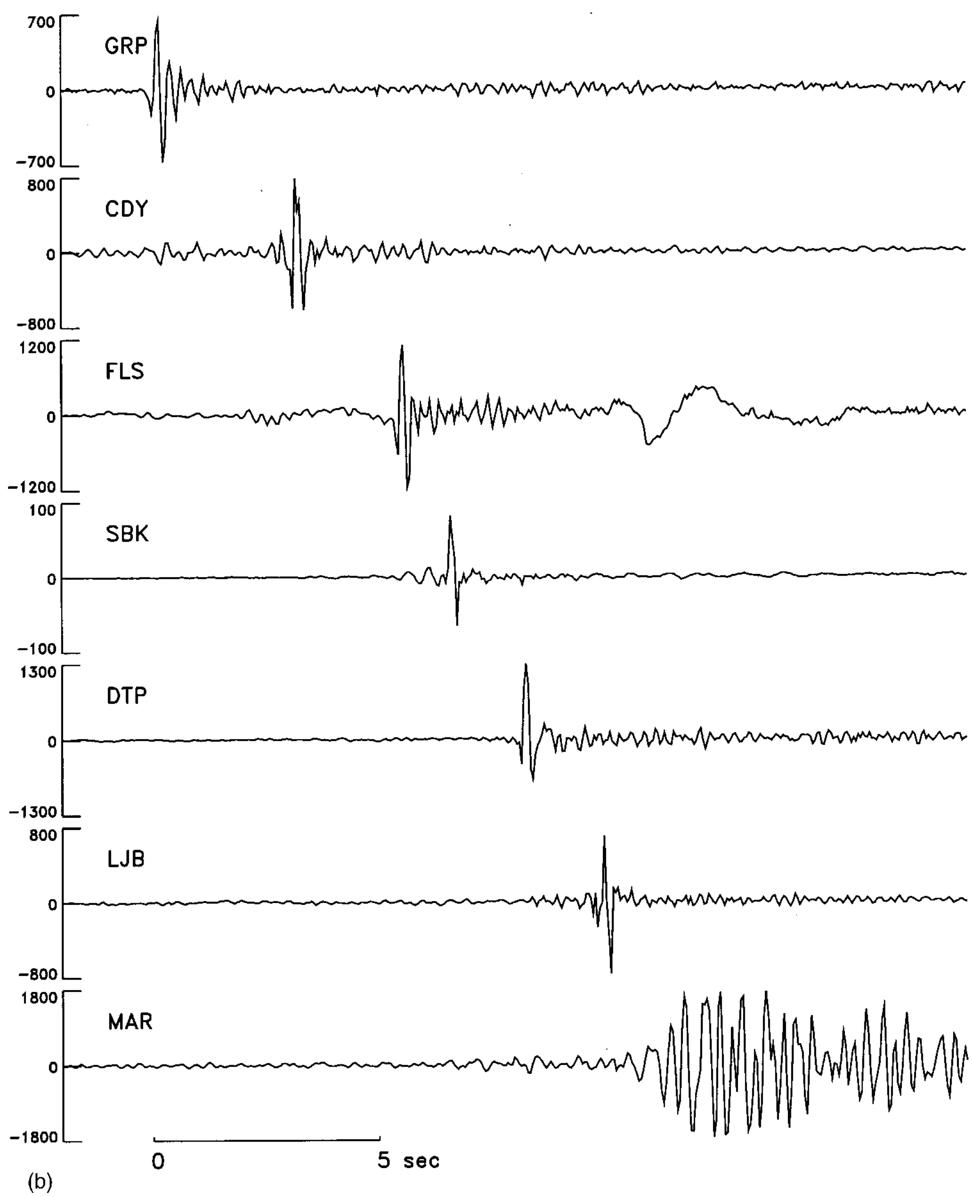

FIG. 8. (a) Seismic station locations relative to SR-71 trajectory and (b) time traces from selected seismic stations which detected the primary boom. Time traces record ground motion, vertical scale is voltage output in counts.

In Fig. 5, data are shown for the two TERRAscope stations CAL (CalState LA) and RPV (Rancho Palos Verdes) for the reentry of space shuttle Endeavour on 18 March 1995. (Data provided by Dr. H. Kanamori, Caltech Seismological Laboratory.) The pressure and surface velocity are measured directly and corrected only for instrument response, and the surface displacement is integrated from the velocity. The characteristic double-peaked signature of an N-wave is clearly visible in the surface velocity traces which provides an accurate estimate of the N-wave duration. The features of the N-wave are also captured very well in the surface displacement.

The seismic network used in the current study consists of over 200 stations shown in Fig. 6 from TERRAscope (Caltech's broadband seismic network), the Caltech-U.S.G.S. Southern California Seismic Network (SCSN), and the University of California Los Angeles Basin Seismic Network. The majority of sites are SCSN stations which measure ground motion velocity in the frequency range of 1 to 20 Hz. These instruments record frequencies well within this range, but response falls off above 20 Hz due to an anti-aliasing filter near 30 Hz. Only a limited response is available below 1 Hz. Raw output voltage data were provided at 100 samples per second by Dr. H. Kanamori, Caltech Seismological Laboratory, and Dr. J. Mori, U.S.G.S., Pasadena. For magnitude analysis, the data were corrected for instrument response; otherwise, the raw signal data were used for selecting arrival times.

For the entire network, amplitude information is difficult to extract from the seismic data due to the lack of detailed knowledge of the local surface conditions of the seismic stations. When the site and instrument properties are known, seismic data have been shown to produce accurate estimates of N-wave pressures for the primary sonic booms from shuttle landings (Kanamori *et al.*, 1992). However, for the extensive network used in this study, the sites are typically classified only as hard or soft rock sites. A useful approximation for at least a basic comparison of pressures is available from Goforth and McDonald (1968). In flight tests with a wide variety of aircraft using velocity seismographs with a frequency range of 1 to 100 Hz, the peak ground velocity was found to be proportional to the maximum overpressure: for high-density rock, maximum ground velocity was approximately 1.5 μm/s per Pa of overpressure, and approximately 2 μm/s per Pa for low-density rock.

The seismograph records provide accurate information for arrival time of the pressure disturbances. When the signal characteristic of N-waves is visible, the duration of the N-wave can also be determined. However, at soft-rock sites, the actual N-wave signal itself is often lost in reverberations of the local sediment. Due to the extremely low magnitude of the ground motion, disturbances often are indistinguishable from local sources such as noise or nearby traffic. Events which are not also observed on nearby sites have to be ignored as local noise when choosing arrival times from the time traces.

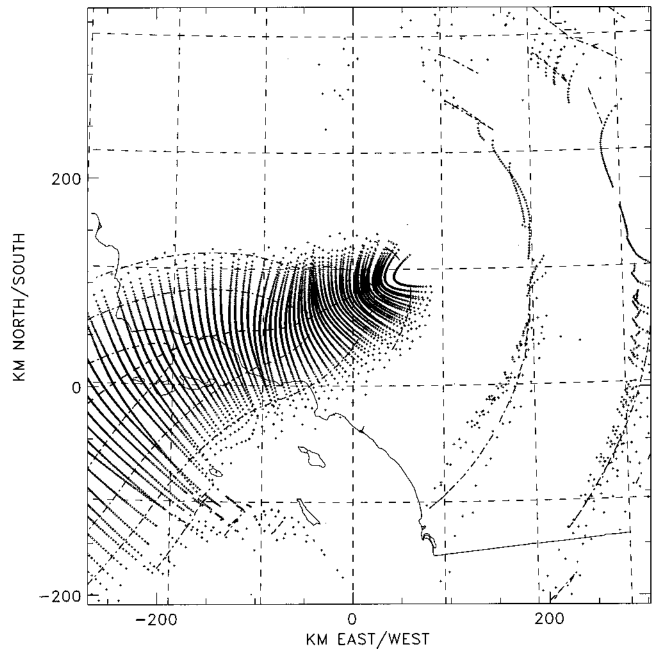

FIG. 9. Ray-tracing results for STS-42 reentry showing points where rays intersected the ground (+) and contours of arrival times (–·–).

IV. FLIGHT RESULTS

A. SR-71 Mach 3.15 overflight

First, due to the relative complexity of the space shuttle reentry trajectories, the results from a portion of a NASA SR-71 flight on 9 December 1993 are presented. As part of a prescheduled flight, the SR-71 flew a high-speed pass from east to west over Edwards AFB at $M=3.15$ at an altitude of 21 km. Through the kind cooperation of Dr. Robert Meyer of NASA Dryden, the SR-71 trajectory was modified to facilitate collection of seismic data.

The seismic data from the overflight are shown in Fig. 7. All seismic stations available are denoted by the triangle symbols, and solid symbols denote the sites which detected the sonic boom. The arrival time data were converted to a regular grid and contoured to produce the solid arrival time contours. Since the majority of the rays are propagating east to west, no indirect carpets are observed. The seismic data clearly show both the north and south edges of the primary carpet.

For comparison, a ray-tracing computation was performed. A cone of rays was launched at the Mach angle at discrete times along the trajectory, and the rays were then propagated using the wind and temperature profiles from the Edwards AFB Range Reference Atmosphere (Meteorology Group, Range Commanders Council, 1983). The small plus symbols in Fig. 7 represent the locations where the computed rays intersected the ground. The majority of the ray ground intersections are direct rays in the primary carpet underneath the aircraft trajectory; only a few indirect rays appear north of the primary carpet. The ground arrival time contours from ray tracing are shown as dashed lines. The ray-tracing contours compare well with the arrival times from the seismic data, with the only significant disagreement being a loss of

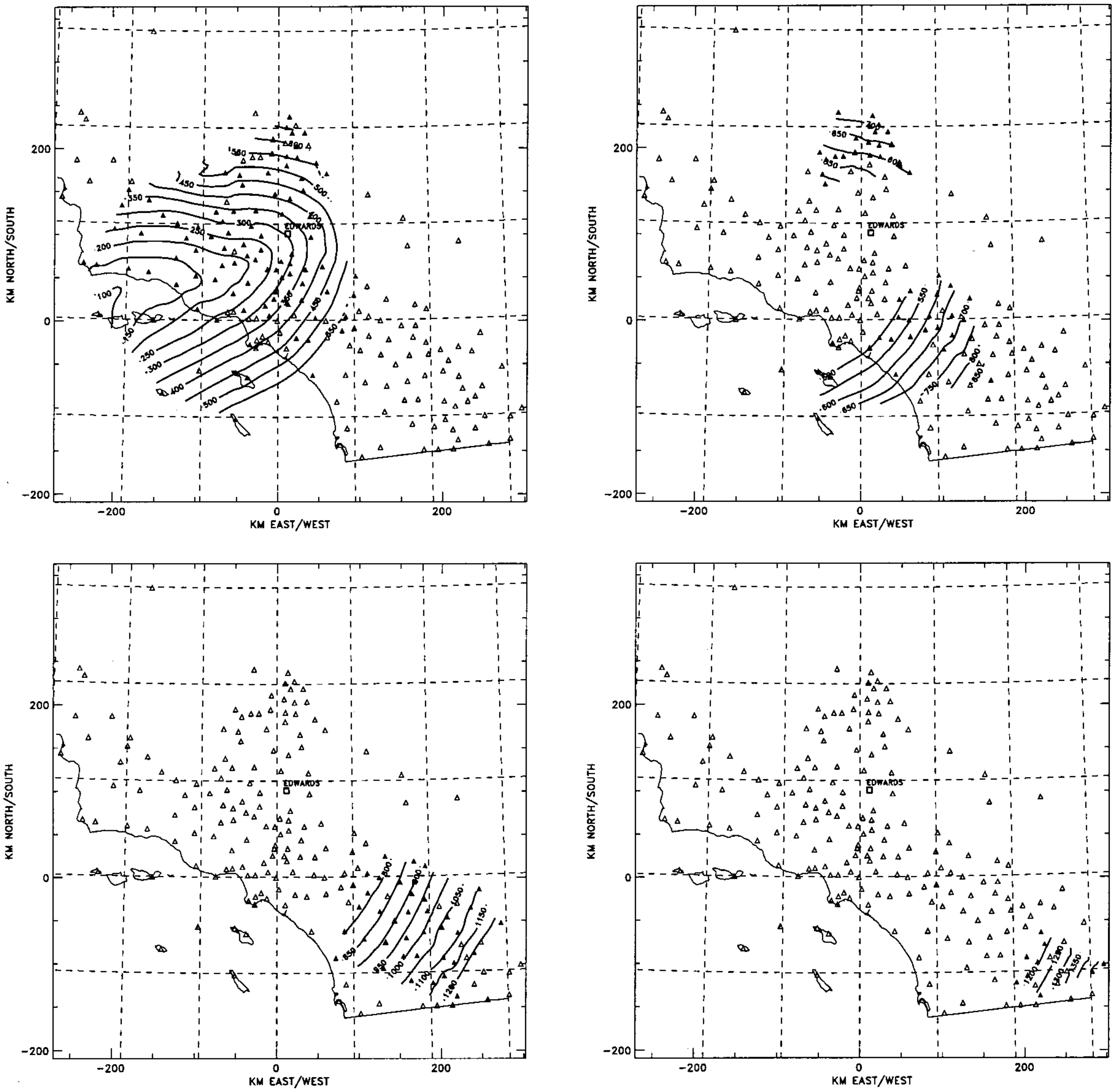

FIG. 10. Contours from seismic arrival times, STS-42 reentry.

resolution due to the lack of sites as the aircraft begins to turn north.

Sections of the seismic traces for seven sites from the SR-71 flight are shown in Fig. 8. The time traces show the ground velocity signal characteristic of an N-wave. The MAR site is shown as an example of a site where the signal is lost in reverberations in the ground layers. Precursor waves are seen before several of the N-wave signatures, most notably at the SBK site. This example provides an important verification that the seismic data do not show spurious signals, but only the signal from the N-wave.

B. STS-42 reentry

The seismic data were examined in detail for the landings at Edwards AFB of space shuttle Discovery, STS-42, on 30 January 1992. The flight approached Edwards AFB from the west over the Pacific Ocean, leading to rays which propagated predominantly from west to east producing a complex set of indirect sonic boom carpets.

Contours of arrival time from ray-tracing results for the reentry of STS-42 are shown in Fig. 9. A cone of rays was launched at the Mach angle at discrete times along the trajectory, and the rays were then propagated through the wind and temperature profiles. The small plus symbols represent the locations where computed rays intersected the ground. The shuttle trajectory is shown as a dashed line. Within the primary carpet, the arrival time contours shown as dashed lines have the characteristic hyperbolic shape, modified by the maneuvering of the shuttle. The shockfront predicted by ray tracing is crossed and folded within the primary carpet, which is manifested as the crossing of the locus of the ground intersection points for rays emitted at subsequent times. As the altitude and Mach number decrease, the width of the primary carpet decreases. In addition to the primary carpet, two indirect carpets to the east are apparent, separated by shadow regions where no rays reach the ground from ray-tracing.

The seismic network detected four booms from the STS-42 landing. Arrival time contours from the seismic data for the four booms are shown in Fig. 10. Arrival times are chosen from the time traces, converted to a regular grid, and contoured at 50 s intervals. The most immediately striking

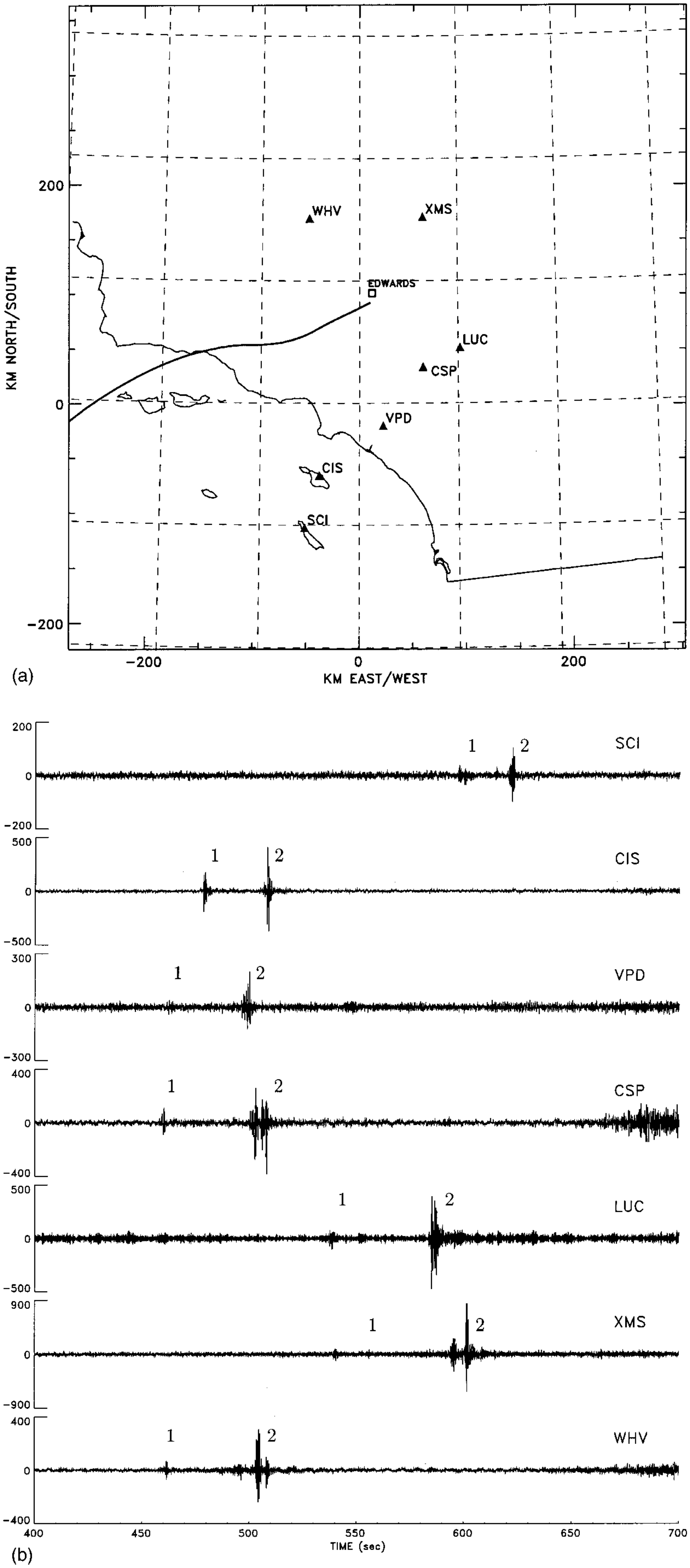

FIG. 11. (a) Seismic station locations relative to the STS-42 trajectory and (b) time traces from selected seismic stations within the shadow region predicted by ray-tracing for STS-42 reentry. Time traces record ground motion, vertical scale is voltage output in counts.

feature of the seismic results is the complete ground coverage. Virtually the entire network detected at least one boom, and no shadow region is visible, which is in contrast to the ray-tracing results (Fig. 9). Within the primary carpet, the contours agree very well with the ray-tracing results, verifying again the ability of the seismic network to accurately map the primary carpet.

Due to the rather unexpected amount of ground coverage of the sonic booms, three sets of representative time traces are shown in Figs. 11–13. The first figure, Fig. 11, shows seven seismic sites situated in the shadow region predicted by geometrical acoustics. The sites, both north and south of the trajectory, show two booms within the shadow region. The first boom is almost certainly the primary boom, labeled boom 1. This is consistent with the underprediction of the carpet width by ray-tracing as was observed for the SR-71 overflight. The second boom, labeled boom 2, may be a creeping wave, although the magnitude appears too large. Attempts to vary the atmosphere profile, such as introducing unusually strong jet stream winds, failed to duplicate the second boom in this region by ray-tracing.

The second figure, Fig. 12, shows seven sites in an area roughly 100 km square, slightly inside the secondary carpet predicted by ray-tracing. Boom 2 appears on each of the sites but splits into two peaks on the eastern sites, for example at the MDA and RAY sites. The low-amplitude disturbance seen on these sites appears to be a third and fourth disturbance, labeled booms 3 and 4, which strengthens and becomes clearly visible further east. The final set of time traces for STS-42 reentry, Fig. 13, shows a line of seven sites stretching 150 km, offering a rare opportunity to view the development of the indirect carpets. The second boom, boom 2, is seen to disappear further from the flight track to be replaced by booms 3 and 4. The indirect booms are split into two segments, which one would assume is caused by discrete bands in the atmosphere profiles.

C. Discovery reentry

A network of seismic stations in Washington and Oregon detected the 9 December 1992 reentry of space shuttle Discovery (Qamar, 1993). Figure 14 shows contours of arrival times from 66 seismic sites covering both sides of the flight track for distances of over 500 km. Arrival times supplied by Qamar have been converted to a regular grid and contoured without any assumptions about the original trajectory. The strong curvature of the contours and the relatively sparse data result in the oscillations seen along the contours; however, the outline of the hyperbolae in the primary carpet is clearly visible.

Sections of the time traces for the seven labeled stations are shown in Fig. 15. The stations are plotted in order of the arrival of the signal, i.e., north to south; however, the time origin is shifted to align the arrival of the primary disturbance. The later stations show two disturbances which Qamar postulated were the two peaks of the N-wave, which would correspond to an N-wave duration of over 1 s.

To the present author's knowledge, such long-duration N-waves have not been observed before. A simple calculation of the Mach angle from the hyperbola contours in Fig. 14 yields a Mach number of approximately $M=14$. From a typical shuttle reentry profile, this Mach number corresponds to an altitude of approximately 55 km. Computing the N-wave duration from the standard approximate relations (Whitham, 1974) gives an N-wave duration of no more than 0.8 s. However, the accuracy of the estimate for such high altitude and Mach number is difficult to assess. Long N-wave durations up to 0.7 s have been observed from the space shuttle reentry using pressure transducers (Garcia *et al.*, 1985), for a sonic boom estimated to have originated from the shuttle at $M=5.87$ at an altitude of 39.4 km, which is still much later in reentry than the sonic booms recorded in Washington. The appearance of the two peaks on such widely separated sites does rule out local geological effects.

V. MYSTERY BOOMS

In the latter half of 1991 and early 1992, the U.S.G.S. office in Pasadena received a number of calls from the general public concerning ‘‘mystery booms’’ heard in southern California. Initially the events were assumed to be earthquakes, but further analysis of the seismograph records suggested sonic booms as the most likely source. An initial analysis of the seismic signals by the U.S.G.S. by attempting to fit hyperbola to the arrival time data for 25 sites near the coast attributed the sonic booms to a source flying at high altitude and high Mach number. These reports were picked up in the popular press and attributed to a top-secret hypersonic Aurora spyplane. A unique feature of the events was that all occurred on Thursday morning at approximately 0700, as shown in Table I.

Following the early claims, the Air Force commissioned MIT Lincoln Labs to investigate the incidents. The available seismograph records for 41 sites for the October 1991 event were analyzed. Again, the arrival times were fit as hyperbola, although an attempt was made to include the effects of vehicle deceleration and atmospheric refraction. The disturbances were attributed to the sonic booms from two F-4 Phantoms returning to Edwards AFB, flying supersonic near Mach 1 overland. None of the sites examined by Lincoln Labs included the third boom mentioned later.

In view of the above-mentioned disagreement, the October 1991 and January 1992 events were analyzed in the present study. The raw seismograph time data were obtained and analyzed for all 209 available sites for both events. Arrival times were chosen from the data and contoured without any assumptions concerning the shape of the time contours.

On the 31 October 1991 event, three booms are clearly distinguished on the time traces. The first boom appears on 90 sites throughout the seismic network. The boom dies out as one moves east and is not seen on the easternmost sites. The first boom is generally followed by a second boom which appears at the largest number of sites, 104, at an average of 83 s later. A third boom appears only at 30 of the easternmost sites, an average of 84 s after the second boom. The contours of arrival times are shown in Fig. 16 for each of the three booms identified. The triangle symbols represent seismic sites for which data were available, and filled triangles show the sites which detected each boom.

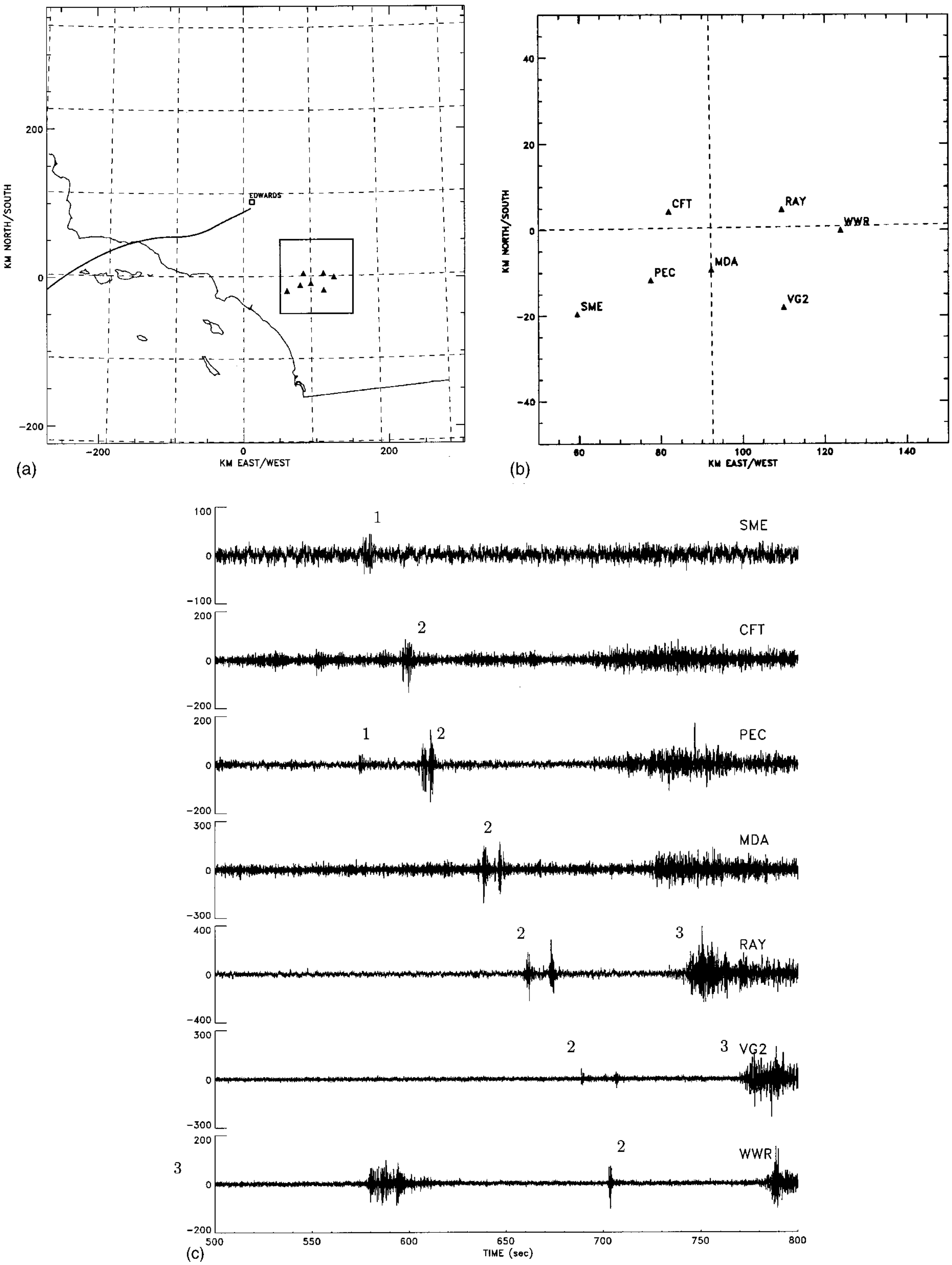

FIG. 12. (a) Seismic station locations relative to the STS-42 trajectory, (b) map inset, and (c) time traces from selected seismic stations within the secondary carpet predicted by ray-tracing for STS-42 reentry. Time traces record ground motion, vertical scale is voltage output in counts.

The northern limit of detection of the sonic boom is clearly defined, since a large number of sites in the northeast did not detect the boom. This is consistent with the low amplitude of the boom observed near the northern boundary. However, the southern edge of the boom carpet is not well defined due to the lack of seismograph sites further south in Mexico. The booms show a relatively high amplitude at the southern sites which suggests the boom carpet may extend further south. Twelve additional sites in Mexico logged no unusual activity for that morning. However, since the actual seismographic data are not available, the sites are not included in this report.

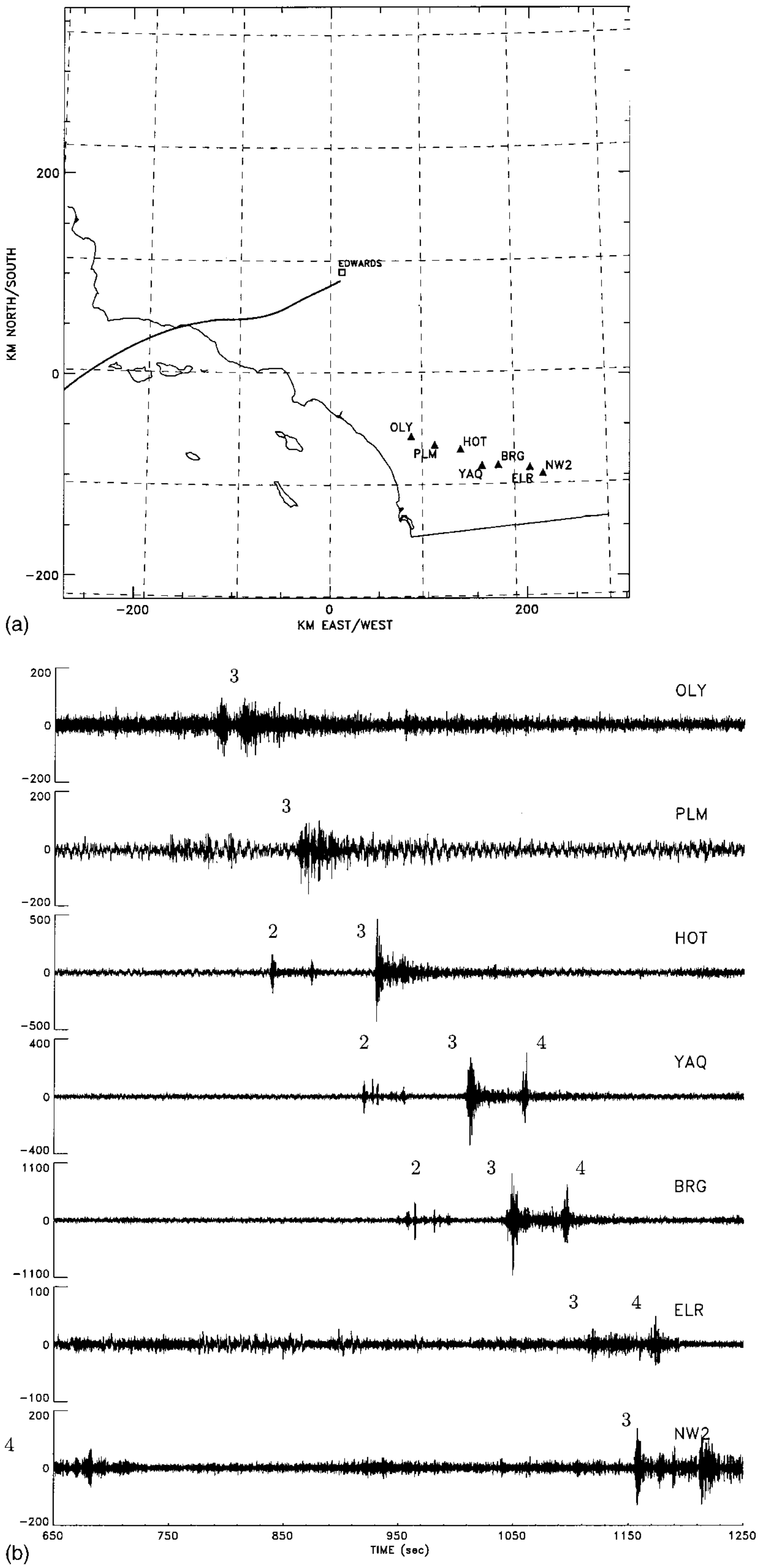

FIG. 13. (a) Seismic station locations relative to the STS-42 trajectory and (b) time traces from line of seismic stations outside the secondary carpet predicted by ray-tracing for STS-42 reentry. Time traces record ground motion, vertical scale is voltage output in counts.

A second event, from 30 January 1992, was also examined in detail and arrival time contours for the three booms observed are shown in Fig. 17. The same pattern of three disturbances is observed: the first boom on the western sites, the second across the entire network, and the third only on the eastern sites. The booms were detected across the entire network from west to east, but the booms were confined to a narrower north to south band.

Only one of the events examined does not display the circular patterns stretching from west to east characteristic of the above two events. The boom from Wednesday, 30 September 1992 is a narrow circular pattern extending from

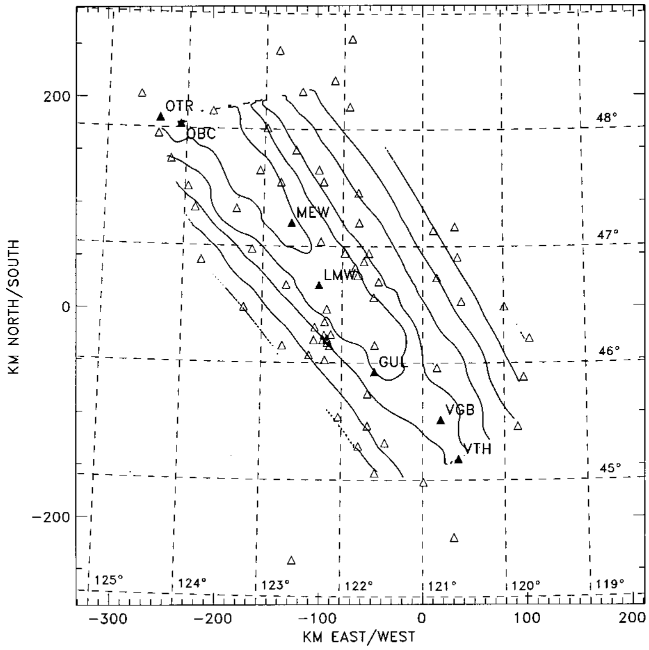

FIG. 14. Arrival time contours from seismic data for the December 1992 reentry of space shuttle Discovery over seismic network in Washington and Oregon. Time traces record ground motion, vertical scale is voltage output in counts. (Data supplied by Dr. A. Qamar, University of Washington.)

south to north. The center of the circular pattern lies offshore, south of Catalina Island.

The analysis of the complete set of data eliminates both of the early theories for the source of the mystery booms. The lack of characteristic N-wave signatures and the fact that no booms were detected on the northwestern sites rules out the original theory of a high-speed aircraft flying north off the coast. At the speeds predicted (Mach 5–6), one would expect to see strong N-wave signatures with high amplitude near the coast, as with the shuttle reentry booms. The Lincoln Lab theory of two aircraft flying essentially down the center of the boom pattern fails to explain the three events detected. The aircraft would have to be flying at a speed of approximately Mach 1 relative to ground sound speed which would place the aircraft at or near the cutoff velocity for their altitude. In the case of a single aircraft, the first boom would be considered the primary boom carpet, and the second and third booms would be secondary booms. However, this single aircraft theory can be ruled out, since indirect booms would not be expected to appear under the aircraft track.

From the complete analysis, all the observed booms appear to be indirect booms from a source offshore propagated

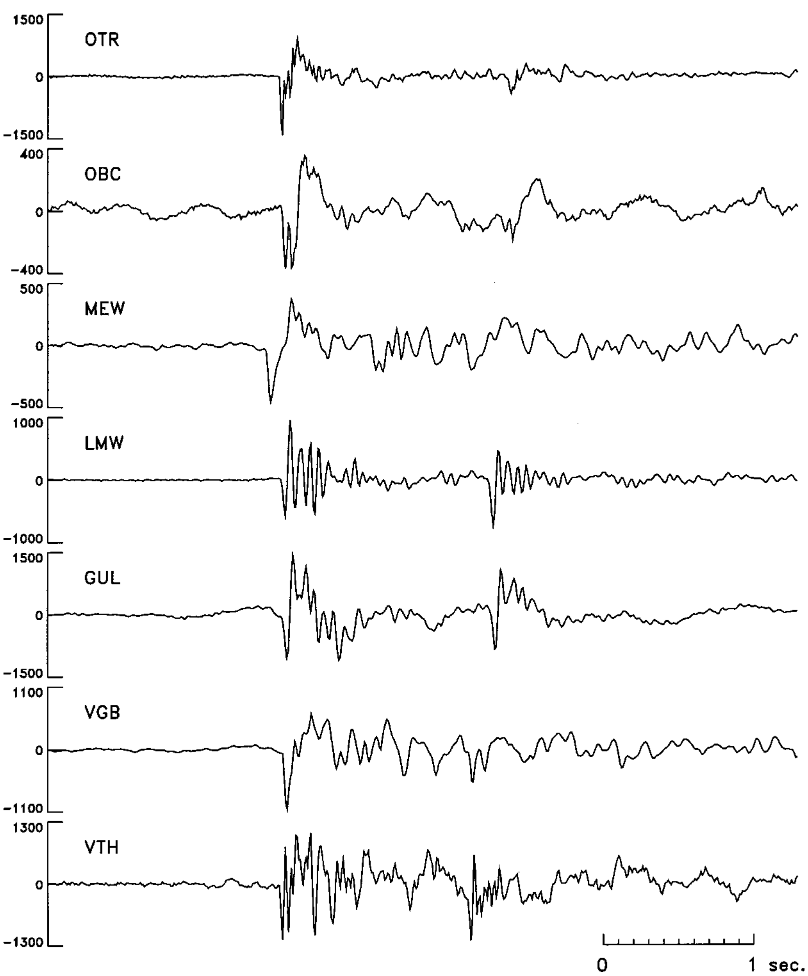

FIG. 15. Seismic traces for stations shown in Fig. 14 for December 1992 reentry of space shuttle Discovery. (Seismic data supplied by Dr. A. Qamar, University of Washington.)

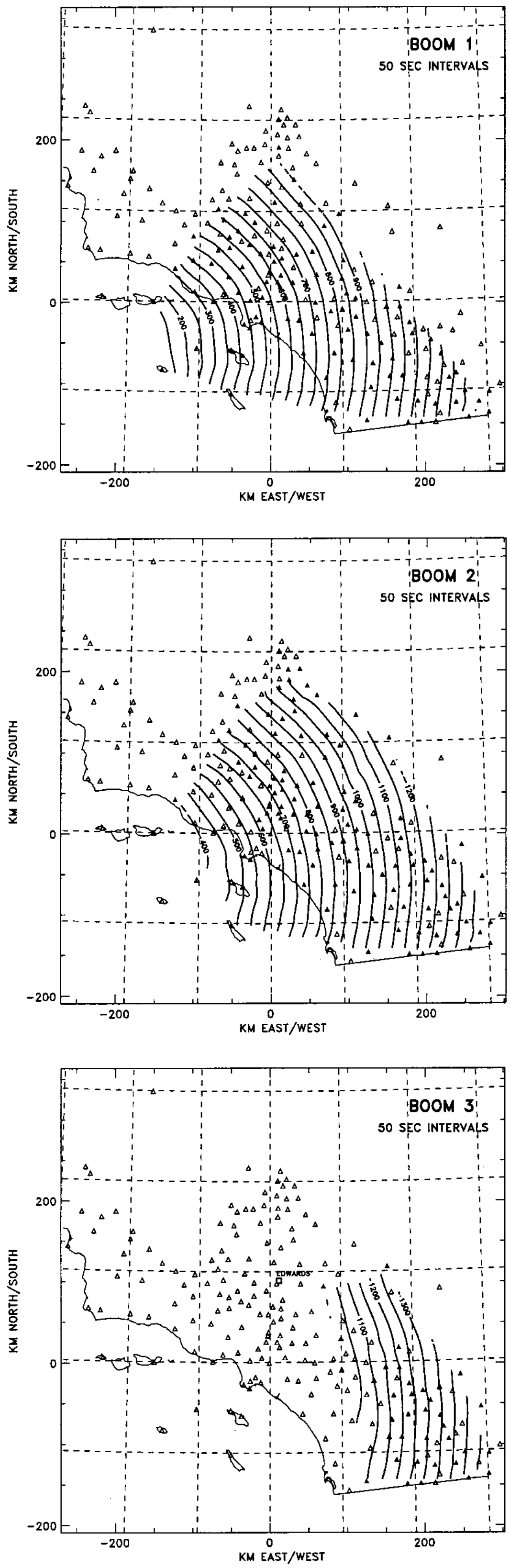

FIG. 16. Arrival time contours generated from seismic data for 31 October 1991 "mystery boom."

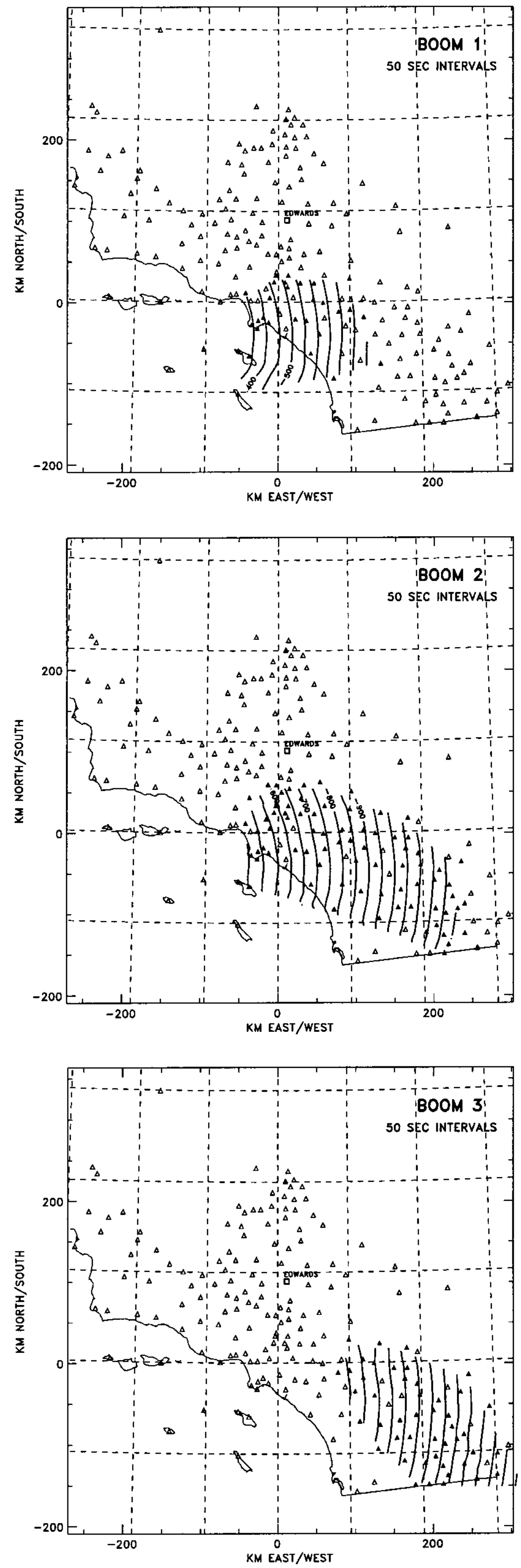

FIG. 17. Arrival time contours generated from seismic data for 30 January 1992 "mystery boom."

inland by high winds. Southern California typically has strong jet stream winds and stratospheric winds blowingfrom west to east. Such anomalous sound propagation is well known, and mystery booms attributed to aircraft are not a new phenomenon. In the late 1970s, a series of East Coast mystery booms occurred. Although a wide range of phenomena were grouped into the "mystery booms," the majority were attributed to indirect sonic booms from the Concorde (Rickley and Pierce, 1980) and sonic booms from military aircraft maneuvering offshore. Similar propagation of sonic

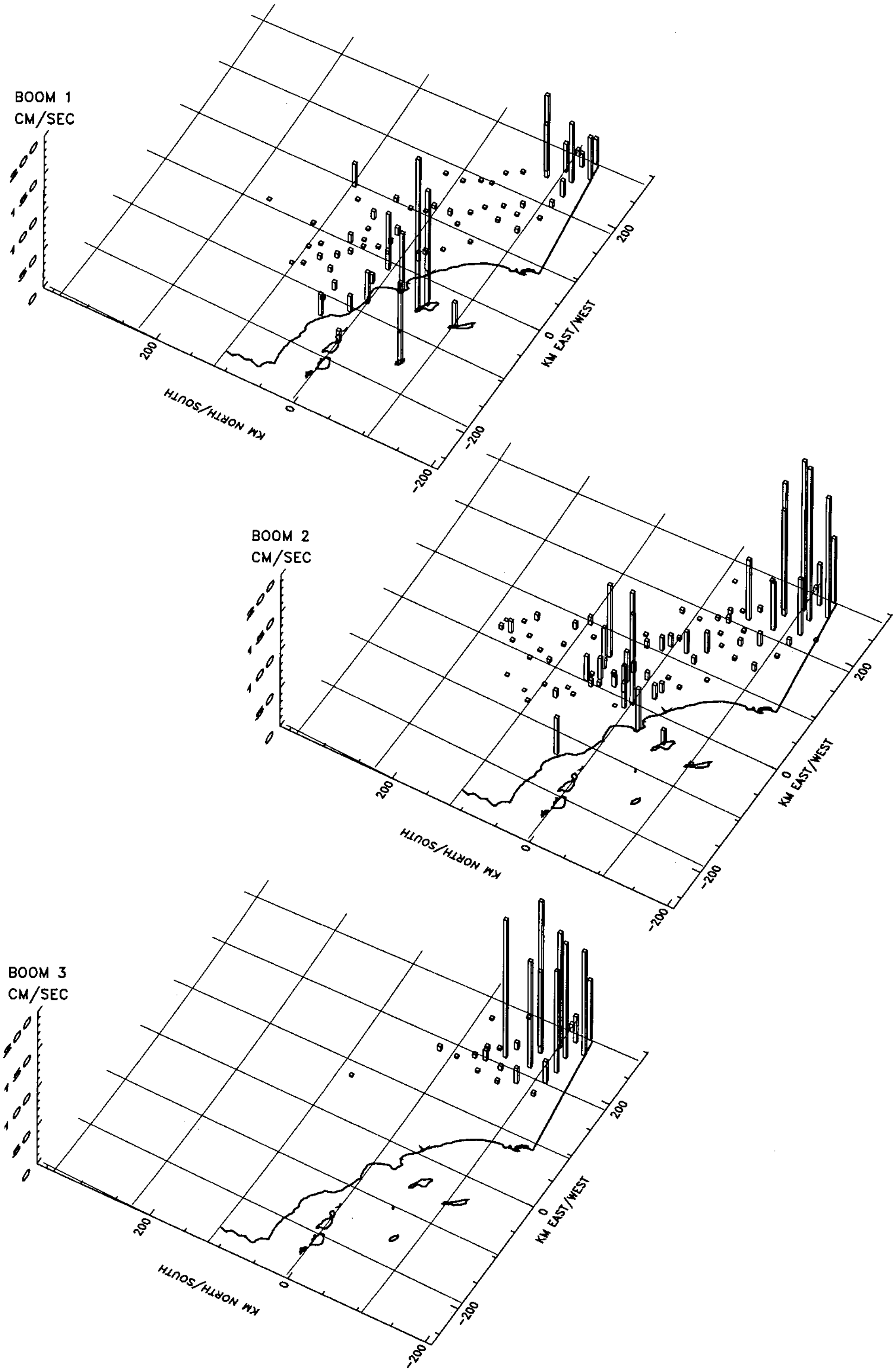

FIG. 18. Ground velocity magnitude (cm/s) for 31 October 1991 events, corrected for instrument response. All amplitudes over 200 are plotted as magnitude 200 for clarity.

booms over 100 km by the high jet stream winds have been observed in Tucson (Wood, 1975).

The magnitudes of the ground velocity for the 31 October 1991 events are shown in Fig. 18. Magnitudes are corrected for instrument response; however, no attempt is made to incorporate local site surface properties. For clarity, all amplitudes over 200 are plotted as 200. Higher ground velocities are found offshore, near the theorized source of the sonic booms. The large amplitudes on the easternmost sites seem to be due to local ground properties near the sites. Using the estimate of 1.5–2 μm/s per Pa of overpressure, the

TABLE I. Mystery boom occurrences. The October 1991 and January 1992 events are analyzed in the current work.

Time	Date
6:34 PDT	Thu 27 June 1991
6:46 PST	Thu 31 Oct. 1991
6:43 PST	Thu 21 Nov. 1991
7:17 PST	Thu 30 Jan. 1992
6:59 PST	Thu 16 Apr. 1992
Unknown	Thu 18 June 1992
6:38 PDT	Thu 15 Oct. 1992

ground velocity amplitudes correspond to the range of average pressures 0.15–0.2 Pa observed for Concorde indirect sonic booms (Rickley and Pierce, 1980).

An attempt to associate the mystery booms with specific flight operations from any of the local military bases has been unsuccessful. Local military bases reported no unusual activity on the dates of the mystery booms; in particular, the Pacific Missile Test Range, which operates offshore from Point Mugu, reported no supersonic flight operations on the mornings of the October 1991 or January 1992 events.

VI. CONCLUSION

The seismic network in southern California has provided the first opportunity to study the size and shape of indirect sonic boom carpets over a large area. The high density of the sites and large ground coverage allow analysis of the direct and indirect boom patterns on both sides of the flight trajectory, and the development of the booms can be followed over several hundred kilometers. The recent addition of pressure transducers at selected TERRAscope sites remedies the only significant weakness of the seismic data, the difficulty of predicting amplitudes.

From analysis of the space shuttle STS-42 reentry, the ground patterns are extremely complex. Ray theory fails to predict indirect sonic boom arrival times, observed multiple booms within the first shadow region, and extensive overlap of the multiple refracted sonic booms. The extensive ground coverage of the ‘‘mystery boom’’ and shuttle reentry booms suggest exposure under the real atmosphere is much larger than previously expected.

The inverse problem of predicting the aircraft trajectory from the ground arrival times is more difficult. Nonetheless, using the seismic network data, we were able to identify the source of the ‘‘mystery booms’’ as indirect booms propagated from offshore operations. However, careful study of the seismic data is required to identify direct and indirect sonic boom carpets before attempting to make predictions about the trajectory.

ACKNOWLEDGMENTS

Seismic data and instrument information for the Southern California seismic network were kindly provided by Dr. H. Kanamori, Caltech Seismological Laboratory, and Dr. J. Mori, U.S.G.S., Pasadena. Seismic data for the Discovery reentry were supplied by Dr. A. Qamar, University of Washington. Shuttle trajectory information was courtesy of Gene Stansbury and Joel Montalbano of NASA. Additional thanks are due to Dr. R. Meyer, Dr. J. Ehernberger, Dr. D. Lux, and Bob Cohn of NASA Dryden, and Dr. J. Greene of JPL for allowing us to participate in the SR-71 flight.

Balachandran, N., Donn, W., and Rind, D. (**1977**). ‘‘Concorde Sonic Booms as an Atmospheric Probe,’’ Science **197**, 47–49.

Ben Menachem, A., and Singh, S. (**1981**). *Seismic Waves and Sources* (Springer-Verlag, New York).

Cook, J., and Goforth, T. (**1970**). ‘‘Ground Motion from Sonic Booms,’’ J. Aircr. **7**, 126–129.

de Violini, R. (**1967**). ‘‘Climactic Handbook for Point Mugu and San Nicolas Island, Volume I, Surface Data,’’ PMR-MR-67-2.

de Violini, R. (**1969**). ‘‘Climactic Handbook for Point Mugu and San Nicolas Island, Volume I, Upper-Air Data,’’ PMR-MR-69-7.

Garcia, F., Jones, J., and Henderson, H. (**1985**). ‘‘Correlation of Predicted and Measured Sonic Boom Characteristics From the Reentry of STS-1 Orbiter,’’ NASA TP-2475.

Goforth, T., and McDonald, J. (**1968**). ‘‘Seismic Effects of Sonic Booms,’’ NASA CR-1137.

Kanamori, H., Mori, J., Sturtevant, B., Anderson, D., and Heaton, T. (**1992**). ‘‘Seismic excitation by space shuttles,’’ Shock Waves **2**, 89–96.

Meteorology Group, Range Commanders Council (**1983**). ‘‘Range Reference Atmosphere 0–70 Km Altitude: Edwards AFB, California,’’ Doc. 366-83.

Onyeowu, R. (**1975**). ‘‘Diffraction of sonic boom past the nominal edge of the corridor,’’ J. Acoust. Soc. Am. **58**, 326–330.

Pierce, A. (**1981**). *Acoustics: An Introduction to Its Physical Principles and Applications* (McGraw–Hill, New York).

Qamar, A. (**1993**). ‘‘Seismic excitation by atmospheric disturbances: the Dec. 1992 Space Shuttle and a fireball in Jan. 1989,’’ SSA abstr, April 1993.

Rickley, E., and Pierce, A. (**1980**). ‘‘Detection and Assessment of Secondary Sonic Booms in New England,’’ FAA-AEE-80-22.

United States Committee on Extension to the Standard Atmosphere (**1966**). *U.S. Standard Atmosphere Supplements* (U.S. Govt. Printing Office, Washington, DC).

Whitham, G. (**1974**). *Linear and Nonlinear Waves* (Wiley, New York).

Wood, R. (**1975**). ‘‘Jet Stream—Sonic Boom Phenomena, Tucson, Arizona, April 1975,’’ Weatherwise **28**, 152–155.

Acoustic propagation and atmosphere characteristics derived from infrasonic waves generated by the Concorde

Alexis Le Pichon[a]
CEA/DASE-LDG, BP12, 91680 Bruyères-le-Châtel, France

Milton Garcés[b]
Infrasound Laboratory, HIGP, University of Hawaii, Manoa, 73-4460 Queen Kaahumanu Hwy., #119, Kailua-Kona, Hawaii 96740-2632

Elisabeth Blanc and Maud Barthélémy
CEA/DASE-LDG, BP12, 91680 Bruyères-le-Châtel, France

Doug P. Drob
Naval Research Laboratory, Washington, DC 20375

(Received 20 April, 2000; revised May 29, 2001; accepted 19 July 2001)

Infrasonic signals generated by daily supersonic Concorde flights between North America and Europe have been consistently recorded by an array of microbarographs in France. These signals are used to investigate the effects of atmospheric variability on long-range sound propagation. Statistical analysis of wave parameters shows seasonal and daily variations associated with changes in the wind structure of the atmosphere. The measurements are compared to the predictions obtained by tracing rays through realistic atmospheric models. Theoretical ray paths allow a consistent interpretation of the observed wave parameters. Variations in the reflection level, travel time, azimuth deviation and propagation range are explained by the source and propagation models. The angular deviation of a ray's azimuth direction, due to the seasonal and diurnal fluctuations of the transverse wind component, is found to be $\sim 5°$ from the initial launch direction. One application of the seasonal and diurnal variations of the observed phase parameters is the use of ground measurements to estimate fluctuations in the wind velocity at the reflection heights. The simulations point out that care must be taken when ascribing a phase velocity to a turning height. Ray path simulations which allow the correct computation of reflection heights are essential for accurate phase identifications. [DOI: 10.1121/1.1404434]

PACS numbers: 43.28.Dm, 43.28.Mw, 43.28.Vd [LCS]

I. INTRODUCTION

The Concorde supersonic transport is the result of a 1962 initiative undertaken by the governments of Great Britain and France to build a civil transport airplane that could fly at twice the speed of sound. It cruises at about 18 km, where it rarely encounters either other commercial planes or bad weather. Systematic infrasonic array observations in Flers, France (Fig. 1) show some clear signals occurring several times a day. These signals are associated with the regular Air France and British Airways flights between North America (New York) and Europe (London and Paris). Like any supersonic aircraft, the Concorde has a system of shock waves associated with it. The exact pressure distribution of these shock waves is determined by the aircraft geometry (Maglieri and Plotkin, 1995). As waves approach a shock condition, nonlinear effects become predominant so that wave shape is distorted and the spectrum of the wave changes (Carlson, 1972). Thus, the radiated pressure wave form may be quite complicated close to the aircraft. However, the finite-amplitude pressure disturbance evolves into an N-wave at a distance of 50 to 100 airplane lengths (Weber and Donn, 1982). The N-wave pulse is then reflected by the ground and the atmosphere, and is thus transformed into a long-duration acoustic signal consisting of multiple arrivals. Acoustic wave guides may be formed between the ground and high temperature and wind speed regions in the troposphere, stratosphere, and thermosphere. For the purposes of tracing rays to long ranges, we make the standard simplifying assumption that acoustic energy is radiated away from the Concorde in a direction normal to the Mach cone. Past sonic boom literature identifies two distinct carpets of sound. The first carpet is associated with the direct downwards-propagating acoustic arrival along the track of the Concorde. The second carpet is associated with reflection from the stratosphere. However, acoustic reflections from the lower thermosphere (~ 120 km) have been consistently observed with sensitive infrasonic arrays.

Previous works investigated the effects of shock wave propagation (Blanc, 1985; Besset and Blanc, 1993) on the environment and the greenhouse effect (Warren, 1972; Shapley, 1978; Rogers and Gardner, 1980). In New York (Weber and Donn, 1982) and in Sweden (Liszka, 1974, 1978; Liszka and Wlademark, 1995), Concorde flights have been routinely observed with infrasonic arrays. Multiple reflections in the atmosphere have allowed Concorde detections as distant as

[a]Electronic mail: lepichon@dase.bruyeres.cea.fr
[b]Electronic mail: milton@kona.net

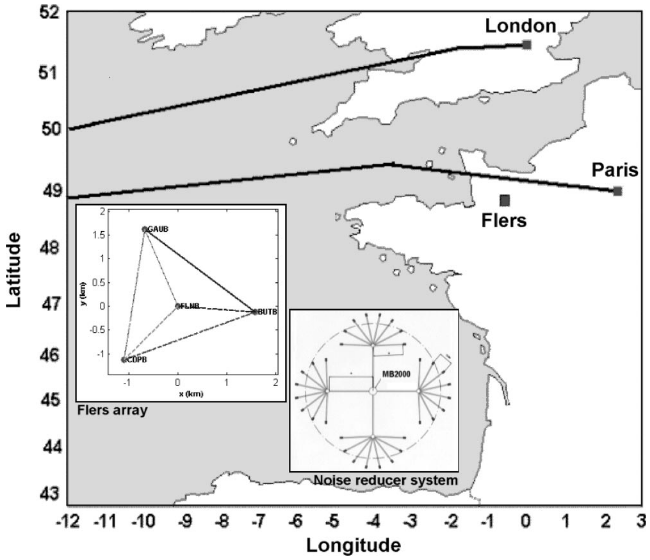

FIG. 1. Schematic view of the flights routes of the Air-France and the British-Airways Concorde across the English-Channel. The microbarographic array is located at Flers (48.76 °N and 0.48 °E). Each microbarograph is connected to an 8 m-diameter noise reducing system.

4000 km (Liszka, 1974, 1978). Diurnal changes in the state of the atmosphere can cause great signal variability. A daily review of automated Concorde detections made at Flers shows a high variability in the number, amplitude, azimuth, and arrival time of observed phases. Some of this variability is caused by local weather conditions, small changes in the wind structure, and turbulence in the lower atmosphere, which also produces irregularities in the sonic boom signature (Pierce and Maglieri, 1972). Other studies investigated the effects of a variable and stratified atmosphere on sonic boom signature (Friedman *et al.*, 1963; Hayes and Runyan, 1970, 1972; Weber and Donn, 1982). The present work focuses on the arrival time, apparent horizontal phase velocity (also referred to as the trace velocity), arrival azimuth, and frequency band of infrasonic waves associated with supersonic Concorde flight.

A valuable feature of Concorde signals is their regularity. Daily recordings associated with known flight routes are useful for calibrating sensors and for investigating sonic boom propagation in a stratified, temporally varying atmosphere. Statistical studies of sonic booms in Sweden have clearly demonstrated the marked effects of zonal wind changes on infrasonic wave propagation (Waldemark, 1997). The Concorde flights provide a known acoustic source that provides a unique means for quantitative studies of the seasonal and diurnal variations in the structure of the upper atmosphere.

The aim of this paper is to correlate seasonal and diurnal atmospheric fluctuations of the upper atmosphere to variations in the arrival time, trace velocity, and arrival azimuth of the infrasonic Concorde signals. Multiple arrivals, referred to as phases, are generally recorded at the Flers array. Each phase corresponds to a specific family of ray paths and turning height levels in the atmosphere, and is characterized by specific values of frequency, coherence, amplitude, trace velocity, and arrival azimuth along the array beam. These phase-specific values are referred to as phase parameters. This paper concentrates on the study of two types of phases. Thermospheric phases correspond to infrasonic waves trapped between the lower thermosphere and the ground (or ocean), which acts as a near-perfect acoustic reflector. Thermospheric phases, abbreviated as *It* (Brown, 1999), are always predicted to exist because of the high sound speed values of the lower thermosphere. However, they may not always be observed because of enhanced attenuation by the rarefied gas of the thermosphere. Stratospheric phases correspond to infrasonic waves trapped between the stratopause and the ground. These phases, abbreviated as *Is*, are observed when the stratospheric winds blow along the direction of propagation and are suppressed by counter-propagation winds.

We model the shock wave source along the aircraft trajectory and compare our observations with the predictions obtained from tracing rays through realistic atmospheric models (Garcés *et al.*, 1998, 1999, 2001). The seasonal trends of the phase parameters are explained through the use of realistic empirical winds and temperature profiles. The observed seasonal and diurnal variations in the infrasonic recordings can be used to correct or validate the wind profiles provided by the atmospheric models. Past works investigated the feasibility of using microbaroms (Donn and Rind, 1971, 1972; Rind *et al.*, 1973; Rind and Donn, 1975) or sonic booms (Balachandran *et al.*, 1977; Donn, 1978) to define characteristics of upper air winds.

In the present study, we first discuss typical features of infrasonic Concorde signals recorded in May and November. Then, we present a statistical analysis of the seasonal changes in the trace velocity and the azimuth deviation of arrivals recorded over a period of 21 months. By modeling the shock wave source along the aircraft trajectory, we compare the measurements to the results of ray-tracing through empirical atmospheric wind and temperature profiles. Temporal variations of the Concorde signals are then related to tidal and seasonal fluctuations in the atmosphere structure. Finally, we compare the zonal and meridional wind profiles at the reflection heights with estimates deduced from ground measurements and ray-tracing.

II. MICROBAROGRAPHIC ARRAY AND DATA PROCESSING

Infrasonic signals are continuously recorded by a four-element array located at Flers, in the West of France (−0.48 °W and 48.76 °N). The Flers array has been set up to characterize infrasonic sources and to improve atmospheric and propagation models. This array is a prototype CTBT (Comprehensive Nuclear Test Ban Treaty) station. The CTBT global infrasonic network will permit the detection and location of both ground surface and middle atmosphere explosions.

The array, which has an aperture of ∼3 km, has been operating continuously since April 1996. Each sensor is a MB2000 microbarograph that can measure both absolute and relative pressure. The MB2000 has been designed to operate from DC up to 27 Hz with an electronic noise level of 2 mPa

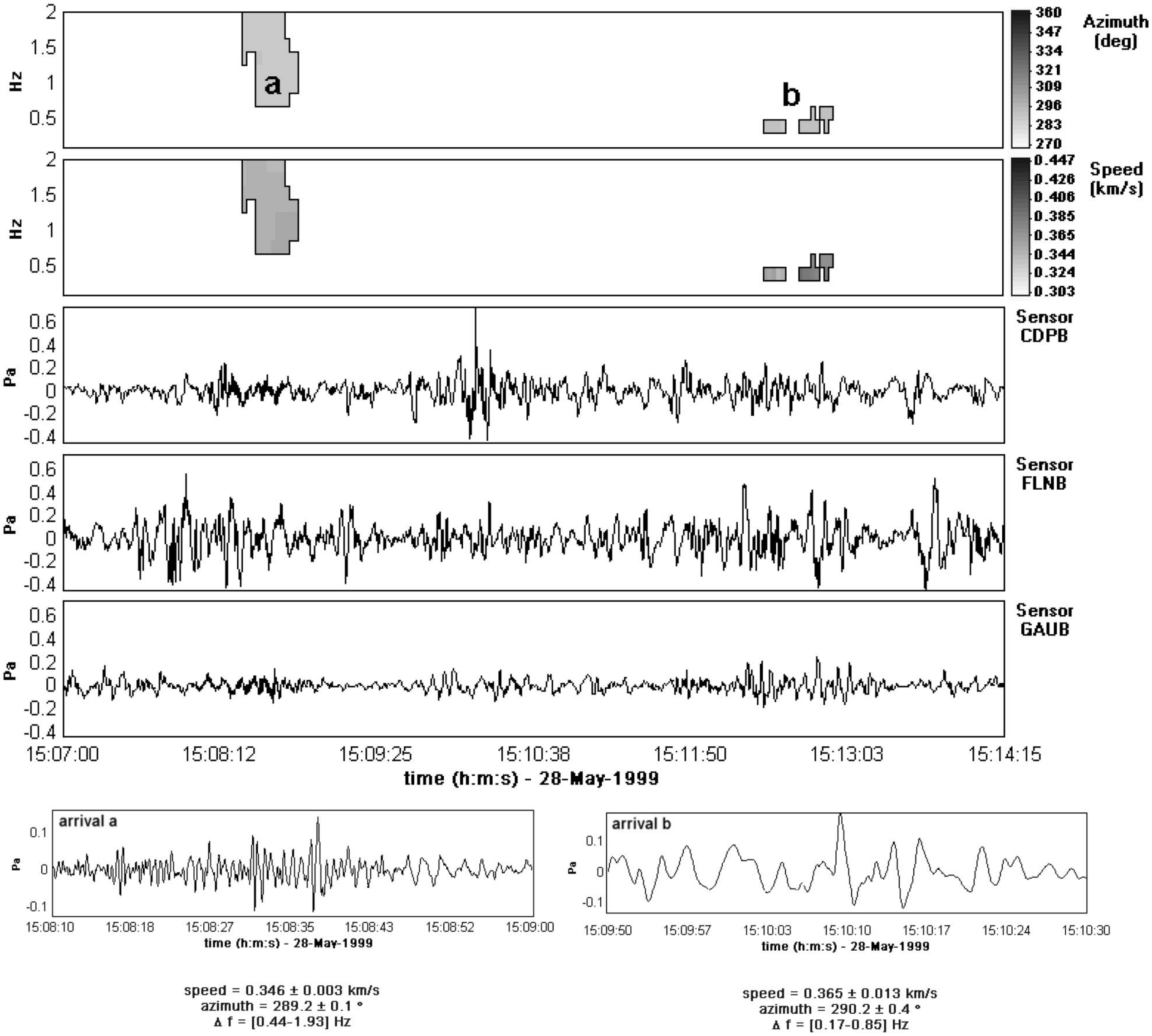

FIG. 2. The upper part of the figure shows typical results of the PMCC cross-correlation calculation for infrasonic waves recorded in May from the Air-France Concorde sonic boom. Trace velocity and azimuth are shown as a function of the time and frequency. The lower part of the figure shows two successive arrivals stacked along the array beam. The waveforms are band-pass filtered between 0.1 Hz and 5 Hz.

rms in the 0.02–4 Hz frequency band. The sensor provides relative pressure at ground level with a sensitivity of 20 mV/Pa and a dynamic range of 134 dB. The digitized data are sent to the central station, where they are stored in a buffer and transmitted in real time to the base geophysical laboratory over a shared VSAT satellite link. In order to minimize pressure changes due to surface wind effects, each sensor is connected to an 8m-diameter noise reducing system equipped to 32 inlet ports (Fig. 1). A comparison of the performance of this pipe array with completely open ports demonstrated that the pipe array with screened inlet ports reduces substantially reduces high frequencies noise (Alcoverro, 1998). For a surface wind speed of 1 m/s and for frequencies greater than 0.3 Hz, this filtering system significantly improves the signal to noise ratio (~ 20 dB at 1 Hz).

The phase parameters are computed by using the Progressive Multi-Channel Correlation Method (PMCC) used as a real-time detector (Cansi, 1995; Cansi, 1997; Le Pichon and Cansi, 1999), that summarizes all detected coherent signals. This method, originally designed for seismic arrays, proved to be very efficient for infrasonic data and is well adapted for analyzing low-amplitude signals waves within noncoherent noise. To avoid ambiguity problems when correlating the records from sensors too far apart, the analysis is initialized on the smallest groups of three sensors. The correlation function is used to calculate the propagation time Δt_{ij} of the wave between sensors i and j. For each subnetwork (i,j,k), the closure relation $\Delta t_{ij}+\Delta t_{jj}+\Delta t_{ki}=0$ should be obtained. In the presence of background noise the phase is unstable. Therefore, the shifts Δt_{ij} measured are the result of random phase combinations. Such a detector is independent of the signal amplitude and uses only the intrinsic information of the processed recordings. As long as the closure relation is valid, the use of sensors increasingly further apart gives more precise wave parameters (trace velocity V_i and azimuth θ_i) since the aperture of the network increases

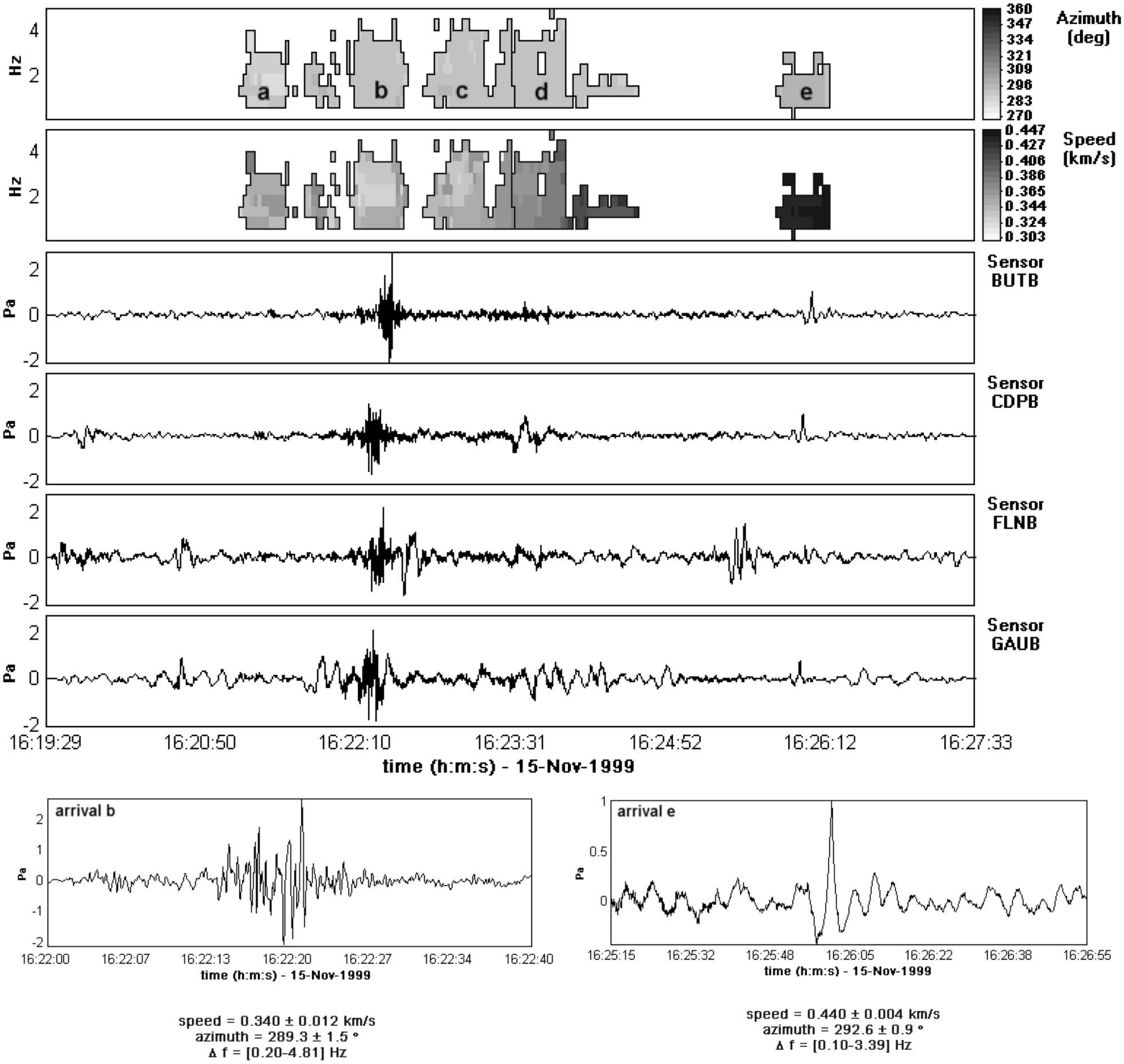

FIG. 3. Same as Fig. 2 for signals recorded in November.

with each new sensor. The processing is performed consecutively in several frequency bands f_i, from 0.1 to 5 Hz, and in adjacent time windows t_i. At this stage of the process, a set of elementary detections in the time-frequency domain is used to represent one detected wave. For each of them, to avoid unrealistic wave detection, a further condition is introduced. A given wave is represented by several elementary detections. The final detection is the result of a nearest-neighbor search of elementary detections in the $(t_i, f_i, V_i, \theta_i)$ domain. In this domain, a weighted distance is used to connect all the close-enough points.

We now focus on the fine fluctuations in the phase parameters of infrasonic phases recorded in May and November. Figures 2 and 3 show the results of the PMCC calculation in the 0.1–5 Hz frequency band for typical phases recorded during these months. These phases are associated with the regular Air France flight between New York and Paris (Fig. 1).

Figure 2 shows coherent wave trains, with a peak-to-peak amplitude of about 0.2 Pa, detected across the array in May. Two successive arrivals (a,b) are selected and time-delayed along the array beam. The maximum signal amplitude noted in May rarely exceeds 0.5 Pa peak to peak.

Figure 3 shows successive arrivals detected in November with a maximum peak to peak amplitude of ~ 3 Pa, which is about 15 times larger than the amplitude observed in May. All arrivals are detected with almost the same azimuth. The number of arrivals and the duration of the recorded signals are also found to be larger in November. The recordings present variations with time in the trace velocity for each phase, ranging from the ground-level sound speed value to 440 m/s. Multiple arrivals with a trace velocity increasing in time are generally associated with increasing reflection heights, or increasing launch angles. The most obvious difference between both seasons is the larger amplitude of the first relatively high-frequency wave trains in Novem-

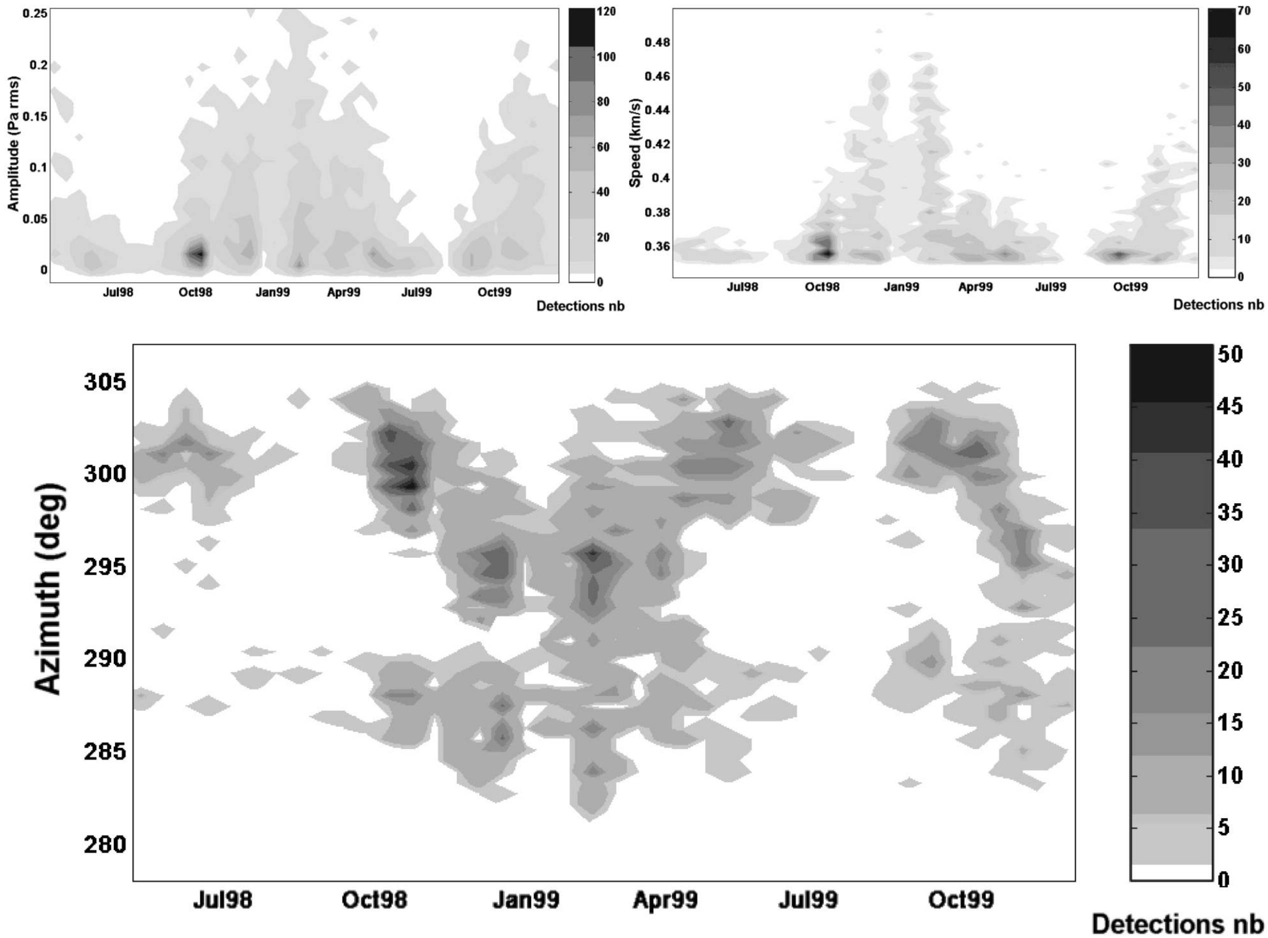

FIG. 4. Contour plot histogram representation of the Concorde recordings over 21 months. The upper part of the figure shows the amplitude (Pa) and the trace velocity variations (km/s). The lower part presents the fluctuations of the direction of the wave arrival of the Air-France and British-Airways Concorde flights. The bar indicates the number of phases detected.

ber. Another interesting feature of the signals recorded in November is that their frequency decreases with time. The energy of the phases is mostly contained below 5 Hz, with a broader frequency range than the signals observed in May. The later low-frequency signal (e) follows the earlier high-frequency group (a–c). The frequency of the recorded signals is a function of the level of reflection, as the high frequency components are more strongly attenuated by viscous and thermal losses in the highly rarefied gas above 100 km (Otterman, 1959; Daniels, 1969; Cotton and Donn, 1971). At about 300–400 km from the launch point, the main expected period is about 10 s (Rogers and Gardner, 1980).

Although the diurnal properties of the signals shows some fluctuations in the number and the amplitude of the arrivals, the variability of the Concorde phases is mainly seasonal, as shown by the recordings of May and November. Those measurements will be compared in Sec. IV to the results of the ray-tracing model.

III. STATISTICAL ANALYSIS

Approximately 6270 phases generated by the Concorde from April 1998 to December 1999 were automatically detected and later reviewed by an analyst. Seasonal trends of the Concorde phase parameters were then obtained from statistical studies. Figure 4 shows the RMS amplitude, the trace velocity and the arrival azimuth of infrasonic arrivals as a function of the time of the year.

In contrast to the large number of phases recorded from October to April, few arrivals were detected from May to September, with no detection in August. The amplitude distribution shows a maximum around 0.15–0.25 Pa RMS in January and a mean amplitude lower than 30 mPa RMS in summer. A strong seasonal variation of the trace velocity is also observed, with an upper limit of 450–500 m/s in January–February. In summer most of the recordings have a trace velocity close to the sound speed near the ground, corresponding to shallow launch angles. Two curves emerge from the azimuth contour plot in Fig. 4. The first one, near 287°, is associated with the Air France flight landing at Paris around 16 h UT. The second one, near 295°, is associated with the British Airways flight landing at London around 21 h UT. Both present a seasonal deviation from the direction of propagation. These deviations are due to the component of the wind transverse to the propagation direction, which deflects the ray from the original launch azimuth. As a result, the apparent arrival direction of the wave does not correspond to the original launch direction and should be corrected by $\sim 5°$. Daily observations show seasonal trends in the frequency range, number of arrivals and trace velocity of

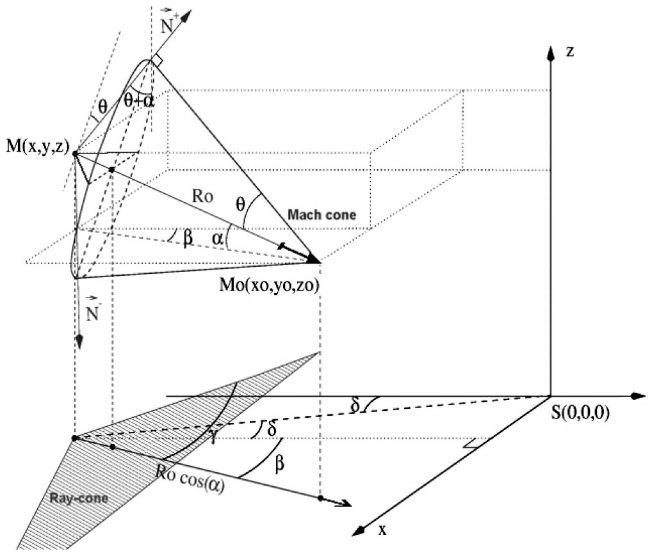

FIG. 5. The geometry of the Mach cone at one point along the flight trajectory. From the launch point M, under the condition $\gamma > \delta + \beta$, two vectors of the ray-cone $\vec{N}^+$ and $\vec{N}^-$ are selected, corresponding to rays propagating upward and downward from the Mach cone and pointing towards the receiver S.

infrasonic detections. The weak number of arrivals observed at 16 h ($\sim$2500) compared to those noted at 21 h ($\sim$3700) are partly explained by the diurnal variations of the local surface wind, which generally decreases at the end of the day. Between 16 and 21 h, a mean difference of 10–15 dB has been found in the acoustic noise level at 1 Hz. The best signal to noise ratio is then expected at 21 h. Due to refraction at different levels of the stratified atmosphere, the initial shock wave is converted into a package of infrasonic waves in the frequency band of 0.1 to 10 Hz and with amplitude ranging from 0.1 to 5 Pa. The multiple arrivals are separated by a few tens of seconds, with time differences entirely determined by the atmospheric conditions along the ray paths. Depending on the propagation conditions and the local background noise, the arrivals can be measured over periods of a few minutes and up to one hour.

IV. SOURCE AND ATMOSPHERIC MODELS

A. Source model

At supersonic speeds, pressure waves combine at the leading edge of a body of rotation and form a shock-wave cone that travels forward from the generation point. Since the acoustic waves are propagated ahead of the shock wave, infrasonic waves can only be recorded at Flers during the aircraft descent towards London and Paris. The sound heard on the ground as a sonic boom is the ear's response to the sudden onset and release of the sharp peak overpressure. However, at large distances of propagation, sonic booms from supersonic aircraft do not present the typical N-wave signature, but rather appear in the form of infrasonic pulses (Pierce and Maglieri, 1972). During a supersonic flight, the opening angle of the cone θ (Fig. 5), is given by

$$\sin(\theta) = \frac{c}{v} = \frac{1}{M}, \tag{1}$$

where M is the Mach number, c and v are the sound and aircraft speeds.

Defining the ray parameter p as the inverse of the trace velocity V_t for a ray propagating in a moving medium, θ as the wave front angle measured from the vertical, and u as the wind component in the direction of propagation, we have

$$V_t = \frac{1}{p} = \frac{c}{\sin(\xi)} + u. \tag{2}$$

For a horizontal flight trajectory without wind, the wave propagated into the atmosphere will have a maximum value of trace velocity V_t equal to $c/\sin(\xi)$. The ray parameter is conserved along the ray path, thus an increase in the sound speed for a ray propagating upward helps bend the waves downward. According to Eq. (1), the trace velocity of the signal across the array is equal to the acoustic velocity at the reflection height, plus the wind component in the direction of propagation. Thus for a known source position and frequency, ground measurements of the observed signal frequency could be used to estimate the wind speed at the reflection levels.

In our source model the shock wave is launched into the atmosphere at different angles with respect to the flight direction. Precise coordinates of the Air France Concorde trajectory were obtained for this study. We will assume that waves are emitted along the normal of the Mach cone, whose angle is set by the flight trajectory. The inclination of the wave vector belonging to the ray-cone will be $\pi/2 - \theta$ with respect to the flight direction (Friedman *et al.*, 1963; Liszka, 1974). In the horizontal plane, the acoustic energy will be radiated in a sector limited by $\pm(\pi/2 - \theta)$ around the flight direction (Fig. 5). Only rays propagating towards the array are used for the calculation. We allow a gap of $\pm 5°$ to take into account the transverse wind effect on the deflection of the ray direction. The variation of the aircraft velocity combined with the source displacement will change both the incidence at the launch point angle and the trace velocity measured on the ground.

The source is approximated by a linear distribution of elementary Mach cones along the flight trajectory. We define $S(0,0,0)$ as the receiver point, $M(x,y,z)$ as the source point, $M_0(x_0,y_0,z_0)$ as the top of the elementary Mach cone, and R_0 as the distance between M and M_0. α and β are the angles between the flight direction with respect to the (Oxy) and (Oyz) planes. γ is the aperture of the ray-cone projected onto the horizontal plane, and δ is the angle between the line $SM(x,y,0)$ and the (Oy) axis. The two waves normal to the Mach cone propagate upward and downward from M to the receiver point S under the condition $\gamma > \delta + \beta$. Otherwise, the Mach number is not large enough (i.e., the aperture of the ray-cone is too small) to keep the receiver point outside the shadow zone.

The horizontal projection of the wave vector is given by the direction between the array and the launch point. Thus the x and y components of the wave normal $\vec{N}(n_x, n_y, n_z)$ are $-x$ and $-y$, respectively. The z-components n_z^- and n_z^+ are then calculated from the following equation:

$$\vec{N}\cdot\overrightarrow{MM_0}=\|\vec{N}\|\|\overrightarrow{MM_0}\|\sin(\theta). \tag{3}$$

Equation (3) yields the two solutions

$$n_z^{\pm}=\frac{2(z-z_0)(x(x-x_0)+y(y-y_0))\pm\sqrt{\Delta}}{2((y-y_0)^2-R_0^2\sin^2(\theta))}, \tag{4}$$

where $\Delta=(x(x-x_0)+y(y-y_0))^2+(z-z_0)^2(x^2+y^2)-R_0^2(x^2+y^2)\sin^2(\theta)$ must be greater than zero. The components of two waves normals propagating upward and downward are $\overrightarrow{N^+}(n_x,n_y,n_z^+)$ and $\overrightarrow{N^-}(n_x,n_y,n_z^-)$. It can be shown, that the condition $\gamma>\delta+\beta$ is then fulfilled.

As the Concorde slows down during its descent phase the Mach cone angle θ increases. The variation of the launch angle with respect to the flight direction will influence the horizontal trace velocities recorded on the ground. Because the ray launch direction is almost parallel to the flight track, the ray parameter is also increasing as the aircraft is approaching the western coast of France. Due to the supersonic speed of the aircraft, the signal generated last generally arrives first. Thus, under favorable propagation conditions, the source of the last arrivals should be located far away along the flight path, producing an increase with time of the trace velocity. Since the array is close to the flight direction, a weak azimuth variation associated with the source trajectory is expected. Since the azimuth deviation is determined by the component of wind transverse to the propagation direction, its variability is mainly driven by diurnal and seasonal changes in the wind conditions.

B. Atmospheric models

Sound waves are affected by the temperature, wind velocity, and composition of the atmosphere. Infrasonic waves originating from a low-altitude source may be ducted in at least four regions of the atmosphere (Garcés *et al.*, 2001). Strong winds and boundary layer effects can trap sound waves anywhere in the troposphere. The prevailing stratospheric winds in Winter and Summer will produce well defined waveguides below the stratopause ($\sim$50 km), but predominantly along the dominant wind direction. In the thermosphere, the drastic increase in sound speed will reflect sound waves back to the ground, and wave guides will form below 120 km and above 120 km. However, waves propagating in the higher of these wave guides can be severely attenuated. Phases associated with waves refracted from the troposphere, stratosphere, below 120 km in the thermosphere, and above 120 km in the thermosphere are referred to as *Iw*, *Is*, *Ita*, and *Itb*, respectively. *Iw* phases are strongly dependent on local atmospheric conditions, and may not extend to very long ranges. Is phases are dependent of the season of the year and may fluctuate with the passing of storms and other large-scale atmospheric disturbances. *It* phases are always predicted, but their amplitudes may not be observable. In this study, we concentrate on the interpretation of *Is* and *It* phases and invoke atmospheric models that account for well known sources of variability in the Mesosphere and Lower Thermosphere (MLT) region of the atmosphere.

Because fluctuations in the sound speed are generally much smaller than wind variations in the upper atmosphere, it is important to utilize realistic wind profiles in order to match predicted arrivals with observed phases. Wind and temperature profiles used for our simulations are computed from the MSISE-90 and HWM-93 empirical reference models (Hedin, 1991; Hedin *et al.*, 1996). These models include detailed parametrizations of seasonal changes in the mean state, dominant solar migrating tides, and low-order stationary planetary waves. These empirical models provide time-dependent temperature, composition and zonal (E–W) and meridional (N–S) winds estimates up to elevations of 200 km that account for the drastic effects of seasonal wind reversals above the troposphere and daily solar tide variability in the MLT. Enhanced versions of these models, now being developed at the Naval Research Laboratory, include recent atmospheric data sets, improved parametrization of the atmospheric vertical structure, and capabilities for near-real time global assimilation of tropospheric and stratospheric winds up to 55 km. A prototype version of these models was used in a theoretical study by Garcés *et al.* (1999, 2001) to investigate the time-dependent variability of infrasound propagation. These recent model enhancements are neglected for the current study but will be used in later works.

Statistical observations averaged over one year show that the launch azimuths (measured from North) of acoustic waves originating from Air France (16h UT) and British Airways (21h UT) supersonic Concorde flights are approximately 105° and 120°, respectively. Figure 6 shows the atmospheric wind velocity at the landing time of both flights as a function of height and month of the year. The wind components are evaluated along and perpendicular to the direction of propagation. Since the direction of propagation is close to the (W–E) direction, the wind component along the launch azimuth nearly corresponds to the zonal wind and the transverse component to the meridional wind.

The transition between the summer and winter trends in the stratospheric general circulation can be observed around the months of September and April. A reversal of the wind direction around and above the stratopause (altitude of 40–70 km) is observed in spring and autumn. The westward-migrating solar tides, with dominant periods of 24, 12, and 8 hours, are the primary source of daily variability in the MLT. Around 120 km at 16 h, a wind speed of 40 m/s is blowing eastward in the direction of propagation [Fig. 6, diagram (a)]. Around the same altitude but at 21 h, strong winds are blowing against the propagation direction, affecting the turning height and thus modifying the horizontal trace velocity of the ray that would be observed at the array [diagram (c)]. At 16 h, the highest transverse winds noted in the thermosphere are blowing northerly at 30–45 m/s between 130 and 140 km, and southerly between 100 and 120 km. At 21 h, the strongest transverse winds reach 50 m/s at 120 km.

These daily tidal fluctuations in the upper atmosphere winds are the direct result of the solar heating of water vapor, ozone, and other molecular species in the middle and upper atmosphere (Forbes, 1995). These tides are the dominant source of predictable daily variability in the upper atmosphere. These seasonal and daily variations of the transverse

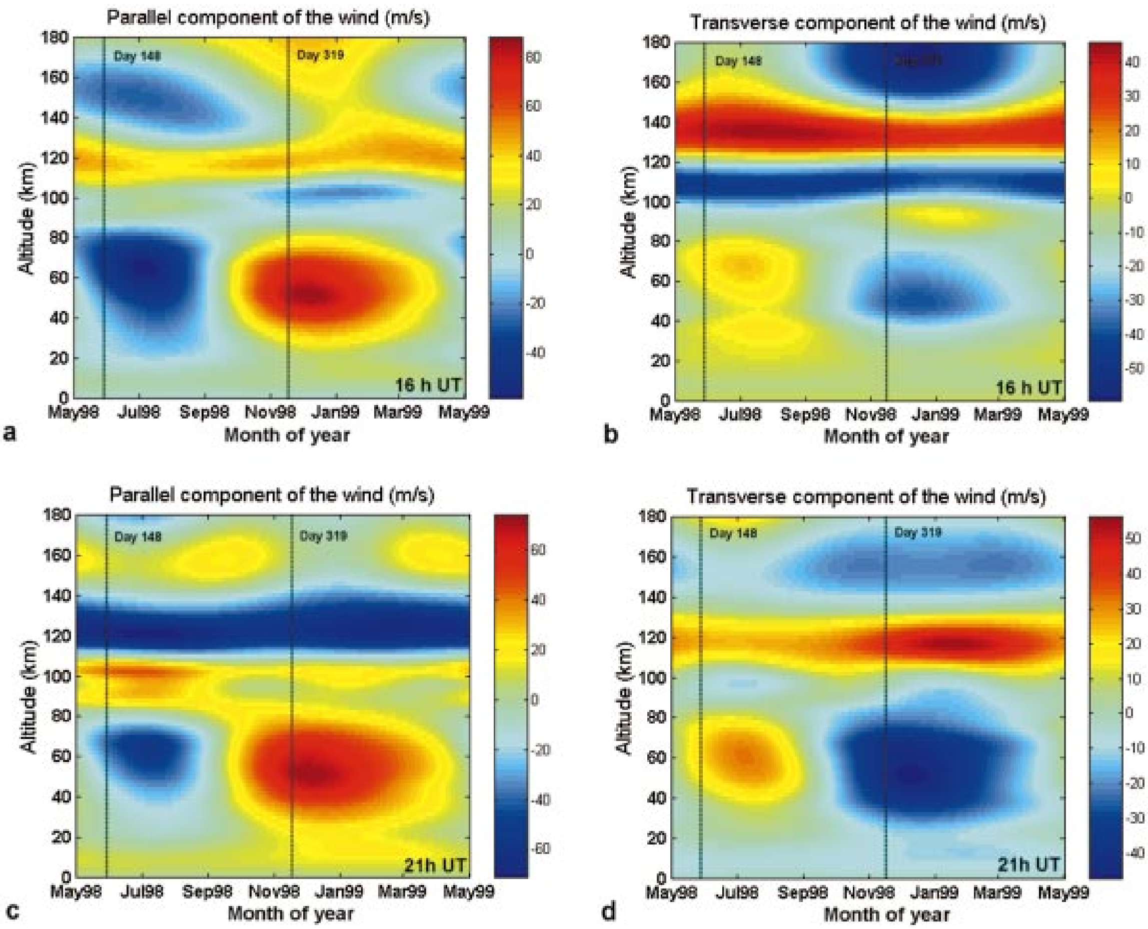

FIG. 6. Seasonal and diurnal variations of the wind profiles as a function of altitude. Wind components are shown along (a,c) and perpendicular (c,d) to the ray paths at a latitude of 48.7 °N and a longitude of 0.48 °E. Data are given each day of the year at 16 h (arrival time of the Air-France aircraft at Paris) and 21 h UT (arrival time of the second British-Airways aircraft at London). Positive values of the parallel component correspond to winds blowing in the direction of propagation. Positive values of the transverse component correspond to winds blowing to the right of the ray direction.

wind component may strongly affect the deflection of the wave in a direction perpendicular to the ray direction (Garcés *et al.*, 2001). According to the atmospheric models used herein, the largest azimuth deviations should be expected at 21 h with high-altitude turning points. Consequently, the apparent arrival direction will depend on the transverse wind component along the ray path for a specific time of day, and may not correspond to the original launch direction.

V. MODEL RESULTS

We focus on the simulation of acoustic signals generated by the Air France and the British Airways flights when they cross the English Channel around 16h and 21h UT, respectively. The flight routes are shown in Fig. 1. They are relatively straight during most of the flight time, but turn to different directions near the end of their flights. Previous works focused on simplified ray-tracing models for waves generated by the Concorde (Chène, 1996; Liszka and Waldemark, 1995). The results of the present simulations are improved by the more realistic atmospheric models and the knowledge of the accurate trajectory, speed and rate of descent of the aircraft. Ray paths are computed with the reformulated *tau-p* method for waves propagating in a stratified atmosphere under the influence of a height-dependent wind profile (Garcés *et al.*, 1998, 1999, 2001). The third order effects of horizontal gradients of wind and temperature have been neglected in these calculations. The sound speed and wind velocity is evaluated every 1 km from the sea level and up to 200 km heights. From Eq. (4), the z components of the original launch vector and the ray parameter are calculated for 200 source points. Those are uniformly distributed along the flight path during its descent phase. The ray paths originating from each source point are then calculated each day of the year. In order to evaluate seasonal effects on sound propagation, we concentrate on the simulations performed for May and November, when the largest differences in the propagation conditions are expected. By tracing rays through the empirical atmospheric models, we can then interpret the different observed phases shown in Figs. 2 and 3.

Diagrams (a,c) of Fig. 7 compare the predicted acoustic ray paths in May and November, respectively. The location of the microbarographic array is indicated by white dotted lines at an estimated distance of 200 km and 400 km from the Air France and British Airways point of transition from supersonic to subsonic flight. The day number is counted from January 1. Ray paths originate from source points distributed along the flight path indicated by the white arrow. The phases are (i) downward-propagating rays reflected in

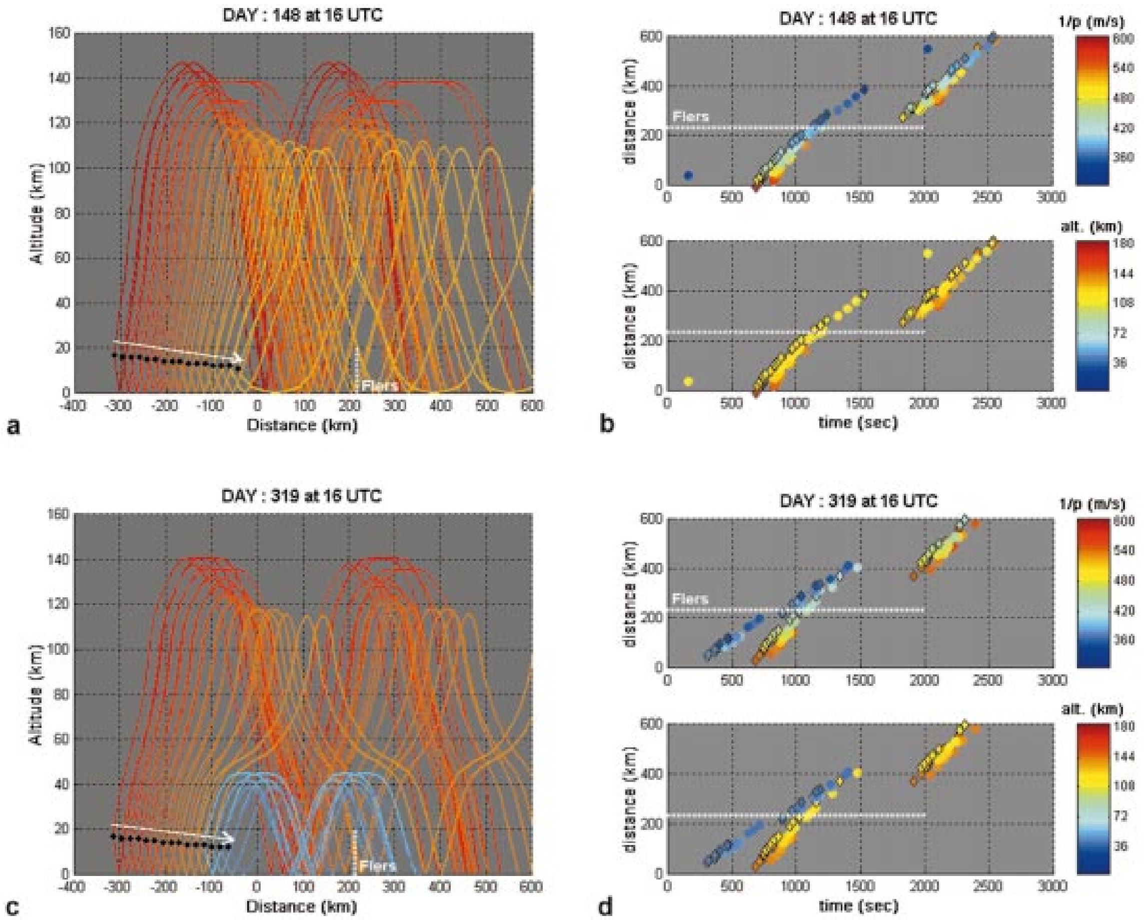

FIG. 7. Ray traces (a,c) and travel time curves (b,d) for infrasonic waves generated by the Air-France Concorde in May and November at 16 h UT. The dotted lines indicate the position of the Flers array at an estimated distance of 210 km. The dots represent some of the positions of the sources. Diagrams (a,b) and (c,d) are obtained from atmospheric models on days 148 and 319, respectively. The distance is relative to the last point of the Concorde supersonic flight. The travel time is relative to launching time point of the last source point. The horizontal trace velocity and the turning height of each ray are given by the color scales.

the stratosphere or in the thermosphere after being first reflected off the surface of the ocean, and (ii) upward-propagating rays, which return to the ground after one or two reflections in the stratosphere or thermosphere. Since the aircraft is traveling at supersonic speeds, the successive arrivals are interpreted as reflections originating from points farther out on the flight path. Diagrams (b,d) of Fig. 7 show the range measured from the last launch point beyond which the aircraft flight becomes subsonic as a function of the travel time of rays originating from the Mach cone. Each dot indicates the first and second bounce location of the distinct phases (*Is*, *Ita*, and *Itb*) expected at the array.

In May, on day 148, no stratospheric phases are predicted propagating against the dominant westward stratospheric wind. The strong prevailing easterly winds reduce the effective sound speed at the stratosphere and suppress downwards refraction in the stratopause, so rays are only returned back to the ground after refraction in the thermosphere. At 16 h, the predicted ray paths are thermospheric phases reflecting near 110 km height with horizontal trace velocities of 360–380 m/s. Thus, arrival (b) may be a thermospheric reflection (*Ita*), as suggested by its low frequency content and its reflection height (Fig. 2). The measured trace velocity of 365 m/s is consistent with the predicted phase, which would have a travel time of $\sim$17 minutes. Arrival (a) may be ascribed to a weak diffracted or scattered signal inside the shadow zone, or to a troposphere ducted wave *Iw* (Pierce and Maglieri, 1972; Donn, 1978). According to the simulations, the arrivals are a combination of waves radiated upward and downward from the launch point and ducted between the surface of the ocean and the lower thermosphere [diagram (a) of Fig. 7]. The turning height of a ray is determined by its launch angle. The steepest rays, generated when the aircraft is cruising at Mach 2, have a turning region near and above 140 km. However, the predicted ground arrival of these rays is too far from the array to be measured.

When the structure of the wind system changes, the turning point of a ray shifts in height and in its geographic position with respect to the source. In November, on day 319, the prevailing stratospheric eastward winds produce returns along the dominant wind directions and allow the formation of a stratospheric waveguide below $\sim$40 km height. The first group (a–c) of Fig. 3 is ascribed to a combination of initially downward- and upward-propagating rays which are refracted back to the ground at the stratosphere [*Is* phases, diagram (c) of Fig. 7]. The reflection levels for these high-frequency wave trains correspond to a temperature maximum

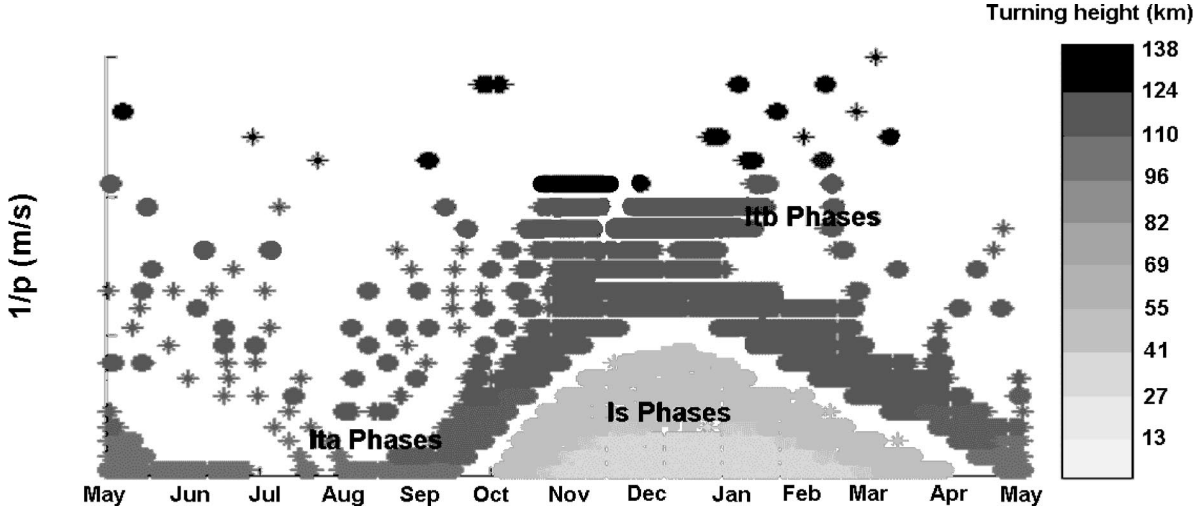

FIG. 8. Trace velocity as a function of month of the year for infrasonic waves generated by the Air-France Concorde at 16 h UT. The scale indicates the height of reflection of each ray.

on the stratopause and prevailing winter westerly zonal winds in the stratosphere. Stratospheric-ducted phases arrive earlier with a travel time of about 12 minutes. The predicted trace velocities are ~ 350 m/s and are consistent with the measurement [340 m/s for arrival (b), Fig. 3]. Additional acoustic arrivals are predicted a few minutes after the first stratospheric arrivals. They propagate upward and downward from the launch points and turn at an altitude of ~ 120 km with a range of ~ 350 km. The later low-frequency arrival (e) is associated with a thermospheric reflection (*Ita* or *Itb*). Its trace velocity is ~ 450 m/s and its travel time is ~ 16 minutes. Those predictions are in good agreement with the measured trace velocity (440 m/s) and the 4–5 minutes time delay measured between the first and last arrivals (Fig. 3). These wave trains may loose 90% of their energy by the time they reach 100 km heights. The largest predicted pressure level of waves radiated by the Concorde and reflected from the thermosphere is on the order of 0.2 Pa (Donn, 1978; Rogers and Gardner, 1980). Those results are in agreement with previous studies of propagation of microbaroms (Donn and Rind, 1971), rockets (Balachandran *et al.*, 1971) or artificial sources (Liszka, 1974), which discuss the formation of stratospheric and upper sound channels according to the season.

Figure 8 presents the variations of the trace velocity as a function of time. The stratospheric phases are only predicted from October to April. For a given ray parameter, the turning height of the stratospheric phases depend on the seasonal changes in the wind structure. For a 360 m/s trace velocity, a decrease of the turning height is observed from 53 km in October down to 32 km in December. The associated decrease of the sound speed is about 20 m/s. This change in the sound speed is compensated by an increase in the stratospheric wind component at 32 km that yields a value for the ray parameter equivalent to that previously found at 53 km [diagram (a) of Fig. 6]. From May to October, all waves are reflected between 90 km and 125 km. An interesting point is the seasonal variation in the phase velocity of thermospheric arrivals. This change is due to the inversion of the wind component along the propagation direction. As shown by Fig. 6, the parallel component of the wind depends on both the season and the level of reflection. In addition to the increase of the sound speed with altitude, the difference in trace velocities between May and November is enhanced by the winds induced by the solar tides in the upper atmosphere, in a range of 50 m/s. In June, near 110 km, the wind blowing against the propagation direction provides a decrease of 20 m/s of the apparent velocity [diagram (a) of Fig. 6]. In November, near 130 km, the parallel wind component reaches 30 m/s.

In order to study the transverse deflection of sound waves from the propagation axis, all bounces within a circle of radius 50 km around Flers have been selected. Figure 9 compares the detected and predicted azimuth of waves generated by the Air France and British Airways Concorde at 16 h and 21 h UT, respectively. Although an azimuth dispersion of about 5° is measured at a given observation time, good agreement is found between simulations and observations. The scatter in the azimuth data is also due to daily fluctuations of the atmosphere which are not represented by the models. The azimuth deviation is caused by the component of the wind transverse to the propagation direction. Some differences due to the tidal fluctuations of the winds in the upper-atmosphere can be observed between 16 h and 21 h. Figure 9 shows that the transverse winds are more influential at 21 h. The highest and lowest values of azimuth are reached in July and September, respectively, when the meridional wind speed amplitudes are the largest. Average azimuth deviations of 3° and 7° are observed for the Air France and British Airways flights, respectively. Over the whole year, the range of deviation for phases reflected in the upper atmosphere is about 25 km at 16 h, and 35 km at 21 h. The highest values of the deviation are reached in summer (from 0 to $+20$ km) and the lowest values are reached in winter (from -5 to -20 km). Since the Concorde routes are quite similar, these differences are mainly explained by daily variations in the wind profiles near 120 km. As shown in Fig. 6, due to the strong eastward and southward winds at 16 h, the resulting wind component is flowing along the wave propagation and will not significantly deflect the ray paths.

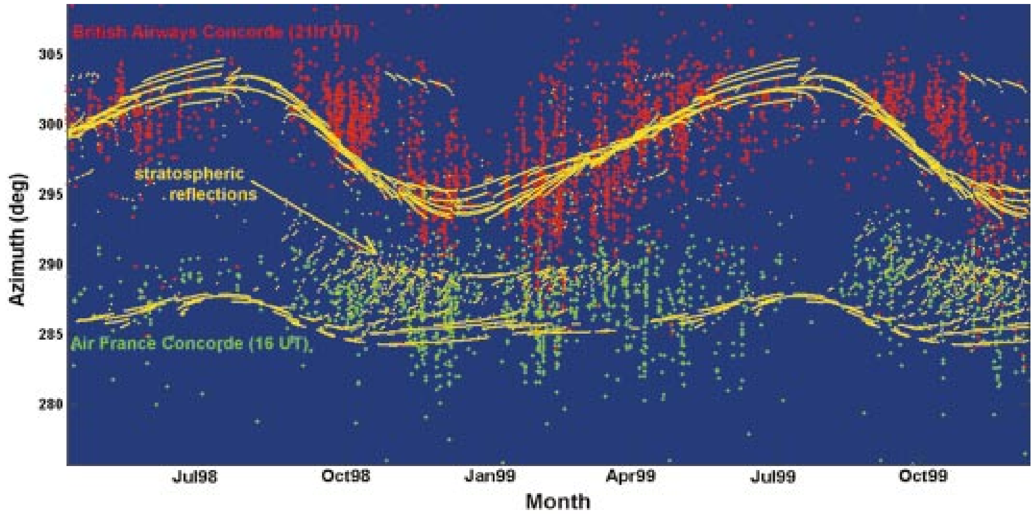

FIG. 9. Comparison between predicted azimuth (yellow dots) and the measured azimuth for the Air-France (green dots) and British-Airways (red dots) Concorde.

At 21 h, northward meridional winds are the strongest at 120 km, causing a significant azimuth deviation to the right of the ray direction [diagram (d) of Fig. 6]. Some discrepancies can be noted in July between the observations and the model. The decrease in the observed azimuth is about one month late as compared to the prediction. These differences may be explained by a month's delay of the seasonal inversion of the transversal winds, initially predicted around September.

We propose that shock waves generated by the Concorde and refracted from the stratosphere and thermosphere can be used as an atmospheric probe. According to Eq. (2), tidal changes can be monitored in the upper atmosphere from the measured trace velocity and the sound speed at the level of reflection. The successive arrivals from the Concorde originating from source points distributed along the flight path can thus be analyzed to determine the wind speed at different levels of reflection. The uncertainties of this procedure are determined by the accuracy of the initial atmospheric models. The simulations can first be used to evaluate the reflection heights, after which the wind speed at particular turning points can be determined from the knowledge of the vertical temperature profile.

As an example, we first consider the recordings of the 28th of May (Fig. 2). Ray tracing has shown an uncertain origin of arrival (a), but suggested that arrival (b) may be ascribed to a phase reflected at 110 km. At that altitude, the speed of sound due to temperature alone is around 335 m/s. As the trace velocity indicates an apparent sound velocity of 365 m/s at the reflecting level, a wind speed of 31 m/s is found at 110 km in the direction of the ray propagation. This agrees well with the 33 m/s given by the atmospheric model at 16 h UT on the 28th of May [diagram (a) of Fig. 6]. On the 15th of November at 16 h (Fig. 3), two phases have been identified. Arrivals (a) and (e) have been reflected at 40 km and 115 km where the sound speed is around 310 m/s and 395 m/s, respectively. Subtracting the sound speed at the turning point from the measured trace velocities, 340 m/s and 440 m/s, a wind speed of 30 m/s and 55 m/s is obtained at 40 km and 115 km, respectively. Because of the uncertainty of the reflection height estimates, one may consider those values consistent with the 45 m/s and 55 m/s wind speed in the stratosphere and thermosphere [diagram (c) of Fig. 6].

VI. CONCLUSION

The infrasonic signals generated by the Concorde offer a unique opportunity to study acoustic propagation in the atmosphere. This study provides further confirmation that long-range sound propagation depends strongly on the atmospheric conditions, primarily on the variability of the meridional and zonal winds. We successfully associated the seasonal and diurnal fluctuations in the phase parameters of the Concorde recordings to the variations of the HWM/MSIS empirical atmospheric models. The horizontal trace velocity, arrival times, and number of observed infrasonic phases were found to vary with the time of the year. The height at which sound waves with specific launch directions were reflected back to the ground also depend on the season and the time of the day. Depending on the angle of incidence, the direction of propagation, and the temperature and wind profiles, ray-tracing has shown wave reflections in two broad regions of the atmosphere. In winter, infrasonic waves propagate both in the stratosphere and in the thermosphere sound channels. In summer, the propagation model explains only reflections in the thermosphere. There were no predicted returns from the stratosphere when the propagation direction was against the predominant stratospheric winds. No attempt was done to predict scattered waves or tropopause ducted waves diffracted inside the shadow-zone. This type of surface-guided waves depend strongly on the tropospheric wind field, which may be highly variable.

The source model benefited from accurate knowledge of the location and speed of the aircraft. Simulations based on realistic winds and temperature profiles and a simple Mach cone model explained most of the daily and seasonally variations of the measured phase parameters. The trace velocities, azimuths and arrival times of the measured signals were satisfactorily interpreted using the ray-tracing model and the empirical atmospheric profiles. At the receiver point, we focused on the successive arrivals originating from source points distributed along flight path. Due to more regular winds along the propagation direction, signals from more distant portions of the flight trajectory may be recorded during the winter.

The daily variations of the signal characteristics were successfully predicted after accounting for the parallel and transverse wind components. For example, the deflection of the waves in a direction perpendicular to the ray path has been explained by the seasonal and tidal fluctuations of the wind profiles. The good agreements found between measurements and simulations demonstrate the validity of the source model. An average azimuth deviation of 5° has been observed and predicted for propagation ranges lower than 1000 km. Therefore, it is of great importance to evaluate precisely the effects of the winds on the angular deviation. Our study of seasonal variations in the Concorde recordings has shown that the apparent arrival direction of the wave does not correspond to the original launch direction. Thus, an azimuth correction is necessary to improve source locations with intersecting array beams. Phase identifications obtained from ray traces demonstrate how a labeling process based only on the horizontal speed classification can provide erroneous results. Low trace velocities may be incorrectly associated to stratospheric phases where a propagation model would predict phases reflected in the thermosphere. In some conditions, the simulations pointed out that there is no unambiguous connection between turning heights and low trace velocities measured on the ground.

Another conclusion of this study is that ground measurements may be utilized as an atmospheric probe to estimate the wind speeds in the direction of the ray at the reflection height. Infrasonic measurements may be utilized to correct or validate atmospheric models. An initial estimate of the turning height can first be performed with ray-tracing model and the best available atmospheric profiles. The successive arrivals from the Concorde can then be analyzed to determine more precisely the wind speed at different levels.

In conclusion, it should be stressed that the great variability of the observed infrasonic signals is a result of the complexity of the atmosphere. This variability indicates that small changes in the wind structure will influence the wave propagation in both lower and upper atmospheric sound channels. However, because of the drastic variability of the phase's amplitude from day to day, this study doesn't deal with signal intensity. In the case of long-range propagation of sonic booms, further work could investigate whether the formation of caustics, diffraction and scattering effects, and wave-front folding phenomena (Pierce and Maglieri, 1972; Donn, 1978; Broutman *et al.*, 2000) are significant and well-understood enough to be integrated in a more realistic propagation model.

ACKNOWLEDGMENTS

The authors gratefully acknowledge Dr. J. Guilbert for his interest in this work and for the many helpful discussions we had during the completion of this work. Many thanks also to Dr. B. Feignier for his improvements to the original text. The authors wish to thank Yves Cansi for his helpful advice with the use of the PMCC algorithm. The authors are also grateful to T. Laplaige of DTNI from Air France for consultations of various aspects of the flight trajectory. M. Garcés work is supported by U.S. Department of Energy Grant No. DE-FC04-98AL79801.

Alcoverro, B. (**1998**). ''Proposition d'un système de filtrage acoustique pour une station infrason IMS,'' CEA-DASE Scientific Report No. 241.

Balachandran, N., Donn, W.L., and Rind, D. (**1971**). ''Characteristics of infrasonic signals from rockets,'' Geophys. J. R. Astron. Soc. **26**, 135.

Balachandran, N., Donn, W.L., and Rind, D. (**1977**). ''Concorde sonic booms as an atmospheric probe,'' Science **197**, 47–49.

Besset, C., and Blanc, E. (**1993**). ''Propagation of shock waves in the atmosphere,'' J. Acoust. Soc. Am. **95**, 1830–1839.

Blanc, E. (**1985**). ''Observations in the upper atmosphere of infrasonic waves from natural or artificial sources,'' Ann. Geophys. (France) **3**, 673–687.

Broutman, D., Rottman, J., and Eckermann, S.D. (**2000**). ''A hybrid method for wave propagation from a localized source, with applications to mountain waves,'' Q. J. R. Meterol. Soc., submitted.

Brown, D.J. (**1999**). ''Summary of infrasound source location meeting, San Diego, November 9–10, 1998,'' Arlington, VA, Center for Monitoring Research, p. 10.

Cansi, Y. (**1995**). ''An automatic seismic event processing for detection and location: The PMCC method,'' Geophys. Res. Lett. **22**, 1021–1024.

Cansi, Y. (**1997**). ''An automated data processing method for mini-arrays,'' CSEM/EMSE European-Mediterranean Seismological Centre, NewsLetter **11**, 1021–1024.

Carlson, H.W., and Maglieri, D.J. (**1972**). ''Review of sonic-boom generation theory and prediction methods,'' J. Acoust. Soc. Am. **51**, 675–685.

Chène, R. (**1996**). ''Interprétation des mesures d'infrasons associés au vol supersonique du Concorde,'' CEA-DASE Scientific Report No. 5/96.

Cotten, D., and Donn, W.L. (**1971**). ''Sound from Apollo rockets in space,'' Science **171**, 565–567.

Daniels, F.B. (**1969**). ''Lengthening of shock waveforms caused by their propagation to high altitudes,'' J. Acoust. Soc. Am. **45**, 241–242.

Donn, W.L., and Rind, D. (**1971**). ''Natural infrasound as an atmospheric probe,'' Geophys. J. R. Astron. Soc. **26**, 111–133.

Donn, W.L., and Rind, D. (**1972**). ''Microbaroms and the temperature and wind of the upper atmosphere,'' J. Atmos. Sci. **29**, 156–172.

Donn, W.L. (**1978**). ''Exploring the atmosphere with sonic booms,'' Am. Sci. **66**, 724–733.

Friedman, M.P., Kane, E.J., and Sigalla, A. (**1963**). ''Effects of atmosphere and aircraft motion on the location and intensity of a sonic boom,'' AIAA J. **1**, 1327–1335.

Forbes, J.M. (**1995**). ''Tidal and Planetary Waves,'' The Upper Mesosphere and Lower Thermosphere, A Review of Experiment and Theory, AGU Geophysical Monograph 87, edited by R. Johnson and T.L. Killeen.

Garcés, M., Hansen, R., and Lindquist, K. (**1998**). ''Traveltimes for infrasonic waves propagating in a stratified atmosphere,'' Geophys. J. Int. **135**, 255–263.

Garcés, M., Hansen, R., Lindquist, K., Drob D., and Picone, M. (**1999**). ''Variability of the lower atmosphere and its effect on the propagation of infrasonic waves,'' Proceedings of the 21st Annual Research Symposium: Technologies for Monitoring the Comprehensive Nuclear-Test-Ban Treaty, 21–24 September 1999, Las Vegas, Vol. 2, pp. 105–111. Sponsored by the US DoD and DoE, LA-UR-99-4700.

Garcés, M., Drob, D.P., and Picone, J.M. (**2001**). ''A theoretical study of the effect of geomagnetic fluctuations and solar tides on the propagation of infrasonic waves in the upper atmosphere,'' Geophys. J. Int. (in press).

Hayes, W.D., and Runyan, H.L. (**1970**). ''Sonic-boom propagation through a stratified atmosphere,'' Proc. Analytical Methods in Aircraft Aerodynamics Symp., NASA SP-228, 229–244.

Hayes, W.D., and Runyan, H.L. (**1972**). ''Sonic-boom propagation through a stratified atmosphere,'' J. Acoust. Soc. Am. **51**, 695–701.

Hedin, A.E. (**1991**). ''Extension of the MSIS thermosphere model into the middle and lower atmosphere,'' J. Geophys. Res. **96**, 1159.

Hedin, A.E., Biondi, M. A., Burnside, R. G., Hernandez, G., Johnson, R. M., Killeen, T. L., Mazaudier, C., Meriwether, J. W., Salah, J. E., Sica, R. J., Smith, R. W., Spencer, N. W., Wickwar, V. B., and Virdi, T. S. (**1996**). ''Reviesed global model of upper thermospheric winds using satellite and ground-based observations,'' J. Geophys. Res. **96**, 7657–7688.

Le Pichon, A., and Cansi, Y. (**1999**). ''One-year analysis of systematic detection and location of infrasounds in a prototype CTBT station,'' Acustica **85**, (Suppl. 1), 178.

Liszka, L. (**1974**). ''Long-distance propagation of infrasound from artificial sources,'' J. Acoust. Soc. Am. **56**, 1383–1388.

Liszka, L. (**1978**). ''Long-distance focusing of Concorde sonic boom,'' J. Acoust. Soc. Am. **64**, 631–635.

Liszka, L., and Waldemark, K. (**1995**). ''High resolution observations of infrasound generated by the supersonic flights of Concorde, ''J. Low. Freq. Noise & Vibr. **14**, 181–192.

Maglieri, D.J., and Plotkin, K.J. (**1995**). ''Sonic Boom,'' in *Aeroacoustics of Flight Vehicles, Theory and Practice*, Vol. 1, edited by H.H. Hubbard (NASA/WADC, NY), pp. 519–561.

Otterman, J. (**1959**). ''Finite-amplitude propagation effect on shock-waves travel times from explosions at high altitudes,'' J. Acoust. Soc. Am. **31**, 470–474.

Pierce, A.D., and Maglieri, D.J. (**1972**). ''Effects of atmospheric irregularities on sonic-boom propagation,'' J. Acoust. Soc. Am. **51**, 702–720.

Rind, D., Donn, W.L., and Dede, E. (**1973**). ''Upper air wind speeds calculated from observations of natural infrasound,'' J. Atmos. Sci. **30**, 1726–1729.

Rind, D., and Donn, W.L. (**1975**). ''Further use of natural infrasound as a continuous monitor of the upper atmosphere,'' J. Atmos. Sci. **32**, 1694–1704.

Rogers, P.H., and Gardner, J.H. (**1980**). ''Propagation of sonic booms in the thermosphere,'' J. Acoust. Soc. Am. **67**, 78–91.

Shapley, D. (**1978**). ''East coast mystery booms: a scientific suspense tale,'' Science **199**, 1416–1417.

Waldemark, K. (**1997**). ''A statistical study of propagation of infrasound generated during supersonic flights,'' IFR Scientific Report 243.

Warren, C.H. (**1972**). ''Recent sonic-bang studies in the United Kingdom,'' J. Acoust. Soc. Am. **51**, 783–789.

Weber, M.E., and Donn, W.D. (**1982**). Ducted propagation of Concorde-generated shock waves, J. Acoust. Soc. Am. **71**, 340–347.